Proceedings of
ECOS 2005

the

18th International Conference on Efficiency, Cost, Optimization, Simulation, and Environmental Impact of Energy Systems

Trondheim, Norway
June 20–22, 2005

Volume I-III

EDITORS
Signe Kjelstrup, Johan E. Hustad, Truls Gundersen, Audun Røsjorde,
George Tsatsaronis

ORGANISED BY
Norwegian University of Science and Technology
NTNU

These Proceedings are available from:
Department of Chemistry
Norwegian University of Science and Technology
NO-7491 Trondheim
Norway

ISBN 82-519-2041-8

Graphical Design by Sara Gjerstad Kjelstrup
Printed by Tapir Uttrykk, Norway
Bounded by Grafisk Produksjonsservice AS, Norway

Tapir Academic Press
NO-7005 TRONDHEIM
NORWAY
Tel.: + 47 73 59 32 10
Fax: + 47 73 59 32 04
E-mail: forlag@tapir.no
Web: www.tapirforlag.no

Organising Committee

Chairman: S. Kjelstrup (Norway)

A. Langseth	(Norway)	G. Valsø Engdal	(Norway)
O. Bolland	(Norway)	E. Hertwich	(Norway)
T. Gundersen	(Norway)	J.E. Hustad	(Norway)
T. Sundset	(Norway)	M.J. Moran	(USA)

International Advisory Board

G. Tsatsaronis	(Germany)
N. Houbak	(Denmark)
R. Rivero	(Mexico)

Scientific Council

Chairman: J.E. Hustad (Norway)

B. Andresen	(Denmark)	P. Mathieu	(Belgium)
Ö. Arnas	(USA)	M. Moran	(USA)
P. Alvfors	(Sweden)	T. Morosuk	(Ukraine)
H. Auracher	(Germany)	S.A. Nebra	(Brasil)
M. Bailey	(USA)	B. Qvale	(Denmark)
A. Bejan	(USA)	R. Rivero	(Mexico)
T. Berntsson	(Sweden)	M. Rubi	(Spain)
D. Favrat	(Switzerland)	P. Salamon	(USA)
C.-J. Fogelholm	(Finland)	E. Sciubba	(Italy)
C. Frangopoulos	(Greece)	S. Sieniutycz	(Poland)
H. Heperkan	(Turkey)	M. von Spakovsky	(USA)
M. Hupa	(Finland)	G. Tsatsaronis	(Germany)
M. Ishida	(Japan)	D. Tondeur	(Franrike)
K. Jordal	(Sweden)	A. Valero	(Spain)
J. Klemes	(Great Britain)	N. Zhang	(China)
A. Lazzaretto	(Italy)	T. Zhelev	(Ireland)
N. Lior	(USA)		

List of Reviewers

Adam, J.	(Norway)	Manfrida, G.	(Italy)
Almås, T.	(Norway)	Massardo, A.	(Italy)
Alvfors, P.	(Sweden)	Mathieu, P.	(Belgium)
Anantharaman, R.	(Norway)	Mathisen, H.M.	(Norway)
Andresen, B.	(Denmark)	Maurstad, O.	(Norway)
Arnas, Ö.	(USA)	Melhus, O.	(Norway)
Assadi, M.	(Sweden)	Moe, S.	(Norway)
Auracher, H.	(Germany)	Moran, M.	(USA)
Bailey, M.	(USA)	Morosuk, T.	(Ukraine)
Barrio, M.	(Norway)	Næss, E.	(Norway)
Bedeaux, D.	(The Netherlands)	Nebra, S.	(Brazil)
Bejan, A.	(USA)	Nekså, P.	(Norway)
Berntsson, T.	(Sweden)	Nielsen, T.	(Norway)
Bolland, O.	(Norway)	Pagonabarraga, I.	(Spain)
Brattebø, H.	(Norway)	Paronen, M.	(Finland)
Bysveen, M.	(Norway)	Pettersen, Joh.	(Norway)
Carnevale, E.	(Italy)	Pettersen, J.	(Norway)
Costea, M.	(Romania)	Qvale, B.	(Denmark)
Desideri, U.	(Italy)	Rørtveit, G.J.	(Norway)
Ditaranto, M.	(Norway)	Røsjorde, A.	(Norway)
Ertesvåg, I.S	(Norway)	Reguera, D.	(Spain)
Favrat, D.	(Switzerland)	Rivero, R.	(Mexico)
Fogelholm, C.-J.	(Finland)	Rubi, M.	(Spain)
Fossum, M.	(Norway)	Salamon, P.	(USA)
Frangopoulos, C.	(Greece)	Sciubba, E.	(Italy)
Grønli, M.	(Norway)	Sieniutycz, S.	(Poland)
Gundersen, T.	(Norway)	Skaugen, G.	(Norway)
Hägg, M.-B.	(Norway)	Skreiberg, Ø.	(Norway)
Hanssen, S.O.	(Norway)	Solli, C.	(Norway)
Haug-Warberg, T.	(Norway)	Span, R.	(Germany)
Heperkan, H.	(Turkey)	von Spakovsky, M.	(USA)
Hernandez-Guerrero, A.	(Mexico)	Stene, J.	(Norway)
Hertwich, E.	(Norway)	Stiller, C.	(Norway)
Hoffmann, K.H.	(Germany)	Strømman, A.	(Norway)
Houbak, N.	(Denmark)	Sørensen, L.H.	(Denmark)
Hupa, M.	(Finland)	Sørum, L.	(Norway)
Hustad, J.E.	(Norway)	Svendsen, H.F.	(Norway)
Ishida, M.	(Japan)	Svensson, A.M.	(Norway)
Jakobsen, A.	(Norway)	Tondeur, D.	(France)
Jansen, D.	(The Netherlands)	Tsatsaronis, G.	(Germany)
Johannessen, E.	(Norway)	Tunold, R.	(Norway)
Jonsson, M.	(Norway)	Ulseth, R.	(Norway)
Jordal, K.	(Sweden)	Undeland, T.	(Norway)
Kjelstrup, S.	(Norway)	Valero, A.	(Spain)
Klemes, J.	(Great Britain)	Vogstad, K.-O.	(Norway)
De Koeijer, G.	(Norway)	Wall, G.	(Sweden)
Van der Kooi, H.	(The Netherlands)	Warmuzinski, K.	(Poland)
Kvamsdal, H.	(Norway)	Zhang, N.	(China)
Lazzaretto, A.	(Italy)	Zhelev, T.	(Ireland)
Lior, N.	(USA)	Zvolinschi, A.	(Norway)
Lombardi, L.	(Italy)		

Preface

The organising committee for "The 18th International Conference on Efficiency, Cost, Optimization, Simulation, and Environmental Impact of Energy Systems" – ECOS 2005 – welcomes you to Trondheim! The motto of ECOS 2005 is *Shaping our future energy systems*. The participants of ECOS 2005, *you*, are central for the realisation of future energy systems that our world, our ecosystem, can sustain.

ECOS 2005 features more sessions on renewable energy sources than in previous ECOS events. In particular, the session on CO_2 handling and storage is expanded. Industrial ecology and environmental issues are high on the agenda. Special activities in the Nordic regions of Europe colour the program through these sessions. Still, the core of ECOS consists of contributions showing state-of-the-art engineering methods that rest on the foundation provided by thermodynamics.

This year we honour the developers of non-equilibrium thermodynamics: Prigogine, de Groot, and Mazur. This theory, which forms a bridge between the nano-, micro-, and macroscales, may prove invaluable as engineering problems become more molecular in character.

The organising committee is grateful to the sponsors that have helped realise the meeting. Special thanks also go to our reviewers, without whom this conference could not be at its high-quality level, and to Enrico Sciubba and Noam Lior for organising panel sessions. The panel discussions together with the other formal and informal discussions at ECOS 2005 sharpen our critical thinking about energy systems and help us prepare for dealing prudently with future societal power needs.

The organising committee wishes new and old members of the ECOS family
a fruitful stay in Norway,

Signe Kjelstrup

Anne Langseth Gunhild Valsø Engdal Olav Bolland Edgar Hertwich

Johan E. Hustad Truls Gundersen Trude Sundseth Michael Moran

Papers

Volume I 1

Key note lectures

Proceedings of ECOS 2005
Trondheim, Norway
June 20–22, 2005

CONTRIBUTIONS TO NON-EQUILIBRIUM THERMODYNAMICS BY deGROOT-MAZUR-PRIGOGINE: IN MEMORIAM

A. Özer Arnas
United States Military Academy at West Point
Department of Civil and Mechanical Engineering
West Point, NY 10996
USA

ABSTRACT

The three pillars of non-equilibrium thermodynamics have passed away within the last decade. Although they all followed in the footsteps of Onsager, they were able to extend the horizons beyond his contributions through their own research, students, and publications. As engineers, however, we have not been very enthusiastic or seem not to be too concerned with non-equilibrium situations; nevertheless, it seems that we have to be able to respond to new technological developments in material science and engineering as well as emerging applications to engineering processes and systems that are challenging us in today's world. To be able to do this, we at least must teach the appropriate material to our students in class and through research problems. It is only then that we will have prepared the future generation to tackle the problems at hand today and those that will appear in the future.
Keywords: De Groot, Mazur, Prigogine, Onsager, non-equilibrium thermodynamics

INTRODUCTION

In this presentation we will pay homage to three people, Sybren de Groot, Peter Mazur, and Ilya Prigogine, who have contributed so much to the use of the Onsager [1] principles in application to non-equilibrium situations in natural phenomena through their individual work, the contributions with their students, and various publications they have produced over very productive years. However, the concept of *irreversibility* started much earlier by Clausius [2] in the discussion of *non-compensated heat*, by Stokes [3] in the discussion of *energy transfer in crystals*, and by Thomson (Lord Kelvin) [4] in the discussion of *a coupled thermo-electric phenomena,* where a direct reference to non-equilibrium situations were made. Much later, Duhem [5] was able to combine the second law of thermodynamics with the three laws of conservation of mass, momentum, and energy to obtain the *local rate of entropy generation*. De Donder [6] was able to extend this by the introduction and use of *affinity* in chemical reactions for the first time. Another decade had to pass before Onsager formulated and published in two concurrent papers [1, 7] his Nobel Prize worthy seminal *reciprocal relations* which connect the coefficients of linear phenomenological laws that characterize coupled irreversible processes. About another decade later, Meixner [8], in a series of articles, followed by Prigogine [9], in his thesis presented at the l'Université Libre de Bruxelles, were able to obtain a consistent set of phenomenological coefficients for irreversible phenomena that successfully incorporated Onsager's reciprocity relations. As a result, they were able to determine the *entropy source strength* for a number of physical situations of interest thus laying the fundamental groundwork for the study of *irreversible*

E-mail: ozer.arnas@usma.edu
Phone: 845-938-5518 Fax: 845-938-5522

thermodynamics of natural systems. Simultaneously with Prigogine in 1945, de Groot published his thesis research [10], presented at the Gemeentelijke Universiteit te Amsterdam, on the flow of matter caused by a temperature gradient, a coupled non-equilibrium situation. One of de Groot's students Mazur, who also worked with Prigogine in Brussels, published his thesis at Universiteit Utrecht [11] on the *thermodynamics of transport phenomena in liquid helium-2*, particularly the so called fountain effect, that verified the experiments performed at the Kamerlingh-Onnes Laboratory in Leiden. Now that we have seen how these three great men of non-equilibrium thermodynamics have started their careers, we can discuss the life and contributions of each.

Sybren de GROOT

Sybren de Groot was born on April 8, 1916 in Amsterdam. He studied theoretical physics at the Gemeentelijke Universiteit te Amsterdam with J. D. van der Waals. During 1942-1947 he was an assistant in the van der Waals Laboratory under the direction of A. Michels. During this time, he received his doctorate upon presentation of his thesis [10] to C. J. Gorter. The topic of the Soret effect on the macroscopic theory of thermal diffusion was very important and of interest in isotope separation. Because of this and at the invitation of Fréderic Joliot-Curie, the Haut-Commisaire à l'Energie Atomique of the Laboratoire de Chimie Nucléaire, de Groot was appointed Chef de Service at the Collège de France in Paris. He was able to continue his doctoral research making calculations on beta- and gamma-rays including angular effects as observed in the emission of oriented and polarized nuclei. A year later, he returned to Utrecht as a Lecturer and was appointed Professor of Theoretical Physics in 1949. In 1953, he moved to Leiden and was appointed Professor of Theoretical Physics following H. A. Kramers and took over the institute which would later be renamed Instituut-Lorentz. He continued, as the organizer for the famous Colloquium Ehrenfestii at Leiden that was founded by Paul Ehrenfest in 1912. He held these positions until 1964 when he went back to Amsterdam where upon his retirement he was appointed as Professor Emeritus in 1984. In 1951, at a very early age, he published his first book on the thermodynamics of irreversible processes [12]. This book contains both the statistical basis and particular topics of the macroscopic theory of irreversible processes. It contains a wide range of transport processes along with appropriate averaging procedures and effects of microscopic symmetries. It is this topic that has brought worldwide recognition to de Groot. It is also interesting to note that this book came out at the same time as his student Mazur was presenting his own thesis [11]. This actually set the stage for all developments on this topic in the Netherlands and in the scientific community for years to come and which still continues through his students and their students. In 1962, de Groot and Mazur were able to further diversify the study of irreversible processes and published their work [13]. In this book, the principles of the macroscopic derivation of Onsager [1, 7] along with the property of time reversal invariance as discussed by Casimir [14] and further remarks of Wigner [15] are all included. The macroscopic Curie principle was derived from microscopic crystal symmetries. Entropy production was also evaluated as were the statistical foundations of kinetic and fluctuation theories, the stochastic laws, and causality conditions. The applications to transport phenomena, including electromagnetic, chemical, and acoustical processes are also included. De Groot and Mazur were comprehensive and original in the proofs presented [13]. De Groot's work in Amsterdam covered the topics of micro-theory, transition from micro- to macro-theory, and macro-theory that permitted him to continue his publications of books on Maxwell's equations [16], on the fundamentals of electrodynamics with Suttorp [17], on the Weyl transformation and the Wigner function [18], and on relativistic kinetic theory principles and applications with van Leeuwen and van Weert [19], after the publication of a number of papers on relativistic transport processes. His collaborative work with Mazur that started in 1950 continued through 1966, even after he had left to go back to Amsterdam, and culminated in some twenty-six additional publications. Most of these were included in their book [13]. Through his personal initiative and those of his students, particularly Mazur, the oldest institute for theoretical physics in the Netherlands, founded in 1921, was renamed Instituut-Lorenz and became known throughout the world. Through his personal relationships, de Groot made the Lorentz Professorship an enviable position that invited persons recognized in

their fields. Among many of these visitors were Uhlenbeck who developed the theory of electron spin, Wigner who was the famous nuclear physicist and the pioneer of microscopic quantum theory, and van Vleck famous for atomic magnetism. It is interesting to note that two of the three were later selected to receive the Nobel Prize in physics, and two were awarded the Royal Netherlands Academy of Science's Lorenz Medal. De Groot was awarded an honorary doctorate by the University of Strasbourg where he was a Visiting Professor during 1958-1963. In 1958, he became a member of the Royal Netherlands Academy of Science. He was honored by the French Académie Européenne des Sciences, des Arts et des Lettres. He was made a Chevalier de la Légion d'Honneur. Upon his retirement he became an Officier and was made a Knight of the Order of the Netherlands Lion. De Groot was a special person; his lectures were exceedingly lucid, without extraneous details but mixed with subtle jokes. He was a superb physicist who freely shared his vast knowledge with his friends, students, and colleagues. His students could count on his loyalty and support and were inspired by his example. He died on May 9, 1994 leaving behind a legacy carried on by his students.

Peter MAZUR

Peter Mazur was born on December 11, 1922 in Vienna. He attended high school in Paris and The Hague. After going into hiding in the Dutch countryside for a few years during the war, Mazur started his studies in chemistry at the University of Utrecht. He did his research in theoretical physics with de Groot. His major contribution at this time was on the application of irreversible phenomena to spatially continuous systems such as superfluids. Prior to defense of his thesis research in 1951, he spent two years as a research associate with Prigogine at the Université Libre de Bruxelles. These two experiences were the start of a long and illustrious career that spanned five decades. He returned to Utrecht from Brussels as the Senior Scientific Associate in 1952 and spent the next year at the University of Maryland, the first of his many visits to the United States. In 1954 he was appointed Lecturer at the University of Leiden, a position he held until 1961 when he was promoted to Professor of Theoretical Physics. Upon Professor de Groot's departure to Amsterdam, Mazur became the Director of Instituut-Lorentz for Theoretical Physics in 1964, a position he held for a quarter of a century, before he became a Professor Emeritus in 1988. During the period of 1962 through 1991, he was appointed a Visiting Professor in France, Italy, Japan, Canada and the United States on a number of occasions, even after he had retired from Leiden. Mazur was the organizer of the Colloquium Ehrenfestii from 1964 until 1978, a tradition that was started by Ehrenfest in 1912. Like de Groot, Mazur collaborated with many people including Prigogine during early years in Brussels. In all, Mazur published one hundred fifty seven papers. He published twenty-six papers with de Groot, and twenty-nine papers with Bedeaux, a post-doctoral student and prolific collaborator of his since 1973. He published another six papers with Prigogine starting in 1951. Mazur's work started with liquid helium and its characteristics. Next he developed a microscopic basis for systems based on non-equilibrium thermodynamics within the framework of classical mechanics. This was later extended into quantum mechanics. Thermodynamics of thermo-magnetic and galvano-magnetic effects and the extension of Onsager relations to these phenomena along with relativistic thermodynamics of irreversible processes followed. In subsequent years, a great breadth of subjects within statistical physics were tackled with remarkable unity of style starting with a very clear statement of the problem followed by a detailed and complete derivation of results. In his last years, the emphasis of research was centered on Brownian motion [20] ending with the last paper on non-equilibrium thermodynamics of quantum systems [21], published after his death. Mazur was recognized by his election as member of the Royal Academy of Sciences of the Netherlands in 1970, his appointment to the Board of the International Union of Pure and Applied Physics during 1966-1984, and the Dutch Foundation for Fundamental Research of Matter during 1970-1985. He was also honored by the French Académie Européenne des Sciences, des Arts et des Lettres in 1987. Prior to his retirement in 1988, he was made a Knight of the Order of the Netherlands Lion. In 1991, he was elected to be a Member of Academia Europaea. Peter Mazur was an authoritative scientist, a superb teacher and colleague to his students and collaborators, and was an animated and flamboyant physicist. He showed his caring and interest in his students, sometimes very formally and often with a warmhearted elegance. His knowledge

and interests encompassed not only science in general and physics in particular, but also almost all fields of intellectual endeavor including literature, art, music, and history. He died on August 15, 2001 leaving behind him his students and other collaborators to carry the torch.

Ilya PRIGOGINE

Ilya Prigogine was born on January 25, 1917 in Moscow. He studied chemistry and physics earning his doctoral degree in 1941 and presenting his thesis for habilitation in 1945 [9], all at the Université Libre de Bruxelles. In 1951 he was appointed Professor in the Faculty of Sciences of the same university until his retirement in 1987. One of his first collaborators was Mazur, who came to Brussels in 1950. Prigogine and Mazur were able to publish six papers within two years. After Mazur's return to Utrecht, Prigogine and his students continued a very productive and successful path in studying many practical problems in physical chemistry and the foundations of quantum mechanics. This produced a series of sixteen authored or co-authored books along with hundreds of specialized papers with students and associates throughout the world. The great contribution of Prigogine to thermodynamic theory is his successful extension of it to systems that are far from thermodynamic equilibrium. Prigogine and his students were able to demonstrate that a new form of ordered structures can exist under such conditions. He gave them the name, *dissipative structures*. An example is Benárd instability, in which the structure is wholly dependent on the supply of energy and disappears when it ceases. Dissipative structures exist only in conjunction with their environment. Close to equilibrium, order in dissipative structures tends to be destroyed. Far from equilibrium, order can be maintained and new structures formed. Prigogine and his group's researches into irreversible thermodynamics have fundamentally transformed and revitalized the science, giving it a new relevance and creating theories to bridge the gaps between chemical, biological, and social scientific fields of inquiry with a distinguished and unequalled elegance and lucidity [22]. Under the influence of de Donder, Prigogine focused his attention on the macroscopic and microscopic aspects of the second principle of thermodynamics. He extended its validity to new situations, and other fundamental approaches to theoretical physics, such as classical and quantum dynamics. Timmermans, another teacher of his, was an experimentalist and was interested in the application of classical thermodynamics to liquid solutions of complex systems. Timmermans confronted him with the precise application of thermodynamic methods including the solutions theory, the theory of corresponding states, and isotopic effects in the condensed phase [23]. Prigogine, contrary to the standard approach which discussed degradation and *loss of useful work*, attributed to irreversible processes a constructive role. He believed that living things provided us with striking examples of systems that were highly organized and in which irreversible phenomena played an essential role. Thus, following the concepts of linear thermodynamics of irreversible processes as studied by Meixner [8] and de Groot and Mazur [13], Prigogine simultaneously published his work on non-equilibrium statistical mechanics purely from a dynamical point of view [24]. Later Prigogine and Glansdorff were able to develop a general evolution criterion valid far from equilibrium and out of the validity domain of the minimum entropy production theorem. Stability criteria that resulted led to the discovery of critical states [25]. Next he built a new kinetic model generated through diffusion-reaction processes that caused the rapid development of the study of dissipative structures. Prigogine and Nicolis were able to show that an unexpected phenomenon appeared when the fluctuation problem in nonlinear systems far from equilibrium was considered, such as chemical kinetics of non-equilibrium phase transitions [26]. Prigogine believed throughout his life that he could find a connection between the physical sciences, biology, and human science. He was able to accomplish this by many publications as stated in his Nobel Prize recognition [22]. Prigogine's last collaborations with his students led to topics of irreversibility of states in quantum mechanics [27], which appeared after his death. Starting in 1967, he was a Regental Professor and Ashbel Smith Professor of Physics and Chemical Engineering at the University of Texas-Austin and founded the Ilya Prigogine Center for Studies in Statistical Mechanics and Complex Systems. Since 1959, he was the Director of the International Solvay

Institute in Brussels. Among other awards, Prigogine was awarded the title of Viscount by the King of Belgium. Recipient of fifty three honorary degrees, he was a member of sixty four national and international professional organizations including the National Academy of Sciences and the American Academy of Arts and Sciences. He was a Special Advisor to the European Community and an Honorary Member of the World Commission of Culture and Development of UNESCO. He received various medals from Sweden, England, Italy, Russia, and France culminating in the award of Commander of the World Order "Science, Culture, Education" of the European Academy of Information in 2002. The University of Siena and the Wessex Institute of Technology in Southampton, UK have instituted two special medals and prizes in his name for best papers submitted on the topic of *ecological systems*. Prigogine died on May 28, 2003 in Brussels. There is no question that his students of the first and second generation are now working with those of the third generation throughout the world to continue his legacy.

HOW I REMEMBER PRIGOGINE, de GROOT and MAZUR

It is not too often that one gets an opportunity to meet with people of renown in their lifetimes. I personally was very fortunate and privileged to have met with each one of these three giants of irreversible thermodynamics first in the Netherlands and Belgium and then in the United States. As a Professor of Mechanical Engineering at Louisiana Sate University-Baton Rouge, I spent my sabbatical years as a Visiting Professor and Research Fellow at the Institute of Thermodynamics of the University Liége with Professor Burnay and as a Visiting Research Professor at the Institute of Heat Technology of Eindhoven University of Technology with Professor van Koppen during the two academic years, 1972-73 and 1979-80. Since my doctoral work was *on non-equilibrium thermodynamics of magneto-solid-mechanics* as applied to special power systems [28], I specifically wanted to go to Europe to have an opportunity to meet these three masters of the topic. It turned out that opportunities did present themselves in different ways. My contact with Prigogine was on personal initiative. After learning more about his personality from people at Liége, I contacted him in writing and followed up by phone. He invited me to visit him at Brussels in his university office. As is my personal custom, I arrived a little early and started looking through the corridors. When the time came, I went to his office. He was very friendly and kind although I noticed that he was very uneasy. Finally he said that we needed to get away from the university since he had told the King that he "could not meet with him that day" because he was going to be busy with me. So we left his office, rushed through the corridors, not the ones used by everyone, and got to his car. He drove away in haste to a restaurant where they knew him. Promptly and at his request we were seated at the very back, away from the crowds. We had not only a wonderful lunch but also discussed many topics for which I had questions and those that he offered on his own. I believe we stayed there about four hours. A few years later, at the invitation of the Chemical Engineering Department at Louisiana State University-Baton Rouge, Prigogine came to present a seminar. Coincidentally at the same time Professor E. P. Wigner, a Nobel Laureate himself, was spending the semester in the Physics Department. The seminar room was packed with Wigner seated at the very front. Prigogine made his presentation with no sound in the room. When he finished, a question/answer period was to follow. Before anyone had a chance, Wigner challenged Prigogine on some issues. The discussion, question-counter question went on longer than the seminar. Finally, Wigner said that it was best "to continue their agreement to disagree" which was received with a lot of laughter and applause. That evening, we went to dinner. Sitting around the table and enjoying the food and the conversation, we noticed a commotion in the restaurant. Prigogine saw immediately that a man was suffocating. Without hesitation he took off and did the appropriate things to relieve the food from the throat of the man. He returned to our table and continued his wonderful discussions into the late hours of the evening as if nothing had happened. Towards me he was most kind and generous with his thoughts. He highly encouraged my research and teaching at that time, including continuing my doctoral research work into new directions and teaching advanced courses in all fields of thermodynamics including non-equilibrium

thermodynamics. His thoughts on all these issues were most beneficial to me. During my stay at Eindhoven, Professor van Koppen gave me much latitude in my work and studies. We had decided that I would investigate the validity of two-phase correlations used in the design of heat exchangers and would determine under what conditions the second principle would be violated so as to have a string of correlations that should be used depending on flow characteristics. When I found out that de Groot was to present a seminar in the Physics Colloquium, I made arrangements to attend and asked for time to meet with him personally. My request was accepted by de Groot and, upon completion of his seminar, we spent a couple hours on the problem on which I was working. I found him to be a very generous person as well. His precise remarks as well as no nonsense attitude were what impressed me the most. He understood my point of view on the problem and made remarks that would prove to be very valuable and precise. He was not as flamboyant as Prigogine but rather reserved. A couple of months later, I found out that Mazur was coming to present a seminar. Again, as I had done with the other two, I arranged to meet with him personally after his seminar presentation. Mazur seemed to be enjoying life to the fullest. He was smiling, making remarks and jokes, and just seemed happy. After he found out who I was and what I was doing in the crowd of chemists and physicists, he became very friendly and made the remark that he "always wanted to have engineers working with him because they could do, understand, and think about situations differently." Again, we spent a few hours discussing mostly my questions. He provided different situations based on his experiences. Indeed Mazur was very kind, accommodating, and just a pleasant person. I cherish these encounters and wish that I had had more contact with each of them so that I could have expanded my understanding of nature through thermodynamics. For me, these are very fond memories of these three pillars of thermodynamics to whom we all owe much.

THERMODYNAMICS IN ENGINEERING

It is a very well known fact that thermodynamics education in the United States, in particular, is not in a healthy state. This situation starts at the undergraduate level and goes through the graduate programs in mechanical engineering. It may be the same situation in chemical engineering, but I will let those knowledgeable about that situation speak and write about it. In the last decade in the United States, most undergraduate mechanical engineering departments have reduced the required coverage of thermodynamics from an equivalent six semester credit hours to four or even three. At the same time some textbooks, written by people who did not understand the field and who have never studied it, were adopted extensively due to their "ease of reading". Since those who studied thermodynamics at the graduate level have decreased dramatically over the last two to three decades, the faculty to teach thermodynamics have been those who themselves never learned the subject. Thus, these textbooks fit the needs of the instructors very well since the students would not challenge them with questions that they could not answer. Therefore, as undergraduates were not taught complete material and graduates were not given the opportunity to study at a higher level, the quality of teaching thermodynamics has deteriorated. During my graduate years in late 1950s and early 1960s, mechanical engineering programs taught classical, statistical, and non-equilibrium thermodynamics at the graduate level. The books that taught us were those of Callen [29] and de Groot and Mazur [13] along with those in statistical thermodynamics, mostly written by physicists and chemists. When my generation started their academic careers, we continued in this mode. However, as time went on due particularly to the lack of research funding in the field, the number of graduate students has dwindled. Today in most universities, one cannot find more than one course offered at the graduate level. The numbers who take this course is way down from what it used to be making the situation even worse since we are not educating thermodynamicists. This situation perpetuates itself by having people who have not studied thermodynamics teaching those at the undergraduate level and beyond; a vicious circle. What my hope is to have this dialogue here so that we all can find an appropriate approach to resolve this problem. However, there are encouraging developments. Recently Bejan [30] has written a text that could be used at the graduate level. However, in some places, the contents are not in

sufficient depth to bring the student to a high level of understanding of thermodynamics. Demirel and Sandler [31], both chemical engineers, have written a review article on *non-equilibrium thermodynamics in engineering and science*. In this detailed study, they describe the importance of the topic in engineering, which is very encouraging indeed. I am hopeful that they are actually offering courses at their institutions which are available to mechanical engineering students as well. It would be a great pity if students are not taking advantage of these professors' interests and expertise in the field. It is really a great shame, in my opinion, that we have permitted the deterioration of the teaching of thermodynamics at all levels in universities. We have not been able to fight the faculty and administrators that make these decisions. The undergraduates are not taught why certain processes occur the way they do in thermodynamics and if a given process or system can actually exist, the use of the second principle. The graduate students are not given the chance to understand and apply thermodynamic principles within problems of research. The research that is required for materials engineering and challenges that we face in new materials by design of novel energy systems at the nano-scale, for example, definitely require innovation that can only occur if we teach the appropriate material. Even for the simplest case of linear non-equilibrium situation of thermo-electricity, the material needed has to have inverse characteristics of thermal and electrical conductivities. As long as we cannot develop this type of material, we cannot expect this energy conversion system to be successful. In other non-equilibrium situations, similar problems are faced. This is what is meant above when we discuss materials by design. I believe that intelligent study of thermodynamics will permit us to at least know what is needed so that others can develop the appropriate solutions to help us in various energy conversion schemes. In my opinion, we are not going to be successful if we do not teach the required thermodynamics at the graduate level. I am not proposing three courses; however, I am proposing the appropriate coverage of topics, not necessarily as separate courses, but as integrated topics. One such course could use the book of Callen [29] which I still believe is the best that there is and that has been written to date. This book contains not only a novel approach to classical thermodynamics but presents an exceptionally good introduction to both statistical and non-equilibrium thermodynamics. In this fashion, the student gets a good overall appreciation of what thermodynamics is and can easily expand into areas of advanced thinking and of research. We, as thermodynamicists particularly in this group of participants from throughout the world, must take control of our own destiny and make sure that we teach and research what we should. My hope is that we can actually accomplish this very soon at the undergraduate and graduate levels for the challenges of the 21st century.

ACKNOWLEDGEMENTS

I would like to acknowledge Professor Kjelstrup and Bedeaux for asking me to make this presentation at the dinner of ECOS 2003 in Copenhagen. My thanks also to Professor Eric Mazur, of Harvard University, who supplied me with information about his father and helped with the translation of the obituaries that were written in Dutch that Professor L. G. Suttorp of the University of Amsterdam sent me. Other obituaries that are in the literature about these three men were also used. Without their help, I could not have paid appropriate and personal respects to de Groot, Mazur, and Prigogine.

The views expressed herein are those of the author and do not purport to reflect the position of the United States Military Academy at West Point, the Department of the Army, or the Department of Defense.

REFERENCES

[1] Onsager L. *Reciprocal relations in irreversible processes.* Physical Review 1931; 37: 405-426.

[2] Clausius R. *On the moving force of heat and the laws regarding the nature of heat itself which are deducible therefrom.* Philosophical Magazine 1851; 2: 1-20.

[3] Stokes G. G. *On the conduction of heat in crystals*. Cambridge Dublin Mathematical Journal 1851; 6: 215-238.

[4] Thomson W. (Lord Kelvin). *Thermo-electric currents*. Transactions of Royal Society of Edinburgh 1854; 21: 232-291.

[5] Duhem P. *Enegétique.* Paris: Gauthier-Villars 1911.

[6] De Donder Th. *L'affinité, applications aux gaz parfaits*. Académie Royale Belge Bull. Cl. Sc. 1922; 7: 197-205.

[7] Onsager L. *Reciprocal relations in irreversible processes.* Physical Review 1931; 38: 2265-2279.

[8] Meixner J. *Zur thermodynamik der thermodiffusion.* Annalen der Physik 1941; 39: 333-356.

[9] Prigogine I. *Etude thermodynamique des phénomène irréversible*. Académie Royale Belge Bull. Cl. Sc. 1945; 31: 600.

[10] de Groot S. R. *L'effet Soret, diffusion thermique dans les phases condensées.* Amsterdam: North-Holland Publishing Company, 1945.

[11] Mazur P. *Thermodynamique des phénomènes de transport dans l'hélium II liquide.* Universiteit Utrecht 1951

[12] de Groot S. R. *Thermodynamics of irreversible processes.* Amsterdam: North Holland Publishing Company 1951.

[13] de Groot S. R. and Mazur, P. *Non-equilibrium thermodynamics*. Amsterdam: North Holland Publishing Company 1962.

[14] Casimir, H. B. G. *On Onsager's principle of microscopic reversibility*. Review of Modern Physics 1945; 17: 343-350.

[15] Wigner, E. P. *Derivations of Onsager's reciprocal relations.* J. Chem. Phys. 1954; 22:191-215.

[16] de Groot, S. R. *The Maxwell equations*. Amsterdam: North Holland Publishing Company 1969.

[17] de Groot S. R. and Suttorp L. G. *Foundations of electrodynamics*. Amsterdam: North Holland Publishing Company 1972.

[18] de Groot S. R. *La transformation de Weyl et la fonction de Wigner*. Montreal: Les Presses de l'Université 1974.

[19] de Groot S. R., van Leeuwen W. A., and van Weert C. G. *Relativistic kinetic theory: Principles and applications*. Amsterdam: North Holland Publishing Company 1980.

[20] Mazur, P. *On the motion and Brownian motion of N spheres in a viscous fluid*. Physica 1982; A110: 128-146.

[21] Bedeaux D. and Mazur, P. *Mesoscopic non-equilibrium thermodynamics for quantum systems*. Physica 2001; A298: 81-100.

[22] The Royal Swedish Academy of Sciences, Press Release: The 1977 Nobel Prize in Chemistry http://nobelprize.org/chemistry/laureates/1977. 11 October 1977.

[23] Timmermans, J. *Les solutions concentrées*. Paris: Masson 1936.

[24] Prigogine, I. *Non-equilibrium statistical mechanics*. London: Interscience 1962.

[25] Glansdorff, P. and Prigogine, I. *Structure, stabilité et fluctuations*. Paris: Masson 1971.

[26] Nicolis, G. and Prigogine, I. *Self-organization and non-eauilibrium systems: From dissipative structures to order through fluctuations*. New York: Wiley 1977.

[27] Petrosky, T., Ordonez, G. and Prigogine, I. *Irreversibility, probabilities and dressed unstable states in quantum mechanics*. Journal Physical Society Japan 2004; 72: 12.

[28] Arnas, Ö. *Non-equilibrium thermodynamic analysis of magneto-solid-mechanics with device applications*. Dissertation Abstracts 1965; 26: 962, No: 65-8947.

[29] Callen, H. *Thermodynamics*. New York: Wiley 1960.

[30] Bejan, A. *Advanced engineering thermodynamics*. New York: Wiley 1997.

[31] Demirel, Y. and Sandler, S. *Non-equilibrium thermodynamics in engineering and science.* Journal of Physical Chemistry 2004; 108: 31-43.

Proceedings of ECOS 2005
Trondheim, Norway
June 20–22, 2005

CLIMATE CHANGE AND ENERGY POLICY: THE IMPORTANCE OF SUSTAINABILITY ARGUMENTS

Professor Roland Clift*,
Centre for Environmental Strategy,
University of Surrey, GUILDFORD,
Surrey GU2 7XH, UK

ABSTRACT

It is the stated policy of the UK government to reduce emissions of carbon dioxide by 60% by 2050. This policy, which goes far beyond commitments under the Kyoto agreement, was originally advocated by the Royal Commission on Environmental Pollution, of which the author was a member. Its acceptance was seen by many as a surprising development, possibly reflecting strength of the underlying case. The target was developed by a three-legged argument which reflects the three components of sustainability:

Environmental constraints: limits on emissions to avoid risk of major climate change;
Social equity: equal per-capita allocation of emissions;
Techno-economic: the feasibility and cost of reduction on this scale.

Assessment of techno-economic feasibility required a new evaluation of the role of different primary energy sources in the UK, including the contribution of biomass and recognising the importance of heat in the national energy balance. It also showed clearly the decisions to be made over both carbon dioxide sequestration and the future of nuclear power.

INTRODUCTION

The author was, until recently, a member of the Royal Commission on Environmental Pollution (RCEP), a uniquely UK institution appointed *to advise on matters, both national and international, concerning the pollution of the environment; on the adequacy of research in this field; and the future possibilities of danger to the environment*. The RCEP has been in continuous existence but with rotating membership since 1971. It is constituted as a body of independent experts, standing outside the political mainstream but intended to provide advice to guide long-term environmental policy. An important role for the RCEP is to present scientific evidence and its implications which may be obvious to the scientific community but politically inconvenient. Some of the RCEP's reports have had a significance which extends outside the UK; for example the concepts of Integrated Pollution Control and Best Practicable Environmental Option originated with the RCEP.

In one of its more recent reports [1], the Royal Commission addressed the issue of climate change and its relationship to energy supply. The principal recommendation of the RCEP's analysis was that carbon dioxide emissions from human activities in the UK must be reduced by 60% below 1998 levels by 2050. The year 2050 was itself chosen carefully: even the most enthusiastic advocates of nuclear fusion did not consider that it would be available before 2050, so that the target would have to be met by known energy technologies[1]. At the time, this target appeared to be too radical to be politically acceptable; for example, it goes way beyond current negotiations under the Kyoto protocol. However, it was accepted and is now UK Government policy. The present paper reviews the argument which presumably led to its acceptance and some of the implications of this policy.

* Corresponding author: Phone: +44 1483 689271 Fax: +44 1483 686671 E-mail: r.clift@surrey.ac.uk

[1]RCEP also recommended a decrease of 80% by 2100, but the reasons for proposing this very long-term target are not discussed in this paper.

THE CONTEXT: SUSTAINABLE DEVELOPMENT

The concept of sustainable development is now sufficiently well known that it will not be rehearsed here. However, a particular interpretation of sustainable development which has proved useful in teaching the concept to engineers and scientists [2] will be reviewed, because it happens to illustrate and support the argument developed by the RCEP [1].

The basic idea is that human activities are limited by three sets of long-term constraints, summarised by the Venn diagram in Figure 1. **Eco-centric concerns** represents the constraints imposed by the fact that the earth is, in thermodynamic terms, a closed system. Thus, energy flux is received from the sun, but the "capital" resources available to us on a global scale are finite, as is the capacity of the biosphere to absorb or adapt to the emissions from human activities. **Techno-centric concerns** represents the constraints imposed by finite human abilities: the technology which we are able to deploy and the economic system within which we deploy that technology. This lobe represents the traditional scope of engineering. **Socio-centric concerns** represents human expectations: the need to provide *a better quality of life for everyone, now and in the future* (to quote from the UK Government's interpretation of sustainable development). This lobe incorporates the principle of inter- and intra-generational equity which are central to the concept of sustainable development. Sustainability is to be found in the central area of Figure 1, which meets all the sets of constraints, while sustainable development is a process of moving towards that region. While it is recognised that Figure 1 is a simplistic representation of a very rich concept, it has nevertheless proved to be useful as an educational device.

Although not stated explicitly in the RCEP report, it is implicit that future use of fossil hydrocarbons will be constrained not by their availability but by the capacity of the biosphere to adapt to the emissions, specifically carbon dioxide. In other words, we already know the whereabouts of more fossil fuels than can be burned without risking disastrous climatic impacts. The driver for change in energy technology is therefore the effect of the emissions, not limited supply; as Sheikh Yamani famously put it, "The stone age did not end because we ran out of stones". To support this argument, current crude oil prices make it not only economic but very profitable to exploit oil sands; the quantity of "synthetic crude" available in Alberta is of the same order as the oil reserves in Saudi Arabia – a simple fact which is sometimes overlooked in discussions over the extent of remaining oil reserves. While the conventional market system can deal with scarcity of supply through rising prices which make new reserves economic, it is necessary to invent a new mechanism to deal with scarcity of "carrying capacity" to absorb emissions. It remains to be seen whether emission trading systems like that being introduced in Europe will constitute an effective market, whether the price will be sufficiently high to influence energy use and whether prices will be too unstable for effective long-term planning and restructuring.

The Royal Commission sidestepped the economic arguments over the damage costs of carbon dioxide emissions by approaching the issue of energy policy and climate change in a different way, using the approach of recognising and trying to estimate the constraints.

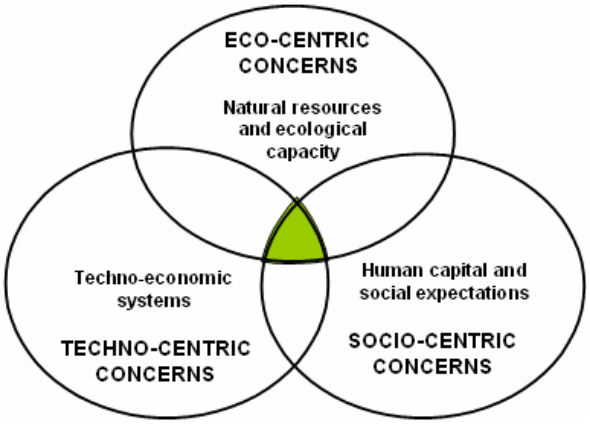

Figure 1: Sustainability expressed as long-term constraints [2]

POLICY RECOMMENDATIONS

The Royal Commission's report starts with an analysis of the evidence that emissions of climate-forcing "greenhouse gases" from human activities are causing changes in the global climate and regional weather patterns. In effect, it endorsed the conclusions of the UN Intergovernmental Panel on Climate change (IPCC). To quote the RCEP report

[1], *the world is now faced with a radical challenge of a totally new kind which requires an urgent response… By the time the effects of human activities on the global climate are clear and unambiguous it would be too late to take preventive measures*. This statement may not be news to the scientific community in Europe, but was necessary at the time of publication (2000) to underpin the Commission's recommendations; although the UK government now stresses its belief that climate change represents a real and serious threat, this commitment has emerged since publication of the RCEP report.

Of more interest here is the analysis which followed, which had three principal steps.

1. If the concentration of carbon dioxide in the atmosphere gets too high, then there will be a risk of really catastrophic climate change associated, for example, with changes in ocean circulation patterns. RCEP proposed 550ppm as the ceiling, a constraint which must not be breached. Some would prefer a lower limit – at 550ppm, the predicted rise in sea level is still bad news for low lying Pacific islands, for example – but there was also a measure of political realism behind the figure (see below).

2. Working back from the 550ppm constraint, RCEP estimated the total tolerable CO_2 emissions, and then divided them by total global population to get the *per capita* ration. Multiplying by the population of the UK gave about 40% of current emissions – hence the recommended target of a 60% reduction. This is known as the "contract-and-converge" principle. It simply ignores economists' attempts to calculate an optimal level of CO_2 emissions, on the basis that the damage cost figures mean little when the whole system is so complex and non-linear (and therefore chaotic) that detailed predictions of climate change (as distinct from estimating thresholds or constraints) are meaningless.

3. To explore the practicality of the 60% reduction target, RCEP developed representative scenarios to illustrate how it might be achieved (see below). Based on these scenarios, the cost of shifting to a low-carbon energy economy was subsequently estimated as about 2% of GDP from now to 2050. The cost is sometimes described as "enormous" but, as an economist will always ask, compared to what? The economists who produced these estimates also project 4% annual growth in GDP. So taking action to limit the potentially catastrophic effects of global climate change would merely slow down the rise in consumer spending in developed countries. Given that most forms of consumer spending lead to carbon dioxide emissions, there is a possible argument that this will in itself have some effect in constraining the growth of climate-forcing emissions.

It is interesting that, although not consciously formulated in terms of the approach to sustainability summarised in Figure 1, the three steps in the argument map exactly onto the three sets of constraints: ecological, societal and techno-economic. Perhaps this illustrates the strength of this approach to sustainability analysis. To quote the RCEP report again [1], … *the UK could cut its carbon dioxide emissions by 60% by 2050. Achieving this will require vision, leadership, and action which begins now*. Acceptance of the target of 60% reduction by 2050 has, so far at least, survived subsequent discussions over commitments under the Kyoto process and softening of UK government targets for shorter term reductions. In fact, the UK government has been advocating international acceptance of the 2050 target, and the Swedish government has also adopted it as a basis for energy policy.

ENERGY SCENARIOS

In order to explore the implications of a 60% reduction in carbon dioxide emissions, the RCEP constructed four scenarios to illustrate measures by which it might be achieved. These scenarios are only illustrations, not intended to be interpreted as predictions or projections, but they enabled rough estimates of the cost of the change (see above). They had a number of common features. They were based on known technologies, assuming that electrical generation by nuclear fusion is not available by 2050 (see above). They took as their starting point the 1998 pattern of energy use in the UK, summarised in Table 1. Figure 2 shows energy use updated to 2003, while Figure 3 shows how UK carbon dioxide emissions have changed since 1990. Compared to continental European countries at comparable latitudes, domestic energy use is high because of the relatively poor energy performance of the UK building stock and the almost complete absence of heating systems using

"low-grade" heat; the principal fuels for space and water heating are natural gas and electrical resistive heating[2]. For obvious geographical reasons, the electricity grid in the UK is separate from that of continental Europe (apart from limited imports via a cross-channel link from France). Most of the decline in carbon dioxide emissions since 1990 is attributable to replacement of coal by natural gas in electricity generation (Figure 3). However, the proportion of renewable sources in the UK electricity system is still low by European Standards: only just over 1% of total inland energy use even in 2004. These features of the UK energy sector present possible savings in carbon intensity which are not available in other European countries, and which just might enable economic growth to be decoupled from carbon dioxide emissions.

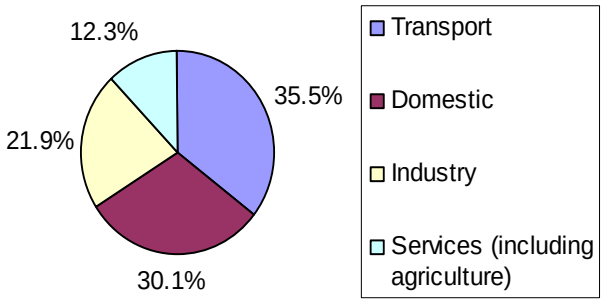

Figure 2: Final energy consumption in the UK, 2003 [3]

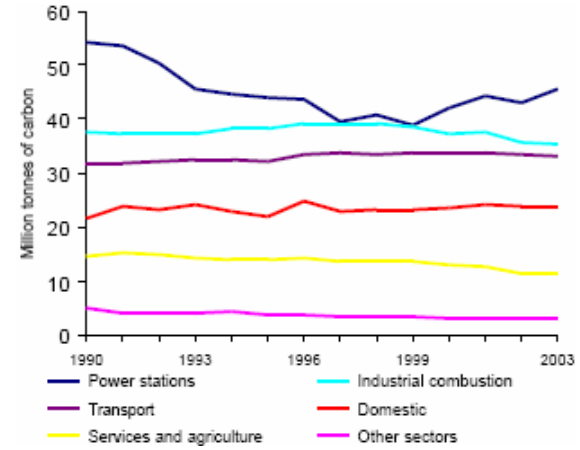

Figure 3: UK carbon dioxide emissions by source [3]

The final energy demands in the RCEP's scenarios are summarised in Table 1. They are based on a number of simplifying but not unrealistic assumptions. High-grade heat (i.e. heat for energy-intensive industrial processes) in all scenarios is supplied by natural gas. Industrial, commercial and domestic demand for electrical energy is reduced in some scenarios through improvements in the efficiency of appliances and machines – but it is recognised that any reductions in demand represent a reversal of current trends. Low grade heat is used primarily for space- and water-heating in domestic and service sectors. The reductions in some scenarios are assumed to be achieved primarily by improving the relatively inefficient UK building stock. Transport is seen as continuing to be dependent on fossil hydrocarbons, although the carbon efficiency of transport is assumed to improve through a combination of incremental technological development, larger shifts such as use of hydrogen produced from fossil fuels but with higher well-to-wheel carbon efficiency, and modal shifts (primarily from road to rail) to carry both people and goods with lower carbon dioxide emissions.[3]

End-use category	**Scenario**			
	1 (as 1998)	2	3	4
High-grade heat	87	44	44	30
Electricity	32	24	24	21
Low-grade heat	16	12	12	11
Transport	70	53	53	47
TOTAL	**205**	**132**	**132**	**109**

Table 1: Final energy consumption in 2050 by end-use (annual averages in GW) [1]

Energy supply in the four scenarios is summarised in Table 2[4]; all scenarios include the 60% reduction below 1998 emissions. Scenarios 1 and 3 assume that intermittent renewable generation of electricity is "backed up" by controllable generating stations fuelled either by nuclear fission

[2] Off-peak "night storage" heating is common in the UK. It has been argued, principally by advocates of nuclear power, that this is to be encouraged, on the basis that future energy systems will be dominated by low-carbon fixed-output electricity generation. RCEP did not subscribe to this view, rejecting its implication that new buildings should be equipped with electrical heating to fit a hypothetical energy system which might possibly exist at some future date.

[3] The role of air transport was considered in a subsequent RCEP study [4], which has also triggered an intense debate.

[4] The figures in Table 2 refer to outputs of electricity, heat and intermediate energy carriers. For the correspondence between Table 1 and 2, see [1]; it requires detailed explanation, primarily because of the use of CHP and the efficiencies assumed in the different scenarios and technologies.

Source	1998	Scenario			
		1	2	3	4
Intermittent renewables:					
On-shore wind	0.10	6.5	3.3	0.2	3.3
Off-shore wind		11.4	11.4	11.4	5.7
Photovoltaic		10.0	5.0	0.5	0.5
Wave		3.75	3.75	3.75	3.75
Tidal stream		0.25	0.25	0.25	0.25
Tidal barrage		2.2	2.2	0.0	2.2
TOTAL	**0.10**	**34.1**	**25.9**	**16.1**	**15.7**
Other renewables:					
Hydro	0.61	0.89	0.89	0.89	0.79
Energy crops	-	10.2	10.2	1.8	1.8
Bio-waste	0.04	5.7	5.7	5.7	1.2
MSW	0.15	1.9	1.9	0	0
TOTAL RENEWABLE	**0.90**	**52.8**	**44.6**	**24.5**	**19.5**
Low-C large scale electrical generation	11.4	52	0	19	0
Other fossil	266	106	106	106	106

Table 2: Outputs from energy sources in 2050 (annual averages in GW) [1]

or by fossil fuels with the carbon dioxide captured and sequestered in geological strata, primarily saline aquifers; the estimated capacity in the UK sectors of the North and Irish seas is sufficiently large to accommodate emissions way beyond 2050. Thus the scenarios illustrate that the significant technological choice, at least for the UK, is between nuclear power and fossil-fired generation with carbon sequestration. The scenarios also implicitly assume that hydrogen used in transport is produced from hydrocarbons but in dedicated reforming plants from which the carbon dioxide is sequestered. Thus the feasibility of carbon dioxide sequestration is a central concern, as is the question of how much generating capacity is needed to "back up" intermittent renewable sources. The latter depends, in turn, on the development of high-density energy storage technology; there is some pumped storage capacity in the UK, but little real prospect of significant expansion. "Other fossil" in Table 2 refers to uses from which the carbon dioxide is emitted to the atmosphere.

The use of renewables in the four scenarios is based on assessments of the cost-effective available resource in the UK [5]. There is limited hydro-electric generation capacity available, and the scenarios assume modest expansion. On-shore and off-shore wind is assumed to expand, a development which has already started in the UK. Wave generation is assumed to have developed to make a modest contribution by 2050, with a further small contribution from tidal-stream turbines. Some scenarios also assume construction of tidal barrages; there is significant technical scope for developing this resource but it may not prove to be environmentally or socially acceptable (compare with Figure 1).[5] Agricultural waste, energy crops and municipal solid waste (MSW) represent significant resources which are currently essentially unused in the UK; their significance is discussed further below.

Scenario 1 represents a "technology can fix it" approach. It is based on final demand held at the 1998 level with the maximum deployment of renewables and maximum use of electrical generation using nuclear sources or fossil fuels. In this scenario, energy crops, agricultural and

[5] One of the areas which has been considered for a tidal barrage but rejected on environmental grounds is the Bristol Channel in the South West of England. However, it is possible that this project might be revisited, on the argument that it would actually provide environmental protection against some of the effects of rising sea level.

forestry waste and municipal solid waste (MSW) are used as fuels in CHP plants or heat-only plants generating low-grade heat output.

Scenario 2 and 3 assume that energy demand can be reduced by 36% below the 1998 level. The largest reduction is in low-grade heat (see Table 1) brought about primarily by improving the energy efficiency of the building stock. In scenario 2 the reduced demand is met by a combination of renewable sources and fossil fuels, while scenario 3 is based on renewable sources plus large controllable generating plants using nuclear fission or fossil fuel with sequestration of carbon dioxide.

Scenario 4 represents the most extreme case: a very large reduction in demand (corresponding, *inter alia*, to replacing or retrofitting all the UK building stock to Nordic standards) supplied from renewable sources with no large generating stations. However, the reduction in demand means that the energy provided by renewable sources can still be less than in scenario 1.

The significance of this analysis is that, with the possible exception of scenario 4, it shows that the 60% reduction is achievable without totally novel technologies and without complete change in social and economic structures or lifestyles. As noted above, these scenarios provided the basis for assessment of the economic cost of switching to a lower-carbon economy. There is little doubt that the assessment of the cost of the transition was an important consideration leading to the political acceptance of the RCEP's "headline" recommendation of a 60% reduction in carbon dioxide emissions by 2050.

USE OF BIOFUELS

A feature of the RCEP report [1], not usual in policy documents, is frequent reference to the laws of thermodynamics. The primary reason for this is that UK energy policy has concentrated on the electricity sector, almost as if heat is not a form of energy. Results of this focus on electrical generation can be seen in the relatively slow development of the Combined Heat and Power (CHP) sector in the UK, the general resistance of local authorities and the construction sector to contemplate anything other than single-dwelling space and water heating, and cooling towers - those obvious symbols of energy waste - at electrical generating stations. The RCEP study tries to bring heat provision more centrally into energy policy.

As a further result of the policy neglect of heat, biological energy resources remain essentially untapped in the UK: agricultural wastes, energy crops and MSW[6]. A more recent RCEP report [6] examined biomass, to investigate its possible contribution to energy supply in the UK and why the sector has been so slow to develop compared to other European countries.

Austria has the most developed biomass sector in Europe. Starting from small-scale heating plants, the sector in Austria has grown over 20 years to the point where biomass provides some 15% of primary energy. This has enabled certain Austrian provinces to achieve one of the holy grails of sustainable development: decoupling economic growth from carbon to the point where GDP has increased but carbon dioxide emissions have decreased. In Denmark, biomass is now widely used, often co-fired with coal, primarily in CHP plants. These are usually built for their heat output, for example into community heating systems, with electrical output used to back-up intermittent renewables, primarily wind. In Sweden, biomass has developed more recently but rapidly, initially for community heating and then CHP plants operated, as in Denmark, over a range of heat/power ratio. But in the UK, renewables still only account for 1.1% of total inland energy use and biomass is only a small fraction of that. Why?

The RCEP diagnosed one of the reasons for this failure as the complex and confused government support for biomass, exacerbated by the focus on generating electrical power with no corresponding incentives for renewable heat production. The focus on power generation seems to have been amplified by the notion that "high technology" processes can be developed for exploitation of biomass leading to possible export markets. One result of this approach has been the conspicuous failure of the ARBRE project in South Yorkshire,

[6] For these purposes, MSW is treated as a renewable fuel, on the basis that it is available anyway but currently consigned mainly to landfill. Public resistance to recovering energy from solid waste is a UK peculiarity, not discussed here.

an electricity generating plant fuelled by short-rotation coppiced willow and using Swedish biomass gasification technology. The plant failed to progress beyond start-up to enter service – for reasons which are hotly discussed.

The RCEP argued that, rather than being seen as a possible fuel for power generation, biomass should be seen primarily as a local fuel for heating or CHP. Local supply chains must therefore be developed and, until the demand is clear, it is unreasonable to expect farmers to plant energy crops even when planting grants are available. Although credits are available to promote the development of renewable electricity generation, there has so far been a marked reluctance on the part of the UK government to extend a similar approach to renewable heat sources – a further manifestation of the neglect of heat as a significant part of the total national energy budget.

More detailed analysis of the possible availability of bio-energy broadly confirmed the earlier estimates summarised in Table 2. In fact significant quantities of biomass will become available over the next 20 years or so from forest plantations, primarily of Sitka spruce, developed to provide pulpwood based on projections of demand which now appear to have been too high. Figure 4 shows estimates by the Forestry Commission for the availability of wood in the UK. Clearly there is already a surplus of supply over demand, and the surplus becomes much larger if agricultural residues – primarily straw – are included. This persuaded the RCEP of the need to develop a market to stimulate demand before there is any point in encouraging planting of energy crops.

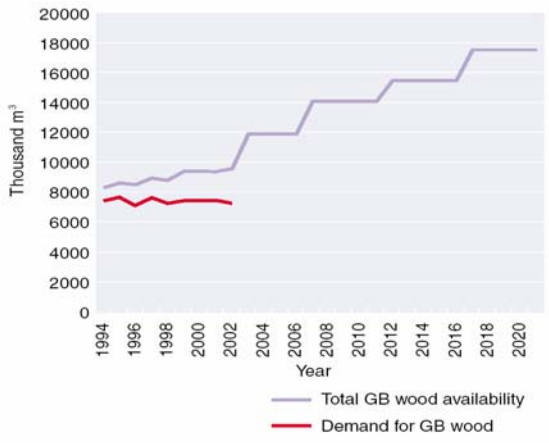

Figure 4: Supply and demand of wood in Great Britain (i.e. England, Wales and Scotland).

However, energy crops will also be needed. Based on assessments of energy yield per hectare, short-rotation coppiced (SRC) *salix* (willow) appears to be generally the highest yielding crop but other plants such as *miscanthus* may be preferred where favoured by local climate and soil conditions. Figure 5 shows the way in which the biomass sector could develop in the UK, using current supplies of wood and agricultural residues as a basis for developing the market for energy crops, up to the level of primary energy supply in 2050 needed to provide the delivered energy required by scenarios 1 and 2 in the earlier RCEP report [1]. A phased approach to the development of bioenergy in the UK was foreseen:

Phase 1 (2004 – 2012): increasing use of both agricultural and forestry resources, and of set-aside land for energy crops;

Phase 2 (2012 – 2018): area producing energy crops increases to include all set-aside land;

Phase 3 (2018 – 2025): energy crops become established as accepted main crops;

Phase 4 (2025 – 2050): the area of land under energy crops becomes a significant proportion of total available agricultural land.

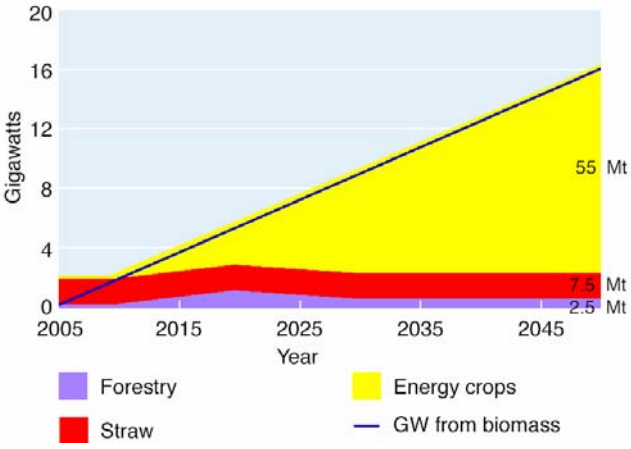

Figure 5: Scenario to achieve 16 GW of energy from forestry, straw and energy crops

It is clear that the competition for land use will be a constraint on the development of the bioenergy sector if anything like the scenario in Figure 5 develops. Contrary to current EU policy, the RCEP analysis leads to the conclusion that the focus should be on biofuels for heat or CHP rather than for transport: only if surplus land is available once the heat demand is met should transport fuels be considered, because the energy yield and carbon

reduction per hectare are lower than for *salix* or *miscanthus*. The RCEP analysis suggests that this will never be the case, providing a *post hoc* justification for the assumption in Tables 1 and 2 that transport will continue to represent the primary demand for hydrocarbons. This conclusion runs counter to the EU's policy of promoting biofuels for transport, and therefore begs the question of why transport fuels, with their less efficient use of agricultural land, have developed ahead of fuels for heat and CHP. One possible reason, which seems plausible to many involved in this sector, is that biofuels for transport have provided a way to support agricultural activities in spite of the Common Agricultural Policy, and that fuels such as biodiesel have developed because the supply chain for vegetable oils was already in place. This serves to underline the importance of developing the supply chain for other bioenergy crops.

CONCLUDING REMARKS

The work of the Royal Commission on Environmental Pollution reviewed here provides both positive and negative examples of success in using scientific analysis to underpin policy recommendations: positive in the sense that the "headline" recommendation on carbon dioxide emissions has been accepted by the UK Government; negative in the sense that more specific recommendations, such as actions to promote the development of biomass as a renewable energy source, have not been implemented. However, the overall message, that climate change is a real threat and that action to mitigate it is possible, does now appear to be widely accepted. The key question is not whether new energy technologies can be developed; on the contrary, the necessary reductions in carbon dioxide emissions could be achieved using known technology. The real question is whether the political will can be found to take the necessary action.

REFERENCES

[1] Royal Commission on Environmental Pollution *Energy – the changing climate.* London: The Stationery Office, 2000.

[2] Mitchell, C.A., Carew A.L. and Clift, R. T*he role of the professional engineer and scientist in sustainable development*, chapter 2, pp.29-55 in "Sustainable development in practice – case studies for engineers and scientists", ed. A. Azapagic, S. Perdan and R. Clift, John Wiley & Sons, Chichester, 2004.

[3] Department of Trade and Industry *Digest of UK Energy Statistics (DUKES)*, DTI, 2004.

[4] Royal Commission on Environmental Pollution *The environmental effects of civil aircraft in flight*, London: RCEP, 2002.

[5] Energy Technology Support Unit (ETSU) *New and renewable energy: prospects in the UK for the 21st century – supporting analysis*, ETSU, Marwell, 1999.

[6] Royal Commission on Environmental Pollution *Biomass as a renewable energy source*, London: RCEP, 2004.

Proceedings of ECOS 2005
Trondheim, Norway
June 20–22, 2005

COMPUTATIONAL FUEL CELL ENGINEERING: CHALLENGES AND OPPORTUNITIES

N. Djilali*
University of Victoria
Institute for Integrated Energy Systems & Dept. of Mechanical Engineering
Victoria, BC Canada V8W 3P6

ABSTRACT

Fuel cell are still in early development stages, and the combination of new and optimized materials, improved product development, novel architectures, more efficient transport processes, and design optimization and integration are expected to lead to major gains in performance, efficiency, reliability, manufacturability and cost-effectiveness. Computational Fuel Cell Engineering tools that allow systematic simulation, design and optimization of fuel cell systems would be very valuable in the integration of such advances, allow less heavy reliance on hardware prototyping, and reduce development cycles.

Computational Fuel Cell Engineering (CFCE) requires the robust integration of models representing a variety of complex transport processes, and characterized by a broad spectrum of length and time scales. These processes include a fascinating, but not always well understood array of phenomena involving fluidic, ionic, electronic and thermal transport, in concert with electrochemical reactions. In this paper, we report on some progress in both fundamental modelling as well as in the development of integrated, CFD based PEM fuel cell models. A new rational model for coupled protonic and water transport in polymer electrolyte membranes, as well direct numerical simulations of two-phase flow in porous gas diffusion electrodes are discussed. Illustrative applications of CFD based simulations are presented for conventional fuel cells as well as novel micro-structured fuel cells. The paper concludes with a perspective on some of the remaining theoretical, experimental and numerical challenges to achieve truly functional CFCE tools.

NOMENCLATURE

c	molar concentration	s	saturation
I, i	current; current density	T	Temperature
k	permeability	u	velocity
F	Farraday's constant	ε	porosity
N_p	protonic flux	Φ	potential
N_λ	water flux	μ	viscosity
P	pressure	ρ	density
		σ	conductivity; interfacial tension

* Phone: +1 250 721-6034 Fax: +1 250 721 6323
E-mail: ndjilali@uvic.ca

INTRODUCTION

Fuel cells and hydrogen technologies hold the promise of zero emission power to meet the increasing demand for energy services such as transportation, heating, manufacturing, and communication in both developed and developing countries. Many socio-political, economic, engineering and scientific obstacles need to be surmounted before wide spread use of these technologies becomes possible. The leading contender for replacing the ubiquitous battery and internal combustion engine is proton exchange membrane fuel cell (PEMFC) technology. In addition to the important question surrounding the development of a hydrogen fuelling infrastructure discussed elsewhere [1], the main obstacles to the deployment and commercialization of PEMFCs are cost, durability, and performance [2]. In this paper we will focus on the role of computational tools in addressing some of the engineering and scientific challenges in the development of better performance and cheaper PEMFC technology.

The overall operating principle of a PEMFC is relatively simple. Hydrogen is to the cell and oxidized at the anode, and oxygen, usually carried in an air stream, is reduced at the cathode. The protons released by the oxidation of hydrogen are conducted through the proton exchange membrane (PEM) to the cathode. Since the membrane is not electronically conductive, the electrons released at the anode have to flow along an external circuit, thereby generating electric power, and eventually recombine with the protons on the cathode side to produce water. These reactions and pathways are illustrated schematically in Figure 1.

Broadly speaking, improved performance in PEMFC can be achieved by enhancing the rates of transport and/or reaction, and by increasing the surface/volume ratio of interfacial areas where reactions/transport take place. This can be achieved by, e.g., engineering the transport properties or processes in specific areas, or by introducing new materials or designs. A particularly promising avenue is the use of micro-structured features [3] as will be discussed later. In any case, it is first necessary to identify the prevailing limitations, their location and their cause. *In-situ* measurements to obtain the relevant information are exceedingly difficult due to the confined and electrochemically active

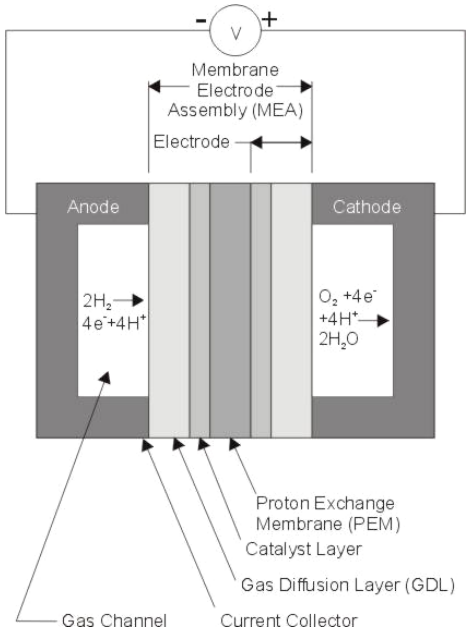

Figure 1: Schematic of a PEM fuel cell

environment of fuel cells, the complexity of the couplings, and the often transient nature of the processes. Rational models based on the fundamental physico-chemical processes together with experimental observation are thus an essential tool to gain a more complete understanding of the operation of a fuel cell. Coupling these models with modern computational fluid dynamics (CFD) and multi-disciplinary optimization methods would allow the creation of powerful Computational Fuel Cell Engineering tools that could lead to dramatic reductions in lead times and development costs, and spur innovative design.

While much progress has been made in recent years in CFD based modelling of fuel cells, truly functional and *predictive* capabilities remain a challenge due to, amongst others things:

- lack of general models for ionic and water transport in polymer membranes;
- deficient models for two phase transport in porous gas diffusion electrodes and gas flow channels;
- lack of general models for ionic and water transport in polymer membranes;

- deficient models for two phase transport in porous gas diffusion electrodes and gas flow channels;
- inadequate macroscopic modelling and resolution of catalyst layers;
- limited data for material and transport parameters; lack of *in situ* data for validation;
- wide disparity in length and time scales.

Many notable advances have been made in CFD based methods over the last few years [4]-[8]. In this paper, we provide an overview primarily focused on progress made at the University of Victoria in addressing some of the key transport phenomena issues and in the development of CFD based modelling strategies. The first part of the paper focuses on fundamental modelling of specific transport phenomena encountered in component layers of the membrane electrode assembly (MEA). In the second part, we discuss the integration of some of these models into multi-dimensional CFD codes and illustrate their application. The paper closes with a perspective on some of the remaining challenges.

TRANSPORT PHENOMENA IN PEMFCs

The cathode side of the membrane electrode assembly (MEA) provides a good illustration of the complex interplay of various transport phenomena in a PEMFC. The MEA consists of a proton exchange membrane sandwiched between catalyst and gas diffusion layers (GDL), and the latter two components essentially form the electrode. This electrode is a buffer zone that facilitates a number of transport processes:

- The conduction of electrons between the current collectors and the reaction sites.
- The conduction of protons between the membrane and catalyst layer.
- The transport of the reactants to the catalyst layer
- The transport of heat away form the reaction site primarily through the solid matrix
- condensation/evaporation and transport of liquid water and vapour.

Optimal tailoring of an effective electrode requires therefore balancing of often conflicting requirements. On the cathode side for instance, the reaction is prone to mass transport limitations at high current densities, when depletion of oxygen in the air stream becomes significant. This can be further compounded by flooding of the electrode pores by the product water and blocking of pathways for oxygen transport. Effective removal of excess water is thus essential, but must be balanced against the need to prevent drying of the proton conducting media (membrane), which causes not only deterioration in protonic conductivity (and thus higher heat generation and lower efficiency), but also impacts durability.

Computational design of fuel cells with effective reactant distribution, optimized structures and proper heat and water management, requires understanding of the various transport processes in each of the components, the development of physically representative models for these processes, and, finally, proper coupling of the models.

Polymer Electrolyte Membranes

Polymer electrolyte membranes (PEM) provide the key functions of conducting protons from anode to cathode, and of preventing reactant crossover. These membranes consist of microphase-separated structures, comprising hydrophobic polymer chains (PTFE/Teflon) and hydrophilic sulfonic acid groups.

A thorough review of transport phenomena in PEM was recently provided in [9]. The protonic conductivity characteristics of a PEM are intimately dependent on the membrane hydration given in terms of λ (number of sorbed waters per sulfonate head). Excess protons in bulk water are primarily in the form hydronium ions (H_3O^+), and higher complexes such as "Eigen" ion $(H_9O_4)^+$ may also participate.

A phenomenon closely linked to membrane conductivity is electro-osmotic drag (EOD), the process whereby a given number of water molecules associated with a proton are dragged as the proton migrates from anode to cathode. This EOD mechanism plays a major role in determining overall water balance.

The breadth of PEM transport models proposed to date ranges from molecular dynamics simulations and statistical mechanics models, to empirical macroscopic models. Our focus is on the development of macroscopic models required for computational simulations of complete fuel cells,

based on micrsoscopic insight. The most widely used model to date for determining membrane conductivity in fuel cell simulations is due to Springer, Zawodzinski and Gottesfeld [10]. This "diffusion" model has limited predictive abilities as it relies on empirical correlations obtained for Nafion membranes.

A more fundamental and general approach to modelling transport in membranes requires consideration of the dominant interactions between the aqueous system and the polymer and how they affect the conductivity and transport properties. A general model that considers such interactions based on the fundamentals of multi-component diffusion was recently derived. This new Binary Friction Membrane Model (BFM2) [11] couples the protonic flux N_p , which is proportional the ionic current i_m, and the water flux through a general constitutive law of the form:

$$\begin{bmatrix} N_p \\ N_w \end{bmatrix} = -c \begin{bmatrix} fD_{pp} & D_{pw} \\ fD_{wp} & D_{ww} \end{bmatrix} \begin{bmatrix} \nabla \Phi_m \\ \nabla \lambda \end{bmatrix} \qquad (1)$$

Where c is the molar concentration of water, $f = F/(RT)$, and Φ_m and λ are the membrane potential and water content. The coupling between the protonic and water transport is through the diagonal transport parameters D_{pw} and D_{wp} which are considered to be functions of water content λ and temperature T. A feature of the model is that all parameters can be obtained using a simplified conductivity model version of the model that represents conditions found in AC impedance conductivity measurements.

The BFM2 has a number of features that make it promising. This model:

- relies on rationally derived transport equations based on the physics of multi-component transport in the membrane;
- is not restricted by the assumption of equimolar counter diffusion;
- accounts for the effect of temperature on the sorption isotherm;
- is not restricted to Nafion, but applies to the entire family of perfluoro-sulfonated membranes.

Figure 2 illustrates the enhanced capabilities of the BFM2 model which captures the variation of

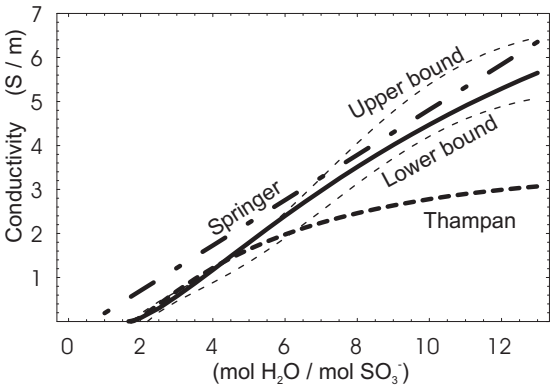

Figure 2: Calculated conductivity using BFM2 (solid) and models of Springer [10] and Thampan [12] against experimental data [13] for Nafion 117 (dashed bounds)

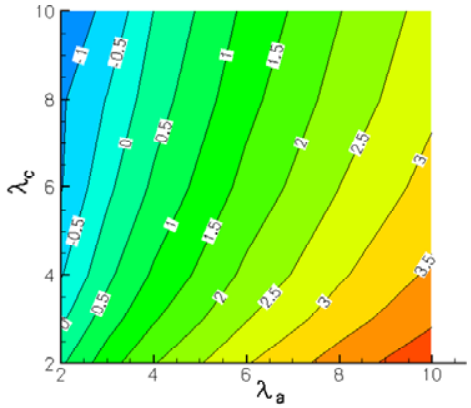

Figure 3: BFM2 computed water crossover (+ve from anode to cathode) for various cathode and anode side water content boundary conditions.

the conductivity for *all* water contents. Figure 3 illustrates the predicted water crossover coefficient $WC = N_\lambda / [I/(2F)]$. In the second part of this paper, the BFM2 is coupled to a fuel model and we will see that the resulting overpotentials and overall performance predicted by the BFM2 can, for some operating conditions, differ significantly from those obtained using the classical Springer model.

Gas Diffusion Electrodes

The gas diffusion layers (GDLs) consist of an anisotropic fibrous structure, either in the form of a "paper" or a "woven cloth", that allows distribution of reactant gases through the porous matrix and collection of current through the fibres. At higher current densities, or when local

water and heat management is inadequate, water condensation takes place leading to potential "flooding" within the GDL (and catalyst layer) as discussed earlier. In order to remedy this, GDLs are commonly treated with PTFE (Teflon) to impart hydrophobicity, and force water droplets to agglomerate at the free surface of the GDL. However, the hydrophilic Nafion in the catalyst layer will absorb and retain liquid water. Thus, liquid water produced is transported from a saturated catalyst layer to the free surface of the GDL.

A major stumbling block in the reliability of two-phase models is the necessity to rely on empirical correlations and experimental observations obtained in soil and sand samples—media with a structure that differs significantly from GDLs.

The phase distribution in a porous media is potentially the result of viscous, capillary, and gravitational forces. When modelling the diffusion layer of a PEMFC, the second (liquid) phase is taken to consist of a single component, with transfer of water only across the phase boundary through evaporation/condensation. For porous media in which the void space is occupied by two-phases, the bulk porosity ε is divided between the liquid ε_l and gas ε_g volume fractions, and the liquid saturation is defined as $s_l = \varepsilon_l / \varepsilon$. Depending on saturation, and also to some degree on wettability, two-phase flow can exist in three possible regimes [14].

Extending classical relationships for the hydrodynamics of a single-phase in porous media to each phase, and using the definition of macroscopic capillary pressure, the momentum conservation equations for the gas and liquid phases take the form [14]:

$$u_g = -\frac{k_g}{\mu_g}\nabla P_g$$
$$u_l = -\frac{k_l}{\mu_l}\nabla P_g - \frac{k_l}{\mu_l}\nabla P_c \qquad (2)$$

Where u_g and u_l are the gas and liquid phase superficial velocities, and P_g and P_c are the gas and cappliary pressures, and k_g and k_l are phase specific permeabilities, obtained by correcting the bulk permeability (k) for the effect of the reduced area open to each phase due to the presence of the other phase.

The last term in equ. (2) represents capillary diffusion. Assuming the capillary pressure gradient depends solely on the saturation gradient, the liquid phase momentum equation becomes:

$$u_l = -\frac{k_l}{\mu_l}\nabla P_g - D(s_l)\nabla s_l \qquad (3)$$

$$D(s_l) = \frac{k_l}{\mu_l}\left(\frac{dP_c}{ds_l}\right) \qquad (4)$$

And $D(s_l)$ is a capillary diffusivity

$$D(s_l) = \frac{k_l}{\mu_l}\left(\frac{dP_c}{ds_l}\right) \qquad (5)$$

Equations (2) are the basis of the most general multi-fluid formulation used so far in complete fuel cell models [15]. One of the key problems in all models of two-phase transport in GDLs is the determination of a constitutive relation for capillary pressure as a function of saturation. So far this has relied on the so-called Leverett J-function, specifically in the form proposed by Udell [16], i.e.

$$J(s) = \frac{P_c}{\sigma}\left(\frac{k}{\varepsilon}\right)^{1/2} \qquad (6)$$

with

$$J(s) = 1.417(1-s) - 2.120(1-s)^2 + 1.263(1-s)^3 \qquad (7)$$

This is then used to compute the capillary pressure, and in turn determine the capillary diffusivity.

Considering the key phenomenon of capillarity associated with interfacial tension, the microscopic capillary pressure is directly proportional to the interfacial tension (σ) and inversely proportional to the radius curvature of the interface (r), i.e. $P_c \propto \sigma / r$. A schematic illustration of capillary motion in a pore is shown in Figure 4. At the end of the pore where the liquid radius is smaller (lower local saturation), the capillary pressure is greater than at the end with the larger liquid radius (greater local saturation). Because $P_c = P_l - P_g$, the hydrodynamic pressure of the liquid is greater at the end of the pore with the smaller radius. Therefore, the bulk motion of the liquid is toward the end with the greater radius (and local saturation). This liquid water transport from low to high saturation is counter-intuitive, and illustrates the tendency for water, in *hydrophobic*

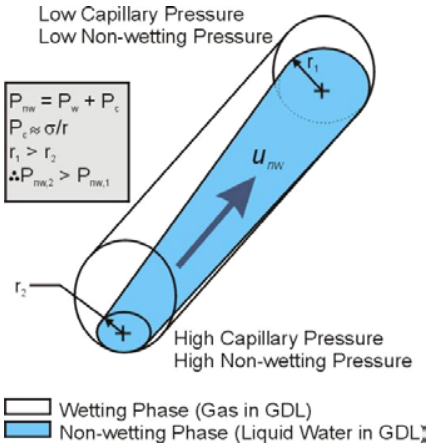

Figure 4: Schematic of capillary diffusion, in which the liquid is the non-wetting phase.

media such as those used for gas diffusion layers, to move to ever-increasing pore diameters according to the capillary pressure's inverse proportionality to the liquid radius. This analysis will be instructive in the subsequent interpretation of visualizations and simulations of flow between fibres composing a GDL.

There are a number of issues with Udell's relation [14], not the least of which is that the experimental data upon which it is based was obtained in porous samples of soils, which have a radically different structure from fibrous media used in GDLs.

The second key issue in the application of two-phase transport models is the determination of the phase specific permeabilities. These must be corrected for the volume fractions occupied by different phases. One of the approaches we have recently used is based on stochastic pore network model simulations. A more fundamental approach consists of resolving the two phase transport by performing direct numerical simulations that explicitly resolve the flow, including dynamic interface tracking, between the fibres. A Volume of fluid (VOF) technique in conjunction with sub-models for surface tension and wall adhesion is used to track the evolution of the two phase flow, including the interface. The instantaneous pressure field obtained from such simulations, Figure 5, clearly shows the two-phase interface. 2D, as well as 3D simulations provide fundamental understanding of the two-phase

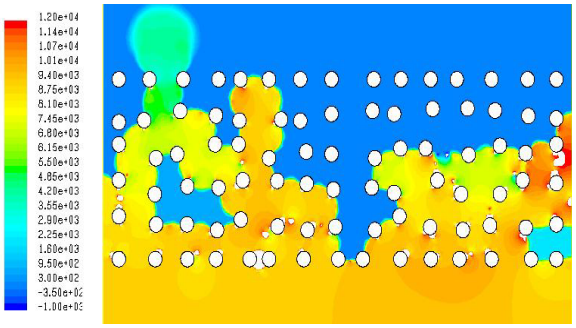

Figure 5: Two phase flow in GDL: instantaneous pressure field liquid phase (gas phase in blue).

transport, and parametric simulations that directly account for detailed features, such as degree of hydrophobicity, can yield data for determining capillary functions that are more representative of GDLs than equation (7).

In recent studies of diffusion layers and two-phase fuel cell models [17][18] it was proposed that liquid water in a GDL evolves in an "inverted tree" structure; i.e. a high number of small capillaries disperse evenly within the GDL and eventually converge into larger capillaries and eventually result in one very large capillary that reaches the surface. The VOF simulations together with quantitative visualization experiments performed at UVic using laser induced fluorescence [19] have recently revealed that transport is in fact dominated by fingering and channeling, and features numerous "dead ends" where water transport recedes when an adjacent breakthrough channel forms.

For a hydrophobically treated GDL, assuming well dispersed PTFE coating (i.e. uniform contact angle), the transport within the GDL is a process of pressure buildup and breakthrough. This process results from the fact that capillary forces provide the main resistance to the progression of the interface in the fibrous hydrophobic structure. As water is produced in the catalyst layer, the pressure in the liquid increases, the fluid surface slowly passes through the constrictions of the cross-sections generated by intersecting fibers. When the water has passed halfway through each constriction, the curvature of the surface decreases due to the expanding radius of the surface. Thus, the liquid pressure at the interface drops and induces hydrodynamic flow in the direction of the

expanding surface. Subsequently, the liquid expands rapidly above this cross-section until the fluid interface contacts the next set of fiber intersections. The process then begins again. The fluid will preferentially pass through the fiber cross-sections featuring the greatest spacing, as this reduces capillary pressure resistance.

PUTTING IT TOGETHER: INTEGRATION INTO CFD BASED FUEL CELL MODELS

One of the most challenging computational aspects is the coupling between the various transport phenomena within a PEMFC as illustrated Figure 6, where each box represents a transport equation governing a particular phenomenon, and the arrows represent the effects of the particular transport on other equations. The equations for gas species, water in liquid and solid (membrane) phases, and energy are closely coupled with all other transport equations. The transport of water, which is present in the system in both vapour and liquid forms, is central to all other coupled transport processes. Unsaturated water in the vapour phase affects local relative humidity in the vicinity of the membrane, and thus its hydration and protonic conductivity, which in turn impacts the electric potential. The liquid water transport in the GDL affects mass transport of gas species, while liquid water in the gas channels affects the pressure field and may affect the overall flow distribution in a unit cell.

Transport of water across the membrane is, as noted earlier, a key phenomenon linking the transport processes between anode and cathode sides. Polarization curves obtained using a complete fuel cell model incorporating the Binary Friction Membrane Model (BFM2) discussed earlier are presented in Figures 15. A particularly important issue here is coupling water transport within the membrane to transport of water vapor in the electrodes, in such a way that mass conservation is ensured and an experimental membrane sorption isotherm is enforced. Figure 7 compares the effects of different humidification regimes on the anode and cathode sides (25% and 75% relative humidity). The Springer model predicts similar polarization curves for both regimes, while the BFM2 predicts a substantial polarization loss for the RH = 25/75 regime (dry anode). An analysis of the source of this loss reveals that it is primarily due to larger ohmic losses predicted through the membrane as a result of drying on the anode side. In this case, there is no water to hydrate the anode CL, unlike the case of the dry cathode (RH = 75/25), where the water production from the oxygen reduction and the cathode–to–anode back-diffusion help to maintain a more uniform membrane saturation. This highlights the crucial importance of membrane modelling, particularly for fuel cell systems that rely on passive water management, such as air breathing cells considered next.

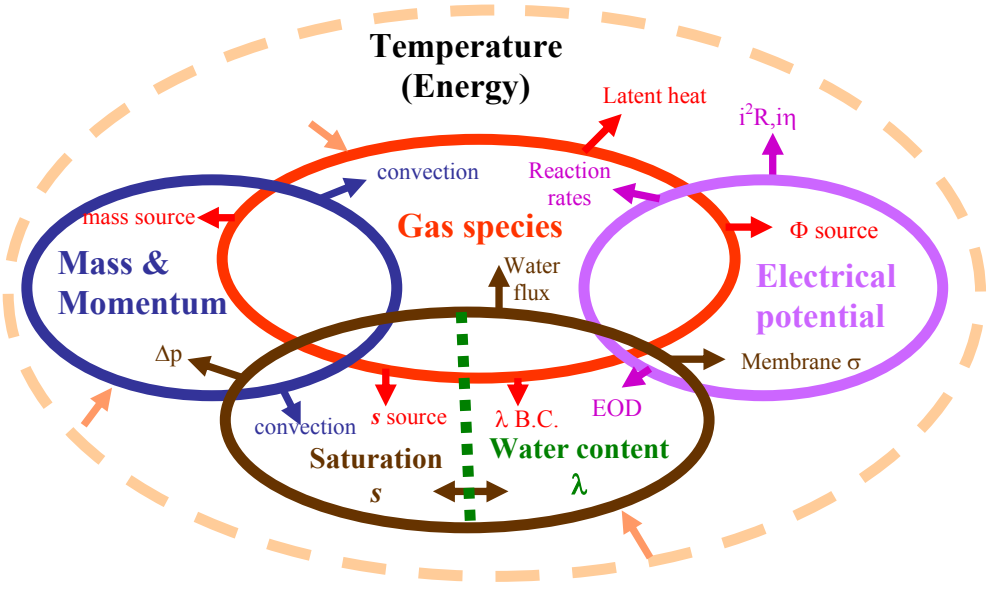

Figure 6: Coupling of Transport Phenomena in a PEMFC

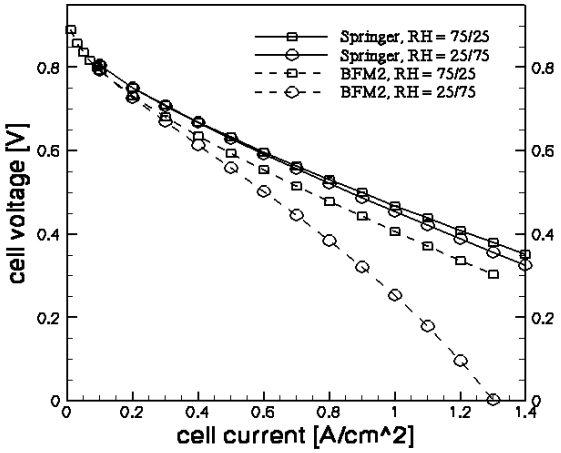

Figure 7: Polarization curve predicted using Springer's membrane model and BFM2

Adaptation of plate and frame PEM fuel cell designs for smaller applications is restricted by the macro-scale materials and manufacturing processes they utilize. Exploitation of microscale transport in conjunction with macro-manufacturing makes it possible to conceive high power density and potentially lower cost fuel cells [3]. Micro-fabrication of flow fields, current collectors, and electrical interconnects have been used in a number of designs, but these have generally relied on the traditional planar MEA architecture. Non-planar designs can achieve much higher active area to volume ratios and volumetric power densities, as was demonstrated in our waved cell topology [20]. Another approach for increasing the volumetric power density, particularly for low power applications, is passive air-breathing operation which allows elimination of manifolding and ancillaries such as fans and compressors. Mass transfer limitations are however an issue in such designs.

One of the concepts to which computational models has been applied is a novel micro-structured electrode, illustrated in Figure 8, that exploits the microscale transport principles in an air-breathing non-planar patented design. The micro-structured electrodes consist of a nano-porous GDL featuring with mean pore diameter on the order of 100nm, i.e. two order of magnitude smaller than in a typical GDLs (Figure 6). With comparable levels of porosity, the nano-porous GDL can increase the active area of the

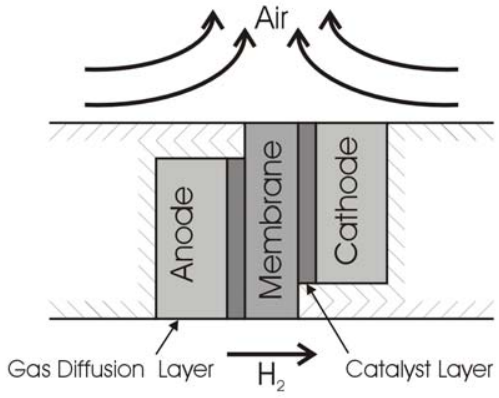

Figure 8: Schematic of micro-structured PEM electrodes.

deposited catalyst by exploiting the surface to volume ratio [3]. The higher functionality of such a GDL can be impeded by:

- the inability of nano-scale porous media to effectively transport reactant and product gases to the entire active area.
- the limited ability of natural convection to passively regulate temperature and supply adequate amounts of oxygen to the cathode.

The CFD based tools were adapted to this problem to assess the functionality of the design, determine the severity of potential transport limitations, and to identify design parameters to alleviate these. In addition to the coupled transport processes discussed earlier, two specific process that have to be accounted for in this case are natural convection in the ambient air, and Knudsen diffusion though the GDL.

Figure 9 illustrates the distribution of oxygen for a system consisting of three electrodes subjected to non-uniform convective heat and mass transport currents. The catalyst layer is located along the left hand vertical axis for each electrode. A minimum oxygen mass fraction of 0.089, a 61% drop from the ambient, is obtained in the central cathode. Though the reduction in oxygen concentration is significant, the fuel cell is still far from being oxygen starved, indicating that the GDL parameters and dimensions considered will not result in insurmountable mass transport limitations.

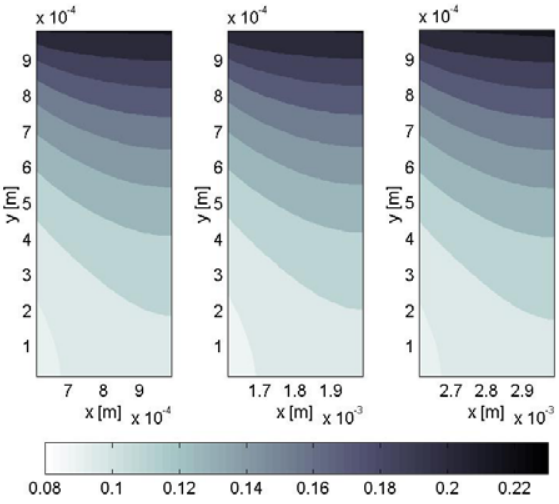

Figure 9: Mass fraction distribution of oxygen in three adjacent electrodes. The ambient oxygen mass fraction in the convective air flow (top) is 0.2303.

CONCLUDING PERSPECTIVE

Fuel cells are at the vanguard of the next generation energy technologies, but must surmount a number of key challenges in order to successfully compete against incumbent technologies such as IC engines and batteries. The availability of reliable and functional computational tools could help achieve dramatic reductions in development cycles and costs, and could spur innovative design required to surmount some of the cost and performance challenges. In this paper we have discussed the array of transport phenomena that are encountered in PEM fuel cells, and presented some of the progress made in our laboratory in addressing some of the fundamental issues that still limit the capabilities of computational fuel cell engineering (CFCE).

A new model for coupled protonic and water transport in polymer membranes was presented. This general model is based on rational and physical consideration, removes several of the limitations of the empirical models used to date, and should provide a good foundation for modelling all purfluoro-sulfonic acid membranes.

Approaches combining pore network modelling, direct numerical simulation of two phase flow in reconstructed gas diffusion layers, and quantitative visualization have been described, and sample results have been presented revealing a fundamental mechanism of liquid water transport in hydrophobic GDLs.

The important issue of integration and coupling was also discussed in the context of CFD based fuel cell models, and we have shown that used judiciously, current models and computational tools can be used in both conventional designs and in novel micro-structured fuel cells to provide detailed information and to analyze design features.

Clearly, numerous outstanding issues remain to be resolved before truly functional computational fuel cell engineering capabilities are achieved.

The broader applicability of the multi-fluid model comes at the cost of solving for an additional set of field equations and the required coupling of the phases. This makes the numerical solution much more challenging and computationally intensive. In particular, the convergence rates and the numerical stability of the model can be problematic under some operating conditions. Alternative models based on various levels of simplifications should be better assessed, and their range and regimes of validity fully established in order to allow multiple levels of modelling and practical simulations, particularly for complete cells and stacks. In any case a critical issue for all two-phase models is the determination of appropriate transport parameters for the various electrode materials (including the catalyst layer), amongst which the relative permeability and the capillary pressure function.

One of the inherent advantages of the Binary Friction Membrane Model is that it can be reduced to represent condition under which AC impedance measurements are conducted, thus allowing determination of some of the transport parameters using conductivity data. Experiments and fundamental micro/nanoscale simulations, such as molecular dynamic simulations, are required to determine the fundamental properties of specific PFSA membranes, including the diffusion and interaction coefficients, and the sorption isotherms.

PEMFC catalyst layers consist of a complex composite network structure of interconnected, microporous agglomerates surrounded by macropores. Charged species, heat, liquid water, and gas all flow through this layer. Space did not allow inclusion of recent work performed using a multiple-thin film agglomerate model for this layer, but in any case modelling and experimental characterization of this layer is one of the most

difficult problems in PEMFCs. Multi-scale modeling strategies are required to resolve the catalyst structure and guide the formulation of improved macroscopic models suitable for use in a CFCE framework.

Finally, the effective and robust integration of the various submodels in a CFCE framework, requires the development of novel algorithms that take into account the specific nature of the couplings and the large range of scales encountered in PEMFCs fuel cells.

ACKNOWLEDGEMENTS

The work presented in this paper is the result of collaboration with a number of former and current graduate students, research associates and collegues. I would like to particularly acknowledge the contributions of: Torsten Berning, Brian Carnes, Jeff Fimrite, Shawn Litster, Ged McLean, Bojan Markicevic, Børge Sivertsen, Henning Struchtrup Jay Sui, and Phong Nguyen.

Financial support from the following is also gratefully acknowledged: the MITACS Network of Centres of Excellence; the Natural Sciences and Engineering Research Council (NSERC) of Canada; Angstrom Power; and Ballard Power Systems.

REFERENCES

[1] Sperling D., and Cannon, J.S. (Eds). The Hydrogen Energy Transition, Elsevier, 2004.

[2] Stone C. and Morrison A.E. Solid State Ionics 2002; 152: 1-13.

[3] McLean, G., Djilali, N, Whale, M. and Niet, T. Proc. 10th Canadian Hydrogen Conference. Quebec City, 2000; 349-358.

[4] Liu, H.T. and Zhou, T.H. J. Enhanced Heat Transfer 2003; 10: 257-274.

[5] Meng H.and Wang, C.Y., Chem. Eng. Science 2004; 59: 3331-3343.

[6] Shimpalee, S., Greenway, S., Spuckler, D. and Van Zee, J. W. J. Power Sources 2004; 135: 79-87.

[7] Nguyen, P.T., Berning. T. and Djilali, N. J. Power Sources 2004; 130:149-157.

[8] Sivertsen, B. R. and Djilali, N. J. Power Sources 2005; 141:65-78.

[9] Kreuer, K.D., Paddison, S.J., Spohr, E. and Schuster, M. Chem. Rev. 2004; 104:4637-4678.

[10] Springer, T. E., Zawodzinski, T. A. and Gottesfeld, S. J. Electrochem. Soc. 1991, 138:2334.

[11] Fimrite, J., Carnes, B., Struchtrup, H. and Djilali, N. J. Electrochem. Soc. 2005, *submitted.*

[12] Thampan, T., Malhotra, S., Tang, H. and Datta, R. J. Electrochem. Soc. 2000; 147: 3242

[13] Sone, Y., Ekdunge, P. and Simonsson, D. J. Electrochem. Soc. 1996; 143: 1254

[14] Litster, S. and Djilali, N. in Transport Phenomena in Fuel Cells (Eds. M. Faghri & B. Sundén) 2005, Vol. 17 of Dev. In Heat Transfer, WIT Press, *in print*.

[15] Berning, T and Djilali, N. J. Electrochem. Soc. 2003; 150: A1589-A1598.

[16] Udell, K.S. Int. J. Heat Mass Transfer 1985; 28:485-495.

[17] Nam, H. and Kaviany, M. Int. J. Heat Mass Transfer 2003; 46: 4595-4611.

[18] Pasaogullari, U. and Wang, C.Y. J. Electochem. Soc. 2004, 151: A399-A406.

[19] Litster, S., Sinton, D. and Djilali. N. J. Power Sources 2005; *in print*

[20] Mérida, W. R., McLean, G. and Djilali, N., J. Power Sources 2001; 102:178-185

Proceedings of ECOS 2005
Trondheim, Norway
June 20–22, 2005

CO_2 – FROM PROBLEM TO BUSINESS OPPORTUNITY?

Hanne Lekva*, Olav Kårstad, Bjørn Berger and Trude Sundset
Statoil ASA, 4035 Stavanger, Norway
*Corresponding author: Phone: +47 4155 8364, E-mail: halek@statoil.com

ABSTRACT
The first decision to apply underground storage of carbon dioxide (CO_2) captured from natural gas - as a climate change mitigation effort - was taken by Statoil (operator) and partners in the Sleipner North Sea licence in 1990. The second such decision was taken by Statoil (operator) and partners in the Snøhvit licence in the Barents Sea in the fall of 2001. A third project of this type was put in operation in the In Salah field in Algeria. This paper presents these injection projects and possible solutions to how CO_2 can be turned into a business opportunity. The whole chain of CO_2 management will be covered, including capture, transportation, storage and end use of CO_2.

Keywords: CO_2 capture, CO_2 geological storage, Sleipner, Snøhvit, In Salah.

TERMINOLOGY

CCP	CO_2 Capture Project
CCS	CO_2 Capture and Storage
CASTOR	Capture and Storage
CO_2	Carbon Dioxide
CO2ReMoVe	CO_2 Registration, Monitoring & Verification
EOR	Enhanced Oil Recovery
ENCAP	Enhanced CO_2 capture
EU	European Union
IEA	International Energy Agency
R&D	Research and Development
SACS	Saline Aquifer CO_2 Storage

INTRODUCTION

Anthropogenic emissions of greenhouse gasses is widely thought to be a contributory factor to changes in the climate. The major contributor is carbon dioxide (CO_2), which arises mainly from use of fossil fuels. Recognising that about 85% of the world's commercial energy needs are met by fossil fuels, a rapid move away from oil, natural gas and coal is unlikely to be achievable without serious disruption to the global economy. Today it is starting to be recognised that emissions of CO_2 from fossil fuel combustion could be much reduced by its capture and safe storage in geological formations. The technology is called CO_2 Capture and Storage (CCS). The aim of this paper is to give an overview of the current CCS operational projects, R&D projects and concept of CO_2 value chain from an industrial perspective. Statoil is a Norwegian oil & gas company and is leading in this area. More extensive information can be found in Buller et al [1].

THE SLEIPNER CO_2-INJECTION

Since 1996 about 1 million tonnes (metric tonnes is used throughout this article) per year of CO_2 has been separated from the natural gas and stored in a saline aquifer (the Utsira formation) at the Sleipner field, see also Baklid et al [2]. Figure 1 gives its location in the North Sea.

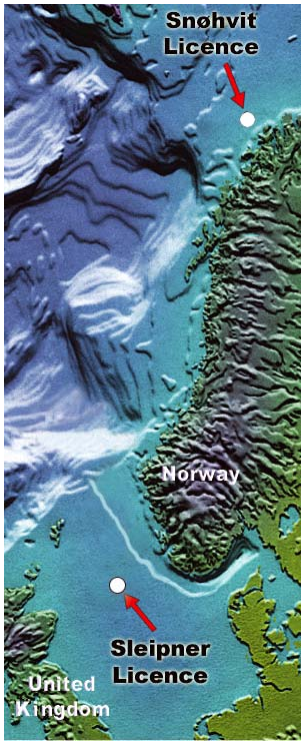

Figure 1: location of Sleipner and Snøhvit CO2 capture and storage sites

Figure 2 gives a drawing of the platform, gas reservoir and Utsira aquifer, which is the storage site. The main motivation for starting this project was an offshore CO_2 tax imposed by the Norwegian government. Valuable experience has been gained both through the operation of this project as well as from the monitoring of the injection through the so-called SACS project. The SACS project is a 4,5 million € R&D programme run under the European Union R&D 5th Framework programme, involving numerous European geological survey institutions and energy companies together with the IEA Greenhouse Gas R&D Programme, see also its website [3]. So far, the SACS programme has carried out two seismic surveys in addition to the pre-injection survey. The results revealed that the CO_2 is trapped in the aquifer and that it is not leaking.

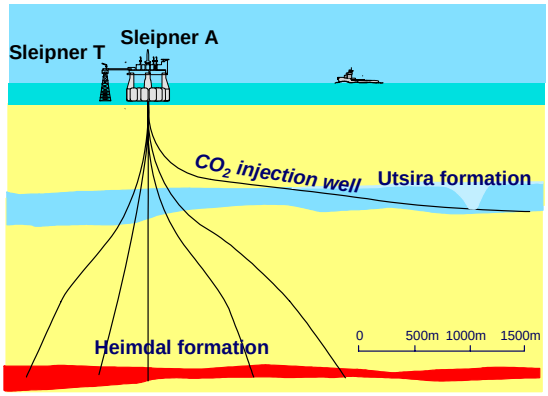

Figure 2 : Drawing of CO_2 injection captured from Sleipner natural gas into the Utsira formation.

THE SNØHVIT CO_2-INJECTION

Since Sleipner, two additional and large CO_2-injection projects of the same type as Sleipner have materialised. The Snøhvit gas field in the Barents Sea north of Norway (see Fig. 1) was the first after Sleipner to be decided for development with CCS. About 0,7 mill tonnes per year will be injected from 2006. The natural gas will flow out of the reservoir via sub-sea wells and a multi-phase pipeline to shore, see Fig. 3. CO_2 captured from the Snøhvit natural gas is captured at the LNG plant (background) and will be piped back 150 km to the field in a separate pipeline.

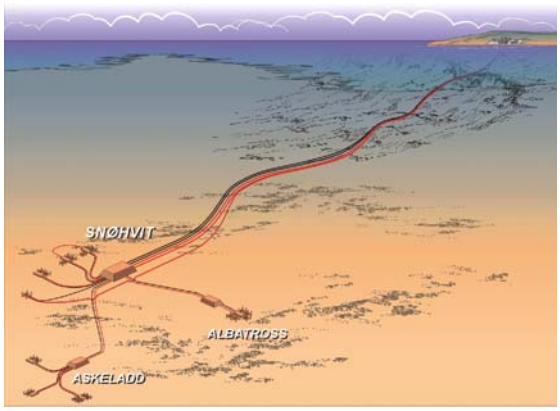

Figure 3 : Overview of offshore Snøhvit field with pipelines and onshore LNG plant in background.

THE IN SALAH CO_2-INJECTION

The In Salah gas field is jointly operated by BP, the Algerian oil & gas company Sonatrach, and Statoil. It is a natural gas field in the middle of Sahara. Like in the Sleipner and Snøhvit fields, this is also a gas field in which CO_2 naturally occurs. The CO_2 is removed, compressed and in this case injected into a remote corner of the gas field. About 1,2 mill tonnes per year of CO_2 is injected. The actual injection operation started in 2004, and will continue for the life of the field. A short comparison of the three CCS projects can be found in De Koeijer and Solbraa [4]

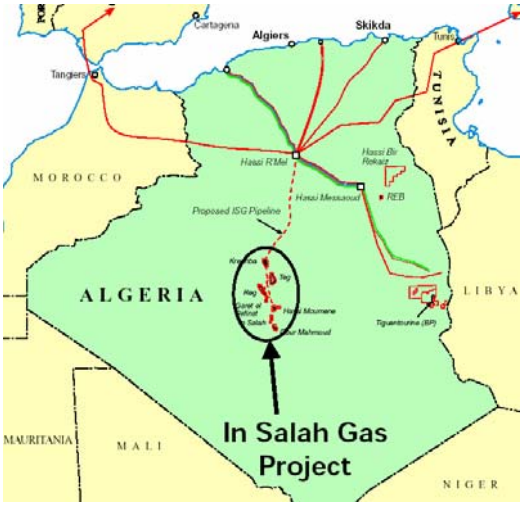

Figure 4: Map with the In Salah CO_2-injection project. The storage takes place at the Kreshba field, north of the In Salah field.

REDUCTION OF CO_2 EMISSIONS

CO_2-injection, together with energy efficiency measures and the electrification of the Troll A offshore gas platform as well as the Kollsnes gas terminal from the land grid will by 2010 have reduced Statoil's CO_2-emissions by 1/3, as is shown in Figure 5

RESEARCH AND DEVELOPMENT

From the start of the Sleipner CO_2-injection project it became clear that it was viewed globally as a demonstration project for a promising new climate technology.

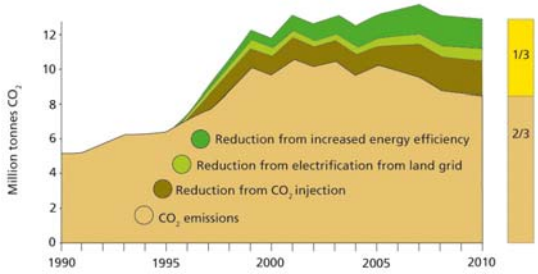

Figure 5: Reduction of CO_2-emissions from Statoil operated facilities 1990-2010.

It was also realised that if this technology were to become widespread in the years to come, questions would be asked about the long-term security of storage in general. Statoil therefore embarked on a long road of research and development with regard to storage security and low-cost CO_2 capture. In this process we realised that in order to gain the consent from the society it was important to conduct an open process (e.g. CO_2 Capture Project [5]). The method chosen was to establish R&D projects with wide participation to follow up these injections. Figure 6 illustrates how, in this case, various EU-funded projects have been established to carry out R&D within the areas of CO_2 storage and capture, see also the project websites [3, 6, 7, 8]. The possible future projects are being prepared and have no reference yet.

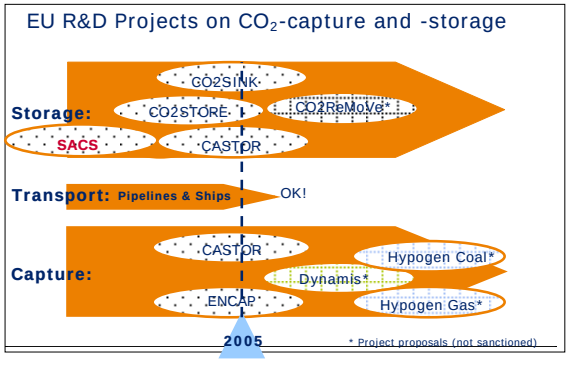

Figure 6 : R&D projects within the EU framework programmes. Dotted backgrounds are running (or already closed) projects. Backgrounds with squares are possible future projects

CO_2 FOR ENHANCED OIL RECOVERY

Carbon dioxide has such properties that it can be used for enhanced oil recovery, see Figure 7. It is extensively used in North America, primarily West Texas for enhanced oil recovery, see Figure 8.

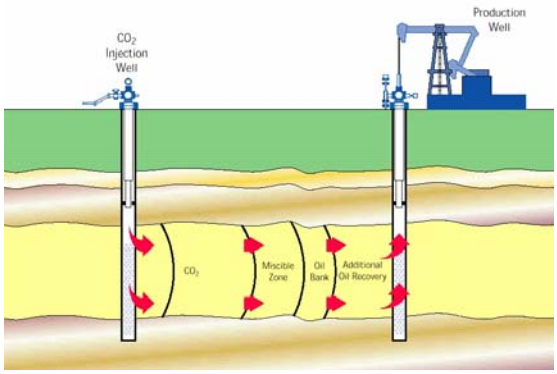

Figure 7 : The principle of using CO_2 for enhanced oil recovery.

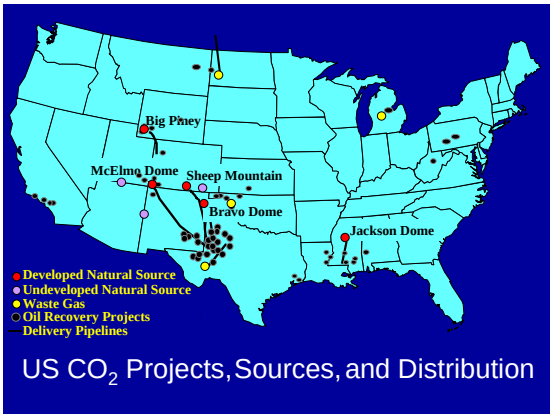

Figure 8 : CO_2 for enhanced oil recovery infrastructure in West Texas

Most of the CO_2 used for enhanced oil recovery in the United States is from naturally occurring reservoirs with nearly pure CO_2, but there is also some industrial CO_2 being used in the system. All in all over 70 oil fields are using CO_2 in this area at present even without any climate change incentive!

So far CO_2 has not been utilised for EOR purposes in the North Sea, but things may change. One thing that makes the North Sea very different from the North American situation is that we lack those large, natural CO_2-reservoirs.

Statoil and partners have carried out studies to see if the Tampen offshore area in the North Sea (North of Sleipner) can benefit from the use of CO_2. A very large amount of work was done in this connection both with respect to reservoir simulation, rebuilding of platforms, transportation of CO_2 and - not the least - in accessing the best CO_2-sources for a total need of 5 million tonnes per year, see Agustsson and Grinestad [9]. This effort identified that more oil can be produced by CO_2-injection than any other method, but the cost of CO_2 in this remote setting far from major industrial sources was shown to be too high for a commercially viable project.

THE CO_2 VALUE CHAIN CONCEPT

In most regions of the world, there are not yet any infrastructures for capturing, transporting and permanently storing large quantities of CO_2. In order to build the necessary infrastructure, large investments must be made, see also Berger et al [10]. Oil fields in the right phase of their lifespan for CO_2 flooding may improve the economics for investment in CO_2 infrastructure. In a near-term time perspective, using CO_2 for enhanced oil recovery is an option that can help us start building the sort of infrastructure needed. The total CO_2 value chain is illustrated in Figure 9.

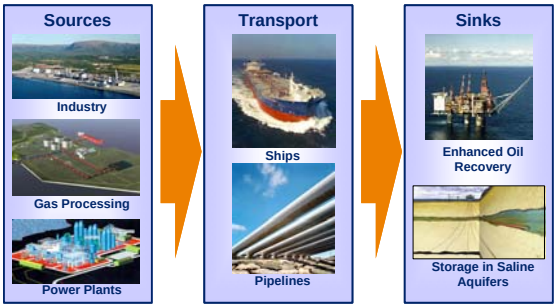

Figure 9 : The CO_2 value chain concept

In order to supply the Gullfaks field in the Tampen offshore area with sufficient amounts of CO_2 for miscible-flood EOR within the limiting time-window, Statoil has, from 2002 to 2004, performed detailed studies on such CO_2 value chain elements as:

- CO_2 sources in northern Europe

- Pure and/or small sources versus large (often dilute) sources
- Liquefaction and compression of CO_2
- Intermediate storage of CO_2
- Ship and pipeline transportation
  - Flexibility versus fixed installations and investments
  - Intermediate CO_2-storage solutions for ship-based chains
- Supply scenarios using combination of ships and pipelines.

Based on the experience from CO_2 pipeline transportation in North America and on the pipe-laying history in the North Sea area, it can be assumed that building pipelines of the lengths and dimensions required for these EOR purposes would not be a difficult undertaking. Pipelines could start at source and go directly to the oil field, or, alternatively, via an onshore CO_2 hub in Norway. For pipeline transportation of CO_2, only compression is needed. One large pipeline carrying several Mt of CO_2 per year could supply a field with all the CO_2 needed over the lifetime of the CO_2 injection. However, the costs associated with the pipeline infrastructure increase significantly when CO_2 is supplied from multiple and geographically spread sources.

Ship transport on a large scale is not as mature as pipeline transportation, but there are already some experiences to learn from Yara International (previously Hydro Agri) routinely transports CO_2 by three small ships (900-1200 tonnes capacity) for the North European market. Loading takes place at Yara's ammonia plants in the Netherlands and in Norway. The experience of Yara has been taken further in the so-called CO_2 ship-transportation project with ships having a carrying capacity of 10 000 to 30 000 m^3. Such ships are not found today, but their design is not a long stretch from an existing type of liquefied petroleum gases (LPG) ships. Ships have the advantage of introducing flexibility in the CO_2 value chain, allowing collection of concentrated CO_2 from various sources at volumes below the critical size for pipeline transportation. A disadvantage is that liquefaction plants and intermediate storage facilities would have to be built at each loading site, adding cost. If an onshore CO_2 hub were to be introduced, intermediate storage facilities matching the incoming amounts of liquefied CO_2 would also be needed there.

The results of these studies have been used to estimate the cost/price range for supplying 5 million metric tonnes (Mt) of CO_2 per year from industrial sources through a 10-year period for the Gullfaks EOR operations. As mentioned above this particular project did not turn out to be commercially viable, but others may be so in the future, in particular as the cost of emitting CO_2 to the atmosphere increases.

CONCLUSION: THE WORLD ON A LOW CARBON DIET?

Capturing and injecting CO_2 from natural gas may not seem to be terribly exciting by itself. Sense is first made when seen in a larger context of decarbonising fossil fuels (coal, oil, natural gas) from major point sources such as energy intensive industries and power plants in order to keep more massive amounts of CO_2 out of the atmosphere.

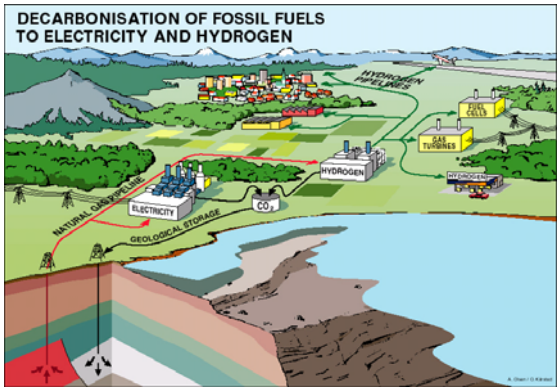

Figure 10 : A vision of a lower carbon future where electricity and hydrogen are the major energy carriers.

Figure 10 seeks to show in a simplified way how electricity and hydrogen may become the favoured energy carriers based on fossil fuels in combination with CO_2-capture and –storage. These energy carriers are essentially the only ones that do not carry the carbon with them to the point of end use. From an oil and gas company perspective this allows our main

products of oil and natural gas to be still attractive while at the same time taking a lead in climate change mitigation. As a result the world might be put on a low carbon diet [11].

REFERENCES

[1] Buller AT, Kårstad O, De Koeijer G. *Carbon Dioxide Capture Storage and Utilization.* Statoil Research & Technology Memoir No. 5, Statoil Research Centre, 7005 Trondheim, Norway, 2004.

[2] Baklid A., Korbøl R., Owren G. 1996. *Sleipner Vest CO_2 Disposal, CO_2 Injection into a Shallow Underground Aquifer*, SPE Annual Technical Conference and Exhibition, Denver, Colorado, USA, SPE 36600, 1996:269-277.

[3] SACS, http://www.iku.sintef.no/projects/IK23430000/, 2003

[4] De Koeijer G, Solbraa E, High Pressure Gas Sweetening With Amines For Reducing CO_2 Emissions, In: Proceedings of GHGT-7, Vancouver, Canada, http://uregina.ca/ghgt7/PDF/papers/nonpeer/267.pdf, 2004

[5] CCP, *Carbon Dioxide Capture for Storage in Deep Geologic Formations - Results from the CO_2 Capture Project.* Volume 1 and 2, ISBN: 0-08-044570-5, Editors: Thomas DC, Benson SM. Elsevier, 2005

[6] ENCAP, http://www.encapco2.org/, 2005

[7] CASTOR, http://www.co2castor.com, 2005

[8] CO2STORE, http://www.co2store.org/ , 2005

[9] Agustsson H, Grinestaff GH, 2004. *A Study of IOR by CO_2 Injection in the Gullfaks Field, Offshore Norway*, SPE/DOE Fourteenth Symposium on Improved Oil Recovery, Tulsa, Oklahoma, USA, SPE 89338, 2004: 1-14

[10] Berger B, Kårstad O, Haugen HA, *Creating a Large-Scale CO_2 Infrastructure for Enhanced Oil Recovery*. In: Proceedings of GHGT-7, Vancouver, Canada, http://uregina.ca/ghgt7/PDF/papers/peer/108.pdf, 2004

[11] Yeomans M, *Putting the World on Low Carbon Diet*, TIME, 17th May 2004: 57-59

Proceedings of ECOS 2005
Trondheim, Norway
June 20–22, 2005

PROCESS INTEGRATION: CURRENT STATUS AND FUTURE POTENTIAL

Robin Smith

Centre for Process Integration, School of Chemical Engineering and Analytical Science, University of Manchester, Manchester, UK.

ABSTRACT

Process integration as a systematic approach to the development of chemical process flow sheets, first a merged in the late 1970's. Emphasis in the earliest applications was on energy conservation. By exploiting thermodynamics and graphical techniques, methods were developed to allow designs to maximise energy recovery. These techniques have now found widespread industrial practice. In parallel with the graphical and thermodynamic techniques, approaches based on the optimization of a superstructure were developed. These allowed automation of the whole design process and allowed both economic trade-offs and complex constraints to be included in the design methods. However, it is only recently that such methods have found their way through to industrial practice. Stemming from the early interest in energy conservation, process integration techniques were extended to encompass mass exchange. Techniques were developed for minimizing water consumption and these have found industrial practice. Another area that has found industrial practice is that of hydrogen integration in petroleum refining. Even though these tools are now well established in process engineering, with commercial software available, the understanding of such tools is still very patchy around the process engineering community. Whilst academic research has forged ahead into new areas, such as reaction systems, there seems to be little attention paid to this so far in industrial applications in these new areas.

INTRODUCTION

Before systematic approaches were developed for process integration, process designers only had heuristics, experience and intuition to guide the creation of new designs. Heuristics are guidelines based on the generalization of past experience. The first attempts to develop process integration methodologies attempted to formalize the use of heuristics in a structured approach [1]. This early work achieved only a limited success in synthesizing flow sheets. The fundamental problem with using heuristics is they do not have a sound scientific basis, are often qualitative in their guidance and different heuristics can often be contradictory. However, the approaches developed required decomposing the problem into sub-problems [1]. These sub-problems (e.g. reaction system synthesis, separation system synthesis, heat exchanger network synthesis) are still the most common exploited today. Much of the research into process integration methodologies has concentrated on removing the need for heuristics to develop designs for the sub-problems and provide a sound theoretical basis.

Whilst new scientifically-based procedures have been helpful in removing the need for heuristics in process integration, heuristics nevertheless have an important role to play for the process designer. Heuristics provide the process designer with a feel for the problem and a benchmark against which to measure features of the process design. It might be that a design feature agrees well with known heuristics, or perhaps disagrees. If the design agrees, then it gives the designer some assurance that the procedure is not producing misleading answers. If the design departs significantly from the heuristics, then the designer should try to understand why.

The first scientifically-based procedures to be developed for process integration developed new thermodynamic principles to solve the heat exchanger network synthesis problem. The composite curves [2-8] are perhaps the best known tool of process integration, see Figure 1. The composite curves give in a single picture the cumulative cooling and heating requirements of a complete process. The overlap between the curves provides us with a target for the heat recovery opportunities, and the residual heating and cooling in the composite curves give us the targets for external heating and cooling requirements.

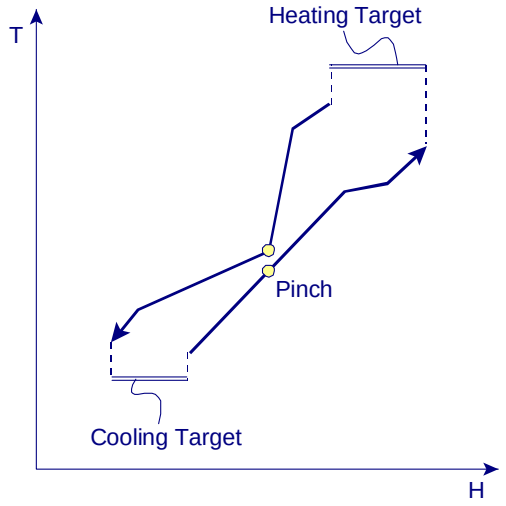

Figure 1: Composite curves allow energy targets to be set before design.

The pinch design method was then developed in order to allow the energy targets to be achieved in practice [9]. The pinch design method followed the pinch principle [4-8], which required that heat should not be transferred across the pinch by process heat recovery and that we should not make inappropriate use of utilities. Another early application was the grand composite curve [10], Figure 2. The grand composite curve presents a temperature enthalpy profile of the external heating and cooling utility requirements after heat recovery has been carried out. This gives a clear picture of the interface between the process and utility system and allows the most appropriate mix of utilities to be selected. So far, all of this relates to individual processes in isolation.

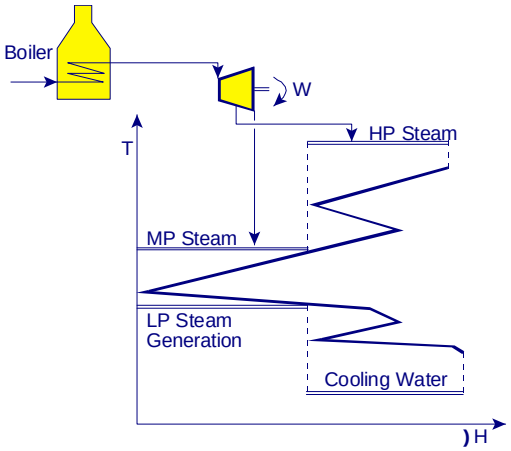

Figure 2: The grand composite curve allows us to select the utility mix before design.

The idea of the grand composite curve was found to be readily extended to total sites in which the grand composite curves of the individual processes could be combined together to produce the site composite curves and give a complete picture of the total site utility requirements as temperature enthalpy profiles [11]. These site composite curves then allow targets to be set for the utility requirements for the complete site and also allow targets for cogeneration from steam turbines to be set.

This process integration technology for energy efficiency has seen widespread application throughout the world. There have now been thousands of successful applications in a wide range of industries from petroleum, petrochemical, chemical, fine chemical, through to steel manufacture, food and drink, pulp and paper. The financial benefit has been both in terms of reduced energy costs and debottlenecking for increased throughput. In a few cases, studies have been driven by the requirement to reduce the emissions of combustion gases. Although applications for reduction in combustion

emissions have so far been few in number, it seems inevitable that this will be a major driving force for future studies as governments seek to reduce national levels of the emissions of greenhouse gasses.

In parallel with the thermodynamic approach that was developed for process integration, an alternative approach based on the optimisation of superstructures using mathematical programming was developed [12]. In this approach a structure, known as a superstructure, is first created that has embedded within it all feasible operations and all feasible interconnections that are candidates for an optimal design. The problem is formulated mathematically and the superstructure optimised in a structural and parameter optimisation. The optimisation then removes redundant features, reducing the complexity of the design and setting operating conditions. Thus, the decision-making aspects of design are carried out by automated procedures in software.

RECENT DEVELOPMENTS IN ENERGY INTEGRATION

Investigating improvements in energy integration should start by investigating the utility system that services the process. Only in this way can the true incentives to improve the energy performance of individual processes be established. Figure 3 illustrates a typical industrial utility system in which different process production units are linked to a common steam system.

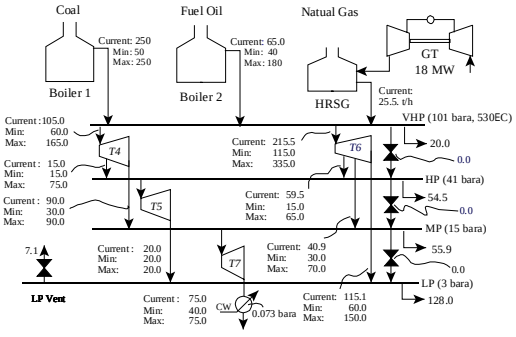

Figure 3: Existing steam system at its optimized conditions (flows in t/h).

Steam is distributed around the site at different pressures. The process units use steam from different pressures, and in some cases, generate steam from sources of waste heat at high temperatures that is fed to steam mains. High temperature heating demands within process units may require furnace heating. Power is generated in the utility system in Figure 3 in backpressure steam turbines from the expansion of steam from high to low pressures. The steam turbines in Figure 3 also feature some condensing power generation. Large sites might also feature gas turbines, Figure 3. Power might be imported to the site from centralized power generation, or in some cases, power exported from the site. On such a site, what is the true value of steam saving? The answer turns out to be not so obvious.

To analyze a utility system, it is first necessary to develop a simulation model [13]. Commercial software is available to allow such models to be developed. The simulation model should allow part-load performance of the steam system components and should provide a simulation of the complete material and energy balance around the steam system, capable of predicting the fuel, power generation, water requirements, etc. for any condition of the steam system. The model must take account of the operating constraints around the system. Once such a simulation model has been developed, it can be subjected to optimization [13]. The value of such an optimization model is that it can be used to identify the true value of energy saving from different pressure levels. The steam usage from each main can be gradually reduced and the system re-optimized at each step [14]. This sounds like a lot of work, but it is straightforward given appropriate software. Figure 4 shows a typical result. Two things need to be noted.

1. There is not a single value for steam at a given level. It depends on how much is being saved, the various costs, equipment performance and the constraints in the utility system.
2. Steam saving is limited by equipment constraints in the utility system. The

steps in Figure 4 are created by the optimization encountering constraints in the utility system.

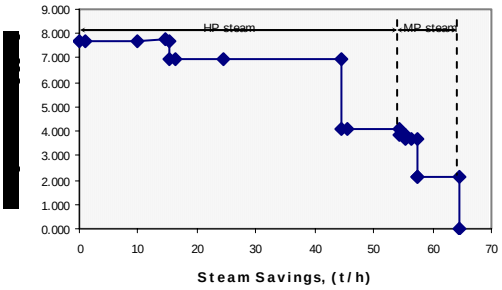

Figure 4: Steam marginal costs for a site.

Figure 4 provides the basis of a strategy for steam saving on a site, but does not show how to go about making the saving. That requires detailed analysis of heat recovery systems, etc.

Process integration techniques for heat exchanger network retrofit have improved significantly. This problem was difficult to address using the thermodynamic methods developed in the 1980's, since when they were applied to retrofit they effectively considered the problem as a pseudo new design. Heat transfer across the pinch was identified as inefficiency in the design and, where appropriate, attempts made to correct it in order to reduce the energy consumption. However, the process pinch relates to an ideal new design and not to what is existing in an existing heat exchanger network. One of the methods proposed to overcome these drawbacks is the so-called network pinch [15, 16]. The network pinch starts by identifying the bottlenecking exchangers within the existing structure. To overcome the network pinch requires a modification to the network structure. This could be relocation of an existing heat exchanger to a new duty, addition of a new exchanger, or introduction of a stream split. To identify the most appropriate structural modification is not straightforward. At this point mathematical programming can be used to identify the most beneficial structural changes, but guided by thermodynamic insights. This approach allows retrofit to be carried out one step at a time, leaving the designer in control to accept or reject options at each stage in the development of a retrofit design.

MASS INTEGRATION

The heat integration developments in the 1980's were later extended to processes involving exchange of mass. El-Halwagi and Manousiouthakis [17] took some of the fundamental ideas from the thermodynamic analysis of heat exchanger networks to create a new area of mass exchange networks. Later work took these ideas and focused on the particular problem of water networks [18, 19]. The design objective in water-using networks is to minimize the water consumption by maximizing the re-use of water. Further reduction in water use can be obtained by introducing processes for partial treatment of the wastewater, termed regeneration, allowing further re-use or recycling of water.

Various water-using processes can be combined together to give a composite curve for the entire system, allowing targets to be set for minimum water supply. Extension of the methods of energy integration to water integration is thus, in principle, quite straightforward. However, this approach rapidly runs into problems. It is possible, although very difficult, to extend this approach to deal with multiple contaminants, rather than a single contaminant [19]. It is also possible, but also difficult, to allow the introduction of the flowrate constraints which are often encountered with water-using operations. Add to this the desire to introduce cost optimization and forbidden matches, etc., and the simplistic extension of the energy integration approach to the

water minimization problem rapidly runs into problems.

However, it is possible to formulate the problem using mathematical programming that allows all of the complexities of water system design to be included [20]. Multiple contaminants, multiple water sources, flowrate constraints, forbidden matches, water costs, effluent treatment costs and piping costs can all be included in the problem.

HYDROGEN INTEGRATION IN PETROLEUM REFINING

The changes taking place in the specifications for gasoline and diesel are causing fundamental changes in petroleum refining throughout the world. When product specifications are changed in a petroleum refinery or the refinery optimized or debottlenecked, the supply of hydrogen is often a limiting factor, particularly when producing low sulphur, low aromatics products. The recovery of hydrogen from off-gases for reuse in refinery processes is a problem analogous to the recovery of process heat. Similar benefits can be achieved by developing integrated designs that make better use of available resources. The problem of hydrogen management is therefore to find a network that will allow the best overall operation of the refinery to be achieved. Sources of hydrogen include recovery from fuel gas and tail gas, dehydrogenation processes, heavy end gasification, steam reforming and outside purchase. Systematic methods of identifying hydrogen needs and available production are required in order to optimize site performance and maintain the flexibility to run different crude oil feed stocks, while maintaining maximum equipment utilization.

Graphical targeting can be used to analyse the hydrogen resources available in the refinery and suggest which off gases should be sent to hydrogen recovery processes [21]. Targets for required hydrogen plant production or off-site purchase can also be set. As with other network design problems, mathematical programming can be used to include the details of the pipework, compressors and the capital cost associated with hydrogen recovery processes. Although the methodology is new, it has already seen many successful applications. To take the best opportunities from hydrogen network design, process changes for the hydrogen consumers needs to be included in the methodology.

INTEGRATION OF DISTILLATION SYSTEMS

Turning now to distillation system design, it is first useful to distinguish between simple and complex columns. A simple column takes a single feed, produces two products with key components adjacent in volatility and the column has a reboiler and a condenser. If consideration is restricted to simple columns, then a system requiring the separation of a mixture into a number of products can be configured in a number of different ways. Although different configurations are possible when using simple columns, the problem still remains of a manageable size. Once complex distillation arrangements are introduced, each simple configuration can be evolved into many complex arrangements involving thermal coupling, side strippers, side rectifiers, pre-fractionaters and dividing wall columns. Thus, as the number of products increases for the distillation system, the number of possible complex column configurations explodes. Added to this problem, the most appropriate pressure for each separation in a complex arrangement needs to be chosen and heat integration considered simultaneously.

Whilst significant progress has been achieved in the development of process integration design methods for the synthesis of heat integrated distillation systems, there is still much work required before the full potential can be exploited commercially. Methods are available to synthesize systems of complex columns, but not heat integrated. Some progress has been made for a particular case of heat integrated refinery distillation, but further development work is required [22].

One of the most significant developments in distillation in recent years has been the application of partition, or dividing wall, distillation columns [23-26]. These allow three essentially pure products to be taken from a single column with efficiency greater than that possible with conventional designs. Such columns allow energy reductions of the order of 30%, together with capital cost reductions, when compared with the equivalent arrangement of simple distillation columns. Although the basic idea has been known since 1947, it is only in recent years that the arrangement has been exploited commercially [23, 25, 26].

The distillation systems considered so far have been restricted to non-azeotropic systems. When azeotropic systems are considered, a whole new set of problems emerge. Graphical techniques have been developed to help designers visualize the problems associated with azeotropic and extractive distillation [27]. Unfortunately, these tools are restricted largely to ternary systems. With the use of elaborate graphics, the principles can be extended to quaternary systems. However, the most complex cases cannot be considered by such simple graphical tools. Even though much progress has been made in recent years towards a better understanding of azeotropic and extractive distillation, much work is still required. Better understanding of heterogeneous systems needs to be developed in order that the potential for simple phase separations can be fully exploited.

GRAPHICAL TECHNIQUES VERSUS OPTIMIZATION

The early systematic procedures developed for process integration were based on graphical techniques. Graphical techniques were developed for energy integration, water minimization and hydrogen integration. Such techniques provide valuable insights and leave the designer under full control. However, graphical techniques also have very severe limitations. Multi-dimensional information is difficult or impossible to represent. Economic trade-offs and constraints are difficult or impossible to include. Thus, to deal with the size and complexity of industrial design problems, the trend is to increasingly exploit approaches to process integration that are based on optimization of a superstructure. This approach has a number of advantages. Many different design options can be considered at the same time. The complex multiple trade-offs usually encountered in chemical process design can be handled by this approach. Also, the entire design procedure can be automated and is capable, in principle, or producing designs quickly and efficiently. However, there are also fundamental problems associated with approaches to process integration based on the optimization of a superstructure. The engineer looses control and the intuitive feel that a graphical representation provides. There is still an incentive to provide the designer with a graphical picture that gives some indication of the physical aspects of the design, for example, in the same way as the composite curves would. In many cases, such graphical representations can be developed from the output of an optimization calculation. This combines the advantages of both the graphical and optimization approaches to process integration.

Another feature of the graphical techniques used in process integration is that they are based on a two-step approach. In the first step, targets are set to scope and screen alternatives. In the second step, a design is developed to achieve the targets set by the graphical approach. Once an approach is adopted that is based on the optimization of a superstructure, structural issues relating to the design are readily included in the process integration technique. This means that the targeting and design steps that were a feature of the early techniques are combined into a single step.

FUTURE POTENTIAL

Challenges remain in process integration, even in the established areas discussed above. Enormous challenges still lie ahead

in new areas. There are many areas of process integration that have hardly been addressed in terms of producing methods that can be exploited commercially.

Process integration of reactions systems is still in its infancy. It is desirable to be able to synthesize the design of the reaction and the associated separation systems simultaneously. This is particularly important when the separation system is extremely complex and costly, as is the case with many azeotropic systems. Reactor design is generally carried out by considering the reactor in isolation. Yet, in most cases the reactor design interacts strongly with the rest of the process. Taking this a step further, the catalyst is often designed prior to the reactor design and without too much consideration of the reactor design to follow. Yet, the catalyst design, reactor design and separation system design should only be carried out simultaneously in an integrated fashion. Biochemical reaction systems present similar, but more daunting challenges.

Besides reaction systems the process integration of separation systems other than distillation has hardly been considered. Membranes, crystallization processes, and solids processing operations in general all need further development. Hybrid separations offer potential advantages in some applications. Yet, the potential for hybrid separation has hardly begun to be exploited

It is often considered that process integration techniques only apply to large scale continuous processes. This is not the case. Whilst it is true that heat integration of batch processes is usually not worthwhile, batch processes still have significant potential for improvement through better process integration. Most batch processes are designed through scale-up. The time element in batch processes provides flexibility in the design and operation. However, the flexibility that the time dimension offers is often taken as an excuse from not doing a thorough design and optimization of the design. In these applications, data is often the biggest problem. How can we design and optimize such a process if we do have basic information, such as reaction kinetic data? Such problems require that experimental investigation (and the design of the experiments) be conducted in parallel with the design of the process and its integration. The experimental design and the process design must be integrated in a co-ordinated activity.

Lack of software for the newer areas of process integration is a bottleneck. There is plenty of commercial software available for energy integration. More recently, commercial software has become available for water system integration, hydrogen system integration and the design of distillation systems.

Unfortunately, commercial software on its own is not enough. Even with the best commercial software, process engineers need to be educated in process integration techniques. Crowded university curricula in too many cases mean that students are not exposed at all to process integration techniques. But this is where awareness must start [28]. Education and updating must continue through professional training. Otherwise, significant opportunities will be missed in process engineering.

REFERENCES

1. Rudd DF, Powers GJ and Siirola JJ. *Process Synthesis*, Prentice Hall, 1973.
2. Hohman EC. *Optimum Networks of Heat Exchange*, PhD Thesis, University of Southern California, 1971.
3. Huang F and Elshout RV. *Optimizing the Heat Recover of Crude Units*. Chem Eng Progr 1976; 72: 68.
4. Linnhoff B, Mason DR and Wardle I. *Understanding Heat Exchanger Networks*, Comp Chem Engg 1976; 3: 295.
5. Umeda T, Itoh J and Shiroko K. *Heat Exchange System Synthesis*, Chem Eng Progr 1978; 74: 70.

6. Umeda T, Harada T and Shiroko K. *A Thermodynamic Approach to the Synthesis of Heat Integration Systems in Chemical Processes.* Comp Chem Engg 1979; 3: 273.
7. Umeda T, Niida K and Shiroko K. *A Thermodynamic Approach to Heat Integration in Distillation Systems*. AIChEJ 1979; **25**: 423.
8. Itoh J, Shiroko K and Umeda T. *Extensive Application of the T-Q Diagram to Heat Integrated System Synthesis*. Int Conf Proc Systems Engineering (PSE – 82) Kyoto:92,1982.
9. Linnhoff B and Hindmarsh E. *The Pinch Design Method of Heat Exchanger Networks*. Chem Eng Sci 1983; 38: 745.
10. Townsend DW and Linnhoff B. *Heat and Power Networks in Process Design*. AIChEJ 1983; 29: 742.
11. Klemes J, Dhole VR, Raissi K, Perry SJ and Puigjaner L. *Targeting and Design Methodology for Reduction of Fuel, Power and CO_2 on Total Sites*. J Applied Thermal Engg 1997; 17: 993.
12. Biegler LT, Grossmann IE and Westerberg AW. *Systematic Methods of Chemical Process Design*, Prentice Hall, 1997.
13. Varbanov PS, Doyle S and Smith R. *Modelling and Optimization of Utility Systems*. Trans IChemE 2004; 82A: 561.
14. Varbanov PS, Perry S, Makwana Y, Zhu,XX and Smith R. *Top-level Analysis of Site Utility Systems*. Trans IChemE 2004; 82A: 784.
15. Asante NDK and Zhu XX. *An Automated and Interactive Approach for Heat Exchanger Network Retrofit*. Trans IChemE, 1997; 75:349.
16. Zhu XX and Asante NDK. *Diagnosis and Optimization Approach for Heat Exchanger Network Retrofit*. AIChE*J*, 1999; 45:1488.
17. Elhalwagi MM and Manousiouthakis V. *Synthesis of Mass Exchange Networks*. AIChEJ 1989; 8:1233.
18. Takama N, Kuriyama T, Shiroko K and Umeda T. *Optimal Water Allocation in a Petroleum Refinery*. Comp Chem Engg 1980; 4: 251.
19. Wang YP and Smith R. *Wastewater Minimization*. *Chem Eng Sci* 1994; 49: 981.
20. Doyle SJ and Smith R. *Targeting Water Reuse with Multiple Contaminants*. Trans IChemE 1997; B75: 181.
21. Alves JJ and Towler GP. *Analysis of Refinery Hydrogen Distribution Systems*, Ind Eng Chem Res, 2002; 41: 5759.
22. Gadalla M, Jobson M and Smith R. *Increase Capacity and Decrease Energy in Existing Refinery Distillation Columns*. Chem Eng Progr 2003; April, 44-50.
23. Kaibel G. *Distillation Columns With Vertical Partitions*. Chem Eng Technol 1987; 10: 92.
24. Triantafyllou C and Smith R. The *Design and Optimization of Fully Thermally-coupled Distillation Columns*. Trans IChemE 1992; 70A: 118.
25. Becker H, Godorr S, Kreis and Vaughan J. *Partitioned Distillation Columns – Why, When and How*. Chem Engg 2001; Jan: 68.
26. Shultz MA, Stewart DG, Harris JM, Rosenblum SP, Shakur MS and O'Brien DE. *Reduce Costs with Dividing-Wall Columns*. Chem Eng Progr 2002; May: 64.
27. Doherty, MF and Malone MF. Conceptual Design of Distillation Systems. McGraw-Hill, 2001.
28. Smith R. *Chemical Process Design and Integration*. John Wiley, 2005.

Industrial ecology

Proceedings of ECOS 2005
Trondheim, Norway
June 20–22, 2005

LIFE CYCLE ENVIRONMENTAL AND ECONOMIC ASSESSMENT OF HIGH-PERFORMANCE WINDOWS USED IN TYPICAL HOUSES IN ANDEAN ARID REGIONS OF WESTERN ARGENTINA.

Alejandro Pablo Arena

Laboratorio de Ambiente Humano y Vivienda. INCIHUSA
Cricyt (CONICET)
Av. Ruiz Leal s/n. Parque Gral. San Martín 5500, Mendoza
Tel +54 (261) 4239596, e-mail: aparena@frm.utn.edu.ar
Argentina.

ABSTRACT

The environmental impact produced in the residential sector is among the biggest in modern society. The energy consumption in this sector accounts for about 40 % of the total energy consumed in a country. Windows are among the main responsible of the energy losses and gains in buildings, affecting both their summer and winter energy balances, and being responsible for up to 25-50 % of the energy consumption due to thermal conditioning purposes, depending on the climate conditions. Modern technology have produced a variety of models aimed at controlling these energy transfers, like double and triple glazed windows filled with heavy inert gases, low-emittance coatings, thermal breaks in frames, etc. However, the fabrication of these new windows requires new consumptions and releases new emissions, and their real environmental and economic benefits are not always guaranteed. For instance, the production of heavy inert gasses like Ar, Kr and Xe requires huge amounts of energy, and therefore is responsible for the associated emissions of pollutants. In this paper, the environmental and economic assessment of the application of double-glazed windows filled with air, Ar, Kr and Xe in typical houses of the Andean arid region of western Argentina is performed. The methodology used for the evaluation of the environmental impact is Life Cycle Assessment, while the economic assessment is performed using the Life Cycle Costing method.
Key words: high performance windows, Life Cycle Assessment, Life Cycle Costing.

INTRODUCTION

Among the many problems arising from sustainable development connected to social, economic and environmental issues, those concerning habitat and energy become of utmost importance. Firstly –and due to its size and permanence- development of the habitat is the physical, most significant impact on natural environment. Secondly, energy is essential for the survival of present-day society. The eventual exhaustion of fossil fuels, together with the negative environmental impact produced by the massive use of such fuels, make it necessary for people to start implementing strategies to control and even undo the harmful processes which are now at work. It becomes obvious, therefore, that those sectors responsible for the production and management of habitat and energy will have to acquire further knowledge of these topics. The built environment probably has the greatest impact on ecosystems of all of society's enterprises, a phenomenon in progress due to the increasing rate of urbanization. According to data provided by the United States Green Building Council (USGBC), the construction of buildings takes up 40% of the energy and materials, 25% of the virgin wood, and 15% of the water used around the world annually [1].

Energy use in the built environment is undoubtedly one of the key issues to be addressed by planners and designers on the path towards such ambitious but elusive goal of sustainable development.

Some official figures on energy consumption in the urban domestic sector in Mendoza (Argentina) show that the domestic sector is responsible for 29.1% of the total end use energy consumed in the province. Within it, the participation in the net consumption by domestic uses is as follows: space heating 41.1%, domestic water heating 32.6%, cooking 11.3%, food conservation 6.1%, lighting 1.7%, space cooling and ventilation 0.5%, other appliances: 6.8 %. It can be seen that space heating and domestic water heating add-up to 73.7% of the total consumption and share a 90.0% of the natural gas consumed by the sector [2].

In general, factors influencing energy consumption in a building in use are as follows:

1. The influence of the building's shape and orientation on the load of heating and air-conditioning.
2. The role of building's design on the utilization of daylighting, solar energy and of natural ventilation.
3. The energy-effectiveness of the heating, cooling, lighting and domestic hot water systems.
4. The role of the users and their strategy to control the building's temperature.

If we consider the quantity of energy required to manufacture the materials and components used in the construction of a building, and the huge amount of materials involved, it becomes evident that it could be as effective to reduce the amount of energy required by buildings through a reduction of the energy consumption during their use –for instance through a bioclimatic design; as to reduce the energy content of the materials used. A study performed by Cole and coworkers shows an example for the Canadian climate [3]. The relation between the energy consumed in the energy content of the building varies according to factors concerning climate, use, tradition and social status; and is common that strategies to reduce the former are based on a higher consumption of energy to manufacture the building's materials and components. Therefore, it becomes necessary to make a deep analysis of all the stages involved in the building's lifecycle, in order to fully determine the value of the strategies at stake.

This paper will discuss the second of the above mentioned factors, focusing on one of the components: the window. Considerations will also be made about the environmental impact of the materials used to manufacture windows. Although this component takes up only 10-25% of the surface of new buildings' outer walls, it is responsible for up to 25% of the values for heating in cold climates and up to 50% of the values for air-conditioning in warm climates [4]. There exist different technologies to improve the termal behaviour of windows, all of which are tending to reduce the speed of heat flowing through the window as a consequence of the temperature difference between the interior and the exterior of the building, measured by the U-value, and the solar energy gain through the window, measured by the Solar Heat Gain Coefficient (SHGC). Among them, we can mention two and three-glazing windows, Low-emittance coatings, insulating gases between the panes, frames with thermal breaks, insulating spacers, etc. Figure 1 shows some of these strategies. This paper will discuss the effect of the reduction of the U-values through the use of a two-pane window and different gases between the panes.

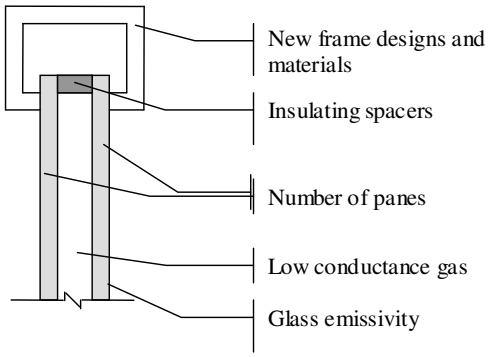

Figure 1

It is a common practice in Argentina to use single-glazing windows and only occasionally can two-glazing windows with air inside be found in sectors with a high purchase power. The second group shows a better performance than the first; yet, convective air currents form between the glazings and let heat flow through them. Using instead a less conductive, more viscous gas, such convective currents are reduced and, therefore, the transfer of heat between the interior and the exterior. There are in the current market high performance windows which make use of heavy inert gases, such as Argon, Kripton and Xenon, all of which have more insulating properties than air. As the molecular weight of the gas used increases, thermal conductivity dramatically decreases, together with cavity gap required. Therefore, high-performance windows can be manufactured with no need for increase significantly the weight of the

frames. The following picture shows the U-value for a window built with air, Ar, Kr y Xe, a low-emissivity coating on both glazings, and with a cavity gap of 20, 16, 12 and 8 mm, respectively [5].

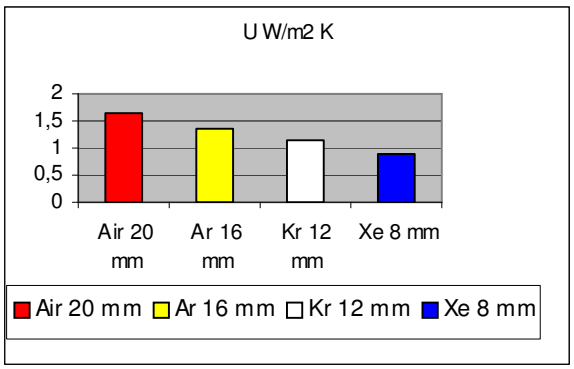

Figure 2. U values for window filled with different gases

Window sellers assure that having high performance windows at home is an intelligent investment, since they help save so much money on heating and cooling regular homes that they represent a far better investment than most available in the market today. They provide more comfort, reduce condensation on the windows, they transmit a smaller amount of UV radiation, responsible for colour fading of drapes and carpets, they reduce the amount of noise coming from outside, etc. This analysis, however, does not take into consideration the fact that to manufacture an efficient window a new set of materials and components are necessary, which, in turn, demand more energy consumption and release harmful emissions. The production of low conductive inert gases, for instance, which are natural components of the air, are obtained through a separation method which requires huge amounts of energy. According to Weir et al 1998, the specific amount of energy required to obtain these gases is 0.672; 38,500 and 511,400 kJ/lt, for Ar, Kr and Xe, respectively. The following questions arise: how is the amount of energy consumed for making a high performance window as compared with the energy saving produced by using that window in a house in normal conditions in Mendoza? How is the CO2 balance like? What about the impact of other environmental factors? Are return rates that significant? What kind of window would be best to have around the house: with air, Ar, Kr or Xe? To answer these questions, we need to know about the processes involved in the manufacturing of the materials and components of the windows, as well as about the energy consumption in the house when each type of window is installed on it. To do so, a windows maker from Mendoza is studied. Information about the processes carried out in this firm will be given later.

OBJECTIVES

This paper will discuss the following topics:

1. Environmental and energy impact of the manufacturing and use of four different types of two-glazing windows, using different types of gases between the panes: air, argon, kripton, xenon. The window discussed is built with aluminium frame, sheet and spacers. A house in Mendoza will be the location for this study case. For the use phase of the windows, only the energy consumption required for heating purposes on a house located in Mendoza will be analyzed, since according to the data given in [2] the energy consumed for cooling accounts for a small share in the region.
2. Economic advantage of each type of window, including different scenarios with different discount rates and the projection of different rates of increase in the cost of energy.

SCOPE OF THE STUDY

The utilized data account, if possible, for present technologies used in Argentina. When these data were not available, foreign values were used, taking into account the local energy mix for calculating the environmental effects associated with energy consumption. Average data have been used, except when the supplier was known and its data were available.

The environmental aspects included in this study account only for external effects, and it is assumed that the same comfort conditions are obtained in the house when the different windows are considered, thus conducing to different energy consumption in the building accordingly to their U-value.

Functional Unit: the study will be carried out based on a 1.2-m x 1.2-m window, the standard size in the local market.

INVENTORY ANALYSIS

For the energy calculations, the energy content of the main materials involved in the construction of the windows (aluminium, glass, inert gas) as well

as the energy consumed for balancing the energy losses through each type of window considered are taken into consideration.
For the other environmental categories considered, and according to the objectives and scope, the evaluation will be comparative and the inventory will only include those materials and energy flows which are different for each case studied. The only input flows to be included, therefore, are inert filling gases and the energy involved in heating the building to make it a warm, comfortable place, considering the insulating properties of each window. The aluminium frame, sheet, spacer and the glass are consequently not included in the inventory.

Making of the window

Making the window comprises many stages: obtaining filling inert gases, the aluminium, the frame, the sheets, the spacers, the glasses, the airtight double glaze (ADG) and the final assembling.
The aluminium profiles are made and painted at ALUAR plant - aprox. 1,400 km away from Mendoza, and then shipped by trucks.
The window frame and sheets are made in a plant located in Mendoza, where also the assembling process takes place. To make the window frame and sheets, the aluminium profiles must be cut properly, which requires relatively low energy consumption: 0.2 MJ per window. Out of the total 16.1 kg used, 15% (2.1 kg) is wasted and 14 kg are actually utilized. The material and processes involved at this stage are the same for all the alternatives assessed.

Assembling

There is no consumption of material or energy in this process.

ADG Manufacturing

The ADG is manufactured at a plant located 10 km away from the window manufacturer. The process includes cutting the glass, polishing its edges, washing it to prevent chips and dust from remaining inside the unit, placing the aluminium spacers, filling up with inert gas and sealing. Due to the lack of reliable information received from the company involved and the similarities found with the data published by Weir et al [6], the latter have been taken as a reference. The complete process requires an average energy consumption of 6 MJ per unit. The gap between glasses varies according to the type of gas used, thus varying the quantity of gas required: 22 l are necessary for air, 17.6 for Ar, 13.2 for Kr and 8.8 for Xe. 0.241 kg of aluminium is required for the spacers, plus 3% of waste.
The glass used is manufactured at another local company. The percentage of recycled glass is 56%. The amount of glass required for both layers is 21.2 kg. During the processes of cutting and assembling, some glass is broken and wasted, which represents 5.5% of the total. The total amount of glass required is 22.26 kg.
The quantity of inert gas consumed is the only relevant aspect at this stage, since the other materials are the same for all the alternatives.

Obtaining the inert gas

The gases involved in the study, Ar, Kr and Xe are natural components of the air and they are obtained through a process of separation, which utilizes considerable amounts of energy, depending mainly on the amount of such gas present in the air. According to data provided by Weir et al [5], the specific amount of energy required for obtaining these gases is 0.672; 38,500 and 511,400 kJ/lt for Ar, Kr and Xe, respectively.

Energy Required for Heating

The energy performance calculations were carried out in a conventional manner (Excel Worsheet) using the Solar Load Ratio method of LANL [7] for a normal 24 hr period The base temperature chosen was 18 ºC.
It is assumed that the window is placed in an outer wall with no solar gain.

LIFE CYCLE IMPACT ASSESSMENT

Classification

The following categories have been considered in the assessment of impacts:

1. Global Warming.
2. Acidification
3. Energy Consumption. All energy subsystems (heat, electricity, transport) are taken into consideration to reach a total amount of energy used. Values thus obtained are absolute and do not merely show differences between a window and a reference. In the other environment categories, instead, the results are comparative using the double-glazed window filled with air as a reference.

Characterization

The potential characterization factors of the CML [8] method have been used.

ECONOMIC ANALYSIS

The method used to carry out the economic analysis is the so-called Life Cycle Costing (LCC) [9]. LCC is used to assess alternative systems competing on the basis of cost, which requires such systems to be functionally equivalent (efficiency, safety, comfort, reliability, etc). Therefore, the system chosen can be that which, from the point of view of the cost, shows the best behaviour in the long term. It is a useful method to compare alternatives in projects which show different costs, and specially useful to determine if an alternative with a higher starting cost can later become more convenient after reducing future costs. The method adds up every cost related to the studied system's possession and operation for a certain period. Such costs are adjusted to the value of money at different times. The most cost-effective alternative will be the one whose life cycle cost –including the starting investment costs and all the expenses during its useful life- is the lowest.

For the economic analysis, several scenarios have been presented, where the discount rate and projections for rate increase of energy costs varied. The first scenario includes no increase in the real price of energy during the building's life time and a real discount rate of 2%, which is the one that the middle investor can obtain at local banks today. Considering no increase in the energy prices in this scenario does not favour conservative measures. In a second scenario it was assumed that energy prices will follow the tendencies shown in the past. Therefore, and according to data from the State Energy Department, a track record was made of natural gas prices for end-consumers in the last 15 years and then extrapolated to the future, following the minimum square method, resulting in an average increase rate in energy prices of 3%. The discount rate used is the same as the one for the previous scenario. The discount rate considered for the third scenario is nil, thus comparing the cost of investment with the non-discounted cost of the energy saved. Rate increase of energy cost is the same as in the previous case. This scenario favours investments in conservative projects, due to its nil discount rate. The last scenario considered here takes into account the present Argentinean situation concerning prices and rates, since the devaluation of the peso at the end of 2001 and the resulting modification of prices had a direct impact on companies which provided public services: the so-called "Economic Emergency Law" established that these companies' prices had to remain unchanged. Therefore, only in the initial period energy prices were around 30-55 % "backwards" – in terms of local currency- according to the inflation rates between 2001 and 2002 [10].

Businessmen in the sector are claiming since then for an increase in rates, and some official announcement are coming on the issue. The percentage of such increase, however, is still under discussion. According to an agreement between the State and the Techint group to install a gas duct in the Northwest, gas rates for domestic consumption will be gradually increasing to over 100% in a period of two years. By mid-2006, they will have reached 80% of their 2001 price in US dollars, which means a 114% overall increase from today's prices [11]. This information has caused some controversy and has even been denied. The truth is that there has been no increase yet. The last scenario suggests a relatively moderate increase: 20% during the first year; 20% after the following two years. After this initial augmentation, the increase would follow the historical tendency (3 %). The discount rate is 2%.

As regard the investment cost of the windows, and according to suppliers, the extra cost for a double-glazed window with air is 14 $/m2 with Argon, 140 $/m2 with Kripton and 556 $/m2 with Xenon [12].

RESULTS

Environmental Aspects

The figures below show the results for each of the studied categories and the influence of each stage (manufacturing and use) in the different categories of impact.

Figure 3 shows the distribution of the energy required for the fabrication of the windows filled with different gasses. It can be seen that in the case of a window filled with Ar, most of the energy consumed is due to the high energy content of aluminium. In the case of Kr and Xe the inert gas is the predominating material instead, due to the big amount of energy required for the separation of these gases from the other constituents of air. The influence of other materials and processes involved

in the fabrication of the windows as glass, transportation and cutting is irrelevant.

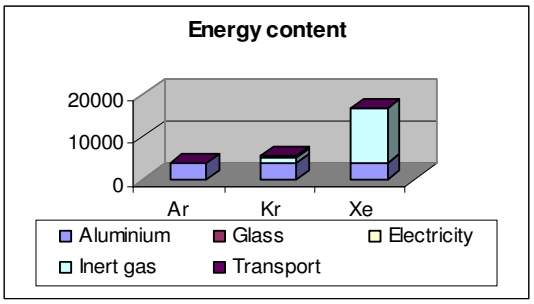

Figure 3. Energy content of the window filled with different gases

When the energy losses through the window during the heating seasons of 50 years are included into the analysis, the values shown in Figure 4 are obtained.

It can be seen that the energy content of the window represents only 25 % of the total in the Air case, and it increases progressively for the Ar, Kr and Xe until reaching up to 72 % in the latest case. Figure 4 shows that the minimum energy consumption is reached in the Argon case. This means that energy investments in inert gases are worth only up to the Ar case, but the additional investments required in terms of energy for the Kr and Xe cases are too expensive compared to the energy savings obtained during the heating seasons.

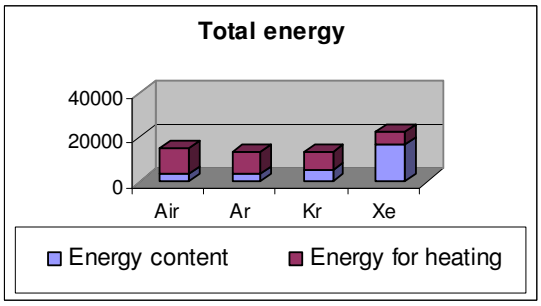

Figure 4. Energy content of the window filled with different gases

Performing now a comparative assessment, considering only the processes and materials used for the Ar, Kr and Xe windows in addition to those used in the window filled with air, and analyzing the global warming potential and acidification categories, tendencies similar to the energy analysis are obtained, as it can be seen in Figures 5 and 6. In all three categories of impact considered, Argon is the preferred alternative from the environmental point of view. These results make weighting and normalization stages of LCA unnecessary.

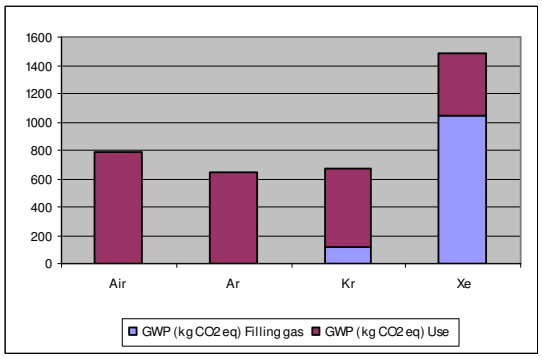

Figure 5. Global Warming Potential. Comparative analysis.

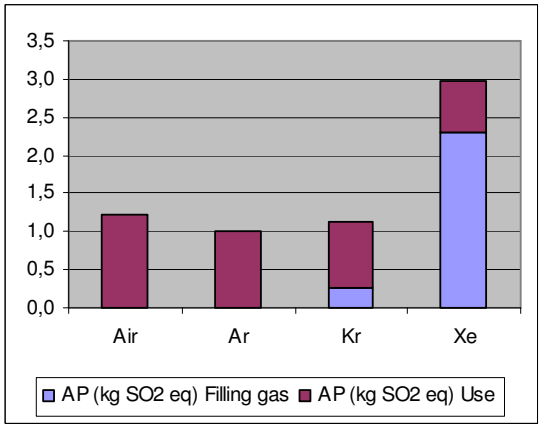

Figure 6. Acidification potential. Comparative analysis.

Economic Aspects

Table 1 shows the results, in present values, in the four considered scenarios. Scenarios 1, 2 and 4 show a preference for windows with air, which explain why this is the preferred window in Mendoza. Scenario 1 does not favour conservative measures since considers no increase in the cost of energy in the future. Neither scenario 2 gives preferentiality to conservative measures, since considers that in the coming 50 years fossil fuels prices will follow the same tendency than in the past, thus assuming that fossil fuels wells are plenty of resources and no scarcity will be in the coming future. Scenario 4 is similar to Scenario 2 with the only difference that takes into consideration initial increases in the energy costs, but the same tendency in the long term. All of these three scenarios consider a real discount rate

of 2 %. Scenario 3, on the other hand, shows that, from the economic point of view, the use of argon as filling gas in double glass windows is preferable when the discount rate is nil, even if the assumption on the increase in the energy costs is the same as in the past. Exploring for the lowest annual increase rate in energy cost that would justify the additional investment needed for the Argon window when a discount rate of 2 % is considered, a value of 5.5 % was found.

Scenario 1		
Project alternative	Initial cost	LCC
Air	0	33 (*)
Argon	20	47
Kripton	200	223
Xenon	801	819
Scenario 2		
Project alternative	Initial cost	LCC
Air	0	68 (*)
Argon	20	76
Kripton	200	247
Xenon	801	838
Scenario 3		
Project alternative	Initial cost	LCC
Air	0	121
Argon	20	120 (*)
Kripton	200	285
Xenon	801	867
Scenario 4		
Project alternative	Initial cost	LCC
Air	0	79 (*)
Argon	20	85
Kripton	200	255
Xenon	801	844

Table 1. Comparative Present-Value Costs of Alternative Projects (* = Lowest LCC)

CONCLUSIONS

Results show that, although there are some environmental and energetic advantages in the use of double-glazed, argon-filled windows, the economic aspect is a disadvantage to its introduction to the market. Even in the case of the most favourable scenario (number 3), with a nil discount rate (which considers no difference between the value of money today and that to be saved in the future), economic results for the argon window and for the air window are almost identical. Kripton windows show small environmental advantages compared to air windows, but their use is not justifiable from the economic point of view. Xenon windows are the least convenient from both the environmental and the economic points of view, even though they are the most energy-effective during the use phase.

REFERENCES

[1]. USGBC. Sustainable Building Technical Manual. Green building design, construction and operations. Produced by Public Technology Inc., US Green Building Council. 1996

[2] J. Fernandez et al., An assessment of the Solar Potential of the Built Environment in the City of Mendoza, Argentina. A study in advance. Proceedings of the 18th PLEA Conference, Florianopolis, Brazil, 2001.

[3] Cole, R., Kernan, P. *Life-Cycle energy use in office buildings.* Building and Environment 1995, 31 (4):307-317.

[4]. EPA, Efficient Windows Collaborative – www.Buildcentral.com/windows/about.asp.

[5]. Muneer, T., Han, B., Truslove, T. Proceedings of the International Workshop on Sustainability of Cities and Buildings, University of Florence, 13-15 September (1995).

[6]. Weir, G., Muneer, T. *Energy and environmental impact analysis of double-glazed windows.* Energy Conversion and Management, 1998;39(3-4):243-256.

[7] Balcomb, J.D. et al. *Passive Solar Design Handbook*. Vol. 3. ASES, Boulder, Co. 1983.

[8] Van den Berg N.W., Duttilh C.E., Hupes G. *Beginning LCA: a guide into environmental Life Cycle Assessment*. Centre of Environmental Science (CML), Leiden, 1995.

[9] Marshall, H. *Life-Cycle Costing*. *Mechanical Estimating Guidebook for Building Construction*, 6th edition Mc. Graw Hill, Inc., 1995.

[10]. Urbiztondo S. *Las tarifas de servicios públicos pre y post devaluación: comparación Internacional*. Julio 2003. http://24.232.76.6/server1/notes/coyuntu58.pdf

[11]. *Escenarios*. Nov 2003. *Panorama financiero y monetario*. N° 130/ Monthly newsletter from the CFI (Consejo Federal de Inversiones). www.cfired.org.ar/esp2/escena/ultimo/pdf/Panofinmone.pdf

[12]. Green Building Store www.greenbuildingstore.co.uk

Proceedings of ECOS 2005
Trondheim, Norway
June 20–22, 2005

AN ECOLOGICAL THERMOECONOMIC OPTIMIZATION OF SOME POWER PLANT MODELS

M.A. Barranco-Jiménez*
Departamento de Ciencias Básicas, Escuela Superior de Cómputo
Instituto Politécnico Nacional
UP Zacatenco. CP 07738 México DF, México.
e-mail: mbarrancoj@ipn.mx
F. Angulo-Brown
Departamento de Física, Escuela Superior de Física y Matemáticas
Instituto Politécnico Nacional
UP Zacatenco, CP 07738 México DF México
e-mail: angulo@esfm.ipn.mx

ABSTRACT

By means of a finite-time thermodynamics formalism we analyze the performance of an endoreversible power plant model (the Novikov model) under thermoeconomical criteria. This is accomplished by using the concept of the profit function defined in terms of the performing costs of the plant. Our study is based upon two optimization criteria: the maximum power regime and the so-called modified ecological regime. We show that under ecological conditions the plant dramatically reduces the rejected heat to the environment, and a lost of profits is translated in an usage of the fuels reducing the rejected heat towards the environment in 50-55% respect to that of a maximum power regime. This reduction depends on the heat transfer law used in the Novikov engine.
Keywords: thermoeconomics, endoreversible cycles, optimization.

INTRODUCTION

It is well known that due to practical and economical considerations actual power plants work under conditions which are between the maximum power (MP) regime and the point corresponding to maximum efficiency[1]. An analysis in this sense was reported by De Vos[1] by means of a thermoeconomical study of an endoreversible power-plant model, obtaining an optimum operation point in terms of relative investment costs and the fuel consumption of the plant. A similar criterion can be used for this thermoeconomical analysis by means of the so-called ecological function introduced in ref.[2], which is defined by

$$E(\tau,\eta) = W(\tau,\eta) - T_2\sigma(\tau,\eta), \qquad (1)$$

where W is the plant's power output, T_2 is the absolute temperature of the cold reservoir, τ is the temperature ratio of the cold (T_2) and hot (T_1) reservoirs of the endoreversible power plant model, η is the efficiency of the endoreversible model and σ is its total entropy production. In general, the maximization of the ecological function given by Eq. (1) leads to an engine configuration with a power output around 75% of the maximum power output and an entropy production around 25% of the entropy produced in the maximum power regime[2, 3]. Another important property of the so-called ecological regime is that at the maximum-E regime the engine's efficiency is approximately the semisum of the efficiencies corresponding to the maximum power regime, $\eta = 1-\sqrt{\tau}$, and the Carnot efficiency, $\eta = 1-\tau$, respectively[2, 3]. Recently, in ref.[3], Angulo-Brown and Arias-Hernández showed that a more suitable ecological optimization criterion must depend on the heat transfer law used to model the irreversible heat fluxes between the heat reservoirs and the working fluid, through a generalization of Eq.

(1), given by

$$E(\tau,\eta) = W(\tau,\eta) - \varepsilon(\tau) T_2 \sigma(\tau,\eta). \qquad (2)$$

This expression is called the modified ecological (EM) function, and the function $\varepsilon(\tau)$ contains the dependence on the particular heat transfer law[3]. As it was shown in [3] the function $\varepsilon(T_1, T_2)$ for the case of a linear Newtonian heat transfer law is given by

$$\varepsilon(\tau) = \sqrt{\frac{1}{\tau}}. \qquad (3)$$

If the heat transfer law is given by one of the Dulong-Petit (DP) type, then the function $\varepsilon(\tau)$ is given by[4]:

$$\varepsilon(\tau) = \frac{\sqrt{\tau(80+\tau)} - \tau}{10\tau}. \qquad (4)$$

The modified ecological criterion also leads to a good compromise between high power output ($\sim 0.75 P_{\max}$) and low entropy production ($\sim 0.25 \sigma_{P_{\max}}$) [4]. In the present work we analyze an endoreversible power plant under thermoeconomical criteria by using both a De Vos-type economical criterion and the modified ecological criterion. The paper is organized as follows: In section 2, we review the results obtained by De Vos[1] by means of a thermoeconomical study of an endoreversible model for a power plant operating under maximum power conditions, by considering both a Newton's and a Dulong-Petit's heat transfer laws. In section 3, we study the same system but using the modified ecological criterion, and we obtain an optimum efficiency in terms of the relative investment and fuel consumption costs of the power plant. We also compare these results by means of the both mentioned criteria. In section 4, we calculate the quantity of energy rejected to the environment of the power plant under the same both criteria. Finally, in section 5, we present our conclusions.

MAXIMUM POWER REGIME

The De Vos model, which was firstly introduced by Novikov[5] for a nuclear power plant, consists of two thermal reservoirs: a hot reservoir at temperature T_1 and a cold reservoir at temperature T_2, both T_1 y T_2 are taken as constants and with known values. Between the two reservoirs we have two components: A reversible Carnot engine and a thermal

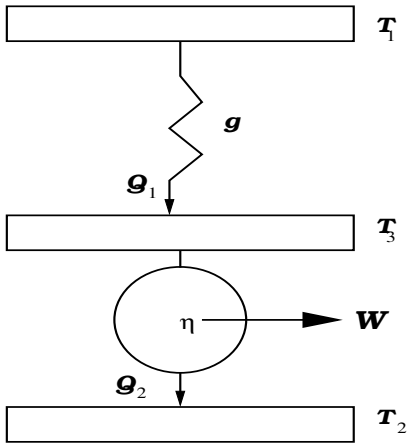

Figure 1: Scheme of the Novikov engine model.

conductor (with conductance g), which is an irreversible component (see Fig. 1). In the Novikov model, the hot side of the Carnot engine is at temperature T_3. In the De Vos thermoeconomical approach a profit function, q, is maximized, this function is given by the quotient between the power output and the costs involved in the performance of the power plant, that is,

$$q = \frac{W}{C}, \qquad (5)$$

where W is the plant's power output and C are the costs, which have two contributions: a).- the cost of the investment which is assumed as proportional to the size of the plant and b).- the cost of the fuel consumption which is assumed as proportional to the quantity of heat Q_1 (see Fig. 1).
If one takes that $Q_{\max}$ is a proper measure of the plant's size, then the costs C can be expressed by

$$C = aQ_{\max} + bQ_1, \qquad (6)$$

where the proportionality constants a and b have units of $\$/Joule$, and $Q_{\max} = g(T_1 - T_2)$.
If in Fig.1 we assume that Q_1 is given by a linear Newtonian heat transfer law, we have

$$Q_1 = g(T_1 - T_3). \qquad (7)$$

On the other hand, from the heat to work conversion in the reversible part of the model we get

$$W = \left(1 - \frac{T_2}{T_3}\right) Q_1. \qquad (8)$$

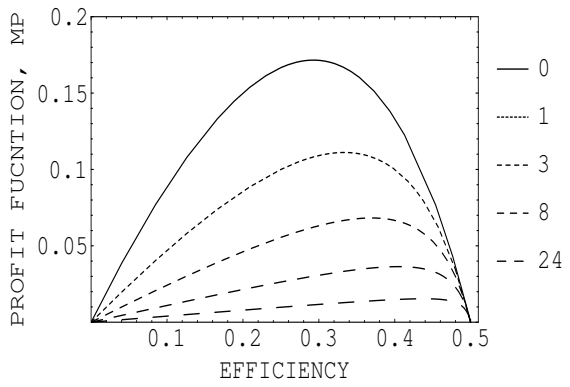

Figure 2: Profit function at maximum power versus efficiency η for several β-values.

If we use the Carnot's efficiency formula for Fig.1 and Eq.(6), the expression for the power output becomes

$$W(\tau,\eta) = gT_1\eta\left(1-\frac{\tau}{1-\eta}\right), \qquad (9)$$

where W is function of the efficiency η and thus of the temperature T_3.
From Eq.(6) the function of costs C becomes

$$C(\tau,\eta) = agT_1\left[(1-\tau)+\beta\left(1-\frac{\tau}{1-\eta}\right)\right], \quad (10)$$

where $\beta = \frac{b}{a}$. From Eqs. (5), (9) and (10), the expression for the De Vos profit function is given by

$$q_V(\tau,\eta,\beta) = \frac{1}{a}\frac{\eta\left(1-\frac{\tau}{1-\eta}\right)}{\left[(1-\tau)+\beta\left(1-\frac{\tau}{1-\eta}\right)\right]}. \quad (11)$$

Fig. 2 shows the form of $aq_V(\tau,\eta,\beta)$ for several values of β, in the case of $\beta = 0$, we have

$$q_V(\tau,\eta) = \frac{1}{a}\frac{W(\tau,\eta)}{Q_{\max}},$$

which has a maximum value at $\eta = 1-\sqrt{\tau}$, that is, the Curzon-Ahlborn efficiency [6], which is the efficiency of an endoreversible engine model working under maximum power conditions. When $\beta \to \infty$, the maximum point of the function aq_V tends to the Carnot efficiency, $\eta = 1-\tau$.

We can calculate in an explicit manner the maximum of the function given by Eq.(11) in terms of the adimensional parameter β. Nevertheless, this parameter is not easy to evaluate and it is more convenient to work in terms of the so-called fuel fractional cost f defined by [1]

$$f = \frac{bQ_1}{aQ_{\max}+bQ_1}, \qquad (12)$$

which is the ratio of the fuel cost between the total cost of the plant. The value of f for several types of fuel is shown in Table I. Therefore, the De Vos optimum efficiency[1] in terms of the fractional cost f, is given by

$$\eta_{opt}^{DV}(\tau,f) = 1-\frac{f}{2}\tau-\frac{\sqrt{4(1-f)\tau+f^2\tau^2}}{2}. \quad (13)$$

Fig. 3 shows how the optimum efficiency changes between $f = 0$ (free costs case) and $f = 1$ (the Carnot case).
Eq. (13) gives us the optimum efficiency of the Novikov's model in terms of the fractional cost of fuel f, when the power plant works in a maximum power regime and the heat exchange between the thermal reservoir and the working fluid is given by a Newton-type heat transfer law.

Fuel	f (%)
Renewable	0
Uranium	25
Coal	35
Natural Gas	50

Table 1. Relative cost of fuel for several energy resources, taken from [1].

We now consider in the Novikov engine a Dulong-Petit transfer law of the type $Q_1 = g\,(T_1-T_3)^{\frac{5}{4}}$, performing in a MP regime, then the profit function is given by[7]:

$$q_{mp}^{DP}(\tau,\eta,\beta) = \frac{1}{a}\frac{\eta(1-\frac{\tau}{1-\eta})^{\frac{5}{4}}}{\left[(1-\tau)^{\frac{5}{4}}+\beta(1-\frac{\tau}{1-\eta})^{\frac{5}{4}}\right]} \qquad (14)$$

This function has a similar behavior as that given by Eq. (11), with a maximum value at $\beta = 0$, which is the MP point, in addition, if $\beta \to \infty$, the maximum value of the curve tends to the reversible Carnot point, that is, to the point $\eta_C = 1-\tau$, see ref. [7]. From the maximization of Eq. (14) we obtain the optimal efficiency in terms of

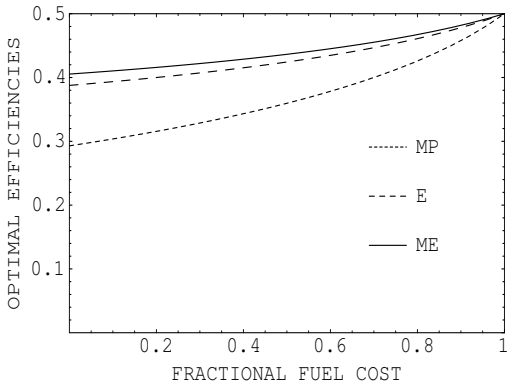

Figure 3: Comparison between η_{opt}^{DV}, η_{opt}^{EM} and η_{opt}^{E} for a Newton heat transfer law, for $\tau = \frac{1}{2}$.

the adimensional parameter β, and by using Eq. (12), we get[7]:

$$\eta_{mp}^{DP}(\tau,f) = 1+\frac{\tau(1-5f)}{8} - \frac{\sqrt{\tau^2(1+25f^2-10f)+80\tau(1-f)}}{8} \quad (15)$$

The function $\eta_{mp}^{DP}(\tau,f)$ has a similar behavior that Eq. (13). From Eq. (15), if $f=0$ (equivalently to $\beta=0$) we obtain the maximum efficiency value of the Novikov engine for a heat transfer law of the Dulong-Petit type, this efficiency is given by [7],

$$\eta_{mp}^{DP}(\tau) = \frac{8+\tau-\sqrt{\tau(\tau+80)}}{8} \quad (16)$$

This expression also was recently obtained by Arias-Hernández et al.[4].

THE ECOLOGICAL CRITERION

Following the same procedure employed in the previous section, now we calculate the optimum point of operation of the Novikov model in terms of the fractional fuel cost assuming that the power plant model works under the maximum modified ecological function (see Eq. 2). We again take the Newton's heat transfer law to describe the heat exchanges between the heat reservoir and the working fluid (see Eq. 7). By using Eqs. (2) and (3), the modified ecological function becomes[7, 8]:

$$E(\tau,\eta) = gT_1\left(1-\frac{\tau}{1-\eta}\right)\left[\eta\left(1+\sqrt{\frac{1}{\tau}}\right)+\sqrt{\tau}\left(1-\frac{1}{\tau}\right)\right], \quad (17)$$

where we also employ the mean entropy production given by $\sigma = \frac{Q_2}{T_2}-\frac{Q_1}{T_1} = \frac{Q_1-W}{T_2}-\frac{Q_1}{T_1}$, which by using Eqs. (7) and (9), becomes $\sigma = \frac{Q_1}{T_2}[1-\tau-\eta]$.

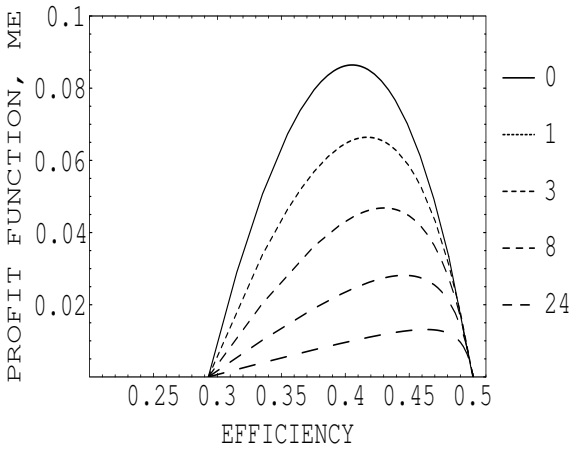

Figure 4: Profit function at maximum modified ecological function versus efficiency η for several β-values.

Thus, by means of Eqs. (10) and (17), the profit function in this case is,

$$q_E(\tau,\eta,\beta) = \frac{1}{a}\frac{\left(1-\frac{\tau}{1-\eta}\right)\left[\eta\left(1+\sqrt{\frac{1}{\tau}}\right)+\sqrt{\tau}\left(1-\frac{1}{\tau}\right)\right]}{\left[(1-\tau)+\beta\left(1-\frac{\tau}{1-\eta}\right)\right]}. \quad (18)$$

Figure 4 shows the behavior of the function $aq_E(\tau,\eta,\beta)$ for several values of β, as we can see, this function has a completely equivalent behavior to the function $aq_V(\tau,\eta,\beta)$ (see Fig. 2) based in the De Vos approach. If $\beta=0$, the profit function becomes

$$q_E(\tau,\eta,\beta) = \frac{W(\tau,\eta)-\varepsilon(\tau)T_2\sigma(\tau,\eta)}{aQ_{\max}},$$

with a maximum value at η given by

$$\eta = 1-\tau^{\frac{3}{4}}, \quad (19)$$

which is the efficiency of an endoreversible heat engine model with Newtonian heat transfer as reported in [3] and also obtained by Velasco et al. [9] by means of a different optimization criterion. If we maximize in an explicit manner Eq. (18), we obtain an expression for the optimum efficiency in terms of the adimensional parameter β and by means of the definition of the fractional fuel cost given by Eq. (11), we get[8]

$$\eta_{opt}^{EM}(\tau,f) = 1-\frac{f}{2}\tau-\frac{\sqrt{4\tau^{\frac{3}{2}}(1-f)+f^2\tau^2}}{2}, \quad (20)$$

that is, the optimum efficiency under the so-called modified ecological regime. Figure 3 shows the form of the function $\eta_{opt}^{EM}(\tau,f)$, which has the same behavior of

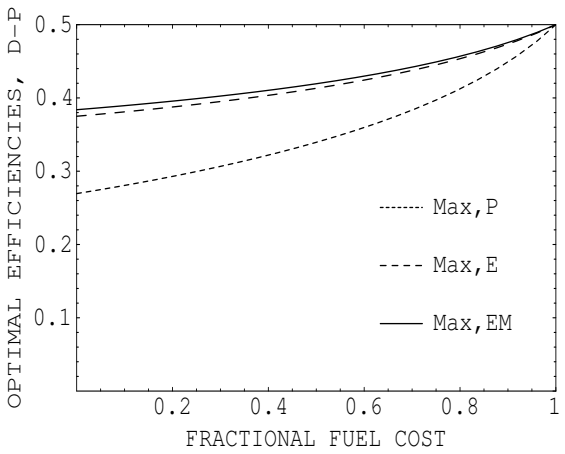

Figure 5: Comparison between η_{mp}^{DP}, η_{ME}^{DP} and η_{E}^{DP} for a DP heat transfer law, for $\tau = \frac{1}{2}$.

$\eta_{opt}^{DV}(\tau, f)$ also showed in Fig. 3. The optimum efficiency smoothly varies from the case $f = 0$ (free cost fuel) where the investment is the predominant cost until the Carnot case with $f = 1$, where the fuel cost is the predominant cost. We can see that in the case $f = 0$ (or $\beta = 0$) we obtain the ecological efficiency given by Eq. (19).
Analogously to the MP-regime, if the heat transfer law is of the Dulong-Petit type, the profit function under an ecological regime is given by[7],

$$q_E^{DP}(\tau,\eta,\beta) = \frac{1}{a}\frac{\frac{(\tau-1)(1-\frac{\tau}{1-\eta})^{\frac{5}{4}}\left[8(\eta-1)-\tau+\sqrt{\tau(8+\tau)}\right]}{\sqrt{\tau(8+\tau)}-9\tau}}{\left[(1-\tau)^{\frac{5}{4}}+\beta(1-\frac{\tau}{1-\tau})^{\frac{5}{4}}\right]}. \tag{21}$$

This function has the same behavior that the function given by Eq. (14). From the maximization of Eq. (21) we arrive to the optimal ecological efficiency in terms of f, given by

$$\eta_{EM}^{DP}(\tau,f) = 1+\frac{\tau(1-5f)}{8} - \frac{\sqrt{10\tau(1-f)\sqrt{\tau(\tau+80)}+(9-25f^2)\tau}}{8} \tag{22}$$

Fig. 5 shows the function $\eta_{EM}^{DP}(\tau, f)$ in terms of the parameter f, it is remarkable that this function has a similar behavior that Eqs. (13), (15) y (20). In Fig. 5 we compare the optimal efficiencies both under the MP and the ecological regimes by using a Dulong-Petit heat transfer law. In Fig 5 we also can observe the optimal efficiency under the former ecological function, given by Eq. (1)[7]. In additon, from the Eq. (22), if $f = 0$ (equivalently to $\beta = 0$), we obtain the maximum ecological efficiency for a Dulong-Petit heat transfer law, which is given by[7]:

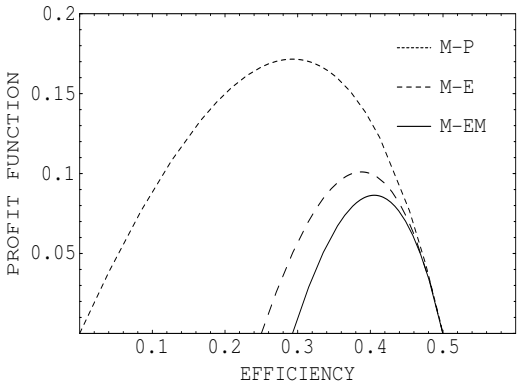

Figure 6: Comparison of the profit functions for the Newtonian case.

$$\eta_{\max}^{DP}(\tau) = \frac{8+\tau-\sqrt{10\tau\sqrt{\tau(\tau+80)}-9\tau}}{8}. \tag{23}$$

If we compare the profits both under the MP and the ecological regimes for a same value of f, it can be observed that the ecological profits are lesser than the profits at MP-regime (see Fig. 6). However, this lost of profits is concomitant whit a better efficiency for a given f (see Fig. 5). This means that the fuel consumption is better used by the power plant at maximum ecological regime.
The relationship between the mentioned optimum efficiencies is as follows,

$$\eta_{CA} < \eta_{DV} < \eta_E < \eta_C.$$

The fact of reducing the system's entropy without an important reduction of the power output has significant consequences in regard to the environmental impact.

ENVIRONMENTAL IMPACT

Nowadays, it is believed that the production of greenhouse gases, as CO_2 for example, can have an important impact over the global climate of the Earth. A great part of the atmospheric CO_2 is produced by human activities based on the combustion of fossil fuels occurring for instance in internal combustion engines. Thus, the aim of designing more efficient engines is concomitant with long-range ecological objectives. In this context, the ecological criteria seem a suitable procedure for the search of insights about an engine's performance with a less aggressive interaction with the environment. In this context, we propose the following simplified analysis. If we apply the first law of the thermodynamics to Fig. 1, we get

$$Q_2 = Q_1 - W. \tag{24}$$

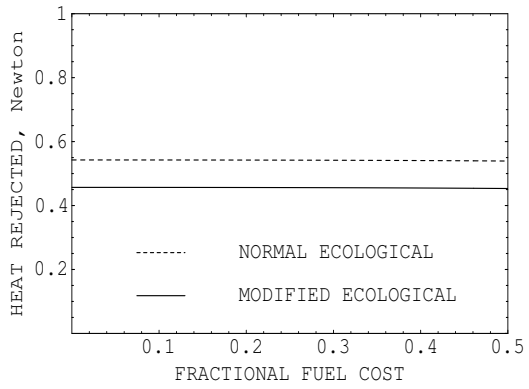

Figure 7: Quotient between the ecological rejected heat and the maximum-power rejected heat for a lineal heat transfer law.

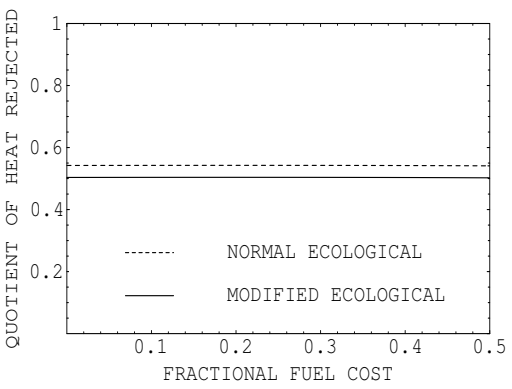

Figure 8: Quotient between the ecological regected heat and the maximum-power regected heat in the case of a DP heat transfer law.

By using Eqs. (8) and (9) in Eq. (24) we obtain

$$Q_2(\tau,\eta) = gT_1(1-\eta)\left(1-\frac{\tau}{1-\eta}\right), \qquad (25)$$

where $Q_2(\tau,\eta)$ is the heat rejected to the environment by the power plant. Therefore, if the power plant works in the maximum power regime, Q_2 becomes

$$Q_2(\tau,\eta_{opt}^{DV}) = gT_1(1-\eta_{opt}^{DV})\left(1-\frac{\tau}{1-\eta_{opt}^{DV}}\right). \qquad (26)$$

Analogously, if the power plant works under maximum modified ecological function conditions,

$$Q_2(\tau,\eta_{opt}^{EM}) = gT_1(1-\eta_{opt}^{EM})\left(1-\frac{\tau}{1-\eta_{opt}^{EM}}\right). \qquad (27)$$

From Eqs. (26) and (27), we can calculate the rejected heat to the environment for each value of f and under different manners of operation of the power plant. From Eqs. (13) and (20), the quotient between both the rejected heats in the modified ecological and maximum power cases can be expressed as

$$R_N(\tau,f) = \frac{(f-2)\tau+\sqrt{4\tau^{\frac{3}{2}}(1-f)+f^2\tau^2}}{(f-2)\tau+\sqrt{4(1-f)\tau+f^2\tau^2}}. \qquad (28)$$

Figure 7 shows the plot of $R_N(\tau,f)$ versus the parameter f for $\tau=\frac{1}{2}$. This plot shows that

$$\frac{Q_2(\tau,\eta_{opt}^{EM})}{Q_2(\tau,\eta_{opt}^{DV})} = 0.45, \qquad (29)$$

that is, the heat rejected to the environment (a river, a lake, the sea, etc.) by the plant under ecological conditions is around a half of the heat rejected under maximum power conditions. This same result was obtained by Velasco et al.[7] by means of another optimization procedure. Fig. 7 also shows the ratio between rejected heats corresponding to the former ecological regime (Eq. (1)) and the Q_2 at maximum power output.

In the same way, if we consider in the Novikov engine a Dulong-Petit heat transfer, we also calculate the quotient between both the rejected heats in the ecological and MP cases. Sustituting the Eqs. (15) and (22) in the Eqs. (26) and (27) respectively, this quotient can be expressed as,

$$\begin{aligned} R_{DP}(\tau,f) &= \frac{Q_2(\tau,\eta_{EM}^{DP})}{Q_2(\tau,\eta_{mp}^{DP})} \\ &= \frac{\sqrt{10\tau(1-f)\sqrt{\tau(\tau+80)}+(9-25f^2)\tau}}{\sqrt{\tau^2(1+25f^2-10f)+80\tau(1-f)}} \end{aligned} \qquad (30)$$

Fig. 8 shows the plot of $R_{DP}(\tau,f)$in terms of the parameter f for a $\tau=\frac{1}{2}$. This plot shows that

$$\frac{Q_2(\tau,\eta_E^{DP})}{Q_2(\tau,\eta_{mp}^{DP})} = 0.5, \qquad (31)$$

that is, the heat rejected to the environment by the plant under ecological conditions is now a half of that rejected under maximum power conditions. This fact can be used for designing some kind of ecological taxes based in the way of performance of heat engines [7, 10].

CONCLUDING REMARKS

Within a finite-time thermodynamics context we have determined an economically optimum regime for a power plant model (the Novikov model) following the De Vos procedure, but by means of an ecological-type optimization criterion. We have found that when the Novikov model maximizes the so-called modified

ecological criterion it reduces the rejected heat to the environment between 50 and 55% of the heat rejected in the case of a power plant model working under maximum power conditions. This represents a great advantage if the aim of the engine's performance is to diminish the impact on the environment.

Aknowledgments: This work was supported in part by COFAA and EDI-IPN-México. MABJ thanks support by SUPERA-SEP and hospitality of the doctoral program of UAEM-Toluca.

REFERENCES

[1] A. De Vos, Energy. Convers. Mgmt. 36 (1995) 1.

[2] F. Angulo-Brown, J. Appl. Phys. 69 (1991) 7465.

[3] F. Angulo-Brown and L.A. Arias-Hernández, J. Appl. Phys. 89 (2001) 1520.

[4] L.A. Arias-Hernández, G. Ares de Parga, and F. Angulo-Brown, Open. Sys. Information Dyn. 10, 351 (2003)

[5] I. Novikov, Atomimaya Energiya. 3 (1957) 409: in english traslation; J. Nucl. Energy II. 7 (1958) 125.

[6] F. Curzon and B. Ahlborn, Am. J. Phys. 43 (1975) 22.

[7] M.A. Barranco-Jiménez, Tesis de Doctorado, UAEM, México 2005 (in spanish, unpublished)

[8] M.A. Barranco-Jiménez and F. Angulo-Brown, Rev. Mex. Fis. (in press)

[9] S. Velasco et al. J. Phys. D: Appl Phys. 33 (2000) 355.

[10] M.A. Barranco-Jiménez and F. Angulo-Brown, Proceedings of 17^{th} International Conference on Efficiency, Costs, Optimization, Simulation and Environmental Impact of Energy and process Systems, ECOS2004 vol. 1 (2004) 351-357.

Proceedings of ECOS 2005
Trondheim, Norway
June 20–22, 2005

MULTI CRITERIA ASSESMENT OF ENERGY CONVERSION SYSTEMS USING AGGREGATED INDICATORS

Alessandro Franco*, Ana R. Diaz
Università di Pisa
Dipartimento di Energetica "L. Poggi"
Via Diotisalvi, 2 - 56126 PISA
ITALY

ABSTRACT

Today decisions concerning energy systems are mainly based on economic analyses, paying minor attention to the Laws of Thermodynamics. This represents a serious conceptual drawback to the possibility of increasing thermal efficiency, reducing pollution emission and making a correct use of energy resources, because those are often subordinate to economic decisions. After a short overview of the methods present in the literature, concerning the multi-dimensional analysis of energy system, the utilization of aggregated indicators is discussed with reference to the case of "clean coal conversion technologies" analysis. The utilization of a different method based on a multi-criteria utility function is also discussed and analyzed with reference to the case of CGAM power plant.

Keywords: Multi-criteria analysis, environment preservation, sustainability, exergy

NOMENCLATURE

ACP	Aggregated Coefficient of Power Generation
c	concentration [% weight]
e_{ch}	specific chemical exergy [kJ/kmol]
Ex	exergy flow [W]
f	penalty factor in Eq. (3)
I	Exergy loss flow rate [W]
k	specific cost [€/kg/kwh]
m	mass flow rate [kg/s]
M	molecular weight [kg/kmol]
NI	Normalised indicator
p	pollutant measure in Eq. (3) [kg/kwh]
P	pressure [bar]
Q	utility function in Eq. (4)
q	generic indicator in Eq. (4)
T	Temperature [K]
U	utility function
w	weight factor
W	power [W]
Z	monetary cost [€]

Greek symbols

β_p	pollution indicator [W]
ε	quality index of fuel utilization
γ	Index of the energy input
η	efficiency
$\eta_c, \overline{\eta}_c$	Carnot efficiency
Γ	cost function [€]
Ψ	utility function

Subscripts

a	of the reference air
ad,f	adiabatic flame
ch	chemical
e	relative to the environment
ex	of the exhaust
in	input
max	maximum
out	output
p	pollutant
ph	physical
r	the r-th unit (r=0 environment)
0	reference

*Corresponding author: phone +39-050-2217154
e-mail: alessandro.franco@ing.unipi.it

INTRODUCTION

Beyond thermodynamic and economic, new criteria are going to influence the evolution of energy production; concepts as the depletion of resources associated with highly intensive use of energy, the

need to preserve the environment or the social issues related to investment decisions and political actions (taxes, incentives, etc.) are also significant subjects concerning the power generation. The general approach to the design of thermal energy systems is based on the idea that it has to be realized with high efficiency, low environmental impacts and acceptable costs. The design of a complex energy system represents a kind of multi-objective optimisation. In this sense the major effort of the EU energy policy is concentrated towards the direction of eco-efficiency. In general no unique solution exists that satisfy all the objectives, because some of them are in "structural" contradiction. In this sense, the problem of considering different viewpoints in the design and analysis of energy systems appears to be crucial and requires the elaboration of specific instruments. Multi-criteria assessment methods were recently proposed in the literature to compare different energy production technologies in the field of fossil fuels or renewable energy sources by the aggregation of thermodynamic, economic and environmental indicators [1-4]. First and Second Law efficiency, emissions to the atmosphere or to the water, heat rejected to the environment, cost of fuel or the specific cost of the energy produced are some of the main indicators used to compare the various energy conversion systems. The method is interesting, but it requires a careful application. First, the indicators considered are not dimensionally homogeneous and they must be recasted to a common normalized base. Second it is necessary to give to every indicator a relevance (i.e. weight) that accounts its influence. In general, it seems difficult to develop an unequivocal weight theory. Different methods for a multi-criterial analysis assessment of energy system are analyzed and discussed in detail with reference to the comparison among common and advanced technologies for the conversion of fossil fuels. The use of composed utility functions appears to be most suitable, owing to the possibility of introducing also the design variables of the system, even if open difficult questions [5-8].

MULTICRITERIA ANALYSIS OF ENERGY SYSTEMS: A CONCISE OVERVIEW

In the last years, methods of analysis and optimisation have been developed taking into account together with the technical elements related to the energy use (thermodynamic dimension), the financial resources expended (economic dimension), the correct use of physical resources and energy sources as well as any pollution and degradation of the environment resulting from the energy systems (environmental dimension). Other dimensions like sanitary, biological or social can also be directly linked to those three macro-dimensions, but they cannot be so simply related to the design of the plant. All the methods discussed in the literature to analyze the energy systems under that multi-dimensional point of view can be reconnected to a multi-objective optimisation. Some of them are based on the maximisation or the minimisation of a utility function in the form also known as "weighting function method" [9]

$$U = \sum_{i=1}^{k} U_i = -\sum_{i=1}^{k} w_i f_i(x) \qquad (1)$$

where w_i is a scalar weighting factor and $f_i(x)$ the i-th objective function. In the literature it is largely diffused the optimization of power plants and energy system basing on utility functions. The aggregation of the different dimensions has been object of the **environomic analysis** [6-7]. This analysis performs an optimisation of the plants by searching for the minimum of a utility function U

$$U = \sum_{r} Z_r + \sum_{r}\sum_{k} \Gamma_{ok,r} + \sum_{e} \Gamma_e - \sum_{r} \Gamma_{ro} \qquad (2)$$

where Z_r is the capital cost of the system associated to the r-th unit of the system, including charges and maintenance cost, $\Gamma_{ok,r}$ is the cost of resource and services, Γ_{ro} is the revenue from products or services that the system furnish (energy, steam etc.), Γ_e is the environmental costs. This term distinguish the environomic from the thermoeconomic approach and is defined as [5]

$$\Gamma_e = f_p k_e p_e \qquad (3)$$

where f_p is a penalty factor related to the pollutant, k_e is an environmental unit cost and p_e is a pollution measure [6]. The selection of the coefficients of Eq. (3) and its evaluation give place to misleading. Till now, the method was developed in a satisfactory way only with reference to some particular systems. A different method, the **aggregative utility function method**, takes into account the different feature of energy production by means of defined indicators. A multi-criteria analysis of energy system could include resource, environment, social and efficiency indicators. A selection among the

different indicators permits of including all the relevant dimensions of the system in a cumulative index. The general indices method comprises the formation of an aggregative function

$$Q(q,w)=\sum_{i=1}^{m} p_i q_i \qquad (4)$$

where p_i is weight-coefficients elements of vector w and q_i is the indicator of the specific criteria [1-2]. A rational work with indicators will confront us with two main problems, the aggregation problems and, the choice of a correct number of indicators.
In the literature some papers are present providing a selection of criteria and options for the comparison of fossil and renewable energy technologies [1-4]. But the comparison of different technologies carried out in those papers raises to a number of questions about the reliability of the method and the final result is strongly influenced by the priority given to a particular dimension or indicators.
Another approach is represented by the **Integrated environmental assessment (IEA).** The purpose of some researchers is to provide a method to evaluate the ability of a set of indicators to support decision-making and measure progress toward more sustainable systems of production. In its current state, the framework focuses on economic, environmental, health and safety aspects of energy production. [10]. The problems, induced on the environment by the pollutant emissions, and the related costs, represent an external costs of the energy systems. The economic approach has to decide how to estimate the external costs of pollutant emissions and how to internalise them into the economic evaluation of the system.
Models aiming at structuring these cross-boundary problems of an economic and environmental nature are usually called 'economic-environmental' or 'economic-ecological' models. The quantitative tradition in economics has enabled researchers to include environmental elements as costs. Nevertheless, in integrating economic and environmental models, some methodological problems are usually met, such as differences in time and spatial scales and differences in measurement levels of relevant variables. The typical approaches for the internalisation of pollution externalities are market based. The charge approach (taxes assigned to the pollutants) is the most commonly used and in this way the technical elements are considered only in a marginal way and the analysis could be very fragmented.

THE AGGREGATED COEFFICIENT OF POWER GENERATION (ACP)

Considering the methods available in the literature joining the idea of aggregative function with the integrated environmental assessment appears interesting. But doubts have been raised about the comparison among different type of power generation plants described in the literature [1-4].
A correct development of the ideas rises to compare systems of similar technologies, including indicators appreciating also some technical details. In general the indicators are not homogeneous and its aggregation to a common basis is a difficulty. This problem is object of the environomic analysis [6-7]. A possibility of aggregating the values of non-homogeneous indicators is to refer them to a normalized basis, using linear or non-linear approach. The Aggregated Coefficient of Power Generation (ACP) is obtained as sum of the different normalized indicators required in the analysis. This provides a simple method to compare different power plants belonging to a similar category depending on fuel used and size. The ACP for the j-th power system can be defined as:

$$ACP_j = \sum_{i=1}^{n} w_i NI_i \Big/ \sum_{i=1}^{n} w_i \qquad (5)$$

where NI_i is a generic normalised indicator, w_i is the weight coefficient for the i-th indicator and *n* is the number of used indicators. Once that the indicators have been defined the best power plant results the one with the highest ACP coefficient.
According to the method, the indicators can be normalized into a linear or no-linear scale [3]. A worst and a best value have to be identified for each indicator. The best value of each indicator is normalised at 1, while the value –1 identifies the worst value. An identification of a reference value (normalized value equal to 0) is also necessary, when a non-linear scale is used; these reference values are fundamental implying a preference among the various energy policies (rising the efficiency, reducing the environmental impact and the costs). In an analysis involving a lot of energy conversion systems the identification of reference values represents a key point too. An exaustive analysis can be obtained using a quite high number of indicators, causing a significant advance in the description of the different power systems, but also the risk of a very fragmented analysis. A definition of the indicators belonging to each dimension and an analysis about their meaning is given below.

The indicators used for the analysis

Among the possible indicators, thermodynamic indicators must be considered. If the comparison concern energy systems using the same input fuel First Law efficiency seems to be more appropriated, while a Second Law efficiency, permits to appreciate some peculiar differences among the technologies when the same fuel is used. For example using as reference the different values of the maximum operating temperature of the system (T_{max}). An indicator that can be introduced in the analysis is a quality index of the fuel utilization. Such an indicator can be related to intrinsic properties of the fuel, like calorific value, exergetic value or adiabatic flame temperature, but also to different data related to the fuel and its utilization in the energy system. Referring to this indicator it is possible to give a significant importance, based on a non-economic dimension, to the fuel used and the different technologies used to convert it to energy, represented for example by the maximum operating temperature of the system

$$\varepsilon = \left(1 - \frac{T_0}{T_{max}}\right) \Big/ \left(1 - \frac{T_0}{T_{ad,flame}}\right) = \eta_c / \overline{\eta}_c \qquad (6)$$

As economic indicators those based on a microeconomics analysis of the system could be used: the total capital cost of the plant for unit power, the energy unit cost, the internal rate of return of the investment related to the plant, the price of the fuel etc. More complex indicators can be defined taking into account the life cycle of the plant, but this is not argument of the present study.

The environmental indicators try to quantify all the "externalities" related to the energy system. In this sense, the pollutant and thermal emissions are considered environmental indicators, and included in the non-energetic dimension. Some typical example could be air pollution emissions (CO_2, NO_x, SO_x, etc.) and heat rejected to the atmosphere or to the water. A detailed report containing the indicators that can be considered for the analysis of energy systems that could be considered in the environmental dimension is outlined in [11].

In the definition of the ACP coefficient, the influence of each indicator is defined by a weight w_i. This underlines the relevance of each dimension considered in the analysis and of the various indicators considered. Methodological issues and data limitations complicate the perspective for the definition of a non-arbitrary weight theory. A first approach is to give an equal weight distribution to every macro-dimension and to each indicator inside the macro-dimension.

APPLICATION OF THE ACP METHOD TO COMPARE DIFFERENT POWER PLANTS

The analysis of the ACP method can be applied in the framework of various fossil fuel based conversion technologies as the advanced coal conversion ones: the Ultra Super Critical (USC), the Pressurized Fluidized Bed Combined Cycle (PFBC) and the Integrated Gasification Combined Cycle (IGCC). In order to show the reliability of the ACP method for high efficiency coal power plants, the Natural Gas Combined Cycle (NGCC) power plant, which is today the most competitive energy conversion technology, and the sub-critical pulverized coal combustion plant (PCC), are used as upper and lower border reference technologies. Values considered for various parameters of the plants are shown in Table 1 [12-15]. The analysis is carried out considering for each dimension the various indicators reported together with the reference values for their normalization in Tables 2-3. Different reference values are considered if coal generation systems are compared with technologies based on the use of a different fuel like NGCC (Table 2) or if only coal technologies are compared (Table 3). In the first case the reference values for adimensionalisation are chosen considering a larger range of variability.

INDICATORS	Power	Thermal efficiency	Total capital cost	Quality index ε	Fuel price	Heat reject factor (1-η)/η	CO_2	SO_2
Power plant type	[MW]	[%]	[€/kW]	[-]	[€/GJ]	[-]	[g/kWh]	[g/kWh]
PCC	400	40	1200	0.78	1.2	1.500	850	2.5
USC	400	47	1400	0.82	1.5	1.127	780	2.0
PFBC	350	43	1500	0.90	1.2	1.326	730	0.3
IGCC	300	45	1700	0.95	1.35	1.247	700	0.2
NGCC	380	58	650	0.93	4.5	0.724	350	0
IGCC CO_2 capture	300	38	2100	0.95	1.35	1.632	100	0.2

Table 1: Power plants and parameters used for ACP analysis

INDICATORS		NI=-1	NI=0	NI=1
Thermal efficiency	[%]	38	43	58
Total capital cost	[€/kW]	2100	1400	650
CO_2 Emissions	[g/kWh]	840	350	100
SO_2 Emissions	[g/kWh]	2.5	1.25	0
Heat Rejected factor	[-]	1.632	1.247	0.724
Index of fuel utilisation ε	[-]	0.78	0.90	0.95
Fuel cost	[€/GJ]	4.5	2.85	1.2

Table 2: Indicators used for fossil fuel plants

INDICATORS		NI=-1	NI=0	NI=1
Thermal efficiency	[%]	38	43	47
Total capital cost	[€/kW]	2100	1727	1410
CO_2 Emissions	[g/kWh]	840	700	100
SO_2 Emissions	[g/kWh]	2.5	1.25	0
Heat Rejected factor t	[-]	1.632	1.326	1.127
Index of fuel utilisation ε	[-]	0.78	0.90	0.95
Fuel cost	[€/GJ]	1.5	1.35	1.2

Table 3: Indicators for coal-based plants

Results and discussion

The results of the comparison among the various energy systems from the perspective of the ACP method are reported in the Figures 1 and 2.

In Fig. 1 the analysis of five coal-based power plants in comparison with the NGCC is outlined in term of ACP coefficient. The cumulative indicator is obtained considering the same weight for the three dimensions (thermodynamic, economic and environmental) and for the various indicators.

Obviously the NGCC power plant has the higher ACP, due to its lower environmental impact and its higher efficiency and represents today the more advantageous option for power generation but unfortunately natural gas reserves are not infinite. Further considerations can be carried out comparing only the coal conversion options. Joining the results of Figs. 1-2, the development of USC plant appears to be not really convenient, even if, at present, they show the higher efficiency.

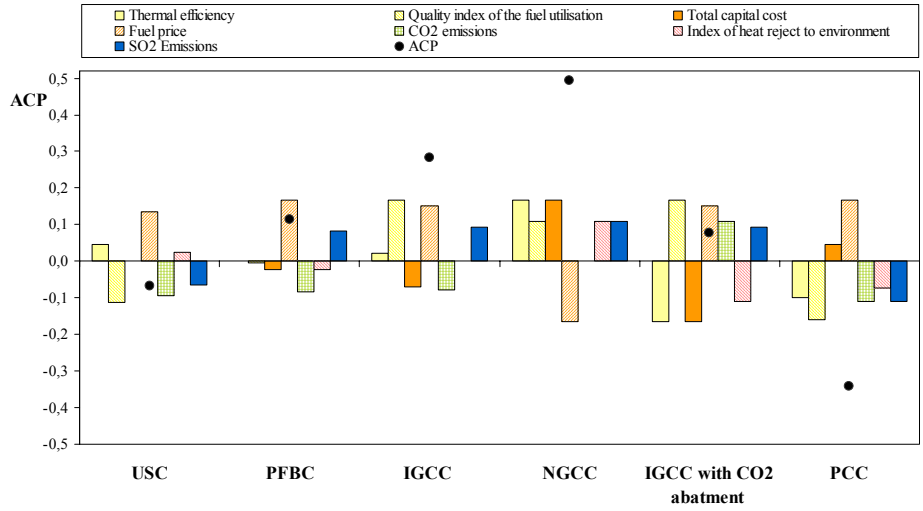

Figure 1: Comparison of coal conversion technologies and natural gas combined plants (ref. Table 2)

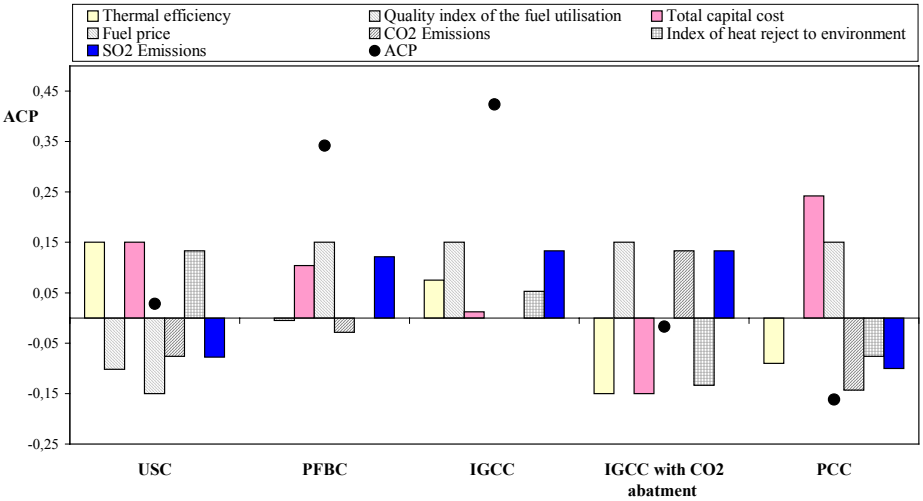

Figure 2: Comparison of coal technologies (ref. Table 3)

The increase of the efficiency and the low reduction of CO_2 emissions, with respect to a conventional PCC plant, do not compensate the increase of the costs and the technological efforts required.
Concerning to the comparison between PFBC and IGCC, a difference between the two technologies cannot be defined in absolute terms even if IGCC seems better than PFBC. The use of abatement technologies, like CO_2 capture, at present, can be considered only if a great weight is attributed to the environmental dimension. With the actual technologies, CO_2 capture seems not always a profitable option: the reduction of CO_2 emissions cannot compensate the lower thermodynamic efficiency and the increase of costs. But clearly appears the difficulty in giving indications about the correct approach to the energetic problem, the guidelines for the development of new technologies and the more efficient use of well known ones. The instrument of ACP seems to really lead towards the direction of eco-efficiency meaning the concept of making the same energetic "service" with a minor use of resources and impact on the environment.

USE OF COMPOSED UTILITY FUNCTIONS FOR POWER PLANTS ANALYSIS

The previous analysis shows that the ACP method, even if it can furnish an element for the comparison of technological solutions for energy conversion, suffers of some limitation related to:

a) the selection of the indicators;
b) the definition of the weight distribution;
c) the adimensionalisation of the indicators.

The quest is open for what concerns the selection of the correct number of the indicators; concerning both the selection of opportune reference values and the normalization (linear or non linear), in general it is simple to compare indicators of economic performance, due to the fact that all of them are referred to a common basis. The same cannot be said for thermodynamic and environmental indicators. A different approach is represented by the development of composed indicators that reconnect to common basis the three dimensions considered.
Considering a thermodynamic point of view, an index that can furnish a simplified comparison between plants using different fuels, like coal or natural gas, can be carried out making reference to the minimisation of a function that aggregate the three main elements involved in the operation of the system: power production (W_{out}), the physical (thermal and pressure) exergy losses (I_{ph}) and the power input (W_{in}). Obviously, this last term have to be weighted by attributing it a weight index to the fuel used (γ). An interesting idea can be represented by the use of the function:

$$\Psi = W_{out} - I_{ph} - \gamma \cdot W_{in} \qquad (7)$$

The Ψ function can be an interesting tool to carry out a thermodynamic optimisation of energy conversion systems, as diffusely discussed in [8].
The Ψ function, due to the consideration of the term γ, can assume an economic connotation. In general it may assume any possible value between 0 and the Carnot factor related to the fuel used ($0< \gamma < \eta_c$). More properly this coefficient γ may account the value of the power input with respect to the output basing on both the characteristics of the input fuel and on the current technological status of energy conversion. The higher is γ the higher is the value of the fuel used and of the technology used to convert it. In general a possible value of γ is a mean efficiency of the plants used to convert the fuel (e.g. natural gas can be converted in gas turbine based plants so $\gamma \approx 0.3$ or in combined plants, $\gamma \approx 0.5$).
The use of the function Ψ, examined in a previous work by the authors, seems to be particularly important due to the possibility of introducing directly the term of input energy. This represents an important conceptual goal, because it couples eco-efficiency policy with a policy aimed at reduction of energy use [8]. The Ψ function does not take directly into account environmental impact issue. In order to introduce environmental concerns, the utility function Ψ can be modified by adding a term that take into account the pollutant emission.

$$\Psi_p = W_{out} - I_{ph} - \beta_p - \gamma \cdot W_{in} \qquad (8)$$

According to the simplified description of Fig. 3 the optimum system is the one that maximize the output power (W_{out}) with the minimum amount of losses (I_{ph}), environmental damage (β_p) and energy consumption (W_{in}). A methodological problem evidenced by the application of ACP analysis was the weight given to each pollutant emissions: this can be considered as an element of inaccuracy.
In order to define the term β_p, an attempt to give a common (physical) basis to the various emissions is necessary. Significant attention has been directed towards the use of exergy analysis in the assessment of thermal systems and their environmental impacts. ([16-17]).

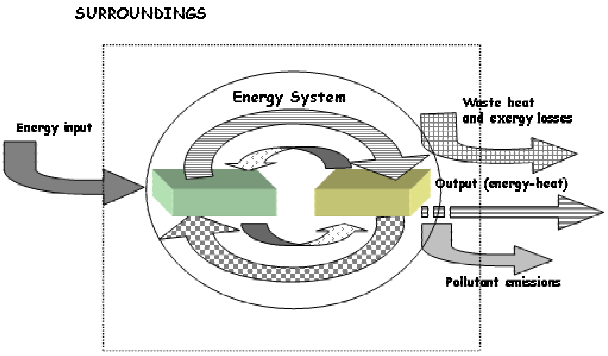

Figure 3: System definition for Ψ functions

Considering, that the exergy content of a chemical species determines the minimum amount of energy needed to construct that chemical from a soup of stable elements the chemical exergy is defined as the minimum work to be supplied if a material has to be produced from the inert reference system.
The impact of the generic pollutants, could be evaluated with reference to the energy required to re-establish the reference system environmental conditions analyzing the single chemical species. Conceptually, this means that a pollutant must be eliminated while the concentration of reference state components must be re-established. In this way the impact of the pollutant is strictly related with the minimum work required to eliminate or to restablish the concentration of the single pollutant. Basing on the definition of a reference state [18] a cumulative pollutant emissions indicator could be:

$$\beta_p = \sum_i \left| e_{ch,i} \left[c_{ip} \frac{m_p}{M_p} - c_{ia} \frac{m_a}{M_a} \right] \right| \qquad (9)$$

where i is the generic chemical species, $e_{ch,i}$ is the standard chemical exergy of the generic chemical species (pollutants as CO_2, SO_x, NO_x or substance contained in the environment as N_2, O_2 or H_2O) [19-20], and c_{ip} and c_{ia} is the concentration of the substances in the exhaust gas and in the reference state respectively. In general the values obtained by Eq. (9) furnish results substantially different from the chemical exergy of the fuel.

Application to a test case

In this section an example for the calculation of the pollutant emission factor in the form of Eq. (9) and for the total function Ψ_p is given. The system used as reference, schematically described in Fig. 4 is a cogeneration system. It operates with natural gas and produces electricity and heat in the form of saturated steam. The thermodynamic specifications are given in Table 4.

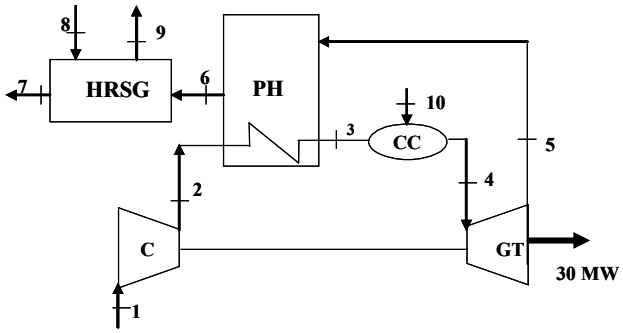

Figure 4: Flow diagram of the CGAM system

Pt.	Substance	m [kg/s]	T [K]	P [bar]	Ex [MW]
1	Air	91.2757	298.15	1.013	0.0000
2	Air	91.2757	603.7	10.130	27.5382
3	Air	91.2757	850.0	9.623	41.9384
4	Exhaust	92.9176	1520.0	9.142	101.4538
5	Exhaust	92.9176	1006.2	1.099	38.7823
6	Exhaust	92.9176	779. 8	1.066	21.7516
7	Exhaust	92.9176	426.9	1.013	2.7726
8	Water	14.0000	298.15	20.000	0.0616
9	Sat. steam	14.0000	485.6	20.000	12.8102
10	Methane	1.6419	298.15	12.000	84.9939

Air: Ma = 28.649 (%) 77.48 N_2, 20.59 O_2, 0.03 CO_2, 1.90 H_2O
Exhaust Mp = 28.254 (%) 75.07 N_2, 13.72 O_2, 3.14 CO_2, 8.07 H_2O

Table 4: Thermodynamic parameters of CGAM [5]

According to the data reported in Table 5, the pollutant emission factor is β_p = 2.65 MW; this value quite low but different from the chemical exergy of the fuel [5] ($e_{ch,}$ = 0.3665 MW). Table 6 provides all the terms of the function given by Eq. (8) considering two different values of the parameter γ and two different plant configurations (with and without HRSG). The two different values of the parameter are considered (γ=0.3 and γ=0.5).
As we can see, in all the cases the Ψ function assumes a negative value and the pollutant emission factor is rather lower than the exergy loss term (I_{ph}).

		CO_2	N_2	O_2
$e_{ch,0}$ [19]	[kJ/kmol]	14176	639	3951
c_a	[%]	0.0003	0.7748	0.2059
$c_a * e_{ch} * m_a / M_a$	[kW]	13.56	1578.38	2593.49
c_p	[%]	0.0314	0.7507	0.1372
$c_p * e_{ch} * m_p / M_p$	[kW]	1513.4	1630.9	1843.4

Table 5: Data for the calculation of β_p index

	Ψ_p [MW]	W_{out} [MW]	I_{ph} [MW]	β_p [MW]	γW_{in} [MW]
Gas Turbine γ=0.3	-51.82	30	54.99	2.65	24.18
CGAM γ=0.3	-39.07	30	42.24	2.65	24.18
Gas Turbine γ=0.5	-67.94	30	54.99	2.65	40.30
CGAM γ=0.5	-55.19	30	42.24	2.65	40.30

Table 6: Values of the terms of utility function Ψ_p

The introduction of the term β_p does not determine a sensible difference between Ψ_p and Ψ, but this is not properly the case for plants using coal where this term has a well higher weight. In this last case the methodological consideration of pollutant emission could become the opportunity to promote the high efficiency design of conventional plants and the dissemination of advanced technologies, like CO_2 capture, that have difficulties to compete in the energy market.

CONCLUSIONS

The problem of considering aspect connected to energy systems like economic, thermodynamics and impact on environment, in term of both energy use and environmental emissions is analyzed. Two approaches for the multi-dimensional analysis of energy systems are considered: the method of the aggregated indicators (ACP method), also referred in the literature and the method of the multi-criterial utility functions (Ψ_p method), originally proposed in this paper. The two methods permit to aggregate different dimensions in order to find a compromise between the increase of the benefits and the reduction of the undesirable elements, present at the energy production assessments with different targets.

The method of aggregated indicators in the form of the Aggregated Coefficient of Power Generation, represents a powerful instrument to compare different energy system of similar technology and to define the technological goal that must be pursued, but it introduces several elements of arbitrariness. An example of application to the comparison of coal technologies delineated in the paper permits to better understand its potentiality.

The second method is more interesting in perspective representing not only an instrument for analysis and comparison of energy system but a real instrument for the design and optimization of energy systems, taking into account also design variables of the system. An example of application is carried out and tested with reference to CGAM.

REFERENCES

[1] Afgan NH, Carvalho MG, Hovanov NV. *Energy system assessment with sustainability indicators*, Energy policy 2000; 28: 603-612.

[2] Afgan NH, Carvalho MG. *Multi-criteria assessment of new and renewable energy power plants*, Energy 2002; 27:739-755.

[3] Giannantoni C, Mirandola A, Tonon S, Ulgiati S. *Energy-based, four sector Diagram of Benefits as a Decision Making Tool*. In: Proc. of Advances in Energy Studies, Portovenere, pp. 575-586, 2002.

[4] Tonon S, Brown MT, Luchi F, Mirandola A, Stoppato A, Ulgiati S. *An integrated assessment of energy conversion processes by means of thermodynamic, economic and environmental parameters*, Energy 2005; in press corrected proof.

[5] Bejan A, Tsatsaronis G, Moran M. *Thermal Design and Optimization*. New York: J. Wiley, 1996.

[6] Frangopoulos CA. *An introduction to environomic analysis and optimisation of energy-intensive systems*. In: Proc. of ECOS '92, 231-239, 1992.

[7] Pelster S, Favrat D, von Spakovsky MR. *Thermoeconomic and environomic modelling and optimisation of the synthesis, design, and operation of CC with advanced options*, ASME Jour. for Eng. of Gas Turbines and Power 2001; 123: 717-726.

[8] Franco A, Giannini N. *An approach for the analysis and the optimum design of power plants incorporating 1st and 2nd Law of Thermodynamics*. In: Proc. of 3rd HPC Conference, Larnaca, 2004.

[9] Rao S. *Engineering Optimization Theory and Practice*. New York: John Wiley & Sons, 1996.

[10] Munda G. *Cost-benefit analysis in integrated environmental assessment: methodological issues*, Ecological Economics 1996;19: 157-168.

[11] McNeill JR. *Something new under the sun – An environmental history of the twentieth century*. London: Penguins Books, 2000.

[12] Longwell JP, Rubint ES, Wilson J. *Coal: energy for the future*, Prog. Energy Combust. Science Vol. 21, pp. 269-360, 1995.

[13] Lako P. *Coal-fired power technologies Coal-fired power options on the brink of climate policies*, Rep. ECN-C-04-076, Clean coal technologies, 2004.

[14] Hasegawa T, Sato M, Nakata T. *A Study of Combustion Characteristics of Gasified coal Fuel*, Transactions of the ASME, Jour. of Eng. for Gas Turbines and Power, 2001; 123: 22-32.

[15] Pfleger D. *Clean Coal Technologies. Development Status*, In: Proc. of World coal institute workshop, Essen, Germany, 2002.

[16] Rosen MA, Dincer I. *Exergy analysis of waste emissions*, Int. Jour. of Energy Research 1999; 23 (13): 1153-1163.

[17] Rosen MA, Dincer I. *On exergy and environmental impact*, Int. Jour. of Energy Research 1997; 21(7): 643-654.

[18] Van Gool W. *Thermodynamics of chemical references for exergy analysis*, Energy Conv. and Mgt, 1998; 39 (16-18): 1719-1728.

[19] Ahrendts J. *Reference states*. Energy, 1980; 5: 667-677.

[20] Szargut J, Morris DR. *Standard Chemical Exergy of some elements on the planet Earth*. Energy 1986; 11: 733-755.

Proceedings of ECOS 2005
Trondheim, Norway
June 20–22, 2005

THERMODYNAMIC ESTIMATION OF THE ENVIRONMENTAL IMPACT OF MINERAL FERTILIZERS PRODUCTION

Zornitza Kirova - Yordanova*,
University "Prof. Assen Zlatarov"
Department of Inorganic Technology
8010 Bourgas
Bulgaria

ABSTRACT

In a previous work the cumulative exergy concept was used to estimate the environmental impact of the mineral fertilizers production on the natural resources consumption [1]. In this work an attempt is made to apply the exergy method to estimate the environmental impact of emissions from mineral fertilizers production. The environmental impact of emissions is estimated by three different approaches: by exergies of the emissions and waste flows; by the exergy of the natural resources, accumulated in waste flows; by the exergy and cumulative exergy consumption of natural resources in some processes of purification, utilisation and recycling of waste flows.
Keywords: Exergy, Cumulative exergy, Mineral fertilizers, Environment, Emissions, Pollutants

NOMENCLATURE

AN	ammonium nitrate
CExC	cumulative exergy consumption [MJ/t]
D	exergy losses [MJ/t]
E	exergy [MJ/t]
LP,MP	Low pressure, Middle pressure
TSP	triple superphosphate

INTRODUCTION

The mineral fertilizers play a critical role in the global food provision. It is estimated [2], that about 40% of the world's protein needs are derived from atmospheric nitrogen fixed by the Haber-Bosch process and its successors to produce ammonia.

In 2002/2003, the world fertilizer industry produced about 144 Million metric tonnes (Mt) of primary plant nutrients, including: 85 Mt nitrogen (N), 34 Mt phosphate (P_2O_5) and 25 Mt potash (K_2O), contained in about 380 Mt various fertilizers products [3,4].

The mineral fertilizers production and use have a versatile and specific environmental impact. As other process industries, the environmental impact of the mineral fertilizers production processes is twofold and concern the consumption of natural resources as well as the discharges to air, water and land. Besides that, the use of mineral fertilizers arises one more relation to environment, because they are introduced directly into the arable land and thus interact immediately with the environment.

Since 1960s, the production of mineral fertilizers have made enormous progress in reducing natural resources consumption as well as emissions [5-7]. As the pollutants, released into the environment from the fertilizers plants, are usually products, semi-products or feed stocks of the production processes, the recycling and recovery of the emissions leads to decreasing both the feedstocks and energy consumption.

In the last decade intensive investigations of the environmental impact of the mineral fertilizers production, distribution and use, made by some

* Corresponding author: Phone +359-56-858274
Fax +359-56-880249 E-mail zkirova@btu.bg

fertilizers producers, are partially inspired by their international organizations in the EU and USA as EFMA, IFA, etc., as well as by FAO, UNEP and UNIDO [8-10]. The various methods and indicators are used, but in most of them some subjective or economic criteria are also used.

New methods have been developed in the last years with the intention to obtain environmental impact indicators based on both the First and Second Laws of Thermodynamics.

The exergy method and the cumulative exergy concept (Szargut et al. [11]) are useful means for evaluation of the overall consumption of all kinds of natural resources at every step of a production process. Szargut proposed also the term *ecological* costs as a measure of their depletition [11,12].

The application of exergy as a measure of the impact of the emissions and wastes is proposed from R. Ayres [13], R. Ayres et al. [14], Rosen [15], etc. As the exergy is the potential of a system with respect to the environment, the higher the exergy of the emissions or the wastes, the greater their influence on the environment. However, some problems, as lack of specifying, are still open. R Ayres [13] pointed out, that the exergy content of a waste stream could be a rough measure about its potential to causing harm, despite of its impossibility to measure the human or eco-toxicity. Szargut [12] proposed to evaluate the impact of waste products by means of their monetary index of harmfulness. Another approach is developed from Valero and Botero [16]. They regard the exergy of resources, consumed by the processes of the emissions abatement, as a measure of environmental impact of technical systems. Cornelissen [17], Gong and Wall [18], etc., use exergy method in the context of Life Cycle Analysis in order to specify a Second-Law based ecological indicator.

In a previous work [1] the cumulative exergy concept was used to estimate the environmental impact of the mineral fertilizers production on the natural resources consumption.

This work is an attempt to use the exergy method and cumulative exergy concept for estimation of environmental impact of emissions and wastes from some basic nitrogen and phosphorous fertilizers production processes.

NITROGEN AND PHOSPHOROUS FERTILIZERS PRODUCTION PROCESSES: FEATURES, INTERACTIONS, INPUTS, OUTPUTS AND DISCHARGES

Urea and fertilizer grade ammonium nitrate (AN) are the most intensive used nitrogen fertilizers, with 100 and 30 million tonnes annual world production respectively. The production and use of di- and monoammonium phosphates (DAP and MAP) rose in the last two decades to about 29 million tonnes/year. The annual world production of the triple superphosphate (TSP), the major phosphorous fertilizer in the past, now decreases down to about 5 million tonnes [3,4].

Ammonia production is a process central to the manufacture of all nitrogen fertilizers, as well as of NP and NPK fertilizers. Besides urea and various ammonium-containing fertilizers, obtained directly from ammonia, it is also used for production of nitric acid, which is the base chemical for the manufacture of ammonium nitrate and other nitrates used as fertilizers, as well as of various NP and NPK fertilizers. Two thirds of phosphate fertilizers, including DAP, MAP and TSP, are derived from phosphate rock treated with phosphoric acid; hence the production of wet-process phosphoric acid is also a base process in the fertilizers manufacture. All these fertilizers production processes are chemically interlinked and sometimes are co-located on the same site forming an integrated complex [6].

Ammonia is produced from water, air and hydrocarbons or coal. Currently about 77% of world ammonia production is based on the steam reforming of natural gas. It takes 28 - 30 GJ/te (only about 40% above the thermodynamic minimum) in modern ammonia plants to make ammonia from natural gas by the overall reaction:

$$\text{Natural gas} + \text{Water (Steam)} + \text{Air} \Rightarrow$$
$$\Rightarrow 3\,H_2 + N_2 + CO_2 \Rightarrow \text{Ammonia} + CO_2 \quad (1)$$

The production of ammonia is relatively clean compared to many other chemical processes, as well as to other production processes in fertilizer industry.

Carbon dioxide (about 99% CO_2), produced in stoichiometric ratio by the main reaction, flue gas from the steam reforming furnace and process condensate are the only discharges from natural gas based modern ammonia plants (Figs.1 and 2). If the produced ammonia is used at the same site for urea production, the carbon dioxide is completely used

and is not venting to the atmosphere. The process condensate is formed by condensation of the extra steam, after the $H_2 + N_2$ mixture is cooled, of the order of about 1 m^3 per tonne NH_3 and contains up to 0.1% ammonia and methanol. In modern ammonia plants the process condensate is treated with steam and then recovered as boiler feed water, after polishing. As the fuel in the steam reforming furnace is preferably natural gas, there is practically no SO_2 emission and CO_2 and NO_x are the only pollutants in the flue gas [6,7].

Fertilizer grade nitric acid (45 - 60%) is produced (Fig.1) by oxidation of ammonia with air to NO_x and subsequent absorption of NO_x with water by the overall reactions:

$$4NH_3 + 5O_2\,(Air) \Rightarrow 4NO + 6H_2O \quad (2)$$

$$2NO + O_2 \Rightarrow 2NO_2 \quad (3)$$

$$4NH_3 + 5O_2\,(Air) \Rightarrow 4NO + 6H_2O \quad (4)$$

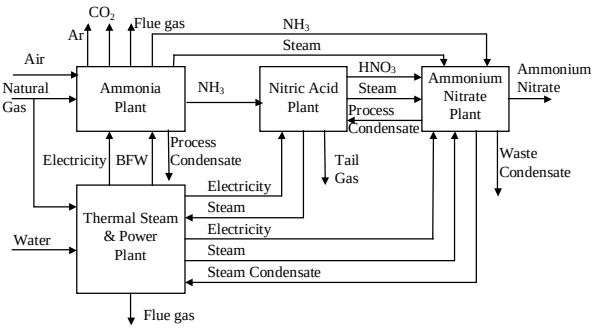

Fig. 1. Block flow diagram of nitric acid and AN production

The nitric acid production is a known source of nitrogen oxides (NO_x and N_2O) emissions into the atmosphere. The waste gas (tail gas) from nitric acid plants can contain various quantities of these pollutants, depending on the process parameters, mainly on the absorption pressure and on the waste gas treatment. The NO_x emissions are attributable to the production process, as by the third reaction one mole NO is produced for every three moles of NO_2 and then complete absorption of NO_x is impossible. The N_2O emissions are also attributable to the nitric acid production, however by another reason: N_2O is an undesirable, but unavoidable by-product of the first reaction, as a result both of the thermodynamic and kinetic features of the ammonia oxidation reaction and of the quality and condition of the catalyst used. Three methods are currently used for NO_x abatement from the tail gas from new as well from existing nitric acid plants and the NO_x emission level strongly decreased in the last decade. However, there are still not reliable commercial methods for N_2O decreasing. Excluding some occasional emissions, no continuous liquid effluents are released from a nitric acid plant [6,7].

Fertilizer grade ammonium nitrate (AN) is produced from ammonia and 45-60% nitric acid (Fig. 1) by the reaction:

$$NH_3 + HNO_3 \Rightarrow NH_4NO_3 \quad (5)$$

The main releases into atmosphere from prilling towers are AN particulate matter and ammonia. Another source of the discharges into atmosphere is the process steam formed in neutralizers and evaporators from water entering into neutralizers with the nitric acid. Two approaches are used to the emission abatement: process steam purification or steam condensation and subsequent purification of the formed condensate. In the last case the condensation heat can to be used in the process. Condensed process effluents and exhaust vapors are used in some cases in nitric acid production. However, there exist various problems and the emissions to the atmosphere as well as to water are still significant [6,7]).

The production of urea from ammonia and CO_2 (Fig.2) by the overall reaction:

$$2NH_3 + CO_2 \Rightarrow NH_2CONH_2 + H_2O \quad (6)$$

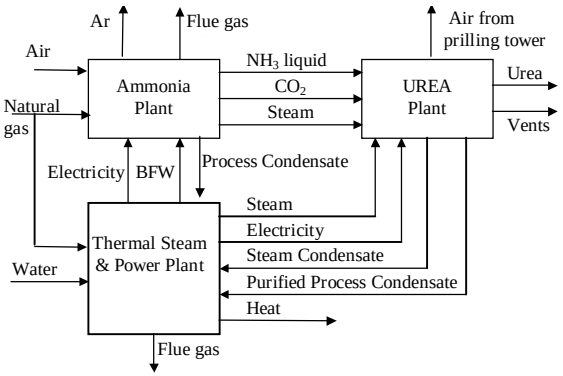

Fig. 2. Block flow diagram of urea production

achieves the most progress in the last years in minimization of both feedstocks consumption and pollutants. The ammonia consumption in the new plants is reduced down to nearly stoichiometric quantity of 567 kg/ tonne urea as a result from diminishing of ammonia and urea emissions both to air and to water.

The main problem in pollution prevention in urea production is the formation of water as a by-

product (Fig.1). The urea synthesis reaction produces process condensate water of 300 kg/tonne urea. Additional water inputs are necessary to remove ammonia from absorbers vents as well as to remove ammonia and urea dust from air, discharged from prilling towers. These sources may increase the final quantity of process water to about 500 kg/te, which has to be discharged to the environment. However, some quantities of ammonia and urea dust are still emitted into atmosphere from vents and prilling towers. The process water treatment to very low emissions limit levels is very difficult and requires big quantities of middle pressure steam [6,7].

Wet process phosphoric acid is produced by decomposition of phosphate rock with sulphuric acid. Depending on the process parameters, five process routes exist, but the dihydrate process is still the most popular one, with by-product $CaSO_4.2H_2O$ (phosphogypsum):

$$3Ca_3(PO_4)_2.CaF_2 + 10\ H_2SO_4 + 20\ H2O \Rightarrow$$
$$\Rightarrow 6\ H_3PO_4 + 10\ CaSO_4.2H_2O + 2\ HF \quad (7)$$

The phosphogypsum is a undesirable, but unavoidable by-product of the reaction. As the quantity of the formed phosphogypsum is very big (about 5500 kg/te phosphoric acid) and it contains various impurities, many problems exist about utilization or deposition of this process waste on land or into the sea. Liquid effluents, containing fluorides and phosphates are formed by the filtration of the phosphogypsum. Some emissions of phosphate dust into atmosphere are formed by handling and grinding of phosphate rock as well as of gaseous fluorides, released by the reaction [6,7].

As is clear from the Table 1, the discharges into environment from both nitrogen and phosphorous fertilizers industry, fall into three groups and therefore, various methods have to be used for treating of the discharges.

Large volume by-products from the main reactions, e.g. CO_2 from ammonia production, phospho-gypsum from wet process phosphoric acid, etc., are suitable for using as feedstocks in another processes or, if possible, as final products. The pollutants, which are by-products from some parallel reactions, usually exist in low concentrations in the emissions. If their formation is unavoidable, they have to be removed and recycled or transformed to harmless components. The pollutants, which are products, semi-products or residuals of feedstocks, have to be removed from gaseous emissions and liquid effluents and recycled into the process. This is the case in the urea and ammonium nitrate production.

DATA SOURCES AND CALCULATION PROCEDURES

Most of the data, used in this work, are collected from Bulgarian fertilizers plants in 1996-2003. In 1996 there were four nitrogen and one phosphorous fertilizers plants in Bulgaria with total capacity of about 1.2 Mt/y ammonia and about 0.1 Mt/y (as P_2O_5) wet process phosphoric acid and TSP. Urea and AN were manufactured from ammonia with a capacity of 0.8 Mt/y and 1.1 Mt/y, respectively. Currently one of the ammonia/ AN plants is closed and dismantled, also the production of ammonia and urea in another plant is temporary stopped. Within the last two years the total ammonia production in Bulgaria are converged to a stable amount at about 0.45 Mt/y. Total production of fertilizers grade AN is about 0.8 Mt/y, with half of this quantity stabilized with phosphate (2-3 % as P_2O_5). The real data about natural resources consumption and emissions in Bulgarian fertilizers plants had been collected yearly and verified by fitting the material and energy balances of all the production unit in the technological chain. Also, some of data used are from EFMA publications about emissions level in the new and existing plants [6,7].

We calculate the chemical and physical exergies of the material flows released to the environment (gaseous and liquid flows, and solid wastes) by Szargut‘s method [11]. Gaseous emissions are released at pressures close to atmospheric pressure and are treated as ideal mixtures of real gases. Liquid effluents are extremely diluted and are treated as ideal mixtures, despite off some lack of precision. The solid waste (phosphogypsum) is also treated as ideal mixture. The environment parameters are assumed as follows: P_0 = 101325 Pa, T_o = 298.15 K and relative humidity 0.301. The cumulative exergy consumption (CExC) of natural resources is also calculated by the method, proposed from Szargut [11]. In addition, we use some results about CExC of mineral fertilizers obtained in a previous work [1].

Reactions	Emission or pollutant	Discharges	Methods for utilization, removal or recycling
BY-PRODUCTS FROM MAIN REACTIONS			
Steam reforming of natural gas and shift conversion	CO_2 98,5 – 99%	Vent gas from CO_2 removal unit in ammonia plants	Urea, soda ash or pure CO_2 production, *or emission to air*
Combustion	CO_2 8-12%	Flue gas from reforming furnace in ammonia plants	Utilization for pure CO_2 production *or emission to air*
Phosphate rock decomposition with H_2SO_4	$CaSO_4.2H2O$ and contaminants	Phosphogypsum from wet process phosphoric acid production	Utilization in cement industry, road making, sulphur recycling *disposal on land or into the sea*
	HF and SiF_4	Vent gas from wet process phosphoric acid production	Fluor compounds production
BY-PRODUCTS FROM PARALLEL REACTIONS			
N_2O formation by ammonia oxydation	N_2O	Tail gas (waste gas) from nitric acid production	NSCR of N_2O *or emission to air*
CH_3OH and NH_3 synthesis in H_2-N_2 preparing units	CH_3OH 0.1% NH_3 0.1%	Process condensate from ammonia production	Condensate purification and recylcing
NOx formation from air	NOx	Flue gas from reforming furnace in ammonia plants	SCR or NSCR of NOx *or emission to air*
RESIDUALS OF PRODUCTS, SEMI-PRODUCTS OR FEEDSTOCKS OF THE PRODUCTION PROCESS			
	NH_3 and urea	Waste water and vents from urea production	Waste water purification with NH_3 and urea recycling
	NH_3 and NH_4NO_3	Waste water and vents from AN production	Waste water purification with NH_3 and NH_4NO_3 recycling
	NOx	Tail gas (waste gas) from nitric acid production	SCR or NSCR of NOx or extended absorption (recycling)
	Urea dust	Air from prilling towers from urea production	Air purification with NH_3 and urea recycling
	NH_4NO_3 dust	Air from prilling towers from AN production	Air purification with NH_3 and NH_4NO_3 recycling

Table 1. Emissions, pollutants and wastes from mineral fertilizers production processes

RESULTS AND DISCUSSION

Some of the collected data were used to calculate various Second-Law based indices:

- exergies of the emissions and waste flows;
- exergies of the natural resources, accumulated in the waste flows;
- exergy and cumulative exergy consumption of natural resources in some processes of the waste flows treatment.

Exergies of the emissions and waste flows

The exergy of the waste flows released to the environment from chemical plants account for the main fraction of the external exergy losses. In most cases the temperature and the pressure of the discharged fluids or solids are close to the environmental parameters, therefore, their physical exergy is rather small. Besides that, the potential of the emissions to damage the environment, depends on their chemical composition and especially, on the concentration and properties of the pollutions. Because of that, the chemical exergy of pollutants as well as of the flows, released to the environment, appears to be a more representative index, than their total exergy.

In Table 2 and Figs 3 and 4 are shown some results of calculation of chemical exergy of gaseous, liquid and solid flows, released to the environment, as well as the chemical exergy of the individual pollutants.

The chemical exergies of the pure pollutions (ammonia, urea, AN, etc.) are usually very high, which is in agreement with their harmfullness, at least qualitatively. The chemical exergies of the same pollutions, referred to the 1 tonne of the product, are small, because of the low contents of the pollution in the released flows. The exergies of the emitted flows as a hole, are rather high, especially in the case of the liquid effluents, higher than the exergies of all the pollutants in them. The reason is that the exergy of the pure liquid water is rather high at the specified environmental parameters.

Gaseous emissions, liquid effluents and solid wastes	Pollutant	Concen-tration of the pollutants	Chemical exergy of the pollutants		Chemical exergy of the emissions flows		Mixing exergy
			GJ/t pollutant	GJ/t product	GJ/t flow	GJ/t product	GJ/t product
Gaseous emissions to atmosphere and liquid effluents from ammonia production							
Vent gas from CO_2 removal	CO_2	98.5-99%	0.4576	0.6030	0.4945	0.6590	0.0024
Flue-gas from the primary reforming furnace	CO_2 NOx ($asNO_2$)	8 -12% <300 mg/Nm^3	0.4576 1.2192	0.2480 0.0012	0.1342	0.5399	0.0755 0.0005
Process condensate	CH_3OH NH_3	1 kg/m^3 1 kg/m^3	22.649 20.024	0.0226 0.0200	0.2035	0.2035	0.0006 0.0010
Total exergy of emissions from ammonia production (CO_2 used in the urea production)				0.3008	0.3377	0.7434	0.0783
Total exergy of emissions from ammonia production (CO_2 vented)				0.9038	1.8322	1.4024	0.0807
Gaseous emissions to atmosphere from nitric acid production							
Tail gas before the treating	NO_x	800-2500 ppmv	NO 2.966 NO_2 1.219	0.01-0.03	0.029-0.040	0.120-0.167	0.002-0.005
Tail gas before the treating	NO_x	50-200 ppmv	NO 2.966 NO_2 1.219	0.0007-0.0022	0.028-0.138	0.116-0.542	0.0002-0.0006
Tail gas before the treating	N_2O	700-1300 ppmv	2.4104	0.01-0.02			0.0018-0.0030
Emissions to atmosphere from ammonia nitrate (AN) production							
Air from prilling towers in AN production (34.5% N)	 NH_3 NH_4NO_3 dust	mg/Nm^3 43 82	 20.024 3.73	 0.0056 0.0020	0.0009	0.0076	0.00040 0.00018
Air from prilling towers in stabilized AN production (31.5% N, 3%P_2O_5)	NH_4NO_3 dust	mg/Nm^3 18-20	3.574	0.0010	0.00054	0.0010	0.00011
Emissions to atmosphere and liquid effluents from urea production							
Air from prilling towers in urea production (46.5% N)	 NH_3 urea dust	mg/Nm^3 8-13 12-110	 20.024 11.372	 0.0087 0.0315	0.00078	0.0402	0.0007 0.0012
Vents from NH_3 absorbers	NH_3	14 g/Nm^3	20.024	0.037	0.0003	0.044	0.0011
Waste process waters before treating	 NH_3 urea	mg/l 110-340 200-770	 20.024 11.372	0.006-0.018 0.006-0.024	0.166-0.177	0.447-0.477	0.00014-0.00039 0.00008-0.00026
Waste process waters after treating in new plants [6,7]	NH_3 urea	5 mg/l 1 mg/l	20.024 11.372	0.00005 $5.6.10^{-6}$	0.1614	0.0807	0.00002 0.00003
Emissions, liquid effluents and wastes from wet process phosphoric acid production							
Vents	HF	mg/Nm^3 0.5-3	3.8544	0.00003-0.00015	$1.5.10^{-6}$ - 9.10^{-6}	0.00003-0.00015	0.00014-0.00076
Waste process waters	phosphates as H_3PO_4 fluor as HF	mg/l 1200-2300 200-900	GJ/t P_2O_5 2.648 - 3.8544	0.0049-0.0094 0.0012-0.0019	0.1650-0.1682	0.2542-0.2594	0.00039 0.00032
Phosphogypsum	$CaSO_42H_2O$ P_2O_5 F	82.78 % 2.0 % 0.56 %	0.1501 0.0203 as $Ca_{10}(PO_4)_9F$ 1.407F as $CaSiF_6$	GJ/t P_2O_5 0.7455 0.0057 0.0514	0.151	0.903	0.00003 4.10^{-6} 0.00001

Table 2. Chemical exergy of the emissions and liquid effluents from ammonia, nitric acid, ammonium nitrate, urea and wet process phosphoric acid production

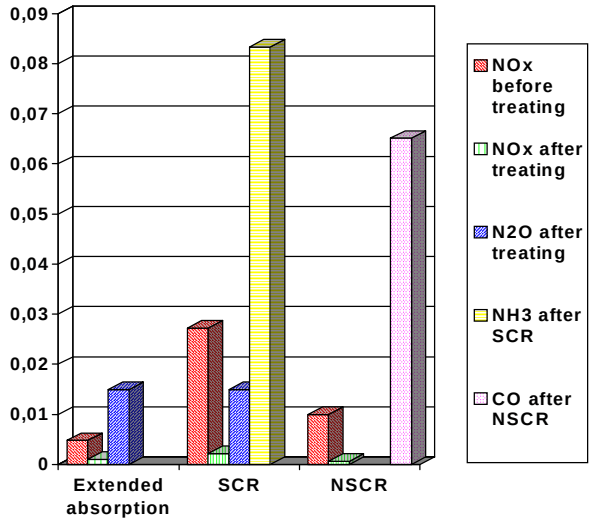

Fig. 3. Chemical exergy (GJ/t 100%HNO_3) of the gaseous pollutants from dual pressure nitric acid production plants before and after the tail gas treating: 1–MP/HP plant with extended absorption; 2–LP/MP plant with SCR; 3–MP/HP plant with NSCR.

- SCR – Selective catalytic reduction of NO_x
- NSCR – Non-selective catalytic reduction of NO_x [6,7]

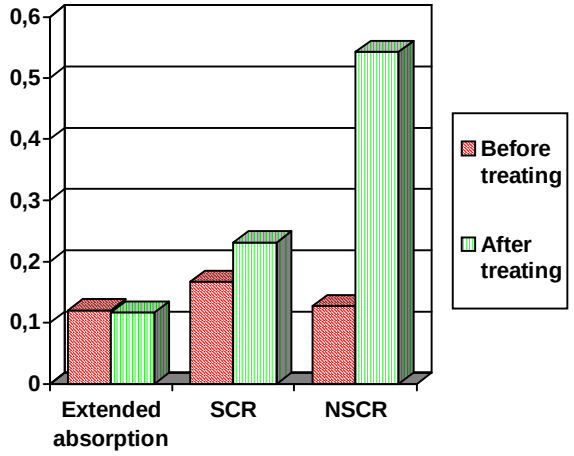

Fig.4. Chemical exergy (GJ/t 100%HNO_3) of the tail gas from nitric acid production plants before and after the tail gas treating. The rest of the explanations are as in fig. 3.

Cumulative exergy

Cumulative exergy of the gaseous pollutions from three different nitric acid production plants before and after the tail gas treating by three different methods are shown in fig.5. The cumulative exergies of ammonia after the SCR and of CO after the NSCR are higher than the cumulative exergies of NOx before treating. Fig.6 shows, that the exergy and cumulative exergy consumption are highest, if NSCR method for NO_x abatement is used. Cumulative exergy of the emissions from urea production (Fig.6) in the existing plants is higher than from AN production, but in the new plants it is lower. The cumulative exergy of the emissions from nitrogen fertilizers production in the existing plants is about 1 % from the total cumulative exergy consumption (CExC) of these fertilizers production [1].

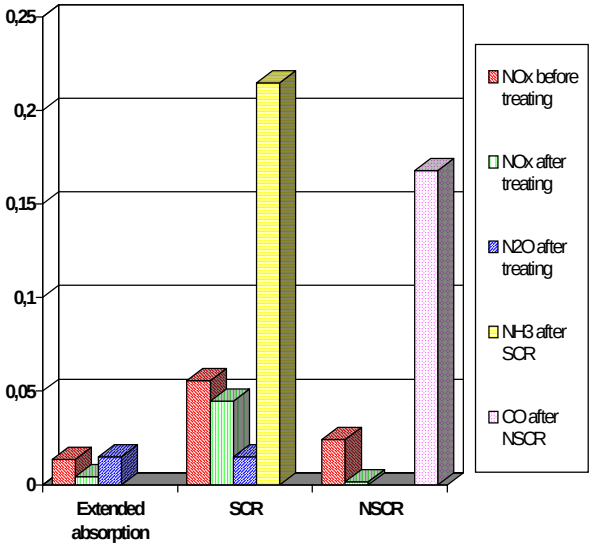

Fig.5. Cumulative exergy (GJ/t 100%HNO_3) of the gaseous pollutants from nitric acid production plants before and after the tail gas treating. The rest of the explanations are as in fig. 3.

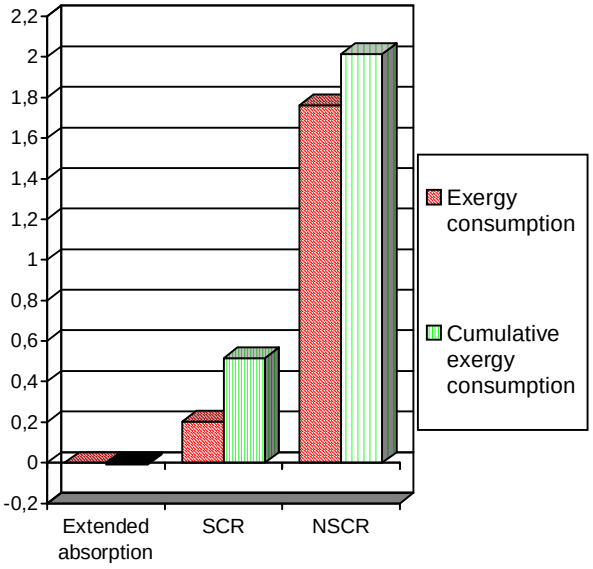

Fig.6. Exergy consumption and cumulative exergy consumption (GJ/t 100% HNO_3) for NOx abatement in nitric acid production plants before and after the tail gas treating. The rest of the explanations are as in fig. 3

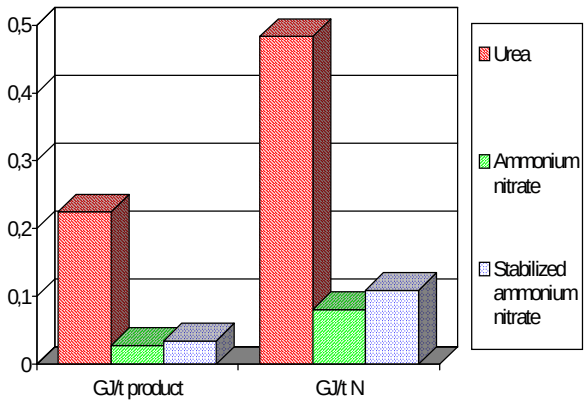

Fig.7. Cumulative exergy (GJ/t) of the emissions from nitrogen fertilizers production

CONCLUSIONS

An attempt is made to estimate the environmental impact of mineral fertilizers production by the Second-Law based indices. The chemical exergy of emissions flows and of pollutants, referred to an unit produced product or primary nutrient, as well as cumulative exergy consumption of the emissions and pollutants, appear to be the representative indices. The cumulative exergy consumption for the emissions abatement could be used to compare different methods.

REFERENCES

[1] Kirova-Yordanova, Z., Cumulative Exergy Consumption in Fertilizers Production Processes, Proc. of The Int. Congress ECOS'98, July 8-10, 1998, Nancy, France. A.Bejan, M. Feidt, M.J. Moran, G. Tsatsaronis Eds., Vol. 1, 195-201.

[2] Smil, V., Long-Range Perspective on Inorganic Fertilizers in Global Agriculture, International Fertilizer Center, 1999 Travis P. Hignett Lecture, November 1, 1999, Florence, Alabama, USA http://www.ifdc.org/Download/LS2/LS-2.pdf

[3] Industry as a Partner for Sustainable Development, Fertilizer Industry. IFA and UNEP, The Beacon Press, UK, 2002.

[4] IFA statistics, http://www.fertilizer.org/ifa/statistics.asp

[5] Isherwood, K. F., Mineral Fertilizer Production and Environment. Part 1. The Fertilizer Industry's Manufacturing Processes and Environmental Issues, UNEP/UNIDO/IFA Technical Report No 26, Paris, February 1999.

[6] Intergrated Polution Prevention and Control. Draft Reference Document on Best Available Techniques in the Large Volume Inorganic Chemicals, Ammonia, Acids and Fertilizers Industries, European Comission, Directorate-General JRC, Draft, March 2004.

[7] Best Available Techniques for Pollution Prevention and Control in the European Fertilizer Industry: Booklet N 1: Production of Ammonia; N2: Production of Nitric Acid; N 4: Production of Phosphoric Acid; N 5: Production of Urea and Urea Ammonium Nitrate; N 6: Production of Ammonium Nitrate and Calcium Ammonium Nitrate. 2000, EFMA, Brussels, Belgium

[8] Kuesters, J., Jenssen, Selecting the right fertilizer from an environmental life cycle perspective, Hydro Agri Belgium, 4 May, 1998.

[9] Autti, M., Practical aspects of fertilizer production and environmental care, IFA Technical Sub-Committee and Committee Meeting, 15-17 September 1999, Novgorod, Russia.

[10] Konshaug, G., Energy Consumption and Greenhouse Gas Emissions in Fertilizer Production, EFMA Seminar on EU Legislation and the Legislation Process in the EU relative to Fertilizer, Prague, October 19-21, 1998.

[11] Szargut, J., Morris, D. R., and Steward, F. R., Exergy Analysis of Thermal, Chemical and Metallurgical Processes, Hemisphere Publishing Co., N. Y., 1988.

[12] Szargut, J., Exergy Analysis of Thermal Processes; Ecological Cost, Int. Workshop "Advances in Energy Studies", Porto Venere, Italy, 29-31 May 1998.

[13] Ayres, R. U., Resources, Scarcity, Growth and the Environment, Center for the Management of Environmental Resources, INSEAD, France, 2001 http://europa.eu.int/comm/environment/enveco/waste/ayres.pdf

[14] Ayres, R.U., L. W. Ayres and K. Martinas, Exergy, Waste Accounting, and Life-Cycle Analysis, Energy, 1998, Vol. 23, No.5, 355-363.

[15] Rosen, M.A., Second-Law Analysis: Approaches and Implications, Int. J.of Energy Res., 1999, Vol. 23, No. 5, 415-429.

[16] Valero, A., Botero, E., An Assessment of the Earths Clean Fossil Exergy Capital Based on Exergy Abatement Costs, Proceedings of ECOS 2002, July 3-5,2002, Berlin, Germany, 151-157.

[17] Cornelissen, R. L., Thermodynamics and Sustainable Development. The use of exergy analysis and the reduction of irreversibility, Ph. D. Thesis, Univ. of Twente, Enschede, The Netherlands, 1997.

[18] Gong, M., Wall, G., On Exergy and Sustainable Development - Part 2: Indicators and Methods, Exergy Int.J., 2001, Vol. 1, No.4, 217-233.

Proceedings of ECOS 2005
Trondheim, Norway
June 20–22, 2005

NEW IDEAL PROCESS DESIGN BASED ON THE EXERGETIC ANALYSIS. COLD PRODUCTION USING RENEWABLE ENERGY HEAT.

Nolwenn Le Pierrès*, Driss Stitou and Nathalie Mazet
PROMES (laboratoire PROcédés, Matériaux et Energie Solaire), UPR CNRS 8521
Rambla de la Thermodynamique, Tecnosud, 66100 Perpignan (France)

ABSTRACT

Cold production processes generally use harmful refrigerants that increase ozone depletion and global warming effect and it is thus important to design new systems that are more environmentally-friendly. A major issue is to use refrigerant fluids which are neutral with respect to ozone depletion and global warming problems. Another goal is to correlate the quality of the energy used to the quality of energy produced by these processes.
The exergy analysis applied to ideal thermochemical dipoles is an efficient way to deal with these questions. Thermochemical dipoles connect two thermal processes exchanging gas with each other. The working gas can be environmentally inert, ammonia or water for example. Original couplings of the dipoles enable to design new processes, for heat or cold production at a desired temperature level.
Our work is aimed to create an original process that could use low-grade energy (produced for instance from a thermal solar collector or a geothermal drilling at around 70°C) to provide low-temperature heat (below -23°C, in order to store deep-frozen food). Indeed, existing solar cooling systems can provide cold at a temperature of around 0°C and produce ice but up to now none is able to ensure long term food conservation. Analysing several possible dipole couplings, one cycle was found to be particularly adapted to a solar heat source. The whole exergy entering this ideal system is used and no cold in excess or unused energy are produced. The ideal coefficient of performance of this system is 0.5.
A numerical simulation of the process evolution proved the feasibility of the concept and showed that its expected coefficient of performance is about 0.11, which is similar to the up-to-date solar cooling systems, but at higher cold temperatures. The system exergetic yield is expected to attain 0.4 in average over the year.
Keywords: exergetic analysis, ideal process, thermochemical dipole, deep freezing.

NOMENCLATURE

COA	coefficient of amplification of heat
COP	coefficient of performance
D	exergetic losses [J]
d	relative exergy losses =D/E’
e_w	exergy selectivity
E’	inlet exergy [J]
E'_{nu}	unused exergy [J]
E’’	outlet exergy [J]
E''_{ex}	excess produced exergy [J]
E''_{un}	untapped produced exergy [J]
E''_{u}	useful produced exergy [J]
P	pressure [Pa]
Q	heat quantity [J]
T	temperature [K]
T_0	reference temperature [K]
x_e	exergy conversion factor
η	exergy yield
θ	Carnot factor
ΔH	heat of transformation [J/mol]

subscripts :

c	cold
h	hot
i	ideal

* Corresponding author : Phone : +33 4 68 68 22 59 Fax : +33 4 68 68 22 13 E-mail : lepierre@univ-perp.fr

INTRODUCTION

When one designs new processes, one has to take into account environmental questions and thus the type of the energy used and of the energy produced involved in this process. It is important to design new systems that are more environmentally-friendly and the utilisation of renewable energies is an interesting option. In the case of solar energy, either transformed into heat or converted into electricity, the question of the quality of the energy source is of particular importance. Indeed, the energy produced by the new process should be of the quantity and quality adapted to its use, of variable power and usable at the time when it is needed, independently from the discontinue time availability of the energy source.

In this study, focus will be directed toward the conversion of solar energy into heat. Nowadays, solar energy is only commonly used in domestic water heating systems and recent developments were made concerning solar cold production and particularly solar climatisation systems. Solar liquid-gas absorption systems were developed more than 50 years ago to transform solar heat into cold, but still present major drawbacks and constraints. Indeed, this type of process works in a continuous way, thus with a continuous heat source. For solar systems, the storage of the needed heat or of the cold produced allows a good functioning of the process, but necessitates heavy and voluminous storage capacities. Moreover, the needed temperature of the heat source is high: from 90 to 140°C [1], what imposes the use of expensive solar collectors, as parabolic concentrators or with vacuum tubes glazing. Problems are of the same kind concerning the solid-gas adsorption systems, with however a lower temperature of the heat source, around 80°C in this case [2]. Adsorption and absorption systems allow to obtain cold at a minimum temperature of about -5°C.

Sorption based on the chemical reaction between a solid and a gas also allows the production of cold at around –5 to –10°C from heat at 80° to 90°C [3], and a solar prototype proved the effectiveness of that concept as soon as 1986 [4]. The reactive gas used is ammonia. This refrigerant fluid is totally neutral with respect to ozone depletion and global warming problems. Lower temperature levels were also obtained using this thermochemical technology, but from higher temperature levels of the heat source, at about 140 to 160°C [5].

The aim of this study is to determine the possibilities to design a new process concept to produce cold at low temperature (at about -30°C for storage of frozen food) from a heat source at about 70°C compatible with the use of flat simple glazed solar collectors. This process separates the time of solar heat availability and the time of cold production.

Recent research work based on the exergetic analysis characterised classical and original processes. Studies were directed toward cold production systems with ideal coefficient of performance (COP) of 1, 2 and 3 [6], and systems producing both cold and heat at higher temperature level (with a coefficient of amplification of heat COA of 0.5) presenting the possibility of heat transport over long distances [7,8].

ANALYSIS BASIS

The first basis of the analysis comes from the definition of the exergetic efficiency, yield and effectiveness [9] based on the work of Brodyanski et al. [10]. These definitions take into account the concept of transiting exergy in the process : the ranking of ideal processes by the determination of the ideal exergy conversion factor x_e [11] allows the optimisation of the ideal and practical exergetic yields of a process, as soon as its conception.

Considering an ideal process, the inlet exergy E' leads to the production of (figure 1):
- exergy that is converted or transformed in the process $E'-E'_{nu}$,
- unused exergy E'_{nu} that only transits through the ideal system.

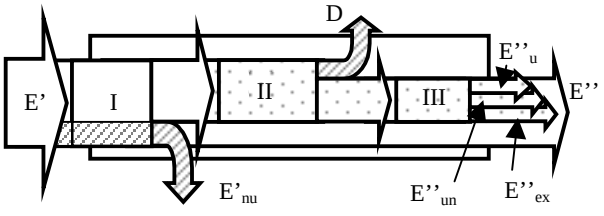

Figure 1: Exergies within (I) an ideal system, (II) a real system and (III) with the different output exergies

The ideal exergy conversion factor x_e defined as:

$$x_e = \frac{E' - E'_{nu}}{E'} \quad (1)$$

should be maximised up to 1.

In real processes, destroyed exergy D, exergy produced in excess E''_{ex} and untapped E''_{un} must be minimised, such that the useful produced exergy E''_u is maximal.

The exergetic yield η is defined as :

$$\eta = \frac{E''_u}{E'} = x_e - d - e_w \quad (2)$$

where $d = \frac{D}{E'}$

and the exergetic selectivity $e_w = \frac{E'_{ex} + E''_{un}}{E'}$

The exergetic yield applied to an ideal system (where d=0), is η_i :

$$\eta_i = x_e - e_w \quad (3)$$

η_i should be maximised, such that the ideal exergy conversion factor x_e approaches 1 and the exergetic selectivity e_w approaches 0.

The second basis of the analysis is the exergetic dipole, used for the study of heat transformation processes by Spinner et al [8]. An exergetic dipole results in the coupling, via an active gas transfer (figure 2.a), of an endothermic process such as:

- an evaporation or
- a gas-liquid or gas-solid desorption

and an exothermic process such as :

- a condensation or
- a gas-liquid or gas-solid absorption.

We will focus on the gas-solid reaction, a monovariant process, and which can be coupled to a liquid-gas phase change, also a monovariant process, or to another gas-solid reaction involving the same fluid but a different reactive solid. The representation of the thermodynamic equilibrium of these reactions in Clausius-Clapeyron diagram are linear (figure 2.b).

Thermodynamic conditions applied to each pole of a closed dipole lead either to a useful heat or cold production phase, or to a regeneration phase. The two phases are independent temporally from each other (figure 2.c). For cold production cycles, the useful cold production phase ‘b’ is followed by the regeneration phase ‘a’ of the dipole.

Transfers from a pole to the other are characterised by the quantity and quality of heat transferred. The quantity of heat transferred is proportional to the enthalpy of the involved transformation. The quality of the heat transferred depends on the temperature levels involved at each pole.

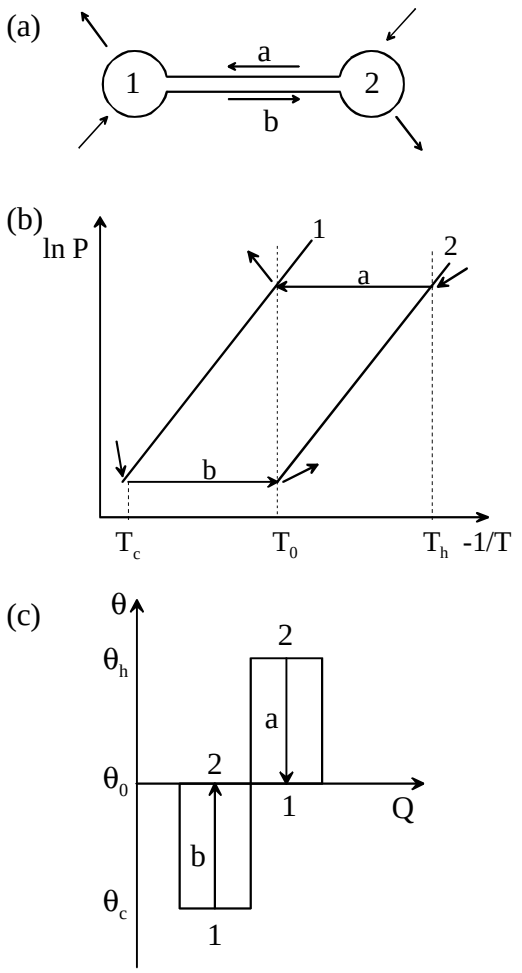

Figure 2:
(a) Dipole functioning between the physico-chemical processes (2) and (1). It is regenerated when gas flows in direction (a) and produces cold in direction (b).
(b) Thermodynamic conditions of the dipole phases in the Clausius-Clapeyron diagram.
(c) Exergies Q.θ involved in the ideal process with cold production at θ_c from heat at θ_h in the diagram $\theta = f(Q)$.

T_h is the regeneration temperature, the highest temperature level involved. T_c is the cold production temperature. T_0 is the reference or ambient temperature. If the heat released by the process is at T_0, the corresponding Carnot factor equal zero and thus the unused and untapped exergies E'_{nu} and E''_{un} equal zero. Thus, x_e equals 1 following equation (1). Moreover, if T_c is the cold temperature level which is necessary to the user, the excess exergy production E''_{ex} is zero and consequently, following equations (2) and (3) in the ideal case, the selectivity e_w equals 0 and the exergetic yield η_i is maximum.

The basic dipole COP_i is defined as :

$$COP_i = \frac{\Delta H_1}{\Delta H_2} \quad (4)$$

for the poles 1 and 2 of the basic dipole represented figure 2, where pole 1 is the one where cold production occurs and 2 is the one that has to be heated for regeneration.

In the ideal case, the COP_i is proportional to the exergetic yield η_i:

$$COP_i = \frac{\Delta H_1}{\Delta H_2} = \eta i \frac{\theta_h}{|\theta_c|} \quad (5)$$

as exergies E' and E''_u in the case of this dipole, equal respectively ΔH_2. θ_h and ΔH_1. θ_c.

In real processes, the transformation enthalpies ΔH vary with the process and the temperature. Moreover, the liquid/gas transformation heat is always smaller than the solid/gas reaction enthalpy [12]. However, in a first analysis of the ideal processes, all enthalpies are considered equal. Real values will be studied in a second step.

DEFINITION OF THE ORIGINAL PROCESS

From equation (5), we can see that, for an ideal system with an exergetic yield of 1, if the desired ideal system COP is of 1 and if the cold temperature level is at -22°C for example, the high temperature level should be at least at 79°C, for a reference temperature T_0 of 20°C. It is supposed that the process enthalpies ΔH_1 and ΔH_2 involved are equal, as precised above.

For the purpose of designing a deep-freezing process using heat at about 70°C, this necessary heat source temperature of 79°C is a lot too high, taking into account the external irreversibilities of such systems [12]. Thus, to design a deep-freezing solar system using low temperature solar heat, the ideal system COP_i has to be lower than 1. A study of ideal processes with a COP_i lower than 1 must thus be done. A particular focus can be drawn on systems with COP_i equal to 0.5. In that case, the high temperature level necessary to produce cold at -22°C is of 47°C for a reference temperature of 20°C. This is compatible with the limit temperature of 70°C for simple flat plate solar collectors. An extensive study of these systems has been lead [13]. This study uses the concept of a thermal coupling between two dipoles presenting respectively an exothermal and an endothermic process. This type of study has already been lead before [7]. A particularly interesting process concept has been extracted from the different possible dipole configurations, and is presented on figure 3.

Following equation (5), an ideal system with a COP_i of 0.5 needs the introduction of twice as much heat as the useful amount of cold produced. On figure 3.a, we can see in the $\theta = f(Q)$ diagram that the process needs twice the heat quantity ΔH at θ_h and once at θ_c. The Carnot factor $|\theta_c|$ can thus be twice as big as θ_h. In that case, the inlet and produced exergies, equal to the area $\theta.Q$ on the diagram, are equal since the exergetic yield is equal to 1. This system involves two dipoles. Both dipoles are (figure 3.c):

- without any thermal connections during the regeneration phase
- with a thermal connection between an endothermal and an exothermic process during the cold production phase.

This ideal process thus allows the production of cold at -22°C using ideally low-grade heat at 47°C from simple flat plate solar collectors. In that case, since solar radiation is the thermal energy supply, the cold production and regeneration phases correspond respectively to the natural diurnal solar radiation and nocturnal sky cooling periods. The monovariant processes chosen for this deep-freezing purpose are one solid-gas reaction coupled to a liquid/gas transformation in each dipole.

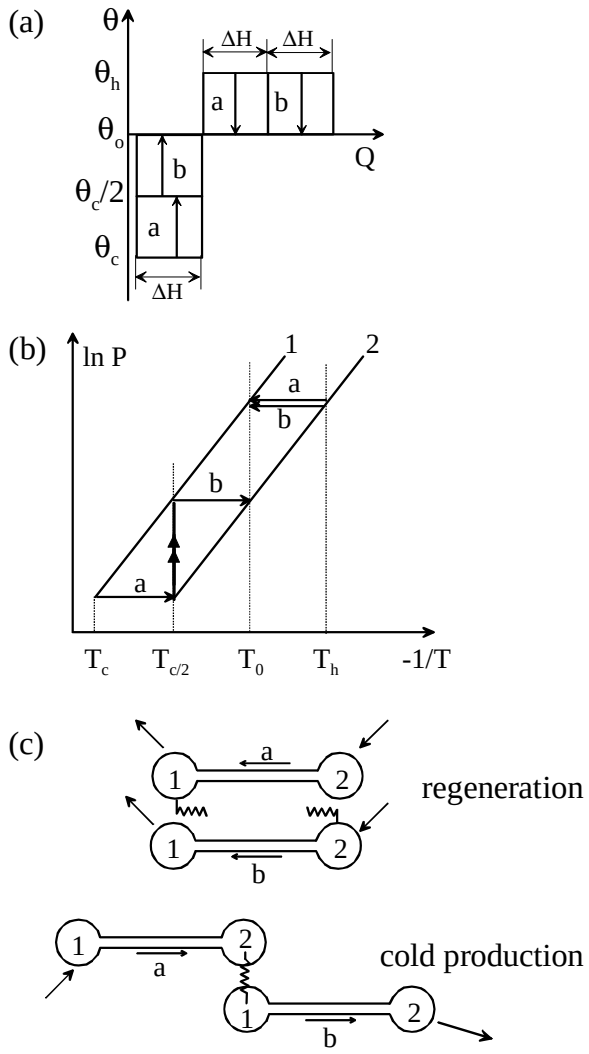

Figure 3:
(a) Exergies (Q.θ) involved in the ideal process with cold production at θ_c from heat at θ_h in the diagram $\theta = f(Q)$.
(b) Thermodynamic conditions of the two dipoles phases in the Clausius-Clapeyron diagram.
(c) Dipoles functioning without thermal connection in regeneration phase and with a thermal connection between processes 'a' and 'b' during the cold production phase.

The fixed bed solid-gas reaction poles (2) of each dipole are situated inside the solar collectors. Evaporator (1) of dipole 'a' (named pole (1a) in the following) is placed in a cold box, where cold is produced at -22°C, and the other evaporator (1b) is coupled to reactor (2) of process 'a', to insure its cooling during the night phase. As can be seen from figure 3.b and 3.c, both systems are brought to high pressure and temperature during the day phase, using the solar radiation received. Gas is desorbed from the reactor beds, and condensates at T_0 (ambient temperature) in the condensers (1). During the night phase, the reactor (2b) is brought to ambient temperature by convection with outside air and radiation to the nocturnal sky. Thus, it absorbs the gas present in dipole 'b' and that leads to the evaporation of the liquid in pole (1b). The thermal connection between system 'a' and 'b' during the night phase allows the cooling of pole (2a) through the boiling of the fluid in pole (1b) at low temperature $T_{c/2}$. Consequently, synthesis happens in the reactor (2a) and boiling at T_c of the liquid in evaporator (1a) can proceed.

This process has been studied and the reactive components have been chosen [14]. The gas used in these systems is ammonia, and the reactive salt chosen is $BaCl_2$, reacting with NH_3 to form $BaCl_2$-$8NH_3$. The reaction equilibrium lines of these components are represented on figure 4. The condensation/boiling enthalpy of NH_3 is about 23 kJ/mol, and the the reaction enthalpy of the $BaCl_2$ with NH_3 is of about 37 kJ/mol of ammonia. Thus, equilibrium lines on figure 4 are not parallel, as for ideal cases and following (4), the ideal COP of this process is 0.31.

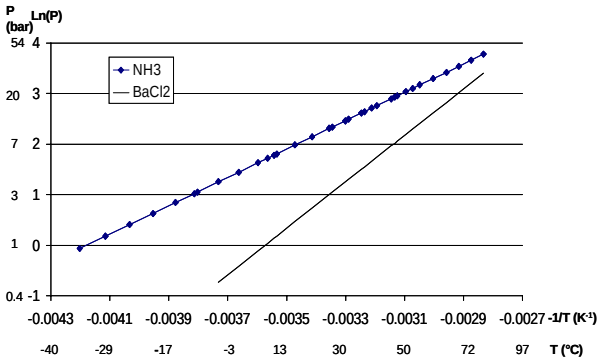

Figure 4: Clausius-Clapeyron diagram of NH_3 liquid-gas transformation and $BaCl_2$-NH_3 reaction.

NUMERICAL ANALYSIS OF THE PROCESS PERFORMANCES

Numerical simulations were performed to characterise the real process corresponding to the ideal process presented above. The development of the modelisation has already been described [14]. Simulations allowed the dimensioning of the process (table 1) and the calculation of its performances depending on the meteorological situation around the solar collectors.

Area solar collector of pole (2a)	1.8 m^2
Area solar collector of pole (2b)	3.8 m^2
Salt mass in pole (2a)	10.4 kg
Salt mass in pole (2b)	20.8 kg
Cycled NH_3 dipole a	5.4 kg
Cycled NH_3 dipole b	10.9 kg

Table 1: Dimensions of the simulated system.

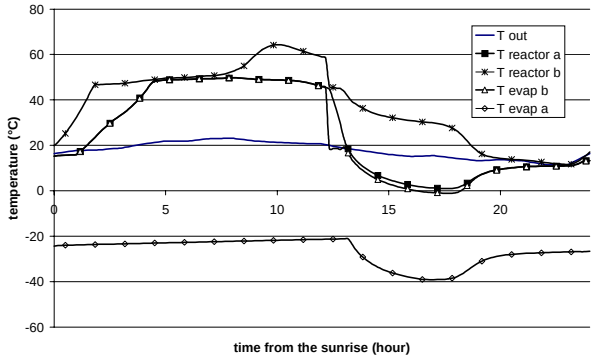

Figure 5: Evolution of the temperatures of the system on the 21th of April, 1996.

Figure 5 shows the temperature evolution of the process on the simulation obtained for the meteorological conditions of the 21th April 1996. This evolution is presented starting from the sunrise (at t=0). During the first hours of insolation, both reactors 'a' and 'b' reach high temperature around 50°C (corresponding to T_h on figure 3). Then, the temperature stabilises and regeneration can occur through the endothermic decomposition of the salts in both reactors. Condensation occurs in the corresponding condensers at outside temperature (T_0 on figure 3). There are no thermal or mass connections between the two dipoles during this phase.

After the beginning of the night, around hour 12, both systems are cooled by convection with outside air and radiation to the nocturnal sky. Temperature of reactor 'b' decreases to approach the ambient temperature T_0. Then, solid absorption begins and evaporator 'b', where evaporation of ammonia happens, is brought to about 0°C ($T_{c/2}$ on figure 3) and absorbs heat from reactor 'a', which is thus brought to about 0°C at minimum. This allows the evaporation of ammonia at about -30°C in evaporator 'a'. This pole reaches a minimum of -40°C during that night. Thus, simulations proved the possibility to reach deep-freezing temperatures using low grade heat from simple flat plate solar collectors.

Figure 6 shows the power involved in the process during an average day of May, obtained from the dynamic simulation of the hour-by-hour evolution of the process. During the day phase, we can see the solar radiations received by the process. As the heat of reaction is twice as big as the evaporation/condensation heat, system 'b' needs to provide twice as much cold to system 'a' as the cold produced at -23°C by system 'a'. Thus the solar collector of system 'b' is twice as big as the solar collector of system 'a' and thus receives twice as much solar heat. The heat used by the system for the thermochemical reactions in both dipoles is lower than the heat received, as the collector efficiency, the thermal amplitude and the heat masses of the process are taken into account in the model. For an average day of May, we can also see that the heat necessary for the reaction is totally obtained by the system after only 8h, though solar heat is received during a longer time.

This is due to the dimensioning of the process for a good functioning over 6 months of the year, and the system is thus over-sized for an average day of May. The cold is produced during the night phase, in the evaporators.

The system practical COP is defined as the ratio:

- of the cold produced by evaporation in evaporator 'a'
- to the heat absorbed by the two solar collectors.

The numerical study of the performances of that process showed a practical system COP of 0.11 in average over the year.

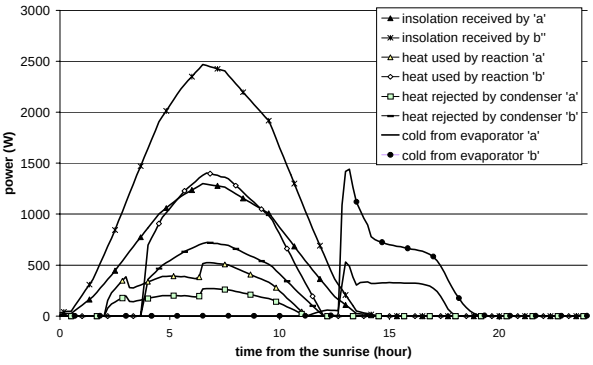

Figure 6: Evolution of the power inlets and outputs of the system during an average day of May.

The net solar COP of the solar system is defined as the ratio of :

- the cold produced by evaporation in evaporator 'a'
- to the solar radiations received by the solar collectors of both dipoles.

Considering an average solar collector efficiency of 0.55 over the year, the net solar COP of the process would be of 0.06, for the production of cold at the deep-freezing temperature of -30°C from low grade solar heat at about 70°C.

An exergetic analysis of the process leads to the determination of its exergetic yield. Figure 7 shows the evolution of the exergies inlets and outlets of the process for an average day of April. During the day phase, the system absorbs exergy through the reactor poles (2a) and (2b). During the night phase, exergy is rejected to the environment by reactor (2b), transferred from pole (2a) to pole (1b) through a thermal connection and useful exergy is produced by pole (1a) at deep-freezing temperature.

The exergetic yield of the process is defined as the ratio of:

- the exergy produced by pole (1a) during the night phase at low temperature
- to the exergies absorbed by poles (2a) and (2b) during the diurnal phase.

For this average day of April, the practical simulated exergetic yield is of 0.35. A simulation of the process during the whole year, using average data for each month of the year, showed that the average system yield would be of about 0.42.

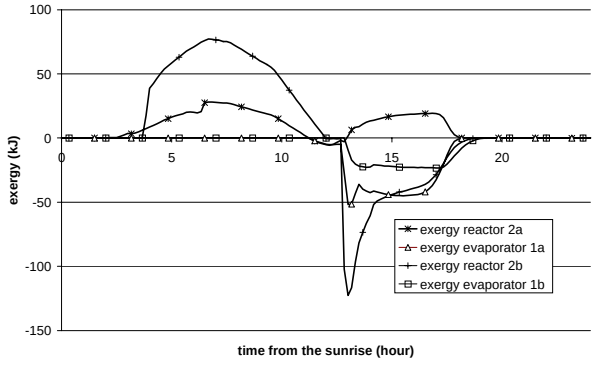

Figure 7: Evolution of the exergetic inlets and outlets of the system during an average day of April, starting from the sunrise at t=0.

CONCLUSIONS

The analysis of the exergies involved in a thermochemical process for cold production allows to distinguish between the quantity and quality of the inlet and outlet energies. A low quality of heat (near the ambient temperature) at the inlet must be balanced by a high quantity, if the quality of the heat desired at the outlet is also high at a given quantity. The study of the $\theta = f(Q)$ diagram allowed to design a new process to produce cold at deep-freezing temperature using low grade heat from simple flat solar collector. This process presents an ideal COP of 0.5 and for the chosen reacting components $BaCl_2$ and NH_3, a COP of 0.31. A numerical simulation of the designed process allowed to calculate the practical COP of the process, taking into account the dynamic of the functioning and the metal, reactive medium and fluids masses involved in the real process. This practical COP was found to be about 0.11 in average over the year.
A numerical exergetic analysis also showed that the designed deep-freezing process could have an exergetic yield of about 0.35, to be compared with the ideal exergetic yield of 1 fixed during the process design.
This process is now being build at PROMES laboratory to experiment this first type of process allowing deep-frozen food conservation using low grade solar heat.

ACKNOWLEDGEMENTS

This work was supported by the French governmental agency for energy management and environment ADEME and the 'ENERGIE' program of the research ministry – CNRS – DGA through PRI 'Froid Solaire' 6.1.

REFERENCES

[1] Alefeld G. and Radermacher A. *Heat conversion systems.* Florida: FL CRC Press Inc., Boca Raton,, 1994.

[2] Meunier F. *La sorption solide: une alternative aux CFCs*, Proceedings of the Symposium 'Le froid à sorption solide', Paris, 1992.

[3] Crozat G., Spinner B., Amouroux M. *Systèmes de gestion de l'énergie thermique basés sur des réactions solide-gaz*, Proceedings of 'pompes à chaleur chimiques de hautes performances', Perpignan, 1988.

[4] Balat M., Crozat G., *Testing of a prototype of a solar powered solid-absorption refrigeration system*, Proceedings of the ISES Solar World Congress, Hamburg, 1987.

[5] Stitou D., Spinner B., Neveu P., Patent FR 02 09392, *Installation et procédé pour la production de froid par un système à sorption renversable*, 24/07/2002 - CNRS.

[6] Stitou D., Spinner B., Sorin M. *An approach for structural design of cooling sorption processes*, I.J.Heat and Technology June 2005; 23 (1).

[7] Spinner B., Stitou D., Mazet N. *New sorption cycles for heat and/or cold production adapted for long distance heat transmission*, Proceedings of IMECE2002, ASME International Mechanical Engineering Congress and Exposition, New Orleans, Louisiana, 2002.

[8] Spinner B., Stitou D., Sorin M. *New processes for heat transformation: exergetic analysis of cold production, heat upgrading, with long distance transportation from a discontinuous heat source at low temperature*, Proceeding of the 53rd Canadian Chem. Eng. Conference, Hamilton, Canada, 2003.

[9] Le Goff P., Cachot T., Lasalle A. and Rahbar M.S., Proceedings of JETC IV conference, pp. 354-362, Nancy, France, 1995,

[10] Brodyanski V.M., Sorin M., Le Goff P. *The efficiency of industrial processes: exergy analysis and optimisation*, Elsevier Science, New York, 1994.

[11] Sorin V.M., Spinner B., Stitou D. *Thermodynamic techniques for the conceptual design of thermochemical refrigerators using two salt materials*, Chem. Eng. Sci. 2002; 57: 4243-4251.

[12] Stitou D., Spinner B. *A new characterization of real energy conversion processes: A contribution of finite size thermodynamics*, Proceedings of the 53rd Canadian Chem. Eng. Conference, Hamilton, Canada, 2003.

[13] Le Pierrès N, Stitou D., Spinner B. *Conception de procédés idéaux basés sur l'analyse exergétique. Nouveaux cas de gestion de dipôles thermochimiques en vue de la production de froid à partir de chaleur basse température*, Proceedings of COFRET'04, Nancy, France, 2004.

[14] Le Pierrès N., Stitou D., Mazet N., *Modelling and performances of a deep freezing process using low grade solar heat*, submitted to Energy, 2005.

Proceedings of ECOS 2005
Trondheim, Norway
June 20–22, 2005

ENVIRONMENTAL EXERGY ANALYSIS OF WASTEWATER TREATMENT PLANTS

C. H. Mora. B. [1], S. de Oliveira Jr [2].
[1] carlos.bejarano@poli.usp.br; [2] silvio.oliveira@poli.usp.br
Polytechnic School of the University of São Paulo, Brazil

ABSTRACT

This work evaluates the environmental impact of Wastewater Treatment Plants (WTP) based on data generated by the exergy analysis, calculating and applying environmental impact indexes for two WTP located in the Metropolitan Area of São Paulo. The environmental impact of the waste water treatment plants was done by means of evaluating two environmental impact exergy based indexes: the environmental exergy efficiency ($\eta_{env,exerg}$) and the total pollution rate ($R_{pol,t}$). The environmental exergy efficiency is defined as the ratio of the exergy of the useful effect of the WTP to the total exergy consumed by human and natural resources, including all the exergy inputs. That relation is an indication of the theoretical potential of future improvements of the process. Besides the environmental exergy efficiency, it is also used the total pollution rate, based on the definition done by Makarytchev [1], as the ratio of the destroyed exergy associated to the process wastes to the exergy of the useful effect of the process. The analysis of the results shows that this method can be used to quantify and also optimise the environmental performance of Wastewater Treatment Plants.

Keywords: exergy efficiency; environmental impact; wastewater treatment plants

NOMENCLATURE

$B_{Deact.}$ exergy of additional natural resources destroyed during waste deactivation [kW]
$B_{Disp.}$ exergy related to waste disposal of the process [kW]
$B_{Nat.Res}$ exergy of the natural resources consumed by the processes [kW]
BOD Biochemical Oxygen Demand [mol/L]
$B_{Prep.}$ exergy required for extraction and preparation of the natural resources [kW]
$B_{Product}$ exergy of the useful effect of a process [kW]
B_{Waste} exergy of waste, which includes the exergies of solid wastes, rejected heat, and emissions [kW]
COD Chemical Oxygen Demand [mol/L]
$\eta_{env,exerg}$ environmental exergy efficiency
$R_{pol,t}$ total pollution rate
WTP Wastewater Treatment Plants

INTRODUCTION

There is an increasing demand for more sustainable wastewater treatment systems. However, the criteria needed to characterize such a system are not fully developed. One important tool in the analysis of the sustainability of a wastewater treatment system is the exergy analysis. Hellström [2] showed how an exergy analysis could be used to estimate the consumption of physical resources at a wastewater treatment plant.

Some authors have suggested that the quantification of the environmental impact of energy conversion processes can be better driven by the use of the exergy concept (Rosen; Dincer [3]; Gong [4]; Wall; Gong [5]). Others went beyond and calculated that impact based on the exergy (Botero [6]; Creyts; Carey [7]; Gong; Wall [8]; Makarytchev [1]); Rosen; Dincer [9]; Valero; Arauzo [10]). According to Szargut [11], exergy is

defined as the amount of work obtainable when some matter is brought to a state of thermodynamic equilibrium with the common components of the natural surroundings by means of reversible processes, involving interaction only with those components of nature.

Exergy can be defined as a sustainable development registration that emphasizes the connection between generated services/products and used resources. This fact makes exergy a better measure of the damage and a good ecological index since a high exergy efficiency means less exergy wastes to the environment or less environmental damage (Gong [4]; Gong; Wall [8]).

Based on this premise, in this work the "exergy efficiency" is proposed as an environmental performance index which includes the aspects of energy efficiency and environmental impact of the energy conversion processes.

The evaluation of the environmental impact of energy conversion processes using the environmental exergy efficiency, $\eta_{env,exerg}$, is complemented with the calculation of the total pollution rate $R_{pol,t}$ (Makarytchev [1]).

WASTEWATER TREATMENT PLANTS

The analysis of environmental impact was applied to two Wastewater Treatment Plants (WTP), located in the Metropolitan Area of São Paulo, that belong to Tietê River Depollution Program.A detailed description of WTPs Barueri and Parque Novo Mundo is presented in Mora [12]. In Fig. 1, it is illustrated the flowchart of WTPs Barueri and Parque Novo Mundo.

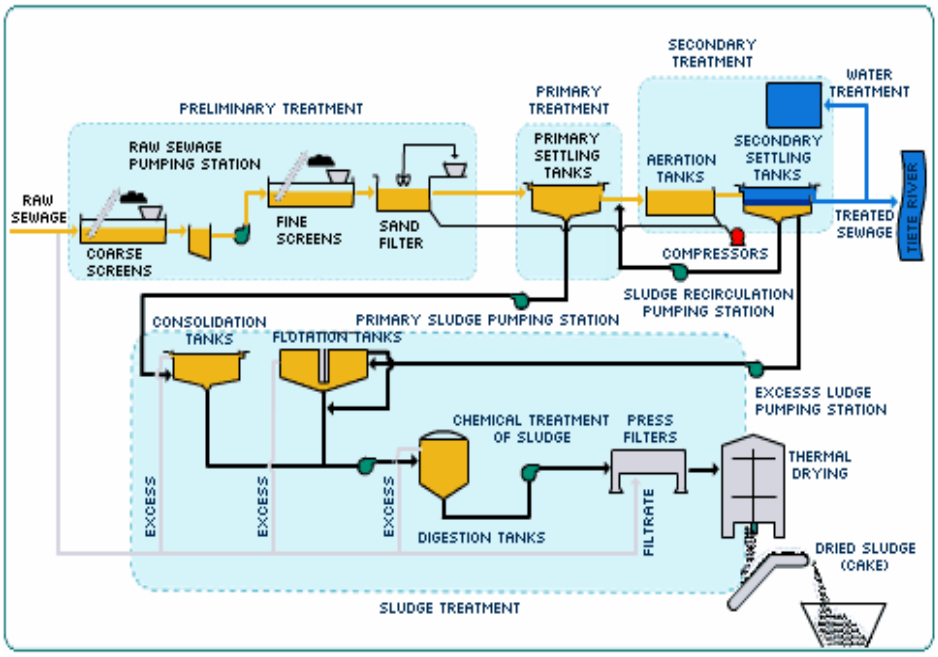

Fig. 1 Wastewater Treatment Plant (SABESP [13])

The plant type illustrated are conventional and secondary activated sludge treatment with organic material removal of 90% Biochemical Oxygen Demand (BOD). The treatment process that take place in the plants consist of the following stages: a) The Preliminary Treatment consist of two

phases: screening and sand removal. Screening removes large solids, which are retained by the screens. The main reasons for screening are to protect the pumps and tubes, later treatment units and the tanks. In sand removal, the sand is removed by sedimentation. The aims of sand removal are to protect equipment from wear and turbulence, eliminate or reduce the risk of blockages in pipes, tanks, siphons and passages, and simplify the liquid transportation, especially transfer of sludge (see Fig.1).

b) The Primary Treatment consist of primary settling tank which tanks are rectangular or round. Sewage flows slowly through the tanks, allowing suspended solids to gradually settle to the bottom of the tank. This solid mass, called primary sludge, can be consolidated at the bottom of the tank and sent directly for digestion, or can be sent to the consolidation tanks. A large part of these solids is made up of organic matter. Depending on the nature and size of the suspended solids, rotating sieves may be used instead of the screening system or the primary settling tanks (WTP PNM). The aim is to separate the larger suspended solids, by means of flowing them through the moving sieves, from the center to the outside. The retained solids are continuously removed in buckets.

c) The Secondary Treatment is made of three phases. In the aeration tank (phase one), organic matter is removed by biochemical reaction, using microorganisms (bacteria, protozoans, fungi) in the aeration tank. This process relies on contact between the microorganisms and the organic material in the sewage, which forms their food. They convert the organic material into carbon dioxide, water and their own cell structure. The secondary settling tanks perform an important function in the activated sludge process (phase two), being responsible for the separation of the suspended solids present in the aeration tank, allowing a clarified liquid to flow out, leaving sediments solids at the base of the tank, which can be returned in a higher concentration. The effluent from the aeration tanks is settled, so that the activated sludge is separated and returns to the aeration tanks. The return of this sludge is necessary to supply the aeration tanks with a sufficient quantity of microorganisms to keep the feeding process going in sufficient strength to decompose the organic material efficiently. The liquid effluent from the secondary settling tanks is either released directly or conveyed for treatment so that it can be reused internally or sold for uses such as washing streets and watering gardens. In the excess sludge pumping station hapes the third stage of the secondary treatment: the sludge formed from the suspended solids by means of the alimentation of microorganisms must be removed to maintain equilibrium in the system (solids in = solids out). The sludge is extracted and sent for treatment (see Fig.1).

d) The Sludge Treatment consists of five phases: i) Consolidation: this stage takes place in consolidation and flotation tanks. As the sludge still contains large quantities of water, its volume must be reduced. The consolidation process increases the solid content in the sludge, reducing its volume. This process can increase the proportion of solids from 1% to 5%. In this way, subsequent units, such as digester tanks and drying units have less work to do. The most common methods include gravity consolidation and flotation. Gravity consolidation is based on the principle of zone sedimentation, as in the conventional settling tanks. The consolidated sludge is removed from the base of the tank. Flotation involves the introduction of air in a compression chamber. When the solution is depressurized, the dissolved air forms micro bubbles that carry the clumps of sludge to the surface, where they are removed. ii) Anaerobic Digestion: digestion has the following aims: to destroy dangerous microorganisms, to stabilize unstable substances and organic material present in the crude sludge, reduce the volume of the sludge through liquefaction, gasification and consolidation, to enable the sludge to reduce its liquid level, and to allow the use of the sludge – after stabilization – as a fertilizer or soil conditioner. Without oxygen, only anaerobic bacteria survive, which are able to use combined oxygen. Acidogenic bacteria break down carbohydrates, proteins and lipids, turning them into volatile acids. Methanogenic bacteria convert a large part of these acids into gases, principally methane. The stabilization of these substances can also be performed by addition of chemicals, a

process known as chemical stabilization. iii) Chemical Conditioning: chemical conditioning results in the coagulation of solids and the freeing of absorbed water. Conditioning is used before the mechanical drying systems, such as filtration, centrifuging, etc. The chemicals used include iron chloride, line, aluminum sulfate and organic polymers. iv) Press Filters: drying in the press filters occurs under high pressure. The advantages of this system include: high concentration of solids in the sludge cake, low turbidity in the filtrate and high solid retention. The resulting proportion of solids is between 30% and 40% for a 2 to 5 hour filtration cycle – the time needed to fill the press, maintain it under pressure, open it, remove the cake and close the press. v) Thermal Drying: thermal drying of the sludge is the process of reduction through evaporation of water into the atmosphere by means of heat, resulting in a proportion of solids between 90% and 95%. This reduces the final volume of the sludge significantly SABESP [13].

	Composition (mol/L)	
	Raw sewage	**Treated sewage**
BOD	0.00756	0.00048
COD	0.01219	0.00143
NH_3	0.00155	0.00021
NO_3	1.6E-06	1.7E-06
NO_2	1.1E-07	2.3E-06
S_2	1.6E-05	1.6E-05
SO_4	0.00043	0.00027
Cd	5.3E-08	5.3E-08
Ni	6.3E-07	6.6E-07
Ag	1.0E-07	3.7E-08
Zn	3.6E-06	1.4E-06
Mg	1.7E-06	1.2E-06
Mo	2.1E-07	2.1E-07
Pb	1.7E-07	1.4E-07
Cu	8.7E-07	4.1E-07
Cr	1.6E-06	5.7E-07
Fe	5.4E-05	8.6E-06
Alcohol	3.4E-06	5.1E-07
P	0.00012	5.8E-05
Detergent	0.00042	3.7E-05
Sn	1.1E-06	1.1E-06
Overall	**0.02236**	**0.00252**

Table 1. Composition of the raw and treated sewage for Barueri Wastewater Treatment Plant

Components	**Composition (mol/kg)**
Cd	0.00011
Pb	0.00079
Cu	0.00871
Cr	0.00899
Mg	0.00443
Fe	0.58161
Ni	0.00480
Zn	0.03183
Ag	0.00059
Mo	0.00016
Overall	**0.64203**

Table 2 Sludge composition of Barueri Wastewater Treatment Plant

Tables 1, 2, 3 and 4 present the composition of the raw and treated sewage as well as the sludge composition of Barueri and Parque Novo Mundo Wastewater Treatment Plants.

ENVIRONMENTAL EXERGY ANALYSIS OF WASTEWATER TREATMENT PLANTS

Environmental impact exergy based indexes

The environmental impact of the waste water treatment plants was done by means of evaluating the values of two environmental impact exergy based indexes: the environmental exergy efficiency ($\eta_{env,exerg}$) and the total pollution rate ($R_{pol,t}$), as proposed by Makarytchev [1] and Mora and Oliveira Jr. [14]. The environmental exergy efficiency is defined as the ratio of the final product exergy (or useful effect of a process) to the total exergy of natural and human resources consumed, including all the exergy inputs. That ratio is also an indication of the theoretical potential of future improvements

for a process. The environmental exergy efficiency is calculated according to Eq. (1).

$$\eta_{env,exerg} = \frac{B_{Product}}{B_{Nat,Res} + B_{Prep} + B_{Deact} + B_{Disp}} \quad (1)$$

	Composition (mol/L)	
	Raw sewage	**Treated sewage**
BOD	0.00360	0.000734
COD	0.00909	0.001359
NH_3	0.00077	0.000357
NO_3	9.2E-06	5.93E-05
NO_2	1.0E-06	7.98E-06
S_2	1.7E-05	8.73E-06
SO_4	0.00049	0.000460
Cd	7.1E-08	7.12E-08
Hg	2.7E-08	1.36E-08
Ni	2.3E-06	2.54E-06
Ag	1.7E-07	1.67E-07
Zn	3.7E-06	1.84E-06
Mg	2.2E-06	1.82E-06
Se	8.5E-09	6.33E-09
Pb	3.9E-07	3.86E-07
Cu	1.7E-06	4.72E-07
Cr	1,8E-06	1.46E-06
Fé	3.9E-05	8.85E-06
Alcohol	1.8E-06	1.29E-06
P	0.00010	4.11E-05
Detergent	0.00012	3.73E-06
Sn	4.0E-06	4.00E-06
Overall	**0.01428**	**0.0030553**

Table 3. Composition of the raw and treated sewage for Parque Novo Mundo Wastewater Treatment Plant

The total pollution rate is defined as the ratio of the destroyed exergy associated to the process wastes to the exergy of the useful effect of the process. It is determined according to Eq. (2).

Components	**Composition (mol/kg)**
Cd	6.1E-05
Pb	4.0E-04
Cu	4.4E-03
Cr	4.4E-03
Mg	4.8E-03
Fé	8.4E-01
Ni	1.5E-03
Zn	1.2E-02
Ag	9.5E-05
Mo	1.5E-04
As	1.4E-04
Co	1.1E-04
Hg	4.8E-09
Se	6.8E-09
Overall	**0.86588**

Table 4 Sludge composition of Parque Novo Mundo Wastewater Treatment Plant

$$R_{pol,t} = \frac{B_{Waste} + B_{Deact}}{B_{Product}} \quad (2)$$

Exergy evaluation of the environmental impact of the WTP

The analysis of the environmental impact was realized for the Wastewater Treatment Plants Barueri and Parque Novo Mundo (PNM). Based on the data supplied by SABESP (São Paulo Wastewater Treatment Co.), an exergy analysis of the two WTP was realized considering operation in steady state conditions. The chemical exergies of the substances were determined according to data presented by Szargut et al. [11].

A detailed description of exergy calculations of WTPs Barueri and Parque Novo Mundo are showed in Mora [12].With the information generated by this exergy analysis, the environmental exergy efficiency and the total pollution rate were determined and compared.

In Fig. 2 and Fig. 3, are presented the exergy balances for the two Wastewater Treatment Plants

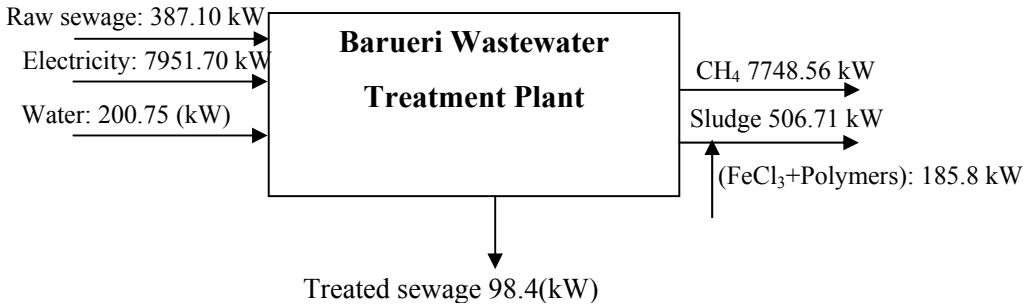

Fig 2. Exergy balance of the Parque Novo Mundo Wastewater Treatment Plant

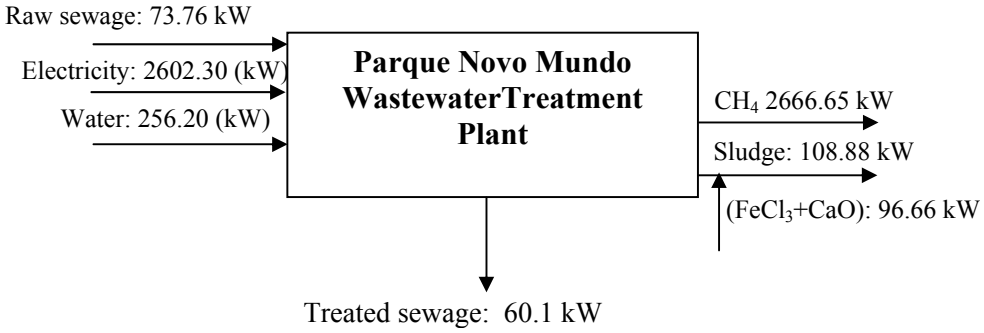

Fig. 3 Exergy balance of the Barueri Wastewater Treatment Plant

In Table 5 are presented the values of the input, output, destroyed and lost exergy flows for Parque Novo Mundo and Barueri. Wastewater Treatment Plants.

In Table 6 are presented the values of the calculated exergy indexes based on the results of the exergy balances. These indexes were used in the evaluation of the environmental impact of the two Wastewater Treatment Plants.

Another important term in the calculation of the exergy indexes is the exergy associated to the wastes of the processes (produced gas and dehydrated mud). If all this exergy was associated to an useful exergetic effect, the values of the $\eta_{env,exerg}$ for WTP Barueri and PNM would increase significantly. These values are presented in Table 7.

	Exergy		
Process	**Input (kW)**	**Output (kW)**	**Destroyed and lost (kW)**
Parque Novo Mundo WTP	2932.3	60.1	2872.2
Barueri WTP	8539.5	98.4	8441.1

Table 5. Values of the input, output, destroyed and lost exergy flows for Parque Novo Mundo and Barueri Wastewater Treatment Plants

	Environmental index	
Process	$\eta_{env,exerg}$	$R_{pol,t}$
Parque Novo Mundo WTP	0.02	47.8
Barueri WTP	0.01	85.8

Table 6. Values of the environmental exergy efficiency and total pollution rate for the analysed Wastewater Treatment Plants

	Environmental index	
Process	$\eta_{env,exerg}$	$R_{pol,t}$
Parque Novo Mundo WTP	0.97	0.00
Barueri WTP	0.98	0.00

Table 7. Environmental exergy efficiency and total pollution rate for Parque Novo Mundo and Barueri Wastewater Treatment Plants considering the use of the produced gas and dehydrated mud

CONCLUSIONS AND RECOMMENDATIONS

The present work proposes a scientific methodology based on an exergy criterium to evaluate and quantify the environmental impact of energy conversion processes that take part in waste water treatment plants In this way, it is possible to compare and characterize the environmental exergy performance, and the destruction of the exergy of these processes in the environment.

An overall comparison of the results obtained through the calculation of the indexes of environmental impact ($\eta_{env,exerg}$, $R_{pol,t}$), (see Table 6 and 7), shows that the process that causes the smallest impact in the environment (not considering the cases where the methane and the mud of WTPs are useful effects) is the Parque Novo Mundo, Wastewater Treatment Plant since it presents the largest $\eta_{env,exerg}$ (0.02) and the smallest $R_{pol,t}$ (47.8). In this comparison it is also observed that in agreement with the $\eta_{env,exerg}$ values, (0.01), and $R_{pol,t}$ (85.8), the process that causes the largest impact in the environment is the Wastewater Treatment Plant Barueri, if the by-products (methane and mud) are not considered as useful effect.

The low values of the environmental exergy efficiency ($\eta_{env,exerg}$) for two WTP , are due mainly to the high consumption of electricity for the small generated product, besides the great amount of methane and mud wasted. The electric power consumption represents the largest percentage of the input exergy in the WTP.

Another important fact to be considered in the low values obtained in the environmental exergy efficiency of WTPs, is that the exergy contained in the by-products generated (methane and the mud) is not being used at the moment. If that exergy was considered as a part of the useful effect of the processes of WTP, the values of the $\eta_{env,exerg}$ for WTP Barueri and PNM would be 0.98 and 0.97, and the values of the pollution rate ($R_{pol,t}$) would be zero. From the analysis of these last results, it is observed the great potential improvement that these processes would have, by using the mud for agricultural purposes and the methane as a fuel.

Finally, it was concluded that the exergy analyses of the environmental impacts supply a coherent approach with the technological options that excel for the sustainability of environmental solutions, allowing an efficient environmental performance evaluation.

From the analysis of the obtained exergetic indexes, it can be observed that in spite of the limitations of the exergy concept with respect to the toxicity and the biological quality of any substance, it is an useful tool in the quantification of the environmental impact of the energy conversion processes, from the point of view of the processes environmental performance ($\eta_{env,exerg}$), as well as in the characterization of the required exergy to deactivate the process wastes ($R_{pol,t}$).With the obtained results of this evaluation and quantification, it can be made the optimization of the environmental performance of the process, what is reflected directly in its economical analysis.

To complement this work, it is proposed to include a thermoeconomic analysis in the methodology presented for the environmental evaluation of

energy conversion processes that take place in wastewater treatment plants.

ACKNOWLEDGEMENT

The authors acknowledge CNPq for the financial support that allowed the accomplishment of this work.

REFERENCES

[1] Makarytchev S. V. Environmental impact analysis of ACFB-based gas and power cogeneration. Energy 1997;23(9): 711–717.

[2] Hellström D. An exergy analysis for a wastewater treatment plant : an estimation of the consumption of physical resources. Water Environment Research 1997;(69): 44-51.

[3] Rosen M. A, Dincer I. On exergy and environmental Impact. International Journal of Energy Research 1997;21(7): 643-654.

[4] Gong M. On exergy as an ecological indicator. Göteborg, Suécia, 1999. Master of Science Thesis -Department of Physical Resource Theory, Chalmers University of Technology and Göteborg University. See also: ftp://exergy.se/pub/eei.pdf.

[5] Wall G, Gong M. On exergy and sustainable development-part 1: conditions and concepts. Exergy 2001;1:128-145.

[6] Botero E. A. Valoración exergética de recursos naturales, minerales, agua y combustibles fósiles. Zaragoza, 2000. Tese (Doutorado) - Departamento de Ingeniería Mecánica,Universidad de Zaragoza. See also: http://www.circe.cps.unizar.es/pub/publicir.nsf.

[7] Creyts J. C, Carey V. P. Use of extended exergy analysis as a tool for assessment of the environmental impact of industrial processes. Advanced Energy Systems Division 1997;37:129-137.

[8] Gong M, Wall G. On exergy and sustainable development-part 2: indicators and methods. Exergy 2001;1:217-233.

[9] Rosen M. A, Dincer I. Exergy analysis of waste emissions. International Journal of Energy Research 1999;23(3):1153-1163.

[10] Valero A, Arauzo I. Consecuencias Exergeticas Asociadas al Efecto Invernadero. 1991. Departamento de Ingeniería Mecánica, Universidad de Zaragoza. Zaragoza. See also: http://www.circe.cps.unizar.es/pub/publicir.nsf.

[11] Szargut J, Morris D. R, Steward F. R. Exergy analysis of thermal, Chemical, and metallurgical processes. New York: Hemisphere., 1988.

[12] Mora, B. C. H. Exergy indexes as indicators of the environmental impact of energy conversion processes (in Portuguese) 2004. Master dissertation Polytechnic School of the University of São Paulo. São Paulo, Brazil.

[13] Companhia de Saneamento Básico do Estado de São Paulo, "Seawage treatment" http://www.sabesp.com.br/english/o_que_fazemos/coleta_e_tratamento/tratamento_de_esgotos/default.htm., 2004.

[14] Mora, B. C. H. and Oliveira Jr, S. Exergy Efficiency as a Measure of the Environmental Impact of Energy Conversion Processes. 17th International Conference on Efficiency, Costs, Optimization and Environmental Impact of Energy Systems- ECOS 2004, pp.423-431, July 7-9, 2004, Guanajuato, Mexico. ISBN-968-489-027-3

Proceedings of ECOS 2005
Trondheim, Norway
June 20–22, 2005

ENERGY AND POLLUTION EMBODIED IN TRADE: THE CASE OF NORWAY

Glen P. Peters* **and Edgar Hertwich**
Industrial Ecology Programme
Norwegian University of Science and Technology
NO-7491 Trondheim
Norway

ABSTRACT

Access to resources and energy, but also policy and historical development, shape the industrial structure of countries. This implies that some countries specialize in energy-intensive and pollution-intensive products. National environmental regulation and international agreements are also expected to shape the global patterns of production, as the concern about "carbon-leakage" under the Kyoto Protocol indicates. Most empirical investigations of the energy and pollution embodied in trade have assumed that imports are produced with the same technology as exports. These investigations were able to reflect differences in the composition of imports and exports, but not differences in pollution control technology, efficiency, or energy mix. We calculate the energy and pollution embodied in trade for Norway, taking into account the energy and pollution intensity of important trading partners. Our investigations indicate that Norwegian exports are more energy intensive than imports. In contrast, due to Norways energy mix and technology, Norwegian exports are often less pollution intensive than imports. This leads us to the hypothesis that, for the case of Norway, there are environmental benefits from trade and a specialization in energy-intensive production is environmentally preferable.

Keywords: Embodied energy, Embodied emissions, CO_2, Kyoto Protocol, Input-output analysis, Environment, Industrial Ecology

NOMENCLATURE

CH	China
DC	Developing Countries
DE	Germany
DK	Denmark
JP	Japan
NA	North America
NO	Norway
SE	Sweden
UK	United Kingdom
US	United States of America
i	Index over different regions
s_i	Share of imports from region i to NO
A_i	Interindustry requirements in region i
A^d_{NO}	Domestic industry requirements in NO
A^i_{NO}	Imported industry requirements in NO
F_i	The pollution intensities in region i
x_i	Output of a region i
y^d_{NO}	Domestic demand on domestic production
y^e_{NO}	Export demand on domestic production
y^i_{NO}	Domestic demand on imported production

*Corresponding author: Phone: +47 7355 1169
E-mail: glen.peters@ntnu.no

INTRODUCTION

As time passes it is becoming increasingly accepted that global climate change is of major concern and not just a scientific hypothesis. Most governments and many companies are publicly acknowledging the importance of reducing global air pollutants. With the increase in global free trade, many are questioning the effects of trade on the environment. On an economic level, most economists would argue that free trade is beneficial to both the exporting and importing countries. However, do these benefits also

occur on the environmental level?

Many authors have estimated the pollution embodied in trade [16, 8]. For instance, approximately 70% of the reported CO_2 emissions in Norway occur in the production of Norwegian exports [4]. Similarly, a portion of each countries consumption is imported; hence a significant portion of a countries environmental impacts may occur in foreign regions. Further, it has been found as global trade has increased, so has the pollution embodied in trade [2].

For countries with relatively low emissions in energy production, it is likely that an imported good will have a higher environmental impact than if the good was produced domestically. In the case of Norway, where hydropower represents nearly 100% of the electricity mix, imports from China will have a significantly higher environmental impact than if the import was produced domestically. Whilst it may be economical to increase trade with China, the resulting environmental impacts may be detrimental.

Current global climate change policies, such as the Kyoto Protocol, have been criticized from many aspects. One notable criticism is that developing countries are not required to reduce emissions. Another notable, but less debated criticism is the role of trade and the concept of "carbon leakage" [16, 2]; it is possible for a country to reduce its overall reported emissions by increasing imports. One way around this issue is to make the consumer responsible for emissions instead of the producer [10]. From an environmental perspective it is desirable for consumers to choose goods that have the lowest impacts.

Norway is an ideal country to study issues of trade and the environment. Due to its unique energy mix, Norway should have a comparative advantage in energy intensive goods. This article determines the energy and emissions embodied in Norwegian trade. By comparing the results with Norway's major trading partners, it is argued that Noway should produce energy intensive goods.

This article is structured as follows: First, the theoretical methodology is presented. Second, the data sources and data manipulations are discussed. Then, calculations of energy and emissions embodied in trade are shown. The results are then discussed and interpreted.

METHODOLOGY

The theoretical framework has been presented in detail in [13] and so only the main equations are shown here. Several applications of this framework are presented in [12]. The model is based on input-output analysis (IOA) [9, 15]. In summary, the total output of the economy is given by intermediate consumption and final consumption,

$$x = Ax + y \tag{1}$$

where A is the interindustry requirements matrix and y represents various demands on the economy. Solving for the total output, x, gives

$$x = (I - A)^{-1} y \tag{2}$$

The interindustry requirements matrix A represents the technology of an economy. It can be broken down into two components representing the interindustry requirements of domestically produced goods and the interindustry requirements of imported goods, $A = A^d + A^i$.

In this article Norway (NO) is the domestic economy. Norway trades with other regions which have different technologies. It is assumed that there is interindustry trade between Norway and the other regions, but the other regions do not trade with each other [13, 8]. The individual outputs in Norway and the trading regions is given by,

$$x_{NO} = (I - A^d_{NO})^{-1} y^d_{NO} \tag{3}$$

$$x_i = (I - A_i)^{-1} M_i \tag{4}$$

where $M_i = s_i(A^i_{NO} x_{NO} + y^i_{NO})$ is the total imports into Norway from region i, $A^i_{NO} x_{NO}$ are the imports into industry, y^i_{NO} are the imports to final demand, and s_i is the share of imports from each region. The pollution embodied in trade is then calculated as,

$$E_i = F_i x_i \tag{5}$$

For some calculations, it is assumed that each region has the same technology as Norway, in which case,

$$A_i = A_{NO} \qquad F_i = F_{NO} \tag{6}$$

DATA

To reduce the required data, data was only collected for Norway's seven major importing partners:

Region	Code	Import	s_i
Sweden	SE	14%	19%
United Kingdom	UK	13%	14%
North America (US)	NA	10%	12%
Germany	DE	10%	25%
Denmark	DK	7%	14%
Japan	JP	4%	7%
Developing (CH)	DC	4%	10%
Total		61%	∼100%

Table 1: The aggregation of Norway's import trade.

Sweden (SE), United Kingdom (UK), United States (US), Germany (DE), Denmark (DK), Japan (JP), and China (CH). These countries represent 61% of the import value of Norway's commodity and services imports. The minor trading partners were then aggregated under one of the seven major importing partners according to energy use per capita, CO_2 emissions per capita, and gross domestic product per capita[1]; see Table 1. Using this method 100% of Norway's imports are captured. The aggregated importing regions are: Sweden (SE), United Kingdom (UK), North America (NA), Germany (DE), Denmark (DK), Japan (JP), and Developing Countries (DC). Most European countries were assumed to have German, Danish, or Swedish technology and most developing countries were assumed to have Chinese technology; this explains the large increase in import shares for those regions.

Trade data

To use the framework described above requires the share of imports directly into industry and final demand categories from each of Norway's main import partners. This data was unavailable, but Statistics Norway[2] publishes data on the total share of imports from all countries into Norway. Using this trade data, for both commodities and services, the share of imports from each region was estimated using

$$s_i = \frac{M_i}{M_{total}} \tag{7}$$

where M_i is the total imports from region i and M_{total} is the total imports into Norway; the calculated values are shown in Table 1. From this data the share of imports directly into industry, $A_{i,NO} = s_i A^i_{NO}$, and to final demand, $y_{i,NO} = s_i y^i_{NO}$, can then be estimated.

[1] From the World Bank data query service; `http://devdata.worldbank.org/data-query/`

[2] `http://www.ssb.no/`

Country	Original Sectors	Valuation	Energy Data	Year
NO	56	Basic	Yes	2000
SE	58	Basic	No	2000
UK	58	Basic	Yes	1995
US	91	Producer	No	1996
DE	58	Basic	Yes	2000
DK	58	Basic	Yes	2000
JP	93	Producer	Yes	1995
CH	124	Producer	No	1997

Table 2: A summary of the data used.

Input-output, energy and emissions data

The input-output (IO), energy and emissions data came from a variety of sources. As a result the data required several manipulations to make the complete data set consistent. First, the data was mapped into a common industry classification with 49 sectors[3]. Second, the Consumer Price Index (CPI) in each country was used to convert the monetary data from the base year into 2000 values [4]. Finally, the currencies were converted into Norwegian Crown (NOK) for the base year of 2000[5]. Unfortunately, not all the data was available in basic prices. The producer prices include taxes and subsidies and so are higher than the basic prices. Where possible, adjustments were made for Financial Intermediation Services Indirectly Measured (FISIM) [1]. For this project, it was not possible to obtain energy data for all regions. The data is summarized in Table 2. The main sources of data for each region are now discussed.

Norway

All the Norwegian data was supplied by Statistics Norway for the year 2000 in basic prices. Domestic production data was provided for interindustry flows Z^d, final demand categories, and gross fixed capital formation, K^d. Capital was internalized into the in-

[3] We used a modified NACE classification [12].

[4] CPI values taken from the OECD's sourceOECD database; `http://caliban.sourceoecd.org/`

[5] `http://www.oanda.com/convert/fxhistory`

terindustry coefficients using

$$A^d_{NO} = (Z^d + K^d)\hat{x}^{-1}_{NO} \tag{8}$$

where x_{NO} is the total output of the Norwegian economy and the hat $\hat{\cdot}$ represents diagonalization [7, 13]. In addition, Statistics Norway provided data for the flow of imports into industry, Z^i, and into final demand categories. Capital investments were not distributed by industry for imports and so the interindustry coefficient matrix for imports is given by

$$A^i_{NO} = Z^i\hat{x}^{-1}_{NO} \tag{9}$$

Foreign regions

The IO data for Denmark, Germany, Sweden, and United Kingdom came from the European Unions' Eurostat database[6]. The data was provided in basic prices for 2000; except for the United Kingdom which was 1995. The energy and emissions data was obtained from each countries central statistical offices.

The data for the United States of America was taken from two sources. The IO data came from the Bureau of Economic Analysis[7] (BEA) and the emissions data from Missing Inventory Estimation Tool (MIET) Version 2 [14]. The MIET uses 1996 data and is at the product level. Manipulations were made using the IO data to convert the MIET data into the industry level. Unfortunately, the US data is only available in producer prices and not basic prices. Energy data was not available for this study.

The Japanese data was obtained from the Embodied Energy and Emissions Intensity (3EID) project[8] [11]. The data was only available for 1995 and in producer prices.

The Chinese data was constructed at the International Institute for Applied Systems Analysis (IIASA) [5]. The IO data was taken from 1997 and was only available in producer prices. The emissions data was constructed from 1995 and 2000 data and then interpolated for 1997 to allow combination with the 1997 IO data.

[6] http://europa.eu.int/comm/eurostat

[7] http://www.bea.doc.gov/bea/dn2/i-o.htm

[8] http://www-cger.nies.go.jp/publication/D031/CGER/Web/eng/index-e.htm

Country	Multiplier kg CO_2/NOK	Electricity kg CO_2/NOK
NO	1.5	0.01
SE	1.7	0.11
JP	2.3	0.26
DK	2.7	0.73
UK	3.1	0.51
DE	3.2	0.82
US	5.7	0.98
CH	24.9	3.25

Table 3: The emission intensities in each region.

CALCULATIONS

Emission intensities

An important quantity in this analysis is the emission intensity; the total, direct plus indirect, CO_2 produced per Norwegian Crown (NOK),

$$F_{i,total} = F_i(I - A_i)^{-1} \tag{10}$$

This is a row vector, with each element representing the emissions per unit of output of that sector. The emission intensity multiplier is defined as the sum of the vector elements,

$$F_{i,multiplier} = \sum_j \{F_{i,total}\}_j \tag{11}$$

and gives an indication of the overall emission intensity in a given region.

Table 3 shows the multiplier of the emissions intensity for each of the regions collected for the following analysis; also shown is the emissions intensity for the electricity and hot water production sector. Due to Norway's high use of hydropower to generate electricity, it has significantly lower emissions intensity in the electricity sector. Despite this, the emission intensity multiplier for all Norwegian industries is comparable to some other regions; this is due to the high emissions from some transport and export industries and the aggregating effect of the multiplier. This highlights that the emission intensity multiplier can be misleading and only gives a general comparison. For instance, compared to China, Norway releases over 300 times less CO_2 in the production of an equivalent value of electricity, and 17 times less CO_2 in the production of an equivalent value of total goods. These differences show

Country	Multiplier MJ/NOK	Electricity MJ/NOK
NO	39.9	12.2
DK	31.6	9.4
DE	49.5	8.5
UK	42.1	6.8
JP	32.5	4.5

Table 4: The energy intensities in each region.

that it is crucial to incorporate the different technology of different regions when determining emissions embodied in trade.

Table 4 shows the multiplier for energy intensity and the energy intensity of the electricity sector for the countries with readily available data. The last column represents the output of electricity compared to the value; reflecting Norway has cheaper electricity and Japan dearer. Of more interest is the total multiplier for energy intensity; which is roughly the same in each region. This reflects the fact that most industrial processes compared across regions have similar energy intensities. In an energy analysis, it is not as important to include the individual technologies from each country.

Emissions embodied in trade

Table 5 shows the emissions embodied in Norwegian trade. The columns represent emissions from the production of domestic demand, the production of export demand, and the production of imports. In each column, the emissions from each region represents the emissions to produce the import requirements for each demand; for instance, Germany (DE) emits 2.0 million tonnes of CO_2 to produce imports directly into the Norwegian production of exports and emits 1.3 million tonnes of CO_2 to produce imports for Norwegian final demand. Recall that the share of imports for each region is increased through aggregation; refer to Table 1. These same calculations can be performed assuming that imports are produced with Norwegian technology; Table 6.

Several results can be drawn from these tables. First, of the Norwegian domestic emissions, 72% of the emissions result from exports; however, only 38% of Norway's domestic output is from exports. This signifies that production of Norwegian exports are more CO_2 intensive than production of domestic

	Domestic y^d_{NO}	Export y^e_{NO}	Import y^i_{NO}
NO	14.0	35.8	0.0
SE	0.6	0.8	0.5
UK	0.8	1.2	0.8
NA	1.9	1.8	1.2
DE	1.4	2.0	1.3
DK	0.5	0.5	0.5
JP	0.4	0.5	0.4
DC	5.8	6.8	7.7
Foreign	11.4	13.7	12.4
Total	**25.4**	**49.5**	**12.4**

Table 5: The emissions embodied in Norwegian consumption and trade (million tonnes CO_2).

	Domestic y^d_{NO}	Export y^e_{NO}	Import y^i_{NO}
NO	14.0	35.8	0.0
Foreign	3.8	5.4	3.3
Total	**17.8**	**41.2**	**3.3**

Table 6: The emissions embodied in Norwegian consumption and trade assuming that imports are produced with Norwegian technology (million tonnes CO_2).

demand. Second, about 50% of the impacts from Norwegian consumption activities occur in other regions. Over half of these impacts occur in developing countries which represent only 10% of Norwegian imports. Third, assuming other regions have Norwegian technology, greatly underestimates the impacts of Norwegian imports.

These results highlight an important issue resulting from climate change policies such as the Kyoto Protocol; namely, "carbon leakage" [16]. A country that is a part of the Kyoto Protocol may reduce its emissions by importing from a foreign region. If the foreign country has a worse emissions profile than the domestic economy, then total global emissions will increase due to trade. This problem can be lessened by including all countries in the Kyoto Protocol. An alternative approach is to make the consumer, and not the producer, responsible for emissions [10].

Currently, the producer is responsible for CO_2 emissions. Total emissions in a country are determined from all producing industries; whether for domestic production or export. If the consumer is respon-

	Producer $y^d_{NO}+y^e_{NO}$	**Consumer** $y^d_{NO}+y^i_{NO}$	**Net** $y^e_{NO}-y^i_{NO}$
NO	49.8	14.0	35.8
Foreign	25.1	23.8	1.3
Total	**74.9**	**37.8**	**37.2**

Table 7: Balance of trade calculations for Norway (million tonnes CO_2).

	Domestic y^d_{NO}	**Export** y^e_{NO}	**Import** y^i_{NO}
NO	484.4	438.5	0.0
Foreign	82.7	91.5	77.0
Total	**567.1**	**530.1**	**77.0**

Table 8: The energy embodied in Norwegian consumption and trade assuming the foreign regions have the same technology as Norway (PJ).

	Producer $y^d_{NO}+y^e_{NO}$	**Consumer** $y^d_{NO}+y^i_{NO}$	**Net** $y^e_{NO}-y^i_{NO}$
NO	922.9	484.4	438.5
Foreign	174.3	159.7	14.6
Total	**1097.2**	**644.0**	**453.1**

Table 9: The balance of trade for energy embodied in Norwegian trade (PJ).

sible, then the total emissions for a given country are the emissions emitted producing goods for domestic consumption and the emissions emitted in the production of imports for domestic consumption. If CO_2 emissions are taken from a consumer perspective, then the consumer must seek the countries with the most CO_2 efficient production processes. The net difference between producer responsibility and consumer responsibility is the balance of trade for emissions. Table 7 shows that from a consumers' perspective Norway has a better emissions performance. This is due to the CO_2 intensive nature of Norway's export industry. Overall, this implies that Norway is a net exporter of CO_2.

Table 3 indicates that Norway has an overall superior emissions performance than other regions. This need not be the case for specific industries. Considering that Sweden, for instance, has a very similar overall emissions intensity multiplier to Norway indicates that it may be more CO_2 efficient in many sectors. Inspection of the raw data shows this to be the case; the emissions intensity in many industries is lower in Sweden than in Norway.

Energy embodied in trade

Unfortunately, for this study, data could not be collected for the energy use by industry sector in China, United States, or Sweden; see Table 2. The energy intensities for the remaining countries is shown in Table 4. Between separate countries, the energy intensity is very similar. Further, Norway does not have the lowest energy intensity. This perhaps reflects the fact that Norway does not have the highest energy efficiency; which may be driven by a low electricity cost. Given that most industrial processes of the same type require similar energy inputs, regardless of the producing country, it is not surprising that the energy intensities are roughly equal. Difference would arise due to problems with aggregation, different product mixes, slightly different technologies, and different energy efficiencies in industrial processes. Given this, it is reasonable to assume that, for energy use, separate regions have the same technology as Norway. For the calculations below, this assumption is followed unless otherwise specified.

Table 8 shows the energy embodied in Norwegian production and consumption with imports produced using Norwegian technology. The shares for the energy embodied in imports from the separate regions can easily be calculated assuming a linear scaling using the import shares; see Table 1. Comparison with Table 5 shows that a significantly smaller portion of energy is embodied in trade compared to carbon emissions. This again highlights the low CO_2 intensity of Norway's production compared to imports. Table 9 shows the corresponding balance of trade calculations for energy. It is clear that Norway is a net exporter of embodied energy.

Another interesting way to look at the embodied emissions and energy data is to consider the ratio of CO_2 emitted to energy used. Table 10 shows this for Norway; a ratio of Table 5 and Table 8. Several conclusions can be drawn from this table. First, Norwegian imports are more CO_2 intensive then domestic production. Second, Norwegian exports emit more CO_2 per energy input than Norwegian domestic production (due largely to Norway's offshore activities). These two points imply that, from an environmental perspective, Norway should supply more

	Domestic y^d_{NO}	**Export** y^e_{NO}	**Import** y^i_{NO}
NO	28.9	81.7	0.0
Foreign	137.9	149.5	160.5
Total	**44.8**	**93.4**	**160.5**

Table 10: The CO_2 emitted per energy used for Norway (kg/GJ).

of its own products; further, Norway should be encouraged to export more energy intensive goods.

DISCUSSION

From an environmental perspective, it is desirable to produce goods where they have the lowest environmental impacts. However, care needs to be taken when comparing energy and emissions intensities from a monetary perspective. If it is assumed that, in a given sector, one unit of monetary output gives the same physical output in each country, then the monetary perspective would be valid. However, this need not be the case[9]. One possible way around this issue is to use Purchasing Price Parity (PPP) instead of Market Exchange Rates (MER) for the currency conversions [6]. Although, it is likely that the PPP would vary from sector to sector. This area requires more research.

If it is assumed that the industry classification is so disaggregated that the same technologies are used in each country to produce the output from a given industry then an analysis of the CO_2 to energy input may be a valid measure of where to produce with the lowest environmental impacts. For the data currently available, this is unlikely to be a reliable measure.

For the current data available, it is best to assume that, for each industry, one unit of monetary output gives the same physical output in each country. This implies that production of a given good should occur in the country with the lowest emissions intensity. For many industries (not all), this would imply that Norway should be encouraged to produce and export more[10]. Further, due to Norway's extensive use of hydropower it can be generalized that Norway should have a comparative advantage in the production of energy intensive goods; Table 10. However, in the current political climate this may not automatically happen.

In the Kyoto Protocol, it is possible for a region to reduce its overall emissions by increasing imports, possibly from a country with worse environmental performance. One way to encourage greater exports from regions with low emissions intensities is to make the consumer responsible for emissions. This approach would encourage consumers to seek the countries with the lowest emission intensities. Although, from a computational point of view the calculations are far more complex with this approach; difficulties include: trade data, transportation, exchange rates, and inflation. Perhaps a better solution is to make the Kyoto Protocol apply across all regions. This would have a similar effect of encouraging all regions to reduce CO_2 emissions; automatically, this would include the export sectors in current non-Kyoto countries.

CONCLUSION

A theoretical framework was presented to calculate energy and emissions embodied in trade. This framework was applied to Norway. It was shown that a significant portion of Norway's induced emissions result from imports; a disproportionate share coming from developing countries. Further, it was found that Norway is a net exporter of carbon emissions. Similar calculations were performed for embodied energy; although, it was found that the energy intensities across countries is roughly constant compared to emission intensities.

The results were then discussed in terms of current climate change policies. It was argued that Norway should be encouraged to produce and export more due to its extensive use of hydropower. One way to achieve this is to make the consumer, and not the producer, responsible for environmental impacts. Alternatively, a possibly less data intensive approach, is to have all countries comply with global climate change policies, such as the Kyoto Protocol.

[9] For instance, the export price of unwrought aluminium in 2000 varied considerably across regions (in kg/US$); NO 1.73, SE 1.70, UK 1.61, US 1.44, DE 1.67, DK 1.42, JP 2.55, CH 1.45. Source: `http://www.unctad.org/`

[10] It is noted that hydropower is a finite resource; however, efficiency impovements would make more energy available for increased production.

ACKNOWLEDGEMENTS

This work is part of the FESCOLA project financed by the European Union's sixth framework programme through grant NMP2-ct-2003-505281. Some of the data was originally prepared and manipulated by Eirik Haukland for a Masters Thesis [3].

REFERENCES

[1] N. Ahmad. The OECD input-output database. In *The fourteenth international conference on input-output techniques*, Montreal, Canda, 2002.

[2] N. Ahmed and A. Wyckoff. Carbon dioxide emissions embodied in international trade. DSTI/DOC(2003)15, Organisation for Economic Co-operation and Development (OECD), 2003.

[3] E. Haukland. Trade and environment: Emissions intensity of Norway's imports and exports. Master's thesis, Industrial Ecology Programme, Norwegian University of Science and Technology (NTNU), Trondheim, Norway, 2004.

[4] E. Hertwich, K. Erlandsen, K. Sørensen, J. Aasness, and K. Hubacek. Pollution embodied in Norway's import and export and its relevance for the environmental profile of households. In E. Hertwich, editor, *Life-cycle Approaches to Sustainable Consumption Workshop Proceedings*, Interim Report IR-02-073, pages 63–72, Laxenburg, Austria, November 2002. International Institute for Applied Systems Analysis.

[5] K. Hubacek. Emission intensities for China (unpublished data). International Institute for Applied Systems Analysis, Laxenburg, Austria. 2002.

[6] R. Lafrance and L. Schembri. Purchasing-power parity: Definition, measurement, and interpretation. *Bank of Canada Review*, (Autumn):27–33, 2002.

[7] M. Lenzen. A generalized input-output multiplier calculus for Australia. *Economic Systems Research*, 13(1):65–92, 2001.

[8] M. Lenzen, L.-L. Pade, and J. Munksgaard. CO_2 multipliers in multi-region input-output models. *Economic Systems Research*, 16(4):391–412, 2004.

[9] R. Miller and P. Blair. *Input-output analysis: Foundations and extensions*. Englewood Cliffs, NJ, Prentice-Hall, 1985.

[10] J. Munksgaard and K. A. Pedersen. CO_2 accounts for open economies: Producer or consumer responsibility? *Energy Policy*, 29:327–334, 2001.

[11] K. Nansai, Y. Moriguchi, and S. Tohmo. Compilation and application of Japanese inventories for energy consumption and air pollutant emissions using input-output tables. *Environmental Science and Technology*, 37(9):2005–2015, 2003.

[12] G. Peters, T. Briceno, and E. Hertwich. Pollution embodied in Norwegian consumption. Technical report, Industrial ecology Programme, Norwegian University of Science and Technology (NTNU), Trondheim, Norway, 2004.

[13] G. P. Peters and E. Hertwich. Production factors and pollution embodied in trade: Theoretical development. Technical report, Industrial Ecology Programme, Norwegian University of Science and Technology, 2004.

[14] S. Suh and G. Huppes. Missing inventory estimation tool using extended input-output analysis. *International Journal of Life Cycle Assessment*, 7(3):134–140, 2002.

[15] United Nations. *Handbook of input-output table compilation and analysis. Studies in Methods Series F, No 74. Handbook of National Accounting*. United Nations, 1999.

[16] A. W. Wyckoff and J. M. Roop. The embodiment of carbon in imports of manufactured products: Implications for international agreements on greenhouse gas emissions. *Energy Policy*, 22:187–194, 1994.

Proceedings of ECOS 2005
Trondheim, Norway
June 20–22, 2005

MEXICAN BOTTOM OF BARREL LIFE CYCLE ENVIRONMENTAL IMPROVEMENT PROPOSAL

Ricardo Pulido*
Instituto Mexicano del Petróleo
Eje Central Lázaro Cárdenas 152
México, D.F.;C.P. 07730
México

Georgina Fernández
Universidad Nacional Autónoma de México
Facultad de Ingeniería
Ciudad Universitaria
México, D.F.;C.P. 07730
México

ABSTRACT

Growing economies have the dual challenge of economical and industrial growing, but in a sustainable way and with protection of Ecosystems, all prior requirements are a must that either are satisfied or Human Kind will suffer the irreparable loss of Earth Biosphere. Prospective studies show that for the period 1990 – 2010 the petroleum will be heavier and richer in sulphur. Mexican petroleum company, PEMEX, has been making serious efforts in order to reduce environmental negative impact through a better use of energy in all his infrastructure and the use of bottom of barrel technologies in order to make a better use of heavier petroleum, but PEMEX must still deal with the burning of heavy fuel oil with a high sulphur content and the bottom of barrel sub products. In order to make a more sustainable use of Mexican heavy petroleum the actual "Life Cycle" of Mexican Bottom of Barrel crude oil can be modified though the proposal of producing an activated carbon (CAFOB) from Mexican petroleum vacuums residue and Mexican petroleum coke and apply it in the flue gases desulphuration. To achieve this goal, activated carbon was made from Mexican petroleum vacuums residue and petroleum coke. Desulphuration adsorption tests were made with experimental (CAFOB) and commercial activated carbons and a synthetic flue gas mixture (SO_2=2000 ppm) similar in composition to flue gases produced from the burning of Mexican heavy fuel oil. Commercial activated carbons were used as reference materials for adsorption tests. The CAFOB180M experimental activated carbon showed a good desulphuration capacity compared to commercial activated carbon showing in this way the potential use of CAFOB for Mexican heavy fuel oil flue gas desulphuration in the processing and use in a more sustainable way of Mexican heavy petroleum through the modification of actual "Life Cycle" of Mexican Bottom of Barrel crude oil.

Nomenclature

LCA	Life Cycle Assessment
CAFOB	Bottom of barrel Activated carbon

*Corresponding autor: Phone: 52-55-91-75-83-72 E-mail:rpulido@imp.mx

INTRODUCTION

Growing economies have the dual challenge of economical and industrial growing, but in a sustainable way and with protection of Ecosystems, all prior requirements are a must that either are satisfied by all economies, or Human Kind will suffer the irreparable loss of Earth Biosphere [1]. Nowadays and in a near future the main source of energy is and will be the petroleum, fact that will produce direct and indirect environmental pressures, because prospective studies of petroleum worldwide markets show that for the period 1990 – 2010 the petroleum will be heavier, with a diminishing of about 0.4 ºAPI, and richer in sulphur with an increase of about 25% in weight content [2, 3].

During the First Global Ministerial Environment Forum in Malmö, Sweden from 29 to 31 May 2000, more than 100 Ministers of Environment signed the Malmö Declaration, recalling the Stockholm Declaration of the United Nations Conference on the Human Environment and the Rio Declaration of the United Nations Conference on Environment and Development, the Barbados Declaration on the Sustainable Development of Small Island Developing States as well as the Nairobi Declaration on the Role and Mandate of the United Nations Environment Programme. [4].

The Life Cycle Initiative is a response to the call from governments for a life cycle economy in the Malmö Declaration. It contributes to the 10 year framework of programmes to promote sustainable consumption and production patterns, as requested at the World Summit on Sustainable Development (WSSD) in Johannesburg in 2002. Its mission is to develop and disseminate practical tools (Life Cycle Thinking, Life Cycle Management and Life Cycle Assessment) for evaluating the opportunities, risks, and trade-offs, associated with products and services over their whole life cycle.
[5].

Life Cycle Assessment (LCA) is a "cradle-to-grave" approach for assessing industrial systems. "Cradle-to-grave" begins with the gathering of raw materials from the earth to create the product and ends at the point when all materials are returned to the earth. LCA evaluates all stages of a product's life from the perspective that they are interdependent, meaning that one operation leads to the next. LCA enables the estimation of the cumulative environmental impacts resulting from all stages in the product life cycle, often including impacts not considered in more traditional analyses (e.g., raw material extraction, material transportation, ultimate product disposal, etc.). By including the impacts throughout the product life cycle, LCA provides a comprehensive view of the environmental aspects of the product or process and a more accurate picture of the true environmental trade-offs in product selection [6].

MEXICAN BOTTOM OF BARREL LIFE CYCLE

Mexican petroleum company, PEMEX, has been making serious efforts in order to reduce environmental negative impact through a better use of energy in all his infrastructure and the use of bottom of barrel technologies in order to make a better use of heavier petroleum, but PEMEX must still deal with the burning of heavy fuel oil with a high sulphur content and the bottom of barrel sub products like coke.

The actual Life Cycle of Mexican Bottom of Barrel, as shown in Figure 1, begins with the petroleum extraction and stabilization, thereafter it is send to refineries. In refineries different qualities of petroleum are blended, desalted and send to atmospheric and vacuum distillation plants. The bottom of barrel is produced in these plants and contains all metals and heavy fractions of petroleum. Atmospheric and vacuum residues are processed in a coking process that produces light fractions and coke. The coke does have a good low heating values, therefore it has been used as base fuel for thermoelectrical plants, like the one called Tamuin, localized in San Luis Potosi Mexico, that will burn the coke in fluidised bed boilers at low temperature with the consequence of producing very low NOx quantities, and will neutralized the

acid flue gases with lime. Finally the residues will be used in a clinker process.

In order to make a more sustainable use of Mexican heavy petroleum the actual "Life Cycle" of Mexican Bottom of Barrel crude oil can be modified through the proposal of producing an activated carbon (CAFOB) from Mexican petroleum vacuum residues and Mexican petroleum coke and apply it in flue gases desulphurization of refineries.

METHOD

In order to sustain such an hypothesis, experimental work was done to achieve this goal. Activated carbon made from Mexican petroleum vacuum residues and petroleum coke, named as CAFOB and a synthetic flue gas was produced and desulphurized in a reactor by using the CAFOB as adsorbent. The synthetic flue gas composition is shown in Table 1.

CAFOB was produced from Mexican petroleum vaccuum residue and Mexican petroleum coke, carbonized at 823 K and steam activated at 1123 K.

In order to have an idea of the desulphurization potential of CAFOB, commercial activated carbons were used for the desulphurization of the same kind of flue gases and compared.

Commercial activated carbons, NORIT RB3 y RBHG3, were used as reference materials for the SO_2 adsorption capacity tests.

The NORIT RB3 is an extruded water steam activated carbon produced from vegetable matter and suggested for gas desulphurization applications; on the other hand the NORIT RBHG3 is extruded sulphur impregnated steam activated carbon.

Synthetic gas mixture desulphurization tests were carried out on experimental and commercial sorbents. The SO_2 exit concentration was measured, with constant inlet gas mixture temperature.

RESULTS ANALYSIS

The experimental CAFOB showed a better desulphurization capacity compared with the commercial activated carbon NORIT RBHG, and an almost similar capacity compared with the NORIT RB3, as shown in Figure 2, Figure 3 and Table 3. The experimental results were statistically analyzed and showed significant statistical differences. The RB3 and CAFOB 120 showed a similar efficiency and both showed a difference if compared to the other experimental CAFOB´s and the RBHG3, showing a removal capacity (circa 70%) that is higher than the one showed by the RBHG3 (circa 48%) and not so far away from the one showed by the RB3 (circa 80%), therefore the potential application of CAFOB for Mexican heavy fuel oil flue gas desulphurization is good prospective and the actual "Life Cycle" of Mexican Bottom of Barrel crude oil could be modified as shown in Figure 4, by introducing the CAFOB process instead of the coke product.

Some of the principal impacts in the Mexican bottom of barrel Life Cycle Environmental improvement proposal are shown in Table 4. One of the most important impact can be detected in the removal of SOx from flue gases. SOx can have negative impact either in ecosystems, human health, cultural heritage or infrastructure, and the cost of correction such negative impacts can be high.

Also there are other positive impact in the economical aspect, because more valuable light products can be recovered during the CAFOB production, and also commercial sulphur can be obtain by making use of refineries sulphur plants, were SOx and H_2S are converted to elemental sulphur.

If internal refinery costs of raw materials for CAFOB production are taking into consideration, the preliminary CAFOB production cost is appropriate to be considered as a possible candidate for flue gas treatment as shown in Table 5, if compared to the production costs of 300 USD/ton for a lower cost sorbent such as activated char made from Illinois coal, $326 USD/ton, or less than $300

USD/ton low surface area (270 m^2/g) activated carbon made from German brown coal produced by a STEAG for their U.S. market, STEAG has pioneered flue gas cleanup in Europe. Other technological options has the disadvantage that the required material for the gas treatment must be imported into the refinery, materials that are considered as wastes cannot be incorporated to the specific refinery bottom of barrel Life Cycle and some technologies and the produced wastes cannot so easily be incorporated into other processes and the by-product (waste) and waste water generated by other FGD requires environmentally friendly disposal system which further increases both capital and operational cost. [6,7]

When CAFOB cannot be recycled anymore , it can be used as a fuel and flue gases can be treated by lime injection, as in Tamuin plant, and the ashes can be introduced completely to the clinker process.

CONCLUSIONS

Nowadays Mexico and other countries must deal with the challenge of making a better use of heavier petroleum. One option is to make a modification to the bottom of barrel Life Cycle with the introduction of CAFOB production that could have positive environmental, energetic and economical impacts

BIBLIOGRAPHY

[1] Pulido Pérez, Ricardo. *Carbón activado: una opción para el control de emisiones de especies contaminantes en gases de combustión*. Revista del Instituto Mexicano del Petróleo. 1995;XXVII (1): 30-38.

[2] Felten,J.R.; Mc Carthy,K.M.; Barrett,E.J. *Residual fuels in a clean-fuels environmet*. Hydrocarbon Processing 1993; 72(6): 82-B - 82-J.

[3] Inomata, Makoto; Sato Kyohei, Yamada, Yu ; Sasaki, Hajime. *Engineering firm has designed refinery of the future*. April 28, 1997. Oil & Gas Journal.

[4] Malmö Ministerial Declaration. United Nations Environment Programme. See: **http://www.unep.org/malmo/malmo_ministerial.htm**

[5] Life Cycle Thinking as a Solution. UNEP's Sustainable Consumption (SC) programme See: **http://www.uneptie.org/pc/sustain/lcinitiative/background.htm**

[6] U.S. Environmental Protection Agency and Science Applications International Corporation. *LCAccess - LCA 101*. 2001. See: http://www.epa.gov/ORD/NRMRL/lcaccess/lca101.htm.

[7] Anthony A. Lizzio, et al. ISGS FINAL TECHNICAL REPORT: DEVELOPMENT OF ACTIVATED CHAR FOR COMBINED SO2/NOx REMOVAL. ICCI Project Number: 95-1/2.1A-11.September 1, 1995, through August 31, 1996 See: http://www.icci.org/96final/lizzio2.htm

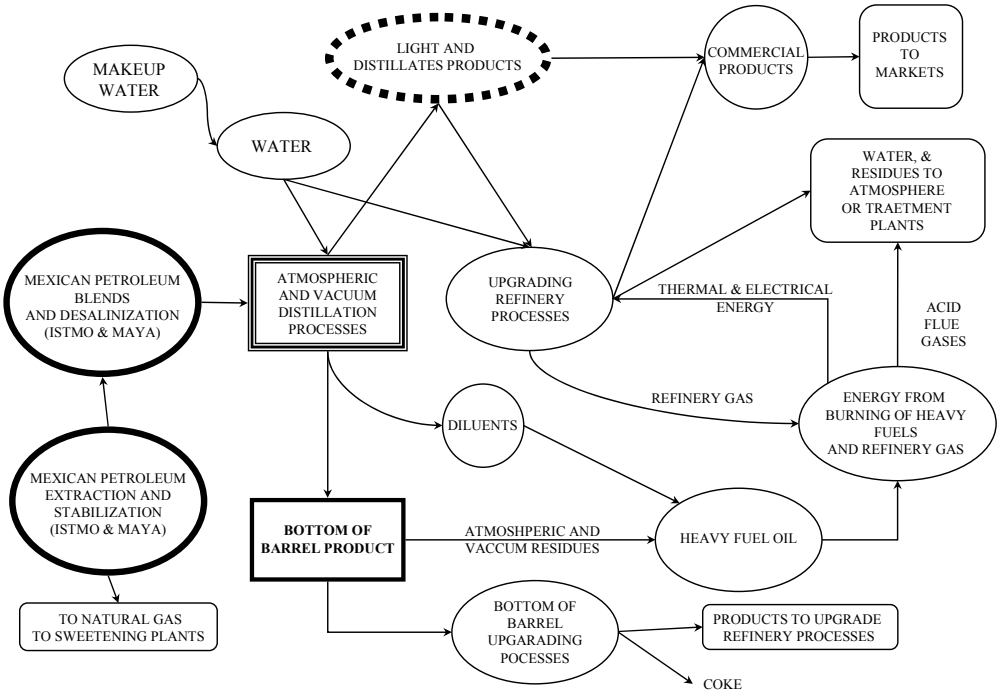

Figure 1 Mexican Bottom Of Barrel Life Cycle

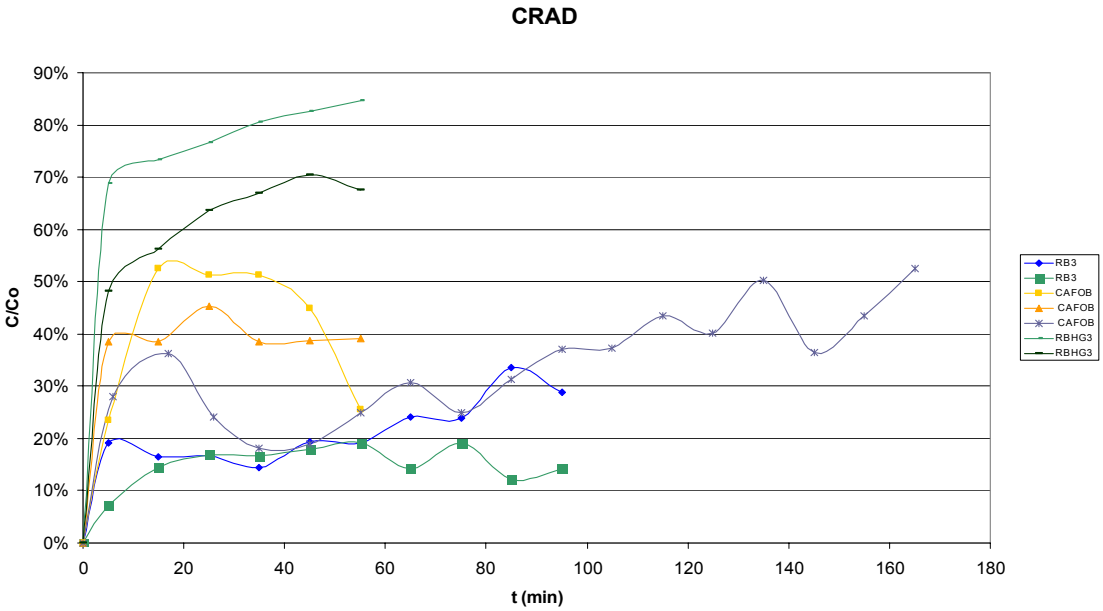

Figure 2 SO_2Adsorption curves

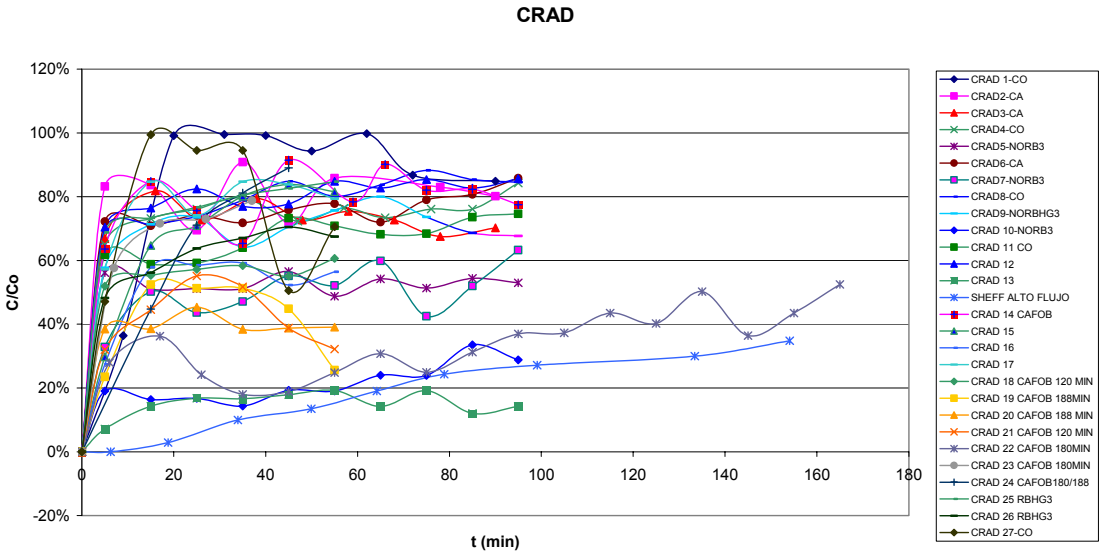

Figure 3 SO_2Adsorption curves

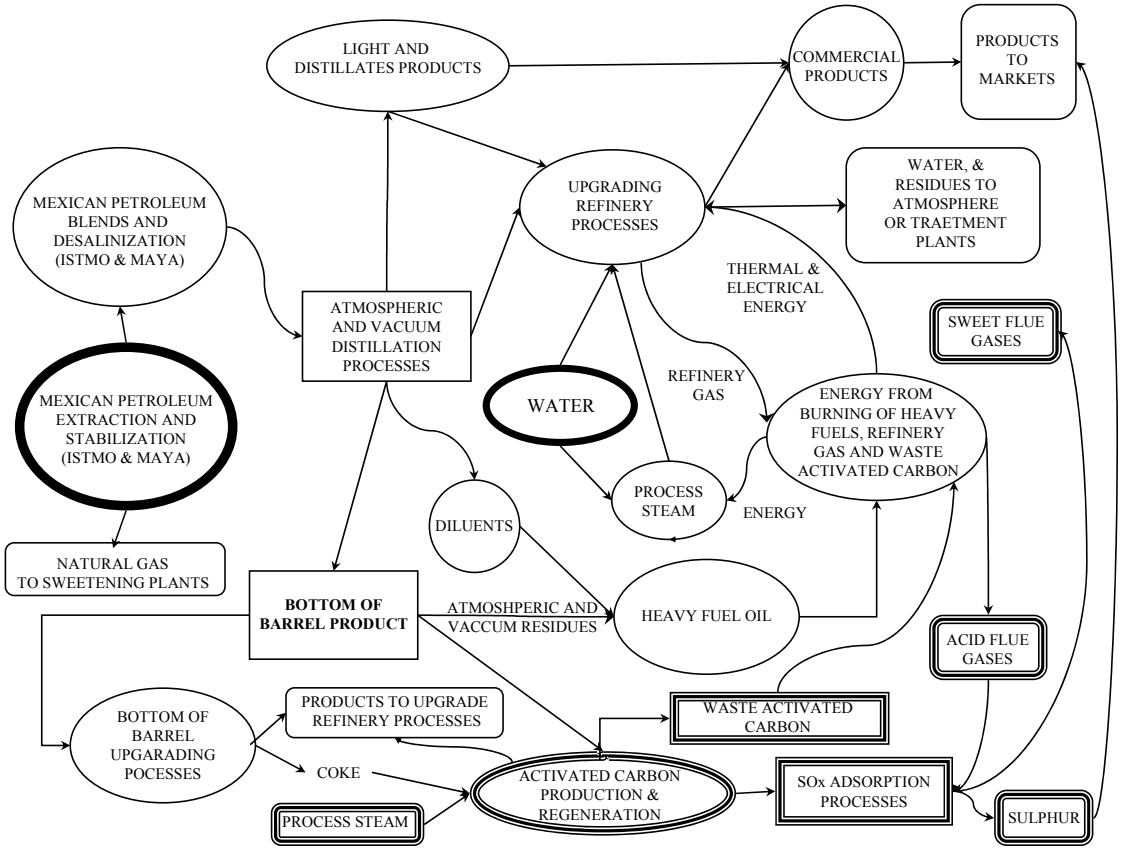

Figure 4 Modified Bottom of Barrel Life Cycle with insertion of CAFOB production and application

Table 1 Synthetical flue gas composition

Chemical species	Composition
SO_2	2 000 ppm
H_2O	8.0 % vol
O_2	4.5 % vol
N_2	77.3 % vol
CO_2	10.1 % vol

Table 2 Experimental Adsorption results

Material	Flue gas flow ($L*min^{-1}$)	Flue gas composition					Flue gas Temperature	SO_2 / C (mg/g)	Removal (%)
		SO_2 (ppm)	CO_2 (%vol)	O_2 (%vol)	N_2 (%vol)	H_2O (%vol)	(K)		
RB3	1	1968	10.82	4.43	83.50	1.06	395.2	0.0076	79.4
RB3	1	1969	10.83	4.43	83.53	1.02	395.8	0.0078	85.0
RBHG3	1	1963	10.80	4.42	83.30	1.29	393.6	0.0045	49.8
RBHG3	1	1963	10.80	4.42	83.29	1.41	394.0	0.0038	46.1
CAFOB	1	1967	10.82	4.43	83.45	1.11	392.6	0.0052	61.9
CAFOB	1	1953	10.74	4.39	83.12	1.55	397.5	0.0068	75.9
CAFOB	1	1965	10.81	4.42	83.38	1.20	393.8	0.0083	76.3

Table 3 Principal impacts in the Mexican bottom of barrel Life Cycle Environmental improvement proposal

Life Cycle Step	Life Cycle Impact		
	Environmental	Energetic	Economical
Mexican petroleum processing	Sulphur in petroleum that is send to atmosphere when heavy fuel oil is burned can be reduced by introduction of CAFOB in the cycle.	The upgrade of residuals to commercial products in the Mexican petroleum Processing without importing energy into the Cycle, gives the possibility of making a better use of energy..	Acid emissions economical environmental impact can be reduced through the CAFOB flue gases desulphurization. Recoverd sulphur can be commercialized
CAFOB Generation	CAFOB production process will generate flue gases incide the cycle.	CAFOB production process will generate light hydrocarbons that can be used as fuels.	CAFOB production process will generate light hydrocarbons with commercial value
CAFOB Application	SOx emissions are reduced and recovered as comercial sulphur products.	More energy can be recovered from flue gases without corrosion problems.	CAFOB application could have a commercial value.
CAFOB Regeneration	CAFOB regeneration process requires less energy, therefore the flue gases emissions are reduced if compered with CAFOB production.	Energy is required during the regeneration process.	Sulphur comercial products are recovered during the process
CAFOB Disposition	CAFOB can be used as fuel in a fludized bed with lime inyection. NOx emissions are reduced and solid subproducts can be used as raw material in clinker production.	CAFOB can be burned as fuel	Either CAFOB or ashes produced from CAFOB burning can be considered as raw material in clinker process.

Table 4 CAFOB cost production

Raw material	Unitary Cost	Requirements	Cost (USD/ton CAFOB)
Coque	3 to 5 USD/ 1000 kg	1 098 $kg*h^{-1}$	5.49
Vacuum Residue	8 to 9 USD/barrel	470.6 $kg*h^{-1}$	24.80
Natural Gas	4 USD/MMBTU	347.9 kW	4.75
Steam	12 USD/1000 kg	494.1 kg	5.93
TOTAL			40.97

Proceedings of ECOS 2005
Trondheim, Norway
June 20–22, 2005

LIFE CYCLE ASSESSMENT OF HYDROGEN PRODUCTION

Christian Solli*, Anders H. Strømman and Edgar G. Hertwich
Industrial Ecology Programme
Norwegian University of Science and Technology
7491 Trondheim
Norway

ABSTRACT

A comparative hybrid life cycle assessment was conducted to assess two different methods for hydrogen production. Environmental impacts from nuclear assisted thermochemical water splitting are compared to hydrogen production from natural gas steam reforming with CO_2-sequestration. The results show that the two methods have significantly different impacts. The nuclear alternative has lower impacts on global warming potential, acidification and eutrophication, and much higher impacts from radiation and human toxicity. A weighting procedure is not applied, hence no overall "winner" can be proclaimed. The relative importance of different impacts remains a challenge for eventual decision makers. Further, the assessment has demonstrated the importance of including economic inputs in a comparative assessment; ordinary process-LCA may produce distorted results since a larger fraction life cycle impacts may occur in one study compared to another.
Keywords: Hydrogen Production, Life Cycle Assessment, Nuclear fission

NOMENCLATURE

$\mathbf{A}_{ff}$	Foreground matrix
$\mathbf{A}_{pp}$	Background matrix
$\mathbf{A}_{nn}$	Input-output matrix
$\mathbf{y}$	Final demand vector
$\mathbf{x}$	Total output vector
$\mathbf{e}$	Environmental flows vector
$\mathbf{E}_f$	Environmental interventions of the foreground processes
$\mathbf{E}_p$	Environmental interventions of the background processes
$\mathbf{E}_n$	Environmental interventions of the input-output processes
$\mathbf{A}_{pf}$	Cut-off from foreground system to background system
$\mathbf{A}_{nf}$	Cut-off from foreground system to input-output system
$\mathbf{C}$	Characterization matrix
VA	Value Added
EC	Equipment Cost
W_i	Weight of material i
MC_i	Material cost of equipment i
GWP	Global Warming Potential
HTP	Human Toxicity Potential
AP	Acidification Potential
EP	Eutrophication potential
R	Human Health Impacts as a result of ionizing radiation

INTRODUCTION

Hydrogen is currently being promoted as a possible future energy carrier. It provides the opportunity for high efficiency conversion to electricity in a fuel cell without any emissions to air except from water vapor. In light of a growing fear of the environmental consequences from the release of greenhouse gases, it's use is favorable in applications such as the transport sector. Hydrogen is not an energy source. It does not occur naturally in great pro-

*Corresponding author: Phone: +4791567304
Email: christian.solli@ntnu.no

portions, and has to be produced from primary energy sources. For hydrogen to be environmentally preferable as an energy carrier, it therefore has to be *produced* in such a manner that the total environmental repercussions is lower than those of other energy carriers such as gasoline. Hydrogen can be produced from fossil fuels, biomass and splitting of water. Several publications provide comprehensive reviews of hydrogen production methods [13, 5, 19]. Two candidates for large-scale production of hydrogen in the near future are nuclear assisted thermochemical water splitting and natural gas steam reforming. They may both serve as hydrogen producing technologies in the transition to a hydrogen fueled future. It is therefore interesting to investigate their relative environmental performance to gain a better understanding of the possible roads to the hydrogen society.

HYBRID LIFE CYCLE ASSESSMENT

Life cycle assessment (LCA) is an analytic tool developed for assessing the environmental impacts of a product or service throughout its entire life cycle, from resource extraction to final disposal. LCA is formalized in the International Organization for Standardization standards 14040-43 and the theory will not be discussed in further detail here.

Another way to determine system-wide environmental impacts is to combine economic input-output analysis with environmental data on the different economic sectors of the economy. This approach was first introduced by Wassily Leontief in 1970 [18]. The idea is that a given demand of commodities from an economic sector will induce economic activity in other sectors. If it is possible to calculate the total induced economic activity from a given demand, one could combine these results with environmental data of the sectors in the economy to produce total environmental impacts for a given demand. The methodology has been further developed since 1970; see for example [28] and [15].

Recent efforts have combined the strengths of process LCA and environmental input-output analysis (see for example [12, 25]). While process LCA provides detailed data on the "close" parts of the system that is assessed, input-output analysis can offer to calculate the environmental burdens arising further out in the system. The construction of an industrial facility will not only require materials such as cement, steel, wood etc., usually accounted for in a process-LCA, but also a significant amount of services from carpenters, electricians, financial sectors and others. They all use equipment and energy doing their job, and the input-output approach offers the possibility to include these inputs through demanding services from an economic sector. The difference between the cost of some sort of equipment and the cost of the materials needed for its construction could be demanded from a sector such as, for example, *construction services*. This results in an induced demand in the whole economy and a set of environmental impacts that can be added to the impacts from process-LCA to yield total environmental impacts.

METHOD OF CALCULATION

The computations of LCA are best performed within a matrix framework, allowing for more flexible and sophisticated analysis.

Unit processes along the life cycle of a product or service can be identified. These are called *foreground processes*. They may all have inputs of products from each other or other processes not specified as a part of the foreground system. The foreground processes can be organized in a matrix $\mathbf{A}_{ff}$ describing the flows between the different processes in the system on a unit output basis. The environmental flows (emissions and raw material use) are assembled in a matrix $\mathbf{E}_f$; also on a unit output basis.

Various LCA-databases have been developed, containing standard LCI-data for different processes. These are contained in matrices called $\mathbf{A}_{pp}$. Their corresponding emissions are given in $\mathbf{E}_p$. These databases can be used to model background processes needed as inputs to the foreground system. The demands from the foreground system to the background system are assembled in matrix $\mathbf{A}_{pf}$.

In order to estimate the environmental impacts of activities not covered in the foreground system or the LCA databases, a combination of input-output analysis and ordinary process-LCA is applied. The difference between the price of a unit equipment and

the cost of its material inputs can be called the *value added* (*VA*),

$$VA = EC - \sum_i W_i \cdot MC_i \tag{1}$$

where EC is the total cost of a unit equipment, W_i is the weight of material i used in the equipment and MC_i is the unit cost of material i. We can now calculate VA for each of the unit processes. The VA must be assigned to an industrial sector or a commodity group, e.g. *Equipment manufacturing* if there is such a sector present in the input-output matrix.

A matrix $\mathbf{A}_{nn}$ describes the interindustry demands in the economy and its corresponding emission matrix, $\mathbf{E}_n$, the environmental flows arising from the one unit output of each process. The demand of the different foreground processes from the background economy can now be assembled of the VA values into a matrix $\mathbf{A}_{nf}$. Matrices $\mathbf{A}_{ff}$, $\mathbf{A}_{pp}$, $\mathbf{A}_{nn}$, $\mathbf{A}_{pf}$ and $\mathbf{A}_{nf}$ can be arranged into a matrix,

$$\mathbf{A} = \begin{pmatrix} \mathbf{A}_{ff} & 0 & 0 \\ \mathbf{A}_{pf} & \mathbf{A}_{pp} & 0 \\ \mathbf{A}_{nf} & 0 & \mathbf{A}_{nn} \end{pmatrix} \tag{2}$$

Corresponding **E**-matrices can be arranged into one large **E**-matrix. With a given demand of foreground processes **y**, the total induced demand of processes, **x**, can now be calculated as,

$$\begin{pmatrix} \mathbf{x}_f \\ \mathbf{x}_p \\ \mathbf{x}_n \end{pmatrix} = \left[I - \begin{pmatrix} \mathbf{A}_{ff} & 0 & 0 \\ \mathbf{A}_{pf} & \mathbf{A}_{pp} & 0 \\ \mathbf{A}_{nf} & 0 & \mathbf{A}_{nn} \end{pmatrix} \right]^{-1} \cdot \begin{pmatrix} \mathbf{y}_f \\ 0 \\ 0 \end{pmatrix} \tag{3}$$

The total environmental flows, **e**, arising as a result of the induced process activity are calculated by

$$\mathbf{e} = \mathbf{E} \cdot \begin{pmatrix} \mathbf{x}_f \\ \mathbf{x}_p \\ \mathbf{x}_n \end{pmatrix} \tag{4}$$

The impact assessment results, **c**, are now calculated by multiplying the **e**-vector with a characterization matrix **C**,

$$\mathbf{c} = \mathbf{C} \cdot \mathbf{e} \tag{5}$$

The matrix structure of the computations is ideal for further analysis. Exploration of process contributions to the different impacts and contributions from foreground, background and input-output parts of the system can be performed with simple straightforward matrix manipulations. This is not explained further in this paper.

SYSTEM DESCRIPTION

The assessment has been conducted with the aim of comparing hydrogen production from natural gas steam reforming and nuclear power. The natural gas based system includes inputs and outputs from natural gas extraction, processing to produce hydrogen, separation and CO_2 sequestration. Data from this case was obtained from a previous study [24].

Hydrogen can be produced from nuclear heat via thermochemical water cracking; a technology described by the industry itself as a promising and realistic option for large scale hydrogen production in the future [4, 20]. Numerous chemical cycles can, combined with heat, produce hydrogen from water. Through a large survey a process called the Iodine-Sulphur (I-S) cycle was found most attractive [4]. The process needs a coolant outlet temperature at least above 850 degrees celcius. This implies new reactor technology to supply the heat. General Atomics (GA) has performed a feasibility study and found a helium cooled high temperature reactor most suited for the task [4]. The concept is called the Hydrogen-Modular Helium Reactor (H_2-MHR) and will deliver the required high temperatures (950 degrees outlet temperature). The reactor will use uranium as fuel with an average enrichment of approx. 13 % U-235 [21]. In principle this system shares most of the current nuclear systems' processes. The main difference is that the electricity producing unit is replaced by hydrogen production. However, it also differs in the internal characteristics of the unit processes e.g. reactor technology and enrichment level. The system analyzed can be divided into seven main stages:

1. Mining and milling produce concentrated uranium in the form of U_3O_8.

2. The conversion stage converts U_3O_8 to the form UF_6 needed in the enrichment process.

3. Enrichment brings concentration of the fissile isotope U-235 to a desired level.

4. In fuel production the chemical composition is altered once again to UO_2 (light water cooled reactors) or UC, UC_2 or UCO (gas cooled reactors).

5. The fuel is then irradiated through use in a nuclear reactor, generating heat for the hydrogen production process.

6. Hydrogen is produced through thermochemical water splitting. Different chemical reactions supported by catalyst chemicals and heat produce hydrogen and oxygen from the input of pure water.

7. Spent fuel is treated in several stages before final storage in a deep geological repository.

The production of 1 TJ hydrogen (higher heating value, HHV) delivered at approx. 37 bars is the basis for the assessment.

Two LCA-databases and one input-output database are used to provide background processes and economic inputs to the foreground processes[1]. It is assumed zero loss of uranium throughout the fuel cycle.

It should further be noted that the hybrid approach is only applied to the nuclear heat facility and the hydrogen production unit. It proved difficult to obtain inventory data and prices for the inputs from the fuel cycle. Fuel cycle foreground processes are therefore modeled entirely with inputs from LCA-database processes. It is, however, assumed that the input data in the LCA-database are covering most subprocesses thus minimizing the *VA* discussed earlier. The construction and demolition of the fuel cycle facilities are included in the LCA-database data. Full system description and inventory data can be viewed in [22].

RESULTS

Not much has been done to evaluate the life cycle environmental burdens arising from nuclear hydrogen production, but some publications assess nuclear electricity production. This includes the ExternE studies [6], which focus mainly on the life cycle external costs arising from the release of radionuclides in the nuclear fuel cycle and the potential for accidents, excluding numerous other possible environmental issues. The Swedish electrical company Vattenfall has conducted LCAs for their different electricity producing technologies, including nuclear power [3]. Some work has also been done in Korea [17, 16]. Other studies apply a life cycle approach to assess nuclear power generation, but fails to include a comprehensive list of impacts, focusing on selected impact categories [29, 23, 10]. There is also nuclear LCA data as a part of the database ETH-ESU 96 [9] and Ecoinvent [7].

For the impact assessment two different methods were used; the CML 2000 baseline method[2] and the Eco-Indicator 99 method[3] Only results for selected impact categories are presented in this paper, for a more comprehensive presentation of the results consult [22]. To be able to assess impacts from radiation, the radiation impact category from Eco-Indicator 99 has been used. The indicators are shown in Table 1.

Impact category	**Indicator**
GWP	kg CO_2-equivalents
HTP	kg 1,4 DB-equivalents[a]
AP	kg SO_2-equivalents
EP	kg PO_4^{3-}-equivalents
R	Disability Adjusted Life Years (DALY)

[a] 1,4 Diclorobenzene- equivalents

Table 1: The Impact Categories used in the assessment.

Comparison with hydrogen production from natural gas

Environmental impacts arising from the production of 1 TJ (HHV) hydrogen were calculated. The results are shown in Table 2. The natural gas based

[1] ETH-ESU 96 [9], Idemat 2001 [2], IO OECD Europe [1]

[2] This method is developed by Center for Environmental Studies at University of Leiden. For more information and background reports consult the LCA website at Leiden, `http://www.leidenuniv.nl/interfac/cml/ssp/projects/lca2/index.html`

[3] For details see methodology report [11].

	N	NG	Ratio, NG/N
GWP	2.46E+03	1.3E+04	5.32
HTP	3.88E+03	1.0E+03	0.26
AP	1.61E+01	2.4E+01	1.49
EP	7.88E-01	3.3E+00	4.17
R	7.89E-03	8.5E-09	1.1E-6

Table 2: Impact assessment results for the production of 1 TJ (HHV) hydrogen from nuclear thermochemical water splitting (N) and natural gas steam reforming (NG).

system performs better for human toxicity and radiation whereas the nuclear alternative has a better score for global warming, acidification and eutrophication.

It is also interesting to investigate the difference in where the impacts occur for the two options. Figures 1 and 2 shows the contribution of foreground-, background- and input-output processes to the different environmental impacts. The GWP shows

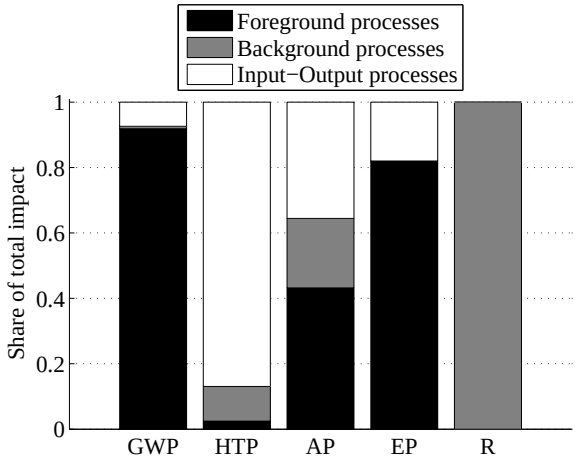

Figure 1: Impacts of hydrogen production from natural gas from foreground, background and economic inputs.

a large difference between the systems. Almost all greenhouse gas emissions in the natural gas case occur in the foreground processes whereas for the nuclear case, economic inputs and background processes dominate the impacts. This is not so strange considering the use of natural gas to fuel the boilers in the steam reforming process for natural gas. For the HTP we see that the foreground processes play

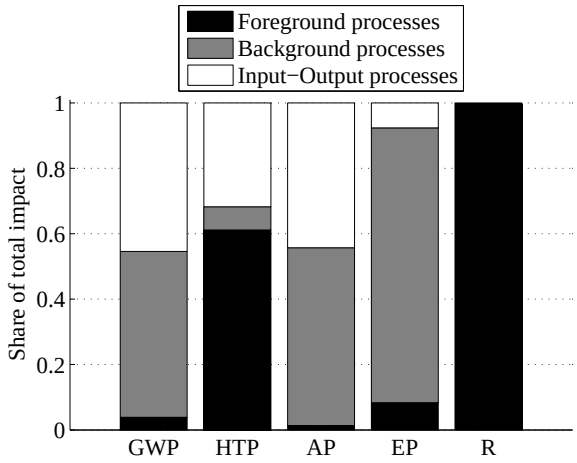

Figure 2: Impacts of nuclear hydrogen production from foreground, background and economic inputs.

a much more important role in the nuclear system. The major part of the impacts comes from fuel cycle activities. In impact categories AP and EP however, foreground processes contribute larger in the natural gas case. The radiation impacts from the nuclear system is dominated by foreground contributions, especially the mill tailings that continue to exhale radon for thousands of years. For the natural gas case, radiation impacts occur only in the background system. Generally we see that input-output contributions are significant for both systems.

Details of nuclear hydrogen production

To gain a better understanding of the environmental performance of the nuclear system, as well as identifying areas of improvement, it is interesting to identify the upstream impacts for each foreground process. These results are shown in Table 3.

Global warming potential (GWP)
For the global warming potential the most important contributions occur upstream the operation of the power plant, hydrogen plant, conversion and milling. Most of this is due to induced activity in background- and input-output matrix. The GWP impacts are quite evenly distributed, i.e. not many large contributors; the ten largest contributors account for

Foreground process	GWP	HTP	AP	EP	R
Constr. NPP	5	3	6	1	0
Constr. H2-plant	6	3	6	1	0
Mining	5	26	6	25	1
Milling	16	38	25	38	0
Mill tailings	0	0	0	0	99
Conversion	16	2	8	16	0
Enrichment	6	1	3	2	0
Fuel fabrication	0	0	1	0	0
Spent fuel mgmt.	9	2	10	11	0
Mgmt. of LLW	0	0	0	0	0
Operation NPP	18	15	20	3	0
Operation H2-plant	19	11	16	3	0

Table 3: Total upstream impacts for the different foreground processes (in % of total)

about 60 % of total.

Human toxicity potential (HTP)
Mining and milling are the most important contributions to this impact category, alone accounting for more than 60 % of impacts. This is mostly the direct impacts from the mining and milling processes. Further, there is a significant difference between open pit and underground mining, meaning that the HTP is somewhat sensitive to the type of mining technology. Open pit mining is significantly better than undergroundmining in this impact category. The impacts from the operation of reactor and hydrogen plant are mostly due to induced economic activity.

Acidification potential (AP)
Impacts caused by inputs to spent fuel management, milling and operation of reactor/hydrogen plant dominate this impact category (about 70-80 % of total). It is therefore sensitive to the assumption that fuel rods are not pushed out of the fuel assembly before managing the spent fuel. Impacts occur almost entirely in background and input-output processes. This is further emphasized in Figure 2.

Eutrophication potential (EP)
Mining and milling contribute most to the eutrophication potential, closely followed by the conversion process and spent fuel management. The dominating direct impacts mainly come from background processes in the LCA-database.

Radiation (R)
Milling of uranium is the most important contributor to human health impacts from radiation. This implies that efforts towards reducing the radiation impacts from from the nuclear cycle should be directed at improved management of mill tailings. UNSCEAR [27] points out that radon emissions from tailings are highly dependent on how they are treated. It also follows that radiation impacts are not sensitive to mining and enrichment technology.

DISCUSSION AND CONCLUSIONS

The assessment has shown that a hybrid approach to LCA is needed to assess the total environmental impacts from the life cycle. For some impact categories a significant amount of the impacts come from the acquisition of economic activities. One of the most important lessons from this is that ordinary process-LCA fails to calculate all impacts from the life cycle. This may not be a problem if the goal of the LCA is to learn more about a product and identify areas of improvement potential; but in a comparative assessment, a significantly larger fraction of impacts may be accounted for in one system or for one impact category than in another through process-LCA. Figures 1 and 2 illustrate that a comparative assessment based on process-LCA alone may give misleading results. It is obvious that only performing a process-LCA can lead to wrong conclusions.

Since the input-output processes are important contributors to some of the impact categories, the results are sensitive to the assignment of costs to economic sectors. This procedure has been done based on our subjective understanding of correlation between different costs and the names of the economic sectors.

It should be kept in mind that the results are quite sensitive to the quality of the databases used since much of the inventory has been constructed using these databases. The input-output database contains highly aggregated data and it is also assumed that the structure of the economy in which the plant is built is equal to that of OECD Europe. Results could therefore be seen more as indicative than exact quantification of impacts.

Natural gas derived hydrogen performs better for human HTP and R, the nuclear system is better on GWP, AP and EP. Results from the impact assessment does, however, not prioritize between the dif-

ferent impact categories; i.e. no weighting procedure is applied. It is therefore impossible to claim an overall best alternative for hydrogen production, comparison between the two alternatives can only be performed impact category by impact category. For an introduction to weighting in LCA, consult [8] or [26].

Improved management of mill tailings is clearly the most important strategy for reducing the human health impacts from ionizing radiation. This is due to the long term exhalation of radon gas from the tailings.

It is hard to discuss aspects of nuclear power without commenting on the politically hot issues of accidents, proliferation and spent fuel management. In an LCA context only impacts resulting from routine operation are accounted. It should be mentioned that the reactor concept assessed in this paper is described as meltdown proof and that it offers high proliferation resistance. The use of coated particles in the fuel is also said to maintain its integrity for at least a million years in a geologic repository [14]. It has not been our ambition to question this information and only routine impacts have been included.

REFERENCES

[1] Dutch input output table (105 sectors). In SIMAPRO 5.1 LCA software, 1995. Linked to Input Output tables (30 sectors) in the rest of the world divided into 3 regions, OECD Europe, rest-OECD and Non-OECD.

[2] Idemat 2001 LCA database. In SIMAPRO 5.1 LCA software, 2001. See `http://www.io.tudelft.nl/research/dfs/idemat/index.htm` for details.

[3] B.-M. Brännström-Noreng, U. Dethlefsen, R. Johansson, C. Setterwall, and S. Tunbrant. Life Cycle Assessment for Vattenfalls‘ Electricity Generation, Summary Repor. Technical report, Vattenfall, Stockholm, Sweden, 1996.

[4] L. Brown, G. Besenbruch, R. Lentsch, K. Scultz, J. Funk, P. Pickard, A. Marshall, and S. Showalter. High efficiency generation of hydrogen fuels using nuclear power - final technical report for the period august 1, 1999 through september 30, 2002. Technical Report GA-A24285 Rev.1, General Atomics, San Diego CA, USA, December 2003. Prepared under the Nuclear Energy Research Initiative (NERI) Programme for the U.S. Department of Energy.

[5] I. Dincer. Technical, environmental and exergetic aspects of hydrogen energy systems. *International Journal of Hydrogen Energy*, 27(3):235–285, 2002.

[6] M. Dreicer, V. Tort, and P. Manen. ExternE, Externalities of Energy. Technical Report 5, Nuclear, European Commision, 1995.

[7] Ecoinvent Centre. Ecoinvent data v1.1, 2004. Swiss Centre for Life Cycle Inventories.

[8] G. Finnveden. A critical review of operational valuation/weighting methods for life cycle assessment. Technical Report AFR-report 253, Forskningsgruppen för miljöstrategiska studier, Stockholms universitet, Stockholm, Sweden, 1999.

[9] R. Frischknecht et. al. Öko-inventare von energiesystemen. In SIMAPRO 5.1 LCA software, 1996. ETH-ESU 1996 LCA database.

[10] L. Gagnon, C. Bélanger, and Y. Uchiyama. Life cycle assessment of electricity generation options: The status of research in year 2001. *Energy Policy*, 30:1267–1278, 2002.

[11] M. Goedkoop and R. Spriensma. The Eco-indicator 99. A damage oriented method for Life Cycle Assessment. Methodology Report. Technical report, Prè Consultants, Amersfoort, NL, 2001. Available from `www.pre.nl`.

[12] R. Heijungs and S. Suh. *The Computational Structure of Life Cycle Assessment*, volume 11 of *Eco-Efficiency in Industry and Science*. Kluwer Academic Publishers, Dordrecht, The Netherlands, 1st edition, 2002.

[13] B. Kruse, S. Grinna, and C. Bush. Hydrogen-status og muligheter. Bellona rapport 6, Miljøstiftelsen Bellona, 2002.

[14] M. P. LaBar. The gas turbine-modular helium reactor: A promising option for near term deployment. Technical Report GA-A23952, General Atomics, San Diego CA, USA, April 2002.

[15] M. Lahr and E. Dietzenbacher, editors. *Input-Output Analysis: Frontiers and Extensions*. Palgrave, New York (USA), 2001.

[16] Y. E. Lee and K.-K. Koh. Decision-making of nuclear energy policy: Application of environmental management tool to nuclear fuel cycle. *Energy Policy*, 30:1151–1161, 2002.

[17] Y. E. Lee, K. J. Lee, and G. W. Lee. Environmental Assessment of Nuclear Power generation in Korea. *Progress in Nuclear Energy*, 37(1-4):113–118, 2000.

[18] W. Leontief. Environmental repercussions and economic structure: An input-output approach. *Review of Economics and Statistics*, 52(3):262–271, 1970.

[19] M. Momirlan and T. N. Veziroglu. Current status of hydrogen energy. *Renewable and Sustainable Energy Reviews*, 6(1-2):141–179, 2002.

[20] K. Schultz. Thermochemical production of hydrogen from solar and nuclear energy. General Atomics, April 2003. Presentation to the Stanford Global Climate and Energy Project.

[21] K. Shultz. Personal communication, Spring 2004. General Atomics.

[22] C. Solli. Fission or Fossil: A Comparative Hybrid Life Cycle Assessment of Two Different Hydrogen Production Methods. Master's thesis, Norwegian University of Science and Technology, Trondheim, Norway, June 2004. online: `http://www.indecol.ntnu.no/indecolwebnew/publications/mastertheses/Christian%20Solli%20var04/masterthesis.pdf`.

[23] J. V. Spadaro, L. Langlois, and B. Hamilton. Greenhouse gas emissions of electricity generation chains- Assessing the difference. *IAEA Bulletin*, 42(2):19–24, 2000.

[24] A. H. Strømman. Hybrid life cycle assessment of natural gas based value chains for transportation. University of Michigan, Ann Arbor, MI, USA , June 29-July 2 2003. International Society for Industrial Ecology. Presentation at the second international conference of the International Society for Industrial Ecology.

[25] A. H. Strømman and E. G. Hertwich. Hybrid Life Cycle Assessment of Large Scale Hydrogen Production Facilities. *Submitted to Journal of Cleaner Production*, 2004.

[26] H. A. Udo de Haes, G. Finnveden, M. Goedkoop, M. Hauschild, E. G. Hertwich, P. Hofstetter, O. Jolliet, W. Klöppfer, W. Krewitt, E. Lindeijer, R. Müller-Wenk, S. I. Olsen, D. W. Pennington, J. Potting, and B. Steen, editors. *Life-Cycle Impact Assessment: Striving Towards Best Practice*, chapter 7, Normalization, Grouping and Weighting in Life Cycle Impact Assessment, pages 177–208. Society of Environmental Toxicology and Chemistry (SETAC), Pensacola FL, USA, 2002.

[27] United Nations. Sources and Effects of Ionizing Radiation, UNSCEAR 1993 Report to the General Assembly, with scientific annexes. Technical Report Annex B, United Nations Scientific Comittee on the Effects of Atomic Radiation, New York, 1993.

[28] United Nations. *Handbook of input-output table compilation and analysis- Studies in methods*. F. New York, USA, 1999.

[29] K. R. Voorspools, E. A. Brouwers, and W. D. D'haeseler. Energy content and indirect greenhouse gas emissions embedded in "Emission Free" power plants: Results for the low countries. *Applied Energy*, 67:307–330, 2000.

Proceedings of ECOS 2005
Trondheim, Norway
June 20–22, 2005

THERMOECOLOGICAL COST OF ELECTRICITY GENERATION IN COAL FIRED STEAM POWER PLANTS

Wojciech STANEK*
Technical University of Silesia
Institute of Thermal Technology
ul. Konarskiego 22, 44-100 Gliwice
Poland

ABSTRACT

The depletion of the limited non-renewable resources is one of the most important factor for the future existence of mankind. Exergy can be applied as a measure of the quality of limited natural resources. The thermoecological cost can be defined as cumulative exergy consumption of non-renewable natural resources connected with the production of some particular product and the additional cumulative exergy consumption connected with prevention and compensation of environmental losses. The paper presents the analysis of the thermoecological cost of electricity production in coal-fired steam power plants. The methodology of evaluating the thermoecological cost taking into account life cycle of considered product is discussed. The paper includes also the description of the method of calculation of the thermoecological cost resulting from rejection of harmful substances to natural environment. In this case two methods are discussed: the first method is based on monetary indices of harmful impacts of the waste products rejected to natural environment and the second is based on the idea of abatement cost. Results of calculations of the thermoecological cost of electricity taking into account life cycle of installation have been presented. Calculations have been made for Polish conditions, where majority of electricity is produced in coal fired (energy hard coal and lignite) steam power plant.

Key words: natural resources, cumulative exergy consumption, thermoecological cost, life-cycle assessment.

NOMENCLATURE

a_{ij}	coefficient of the consumption and of *i*-th product per unit of *j*-th major product
f_{ij}	coefficient of by-production of *i*-th product per unit of *j*-th major product
a_{rj}	coefficient of the consumption of *r*-th imported semi-finished product per unit of *j*-th major product,
b_{sj}	exergy of *s*-th non-renewable natural resource immediately consumed in the process under consideration per unit of *j*-th product
B	annual exergy consumption of non-renewable natural resources
ec	energy hard coal
lig	lignite
GDP	annual gross domestic product,
P_k	annual production of *k*-th aggressive component of waste products rejected to the environment in the considered region

*Corresponding author: Phone:+48 32 237 28 52,
Fax: +48 32 237 28 72 E-mail: stanek@itc.polsl.pl

p_{jk} amount of *k*-th aggressive component rejected to natural environment per unit of *j*-th product

ρ_j specific thermoecological cost of the *j*-th product

ρ_r specific thermoecological cost of imported *r*-th good

ρ_{ex} thermoecological cost burdening exploitation of the plant (mainly fuel consumption)

ρ_{LCA} total thermoecological cost taking into account total life time of the plant

w_k monetary coefficient of ecological damages per unit of the *k*-th aggressive waste product

ζ_k cumulative exergy consumption of non-renewable resources due to the emission of unit of the *k*-th waste product

INTRODUCTION

The paper deals with the problem of depletion of natural resources resulting from production of electric energy. Methodology of evaluation of unfavourable ecological effects of human activity basing on thermoecological cost is discussed. Such a unfavourable effects result from two reasons: consumption of non-renewable natural resources and rejection of harmful waste material to the natural environment. Rejection of harmful substances to the natural environment causes losses in fields of human health, nature, buildings, agriculture etc. For this reason we should pay additional expenses for decrease or compensate these unfavourable effects as far as it is profitable from the environmental point of view. The measure of such a profitability is discussed by means of definitions of two kinds of environmental factor: thermoecological cost of rejection of waste products and thermoecological cost of decrease of harmful impacts.

Production of electricity influences the depletion of natural resources mainly due to consumption of non-renewable fossil fuels. In Polish conditions majority of electricity is generated in energy hard coal- and lignite-fired steam power plants. Installed power in Polish power plants at the end of the year 2003 amounted to 32268 MW [23]. Of which [23] 28803 MW (64%) was installed in energy hard coal-fired power plant and 9304 MW (45%) in lignite-fired power plant. Yearly average load reached 62% of installed power [23]. Average net energy efficiency of electricity generation in Polish conditions is equal 34.5%.

These are the main Polish power plants with installed power greater than 150 MW [22]: 1. Power Plant Bełchatów SA 4420 MW (lig.), 2. Power Plant Kozienice SA 2820 MW (ec), 3. Power Plant Turów SA 2166 MW (lig.), 4. Power Plant Połaniec SA 1800 MW (ec), 5. Power Plant Rybnik SA 1775 MW (ec), 6. Power Plant Dolna Odra SA 1742 MW (ec), 7. Power Plant Jaworzno SA 1635 MW (ec), 8. Power Plant Opole SA 1479 MW (ec), 9. Power Plant Pątnów SA 1200 MW (lig.), 10. Power Plant Łaziska SA 1155 MW (ec), 11. Power Plant Łagisza SA 840 MW (ec), 12. Power Plant Siersza SA 786 MW (ec), 13. Power Plant Adamów SA 600 MW (lig), 14. Power Plant Ostrołęka SA 600 MW (ec), 15. Power Plant Skawina SA 590 MW (ec), 16. Power Plant Konin SA 523 MW (lig), 17. Power Plant Stalowa Wola SA 341 MW (ec), 18. Power Plant Halemba SA 200 MW (ec), 19. Power Plant Blachownia SA 158 MW (ec).

Power Plant Opole is characterized by highest (in Polish conditions) value of net energy efficiency of about 36.5% [22]. The longest distance between coal mines located in Southern Poland and Power Plant Dolne Odra located in north of Poland is about 600 km.

Besides of consumption of fossil fuels the generation of electricity is burdened by additional consumption resulting from rejection of harmful substances to natural environment and external costs due to expenditures for construction of plant, transportation, redecorations during life cycle and recycling of materials after decommissioning of existing plant.

As different resources and products are consumed in each of mentioned steps of lifetime of power plant we have to take common measure that let us compare all of these unfavourable effects. For this purpose we can apply exergy [11],[12],[13],[14]. Not only the consumption of fossil fuels influences the total expenditures burdening the thermoecological cost so the author propose to connect the methodology of exergo-ecology analysis with the methodology of life cycle assessment to determine full impacts. The author propose the concept of Thermo Ecological

Life Cycle Assessment (*analysis from the cradle to the grave*) as a tool for for comprehensive evaluation of environmental contribution of human activity. Cumulative Exergy Life Cycle Assessment has been also taken into account in [2].

CONCEPT OF THERMOECOLOGICAL COST

According to J. Szargut [12],[14] the *thermo-ecological cost* is defined as the cumulative consumption of non-renewable exergy connected with the fabrication of a particular product including additionally the consumption resulting from the necessity of compensation of environmental losses caused by rejection of harmful substances to the environment (Fig 1.)

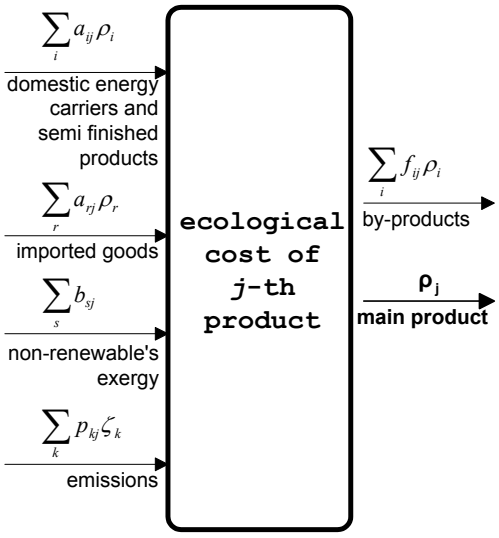

Fig. 1 Balance of thermoecological cost

The index of thermo-ecological cost can be determined by solving the set of thermoecological cost balance equations:

$$\rho_j + \sum_i \left(f_{ij} - a_{ij}\right)\rho_i - \sum_r a_{rj}\rho_r = \\ = \sum_s b_{sj} + \sum_k p_{kj}\zeta_k \qquad (1)$$

This set should comprise all the branches of domestic economy. However, it would be difficult to solve such a problem. For this reason in practical calculation only strongly connected production processes are taken into account. In analysis described in next sections 33 branches of domestic economy are taken into account. Method of determination of the factor ζ_k is discussed in details in next sections of the paper.

The thermodynamic evaluation of environmental losses and natural resources has been also considered in [1],[2],[3],[4],[5],[17],[18].

Some of thermoecological cost balance equations include the thermo-ecological cost of imported goods which represent additional unknowns in the equation set. These unknowns may be determined using an iterative method described in [8].

THERMOECOLOGICAL LIFE CYCLE ASSESSMENT

The Thermo Ecological Life Cycle Assessment (TELCA) based on methodology, described in previous section, comprises the following phases:

1. **Construction Phase** encompasses project, extraction of raw materials, semi-finished products fabrications, transport expenditures in the construction phase. All of these expenses influence the final thermoecological cost burdening the final useful consumptive product. This phase has a significant contribution in case of processes that are based on renewable sources of energy. For instance, in case of wind power plant the thermoecological cost results mainly from expenses in construction phase.
2. **Operation phase** is defined as a period of time between the end of construction phase and the beginning of decommissioning phase. In processes utilising non-renewable resources this phase is predominant in the cumulative consumption of natural resources, mainly energy carriers.
3. **Decomissioning phase** of plant concerns the period at the end of life of installation. Thermoecological cost in this phase results from expenditures for develop the remains of the system and e.g. some expenditures for reclamation of terrain.

The general form of the objective function in case of thermoecological cost minimisation taking into account the life – time of product has been formulated by J. Szargut and presented in [13].

Basing on the concept presented in [13] in order to taking into account total resources expenditure during whole life-time the thermoecological cost balance equation (1) used so far [8],[9],[10] should be extended by the following components:

1) cumulative consumption of exergy of non-renewable resources in the construction phase:

$$a_{1j} = \frac{\frac{1}{\tau}\sum_m G_m \rho_m}{P_j} \quad (2)$$

where: τ – total life time of j – th productive process, G_m – consumption of construction materials during the construction phase, ρ_m – index of thermoecological cost of m – th material consumed in construction phase, P_j – total annual productivity of j – th process,

2) cumulative exergy consumption of non-renewable natural resources resulting from necessity of redecoration during operational phase of j – th productive process:

$$a_{2rj} = \frac{\frac{1}{\tau}\sum_r G_r \rho_r}{P_j} \quad (3)$$

where: G_r, ρ_r – consumption and thermoecological cost of materials used for redecoration during total life time of considered plant,

3) cumulative consumption of exergy of non-renewable resources during decommissioning of considered plant:

$$a_{3j} = \frac{\frac{1}{\tau}\left(\sum_l G_l \rho_l - \sum_u G_u \rho_u u_{rec}\right)}{P_j} \quad (4)$$

where: $\sum_i G_i \rho_i$ – additional thermoecological cost resulting from decommissioning of installation of j – th productive process, $G_u u_{\mathrm{rec}}$ – amount of u – th recyclable material that will be recycled, ρ_u – thermoecological cost of u – th recyclable product.

Each productive process is inseparably connected with additional consumption resulting from the needs for transportation. These expenses resulting both from construction of means of transport as well as resource expenses during the period of its operation (fuel consumption, emissions of harmful substances, expenses for redecoration of transportation). For example the thermoecological cost resulting from needs for transportation of fuel to power plant by means of cars results from the following formulas:

a) cost dependent on fuel consumption:

$$\rho_{t1} = \frac{\bar{e}_f}{\eta_{Eek} W_{dek}} l\left(\gamma_f + \sum_k p_k \zeta_k\right) \quad (5)$$

where: $\bar{e}_f$ – average specific consumption of chemical energy of fuel by means of transportation e.g. MJ/(t·km), η_{Eek} – energy efficiency of considered power plant, $W_{d\mathrm{ek}}$ – lower heating value of fuel transported to considered power plant, l – average distance of transportation of fuel to power plant, γ_f – ratio of thermoecological cost per unit of chemical energy of fuel, p_k – specific emission of k – th harmful substance per unit of consumed chemical energy of fuel, ξ_k – thermoecoloical cost of k – th harmful substance;

b) cost independent on amount of consumed fuel:

$$\rho_{t2} = \frac{1}{\tau_{LT}} \frac{\sum_i G_i \rho_i (1 - u_i)}{\eta_{Eek} W_{dek}} \frac{l}{V \tau_d \mu G \tau_R} \quad (6)$$

where: τ_{LT} – life time of transportation means, $\sum_i G_i \rho_i$ – thermoecological cost burdening the construction of transportation means, u_i – index of recycling of materials after life time of transportation means, $V\tau_d$ – average daily mileage, μ – degree of utilising the transportation means, G – carrying capacity of transportation means, τ_R – annual operational time.

Formulas (5) and (6) expresses the thermoecological cost burdening the transportation of fuel required for production of 1 MJ of electric energy. Such a relations can be applied for determination of any transportation replacing in denominator the term of $\eta_{Eek} W_{dek}$ by means of adequate amount of other transported good. Quoted formulas let to investigate the influence of the transportation distance between mine and plant on the indices of thermoecological cost of electricity.

THERMOECOLOGICAL ASSESMENT OF REJECTION OF HARMFUL SUBSTANCES

Fig. 2 presents the connections between j – th productive process and rejections of harmful substance to the natural environment.

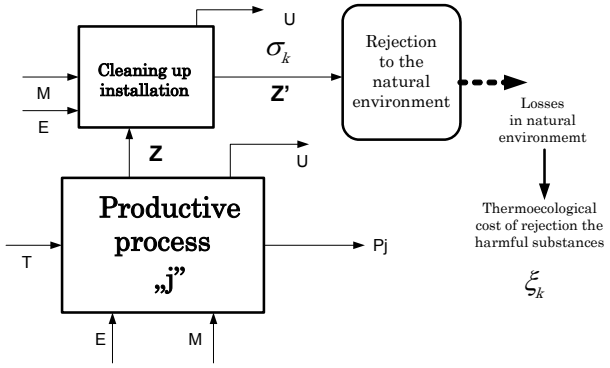

Fig. 2 Rejection of harmful substances to natural environment

Symbols in Fig. 2 concerns: *E* – energy, *M* – raw materials or semi-finished products, *U* – by-products, *T* – transport, P_j – main product of *j*-th productive process, ***Z*** – harmful waste products generated in *j*-th productive process transferred to cleaning up installation, ***Z'*** – harmful waste products rejected to natural environment.

From the thermoecological point of view this chain (Fig. 2) can be divided in two characteristic stages. The first stage encompasses the thermoecological cost resulting from the necessity of cleaning of harmful products of *j* – th productive process while the second stage is the rejection of harmful substance *k* to the natural environment. The environmental losses are caused by both of such phases. The first phase require some expenditure of exergy of natural resources [4],[5],[19] to cleaning up of the stream ***Z*** (abatement cost). The rejection of harmful substance causes environmental losess in the fields of human health, useful industrial and other manufactured products (machines, buildings, transportation equipment) and losses in agriculture and forestry. All of such losses required some additional resources expenditure to compensate them. Thermoecological cost resulting from rejection of harmful substances to natural environment can be evaluated by means of monetary indices of harmful impacts w_k [14],[15]:

$$\zeta_k = \frac{Bw_k}{GDP + \sum_k P_k w_k} \qquad (7)$$

The value of ζ_k has been calculated in [8],[10],[15]. For the main harmful substances (NO_X, SO_2, dust), the following values have been obtained: $\zeta_{SO2} = \zeta_{NOx} = 45$ MJ/kg, $\zeta_d = 9{,}3$ MJ/kg.

Table 1 presents the expenditures necessary for cleaning the main harmful substances SO_2, NO_x, dust and CO_2 (*abatement cost* = thermecological cost burdening the operation of cleaning installation), thermoecological cost and sustainability index. Sustainability index is defined as a ratio of thermoecological cost per abatement cost. The concepts of abatement has been proposed and discussed in [19]. The indices of thermoecological abatement cost were determined in [10]. For example, in case of CO_2 removal the thermoecological abatement cost can be determined by means following formula:

$$\sigma_{CO_2} = \beta_{\mathrm{el}}\rho_{el} = \frac{\sum N + N_t}{\frac{N_{\mathrm{el}0}}{\eta_{\mathrm{Eel}} W_d} m''_{CO_2}\eta_{\mathrm{CO}_2}}\rho_{el} \qquad (8)$$

where: $\sum N$ - total electric consumption resulting fm CO_2 removal, N_t - additional electric energy consumption resulting from CO_2 transportation, N_{el0} - electric power of plant before without CO_2 removal, η_{Eel} - net energy efficiency of power plant, W_d - net calorific value, m''_{CO_2} - amount of CO_2 generated per unit of fuel, η_{CO_2} - efficiency of CO_2 removal.

The value of σ_{CO_2} has been determined basing on data presented in [7].

Harmful substance	Abatement cost	Thermoeco--logical cost	Sustaina-bility
	MJ/kg	MJ/kg	%
CO_2	4.4	= =	= =
SO_2	17.5	45.0	38.0
NO_x	26.0	45.0	58.0
dust	0.5	9.5	5.0

Table 1: Comparison of abatement and thermoecological cost

Cleaning of waste product is profitable when the sustainability index is less than 1. Presented results show that cleaning of flue gases from dust using electrostatic precipitator is relatively high efficient from ecological point of view in comparison with other pollutants taken into account.

Because it is impossible to determine the thermoecological cost of CO by means of monetary indices of harmful impact (eq. 7) the method of abatement cost can be applied as a approximate method of evaluation of

thermoecological cost of rejection of CO_2 to the natural environment.

EXAMPLE CALCULATIONS OF THERMOECOLOGICAL COST OF ELECTRIC ENERGY PRODUCED IN COAL FIRED POWER PLANT

As it has been pointed out in previous sections of the paper in Polish conditions majority of electric energy is produced in conventional steam power plant fired by coal extracted in domestic coal mines. Power plants fired by lignite are located in neighbourhood of coal mines. The share of lignite-fired power plants in total production is about 40%. Majority of the rest of production is produced basing on energy hard coal extracted in Southern Poland. Table 2 presents selected properties of typical energy coal (lignite – lig. and four types of energy hard coal – ec extracted in Polish coal mines.

Fuel parameter	Unit	lig.	ec-1	ec-2	ec-3	ec-4
moisture fraction, w	kg/kg	52.1	20.0	7.0	5.0	7.0
ash fraction, p	kg/kg	8.6	20.0	20.0	20.0	20.0
coal fraction, c	kg/kg	25.9	45.9	58.8	61.5	58.0
LHV, W_d	MJ/kg	7.8	17.4	22.0	24.4	23.0
emission of CO_2	kg/kg	0.95	1.68	2.15	2.26	2.13
emission of CO_2	kg/MJ	0.12	0.10	0.10	0.09	0.09

Table 2: Parameters of typical Polish lignite and energy coal

For each type of coal presented in table 2 calculations of thermoecological cost have been done using methodology of life cycle assessment described in previous sections. It has been taken into account (table 3 and 5) that the average net energy efficiency of electricity production in Polish conditions is equal to 34.5%. In each variant of calculation presented in table 3 and 5 it has been assumed that the distance between coal mine and power plant is equal 50 km. In case of lignite power plant car transport of fuel has been taken into account while in case of hard energy coal both car and train transport has been taken into considerations. Data concerning the resources investment expenditures in the construction phase of the plant as well as energy consumption in this phase has been evaluated basing on [6], [20], [24].

Results of calculations of thermoecological cost presented in table 3 - 5 encompasses the value of thermoecological cost ρ_{LCA} taking into account life cycle of product and ratio $r_{el} = \rho_{LCA}/\rho_{ex}$ of total thermoecological cost ρ_{LCA} per thermoecological cost ρ_{ex} resulting from operational expenditures of the plant. Tables 3 - 5 also present the share of exploitation, construction phases, expenditures for transport and thermoecological cost of CO_2 in the total thermoecological cost ρ_{LCA} of electricity.

The results of calculations of the influence of kind of coal (included in table 2) upon the thermoecological cost are presented in table 3.

Parameter	lig.	ec-1	ec-2	ec-3	ec-4
ρ_{LCA}	4.71	4.11	4.11	4.08	4.09
ρ_{LCA} / ρ_{ex}	1.25	1.23	1.23	1.22	1.22
Structure of ρ_{LCA}, %					
Plant operation	80.0	81.4	81.4	82.0	82.0
CO_2	13.2	12.0	12.2	11.5	11.5
Construction	6.2	6.1	6.1	6.1	6.1
Transport	0.6	0.5	0.4	0.3	0.4

Table 3: Electricity thermoecological life cycle assessment for different types of coal

Thermoecological cost of electric energy produced in lignite-fired power plant is about 15% greater than in case of hard energy coal-fired power plant because of differences in thermoecological cost [8], [10] of lignite (γ_{lig}=1.2 MJ/MJ) and hard energy coal (γ_{ec}=1.12 MJ/MJ). The share of operation phase of power plant presents about 80% of total thermoecological cost ρ_{LCA}. This number confirmed that the resource expenses in other phases than operational one are not negligible. Significant influence on the results of calculation has the thermoecological cost of CO_2, especially in the case of lower quality fuel (lig., ec-1). In such a cases the amount of combusted fuel is higher than in high quality ones.

Table 4 presents results of calculations of thermoecological cost of electric energy for different values of net energy efficiency in the range of 30 to 40%. The value η_{Eel} = 36.5% corresponds to the highest value in domestic conditions while the average values for whole energy system is equal to 34.5%. The highest value of net energy efficiency is achieved in Power Plant Opole.

Shift of the production of electricity from the "average" power plant (η_{Eel} = 34.5%) to power plant characterized by efficiency equal to 36.5% leads to decrease of thermoecological cost of

electricity by 0.21 MJ/MJ (5.2% in relation to the index calculated for η_{Eel} = 34.5%).

Net energy efficiency, %	30.0	34.5	36.0	36.5	40.0
ρ_{LCA}	4.66	4.08	3.92	3.87	3.56
ρ_{LCA} / ρ_{ex}	1.21	1.22	1.22	1.22	1.23
Structure of ρ_{LCA}, %					
Plant operation	82.6	82.0	81.8	81.7	81.2
CO_2	11.6	11.5	11.5	11.5	11.4
Construction	5.4	6.1	6.4	6.4	7.0
Transport	0.4	0.3	0.3	0.3	0.3

Table 4: Electricity thermoecological life cycle assessment for various net energy efficiency

Annual consumption of exergy of natural resources was on average [10], [21] on the level of about 3500 PJ/year in last five years. The annual savings of exergy of natural resources due to increase the net energy efficiency from η_{Eel} = 34.5% up to 36.5% would be on the level of 14% of total present consumption of exergy of domestic natural resources.

Table 5 presents the results of calculations of thermoecological cost in dependence on distance of transportation between coal mine and power plant.

Distance, km	50	100	300	600
ρ_{LCA}	4.08	4.10	4.15	4.24
ρ_{LCA} / ρ_{ex}	1.22	1.22	1.24	1.27
Structure of ρ_{LCA}, %				
Plant operation	82.0	81.7	80.6	79.0
CO_2	11.5	11.5	11.3	11.1
Construction	6.1	6.1	6.0	5.9
Transport	0.3	0.7	2.0	4.0

Table 5: Electricity thermoecological life cycle assessment for various distance between coal mine and power plant

It has been assumed that the longest distance between coal mine located in Southern Poland and power plant No 6 (Fig. 1) located in the north of Poland is equal to 600 km.

In case of $L = 50$ km the share of resource expenditures connecting with transport of fuel in total thermoecological cost of electricity ρ_{LCA} is about 0.4% and has not significant influence on final result of ρ_{LCA}, while in the case of $L = 600$ km the share amounts to 4% and for this reason can not be neglected in considerations concerning evaluation of ρ_{LCA}.

In all of considered cases (table 3,4,5) the share of thermoecoogical cost of CO_2 is between 11÷13% of total thermoecological cost of electricity, while the share of resource expenditures connected with construction and decommissioning of the plant are between 6÷7%

All the presented numbers show that although dominating influence of energy carriers in productive processes (operation phase) based on utilization of non-renewable natural resources also external costs (eg. manufacturing of semi-finished products for construction of power plant, transport, etc.) can not be neglected. The real environmental load measured as depletion of non-renewable natural resources can be evaluated by means of combination of thermoecological cost analysis [10], [14] and Life Cycle Assessment Methodology (THELCA).

SUMMARY AND CONCLUSIONS

Methodology of evaluation of unfavourable ecological effects of human activity by means of concept of thermoecological cost analysis has been discussed. The detailed description of method of evaluation the thermoecological cost resulting from rejection of harmful substances to natural environment is also presented. The description of the method of determination of full environmental load caused by productive processes are proposed by combination of the concepts of thermoecological cost analysis and concept of Life Cycle Assessment (THELCA). The example calculation has been made in case of electric energy productions. Considerations comprises the direct and indirect resource expenditures connected with fabrication of considered product. In the set of balance equations of thermoecological cost 33 additional productive processes have been introduced. Obtained results confirmed that although the production of electricity in Polish conditions is mainly based on consumption of non-renewable energy resources the external costs can not be neglected ($r_{el} = \rho_{LCA} / \rho_{ex}$ = 1.21÷ 1.27) The full thermoecological cost of electricity is approximately divided between 80% - plant operation, about 12% - CO_2 thermoecological cost, 6% - construction and decommissioning of the plant, 0.5 – 4 % - transport of fuel to power plant. The results are dependent on the accuracy of data introduced into consideration. There are a significant difference between sources of data

especially in the case of data concerning the construction phase. For this reason it is planned to continue the investigation concerning THELCA analysis. It seem to be important to introduce the sensitivity analysis in order to determine the importance of particular input data on final results of THELCA analysis.

Acknowledgement
The paper was created within the frame of realisation of Grant 4T10B01925. The author would like to express gratitude to the Ministry of Science and Informatics.

REFERENCES

[1] Conelly, L., Koshland, C. P., "Exergy and industrial ecology", Exergy Int. J., Vol. 1, 2001
[2] Cornelissen R. L. Thermodynamics and sustainable development. The use of exergy to reduce irreversability. PhD Thesis. Enshede Netherlands 1997.
[3] Frangopoulos, C.A., "An Introduction to Environment Analysis and Optimization of Energy Intensive Systems". Proc. Conf. ECOS'92, Zaragoza 1992.
[4] Sciubba, E., "Beyond thermoeconomics? The concept of Extended Exergy Accounting and its application to the analysis and design of thermal systems", Exergy Int. J., Vol.1., 2001.
[5] Sciubba E. Exergo_Economics: Thermodynamically sound system Analysis as a Step Toward More Rational Resource Use. Int. Summer School on Thermodynamic Optimization and Construction Design. Istanbul 2004.
[6] Spath P. L., Mann M., K.: Capturing and Sequestering CO2 from a Coal-fired Power Plant – Assessing the Net Energy and Greenhouse Gas Emissions
[7] Spath P., Mann M., Kerr D. Life Cycle Assessment of Coal-fired Power Production. National Renewable Energy Laboratory. Colorado 1999.
[8] Stanek, W., 2001, "Iterative Method of Evaluating the Ecological Cost of Imported Goods", Proc. Conf. ECOS'2001, Istanbul, Turkey 2001.
[9] Stanek W. Selected Application of ThermoEcological Cost Analysis. Proc. Conf. Contemporary Problems of Thermal Engineering. Centre of Excellence OPTI_Energy, Gliwica-Ustron, June 2004.
[10] Stanek W. Application of exergy analysis for evaluation of ecological effects in thermal processes. Techn. Report. Institute of Thermal Technology. Gliwice 2005.
[11] Szargut J. Minimization of the Consumption of Natural Resources. Bulletin of the Polish Academy of Sciences, Technical Sciences, v. 26 (1978), No 6.
[12] Szargut, J., Application of Exergy for the Determination of Ecological Cost", Bull. Polish Acad., Techn. Sciences, 34, No. 7-8., 1986.
[13] Szargut, J., Minimization of the depletion of non-renewable resources by means of the optimization of design parameters. Proc. Conf. ECOS 2002, Berlin 2002.
[14] Szargut, J., "Depletion of Unrestorable Natural Exergy Resources", Bulletin of the Polish Academy of Sciences, Vol. 45, No. 2., 1997.
[15] Szargut, J., Ziębik A., *Fundamentals of Thermal Engineering*, PWN, Warsaw 2000 (in Polish).
[16] Szargut, J., Ziębik, A., Stanek, W. Depletion of the Unrestorable Natural Exergy Resources as a Measure of the Ecological Cost", Energy Conversion & Management 43 (2002).
[17] Wall, G., Gong M., "On exergy and sustainable development", Exergy Int. J., Vol.1., 2001.
[18] Valero A., Botero E. Exergetic evaluation of natural mineral capital (2): Application of the methodology to current world reserves. Proc. Conf. ECOS'2002.
[19] Valero A., Botero E., An assessment of the Earth's clean fossil exergy capital based on Exergy Abatement Cost. Proc. Conf. ECOS'2002.
[20] Voss A. LCA and External Costs in Comparative Assessment of Electricity Chains. IEA Conference, Paris, Nov. 2001.
[21] GUS (Central Statistical Office), 2004, Statistical Yearbook (in Polish), www.stat.gov.pl.
[22] http://www.elektrownie.com.pl
[23] The Energy Regulatory Office. www.ure.gov.pl
[24] ExternE – Externalities of Energy. EU Commission. www.externe.jrc.es

Proceedings of ECOS 2005
Trondheim, Norway
June 20–22, 2005

SOLID RESIDUES UTILIZATION ORIENTATED BY INDUSTRIAL ECOLOGY PRINCIPALS: A CASE STUDY

Thompson Copperfield von Agner*
CEFET PR Ponta Grossa – Parana – Brazil

Carlos Stadler Prof. Dr.
CEFET PR Ponta Grossa – Parana – Brazil

Rui Francisco Martins Marçal, Prof. Dr.
CEFET PR Ponta Grossa – Parana – Brazil

João Luis Kovaleski, Prof. Dr.
CEFET PR Ponta Grossa – Parana – Brazil

ABSTRACT

The present work is based on the application of Industrial Ecology with the vision of the solid waste management in a medium size lumber company. This organization this located in the municipal district of Ponta Grossa, State of Parana, south of Brazil. The sawmill's activity is the production of fences from reforested pine, that are destined to the North American and European markets. The daily amount of residues generated in the production process is of approximately $50m^3$, generating a monthly volume of $1200m^3$. The fact of not practicing a segregation process of the residues makes this reuse unfeasible for processes such as the production of OSB and MDF in local industries. A great amount of this material is dispersed in an open field at the sawmill's perimeter and set fire to without producing any benefits. This only brings safety risks to the low-income population that lives in the neighborhood and also a great amount of pollution, due to smoke that is dispersed over the area that is constituted by low-income residences. The objective of this work was in finding an economical solution that reduced the environmental pollution via the vision of Industrial Ecology. The results found result were the generation of electric power in a local thermo-electrical facility.

Key words: Industrial Ecology, Wood residue, Clusters

INTRODUCTION

With to growing reduction of the world's fossil fuels new alternatives of energy supply are appearing and being refined. These alternatives contribute to the carbon dioxide reduction in the atmosphere. Due to Brazil's geographical characteristics, a vast energy production capacity through hydroelectric generation is available. Not all Brazilian regions are provided with the capacity to generate hydropower so other alternatives have to be implemented. According to data from the National Agency of Electric Power (ANEEL) [1], the electric power consumer market presents a growth of 4.5% per year and it will surpass the need of 100 thousand MW in the year of 2008. The Brazilian government, through technical studies, verified that in a medium period there is going to be the need of investments of around two billion and half American dollars to accomplish the expansion of the electrical grid and to attend the growing demand of the consumer market. To accomplish this, alterations in the investment structure in electric power will happen with the installation of thermo electrical generation units. It

* Corresponding author: Phone +55 42 8801-2523
e-mail: tomagner@yahoo.com

is verified, that due to the need of supplying internal demand for electric power, cost reduction and a better management of residues a range of lumber processing industries are installing electric co-generation units in their productive units. In the area where the study was accomplished, two large organizations possess such co-generation systems.

JUSTIFICATION AND DELIMITATION

The intention of this study is to demonstrate that the application of Industrial Ecology (IE) principals can go beyond pollution control. Applying IE it is possible to develop new products or new possibilities of commercial partnerships among organizations; in addition, they develop great benefits, such as economical and environmental, due to better use of the resources.

This work is delimited to analyzing the interaction possibility among a medium size lumber industry with possible industries that can use the not segregated residues that are generated.

INDUSTRIAL ECOLOGY

The analogy with the natural ecosystems is the base for the conception of a new industrial model that breaks the unsustainable path promoted by societies since the beginning of the industrial revolution. Fosch and Gallopoulos popularized the concept of Industrial Ecology, which in synthesis explains that the traditional models of industrial activities; accomplish the extraction of raw materials, develop products to be sold, adding to the production process the disposition of the generated residues. For them this productive model should be transformed in a model that integrates all of the productive activities in a holistic way by this way generating an Industrial Ecosystem [2]. Erkman [3] uses a vision of immediate use for the concept of Industrial Ecology, explaining the exchange among organizations for the creation or reorganizations of industrial districts for the use of residues or by-products.

It is observed by this that Industrial Ecology provides a holistic vision of the industrial systems. By this way, Industrial Ecology is a principal that guides industrial systems towards a sustainable use of natural resources. For the development of a holistic industrial producing vision, there is the need for the development of new productive conglomerates that are integrated production wise.

The concepts of Industrial Ecology can guide business strategies and operational practices for a growing approach to sustainability. The application of this concept is largely associated to the development of industrial conglomerates (clusters) and the reorganization of the existing conglomerates. Promoting the dismemberment of the open lineal industrial systems model, to similar systems found in the natural environment, that is, cyclical systems. Where the productive cycle (extraction/processing/discard) interacts with other processing units in the same system or in other industries. Searching to reduce to the maximum, possible, the entropy and with this resembling the synergy found in natural ecosystems.

With the development of an intra-organizational synergy through the generated residues, there is the possibility of reduction of the energy demand, the reduction of environmental impacts, the development of new business opportunities and the possibility of development of new products. Assuming the form of an industrial symbiosis system.

Chertow [4] explains that industrial symbiosis is constituted by a group of organizations that work in a collaborative form through the exchange not only of residues. They seek the reduction of consumption of natural resources and the reduction in pollutant emissions. In the network formed by this symbiosis there is the union of industries that look for competitive advantage involving the exchange of materials, energy, water and by-products. With this intra-organizational symbiosis, there is the formation of an industrial ecosystem where the cycle is as closed as possible. Gertler [5] explains that a community or a network of companies and other organizations in a region that decide to interact through exchange making use of by-products and or energy, in way to reach benefits, are accomplishing an Industrial Ecology system.

Industrial Ecology can be visualized as being a holistic vision of the industrial process that considers the integration of the components that configure industrial economy in a way that imitates the existent relationships in the biosphere. Another observed factor is the consideration of the technological dynamics that promotes the evolution of technological clusters. Being these

clusters key elements for the transition from the traditional industrial system, to an industrial ecosystem that promotes sustainability.

SUSTAINABILITY

Management in a sustainable manner began to be a requirement so that the organizations prolong permanence in the national and international markets. According to the Brundtland Commission [6], sustainable development is the development that assists to the needs of the present generation without committing future generations. Kraemer [7] comments that society is in a transition period, because the current lifestyle paradigm that promotes individualism, consumption, that all things are disposable and of economic development at any price is shifting in a sustainable direction. The short-term development, of excluding capitalism, does not answer in a satisfactorily manner the concerns with the future. The need for a new direction with a new paradigm, is not yet defined.

By this, it is observed that there is the need for society to act in an integrated manner in all levels and not in the Cartesian method. Robèrt [8] comments that there should not be any conflicts among environmental and economical interests, since human affluence depends on the capacity of nature to recycle debris in the form of generating resources and to provide the indispensable resources for the maintenance of life.

The concern for the environment together with socioeconomic factors made the concept of sustainable development appear. Montibeller Filho[9] and Lerípio [10] explain that the main factor for organizations to alter the perception regarding residues is the search for sustainability.

In synthesis, the vision that the principals of Industrial Ecology promote are the development of a maintainable industrial system. This is due to the maximum sustainable use of all resources.

USING THE CURRENT DEVELOPING LUMBER CLUSTER

Clusters are concentrated groupings of interrelated companies and correlated institutions, in a certain sector, linked by common and complementing elements. The formation of a cluster varies from a single city or state to an entire country or even a net of neighboring countries [11].

Porter explains that the interconnections of a group of companies and institutions in a cluster, accentuates the coordination opportunities and mutual refinement. The interconnections create refinement in areas of common interest, without threatening, distorting competition or restricting the intensity of rivalry, providing an efficient system for dialogue among correlated companies and suppliers. These interconnections bring the opportunity of developing industrial symbioses for residue and energy harness.

A Local Productive Arrangement (LPA) defined by Melo & Casarotto Filho [12] as being a concentration of companies of the same sector, under the form of a structured system, with the presence of interrelations in this group of companies. Cassarotto Filho [13] complements this concept with the following vision: A LPA is a great associative network, through mechanisms of integration of all of the representative entities of the area that are seeking development. The local productive system can be defined as an area strongly structured, containing one or more clusters, with territorial planning, high public and privet interaction, and respecting local culture with the objective of assuring the inhabitants quality of life. In this way, the structured system in the LPA can combine all elements of residue in a manner that a holistic and sustainable vision is achieved.

Albagli and Brito [14] define LPA as being a significant grouping of organizations that act around a main productive activity, as well as correlate companies in the same geographical space (a municipal district, group of municipal districts or region). A LPA possesses a local cultural identity, articulation bonds, interaction, cooperation and learning amongst themselves and with other local organizations. These local organizations can be public and privet institutions, promotion and consultancy, technical schools and universities, research institutions, class entities and support institutions to organizations. The possibilities of the implementation of Industrial Ecology as a policy are possible due to the fact that public, private and educational organizations can promote and develop the needed support for the integration and development of a sustainable management system.

LPA or clusters possess the function of strengthening key organizations and the organizations and institutions that supply their needs, such as technological demands and of raw materials. According to Porter [15], the more the groupings grow more resources tend to flow to them and moves away from organizations that work in an isolated manner. This aspect detaches the importance of the geographical proximity among the industries, many times, in a single city or area of a country. The geographical concentration integrates and strengthens the process, this way maintaining the developed competitive advantages and facilitating the implementation of the processes needed in Industrial Ecology.

THE LUMBER LPA

In spite of the lumber cluster in the region is still growing according to the Institute of Forest Handling and Agricultural Certification (IMAFLORA), the state of Parana, is responsible for more than 60% of the national production of lumber blocks. The lumber used in the LPA is from plantation pine forests of *Taeda and Eliottis Pine.* These are the main species grown in the South and Southeast of the country. The States of Parana is one of the largest cultivators of forests with these species and it is in this area that the industry is concentrated. This wood is utilized due to the great acceptance in the international market, besides being the species that is planted abundantly in the region because its adaptation to climate condition.

This opens opportunities for the implementation of Industrial Ecology because the lumber cluster is still in development in the Ponta Grossa region, and adaptation is still possible.

LPA EVOLUTION

It is observed, through field research, that the lumber LPA of the Ponta Grossa area is in an intermediate state of evolution. It is between Phase 02 and the Phase 03 as it can be observed in illustration 01, where not all of the organizations are interlinked, but begin the process in a slow manner, mainly because the lack of a clustering development policy.

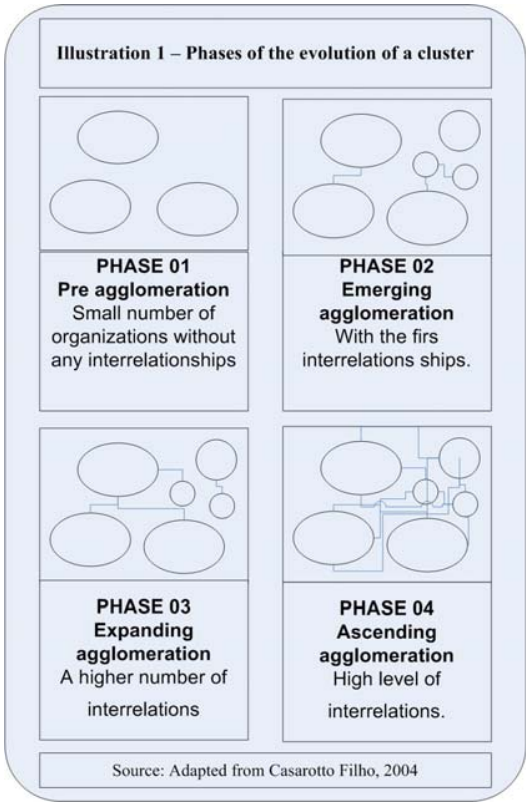

The interrelation process in the LPA is in a stage that only the raw material suppliers are interlinked. This initial stage opens the possibility to develop not only clustering policies but also policies that encourages lumber organizations to develop internal waste management systems. These management systems would treat waste as new raw materials for other organizations and not only as a problem to be solved.

This LPA is intensity more developed in the production sector. It is in this area that the largest interrelations are observed among organizations. The organizations that in the initial production phases accomplished the totality of the production process are now modifying their systems. A segregation of the production process is happening in the LPA. Countless companies are only accomplishing the unfolding of the logs and the drying of the boards and reselling this material. Other organizations are acquiring the boards and transforming them in goods.

This growing segregation of the production processes is opening opportunities for new organizations that can develop new products with

the generated waste. In this phase, only energy is being produced.

OBJECTIVE

The general objective of this study is to verifying the possibility in developing a symbiosis between the studied organization and a larger organization that can take advantage of the generated residues.

To accomplish such objective the following specific objectives were elaborated:

- Verify the current model of residue management of the organization;
- Analyze through the principals of Industrial Ecology the possible alternatives for the destination of the residues.

THE CASE STUDY

The analyzed organization will be a medium size organization, possessing 25 employees. It is located in the municipal district of Ponta Grossa State of Parana, a southern state of Brazil, in a periphery neighborhood with a low-income population.

The industrial activity is the production of wooden fences for the North American and European markets. The wood used is Taeda Pine and Eliotis Pine, from reforestations in the vicinity of the city.

The fences are the "Dog Ear" model. This fence possesses a simple, economical and easy production design. One of the extremities of the fence is cut in an angle that results in the aspect of a dog-ear. The following dimensions are processed; 1280 mm of length, 150 mm of width and 254 mm of thickness and the finish is accomplished through a planer.

For the fence production, it is necessary only the superior part of the log, this is because this section possesses the necessary dimensions and has a reduced market price due to the limited use for other products. After having dismembered the logs in to boards of varied dimensions, they are exposed outdoors for air-drying until reaching a medium coefficient of humidity of 18% in a period of 7 to 10 days, to achieve the final product with the intended quality.

CURRENT MODEL OF RESIDUE MANAGEMENT

During the productive process, daily there is a generation of approximately $50m^3$ of residues. The average total volume of residues generated monthly is of $1200m^3$, and these residues do not possess a specific destiny. Such fact is due to the non-accomplishment of a segregation of the material, that it is constituted of several types of sawdust. This sawdust is composed of small particles of dust to larger pieces with an average of 15 cm x 40 cm x 2,54cm. The non-segregation incapacitates the possibility to designate the residue for the traditional processes of reuse, which is the production of OSB and MDF in a local industry that needs this material with appropriate characteristics.

In the process of drying the wood a dry kiln is not used, what impedes in not using the sawdust for feeding of a boiler system. By this way a percentage of this material is dispersed in an open field on the perimeter of the sawmill, that later fire is set to, not producing any environmental or economical benefit. It is noticed that this action brings risks to the safety of the industry, to the employees and generates atmospheric pollution due to smoke that disperses in the whole area of the factory and to the neighboring houses. A percentage of the residue is given freely to local farmers that use the sawdust as animal beds for poultry and swine breading. A percentage is taken to a sanitary landfill, generating transport increment cost and occupying the landfill with useful material.

This management model is common among the small and medium lumber mills found in the area of the study. Such model is unsustainable due to the non-use of existing opportunities and of the generated pollution. The development of a local and regional policy that foments the principal of Industrial Ecology would generate the possibility to reformulate the current models of residue management.

WASTE MANAGEMENT WITH INDUSTRIAL ECOLOGY PRINCIPALS

Following the principals proposed by Industrial Ecology an initial management plan for the sawdust residues was developed, where low cost modifications were proposed to be implemented.

The first modification to be accomplished is the construction of an enclosed area where the residues are gathered. This allocation of the sawdust in a single enclosed area avoids the danger of possible fires and makes possible a calculation with larger precision of the generated volume.

The second modification in the process is to enter in contact with other larger mills, which possess a thermo electrical unit fed with wood residues. It is observed that the samples of the residue should be tested and approved for the used in the electric power generation, generating the first symbiosis among organizations.

The third modification is the contact with a factory that produces boxes for the accommodation of fruits. Usually this type of organization possesses conditions of using the 150 mm x 400 mm boards that are discarded in the production of the fences. This action generates the second symbiosis among organizations.

The next stage is the proposal for the development of a log debarker. The process of removing the tree bark will make it possible that the bark is sold to local breeders in the area and part of the sawdust can be sold to the local MDF/OSB production facility.

It is proposed that the project for the development of the debarker equipment is accomplished by the local CEFET PR (Federal Center of Technological Education) generating the possibility of a greater interaction between the industry and university.

CONCLUSION

This study allowed the visualization of the opportunities for the development of Industrial Ecology with simple actions in developing countries. The possibility to create a symbiosis between organizations and universities that develop a change in the current non-sustainable paradigm. This change modifies the vision of the generation of residues without destination to the generation of new raw materials, which will produce business opportunities will still reduce the negative impact over the environment.

It is observed that the rearrangement of the current industrial agglomerates in the molds of Industrial Ecology and of sustainable development should also be a focus for the development local and regional policies. Without this collaboration and stimulation, industries that need modification in the production cycle will not be reached.

Another observed factor is the non-existence of professionals, inside of organizations of this activity, responsible for the management and development of new destinies for the generated residue. In addition there is no simulation, on behalf of the municipality responsible for industrial development, in the readapting the industrial system for a sustainable reality.

REFERENCES:

[1]ANEEL - http://www.aneel.gov.br/ access on the 03rd of October 2004

[2] Korhonen J., Savolainen I., Ohlstro M. *Applications of the industrial ecology concept in a research project: Technology and Climate Change (CLIMTECH) Research in Finland.* Journal of Cleaner Production 12 2004

[3] Erkman S. *Industrial ecology: a historical view.* Journal of Cleaner Production 05 1997

[4] Chertow, M. et al. *Thinking ecologically.* New Haven. Yale University Press 1997

[5] Gertler, N. *Industrial ecosystems: Developing sustainable industrial structures.* Massachusetts Institute of Technology, Cambridge, MA 1995.

[6] CMMAD. *Nosso Futuro Comum.* FGV São Paulo, 1991

[7]Kraemer, T. H. *Modelo Econômico De Controle E Avaliação De Impactos Ambientais - MECAIA* - Tese Doutorado - Programa de Pós-Graduação em Engenharia de Produção da Universidade Federal de Santa Catarina – 2002.

[8]Robèrt K. *The Natural Step: A historia de uma revolução silenciosa.* Cultrix, São Paulo 2002

[9]Montibeller Filho, G. *O mito do desenvolvimento sustentável: meio ambiente e custos sociais no moderno sistema produtivo de mercadorias.* Florianópolis. Ed. da UFSC 2001.

[10]Leripio, A. *GAIA - um método de gerenciamento de aspectos e impactos ambientais.* Tese de Doutorado em Engenharia de Produção. Programa de Pós-Graduação em Engenharia de Produção, UFSC, Florianópolis 2001.

[11] Porter, M. E. *Clusters and the new economics of competition.* Harvard Business Review USA 1998.

[12] Melo and Casarotto Filho, N. *Cluster e a importância das pequenas e médias empresas: a variante italiana***.** Florianópolis: UFSC, 2000.

[13] Casarotto Filho, N. *Instrumentos De Integração E Governança Em Aglomerações Competitivas* Departamento de Engenharia de Produção e Sistemas, UFSC www.ucdb.br/coloquio/arquivos/Casarotto.pdf

[14] Albagli, S. and Brito, J**.** *Arranjos Produtivos Locais: Uma nova estratégia de ação* RedeSist, 2002.

[15] Porter, M. *A vantagem competitiva das nações.* Rio de Janeiro: Campus, 1993.

Proceedings of ECOS 2005
Trondheim, Norway
June 20–22, 2005

ENVIRONMENTAL AND ECONOMIC ASSESSMENT OF AN INTER-INDUSTRIAL AND INTER-REGIONAL WASTE RECYCLING SYSTEM IN JAPAN

Takuya Hara, Yoshikuni Yoshida and Ryuji Matsuhashi
The University of Tokyo
Graduate School of Frontier Sciences
113-0033 Tokyo
Japan

Hirokazu Shima
Mitsubishi Materials Corporation
Omiya Research Center
Japan

ABSTRACT

In this study we investigate an inter-industrial and inter-regional recycling system for industrial waste by the cement industry in Japan. We develop a linear programming model that represents cement production processes and waste transportation of all cement factories in Japan. We assess inter-regional material flows of industrial waste, and environmental effects of recycling.
Keywords: Recycling, Cement, Transportation, Linear programming

NOMENCLAUTURE

Index

h	index of cement factory (1-36)
i	index of steel factory (1-18)
j	index of coal-fired power station (1-32)
k	index of cement production process (1-6)
m	index of railway station (1-72)
n	index of port (1-64)
p	class of node of transport network (*h, i, j, , m, n*)
q	class of node as waste generation (*i, j*)
prod	index of cement product (*clinker, portland cement, blast-furnace cement, flyash cement*)
w	index of waste (*slag, flyash*)

Variable

cementCO2	total CO_2 of cement production [tCO_2]
cementCost	total cost of cement production [¥]
railCO2	CO_2 of transport by railroad [tCO_2]
railCost	cost of transport by railroad [¥]
roadCO2	CO_2 of transport by truck [tCO_2]
roadCost	cost of transport by truck [¥]
seaCO2	CO_2 of transport by internal navigation [tCO_2]

seaCost cost of transport by internal navigation [¥]

totalCO2 Total CO_2 of cement production and waste transportation [tCO_2]

totalCost Total cost of cement production and waste transportation [¥]

tRail(*w,m,m'*) amount of waste transported by railroad from m to m' [t]

tRoad(w,p,p') amount of waste transported by road from p to p' [t]

tSea(*w,n,n'*) amount of waste transported by railroad from n to n' [t]

x(*h, k*) amount of cement production at cement factory h, process k [t]

y(*w, h*) amount of waste utilization at cement factory h [t]

Constant

*cCemen*t cost of cement production [¥/t]

cRail cost of transport by railroad(proportional factor) [¥/t]

cRailInt cost of transport by railroad(intercept) [¥/t]

cRoad cost of transport by road(proportional factor) [¥/t]

cRoadIn t cost of transport by road(intercept) [¥/t]

cSea cost of transport by internal navigation(proportional factor) [¥/t]

cSeaInt cost of transport by internal navigation(intercept) [¥/t]

co2Cement CO_2 of cement production [tCO_2/t]

co2Rail CO_2 of transport by railroad [tCO_2/t]

co2Road CO_2 of transport by road [tCO_2/t]

co2Sea CO_2 of transport by internal navigation [tCO_2/t]

a(l,k) input output coefficient of cement production at process k (*l :prod, w*) [t/t]

d(*p,p'*) distanceof p and p' (*p:h, i, j, m, n*) [km or mile]

Demand(*prod*) amount of demand of cement product [t]

f(*w, j*) amount of waste generated at coal-fired power station [t]

s(*w, i*) amount of waste generated at steel factory [t]

INTRODUCTION

In Japan, there is a growing concern that a shortage of landfill space will become a big issue in the near future, due to the great amount of waste generated and the difficulty of the expansion of landfill capacity. Recycling is considered as a key way to decrease the final disposal waste

Industrial ecology, a recent and interdisciplinary field, provides a concept to deal with such problems: The basic idea is to design an inter-industrial recycling system that utilizes waste from one industry as a resource for other industries, and that reduces the amount of waste emitted from the entire system, as well as the resources extracted from the environment. Seen from such a perspective, the cement industry can represent the central part of the system, because diverse wastes can be used as raw materials in the cement production processes.

The Japanese cement industry already utilizes substantial amounts of industrial waste, such as blast furnace slag from the steel industry, and fly ash from coal-fired power stations and other industries. Increased recycling of waste in the cement industry is expected to reduce energy consumption and CO_2 emissions, and to reduce the final disposal of waste from other industries.

When assessing the feasibility and environmental effects of recycling, it is important to consider the long-distance transport of waste that occurs as a consequence of the disparate location of cement factories in Japan. The increasing cost of waste transportation can be a bottleneck for encouraging the spread of recycling systems. In order to design an inter-industrial and inter-regional recycling system, it is essential to appraise the information about the location and the amount of sources of waste, and the capacity of recycling at the cement factories.

There are several studies that deal with environmental effects of the recycling of industrial wastes in the cement industry. Although Fujiwara et al [1] developed environmental input-output table and estimated the reduction of CO_2 emission by the recycling, the cement process model developed in this study is insufficient to describe the real process. Wada et al [2] developed a linear programming model including a sub-model of waste transportation to evaluate environmental effects caused by the increasing of waste-mixed cement production. The sub model of waste transportation can consider all possible transport between sources of blast furnace slag or coal fly ash and cement factories in Japan. This model, however, is inadequate because it considers only road transport.

In this study we investigate an inter-industrial and inter-regional recycling system for industrial waste recycled by the cement industry in Japan. We develop a linear programming model that represents cement production processes and waste transportation of all cement factories in Japan. We assess inter-regional material flows of industrial waste, and environmental effects of recycling.

MODEL

Overview

The model in this study consists of two parts; one part is a model of transport process between sources of blast furnace slag or coal fly ash and cement factories, and the other part is a model of cement production processes that utilize natural resources or wastes. The model is a linear programming model combining two problems: 1) the optimal transport of wastes and 2) the optimal production of cement factories. These two problems are solved simultaneously. We set two objective functions; minimizing the total system cost and minimizing the total CO_2 emission from the system.

Formulation

The formulation of the model is as follows.

Objective function I

minimize $totalCost$

$$totalCost = cementCost + roadCost + railCost + seaCost \quad (1)$$

$$cementCost = \sum_h \sum_k cCement(k) \cdot x(h,k) \quad (2)$$

$$roadCost = \sum_w \sum_p tRoad(w,p,p') \times [d(p,p') \times cRoad + cRoadInt] \quad (3)$$

$$railCost = \sum_w \sum_m tRail(w,m,m') \times [d(m,m') \times cRail + cRailInt] \quad (4)$$

$$seaCost = \sum_w \sum_n tSea(w,n,n') \times [d(n,n') \times cSea + cSeaInt] \quad (5)$$

Objective function II

minimize $totalCO2$

$$totalCO2 = cementCO2 + roadCO2 + railCO2 + seaCO2 \quad (6)$$

$$cementCO2 = \sum_h \sum_k co2Cement(k) \cdot x(h,k) \quad (7)$$

$$roadCO2 = \sum_w \sum_p tRoad(w,p,p') \times co2Road \quad (8)$$

$$railCO2 = \sum_{w} \sum_{m} tRail(w,m,m') \times co2Rail \quad (9)$$

$$seaCO2 = \sum_{w} \sum_{n} tSea(w,n,n') \times co2Sea \quad (10)$$

Constraints

1) a model of cement production processes

$$\sum_{k} a(w,k) \cdot x(h,k) = y(w,h) \quad (11)$$

$$\sum_{h} \sum_{k} a(prod,k) \cdot x(h,k) \geq Demand(prod) \quad (12)$$

2) a model of waste transportation process

$$y(w,h) = \sum_{i} tRoad(w,i,h) + \sum_{m} tRoad(w,m,h) + \sum_{n} tRoad(w,n,h) \quad (13)$$

$$s(w,i) \geq \sum_{h} tRoad(w,i,h) + \sum_{m} tRoad(w,i,m) + \sum_{n} tRoad(w,i,n) \quad (14)$$

$$f(w,j) = \sum_{h} tRoad(w,j,h) + \sum_{m} tRoad(w,j,m) + \sum_{n} tRoad(w,j,n) \quad (15)$$

$$\sum_{i} tRoad(w,q,m) + \sum_{n} tRoad(w,n,m) + \sum_{m'} tRail(w,m',m) = \sum_{i} tRoad(w,m,q) + \sum_{n} tRoad(w,m,n) + \sum_{m'} tRail(w,m,m') \quad (16)$$

$$\sum_{i} tRoad(w,q,n) + \sum_{m} tRoad(w,m,n) = \sum_{n'} tSea(w,n,n') \quad (17)$$

$$\sum_{n'} tSea(w,n',n) = \sum_{h} tRoad(w,n,h) + \sum_{m} tRoad(w,n,m) \quad (18)$$

Equation (11) expresses the material balance between processes of the cement production. Equation (12) is a constraint that the total amount of cement produced must be larger than the total demand of cement. Equation (13) expresses that the amount of waste utilized for a factory h equals to that of waste transported to a factory h. Equation (14) and (15) expresses that the total amount of waste transported from a source i or j is less than that of waste generated at i or j. Equations from (16) to (18) are constraints on waste transportation processes, which set the material balance at the nodes of the transport network.

Cement production processes

The flow diagram of the cement production is shown in Figure 1. The cement production processes consist of the clinker production process and the cement mixing process. At the clinker production process, clinker is produced by calcinating limestone, clay and other raw materials. At the cement production process, cement is produced by crushing and mixing clinker and gypsum. The cement mixed with wastes at the cement production process is called blast furnace cement or fly ash cement, because of its unique characteristics. These cement types are mainly utilized in public civil engineering and construction because of their strength and workability. In this model, we distinguish three types of cement, and set their demands respectively. Despite the difference of raw materials used in blending, we assume that there is only one type of clinker with average characteristics.

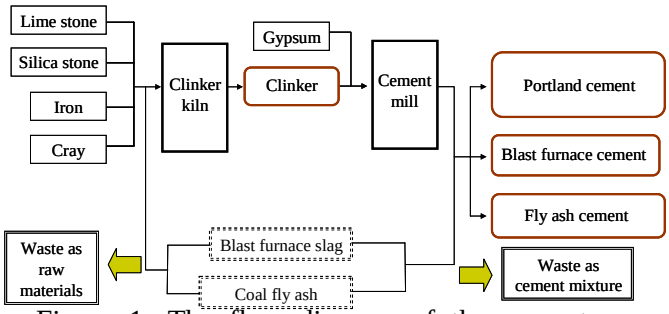

Figure 1: The flow diagram of the cement production

Input-output data of the cement production processes are shown in Table 1. In this table, a negative number means input to the process. For example, material inputs are gypsum (0.02), blast furnace slag (0.40) and clinker (0.58) for a unit amount of the product of the blast furnace cement. The process costs are represented by ¥(yen)/t (1,000yen 7.17euro). The data sources are the Japanese input-output table [3], blending calculation of cement [4], and statistics of cement

industry [5].

Table 1: The input output table of the cement production processes

		cement production processes					
		1	2	3	4	5	6
		clinker (natural resource)	clinker (blast furnace slag)	clinker (coal fly ash)	portland cement	blast furnace cement	fly ash cement
raw materials	limestone	-1.20	-0.98	-1.21	0	0	0
	other materials	-0.34	-0.16	-0.18	0	0	0
	gypsum	0	0	0	-0.04	-0.02	-0.04
wastes	blast furnace slag	0	-0.29	0	-0.02	-0.40	0
	coal fly ash	0	0	-0.14	0	0	-0.20
products	clinker	1	1	1	-0.94	-0.58	-0.77
	portland cement	0	0	0	1	0	0
	blast furnace cement	0	0	0	0	1	0
	fly ash cement	0	0	0	0	0	1
unit		t	t	t	t	t	t
CO2 intensity (t-CO_2/t)		0.87	0.72	0.87	0	0	0
cost (\/t)		7,097	6,848	7,106	1,058	1,169	929

Waste transportation process

The overview of the waste transportation process model is shown in Figure 2.

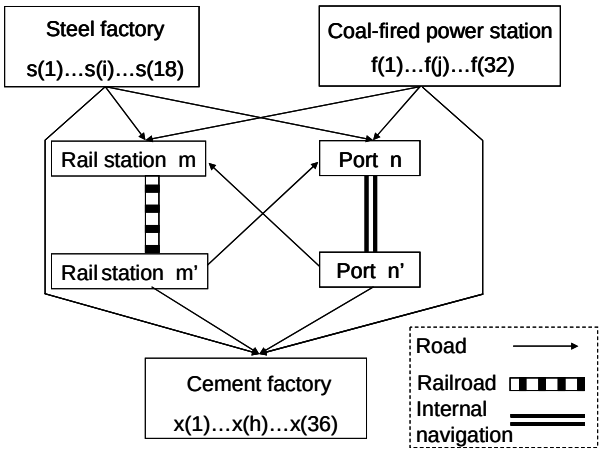

Figure 2: The overview of the waste transportation process

The model deals with three transportation modes; road, rail, and internal navigation (shipping). We use data for the fiscal year 2000 about the amount of waste generated in the steel factories and the coal-fired power stations. In Japan, there are 36 cement factories, 18 steel factories with blast furnaces, and 32 coal-fired power stations. The model includes 72 major railway stations and 64 ports as nodes of the transport network.

The transport costs and the CO_2 intensity of transport are shown in Table 2 [6].

Table 2: Transport cost and CO_2 intensity

Transport cost function	
Road (\/t)	1500 + 18.5×d(km)
Railroad (\/t)	951 + 4.34×d(km)
Internal navigation (\/t)	1300 + 4.26×d (mile)

CO_2 intensity of transport		
Road	(t-CO_2/t-km)	1.74×10^{-4}
Railroad	(t-CO_2/t-km)	2.10×10^{-5}
Internal navigation	(t-CO_2/t-mile	7.04×10^{-5}

SIMULATION AND RESULT

We apply the model to simulate an inter-industrial and inter-regional recycling system in Japan. The demand of cement products and the amount of waste recycled as cement materials are valid for the fiscal year 2000. Using GAMS (General Algebraic Modeling System) [7], an optimization software, we calculate the system that minimizes both cost and CO_2–emissions. The amounts of waste generated and utilized at each factory are aggregated into 10 regions as shown in Figure 3. The amount of waste transportation of each region and each mode will be shown as the result of the simulation.

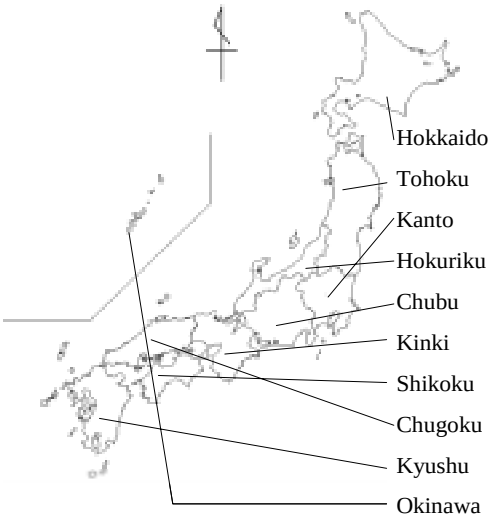

Figure 3: 10 regions in Japan

The capacity of cement production of all factories is shown in Figure 4.

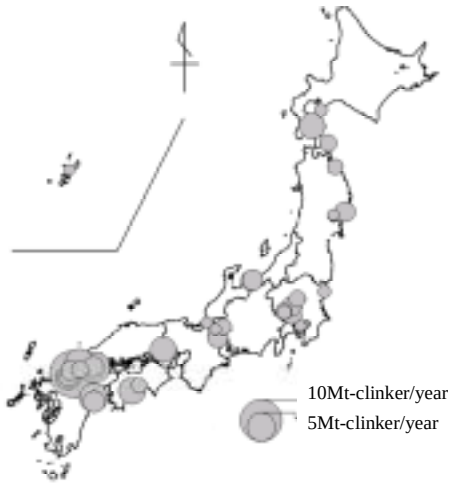

Figure 4: The capacity of the cement production of all factories

Cost-minimizing system

The amounts of waste generated and transported to cement factories in each region are shown in Figure 5. The amounts of waste utilized for cement production in each region are shown in Figure 6. There are wastes transported inter-regionally, so that the amount of waste in one region in Figure 5 and Figure 6 is not necessarily the same.

Blast furnace slag generated in Kanto and Chugoku , and coal fly ash generated in Tohoku are not utilized in the cement industry as much as other regions.

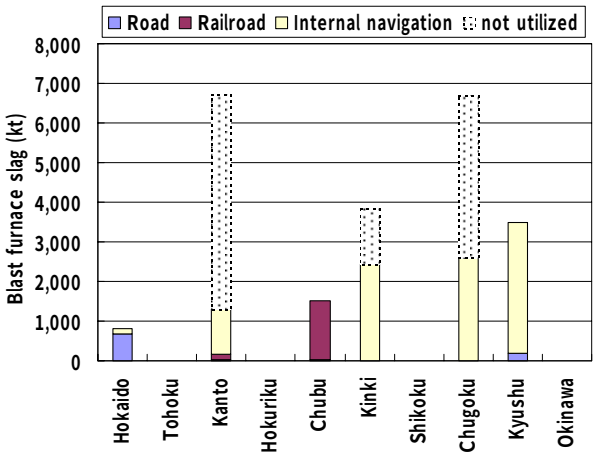

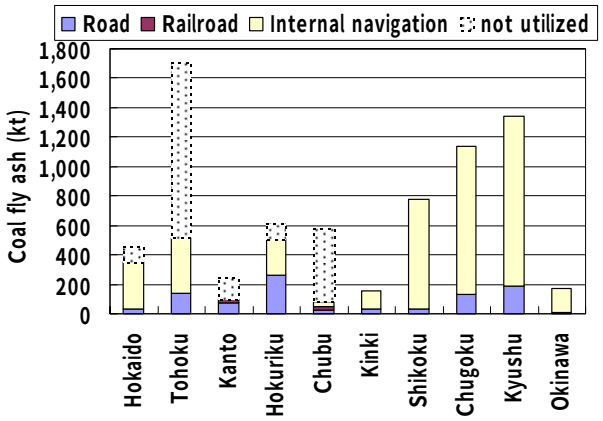

Figure 5: The amounts of wastes generated and transported to cement factories
(upper: blast furnace slag, lower: coal fly ash)

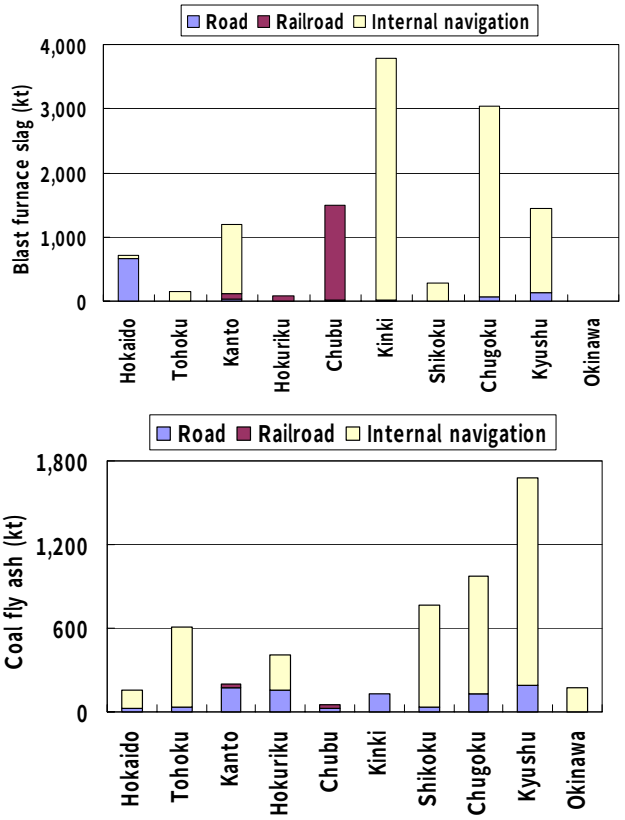

Figure 6: The amounts of wastes utilized for cement production
(upper: blast furnace slag, lower: coal fly ash)

The main transportation mode used is internal navigation, because road and rail are associated with high cost.

CO_2-minimizing system

The amounts of wastes generated and transported to cement factories in each region are shown in Figure 7. The amounts of waste utilized for cement production in each region are shown in Figure 8. There are wastes transported inter-regionally, so that the amount of waste in one region in Figure 7 and Figure 8 is not necessarily the same.

Blast furnace slag generated in Kanto and Chugoku , and coal fly ash generated in Tohoku are not utilized as much as other regions.

Contrary to the result of the cost-minimizing system, rail transport is used more because of its low CO_2 intensity.

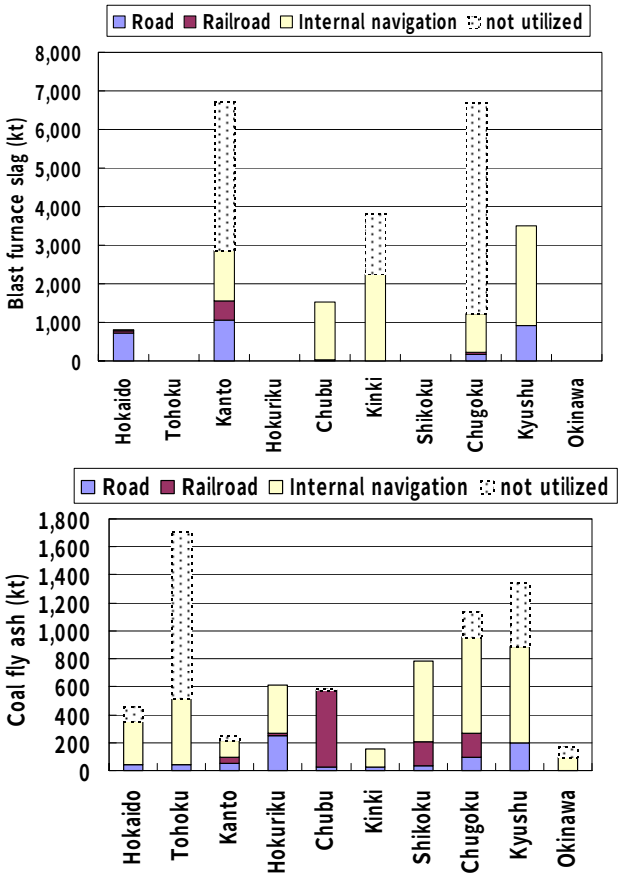

Figure 7: The amounts of wastes generated and transported to cement factories

(upper: blast furnace slag, lower: coal fly ash)

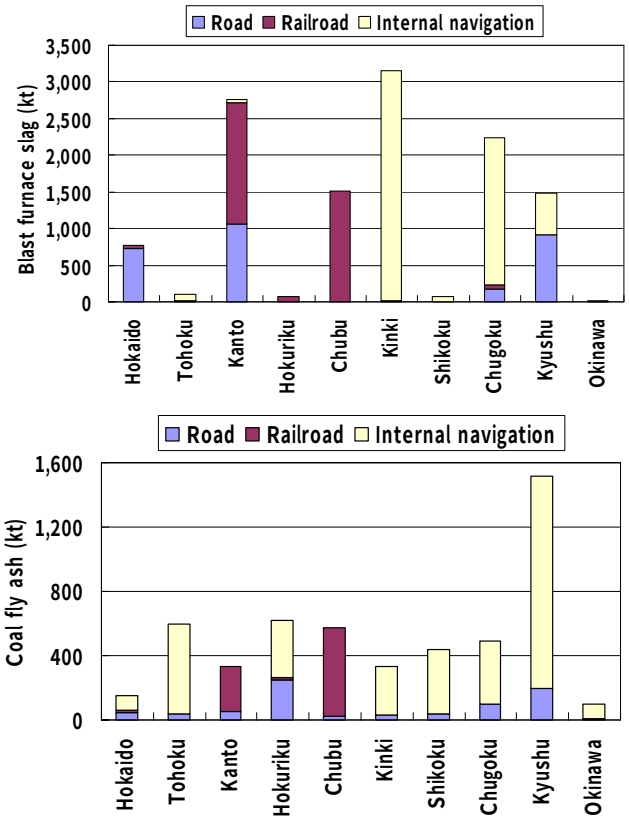

Figure 8: The amounts of wastes utilized for cement production

(upper: blast furnace slag, lower: coal fly ash)

DISCUSSION

We discuss differences between the result of the cost-minimizing and the CO_2-minimsing systems. The difference between the amounts of wastes utilized for cement production in each region is apparent, whereas the difference between the amounts of wastes generated and transported in each region is not significant. With regard to blast furnace slag, the amount utilized in Kanto is higher in the CO_2-minimizing system compared to the cost-minimizing system. Regarding coal fly ash, he amount utilized in Chubu and Kinki is higher in the CO_2-minimizing system. The difference is due to the difference of the transportation, that is whether rail is used or not. With respect to the

CO_2-minimizing system, waste transportation to the inland cement factories by railway is high.

The total cost and total CO_2 emissions of each system are shown in Table 3. The total cost of the CO_2-minimizing system is 2% higher than that of cost-minimizing system; on the other hand, the CO_2 emissions of each system are almost same. That is because the ratio of the transport cost to the total cost is much higher than that of the transport CO_2 to the total CO_2.

The CO_2 emissions from the transport process are negligibly small compared with those occurring during the cement production processes. Hence, when considering the reduction of CO_2 emission, it is more important to increase the usage of the mixed cement and the recycle of wastes for the cement production. The waste transportation is less important to CO_2 emission, but affects the total cost. In conclusion, the waste transportation is important in order to encourage recycling waste for a cement production, in respect of the cost, and the recycle leads to CO_2 reduction.

Table 3: Total cost and CO_2 emission

Cost (10^{10}yen)

	Cement production process	Waste transportation process	Total
Cost minimum sytem	58.8	2.7	61.5
CO_2 minimum sytem	58.8	4.0	62.8

CO_2 emission (10^6 t-CO_2)

	Cement production process	Waste transportation process	Total
Cost minimum sytem	60	0.066	60
CO_2 minimum sytem	60	0.051	60

CONCLUSION

We have developed inter-industrial and inter-regional waste recycling model. We simulate cost and CO_2-minimizing systems, and find viable solutions. In conclusion, the waste transportation is important in order to encourage recycling waste for cement production, with respect to the cost, as well as to CO_2 reductions. Thus, making waste transportation more efficient is an effective means for CO_2 reduction.

REFFERENCES

[1] Fujiwara K et al. *Recommending the Use of Blast Furnace Cement to Reduce CO2 Emission*. Keio Economic Observatory Occasional Paper No.21. Tokyo: Keio University, Institute for Economic and Industry Studies, 1995.

[2] Wada M and Hammad *A. Study on the Recycling Planning of Industrial By-products in the Cement Industry*. Environmental Systems Research 2000;28:33-38. (in Japanese)

[3] Management and Coordination Agency Government of Japan. *1995 Input-Output Tables.* Tokyo: Research Institute of Economy, Trade and Industry., 1999

[4] Shima H. *Study on Concrete Recycling System by High Quality Recycled Aggregate*. Ph.D thesis at the University of Tokyo., 2004. (in Japanese)

[5] Japan Cement Association. *Cement Handbook*.Tokyo: Japan Cement Association., 2001. (in Japanese)

[6] *Ministry of Land, Infrastructure and Transport*.CO_2 intensity of transportation. See also: http://www.mlit.go.jp/seisakutokatsu/freight/butsuryu-deta.html (in Japanese)

[7] Brooke A et al. GAMS a user's guide. Washington: GAMS development corporation., 1998.

Process integration

Proceedings of ECOS 2005
Trondheim, Norway
June 20–22, 2005

ENERGY LEVEL COMPOSITE CURVES – FROM THEORY TO PRACTICE

Rahul Anantharaman[1], Ola Sørås and Truls Gundersen
Norwegian University of Science and Technology
Department of Energy and Process Engineering
N-7491 Trondheim
Norway

ABSTRACT

Energy Level Composite Curves (ELCC) – a synergy of Exergy Analysis and the Composite Curves of Pinch Analysis – is a novel method for the integration of energy intensive processes that was recently developed by our group. This was the first methodological attempt to represent thermal, mechanical and chemical energy in a graphical form similar to Composite Curves.
In this paper, we present a simplified methodology that represents the thermal and mechanical energy of a process in a graphical form and a preliminary energy targeting strategy is developed for use with the ELCC. Results and our experiences of applying this new methodology for the energy integration of a methanol plant in Norway are also presented.
Keywords: Energy Integration, Energy Level, Composite Curves, Utility Targeting

NOMENCLATURE

Ex	Exergy (kW)
H	Enthalpy (kW)
P	Pressure (bar)
Q	Heat (kW)
T	Temperature (ºC)
S	Entropy (kW/ºC)
W	Shaft work (kW)
η_c	Carnot Efficiency
Ω	Energy Level

Subscripts

$_0$	Reference State

Superscipts

^{s}	Supply condition
^{t}	Target condition

INTRODUCTION

Pinch Analysis is a thermodynamic approach to energy integration based on simple, yet powerful, graphical representations; but fails to account for changes in pressure and chemical composition in the process under consideration. Exergy Analysis identifies major causes of thermodynamic imperfections in thermal and chemical processes. Exergy based methodologies, however, lack the simple representations that have made Pinch Analysis well recognized and applied in the process industries. Further, there is no direct link between exergy and cost; in many cases exergy and cost are competing properties of a plant. Optimization methodologies enable the engineer to address the multiple trade-offs that are an integral part of energy integration which would not be possible to solve manually. The downside of this is that optimization is not simple and at present cannot solve large industrial problems due to combinatorial explosion (binary variables used to model discrete decisions) and local optima problems (non-linear and non-convex models).

ENERGY LEVEL COMPOSITE CURVES

The Energy Level Composite Curves (ELCC) [1] is a novel method for energy integration developed by our group that incorporates pressure and composition changes in the process in addition to temperature. ELCC, a graphical tool, draws on

[1] Corresponding author: Phone: +47 7359 6937 Fax: +47 7359 8390 E-mail: rahul.anantharaman@ntnu.no

earlier strategies of Combined Pinch and Exergy Analysis [2] and Composite Curves of Pinch Analysis [3], [4], [5].

Energy Level

Energy Level (Ω) is defined as [2]:

$$\Omega = \frac{Exergy}{Energy} \qquad (1)$$

This definition of energy level enables graphical representation of processes involving energy in terms of heat and work. Table 1 lists energy levels for some special cases.

Case	Energy Level
Work	1
Heat	$\eta_c = 1 - T_0 / T$
Steady state flow system	$\Delta Ex / \Delta H$

Table 1: Energy levels for special cases

The Energy level concept was introduced [2] to visualize energy quality loss in a process unit and screen for potential process modifications.
Rather than evaluate the energy level of a process unit, it was observed by Anantharaman et al. [1], that evaluating energy level at the supply and target conditions of a process stream gives a better understanding of the energy requirements and behavior of the stream. This is similar to Pinch Analysis where stream supply and target temperatures are considered to evaluate the heat content of the stream.
A stream with increasing energy levels is an energy sink and a stream with decreasing energy levels is an energy source. Further extending the analogy to Pinch Analysis, an energy source at higher energy levels can be integrated with an energy sink at lower energy levels.
Thus, energy level in ELCC is equivalent to temperature in Composite Curves of Pinch Analysis.

Evaluating Energy Level
Energy level at supply and target conditions is evaluated as:

$$\Omega = \frac{(H - H_0) - T_0 (S - S_0)}{H - H_0} \qquad (2)$$

In this paper, only pressure and temperature contributions to exergy are taken into account for evaluating energy level as the focus is mainly on identifying opportunities for pressure exchange (in the form of shaft work) in addition to heat exchange. This simplification is a necessary first step to develop a systematic method for temperature and pressure exchange before considering composition. The implication is that streams undergoing composition change cannot be analyzed by this method.
This simplification would be unacceptable in the exergy analysis of a chemical plant where exergy and energy accounting is carried out.
Evaluating energy level using Equation 1, incorporating chemical exergy, involves developing a new and common reference state calculation procedure for enthalpy and exergy that ensures positive values. This is a principle area of research in our group.

ELCC – construction and analysis

The Energy Level – Enthalpy diagram is constructed by plotting energy level intervals of process streams against cumulative values of enthalpy differences – similar to the construction of Composite Curves in Pinch Analysis. There are two curves – one for energy level increasing streams (energy sink curve) and the other for energy level decreasing streams (energy source curve).
A step-by-step procedure for constructing an ELCC is detailed in [1] with an example.
The analysis of an ELCC is similar to Composite Curves in Pinch Analysis. The ELCC provides physical insight to the engineer regarding energy integration between the streams on the energy source curve and the energy sink curve.
When considering heat transfer between streams, Table 1 shows that the principle of transferring energy from a higher energy level value to a lower value is valid as higher temperature streams will have higher energy level.
Similar to the idea of vertical heat transfer between Composite Curves to minimize heat transfer area, one would expect that streams on the

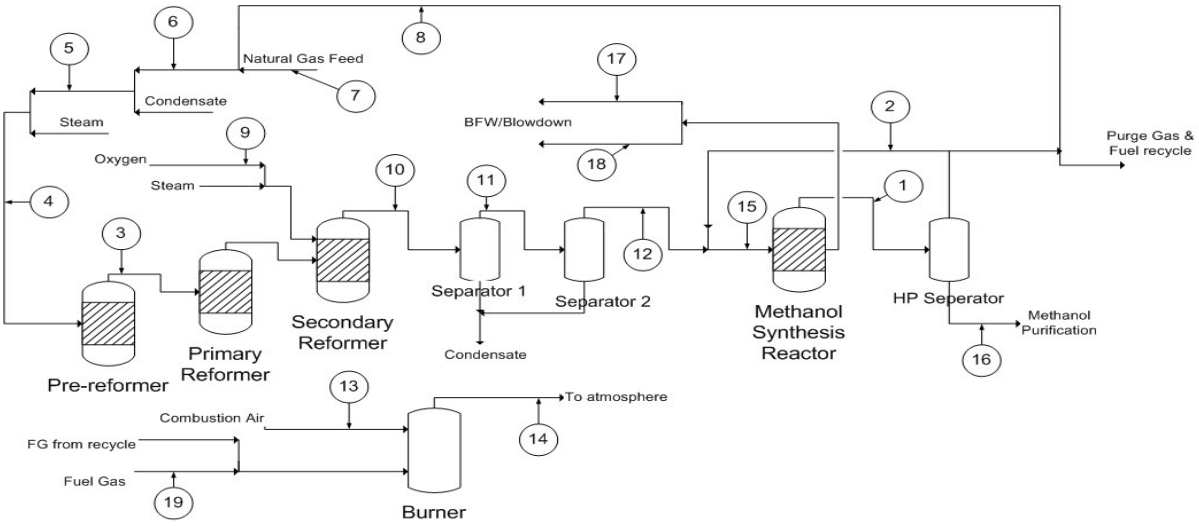

Figure 1: Methanol Plant case study process flow sheet with stream numbers

energy source curve should be integrated with streams placed adjacently below on the energy sink curve to maximize total energy integration. Further, one would also expect that, integration between energy sources and sinks should start where the vertical distance is the least.

An important aspect of the ELCC is that it functions as an idea generator rather than a design generator. This methodology cannot give any explicit recommendation for integration between process units. A high energy level of a stream can be caused by high pressure or high temperature or a combination of these. Obviously, we have to distinguish between pressure exchange and heat exchange.

To alleviate this drawback, and to identify scope for integration, a preliminary targeting methodology has been developed in this paper that can be used together with the ELCC.

The authors have developed an Excel Add-in, called HYSYSLink, to construct the ELCC from a HYSYS simulation.

METHANOL PLANT CASE STUDY

The methanol process is ideally suited for energy integration studies using this methodology as it is an energy intensive process with an enormous interplay of thermal, mechanical and chemical energy in the plant. In our earlier work, [1] and [6], we tested the methodology on a simple literature based simulation of a methanol plant.

In this work, a methanol plant in Norway is used to test the efficacy of the methodology for industrial cases. The utility system was not included in these energy integration studies to simplify the case under consideration.

Figure 1 shows the process flow diagram for the methanol plant under consideration. The 900,000 tonnes/year plant has a reforming section consisting of combined reforming with a pre-reformer and a Lurgi low pressure methanol synthesis section.

A HYSYS simulation model of the plant was used to perform energy integration studies. As the simulation model did not have detailed distillation column models in the purification section, the energy integration studies did not consider that section.

Energy Integration study using ELCC

The Excel Add-In, HYSYSLink, is used to construct the ELCC for the plant as shown in Figure 2. The stream data is given in Appendix A.

From the curves and stream data, it can be deduced that Streams 14, 10 and 11 are large energy sources and it is possible to transfer energy to the energy sinks. As discussed earlier, starting where the distance between the curves is minimum (Ω pinch*)* Stream 14 can potentially be integrated with Streams 3, 4, 7 etc in that order.

A study of all the potential matches shows that the plant is already well integrated with minimum scope for further integration. A targeting method

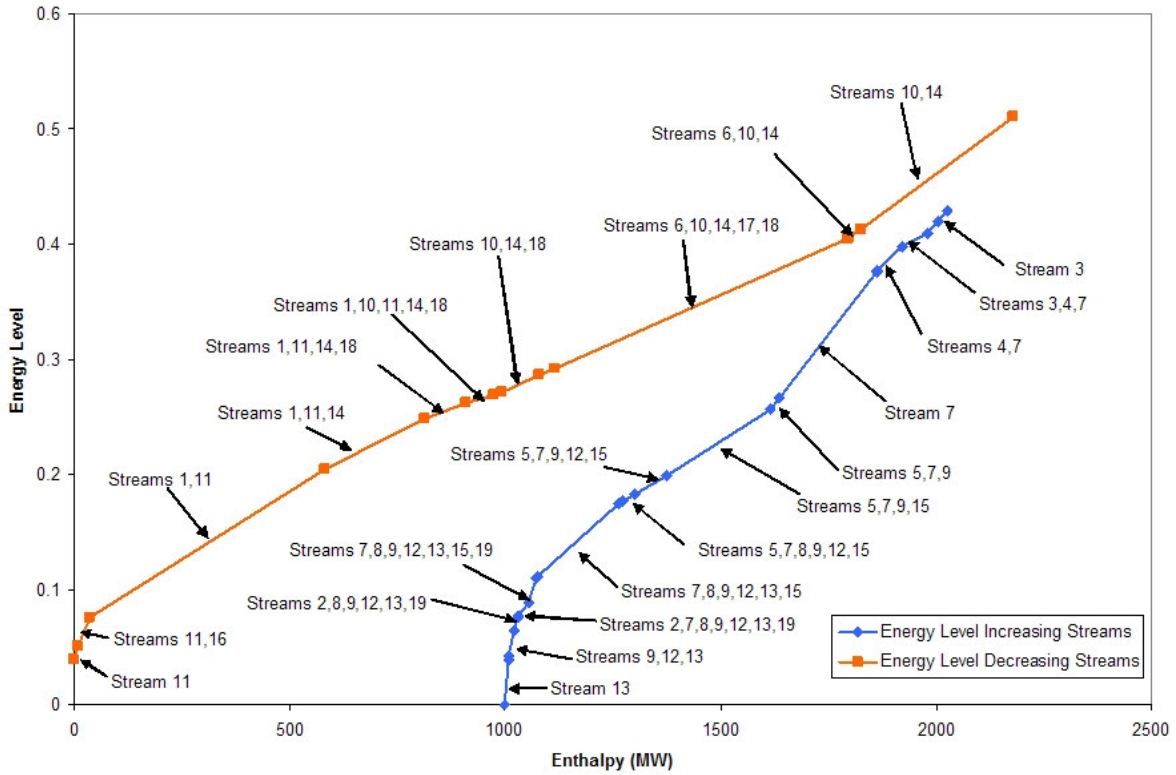

Figure 2: Energy Level Composite Curves for Methanol Plant Case Study

is required in such cases to verify if the plant is sufficiently integrated or if further scope for integration exists.

Streams 2, 12, 14 and 19 involve an increase in pressure. Electricity is imported from the utility section to supply their needs.

Many streams undergo a small change in pressure that can be attributed to pressure drops in heat exchangers.

Stream 16 represents an interesting possibility. It is the only stream in the process undergoing a substantial pressure drop (7751 kPa to 1100 kPa). The stream is a liquid and hence cannot be expanded to generate shaft work that could have been used to satisfy pressure increasing streams. This is indicated by the low energy level of Stream 16.

It could be possible to vaporize the liquid stream and superheat it (increase its energy level), expand the stream to generate electricity and then further cool it to the target temperature.

The effectiveness of this scheme depends on whether the excess energy required for vaporizing and cooling the stream is available in the process at the required level – without any additional heating or cooling utilities. This can also be verified with a targeting method.

MINIMUM ENERGY TARGETS

The minimum energy target consists of four components – hot utility, cold utility, work consumed and work obtained.

Linnhoff and Dhole [7] extended Pinch Analysis for the design of low-temperature processes to yield shaft work targets directly from basic process data. The Exergy Grand Composite Curves is used generate shaft work targets for retrofit schemes in refrigeration systems. This procedure cannot be extended to chemical process systems where a change in pressure translates into shaft work.

The following is a preliminary utility target procedure based on heuristics and Pinch Analysis.

Pressure – Temperature relationship

Before developing an algorithm to obtain minimum energy requirement, it would be worthwhile to refresh the pressure-temperature relationship in process plants.

1. Temperature change from supply to target temperature is possible with very small pressure drop – one dimensional in temperature.
   ⇒ Heat transfer
2. For incompressible fluids (liquids), pressure change does not cause any significant change in temperature – one dimensional in pressure.
   ⇒ Pumping liquids
3. For compressible fluids (gases), pressure change results in a considerable change in temperature – two dimensional (temperature and pressure).
   ⇒ Adiabatic expansion and compression of gases
4. Simultaneous pressure and temperature change is possible without any change in enthalpy
   ⇒ Isenthalpic expansion of fluids through a valve

Further, streams undergoing a pressure change almost always (except in the isenthalpic expansion case) exchange energy in the form of shaft work in addition to heat. Streams undergoing temperature change only exchange energy in the form of heat.

First Law and Target for available energy

The enthalpy change of a process stream is given by the first law of thermodynamics for flow processes as

$$\Delta H = Q - W \tag{3}$$

Q is defined to be positive when heat is added to the system and W is defined to be positive when work is done by the system.

The enthalpy change is a constant for a stream with a given set of process conditions (process path).

Earlier work [8] approaches the criteria of the optimal process path from an exergy perspective. Work W is total exergy while the exergy of heat Q is $\eta_c Q$. For a process with $\Delta H>0$, e.g. a compression process, the thermodynamic criterion for optimal path between supply and target conditions would be where the following functional would be minimum

$$\int_{\text{supply}}^{\text{target}} (\eta_c \delta Q - \delta W) \tag{4}$$

As work is done on the system in a compression process and Carnot efficiency is normally less than 0.7 for typical process conditions, paths involving more heat and less work are optimal. The opposite is true for processes where $\Delta H<0$.

This is valid from a simple economic perspective too. Electricity is usually the most expensive utility and hence its consumption must be minimized and, conversely, its production must be maximized.

If work is done by the system for a process with $\Delta H>0$, minimization of Eq. 4 is unconstrained and would require additional process constraints for solution. Similarly to the above discussion, the converse is true for processes with $\Delta H<0$.

This work presents a completely new stream data situation, compared to Pinch Analysis, as it deals with varying pressures and temperatures. There are many possible paths from supply to target conditions. It is elaborated in the next section.

Optimal path heuristics

As seen from the earlier section, optimal path heuristics imply minimizing or maximizing work for a given process stream from its supply to target conditions.

For a stream at supply conditions (T^s, P^s) and target conditions (T^t, P^t) there are four possible situations above atmospheric pressure [8]:

1. $T^s < T^t$, $P^s < P^t$ *(heating + compression)*
2. $T^s > T^t$, $P^s > P^t$ *(cooling +expansion)*
3. $T^s > T^t$, $P^s < P^t$ *(cooling+ compression)*
4. $T^s < T^t$, $P^s > P^t$ *(heating + expansion)*

Outlined below are heuristics for each of the above cases.

1. To increase pressure from P^s to P^t, shaft work is always necessary – either by pumps or compressors. For vapor streams,

compression at lower temperatures is optimal since this requires lesser work. Further, temperature is also increased in the process. To obtain minimum work, interstage cooling can be considered, particularly in cases where temperature at the outlet of a single stage compression is greater than T^t.

2. A supply pressure higher than the target pressure offers a potential to gain shaft work in an expander. In the case of a vapor stream, expansion must be done at the highest possible temperature to extract maximum work. Liquid streams can be expanded isenthalpically in a valve. Alternatively, the liquid stream can be vaporized and superheated, passed through an expander and cooled to the target temperature.
3. In case of vapor streams cool to temperature below T^t and then compress for minimum shaft work. For liquid streams, the sequence of pumping and cooling is not important.
4. As $P^s > P^t$ shaft work can be extracted. To get maximum work for a vapor stream, heat the stream to a temperature greater than T^t and then expand the stream. A liquid stream can be heated and then expanded isenthalpically or vaporized and superheated, expanded and then cooled. The choice of path depends on heating and cooling availability in the system under consideration.

In all the above instances, it is clear that by assuming optimal path heuristics based on shaft work, opportunities for process heat integration are ignored. For a rigorous calculation, optimization methods will have to be employed.

There are many possible paths for going from the supply state to the target state. Only a few paths, relevant to the case study on hand, are dealt with here. As the methodology is applied to other case studies, the path possibilities will be expanded.

Algorithm for Energy Targeting

1. For each stream
   a. If $P^s < P^t$ use the suitable optimal path heuristic 1 or 3 to evaluate the minimum shaft work. Based on information from the optimal path heuristics, split the stream into one or more work streams and one or more heat streams.
   b. If $P^s > P^t$ and $(P^s - P^t) > 5$ bar*, use the suitable optimal path heuristic 2 or 4 to evaluate the maximum shaft work. Based on information from the optimal path heuristics, split the stream into one or more work streams and one or more heat streams.
   c. If $P^s > P^t$ or $(P^s - P^t) < 5$ bar*, treat the entire stream as a heat stream.
2. At the end of Step 1, the minimum work consumed and maximum work obtained can be evaluated.
3. Use the Heat Cascade method of Pinch Analysis for all the heat streams to evaluate the minimum hot and cold utilities.

METHANOL PLANT ENERGY TARGET

The HYSYSLink Excel Add-in is modified to evaluate the energy targets for a HYSYS simulation.

Applying the optimal path heuristics detailed earlier to Streams 12, 13 and 14, it is seen that

- Stream 12 uses heuristic 2 and requires no subsequent heating. It is entirely a work stream.
- Stream 13 follows heuristic 2 and requires subsequent heating.
- Stream 14 follows heuristic 3.

Base case – existing plant

Table 2 shows the energy targets obtained for the plant (as in Figure 1) using the new algorithm (with a ΔT_{min} of 40ºC for heat cascade calculations) and actual consumption from the simulation model.

Detailed examination of the process flowsheet and the ELCC shows that the target is not achieved as

* The maximum pressure drop through a set of heat exchangers for a stream is taken to be 5 bar for this case study. This will change depending on the case on hand and can be evaluated as a function of $(T^t - T^s)$ and P^t / P^s. This function has not been developed in this work.

energy source, Stream 10, is not integrated with any energy sink. This stream is instead used to generate HP steam and supplies energy to reboilers in the methanol purification section. In addition, a few other streams are not integrated because of locational and process constraints.

	Target	Actual
Hot Utility (MW)	0.0	1.84
Cold Utility (MW)	240	284.22
Work Consumed (MW)	17.34	17.4
Work Obtained (MW)	-	-

Table 2: Base case actual and theoretical energy targets

The results show that the energy targeting model can be applied to generate good estimates for utility consumption that can be realized.

With proposed modification from the ELCC

The energy source Stream 16 is considered for integration as indicated in the case study section. The optimal path heuristic for Stream 16 is 2. The stream is split up into three parts – two heat streams and one work stream.
Table 3 shows the energy targets obtained after process modification with a ΔT_{min} of 40ºC for heat cascade calculations.

	Target after modifications	Base Case Target
Hot Utility (MW)	0.0	0.0
Cold Utility (MW)	234.47	240
Work Consumed (MW)	17.34	17.34
Work Obtained (MW)	5.5	-

Table 3: Energy targets for base case and after process modification

The results show that no additional hot or cold utility is consumed as compared to the base case and hence the proposed modification is theoretically possible.
The plant is tightly integrated with the utility system and unless a detailed heat exchanger network synthesis study is performed, it is not possible to evaluate the actual effect on the overall plant energy consumption. This is outside the scope of this paper.

CONCLUSION

The Energy Level Composite Curve methodology was modified and extended to incorporate energy targets to be used with the ELCC for energy integration. Energy integration study of a methanol plant in Norway was performed using this methodology. An integration scheme was proposed that would have been difficult to visualize by other techniques. The energy targets for the base case and proposed integration scheme was evaluated. The proposed modification reduced the theoretical cold utility target by 5.53 MW and 5.5 MW of work is obtained.
The ELCC and targeting methodology can be fine tuned and modified with insights gained from energy integration studies of the entire plant including the utility section.
The targeting methodology must be modified to take heat integration into consideration while developing the work targets. An optimization scheme would be best suited for this.
Finally, the methodology should be expanded to include composition change in addition to pressure and temperature change to ensure that the entire chemical plant can be analyzed for energy integration.
This energy integration strategy, still in its early phase of development, has shown considerable promise when applied to an industrial case study. Substantial work is required to develop a complete systematic framework that incorporates thermal, mechanical and chemical energies.

REFERENCES

[1] Anantharaman R, Abbas OS, Gundersen T. *Energy level composite curves – a new graphical methodology for the integration of energy intensive processes.* Proceedings of the 16th International Congress of Chemical and Process Engineering (CHISA/PRES 04), Prague, 2004.

[2] Feng X, Zhu XX. *Combining Pinch and Exergy Analysis for Process Modifications*. Applied Thermal Engineering 1997;17(3):249-261.

[3] Huang F, Elshout R. *Optimizing the heat recovery of crude units.* Chem. Engng Prog. 1976; 72(7): 68-74.

[4] Umeda T, Harada T, Shiroko K. *A thermodynamic approach to the synthesis of heat integration schemes in chemical processes.* Comput. Chem. Engng. 1979;3:273-282.

[5] Linnhoff B, Townsend DW, Boland D, Hewitt GF, Thomas BE, Guy AR, Marsland RH. *User guide on process integration for the efficient use of energy*. IChemE, Rugby. 1982.

[6] Anantharaman R, Abbas OS, Gundersen T. *Energy level composite curves – a new graphical methodology for the integration of energy intensive processes.* Submitted to Applied Thermal Engineering. Dec 2004.

[7] Linnhoff B, Dhole VR. *Shaftwork targets for low-temperature process design.* Chemical Engineering Science 1992; 47(8):2081-2091.

[8] Václavek V, Novotná A and Dedková J. *Pressure as a further parameter of composite curves in energy process integration.* Applied Thermal Engineering 2003;23:1785-1795.

APPENDIX A – Stream data for Methanol Plant case study

	Supply				Target			
	Temp (ºC)	Pressure (bar)	Enthalpy (MW)	Omega	Temp (ºC)	Pressure (bar)	Enthalpy (MW)	Omega
Stream 1	247.8	79.02	173.21	0.2707	45.0	77.52	19.63	0.0762
Stream 2	45.0	77.52	17.17	0.0762	54.5	83.50	21.18	0.0882
Stream 3	460.5	40.00	122.18	0.3978	587.0	39.00	139.12	0.4285
Stream 4	329.0	41.00	111.62	0.3767	487.0	40.00	131.79	0.4095
Stream 5	117.8	45.00	20.14	0.1750	328.0	41.00	107.74	0.3756
Stream 6	422.9	46.00	18.79	0.4125	238.0	45.00	9.13	0.2859
Stream 7	48.0	50.00	0.71	0.0768	435.0	46.00	18.51	0.4193
Stream 8	45.0	77.52	0.09	0.0762	136.0	77.42	0.29	0.1833
Stream 9	25.0	40.00	0.13	0.0430	220.0	39.40	2.31	0.2662
Stream 10	972.9	35.48	222.05	0.5106	158.6	32.58	62.88	0.2620
Stream 11	158.6	32.58	55.33	0.2685	22.6	31.98	2.57	0.0393
Stream 12	22.6	31.98	1.94	0.0394	148.0	80.50	14.34	0.1991
Stream 13	0.0	1.01	0.00	0.0000	125.0	1.04	8.18	0.1772
Stream 14	1029.6	0.99	106.84	0.5109	237.6	1.01	38.04	0.2041
Stream 15	72.2	80.50	35.52	0.1103	212.5	80.00	111.10	0.2560
Stream 16	45.0	77.52	8.41	0.0762	46.7	11.00	8.41	0.0503
Stream 17	242.6	35.00	1.67	0.4051	241.8	34.50	0.61	0.2917
Stream 18	245.9	35.00	105.75	0.4053	194.7	34.50	30.14	0.2487
Stream 19	40.0	50.10	0.07	0.0641	73.8	50.00	0.31	0.1116

APPENDIX B – Stream data for streams 13, 14 and 16 split into heat and work streams

	Supply				Target			
	Temp (ºC)	Pressure (bar)	Enthalpy (MW)	Omega	Temp (ºC)	Pressure (bar)	Enthalpy (MW)	Omega
Stream 13 A	0.0	1.01	0.00	0.0000	9.2	1.11	0.59	0.0165
Stream 13 B	9.2	1.11	0.59	0.0165	125.0	1.04	8.18	0.1772
Stream 14 A	1029.6	0.99	106.84	0.5109	233.4	0.99	37.71	0.1946
Stream 14 B	233.4	0.99	37.71	0.1946	237.6	1.01	38.04	0.2041
Stream 16 A	45.0	77.52	8.41	0.0762	300.0	77.52	70.59	0.2079
Stream 16 B	300.0	77.52	70.59	0.2079	154.2	11.00	65.09	0.1666
Stream 16 C	154.2	11.00	65.09	0.1666	46.7	11.00	8.41	0.0503

Proceedings of ECOS 2005
Trondheim, Norway
June 20–22, 2005

PROCEDURES FOR EFFICIENT AND ECONOMIC RECOVERY OF HEAT FOR REUSE IN BATCH PROCESSES FOR CLEANING

H. Dalsgård,
COWI A/S[1]
2800 Lyngby
Denmark

B. Qvale[2]
Technical University of Denmark
Department of Mechanical Engineering
2800 Lyngby
Denmark

ABSTRACT

The expenditure of primary energy can be reduced and the economics of process plants in the food industry can be improved by intelligent application of Process Integration (PI). Since a greater part of the products in the food industry is processed in batches, the use of Thermal-Energy Storage (TES) may be required to achieve these improvements. Further improvements may be achieved if there is a need, in the plant, for heating water at low-or-medium-level temperatures for cleaning purposes and there are significant quantities of medium-to-low-temperature heat recoverable. Such conditions are often encountered in the food industry. However, the extent to which PI is utilized is much smaller than the number of potential applications. The present paper will address this topic, give some reasons for the underuse of PI, and indicate some principles, methods, and directions that, when applied, could increase the use and usefulness of PI by incorporating TES, thus fulfilling PI's promises of improved operation, reduced energy consumption, reduced environmental impact, and improved economics. The application of these procedures is illustrated through the description of two cases.
Keywords: Heat Recovery. Industrial Process Integration. Batch Processes, Hot Water

NOMENCLATURE

C_{XHR}= Cost of heat exchanger for recovery of heat
C_S = Cost of heat store
C_{XC} = Cost of cleaning-water heat exchanger
C_{XU} = Cost of utility heat exchanger
I_i=Investment, improved plant
I_o= Investment, original plant
N_{HR} = Number of streams that are to be integrated
NPV=Net Present Value
PBP= Pay-Back Period
PBP_o= Pay-Back Period, original plant
S_i=Savings, improved plant
S_o=Savings, original plant
τ= Delay

INTRODUCTION

The Present Study

A number of reasons can be given for heat recovery (HR) not achieving wide-spread use in the food industry (or in industry in general for that matter) thus not realizing its potential benefits with respect to energy savings, emission reduction, resource depletion, and economic gain. The prime reason is that production in the food industry most often is based on batch processes that in turn lead to operational complexity or expensive hardware. Other reasons that may be given are unproven system design, high cost of engineering, design, and construction, insecure feelings caused by

[1] Parallelvej 2, hda@cowi.dk
[2] Building 402, Nils Koppel´s Allé, bq@mek.dtu.dk

unproven system configurations, and operational complexity. All these reasons may be true to some extent, but some simple considerations, described in the first section below, show that the delay caused by the time required for engineering, design and construction may be a decisive factor. The central theme of the present work is then to present and justify some measures by which this time can be reduced to a minimum. This will be done by developing standard off-the-shelf components and systems. Since these solutions are off-the-shelf, they will only achieve almost-optimal operation. However, it can easily be demonstrated that it is better to have high number of industrial plants achieve almost-optimal energy recovery, than to have a small number of plants achieve optimal energy recovery.

Background

During the last 10 years, the Process-Integration projects in the Department of Mechanical Engineering of the Technical University of Denmark have focused on heat recovery in Batch Processes. These projects were initially directed towards the development of computationally efficient algorithms for the synthesis of energy-efficient process networks. The resulting algorithms that utilized both direct[3] and indirect[4] heat recovery, have always included one or more TES´s.

In the Ph.D. study of Mikkelsen (1998), methods for the generation of Heat Exchanger Networks (HENs) for industrial batch processes incorporating TES were developed.

The Ph.D. study of Krummenacher (2001) of EPFL, Switzerland, refined and extended the studies and confirmed the results of the previous Danish studies.

The latest studies have been carried out as a part of a Ph.D.thesis that has been completed recently by Dalsgård (2002). In this work, 11 industrial process plants in Lithuania and Denmark were studied and recommendations for modifications of the existing energy systems, or the design of novel systems, were given. A number of these recommendations have been implemented. The observations and conclusions of the rather theoretically oriented work of Mikkelsen and Krummenacher and rather practical work of Dalsgård point in the same direction.

Efficient, expedient, and appropriate procedures are crucial for the profitability of heat recovery in industrial process networks. The results of these three studies represent an important base of knowledge for deciding the priorities of the different heat recovery schemes and the selection of the order in which the various excess heats should be recovered

Since the selection and design decisions of a heat-recovery scheme for one subsystem invariably limit the choices available for the remaining subsystems, it was concluded that the challenge was, and will be, also in the future, the development of a selection procedure for the order in which the various heat-recovery measures are to be introduced into the system design.

The paper will discuss these issues and will present qualitative considerations and the logical chains of arguments that have led to a number of simplified mathematical expressions to be used in the preliminary evaluation and conceptual design of heat recovery systems incorporating TES in industrial process networks resulting in the concrete recommendation of using heating of water for cleaning purposes to achieve economical heat recovery by introduction of TES in batch-process networks.

The basic ideas contained in the present paper have been presented at the energy-storage conference FUTURESTOCK 2003 by Dalsgård and Qvale (2003), but the treatment has been shifted from TES towards PI as a result of responses from colleagues and experiences gained during the past year, and also with the aim of making the basic thoughts accessible to the new and different audience of ECOS 2005.

THE IMPORTANCE OF TIME

Many aspects of the activities concerned with the preliminary studies, with the design, and with the implementation of energy recovery and energy management in industrial process plants are often considered only after the completion of the design of the plant or even after the completion of the

[3] Direct heat recovery implies that heat is exchanged directly between the hot process stream and the water stream to be heated. The TES in the water stream is used to adjust the water flow to the, usually time-varying, demand.

[4] Indirect heat recovery implies that the heat is first transferred to a TES system, normally with storage of water at two temperature levels. Thereafter, heat is transferred to the water stream in accordance with the time-variations of the demand.

construction of the plant. A process-integration study, followed by design and implementation can easily last many months, maybe as much as an entire year. The situation could then pretty much be as shown in Figure 1. The curve labeled NPV1 shows the development of the Net Present Value of the originally designed process (1). It starts, at time zero, with a rather substantial deficit in the form of the initial investment required for the installation of the process equipment. This deficit is reduced with time until the initial investment has been paid. In the present case this Pay-Back Period is 7.28 years

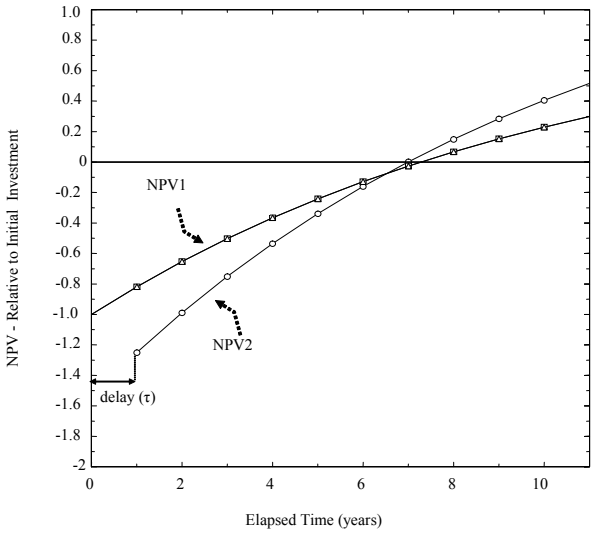

Figure1: The Development of the Net Present Value of the Two Projects
(The interest rate equals 10 percent/year).

In order to improve the performance of this industrial process plant, Process Integration studies are initiated. The engineering activities associated with these Process Integration studies lead to a delay. The activities are only interesting if they lead to improved energy utilization (and associated improved resource utilization and reduced environmental strain). The initial investment may or may not be reduced relative to the original. The consequence of the delay caused by engineering is that the Net Present Value of the improved project may lag behind the original project for a number of years. Figure 1 illustrates the case for the delay equal to one year, a considerable improvement of running surplus of 44 percent, and an increase of the initial investment of 25 percent. It is seen that even for this very successful application of Process Integration, it takes more than six years before the economic balance of the improved project (2) overtakes the original project(1).

In Figure 2, the time required to recover the cost of the improvement is presented as a function of the delay caused by engineering. Both a decrease and an increase of the initial investment are considered (plus/minus 25 percent) and two levels of interest rates (0.0 percent and 10.0 percent). It is seen that, in cases where the investment costs decrease or remain constant, the improved solution very quickly overtakes the original version. But in cases where the costs increase, the improved version will overtake the original version only after a period of time that may exceed the pay-back period for the original project. It is seen that when the interest rate is varied over a limited range, the effect is only of secondary importance.

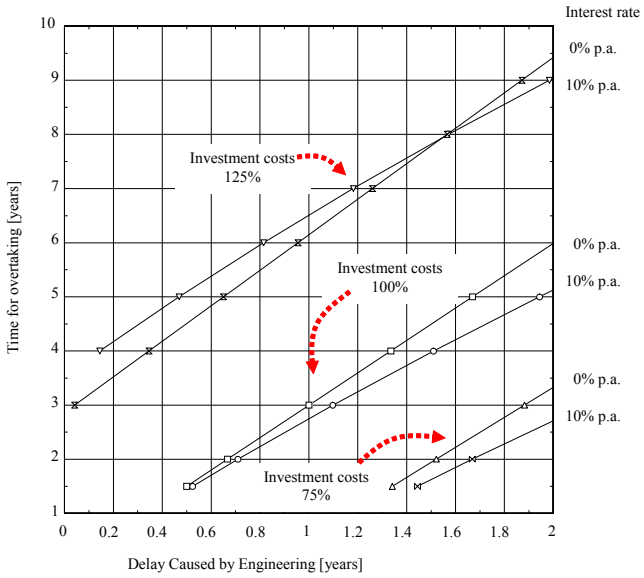

Figure 2: Time Required for the Net Present Value of an Improved Project (2) to Overtake that of the Original Project (1) for different real-interest rates.

This situation can also be regarded from a different viewpoint. It would be reasonable to postulate that for the delay caused by Process Integration to be acceptable, the investment should be paid back at the latest at the same point in time as the investment in the original plant. This situation is illustrated in Figure 3, which shows the acceptable delay for a given increase of cost and expected gain in performance. The payback period is chosen to be three years, the delay τ is one year, and the real interest rate is assumed to be zero, which is in

quite close agreement with the prevailing conditions in the industrial world at present.
As shown in Figure 3 it will be necessary to increase the relative savings (Savings/Investment) if the PI-project is delayed and if the invested money has to be paid back at a given time. This can e.g. be done by reducing the investment and at the same time keeping actual annual savings (illustrated by the straight lines). If the suggested solutions are more expensive than the original one it will be necessary to increase the annual savings even more (jump to line with a greater slope).

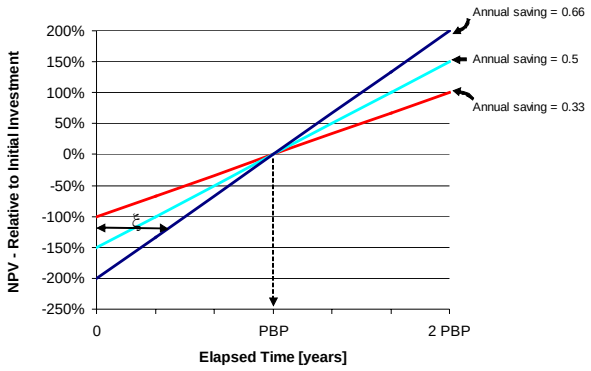

Figure 3: The return of investment (profit) related to the time for implementation (or delay) and the annual saving potential.

In this view, all relationships between variables are linear. As a consequence, the results may be condensed in the very simple non-dimensional curve shown in Figure 4.

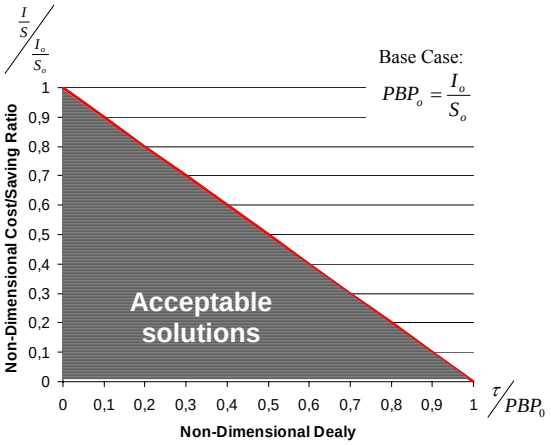

Figure 4: Non-dimensional decision diagram

Figure 4 shows the relationship between acceptable time delay (τ), investment (I), and saving potential (S). It is seen from the above that, it would be very difficult to convince managers (that want to show the company stockholders, represented by the Board of Directors, how clever and competent they are) that Heat Recovery and Process Integration are for the best of the company.
What can be done to change or ameliorate the situation?

1. Provide information and education so that the principles of Process Integration are known in the companies
2. Reduce the time required for Engineering by developing efficient methods and user-friendly computer programs.
3. Develop Standard Systems Solutions.
4. Apply Proven Technology (Known characteristics with respect to operability, controllability, and flexibility)
5. Initiate the PI activities simultaneously with the design of the plant, and avoid the introduction the energy-efficiency measures as an afterthought.

The ultimate goal would be to have Process Integration enter as a natural, generally accepted, and indispensable element in the initial stages of the planning of the new plant.
Using Standard System Solutions may lead to systems that are not absolutely optimal, but both for the plant in question and for society in general, such a procedure may result in the best overall performance. Albeit not rigorously, logically, and mathematically the optimal system, it may still be better than any realistic alternative.

THE RECOVERY OF HEAT IN BATCH PROCESSES FOR CLEANING WATER APPLICATION, USING INDIRECT HEAT RECOVERY

The general observation that has been documented in a number of articles is that, when applied intelligently, Process Integration may improve the economics of industrial process plants very significantly. Mikkelsen (1999) developed methods for PI in batch by incorporation of TES into Heat-Exchanger Networks (HEN). However, the methods although being very effective, required a deep and thorough understanding of thermodynamics AND Process Integration. Krummenacher (2001) substantiated these results. He, furthermore, observed that the application of

heat recovery by heating of water for cleaning purposes could represent an alternative, that in many situations would be extremely interesting both thermodynamically, technically, and economically. Simultaneously, Dalsgård (2002) carried out Process Integration studies of a number of plants in Lithuanian and Danish food industry. These studies showed, through extensive case studies, that heating water for cleaning purposes was an interesting alternative. In particular, this alternative was perceived as proven technology and, therefore, without risk. Furthermore, the solutions that were proposed and subsequently implemented were based on standard components and available on short notice. Thus, the solutions were psychologically digestible and would not entail delays and high costs caused by extensive engineering work.

Let us consider the conceptually simple situation taken from a process plant operating with batch processes, shown in figure 5. One hot process stream is going to be cooled and one cold stream has to be heated. The processes do not take place at the same time. The heating and cooling can be achieved by using available utilities. This will require the expenditure of primary energy. This is the solution with the lowest investment and the most flexible operation, but has the highest energy demand. This solution could serve as reference. We assume that Process-Integration studies of the system have resulted in the selection of these two streams for heat recovery. If the processes were taking place simultaneously, this heat recovery could take place directly. Thus it is called Direct Heat Recovery (DHR) and is illustrated in Figure 6. This is the best solution seen from an energy-demand point of view and could thus serve as a second reference point. However, if the processes do not take place simultaneously, heat will have to be removed during one period, stored in a system for storage of thermal energy storage, and given off to the cold stream during a later period. This is labeled Indirect Heat Recovery (IHR). This is shown in Figure 7. It is clear from this illustration that the temperature differences over which the heat is exchanged in the heat exchangers could be reduced to one half of what it was with DHR thus leading to the need for a heat exchanger that is twice as big. However, this will not be the case in real life. The heat exchanger will be optimized leading to approximately the same size as in the case of DHR. Therefore, the unit cost of the optimized heat exchanger used for recovery of heat is the same in the four situations depicted in Figures 6, 7, and 8 However the amount of heat transferred will be reduced.

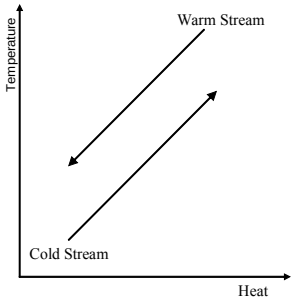

Figure 5: Process Streams. No Heat Recovery.

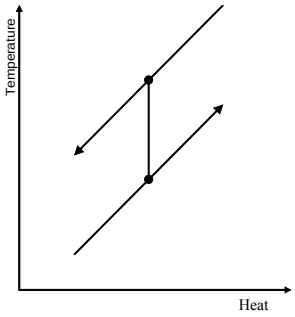

Figure 6: Direct Heat Recovery.

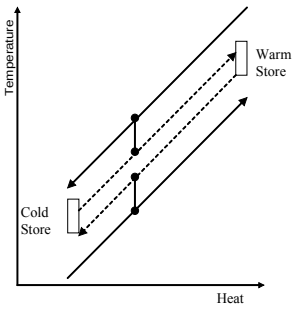

Figure 7: Indirect Heat Recovery, Using TES.

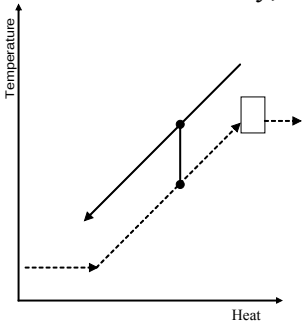

Figure 8: Direct Heat Recovery for Cleaning Water, Using TES.

If the two streams were perfectly matched initially, the heat recovered would be reduced for the optimized heat exchangers, thus requiring supplementary heating and cooling by utilities. But as noted before, the establishment of this supplement would be quite cheap.

These situations have been studied and evaluated. The parameter values are shown in the section DATA. The resulting simplified expressions have been developed assuming that the food processing plants include a number N_{HR} of similar processes that can be used for energy recovery, thus $N_{HR}>>1.0$ and that the cost of the cleaning-water heat exchanger C_{XC} is the same as that of the heat-recovery heat exchanger C_{XHR}. The resulting simplifying expressions are shown in the Table 1.

It is seen that the cheapest in terms of investment is the heating and cooling by utilities, but that the second cheapest solution and, therefore, the second most attractive short-term solution for industrial batch processes is the heat recovery by heating of water.
When the savings of energy is included through the cost of heating and cooling by utilities, the other alternatives become attractive and the investments can be written off. And these savings have to be allowed to be accumulated over an extended period of time periods such as, for example, four or eight years.

CASES

Superstructure

A superstructure was developed. This superstructure could have been the base for the design of the two examples in the present section, but the situation was actually the reverse. These two examples, together with a number of other cases formed the basis for the suggested superstructure. The superstructure can be put to use in similar situations in the future, Dalsgård (2002).

Example A

The company DANPO was to establish a new chicken processing plant in 1999. A Process Integration project was started up quite early in the planning phase. The resulting water heating system was quite simple as seen from Figure 9. The structure of the heat recovery network was not much different from the ordinary heating and hot water systems.

	Investment Cost (Simplified Expressions)	Saved Cost of Investment Relative to the next Higher Case (Simplified Expressions)	Minimum Required Load Duration (hours)
Indirect Heat Recovery (IDH)	$N_{HR}(2C_{XHR}+C_S)$		817
		$½N_{HR}(3C_{XHR}+2C_S)-C_S$	
Heat Recovery by Heating of Water for Cleaning (C)	$½N_{HR}(C_{XC}+C_{XU})+C_S$		375 (817 for Closed System)
		$½N_{HR}C_{XU}+C_S$	
Direct Heat Recovery (DH)	$½N_{HR}C_{XHR}$		347
		$½N_{HR}C_{XHR}$	
Heating and Cooling by Utilities (U)	$N_{HR}C_{XU}$	With the numbers used in this study the required load duration would be infinite, implying that the costs of fuel and equipment would never be recovered.	

Table 1: Simplified Expressions of Cost Functions and Reduction of Investment.

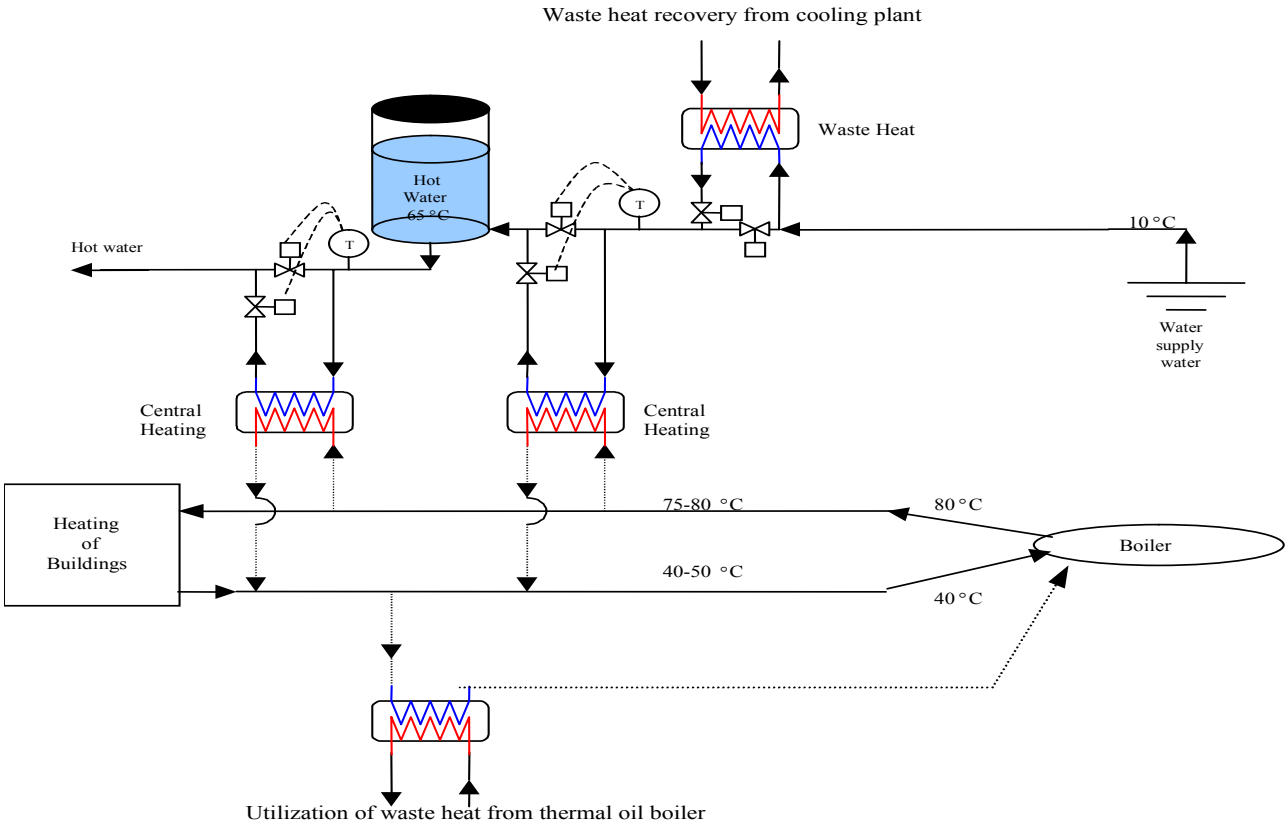

Figure 9: Heat Recovery Network at Poultry Factory (Danpo).

Integration between the cooling plant, which is present in most food factories, and the hot water production formed the basic structure for the heat recovery. The hot water system was successfully integrated with a boiler flue-gas heat recovery system. The heat from the flue gas was passed on to the hot water through the central heating system.

The amount of excess heat from the cooling plant increased dramatically as a result of the decision to install an ammonia-based cooling system instead of CO_2-freezers.

The excess heat from a cooling plant is generated at three points:

- from the cooling of lubrication oil in the NH_3 system's compressors,
- from cooling of superheated NH_3 gas
- from the compressors, from condensing of NH_3

The Danpo A/S Farre facilities need approx. 120 m^3 of hot water per 24 hours for cleaning purposes. This amount corresponds closely to the excess heat available from the NH_3 cooling system. Calculations showed that 2,500 MWh/year could be drawn from the excess heat, and a 120-m^3 storage tank was subsequently included in the facility layout. The water in the tank is kept at approx. 65°C by the excess heat (backed up by the natural gas boiler). Savings on natural gas expenses have been calculated to 2500 MWh or EURO 70,000 per year. Payback for the water tank system is 3.2 years. However, the pay-back period was, due to a grant from the Danish Energy Agency, reduced to 2.3 years.

The facilities are not able to use all their excess heat and some of the heat is led to the nearby Danpo A/S chicken slaughterhouse via a rediscovered, old pipeline. Natural gas savings there have been calculated to EURO 6,000 per year.

Example B

Danish Crown was going to build a new slaughterhouse in Denmark, this being one of the biggest in Europe. The resulting hot-water system is shown in the figure below.
Beside the illustrated heat recovery system for cleaning water, it is planned to use the central heating system to recover and distribute waste heat form the singeing ovens in the black slaughtering hall (Ovens for hair removal and decontamination of pigs).

The overall heat recovery systems supply the slaughterhouse with 20.000 MWh/year worth 500,000 EURO per year (excl. energy tax). The recovered heat corresponds to approximately 35% of the total heat demand. The pay back period is less than 3 years.

SUMMARY AND CONCLUSIONS

The present paper is striving to translate and generalize the results of past studies and particularly three Ph.D. theses (Mikkelsen (1998), Krummenacher (2001), and Dalsgård (2002)), into practical methods and procedures for developing efficient energy systems for batch processes in the food industry.
The goal is actually twofold: First, to develop energy-efficient and economically interesting energy systems through the application of Process Integration to improve the economics of TES system by increasing the return on investment.
Second, to raise the level of knowledge, acceptance, and interest for the use of Process Integration for retrofit of energy systems and the use of TES.

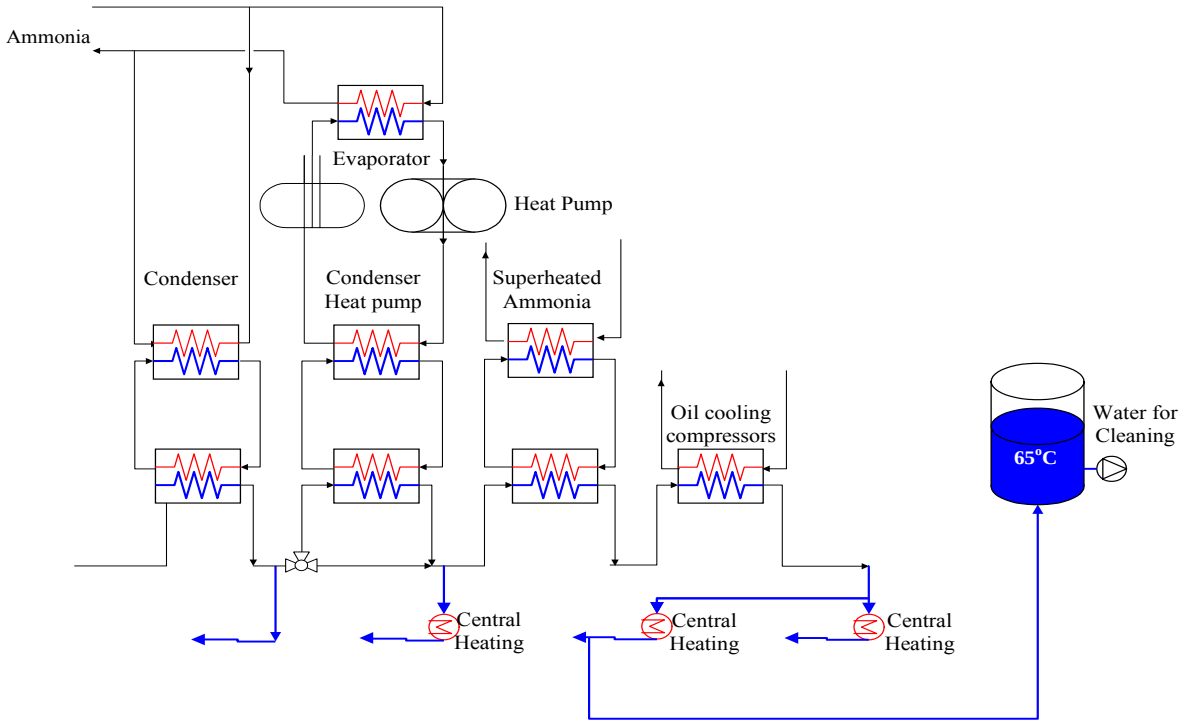

Figure 10. Heat Recovery from Danish-Crown Cooling Plant

In the present context, the first goal may be the most interesting. Over the years, the improvement of the economics of PI through the application of TES has been amply documented, for example in Mikkelsen (1999). It has been shown that a reduction of Pay-Back periods for the return on investment of the redesigned energy system including TES with a factor of two and three can be achieved.

The second task is aimed at raising the general awareness and use of PI and TES, thereby increasing the efficiency and economics of energy systems thus improving the economics of existing industrial process plants and decreasing their consumption of resources (primary energy).

The third task is aimed at improving the effectiveness of PI, first, by decreasing the time required for studies. The importance of this was demonstrated through some simple annuity consideration in the introduction of the present paper. The central theme here is the development of standard solutions based on "Proven Technology".

The standard system solution found to be the most interesting in the present context, was the use of heat recovery for heating of water for cleaning purposes. This was advocated theoretically by Krummenacher and, practically, by Dalsgård.
The simple considerations of the present study show that their recommendations have a general validity: If there is a need for warm cleaning water, the use of heat recovered from the cooling of warm process streams to heat the cleaning water will always be economically superior to heating a cool process stream.

APPENDIX. DATA AND ASSUMPTIONS SELECTED FOR THE STUDIES.

Data

Temperatures in the store 90C and 30C
Temperature difference over water-to-water heat exchanger 3 C
Temperature difference over gas-to-water heat exchanger 30 C
Temperature difference over gas-to-gas heat exchanger 30 C
Cost of heat exchangers:
- Water-to-water 200DKK/kJ/s
- Gas-to-water 1000DKK/kJ/s
- Gas-to-gas 2000DKK/kJ/s
- Water-to-cleaning water 200DKK/kJ/s
- Gas-to-cleaning water 1000DKK/kJ/s
- Utility 50 DKK/kJ/s

Cost of heat store 12x 10^{-3} DKK/kJ
Cost of hot utility $20*10^{-6}$ DKK/kJ
Cost of cold utility $20*10^{-6}$ DKK/kJ
Capitalization factor 4
Number of batches per year 1000

References

[1] Mikkelsen, J.B., (1998), Thermal-Energy Storage Systems in Batch Processing, PhD Thesis, Department of Mechanical Engineering, Technical University of Denmark, Report ET-PhD 98-4, ISBN 87-7475-205-7.

[2] Krummenacher, P.,(2001), Contribution to the Heat Integration of Batch Processes (with or without Heat Storage), Ph.D Thesis, Laboratoire d´Énergétique Industrielle, École Polytechnique Fédérale de Lausanne, Thesis No 2480.

[3] Dalsgård, H.,(2002), Simplification of Process Integration in Medium-Size Industry, PhD Thesis, Department of Mechanical Engineering, Technical University of Denmark, Report MEK-ET-PhD-2002-01, ISBN 87-7475-290-1.

[4] Dalsgård, H. and Qvale, B. (2003), The Use of TES for the Recovery of Heat for Industrial Processes and Cleaning Water, Proceedings of Futurestock 2003, Warsaw, pp. 109-118.

[5] Mikkelsen, J.B, Dalsgård, H., and Qvale, B.,(1999), Coordinated Incorporation of Thermal Energy Storage in Networks for Batch Processes, Entropie, Volume 35, pp36-41.

Proceedings of ECOS 2005
Trondheim, Norway
June 20–22, 2005

SELECTION OF MASS SEPARATING AGENTS IN MASS EXCHANGER NETWORK SYNTHESIS

Duncan Fraser[1], Michael Howe and Andre Hugo
Department of Chemical Engineering, University of Cape Town
Rondebosch, 7701 South Africa

Uday Shenoy
Department of Chemical Engineering, Indian Institute of Technology, Bombay

ABSTRACT

In this paper we set out the principles for using the grand composite curve (GCC) of mass exchange network synthesis (MENS) for selection of mass separating agents (MSAs). These principles enable us to systematically choose between alternative MSAs as well as the minimum flow rate for each MSA selected. This has not been possible using procedures developed so far. Of particular note is that the cheapest MSA is not necessarily the one with the lowest cost per unit mass of MSA, but rather the one with the lowest overall cost of removal of the mass load, which depends on both the MSA cost and its permissible concentration change. We illustrate the principles presented by application to two example problems.
Keywords: Mass Exchange Network Synthesis, Grand Composite Curve, Mass Separating Agents

INTRODUCTION

Up till now it has not been possible to systematically choose between available external Mass Separating Agents (MSAs) in Mass Exchange Network Synthesis (MENS).

In Heat Exchange Network Synthesis (HENS) the Grand Composite Curve (GCC) has long been established as a tool for choosing how much of each utility to use (Linnhoff, et al., 1982). The power of the HENS GCC is that it provides a visual means of identifying the flow of energy in a heat exchange network and allows for easy selection of HEN utilities. In spite of the many analogies between HENS and MENS, there has been limited application of the GCC to the selection of MSAs in Mass Exchange Network Synthesis (MENS) (Shenoy, 1995). Shenoy developed the GCC for MENS based on the minimum composition difference in the lean phase, ε, and applied it to one example problem and two other problems. He assumed that in placing the alternative MSAs the order of selection was cheapest cost in terms of MSA cost per unit mass.

We propose to show that a GCC for MENS has similar benefits to the GCC for HENS, especially with regard to selection between alternative external MSAs. As before, we expect that the HENS procedures will provide a foundation from which to work, but there will be features of MENS requiring different approaches (Hallale and Fraser, 1998, 2000a, 2000b, Fraser and Hallale, 2000).

In this paper we will first describe the use of the Grand Composite Curve in HENS. We will then discuss the features of the MENS Composite Curve on which the GCC will be based, pointing out differences between the HENS and MENS cases. Finally, we will present our proposal for use of the MENS Grand Composite Curve, and illustrate this with two examples.

The HENS Grand Composite Curve

The Grand Composite Curve, which is derived directly from the Problem Table, shows the cascade of energy in a heat exchanger network (Figure 1, Linnhoff et al., 1982). It clearly shows the process heat sink above the pinch and the

[1] Corresponding author: Phone: +27-21-650-2515, Fax: +27-21-650-5501, Email: dmf@chemeng.uct.ac.za

process heat source below the pinch, where the pinch is the point that the curve touches the vertical temperature axis. It also shows regions in which the process streams may satisfy their own needs (the two shaded portions of the curve). Most importantly, it allows you to choose the most appropriate combination of utilities from a variety of possibilities, e.g. steam at different temperature and pressure levels. Note that the Problem Table (and hence the GCC) uses modified stream temperatures to bring hot and cold stream temperatures to a common basis, with $\frac{1}{2}\Delta T_{min}$ being subtracted from hot stream temperatures and added to cold stream temperatures.

Figure 1 illustrates how a number of utilities are used to satisfy the heat surplus and demand below and above the pinch respectively. Note how the supply and target levels of each utility are represented. In most cases the shape of the curve dictates the most appropriate choice of utility level and load. Where the selection is not as apparent, a more rigorous set of guidelines is required. Linnhoff et al. (1982) proposed the following set of principles for this purpose:

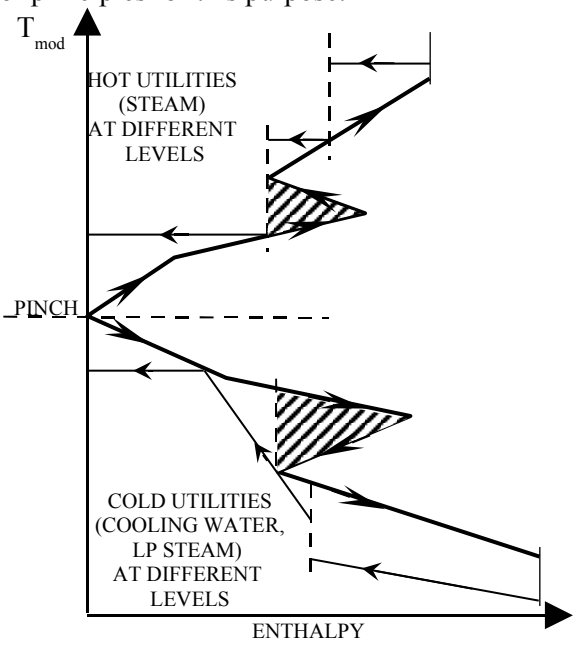

Figure 1. HENS Grand Composite Curve (from Linnhoff et al., 1982)

1. Maximise the use of the least expensive utilities. Note that in HENS it is generally true that the further away from ambient conditions you are, the more expensive the utility is (whether hot or cold), so it is obvious which are the least expensive utilities.
2. Minimise the flow of a particular utility by maximising the slope of the operating line, i.e. attempt to have an operating line with the most negative slope below the pinch and most positive slope above the pinch.
3. Where several choices and combinations are possible, evaluate whether the reduced operating cost achieved by the addition of more levels (i.e. use of more utilities) justifies the added capital costs required (because of the lower driving forces for heat transfer).
4. Each time a utility operating line touches the energy cascade curve a new pinch is created and the number of units – and the capital cost – required to satisfy the exchange increases. In these cases it might be beneficial to relax either the load or target level of the utility to avoid an additional pinch (which also leads to a more constrained system of matches).

This set of principles will form the foundation for the use of the MENS GCC presented in this paper.

The MENS Composite Curves

We will use the most general MENS Composite Curves (see Figure 2), namely the y-y* composite curve for overlapping MSAs (i.e. where different MSAs exist in the same composition interval), developed by Hallale and Fraser (2000a, 2000b). Here the MSA composition is expressed as the corresponding rich stream composition with which it is in equilibrium, allowing overlapping MSAs to be plotted on a common basis. Note that for MENS the excess capacity of the process MSAs is the equivalent of hot utility in HENS, and the load for external MSAs is the equivalent of cold utility.

As opposed to the minimum composition difference, ε, in the lean phase (introduced by El-Halwagi and Manousiouthakis, 1989), we use the minimum composition difference, Δy_{min}, in the rich phase. For a linear equilibrium function relating the composition in the rich phase to the composition in the lean phase (MSA):

$$y^* = m_j x + b_j \qquad (1)$$

(where the subscript j denotes the different MSAs), these minimum composition differences are related to each other as follows:

$$\Delta y_{min} = m_j \varepsilon \qquad (2)$$

This implies that for a fixed value of ε each MSA has a different value of Δy_{min}, but in this approach we use a global value for Δy_{min} instead (so each MSA effectively has a different value of ε).

Construction of the Grand Composite Curve (GCC) for MENS

As mentioned above, one of the main purposes for developing the GCC for MENS is that it will aid in external MSA selection. For this reason, only the data for rich streams and process MSA streams must be used in its construction. The construction involves using the Composition Interval Table (CIT), set up in much the same way as the HENS Problem Table. The mass cascade from this table is plotted against a modified y value, y_{mod}, similar to the modified HENS temperature. This value is calculated as shown in Equations 3 and 4 below:

$$y_{mod} = y - \tfrac{1}{2}\Delta y_{min} \quad \text{Rich streams} \quad (3)$$

$$y^*_{mod} = y^* + \tfrac{1}{2}\Delta y_{min} \quad \text{Lean streams} \quad (4)$$

Note that the value of Δy_{min} used in Equations 3 and 4 should preferably be the optimum value obtained from supertargeting of the problem being considered (Hallale and Fraser, 2000c, 2000d). The MENS GCC is plotted directly from the CIT, with y_{mod} being plotted against mass exchanged, as shown in Figure 2. The Pinch is where the curve touches the vertical composition axis. Also note that we are using Δy_{min} in determination of y_{mod}, and not ε as used by Shenoy (1995).

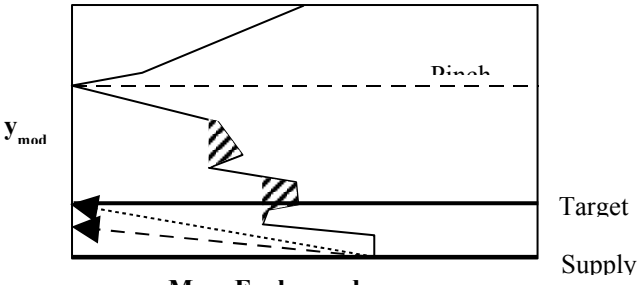

Figure 2. MENS Grand Composite

Procedure for using the MENS Grand Composite Curve to target MSAs

1. Construct the GCC and adjust the process MSA flow rates (if desired):

The first step in using the Grand Composite Curve (GCC) is to decide on any reduction in process MSA flow rates. This is decided as follows:

- For process MSAs that exist entirely above the pinch: The use of any one of them may be reduced to eliminate the excess capacity of the process MSAs. In this case you could choose to redraw the GCC to reflect the change above the pinch. If the excess capacity of the process MSAs has been eliminated, the GCC will start from the vertical composition axis at the top.
- For process MSAs that exist only below the pinch: Their use should not be reduced, as it will lead to an increase in the loading on the external MSAs.
- For process MSAs that cross the pinch: A reduction in flow rate will cause the load on the external MSAs to be increased. There appears to be no point in reducing the flow rate of such an MSA, even if it is the only MSA above the pinch. If it is decided to reduce the flow rate of such an MSA, the GCC will need to be recalculated before proceeding to the next step.

2. Eliminate self-sufficient areas below pinch on GCC:

Determine which areas of the Grand Composite Curve (GCC) are self-sufficient (i.e. no external MSA is required for these mass transfers). As for HENS, these are pockets (areas that overlap), shown by the shaded regions in Figure 2.

3. Identify and cost possible external MSA technologies:

The next step of the analysis is to identify all external MSA technologies that will perform the required mass transfer, check if their operating composition range is suitable for the problem in hand, and then rank those that remain in terms of cost of removal of the required mass. For each external MSA the following data is needed: supply and target compositions, equilibrium relationship for transferred component, cost.

Check the supply and target compositions of the available technologies and eliminate any MSA where the supply composition is above the pinch composition (since the region above the pinch is satisfied with process MSAs, supplying an external MSA in this region is redundant). If the target composition of an MSA is above the pinch it should be reduced to less than or equal to the pinch composition (no mass transfer across the pinch).

Calculate the minimum removal cost for each remaining MSA, C_{min}, as given by Equations 5 to

7. This cost is obtained by assuming that each MSA would remove the total mass required by external MSAs, $M_{removed}$, over its maximum concentration range, Δx_{max}. The total mass required is the last entry in the CIT, and the final point of the GCC. Note that L_{min} represents the minimum MSA flow rate (kg/s) and C_{MSA} the unit cost of the MSA ($/kg).

$$\Delta x_{max} = x_t - x_s \quad (5)$$

$$L_{min} = M_{removed}/\Delta x_{max} \quad (6)$$

$$C_{min} = C_{MSA} * L_{min} \quad (7)$$

Finally in this step, rank the MSAs in terms of increasing minimum removal costs, C_{min}. This order will not necessarily be the same as you would get if you simply ranked them according to their unit costs, C_{MSA} (Shenoy, 1995); rather the order is in terms of increasing ($C_{MSA}/\Delta x_{max}$).

4. Select how much of each external MSA is to be used:

Now select which of the MSAs is to be used to transfer the required mass and determine the minimum flow rate for each selected MSA. It is helpful to plot each of the MSAs on the GCC to assist in this process, over the full range of mass to be exchanged.

The slope of the operating line of MSA S_j is $-m_j/L_j$. Since m_j is given, once the slope is known, the flow rate of the MSA can be determined. A line with the steepest possible slope therefore corresponds to the minimum, and hence cheapest, MSA flow rate. Here $L_j = L_{min}$ (as defined in Equation 6). A line of lower slope also transfers the required mass, but would correspond to a greater MSA flow.

Start at the supply composition of each MSA and attempt to reach its target composition. If the target composition cannot be met, then calculate the highest final composition that the MSA can reach, by just touching the GCC at the closest approach so as to maximise the slope, as shown in Figure 4 (if the operating line crossed the GCC it would represent infeasible mass transfer). In this case $L_j > L_{min}$.

Two options are available in this situation, neither of which is ideal in that the target composition cannot be met for the complete mass transfer. The first of these options is to use the MSA in a mass exchange operation that pinches with the GCC, as shown in the dotted line in Figure 3. The second is to split the MSA and to use two exchange operations, the first also pinches with the GCC, while the second completes the necessary mass transfer (dashed lines in Figure 3).

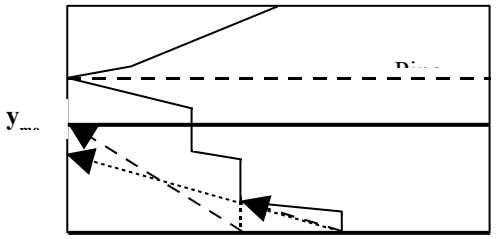

Figure 3. Alternatives when target composition cannot be reached directly

Choosing between the alternatives shown in Figure 3 is not a simple matter. The slopes of the lines touching the GCC are clearly equal. The second dashed line is essentially ideal for its part of the mass transfer. This does not necessarily mean that the configuration given by the dashed lines is the best alternative, however. For example, the capital cost of using two mass exchange operations may make the second alternative less cost effective than the first. The total MSA usage for the two dashed lines is also greater than the usage for the dotted line. Decisions in these circumstances therefore require more thorough economic evaluation.

Complete the problem using the cheapest possible MSAs, in order. In Figure 4 we see an example of this. The number of "$" symbols represents the relative cost of each MSA. For example, depending on the costs of the MSAs shown in Figure 4, it may be cheaper to transfer the entire amount using the more expensive MSA (represented by the dashed line) as only a single exchanger type may be necessary, rather than use two different MSAs (shown by the dotted line). These alternatives also have capital cost implications which need to be taken into account.

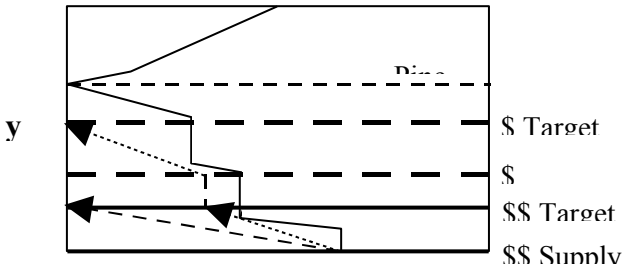

Figure 4. Single versus Multiple MSAs

Occasionally the most expensive MSA must be used, because of the concentration levels of the MSAs on the supply side.

5. Choose between possible options:

If more than one possible combination of MSAs has been identified, calculate the operating cost associated with each option. Perform a final comparison between all the possible options based on their individual operating costs as well as their capital cost implications.

Examples

In order to demonstrate the validity of the proposed procedure, two problems will be presented.

Example Problem 1 (Dephenolisation of rayon wastes, El Halwagi, 1997)

In El Halwagi's solution of this problem activated carbon is the only external MSA. Air, light oil, and ion exchange resin are all possible external MSAs that are technologically feasible candidates for the required separation (El-Halwagi, 1997; Hallale, 1998). We will demonstrate the use of the Grand Composite Curve to choose between these four alternatives.

Step 1: The GCC is constructed, taking only the two process MSAs (S_1 and S_2) and the two rich streams (R_1 and R_2) into account. The optimum Δy_{min} value of 0.000255 is used to determine the targets (Hallale, 1998). The supply composition of S_2 is at the pinch ($y_{mod} = 0.015428$), so its load may be reduced from 3.0 to 2.48 kg/s (the MSA flow rate that exactly removes the required amount of phenol). Figure 5 shows the GCC both before (solid line) and after (dotted line) adjustment of the process MSA flow rate. Note that there is now no surplus capacity of process MSAs and that the curve does not change below the pinch.

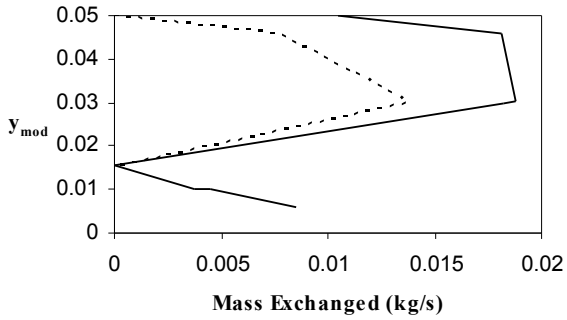

Figure 5. GCC for Example 1

Step 2: There are no regions below the pinch where there are any pockets.

Step 3: For the removal of phenol from aqueous streams, the MSAs listed in Table 1 are possible candidates. All the possible external MSAs listed in Table 1 fall within the region below the pinch. This is verified by converting their individual supply and target compositions to the equilibrium composition in the rich phase, y*, and then to y^*_{mod} values using Equation 4 (as given in Table 1).

Table 1. Available technologies for the removal of phenol from aqueous streams

Technology	MSA	x_s (mass ratio)	x_t (mass ratio)	m_j	b_j	$y^*_{s,mod}$	$y^*_{t,mod}$
Activated Carbon	S_3	0	0.110	0.02	0	0.0001275	0.002328
Air	S_4	0	0.029	0.04	0	0.0001275	0.001288
Light Oil	S_5	0.0013	0.015	0.71	0.001	0.0020505	0.011778
Ion Exchange Resin	S_6	0	0.170	0.09	0	0.0001275	0.015428

Table 2. Minimum operating cost for each MSA

Technology	MSA	Δx_{max}	L_{min} (kg/s)	C_{MSA} ($/kg)	$C_{MSA}/\Delta x_{max}$ ($/kg)	C_{min} ($/hr)
Activated Carbon	S_3	0.110	0.077	0.081	0.736	22.5
Air	S_4	0.029	0.292	0.060	2.067	63.1
Light Oil	S_5	0.0137	0.619	0.010	0.730	22.3
Ion Exchange Resin	S_6	0.170	0.050	0.212	1.247	38.1

Table 2 shows the minimum operating cost for each of the available MSAs, based on $M_{removed} = 0.008475$ kg/s. The order of increasing MSA costs is: S_5, S_3, S_6, S_4. Note that the second last column in Table 2 ($C_{MSA}/\Delta x_{max}$) can be used for this ranking, rather than the last column (C_{min}), which requires a knowledge of $M_{removed}$, and that while the minimum flow of S_5 is much greater than that of S_3, their relative costs mean that the overall costs for the two are very close. This closeness of costs

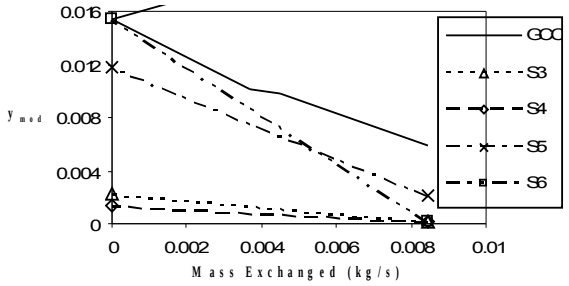

Figure 6. GCC for Example 1 below pinch showing all external MSAs

for S_5 and S_3 means that other considerations may be significant in choosing between them.

Step 4: Plot each of the available MSAs on the Grand Composite Curve. Since only the region below the pinch is of interest, it is most convenient to focus on this part of the curve as presented in Figure 6. Each MSA is plotted over the full range of mass to be exchanged and its full composition range. In this case any of the MSAs could remove the total load on its own, as is evident in Figure 6. On the basis of operating costs, either S_3 or S_5 would be the preferred choice.

Step 5: Looking at Figure 6, with the operating costs for S_3 and S_5 being so close, it seems that S_3 would have the larger driving forces and should have the edge over S_5 in terms of capital investment. This is as far as we need to go with this problem, and the procedure proposed has proved effective in determining the most cost effective MSA from a set of four possibilities.

Example Problem 2 (Howe and Hugo, 2000)

The data for this problem can be found in Table 3.

Table 3. Data for Example Problem 2 ($\Delta y_{min} = 0.001$)

Rich Streams	G_i (kg/s)	y_s (mass ratio)	y_t (mass ratio)	Lean Streams	L_j (kg/s)	x_s (mass ratio)	x_t (mass ratio)	m_j	b_j	C_{MSA} ($/kg)	$y^*_{s,mod}$	$y^*_{t,mod}$
R_1	3.00	0.05	0.0015	S_1	0.35	0.00795	0.200	0.51	0.010		0.014555	0.11250
R_2	1.00	0.07	0.003	S_2	0.60	0.008	0.100	0.13	0.001		0.00254	0.01450
R_3	1.40	0.02	0.003	S_3	0.20	0.0001	0.125	0.40	0.002		0.00254	0.05250
R_4	0.20	0.15	0.002	S_4	0.149	0.001	0.300	0.30	0.002		0.00280	0.09250
R_5	0.10	0.27	0.010	S_5	0.61	0.003	0.125	0.17	0.001		0.00201	0.02275
R_6	0.90	0.01	0.001	S_6	∞	0.125	0.275	0.14	0.010	1.4	0.02800	0.04900
R_7	0.10	0.02	0.0045	S_7	∞	0.022	0.047	0.89	0.001	2.1	0.02108	0.04333
R_8	0.01	0.021	0.0012	S_8	∞	0.000	0.00425	2.00	0.000	5.0	0.00050	0.00900

Step 1: The GCC is constructed from the CIT for a Δy_{min} of 0.001, and shown in Figure 7. Note that in this case all the process MSAs except S_1 and S_4 are entirely below the pinch, at $y_{mod} = 0.0695$, and S_1 and S_4 both cross the pinch. There is therefore no incentive to reduce the flow rate of any of the process MSAs, and the GCC does not change.

Step 2: Remove self-sufficient areas, as shown in Figure 8, which only shows the GCC below the pinch. The dotted lines indicate the regions that no longer need to be considered.

Step 3: The possible external MSAs are identified in Table 3, together with the required data. The supply and target compositions of the external MSAs (converted to y^*_{mod}) are also shown in Table 3. They are all below the pinch. Table 4 shows the relative costs for removal of all the mass by each of the external MSAs. For this problem $M_{removed}$ is 0.040313 kg/s. Note that in this case the relative costs per unit mass are amplified in the minimum removal costs, and that the costs increase by an order of magnitude for each successive MSA. The cheapest MSA is S_6, followed by S_7 and then S_8.

Table 4. Minimum operating cost for each external MSA in Example 2

MSA	Δx_{max}	L_{min} (kg/s)	C_{MSA} ($/kg)	$C_{MSA}/\Delta x_{max}$ ($/kg)	C_{min} ($/s)
S_6	0.150	0.269	1.4	9.33	0.376
S_7	0.025	1.612	2.1	84.0	3.39
S_8	0.00425	9.485	5.0	1176	47.4

Step 4: The maximum possible transfer of mass to all of the MSAs is shown in Figure 9, using the full composition range in each case. It will be noted that neither S_6 nor S_7 can carry the full load because their supply compositions are too high.

First use S_6 to transfer as much mass as possible, starting from where it touches the GCC. No

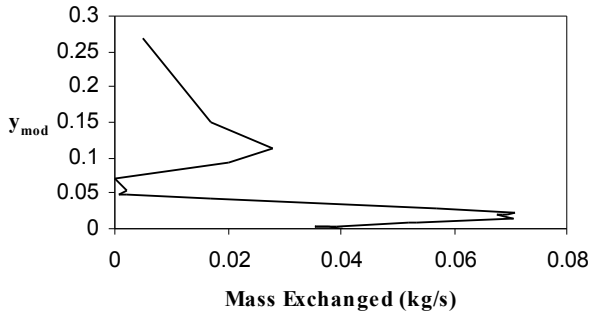

Figure 7. GCC for Example 2

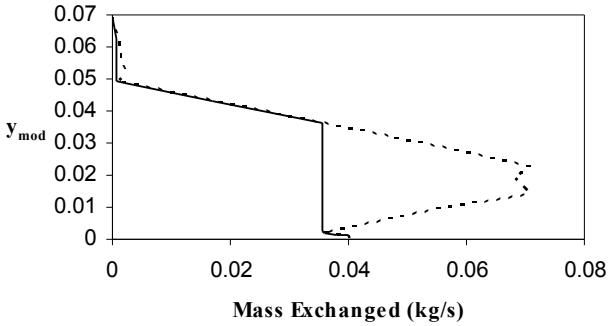

Figure 8. GCC for Example 2 below pinch showing elimination of self-sufficient areas

further mass can be transferred using S_7, as it also touches the GCC at the same mass exchanged. The remaining mass must therefore be transferred using S_8, even though it is the most expensive MSA. The complete mass transfer operation is represented in Figure 10. This is Option 1.

Figure 11 shows the region in which S_8 is used in greater detail. This illustrates that you must be careful not to let the MSA cross the GCC line.

Another possibility is shown in Figure 10, where S_8 is allowed to reach its target composition. This does not increase the flow of S_8, but it does mean that less S_6 will be used (note the higher slope for S_6 in Figure 10). This is Option 2.

Step 5: Finally we compare the total operating cost of each of the alternatives identified. The four alternatives investigated are the two options shown in Figures 12 and 14, and another two options using S_7 instead of S_6 (Options 3 & 4). The results are presented in Table 5.

It is clear from Table 5 that, as anticipated, Option 2 is in fact the cheapest from an operating cost point of view ($107 900/hr). This shows that it may not be best to always transfer the maximum amount of mass using the cheapest MSA. Seeing as Options 1 and 2 are quite close in terms of operating costs, consideration will need to be given to the capital costs of each of these alternatives before making a final decision between them.
Table 5 also shows the costs of using S_7 instead of S_6 (Options 3 and 4). Given the dominance of the S_8 costs in this problem, the total costs using S_7 do not increase by much and the larger driving forces for S_7 compared to S_6 might make Option 4 the most attractive.

Table 5. Actual operating cost of alternatives in Example 2

Option	MSAs	Δy^*_{mod}	Slope (s/kg)	L_j (kg/s)	C_{MSA} ($/kg)	Operating Cost ($/hr)	Total Operating Cost ($/hr)
1	S_6	0.0210	-0.593	0.236	1.4	1190	108 600
	S_8	0.001635	-0.335	5.966	5.0	107380	
2	S_6	0.0210	-1.404	0.100	1.4	500	107 900
	S_8	0.0085	-0.335	5.966	5.0	107380	
3	S_7	0.02225	-0.628	1.417	2.1	10720	118 100
	S_8	0.00204	-0.335	5.966	5.0	107380	
4	S_7	0.02225	-1.487	0.598	2.1	4520	111 900
	S_8	0.0085	-0.335	5.966	5.0	107380	

CONCLUSION

We have proposed a set of procedures for using the MENS Grand Composite Curve for choosing between possible external MSAs, just as the HENS GCC is used for choosing between available hot utilities and available cold utilities. These procedures not only determine the best MSAs to use, but also the minimum flow rates for each of them. We have shown that care should be taken when determining the cheapest MSA. This may not be the MSA with the lowest cost per unit mass of MSA, but rather the one with the lowest cost for removal of the required mass load. This removal cost depends on both the cost of the MSA as well as the concentration range over which it can work.

We have demonstrated the validity of these procedures by application to two examples.

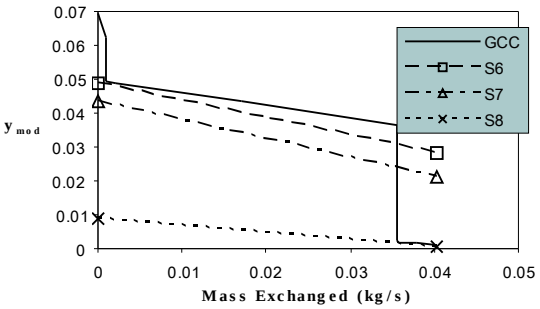

Figure 9. GCC for Example 2 showing all the external MSAs carrying the full load

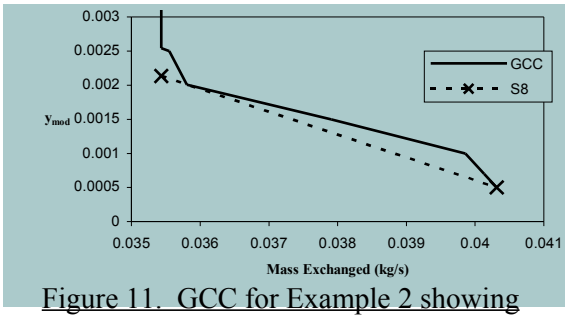

Figure 11. GCC for Example 2 showing expanded region for S_8

This paper has again shown that HENS procedures form a good basis for MENS procedures, but that they need to be extended to cover the significant differences between HENS and MENS.

REFERENCES

El-Halwagi, M. M., 1997, *Pollution Prevention through Process Integration: Systematic Design Tools* (Academic Press, San Diego, USA).

El-Halwagi, M. M. and Manousiouthakis, V., 1989, Synthesis of Mass Exchange Networks, *AIChE Journal*, **35**(8): 1233-1244.

Fraser, D. M. and Hallale, N., 2000, Retrofit of Mass Exchange Networks Using Pinch Technology, *AIChE Journal,* **46**(10): 2112-2117.

Hallale, N., 1998, *Capital Cost Targets for the Optimum Synthesis of Mass Exchange Networks*. PhD thesis (Department of Chemical Engineering, University of Cape Town, South Africa).

Hallale, N. and Fraser, D. M., 1998, Capital cost targets for mass exchange networks. A special case: Water minimisation, *Chem. Eng. Sc.*, **53**(2): 293-313.

Hallale, N. and Fraser, D. M., 2000a, Capital and Total Cost Targets for Mass Exchange Networks, Part 1: Simple Capital Cost Models, *Computers and Chemical Engineering*, **23**(11-12): 1661-1679.

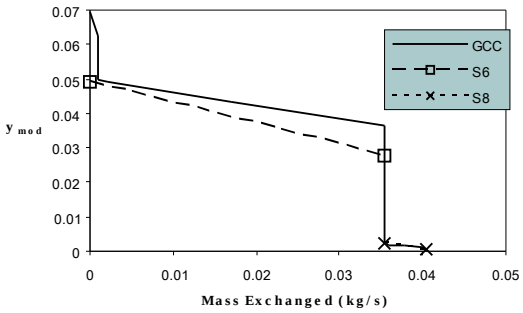

Figure 10. GCC for Example 2 showing maximum use of cheapest MSA

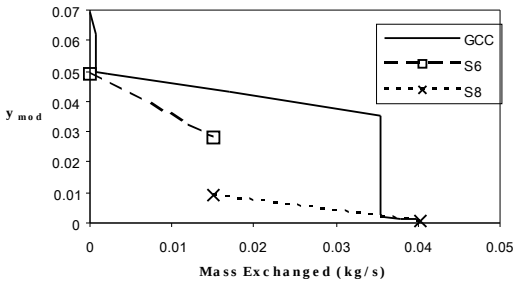

Figure 12. GCC for Example 2 showing full use of most expensive MSA

Hallale, N. and Fraser, D. M., 2000b, Capital and Total Cost Targets for Mass Exchange Networks, Part 2: Detailed Capital Cost Models, *Computers and Chemical Engineering*, **23**(11-12): 1681-1699.

Hallale, N. and Fraser, D. M., 2000c, Supertargeting for Mass Exchange Networks: Part I – Targeting and Design Techniques, *Trans IChemE, Part A, Chem Eng Res Des*, **78**(Mar): 202-207.

Hallale, N. and Fraser, D. M., 2000d, Supertargeting for Mass Exchange Networks: Part II – Applications, *Trans IChemE, Part A, Chem Eng Res Des*, **78**(Mar): 208-216.

Howe, M. and Hugo, A., 2000, *Pollution Reduction and the Retrofit Design of Mass Exchange Networks*, Project Report (Department of Chemical Engineering, University of Cape Town, South Africa).

Linnhoff, B. Townsend, D.W., Boland D., Hewitt G.F., Thomas B.E.A., Guy, A.R., and Marsland, R.H., 1982, *A User Guide on Process Integration for the Efficient Use of Energy* (Institution of Chemical Engineers, Rugby, UK).

Shenoy, U.V., 1995, *Heat Exchanger Network Synthesis*, (Gulf Publishing Co., Houston, USA).

Proceedings of ECOS 2005
Trondheim, Norway
June 20–22, 2005

SYSTEM ANALYSIS OF A NEW SCHEME FOR PLASTIC RECOVERY

Kristin Kaggerud[*] and Truls Gundersen
Norwegian University of Science and Technology
Department of Energy and Process Engineering
NO-7491 Trondheim
Norway

Per Sandberg and Unni Musdalslien
Norsk Hydro Corporate Research Centre
NO-3908 Porsgrunn
Norway

ABSTRACT

The recycling concept presented here converts mixed plastic waste chemically to new plastic, the Plastic waste to Plastic concept (PtP). The PtP concept has been developed by Norsk Hydro. After a suitable pre-treatment, the waste is converted thermally to synthesis gas in a gasifier. The synthesis gas is used in methanol production, which is then converted to olefins by use of a patented MTO (Methanol to Olefins) process. Olefins are the raw material in production of new plastic. The UOP/Hydro MTO process makes the system innovative as it provides a closed-loop recycling process for plastic. All the technology steps exist, though not yet realized in a continuous process train. The recycling concept facilitates production of virgin plastic from old, mixed and contaminated plastic waste. The carbon in the plastic waste is captured thereby preventing releases of CO_2 to the atmosphere, additionally CO_2 releases from alternative production of plastic is avoided.

Keywords: Plastic recycling, MTO, Gasification, Legislation, System analysis

NOMENCLATURE

APME:	Association of plastics manufacturers in Europe
HC:	Hydrocarbons
H/C:	Hydrogen to carbon ratio
ELV:	End of life vehicles
MeOH:	Methanol
MTO**:**	Hydro/UOP patented Methanol to Olefins process
n:	moles [mol]
Olefins:	Alkenes, usually ethene and/or propene
p:	Number of units in polymer
PE**:**	Polyethylene
PET**:**	Polyethylene terephthalate
PP**:**	Polypropylene
PtP**:**	Plastic waste to plastic concept
PVC**:**	Polyvinylchloride
VCM:	Vinyl chloride monomer
WGS**:**	Water gas shift
WEEE:	Waste electrical and electronic equipment
x:	Number of carbon atoms
y:	Number of hydrogen atoms
η:	Efficiency
Π:	Product

Subscript/Superscript

C:	Carbon
i:	Unit i
in:	Mass flow into the unit
out:	Mass flow out of the unit
p:	Number of units in polymer
x:	Number of carbon atoms
y:	Number of hydrogen atoms

[*] Corresponding author: Phone: +4773592745
E-mail: kristin.kaggerud@ntnu.no

INTRODUCTION

Plastic waste is a valuable source of both energy and chemicals. The present situation, however, shows that more than 60% of the plastic waste in Western Europe is landfilled or burned without recovering the energy or material [1]. This paper presents a new concept for recovery of plastic waste, where co-production of chemicals and energy is utilizing the potential of plastic waste.

Most of the plastic waste recycled today is treated mechanically by a melting process. This treatment requires a high purity feedstock, since any impurities that remain in the feed will result in down-cycling of the material; this is true even if the impurities are other plastic material. The result is that only relatively pure and large plastic waste streams are economical to treat in a mechanical process, and the material produced is of lower quality than the virgin material. In addition, the capacity of mechanical recycling is limited. In this paper a recycling concept for large scale, mixed and contaminated waste is presented, where the quality of the recycled material is equal to plastic produced from virgin sources.

PLASTIC WASTE TO PLASTIC, PtP

The Plastic waste to plastic (PtP) concept is developed by Norsk Hydro and offers a closed-loop system for a large scale recycling of mixed plastic waste back to plastic. The concept envisages combining existing technologies for waste treatment and production of valuable chemicals. The produced chemicals provide new feedstock to the plastic industry. The concept is outlined in Figure 1. The black arrows and text show the core strategy, taking plastic waste back to plastic. The mixed plastic waste is collected and pre-treated making it usable in a gasification process. The plastic waste is broken down to the chemical components, CO and H_2, in the gasifier. In order to produce new plastic material, the CO and H_2 are converted to methanol which is further reacted over a catalyst to produce olefins by use of the patented UOP/Hydro Methanol to Olefins process (MTO). Olefins are the feedstock in the production of plastic; e.g. PVC, PE, PP and PET. The mixed plastic waste also contains metals and other inorganics, which will be separated from the synthesis gas in the gasifier and recovered. The metals can replace virgin metals and the other inorganics are recovered as a glasified slag, known as frit and usable e.g. in roadbeds or in cement production.

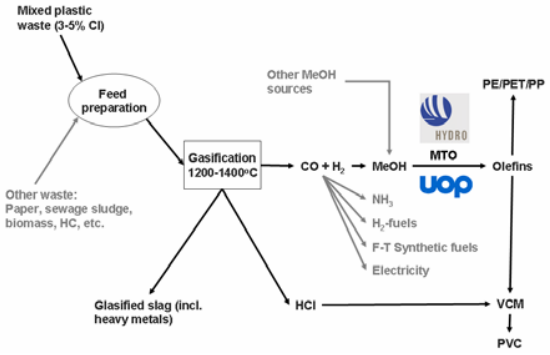

Figure 1: The Plastic waste to plastic (PtP) concept is shown schematically. The black path is the original PtP concept, whereas the grey paths are options included to increase the flexibility of the concept.

The grey arrows given in Figure 1 are the possible add-ons both as input and output. The extended PtP concept offers increased flexibility with its possibilities for alternative feedstock and product extractions at various stages in the process chain. All carbonaceous material is a potential feedstock in the concept. These other waste sources include paper, sewage sludge, wood, biomass and all other hydrocarbons, both renewable and non-renewable. The synthesis gas can be used to produce a number of products including methanol, ammonia, hydrogen, Fischer-Tropsch synthetic fuels and electricity. The possibility for extracting intermediates makes it possible from the single core technology, to add flexible downstream technologies that match market needs, technology developments, and existing legislation (which e.g. specifies targets for plastic-to-plastic, plastic-to-other material products, and plastic-to-energy recovery). Every intermediate can also be produced from alternative feedstocks, like introduction of methanol as shown in Figure 1. The possibility to use alternative feedstocks provides opportunities for varying the scale of different parts of the process train.

Substances (e.g. heavy metals) in the plastic waste not wanted in new polymers can be removed from the recycling chain in the gasifier. Reasons for wanting to remove substances can be based on environmental and/or product quality concerns.

An additional benefit of this concept when the waste material is recycled back to new plastic, instead of being burned, is the opportunity to capture the carbon and thereby preventing releases of CO_2 to the atmosphere. Since the carbon is captured, the

ethylene produced could be seen as green sourced. At the same time, CO_2 emissions from alternative production of ethylene are avoided.

Two operating processes worldwide produces chemicals from plastics waste, one in Germany and one in Japan. SVZ in Germany produces methanol from mixed waste [2] and Ebara in Japan produces ammonia from plastic waste [3], they are both gasifying the plastics waste.

UNITS AND REACTIONS

All carbonaceous material, including all sorts of polymers, can be treated in this concept. In order to be able to gasify the waste, a calorific value of at least 20MJ/kg is required. High calorific material such as PE, coal and oil can be added to increase the calorific value if low calorific material like PVC and polymers with high filler content (inorganics) is treated. Most gasifiers have a chlorine limit of 3% in order to avoid severe corrosion. Plastic material with brominated flame retardants are destructed in the process.

A minimum of feed pre-treatment is needed for gasification processes [4]. The level of pre-treatment is dependent of the gasification process chosen as the various reactors can treat various feeds. Large metal and other inorganic parts are removed, and the material crushed down to suitable particle sizes, ranging from 5mm to 10cm. Fixed bed gasifiers generally need less feed treatment than fluidised bed gasifiers, as the former can treat larger particles. The latter will, however, give syngas with higher and more uniform quality [5].

Gasification is a thermal upgrading process using oxygen, air, steam, or a combination thereof, in the reaction with the carbonaceous material. The product gas consists mainly of CO and H_2, normally called synthesis gas, and small amounts of CO_2, H_2O and CH_4 [6]. Pure O_2 is chosen as the oxygen source in this concept to assure a high calorific syngas; hence the following overall, strongly exothermic, reaction will take place in the gasifier. In the Equation the subscript p is used to indicate that this is a reaction with various polymers, which consists of different monomers (C_xH_y).

$$\left(C_xH_y\right)_p + \frac{x \cdot p}{2} O_2 \rightarrow (x \cdot p)CO + \left(\frac{y \cdot p}{2}\right) H_2 \quad (1)$$

By adding water to the synthesis gas produced, the H_2/CO ratio can be controlled. The slightly exothermic reaction is known as the Water-Gas-Shift (WGS) reaction, and is given below.

$$CO + H_2O \leftrightarrow CO_2 + H_2 \quad (2)$$

When plastic waste is used as the carbonaceous material in the gasification, other components than carbon and hydrogen will also be present. The chlorine present will form HCl in the gasifier. Due to the high temperatures in the reactor and direct quench [7] the level of dioxin reported is well below the legal limits [8]. The detailed reactions involved in the conversion are given in Aguado and Serrano [4]. More details on the gasification unit in the PtP concept are also given in Kaggerud et al. [9].

Dependent on the feedstock various gas treatment is necessary. Chlorine will always be present as HCl in the syngas, and has to be removed. It is normally removed by an aqueous solution of $Ca(OH)_2$ which forms $CaCl_2$ with HCl. This can either be done in a direct quench, or in a separate gas treatment unit. Thermodynamically the latter is advantageous [10]. Small amounts of sulphur can also be present in the feedstock. Sulfur forms H_2S and small amounts of COS in the gasifier, which has to be removed. Solid particles are removed in a filter.

The next step in the concept is the production of methanol from syngas, which is achieved by a conventional methanol process. The main reactions are given below, both are exothermic reactions. In order to obtain maximum catalyst activity, 5% of the feed should be CO_2 [11].

$$CO + 2H_2 \rightarrow CH_3OH \quad (3)$$

$$CO_2 + 3H_2 \rightarrow CH_3OH + H_2O \quad (4)$$

The UOP/Hydro Methanol to Olefins process, MTO, is designed to selectively convert methanol, either crude or refined, into olefins. The reaction takes place in a circulated fluidized bed, with a yield of 80% ethene and propene. The yield can be increased to above 90% by use of an olefin cracking process (OCP) for the C_{4+} reactor product [12]. The yield is higher than traditional thermal cracking of ethane and propane to olefins, which is of course beneficial for the energy usage in the separation sequence. The process is robust with regard to methanol quality, making it possible to operate with crude methanol.

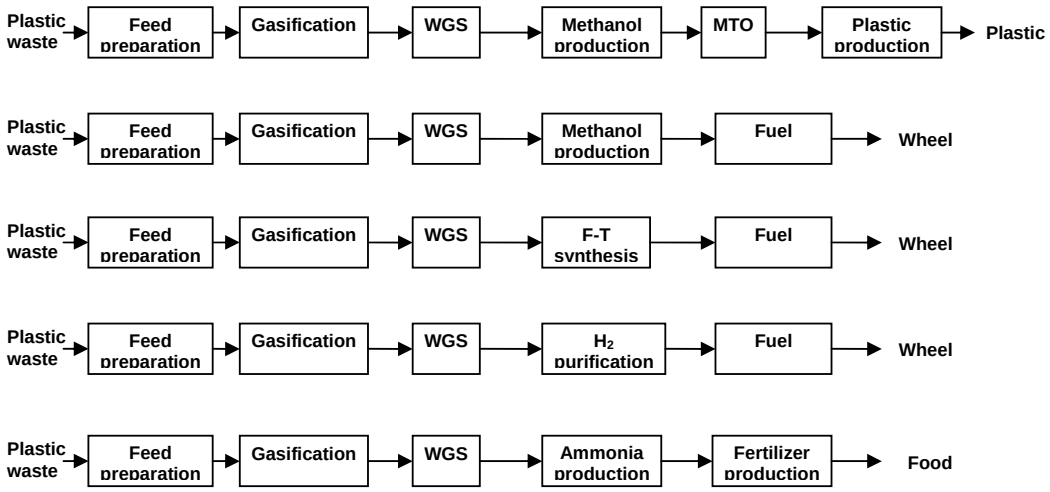

Figure 2: Possible process trains for processing of plastic waste

The olefins produced in the MTO-process will be used in production of new plastic, like PVC, PE, PET and PP. The catalyst used in the MTO process is based on a silicoaluminophosphate, SAPO-34. The principal reaction is given below [12].

$$5CH_3OH \rightarrow CH_2CH_2 + CH_2CHCH_3 + 5H_2O \quad (5)$$

Based on extensive tests in the demonstration plant, the MTO process is to be scaled up to a single train unit with capacity of up to one million tonnes of light olefins per year [12]. Basic engineering of the first planned commercial MTO plant based on stranded gas has been carried out. The plant will be part of a petrochemical complex in Nigeria, and is scheduled to come on stream in 2006. The plant will convert 2.5 million tonnes methanol into 400,000 tonnes of ethylene and 400,000 tonnes of propylene [13]. The MTO plant is flexible wit regard to the C_2/C_3-ratio, and typically the ratio can be modified within a range of 0.75-1.5 by adjusting the operating severity, with higher temperature leading to higher C_2/C_3-ratio [12].

SYSTEM EVALUATION

The core strategy in the PtP concept is shown in Figure 1 together with potential add-ons both in input and output. When the various process trains in Figure 1 are broken down to single process trains, the result is as shown in Figure 2, the core strategy is given as the first line. Of course, Figure 2 is not exhaustive and even further alternatives are possible. The core concept has been evaluated with respect to carbon efficiency in the various steps.

Definition of the carbon efficiency for step i:

$$\eta_C^i = \frac{(n_C)_{out}^i}{(n_C)_{in}^i} \quad (6)$$

The total carbon efficiency in the entire process train is then:

$$\eta_C = \prod_i \eta_C^i \quad (7)$$

The evaluation of the core PtP concept has been done by using the stoichiometric reactions given as Equations 1, 2, 3 and 5. For simplicity Equation 4 is omitted. The carbon efficiency is based on atom balances. In order to show the maximum potential for the core concept, all unit efficiencies are set to 1. In Figure 3 the stepwise decrease in carbon efficiency for various feed compositions is given. Compared with Figure 2, WGS is included in the methanol production unit as WGS is done to adjust the H/C-ratio for the methanol process. The maximum efficiency that can be achieved by this route is when the unit efficiency for all process steps equal 1, this is shown in Figure 3. Unit efficiency is the internal efficiency in the process, e.g. gasification. As can be seen from the figure, for all feed compositions lower than 80/20 the carbon

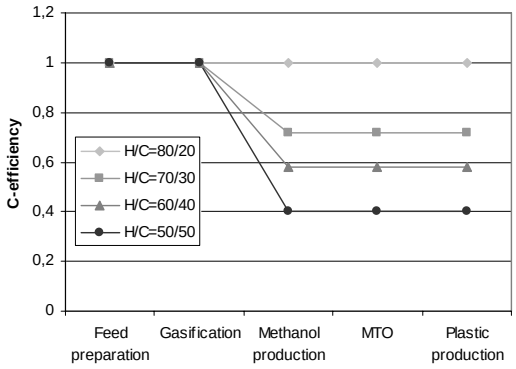

Figure 3: Stepwise decrease in carbon efficiency for various feed compositions, all unit operations have an efficiency set to 1. (The WGS is included in the methanol production unit)

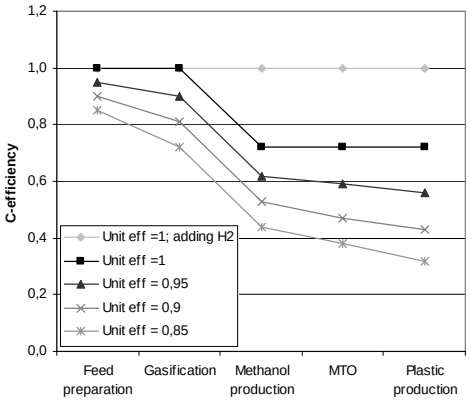

Figure 4: Carbon efficiency with decreasing unit efficiency in the PtP concept, H/C-ratio in the feed set to 70/30.

efficiency drops in the methanol production. The reason for this is the low hydrogen content in the waste compared to methanol; hence CO in the syngas has to be shifted to hydrogen by use of the WGS-reaction (Eq. 2), producing equal amounts of CO_2.

A high H-content in the feed gives a higher C-efficiency due to the high H/C-ratio needed in the methanol production. For an H/C-feed composition of 80/20 there is enough hydrogen available in the waste material to produce methanol without shifting the synthesis gas stream towards more hydrogen, hence no drop in efficiency will take place. Plastic waste will typically have a H/C-ratio of 65/35-70/30, hence a drop in efficiency will occur in methanol production. In order to avoid this drop in efficiency, a hydrogen-rich feed can be added to the plastic waste feedstock.

As the unit efficiency drops, the total carbon efficiency will of course drop as well. For calculations where the H/C-ratio is set to 70/30, the total carbon efficiency will drop from 0.72 at unit efficiency 1 to 0.43 at unit efficiency of 0.9; this is shown in Figure 4. Due to the long process train a small decrease in unit efficiency will result in a large drop in the total carbon efficiency. The main drop in efficiency is still the methanol production, for the same reasons as explained above. However; as the unit efficiency drops substantially, the other steps in the process will contribute more to the efficiency drop. For a unit efficiency of 0.85 the total carbon efficiency is as low as 0.32. For such low unit efficiencies the drop in carbon efficiency is spread more uniformly along the process train.

In Figure 4 it can be seen that the absolute difference in carbon efficiency is larger in the gasification step than in the methanol production, the relative difference is however larger in the methanol production step. The relative difference in efficiency shows the stepwise decrease in efficiency throughout the process train. To overcome the decrease in efficiency in the methanol production step, H_2 can be added to the syngas in order to adjust the H/C-ratio in favour of the methanol production unit. The effect of the additional H_2 is shown as the upper line in Figure 4. The efficiency drop in the methanol production can be solved by additional H_2, however, the challenge with a long process train remains. The production of hydrogen is not included in the efficiency calculations.

The evaluation above concentrate on the carbon efficiency. In the MTO-process, however, H_2O is being split off. This water has to be recycled in within the concept in order to maintain a high overall efficiency.

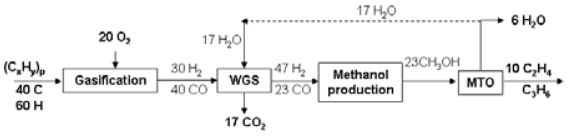

Figure 5: Simplified flow diagram for the core process train in the PtP concept. (Figures rounded up to the nearest whole number.)

In Figure 5, a simplified flow diagram shows the material flow in the concept. The input to the process train is plastic waste $(C_xH_y)_p$, oxygen and steam (steam might be recycled from the MTO

reactor). The output is the olefin product (C_2H_4 and C_3H_6), CO_2 and water. A rough stoichiometric molar balance is given in Figure 5. For simplicity the main product is ethene, however, as mentioned before different compositions of the olefin product is possible. The feed composition used is H/C=60/40, and all unit efficiencies are set to 1. The overall carbon efficiency is ~0,6 for the material balance in Figure 5, which is in agreement with the efficiency given in Figure 3. As indicated above, the reason for the low carbon efficiency is the high hydrogen content in the intermediate product methanol. In order to produce enough H_2 for the methanol production, water is reacted with CO (Eq. 2) and consequently equal amounts of CO_2 are produced.

In the MTO process, equal amounts of water are being split off as methanol is converted to olefins. The water can however be recycled to the WGS reactor, reducing the loss of water significantly. Recycling of water from the MTO to the WGS reactor will decrease the overall loss of atoms in the process train.

The main obstacle in the concept is the high hydrogen content in the intermediate product methanol, compared to both the waste plastic and the plastic product. To increase the carbon efficiency in the system various actions can be taken. Chemical integration with other process trains where the high carbon content can be utilized in other products is one option. Additional input of hydrogen or hydrogen-rich chemicals, or utilization of the intermediate products are other possibilities. These are shown as the grey arrows in Figure 1. The introduction of other feed and by-products can increase the efficiency of the concept; the extended PtP concept. As the high hydrogen content in the methanol is a main obstacle in the concept, another way to improve the efficiency of the concept is to avoid the formation of methanol by using alternative pathways from syngas to olefins. A catalytic process which converts synthesis gas into olefins by a direct route will of course be beneficial; however, this process does not exist for commercial operation.

DISCUSSION

Western Europe generates around 20 million tonnes of plastic waste annually. In 2002, 13% was recycled and 22% incinerated with energy recovery while the major part is still landfilled [14]. The EU post-consumer waste Directives will force more plastic waste to be recycled. These Directives include; The Packaging and Packaging Waste (1994), End-of-life Vehicles, ELV, (2000), Waste Electrical and Electronic Equipment, WEEE, (2003). The Packaging and Packaging waste Directive is at present being revised. The new recycling target for plastic will be 22.5%, up from today's 15% [15]. This target is only to be achieved by recycling plastic waste back to plastic. As a result of these post-consumer waste Directives, we have estimated that an additional recycling capacity in the order of 2 million tonnes is requested in 2008. It is envisaged that only a limited part of this could be achieved by mechanical recycling. This is due to lack of end-markets for the recycled material and the presence of large quantities of mixed plastic waste [1].

Household waste accounts for almost 70% of the total amount of plastic waste. This waste stream is often contaminated with food, detergents, metals, paper etc. Only 8% of the plastic waste from households is recycled at present [14]. This source is an excellent feedstock for the PtP concept. The most important driver for increased recycling might be the ban on landfilling of carbonaceous material. Several European countries are about to illegalise the deposit of plastic material, hence the plastic waste will have to be recovered [16].

In the future, there will be even more plastic waste generated than there is today. Furthermore, consumer choice increases the variety of polymers and additives. This can sometimes be for good reasons such as longer shelf-life of food in packaging or merely for aesthetic purposes. These changes create a major challenge for mechanical recycling, since everything that goes into such recycling is bound to come out in the recyclate. This also applies to additives that may have been phased out or become obsolete. Mechanical recycling hence often implies down-cycling. APME has recently raised a concern that the availability of end-markets for plastic waste recyclate may be a limiting factor for the long term sustainability of high rates of mechanical plastic waste recycling [1]. In the PtP concept, plastic waste is broken down to the chemical components CO and H_2, which can be purified and used to produce a variety of products. As the market requires high quality plastic material, the plastic waste can be used as a feedstock to meet this requirement.

The PtP can be used to produce high quality plastic as all the impurities are removed in the process train, whereas products from mechanical recycling will decrease in quality for each time is it recycled. The decrease in quality is with respect to both chemical and physical properties, like mixing of polymers,

fillers, banned chemicals, colour, strength, etc. To compensate for the decrease in strength, more recycled material than virgin material is needed to fulfil the same function. The consequence is that 1 kg of virgin material in a car cannot be replaced by only 1 kg of recycled material, but i.e. 1,1 kg of recycled plastic. This means that when different processes are to be compared, the real material consumption has to be taken into account, focusing on the functional unit the material shall fulfil. In order to account for this difference, a substitution factor has been proposed, defined as "*the quantity of virgin material (kg) that can be replaced by one kilo of recycled plastic in order to achieve equivalent performance*". [17]

Energy recovery

Why do we not just recover the energy of the waste material? There are several reasons for recovering the material in the plastic waste. First of all, according to the EU waste hierarchy material recycling is preferred to energy recovery. The waste hierarchy have the following preferred order:

1. *Waste prevention*

2. *Recovery*
   i) reuse
   ii) material recycling
   iii) energy recovery

3. *Disposal*

The waste hierarchy has been criticized lately as it would prevent development of more efficient waste management systems [18, 19]. The waste hierarchy gives general guidelines for treatment of waste. More careful investigation is of course needed for each specific case.

Second, the need for feedstock for production of materials also after the fossil fuel age argues that plastic waste should be recycled as material. The waste will always be present, even after the oil and gas are consumed. In addition, less CO_2 emissions than in production of plastic from virgin resources, are formed as the plastic waste is used as feedstock in production of plastic.

To become sustainable, energy and materials will have to be produced from renewable resources. In addition we will have to take care of the waste that we are generating. As the waste is at a high energy level, it should be kept at this high energy level by recycling it back to new materials. Polymers will be seen as highly efficient materials with respect to natural resources, cost, weight and greenhouse gas emissions. To safeguard that impression, cost-efficient recycling solutions that handle large volumes of diverse polymers will have to be developed, to demonstrate that plastic wastes do not have inherent recycling limits.

The plastic recycling system can be extended by use of alternative feedstock and product extractions at various stages in the process chain. This will offer an increased flexibility of the process. As the plastic waste or an alternative carbonaceous feedstock is converted to synthesis gas in the process, it opens up for a variety of products. Bulk chemicals like methanol and ammonia are produced from synthesis gas. In addition, H_2, various fuels, heat and electricity can be produced from synthesis gas. Plastic waste is an interesting substitute for natural gas feed, as the waste always will be present. A superstructure similar to the one given in this paper has been set up for natural gas [20]. More ideas for chemical and process integration through co-production of energy and materials are outlined in the paper referred to above.

CONCLUSION

In this paper, a new concept is presented for closed-loop large scale recycling of mixed plastic waste, with a gasifier and the MTO process as key process steps. The concept facilitates production of new modern plastic from old, mixed and contaminated plastic waste. Organic constituents in the plastic waste e.g. polybrominated flame retardants are destructed and inorganic constituents e.g. heavy metals are extracted and immobilized. In comparison to mechanical recycling, no sorting is needed and down-cycling is avoided. The concept will fill the gap between what is achievable by mechanical recycling and the targets for recycling given in EU post-consumer waste directives.

The main obstacle for a high carbon efficiency in the core PtP concept is the high H/C-ratio needed in the intermediate product methanol compared to the ratio in both the feedstock and end-product. The carbon efficiency drops rapidly with decreasing unit efficiency due to the long process train. To overcome this challenge, integration with other process trains, production of products with a high carbon content or supply of additional hydrogen-rich

feedstock to the process train are obvious possibilities.

In this paper, focus has been on chemical integration and utilisation of the atoms that enters the process train. Of particular interest is of course also the energy flow and possibilities for process integration in the PtP concept. This is published in [10], and will be examined in detail in further work.

REFERENCES

[1] **APME**, *Assessing the potential for post-use plastics waste recycling-predicting recovery in 2001 and 2006,* Summary report, Brussels: APME, 1998.

[2] **Malkow**, T., *Novel and innovative pyrolysis and gasification technologies for energy efficient and environmentally sound MSW disposal*, Waste Management, 2004;24(1):53-79.

[3] **Parkinson**, G., *Plastic wastes will be the new raw material for ammonia production*, Chemical Engineering, 2002;109(13):13.

[4] **Aguado**, J. and Serrano, D.P., *Feedstock Recycling of Plastic Waste.* Cambridge: Royal Society of Chemistry, 1999.

[5] **Kunii**, D. and Levenspiel, O., *Fluidization Engineering*, 2 Ed., Newton, Butterworth-Heinemann, 1991.

[6] **Menges**, G., Michaeli, W. and Bittner, M., *Recycling von Kunststoffen*, Wien, Carl Hanser Verlag München, 1992.

[7] **Lighty**, J. S., Veranth, J.M., *The role of research in practical incineration systems-a look at the past and the future.* In: Proceedings of the Twenty-seventh International Symposium on Combustion, Colorado, 1998.

[8] **Yamamoto**, T., Sato, H., Matsukura, Y., Ujisawa, Y., Ishida, H., Sasaki, S. and Hata, Y., *Energy and chlorine recovery from plastics waste including polyvinyl chloride by using Sumitomo metals' waste gasification and smelting system*, In: Clean Air 2003, Proceedings of Seventh Conference on Energy for a Clean Environment, Lisbon, 2003.

[9] **Kaggerud**, K.H., Sandberg, P., Musdalslien, U.I., Nilsen, H.R. and Leadbitter, J., *A New Concept for Plastic Waste to Plastic Recycling*, In: Proceeding of Gasification, A versatile solution conference, Brighton, 2004.

[10] **Kaggerud,** K.H., Sisjord I.L., Musdalslien U.I. and Gundersen T., *Process Integration Opportunities in the Plastic Waste to Plastic Production Chain,* In: Proceedings of PRES'05, Sicily, 2005.

[11] **Moulijn**, J.A., Makkee, M. and van Diepen, A., *Chemical Process Technology*, 2 Ed, England, John Wiley & Sons, 2003.

[12] **Kvisle**, S., Nilsen, H.R., Fuglerud, T., Grønvold, A., Vora, B.V., Pujado, P.R., Barger, P.T. and Andersen, J.M., *Methanol to Olefins: State of the Art and Perspectives*, Erdöl Erdgas Kohle, 2002;118(7/8):361-364.

[13] **Chementator**, *Methanol-to-olefins project moves forward*. Chemical Engineering 2003;110(3):21.

[14] **Delavelle**, C. and Shaw, P., *Information System on Plastic Waste Management in Europe; European Overview 2000 Data*. France: TN SOFRES Consulting for APME, 2002.

[15] **Commission**, *Proposal for a Directive of the European Parliament and of the Council amending Directive 94/62/EC on packaging and packaging waste*, Brussels: European Union, 2001.

[16] **Brown** K.A et al., *Economic evaluation of PVC Waste Management*, A report produced for European Commission Environment Directorate, Brussels: European Commission, June 2000.

[17] **APME**, *An Examination of waste treatment scenarios for plastics from end-of-life electrical and electronic equipment using an eco-efficiency model*, Summary report, Brussels: APME, 2003.

[18] **Davoudi**, S., *Planning for waste management: changing discourses and institutional relationships*, Progress in Planning, 2000;53(3):165-216.

[19] **Malkow,** T., *Novel and innovative pyrolysis and gasification technologies for energy efficient and environmentally sound MSW disposal*, Waste Management, 2004;24(1):53-79.

[20] **Kaggerud**, K.H, Bolland, O. and Gundersen, T., *Chemical and process integration: Synergies in co-production of power and chemicals from natural gas with CO2 capture*. In: PRES 2004, Proceedings of CHISA 2004 conference, Prague, 2004 (To be published in Applied Thermal Engineering).

Proceedings of ECOS 2005
Trondheim, Norway
June 20–22, 2005

COMBINED EXERGY AND PINCH ANALYSIS FOR OPTIMAL ENERGY CONVERSION TECHNOLOGIES INTEGRATION

François Marechal*, Daniel Favrat
Laboratory for Industrial Energy Systems, Ecole Polytechnique Fédérale de Lausanne
CH-1015 Lausanne

ABSTRACT

Exergy concept combined with pinch based approach are used for studying the optimal integration of energy conversion systems. The analysis first considers the representation of the hot and cold composite curves of the process and defines the energy and the exergy requirements. The basic assumption of the $\Delta T min$ required for the pinch analysis is represented as an exergy loss that increases the exergy requirement of the process. The exergy composite curves put the focus on the opportunities for heat pumping in the process. The optimal integration of the utility system is then realised by extracting the energy conversion system configuration from a superstructure using a Mixed Integer Linear Programming formulation in which the heat cascade definition and the combined heat and power production balances are introduced as constraints and where the exergy losses minimisation is used as an objective function. The balanced exergy composite curves are used to visualise the exergy losses in the heat exchanges and the analysis of the results is made using a definition of the exergy efficiency that accounts for the pinch point location, the process exergy and the exported energy services.

Keywords: process integration, energy conversion integration, exergy analysis, second law analysis

NOMENCLATURE

CHP	Combined heat and power
ΔT_{min}	Minimum heat recovery approach temperature
e_{fuel}	specific exergy of the fuel (kJ/kg)
f_{fuel}	fuel flowrate (kg/s)
E_{cool}	exergy available below the pinch point (kW)
E_{frg}	exergy required for the refrigeration(kW)
E_{heat}	exergy required above the pinch point (kW)
E_{res}	exergy resource consumed by the process(kW)
GT	Gas turbine
HP	Heat pump system
LHV	Lower Heating Value (kJ/kg)
MER	Minimum Energy Requirement
MILP	Mixed Integer Linear Programming
W	Electrical power (kW)

INTRODUCTION

When considering the energy efficiency of a process, pinch based approaches [1] target the identification of the possible energy recovery by heat exchange and define this way the minimum energy requirement (MER) of a process. The integration of the energy conversion technologies concerns the way the minimum energy requirement will be satisfied by converting energy resources into useful energy for the process, considering the combined heat and power production, the integration of steam networks, heat pumps and refrigeration systems. It represents a major step in a process integration study because it defines the cost of the energy requirement together with the complete list of streams to be considered in the heat exchanger network design. It is usually solved by applying optimisation techniques based on mixed integer linear programming techniques [2, 3] that aim at selecting the most appropriate technology and to determine the optimal flowrates in the energy conversion technologies.

By allowing the comparison of different forms of energy, exergy is a rigourous way of analysing energy conversion systems. In the context of process integration analysis, the exergy concept is combined with the pinch analysis for reducing the energy requirement of the process [4, 5], optimising the energy conversion system integration and realis-

*Corresponding author: Phone: +41 21693 3516 Fax: +41 21693 3502 E-mail: francois.marechal@epfl.ch

ing combined heat and power production. The exergy composite curve concept has been introduced by Dhole [6] for this purpose. The exergy delivered (E) by a stream delivering heat (Q) from T_{in} to T_{out} is computed by : $E = Q(1 - \frac{T_a}{T_{lm}})$ where T_{lm} is the logarithmic mean of temperatures computed by $T_{lm} = \frac{T_{in} - T_{out}}{ln(\frac{T_{in}}{T_{out}})}$ and T_a is the ambient temperature, all temperatures being expressed in K. When considering the hot composite curve, the heat delivered is represented by the temperature-enthalpy diagram, the exergy delivered is computed by replacing the temperature axis by the Carnot efficiency $(1 - \frac{T_a}{T})$. It corresponds then to the area between the composite curve and the enthalpy axis (figure 1, right). The same procedure is followed for the cold streams to define the exergy required by the cold streams. Favrat and Staine [4] have added to this representation, the exergy losses related to the compression work (as a function of the pressure drop) and the grey exergy. The grey exergy is the exergy required to construct the heat exchangers. It includes the raw materials exergy content as well as the exergy consumed in the construction process. This concept is then used to determine the optimal value of the ΔT_{min}. The exergy analysis has been extended to account for the chemical reactions or the physical separations of the process operations [7, 5]. The graphical representation in [7] uses $\frac{\Delta H - T_a \Delta S}{\Delta H}$ as Y-axis that is an extension of the Carnot factor $(1 - \frac{T_a}{T})$. Marechal et al. in [8] use the concept of exergy to target the combined heat and power production by integrating rectangles in the Grand composite curve. The area of the rectangles is proportional to the mechanical power production, the height referring to the Carnot efficiency and the width being proportional to the heat load.

The goal of this paper is to discuss the application of exergy concepts for helping in the design of optimal energy conversion systems for a given process.

MINIMUM ENERGY REQUIREMENT

Based on the definition of a minimum approach temperature difference (ΔT_{min}), composite curves are used to compute the maximum energy recovery between the hot and the cold streams of a process. The temperature is a topological indicator in the sense that it allows to pinpoint the process operations concerned with the pinch points or the pseudo pinch points. Four zones are of importance in the hot and

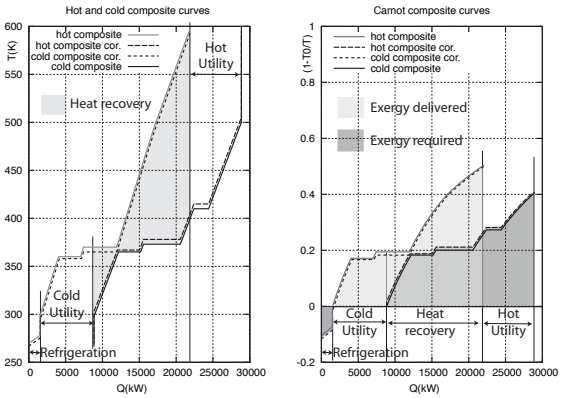

Figure 1: Exergy composite curves defining the process requirements

cold composite curves (figure 1, left). On the right, we visualise the hot utility requirement. The heat recovery zone represents the possible heat recovery by exchange between hot and cold streams of the process. The remaining heat of the hot stream has to be evacuated by cold utility. The left part of the graph defines therefore the cold utility requirement, the later being divided between cooling requirements above the ambient temperature and the refrigeration requirements below the ambient temperature. When using the Carnot efficiency ($(1 - \frac{T_a}{T})$) as the Y-axis, the area between the Xzero-axis and the cold composite curve (figure 1,right) represents the exergy required to heat up the process cold streams while the area below the hot composite and the zero axis represents the exergy delivered by the hot streams of the process. The difference between the two areas represent the net exergy balance available from the process streams through heat exchange. From this available exergy, a first exergy loss will be associated to the passage in the corrected temperatures domain that is obtained by shifting vertically the hot streams downwards and the cold streams upwards from a value of $\Delta T_{min}/2$. More rigourously, the exergy loss is computed considering the contribution $\Delta T_{min}/2_j$ of each stream j that is proportional to its heat film transfer coefficient.

The Grand composite curve (figure 2, left) describes as a function of the temperature, the way energy has to be supplied to or removed from the system. The process Grand composite curve is divided into three zones : above the process pinch point, the system is

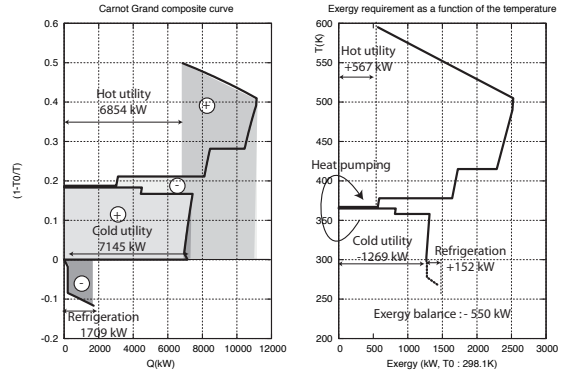

Figure 2: Exergy Grand composite curves of the process requirements

a heat sink to be supplied by a hot utility. Below the process pinch point and above the ambient temperature, the process is a heat source. Below the ambient temperature, the process requires refrigeration. The feasibility rule of the utility integration is that the Grand composite curve of the utility system should envelop the process Grand composite curve.

When considering the exergy Grand composite curve (figure 2,left), the process exergy requirement is defined by a difference of areas. In this diagram, it should be noted the special role of the self-sufficient pockets (right part of the graph), the area of which represents the possible mechanical power recovery by combined heat and power production. The composite curve on figure 2,right represents the cumulated exergy required by the process as a function of the temperature. The exergy balance shows an overall exergy availability. However, from the definition of the pinch point, it is necessary to divide the system into three sub-systems, considering the exergy balance for each of the systems. Comparing the energy requirement and the exergy requirement allows to set efficiency target for the energy conversion system. This exergy may be recovered partly by properly integrating combined heat and power devices (Rankine cycles), while exergy transfer between sub-systems will only be possible by heat pumping.

INTEGRATION OF ENERGY CONVERSION SYSTEMS

The integration of the energy conversion system aims at defining the complete list of streams to be considered including the hot and cold streams of the utility sub-system, prior any heat exchanger network design. The utility streams are defined so that they will minimise the cost of the energy requirement and/or make the best use of the process exergy. The calculation of the best system will start with the definition of a utility system superstructure that will include the possible conversion technologies that are envisaged. The analysis of the grand composite curve, applying the rules for optimal placement of Townsend et al. [9] and other rules for the optimal CHP integration, help in defining the list of energy conversion technologies able to supply the energy requirement of the process with a maximum of efficiency. In order to solve problems where several utilities are considered, MILP formulations have been proposed [2, 10]. The mathematical formulation (eq. 1) of the targeting problem exploits the concept of Effect Modelling and Optimisation (EMO) [3, 11]. It is used to select the equipments in the superstructure and determine their optimal operating flowrates in the integrated system. This approach assumes that the temperature and pressure levels of the energy conversion technologies are known. Two variables are associated with any utility technology w : the integer variables y_w represents the presence of the technology w in the optimal configuration and f_w its level of utilisation ($fmin_w \leq f_w \leq fmax_w$). The objective function is the total cost including the operating costs and the annualised investment cost, both expressed in $€/year$. Other objective functions like minimum operating cost or minimum of emissions may also be used. The annualising factor is computed knowing the interest rate i and the expected life time of the investment n_{years}.

$$\min_{R_r, y_w, f_w} \sum_{w=1}^{n_w} (C2_w f_w) + Cel_i Wel_i - Cel_s Wel_s) * t + \sum_{w=1}^{n_w} (C1_w y_w) + \frac{i(1+i)^{n_{years}}}{(1+i)^{n_{years}} - 1} \sum_{w=1}^{n_w} (ICF_w y_w + ICP_w f_w) \quad (1)$$

subject to

Heat balance of the temperature intervals

$$\sum_{w=1}^{n_w} f_w q_{w,r} + \sum_{i=1}^{n} Q_{i,r} + R_{r+1} - R_r = 0 \qquad \forall r = 1,...,n_r \quad (2)$$

Electricity consumption:

$$\sum_{w=1}^{n_w} f_w w_w + Wel_i - Wc \geq 0 \quad (3)$$

Electricity exportation

$$\sum_{w=1}^{n_w} f_w w_w + Wel_i - Wel_s - Wc = 0 \quad (4)$$

Existence of technology w

$$fmin_w y_w \leq f_w \leq fmax_w y_w \quad {}^{\forall w=1,...,n_w}_{y_w \in \{0,1\}} \quad (5)$$

Thermodynamic feasibility of the heat recovery and utility systems

$$Wel \geq 0, Wel_s \geq 0 \quad (6)$$

$$R_1 = 0, R_{n_{r+1}} = 0, R_r \geq 0 \qquad \forall r = 1,...,n_{r+1} \quad (7)$$

R_r $[kW]$ (r=1,n_r+1) is the heat cascaded from the temperature interval r to the lower temperature intervals, n is the number of process streams, Q_{ir} $[kW]$ is the heat load of the process stream i in the temperature interval r ($Q_{ir} > 0$ for hot streams), Wel_s and Wel_i are respectively the net production and net import of electricity $[kW]$; $C1_w$ and $C2_w$ are respectively the fixed and the proportional cost of using the technology w; ICF_w and ICP_w are respectively the fixed and the proportional cost related to the investment of using technology w. Although the formulation is linear, it allows this way to account for size effect in the investment; n_w is the number of technologies proposed in the utility system superstructure; q_{wr} is the heat load of the technology w in the temperature interval r for a given reference flowrate, ($q_{wr} > 0$ for a hot stream) ;w_w is the mechanical power produced by the reference flowrate of technology w; ($w_w > 0$ for a mechanical power producer); Cel_s and Cel_i are respectively the selling price and the import price of electricity $[€/kW]$; t is the total annual operation time $[s/year]$; Wc $[kW]$ is the overall mechanical power needs of the process; ($Wc < 0$ if the overall balance corresponds to a mechanical power production).

This method may be applied to any kind of energy conversion technologies. It is based on the assumption that the operating conditions have been defined for each of the equipment concerned and that only the flowrates are unknown. This is a limiting assumption but it allows to solve most of the problems of energy conversion integration mainly because non linearities may usually be solved by discretising the search space. The method has been further adapted to compute the optimal integration of steam networks [12], to incorporate restricted matches constraints [13], to integrate refrigeration cycles [14] and Organic Rankine Cycles[15] as well as heat pumps [16].

The grand composite curve resulting from the optimisation is the balanced composite curves. An example of such curves is given on figure 3, left. This representation is characterised by a number of pinch points, one being the process pinch point, the others corresponding to the maximum use of the cheapest utilities to satisfy the process requirement. In the Carnot representation (figure 3, right) the area between the curve and the Y-axis represents the exergy losses in the system heat transfer. Two curves are presented, the external one represents the overall exergy losses, while the internal one that feature pinch points represents the one computed with the corrected temperatures. The area between the two curves represents therefore the exergy losses relating to the assumptions of the $\Delta T_{min}/2_j$ contributions of the streams. Analysing the inner curve allows to identify further improvement for the energy conversion by modifying for example the operating conditions (pressures or temperatures) in the energy conversion technologies. Integrated composite curves [17] may be used to analyse the integration of subsystems in the process. The figure 4 shows for example the integration of the steam network in the system under study. The energy balance of the hot and cold streams of the steam network is the net mechanical power production. When appropriately placed, it corresponds to a supplement of energy to be supplied to the system. The fact that it appears on the left of the temperature axis proves that the steam network characteristics are appropriate for the optimal production of mechanical power. In the Carnot factor ordinate, the area between the two curves gives an indication of the quality of the exergy use in the corresponding sub-system.

One heuristic rule resulting from the exergy analysis is to try to reduce to a minimum the area between the hot and cold composite curves of the integrated

systems including the energy conversion system.

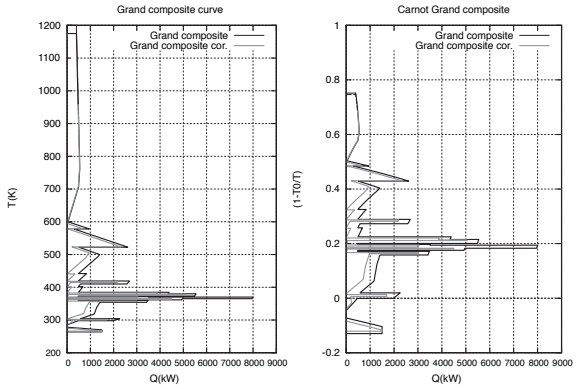

Figure 3: Balanced Grand composite curves of the integrated system

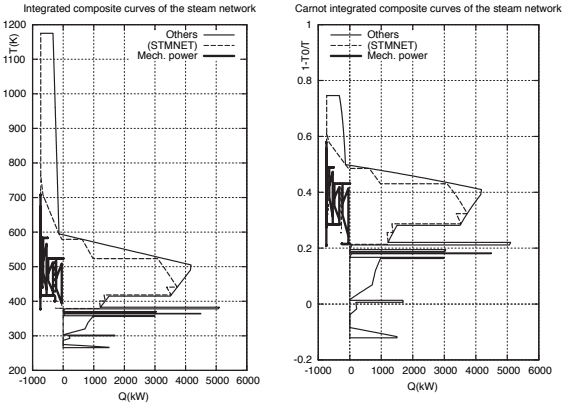

Figure 4: Integrated composite curves of the steam network

Using the exergy losses as an objective function

Due to the linear nature of the problem, the use of the energy cost as an objective function may reveals some difficulties [16]. When the cost of fuel and electricity is such that the electrical efficiency of a cogeneration unit is attractive without the use of heat (i.e. when the electrical efficiency of the unit $\eta_{el} = \frac{W_{el}}{LHV_{fuel}}$ is greater than $\frac{C_{LHV}(€/kJ)}{C_{el}(€/kJ_e}$)) there is an economical interest to produce electricity even without cogeneration). In this case, the linear programming procedure leads to a situation where the cogeneration unit is used at its maximum. This situation usually does not occur when the investment cost are properly considered or when the cost of the different forms of energy are coherent with respect to the electrical efficiency. Nevertheless, the relative price of the different forms of energy will influence the technology selection and their level of usage in the integrated solution. When the target is the maximisation of the system efficiency, alternative formulations that take into account the value of energy in the objective functions have to be considered. The minimisation of the exergy losses (eq. 8) is an alternative way of formulating the objective function.

$$\underset{R_k, y_w, f_w}{Min} \sum_{w=1}^{n_w} (f_w * (\Delta Ex_w - \sum_{k=1}^{n_k} \Delta ex_{wk} + w_w)) \qquad (8)$$

In this relation, ΔEx_w is the exergy consumed to produce the hot and cold streams and the electricity of the conversion unit w, Δex_{wk} is the heat-exergy supplied by the ns_w hot and cold streams of the conversion unit w in the temperature interval k. Δex_{wk} is given by (9).

$$\Delta ex_{wk} = \sum_{s=1}^{ns_w} q_{sk} * (1 - \frac{T_a * ln(\frac{T_{k+1}+\Delta T_{min}/2_s}{T_k+\Delta T_{min}/2_s})}{T_{k+1} - T_k}) \qquad (9)$$

Using this formulation, it is possible to define the set of energy conversion technologies that minimises the exergy losses of the system. It is even possible to introduce the aspects related to the investment by adding the grey exergy into the ΔEx_w term.

EXAMPLE

Let us consider the system requirements defined on table 1. These result from the hot and cold composite curves of figure 1 and the Grand composite curve of figure 2. For the calculations, we assumed that all the possible process improvements were already implemented before analysing the energy conversion technologies integration.

Table 1: Minimum energy and exergy requirements of the process

	Energy	Exergy
Heating (kW)	+6854	+567
Cooling (kW)	-6948	- 1269
Refrigeration (kW)	+1709	+ 157

Several optional energy conversion system configurations are studied, the results are summarized in table 5 where the energy consumption of the energy

conversion sub-systems are presented. The simplest solution (option 1) is to integrate a boiler using natural gas (with a LHV of 44495 kJ/kg) and to cool the process with cooling water. The refrigeration needs will be supplied with a refrigeration cycle using ammonia (R717). The operating conditions of the refrigeration cycle (table 2) have been obtained by simulation considering the temperature levels in the composite curve and the ΔT_{min} to be reached in the heat exchangers. The integrated composite curves presenting the results of the optimisation are presented on figure 5 (left). The refrigeration cycle consumption is of 314 kW corresponding to an exergy efficiency of 50 %. It should be noted that the energy consumption is higher than the MER due to the losses at the boiler stack (398 K). The solution accounts for the possibility of air preheating to valorise the energy excess available in the process. The heat load of air preheating is of 131 kW. In order to valorise the exergy potential, a steam network has been integrated (Option 2). The steam network headers are given on table 3, the isentropic efficiency of the turbines are assumed to be of 70 %.

Table 2: Refrigeration cycle characteristics

Refrigerant			R717	Ammonia	
Reference flowrate			0.1	kmol/s	
Mechanical power			394	kW	
	P	T_{in}	T_{out}	Q	$\Delta T min/2$
	(bar)	(°K)	(°K)	kW	(°K)
Hot str.	12	340	304	2274	2
Cold str.	3	264	264	1880	2

Applying the rules of the appropriate placement of heat pumping devices, 3 heat pumping cycles have been proposed and simulated (table 4).

The high values of the COP are explained by the very small temperature raise to be obtained from the heat pump when considering small $\Delta T_{min}/2$ values for the heat exchangers. Using the optimisation tool, the optimal flowrates in the three cycles have been computed together with the new value of the fuel in the boiler house (Option 4). In the example considered, this leads to a situation where the whole heat requirement may be provided by the heat pumps. When the steam network is considered together with the heat pumps (Option 5), the results are slightly

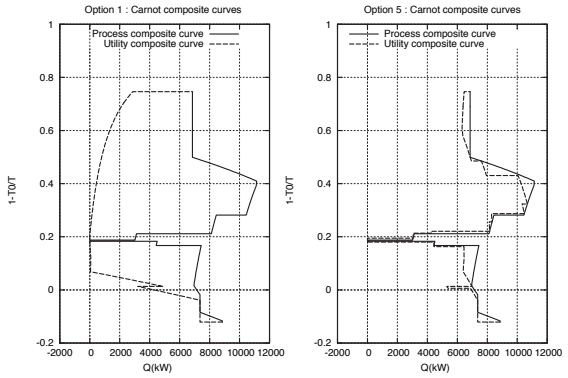

Figure 5: Carnot integrated composite curves of the energy conversion system for options 1 (left) and 5 (right)

different since in this case, an additional amount of energy is required by the system to balance the mechanical power produced by expansion in the steam network. The solution of heat pumping is then compared with a combined heat power production using a gas turbine (Option 3). In this situation, the two options are conflicting.

Energy and Exergy efficiency

The summary of the energy conversion system integration is given on table 6. It is shown that a MER of 6854 kW for the heating requirement and of 1709 kW for the refrigeration requirement is finally supplied with an equivalent 893 kW of fuel when considering the possibility of heat pumping and when converting the exergy content of the process streams. Compared to the boiler house solution, the new situ-

Table 3: Steam cycle characteristics

Header	P	T	Comment
	(bar)	(K)	
HP2	92	793	superheated
HP1	39	707	superheated
HPU	32	510	condensation
MPU	7.66	442	condensation
LPU	4.28	419	condensation
LPU2	2.59	402	condensation
LPU3	1.29	380	condensation
DEA	1.15	377	deaeration

Table 4: Characteristics of the heat pump system, based on R123 as working fluid

	P_{low} (bar)	T_{low} (°K)	P_{high} (bar)	T_{high} (K)	COP -	kWe
Cycle 3	5	354	7.5	371	15	130
Cycle 2	6	361	10	384	12	323
Cycle 0	6	361	7.5	371	28	34

Table 5: Results of the energy conversion system integration for different options

Opt	Fuel kW_{LHV}	GT kWe	CHP kWe	Cooling kW	HP kWe
1	7071	-	-	8979	-
2	10086		2957	9006	-
3	16961	5427	2262	9160	-
4	-	-	-	2800	485
5	666	-	738	2713	496

ation corresponds to a reduction by a factor 8 of the fuel consumption. These data have been computed by considering a fuel equivalence of 55% for the electricity production (column Total 1). The order of the solutions will be different if we consider the European mix (38.7%) for the fuel equivalence (Table 6, column Total 2). In order not to rely on the definition of a fuel equivalence, an exergy efficiency η_{ec} of the energy conversion system will be computed considering the exergy of the process. In this definition, we consider that the energy services delivered, i.e. the process exergy requirement ($E_{heat} + E_{frg}$) and the export of electricity (Wel_s), will be satisfied with an efficiency of η_{ec} leading to an exergy consumption of $\frac{E_{heat}+E_{frg}+Wel_s}{\eta_{ec}}$, while the exergy excess (E_{cool}) will be converted with an efficiency of η_{ec}. The balance (eq. 10) is equal to the energy resources ($E_{res} = f_{fuel} * e_{fuel} + Wel_i$) converted in the energy conversion system. Solving (10) gives the definition of the exergy efficiency of the system (eq. 11). In Table 6, it can be seen that the options that do not convert the exergy excess (E_{cool}) have smaller exergy efficiencies. The best solutions are the one that realise heat pumping that "pump" the excess of exergy from below to above the pinch point.

$$E_{res} = \frac{E_{heat} + E_{frg} + Wel_s}{\eta_{ec}} - E_{cool} * \eta_{ec} \qquad (10)$$

$$\eta_{ec} = \frac{E_{res} - \sqrt{(E_{res})^2 + 4E_{cool}(E_{frg} + E_{heat} + Wel_s)}}{-2E_{cool}} \qquad (11)$$

CONCLUSIONS

The application of the exergy concept combined with pinch based methods for analysing the optimal integration of energy conversion system of industrial processes has been studied. The exergy composite curves is used to compute the minimum exergy requirement of the process, considering the pinch point location. The exergy requirement is obtained by first considering an exergy loss resulting from the definition of the ΔT_{min}. The remaining exergy requirement is divided into three contributions: the exergy required above the pinch point, the exergy produced as energy excess between the pinch point and the ambient temperature and the exergy required for refrigeration. Starting with an energy conversion system superstructure, a linear programming formulation is used to extract the optimal energy conversion system configuration that supplies the process energy requirement and that integrates the combined heat and power production and the heat cascade. In this formulation, it is possible to use either the energy cost or the exergy losses as an objective function. The exergy balanced composite curves and the exergy integrated curves are used to visualise the exergy losses in the system. The exergy efficiency of the conversion system is defined by comparing the exergy resource consumption with the exergy export and the process exergy, making the distinction between the exergy available and the exergy required. This efficiency definition sets the focus on the ex-

Table 6: Energy and exergy efficiency of the different options

Opt	Fuel kW_{LHV}	Net El. kWe	Total 1 kW_{LHV}	Total 2 kW_{LHV}	η_{ec} %
1	7071.0	371.0	7745.5	8030	9.6
2	10086.0	-2481.0	5575.1	3675	30.6
3	16961.0	-7195.0	3879.2	-1630	45.16
4	0.0	832.0	1512.7	2149	49.6
5	666.0	125.0	893.3	989	50.5

ergy available in the process, promoting solutions that integrate heat pumps, thereby converting the exergy excess into useful energy.

REFERENCES

[1] Boland P., Hewitt G.F., Thomas B.E.A., Guy A.R., Marsland R.H., Linnhoff B., Townsend D.W. A user guide on process integration for the efficient use of energy. *The Institution of Chemical Engineers*, 1982.

[2] Grossmann I.E., Papoulias S.A. A structural optimization approach in process synthesis - i. utility systems. *Comp. Chem. Engng.*, 7(6):695–706, 1983.

[3] B. Kalitventzeff, Marechal F. Heat and power integration : a milp approach for optimal integration of utility systems. *proceedings COPE'91 (Barcelona)*, 1991.

[4] Favrat D., Staine F. Energy integration of industrial processes based on the pinch analysis method extended to include exergy factors. *Applied Thermal Engineering*, 16:497–507, 1996.

[5] Lavric V., Baetens D., Plesu V., De Ruyck, J. Broadening the capabilities of pinch analysis through virtual heat exchanger networks. *Energy Conversion and Management*, 44:2321-2329,2003.

[6] Linnhoff B., Dhole V.R. Total site targets for fuel, co-generation emissions, and cooling. *Comp. Chem Engng*,17:s101-s109, 1992.

[7] Ohba T., Ishida M. A new approach to energy-utilization diagrams for evaluation of energy of chemical systems. In *ECOS 04 Proceedings*, 845–852., 2004.

[8] Kalitventzeff B., Marechal F. Identification of the optimal pressure levels in steam networks using integrated combined heat and power method. *Chemical Engineering Science*, 52(17):2977–2989, 1997.

[9] Linnhoff B., Townsend D.W. Heat and power networks in process design. part 1: Criteria for placement of heat engines and heat pumps in process networks. *AIChE Journal*, 29(5):742–748, 1983.

[10] Mason D., Linnhoff B., Cerda J., Westerberg A.W. Minimum utility usage in heat exchanger network synthesis. a transportation problem. *Chemical Engineering Science*, 38(3):378–387, 1983.

[11] Kalitventzeff B., Marechal F. Process integration : Selection of the optimal utility system. *Comp. Chem. Engng.*, 22:S149–S156, 1998.

[12] Kalitventzeff B., Marechal F. Targeting the optimal integration of steam networks,. *Comp. Chem. Engng.*, 23:s133–s136, 1999.

[13] Kalitventzeff B., Marechal F. Restricted matches and minimum cost of energy requirements: tools and methodology for producing practical solutions. *PRES'99 proceedings*, 433–438, 1999.

[14] Kalitventzeff B., Marechal F. A tool for optimal synthesis of industrial refrigeration systems. *Computer Aided Chemical Engineering series, Ed. Elsevier*, 90:457–463, May 2001.

[15] Kalitventzeff B., Marechal F., Favrat D. A methodology for the optimal insertion of organic Rankine cycles in industrial processes. *2nd International Symposium on Process Integration, Halifax*, 2001.

[16] Kalitventzeff B., Marechal F. Targeting the integration of multi-period utility systems for site scale process integration. *Applied Thermal Engineering*, 23:1763–1784, 2003.

[17] Kalitventzeff B., Marechal F. Targeting the minimum cost of energy requirements : a new graphical technique for evaluating the integration of utility systems. *Comp. Chem. Engng.*, 20(Suppl.):S225–S230, 1996.

Proceedings of ECOS 2005
Trondheim, Norway
June 20–22, 2005

THEORETICAL ANALYSIS OF A NOVEL INTEGRATED ENERGY SYSTEM FORMED BY A MICROTURBINE AND A EXHAUST FIRED SINGLE-DOUBLE EFFECT ABSORPTION CHILLER

Marc Medrano, Josh Mauzey, Vince McDonell, Scott Samuelsen[1]
Advanced Power and Energy Program
University of California, Irvine

Dieter Boer
Department of Mechanical Engineering; ETSEQ
University of Rovira i Virgili, Tarragona (Spain)

ABSTRACT

Integrated Energy Systems (IES) combine a distributed power generation system (DG) such as a microturbine generator (MTG) or a fuel cell with thermally activated technologies (TAT) such as absorption cooling. This integration maximizes the efficiency of energy use by utilizing on-site most of the waste heat generated by DG, and reduces harmful emissions to the environment.

This study investigates the energy and exergy performance of an IES. This system is comprised of an MTG with internal recuperator and a novel absorption cooling cycle. The absorption cycle is a single effect-double effect exhaust fired cycle, which increases the heat exchanged from the MTG exhaust gases using two generators at two different levels of temperature.

The selection of the DG element, the TAT element and their internal configurations is based upon a real IES commercial unit that has been tested in the APEP-UCI DG testing facilities in Irvine, California. This unit has an electrical power capacity of 28 kW and a cooling capacity of 14 refrigeration tons (49.2 kW).

Inputs for the thermodynamic models developed for the MTG and for the absorption cycle are derived from experimental variables that will be controlled in the testing phase. The MTG model is using empirical correlations for key model parameters (pressure ratio, turbine inlet temperature, etc.) from previous studies in order to predict the observed change in performance with part load operation. The calculated mass flow rate and temperature of the exhaust gases are inputs for the absorption cycle model, together with cooling and chilled water inlet temperatures and flow rates. Heat and mass transfer efficiencies along with heat transfer coefficients for the suite of heat exchangers comprising the single-double effect absorption cycle are determined from proprietary testing data provided by the manufacturers.

Keywords: Integrated Energy Systems, distributed generation, thermally activated technologies, microturbine, absorption chiller, exhaust fired chiller, single effect-double effect cycle, model

[1] Corresponding author: Phone: 949-824-5468, Fax: 949-824-7423 email: gss@apep.uci.edu

NOMENCLATURE

$\dot{E}$	Exergy flow (kW)
e	Exergy / specific exergy(kJ/kg)
HHV	Higher Heating Value (kJ/kg)
LHV	Lower Heating Value (kJ/kg)
m	Mass flow rate (kg/s)
Q	Heat power (kW)
P	Pressure (kPa)
T	Temperature (°C)
X	LiBr solution concentration (kg/kg)
W	Power (kW)
Greek letters	
Ψ	Exergy efficiency of the cycle (-)
η	Efficiency (-)
Subscripts	
chw	Chilled water
eq	Equilibrium conditions
E	Evaporator
G1	Generator at high temperature
G2	Generator at low temperature
in	Inlet
m	Mass
out	Outlet

INTRODUCTION

Integrated Energy Systems (IES) combine a distributed power generation system (DG) such as a microturbine generator (MTG) or a fuel cell with thermally activated technologies (TAT) such as absorption cooling, water heating, or desiccant dehumidification. Other acronyms often used in the literature to refer to the same IES concept are CHPB (cooling, heating, and power for buildings), BCHP (building cooling, heating, and power) and CCHP (combined cooling, heating, and power). This integration maximizes the efficiency of energy use by utilizing on-site most of the waste heat generated by DG, and subsequently reduces harmful emissions to the environment.

In the past decades the implementation of an IES in a particular facility involved the selection and purchase of the disparate components of an IES (i.e.: the prime mover, the heat exchanger, the chiller), followed by a customized, rather costly installation onsite. However, the current trend of Japanese and US DG manufacturers is to develop pre-engineered packaged units that will significantly reduce costs, boost system efficiency, and simplify the installation process to the point of a plug-and-play process. This integration will likely encourage many building and industry owners to adopt IES rapidly [1]. Some integrated products are in the development phase, and a few are already commercial.

The Advanced Power and Energy Program (APEP) at the University of California, Irvine (UCI) has developed a test rig facility in order to test and evaluate the operational and emissions performance of both DG power-only and IES units. After several years of experience with power-only and CHP tests of MTGs from several manufacturers [2], the first tests with a CCHP commercial unit will be accomplished in 2005. This IES unit is manufactured by Takuma Company, Ltd. for the Japanese market and consists of a 28 kW MTG with recuperator and a novel single effect-double effect exhaust fired absorption chiller with a cooling capacity of 14 refrigeration tons (49.2 kW) and a nominal coefficient of performance (COP) of 1.

As a first step prior to the test phase, thermodynamic models for the MTG and the chiller integrating characteristics of the commercial unit were developed. The purpose of this paper is to present these models and to investigate the energy and exergy performance of the integrated energy system at different operating conditions.

DESCRIPTION OF THE INTEGRATED ENERGY SYSTEM TO BE TESTED

The IES commercial unit to be tested consists of a MTG element, Takuma TCP30 model, and an exhaust fired absorption chiller/heater element, Takuma EGT-15 model.

The first element is a 30 kW capacity single-shaft turbine with recuperator manufactured by Capstone Turbine Corporation. This assembly uses air bearings, has a rotating speed of 96000 revolutions per min, and has a permanent magnet type high-speed generator [3].

The absorption chiller/heater is a single effect-double effect exhaust fired unit with 49.8 kW of heating capacity and 49.2 kW (14 refrigeration tons) of cooling capacity and uses the system

water-LiBr as working fluid mixture. The single-double effect cycle used in this chiller increases the heat exchanged from the MTG exhaust gases using two generators at two different temperature levels. The exhaust gases leaving the high temperature generator of the double effect cycle can then be further utilized to drive the single effect cycle and produce an extra cooling effect.
The exhaust gases from the MTG are directed to the absorption chiller through insulated ducting to minimize losses. Figure 1 shows a picture of the Takuma IES unit already located in APEP's test facilities. Figure 2 presents a schematic flowchart with energy fluxes of the MTG and the absorption chiller integrating the unit.

Figure 1: IES unit installed in APEP's test facilities (4th and 5th units starting from bottom to top of picture).

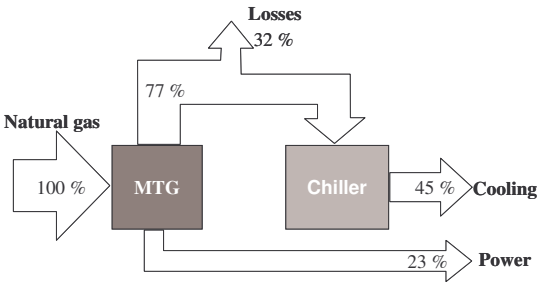

Figure 2: Schematic heat fluxes of the MTG and the absorption chiller cycle integrating the IES unit working in cooling mode.

MICROTURBINE

Thermodynamic cycle

Figure 3 shows the components of the microturbine generator that are included in the thermodynamic model. The air entering the MTG (state point 1) is compressed in the air compressor to state point 2. Then, air goes to the recuperator, where it is heated by the heat of the rejected exhaust gases (state point 3). Air enters with compressed natural gas into the adiabatic combustion chamber. The resulting high temperature combustion gases (state point 4) are then fed to the gas turbine, where they are expanded from state point 4 to state point 5. After the turbine, the rejected gases flow through the recuperator where heat is transferred to incoming air. The temperature of the exhaust gas downstream of the recuperator is still high enough to drive an absorption cycle, as explained in next section.

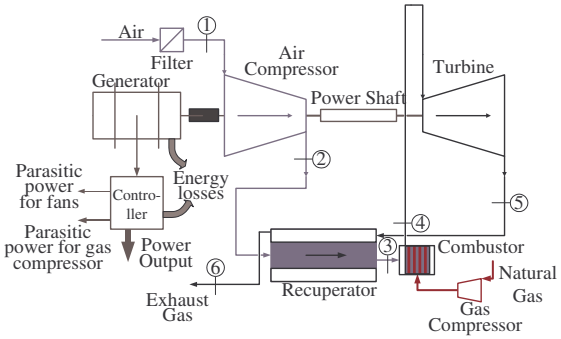

Figure 3: Schematic of the microturbine generator process.

MTG Simulation Methodology

A thermodynamic model was developed for the MTG using the program Equation Engineering Solver (EES). Most of the mathematical equations used to describe the cycle can be found elsewhere [4]. The combustion process is not treated as a black box, however. The chemical reaction between the fuel and the air in the chamber is modeled and excess air and exhaust gases compositions are obtained. Some input parameters of the cycle (air compressor and turbine isentropic efficiencies, recuperator efficiency, combustor efficiency, and fuel compressor isentropic efficiency) were determined on the basis of manufacturers' data at full load conditions, and were assumed constant for the operating range

studied. To account for changes in performance of the MTG unit with part-load operation some other parameters (i.e. turbine inlet temperature, pressure ratio, recuperator heat loss coefficient, generator heat losses, and controller heat losses) were correlated to net power output using literature experimental data for the same MTG unit [4].

Input data are presented below. The first three parameters will vary during the future experimental testing process and their effect on the performance parameters will be analyzed. The rest are assumed constant for the range of operating conditions investigated:

- Net power output
- Air inlet temperature
- Fuel inlet temperature
- Air compressor isentropic efficiency
- Turbine isentropic efficiency
- Recuperator efficiency
- Combustor efficiency
- Fuel compressor isentropic efficiency
- Inlet compressor pressure

Output data are:

- Pressures, temperatures, gas compositions, mass flows, enthalpies, entropies, exergies of the flows
- Mechanical or thermal power and irreversibility rate of the main components
- Electric efficiency of MTG based on natural gas higher heating value (HHV)

The principal assumptions of the MTG model are:

- No pressure losses
- No heat losses in turbine, compressors and combustion chamber
- Natural gas is treated as pure methane
- Air, methane and combustion gases are treated as ideal gases

ABSORPTION CHILLER

Thermodynamic Cycle

The novel configuration of the single-double effect absorption cycle shown in Figure 4 combines a series flow double effect cycle with a single effect cycle. Detailed description of the separated cycles can be found elsewhere [5].

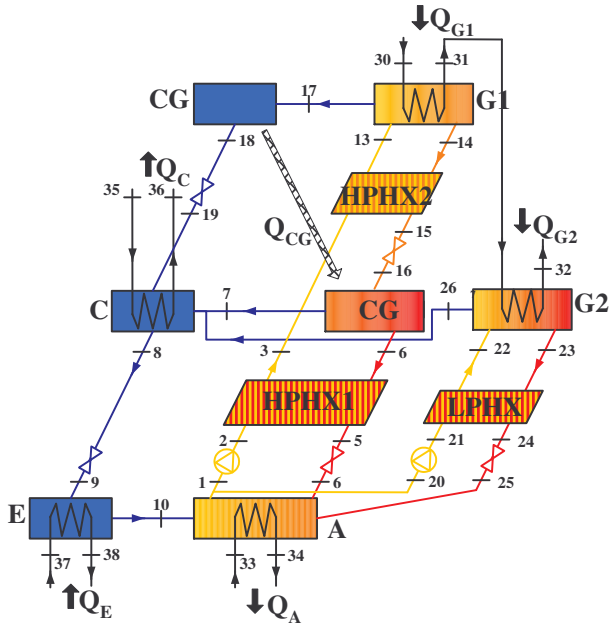

Figure 4: Components, state points and heat exchanges of a single-double effect absorption cycle.

Both cycles share common components, namely the absorber, the evaporator, and the condenser. The single-double effect cycle is comprised of 9 main components. The names of each of the components, the cycle they belong to, and the abbreviations used in Figure 4 are shown in Table 1.

Abbreviation	Complete Name	Belongs to
A	Absorber	Single & Double effect cycles
C	Condenser	Single & Double effect cycles
CG	Condenser-Generator	Double effect
E	Evaporator	Single & Double effect cycles
G1	High Pressure Generator	Double effect
G2	Low Pressure Generator	Single effect
HPHX1	High pressure solution heat exchanger 1	Double effect

HPHX2	High pressure solution heat exchanger 2	Double effect
LPHX	Low pressure solution heat exchanger	Single effect

Table 1: Abbreviations used in Figure 4.

The following heat transfers take place with external fluids. Heat is supplied at high temperature (270-280 °C) in generator G1 from the exhaust gases exiting the MTG. After G1, the relatively lower temperature gases (160-170 °C) supply extra heat in generator G2, which drives the single effect cycle and provides extra cooling (Figure 5).

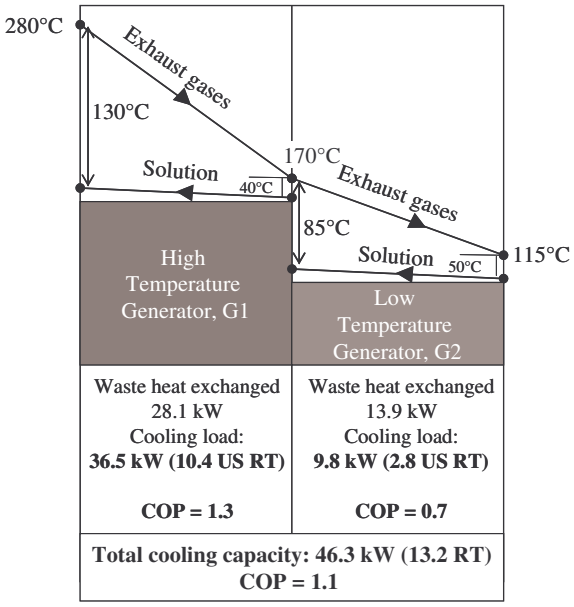

Figure 5: Temperature distribution and heat exchanged of exhaust gases in the two generators of the EGT15 chiller.

This novel cycle arrangement enables a better utilization of the MTG exhaust gases exergy. Heat is dissipated in absorber A and condenser C to cooling water in a series flow arrangement of cooling water. Chilled water is produced in the evaporator E.

Internal heat is transferred from condensing refrigerant vapor to the absorbent solution in the condenser-generator assembly CG. In the CG, part of the refrigerant is evaporated from the incoming solution on the cold side. On the hot side superheated refrigerant vapor is condensed. Between hot and cold solution streams heat is recovered in the solution heat exchangers HPHX1, HPHX2 and LPHX. The absorbent solution is in a series flow arrangement. The rich-in-water solution leaving the absorber A is preheated by the solution heat exchangers and then directly enters the generator G1. Now the rich-in-water solution will be gradually concentrated in salt in the different generators G1 and CG.

Chiller Simulation Methodology

A computer code for the simulation of the cycle has been established using the program EES. Properties for water-LiBr are integrated in EES, except the specific entropy, which has been calculated following Kaita [6]. The specific exergy calculation is given by Misra et al. [7].

Some input parameters in the model coincide with the experimental variables that will be controlled in the experimental testing phase. Others such as mass exchange efficiencies along with heat transfer coefficients for the suite of heat exchangers comprising the cycle are determined from proprietary manufacturer's testing data at nominal conditions and are assumed constant for the studied working range. The list of input variables of the model is presented below:

- Inlet temperatures and flow rates of external fluids.
- Temperature difference for subcooling in condensers and superheating in evaporator.
- Overall heat transfer coefficients in heat and mass exchangers.
- Mass exchange efficiencies, η_m, defined as:

$$\eta_m = \frac{X_{out} - X_{in}}{X_{eq,out}(T_{out}, P_{out}) - X_{in}} \quad (1)$$

- Percentage of heat loss in exhaust gas-driven generators, α.
- Ratio of outlet absorber solution flow rate to double effect cycle over flow rate to single effect cycle, f.

The same type of output data for each state point presented above for the MTG model is also obtained for the chiller model. The principal performance parameter for the absorption chiller is the COP. This parameter is defined as the ratio

of driving heat supplied by exhaust gases in generators G1 and G2 over cooling produced:

$$COP = \frac{Q_E}{Q_{G1} + Q_{G2}} \quad (2)$$

Principal assumptions of the chiller thermodynamic model are:

- The refrigerant vapor leaving the evaporator is pure water.
- Exhaust gas fired generators operate in cross-current flow.
- No liquid carryover from evaporator
- The solution and refrigerant valves are adiabatic
- No heat losses
- No pressures losses

Exergy Analysis

Assessment of overall IES efficiency based on exergy efficiency is recommended ([8], [9]), as this approach takes into account the disparate energy qualities of the driving natural gas chemical energy, the electric power generated in the MTG, and the cooling produced in the single-double effect absorption chiller. The exergy efficiency is defined as the useful exergy output divided by the exergy input, enabling us to compare cycles with different types of energy inputs. For the selected IES the exergy efficiency can be expressed as:

$$\Psi_{IES} = \frac{\dot{E}_{chw} + \dot{E}_{MTG}}{\dot{E}_{fuel}} = \frac{m_{chw}(e_{out} - e_{in})_{chw} + W_{MTG}}{m_{fuel} LHV \cdot 1.04} \quad (3)$$

The expression for exergy flow of natural gas ($\dot{E}_{fuel}$) is taken from Kotas [9].

RESULTS AND DISCUSSION

MTG model results show good agreement with manufacturer's nominal values at full load and with literature experimental values at part load performance [4]. Figure 6 shows predicted values for electric efficiency (based on the HHV of natural gas), and mass flow rate and temperature for the exhaust gases leaving the recuperator, all as a function of MTG net power output. These last two output variables, which characterize the heat content of the waste heat stream, are used as inputs in the chiller model and have a significant effect on the performance of the chiller. As some parasitic losses such as fan electric motors are practically independent of power output, electric efficiency decreases slightly with decreasing power outputs. Both air flow rate and natural gas flow rate (not shown) vary in a fairly linear fashion with MTG output power. The non-linear increase of exhaust gas temperature with output power responds to the empirical correlation of inlet turbine temperature as a function of power used as an input to the model.

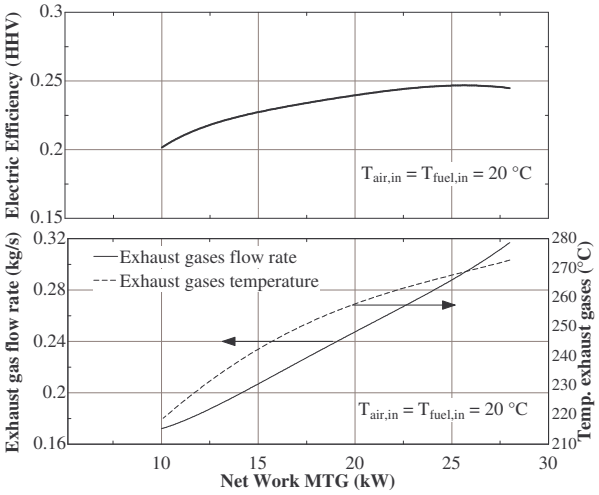

Figure 6: MTG electric efficiency based on HHV (above) and exhaust gases flow rate and temperature (below) versus net MTG power output.

The MTG model also predicts well the expected reduction in electric efficiency with an increase in ambient air temperature (not shown).

Figure 7 presents predicted results for chiller cooling load and coefficient of performance as a function of inlet chilled water temperature when the MTG is operating at full load and cooling water temperature is at nominal conditions. Similarly, Figure 8 shows how the same performance parameters are affected by inlet cooling water temperature. An increase of inlet chilled water temperature with constant intermediate level temperature or a decrease of inlet cooling water temperature with constant low temperature level both result in higher COPs and higher cooling loads. This is due to the decrease in the temperature lift between low and intermediate temperature levels, which is

thermodynamically more favorable. The study of the effect of cooling water temperature is limited to values above 26.5 °C as lower temperatures lead to crystallization of LiBr for the solution streams at the absorber inlet (state points 5 and 24 in Figure 4).

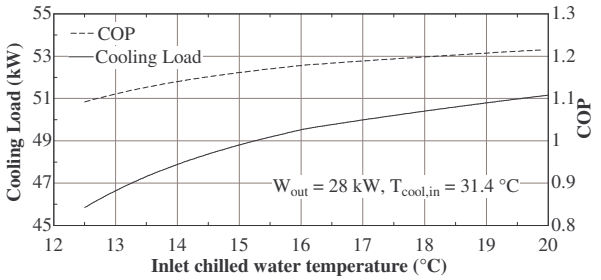

Figure 7: Effect of chilled water inlet temperature on chiller cooling load and on COP for full load MTG conditions.

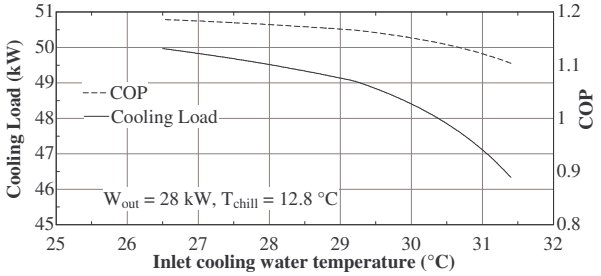

Figure 8: Effect of cooling water inlet temperature on chiller cooling load and on COP for full load MTG conditions.

Unlike the MTG model, which includes empirical correlations of some parameters to account for the control strategy of the real unit, these types of correlations are not available for the chiller model. This means that the model is predicting how the chiller would behave if no controls had been implemented. For that reason predicted results for chiller performance at part load MTG operating conditions (Figure 9) are restricted to a very narrow range (25.6-28 kW). With mass flow rates and temperatures of the exhaust gases corresponding to MTG loads below 25.6 kW the model predicts crystallization will occur at solution stream 24, which leaves the solution heat exchanger of the single effect cycle. The control devices implemented in the real unit prevent crystallization by changing flow rates and, according to manufaturer's data, should enable some cooling production at MTG part load performances as low as 15 kW. However, Figure 9 estimates correctly the expected trends of decreasing cooling capacity with decreasing MTG power output.

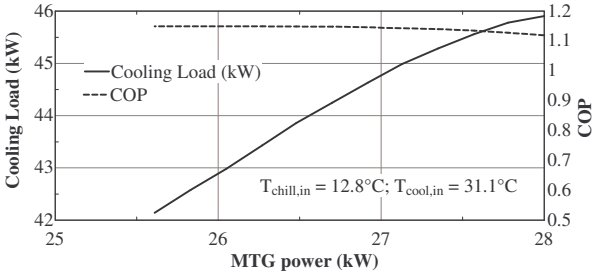

Figure 9: Effect of MTG power output on chiller cooling load and on COP.

Energy efficiencies have been assessed individually for the MTG cycle and the absorption cycle that integrate the IES presented in this study. The exergy efficiency is applied to compare overall efficiencies of three similar IESs that vary in the configuration of the chiller. The chiller absorption cycles chosen are the single-double effect studied in this work, the single effect cycle and the double effect cycle. The MTG power is the same for the three IESs. presents exergy results for the three IES configurations. As expected, the IES with the novel single-double effect absorption cycle is the one with the highest overall exergy efficiency, as it produces the largest cooling for the same amount of natural gas driving energy.

CONCLUSIONS

A theoretical analysis of a commercial integrated energy system consisting of a microturbine and an absorption chiller was presented as a first step for planning and executing performance tests of the real unit at the APEP DG-IES test facility. Steady-state models for the MTG and the chiller were developed and results analyzed. The principal findings of this study are:

- The MTG model predicts that the electrical efficiency, as well as the exhaust gas flow rate and temperature increase with power output, in good agreement with published experimental data.

	IES with Single-Double effect chiller	IES with Double effect chiller	IES with Single effect chiller
m_{fuel} (kg/s)	0.0027	0.0027	0.0027
$\dot{E}_{fuel}$ (kW)	106.6	106.6	106.6
$\dot{E}_{MTG}$ (kW)	28	28	28
Cooling (kW)*	46.2	37.6	29.4
$\dot{E}_{chw}$ (kW)	2.35	1.91	1.49
Ψ_{IES}	0.285	0.281	0.277

* Cooling refers to an energy flow and not to an exergy flow.

Table 2: Determination of overall IES exergy efficiencies with three different cycle configurations for the absorption chiller.

- The absorption chiller model predicts the increase of COP and cooling load with increasing chilled water temperatures and decreasing cooling water temperatures, with maximum COPs above 1.2.
- Part load performance of the chiller is not accurately represented by the current model. The absorption chiller model should be improved with empirical correlations obtained in the future test phase to take into account chiller crystallization and part load controls.
- The overall exergy efficiency of the studied IES with the novel chiller using a single-double effect absorption cycle is higher than the ones resulting from the same MTG and exhaust gas fired single or double effect chillers.

The second part of this project is the actual performance evaluation of the commercial IES. Preliminary results of this test phase will be presented in a second paper.

REFERENCES

[1] Engle D. *The New Trigeneration Players: Integrated Cooling, Heating and Power Systems are Here*. Distributed Energy, The Journal for Onsite Power Solutions, 2004, Forester Communications Inc., http://www.distributedenergy.com/de_0405_trigeneration.html

[2] McDonell VG, Hack RL, Lee SW, Mauzey JL, Wojciechowski JS, Samuelsen GS. *Experiences with Microturbine generators systems installed in the South Coast Air Quality Management District*. In: TURBOEXPO 2003-Land, Sea, and Air, 49th ASME International Gas Turbine & Aeroengine Technical Congress. 2003. Atlanta, Georgia, US.

[3] Gillette S. *Microturbine Advances*. Globalcon 2004, March 24-25, Boston, MA.

[4] Labinov SD, Zaltash A,. Rizy DT, Fairchild PD, Robert PE, DeVault RD, Vineyard EA. *Predictive Algorithms for Microturbine Performance for BCHP Systems*. ASHRAE Transactions 2002.

[5] Boer D, Medrano M, Nogues M. *Comparative Exergy Analysis of the Principal Water-LiBr Absorption Cycles*. In: International Conference on Thermal Engineering Theory and Applications, Beirut (Lebanon), May 30-June 3, 2004.

[6] Kaita Y. *Thermodynamic properties of litium bormide-water solutions at high temperatures*. International Journal of Refrigeration 2001, 24, 374-390.

[7] Misra RD, Sahoo PK, Sahoo S, Gupta A. *Thermoeconomic optimization of a single effect water/LiBr vapour absorption refrigeration system*. International Journal of Refrigeration 2003, 26, 158-169.

[8] Bejan A, Tsatsaronis G, Moran M. *Thermal Design & Optimization*, John Wiley & Sons Inc., New York, 1996.

[9] Kotas TJ. *The Exergy Method of Thermal Plant Analysis*, Krieger Publishing Company, Melbourne, Florida, 1995.

Proceedings of ECOS 2005
Trondheim, Norway
June 20–22, 2005

ADVANCED PINCH TECHNOLOGY BASED COMPOSITE CURVES FOR EVALUATING THE USABLE EXCESS HEAT POTENTIAL

Nordman R.*, Berntsson T.

Heat and Power Technology
Department of Energy and Environment
Chalmers University of Technology, SE 41296 Göteborg, Sweden

* Corresponding author. Tel.: +46 31 772 30 22; Fax: +46 31 82 19 28.
E-mail address: roger.nordman@chalmers.se (R.Nordman)

ABSTRACT

This paper describes the application of a set of advanced composite curves to evaluate the potential to release usable excess heat (hereafter referred to as Q_{xs}) from an existing process industry. Throughout this paper Q_{xs} is defined as heat at enough high temperature to be interesting for use e.g. for district heating. Studies using the advanced curves reveal information about the existing HEN that traditional graphical methods are not able of, and that for almost the same collected information from the process. This allows for estimations on the heat recovery potential and existing pinch violations before detailed calculations.

These curves have earlier been presented in connection with integration of CHP, HP and retrofitting HEN's. The curves have also been used to evaluate the Q_{xs} potential in one doctoral thesis, but the methodology was not explained in detail, but rather used as a tool among many.

In this paper we broaden the discussion on how to use the curves, which traps there might be and how to interpret and use the results.

Important questions that are answered are for example:

- How does the Q_{xs} potential change when the pinch temperature changes?
- At which temperature is it possible to release Q_{xs}?
- How could the Q_{xs} be made available?
- How can the Q_{xs} potential be revealed?

Keywords: Advanced composite curves, Pinch technology, Process integration

INTRODUCTION

Process energy savings have been high listed on plant managements' agenda since the oil crisis in the 1970's. In the years following, the first systematic methods for energy savings appeared [1-3], and during the 1980-1990's a number of methods developed, using pinch technology, mathematical programming or exergy analysis. Global warming due to anthropogenous release of greenhouse gases has later become an important issue. The reduction of fossil fuel use is becoming increasingly important in an economic perspective due to CO_2 emission trading systems [4]. For industries using biofuels, energy reductions could lead to incomes from sold released biomass. Revamp of plants is a highly complex task, including evaluation of many different measures that some time compete, some time have synergistic effect. In most cases not only one measure is considered, but rather a combination of different measures.

All this motivates for finding methods that are even better than existing in finding cost-effective energy recovery potentials, and could take many different measures into consideration.

This paper present results from work by the authors [5, 6] in HEN retrofit, and by Nordman and Bengtsson [7] in the area of assessing the

potential for releasing usable excess heat. The paragraphs about HEN retrofit and HP and CHP integration should be seen as an overview of the usefulness of the advanced curves.

EARLIER WORK

Pinch analysis have for the last decades provided new modes for analysing energy systems systematically. Most of the techniques developed origin from grass-root design and analysis, where no existing equipment constrain the potential for energy recovery projects. Methods that take existing equipment (heat exchangers) into consideration are the α-method [8], the path analysis method [9], the RTD method [10, 11] and the network pinch concepts [12]. The Matrix method [13] also takes piping cost, which can be a large part of a retrofit, into consideration. These methods are all specific for HEN retrofit. At Chalmers, a graphical method, consisting of advanced composite curves, for analysing energy systems in retrofit situations have been developed. These curves have proven useful not only for HEN retrofitting [5] but also for integration of Heat Pumps (HP) [14] and Combined Heat and Power (CHP) [15].
In this paper, the curves' ability to predict the potential to release usable excess heat, Q_{xs}, is presented. Integration of HP and CHP is also discussed briefly.

ADVANCED COMPOSITE CURVES

Construction of the Advanced Curves and Differences from "Traditional" Curves

The method uses four composite curves above and below the pinch respectively.
Only the construction of the curves above the pinch is explained, the curves below the pinch are constructed in the same way as described for the curves above pinch.
The four curves above the pinch are called Hot Utility Curve (HUC), Theoretical Heat Load Curve (THLC), Actual Heat Load Curve (AHLC) and Extreme Heat Load Curve (EHLC). The corresponding names below the pinch is Cold Utility Curve (CUC), Theoretical Cooling Load Curve (TCLC), Actual Cooling Load Curve (ACLC) and Extreme Cooling Load Curve (ECLC).

The Hot Utility Curve (HUC) is a composite curve of the *utility* streams in the existing heaters plotted at real temperatures. Correspondingly, the Actual Heat Load Curve (AHLC) is a composite of the parts of the *process* streams that run in the existing heaters.

The EHLC shows the temperatures where heat would be supplied if the heat exchange were carried out so that all external heat was supplied at the highest possible temperature (with the same Q_H as the AHLC). This corresponds to the overshooting part of the cold CC. Traditional grass-root theory refers to this as vertical heat exchange (provided all streams have the same heat transfer coefficient).

The THLC shows the lowest possible temperatures where heat would be supplied if all thermodynamic possible measures for energy conservation had been used (for the present Q_H) with a given EMAT (<HRAT). The THLC should be plotted with as low EMAT that would be acceptable when building a new heat exchanger, e.g. 5K according to Gundersen [16]. Theoretical minimum could of course be 0K, but that would yield unrealistic targets in practice. The THLC can therefore be seen as a GCC for the process, but plotted with ΔT_{min} = EMAT instead of ΔT_{min} = HRAT although Q_H is set the same as for ΔT_{min} = HRAT, with the pockets removed, and plotted at real temperatures. It is important to notice that the Q_H is the same as for the actual ΔT_{min} (= HRAT), but that the heat demand is now at lower temperatures. The difference in Q_H between systems of ΔT_{min} = EMAT and ΔT_{min} = HRAT corresponds to the amount of heat that could be saved in a correct built network when the ΔT_{min} decreases from the actual value (HRAT) to ΔT_{min} = EMAT. The construction of the THLC requires that the problem be not divided in the pinch. The reason is when HRAT is greater or much greater than EMAT, there is a possibility to successively shift heat from below the pinch to above, until ΔT_{min} = EMAT is reached. This amount of heat could ultimately be saved as utility; therefore it is plotted at the utility temperature level. When multiple utility levels are present it is not obvious which of the utility levels should be chosen. This is discussed further below.
The major difference between the advanced curves and traditional curves is that information

about the existing network structure is included in the advanced curves via the HUC/CUC and the AHLC/ACLC. Construction of these curves requires gathering of information on both utility and process streams in heaters and coolers. This is however the only additional information that is needed compared to traditional methods, but allows for more details in the analysis of measures, both stand-alone and combinations of measures.

The fact that the curves are all plotted at the real temperatures removes any hesitation that occur when measures is integrated versus the GCC, e.g. the correct integration temperature of HP and CHP is directly assessed.

Four possible measures are discussed in this paper, increased heat recovery by heat exchange, HP, CHP and introduction of new processes using excess heat from the existing process.

APPLICATIONS

Figure 1 shows an example of a network, Figure 2 shows all the corresponding advanced curves and Figure 3 shows the CC with the parts that constitutes the EHLC and ECLC indicated.

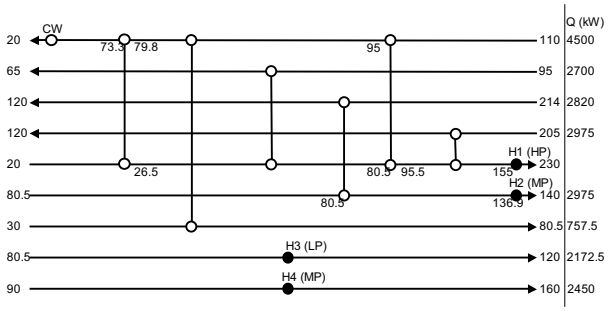

Figure 1: Grid diagram of the HEN in example 1.

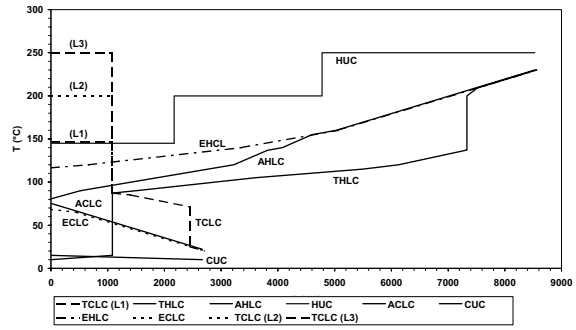

Figure 2: Advanced Curves for Example 1.

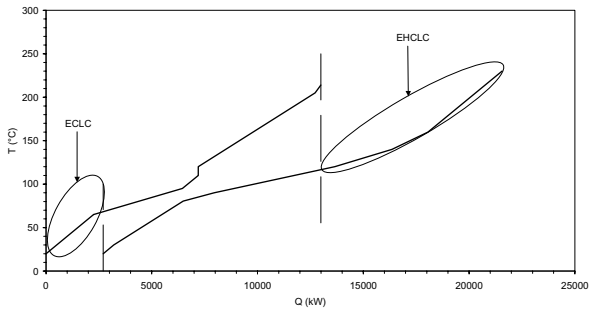

Figure 3: Composite Curves for Example 1, showing the EHLC and ECLC.

HEN Retrofit

The intersection between the THLC and the TCLC gives the practical heat saving potential by increased heat recovery. The amount of heat to the left of the intersection corresponds to the pinch violations that would be possible to remove when lowering the Q_H from present HRAT to HRAT = EMAT. It has been shown that it is not always economically feasible to remove all pinch violations [13], instead, one could evaluate the portion of the pinch violations that could be removed by HEN retrofit, given a certain PBP (Figure 4). By this approach, some pinch violations may be left unchanged, but this heat could be used for other measures as discussed below.

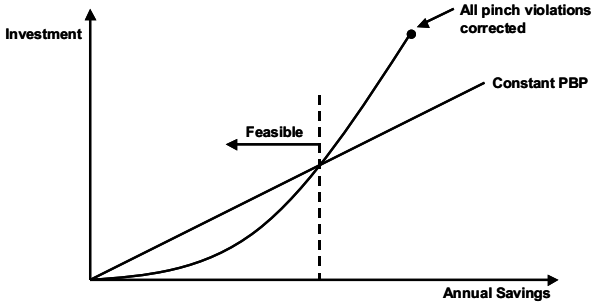

Figure 4: Investment cost vs Annual Savings Plot.

By plotting the EHLC, the AHLC and the THLC, the temperature-wise limits as well as the actual placement of heaters is shown. The AHLC cannot lie outside the EHLC, and generally not outside the THLC (unless a very small approach temperature is used in existing heat exchangers). It has been shown that it is relatively cheaper to save one unit of heat when the AHLC lies close to the THLC. When the AHLC closes in on the EHLC, the cost per saved unit heat increases, sometimes drastically. Heaters placed low in

temperature should therefore generally be considered for retrofit first [5, 6].

Multiple Utility Levels

When there are multiple hot utility levels present, as in the example, it is not evident which temperature level the part of the ACLC that corresponds to pinch violations should be plotted at. The utility level(s) that can be released by cutting the AHLC from the left is what should be chosen. One must therefore look at which utilities the streams composing the AHLC are connected to. The important thing to remember is that the cold streams composing the AHLC are governing, not the HUC streams. In the example, the part of the AHLC that could be saved by correcting pinch violation corresponds to about 1100kW. In the low temperature region this corresponds to saving heat in one ore more of the heaters H2, H3 or H4, Figure 1.

From the grid diagram, Figure 1 it can however be concluded that the only heater already connected to a cooler through a path is the one using HP steam. This heater may seem to be cheaper to unload, since it "only" requires area enhancement in existing heat exchangers. Unloading any of the three other heaters first requires insertion of a new heat exchanger to create a path between the cooler and the heater in question, then probably also area enhancement in existing heat exchangers. It has however been showed that heaters low in temperature are in general cheaper to release [6]. The reason is twofold, releasing heaters placed high requires many rearrangements of existing units, and poorer temperature driving forces result in large heat exchanger areas.

Heat Pump Integration

In general, heat pumps should be integrated so that the evaporation takes place where there is a surplus of heat, and the condensation where there is a deficit of heat. In most industrial cases this means around the pinch. There is also the possibility to integrate a HP around a "nose" in the GCC, but that is not discussed further here.

When using the advanced composite curves, integration can generally be carried out at three levels; integration against the HUC/CUC, against the AHLC/ACLC and against the THLC/TCLC. A combination of the curves could also be used, e.g. integration against the HUC/ACLC. Integration against the HUC/ CUC would require least changes in the HEN, but the COP would be lower due to the higher temperature lift required, and the HP size may not be as big as could be achieved by integration against the AHLC/ACLC (Figure 5). The most extreme case is to integrate the HP against the THLC/TCLC curves, but that would in most cases require a large retrofit of the HEN so the heat/cooling demand changes from the AHLC/ACLC situation to the THLC/TCLC ditto to *create* a foundation for successful HP integration.

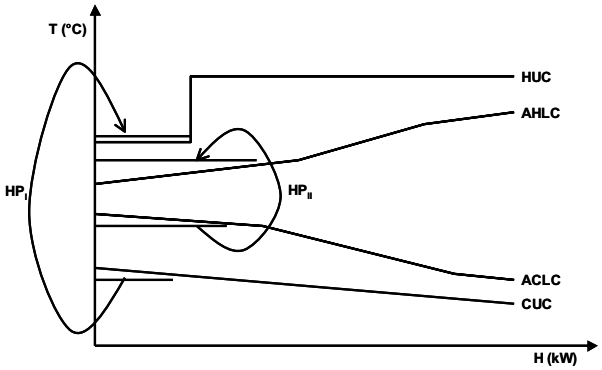

Figure 5: Heat Pump Integration Potential using Advanced Curves.

Which level of the abovementioned should be used is a trade-off between the COP and size of the HP, and the cost of the necessary rearrangements in the HEN to facilitate the HP. Which complexity levels that results in best project economy could be determined by the method developed by Wallin [14].

CHP Integration

As an example of CHP integration, a simple GT is used. When a GT is to be integrated, a number of key figures must be determined, e.g. GT size (MW), stack and exhaust temperature and the quantity of supplementary firing needed. Supplementary firing could be left out in a simple GT cycle if the GT size exactly match the heat demand, but this is almost never the case, since GTs are manufactured and delivered in fixed sizes. Another situation when supplementary firing could be left out is if there is already a heat generation system available, and the GT is integrated primary for electricity generation.

The size of the GT is determined from the T-H diagram, where the slope of the GT line equals 1/(F*Cp). A steep slope of the line indicates a

small GT and correspondingly a flat slope indicates a large GT.
The GT could be integrated against the HUC, AHLC or THLC respectively (Figure 6).

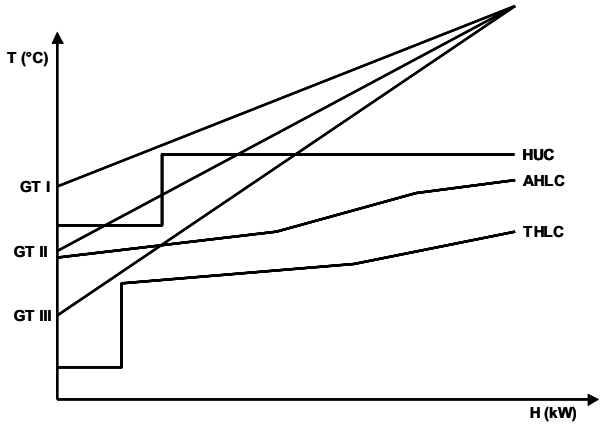

Figure 6: Gas Turbine Integration using Advanced Curves.

Which curve to integrate against is a matter of project economy, which is a function of not only the GT investment cost, but also the cost of retrofitting the HEN. Integration against the HUC requires little or no changes in the HEN but may give a less profitable GT than if the integration is done against the AHLC or THLC. To analyse the most profitable investment, many combinations should be looked upon, and the total project economy be evaluated for each of these combinations. A method to carry out this complex integration task has been presented by Strömberg and Berntsson [15].

Usable Excess Heat

When the potential for releasing usable excess heat is assessed, the THLC and TCLC are used.
Two ways of increasing the total efficiency in the plant exist; to decrease the heat demand for the current process, or to utilize the currently added heat more efficiently. Using the added heat more efficiently requires release of usable excess heat. Basic pinch theory establishes the pinch rule that says that heat surplus only appears below the pinch, whereas deficit appears above the pinch.
The surplus can then not be used for heating purposes. This rule is only valid for a given, fixed set of stream data. The heat surplus below the pinch *may* be used if:

1. New processes are added to the overall process (New cold streams are added to the stream set).
2. New design of existing processes lead to existing hot and cold streams' data changes.

Instead of correcting pinch violations, it might be economically justified to keep the current heat demand, and instead integrate new processes. This is done against the curves using background/foreground analysis. Non-conventional evaporation is a good example of such integration [7, 17]. A combination of removing some amount of pinch violations, and use the remaining heat for integration of new processes could of course also be considered. Which combination of measures should ultimately be chosen is determined by the economic evaluation of possible and viable combinations.
It is important to notice that all cooling demand depicted in the TCLC is excess heat. However, the amount of this excess heat that is useful for other applications depend on the temperature level at which it is released. In different industries, the operating conditions for particular process parts and unit operations are believed well known. However, when using other, new sources of heat, e.g. excess heat, for a certain process, one must also relax the design and operating conditions for that process. For example, in the pulp and paper industry, excess heat of 80 °C is not of much use when the existing process is analysed. Excess heat of 60-80°C could however be used for pre-evaporation of black liquor or effluents, district heating or heating of facilities in the plant if new or redesigned processes are integrated. The key question here is to relax the process under consideration from the background, and study it as a foreground process. Process integrated evaporation of black liquor is taken as an example here and explained using the GCC. From the existing GCC Figure 9, the evaporation is excluded and added as a stand-alone unit, Figure 7. When this is done, changing the design of and operating conditions for the evaporators, a process integrated design using now usable excess heat could be derived, Figure 8. Work by Algehed [17] and Bengtsson [18] has shown that substantial live steam savings, between 16 and 90 % of initial consumption, could be achieved by this approach.

In the same way new processes should be added and integrated as foreground processes to the existing process (background).

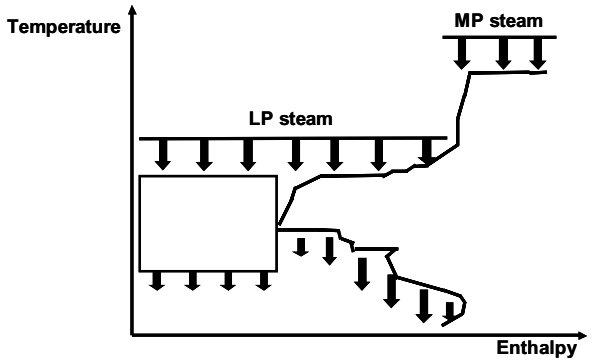

Figure 7: Conventional evaporation plant as foreground.

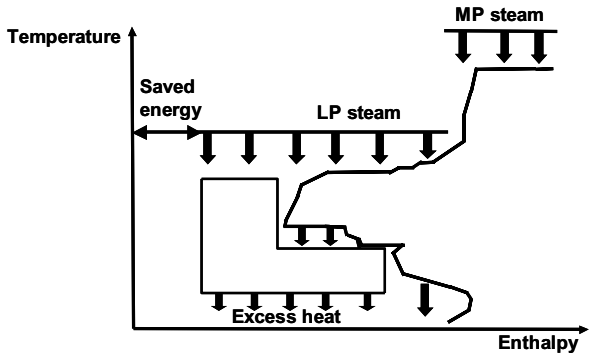

Figure 8: Process Integrated Evaporation.

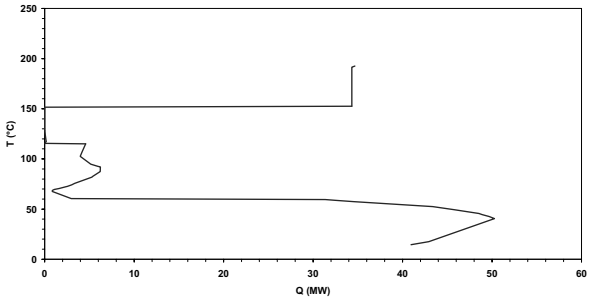

Figure 9: GCC for the Pulp Mill Example.

In many industrial projects Chalmers have participated, there has often been an attitude that there is no usable excess heat available in the plant. This is often based on studying the GCC, plotted for the HRAT that corresponds to the existing heat demand. If instead the same process is examined using the advanced curves, a quite different picture could be the result, especially if the difference between the HRAT and EMAT is large.

As an example of this, Figure 9 and Figure 10 present the GCC and the THLC/TCLC for a pulp and paper plant. The GCC is plotted for a HRAT of 15°C, so that the existing heat demand is met.
When the GCC is analysed, about 0.9 MW of excess heat is available above 67.5°C (this heat could be released up to 115°C) out of a total of about 41 MW. All temperatures are in this case adjusted. This amount of excess heat would probably not be very efficient to use for other processes, and the analysis might stop here.
If, on the other hand, the advanced curves were used, a completely different picture appears.
The THLC and TCLC in Figure 10 shows a potential to release 7.5 MW above 98°C, whereof 4.7 MW at or above 122°C. All temperatures are in this case real temperatures.

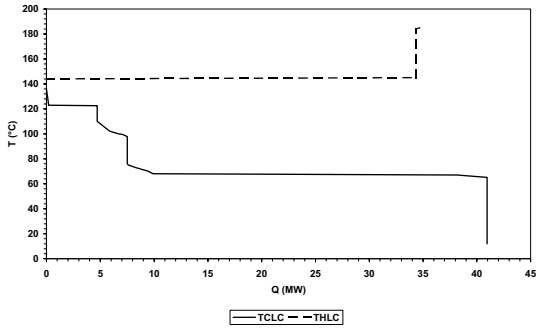

Figure 10: THLC and TCLC for the Pulp Mill Example.

Important to remember is that both the GCC and the advanced curves are constructed out of stream data only, so what is causing the difference in the results?
The answer to this is the advanced curves show the potential excess heat release if a given EMAT is used to retrofit the HEN. This means that in the existing HEN it might not be possible to release the excess heat at the temperatures indicated in the advanced curves, but there is the possibility to do this. A new process using excess heat at high temperatures could therefore be considered, but when the investment is evaluated, the cost of retrofitting the HEN to fit the new process must be added.

Shifting Pinch Point

One additional "phenomenon" that should be recognised is when the pinch point shifts from one stream to another. In the example above, the pinch point remains the same from 15K down to

5K, but the situation could have been quite different. Figure 11 shows the pinch point temperature versus the HRAT for the example. It can bee seen that between HRAT = 15K and HRAT = 17K, there is a shift in pinch temperature from 128.5 °C to 67.5 °C.

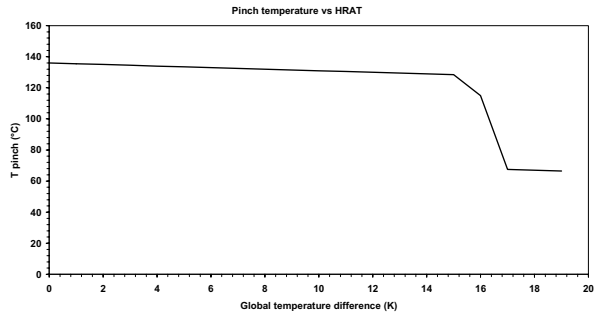

Figure 11. Pinch Temperature vs HRAT.

If the existing heat demand had been e.g. 35.9 MW, corresponding to a HRAT of 18K, the GCC would look as depicted in Figure 12. According to this GCC, practically no usable excess heat could be released. By plotting the GCC for a lower HRAT, e.g. 5K would help seeing the potential, but this curve would miss the true potential by the amount of heat that differs between the existing HRAT and the HRAT that the curve is plotted with.

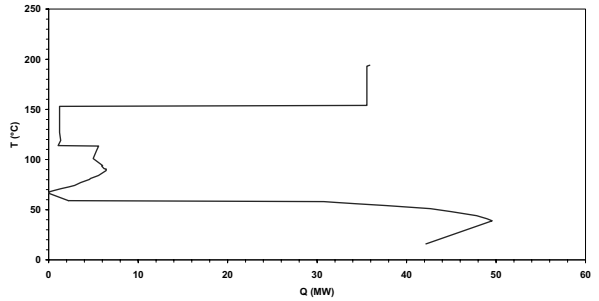

Figure 12: Pulp Mill GCC for HRAT = 18K.

CONCLUSIONS

In this paper, a set of advanced curves for energy integration has been presented. The usefulness of these curves, especially in the case of identifying useful excess heat and integration of new processes, but also for evaluating the HEN retrofit potential has been demonstrated. A brief discussion of Heat Pump and Gas Turbine integration was also presented to demonstrate the broad application range of these curves. The importance of taking all possible measures into consideration in a heat recovery project has been stressed.

ACKNOWLEDGEMENT

Financial support from STEM project PI-10093-1-10093-4 is gratefully acknowledged.

REFERENCES

[1] Umeda, T., J. Itoh, and K. Shiroko, *Heat Exchange System Synthesis.* Chemical Engineering Progress, 1978(July): 70-76.

[2] Flower, J.R. and B. Linnhoff, *A Thermodynamic-Combinatorial Approach to the Design of Optimum Heat Exchanger Networks.* AIChE Journal, 1980. **26(**1): 1-9.

[3] Flower, J.R. and B. Linnhoff, *Thermodynamic Analysis in the Design of Process Networks.* Computers & Chemical Engineering, 1979. **3**: 283-291.

[4] *European Union, 2003. Directive 2003/87/EC of European Parliament and the Council of 13 October 2003 establishing a scheme of greenhouse gas emission allowance trading within the Community and amending Council Directive 96/61/EC. Official Journal of the European Union 25.10.2003 L275/32*, Directive 2003/87/EC, 2003.

[5] Nordman, R. and T. Berntsson, *New Pinch Technology Based HEN Analysis Methodologies for Cost-Effective Retrofitting.* Canadian Journal of Chemical Engineering, 2001. **79**(4): 655-662.

[6] Nordman, R. and T. Berntsson, *Use of Advanced Composite Curves for Assessing Cost-Effective HEN Retrofit.* Submitted for publication, 2005.

[7] Bengtsson, C., R. Nordman, and T. Berntsson, *Utilization of excess heat in the pulp and paper industry--a case study of technical and economic opportunities.* Applied Thermal Engineering, 2002. **22**(9): 1069-1081.

[8] Tjoe, T.N., *Retrofit of Heat Exchanger Networks*, PhD Thesis, UMIST, 1986.

[9] Van Reisen, J.L.B., et al*., The placement of two-stream and multi-stream heat-exchangers in an existing network through path analysis.* Computers & Chemical Engineering, 1995. **19**: S143-S148.

[10] Lakshmanan, R. and R. BanaresAlcantara, *A novel visualization tool for heat exchanger network retrofit.* Industrial & Engineering Chemistry Research, 1996. **35**(12): 4507-4522.

[11] Lakshmanan, R. and R. BanaresAlcantara, *Retrofit by inspection using thermodynamic process visualisation.* Computers & Chemical Engineering, 1998. **22**: S809-S812.

[12] Asante, N.D.K. and X.X. Zhu, *An automated approach for heat exchanger network retrofit featuring minimal topology modifications.* Computers & Chemical Engineering, 1996. **20**: S7-S12.

[13] Carlsson, A., *Optimum Design of Heat Exchanger Networks in Retrofit Situations*, Ph.D. Thesis, Chalmers University of Technology, 1996.

[14] Wallin, E., *Process Integration of Industrial Heat Pumps in Grass-root and Retrofit Situations*, Ph.D. Thesis, Chalmers, 1996.

[15] Strömberg, J.B., T. *A process integration methodology for optimizing industrial CHP systems*. In: *IEA workshop on Industrial CHP*. Santa Margarita, Italy, March 1995.

[16] Gundersen, T. and I.E. Grossmann, *Improved Optimization Strategies for automated heat exchanger network synthesis through physical insights.* Computers & chemical engineering, 1990. **14**(9): 925-944.

[17] Algehed, J., *Energy Efficient Evaporation in Future Kraft Pulp Mills*, Ph.D. Thesis, Chalmers University of Technology, 2002.

[18] Bengtsson, C., *Novel Process Integration Opportunities in Existing Kraft Pulp Mills with Low Water Consumption*, Ph.D. Thesis, Chalmers University of Technology, 2004.

Proceedings of ECOS 2005
Trondheim, Norway
June 20–22, 2005

PROCESS INTEGRATION-CASE STUDY SODIUMTRIPOLYPHOSPHATE MANUFACTURE

Predrag Rašković [1]
University of Nis
Faculty of Technological Engineering
16000 Leskovac
Serbia and Montenegro

ABSTRACT

The reference object for Process Integration, in this paper, is the sodium tripolyphosphate manufacture in "*IHP-Prahovo*", the biggest factory for producing base chemical products in Serbia and Montenegro. The sodiumtripolyphosphate-$Na_5P_3O_{10}$ manufacture is one of the most complex processes in the chemical industry. The overall process could be divided in two parts: the wet process part, where the raw material is primarily treated with chemical reactions, and the dry (final) process part based on thermal treating of the material.
The retrofit project, for dry process part, consist of five closely connected phases: modeling, simulation, optimization, Process Integration and energy efficiency analyses.
Process Integration of dry process is realized by Thermodynamic methods, Exergy analyze for the flue gas recirculation models, and Pinch design method for heat exchanger network models. The results indicate much better energy performance for project realized on heat exchanger network models.

Key words: Process Integration, sodium tripolyphosphate, IHP-Prahovo, software tool.

NOMENCLATURE

Cs	cold stream
Hs	hot stream
G	mass flow rate [kg/s]
E	energy flow rate [W]
$Q_{H,min}$	minimum external heating [W]
$Q_{C,min}$	minimum external cooling [W]
HRAT	heat recovery approach temperature [^{0}C]
W	heat capacity flow rate [kW/^{0}C]
$\Delta Tmin$	minimum approach temperature [^{0}C]

INTRODUCTION

The reference object for Process Integration, in this paper, is the sodium tripolyphosphate manufacture in "*IHP-Prahovo*", the biggest factory for producing base chemical products in Serbia and Montenegro.

Sodium tripolyphosphate (*STPP*)- $Na_5P_3O_{10}$, is a solid inorganic compound in regular and compact laundry detergents, automatic dishwashing detergents, also in human foodstuffs, animal feeds, industrial cleaning processes and ceramics manufacture.
The stable form of STPP is the hexahydrated salt. Sodium tripolyphosphate exists in two major crystalline forms, known as Phase I (or Form I) and Phase II (or Form II). Phase I material is formed if the process temperature is maintained above 450^{0}C, while Phase II material is formed at temperatures below 450^{0}C. The transition temperature between them is about 420^{0}C. The two crystalline forms have different properties and in many applications they are not interchangeable.
The annual production of *STTP* in "*IHP-Prahovo*" is about 45000 t/year. The most significant part in

[1] Corresponding author : Phone +381 64 2659230, E-mail: buki@bankerinter.net

plant production cost is the heavy oil consumption (approximately 7000 t per year). More than 90% of the consumption is executed in the final process part (dry part), based on thermal treating of material. Because of that fact, the research is focused on them. The energy system's retrofit project, consist of 5 closely connected phases, presented in flowchart on *Fig.1*.

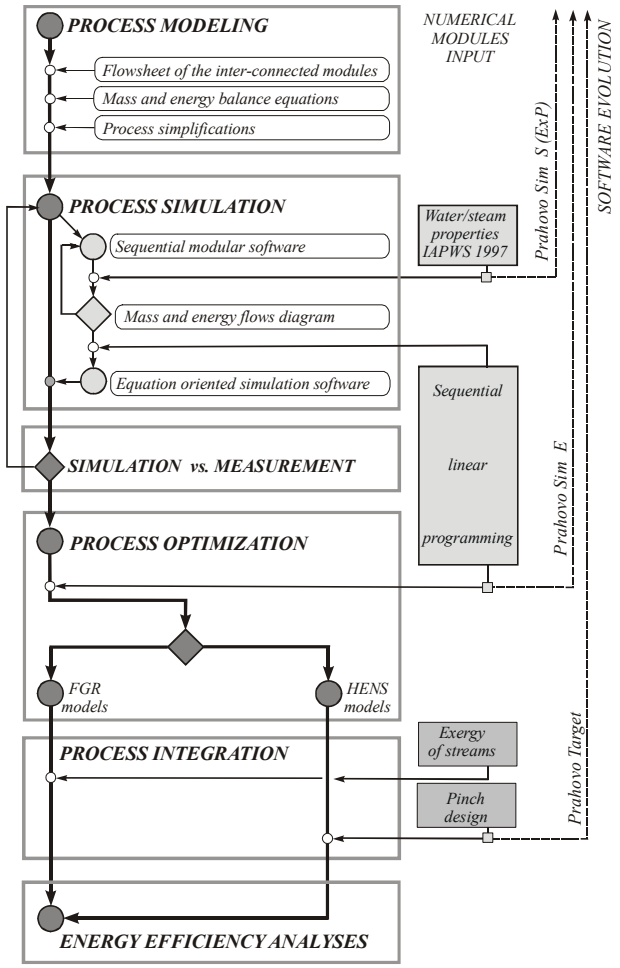

Figure 1. Flowchart of retrofit project

The main part in this paper will be dedicated to the phase of Process Integration, with briefly presentation of important facts from previous phases. As this is the first published work after the research is completed, author decided to present the main ideas without the detailed diagram analyses.

TECHNOLOGICAL SCHEME OF SODIUM TRIPOLYPHOSPHATE MANUFACTURE

Existing production plant for *STPP* [1] in "*IHP-Prahovo*" (*Fig. 2*) essentially consists of a two parts:

- *Wet proces part*, where the raw material is primarily treated with chemical reactions,
- *Dry (final) process part,* based on thermal treating of semifinished product from previous part.

In the *Wet process plant***,** phosphoric acid is first purified and then neutralized with alkaline compound such as sodium hydroxide or sodium carbonate. The result of this operation is an aqueous solution (orthophosphate solution also called "make up liquor"), such that the mole ratio of sodium to phosphorus is on the order of about 1.67:1. This solution contains the equivalent of monosodium orthophosphate and disodium orthophosphate in a mole ratio of 1:2.

In the *Dry process plant***,** the solution is sprayed into the spray dryer (atomizer) in a finally atomized state and dried into a predominately orthophosphate material[2]. Heated gas (flue gas), from atomizer oil firing unit[3], is employed in the spray dryer to accelerate the heating of sodium orthophosphate solution.

The moisturized product is then calcined in the rotary kiln (calciner) in order to convert orthophosphate into sodium tripolyphosphate[4]. Heating agent in calciner is the flue gas from another, calciner firing unit. The final temperature, within the range of from about 300 ^{0}C to about 600^{0}C, is selected in order to produce the desired Form I, and/or Form II, content in the final *STPP* product. The obtained product is generally in agglomerated form. The agglomerates are cooled and sized to yield a sodium tripolyphosphate product which is separated into granules (size about 1mm in diam.).

The gas stream emanating from either the spray dryer or the calciner is passing through a solid recovery zone (cyclone battery of centrifugal separators) to remove the bulk of any sodium tripolyphosphate powder that has been entrained in the gas stream. Such treated gas stream is then passing through a scrubber, containing a liquid scrubbing solution which contacts the gas. The scrubber also takes up remaining amounts of finally powdered sodium tripolyphosphate which were not caught in the centrifugal separator.

---

[2] mixture $2Na_2HPO_4 \div NaH_2PO_4$

[3] In the spray dryer the flue gas is coming as the mixture of recirculation and *fresh* flue gases from mixture chambers.

[4] $2Na_2HPO_{4(s)}+2NaH_2PO_{4(s)} \rightarrow 2Na_4P_2O_{7(s)}+2Na_2H_2P_2O_{7(s)}+3H_2O$

$2Na_4P_2O_7+ 2Na_2H_2P_2O_7 \rightarrow 2Na_5P_3O_{10}+H_2O$

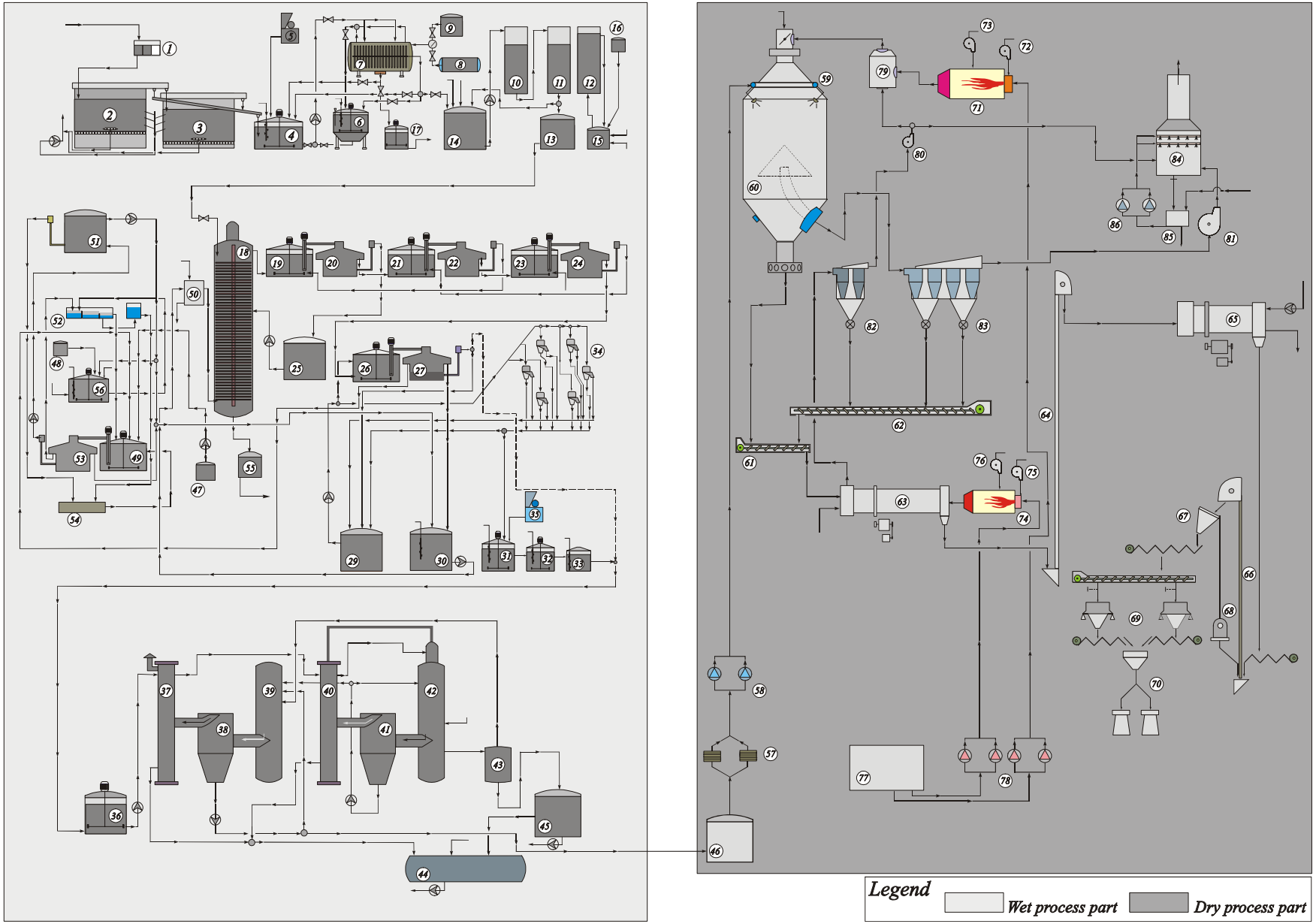

Figure 2: Technological scheme of sodium tripolyphosphate manufacture in *IHP Prahovo*

RETROFIT PROJECT OF DRY PROCESS PART

Retrofit project of dry process part (*Fig. 1*), start with modeling phase [5]. Physical model is created as the network of inter-connected modules (*Fig. 3a*). Mathematical model is based on mass and energy balance equations with, according to the technology limits, some simplifications. The most important are:

- Model is a continuous and steady state,
- Some of the streams are the ideal mixtures of air, dry flue gases, vapor in gases and sodium tripolyphosphate powder. For such stream, balance equations are created for each component,
- bulk mass flow and the vapor content in flue gases are the function of belonging stream mass flow and fuel specification respectively.

Process simulation is primary made by the use of spreadsheet software tool-*Prahovo sim S (ExP)*[5] [2] which includes the water/steam simulator.

The results of the software confirmed the proposed mathematical models of process units, and enabled the global connection of mass and energy flows (*Fig. 3b* and *3c*). Another important conclusion was that the influence of the pumps, fans and pipes heat loses are negligible in the overall heat balance.

Numerical integration of equation-oriented software (named *Prahovo sim E*) is developed on *Visual Studio C++* programming platform. It's solving procedure is based on *Sequential Linear Programming* (*SLP*) technique for non-linear simulation/optimization.

The results obtained by the use of *Prahovo Sim E* are compared with plant operating measurement, which are made in present and past time, for production of both crystal form of *STTP*. The author concluded, that the average mistake of about 5.84%, could be good starting point for the next retrofit project phases.

Energy system optimisation was done in two ways: one by adding the new possibilities for flue gas recirculation (*FGR* models) and another by adding the new heat exchangers in existing plant (*HENS* models).

The additional improvements for the next, Process Integration phase, are realized by the use of Thermodynamic methods. For the first, *FGR* models, numerical module for exergy calculation enabled the use of Exergy analyze. For the second, *HENS* models, pinch numerical module[3] enabled Process Integration by Pinch design method. On that way software *Prahovo sim E* evolved in a final form named *Prahovo Target.*

PROCESS INTEGRATION OF *HENS* MODELS

Process Integration of *HENS* models, by the ordinary use of pinch design method, was limited for only 3 streams of existing model. These streams passed through the complex chemical operation (combustion, spray drying, calcining, scrubbing), and their possible matching are in accordance with mass and energy balance of the plant. The results of their integration would be the slight increase of the plant energy efficiency.

On the other side, involving the new, let me call them *promising*, streams, in Pinch design task, is limited by two reasons:

- Their fixed input/output energy parameters, doesn't enabled matching with other streams,
- Changing of their parameters[6], will complete the pinch design task, but the final solution would break the overall mass and energy balance, due to existence of chemical operation.

To exceed these limitations, plant was first reconfigured by adding the modules of new heat exchangers (*Fig 5a* and *b*) in existing physical and mathematical model. These exchangers present just fictive elements, for possible heating/cooling of the streams. Their purpose is to ensure the overall plant balance equations. Energy parameters of *promising* streams becomes the preassigned parameters (included in software input menu) of new formed optimization task. The optimization result automatically generates the base Pinch design task, and enabled future improvements by other Pinch design phases [6].

Software flowchart for that operation is presented in *Fig 3* (stages are on light gray background, connected with dashed dark gray line).

[5] Developed on *Microsoft Excel* programming platform by sequential modular approach

[6] On example changing the temperature or mass flow rate of primary and secondary air in combustion chambers

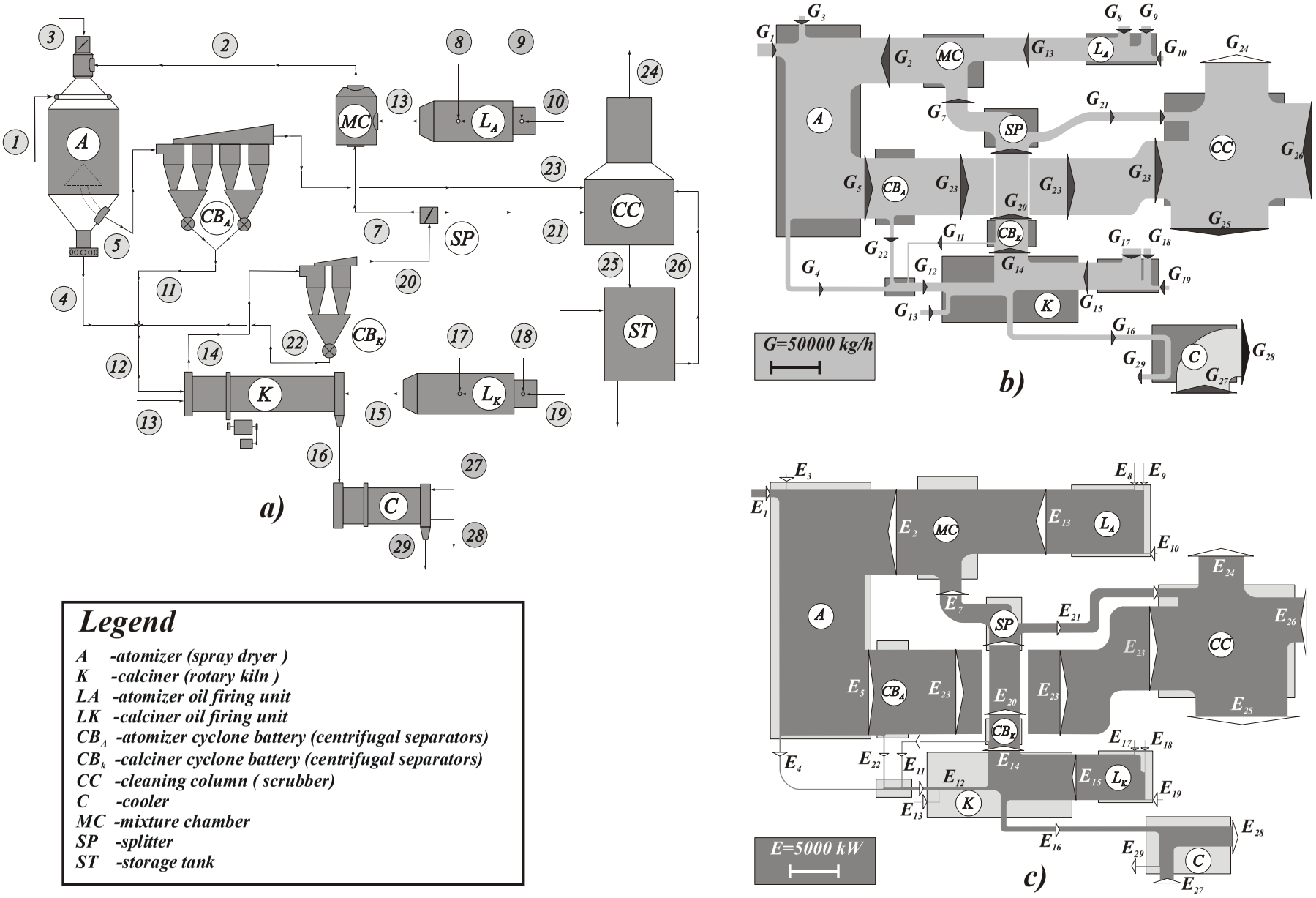

Figure 3: Physical model of dry process part (*a*) with mass flow (*b*) and energy flow (*c*) diagrams

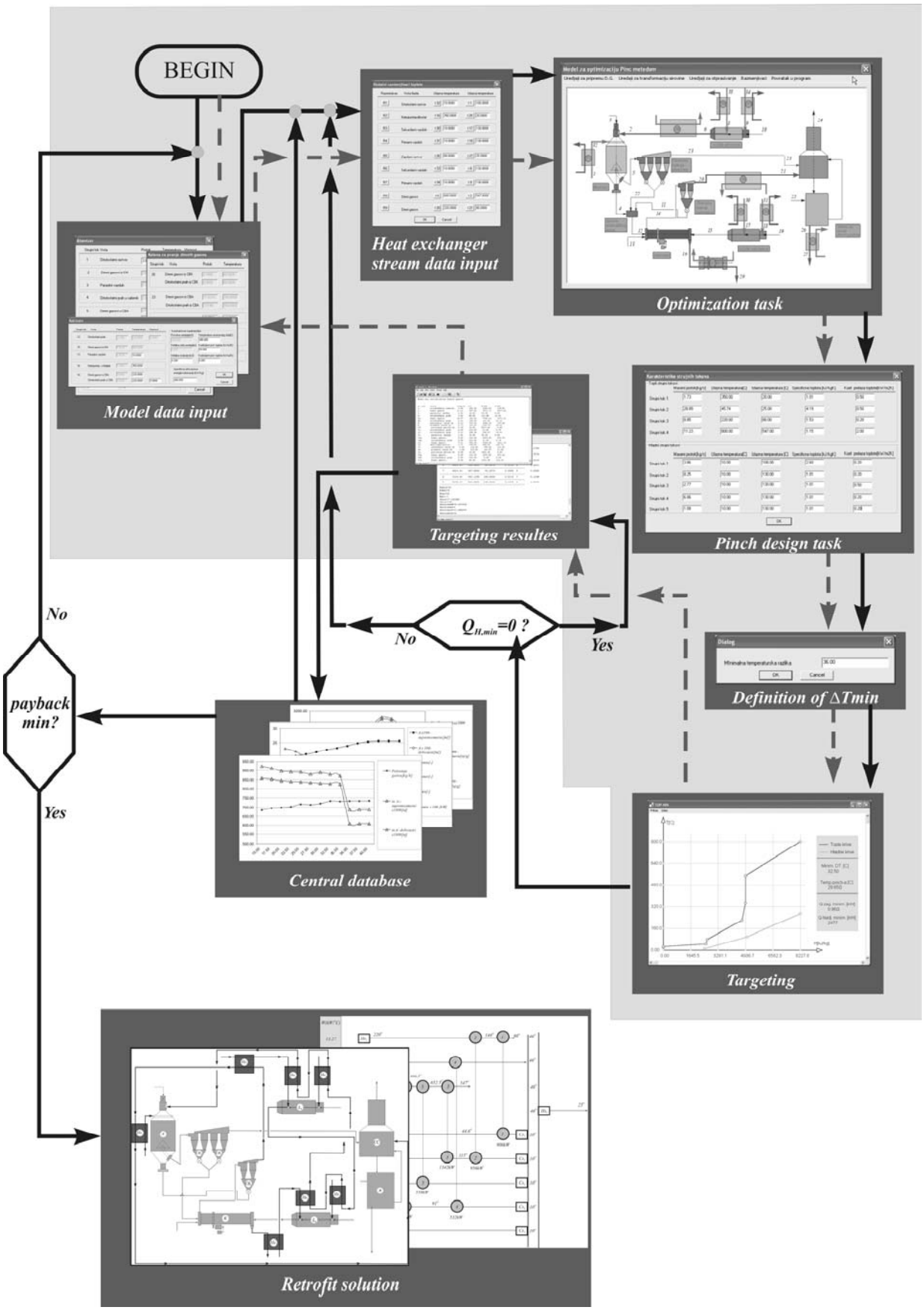

Figure 4: Software flowchart of Process Integration for HENS models

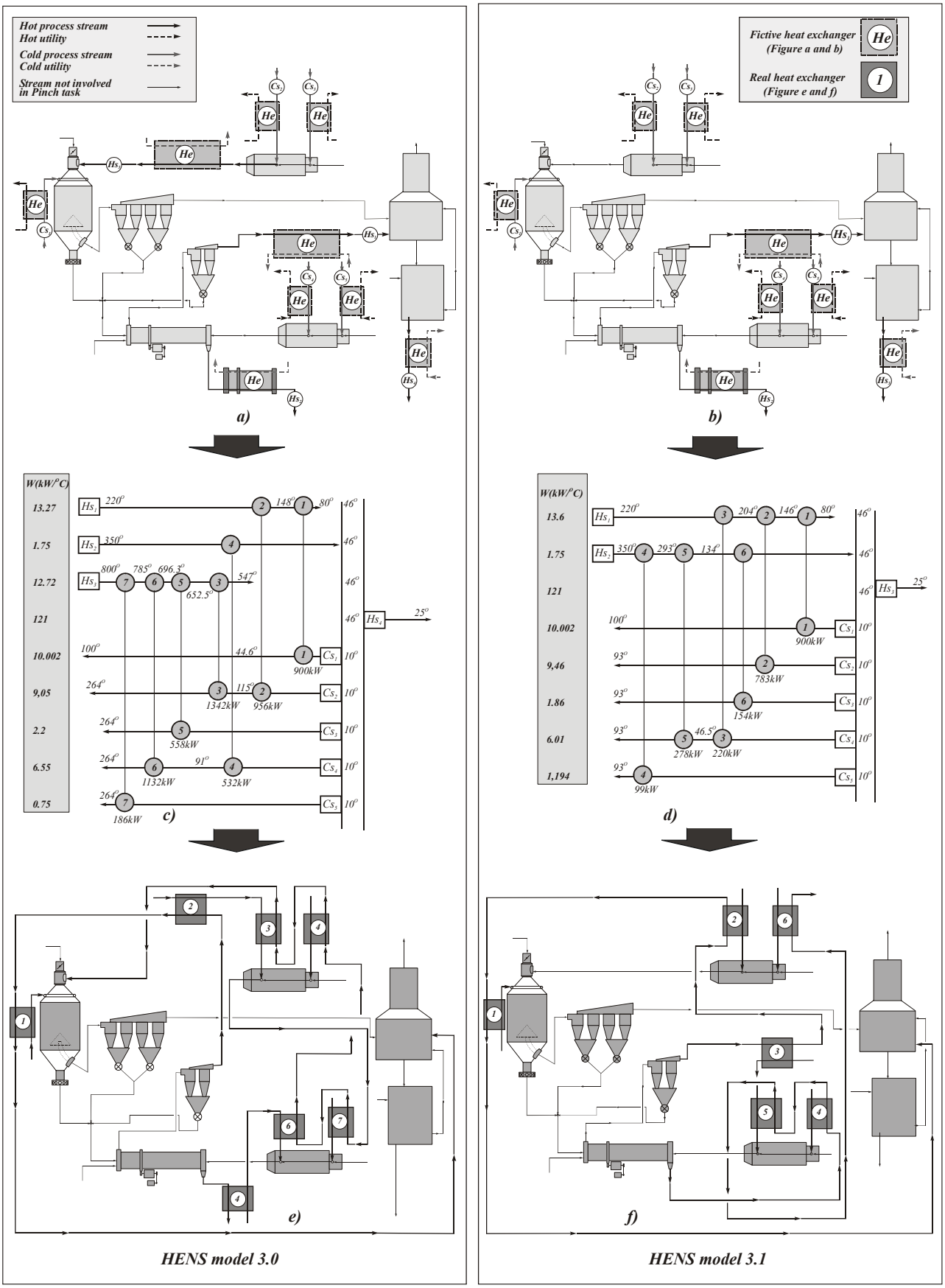

Figure 5: Retrofit project for HENS models

After the development of software *Prahovo Target,* next goal was the creation of retrofit solution without use of any new external heating/cooling. Elimination of the external heating conect the operating cost with oil consumption in the system.
By previously explained procedure, in first research circle, composite curves are put in threshold problem statement for specific *ΔTmin*. Operating and investment cost for that state, obtained from targeting phase, are loaded in intermediary (*Targeting results*) and central database for energy efficiency analyses. The research circle is then repeated for different value of *ΔTmin.* In the second research circle procedure is the same, but this time with different process parameters. Graphical explanation of this investigation is presented by software flowchart in *Fig. 4* (stages are connected with dark solid line).

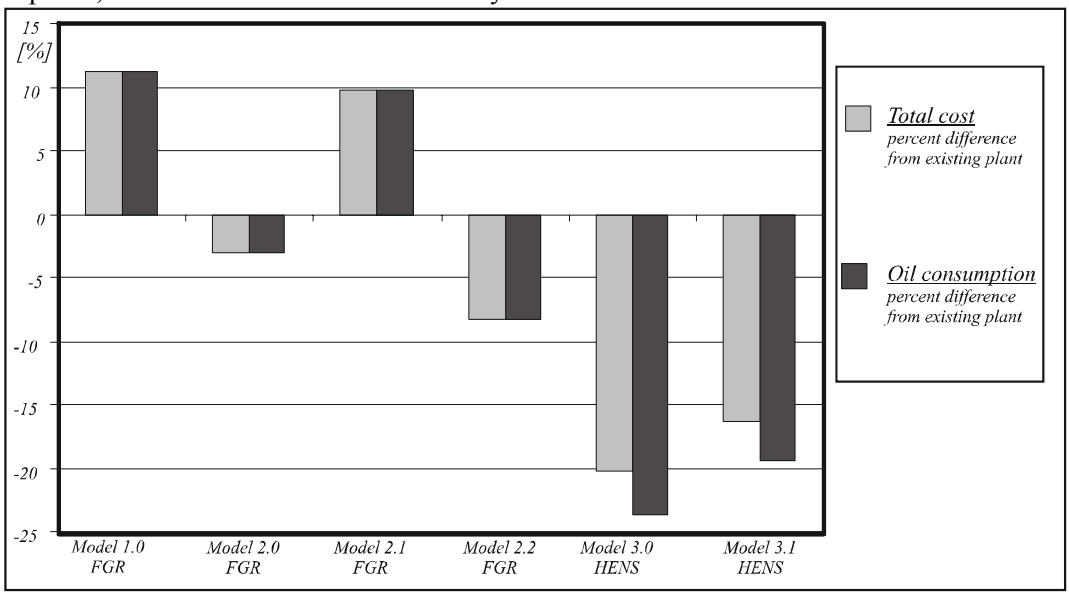

Fig 6: Economic analyses of retrofit solutions

RESULTS AND DISCUSSION

Process Integration was applied on two different *HENS* models, presented in *Fig 5* (*named Model 3.0* and *Model 3.1*). The economic analysis of targeting results, indicated $\Delta Tmin=36^0C$ as the optimal *HRAT* value for the both models. By that value, in grid diagrams (*Fig. 5c* and 5d) there is only one stream (stream from storage tank) which needs external cooling. As the technology process doesn't limit its target temperature, the purpose for cooling could be neglected. This fact has important effect on the investment cost of design. The final retrofit solutions are presented in *Fig. 5e and 5f.*
General comparing of *FRG* and *HENS* models solutions, was done on the basis of the same important energy inputs, and the same physicochemical property of raw and final materials. The results are presented in *Fig. 6*. They clearly indicated better energy performance for retrofit project realized by the use of *HENS* models.

REFERENCES

[1] Rašković P. *Industrial energy system optimization based on heat exchanger network synthesis.* Ph.D.Thesis: Mechanical Engineering, University of Niš, 2002.

[2] Rašković P, Živković D, Milojević M. *Software tool for energy process simulation of sodium tripolyphosphate producing factory*. In: Energy Forum, Varna, 2000.

[3]. Rašković P. *Ni Pinch-software tool for heat exchanger network synthesis* In: CFD and energy technology, First professional seminar, Niš, 2004.

[4] Atanasova L, Rasheva D. *Exergy Analysis of Sodiumtripoliphosphate Manufacture*. In: ECCOSE 2000, Holand,2000.

[5] Smith R. *Chemical Process Design*, New York: McGraw-Hill, 1995.

[6] Gundersen T. *Process Integration PRIMER*, In:SINTEF Energy Research, 2000.

Proceedings of ECOS 2005
Trondheim, Norway
June 20–22, 2005

ENERGY INTEGRATION AND SUSTAINABILITY IMPROVEMENT OF AN ECO-INDUSTRIAL NETWORK

Toshko Zhelev, Bernadette O'Regan, Richard Moles
Center for Environmental Studies
University of Limerick, Limerick, Ireland

Abstract:
The paper focuses on problems and challenges related to the integration, resources management and environmentally benign operation of urban based SMEs forming clusters of mutual trust and benefits known as Eco-industrial network. Presented analysis is based on the conceptual approach of design and redesign and utilises the experience in energy integration of remote areas of integrity, reuse/recovery/utilization of resources between partner factories, guided design changes for beneficial solutions and incorporates an optimality criteria (multiple resources management – water, energy, effluents) with environmental impact considerations. It proposes a procedure assisting decision making when centralized versus distributed waste treatment competes with balanced/mixed options. This procedure is tailored to assist partner companies to decide what part of waste to treat on their own production site and what part of it to send to a centralized service or neighboring company for treatment. An attempt is reported to bring together in one analysis the products, raw materials and services, accounting for their sustainable origin (history) and required treatment (future), considering possibilities for guided waste recovery and utilization in other areas of integrity and finally focusing on production/process management for maximum efficiency and sustainability through combined Emergy-Pinch analysis.

INTRODUCTION

The International Energy Agency (IEA) defined process integration as *Systematic and general methods for designing integrated production systems, ranging from individual processes to total sites, with special emphasis on the efficient use of energy and reducing environmental effects* (Gundersen, 1997). Currently, process integration can be seen as a holistic approach to process design, retrofitting and operation, which emphasizes the unity of the process. It can be seen as a common term for the application of methodologies developed for system-oriented process plant design. The three major features of process integration methods are: The use of heuristics (insight) about design and economy; the use of thermodynamics (e.g. pinch analysis, exergy analysis) and the use of optimisation techniques. Examples of the efficiency criteria used are capital investment, energy efficiency, emissions, operability, flexibility, controllability, safety and yields (Gundersen, 1997). Recently, a new wider concept specified as *comprehensive process integration* was introduced by Markka Hurme (2005) and defined as design, operation and management of industrial processes with system-oriented and integrated methods, models and tools. It covers not only energy and utility flows but also all material and information flows with the aim to balance their use for optimised process performance. Comprehensive process integration aims to integrate different elements of production (raw materials,

utilities) using various performance criteria and different scopes and areas of application (process, site, community) during the whole life cycle of the plant (industrial activity). Finally the process integration principles can be seen in accordance with the principles of sustainable development and industrial ecology; especially, when the definition "site" is extended to include the environment and society.

In the case of this research, the intention is to utilise the concept of integrating areas, sites and industrial activities of particular integrity with the view of better and more efficient performance accompanied with more environmentally friendly operation that is recognised by the local society. The core element of such integration remains at the systematic approach to energy and material flows, where the effluent's flows and waste management becomes a new dimension.

ECO-INDUSTRIAL NETWORK

The drive for integration leading to possible economic and environmental benefits has turned our focus onto local small and medium enterprises (SMEs) located in the Mid-West region of Ireland. The Mid-West region of Ireland comprises County Limerick, County Clare and County Tipperary and includes approximately 10% of the national land area and population of Ireland. The industrial base is dominated by light industry such as electronics, instruments, pharmaceutical and healthcare, metals and engineering. The attractiveness of the Mid-West as a location for industry is demonstrated by the large number of foreign-owned plants established in the region. It is estimated that there are approximately 400 SMEs in the Mid West region.

While SMEs contribute to growth, employment and rural development they also exert quite significant impacts on the environment. It is estimated that in total SMEs are responsible for 70% of all industrial pollution across the EU (EC Enterprise Directorate General. 2004).

The announcement of our research in the area of industrial integration has attracted significant interest in the region and already 22 SMEs from the Mid West region formally expressed commitment to this project. Many of these companies already work together in areas other than sustainability and this basis has established such crucial advantages as mutual trust.

There are many successful international examples of SMEs integration to form Eco-Industrial networks and these have been successful in terms of the reduction of environmental impacts. e.g. waste reduction, resource use reduction, improved transport management, etc. and improved competitiveness for the companies involved. Such are: Kalundborg - Denmark and Styna - Austria; the INES project in Rotterdam Harbour and the UK National Industrial Symbiosis Programme (Internet Reference 6). But there is still significant work to be done in terms of integration methodology development and methodology generalisation.

THE CONCEPT

Eco-Industrial development is characterised by closely co-operating manufacturing and service industries working together to improve their environmental and socio-economic performance by improving their energy resource use and waste disposal efficiency through identification of options for reuse recycling or regenerative reuse of resources across areas of integrity. This may be as simple as identifying one SME's waste which could be used as a raw material by another business, or as complex as rethinking the transport and supply

logistics for the entire cluster or maximising economic and environmental performance using grass-root multi-objective optimisation methodology.

The attraction in the concept of Eco-Industrial development lies in its application of the natural ecosystem metaphor to "industrial ecosystems". The ideal of the metaphor is that industrial ecosystems function according to the system development principles of natural ecosystems, i.e. closed loops and waste utilisation between industrial actors (Singhal and Kapur, 2002). A local or regional industrial system is encouraged to move towards an interactive system through cooperative waste material and waste energy utilisation (recycling of matter, cascading of energy) and sustainable use of local renewable natural resources of matter and energy between the industrial actors. By reducing the waste management costs, emission control costs, raw material and energy costs, transportation costs, costs resulting from the implementation of measures required in environmental legislation and by improving the environmental image as well as the "green market situation" of the network, economic gains are possible.

The goal of Eco-Industrial development is, at the minimum, to generate the least damage in industrial and ecological systems through the optimal circulation of materials and energy (Cohen-Rosenthal, 2004).

All companies participating in this project confidently expect that by improving their performance with respect to sustainability they will gain economically through shared marketing initiatives, accessing green markets and gaining recognition as responsible stakeholders within the local community.

SYSTEM ORIENTED METHODS

System oriented methods provide practical ways to find required minimums for energy, raw material and water use in process integration at a system level. Unfortunately, until now most of the methods developed consider each of the resources in question separately.
The information available for the process design changes during the process life cycle stages because of process development, design, operation and retrofit. In the case of an existing network of companies this increases the level of complexity. Therefore to guide the decision maker towards the total optimum, a more complex view of analysing process integration efficiency is required.

First the alternatives are generated, analysed by calculation and evaluation of indicators. In the beginning of the project the process design activities are first aligned with the strategic targets of the company. To facilitate this, the company management has to define strategic goals and priorities for the design/redesign/operation. At the same time, this information will identify many design constraints.

AREAS OF INTEGRITY

An energy integration concept developed by (Ahmad and Hui, 2001) may have an important impact on the task of beneficial integration within the Eco-Industrial Network. The concept utilises the natural division of process plants in logically identifiable regions (areas of integrity) and the potential for heat (energy) recovery between these areas. The optimisation task in this case is defined as the identification of schemes of energy recovery between areas of integrity which offer maximum heat flow between these areas (maximum integrity) that secures minimum energy import to the system with least number of

interconnections between the regions. Ahmad and Hui, 2001 propose procedures, which translate the heat-flow-schemes into actual heat exchanger network designs.

The proposed methodology generates solutions ensuring maximum energy recovery between areas of integrity with minimum capital investments. This concept can be adapted without changes for the purposes of energy conservation within an Eco-Industrial Network. The areas of integrity in this case are the SMEs themselves and the integration of energy will be done with minimum re-piping or other type of interconnections between them.

EMERGY ANALYSIS FOR INTEGRATION

To address the levels of integration and sustainability a logical question arises – is there a way to address and analyse the vast majority of resources and goods, as well as the services, treatment and operations involving these resources? It is known for quite some time that the concept of *emergy* provides resources for such a combination.

The available solar energy used up directly or indirectly to make a service or product available, defined as *emergy* by (Odum, 1996), was applied by a number of authors to compare inputs of different origin, such as human labour, trucks, energy, fuels, chemicals, utilities, plant cost, etc. *Solar emergy* is the solar energy directly or indirectly necessary to obtain a product or a flux of energy in a process; it is an extensive quantity and its unit is the *solar emergy joule* [sej]. To convert inputs and other kind of flows into the solar equivalent, it is necessary to know the solar transformity, which is the *emergy* necessary to obtain one unit of product. Unlike the *emergy*, transformity is an intensive quantity and usually measured in [sej/J]. Transformity calculation is a difficult task stimulating researchers to exchange data and build databases establishing a common ground for analysis.

An interesting feature of *emergy analysis* is that it gives historical information about the resource or activity in question. Any *emergy* in the particular moment of interest contains all emergies of stage changes occurring on the way to that stage. The *emergy* value associated with a product is the sum of the all energies that were used to produce it. Another useful feature of *emergy analysis* is the ability to identify critical processes/stages/units. This makes it suitable for the purposes of environmental pre- and post-impact consideration in the Eco-Industrial Network.

In 2004, Zhelev & Ridolfi (2004) promoted the concept of combining emergy analysis with Pinch analysis – a recognised tool for resource management in industry. These two methods give the missing link between the industrial resources management for economic benefits and the environmental impact assessment comparing alternative solutions. The restriction in this particular case is that the combined analysis addresses energy resource only.

EMERGY-PINCH ANALYSIS FOR ENERGY CONSERVATION

As suggested earlier by Zhelev & Ridolfi (2004) the amalgamation between *Emergy* and *Pinch* concepts can provide a range of benefits. Details about technicalities of the combined procedure are provided again here. To apply the Pinch concept one needs to construct the Composite curve. The streams, being either wastewater or energy, are defined in emergy units and in the way that can support emergy composite construction for the purpose of further targeting. Each stream is represented in a specific way. There is a portion of information (transformity) describing the past emergy investment, the "history" of the stream; a second portion, showing the "market" potential of the stream in terms of usability,

as it is the heat (temperature) potential for a thermal stream or the concentration limits, if it is a water stream; the final, third portion of information is associated with the stream's future – it is linked to the future of the stream and its further usability (regenerative reuse). In the case of thermal Pinch analysis, the hot and cold streams will have different sign of this component of final emergy investment. The required emergy investment to heat the cold streams will possess a different sign than the available emergy, allowing at this level of analysis to relax particular constrains such as ΔT_{min} that can lead to minimisation of the usage of expensive hot utility.

Emergy analysis seldom addresses industrial systems and do not consider the impact of wastes - that third portion of information we impose to the stream definition. An important issue is the possibility in the third portion (stage) of any resource stream to consider waste reuse options (positive emergy associated with it) and another portion that is to be lost when disposed to the environment. The emergy loss can be considered through the investment in waste treatment. At the same time this treatment may not only recover an ecologically acceptable level of the resource, but also raise its potential for regenerative reuse.

Applying Pinch analogy, the projection of any stream-representing vector on X-axis shows the Solar Emergy, the projection on Y-axis gives the solar transformity. The solar transformity is a quality characteristic. The slope (reverse of the slope) of the line represents the amount/flowrate, quantity of the resource. It should be noted that the solar emergy has a relative (not absolute) value, so the allocation of the line representing a resource would be not fixed in horizontal plane.

In the general case of emergy analysis similar to classical Pinch analysis the processes "overlap" in the horizontal plane (temperature range, concentration range, here - transformities range). The emergy loads, or investments, for different processes are characterized by relative values. Then their graphical representation can be freely shifted left and right in their SolarTransformity/SolarEmergy plot.

Targetting

The total emergy investment would be targeted drawing the line touching the composite and accounting for its slope. As bigger the slope of total emergy investment line is as smaller the rate of total emergy investment. This means the supply of combined resource and corresponding costs associated with it will be minimised lifting the emergy supply line to its maximum. The limit is manifested by the touching point between the supply line and the composite curve, the point known as Pinch. Measuring the allocation of the emergy supply line and its slope can help to compare alternative design or operation options. In other words, transformity is accepted as a parameter involving quality and plotted against the emergy investment allows targeting of total emergy investment and determination of maximum total transformity need to run the process.

Design guidelines

The treatment and reuse of wastes is the key to the evaluation of systems sustainability. The emergy loss is considered through the investment of waste treatment, but in the same time this treatment may not only recover ecological acceptable levels of the resource, but raise its potential for regenerated usage (application).

The Pinch concept also provides unequivocal design guidelines which help to design a system fulfilling the targets defined earlier. The design guidelines will come from a

classical pinch grid diagram. The emergy composite will identify potential processes to be changed before fixing temperatures and flowrates of streams. The design issue of combined emergy-pinch analysis is of particular importance and complications may arise that require special attention. A single emergy composite is drawn for all streams and an emergy investment supply line is matched accordingly. Such an analysis would show the targets in terms of emergy investment.

An interesting point for discussion is if one can consider processes generating Emergy, not only those consuming Emergy. For example, these can be any exothermic reaction, water generation as a result of chemical reaction, money generated through sale, power co-generation, etc. In such a case it might be better to consider first the optimal utilization of internal resources of emergy and then – the minimization of the external ones. The design guidelines suggested by this approach are associated with the classical concept of the pinch grid diagram. The Emergy composite helps to identify potential processes to be changed before fixing temperatures and flowrates of process streams. A single emergy composite is drawn for all streams and an emergy investment supply line is matched accordingly. Such an analysis will show the targets in terms of emergy investment.

Bottlenecks identification

The identification of bottlenecks is of great concern in all methods of analysis and evaluation. The Pinch does it through its third graphical tool – the Grid diagram. It shows the cross-pinch energy transfer leading to cost implications and penalties. The emergy analysis identifies the critical processes through the value of emergy investment. Combining Emergy and Pinch concepts we are able to identify more precisely the combined influence of critical processes or phases through allocation of constrained processes (these touching the total emergy investment supply line and preventing its further lift up). The Pinch-type of targeting gives several important evaluation parameters: (1) the ultimate minimum emergy supply to run the entire process at any time (the slope of the total emergy investment). This is the flow of resources, services and work to run the entire system); (2) The total emergy investment for the entire process for the entire period; (3) The maximum transformity (the "amplitude" of transformity, giving the total "power" of resources to run the process – another criteria to compare alternatives, identifying what process needs resources of highest quality) – the horizontal projection of the right end point of the emergy investment supply line; (4) Limiting stages/resources (restricting the emergy investment supply line to increase its slope). This one gives indication about processes and resources which utilisation is to be intensified in order to improve the efficiency of the entire process; (5) Pinch point allocation; there is some substantial difference in the possibilities for improvement (minimisation) of the total emergy supply for Pinch points allocations characterised with lower transformity compare to those with high transformity. Details of these cases can be found in (Zhelev & Ridolfi, 2004).

OXYGEN-WATER PINCH ANALYSIS OF WASTEWATER MANAGEMENT IN ECO-INDUSTRIAL NETWORKS

As Thermal Pinch Analysis addresses heat exchange from a hot stream to a cold stream, so does the Water Pinch Analysis addressing mass exchange from a rich stream to a lean stream. A rich stream is a stream that has higher concentration of contaminant while a lean stream has lower concentration of the contaminant. The initial methodology (El-Halwagi and Manousiouthakis, 1989) considered the transfer of only a single contaminant from a

rich stream to a lean stream. The method is analogous to Thermal Pinch Analysis and uses the same basic steps. Wastewater may be minimised using any of the following redesign methods (Wang and Smith, 1994):

- *Reduction in Fresh Water Used.*

A reduction in the water supply will result in a decrease of the quantity of wastewater being produced. Optimising processes may change the fresh water demand for the process.

- *Reuse of process water*

Certain process streams require water of any quality, such as in the case of floor washing processes. The water supplied for these processes needs not be fresh water. Thus there is an opportunity to reuse water. The opportunity can be found in the neighbour factory. The benefit of water reuse has to be assessed accounting for the piping and pumping costs.

- *Regeneration recycling*

Water that leaves a process is often termed as wastewater. The quality of this water determines whether this water may be reused in other processes or neighbour factory. If the wastewater from a process can be treated easily and at a low cost, then the water may be "cleaned" or regenerated and used again. Simple regeneration can be settling or filtration.

- *Regeneration and reuse*

The water that is regenerated may be used in another process or factory and need not be recycled to the process/factory it originated from.

- *Oxygen Pinch Analysis*

The intent to design more cost attractive wastewater treatment systems was approached by extending Pinch principles towards so-called Oxygen Pinch analysis (Zhelev and Ntlhakana, 1999). The idea is to target prior to design the idealistic minimum oxygen required by the micro-organisms to degrade organic waste and to suggest treatment flowsheet and design changes ensuring efficiency of operation close to the earlier stated target. In most of the cases the oxygen is supplied to the micro-organisms through agitation. Agitation and other forms of aeration require energy, so finally the analysis based on Oxygen Pinch principles leads again to their original application associated with energy conservation. Apart from this, Oxygen-Pinch concept allows for the first time targeting a quality characteristic – the growth (the reproduction rate, or heath) of micro-organisms.

- *Combined Water-Oxygen Pinch Analysis*

The aim of this methodology is to help decision making about the strategy and the organisation of wastewater treatment within an Eco-Industrial Network. Major factors contributing to the cost of wastewater treatment and pollution levels are the wastewater quantity and the wastewater quality. The wastewater quantity is directly linked to the amount of energy required for the wastewater treatment. The objective to minimise the wastewater quantity can be achieved using the Water-pinch analysis. Water Pinch helps to increase concentration levels of wastewater and decrease its quantity. In contrary, wastewater quality is inversely proportional to the energy required for wastewater treatment as well as pollution levels. There is no integration technique that would facilitate wastewater quality improvement. A mechanism to negate this effect is required. This objective can be achieved by the application of Oxygen Pinch Analysis. Thus the overall effect of increasing the cost effectiveness of wastewater treatment can be addressed through combination of Water and Oxygen Pinch Analysis. The expected result is a decision-making procedure suggesting within particular market circumstances what amount of

wastewater to be taken for treatment within particular member factory of the Eco-Industrial network and what part of it to be sent to the servicing wastewater treatment plant.

- *Combined Methodology*

The link between Water Pinch Analysis and Oxygen Pinch Analysis is the common concentration variable, namely - the Chemical Oxygen Demand (COD). This concentration variable is duplicated in Oxygen Pinch Analysis as COD of the wastewater. The link between these two Pinch techniques, is the usage of COD as a single concentration variable. To demonstrate this amalgamation two configurations of wastewater treatment can be investigated – one based on centralised wastewater treatment strategy and second – using the strategy of the distributed wastewater treatment. The quantity of wastewater treated and the quantity of oxygen required are chosen as variables of the analysis of the most suitable wastewater treatment strategy. The quantity of wastewater can be minimised on particular factory site using the Water-Pinch concept. The quantity of oxygen required (respective the aeration energy required) for different quantities and qualities of wastewater can be targeted with the help of Oxygen-pinch concept. Both, the quantity and the quality of the wastewater treated are related to the cost of the treatment process. The configuration of wastewater treatment serves as an aid to establish whether there was a significant difference in wastewater treatment cost when the service charge is based on quality rather than on quantity only.

The above methodology may be particularly useful for the Eco-Industrial network as a convincing argument for or against the idea for commissioning a centralised wastewater treatment plant, its location, etc. It can help particular member companies decisions to join the group of factories served by such a plant as well as providing cost-effective quality and quantities of wastewater to be sent to this servicing plant under particular market circumstances. It can also serve as a firm ground for targeting the minimum electrical energy (respective cost) for treatment of different quantities and qualities of wastewater, which may provide a tool for the determination of service charges.

WATER PINCH AND EMERGY

Water Pinch principles have established a standard for drawing the limits for water reuse in industries and setting pre-design targets of minimum fresh water demand - an important feature for addressing alternative solutions of design changes and production expansion. One important feature of Water Pinch, inherited from the classical Pinch analysis is that this method, apart from the preliminary targets setting gives design guidelines which is an important advantage over Emergy analysis. Water Pinch considers mainly the contamination levels of streams, and helps identify when this level is below acceptable limits. It is more than obvious that different contaminations and concentration levels would require different levels of water treatment depending on the nature of contamination, composition, chemical bounds, etc., not just on concentration levels and limits. Emergy analysis can be useful under these circumstances. The ability to assess the history and the effort associated with making water resources available (boring dept, pumping, pre-treatment, softening, filtration, chlorinating, etc.) provides a good baseline to compare resources of equal quality.

The confidence to use transformity as an analogue to the temperature in thermal Pinch analysis or concentration in Water Pinch targeting comes from the fact that the transformity is an intensive unit of emergy and measures the quality of energy. The emergy of the wastewater may be determined from the knowledge of the concentration and nature

of the effluent, and the transformity of the relevant ecological services (water treatment process). The importance of water as a limiting resource in Ireland is growing and its management is becoming increasing important with the introduction of the Water Framework Directive. Consequently, Water-Emergy Pinch analysis may be effectively used as an aid in decision-making in the constrained cases of plant development and expansion, when the water resources are limiting these decisions.

INTEGRATION WITHIN THE ECO-INDUSTRIAL-NETWORK

The first level of analysis focuses on the possible on-site integration of processes inside the factories in question. This time consuming process is based on iterative evaluation of data collected through detailed questionnaire, interviews of staff and documentation design. Currently we collected data from 8 out of 22 member factories. We constrained the possible integration into four different vertical levels: (a) energy; (b) water; (c) waste treatment; (d) transportation. With the help of geographic information systems we first considered the possibility of horizontal integration between the indistries. First, decomposition in clusters of member SMS was proposed accounting for their geographic location. Second level of decomposition was based on common landfill waste-disposal sites. The third level of decomposition accounted for potentials of inter-factories waste-reuse/waste and utilities utilisation options. The optimisation problem of maximum cost benefit can be formulated as a problem of finding the maximum of the "vertical sum" of "horizontal integration benefits". The proposed principle for redistribution of the achieved savings amongst the member enterprises was proportional to the integration investments.

OTHER INTEGRATION ACTIVITIES (FUTURE WORK)

These may include investigating possibility for integration of not only energy, water and waste recovery, but possible sharing of information and information technology investments. The diffusion of information and communication technologies (ICT) offers opportunities to transfer, collect and manage a great amount of information and to reduce the space and time barriers. Participating firms may reduce their ICT costs by forming a joint Management Information System (intranet) for the Cluster and this will identify further opportunities for sharing information and resources.

The next level of integration expansion will be common purchase of materials and shared transportation, shared commuting, shared inventories, shared shipping through integrating the transportation logistics of the participating SMEs. Each of these provides for a reduction in environmental impacts through reduced fuel cost, transport related emissions while also reducing the transportation costs of the companies and providing additional social benefits in reducing the number of vehicles on the roads.

CONCLUSION

Adopting the principles of Eco-Industrial networks, this paper builds a set of appropriate methodologies and develops procedure suitable to identify synergies and opportunities for symbioses between collaborating SMEs which would result in enhancing the environmental performance of the companies, targeting opportunities for socio-economic benefits. The paper reports progress in tailoring and application of three integration concepts originally developed for smaller and more compact systems to larger systems, such as the Eco-Industrial Network of factories, situated in restricted geographic region. The major difference to other well-configured systems is the principle of open-side system integration.

That means – the system is to allow provision for flexibility (including or excluding neighbor factories) and include other integration dimensions. The three methodologies in question are: (a) Energy integration of distant areas of process-supported integrity; (b) Emergy-Pinch analysis (a novel amalgamation of two conceptual design approaches), and (c) Oxygen-Water Pinch analysis. These three integration methodologies are designed to consider the economic and environmental impact to decision making. The idea behind the integration of these methodologies is the merge between sustainability concerns at regional level with environmental concerns first at process level and second at SME level (horizontal and vertical integration).

The effort of such a project can demonstrate the practicality of the proposed framework through implementation it with a view to providing a platform for the eventual set up of an Industrial Ecology Park.

ACKNOWLEDGEMENT

This project is being undertaken as part of the Irish EPA's research programme entitled the Environmental Research, Technological Development and Innovation Programme 2000-2006. The programme is financed by the Irish Government under the National Development Plan.

REFERENCES

Ahmad, S. and DCW Hui, 2001. "Heat recovery between areas of integrity", *Comput & Chem.Eng.*, 15(12): 809-832.

Cohen-Rosenthal, E., 2004. "Making sense out of industrial ecology: a framework for analysis and action", *Journal of Cleaner Production*, In Press.

EC Enterprise Directorate General, January 2004. "*Public Policy Initiatives to Promote the Uptake of Environmental Management Systems in Small and Medium-Sized Enterprises",* Final Report of the Best Project Expert Group, EU.

El-Halwagi,M.M. and V.Manousiouthakis, 1989. "Synthesis of Mass-Exchange Networks", *AIChE Journal,* 35 (8): 1233.

Gundersen, T., 1997. "A Worldwide Catalogue on Process Integration", *The International Energy Agency* / Telemark Institute of Technology, Porsgrunn, Norway.

Hurme, M., M.Tuommla and P.Ahtila, 2005. "Process Efficiency by comprehensive process integration", *PRES'05*, Sicily, Italy (in press).

Odum H.T., 1996. "Environmental Accounting: Emergy and Environmental Decision Making", John Wiley and Sons, New York.

O'Regan, January 22nd 2004. B., "Environmental Management - Opportunities for SMEs" *presented at Analog Devices*.

Singhal, S., Amit Kapur, 2002. "Industrial estate planning and management in India—an integrated approach towards industrial ecology", *Journal of Environmental Management,* 66(1): 19-29.

UK National Industrial Symbiosis Programme (http://firstsupply.co.uk/nisp/)

Wang,Y.P. and R.Smith, 1994."Wastewater minimisation", *Chem Eng Sci*, 49(7):981-1006.

Zhelev T.K. and L.Ntlhakana, 1999. "Energy-Environmental Closed-Loop through Oxygen Pinch", *Comput. & Chem.Eng.*, 23: s79-83.

Zhelev, T.K., R.Ridolfi and N.Marchettini, 2003. "Combined Pinch-Emergy Assessment for Integrated Waste Management", *Chemical Engineering Transaction*, 1: 691-696.

Non-equilibrium thermodynamics

Proceedings of ECOS 2005
Trondheim, Norway
June 20–22, 2005

THERMODYNAMICS OF SUBCOOLED FLOW BOILING

Francisco J. Collado[1]
CPS-B, Universidad de Zaragoza
Departamento de Ingeniería Mecánica-Motores Térmicos
María de Luna s/n
50018-Zaragoza
Spain

ABSTRACT

Forced convective subcooled boiling is of interest for many applications in the power and process industry. However the existence of mechanical and thermal non-equilibrium between the phases complicates its treatment. So the fundamentals of subcooled flow boiling through channels are still in dispute and several models are keep on proposed. This work will try to determine which is the actual heat balance comparing the specific absorbed heat against mixture enthalpy using data measured by General Electric in the sixties. Two key points of this analysis will be the Law of Stable Equilibrium (LSE) for obtaining true equilibrium states, and to define mixture thermodynamic properties through the thermodynamic vapor mass fraction. The main result is that the standard heat balance cannot explain at all the complex subcooled flow boiling physics. The slip ratio, i.e. the vapor-liquid average velocity ratio, could close the relation between heat and enthalpy in this kind of two phase flows.

Keywords: subcooled flow boiling, mass fraction, heat balance, slip ratio, Law of Stable Equilibrium

NOMENCLATURE

A_c Cross-sectional area of the channel [m^2]
c Cross-sectional mean velocity [m/s]
h Specific enthalpy [kJ/kg]
p Pressure [kPa]
Q Heat [kW]
q' Specific heat per unit length [kJ/kg-m]
q'' Heat flux [kW/m^2]
S Slip ratio: vapor-liquid mean velocity ratio
T Temperature [ºC]
T_{wall} Average temperature of the heated wall [º C]
T_{sat} Saturation temperature [º C]
u Specific internal energy [kJ/kg]
v Specific volume [m^3/kg]
V Volume [m^3]
W Mass flow rate [kg/s]
x_{th} 'Thermodynamic' quality (dryness fraction)
x 'Flow' quality
x_e 'Equilibrium' quality
z Axial coordinate along the channel (m)
– Mean vapor volumetric fraction (void fraction)
– T_{sub} Local subcooling: T_{sat}-T_L (ºC)
– Density [kg/ m^3]

subindex

eq Equilibrium state through the LSE
i Inlet
F Saturated liquid
G Saturated vapor
L Subcooled liquid
m Vapor-liquid mixture (wheighted with x_{th})
o Outlet
sat Saturation

INTRODUCTION

Subcooled flow boiling [1-2], with a large amount of applications of industrial interest, takes place when a subcooled liquid enters in a heated channel with the wall temperature exceeding the saturation temperature in a certain amount. In this flow, vapor bubbles at saturation steadily co-exist with subcooled bulk liquid. In addition to this thermal non-equilibrium between the two phases, there is also a mechanical non-equilibrium due to

[1] Phone: +34 976 762551 Fax: +34 976 762616 E-mail: fjk@unizar.es

the difference of velocities between them i.e., the so-called 'slip'. This double non-equilibrium makes rather complicated its analysis, so that empirical approaches are usual.

Void fraction and standard heat balance

For example, the capability to predict the volumetric fraction of vapor [1-7], or void fraction, in subcooled boiling is of considerable interest to nuclear water-cooled reactors, because the void fraction significantly affects neutron absorption, heat transfer and pressure drop. Yet the proposed heat balance for these non-equilibrium flows is not clear.

So a 'true flow fraction' x, or 'flow' quality, is used [1-5], which is defined as a mass flow rate ratio,

$$W_G = \rho\rho_G c_G A_c, \quad (1)$$

$$W_L = (1\,\rho\,\rho)\rho_L c_L A_c, \quad (2)$$

$$S = c_G / c_L, \quad (3)$$

$$x = W_G/(W_G + W_L) = (--_G S)/\left[--_G S + (1--)-_L\right], \quad (4)$$

where we have previously stated the standard mass flow rates for the vapor and the liquid W_G and W_L, respectively, and then included the definition of the slip ratio S [1-7].

Then deriving – from Eq. (4),

$$- = \left[x(-_L/-_G)\right]/\left[(1-x)S + x(-_L/-_G)\right]. \quad (5)$$

Thus – depends on the 'flow' quality x, the 'slip' ratio S and the liquid density i.e., the subcooled liquid temperature, which will change throughout the channel until reaching saturation.

By convenience, we also derive S from Eq. (4),

$$S = \left[x(1\,\rho\,\rho)\rho_L\right]/\left[(1\,\rho\,x)\rho\rho_G\right]. \quad (6)$$

x could be derived from some heat balance, but S should be correlated against void fraction measurements.

The standard heat balance for a vertical heated channel [1-7] when a total mass flow rate W of fluid enters in,

$$\frac{d}{dz}\left[W_G\left(h_G + c_G^2/2\right) + W_L\left(h_L + c_L^2/2\right) + Wg\right] = \frac{dQ}{dz}. \quad (7)$$

At steady state, the kinetic and gravity terms are usually considered negligible [1-7]. Dividing Eq. (7) by the total or inlet mass flow rate W and including the 'flow' quality definition, Eq. (4), we have

$$\frac{d}{dz}\left[x h_G + (1-x)h_L\right] = \frac{1}{W}\frac{dQ}{dz} = q'. \quad (8)$$

Assuming also an uniform heat flux applied, i.e. an uniform specific heat per unit length q', Eq. (8) becomes

$$\frac{d}{dz}\left[x h_G + (1-x)h_L\right] = q' = cons\tan t. \quad (9)$$

Integrating from the inlet to some point at a distance z, also assuming only subcooled liquid at inlet with enthalpy $h_{L,i}$,

$$x h_G + (1-x)h_L = q' z + h_{L,i}. \quad (10)$$

In this case, the derivation of x from Eq. (10) is immediate,

$$x = \left[q' z - (h_L - h_{L,i})\right]/(h_G - h_L). \quad (11)$$

Unfortunately x also depends on subcooled liquid enthalpy (temperature), which is not known unless it was assumed that the vapor content is negligible [1-7] i.e., x≈0.

Therefore the standard heat balance, Eqs. (10)-(11), is not used for deriving x and so – [1-7].

As an alternative way to relate – with x, first an 'equilibrium' quality is defined [1-7],

$$x_e = (q' z\,\Delta h_F)/\Delta h_{FG}, \quad (12)$$

which obviously takes negative values until the liquid reaches saturation. In [3], it is asserted that '*this is the quality that we would obtain if the flowing mixture were removed adiabatically, thoroughly mixed, and allowed to reach a condition of thermodynamic equilibrium*'. However a negative mass fraction has no physical meaning at all.

Finally to relate 'flow' quality with heat, i.e. with the equilibrium quality, several empirical expressions, exponential [6] or hyperbolic tangent [5], have been suggested.

Indeed the current procedures [4-5] to calculate – are more complicated because a modified form of Eq. (5), through the Zuber and Findlay drift flux model [7], is used.

Heat balance between equilibrium states

It is evident that the complexities in this kind of flows arise due to the double non-equilibrium between the phases commented before.

In addition of the lack of physical sense of the former 'equilibrium' quality and the empirical way of connecting it with the 'flow' quality, it is

questionable to pose a thermodynamic heat balance, Eq.(7), including a vapor-liquid mixture in non-equilibrium state. Notice that first principles were postulated for systems in thermodynamic equilibrium [8].

Therefore we would face two main problems about subcooled flow boiling fundamentals namely, which are the correct thermodynamic properties we should use and which would be the right balance between heat and properties.

About properties, here we will follow the proposal of Bilicki et al. [9] of using the so-called 'dryness fraction' or 'thermodynamic' quality x_{th} defined as

$$x_{th} = (--_G)/-_m = (--_G)/[--_G + (1--)-_L], \quad (13)$$

where $-_m$ is the usual density of the two-phase system [1-8]. Lahey Jr and Moody [3] call x_{th} the 'static' quality.

As pointed out in [10], we are able to measure the void fraction – by gamma-ray or X-ray attenuation and then to calculate the dryness fraction in terms of –, see Eq. (13).

Assuming 'instantaneous' measurement of – in a control volume V and the condition of local equilibrium [9], the actual mass fraction of vapor in it would be x_{th}, not x, the difference between them lying in the slip ratio, Eq. (4).

According to Bilicki et al. [9], the extensive quantities of system V will be expressed in terms of the properties of the two co-existing systems wheighted with x_{th}. In particular, the specific internal energy of the mixture, u_m

$$u_m = x_{th}\, u_G + (1 - x_{th}) u_L, \quad (14)$$

and the specific mixture volume, v_m

$$v_m = x_{th}\, v_G + (1\rho\, x_{th}) v_L = 1/\rho_m. \quad (15)$$

u_m would be the specific internal energy content, and v_m would be V divided by the total mass content, respectively of our non-equilibrium (mechanical and thermal) system. Eq.(15) would highlight again the close connection between actual mean void fraction measurements through X-ray or gamma-ray attenuation and the actual vapor mass fraction i.e., x_{th}.

However for the rest of the extensive and intensive thermodynamic properties of our thermodynamic system herewe will follow the Law of Stable Equilibrium (LSE) proposed by Hastopoulos and Keenan [11] and commented by Haywood [8], closely connected to classic equilibrium Thermodynamics.

The LSE allows define a unique equilibrium state corresponding to any non-equilibrium one. Thus, at difference from extended non-equilibrium Thermodynamics [9], the mixture equilibrium temperature, an intensive property, can be clearly obtained from measurements and thermodynamic tables, as we have already shown in [12].

Finally, using the accurate void fraction measurements of General Electric taken in the sixties [13], the mixture properties in these equilibrium states can be compared with the applied heat.

The main results are two: first, the standard heat balance, Eq. (10), cannot explain at all the complex subcooled flow boiling physics. Second, to balance heat with the equilibrium mixture enthalpy increment, a parameter should be included. It is suggested that it could be the slip ratio. This was already proposed in a preliminary work [14].

GENERAL ELECTRIC DATA-TASK I

Under Task I of an experimental program conducted by General Electric for the join U.S.-Euratom Research and Development Program [13], the measurement of the initiation and early development of the subcooled void profile was carried out, including all required profile measurements and observations, with low-pressure water (0.12-0.31 MPa). A vertical, one-side uniformly heated ten-to-one aspect ratio, rectangular cross section of D_h=0.01385 m (0.5454") was employed to permit the accurate measurements of transverse and axial void fraction profiles (with an accuracy of ±3% voids), and liquid phase temperature profiles (±0.1ºC). The measurement accuracy of test section heat addition and flowrate was 1 %. The test section was 0.0762 m x 0.00762 m x 0.3429 m-long (3" x 0.3 " x 13.5"). It was used to satisfy a maximum heat flux capability of 3.15 MW/m^2 (10^6 Btu/hr-ft^2), and a maximum mass velocity of 3391 kg/s-m^2 ($2.5*10^6$ lb/hr-ft^2).

In the final report, Staub et al. [13] gave the general data for each run namely, inlet conditions, uniform heat flux applied, average heater surface

temperature, and the average pressure gradient in the first and second half of the channel. Also for each run, the cross-sectional averages of the saturation temperature (so pressure), subcooling (so liquid temperature), and vapor void fraction along the height of the channel –normally four to six positions- were reported. These cross-sectional averages of void fraction and liquid temperature were worked out by the own authors through numerical integration of the measured transversal profiles at each cross section, which were also presented in the report. The liquid temperatures transversal profile normally included ten points, whereas for the vapor void fraction about seven transversal measurements were taken. Both were non-symmetric due to the one-side heating. In this work, it is assumed the same pressure for the two phases [1-7, 13].

THE LAW OF STABLE EQUILIBRIUM (LSE)

The Law of Stable Equilibrium (LSE) states [8, 11] that when a system, which remains subject to a fixed set of constraints and has an upper bound in volume, is in some non-equilibrium allowed state and is then suddenly isolated from its environment, the system would always ultimately settle to one and the same stable state.

Then the energy of a system in a non-equilibrium state is defined as being equal to the energy of that stable state to which the system would ultimately settle if it were suddenly isolated from its environment and the constraints to which it was subject remained unaltered.

As these final states will be equilibrium ones, to know the final stable state (all the properties of this state) we can enter in thermodynamic tables [15] with the two fixed constraints-properties (u_m, v_m), calculated with Eqs. (14)-(15) i.e., $u_{eq} = u_m$ and $v_{eq} = v_m$ and read the rest of equilibrium properties.

This would be equivalent to isolate our system with rigid, adiabatic and non-permeable walls thus ensuring through the LSE that the internal energy of the original equilibrium state is equal to the energy of the equilibrium state to which the system would ultimately settle down. In this case, the environment would rest unaltered.

However this would not be exactly true due to the kinetic terms. In task I, the greatest inlet liquid velocity was 2.9 m/s, i.e., 0.0042 kJ/kg. However the energy we should add to the final equilibrium energy by, for example, the deceleration of the liquid until reaching the vapor velocity, so getting mechanical equilibrium, would be much more lesser. It is necessary to have into account that the 'slip' ratio in subcooled flow boiling is about 0.9 [1-2].

For mass systems in the subcooled region but with a net content of vapor, we have checked that the equilibrium state results in saturation, this saturation temperature being nearly equal to the non-equilibrium subcooled liquid one, although now the equilibrium pressure is clearly lower than the non-equilibrium one.

$$p_{eq} < p. \tag{16}$$

Due to the low pressures used in these tests, the equilibrium enthalpy is almost equal (differing from the second or third decimal figure) to the non-equilibrium one calculated as

$$h_{eq} - h_m = x_{th} h_G + (1 - x_{th}) h_L. \tag{17}$$

Finally the so-called 'equilibrium' quality definition [1-7], which would take a negative value at this state chosen as example, is not supported. The equilibrium quality is logically positive and extremely low, and slightly different from the calculated one in the non-equilibrium state through the measured void fraction and the corresponding densities. Although highlight that the void fraction in equilibrium is practically equal to the non-equilibrium one.

HEAT BALANCE FROM MEASUREMENTS

Now we are going to check against these accurate measurements the actual energetic relation between the mixture enthalpy h_m with the specific linear heat applied q'. We should search for some relation between the mixture enthalpy slope and q' i.e., $dh_m/dz \sim q'$.

Figures 1 to 8 compares the standard heat balance, Eq. (10) (straight red line), with the evolution of h_m, Eq. (19) (black line), and that of h_L (blue line) along the heated channel for several tests of General Electric-Task I [13]. The conditions of the tests analyzed are shown in Table 1.

# Test	p_i [MPa]	$c_{L,i}$ [m/s]	G [kg/m^2-s]	$-T_{sub,i}$ [º C]	q'' [kW/m^2]	q' [kJ/kg-m]	$T_{sat,i}$ [º C]	$T_{wall,av}$ [ºC]
1–S–45	0.129	2.92	2848.0	30.8	315.4	14.1	106.8	93.9
1-T-55	0.119	0.36	345.8	11.3	753.7	276.5	104.5	130.6
1-T-65	0.117	0.71	683.6	10.7	734.8	136.4	104.0	134.6
1-T-66	0.12	0.36	349.9	11.4	728.5	264.1	104.9	136.1
1-T-71	0.136	0.96	922.3	7.8	725.3	99.8	108.4	138.3
1-T-72	0.308	0.37	343.1	9.2	369.0	136.4	134.4	151.7
1-T-76	0.309	0.36	343.1	12.1	737.9	272.8	134.5	161.1
1_T-84	0.305	0.36	343.1	9.2	422.6	158.1	134.1	160.6

Table 1. Conditions of the tests reaching saturation in Task I of General Electric [14]

In all these tests, saturation was clearly reached or nearly. The exception is test 1-S-45, in which no vapor was formed i.e., it was a single flow. The energy balance closure for this single flow through measurements is excellent, confirming the outstanding accuracy of the data taken.

For the rest of tests, the behavior of subcooled flow boiling is quite surprising in reaching saturation and, until the knowledge of the author, never reported before.

First, the subcooled liquid enthalpy h_L (in blue) is greater than the linear specific heat applied ($q'*z+h_{L,i}$, in red). Thus at subcooling, the slope of mixture enthalpy h_m, Eq. (19), (in black) is also greater than q'. This experimental finding would invalidate the standard heat balance, which would give negative 'flow' qualities, Eq. (10).

Then when liquid reaches saturation, the mixture enthalpy suffers such a dramatic change that the h_m slope becomes lower than q'.

This strong change of slope could be physically justified because the mixture reaches thermal equilibrium.

Therefore, for uniformly applied heat flux at steady state, the standard heat balance could not respond at all to this abrupt slope change, see Eq. (9).

Elsewhere the author has already suggested including explicitly the slip ratio S in the heat balance of subcooled [14] and saturated [16] flow boiling,

$$q' z / S \sim \Delta h_m . \qquad (19).$$

Eq. (19) would allow follow the physical behavior of the flow boiling because in reaching saturation the slip ratio changes [1-7]. So for subcooled flow boiling, photographic measurements have shown a slip ratio about 0.9 (less than one) [2].

For saturated flow boiling the slip ratio is greater than one, lower the pressure greater the slip ratio [1-2, 16].

A possible justification [14, 16] of this new proposal could be the fact that we are treating two different velocities (vapor and liquid) in the same control volume i.e., the same length. Then it is impossible that they cover the same distance at the same time. Thus the slip ratio would also be a time scale ratio, acting as a time scale conversion factor between the phases.

Eq. (19) would reflect the fact that heat enters in the control volume through condensing bubbles migrating from the heated wall i.e., entering with the vapor time scale.

Modeling the mixture enthalpy in flow boiling

The change of the mixture enthalpy slope in Figures 2 to 8 suggests using two different slip ratios: S_1 for the subcooled zone and S_2 for saturation. So the heat balance at subcooling

$$h_m = q' z / S_1 + h_{L,i} \quad - \quad S_1 = q' z / \left(h_m - h_{L,i} \right) . \quad (20).$$

After saturation, the energetic relation would be

$$h_m = q' \left(z = z_{sat} \right) / S_2 + h_m \left(z_{sat} \right) \Rightarrow$$
$$S_2 = q' \left(z = z_{sat} \right) / \left[h_m = h_m \left(z_{sat} \right) \right] . \qquad (21).$$

From Figures 2-8, it is clear that z_{sat} could be

$$h_F - q' z_{sat} + h_{L,i} \quad - \quad z_{sat} - \left(h_F - h_{L,i} \right) / q' . \quad (22).$$

Then substituting Eqs. (20) and (22) in Eq. (21), we had

$$S_2 = \left[q' z - \left(h_F - h_{L,i}\right)\right] \Big/ \left[h_m - h_{L,i} - \left(h_F - h_{L,i}\right)/S_{1,sat}\right] . \quad (23).$$

Figures 9-15 show the evolution of S_1, S_2 (assuming $S_{1,sat} \approx 1$) and S, Eq. (6).

At full saturation, note that S_2, Eq. (23), assuming $S_{1,sat} \approx 1$, coincides with the standard S, Eq. (6), which has been calculated with the 'flow' quality x from Eq. (11) and including the measured void fraction –.

Finally, Figure 16 would confirm the role of the slip ratio as a time scale factor between the phases, the quotient between 'flow' quality and thermodynamic quality being the standard slip ratio. Notice that the 'flow' quality and so the standard slip ratio takes negative values at subcooling.

REFERENCES

[1] Bergles AE, Collier JG, Delhaye JM, Hewitt G, Mayinger F. *Two-phase flow and heat transfer in the power and process industries*. Washington: Hemisphere, 1981.

[2] Collier JG, Thome JR. *Convective boiling and condensation*, third ed. Oxford: Clarendon Press, 1994.

[3] Lahey Jr. RT, Moody FJ. *The thermal hydraulics of a boiling water nuclear reactor*, LaGrange Park: American Nuclear Society, 1977.

[4] Situ R, Hibiki T, Sun X, Mi Y, Ishii M. *Flow structure of subcooled boiling flow in an internally heated annulus*. International Journal of Heat and Mass Transfer 2004; 47:5351-5364.

[5] Delhaye JM, Maugin F, Ochterbeck JM. *Void fraction predictions in forced convective subcooled boiling of water between 10 and 18 MPa*. International Journal of Heat and Mass Transfer 2004;47:4415-4425.

[6] Levy S. *Forced convection subcooled boiling-prediction of vapor volumetric fraction*. International Journal of Heat and Mass Transfer 1967;19(1):99-113.

[7] Zuber N, Findlay JA. *Average volumetric concentration in two-phase flow systems*. Journal of Heat Transfer-Transactions of ASME 1965;87:453-468.

[8] Haywood RW. *Equilibrium Thermodynamics for engineers and scientists*. New York: Wiley, 1980.

[9] Bilicki Z, Giot M, Kwidzinski R. *Fundamentals of two-phase flow by the method of irreversible thermodynamics*. International Journal of Multiphase Flow 2002;28:1983-2005.

[10] Bilicki Z, Michaelides EE. *Thermodynamic nonequilibrium in liquid-vapour flows*. Journal of Non-Equilibrium Thermodynamics 1997;22:99-109.

[11] Hatsopoulos GN, Keenan JH. *Principles of general Thermodynamics*. Malabar: Krieger, 1983 reprint [original edition published 1965].

[12] Collado FJ. *The law of stable equilibrium and the entropy-based boiling curve for flow boiling*. Energy 2005; 30: 807-819.

[13] Staub FW, Wamet GE, Niemi RO. *Heat transfer and hydraulics-the effects of subcooled voids,* final report. New York: General Electric, NYO-3679-8, 1969.

[14] Collado FJ. *Mixture enthalpy in subcooled boiling flow*. Transactions of American Nuclear Society 2000;82: 254-256.

[15] The International Association for the Properties of Water and Steam (IAPWS). *The 1995 formulation for the thermodynamic properties of ordinary water substance for general and scientific use.* 1995.

[16] Collado FJ. *Mass quality, void fraction and slip ratio in bulk flow boiling.* In: Symposium on Fluid Physics and Heat Transfer for Macro- and Micro-Scale Gas-Liquid and Phase Change Flows, Proceedings of ASME IMECE 2001, New York, 2001.

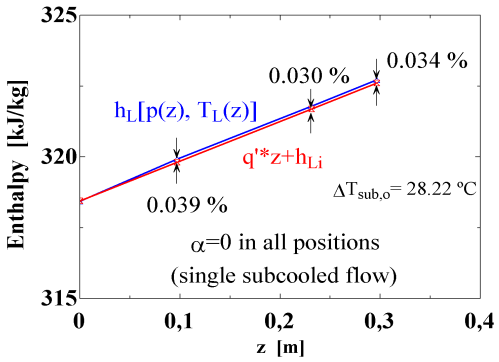

Figure 1: Closure of heat balance for Test 1-S-45

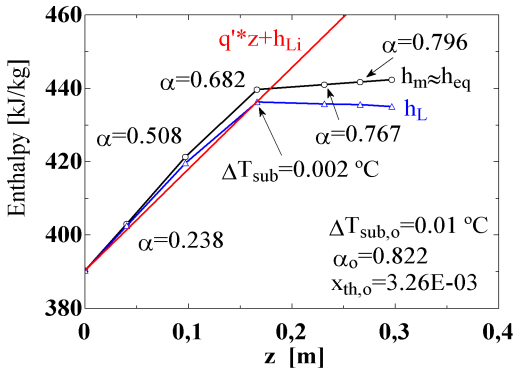

Figure 2: Closure of heat balance for Test 1-T-55

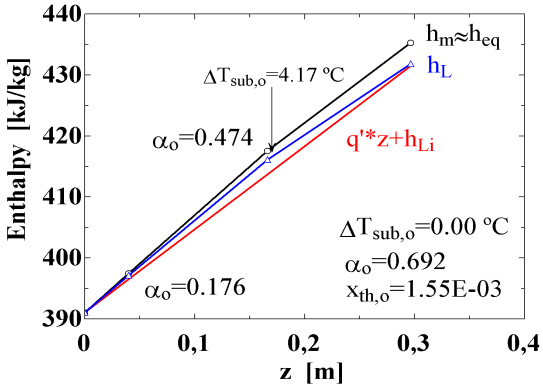

Figure 3: Closure of heat balance for test 1-T-65

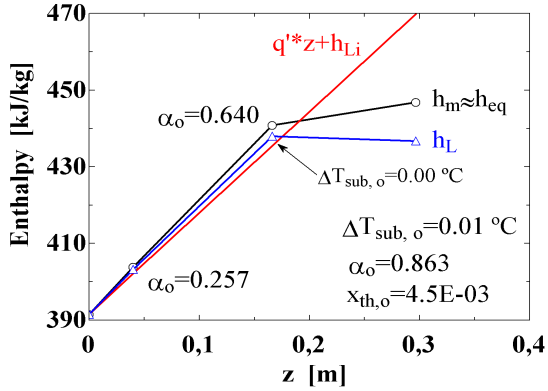

Figure 4: Closure of heat balance for test 1-T-66

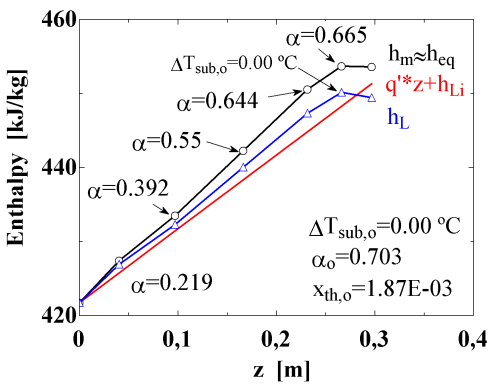

Figure 5: Closure of heat balance for test 1-T-71

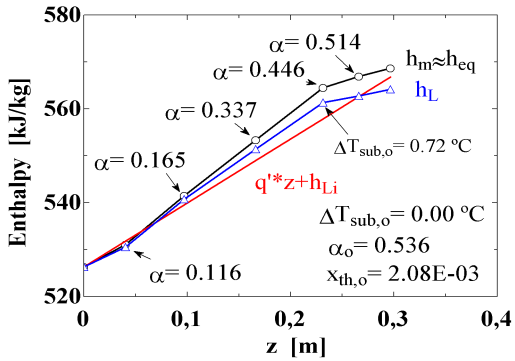

Figure 6: Closure of heat balance for test 1-T-72

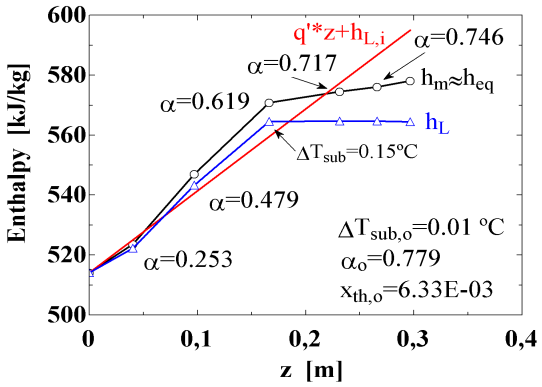

Figure 7: Closure of heat balance for test 1-T-76

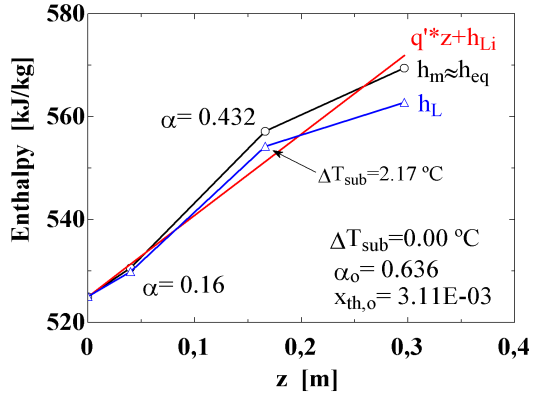

Figure 8: Closure of heat balance for test 1-T-84

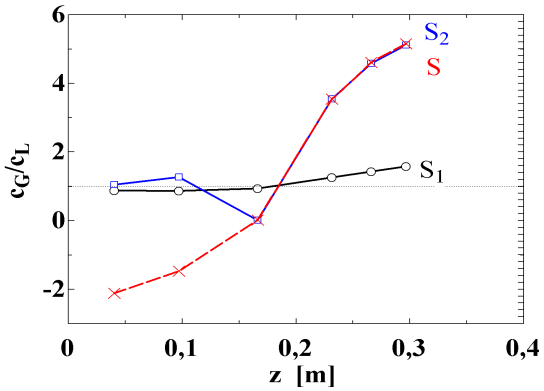

Figure 9: Slip ratios for Test 1-T-55

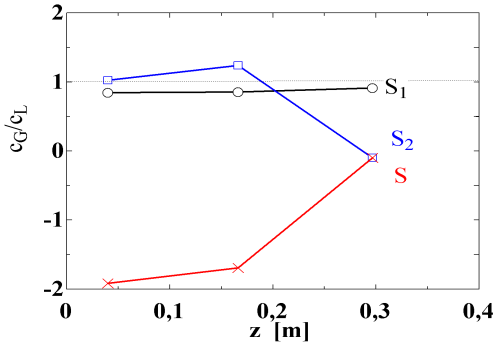

Figure 10: Slip ratios for Test 1-T-65

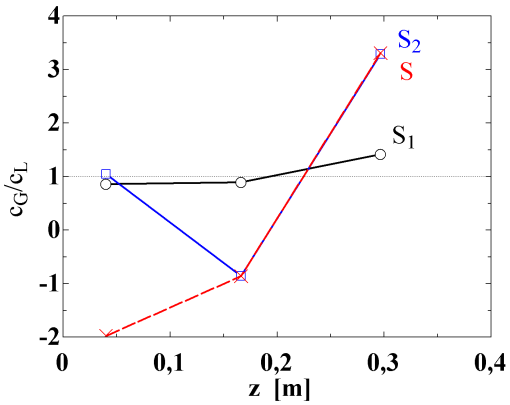

Figure 11: Slip ratios for Test 1-T-66

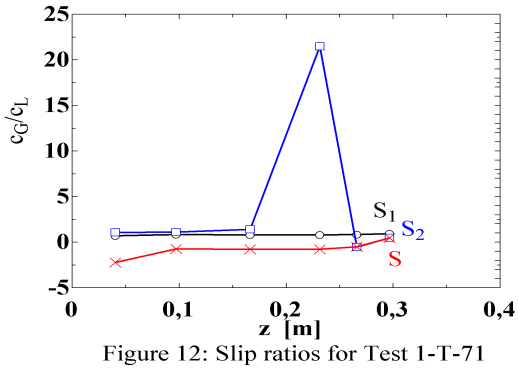

Figure 12: Slip ratios for Test 1-T-71

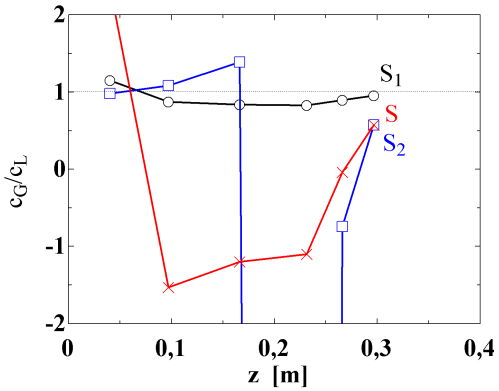

Figure 13: Slip ratios for Test 1-T-72

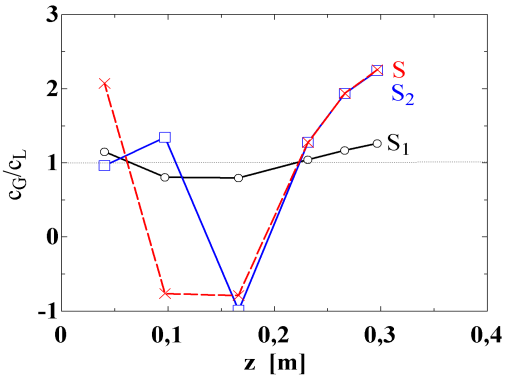

Figure 14: Slip ratios for Test 1-T-76

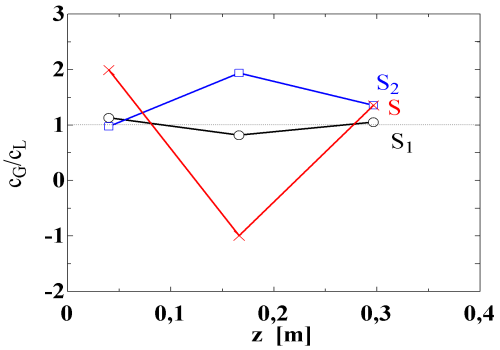

Figure 15: Slip ratios for Test 1-T-84

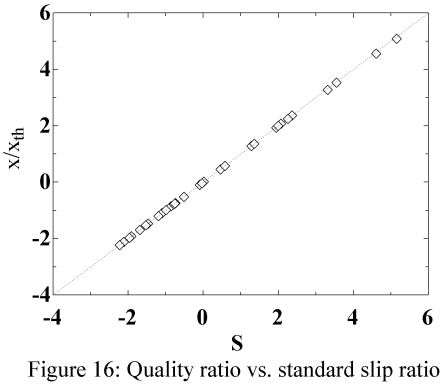

Figure 16: Quality ratio vs. standard slip ratio

Proceedings of ECOS 2005
Trondheim, Norway
June 20–22, 2005

ACTIVE TRANSPORT IN SLIPPING BIOLOGICAL PUMPS

S. Kjelstrup [*], J.M. Rubi[§] and D. Bedeaux
Department of Chemistry, Faculty of Natural Science and Technology,
Norwegian University of Science and Technology, Trondheim, 7491- Norway,
[§] Department de Fisica Fonamental, Universitat de Barcelona,
Diagonal 647, 08028 Barcelona, Spain

ABSTRACT

We present a model for active transport in cation pumps in biological membranes, using mesoscopic nonequilibrium thermodynamics. The model describes energy dissipation and slippage in the pump under isothermal as well as nonisothermal conditions. Coupling of scalar and vectorial processes, like reactions and diffusion, must for symmetry reasons, take place at the membrane surface. They are governed by the excess entropy production of the surface. We take as example the well studied active transport of Ca^{2+} across a biological membrane by means of its ATPase, and find expressions for the entropy production of pumps at static head, for tight as well as slipping pump conditions.
Keywords: Active transport, slippage, scalar-vectorial coupling, stochastic processes.

NOMENCLATURE

c_j	concentration, mol/mg protein
D_{ij}	diffusioncoefficient in γ-space
$G_i(\gamma)$	Gibbs energy of ensemble at position γ
ΔG	Gibbs energy of reaction, J/mol
H_k	partial molar enthalpy of k, J/mol
ΔH	enthalpy of reaction, J/mol
i	phase i, left of the interface
J_k	flux of component k, mol/s mg
J'_q	flux of heat, J/s mg
J_q	total heat flux, J/s mg
J_s	flux of entropy, J/K s mg
l_{ij}	phenomenological coefficient
n	number of components
o	phase o, right of the interface
r	reaction rate, mol/s mg
s^s	entropy density of surface, J/K mg
T	temperature, K
u^s	energy density of surface, J/mg
z	fugacity of phosphorylated enzyme ensemble
γ	dimensionless internal coordinate
ϕ	activation energy barrier, J/mol
μ_k	chemical potential of k, J/mol
σ^s	entropy production of surface, J/K mg

[*]Corresponding author: Telephone 47 75594179, email: signekj@phys.chem.ntnu.no

INTRODUCTION

The aim of the present work is to describe the energy dissipation and coupling that takes place in biological membranes. In particular we want to describe the slipping of these pumps, not only for isothermal conditions, but also for nonisothermal conditions. A slipping pump, in contrast to a tight one, does not deliver to the other side of the membrane, a constant number of ions per adenosine tri phosphate molecule (ATP) reacted. It is well documented that the heat production during pump operation is significant and varies (de Meis et al.,1997), and we want to make a connection between this energy dissipation and the slipping pump. Berman (2001) summarized the understanding of slipping pumps in a recent review. No systematic theory is available for a description of socalled “non-shivering thermogenesis”. The common Post-Albers scheme based on chemical kinetics (see e.g. Peinelt and Apell, 2004) does neither address coupling, nor energy dissipation or slippage. The aim of this article is to provide a theoretical basis for measurements of slip at isothermal and nonisothermal conditions, by showing how tight and slipping pumps can be characterised by their entropy production. We have recently used mesoscopic non-equilibrium thermodynamics (MNET) to derive a non-linear equation for

active transport across biological membranes (Kjelstrup et al., 2005), an equation that is consistent with many experimental observations. In this manner a theoretical description of this important phenomenon was obtained, and a long-standing problem with the theory of non-equilibrium thermodynamics (NET) (Caplan and Essig, 1983; Westerhoff and van Dam, 1987; Walz, 1990) was resolved. We were able to show that *non-linear* flux-force relations are normal for such transport phenomena, and that they also are completely in accordance with Onsager's original principles. This work is a continuation of this work. We take as example the well studied (Berman, 2001) active transport of Ca^{2+}, across a biological membrane by means of its ATPase. Calcium ions are transported across the membrane against a chemical potential difference, from side (i) to side (o), via the surface (s), for a wide range of solute concentrations:

$$Ca^{2+}(\mathrm{i}) \rightleftharpoons Ca^{2+}(\mathrm{s}) \rightleftharpoons Ca^{2+}(\mathrm{o}) \qquad (1)$$

Counter-transport of protons maintains electroneutrality (Peinelt and Apell, 2004). The rate of transport can be large, up to 8 10^{-8} mol/s mg (Berman, 2001), mainly because the density of ATPases in the membrane is so high (Peinelt and Apell, 2004). The transport obtains energy from the hydrolysis of ATP on the membrane surface:

$$\mathrm{ATP}(\mathrm{s}) \rightleftharpoons \mathrm{ADP}(\mathrm{s}) + \mathrm{P}(\mathrm{s}) \qquad (2)$$

The coupling must, for symmetry reasons, take place in the *membrane surface*, according to the Curie principle (Albano and Bedeaux, 1987). The reaction Gibbs energy of the hydrolysis reaction is ca. -56 kJ/mol (Berman, 2001):

$$\Delta G^{\mathrm{s}} = \mu^{\mathrm{s}}_{\mathrm{P}} + \mu^{\mathrm{s}}_{\mathrm{ADP}} - \mu^{\mathrm{s}}_{\mathrm{ATP}} \qquad (3)$$

The charge numbers have been omitted in the subscripts. The total process has a very high activation energy, 80-90 kJ/mol, attributed to the enzyme conformational changes that are required for the transport (Peinelt and Apell, 2004). The molecular mechanism involves most likely a gradually increasing bond between ATP and the ATPase and a rotation of the enzyme "shaft" (Sun et al., 2004). A realistic theory for active transport must describe:

1. The large degree of coupling between the ion transport and chemical reaction, and the reversible property of the pump
2. The stochastic nature of the pump.
3. The energy dissipation in the system
4. The constant performance of tight pumps at small net driving forces

We shall take as a starting point the excess entropy production rate for the surface (Albano and Bedeaux, 1987) found by NET. The normal component of a three-dimensional vector into the surface has the symmetry of a scalar at the surface, and coupling is therefore possible between a scalar chemical reaction and a vectorial process here and *only here.* We shall then see that MNET enables us to go beyond the overall or 'black box' description of the membrane offered by NET. MNET allows us to use Onsager's formalism on the mesoscopic level. It describes processes like the present one, where one must consider a distribution over states of the ATPase enzymes for the distribution of the reactants, the adsorbed Ca^{2+}-ions and the temperature.

THE MEMBRANE SURFACE

The membrane surface is the layer next to the biological membrane, for which we can define excess thermodynamic variables. It consists of the phospholipids and enzymes in the layer, plus adsorbed water, ions, reactants and products. We assume *local equilibrium* in this layer, meaning that all normal thermodynamic relations apply for the surface excess variables. The gradients across the thin biological membrane are enormous (about 10^8 V/m for the electric field), but various evidence is emerging that the assumption of local equilibrium in the surface is good (Røsjorde et al., 2000; Johannessen and Bedeaux, 2003). Local thermodynamic equilibrium in the surface does not necessarily imply that there is *chemical* equilibrium. The Gibbs equation for the surface element is:

$$ds^{\mathrm{s}} = \frac{1}{T^{\mathrm{s}}}du^{\mathrm{s}} - \frac{\mu^{\mathrm{s}}_{\mathrm{ATP}}}{T^{\mathrm{s}}}dc^{\mathrm{s}}_{\mathrm{ATP}} - \frac{\mu^{\mathrm{s}}_{\mathrm{ADP}}}{T^{\mathrm{s}}}dc^{\mathrm{s}}_{\mathrm{ADP}} - \frac{\mu^{\mathrm{s}}_{\mathrm{P}}}{T^{\mathrm{s}}}dc^{\mathrm{s}}_{\mathrm{P}} - \frac{\mu^{\mathrm{s}}_{\mathrm{Ca}}}{T^{\mathrm{s}}}dc^{\mathrm{s}}_{\mathrm{Ca}} \qquad (4)$$

where s^{s} the excess surface entropy density, T^{s} is the temperature of the surface, u^{s} is the excess energy density, μ^{s}_j is the chemical potential at the surface of component j, and c^{s}_j the excess surface density. All densities or concentrations, as well as fluxes, are

given per mg of protein studied. This assumes that the surface area is proportional to the amount of enzyme. We assume that the total entropy of the surface and the i-side is unaltered if the various components are moved from the i-side to the surface and back, without moving internal energy (partial equilibrium for the adsorption/desorption, cf. deGroot and Mazur, 1984, Ch.15). This implies that: $\mu_j^{\mathrm{s}}/T^{\mathrm{s}} = \mu_j^{\mathrm{i}}/T^{\mathrm{i}}$. On the other side of the surface, we assume that internal energy can be moved, without moving ions, to the o-side without altering the entropy. This implies that $T^{\mathrm{s}} = T^{\mathrm{o}}$. The Gibbs equation becomes

$$ds^{\mathrm{s}} = \frac{1}{T^{\mathrm{o}}}du^{\mathrm{s}} - \frac{\mu^{\mathrm{i}}_{\mathrm{ATP}}}{T^{\mathrm{i}}}dc^{\mathrm{s}}_{\mathrm{ATP}} - \frac{\mu^{\mathrm{i}}_{\mathrm{ADP}}}{T^{\mathrm{i}}}dc^{\mathrm{s}}_{\mathrm{ADP}} - \frac{\mu^{\mathrm{i}}_{\mathrm{P}}}{T^{\mathrm{i}}}dc^{\mathrm{s}}_{\mathrm{P}} - \frac{\mu^{\mathrm{i}}_{\mathrm{Ca}}}{T^{\mathrm{i}}}dc^{\mathrm{s}}_{\mathrm{Ca}} \qquad (5)$$

The Gibbs reaction energy then becomes $\Delta G^{\mathrm{i}} = \mu^{\mathrm{i}}_{\mathrm{P}} + \mu^{\mathrm{i}}_{\mathrm{ADP}} - \mu^{\mathrm{i}}_{\mathrm{ATP}}$. This quantity can be found by experiments.

THE EXCESS ENTROPY PRODUCTION RATE IN THE SURFACE

The excess entropy production rate for the surface, σ^s, is determined the normal way (de Groot and Mazur, 1984), by substituting the first law and the mass balances into Gibbs equation, and comparing the result with the entropy balance:

$$\frac{ds^{\mathrm{s}}}{dt} = -J_s^{\mathrm{o}} + J_s^{\mathrm{i}} + \sigma^s \qquad (6)$$

Here J_s^{i} and J_s^{o} are the entropy fluxes in and out of the surface. The result for the excess entropy production rate is:

$$\sigma^{\mathrm{s}} = J_q^{\mathrm{i}}\left(\frac{1}{T^{\mathrm{o}}} - \frac{1}{T^{\mathrm{i}}}\right) - r\frac{1}{T^{\mathrm{i}}}\Delta G - J^{\mathrm{o}}_{\mathrm{Ca}}\left(\frac{\mu^{\mathrm{o}}_{\mathrm{Ca}}}{T^{\mathrm{o}}} - \frac{\mu^{\mathrm{i}}_{\mathrm{Ca}}}{T^{\mathrm{i}}}\right) \qquad (7)$$

where J_q^{i} is the total heat flux into the surface from the i-side, r is the reaction rate and $J^{\mathrm{o}}_{\mathrm{Ca}}$ is the calcium flux out of the surface to the o-side. The total heat flux, J_q^{l}, is the sum of the measurable heat flux and the partial molar enthalpies carried along with the components, and it is also equal to the temperature times the entropy flux plus the chemical potentials carried along with the components.

$$J_q^{\mathrm{l}} = J_q'^{\mathrm{l}} + \sum_k H_k^{\mathrm{l}} J_k^{\mathrm{l}} = T^{\mathrm{l}} J_s^{\mathrm{l}} + \sum_k \mu_k^{\mathrm{l}} J_k^{\mathrm{l}} \qquad (8)$$

Here k refers to all components, and l = i or o. All expressions on a finer level of description must integrate to give Eq.(7). In active transport, the last term in the entropy production rate is negative due to the concentration differences (the entropy differences) between the two sides, while the term containing the reaction Gibbs energy is positive and more than double the value of the last term (Berman, 2001).

The resistance to transport of Ca^{2+} in the channel leading to side o from the surface is small. The entropy production rate in the channel can therefore be neglected, and the entropy production rate given in Eq.(7) therefore applies to the whole membrane. Equation (7) is not detailed enough for our purpose, however. We proceed to give a finer description of for σ^s valid at the mesoscopic level.

A MESOSCOPIC DESCRIPTION

The transduction of energy from the chemical reaction to transport, is a stochastic process, where fluctuations in state variables play a crucial role. We introduce the familiar reaction coordinate γ, introduced by Eyring and Eyring (1965), in order to address the distribution over states along this coordinate for each enzyme (Ca^{2+}-ATPase). We use the concentration, $c_r(\gamma)$, of enzymes with a given coordinate γ. The dimensionless reaction coordinate γ has values between 0 (the start) and 1 (the end) of the reaction. We consider also the concentration, $c^{\mathrm{s}}_{\mathrm{Ca}}(\gamma)$, of Ca^{2+} bound to enzymes with a given coordinate. Both concentrations are in mol/mg. They are, in principle, independent of each other. Furthermore we use the internal energy, $u^{\mathrm{s}}(\gamma)$, of the enzymes with a coordinate γ.

The Gibbs equation written for a state γ on this scale is:

$$ds^{\mathrm{s}}(\gamma) = \frac{du^{\mathrm{s}}(\gamma)}{T^{\mathrm{s}}(\gamma)} - \frac{G^{\mathrm{s}}(\gamma)}{T^{\mathrm{s}}(\gamma)}dc_r(\gamma) - \frac{\mu^{\mathrm{s}}_{\mathrm{Ca}}(\gamma)}{T^{\mathrm{s}}(\gamma)}dc^{\mathrm{s}}_{\mathrm{Ca}}(\gamma) \qquad (9)$$

In order to regain the excess variables for the whole surface, one has to integrate the γ dependent variables over γ. The function $G^{\mathrm{s}}(\gamma)$ decreases monotonously with γ. Were it not for the coupling between the phenomena, it would give a purely dissipative contribution to σ^{s}. We again assume that the entropy does not change when we move ATP, ADP and P from the i-side to the surface or back, so that $\mu_j^{\mathrm{s}}(0)/T^{\mathrm{s}}(0) = \mu_j^{\mathrm{s}}(1)/T^{\mathrm{s}}(1) = \mu_j^{\mathrm{i}}/T^{\mathrm{i}}$. For Ca^{2+}

we assume $\mu^{\rm s}_{Ca}(\gamma)/T^{\rm s}(\gamma) = \mu^{\rm i}_{Ca}/T^{\rm i}$. We furthermore assume that the entropy does not change when we move internal energy from the surface to the o-side. This implies that $T^{\rm s}(\gamma) = T^{\rm o}$. These assumptions are extensions of the assumptions made above Eq.(5). We finally define $G(\gamma)/T^{\rm i} = G^{s}(\gamma)/T^{\rm s}(\gamma)$. The Gibbs equation then becomes

$$ds^{\rm s}(\gamma) = \frac{du^{\rm s}(\gamma)}{T^{\rm o}} - \frac{G^{\rm i}(\gamma)}{T^{\rm i}} dc_r(\gamma) - \frac{\mu^{\rm i}_{\rm Ca}}{T^{\rm i}} dc^{\rm s}_{\rm Ca}(\gamma) \tag{10}$$

At the beginning and end of the coordinate, the Gibbs energies are $G^{\rm i}(0) = \mu^{\rm i}_{\rm ATP}$ and $G^{\rm i}(1) = \mu^{\rm i}_{\rm P} + \mu^{\rm i}_{\rm ADP}$, respectively. Along the reaction coordinate, it is customary in MNET to write the Gibbs energy as a combination of the activation energy per mole of mixture, $\Phi(\gamma)$, and an (ideal) contribution to the energy, $RT \ln c_r(\gamma)/c^o$. Here c^o is a standard concentration. For the potential profile, correct boundary conditions for $G^{\rm i}(\gamma)$ are obtained with $\Phi(0) = \mu^0_{\rm ATP}$ and $\Phi(1) = \mu_{\rm ADP^0_P}$. The activation energy has a large maximum at the transition state, γ_{tr} (Peinelt and Apell, 2004). At this peak, the concentration $c_{tr}(\gamma)$ is correspondingly low. The dimensionless fugacity of the ensemble of phosphorylated enzymes is:

$$z(\gamma) = \exp[G^{\rm i}(\gamma)/RT^{\rm i}] = \frac{c_r(\gamma)}{c^o} \exp[\Phi(\gamma)/RT^{\rm i}] \tag{11}$$

In equilibrium, $G^{\rm i}(\gamma) = G_{eq}$ and $T^{\rm i} = T_{eq}$ and therefore $z(\gamma) = z_{eq}$ is constant. It follows that

$$c_{eq}(\gamma)/c^o = z_{eq} \exp[-\Phi(\gamma)/RT_{eq}] \tag{12}$$

The balance of the entropy along the γ-coordinate is

$$\frac{ds^{\rm s}(\gamma)}{dt} = \sigma^{\rm s}(\gamma) - \frac{\partial}{\partial\gamma} J_s(\gamma) + J^{\rm i}_s(\gamma) - J^{\rm o}_s(\gamma) \tag{13}$$

The entropy change along the γ-coordinate is equal to the entropy production rate, $\sigma^{\rm s}(\gamma)$, minus the divergence of an entropy flux along the γ-coordinate, plus the entropy flux into the element from the i-side, $J^{\rm i}_s(\gamma)$, and from the element into the o-side, $J^{\rm o}_s(\gamma)$, respectively. Equation (13) is the most general form for a balance equation along the γ-coordinate. When an enzyme changes its state γ entropy is not only produced, but also carried along. Furthermore internal energy and Ca^{2+} ions can go from an enzyme in the state γ directly into the i- or the o-phase. The pump slips if the ion goes to the i-phase. The transports produce entropy (heat) and give entropy flows into these phases. All excess densities of the surface are given by integrals of the corresponding densities along the γ coordinate. For the excess entropy of the surface and the excess entropy production rate we therefore have

$$s^{\rm s} = \int_0^1 s^{\rm s}(\gamma) d\gamma \quad \text{and} \quad \sigma^{\rm s} = \int_0^1 \sigma^{\rm s}(\gamma) d\gamma \tag{14}$$

THE MODEL

Enzymes in the state γ change their state only by the reaction flux along the γ coordinate, this gives Eq.(15a). The Ca^{2+} ions do not flow along the γ-coordinate. They are bound to and escape from an enzyme in the state γ directly. This gives Eq.(15b).

$$\frac{dc_r(\gamma)}{dt} = -\frac{\partial r(\gamma)}{\partial\gamma} \quad \text{and} \quad \frac{dc^{\rm s}_{\rm Ca}(\gamma)}{dt} = J^{\rm i}_{\rm Ca}(\gamma) - J^{\rm o}_{\rm Ca}(\gamma) \tag{15}$$

The fluxes of calcium ions used in Eq.(7), $J^{\rm i}_{\rm Ca}$ and $J^{\rm o}_{\rm Ca}$, are obtained by integrating $J^{\rm i}_{\rm Ca}(\gamma)$ and $J^{\rm o}_{\rm Ca}(\gamma)$ over γ. The reaction rate along the γ coordinate satisfies the boundary condition $r(0) = r(1) = r$ where r is the reaction rate in Eq.(7). The internal energy balance contains the total heat fluxes.

$$\frac{du^{\rm s}(\gamma)}{dt} = J^{\rm i}_q(\gamma) - J^{\rm o}_q(\gamma) \tag{16}$$

There is no such heat flux along the γ coordinate. These expressions are now introduced into the Gibbs equation 9 and the result is compared with the balance equation (13) for the entropy. We can then, after some algebra, identify the net entropy fluxes

$$\begin{aligned} J_s(\gamma) &= -r(\gamma)\frac{G(\gamma)}{T^{\rm i}} \\ J^{\rm i}_s(\gamma) &= \frac{1}{T^{\rm i}}\left(J^{\rm i}_q(\gamma) - J^{\rm i}_{\rm Ca}\mu^{\rm i}_{\rm Ca}\right) \\ J^{\rm o}_s(\gamma) &= \frac{1}{T^{\rm o}}\left(J^{\rm o}_q - J^{\rm o}_{\rm Ca}(\gamma)\mu^{\rm o}_{\rm Ca}\right) \end{aligned} \tag{17}$$

and the entropy production in γ-space

$$\sigma^{\rm s}(\gamma) = -r(\gamma)\frac{1}{T^{\rm i}}\frac{\partial G(\gamma)}{\partial\gamma} - J^{\rm o}_{\rm Ca}(\gamma)\left(\frac{\mu^{\rm o}_{\rm Ca}}{T^{\rm o}} - \frac{\mu^{\rm i}_{\rm Ca}}{T^{\rm i}}\right) + J^{\rm i}_q(\gamma)\left(\frac{1}{T^{\rm o}} - \frac{1}{T^{\rm i}}\right) \tag{18}$$

This is the expression for the entropy production on the mesoscopic level, for the model. When the probability distribution along the γ coordinate is stationary, $r(\gamma) = r$ is constant and integration of Eq.(18)

over γ gives Eq.(7). In this context, $J_q^{\mathrm{i}}(\gamma)$, $J_s^{\mathrm{o}}(\gamma)$, $J_{\mathrm{Ca}}^{\mathrm{o}}(\gamma)$ integrate out to J_q^{i}, J_s^{o}, $J_{\mathrm{Ca}}^{\mathrm{o}}$. For the entropy flux on the i-side we have, however,

$$J_s^{\mathrm{i}} = \int_0^1 \left[-\frac{\partial}{\partial \gamma} J_s(\gamma) + J_s^{\mathrm{i}}(\gamma) \right] d\gamma \qquad (19)$$

The fluxes and forces on the mesoscopic level

The flux-force relationships that follow from Eq.(18) are:

$$\begin{aligned}
r(\gamma) &= -\frac{l_{rr}(\gamma)}{T^{\mathrm{i}}} \frac{\partial G(\gamma)}{\partial \gamma} - l_{rd}(\gamma)\left(\frac{\mu_{\mathrm{Ca}}^{\mathrm{o}}}{T^{\mathrm{o}}} - \frac{\mu_{\mathrm{Ca}}^{\mathrm{i}}}{T^{\mathrm{i}}}\right) \\
&\quad + l_{rq}(\gamma)\left(\frac{1}{T^{\mathrm{o}}} - \frac{1}{T^{\mathrm{i}}}\right) \\
J_{\mathrm{Ca}}^{\mathrm{o}}(\gamma) &= -\frac{l_{dr}(\gamma)}{T^{\mathrm{i}}} \frac{\partial G(\gamma)}{\partial \gamma} - l_{dd}(\gamma)\left(\frac{\mu_{\mathrm{Ca}}^{\mathrm{o}}}{T^{\mathrm{o}}} - \frac{\mu_{\mathrm{Ca}}^{\mathrm{i}}}{T^{\mathrm{i}}}\right) \\
&\quad + l_{dq}(\gamma)\left(\frac{1}{T^{\mathrm{o}}} - \frac{1}{T^{\mathrm{i}}}\right) \\
J_q^{\mathrm{i}}(\gamma) &= -\frac{l_{qr}(\gamma)}{T^{\mathrm{i}}} \frac{\partial G(\gamma)}{\partial \gamma} - l_{qd}(\gamma)\left(\frac{\mu_{\mathrm{Ca}}^{\mathrm{o}}}{T^{\mathrm{o}}} - \frac{\mu_{\mathrm{Ca}}^{\mathrm{i}}}{T^{\mathrm{i}}}\right) \\
&\quad + l_{qq}(\gamma)\left(\frac{1}{T^{\mathrm{o}}} - \frac{1}{T^{\mathrm{i}}}\right) \qquad (20)
\end{aligned}$$

The Onsager relations are $l_{ij}(\gamma) = l_{ji}(\gamma)$. The coefficients are independent of the forces. From the isothermal case we know that the cross coefficient $l_{rd}(\gamma) = l_{dr}(\gamma)$ is large. Through a non-zero $l_{dq}(\gamma) = l_{qd}(\gamma)$, a low temperature on the i-side promotes transport of Ca^{2+} ions, while conversely a chemical potential difference of the calcium ions leads to heat transport and entropy production. The values of the coefficients that couple the heat flux to the other fluxes are not known. But the foundation is led for a description of thermogenesis, see de Meis et al. (2001).

Transport equations on the macroscopic level

The linear equations (20) give nonlinear laws on the macroscopic level. Substituting Eq.(11) into Eq.(20) gives

$$\begin{aligned}
r(\gamma) &= -\frac{l_{rr}(\gamma) R c^o}{c_r(\gamma) \exp[\Phi(\gamma)/RT^{\mathrm{i}}]} \frac{\partial z(\gamma)}{\partial \gamma} - l_{rd}(\gamma) \\
&\quad \left(\frac{\mu_{\mathrm{Ca}}^{\mathrm{o}}}{T^{\mathrm{o}}} - \frac{\mu_{\mathrm{Ca}}^{\mathrm{i}}}{T^{\mathrm{i}}}\right) + l_{rq}(\gamma)\left(\frac{1}{T^{\mathrm{o}}} - \frac{1}{T^{\mathrm{i}}}\right) \\
J_{\mathrm{Ca}}^{\mathrm{o}}(\gamma) &= -\frac{l_{dr}(\gamma) R c^o}{c_r(\gamma) \exp[\Phi(\gamma)/RT^{\mathrm{i}}]} \frac{\partial z(\gamma)}{\partial \gamma} - l_{dd}(\gamma) \\
&\quad \left(\frac{\mu_{\mathrm{Ca}}^{\mathrm{o}}}{T^{\mathrm{o}}} - \frac{\mu_{\mathrm{Ca}}^{\mathrm{i}}}{T^{\mathrm{i}}}\right) + l_{dq}(\gamma)\left(\frac{1}{T^{\mathrm{o}}} - \frac{1}{T^{\mathrm{i}}}\right) \\
J_q^{\mathrm{i}}(\gamma) &= -\frac{l_{qr}(\gamma) R c^o}{c_r(\gamma) \exp[\Phi(\gamma)/RT^{\mathrm{i}}]} \frac{\partial z(\gamma)}{\partial \gamma} - l_{qd}(\gamma) \\
&\quad \left(\frac{\mu_{\mathrm{Ca}}^{\mathrm{o}}}{T^{\mathrm{o}}} - \frac{\mu_{\mathrm{Ca}}^{\mathrm{i}}}{T^{\mathrm{i}}}\right) + l_{qq}(\gamma)\left(\frac{1}{T^{\mathrm{o}}} - \frac{1}{T^{\mathrm{i}}}\right) \qquad (21)
\end{aligned}$$

Conductivities are normally in good approximation proportional to the concentrations, and we shall use this property. The symmetric d-matrix is then introduced, using:

$$d_{ij} \equiv l_{ij}(\gamma)/c_r(\gamma) \qquad (22)$$

with d_{ij} independent of γ. Equation (21) becomes:

$$\begin{aligned}
r(\gamma) &= -\frac{d_{rr} R c^o}{\exp[\Phi(\gamma)/RT^{\mathrm{i}}]} \frac{\partial z(\gamma)}{\partial \gamma} \\
&\quad - d_{rd} c_r(\gamma)\left(\frac{\mu_{\mathrm{Ca}}^{\mathrm{o}}}{T^{\mathrm{o}}} - \frac{\mu_{\mathrm{Ca}}^{\mathrm{i}}}{T^{\mathrm{i}}}\right) + d_{rq} c_r(\gamma)\left(\frac{1}{T^{\mathrm{o}}} - \frac{1}{T^{\mathrm{i}}}\right) \\
J_{\mathrm{Ca}}^{\mathrm{o}}(\gamma) &= -\frac{d_{dr} R c^o}{\exp[\Phi(\gamma)/RT^{\mathrm{i}}]} \frac{\partial z(\gamma)}{\partial \gamma} \\
&\quad - d_{dd} c_r(\gamma)\left(\frac{\mu_{\mathrm{Ca}}^{\mathrm{o}}}{T^{\mathrm{o}}} - \frac{\mu_{\mathrm{Ca}}^{\mathrm{i}}}{T^{\mathrm{i}}}\right) + d_{dq} c_r(\gamma)\left(\frac{1}{T^{\mathrm{o}}} - \frac{1}{T^{\mathrm{i}}}\right) \\
J_q^{\mathrm{i}}(\gamma) &= -\frac{d_{qr} R c^o}{\exp[\Phi(\gamma)/RT^{\mathrm{i}}]} \frac{\partial z(\gamma)}{\partial \gamma} \\
&\quad - d_{qd} c_r(\gamma)\left(\frac{\mu_{\mathrm{Ca}}^{\mathrm{o}}}{T^{\mathrm{o}}} - \frac{\mu_{\mathrm{Ca}}^{\mathrm{i}}}{T^{\mathrm{i}}}\right) + d_{qq} c_r(\gamma)\left(\frac{1}{T^{\mathrm{o}}} - \frac{1}{T^{\mathrm{i}}}\right) \qquad (23)
\end{aligned}$$

Since the potential barrier along the reaction coordinate is high, the system will be in a quasi-stationary state after a short time. The reaction flux is then indepent of γ, i.e. $r(\gamma) = r$. As the Gibbs energy of the reaction is needed to enable the Ca^{2+} ions to move from the i-side to the o-side, where the chemical potential is higher, it is reasonable to assume that the Ca^{2+} flux and the heat flux are proportional to the reaction flux and therefore also in good approximation independent of γ, $J_{\mathrm{Ca}}^{\mathrm{o}}(\gamma) = J_{\mathrm{Ca}}^{\mathrm{o}}$ and $J_q^{\mathrm{i}}(\gamma) = J_q^{\mathrm{i}}$. Multiplying left and right with $\exp[\Phi(\gamma)/RT^{\mathrm{i}}]$ and

integrating then gives

$$r = -D_{rr}\left(1-\exp\frac{-\Delta G^{\mathrm{i}}}{RT^{\mathrm{i}}}\right) - D_{rd}\left(\frac{\mu^{\mathrm{o}}_{\mathrm{Ca}}}{RT^{\mathrm{o}}} - \frac{\mu^{\mathrm{i}}_{\mathrm{Ca}}}{RT^{\mathrm{i}}}\right) - D_{rq}\left(1-\frac{T^{\mathrm{i}}}{T^{\mathrm{o}}}\right)$$

$$J^{\mathrm{o}}_{\mathrm{Ca}} = -D_{dr}\left(1-\exp\frac{-\Delta G^{\mathrm{i}}}{RT^{\mathrm{i}}}\right) - D_{dd}\left(\frac{\mu^{\mathrm{o}}_{\mathrm{Ca}}}{RT^{\mathrm{o}}} - \frac{\mu^{\mathrm{i}}_{\mathrm{Ca}}}{RT^{\mathrm{i}}}\right) - D_{dq}\left(1-\frac{T^{\mathrm{i}}}{T^{\mathrm{o}}}\right)$$

$$J^{\mathrm{i}}_{q} = -D_{qr}\left(1-\exp\frac{-\Delta G^{\mathrm{i}}}{RT^{\mathrm{i}}}\right) - D_{qd}\left(\frac{\mu^{\mathrm{o}}_{\mathrm{Ca}}}{RT^{\mathrm{o}}} - \frac{\mu^{\mathrm{i}}_{\mathrm{Ca}}}{RT^{\mathrm{i}}}\right) - D_{qq}\left(1-\frac{T^{\mathrm{i}}}{T^{\mathrm{o}}}\right) \quad (24)$$

where

$$\begin{aligned} D_{jr} &= d_{jr}\frac{R\exp\left((\mu^{\mathrm{i}}_{\mathrm{ATP}}+\mu^{\mathrm{i}}_{\mathrm{P}})/RT^{\mathrm{i}}\right)}{\int_0^1\exp[\Phi(\gamma)/RT^{\mathrm{i}}]d\gamma} \\ D_{jd} &= d_{jd}\frac{R\int_0^1 z(\gamma)d\gamma}{\int_0^1\exp[\Phi(\gamma)/RT^{\mathrm{i}}]d\gamma} \\ D_{jq} &= d_{jq}\frac{\int_0^1 z(\gamma)d\gamma}{T^{\mathrm{i}}\int_0^1\exp[\Phi(\gamma)/RT^{\mathrm{i}}]d\gamma} \end{aligned} \quad (25)$$

where j= r,d,q. The D-matrix is not symmetric. This model obeys the conditions 1-4 in the introduction. It is a description using distributions in reaction coordinate space. It describes through the matrix of coefficients a process that can be reversed by altering the driving forces. The coupling coefficients are probably large. The conditions at static head and during pump operation far from linear conditions can now be described in more detail.

SLIPPAGE AT ISOTHERMAL CONDITIONS

A tight pump has a constant ratio $J^{\mathrm{o}}_{\mathrm{Ca}}/r = n$. In order to find an expression for the flux ratio in the isothermal case, we use the coefficients of the corresponding 2×2 matrix of Eqs.(24) and Eq.(22). The ratio n is then defined as follows. We can also define the factor α_d by:

$$n \equiv \frac{l_{dr}(\gamma)}{l_{rr}(\gamma)} = \frac{d_{dr}}{d_{rr}} \text{ and } n(1+\alpha_d) \equiv \frac{l_{dd}(\gamma)}{l_{rd}(\gamma)} = \frac{d_{dd}}{d_{rd}} \quad (26)$$

The tight pump has $\alpha_d = 0$. It follows from Eq.(25) that

$$n = \frac{D_{dr}}{D_{rr}} \text{ and } n(1+\alpha_d) = \frac{D_{dd}}{D_{rd}} \quad (27)$$

By using these relations and Eq.(24) we find to linear order in α_d a deviation from a constant ratio n

$$\frac{J^{\mathrm{o}}_{\mathrm{Ca}}}{r} = n\left\{1+\alpha_d\left[1+\frac{D_{dr}RT}{nD_{rd}}\frac{1-\exp(-\Delta G^{\mathrm{i}}/RT)}{\mu^{\mathrm{o}}_{\mathrm{Ca}}-\mu^{\mathrm{i}}_{\mathrm{Ca}}}\right]^{-1}\right\} \quad (28)$$

This gives a more accurate expression for pump slippage than is possible to obtain from NET. The value of $\alpha_d < 1$ measures the degree of slip, or the deviation from the "stochiometric" pump value n. Under normal operating conditions $\left(1-\exp\left(-\Delta G^{\mathrm{i}}/RT\right)\right)$ is large and negative, while $\left(\mu^{\mathrm{o}}_{\mathrm{Ca}}-\mu^{\mathrm{i}}_{\mathrm{Ca}}\right)$ is positive and smaller. This explains how the flux ratio deviates from the constant n when the temperature is constant.

The static head condition is defined by $J^{\mathrm{o}}_{\mathrm{Ca}} = 0$ (Caplan and Essig, 1983). Equation 28 gives the following ratio of thermodynamic forces at static head at constant temperature:

$$RT\left(1-\exp\frac{(-\Delta G^{\mathrm{i}})}{RT}\right)/(\mu^{\mathrm{o}}_{\mathrm{Ca}}-\mu^{\mathrm{i}}_{\mathrm{Ca}}) = -n(1+\alpha_d)\frac{D_{rd}}{D_{dr}} \quad (29)$$

to linear order in α_d. By substituting Eq.(29) into Eq.(24a) and using Eq.(26) one obtains for the reaction rate at static head

$$r = -\alpha_d D_{rr}\left(1-\exp\frac{(-\Delta G^{\mathrm{i}})}{RT}\right) \quad (30)$$

to linear order in α_d. The entropy production of the slipping pump at static head is obtained by integrating Eq.(18), which gives

$$\sigma^{\mathrm{s}} = \alpha_d D_{rr}\frac{\Delta G^{\mathrm{i}}}{T}\left(1-\exp\frac{(-\Delta G^{\mathrm{i}})}{RT}\right) \quad (31)$$

The tight pump has $\sigma^{\mathrm{s}} = 0$, at static head. For all other conditions there is a positive entropy production. Not all of the energy that is latent in the enthalpy of reaction is then converted to energy storage, in terms of raising the chemical potential of the ion. This mismatch makes a heat source at the surface. We proceed to study the slippage under such conditions.

NON-ISOTHERMAL SLIPPAGE

The non-isothermal case was investigated by De Meis and coworkers (1997). They found that the heat released per mol ATP hydrolyzed was constant, and depended on the state of the vesicles

with reconstituted ATPase. The heat production per mol was 118 kJ/mol, about three times higher in the leaky vesicles than in the intact ones where it was 42 kJ/mol. These observations are important; they show that the pumping activity is correlated to a significant heat production. It is thus likely that small temperature differences exists as a consequence. The authors demonstrated large heat effects not only under forward, but also under reverse pump operating conditions. The authors went on to show that the heat production did not depend on the Ca^{2+}-gradient. We may speculate that this corresponds to setting $D_{dq} = D_{qd} = 0$ and $D_{rq} = D_{qr}$ being finite. The temperature increase of the surface and the o-side induced by the reaction can then be written as

$$T^{\mathrm{o}} - T^{\mathrm{i}} = -\alpha_T r \Delta H \tag{32}$$

where the reaction enthalpy is negative and α_T is a factor defined by this equation. By combining this with Eq.(24), we obtain

$$\frac{J^{\mathrm{o}}_{\mathrm{Ca}}}{r} = n + n\left[\alpha_T \frac{D_{rq}}{T^{\mathrm{o}}}\Delta H\right] + n\alpha_d\left[1 + \frac{D_{dr}R}{nD_{rd}}\frac{(1-\exp(-\Delta G^{\mathrm{i}})/RT^{\mathrm{i}})}{\mu^{\mathrm{o}}_{\mathrm{Ca}}/T^{\mathrm{o}} - \mu^{\mathrm{i}}_{\mathrm{Ca}}/T^{\mathrm{i}}}\right]^{-1} \tag{33}$$

This expression shows that the presence of a temperature difference also leads to a reduction in the stoichiometric number *n*, or to an increased slip in the pump. The issue of slipping pumps has not been adressed by MNET before.

DISCUSSION

We have shown above that active transport in biological systems can be described with MNET on a stochastic level by introducing the reaction coordinate γ. We have considered the density of ATPase enzymes in the state γ along the reaction coordinate, $c(\gamma)$, the concentration, $c_{\mathrm{Ca}}(\gamma)$, of Ca^{2+} adsorbed to enzymes in the state γ and the temperature, $T^{\mathrm{s}}(\gamma)$, of these enzymes in states given by the variable γ. The description gave a nonlinear relation between the ion flux and the chemical driving force, and, if present, also a thermal driving force. The description can be seen as a generalization of the linear description given by Caplan and Essig (1983). MNET does not have transport coefficients that depend on the force. This can be used to argue against non-linear coefficients as a possible explanation of non-linear behaviour, cf. Walz (1990) and references therein. A nonlinear flux-force relation is not enough to infer slippage, however, as is evident from Eq.(28). This was also pointed out by Garlid et al. (1992) who studied leak pathways in mitochondria.

We have stated that the coupling takes place *in the surface*. The surface must be understood as the space covered by the ATP-binding site(s) plus the molecular links to the ion binding site(s), all positions where the fluctuations in γ-space takes place. The gradients at the surface are probably very large. Long-range correlations are then typical (Torner and Rubi, 1991). An interdependency of fluctuations at different points, that follow from long-range correlations, may capture the interplay between a gradually increasing bond strenght for ATP during conversion and the known motion at another part of the enzyme that pumps the ion across (Sun et al.2004). It is reasonable that a stochastic pump process has a certain probability for slippage. We have here calculated how slippage may depend on the value of the driving forces.

When the equality $l^2_{rd}(\gamma) = l^2_{dr}(\gamma) = l_{rr}(\gamma)l_{dd}(\gamma)$ holds, the pump is tight. The process is close to being reversible, and the entropy production rate is small, compatible with the observation of de Meis and coworkers (1997). In such a situation, when the stress on the system is not too large, there is probably enough time for a molecule, or an ion, to seek new favorable attachments, without necessarily loosing too much of the energy. Under extreme solution conditions, the fluctuation pattern may change, making reversible transitions less favorable, and the entropy production larger.

There is always dissipation of energy connected to the pump, and the present theory describes this as well as the heat fluxes. A large heat production was measured during active transport (de Meis et.al 1997). Also Antes et al. (2003) describe the need to thermostat the hot spots in the ATPase regions in molecular dynamics simulations of the hydrolysis. These measurements and calculations give support to the present description. The reversible property of the pump can be compared to a reversible electrochemical system. The electrode reaction gives electric energy in the electrochemical cell, here the chemical reactions gives an increased chemical potential for Ca^{2+}. In an electrochemical cell, there is a reversible heat effect, due to the entropy of reaction, a Peltier heat. Here, there is a reversible heat

effect connected to the energies of transfer. This will be elaborated on in the future.

Since there is often a significant heat production during operation, and because of the stochastic nature of the process, one might consider overheating as an additional cause of slippage, as demonstrated by Eq.(33). This is a new explanation for slippage. Most likely is $T^{\mathrm{o}} > T^{\mathrm{i}}$. The higher the temperature becomes, the smaller is the likelihood for the right detachment / attachment of chemical bonds, and a higher probability for slip arise.

Models discussed in the literature can be discussed on the background of the present theory. The alternating access model (see Berman, 2001) fits only with the picture of a tight pump, and is thus unrealistic. The binding-zipper model (see Sun et al. 2004), where the chemical energy is uniquely transferred to the shaft of the rotating pump, is also pictured as a tight pump, even if the authors do not address ion transport explicitly. Berman emphasized the stochastic nature of a slipping pump and proposed a continuum of states rather than a cycle of discrete states. The events described here in $\gamma-$space are of this nature. The present theory may cover most of the energy-barrier model of Lauger (see Berman, 2001).

CONCLUSION

The aim of this paper was to show that nonlinear expressions for the fluxes in terms of their driving forces can be derived for active transport in biological systems. We have shown this using MNET, a theory that capture nonlinearities that otherwise remain hidden in the macroscopic NET-theory. We have used MNET for the first time to analyze phenomena related to slippage and uncoupling of ion pumps. Active transport means coupling at the membrane surface and positive coupling coefficients. We propose a hypothesis for slipping pumps, where also the temperature of the surface may play a role for the slip. The hypothesis may be tested with the equations that are provided. We have somewhat arbitrarily taken active transport of Ca^{2+} as an example, but the scheme should be transferable to many kinds of transport processes that obtain their energy from chemical reactions, as molecular motors. We hope in this way to provide more options for analysis of experiments in this important domain.

Acknowledgement

SK and DB are grateful to MECD Grants number SAB 2002-0191 and SAB 2003-0051 for their sabbatical stay at University of Barcelona.

REFERENCES

Albano, A.M. and D. Bedeaux. Physica A 147:407-435, 1987.

Antes, I., D. Chandler, H. Wang, and G. Oster. Biophysical J. 85:695-706, 2003.

Berman, M.C.Biochim. Biophys. Acta. 1513:95-121, 2001.

Caplan, S.R. and A. Essig. Bioenergetics and linear nonequilibrium thermodynamics. The steady state. Harvard University Press, Cambridge, Massachusetts, 1983.

De Meis, L., Bianconi, M.L., and Suzano, V.A. FEBS Letters, 406: 201-204, 1997.

Eyring, H. and E. Eyring. Modern Chemical Kinetics. Chapman and Hall, London, 1965.

Garlid, K.D., C.S. Semrad, and V. Zinchenko. Does redox slip contribute significantly to mitochondrial respiration? In: Modern Trends in Biothermokinetics. S. Schuster, M. Rigoulet, R. Ouhabi, and J.-P. Mazat, editors. Plenum press, New York. 287-293, 1992.

Kjelstrup, S., J.M. Rubi, D. Bedeaux. J. Theor. Biology, 234: 7-12, 2005.

Johannessen, E. and D. Bedeaux. Physica A. 330:354-372, 2003.

Peinelt, C. and H.J. Apell. Biophysical J. 86:815-824, 2004.

Røsjorde, A., D.W. Fossmo, S. Kjelstrup, D. Bedeaux and B. Hafskjold. J. Colloid Interf. Sci.232:178-185, 2000.

Sun, S.X., H. Wang, and G. Oster. Biophysical J. 86: 1373-1384, 2004.

Torner, L. and J.M. Rubi, Phys.Rev. A 44: 1077-1085, 1991.

Westerhoff, H.V. and K. van Dam. Thermodynamics and control of biological free-energy transduction. Elsevier, Amsterdam, 1987.

Walz, D. Biochim. Biophys. Acta 1019: 171-224, 1990

Proceedings of ECOS 2005
Trondheim, Norway
June 20–22, 2005

NUMERICAL STUDY OF MICRO-EXPLOSION DELAY OF WATER-IN-FUEL EMULSION DROPLETS

Dominique Tarlet, Jérôme Bellettre[1] and Mohand Tazerout
Ecole des Mines de Nantes / Dept. of Energetics and Environmental Engineering
BP 20722 - 4, rue Alfred Kastler – 44307 Nantes cedex 3- FRANCE

Camal Rahmouni
Véolia Environnement / C.R.E.E.D.
291, avenue Dreyfous Ducas – 78520 Limay - FRANCE

ABSTRACT

Spray combustion of water-emulsified fuel induces an effective decrease in total combustion time, carbonaceous residues and NO_X compared to pure fuel, thanks to the micro-explosion phenomenon. Designing emulsion-burning appliances requires to calculate the micro-explosion delay included in total combustion time. This rather technical contribution addresses the problem of how to model the process of microexplosions in emulsions. The authors describe a numerical method to account for thermal conduction effects and analyze its effect upon the microexplosion delay. Some of the expressed physical quantities may be useful for other researchers in this field. The evolution of the emulsion droplet (radius and temperature through the time) is faced with experimental micro-explosion delay, for three cases of emulsion droplet (different initial diameters and temperatures). Finally, observations resulting from this comparison are discussed.

Keywords : waste oils, heavy fuels, emulsion, combustion, micro-explosion delay

NOMENCLATURE

c_p	Specific heat [$J.kg^{-1}.K^{-1}$]
C	Concentration [$kmole.m^{-3}$]
f	Mass fraction of water in emulsion
k_C	Diffusion coefficient [$m.s^{-1}$]
L	Latent heat [$J.kg^{-1}$]
M	Molar mass [$kg.mole^{-1}$]
m	Mass [kg]
N	Number of water droplets
P	Pressure [Pa]
Q	Heat flux [W]
R	Gases constant [$J.kmole^{-1}.K^{-1}$]
r	Radius [m]
S	Surface area [m^2]
T	Temperature [K]
t	Time [s]
V	Volume [m^3]
W	Molar flux [$kmole.s^{-1}$]
α	Convective coefficient [$W.m^{-2}.K^{-1}$]
λ	Thermal conductivity [$W.m^{-1}.K^{-1}$]
σ	Constant of Stefan-Boltzmann [$W.m^{-2}.K^{-4}$]
ρ	Density [$kg.m^{-3}$]
υ	Characteristic volume of diffusion [m^3]

Subscripts

bp	Boiling point
CH	Fuel
ext	Surface layer
G	Gaseous phase
l	Fuel spherical layer
p	Emulsion droplet
vap	Fuel vapour
W	Water

[1] Phone : +33 2 51 85 82 96 Fax : +33 2 51 85 82 99
E-mail : Jerome.Bellettre@emn.fr

∞ Away in the gaseous phase

INTRODUCTION

Residual oil and heavy fuels from engines, cooking, refineries and other sources represent pollutant combustibles. Burning of a water-in-oil emulsion enables environmental advantages, such as reduction in NOx formation [1,2].

The difference in volatility between oil and water causes the water to vaporise and fragment the around oil, namely to generate the physical phenomenon of micro-explosion. The water droplets are not supposed to vaporise at boiling point inside the emulsion [3], so they reach a metastable state that breaks up at a temperature between their boiling point and their well-known spinodal limit [4]. Micro explosion delay lies between these bounds, but nucleation can be induced by random solid impurities. So micro-explosion criteria still have to be defined and validated.

In all cases, the micro-explosion phenomenon creates numerous small child droplets from one initial emulsion droplet [5] : It also induces more fragile-shaped carbonaceous residues, expected to burn out faster [6].

Law [4] indicates whether, but not when micro explosion occurs. Using nucleation theory, Wei Biao Fu [3] gives a criterion for micro explosion based on the size of the emulsion droplet and its volume fraction of water. As far as we know, no thermal model of the emulsion droplet does provide any micro-explosion delay.

This paper exposes first a modelisation of heat transfer at the surface and inside of the emulsion droplet. Thus, the results of the model are faced with experimental micro-explosion delay from Gollahalli [7]. Finally, observations of these comparisons are discussed.

Authors would like to emphasize the fact that all thermo-physical properties of fuel and gaseous phase are implemented as pressure and temperature dependent.

THE SPHERE LAYERS MODEL

The dispersed phase is inserted as spheres of water subtracting volume and showing heat-exchanging surface within the spherical layers of fuel (figure 1). These volumes and surfaces are re-calculated without any geometrical approximation at every step of time, taking thermal expansions of fuel and water into account. In each sphere layer, the number of water droplets is assumed to maintain the same volume fraction of water in the whole emulsion droplet. The water droplets are assumed to be all the same initial radius R_W.

Governing equations and hypotheses

Heat balance is calculated for a sphere layer l, considering conductive heat transfer from

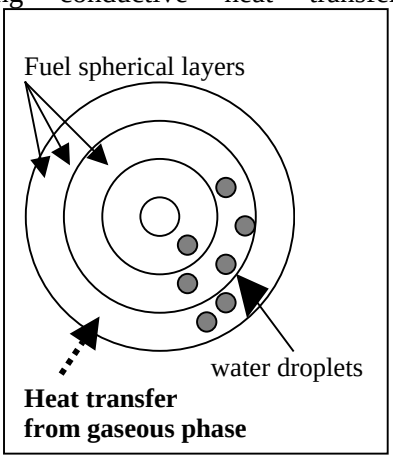

Figure 1 : The sphere layers model

neighbourhood l+1 and l-1, and heat transfer to dispersed phase Q_l (equation 1).

$$m_l c_{Pl} \frac{dT_l}{dt} = \frac{\lambda_{CH}}{dr}(S_{l-1}(T_{l-1} - T_l) + S_l(T_{l+1} - T_l)) - Q_l \qquad (1)$$

Conductive heat tansfer is modelled across the surface between sphere layers. Later in this paper, the error induced by spatial discretisation is evaluated by comparison with analytical conduction in a sphere.

The hypothesis consisting of no convection inside the emulsion droplet is adopted. It is made by numerous authors [8,9] considering fuel as viscous enough to prevent internal circulation. This is especially true for heavy fuel oil because of their higher viscosity compared to lighter ones [10]. Similarly, only conduction in taken into account at the surface of internal droplets of water (equation 2):

$$Q_l = N_{W,l} \frac{\lambda_{CH}}{r_W} S_{W,l} \left(T_l - T_{W,l}\right) \qquad (2)$$

This heat transfer to water droplets enables to determine their thermal expansion.

At the surface of the emulsion droplet, both convective and radiative heat transfer from gaseous phase are calculated (equation 3). The correlation of Ranz and Marshall [11] is used for convective coefficient α. This gradient boundary condition is implemented using T_{ext} and T_{ext-1}, respectively

temperature of surface and under-surface layers, provided by the sphere layers model.

$$\frac{T_{ext}-T_{ext-1}}{dr}=\frac{\sigma E_{CH}E_G}{\lambda_{CH}}\left(T_G^4-T_{ext}^4\right)+\frac{\alpha}{\lambda_{CH}}\left(T_G-T_{ext}\right) \qquad (3)$$

Vaporization and boiling

Heavy fuels consisting of long hydrocarbonated chains have a higher boiling point compared to lighter fuels, especially at pressures higher than 1 bar. Hence, diffusion-limited evaporation mass flux (equation 4) W_{vap} at the surface of the emulsion droplet is of crucial relevance to determine the quantity of fuel evaporated prior to micro-explosion.

$$W_{vap}=k_C S_P\left(\frac{P_{sat,CH}\left(T_{ext}\right)}{RT_{ext}}-C_\infty\right) \qquad (4)$$

The binary gas-phase diffusion coefficient k_C is obtained by correlation of Fuller et al. (equation 5) [12]. This correlation enables to take into account variations in diffusion coefficient k_C caused by temperature and pressure in gaseous phase.

$$k_C=\frac{1.10^{-3}\times\left(\frac{1}{M_{CH}}+\frac{1}{M_G}\right)^{\frac{1}{2}}}{\left[\left(\sum_G v\right)^{\frac{1}{3}}+\left(\sum_{CH} v\right)^{\frac{1}{3}}\right]^2}\times\frac{T_G^{1.75}}{P_G} \qquad (5)$$

The surface layer is applied the following heat balance (equation 6). Once boiling point T_b is reached by the surface layer, heat imput from gaseous phase is considered to compense latent heat, plus droplet heating. So, while boiling, the surface layer keeps the constant temperature T_b.

$$S_{ext}\sigma E_{CH}E_F(T_G^4-T_{bp}^4)+S_{ext}\alpha(T_G-T_{bp})$$
$$-\frac{\lambda_{CH}}{dr}S_{ext-1}(T_{bp}-T_{ext-1}) \qquad (6)$$
$$=-L_{CH}\frac{dm_{CH,ext}}{dt}-L_W\frac{dm_{W,ext}}{dt}+\frac{m_{W,ext}Cp_{W\left(T_{W,ext}-T_{bp,W}\right)}}{dt}$$

$dm_{W,ext}$ is the mass of water removed whith a mass $dm_{CH,ext}$ evaporated, so $dm_{W,ext} = f\,(dm_{CH,ext}+ dm_{W,ext})$ When removed from the surface, liquid water is embedded in fuel, being above the boiling point of water. So these removed water droplets are considered to break up their metastable state. The last term on the right in equation 6, which accounts for this breaking up, will be explained later in the part about metastable states.

The surface sphere layer thickness dr is to be noticed : Contrary to inside layers in equation 1, dr decreases in equation 6, because the surface layer is evaporating or boiling. So, dr decreases until tiny values putting computations at risk of divergence. A criterion of critical thickness for the surface layer is defined (inequation 7).

$$V_{l=ext}\le 1\%\,V_{l=ext,t=0} \qquad (7)$$

Once this criteria reached because of a tiny enough dr, the remaining liquid fuel is considered as instantly depleted, so the under-surface layer is becoming the surface layer.

Results and tests for time and space steps

Results are obtained through a finite-differences numerical method, forward in time and centered in space. Considering the results shown in Figure 3, the space step is set to 10 µm or less. Thermal expansion of fuel and water, evaporation and boiling result altogether in variation of droplet radius through the time (figure 2). In figure 2, a test for the time step is made, using a constant space step of 10 µm, which is a maximum as determined from Figure 3.

In figure 2, the radius is slightly increasing due to thermal expansion until 5 ms, when evaporation compensates, then counter-balances expansion, making the radius decrease. This decreasing of

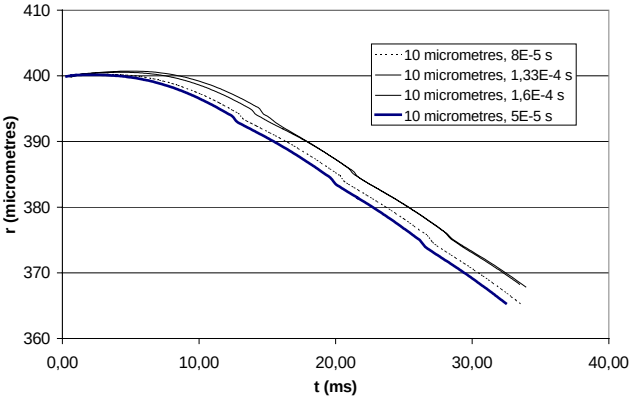

Figure 2 : Test for time step

radius is determined by the quantity of fuel evaporated.

Time and space steps are ensured to enable modelisation of conduction by Fourier's law. Fourier's law is not valid under some hundreds of nanometers in gases, and this critical distance still decreases for liquids and solids. In this paper, 2 µm is a minimum for the sphere layer thickness, which is the space step. The relaxation time of particles responsible for conduction of heat are : 10^{-11} s (phonons), 10^{-13} s (electrons). In this model, 10^{-6} s is a minimum.

So, equations 1-6 can be properly used to modelize heat transfer, and space and time steps are respectively chosen as : 10 µm and 1,33.10^{-4}s.

Validation with analytic conductive heat transfer

The phenomena influencing micro explosion delay (evaporation and boiling rate, heat transfer to dispersed phase, a.s.o…) are determined by temperature. So special care is taken to ensure a validated heat transfer across the emulsion droplet.
The well-known analytical conductive heat transfer within a sphere (equation 8) is used in [9] :

$$\rho C_p \frac{dT}{dt} = \lambda_{CH}\left(\frac{\partial^2 T}{\partial t^2} + \frac{2}{r}\frac{\partial T}{\partial t}\right) \qquad (8)$$

Figure 3 shows the temperature at the center of a pure oil droplet, both calculated by Jacques [9] using equation 8, and by the sphere layers model, using the same thermophysical properties and heat input at the surface. The influence of decreasing sphere layer thickness can be noticed as a convergence.

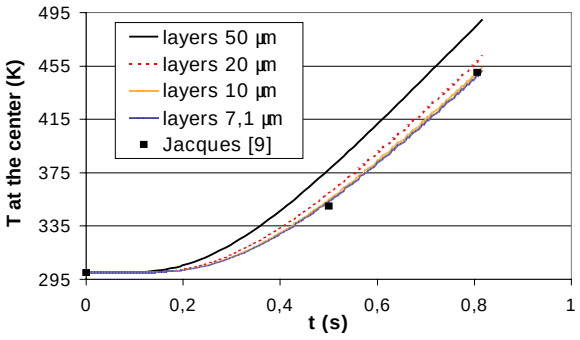

Figure 3 : Space step vs. analytical results

Criteria for micro-explosion

The metastable state of inside water is favourized by enclosure in around oil, fast heat transfer and micrometric scale [5]. It is broken up, (e.g. sudden phase change to steam) between boiling point and well-known spinodal limit [4]. Between these two bounds, the nucleation sites may consist of impurities, randomly dispersed across the emulsion droplet. Although a metastable droplet put in contact with the gaseous phase by means of evaporation, or by violent disruption in the neighborhoud [2] is clearly not supposed to remain in metastable state.
As it is done in this paper, micro explosion delay is not –unless from experimental data- indicated as precise delay, but between these bounds, also considering radius decreasing.

Production of steam out of metastable state

As considered by Wolfe [13] at breaking up of metastable state, enthalpy above boiling point compenses latent heat, so liquid water of mass m_W is partly, but suddenly vaporized (equation 9) into a mass of steam m_{steam} .

$$m_{steam} = \frac{m_W Cp_W (T_{W,l} - T_{bp,W})}{L_W} \qquad (9)$$

The remaining liquid water is supposed to lower its temperature until boiling point. The last term on the right in equation 6 represents the latent heat furnished by this breaking up of metastable state.
Considering pressure in the gaseous phase, the volume of potentially produced steam V_{steam} is then obtained from tables. In this model, V_{steam} would be the steam produced from all the liquid water above boiling point in the emulsion droplet.

VALIDATION OF MICRO-EXPLOSION DELAY

Experiments of Gollahalli [7] enable us to an experimental validation ensuring all the necessary variables (table 1). Moreover, these experiments were carried out using the drop tower technique, without suspending filament for the droplet, which is known as a nucleation site that shortens the micro explosion delay [14]. Furthermore, Gollahalli did not use any additional surfactant to prepare the emulsions. Although the gaseous phase is a flame of natural gas in [7], only convective heat transfer is taken into account in equation 3.
Three different cases of emulsion droplet (e.g. with different initial temperatures and diameters, cf. table 1) are computed and faced with experimental micro-explosion delays obtained by Gollahalli [7].
For each case, two curves are provided through the time since injection :

(a) The variation of droplet radius (r_p), plus the radius at which internal water droplets attain 373,15 K (r_{bp}), thus entering metastable state

(b) The variation of droplet volume (V_p), plus the variation of the volume of potentially produced steam V_{steam} (cf. equation 7)

In his experiments, Gollahalli observed evaporation of the emulsion droplets prior to micro-explosion, which accounts for the importance of evaporation in equations 4 and 5.

The micro-explosions he observed were unique, e.g. without any secondary or tertiary explosions, which indicates disruption of the whole droplet. Although Gollahalli does not indicate the range of reproducibility of his experimental results in [7], observed gaps between measurements lie up to 30 ms.

Parameter	**Value**
Initial diameter of emulsion droplet	1000 μm or 800 μm
Initial emulsion temperature	300 K or 330 K
Dispersed phase	10 μm – diametered water droplets mass fraction : 0,1
Gaseous phase temperature	1400 K
Relative velocity to gaseous phase	5 $m.s^{-1}$
Case of emulsion burning in [7]	**Initial temperature and diameter of emulsion droplet**
Case #1	300 K , 800 μm
Case #2	300 K , 1000 μm
Case #3	330 K , 1000 μm

Table 1 : Experiments of Gollahalli [7]

In Figures 5.a and 6.a (cases #1 and #2), experimental micro-explosion delay is observed when R_{bp} is the half of the initial radius of the emulsion droplet, according to the model. In case #3 (Figures 7.a), at the experimental micro-explosion, R_{bp} is more than half of the initial radius of the emulsion droplet.
In all cases #1, #2 and #3, experimental micro-explosion is observed after V_{steam} is more than V_p, so micro-explosion could theoretically happen (Figures 5.b, 6.b and 7.b). In 2 cases out of 3, micro-explosion happens when $r_{bp} = 50\% \; r_{p,t=0}$.
In the future, more situations with other varying parameters (temperature in gaseous phase, mass fraction of water, a.s.o.) should be examined and faced with the time of occurrence of micro-explosion.

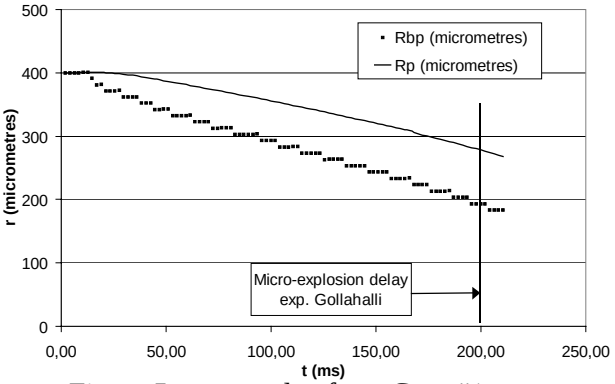

Figure 5.a : r_{bp} and r_p from Case #1

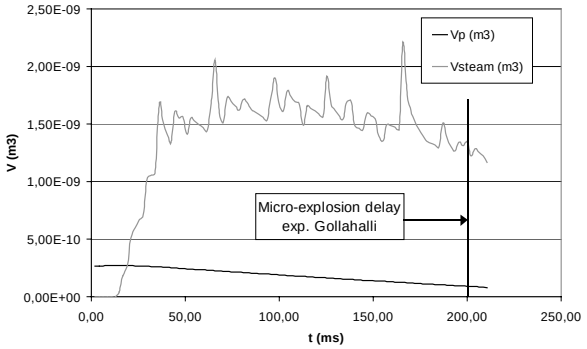

Figure 5.b : V_p and V_{steam} from Case #1

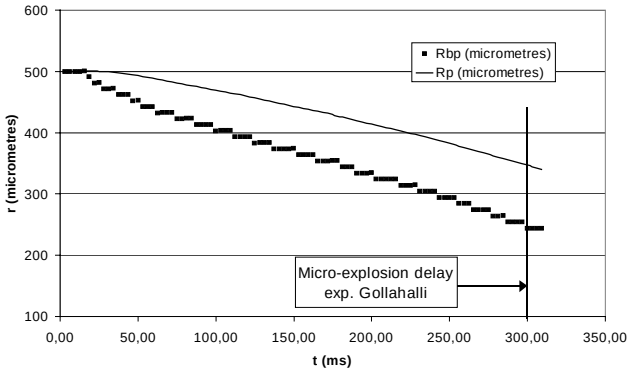

Figure 6.a : r_{bp} and r_p from Case #2

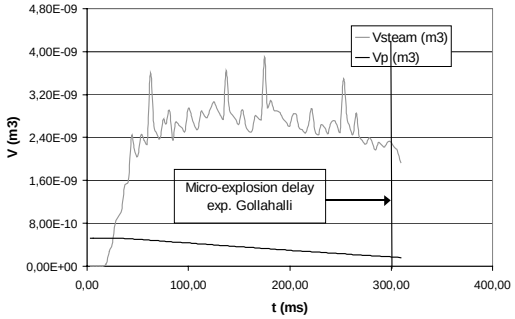

Figure 6.b : V_p and V_{steam} from Case #2

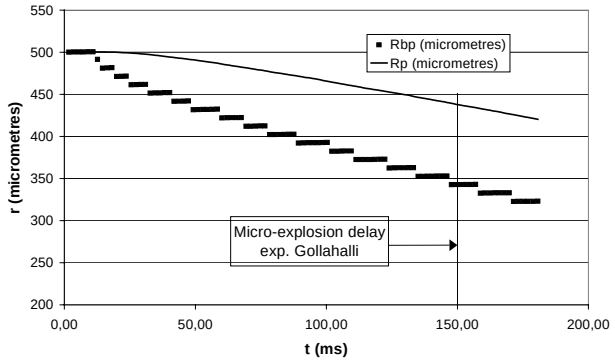

Figure 7.a : r_{bp} and r_p from Case #3

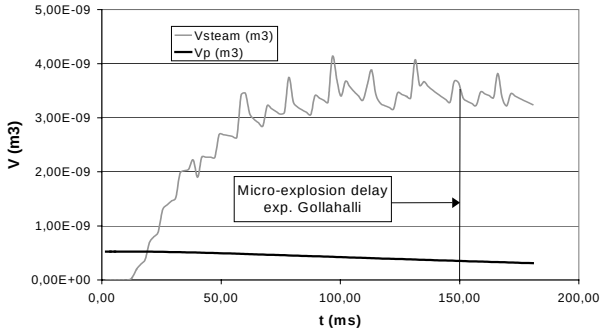

Figure 7.b : V_p and V_{steam} from Case #3

CONCLUSION

A thermal modelisation of the emulsion droplet is made, enabling to determine temperature distribution, radius distribution and potentially-produced steam through the time.

A comparison is made with experimental measurements of micro-explosion delay, without suspending filament or additional surfactant that could start nucleation.

Results from the model are in accordance with the experimental micro-explosion delay, although they indicate that micro-explosion is also possible before experimental observations.

Further work should consist of modelisation and validation of more situations, to closer inquire criteria for the onset of micro-explosion.

REFERENCES

[1] A. Kerihuel, M. Senthil Kumar, J. Bellettre and M. Tazerout, *Investigations On a CI Engine Using Animal Fat And Its Emulsions with Water and Methanol as Fuel*, SAE Paper (No. 2005-01-1729), Detroit 2005.

[2] V.M. Ivanov and P.I Nefedov , *Experimental investigation of the combustion process of natural and emulsified liquid fuels*, from Trudy Goryachikh Iskopayemykh 1962 ;19 :35-45.

[3] Wei Biao Fu, Ling Yun Hou, Lipo Wang, Fan Hua Ma, *A unified model for the micro-explosion of emulsified droplets of oil and water*, Fuel processing technology 2002 ;79 :107-119

[4] C.K. Law, *A model for the combustion of Oil/Water Emulsion droplets*, Combustion science and technology 1977 : 29-38

[5] T. Kadota, H. Yamasaki, *Recent advances in the combustion of water fuel emulsion* Progress in energy and combustion science 2002 ;28 :385-404

[6] R. Ocampo-Barrera, R. Villasenor and A. Diego-Marin, *An experimental study of the effect of water content on combustion of heavy fuel oil/water emulsion droplets*, Combustion and flame 2001 ;126 :1845-1855

[7] S.R. Gollahalli, *An experimental study of the combustion of unsupported drops of residual oils and emulsions*, Combustion science and technology 1979 ;19 :245-250

[8] S.S. Sazhin, *Transient heating of diesel fuel droplet* , International journal of heat and mass transfer 2004

[9] M.T.Jacques, *Transient heating of emulsified water-in-oil droplet*, Combustion and flame 1977 ;29 : 77-85

[10] M. Ikegami, G. Xu, K. Ikeda, S. Honma, H. Nagaishi, D.L. Dietrich, Y. Takeshita, *Distinctive combustion stages of single heavy oil droplet under microgravity*, Fuel 2003 ;82 : 293-304

[11] W. E. Ranz, W. R. Marshall, Jr., *Evaporation from drops*, Chemical engineering process ;48(3) : 141-180

[12] E.N. Fuller, P.D. Schettler, J.C. Giddings, *A new method for prediction of binary gas-phase diffusion coefficients*, Industrial and engineering chemistry 1966 ; 58 (5)

[13] *Superheating and microwave ovens*, some notes by Joe Wolfe, School of physics, The University of New South Wales, Sydney. See also :`http://www.phys.unsw.edu.au/~jw/superheating.html`

[14] J.C. Lasheras, A.C. Fernandez-Perello, F.L. Dryer, *Initial observations on the free droplet combustion characteristics of water-in-fuel emulsions*, Combustion science and technology 1979 ; 21 : 1-14

Proceedings of ECOS 2005
Trondheim, Norway
June 20–22, 2005

RATE LIMITING PROTON HYDRATION IN THE HYDROGEN ELECTRODE OF THE POLYMER ELECTROLYTE MEMBRANE FUEL CELL

A.K. Meland, D. Bedeaux, S. Kjelstrup*
Department of chemistry, Norwegian University of Science and Technology, Trondheim, Norway

ABSTRACT

We show how one can obtain information on the three-phase contact of the electrode in the polymer electrolyte fuel cell, using nonequilibrium thermodynamics in combination with impedance spectroscopy. The isothermal hydrogen adsorption and reaction at the E-TEK electrode of a polymer electrolyte fuel cell with a Nafion®117 membrane is investigated at 30°C and 1 bar. We have earlier reported that adsorption and diffusion of gas to the three-phase contact is rate-limiting. We proceed to show how charge transfer and hydration and transport into the membrane play a role. The adsorption/diffusion step takes place in a layer located before the platinum surface, while the charge transfer takes place at (predominantly) the metal particle surface, while the third step is on the membrane side of the metal surface.

Keywords: Entropy production, non-isothermal fuel cell, heat production, irreversible thermodynamics

NOMENCLATURE

c_i	concentration, mol/m^3
c^s	capacitance, F m^2
D	diffusion coefficient, m^2/s
F	Faraday's constant, 96500 C/mol
ϕ	electric potential, V
ΔG	reaction Gibbs energy, J/mol
Γ	surface adsorption, mol/m^2
j	current density, A/m^2
J_i	flux of i, mol/s m^2
k_i	rate constant, s^{-1}
μ_i	chemical potential, J/mol
R	gas constant, 8.314 J/K mol
r	reaction rate, mol/s m^3
ρ	resistivity of surface process, ohm m^2
σ^s	entropy production rate of surface, J/K m^2
t	time, s
τ	relaxation time, s
T	temperature, K
x	coordinate axis, m
Y_0	admittance, ohm^{-1} m^{-2} s$^{1/2}$
Z	impedance, ohm m^2

*email:signekj@phys.chem.ntnu.no, Tel: +47-73594179

INTRODUCTION

Electrochemical impedance spectroscopy (EIS) is an experimental technique that can separate phenomena with different relaxation times, and is thus useful for determination of rate-limiting steps at electrode surfaces [1]. It has been used widely, also in studies of rather complicated three-phase contacts, which are typical for fuel cell electrodes.

The fuel cell electrodes consist of a porous matrix of carbon black that allow gas diffusion up to the catalyst (Pt) particles. The gas reacts at the catalyst, which is in contact with the proton-conducting membrane. We have started a systematic study of this nanoporous material, by investigating the hydrogen electrode in a cell with two such electrodes [2]. Our aim is to study the CO tolerance of this electrode [3, 4].

We predict first the impedance spectrum for the two electrodes. Details of the mechanism shall be concluded by comparing experimental and theoretical results. We consider a common membrane electrode assembly, namely the E-TEK electrode with 0.5 mg Pt/cm^2 and a Nafion®117 membrane. It has been common to assume that the rate limiting pro-

cess in the electrode backing of the anode (as well as the cathode) is diffusion in the gas phase. In our previous analysis [2], we argued that the good fit to a Gerischer phase element, indicated that the reversible adsorption reaction of hydrogen to carbon black along the pore walls and the subsequent diffusion along the surface to the catalyst plays a more important role.

In the previous paper [2], we did not consider in detail the steps following the adsorption and diffusion. We shall now proceed to do so. We analyze in particular how water affects the behavior of the system. The paper is organized as follows. We derive in sections 2 and 3 the impedance of the hydrogen electrode using a two-layer model. The first layer is that of the porous carbon layer supporting the catalyst particles, the so-called adsorption-diffusion layer. The next layer is the surface layer of the catalyst, where the charge transfer reactions take place. The experiments and the results are described in section 4 and 5 and discussed in section 6.

THE STEPS IN THE ELECTRODE REACTION

According to earlier evidence, we assume first that hydrogen gas is absorbed as hydrogen along the pores in the carbon matrix:

$$\frac{1}{2}\mathrm{H_2(g)} \rightarrow \frac{1}{2}\mathrm{H_2(a)} \qquad \text{(ad)}$$

The adsorption reaction is labelled "ad". The hydrogen proceeds to diffuse along the pore surface to the platinum catalyst, located between the porous carbon matrix and the cation exchange membrane. During the diffusion process some of the hydrogen desorbs back to the gas phase. We assume that the process is a first order reaction in both directions:

$$r = k^{\mathrm{a}}_{\mathrm{H_2}} c^{\mathrm{g}}_{\mathrm{H_2}} - k^{\mathrm{d}}_{\mathrm{H_2}} c^{\mathrm{a}}_{\mathrm{H_2}}(x,t) \qquad (1)$$

Here $k^{\mathrm{a}}_{\mathrm{H_2}}$ and $k^{\mathrm{d}}_{\mathrm{H_2}}$ are rate coefficients (superscripts a and d refer to adsorb and desorb, respectively). We use a course-grained description in which both concentrations are given in mol/m^3. The course-grained concentration $c^{\mathrm{g}}_{\mathrm{H_2}}$ is the concentration in the pores times the porosity of the layer. The course-grained concentration $c^{\mathrm{a}}_{\mathrm{H_2}}$ is the surface excess concentration in mol/m^2 times the surface area of the pores per unit of volume in m^{-1}. The adsorption reaction was assumed to take place on the metal surface, see e.g. [5], while we located this reaction to the surface of the pores in the carbon. In the following we assume the Volmer mechanism, where the molecule dissociates into protons and electrons in active sites on the surface of the platinum:

$$\frac{1}{2}\mathrm{H_2(a)} \rightarrow \mathrm{H^+(s)} + \mathrm{e^-(a)} \qquad \text{(ct)}$$

This charge transfer reaction is labelled ct. An excellent discussion of the relevant sites on Pt, that are active in the reaction, was given by Chen and Kucernak [5]. The protons are next bound to a water molecule and move into the cation exchange membrane (m) as hydronium ions

$$\mathrm{H^+(s)} + \mathrm{H_2O(m)} \rightarrow \mathrm{H_3O^+(m)} \qquad \text{(cm)}$$

This proton hydration reaction is labelled cm. Protons may bind to more than one water molecule. Electrons are transported into the anode carbon matrix (also indicated by a).

The thickness of the carbon matrix in the experiment is in the order of 0.5 mm, while the thickness of the catalyst layer is in the order of 0.01 mm. In the theory given below we use a continuous model for the carbon matrix. It is sufficient to use a sharp interface for the catalyst layer. Such a description is obtained from the excess entropy production rate, and the resulting fluxes and forces, for the electrode surface.

The reaction Gibbs energy of the absorption reaction in front of the metal surface is:

$$\Delta_r G^{\mathrm{s}}_{\mathrm{ad}} = \frac{1}{2}\mu^{\mathrm{s}}_{\mathrm{H_2}} - \frac{1}{2}\mu^{\mathrm{g}}_{\mathrm{H_2}} \equiv \frac{1}{2}\mu^{\mathrm{a}}_{\mathrm{H_2}}(x=0) - \frac{1}{2}\mu^{\mathrm{g}}_{\mathrm{H_2}} \qquad (2)$$

where $x = 0$ indicates the position of the catalyst surface. The chemical potential of hydrogen just before the surface and at the surface are the same, $\mu^{\mathrm{s}}_{\mathrm{H_2}} = \mu^{\mathrm{a}}_{\mathrm{H_2}}(x=0)$. The hydrogen gas in the experiment has a constant (position and time independent) pressure, leading to a constant $\mu^{\mathrm{g}}_{\mathrm{H_2}}$ as well as constant $c^{\mathrm{g}}_{\mathrm{H_2}}$. The superscripts s indicates a property of the surface. The bulk anode is located at $x < 0$ and the membrane at $x > 0$. In our coarse grained description, transport takes place along a coordinate normal to the surface of the membrane. All variables are then independent of coordinates parallel to the surface.

In the description of the electrochemical processes at the surface, we need the change in Gibbs energy

at the surface from the reaction of neutral species. For the ct reaction we then have:

$$\Delta_n G^{\rm s}_{\rm ct} = -\frac{1}{2}\mu^{\rm s}_{\rm H_2} \equiv -\frac{1}{2}\mu^{\rm a}_{\rm H_2}(x=0) \qquad (3)$$

and for the cm reaction we have:

$$\Delta_n G^{\rm s}_{\rm cm} = -\mu^{\rm s}_{\rm H_2O} \equiv -\mu^{\rm m}_{\rm H_2O}(x=0) \qquad (4)$$

For the total electrode reaction, we have the sum of the above terms:

$$\Delta_n G^{\rm s} = -\frac{1}{2}\mu^{\rm g}_{\rm H_2} - \mu^{\rm m}_{\rm H_2O}(x=0) \qquad (5)$$

At the surface there is an adsorption of protons, $\Gamma_{\rm H^+}$, hydronium ions, $\Gamma_{\rm H_3O^+}$, and electrons, $\Gamma_{\rm e^-}$. We can take the catalyst surface to be electroneutral, by choosing its thickness such that the total adsorptions (in mol/m^2) of positive ions is equal to the adsorption of electrons:

$$\Gamma_{\rm H^+} + \Gamma_{\rm H_3O^+} = \Gamma_{\rm e^-} \qquad (6)$$

The polarization of the surface is an important property. There are here two contributions to this polarization, one is due to proton-electron pairs and the other one is due to hydronium ion-electron pairs. The number of moles of the proton-electron dipoles per unit of surface area is given by $\Gamma_{\rm H^+}$ and the number of moles of hydronium ion-electron dipoles by $\Gamma_{\rm H_3O^+}$. The charge densities of the proton and the hydronium layer are equal to the potential difference between these layers and the electron layer times the capacitances, $c^{\rm s}_{\rm H^+}$ and $c^{\rm s}_{\rm H_3O^+}$, of these two dipole layers

$$F\Gamma_{\rm H^+} = c^{\rm s}_{\rm H^+}\Delta_{\rm s,H^+}\phi \quad \text{and} \quad F\Gamma_{\rm H_3O^+} = c^{\rm s}_{\rm H_3O^+}\Delta_{\rm s}\phi \qquad (7)$$

where F is Faraday's constant. The ct reaction increases the number of adsorbed dipoles of the first kind while the cm reaction decreases it. We therefore have

$$\frac{d}{dt}\Gamma_{\rm H^+} = r^{\rm s}_{\rm ct} - r^{\rm s}_{\rm cm} \qquad (8)$$

where $r^{\rm s}_{\rm ct}$ and $r^{\rm s}_{\rm cm}$ refer to the reaction rates. Similarly the cm reaction increases the number of dipoles of the second kind while the electric current decreases it. This gives

$$\frac{d}{dt}\Gamma_{\rm H_3O^+} = r^{\rm s}_{\rm cm} - \frac{j}{F} \qquad (9)$$

It therefore follows from Eqs.(7)-(9) that

$$r^{\rm s}_{\rm ct} = r^{\rm s}_{\rm cm} + \frac{c^{\rm s}_{\rm H^+}}{F}\frac{d\Delta_{\rm s,H^+}\phi}{dt} \quad r^{\rm s}_{\rm cm}F = j + c^{\rm s}_{\rm H_3O^+}\frac{d\Delta_{\rm s}\phi}{dt} \qquad (10)$$

As the hydronium ions are on the surface with the membrane, the potential difference between this layer and the electron layer is the full potential difference $\Delta_{\rm s}\phi$ across the surface. The protons are closer to the electron layer, so the potential difference between this layer and the electron layer $\Delta_{\rm s,H^+}\phi$ is smaller.

THE ELECTRODE IMPEDANCE

The variables in the oscillating field

Impedances are measured as a function of the frequency ω of the alternating potential, in the presence of a constant applied potential. The cell under investigation is symmetric, so we consider the potential difference between the anode and the center of the membrane:

$$\Delta\phi = \Delta\phi_{\rm dc} + \Delta\phi_{\rm ac}\exp(i\omega t) \qquad (11)$$

The potential difference between the center of the membrane and the cathode is the same. We disregard here the *emf* of both surfaces, which are equal and opposite. The contributions due to the bulk anode (and cathode) are negligible. Both contributions are the sum of the potential difference across the anode surface and (half) the membrane

$$\Delta\phi_{\rm dc} = \Delta_{\rm s}\phi_{\rm dc} + \frac{1}{2}\Delta_{\rm m}\phi_{\rm dc} \quad \Delta\phi_{\rm ac} = \Delta_{\rm s}\phi_{\rm ac} + \frac{1}{2}\Delta_{\rm m}\phi_{\rm ac} \qquad (12)$$

The electric current, as well as all other variables, similarly have a dc and an ac contribution. In the membrane, which conducts only protons, one has

$$\Delta_{\rm m}\phi_{\rm dc} = r_{\rm m}\, j_{\rm dc} \ \text{ and } \ \Delta_{\rm m}\phi_{\rm ac} = r_{\rm m}\, j_{\rm ac} \qquad (13)$$

The corresponding relations for the potential differences across the surface shall be derived below. For the dc and the ac contributions to the reaction rates one has, using Eq.(10),

$$Fr^{\rm s}_{\rm ct,dc} = Fr^{\rm s}_{\rm cm,dc} = j_{\rm dc} \qquad (14)$$

and

$$\begin{aligned} Fr^{\rm s}_{\rm ct,ac} &= Fr^{\rm s}_{\rm cm,ac} + i\omega c^{\rm s}_{\rm H^+}\Delta_{\rm s,H^+}\phi \\ Fr^{\rm s}_{\rm cm,ac} &= j_{\rm ac} + i\omega c^{\rm s}_{\rm H_3O^+}\Delta_{\rm s}\phi \end{aligned} \qquad (15)$$

The adsorption-diffusion layer in front of the catalyst

The time dependence of the concentration of hydrogen at position x in the anode is given by

$$\frac{\partial c^{\rm a}_{\rm H_2}}{\partial t} = D\frac{\partial^2 c^{\rm a}_{\rm H_2}(x,t)}{\partial x^2} + \frac{1}{2}k^{\rm a}_{\rm H_2}c^{\rm g}_{\rm H_2} - \frac{1}{2}k^{\rm d}_{\rm H_2}c^{\rm a}_{\rm H_2} \quad (16)$$

where D is the diffusion constant. Equilibrium in the adsorption reaction gives, using Eq.(1), the equilibrium concentration of hydrogen

$$c^{\rm a}_{{\rm H_2},eq} = c^{\rm g}_{\rm H_2}\frac{k^{\rm a}_{\rm H_2}}{k^{\rm d}_{\rm H_2}} \quad (17)$$

A constant hydrogen pressure in the pores gives a constant gas concentration, $c^{\rm g}_{\rm H_2}$ and therefore also a constant value for $c^{\rm a}_{{\rm H_2},eq}$. We introduce the deviation from the equilibrium concentration

$$c^{\rm a}_{\rm H_2}(x,t) \equiv c^{\rm a}_{{\rm H_2},eq} + \delta c^{\rm a}_{\rm H_2}(x,t) \quad (18)$$

Equation (16) then becomes to linear order in $\delta c^{\rm a}_{\rm H_2}$

$$\frac{\partial \delta c^{\rm a}_{\rm H_2}(x,t)}{\partial t} = D\frac{\partial^2 \delta c^{\rm a}_{\rm H_2}(x)}{\partial x^2} - \frac{1}{2}k^{\rm d}_{\rm H_2}\delta c^{\rm a}_{\rm H_2}(x,t) \quad (19)$$

The first paper [2] gave the solutions of this equation for dc and ac currents. We repeat the expressions needed, and refer to the first paper for their derivation. For a dc electric current the total Gibbs energy change of the whole reaction diffusion layer was

$$\begin{aligned}\Delta_r G_{\rm ad,dc} = \delta\mu^{\rm s}_{{\rm H_2},{\rm dc}} &= \delta\mu^{\rm a}_{{\rm H_2},{\rm dc}}(x=0) \\ &= -\frac{j_{\rm dc}RT}{2Fc^{\rm a}_{{\rm H_2},eq}\sqrt{2Dk^{\rm d}_{\rm H_2}}} \end{aligned} \quad (20)$$

The ac contribution to the total Gibbs energy change of the reaction/ diffusion layer was:

$$\Delta_r G_{\rm ad,ac} = \delta\mu^{\rm s}_{{\rm H_2},{\rm ac}} = \delta\mu^{\rm a}_{{\rm H_2},{\rm ac}}(x=0) = -Z_{\rm ad}F^2 r^{\rm s}_{\rm ct,ac} \quad (21)$$

where the contribution to the impedance was

$$Z_{\rm ad} = \frac{RT}{2F^2 c^{\rm a}_{{\rm H_2},eq}\sqrt{2Dk^{\rm d}_{\rm H_2}(1+i\omega\tau_{\rm ad})}} \quad (22)$$

and where the relaxation time in the absorption process was

$$\tau_{\rm ad} = \frac{1}{k^{\rm d}_{\rm H_2}} = \frac{c^{\rm a}_{{\rm H_2},eq}}{c^{\rm g}_{\rm H_2}k^{\rm a}_{\rm H_2}} \quad (23)$$

$Z_{\rm ad}$ is the impedance of a Gerischer element. Experimental results for the hydrogen electrode of the fuel cell fitted well to this asymmetric element [2], while the symmetric constant phase element and the element one obtains for a self-similar fractal surface structures [6] can only be fitted with much larger inaccuracies. A Warburg element does not describe the measurements at all.

The charge transfer reactions at the catalyst surface

Consider next the catalyst surface, or the interface between the membrane and the adsorption-diffusion layer in the electrode. The excess entropy production rate of this surface, $\sigma^{\rm s}$, contains the information about the surface dynamics. For isothermal conditions, the contributions due to the alternating fields are [7]:

$$\begin{aligned} T\sigma^{\rm s}_{\rm ac} &= -r^{\rm s}_{\rm cm,ac}F\left(\Delta_{\rm s}\phi_{\rm ac} - \Delta_{\rm s,H^+}\phi_{\rm ac}\right) \\ &\quad -r^{\rm s}_{\rm ct,ac}\left(F\Delta_{\rm s,H^+}\phi_{\rm ac} - \Delta_r G^{\rm s}_{\rm ad,ac}\right) \end{aligned} \quad (24)$$

Using the fact the two reactions occur consecutively, the coupling of these reactions may be neglected and the theory of non-equilibrium thermodynamics then prescribes that the forces and the fluxes are related by

$$\begin{aligned} \Delta_{\rm s,H^+}\phi_{\rm ac} - \frac{1}{F}\Delta_r G^{\rm s}_{\rm ad,ac} &= -\rho^{\rm s}_{\rm ct}Fr^{\rm s}_{\rm ct,ac} \\ \Delta_{\rm s}\phi_{\rm ac} - \Delta_{\rm s,H^+}\phi_{\rm ac} &= -\rho^{\rm s}_{\rm cm}Fr^{\rm s}_{\rm cm,ac} \end{aligned} \quad (25)$$

where $\rho^{\rm s}_{\rm ct}$ and $\rho^{\rm s}_{\rm cm}$ are the resistivities of the ct and cm reactions. Electrochemical reaction rates are normally not related to their driving forces by linear relations. In this experiment, the alternating contribution to the forces are small (± 5 mV), however, so that we can use a linear theory. Adding the two relations in Eq.(25) one obtains

$$\Delta_{\rm s}\phi_{\rm ac} - \frac{1}{F}\Delta_r G^{\rm s}_{\rm ad,ac} = -\rho^{\rm s}_{\rm ct}Fr^{\rm s}_{\rm ct,ac} - \rho^{\rm s}_{\rm cm}Fr^{\rm s}_{\rm cm,ac} \quad (26)$$

The adsorption-diffusion layer has an impact on $\Delta_{\rm s}\phi_{\rm ac}$, because this layer determines the chemical potential of hydrogen atoms at position $x = 0$. The resistivity is independent of the driving force, but can depend on the temperature and the polarization induced by the dc-field. The dc contribution to the excess entropy production rate is found using $\omega = 0$

and $j_{dc} = Fr^{s}_{ct,dc} = Fr^{s}_{cm,dc}$. This gives

$$T\sigma^{s}_{dc} = -j_{dc}\left[\Delta_s\phi_{dc} + \frac{1}{F}\left(\Delta_n G^{s}_{cm,dc} + \Delta_n G^{s}_{ct,dc}\right)\right] \tag{27}$$

For small dc-currents the linear law is thus:

$$\Delta_s\phi_{dc} + \frac{1}{F}\left(\Delta_n G^{s}_{cm,dc} + \Delta_n G^{s}_{ct,dc}\right) = -\left(\rho^{s}_{ct} + \rho^{s}_{cm}\right) j_{dc} \tag{28}$$

The surface impedance and the surface properties

The impedance of the catalyst surface is defined as:

$$Z^{s} \equiv -\frac{\Delta_s\phi_{ac}}{j_{ac}} \tag{29}$$

We find the surface impedance by adding Eqs.(21) and (26). This gives:

$$\Delta_s\phi_{ac} = -\left(\rho^{s}_{ct} + Z^{s}_{ad}\right) Fr^{s}_{ct,ac} - \rho^{s}_{cm} Fr^{s}_{cm,ac} \tag{30}$$

It furthermore follows from Eqs.(10) and (7) that

$$\begin{aligned} Fr^{s}_{ct} &= Fr^{s}_{cm} + i\omega c^{s}_{H^+}\Delta_{s,H^+}\phi \\ Fr^{s}_{cm} &= j_{ac} + i\omega c^{s}_{H_3O^+}\Delta_s\phi \end{aligned} \tag{31}$$

By combining Eqs.(25) and (29)-(31), we obtain the impedance of the surface

$$Z^{s} = \frac{\rho^{s}_{cm} + Z_{ct}}{1 + i\omega c^{s}_{H_3O^+}\left(\rho^{s}_{cm} + Z_{ct}\right)} \tag{32}$$

where

$$Z_{ct} = \frac{\rho^{s}_{ct} + Z_{ad}}{1 + i\omega c^{s}_{H^+}\left(\rho^{s}_{ct} + Z_{ad}\right)} \tag{33}$$

In the present experiments, we measure the response of two identically made electrodes plus membrane electrolyte. When a dc-current is passing the cell, one electrode will be a sink for hydrogen, while the other will be a source for hydrogen. The impedances of the two electrodes are the same, however. Both electrodes therefore give the same contribution to the measurement, also when the electrodes are polarized. In terms of the measured impedance, Z^{cell}, and the membrane impedance, Z^{mem}, the impedance of one electrode is then;

$$Z^{s} = \frac{1}{2}(Z^{cell} - Z^{mem}) \tag{34}$$

The membrane impedance is found by taking the limit of Z^{cell} for $\omega \to \infty$. The results that are calculated for Z^{s} from Eq.(34), can now be fitted to formulas (32) and (33) using Eq.(22) for Z_{ad}.
A constant phase element (CPE) shall be used for the charge transfer step in Eq.(32), rather than the capacitance. Eq.(33) then becomes:

$$Z_{ct} = \frac{\rho^{s}_{ct} + Z_{ad}}{1 + T_{ct}(i\omega)^{\alpha}\left(\rho^{s}_{ct} + Z_{ad}\right)} \tag{35}$$

When α equals 1, one has $T_{ct} = c^{s}_{H^+}$. The more depressed the semi-circle is, the lower is the α-value. We found α to be typically 0.82. We define the relaxation time for the charge transfer reaction:

$$\tau_{ct} \equiv \left(T_{ct}\,\rho_{ct}\right)^{1/\alpha} \tag{36}$$

The fit of the experimental results to the theoretical expressions gave Y_0 and τ_{ad} in the following expression for Z_{ad}:

$$Z_{ad} = \frac{1}{Y_0\sqrt{\tau^{-1}_{ad} + i\omega}} \tag{37}$$

The expression for the relaxation time, $\tau^{-1}_{ad} = k^{d}_{H_2}$, was given in Eq.(23).
The other variable is

$$Y_0 = \frac{2F^2}{RT} c^{a}_{H_2,eq}\sqrt{2D} \tag{38}$$

We see that knowledge of the diffusion constant for hydrogen along the pores, enables us to calculate $c^{a}_{H_2,eq}$ from this equation.

EXPERIMENTAL

For details about the membrane-electrode assembly, the gas humidifying system and other aspects of the experimental setup we refer to our first paper [2]. The impedance of the cell was measured at 30°C for different dc voltages. The impedance diagrams were recorded using a PAR 263A/94 potentiostat and a Solartron 1260 FRA. Z-plot software from Scribner Ass. Inc. was used to run the experiments. Measurements were made in a two-electrode set-up. The impedance was obtained by sweeping over the frequencies from 10 kHz to 10 mHz, recording 12 steps/decade, for each applied voltage. An amplitude of 5 mV was used in the experiments. The dc voltage varied from 0 to 60 mV in increments of 10 mV. Spectra were also recorded for systems exposed to a series of 30 experiments.

RESULTS

The impedance diagrams of Figs. 1 and 2 [2] were fitted to the expressions above. The spectra are given as Nyquist plots of Z^{cell}. The fitted results are presented in Tables 1-3. Table 1 gives the resistance of

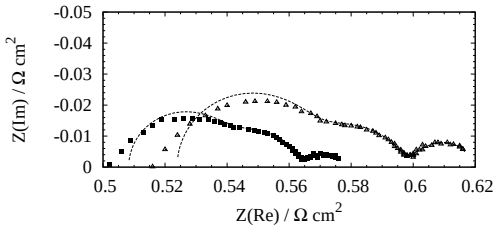

Figure 1: Impedance diagram for a freshly made PEMFC hydrogen electrode at 30^{o}C and 1 bar

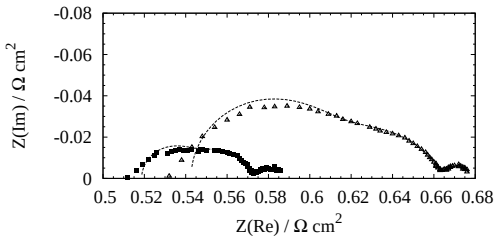

Figure 2: Impedance diagram for the PEMFC hydrogen electrode of Fig.1 used in 30 experiments, at 30^{o}C and 1 bar

the membrane R_Ω. It is, as expected, independent of the dc-voltage within the accuracy.

The first high frequency arc

The first arc in Figs.1 and 2 is, according to the model, related to the proton hydration. It was only possible to fit the first arc using a capacitance and a resistance, and not a constant phase element. When the applied dc potential increased, $c^{\text{s}}_{\text{H}_3\text{O}^+}$ decreased and ρ_{cm} increased.

The second arc: The constant phase element

The second arc in Figs.1 and 2, is according to the model, related to the charge transfer step. It is likely that the heterogeneity of the electrode causes a depression like the one we observe. This is also the motivation by us and others [3] to fit this second semi-circle to a constant phase element. The results show that T_{ct} is constant, while the resistance ρ_{ct} increases a little with the dc-potential. The variable

$\Delta\phi_{\text{dc}}$ (mV)	R_Ω (Ω cm^2)	$c^{\text{s}}_{\text{H}_3\text{O}^+}$ (F cm^2)	ρ_{cm} (Ω cm^2)
0	0.51	0.0071	0.035
10	0.53	0.0061	0.038
20	0.53	0.0057	0.041
30	0.53	0.0053	0.044
50	0.53	0.0049	0.047
60	0.54	0.0047	0.050

Table 1: Fitted results for the high frequency arc of the hydrogen electrode at 30 ^{o}C and 1 bar, for different applied dc potentials (5 % accuracy).

α_{ct} in the fit of the diagram to a CPE was constant (0.82).

$\Delta\phi_{\text{dc}}$ (mV)	T_{ct} (Ω^{-1} cm^{-2} s$^\alpha$)	α_{ct}	ρ_{ct} (Ω cm^2)
0	0.46$\pm$0.10	0.83	0.020$\pm$0.002
10	0.49$\pm$0.11	0.80	0.023$\pm$0.002
20	0.41$\pm$0.08	0.84	0.023$\pm$0.001
30	0.47$\pm$0.09	0.82	0.025$\pm$0.001
50	0.47$\pm$0.12	0.82	0.026$\pm$0.002
60	0.50$\pm$0.12	0.82	0.026$\pm$0.002

Table 2: Fitted results for the second arc of the hydrogen electrode at 30 ^{o}C and 1 bar, for different applied dc potentials

The third arc: The Gerischer element

The parameter Y_0 in the Gerischer element decreases when the dc-voltage increases, while the adsorption time τ_{ad} is constant within the accuracy. These results are essentially the same as those found in the first paper, where we simplified the description by assuming the water to be everywhere in equilibrium. They did also not vary by ageing. The relaxation times for the high an medium frequency phenomena were calculated, see Table 4. For τ_{cm} we used $\rho^{\text{s}}_{\text{cm}} c^{\text{s}}_{\text{H}_3\text{O}^+}$ while the relaxation time for the charge transport, τ_{ct}, was calculated using Eq.(36). The relaxation time for the slowest process was given in Table 3.

Ageing

As the electrode is being exposed to the oscillating field, even in the absence of an applied dc potential,

$\Delta\phi_{dc}$ (mV)	Y_0 (Ω^{-1} cm^{-2} s$^{1/2}$)	τ_{ad} (s)
0	190±20	6 ±2
10	180±16	8 ±1
20	160±10	8 ±1
30	150±10	8 ±1
50	130±10	8 ±1
60	120±10	8 ±1

Table 3: Fitted results for the Gerischer element of the hydrogen electrode at 30 ^{o}C and 1 bar, for different applied dc potentials

$\Delta\phi_{dc}$ (mV)	j (A cm^{-2})	τ_{cm} (10^{-4} s)	τ_{ct} (10^{-3} s)
0	0	2.49	3.5
10	0.016	2.32	3.7
20	0.030	2.34	3.9
30	0.043	2.33	4.4
50	0.070	2.30	4.6
60	0.083	2.35	5.0

Table 4: Calculated relaxation times for the cell at T=30^o C and 1 bar hydrogen gas, for different applied potentials

the first and the second arc obtains an increased resistivity. The Gerischer element remains unchanged.

DISCUSSION

The three arcs can be characterized as follows.

- The first arc has few signs of depression, and its relaxation time is independent of the applied potential. Its resistance depends on ageing, but the relaxation time does not.
- The second arc needs to be modelled with a constant phase element. Its resistance depends on ageing and the applied potential. Among the three relaxation times, only τ_{ct} increases with applied potential.
- The Gerischer element does neither depend on the applied potential, nor on the ageing of the electrode or the assumption of equilibrium for water for all conditions

These properties do all support the model given above, with the three suggested rate limiting steps, if the ageing effect can be explained by a reduction in particle surface, or by particle agglomeration [8]. It is likely that proton hydration relaxation does not depend on the applied potential, but that the resistance of this step depends on the surface area. Pictures of the catalyst particles may further confirm this hypothesis. A rate-limiting role for water was suggested by others [9–11]. It is furthermore natural that the charge transfer step depends on the applied potential, as well as on the current density, as observed. The Gerischer element was discussed earlier [2]. The diffusion coefficient of molecular hydrogen inside the carbon pores is 2×10^{-4} m^2/s [12, 13]

$\Delta\phi_{dc}$ (mV)	$c^a_{H_2,eq}$ (mol m^{-3})	$k^d_{H_2}$ (1/s)	$k^a_{H_2}$ (1/s)
0	300	0.17	0.30
10	290	0.13	0.24
20	240	0.13	0.20
30	240	0.12	0.20
50	210	0.12	0.17
60	190	0.12	0.15

Table 5: Concentrations and rate constants for a pressure of 1 bar at 30^{o}C and varying potential.

where the porosity is 0.4 and the pore diameter 50 nm [13, 14]. The surface of the pores area per cubic meter carbon is about 3×10^7 m^2. The volume fraction of a 0.33 nm thick surface is about 0.01. Scaled for the surface volume and a tortuosity of around 7 [14] the gas diffusion coefficient gave an estimate of the course grained diffusion coefficient of about $D = 3\times10^{-7}$ m^2/s. The equilibrium concentration of adsorbed hydrogen, $c^a_{H_2,eq}$, can now be calculated using Eq.(38). The concentration of molecular hydrogen in the pores is found using the ideal gas law which gives 40 mol m^{-3}. Multiplied with the porosity, we have $c^g_{H_2} = 16$ mol m^{-3}, independent of the dc-potential. The rate constants $k^a_{H_2}$ and $k^d_{H_2}$ then follow from Eq. (23). The calculated results are given in Table 5. The density of adsorbed hydrogen decreases from about 2 to one molecule per square nanometer, when the dc-voltage increases. Concurrently the rate coefficient decreases by a factor of two. The density of the hydrogen in the pores as well as the rate coefficient for desorption are both constant.

CONCLUSION

Electrochemical impedance spectroscopy was performed of the fuel cell electrode E-TEK, Elat/Std/DS/V2 0.5 mg Pt/cm^2, 20 Pt/C, impregnated with 0.6 mg Nafion®/cm^2 (5 wt % solution). The membrane contact was Nafion® 117. The electrode was studied at 30^{o}C and 1 bar.

A model was developed to describe three arcs in the Nyquist plot. We conclude that proton hydration may play a role in the process, in addition to the charge transfer process and the adsorption and diffusion of gas along the carbon surface. The experiments can be taken as a support for the theoretical description of the electrochemical transport processes in the nanoporous material.

ACKNOWLEDGMENTS

A.K. Meland is grateful to Nordic Energy Research and Norsk Hydro ASA.

REFERENCES

[1] D.A. Harrington and B.E. Conway. AC impedance of faradaic reactions involving electrosorbed intermediates-i. kinetic theory. *Electrochim. Acta*, 32:1703–1712, 1987.

[2] A.-K. Meland, D. Bedeaux, and S. Kjelstrup. A Gerischer phase element in the impedance diagram of the polymer electrolyte membrane fuel cell anode. *submitted*, 2005.

[3] M. Ciureanu and H. Wang. Electrochemical impedance study of electrode-membrane assemblies in PEM fuel cells I. Electro-oxidation of H_2 and H_2/CO mixtures on Pt-based gas-diffusion electrodes. *J. Electrochem. Soc.*, 146(11):4031–4040, 1999.

[4] J.-D. Kim, Y.-I. Park, K. Kobayashi, M. Nagai, and M. Kunimatsu. Characterization of CO tolerance of PEMFC by ac impedance spectroscopy. *Solid State Ionics*, 140:313–325, 2001.

[5] S.L. Chen and A. Kucernak. Electrocatalysis under conditions of high mass transport: Investigation of hydrogen oxidation on single submicron Pt particles supported on carbon. *J. Phys. Chem. B*, 108:13984–13994, 2004.

[6] W.H. Mulder and J.H. Sluyters. An explanation of depressed semi-circular arcs in impedance plots for irreversible electrode reactions. *Electrochim. Acta*, 33(3):303–310, 1988.

[7] D. Bedeaux and S. Kjelstrup. The impedance of an electrode surface described by irreversible thermodynamics. *J. Nonequil. Thermodyn.*, 24:80–96, 1999.

[8] J. Xie, D.L. Wood III, D.M. Wayne, T.A. Zawodzinski, P. Atanassov, and R.L. Borpu. Durability of PEFCs at high humidity conditions. *J. Electrochem. Soc.*, 152(1):A104–A113, 2005.

[9] V.A. Paganin, C.L.F. Oliveira, E.A. Ticianelli, T.E. Springer, and E.R. Gonzalez. Modelistic interpretation of the impedance response of a polymer electrolyte fuel cell. *Electrochim. Acta*, 43:3761–3766, 1998.

[10] T.J.P. Freire and E.R. Gonzalez. Effect of membrane chracteristics and humidification conditions on the impedance response of polymer electrolyte fuel cells. *J. Electroanal. Chem.*, 503:57–68, 2001.

[11] M. Brown, S. Primdahl, and M. Mogensen. Structure/performance relations for Ni/yttria-stabilized zirconia anodes for solid oxide fuel cells. *J. Electrochem. Soc.*, 147:475–485, 2000.

[12] R.B. Bird, W.E. Stewart, and E.N. Lightfoot. *Transport Phenomena*. Wiley, Chichester, UK, 1960.

[13] M. Grujicic and K.M. Chittajallum. Design and optimization of polymer electrolyte membrane (PEM) fuel cells. *Applied Surface Science*, 227:56–72, 2004.

[14] T.E. Springer, T.A. Zawodzinski, M.S. Wilson, and S. Gottesfeld. Characterization of polymer electrolyte fuel cells using ac impedance spectroscopy. *J. Electrochem. Soc*, 143:587–599, 1996.

Proceedings of ECOS 2005
Trondheim, Norway
June 20–22, 2005

DYNAMICS OF TRANSLOCATION THROUGH NANOPORES

David Reguera*
Departament de Física Fonamental, Universitat de Barcelona,
Martí i Franquès 1, 08028 Barcelona, SPAIN

Roya Zandi, William M. Gelbart
Department of Chemistry and Biochemistry, University of California,
Los Angeles, CA 90095, USA

Joseph Rudnick
Department of Physics, University of California,
Los Angeles, CA 90095, USA

ABSTRACT

Many biological processes involve the translocation of a biomolecule through a pore or a channel. A common example is the entry of the DNA of a bacteriophage into the cell [1]. Translocation may occur by simple diffusion. However, this mechanism is very slow, and in many cases there are some proteins in the cell that facilitate the entry of the biomolecule by binding reversibly to it. The role played by these proteins is assumed to be the rectification of the diffusion, thus acting as a Brownian ratchet [2].

To analyze in detail the process of translocation, we study the dynamics of the passage of a stiff chain through a pore into a cell containing particles that bind reversibly to it [3]. Using Brownian dynamics simulations we investigate the mean first-passage time as a function of the length of the chain inside for different concentrations of binding particles. We find that, as a consequence of the interactions with these particles, the chain experiences a net force along its length which drives it into the cell significantly faster than by pure or even ratcheted diffusion. These results suggest a role of binding particles in the translocation process that is in general quite different from that of a Brownian ratchet. Furthermore, nonequilibrium effects contribute significantly to the dynamics; e.g., the force that pulls the biomolecule strongly depends on how fast the translocation occurs compared to the binding of proteins. The results of the simulations and the dynamics of translocation can be successfully described using Mesoscopic Non-Equilibrium Thermodynamics (MNET) [4], in terms of a generalized diffusion equation which unveils the origin of the pulling force and provides a complete description of the kinetics of both chain entry and particle binding.

Keywords: Translocation, Brownian ratchet, Mesoscopic Non-Equilibrium Thermodynamics

REFERENCES

[1] Alberts B *et al. Molecular Biology of the Cell.* New York: Garland, 1994.

[2] Simon SM, Peskin CS, Oster GF. *What drives the translocation of proteins?*. Proc. Nat. Acad. Sci.1992; 89(9); 3770-3774.

[3] Zandi R, Reguera D, Rudnick J, Gelbart WD. *What drives the translocation of stiff chains?*. Proc. Nat. Acad. Sci. 2003; 100(15); 8649-8653.

[4] Reguera D, Rubí JM. *Kinetic equations for diffusion in the presence of entropic barriers*. Phys. Rev. E 2001; 64(6); 061106.

*E-mail: dreguera@ub.edu

Proceedings of ECOS 2005
Trondheim, Norway
June 20–22, 2005

NON-EQUILIBRIUM THERMODYNAMICS FOR NANOSYSTEMS

J.M. Rubi

Departament de Fisica Fonamental, Universitat de Barcelona, Diagonal 647, 08028, Barcelona, Spain

Nonequilibrium thermodynamics was proposed as a theoretical framework to analyze irreversible processes taking place in large scale systems. The theory has been successfully applied to systems of a very different nature, pertaining to different areas such as physics, physical-chemistry, biology and engineering. The scheme of non-equilibrium thermodynamics was extended to incorporate internal degrees of freedom to the set of thermodynamic variables. These degrees of freedom can, for exemple, represent the orientation of a macromolecules or a reaction coordinate and were assumed to undergo a diffusion process along an internal coordinate. We have shown that when endowed with probabilistic elements the method can also be used to analyze the irreversible behaviour of nanosystems for which the presence of fluctuations and the nature of the environment become elements of primary importance in the dynamics of the system. In this scheme the chemical potential and the probability density play the role of conjugate mesoscopic thermodyamic variables. The proposed theory: mesoscopic nonequilibrium thermodynamics (MNET) is offered as a general formalism able to characterize the irreversible behavior of small scale systems.
In the last years, we have shown the applicability of mesoscopic non-equilibrium thermodynamics to a broad variety of situations such as chemical kinetics electrochemistry, nucleation and growth, evaporation and condensation phenomena, active transport in biological systems and diffusion in the presence of entropic barriers. Our approach opens the way to the study of nanosystems through non-equilibrium thermodynamics methods.

1. de Groot, S.R.; Mazur, P., Non-Equilibrium thermodynamics, Dover: New York, 1984.
2. Prigogine, I.; Mazur, P., Physica (1953), XIX, 241.
3. Reguera, D.; Rubi, J.M., Phys. Rev. E (2001), **64**, 061106.
4. Vilar, J.M.G.; Rubi, J.M., Proc. Nat. Acad. Sci. (2001), **98**, 11081.
5. Rubi, J.M.; Kjelstrup, S., J. Chem. Phys B (2003), **107**, 13471.
6. Bedeaux, D.; Kjelstrup, S.; Rubi, J.M., J. Chem. Phys. (2003), **119**, 1.
7. Kjelstrup, S.; Rubi, J.M.; Bedeaux, D., J. Theor. Biol. (2005), **234**, 7.

Second law analyses

Proceedings of ECOS 2005
Trondheim, Norway
June 20–22, 2005

MAXIMUM POWER PROCESSES FOR MULTI-SOURCE ENDOREVERSIBLE HEAT ENGINES

B. Andresen
Niels Bohr Institute, University of Copenhagen,
Universitetsparken 5, DK-2100 Copenhagen Ø, Denmark

S. A. Amelkin, A. M. Tsirlin
Program Systems Institute,
RU-152140 Pereslavl-Zalessky, Russia

J. M. Burzler, K. H. Hoffmann
Institute of Physics, Technical University of Chemnitz,
D-09107 Chemnitz, Germany

ABSTRACT

The maximum power processes of multi-source endoreversible engines with stationary temperature reservoirs are investigated. We prove that the optimal solution is always time independent with a single hot and a cold engine contact temperature. The heat reservoirs fall into three groups: The hot reservoirs which are connected at all times for heat delivery, the cold reservoirs which are connected at all times for heat drain, and possibly a group of reservoirs at intermediate temperatures which are unused. This phenomenon is demonstrated for a three-source system. We find that for a commonly used class of heat transfer functions, including Newtonian, Fourier and radiative heat transport, the efficiencies at maximum power are the same as for two-reservoir engines with appropriately chosen properties.
*Keywords:*heat engine, endoreversible, optimization, reservoirs

INTRODUCTION

Heat engines with several heat sources are common for many real-world applications such as industrial heat-recovery systems and solar energy installations. In such installations several different heat sources are present, which provide heat at different rates, and, even more importantly, at different temperatures. For instance in solar energy installations these differences can come about because the angle towards the sun may differ or because some solar collectors might be at a larger distance from the central plant and thus the losses along the transport pipes cause a change in the effective temperature at the engine.

This paper investigates the performance limits for such engines. In particular we study maximum power processes for an endoreversible engine [1–3] operating between several heat reservoirs. The average power output is used as a criterion of thermodynamic merit. Methods of averaged nonlinear programming [4–6], which are already well established for the optimization of thermal systems with two heat reservoirs [7–9], are applied to determine the maximum possible average power output and the corresponding optimal contact functions between the heat reservoirs and the power converting subsystem.

In this model all irreversible processes are associated with the interactions between the heat engine and the heat reservoirs while the processes inside the reservoirs and power converting subsystem are reversible (i.e. the endoreversibility hypothesis [1]). This study thus complements earlier work on staged and combined systems, see for instance [10–19].

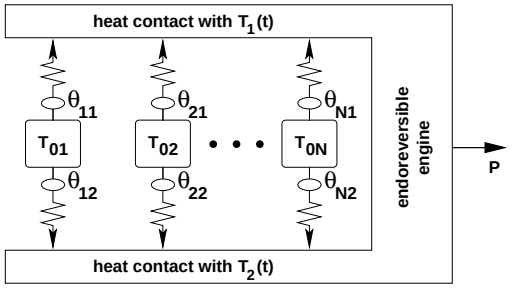

Figure 1: A multi-source endoreversible engine.

MODEL

A model of a multi-source endoreversible heat engine is depicted in figure 1. It consists of a power converting subsystem operating reversibly between two temperature contacts $T_1(t)$ and $T_2(t)$ and of N heat sources/sinks at constant temperatures T_{0i} where $i \in [1,N]$. The heat transfer laws between source i and engine contact $\alpha \in \{1,2\}$ have the form

$$\tilde{q}_{i\alpha}(T_{0i},T_\alpha,\theta_{i\alpha}) = \theta_{i\alpha} q_{i\alpha}(T_{0i},T_\alpha), \quad i \in [1,N]\,. \quad (1)$$

The contact functions $\theta_{i\alpha}$ describe the extent of the contact between reservoir and engine. They are equal to one if the i-th reservoir is fully connected to contact α and are equal to zero if there is no contact. Thus $0 \le \theta_{i\alpha}(t) \le 1$.

In the following we assume that the functions $q_{i\alpha}(T_{0i},T_\alpha)$ show the standard behavior of heat transfer as a function of T_{0i} and T_α, i.e. heat flows from high to low temperature: $q_{i\alpha}(T_{0i},T_\alpha) > 0$ if $T_{0\mathrm{i}} > T_\alpha$, $q_{i\alpha}(T_{0i},T_\alpha) < 0$ if $T_{0\mathrm{i}} < T_\alpha$, and $q_{i\alpha}(T_{0i},T_\alpha) = 0$ if $T_{0\mathrm{i}} = T_\alpha$.

POWER OPTIMIZATION

Our aim is to determine maximum power processes for this multi-source engine as well as the efficiency at maximum power. The system is operated under cyclic conditions with a fixed cycle time τ_{tot}, i.e. internal energy and entropy of the endoreversible engine is the same at the beginning and the end of the cycle. The system is optimized for maximum average power output $\bar{P}$. This is equivalent to the maximization of the time-averaged sum of the heat flows

$$q_\Sigma(T_0,T_1(t),T_2(t),\theta_1(t),\theta_2(t)) = \sum_{i=1}^{N} \tilde{q}_{i1}(T_{0i},T_1,\theta_{i1}) + \tilde{q}_{i2}(T_{0i},T_2,\theta_{i2})\,, \quad (2)$$

where the vectors θ_α of the contact functions and the vector T_0 of the reservoir temperatures are defined as

$$\theta_\alpha = (\theta_{1\alpha},\theta_{2\alpha},\ldots,\theta_{N\alpha}) \quad \text{and} \quad (3)$$
$$T_0 = (T_{01},T_{02},\ldots,T_{0N})\,. \quad (4)$$

The optimization problem can be stated formally as the maximization of the functional

$$I = \bar{P} = \overline{q_\Sigma}\,,[T_0,T_1(t),T_2(t),\theta_1,\theta_2] = \frac{1}{\tau_{\mathrm{tot}}}\int_0^{\tau_{\mathrm{tot}}} \sum_{i=1}^{N} (\tilde{q}_{i1}(T_{0i},T_1,\theta_{i1}) + \tilde{q}_{i2}(T_{0i},T_2,\theta_{i2}))\,\mathrm{d}t \to \max_{\{T_\alpha,\theta_\alpha\}} \quad (5)$$

by varying the engine contact temperatures T_1 and T_2 and all the contact functions θ_α subject to the restriction of entropy balance

$$\overline{s_\Sigma} = \overline{s_\Sigma}[T_0,T_1(t),T_2(t),\theta_1,\theta_2] = \frac{1}{\tau_{\mathrm{tot}}}\int_0^{\tau_{\mathrm{tot}}} \sum_{i=1}^{N} \left(\frac{\tilde{q}_{i1}(T_{0i},T_1,\theta_{i1})}{T_1} + \frac{\tilde{q}_{i2}(T_{0i},T_2,\theta_{i2})}{T_2}\right)\mathrm{d}t = 0\,. \quad (6)$$

This restriction is due to the cyclic operation of the system.

The temperatures $0 < T_1(t), T_2(t) < \infty$ of the endoreversible engine and the elements of the vector θ_α of contact functions are the $2N+2$ controls of the system. These elements satisfy the conditions

$$0 \le \theta_{i\alpha}(t) \le 1\,, \quad i \in [1,N] \quad \alpha \in \{1,2\}\,. \quad (7)$$

Equations (5–7) can either be optimized by using optimal control theory or by a special kind of nonlinear programming. As the objective as well as the constraint are both in the form of a time average over a given interval, we will here use averaged nonlinear programming. The Lagrangian for this problem has the form [4–6]

$$\mathscr{L} = \sum_{i=1}^{N} (\tilde{q}_{i1}(T_{0i},T_1,\theta_{i1})\left[1-\frac{\lambda}{T_1}\right] + \tilde{q}_{i2}(T_{0i},T_2,\theta_{i2})\left[1-\frac{\lambda}{T_2}\right]) \to \max_{\{T_\alpha,\theta_\alpha\}}\,, \quad (8)$$

where λ is a kind of Lagrange multiplier associated with the entropy balance, eq. (6).

The theory of averaged programming [4, 5] states that the solution for the optimal controls are piecewise constant functions taking values out of a set of

no more than $m+1$ *base points* where m is the number of averaged constraints of the problem (see [6], p. 78 ff).

The first point to note is thus that T_1 and T_2 are piecewise constant in time. The second point is that there is only one averaged constraint (6) here, and consequently there are no more than two base points for the controls and in particular for the temperatures $T_1(t)$ and $T_2(t)$. Let us call them T_h and T_c. As the optimization problem set up above is fully symmetric in the two contacts 1 and 2, the two base points are either of the form $(T_1,T_2)=(T_\mathrm{h},T_\mathrm{c})$ and $(T_1,T_2)=(T_\mathrm{c},T_\mathrm{h})$, or there is only one base point which then must have $T_1=T_2$. In the latter case the engine does not produce any power, so we exclude this case from our further considerations. In the first case we need to discuss only one of the base points and can thus assume $T_\mathrm{c}<T_\mathrm{h}$ without loss of generality.

From a physical point of view this means that, even though in principle the temperatures at the contacts of the endoreversible engine could change, it is optimal to run the engine in a stationary mode with fixed temperatures.

OPTIMAL CONTACT FUNCTIONS

We now turn to the variation of $\mathscr{L}$ with respect to the controls $\theta_{i\alpha}$. The Lagrangean $\mathscr{L}$ depends linearly on each $\theta_{i\alpha}$, so that $\mathscr{L}$ will attain its maximum only at the boundary values $\{0,1\}$ of the admissible range of $\theta_{i\alpha}$. This determines a rule for the contact functions:

$$\theta_{i\alpha}(T_{0i},T_{i\alpha})=\begin{cases}1 & \text{if} \quad \left[1-\frac{\lambda}{T_\alpha}\right]q_{i\alpha}(T_{0i},T_\alpha)>0\\ 0 & \text{if} \quad \left[1-\frac{\lambda}{T_\alpha}\right]q_{i\alpha}(T_{0i},T_\alpha)<0\end{cases}$$

$$\in[1,N] \quad \alpha\in\{1,2\}. \tag{9}$$

Let us take a closer look at this rule. $q_{i\alpha}(T_{0i},T_\alpha)<0$ means that the contact α connects with reservoirs which serve as heat sinks and thus fulfill the condition $T_{0i}<T_\alpha$. In the opposite case, i.e. $q_{i\alpha}(T_{0i},T_\alpha)>0$, this implies the condition $T_{0i}>T_\alpha$. The working fluid then connects to reservoirs which act as heat sources.

We now distinguish three cases:

$T_\mathrm{h}>T_\mathrm{c}>\lambda$:

$$\left[1-\frac{\lambda}{T_\mathrm{h}}\right]>0 \quad\Rightarrow\quad \begin{cases}\theta_{i\mathrm{h}}(T_{0i},T_\mathrm{h},\lambda)=1\\ \quad\text{if } q_{i\mathrm{h}}>0 \text{ i.e. } T_{0i}>T_\mathrm{h}\\ \theta_{i\mathrm{h}}(T_{0i},T_\mathrm{h},\lambda)=0\\ \quad\text{if } q_{i\mathrm{h}}\le 0 \text{ i.e. } T_{0i}\le T_\mathrm{h},\end{cases} \tag{10}$$

$$\left[1-\frac{\lambda}{T_\mathrm{c}}\right]>0 \quad\Rightarrow\quad \begin{cases}\theta_{i\mathrm{c}}(T_{0i},T_\mathrm{c},\lambda)=1\\ \quad\text{if } q_{i\mathrm{c}}>0 \text{ i.e. } T_{0i}>T_\mathrm{c}\\ \theta_{i\mathrm{c}}(T_{0i},T_\mathrm{c},\lambda)=0\\ \quad\text{if } q_{i\mathrm{c}}\le 0 \text{ i.e. } T_{0i}\le T_\mathrm{c}.\end{cases} \tag{11}$$

In this case all $\tilde{q}_{i\alpha}$ are either positive or vanishing which means that due to the entropy constraint all $\tilde{q}_{i\alpha}$ have to equal zero and thus no power is produced. We therefore exclude this case from our further consideration.

$\lambda>T_\mathrm{h}>T_\mathrm{c}$:

$$\left[1-\frac{\lambda}{T_\mathrm{h}}\right]<0 \quad\Rightarrow\quad \begin{cases}\theta_{i\mathrm{h}}(T_{0i},T_\mathrm{h},\lambda)=0\\ \quad\text{if } q_{i\mathrm{h}}>0 \text{ i.e. } T_{0i}>T_\mathrm{h}\\ \theta_{i\mathrm{h}}(T_{0i},T_\mathrm{h},\lambda)=1\\ \quad\text{if } q_{i\mathrm{h}}\le 0 \text{ i.e. } T_{0i}\le T_\mathrm{h},\end{cases} \tag{12}$$

$$\left[1-\frac{\lambda}{T_\mathrm{c}}\right]<0 \quad\Rightarrow\quad \begin{cases}\theta_{i\mathrm{c}}(T_{0i},T_\mathrm{c},\lambda)=0\\ \quad\text{if } q_{i\mathrm{c}}>0 \text{ i.e. } {}_{0i}>T_\mathrm{c},\\ \theta_{i\mathrm{c}}(T_{0i},T_\mathrm{c},\lambda)=1\\ \quad\text{if } q_{i\mathrm{c}}\le 0 \text{ i.e. } T_{0i}\le T_\mathrm{c}.\end{cases} \tag{13}$$

In this case all $\tilde{q}_{i\alpha}$ are either negative or vanishing which means that due to the entropy constraint all $\tilde{q}_{i\alpha}$ have to equal zero and thus no power is produced. Again we therefore exclude this case from our further consideration.

$T_\mathrm{h}>\lambda>T_\mathrm{c}$:

$$\left[1-\frac{\lambda}{T_\mathrm{h}}\right]>0 \quad\Rightarrow\quad \begin{cases}\theta_{i\mathrm{h}}(T_{0i},T_\mathrm{h},\lambda)=1\\ \quad\text{if } q_{i\mathrm{h}}>0 \text{ i.e. } T_{0i}>T_\mathrm{h}\\ \theta_{i\mathrm{h}}(T_{0i},T_\mathrm{h},\lambda)=0\\ \quad\text{if } q_{i\mathrm{h}}\le 0 \text{ i.e. } T_{0i}\le T_\mathrm{h},\end{cases} \tag{14}$$

$$\left[1-\frac{\lambda}{T_\mathrm{c}}\right]<0 \quad\Rightarrow\quad \begin{cases}\theta_{i\mathrm{c}}(T_{0i},T_\mathrm{c},\lambda)=0\\ \quad\text{if } q_{i\mathrm{c}}>0 \text{ i.e. } T_{0i}>T_\mathrm{c}\\ \theta_{i\mathrm{c}}(T_{0i},T_\mathrm{c},\lambda)=1\\ \quad\text{if } q_{i\mathrm{c}}\le 0 \text{ i.e. } T_{0i}\le T_\mathrm{c}.\end{cases} \tag{15}$$

In this case only reservoirs with positive $q_{i\mathrm{h}}(T_{0i},T_\mathrm{h})$ are connected to the engine contact at T_h, i.e. those with $T_{0i}>T_\mathrm{h}$. In the same way only negative $q_{i\mathrm{c}}(T_{0i},T_\mathrm{c})$ are connected to the engine contact at T_c, i.e those with $T_{0i}<T_\mathrm{c}$.

Note that due to the stationarity of T_h, T_c, and λ the contact functions are also independent of time.

HOT, COLD, AND UNUSED RESERVOIRS

We can now draw a number of interesting and surprising conclusions from the structure of the optimal contact functions. First of all it is clear that a reservoir will be at most connected to one heat contact. Those reservoirs with temperatures above the hot contact temperature will deliver heat, those with temperatures below the the cold temperature contact will receive heat. All reservoirs with temperatures in the range between T_c and T_h are therefore never connected during a cycle; these reservoirs are referred to as *unused reservoirs*.

As a consequence the set of N heat reservoirs is divided into three subsets R_h, R_c, and R_u of *hot*, *cold* and *unused* reservoirs, respectively. Note that the unused set may be empty depending on the temperatures of the reservoir. Also, it is clear that the hotest and coldest reservoirs are always active in a finite power producing solution.

CONSTRUCTION OF HEATING AND COOLING FUNCTIONS

To determine the heat flows resulting from the above rule, the heat transfer functions for each reservoir are separated into heat input and output functions,

$$q^+_{i\mathrm{h}}(T_{0i},T_\mathrm{h}) = \begin{cases} q_{i\mathrm{h}}(T_{0i},T_\mathrm{h}) & \text{if} T_{0i}\geq T_\mathrm{h} \\ 0 & \text{if} T_{0i}<T_\mathrm{h} \end{cases} \quad (16)$$

$$q^-_{i\mathrm{c}}(T_{0i},T_\mathrm{c}) = \begin{cases} 0 & \text{if} T_{0i}>T_\mathrm{c} \\ q_{i\mathrm{c}}(T_{0i},T_\mathrm{c}) & \text{if} T_{0i}\leq T_\mathrm{c} \end{cases} \quad (17)$$

for each $i\in[1,N]$. The total rate of heat input to and from the endoreversible engine are calculated as the sum of all contributions $q^+_{i\mathrm{h}}(T_{0i},T_\mathrm{h})$ and $q^-_{i\mathrm{c}}(T_{0i},T_\mathrm{c})$,

$$q^+(T_0,T_\mathrm{h}) = \sum_{i=1}^{N} q^+_{i\mathrm{h}}(T_{0i},T_\mathrm{h}) \quad (18)$$

$$q^-(T_0,T_\mathrm{c}) = \sum_{i=1}^{N} q^-_{i\mathrm{c}}(T_{0i},T_\mathrm{c})\,. \quad (19)$$

The heat exchange causes an entropy change of the working fluid. The rates of entropy flow to the working fluid are easily obtained by dividing the corresponding heat exchange rate by the current temperature of the working fluid. Specifically, the rates of entropy change are

$$s^+(T_0,T_\mathrm{h}) = \frac{q^+(T_0,T_\mathrm{h})}{T_\mathrm{h}} \quad (20)$$

$$s^-(T_0,T_\mathrm{c}) = \frac{q^-(T_0,T_\mathrm{c})}{T_\mathrm{c}}\,. \quad (21)$$

OPTIMAL TEMPERATURES FOR THE ENGINE CONTACTS

The Lagrange function (8) can now be expressed in terms of the above defined functions:

$$\mathscr{L} = q^+(T_0,T_\mathrm{h})\left[1-\frac{\lambda}{T_\mathrm{h}}\right] + q^-(T_0,T_\mathrm{c})\left[1-\frac{\lambda}{T_\mathrm{c}}\right]. \quad (22)$$

Already at this point it is apparent that the optimization of a multi source heat engine is equivalent to the optimization of a two-reservoir heat engine with the heat transfer functions defined above.

In order to determine the optimal temperatures we use the optimality condition $\partial\mathscr{L}/\partial T_\mathrm{h}=0$ and $\partial\mathscr{L}/\partial T_\mathrm{c}=0$ which can be rewritten as

$$\lambda = \frac{\partial q^+(T_0,T_\mathrm{h})}{\partial T_\mathrm{h}} T_\mathrm{h}\left(\frac{\partial q^+(T_0,T_\mathrm{h})}{\partial T_\mathrm{h}} - \frac{q^+(T_0,T_\mathrm{h})}{T_\mathrm{h}}\right)^{-1}, \quad (23)$$

and

$$\lambda = \frac{\partial q^-(T_0,T_\mathrm{c})}{\partial T_\mathrm{c}} T_\mathrm{c}\left(\frac{\partial q^-(T_0,T_\mathrm{c})}{\partial T_\mathrm{c}} - \frac{q^-(T_0,T_\mathrm{c})}{T_\mathrm{c}}\right)^{-1}. \quad (24)$$

Together with the constraint on the entropy as given by eq. (6) these equations determine the values of λ, T_h, T_c for given laws of heat conduction $q_i(T_{0i},T)$ and reservoir temperatures T_{0i}. These equations are used to analytically or numerically calculate optimal solutions.

A SPECIAL CLASS OF HEAT TRANSPORT EQUATIONS

We now restrict our analysis to an important subclass of heat transport equations. This class is characterized by a special structure in which the net heat flow is a sum or difference of two terms, where each system contributes to the heat flow based on just its own temperature:

$$q_{i\alpha}(T_{0i},T_\alpha) = q^{(\mathrm{r})}_{i\alpha}(T_{0i}) + q^{(\mathrm{s})}_{i\alpha}(T_\alpha). \quad (25)$$

This structure includes for instance Newtonian heat transfer, Fourier heat transfer, and heat transport by radiation. An example of a transport rule which does not comply with this structure is due to Anand:

$$q_{i\alpha}(T_{0i},T_\alpha) = (T_{0i}-T_\alpha)^\gamma. \quad (26)$$

For transport equations of the form (25) the summed up heat flows obey

$$q^+(T_0,T_\mathrm{h}) = \sum_{i\in R_\mathrm{h}} q^{(\mathrm{r})}_{i\mathrm{h}}(T_{0i}) + \sum_{i\in R_\mathrm{h}} q^{(\mathrm{s})}_{i\mathrm{h}}(T_\mathrm{h})$$

$$= q_{\rm h}^{(\rm r)}(T_0) + q_{\rm h}^{(\rm s)}(T_{\rm h}) \qquad (27)$$

$$q^-(T_0, T_{\rm c}) = \sum_{i\in R_{\rm c}} q_{i{\rm c}}^{(\rm r)}(T_{0i}) + \sum_{i\in R_{\rm c}} q_{i{\rm c}}^{(\rm s)}(T_{\rm c})$$

$$= q_{\rm c}^{(\rm r)}(T_0) + q_{\rm c}^{(\rm s)}(T_{\rm c})\,. \qquad (28)$$

Thus the system behaves as if connected to only two reservoirs.

If further the multiple sources are coupled to the engine by transport rules with the same T dependent function f, i.e.

$$q_{i\alpha}(T_{0i}, T_\alpha) = a_{i\alpha}(f(T_{0i}) - f(T_\alpha)). \qquad (29)$$

then the summed up heat transfer functions q^+ and q^- have the same structure

$$q^+(T_0, T_{\rm h}) = a_{\rm h}(f(T_{0{\rm h}}) - f(T_{\rm h})) \qquad (30)$$

$$q^-(T_0, T_{\rm c}) = a_{\rm c}(f(T_{0{\rm c}}) - f(T_{\rm c})) \qquad (31)$$

with $a_\alpha = \sum_{i\in R_\alpha} a_{i\alpha}$ and

$$T_{0\alpha} = f^{-1}\Big(\sum_{i\in R_\alpha} a_{i\alpha} f(T_{0i}) \Big/ \sum_{i\in R_\alpha} a_{i\alpha}\Big). \qquad (32)$$

Note that Newtonian, Fourier, and radiation heat transfer have this property.

As an example let us consider a system with three heat reservoirs. The temperatures of these reservoirs are T_{01}, T_{02}, and T_{03}. Whenever they are connected to either of the two contacts of the engine, the heat exchange is assumed to obey a linear transport law,

$$q_i(T_{0i}, T) = \alpha_i(T_{0i} - T). \qquad (33)$$

The temperatures of the three reservoirs are chosen to be $T_{01} = 1$, $T_{02} = 1.6$, and $T_{03} = 4$. We set the heat conductances $\alpha_1 = \alpha_3 = 1$ by an appropriate choice of units. We then vary the heat conductance α_2 of the intermediate reservoir T_{02} between 0 and 5 in steps of 0.1 and study how the behavior of the system changes.

The power output of these systems have been numerically determined. In this particularly simple example we used a less general method than the one introduced above in eqs. (23) and (24). Here we expressed the heat flows at the two contacts in terms of the respective entropy flows: $q^+(s^+)$ and $q^-(s^-)$. Whether such an approach is possible depends on the heat transport equations: one cannot always determine the heat flow as a single-valued function of the entropy flow. If one can then the advantage of this approach lies in the fact that the entropy constraint can explicitely be fulfilled by setting $s^+ = -s^-$. In our case the power output $q^+(s^+) + q^-(-s^+)$ was easily optimized by a line search varying s^+. However the reader should be aware that the power output might not be a unimodal function.

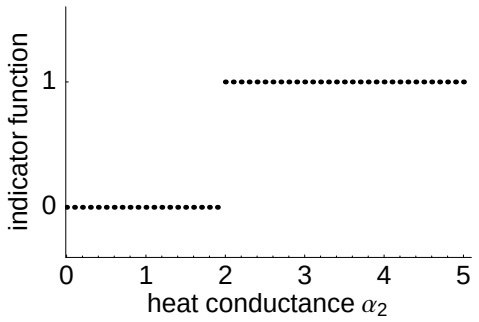

Figure 2: The indicator function $ind(\alpha_2)$ takes the value equal to the reservoir together with which reservoir 2 is used or zero in case it is not used at all.

In the following we analyze the dependence of the results on the value of the heat conductance α_2. The system shows a cross-over behavior at a critical heat conductance. This cross-over is intimately connected to the phenomenon of unused heat reservoirs.

In figure 2 the indicator function $ind(\alpha_2)$ shows how the intermediate heat reservoir is used: For small heat conductances the second reservoir is not used at all, here indicated by $ind = 0$, only reservoir 1 is connected to the cold contact and reservoir 3 is connected to the hot contact. With increasing heat conductance α_2 the reservoir becomes more and more important and – at the critical point – it is connected to the cold engine contact together with reservoir 1, here indicated by $ind = 1$.

Figure 3 shows the resulting maximal power output as a function of α_2. The dots represent the results of the numerical optimization. With increasing α_2 the power stays constant at 0.5 until reservoir 2 is switched on, then the power increases.

In figure 4 the corresponding efficiency at maximum power is shown. The behavior discussed above can be understood in terms of a Curzon-Ahlborn engine operating between two heat baths.

Initially the system uses only two of the three heat

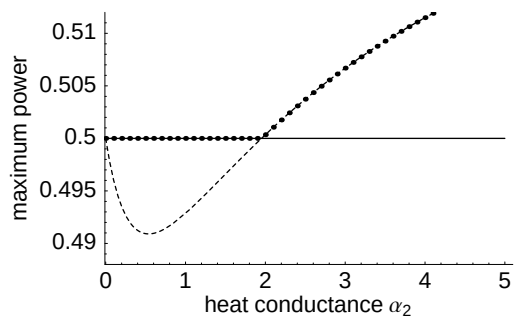

Figure 3: The maximal power output as a function of heat conductance α_2. Dots show the numerical solution for three reservoirs at $T_{01} = 1$, $T_{02} = 1.6$, and $T_{03} = 4$ and conductances $\alpha_1 = \alpha_3 = 1$. The solid line is the optimal solution of a Curzon-Ahlborn engine operating between reservoirs 3 and 1 only, while the dashed line is the optimal solution for operation between reservoirs 3 and the combined reservoirs 1 and 2.

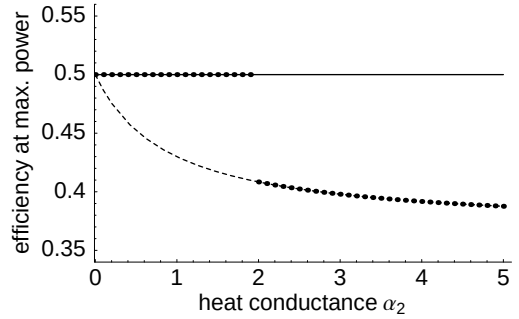

Figure 4: The efficiency at maximum power. Same nomenclature as in Fig. 3.

reservoirs: the hottest and the coldest. Then power and efficiency at maximum power are those of the Curzon-Ahlborn engine:

$$\begin{aligned} P_{\rm opt} &= \frac{\alpha_1\alpha_3}{\alpha_1+\alpha_3}(\sqrt{T_{01}}-\sqrt{T_{03}})^2, \\ \eta_{\rm CA} &= 1-\sqrt{\frac{T_{01}}{T_{03}}} = 1-\sqrt{\frac{1}{4}} = 0.5. \end{aligned} \quad (34)$$

These values are displayd as a solid line in figures (3) and (4). The dashed line corresponds to a Curzon-Ahlborn engine which operates between reservoir 3 as the high temperature reservoir and reservoirs 2 and 1 combined as the cold reservoir.
The results demonstrate very nicely that as soon as the dashed line crosses the solid line, reservoir 2 is put into use. This reservoir shows a cross-over from unused to used at which the power output is nondifferentiable but continuous, not unlike a second order phase transition. The efficiency on the other hand changes in a step-like fashion.

SUMMARY

In this paper a power-producing endoreversible engine which exchanges heat with several (two or more) constant temperature heat sources was considered. The heat transport is general and includes heat transfer processes obeying Newtonian, Fourier, and radiative heat transport. One of the interesting questions for such systems is how the different heat reservoirs are used in an optimal fashion. The system was optimized for maximum power output in case of cyclic operation using averaged nonliear programming methods. The optimal solution shows a number of interesting properties: First, it was shown that there are conditions where some reservoirs should not be connected at all in order to achieve an optimal performance of the system. These reservoirs are referred to as *unused reservoirs*. The hottest and the coldest reservoir will always be used.
The second important finding is that the optimal operation is a stationary one, where the *used* reservoirs and the power-producing subsystem contact temperatures are time-indepent.
We analysed a special class of heat transfer functions which includes the often used Newtonian, Fourier, and radiative heat transport. For this class of transport laws we showed that a multi-source endore-

versible engine is equivalent to a two-source engine with a particular choice of transport laws.
These results were finally exemplified by a simple three-heat source engine for which the heat conductance to the reservoir with the intermediate temperature was varied.

REFERENCES

[1] Morton H. Rubin. Optimal configuration of a class of irreversible heat engines. I. *Phys. Rev. A*, 19(3):1272–1276, 1979.

[2] M. J. Ondrechen, M. H. Rubin, and Y. B. Band. The generalized Carnot cycle - a working fluid operation in finite-time between finite heat sources and sinks. *J. Chem. Phys.*, 78:4721–4727, 1983.

[3] K. H. Hoffmann, J. M. Burzler, and S. Schubert. Endoreversible thermodynamics. *J. Non-Equilib. Thermodyn.*, 22(4):311–355, 1997.

[4] A. M. Tsirlin. Conditions for optimality of the solution of averaged problems of mathematical programming. *Dokl. Akad. Nauk SSSR*, 323(1):43–47, 1992. in Russian.

[5] A. M. Tsirlin. *Methods of Averaged Optimization and their Applications*. Nauka-Fizmatlit, 1997. in Russian.

[6] R. S. Berry, V. A. Kazakov, S. Sieniutycz, Z. Szwast, and A. M. Tsirlin. *Thermodynamic Optimization of Finite-Time Processes*. John Wiley & Sons, Chicester, 2000.

[7] L. I. Rozonoer and Anatolii M. Tsirlin. Optimal control of thermodynamic processes I. *Automat. Remote Control*, 44(1):55–62, 1983. Translated from Avtomatika i Telemekhanika.

[8] L. I. Rozonoer and Anatolii M. Tsirlin. Optimal control of thermodynamic processes II. *Automat. Remote Control*, 44(1):209–220, 1983. Translated from Avtomatika i Telemekhanika.

[9] L. I. Rozonoer and Anatolii M. Tsirlin. Optimal control of thermodynamic processes III. *Automat. Remote Control*, 44(1):314–326, 1983. Translated from Avtomatika i Telemekhanika.

[10] M. J. Ondrechen, B. Andresen, M. Mozurkewich, and R. S. Berry. Maximum work from a finite reservoir by sequential Carnot cycles. *Am. J. Phys.*, 49(7):681–685, 1981.

[11] Morton H. Rubin and Bjarne Andresen. Optimal staging of endoreversible heat engines. *J. Appl. Phys.*, 53(1):1–7, 1982.

[12] Jincan Chen and Zijun Yan. Optimal performance of an endoreversible-combined refrigeration cycle. *J. Appl. Phys.*, 63(10):4795–4798, 1988.

[13] Chih Wu. Power performance of a cascade endoreversible cycle. *Energy Conversion and Management*, 30(3):261–266, 1990.

[14] S. Jeong and J. L. Jr Smith. Optimum temperature staging of cryogenic refrigeration system. *Cryogenics*, 34(11):929–933, 1994.

[15] G. De Mey and Alexis De Vos. On the optimum efficiency of endoreversible thermodynamic processes. *J. Phys. D: Appl. Phys.*, 27(4):736–739, 1994.

[16] J. Chen and C. Wu. Performance of a cascade endo-reversible heat-pump system. *J. Inst. Energy*, 68(476):137–141, 1995.

[17] Bahri Sahin and Ali Kodal. Steady-state thermodynamic analysis of a combined Carnot cycle with internal irreversibility. *Energy*, 20(12):1285–1289, 1995.

[18] O. M. Ibrahim and S. A. Klein. High-power multistage rankine cycles. *J. Energy Resources Technology*, 117:192–196, 1995.

[19] Adrian Bejan. Theory of heat transfer-irreversible power plants - II. the optimal allocation of heat exchange equipment. *Int. J. Heat Mass Transfer*, 38(3):433–444, 1995.

Proceedings of ECOS 2005
Trondheim, Norway
June 20–22, 2005

ENTROPY PRODUCTION MODELING IN CFD OF TURBULENT COMBUSTION FLOW

Ivar S. Ertesvåg*, Jostein Kolbu†
Department of Energy and Process Engineering
Norwegian University of Science and Technology
NO-7491 Trondheim, Norway

Abstract

A model for predicting the detailed field of entropy production by computational fluid dynamics (CFD) of turbulent flows with combustion is developed. The model is based on the widely used Eddy Dissipation Concept for turbulent combustion (EDC) by Magnussen and co-workers. It can be applied with an infinitely-fast-chemistry assumption or in conjunction with a detailed chemical mechanism (e.g. GRI Mech). The model is tested for a simple laboratory flame. The results are good when compared with results from a conventional box-model (overall) entropy-balance analysis.
Keywords: Turbulent combustion, EDC, CFD, entropy production, irreversibility

INTRODUCTION

For several decades, the methods of 2nd-law or exergy analysis of thermal and chemical systems have been developed and utilized. These methods are primarily flowsheeting approaches, where energy and exergy balances are put up for a number of interconnected subsystems or components (*e.g.* compressors, combustors, heat exchangers). Then the entropy production or the irreversibility (a.k.a. "lost work") of each component can be computed.

In parallel, methods for computing detailed flowfields without and with chemical reactions have been developed (known as computational fluid dynamics, CFD). In the context of turbulent combustion, Magnussen's EDC has become a standard model for technological applications. These methods provide detailed fields of velocity, temperature and concentrations of species throughout combustors or other devices.

For accurate optimization, a more detailed knowledge of the entropy production may be desired. The CFD approach can be extended to provide a detailed field of the entropy production as well. The basic formulation for this is known from several textbooks. For laminar flows, these equations can be solved numerically, see *e.g.* [9]. However, as most flows are turbulent, a model for entropy production is required, along with the models for turbulent transport, mixing, and combustion. One of the few attempts (the only?) is presented in [8], where combustion modeling was based on a prescribed-pdf method. In the present study, entropy modeling is based on the EDC [2–4, 6].

*ivar.s.ertesvag@ntnu.no
†jostein.kolbu@ntnu.no

BASIC THEORY

Transport equations

The notation, terminology and basic assumptions are primarily those customarily used in fluid-mechanics and combustion literature (*e.g.* [2, 7, 10]). In some instances this differs from the irreversible-thermodynamics literature. The exposition follows an Eulerian and barycentric description, and continuity is assumed. The flow and scalar fields of reacting flows can be described by the following partial differential equations, often known as transport equations.

Momentum:

$$\underbrace{\frac{\partial}{\partial t}(\rho u_i)+\frac{\partial}{\partial x_j}(\rho u_i u_j)}_{\rho Du_i/Dt}=\frac{\partial}{\partial x_j}(-p\delta_{ij}+\tau_{ij})+\rho f_i. \quad (1)$$

Here, ρ is density, u_i Cartesian velocity components,

p pressure, τ_{ij} is the viscous stress tensor, f_i body-force acceleration, and δ_{ij} is the Kronecker tensor.
Mass of species:

$$\rho\frac{DY_k}{Dt} = \frac{\partial}{\partial x_j}(-j_{k,j}) + R_k. \tag{2}$$

Here, Y_k is the species mass fraction, $j_{k,j}$ the mass flux, and R_k the volumetric reaction rate. When this equation is summed for all species, the continuity equation is obtained:

$$\frac{\partial\rho}{\partial t} + \frac{\partial}{\partial x_j}(\rho u_j) = \frac{D\rho}{Dt} + \rho\frac{\partial u_j}{\partial x_j} = 0. \tag{3}$$

Energy:

$$\rho\frac{De}{Dt} = \frac{\partial}{\partial x_j}\left(-q_j - \sum_k h_k j_{k,j}\right) - p\frac{\partial u_j}{\partial x_j} + \tau_{ij}\frac{\partial u_i}{\partial x_j} + Q \tag{4}$$

Here, e is the specific internal energy of the mixture, q_j the heat flux, h_k the specific enthalpy, and Q the volumetric energy production, either by internal sources (heating) or by radiation. The second last term is the dissipation term, in the following denoted Φ. This equation can readily be rewritten into an equation for the enthalpy, $h = e + p/\rho$.

Flux relations

The preceeding equations includes terms for molecular fluxes. For most combustion cases, and indeed turbulent combustion cases, the following models are appropriate. For Newtonian fluids, the viscous stress tensor is expressed

$$\tau_{ij} = \mu\left(\frac{\partial u_i}{\partial x_j} + \frac{\partial u_j}{\partial x_i}\right) - \tfrac{2}{3}\mu\frac{\partial u_l}{\partial x_l}\delta_{ij}. \tag{5}$$

Mass diffusion is modeled by Fick's law,

$$-j_{k,j} = \rho\mathscr{D}_k\frac{\partial Y_k}{\partial x_j}, \tag{6}$$

and heat transfer by Fourier's law,

$$-q_j = \lambda\frac{\partial T}{\partial x_j}. \tag{7}$$

Here, the dynamic viscosity μ, the thermal conductivity, λ, and the specific heat capacity, c_p, are for the mixture, whereas the diffusion coefficient, $\mathscr{D}_k$, is for the individual species.

Entropy

Later on, we will make use of the fact that the chemical potential (here used on a mass basis) for ideal gases is equal to the specific Gibbs function: $\mu_k = g_k = h_k - Ts_k$. With material derivatives, the classical Gibbs' equation can be expressed

$$T\rho\frac{Ds}{Dt} = \rho\frac{De}{Dt} - \frac{p}{\rho}\frac{D\rho}{Dt} - \rho\sum_k \mu_k\frac{DY_k}{Dt}. \tag{8}$$

From this and the energy and mass balances, an entropy equation can be developed on the form

$$\rho\frac{Ds}{Dt} = \frac{\partial}{\partial x_j}\left(-\frac{q_j}{T} - \sum_k s_k j_{k,j}\right) + \left(-\frac{q_j}{T^2}\right)\frac{\partial T}{\partial x_j} + \frac{1}{T}\sum_k\left(-j_{k,j}\right)\left(\frac{\partial\mu_k}{\partial x_j}\right)_T + \frac{Q}{T} + \frac{\Phi}{T} - \frac{1}{T}\sum_k \mu_k R_k. \tag{9}$$

TURBULENCE MODELING

Averaging

For turbulent reacting flows, it is convenient to include the density in the averaged quantities. This is known as mass-weighted Reynolds average or Favre average [2, 7]. The quantities such as velocity, specific enthalpy, species mass fraction, and temperature are decomposed into mean and fluctuating values as $\phi = \tilde{\phi} + \phi''$, where ϕ is a general variable. The mass-weighted mean value is defined

$$\tilde{\phi} = \frac{\overline{\rho\phi}}{\overline{\rho}}. \tag{10}$$

A consequence of this definition is that $\overline{\rho\phi''} = 0$, whereas in general, $\overline{\phi''} \neq 0$. The overbar shows average (statistical expectation). If the density does not fluctuate, or does not correlate with the other quantity, the Favre average is equivalent to the Reynolds average.

Continuity

The mass-weighted Reynolds-averaged (Favre-averaged) continuity equation is

$$\frac{\partial\bar{\rho}}{\partial t} + \frac{\partial}{\partial x_j}(\bar{\rho}\tilde{u}_j) = 0. \tag{11}$$

Momentum and turbulence transport

The mass-weighted Reynolds average (Favre average) momentum equation can be written

$$\frac{\partial}{\partial t}(\bar{\rho}\tilde{u}_i)+\frac{\partial}{\partial x_j}(\bar{\rho}\tilde{u}_i\tilde{u}_j)=-\frac{\partial \overline{p}}{\partial x_i} + \frac{\partial}{\partial x_j}\left(\overline{\tau}_{ij}-\overline{\rho u_i'' u_j''}\right)+\overline{\rho f}_i. \quad (12)$$

This is a derivation from Eq. (1). The new quantities appearing in this equation, $\overline{\rho u_i'' u_j''}$, represent convective transport of mean momentum by the action of turbulent motion. Their effect is similar to the (viscous) stresses, and they are known as Reynolds or turbulence stresses. From these, the turbulence energy is defined $\bar{\rho}\tilde{k}=\frac{1}{2}\overline{\rho u_i'' u_i''}$. A simple and frequently used model for the Reynolds stresses is the turbulence-viscosity model:

$$-\overline{\rho u_i'' u_j''}=\mu_t\left(\frac{\partial \tilde{u}_i}{\partial x_j}+\frac{\partial \tilde{u}_j}{\partial x_i}\right)-\frac{2}{3}\left(\bar{\rho}\tilde{k}+\mu_t\frac{\partial \tilde{u}_l}{\partial x_l}\right)\delta_{ij}. \quad (13)$$

This model is an analogy to Eq. (5). However, the turbulence viscosity, μ_t, is not a material property but a quantity characteristic of the flow. It can be regarded as a product of a turbulence length scale and a turbulent velocity scale. These scales can be expressed from lengths and velocities of the flow situation. However, a more general approach is to solve these scales from transport equations. The by far most popular model, which will be used here, is the k-ε model. Then the turbulence viscosity is modeled

$$\mu_t=\bar{\rho}C_\mu\frac{\tilde{k}^2}{\tilde{\varepsilon}} \quad (14)$$

Similar quantities, representing turbulence transport of scalars, will appear in mean-scalar transport equations in the following. When a general scalar is denoted ϕ, the Reynolds or turbulence fluxes are modeled

$$-\overline{\rho\phi'' u_j''}=\Gamma_{\phi,t}\frac{\partial\tilde{\phi}}{\partial x_j}=\frac{\mu_t}{\sigma_\phi}\frac{\partial\tilde{\phi}}{\partial x_j}. \quad (15)$$

This is known as the general gradient model. The turbulence Prandtl/Schmidt numbers, σ_ϕ, have to be specified in the model. The mean molecular diffusive flux may also be modeled by the same formalism or by more exact expressions of that term.
It should be noted that models solving transport equations for the Reynolds stresses are also an realistic option for turbulent combusting flows. However, these aspects of turbulence modeling are beyond the scope of this study.

Turbulence energy and dissipation rate

The modeled transport equation for turbulence energy can be written

$$\frac{\partial}{\partial t}\left(\bar{\rho}\tilde{k}\right)+\frac{\partial}{\partial x_j}\left(\bar{\rho}\tilde{k}\tilde{u}_j\right)=P^k+D^k+\Pi^k-\bar{\rho}\tilde{\varepsilon}. \quad (16)$$

In this equation, the production term,

$$P^k=-\overline{\rho u_i'' u_j''}\frac{\partial\tilde{u}_i}{\partial x_j}, \quad (17)$$

is closed as the Reynolds stresses already are modeled. The model expressions for the remaining terms vary according to the chosen model. The diffusion term is usually modeled by a molecular term and a turbulence term according to the general-gradient model,

$$D^k=\frac{\partial}{\partial x_j}\left(\left(\mu+\frac{\mu_t}{\sigma_k}\right)\frac{\partial\tilde{k}}{\partial x_j}\right). \quad (18)$$

The pressure term, Π^k, is very often neglected, as a generic and fully accepted model is still to be developed. Finally, the dissipation rate of turbulence energy,

$$\bar{\rho}\tilde{\varepsilon}=-\overline{\tau_{ij}\frac{\partial u_i''}{\partial x_j}}, \quad (19)$$

is solved from a separate transport equation. The terms as shown here follows the "standard" k-ε model for high-Reynolds number flows [5].
The dissipation-rate equation can be written

$$\frac{\partial}{\partial t}\left(\bar{\rho}\tilde{\varepsilon}\right)+\frac{\partial}{\partial x_j}\left(\bar{\rho}\tilde{\varepsilon}\tilde{u}_j\right)=D^\varepsilon+S^\varepsilon, \quad (20)$$

where the diffusion term is modeled analogously to Eq. (18) in the turbulence energy equation,

$$D^\varepsilon=\frac{\partial}{\partial x_j}\left(\left(\mu+\frac{\mu_t}{\sigma_\varepsilon}\right)\frac{\partial\tilde{\varepsilon}}{\partial x_j}\right), \quad (21)$$

and the source term is modeled as a balance between production and destruction:

$$S^\varepsilon=\frac{\tilde{\varepsilon}}{\tilde{k}}\left(C_1P^k-C_2\bar{\rho}\tilde{\varepsilon}\right). \quad (22)$$

Mass of species

The transport equation for mean mass fraction is

$$\frac{\partial}{\partial t}(\bar{\rho}\tilde{Y}_k)+\frac{\partial}{\partial x_j}(\bar{\rho}\tilde{Y}_k\tilde{u}_j)=\frac{\partial}{\partial x_j}\left(-\overline{j_{k,j}}-\overline{\rho Y_k''u_j''}\right)+\overline{R_k}. \tag{23}$$

The diffusive molecular and turbulence fluxes of species mass are often modeled according to the general gradient model, corresponding to Eq. (15) or Eq. (18) above. Moreover, the reaction term (species production term) has to be modeled, see below.

Energy

The energy equation, Eq. (4), can be rewritten to an enthalpy equation. The averaged version of this equation is

$$\frac{\partial}{\partial t}(\bar{\rho}\tilde{h})+\frac{\partial}{\partial x_j}(\bar{\rho}\tilde{h}\tilde{u}_j)=\frac{\partial \bar{p}}{\partial t}+\tilde{u}_j\frac{\partial \bar{p}}{\partial x_j}+\overline{u_j''\frac{\partial p}{\partial x_j}}$$
$$+\frac{\partial}{\partial x_j}\left(-\overline{q}_j-\sum_k\overline{h_k j_{k,j}}-\overline{\rho h''u_j''}\right)+\overline{\Phi}+\overline{Q} \tag{24}$$

In this equation, the third term at the right-hand side is equivalent to the pressure term Π^k in Eq. (16), and has to be modeled (often neglected).
The treatment of the diffusive fourth term depends both on the approximations for the heat and the molecular flux and on the numerical approach. However, the third part, the turbulence diffusion of enthalpy, is modeled according to the general gradient model, Eq. (15).

Combustion modeling

The Eddy Dissipation Concept for turbulent combustion (EDC) [2–4, 6] can be used to model the interaction between turbulence and combustion. A cascade model is used to link the fine turbulence structures (where reactions are assumed to occur) to the mean flow and large-scale turbulence (that is described by turbulence models). The fine structures are modeled as a reactor, Fig. 1. The reaction rate is obtained from a mass balance for each species.
When a fast-chemistry assumption (*i.e.* "mixed is burnt") is applied, the average reaction rate in Eq. (23) is modeled

$$\overline{R}_{\mathrm{fu}}=-\frac{\bar{\rho}\gamma^*\dot{m}^*\chi}{1-\gamma^*\chi}\tilde{Y}_{\mathrm{min}}, \tag{25}$$

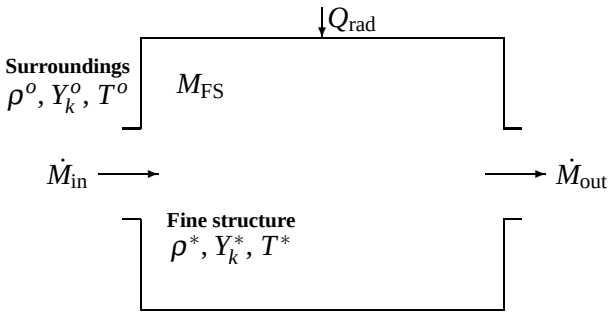

Figure 1: Schematic fine structure reactor of EDC

where

$$\tilde{Y}_{\mathrm{min}}=\min\left(\tilde{Y}_{\mathrm{fu}},\frac{1}{r}\tilde{Y}_{\mathrm{ox}}\right). \tag{26}$$

Here, r is the stoichiometric oxidizer (*i.e.* air or oxygen) requirement on a mass basis for the specific fuel, and subscripts "fu" and "ox" denote fuel and oxidizer, respectively. The quantities γ^* and $\dot{m}^*$ are the mass fraction of turbulence fine structures and its mass exchange with the surrounding fluid, respectively (cf. Fig. 1). These are related to the turbulence-cascade model of the EDC [2, 3] and are expressed as functions of the turbulence energy $\tilde{k}$ and its dissipation rate $\tilde{\varepsilon}$. The chemical reactions are assumed to occur in the fine structures, *i.e.*, the small turbulence scales. The mass exchange is the reciprocal of the fine-structure residence time, $\tau^*=1/\dot{m}^*$, which is proportional to the Kolmogorov time scale. The quantity χ is the fraction of fine structure that is reacting, and is a function of the concentrations of fuel, oxidizer, and product. The implementation of chemical kinetics is described by [4]. Then the reaction rate for a chemical species is expressed

$$\overline{R}_k=-\frac{\bar{\rho}\gamma^*\dot{m}^*}{(\gamma^*)^{1/3}}(Y_k^o-Y_k^*). \tag{27}$$

Here, Y_k^o and Y_k^* are the mass fraction of species k entering into and leaving the fine-structure reactor, respectively. The reacting turbulence fine structures are regarded as a perfectly stirred reactor, and the species mass balances of the reactor is solved with the use of data from a chemical-kinetics mechanism (*e.g.* GRI-Mech).
The model in Eq. (27) is obtained from a species mass balance for the reactor (Fig. 1), while Eq. (25) is the special case for fast chemistry. An energy balance for the reactor provide a model for the reactor

and mean temperatures. Similarly, we will use an entropy balance to model the entropy production.

Mean Entropy Equation

Above, the transport equation for entropy was expressed from the equations for species mass, continuity, and energy, by using Gibbs' relation. However, for the mean quantities, there exist no simple relation corresponding to the Gibbs relation or Eq. (8.)

The equation for the average of the entropy, can be written as the mean of Eq. (9),

$$\begin{aligned}\frac{\partial}{\partial t}(\bar{\rho}\tilde{s}) + \frac{\partial}{\partial x_j}(\bar{\rho}\tilde{s}\tilde{u}_j) \\ = \frac{\partial}{\partial x_j}\left(\overline{-\frac{q_j}{T} - \sum_k s_k j_{k,j}} - \overline{\rho s'' u_j''}\right) \\ + \overline{\left(-\frac{q_j}{T^2}\right)\frac{\partial T}{\partial x_j}} + \overline{\sum_k \left(-\frac{j_{k,j}}{T}\right)\left(\frac{\partial \mu_k}{\partial x_j}\right)_T} \\ + \overline{\left(\frac{Q}{T}\right)} + \overline{\left(\frac{\Phi}{T}\right)} - \overline{\left(\frac{1}{T}\sum_k \mu_k R_k\right)} \end{aligned} \quad (28)$$

The five last terms are the mean entropy production. It should be noted that the average of the products and ratios are not readily rewritten into terms containing products of mean values. This means that models for transport and production of mean entropy have to be developed.

As an example of the required modeling, the viscous-dissipation term can be inspected: The dissipation term of the entropy equation can be split in a mean-flow term and a turbulence term,

$$\overline{\left(\frac{\Phi}{T}\right)} = \overline{\left(\frac{\tau_{ij}}{T}\right)}\frac{\partial \tilde{u}_i}{\partial x_j} + \overline{\frac{\tau_{ij}}{T}\frac{\partial u_i''}{\partial x_j}}. = \overline{\left(\frac{\tau_{ij}}{T}\right)}\frac{\partial \tilde{u}_i}{\partial x_j} + \overline{\left(\frac{\rho\varepsilon}{T}\right)}. \quad (29)$$

Notice here that ε denotes the non-averaged dissipation rate of turbulence energy, cf. Eq. (19).

Provided that, but only then, the correlations between temperature and the other quantities are weak, the mean temperature can be left outside. For the viscous term, this is a reasonable assumption. However, for the other terms, the assumption would imply that the fluctuations of temperature and species mass fractions were small – which is certainly not the case in turbulent combustion.

ENTROPY MODELING WITH THE EDDY DISSIPATION CONCEPT

Overall approach

Turbulent motion may be regarded as eddies of sizes ranging from the external dimensions of the flow down to the smallest scales where the eddies are disrupted by viscous forces. This can be depicted as an energy cascade [3]. Combustion takes place at all scales, but mainly in the smallest scales. There, the gradients, and hence, the molecular fluxes, are the largest. Similarly, entropy is produced at all scales but mainly in the smallest eddies of turbulence.

When modeling the entropy production with the EDC, the approach will be to split the production into a large-scale (i.e. mean-flow and large-scale turbulence) contribution and a fine-structure contribution.

$$P^{\tilde{s}} = P^{\tilde{s}}_{\mathrm{LS}} + P^{\tilde{s}}_{\mathrm{FS}} \quad (30)$$

The large-scale contributions to entropy production are modeled by using the mean values in the production terms:

$$P^{\tilde{s}}_{\mathrm{LS}} = \frac{\overline{\tau}_{ij}}{\tilde{T}}\frac{\partial \tilde{u}_i}{\partial x_j} + \frac{\lambda}{\tilde{T}^2}\left(\frac{\partial \tilde{T}}{\partial x_j}\right)^2 + \sum_k \frac{\mathscr{R}_u}{M_k}\frac{\bar{\rho}\mathscr{D}_k}{\tilde{Y}_k}\left(\frac{\partial \tilde{Y}_k}{\partial x_j}\right)^2. \quad (31)$$

Here, $\mathscr{R}_u$ is the universal gas constant, and M_k is the molar mass. The radiation term is neglected in this study. In the EDC, the reactions are assumed to take place in the fine structures, and hence, there are no large-scale contributions from reactions.

Turbulence fine-structure entropy modeling

In the EDC, a mass-weighted (Favre) average (cf. Eq. 10) is expressed [2, 6] as

$$\tilde{\varphi} = \gamma^*\chi\varphi^* + (1-\gamma^*\chi)\varphi^o. \quad (32)$$

The general variable ϕ can represent the entropy production, σ. Thus, $\bar{\rho}\tilde{\sigma} = \overline{\rho\sigma}$ is the mean of the sum of entropy-production terms of Eq. (9), and σ^* and σ^o are the entropy production rates on a mass basis of the reactor and its surroundings, respectively. Here, in conjunction with Eq (30), the contribution of fine-structures to mean entropy production will be modeled by

$$P^{\tilde{s}}_{\mathrm{FS}} = \bar{\rho}\tilde{\sigma}_{\mathrm{FS}} = \bar{\rho}\left(\gamma^*\chi\sigma^* + (1-\gamma^*\chi)\sigma^o\right). \quad (33)$$

This formulation is based on the assumption in EDC that all reactions take place in the reactor. Furthermore, the major part of localized heat and mass exchange due to reactions also take place in the reactor or its vicinity. After exiting the reactor, the products are mixed with the surroundings.
Similar to the mass and energy balances [2], an entropy balance for the reactor can be put up to determine the reactor entropy production,

$$\sigma_1^* = \dot{m}^* \sum_k (Y_k^* s_k^* - Y_k^o s_k^o) - \frac{Q_{\text{rad}}}{\rho^* T^*} \qquad (34)$$

Here, the notation of the EDC is followed: The superscripts * and ^{o} refer to properties of the reactor and the surroundings of the reactor, respectively. $\dot{m}^*$ is the mass inflow rate to the reactor divided by the mass of the reactor. Its reciprocal is the residence time of the reactor. The last term is entropy transferred by radiation inflow, cf. Fig. 1. In this study, radiation term is neglected. However, when a radiation model is implemented with the combustion model (for energy exchange), it can readily be implemented in the entropy production model as well.
The expression above does not include the post-reaction mixing. This can be modeled

$$\sigma_2^* = \dot{m}^* \sum_k (Y_k^* (s_k^* - \tilde{s}_k)) \qquad (35)$$

for the mass exiting from the fine-structure reactor. Here, $\tilde{s}_k$ denotes the entropy of the species based on mean composition, pressure and temperature. The two contributions should be added; $\sigma^* = \sigma_1^* + \sigma_2^*$. At this stage, the last term of Eq. (33), σ^o, is left for future considerations.
The model in Eqs. (33)-(35) is decoupled from the specific formulation of the terms in Eq. (9). The idea of this model is that reactants enter the reactor with properties of the surroundings, whereas products leave the reactor with properties of the reactor.
The model can be used both with the "fast chemistry" assumption, and with a detailed mechanism for chemical kinetics. When EDC is implemented in a code, the quantities Y_k^*, Y_k^o, T^*, and T^o are already computed. Then, the mole fractions X_k^* and X_k^o and the partial pressures p_k^* and p_k^o can readily be calculated. Eventually, the only task remaining is to determine the specific entropies

$$s_k^* = s_k(T^*, p_k^*) \quad \text{and} \quad s_k^o = s_k(T^o, p_k^o). \qquad (36)$$

For readers familiar with the EDC, it can be mentioned that a simpler expression involving $\tilde{Y}_{\text{min}}$ (cf. Eq. 25) is not obtainable for the model in Eq. (34).

The investigations of [1] indicate that the reactions as such only give a minor contribution to entropy production, compared to the associated mass and energy exchange. Basically, the model in Eqs. (33)-(35) should be a model including all the localized (small-scale) entropy-producing processes in the turbulent combusting flow. That is, all processes (*e.g.* local mass transfer) that affects the field of temperature and partial pressures. Even though the individual processes are not specified, when their effects are seen in the temperature and composition fields, they are also included in the entropy-production model.

PREDICTIONS

For exemplary calculations, the model was applied to a jet flame. The fuel is a 1:1 mixture of H_2 and N_2, and the fuel jet diameter, bulk velocity, and Reynolds number are 8 mm, 34.8 m/s, and 10000, respectively. The jet is situated in a air coflow with diameter 400 mm, and velocity 0.2 m/s. Both flows have temperature 300 K. This is case "H3" in the database of the International Workshop on Measurement and Simulation of Turbulent Nonpremixed Flames. The predictions were made using the general-purpose CFD code Spider, which is based on finite volumes and non-orthogonal curvilinear computational mesh. In this case, a 2-dimensional rectangular mesh with axial symmetry was used. The turbulence model was the standard k-ε model, except for the round-jet modification of the constant $C_2 = 1.83$ (Eq. 22) and turbulence Prandtl and Schmidt numbers of 0.5. Buoyancy was included in the momentum equation. Combustion was modeled with the EDC and fast-chemistry assumption (Eqs. 25–26). Thermophysical data, including enthalpy and entropy, were obtained from the Chemkin Library.

The inlet boundary was specified as fixed values. For the jet flow, these were approximated to calculations of a fully developed pipe flow. The outlet was a parallel flow, and at the outer boundary zero radial transport was assumed.

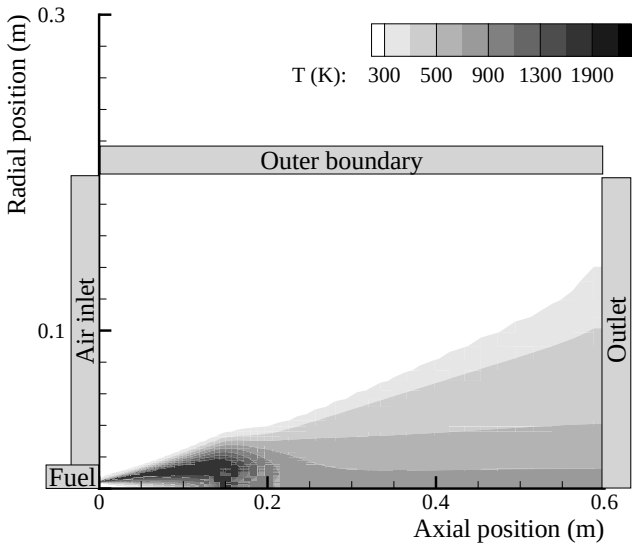

Figure 2: Geometry and computed mean temperature field of the flame

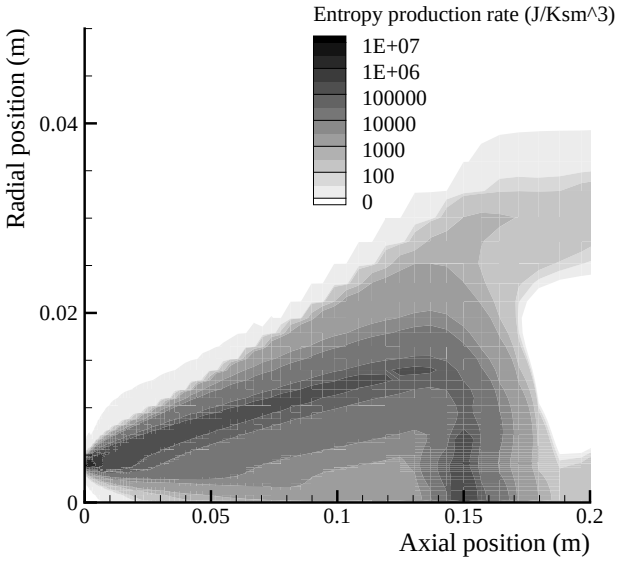

Figure 4: Zoomed excerpt from Fig. 3

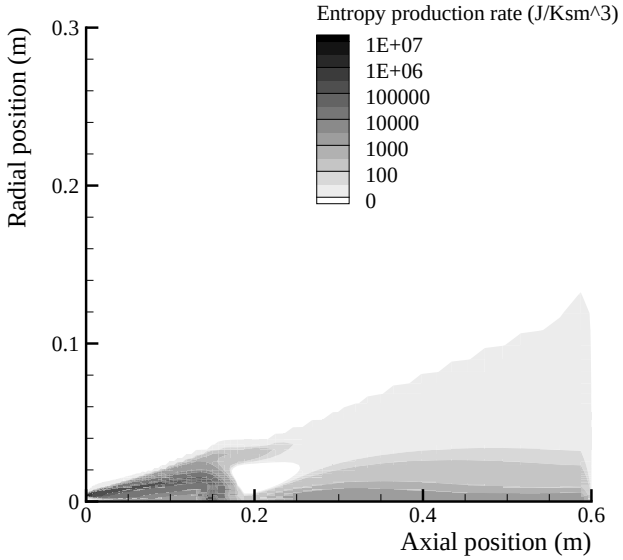

Figure 3: Mean entropy production rate

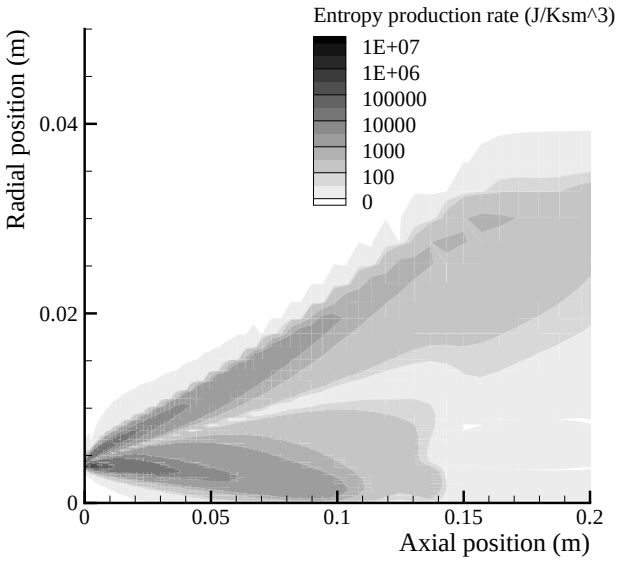

Figure 5: Entropy production due to mean temperature gradients, 2nd term of Eq. (31)

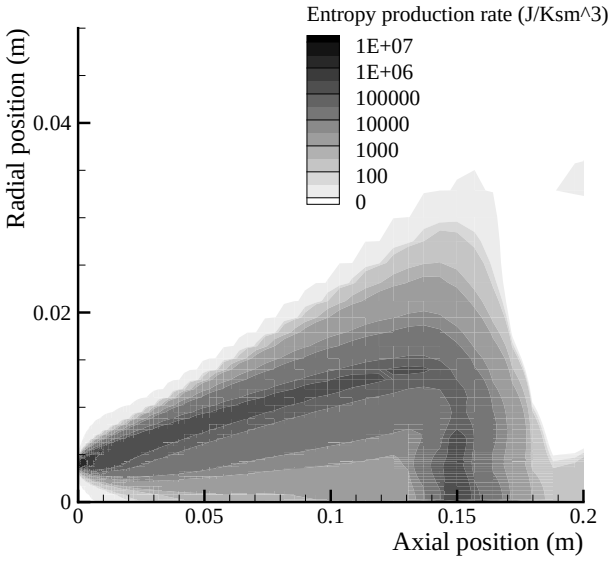

Figure 6: Fine-structure contribution to entropy production model in Eqs. (33)-(35)

RESULTS AND DISCUSSION

The geometry and the simulated mean temperature field of the jet are shown in Fig. 2. This and the species field (not shown) resembled experimental data quite well. The modeled mean entropy production is shown in Figs. 3–4. This is the sum of the contributions from the mean-field, Eq. (31), and from turbulence fine structures, Eqs. (33)-(35). In the former, the heat-flux contribution, that is, the 2nd term of Eq. (31), was by far the largest. This term gave some relatively large local values and is shown in Fig. 5. The major production, however, was found in the fine-structures, shown in Fig. 6. Here, the effects of chemical reactions and pre-reaction mixing are included through the model in Eq. (34). However, the main contributor was the post-reaction mixing term, Eq. (35). This finding corresponds well with the result obtained in [1].

No experimental data are available on entropy production. However, when the volumetric entropy production rate is integrated over the computed domain, it should be comparable to results of an overall entropy balance for the same case. Here, such a balance was evaluated based on the mean values. Then, the sum of entropy inflow to all inflow cells minus the entropy outflow from all outflow cells was 8.62 W/K. The inflow has no concentration fluctuations and only small temperature fluctuations. In the outlet, these fluctuations will be larger, and hence, the outflow entropy somewhat larger. Thus, the entropy production was somewhat overestimated when using the overall balance based on mean values. Nevertheless, it should be a good indication of the correct result.

The entropy production computed from the model presented above, was 6.14 W/K, or 71 % of that found from the simple balance. The fine-structure model gave 5.88 W/K, of this 2.36 W/K from Eq. (34) and 3.52 W/K from Eq. (35), while the mean-temperature term (Eq. 31) gave 0.25 W/K.

CONCLUDING REMARKS

The Eddy Dissipation Concept (EDC) for turbulent combustion has been extended to include modeling of entropy production. The results obtained are very good when compared with an overall entropy balance of the same case.

REFERENCES

[1] Dunbar WR, Lior N. (1994) *Combust. Sci. Tech.* 103:41-61, 1994.

[2] Ertesvåg IS. *Turbulent flow and combustion* (in Norwegian.) Tapir Academic Publisher, Trondheim, Norway, 2000.

[3] Ertesvåg IS, Magnussen BF. *Comb. Sci. Technol.* 159:213-236, 2000.

[4] Gran IR, Magnussen BF. *Comb. Sci. Technol.* 119:191-217, 1996.

[5] Launder BE, Spalding DB, *Comput. Meth. in Appl. Mech. and Eng.* 3:269-289, 1974.

[6] Magnussen BF, "Modeling of NO_x and soot formation by the Eddy Dissipation Concept," Int. Flame Research Foundation, 1st Topic Oriented Technical Meeting, 17-19 Oct., Amsterdam, Holland, 1989.

[7] Poinsot T, Veynante D. *Theoretical and numerical combustion.* Edwards, Philadelphia PA, 2001.

[8] Stanciu D, Isvoranu D, Marinescu M, Gogus Y. *Int. J. Appl. Thermodyn.* 4(1):1-18, 2001.

[9] Teng H, Kinoshita CM, Masutani SM, Zhou J. *ASME J. Energy Resour. Tech.* 120:226-232, 1998.

[10] Williams F.A. *Combustion theory.* 2nd ed. Benjamin/Cummings Publ. Comp., endthebibliography Menlo Park CA, 1985.

Proceedings of ECOS 2005
Trondheim, Norway
June 20–22, 2005

THE SECOND LAW OF THERMODYNAMICS AND EVOLUTION OF LIVING SYSTEMS

Georgi P. Gladyshev*
International Academy of Creative Endeavors
San Diego, USA – Moscow, Russia
N. N. Semenov Institute of Chemical Physics, Russian Academy of Sciences

ABSTRACT

The classical formulations of the second law of thermodynamics are presented. Some mistakes in the understanding the physical meaning of this general law of nature are noted. It is asserted that many misunderstandings of the second law of thermodynamics are related to terminological confusion and the underestimation (the disregard) of the theory developed by J.W. Gibbs and other founders of "true thermodynamics," which is impossible to disprove. To a certain approximation, R.Clausius and J.W. Gibbs' thermodynamics is applied to describing the evolution of living systems. This is possible due to the law of temporal hierarchies and the premise that the functions of state of living systems have real physical meaning at practically all hierarchical levels and at every moment of time. Making no pretensions to perfection, the author offers some advice to researchers dealing with thermodynamics. The author believes that, when considering thermodynamic problems, "ambiguous" terms and definitions should be clarified preliminarily in order to preclude possible misunderstandings. It is also advisable to refer to the classical works (including textbooks and encyclopedias) that the authors of publications have used. This will allow the correctness of the results reported to be estimated at least preliminarily.
Keywords: Second law, thermodynamics, chemical thermodynamics, entropy, Gibbs function, Gibbs energy, full differential, law of temporal hierarchies, evolution, living systems, quasi-closed systems.

"… the true and only goal of science is
to reveal unity rather than mechanisms"

Henri Poincaré

Classics of science enunciated the second law of thermodynamics, one of general laws of nature, in the first half of the 19th century. Well-known formulations of this law are associated with the names of N.L.S. Carnot (1824), R. Clausius (1850), and W. Thomson (Lord Kelvin) (1851). *

Although the formulations themselves are different, mainly because of the difference in phrasing, they may be considered equivalent. Many authors have attempted to change or improve the formulations as regards their physical meaning, yet none has succeeded. The meaning (essence) of these formulations has not been disproved to date [1–23]. However, new concepts have extended the possible applications of the second law of thermodynamics

* Georgi P. Gladyshev: E-mail: academy@endeav.org

to different sciences, especially chemistry and, as it turned out later, biology. This became possible mainly due to J.W. Gibbs' works performed in 1873–1878. To a certain approximation, the methodology of Gibbs thermodynamics [2] has been extended to date to all hierarchies of natural systems, which are generally open ones [17]. The discovery of the law of temporal hierarchies, which may be considered a new general law of nature, has determined the extension of Gibbs's theory to living systems [17, 22–28]. This law [17] makes it possible to apply thermodynamics (more precisely, the hierarchic thermodynamics of quasi-closed systems), to all hierarchies of the real world, particularly, living objects and biological systems, to quite a good approximation. I believe that the discovery of this law confirms the universality of classical thermodynamic methods, and the name of Josiah Willard Gibbs even more vividly symbolizes the future of science that confirms the validity of general laws of nature as applied to the evolution of all material systems at all organizational levels of our world. Advances in classical thermodynamics (as well as approximate thermodynamics, i.e., the quasi-equilibrium thermodynamics of quasi-closed systems) are described in a number of textbooks and monographs. They are certainly numerous; I would especially recommend the works [1–17], which will be very useful for all beginner researchers.

Clausius' formulation of the second law of thermodynamics, also known as the Clausius principle, states that a process that involves no changes except for the transfer of heat from a warmer body to a colder body is irreversible, i.e., heat cannot spontaneously pass from a colder body to a warmer one [7--10].

Clausius introduced the concept of entropy (S), a function of state of a system (a function that has a full differential). According to the Clausius inequality,

$$dS \geq \delta Q / T, \qquad (1)$$

where the equality sign pertains to reversible processes and the inequality (greater-than) sign, to irreversible ones.

Expression (1) is suitable for a simple isolated system, which can exchange neither substance nor energy with the environment and whose internal energy (U) and volume (V) are constant. In such systems only the work of expansion or no work at all is performed In this case, the second law of thermodynamics may be written as

$$dS_{U,V} \geq 0 .$$

Thus, the entropy of this system increases when irreversible processes occur, and it is maximum in the state of thermodynamic equilibrium.

The second law of thermodynamics according to Thomson (Thomson's principle) states that the process during which work is transformed into heat without any other changes in the system's state is irreversible. This means that all heat withdrawn from a body cannot be entirely transformed into work unless the system is changed in other respects. This formulation is equivalent to the statement that the perpetuum mobile of the second kind is impossible [7-10].

Carnot's theorem is also equivalent to the impossibility of the perpetuum mobile of the second kind. According to this theorem, no heat engine can have a higher efficiency than that of the Carnot cycle, $\eta = (T_1 - T_2)/T_1$, which is determined only by the temperatures of the heater and the cooler (T_1 and T_2, respectively). Carnot's theorem lays the basis for the absolute temperature scale.

Sometimes, the second law of thermodynamics is formulated as the well-known C. Caratheodory's principle (1909).

In the kinetic theory of gases, the second law of thermodynamics is substantiated by Boltzmann's H theorem. Here, H is the Boltzmann H function (to be precise, functional) determined from the mean logarithm of the particle distribution function. The Boltzmann H function is proportional to the entropy of a perfect gas.

The physical meaning of entropy is revealed in statistical physics. Boltzmann demonstrated that the entropy is related to the logarithm of thermodynamic probability (W):

$$S = k \ln W,$$

where k is the Boltzmann constant.

Note that the Boltzmann's substantiating the statistical basis of the second law of thermodynamics, as well as the statistical substantiation of phenomenological thermodynamics suggested by Gibbs, involves ideal models, e.g., a perfect gas. In the case of more complex systems [3-4, 8], where pronounced (especially, strong) interactions

between particles (molecules) are observed, it is difficult to perform the calculations. Therefore, it is obvious that these models are unlikely to be effective when studying most natural systems (e.g., biological), i.e., the systems that are far from corresponding to ideal or simple models.

The thermodynamics of nonequilibrium processes deals with the rate of increase in or (which is the same) production of entropy. Therefore, it is sometimes asserted that nonequilibrium thermodynamics provides "the quantitative characteristic of the second law of thermodynamics" [7]. In the given case, however, this statement is reasonable only when applied to transformations in simple isolated systems where all processes are close to equilibrium. Only in a system that is close to equilibrium can the differential of this function of state of the system (entropy) be considered to be a full one, to an acceptable approximation. However, all the aforesaid is usually underestimated; therefore, many works on nonequilibrium thermodynamics, especially the thermodynamics of systems that are far from equilibrium, remain a faint "future hope." Some of these works, I daresay, are mere "mathematically trimmed" fantasies useless for real life [22–24].

Historically, the formulations of the second law of thermodynamics were closely associated with the study of heat engines. This approach has been developed by physicists, mainly thermal physicists, and heat engineers. Another trend in the use of the second law of thermodynamics is related to the attempts of some mathematicians and physicists constructing ideal and simple models to explain many natural phenomena in statistical terms. However, since all interactions in real systems are impossible to take into account, there is but little hope that calculations in the framework of these models will successfully solve the problem. Hence, only the phenomenological thermodynamics of systems close to equilibrium (equilibrium or quasi-equilibrium thermodynamics) is likely to ensure the insight into many natural phenomena and make reliable quantitative predictions.

The above formulations of the second law of thermodynamics are, in a sense, somewhat outside the realm of the chemistry of molecular and supramolecular systems. These formulations may seem to be even farther from biology, sociology, and other sciences that are mainly based on chemistry (both molecular chemistry per se and the chemistry of supramolecular structures), which we perceive as "chemistry around us." Therefore, it is not unexpected that a purely physical (rather than physicochemical) approach to the origin of life, biological evolution, and aging of living organisms has lead to numerous misunderstandings—one might say, even to tragic errors—in life science. It should suffice to mention L. Boltzmann's, E. Schrödinger's, I. Progogine's [29–31], and other researchers' fallacies accounted for by neglecting (to some or another extent) Gibbs's works and underestimating the possibilities offered by thermodynamics. In some of my publications, I emphasized the substantial misunderstandings in this field [11, 20, 22, 23] that the founders of classical thermodynamics noted long ago [1, 2, 10–13].

To justify these statements, let me make a digression to cite the renowned scientists Boltzmann and Schrödinger [31] who asserted that living organisms struggle for negative entropy (also called negentropy). I will also cite some Prigogine's [29] quotations that appeared even on the cover of his books. The reader will find references to them in the Internet [31, 32].

I would like to note that the quotations presented below do not pertain to the second law of thermodynamics in its classical form [2, 9, 10]. Today, they may seem surprising, especially taking into account that all this was written several years after Gibbs published his works.

For example, Boltzmann (1886) wrote,

"The general struggle for existence of animate beings is therefore not a struggle for raw materials - these, for organisms, are air, water and soil, all abundantly available—nor for energy which exists in plenty in any body in the form of heat (albeit unfortunately not transformable), but a struggle for entropy, which becomes available through the transition of energy from the hot sun to the cold earth.".

Then, in 1944, Schrödinger wrote that *"the only way a living system stays alive, away from maximum entropy or death is to be continually drawing from its environment negative entropy. Thus the device by which an organism maintains itself stationary at a fairly high level of orderliness (= fairly low level of entropy) really consists in continually sucking orderliness from its environment. …Plants of course have their most powerful supply in negative entropy in sunlight…"*.

Later, Prigogine also supposed (on the basis of previous notions of Boltzmann, Schrödinger, and their followers in life science) that the phenomenon

of life is hardly consistent with the second law of thermodynamics. He noted, *"During the last decades, an opinion has widely spread that there is the apparent contradiction between biological order and laws of physics—particularly the second law of thermodynamics"* (1980). Prigogine also emphasized that *"this contradiction cannot be removed as long as one tries to understand living systems by the methods of equilibrium thermodynamics"*.

In order to solve these "contradiction", Prigogine [29] developed the theory of dissipative structures, i.e., the structures that appearing in systems that are **far from equilibrium.** Later, it turned out that the theory did not allow overcoming the aforementioned "contradictions." In fact, it made the imbroglio even more intricate. It later became obvious that Prigogine's views do not agree with the second law of thermodynamics [20, 22, 24]. This is so in many respects. Suffice it to say that, in the general case, the Prigogine entropy (S' or S_i) has no full differential. Therefore, his theory cannot be regarded as thermodynamic. This is a kinetic theory based on an "entropy" (Prigogine's entropy, S') which can be neither calculated nor measured.

Prigogine considered Gibbs's work to be mainly theoretical and stated that Gibbs's method is inapplicable to studying physicochemical transformations, such as chemical reactions, because the values used in this method are the functions of state pertaining to the whole system or its individual component. Prigogine actively publicized his views via scientific literature and textbooks [30]. As a result, many researchers refer to Prigogine's formulation of the second law of thermodynamics. Actually, this formulation applies to a particular speculative model and may be accepted only on certain premises that cannot be proved. Unfortunately, this concept (which, in a sense, contradicts the principles of science itself [5, 6]) was supported by many researchers. Owing to efficient publicity, these colleagues were convinced by hardly comprehensible (in physical terms) formulas and doubtful argumentation. In my opinion, the supporters of Prigogine's theory were, in a sense, deceived. Although Prigogine's theory proved an impasse, it still has its followers. Nevertheless, no numerical data obtained from either experiment or observations have confirmed the theory even at the qualitative level [20, 22]. Moreover, many physicochemical processes of the formation of spatially periodic structures (which Prigogine and his coauthors regarded as dissipative) were explained long ago in terms of the thermodynamic models of quasi-equilibrium systems (without involving the concept of dissipative structures). It is generally known that W.Ostwald (1897) used the notion of supersaturation to explain the existence of such systems in nature.

Thus, the aforementioned concepts by Boltzmann, Schrödinger, Prigogine, and their followers turned out to be at best tentative ones, or even a dead end. They hampered for many decades the search for the ways to explaining the evolution of living systems in physicochemical terms on the basis of the second law of thermodynamics. As noted above, only in recent decades were the principles of hierarchical thermodynamics (macrothermodynamics) formulated. I have managed to extend Gibbs's methodology so that it might be used for creating the physical (physicochemical) theories of the origin of life, biological evolution, and aging of living organisms [17, 22–28].

As noted above, the physical substantiation of the second law of thermodynamics deals with ideal processes and is based on the concept of statistical entropy. The nonequilibrium thermodynamics of systems that are far from equilibrium tries to study the changes in "kinetic entropy" (e.g., Prigogine's entropy S' or (S' or S_i), which, as mentioned above, has no full differential (even an approximate one) and cannot be calculated in principle! In addition, the approaches used in the nonequilibrium thermodynamics of systems far from equilibrium create difficulties related, e.g., to the notions on the thermodynamics of processes and the thermodynamics of systems.

One of the greatest merits of Gibbs and other renowned founders of classical thermodynamics is that they used the works by J.L. Lagrange, L. Euler, and other outstanding mathematicians (specifically, the variation principles developed by them) as a basis for the concepts on the functions of state of the system other than entropy (which, like entropy, have full differentials). The functions of state permit determining the directions of spontaneous processes and estimating the extent of their advancement in individual thermodynamic systems identified in the real world. In other words, the evolution of systems themselves can now be studied, to a certain approximation, if certain natural (independent) variables are constant. The

Gibbs function G (the Gibbs free energy or, more briefly, the Gibbs energy) can be used for studying equilibrium (quasi-equilibrium) processes and closed systems (the quasi-closed systems in which quasi-equilibrium transformations occur) at constant temperature and pressure. The Helmholtz function F (A) is applicable to studying these processes and systems at constant temperature and volume. Certainly, this is only true on the assumption that the functions of state (of the systems studied) have actual physical sense at any moment of time. This is true for systems close to equilibrium but not for those far from equilibrium. I would like to emphasize once more that the law of temporal hierarchies gives grounds for the use of the functions of state when the direction and the extent of advancement of the evolutionary processes that occur in quasi-closed systems are estimated at different hierarchical levels of living matter [17]. For clarity, let us make a digression on the law of temporal hierarchies.

The law of temporal hierarchies makes it possible to identify quasi-closed thermodynamic systems (subsystems) within open biological systems and to study the individual development (ontogenesis) and evolution (phylogenesis) of these subsystems via studying the changes in the specific (calculated per unit volume or mass) Gibbs function for the formation of a given higher monohierarchical structure out of lower monohierarchical structures. For example, it has been found that the specific Gibbs function for the formation of supramolecular structures of biological tissues ($\overline{\tilde{G}}_i^{im}$) tends towards its minimum in the course of ontogenesis (as well as phylogenesis and evolution as a whole):

$$\overline{\tilde{G}}_i^{im} = \frac{1}{V}\int_0^V \frac{\partial \tilde{G}^{im}}{\partial m}(x, y, z)dxdydz \to \min, \quad (2)$$

where V is the volume of the system, m is the mass of the microvolumes identified, x, y, and z are coordinates, the symbol "–" means that $\overline{\tilde{G}}_i^{im}$ is a specific value (i.e., calculated per unit macrovolume), and the symbol "~" emphasizes that the system is heterogeneous. Note that expression (2) implies that the intermolecular (supramolecular) interactions in all hierarchical structures of biological tissues (both intracellular and intercellular interactions) are taken into account. This is justified because the structural hierarchy does not necessarily coincide with the temporal one. For example, cells of some types do not divide; like organs, they age simultaneously with the body as a whole. However, for each supramolecular hierarchy (j–1), there exists a higher hierarchy (j+x) such that

$$t^{j-1} << t^{j+x},$$

where t^{j-1} and t^{j+x} are the mean lifetimes (or lifespan) of the elementary structures of the respective structural hierarchies in the living system; x = 0, 1, 2, etc.

Note that the internal medium and many fragments of nondividing cells are nevertheless renewed due to metabolism.

The use of expression (2) actually means that, in the given case, the law of temporal hierarchies assumes the following form:

$$\ldots << t^{m} << t^{im} << t^{organism} << t^{pop} << \ldots . \quad (3)$$

Here, t^{m} (t^{ch}) is the mean lifetime of molecules (chemical substance) involved in metabolism in the body, t^{im} (t^{supra}) is the mean lifetime of all intermolecular (supramolecular) structures of tissues renewed during individual growth and development, $t^{organism}$ is the mean lifetime of individual organisms in a population, and t^{pop} is the mean population lifetime. I have deliberately excluded the lifetimes of cells and some other complex supramolecular structures from the series of strong inequalities (3) for the reasons indicated above. However, this series certainly represents a general law of nature consistent with reality and reflecting the existence of temporal hierarchies in living systems.

The law of temporal hierarchies is related to the presence of metabolism or other forms of substance transformation at all hierarchical levels. Note that metabolism is an essential characteristic of living organisms.

This law (Gladyshev's law) allows strict demonstration of the possibility to identify (discern) quasi-closed monohierarchical systems (subsystems) within open polyhierarchical biological systems. This statement entirely agrees

with the experience accumulated in theoretical and experimental physics [3, 5]. I am convinced that this assertion cannot raise any objections.

It is impossible in this short article to list all important conditions for the use of some or another function of state of the system. Moreover, I do not think I have noted all of the main "delicate" points that beginners should take into account. Besides, I refer to just a few publications, those that are most important for me. It should also be noted that my paper, as well as most publications on thermodynamics, may contain some inaccuracies of wording resulting from the ambiguity of translation. For example, most professional scientists know about inexcusable confusions with the terms *isolated system* and *closed system* (originally English). Both terms are sometimes translated into Russian as *замкнутая система* (literally, *closed system*). So the terms are often regarded as equivalent or identical. Other errors result from semantic coincidence of some terms. For example, the Gibbs (or Helmholtz) free energy is often confused with energy in the ordinary sense. This is why many researchers have attempted to replace this term with the term *the Gibbs function* [19]. Another example is the term *complex system.* Here, the word *complex* has a double meaning. In thermodynamics, a complex system (as opposed to a simple one) usually means a system in which (or on which) a work other than the work of expansion is done [15, 16]. Sometimes, however, the word *complex* is used to emphasize a structural or some other heterogeneity of the system itself or the diversity of its elements. This also applies to the term *simple system,* and so on. Certainly, these and other such confusions may lead to blunders that escape a nonprofessional's notice. These and other similar errors creep into some textbooks, reference books, and then into the Internet. I presume the possible inaccuracy of my English in this paper is insignificant, and I hope that the above remarks will warn beginners about the erroneous views that may exist in thermodynamics. I think that all physicists, chemists, biologists, and other specialists that deal with thermodynamics should study the Gibbs phenomenological thermodynamics first of all. As noted above, this authentic (in a certain sense, true) thermodynamics is based on the notion of full differentials. Note that this approach to understanding the world surrounding us is intrinsically irrefutable. We may only discuss the accuracy of the Gibbs thermodynamics as applied to, e.g., quasi-closed systems the processes in which are close to equilibrium. In accord with the very essence of full differential (its mathematical meaning), as well as the first law of thermodynamics, the change in the function of state of the system accompanying the transition from one equilibrium state to another is independent of the way or mechanisms of this transition. Probably, the lack of our knowledge on actual complex systems may be partly attributed to the changes in entropy during this transition, because the entropy cannot be measured directly. The changes in phenomenological entropy accompanying transformations in both simple and complex systems may be calculated only if one has studied the corresponding thermal processes. In statistical terms, the entropy is calculated only for ideal systems (or systems close to ideal). It is impossible to perform any precise calculations of this function of state for systems with strong interactions between particles (molecules and supramolecular structures) on a statistical basis. I would like to emphasize that this applies to complex thermodynamic systems, i.e., the systems in which strong interactions occur.

Thermodynamics, owing to its impeccably reliable mathematical basis, may be regarded as a "machine" that always yields the right result if the premises are correct. Physical chemistry has repeatedly confirmed this [8–10, 14, 19]. Unfortunately, some physicists, biophysicists, biologists, and, especially, modern "philosophers" are still unaware of this experience of chemists and chemical technologists.

I would like to repeat that the aforementioned ambiguities, which are mainly related to the disregard of the correct use of many terms that are semantically similar but differ in physical meaning, result in confusion and misunderstandings. These misunderstandings discredit, at least in nonprofessionals' opinion, thermodynamics itself and science as a whole. Hence the numerous incorrect interpretations of the second law of thermodynamics, various dubious "views" on entropy [11, 13, 20, 22], and far-fetched "the functions of state of the system" in literature are appeared. Many authors, ignoring classical works in this field, apply different formulations of the second law of thermodynamics to systems where they are inherently inapplicable. Some of these authors suggest their own interpretations of this general law of nature. This debases science and education. Moreover, it can be said that several

"second laws of thermodynamics" have appeared, none of which having anything to do with reality. A good example is the aforementioned Prigogine's [29] interpretation of the second law of thermodynamics. This interpretation "extends" the well-known incorrect and indemonstrable statement by the great Boltzmann [31], who neglected the important concepts put forward by Clausius and Gibbs. The interpretation suggested by Prigogine has practically conquered the "scientific" world and still remains one of the trendiest interpretations of the second law of thermodynamics. I am well aware that it would be hopeless to argue with the visionaries that create or support these concepts: they have developed an excellent method for leading such debates. They unfailingly give lots of arguments, which are mostly quotations from published or oral statements made by other visionaries or by insufficiently informed scientists. It is often emphasized that those scientists are well known or even famous. However, the visionaries forget that scientists that are well known and famous in one field are not necessarily professionals in others. The only way to withstand this conjuncture is to refer the readers to classical works and serious textbooks written in a highly professional milieu of world-renowned scientific schools with centuries-long traditions.

Thus, making no pretensions to perfection, I would like nevertheless to offer advice to researchers dealing with thermodynamics, as well as other branches of science, and the editors of scientific periodicals. My advice is the following. **When discussing the problems of thermodynamics or using its mathematical tools for calculations, it is necessary to clarify "ambiguous" terms and definitions. It is also advisable to refer to the classical works (including textbooks, reference books, and encyclopedias) that the authors of publications used.** In this case, the correctness of the results reported in the publications can be at least preliminarily estimated.

I am grateful to Prof. M.M. Abdildin, Prof. G. Arrhenius, Prof. N.N. Bogolyubov, Jr., Prof. K.G. Denbigh, Prof. V.P. Kazakov, Prof. Yu.S. Lipatov, Prof. A.A. Logunov, Prof. V.V. Sychev, and Prof. V.M. Frolov for the support, systematic fruitful discussions, and valuable advice.

REFERENCES

[1] Poincare' A. *On Science*. Moscow: Nauka, 1983.

[2] Gibbs JW. *The Collected Works of J. Willard Gibbs*. *Thermodynamics, Vol.1*. New York: Longmans, Green and Co., 1928.

[3] Bogolubov NN. *Selected works. Part 1, Dynamical Theory.* New York: Gordon and Breach Science Publishers, 1990.

[4] Bogolubov NN. and Bogolubov NN., Jr. *An Introduction to Quantum Statistical Mechanics.* Library of Congress Catalog ISBN, 2-88124-879-9, QC 174.4.B6413: Gordon and Breach Science publishers, 1992.

[5] Sedov LI. *The Thoughts on Science and on Scientists.* Moscow :Nauka, Russian Academy of Sciences, V.A. Steklov Mathematical Institute, 1980.

[6] Sedov L.I. *New theories, model and reality*. Nature (Russ.)1984; 11: 3-10.

[7] Zubarev DN. *The Carnot theorem.* In: Physical Encyclopedia. Moscow: Soviet Encyclopedia, 1990, Vol. 2, p. 242-243.

[8] Alberty RA. *Physical Chemistry,* 7th *Ed*. New York, Etc: Wiley, 1987.

[9] Silbey RJ., Alberty RA. *Physical Chemistry, 3rd Ed.* New York: John Wiley & Sons, 2001.

[10] Denbigh KG. *The Principle of Chemical Equilibrium, 3ed Ed*. Cambridge: University Press, Cambridge, 1971.

[11] Denbigh KG. *Note on Entropy, Disorder and Disorganization.* Brit. J. Phyl. Sci. 1989; 40: 323 -332.

[12] Denbigh KG. *The Many Faces of Irreversibility*. Brit. J. Phil Sci. 1989;40:501-518.

[13] Denbigh KG., Denbigh JS. *Entropy in Relation to Incomplete Knowledge.* Cambridge: University Press, Cambridge, 1985.

[14] Cantor ChR. , Schimmel PR. *Biophysical Chemistry, Vol. 1-3*. Moscow: Mir, 1984-1985.

[15] Sychev VV. *Thermodynamics of Complex Systems.* Moscow: Energoatomizdat, 1986.

[16] Sychev VV. *Differential Equations of Thermodynamics.* Moscow: Nauka, 1981.

[17] Gladyshev GP. *Supramolecular thermodynamics is a key to understanding phenomenon of life. What is Life from a Physical Chemist's Viewpoint; Second Ed.* Moscow – Izhevsk: "Regular and Chaotic Dynamics", 2003 (In Russian).

[18] Lipatov Yu. S. *Phase-Separated Interpenetrating Polymer Network..* Dnepropetrovsk: USChTU (ISBN 966-8018-12), 2001, 326p.

[19] Jones MN., Ed., *Biochemical Thermodynamics.* Amsterdam – Oxford – New York: Elsevier Scientific Publishing Company, 1979 (Russian translation. Moscow: Mir, 1982).

[20] Shu-Kun Lin. *Diversity and Entropy.* Entropy 1999; 1:1-3. www.mdpi.org/entropy

[21] Alberty AR, *Research Summary*; Massachusetts Institute of Technology, Chemistry : Internet, 2004 http://web.mit.edu/chemistry/www/faculty/alberty.html

[22] Gladyshev GP. *Macrothermodynamics of Biological Evolution: Aging of Living Beings.* International Journal of Modern Physics B 2004;18(6):801-825.

[23] Gladyshev GP. *Thermodynamic self-organization as a mechanism of hierarchical structures formation of biological matter.* Progress in Reaction Kinetics and Mechanism (An International Review Journal. UK, USA) 2003;28: 157-188.

[24] Gladyshev GP. *Macrothermodynamics of Biological Evolution and Aging of Living Beings. Physical Chemistry of Dietaries.* Proceedings of International Higher Education Academy of Sciences 2003;4 (26):19-46.

[25] Gladyshev GP. *Thermodynamics of biological evolution and aging.* Electron. J. Math. Phys. Sci. (USA) 2002; Seminar, 2: 1-15. www.ejmaps.org .

[26] Gladyshev GP. *The Hierarchical Equilibrium Thermodynamics of Living Systems in Action.* SEED Journal 2002;3:42-59 (Toborsky E., co-editor SEED. Editorial, № 3, 1-2). http://www.library.utoronto.ca/see/pages .

[27] Gladyshev GP. *On the Thermodynamics, Entropy and Evolution of Biological Systems: What is Life from a Physical Chemist's Viewpoint.* Entropy 1999; 1(2): 9-20. www.mdpi.org/entropy.

[28] Gladyshev GP. *Thermodynamic Theory of Biological Evolution and Aging. Experimental Confirmations of Theory.* Entropy 1999;4:55-68. www.mdpi.org/entropy .

[29] Prigogine I. *From Being to Becoming: Time and Complexity and the Physical Sciences.* San Francisco: W.H. Freeman & Co., 1980.

[30] Prigogine I., Defey R. *Chemical Thermodynamics.* Novosibirsk: Nauka, 1966.

[31] References of works of L.Boltzmann, E.Schrödinger end I.Prigogine one can find in web-page: http://www.redfish.com/research/SchneiderKay1995_OrderFromDisorder.htm (E.D. Schneider, J.J. Kay, 1995, "Order from Disorder: The Thermodynamics of Complexity in Biology", in Michael P. Murphy, Luke A.J. O'Neill (ed.), *"What is Life: The Next Fifty Years. Reflections on the Future of Biology"*; Cambridge University Press, pp. 161-172).

[32] Information in Internet. *The problems of Thermodynamics of Biological Evolution* http://www.endeav.org/evolut

Proceedings of ECOS 2005
Trondheim, Norway
June 20–22, 2005

USING ENTROPY PRODUCTION TO MODEL INTERACTION BETWEEN COMBUSTION AND ACOUSTICS

Carmine Luca Iandoli[1] and Ivar Ståle Ertesvåg[2]
Department of Energy and Process Engineering, NTNU
Trondheim, Norway

Enrico Sciubba[3]
Department of Mechanical & Aeronautical Engineering
University of Roma 1 "La Sapienza"
Roma, Italy

ABSTRACT

Considerations on entropy production are made to understand and model the reaction-rate enhancement observed in turbulent combustion affected by acoustic waves. The Eddy Dissipation Concept for turbulent combustion (EDC) is extended to account for the acoustic waves. It is argued that in combustors, acoustic waves often occur at length scales at the order of magnitude of the mean flow. Hence, the small-scale behaviour, including chemical reactions, is affected through the kinetic energy cascaded to turbulence fine structures. The energy input is enhanced by the large-scale entropy production due to acoustic waves, and increases the dissipation. Testing the modified model against available experimental data gave the correct response to acoustic waves.

Keywords: Combustion modeling, acoustics, local entropy generation rate, EDC, CFD

NOMENCLATURE

a	attenuation of acoustic energy [m^{-1}]
c	speed of sound [m/s]
k	turbulence kinetic energy [m^2/s^2]
m^*	mass exchange of the fine structures [s^{-1}]
p	pressure [Pa]
q_n	dissipation (EDC) [m^2/s^3]
T	temperature [K]
u	velocity [m/s]
w_n	energy transfer (EDC) [m^2/s^3]
γ_λ	mass fraction (EDC) [-]
ε	turbulence energy dissipation rate [m^2/s^3]
Φ	dissipation function [W/m^3]
λ	thermal conductivity [W/(m K)]
ν	kinematic viscosity [m^2/s]
ρ	density [kg/m^3]
σ	entropy production rate [$W/(m^3 K)$]
τ^*	reactor residence time (EDC) [s]
τ_{ij}	viscous stress tensor [N/m^2]
ω_n	characteristic frequency of turbulence [s^{-1}]

1 INTRODUCTION

In the field of turbo-machinery, as in any other field, the efficiency of turbines, compressors and other components is inversely proportional to the distance of the real process from its ideal counterpart. This implies that the design goal is that of minimizing the exergy destruction in the device [2]. In order to achieve this, the detailed accounting for the local entropy production proposed by the authors [8-9,12,15] has been shown to provide additional insight into the dissipative mechanisms and consequently to be a proper designer's guideline to process improvement.

In this paper we suggest how entropy production can be used to model mixing mechanisms such as interaction with acoustic waves.

Our goal here is not to investigate efficiency, but to explore whether an entropic approach can provide a better understanding of combustion and

[1] Carmine.L.Iandoli@ntnu.no
[2] Ivar.S.Ertesvag@ntnu.no
[3] Enrico.Sciubba@uniroma1.it

lead to more accurate modeling of turbulent flames. As a first step we will show how the Eddy Dissipation Concept for turbulent combustion (EDC) by Magnussen and co-workers [5,11] can be related to the entropy generation and how considerations on entropy generation can improve such a model.

2 ENTROPY GENERATION AND ACOUSTIC WAVES

2.1 Turbulence cascade

Turbulent combustion is controlled by mass transfer from the large to the small scales of the flow. This is an intrinsically dissipative process which is governed by the turbulent characteristics of the flow. The large scales of the motion are loosing their energy by "cascading" it towards ever smaller scales, until the smallest viscous scales are reached where mechanical energy is fully converted into heat. In the absence of an energy input mechanism ("forcing") at some large scale, the turbulence is known to decay quite rapidly.

A possible modeling of the energy decay is the EDC [5,11]. This model provides a link between the local level of turbulent energy and dissipation rate and the time needed to achieve perfect mixing. The concept involves the explicit consideration of an energy cascade that transfers mechanical energy from the largest to the smallest scales. The model has been widely applied. However, the EDC in its present formulation does not seem to yield proper results when applied to the solution of problems involving highly unsteady processes such as pressure waves and their interaction with the heat release. In order to understand if, where, and how EDC can be improved, the general picture of the mixing process will here be observed from a different perspective.

By following a given control volume $\mathcal{V}$ in time, we see that it exchanges energy and momentum with the surroundings, changing its turbulence level in the process. What actually happens at the smallest scales is that the dynamics of the turbulence evolves not under the direct effect of the main flow, but just because of the evolution of the energy cascade. This evolution is a natural process that involves production of entropy and depends on the very structure of the flow. The turbulence cascade posses its own continuous set of time scales, and it is maintained as long as the main flow keeps "feeding" the turbulence energy. What happens is that part of the energy of the mean flow, the turbulence kinetic energy, is dissipated and converted into heat inside of each volume $\mathcal{V}$. In other words, turbulence is converting kinetic energy into heat while producing entropy. If the volume could reach a condition of equilibrium where no more turbulence energy is being added from the outside, all the turbulence energy would be converted very quickly into heat, until the flow within $\mathcal{V}$ first re-laminarises and then finally comes to a stillstand. In this sense, the turbulence kinetic energy may be considered as a measure of the potential entropy of the flow, or, in other words, as a measure of the distance from local thermodynamic equilibrium.

But we know that it is the turbulence energy dissipation rate that physically represents the local entropy production rate due to the transfer of momentum at the smallest scales: therefore, the ratio between dissipation rate and turbulent kinetic energy must functionally represent a measure of the distance between local and global equilibrium.

The above ideas may be applied when dealing with the calculation of the fine-structure volume fraction and the reactor residence time in the framework of the EDC (see expressions below).

In this sense, the energy cascade already represents the link between local entropy production (ε) and its distance from equilibrium (k).

The original formulation of the EDC given by Magnussen [10] can be revised on the basis of the concepts outlined above, but before doing that it is useful to show how the entropy production and the dissipation rates are related.

2.2 Entropy production

Entropy is generated due to reactions, mass fluxes, energy fluxes, and viscous dissipation. Here, it will be argued that the contributions from reactions and mass fluxes are mainly found in

smaller scales. Moreover, it is observed that pressure waves occur at the mean-flow scale level. Hence, the volumetric entropy production associated with pressure waves can be expressed

$$\sigma = \frac{\lambda}{T^2}\left(grad\left(T\right)\right)^2 + \frac{\Phi}{T} \qquad (1)$$

Here, the dissipation function is expressed

$$\Phi = \tau_{ij}\frac{\partial u_i}{\partial x_j}, \qquad (2)$$

and the velocity and temperature are used with their mean values. It can be noted that neglecting of the heat-transfer term implies that the compression is considered adiabatic.
Further considerations of entropy and CFD modeling of turbulent combustion with EDC are provided in [4].

2.3 Attenuation of pressure waves

The attenuation of pressure waves traveling through a fluid involves both thermodynamic and viscous effects. The pressure change resulting from the volume reduction ("compression") is not quite in phase with the change of density, and volume deformation energy is thereby converted into heat. Through interaction with the surrounding gas, the compressed portion loses thermal energy by diffusion, and a corresponding "relaxation" of the sound pressure results [8].
The effects of viscosity involve a similar diffusion from the moving part to the rest of the gas: They amount to irreversible transfers of kinetic energy from the organized motion of the sound wave to the disorganized translational motion of the molecules which constitutes their thermal energy.
The general picture of the pressure attenuation should also include the relaxation due to chemical reactions and the effects related to mixtures including non-monatomic gases, where there are other degrees of freedom of the molecules, other than the translational ones.
Neglecting for the moment chemical effects, we can say that an increase of the entropy generation rate is generated by a rate of variation of thermal energy per unit volume that must be equal to the loss of power (energy per unit time) per unit volume from the sound wave. In this case both temperature and momentum fluxes must be included into the entropy production term, Eq. (1)
For a simple-harmonic plane wave propagating through a perfect gas, the attenuation can be expressed as a fraction of its energy [6]:

$$2a = \frac{dQ}{I} = \frac{\sigma \cdot T}{I}, \qquad (3)$$

where the intensity is $I = \rho c u_0^2$. It is worth noticing that the attenuation is computed by comparing the local entropy production of the disturbance with its intensity, which is the same concept used in the EDC framework to evaluate the turbulence cascade.

Fluid motion is characterized by a continuous production of entropy: when the process involves a mixture, global equilibrium is achieved when the velocity, temperature and concentration gradients are identically zero. In this condition, each volume of fluid may potentially burn if the temperature is high enough. By following the evolution of a fluid volume, one may observe that the local entropic level increases in time, because of the local entropy production rate, which includes all of the dissipative effects. The conversion of the kinetic energy of the fluid into thermal energy can therefore be seen as a measure of the mixing achieved at the smallest scales. The way this mixing is achieved depends on the nature of the process itself: in the case of turbulence it is modeled by the energy cascade, while in the case of acoustic disturbances it still needs to be modeled. However, in the next paragraph we will show that acoustic waves do increase both the turbulent kinetic energy and the dissipation of the flow they travel through. It should be kept in mind that the attenuation of acoustic waves is a process which includes a transfer of energy to other frequencies, but in general is not governed by the turbulent energy cascade.
In fact, it must be remarked that viscosity and thermal conductivity are actually transmitting energy from the large scales of motion to the molecular scales. This can be easily proved without assuming any cascade model.
Equation (3) shows that the attenuation is governed by non-linear terms. This means that the larger the gradients, the larger the attenuation. In

this sense the higher frequencies, which are characterized by higher gradients, are attenuated faster. Similar considerations apply in the case of both pressure and velocity waves, but in this latter case it is easier to understand how the dissipation is achieved.

3 ACOUSTIC WAVES AND TURBULENCE DYNAMICS

The attenuation of sound waves is a process of energy transfer from large to small scales. This transfer is represented by the dissipation of the velocity fluctuations (turbulence energy) and is enacted by the dissipation function Φ which can be easily linked to the viscous entropy production, Eqs.(1)-(2).

Numerical tests [8] shown that the decay of acoustics waves follows a path similar to the decay of turbulent energy. In particular in a frequency range lower than the Taylor scales, which is related to the inertial sub range, acoustic energy is mostly transferred from a lower to a higher frequency with little dissipation, while in the dissipative range not all of the energy is transferred, but part of it is also dissipated and converted into heat.

However, the interaction between the kinetic energy produced in that case by the boundaries and the acoustic energy is yet to be modeled and in fact the turbulent kinetic energy k as well as the dissipation ε were not affected by the acoustic waves.

Direct interaction between shear stress due to acoustic waves and turbulence should be expected when the reciprocal of the mean strain rate (S^{-1}) and the turbulence time (k/ε) scale are in the same range [12].

In industrial combustion chambers these time scales are usually close enough to interact, but the intensity of such an interaction and its effect depend on the relative magnitude among the two energies involved. A first evaluation can be performed comparing the amplitude of velocity fluctuations due to turbulence and acoustics. In the operational range of a gas turbine burner, a high turbulence level is required to improve mixing, thus we can expect velocity fluctuations u' to be in the range of 1-2 m/s. As a very rough first approximation, the acoustically induced velocity fluctuations for plane waves such as those observed in combustors can be computed on the basis of [6]:

$$u_{acoustics} = p_{acoustics} / (\rho c) \qquad (4)$$

Acoustic pressure rarely exceeds *100 Pa*, while density is in the order of *0.2-0.3kg/m*^{3} and speed of sound is about *500 m/s*. Under these conditions the maximum $u'_{acoustics}$ we can expect is in the range 0.7—0.5 m/s, which is not far from the turbulence-induced velocity scale. Preliminary experiments have been performed to evaluate how acoustics affects turbulence. A turbulent stream was perturbed with acoustic drivers confirming that it is possible to modify the turbulent energy spectrum with acoustic waves [8]; an example of this interaction is reported in Fig. 1. In this case, the turbulent field is generated by a grid and an acoustic driver is perturbing the flow at different frequencies, in the figure we reported the effect of forcing at 263 Hz.

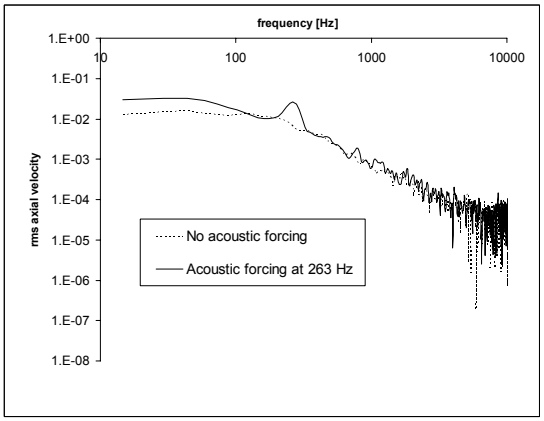

Figure 1: Axial velocity spectrum with and without acoustic forcing

The velocity spectrum shows that when perturbing the turbulent flow with an acoustic fluctuation, the effect of the perturbation is directly felt on the spectrum (the continuous line shows a peak in correspondence of the frequency of the perturbation). However this is the only appreciable effect on the stream.

The effect of the acoustic forcing on turbulence needs further investigations however theoretical analyses suggested that two kinds of effects can

be expected depending on the relative magnitude of acoustics and turbulence [12]. If the acoustic shear is strong enough, the flow should suffer a strong and highly dissipative distortion which has been treated by the rapid distortion theory. In this case a huge production of kinetic energy follows the distortion and then the turbulence field becomes anisotropic. However our experiments did not show any anisotropy in the flow field.
On the other hand, if the shear is not strong enough, the tiny anisotropy induced by acoustics will be redistributed among the Reynolds stresses, in this case the flow is experiencing a return to isotropy and the energy of acoustics does not appear in the turbulent kinetic energy budget [12]. Nevertheless the acoustic shear affects the energy flux among the stresses, and once isotropy is recovered, we should except that the decay of acoustic and turbulent energy should follow the same path.

4 ACCOUNTING FOR ACOUSTIC EFFECTS IN THE EDC

4.1 Kinetics of acoustic waves

In the framework of the EDC, the combustion rate is ruled by the amount of energy cascading to the fine structures, which are modeled as a reactor [5,11]. Any changes in the dissipation of turbulent energy should therefore affect the reactor parameters. Hence, the turbulence Reynolds number provides a measure of the distance of the reactor from global equilibrium and an acoustic wave does change such a distance. In particular, in the case of acoustic waves, the distance from equilibrium is increased as well as the entropy generation; therefore we should expect combustion to be enhanced.
Experimental tests have shown that acoustic waves indeed enhance combustion rate [1,7,14].
A possibility for modeling such an effect could be to include the increase in dissipation due to acoustics. Its modeling requires care because both dissipation and distance from equilibrium are increased by acoustic waves. We propose using the viscous term for the entropy generation as a measure of the dissipation and

$$k_{acoustic} = \tfrac{1}{2}\rho u^2_{acoustic} \qquad (5)$$

as a measure of the acoustic energy. Both terms however need to couple with turbulence, and thus in the following we will show a possible way to include them in the energy cascade.

4.2 The EDC cascade model

In the EDC, dissipation is pictured as a multi-step cascade, at each level of which a fraction of the turbulent energy is dissipated into heat (q_n) while the rest feeds mechanical energy (w_n) into the lower scale. For each level, the energy converted into heat is calculated by [5]

$$q_n = C_{D2}\nu\omega_n^2, \qquad (6)$$

while mechanical energy transfer is

$$w_n = \tfrac{3}{2} C_{D1}\omega_n u_n^2 . \qquad (7)$$

Here, C_{D1} and C_{D2} are model constants equal to 0.134 and 0.50, respectively. This mechanism proceeds until all the mechanical energy has been dissipated. Complete dissipation is achieved in the fine structures where, in the hypothesis that the Reynolds number is sufficiently high, the amount of turbulent energy converted into heat is

$$q^* = \tfrac{3}{4} w'' \approx \tfrac{3}{4}\varepsilon = 0.75 u'^3 / L' \qquad (8)$$

This equation links the dissipation at fine structures (q^*) and the turbulence velocity scale u'. The cascade also provides [5] a measure of the velocity fluctuations at the fine scales:

$$u^* = \left(C_{D2}/3C_{D1}^2\right)^{1/4} (\nu\varepsilon)^{1/4} \qquad (9)$$

In order to include the effect of acoustics, it should be considered that the velocity fluctuations associated with sound waves have a specific frequency which essentially depends on the geometry of the combustor. However, in practical applications sound is always produced at large scales, which allows us to assume that acoustics will affect the top of the cascade. This implies that the dissipation of acoustic energy will follow the same path as the turbulent energy, and in particular that fine structure velocity fluctuations can be expressed as:

$$u^* = \left(C_{D2}/3C_{D1}^2\right)^{1/4} \left(\nu\left(\varepsilon + T\sigma_{acoustic}/\rho\right)\right)^{1/4} \qquad (10)$$

The EDC model then uses u^* to evaluate the amount of mass that is molecularly mixed [5]:

$$\gamma_\lambda = u^*/u' = \left(3C_{D2}/4C_{D1}^2\right)^{1/4}\left(\nu\varepsilon/k^2\right)^{1/4}. \quad (11)$$

This quantity is interpreted as the ratio between mass of fine-structure regions and total mass. The ratio of the mass of the active reactor and total mass, and hence the reaction rate, is taken proportional to the square of γ_λ.

In order to account for the acoustic forcing, it is necessary to modify the turbulence velocity scale $u' = (2k/3)^{1/2}$. Here, we suggest modeling it as

$$u' = (2k/3)^{1/2} + p/\rho c, \quad (12)$$

where the additional term accounts for the velocity fluctuations due to a plain acoustic wave with intensity p. It is worth noticing that the amplitude of the fluctuations increases with decreasing density.

Although such a measure of the amplitude of an acoustic wave is not correct for sound propagation in open spaces, in combustors, sound is coupled to the acoustic modes of the burner, so that acoustic waves may be roughly approximated as plane. For more general cases, a strategy for a more accurate computation of velocity fluctuations should be considered.

The new mass fraction thus will be

$$\gamma_{\lambda,acoustic} = \left(\frac{3C_{D2}}{4C_{D1}^2}\right)^{1/4}\left(\frac{\nu\left(\varepsilon+\sigma T/\rho\right)}{k+\frac{1}{2}\left(p/\rho c\right)^2}\right)^{1/4} \quad (13)$$

Once the mass fraction is defined, the EDC model introduces a time scale, which is needed to define how long fuel and oxidizers are hosted in the reactor $\tau^* = (m^*)^{-1}$, where m^* is the mass flow to the fine structures modeled as

$$m^* = 2\frac{u^*}{L^*} = \left(\frac{3}{C_{D2}}\right)^{1/2}\left(\frac{\varepsilon}{\nu}\right)^{1/2}. \quad (14)$$

By substituting here the dissipation ε with the extended dissipation that includes the entropy generation ($\varepsilon+T\sigma_{acoustic}/\rho$), the new residence time becomes:

$$\tau^{*-1} = m^* = \left(\frac{3}{C_{D2}}\right)^{0.5}\left(\frac{\varepsilon+T\sigma_{acoustic}/\rho}{\nu}\right)^{0.5} \quad (15)$$

This expression shows that an increased energy forcing to the top of the cascade will indeed affect the fine structures and ultimately enhance combustion.

Notice that our main hypothesis is that acoustic is feeding the energy cascade from the level of the mean flow, and therefore our model cannot be used for high frequency acoustic waves, where the interactions of the wave trains with the cascade are different.

4.3 Entropy and acoustic waves

The calculation of the viscous dissipation in numerical simulation requires a careful evaluation of the amount of dissipation occurring at the large scales compared with the small ones. As a matter of fact, except for DNS, the latter are accounted by the turbulence model while only large scales variations are directly computed by means of the mean quantities of the motion.

A first remark is that acoustic waves observed in combustors are often related to the acoustic modes of the combustion chamber, which are in the range of 100 to 500 Hz. These frequencies correspond to rather long waves (in the order of 1 meter). In numerical computation of combustion chambers, such long scales of motion are easily calculated by the mean quantities and thus should not require any subgrid modeling.

Therefore it might be possible to evaluate the relevant entropy production only by means of the average quantities. In particular, the viscous dissipation term can be split into a contribution from the large and one from the small scales. The small-scale part is accounted for by the dissipation-rate of turbulence energy. The part associated with acoustic waves is the large-scale (mean) part

$$\frac{T\sigma_{acoustic}}{\rho} = \frac{\Phi_{acoustic}}{\rho} = \left(\frac{\Phi}{\rho}\right)_{LS} = \frac{\tau_{ij}}{\rho}\frac{\partial u_i}{\partial x_j} \quad (16)$$

where, again, the mean values of the quantities are used. The expression assumes density fluctuations are small compared with the mean.

5 TESTING THE EXTENDED EDC MODEL

Although the computation of $\gamma_{\lambda,acoustic}$ can be performed rather easily, the problem is to reproduce the behavior of the acoustic waves.

The investigation discussed in [8] shows that pressure waves and their decay can be computed with the available numerical tools, but that extreme care should be exercised to avoid the occurrence of erroneous results. In an acoustic field, sound is locally generated by density variations, but in the far field it propagates by velocity rather than density fluctuations. Acoustic signals are thus convected as velocity waves that travel through the field and are either reflected or absorbed by the boundaries. This implies that, regardless of the capability of the boundaries to reflect or adsorb pressure waves, in our case we need a numerical boundary treatment that allows both velocity and pressure to fluctuate freely.

The first step towards the evaluation and the validation of the suggested model is by testing statically the EDC reactor by assuming a given level of acoustic pressure and turbulence.

In order to test our model, we thus assume that the link between pressure and velocity waves is given by Eq. (4), which allows us also to estimate the magnitude of the velocity gradients.

The set up for our perfectly stirred reactor was taken accordingly with the experiments performed by [13]. In their work they acoustically forced a highly turbulent flame (Re 20000) by means of two loudspeakers at relatively low frequency (22-50 Hz). Their results indicate that the acoustics was enhancing combustion. On the basis of the combustor data reported in that paper, we assumed that reasonable values for the turbulent kinetic energy and dissipation were, respectively, 1.5 m^2/s^2 and 4 m^2/s^3. These values provide a measure of the turbulence level within the combustion chamber, and of course are not constant in space; however they should provide a reasonable input for the evaluation of τ^* and γ_λ (Eqs. (12) and (9)). In particular:

$$\begin{aligned} \gamma_\lambda &= 0.25 \\ \tau^* &= 17.32 \cdot 10^{-3} \text{s} \end{aligned} \tag{17}$$

Different frequencies are tested in [13], in particular we have investigated the effect of acoustic fluctuations at 22 Hz whit a measured pressure level of 35 Pa. Assuming the density and the speed of sound to be 0.5 kg/m^3 and 500 m/s, respectively, the amplitude of velocity fluctuations due to the acoustic wave can be computed as:

$$u'_{acoustic} = \frac{p}{\rho c} = \frac{35}{500 \cdot 0.5} \text{m/s} = 0.14 \text{m/s} \tag{18}$$

Velocity fluctuations will occur at the same frequency as pressure waves, thus the spatial behavior of the velocity wave will be:

$$\begin{aligned} u(x) &= u'_{acoustic} \sin(2\pi \cdot f \cdot x / c) = \\ &= 0.14 \sin(2\pi \cdot 22 \cdot x / 500) \end{aligned} \tag{19}$$

The analytical expression of the velocity wave allows us to evaluate the attenuation:

$$\frac{\sigma T}{\rho} = 5.8 \cdot 10^{-3} \tag{20}$$

From Eqs. (18) and (20), we can finally evaluate the new values for the mass fraction, Eq. (13) and the residence time, Eq. (15):

$$\begin{aligned} \gamma_{\lambda,acoustics} &= 0.268 \\ \tau^*_{acoustics} &= 1.730 \cdot 10^{-3} s \end{aligned} \tag{21}$$

The new values show that acoustics increases the volume fraction of about 7%, which may explain the enhancement of combustion observed in experiments [1]. The residence time is slightly reduced, but in this case such effect is too small to affect the reactor.

The effect of the changes in the parameters of the EDC was tested on an in-house finite-volume CFD code Spider.

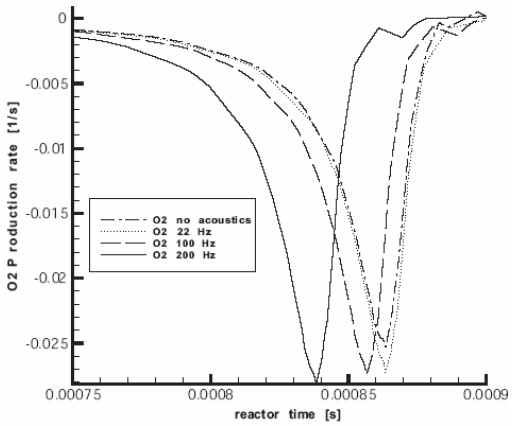

Figure 2: Consumption of O2 at different frequencies of acoustic forcing

Tests were performed with a stoichiometric mixture of CO_2, CH_4, and air, the production rates at different acoustic frequencies are reported in Fig.2.

Acoustics is affecting both the production of turbulent energy and its dissipation. In particular, while the residence time, Eq. (15), depends only on dissipation, the mass fraction, Eq. (13), is a function of both kinetic energy and dissipation. The evolution of each elemental reactor is ruled only by the residence time, while the volume fraction is a scale factor which does not affect the time behavior of the single reactor. For this reason, the differences in time observed for the different frequencies are due only to the residence time and thus to the dissipation. As a matter of fact the variations of the production rate across the frequency spectrum are quite small, and this can agrees with the fact that dissipation at the acoustic scale is almost negligible. Therefore, the trend of the O_2 consumption is related to the effect of the acoustic energy more than to its dissipation.

6 CONCLUSIONS

The EDC model for combustion can be re-interpreted as a measure of the distance between local and global equilibrium of a turbulent flow. Following this approach, we proposed a model that accounts for the mixing effects caused by acoustic waves. We used the viscous entropy production as a measure of the local distance from equilibrium, and the energy of the acoustic wave as a measure of the total equilibrium. The improved mixing was then evaluated using the turbulent energy cascade. The model seams to generate the correct response to acoustic forcing, and although further investigations must be performed, it may provide a feasible modeling for acoustic-flame interaction.

REFERENCES

[1] Baillot F, Demare D. Physical mechanisms of a lifted nonpremixed flame stabi-lized in an acoustic field, Comb. Sci. Tech, 174 (8):73-98, 2002.

[2] Bejan A. *Entropy generation through heat and fluid flow*, Wiley, 1982.

[3] de Groot SR, Mazur P. *Non-Equilibrium Thermodynamics*, Dover Publ., 1984.

[4] Ertesvåg IS, Kolbu J. Entropy production modeling in CFD of turbulent combustion flow. ECOS 2005, Trondheim, Norway.

[5] Ertesvåg IS, Magnussen BF. The eddy dissipation turbulence energy cascade model. Comb. Sci. Tech. 159: 213-235, 2000.

[6] Fahy F. *Foundations of Engineering Acoustics*, Academic Press, 2001.

[7] Hardalupas Y, Selbach A. *Imposed oscillation and non-premixed flames*, Prog. Energy Comb. Sci. 28:75-104, 2002

[8] Iandoli CL. Thesis for PhD. Norwegian University of Science and Technology, Torndheim, 2005.

[9] Iandoli CL, Sciubba E, *3-D Numerical calculation of the local entropy generation rates in a radial compressor stage*, ECOS 2004.

[10] Magnussen BF. *Modeling of pollutant formation in gas turbine combustors based on the eddy dissipation concept*, Int. Flame Research Foundation, 1st Topic Oriented Tech. Meeting, 17-19.Oct., Amsterdam, 1989.

[11] Natalini G, Sciubba E. Minimization of the local rates of entropy production in the design of air-cooled gas turbine blades. ASME J. Eng. Gas Turbines and Power 121: 461-475, 1999.

[12] Pope SB. *Turbulent Flows*. Cambridge University Press, 2001

[13] Pun W, Palm SL, Culik FEC. Combustion Dynamics of an acoustically forced flame. Comb. Sci. Tech. 176: 499-521, 2003.

[14] Sciubba E. *Optimization of gas turbine components via constrained minimization of the local entropy production rate*, Proc. NATO-ASI W.shop on Thermodyn. and Optim. of Complex Energy Systems, Costanza Romania, 1998

Proceedings of ECOS 2005
Trondheim, Norway
June 20–22, 2005

ON THE ENTROPY GENERATION MINIMIZATION IN STEADY STATE AND TRANSIENT HEAT CONDUCTION PROCESSES

Zygmunt Kolenda*, Janusz Donizak, Adam Hołda
and
Marcin Zembura
University of Science and Technology
Department of Theoretical Metallurgy and Metallurgical Engineering
Av. Mickiewicza 30 , 30054 Kraków, Poland

ABSTRACT

On the basis of minimum entropy generation principle, a new formulation of the boundary and initial-boundary value problems of heat conduction is proposed. Two independent approaches are presented-first is based on the first law of thermodynamics and second on Euler-Lagrange variational formalism. It is shown that minimization of entropy generation in steady and transient heat conduction processes is always possible by introducing additional heat sources. It means that irreversibility ratio according to the Gouy-Stodola theorem can be decreased. Numerical examples are presented.
Keywords: entropy generation minimization, heat conduction, boundary and initial-boundary value problems.

NOMENCLATURE

a - thermal diffusivity coefficient [m^2/s]
c_p – specific heat capacity under constant pressure [J/kgK]
h – specific enthalpy [kJ/kg]
k – heat conduction coefficient [W/mK]
$\dot{q}$ - heat flux [W/m^2]
$\dot{q}_V$ - intensity of internal heat source [W/m^3]
s - specific entropy [kJ/kgK]
T – absolute temperature [K], also dimensionless
x_i – Cartesian coordinates (i=1,2,3)
Δ – change of the function
σ, σ_t – local and global intensity of entropy generation rate [W/m^3]
ρ - density of solid [kg/m^3]
τ – time [s]
∇ - operator nabla

INTRODUCTION

Differential equations describing heat conduction processes are usually derived from the first law of thermodynamics and in general take the forms

- transient processes

$$\mathrm{div}\left[k(T)\mathrm{grad}T(x_i,\tau)\right]+\dot{q}_V(T,x_i,\tau)=\rho c_p\frac{\partial T(x_i,\tau)}{\partial\tau} \quad (i=1,2,3) \tag{1}$$

- steady-state

$$\mathrm{div}\left[k(T)\mathrm{grad}T(x_i)\right]+\dot{q}_V(T,x_i)=0 \quad (i=1,2,3) \tag{2}$$

Eqs. (1) or (2) are usually derived by integral or differential ways but in both cases on the basis of enthalpy balances, [5,6].
Temperature scalar fields, transient or steady-state, result of the solution of Eqs. (1) or (2) with respect to the required initial and boundary conditions. Transient and steady state problems are known in literature as initial-boundary and boundary value problems, respectively. Different formulation to the classical boundary value problems can be obtained when differential heat conduction equation is derived from the minimum entropy generation principle [4]. According to the thermodynamics of irreversible processes [1],

entropy generation at steady state is at minimum. Introducing expression for local entropy generation

$$\sigma = \sigma(T, T_{x_i}) \equiv \frac{d_i s}{dt} = \frac{k(T)}{T^2}\left(\text{grad}T\right)^2 \qquad (3)$$

or

$$\sigma = \frac{k(T)}{T^2}\nabla T \circ \nabla T \qquad (4)$$

where T_{x_i} denotes gradient components $\partial T / \partial x_i$, the problem can be formulated in the following way: *find such a function* $T = T(x_i)$ *which satisfying required boundary conditions minimizes simultaneously integral*

$$\sigma_t = \int_{\Omega} \sigma(T, T_{x_i}) d\Omega \qquad i=1,2,3 \qquad (5)$$

over the whole domain Ω. Here σ_t represent global entropy production of the process.

MATHEMATICAL CONSIDERATIONS

Steady state processes

For 3D problem in Cartesian coordinates (*k=const*) the global entropy generation rate is

$$\sigma_t = \iiint_{\Omega} \sigma d\Omega = k \iiint_{\Omega} \frac{1}{T^2}\nabla T \circ \nabla T d\Omega \qquad (6)$$

$$T = T(x,y,z)$$

and its minimization leads to the Euler type heat conduction equation

$$\frac{\partial \sigma}{\partial T} - \frac{\partial}{\partial x}\left(\frac{\partial \sigma}{\partial T_x}\right) - \frac{\partial}{\partial y}\left(\frac{\partial \sigma}{\partial T_y}\right) - \frac{\partial}{\partial z}\left(\frac{\partial \sigma}{\partial T_z}\right) = 0$$

After calculation

$$\nabla^2 T - \tfrac{1}{T}\nabla T \circ \nabla T = 0 \qquad (7)$$

Second term describes intensity of the additional external heat source

$$\dot{\boldsymbol{q}}_V = -\tfrac{k}{T}\nabla T \circ \nabla T < 0 \qquad (8)$$

Eq.(7) can be written in the shorter form

$$\frac{\partial}{\partial x}\left(\frac{1}{T}\frac{\partial T}{\partial x}\right) + \frac{\partial}{\partial y}\left(\frac{1}{T}\frac{\partial T}{\partial y}\right) + \frac{\partial}{\partial z}\left(\frac{1}{T}\frac{\partial T}{\partial z}\right) = 0 \qquad (9)$$

or

$$\text{div}\left(\frac{\dot{\boldsymbol{q}}}{\boldsymbol{T}}\right) = 0 \qquad (10)$$

where $\dot{\boldsymbol{q}}$ is given by the Fourier's law ($\dot{\boldsymbol{q}} = -k\,\text{grad}\,T$), ($T = T(x,y,z)$).

Solutions to the 1D and 2D boundary problems with constant and temperature dependent thermal conductivity coefficient have been presented in details in the authors' paper [7] (also presented at ECOS'02). The problem of entropy generation at steady state heat conduction problem has been formulated in literature, for the first time, by Bejan [1,2].

In the following text, the initial-boundary and boundary value problems will be considered. An analysis of transient problem is a new extension of the method of entropy generation minimization principle.

Physical interpretation of Eq.(8) results from the Principle of Entropy Compensation [9] that:

"*The entropy of a system can be reduced only if it is made to interact with one or more auxiliary systems in a process which imparts at least a compensating amount of entropy*."

Graphical interpretations of classical heat conduction equation (Eq.(1) where *k=const*, $\dot{\boldsymbol{q}}_V = 0$ and $\partial T / \partial \tau = 0$) and Eq.(7) are presented in Fig.1.

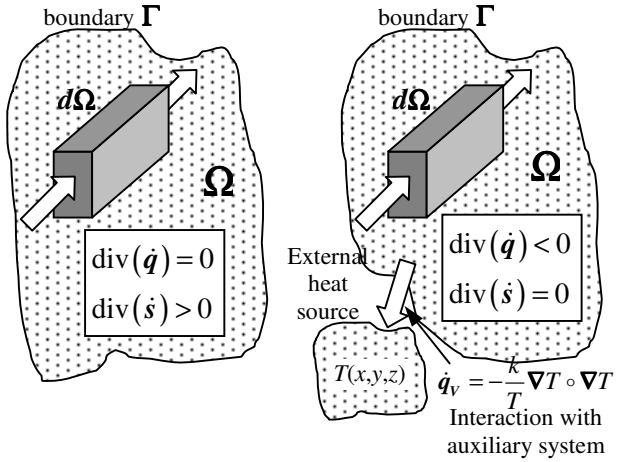

Figure 1: Graphical interpretation

Transient heat conduction - variational calculus approach

Global entropy generation rate is given by the integral

$$\sigma_t = \int_{\Omega}\int_{\tau} \frac{1}{T^2}\nabla T \circ \nabla T d\tau d\Omega \qquad (11)$$

$$T = T(x,y,z,\tau)$$

with the integral constraint

$$\Delta s = \int_{\Omega}\int_{\tau} \frac{\rho c_p}{T}\frac{\partial T}{\partial \tau} d\Omega\, d\tau = C \qquad (12)$$

where C is constant and its value is the same both for reversible and irreversible path (σ_t=0 or σ_t>0).
Variational calculus requires the function

$$K = \frac{k}{T^2}\nabla T \circ \nabla T + \lambda \frac{\rho c_p}{T}\frac{\partial T}{\partial \tau} \qquad (13)$$

to satisfy Euler-Lagrange equation

$$\frac{\partial K}{\partial T} - \frac{\partial}{\partial x}\left(\frac{\partial K}{\partial T_x}\right) - \frac{\partial}{\partial y}\left(\frac{\partial K}{\partial T_y}\right) - \frac{\partial}{\partial z}\left(\frac{\partial K}{\partial T_z}\right) = 0 \qquad (14)$$

where λ is a Lagrange multiplier [2]. After calculation we have

$$k\nabla^2 T - \tfrac{k}{T}\nabla T \circ \nabla T + \frac{\lambda}{2}\rho c_p \frac{\partial T}{\partial \tau} = 0 \qquad (15)$$

and from the fact, that Δs (see Eq.(12)) does not depend on the path of the process, λ must be equal to –2.
Thus, Eq.(15) becomes in the final form

$$a\nabla^2 T - \tfrac{a}{T}\nabla T \circ \nabla T = \tfrac{\partial T}{\partial \tau} \qquad (16)$$

$$T = T(x,y,z,\tau)$$

where additional external heat source is

$$\dot{q}_V = -\tfrac{a}{T}\nabla T \circ \nabla T \qquad (17)$$

Again, graphical interpretations are presented in Fig.2.

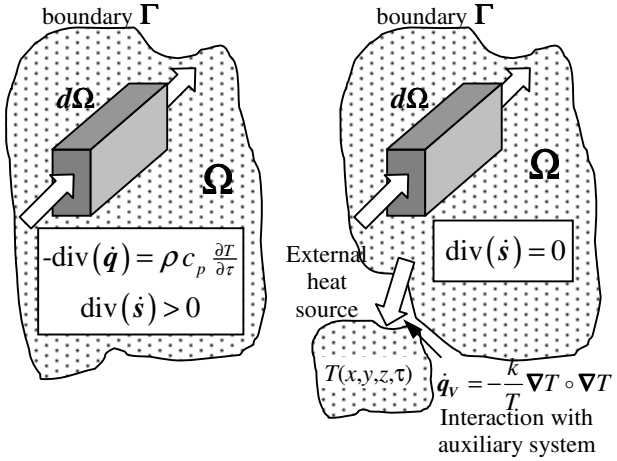

Figure 2: Graphical interpretation

NUMERICAL EXAMPLES

To illustrate differences between the solutions of classical and entropy generation minimization initial-boundary and boundary value problems two numerical examples will be considered.

Steady state problem.
Solve the boundary value problem

$$T = T(x,y) \quad (x,y) \in \Omega$$

$$\frac{\partial^2 T}{\partial x^2} + \frac{\partial^2 T}{\partial y^2} = 0 \qquad x \in (0,1) \quad y \in (0,1) \qquad (18)$$

$$T \in (1,e)$$

in the square (Fig.3)

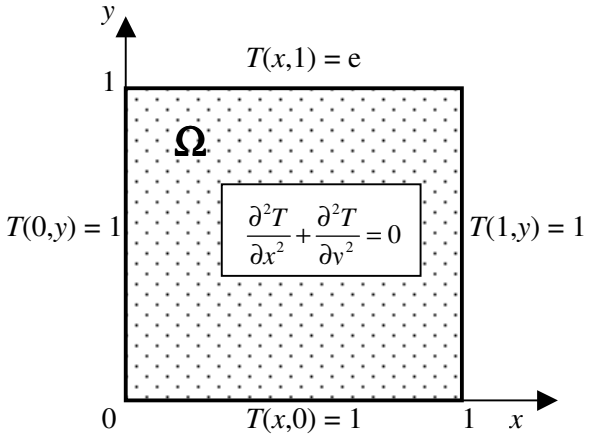

Figure 3: Classical boundary value problem.

with boundary conditions

$$T(0,y) = 1 \quad T(1,y) = 1$$
$$T(x,0) = 1 \quad T(x,1) = e \qquad (19)$$

Introducing from definition a new dependent variable

$$T^*(x,y) = T(x,y) - 1$$

the boundary value problem becomes (Fig.4)

$$\frac{\partial^2 T^*}{\partial x^2} + \frac{\partial^2 T^*}{\partial y^2} = 0 \qquad (20)$$

$$T^*(0,y) = 0 \quad T^*(1,y) = 0$$
$$T^*(x,0) = 0 \quad T^*(x,1) = e - 1 \qquad (21)$$

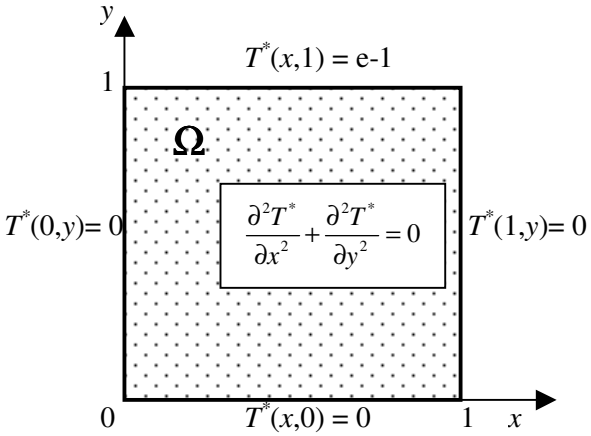

Figure 4: Simplified boundary value problem.

Similar problem formulated on the principle of entropy generation minimization is (Fig. 5)

$$\frac{\partial^2 T_1}{\partial x^2}+\frac{\partial^2 T_1}{\partial y^2}-\frac{1}{T_1}\left[\left(\frac{\partial T_1}{\partial x}\right)^2+\left(\frac{\partial T_1}{\partial y}\right)^2\right]=0 \qquad (22)$$

$$T_1 = T_1(x, y)$$

with the same boundary conditions (see Fig.5).

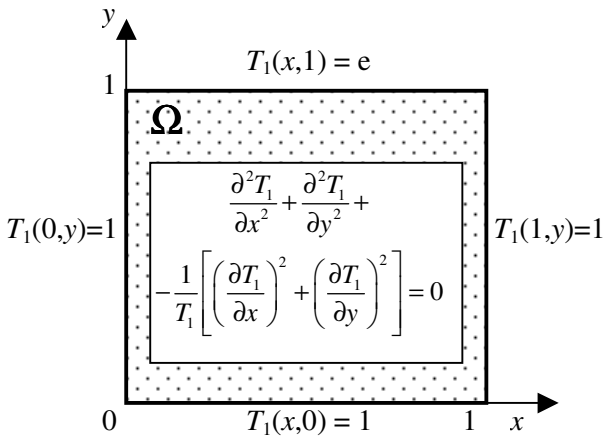

Figure 5: Modified boundary value problem.

Introducing from definition a new variable

$$Y = \ln T_1 \qquad Y = Y(x, y)$$

boundary value problem (22) and (19) becomes in the form (Fig.6)

$$\frac{\partial^2 Y}{\partial x^2}+\frac{\partial^2 Y}{\partial y^2}=0 \qquad (23)$$

$$Y(0, y)=0 \quad Y(1, y)=0$$
$$Y(x,0)=0 \quad Y(x,1)=e-1 \qquad (24)$$

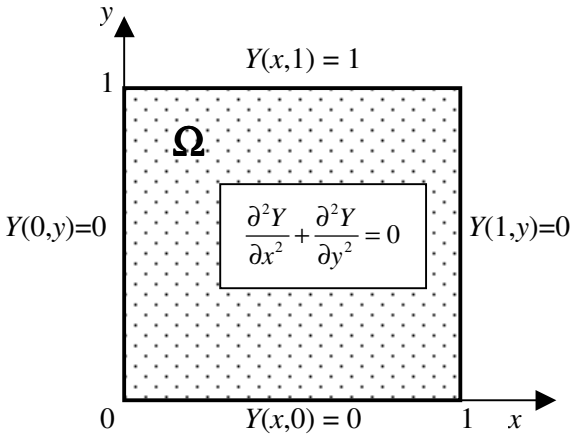

Figure 6: Modified boundary value problem.

Analytical solutions to the above two boundary value problems are known and have the form [5]

$$T^*(x, y)=\frac{4(e-1)}{\pi}\sum_{i=1,3,5...}^{\infty}\frac{1}{n}\frac{\sinh(n\pi y)}{\sinh(n\pi)}\sin(n\pi x) \qquad (25)$$

and

$$Y(x, y)=\frac{4}{\pi}\sum_{i=1,3,5...}^{\infty}\frac{1}{n}\frac{\sinh(n\pi y)}{\sinh(n\pi)}\sin(n\pi x) \qquad (26)$$

For the points of the same x,y coordinates

$$\frac{T(x, y)-1}{Y(x, y)}=e-1$$

and

$$\frac{T(x, y)-1}{\ln T_1(x, y)}=e-1$$

Thus

$$\delta T(x, y)=T_1(x, y)-T(x, y)=$$
$$=\exp\left(\frac{T(x, y)-1}{e-1}\right)-T(x, y)<0 \qquad (27)$$

Physical explanation that δT is always negative is simple as in the system an additional internal heat source exists $\dot{q}_V=-a/T\left(\partial T/\partial x\right)^2$, (see Eq.(17)).

Differences between solutions for $T \in (0,e)$ are shown in the Table 1.

T(x,y)	δT	%
1.0	0	0
1.2	-0.077	6.45
1.4	-0.140	10.00
1.6	-0.185	11.60
1.8	-0.212	11.80
2.0	-0.218	10.90
2.2	-0.200	9.05
2.4	-0.154	6.41
e	0	0

Table 1: Solution differences.

Transient problem

Solve the initial – boundary value problem of linear flow of heat in the solid bounded by two parallel planes.
Classical formulation:

$$a\frac{\partial^2 T}{\partial x^2}=\frac{\partial T}{\partial \tau} \quad T=T(x,\tau) \qquad (28)$$
$$x\in(0,1) \quad T\in(1,e)$$

$$T(0,\tau)=1$$
$$T(1,\tau)=1 \qquad (29)$$
$$T(x,0)=\mathrm{e}$$

Introducing

$$T^*(x,\tau)=T(x,\tau)-1$$

the problem is

$$a\frac{\partial^2 T^*}{\partial x^2}=\frac{\partial T^*}{\partial \tau} \qquad (30)$$

and

$$T^*(0,\tau)=0$$
$$T^*(1,\tau)=0 \qquad (31)$$
$$T^*(x,0)=\mathrm{e}-1$$

Entropy generation minimization formulation

$$a\frac{\partial^2 T}{\partial x^2}-\frac{a}{T}\left(\frac{\partial T}{\partial x}\right)^2=\frac{\partial T}{\partial \tau} \qquad (32)$$

$T=T(x,\tau) \qquad x\in(0,1) \qquad T\in(1,\mathrm{e})$

and using new variable

$$Y(x,\tau)=\ln T(x,\tau)$$

Eq. (32) takes the form

$$a\frac{\partial^2 Y}{\partial x^2}=\frac{\partial Y}{\partial \tau} \qquad (33)$$

with boundary conditions

$$Y(0,\tau)=0$$
$$Y(1,\tau)=0 \qquad (34)$$
$$Y(x,0)=1$$

The solution of (30) and (31) is [6]

$$T^*(x,\tau)=\frac{4}{\pi}(e-1)\cdot \cdot\sum_{n=0}^{\infty}\frac{1}{2n+1}\exp\left[-a(2n+1)^2\pi^2\tau\right]\sin(2n+1)\pi x \qquad (35)$$

and of (33) and (34)

$$Y(x,\tau)=\frac{4}{\pi}\cdot \cdot\sum_{n=1}^{\infty}\frac{1}{2n+1}\exp\left[-a(2n+1)^2\pi^2\tau\right]\sin(2n+1)\pi x$$

The difference of the above two solutions is also given by Eq. (27)

$$\delta T(x,\tau)=\exp\left(\frac{T(x,\tau)-1}{e-1}\right)-T(x,\tau)<0$$

and numerical values are listed in Table 1. As in the case of steady state conduction, the values of $\delta T(x,\tau)$ are negative resulting from the additional external heat source

$$\dot{q}_V^*=-\frac{a}{T}\nabla T\circ\nabla T \quad \text{(see Eq.(17))}$$

CONCLUSIONS

Minimization of entropy generation both in study state and transient heat conduction processes by introducing additional external heat sources. The most important conclusion is that the entropy generation principle can also be used in the case of transient problems. Many practical applications decreasing irreversibility ratio are possible, as for example: thermal insulation systems, storage systems, power generation (maximizing the power output), optimal combustion chamber temperature, solar-thermal power generation and refrigeration systems.

ACKNOWLEDGEMENTS

This work was supported by the Polish Scientific Committee (KBN) under the Grant No 4T08B02725.

REFERENCES

[1] Bejan A., *A General variational principle for thermal insulation system design*, Int J Heat Mass Transfer 1979; 22:217-227.

[2] Bejan A., *Entropy generation minimization*, Chapter 6, Boca Raton, Florida (USA), CRC Press, 1996.

[3] Margenau H., Murphy GM., *The mathematics of physics and chemistry,* Chapter 6, D. Van Nostrand Co. Ins, 1959.

[4] Prigogine J., *Introduction to thermodynamics of irreversible processes*, Springfield, Ill, C. Thomas Publisher, 1955.

[5] Bejan A., *Heat transfer*, John Wiley & Sons, Inc, New York, 1993.

[6] Carslaw H. S., and Jaeger J. C., *Conduction of heat in solids*, Clarendon Press, Oxford, II Ed., 1959.

[7] Kolenda Z., Donizak J. and Hubert J., *On the minimum entropy production in steady state conduction processes*., Energy 2004; 29:2441-2460.

[8] de Groot S. R., *Thermodynamics of irreversible processes*, North-Holland Publ Co., Amsterdam, 1952.

[9] Reif F., *Statistical physics,* Berkeley physics course, Vol. 5, 1967.

Proceedings of ECOS 2005
Trondheim, Norway
June 20–22, 2005

MODIFIED THERMODYNAMIC PRINCIPLES UNIFYING ORDER EXISTENCE AND EVOLUTION

S.P. Mahulikar[†]
Indian Institute of Technology – Bombay
Dept. of Aerospace Engineering
P.O. IIT, Powai, Mumbai – 400 076
India

H. Herwig
Technische Universität Hamburg-Harburg
Technische Thermodynamik
Arbeitsbereich 6-08, Denickestr. 17, 21073 Hamburg
Germany

ABSTRACT

The 'negentropy' proposed first by Schroedinger is re-examined, and its conceptual and mathematical definition are proposed; which is shown to integrate Schroedinger's intention of its introduction, and the subsequent diverse notions in literature. This definition of negentropy is corroborated by its unique ability to state direct thermodynamic principles for order existence: '*Negentropy Principle*', and order evolution: '*Principle of Maximum Negentropy Production*'. These principles are the respective counterparts of the '*Entropy Principle*', and the '*Law of Maximum Entropy Production*'. The *Principle of Maximum Negentropy Production* combines the basic philosophies of the evolution theories postulated by *Darwin* and *de Vries*. The prime advantage of these two additional thermodynamic principles, is the resulting unified explanation of order creation, existence, evolution, and destruction; using thermodynamic principles only.

Keywords: autocatakinetic, cosmology, creation, destruction, disorder, entropy, evolution, existence, irreversibility, living organism, *negentropy*, non-equilibrium, order, self-organising, space-time structure, spontaneous order, thermodynamics of organized complexity
PACS ref. 05.70.*Ln*, 87.23.*Kg*, 05.65.+*b*

NOMENCLATURE

F	symbol for field variable/s
J	symbol for rate/s of irreversible process/es
m	mass [kg]
S	entropy [J/K]
s	specific entropy [J/kg·K]
s_n	negentropy of ordered sub-system [J/kg·K]
t	time [s]

Subscripts

d	surrounding disorder
IP	Inflection Point
IS	Isolated System
max	maximum
o	ordered sub-system
thr	threshold value
1,2,…,N	different ordered sub-systems

INTRODUCTION

The laws that govern an organization are derived from the two Laws of Thermodynamics. The First Law states that the total *quantity* of energy in an isolated system remains constant. The 2nd *Law of Thermodynamics* is also called the *Entropy Principle* (EP), and it came in to existence after the First Law was established. The 'entropy' refers to the diminished gradients of field variables, Grad(*F*), in a dissipation process, and is

[†]Corresponding author: Tel. ++91 (0)22 2576 7122, Fax. ++91 (0)22 2572 2602
E-mail: spm@aero.iitb.ac.in

the classical signpost of natural change [1]. The EP is a re-statement of a unifying law of nature; which implies that on a global basis, gradients of field variables are always diminished. Diminishing Grad(F) leads to dispersion, i.e. entropy increase. Thus, reducing Grad(F) and entropy increase are concurrent and synonymous.

The '*negentropy*' first came from Schroedinger [2], who stated: 'what an ordered sub-system feeds upon is negentropy; thereby succeeding in freezing itself from the entropy it cannot help producing'. However, in a footnote later, Schroedinger explains that neg*entropy* is free *energy*. Subsequently, others took *neg*entropy as entropy with a *negative sign* [3,4]; as they felt it erroneous to refer to neg*entropy* as free *energy*. However, *entropy with a negative sign* does not capture the intention of Schroedinger [2], who introduced it to identify the ability of the living system to increase organization. Later, Ho [5] explains that neg*entropy* is mobilisable stored *energy* in an organized system. However, views based on neg*entropy* as a form of *energy* are inappropriate to its nomenclature; since, stored *energy* should then be referred as 'neg' / 'pos' *energy*. Further, free / stored energy need not necessarily be utilised for increasing organisation; and hence, cannot always be associated with negentropy.

Earlier [6], order was explained indirectly (using the concept of '*entropy*' only), by identifying the effect of order creation and its' existence, on disorder increase. This explanation was demonstrated by a mathematical model.

Objectives, scope, and formulation

There is a lack of consensus on what should be the conceptual and mathematical definition of *negentropy*. The objective here is to propose its definition that unifies the existing assorted notions, and the concepts of order creation / origin, existence, evolution, and destruction; exclusively by thermodynamic principles. Since, thermodynamic principles are universally valid, the principles for order creation, existence, evolution, and destruction, are valid for all scales; ranging from biology to cosmology.

The two legitimate assumptions made, regarding the isolated system (ref. Fig. 1) that may comprise of ordered sub-systems, are elaborated below; thereby defining the scope of this investigation. These assumptions are the pre-requisites for ordered sub-systems to be created,

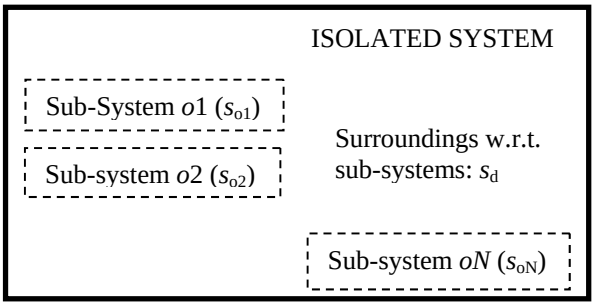

Figure 1: Schematic illustration of sustainable order in disorder, in an isolated system

and to co-exist with disorder [7].

Assumption *i*): $\ddot{S}_{IS} > 0$, (1)

as illustrated in Fig. 2. This assumption implies that the isolated system is sufficiently far from equilibrium. It is demonstrated that $\delta^2 S_{IS}$ is the Lyapounov function, especially when large deviations from equilibrium are considered [7]. As the isolated system approaches equilibrium, the sign of $\ddot{S}_{IS}$ changes at a particular Inflection Point (IP in Fig. 2); and thereafter,

$$\ddot{S}_{IS} < 0. \quad (2)$$

To the left (and bottom quadrant) of IP, the non-equilibrium system follows the *Law of Maximum Entropy Production* (LMEP), which states [8]: "the system will select the path or assemblage of paths out of available paths that minimises the potential or maximizes the entropy at the fastest rate for given constraints". This statement is a reflection of nature's law of preference for path of least resistance, for minimizing Grad(F). For given Grad(F), minimising resistance leads to maximising J; i.e. $\dot{S}_{IS} = J \cdot \text{Grad}(F)$ is maximised.

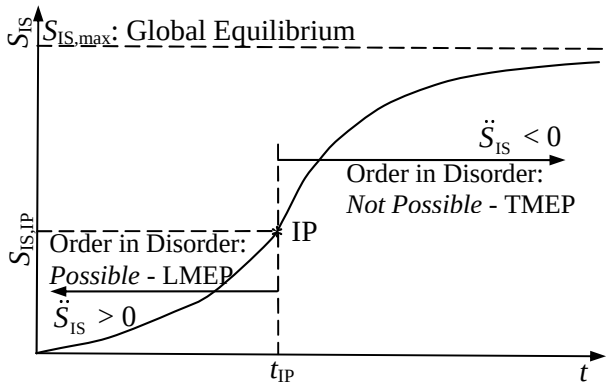

Figure 2: Schematic illustration of two distinct regimes, on S_{IS} vs. t plot

To the right (and top quadrant) of IP, S_{IS} increase gradually approaches the asymptote (global equilibrium). In this regime, the system characteristics are determined by its inertia; which prevents the system from reaching global equilibrium ($\dot{S}_{IS} = 0$). Hence, the system settles down to the tendency based on the Theorem of Minimum Entropy Production (TMEP), which states that [9] 'the variation of $\dot{S}_{IS}$ is negative or zero in non-equilibrium stationary states, in the vicinity of equilibrium (after crossing IP)'. Since, entropy production is minimised in this regime, dynamic order cannot be created; since, the objective of creation and existence of dynamic order is entropy production at a rate faster than had they not existed (ref. Statement 9 in [6]). Thus, creation and existence of dynamic order (in disorder) satisfy the inequality given by Eq. (1). The only possible ordered structures in the regime determined by the inequality in Eq. (2), are 'equilibrium-static-ordered-structures', e.g. crystals; which are characterised by the minimum of the Helmholtz free energy. Thus, dynamic ordered structures are feasible only to the left of IP, as indicated in Fig. 2. A practical illustration is the creation and existence of dynamic order only during the acceleration-phase of universe expansion [10].

Assumption *ii*): *The isolated system is dynamically unstable and chaotic*. This pre-requisite is a subset of *i*); the additional condition imposed by this assumption, is the requirement for large number of interactions within the isolated system. Stable existence of order in disorder necessitates stable exchange of mass and energy between ordered sub-systems and their surroundings (disorder), which is stabilised as per the Law of Large Numbers [7].

Introduction to 'negentropy'

The '*negentropy*' once appropriately defined, must encompass the following perspectives, with which it is associated:

i) It should have *negative* sign, but its implication/s should extend beyond *entropy with a negative sign*.
ii) It should have units of *entropy* or specific *entropy*.
iii) It should account for the existence of ordered sub-systems like living organisms and the solar system, by encapsulating Schroedinger's intentions [2].
iv) Since, S can never be negative, as per the 3rd *Law of Thermodynamics* {ref. e.g. [11]}, negentropy is a *relative* measure of deviation from equilibrium of ordered sub-system/s with respect to their surroundings.

In [6], the term, $s_d - s_o$, was identified as the criterion for sustainability of order in disorder. It is now proposed: $\boldsymbol{s_n = s_o - s_d}$. (3)

The negentropy is defined as "*the specific entropy deficit of ordered sub-system with respect to its surroundings*". This deficit is created due to creation of order, and exists for ordered sub-systems, *o*1-*oN* (ref. Fig. 1) so long as these ordered sub-systems exist; and reduces to zero when they completely merge with disorder. Since, s_n is a difference of two state functions, s_n is also a state function. Since, $s_o << s_d$, (3.1) s_n is always negative. This proposal for negentropy has the following direct implications:

a. Negentropy is based on *specific entropy*.
b. Negentropy is a *relative* concept: the term, $-s_n = s_d - s_o$, is specific entropy of surrounding disorder relative to ordered sub-system/s, and is the absolute value of negentropy. *Negentropy*, s_n, is a *relative* measure (contrast) of localised ordering / organization, with respect to surroundings (disorder).
c. For ordered sub-systems, *neg*entropy is *negative*: negentropy is zero when order is in equilibrium with disorder (order is destroyed).

The entropy of the isolated system comprising of order existing within disorder (ref. Fig. 1) is given as, $S_{IS} = m_o \cdot s_o + m_d \cdot s_d$. (4)

From Eq. (3), $S_{IS} = m_d \cdot (-s_n) + m_{IS} \cdot s_o$; where, $m_{IS} = m_o + m_d$. Hence, $s_{IS} = (m_d/m_{IS}) \cdot (-s_n) + s_o$. (4.1)

NEGENTROPY BASED PRINCIPLES

The s_n [Eq. (3)] has immediate implication in its ability to state thermodynamic principles for order existence and evolution, complementary to the existing, EP and LMEP; by referring to its negentropy. The increase / decrease of negentropy discussed hereafter are its modulus.

Negentropy Principle (NEP)

"*For order to exist* (*or when order exists*), *negentropy must increase* ($\dot{s}_n > 0$)."

Conversely, "when order ceases to exist, its negentropy begins to decrease ($\dot{s}_n < 0$), until $s_n = 0$". The s_{IS} [Eq. (4.1)] always increases, since S_{IS} always increases (EP) and m_{IS} is fixed

(*Conservation of Mass*). Further, $(m_d/m_{IS}) \approx 1$; since, $m_o << m_d$; {ref. [6]}, and Eq. (3.1). From Eq. (4.1), increasing s_{IS} implies the following two exclusive possibilities:

a. The $-s_n$ must increase (NEP), and order exists; since, s_o reduces, or remains the same, or may increase at a rate that is small enough for order to continue existing in disorder.
b. If $-s_n$ reduces or remains the same, the increase of s_o is faster than or the same rate as s_{IS} [from Eq. (4.1)], and order is converted in to disorder. Thus, compliance with NEP is a special case of EP.

For order to exist, $s_o \leq s_{o,thr}$ [6], where $s_{o,thr}$ is the threshold value of specific entropy above which, order begins to merge with disorder. This is the same as, $\text{Grad}(F)|_o \leq \text{Grad}(F)|_{o,thr}$; (5)
i.e. gradients of field variables across ordered sub-systems are lower than a threshold, but exist. Consequently, to satisfy the 2nd Law, the gradients of these field variables in the surrounding disorder are lower than the gradients of field variables in total (only) disorder (when localised order does not exist, represented by superscript '*'); i.e.

$$\text{Grad}(F)|_d < [\text{Grad}(F)|_d]^*. \quad (5.1)$$

Equation (5.1) results from the need to compensate for existing and maintained gradients of field variables across ordered sub-systems, given by Eq. (5); which reduce entropy production by reducing '*J*'. This deduction is an outcome of the inequality,

$$S_{IS} > S^*_{IS}; \quad (5.2)$$

which is Statement 2 in ref. [6]; where, $S^*_{IS} = m_{IS} \cdot s^*_{IS}$. Only if the inequality given by Eq. (5.2) is satisfied, the system may select the bifurcation branch that results in 'order in disorder'. From Eqs. (4) and (5.2),

$$(m_d/m_{IS}) \cdot (-s_n) + s_o > s^*_{IS}. \quad (5.3)$$

Since, $m_d < m_{IS}$, Eq. (5.3) also leads to, $(-s_n) + s_o > s^*_{IS}$. The s_n increase, increases the ensemble average of gradient of field variables, $\text{Grad}(F)|_o$, across the boundary between ordered structures and their surroundings [6].

Principle of Maximum Negentropy Production (PMNEP)

"*The isolated system comprising of order co-existing in disorder* '*will select the path or assemblage of paths out of available paths*' *that maximizes the negentropy at the fastest rate for given constraints*".

This statement is the counterpart of LMEP. Since, S_{IS} increases at the fastest rate for given constraints, s_{IS} also increases at the fastest rate for the same given constraints. From Eq. (4.1), there are again two possible ways of realising LMEP:

a. The $(-s_n)$ must increase at the fastest rate for given constraints (PMNEP); then s_o can remain the same, or reduce, or increase at a relatively slow rate. Thus, when order exists, LMEP reduces to PMNEP.
b. If $(-s_n)$ reduces or remains the same, s_o increases at the fastest rate given constraints [from Eq. (4.1)], and order is destroyed into disorder. Thus, compliance with PMNEP is a special case of the LMEP. From Eq. (4),

$$\dot{S}_{IS} = m_o \cdot \dot{s}_o + m_d \cdot \dot{s}_d; \quad (6)$$

assuming that m_o and m_d are constant. This assumption is discussed in [6]; as a case when the number / mass of ordered sub-systems destroyed, is the same as the number / mass of ordered sub-systems created. Further,

$$\dot{S}^*_{IS} = m_{IS} \cdot \dot{s}^*_{IS}. \quad (7)$$

Since, $\dot{S}_{IS} > \dot{S}^*_{IS}$ (from LMEP), from Eqs. (6) and (7), $(m_o/m_d) \cdot \dot{s}_o + \dot{s}_d > (m_{IS}/m_d) \cdot \dot{s}^*_{IS}$. (7.1)

Since, $m_o << m_d$, and consequently, $m_{IS} \approx m_d$ [6],

$$\dot{s}_d > \dot{s}^*_{IS}; \quad (8)$$

which states that specific entropy of surrounding disorder that has localised ordered sub-systems, increases at a faster rate than the alternative bifurcation branch that comprises of only disorder. Differentiating Eq. (3), and from Eq. (8), $-\dot{s}_n > \dot{s}^*_{IS} - \dot{s}_o$; i.e. rate of negentropy increase, exceeds the difference in rates of specific entropy increase of isolated system in state of total disorder, and specific entropy increase of order.

EVOLUTION AND THERMODYNAMICS

Several features of ordered organisms show an evolutionary trend, and many *rationales* are proposed. Schneider & Kay [12] state that ecosystems develop in ways, which increase their ability to degrade the incoming solar energy. They also state that '*Thermodynamics*' *can* make it possible for the study of ecosystems to be developed from a descriptive to predictive

science, founded on basic principle/s of physics. Toussaint & Schneider [13] state that as bio-systems develop, they follow certain trends: e.g. increase their total dissipation, develop more complex structures with more energy flow, increase their cycling activity, develop greater diversity, and generate more hierarchical levels. McShea [14] reviewed 8 candidate features that constitute these trends: entropy, energy intensiveness, evolutionary versatility, developmental depth, structural depth, adaptedness, size, and complexity. Later, McShea [15] states that "evolution shows a trend in hierarchical organization, revealed by the successive emergence of organisms with greater levels of *nestedness*, and greater development or *individuation* of the highest level."

There has been no basic guiding principle of physics dedicated to the explanation of existence of order, and in particular for evolution of ordered structures in to superior forms. By evolution of ordered structures to superior forms, the following two features, based on Schroedinger's intention of introduction of negentropy, are combined [2]: (*1*) superior ability to avoid spontaneously created gradients of field variables, that exceed the threshold value up to which order can withstand, $\text{Grad}(F)|_{o} \leq \text{Grad}(F)|_{o,thr}$ {discussed in [6]}, thereby prolonging the existence of ordered structures; and (*2*) ability to generate negentropy at increasing rates. So far, attempts to explain order evolution have been limited only to postulates / hypotheses / conjectures. One such popular theory is by Darwin [16], which begins with a postulate that life on Earth arose from non-living matter by an *unknown* process, and then proceeded to evolve into more complex life forms; by random mutation and natural selection process. This postulate is widely known as *the survival of the fittest*. Demetrius [17,18] showed that the use of evolutionary entropy (uncertainty in the age of the mother of a randomly chosen newborn), rather than the Malthusian parameter (parameter in the exponential equation of population growth), represents a non-equilibrium analogue of EP; and constitutes the operationally valid measure of Darwinian fitness (which is the relative probability of survival and reproduction for a genotype). The other exclusive theory is by *de Vries*: the *Mutation Theory*, which believes that mutations alone can bring about the abrupt changes in ordered structures; thereby divorcing evolution from *natural selection*. The role of *mutations* was later explained by experiments with mutability [19]. It is stated by a strong defender of Darwinism [20]: 'A biological explanation should invoke no factor other than the *laws of physical science*, natural selection, and the contingencies of history.'

Role of PMNEP in order evolution

The review on order evolution indicates divergence of view-points, primarily because they are not based on firm foundations (*Law/s of Physics*). *It is proposed here that PMNEP is the thermodynamic principle governing evolution of ordered structures in to superior forms*, which will now be elaborately justified. In PMNEP, '*The selection of path or assemblage of paths out of available paths, under given constraints*' (these constraints are determined jointly by ordered structures and their surrounding disorder), is the evolution of ordered structures, in to superior forms. Alternatively, ordered structures continue to evolve in to superior forms, as they select different path/s or assemblages of paths (under given constraints); with the objective of maximising *negentropy*. The evolution refers to the increasing ability of increasingly superior ordered structures, to simultaneously manage high negentropy production and yet avoid the resulting high values of spontaneously created '$\text{Grad}(F)|_{o}$' that can lead to their destruction.

Noticeable evolutionary trends are observed [21] over large geological time, as certain constraints are removed and / or minimal thresholds of parameters are reached [22]; which enable ordered structures to take *significantly*, and hence, noticeably different paths or their assemblages that enables negentropy increase at the fastest rate (under varying constraints). The PMNEP also integrates the basic notions in the theories by *Darwin* [16], and *de Vries* [19]. For instance, the notion of *survival of fittest* in *Darwin's Theory of Evolution* is explained by PMNEP; since, fitter ordered structures generate higher negentropy and still survive (for longer duration). The notion of mutation in the theory by *de Vries* refers to 'some constraints being removed / revised' in PMNEP, which enables selection of entirely different path or assemblages of paths that dramatically increase the rate of negentropy production; thereby leading to noticeable evolution.

ORDER AND NEGENTROPY PRINCIPLES

The governing principles for order creation, existence, and total destruction {formulated in [6]}, are now re-discussed; but using NEP and PMNEP, to the extent possible.

Statements of Directives

Statement 1 (*Creation of order*)

"*As the localised disequilibrium in an isolated system increases and exceeds a particular threshold, sustainable order is created within disorder, whenever there is a chance*."

The role of localised disequilibrium in this statement is explained by LMEP. Since, ordered flow produces higher entropy (and faster rate of approach to equilibrium) than only disorder, ordered structures are created when localised disequilibrium exceeds a certain threshold. For low disequilibrium, the inequality given by Eq. (1) is not satisfied, and disorder alone diminishes the low gradient/s of field variable/s. In particular, the system inertia prohibits formation of ordered structures. Hence, net excess entropy due to localised order (relative to state of total disorder) cannot be generated. Schneider & Kay [12] state the reformulated EP to extend it to non-equilibrium regions: 'As systems are moved away from equilibrium, they take advantage of all available means {*including localised ordering* [8]}, to resist externally applied gradients. Later, Toussaint & Schneider [13] re-state that in systems moved away from equilibrium, the system organizes in a way that reduces the effect of the applied 'Grad(F)'. When ordered structures are created and sustained, negentropy is initialised and begins to increase. The event of creation of order is the bifurcation point when *negentropy* is introduced, EP reduces to NEP, and LMEP reduces to PMNEP.

Statement 2 (*Creation of order*)

"*In an isolated system, created order within disorder is a state of higher net disorder than the preceding state of total disorder*."

The higher net disorder is an outcome of negentropy increase, due to creation (and sustained existence) of ordered sub-systems [6]. Alternatively, from Eq. (5.1), gradients of field variables are more diminished than in the state of total disorder. It was suggested by Schroedinger [2] that sustainable orders like flames are permitted to exist away from equilibrium, because they feed on negentropy in their environments; which was later popularised by Prigogine [7] by the term 'dissipative structures'. Schroedinger's [2] important point was that as long as sustainable orders produce entropy at a sufficient rate to compensate for their own internal ordering, i.e. negentropy increase, then the balance equation based on EP is not violated.

Statement 3 (*Existence of order*)

"*In an isolated system, order must coexist with disorder, but disorder can exist alone as total disorder*; *or total order does not exist*."

When order co-exists with disorder, negentropy exists; which is a relative concept: between order and disorder. However, EP holds regardless of whether negentropy exists or not.

Statement 4 (*Existence of order*)

"*In an isolated system, order and / or disorder must create more order and disorder for sustenance of created order*; *else, created order is converted in to disorder*."

When order exists, negentropy increases (EP); i.e. localised ordering / organization relative to surroundings (disorder) increases. Hence, more order is necessarily created. The s_o level is maintained locally by continuously draining out entropy to the surroundings (disorder), which is the sustenance of the fleeting disequilibrium [23]. Swenson [24] presented an ecological physical view which showed that - 'purposive, creative behaviour is a consequence of *a natural law* as per which, order is produced such that order acts back upon order to produce more order; i.e. for increasing negentropy.

Statement 5 (*Existence of order*)

"*In an isolated system, order can create more order only through disorder*."

Creation of more order results in negentropy increase by increasing s_d; since, order and its surroundings interact. Negentropy increase is due to intake of mass and energy from surroundings (processed to increase organisation), and by draining out 'excess entropy' to the surroundings. Thus, order is an open system, which interacts with its surroundings (disorder), for its existence.

Statement 6 (*Total destruction of order*)

"*As the disorder of an isolated system containing order increases and exceeds another higher threshold, all order is destroyed in to total disorder again, if there is a chance*."

The s_d increase due to creation and existence of order, is elaborated in [6]. The s_d also increases due to several other irreversible processes (not related to the operations of order in

disorder). The selection of path or assemblages of available paths to withstand increasing Grad(F)$|_o$ [$\leq$ Grad(F)$|_{o,thr}$] due to s_n increase, enables simultaneous existence of order, and compliance with NEP and PMNEP; which is order existence and evolution. Evolution enables superior forms of ordered structures to avoid with increasing probability, the spontaneously created high values of Grad(F)$|_o$ by surroundings, effectively by increasing Grad(F)$|_{o,thr}$. Over increasing geological times, the possibility of a mismatch between evolution and Grad(F)$|_o$ increases; in which case, the probabilistically created high Grad(F)$|_o$ [>> Grad(F)$|_{o,thr}$], destroy all order in to total disorder. Especially due to increasing s_n, i.e. due to increasing s_d, the probability that such an event occurs increases; since, the ensemble averaged Grad(F)$|_o$ increases with s_n. The event of total destruction of order is the bifurcation point, when *negentropy* vanishes together with NEP and PMNEP; leaving only EP and LMEP.

Statement 7 (*Creation, existence, and total destruction of order*)

"*In an isolated system, creation, existence and total destruction of order within disorder is a sequential train with increasing entropy thresholds for order creation and total destruction.*"

The sequential train with repeating compartments is illustrated in Fig. 3. The '$S = 0^+$' is the beginning, and the destination of this train is *equilibrium*. This train begins and ends with *Total Disorder*, and the ending is before the point IP in Fig. 2. The sequence of repetition of NEP and PMNEP, when order co-exists with disorder, is shown.

Statement 8 (*Existence of order*)

"*In an isolated system, disorder exists forever*; *but existence of order is fleeting*."

This statement spells the integral broken symmetry, between the principles based on entropy and *neg*entropy; since, negentropy exists only when order co-exists with disorder. In the sequential train in Fig. 3, principles based on

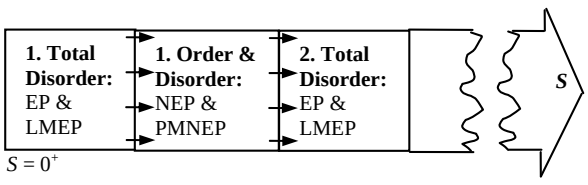

Figure 3: Sequential train illustrating repetitive sequence of validity of thermodynamic principles

entropy are valid in all compartments; but principles based on negentropy hold only in alternate compartments.

Statement 9 (*Creation, existence, & total destruction of order*)

"*In an isolated system, the role of creation and fleeting existence of order, is to increase the system entropy at a faster rate than had order not existed*."

This statement consolidates investigations on the role of order in disorder. During creation & fleeting existence of order, negentropy increases; which increases the system entropy faster (than the case without negentropy). Alternatively, the approach of the destination (vicinity of equilibrium) of the sequential train illustrated in Fig. 3, is hastened by order.

CONCLUSIONS

Schroedinger's negentropy is defined, to unify the intentions behind its introduction; and the diverse interpretations of researchers. The proposed definition enables formulation of two additional thermodynamic principles: *Negentropy Principle*, and *Principle of Maximum Negentropy Production*. The later is the basis for evolution of ordered structures in to superior forms, and combines the ideas behind the evolution theories postulated by *Darwin* and *de Vries*. The resulting unification of order creation, existence, evolution, and total destruction, by thermodynamic principles, is summarised by the block diagram in Fig. 4. The hierarchy of the 4 principles is based

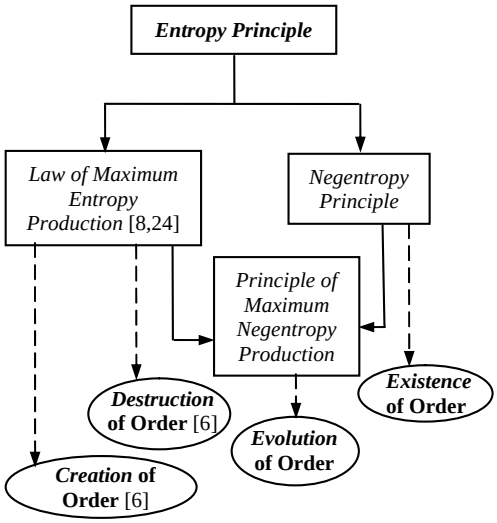

Figure 4: Unification of order creation, existence, evolution, and destruction; by thermodynamic principles

on their validity. The *Entropy Principle* continues as the ruling paradigm [25], since it is valid in all other principles below it. The *Law of Maximum Entropy Production* and *Negentropy Principle*, hold in *Principle of Maximum Negentropy Production*.

Acknowledgements: The authors thank the *A. von Humboldt Foundation, Germany*; for supporting this collaborative research. The authors are also grateful to Dean Faculty, IIT-Bombay, for the financial support; and ECOS-2005 conference organizing committee, for their extended support and encouragement towards participation.

REFERENCES

[1] Clausius R. *Über die bewegende kraft der wärme*. Annalen der Physik 1854;93:481.

[2] Schroedinger E. *What is life*? *The physical aspect of the living cell*. Cambridge: University Press, 1945.

[3] Brillouin L. *Science and information theory*. 2nd ed. New York: Academic Press, 1962.

[4] Penrose O. *Foundations of statistic mechanics*: *A deductive approach*. Oxford: Pergamon Press, 1970.

[5] Ho M-W. *What is* (*Schroedinger's*) *negentropy*? Modern Trends in BioThermoKinetics 1994;3:50-61.

[6] Mahulikar SP, Herwig H. *Conceptual investigation of the entropy principle for identification of directives for creation, existence and total destruction of order*. Physica Scripta 2004;70(4):212-221.

[7] Prigogine I. *Time, structure and fluctuations*. Science 1978;201(4358):777-785.

[8] Swenson R. *Emergent attractors and the law of maximum entropy production*: *Foundations to a theory of general evolution*. Systems Research 1989;6:187-197.

[9] Prigogine I. 1961 *Introduction to thermodynamics of irreversible processes*. New York: Interscience Publishers, 1961.

[10] Layzer D. *Cosmogenesis*: *The growth of order in the universe*. Oxford: University Press, 1991.

[11] Tamir A. *The third law*: *No way to absolute zero*. Canadian J. Chemical Engg. 2002;80:1002.

[12] Schneider ED, Kay JJ. *Life as a manifestation of the 2nd law of thermodynamics*. Mathematical and Computer Modelling 1994;19(6-8):25-48.

[13] Toussaint O, Schneider ED. *The thermodynamics and evolution of complexity in biological systems*. Comparative Biochemistry and Physiology A - Molecular & Integrative Physiology 1998;120(1):3-9.

[14] McShea DW. *Possible largest-scale trends in organismal evolution*: *Eight* '*live hypothesis*'. Annual Review of Ecology & Systematics 1998;29:293-318.

[15] McShea DW. *The minor transitions in hierarchical evolution and the question of a directional bias*. Journal of Evolutionary Biology 2001;14(3):502-518.

[16] Darwin C. *The origin of species*. 6th ed. New York: University Press, 1988.

[17] Demetrius L. *Directionality principles in thermodynamics and evolution*. Proceedings of the National Academy of Sciences of the U.S.A. 1997;94(8):3491-3498.

[18] Demetrius L. *Mortality plateaus and directionality theory*. Proceedings of the Royal Society (London) Ser. B: Biological Sciences 2001;268(1480):2029-2037.

[19] Morgan TH. *The physical basis of heredity*. Philadelphia: JB. Lippincott Co., 1919.

[20] Williams GC. *Adaptation and natural selection*. Princeton: University Press, 1966.

[21] McShea DW. *Mechanisms of large-scale evolutionary trends*. Evolution 1994;48(6):1747-1763.

[22] Runnegar B. *The Cambrian explosion*: *Animals or fossils*? J. Geological Soc. Australia 1982;29:395-411.

[23] Atkins PW. *The 2nd law*: *Energy, chaos, and form*. New York: Scientific American Books, 1984.

[24] Swenson R. *Autocatakinetics, yes-autopoiesis, no*: *Steps towards a unified theory of evolutionary ordering*. International Journal of General Systems 1992;21(2):207-228.

[25] Rifkin J. *Entropy*: *A new world view*. New York: Viking Press, p. 6, 1980.

Proceedings of ECOS 2005
Trondheim, Norway
June 20–22, 2005

LOCAL STABILITY ANALYSIS OF AN ENDOREVERSIBLE CURZON-AHLBORN-NOVIKOV ENGINE WITH DULONG-PETIT HEAT TRANSFER LAW

R. T. Páez Hernández[1], L. A. Arias Hernández[2] and F Angulo Brown[2]
[1]Area de Física de Procesos Irreversibles, Departamento de Ciencias Básicas Universidad Autonóma Metropolitana-A. Av. San Pablo #180 DF MEXICO, CP 02200

[2]Instituto Politecnico Nacional, Escuela Superior de Física y Matemáticas, Departamento de Física, UP Zacatenco, Edificio #9, 2° Piso, DF, MEXICO, CP 07738

ABSTRACT

A local stability analysis of an endoreversible Curzon-Ahlborn-Novikov (CAN) engine, with Dulong-Petit heat transfer law, is presented. In this study, we consider two different optimum performance regimes. A CAN engine consists of a Carnot engine exchanging heat with external heat reservoirs T_1 and T_2 ($T_1 > T_2$), through a couple of thermal conductors both having the same conductance (α). In addition, the working fluid has the same heat capacity (C) in the two isothermal branches of the cycle. From the local stability analysis we conclude that the CAN engine is stable for every value of α, C, and $\tau \in [0.3,0.6]$ ($\tau = T_2 / T_1$). Moreover, our results also emphasize the importance of the heat transfer law on the engine stabilty. The results obtained with the Dulong-Petit heat transfer law are quite different from those obtained with Newton's law when $\tau \to 0$ and $\tau \to 1$.

NOMENCLATURE

E	Ecological function (W)
P	Power output(W)
T_1	Hot reservoir temperature(K)
T_2	Cold reservoir temperature(K)
η	Thermal efficiency
C	Heat Capacity (JK^{-1})
τ	Ratio of reservoir's temperatures
J_1	Heat flux from hot reservoir(W)
J_2	Heat flux towards cold reservoir(W)
α	Thermal conductance ($W/m^2K^{5/4}$)
T_0	Temperature(K)
t	Time(s)
λ_1, λ_2	Relaxation times(s)

INTRODUCTION

It is known that the limits imposed by Clasical Equilibrium Thermodynamics (CET) correspond to reversible processes. This represents a limitation for CET and leads to process-variable values too remote from the values reported in the literature. This limitation has been overcome, in great part, by the so called Finite Time Thermodynamics (FTT). Most of the studies in FTT have been focused on the steady-state energetic properties [1-7], which are important from a good-design viewpoint. Conversely, only a few of these studies had taken into consideration the system's dynamic properties: like the system respons to noisy perturbations or the steady-state stability. Most of the papers in this field consider that the heat flow between the working substance

[1] All correspondance should be addressed to R. T. Páez Hernández
email: phrt@correo.azc.uam.mx

and its surroundings is governed by Newton's cooling law [4-10]. However, Dulon-Petit heat transfer law is more realistic because it takes into account both conduction and radiation [11]. This cooling law is given by:

$$\frac{dQ}{dt} = \alpha\left(T_0 - T\right)^k, \qquad (1)$$

where dQ/dt is the heat exchange rate, α is the conductors' thermal conductance, T_0 is the environmental temperature, T is the body temperature, and k is an exponent in the range from 1.1 to 1.6 [11]. In 1993, Angulo-Brown and Páez-Hernández showed that a Dulong-Petit CAN engine renders more realistic efficiency values than those of a Newtonian model. They considered both the maximum-power and the ecological [12] regimes, and compared with values reported for different steam plants. The present work is structured as follows. In section II we analize the steady-state thermodynamic properties of a CAN endoreversible engine performing in a maximum power like regime. In section III we derive the differential equations governing the engine dynamics. In section IV, the local stability analysis is carried out. Finally, in section V we present the results corresponding to the ecological regime.
A schematic representation of a CAN engine is shown in Figure 1.

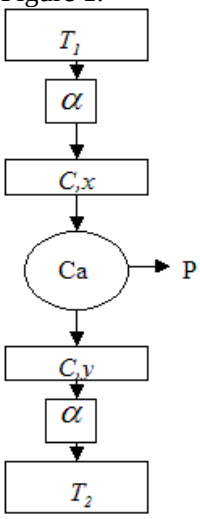

Figure 1. Schematic representation of a CAN engine. This machine consists in a Carnot cycle (Ca) which in every cycle exchanges the heat flows J_1 and J_2 with the reservoirs T_1 and T_2 respectively $\left(T_1 > T_2\right)$. This exchange of heat takes place through the thermal conductors, both with conductance (α). x and y represent the temperatures of working fluid along the isothermal branches of the Ca-cycle, and we take C as the heat capacity of the working fluid.

II STEADY-STATE ENDOREVERSIBLE CAN ENGINE

Consider the endoreversible engine depicted in the figure 1. The engine operates between temperatures T_1 and T_2, with $T_1 > T_2$. Heat flows irreversibly from T_1 to $\bar{x}$ and from $\bar{y}$ to T_2 ($T_1 > \bar{x} > \bar{y} > T_2$). Here and thereafter we use overbars to indicate steady-state values. The endoreversibility hypothesis states that the system is internally reversible. That is, a Carnot cycle operates between temperatures $\bar{x}$ and $\bar{y}$. This hypothesis further implies that the heat flows can be expressed as [13]

$$\bar{J}_1 = \frac{\bar{x}}{\bar{x} - \bar{y}}\bar{P} \qquad (2)$$

and

$$\bar{J}_2 = \frac{\bar{y}}{\bar{x} - \bar{y}}\bar{P}, \qquad (3)$$

where $\bar{J}_1$ and $\bar{J}_2$ are the heat flows from $\bar{x}$ to the engine and from the engine to $\bar{y}$, and $\bar{P}$ is the power output. In this study we consider heat transfer law that in steady-state heat flows are given by:

$$\bar{J}_1 = \alpha(T_1 - \bar{x})^k \qquad (4)$$

and

$$\bar{J}_2 = \alpha(\bar{y} - T_2)^k, \qquad (5)$$

with α the thermal conductance.
From equations (2)-(5) and the definition of efficiency given in [14],

$$\bar{\eta}_{MP} = 1 + (k-1) - \frac{\tau}{2} - \sqrt{\left(1 + (k-1)\frac{\tau}{2}\right)^2 + (\tau - 1)}, \quad (6)$$

it is possible to express temperatures $\bar{x}$ and $\bar{y}$ as

$$\bar{x} = \frac{T_1\left((1-\eta)^{1/k} + \tau\right)}{(1-\eta)^{1/k} + (1-\eta)} \quad (7)$$

and

$$\bar{y} = \frac{T_1(1-\eta)\left((1-\eta)^{1/k} + \tau\right)}{(1-\eta)^{1/k} + (1-\eta)}, \quad (8)$$

with $\tau = T_2/T_1$.

Moreover, we have that the power output is

$$\bar{P} = \bar{\eta}\,\bar{J}_1. \quad (9)$$

After a little algebra we obtain a expression for the power in terms of $\bar{x}$ and $\bar{y}$:

$$\bar{P}(\bar{x}, \bar{y}) = \alpha\left[\frac{\bar{y} - \bar{x}\tau}{\bar{y}^{1/k} + \bar{x}^{1/k}\tau}\right]^k. \quad (10)$$

III DYNAMICS OF THE CAN ENGINE WORKING IN THE REGIME OF MAXIMUM POWER.

Consider again figure 1. Now, the resrvoirs *x* and *y* are not real heat reservoirs but macroscopic objects with a heat capacity *C*. Therefore, their temperature changes according the following equations

$$\frac{dx}{dt} = \frac{1}{C}\left[\alpha(T_1 - x)^k - J_1\right] \quad (11)$$

and

$$\frac{dy}{dt} = \frac{1}{C}\left[J_2 - \alpha(y - T_2)^k\right]. \quad (12)$$

Both of these derivatives cancel when *x* and *y* take their steady-state values. We use the criterion that the flow from *x* to the work substance (J_1) and from the Carnot engine to *y* (J_2) are given in terms of the output power *P* by (see equations (2) and (3))

$$J_1 = \frac{x}{x - y}P \quad (13)$$

and

$$J_2 = \frac{y}{x - y}P. \quad (14)$$

Following of Santillán et al [13] we assumed that out of the steady state but no too far away, the power of a CAN engine depends on *x* and *y* in the same way that it depends on $\bar{x}$ and $\bar{y}$ in the steady state ($\bar{P}(\bar{x}, \bar{y}) \to P(x, y)$), applicable only in the neighborhood of the steady state:

$$P = \alpha\left[\frac{y - x\tau}{y^{1/k} + x^{1/k}\tau}\right]^k. \quad (15)$$

Substituting equations (13), (14), and (15) into (11) and (12) we obtain the next pair of differential equations for *x* and *y* in the maximum power regime:

$$\frac{dx}{dt} = \frac{\alpha}{C}\left[(T_1 - x)^k - x\left[\frac{y - x\tau}{y^{1/k} + x^{1/k}\tau}\right]^k\right] \quad (16)$$

and

$$\frac{dy}{dt} = \frac{\alpha}{C}\left[y\left[\frac{y - x\tau}{y^{1/k} + x^{1/k}\tau}\right]^k - (y - T_2)^k\right]. \quad (17)$$

IV LOCAL STABILITY ANALISIS

Let $f(x, y)$ and $g(x, y)$ be defined as

$$f(x, y) = \frac{\alpha}{C}\left[(T_1 - x)^k - x\left[\frac{y - x\tau}{y^{1/k} + x^{1/k}\tau}\right]^k\right] \quad (18)$$

and

$$g(x, y) = \frac{\alpha}{C}\left[y\left[\frac{y - x\tau}{y^{1/k} + x^{1/k}\tau}\right]^k - (y - T_2)^k\right]. \quad (19)$$

By construction, the values of the steady-state x and y are given by equations (7) and (8). If x and y are very close to the steady-state value, we can write $x(t) = \bar{x} + \delta x(t)$ and $y(t) = \bar{y} + \delta y(t)$, where $\delta x(t)$ and $\delta y(t)$ are small perturbations. By substituting into equations (18) and (19), and using the smallness of $\delta x(t)$ and $\delta y(t)$ we can make a first order approximation a Taylor series expansion obtaining following differential equations for $\delta x(t)$ and $\delta y(t)$:

$$\frac{d\delta x}{dt} = f_X \delta x(t) + f_Y \delta y(t) \qquad (20)$$

and

$$\frac{d\delta y}{dt} = g_X \delta x(t) + g_Y \delta y(t) \qquad (21)$$

where $f_X = \left.\frac{\partial f}{\partial x}\right|_{\bar{x},\bar{y}}$, $f_y = \left.\frac{\partial f}{\partial y}\right|_{\bar{x},\bar{y}}$, $g_X = \left.\frac{\partial g}{\partial x}\right|_{\bar{x},\bar{y}}$, and $g_y = \left.\frac{\partial g}{\partial y}\right|_{\bar{x},\bar{y}}$ are given by:[*2]

Assume that $\delta x(t)$ and $\delta y(t)$ are of the form [15],

$$\delta x(t) = a e^{zt} \qquad (26)$$

and

$$\delta y(t) = b e^{zt} \qquad (27)$$

with z a complex number that will be determined.

Substitution of equations (26) and (27) into equations (20) and (21) leads to the following set of homogeneous linear algebraic equations for a and b:

$$(f_X - z)a + f_Y b = 0 \qquad (28)$$

and

$$g_X a + (g_X - z)b = 0\,. \qquad (29)$$

This system of equations has non-trivial solutions only if the determinant of the matrix of coefficients is equals zero [16], i.e.

$$(f_X - z)(g_Y - z) - g_X f_Y = 0\,. \qquad (30)$$

This equation is called the characteristic equation. In conclusion, the only possible solutions to equations (20) and (21) are those with a z which is the solution of the characteristic equation (30). Denote the solutions of equation (30) as z_1 and z_2. They are numerically calculated, and both are real and negative. It follows then from equation (26) and (27) that any perturbation decays exponentially with time. The relaxation time depends on the absolute value of z_1 and z_2. Indeed, we can define two relaxation times λ_1 and λ_2 as

$$\lambda_1 = -\frac{1}{z_1} \quad \text{and} \quad \lambda_2 = -\frac{1}{z_2}\,. \qquad (33)$$

The smaller λ_1 and λ_2, the more quickly the system returns to the steady state after a perturbation.

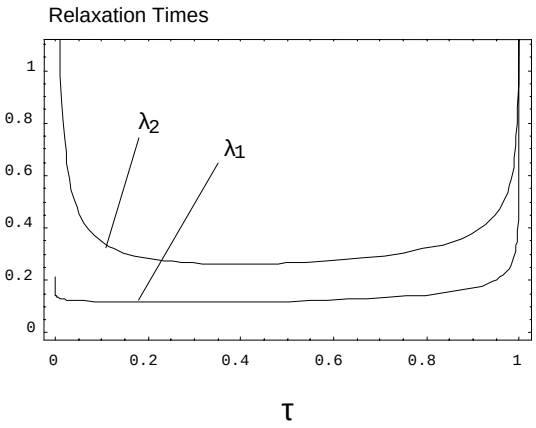

Figure 2.- This figure shows the dependency of the relaxation times λ_1 and λ_2 with the temperatures of both reservoirs for the maximum power regime for a Dulong-Peti's heat transfer law..

The plots of λ_1 and λ_2 are shown in figure 2. λ_1 and λ_2 are concave with a minimum value, depending of τ, with $\tau \in [0.3, 0.6]$ ($\tau = T_2 / T_1$). In conclusion, the engine's stability properties can be guaranteed.

V ECOLOGICAL CRITERION

Consider now the ecological regime, proposed by Angulo Brown [12], which consists in optimizing the function $E = P - \varepsilon T_2 \sigma$, that represents an

[*2] Due the size of equations (22), (23), (24) and (25) these are included in the appendix A at the end of the paper.

austere compromise between power output and energy of the engine, E is the so-called ecological function, P is the power output, T_2 is the cold reservoir temperature, ε is a parameter, and σ the entropy production. Following step by step the procedure shown in the last sections, with the exception that the expression for the maximum ecological efficiency $\eta_E = \eta_E(\tau, k)$, is used [19]. We obtain that z_1 and z_2 also are real and negative. Figure 3 shows the plots of the relaxation times λ_1 and λ_2 vs. τ. We can see that are concave with a minimum value, depending of τ, with $\tau \in [0.3,0.6]$ ($\tau = T_2 / T_1$).

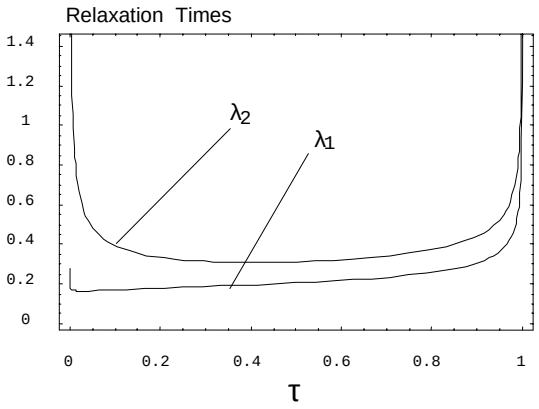

Figure 3.- Plot of the relaxation times λ_1 and λ_2 vs. τ, for the ecological regime governed by a Dulong-Petit's heat transfer law between the reservoirs and the work substance.

Then the engine's stability is guaranteed. In figure 4 (see appendix B) we present a qualitative phase portraits for different regimes and different heat transfer laws.

CONCLUSIONS

We have presented a local stability analysis for an endoreversible CAN engine, governed by a Dulong-Petit heat transfer law. The results were compared with those corresponding to the Newton's heat transfer law. We conclude that both regimes are quite susceptible to the governing heat transfer law. The curves that represent the relaxation times λ_1 and λ_2 are concave with a minimum value, so the CAN engine is stable for quite value of α, C, and $\tau \in [0.3,0.6]$ ($\tau = T_2 / T_1$), which agree with the data reported in references [17,18]. As shown in figure 3, when $\tau \approx 1$ the relaxation times λ_1 y $\lambda_2 \to \infty$. This means that, in this limit ($T_1 \approx T_2$), the hypothesis of little perturbations is not satisfied. because any perturbation would be as big as the system, which the local stability is nullified. Future work would involve studying, a no-endoreversible CAN engine will be considered for the same analysis.

ACKNOWLEDGEMENTS

We thank M Santillán for suggestions and help in the preparation of the manuscript. This work was sponsored by COFAA, the EDI system and the Investigation Project CGPI #20040282 of Instituto Politécnico Nacional, and SNI-CONACYT.

REFERENCES

[1].- De Vos A Endorreversible Thermodynamics of Solar Energy Conversion (Oxford: Oxford University Press) (1992).
[2].- Sieniutycs S and De Vos A (eds) 2000 Thermodynamics of Energy Conversions and Transport(New York: Springer).
[3].- Bejan A V 1996 J. Appl. Phys. **79** 1991.
[4].- Hofmann KH, Burzler JM and Shubert S 1997 J. Nonequilib. Thermodynam. **22** 311
[5].- Wu C, Chen L and Chen (eds) 1999 Recent Advances in Finite Time Thermodynamics (New York: Nova)
[6].- Andresen B, Salamon P and Berry R. S., Thermodynamics in Finite Time, Phys. Today **37**, 62 (1984).
[7].- Bejan A 1996 Entropy Generation Minimization (Boca Raton, FL CRC)
[8].- Curzon F. L. and Ahlborn B., Efficiency of Carnot Engine at Maximum Power Out, Am. J. Phys. **43**, 22 (1975).
[9].- Rubin M.H 1979 Phys. Rev. A **19** 1277

[10].- Angulo Brown F. and Páez Hernández R. 1993 J. Appl. Phys. **74** 2216
[11].- .- Colm T. O'Sullivan, Am. J. Phys.**58** 956 (1990)
[12].- F. Angulo Brown, J. Appl. Phys. **69** 7465 (1991)
[13].- Moisés Santillán, Gabriela Maya and Fernando Angulo Brown., Local stability analysis of an endoreversible Curzon-Ahlborn-Novikov engine working in maximum power like regime J. Phys. D: Appl. Phys. **34** 2068-2072 (2002).
[14].- L. A. Arias Hernández, G. Ares de Parga and F. Angulo Brown Open Sys. & Information Dyn. **10** 351
[15].-Strogatz H S 1994 Non Linear Dynamics and Chaos: With Applications to Physics, Chemistry and Engineering (Cambridge, MA:Perseus)
[16].- Lang S 1987 Linear Alebra (New York:Springer)
[17].- Bejan A 1998 Advance Engineering Thermodyanmics (New York Wiley)
[18].- Velasco S, Roco JMM, Medina A, White JA and Calvo Hernández A 2000 J. Phys. D: Appl. Phys. **33** 355
[19].- L. A. Arias Hernández, G. Ares de Parga and F. Angulo Brown Open Sys. & Information Dyn. **11** 1 (en prensa).

APPENDIX A
EQUATIONS DON'T SHOWED IN BODY PAPER

$$f_X = \left.\frac{\partial f}{\partial x}\right|_{\bar{x},\bar{y}} = \left\{\left[k\alpha(T_1 - x)^k (y - \tau x)\left(y^{1/k} + \tau x^{1/k}\right) - \alpha(T_1 - x)(y - \tau x)\left(\frac{y - \tau x}{y^{1/k} + \tau x^{1/k}}\right)^k\right]\bullet\right.$$

$$\left.\bullet\left(kx^{1+1/k}\left(\tau^2 + \tau xy\right) + y^{1/k}\left(x - y\left(\tau + k\tau + \tau kx^2\right)\right)\right)\right\}/\left(\mathrm{C}(\mathrm{T}_1 - x)(\tau x - y)\left(y^{1/k} + \tau x^{1/k}\right)\right) \quad (22)$$

$$f_y = \left.\frac{\partial f}{\partial y}\right|_{\bar{x},\bar{y}} = \left[\alpha x\left(\frac{y - x\tau}{y^{1/k} + x^{1/k}\tau}\right)\right]^{1+k}\left(kyx^{1/k}(y\tau y - \tau) + y^{1/k}(y - ky - x\tau + kxy\tau y)\right)/\left(Cy(y - x\tau)^2\right) \quad (23)$$

$$g_X = \left.\frac{\partial g}{\partial x}\right|_{\bar{x},\bar{y}} = -\frac{1}{Cx}(y - x\tau)^2\left(\alpha y\left(\frac{y - x\tau}{y^{1/k} + x^{1/k}\tau}\right)^{1+k}\left(kxy^{1/k}(\tau + x\tau x) + x^{1/k}\left(\tau(y + (k-1)x\tau) + kxy\tau x\right)\right)\right) \quad (24)$$

$$g_y = \left.\frac{\partial g}{\partial y}\right|_{\bar{x},\bar{y}}\left[\alpha k(y - T_2)^k\right](y - x\tau)\left(y^{1/k} + x^{1/k}\tau\right) + \alpha(y - T_2)\left(\frac{y - x\tau}{y^{1/k} + x^{1/k}\tau}\right)^k\left(ky^{1+1/k}(x\tau y - 1) + \right.$$

$$\left.x^{1/k}\left(-(k+1)y\tau + x\tau^2 + ky^2\tau y\right)\right)/\left(C(T_2 - y)(y - x\tau)\left(y^{1/k} + x^{1/k}\tau\right)\right) \quad (25)$$

Observation, here we have supposed that, $\tau = \tau(x, y)$, this is the variation of the work's temperature with respect to T_2/T_1, once fixed the operation regime

APPENDIX B
PHASE PORTRAITS

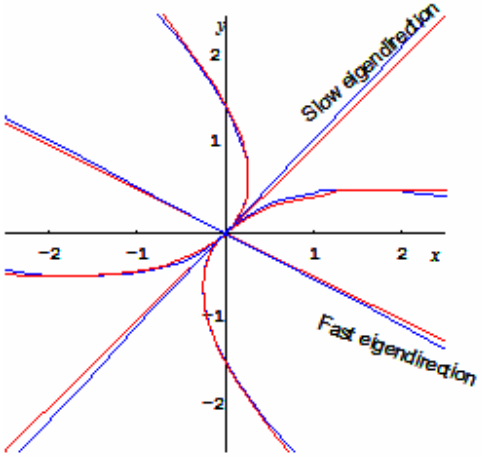

Figure 4a.-Maximum power regime for Newton's law and Dulong-Petit law

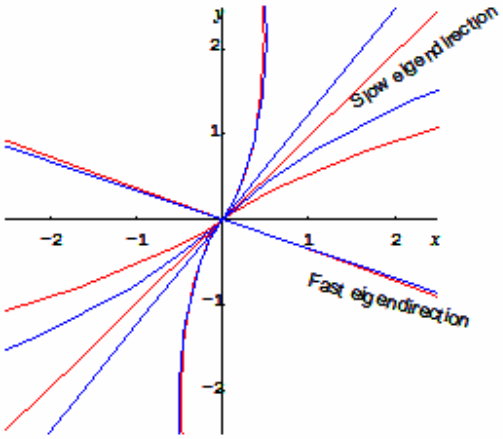

Figure 4b.-Maximum ecological function for Newton's law and Dulong-Petit law

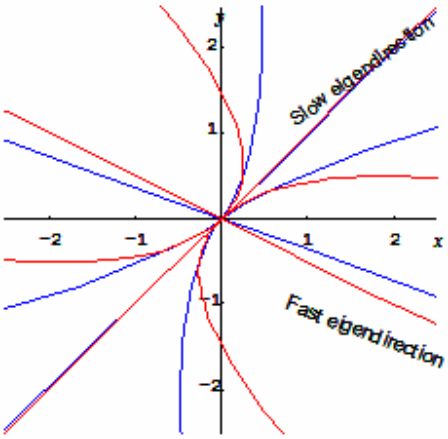

Figure 4c.-Maximum power regime and Maximum ecological function for Newton's law

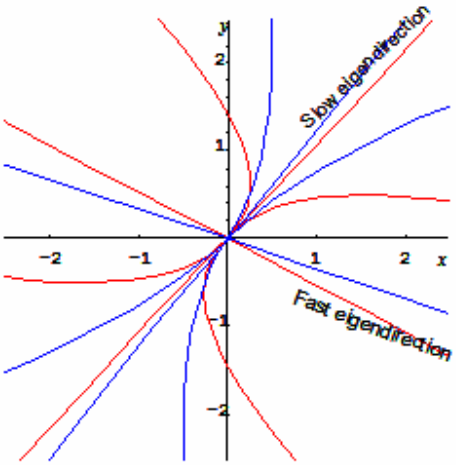

Figure 4d.-Maximum power regime and Maximum ecological function for Dulong-Petit law

Proceedings of ECOS 2005
Trondheim, Norway
June 20–22, 2005

GENERALIZED GIBBS ENTROPY, IRREVERSIBILITY AND STATIONARY STATES

A. Pérez-Madrid
Departament de Física Fonamental. Facultat de Física. Universitat de Barcelona.
Diagonal 647, 08028 Barcelona. Spain

ABSTRACT

A generalization of the Gibbs entropy postulate is proposed based on the BBGKY hierarchy as the nonequilibrium entropy for a system of N interacting particles. This entropy satisfies the basic principles of thermodynamics in the sense that it reaches its maximum at equilibrium and is coherent with the second law. By using this entropy and the methods of nonequilibrium thermodynamics in the phase space, a generalization of the Liouville equation describing the evolution of the distribution vector in the form of a master equation is obtained. After neglecting correlations in this master equation the Boltzmann equation was obtained. Moreover, this entropy remains constant in nonequilibrium stationary states and leads to macroscopic hydrodynamics. Nonequilibrium Green-Kubo type relations and the probability for the nonequilibrium fluctuations are also derived.

INTRODUCTION

According to the mechanicistic interpretation of the physical world, the basic laws of nature are deterministic and time reversible. However, at the macroscopic level we observe irreversible processes related to energy degradation which generate entropy. How do we reconcile the 'spontaneous production of entropy' with the time reversibility of the microscopic equations of motion?. At the end of the nineteenth century, Boltzmann tried to answer this question from a probabilistic point of view. According to him, entropy is a measure of the lack of knowledge of the precise state of matter and can be defined as a function of the probability of a given state of matter. This function associates a number $S_B(X) = \log|\Gamma_{M(X)}|$ to each microstate X of a macroscopic system, with $|\Gamma_M|$ being the volume of the region of the phase space Γ_M corresponding to the macrostate $M = M(X)$. The macrostate M is all of a group of states Y such that $M(Y) = M(X) = M$. In this sense, the Boltzmann entropy is a function of the microstate which at equilibrium coincides with the thermodynamic entropy. All systems in their irreversible evolution tend to a state of maximum probability or maximum entropy -the state of equilibrium- .

In contrast to the Boltzmann entropy, the Gibbs entropy is not a function of the individual microstate but rather a function of the probability distribution in a statistical ensemble of systems with both entropies coinciding at equilibrium. As a consequence of the incompressible character of the flow of points representing the natural evolution of the statistical ensemble in phase space , the Gibbs entropy is a constant of motion. Thus, it has been argued that the relevant entropy for understanding thermodynamic irreversibility is the Boltzmann entropy and not the Gibbs entropy [1], [2], [3].

In addition, the problem of the diverging character of the Gibbs entropy related to the negative sign of the entropy production in nonequilibrium stationary states apparently excludes the use of the Gibbs entropy in the statistical description of nonequilibrium systems [4], [5]. This raises the question as to how to define the nonequilibrium entropy and if possible, to give a thermodynamic description of nonequilibrium fluctuations. In other words: can Thermodynamics describe systems far from equilibrium? [6], [7].

Thus, from the moment when Gibbs first postulated his entropy formula, the definition of the nonequilibrium entropy and its relation to irreversibility has been an outstanding problem, now compounded by the fact that the entropy production is negative in nonequilibrium stationary states in apparent viola-

tion of the second law of Thermodynamics [8], [9]. This constitutes an open problem which must be solved.

A huge amount of work has been done on this subject trying to address the problem. On one hand, there have been attempts to extend the equilibrium entropy [10], [11], [12], [13] to nonequilibrium situations in order to avoid the divergence of the Gibbs entropy. On the other hand, work has been done to establish fluctuation theorems for the probability of the entropy production fluctuations [14]. In a previous work [16] we showed a way to circumvent the difficulty of reconciling the second law of thermodynamics with the reversible microscopic equations of motion in the framework of the BBGKY hierarchy. We proposed a functional of the set of s-particle reduced distribution functions as the entropy for a system of N interacting particles. This entropy does not enter into contradiction with thermodynamics, and as we show here, in addition to being time-dependent it enables one to perform a thermodynamic analysis of the stationary nonequilibrium states. In this sense, our theory constitutes an extension of the scope of thermodynamics to systems away from equilibrium.

I begin this contribution introducing the representation of the state of the isolated system in terms of the hierarchy of reduced distribution functions. Afterwards I develop the thermodynamic analysis and derive the entropy production which enables us to draw kinetic equations, in particular the Boltzmann equation. After that comes the analysis of the nonequilibrium stationary states of the system. Finally I stress the main conclusions.

HAMILTONIAN DYNAMICS

Let's consider a dynamical system of N identical particles whose Hamiltonian $H_N(\{\underline{q}^N,\underline{p}^N\})$ is given by

$$H_N=\sum_{j=1}^{N}\frac{\underline{p}_j^2}{2m}+\frac{1}{2}\sum_{j\neq k=1}^{N}\phi\left(\left|\underline{q}_j-\underline{q}_k\right|\right)\ , \qquad (1)$$

where m is the mass and $\phi\left(\left|\underline{q}_j-\underline{q}_k\right|\right)\equiv\phi_{jk}$ is the interaction potential. The state of the system is completely specified at a given time by the N-particle distribution function $F\left(\{\underline{q}^N,\underline{p}^N\};t\right)$ which evolves in time according to the Liouville equation. Nonetheless, an alternative description of the state of the system can be given in terms of the distribution vector [15]

$$\underline{f}\equiv\{f_0,f_1(\Gamma_1),f_2(\Gamma_2),.....,f_N(\Gamma_N)\}\ , \qquad (2)$$

with $\Gamma_s=(x_1,x_2,.....,x_s)$ and $x_j\equiv(\underline{q}_j,\underline{p}_j)$. Additionally, the set of quantities Γ_s can be grouped as the vector $\underline{\Gamma}\equiv\{\Gamma_1,\Gamma_2,.....,\Gamma_N\}$, and correspondingly $\underline{H}\equiv\{H_1,H_2,.....,H_N\}$ can be defined with H_s being the s-particle Hamiltonian. The distribution vector represents the set of all the s-particle reduced distribution functions $f_s(\Gamma_s)$ $(s=0,....,N)$, defined through

$$f_s=\frac{N!}{(N-s)!}\int F(x_1,..,x_s,x_{s+1},..,x_N)\,dx_{s+1}...dx_N\ . \qquad (3)$$

The evolution equations of these functions can be obtained by integrating the Liouville equation thereby constituting a set of coupled equations: the BBGKY hierarchy which can be written in a compact way as a generalized Liouville equation [16]

$$\left(\frac{\partial}{\partial t}-\mathscr{P}\mathscr{L}\right)\underline{f}(t)=\mathscr{Q}\mathscr{L}\underline{f}(t)\ , \qquad (4)$$

with

$$\begin{aligned}\langle s\,|\,\mathscr{P}\mathscr{L}\,|\,s'\rangle&=\delta_{s,s'}\left\{\sum_{j=1}^{s}L_j^o+\sum_{j<n=1}^{s}L'_{j,n}\right\} \qquad (5)\\ &=\delta_{s,s'}\,[H_s,...]_P\,,\end{aligned}$$

and

$$\langle s\,|\,\mathscr{Q}\mathscr{L}\,|\,s'\rangle=\delta_{s',s+1}\int\left\{\sum_{j=1}^{s}L'_{j,s+1}\right\}dx_{s+1}\ . \qquad (6)$$

where $|\ s\rangle$ represents the s-particle state defined through $\langle\Gamma_s|s\rangle=f_s(\Gamma_s)$ and where the projection operators $\mathscr{P}$ and $\mathscr{Q}$, its complement with respect to the identity, give the diagonal and nondiagonal part of the generalized Liouvillian $\mathscr{L}$, respectively. Here, $L_j^o=\left[H_j^o,...\right]_P$,where $[...,...]_P$ is the Poisson bracket, $H_j^o=\frac{\underline{p}_j^2}{2m}$, and $L'_{j,n}=\left[H'_{j,n},...\right]_P$, with $H'_{j,n}=\frac{1}{2}\phi_{j,n}$. Unlike the Liouville equation which remains invariant under time reversal

$$\begin{aligned}t\ &\longrightarrow\ -t\equiv t^*\ , \qquad (7)\\ \underline{p}_j\ &\longrightarrow\ -\underline{p}_j\ ,\ j=1,...,N\ \ ,\end{aligned}$$

this symmetry is broken in Eq. (4) due to the term on their right hand side

$$\left(\frac{\partial}{\partial t^*} - \mathscr{P}\mathscr{L}\right)\underline{f}(t^*) = -\mathscr{Q}\mathscr{L}\underline{f}(t^*) \,.$$

This means that under the operation of time reversal the densities f_s do not reverse their evolution. Thus, the diagonal part of the generalized Liouvillian accounts for the reversible evolution of the distribution vector while the nondiagonal part introduces irreversibility in the dynamics of $\underline{f}$ leading to dissipation. Hence, in the sense that the time-reversal symmetry is broken, the generalized Liouville equation given through Eq. (4) is irreversible. Irreversibility is manifested in the dynamics of the system when the adequate description, *i.e.* in terms of the distribution vector is used. Some degree of coarse graining is inherent to this description.

NONEQUILIBRIUM THERMODYNAMICS

As the expression for the nonequilibrium entropy I propose

$$\begin{aligned} S &= -k_B \mathrm{tr}\left\{\underline{f}\log\left(\underline{f}_o^{-1}\underline{f}\right)\right\} + S_o \\ &= -k_B \sum_{n=1}^{N} \frac{1}{n!}\int f_n \log\frac{f_n}{f_{o,n}}\, dx_1.....dx_n \; + S_o \,, \end{aligned} \quad (8)$$

a functional of $\underline{f}$, analogous with the Gibbs entropy postulate [17], [18], based on the fact that the distribution vector determines the state of the system. Here, k_B is the Boltzmann constant, $\underline{f}_o = \{f_{o,0}, f_{o,1}, f_{o,2}, ...\}$ is assumed to be the equilibrium distribution vector which corresponds with the equilibrium entropy S_o, satisfying $\mathscr{L}\underline{f}_o = 0$ whereas $\underline{f}_o^{-1}$ denotes the vector whose components are the inverse of the reduced distribution functions $f_{o,n}^{-1}$. Moreover, S is maximum at equilibrium when $\underline{f}$=$\underline{f}_o$ giving $S = S_o$, which can be proven by taking the first and second variation of S with respect to $\underline{f}$ while S_o and $\underline{f}_o$ remain fixed. This entropy is also coherent with the second law according to which S increases in irreversible processes such as the relaxation to equilibrium from an initially nonequilibrium state. This expression based on the BBGKY hierarchy is different from other developments in the literature such as the paper by Green and Nettleton [19]. Therefore, the rate of change of S which can be obtained by differentiating Eq. (8) with the help of Eq. (4) is

$$\begin{aligned} \sigma &= -k_B \mathrm{tr}\left\{\frac{\partial \underline{f}}{\partial t}\log\left(\underline{f}_o^{-1}\underline{f}\right)\right\} \\ &= -k_B \mathrm{tr}\left\{\mathscr{Q}\mathscr{L}\underline{f}\log\left(\underline{f}_o^{-1}\underline{f}\right)\right\} \,. \end{aligned} \quad (9)$$

This constitutes the entropy production corresponding to the relaxation passing from a nonequilibrium state to equilibrium. Here, the only contribution to the entropy production comes from the irreversible change of the distribution vector. The reversible change of the distribution vector is given by the mainstream current induced by the s-Hamiltonian flow in each one of the s-particle subspaces of the total phase space, in light of the fact that the Hamiltonian flow does not create entropy.
At equilibrium $\mathscr{P}\mathscr{L}\underline{f}_o = -\mathscr{Q}\mathscr{L}\underline{f}_o$ according to Eq. (4), neither $\mathscr{P}\mathscr{L}\underline{f}_o$ nor $\mathscr{Q}\mathscr{L}\underline{f}_o$ vanish, but rather both terms balance together. Hence, the thermodynamic current $\mathscr{Q}\mathscr{L}\underline{f}$ appearing in Eq. (9) contains an equilibrium contribution. Therefore, in order to get a completely nonequilibrium current maintaining the invariance of the entropy production, I define the new current $\underline{J}'$ through $\mathscr{Q}\mathscr{L}\underline{f} - \underline{J}' = -\mathscr{P}\mathscr{L}\underline{f}$, entering a continuity equation for $\underline{f}$

$$\frac{\partial}{\partial t}\underline{f} = \underline{J}' \,. \quad (10)$$

Thus for small deviations from equilibrium, Eq. (9) with the aid of Eq. (10) becomes

$$\sigma = k_B \mathrm{tr}\left\{-\underline{J}'\underline{X}\right\} \,, \quad (11)$$

where $\underline{X} = \underline{f}_o^{-1}\left(\underline{f}_o - \underline{f}\right)$ is the thermodynamic force conjugated with the current $\underline{J}'$. Following the methods of nonequilibrium thermodynamics [17], [20] in the phase space, from Eq. (9) the linear relation

$$\underline{J}' = -\underline{M}\,\underline{X} \quad (12)$$

is inferred, where the master or mobility matrix $\underline{M}$ acts on an arbitrary vector $\underline{Y}$ according to

$$\langle s\,|\underline{M}|\,s'\rangle\langle s'\,|\,\underline{Y} = \int M(s|s')Y_{s'}(x'_1,....,x'_{s'})dx'_1.....dx'_{s'} \,. \quad (13)$$

Note that in view of the definition of the current $\underline{J}'$ and the orthogonal character of the operators $\mathscr{P}$ and $\mathscr{Q}$, Eq. (12) leads to $\mathscr{Q}\underline{M}\,\underline{X} = \mathscr{Q}\mathscr{L}\underline{f}$ and $\mathscr{P}\underline{M}\,\underline{X} = -\mathscr{P}\mathscr{L}\underline{f}$.

Substituting the linear relation Eq. (12) into Eq. (11) and using the cyclic invariance of the trace, the entropy production is

$$\mathrm{tr}\,(\underline{X}\,\underline{M}\,\underline{X}) = \mathrm{tr}\,(\underline{X}\underline{\mathscr{Q}}\underline{M}\,\underline{X}) \geq 0\,, \qquad (14)$$

according to the second law of Thermodynamics. Therefore, M is a positive semidefinite matrix. In addition, the master matrix should be Hermitian

$$M(s|s') = M^{\dagger}(s|s') = M^{*}(s'|s)\,, \qquad (15)$$

as predicted by the Onsager symmetry relations. Here † refers to the Hermitian conjugate and * stands for the complex conjugated. Furthermore, due to the fact that $\underline{f}$ should be normalized, $\mathrm{tr}(\underline{f})$ is a constant quantity which is a function of N. It can be inferred from Eqs. (10) and (12) that $\mathrm{tr}(\underline{M}\,\underline{X}) = 0$ which, when the Hermitian character of the master matrix is taken into account, leads to the following constraints

$$\int M(s\mid s')dx_1.....dx_s = \int M^{\dagger}(s\mid s')dx'_1.....dx'_{s'} = 0\,. \qquad (16)$$

Hence, by using Eq. (12) the generalized Liouville equation (4) can be written

$$\left(\frac{\partial}{\partial t} - \underline{\mathscr{P}}\underline{\mathscr{L}}\right)\underline{f} = \underline{\mathscr{Q}}\underline{M}\underline{X}\,, \qquad (17)$$

with

$$\langle s\,|\underline{\mathscr{Q}}\underline{M}|\,s'\rangle\langle s'\mid \underline{X} = \delta_{s',s+1}\int M(s+1|s')X_{s'}dx'_1.....dx'_{s'}dx_{s+1}\,, \qquad (18)$$

written in analogy with Eq. (6). It should be mentioned that the presence of the master matrix in Eq. (17) notably simplifies the BBGKY hierarchy. In fact, the master matrix introduces a relaxation time scale. Hence, our theory is equivalent to a relaxation time approach to the study of the BBGKY hierarchy valid when there is a broad separation between the hydrodynamic and microscopic scales.

Here, Eq. (17) can be put into a more common form by introducing a new function $\underline{W}$ defined through [21]

$$f_{o,s'}W\left(s'\mid s\right) = -M\left(s\mid s'\right) + \delta\left(x'_1 - x_1\right).....\delta\left(x'_{s'} - x_s\right)\psi_s\left(x_1,....,x_s\right)\,, \qquad (19)$$

where the auxiliary function ψ_s is not arbitrarily selectable because of the constraints given by Eq. (16). Instead

$$\psi_s\left(x_1,...,x_s\right) = f_{o,s}(x_1,...,x_s)\int W(s|s')dx'_1...dx'_{s'} \qquad (20)$$

can be applied. Thus, Eq. (17) may be written in terms of the transition matrix as follows

$$\left(\frac{\partial}{\partial t} - \underline{\mathscr{P}}\underline{\mathscr{L}}\right)\underline{f}(t) = \underline{\mathscr{Q}}\underline{W}\underline{f}(t)\,, \qquad (21)$$

where

$$\langle s\,|\underline{\mathscr{Q}}\underline{W}|\,s'\rangle\langle s'\mid \underline{f} = \delta_{s',s+1}\int\{f_{s'}(x'_1,...,x'_{s'})W(s'|s+1) - f_{s+1}(x_1,...,x_{s+1})W(s+1\mid s')\}dx'_1...dx'_{s'}dx_{s+1}\,. \qquad (22)$$

The introduction of the transition matrix enables us to write Eq. (17) as a master equation.

A particularly interesting case corresponds to $s = 1$ where Eqs. (21) and (22) reduce to

$$\left(\frac{\partial}{\partial t} - L_1^o\right)f_1(x_1)) = \int\{f_2(x'_1,x'_2)W(x'_1,x'_2|x_1,x_2) - f_2(x_1,x_2)W(x_1,x_2\mid x'_1,x'_2)\}dx'_1dx'_2dx_2\,. \qquad (23)$$

This is not yet a kinetic equation; however, its uncorrelated part can be written as

$$\left(\frac{\partial}{\partial t} - L_1^o\right)f_1(x_1) = \int\{f_1(x'_1)f_1(x'_2)W(x'_1,x'_2|x_1,x_2) - f_1(x_1)f_1(x_2)W(x_1,x_2\mid x'_1,x'_2)\}dx'_1dx'_2dx_2\,, \qquad (24)$$

which is the famous Boltzmann equation. Analogous procedure can be followed to obtain the kinetic equations for the correlations coming from the components of $\underline{f}$ of an order higher than one.

NONEQUILIBRIUM STATIONARY STATE

Let us assume that a nonconservative field $h(t)$ acts on the system, modifying the Hamilton equations of motion

$$\dot{\underline{q}}_i = \frac{\partial H_N}{\partial \underline{p}_i} + \underline{C}_i(x_1,...x_N)h(t)\,,$$
$$\dot{\underline{p}}_i = -\frac{\partial H_N}{\partial \underline{q}_i} + \underline{D}_i(x_1,...x_N)h(t)\,, \qquad (25)$$

where $\underline{C}_i(x_j)$ and $\underline{D}_i(x_j)$ are coupling functions. This drive introduces a compressible contribution to the flow in the phase space which is reflected in the Liouville equation characterizing the phase space flow

$$\frac{\partial}{\partial t}F - [H_N, F]_P = -\frac{\partial}{\partial \Gamma_N}\cdot \dot{\Gamma}_N^{nc} F \ , \qquad (26)$$

where $\dot{\Gamma}_N^{nc} = (\dot{x}_1^{nc}, ..., \dot{x}_N^{nc})$, $\dot{x}_i^{nc} = (\underline{C}_i(x_j), \underline{D}_i(x_j))\, h(t)$. To Eq. (26) corresponds

$$\left(\frac{\partial}{\partial t} - \mathscr{P}\,(\mathscr{L} - \underline{G})\right)\underline{f} = \mathscr{Q}\mathscr{L}\underline{f} \qquad (27)$$

for the distribution vector, where $\underline{G}\underline{f} = \frac{\partial}{\partial \underline{\Gamma}}\dot{\underline{\Gamma}}^{nc}\underline{f}$ and $\langle s'|\mathscr{P}\underline{G}\underline{f}|s\rangle = \delta_{s,s'}\frac{\partial}{\partial \Gamma_s}\cdot \dot{\Gamma}_s^{nc}\ f_s$. Eq. (26) admits a stationary solution satisfying

$$[H_N, F_{st}]_P = \frac{\partial}{\partial \Gamma_N}\cdot \dot{\Gamma}_N^{nc} F_{st} \ , \qquad (28)$$

or equivalently

$$\dot{\Gamma}_N \cdot \frac{\partial}{\partial \Gamma_N}\ln F_{st} - \frac{\partial}{\partial \Gamma_N}\cdot \dot{\Gamma}_N^{nc} = 0 \ . \qquad (29)$$

Up to order one with respect to the external force, Eq. (28) becomes $[H_N, \ln F_{st}]_P = \frac{\partial}{\partial \Gamma_N}\cdot \dot{\Gamma}_N^{nc}$. To this stationary distribution function F_{st}, there is a corresponding stationary distribution vector $\underline{f}_{st}$ which can be obtained as a solution of the stationary version of Eq. (27) or computed directly from F_{st} by using Eq. (3), $\underline{f}_{st} \neq \underline{f}_o$.

In this stationary state the rate of change of the internal energy $U = \int H_N(x_1, ...x_N)F(x_1, ...x_N)dx_1....dx_N$, is given by

$$\frac{dU_{st}}{dt} = \int H_N(x_1, .., x_N) \qquad (30)$$
$$\times \frac{\partial}{\partial t}F_{st}(x_1, .., x_N)dx_1...dx_N = 0 \ ,$$

i.e. the energy is constant. Moreover, the total rate of change of the entropy is given by

$$\frac{dS_{st}}{dt} = -k_B \mathrm{tr}\left\{\frac{\partial \underline{f}_{st}}{\partial t}\log\left(\underline{f}_o^{-1}\underline{f}_{st}\right)\right\}$$
$$= k_B \mathrm{tr}\left\{\underline{G}\underline{f}_{st}\log\left(\underline{f}_o^{-1}\underline{f}_{st}\right)\right\} + \sigma_{st} = 0 \ , \quad (31)$$

which is also constant showing that entropy does not diverge. Hence, the stationary state coincides with the state of constant internal energy and entropy . In fact, In general the stationary average of any phase function remains constant. According to Eq. (31) the entropy production (9) reduces to

$$\sigma_{st} = -k_B \mathrm{tr}\left\{\underline{G}\underline{f}_{st}\log\left(\underline{f}_o^{-1}\underline{f}_{st}\right)\right\}$$
$$= k_B \mathrm{tr}\left\{\underline{f}_{st}\dot{\underline{\Gamma}}^{nc}\frac{\partial}{\partial \underline{\Gamma}}\log\left(\underline{f}_o^{-1}\underline{f}_{st}\right)\right\} \ , \qquad (32)$$

where $\underline{f}_{st}\dot{\underline{\Gamma}}^{nc}$ plays the role of a thermodynamic current $\underline{J}$ and $\frac{\partial}{\partial \underline{\Gamma}}\log\left(\underline{f}_o^{-1}\underline{f}_{st}\right)$ is the corresponding conjugated force $\underline{X}$. A mobility $\underline{M}$ matching both quantities and a diffusion coefficient $\underline{D}$ related to this mobility through an effective temperature T_{st} as $T_{st}\underline{f}_{st} = \underline{M}\cdot\underline{D}$ can be defined. Thus, one gets the phenomenological law

$$\dot{\underline{\Gamma}}^{nc} = T_{st}\underline{D}^{-1}\cdot\frac{\partial}{\partial \underline{\Gamma}}\log\left(\underline{f}_o^{-1}\underline{f}_{st}\right) \qquad (33)$$

allowing us to rewrite Eq. (32)

$$\sigma_{st} = \frac{k_B}{T_{st}}\mathrm{tr}\left\{\underline{f}_{st}\dot{\underline{\Gamma}}^{nc}\underline{D}\dot{\underline{\Gamma}}^{nc}\right\} \sim \frac{h(t)^2}{T_{st}} \ . \qquad (34)$$

By approximating $\underline{D}$ by its average value $D = \mathrm{tr}\left\{\underline{f}_{st}\underline{D}\right\}$ and by using Eq.(9), I find

$$D^{-1} = \frac{1}{T_{st}}\left(\frac{\mathrm{tr}\left\{\underline{f}_{st}\dot{\underline{\Gamma}}^{nc}\dot{\underline{\Gamma}}^{nc}\right\}}{-\mathrm{tr}\left\{\mathscr{Q}\mathscr{L}\underline{f}_{st}\log\left(\underline{f}_o^{-1}\underline{f}_{st}\right)\right\}}\right) \ , \qquad (35)$$

which constitutes a kind of Green-Kubo relation. Thus, I can assume that for small deviations from the stationary state

$$\widehat{\sigma} \equiv \frac{dS}{dt} - \sigma = -\frac{Dk_B}{T_{st}}\mathrm{tr}\left\{\underline{f}\,\dot{\underline{\Gamma}}^{nc}\dot{\underline{\Gamma}}^{nc}\right\} \ . \qquad (36)$$

This is a powerful relation because following Boltzmann, the probability of the nonequilibrium fluctuations can be defined

$$P_\tau(\dot{\underline{\Gamma}}^{nc}, t) \sim \exp\left(\frac{\widehat{\sigma}\tau}{k_B}\right) \qquad (37)$$
$$= \exp\left(-\frac{D\tau}{T_{st}}\mathrm{tr}\left\{\underline{f}\,\dot{\underline{\Gamma}}^{nc}\dot{\underline{\Gamma}}^{nc}\right\}\right) \ ,$$

where τ is a time scale shorter than the time scale in which $h(t)$ varies considerably. This probability enables us to compute the average value of any phase

function $\psi(\dot{\underline{\Gamma}}^{nc})$, as for example the compressibility factor $\underline{G}$, .
Since macroscopic hydrodynamics occurs in the N-particle subspace, it can be concluded that one can also recover macroscopic hydrodynamics from this description.

CONCLUSIONS

Here, I have presented a representation of the statistical description of a many-body system in terms of the distribution vector which reveals the irreversible component of the motion of this system. This component is hidden when one works with the standard Liouville equation but at the level of the generalized Liouville equation which entails a certain degree of coarse graining, this irreversible component becomes obvious. The Liouville equation is a closed equation for the phase space distribution function while the generalized Liouville equation encloses a set of coupled equations, each one in itself represents a contraction of the statistical description. But, as I have mentioned previously, the full statistical description in terms of the phase space distribution function is equivalent to the description in terms of the set of all the reduced s-particle distribution functions. In this scenario, I show that the Gibbs entropy given by the Gibbs entropy postulate is a non-conserved quantity throughout the motion in phase space. This entropy should increase up to its maximum value at equilibrium according to the second law. The consequences I have drawn from the Gibbs entropy are compatible with the explanation of irreversibility which follows from Boltzmann's entropy postulate.
By applying the methods of nonequilibrium thermodynamics in phase space, *i.e.* in the framework of the mesoscopic nonequilibrium thermodynamics MNET [22], [23], I obtain a linear relation between the irreversible rate of change of the distribution vector and the conjugated thermodynamic force which introduces a master matrix which should satisfy the properties required by the Onsager theory. This result simplifies the BBGKY hierarchy and enables us to break the hierarchy by neglecting higher order correlations thus obtaining the Boltzmann equation for the one-particle distribution function. This last result constitutes a test of our theory. Hence, based on the MNET I have founded a way for deriving kinetic equations.
I also point out that in our mesoscopic approach, the master matrix introduces a relaxation time scale which shows that our theory is valid when there is a broad separation between the hydrodynamic and microscopic scales. The existence of such a separation of time scales allows the rate of change of the distribution vector due to the main stream flow velocity in phase space to balance the irreversible change in order to achieve a stationary distribution at long time. This is precisely what is assumed to happen in the context of the phenomena described by the kinetic equations.
I have also shown that the entropy defined in terms of the distribution vector remains constant in a non-equilibrium stationary state, hence, divergences are avoided and the second law is satisfied. Also a kind of Green-Kubo relation was derived for a transport coefficient that can be defined in the system relating the power supplied to the system with the entropy production with the aid of a stationary temperature. Finally, following the Boltzmann principle I derive the expression of the probability for the nonequilibrium fluctuations. Therefore, the answer to the question raised at the beginning, can Thermodynamics describe systems far from equilibrium?, is obviously yes if one works at the adequate level of description, which corresponds to the distribution vector.

REFERENCES

[1] J.L. Lebowitz,, Physica A **263**, 516 (1999).

[2] J.L. Lebowitz, Rev. Mod. Phys. **71**, S346 (1999).

[3] S. Goldstein, *Boltzmann's Approach to Statistical Mechanics*, in Chance in Physics: Foundations and Perspectives, edited by Jean Bricmont et al., Lectures Notes in Physics **574**, (springer-Verlag, 2001).

[4] L. Andrey, Phys. Letters **111A**, 45 (1985).

[5] W.G. Hoover, H.A. Posch, C.G. Hoover, Chaos **2**, 245 (1992).

[6] G. Gallavotti, "*Nonequilibrium thermodynamics ?,*" arXiv: cond-matt/0301172, also Meteorological and geophysical fluid dynamics, ed. W. Schröder (Science, 2004).

[7] D. P. Ruelle, Physica A **263**, 540 (1999).

[8] D.J. Evans and D.J. Searles, Phys. Rev. E **50**, 1645 (1994).

[9] G.M. Wang, E.M. Sevick, E. Mittag, D.J. Searles and D.J. Evans, Phys. Rev. Lett. **89**, 050601 (2002).

[10] L. Rondoni and E.G.D. Cohen, Nonlinearity **13**, 1905 (2000).

[11] D.P. Ruelle, Proc. Nat. Acad. Sci. **100**, 30054(2003).

[12] M.E. Tuckerman, C.J. Mundy and M.L. Klein, Phys. Rev. Lett. **78**, 2042 (1997).

[13] P. Gaspard, J. Stat. Phys. **88**, 1215 (1997).

[14] Advances in Phys. **51**, 1529 (2002).

[15] R. Balescu, *Equilibrium and Nonequilibrium Statistical Mechanics,* Wiley-Interscience, New York, 1975.

[16] A. Pérez-Madrid, Physica A **339**, 339 (2004).

[17] S.R. de Groot and P. Mazur, *Non-Equilibrium Thermodynamics* (Dover, New York, 1984), Sect. VII.8, pag 126.

[18] N.G. van Kampen, *Stochastic Processes in Physics and Chemistry* (North-Holland, Amsterdam, 1990), Sect. VII.6, pag. 202.

[19] R.E. Nettleton and M.S. Green, J. Chem. Phys. **29**, 1365 (1958).

[20] D. Bedeaux, and P. Mazur, Physica A **298**, 81 (2001).

[21] J. Meixner, Zeitschr. Physik **149**, 624 (1957).

[22] A. Pérez-Madrid, J.M. Rubí, P. Mazur, Physica A **212**, 231 (1994).

[23] P. Mazur, Physica A **274**, 491 (1999).

Exergy analysis

Proceedings of ECOS 2005
Trondheim, Norway
June 20–22, 2005

DEFINITIONS AND NOMENCLATURE IN EXERGY ANALYSIS AND EXERGOECONOMICS

George Tsatsaronis, Project Coordinator
Technische Universität Berlin
Institute for Energy Engineering
Marchstr. 18, 10587 Berlin
Germany

SUMMARY

This paper presents the definitions of some terms used in exergy analysis and exergy costing, discusses options for the symbols to be used for exergy and presents the nomenclature for the remaining terms.

1 INTRODUCTION

The number of publications dealing with exergy analysis and exergoeconomics has been increasing continuously in the last years. The symbols used in these publications and in textbooks (see Table 1) cover a rather large spectrum of the Latin and Greek alphabets. There is an urgent need for some consensus on the symbols to be used in the future. This will facilitate (a) the communication among practitioners, and (b) the further development of the disciplines of exergy analysis and exergoeconomics. The symbols used in section 2 and 3 are suggested for publications in journals and conference proceedings. In section 4 some alternatives are presented for use in textbooks.

2 EXERGY

Exergy of a thermodynamic system is the maximum theoretical useful work (shaft work or electrical work) obtainable as the system is brought into complete thermodynamic equilibrium with the thermodynamic environment while the system interacts with this environment only. The total exergy of a system consists of

- physical exergy (due to the departure of the temperature and pressure of the system from those of the environment),
- chemical exergy (due to the departure of the chemical composition of the system from that of the environment)
- kinetic exergy (due to the system velocity measured relative to the environment), and
- potential exergy (due to the system height measured relative to the environment).

The physical exergy consists of

- mechanical exergy (associated with the system pressure) and
- thermal exergy (associated with the system temperature).

For a given thermodynamic state at a temperature T and pressure p, the thermal exergy is usually calculated along the isobaric line at p (from state [T, p] to state [T_0, p]), whereas the mechanical exergy is calculated along the isothermal line at T_0 (from state [T_0, p] to state [T_0, p_0]).

Distinction between thermal and mechanical exergy might not always be unambiguous.

The chemical exergy of a system can be split into

- reactive exergy (associated in its calculation with chemical reactions), and
- nonreactive exergy (associated in its calculation with nonreactive processes such as expansion, compression, mixing and separation).

An option for splitting the chemical exergy into reactive and nonreactive exergy is presented in Reference [1]. The splitting of physical and chemical exergy might be useful for defining more accurate exergetic efficiencies and for improving the costing approach.

The symbol for exergy has been the subject of a lot of controversy in the past. The exergy symbol should be easy to use and recognize. We should not use two letters for this symbol (e.g., Ex) because (a) this is not common for important variables in thermodynamics, and (b) there is a potential for missinterpretations when it is used with superscripts and subscripts.

With exergy we mean the potential to generate work regardless of the cases, systems, or exergy components being actually considered. Therefore, it is logical to use only one and the same symbol for all cases, systems and exergy components, as well as for exergy destruction and exergy loss. The fact that in energy analysis we use traditionally different symbols for total energy, internal energy and enthalpy should not lead us to use different symbols for the physical exergy of a system and the physical exergy of a material stream simply because the equations used to calculate each of these physical exergies are different. If we would follow this way, we should use different symbols also for the exergy associated with both heat transfer and work, and we would soon come to a completely unacceptable situation regarding symbols for exergy.

If we now agree that a one-letter symbol should be used in all cases in conjunction with exergy, the question arises what letter should this be. The easiest and more natural approach for publications in journals and conference proceedings would be to use the letter E for exergy, as it has been used in Germany and some other countries from the very moment the exergy concept was introduced.

It should be considered that the vast majority of these publications involving exergy refer usually to control volumes at steady state. In these applications the relevant energy terms are only enthalpy, heat and work. Therefore, there is no danger of confusing total e**n**ergy, which is also denoted by E, with any form of e**x**ergy. In cases where both exergy and total energy appear in the same publication, a slightly different font can be employed for total energy, unless energy is mainly used and exergy is mentioned only in passing. In the last case, a slightly different symbol (for example, the roman font) can be used for exergy. This should not result in confusion because it is always clear from the context whether exergy or total energy is meant.

Thus, for publications in journals and conference proceedings, where a simple approach is very important, the following equations should be employed in exergy analysis. Alternatives are presented in section 4.

Total exergy of a system:

$$E_{sys} = E_{sys}^{PH} + E^{KN} + E^{PT} + E^{CH} \quad (1)$$

$$e_{sys} = e_{sys}^{PH} + e^{KN} + e^{PT} + e^{CH} \quad (1a)$$

To distinguish the physical exergy and total exergy of a system from the same exergies associated with a stream of matter, a subscript "*sys*" is used here for the exergies of the system.

Physical exergy of a system:

$$E_{sys}^{PH} = (U - U_0) + p_0(V - V_0) - T_0(S - S_0) \quad (2)$$

$$e_{sys}^{PH} = (u - u_0) + p_0(v - v_0) - T_0(s - s_0) \quad (2a)$$

Mechanical and thermal exergy of a system:

$$E_{sys}^{PH} = E_{sys}^{T} + E_{sys}^{M} \quad (3)$$

$$e_{sys}^{PH} = e_{sys}^{T} + e_{sys}^{M} \quad (3a)$$

Reactive and nonreactive exergy:

$$E^{CH} = E^{R} + E^{N} \quad (4)$$

$$e^{CH} = e^{R} + e^{N} \quad (4a)$$

In applications of the exergy concept, the subscript "*sys*" will be replaced by the abbreviation used for the component being considered (e.g., *ac* for air compressor, *hrsg* for heat-recovery steam generator, and *sr* for storage vessel).

Total exergy of a material stream:

$$E = E^{PH} + E^{KN} + E^{PT} + E^{CH} \quad (5)$$

$$e = e^{PH} + e^{KN} + e^{PT} + e^{CH} \quad (5a)$$

Physical exergy of a material stream:

$$E^{PH} = (H - H_0) - T_0(S - S_0) \quad (6)$$

$$e^{PH} = (h - h_0) - T_0(s - s_0) \quad (6a)$$

Mechanical and thermal exergy of a material stream:

$$E^{PH} = E^{T} + E^{M} \quad (7)$$

$$e^{PH} = e^{T} + e^{M} \quad (7a)$$

Please note that the terms E^{KN} and E^{PT} (e^{KN} and e^{PT}) in Equations (1) and (5) are calculated by

$$E^{KN} = \frac{1}{2} m \vec{v}^{\,2} \quad (8)$$

$$e^{KN} = \frac{1}{2} \vec{v}^{\,2} \quad (8a)$$

and

$$E^{PT} = mgz \quad (9)$$

$$e^{PT} = gz \quad (9a)$$

Here $\vec{v}$ is the system velocity measured relative to the environment and z represents the system height also measured relative to the environment.

3 OTHER EXERGETIC VARIABLES

3.1 The *product exergy* represents the desired result (expressed in terms of exergy) generated by the exergy system. The product exergy is denoted by E_P.

3.2 The *fuel exergy* represents the resources (expressed in terms of exergy) expended to provide the product exergy. The fuel exergy is denoted by E_F. The term "fuel exergy" here is not limited to fossil fuels but represents in general the exergetic resources used to drive (to "fuel") the process being considered.

3.3 The exergetic efficiency is the ratio between product exergy and fuel exergy and is denoted by ε (Greek epsilon). The inverse of the exergetic efficiency is denoted by the symbol κ (Greek kappa). The terms second-law efficiency and rational efficiency are not precise and should be avoided when an exergetic efficiency is implied by them.

3.4 The energetic efficiency, defined in a similar way as the exergetic efficiency but using only energy terms, is denoted by η (Greek eta).

3.5 The thermodynamic inefficiencies of a system consist of exergy destruction (E_D) associated with the irreversibilities (entropy generation) within the system and of exergy losses (E_L) associated with the transfer of exergy (through material and energy streams) to the surroundings. The use of the term irreversibility (instead of exergy destruction) and the symbol I should be avoided. The term irreversibility does not imply that the exergy concept is used because the exergy destruction can be calculated from entropy values alone.

4 ALTERNATIVES IN THE NOMENCLATURE

The suggestions made above refer to publications in journals and conference proceedings when exergy is mainly used and total energy is mentioned, if at all, in passing. For such applications addressed mainly to exergy

practioners, the letter E can used for exergy without creating confusion.

The situation might be different if we deal with students who might be easily confused by differences in notations. For textbooks an E should be used for total energy. This is in accord with current use in most textbooks.

Then we have the following options for the exergy symbol. The options presented in order of decreasing simplicity and degree of preference.

Option 1: Use the letter E in a different font, for example the roman font E (instead of an italic E). Experience with textbooks using this option (e.g., [2]) shows that this seldom results in confusion. Texts and instructors simply need to point out the different fonts being used.

Option 2: Use a Greek epsilon ($\mathcal{E}, \varepsilon$). This option requires that a letter different than ε (for example, Greek zeta ζ) is used for the exergetic efficiency since now ε represents the specific exergy.

Option 3: Use the letter X (x) which is the second one in the word exergy. This letter is used, however, to denote an unknown variable in mathematics.

Option 4: Use a Greek epsilon ($\mathcal{E}, \varepsilon$) for the exergy associated with material and energy streams and a Greek psi (Ψ, ψ) for the exergy associated with a system, to avoid the use of subscript "sys".

Option 5: Use the two letters Ex (ex).

It is apparent that several more options exist for exergy and also for the other variables associated with exergy costing. Authors should consider that simplicity and ease of use are very important factors in selecting the exergy symbol.

5 EXERGOECONOMICS: EXERGY COSTING

Exergoeconomics is the branch of engineering that appropriately combines thermodynamic evaluations based on an exergy analysis with economic principles to provide the designer or operator of an energy system with information (a) useful to the design and operation of a cost-effective system, and (b) not obtainable by regular energy analysis and economic analysis. Exergoeconomics rests on the notion that exergy is the only rational basis for assigning monetary costs to the interactions that a system experiences with its surroundings and to the sources of thermodynamic inefficiencies within it. We call this approach *exergy costing*. When exergy costing is **not** applied, authors should use a different term (e.g., thermoeconomics). Thermoeconomics, being a more general term and characterizing any combination of a thermodynamic analysis with an economic one, might also be used instead of the term exergoeconomics (but not vice-versa). The following definitions and symbols are recommended in publications dealing with exergoeconomics:

5.1 The exergetic cost of a stream represents the fuel exergy that needs to be supplied to the overall system to generate the exergy associated with that stream. The exergetic cost is denoted by E^c. The product and fuel exergetic costs are denoted by E_P^c and E_F^c, respectively. The unit of exergetic cost is the ratio between exergetic cost and corresponding exergy and is denoted by the symbol k^c.

5.2 The cost associated with an equipment item is denoted by Z.

5.3 The cost associated with a material or energy stream in exergoeconomics is denoted by the symbol C. The average unit cost (usually a cost per unit of exergy) is denoted by c.

5.4 When marginal costs are used, these must be explicitly defined. A λ (Greek lambda) may be used for this purpose.

The following section summarizes the symbols suggested here for publications in journal and conference proceedings.

6 NOMENCLATURE

c	average cost per exergy unit
C	cost associated with a stream
e	specific exergy
E	exergy
E_{sys}	total exergy of a system
E_{sys}^{PH}	physical exergy of a system
E^c	exergetic cost
h	specific enthalpy
H	enthalpy
k^c	unit of exergetic cost
p	pressure
s	specific entropy
S	entropy
T	temperature
u	specific internal energy
U	internal energy
v	specific volume
V	volume
$\vec{v}$	velocity relative to the environment
z	height relative to the environment
Z	cost associated with equipment

Greek letters

ε	exergetic efficiency
η	energetic efficiency
κ	inverse of the exergetic efficiency
λ	marginal cost (optional)

Subscripts

D	exergy destruction
F	fuel exergy
L	exergy loss
P	product exergy
sys	system
0	conditions of the thermodynamic environment

Superscripts

c	exergetic cost
CH	chemical exergy
KN	kinetic exergy or energy
M	mechanical exergy
N	nonreactive exergy
PH	physical exergy or energy
PT	potential exergy
R	reactive exergy
T	thermal exergy

ACKNOWLEDGEMENT

This project was initiated by Noam Lior. In addition to him, input was provided by many exergy practioners including the following:

Cai Ruixian
Michel Feidt
Christos Frangopoulos
Richard Gaggioli
Signe Kjelstrup
Andrea Lazzaretto
Giampaolo Manfrida
Alberto Mirandola
Michael Moran
Silvia Azucena Nebra
Gordon Reistadt
Ricardo Rivero
Enrico Sciubba
Antonio Valero
Michael von Spakovsky

Some of the above listed practioners disagree with some of the suggestions made here.

REFERENCES

1. Bejan, A., Tsatsaronis, G. and Moran, M., *Thermal Design and Optimization*, John Wiley & Sons, New York, 1996.

2. Moran, M. and Shapiro, Fundamentals of Engineering Thermodynamics, 5th edition, John Wiley & Sons, New York, 2004.

Table 1. Symbols for exergy and exergetic efficiency used in textbooks [initially compiled by Noam Lior]

specific exergy, [kJ/kg] or [J/mole]	exergy [J]	the specific exergy function [J/kg]	the exergy function [J]	specific energy [kJ/kg]	energy [J]	exergy destruction	exergetic efficiency	Textbook reference
Δb	-	b		e	$\boldsymbol{E}$	*Irreversibility*	ε	Keenan
	Λ	Φ, b		e	$\boldsymbol{E}$	I		Hatsopoulos & Keenan, 1965
							ψ	Kotas, 1985
							ε	Moran
e	E			e	E	E_d	ε	Moran and Shapiro
e_x for open systems, ξ for closed	E_x for open systems, Ξ for closed	b for open systems, a for closed	B for open systems, A for closed	e	E	W_{lost}	η_{II}	Bejan
e	E	e	E			E_D	ε	Bejan, Tsatsaronis, and Moran
	B					δb	η_B, η_p	Szargut et al.
ψ for open systems, φ for closed	X			e	E	I, $X_{destroyed}$	η_{II}	Cengel and Boles
ψ for open systems, φ for closed	Ψ, ϕ			e	E		η_{2nd}	Anderson
	Ψ, Ω				E		ε	Gyftopoulos and Beretta
	E						ζ	Bosnjakovic
ϕ							η_{II}	Sussman
ψ for open systems, φ for closed	ϕ			e	E	I	$\eta_{2nd\ law}$	Sontag, Borgnakke, van Wylen
e	$\dot{E}$ *(only for streams)*			e	E			Baehr

Proceedings of ECOS 2005
Trondheim, Norway
June 20–22, 2005

EXERGY ANALYSIS OF ZERO CO_2 EMISSION POWER PLANTS

V. Amati, P. Fiorini(*), E. Sciubba
University of Roma 1 "La Sapienza"
Mechanical and Aeronautical Engineering Department
Italy

ABSTRACT

A modular simulator code, CAMEL®, developed by the University of Roma 1, has been applied to a simulation of a series of "zero emissions" and high efficiency cycles. The code libraries have been augmented by adding property data for all working media involved (H_2, high temperature steam) and by developing some additional component models.
Due to the social, political and economic changing attitude towards greenhouse emissions, more and more processes are being considered that include CO_2 removal in some form. Of the different solutions for CO_2 separation recently presented in the literature, we chose here to analyze the one based on chemical or physical absorption upstream of the combustion process: pure hydrogen is burnt in presence of pure oxygen to produce superheated steam. Three different solutions are considered, all based on non-conventional plant configurations: two of them are H_2/O_2 cycles and the third one is the so called ZECOTECH® cycle. The main features of all three configurations are presented and their thermodynamic cycles are simulated in order to perform an exergetic analysis and to carry out a better insight of the losses and of their relative importance on the process performance indicators.
Keywords: simulation, innovative and "Zero Emission" cycles, exergetic analysis.

NOMENCLATURE

C	Compressor
cc	Combustion chamber
CSB	Coefficient of structural bond
E_d	Exergy destroyed in a component [kW]
E_F	Exergy resource [kW]
E_U	Useful exergy production [kW]
ex	Specific exergy [kJ/kg]
h	Specific enthalpy [kJ/kg]
HPT	High pressure turbine
HRSG	Heat recovery steam generator
K	Condenser
k	Specific heat ratio
LHV	Lower heating value [kJ/kg]
LMTD	Logarithmic mean temperature difference [°C]
LPT	Low pressure turbine
m	Mass flow rate [kg/s]
MPT	Medium pressure turbine
N	Number of stages
P	Net power output [kW]
$p_{out,MPT}$	Medium pressure turbine outlet pressure [bar]
q	Heat transfer for unit of mass [kJ/kg]
ST	Steam turbine
T	Temperature [K]
Tmax	Top cycle temperature [°C]
TTD	Terminal temperature difference [°C]
β	Total pressure ratio
ε	Exergetic efficiency
η	Energetic efficiency
η_s	Stage adiabatic efficiency

(*) Corresponding Author, 39-06-44585272, fax 39-06-44585249, *e-mail: paolo.fiorini@casaccia.enea.it*

$\pi_{k,i}$ Coefficient of structural bond for component k, with the variation of the parameter x_i

INTRODUCTION

The need to cover an ever-increasing final energy demand and the consciousness of the necessity of setting a limit to the related emissions is prompting design engineers to concentrate their attention not only on the repowering of technically obsolete power plants but also on the development of "innovative" solutions. A long time perspective directs these studies towards the possibility of using renewable and "clean" energy sources. If one considers the present world energetic situation (energy resource availability, current state of art of the energy conversion technologies) and the foreseen developments in the short and medium term, it is immediately clear that the energy resources that can be realistically exploited for large scale production are still those of fossil origin, in particular coal. One of the problems related to the use of fossil fuels is of course the technology employed for the fuel treatment and combustion: any process involving a carbon-rich fuel implies CO_2 emission in the atmosphere. Several removal and sequestration techniques have been proposed, some based on chemical or physical fuel treatment upstream the power cycle, that is fed by a carbon-free syngas (for example coal gasification with production of H_2 and CO_2 removal through MEA or $CaCO_3$-methods [3], natural gas decarbonisation [8]). Others techniques are based on CO_2-capture in an intermediate phase of the power cycle [1].

In the present paper, the energetic and exergetic performance of some of the so-called "Zero Emission" innovative cycles of the first category are analyzed. All process calculation are performed by means of a modular code for the simulation of energy conversion processes; the code, CAMEL®, has been developed by the Authors' group at the Mechanical and Aeronautical Engineering Department of the University of Roma 1, "La Sapienza"[4,5]. The work is the result of three consecutive stages:

1) Up-dating of the code: it has been necessary in order to perform, with the same simulator, the analysis (and consequently the comparison) of innovative cycles that, until now, have been studied by using different codes. In this step the selected cycles have been used as a "test bench" to verify the performances of CAMEL®; for this reason they were chosen between those cycles for which a simulation was already performed; see that their plant configurations are the results of accurate and published analysis [3,6] only a brief description of them will be here reported. For all the details concerning the optimization and the methodology used in the plant design we recommend [3,6].

2) Simulation of the cycles and testing of the code: the results of the simulations have been compared with the available data. This stage has been positively completed: the code allows the simulation of different typology of power plants while the integration of other modular elements is actually in execution; they will make possible the simulation of the whole power generation process including all the sub-processes (coal gasification, CO_2 sequestration, O_2 production) that here cannot been considered.

3) After these works of implementation, calculation and testing, the new possibilities offered by the code have been exploited to develop the plant analysis by adding an exergetic evaluation of the cycles that will be here discussed more in detail.

THE PROCESSES SELECTED FOR THE ANALYSIS

The proposed plant configurations enact an internal combustion steam cycle fed by hydrogen: the oxidizer being pure oxygen, superheated steam is the product of the combustion, while cogenerated steam is injected in the combustion chamber as an "inert" to control the gas temperature and to limit oxygen consumption. The selected cycles are:

1-2) H_2/O_2 Cycle-case a (T_{max} = 1350°C, Figure 1) and case b (T_{max} = 1700°C). Both were proposed by the research group of the Science and Energy Technologies Department of the University of Roma 2, "Tor Vergata"[6].

3) ZECOTECH® Cycle, jointly developed by the Energy Department of ENEA (Italian National Agency for New Technologies, Energy and Environment), the Ansaldo Group and the Department of Mechanical and Aeronautical Engineering of the University of Roma 1, "La Sapienza"[3].

DESCRIPTION OF THE PLANT LAYOUTS

The proposed plant layouts are described in this section: Tables 1-3 contain the values of the most relevant thermodynamic parameters evaluated during the simulations.

Cycle n°1 and 2 (H_2/O_2 cycles)

The two examined cycles, (cycle n°1 in Figure 1), result in similar plant layout; but while Cycle (1) is designed by respecting the present or the short-term state of the art (T_{max}=1350°C and β=30), Cycle (2) is developed by considering the possible development for the gas turbine technology in the medium and long term (T_{max}=1700°C e β=70) [9]. It differentiates from Cycle (1) for the addition of a low pressure section (steam turbine and condenser) downstream the HRSG.

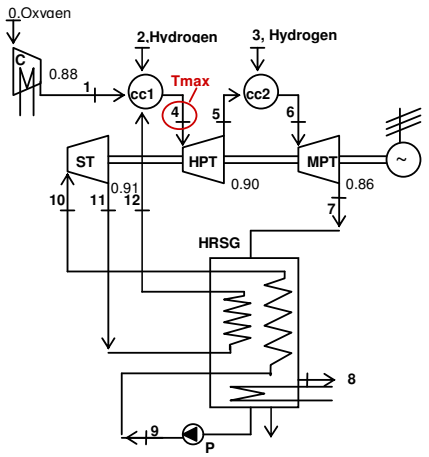

Figure 1: Plant layout of Cycle n°1

	m[kg/s]	p[bar]	T[K]	h[kJ/kg]	ex[kJ/kg]
0	1.000	1.01	298.15	0	122.42
1	1.000	33.60	633.75	332	501.6
2	0.0601	31.30	553.15	4081	140000
3	0.0411	5.64	513.15	3496	140000
4	3.515	30.40	1623.15	4919	2605
5	3.515	2.00	1050.15	3615	1228
6	3.556	2.02	1623.15	5293	2439
7	3.556	1.07	1473.15	4912	2037
8	1.100	1.01	370.75	2182	388
9	2.455	346.0	315.95	209	36.4
10	2.455	294.0	838.15	3346	1517
11	2.455	36.70	541.15	2884	1020
12	2.455	33.80	773.15	3451	1317

Table 1: Relevant thermodynamic parameters for process n°1

Cycle n°3 (ZECOTECH®)

A first study [3] was conducted on the potentialities of the cycle, considering both the power section than its necessary coupling with the chemical section in which the hydrogen synthesis and the sequestration processes take place. The resulted optimal plant configuration is shown in Figure 2.

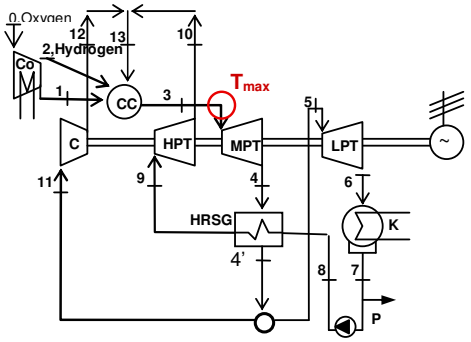

Figure 2: Plant layout of ZECOTECH® Cycle

The pressure level required by the sub-processes upstream the power unit (gasifier and decarbonator) limit the pressure in the combustion chamber to 30 bar. The MPT outlet pressure ($p_{out,MPT}$) was found to be one of the most influential parameters on cycle efficiency; for this reason, as a first step in this work, a sensitivity analysis was carried out to quantify the dependence of the cycle efficiency on the variation of $p_{out,MPT}$ for different T_{max}. Throughout the tests, the following assumptions were made:

a) Turbine and compressor adiabatic efficiencies are function of the total pressure ratio and of the consequent number of stages as reported in formulas (1) and (2), [10]. For the expansion and compression ratio of individual stages, the value of 2 for the turbine and of 1.25 for the compressor have been assumed. For a turbine we have:

$$\eta_{ad,TOT} = \frac{1-[1-\eta_s(1-\beta^{(1-k)/Nk})]^N}{1-\beta^{(1-k)/k}} \qquad (1)$$

Whereas for a compressor we have:

$$\eta_{ad,TOT} = \frac{\beta^{(k-1)/k}-1}{[1+(\beta^{(k-1)/Nk}-1)/\eta_s]^N-1} \qquad (2)$$

The stage adiabatic efficiency was assumed equal to 0.90 for the turbines and to 0.89 for the compressors.

b) Pressure losses along the circuit have been neglected; in the exchangers and in the combustion chamber they are equal to 2%:

c) Combustion energy efficiency is equal to 0.98;
d) The hydraulic efficiency of the pump is equal to 0.85;
e) The energy efficiency of the generator is equal to 0.98;
f) The coolant used in the intercooler and in the condenser is water at ambient conditions (298.15 K and 1.01 bar).
Figure 3 shows the results of the analysis: the optimal MPT discharge pressure decreases with increasing T_{max} : for T_{max}=1350°C the optimal pressure is equal to 1.5 bar, while for T_{max}=1700°C it is equal to 1 bar.

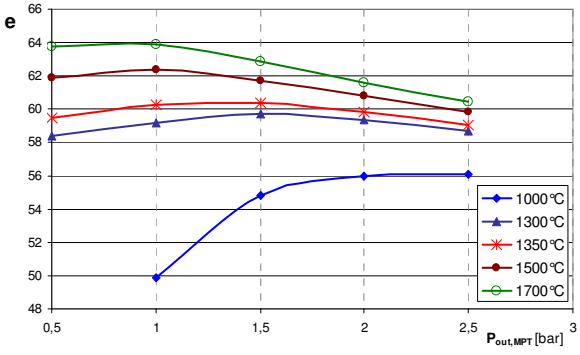

Figure 3: Exergetic efficiency as function of $p_{out,MPT}$

The following simulations of cycle (3), whose results are reported in Tables 2 and 4, have been performed with T_{max} respectively equal to those reached in cycles (1) and (2) (and with the optimal values of $p_{out,MPT}$), to compare the overall performances .

	m[kg/s]	p[bar]	T[K]	h[kJ/kg]	ex[kJ/kg
0	4.498	1.01	298.15	0	122.0
1	4.498	30.0	633.00	332.0	492.4
2	0.56222	30.0	553.15	6644.0	140000
3	32.164	30.0	1623.15	5541.6	2853.3
4	32.164	1.5	985.62	3956.9	1223.8
5	14.744	1.5	518.35	2962.6	634.3
6	14.744	0.05	306.03	2436.7	59.5
7	14.744	0.05	305.38	135.0	0.3
8	9.684	170.0	305.81	152.1	17.3
9	9.684	170.0	833.00	3454.6	1528.6
10	9.684	30.0	578.84	3006.9	1054.9
11	17.419	1.5	518.35	2962.6	634.3
12	17.419	30.0	1062.12	4120.2	1750.8
13	27.103	30.0	871.72	3238.4	1295.3
Adiab. efficiency: C:0.85; MPT:0.90; HPT:0.91; LPT:=0.87					

Table 2: Relevant thermodynamic parameters for process n°3- T_{max} = 1350°C

ENERGETIC ANALYSIS

On the basis of the results of the simulations the energetic performances have been examined and summarized in Table 3. For better comparison, the results obtained for the three plants are all referred to the unit of oxygen consumed. For LHV, the value of 114703 kJ/kg was assumed, in accordance to [6] and in order to compare their results with the ones of CAMEL®, even if we recognize that the usual value should be 120 MJ/kg.

	Cycle 1	Cycle 2	ZECOTECH®	
T_{max}[°C]	1350	1700	1350	1700
β	30	70	30	30
P [kW]	5865	8834	8645.5	9146.4
m_{fuel} [kg/s]	0.1012	0.1245	0.125	0.125
η=P/(m_{fuel} LHV)	**50.53**	**61.86**	**60.38**	**63.87**

Table 3: Energetic efficiencies of the plants

	m[kg/s]	p[bar]	T[K]	h[kJ/kg]	ex[kJ/k
0	4.498	1.0	298.15	0.0	122.0
1	4.498	30.0	633.00	332.0	492.4
2	0.5622	30.0	553.15	6644.0	140000
3	20.259	30.0	1973.15	6509.4	3660.3
4	20.259	1.0	1161.31	4369.0	1465.5
5	13.677	1.0	518.35	2964.3	579.5
6	13.677	0.05	306.03	2488.3	60.9
7	13.677	0.05	305.38	135.0	0.3
8	8.617	170.0	305.81	152.1	17.3
9	8.617	170.0	833.00	3454.6	1528.6
10	8.617	30.0	578.84	3007.0	1054.9
11	6.582	1.0	518.35	2964.3	579.5
12	6.582	30.0	1156.93	4347.4	1917.0
13	15.199	30.0	805.89	2841.8	1129.8
Adiab. efficiency: C:0.84; MPT:0.89; HPT:0.91; LPT:=0.87					

Table 4: Relevant thermodynamic parameters for process n°3 - T_{max} = 1700°C

EXERGETIC ANALYSIS

Purpose of this work is to perform an explicit exergy analysis of the plant, to identify the components that in each of the proposed solutions are affected by the highest irreversible losses and that consequently ought to be given more attention during the design phase. The results of such an analysis provide the designer with a better insight as of where a design modification is necessary, both at the single component and at a process level, to the purpose of better exploiting the available resources. For each cycle the following evaluations were made [2]:

a. Exergetic efficiency of each component, ε:
   $\varepsilon = E_U / E_F$
   with E_U and E_F respectively the useful product and the resource of the component, always evaluated in exergetic terms.

b. Exergy destroyed in each component, E_d (kW), and in the whole plant, $E_{d,tot}$ (kW).
c. Dimensionless loss parameters:
   - $E_d\% = E_{d(component)} / E_{d,tot} \times 100$
     Ed% is thus the percentage of exergy destroyed in the component with respect to the total exergy destroyed in the plant.
   - $E'_d\% = E_{d(component)} / E_F \times 100$
     This is the percentage of exergy destroyed with respect to the total exergy resource influx into the process.
d. Evaluation, for cycle (1) and (3), with T_{max}=1350°C, of the coefficient of structural bond or CSB, defined as [7,11]:

$$\pi_{k,i} = \frac{\left(\frac{\partial E_{d,tot}}{\partial x_i}\right)}{\left(\frac{\partial E_k}{\partial x_i}\right)} = \left(\frac{\partial E_{d,tot}}{\partial E_k}\right)_{x_i=var} \approx \left(\frac{\Delta E_{d,tot}}{\Delta E_k}\right)_{x_i=var} \quad (3)$$

π represents the ratio between the variation of the exergy destroyed in the plant ($E_{d,tot}$) to that destroyed in the k^{th} single component (E_k) when only the changing of parameter x_i is imposed. The CSB allows an examination of the positive or negative influence of each single component on the overall plant performance when some of the working parameters are changing. It is useful to recall the values π can assume and their meaning:

- $\pi_{k,i} > 0$: when the parameter x_i is changing, to a decrease in the exergy destruction in the k^{th}-component corresponds a decrease in the total exergy destruction of the plant. A value much higher than one can be explained as follows:
  1. Considering the third member in Formula 3, a small variation of E_k corresponds to a large variation of $E_{d,tot}$;
  2. Considering the second member of Formula 3, a high value of $\pi_{k,i}$ means that the derivative $\partial E_k/\partial x_i$ is much lower than $\partial E_{d,tot}/\partial x_i$: the parameter x_i has a much lesser influence on the exergy losses of the k^{th}-component than the one it has on the whole plant.

  When $0 < \pi_{k,i} < 1$, to a decrease of E_k corresponds a lower decrease of $E_{d,tot}$: this is due to the fact that other components at the same time are causing a $\Delta E_{d,tot}$ of opposite sign respect the one caused by the k^{th}-component.
- $\pi_{k,i} = 0$: the k^{th}-component does not influence the variation of $E_{d,tot}$.
- $\pi_{k,i} < 0$: when the parameter x_i is changing, to a decrease in the exergy destruction in the component k corresponds an increase in the total exergy destruction of the plant, that is higher for high values, in absolute terms, of $\pi_{k,i}$.

Cycle n°1 and 2° (H_2/O_2)

	ε	E_d[kW]	E_d%	E'_d%
C (I)	*0.9124*	*17.79*	*0.31*	*0.13*
C (II)	*0.9273*	*18.46*	*0.32*	*0.13*
Intercooler	*0.0502*	*38.78*	*0.68*	*0.28*
Interc. C	0.8276	75.03	1.31	0.55
HPT	0.9280	348.27	6.08	2.54
MPT	0.9288	101.77	1.78	0.74
ST	0.9110	108.61	1.90	0.79
PUMP	0.7600	1.75	0.03	0.01
HRSG	0.7625	1346.51	23.51	9.81
cc1	0.7836	2528.84	44.14	18.42
cc2	0.8769	1217.81	21.26	8.87
$E_{d,tot}$		**5728.59**	**100.00**	**41.74**

Table 5: Syntesis of the exergetic analysis of Cycle n° 1

For the intercooled compressor the analysis has been performed first on each single stage and the connected intercooler, and then for the multistage machine as a whole, in order to evaluate the effect of intercooling on the exergetic efficiency: it is well known that intercooling reduces the overall power absorption, but the exergetic cost of the use of an external coolant is such that it decreases the total efficiency: all single stages have an ε higher than 90% and intercooling decreases this value to 82.7%. The thermodynamic reason is clear: heat is transferred to a cooler medium (the cooling water) and dispersed in the environment with no further recovery. However, it must be considered that the ratio between the power-gain obtained with the intercooling (ΔP) and the exergetic cost associated to it ($\Delta ex_{coolant}$) is much higher than one:

$\Delta P = P_{non\ interc} - P_{interc} = 496 - 442 = 54$ kW

$\Delta ex_{coolant} = 3.5$ kW

And therefore there is a global advantage, at process level, in adopting an intercooled configuration.

The major percentage of loss is found, as expected, in the two combustion chambers and in the heat-recovery exchanger (HRSG); the former enacts an irreversible process (the transformation of

chemical into thermal exergy); the lower the temperature of the reactants, the higher the exergy losses: the temperature of the mixture steam-O_2 at the inlet of the cc2 is 1050°C versus 500°C at the inlet of cc1: the value of E_d for this last component is in fact much higher than for cc2.
In the HRSG the losses are, percentage wise, even higher than in cc2: such a high value is caused by the high temperature difference between the two streams inside of the heat exchanger: both the terminal temperature differences and the LMTDs for the two media (gasification with superheating and re-superheating) are very high:
$LMTD_1$ (gas, sh)=236 °C; TTD_1 (gas,sh)= 615°C;
$LMTD_2$ (rh) = 200 °C; TTD_2 (rh) = 700°C.
Such an analysis is useful because it directly suggests a process modification: that of substituting the hypercritical boiler with a subcritical one, with more than one pressure level. With this latter solution the thermal profiles of the two streams are shifted towards lower LMTDs.
All turbines present a very high efficiency that, as expected, increases with the respective outlet temperatures: exergy evaluates not only the enthalpic term (real enthalpy drop with respect to the ideal one): in the term in the denominator of ε, that represents the exergy input in the machine, an entropic term is also present that accounts for the real conditions of the stream at the outlet and for the possibility that it can be still used for another thermodynamic process. For this reason, the higher the outlet temperature, the higher the exergetic efficiency (for equal inlet conditions).
For cycle (2) the typology and the distribution of the losses are similar to those of cycle (1) but result in a lower amount (E'd= 40.9%).

Cycle n°1: evaluation of CSB

In this section we shall examine the modification of the plant working conditions with a variation of the top cycle temperature: we shall do this by evaluating the values of the CSBs for each component. All the other working parameters imposed as input in the simulation have been maintained constant while T_{max} is changed about its nominal value of 1350°C (± 10%). All the analysis has been performed considering equal exergetic input for each test (equal fuel consumption); for each run all the variations of the working parameters not fixed as input (as the steam mass flow rate) have been registered in order to evaluate π.

It is well known that increasing the top cycle temperature leads to an increase of the overall plant efficiency; also from an exergetic point of view, it results that the total losses decrease. The analysis of the signs and of the magnitude of CSB are useful to examine which components provide a higher contribution to this improvement and which ones, on the contrary, present a trend of their losses E_k discordant with the $E_{d,tot}$: for the latter, a negative value of CSB means that the optimization of their configuration and characteristic working parameters cannot be conducted by varying the chosen parameter x_i (in this case T_{max}), because this causes negative effects on the overall plant performance. Figure 4 presents the trends of CSB for the components more influenced by the variation of T_{max}: the intercooled compressor is not interested at all by this parameter while HPT, MPT, LPT present CSB >>1, which reflect their secondary influence on the value of $E_{d,tot.}$. On the contrary it is interesting to investigate about the CSB of the other components; we can observe the following:
a) Combustion chambers: they presents opposite signs of CSB: to an increase of T_{max} corresponds a decrease of the exergy destruction (CSB>0) for the first cc and an increase for the second one (CSB<0). This can be justified as follows: considering equal total fuel consumption, the necessity of reaching higher temperature for the combustion products has opposite consequences on the streams that flow through the two chambers; in the first cc there is a decrease of the fuel consumption and a higher T_{max} is guaranteed by injecting a lower rate of steam as inert: limiting the fuel mass flow rate leads here to a decrease of the combustion irreversibility rate. In the second cc, even if the reactants enter with a higher value of enthalpy, it is however necessary, to increase the temperature of the products, to increase fuel consumption and consequently the irreversible conversion of chemical to thermal exergy.

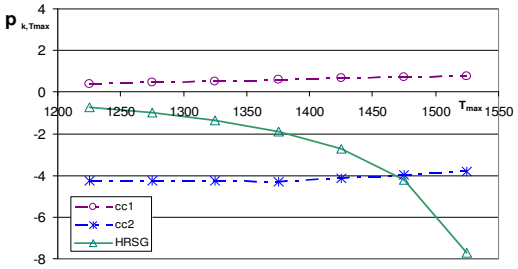

Figure 4: CSB for the components of Cycle 1.

b) HRSG: CSB<0, and its losses are always increasing with $T_{max.}$ This trend is due to the departure of the thermal profiles of the two streams, due to the fact that the hot gas outlet temperature (section n° 8 in Figure 1) is maintained equal for each test (to ensure equal inlet conditions into the pump) while the inlet temperature continues to increase. Consequently, the total heat transfer for unit of mass, q, is increasing in the exchanger. The outlet temperatures of the SH and RH steams (points 10 and 12) are maintained fixed because they represent respectively the value of the TIT for the ST and the temperature of the steam injected in the cc; this means that the higher value of q is exchanged with the external coolant in the phase of condensation and undercooling of the hot steam.
It is clear that, in a global perspective, a higher value of the top cycle temperature has positive effects on the plant performance; the negative value of the CSB characteristic of the HRSG is in fact more than counterbalanced by the value of the coefficients for the other components.
Such an analysis can guide designers' attention on the HRSG design: it is the only element that suffers from higher values of $T_{max,}$ and finding new solutions for its design could permit to better exploit the technological efforts connected with the reaching of higher TIT.

Cycle n°3 (ZECOTECH®)
The highest contribution to the total exergy destruction is again provided by the cc, the only one, in this case, of the plant. The losses in the HRSG on the contrary are much lower with respect to Cycles n°1 and 2, even if a direct comparison makes little sense due to the different connectivity.
The thermal profiles of the two streams are closer for the case 1350°C (LMTD=180°C) than for the case 1700°C (LMTD=260°C), and in this latter case the losses of the component are consequently higher (E_d=15%).

	ε	E_d	E_d%	E'_d%
C	0.9453	1125.7	3.22	1.48
HPT	0.9261	339.0	0.97	0.45
MPT	0.9530	2461.7	7.03	3.24
LPT	0.8967	875.0	2.50	1.15
PUMP	0.4746	182.4	0.52	0.24
HRSG	0.7718	4327.4	12.36	5.70
K	0.0517	642.7	1.84	0.85
cc	0.7855	25057.7	71.57	33.01
$E_{d,tot}$	-	***35011.6***	100.00	46.13

Table 6: Synthesis of the exergetic analysis of Cycle 3-T_{max} =1350°C

In percentage, the losses for the MPT are quite high; this is the turbine with the highest outlet temperature and also the highest efficiency (that is higher in the case of T_{max}=1700°C, ε=0.96); such high losses can be explained considering that while the MPT processes the entire mass flow rate of steam, only a fraction of the total mass flow rate flows in the other two turbines and in the compressor: 36% of the total is directed to the LPT and evolves in the HPT too, while the remaining 64% constitutes the flow rate of the compressor.

Cycle n° 3: evaluation of CSB
Even for this plant we shall evaluate the CSB considering the variation of $T_{max.}$ Figure 5 reports the results obtained by changing T_{max} around its nominal value and maintaining $p_{out,MPT}$ at the optimal value (1.5 bar).

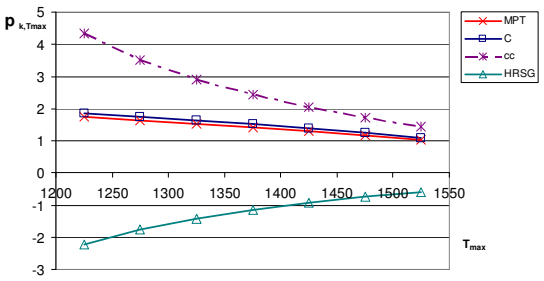

Figure 5: CSB for the components of Zecotech® Cycle, with a variation of T_{max}.

As expected, increasing the top cycle temperature leads to an improvement of the overall efficiency and it is accompanied by a decrease in the total exergy losses.
The components not displayed are those that are less influenced by a variation of T_{max} (LPT, HPT, K): the conditions of the streams at their inlet and outlet in fact remain constant during the tests (the TIT and expansion ratio of these two turbines are fixed as well as the outlet temperature of the water condensed), so that their decreasing losses are due only to the decrease of the steam mass flow rate in the plant.
The components which present CSBs closer to one have their performances more influenced by the variation of T_{max}, and this is the case for cc, MPT, HRSG and C (Figure 5). The cc and the MPT are directly influenced by this parameter, because it represents the gas outlet temperature of the burner and the inlet temperature of the downstream

turbine; the compressor is influenced only by the decrease of the steam mass flow rate (that is necessary to guarantee, with equal fuel consumption, a higher top cycle temperature), but more than the other components already analyzed: the decreasing steam rate is higher for the stream directed to the compressor than for the one fed into the LPT. Also in this plant, the HRSG has a negative CSB. It is possible to observe that the total heat transfer decreases with increasing T_{max}: the inlet condition of the water pumped (section 8, Figure 2) and the outlet temperature of the SH-steam (section 9) remain constant while the water mass flow rate decreases; the hot gas outlet temperature (section 4') is fixed too (because it coincides with the fixed LPT inlet temperature), while the inlet gas temperature (section 4) is increasing with T_{max}: the heat transfer is lower with respect to the base case because of the contemporary decreasing of the hot gas mass flow rate. Consequently, the growing irreversibility rate is due to the departure of the thermal profiles of the two streams.

CONCLUSION

The importance of the analysis of "innovative power cycles" has been discussed: the energy resources ought to be exploited with the maximum reachable efficiency compatible with the concepts of sustainability and eco-compatibility. The H_2-fed cycles examined belong to this new category of plant, but to define them as "high efficiency cycle" is not proper at all. The isolated power plants have demonstrated to have really high efficiency, but the analysis ought to be carried out considering all the sub-processes connected with the power generation unit: fuel treatment, gasification of coal, oxygen separation, CO_2 sequestration and removal. The principle of the exergetic analysis can highlight possible ways to follow to improve the plant design. The use of a complex simulation code proved to be a very useful instrument to execute all the necessary analysis, allowing for a fast and accurate evaluation of all the fundamental working parameters; moreover, the possibility of use a "home-made" code, CAMEL®, guaranteed a large flexibility of analysis: it has been used not only as a simple simulator of processes but even as a post-processing instrument for carrying out the desired energetic and exergetic analysis. It's necessary to complete the extension of the code to simulate the other sub-processes mentioned.

REFERENCES

[1] Anderson, R.E., Hoffman, L.C., Viteri, F., *Integration of Clean Energy System Technology with Air Separation Units, Gas Turbine and Steam Turbine into Zero-Emission Power Plants*, presented at Natural Gas Technologies Conf. II, Pointe South Mountain Resort, Phoenix Arizona, February 8-11, 2004.

[2] Bejan, A., Tsatsaronis, G., Moran, M., *Thermal design and optimization*, John Wiley & Sons Inc., New York, 1996.

[3] Calabrò, A., Fiorini, P., Girardi, G., Sciubba, E., *Exergy analysis of a CO_2 zero emission high efficiency plant*, Proc. ECOS 2004 Guanajuato, Mexico, July 7-9, 2004.

[4] Falcetta, M., Sciubba, E., "A Computational, Modular Approach to the Simulation of Power Plants", «Heat Recovery Systems & CHP», V.15, n°2, 1995.

[5] Falcetta, M., Sciubba, E., "Exergy Analysis of the Start-up Transient of a Combined Cycle Plant", Proc. ECOS 1998, Nancy, 8-10 July 1998.

[6] Gambini, M., Guizzi, G.L., Vellini, M., *H_2/O_2 Cycles: Thermodynamic Potentialities and Limits*, Proc. IJPGC'03, Atlanta, Georgia, USA, June 16-19, 2003.

[7] Kotas, T.J., *The exergy method of thermal plant analysis*, Krieger Publishing Company, Malabar Florida 1995.

[8] Lozza G, Chiesa P., *Natural gas decarbonisation to reduce CO_2 emission from combined cycle. Part 2: methansteam reforming.* ASME journal of Eng. For Gas Turbines and Power 2002; 124:89-95.

[9] Okamura, T., Koga, A., Itoh, S., and Kagagishi, H., *Evaluation of 1700 C Class Turbine Blades in Hydrogen Fueled Combustion Turbine Sysyem* (Toshiba Corp.), ASME 2000-GT-615, presented at the Int. Gas Turbine & Aeroengine Congr. & Exhib., Munich, Germany, May 8-11, 2000.

[10] Sciubba, E., *Lectures on turbomachinery*, EUROMA, Roma 2002.(in Italian).

[11] Szargut, J., Morris, D.H., Steward, F.R., *Exergy analysis of thermal, chemical, and metallurgical processes*, Spinger-Verlog, 1988.

Proceedings of ECOS 2005
Trondheim, Norway
June 20–22, 2005

EXERGY AND STRUCTURAL ANALYSIS OF AN ABSORPTION COOLING CYCLE AND THE EFFECT OF EFFICIENCY PARAMETERS

Dieter Boer[1]
Department of Mechanical Engineering; ETSEQ
University of Rovira i Virgili, Tarragona (Spain)

Marc Medrano, Miquel Nogués
Departament d'Informàtica i Enginyeria Industrial;
Universitat de Lleida; Lleida (Spain)

ABSTRACT

Absorption cycles are an alternative to compression cycles in cooling and refrigeration applications. The thermoeconomic analysis could contribute in improving their cost effectiveness. Our approach is based on the exergy and the structural analysis. Once the exergy analysis has been achieved by a structural analysis, the coefficients of structural bonds (CSB's) of the main heat and mass exchangers can be determined. The CSB's show how the modification of the irreversibility of one component, by means of a variation of its efficiency, affects the whole cycle. It will be wise to put much of the design effort in improving the efficiency of a component, knowing that a slight decrease of the irreversibility of that component, thanks to a higher efficiency, results in an important improvement in the total irreversibility of the cycle. This methodology is applied to a single effect ammonia-water absorption cooling cycle. We also study how the selection of efficiency parameters affects the results comparing CSB's of heat exchangers obtained from the minimum temperature differences or the UA-values.
Results show that the UA is a more suitable parameter than the minimum temperature difference. Concerning the CSB values, we obtain very high values for the condensate subcooler. Values above one are also observed for the absorber, condenser and generator. Lower values are found for the generator and the solution heat exchanger. A more detailed analysis should investigate the dependence of the CSB values on the range of efficiencies. As a further step, these results could be used in the thermoeconomic analysis and optimization.

Keywords: Absorption cycle, Ammonia-water, single effect, Cooling, model, Exergy Analysis, Structural Analysis, Thermoeconomic optimization, Coefficients of structural bonds

[1] Corresponding author: e-mail: Dieter.Boer@urv.net, phone (+34) 977 559631

NOMENCLATURE

CSB	Coefficients of structural bonds
CP	Product of mass flow and specific heat (kW K^{-1})
e	Specific exergy (kJ kg^{-1}, kJ $kmol^{-1}$)
$\dot{E}$	Exergy flow (kW)
h	Specific enthalpy (kJ kg^{-1})
$\dot{I}$	Irreversibility (kW)
$\dot{m}$	Mass flow
p	Pressure (bar)
$\dot{Q}$	Heat flow (kW)
R	Gas constant (kJ/kmol K)
s	Specific entropy (kJ kg^{-1} K^{-1})
T	Temperature (ºC or K)
UA	Product of heat transfer coefficient and heat transfer area (kW/K)
$\dot{W}$	Mechanical power (kW)
x_i	Parameter in the efficiency variation of the CSB, molar concentration
z	Concentration (mass fraction ammonia) (kg/kg)

Greek letters

γ	activity coefficient (-)

Indices

0	environmental state (25ºC, 1 bar)
ch	chemical
e	exit
i	inlet, component of the mixture
k	component k
ph	physical
t	total

Italic Numbers

1	Absorber
2	Condenser
3	Rectification reboiler (Generator)
4	Evaporator
5	Rectification condenser
6	Condensate subcooler
7	Solution heat exchanger
8	Solution pump
9	Refrigerant expansion valve
10	Solution expansion valves
11	Adiabatic rectification plates

INTRODUCTION

Cycles used for cooling and refrigeration are mostly based on mechanically driven compression cycles. As the cooling demand in summer in southern countries leads to a peak in electricity consumption, alternative technologies use should be favoured.

One possibility consists in absorption cycles ([1, 2]). Their principal advantages compared to mechanically driven compression cycles are that they use natural refrigerants and, consequently, they do not contribute to the destruction of the ozone layer, and that they are thermally driven and consume only a little electrical energy. Besides some circulating pumps do not have moving parts.

Absorption cycles use a working pair consisting on a refrigerant and an absorbent. Generally these are water-Lithiumbromide (LiBr) and ammonia-water. They are not contributing to the destruction of the ozone layer and to the global warming effect. The basic absorption cycle structure is the single effect, with four basic components: absorber, generator, evaporator and condenser.

One important drawback in the actuality is the comparatively higher initial cost of absorption cycles compared to compression cycles. In order to reduce the cost of the absorption cycles we try to apply the thermoeconomic analysis and optimisation in order to get more cost-effective designs ([3, 4]). This has been done to some extent for compression systems ([5-10]), but less for absorption systems ([11-14]).

In this work we will present how we use the structural method of thermoeconomic optimisation

The exergy analysis can simplify this optimization by structural coefficients ([15, 16]). They show how local irreversibilities in components affect the overall irreversibility rate of the cycle.

In our case we will use the coefficients of structural bonds (CSB). The CSB of a component k, which is obtained by a parameter x_i, is defined by

$$CSB_{k;i} = \left(\frac{\partial \dot{I}_t}{\partial \dot{I}_k} \right)_{xi=\text{var}} \quad (1)$$

I_k is the irreversibility rate of the component k, I_t is the Irreversibility rate or also called the exergy loss of the whole cycle. In order to obtain the CSB we study the effect of a variation of a parameter x_i, which can be an efficiency-related parameter, on the irreversibility rate in the component under consideration and on the whole cycle.

Structural coefficients consider how the irreversibility of the whole cycle changes when we modify the irreversibility of one component by means of a variation of its efficiency. If a slight decrease of the irreversibility of one component due to a higher efficiency causes an important improvement in the total irreversibility of the cycle, it will be wise to put much of the design effort in improving the efficiency of this component. In the case of a high coefficient of structural bonds the benefit of a more efficient and thus more expensive component on the performance of the whole cycle will be considerable. Otherwise, if the coefficient of structural bonds is low, near unity, an improvement of the efficiency of the considered component is not economically worthwhile.

Modelling starts with first law analysis ([17-20]). Once obtained the corresponding results we can achieve the exergy analysis in order to obtain the irreversibilities ([21-24]). Now we can achieve the structural analysis using the coefficients of structural bonds.

In our study this methodology will be applied to an ammonia-water single effect cycle.

DESCRIPTION OF THE ABSORPTION CYCLE

Figure 1 shows a single-effect ammonia-water absorption cycle. The components are numbered in italics. Basic components are the absorber (*1*), the condenser (*2*), the generator (*3*), and the evaporator (*4*). The cycle is completed by the condensate subcooler (*6*), the solution heat exchanger (*7*), the condenser of the rectification column (5) and the adiabatic rectification plates. There are three adiabatic plates, which is the optimum number for this configuration ([20]).

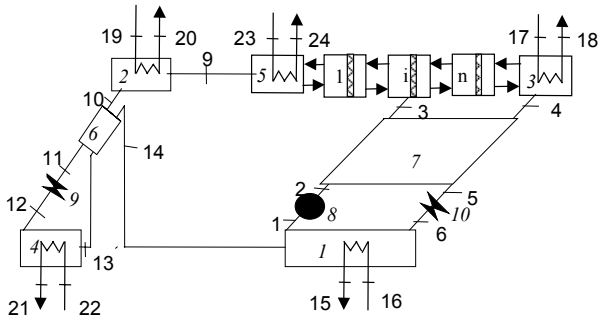

Figure 1: Single effect absorption cycle

The figure presents the cycle in a pressure-temperature plot. The pressure increase upwards and temperatures increase to the left. In the following description cursive letters refer to the components, normal ones to the state points.

The solution circulates between the absorber (*1*), where the refrigerant is absorbed at low pressure, and the generator (*3*), where the refrigerant is desorbed at high pressure (state points 1 to 6). The strong solution leaves the absorber (*1*), is preheated in the solution heat exchanger (*7*), and enters the rectification column in central plate two. Temperature and water concentration increases from plate one to plate three. The generator acts as the reboiler of the rectification column. The weak solution (4) leaves towards the absorber. In the condenser of the rectification column, we obtain the necessary liquid reflux, while the rest of the vapour (9) condenses completely in the condenser (10) and is cooled in the condensate subcooler (*6*). The condensate expands in the refrigerant throttle valve and enters the evaporator(*4*). Due to the water content of the mixture, the evaporation takes place with a temperature glide. The temperature increases during the vaporisation process as the liquid contains less and less ammonia, which is the more volatile component. Vaporisation in the evaporator is only partial. For total evaporation, the temperature glide would be too high. The cycle is closed when the vapour with a small liquid fraction (13) passes through the condensate subcooler (*6*) and enters the absorber (*1*). Streams 15 to 22 are the external heat transfer fluids (in all cases we assume this is water), which deliver or extract the heat.

The useful production of cooling takes place in the evaporator (*4*), heat is supplied in form of hot water to the generator (*7*), and heat is dissipated at an intermediate temperature in condenser (*2*) and absorber (*1*).
To obtain the necessary pressure changes, the cycles include the solution pump (*8*), the refrigerant expansion valve (*9*) and solution expansion valve (*10*).

Methodology of simulation for absorption cycle
A thermodynamic model was developed for the absorption cycle using the program Engineering Equation Solver (EES). Properties for ammonia water are given by Tillner-Roth and Friend [25].
We evaluated properties for all state point including specific exergies. After conducting the exergy analysis, we computed the irreversibilities.

The input data, output data, main assumptions and operating conditions are presented below.

The input data are:
- The cooling power of the evaporator, which is fixed in all calculations
- The inlet and outlet temperatures of the external fluids
- The minimum temperature difference in the heat and mass exchangers

The output data are:
- The pressures, temperatures, concentrations, mass flows, enthalpies, entropies and exergies of each current
- The thermal or, in the case of the solution pump, mechanical power and irreversibility rate of the main components.
- The COP and exergetic efficiency

The main assumptions are:
- Steady state
- There are no heat losses
- There are no pressure losses
- The refrigerant leaving the condensers is saturated liquid
- The solution leaving the generators is boiling
- The solution leaving the absorber is saturated
- On adiabatic rectification, plates leaving liquid and vapour are in equilibrium
- The solution and refrigerant valves are adiabatic

The operating conditions are:
- Evaporator cooling capacity 1000 kW

Temperatures:
- Chilled water inlet/outlet 6/12ºC
- Cooling water (parallel flow through absorber and condenser inlet/outlet) 27/35ºC
- Hot water inlet 90ºC
- Minimum temperature difference in the heat exchangers 5 K

The hot water outlet temperature is adjusted to minimise the CP-mismatch in the generator.

Steady state mass and energy balances for the components of the cycles are established as follows:
Global mass balance:

$$\Sigma \dot{m}_i = \Sigma \dot{m}_e \qquad (2)$$

Mass balance for ammonia:

$$\Sigma \dot{m}_i z_i = \Sigma \dot{m}_e z_e \qquad (3)$$

Energy balance:

$$0 = \dot{Q} - \dot{W} + \sum_i \dot{m}_i h_i - \sum_e \dot{m}_e h_e \qquad (4)$$

Exergy balance:

$$0 = \sum_i (1 - \frac{T_0}{T_i})\dot{Q}_i - \dot{W} + \sum_i \dot{m}_i e_i - \sum_e \dot{m}_e e_e - \dot{I} \qquad (5)$$

Specific exergy (eq.6) is made up of a physical (eq.7) and a chemical component (eq.8).

$$e = e_{ph} + e_{ch} \qquad (6)$$

$$e_{ph} = h - h_0 - T_0(s - s_0) \qquad (7)$$

$$e_{ch} = \sum_i x_i e_{ch,i} + RT_0 \sum_i x_i \ln(\gamma_i x_i) \qquad (8)$$

The properties indicated with the subscript 0 refer to the environmental state, which is defined as 25ºC and 1bar.

RESULTS AND DISCUSSION

Energetic analysis
Results of the energetic analysis for the different state points are presented in Table 1. These results

as well as the results for exergy analysis are obtained by fixing a minimum temperature difference in the heat exchangers of 5K, with the exception of the rectifier condenser, which has a minimum temperature difference of 20K.

State point	T [C]	p [bar]	z [kg/kg]	m [kg/s]	h [kJ/kg]	e [kJ/kg]
1	32	4,45	0,519	5,048	72,01	27,32
2	32,1	12,36	0,519	5,048	72,99	28,29
3	68,7	12,36	0,519	5,048	259,4	43,41
4	85	12,36	0,422	4,201	289	61,09
5	37,1	12,36	0,422	4,201	64,92	37,16
6	37,2	4,45	0,422	4,201	64,92	36,26
9	47	12,36	0,999	0,847	1678	189,6
10	32	12,36	0,999	0,847	493,1	160,4
11	19,3	12,36	0,999	0,847	432,4	160,3
12	1	4,45	0,999	0,847	432,4	155,9
13	7	4,45	0,999	0,847	1613	53,47
14	27	4,45	0,999	0,847	1674	51,69
15	27	1	0	63,486	113,3	0,0279
16	32	1	0	63,486	134,2	0,3382
17	90	1	0	21,503	377,1	26,05
18	74,5	1	0	21,503	311,9	15,56
19	27	1	0	48,011	113,3	0,0279
20	32	1	0	48,011	134,2	0,3382
21	12	1	0	39,71	50,51	1,222
22	6	1	0	39,71	25,32	2,652
23	27	1	0	3,664	113,3	0,0279
24	32	1	0	3,664	134,2	0,3382

Table 1: Results of energetic analysis

Exergy analysis

The next step was the exergy analysis. After determining the exergies of the state points, we conducted the exergy analysis. Irreversibilites for the main components are shown in Table 2.

The highest irreversibilities are found in the absorber (*1*), followed by the evaporator (*4*), the solution heat exchanger (*7*) and the generator (*3*). This already includes nearly all the main heat exchangers. The irreversibility of condenser (*2*) and the condenser of the rectification column (*5*) were lower. Smaller contributions were made by the condensate subcooler, the solution pump (*8*) and the expansion valves (*9* and *10*). Irreversibilities in the adiabatic rectification plates (*11*) were also low. Table 3 present exergy in- and output to main components, including as reference also their thermal power and the design UA value.

Component	$\dot{I}$ [kW]
1	38,5
2	9,82
3	18,1
4	30,0
5	6,23
6	1,61
7	24,2
8	3,29
9	3,68
10	3,80
11	1,97

Table 2. Irreversiblities of the components of the absorption cycle.

component	$\dot{Q}$ [kW]	UA [kW K^{-1}]	Exergy Input [kW]	Exergy Output [kW]	$\dot{I}$ [kW]
1	1327	259,8	58,2	19,7	38,5
2	1003	110,2	24,7	14,9	9,8
3	1402	280,4	225,6	207,4	18,2
4	1000	200	86,8	56,8	30

Table 3. Energy and exergy flow of main components (in kW) .

The irreversibilities are interesting information as they indicate us where exergy is destroyed. But their usefulness is limited in the sense that they do not show the best way to improve the cycle. For example it is not necessarily the best choice to increase the efficiency of the component with the highest irreversibility, in our case the absorber, as we do not know the interactions with the rest of the system.

Structural analysis

Once the irreversibilities are obtained, we can check how a change of the irreversibility of one component affects the rest of the cycle. This is done using the coefficients of structural bonds, as proposed by [15, 16]. In our case this means that we will vary the efficiency of the different heat

exchangers maintaining the efficiencies of the others constant. We will compare two different approaches. In the first one we use as parameter the minimum temperature difference ΔT_{min}, which will be varied in one component and fixed in the others. In the second case we will use the value of UA for the same purpose.

Figure 2 represents a plot of the irreversibility in the absorber versus the total irreversibility for different minimum temperature differences. We also include on the right scale the corresponding values of ΔT_{min}. As pressure loss is neglected with lower ΔT_{min} the irreversibility of the absorber is reduced. But more interesting is in which way the total irreversibility is affected. This information can be obtained quantitatively by the CSB:

$$CSB_{A;\Delta T_{\min,A}} = \left(\frac{\partial \dot{I}_t}{\partial \dot{I}_A} \right)_{\Delta T_{\min,A}=\text{var}} \qquad (9)$$

We achieved in Figure 2 a lineal interpolation of the values of I[1] versus I_t. The value of 1,51 represents the slope and gives us the mean values of the CSB of the absorber. This means if the irreversibility of the absorber can be reduced by 1kW due to an efficiency increase, the total irreversibility will decrease by 1,51kW. So the benefit for the total cycle is even greater than for the component due to their interactions.

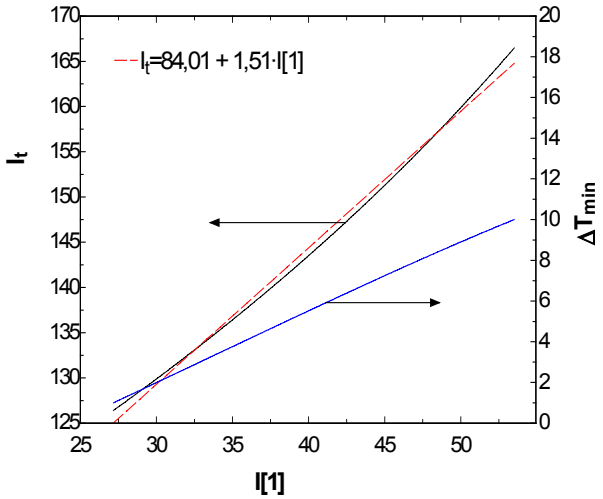

Figure 2 Irreversibility of the Absorber versus total Irreversibility varying ΔT_{min}

Figure 3 represents a similar plot with the difference that the parameter which is varied is UA of the absorber, and the UA-values of the other components are fixed. In order to be able to compare both figures we plotted in the right scale also the corresponding ΔT_{min} values.

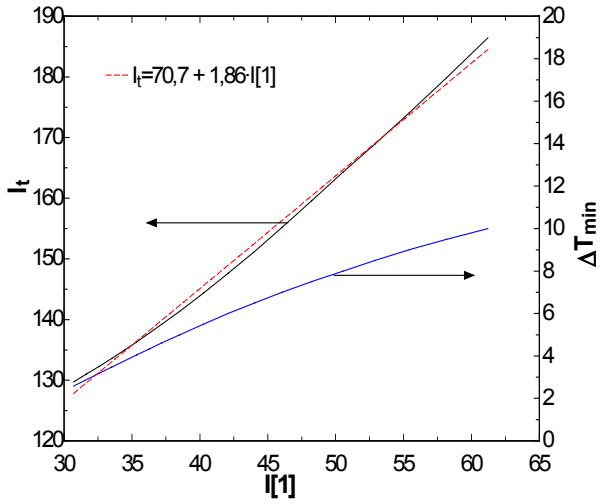

Figure 3 Irreversibility of the Absorber versus total Irreversibility varying UA

The CSB is now defined by

$$CSB_{A;UA_A} = \left(\frac{\partial \dot{I}_t}{\partial \dot{I}_A} \right)_{UA_A=\text{var}} \qquad (10)$$

The value obtained by a lineal interpolation is 1,86, which differs considerably from the formerly obtained value. The difference lies in the behavior of the other components. In the case of fixing ΔT_{min} their efficiencies will remain similar, but their exchange area can be different. In the case of fixing UA their size will be similar, but not their efficiencies. Table 4 presents the results for both parameters, which in some cases differs significantly.

Component number	ΔT_{min} [K]	UA [kW/K]
1	1,51	1,86
2	1,30	1,62
3	0,66	0,875
4	1,43	1,76
6	8,34	9,99
7	2,83	0,80

Table 4 Coefficients of structural bonds CSB for main components of the cycle

But which is the better parameter choice? Our purpose is the use of the CSB in the thermoeconomic optimization of the components. Thus we would like to know how the change of the design parameters of one component affects the whole cycle, while the rest of the cycle is unchanged. The term unchanged fits better to the parameter UA, as this means constant capital cost of the other components. So for us results obtained by variation of UA are more useful.
It is also worthwhile to observe the values. For example, it seems especially interesting to improve the condensate subcooler having a CSB of nearly 10. We can explain this the following way: As a design parameter we fix the cooling output. As a better condensate subcooler achieves lower enthalpies in the inlet of the evaporator, we need less refrigerant to obtain the needed cooling power. Proportionally to the refigerant flow also the solution flow rates will be reduced, and maintaining the UA of the heat exchangers their efficiency will increase.
In similar ways the CSB's of the other components can be explained. These results will be discussed in more detail in a later publication.

CONCLUSIONS

In our work we achieved the energy, exergy and structural analysis of an ammonia-water single effect cooling cycle. The exergy analysis helps us to determine the irreversibilities of the components of the cycle and the total cycle. As a further step we achieve the structural analysis using the coefficients of structural bonds. They indicate us how the irreversibility change in one component affects the rest of the system. The effect of two different parameters have been tested and compared: the minimum temperature difference in the heat exchangers and their UA value. We concluded that for the purpose of a thermoeconomic optimization of the cycle the UA values are more appropriate, as fixing the UA value of a component its capital cost is approximately constant.
Other interesting results of our work are the values of the CSB, which in the case of some components show relatively high values. In the case of a high coefficient of structural bonds the benefit of a more efficient and thus more expensive component on the performance of the whole cycle will be considerable.
This work will be continued for other cycle configurations. Once a set of CSB's is obtained they can be used in the optimization of the components.

ACKNOWLEDGEMENTS

This research project is financially supported by the "Ministerio de Ciencia y Tecnología – Dirección general de investigación" (DPI2002-00706).

REFERENCES

[1] Herold, K., R. Radermacher, and K. SA, *Absorption chillers and heat pumps*, ed. CRC Press. 1996.
[2] Ziegler, F., *State of the art in sorption heat pumping and cooling technologies.* International Journal of Refrigeration, 2002. **25**: 450-459.
[3] Bejan, A., G. Tsatsaronis, and M. Moran, *Thermal Design & Optimization*, ed. N.Y. John Wiley & Sons Inc. 1996.
[4] Kotas, T., *The Exergy Method of Thermal Plant Analysis*, ed. M. Krieger Publishing Company, Florida. 1995.
[5] Dentice d'Accadia, M. and F. de Rossi, *Thermoeconomic optimization of a refrigeration plant.* International Journal of Refrigeration, 1998. **21**(3): 42-54.
[6] Dentice d'Accadia, M. and L. Vanoli, *Thermoeconomic optimisation of the condenser in a vapour compression heat*

pump,. International Journal of Refrigeration, 2004. **27**(4): 433-441.
[7] Dingeç, H. and A. Leri, *Thermoeconomic optimization of simple refrigerators.* International Journal of Energy Research, 1999. **23**(11): 949-962.
[8] Ferrer, M.A., M.A. Lozano, and R. Tozer, *Thermoeconomics applied to Air-Conditioning Systems.* ASHRAE Transactions AT-01-9-2, 2001.
[9] Wall, G., *Thermoeconomic optimisation of a heat pump system*. 1995.
[10] Zhang, G.Q., et al., *Thermoeconomic optimization of small size central air conditioner.* Applied Thermal Engineering, 2004. **24**(4): 471-485.
[11] Misra, R.D., et al., *Thermoeconomic optimization of a single effect water/LiBr vapour absorption refrigeration system.* International Journal of Refrigeration, 2003. **26**(2): 158-169.
[12] Sahin, B. and A. Kodal, *Thermoeconomic optimization of a two stage combined refrigeration system: a finite-time approach.* International Journal of Refrigeration, 2002. **25**(7): 872-877.
[13] Tozer, R. and M.A. Lozano. *Thermo-economic optimisation of a single effect absorption chiller and cooling tower.* in *International Sorption Heat Pump Conference. Munich:ZAE Bayern*. 1999.
[14] Boer, D., M. Medrano, and M. Nogues. *Structural analysis of triple effect water-LiBr absorption cooling cycles*. in *3rd International Heat Powered Cycles Conference*. 2004. Larnaca (Cipre).
[15] Beyer, J., *Strukturuntersuchungen-notwendiger Bestandteil der Effektivitaetsanalyse von Waermeverbrauchersystemen.* Energieanwendung, 1970. **19**(12): 358-361.
[16] Beyer, J., *Struktur wärmetechnischer Systeme und ökonomische Optimierung der Systemparameter.* Energieanwendung, 1974. **23**(9): 274-279.
[17] Chua, H.T., H.K. Toh, and K.C. Ng, *Thermodynamic modeling of an ammonia–water absorption chiller.* International Journal of Refrigeration, 2002. **25**(7): 896-906.
[18] Fernandez-Seara, J. and M. Vazquez, *Study and control of the optimal generation temperature in NH3-H2O absorption refrigeration systems.* Applied Thermal Engineering, 2001. **21**: 343-357.
[19] Fernández-Seara, J., J. Sieres, and M. Vázquez, *Distillation column configurations in ammonia–water absorption refrigeration systems.* International Journal of Refrigeration, 2003. **26**(1): 28-34.
[20] Laouir, A., P. LeGoff, and J.-M. Hornut, *Cycles de frigopompes à absorption en cascades matérielles - détermination du nombre d'étages optimal pour le mélange ammonoiac–eau: Absorption heat pump cycles using an ammonia-water mixture and linked in a material cascade.* International Journal of Refrigeration, 2002. **25**(1): 136-148.
[21] Ataer, O.E. *Exergy Analysis Of An Aqua-Ammonia Absorption Refrigeration System*. in *Progress In The Science And Technology Of Refrigeration In Food Engineering. Dresden, Germany*. 1990.
[22] Best, R., J. Islas, and M. Martinez, *Exergy Efficiency Of An Ammonia-Water Absorption System For Ice Production.* Applied Energy, 1993. **45**: 241-256.
[23] Ercran, Ö. and Y. Gögus, *Comparative study of irreversibilities in an aqua-ammonia absorption refrigeration system.* International Journal of Refrigeration, 1991. **14**(2): 86-92.
[24] Karakas, A., N. Egrican, and S. Uygur, *Second law analysis of solar absorption-cooling cycles using Lithium Bromide/Water and Ammonia/Water as Working Fluids.* Applied Energy, 1990. **37**: 169-197.
[25] Tillner Roth, R. and D.G. Friend, *Survey and assessment of available measurements on thermodynamic properties of the mixture water + ammonia.* J. Phys. Chem. Ref. Data, 1998. **27**(1): 45-61.

Proceedings of ECOS 2005
Trondheim, Norway
June 20–22, 2005

EXERGETIC ANALYSIS OF A CRYOGENIC REFRIGERATION SYSTEM

Alexandru Dobrovicescu

University POLYTECHNICA of Bucharest
Faculty of Mechanical Engineering
Department of Thermodynamics and Refrigeration Systems
Splaiul Independentei 313, Sect 6, Bucharest, Romania
e-mail: dobrovicescu@yahoo.com

ABSTRACT

The paper deals with the problem of the optimized design and conduct of a Claude refrigeration system. The performance of the system is related to the technical characteristics of the key pieces of the refrigeration equipment and is based on the laws of variation of the shares of the exergy destructions in the mechanical work input.
The studied working conditions have resulted from the optimization of the throttling stage after eliminating the technical incompatible variants from the point of view of the heat transfer in the recuperative stage.
This detailed analysis, based on the exergetic balance equation, succeeds in rendering evident the optimum design and operating condition of the whole cryogenic system.
Keywords: cryogenics, optimization, exergy, recuperative heat exchanger

NOMENCLATURE

A	heat exchange area [m^2]
An	anergy [J]
C	cooler
Cp	compressor
d	tube diameter [m]
E	heat exchanger
Ex	expander
$\hat{E}x$	exergy [J/(kg of compressed gas)]
ex	specific exergy [J/kg]
F	fraction of the compressed gas flow expanded in the expander [(kg of expanded gas)/(kg of compresed gas)]
f	friction factor
$\hat{I}$	exergy destruction due to internal irreversibility [J/(kg of compressed gas)]
i	specific exergy [J/kg]
K	compressor mechanical work input for 1 kJ of refrigeration duty
L	tube length [m]
$\hat{L}$	exergy loss [J/(kg of compressed gas)]
l	specific exergy loss [J/kg]
$\dot{m}$	mass rate [kg/s]
n	number of tubes in the flow direction
P	power input for 1 kW of refrigeration duty
p	pressure [N/m^2]
$\hat{Q}$	heat [J/(kg of compressed gas)]
$\hat{Q}_0$	refrigeration load [J/(kg of compressed gas)]
RC	refrigeration chamber
T	absolute temperature [K]
TV	throttle valve
$\hat{W}$	shaft work [J/(kg of compressed gas)]
w	specific shaft work [J/kg]
x_1	radial path
x_2	axial path
ΔP	pressure drop [N/m^2]
ΔT	temperature difference [K]
ΔT_n	temperature difference at the warm extremity of the heat exchanger [K]

η_{Ex} exergetic efficiency, isentropic efficiency of the expander

η_m part of the expander mechanical work returned to the cycle

η_T isothermal efficiency of the compressor

ξ_c coefficient accounting for the tube curvature

ρ density [kg/m^3]

Ω mass velocities ratio

Subscripts

0 environment

c Carnot

cp compressor

Ex expander

f forward gas stream

r return gas stream

v evaporation

R refrigeration

Q heat

Q_0 heat extracted from the refrigeration chamber

Q_s heat inleak due to imperfect insulation

Q_n unrecovered heat

ΔP pressure drop

ΔT temperature difference

INTRODUCTION

The comparative study based on the irreversibility of the working process shows that a way to improve the performance of the Linde refrigeration system is precooling of the forward cryogenic stream with an independent system or by its adiabatic expansion in an expander.

REFRIGERATION CYCLE FLOW DIAGRAM

Figure 1 presents the flow diagram and the T-s diagram for a refrigeration system by adiabatic expansion and throttling with the expander connected in parallel.

The exergetic analysis of the recuperative stage that operates below the environmental temperature reveals that the exergy destruction, that is equal to the anergy generation, increases with the decrease in temperature (eq. 1)

$$I = An_{gen} = T_0 \frac{Q}{T} \qquad (1)$$

Because the major cause of irreversibility is the temperature difference in the recuperative heat exchanger, this should decrease with temperature [1,2].

The expander of the Claude cryogenic system achieves this desideratum by precooling the return current and by the reduction of the incoming mass flow rate in the heat exchanger of the recuperative stage.

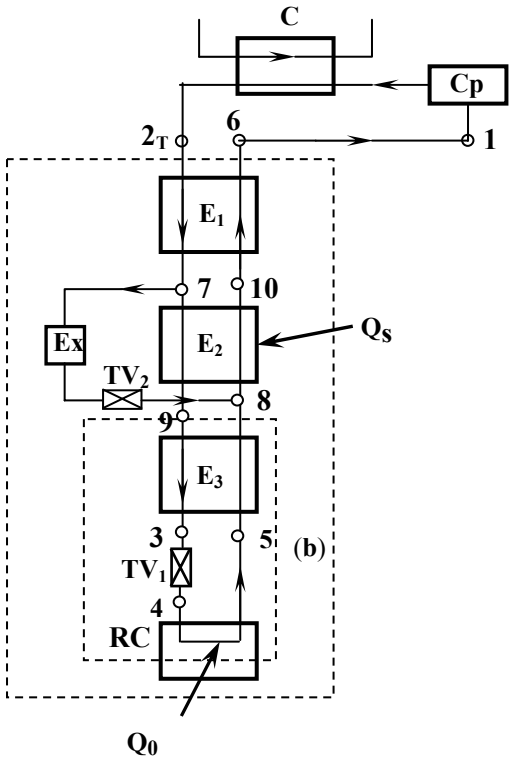

Figure 1,a

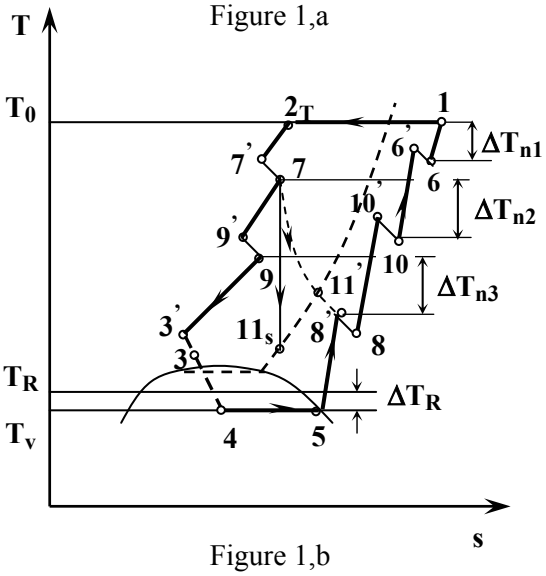

Figure 1,b

For 1kg/s of compressed gas the study was performed under the following assumptions:

- the gas is compressed in the compressor *Cp* and then cooled in the cooler *C* to the temperature of the surroundings $T_0 = T_{2T}$;
- the temperature difference ΔT_n at the warm end of the heat exchangers is due to the finite size of the apparatuses;

- for the engine expansion cycle (*Figure* 1,a) for every 1kg/s of compressed gas a fraction *F* is led to the expander *Ex* where is adiabatically expanded, producing mechanical work and cooled down; the rest is cooled in the recuperative heat exchangers *E*2 and *E*3 and then throttled in *VL*1.
- the pressure drops in the recuperative heat exchangers are schematized by throttlings.

EXERGETIC BALANCE

The exergetic balance equation [3] for 1kg/s of compressed gas gives:

$$\sum \hat{\mathrm{E}}\mathrm{x}_{\mathrm{Q}} = \hat{\mathrm{W}} + \sum \hat{\mathrm{I}} \qquad (2)$$

where

$$\sum \hat{\mathrm{E}}\mathrm{x}_{\mathrm{Q}} = \hat{\mathrm{E}}\mathrm{x}_{\mathrm{Q_0}} + \mathrm{ex}_{\mathrm{Qs1}} + \mathrm{ex}_{\mathrm{Qs2}} + \hat{\mathrm{E}}\mathrm{x}_{\mathrm{Qs3}} + \\ + \mathrm{ex}_{\mathrm{Qn1}} + \mathrm{ex}_{\mathrm{Qcp}} \qquad (3)$$

represents the sum of the heat exergies exchanged with the surroundings by 1kg/s of compressed gas while undergoing the refrigeration cycle (indices *1,2,3* refer to the engine expansion stage (*1,2*) and throttling expansion stage (*3*) respectively);

$$\sum \hat{\mathrm{W}} = \mathrm{w}_{\mathrm{cp}} + \hat{\mathrm{W}}_{\mathrm{Ex}} = -\left|\mathrm{w}_{\mathrm{cp}}\right| + \hat{\mathrm{W}}_{\mathrm{Ex}} \qquad (4)$$

is the whole technical mechanical work composed of the expended work w_{cp} in the compressor and the produced mechanical work in the expander $\hat{W}_{Ex}$;

$$\sum \hat{\mathrm{I}} = \mathrm{i}_{\Delta \mathrm{Pf1}} + \hat{\mathrm{I}}_{\Delta \mathrm{Pf2}} + \hat{\mathrm{I}}_{\Delta \mathrm{Pf3}} + \mathrm{i}_{\Delta \mathrm{Pr1}} + \\ + \mathrm{i}_{\Delta \mathrm{Pr2}} + \hat{\mathrm{I}}_{\Delta \mathrm{Pr3}} + \mathrm{i}_{\Delta \mathrm{T1}} + \hat{\mathrm{I}}_{\Delta \mathrm{T2}} + \hat{\mathrm{I}}_{\Delta \mathrm{T3}} + \\ + \hat{\mathrm{I}}_{\mathrm{t}} + \hat{\mathrm{I}}_{\mathrm{Ex}} + \hat{\mathrm{I}}_{\mathrm{ti}} + \mathrm{i}_{\mathrm{cp}} \qquad (5)$$

where the terms from the right hand member represent in order the exergy destructions due to: pressure drops in the forward $\left(\hat{I}_{\Delta P_f}\right)$ and return $\left(\hat{I}_{\Delta P_r}\right)$ gas streams of the recuperative heat exchangers, heat transfer at a finite temperature difference between the two currents of gas $\left(\hat{I}_{\Delta T}\right)$, throttle expansion in the throttling valve $\left(\hat{I}_t\right)$, compression process $\left(\hat{I}_{cp}\right)$ and expansion in the expander $\left(\hat{I}_{Ex}\right)$.

Inserting Equations. 3-5 into Equation. 2, gives:

$$\left|\mathrm{w}_{\mathrm{cp}}\right| = -\hat{\mathrm{E}}\mathrm{x}_{\mathrm{Q_0}} - \mathrm{ex}_{\mathrm{Qs1}} - \mathrm{ex}_{\mathrm{Qs2}} - \hat{\mathrm{E}}\mathrm{x}_{\mathrm{Qs3}} - \\ - \mathrm{ex}_{\mathrm{Qn1}} - \mathrm{ex}_{\mathrm{Qcp}} + \hat{\mathrm{W}}_{\mathrm{Ex}} + \mathrm{i}_{\Delta \mathrm{Pf1}} + \hat{\mathrm{I}}_{\Delta \mathrm{Pf2}} + \\ + \hat{\mathrm{I}}_{\Delta \mathrm{Pf3}} + \mathrm{i}_{\Delta \mathrm{Pr1}} + \mathrm{i}_{\Delta \mathrm{Pr2}} + \hat{\mathrm{I}}_{\Delta \mathrm{Pr3}} + \mathrm{i}_{\Delta \mathrm{T1}} + \\ + \hat{\mathrm{I}}_{\Delta \mathrm{T2}} + \hat{\mathrm{I}}_{\Delta \mathrm{T3}} + \hat{\mathrm{I}}_{\mathrm{t}} + \hat{\mathrm{I}}_{\mathrm{Ex}} + \hat{\mathrm{I}}_{\mathrm{ti}} + \mathrm{i}_{\mathrm{cp}} \qquad (6)$$

In *Equation* 6 the heat exergies have the following significance:

- $-\hat{\mathrm{E}}\mathrm{x}_{\mathrm{Q_o}} = \left|\hat{\mathrm{E}}\mathrm{x}_{\mathrm{Q_o}}\right|$, represents the exergy of the cooling capacity at the temperature level T_v, with the significance of the minimum work consumption necessary to undergo an inverse Carnot cycle limited by the evaporation temperature T_v and the surroundings temperature T_0;
- $-\hat{\mathrm{E}}\mathrm{x}_{\mathrm{Q_s}} = \left|\hat{\mathrm{E}}\mathrm{x}_{\mathrm{Qs}}\right| = \hat{\mathrm{L}}_{\mathrm{Q_s}}$, represents the lost exergy from imperfect thermal insulation;
- $-\mathrm{ex}_{\mathrm{Qn1}} = \left|\mathrm{ex}_{\mathrm{Qn1}}\right| = \mathrm{l}_{\mathrm{Qn1}}$, denotes the lost exergy with the heat coming from outside in process (6-1) and so unrecovered from the forward stream;
- $-\mathrm{ex}_{\mathrm{Qcp}} = \left|\mathrm{ex}_{\mathrm{Qcp}}\right| = \mathrm{l}_{\mathrm{cp}}$, represents for the compressor, the exergy of the heat transferred to the refrigeration system (a loss).

Taking into account the exergy destruction from heat transfer across a finite temperature difference $\Delta T_R = T_R - T_v$ in the refrigerating chamber $\hat{I}_{\Delta T_R} = \left|\hat{E}x_{Q_0}^{T_v}\right| - \left|\hat{E}x_{Q_R}^{T_R}\right|$, where $\hat{E}x_{Q_R}^{T_R}$ represents the exergy of the specific refrigerating power $\hat{Q}_0 = \hat{Q}_R$, at the temperature level T_R, and denoting that $(i,l)_{cp} = i_{cp} + l_{cp}$, *Equation* 6 becomes:

$$\left|\hat{\mathrm{W}}\right| = \left|\hat{\mathrm{E}}\mathrm{x}_{\mathrm{Q_R}}^{\mathrm{T_R}}\right| + \hat{\mathrm{I}}_{\Delta \mathrm{TR}} + \mathrm{l}_{\mathrm{Qs1}} + \mathrm{l}_{\mathrm{Qs2}} + \hat{\mathrm{L}}_{\mathrm{Qs3}} + \mathrm{l}_{\mathrm{Qn1}} + \\ + \mathrm{i}_{\Delta \mathrm{Pf1}} + \hat{\mathrm{I}}_{\Delta \mathrm{Pf2}} + \hat{\mathrm{I}}_{\Delta \mathrm{Pf3}} + \mathrm{i}_{\Delta \mathrm{Pr1}} + \mathrm{i}_{\Delta \mathrm{Pr2}} + \hat{\mathrm{I}}_{\Delta \mathrm{Pr3}} + \\ + \mathrm{i}_{\Delta \mathrm{T1}} + \hat{\mathrm{I}}_{\Delta \mathrm{T2}} + + \hat{\mathrm{I}}_{\Delta \mathrm{T3}} + \hat{\mathrm{I}}_{\mathrm{t}} + \hat{\mathrm{I}}_{\mathrm{Ex}} + \hat{\mathrm{I}}_{\mathrm{it}} + \mathrm{i}_{\mathrm{cp}} = \\ = \left|\hat{\mathrm{E}}\mathrm{x}_{\mathrm{Q_R}}^{\mathrm{T_R}}\right| + \sum_{1}^{14} \hat{\mathrm{I}}_{\mathrm{j}} + \sum_{1}^{4} \hat{\mathrm{L}}_{\mathrm{k}} \qquad (7)$$

where $\left|\hat{W}\right| = \left|w_{cp}\right| - \eta_m \cdot \hat{W}_{Ex}$ represents the mechanical work expended in the refrigeration cycle and $\hat{I}_{Ex} = (1 - \eta_m)\hat{W}_{Ex}$, the lost part of the mechanical work produced by the expander.

COEFFICIENTS OF PERFORMANCE FOR THE CLAUDE REFRIGERATION CYCLE

Exergetic efficiency

$$\eta_{\mathrm{Ex}} = \frac{\left|\hat{\mathrm{W}}_{\min \mathrm{C}}\right|}{\left|\hat{\mathrm{W}}\right|} = \frac{\left|\hat{\mathrm{E}}\mathrm{x}_{\mathrm{Q_R}}^{\mathrm{T_R}}\right|}{\left|\hat{\mathrm{W}}\right|} = 1 - \sum(\hat{\mathrm{I}}, \hat{\mathrm{L}}) \qquad (8)$$

Specific mechanical work input

$$K = \frac{\left|\hat{W}\right|}{\hat{Q}_R} = \frac{T_0 / T_R - 1}{1 - \sum\left(\hat{I}, \hat{L}\right)} \qquad (9)$$

OPTIMIZATION OF THE CRYOGENIC SYSTEM OPERATING

The considered refrigeration system (*Figure* 1) is equipped with coil type recuperative heat exchangers [4] (*Figure* 2). The forward (high pressure) gas stream flows inside the tubes.

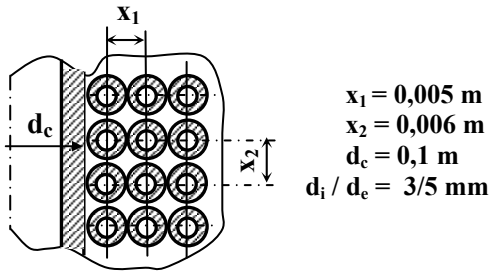

Figure 2

For this type of heat exchanger the heat transfer characteristics and gas-dynamic resistance are given by the following equations:

- for the forward gas stream

$$\Delta p_f = f_f \frac{L_m \cdot w_f^2}{2 d_i \cdot \rho_f}, \quad \text{where}$$

$$f_f = 0{,}34804\, Re_f^{-0{,}25} \qquad (10)$$

$Nu_f = 0{,}023\, Re_f^{0,8}\, Pr_f^{0,4}\, \xi_c$ - for the turbulent regime, and

$Nu_f = \frac{Re_p}{300} Pr_f^{0,37}\, \xi_c$ - for the transitory regime

- for the return gas stream (of low pressure)

$$\Delta p_r = 19{,}4 \cdot n \cdot Re_r^{-0{,}1} \frac{w_r^2}{\rho_r} \quad \text{and}$$

$$Nu_r = 0{,}009\, Re_r^{-1{,}1} \qquad (11)$$

The refrigerating agent is nitrogen [5,6]

Observing that the throttling stage has a major influence upon the overall efficiency of the system, the analysis starts with the optimization of the throttling stage.

The exergetic balance equation for the throttling stage gives:

$$\hat{Ex}_9 + \hat{Ex}_{Q0} + \hat{Ex}_{Qs3} = \hat{Ex}_8 + \sum \hat{I} \qquad (12)$$

where the exergy destruction is

$$\sum \hat{I} = \hat{I}_{\Delta Pf3} + \hat{I}_{\Delta Pr3} + \hat{I}_{\Delta T3} + \hat{I}_t \qquad (13)$$

Observing that

$$-\hat{Ex}_{Q_R}^{TV} = \left|\hat{Ex}_{Q_R}^{TV}\right|, \text{ and}$$

$$-\hat{Ex}_{Qs3} = \left|\hat{Ex}_{Qs3}\right| = \hat{L}_{Qs3}$$

equation 12 becomes:

$$\hat{Ex}_9 - \hat{Ex}_8 = \left|\hat{Ex}_{Q_R}^{T_R}\right| + \hat{I}_{\Delta T_R} + L_{Qs3} +$$

$$+ \sum \hat{I} = \left|\hat{Ex}_{Q_R}^{T_R}\right| + \hat{L}_{Qs3} + \sum \hat{I}_{t_{st}} \qquad (14)$$

The exergetic efficiency for the throttling stage becomes:

$$\eta_{Ex,t} = \frac{\left|\hat{Ex}_{Q_R}^{T_R}\right|}{\hat{Ex}_9 - \hat{Ex}_8} \qquad (15)$$

The optimal parameters of the throttling stage correspond to the maximum exergetic efficiency $\eta_{Ex,t}$

OPTIMIZATION OF THE OPERATING PARAMETERS

The analysis, achieved for T_R = 82 K, T_0=300K and q_s=2 kJ/kg, was looking for the operating parameters at the inlet of the forward gas stream in the recuperative heat exchanger of the throttling stage (p_9, T_9), for the temperature differences ΔT_{n3} and ΔT_R, and for the mass velocity w_{r3} in the return gas stream, for which the exergetic efficiency $\eta_{Ex,t}$ of the throttling stage is maximum.

The optimization attempt has been achieved in the following stages:

a) `For every variant of study, the optimum value for w_{r3} has been determined for the minimum exergy destruction in the recuperative heat exchanger of the throttling stage $\left(\hat{I}_{E3} = \hat{I}_{\Delta Pf3} + \hat{I}_{\Delta Pf3} + \hat{I}_{\Delta T3}\right)_{min}$

b) The exergetic efficiency $\eta_{Ex,t}$ for the throttling stage is calculated at the variation of the decisional parameters $p_9, T_9, \Delta T_{n3}$ and w_{r3}. For pressure p_9 =12MPa the procedure is presented in *Figure* 3. Figure 3 reveals that for p_9=12MPa, for every temperature differences ΔT_R, the maximum value for $\eta_{Ex,t}$, called local maximum, is reached for the lowest values for ΔT_{n3} and w_{r3}.

c) In *Fgure* 4,a,b for different pressures p_9 for the forward gas stream, the variation of the local maximum for $\eta_{Ex,t}$ is presented for different values for ΔT_R and T_9. One observes that for every pressure p_9 the maximum value for $\eta_{Ex,t}$ is reached for the lowest temperature T_9 at the lowest ΔT_R (*Figure* 4,a,b).

d) The comparison of the maximum value for $\eta_{Ex,t}$ for different pressures p_9 points out that the maximum exergetic efficiency $\eta_{Ex,t}$ in the throttling stage corresponds to pressure p_9=12bar (*Figure* 5) and for minimum values for w_{f3}, ΔT_{n3}, ΔT_R, T_9. For economic reasons, the variation of the heat exchange surface in the throttling stage, for a refrigerating load of 1 kW $(A_{f3} / \dot{Q})$, is represented too.

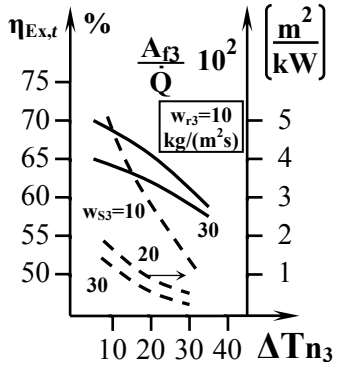

p_9=12MPa T_9=135 K

ΔT_R=3 K

Figure 3

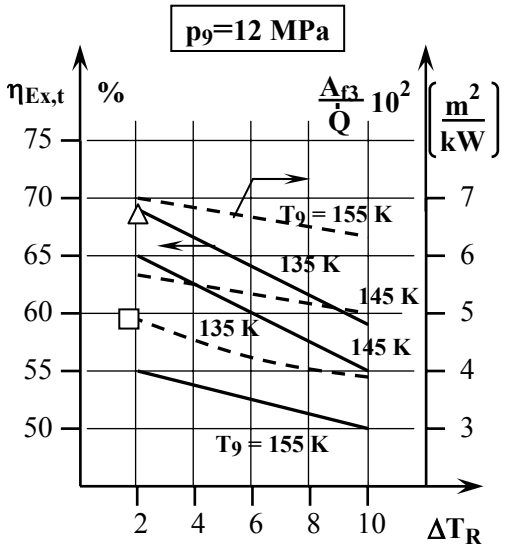

Figure 4,a

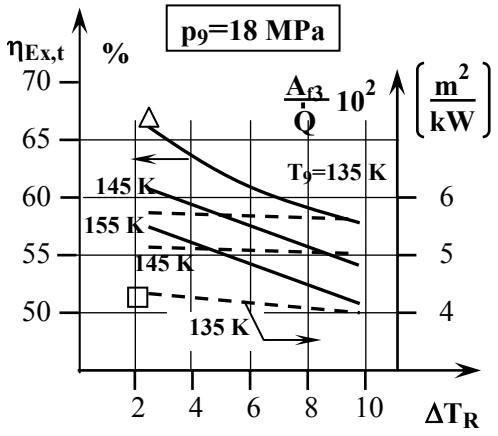

Figure 4,b

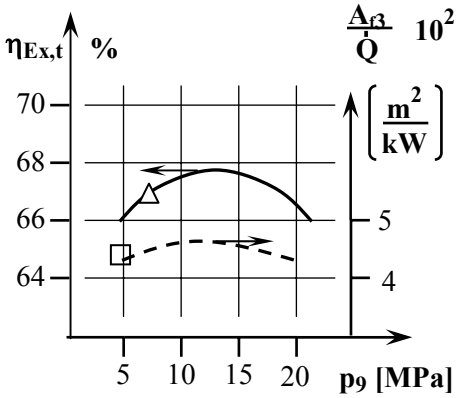

Figure 5

THE CONDUCT OF THE REFRIGERATION SYSTEM FOR OPTIMUM OPERATING OF THE THROTTLING STAGE

After optimization of the throttling stage, corresponding to the main throttling valve TV1, the whole system is optimized.

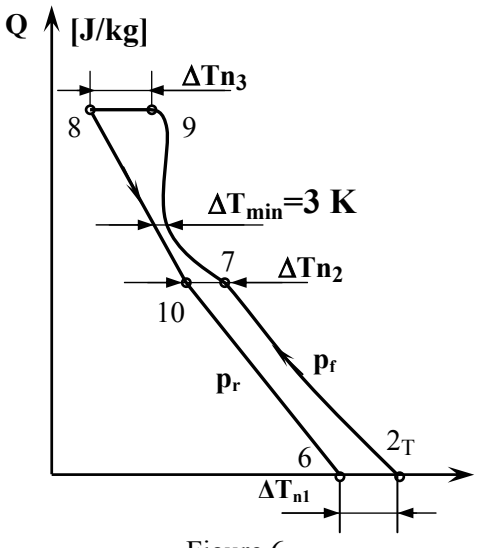

Figure 6

The analysis of the heat transfer in the recuperative heat exchangers points out that due to the variation of the thermophysical properties and to the inequality between the mass flow rates in the forward and return gas streams, the temperature difference in the recuperative stage with the expander located in parallel, can decrease below a minimum admissible (*Figure* 6).

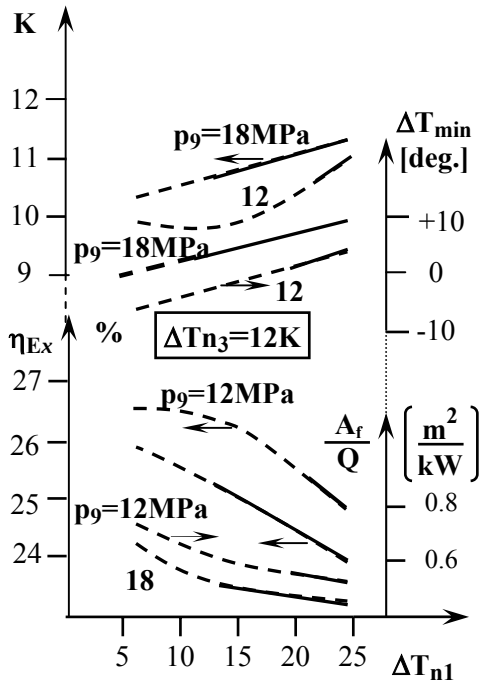

Figure 7,a

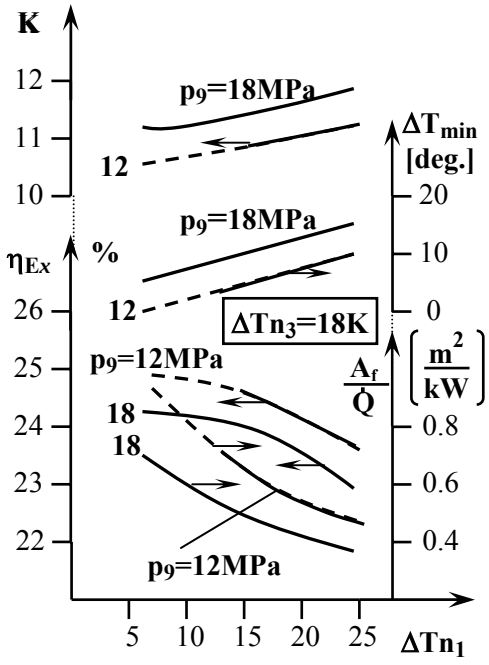

Figure 7,b

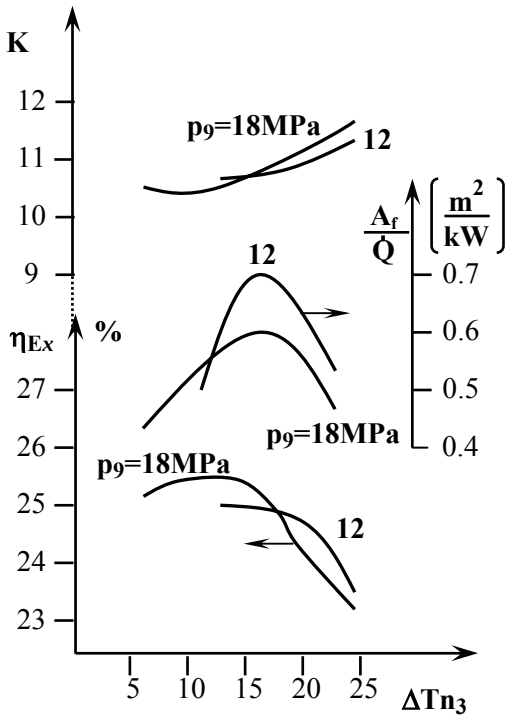

Figure 8

This technical incompatibility leads to the elimination of some of the variants, otherwise characterized by reduced exergy destruction. The eliminated variants are represented with dotted line (Figure 7,a,b).

The comparison of the maximum values for the exergetic efficiency $\eta_{Ex,t}$ for different pressures p_9 and temperature differences ΔT_{n1} reveals that the highest maximum is reached for p_9 = 18MPa, $\Delta T_{n3} \cong 12K$ and $\Delta T_{n1} \cong 12K$. For higher temperature differences ΔT_{n3}, the use of pressure p_9 = 12 MPa becomes economical (*Figure* 8).

INFLUENCE OF THE OPERATING CONDITIONS UPON THE CRYOGENIC REFRIGERATION SYSTEM

The analysis is performed in the following conditions: heat inleaks due to incomplete insulation $q_{s1} = q_{s2} = 2kJ/kg$, η_T =0.6, η_{Ex}=0.8, η_m =0.8, heat transfer surfaces are of the same type in all stages (*Figure* 2), p_9 =18 MPa, T_9 =135K, T_R = 82 K and ΔT_R = 3 K.

Influence of the temperature difference ΔT_{n3} at the warm bottom of the recuperative heat exchanger of the throttling stage

This influence ($\Delta T_{n3} = 12...24K$) analyzed for T_0=300K, ΔT_{n1}=6K, w_{r1}=7,5kg/(m^{2}s), w_{r2} = 5 kg/(m^{2}s), w_{r3} = 15 kg/(m^{2}s), p_{11} = 0,75 MPa, is presented in *Figure* 9.

One observes:

- the constancy of the efficiency η_{Ex} and of the forward gas stream state at the inlet in the throttling stage (p_9, T_9), and the increase in ΔT_{n3}, lead to a decrease in the specific thermal load of the second recuperative heat exchanger on the forward gas side, leading to a decrease in the fraction *F* of gas expanded (*Figure* 9,b); the decrease of fraction *F* explains the decrease in $\hat{W}_{Ex}$ and $\hat{I}_{Ex}$ (*Figure* 9,a);
- the increase in ΔT_{n3} has as consequence the augmentation of the enthalpy at the inlet of the throttling valve *TV*1 conducing to a reduction in the refrigeration power $\hat{Q}_R$ (*Figure* 9,a);
- as expected, the increase in ΔT_{n3} leads to an augmentation of the exergy destructions $\hat{I}_{\Delta T1}, \hat{I}_{\Delta T2}, \hat{I}_{\Delta T3}$, due to heat transfer across a finite temperature difference in the recuperative heat exchangers (*Figure* 9,a);
- for all recuperative heat exchangers, the optimum velocity ratios $\Omega = w_f / w_r$ for which the exergy destruction due to heat transfer across a finite temperature difference and gas-dynamic resistance are minimum, decrease at the augmentation of ΔT_{n3}; the maximum value for Ω is registered for the first heat exchanger (*Figure* 9,b);
- at the augmentation of ΔT_{n3}, for both the forward and return gas streams, the pressure drops in the recuperative heat exchangers *E*2 and *E*3 decrease while for *E*1 increases (*Figure* 9,b);
- at the augmentation of ΔT_{n3}, the heat transfer surface on the return gas side A_{r1} increases, while A_{r2} and A_{r3} decrease, a fact due primarily to the variation in the same sense of the refrigerating loads of the three heat exchangers (*Figure* 9,b).

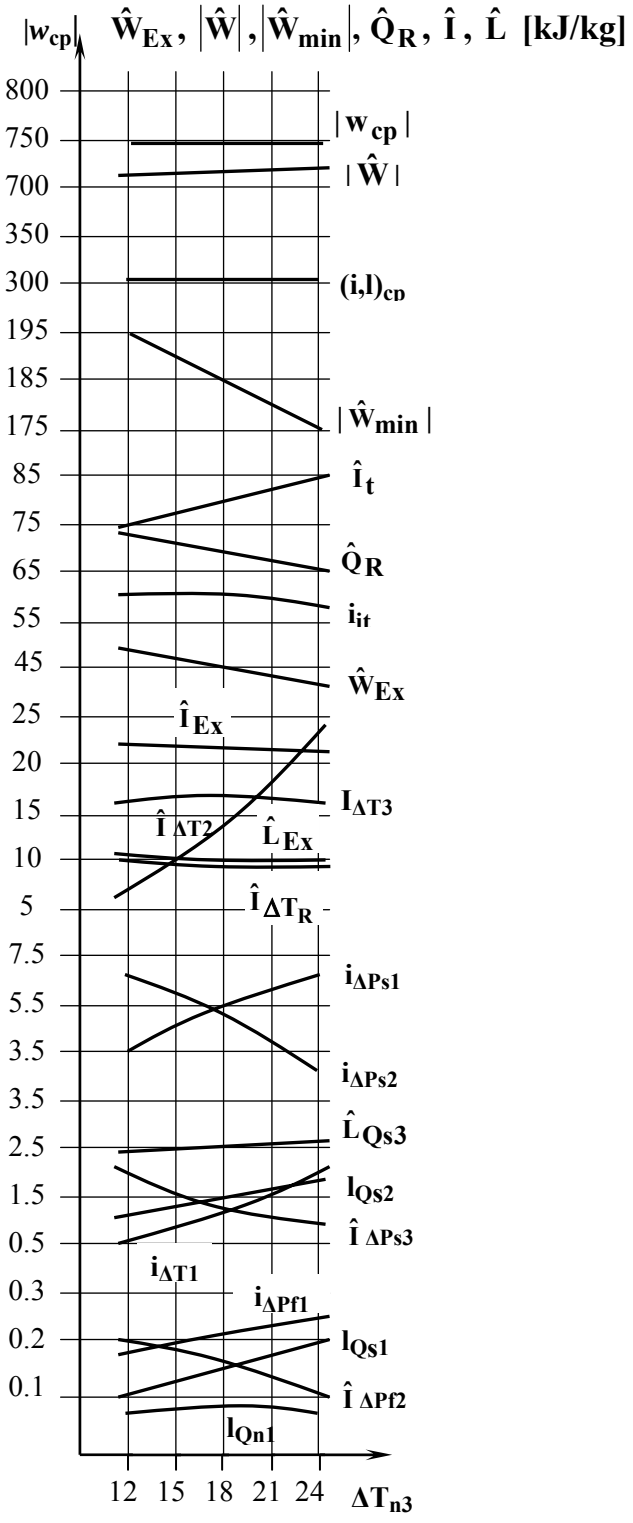

Figure 9,a

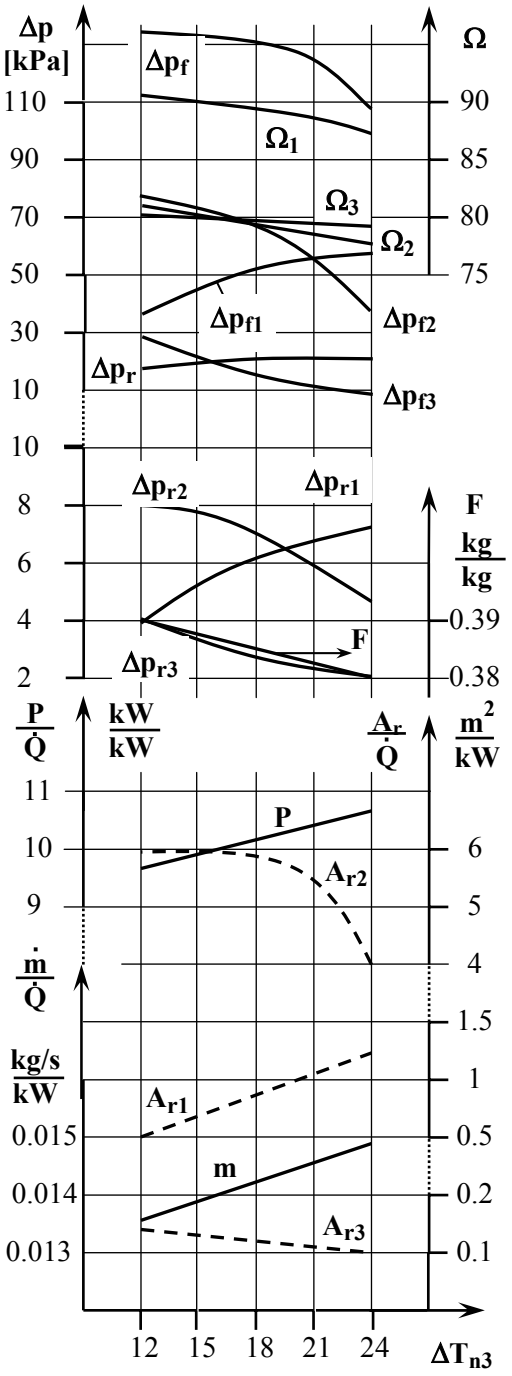

Figure 9,b

CONCLUSIONS

The throttling stage of the Claude cryogenic refrigeration system plays a decisive influence on the entire system performance.

In the aim of optimizing the whole refrigeration system, the operating parameters of the throttling stage have been determined on the basis of the maximization of the exergetic efficiency.

The optimum operating conditions can lead in the upper stages to technical incompatibilities such that the annulment of the heat transfer in the expander stage.

The specific geometry chosen for the recuperative heat exchangers, made possible the calculation of the pressure drops and associated exergy destructions and the size of the heat transfer surfaces. These data are capital for further thermoeconomic analysis where the investment and operating costs have to be balanced.

REFERENCES

[1] Arkharov, A., Marfenina, I., Mikulin, Ye., *Theory and Design of Cryogenic Systems*, Moscow, MIR, 1987

[2] Bejan, A., *Advanced Engineering Thermodynamics*, New York, Wiley, 1988

[3] Bejan, A., Tsatsaronis, G., Moran, M., *Thermal Design and Optimization*, New York, Wiley, 1996

[4] Usiuchin,I,P., *Ustanovschi masini I aparati crioghenoi tehnichi, Moscova*, Piscevaia promislemnost, 1982

[5] Hands,B.A., *NIPROP – computer package for the thermodynamic and thermophysical properties of nitrogen*, Oxford, Cryogenics Laboratory Department of Enginering Science, Departmental Report Number 1485/83

[6] Jacobsen, R.T., Stewart,R.B., Thermody-namic Properties of Nitrogen Including Liquid and Vapor Phases from 63 K to 2000 K with Pressures to 10,000 Bar*, J.Phys. Chem. Ref. Data*, 2,4 757-922, 1973

[7] Dobrovicescu, A., An Analysis of a Gaseous Helium Refrigeration System, *Design of Energy Systems*, editor G. Tsatsaronis, AES 64-3, London, 1994

[8] Dobrovicescu, A., *Analysis of the operating and design of cryogenic systems based on entropy generation minimization*, CNCSIS Report Nr. 37124/2000

Proceedings of ECOS 2005
Trondheim, Norway
June 20–22, 2005

EXERGETIC COMPARISON OF ENERGY-BASED EFFICIENCY INDICATORS FOR COMBINED HEAT AND POWER (CHP)

Ivar S. Ertesvåg*
Department of Energy and Process Engineering
Norwegian University of Science and Technology,
NO-7491 Trondheim, Norway

Svein Jacob Nesheim
Statoil, NO-4035 Stavanger, Norway

ABSTRACT

In many countries, legislative regulations in favor of combined heat and power production (CHP) have been implemented. Although these regulations put different emphasis on power production vs. process heat production, they are based on energy quantities and not on exergy. In order to analyze and compare the exergetic consequences of the various legislations, a relative avoided irreversibility (RAI) is defined. This can be regarded as the irreversibility that is avoided when a reference plant with separate production is replaced by an actual CHP plant. A series of natural-gas fired industrial and district heating CHP plants, under varying operational conditions, are used as test cases, and the consequences of the various legislations are shown. It is seen that some, but not all, CHP cases are exergetically beneficial to separate generation. The exergetic improvements were only to a limited degree captured by the various energy-based efficiency indicators. Some legislatively defined indicators appeared to discourage thermodynamic improvements.
Keywords: Exergy, CHP, cogeneration, efficiencies, legislation, comparison, evaluation

1 INTRODUCTION

Cogeneration or CHP is sometimes regarded as the materialization of the 2nd law of thermodynamics. First, electricity is produced from the high-exergy heat, and next, thermal energy is produced from heat at lower temperatures. On a 1st-law basis, CHPs provide a substantially higher output than plants for separate electricity generation.

Several countries have implemented legislations promoting CHP. The new EU CHP directive [1] contributes to this and describes the process for developing a future standard for CHP efficiencies. However, to define the "useful output" and "input", raises a number of methodological considerations that can be measured and expressed in a number of different ways, with also the potential for misleading or faulty comparisons. An increasing number of national definitions shows considerable differences in how to evaluate CHP efficiency. A common feature, though, is that they are not based on the 2nd law. A 2nd-law efficiency can be used to measure the performance of a plant and to compare with other plants. This can give a qualitative comparison and assessment of the various concepts of CHP evaluation mentioned above. The present study is an attempt to do a quantitative investigation of these concepts of evaluation. Then, the exergetic concequences of the various legislations can be discussed.

* Corresponding author: Ivar.S.Ertesvag@ntnu.no

2 COMPARISON OF SYSTEMS FOR ENERGY CONVERSION

2.1 Relative Avoided Irreversibility

The exergy loss (irreversibility) of a certain case can be expressed $(1-\psi)E_{\text{in}}$, where ψ is the exergy efficiency, that is, the ratio of usable exergy output to exergy input, and E_{in} is the exergy input (usually the fuel exergy).

A case or process can be compared to a specified reference case. The irreversibility that is avoided by replacing the reference case by the new case will be

$$(1-\psi_{\text{ref}})E_{\text{in,ref}} - (1-\psi)E_{\text{in}} \quad (1)$$

where the subscript "ref" denotes a reference case. The term avoided irreversibility presumes that the case is an improvement from the reference case. However, the quantity will be negative if the utilization is worsened.
The term can be made dimensionless by the input to the reference case, and the Relative Avoided Irreversibility is expressed

$$\text{RAI} = (1-\psi_{\text{ref}}) - (1-\psi)E_{\text{in}} / E_{\text{in,ref}} \quad (2)$$

In a general notion, this quantity can be regarded as the irreversibility of the specific case or system, subtracted from the irreversibility that would have been there if the case or system was not applied.

2.2 Comparison with energy-based efficiencies or improvement indicators.

Quite a few efficiencies and efficiency-improvement indicators are defined on a technical or legislative basis. In most instances, these are based on energy considerations. Thus, all forms of usable energy, *e.g.* fuel, electricity, and heat, are accounted for by their energy value (*i.e.* heating value).

Similar to the outline above, a Relative Avoided Loss can be expressed

$$\text{RAL} = (1-\eta_{\text{ref}}) - (1-\eta)H_{\text{in}} / H_{\text{in,ref}} \,. \quad (3)$$

Here, η is some defined efficiency, H_{in} is the energy input (usually the fuel LHV), and subscript "ref" again denotes a reference case. This formulation can be used for the variety of efficiencies shown below. RAL is the loss of energy, according to the chosen definition of efficiency, that is avoided when the reference case is replaced by the actual case.

If the efficiency η in Eq. (3) is the total energy efficiency (e.g. electric energy plus heat divided by the fuel LHV), the RAL is the loss of energy that is avoided because the actual case has replaced the reference case. This is known as the Relative Primary Energy Savings (RPES). In most cases, the energy efficiency is different from the exergy efficiency. Other definitions of efficiency, based on technology or policy reasoning, give different evaluations of energy, and accordingly, of the utilized and lost energy.

For a thermodynamic comparison of the different indicators, the ratio of RAI to RAL can be used as metric. Thus, if

- RAI>RAL, the improvement is underestimated by the indicator,
- RAI=RAL, the improvement is evaluated in accordance with thermodynamics,
- RAI<RAL, the improvement is overestimated by the indicator,
- RAI/RAL<0, the emphasis of the indicator is in the wrong direction.

2.3 Efficiency indicators for combined heat and power (CHP)

The ratio of delivered useable energy to the energy input can be termed the total energy efficiency or CHP efficiency. For a system producing heat and power this can be expressed

$$\eta_{\text{CHP}} = (W+Q)/H \,, \quad (4)$$

where W is the mechanical power or electricity produced, Q is the thermal energy in delivered steam, and H is the input energy, usually the LHV of the fuel. In the context of CHP, the fractions of input energy that are converted to electric energy and heat can, respectively, be called electric efficiency and heat efficiency and expressed

$$\eta_{\text{el}} = W/H \quad (5)$$

$$\eta_{Q} = Q/H \quad (6)$$

These expressions are useful when evaluating the different methods of qualifying CHP.
To describe the quality difference between electricity and heat, the exergy efficiency can be defined. This is the ratio of exergy in the products

electricity and thermal energy to the exergy of the input

$$\psi = (W + E_Q) / E_F \quad (7)$$

Here, E_Q and E_F are, respectively, the exergy of the delivered thermal energy and the input exergy, while the exergy of electricity or mechanical energy is equal to its energy W.

Both thermodynamically, technically, and economically, electric energy differs from thermal energy. Several other parameters have been defined to account for this difference without making use of the exergy concept.

While electricity generation can be conducted nearly anywhere, the heat has to be generated near the user, and it has to be scaled according to the consumption. Thus, it may be useful to regard a CHP as a heat generator with surplus electricity generation. This is expressed by defining an Equivalent electrical efficiency (EEE) [3],

$$\eta_{\text{eel}} = W / (H - Q / \eta_{\text{Qref}}) \quad (8)$$

Here, the fuel energy to the CHP plant is supposed to be reduced by the fuel needed to produce the heat in a separate boiler with efficiency η_{Qref}. In the legislations of Spain and (with a slight modification) Portugal, this concept is used (cf. [4][5]). While in Eq. (8), a portion of the fuel (fuel for heating) is subtracted in the denominator, a fraction of the energy in the steam is added in the numerator in the efficiency defined by the US legislation PURPA,

$$\eta_{\text{PURPA}} = (W + 0.5 \cdot Q) / H \quad (9)$$

Also in Brazil, an efficiency close to this is used. Such efficiencies can be seen as a simplified exergy efficiency, without really taking into account the actual exergy content of the heat.

Feng et al.[6] suggested an adjusted exergy efficiency with the definition

$$\eta_{\text{adex}} = (W + E_Q + \xi \cdot (Q - E_Q)) / H \quad (10)$$

where ξ=0.12 is an adjusted exergy factor.

For all these efficiencies, an RAL can be defined according to Eq. (3). Other indicators may focus on the savings of energy or emissions. The relative primary energy savings (RPES) [3][4]can be written

$$\text{RPES} = 1 - H / H_{\text{ref}} \quad (11)$$

This is the fuel energy that is saved by the CHP when comparing to separate generation. The RPES is used as an indicator for the goodness of CHP systems in the Flemish legislation (Belgium). Other such indicators are (see [4][5]) the Relative CO_2 Emissions Savings (RCES; Walloon and Brussels-region legislations), the fuel-free electricity (Dutch legislation), and the Quality Index (QI; British legislation).

For natural-gas fired CHP, the Brussels RCES can be expressed equal to the RPES, while the Walloon RCES can be expressed equal to $\text{RPES} \cdot (H_{\text{ref}} / H_{\text{elref}})$. The RPES and the RCESs can be regarded as RALs, and the fuel-free electricity W_{free} can be related through

$$W_{\text{free}} / H_{\text{ref}} = \eta_{\text{elref}} \cdot \text{RPES} \quad (12)$$

where η_{elref} is defined below.

The Quality Index (QI) can be expressed as a relative Quality-Index improvement by

$$\text{RAL} = \text{QI} / \text{QI}_{\text{ref}} - 1 \quad (13)$$

All these RALs are based on energy considerations. At first sight, e.g. the RPES seems to represent mass of fuel and thus energy and exergy of the fuel as well. However, when the "saved" energy is evaluated, all forms of usable energy are accounted equally. That is, electric energy, fuel energy, and thermal energy in MP and LP steam are considered equal. From a thermodynamic consideration (1st and 2nd law), a system delivering an amount of heat in LP steam has higher losses than a system delivering heat in MP steam at a higher temperature. And actually, the system has a lower (1st-law) capacity when producing MP steam (see below).

2.4 Reference plants for separate generation of heat and power

For energy analyses, it is convenient to define reference plants for separate heat and power generation, with the electric and heat efficiencies η_{elref} and η_{Qref}, respectively. The reference amounts of fuel energy can be defined, $H_{\text{elref}} = W / \eta_{\text{elref}}$ and $H_{\text{Qref}} = Q / \eta_{\text{Qref}}$, and the sum $H_{\text{ref}} = H_{\text{elref}} + H_{\text{Qref}}$. These are the amounts required to produce the

same electricity and heat separately in the reference plants. The ratio of the actual to the reference fuel energy is

$$H / H_{\text{ref}} = (\eta_{\text{el}} / \eta_{\text{elref}} + \eta_Q / \eta_{\text{Qref}})^{-1} \quad (14)$$

Similarly, the reference fuel exergy for separate electricity generation can be expressed

$$E_{\text{F,elref}} = \alpha_{\text{F}} H_{\text{elref}} = \alpha_{\text{F}} W / \eta_{\text{elref}} \quad (15)$$

where α_F is a constant, usually close to unity (e.g. 1.04 for natural gas at standard state). The fuel exergy for separate heat generation will be discussed below.

The values of the reference efficiencies can be determined based on the notion of Best Available Technology (BAT) or based on an average of existing installations. In legislative regulations, the choice of reference values may be based on a compromise between existing technology and BAT. As the choice will affect the regarded goodness of any CHP plant, it is quite often an outcome of intense lobbying by the involved parties.

This procedure does not recognize the exergetic value or "quality" of thermal energy. The reference amount of fuel for separate heat generation is taken as the same value regardless of the temperature of the steam (or other heating media: water, oil, air, etc.). It can be argued that a conventional boiler has about the same efficiency for HP steam and LP steam, and even for hot water. Actually, this efficiency is determined more by the state of the outflow flue gas than by the state of the heating medium. However, it can be observed that for a CHP producing LP steam, the electricity generation is relatively lower than for a similar CHP producing MP or HP steam.

Moreover, low-temperature thermal energy can be generated by heat pumps. A system of separate electricity generation and heat pumps can supply an amount of heat that is larger than the fuel LHV used. Thus, for a proper exergetic comparison, the reference heat efficiency has to depend on the exergy of the heat. This corresponds to defining a reference heat-pump exergetic efficiency.

The exergy of heat can be written $E_Q = \alpha_Q Q$, which defines the exergy-to-heat ratio, α_Q. When provided by a heat pump, this heat requires the amount of work W_{QP}. These quantities can be related by the exergetic efficiency of the heat pump,

$$\psi_{QP} = E_Q / W_{QP} = \alpha_Q Q / W_{QP} \quad (16)$$

Furthermore, the heat-pump work can be assumed generated in a reference power plant as described above. Hence, the amount of fuel for separate generation of heat varies with the exergy of the steam (or other heating medium). It also depends on the exergetic efficiency of the heat pump. This efficiency may vary with the temperature levels involved but will, for convenience, be assumed constant in the following.

Two approaches can be followed to determine the reference fuel exergy for heat generation: 1) specify a reference exergy-to heat ratio, $\alpha_{Q\text{ref}}$ for heat generation, or 2) specify a reference exergetic efficiency $\psi_{QP\text{ref}}$ for a heat pump providing the heat.

In the first approach, the reference exergy efficiency for separate heat generation in a boiler can be expressed

$$\psi_{Q\text{ref,B}} = \frac{\alpha_{Q\text{ref}} Q}{\alpha_F Q / \eta_{Q\text{ref}}} = \frac{\alpha_{Q\text{ref}} \eta_{Q\text{ref}}}{\alpha_F} \quad (17)$$

Here, the reference is separate generation of the same amount of heat at the specified exergy-to heat ratio and a specified energy efficiency. This will give a reference amount of fuel exergy for the boiler (subscript "B") approach

$$E_{F,Q\text{ref,B}} = \frac{\alpha_Q Q}{\psi_{Q\text{refB}}} = \frac{\alpha_F \alpha_Q Q}{\alpha_{Q\text{ref}} \eta_{Q\text{ref}}} \quad (18)$$

When the actual heat generation is conducted by a heat pump using electricity (work) from a reference plant for separate power generation, the heat-generation exergy efficiency is

$$\psi_{Q\text{ref,QP}} = \frac{\alpha_Q Q}{\alpha_F (W_{\text{QPref}} / \eta_{\text{elref}})} = \frac{\eta_{\text{elref}} \psi_{QP\text{ref}}}{\alpha_F}. \quad (19)$$

The reference fuel exergy for separate heat generation in the heat-pump (subscript "QP") approach can then be expressed

$$E_{F,Q\text{ref,QP}} = \frac{\alpha_F W_{\text{QPref}}}{\eta_{\text{elref}}} = \frac{\alpha_F \alpha_Q Q}{\eta_{\text{elref}} \psi_{\text{QPref}}}. \quad (20)$$

The two approaches can be joined by setting $\alpha_{Q\text{ref}}\eta_{Q\text{ref}} = \eta_{\text{elref}}\psi_{\text{QPref}}$. This also leads to an expression for the coefficient of performance of the reference heat pump,

$$\text{COP}_{\text{ref}} = Q / W_{\text{QPref}} = \psi_{\text{QPref}} / \alpha_{Q\text{ref}} = \eta_{Q\text{ref}} / \eta_{\text{elref}} \quad (21)$$

Although this ratio is fixed to the reference efficiencies for heat and electricity, the requirement will be more demanding as the exergy ($\alpha_{Q\text{ref}}$) increases.

Now, reference amounts of fuel exergy for separate heat and power generation are defined, and the reference efficiency can be expressed

$$\psi_{\text{ref}} = \frac{\eta_{el} + \alpha_Q \eta_Q}{\alpha_{\text{F}}(\eta_{el} / \eta_{\text{elref}} + \alpha_Q \eta_Q / (\alpha_{\text{Qref}} \eta_{\text{Qref}}))} \quad (22)$$

This procedure allows a comparison of different systems and recognizes the quality of the thermal energy. The ratio of actual fuel-exergy input to the reference input is

$$E_{\text{F}} / E_{\text{F,ref}} = (\eta_{el} / \eta_{\text{elref}} + \alpha_Q \eta_Q / (\alpha_{\text{Qref}} \eta_{\text{Qref}}))^{-1} \quad (23)$$

It is readily seen that for a heating medium with $\alpha_Q = \alpha_{Q\text{ref}}$, the fuel-exergy ratio of Eq.(23) is equal to the fuel-energy ratio of Eq.(14).

Still, the reference exergy-to heat ratio, $\alpha_{Q\text{ref}}$, (or alternatively, the reference heat-pump exergetic efficiency ψ_{QPref}) has to be specified. In this study, a value of $\alpha_Q = 0.28$ was adopted. This is the ratio of exergy to enthalpy differences for instance of steam at 2.5 bar 140 °C (LP steam), when the environmental pressure and temperature are 1 bar and 15 °C. In combination with a reference electric and heat efficiencies of 0.55 and 0.90, respectively, this corresponds to a heat-pump exergy efficiency ψ_{QPref} of 0.46 and a reference COP of 1.64. These figures are technically achievable and are chosen here to enable a quantified analysis.

This choice of "quality" for the reference is modest. An alternative choice of $\alpha_Q = 0.40$ (MP steam, 21 bar, 330 °C) corresponds to a ψ_{QPref} of 0.65. Even at this level, a reference COP of 1.64 is technically feasible. On the other side, a low-exergy reference, e.g. hot water with $\alpha_Q = 0.15$ was an alternative. The choice of reference for exergy is largely arbitrary and a matter of taste, at least within the technically possible range. The issue is whether a medium-exergy thermal system should be accounted "neutral", "positive" or "negative". From a pedagogical viewpoint, it is preferred to have both "negative" and "positive" categories, as the choice made here implies.

3 TEST CASES OF CHP

3.1 Cases of industrial CHP

Two different configurations for a CHP plant have been considered in this study: A boiler with back-pressure steam turbine (ST) and condensing ST (BST plant), and a plant with gas-turbine with a flue-gas heat-recovery steam generator (HRSG) and condensing steam turbine (GT-plant) [4][5].

Table 1 Cases of industrial CHP, Boiler/steam-turbine (B3-) and gas-turbine with HRSG (GT2-) series with low-pressure (LP) and medium-pressure (MP) steam delivery. From [4][5].

	Steam delivery load (tonnes/h)				
	40	55	70	85	100
B3-LP (α_Q=0.28)					
W/H	0.240	0.224	0.207	0.191	0.174
Q/H	0.281	0.386	0.491	0.597	0.702
E_Q/H	0.079	0.108	0.138	0.167	0.197
B3-MP (α_Q=0.39)					
W/H	0.144	0.128	0.111	0.095	0.079
Q/H	0.319	0.439	0.559	0.678	0.798
E_Q/H	0.125	0.172	0.218	0.265	0.312
GT2-LP (α_Q=0.28)					
W/H	0.462	0.449	0.438	0.423	0.409
Q/H	0.241	0.332	0.418	0.452	0.483
E_Q/H	0.068	0.093	0.117	0.127	0.135
GT2-MP (α_Q=0.39)					
W/H	0.410	0.396	0.373	0.351	0.332
Q/H	0.274	0.377	0.464	0.512	0.545
E_Q/H	0.107	0.147	0.182	0.200	0.213

The fuel for all cases was natural gas. The cases selected are the operational mode III of the BST plant (maintained firing, reduced condensing ST load to increase steam delivery load), and the operational mode II for the GT/HRSG/ST plant, both with LP and MP steam delivery. The fuel-energy (LHV) consumption rate was 101 MW for the BST and from 117 to 147 MW for the GT

plant. Within each of the four series of cases, the steam delivery load increased from 40 to 100 ton/h. As the issue here is to investigate the efficiency indicators, most details of the plants will be left out. The key data are shown in Table 1. The RAIs for all 20 cases are seen in Fig. 1 (abscissa). Increased steam delivery load increases utilization compared to separate production. In the cases presented (except higher GT cases), reduced steam delivery was obtained by increasing load on the condensing steam turbine. It is seen that this reduces the RAI, which for the BST, becomes negative. Furthermore, it is seen that MP steam delivery gave higher RAI than LP steam, and that the GT systems gave higher RAI than the BST systems.

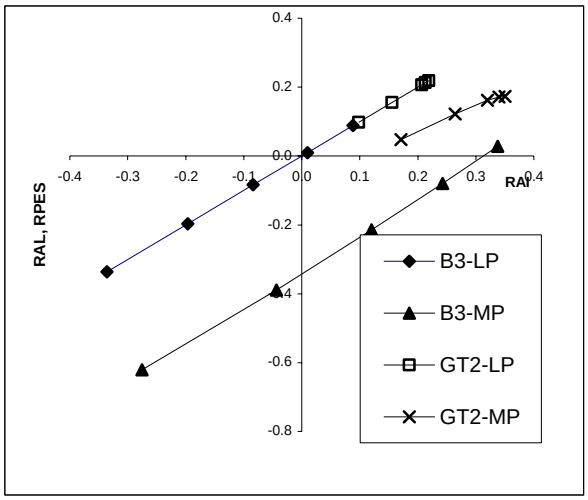

Figure 1 RAL based on the total energy (or CHP) efficiency vs. RAI for the industrial CHP cases. This RAL equals the RPES (Flandern, Brussels).

Figures 1 to 5 show the comparison between the exergy-based and energy based indicators. Here it should be noted that all indicators are defined or chosen with the purpose of promoting CHP. Each of the four series of cases has an RAI that is increasing with increasing steam delivery load. The closer a line between two cases is the diagonal line RAL=RAI, the closer the indicator resembles to the exergetic evaluation.

The Dutch fuel-free electricity (normalized with the reference amount of fuel energy) is proportional to the RPES and exhibit the corresponding behaviour.
The first graph, Fig. 1, shows the RAL based on the total energy efficiency or CHP efficiency. This RAL is equivalent to the RPES (used in Flandern legislation) and to the Brussels-region RCES. As the reference exergy-to-enthalpy ratio is chosen

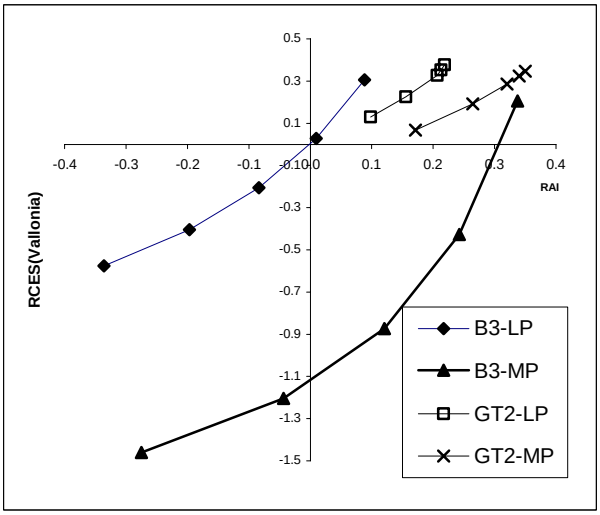

Figure 2 Walloon-legislation RCES vs. RAI.

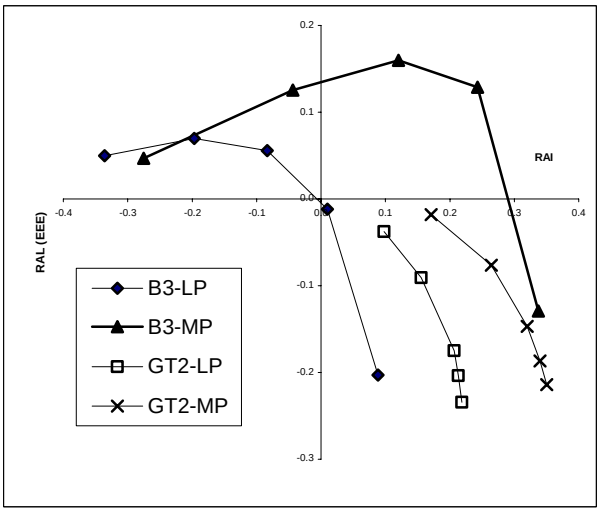

Figure 3 RAL based on EEE (Spain, Portugal) vs. RAI

equal to that of the LP steam, the LP cases lie on the line RAL=RAI. Hence, increased steam delivery for a specific plant is evaluated in accordance with exergy analysis. Improving a plant by replacing the boiler with a GT/HRSG is also encouraged by this indicator. However, it is seen that steam delivery at a higher temperature and exergy (MP steam) is punished by the energy indicator, giving a lower RAL in spite of increased RAI. The higher B3-MP cases are even found in the 4th quadrant, as the RAL takes negative values for positive RAI.

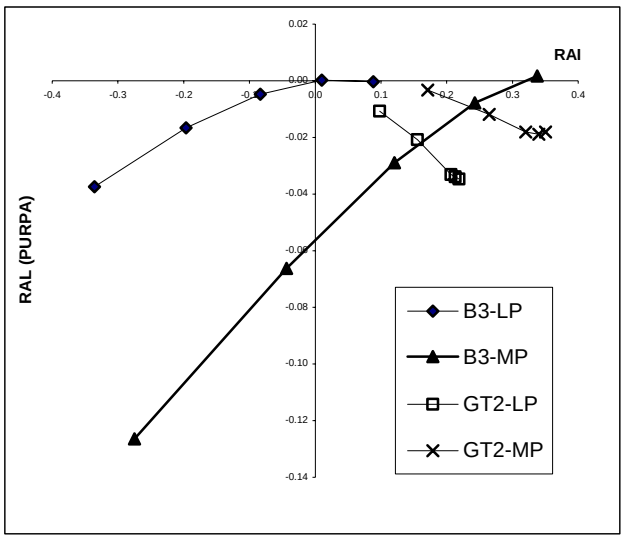

Figure 4 RAL based on US PURPA efficiency vs. RAI

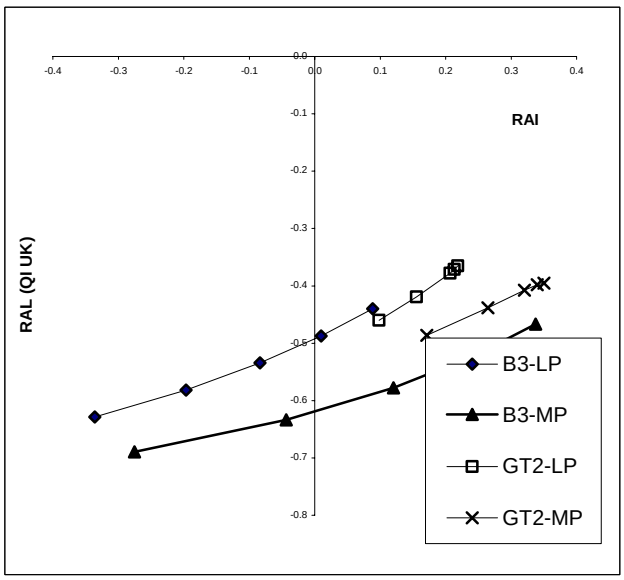

Figure 5 RAL based on British QI vs. RAI

Next, Fig. 2 shows the RCES of the Walloon legislation. This is similar to the RPES above, except that the points are moved clock-wise such that the impact of improvements are enhanced and several cases are raised above the RAL=RAI line in the first quadrant and below on the negative side.

For the present cases, with no in-house derived fuel, the efficiency of the Portuguese legislation becomes equal to the Equivalent electric efficiency (EEE), which is also used in Spain. The RAL based on this efficiency is shown in Fig. 3. This remarkable figure shows that most cases are found in the 2nd and 4th quadrant. Moreover, almost any improvement in terms of exergy utilization is answered with a poorer RAL. One exception in this picture is that the RALs for the higher boiler-MP cases are higher than those of the corresponding LP cases.

The efficiency of the US PURPA is somewhat related to the EEE above, and some of the same tendencies are seen in Fig. 4. In particular, the use of GT/HRSG is discouraged by this indicator, although not to the extent seen with the RAL based on EEE. For the BST configuration, we see some of the same picture as for the total efficiency and RPES above (Fig. 1). The efficiency proposed by Feng, Eq. (10), showed much the same picture as the PURPA efficiency, and is not included here.

The RAL based on the British Quality Index is shown in Fig. 5. It can be noted that higher steam load and higher RAI provide a less negative RAL. However, any other improvement is disregarded by this indicator.

It should be noted that the RAI values are affected by the choice of reference exergy-to-heat ratio, $\alpha_{Q\mathrm{ref}}$. A higher value will reduce the RAI, whereas the various RALs are not affected. Consequently, in all graphs, each point will be moved to the left. The change has less impact with a higher power-to-heat ratio. Nevertheless, the main picture described above will remain the same with a higher or lower value chosen for reference exergy-to-heat ratio.

3.2 Cases of CHP with district heating

In some countries, particularly Denmark, the legislation has been designed to promote small-scale CHP for district heating. This has brought forth a substantial number of natural-gas fired power-plants in the range 3-30 MW electric power, supplying their neighbourhood with space heating. Often, such plants are only operating during the heating season. A number of such cases are specified in Table 2. These data were taken from [7] and are long-term averages for plants in operation. Most of the cases are based on the K type (one B type) of natural-gas fired motor from Rolls Royce Marine Diesel of Bergen, Norway. We will regard these as representative for a number of existing plants. For such plants, the water supply and return temperatures, respectively, are typically 95°C and 50 °C. Here we have

assumed $\alpha_Q = 0.19$, although the value may be lower during parts of the heating season.

Table 2 Cases of district heating (α_Q=0.19).

Case	RR1	RR2	RR3	RR4	RR5	RR6
W/H	0.419	0.416	0.397	0.407	0.413	0.450
Q/H	0.341	0.445	0.531	0.521	0.515	0.450
E_Q/H	0.065	0.085	0.101	0.099	0.098	0.086

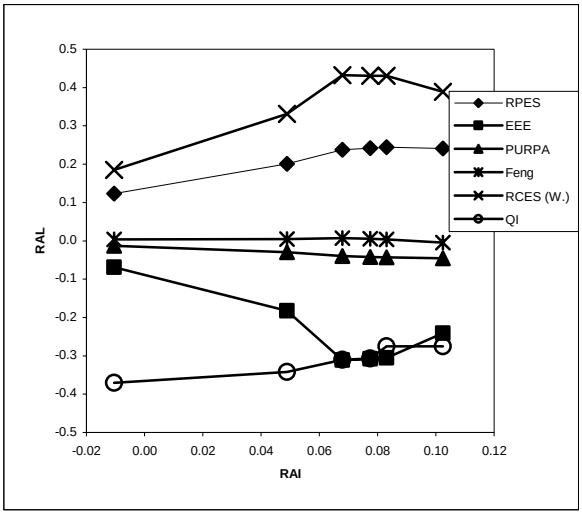

Figure 6 RAL based on various indicators vs. RAI for six cases of disctrict heating.

In Fig.6, these cases are presented from lowest (Case RR1) to highest (RR6) RAI. The corresponding RALs based on six different indicators are shown. It is seen that the total efficiency RAL (equivalent to RPES), encourage but overestimates the improvement, and the Walloon RCES even more. The RALs based on PURPA, EEE, and QI discourage improvements as five of the cases are found in the fourth quadrant of the graph. The RAL based on Feng's efficiency is close to zero for all cases.

It can be argued that for space heating, separate production will give more than 90% of the LHV. In fact, more than 105% can be achieved by using furnaces that condense some of the flue-gas water vapour. Even with his reference, the plant will turn out with positive RAL and RAI. However, the most efficient means for space heating is heat pumps. A relatively modest COP of 3.7 or less, combined with separate electricity production, will give the same RAL or fuel savings as in the cases specified. This shows that from a thermodynamic viewpoint, small-scale power plants with low-temperature heat production are advantageous to on-site heating by combustion, while the best way to provide space heating is heat pumps.

4 CONCLUDING REMARKS

The purpose of this study was to assess various 1st-law-based metrics for evaluating CHP systems. An expression for relative avoided irreversibility (RAI) was developed to enable exergetic comparison of alternative energy conversion systems. Similarly, the relative performance according to various technically or legislatively defined efficiency indicators can be expressed and compared to the RAI.

From a series of industrial and district-heating CHP test cases, it was seen that exergetic improvement (or disprovements) only to a limitied degree was captured by the various energy-based efficiency indicators. Some legislatively defined indicators appear to discourage thermodynamically based improvements.

REFERENCES

[1] EU CHP Directive 2004/8/EC 11 Feb 2004.

[2] Kotas TJ. *The exergy method of thermal plant analysis.* 2nd ed. Malabar, FL: Krieger, 1995.

[3] Horlock JH. *Cogeneration – Combined heat and power (CHP)*. 2nd ed. Malabar, FL: Krieger, 1997.

[4] Nesheim SJ. *Combined heat and power fired with natural gas - Thermodynamical, industrial, and societal consideration.* Thesis submitted for PhD. Trondheim: Norwegian University of Science and Technology, 2005.

[5] Nesheim SJ, Ertesvåg IS. *Efficiencies and indicators defined to promote combined heat and power (CHP).* To be submitted for publication, 2005.

[6] Feng X, Cai Y-N, Qian L-L *A new performance criterion for cogeneration system.* Energy Conv. Mgm. 1998;39(15):1607-9.

[7] Rolls-Royce, Power Generation `http://www.rolls-royce.com/`

Proceedings of ECOS 2005
Trondheim, Norway
June 20–22, 2005

EFFECT OF ENVIRONMENTAL CONDITIONS ON THE CALCULATION OF CHEMICAL EXERGY

Marisol Garfias* and Ricardo Rivero
Instituto Mexicano del Petróleo
Eje Central Lázaro Cárdenas 152
México, D.F.

ABSTRACT

Chemical exergy of any substance, in its standard state, is normally estimated from tabulated values obtained for normal conditions (298.15 K and 1 atm) and taking into account a model of reference species that considers the concentration of the most common components of real environment. In the present work, the effect on the chemical exergy of elements and compounds of ambient temperature, atmospheric pressure, air humidity, CO_2 concentration in the air and oceans salinity, is studied considering the Szargut model for determining the chemical exergy of a substance. Ambient temperature is the condition that has the greatest effect on the chemical exergy of a substance. This is due to the fact that Gibbs free energy for the formation reaction of the reference species and its environmental concentration depend on this condition. Furthermore, the chemical exergy value changes little when atmospheric pressure, air humidity, CO_2 concentration in the air and seawater salinity vary. Finally, at atmospheric pressure and constant relative humidity, the chemical exergy of any hydrocarbon increases when ambient temperature decreases.

Keywords: Standard chemical exergy, elements, environmental conditions.

NOMENCLATURE

b_y	Number of molecules of the additional element *y* present in a molecule of the reference species in seawater
Ex	Exergy [kJ/gmol]
ΔG	Gibbs free energy [kJ/gmol]
ΔH	Enthalpy [kJ/gmol]
h	Altitude [m]
j	Number of reference ions derived from one molecule of the element under consideration
K	Thermodynamic equilibrium constant of a reaction
m	Molal concentration or molality [mol/kg_{H2O}]
n	Number of moles
P	Atmospheric pressure [kPa]
$P°_{H2O}$	Water vapor pressure [kPa]
pH	Negative logarithm of hydrogen ion concentration
R	Ideal gas constant [kJ/gmol K]
S	Conventional seawater salinity [‰: parts per thousand]
T	Absolute ambient temperature [K]
x	Mole fraction
z	Charge, in electric units, of reference ion present in seawater

Greek symbols

ϕ	Atmospheric air relative humidity
γ	Activity coefficient (molal scale)

Superscripts

o	Standard state

Subscripts

c	Concentrational
el	Element
f	Reaction of formation
i	Species or component of a mixture

*Corresponding author. Tel.: +52(55)9175 8153; Fax: +52(55)9175 8067. *E-mail*: mgarfias@imp.mx

n Normal conditions of temperature (298.15 K), pressure (101.325 kPa) and concentration of the species
q Chemical
r Reactional
y Additional reacting species in the reference reaction

INTRODUCTION

Chemical exergy (Ex_q) of any substance is the maximum work that can be obtained by taking the system to chemical equilibrium with the environment at constant temperature and pressure. This has two contributions: reactional exergy (Ex_r), resulting from the chemical reactions necessary to produce species existing as stable components in the environment, from the initial composition of the substance; and concentrational exergy (Ex_c), which is a result of the processes requiered to match the chemical concentration of the produced species to their chemical concentration in the environment [1].
The calculation of Ex_q of a substance in its standard state ($Ex_q°$), is carried out considering the environmental conditions and species concentration in the reference environment, which are usually the normal temperature and pressure conditions, this is, 298.15 K and 101.325 kPa, and the mean concentration of the species in the environment at these conditions. It is important to point out that the standard state of a substance is its particular state at temperature *T* defined by general use at reference conditions of pressure, composition and physical state [2]. In this work, the standard state for gases is taken as the pure gas in the ideal-gas state at 101.325 kPa; while for liquids and solids, the standard state is taken as the pure liquid or solid in the real state at 101.325 kPa. The Ex_q of a substance is estimated at normal conditions (T_n and P_n) due to the fact that most of the information about thermodynamic properties and species concentration in the environment is available at these conditions; besides, these are considered the average in the environment. However, depending on the geographical place and season of the year, the environmental conditions may be different from the average. For example, in north hemisphere regions, the ambient temperature has a mean value of –20°C or less during winter, while, places that are close to the Equator, the environmental temperature can be higher than 40°C in the summer [3,4]. Besides, superficial seawater temperature varies between 30°C or more in tropical regions and –2°C under the Artic Ice [3,5].
The effect on $Ex_q°$ of elements and compounds of ambient temperature, atmospheric pressure and reference species concentration –air humidity, carbon dioxide concentration in the air and seawater salinity–, is studied considering the model proposed by Szargut for the calculation of chemical exergy of a substance.

CHEMICAL EXERGY OF COMPOUNDS AND ELEMENTS

According to Szargut [6, 7], to calculate Ex_q of any substance, reference species should be chosen as the most probable products of the interactions between the considered substance and the components of the natural environment. Reference species can be either gaseous components from the atmosphere, or species dissolved in seawater, or solid compounds present on the earth's surface.
Knowing the $Ex_q°$ values of elements, the $Ex_q°$ of any chemical compound can be determined by means of an exergy balance of its formation reaction, this is,

$$Ex_q^o = \Delta G_f^o + \sum_{el} n_{el}\ Ex_{q\,el}^o \qquad (1)$$

Now, the $Ex_q°$ of any element can be determined from $Ex_q°$ values of its reference species and from other elements present in the reference species, as well as from the $\Delta G_f°$ value of the reference species. Considering that species in atmospheric air follow the ideal gas behaviour, their $Ex_q°$ can be evaluated by:

$$Ex_{q\,i}^o = R\,T_n\,\ln\frac{P_n}{P_{i\,n}} = R\,T_n\,\ln\frac{1}{x_{i\,n}} \qquad (2)$$

The partial pressure of water in air, P_{H2O}, is obtained from the relative humidity definition (see Equation 3). The effect of temperature on the vapor pressure of water follows Antoine's expression [8].

$$\phi = \frac{P_{H_2O}}{P_{H_2O}^o} \qquad (3)$$

Standard chemical exergy of elements, whose reference species are dissolved in seawater, are obtained by means of Equation 4, which is derived from the model proposed by Morris, Steward and Szargut [7].

$$Ex^{o}_{q\,el} = -j\Delta G^{o}_{f\,i} + \tfrac{1}{2}\, jz_i Ex^{o}_{q\,H_2} - j\sum_y b_y Ex^{o}_{q\,y} - 2.303RT_n jz_i (pH) - jRT_n \ln(m_{i\,n}\gamma_i) \quad (4)$$

One example of the reaction used in Equation 4 is the formation of sulphate ion, species dissolved in seawater that contains the element sulphur and whose global formation reaction in an electrochemical cell is:

$$S + 2O_2 + H_2 \rightarrow SO_4^{2-} + 2H^+ \quad (5)$$

Activity coefficients of the species dissolved in seawater depend mainly on the ionic strength of the solution. The seawater *pH* (in the range of 7.8-8.2 [9, 10]) is controlled mainly by the carbon dioxide system with minor contributions from boric acid. Presently, molality, *pH* and γ_i values are calculated as function of salinity and temperature, in the same way as Rivero and Garfias determinated these values for the $Ex_q°$ estimation of elements [11], using the total hydrogen ion concentration scale for *pH* and the Pitzer's model for electrolyte mixtures in the case of activity coefficient. Moreover, in this study, the proportion among the species dissolved in seawater is considered constant for any salinity. Also, due to the fact that the concentration of the species dissolved in seawater changes slightly between 273.15 and 323.15 K at constant salinity [12], the proportion among the species present in the hydrosphere is assumed to be constant when seawater temperature varies.

Finally, Szargut [6, 7] establishes that $Ex_q°$ of the solid species in the environment (as an ideal solution) can be determined by means of the following expression:

$$Ex^{o}_{q\,i} = -R\,T_n \ln x_{in} \quad (6)$$

EFFECT OF AIR HUMIDITY ON $Ex_q°$

The water content in the atmospheric air depends on the geographical location and on the season of the year. Normally, the value of 0.7 is used for calculating the $Ex_q°$. Figure 1 shows the $Ex_q°$ as a function of the relative humidity for the most common elements found in the atmosphere and for those species which are directly affected for changes in humidity. In order to see the effect of relative humidity on $Ex_q°$ of a hydrocarbon, methane is included in the analysis ($\Delta G^{o}_{f\,CH4}$ = -50.79 kJ/gmol [13]).

Figure 1 shows that the lower the water content in the atmospheric air, the lower $Ex_q°$ of the elements (except for hydrogen), since the content of the rest of the species of the air increases, and therefore the reference species Ex_c decreases. Moreover, in the case of hydrogen, water itself and methane, the lower air humidity the higher the $Ex_q°$ because these substances are directly related either with the water concentration or with the $Ex_q°$ of hydrogen; e.g. methane, which is formed from two hydrogen molecules and one carbon molecule.

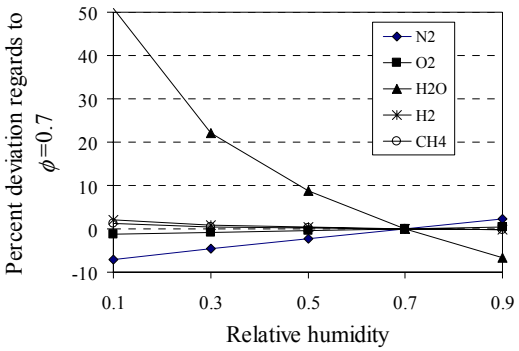

Figure 1: Atmospheric effect of water content on $Ex_q°$

It is important to note that $Ex_q°$ of carbon is not affected by the change of air relative humidity, because the difference between $Ex_q°$ of carbon dioxide and oxygen, from which $Ex_q°$ of carbon is obtained, remains constant whenever humidity varies.

EFFECT OF CO_2 CONCENTRATION ON $Ex_q°$ OF ELEMENTS

Due to the increase of the emissions from the fossil fuels combustion, the CO_2 concentration in the atmosphere has been increasing since the beginning of the industrialization process. Figure 2 shows how the $Ex_q°$ of CO_2 decreased only 2.2 % during the last century even though its

concentration in the air increased 19.4% during the same period [14].

Figure 2 shows that the value of $Ex_q°$ of other substances does not change significantly if the CO_2 concentration is different from 345 ppmv (Szargut's value) [6, 7]. Moreover, in the case of carbon and methane, whose $Ex_q°$ values strongly depend on $Ex_q°$ of carbon dioxide, the effect of CO_2 concentration on the $Ex_q°$ is less than 0.1%.

$Ex_q°$ of water is not affected by changing CO_2 concentration because humidity is kept constant, so it does not depend on the rest of the species of dry air, but on temperature and the total pressure of the medium.

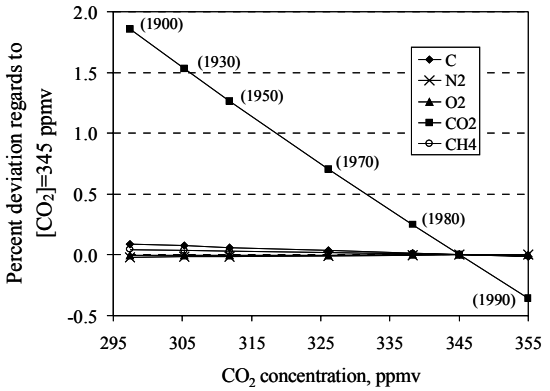

Figure 2: Effect of CO_2 concentration during the last century on $Ex_q°$

EFFECT OF SEEWATER SALINITY ON $Ex_q°$ OF ELEMENTS

Water salinity in the oceans is associated with latitude. Low salinity values are found in zones where rain precipitation is continuous or in the polar areas where salts are diluted by the fusion of ice, although during the winter salinity increases due to the opposite process. An example of this is the Baltic Sea of which salts content varies between 5 and 15‰. In contrast, in the subtropical regions where rain is scarce and water evaporation is high, the salinity can reach a value of 40‰, as it is the case of the Red Sea where, besides of being surrounded by earth, there are not fresh water supplies. The mean value of seawater salinity on Earth is 35‰.

In the present work, the effect of environmental conditions on $Ex_q°$ is analysed only for those elements, whose reference species dissolved in seawater were recommended by Rivero and Garfias in 2002 [11, 12]. The work obtained to change species concentration from pure substance to its concentration in the environment (Ex_c) decreases when the species concentration is increased in the environment, whenever the considered formation reaction of the reference species is the same. The effect of changing seawater salinity on $Ex_q°$ of the elements found in the ocean is very low (Figure 3), regardless of its value at T_n (298.15 K). The maximum deviation (1.1%) of the $Ex_q°$ value by increasing the salinity from 35 to 40‰ occurs for the bromide element.

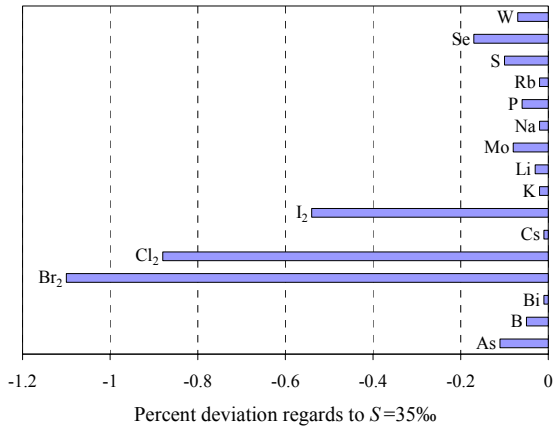

Figure 3: Effect on $Ex_q°$ of elements contained in the hydrosphere by increasing S to 40‰

EFFECT OF ENVIROMENTAL TEMPERATURE ON $Ex_q°$

The $Ex_q°$ of any substance strongly depends on the environmental temperature because its value fixes the change in the $\Delta G°$ of the reference reaction at equilibrium and to some extent also the concentration of the references species in the medium. In this work, the extreme conditions considered for terrestrial systems are 233.15 K (-40°C) as minimum temperature and 323.15 K (50°C) as maximum temperature.

The effect of temperature on the equilibrium constant of the reference reaction is given by [2]:

$$\frac{d(\ln K)}{dT} = \frac{\Delta H^o}{RT^2} \qquad (7)$$

If it is assumed that the $\Delta H°$ of the reaction is constant in the temperature range considered and its value is equal to the heat of reaction at normal

temperature T_n, the integral of Eq. (7) from the normal temperature T_n to the ambient temperature T becomes,

$$\ln \frac{K}{K_{T_n}} = \frac{\Delta H^o_{T_n}}{R}\left(\frac{1}{T_n} - \frac{1}{T}\right) \qquad (8)$$

Finally, using the relationship (Eq. (9)) between $\Delta G°$ and K of the reaction, the value change of $\Delta G°$ at a different temperature in reference to the normal is obtained by Eq. (10).

$$\ln K = -\frac{\Delta G^o}{RT} \qquad (9)$$

$$\Delta G^o = \Delta G^o_{T_n}\frac{T}{T_n} + \Delta H^o_{T_n}\left(1 - \frac{T}{T_n}\right) \qquad (10)$$

In general, the values of standard enthalpy and standard Gibbs energy for the formation reaction were taken from the same reference [8, 13, 15-18]; however, for some species $\Delta H_f°$ was obtained from $\Delta G°$ and entropy change of the reaction at 298.15 K.

Effect of temperature on $Ex_q°$ of elements and substances in the atmosphere

Figure 4 shows the percent deviation of the $Ex_q°$ of elements and reference species present in the atmosphere, as a function of environmental temperature. In the same figure, the $Ex_q°$ of methane is included.

When the environmental temperature varies, at atmospheric pressure and constant relative humidity (not constant absolute humidity), $Ex_q°$ value of the elements in the air changes significantly due to an important change of the water content in the atmosphere. For instance, at 323.15 K (50°C), the P_{H2O} increases almost 300% with respect to its value at 298.15 K (25°C), then the partial pressure in the air of the rest of the species decreases about 7% and consequently their $Ex_q°$ is increased. In the case of nitrogen, oxygen, and argon, the increase in $Ex_q°$ at 323.15 K is 35, 13 and 10%, respectively, whereas water $Ex_q°$ value decreases 30%, with respect to the normal temperature. Although, the $Ex_q°$ of carbon dioxide increases 9.3% at the same temperature, the $Ex_q°$ of the element carbon only increases 0.3%.

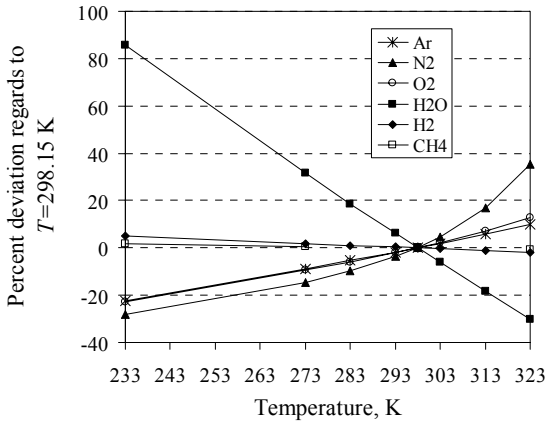

Figure 4: Effect of environmental temperature on $Ex_q°$ of elements and substances in the atmosphere

In the case of methane, the temperature effect is also small with a maximum variation at –40°C (1.7%), which is higher than its value at 25°C. When the environmental temperature and the water concentration, at constant atmospheric pressure and relative humidity, decrease and then the $Ex_q°$ of hydrogen increases, the value of the $Ex_q°$ of methane (Figure 4), as well as its $\Delta G_f°$ becomes higher. Since the $Ex_q°$ of carbon changes slightly with temperature and methane is formed by the double of molecules of hydrogen than carbon molecules, the change in the $Ex_q°$ value of the methane depends mainly on the change of the $Ex_q°$ of hydrogen. It is important to mention that if the P_{H2O} in the air is kept constant, and consequently its absolute humidity is kept constant during temperature change, the $Ex_q°$ of methane will show the opposite behaviour of the one shown in Figure 4, i.e., the higher temperature, the higher is $Ex_q°$ of methane [19]. However, maintaining a constant absolute humidity of air would imply a change in its relative humidity because of the variation of the $P°_{H2O}$.

Effect of temperature on $Ex_q°$ of elements present in the hydrosphere and lithosphere

When the environmental temperature is below zero degrees Celsius, a problem arises in the calculation of $Ex_q°$ of the elements of the hydrosphere and lithosphere, since seawater freezes at –2°C and so the reference species dissolved in seawater no

longer exits as such. This has no effect in the case of the elements in the atmosphere, since their $Ex_q°$ values do not depend on the $Ex_q°$ of the elements of the hydrosphere; however, the $Ex_q°$ of some elements of the Earth's crust (Ag, Ba, Cr, F_2, Hg, and Ra) depends on the exergy value of chlorine, potassium, phosphorus and sulphur which exits in seawater.

Information about frozen seawater composition is almost non-existent. Millero [20] indicates that frozen seawater has a higher relation of SO_4^{2-} to Cl^- ions with respect to liquid seawater because the sulphate ions are incorporated into the ice. Also, the relation Ca^+ to Cl^- changes due to the precipitation of calcium carbonate in the frozen sea. Assuming a frozen seawater composition would be extremely complex.

As the $Ex_q°$ of an element at 0°C is lower than its value at 25°C, it could be expected that if the temperature decreases further, this tendency would remain the same and vice versa. The only possibility that fulfills this assumption for all the elements is when the $Ex_q°$ of the elements of seawater and Earth's crust is determined at the same temperature at which the atmospheric air is, assuming that the species dissolved in seawater remain as such even when the temperature is below the seawater fusion point.

Figure 5 shows the percent deviation with respect to the value of $Ex_q°$ of elements on the hydrosphere and lithosphere at 25°C, when the temperature of the environment is –40°C, 0°C and 50°C. Figure 5 illustrates only the elements with the highest variation in the $Ex_q°$ value when changing temperature.

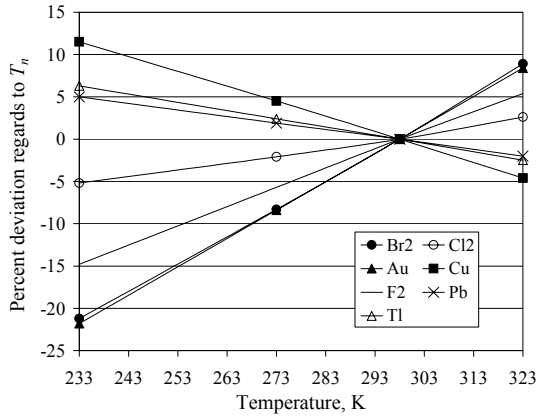

Figure 5: Effect of temperature on $Ex_q°$ of elements in seawater and Earth's crust.

There are two overall effects with temperature: the change of $\Delta G_f°$ and, the change of $Ex_q°$ of the reference species as well as of the others elements contained in the species.

In general, the higher the temperature, the lower the $Ex_q°$ value. This is reasonable since increasing the temperature of the reaction in which the element is transformed to its reference species and decreasing spontaneously (lower $\Delta G_f°$) more work from the surroundings is required for the reaction to take place and then the Ex_r decreases, i.e. the maximum useful work that can be obtained from that reaction.

In the case of elements Br_2, Cl_2, Cs, Rb, Ag, Au, F_2, Ir, Ni, Pd, Pt, Pu, Ra, Ru, and Te, the higher temperature the higher their $Ex_q°$. For the case of cesium and rubidium, when temperature increases, the $\Delta G_f°$ also increases. However, the behaviour of the $Ex_q°$ when temperature changes cannot be explained only by the tendency and magnitude of the $\Delta G_f°$ value, since in the case of Br_2, Cl_2, K, Li, Na, Ag, F_2, Ir, Ni, Pd, Pt, Pu, Ra, Ru, and Te, when temperature varies, the change in $Ex_q°$ and $\Delta G_f°$ do not follow the same tendency. Then, the change of $Ex_q°$ with temperature depends also on $Ex_q°$ of the reference species and of the other elements that are contained in the species.

In the case of gold, whose reference species is solid gold, the percent variation in its $Ex_q°$ is the only result of the temperature difference since its concentration remains constant. For the rest of the elements of the periodic table, the variation of $Ex_q°$ with environmental temperature is low, lower than 5%.

EFFECT OF ATMOSPHERIC PRESSURE ON $Ex_q°$

Although there are regions on the Earth with a height over sea level higher than 4,000 meters, in this work only altitudes where population live and chemical processes can be carried out, are considered. So, the values of 3,625 m (La Paz, Bolivia) and –244 m (Jericho, Israel) are assumed as maximum and minimum altitudes, respectively, with an atmospheric pressure of 0.65 and 1.03 atm. The pressure is related to altitude by [21]:

$$P_2 = P_1 \, e^{-Bh} \qquad (11)$$

P_2 is the atmospheric pressure at h, P_1 atmospheric pressure at sea level (1 atm), B a constant that

includes the air molecular weight, gravitational acceleration, R and T. At 25°C, B is equal to 1.168×10^{-4} m^{-1}. In general, the effect of atmospheric pressure on $Ex_q°$ of elements is very low or zero. In the case of elements whose reference species are in the air, the lower the pressure, the higher $Ex_q°$ of the rest of elements being in the atmosphere. The higher deviation (4.5%) on $Ex_q°$ is for nitrogen at 0.65 atm with respect to its value at 1 atm (see Figure 6).

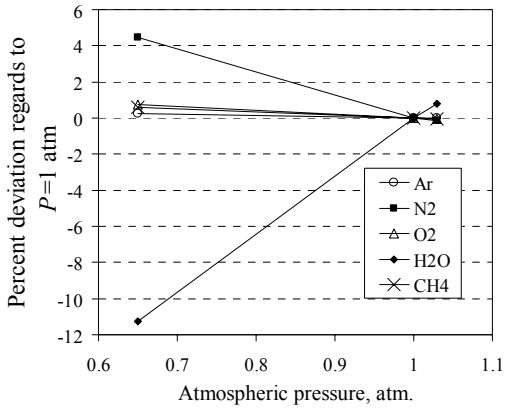

Figure 6: Effect of atmospheric pressure on $Ex_q°$ of elements and substances in the air

Changing atmospheric pressure, the $P°_{H2O}$ in the air keeps constant since its value depends only on temperature and relative humidity; however, the partial pressure and then the mole fraction value of the rest of species present in the atmosphere is modified, even though the proportion among them remains constant. Decreasing atmospheric pressure from 1 to 0.65 atm, the partial pressure of species different to water decreases by 35%. The molar fraction value of these species decreases, only by 1.2 % in this case, whereas the increment on x_{H2O} is almost 54%. The result is that $Ex_q°$ of water decreases 11% (see Figure 6) due to the increment of the water concentration in the medium, thus reducing its Ex_c. The lower molar fraction of the rest of species, the higher is their $Ex_q°$.

The variation on $Ex_q°$ value of elements present in the hydrosphere and lithosphere, by changing pressure, depends only on the variation of $Ex_q°$ of elements whose references species are in the atmosphere and which constitute reference species present in seawater and Earth's crust. If atmospheric pressure decreases to 0.65 atm, elements with the higher deviation in their $Ex_q°$ values are fluorine (1.8%), bromide (1.1%) and mercury (1%). In this case, the $Ex_q°$ of methane changes only 0.3% regards to its value at 1 atm, because this value is affected only by $Ex_q°$ of hydrogen, not by $Ex_q°$ of carbon or by $\Delta G_f°$, both of which do not change.

CONCLUSIONS

Ambient temperature is the condition that has the most important effect on the $Ex_q°$ of a substance, this is due to the fact that $\Delta G_f°$ of the reference species and its environmental concentration depend on this condition. If the substance is a component of the environment, such as nitrogen, oxygen and water, the effect of considering a temperature value different from 298K is higher than when the substance is not present. Moreover, when atmospheric pressure, air relative humidity, CO_2 concentration in the air and seawater salinity vary, the effect on $Ex_q°$ is very small.

Standard chemical exergy of water is the most sensitive value to changes in environmental conditions because its concentration in the environment is the one that changes more when any environmental property varies. In the case of steam water, the variation of its $Ex_q°$ value can be as high as 50%. Finally, at atmospheric pressure and constant relative humidity (not constant absolute humidity), $Ex_q°$ of any hydrocarbon increases when ambient temperature decreases. However, reducing temperature at constant air absolute humidity and atmospheric pressure, the $Ex_q°$ of a hydrocarbon decreases too; this is because of a change in relative humidity by the variation of water partial pressure.

REFERENCES

[1] Rivero R, Anaya A. *Exergy Analysis of Industrial Processes: Energy-Economy-Ecology*. Latin American Applied Research 1997; 27 (4): 191-205.

[2] Smith J M, Van Ness H C. *Introduction to Chemical Engineering Thermodynamics*. USA: McGraw-Hill, Inc., 4th Ed., 1987.

[3] Grant Gross M. *Oceanography: A View of the Earth*. N.J.: Prentice-Hall, Inc., Englewood Cliffs, 3rd Ed., 1982.

[4] Microsoft Corporation. *Encarta 98 Encyclopedia.* 1998 edition.

[5] Whitfield M, Turner D R. *Sea Water as an Electrochemical Medium*. In: Whitfield M, Jagner D, editors. Marine Electrochemistry: A practical introduction. *John Wiley y Sons Ltd.*, 1981.

[6] Szargut J. *Chemical Exergies of the Elements*. Applied Energy1989; 32: 269-286.

[7] Szargut J, Morris D R, Steward F R. *Exergy Analysis of Thermal, Chemical, and Metallurgical Processes*. New York: Hemisphere, 1988.

[8] Reid R C, Prausnitz J M, Sherwood T K. *The Properties of gases and Liquids*. U.S.A.: *McGraw-Hill Book Company*, 3rd. Ed., 1977.

[9] Riley J P. *Introduction to Marine Chemistry*. London: Academic Press, 1971.

[10] The Open University Course Team. *Seawater: its composition properties and behaviour*. Pergamon Press, 1989.

[11] Rivero R, Garfias M. *Standard Chemical Exergy Updated. Part I and II*. In: Energy-Efficient, Cost-Effective, and Environmentally-Sustainable Systems and Processes, Mexico, 2004, pp.761-785.

[12] Garfias M. *Efecto de las condiciones ambientales en la determinación de la exergia química y su impacto en el análisis exérgico de equipos y procesos*. Master degree thesis in Chemical Engineering, Universidad Nacional Autónoma de México, 2002.

[13] Perry R H, Chilton C H. *Manual del Ingeniero Químico*. Mexico: McGraw-Hill de México, 2nd Ed., 1982.

[14] CESPEDES. *Cambio Climático Global: El Reto del Sector Privado en América Latina*. Mexico: Centro de Estudios del Sector Privado para el Desarrollo Sustentable, Fuente original: Instituto Nacional de Ecología, 1998.

[15] Wagman D D, William H E, Parker V B, Schumm R H, Halow I, Bailey S M, Churney K L, Nuttall R L. *The nbs tables of chemical thermodynamic properties: Selected values for inorganic and C1 and C2 organic substances in SI units*. New York: American Chemical Society and the American Institute of Physics for the National Bureau of Standards, 1982.

[16] *CRC Handbook of Chemistry and Physics*. Robert C Weast, editor, CRC Press, 55th. Ed., 1975.

[17] Barner H E, Scheuerman R V. *Handbook of Thermochemical Data for Compounds and Aqueous Species*. N. Y.: John Wiley, 1978.

[18] Latimer W M. *The oxidation states of the elements and their potentials in aqueous solutions*. New York: Prentice-Hall, 1952.

[19] Rivero R, Montero G, Garfias M. *Efecto de la temperatura ambiental en la determinación de la exergia química de parafinas*. Revista del Instituto Mexicano de Ingenieros Químicos, A.C. 2001; 9-12: 197-205.

[20] Millero F J, Sohn M L. *Chemical Oceanography*. CRC Press, 1992.

[21] Perry J H. *Chemical Engineers' Handbook*. U.S.A.: McGraw-Hill, 3rd. Ed., 1949.

Proceedings of ECOS 2005
Trondheim, Norway
June 20–22, 2005

EXERGY ANALYSIS OF THE BASIC CRGT CYCLE

Wei Han[1,2] Hongguang Jin[1] and Na Zhang[1]
1 Institute of Engineering Thermophysics, Chinese Academy of Sciences Beijing 100080, China
2 Graduate school of the Chinese Academy of Sciences Beijing 100080, China
Tel: 86-10-82622854 E-mail: hgjin@mail.etp.ac.cn

ABSTRUCT: In this paper three advanced power systems, including the chemically recuperated gas turbine cycle (CRGT), the steam injected gas turbine cycle (STIG) and the combined cycle, were investigated through the exergy analysis. By comparing the results, the exergy destruction of combustion in CRGT cycle was lower 6.1% than that of the STIG cycle, which made the exergy efficiency of the CRGT cycle 2.6 percentage points higher. Through the exergy analysis based on the concept of energy level, the cascade utilization of chemical energy of natural gas in CRGT cycle was clarified. The exergy destruction during the mix process before combustion and the exergy loss of the exhausted gas in the CRGT cycle was increased rapidly compared to the combined cycle, which made the exergy efficiency of the CRGT cycle was about 5 percentage points lower than that of the combined cycle. At last the approach to improve the performance of CRGT was pointed out. The results obtained here give a deeper understanding of CRGT cycle and provide a new approach for the synthesis of innovative energy systems.

1 INTRUCTION

Thermal cycle is one of the active domains of energy and environment science. In the past several decades some advanced thermal cycles with gas turbine as core were proposed to improve the thermal efficiency of thermal cycle. These thermal cycles included the combined cycle (CC), steam injected gas turbine (STIG) [1, 2], humid air gas turbine (HAT) [3] and Kalina cycle [4]. The exhaust thermal energy from the gas turbine is used more and more efficiently, and it becomes more and more difficult to improve the performance of the thermal cycle. The current research was mainly focused on how to utilize the thermal energy of exhaust gas of gas turbine more efficiently.

The chemically recuperated gas turbine (CRGT), which was proposed in 1970's, was the first time to combine the thermal cycle with the chemical process of the steam reforming. In this paper we call it as the indirect energy release of the natural gas. Steam reforming was considered by several authors as a possibility to improve the efficiency of gas turbine cycles [5-7]. The basic chemically recuperated cycle was simulated in Ref. [8], and the thermal efficiency was 48.8%, which was higher than that of the steam injected gas turbine (STIG) and lower than of the combined cycle (CC). Then the CRGT was improved [12] by using reheated Brayton cycle as the topping cycle, and the thermal efficiency rose, however lower than that of the CC. Many researchers have noted that the calorific value of the fuel will be increased by the utilization of heat available at the turbine discharge, but the thermal efficiency of the cycle does not rise conspicuously. In order to understand the reason, the system was studied by the traditional exergy analysis [15], but no satisfied result was obtained.

The aims of this paper are (1) to clarify the role of the indirect energy release in the CRGT based on the concept of energy level, (2) to investigate the key factors that affect the performance of the indirect energy release. (3) to point out the method to improve the efficiency of the power cycle with steam reforming.

2 SIMULATIONS OF CYCLES

Three thermal cycles were simulated using ASPEN+ process simulation code, which were the CRGT, the STIG and the CC. The gas turbines in these cycles were without intercooling or reheat. Figures 1a 1b and 1c respectively show the schematic diagrams of the CRGT cycle STIG

cycle and the CC. In the three cycles the compression ratio is 15.0 and the inlet temperature of gas turbine is 1581K. The combustor pressure ratio is 0.97. The compressor isentropic efficiency is 0.89 and the turbine isentropic efficiency is 0.88.

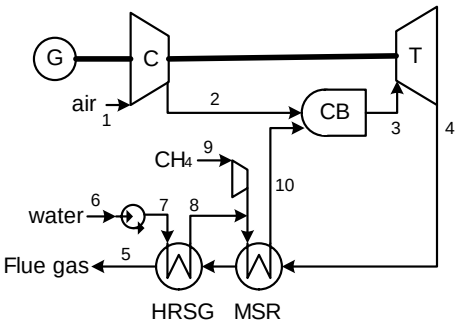

C: compressor T: turbine CB: combustor
MSR: Methane-Steam reformer
HRSG: Heat Recovery Steam Generator
G: generator P: pump

Fig. 1a. CRGT cycle

In the reformer of the CRGT the approach temperature difference is 20K. According to Ref. [8], the chemical nonequilibrium can be described by the chemical equilibrium approach temperature difference ($\triangle T_{eq}$). $\triangle T_{eq}$ can either be specified or calculated from the following equation for a typical reformer using a nickel-based catalyst:

$$\Delta T_{eq} = 0 \qquad \text{if } T_{\text{out},2} \geq 923\text{K}$$

$$\Delta T_{eq} = 43.33(1.0 - \frac{T_{out,2} - 273}{650}) \quad \text{if } T_{\text{out},2} < 923\text{K}$$

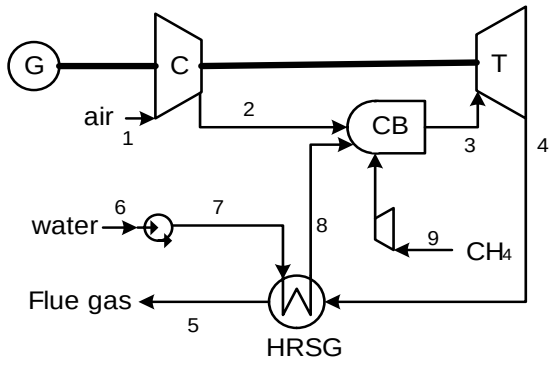

C: compressor T: turbine CB: combustor
HRSG: Heat Recovery Steam Generator
G: generator P: pump

Fig. 1b. Simple STIG cycle

The hot-side reformer pressure ratio is 0.97 and the cold-side reformer pressure ratio is 0.9.

In the STIG cycle the hot-side HRSG pressure ratio is 0.99 and the cold-side HRSG pressure ratio is 0.95. The approach temperature difference of the HRSG is 20K.

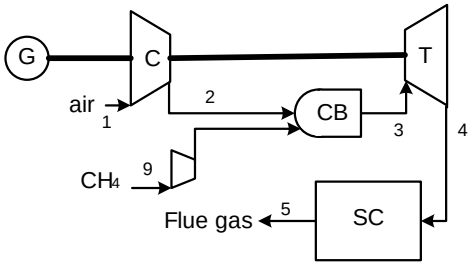

C: compressor T: turbine CB: combustor
SC: Steam cycle G: generator

Fig. 1c.Combined cycle

In the combined cycle the steam cycle (SC) is with dual pressures and reheating. The high pressure is 12MPa and the temperature of the live steam is 535°C. The reheating pressure is 3.9MPa and the reheating temperature is 535°C. The low pressure is 0.5MPa and the temperature of steam is 260°C.

Table 1 presents the main results for the three cycles.

Table 1 Main result for CRGT, STIG and CC cycle

Points	CRGT cycle		STIG cycle		CC cycle	
	P/ atm	T/ K	P/ atm	T/ K	P/ atm	T/ K
1	0.99	288	0.99	288	0.99	288
2	14.7	672	14.7	672	14.7	673
3	14.3	1581	14.3	1581	14.3	1581
4	1.04	860	1.02	875	1.04	869
5	1.0	413	1.0	413	1.0	413
6	1.97	288	1.97	288	--	--
7	22.2	288	22.2	288	--	--
8	21.1	494	21.1	494	--	--
9	4.93	288	4.93	288	4.93	288
10	19.0	840	--	--	--	--

3 ANALYSES OF THE THREE CYCLES BASED ON EXERGY AND THE CONCEPT OF ENERGY LEVEL

3.1 Exergy analysis

Based on the simulation results of the three cycles, the exergy analyses were carried out. In this paper the combustion was divided into two steps. Firstly, the fuel, air and other stream such as the steam in the STIG cycle were mixed before combustion. Secondly, the mixture took reaction and the fuel was oxidated completely.

Table 2 Exergetic comparison of CRGT and STIG

	Exergy / kW		
	CRGT	STIG	CC
Exergy losses			
Mix before Com.	5.69	6.58	1.49
Combustor	24.54	26.14	28.11
Heat recovery	6.83	6.83	3.42
Power subsystem	9.54	8.85	11.06
Stack gas	6.39	7.19	4.09
Total losses	53.00	55.58	48.16
Work output	47.00	44.24	51.84
Exergy of fuel	100.00	100.00	100.00
Exergy efficiency	47.00%	44.42%	51.84%

The exergic analyses of the three cycles were presented in Table 2. The exergy efficiency of the CRGT cycle is 2.58 percentage points higher than that of the STIG cycle. In the CRGT cycle the ratio of steam to methane was 6.1 and in the STIG cycle the ratio was 6.9. As there was more steam mixed with air in STIG cycle, the exergy destruction of mix before combustion is 0.89 kW more than that in the CRGT cycle. For the same reason the exergy loss of stack gas in CRGT cycle was smaller than that of the STIG cycle. The energy destruction in combustor of the CRGT cycle is decreased 6.1% than that of the STIG cycle. Hence, the decrease of the exergy destruction of combustion looks like the primary reason that leads the exergy efficiency of the CRGT cycle higher than the STIG cycle.

With the same inlet temperature of gas turbine, the optimal pressure of the CRGT cycle and the STIG cycle is difference. The optimal pressure of the STIG is higher than that of the CRGT. When the pressure is lower, the efficiency of the CRGT cycle is higher than that of the STIG. As the pressure is increased, the outlet temperature of gas turbine will be decreased. So there will be less methane reformed, and the advantage of the CRGT cycle is weakened. As the pressure is high enough, the reforming reaction does not take place and the CRGT cycle does not work.

Comparing the CRGT cycle and the CC, the exergy destruction of combustion of CRGT is decreased by 3.571kW. As there is no steam in the mix before combustion, the exergy destructions in the process and the exergy loss of stack gas in CC are respectively decreased by 4.2kW and 2.3 kW compared with CRGT. The decrement of the exergy destruction in combustion is counteracted by the increment of the exergy destruction in mix. In the CRGT and STIG cycles the HRSG is single pressure, but in CC the HRSG is dual pressure. The exergy destruction in HRSG of the CC is decreased by 3.41 kW than the CRGT cycle.

3.2 The role of the steam reforming in CRGT cycle

In order to disclose the cascade utilization of natural gas in CRGT cycle, we analysis the steam reforming based on the concept of energy level. In Ref. [16] Masaru Ishida introduced the concept of energy level and also introduced many applications on difference thermal processes. The exergy analysis based on this concept can get more detail of the thermal process than the traditional exergy analysis. The defining equation of A is

$$A = \Delta E / \Delta H \tag{1}$$

where ΔH represents the quantity of transformed energy and ΔE represents the quality of transformed energy. When $A=0$, it represents the environmental status.

The steam reforming was presented in the Fig.2.

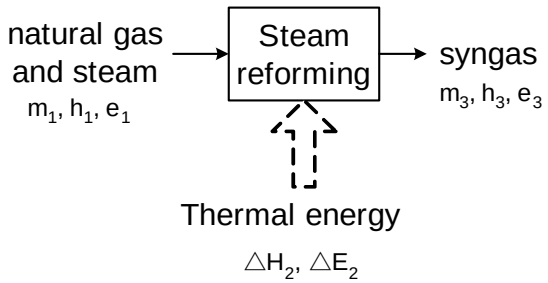

Fig. 2 Sketch map of the steam reforming

We assumed that the temperature of the reforming reaction is constant. The parameters of m, h and e, respectively, represent mass, enthalpy and exergy, and the subscript 1, 2 and 3 respectively represent reactant (mixture of natural gas and steam), thermal energy for reaction and the product of reforming reaction-syngas. Since the temperature has little effect on the enthalpy and exergy of fuel, here the enthalpy and exergy of the fuel are assumed as constants.

The energy balance of the reaction is based on the first law of thermodynamics

$$m_3 * h_3 = m_1 * h_1 + \Delta H_2 . \quad (2)$$

Similarly, the exergy balance of the reaction is based on the second law of the thermodynamics

$$(\Delta E_2 - \Delta E_w) = m_3 e_3 - m_1 e_1 \quad (3)$$

where ΔE_w is the exergy loss in the reaction. Eq. (3) can be rearranged as

$$m_3 e_3 = m_1 e_1 + (\Delta E_2 - \Delta E_w) . \quad (4)$$

Based on the Eq. (1), the energy level of the fuel and the synthetic fuel can be expressed as

$$A_1 = \frac{m_1 * e_1}{m_1 * h_1} = \frac{e_1}{h_1} \quad (5)$$

$$A_3 = \frac{m_3 * e_3}{m_3 * h_3} = \frac{e_3}{h_3} . \quad (6)$$

Substitute Eqs. (2) and (4) into Eq. (6), and yields

$$A_3 = \frac{m_1 * e_1 + \Delta E_2 - \Delta E_l}{m_1 * h_1 + \Delta H_2} . \quad (7)$$

The energy level of the thermal energy for reaction is

$$A_2 = \frac{\Delta E_2}{\Delta H_2} = 1 - \frac{T_0}{T_2} \quad (8)$$

where T_2 is the temperature at which the reaction takes place. The energy level of the thermal energy for reaction is equal to the efficiency of the Carnot cycle which woks between the temperature of reaction and environment.

Here, we define the parameter β which is the ratio of the thermal energy for reaction to the enthalpy of the reactant (fuel). The expression of β is

$$\beta = \frac{\Delta H_2}{m_1 * h_1} . \quad (9)$$

Substitute the Eqs. (5), (8) and (9) into Eq. (7) and predigest it. The following equation is obtained

$$A_3 = \frac{A_1}{1+\beta} + \frac{\beta}{1+\beta}(A_2 - \frac{\Delta E_w}{\Delta H_2}) \quad (10)$$

where $\Delta E_w/\Delta H_2$ is the energy level degradation of the thermal energy for reaction caused by the exergy loss in the chemical reaction. (A_2-$\Delta E_w/\Delta H_2$) can be understood as the energy level of reforming reaction, when the reaction is reversible. As $\Delta E_w/\Delta H_2$ is denoted by ΔA_w, the Eq. (10) becomes

$$A_3 = \frac{A_1}{1+\beta} + \frac{\beta}{1+\beta}(A_2 - \Delta A_w) \quad (11)$$

Eq. (11) can be rearranged as

$$A_3 = A_1(\frac{1}{1+\beta} + \frac{\beta}{1+\beta}\frac{A_2 - \Delta A_w}{A_1}) \quad (12a)$$

Eq. (12a) can be written as

$$A_3 = \alpha * A_1 \quad (12b)$$

where

$$\alpha = (1 + \beta\frac{A_2 - \Delta A_w}{A_1})/(1+\beta) \quad (13).$$

As $(A_2 - \Delta A_w) < A_1$, we can get $\alpha < 1$. From the Eq.(12b) the energy level of natural gas is decreased through the steam reforming.

Eq. (11) can be rearranged as

$$(1+\beta)A_3 = A_1 + \beta(A_2 - \Delta A_w) \quad (14)$$

The left side of the Eq. (14) is the exergy of syngas, and $(1+\beta)$ is the quantity of chemical energy of syngas. The first item on the right side of Eq. (14) is the exergy of methane, and the quantity of chemical energy of methane is equal to 1. The second item on the right side is the exergy of thermal energy absorbed by the reaction theoretically. From Eq. (14) we can see that the exergy of thermal energy and methane are changed into the exergy of syngas. As we know that the energy level of thermal energy is lower than that of syngas, it is upgraded. Here we can conclude that the decrement of the energy level of methane is not destructed, but it is utilized to upgrade the energy level of thermal energy.

When the syngas is combusted, the exergy destruction can be expressed as

$$(1+\beta)(A_3 - A_T) = (1+\beta)A_3 - (1+\beta)A_T \quad (15).$$

Substitute the Eq.(14) into Eq.(15) and predigest it

$$(1+\beta)(A_3 - A_T) = (A_1 - A_T) - \beta(A_T - A_2 + \Delta A_w) \quad (16)$$

The first item of right side of Eq. (16) is the exergy destruction of combustion of methane, as the methane is combusted directly. The combustion temperature is higher than that of the reforming reaction, the second item of right side of Eq. (16) is positive. Then we can say that in the combustion the exergy destruction of syngas is smaller than that of methane. Through the steam reforming the CRGT cycle utilizes the chemical energy of methane before combustion and causes the exergy destruction in combustion to be decreased. It is efficient utilization of the chemical energy of methane that made exergy efficiency of the CRGT cycle higher than that of the STIG cycle.

4 PERFORMANCE OF INDIRECT ENERGY RELEASE

The steam reforming is the key process in the CRGT cycle and it will affect the thermal efficiency of the power cycle. There are some parameters that will affect the utilization of natural gas in the CRGT. The first one is the ratio of steam to methane (s/c) in the reformer, the second one is the temperature of the reforming (tr) and the third one is the pressure of the reaction of reforming. As the pressure of reforming is decided by the pressure ratio of compressor, we assume that the pressure of reforming is 19 atm. Fig. 3 shows the effect of the parameters of s/c and tr to the mix and the combustion. As the temperature of steam reforming is increased from 600K to 1400K, the exergy destruction of combustion is decreased in Fig. 3. The methane/steam reforming is a highly endothermic reaction and the reaction is

$$CH_4 + H_2O = CO + 3H_2$$

$$(\Delta H^0_{298} = 206 \text{ kJ/mol}).$$

The high temperature will get the high conversion rate of natural gas into CO or H_2. When more methane is converted into CO and H_2, the reaction of reforming will absorb more thermal energy and the parameter of β rise. From Eq.(13) the parameter of α will reduce with the increment of the parameter β. From Eq. (14), the exergy destruction of combustion is decreased with the increment of the reforming temperature. On the other hand, when the temperature of reforming is increased, the temperature and the molecule number of syngas are increased. So the exergy destruction of mix is increased rapidly in Fig.4. Fig.5 expresses the effect of temperature of reforming on the sum of mix and combustion. There exists a proper reforming temperature, at which the sum of exergy destruction has minimum.

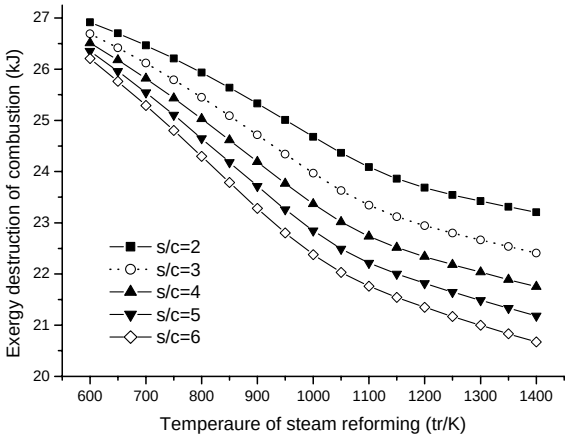

Fig. 3 Exergy destruction of combustion

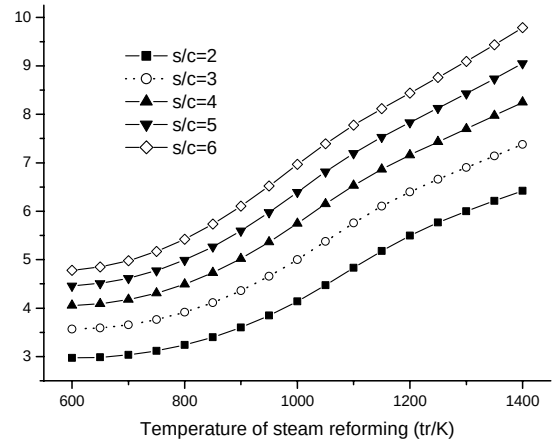

Fig. 4 Exergy destruction of mix

The ratio of steam to methane also affects the steam reforming. The increment of ratio (s/c) drives more methane reacted. The parameter of β is increased and α is decreased. The exergy destruction of combustion is decreased with the increment of s/c shown in Fig. 3. By contraries, the exergy destruction of mix is increased with the

increment of s/c, as the molecule number of syngas is decreased in Fig. 4. In order to reduce the exergy destruction of the sum, the parameter s/c should be smaller as shown in Fig. 5. As the parameter of s/c and tr are respectively 2 and 1000K, the sum of exergy destruction is 28.82kJ which is 0.78kJ less than that of the CC. The exergy exhaust gas is 4.66kJ and is 0.57kJ more than the CC. In a word the proper reforming temperature (950K—1050K) and the lower ratio of steam to methane will improve the performance of the indirect energy release.

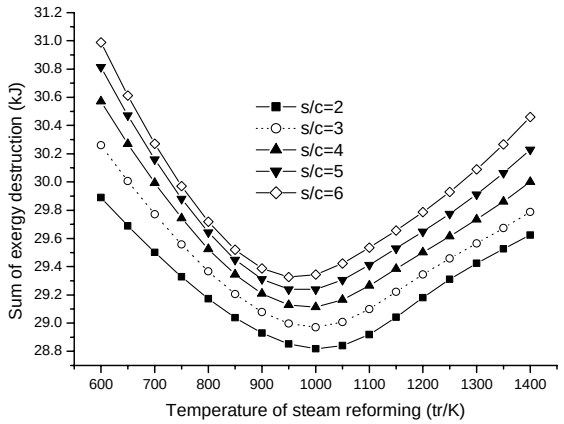

Fig. 5 Sum of exergy destruction

5 APPROACH TO IMPROVE CRGT

In order to improve the performance of the CRGT cycle, we can adopt several methods. (1) Keep the temperature of reforming between 900K and 1050K. In this range the indirect energy release has high performance in Fig. 5. (2) The ratio of steam to methane should be as low as it can be. In the practice it should be higher than 2. If the ratio is lower than 2, the carbon will be generated and the catalyzer will be poisoned. As the steam is decreased, the performance of the indirect energy release is improved. At the same time the exergy destruction of mix and exhaust will also be reduced. (3) The thermal energy of the exhaust gas of gas turbine should be utilized more efficiently in CRGT cycle. The thermal energy with higher temperature can be absorbed by the reaction of steam/methane reforming. A part of the thermal energy with lower temperature can generate steam for the reforming reaction and the other can be used to humidify the air of the combustion.

6 CONCLUSIONS

In this paper the indirect energy release in the CRGT cycle is studied, and it is the key process that makes the thermal efficiency of CRGT cycle higher than the STIG cycle. In the indirect energy release the chemical energy of natural gas is utilized before combustion and the energy level of fuel is decreased. The decrement of energy level of fuel makes the exergy destruction of combustion reduce. The exergy destruction during mix before combustion and heat exchange was increased as while as the exergy loss of exhaust gas. All of these make the thermal efficiency of the CRGT cycle lower than that of the CC. Based on the parameters analysis, the indirect energy release can utilize the natural gas more efficiently, when the temperature of steam reforming is about 1000K and the ratio of steam to methane is equal to 2. This paper gives a deeper understanding of CRGT cycle and provides a new approach for the synthesis of innovative energy systems.

ACKNOWLEDGMENT

*Supported by the National Natural Science Fundamental Research Program (No. 90210032)

REFERENCES

[1] Dah-Yu Cheng et al. Parallel-compound dual-fluid heat engine. U.S. Patent 3978661, 1976

[2] Lin, R. et al. Analysis of the steam injected gas turbine (in Chinese), Journal of engineering thermophysics, 1986, Vol. 7(3):195-200

[3] Y. Mori et al. High efficient regeneration gas turbine system by new method of heat recovery with water injection. In: Tokyo international gas turbine congress, 1983

[4] Kalina A. I. et al. Combined cycle system with novel bottoming cycle, Journal of engineering gas turbines and power, 1984, Vol. 106(10):737-742

[5] Jin H et al. Graphical exergy analysis of complex cycles, Energy-the International Journal, 1993, Vol. 18(6):615-625

[6] Jin H et al. Exergy evaluation of two current advanced power plants: supercritical steam

turbine and combined cycle, Transactions of the ASME, 1997, Vol. 119(12):250-256
[7] Jin H et al. A novel gas turbine cycle with hydrogen fueled chemical-looping combustion, International Journal of Hydrogen, 2000, Vol. 25:1209-1215
[8] K. F. Kesser et al. Analysis of a basic chemically recuperated gas turbine power plant, Journal of engineering for gas turbine and power, 1994, Vol. 116(4):277-284
[9] T. Nakagaki et al. Development of chemically recuperated micro gas turbine, Journal of engineering for gas turbine and power, 2003, Vol. 125(1):391-397
[10] T. Nakagaki et al. Development of methanol steam reformer for chemical recuperation, Journal of engineering for gas turbine and power, 2001, Vol. 123(10):727-733
[11] Janes, J. et al. Chemical recuperated gas turbine, California Energy Commission Staff Report P500-92-015, 1972
[12] Simon Harvey et al. Analysis of a reheat gas turbine cycle with chemical recuperation using Aspen, Energy Convers. Mgmt, 1997, Vol. 38(15-17):1671-1679
[13] C. Carcasci et al. Modular approach to analysis of chemically recuperated gas turbine cycles, Energy Convers. Mgmt, 1998, Vol. 39(16-18):1693-1703
[14] G. Lozza et al. Nature gas decarbonization to reduce CO2 emission from combined cycles-part II:Steam-methane reforming, Journal of Engineering for Gas Turbines and Power, 2002, Vol. 124(1):89-95
[15] H. Abdallah et al. Exergetic optimization of intercooled reheat chemically recuperated gas turbine, Energy Connvers. Mgmt, 1999, Vol. 40:1679-1686
[16] Masaru Ishida. Thermodynamics made comprehensible, Nova Science Publishers, Inc. New York

Proceedings of ECOS 2005
Trondheim, Norway
June 20–22, 2005

GRAPHICAL MODELS FOR SPLITTING PHYSICAL EXERGY

Tatiana Morosuk*
Institute for Low Temperature, Odessa State Academy of Refrigeration
Dvorianskaya 1/3, Odessa 65026, Ukraine

George Tsatsaronis
Institute for Energy Engineering, Technische Universität Berlin
Marchstr. 18, 10587 Berlin, Germany

ABSTRACT

Splitting the physical exergy of a working fluid into its thermal and mechanical components improves the accuracy of and facilitates an exergoeconomic optimization. In this paper graphical models are used to demonstrate the splitting of physical exergy. These models assist in understanding and using theoretical models.
Keywords: physical exergy, thermal exergy, mechanical exergy, isothermal expansion, isobaric heat transfer

NOMENCLATURE

e	specific exegy [J/kg]
h	specific enthalpy [J/kg]
T	temperature [K]
s	specific entropy [J/kg·K]
p	pressure [Pa]
Superscripts	
PH	physical exergy
T	thermal exergy
M	mechanical exergy
Subscripts	
O	environment
☺	point being considered

INTRODUCTION

The accuracy of an exergoeconomic analysis and the quality of optimization may be improved when (a) the physical exergy of a working fluid is split into its thermal and mechanical exergy components, and (b) each exergy component is cost separately. The principles of costing exergy streams are discussed in References [1-8].

The splitting of physical exergy is discussed in References [1-3, 5, 9-14 and 19]. For this purpose either adiabatic and isothermal processes or isobaric and isothermal processes are considered.
The present paper complements the development presented by Paulus and the authors [14] and demonstrates graphically the interpretation of physical exergy splitting. The physical exergy may be graphically shown on various diagrams including the following:

On an *e*-*h*-diagram

The graphical model for splitting physical exergy into its components is used to estimate the effect of changing pressure and temperature of a material stream on the exergy value. The graphical demonstration of physical exergy as the sum of the thermal and mechanical exergy components using an *e*-*h*-diagram is given in References [10] and [11], Fig. 1.
It is necessary to recognize that analysis on an *e*-*h*-diagram is not as objective as the analysis on other thermodynamic diagrams of a working fluid, for example, on an *h*-*s*-diagram, or *T*-*s*-diagram. The

* Corresponding author: Phone: +38 0482 239183
Fax: +38 0482 238931 E-mail: morosuk@paco.net

e-h-diagram is created by fixing the temperature and pressure of point «O» (p_O, T_O). In References [10] and [11] the temperature of environment is T_O=290 K (17°C) a values considered as standard for exergy analysis in the 1960's. Note, that for exergy analysis the following values of T_O: are accepted T_O=15°C (288K) as ISO standard; T_O=27°C (300K) in [17] for simplification of calculation data and T_O=25°C (77°F, 298K) as standard for modern applied thermodynamics [5].

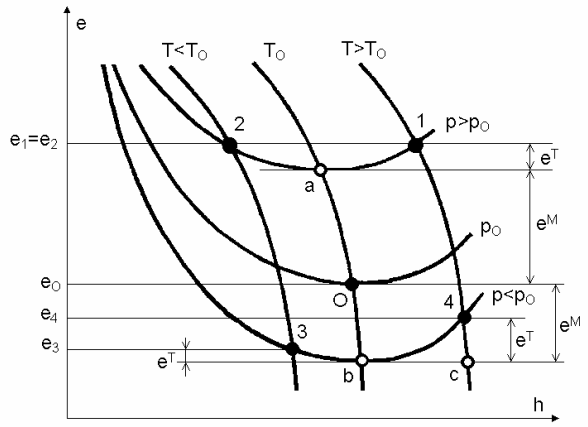

Figure 1: Thermal and mechanical components of physical exergy. Graphical interpretation on *e-h*-diagram by [10-11]:

Point 1 - $T_1>T_O$; $p_1>p_O$; $e^T=e^1-e^a$; $e^M=e^a-e_O$; $e^T+e^M=e^1-e_O$

Point 2 - $T_2<T_O$; $p_2>p_O$; $e^T=e^2-e^a$; $e^M=e^a-e_O$;

Point 3 - $T_3<T_O$; $p_3<p_O$; $e^T=e^3-e^b$; $e^M=e^b-e_O$; $e^T+e^M=e^3$; $e^M<0$; $e^T>0$

Point 4 - $T_4>T_O$; $p_4<p_O$; $e^T=e^4-e^c$; $e^M=e^c-e_O$

On a *p-V*-diagram

If exergy is potential work, then there must be an expansion machine where this work can be produced. This was proposed by Bošnjaković [9] and presented graphically as shown in Fig. 2a. Physical exergy is the area of *p-V*-diagram of an expansion machine. There are two parts:

- work produced by an isentropic expansion ($e^1 \equiv w_{s=const}$);
- work produced by an isothermal expansion ($e^2 \equiv w_{T=const}$).

Thus, the physical exergy is

$$e = -\int_1^3 v dp = -\int_1^2 v dp - \int_2^3 v dp \,, \qquad (1)$$

$$q = h_3 - h_1 - \int_1^3 v dp = h_3 - h_1 + e \,. \qquad (2)$$

If the process 2→3 is an isothermal expansion (*T=const*), then the amounts of heat and work are absolutely taken equal in this process $w_{2\to3}=q_{2\to3} = T(s_3 - s_2)$. Thus, if $T_3=T_O$, we have an equation for calculating physical exergy

$$e = h - h_O - T_O(s - s_O). \qquad (3)$$

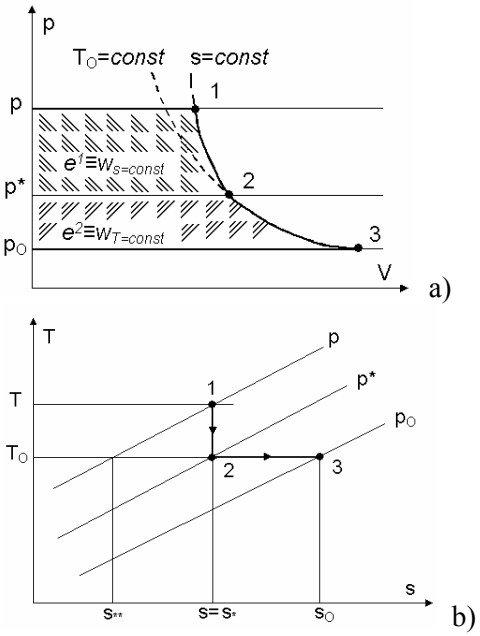

Figure 2: Graphical model of exergy by Bošnjaković [9]

BACKGROUND FOR PHYSICAL EXERGY SPLITTING

There are only three thermodynamic processes that can be used to develop the components of physical exergy: isothermal expansion (or compression), adiabatic expansion (or compression), and isobaric heat transfer.

Isothermal expansion. An isothermal expansion from p to p_O is an ideal process that cannot be realized in practice. The amount of heat required is absolutely taken equal to work generated.

This process can be carried out if there is a heat source of limited size with unlimited heat capacity or a heat source with limited heat capacity but unlimited size. From the theoretical point of view, the isothermal expansion can be carried out at any temperature level. Isothermal expansion at $T<T_O$ or $T>T_O$ demands additional energetic expenses (*T=const* only) that should be taken into account in the analysis. An isothermal expansion at $T<T_O$ or $T>T_O$ is according to Reference [15] a non-

equilibrium process that should not be considered in a theoretical analysis.

Isobaric heat transfer. An isobaric heat transfer process from T to T_O can be carried out at $p<p_O$, $p=p_O$ and $p>p_O$. For heat transfer realization at $p<p_O$ or $p>p_O$ additional energetic expenses are necessary.
Adiabatic expansion. An adiabatic expansion can be considered as the combination of isobaric heat transfer and isothermal expansion; therefore, this process can also be used in the analysis. Reference [18] contains a detailed analysis of an adiabatic compression process as sum of isothermal compression and isobaric heat transfer.

GRAPHICAL MODEL OF EXERGY

A graphical model is the illustration of a theoretical model. In the following, the graphical models of exergy for five different locations of point «☺» (p, T) with respect to the environmental point «O» are given on p-V-diagrams, T-s-diagrams and h-s-diagrams. Let us work "from simple to complex" and systematize the results.

On *p-V*- and *T-s*-diagrams

Model «A» (Fig.3). The coordinates of point «☺» are (p, $T=T_O$, $s<s_O$, h). An isothermal expansion leads from point «☺» to point «O» at T_O. The physical exergy of point «☺» has only a mechanical component. Thus the area on a p-V-diagram is equivalent to the mechanical component of physical exergy only.

The graphical model of exergy is

$$e^{PH} = e^{M} \equiv \text{area (a-☺-O-b)}. \qquad (4a)$$

The theoretical model of exergy is

$$e^{PH} = e^{M} = T_O\left(s_O - s\right) - \left(h_O - h\right)_{T_O=const}. \qquad (4b)$$

Model «B» (Fig.4). The coordinates of point «☺» are (p, T, $s=s_O$, h). An isentropic expansion leads from point «☺» to point «O».
An adiabatic expansion from point «☺» to point «O» must be replaced by a combination of isobaric heat transfer and isothermal expansion for defining the thermal and mechanical components of physical exergy.

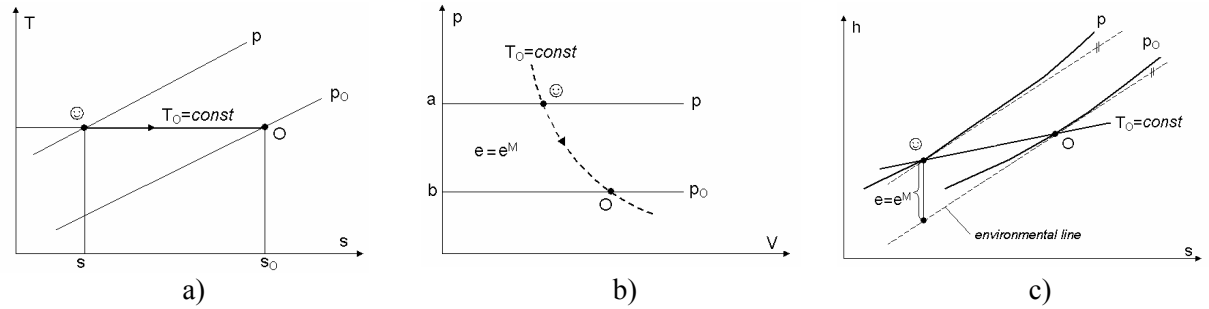

a) b) c)

Figure 3: Graphical model of exergy (*Model «A»*):
a) on T-s diagram; b) on p-V-diagram; c) on h-s-diagram

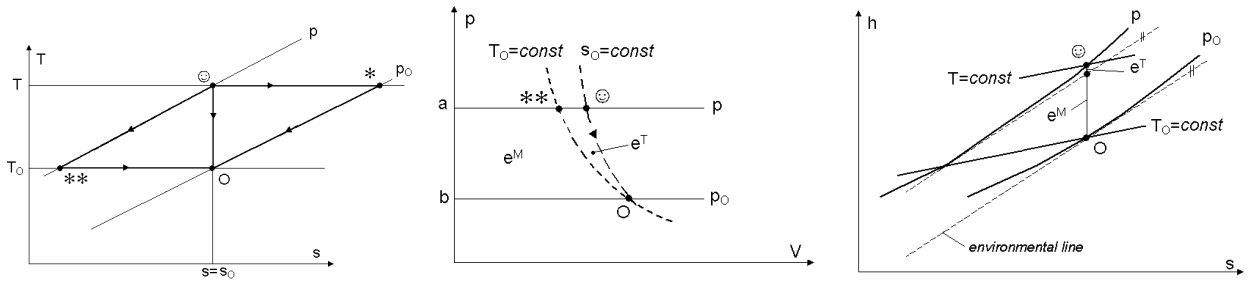

a) b) c)

Figure 4: Graphical model of exergy (*Model «B»*):
a) on T-s diagram; b) on p-V-diagram; c) on h-s-diagram

We may use one of the following two ways:

Way 1:
isothermal expansion $p \rightarrow p_O$ at $T=const$
+ isobaric cooling $T \rightarrow T_O$ at $p_O=const$
= way «☺» → «*» → «O»

This way should be excluded from the analysis because there is an isothermal compression process at $T>T_O$ (see [15]).

Way 2:
isobaric cooling $T \rightarrow T_O$ at $p=const$
+ isothermal expansion $p \rightarrow p_O$ at $T_O=const$
= way «☺» → «**» → «O»

The physical exergy of point «☺» represents the sum of the thermal and mechanical exergy components, hence the area of p-V-diagram consists of two parts.

Graphical model of exergy

$$e^{PH} = e^{T} + e^{M} \equiv$$
$$\equiv \text{area}\,(☺\text{-}**\text{-}O) + \text{area}\,(a\text{-}**\text{-}O\text{-}b). \quad (5a)$$

Theoretical model of exergy

$$e^{PH} = \underbrace{c_p\left(T - T_O\right)}_{e^T} + \underbrace{T_O\left(s_O - s^{**}\right) - \left(h_O - h^{**}\right)_{T_O=const}}_{e^M} \quad (5b)$$

Model «C» (Fig.5). This model was proposed in [9]. The coordinates of point «☺» are (p, T, $s<s_O$, h). An irreversible expansion leads from point «☺» to point «O» at $\Delta s>0$.
We may use the following ways for this model:

Way 1:
adiabatic expansion $p \rightarrow p^*$ at $s=const$
+ isothermal expansion $p^* \rightarrow p_O$ at $T_O=const$
= way «☺» → «*2» → «O»

Way 2a:
isothermal expansion $p \rightarrow p^*$ at $T=const$
+ adiabatic expansion $p^* \rightarrow p$ at $s_O=const$
= way «☺» → «*1» → «O»

Way 2b:
isothermal expansion $p \rightarrow p_O$ at $T=const$
+ isobaric cooling $T \rightarrow T_O$ at $p_O=const$
= way «☺» → «*» → «O»

Way 2 (ways 2a and 2b) should be excluded from the analysis, as an isothermal compression occurs at $T>T_O$.

Way 3:
isobaric cooling $T \rightarrow T_O$ at $p=const$
+ isothermal expansion $p \rightarrow p_O$ at $T_O=const$
= way «☺» → «**» → «O»

Way 1 and way 3 are alternatives. An adiabatic expansion «☺» → «*2» (by way 1) is the sum of isobaric cooling and isothermal expansion «☺» → «**» + «**» → «O». It is clear that the physical exergy of point «☺» is the sum of thermal and mechanical exergy components. The area of indicator diagram consists of three parts: two parts are mechanical exergy components and one part represents the thermal component of physical exergy.

Graphical model of exergy

$$e^{PH} = e^{T} + e^{M1} + e^{M2}$$

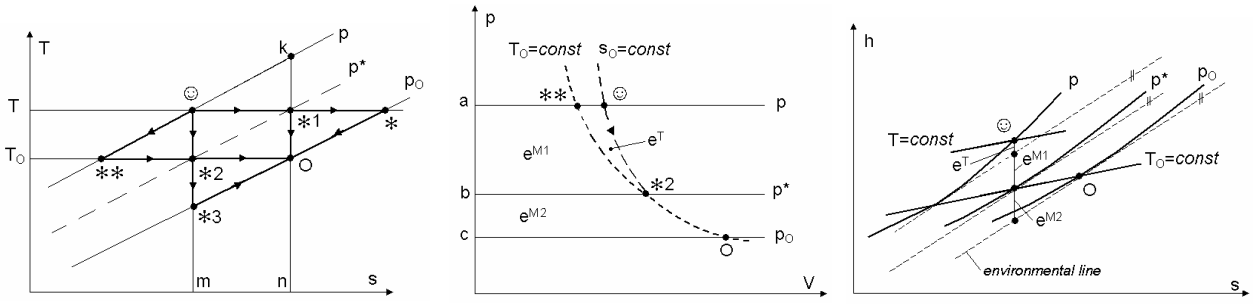

a) b) c)

Figure 5: Graphical model of exergy (*Model «C»*):
a) on T-s diagram; b) on p-V-diagram; c) on h-s-diagram

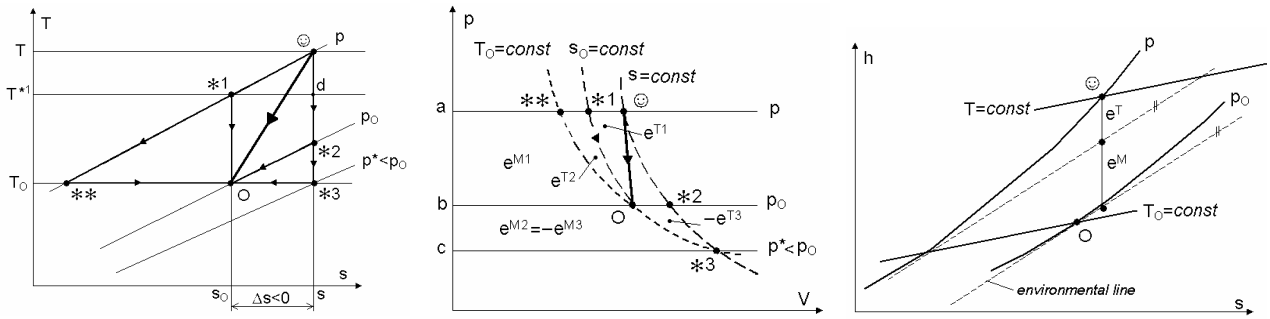

a) b) c)

Figure 6: Graphical model of exergy (Model «D»):
a) on *T-s* diagram; b) on *p-V*-diagram; c) on *h-s*-diagram

$$e^{PH} \equiv \text{area}\,(☺\text{-}**\text{-}*2) + \text{area}\,(a\text{-}**\text{-}*2\text{-}b) + \text{area}\,(b\text{-}*2\text{-}O\text{-}c)$$

or

$$e^{PH} = e^{T} + e^{M}$$

$$e^{PH} \equiv \text{area}\,(☺\text{-}**\text{-}*2) + \text{area}\,(a\text{-}**\text{-}*2\text{-}O\text{-}c). \quad (6a)$$

Theoretical model of exergy

$$e^{PH} = \underbrace{c_p\left(T - T_O\right)}_{e^T} + \underbrace{T_O\left(s_O - s**\right) - \left(h_O - h**\right)_{T_O=const}}_{e^M} \quad (6b)$$

Model «D» (Fig.6). This model was proposed in [15]. The coordinates of point «☺» are (*p, T, s>sO, h*). An irreversible expansion leads from point «☺» to point «O» at $\Delta s<0$. This process does not comply with the second law of Thermodynamics; therefore it is necessary to use a "compensating process" for maintaining $\Delta s=0$.
It is possible to use the following ways in this model:

Way 1:
isothermal expansion $p \rightarrow p_O$ at $T=const$
\+ isobaric cooling $T \rightarrow T_O$ at $p_O=const$
= way «☺» → «*» → «O»

Way 1 (not shown in Fig.6a) is the same way as way 2b in *Model «C»*. Way 1 should be excluded from the analysis, as the isothermal compression occurs at $T>T_O$.

Way 2a:
adiabatic expansion $p \rightarrow p_O$ at $s=const$
\+ isobaric cooling $T^{*2} \rightarrow T_O$ at $p_O=const$
= way «☺» → «*2» → «O»

Way 2b:
isobaric cooling $T \rightarrow T^{*1}$ at $p=const$
\+ adiabatic expansion $p \rightarrow p_O$ at $s_O=const$
= way «☺» → «*1» → «O»

Way 2c:
adiabatic expansion $p \rightarrow p_O$ at $s=const$
\+ isothermal compression $T^{*3} \rightarrow T_O$ at $T_O=const$
= way «☺» → «*3» → «O»

Way 3:
isobaric cooling $T \rightarrow T_O$ at $p=const$
\+ isothermal expansion $p \rightarrow p_O$ at $T_O=const$
= way «☺» → «**» → «O»

The final exergy model is obtained by the following way:

Way 4:
isobaric cooling $T \rightarrow T^{*1}$ at $p=const$
(up to $s^{*1}=s_O$)
\+ isobaric cooling $T^{*1} \rightarrow T^{**}$ at $p=const$
\+ isothermal expansion $p \rightarrow p_O$ at $T_O=const$
\+ isothermal expansion $p_O \rightarrow p^*$ at $T_O=const$
− isothermal compression $p^* \rightarrow p_O$ at $T_O=const$
= way «☺» → «*1» → «**»→ «O» ← «*3»

Graphic model of exergy

$$e^{PH} = e^{T1} + e^{T2} + e^{M1} + e^{M2} - e^{M3}$$

$$e^{T2} + e^{M1} + e^{M2} \equiv \text{area}\,(**\text{-}*1\text{-}O) + \text{area}\,(a\text{-}**\text{-}O\text{-}b) + \text{area}\,(b\text{-}O\text{-}*3\text{-}c)$$

$$e^{T1} \equiv \text{area}\,(☺\text{-}*1\text{-}O),$$

The triangles ☺-*1-d and *2-O-*3 (Fig. 6a) are similar for ideal gases. Thus, if the adiabatic

expansion *2-*3 is the equivalent of isobaric cooling *2-O and isothermal compression *3-O, then the mechanical component of the physical exergy of process *3-O is e^{M3} ≡ area (b-O-*3-c), and the thermal component of the physical exergy of process is *2-O ≡ area (O-*2-*3). The value of the latter is equal to the thermal component of physical exergy of process ☺-*1, i.e. $e^{T1} = e^{T3}$. It is necessary to remember that now we argue not with definition of absolute values of physical exergy and its components but with the areas on the *p-V*-diagram that graphically describe the value of physical exergy.

Finally

$$e^{PH} = e^{T1=T3} + e^{T2} + e^{M1}$$
$$e^{PH} \equiv \text{area (O-*2-*3)} + \text{area (**-*1-O)} + \text{area (a-**-O-b)} \quad (7a)$$

The theoretical model of exergy becomes

$$e^{PH} = \underbrace{c_p(T - T_O) - T_O(s - s_O)}_{e^T} + \underbrace{T_O(s_O - s^{**}) - (h_O - h^{**})_{T_O=const}}_{e^M}. \quad (7b)$$

Model «E» (Fig.7). The coordinates of point «☺» are ($p>p_O$, $T<T_O$, $s<s_O$, h). Irreversible expansion from point «☺» to point «O» occurs at $\Delta s>0$.
It is possible to use following ways for this model:

Way 1:
isothermal expansion $p \rightarrow p_O$ at $T=const$
\+ isobaric heating $T \rightarrow T_O$ at $p_O=const$
= way «☺» → «*4» → «O»

Way 1 should be excluded from the analysis, as the isothermal compression occurs at $T<T_O$.

Way 2:
isobaric heating $T \rightarrow T_O$ at $p=const$
\+ isothermal expansion $p \rightarrow p_O$ at $T_O=const$
= way «☺» → «**» → «O»

Way 3:
adiabatic expansion → p_O at $s=const$
\+ isobaric heating $T^* \rightarrow T_O$ at $p=const$
= way «☺» → «*» → «O»

Way 4a:
adiabatic compression $p \rightarrow p^*$ at $s=const$
\+ isothermal expansion $p^* \rightarrow p$ at $T_O=const$
= way «☺» → «*3» → «O»

Way 4b:
isothermal compression $p \rightarrow p^*$ at $T=const$
\+ isobaric heating $T \rightarrow T_O$ at $p^*=const$
\+ isothermal expansion $p^* \rightarrow p$ at $T_O=const$
\+ isothermal expansion $p \rightarrow p_O$ at $T_O=const$
= way «☺» → «*2» → «*3» → «**» → «O»

However, way 4b requires heat transfer at $T<T_O$ and should be excluded.

Graphic model of exergy is

$$e^{PH} = -e^{M1} - e^{T1} + e^{M2} + e^{M3}$$

The adiabatic compression «☺» → «*3» (area a-*3-☺-b) is the sum

$$e^{M1} + e^{T1} \equiv \text{area (a-*2-☺-b)} + \text{area (*2-*3-☺)}$$

One mechanical component is

$$e^{M2} \equiv \text{area (a-*3-**-☺-b)}.$$

It is visible (by graphical interpretation only)

$$e^{T1} = e^{M2} - e^{M1}$$

Finally

$$e^{PH} = -e^{T1} + e^{M3}$$
$$e^{PH} \equiv -\text{area (*2-*3-☺)} + \text{area (b-☺-**-O-*4-*-c)} \quad (8a)$$

Theoretical model of exergy

$$e^{PH} = \underbrace{-c_p(T_O - T)}_{e^T} + \underbrace{T_O(s_O - s^{**}) - (h_O - h^{**})_{T_O=const}}_{e^M} \quad (8b)$$

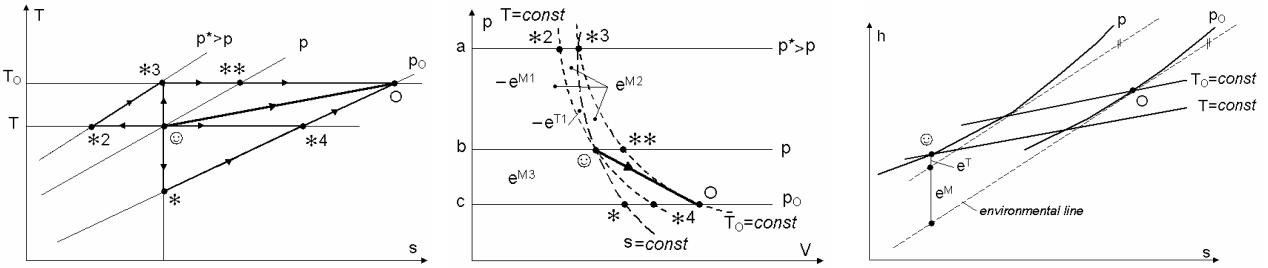

a) b) c)

Figure 7: Graphical model of exergy (*Model «E»*):
a) on *T-s* diagram; b) on *p-V*-diagram; c) on *h-s*-diagram

On the basis of theoretical models of exergy analysis (by eqs. (4b), (5b), (6b), (7b) and (8b)) we conclude that for calculating the thermal and mechanical components of physical exergy it is necessary to have the following data:

- thermodynamic parameters in the point «☺» (p, T, h, s);
- thermodynamic parameters in the point «O» (p_O, T_O, h_O, s_O);
- values of enthalpy (h**) and entropy (s**) in point «**» where p**=p and T**=T_O.

Eqs. (4b), (5b), (6b), (7b) and (8b) can be written for engineering calculations of e^T and e^M (for all models of exergy) for any position of point «☺» (p, T, h, s)

$$e^{PH} = \underbrace{(h-h^{**})-T_O(s-s^{**})+}_{e^T} \qquad (9)$$

$$\underbrace{+T_O(s_O-s^{**})-(h_O-h^{**})_{T_O=const}}_{e^M}$$

Similar results were presented in a Tridimensional exergy diagram by Rivero [20].

On a *h-s*-diagram

Traditional graphical illustration of physical exergy is given on a *h-s*-diagram. The graphical representation of splitting the physical exergy into its components in the *h-s*-diagram is demonstrated in Figures 3c through 7c.

Let us consider an auxiliary line in a *h-s*-diagram as proposed in [9,17]. It is known that this so-called "environmental line" is the tangent on the isobaric line p_O=*const* at the point T_O

$$tg\,\alpha = \left(\frac{\partial h}{\partial s}\right)_{p_O=const} \qquad (10)$$

and

$$arctg\alpha = T_O\,.$$

By moving the environmental line in parallel from point «O» (p_O, T_O) to point "**" (T_O and p) it is possible to separate the thermal and mechanical exergy components as shown in Figures 3c through 7c.

CONCLUSIONS

The paper discusses different approaches to the graphical representation of the thermal and mechanical exergy components associated with the physical exergy of a stream of matter. A general procedure is proposed and its application on different thermodynamic diagrams is demonstrated.

The authors' proposition for calculating the thermal and mechanical components of physical exergy can be used in engineering calculations for analysis and optimization purposes.

ACKNOWLEDGEMENTS

Prof. T. Morosuk grateful acknowledges the support by Alexander von Humboldt Stiftung (IV-UKR/1117838 STR) which enables her scientific work in the year 2005 at the Institute for Energy Engineering, Technical University of Berlin.

REFERENCES

1. Gaggioli R.A., El-Sayed Y.M. *A Critical Rewiew of Second Law Costing Methods – II: Calculus Procedures*. Journal of Energy Resources Technology, 1989; Vol. 111:.9-15.

2. Moran M. *Availability Analysis*. New York: ASME Press, 1989.

3. Dunbar W.R., Lior N., Gaggioli R.A. *That Component Equations of Energy and Exergy*. Journal of Energy Resources Technology, 1992; Vol. 114: 75-83.

4. Tsatsaronis G., Lin L., Pisa J. *Exergy Costing in Exergoeconomics*. Journal of Energy Resources Technology, 1993; Vol.115: 9-16.

5. Bejan A., Tsatsaronis G., Moran M. *Thermal Design and Optimization*, New York: John Wiley and Sons, 1996.

6. Lazzaretto A., Tsatsaronis G. *A General Process - Based Methology for Exergy Costing*. ASME, AES, 1996; Vol.36: 413-428.

7. Lazzaretto A., Tsatsaronis G. *On the Quest for Objective Equations in Exergy Costing*. ASME, AES, 1997; Vol.37: 413-428.

8. Lazzaretto A., Tsatsaronis G. *On the Calculation of Efficiencies and costs in Thermal systems*. ASME, AES, 1999; Vol.39: 421-430.

9. Bošnjaković Fr. *Technische Thermodynamik*, 6. verbesserte Auflage, Dresden: Verlag Theodor Steinkopff, 1972.

10. *Exergy calculation of technical systems*. Technical manual. Eds. Dolinsky A.A., Brodiansky V.M., Kiev: Naukova Dumka, 1991 (in Russian).

11. Kotas T.J. *The Exergy Method of Thermal Plant Analysis*, Florida, USA: Krieger Publishing Company, Malabar, 1985.

12. Lior N. *Irreversibility in Combustion* In Ozturk A. and Gogus Y.A. "Efficiency, Cost, Optimization and Environmental Impact of Energy System", ECOS'01, Istanbul, Turkey, 2001, Vol. I: p.39-48.

13. Szargut, J., Petela, R. *Egzergia*, Warsaw: Wydavnictwa Naukowo-Techniczne, 1965.

14. Paulus D., Tsatsaronis G., Morosuk T. *An overview of methods for splitting physical exergy*. In: Efficiency, Costs, Optimization, Simulation, and Environmental Impacts of Energy and Process Systems, Eds. Rivero R., Monroy L., Pulido R. and Tsatsaronis G. (Instituto Mexicano del Petroleo), 2004, Vol.2: 787-799.

15. Gyftopoulos E.P., Beretta G.P. *Thermodynamics: Foundations and Applications*, New York: Macmillan Publishing Company, 1991.

16. Bejan A. *Advances Engineering thermodynamics*, New York: John Wiley and Sons, 1988.

17. Bošnjaković Fr., Knoche, K.F. *Technische Thermodynamik*, 8. korrigierte Auflage, Darmstadt: Steinkopff, 1998.

18. Rosenfeld L.M., Tkahev A.G. *Refrigeration machines and apparatuses*, Moscow: Gostorgizdat, 1960 (in Russian).

19. Tsatsaronis G., Pisa J.J., Lin L. *The Effect of Assumptions on the Detailed Exergoeconomic Analysis of a Steam Power Plant Design Configuration; Part I: Theoretical Development; Part II: Results and Discussion*, in "A Future for Energy", Proceedings of the Florence World Energy Research Symposium, Firenze, Italy, May 28-June 1, 1990: 771-792.

20. Rivero R. *Tridimensional exergy diagram*. In: Energy systems and ecology, Proceedings of the ENSEC'93 Conference, Eds., Szargut J., Kolenda Z., Tsatsaronis G. and Ziebik A. Krakow, Poland, July 5-9, 1993, Vol. 1: 305-312.

Proceedings of ECOS 2005
Trondheim, Norway
June 20–22, 2005

THE EXERGY OF SUCROSE-WATER SOLUTIONS: PROPOSAL OF A CALCULATION METHOD

S. A. Nebra[*]
State University of Campinas,
Mechanical Engineering Faculty, Energy Department,
P. O. Box 6122, CEP 13083-970, Campinas, SP,
Brazil.

M. I. Fernández-Parra*Universidad de Oriente,*
CEEFE/FIM/UO,
Avenida Las Américas s/n esquina L, Santiago de Cuba,
Cuba.

ABSTRACT

The present paper discusses a calculation method for the sucrose – water solution exergy. To perform this calculation, correlations are presented to obtain some properties: density, solubility, specific heat, boiling point elevation, enthalpy and entropy. These properties permit to calculate the solution physical exergy. Moreover, a correlation for the water activity coefficient in the solution was obtained from the literature and an equation to calculate the sucrose activity coefficient is proposed. Both coefficients are used to determine the mixture exergy. Finally, a discussion of the reference system is performed, to complete the calculation of the chemical exergy.

Keywords: exergy, Sugar cane, sugar cane juice, solubility, specific heat, enthalpy, entropy

NOMENCLATURE

a	Activity
b	Specific exergy [kJ/kg]
c_p	Specific heat [kJ/kg K]
h	Specific enthalpy [kJ/kg]
p	pressure [kPa]
Pz	Purity coefficient [%]
s	Specific entropy [kJ/(kg K)]
t	temperature [°C]
T	temperature [K]
v	Volume [m^3]
x	mass fraction of solids [%]
y	molar fraction of solids
z	solution proportion in the mixture above solubility
$\tilde{\varepsilon}$	molar chemical exergy
γ	Activity coefficient
ρ	density [kg/l]

Subscripts

ch	Chemical
mix	Mixture
w	Water
0	reference state
sol	Solubility
Suc	Sucrose

[*] Corresponding author: Phone: 55 -19 – 37883270 ; e-mail: sanebra@fem.unicamp.br

INTRODUCTION

In the last years, the sugar and alcohol industry has increased in Brazil. Along the 2004/05 sugar crop 327 million tons of sugar cane will be produced, from which 51% will be used to produce ethylic alcohol and 49%, sugar. The sugar produced will be 22.05 million tons and 13.54 billion litres of ethylic alcohol.[1], summing up both types, hydrated and non-hydrated.

At the same time the production is increased, an effort is being made to improve the use of energy in the industry. In order to increase the electric energy cogeneration, a reduction of the process steam consumed is necessary, consequently, studies are being made in this direction [2], introducing also the concept of exergy [3].

To perform a thermodynamic analysis of the process, the calculation of the exergy of sugar – water solutions at different concentrations is essential, so, this paper is devoted to the discussion of a methodology to do that.

Some authors presented calculation methods of sugar-water solutions exergy, as Baloh [4,5]; Baloh and Wittwer [6], and Guallar – Paracuellos [7]. From this time to nowadays, some new correlations to calculate sugar-water solutions properties have appeared in the literature and also, from our point of view, a revision of the reference system adopted by these preview authors is necessary, so, a new calculation proposal is made in the present paper.

DENSITY AND SOLUBILITY

Some authors present the variation of the solution density with the concentration in the form of a table [8, 9], some others in a correlation form [10]. A simpler correlation, due to de Grut, is proposed by Peacock [11].

$$\rho = 1000\left[1+\frac{x(x+200)}{54000}\right]\left[1-\frac{0.036(t-20)}{(160-t)}\right] \quad (1)$$

Equation [1] is valid for temperature less than 100°C, a plot is showed in Figure 1,where the symbols do not indicate experimental values.

Data on solubility are reported for various authors [8,10,11,12]. Hugot [12] proposed a simple correlation:

$$x_{sol} = \frac{10000}{\left[100+0.355(158-t)\right]} \quad (2)$$

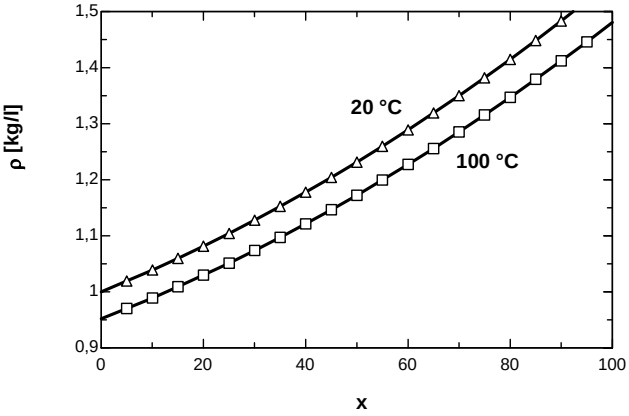

Figure 1: sugar-sucrose solutions density in function of solid mass fraction.

And Peacock [11], based on de Grut's data, developed another one, also simple:

$$x_{sol} = 63.753 + 0.13542 * t + 0.0008869 * t^2 - 2.222 * 10^{-6} * t^3 \quad (3)$$

The different correlations are compared in Figure 2, where the symbols only differentiate one from the other.

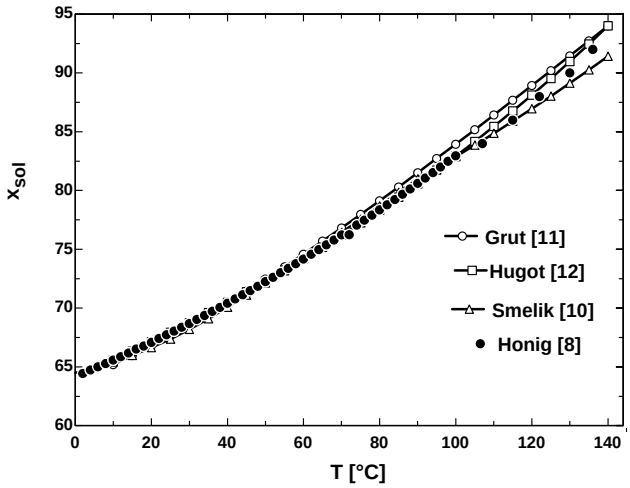

Figure 2: Sucrose in water solubility in function of temperature.

When the solution is above the solubility point, a new phase will appear, constituted by sugar crystals. Anyway, a mean value of the properties of both phases can be calculated.

In a mixture of both phases, the quantity of sucrose-water solution will be given by Eq. 4.

$$z = \frac{100-x}{100-x_{sol}} \quad (4)$$

The mean value of the mixture density can be calculated as following:

$$\rho_{mix} = z\rho_{sol} + (1-z)\rho_{suc} \quad (5)$$

In Equation (5) a value of 1.59 [kg/l] is adopted for the pure sucrose [6].

SPECIFIC HEAT

Various authors have presented values [6, 8, 9] and correlations [7, 10, 11, 12] to get the specific heat of sugar – water solutions. The correlation presented by Hugot [12] has the disadvantage of no taking into account the temperature effect. The correlation due to Janovskij and ArchangelskiJ, reported by Kadlec et al. [10], has the advantage that it takes into account the temperature effect and also it can be applied through a variation of 55 to 100 % in the *purity coefficient*- sugar content in the total solids. This concept is useful to calculate industrial solutions. This correlation is showed in Equation (6).

$$c_p = 4.868 - 0.0297 * x + 4.6 * 10^{-5} x * Pz + 7.5 * 10^{-5} x * t \quad (6)$$

In Figure 3, some of the correlations, above mentioned, are presented, a value of 100 % was considered for the purity coefficient. The symbols do not mean experimental values.

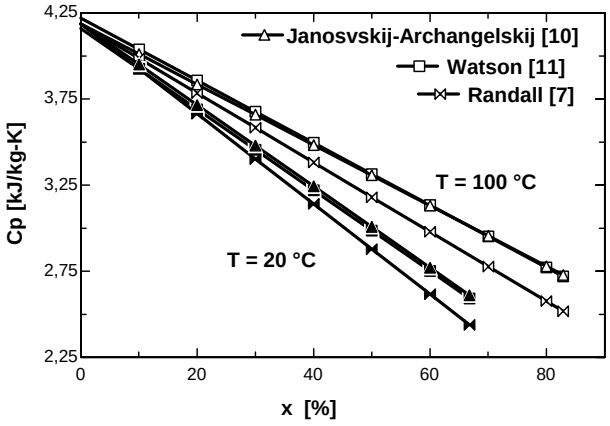

Figure 3: Specific heat in function of the solid mass fraction.

In order to calculate the specific heat of mixtures above the solubility point, a mean value can be obtained, as it was made in Equation (5):

$$c_{p\,mix} = z\,c_{p\,sol} + (1-z)\,c_{p\,suc} \quad (7)$$

Where a value for the pure sugar specific heat is needed. Hugot [12] propose the Equation (8), and Anderson el al. [13], the equation (9).

$$c_{p\,suc} = 1.161837 + 0.0035587 * t \quad (8)$$

$$c_{p\,suc} = 1.244 + 4.819x10^{-3}(t-25) + 6.238x10^{-6}(t-25)^2 \quad (9)$$

As can be seen in Figure 4, the correlation proposed by Anderson et al. [13] agrees well with the experimental data presented by Honig [8].

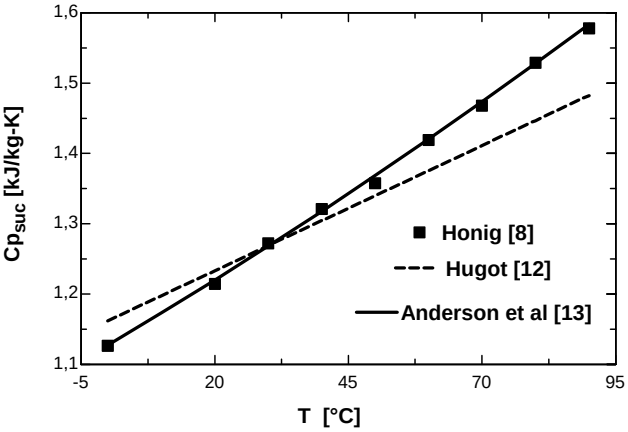

Figure 4: Specific heat of pure sucrose.

ENTHALPY

The enthalpy, at a given pressure, can be obtained from correlations of specific heat and volume varying with the temperature, as indicated in Equation (10) [14].

$$h(T,p) = h(T_0,p_0) + \int_{T_0}^{T} c_p(T',p)dT' + \int_{p_0}^{p}\left[v(T_0,p') - T_0\left(\frac{\partial v(T,p')}{\partial T}\right)_{p'}\Big|_{T=T_0}\right]dp' \quad (10)$$

In Eq. (10), all the authors neglect the second term [4, 5, 7, 10], so, we will do the same, integrating Equation (6), as Kadlec et al. did [10]. The result is showed in Equation (11).

$$h = (4.1868 - 0.0297 * x + 4.6 * 10^{-5} x * Pz)t + 3.75 * 10^{-5} x * t^2 \quad (11)$$

The Equation (12) is another one, proposed by Peacock [11].

$$h = 2.326\left\{\begin{array}{l}\left(\frac{x}{10}\right)\frac{(100+x)}{(900-8x)} \\ +1.8t\left[1-\left(\frac{x}{100}\right)(0.6-0.0009t)\right]\end{array}\right\} \quad (12)$$

For mixtures above the solubility point, a mean value can be obtained, as suggested by Baloh and Wittwer [6]. In the some way that was made in Equation (7), we get Equation (13), [10], where the enthalpy of the sucrose is calculated based in his specific heat, Equation (9).

$$h_{mix} = zh_{sol} + (1-z)h_{suc} \quad (13)$$

In figure 5, a graphic of the enthalpy in function of the solid mass fraction is showed; the Equation (11) is compared with Equation (12). The reference adopted was null enthalpy at 0 °C. The equation proposed by Peacock presents higher values around the maximum solubility point.

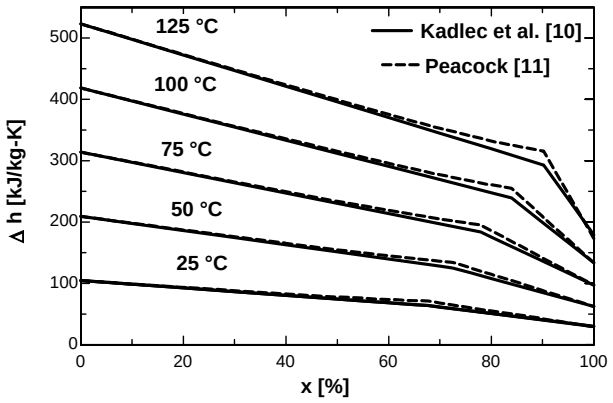

Figure 5: Enthalpy of sucrose – water mixtures in function of the solid mass fraction.

ENTROPY

Few authors treat this property; Baloh gives a Table of water – sucrose mixture entropy [4], whose reference was changed in order to compare with the results of this paper. Tekin and Bayramoğlu [15] reported equations for enthalpy and entropy, but the values obtained with them were without sense.

Anyway, as in the case of enthalpy, the entropy can be obtained through the integration of the Equation (14) [14], where, another time, the second term is neglected [4,5,7]. The result obtained is Equation (15). The Equation (16) calculates the pure sucrose entropy. In both cases, to change temperature scale, before to integrate, is necessary.

$$\Delta s = \int_{T_0}^{T}\frac{c_p(T',p)}{T'}dT' - \int_{p_0}^{p}\left(\frac{\partial v(T,p')}{\partial T}\right)_{p'}\Bigg|_{T=T_0} dp' \quad (14)$$

$$\Delta s = (4.1868 - 0.05018625x + 4.6*10^{-5}xPz)\ln\left(\frac{T}{T_0}\right) + \left(7.5*10^{-5}x\right)(T-T_0) \quad (15)$$

$$\Delta s_{suc} = -0.260000693\ln\left(\frac{T}{T_0}\right) + 0.005046934(T-T_0) \quad (16)$$

A graphic is shown in Figure 6, where the same procedure than before was used for mixtures above the solubility point. The reference adopted was of entropy null for T= 0°C. The results are compared with those of Baloh [4], a good agreement was obtained; some differences appear only around the maximum saturation point, for temperatures greater than 100 °C.

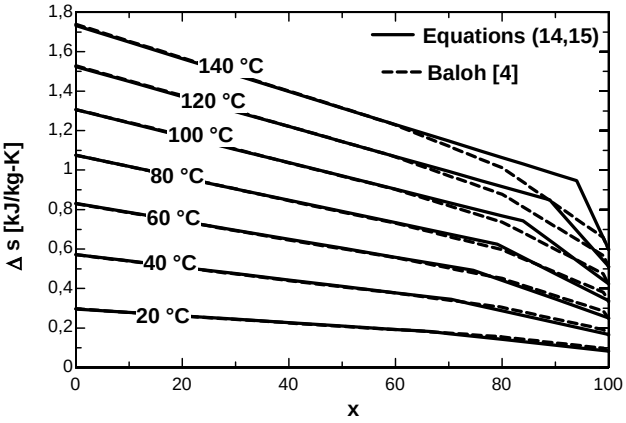

Figure 6: Entropy of sucrose-water mixtures in function of the solid mass fraction.

ACTIVITY

Considering a solution of sucrose-water in equilibrium with his vapour, we can write Equation (16), [7, 16]

$$p_{total}(t_0) = \gamma_w(y_{suc}, t)y_w p_w^0(t) \quad (17)$$

Where $\Delta t_{BPE} = t - t_0$ is the boiling point elevation and $p_w^0(t)$ is the water vapour pressure at temperature t (the vapour phase is constituted only by pure water).

Measurements of boiling point elevation permit to obtain activity coefficient values [7, 16].

Starzack and Peacock [16,17] provide a correlation to calculate the water activity coefficient:

$$\ln \gamma_w = \frac{Q}{RT} y_{suc}^2 \left(1 + A y_{suc} + B y_{suc}^2\right) \quad (18)$$

Where the activity is calculated as: $\gamma\, y = a$.

And the coefficients have the values:

$$\frac{Q}{RT} = \frac{-17638[J/mol]}{8.3143[J/(molK)]T[K]} = \frac{-2121.4052[K]}{T[K]} \quad (19)$$

$$A = -1.0038$$

$$B = -0.24653$$

In Equation (18), the reference values are:

$\gamma_w = 1 \quad for \;\; y_{suc} = 0, \quad so \quad a_w = 1.$

From (18), using the Gibbs – Duhem integrated equation; Equation (20), the value of the sucrose activity coefficient can be obtained, following the method described in [18].

$$\int_{y_{suc}}^{y_{suc}=y_{suc,sat}} d(\ln a_{suc}) = \int_{y_{suc}}^{y_{suc}=y_{suc,sat}} \frac{y_w}{y_{suc}} d(\ln a_w) \quad (20)$$

Where the integration limits were defined between a generic state and the saturated state corresponding to the maximum solubility. The superior limit was adopted in function of the calculation of exergy that will be performed afterwards; in fact, it corresponds to a state where the solution is in equilibrium with the solid pure sucrose; so, the reference value for the sucrose activity corresponds to pure sucrose, as suggested by Hougen et al. [19]. In this way, the condition (21) must be used [19]:

$$\gamma_{suc,sat} = \frac{1}{y_{suc,sat}} \quad (21)$$

Substituting in Equation (20) according to (18), operating and solving the integrals, we get Equation (22).

$$\ln\left(\frac{\gamma_{suc}}{\gamma_{suc,sat}}\right) = -\frac{Q}{RT}\left[2y_{suc} + \frac{(3a-2)}{2} y_{suc}^2 + \frac{(4b-3a)}{3} y_{suc}^3 - b y_{suc}^4\right]_{y_{sac}=y_{sac,sat}}^{y_{suc}} \quad (22)$$

Starzack and Peacock [17] reported another correlation for the water activity coefficient, due to Kadlec et al., which gave similar results to Equation (18), but as the work of the first authors was based in an extended bibliographic research, we decided to adopt their correlation.

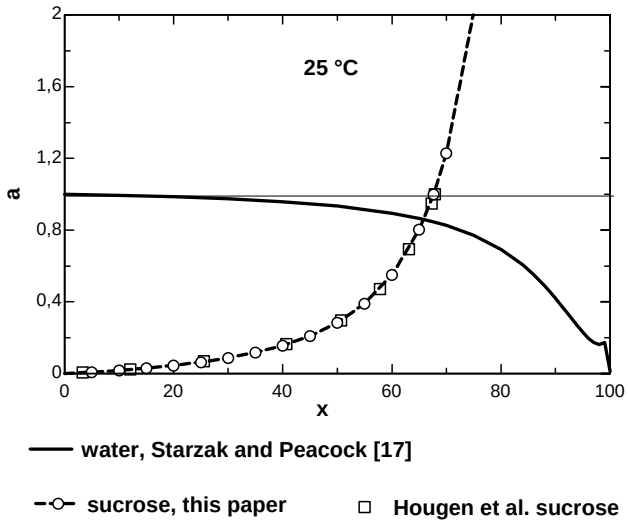

Figure 7: water and sucrose activity in function of the solid mass fraction.

In Figure 7, a graph of the water and sucrose activities correlations, at 25 °C, is presented, the results obtained with Equation (22) are compared with data given by Houghen et al.[19]. The agreement is very good.

EXERGY

Following Szargut et al. [20] and also Kotas [21], the exergy of a sucrose – water solution can be calculated as the sum of three terms:
(i) the physical exergy, which is the changing in exergy value when the system go from (T,p) to (T_0, p_0), (ii) the mixture exergy, which corresponds to the exergy needed to separate the two components, and (iii) the chemical exergy, which correspond to the change in exergy value from the pure components, set apart, to the final equilibrium of them with the pre-defined environmental system (See Figure 8).

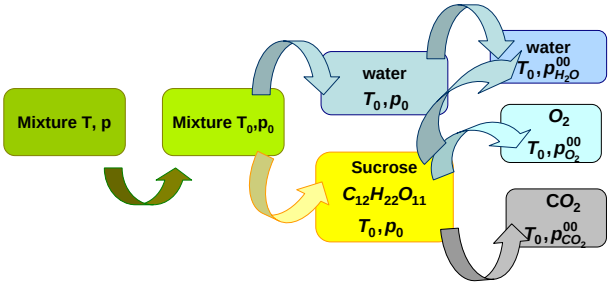

Figure 8: representation of the exergy calculation.

Each one of the above mentioned exergy terms are calculated as follows:

$$ex_{ph} = \int_{T_0}^{T} Cp\left(1 - \frac{T_0}{T}\right)dT = \Delta h - T_0 \Delta s \quad (23)$$

$$ex_{mix} = \frac{RT_0}{M_{mix}}\left[y_{suc} \ln a_{suc} + y_w \ln a_w\right] \quad (24)$$

$$ex_{chem} = \left[y_{suc} ex^{00}_{chem,suc} + y_w ex^{00}_{chem,w}\right] \quad (25)$$

Where the following values were adopted [20]:

$$ex^{00}_{chem,suc} = 6007800\,[\text{kJ/kmol}]$$
$$ex^{00}_{chem,w} = 900\,[\text{kJ/kmol}] \quad (26)$$

A graph of Equation (23) is showed in Figure 9, to get that, the equations (9), (13), (15) and (16) were used. A reference of t= 25 °C and 101,3 kPa was adopted.

The Equation (24) is represented in Figure 10. The equations (18), (21) and (22) were used, joined with the numerical values of (19). Null mixture exergy values are adopted for the pure substances.

In Figure 11, the total exergy is showed. As it can be seen, a unique line represents all the temperature values, this is due to the fact that the values of the chemical reference exergies of the pure products (Equation (26)) are very big.

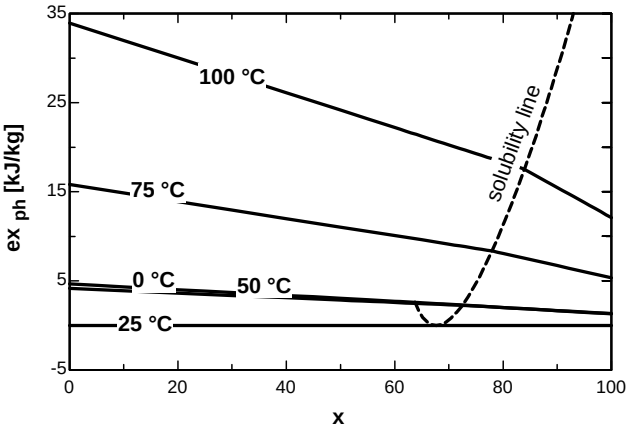

Figure 9: physical exergy of sucrose-water mixtures.

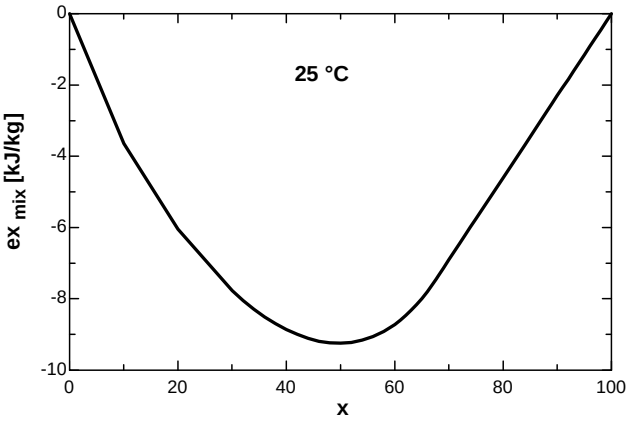

Figure 10: mixture exergy of sucrose – water system.

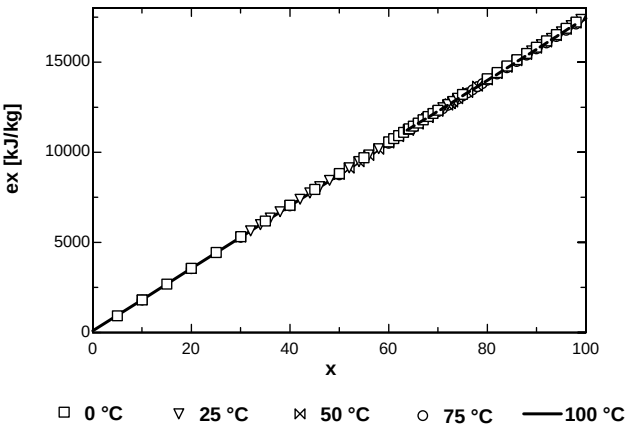

Figure 11: total exergy of the sucrose – water system.

The values of the reference exergies in Equation (25), Equation (26), for sucrose and water, were taken from Szargut et al. [20], so, the reference environment proposed by these authors was

adopted. Considering the elemental substances present in the system, which are carbon, oxygen and hydrogen, the reference substances adopted are: carbon dioxide, oxygen and water (in vapour state), all them diluted in the standard atmosphere detailed in [20]. What this means is that the sucrose was treated as a *fuel*, and, if we think that it is used for human feeding, it acts really as a fuel, because the man produces carbon dioxide when breathes. Anyway, it can also be burnt.

The reference state adopted in this work is different of that of Baloh [5] and Guallar [7], whom adopted the minimum value of mixture exergy at 25 °C (or 20 °C) as zero level, so, the value corresponding to minimum free energy and maximum solubility. Baloh [5] adopted also a null value of exergy for the sucrose at reference temperature. Guallar [7] adopted two different reference systems, when he analysis the sugar production process.

Since our final objective is to perform a complete exergetic analysis of the sugar and alcohol production process from sugar cane, where the elemental substances, carbon, oxygen and hydrogen are present also in the bagasse, used as fuel, we think that a unique reference system must be adopted to perform the exergy calculations.

CONCLUSIONS

A research on the properties of water – sucrose solutions was made; being as final objective to present an exergy calculation methodology. In order to reach this objective, values of density, solubility, specific heat, enthalpy and entropy are presented. Correlation and values from different authors were carefully compared.

An expression for the sucrose activity was developed from a correlation for the water activity in the solution, using the Gibbs – Duhem equation. In order to calculate the exergy, we need to adopt as reference states pure water and pure sucrose, this was also performed in the calculation of the activity coefficient. As this type of solutions have a solubility limit, careful calculations and considerations needed to be done. The reported correlations permit the complete exergy calculation of sucrose-water mixtures at any concentration. Other authors reported only a graphic as Baloh [5] or a description of the method as Guallar [7]. The calculation was performed using the EES® software as base; the authors offer the code developed to people interested on them.

Along the work some doubts appear, new research need to be done on some subjects.

A careful research can be made about the influence of the second integral term in Equations (10) and (14), the Equation (1) would be useful to do that.

The mixture properties, as enthalpy, entropy, free energy can be calculated from calorimetric data or from activity data. See, for example Gyftopoulos and Beretta [14]. The authors of this paper realized part of this work and compare the results, which presented differences. A complete discussion of these results could be done in a next paper.

Finally, in the last times, we have found some important mistakes at the literature in the calculation of the exergy of different types of solutions; we hope this work will contribute to lead the people think about that.

ACKNOWLEDGMENTS

The authors want to express their gratitude to Research Foundation of Sao Paulo State – FAPESP, to Coordination for the Improving of Superior Education - CAPES and to Research Council of Scientific and Technological Development – CNPq, for the financial resources to do this work.

REFERENCES

[1]http://revistagloborural.globo.com/GloboRural, 04/02/2005.

[2] Higa, M.; *Study of the energy consumption in a sugar cane plant using the pinch point and optimization methods*; Master Thesis, Mechanical Engineering Faculty, State University of Campinas, SP, Brazil, 1999 (in Portuguese).

[3] Fernández – Parra, M. I.; *Methodology of exergoeconomic analysis of the sugar production process*; Doctoral Thesis, Mechanical Engineering Faculty, State University of Campinas, SP, Brazil, 2003 (in Portuguese).

[4] Baloh, T.; *Exergetic investi gations in the sugar industry;* Zucker, April, 1963, (16) nr.8; 194-1963 (in German)

[5] Baloh, T.; *A new diagram for sucrose-water solutions*; Zucker, 1974 (27) nr.2; 65-72. (in German)

[6] Baloh, T,and Wittwer E, *Energy manual for sugar factorie*, Edit. Verlag Dr. Albert Bartens, Berlin, 2nd. Edition.,1995.
[7] Guallar P.J. *Exergetic Analysis and Process Thermal Integration in the Sugar industry*, Doctoral Thesis, University of Zaragoza, Zaragoza, Spain (in Spanish), 1987.
[8] Honig, P.; *Principles of Sugar Technology*,Compañia Editorial Continental, S.A.,México, 1969, V. I (in Spanish).
[9] Spencer and Meade, *Handbook of Sugar Cane*; Editorial Montaner y Simón S.A Barcelona. España, 1976 (in Spanish).
[10] Kadlec, P.; Bretschneider, R. ; Dandar, A.; *The measurement and the calculation of the physical – chemical properties of water-sugar solutions*, La Sucrerie Belge, Vol. 100, Feb. 1981; pp. 45-59. (in French).
[11] Peacock, Stephen; *Predicting physical properties of factory juices and syrups*; International Sugar Journal, 1995, Vol. 97, Nr. 1162, pp. 571 – 577.
[12] Hugot E., *Handbook of Cane Sugar Engineering*. Sugar Series 7.Elsevier Science. Publishing, 1986.
[13] Anderson, G.L., Jr.; Howard Higbie and Gebhard Stegeman, *The heat capacity of sucrose from 25 to 90 °C*, J. Am. Chem. Soc, August, 1950, (72), 3798 – 3799.
[14] Gyftopoulos, Elias P. and Beretta, Gian Paolo; *Thermodynamics: Foundations and Applications*, Edit. Macmillan Publishing Company, New York, USA, 1991.
[15] Tekin, T. and Bayramoğlu, M.; *Exergy and structural analysis of raw juice production and steam-power units of a sugar production plant;* Energy 2001 (26) 287-297.
[16] Starzak, M. and Peacock, S.D.; *Water activity coefficient in aqueous solutions of sucrose- A comprehensive data analysis*; Zuckering, 1997 (122), Nr. 5, 380-387.
[17]Starzak, M. and Peacock, S.D.; Boling point elevation for aqueous solutions of sucrose – A comparison of different prediction methos; Zuckerindustrie 1998 (123), Nr. 6, 433-441.
[18] Balzhiser, Richard E.; Samuels, Michael R.; Eliassen, John D.; *Thermodynamics for engineers;* Edit. Prentice / Hall Internacional. Englewood, New Jersey, USA. (In Spanish), 1980.
[19] Hougen, A.; Watson, K.M. e Ragatz, R.A.; *Principles of the chemical process*; Edit. Reverté S.A.; Barcelona, Buenos Aires, México, 1964. (in Spanish)
[20] Szargut J., Morris D.R. Steward F.R., *Exergy Analysis of Thermal, Chemical and Metallurgical Process*, Hemisphere Publishing Corporation, USA, 1988.
[21] Kotas, T. J. ; The exergy method of thermal plant analysis; Krieger Publishing.

Proceedings of ECOS 2005
Trondheim, Norway
June 20–22, 2005

EXERGY ANALYSIS OF SUGARCANE BAGASSE GASIFICATION

Luiz Felipe Pellegrini and Silvio de Oliveira Jr.
Polytechnic School – University of São Paulo
Department of Mechanical Engineering
Brazil

ABSTRACT

The gasification technology has been process of study of many researchers, especially those involved in promoting large-scale electricity generation in sugarcane mills. This paper presents a simplified model for the gasification process based on chemical equilibrium considerations. The model consists in the minimization of the Gibbs free energy of the produced gas, constrained by mass and energy balances for the system. Despite the simplicity of the model, its results are reliable in identifying the tendencies of the working parameters of the system. A parametric study has been carried in order to verify the influence of many variables inherent to the model, such as: gasification temperature, moisture content, and air temperature, among others. The results were compared with those found in literature and real systems. Following this parametric study, an exergy analysis has been performed in order to evaluate irreversibilities associated to the process, and the influence of temperature, moisture, charcoal production, and thermal losses on them. Finally, a first attempt to integrate a gasifier into a sugarcane mill was performed, which showed the potential benefits regarding the use of such technology.
Keywords: biomass gasification, exergy analysis, sugarcane bagasse

NOMENCLATURE

a number of atoms of specie k in molecule j
A total number of atoms of specie k
b specific exergy (kJ/kg or kJ/mol)
B total exergy flow rate (kW)
c_p specific heat (kJ/kmol-K)
f coefficient of thermal losses (from 0 to1)
G Gibbs free energy (kJ/kg)
H total enthalpy flow rate (kW)
I irreversibility or exergy destroyed (kW)
j index for components
k index for atoms
LHV lower heating value (kJ/kg)
m mass flow (kg/s)
n total number of molecules j
p pressure (atm)
Q heat transfer (kW)
R gases constant (kJ/kmol-K)
tc ton of cane
T temperature (°C or K)
y molar fraction
Φ equivalence ratio
β coefficient for calculating chemical exergy
λ Lagrange multiplier
η efficiency

INTRODUCTION

Gasification is a thermo-chemical process in which a solid/liquid fuel is converted, due to the addition of heat in a sub-oxidizing atmosphere, into a mixture of gases (produced gas) with low calorific value. The gasification technology has been object of study of many researchers, especially those involved in promoting large-scale electricity generation in sugarcane mills. However, few of these studies focused on the process itself [1], being more concerned about the application of the produced gas in combined cycles and/or co-firing systems [2] [3].

Most recently, many works have been published in the field of gasification modeling by chemical equilibrium and its analysis. A non-stoichiometric model, which uses empirical relations in order to come closer to real operation of gasification of biomass, based on the operation of a circulating fluidized bed, was proposed in [4]. Gasification and combustion processes for CHO systems are analyzed based on first and second law analysis,

following a stoichiometric approach [5], [6]. These studies provided a fairly comparison between gasification and combustion, showing the principal irreversibilities associated with each process, and the advantages of one and another. The gasification of different biomass materials in an equilibrium model based on equilibrium constants for methane formation and shift reaction is, also, available in [7].

The aim of this paper is to develop a gasification model that might indicate energetic and exergetic behavior of the process. Also, allowing a parametric study in order to provide information regarding parameters that most influence the process. Finally, a first attempt to integrate a gasifier into a sugarcane mill is performed.

ENERGY AND EXERGY MODELING

It has been adopted the non-stoichiometric approach to find the chemical equilibrium, in which:

- ✓ Only gaseous species (CO, H_2, H_2O, CO_2 and N_2) have been considered in equilibrium;
- ✓ The volume of CH_4 and unconverted carbon have been calculated based on experimental data and empirical relations [4];
- ✓ The produced gas was modeled as a mixture of ideal gases;
- ✓ No nitrogen pollutants were presented (NO_x, N_2O).

The approach for the equilibrium calculations consists in solving a system of non-linear equations given by [8]:

– N equations related to equilibrium conditions:

$$\mu_j + \sum_{k=1}^{w} \lambda_k a_{jk} = 0 \text{ , for } j = 1,2,...,N \qquad (1)$$

– w equations related to material balances:

$$\sum_{j=1}^{N} \left(n_j \cdot a_{jk}\right) = A_k \text{ , for } k = 1,2,...,w \qquad (2)$$

As it was considered a mixture of ideal gases, Eq. (1) can be re-arranged [9]:

$$\Delta G_j^0 + RT \ln\left(y_j\right) + \sum_{k=1}^{w} \lambda_k a_{jk} = 0 \text{ , for } j = 1,2,...,n \qquad (3)$$

Same as in [4], the volumes of CH_4 formed and unconverted carbon were found using empirical correlations, according to experimental data from [4]:

$$\beta_{CH_4} = 0.11 \cdot (1 - \phi) \qquad (4)$$

$$n_{CH_4} = \beta_{CH_4} \cdot n_{C,\,initial} \qquad (5)$$

$$\beta_C = 1 - \left(-\phi / 0.1367\right) \qquad (6)$$

$$n_C = \beta_C \cdot n_{C,\,initial} \qquad (7)$$

These relations are taken into account, so non-equilibrium effects are considered [4].

In order to moderate the system, an energy balance was imposed to the problem:

$$\left(\sum \dot{H}_i\right)_{in} = \left(\sum \dot{H}_j\right)_{out} + \dot{Q}_{losses} \qquad (8)$$

$$\left(\sum \dot{H}_i\right)_{in} = \dot{H}_{air} + \dot{H}_{\substack{dry \\ biomass}} + \dot{H}_{\substack{biomass \\ moisture}} + \dot{H}_{steam} \qquad (9)$$

$$\left(\sum \dot{H}_j\right)_{out} = \dot{H}_{\substack{produced \\ gas,\,dry}} + \dot{H}_{\substack{unconverted \\ carbon}} + \dot{H}_{steam} \qquad (10)$$

$$\dot{Q}_{losses} = f \cdot \left(\sum \dot{H}_i\right)_{in} \qquad (11)$$

This balance is responsible for the determination of the temperature of the system for a given air-to-fuel ratio, or the other way round. All relations related to the calculation of thermodynamic properties are shown in the appendix. It must be pointed out here that this procedure is different from the one exposed in [4], in which both temperature and air ratio are considered independent variables.

The exergy analysis was carried out, according to the following equations:

$$\left(\sum \dot{B}_i\right)_{in} = \left(\sum \dot{B}_j\right)_{out} + \dot{I} \qquad (12)$$

$$\left(\sum \dot{B}_i\right)_{in} = \dot{B}_{air} + \dot{B}_{\substack{dry \\ biomass}} + \dot{B}_{\substack{biomass \\ moisture}} + \dot{B}_{steam} \qquad (13)$$

$$\left(\sum \dot{B}_j\right)_{out} = \dot{B}_{\substack{produced \\ gas,\,dry}} + \dot{B}_{\substack{unconverted \\ carbon}} + \dot{B}_{steam} \qquad (14)$$

The reference state was taken as $T_0 = 25°C$ and $p_0 = 1$ bar.

With the aim of evaluating the performance of the process, some parameters were considered [4], [5]:

$$\eta_{\substack{cold \\ gas}} = \frac{\dot{m}_{\substack{produced \\ gas}} \cdot LHV_{\substack{produced \\ gas}}}{\dot{m}_{\substack{dry \\ biomass}} \cdot LHV_{\substack{dry \\ biomass}}} \qquad (15)$$

$$\eta_{energetic} = \frac{\left(\sum \dot{H}_j\right)_{out}}{\left(\sum \dot{H}_i\right)_{in}} \qquad (16)$$

$$\eta_I = \frac{\dot{B}_C + \dot{B}_{\underset{mixture}{gases}} + \dot{B}_{\underset{gas}{steam}}}{\dot{B}_{\underset{biomass}{dry}} + \dot{B}_{air} + \dot{B}_{steam} + \dot{B}_{moisture}} \quad (17)$$

$$\eta_{II} = \frac{\dot{B}_{\underset{mixture}{gases}}}{\left(\dot{B}_{\underset{biomass}{dry}} - \dot{B}_C\right) + \dot{B}_{air} + \dot{B}_{steam} + \dot{B}_{moisture}} \quad (18)$$

$$\eta_{III} = \frac{\dot{B}_C + \left(\dot{B}_{\underset{mixture}{gas}} - \dot{B}_{air} - \dot{B}_{steam} - \dot{B}_{moisture}\right)}{\dot{B}_{biomassa}} \quad (19)$$

$$\eta_{IV} = \frac{\dot{B}_{\underset{mixture}{gases}} - \dot{B}_{air} - \dot{B}_{steam} - \dot{B}_{moisture}}{\dot{B}_{\underset{biomass}{dry}} - \dot{B}_C} \quad (20)$$

Eq. (15) states a relation between LHV of the produced gas and LHV of the biomass (cold gas efficiency). It does not represent a process index [4]. Eq. (16) represents the magnitude of energy losses of the system (if $\dot{Q}_{losses} = 0$, then its value equals 1). Eqs. (17) to (20) represent exergy efficiencies for the process, according to [6]:

- Eq. (17): relation between outlet exergy flow rate and inlet exergy flow rate, i.e., from what is made available, how much is used. It indicates the total destruction of exergy;
- Eq. (18): process efficiency, i.e., useful effect. This equation relates the exergy of the product (produced gas) and the exergy available for the process;
- Eq. (19): represents the degree of conversion of biomass exergy into products (produced gas and unconverted carbon);
- Eq. (20): expresses the difference in the produced gas exergy and exergy of air, steam and moisture divided by the difference between the dry biomass exergy and the unconverted carbon exergy, as defined in [6].

According to [6], the last equation represents the most stringent criterion, as it relates better to the function of the gasifier (conversion of solid/liquid fuels into a gas fuel).

SIMULATION

For the analysis of the gasification process, it was considered that the reduced molecular formula of sugarcane bagasse was: $CH_{1,61}O_{0,7}$ [10]. All equations shown above were solved using EES software [11] and a parametric study performed. The following variables were evaluated:

- Moisture in biomass;
- Temperature of air;
- Temperature of biomass;
- Volume of steam added;
- Thermal losses.

All relevant results are presented in graphics in order to ease visualization.

RESULTS

Base Case

Aiming to validate the model, it was considered a reference case, so that no moisture is presented in the biomass nor steam is added. Fig. (1) shows the molar fractions for different equivalence ratios.

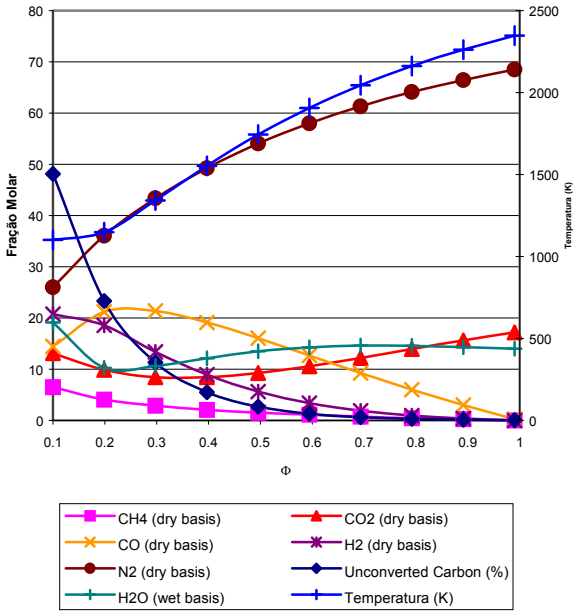

Figure 1 – Molar fractions for base case

As stated in [12], equilibrium models, which assume perfect gas behavior, cannot describe pyrolisis processes, due to the presence of liquid hydrocarbons as pyrolisis products. So, it has not been analyzed very low air-ratio values (below 0.10).

The curves found show the same tendency presented in [4], although some values are different.

Values for CO concentrations are higher than those in [4], while for H_2 they are lower. The different composition of fuel and modeling approach used in each work can explain these differences. Furthermore, both results present CO concentrations lower and H_2 concentrations higher than that found in real systems. However, this behavior does not affect the value of LHV, as

LHV for H_2 and CO are very close to each other [4].

Performance indexes can be evaluated in Fig. (2). For illustration of the destruction of the exergy, it has been used a specific value, which is related to the flow rate of dry bagasse fed to the gasifier. It could have been used the produced gas flow rate, but, as it varies with the air ratio, the results might be misleading. Also, it could have been considered the flow rate of wet bagasse, nevertheless, one proposition of this paper is to present the influence of moisture in the gasification process.

The model does not consider any advantages or disadvantages related to small or large-scale operation. The model is quite general, aiming the visualization of parameters that would enhance performance.

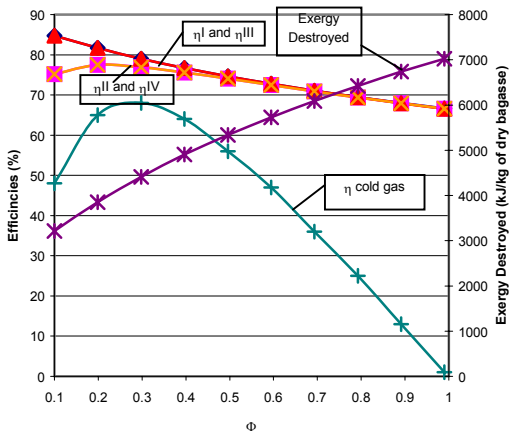

Figure 2 – Performance Indexes for base case

It can be observed from Fig. (2) that the best operating points for the process range between Φ equal to 0.15 to 0.30. In [5], it was found that the carbon boundary[1] lied in Φ equals to 0.255. This point represents the maximum value for process efficiency. This range, also, fits the maximum values for H_2 (Φ≈0.15) and CO (Φ≈0.25) concentrations in Fig. (1). The maximum value for η_{II} and η_{IV} lie in between those two maximum concentrations, what represents a trade-off between the availability of these gases. The existence of such a maximum may be related to the temperature of the process and the conversion of carbon. For air ratio values increasing from 0,15 to 0.30, the conversion of carbon into gas is accelerated (what increases efficiency); for values greater than 0.30, this conversion slows down. As discussed in [6], and also shown by the results of the model, as more air is supplied the process goes from gasification (Φ>0.15) to combustion (Φ >0.5), so temperature increases. This causes an increase in the exergy destruction, due to production of gases with lower chemical exergy and greater temperature differences between products and reactants. So, the presence of those maximum values for the efficiencies shows the trade-off between the conversion of biomass and temperature raise.

In [6], it was suggested operation temperature in the ranges of 1100K – 1200K, for atmospheric gasification, in order to achieve the highest efficiencies. In the model, this range fits exactly the points where Φ range from 0,15 to 0,25. In fact, they suggest operation temperature just above this range (1300K – 1400K) – Φ ranging from 0,25 to 0,35 in the model; so that 75% of the exergy contained in the biomass can be converted into chemical exergy of the produced gas. This statement agrees with the so-called cold gas efficiency in the model.

Parametric Study

Moisture content

One major concern in gasification process is the moisture content in biomass. If it is too high, then there will not be enough energy (low temperatures) to start up the process. To take place, gasification needs temperature above 800 K [13]. Fig. (3) shows the influence of moisture in the process temperature – Φ equal to 0,25:

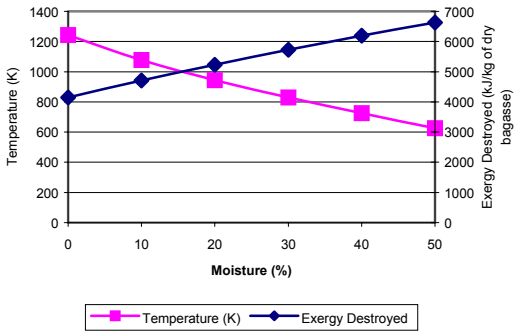

Figure 3 – Influence of moisture on the gasification temperature and exergy destruction

In sugar and alcohol mills, sugarcane bagasse leaves the milling process with 50% moisture, a too high value to start up the process. So, it is

[1] For air-to-fuel ratios greater than the carbon boundary, all carbon is converted into gas.

needed a dryer to operate a gasifier with sugarcane bagasse inside a mill, so biomass could be dried to less than 30% moisture.

Regarding the exergy destruction, an increase in moisture content, increases the destruction of exergy inside the gasifier (Fig. 3). This fact may be explained by:

- Although more H_2 is formed (more atoms of hydrogen are available with an increase in moisture), in order to maintain the process, more energy must be supplied, so exothermic reactions are favored, what promotes CO_2 formation – not a fuel gas.
- More moisture indicates that more energy is to be used in the vaporization of it, and less is available for endothermic reactions, responsible for the production of H_2 and CO.

These conclusions may be visualized in Fig. 4:

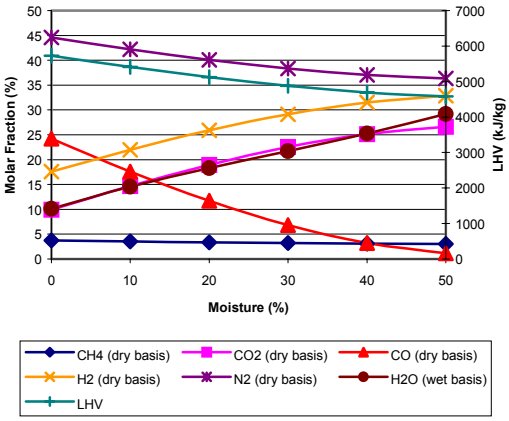

Figure 4 – Influence of moisture on the produced gas

Fig. (5) indicates a displacement of the optimum operation point to the right (and also to a lower efficiency value), as moisture content in biomass increases:

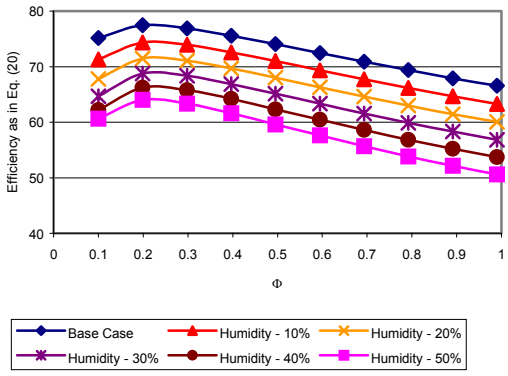

Figure 5 – Influence of moisture on the optimum operating point

From the previous analysis, this displacement is a result of the necessity of more energy to evaporate moisture, increasing the air-to-fuel ratio in order to favor exothermic reactions forming CO_2 and H_2O. The chemical exergies of these gases are lower than chemical exergies of CO and H_2, thus the total exergy of the produced gas is lowered, decreasing the exergy efficiency of conversion (Eq. (20)).

It must be pointed out that Souza-Santos [1] discusses, based in a kinetic gasification model, that if the bagasse drying system could not lead to moisture values below 30%, it might be preferable to feed the gasifier with wet bagasse (50% moisture), as it increases hydrogen availability.

Thermal losses

Despite the increase in H_2 formation, the influence of thermal losses is similar to that of moisture. It reduces the available energy in the process, jeopardizing reduction reactions, and increasing exergy destruction (heat transfer to environment).

Pre-heating of air and/or biomass at the entrance

In [6], the authors state that the main source of exergy destruction, in gasification and oxidation processes, is the presence of chemical reactions. Following them, heat transfer between products and reactants is a second major source of exergy destruction. In this sense, pre-heating air and/or biomass might reduce such destruction, due to lower temperature differences between products and reactants.

However, this reduction is quite small if compared with the increase of exergy destruction due to moisture or thermal losses.

Steam added

In biomass gasification processes, steam is added to the system in order to moderate temperature over the grate, so that no ash fusion occurs [12]. The influence of it in operation is the same that of moisture, but in a much lower scale.

Integration to a Sugarcane Mill

As in [6], the model presented optimum operation points for Φ ranging from 0,15 – 0,25, what represents that almost 75% of the exergy in the biomass is in the produced gas. Coupling this gasification process to a combined cycle, the exergy efficiency of the BIGCC (Biomass Integrated Gasification Combined Cycle), Fig. (6), would be, approximately, 30%; value greater

than the ones found in business practice – Brazilian sugarcane mills based in Rankine Cycles [3]. Fig. (7) is a first attempt to integrate this cycle to a sugarcane mill. For this integration, it has been considered the case of Usina Iracema, located in the state of São Paulo, Brazil. The mill crushes 20,000 t of raw cane per day, producing, approximately, 5,000 t of bagasse (with 50% moisture) per day.

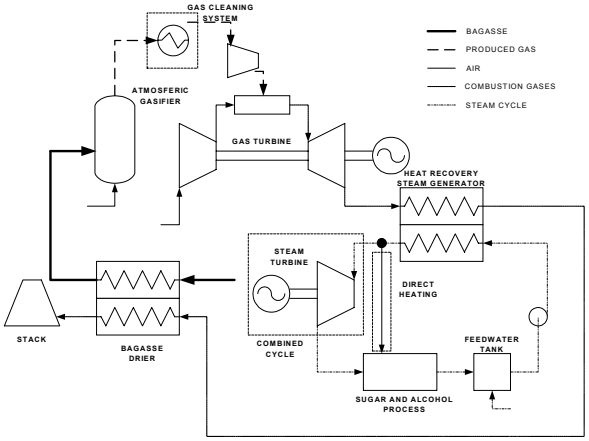

Figure 6 – BIGCC scheme considered in the analysis

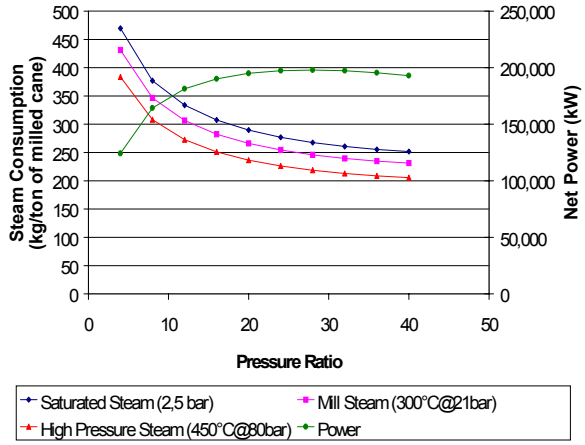

Figure 7 – BIGCC operation for different pressure ratios and steam qualities

It has not been considered any specific commercial gas turbine or HRSG (Heat Recovery Steam Generator) for this analysis. A simple energy balance (considering, inlet turbine temperature equal to 1400 K) was done, so that it could be found the air flow rate required in the gas turbine, the net power produced, and the quantity of steam available, considering different states. As expected, the maximum net power is produced when pressure ratio is, approximately, 30 (value greater than those found for natural gas). The reason for such behavior is the greater amount of produced gas required to achieve the turbine temperature.

It has not been seek, in this work, to analyze the operation/performance of combined cycles operating under low calorific values, even though it has been considered the power input necessary to compress the produced gas into the combustion chamber. More information regarding this subject may be found in [2], [3].

The specific power produced is 216 kWh/tc. This value represents seven times the usual power produced in sugar cane mill considered (30 kWh/tc). However, the steam required in the process (500 kg/tc) cannot be supplied by this system alone.

CONCLUSIONS

Despite the simplicity of the model, its results showed good agreement with results found in literature. This fact allows the following conclusions:

- Moisture is the main problem related to bagasse gasification: it is responsible for an increase in the destruction of exergy inside the reactor, as a result of an increase of the energy required to evaporate the moisture.
- Sugarcane bagasse must be dried to, at least, 30% moisture in order to start-up gasification, according to equilibrium considerations;
- Pre-heating air and/or bagasse may reduce irreversibilities, although it is not sufficient to compensate losses due to high moisture content and/or thermal losses.

It has not been evaluated the influence of moisture on CH_4 formation and the conversion of carbon. For such analysis a stoichiometric approach may be of more use than the one presented here, as it considers the reactions per se. However, the use of empirical relations may be jeopardized.

In Brazil, the steam consumption in sugarcane mills ranges from 400 to 550 kg of steam/tc. From Fig. (5), these values are unrealistic for systems operating with gasification. So, it can be concluded that, before designing a BIGCC System, it is necessary to carry out measures for steam saving, as described in [14], [15], in order to reduce consumption to 200-300 kg of steam/tc.

It is also required to study the influence of low calorific gas operation on commercial gas turbine, in order to evaluate performance and integration of a BIGCC system with processes plant, such as sugarcane mill.

ACKNOWLEDGMENT

The authors wish to acknowledge Fundação de Amparo à Pesquisa do Estado de São Paulo (FAPESP) for the financial support received (grant 03/12094-8), and Usina Iracema for their technical support and data.

REFERENCES

[1] Souza-Santos ML. *A Feasibility Study of an Alternative Pow er Generation System Based on Biomass Gasification/Gas Turbine Concept.*Fuel 1999;78:529-538.

[2] Consonni S, Larson ED. *Biomass-Gasifier/Aeroderivative Gas Turbine Combined Cycles: Part A – Technologies and Performance Modeling and Part B – Performance Calculations and Economic Assessment*. Journal of Engineering for Gas Turbine and Power 1996; 118:507-515 and 516-525.

[3] Rodrigues M, Walter A, Faaij A. *Co-firing of Natural Gas in Biomass Integrated Gasification/Combined Cycle Systems.* Energy 2003; 28:1115-1131.

[4] Li XT, Grace JR, Lim CJ, Watkinson AP, Chen HP, Kim JR. *Biomass Gasification in a Circulating Fluidized Bed.* Biomass and Bioenergy 2004; 26:171-193.

[5] Prins, MJ, Ptasinski KJ. *Energy and Exergy Analysis of Oxidation and Gasification of Carbon.* Energy 2005; 30:982-1002.

[6] Prins MJ, Ptasinski KJ, Janssen FJJG. *Thermodynamics of Gas-char Reactions: First and Second Law Analysis.* Chemical Engineering Science 2003; 58:1003-1011.

[7] Zainal ZA, Ali R, Lean CH, Seetharamu KN. *Prediction of Performance of a Downdraft Gasifier Using Equilibrium Modeling for Different Biomass Materials.* Energy Conversion and Management 2001; 42:1499-1515.

[8] Modell M, Tester JW, *Thermodynamics and its Applications*. Prentice Hall, 3rd edition, 1997.

[9] Abbot MM, Smith JM, Van Ness HC. *Introduction to Chemical Engineering Thermodynamics.* McGraw-Hill, 6th edition, 2001.

[10] Walter ACS. *Viability and Perspectives of Cogeneration and Thermoelectric Generation in the Sugar and Alcohol Sector.* UNICAMP (Ph.D Thesis), 1994.

[11] Klein SA, Alvarado FL. *EES – Engineering Equation Solver for Microsoft Windows Operating Systems.*F-Chart Software, 2004.

[12] Ruggiero M, Manfrida G. An Equilibrium Model for Biomass Gasification Processes. Renewable Energy 1999;16:1106-1009.

[13] Reed TB, Gaur S. *A Survey of Biomass Gasification 2000.* The National Renewable Laboratory and The Biomass Energy Foundation, 2001

[14] Camargo CA (coordinator). *Energy Conservation in The Sugar and Alcohol Industry.* IPT – Institute for Technological Research of São Paulo, 1990 *(in portuguese)*

[15] Baloh T, Wittwer E. *Energy Manual for Sugar Factories.* Berlin: Bartens, 2nd edition, 1995.

[16] Szargut, J, Morris DR, Steward FR. *Exergy Analysis of Thermal, Chemical and Metallurgical Processes.* Hemisphere Publishing Corporation, 1988.

[17] Fock, F, Thomsen KPB. *Modeling a Biomass Gasification System by Means of EES.* In: The Scandinavian Simulation Society, Technical University of Denmark, Kgs. Lyngby, Denmark, 2000.

[18] Karapétiantz M. *Thermodinamique Chimique*. Moscow:MIR, 1978.

[19] Kotas TJ. *The Exergy Method of Thermal Plant Analysis*. Butterworths, 1985.

APPENDIX

In what follows, the main relations for determining the thermodynamic properties of the streams are shown.

Gibbs free energies were evaluated by:

- Carbon Dioxide (CO_2):

$$\Delta G^0_{CO_2} = -1.3503 \cdot T - 394{,}353 \qquad (21)$$

- Carbon monoxide (CO):

$$\Delta G^0_{CO} = -88.381 \cdot T - 111{,}713 \qquad (22)$$

- Steam ($H_2O_{(v)}$):

$$\Delta G^0_{H_2O} = 55.186 \cdot T - 247{,}676 \qquad (23)$$

These relations were obtained through an analysis of the forming reactions of each component. Gibbs free energies for H_2 and N_2 are zero, because they are considered in their standard state [8].

The following values were used for chemical exergies [16]:

Component	Chemical Exergy (kJ/mol)
O_2	3.97
N_2	0.72
CH_4	831.65
CO_2	198.70
CO	275.10
H_2O	9.50
H_2	236.10
$C_{(graphite)}$	410.26

Table 1 – Chemical exergies for different components

Enthalpies for biomass and unconverted carbon were determined by the following relations:

- Biomass (CH_yO_z) [17]:

$$\bar{h}_{f_{biomass}} = h_{CO_2}(25°C,1bar) + \frac{y}{2}\cdot\bar{h}_{H_2O_{(v)}}(25°C,1bar) + PCI_{biomass} \quad (24)$$

$$\Delta h = \frac{0.003867\cdot\left(T_{biomass}^2 - T_0^2\right)}{2} + 0.1031\cdot\left(T_{biomass} - T_0\right) \quad (25)$$

$$\Delta\bar{h} = \bar{c}_{p_{biomass}}\cdot\Delta T \quad (26)$$

- Unconverted carbon ($C_{(s)}$) [18]:

$$\bar{h}_{f_{carbon}} = 0 \quad (27)$$

$$\Delta\bar{h} = \left[4.03\cdot\left(T_C - T_0\right) + \frac{1.14x10^{-3}\cdot\left(T_C^2 - T_0^2\right)}{2} + 2.04x10^5\cdot\left(\frac{1}{T_C} - \frac{1}{T_0}\right)\right]\cdot 4.18 \quad (28)$$

For the exergy of biomass, it was used a coefficient that relates the LHV of biomass to its chemical exergy (the physical exergy has been disregarded from the analysis) [16]:

$$b_{biomass} = \beta\cdot LHV_{biomass} \quad (29)$$

$$\beta = \frac{1.0414 + 0.0177\cdot\frac{H}{C} - 0.3328\cdot\frac{O}{C}\cdot\left[1 + 0.0537\cdot\frac{H}{C}\right]}{1 - 0.4021\cdot\frac{O}{C}} \quad (30)$$

And for carbon, the chemical exergy is 410.26 kJ/mol, and the physical part was obtained by:

$$\bar{b}_{ph} = \int_{T_0}^{T} c_p\cdot dT - T_0\int_{T_0}^{T} c_p\cdot\frac{dT}{T} \quad (31)$$

Using the following relation for c_p [18]:

$$c_p = \left[4.03 + 1.14x10^{-3}\cdot T - \frac{2.04x10^5}{T^2}\right]\cdot 4.18 \quad (32)$$

Enthalpies and entropies for all other components presented in the model were evaluated using the software EES [11].

The evaluation of the exergy of the produced gas was carried out using [19]:

$$\bar{b}_{ph} = \left(\bar{h} - \bar{h}_0\right) - T_0\cdot\left(\bar{s} - \bar{s}_0\right) \quad (33)$$

$$\bar{b}_{ch} = \sum y_j\cdot\bar{b}_j^0 + R\cdot T_0\cdot\sum y_j\cdot\ln\left(y_j\right) \quad (34)$$

$$\bar{b}_{\substack{produced\\gas}} = \bar{b}_{ph} + \bar{b}_{ch} \quad (35)$$

Proceedings of ECOS 2005
Trondheim, Norway
June 20–22, 2005

A DIVISION OF THE THERMOMECHANICAL EXERGY INTO TWO COMPONENTS WITH VERY DIFFERENT QUALITIES

Pedro Pérez-del-Notario and Teresa J. Leo*
Universidad Politécnica de Madrid
Dept. Motopropulsión y Termofluidodinámica
Pza Cardenal Cisneros, 3
28040 Madrid (Spain)

ABSTRACT

The aim of this work is to provide a tool to approach the energy actual market value. As exergy represents the quality of energy, the normal procedure to carry out the thermoeconomic optimization of a given thermal system involves the use of the exergy of each stream as the basic quantity. The usual method evaluates the cost rates appearing in the cost rate balance in terms of the associated rates of exergy transfer and the corresponding unit costs. In this work, the thermomechanical exergy of each stream is divided into two components with very different qualities and, as a consequence, with different unit costs. The component with higher quality can be assigned the same unit cost than work whereas the component with lower quality will usually be assigned a lower unit cost. Therefore, the cost rates of the entering or leaving streams of a system will result closer to actual economic values, especially in processes with important pressure variations. An example related to combined cycles is studied.
Keywords: thermoeconomic optimization, exergy, cost balance, combined cycle

NOMENCLATURE

c	Levelized cost per unit of thermobaric component, per unit of work or per unit of equivalent economic exergy [$/GJ or €/GJ]
c^{ta}	Levelized cost per unit of thermoambient component of thermomechanical exergy [$/GJ or €/GJ]
c_p	Specific heat capacity at constant pressure [kJ/(kg K)] of a gas
c_l	Specific heat capacity of a liquid [kJ/(kg K)]
$\dot{C}_{ik}$	Cost rate of the "fuel" i entering the component k [$/s or €/s]
$\dot{C}_{kj}$	Cost rate of the "product" j leaving the component k[$/s or €/s]
$\dot{C}_{st}$	Cost rate of a stream [$/s or €/s]
h	Specific enthalpy [kJ/kg]
$\dot{I}$	Irreversibility rate [GJ/s]
k	Quotient of equivalent economic exergies, exit to inlet
$\dot{m}$	Mass flow rate [kg/s]
p	Pressure [Pa]
R	Gas constant [kJ/(kg K)]
s	Specific entropy [kJ/(kg K)]
T	Temperature [K]
T_{as}	Temperature [K] defined by the identity $s(T,p)=s(T_{as},p_a)$
v	Velocity [m/s]
$\dot{W}$	Power [GJ/s, GW]
x	Steam quality
z	Elevation [m]
$\dot{Z}_k$	Total capital investment and operating and maintenance costs rate of the k component [$/s or €/s]
δ_0	Temperature increment [ºC]
ρ	Density [kg/m^3]
ϕ	Specific flow exergy [GJ/kg]
$\Delta\phi^{TM}$	Specific thermomechanical flow exergy [GJ/kg]
$\Delta\phi^{CH}$	Specific chemical flow exergy [GJ/kg]
$\Delta\phi^{ta}$	Specific thermoambient component [GJ/kg]
$\Delta\phi^{tb}$	Specific thermobaric component [GJ/kg]

* Corresponding author: Phone: +34 9133 66349 Fax: +34 9133 6371 E-mail: teresa.leo.mena@upm.es

$\Delta\phi^{tb} + \xi\Delta\phi^{ta}$	Specific equivalent economic thermomechanical flow exergy [GJ/kg]
ξ	Quotient of thermoambient to thermobaric components unit costs
Δh^{ta}	Defined by $\left(h(T_{as}, p_a) - h(T_a, p_a)\right)$ [GJ/kg]
Δs^{ta}	Defined by $\left(s(T_{as}, p_a) - s(T_a, p_a)\right)$ [GJ/(kg K)]

Subscripts

a	Ambient
c	Hot gases
l	Liquid
s	Saturated state
t	Total state
v	Vapor
ik	Component *i* towards component *k*
ka	Component *k* towards the ambient
kj	Component *k* towards component *j*
vj	Vapor towards component *j*

INTRODUCTION

The first step to approach the *optimal* design of a complex thermal system is, in many cases, to obtain the minimum irreversibility compatible with "the state of the art" of the system components manufacture. That is, the *thermodynamic* optimization is usually the first step to optimize thermal systems. But usually, a lower irreversibility demands a higher cost, and therefore, the most competitive solution of the new design requires a thorough analysis for a *thermoeconomic* optimization. This thermoeconomic analysis includes the economic evaluation of energy, especially in those systems transforming important quantities of it (thermal engines, chemical industries, etc.). In a number of cases, streams interchanging mass, heat and work are present in many ways in the diverse components of these systems.

A material or a product containing energy has a variable economic value depending on its *quality*. The *thermodynamic quality* of the energetic product is established attending to the product capacity to provide the maximum work interaction, respect to the unit of the product energy. Then, the thermodynamic quality of the energy of a stream is determined by its exergy.

Nevertheless, in the energy market, the *actual quality* of the product is based both on its thermodynamic quality and on the simplicity of the energy transformer required to obtain the above mentioned work interaction.

In this work the actual quality of the exergy of a stream is analyzed. To do so, the thermomechanical flow exergy is written as a sum of two components with different actual qualities. Then, a different unit cost consistent with the actual market value of the energy is proposed for each of these two components of the thermomechanical exergy.

THERMOBARIC AND THERMOAMBIENT COMPONENTS OF THE THERMOMECHANICAL EXERGY OF A STREAM

It is widely known the following distribution of the flow exergy rate by unit of mass flow rate ϕ into its two main components [1-3]

$$\phi = \left[\Delta\phi^{PT} + \Delta\phi^{KN} + \Delta\phi^{PH}\right] + \Delta\phi^{CH} = \Delta\phi^{TM} + \Delta\phi^{CH} \quad (1)$$

where the ensemble of the three first terms is called *thermomechanical exergy* $\Delta\phi^{TM}$, being $\Delta\phi^{PT} = gz$ the potential energy, $\Delta\phi^{KN} = 1/2\,v^2$ the kinetic energy and the physical exergy is $\Delta\phi^{PH} = h(p,T) - h(p_a,T_a) - T_a\left(s(p,T) - s(p_a,T_a)\right)$.

The term $\Delta\phi^{CH}(p_a,T_a)$ represents the chemical exergy in the ambient state $(p_a,T_a,v=0,z=0)$.

The state of reference or dead state is defined by $O(p_a,T_a,v=0,z=0)$ and a chemical composition in chemical equilibrium with the ambient.

Using the concept of total enthalpy h_t, Eq.(1) is written as follows

$$\phi = \left[h_t(p,T,v,z) - h(p_a,T_a) - T_a\left(s(p,T) - s(p_a,T_a)\right)\right] + \Delta\phi^{CH} = \Delta\phi^{TM} + \Delta\phi^{CH} \quad (1b)$$

rion of *actual quality* here introduced, an intermediate state $A(p_a, T_{as}, v=0, z=0)$ is established and then the following division is proposed

$$\Delta\phi^{TM} = \left[\phi(p,T,v,z) - \phi(p_a,T_{as})\right] + \left[\phi(p_a,T_{as}) - \phi(p_a,T_a)\right] \quad (2)$$

being T_{as} the temperature that, without changes in the chemical composition, meets the condition $s(p,T) = s(p_a,T_{as})$. That is, the thermodynamic state $A(p_a, T_{as}, v=0, z=0)$ is the one obtained after an isentropic expansion (or compression) from a state of pressure *p*, temperature *T*, velocity *v* and elevation *z*, to the ambient pressure p_a and kinetic and potential energy levels equal to zero, without changing the chemical composition The Eq.(2) can be written as

$$\Delta\phi^{TM} = \Delta\phi^{tb} + \Delta\phi^{ta} \quad (3)$$

where the first term of the right hand side

$$\Delta\phi^{tb} = h_t(p,T,v,z) - h(p_a,T_{as},v=0,z=0) \quad (4)$$

represents the work obtained (or required) in the adiabatic and isentropic expansion (or compression) process to ambient pressure, zero velocity and zero potential energy level. This component of the thermomechanical exergy has been called *thermobaric* component. The energetic quality of this thermobaric component can be comparable to that of work.

The second term of the right hand side of Eq. (3)

$$\Delta\phi^{ta} = \left[h(p_a,T_{as}) - h(p_a,T_a)\right] - T_a\left[s(p_a,T_{sa}) - s(p_a,T_a)\right] \quad (5)$$

represents an exergetic component of exclusively thermal-type at the ambient pressure p_a. The reversible conversion of it into work interaction becomes a very complex task. This component of the thermomechanical exergy can be designed by *thermoambient* component.

It is evident that the economic value of these two components is different, being higher the thermobaric than the thermoambient one in the thermal engines case.

The thermomechanical exergy $\Delta\phi^{TM}$ can be split in diverse forms, but taking into account the crite

Assuming, as an example, a gas perfect stream (c_p, R), for a (p_t, T_t) state it follows

$$\frac{T_{as}}{T_t} = \left(\frac{p_a}{p_t}\right)^{R/c_p}$$

$$\Delta\phi^{tb} = c_p(T_t - T_{as}) = c_p T_t\left[1 - \left(\frac{p_a}{p_t}\right)^{R/c_p}\right] \quad (6)$$

$$\Delta\phi^{ta} = \Delta h^{ta} - T_a\left[s(p_a,T_{as}) - s(p_a,T_a)\right] = c_p T_a\left(\frac{T_{as}}{T_a} - 1\right) - c_p T_a \ln\frac{T_{as}}{T_a} \quad (7)$$

Numerical values of $\Delta\phi^{ta}$, $\Delta\phi^{tb}$ and ϕ can be either positive or negative depending on the (p_t,T_t) and (p_a,T_a) states. Both thermobaric and thermoambient exergy components can have a wide variety of values in the different systems under study.

In the case of a hot gases stream in a state with $T_t = 1500\,\mathrm{K}$, p_t = 2MPa, $c_p = 1.16\,\mathrm{kJkg^{-1}K^{-1}}$ and $R = 0.287\,\mathrm{kJkg^{-1}K^{-1}}$, and an ambient state ($T_a = 300\ \mathrm{K}$; $p_a = 0.1\ \mathrm{MPa}$), the following results are obtained: $T_{as} = 715.7\,\mathrm{K}$, $\Delta\phi^{tb} = 909.8\ \mathrm{kJkg^{-1}}$ and $\Delta\phi^{ta} = 179.56\ \mathrm{kJkg^{-1}}$.

If a stream of an incompressible liquid at the state (p_t, T) of thermal specific capacity c_l is assumed, the following results are obtained

$$T_{as} = T \qquad \Delta\phi^{tb} = \frac{p_t - p_a}{\rho_l} \quad (8)$$

$$\Delta\phi^{ta} = \Delta h^{ta} - T_a\left[s(p_a,T_{as}) - s(p_a,T_a)\right] = c_l T_a\left(\frac{T}{T_a} - 1\right) - c_l T_a \ln\frac{T}{T_a} \quad (9)$$

In a wide range of technical devices, the processes underwent by the streams can be assumed as adiabatic ones. Even, when a heat exchanger is involved, the ensemble as a whole can also be considered as an adiabatic system. Therefore, the study developed here is applied to *adiabatic processes*.

RELATIVE ECONOMIC EVALUATION OF THERMOMECHANICAL EXERGY COMPONENTS. ADIABATIC PROCESSES

The economic value of energy in a given stream depends on its thermodynamic quality and then, in an early economic evaluation of the stream, exergy is used as a property with economic value.

Economic evaluation of exergy begins by assigning costs to the main components shown in Eq. (1), that is, by giving economic values to thermomechanical exergy $\Delta\phi^{TM}$ and thermochemical exergy $\Delta\phi^{CH}$.

For many energetic products or energetic supplies ("fuel"), the market value or actual economic evaluation of the chemical exergy $\Delta\phi^{CH}$ is based both on their amount of exergy and on other non-thermodynamic characteristics.

Consequently, when an energetic conversion is analyzed from a thermoeconomic point of view, to approach the actual energetic market situation, the chemical exergy component $\Delta\phi^{CH}$ is considered separately from the thermomechanical exergy one, $\Delta\phi^{TM}$.

Many thermodynamic processes take place without changes of chemical composition of the streams involved in. Therefore $\Delta\phi^{CH}$ does not change and does not participate in the thermoeconomic study performed.

Respect to the thermomechanical exergy $\Delta\phi^{TM}$, it must be pointed out that it is usually treated as a whole in the thermoeconomic analyses. But, as has been shown when the thermomechanical exergy has been split in the proposed manner, Eqs. (4) and (5), the thermobaric component $\Delta\phi^{tb}$ includes, in addition to the kinetic and potential energies, the amount of work extracted (or required) in a simple expansion (or compression) process. Therefore, conversion of thermobaric exergy $\Delta\phi^{tb}$ into work implies a direct process without complex processes. On the contrary, the thermoambient exergy $\Delta\phi^{ta}$ is exclusively constituted by thermal exergy at the ambient pressure and converting it into work is a rather complex task. Theoretically at least, it could be completely converted into work by means of a reversible process.

In order to approach the actual market values, different costs to both exergy components should be assigned when a thermoeconomic analysis is performed.

As can be deduced from Eq. (3), a given value of $\Delta\phi^{TM}$ can be the result of the sum of very different $\Delta\phi^{tb}$ and $\Delta\phi^{ta}$ quantities. As the economic value of both components is different, the corresponding economic value of the same quantity $\Delta\phi^{TM}$ can be very different depending on the system under study.

In this work, the economic evaluation of both thermomechanical exergy components is proposed as

$$c\Delta\phi^{tb} + c^{ta}\Delta\phi^{ta} = c(\Delta\phi^{tb} + \xi\Delta\phi^{ta}) \qquad (10)$$

where

$$\xi = \frac{c^{ta}}{c} \qquad (11)$$

is a parameter used to establish the relative economic value of the thermoambient and thermobaric exergy components. The quantities c and c^{ta} in Eq. (11) are the levelized unit costs of these two exergies with different qualities.

It is correct to think that the estimation of the ξ parameter will depend on each specific system and the place where the installation is working. In any case, the same value for all the streams and components in the specific system can be assumed. This hypothesis can be established if the relative cost of mechanical and thermal energy is assumed constant in a given situation (a cogeneration plant in a given country, for example). It must be pointed out that ξ is an economic parameter and not a thermodynamic one.

In power systems, this parameter can be estimated, for example, in the following way

$$\xi = \frac{\text{levelized unit cost of the natural gas energy GJ}}{\text{levelized unit cost of the electric energy GJ}}$$

Values between 0.3 and 0.4 are obtained in typical situations. Sensitive analyses can be performed with this parameter after the thermoeconomic study is made.

The quantity ($\Delta\phi^{tb} + \xi\Delta\phi^{ta}$) is called here *equivalent economic thermomechanical flow exergy*.

The cost rate of a stream, $\dot{C}_{st}$ ($/s o €/s), is generally expressed as the product of a levelized unit cost by the flow exergy of the stream, that is, $\dot{C}_{st} = c(\dot{m}\phi)$. Making use of the formulation proposed here, such cost rate can be written as

$$\dot{C}_{st} = c\left[\dot{m}(\Delta\phi^{tb} + \xi\Delta\phi^{ta})\right] \qquad (12)$$

now being c the levelized unit cost of the equivalent economic exergy. Thus, the levelized unit cost c is referred to the equivalent economic value of the product, which is closer to its actual market value.

Thermodynamic quality of $\Delta\phi^{tb}$ is assumed to be analogous to that of specific work. Thus, when they are obtained as energetic products at the same time, it is also assumed that both have equal economic values.

When a thermoeconomic study is applied to a complex system, the cost balance applied to each component k (energy converter), is based on the well known economic equation [1-3]

$$\sum_i \dot{C}_{ik} + \dot{Z}_k = \sum_j \dot{C}_{kj} \qquad (13)$$

written for a given period of time. When this equation is particularized to *adiabatic systems*, $\dot{C}_{ik}$ represent the cost rates of the streams $\dot{m}_i$ and work interactions $\dot{W}_i$ that, coming from the component i, enter the component k. All of them are known. $\dot{Z}_k$ stands for the investment, operation and maintenance cost rate of such component k. $\dot{C}_{kj}$ are the cost rates of the energetic products obtained (streams and work interactions) in k and entering other components j. $\dot{C}_{kj}$ are the unknowns precisely.

As only one economic equation by component is available, when more than one energetic product are obtained at the exit of the k component, some additional hypotheses are needed. Such hypotheses must relate the various products from the economic point of view in order to determine their unit costs [1-3].

That is, it is a common practice to apply diverse additional hypotheses based on the exergy of each stream to determine unit costs.

If Eq. (12) is introduced into Eq. (13), for a process without change of composition in the k component, the new formulation leads to

$$\sum_i \left[c_{ik}\dot{W}_{ik} + c_{ik}\dot{m}_{ik}(\Delta\phi_{ik}^{tb} + \xi\Delta\phi_{ik}^{ta})\right] + \dot{Z}_k = c_k\left\{\sum_j \left[\dot{W}_{kj} + \dot{m}_{kj}(\Delta\phi_{kj}^{tb} + \xi\Delta\phi_{kj}^{ta})\right]\right\} \qquad (14)$$

where c_{ik} represents the levelized unit cost of the "fuel" entering the k component, which coming from the outside or from other component i, has been calculated or estimated previously. In Eq. (14) c_k is the levelized unit cost of the *equivalent economic thermomechanical flow exergy* of the streams leaving the component k and entering any other component j. It also represents the levelized unit cost of the specific work obtained in this component. In other words, c_k represents the levelized unit cost of the energetic products.

It must be pointed out that Eq. (14) has been written stating a unique hypothesis common to all the products of every component in the whole specific thermal system. Such hypothesis is that a unique value of the ξ parameter is assumed.

Equation (14) makes evident the influence of the division of thermomechanical exergy into two components of different quality (thermobaric and thermoambient exergy), in the unit cost of a stream. As has been said, this feature allows to obtain costs of the products close to actual market values.

In addition to the previous equation, the exergy balance particularized to each component k is available. Using Eq. (3) the following is obtained

$$\sum_i \left(\dot{W}_{ik} + \dot{m}_{ik}\left(\Delta\phi_{ik}^{tb} + \Delta\phi_{ik}^{ta}\right)\right) = \sum_j \left(\dot{W}_{kj} + \dot{m}_{kj}\left(\Delta\phi_{kj}^{tb} + \Delta\phi_{kj}^{ta}\right)\right) + \dot{m}_{ka}\phi_{ka} + \dot{I}_k \qquad (15)$$

where the total exergy thrown to the ambient (lost exergy) and the irreversibility of the process are, respectively $\dot{m}_{ka}\phi_{ka}$ and $\dot{I}_k$.

To use the cost balance expressed as in Eq. (14), knowledge of the magnitudes of the thermobaric and thermoambient exergy components, $\Delta\phi^{tb}$ and $\Delta\phi^{ta}$, in every control section of the system is needed.

Provided the corresponding device efficiencies are available, Thermodynamics makes possible to determine the streams thermodynamic properties in the different control sections of the thermal system. The method of calculation for some simple cases is explained, as examples, in the following section.

As the unit cost of "fuels" is known and the magnitude and kind of the energetic products are also known, the only unknown value of Eq. (14) is c_k.

Thus, writing one equation, Eq. (14), for each system component, a lineal equation system is ob-

tained and then, the unknowns c_k can be determined.

THERMODYNAMIC EVALUATION OF THE THERMOBARIC AND THERMOAMBIENT COMPONENTS. ADIABATIC PROCESSES

A monophase stream without composition change

The following expressions can be written when a stream experiences an adiabatic process 1→2 in a component of the thermal system

$$\begin{aligned} &\dot{m}_1 h_{t1} + \dot{W}_1 = \dot{m}_1 h_{t2} + \dot{W}_2 \\ &\dot{m}_1 \phi_1 + \dot{W}_1 = \dot{m}_1 \phi_2 + \dot{W}_2 + \dot{I}_{12} \end{aligned} \qquad (16)$$

The subscripts 1 and 2 indicate the inlet and the outlet of the system component *k*, respectively. Here $\dot{I}_{12}$ represents the irreversibility rate in the process.

Assuming that thermodynamic properties at the inlet, section 1, are known and particularizing Eqs. (1) and (3) for the control sections 1 and 2, it follows that

$$\begin{aligned} &\Delta\phi_2^{CH} - \Delta\phi_1^{CH} = 0 \\ &\Delta\phi_2^{tb} - \Delta\phi_1^{tb} = \frac{\dot{W}_1 - \dot{W}_2}{\dot{m}} - (\Delta h_2^{ta} - \Delta h_1^{ta}) \\ &\Delta\phi_2^{ta} - \Delta\phi_1^{ta} = (\Delta h_2^{ta} - \Delta h_1^{ta}) - T_a \Delta s_{12}^{ta} \end{aligned} \qquad (17)$$

With any model of substance, at the constant pressure $p = p_a$, the following expressions are derived

$$\begin{aligned} &\Delta h_2^{ta} - \Delta h_1^{ta} = \int_{T_{as1}}^{T_{as2}} c_p(p_a, T)\, dT \\ &\Delta s_{12}^{ta} = \int_{T_{as1}}^{T_{as2}} \frac{c_p(p_a, T)}{T}\, dT \end{aligned} \qquad (18)$$

The value of T_{as2} is obtained calculating previously the state 2t. To do that, the device efficiency to determine the irreversibility process is required.

A two phase stream without chemical composition change

In technical applications, processes where both liquid and vapour phases either together or separated are quite frequently found. This is usual when the ambient state $O(p_a, T_a)$ is near to the biphasic states (vapour, liquid) of the substances.

This circumstance takes place in two cases of technical relevance: steam power plants and refrigerating plants. In the case of steam power plants the ambient state usually corresponds to liquid water, $O(p_a, T_a, \text{liquid})$.

To study a vapour stream with thermomechanical exergy $\Delta\phi_v^{TM}(p,T,v,z)$ is adequate to select the state of separation of the thermobaric and thermoambient components as $B\left[p_v(T_a), T_{as}\right]$. Here $p_v(T_a)$ represents the vapour pressure corresponding to the ambient temperature T_a. The value of T_{as} is given by the condition $s\left(p_v(T_a), T_{as}\right) = s(p,T)$. Therefore, the thermobaric component of a vapour stream is written as

$$\begin{aligned} \Delta\phi_v^{tb} &= \phi_v(p,T,v,z) - \phi_v(p_v(T_a), T_{as}) \\ &= h_v(p,T,v,z) - h_v\left(p_v(T_a), T_{as}\right) \end{aligned} \qquad (19)$$

which represents the specific work that can be obtained directly after an isentropic expansion. For calculation purposes it is evident that $h_v\left(p_v(T_a), T_{as}\right) = h_v\left(p_v(T_a), s(p,T)\right)$.

The thermoambient component is in this case

$$\begin{aligned} \Delta\phi_v^{ta} &= h_v\left(p_v(T_a), T_{as}\right) - h_l(p_a, T_a) \\ &\quad - T_a\left[s_v\left(p_v(T_a), T_{as}\right) - s_l(p_a, T_a)\right] \\ &= h_v\left(p_v(T_a), T_{as}\right) - h_{vs}(T_a) + h_{ls}(T_a) - h_l(p_a, T_a) \\ &\quad - T_a\left[s_v\left(p_v(T_a), T_{as}\right) - s_{vs}(T_a) + s_{ls}(T_a) - s_l(p_a, T_a)\right] \end{aligned} \qquad (20)$$

Here the subscripts "*ls*" and "*vs*" stand for saturated liquid and vapour, respectively, at the temperature T_a.

From Eq. (19) it follows that when $p_v(T_a) \ll p_a$ the value of $\Delta\phi_v^{tb}$ is high, and from Eq. (20) can be deduced that the value of $\Delta\phi_v^{ta}$ is low. That is, the thermomechanical exergy of a high pressure vapour stream that, for example, is to be expanded in a turbine, is mainly thermobaric component, high quality exergy as has been said. In this case the thermoambient component has a very low value, as can be appreciated next. At pressure $p_v(T_a) \ll p_a$ the steam can be taken as perfect gas, then

$$\Delta\phi_v^{ta} = c_{pv}(T_{as} - T_a) - c_{pv}T_a \ln\frac{T_{as}}{T_a} + \frac{p_v(T_a) - p_a}{\rho_l}$$
$$= c_{pv}T_a\left(\frac{T_{as}}{T_a} - 1 - \ln\frac{T_{as}}{T_a}\right) + \frac{p_v(T_a) - p_a}{\rho_l} \quad (21)$$

When $T_{as} = T_a$ (two-phase region) $\Delta\phi_v^{ta}$ is equal to the second member of the right hand side of Eq. (21), with very low value.

Heat exchanger with phase change

The case of a hot gases stream $\dot{m}$ that, at ambient pressure p_a, transfers its exergy (thermoambient component in this case) to a pressurized liquid stream $\dot{m}_l$ in various pressure steps, is studied. In the heat exchanger, this liquid stream at high pressure is transformed into various vapour streams with different pressure levels. This could be the case of the heat recovery steam generator (HRSG) in a combined cycle power plant. Making use of the exergy balance, Eq. (15), and rearranging

$$\dot{m}(\Delta\phi_1^{ta} - \Delta\phi_2^{ta}) = \sum_j \dot{m}_{vj2}\Delta\phi_{vj2}^{tb} + (\sum_j \dot{m}_{vj2}\Delta\phi_{vj2}^{ta} - \dot{m}_l\Delta\phi_{l1}^{tb}) + \dot{I}_{12} \quad (22)$$

Equations (18), (19) and (21) suggest that the exergy of a gas stream $\dot{m}$ at pressure near to ambient (exhaust gas stream of a gas turbine, for example), whose thermoambient component is much higher than its thermobaric component $\dot{m}\Delta\phi^{ta} \gg \dot{m}\Delta\phi^{tb}$, can be transferred directly (without external work) to a pressurized liquid stream until a vapour state is reached for which its thermobaric component is much higher than its thermoambient one, $\dot{m}_v\Delta\phi_v^{tb} \gg \dot{m}_v\Delta\phi_v^{ta}$. Thus, the higher possible value of the thermobaric component is obtained $\sum_j \dot{m}_{vj2}\Delta\phi_{vj2}^{tb} \gg (\sum_j \dot{m}_{vj2}\Delta\phi_{vj2}^{ta} - \dot{m}_l\Delta\phi_{l1}^{tb})$ in this process and a subsequent direct conversion into work can be performed in a turbine. It can be said that this process *regenerates the quality* of the exergy of the hot gases stream.

This possibility, suggested by thermodynamic considerations, gives rise to the denominated *combined cycle*, by means of a relatively simple process.

STUDY OF AN EXAMPLE RELATED TO COMBINED CYCLE POWER PLANTS

To make evident the influence of the thermomechanical exergy division into two components of different qualities, thermobaric and thermoambient ones, a simple case of interest in combined cycle power plants is presented.

A hot perfect gases stream $(\dot{m}, c_p, T_{c1}, p_{c1} \approx p_a)$ enters a unique pressure level steam generator to give a vapour stream $(\dot{m}_v, p_2, T_{v2} = T_{c1} - \delta_0, \delta_0 > 0)$ from a liquid water stream $(\dot{m}_l = \dot{m}_v, p_2, T_a)$. Inlet and outlet thermobaric and thermoambient component values are determined and compared. To reduce irreversibility, a counterflow arrangement is used. The process is constituted by two steps: *a*) heating of the pressurized liquid until the saturation temperature corresponding to the pressure p_2, $T_s(p_2)$ is reached. The corresponding gases temperature is $T_s(p_2) + \delta_1$, (pinch point δ_1); *b*) evaporation and overheating to achieve the final steam temperature.

The total energy balance leads to

$$\frac{\dot{m}_v}{\dot{m}} = \frac{c_p(T_{c1} - T_s(p_2) - \delta_1)}{h_v(p_2, T_{c1} - \delta_0) - h_{ls}(p_2)}$$
$$\Delta T_c = T_{c1} - T_{c2} = \left(T_{c1} - T_s(p_2) - \delta_1\right)\frac{h_v(p_2, T_{c1} - \delta_o) - h_l(p_2, T_a)}{h_v(p_2, T_{c1} - \delta_0) - h_{ls}(p_2)}$$

In addition to this, using Eq. (7)

$$\Delta\phi_1^{ta} - \Delta\phi_2^{ta} = c_p T_a\left[\frac{\Delta T_c}{T_a} + \ln\left(1 - \frac{\Delta T_c}{T_{c1}}\right)\right]$$

Using Eq. (19)

$$\Delta\phi_{v2}^{tb} = h_v(p_2, T_{c1} - \delta_0) - \left[T_a\left(s_v(p_2, T_{c1} - \delta_0) - s_{ls}(T_a)\right)\right] - h_{ls}(T_a)$$

The exergy of a liquid stream can be written in this case as follows

$$\phi_{l1}(p_2, T_a) = h_{l1}(p_2, T_a) - h_l(p_a, T_a) - T_a\left(s_{l1}(p_2, T_a) - s_l(p_a, T_a)\right)$$

For example, if $T_a = 30\,^{o}\mathrm{C}$, $p_a = 0.1\mathrm{MPa}$, $T_{c1} = 515\,^{o}\mathrm{C}$, $p_{c1} = p_a$, $\delta_0 = \delta_1 = 15\,^{o}\mathrm{C}$ and $c_p = 1.16\,\mathrm{kJkg^{-1}K^{-1}}$ it results that $\Delta\phi_1^{tb} = 0\,\mathrm{kJkg^{-1}}$, $\Delta\phi_1^{ta} = 226.6\,\mathrm{kJkg^{-1}}$ and $\Delta\phi_{v2}^{ta} = -0.09618\,\mathrm{kJkg^{-1}}$. To calculate the process irreversibility Eq. (22) is used.

To make evident the different economic value of the streams involved in Eq. (14), the quotient of the equivalent economic exergies leaving and entering the device, *k*, is calculated as

$$k = \frac{\dot{m}_v(\Delta\phi_{v2}^{tb} + \xi\Delta\phi_{v2}^{ta}) + \dot{m}\xi\Delta\phi_2^{ta}}{\dot{m}\xi\Delta\phi_1^{ta} + \dot{m}_v\Delta\phi_{l1}^{tb}}$$

The results obtained from the study of a steam generator with a unique pressure level are presented in Table 1 for different values of liquid water pressure, p_2. This pressure is also the pressure of the resulting steam entering the turbine. It can be observed that when p_2 rises, the steam quality *x* diminishes and more than one pressure level is required.

p_2 **MPa**	$\dot{m}_v/\dot{m}$	ΔT_c **°C**	$\Delta\phi_{v2}^{tb}$ **kJkg^{-1}**	$\frac{\dot{m}_v\Delta\phi_{v2}^{tb}}{\dot{m}\Delta\phi_1^{ta}}$
0.3	0.145	421.05	968.97	0.622
1.0	0.137	395.1	1132.14	0.683
2.0	0.130	375.4	1221.47	0.703
3.0	0.126	361.7	1270.30	0.707
4.0	0.123	351.03	1302.66	0.706
5.0	0.121	341.6	1335.78	0.705
p_2 **MPa**	$\frac{\dot{I}_{12}}{\dot{m}\Delta\phi_1^{ta}}$	x	k $\xi = 0{,}3$	k $\xi = 1$
0.3	0.348	0.98	2.09	0.64
1.0	0.260	0.91	2.32	0.73
2.0	0.216	0.87	2.42	0.77
3.0	0.193	0.85	2.45	0.80
4.0	0.178	0.83	2.46	0.81
5.0	0.164	0.82	2.47	0.83

Table 1: Steam generator with a unique pressure level

In order to make evident the influence of the ξ parameter, the values of *k* for $\xi = 0.3$ and $\xi = 1$ are presented in the last two columns of Table 1. It can be observed that for a standard value of $\xi = 0.3$, *k* is greater than 2. On the contrary, if thermomechanical exergy is not divided into the two components of different quality, $\Delta\phi^{TM} = \Delta\phi^{tb} + \Delta\phi^{ta}$, case for which $\xi = 1$, values lower than unity are obtained for this quotient.

CONCLUSIONS

Thermobaric and thermoambient components of thermomechanical exergy defined here can have very different values giving rise to the same final thermomechanical numeric result. As a consequence, the actual quality of this thermomechanical exergy, quantified by the economic equivalent exergy, may have very different values depending on the relative contribution of these two components.

Division of thermomechanical exergy into two components with different qualities allows to obtain product unit costs closer to market values.

With this formalism a unique hypothesis is assumed: the quotient of the two thermomechanical exergy component unit costs is kept constant all over the specific thermal system. This feature makes unnecessary the particular hypotheses usually assumed for each economic equation in each system component.

REFERENCES

[1] Bejan A.. Tsatsaronis G. and Moran M. *Thermal Design and Optimization*. New York: John Wiley and Sons Inc., 1996.

[2] Frank Kreith. ed. The CRC Handbook of Thermal Engineering. CRC Press: New York, 2000.

[3] Kotas T. J. *The exergy method of thermal plant analysis*. London: Butterworths, 1985.

Proceedings of ECOS 2005
Trondheim, Norway
June 20–22, 2005

TOWARDS AN INTERNATIONAL LEGAL REFERENCE ENVIRONMENT

Jan Szargut*, Antonio Valero, Wojciech Stanek* and Alicia Valero****

***Silesian University of Technology; Institute of Thermal Technology**
Gliwice, Poland

****Centro de Investigación de Recursos y Consumos Energeticos**
Zaragoza, Spain

ABSTRACT

The determination of the natural capital exergy is linked to the definition and thermodynamic properties of the Reference Environment (R.E.) used. Hence the importance of an appropriate selection of the R.E. The aim of this paper is to obtain and propose in ECOS 2005, an agreement on the legal international reference environment for evaluating the natural resources on Earth. For this purpose, all the R.E. models published so far are systematically analyzed, the best suitable methodology for calculating the standard chemical exergy of the chemical elements is chosen and shown and the variables used in the chosen methodology are updated using new geochemistry information and revisions done by other authors.

Keywords: Reference Environment, Reference Substance, Standard Chemical Exergy, Natural capital

INTRODUCTION

The natural capital can be evaluated from different points of view. One of them, and perhaps the most commonly known is the economic point of view. Nevertheless, as Naredo [1] analyzes, standard economy is only concerned with what which being directly useful to man, is also acquirable, valuable and produce-able. For this reason, most of the natural resources, remain outside the object of analysis of the economic system. The price-fixing mechanisms, rarely take into account the concrete physical characteristics which make them valuable. But natural capital has at least two physical features which make minerals or fresh water for example unusual: a particular composition which differentiates them from the surrounding environment, and a distribution which places them in a specific concentration. These intrinsic properties, can be in fact evaluated from a thermodynamic point of view in terms of exergy [2].

The thermodynamic value of a natural resource could be defined as the minimum work necessary to produce it with a specific structure and concentration from common materials in the environment. This minimum amount of work is theoretical by definition and is equal to the material's exergy (Riekert [3]). The exergy of a system gives an idea of its evolution potential for not being in thermodynamic equilibrium with the environment, or what is the same, for not being in a dead state related to the Reference Environment (R.E.). Therefore, for calculating the exergy of any natural resource, a R.E. should be defined. This R.E. must be determined by the natural environment and can be assimilated to a thermodynamically dead planet where all materials have reacted, dispersed and mixed.

Each of the R.E. definitions are fixed by their chemical composition. They have therefore different values of reference exergy and generate different exergies. This implies that the determination of the natural capital exergy is necessarily linked to the definition and thermodynamic properties of the R.E.

Hence the importance of an appropriate selection of a R.E. for evaluating natural resources.

SEARCHING THE BEST SUITABLE R.E. CATEGORY

So far, there have been many contributions to the determination of a R.E. They could be divided into two main groups: *Partial* and *Comprehensive Reference Environments*.

It is well known, that some authors such as Bosnjakovich [4], Gaggioli and Petit [5] and Sussman [6] established that the R.E. should be defined according to the specific characteristics of the analyzed process. This criterion is based on that being the exergy a parameter that quantifies the theoretical evolution of a system with respect to the R.E., some of the possible evolutions of the system, cannot be attained because of process limitations. Hence, only possibilities of evolution that the system can practically attain are analyzed. The R.E. is not a "dead state" anymore. For computing exergy changes of variable composition or chemically reactive steady flow processes, a *Comprehensive Reference Environment* is generally unnecessary. However, this is not the case when the point is to evaluate the natural capital on Earth. In this case, there are no process limitations and the resources can follow an evolution process towards the dead state, thus a comprehensive R.E. is required.

Within the known *Comprehensive Reference Environments*, all authors agree in dividing the Reference Substances (R.S.) that compose the R.E. into gaseous components of the atmospheric air, solid components of the external layer of the Earth's crust, and molecular components of seawater. Nevertheless, there are also criterion differences between the different authors. They could be classified into environments based on 1) *Szargut's criterion*, 2) *Chemical equilibrium* and 3) *Abundance*.

Abundance and *Szargut's criterion* are not opposite criteria. According to *Szargut's criterion*, among a group of reasonable abundant substances, the most stable will be chosen if they also complain with the "Earth similarity criterion". That is, if the stability of the possible different reference substances for a specific element (measured in terms of the formation Gibbs energy) is within a certain threshold, then the most abundant R.S. will be chosen. If the differences exceed this threshold, the most stable substance will be taken as R.S. as long as it does not contradict the "Earth similarity criterion". The stability threshold has not a fix value and depends on each element considered, since it is subjected to geological uncertainties. Thus for example in the case of Sb, the substance Sb_2S_3 is more abundant than Sb_2O_5, nevertheless, according to *Szargut's criterion*, Sb_2O_5, which is much more stable, will be taken as reference substance. This happens also with the substances listed in table 1. Nevertheless nitrates such as $Ca(NO_3)_2$, $NaNO_3$, KNO_3 are discarded, because being most stable but not abundant in the natural environment, would break the similarity criterion if they are taken as R.S. Therefore, Szargut's [7] dead environment is similar to the real physical environment and should represent the products of an interaction between the components of the natural environment and the waste products of the processes. The most probable products of this interaction should be chosen as reference species. Next section explains purposively the well known Szargut's methodology for obtaining the chemical exergy of the elements from the R.E.

Some authors define the chemical exergy by means of the *chemical equilibrium* with the real environment. Szargut stresses that it is not possible to attain an equilibrium with the system being not in the state of internal equilibrium (and the natural environment is far away from such equilibrium). Ahrendts [8] and Diederichsen [9] for example, stated that if the amount of different elements in the reference system is known and the temperature of the system is fixed, the quantity of each chemical compound and the value of each chemical potential is uniquely determined by the condition of *chemical equilibrium*. Even though Ahrendt's R. E. only included 15 elements, they represented more than 99% of the Earth's crust and thus his R.E. can be considered as a *Comprehensive Reference Environment*. Ahrendts calculated the composition of this environment in chemical equilibrium, having as a variable parameter the thickness of the crust layer.

Valero, Ranz and Botero [2], explained already why Ahrendt's R.E. was not suitable to evaluate the natural capital on Earth. Most of the metals cannot be evaluated because they form part of the 1% of the Earth's crust neglected by Ahrendts. His obtained R.E. is very different from the real environment and it is very unlikely an eventual evolution

towards it, since some processes are kinetically, biologically and/or geologically blocked.

Diederichsen updated and extended Ahrendt's model with new geochemical data and obtained among others, a R. E. including 75 elements. Furthermore, he allowed the composition of this environment to change with two variable parameters: thickness of the Earth's crust and ocean's depth. The final chosen environment should comply with the "Earth similarity criterion". The similarity with the Earth was measured with the equilibrium pressure, the oxygen and nitrogen content in the gas-phase and the equilibrium salt content in the oceans.

Even though Diederichsen [9] added more elements than Ahrendts [8] and included a new variable parameter, the composition of his new Reference Environment is still too different from the real Earth. According to the "Earth similarity criterion", the R.E. that best fits with the Earth's environment takes a crust thickness of only 0,1 m and an ocean's depth of 100 m. Greater values would move further away the R.E. from the real Earth, and would have among other features, reduced pressures and oxygen contents. As it happened with Ahrendt's model before, Diederichsen obtained high exergy values for oxygen. This happens because nearly all the oxygen of the air is consumed basically by the formation of nitrates and only in the limit, for a crust thickness of 0 m, the mean Earth pressure matches with that of the model. It seems therefore that achieving a R.E. in *chemical equilibrium* is in disagreement with the "Earth similarity criterion" and is not appropriate for the evaluation of natural capital on Earth. This idea fully fits with Lovelock's Gaia hypothesis [10]: the Earth is a life being and fights against thermodynamic stable equilibrium.

Kameyama et al. [11] proposed a reference environment with the criterion of chemical stability. The references are the most stable compounds among those with thermo-chemical data and can be integrated in the solid, liquid and gaseous environments. As Szargut stated in [12], some of the most stable compounds selected by Kameyama et al. like nitrates, compounds between rare elements (e.g. $PtBr_2$) or compounds with Fr as the reference species for the elements F, Cl, Br, I should not be recommended, because the probability of their formation in the environment is very small. Therefore, Kameyama et al. R.E. is not very suitable either to evaluate the scarcity of the natural capital.

According to Ranz [13], lots of minerals are compounds with the most common components of the upper continental crust, but are not very stable and do not represent the products of an interaction between the components of the natural environment and the waste products of industrial processes. Hence, Ranz [13] proposes a new R.E. very close to the real environment based on *abundance* and following *Szargut's criterion*. The solid phase of this new R.E. reproduces accurately the Earth's upper continental crust, since the solid reference species that make up this environment are the same as the most abundant types found in the Earth's upper continental crust. A problem with the Ranz proposed R.E. is that if we assign zero exergy to the most abundant substances, we are decreasing arbitrarily the natural capital, because many abundant minerals like sulfides naturally evolute to the most stable oxides. Therefore, as proposed by Valero, Ranz and Botero [2], we must return to Szargut's criterion of using the most stable substance, within the limits fixed by the "Earth similarity criterion".

Hence, our goal is to obtain an agreed legal international reference state for evaluating the natural resources on Earth, based on *Szargut's criterion* and methodology and using the more precise data used by Ranz and other authors such as Rivero [14], as well as new geochemical updates.

In the next section, Szargut's R.E. methodology is explained and the variables used are discussed.

CALCULATION METHODOLOGY: STANDARD CHEMICAL EXERGY OF THE CHEMICAL ELEMENTS

Chemical exergy expresses the exergy of a substance at ambient temperature and pressure. It is defined as a maximum work which can be obtained when the considered substance is brought in a reversible way to the state of reference substances present in the environment, using the environment as a source of heat and of reference substances necessary for the realization of the described process. The R.S. most common in the environment are accepted separately for every chemical element, and are mutually independent. Hence, the problem of equilibrium between the reference substances does not exist. It is impossible to formulate a chemical reaction in which only the reference substances take part.

Standard chemical exergy of chemical compounds

Methodology

Standard chemical exergy results from a conventional assumption of a standard ambient temperature and pressure and standard concentration of reference substances in the natural environment.
The standard chemical exergy of any chemical compound can be calculated by means of the exergy balance of a reversible formation reaction;

$$b_{chn} = \Delta G_f + \sum_e n_e b_{chne} \qquad (1)$$

where:
- ΔG_f formation Gibbs energy
- n_e amount of kmol of the element e
- b_{chne} standard chemical exergy of the element.

If the chemical element does not belong to the reference substances, its standard chemical exergy can also be calculated from Eq. 1, however, a reference reaction of this element should be formulated. This reaction contains only reference substances, additional as reactants and final as products. For example, following reference reaction holds for the element C: $C+O_2 = CO_2$, where O_2 is the additional and CO_2 the final reference substance. The standard chemical exergy of the reference substances are calculated prior to the standard chemical exergy of the element.

Discussion of the variables used

The formation Gibbs energy used by Szargut [12] was revised by Rivero [14] using [15], [16], [17], [18] and [19]. No substantial differences were found, except for sillimanite (Al_2SiO_5), whose new value is $\Delta G_f = 2440,9$ kJ/mol. The information source of Ranz [13] for obtaining ΔG_f, was Faure [20], which is a compilation of the literature from several authors. This source corroborates Rivero's revision and thus, it will be considered for the calculation of our particular R.E.

Gaseous reference substances

Methodology

Free chemical elements present in the atmospheric air (O_2, N_2, Ar, He, Ne, Kr, Xe) and the compounds H_2O, CO_2 are assumed as reference substances. Their standard chemical exergy results from the conventional standard concentration in the atmosphere;

$$b_{chn} = -RT_0 \ln \frac{P_{0n}}{P_n} = -RT_0 \ln z_0 \qquad (2)$$

where:
- R gas constant,
- T_0 standard ambient temperature (298,15 K),
- P_{0n} conventional mean ideal gas partial pressure in the atmosphere (kPa),
- P_n standard pressure (101,325 kPa),
- z_0 conventional standard molar fraction in the environment.

The values of standard chemical exergy of gaseous reference substances O_2, H_2O, CO_2, N_2 are calculated before other values because they are necessary in the calculation of standard chemical exergy of non-gaseous reference substances.

Discussion of the variables used

The universal gas constant is used (8,3143 kJ/(kmol K)) and the calculated standard chemical exergy relates to 1 kmol. Rivero and Garfias [14] accepted the reference pressure according to the conventional unit "physical atmosphere", thus 101,325 kPa. We are assuming the mean partial pressure calculated by Szargut and used by Ranz [13], which is the really appearing mean value and is equal to 99,31 kPa.
Table 2 shows the results obtained in this study for the chemical exergy of the gaseous substances. The obtained values are the same of those obtained by Szargut [12] and Valero, Ranz and Botero [2], since the methodology and the values used for this R.E. has been the same. The differences with Rivero and Garfias [14] are due to the different partial pressures in the atmosphere taken.

Solid reference substances

Methodology

For a prevailing part of chemical elements, solid R.S. commonly appearing in the external layer of the continental part of Earth's crust, have been assumed. However, the Earth's crust is a very complicated mixture of solid solutions and an exact calculation of the chemical exergy of its components is impossible. We can only approximately evaluate

that exergy, assuming that the reference species behave as components of an ideal solution. Hence, Eq. 2 can be applied also in this case.

The evaluation of the standard molar concentration of solid R.S. in the external layer of the Earth's crust is difficult. In past geochemical publications we can only find a mean mass concentration of particular chemical elements and some information about the chemical compounds containing the considered elements. Hence, the best considered way so far to obtain the standard molar concentration of R.S. in the solid environment, has been with following equation suggested by Szargut in [12]:

$$z_{0i} = \frac{1}{l_i} n_{0i} c_i M_0 \qquad (3)$$

where:

- n_{0i} mean molar concentration (in mol/kg) of the i-th element in the continental part of the Earth's crust,
- l_i number of the atoms of i-th element in the molecule of the reference species,
- c_i fraction of the i-th element appearing in the form of reference species,
- M_0 mean molecular mass of the upper layer of the continental part of Earth's crust.

The reference reactions of the elements having solid R.S. contain usually the gaseous R.S. Sometimes appear also solid reference species. For example, the solid R.S. of Mg is $Mg_3Si_4O_{10}(OH)_2$ the reference reaction for the element Mg has a form:

$$3\,Mg + 4\,SiO_2 + 1{,}5\,O_2 + H_2O = Mg_3Si_4O_{10}(OH)_2$$

In such case the standard chemical exergy of the appearing solid reference substance should be calculated prior to the calculation of the chemical exergy of the considered element.

Discussion of the variables used

The mean molar concentration of the elements in the upper continental crust n_{0i}, used in Szargut [12], was the recommended by Polanski and Smulikowski [21]. Ranz [13] used updated values mainly from Taylor and McLennan [22], [23]. For the elements: Br, C, Cl, F, S, Pt, Pu, Ra, Rh, Ru, Te, I, Hg and N, Taylor and Mclennan did not provide any information, therefore, Ranz used the values given by Wedepohl [24] for S, Br, C, F, I, Hg, N and for the remainig elements, the values used by Szargut [12]. Some authors like Plank and Langmuir [25] basing on their studies on marine sediments, suggested already in 1998 some revisions of the estimated values by Taylor and McLennan [22], [23] for Nb, Cs,Ti, Ta. As a consequence, McLennan [26] published in year 2001 new mean molar concentrations of the upper continental crust for the elements: Sc, Ti, V, Co, Ni, Nb, Cs, Pb, Ta. Grigor'ev published in year 2000 [27] the average mineral content of the upper continental crust obtained through a great number of quantitative mineralogical analysis of important rocks published mainly in the USSR and USA. Recently, Grigor'ev updated this information; this new analysis comprises 255 minerals corresponding to 99,13% of the total mineral content of the upper continental crust. Although Grigor'ev has not published this information yet, he gave permission to the authors of this paper, to use it. This valuable information will allow to obtain directly the standard molar concentration of the following 12 reference substances in the solid environment without using Eq. 3: $BaSO_4$, $CaCO_3$, Au, Fe_2O_3, $Mg_3Si_4O_{10}(OH)_2$, MnO_2, SiO_2, $SrCO_3$, ThO_2, SnO_2, TiO_2, $ZrSiO_4$. For the rest substances, Eq. 3 must be used, taking n_{0i} from the latest geochemical publications. First the values from McLennan [26] completed with those from Wedepohl [24] will be used. For the remaining elements not appearing in the latter publications, n_{0i} used by Szargut [12] will be applied.

The mean molecular mass of the upper layer of the continental part of the Earth's crust, was first estimated by Szargut [28]. The obtained value was M_0= 135,5 kg/kmol, applying the following estimation method: according to the geochemical data, the mean concentration values (in mol/kg) of particular chemical groups or elements in the external layer of the continental Earth's crust and the chemical compound formed from these groups were assumed. The first considered group was CO_2, which appears in the Earth's crust mainly in carbonates of Ca, Mg and Fe. Per 1 mol of $(CaO + MgO + FeO)$ 0,035 mol of CO_2 are present. The group CO_2 was partitioned between the mentioned groups and elements Zn, Cu, Pb and Cd, appearing also in the form of carbonates. The group SO_3 was partitioned between CaO and MgO forming sulphates. It was assumed that a prevailing part of metals (Sn, Co, Mn, Fe, Ni) appears in form of different oxides (Co_2O_3, Co_3O_4, Fe_2O_3, Fe_3O_4). It was also assumed that 8% of

Fe appears in form of free oxide Fe_2O_3. The remaining part appears in form of $FeTiO_3$, $FeCr_2O_3$ and silicates. For example, following silicates were assumed: $NaAlSi_3O_8$, $KAlSi_3O_8$, $NaFeSi_2O_6$, $MgSiO_3$, $CaO.Al_2Si_2O_7$. Because of the large content of SiO_2, a considerable part of it was assumed in free form. After estimating the composition of a mean sample of the lithosphere, its molecular mass was calculated.

Ranz [13] updated the molecular mass of the upper continental crust using more recent geochemical information and adopting not only a geochemical approach, but also a geological one. The methodology used was as follows: The international accepted norm CIPW [29] was applied to the mass fractions of the principal oxide groups obtained by Carmichael [30] for the cratonic and sedimentary layers, in order to redistribute the chemical components from the oxides to the mineral molecules that are representative in real minerals appearing in a rock. Next, the minerals of the norm and their respective relative masses were modified to adjust them to the real volumes of the principal groups of each rock. Finally, their molar fractions were calculated and the mean molecular mass of the whole was obtained. The resulting M_0 was equal to 145,5 kg/kmol. Even though this methodology used better geochemical values than the ones in Szargut [28], and included the geological approach, we cannot forget that the CIPW norm is an artificial way to obtain the possible minerals that can appear in a rock. It is therefore only an approximation as well.

In the light of Grigor'ev's analysis, a more accurate molecular weight of the upper continental crust, based on experimental results rather than assumptions, can be easily obtained. The new calculated value is M_0= 143,4 kg/kmol, which is very close to the estimation done by Ranz. The difference in the chemical exergy of the elements obtained with the new molecular weight is almost negligible: in average, taking a molecular weight equal to 143,4 instead of 145,5, makes a difference in the exergy of the solid reference substances of only 0,007%.

For the fraction of the i-th element appearing in the form of reference species (coefficient c_i), Szargut [31] associates values comprised between 0,5 for more abundant substances and 0,001 for less frequent substances from geochemical data given by Polanski and Smulikowski [21]. Ranz [13] obtained more accurate c_i coefficients for solid R.S. containing the most abundant elements in the upper continental crust. For this purpose, she used the mineralogical composition of the Earth's upper layer obtained with the CIPW norm before and updated geochemical information, mainly from Taylor and McLennan [23]. For minority elements, due to the lack of information, Szargut's [31] values were used. As long as a better mineralogical composition of the Earth's crust is done and the c_i coefficients are recalculated with this information, we will assume the c_i values obtained by Ranz [13]. Nevertheless, it must be stressed that choosing a certain c_i or another a 100 times greater, throws less differences in the chemical exergy of the elements than choosing another R.S.

Table 4 shows the results obtained in this study for the chemical exergy of the solid substances. The solid R.S. assumed were those taken by Szargut [12], basing on the *Szargut's criterion* mentioned before. The new chemical exergies obtained differ in 1,1% in average with respect to the values obtained by Szargut in [12]. Taking the empirical standard molar concentration of solid R.S. found in Grigor'ev [27] instead of calculating it with Eq. 3, implies a difference in the element chemical exergy of less than 4% except for Au (14%) and F (18%). For the latter elements, the greater difference is due to the greater sensitivity of Au to z_0, since its ΔG is equal to zero and the great proportion of atoms of Ca in the reference substance of F, respectively.

Reference substances dissolved in seawater

Methodology

Assumption of ionic or molecular R.S. dissolved in seawater ensures in many cases more exact determination of standard chemical exergy of chemical elements when compared with solid R.S. The calculation methods of thermodynamic functions of monocharged and bicharged ions are relatively exact. This is the case also when the reference substance is dissolved in molecular form with a very small degree of ionization.

The method of calculation of standard chemical exergy of elements with R.S. dissolved in seawater has been developed by Morris [32]:

$$b_{chn} = j\Bigg(-\Delta G_f + 0.5\,z\,b_{chH_2} - \sum_k \nu_k\, b_{chk} - \\ - R\,T_n\,[2.303\,z\,(pH) + \ln m_n\,\gamma]\Bigg) \quad (4)$$

where:

j	number of reference ions or molecules derived from one molecule of the element under consideration,
ΔG_f	formation Gibbs energy of the R.S.,
z	number of elementary positive charges of the reference ion,
ν_k	number of molecules of additional elements present in the molecule of reference substance,
b_{chH_2}, b_{chk}	standard chemical exergy of hydrogen gas and of the k-th additional element.
m_n	conventional standard molarity of the reference substance in seawater,
γ	activity coefficient (molarity scale) of the reference substance in seawater,
pH	exponent of the concentration of hydrogen ion in seawater (=8,1)

The activity coefficient of single ion can be calculated by means of the Debye-Huckel equation:

$$-\log\gamma_i = \frac{A\,z_i^2\sqrt{I}}{1 + a_i B\sqrt{I}} \quad (5)$$

where:

A	= 0,51 kg$^{1/2}$ mol$^{-1/2}$ for water at 25^{o}C,
B	= 3,287 * 10^9 kg$^{1/2}$ m^{-1} mol$^{-1/2}$ for water at 25^{o}C,
a_i	effective diameter of the ion,
I	ionic strength of the electrolyte.

The ionic strength of the electrolyte results from the following equation:

$$I = \frac{1}{2}\sum_i m_i {z_i}^2 \quad (6)$$

where:

m_i	molarity of the ion, mol/kg H_2O,
z_i	number of elementary electric charges of the ion.

The ion Cl^- prevails among the negative ions in seawater. Therefore, the data of chlorides can be assumed for activity coefficients of the positive ions Na^+, K^+. The activity coefficients of the negative ions Cl^- and SO_4^{-2} can be estimated in reference to the predominant positive ion Na^+.

Discussion of the variables used

The positive ionic R.S. have been assumed for the elements from the first column of the periodic system and for the monocharged and bicharged negative ions formed from acids. The elements from the second column of the periodic system appear in the seawater in form of positive bicharged ions, however, they are not recommended as R.S., because the so calculated standard chemical exergy of the elements leads to negative values of chemical exergy of some solid compounds common in the Earth's crust. Rivero and Garfias [14] have found the influence of salinity of seawater on the calculated values of standard chemical exergy of elements calculated by means of reference substances dissolved in seawater. However, an increased salinity (greater than 35‰ appears seldom (Red Sea), and the deviations are not large (usually less than 1,6%). Every introduction of solid reference substances can decrease the accuracy of calculations. Therefore we are assuming the solid reference substances only for the elements from the second column of the periodic system. Following ionic and molecular reference substances dissolved in seawater have been accepted in the recent publication of Szargut [33] and will be used for this proposal:

Cl^-, $AgCl_2^-$, $B(OH)_3$ aq, BiO^+, Br^-, $CdCl_2$ aq, Cs^+, Cu^{+2}, HPO_4^{-2}, $HAsO_4^{-2}$, $HgCl_4^{-2}$, IO_3^-, K^+, Li^+, MoO_4^{-2}, Na^+, Ni^{+2}, $PbCl_2$ aq, Rb^+, SO_4^{-2}, SeO_4^{-2}, WO_4^{-2}, Zn^{+2}.

Major ions in seawater are ions with fractions greater than 1 ppm. The Seawater Reference Environment taken into account in this proposal comprises the following major ions: Na^+, K^+, $HAsO_4^{-2}$, BiO^+, Cl^-, SO_4^{-2}, Br^-, $B(OH)_3$. Values of the activity coefficients and molarity of these species basing on information presented in Millero [34], Pilson [35] and Mottl [36] were reviewed and compared with those which Ranz and Rivero took into account. With the exception of SO_4^{-2} the differences are negligible from the point of view of the influence on the final exergy of the considered element. In case of SO_4^- Szargut and Ranz assumed a value of m = 1,17e-2, and Rivero m = 1,24e-2. The molarity

calculated basing on the three independent sources [34], [35] and [36] is estimated as m = 2,93e-2 and is almost 2,5 times greater. This difference decreases the chemical exergy of sulfur only about 2 kJ/mol. The rest of the obtained results are very similar to previous investigations and the differences are negligible.

Table 3 shows the results obtained in this study for the chemical exergy of the substances dissolved in seawater.

CONCLUSIONS

A revision of the different R.E. proposed so far has been done. The authors have agreed to choose as best suitable R.E. category for the evaluation of natural capital, a *Comprehensive Reference Environment* based on *Szargut's criterion*. The parameters used in the equations for calculating the chemical exergy of the elements, mainly ΔG, n_0, M_0, c_i, z_{0i} and m, have been revised and updated according to new geochemical information and revisions done by other authors. It has been stated, that the differences on the chemical exergy of the elements between the different authors is not very significant. Therefore, the current authors would like to propose in ECOS 2005 conference, to take the agreement of accepting internationally the R.E. presented in this paper for the evaluation of the exergy resources on Earth. Nevertheless, it has been seen, that this information can be furthered improved if more empirical updates appear. Presently, the authors of this paper are working on improving the data, but other interested authors are invited to join this research.

REFERENCES

[1] J.M. Naredo. *La economía en evolución. Historia y perspectivas de características básicas del pensamiento económico.* Ediciones Siglo XXI, Madrid, 1987. In spanish.

[2] A. Valero, L. Ranz, and E. Botero. Exergetic evaluation of natural mineral capital (1) reference environment and methodology. In *Proceedings of ECOS 2002*, Berlin, July 2002.

[3] L. Riekert. The efficiency of energy utilization in chemical processes. *hem. Eng. Sci*, 29:1613–1620, 1974.

[4] F. Bosjankovic. Reference level of exergy of chemically reacting systems. *Forschung im Ingenieurwesen*, 21:151–152, 1963.

[5] R.A. Gaggioli and P.J. Petit. Second law analysis for pinpointing the true inneficiencies in final comversion systems. *A.C.S. Division of Fuel Chemistry*, 21(2), 1976.

[6] M.V. Sussman. Choosing a reference environment-state for available-energy computations. In *72nd Annual Meeting. American Institute of Chemical Engineers*, San Francisco (USA), November 1979.

[7] J. Szargut. Energy potential balance in chemical processes. *Archiwum Budowy Maszyn*, 4(11):89–117, 1957. In Polish.

[8] J. Ahrendts. The exergy of chemically reacting systems. Technical report, VDI Forschungsheft 579, Düsseldorf, 1977. In German.

[9] C. Diederichsen. Referenzumgebungen zur berechnung der chemischen exergie. Technical Report 50, Fortschr.-Ber. VDI Reihe 19, Düsseldorf: VDI Verlag, 1999.

[10] J. Lovelock. *Gaia: A new look at life on Earth*. Oxford University Press, 1979.

[11] H. Kameyama, K. Yoshida, Yamauchi S., and Fueki K. Evaluation of reference exergy for the elements. *Applied Energy*, 11:69–83, 1982.

[12] J. Szargut. Chemical exergies of the elements. *Applied Enegy*, 32:269–285, 1989.

[13] L. Ranz. *Análisis de los costes exergéticos de la Riqueza Mineral Terrestre. Su aplicación para la gestión de la sostenibilidad.* PhD thesis, Universidad de Zaragoza (Spain), September 1999.

[14] R. Rivero and M. Garfias. Standard chemical exergy updated. part ii. In R. Palido R. Rivero, L. Monroy and G. Tsatsaronis, editors, *Proceedings of ECOS 2004*, pages 773–786, Guanajuato, Mexico, 2002.

[15] C.H. Perry, R.H.; Chilton. *Manual del Ingeniero Químico*. McGraw-Hill de México, México, 2nd edition, 1992.

[16] D.D. Wagman, H.E. William, V.B. Parker, R.H. Schumm, I. Halow, S.M. Bailey, K.L. Churney, and R.L. Nuttall. *The NBS tables of chemical thermodynamic properties: Selected values for inorganic and C1 and C2 organic substances in SI units*. American Chemical Society and the American Institute of Physics for the National Bureau of Standards, New York, 1982.

[17] W.M. Latimer. *The oxidation states of the elements and their potentials in aqueous solutions*. Prentice-Hall, New York, 1952.

[18] I. Barin. *Thermochemical Data of Pure Substances*. VCH Verlagsgesellschaft GmbH, Weinheim, Germany, 1993.

[19] R.C. Weast, editor. *CRC Handbook of Chemistry and Physics*. CRC Press, 1975.

[20] G. Faure. *Principles and Applications of Inorganic Geochemistry*. Maxwell MacMilan International Editions, New York, 1992.

[21] A. Polanski and K. Smulikowski. *Geochemia*. Wydawnictwa Geologicne, Warsaw, 1969.

[22] S.R. Taylor and S.M. McLennan. The geochemical evolution of the continental crust. *Rev. Geophys.*, 33:241–265, 1995.

[23] S.R. Taylor and S.M. McLennan. *The Continental Crust: Its Composition and Evolution*. Blackwell, London, 1985.

[24] K.H. Wedepohl. The composition of the continental crust. *Geochim. Cosmochim. Acta*, 59:1217–1232, 1995.

[25] T. Plank and C.H. Langmuir. The geochemical composition of subducting sediment and its consequences for the crust and mantle. *Chemical Geology*, 145:325–394, 1998.

[26] S.M. McLennan. Relationships between the trace element composition of sedimentary rocks and upper continental crust. *Geochemistry, Geophysics, Geosystems*, 2:2000GC000109, April 2001.

[27] N.A. Grigor'ev. The average mineral composition of the upper continental crust. *Uralian Geological Journal*, (3):3–21, 2000. In Russian.

[28] J. Szargut. Exergy balance of metallurgical processes. *Archiwum Hutnictwa*, 6(1):23–60, 1961. In Polish.

[29] A.R. Philpotts. *Igneous and Metamorphic Petrology*. Prentice Hall, Englewood Cliffs, 1990.

[30] R.S. Carmichael. *Practical handbook of Physical Properties of Rocks and Minerals*. CRC Press, Boca Raton, Florida, 1990.

[31] J. Szargut. Standard chemical exergy of some elements and their compounds, based upon te concentration in earth's crust. *Geochemistry International*, 35(1-2):53–60, 1987.

[32] J. Szargut and D.R. Morris. Calculation of standard chemical exergy of some elements and their compounds based upon seawater as the datum level substance. *Bulletin of the Polish Academy of Sciences. Techical Sciences.*, 33(5-6):293–305, 1985.

[33] J. Szargut. *Exergy method: technical and ecological applications*. WIT-press, Ashurst, UK. In press.

[34] F.J. Millero. *Chemical Oceanography*. CRC Press, 2nd edition, 1996.

[35] M.E. Pilson. *An Introduction to the Chemistry of the Sea*. Prentice Hall, New Jersey, 1998.

[36] M. Mottl. Composition of seawater: Salinity of the major ions. Chemocal Oceanography (OC 623); www.soest.hawaii.edu.

Element	Most abundant species	Most stable species	Exergy difference between both R.E. (kJ/mol)
Sb	Sb2S3	Sb2O5	1235,58
As	FeAsS	As2O5	1201,32
S	FeS2	SO4-2	963,63
Bi	Bi	BiO+	228,88
Cd	CdS	CdCl2	745,75
Ce	PO4Ce	CeO2	258,33
Zn	ZnS	Zn+2	717,22
Co	Co3S4	Co3O4	967,7
Cu	CuFeS2	Cu+2	1423,18
Mo	MoS2	MoO4-2	1675,9
Os	Os	OsO4	306,81
Ag	Ag2S	AgCl2-	330,65
Pt	Pt	PtO2	84,59
Pb	PbS	PbCl2	710,34
Re	ReS2	Re2O7	1556,65
Ru	Ru	RuO2	254,82
U	UO2	UO3.H2O	127,49

Table 1: Exergy difference of selected elements considering either as reference species the most abundant or the most stable substances in the R.E. [2]

CHEMICAL ELEMENT		REFERENCE SPECIES					CHEMICAL EL. EXERGY				
Element	Ch.S.	Formula	State	P_{0i} (kPa)	Chemical exergy, kJ/mol	ΔGf (kJ/mol)	State	This proposal (kJ/mol)	Szargut 1989 (kJ/mol)	Valero et al. 2002 (kJ/mol)	Rivero and Garfias 2004 (kJ/mol)
Argon	Ar	Ar	g	9,06E-03	11,69	0	g	11,69	11,69	11,69	11,64
Carbon	C	CO2	g	3,35E-04	19,87	-394,36	s.,graf.	410,25	410,26	410,26	410,27
Helium	He	He	g	4,85E-06	30,37	0	g	30,37	30,37	30,37	31,31
Hydrogen	H	H20	g	2,20E-02	9,49	-228,59	H2,g	236,10	236,1	236,10	236,12
Kripton	Kr	Kr	g	9,70E-07	34,36	0	g	34,36	34,36	34,36	34,30
Neon	Ne	Ne	g	1,77E-05	27,16	0	g	27,16	27,16	27,16	27,14
Nitrogen	N	N2	g	7,58E-01	0,72	0	N2, g	0,72	0,72	0,72	0,67
Oxygen	O	O2	g	2,04E-01	3,97	0	O2, g	3,97	3,97	3,97	3,92
Xenon	Xe	Xe	g	8,70E-08	40,33	0	g	40,33	40,34	40,33	40,27

Table 2: Chemical exergies of the elements for gaseous reference substances

CHEMICAL ELEMENT		REFERENCE SPECIES						CHEMICAL EL. EXERGY				
Element	Ch.S.	Formula	State	z	γ	m_i mol/kg	ΔGf (kJ/mol)	State	This proposal (kJ/mol)	Szargut 1989 (kJ/mol)	Valero, Ranz and Botero 2002 (kJ/mol)	Rivero and Garfias 2004 (kJ/mol)
Arsenic	As	HAsO4-2	liq	-2	0,138	2,10E-08	-714,7	s	493,83	494,6	**litosphere**	492,60
Bismuth	Bi	BiO+	liq	1	0,52	1,00E-10	-146,4	s	274,92	274,5	274,56	274,80
Boron	B	B(OH)3	liq	0	1	3,40E-04	-968,8	s	628,60	628,5	628,49	628,10
Bromine	Br	Br-	liq	-1	0,73	8,70E-04	-104,0	Br2, l	100,89	101,2	101,25	101,00
Cesium	Cs	Cs+	liq	1	0,6	2,30E-09	-282,2	s	404,58	404,4	404,58	404,60
Chlorine	Cl	Cl-	liq	-1	0,63	5,66E-01	-131,26	Cl2, g	124,03	123,6	123,66	123,70
Cadmium	Cd	CdCl2	liq	0	1	6,90E-11	-359,4	s	293,37	293,8	293,8	**litosphere**
Copper	Cu	Cu2+	liq	2	0,2	7,30E-10	65,5	s	134,25	134,2	134,24	**litosphere**
Iodine	I	IO3-	liq	-1	0,6	5,20E-07	-128,0	I2, s	174,74	174,7	174,76	175,70
Lead	Pb	PbCl2	liq	0	1	4,20E-11	-297,2	s	232,40	232,8	232,83	**litosphere**
Lithium	Li	Li+	liq	1	0,68	2,50E-05	-294,0	s	393,03	393,0	393,03	392,7
Mercury	Hg	HgCl4-2	liq	-2	0,1	3,40E-10	-446,9	l	114,99	115,9	115,86	**litosphere**
Molybdenium	Mo	MoO4-2	liq	-2	0,1	1,10E-07	-836,4	s	730,27	730,3	730,29	731,3
Nickel	Ni	Ni+2	liq	2	0,2	1,20E-07	-45,6	s	232,70	232,7	232,7	**litosphere**
Phosphorous	P	HPO4-2	liq	-2	0,1	4,90E-07	-1089,3	s	861,42	861,4	861,43	861,3
Potash	K	K+	liq	1	0,62	1,06E-02	-282,4	s	366,66	366,6	366,67	366,7
Rubidium	Rb	Rb+	liq	1	0,6	1,40E-06	-282,4	s	388,89	388,6	388,88	388,7
Selenium	Se	SeO4-2	liq	-2	0,1	1,20E-09	-441,4	s	346,47	346,5	346,49	347,5
Silver	Ag	AgCl2-	liq	-1	0,6	2,70E-09	-215,5	s	69,85	70,2	70,28	**litosphere**
Sodium	Na	Na+	liq	1	0,65	4,86E-01	-262,05	s	336,71	336,6	336,66	336,7
Sulfur	S	SO4-2	liq	-2	0,11	2,93E-02	-744,6	s	607,05	609,6	609,56	609,3
Wolfram	W	WO4-2	liq	-2	0,1	5,60E-10	-920,5	s	827,46	827,5	827,48	828,5
Zinc	Zn	Zn2+	liq	2	0,2	1,70E-08	-147,3	s	339,25	339,2	339,24	**litosphere**

Table 3: Chemical exergies of the elements for aqueous reference substances

CHEMICAL ELEMENT			REFERENCE SPECIES						CHEMICAL EL. EXERGY				
Element	Ch.S.	noi(mol/g)	Formula	State	ci	z0	Che-mical exergy, kJ/mol	ΔGf (kJ/mol)	State	This proposal (kJ/mol)	Szargut 1989 (kJ/mol)	Valero et al. 2002 (kJ/mol)	Rivero and Garfias 2004 (kJ/mol)
Aluminium	Al	2,98E-01	Al2SiO5	s	0,01	2,14E-01	3,83	-2440,99	s	790,39	888,20	**RS = Al2O3**	795,7
Antimonium	Sb	1,64E-09	Sb2O5	s	0,001	1,18E-10	56,68	-829,3	s	438,02	438,01	438,01	438,2
Barium	Ba		BaSO4	s		5,88E-06	29,85	-1361,9	s	776,76	775,1	774,25	775,4
Beryllium	Be	3,33E-07	Be2SiO4	s	0,01	2,39E-07	37,80	-2033,3	s	604,53	604,40	**RS=BeO**	604,3
Calcium	Ca		CaCO3	s		5,48E-04	18,61	-1129	s	731,40	729,10	**hydrosphere**	729,1
Cerium	Ce	4,57E-07	CeO2	s	0,02	1,31E-06	33,58	-1024,8	s	1054,40	1054,60	1054,38	1054,7
Chromium	Cr	1,60E-06	K2Cr2O7	s	0,01	1,15E-06	33,91	-1882,3	s	584,49	584,3	**RS=Cr2O3**	584,4
Cobalt	Co	2,89E-07	CoFe2O4	s	0,005	2,07E-07	38,15	-1032,6	s	308,82	312,00	**RS=Co3O4**	313,4
Dysprosium	Dy	2,15E-08	Dy(OH)3	s	0,02	6,17E-08	41,15	-1294,3	s	975,35	975,9	975,32	976
Erbium	Er	1,38E-08	Er(OH)3	s	0,02	3,96E-08	42,25	-1291	s	973,15	972,8	973,12	972,8
Europium	Eu	5,79E-09	Eu(OH)3	s	0,02	1,66E-08	44,41	-1320,1	s	1004,40	1003,8	1004,37	1003,8
Fluorine	F2	3,30E-05	CaF2*3Ca3 (PO)2	s	0,01	2,37E-05	26,40	-12985,3	F2, g	481,54	504,90	**RS = CaF2**	505,8
Gadolinium	Gd	1,93E-08	Gd(OH)3	s	0,02	5,54E-08	41,42	-1288,9	s	970,22	969	969,63	969
Gallium	Ga	2,44E-07	Ga2O3	s	0,02	3,50E-07	36,85	-998,6	s	514,75	514,9	514,73	515
Germanium	Ge	2,20E-08	GeO2	s	0,05	1,58E-07	38,83	-521,5	s	556,35	557,6	556,33	557,7
Gold	Au		Au	s		3,23E-11	59,88	0	s	59,88	50,5	53,39	50,6
Hafnium	Hf	3,25E-08	HfO2	s	0,05	2,33E-07	37,86	-1027,4	s	1061,28	1062,90	1061,26	1063,1
Holmium	Ho	4,85E-09	Ho(OH)3	s	0,02	1,39E-08	44,85	-1294,8	s	979,54	978,6	979,51	978,7
Indium	In	4,36E-10	In2O3	s	0,05	1,56E-09	50,26	-830,9	s	437,60	436,8	437,59	436,9
Iridium	Ir	1,04E-13	IrO2	s	0,005	7,46E-14	74,93	-185,6	s	256,56	246,80	256,53	247
Iron	Fe		Fe2O3	s		7,78E-04	17,75	-742,2	s	376,99	374,8	374,81	374,3
Lanthanum	La	2,16E-07	La(OH)3	s	0,02	6,19E-07	35,43	-1319,2	s	994,53	994,6	994,5	994,7
Lutetium	Lu	1,83E-09	Lu(OH)3	s	0,02	5,25E-09	47,26	-1259,6	s	946,76	945,7	946,73	945,8
Magnesium	Mg		Mg3Si4 O10(OH)2	s		1,75E-04	21,45	-5543	s	629,37	626,1	**hydrosphere**	626,9
Manganese	Mn		MnO2	s		6,81E-07	35,20	-465,2	s	496,42	482	482,93	487,7
Neodymium	Nd	1,80E-07	Nd(OH)3	s	0,02	5,16E-07	35,89	-1294,3	s	970,08	970,1	970,05	970,1
Niobium	Nb	1,29E-07	Nb2O3	s	0,01	9,25E-08	40,15	-1766,4	s	900,29	899,7	899,37	899,7
Osmium	Os	2,63E-13	OsO4	s	0,005	1,89E-13	72,63	-305,1	s	369,78	368,1	369,76	368,4
Palladium	Pd	4,70E-12	PdO	s	0,005	3,37E-12	65,48	-82,5	s	146,00	138,6	145,97	138,7
Platinum	Pt	2,60E-11	PtO2	s	0,005	1,86E-11	61,24	-83,7	s	140,97	141	140,9	141,2
Plutonium	Pu	6,20E-20	PuO2	s	0,01	8,89E-20	108,74	-995,1	s	1099,87	1100	1099,84	1100,1
Praseodymium	Pr	5,04E-08	Pr(OH)3	s	0,02	1,45E-07	39,04	-1285,1	s	964,04	963,8	964,01	963,9
Radium	Ra	4,40E-15	RaSO4	s	0,05	3,15E-14	77,06	-1364,2	s	826,27	823,9	823,69	824,2
Rhenium	Re	2,15E-12	Re2O7	s	0,01	1,54E-12	67,42	-1067,6	s	560,56	559,5	560,27	559,6
Rhodium	Rh	9,70E-12	Rh2O3	s	0,005	3,48E-12	65,41	-299,8	s	179,62	179,7	176,61	179,7
Rutenium	Ru	1,00E-12	RuO2	s	0,005	7,17E-13	69,32	-253,1	s	318,45	318,6	318,42	318,6
Samarium	Sm	2,99E-08	Sm(OH)3	s	0,02	8,58E-08	40,34	-1314	s	994,23	993,6	994,2	993,7
Scandium	Sc	3,03E-07	Sc2O3	s	0,05	1,09E-06	34,04	-1819,7	s	923,89	925,2	924,14	925,3
Silicon	Si		SiO2	s		5,75E-01	1,37	-856,7	s	854,10	854,9	854,18	855
Strontium	Sr		SrCO3	s		1,96E-09	49,71	-1140,1	s	773,59	749,8	748,63	749,8
Tantalum	Ta	5,53E-09	Ta2O5	s	0,01	3,97E-09	47,96	-1911,6	s	974,81	974	973,82	974,1
Tellurium	Te	1,40E-11	TeO2	s	0,005	1,00E-11	62,78	-270,3	s	329,10	329,2	329,08	329,3
Terbium	Tb	4,03E-09	Tb(OH)3	s	0,02	1,16E-08	45,30	-1314,2	s	999,40	998,4	999,37	998,5
Thalium	Tl	3,67E-09	Tl2O4	s	0,01	2,63E-09	48,97	-347,3	s	194,16	194,9	194,15	194,9
Thorium	Th		ThO2	s		1,86E-10	55,54	-1169,1	s	1220,67	1202,6	1202,09	1202,7
Thulium	Tm	1,95E-09	Tm(OH)3	s	0,02	5,59E-09	47,10	-1265,5	s	952,50	951,7	952,47	951,8
Tin	Sn		SnO2	s		2,87E-08	43,05	-519,6	s	558,67	551,9	549,15	551,8
Titanium	Ti		TiO2	s		1,99E-04	21,13	-889,5	s	906,65	907,2	902,89	907,2
Uranium	U	1,18E-08	UO3.H2O	s	0,01	1,69E-08	44,36	-1395,9	s	1196,22	1196,6	1196,19	1196,6
Vanadium	V	2,10E-06	V2O5	s	0,01	1,51E-06	33,23	-1419,6	s	721,45	720,4	722,15	721,3
Yterbium	Yb	1,27E-08	Yb(OH)3	s	0,02	3,64E-08	42,46	-1262,5	s	944,85	944,3	944,83	944,3
Ytrium	Y	2,48E-07	Y(OH)3	s	0,02	7,11E-07	35,09	-1291,4	s	966,39	965,5	966,37	965,6
Zirconium	Zr		ZrSiO4	s		7,88E-05	23,42	-1919,5	s	1080,88	1083,4	**RE = ZrO2**	1083

Table 4: Chemical exergies of the elements for solid reference substances

Proceedings of ECOS 2005
Trondheim, Norway
June 20–22, 2005

EXERGY ANALYSIS OF AN ACETALDEHYDE PRODUCTION PLANT

Uirajara Vieira Jr.
Polytechnic School – University of São Paulo
Mechanical Engineering Department
Brazil

Silvio de Oliveira Jr.
Polytechnic School – University of São Paulo
Mechanical Engineering Department
Brazil

ABSTRACT

This work develops a thermodynamic model to assess the industrial acetaldehyde production by ethanol partial oxidation, and proposes an improved plant configuration in order to use the thermal exergy more efficiently. Exergy analysis was used as the evaluation tool. The model was able to predict all relevant thermodynamic properties of the process streams. The vapor phase was considered ideal, while the non-idealities on liquid phase were corrected by Wilson equation. The irreversibility sums 1076 kW – 5165 kJ/kg acetaldehyde. The irreversibilities are mainly produced in the oxidation reactor (458 kW), the waste heat boiler (118 kW), the acetaldehyde absorption tower (105 kW) and distillation tower (247 kW). The new approach reduces the irreversibilities to 925 kW, which represents a reduction of 14.7%. The modifications were made in the absorption and distillation towers and a new heat exchanger network was added, causing a 28 kW reduction.
***Keywords**:* exergy analysis, acetaldehyde production, modeling and simulation

NOMENCLATURE

a constant of Eq. 6, 12 and 20
A parameter of Eq. 21
b constant of Eq. 6, 12 and 20
BL Column liquid side draw [kmol/s]
c constant of Eq. 6, 12 and 20
cp Specific heat at constant pressure [kJ/kmol.K]
d constant of Eq. 6 and 12
e constant of Eq. 12
ex Specific exergy [kJ/kmol]
F Stage feed flow rate[kmol/s]
G specific Gibbs free energy [kJ/kmol]
h Specific enthalpy [kJ/kmol]
K Equilibrium ratio
L Liquid flow rate [kmol/s]
P pressure [kPa]
Q Heat duty or heat rate [kW]
R Constant [8,314 kJ/kmol.K]
T Temperature [K]
I Irreversibility rate[kW]
UA heat transfer skill [kW/K]
V vapor flow rate [kmol/s]
x liquid phase concentration [kmol/kmol]
y vapor phase concentration [kmol/kmol]
z stage feed concentration [kmol/kmol]
α parameter of Eq. 21
β parameter of Eq. 21
γ activity coefficient
δ percentage of irreversibility rate
θ Carnot factor

Subscript

g gas or vapor phase
i chemical component
in inlet
j equilibrium stage
k unit
l liquid phase
out outlet

Superscript

b boundary
e excess
0 reference (T=298 K, p=101. 3 kPa)

INTRODUCTION

This work has two goals; the first one is to develop a thermodynamic model, which allows estimating

the components and energy balances of a chemical plant for acetaldehyde production, as well as its irreversibilities. The second goal is to propose a new plant configuration with lower exergy destruction [1].

An acetaldehyde production by ethanol partial oxidation plant [2], located in southeastern Brazil, was chosen as the case study. The plant operational data were used to compare and to validate the results of the thermodynamic model.

ACETALDEHYDE PRODUCTION

In the chosen production route, shown in the Figure 1, a mixture of ethanol and air converts into acetaldehyde by going through a catalytic layer; the reactions occur at a temperature range between 800 and 900 K. The reactions are:

$$CH_3CH_2OH_{(g)} \rightarrow CH_3CHO_{(g)} + H_{2(g)} \quad (1)$$

$$H_{2(g)} + \tfrac{1}{2}O_{2(g)} \rightarrow H_2O_{(g)} \quad (2)$$

$$CH_3CH_2OH_{(g)} + 3O_{2(g)} \rightarrow 2CO_{2(g)} + 3H_2O_{(g)} \quad (3)$$

A hot stream of acetaldehyde, water, non-converted ethanol and a mixture of gases - oxygen, nitrogen, hydrogen and carbon dioxide – leaves reactor RX1 to the waste heat boiler HE2, where it is cooled to 443 K and produces low pressure steam (550 kPa).

After that the stream follows to the acetaldehyde absorption tower T2 to be quenched with an alcoholic solution, which comes from the bottom of the distillation tower T3; acetaldehyde, water and ethanol are condensed while gases rise up through the tower. The heat released during condensation is removed by the cooler HE3 and coils installed inside the column. The gases, saturated with water and ethanol, leave the top of tower T2 and go to the next tower T4, to be quenched with chilled water. After that, the gases free from ethanol are released to the atmosphere at 288 K.

The liquid, a mixture of ethanol, water and acetaldehyde, leaves the column, is heated up by the pre-heater HE4, and follows to the distillation tower T3, which operates at 345 kPa. The pure acetaldehyde is removed at the top at 327 K, while the ethanol and water stream at bottom splits into two parts: one part goes to tower T2, and the other one is fed into tower T1.

The function of tower T1 is to strip the ethanol from water and recycle it to the process at azeotropic concentration; the water leaves the tower by the bottom as a waste. New raw ethanol is fed to top of the tower to cool it; the vapor of this tower is a mixture of water and ethanol, which feeds the evaporator EV1. In the evaporator EV1, operating at 340 K, the ethanol is mixed with air, compressed previously by the compressor C1.

Before feeding the reactor RX1, the ethanol-air mixture leaves the evaporator EV1 and goes to the pre-heater HE1 to be heated above dew point (393 K).

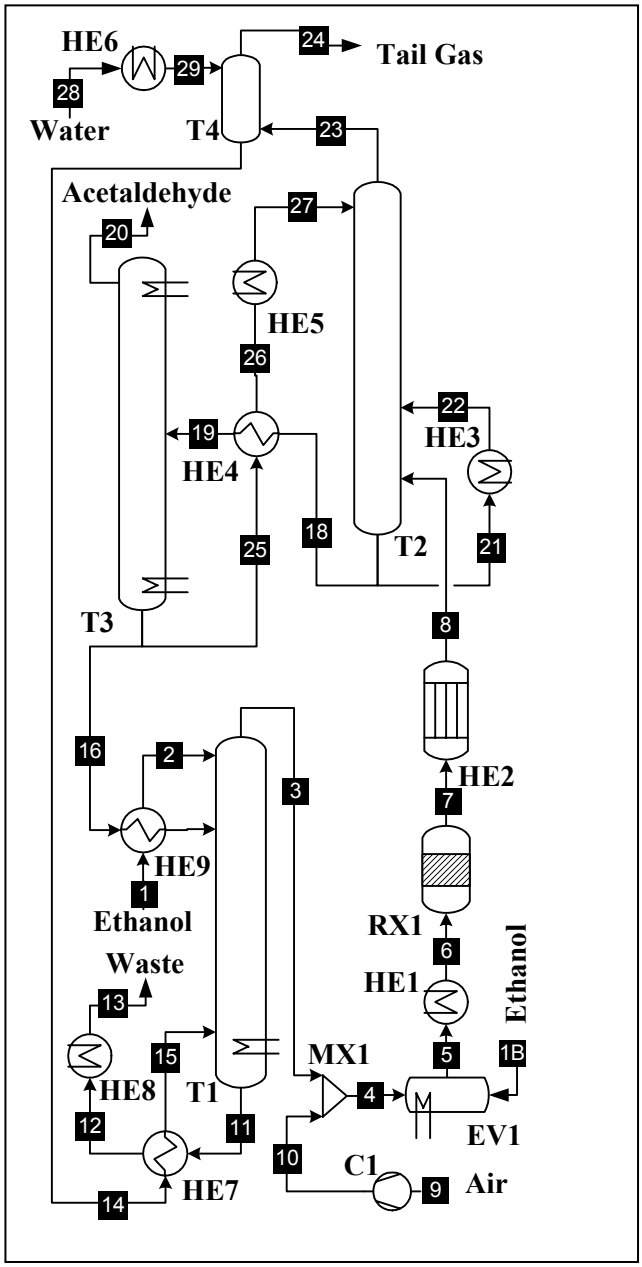

Figure 1: Acetaldehyde production plant

THERMODYNAMIC MODEL

The model [3,4] takes into account the seven main compounds: ethanol, water, acetaldehyde, oxygen, nitrogen, hydrogen and carbon dioxide; other chemical components are presented in a much lower concentration.

The thermodynamic model hypotheses [5] are:

- *Steady state conditions for all processes;*
- *Ideal vapor phase;*
- *Raoult's law corrected by Wilson's equation;*
- *Gas solubility depends only on temperature;*
- *Control volumes are perfectly insulated;*
- *No temperature or concentration gradient inside control volumes (for equilibrium stages);*
- *No short-circuit or carry-over in the equilibrium stages.*

The highest pressure occurs in tower T1 and it is equal to 345 kPa. As this pressure may be considered moderate, it is possible to assume ideal gas behavior for the vapor phase. However, this fact is not true for the liquid phase, in which the non-ideality must be corrected. The Wilson equation was chosen to evaluate the liquid phase activity coefficients.

Henry's law estimated the dissolved gases behavior. The reactor RX1 was considered as a black box in which reactions, done by Eq. 1 to 3, occur with given conversion rates for ethanol and oxigen, and acetaldehyde efficiency [4]. The air compression power was evaluated considering a polytropic compression of an ideal gas [4].

The calculation of the thermodynamic properties was performed as described below.

Vapor phase

The vapor phase enthalpy is evaluated by:

$$h_g = \sum_i y_i . h_{i,g} \tag{4}$$

$$h_{i,g} = h_{i,g}^0 + \int_{T_0}^{T} c_{p_{i,g}} dT \tag{5}$$

$$c_{p\,i,g} = a_i + b_i T + c_i T^2 + d_i T^3 \tag{6}$$

The entropy is calculated as follow:

$$s_g = \sum_i y_i . s_{i,g} - R . \sum y_i . \ln(y_i) \tag{7}$$

$$s_{i,g} = s_{i,g}^0 + \int_{T_0}^{T} \frac{c_{p_{i,g}}}{T} dT - R \int_{P_0}^{P} \frac{dP}{P} \tag{8}$$

Finally, the vapor phase exergy may be calculated by:

$$ex_g = \sum_i y_i . ex_{i,g}^0 + RT_0 . \sum_i y_i . \ln(y_i) + \ldots + \left(h_g - h_g^0\right) - T_0 . \left(s_g - s_g^0\right) \tag{9}$$

Liquid phase

For the liquid phase the properties are calculated as follow:

$$h_l = \sum_i x_i . h_{i,l} + h^e \tag{10}$$

$$h_{i,l} = h_{i,l}^0 + \int_{T_0}^{T} c_{p_{i,l}} dT \tag{11}$$

$$c_{p\,i,l} = a_i + b_i T + c_i T^2 + d_i T^3 + e_i T^4 \tag{12}$$

$$h^e = -R . T^2 . \left(\frac{\partial g^e / RT}{\partial T} \right)_{x,P} \tag{13}$$

$$g^e = RT . \sum_i x_i . \ln(\gamma_i) \tag{14}$$

$$s_l = \sum_i x_i . s_{i,l} - R . \sum_i x_i . \ln(x_i . \gamma_i) + s^e \tag{15}$$

$$s_{i,l} = s_{i,l}^0 + \int_{T_0}^{T} \frac{c_{p_{i,l}}}{T} dT \tag{16}$$

$$s^e = \frac{h^e - g^e}{T} \tag{17}$$

$$ex_l = \sum_i x_i . ex_{i,l}^0 + RT_0 . \sum_i x_i . \ln(x_i . \gamma_i) + \ldots + \left(h_l - h_l^0\right) - T_0 . \left(s_l - s_l^0\right) \tag{18}$$

Vapor-Liquid equilibrium

$$K_i = \frac{y_i}{x_i} = \frac{\gamma_i . P_i}{P} \tag{19}$$

$$P_i = e^{a_i - b_i/(T + c_i)} \tag{20}$$

$$\ln(\gamma_i) = 1 - \ln\left(\sum_{k=1,n} x_k . A_{i,k} \right) - \sum_{l=1,n} \frac{x_l . A_{l,i}}{\sum_{j=1,n} x_j . A_{l,j}} \tag{21}$$

$$A_{l,j} = \beta_{i,j} . e^{-\alpha_{i,j}/RT} \tag{22}$$

Equilibrium stage model

The separation steps are considered as equilibrium stages; the following sketch in the Figure 2 represents one equilibrium stage:

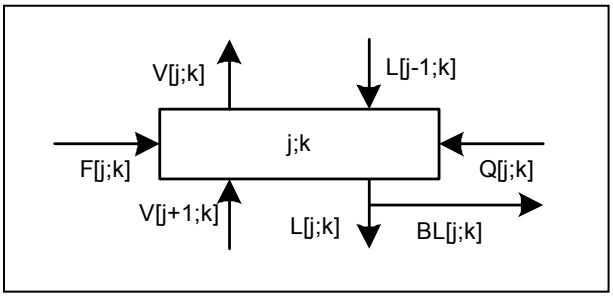

Figure 2: Equilibrium stage

The streams which leave the equilibrium stage $V_{i;j}$ e $L_{i;j}$ are the molar rate of the *i* component in the vapor and liquid phase respectively and they are in thermodynamic equilibrium, and obey the following equations:

$$y_{i,j,k} - x_{i,j,k}.K_{i,j,k} = 0 \qquad (23)$$

$$\sum_i x_{i,j,k} - 1 = 0 \qquad (24)$$

$$\sum_i y_{i,j,k} - 1 = 0 \qquad (25)$$

$$\begin{aligned} &x_{i,j-1,k}.L_{j-1,k} + y_{i,j+1,k}.V_{j+1,k} + z_{i,j,k}.F_{j,k} \\ &...- x_{i,j,k}.(L_{j,k} + BL_{j,k}) - y_{i,j,k}.V_{j,k} = 0 \end{aligned} \qquad (26)$$

$$\begin{aligned} &h_{l\,j-1,k}.L_{j-1,k} + h_{g\,j+1,k}.V_{j+1,k} + h_{l\,j,k}.F_{j,k} \\ &...- h_{l\,j,k}.(L_{j,k} + BL_{j,k}) - h_{g\,j,k}.V_{j,k} + Q_{j,k} = 0 \end{aligned} \qquad (27)$$

Where *i* identifies the chemical components (1 to 7), *j* is the equilibrium stage number and *k* names the unit the stage belongs to. The first equation (23) models the equilibrium liquid-vapor, while the equations (26) and (27) are the material and energy balances respectively. To solve the previous set of equations it is necessary to define all inlet streams $L_{j-1;k}$, $V_{j+1;k}$ and $F_{j;k}$, their concentrations $x_{i;j-1;k}$, $y_{i;j+1;k}$ and $z_{i;j;k}$, the stage pressure $p_{j;k}$, the heat duty $Q_{j;k}$ and the ratio $BL_{j;k}/L_{j;k}$. The solution will be the liquid $x_{i;j;k}$ and vapor $y_{i;j;k}$ concentration profile through the column, the liquid $L_{j;k}$, and the vapor $V_{j;k}$ molar rates, as well as the stage temperature $T_{j;k}$.

The irreversibility rate $I_{j,k}$ is evaluated by the exergy balance:

$$\begin{aligned} &ex_{l\,j-1,k}.L_{j-1,k} + ex_{g\,j+1,k}.V_{j+1,k} + ex_{l\,j,k}.F_{j,k}...- \\ &ex_{l\,j,k}.(L_{j,k} + BL_{j,k}) - ex_{g\,j,k}.V_{j,k} + Q_{j,k}.\theta_{j,k} = I_{j,k} \end{aligned} \qquad (28)$$

where $\theta_{j,k}$ is the Carnot factor, which is defined as follow:

$$\theta_{j;k} = 1 - \frac{T_0}{T^b_{j,k}} \qquad (29)$$

and $T^b_{j,k}$ is the boundary temperature.

Equilibrium multi-stage model

The columns T1, T2 and T3 are considered as an array of equilibrium stage. The set of equations are similar, the only difference is the number of equations. The index *j* represents the stage number inside a unit *k*.

Heat exchangers

The heat exchangers without phase change may be calculated as follow:

$$h_{l1,k}.L_{1,k} - h_{l2,k}.L_{2,k} + Q_{j,k} = 0 \qquad (30)$$

$$h_{l3,k}.L_{3,k} - h_{l4,k}.L_{4,k} - Q_{j,k} = 0 \qquad (31)$$

$$Q_{j,k} - (UA)_{j,k}.\tfrac{1}{2}.\left[(T_3 - T_1) + (T_4 - T_2)\right] = 0 \qquad (32)$$

Where $(UA)_{j,k}$ is heat transfer skill of the heat exchanger. The irreversibility is calculated by:

$$\begin{aligned} &ex_{l1,k}.L_{1,k} + ex_{l3,k}.L_{3,k} \\ &...- ex_{l2,k}.L_{2,k} - ex_{l4,k}.L_{4,k} = I_{j,k} \end{aligned} \qquad (33)$$

For the evaporator and reboilers the equations are simpler, since the heating medium is always low-pressure steam at T_S:

$$h_{l1,k}.L_{1,k} - h_{l2,k}.L_{2,k} + Q_{j,k} = 0 \qquad (34)$$

$$Q_{j,k} - (UA)_{j,k}.\tfrac{1}{2}.\left[(T_S - T_1) + (T_S - T_2)\right] = 0 \qquad (35)$$

$$ex_{l1,k}.L_{1,k} - ex_{l2,k}.L_{2,k} + Q_{j,k}.\theta_{j,k} = I_{j,k} \qquad (36)$$

$$\theta_{j;k} = 1 - \frac{T_0}{T_S} \qquad (37)$$

In case the heat exchanger is a cooler, the heat transfer temperature is not constant but varies between T_1 and T_2, so the Carnot factor should be an average value, estimated by:

$$\theta_{j;k} = \frac{\int_{T_1}^{T_2} Q_{j;k}.\theta_{j;k}.dT}{(T_2 - T_1).Q_{j;k}} = \frac{\int_{T_1}^{T_2} (T - T_1).\left(1 - \frac{T_0}{T}\right).dT}{(T_2 - T_1).(T_2 - T_1)} = \frac{\left[\frac{T_2^2 - T_1^2}{2} - (T_2 - T_1)(T_1 + T_0) + T_1.T_0.\ln\left(\frac{T_2}{T_1}\right)\right]}{(T_2 - T_1)^2}$$

RESULTS

All equations shown above were solved using EES software [6]. Two different plant configurations were simulated: the first one refers to the original plant and it was used for testing and validation of the model; the second one is the proposed configuration, in which exergy destruction is expected to be lower. Table 1 and 2 show the simulation results for the original configuration: mass flow rates (F), enthalpy flow rates (F.h); heat transfer rates (Q), exergy flow rates (F.ex); exergy rates (Q.θ); irreversibility rates (I) and percentage of the irreversibility rate (δ).

Unit	F_{in}	F_{out}	$\Sigma(F.h)_{in}$	$\Sigma(F.h)_{out}$	ΣQ
	[kmol/s]	[kmol/s]	[kW]	[kW]	[kW]
MX1	0.0218	0.0218	-2150	-2150	0
T1	0.0314	0.0314	-8701	-8340	360
EV1	0.0237	0.0237	-2687	-2611	76
C1	0.0129	0.0129	-99	-83	16
HE1	0.0237	0.0237	-2611	-2543	68
RX1	0.0237	0.0270	-2543	-2544	0
T2	0.4778	0.4779	-127588	-127604	-18
HE3	0.4015	0.4015	-109948	-110535	-587
T4	0.0310	0.0310	-5456	-5456	0
T3	0.0632	0.0632	-17060	-16831	224
HE2	0.0270	0.0270	-2544	-3094	-550
HE7	0.0225	0.0225	-6272	-6365	-93
HE8	0.0225	0.0225	-6365	-6413	-48
HE9	0.0087	0.0087	-2368	-2386	-18
HE4	0.0632	0.0632	-17310	-17070	239
HE5	0.0500	0.0500	-13873	-14051	-178
HE6	0.0178	0.0178	-5093	-5109	-16
global	**0.0366**	**0.0395**	**-332670**	**-333187**	**-523**

Table 1: Original configuration material and energy balances

Unit	$\Sigma(F.ex)_{in}$	$\Sigma(F.ex)_{out}$	$\Sigma Q.\theta$	I	δ
	[kW]	[kW]	[kW]	[kW]	[%]
MX1	9703	9669	0	34	3.2
T1	9872	9947	114	39	3.6
EV1	11934	11934	19	19	1.8
C1	2	13	16	4	0.4
HE1	11934	11947	21	7	0.7
RX1	11951	11493	0	458	42.6
T2	247663	247557	-1	105	9.7
HE3	212737	212728	-9	0	0.0
T4	1384	1380	0	4	0.4
T3	33538	33595	304	247	22.9
HE2	11493	11208	-167	118	11.0
HE7	257	242	-12	3	0.3
HE8	242	239	0	2	0.2
HE9	4201	4,198	-1	3	0.3
HE4	33492	33515	44	21	1.9
HE5	24149	24136	-2	12	1.1
HE6	56	56	0	0	0.0
global	**624607**	**623855**	**324**	**1076**	**100.0**

Table 2: Original configuration exergy balance

The above tables show that the main irreversibility rate, 428 kW and 42.6% of the total irreversibility rate of the process, occurs in the ethanol oxidation reactor (RX1); this results were already expected since oxidation reactions on gaseous phase at high temperature are far away from the equilibrium. The reactor, together with the acetaldehyde distillation tower T3, responsible for 347 kW of exergy destruction, the waste heat boiler HE2, responsible for more 118 kW, and the absorption tower T2, for 105 kW of exergy destruction, accounts for more than 86% of the total irreversibility rate of the process.

The simulation results were compared to the plant processes data. The data were collected during 7 days of stable run and their average values are shown in Table 3, as well the standard deviation. The stream number refers to the tags shown in black in Figure 1; the stream STEAM T1 is the steam rate for the T1 reboiler, STEAM T3 refers to the steam rate for the T3 reboiler, while RFLX is the T3 internal reflux. The calculated mass flow rate results show a maximum deviation from the measured data of -14%. The calculated temperature results show a maximum deviation from the measured data of 4.4%.

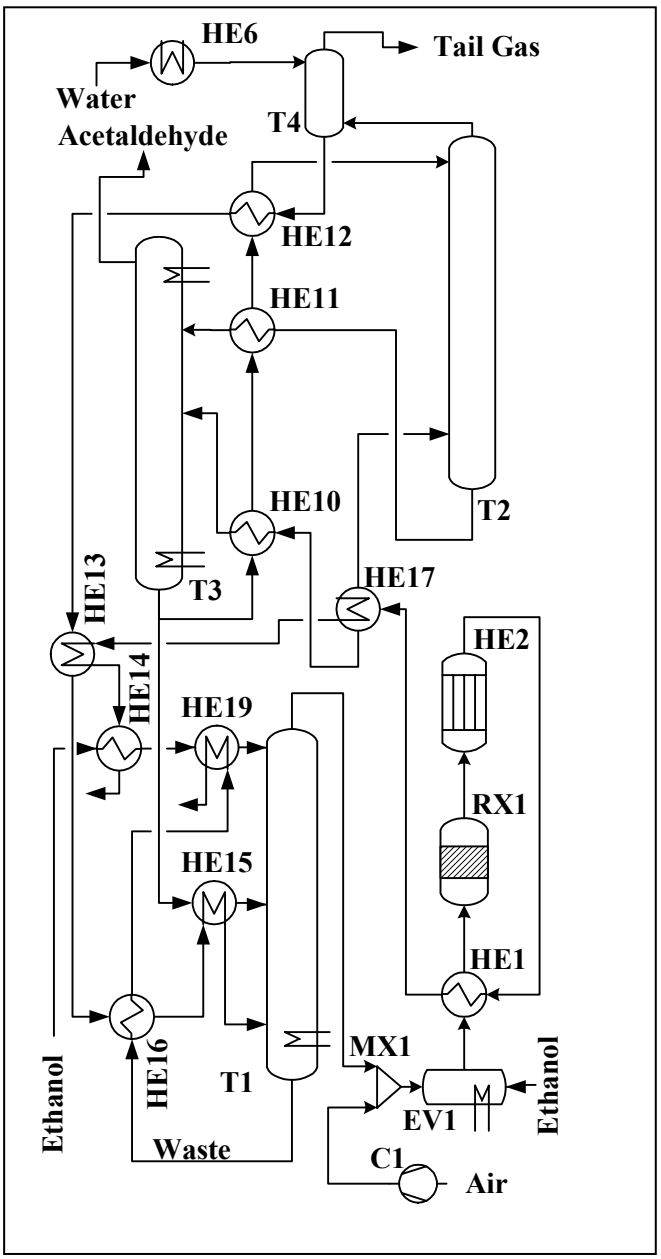

Figure 3: Proposed process configuration

An alternative process configuration was proposed, as shown in the figure 3, based on the following recommendations [1,5]:

- *Optimize the heat exchanger network;*
- *Feed the distillation tower T3 in two different points;*
- *Decrease the recycle between the distillation tower T3 and the absorption tower T2;.*
- *Choose the best feed tray for the tower T3;*
- *Install a condenser between the waste heat boiler and the absorption tower T2;*
- *Pre-heat the reactor by using the hot gases from the waste heat boiler;*
- *Decrease the amount of quench water of tower T4;*
- *Decrease the reflux ratio of the distillation tower T3.*

Stream		Measured		Model result	Dev. (%)
		Avg.	Std. Dev.		
1	[kg/h]	600	1	595	-0.8
1B	[kg/h]	288	89	293	1.7
20	[kg/h]	725	206	755	4.1
9	[kg/h]	1320	47	1324	0.3
19	[kg/h]	7684	294	6608	-14.0
27	[kg/h]	5051	167	5019	-0.6
21	[kg/h]	40007	164	41975	4.9
18+21	[kg/h]	47692	344	48584	1.9
29	[kg/h]	1155	83	1155	0.0
RFLX	[kg/h]	2430	129	2639	8.6
16+25	[kg/h]	5863	230	5890	0.5
16	[kg/h]	811	87	871	7.4
STEAM T1	[kg/h]	695	27	649	-6.6
STEAM T3	[kg/h]	1361	105	1337	-1.8
7	[K]	841	3.9	817.0	-2.9
10	[K]	338	2.4	339.6	0.5
5	[K]	340	0.1	341.6	0.5
6	[K]	402	0.3	402.0	0.0
29	[K]	286	2.7	286.0	0.0
24	[K]	291	6.7	297.0	2.1
22	[K]	305	2.3	299.6	-1.8
19	[K]	351	0.0	353.0	0.7
21	[K]	332	1.6	315.0	-5.1
14	[K]	301	7.1	314.0	4.4
20	[K]	326	1	326.5	0.1
25	[K]	385	0.9	392.0	1.9
3	[K]	356	1.2	362.3	1.9
11	[K]	379	1.7	384.9	1.5

Table 3: Process plant data versus model results

The following tables, 4 and 5, show the simulation results for the proposed configuration operating at the same feeding conditions of the original plant. In Table 5 it can be verified that the total irreversibility rate is lowered to 925 kW.

Unit	F_{in}	F_{out}	$\Sigma(F.h)_{in}$	$\Sigma(F.h)_{out}$	ΣQ
	[kmol/s]	[kmol/s]	[kW]	[kW]	[kW]
MX1	0.0202	0.0202	-1784	-1785	0
T1	0.0439	0.0439	-12216	-11920	297
EV1	0.0222	0.0222	-2322	-2243	79
C1	0.0129	0.0129	-99	-86	12
HE1	0.0222	0.0222	-2243	-2178	65
RX1	0.0222	0.0248	-2178	-2178	0
T2	0.0450	0.0450	-9108	-9163	-55
T4	0.0452	0.0452	-9663	-9663	0
T3	0.0423	0.0423	-11152	-11034	117
HE2	0.0248	0.0248	-2178	-2779	-601
HE17	0.0248	0.0248	-2844	-3320	-476
HE18	0.0098	0.0098	-2627	-2627	0
HE11	0.0322	0.0322	-8788	-8642	145
H10	0.0098	0.0098	-2627	-2572	55
HE12	0.0300	0.0300	-8391	-8415	-25
HE13	0.0336	0.0336	-9535	-9461	74
HE16	0.0336	0.0336	-9461	-9405	56
HE15	0.0336	0.0336	-9405	-9387	18
HE14	0.1300	0.1300	-36694	-36720	-25
HE19	0.0366	0.0366	-10278	-10283	-5
HE6	0.0324	0.0324	-9263	-9288	-24
global	**0.7071**	**0.7098**	**-153593**	**-153862**	**-268**

Table 4: Proposed configuration material and energy balance

Unit	$\Sigma(F.ex)_{in}$	$\Sigma(F.ex)_{out}$	$\Sigma Q.\theta$	I	δ
	[kW]	[kW]	[kW]	[kW]	[%]
MX1	8187	8157	0	31	3.3
T1	8951	9009	90	33	3.6
EV1	10422	10440	38	20	2.1
C1	2	13	12	1	0.2
HE1	10440	10452	18	5	0.6
RX1	10452	10016	-1	436	47.4
T2	18493	18464	0	29	3.2
T4	1397	1392	0	5	0.5
T3	24766	24806	232	193	21.0
HE2	10016	9690	-183	143	15.6
HE17	9672	9618	-49	6	0.6
HE18	5620	5614	0	6	0.6
HE11	17168	17181	18	5	0.5
H10	5614	5625	17	6	0.7
HE12	14490	14489	-1	0	0.0
HE13	1205	1213	11	3	0.3
HE16	1213	1222	11	2	0.2
HE15	1222	1226	3	0	0.0
HE14	439	435	-2	2	0.2
HE19	812	811	-1	0	0.0
HE6	101	102	1	0	0.0
global	**160581**	**159872**	**215**	**925**	**100.0**

Table 5: Alternative configuration exergy balance

CONCLUSIONS

There are several causes of irreversibility on the acetaldehyde production process, and the most important are the oxidation reaction (458 kW), the heat exchange in the waste heat boiler (118 kW), the recirculation for cooling purposes in the absorption tower (105 kW) and the high reflux ratio in the distillation tower T3 (247 kW).

The exergy analysis of the acetaldehyde production plant, as stated here, allows indicating, quantifying and creating a hierarchy of the irreversibilities.

The proposed configuration, operating at the same feeding conditions of the original plant, destroys 925 kW of exergy, what correspond to a reduction of 14.1%.

The specific energy consumption of the plant was reduced in 28% comparing to the original one, from 5622 kJ/kg of acetaldehyde to 4032 kJ/kg. The exergy destruction was reduced from 5165 kJ/kg to 4440 kJ/kg, what corresponds to 14% of reduction.

REFERENCES

[1] Doldrsum, A. “Exergy Analysis Proves Viability of Process Modification”. 1998, Energy Conversion and Management, v 38, p 1781-1789.

[2] Johnson, W. K.; Fink, U. and Sakuma, Y. *Acetaldehyde*, 1998 CEH Product Review, SRI International.

[3] Kotas, T. J., 1985, The Exergy method of thermal plant analysis , Butterworths.

[4] Vieira Jr., U. Exergy Analysis of an Acetaldehyde Production Plant**.** (in Portuguese) 2004. Master dissertation. Polytechnic School of the University of São Paulo. São Paulo, Brazil

[5] Stichlmair, J. e Fair, J. R. Distillation: Principles and Practice, 1998, Wiley-Liss.

[6] Klein SA, Alvarado FL. EES – Engineering Equation Solver for Microsoft Windows Operating Systems. 2004, F-Chart Software.

Proceedings of ECOS 2005
Trondheim, Norway
June 20–22, 2005

EXERGY CONVERSION IN THE THERMOCHEMICAL RECUPERATOR OF A PISTON ENGINE

Shokotov M.
W.Verner str. 70, D-09120 Chemnitz, Germany.
Yantovski E.
Elsass str.58, D-52068 Aachen, Germany, iksvotnay@aol.com
Shokotov V.
Laruper Hauptstr.212, D-22547 Hamburg, Germany.

ABSTRACT

Thermochemical recuperation (TCR) as the use of waste heat for the fuel reforming with H2O or CO2, leading to efficiency increase, is well known for gas turbine units. Less known, that the similar TCR is useful for piston engines(PE) as well. The difference is in low pressure of a mixture of fuel and H2O or CO2.
The paper is aimed at calculating of endothermal reactions of methane as fuel with H2O and CO2 by conditions, suitable for PE. It is shown that exergy of heat of exhaust gases is converted into exergy of reformed fuel (CO + Hydrogen).The results are presented as graphs of exergy efficiency versus temperature of the end of reaction. Within the limits of 800 – 1000 K the exergy efficiency of TCR is increased from 0.23 to 0.77 for CH4+CO2 and from 0.30 to 0.80 for CH4+H2O. Fuel economy in a diesel engine might reach 19%.

Introduction

The initiative to apply to piston engines the principle of thermochemical recuperation, well known from gas turbine systems, belongs to Gas Technology Institute, USA. To save place the literal citation [1] is used: *TCR is a promising concept for application to reciprocating engines. Rejected sensible energy from the engine combustion is recovered to support catalytic reformation of the fuel (natural gas) to a higher energy content fuel.*
Preliminary analysis by GTI indicates, that a TCR system could offer the following advantages over conventional power generating systems:

- *Reduced fuel consumption by virtue of increased cycle efficiency, which results from use of rejected heat from the engine.*
- *Reduced CO2 emissions by virtue of increased efficiency.*
- *Increased power output capacity.*
- *Ultra-low emissions of criteria pollutants (Nox,CO, etc.) and hazardous pollutants (HCs, formaldehyde, etc.) by virtue of improved combustion conditions.*

Theoretically, the TCR can reform all kinds of liquid and gaseous hydrocarbon fuels…
The H2-enriched fuel would increase the ignitability of the mixture due to its broad flammability limits and low ignition energy requirements, and increase flame speed relative to natural gas.

From energy balance point the TCR is a clear measure to decline the temperature of outgoing gases (e.g. losses) by virtue of absorption of their energy by incoming gases. In addition to GTI statements we wish to underline that TCR is promising for the efficiency increase in zero-emission (including automotive) piston engine systems[2], where fuel should be reformed not with steam, but with carbon dioxide.

In application to gas-turbine systems with CO2 capture and TCR the detailed analysis, demonstrating the exergy losses in gas turbine, fuel reactor e t.c. has been made by Bolland and Ertesvag[3]

Present paper is aimed at calculating the exergy balances of TCR for a piston engine to visualise the losses of reformer and select the needed reaction temperature by reforming with water and carbon dioxide as well. For simplicity the only gaseous fuel methane is considered.

Processes in TCR

The two endothermic reactions of fuel methane reforming are known:

$CH_4 + H_2O \Leftrightarrow CO + 3\ H_2$ (1)
$CH_4 + CO_2 \Leftrightarrow 2\ CO + 2\ H_2$ (2)

Schematics of a TCR is presented in Fig.1, where 1 and 2, 3 and 4 are the flows of incoming reactants, 5 is the flow of reaction products, 6,7,8,9 and 10 are flows of exhaust gases of piston engine, giving its sensible heat to support endothermic reactions.The main our assumption is the equilibrium, it means the validity of Hess law. Kinetics of reactions, affected by catalysts is not considered.

The equilibrium constant K by atmospheric pressure depends upon the temperature only [4]:

$$K = e^{-\frac{\Delta G_T^0}{RT_i}} \quad (3)$$

For the reaction (1):

$$\Delta G_T^0 = 188748 + 228{,}75 \cdot T_i - 69{,}61 \cdot T_i \cdot \ln T_i + \frac{80{,}711 \cdot 10^{-3}}{2} \cdot T_i^2 - \frac{22{,}874 \cdot 10^{-6}}{6} \cdot T_i^3 \quad (4)$$

and for the reaction (2):

$$\Delta G_T^0 = 230323 + 193{,}78 \cdot T_i - 71{,}75 \cdot T_i \cdot \ln T_i + \frac{106{,}81 \cdot 10^{-3}}{2} \cdot T_i^2 - \frac{36{,}06 \cdot 10^{-6}}{6} \cdot T_i^3 \quad (5)$$

The fraction of reformed methane till equilibrium for the two reactions is

$$m = \sqrt{\frac{\frac{\sqrt{k}}{2{,}6}}{1 + \frac{\sqrt{k}}{2{,}6}}} \text{ and } m = \sqrt{\frac{\frac{\sqrt{k}}{2}}{1 + \frac{\sqrt{k}}{2}}} \quad (6)$$

The fractions of reaction products for (1) and (2) are:

$$\mu_{CH_4} = \mu_{H_2O} = \frac{1-m}{2 \cdot (1+m)};\ \mu_{CO} = \frac{m}{2 \cdot (1+m)};\ \mu_{H_2} = \frac{3 \cdot m}{2 \cdot (1+m)} \quad (7)$$

$$\mu_{CH_4} = \mu_{CO_2} = \frac{1-m}{2 \cdot (1+m)};\ \mu_{CO} = \mu_{H_2} = \frac{m}{(1+m)} \quad (8)$$

The ratio of the amount of final reaction products to the incoming reactants (chemical coefficient of molecular change) is

$\beta = 1 + m$ (9)

The incoming reactants are at ambient temperature $T_1 = T_2 = To$. Due to heating their temperature increases. It is assumed, that reaction is getting started by $T_3 = T_4 = T_{AR}$, when m = 0.001. In reaction (1) T_{AR} =415 K, whereas in (2) T_{AR} = 515 K.
This heating energy is:

$Q_{H1} = H_2 - H_1 = H_7 - H_9$,
$Q_{H2} = H_4 - H_2 = H_8 - H_{10}$

Reactions in the point R take the energy:

$Qin = H_6 - H_7 - H_8 =$
$Q_R + (H_5 - H_3 - H_4)$

Exergy balance

Exergy flow from cooled flue gases is:
$\Delta E_{CQ} = E_{Qein} + E_{3P} + E_{4P} - E_{5P}$ (10)
Or per one mole

$$\Delta e_{cq} = e_{q_{ein}} + e_{3p} + e_{4p} - e_{rp}\ , \quad (11)$$

$$e_{q_{ein}} = q_{ein} \cdot \eta_c = q_{ein} \cdot (1 - \frac{T_0}{T_i})\ ;$$

$$q_{ein} = q_R + (h_{r5} - h_3 - h_4)\ ;$$

$$h_{r5} = 2 \cdot \beta \cdot h_5 = 2 \cdot \beta \cdot (a_M + \frac{b_M}{2} \cdot T_i + \frac{C_M}{3} \cdot T_i^2) \cdot T_i\ ;$$

$$a_M = \sum \mu_i \cdot a_i;\ b_M = \sum \mu_i \cdot b_i;\ C_M = \sum \mu_i \cdot C_i;$$

$$e_{rp} = 2 \cdot \beta \cdot e_{5p} = 2 \cdot \beta \cdot [(h_5 - h_0) - T_0 \cdot (s_5 - s_0)]\ ;$$

Molar exergy of the flow of a substance consists of the two parts (see Fig.1, c):

$$e_i = e_{ip} + e_{ic} \ , \quad (12)$$

where $e_{ip} = (h_i - h_o) - T_o(s_5 - s_o)$ is the physical exergy, depending upon the pressure and temperature of flow and e_{ic} = chemical exergy, depending on contents. In the Table 1 the standard chemical exergy, recommended by Szargut and Morris [5] is given.

In an endothermic reaction the thermal exergy is converted into exergy of substances and reaction losses:

$$\Delta e_{cq} = \Delta e_c + d_{RC} \ , \quad (13)$$

where

$$\Delta e_c = e_{rc} - e_{3c} - e_{4c} \ , \quad (14)$$

$$e_{rc} = 2 \cdot \beta \cdot e_{5c} = 2 \cdot \beta \cdot \Sigma \mu_i e_i \ .$$

$$e_{q_{ein}} = \Delta e + d_{RC} \ , \quad (15)$$

$$\Delta e = e_5 - e_3 - e_4, \ e_5 = e_{rp} + e_{rc} \ ;$$

$$e_3 = e_{3p} + e_{3c} \ ; \ e_4 = e_{4p} + e_{4c} \ .$$

Exergy efficiency of the TCR is defined as follows:

$$\eta_{ex.1} = \Delta e_c / \Delta e_{cq} = 1 - d_{RC} / \Delta e_{cq} \quad (16)$$

If to relate the gained chemical exergy in reformed fuel to the physical one from flue gases we get

$$\eta_{ex.2} = \Delta e / (\Delta e + d_{RC}) \quad (17)$$

Results of calculations

The results of computwer calculations of endothermic reactions and exergy conversion efficiency versus the temperature of reaction are given in the Table 3 and Fig.2.. It is seen that in the reforming with CO2 in reaction (2) the exergy taken from exhaust gases is greater than that by reforming with H2O. But exergy converted into the new fuel exergy in reaction (2) is less, than in (1), that is why the efficiency η_{ex1} for reaction (1) is higher. This difference vanishes when temperature exceeds 900 K.

If needed,the end of reaction might be by temperature less 1000 K. There are no rapid changes in the curves “contents versus temperature.”.

On the graphs Fig.2 the conversion of methane in reformed fuel in the temperature interval 800-1000 K is presented . By T= 1000 K the exergy efficiency might reach 80% .

In order to evaluate the possible increase of exergy of reformed fuel let us look at the figures, calculated for a gas-fuelled diesel of about 5000 kW capacity. The main exergy flows are in the Table 4.

The chemical exergy flow, which enters the cylinder is about 19%higher, than that of methane fuel (on account of the use of exergy of flue gases). As exergy efficiency of the diesel itself only slightly depends upon used fuel it shows the possible fuel economy by TCR of about 19%.

The percentage distribution of exergy, taken from flue gases E_{Qein} = 2070.23 kW is as follows: 20.75% is used for heating reformed fuel from 515 up to 1000 K, 76.05% is converted into chemical exergy of reformed fuel and 3.2 % is exergy destruction (internal losses due to entropy rise in chemical reaction).

Conclusion

Calculations, based on assumption on equilibrium, show a possibility to reach rather high exergy efficiency (about 80%) of TCR incorporated in a piston engine systems when reaction temperature is 900-1000 K. Fuel methane reforming by CO2 is only slightly less efficient than that by water. Fuel economy by TCR in a gas-fuelled diesel is about 19% due to such increase of exergy of the reformed fuel.

5. Szargut J., Morris D. Cumulative Exergy consumption and cumulative Degree of Perfection of Chemical Processes. Energy Research, 1987, v.11, pp 245-261.

References

1. Gas Technology Institute. A Technology Development Prospectus. High Efficiency; Ultra-Low Emissions, Thermochemically Recuperated Reciprocating Internal Combustion Engine Systems. 2004.

2.Yantovski E., Shokotov M., McGovern J., Vaddella V. A Zero Emission Membrane Piston Engine System (ZEMPES) for a bus .Int.Conf. Vehicles Alternative Fuel Systems and Environmental Protection (VAFSEP) Dublin, 6-9 July 2004, paper 183, pp 129-133.

3.Bolland O., Ertesvag I. Exergy Analysis of gas-Turbine Combined Cycle with CO2 capture using Auto-thermal Reforming of Natural Gas. www.ept.ntnu.no/noco2/poster%20exergy%20Liege202001.ppt

4. Hoverton M.T. Engineering Thermodynamics. Van Nostrand, NY,Princeton1964.

Fig.1. Schematics of the Thermochemical reactor (TCR)

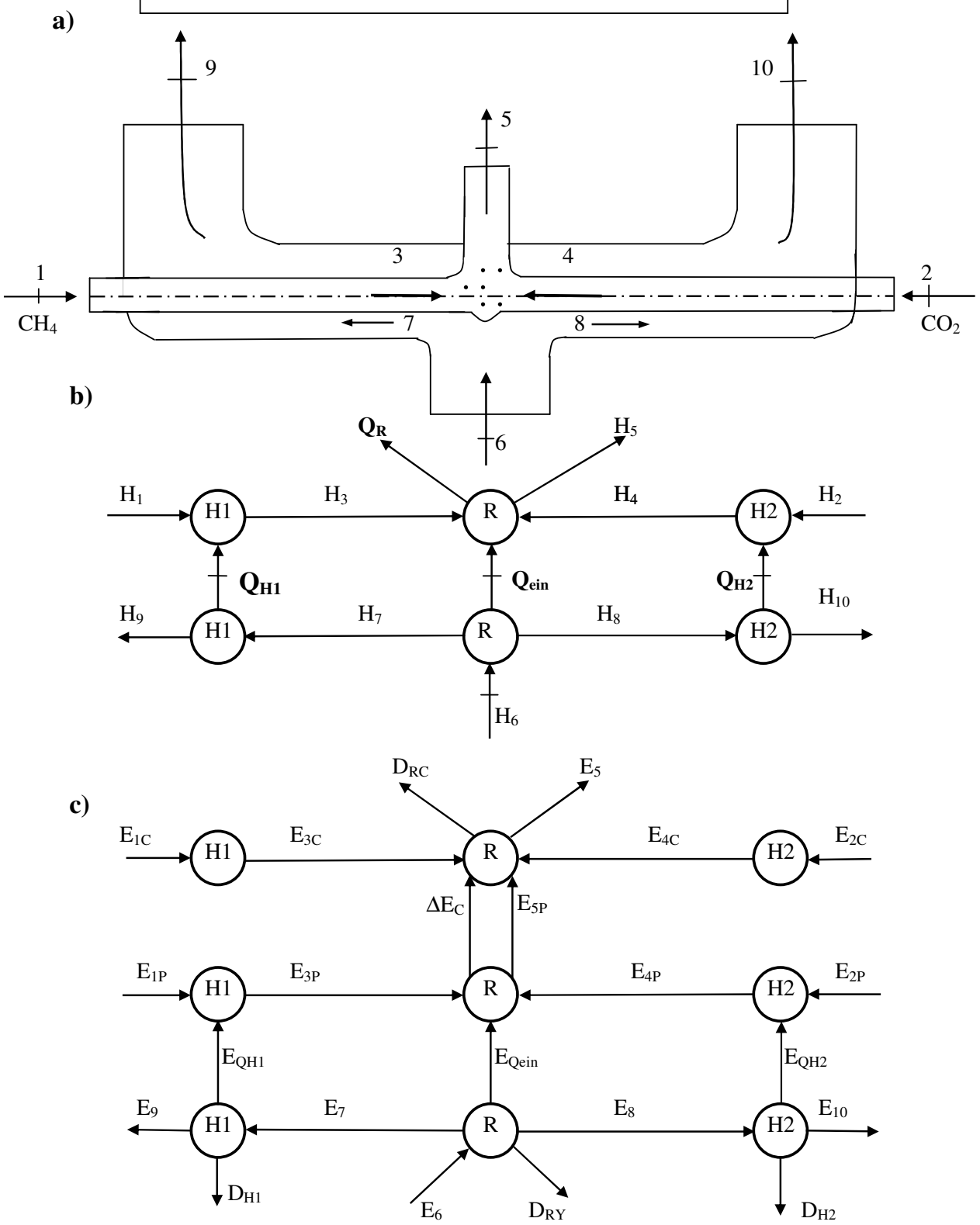

Fig.2. Efficiency and molar fractions versus temperature

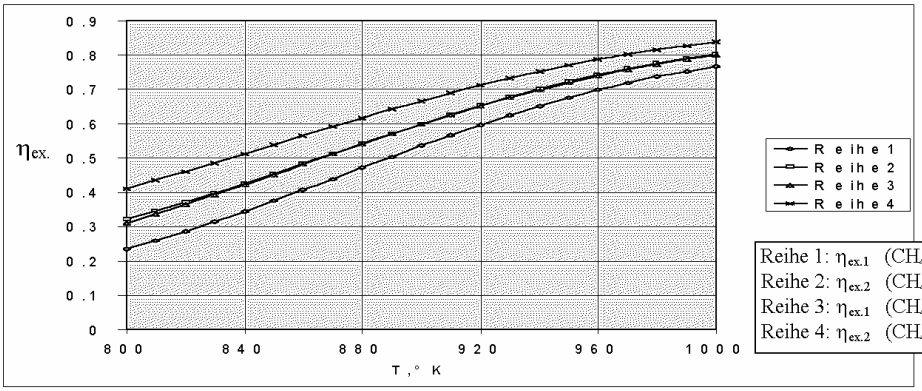

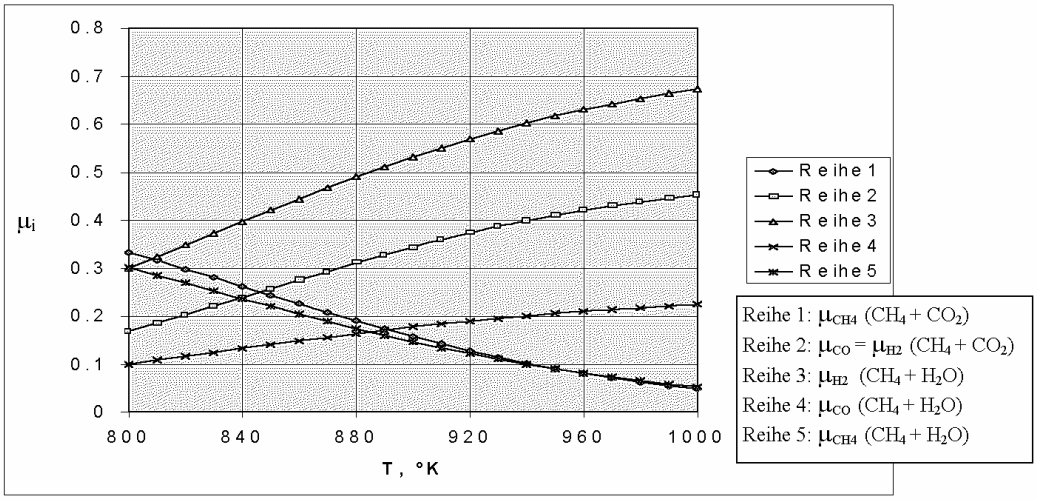

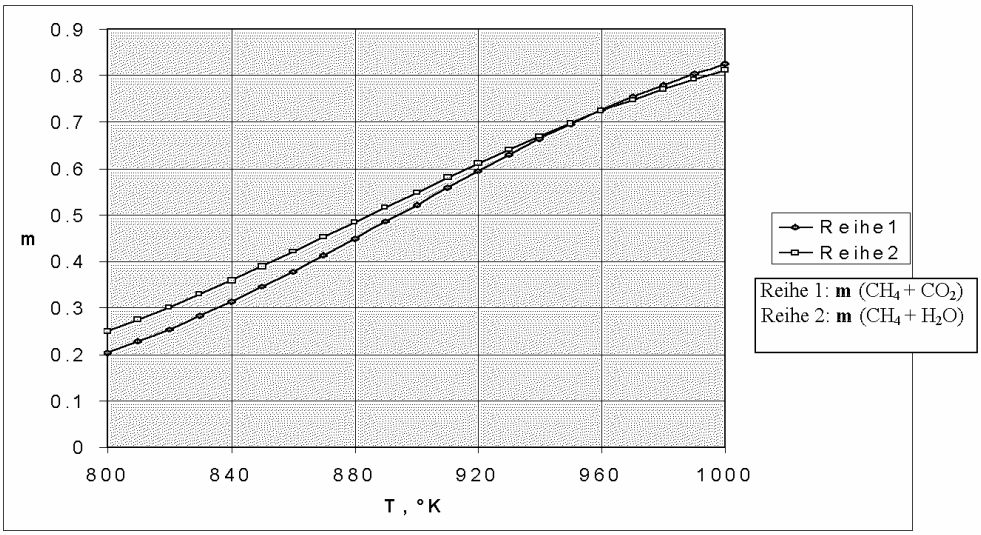

Table 1.

Reaction heat and molar exergy of the fuels constituens (at 298 K, 1 bar)

Substance	h high, kJ/kmol	h low , kJ/kmol	e_i, J/kmol
H2	285900	241800	238350
CO	283000	283000	275350
CH4	890500	802300	836510
CO2	-	-	20170
H2O	-	-	750
O2	-	-	3970
N2	-	-	720

Table 2

Contents of reformed fuel by 1000 K

	CH4	**H2O**	**CO**	**H2**
Reaction CH4 + H2O	0.052	0.052	0.224	0.672
CH4 + CO2	0.0479	0.0479	0.4521	0.4521

Table 3

Exergy conversion versus temperature(e in 100 kJ/Mol)

Ti, K	$\Delta e_{cq} = \Delta e_c + d_{RC}$,		Δe_c		η ex1	
	(1)	(2)	(1)	(2)	(1)	(2)
515	0.835	0	0.00402	0	0.005	0
550	0.85439	1.04996	0.00933	0.00431	0.0109	0.0041
600	0.94599	1.14343	0.02518	0.01386	0.0266	0.0120
650	1.019520	1.23710	0.05813	0.03736	0.0570	0.0302
700	1.0925	1.3177	0.11984	0.08756	0.1097	0.0664
750	1.1647	1.3962	0.2239	0.18293	0.1922	0.1310
800	1.2402	1.4780	0,3822	0.3452	0.3082	0.2335
850	1.3207	1.5671	0.5954	0.5879	0.4508	0.3751
900	1.4043	1.6627	0.8392	0.8909	0.5976	0.5358
950	1.4843	1.7556	1.0677	1.1868	0.7193	0.6759
1000	1.5546	1.8365	1.243	1.4088	0.7995	0.7671

Table 4.

Exergy	Fuel E_3	Reformed E_5	Flue gas E_6	Loss D_R	Outlet gases E_7 and E_8
Total,kW	96157.7 (515 K)	11880.48 (1000 K)	3245.93 (1102 K)	66.42	571.48 (586 K) / 604.22 (586 K)
Chemical	9588.0	11393.58	629.04		305.76 / 323.28
%	100	118.83	27.29		

Proceedings of ECOS 2005
Trondheim, Norway
June 20–22, 2005

ENERGY, EXERGY, AND SECOND LAW PERFORMANCE CRITERIA

Noam Lior
Department of Mechanical Engineering and Applied Mechanics
University of Pennsylvania
Philadelphia, PA 19104-6315
USA

Na Zhang
Institute of Engineering Thermophysics, Chinese Academy of Sciences
Beijing 100080
P.R. China

ABSTRACT

Performance criteria, such as efficiencies and coefficients of performance, for energy systems, are commonly used but often without sufficient understanding and consistence. The situation becomes particularly incoherent when simultaneous energy interactions of different types, such as work, heating and cooling, take place with a system. Also, the distinction between exergy and Second-Law efficiencies is not clearly recognized by many. It is attempted here to clarify the definitions and use of energy and exergy based performance criteria, and of the Second Law efficiency, with an aim at the advancement of international standardization of these important concepts.

Keywords: thermodynamics, efficiency, exergy, Second Law, performance

NOMENCLATURE

a specific exergy, J/kg
A exergy, J
COP coefficient of performance
$\widetilde{COP}$ reversible cycle coefficient of performance, eq. (35)
E energy, J
I irreversibility, J
j the number of useful work or inputs and outputs
$\dot{m}$ mass flow rate of a stream
q heat per unit mass, J/kg
Q heat, J
$\widehat{Q}$ heat invested in plant construction, J
r_c the useful cooling to work output ratio, eq. (22)
r_h the useful heat to work output ratio, eq. (23)
s specific entropy, J kg^{-1} K^{-1}
S entropy, J/K
S_{gen} entropy generation, J/K
t time, s
T temperature, K
$\widehat{T}$ entropic temperature, eq. (31), K
v specific volume, m^3
w specific work, J/kg
W work, J

Greek

ε exergy efficiency
$\hat{\varepsilon}_t$ The "total" (or "overall") unsteady state exergy efficiency
$\tilde{\varepsilon}_t$ The "total" (or "overall") steady state exergy efficiency, including the system exergy
η_I energy (First Law) efficiency
η_{Iu} utilitarian (task) energy efficiency
η_{II} Second Law efficiency
η_Q useful heat production efficiency in a cogeneration cycle, eq. (20)
η_w work production efficiency in a cogeneration cycle, eq. (19)
content of the system is taken into consideration
$\tilde{\eta}_{hp}$ heat input based reversible cycle efficiency definition, eq. (34)
$\tilde{\eta}_{hu}$ heat output based reversible cycle efficiency definition, eq. (36)

Subscripts

0 dead state
a absorber

c cooling, or cold temperature reservoir
con condenser
cu for refrigeration use
cp paid-for refrigeration
d direct
e environment of a system
f heating or cooling fluid
h heating, or high temperature reservoir
hp paid-for heat
hu for heating use
i incoming
I First Law
II Second Law
j index, the *j*-th heat or work exchange
k number of material products of a plant
o outgoing
p paid for
rev reversible
s system
t total
u useful, for u

INTRODUCTION

There are many ways to assess energy system performance, and they must be adapted to the particular use they are put to. While the underlying concepts of such assessments are often well known and documented for a number of systems and cases, there are no clear agreements or rules about efficiency definitions, and authors often use different, and sometimes unsuitable, efficiency definitions for the same systems. The situation becomes particularly incoherent when simultaneous energy interactions of different types, such as work, heating and cooling, take place with a system (cf. [1], [2]). This prevents logical comparison of results at best, and wrong results at worst. This paper, though highly abbreviated due to conference page limitations, is intended to provide some clarifications and uniformity in that area, make a few proposals, and start a discussion that would hopefully lead to accelerated international standardization of these important concepts.

The most common energy system performance assessment criteria are *energy based* ("First Law") and they are useful for assessing the efficiency of energy use, and can be easily converted to energy cost efficiencies if the prices of the energy forms of the useful outputs and paid inputs are known. Here we define as "useful" all energy interactions that have use by the system "owner", usually in terms of monetary value, and "paid" all energy interactions that have a direct cost, usually monetary, to the system owner (cf. [1]). Thus, for example, the heat inputs that come from the environment for which the owner doesn't need to pay aren't included. We hasten to add that analyses that address environmental impact will include exchanges with the environment too.

Since such energy-based criteria do not account for the quality of energy, expressed as exergy, *exergy-based* criteria are also appropriate as they account better for use of energy resources and give much better guidance for system improvement. They also can be converted to exergy cost efficiencies if the exergy values of the useful outputs and paid inputs can be rationally priced (cf. [3]).

Another set of criteria assess the difference between the performance of a system relative to an ideal one (reversible) which operates between the same thermodynamic limits. We shall call these *Second-Law-based* criteria, although many authors use this term for exergy-based criteria.

Ultimately, decisions on best designs are most often based on economical considerations, in which energy (or exergy) are only one part, and sometimes not the most significant one, where the other parts include capital investment, labor, insurance, taxes, etc.

It is also worth noting that while performance criteria are most often applied to the entire system, such as plant or energy conversion device, they can be applied at any level, such as to different components, inside spatial and temporal processes (cf. [4]-[7]), and down to the smallest particle interactions, when there is an interest in that kind of exploration.

2. ENERGY-BASED CRITERIA

2.1 Introduction

Figure 1 describes a generalized system exchanging heat (heating and cooling) and work with other systems and with the environment, and will be used in this paper. The many definitions of energy efficiency, are reasonably well known, and would not be reviewed here due to paper length limitations.

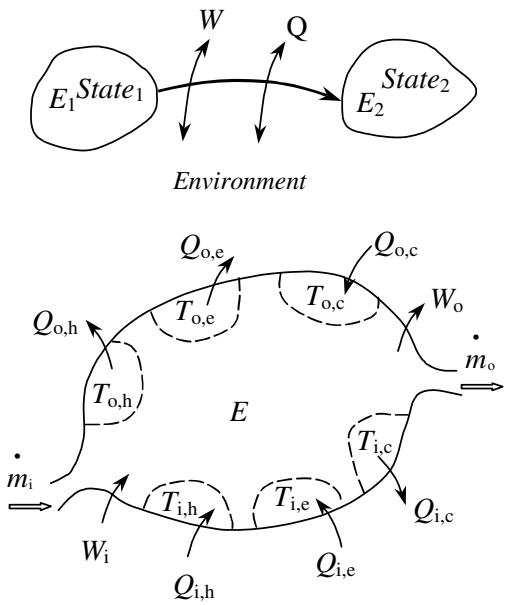

Fig. 1 Energy interactions

They include the

- *Total energy efficiency*, the ratio of all energy outputs to inputs, which is always equal to 1 and is thus useless for system performance assessment, although it should always be used in computations as a part of results validation.
- *Common (utilitarian, or "task") energy (First Law) efficiency* η_{lu} based on the practical energy needs (work, heat, refrigeration) of the system vendor or owner that are satisfied by the system, and that can be given a monetary value, and on the material and energy inputs to the system that must be paid for.
- *Coefficient of performance, COP,* used mostly in evaluating the performance of systems that produce primarily cooling .
- *Embodied energy efficiency*, it is often of interest (or should be…) to include in the energy efficiency assessment also the energy embodied in the production of the plant, in the materials produced by it, and in the materials and labor needed for its operation and for the distribution of its material products to the customer. A more consistent definition would also include the total energy investment, embodied in the fuel, materials and labor needed for the plant operation over its lifetime (L years), as well as the energy embodied in non-energy k products of the plant. A simple energy payback time, or preferably based on life-cycle-cost-analysis (LCA) is usually used as the evaluation criterion (cf. [8], [9]). To create a more equitable comparison between systems that produce different impacts on the environment, these embodied energies should also include the energy needed for restoration of the environment to its original state.
- *Energy criteria considering environmental effects,* since in some circumstances the objective of the analysis may include the energy impact of the system on the environment, including heat rejection to the environment or heat absorption from it, even though no direct (or immediate) monetary cost or benefit may be associated with it. This also would be of interest for finding the effects on ambient cooling or heating water consumption, etc. In that case we can define a thermal environmental impact ratio, all of the heat interactions with the environment (heat rejection and absorption) to the sum of the useful net power, heating and cooling produced.
- *Evaluation criteria based on economics,* include payback period, return on investment (ROI), and life cycle cost analysis (cf. ([3]), and those can be either restricted to the direct energy streams, or to the energy streams included embodied energy.

3. EXERGY EFFICIENCY, ε

3.1 Introduction

Just as there are various definitions of energy efficiencies as discussed above, there are also various definitions of exergy efficiency. We discuss here overall efficiency, the utilitarian (or "task") efficiency, and some ways to define the exergy.

Of help in these definitions is the exergy accounting for the system. For a thermodynamic system going through interactions between an initial state 1 and a later state 2, where the system exergy values are $A_{s,1}$ and $A_{s,2}$, respectively, the equation representing this accounting is

$$A_{s,2} - A_{s,1} = \sum_i A_i - \sum_o A_o - I \qquad (1)$$

where A_i and A_o are the exergy inputs and outputs to and from the system, respectively, and I is the total exergy loss (or destruction). Due to the Second Law, $I \geq 0$.

In steady state $A_{s,1} = A_{s,2}$, and Eq. (1) gives

$$\sum_o A_o = \sum_i A_i - I \qquad (2)$$

The irreversibility I is linked to the entropy generation S_{gen} by the equation

$$I = T_0 S_{gen} \qquad (3)$$

where T_0 is the dead state temperature (in absolute units).

3.2 The "total" (or "overall") exergy efficiency, $\hat{\varepsilon}_t$

$$\hat{\varepsilon}_t \equiv \frac{\left[\begin{array}{l}(\text{the system exergy at state 2}) + \\ \left(\sum_{\text{o}} \text{all exergy outputs}\right)\end{array}\right]}{\left[\begin{array}{l}(\text{the system exergy at state 1}) + \\ \left(\sum_{\text{i}} \text{all exergy inputs}\right)\end{array}\right]} = \frac{A_{s,2} + \sum_o A_o}{A_{s,1} + \sum_i A_i} \quad (4)$$

and the ingoing and outgoing exergy quantities may include work, heat and cooling, with or without mass flows. Incorporating Eq. (1) into (4) gives

$$\hat{\varepsilon}_t = \frac{A_{s,1} + \sum_i A_i - I}{A_{s,1} + \sum_i A_i} = 1 - \frac{I}{A_{s,1} + \sum_i A_i} \quad (5)$$

$\hat{\varepsilon}_t$ is used when the overall exergy efficiency of a system needs to be calculated, without interest in some of the individual outputs of the system. It is especially applicable when the system input and output streams do not maintain their integrity and the major part of the output is useful. It also has a more thermodynamic flavor than other efficiency definitions, in that it evaluates the efficiency of a process giving equal consideration to all outputs and inputs regardless of whether they are being used or paid for. For example, it offers a good starting point for ecological analysis of processes since it takes into equal consideration exergy components as diverse as useful work, heat and product materials on the one hand, and material and heat emissions to the environment on the other, on the output side, and paid fuel, work, and materials on the one hand, and "free" environmental heat on the other, on the input side.

In steady state $A_{s,1} = A_{s,2} = A_s$ and Eqs. (4) and (5) become

$$\tilde{\varepsilon}_t \equiv \frac{1 + \frac{\sum_o A_o}{A_s}}{1 + \frac{\sum_i A_i}{A_s}} \quad (6)$$

and

$$\tilde{\varepsilon}_t = 1 - \frac{I}{A_s + \sum_i A_i} \quad (7)$$

respectively.

Most often, the steady state total exergy efficiency is defined without consideration of the exergy value of the system, A_s, to more clearly focus on the exergy inputs and outputs only, and thus the best known form of the steady state total exergy takes the form

$$\varepsilon_t \equiv \frac{\sum_o A_o}{\sum_i A_i} = 1 - \frac{I}{\sum_i A_i} \quad (8)$$

3.3 The task (or "utilitarian") exergy efficiency, ε_u

Using the same logic as in definition of η_I, ε_u can be defined as the ratio between the exergy outputs useful to the owner, and the exergy inputs paid by the owner. The most common is the steady state definition:

$$\varepsilon_u = \frac{\sum_i |W_{u,i}| - \sum_i |W_{p,i}| + \sum_i |A_{hu,i}| + \sum_i |A_{cu,i}|}{\sum_i |A_{hp,i}| + \sum_i |A_{cp,i}|} \quad (9)$$

3.4 Exergy definitions

Work (including electrical energy) interactions are pure exergy and thus the exergy values of such interactions are equal to their energy values. Non-work energy interactions (heat for example) have values of exergy that depend on both the type of the energy interaction and the definition of the control system under consideration. The latter depends on the objective of the performance analysis. We can classify the types of non-work energy interactions and of typical objectives as follows [4].

Straight heat input or output

In general, the exergy of the system heat interactions of a system at constant temperature T with an environment at the dead state temperature T_0 for a process starting at time t_1 and ending at time t_2 is

$$\hat{A}_{h,i} = \int_{t_1}^{t_2} Q_{h,i}\left(1 - \frac{T_0}{T}\right) dt \quad (10)$$

when $T > T_0$ and $Q_{h,i}$ is the heat output from the system to the environment (or to a heat load at T_0), and

$$\hat{A}_{c,i} = \int_{t_1}^{t_2} Q_{c,i}\left(\frac{T_0}{T} - 1\right) dt \quad (11)$$

when $T < T_0$ and $Q_{c,i}$ is the heat input from the environment (or the cooling load at T_0) to the system, where all the parameters in the integral may vary with time. The efficiency becomes in the first case

$$\hat{\varepsilon}_u = \int_{t_1}^{t_2} \frac{W_u}{Q_{hi}(1-\frac{T_0}{T})} dt \qquad (12)$$

Stream-carried exergy

Exergy can be carried in and out of systems with a mass flow stream at the rate $\dot{m}a$, where $\dot{m}$ is the mass flow rate (in kg/s) and a is the specific exergy. a should include all the relevant exergy components including kinetic, potential, thermal, strain, and chemical as explained in detail in [4]. The sketch in Table 1 shows two common flow configurations: Fig. a. depicts a case in which the stream doesn't mix with the system and maintains its integrity, and Fig. b. depicts a case where a stream enters the systems, loses its integrity in it, and another stream exits the system.

The exergy exchange config-uration	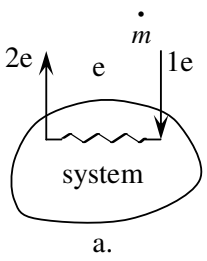 a.	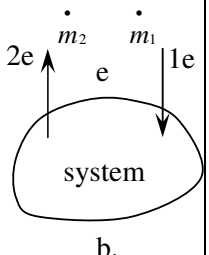 b.
The exergy change, A	$\dot{m}(a_1 - a_2)$ (13)	$\dot{m}_1 a_1 - \dot{m}_2 a_2$ (14)

Table 1 External stream-carried exergy configurations and magnitudes

The configurations described in Table 1 ignore exergy losses during the exchange between the stream and the system, in other words it is implicitly assumed that these losses are either negligible (infinite exchange coefficients) or that the analysis is not aimed at this purpose. A more rigorous model, which includes the exchange exergy losses, is described in Table 2. Figure a. describes a system where the external stream 1e→2e and a system stream 1s→2s interacting while maintaining their integrities. A sample case is when stream 1s→2s is the evaporator in a refrigeration system, and stream 1e→2e is the fluid that is being cooled by the evaporator (refrigerator).

The exergy exchange config-uration	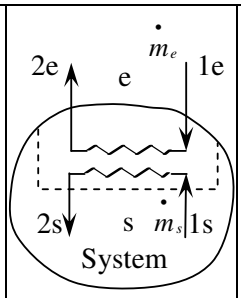 a.	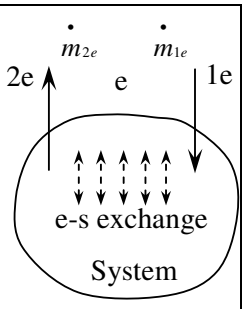 b.
The exergy change, A	$\dot{m}_e(a_{1e} - a_{2e}) =$ $\dot{m}_s(a_{2s} - a_{1s}) + I_{e\leftrightarrow s}$ (15)	$\dot{m}_1 a_{1e} - \dot{m}_2 a_{2e} =$ $A_{s2} - A_{s1} + I_{e\leftrightarrow s}$ (16)

Table 2 External stream-carried exergy configurations and magnitudes

Equation (15) represents the exergy balance in this case, where $I_{e\leftrightarrow s}$ is the irreversibility due to the interaction between the streams, and allows the inclusion of this irreversibility in the system efficiency calculation by ascribing the exergy (input or output) value to the external, rather than the system, stream, as was done in the model of Table 1 Fig. a.

Similar to the model of Fig. b in Table 1, that of the model in Fig. b of Table 2 represents input and output streams that aren't directly connected, but the one of Table 2 Fig. b includes the interactions between these streams and the system, with the associated irreversibility in Eq. (16). A sample case is a combustor with inputs of fuel and oxidant and an output of reaction products, when the exergy losses due to the combustion process (including mixing, chemical reaction, heat transfer) are wished to be taken into account (cf. [5]). Use of such a model is the basis for "intrinsic" exergy analysis that allows detailed (even spatial and temporal) determination of exergy changes in all interaction processes (cf. [4]-[7]).

4. SECOND-LAW EFFICIENCY

4.1 Introduction

Given the objectives of the system under consideration, such as power production, cooling, heating, materials processing, etc., and the thermodynamic limits, such as the top and bottom temperatures, pressures, and other thermodynamic potentials, it is useful to compare the performance of the system with one that would deliver the best thermodynamic performance between the same limits,

i.e. one in which all the processes are reversible. This indicates clearly a potential for improvement.

The Second-Law efficiency is defined here ([2] and many others) as the ratio of the First-Law efficiency of the system to the efficiency of a reversible system operating between the same thermodynamic states,

$$\eta_{II} = \frac{\eta_I}{\eta_{rev}} \tag{17}$$

To compute η_{II}, the cycle for which η_{rev} needs to be calculated must have a close relationship to the cycle under consideration, for which η_I is known, as stated at the outset. Starting with the work by Martinovsky,([10],[11]), Niebergall [12], and Stierlin [13], the definition for that purpose of a "model reversible cycle" was advanced by Morosuk and co-workers ([14],[15]) We now examine several cases for the definition of this reversible cycle.

4.5 Systems that simultaneously produce useful work, cooling and heating

In that case, and abbreviating the notations,

$$\eta_I = \frac{W_u + Q_{hu} + Q_{cu}}{Q_{hp}} = \eta_w + \eta_Q + COP_c \tag{18}$$

where W_u, Q_{hu}, and Q_{cu} are the useful outputs of work, heat and cooling, Q_{hp} is the paid heat input to the cycle, and the efficiency terms on the right hand side of the equation are defined as, the useful work production efficiency,

$$\eta_w \equiv \frac{W_u}{Q_{hp}} \tag{19}$$

the useful heat production efficiency,

$$\eta_Q \equiv \frac{Q_{hu}}{Q_{hp}} \tag{20}$$

and the useful cooling output *COP*,

$$COP_c \equiv \frac{Q_{cu}}{Q_{hp}} \tag{21}$$

It is often of practical utility to define the ratios of the cooling and heating energy outputs to the work output

$$r_c \equiv \frac{Q_{cu}}{W_u} \tag{22}$$

$$r_h \equiv \frac{Q_{hu}}{W_u} \tag{23}$$

and then eq. (18) takes the form

$$\eta_I = (1 + r_c + r_h)\eta_w \tag{24}$$

Equation (24) is useful when comparing efficiencies of systems that have the same values of the output heat-work ratios *r*.

The reversible system efficiency can be expressed similarly as

$$\eta_{rev} = \left(\frac{W_u + Q_{hu} + Q_{cu}}{Q_{hp}} \right)_{rev} = \tag{25}$$
$$= \eta_{w,rev} + \eta_{Q,rev} + COP_{c,rev}$$

where the efficiency terms on the right hand side of the equation, all for the reversible case, are defined as follows:
the useful work production efficiency,

$$\eta_{w,rev} \equiv \frac{W_{u,rev}}{Q_{hp,rev}} \tag{26}$$

the useful heat production efficiency,

$$\eta_{Q,rev} \equiv \frac{Q_{hu,rev}}{Q_{hp,rev}} \tag{27}$$

and the useful cooling output $COP_{c,rev}$,

$$COP_{c,rev} \equiv \frac{Q_{cu,rev}}{Q_{hp,rev}} \tag{28}$$

Similar to the energy balance shown in Fig. 1 but somewhat simplified for clarity, let us assume that a system produces useful work amount W_u, useful cooling Q_{cu} at temperature T_c, and useful heat Q_{hu} at temperature T_{hu}, has a paid heat input Q_{hp} at temperature T_{hp}, and has "free" heat output to- and input from- the environment, $Q_{i,e}$ and $Q_{o,e}$ at temperatures $T_{i,e}$ and $T_{o,e}$, respectively. The entropy balance for this reversible cycle is

$$\left(\frac{Q_{hp}}{T_{hp}} + \frac{Q_{cu}}{T_c} + \frac{Q_{i,e}}{T_{i,e}} - \frac{Q_{hu}}{T_{hu}} - \frac{Q_{o,e}}{T_{o,e}} \right)_{rev} = 0 \tag{29}$$

and energy conservation

$$Q_{hp} + Q_{cu} + Q_{i,e} - Q_{o,e} - Q_{hu} - W_u = 0 \tag{30}$$

In many power cycles the heat input and rejection is not even approximately isothermal. The reversible power cycle named after Lorenz [16] can serve as the "model ideal cycle" in such cases, and also serves well to introduce the "entropic temperature" concept useful in such analyses. This cycle consists of an isentropic compression stroke 1→2, followed by a stroke 2→3 in which heat is transferred to the working fluid at gradually increasing temperature till the top temperature T_3 of the cycle is reached, followed by an isentropic expansion stroke 3→4 to a lower pressure, and closed with a heat rejection stroke 4→1 at variable temperature. One case of the Lorenz cycle is the Brayton cycle (called by some the Joule cycle) in which the heat input and rejection strokes take place isobarically.

A common simplification is to express the efficiency of the Lorenz cycle in terms of an equivalent Carnot cycle operating between the

temperatures $\widehat{T}_h$ and $\widehat{T}_c$, also known as the *entropic temperatures*, defined by

$$\widehat{T}_h \equiv \frac{\int_2^3 TdS}{S_3 - S_2} \qquad \widehat{T}_c \equiv \frac{\int_1^4 TdS}{S_4 - S_1} \tag{31}$$

It is easy to show that the Carnot cycle operating between the temperatures $\widehat{T}_h$ and $\widehat{T}_c$ has the same efficiency as the Lorenz cycle, and the Lorenz cycle efficiency is thus

$$\eta_{rev,Lorenz} = 1 - \frac{\widehat{T}_c}{\widehat{T}_h} \tag{32}$$

Combining eqs. (29) and (30) to eliminate $Q_{o,e}$ yields

$$-Q_{hp}\left(1 - \frac{T_{o,e}}{T_{hp}}\right) + Q_{cu}\left(\frac{T_{o,e} - T_c}{T_c}\right) + Q_{hu}\left(1 - \frac{T_{o,e}}{T_{hu}}\right) + Q_{i,e}\left(\frac{T_{o,e} - T_{i,e}}{T_{i,e}}\right) + W_u = 0 \tag{33}$$

The terms in the parentheses are now named the reversible cycle efficiencies as follows:

$$\tilde{\eta}_{hp} \equiv 1 - \frac{T_{o,e}}{T_{hp}} \tag{34}$$

$$C\tilde{O}P_c \equiv \frac{T_c}{T_{o,e} - T_c} \tag{35}$$

$$\tilde{\eta}_{hu} \equiv 1 - \frac{T_{o,e}}{T_{hu}} \tag{36}$$

$$C\tilde{O}P_e \equiv \frac{T_{i,e}}{T_{o,e} - T_{i,e}} \tag{37}$$

Using Eqs. (33) - (37) we can express the paid heat input required to produce the useful work, cooling and heating outputs of the reversible cycle as

$$Q_{hp} = \left(W_u + \frac{Q_c}{C\tilde{O}P_c} + \tilde{\eta}_{hu}Q_{hu} + \frac{Q_{i,e}}{C\tilde{O}P_e}\right)\frac{1}{\tilde{\eta}_{hp}} \tag{38}$$

Replacing the denominator in Eq. (25) with the last expression gives

$$\eta_{rev} = \frac{\left(W_u + Q_{hu} + Q_{cu}\right)_{rev}}{\left(W_u + \frac{Q_{cu}}{C\tilde{O}P_c} + \tilde{\eta}_{hu}Q_{hu} + \frac{Q_{i,e}}{C\tilde{O}P_e}\right)\frac{1}{\tilde{\eta}_{hp}}} \tag{39}$$

Similar to the derivation of Eq. (24), we define for the reversible cycle the heat-work output ratios as

$$\tilde{r}_c \equiv \left(\frac{Q_{cu}}{W_u}\right)_{rev} \tag{40}$$

$$\tilde{r}_h \equiv \left(\frac{Q_{hu}}{W_u}\right)_{rev} \tag{41}$$

$$\tilde{r}_e \equiv \left(\frac{Q_{i,e}}{W_u}\right)_{rev} \tag{42}$$

and with the substitution of Eqs. (40) - (42), Eq. (39) takes the form

$$\eta_{rev} = \frac{\tilde{\eta}_{hp}\left(1 + \tilde{r}_c + \tilde{r}_h\right)_{rev}}{1 + \frac{\tilde{r}_c}{C\tilde{O}P_c} + \tilde{\eta}_{hu}\tilde{r}_h + \frac{\tilde{r}_e}{C\tilde{O}P_e}} \tag{43}$$

The Second Law efficiency is thus, using Eqs. (17), (18) and (25)

$$\eta_{II} = \frac{\eta_w + \eta_Q + COP_c}{\eta_{w,rev} + \eta_{Q,rev} + COP_{c,rev}} \tag{44}$$

or from Eqs. (24) and (43) gives another equation for η_{II} which is often easier to use:

$$\eta_{II} = \frac{\eta_w\left(1 + r_c + r_h\right)}{\tilde{\eta}_{hp}\left(1 + \tilde{r}_c + \tilde{r}_h\right)}\left(1 + \frac{\tilde{r}_c}{C\tilde{O}P_c} + \tilde{\eta}_{hu}\tilde{r}_h + \frac{\tilde{r}_e}{C\tilde{O}P_e}\right) \tag{45}$$

All of the terms in Eq. (45) except $\tilde{r}_e$ are known from choice or calculation, so if $\tilde{r}_e$ can be determined by some other means, η_{II} can be calculated.

Further simplification of efficiency comparisons is obtained if it is chosen that the heat-power outputs in the actual and reversible cycle are the same, $r_c + r_h = \tilde{r}_c + \tilde{r}_h$, and then Eq. (45) becomes

$$\eta_{II} = \frac{\eta_w}{\tilde{\eta}_{hp}}\left(1 + \frac{\tilde{r}_c}{C\tilde{O}P_c} + \tilde{\eta}_{hu}\tilde{r}_h + \frac{\tilde{r}_e}{C\tilde{O}P_e}\right) \tag{46}$$

If it can be assumed that the heat exchange with the environment occurs at the temperature of the environment, T_e, so $T_{i,e} = T_{o,e}$, Eq. (46) becomes

$$\eta_{II} = \frac{\eta_w}{\tilde{\eta}_{hp}}\left(1 + \frac{\tilde{r}_c}{C\tilde{O}P_c} + \tilde{\eta}_{hu}\tilde{r}_h\right) \tag{47}$$

and now η_{II} can be calculated without knowing $\tilde{r}_e$.

It is of interest to compare these Second Law efficiency equations with those defining the exergy efficiency presented in Section 3.

An example:

This example demonstrates one possible error that can be made when the exergy and Second Law efficiencies are used interchangeably, without realizing their distinct definitions, using the case of a compound cycle for cogeneration of power, heating and cooling proposed by the authors [17]. The plant operates in a parallel combined cycle mode with an ammonia-water Rankine cycle and an ammonia refrigeration cycle, interconnected by the absorption,

separation and heat transfer processes. It is driven by one external heat source fluid. In this paper, the heat source fluid is chosen to be air, entering the system at 450°C/1.043bar, and the net power output is 719 kW. Both refrigeration and heating output are at variable temperatures. The refrigeration output is 266.2kW, the working fluid (rich ammonia stream) provide refrigeration in a evaporator at the temperature range of -22.7°C to -15°C and pressure of 1.6 bar, with the corresponding *entropic temperature* (eq. (31)) T_c=250.5K. The heating fluid provide low level heat at the temperature range of 90° to 50°C and pressure of 1.013bar, the heat output is 308.9 kW, at the corresponding *entropic temperature* T_{hu}=342.8K. The heating fluid finally exhausts to the environment (T_e=298.15K), and the heat addition process is also a temperature variable process, at the *entropic temperature* T_{hp}=492.5K. the total heat input is 3496 kW.

The First Law efficiency:

$$\eta_I = \frac{W_u + Q_u + Q_c}{Q_{ip}} = 37.0\% \quad (48)$$

The refrigeration exergy output is (eq. (11))

$$A_c = Q_c\left(\frac{T_e - T_c}{T_c}\right) = 50.6 \text{ kW} \quad (49)$$

The heating exergy output is (eq. (10)):

$$A_{hu} = Q_{hu}(1 - T_e / T_{hu}) = 40.2 \text{ Kw} \quad (50)$$

The exergy input is

$$A_{hp} = Q_{hp}(1 - T_e / T_{hp}) = 1379.6 \text{ kW}$$

so, the exergy efficiency is (eq. (9).

$$\varepsilon = \frac{W_u + A_{hu} + A_c}{A_{hp}} = 58.7\% \quad (51)$$

To calculate the second law efficiency, we should first find the first law efficiency of a reversible cycle, which operates in the same thermophysical conditions and have the same power, heating and cooling outputs. Using eqs. (29), (30):

$$\begin{cases} \dfrac{Q_{hP,rev}}{T_{hp}} + \dfrac{Q_c}{T_c} - \dfrac{Q_{hu}}{T_{hu}} - \dfrac{Q_{0,rev}}{T_0} = 0 \\ Q_{hp,rev} + Q_c = Q_{hu} + W + Q_{0,rev} \end{cases} \quad (52)$$

where Q_0 is the heat amount exhausted to the heat sink.

(1) If the heat sink is chosen to be the environment with the temperature T_0=T_e=298.15K, then we can calculate the $Q_{hp,\,rev}$ from the above two equations to be $Q_{hp,\,rev}$=2052.1 kW, and the first law efficiency of the reversible system is:

$$\eta_{I,rev} = \frac{W_u + Q_u + Q_c}{Q_{hp,rev}} = 63.06\%$$

therefore, the Second Law efficiency of the system is (eq. (17)):

$$\eta_{II} = \eta_I / \eta_{I,rev} = 58.7\%$$

In this case, the Second Law efficiency is the same as the exergy efficiency.

(2) If the heat sink temperature is chosen to be at a value different than the environment temperature T_e, for example, if the heat sink is sensibly assumed to be the cooling water at T_0=303.15K, then $Q_{hp,\,rev}$=2108.4 kW, and the first law efficiency of the reversible system is thus:

$$\eta_{I,rev} = \frac{W_u + Q_u + Q_c}{Q_{hp,rev}} = 61.4\%,$$

and then the Second Law efficiency of the system is $\eta_{II} = \eta_I / \eta_{I,rev}$ = 60.3%, 2.7% higher than the exergy efficiency despite the smallness of the difference between the temperatures of the reference states (5 K, 1.6%).

5. REFERENCES

[1]. Lior, N. Research and new concepts. In: Löf, G.O.G., editor. Active solar systems. Cambridge MA: MIT Press, 1993. Ch. 17, p. 615-674.

[2]. Vijayaraghavan, S, Goswami, DY. On evaluating efficiency of a combined power and cooling cycle, Trans. ASME J. Energy Resources Technol. 2003:125 (3) 221-227.

[3]. Bejan, A., Tstsaronis, G., Moran, M. *Thermal design and optimization*. New York: John Wiley and Sons, Inc., 1996.

[4]. Dunbar, W.R., Lior, N., Gaggioli, R. The component equations of energy and exergy. ASME J. Energy Resources Technology 1992;114:75-83.

[5]. Dunbar, W.R., Lior, N. Sources of combustion irreversibility. Comb. Sci. Technol. 1994;103:41-61.

[6]. Lior, N. Irreversibility in combustion, invited keynote paper, Proc. of ECOS '01: Efficiency, Costs, Optimization, Simulation and Environmental Aspects of Energy Systems, Istanbul, Turkey, vol. 1, pp. 39-48, 2001.

[7]. Lior, N., Sarmiento-Darkin, W., Al-Sharqawi, H.S. The exergy fields in transport processes: their calculation and use. invited keynote presentation and paper, Proc. ASME – ZSIS International Thermal Science Seminar II, Bled,

Slovenia, June 13 – 16, 2004, pp. 155-169; expanded version accepted for publication in ENERGY – The International Journal.
[8]. Alsema, E.A., Nieuwlaar, E. Energy viability of photovoltaic systems. Energy Policy 2000;28:999-1010.
[9]. Battisti, R.. Corrado, A. Evaluation of technical improvements of photovoltaic systems through life cycle assessment methodology, Energy 2005;30:952-967.
[10]. Martinovsky V.S. *Thermodynamic characteristics of heat and refrigeration machines cycles*. Moscow-Leningrad: Government Energy Publication, 1952.
[11]. Martinovsky V.S., *Cycles, schemes and characteristics of thermotransformers*. Moscow, Energy, 1979.
[12]. Niebergall, W., *Sorptions-Kältemaschinen*, vol. 7 in Ed. Plank, R., *Handbuch der Kältetechnik*, Springer-Verlag, Berlin 1959, p. 23-30.
[13]. Stierlin, H. Beitrag zur Teorie der Absorptions-Kältemaschine, Kältetechnik 1964:16 213-219
[14]. Morosuk T.V. "New at the Thermodynamic Analysis of Absorption Thermotransformers" In A. Ozturk and Y.A. Gogus "Efficiency, Cost, Optimization and Environmental Impact of Energy System", ECOS'01, Istanbul, Turkey, 2001, Vol. II, p.643-649.
[15]. Morosuk, T., Morosuk, C., Feidt, M. New proposal in the thermodynamic analysis of complex heat regeneration systems Energy, Volume 29, Issues 12-15, October-December 2004, Pages 2517-2535.
[16]. Lorenz, H. Die Ermittlung der Grenzwerte der thermodynamischen Energi-umwandlung. Z. Ges. Kälteind. vol. 2 p. 8,27,43 and in Die Ausnutzung der Brennstoffe in den Kühlmaschinen. Z. Ges. Kälteind. vol. 1 (1894) 10-15.
[17]. Na Zhang, Ruixian Cai, Noam Lior, A Novel Ammonia-Water Cycle for Power and Refrigeration Cogeneration, ASME paper IMECE2004-60692, Anaheim, CA, 2004, American Society of Mechanical Engineers, N.Y..

Thermoeconomics/Trade

Proceedings of ECOS 2005
Trondheim, Norway
June 20–22, 2005

COMBUSTION PROCESS OPTIMIZATION FROM THE EXERGY – ECONOMY POINT OF VIEW

Majid Amidpour *
K.N. Toosi University (KNTU)
Mechanical Engineering Department
Tehranpars, Tehran, Iran

Omid Hamidkhani
Iran University of Science and Technology (IUST)
Mechanical Engineering Department
Narmak, Tehran, Iran

ABSTRACT

Identifying and quantification of the losses allows us to improve the design of the systems. Energy losses are not necessarily indicative of the diversion from ideality .For instance; some processes have no energy losses, such as combustion of a fuel in an isolated vessel, yet the process is highly irreversible and therefore non-ideal. Thus energy analysis is not adequate for evaluation of the thermal system. Exergy analysis is a more powerful tool for evaluating of the systems and finding the type, location, and magnitude of the thermal losses in them.
The combustion process is one of the most important parts of the thermal systems; in this research the destruction of availability (exergy) during a combustion process is examined for adiabatic, constant pressure gaseous (methane) combustion. Exergetic efficiency of this irreversible process is obtained as a function of inlet air temperature, combustion pressure, air fuel ratio and the inlet air relative humidity. Since higher combustion pressure results higher exergetic efficiency but higher costs, the optimum combustion pressure is obtained from the exergoeconomic point of view.
*Keywords***:** Combustion, Cost, Exergy, Thermoeconomy, Optimization

NOMENCLATURE

$\dot{I}$	Exergy loss [kW]
$\dot{E}$	Exergy [kW]
C_T	Total cost [$/year]
b	Fixed costs [$/year]
a	Annual recovery factor [1/year]
$t_{op.}$	Operating period [hr/year]
x_i	Effective parameter
C_{in}	Exergy unit cost [$/kWh]
C_c	Capital cost [$]

Subscripts

in	inlet
out	outlet
e.p	electrical power

INTRODUCTION

The design of efficient thermal systems that use nonrenewable energy sources is clearly important.∗ As pointed out earlier, Energy losses are not necessarily indicative of the derivation from ideality .For instance; some processes have no energy losses, such as combustion of a fuel in an isolated vessel, yet the process is highly irreversible and therefore non-ideal. Thus energy analysis is not adequate for evaluation of the thermal system.
Exergy analysis is a more powerful tool for evaluating of the systems and finding the type, location, and magnitude of the thermal losses in them. Identifying and quantification of the losses allows us to improve the design of the systems.

* Corresponding Author: Phone: +98 21 7343300
E-mail Address: amidpour@kntu.ac.ir

Since the thermodynamic optimizations of a thermal system usually appear to correlate in an inverse manner with capital costs, these methods should be integrated with engineering economics principles to determine the potential for cost effective improvement systems.
While it does not make sense to compare the energy cost of 1 kJ of electricity with that of 1 kJ of cooling water, it does make sense to compare them from the exergy point of view. So in the thermoeconomic analysis of the thermal systems the concept of exergy should be used instead of energy.
Work linking exergy and economics stems from researches carried out several decades ago that tied entropy to economics. One of the pioneers in this area was Nicolus G. Rogen whose 1971 book "The Entropy Law and The Economic Process" is cited continually and has motivated many research projects. [1]
Although an extensive literature exists concerning the destruction of availability, only a limited amount of work has been reported on the specific details for combustion processes (e.g. [2]) and no work has been reported on the thermoeconomic optimization of these processes.

EXERGY ANALYSIS

The concept of maximum work and availability can be extended to chemically reacting systems such as combustion process.
Since exergy destruction is a measure of irreversibility, it is important to consider the effect of the variation of the operating parameters on it.
In this study an isobar and adiabatic combustion of methane is evaluated by exergy and exergo-economic analysis.
For an adiabatic control volume, the exergy balance can be written as:

$$\dot{I} = \dot{E}_{in} - \dot{E}_{out} \qquad (1)$$

In a combustion process, inlet exergy is due to the chemical availability of fuel. Chemical availability is a measure of the maximum work when a gas or gas mixture comes to equilibrium with the environmental composition.
Chemical availability of a substance such as a fuel is examined as a chemical reaction occurs and the products of the reaction reach to equilibrium with the environmental composition.
Exergy loss can be simply obtained From Eq. 1. Calculation of products exergy entails calculation of the chemical composition of the products. Chemical composition of the products is obtained from the usual algorithms suggested in textbooks [3] by means of a computer code developed in C^{++}.
In this research the exergetic efficiency - defined as the ratio of the output exergy to inlet exergy - is plotted as a function of the operating parameters. Results are explained below:

Air fuel ratio

Fig. 1 depicts the effect of the air fuel ratio on the exergetic efficiency of the process.
As shown in the figure, increasing of the air fuel ratio leads to efficiency reduction.
This inverse relation is due to the products mass (moles) increase. Since higher products mass results lower flame temperature, a higher air fuel ratio results lower products exergy and so lower exergetic efficiency.

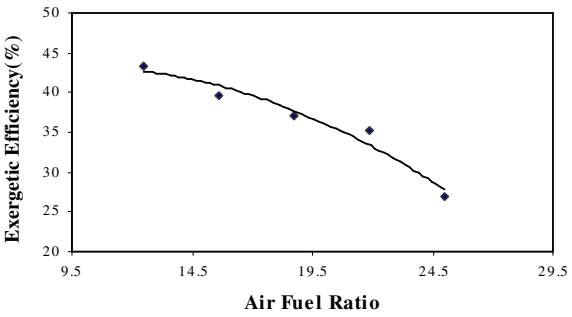

Figure 1: Exergetic efficiency as a function of air fuel ratio

Inlet Air Temperature

The effect of the inlet air temperature on exergetic efficiency is depicted in fig. 2. As shown in this figure, the inlet air temperature increase results in exergetic efficiency increase. Simply it can be understood that this increase is the result of the products temperature increase.

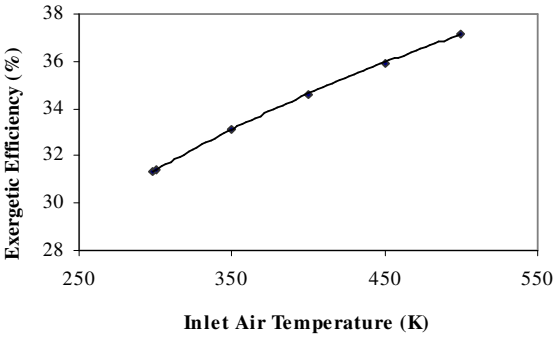

Figure 2: Exergetic efficiency as a function of inlet air temperature

Inlet air relative humidity

Fig. 3 shows the exergetic efficiency variation as a function of inlet air relative humidity.

As it is known, an increase in inlet air relative humidity leads to flame temperature reduction and this will reduce the products exergy. So as shown in the figure higher inlet air relative humidity will result lower exergetic efficiency.

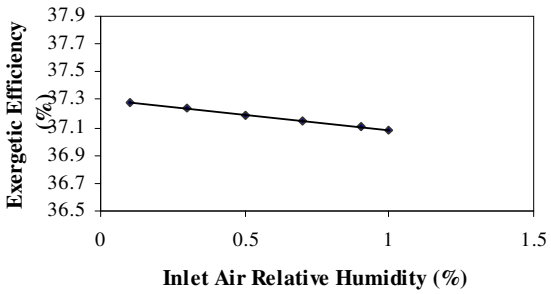

Figure 3:Exergetic efficiency as a function of inlet air relative humidity

Combustion pressure

As shown in fig. 4, higher combustion pressure results higher exergetic efficiency. This is due to flame temperature increase as a result of pressure increase.

According to the results explained above, inlet air temperature increase, inlet air relative humidity decrease and combustion pressure increase will lead to exergetic efficiency decrease. But clearly it is necessary to spend some exergy and even cost to do these improvements. So the combustion process should be analyzed by a more powerful method called exergoeconomy.

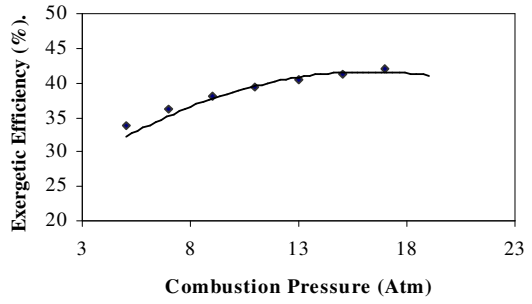

Figure 4: Exergetic efficiency as a function of combustion pressure

COMBINATION OF EXERGY AND ECONOMY

As mentioned before, the exergetic efficiency increase entails higher cost. For example, a higher combustion pressure leads to higher exergetic efficiency but a compressor unit should do this pressure increase.

Since using a compressor results some costs (capital and operating) there is an optimum combustion pressure that will minimize the total cost.

In this section a combustion process is optimized by exergoeconomy method in order to obtain the optimum combustion pressure.

Supposing an adiabatic combustion chamber and a compressor unit, the exergy balance can be written as follows [4]:

$$\dot{I}(x_i) = \dot{E}_{in}(x_i) - \dot{E}_{out}(x_i) + \dot{E}_{e.p}(x_i) \quad \textbf{(2)}$$

Since always there is some exergy loss in the actual processes, it is necessary to consume more input exergy to produce a certain amount of output exergy.

From the economic point of view, an objective function can be defined as follows:

$$C_T(x_i) = t_{op.} C_{in} \left(\dot{E}_{in}(x_i) + \dot{E}_{e.p}(x_i) \right) + aC_C(x_i) + b \quad \textbf{(3)}$$

This objective function represents the total cost required to produce a certain amount of exergy.

In this equation x_i is a parameter affecting the performance of the system. In this study x_i can be supposed to be the combustion pressure.

According to the usual mathematical method, this objective function should be differentiated to find the optimum combustion pressure. Thus:

$$\frac{\partial C_T}{\partial x_i} = t_{op} C_{in} \frac{\partial}{\partial x_i} \left(\dot{E}_{in}(x_i) + \dot{E}_{e.p}(x_i) \right) + a \frac{\partial C_c}{\partial x_i} \quad \textbf{(4)}$$

Differentiation of Eq. 2 also gives:

$$\frac{\partial \dot{I}}{\partial x_i} = \frac{\partial \dot{E}_{in}(x_i)}{\partial x_i} - \frac{\partial \dot{E}_{out}(x_i)}{\partial x_i} + \frac{\partial \dot{E}_{e.p}(x_i)}{\partial x_i} \quad \textbf{(5)}$$

As mentioned before, the optimum operating condition to produce a constant amount of exergy is required, so:

$$\frac{\partial \dot{E}_{out}(x_i)}{\partial x_i} = 0 \quad \textbf{(6)}$$

Thus:

$$\frac{\partial \dot{I}}{\partial x_i} = \frac{\partial}{\partial x_i}\left(\dot{E}_{in}(x_i) + \dot{E}_{e.p}(x_i) \right)$$

(7)

Substituting Eq. 7 in Eq. 4 results:

$$\frac{\partial C_T}{\partial x_i} = t_{op.} C_{in} \frac{\partial \dot{I}}{\partial x_i} + a \frac{\partial C_c}{\partial x_i} \qquad \textbf{(8)}$$

To optimize the objective function, make Eq. 8 zero. hence:

$$\frac{\partial Cc}{\partial \dot{I}} = -\frac{t_{op.} \cdot C_{in}}{a} \qquad \textbf{(9)}$$

Equation (9) shows that in the optimum x_i the slope of the tangential line to the capital cost – exergy loss graph equals $-\frac{t_{op.} \cdot C_{in}}{a}$.

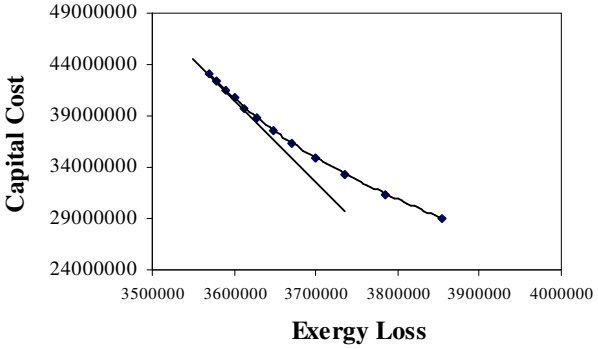

Figure 5: Capital cost as a function of Exergy Loss

The capital cost can be obtained from the experimental capital cost estimation diagrams given in textbooks [5].

Figure 5 depicts the variation of the capital cost as a function of exergy loss for different combustion pressure. The optimum condition is the point in which the slope of the tangential line equals $-\frac{t_{op.} \cdot C_{in}}{a}$ so, from this graph the exergy loss amount in the optimum condition can be graphically obtained.

As it is clear in fig. 5 in the optimum condition the exergy loss amount is approximately 3600000 (kW) that the corresponding combustion pressure will be 12.5 bar. It should be noted that this result obtained for a certain set of operating parameters such as inlet air temperature, air fuel ratio and inlet air relative humidity.

4. CONCLUSION

Adiabatic and isobaric combustion of methane has been considered by exergy analysis. Results showed that an increase in combustion pressure results an increase in exergetic efficiency so consequently lower fuel cost is required to produce a constant amount of exergy. On the other hand increasing the combustion pressure entails more costs due to the compressor set capital cost and its power consumption cost. So it is possible to find an optimum combustion pressure by means of the exergoeconomy method.

It should be noted that different situations such as economical factors (a, C_{in} and . . .) and physical parameters (air fuel ratio, inlet air temperature, inlet air relative humidity and . . .) would definitely conduct to different solutions.

REFERENCES

[1] Rosen MA. Exergy and economics: Is exergy profitable? Exergy 2002; 2:218-220

[2] Caton JA. On the destruction of availability (exergy) due to combustion processes-with specific application to internal combustion engines. Energy, 2000; 25: 1097-1117

[3] Heywood JB. Internal Combustion Engine Fundamentals. New York: McGraw Hill, 1998.

[4] Kotas TJ. The exergy method of thermal plants analysis. London: Krieger, 1995.

[5] Peters MS, Timmerhaus KO. Plant design and economic for chemical Engineers. New York: McGraw Hill, 1991.

Proceedings of ECOS 2005
Trondheim, Norway
June 20–22, 2005

EXERGY AND EXERGO-ECONOMIC ANALYSIS OF A MICRO-COGENERATION SYSTEM BASED ON AN ERICSSON ENGINE

Sébastien Bonnet, Muriel Alaphilippe, and Pascal Stouffs*
Laboratoire de Thermique, Energétique et Procédés (LaTEP),
IUT des Pays de l'Adour, Département Génie Thermique et Energie,
Avenue de l'Université, F-64000 PAU
France

ABSTRACT

Hot air engines (Stirling and Ericsson engines) are well suited for micro-cogeneration applications because they are noiseless, and they require very low maintenance. We study the coupling of an Ericsson engine *(i.e.* a Joule cycle reciprocating engine with external heat supply) with a system of natural gas combustion. In order to design this installation, we carry out energy, exergy and exergo-economic analyses that allow us to plot the exergy GRASSMANN diagram and evaluate the cost of the thermal and electric energy production. These simple analyses confirm the interest of such systems. The main result of this study is thus to draw the attention on Ericsson engines, unfortunately unfairly fallen into oblivion.
Keywords: Joule cycle, Ericsson engine, micro-cogeneration, CHP, exergy analysis

NOMENCLATURE

c_i	exergy cost of stream i [€.J^{-1}]
E	heat exchanger effectiveness
ex, $\overline{ex}$	exergy per mass or mol [J.kg^{-1}], [J.mol^{-1}]
$\dot{E}x_i$	rate of exergy transfer of stream i [W]
h	enthalpy per unit mass [J.kg^{-1}]
$\dot{m}$	mass flow rate [kg.s^{-1}]
p	pressure [Pa]
P	price [€]
$\dot{Q}$	thermal power [W]
R	ideal gas constant [J.kg^{-1}.K^{-1}]
$\overline{R}$	universal gas constant [J. mol^{-1}.K^{-1}]
s	entropy per unit mass [J.kg^{-1}.K]
T	temperature [K]
v	fluid velocity [m.s^{-1}]
$\dot{W}$	mechanical power [W]
x	molar fraction
$\dot{Z}_i$	cost per unit time of constituent i, [€.s^{-1}]

Greeks symbols

η	efficiency
ξ	pressure loss coefficient
ρ	density [kg.m^{-3}]
ψ	valve pressure loss factor

Subscripts and superscripts

amb	ambient conditions
C	compression cylinder
CC	combustion chamber
ch	chemical
chim	chimney
cr	working air between C and R
D	destroyed (exergy)
E	expansion cylinder
e	exhaust comb. gases, between CC and H
ep	exhaust comb. gases, between H and P
er	working air, between E and R
g	gaseous fuel
H	heater
h	working air, heater outlet
IC	intercooler
ind	indicated (work or efficiency)
K	cooler
k	working air, inlet 1st stage of C
k1	working air, between C1 and IC
k2	working air, between IC and C2
mec	mechanical
P	combustion air preheater
pa	preheated air
Ph	physical
R	regenerator or recuperator
rh	working air, between R and H

*Corresponding author: Phone: + 33 5 59 40 71 51 Fax: +33 5 59 40 71 60 E-mail: pascal.stouffs@univ-pau.fr

rk working air, between R and H
0 reference state, standard

INTRODUCTION

In the low electrical power range (500 We … 50 kWe), combined heat and power (CHP), also called co-generation, does not have the same development as for higher power. This lack of success, although the market for residential cogeneration could be strong, is mainly due to the absence of suitable systems for this power range: internal combustion engines generate noise and vibrations. The market seems more promising for systems based on external combustion. Especially a lot of developments are devoted to CHP systems with kinematic or free piston Stirling engines and some of these systems are already commercially available.

We study a micro-cogeneration system based on an Ericsson engine coupled with a system of natural gas combustion. The objective of this system is to produce sanitary and heating hot water and 11 kW of electric output. In order to design this system, we carry out energetic, exergetic and exergo-economic studies.

CONFIGURATION OF THE STUDIED SYSTEM

Figure 1 shows the studied system. On the top of the figure, we can see a sketch of the combustion system with a combustion chamber and a heat exchanger, the air pre-heater. The burned gases transfer thermal energy to the Ericsson reciprocating engine through a heat exchanger called "heater". This Joule cycle [1] engine is located on the low part of the figure.

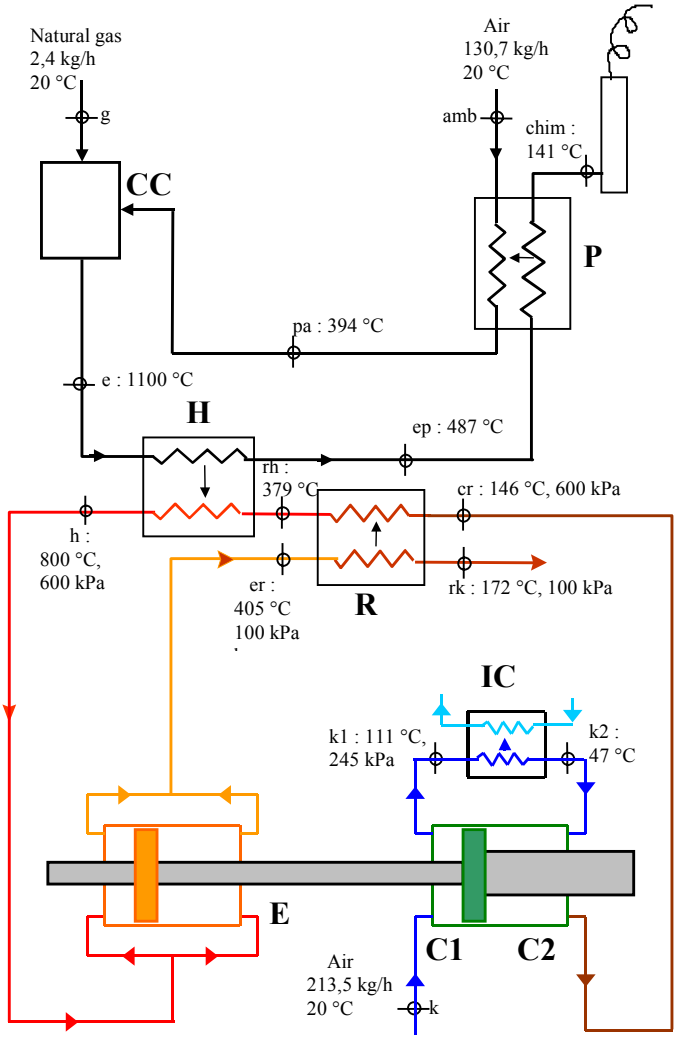

Figure 1: Energy system main features

There are several possibilities for the choice of the working fluid and for the layout of the engine. For instance, hydrogen or helium can be used as working fluid.
This naturally leads to high pressure, compact, engines, requiring a quite high level of technology. This is the usual choice for most Stirling micro-cogeneration systems developed up to now. However, for micro-cogeneration systems, it is not sure that the low size of the system is a determining factor, especially if reduced size is obtained from a high additional cost. We prefer a low-pressure system with air as the working fluid. In this case, we can use an open cycle. The engine is composed of 5 working spaces that we can easily locate on Figure 1: the heater, the recuperator, the inter-cooler, which are heat exchangers, and the expander space *E* and the compression spaces *C1* and *C2*. The engine operating principle is rather simple. Air is allowed at atmospheric temperature and atmospheric pressure and then, it is compressed. The compression is realized into 2 stages with water inter-cooling. Then, air goes through the recuperator where it recovers energy before going through the heater. There, it recovers the energy of the combustion gases before being expanded in the expansion cylinder. On the other hand, the expansion is realized in one stage in 2 parallel expanders without reheating. In the compression and expansion spaces, we have double-acting pistons.

ENERGY ANALYSIS

Modeling

A model is developed in order to obtain a suitable design for the cylinders and the heat exchangers. At this point of the study, the model used is not a dynamic model, but a 0-D global model whose variables are time-independent [1]. In order to study the energetic system under consideration, several quantities are assumed as inlet data. These are:

- The fuel mass flow rate; we consider natural gas with $\dot{m}_g = 0.67\ 10^{-3}$ kg/s.
- The combustion gas temperature at the outlet of the combustion chamber, and the inlet of the heater; we assume T_e = 1100 °C, in accordance with steel whose cost and machining is affordable.
- The compressed air temperature T_h in the engine is also limited for technological reasons of material thermal and mechanical resistance; we assume T_h = 800 °C; the energetic performance of the system obviously deeply depends on this temperature so that a detailed technical-economic study would be necessary to assess this value.
- The minimum working fluid pressure is the atmospheric pressure since the cycle is open; the maximum air pressure is set to $p_{cr} = 6.10^5$ Pa; it is well known that the cycle efficiency slowly decreases as the pressure ratio increases if the recuperator effectiveness is equal to 1 [2, p.538]; if the recuperator effectiveness is lower than 1, there is an optimum pressure that maximizes the power plant thermal efficiency [3, p.636]; for higher pressure values the efficiency decrease is quite slow; however we aim to maximize the global efficiency, not the thermal efficiency. The global efficiency depends also on the mechanical efficiency, which in turn depends on the pressure levels in the engine. Considering all this, our simulation results show that, from a pressure $p_{cr} = 6.10^5$ Pa, the power plant performance does nearly not vary when the pressure ratio increases.
- We set the heat exchanger effectiveness to the following values: E_P = 0.8, E_H =0.85, E_R = 0.9 and E_{IC} = 0.7 respectively for the combustion air pre-heater, the heater, the recuperator and the compressor inter-cooler; these are quite high values for gas/gas heat exchangers, but this high effectiveness of the exchangers is needed in order to obtain a high efficiency of the micro-cogeneration plant. It has been checked out that the chosen effectiveness values for the heat exchangers correspond to the best suitable heat exchangers transfer areas in the system [4].

In order to study the energetic system, the following assumptions are made:

- The combustion gases, the combustion air and the working fluid air are assumed to obey the ideal gas law; the specific heat of these gases is a polynomial function of temperature [5]; the combustion gases composition is computed from the composition of natural gas

and the computed excess air factor assuming a complete combustion;

- The pressure variations are realized in reciprocating piston/cylinder machines [6]; so the compression and the expansion are assumed to be isentropic in the cylinders; however the actual pressure ratio in the cylinders is different from the p_{cr} / p_k due to pressure losses trough the valves;
- Pressure losses trough the inlet and exhaust valves of the cylinders are modeled by

$$\Delta p = \xi \, \rho \frac{c^2}{2} \qquad (1)$$

The working air is assumed to obey the ideal gas law. This yields:

$$\frac{\Delta p}{p} \frac{T}{T_k} = \frac{\xi}{r} \frac{v^2}{T_k} \frac{v^2}{2} = \psi \qquad (2)$$

We consider that the valves around the cylinders can be designed so that the pressure loss factor ψ is the same for each valve and we assume ψ = 0.03; it should be noted that the performance of the system deeply depends on this value.

- A counter-flow shell and tube design is considered for all heat exchangers, the combustion gases (heater, pre-heater) and the low pressure air (recuperator) flowing out of the tubes; thermophysical properties of the fluids are computed at the mean temperature between the inlet and the outlet of the heat exchanger. The dynamic viscosity and thermal conductivity of the combustion gases are assumed to be the same of the ones of air. They are computed as a function of the mean temperature from a Sutherland relationship [7]. Heat transfer coefficients inside and outside the tubes are computed by the Gnielinski correlation [8] for clean pipes. In order to design the heat exchangers, we fix the maximal velocity of the fluid in the tubes and in the shell and we fix the tubes diameter for each heat exchanger.
- Mechanical losses are quite difficult to evaluate as the models developed for internal combustion engines are not appropriate. We consider a separate mechanical efficiency for the expansion and the compression cylinders. The net shaft power is then obtain from:

$$\left|\dot{W}_{net}\right| = \eta_{mec,E} \left|\dot{W}_E\right| - \frac{\dot{W}_C}{\eta_{mec,C}} \qquad (3)$$

In this relation we assume that both compression and expansion mechanical efficiencies are equal to 0.9. It is worth noting that the performance of the power plant deeply depends on this value.

- The cylinder volumes are computed from the working fluid mass flow rate and from the engine rotational speed. For technological reasons, and for mechanical efficiency, we choose a low speed, *i.e.* 1000 rpm. This leads to high cylinder capacities. The number of cylinders is determined by limiting the mean linear piston velocity to 8 m/s.
- The net power delivered by the engine is the shaft power. The electromechanical efficiency of the electric generator and the power consumption of the auxiliary pumps, ventilators, … are not taken into account. They are masked by the uncertainty on the mechanical efficiency.

Configuration chosen

The thermodynamic characteristics of the cycle are given in Figure 1. The energetic performances are reported in Tables 1 to 3. The net efficiency takes into account only the net shaft power, whereas the global efficiency (first principle) also takes into account the heat of the working air at the exhaust of the engine (state *rk*, Figure 1). Indeed the clean, dry, hot air at the exit of the engine can be directly used for heating purposes. The heat evacuated from the inter-cooler by the cooling water is also included in the net efficiency. The whole heat at the chimney (state *chim.*) is assumed to be lost.

	$\dot{Q}$ [kW]
fuel (high calor. value) (*g*)	36.2
heater (*H*)	27.8
engine exhaust (*ck*)	9.2
inter-cooler. (*IC*)	3.8
chimney (*chim*)	8.4

Table 1: Thermal powers

	$\dot{W}$ [kW]
indicated	14.7
net	10.8

Table 2: Mechanical powers

	η
ind	0.529
mec	0.736
net (high cal. val.)	0.299
global 1st principle	0.657

Table 3: Efficiencies

The dimensional characteristics are given in Tables 4 and 5. Even if the technological choices lead to a large engine and the shell-and-tubes heat exchanger configuration is not the best suitable for compactness, it can be seen that the total size of the micro-cogen power plant is acceptable, since the whole power plant can be installed on a floor area of less than 1 m^2.

	C_1	C_2	E
	[mm]	[mm]	[mm]
bore	136	91	207
stroke	207	207	207

Table 4: Cylinders

	Ø shell	Ø tubes	nbr tubes	tubes length
	[mm] int/ext	[mm] int/ext	[-]	[m]
pre-heater P	90/100	10/12	33	3.9
heater H	90/100	7/10	54	3.4
recuperator R	100/110	4/6	126	5.9

Table 5: Heat exchangers dimensional characteristics

EXERGY ANALYSIS

Exergy definition

The exergy concept was developed in order to propose a method of analysis taking the first two principles of thermodynamics into account. Exergy is defined as the maximal quantity of work that one can extract from a system, when it goes from its initial state to a state of equilibrium, if this process is made by interactions with the ambient environment. This maximal theoretical work is obtained during a completely reversible evolution towards the state of equilibrium with the environment reference state [2-3, 9-12]. In the absence of nuclear interactions, electromagnetic interactions, or surface tension interactions, the total exergy results from the sum of the physical exergy, the chemical exergy and the mechanical exergy (kinetic and potential exergy). In our study, the kinetic and potential exergies of the various flows can be neglected. The physical exergy is defined as follows:

$$ex^{ph} = (h - h_0) - T_0(s - s_0) \qquad (4)$$

The chemical exergy is defined by:

$$\overline{ex}^{ch} = \sum x_k \, \overline{ex}^{ch}_{0,k} + \overline{R}\, T_0 \sum x_k \ln x_k \qquad (5)$$

Calculation of exergy transfer rates and exergy efficiencies

The values of exergy transfer rates are calculated from Eqs (4) and (5), and from the results of the energy analysis. Table 6 shows these results. The designation of the streams is defined by reference to the states in Figure 1.

Stream	T	p	$\dot{m}$	$\dot{E}x$
	[K]	[10^5 Pa]	[kg/h]	[W]
g	293	1	2.4	33789
e	1373	1	133.1	27996
ep	760	1	133.1	8184
chim	414	1	133.1	1356
amb	293	1	130.7	94
pa	667	1	130.7	5052
k	293	1	213.5	3
k1	384	2.45	213.5	5196
k2	320	2.45	213.5	4615
cr	419	6	213.5	10310
rh	652	6	213.5	16617
h	1073	6	213.5	34628
er	678	1	213.5	8391
rk	445	1	213.5	1665

Table 6: Exergy transfer rates

For each component of the system, we can determine the exergetic efficiency and the exergy destruction in this component. The definition of the component exergetic efficiency depends on the function of the component. For example, if we consider the heater, its function is to heat air in the engine. Therefore, its exergetic efficiency can be defined as the ratio of the difference of exergy transfer rates

between the cold stream outlet and inlet of the heater, on the difference of exergy transfer rates between the hot stream inlet and outlet of the heater:

$$\eta_H = \frac{\dot{E}x_h - \dot{E}x_{rh}}{\dot{E}x_e - \dot{E}x_{ep}} \quad (6)$$

The heat rejected by the inter-cooler IC and by the exhaust air stream *rk* is assumed to be useful. If the exergy destructions related to the transfer of these thermal energies re not taken into account, the exergetic efficiency of the global system can be defined by the relation:

$$\eta = \frac{\dot{W} + \dot{E}x_{rk} + \dot{E}x_{k1} - \dot{E}x_{k2}}{\dot{E}x_g + \dot{E}x_{amb} + \dot{E}x_k} \quad (7)$$

Assuming no exergy losses in the components of the system under consideration, the rate of exergy destruction is obtained by the difference of the exergy transfer rates of the streams flowing in the component considered and the sum of exergy transfer rates of the streams flowing out of the component considered plus the time rate of energy transfer by mechanical work. For the heater, we obtain:

$$\dot{E}x_H^D = \dot{E}x_e + \dot{E}x_{rh} - \dot{E}x_h - \dot{E}x_{ep} \quad (8)$$

Table 7 shows the results.

Component	Exergetic efficiency	Rate of exergy destruction
	[%]	[W]
combustion chamber CC	71.2	10845
pre-heater P	72.6	1869
heater H	90.9	1801
recuperator R	93.8	420
compr. C1/C2	95.2 / 90.1	544
compression mech. system	90.0	1270
expander	99.6	107
expansion mech. system	90.0	2613
global system	38.5	19469

Table 7: Exergy efficiencies and exergy destructions

In order to visualize the rates of exergy transfer and exergy destruction, we draw the exergy GRASSMANN diagram (Figure 2).

We notice on this figure that the combustion chamber is the main source of exergy destruction. Indeed, the rate of exergy destruction in the combustion chamber amounts to 10.8 kW, that is the same value as the useful mechanical power produced by the engine. The heater and the mechanical systems of compression and expansion, each of them with an exergetic component efficiency of about 90 %, are also responsible for high rates of exergy destruction. But mostly, we can also see that the air pre-heater causes an important rate of exergy destruction in comparison with the exergy rates flowing trough this component. That explains its low exergetic efficiency.

EXERGO-ECONOMIC ANALYSIS OF THE SYSTEM

The exergo-economic analysis allows us to establish a cost balance for each element of the system, in order to determine the monetary value of the kilowatt of produced power and the exergy costs of the various streams *i*.
Assuming as previously that all components are adiabatic (no heat transfer to the environment or to other components, that is no exergy losses), this equation will be as follows [10]:

$$\dot{Z}_k + \left(\sum_i c_i \, \dot{E}x_i \right)_{in,k} = \left(\sum_i c_i \, \dot{E}x_i \right)_{out,k} + c_W \, \dot{W} \quad (9)$$

In Eq. (9), $\dot{Z}_k$ denotes the non-exergy-related cost rate associated with component *k*. It results from the cost rates associated to capital investment and operating and maintenance. For each component, $\dot{Z}_k$ would be known from a previous economic evaluation. The plant under consideration is made up of ten components *k*, namely the air pre-heater P, the combustion chamber CC, the compression spaces C1 and C2, the inter-cooler IC, the recuperator R, the heater H, and the mechanical compression and expansion devices. A linear system of 10 equations with 10 unknown factors, c_i and c_W, the costs per unit exergy of stream *i* or work, has thus to be solved.
To determine these costs, the cost of each component should have been assessed first. For the heat exchangers, we know the raw material cost (shell, tubes, ...), from pipe suppliers list prices, and we multiply this cost by an arbitrary

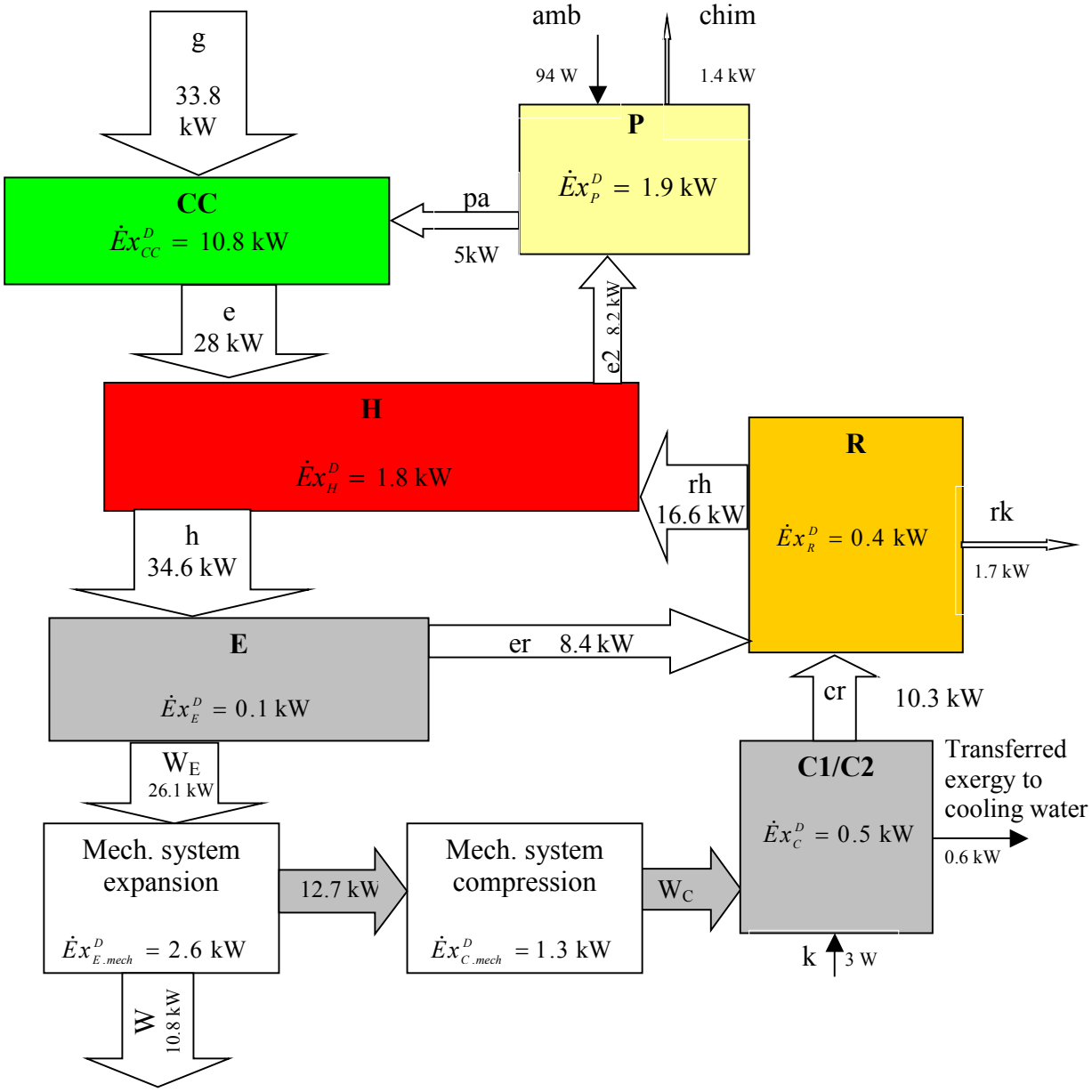

Figure 2: Rates of exergy transfer and exergy destruction

factor to take all costs into account, including heat exchanger manufacturing cost,... In our case, we multiply the raw material cost by 3. On the other hand, for the other components, we use an empirical relation such as:

$$P(X) = P(X)_{known} \left(\frac{X}{X_{known}} \right)^{\alpha} \qquad (10)$$

where $P(X)$ is the searched price of the device of characteristic value X; the couple (X_{known}, $P(X)_{known}$) and the value of the exponent α are evaluated from data taken from [10].

As soon as the price is determined, it is converted into price per unit time, knowing that we take into account a 10 years useful life for each component with 8000 operating hours by year. Table 8 shows the costs of the different exergy streams. The first line indicates the cost of the gaseous fuel, used as input data. The last line gives the cost of one kilowatt-hour of electric energy production. Each kilowatt-hour of electric energy production is accompanied by a (free) production of 1.2 kWh of recoverable thermal energy for heating or sanitary hot water

purposes. If we compare the value of 0.13 € with the domestic prices given by the French electric operator EDF (≈ 0.10 €/kWh of electric energy) and by the French natural gas supplier GDF (≈ 0.03 €/kWh of thermal energy), we notice that these values are close and therefore, the studied system could be profitable. However, the cost of the different component of this micro-cogeneration system should be known more exactly to refine these results.

Exergy stream	Cost [€ / kWh]
c_g	0.03
c_{pa}	0.09
c_e	0.05
c_{k1}	0.16
c_{k2}	0.20
c_{cr}	0.17
c_{rh}	0.17
c_h	0.11
c_{Wc}	0.15
c_{We}	0.12
c_W	0.13

Table 8: Cost of the different exergy streams

CONCLUSION

This communication presents the results of the energy study, the exergy study and the exergo-economic study of a micro-cogeneration system based on an ERICSSON engine. The exergy study allows to draw the GRASSMANN diagram and to observe the exergy streams and the exergy destructions in the system. Finally, the exergo-economic study allows to calculate the cost of the heat and of the electricity produced and to conclude to the possible profitability of the system by comparison with the prices given by the French energy suppliers.

It should be emphasized that the assumptions used in this work are quite severe and conservative. For instance, the assumed mechanical efficiency is low, the valve pressure losses are quite high, the amount of heat rejected at the chimney is important. Nevertheless, the modeled system proves to be interesting. The main issue of this work is to put a new light on an old, but cheap, simple, and efficient technology and to draw the attention on Ericsson engines, unfairly not yet brought out of oblivion.

REFERENCES

[1] Bonnet S., Alaphilippe M., Stouffs P., *Study of a small Ericsson engine for household micro-cogeneration*, Proceedings of the International Stirling Forum 2004, Osnabrück, 8p., 2004.

[2] Van Wylen G.J. Sonntag, R.E., Desrochers P., *Thermodynamique Appliquée*, Ed. du Renouveau Pédagogique, Ottawa, 1992.

[3] Borel L., *Thermodynamique et Energétique*, Vol.1, Presses Polytech. Romandes, Lausanne, 1991.

[4] Bonnet S., Alaphilippe M., Stouffs P., *Distribution of the heat transfer areas in a micro-cogeneration system based on an Ericsson engine : a case study,* in: Heat Transfer in Components and Systems for Sustainable Energy Technologies, Proceedings of the Heat SET 2005 Conference, 5-7 April 2005, Grenoble, France, accepted.

[5] Sandler S.I., *Chemical and Engineering Thermodynamics*, John Wiley and Sons, NY, 1989.

[6] Stouffs P., Tazerout M., Wauters P., *Thermodynamic analysis of reciprocating compressors*, Int. J. Therm. Sci., Vol. 40, N° 1, p. 52-66, 2001.

[7] Organ A.J., *The regenerator and the Stirling engine*, Mechanical Engineering Publications, London, 1997.

[8] Gnielinski V., *Forced convection in ducts*, Heat Exchanger Design, Vol. 2, 1987.

[9] Abdallah H., *Analyse énergétique, exergétique et économique des cycles de turbines à combustion*, PhD Thesis, Université de Nantes, France, 1998.

[10] Bejan A., Tsatsaronis G., Moran M., *Thermal, design and optimization*, John Wiley & Sons, New-York, 1996.

[11] Göran Wall, *Exergetics*, Exergy, ecology, democraty, Mölndal, 1998. See also: `http://www.exergy.se/ftp/exergetics.pdf`

[12] Bejan A., *Entropy generation minimi-zation*, CRC Press, Boca Raton, FL, 1995.

Proceedings of ECOS 2005
Trondheim, Norway
June 20–22, 2005

DESIGN OPTIMISATION OF THE CONDENSER IN VAPOUR COMPRESSION HEAT PUMPS BY THERMOECONOMIC ANALYSIS

Francesco Calise and Massimo Dentice d'Accadia[1]
DETEC - Università degli Studi di Napoli Federico II - P. le Tecchio 80 - 80125 Napoli, Italy
Phone: +39 081 7682299 - Fax: +39 081 2390364 - e-mail: dentice@unina.it

Laura Vanoli
DSA - Università degli Studi di Napoli Federico II – Via Università, 100 – Portici (NA), Italy
Phone: +39 081 2539332 - Fax: +39 081 2539407- e-mail: laura.vanoli@unina.it

ABSTRACT

In the paper, the design optimisation of a heat exchanger is discussed. The investigation is referred to the tube-in-tube condenser of an electric vapour-compression heat pump, with a two-phase refrigerant flowing in the inner tube and the water to be heated flowing in the annulus.
In order to include in the analysis economic aspects, a cost function to be minimised is introduced, defined as the sum of two contributions: i) the amortisation cost of the condenser, related to the heat exchange area; ii) the operating cost of the electric-driven heat pump in which the heat exchanger will work, depending on the overall exergy destruction rate in the system. In the paper, this latter contribution is related to the local irreversibility rate in the condenser, using the so-called structural approach.
The optimal trade-off between amortisation and operating cost is therefore investigated, by minimising the above-mentioned cost function.
A numerical example is discussed, in which, for a commercial heat exchanger, the design improvements needed to obtain a cost-optimal configuration are investigated. The analysis is carried out for two different refrigerants: R134a and-R410A.

Keywords: Exergy, Irreversibility, Cost-function, Condensation, Heat Pump.

NOMENCLATURE

A	heat exchange area, m^2
c_F	unit cost of electric energy, € kWh^{-1}
CSB	coefficient of structural bond
D	diameter, m
F	fuel, W
h	enthalpy, kJ kg^{-1}
I	exergy destruction rate, W
$\dot{m}$	mass flow rate, kg s^{-1}
P	product, W
s	specific entropy, J kg^{-1} K^{-1}
$\dot{Q}$	heat transfer rate, W
$\dot{S}_{gen}$	entropy generation rate, W K^{-1}
T	temperature, K
U	overall thermal conductance per unit area, W m^{-2} K^{-1}
UA	overall thermal conductance, W K^{-1}
y	design variable
Z	cost, €

Subscripts

in	inlet
lm	logarithmic mean
out	outlet
r	refrigerant
sat	saturation
tot	total
w	water
in	inner
i	device index
k	variable index
o	reference value

Superscripts

=	matrix
–	mean value

Greek symbols

α	mean heat-transfer coefficient, W m^{-2} K^{-1}
Δ	difference
ε	thickness, m
ζ	amortisation factor, $years^{-1}$

[1] Author for correspondence

λ thermal conductivity, W m $^{-1}$K $^{-1}$
Π total cost, € year $^{-1}$
τ operation time, h years $^{-1}$
ξ coefficient of external cost, € W $^{-1}$

1. INTRODUCTION

The optimisation of heat exchangers, also including evaporators and condensers of refrigeration and heat pump systems, has been widely studied in recent years. Different approaches were proposed, such as Entropy Generation Minimisation, Lyfe Cycle Analysis and Exergoeconomic or Thermoeconomic Analysis [1 - 7].
In this paper, the problem of determining the optimal trade-off between amortisation and operating costs for the condenser of a vapour-compression heat pump is discussed. Heat exchanger geometry, working fluids and heating capacity were fixed. Namely, the component under study was a tube-in-tube heat exchanger, made-up by two coaxial tubes. The fluid to be heated was water, flowing in the annulus between inner and outer tubes. As for the refrigerant, flowing in the inner tube, the analysis was carried out for two different fluids: R134a and R410A. A heating capacity of 10 kW was assumed.
A cost function to be minimised was introduced, defined as the sum of two contributions: the amortisation cost of the condenser and the operating cost of the electric-driven heat pump in which the component had to work.
For fixed heating capacity and flow arrangement, the amortisation cost related to the condenser was assumed to depend on the heat exchange area.
As for the operating cost, it was necessary to evaluate the influence of condenser design on the electric energy consumption of the heat pump in which it had to operate. For this scope, two different approaches are possible, depending on the hypothesis of the study. When the condenser is designed for a specific heat pump, a detailed simulation is possible for the system, allowing the designer to take into account the mutual interactions among all plant components.
However, this is not possible when the specific model of compressor, evaporator and expansion device to be matched with the condenser are not known at the moment in which it is designed. This is the hypothesis assumed in the paper.
In this case, the optimisation must be performed by isolating the device from the rest of the system. However, the influence of the condenser performance on that of the remaining components must be taken into account: this is possible using the so-called structural approach, in which an approximate correlation is assumed between the local exergy destruction rate in a given component and that of the system as a whole [8].
Two design variables were considered in the optimisation: the saturation temperature of the refrigerant, T_{sat}, and the internal diameter of the inner tube, D_{in}. These variables directly affect the heat exchange area, A, and the exergy destruction rate in the condenser, I. On their turn, A and I directly affect the cost function to be minimised, as previously mentioned. The annulus outer diameter, D_{out}, was kept constant, so that the external size of the heat exchanger, in radial direction, was fixed. Obviously, in general, this parameter could be a further decision variable, affecting the design analysis and optimization of the condenser.
In the following sections, the fundamentals of the structural method for thermoeconomic optimisation are shortly reminded. Then, a numerical example is developed, in which, for a fixed heating capacity of the condenser, optimum design conditions are investigated for two different refrigerants.

2. THE STRUCTURAL METHOD FOR THERMOECONOMIC OPTIMISATION

In this section, the method for structural thermoeconomic optimisation is shortly resumed [8].

For a given thermal system, the overall exergy destruction rate, I_{tot}, can be calculated as:

$$I_{tot}(\bar{\bar{y}}) = F_{tot}(\bar{\bar{y}}) - P_{tot} \quad (1)$$

where P_{tot} is the exergy flow rate representing the product of the process, F_{tot} is the external resource, or Fuel, consumed by the system, and $\bar{\bar{y}}$ is the matrix of all design variables affecting the performance of the system, whose component $y_{i,k}$ represents the k-th variable directly affecting the performance of device i. In the case under study, for example, the product

P_{tot} was represented by the increase of the physical exergy of the fluid to be heated in the condenser, and F_{tot} by the electric power required to driving the compressor.
If maintenance and other accessory costs are neglected, the economic cost of owning and operating the plant can be expressed as follows:

$$\Pi_{tot}(\bar{\bar{y}}) = c_F F_{tot}(\bar{\bar{y}})\tau + \zeta \sum_k Z_k(\bar{y}_k) \quad (2)$$

In eqn. (2), c_F is the cost per unit exergy of the Fuel, that is, in our case, the unit cost of the electric energy used by the heat pump, τ is the equivalent time of full-load operation planned for the system, on a yearly base, ζ is the amortisation factor and Z_k represents the cost of the generic k-th component.
In order to determine the optimal condition with respect to a fixed design variable, say $y_{i,k}$, when holding fixed all the others, the following condition can be obtained by differentiating eqn. (2):

$$\partial \prod_{tot} / \partial y_{i,k} = c_F \left(\partial F_{tot} / \partial y_{i,k}\right)\tau + \zeta \sum_i \left(\partial Z_i / \partial y_{i,k}\right) = 0 \quad (3)$$

This condition identifies a minimum or a maximum value, depending on the sign of the second order derivative.

Assuming a constant overall product, we have:

$$\Delta I_{tot} = \Delta F_{tot} \quad (4)$$

and differentiating with respect to the design variable to be optimised:

$$\partial I_{tot} / \partial y_{i,k} = \partial F_{tot} / \partial y_{i,k} \quad (5)$$

Combining equations (3) and (5) the optimum condition can be expressed as:

$$\partial \prod_{tot} / \partial y_{i,k} = CSB_{i,k}\ c_F \left(\partial I_k / \partial y_{i,k}\right)\ \tau + \zeta \sum_i \left(\partial Z_i / \partial y_{i,k}\right) = 0 \quad (6)$$

in which the coefficient of structural bond, $CSB_{i,k}$, has been introduced, defined as [8]:

$$CSB_{i,k} = \left(\partial I_{tot} / \partial y_{i,k}\right) / \left(\partial I_k / \partial y_{i,k}\right) \quad (7)$$

where I_k is the exergy destruction rate in the k-th component of the plant.
This coefficient allows one to establish a correlation between the local irreversibility rate in the k-th component to the overall exergy destruction. In other terms, it provides a measure of the impact of a change in the local performance on that of the system as a whole.
Eqn. (6) can be also expressed as:

$$\partial \prod_{tot} / \partial y_{i,k} = CSB_{i,k} c_F \left(\partial I_k / \partial y_{i,k}\right)\ \tau + \zeta \left(\partial Z_k / \partial y_{i,k}\right)\ +\ \xi_{i,k}\ (\partial I_k / \partial y_{i,k}) = 0 \quad (8)$$

In eqn. (8) the contribution due to the k-th component directly influenced by variable $y_{i,k}$ has been separated by those referred to the other components and the coefficient of external costs has been introduced:

$$\xi_{i,k} = \sum_{i \neq k} \partial Z_i / \partial I_k \quad (9)$$

The value of coefficient $\xi_{i,k}$ is negligible when the variation of $y_{i,k}$ does not influence significantly the cost of components different from the k-th. This may also happen, for example, when these latter components are available in standard sizes and the variation of the design variable $y_{i,k}$ is not sufficient to induce size variations in other components. If the coefficient $\xi_{i,k}$ can be settled to zero, the following final expressions for optimum conditions can be written:

$$\partial \Pi_{tot} / \partial y_{i,k} \ = \ CSB_{i,k} c_F \left(\partial I_k / \partial y_{i,k}\right)\tau + \zeta \left(\partial Z_k / \partial y_{i,k}\right)\ = 0 \quad (10a)$$

$$\partial^2 \Pi_{tot} / \partial y_{i,k}{}^2 > 0 \quad (10b)$$

By solving eqn. (10a), and controlling that eqn. (10b) is satisfied, the value of the design variable $y_{i,k}$ that minimise the overall cost Π_{tot} can be found.

3. CASE STUDY: PROBLEM DEFINITION

The methodology described in the previous section was applied to a commercial tube-in-tube heat exchanger to be used as the condenser in a conventional electric-driven vapour-compression heat pump. A schematic view of the condenser is provided in Figure 1. The main features of the heat exchanger are resumed in Table 1.
The following assumptions were used: i) Newtonian non-reacting pure fluids; ii) operation in steady-state conditions; iii) mono-dimensional flow conditions; iv) negligible exergy losses toward the environment.

The heating capacity of the condenser, $\dot{Q}$, was fixed, as well as the inlet and outlet temperatures of water. So, the water mass flow-rate and the

exergy flow rate corresponding to $\dot{Q}$ were practically fixed, too, since the contribution of pressure losses to the enthalpy and entropy variation of liquid water was negligible. This exergy flow rate represented the product of the heat pump under study, P_{tot}.

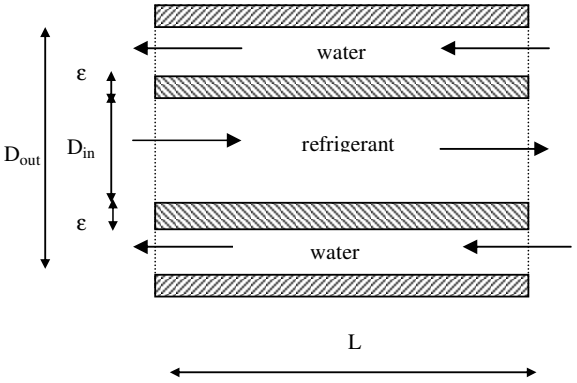

Figure 1. Schematic representation of the condenser analysed

Geometry:	tube-in-tube
Materials:	inner tube: copper
	outer tube: steel
Copper thermal	398 W m^{-1} K^{-1}
Internal diameter, inner	variable from 10 to 20
Thickness, inner tube:	1 mm
Internal diameter, outer	25 mm
Cold fluid (annular	Water
Refrigerant (inner tube):	R134a, R410A
Heating capacity:	10 kW
Water inlet temperature:	40 °C
Water inlet pressure:	1.4 bar
Water outlet temperature:	50 °C
Refrigerant inlet	variable from 55 to 65
Refrigerant inlet quality:	1.0
Refrigerant outlet quality:	0

Table 1. Main features of the condenser under analysis.

In order to focus on the condensation process, de-superheating and sub-cooling were neglected, and therefore the refrigerant was always assumed in two-phase conditions. In other terms, for simplicity, the optimisation procedure was carried out leaving apart the de-superheating and the sub-cooling sections of the heat exchanger.

Referring to eqn. (10a):
- the unit cost of the electric energy required to move the compressor, c_F, was considered as an external parameter, and assumed equal to 0.10 € kWh^{-1} ; however, since this cost may vary sinificantly, depending on the mean electricity rate applied to the end user, the optimisation was also performed for different values of c_F (0.08 and 0.12 € kWh^{-1});
- a reference value of 2.0 was assumed for the *CSB* of the condenser, with respect to both design variables considered (T_{sat} and D_{in}, as discussed below); this reference value was based on the results provided by a simulation programme for conventional heat pump systems (basic configuration, with scroll compressor, tube-in-tube condenser and evaporator and thermostatic expansion valve), in typical operating conditions (evaporation temperature in the range 0 to 5 °C, condensation temperature in the range 55 to 65 °C) [9];
- the coefficient of external cost, $\xi_{i,k}$, was assumed equal to zero;
- the cost of the condenser was expressed as a function of the heat exchange area, measured from the refrigerant side, according to the following equation [10]:

$$Z = Z_o \left(\frac{A}{A_o} \right)^n \qquad (11)$$

where Z_0 = 1500 € and A_0 = 1.0 m^2 are the reference cost and area, respectively, and the exponent n was assumed equal to 0.75 [10];
- an operation time, τ, of 1500 hours per year was assumed;
- finally, a discount rate of 5% and a time horizon of 10 years was assumed, leading to a value of the amortisation factor $\zeta = 0.1295$ $years^{-1}$.

Two independent design variables were considered in the optimisation: i) the saturation temperature of the refrigerant, T_{sat}, at the beginning of the condensation process, directly affecting the heat exchange area; ii) the inner diameter of the inner tube, D_{in}, that also affects the heat exchange area, since both refrigerant and water heat-transfer coefficients depend on it. T_{sat} was assumed to vary in the range from 52 to 65 °C, with a step of 1 °C; D_{in} was assumed to vary in the range from 10 to 20 mm, with a step of 1 mm.

4. CASE STUDY: DESIGN ANALYSIS AND OPTIMISATION

The following procedure was used in the design analysis and optimisation of the condenser.

1) The water mass flow-rate was calculated as the ratio between $\dot{Q}$ and the enthalpy variation; pressure losses, slightly depending on the variables to be optimised, were here neglected.

2) For any value of the initial temperature of the refrigerant, T_{sat}, in the range of interest, the refrigerant mass flow rate was calculated, at first, as the ratio of the condenser heat duty, $\dot{Q}$, to the enthalpy of condensation - at constant pressure - corresponding to that temperature:

$$\dot{m}_r = \dot{Q} / \left(h_{r,in} - h_{r,out}\right) \qquad (12)$$

Since pressure drops induce a slight variation in the difference between inlet and outlet enthalpies, with respect to an ideal condensation at constant pressure, the result provided by eqn. (12) is approximate: so, after calculation of the heat-exchanger length and the corresponding pressure losses for the refrigerant, this mass flow rate was re-calculated, as described in the next point.

3) For any possible set of values of T_{sat} and D_{in}, the heat-exchange area, A, was calculated as follows. First, the overall thermal conductance, UA, was approximately estimated - neglecting all pressure losses - as the ratio of the condenser heating capacity, $\dot{Q}$, to the mean logarithmic temperature difference in the heat exchanger corresponding to the current values of T_{sat} and D_{in}:

$$UA = \dot{Q} / \Delta T_{lm} \qquad (13)$$

Then, the overall length of the condenser, L, was calculated as:

$$L = (\mathrm{UA}) \left[\frac{1}{\alpha_r \pi D_{in}} + \frac{\ln\left(\frac{D_{in} + 2\varepsilon}{D_{in}}\right)}{2\pi\lambda} + \frac{1}{\alpha_w \pi (D_{in} + 2\varepsilon)} \right] \qquad (14)$$

where α_w and α_r are the mean heat-transfer coefficients for water and refrigerant, for the current values of T_{sat}, D_{in} and mass flow rates.

The estimation of mean heat-transfer coefficients was based on the correlations available in the literature. In particular, the model recently proposed by Cavallini et al. [11] for horizontal smooth tubes was used for the two-phase flow: for any value of vapour quality in the range 0 to 1, the local heat-transfer coefficient is calculated with different correlations, depending on the local flow regime (annular, transition, stratified and slug flows). Finally, the arithmetic mean value of the local coefficients is calculated. Classical correlations were used for the single-phase flow in the annular section of the condenser [12].

As for pressure losses, they were obtained multiplying the L value by the mean pressure gradient. For the refrigerant, this latter was evaluated using the correlation proposed by Koyama et al. [13], especially suited for the refrigerants under analysis. For the cold fluid, classical correlations for single-phase flow in annular section were used [12].

An automatic control was introduced in the procedure in order to reject possible geometries characterized by unacceptable pressure losses: a maximum value of 60 kPa was fixed for both cold and hot sides of the condenser, in optimum conditions.

The physical properties needed for the analysis were obtained through tables available in the literature, for the water [14], and the REFPROP software, for the refrigerants [15].

4) At this point, the refrigerant mass flow-rate was re-calculated through eqn. (12), using the actual enthalpy variation between inlet and outlet of the condenser, and all calculations were iterated until satisfactory convergence was attained (difference between new and previous value of $\dot{m}_r$ less than 0.1%).

5) Finally, the heat-exchange area - refrigerant side - corresponding to the given set of T_{sat} and D_{in} values was obtained as:

$$A = \pi D_{in} L \qquad (15)$$

6) The entropy generation rate in the condenser, corresponding to the given values of T_{sat} and D_{in}, was calculated from the entropy balance, as:

$$\dot{S}_{gen} = \dot{m}_w \times \left(s_{w,out} - s_{w,in}\right) - \dot{m}_r \times \left(s_{r,in} - s_{r,out}\right) \qquad (16)$$

7) The exergy destruction rate in the condenser was evaluated as [8]:

$$I = T_0 \dot{S}_{gen} \qquad (17)$$

The ambient temperature, T_0, was settled to 280 K.

8) Once the heat-exchange area, A, and the exergy destruction rate in the condenser, I, were evaluated for any possible couple of T_{sat} and D_{in} values, each term of eqn. (10a) was expressed as a continuous and derivable function of each of these two variables, by regression of the data previously obtained. To this scope, for both dependent variables A and I, a regression with a polynomial of the third order, performed with respect to T_{sat} for fixed D_{in} and vice-versa, was always sufficient to reach a value of the coefficient of determination, R^2, greater than 0,999.

The functions $A = A(T_{sat}, D_{in})$ and $I = I(T_{sat}, D_{in})$ are graphically represented in Figures from 2 to 5. In particular, Figures 2 and 3 respectively show the values of the heat-exchange area and the corresponding exergy destruction rate, as a function of the saturation temperature T_{sat} and the inner diameter D_{in}, for the refrigerant R134a. In Figures 4 and 5, the same quantities are shown for R410A. Obviously, in any case, when the initial saturation temperature rises, the heat exchange area always decreases (Figures 2 and 4). On the contrary, the corresponding exergy destruction rate, mainly due to heat transfer irreversibility, always increases with T_{sat} (Figures 3 and 5). For any given couple of T_{sat} and D_{in} values, the heat exchange area was minimum for R134a.

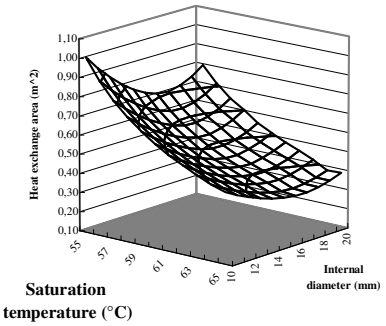

Figure 2. Heat exchange area vs. saturation temperature and internal diameter of the inner tube. Working fluid: R134a.

It is interesting to observe that, for both refrigerants, and for any fixed value of T_{sat}, both heat exchange area, A, and exergy destruction rate, I, have a minimum for a D_{in} value always ranging between 15 and 16 mm.

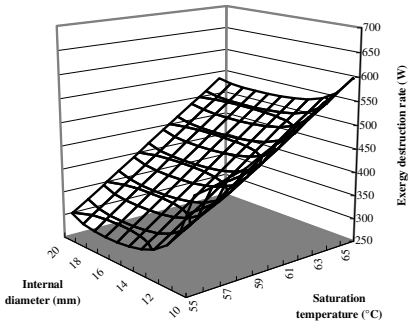

Figure 3. Eergy destruction rate vs. saturation temperature and internal diameter of the inner tube. Working fluid: R134a**.**

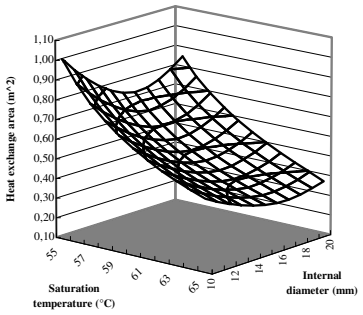

Figure 4. Heat exchange area as a function of saturation temperature and internal diameter of the inner tube. Working fluid: R410A.

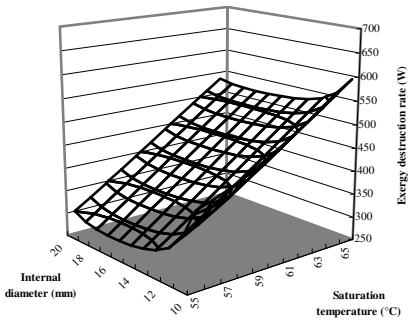

Figure 5. Exergy destruction rate vs. saturation temperature and internal diameter of the inner tube. Working fluid: R410A.

Obviously, these values are not casual. In the case of A, they correspond to the maximum of the overall thermal conductance per unit area, U, compatible with the values fixed for the external diameter of the condenser, D_{out}, and for the mass flow rates of the fluids.
With regard to I, the following comment can be made. For a given saturation temperature, the overall exergy destruction due to heat transfer is practically fixed, too: in fact, also the heat flow rate and the temperature of water are fixed. However, the contribution due to pressure losses still depends on D_{in}, and the minimum of I corresponds to the optimal distribution of the frictional irreversibility between cold and hot fluids. The dependence of I on D_{in} at constant T_{sat} is strong in the range from 10 to 13 mm, when the pressure losses for the two-phase flow are significant; the slope of the curves becomes very small in the range from 14 to 20 mm, when the contribution of the frictional losses to the overall irreversibility becomes very modest (from 2 to 6%).
In the case under study, the correlation between pressure losses and heat transfer coefficients are such that the minimum values of A and I are reached for values of D_{in} falling in a very small range.
Once the functional relationships $A= A(T_{sat}, D_{in})$ and $I= I(T_{sat}, D_{in})$ were obtained, optimum design conditions with respect to T_{sat} for fixed D_{in} - or inversely - could be found by solving eqns. (10). To determine the overall optimum conditions, with respect to both design variables, for a fixed set of all remaining parameters, a simple iterative procedure was followed:
- an initial value of T_{sat} in the range of interest was assigned;
- the corresponding optimum value of the internal diameter was calculated, by solving eqn. (10a) with respect to D_{in} and then verifying that eqn. (10b) was satisfied, too;
- the optimum value of the saturation temperature corresponding to this latter value of D_{in} was calculated by solving eqn. (10a) with respect to T_{sat} and then verifying that eqn. (10b) was satisfied, too;
- the optimum value obtained for T_{sat} was compared with the corresponding initial value and the procedure was iterated until convergence was attained, that is, until initial and calculated values were equal.
In all cases taken into consideration, the convergence of this procedure was practically immediate (less than one second, using a PC equipped with a Pentium III Processor and 256 MB RAM).
The most significant results of the optimisation are discussed in the following.
For any c_F in the range from 0.08 to 0.12 €/kWh, the optimum values of the internal diameter of the inner tube were practically equal to those that minimised A and I, namely optimum D_{in} = 16 mm for both refrigerant fluids.
Not only c_F, but also the remaining parameters CSB, τ, Z_0 and n did not influence the optimum D_{in}, even when varying of ± 20% with respect to the base-case.
As for the optimum values of T_{sat}, and the corresponding values of A and I, the results obtained for different values of the electric energy cost are summarised in Figg. from 6 to 8.
The optimal saturation temperatures (Fig. 6) always decrease with c_F, as expected. The optimum values range from 60 °C to 57 °C for R410A, from 59 °C to 56 °C for R134a.

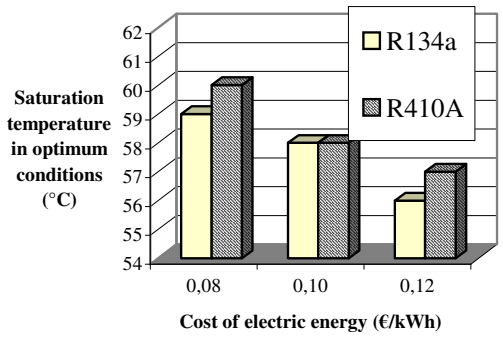

Figure 6. Saturation temperature in optimum conditions, for different values of the electric energy cost.

As a consequence, the heat exchange area required to optimise the thermoeconomic performance of the system increases with c_F (Fig. 7), whereas the corresponding exergy destruction rate decreases (Fig. 8). This irreversibility is mainly due to heat transfer, since, in optimum conditions, the contribution due to friction always ranged between 2 and 3% of the overall value.
So, it may be commented that the higher is the cost of electric energy that the final user has to afford, the greater is the profitability for him of investing money in selecting a condenser with an extended heat-exchange area, therefore

lowering the saturation temperature of the refrigerant: this induces a reduction of the irreversibility in the condenser and in the heat pump, leading to energy and money savings during system operation.

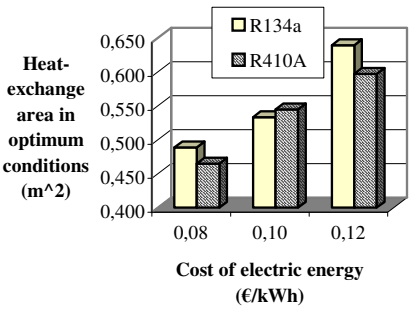

Figure 7. Heat exchange area in optimum conditions, for different values of the electric energy cost.

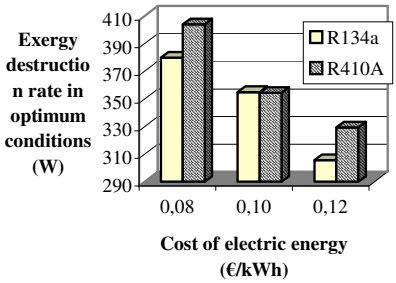

Figure 8. Exergy destruction rate in optimum conditions, for different values of the electric energy cost.

The influence of the working fluid on the optimum design was often remarkable, too, suggesting the importance of strictly relating the design of new condensers to the refrigerant to be used. However, it is useful to emphasize that the analysis presented here cannot be used directly to evaluate or compare the overall thermodynamic or thermoeconomic performance of the fluids: this problem can only be analysed by studying the performance of the overall heat pump system.

It may be also interesting to compare the results of the optimisation with those that would have been obtained by neglecting the structural effect induced by the condenser on the system as a whole (i.e.: assuming for the condenser CSB = 1). It was calculated that, in this case, the "optimum" values of the heat-exchange area would be from 30% to 39% smaller than the actual ones. This result highlights the importance of taking into account the structural effects when optimising single components of thermal systems.

A sensitivity analysis was also performed with respect to some of the independent parameters involved in calculations: Z_0, $CSB_{i,k}$, τ, α_r and c_F, again. As an example, the results obtained for R134a are shown in Fig. 9, referring to the dependent variable A. Diagrams related to the R410a was very similar.

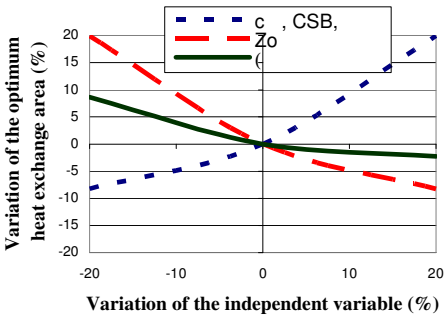

Figure 9. Sensitivity of the optimum heat exchange area to the independent parameters c_F, CSB, τ, Z_0 *and* α_r. Working fluid: R134a.

A unique curve is shown for three parameters: $CSB_{i,k}$, τ, and c_F: in fact, they have the same influence on the optimal values of A, due to the form of eqn. (10a). For example, if the actual CSB were 20% less than the value assumed in the reference case (i.e.: 1.8 instead of 2.0), the optimum heat exchange area would be about 8% smaller than that previously obtained (0.49 m^2 instead of 0.53 m^2).

Obviously, the dependence of the optimum conditions on Z_0 has an opposite sign, with respect to CSB, τ, and c_F: if the reference cost of the heat exchanger rises, the optimal area decreases.

With regard to the heat-transfer coefficient α_r, it can be noted, for example, that the heat exchange area increases if the actual value of α_r is lower than that assumed in the reference case: for instance, a 10% reduction of the heat transfer coefficient for R134a, with respect to the value predicted by correlations, would lead to a difference of about 4% between the optimum value of A calculated in the reference case (0.53 m^2) and the actual one (0.55 m^2).

This latter analysis is of special interest, since actual values of the heat-transfer coefficients can be significantly affected, for example, by the presence of compressor oil. Furthermore, the

correlations available to predict heat-transfer coefficients for two-phase flows are characterised by remarkable uncertainty.

4. CONCLUSIONS

In the paper, the search for the optimum design of a condenser to be used in a conventional vapour-compression heat pump was discussed. In particular, varying the inner tube diameter and the refrigerant saturation temperature, the optimal heat-exchanger area, *A*, was calculated, for a fixed heating capacity of the condenser.
The optimum values obtained for *A* appear greater than those usually adopted in commercial devices, especially for high values of the electric energy cost. In fact, when this latter cost increases, the weight of the irreversibility in the operation cost increases too, whereas the amortisation costs become less important: thus, greater investments, aimed at improving plant efficiency, become more and more advantageous. Although this conclusion could appear obvious, similar considerations are usually neglected, especially when plant designer will not be involved in meeting the expenses of operating the system.
The example presented in the paper should be also intended as a contribution to a wider diffusion of methods for thermoeconomic analysis and optimisation in the field of refrigeration and heat pumps. In this sector, characterised by emerging technologies and by the gradual introduction of new working fluids**,** these methods can be helpful in addressing the design and selection of new equipment, not less than in the field of power plant.
A further development of this study is currently in progress, aiming at including in the analysis environmental aspects, with special attention to those regarding the emissions of greenhouse gases (Total Equivalent Warming Impact).

REFERENCES

1. Aceves-Saborio S, Ranasinghe J, Reistad G M, An Extension to the Irreversibility Minimization Analysis Applied to Heat Exchangers. ASME Journal of Heat Transfer 1989, 111, 29-36.
2. Bejan A, Tsatsaronis G, Moran M. Thermal Design and Optimization. J. Wiley, New York, 1996.
3. Cornelissen RL, Hirs GG. Exergetic Optimisation of a Heat Exchanger. Energy Conversion and Management 1997, 38, 1567-1576.
4. Dentice d'Accadia M, de Rossi F. Thermoeconomic Optimisation of a Refrigeration Plant. Int J Refrigeration 1998, 21, 42-54.
5. Cornelissen RL. Thermodynamic Optimisation of a Heat Exchanger. Int J Heat Mass Transfer 1999, 42, 951-959.
6. Dentice d'Accadia M, Fichera A, Sasso M, Vidiri M. Determining the optimal configuration of a heat exchanger with a two-phase refrigerant through exergonomic approach. Applied Energy, 2002, 71, 191-203.
7. Shah RK, Sekulic DP. Fundamentals of Heat Exchanger Design. J. Wiley, New York, 2003.
8. Kotas TJ. The Exergy method of thermal plant analysis. ISBN 0-89464-941-8, Krieger Publ. C., Florida, 1995.
9. De Rossi F, Mastrullo R, Mazzei P and Sasso M. EASY, Exergetic Analysis of vapour compression SYstems. Liguori Editore, Napoli, Italia, 1999.
10. Bohem, RF. Design Analysis of Thermal Systems. J. Wiley, New york, 1987.
11. Cavallini A, Censi G, Del Col D, Doretti L, Longo GA, Rossetto L, Zilio C. Condensation inside and outside smooth and enhanced tubes - a review of recent research. Int J Refrigeration 2003, 26, 373-392.
12. Hewitt G F. Heat Exchanger Design Handbook. Begell House, New York, 1998.
13. Koyama S, Haraguchi H, Fujii T. Condensation of pure refrigerants inside a horizontal smooth tube. In: Heat transfer in Condensation. Proc. of Eurotherm Seminar 47, oct. 1995, Paris. Marvillet and Vidil Editors, Elsevier, 1995, 132-138.
14. Eckert ERG and Drake RM. Analysis of Heat and Mass Transfer. McGraw-Hill, New York, 1972.
15. McLinden MO, Klein SA, Lemmon EW, Peskins AP. REFPROP 6.01- Thermodynamic properties of refrigerants and refrigerant mixtures database. National Institute of Standards and Technology (NIST), Boulder, CO, 1998.

Proceedings of ECOS 2005
Trondheim, Norway
June 20–22, 2005

EXERGOECONOMIC ANALYSIS OF ABSORPTION SYSTEMS FOR TURBINE AIR INLET COOLING IN TRIGENERATION PLANTS

G. Chiummo, A. Di Nardo, G. Langella*, C. Noviello
Department of Mechanical Engineering and Energetic
University of Naples "Federico II" - ITALY

ABSTRACT

The aim of the work is the analysis of energetic and economic advantage of installing an air cooling system at the inlet of a gas turbine set (compressor – combustor – turbine), in a 5 MW CHP plant. Two different solutions have been compared: the first one is an absorbption chiller fed by heat recovery from the gas turbine, through an heat exchanger; the second one is a traditional cooling system by CFC compression cycle, electrically fed by electrical generator coupled with gas turbine.

Keywords: Cogeneration, trigeneration, air cooling.

NOMENCLATURE

P	power	[kW]
E	energy	[kWh]
T	temperature	[K]
cp	specific heat	[kJ/kg°C]
$\dot{m}$	mass flow	[kg/s]
η	efficiency	
β	compressor ratio	
α	air/fuel ratio	
λ	isoentropic exponent	

Subscrits

t,c	turbine and compressor
a,c,f	air, fuel and exhaust gas
ucr	exit HRSG
e,t,m,ex,pc,p	electrical, thermal, mechanical, exergetic, politropic and primary
0, ml	environment, mean logarithmic
1, 2, 3, 4, ‘	inlet compressor, outlet compressor, inlet turbine, outlet turbine, non isentropic

*Corresponding author: giulange@unina.it

INTRODUCTION

It's well known that electrical output from a gas turbine combined heat and power plant, decreases with environmental temperature increasing, due to the bigger power requested from compressor unit (see Fig.1 below).

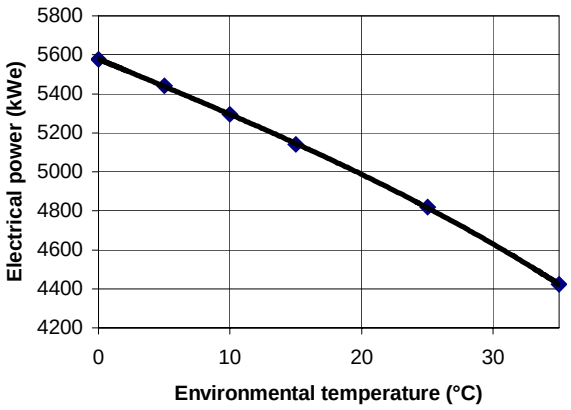

Figure 1: Gas Turbine Electrical power output VS environmental temperature

The relationships regarding the characteristic operating parameters of a gas turbine plant are here analysed. This is to remark the link between these parameters and the environmental temperature, in order to evaluate the benefit of installing an absorbption chiller or a CFC compression one, for inlet air cooling. The first is supposed to be fed by hot water or steam produced by heat recovery which can be performed through an heat exchanger or an heat recovery boiler, taking thermal power from gas turbine flue gas stream. The second option is a traditional chiller working with CFC compression cycle and fed electrically by gas turbine generator itself. Both of them have the task to cool inlet air to the compressor, avoiding electrical power decreasing during worm climate period, especially in summer.

Power output from the plant can be expressed :

$$\boldsymbol{Pe = \eta_e \eta_m \left(Pt - Pc \right)} \tag{1}$$

Mechanical power from the turbine unit and to the compressor unit are respectively:

$$Pt = \dot{m}_f c_p \left(T_3 - T_{4'} \right) = \dot{m}_f c_p T_3 \left(1 - \frac{T_{4'}}{T_3} \right) = \tag{2}$$

$$\dot{m}_f c_p T_3 \left(1 - \frac{1}{\beta^{\lambda \eta_{pt}}} \right)$$

$$Pc = \dot{m}_a c_p \left(T_{2'} - T_1 \right) = \dot{m}_a c_p T_1 \left(\frac{T_{2'}}{T_1} - 1 \right) = \tag{3}$$

$$\dot{m}_a c_p T_1 \left(\beta^{\lambda / \eta pc} - 1 \right)$$

Combining the formula above reported it can be written:

$$Pe = \eta_e \eta_c \begin{pmatrix} \dot{m}_f c_p T_3 \left(1 - \frac{1}{\beta^{\lambda \eta_{pt}}} \right) \\ - \dot{m}_a c_p T_1 \left(\beta^{\lambda / \eta pc} - 1 \right) \end{pmatrix} \tag{4}$$

$$Pe = \eta_e \eta_c \dot{m}_c \begin{pmatrix} (1+\alpha) c_p T_3 \left(1 - \frac{1}{\beta^{\lambda \eta_{pt}}} \right) - \\ \alpha c_p T_1 \left(\beta^{\lambda / \eta pc} - 1 \right) \end{pmatrix} \tag{5}$$

Last formula highlights the relationship among electrical power output, environmental temperature, turbine inlet and outlet temperature, air and fuel rates.
The maximum available heat recovery from flue gas is:

$$\boldsymbol{\dot{Q} = \dot{m}_{gas} c_p \left(T_{4'} - T_{ucr} \right)} \tag{6}$$

where specific heat values are averaged in temperature ranges considered.
From technical data of an existing 5 MW gas turbine CHP gas plant it has been possible to plot by interpolation the diagrams above reported, which represent the electrical power output, the flue gas rate and the T4' temperature vs environmental temperature (see figg. 1,2,3).

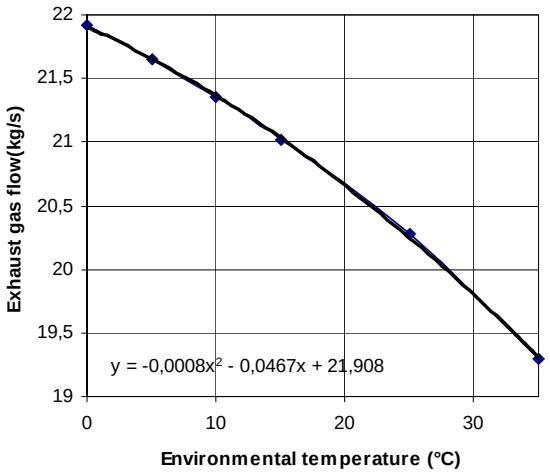

Figure 2: Turbine data.

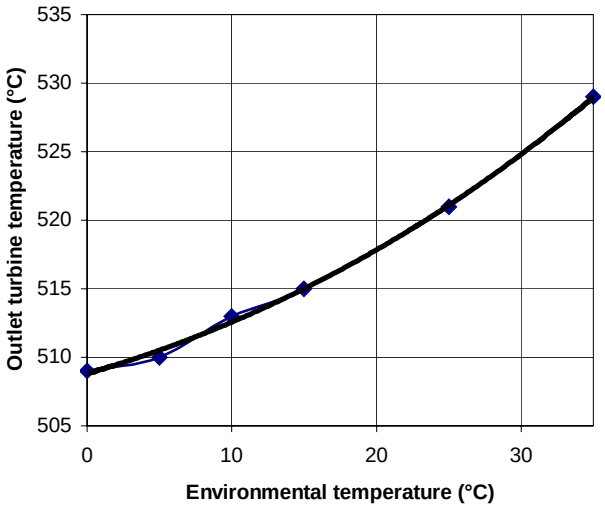

Figure 3: Turbine data.

OPTIONS ANALYSIS

The analysis regards the evaluation of technical and economical advantage coming from the installation of an absorbption cooling system or a CFC one, in order to cool inlet air to the compressor unit in a 5 MWe cogeneration plant. In both cases air temperature after cooling is set on 10 °C or more, so not very hard cooling are considered: that's to avoid turbine surcharge, but also because the temperature of available cool water is in the range 7-12 °C.
Different maximum cooling powers have been considered, together with the chance to reduce the load to 50%, with a minimum air cooled temperature value of 10°C. The two different cooling systems have been compared basing the analysis on electrical and thermal output without inlet air cooling (see Tab.1):

T(environment)	0°C	15°C	35°C
Electrical output	5577 kW	5142 kW	4423 kW
Thermal output	8776 kW	8560 kW	8134 kW

Table1: Nominal power output of the plant without air cooling

1. Absorbption chiller dedicated to air cooling and fed by Heat Recovery Steam Generator (HRSG) integrated by traditional boiler, in order to keep constant the reference thermal energy (see Fig.4).

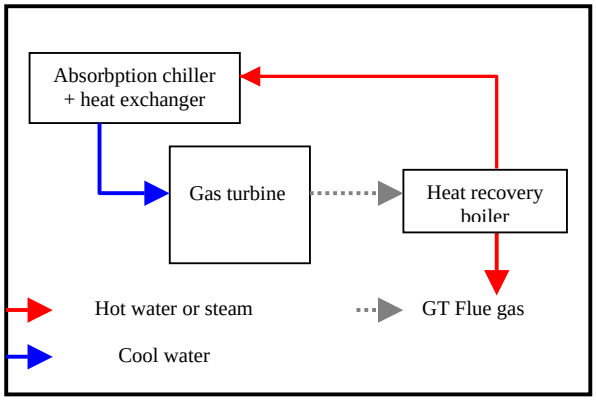

Figure 4: First option scheme.

1. CFC compression cooling system, electrically fed by gas turbine coupled electrical generator (see Fig. 5).

.

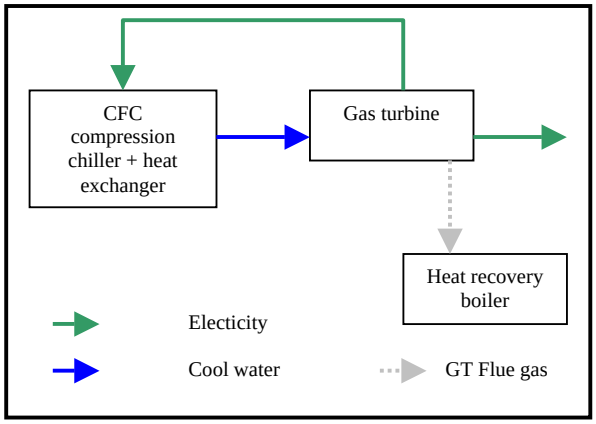

Figure 5: Second option scheme.

Naples meteorological characteristic has been the reference for daily temperature all year long. Temperature graph along the day has been assumed to be variable between a lower and a upper value, as shown in fig.6.

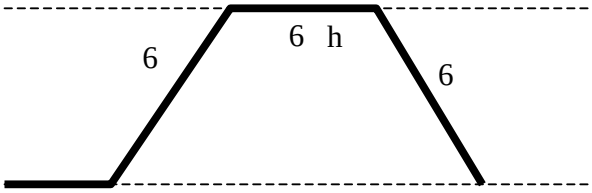

Figure 6: Daily Environmental temperature graph.

For both technical solution and for each cooling power, the number of operating hours of the cooling system has been calculated, in a typical day: for each cooling power (60, 120, 260, 360 KW), air temperature downstream the heat exchanger can decrease lower than 10°C, (which is temperature of the cold water stream) depending on environment initial temperature, limiting the operation time of the system and so this economical advantage; for this reason the cooling system has been considered to be variable in its load thru 50% min.

The positive variation of electrical production gained due to air cooling, with respect to traditional configuration, has been calculated all year long and translated in money considering a 0.12 €/kWh value.

Starting from cooling power required and considering a COP varying from 0.65 to 1.21 for absorption system, the global thermal energy to the cooling system has been calculated and translated in money, considering a 0.35€/kg cost for fuel and a boiler thermal efficiency equal to 0.90. In a similar way the case of electrically fed cooling system, a COP varying from 2.5 to 3.5 has been considered, in order to evaluate the electrical energy required to air cooling, which must be subtracted from total electrical output of the gas turbine coupled generator.

It has been considered also the thermal energy variation obtained from HRSG, due to a lower inlet temperature at the boiler, with respect to traditional configuration; finally the increase of fuel required from gas turbine, due to cooler inlet air, has been evaluated in both cases.

It has to be remarked also the influence of air humidity, which increases cooling power, especially in summer.

COP	0,65	1,1	1,2
P=60kW	16550	26769	28110
P=160kW	12182	33087	35832
P=260kW	361	29311	33113
P=360kW	-8046	25566	29979

Table 2: Annual economical benefit from absorption system (euro).

COP	2,5	3	3,5
P=60kW	23698	26669	28792
P=160kW	26804	32884	37227
P=260kW	20611	29030	35044
P=360kW	15464	25239	32222

Table 3: Annual economical benefit from electrical cooling system (euro).

NUMERICAL RESULTS

Through reported diagrams, electric energy, thermal one and efficiencies of two plant configurations are compared. Data are referred to one year period, with cooling system operating in hours which respect the restrictions before shown.

In the absorbption chiller configuration electrical output is clearly higher than configuration with cooling system (1.3 – 2.3 % more and 1 – 1.4 % more respectively, with respect to reference solution); in fact electrical cooling system is fed by part of electrical output of machine itself which, for not so high cooling power and not so low COP, presents electrical efficiency quite similar to reference configuration and higher thermal output (0.2-0.4%) with thermal efficiency lower than reference values (0.7-1.3%).

About absorbption chiller configuration it can be noticed that both electrical output surplus, and efficiency delta (0.1-0.2%) , increase with cooling power. On the contrary, thermal energy output and thermal efficiency, decrease, as expected, with cooling power increasing. In particular way thermal efficiency decreases by 1.7-2.3 %and energy by 0.6-1%.

About exergetic analysis, exergetic efficiency has been evaluated, as ratio between output exergy and input one for the system:

$$\eta_{ex} = \frac{Ee + Et\left(1 - T_0 / T_{ml}\right)}{Ep} \qquad (7)$$

Exergy associated to electrical energy is equal to electrical energy itself, while exergy associated to thermal one is reduced by Carnot factor, calculated supposing that thermal energy is distributed at T_{ml} =130 °C. Input exergy is considered to be equal to fuel heat value.
From data reported it can be remarked that exergetic efficiency is lower with respect to reference configuration, especially for cooling system case and decreases with cooling power increasing.
About economic benefit derived from installation of such a system, from the analysis of data reported in Tab. 3, we can conclude that it depends strongly upon unit prices applied, once considered the investment cost. Anyway such a system is certainly to be well considered in case that a cooling machine is already available in the plant, with not so low COP efficiency.

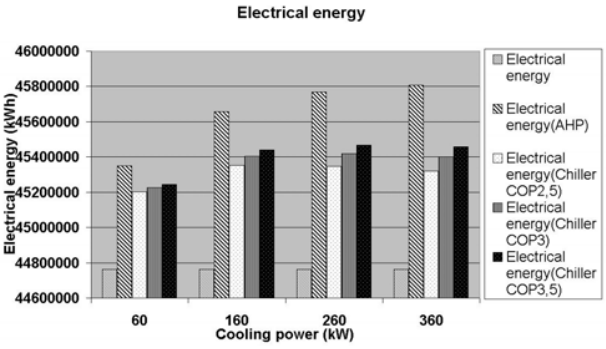

Figure 7. Electrical energy histogram.

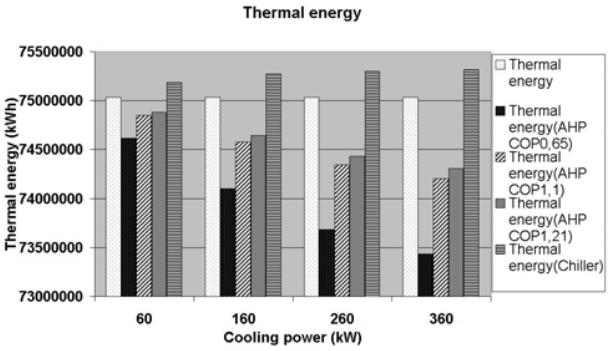

Figure 8: Thermal energy histogram.

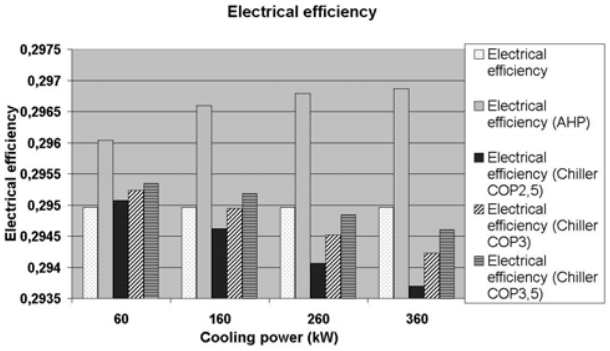

Figure 9. Electrical efficiency.

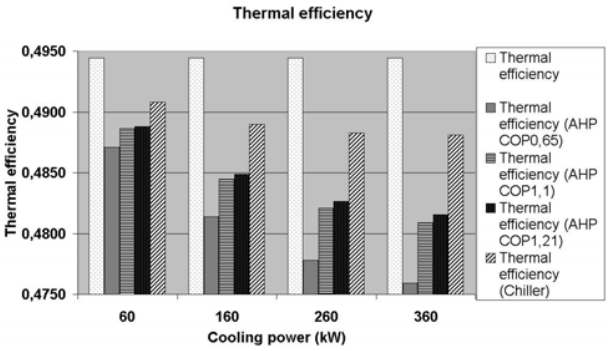

Figure 10. Thermal efficiency.

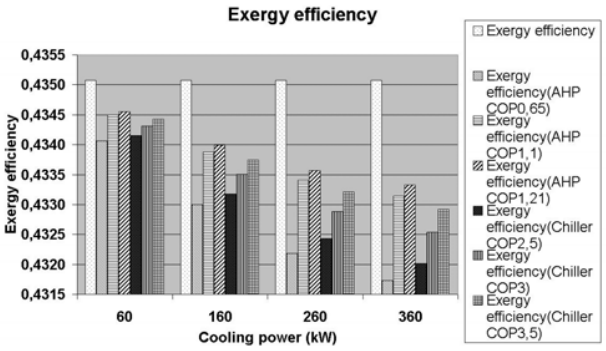

Figure 11: Exergy efficiency.

REFERENCES

[1] M. Dentice d'Accadia, M. Sasso, S. Sibilio, R. Vanoli - *Energetic applications* - Liguori Editions, 1999.Italy

[2]J. A. Orlando - *Cogeneration planners handbook* - The Fairmont Press, 1991.

[3] Bejan .A., Tsatsaronis G., Moran M.: *Thermal design and optimisation*. A Wiley and Sons, INC., New York, 1996

[4]S. Coslovi, A. Zulian - Cogenerazione: Analisi dei parametri significativi per elaborazione degli studi di fattibilità - IV Convegno ATIG Napoli 25-27 Novembre, 1992.

[5]G. Manfrida - *Impianti cogenerativi* - Politecnico Milano - Programma Istruzione Permanente, 1990-1991.

[6]Szargut J., Ziebik A., *Fundamentals of Thermal Engeneering*. PWN, Warszawa, 1998.

[7]El Sayed Y.and Gogus Y., *Demand variability and mismatches in the cogeneration of power and process heat*, Int. J. Of Appl. Thermodynamics, Vol.3, pp 199-208, December 2000. [5]A. Spiewak, L. Weiss - Cogeneration *and small power production* - The Fairmont Press, 1994.

[8] J.Hernandez, C.Heard R.Rivero, *Exergoeconomic c*omparison *of a combined cycle cogeneration system with absorption refrigeration turbine inlet air cooling*, ECOS 2003, Copenhagen, Denmark, June 30 – July 2, 2003.

Proceedings of ECOS 2005
Trondheim, Norway
June 20–22, 2005

THERMOECONOMIC OPTIMIZATION OF A DOUBLE-EFFECT H_2O/LIBR VAPOUR-ABSORPTION REFRIGERATION SYSTEM USING THE EXERGETIC COST THEORY

R. D. Misra*
Mechanical Engg. Deptt., National Institute of Technology Silchar, Silchar – 788 010 (India).
P. K. Sahoo and A. Gupta
Mech. & Ind. Engg. Deptt., Indian Institute of Technology Roorkee, Roorkee - 247 667 (India).

ABSTRACT

In this paper, the thermoeconomic concept is applied to the optimization of a double-effect H_2O/LiBr VAR system, aimed at minimizing its overall product cost. Here, a simplified cost minimization methodology based on the Exergetic Cost Theory with negentropy concept is applied to calculate the economic costs of all the internal flows and products of the system. Once these costs are determined, an improved design configuration of the system is obtained through an iterative improvement procedure using sequential local optimization of the components of the system. Finally, sensitivity analysis shows that the optimal values of the decision variables are negligible with changes in the fuel cost.

Keywords: Thermoeconomic, exergy, exergetic cost

NOMENCLATURE

A = Heat transfer surface area [m^2]
a = Parameter of investment cost equation
B = Exergy [kW]
B^* = Exergetic cost [kW]
c = Unit thermoeconomic cost [Rs. GJ^{-1}]
$\dot{C}$ = Thermoeconomic cost [Rs. hr^{-1}]
h = Specific enthalpy [kJ kg^{-1}]
k^* = Unit exergetic cost [kW]
$\dot{m}$ = Mass flow rate [kg s^{-1}]
M = Molecular weight [kg $kmol^{-1}$]
s = Specific entropy [kJ kg^{-1} K^{-1}]
t = Temperature on Celsius scale [°C]
T = Temperature on Kelvin scale [K]
x = Decision variable
z = Concentration
Z = Investment cost of the components [Rs.]
$\dot{Z}$ = Levelized (annual) investment cost of the system components [Rs. hr^{-1}]

Greek letters

β = Coefficient expressing O&M costs
χ = Effectiveness of heat exchangers
Π = Economic cost [Rs. hr^{-1}]
η = Efficiency
ε = Exergetic efficiency [%]
τ = Annual no. of hours of operations
ξ = Capital recovery factor
Δ = Difference

Superscripts

b = Exponent of investment cost equation
Ch = Chemical component
Ph = Physical component
OPT = Optimum

Subscripts

0 = Environmental state
a = Absorber
$B111, B1211,...$ = Exergy flows [kW]
c = Condenser
D = Exergy destruction
e = Evaporator
F = Fuel
htg = High temperature generator (HTG)
k = The k^{th} component of the system
L = Exergy loss

* Corresponding author. Tel. +91-3842-242677(Res.), E-mail: rdmishra@nits.ac.in, rdmisra@yahoo.com

ltg = Low temperature generator (LTG)
m = Electric motor
p = Pump
P = Product
$S111, S1211, \ldots$ = Negentropy flows [kW]
he = Solution heat exchanger
tot = Overall system

Vector & Matrices

$\overline{A}$ = Incidence matrix
$\overline{\overline{A}}$ = Coefficient matrix
$\overline{B}^{*}$ = Vector for exergetic costs of flows
$\overline{\dot{C}}$ = Vector for thermoeconomic costs of flows
$\overline{\overline{Y}}$ = External assessment vector
$\overline{\dot{Z}}$ = Vector for levelized cost of components
$\overline{\alpha}$ = Sub-matrix for flows
$\overline{\Pi}$ = Vector for economic costs of fuel
$\overline{\omega}$ = Vector for exergy values of fuel

INTRODUCTION

The refrigeration-based industries are facing challenges mainly from the ozone layer depletion and the global warming effects. It has directed the research trend towards the search for alternative refrigerants and alternative technologies [1]. In this regard, vapour-absorption refrigeration (VAR) systems appear to be a promising option. However, these systems still have lower COP with higher investment cost compared to their vapour-compression counterpart. This demands for performance enhancement along with reduction in investment cost. In this respect, the Exergetic Cost Theory (ECT) [2] is one of the better tools as it provides a common platform for both thermodynamics and economics. The research so far has put the thermoeconomic optimization methodologies to a maturity level. The works of Tsatsaronis and his coworkers [3], Valero and his coworkers [4,5], Frangopoulos [6], von Spakovsky [7], ect. have contributed towards this development. The applications are mainly focused on large cogeneration and combined power plants, chemical plants, etc. [3-7]. However, applications like refrigeration and air-conditioning have higher rates of energy consumption and poor efficiency, and therefore, deserve greater attention. Regarding the optimization of refrigeration systems, the notable contributions are seen from d'Accadia and de Rossi [8], and Wall [9] in compression refrigeration, Misra et al. [10,11] in single-effect H_2O/LiBr absorption refrigeration, and Sahoo et al. [12] in NH_3/H_2O absorption refrigeration system.

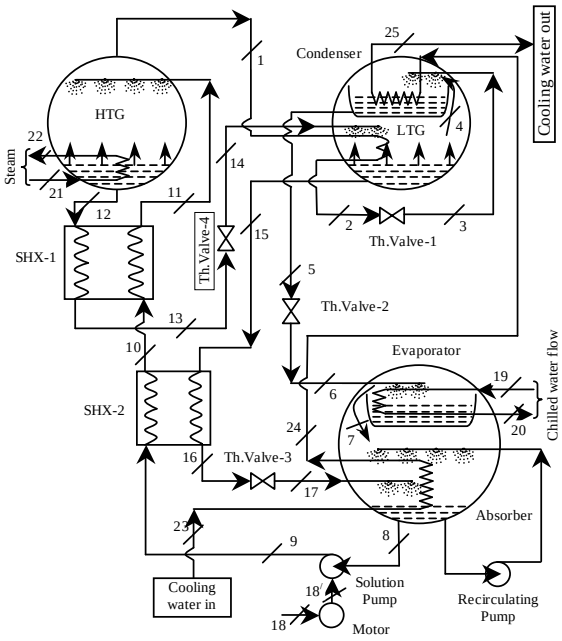

Figure 1: Schematic diagram of a double-effect H_2O/LiBr vapour absorption refrigeration system

ASSUMPTIONS USED IN THE ANALYSIS

Figure 1 shows the schematic diagram of a double-effect H_2O/LiBr VAR system having a cooling capacity of 2731 kW (about 780 TR). For the purpose of analysis the following assumptions are made:

- The system is in steady state.
- The refrigerant at the condenser and the evaporator exits are in saturated states.
- The refrigerant vapour and the weak solution of refrigerant leaving the LTG, and the strong solution of refrigerant leaving the absorber are in saturated states.
- Pressure losses in all the heat exchangers and the pipelines are negligible.
- The reference environmental state is 25^0C (T_0) and 1 atmospheric pressure (p_0).
- To avoid crystallization of the solution, the temperature of the solution entering the throttling valve should be at least 5^0C above crystallization temperature.

- The cooling water first enters the absorber at 27^0C, then passes through the condenser, and finally it is rejected by the system at 35^0C.
- The water to be chilled enters the evaporator at 20^0C and leaves at 10^0C.

Based on these assumptions, a workable initial design, referred as the Base Case, is developed for the system shown in Fig.1 with the following data: t_{htg}=157^{0}C, t_{ltg}=94^{0}C, t_c=40.3^{0}C, t_e=4.1^{0}C, t_a=39.4^{0}C, χ_{he1}=60%, χ_{he2}=60%, η_p=75%, and η_m=90%. In the analysis, the properties of water/steam are obtained from correlations provided by Irvine and Liley [13]. The properties of LiBr solution are taken from the work of Chua et al. [14].

THERMODYNAMIC ANALYSIS

Exergy measures the true thermodynamic losses of a system qualitatively as well as quantitatively. In the absence of magnetic, electrical, nuclear, surface tension effects, and considering the system is at rest relative to the environment, the total exergy of a system becomes:

$$B = B^{Ph} + B^{Ch} \quad (1)$$

The physical exergy component is calculated using the following relation:

$$B^{Ph} = \dot{m}\left[(h - h_0) - T_0(s - s_0)\right] \quad (2)$$

The calculation procedure of the chemical exergy of various substances based on standard chemical exergy values of respective species is widely discussed by Bejan et al. [15], Ahrendts [16], and Szargut et al. [17]. In the VAR system considered here, the chemical exergy of the flows for water can be calculated using the following relation:

$$B^{Ch}_{H_2O} = \dot{m}\left(z_{H_2O} / M_{H_2O}\right) e^0_{Ch,H_2O} \quad (3)$$

where e^0_{Ch,H_2O} is the standard chemical exergy of water and its value is taken from Ahrendts [16]. As there is no chemical reaction in the components of the VAR system, the chemical state of the absorbent remains constant throughout the absorber circuit. But, changes in chemical composition lead to changes in chemical exergies. In this analysis the change in chemical exergy of LiBr is not considered. This assumption, however, introduces a small error [10]. Using these, the exergy at various state points is calculated.

THERMOECONOMIC ANALYSIS

In order to analyze the system from thermoeconomic point of view, its productive structure must be considered by attributing a well defined role, i.e. fuel, product or loss, to each physical flow entering or leaving them [2-6]. This is quite easy for the HTG, LTG, evaporator, pump, solution heat exchanger-1 (SHX-1) and solution heat exchanger-2 (SHX-2), where exergy of the product stream is increased. Since the product cannot be defined readily for the heat dissipative devices, i.e. the four throttling valves, they are considered together with the components they serve. With regard to the condenser and the absorber, which reject heat to the environment, the concept of negentropy is used [8,11]. That is to consider the reduction of entropy induced for the outflow as product of the system. The negentropy flows do not have any significance as for real operation of the plant, nor appear in the energy and exergy balances. But, it represents a physical flow that can be introduced to which the cost of fuels entering these devices is attributed. This cost is then distributed among the remaining components of the system. These considerations lead to the 'Productive Structure' of the system as shown in Fig. 2. The system is considered to be composed of eight productive units and two fictitious units. In the two fictitious units, the homogeneous products are distributed among more than one unit.

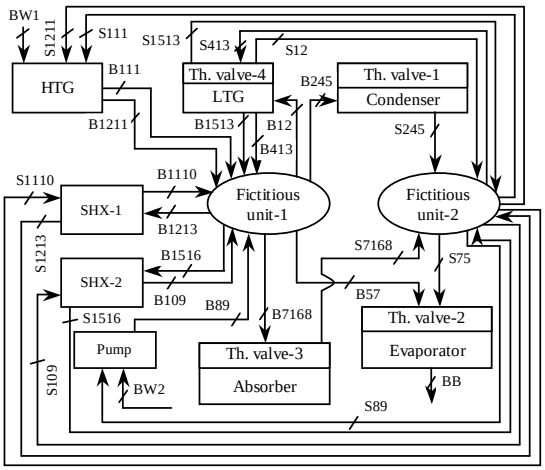

Figure 2: Productive structure of the system

Thus, the flows that interrelate the structure are either exergy flows (denoted by '*B*') or have same dimensions, in case of negentropy flows (denoted by '*S*'). In the fictitious unit-1, the increase of the exergy in the HTG, LTG, pump, and the two solution heat exchangers is divided into six flows (*B*12, *B*245, *B*57, *B*7168, *B*1213, and *B*1516) corresponding to the decrease in the exergy in the LTG, condenser, evaporator, absorber, SHX-1, and

SHX-2. As far as the negentropy flow is concerned, the negentropy produced in the LTG (*S*12 and *S*1315), condenser (*S*245), the absorber (*S*7168), and the two solution heat exchangers (*S*1213 and *S*1516) is distributed among the HTG, LTG, evaporator, pump, and the two solution heat exchangers through flows *S*111, *S*1211, *S*413, *S*75, *S*89, *S*1110, and *S*110 This distribution is done through the fictitious unit-2.

The annual levelized investment cost associated with the k[th] component is calculated as

$$\dot{Z}_k = \dot{Z}_k^{CI} + \dot{Z}_k^{OM} = \xi Z_k + \beta_k Z_k \quad (4)$$

where, ξ is the capital recovery factor and β_k is O&M costs associated with the total investment cost. The calculation of $\dot{Z}_k$ is shown in Appendix-A. For simplicity, we assume β_k =1.25% of total investment cost of each component [3,15].

According to the ECT [2], now it is possible to obtain the exergetic and thermoeconomic costs with their unit values of all the flows that appear in this structure. The exergetic cost, B^*, and the economic cost, $\dot{C}$, of an exergy flow (B) are defined, respectively, as the amount of exergy and the economic resources required to obtain that flow. For a flow, the unit exergetic cost (k^*) is the exergetic cost per unit of exergy and the unit thermoeconomic cost (c) is the thermoeconomic cost per unit of exergy of that flow. These costs are calculated by formulating respective balance equations for each productive unit of the system using the propositions formulated by Lozano and Valero [2]. For example, the exergetic cost balance equation along with other balance equations for the HTG are written as

$$B^*_{BW1} - B^*_{B111} - B^*_{B1211} + B^*_{S111} + B^*_{S1211} = 0 \quad (5)$$

$$B^*_{BW1} = BW1 \quad (6)$$

$$k^*_{B111} = k^*_{B1211} \Rightarrow B^*_{B111} - \left(\frac{B111}{B1211}\right) B^*_{B1211} = 0 \quad (7)$$

$$k^*_{S111} = k^*_{S1211} \Rightarrow B^*_{S111} - \left(\frac{S111}{S1211}\right) B^*_{S1211} = 0 \quad (8)$$

Similarly, the thermoeconomic cost balance equation along with other cost balance equations for the HTG are written as

$$\dot{C}_{BW1} - \dot{C}_{B111} - \dot{C}_{B1211} + \dot{C}_{S111} + \dot{C}_{S1211} = -\dot{Z}_{htg} \quad (9)$$

$$\dot{C}_{BW1} = \Pi_{BW1} \quad (10)$$

$$c_{B111} = c_{B1211} \Rightarrow \dot{C}_{B111} - \left(\frac{B111}{B1211}\right) \dot{C}_{B1211} = 0 \quad (11)$$

$$c_{S111} = c_{S1211} \Rightarrow \dot{C}_{S111} - \left(\frac{S111}{S1211}\right) \dot{C}_{S1211} = 0 \quad (12)$$

In this system, there are ten productive units including two fictitious units and 29 flows. Thus, a total of 10 cost equations are formulated from the cost balances, i.e. $\overline{A}\,\overline{B}^* = 0$ and $\overline{A}\,\overline{\dot{C}} = \overline{\dot{Z}}$. There are two flows entering the system, i.e. the fuels for the system: *BW*1 and *BW*2, which form two equations for the system, i.e. $\overline{\alpha}_f\,\overline{B}^* = \overline{\omega}$ and $\overline{\alpha}_f\,\overline{\dot{C}} = \overline{\Pi}$. The HTG, LTG, SHX-1, SHX-2, fictitious unit-1, and fictitious unit-2 have products composed of several flows, which provide the remaining 17 equations, i.e. $\overline{\alpha}_x\,\overline{B}^* = 0$ and $\overline{\alpha}_x\,\overline{\dot{C}} = 0$. The coefficients of the variables on the LHS of these equations form the coefficient matrix, i.e. $\overline{\overline{A}} = \left[\overline{A} : \overline{\alpha}_f : \overline{\alpha}_x\right]^t$. The terms on the RHS of these equations form the vectors $\overline{\overline{Y}}_B = \left[0 : \overline{\omega} : 0\right]^t$ and $\overline{\overline{Y}}_Z = \left[\overline{\dot{Z}} : \overline{\Pi} : 0\right]^t$ for exergetic cost and thermoeconomic cost, respectively. In matrix form, the exergetic and thermoeconomic cost balances, respectively, are expressed as:

$$\overline{B}^* = \overline{\overline{A}}^{-1}\,\overline{\overline{Y}}_B \quad (13)$$

$$\overline{\dot{C}} = \overline{\overline{A}}^{-1}\,\overline{\overline{Y}}_Z \quad (14)$$

By solving these two matrix equations, B^* and $\dot{C}$ for each flow are determined, which are summarized in Table 1 for the Base Case.

THERMOECONOMIC OPTIMIZATION

The objective function is to minimize the economic cost of the final product of the system. The initial values for the overall optimization can be obtained by means of sequential, local optimization of the individual productive units of the system, each one considered as if it were independent of others. The minimum thermoeconomic product cost of each individual units (say, unit *k*) of the system, with respect to the local decision variable x_k, can be expressed as:

$$\underset{\{x_k\}}{\text{Minimize}} \quad c_{P,k} = \sum_k \left(c_{F,k} \frac{B_{F,k}}{B_{P,k}} \right) + \frac{\dot{Z}_k}{B_{P,k}} = \sum_k \left(c_{F,k}\, k_k \right) + \frac{\dot{Z}_k}{B_{P,k}} \quad (15)$$

where, k_k is function of the decision variable x_k.

Flows	B (kW)	B^*(kW)	$k^*=B^*/B$	$\dot{C}$ (Rs/hr)^	c (Rs/GJ)
*BW*1	779.99	779.99	1.00	1256.4	447.45
*BW*2	1.08	1.08	1.00	5.42	1395.00
*B*111	279.51	424.85	1.52	815.56	810.52
*B*1211	442.46	672.54	1.52	1291.0	810.52
*B*12	306.19	307.36	1.00	609.00	552.50
*B*413	29.90	11.49	0.38	25.52	237.15
*B*1513	201.15	77.29	0.38	171.73	237.15
*B*245	90.93	91.28	1.00	180.86	552.50
*B*57	217.31	218.14	1.00	432.22	552.50
*B*7168	237.58	238.49	1.00	472.54	552.50
*B*89	0.01	1.22	133.58	15.42	467277.3
*B*109	105.19	49.98	0.48	113.47	299.64
*B*1516	115.15	115.60	1.00	229.04	552.50
*B*1110	303.91	130.00	0.43	276.52	252.74
*B*1213	394.98	396.50	1.00	785.61	552.50
*S*111	1311.76	250.46	0.19	576.44	122.07
*S*1211	350.62	66.95	0.19	154.08	122.07
*S*12	1202.61	462.07	0.38	1026.7	237.15
*S*413	1280.29	244.45	0.19	562.62	122.07
*S*1315	2.54	0.97	0.38	2.17	237.15
*S*245	1403.21	91.28	0.07	302.08	59.80
*S*75	2948.31	562.93	0.19	1295.6	122.07
*S*7168	3384.40	238.49	0.07	589.38	48.37
*S*89	0.76	0.15	0.19	0.33	122.07
*S*109	688.94	131.54	0.19	302.75	122.07
*S*1516	678.97	197.15	0.29	447.57	183.11
*S*1110	1289.81	246.27	0.19	566.80	122.07
*S*1213	1198.75	512.77	0.43	1090.7	252.74
BB	95.21	781.07	8.20	1833.6	5349.77

Table 1. Exergetic and thermoeconomic costs of flows of the system (base case).

The term, $\dot{Z}_k$, is expressed as function of the decision variable x_k and the exergetic product of the unit $B_{P,k}$ (Appendix-B). Considering $c_{F,k}$ and $B_{P,k}$ as constants, the cost $c_{P,k}$ becomes sole function of the decision variable x_k. Applying standard procedures, such as, golden section algorithm, polynomial approximation methods etc. Eq. (15) can be easily solved.

^ Rupees (*Rs.) is the Indian Currency. Equivalent approximate U.S. Dollar ($) value is Rs. 45.00*

The local decision variables considered for the double-effect VAR system are: t_{htg} for the HTG, t_{ltg} for the LTG, t_c for the condenser, t_e for the evaporator, t_a for the absorber, η_p for the solution pump, χ_{he1} for the SHX-1, and χ_{he2} for the SHX-2. Using Eq. (15), the objective functions for the local optimization of the components are formulated. For example, the local objective function for the HTG is formulated as

$$\begin{aligned} & c_{B111} \times (B111 + B1211) \\ & = c_{BW1} \times BW1 + c_{S111} \times (S111 + S1211) + \dot{Z}_{htg} \\ & \Rightarrow c_{B111} = c_{BW1} \times \frac{BW1}{B111 + B1211} \\ & + c_{S111} \times \frac{S111 + S1211}{B111 + B1211} + \left(\frac{\xi + \beta}{\tau} \right) a_{htg} \left(\frac{A_{hx,htg}}{A_{hx,tot}} \right)^{b_{htg}} \end{aligned} \quad (16)$$

Now for constant values of the exergetic product and the unit thermoeconomic cost of the fuel, the product cost (c_{B111}) of the HTG becomes sole function of its local decision variable, t_{htg}. Using the golden section algorithm, the optimum values of x_{htg}^{OPT} and $c_{P,htg}^{OPT}$ are found out. For other components same procedure is followed.

However, such one step optimization may not lead to near global optimum solution for the overall system. This is due to the complex interrelations of the various units of the system, such as variation of a local variable of one unit may have serious impact on the thermodynamic as well as economic behaviour of the other units of the system. Thus, an iterative procedure, which leads towards the minimum product cost, is used to find out an improved cost-effective design of the system. In this iterative procedure, the following parameters are evaluated in each iterative step to take necessary judgment regarding the changes in the decision variables from one iterative step to the next:

- The thermoeconomic variable, $\Delta c_{P,k}$, is defined to show the percentage variation of the product cost of a particular unit with its optimum value, i.e.
$$\Delta c_{P,k} = 100 \times \left(c_{P,k} - c_{P,k}^{OPT} \right) / c_{P,k}^{OPT} \quad (17)$$
- The product cost of the overall system, i.e.
$$\dot{C}_{P,tot} = \dot{C}_{F,tot} + \dot{Z}_{tot} \quad (18)$$

In the iterative procedure engineering judgments and critical evaluations are used in deciding on the changes made to the decision variables from one iterative step to the next. The criteria followed for this is as follows:

- Determination of the local optimum by formulating the objective functions for each productive unit.
- Calculation of $\Delta c_{P,k}$ and $\dot{C}_{P,tot}$ for a change in one decision variable in a certain step, while keeping all other decision variables constant.
- If the effect on the above parameter is positive, i.e. $\dot{C}_{P,tot}$ has reducing trend, then in the next iterative step this variable becomes a candidate for a similar change, otherwise, this variable remains unchanged in the next iterative step.
- Repetition of the above three steps for the other decision variables.

RESULTS AND DISCUSSIONS

Variable	Base Case	Itr. Case-1	Itr. Case-2	Itr. Case-3	Itr. Case-4	Itr. Case-5
t_g (C)	157.0	155.0	154.0	152.0	150.0	148.0
t_{gc} (C)	94.0	95.0	95.0	95.0	95.0	95.0
t_c (C)	40.3	40.0	40.0	40.0	40.0	40.0
t_e (C)	4.1	5.0	6.0	7.0	7.5	7.5
t_a (C)	39.4	38.0	36.0	35.0	34.7	34.7
η_p (%)	75.0	72.5	70.0	70.0	70.0	70.0
χ_{he1} (%)	75.0	77.5	80.0	82.5	85.0	90.0
χ_{he2} (%)	65.0	67.5	70.0	72.5	74.0	74.0
	Δc_P	Δc_P	Δc_P	Δc_P	Δc_P	Δc_P
H.T.G.	10.82	13.00	9.76	8.35	7.31	5.89
L.T.G.	58.49	58.68	57.75	58.21	59.16	60.95
Cond.	23.74	5.27	7.25	5.96	4.67	2.55
Evap.	5.95	4.71	3.78	3.29	3.01	1.99
Absr.	12.33	5.55	2.96	1.43	1.04	1.12
Pump	6.32	2.86	0.60	-1.38	-4.72	-3.96
SHX-1	37.23	38.58	49.37	54.60	55.93	56.83
SHX-2	65.30	67.79	69.51	70.53	70.91	70.88
$\dot{C}_{L,tot}$ (Rs/hr)	160.96	155.6	152.6	150.4	149.1	148.0
$\dot{C}_{D,tot}$ (Rs/hr)	947.08	862.8	816.4	781.8	760.8	743.1
$\dot{C}_{P,tot}$ (Rs/hr)	1833.61	1742.6	1692.3	1655.0	1632.6	1613.7

Table 2: Variables obtained during the optimization of the system from base case to the optimum case

Table 2 summarizes the stage-by-stage iteration results from the Base Case to the Optimum Case. With the study of the positive/negative effects of the changes in the decision variables, which is governed by $\Delta c_{P,k}$, on the product cost, the decision has been taken on the changes of these decision variables from one iterative case to the next. The process of iterations continues till the difference in the objective function, i.e. the product cost, between successive iterations becomes negligible.

Properties	Base case	Optimum case	%Variation
OBF (Rs/hr)	1833.61	1613.72	-11.99
ε_{tot} (%)	12.19	14.71	20.68
COP	1.14	1.38	20.65
$\dot{C}_{F,tot}$ (Rs/hr)	1261.85	1044.73	-17.21
$\dot{C}_{D,tot}$ (Rs/hr)	947.08	743.06	-21.54
$\dot{C}_{L,tot}$ (Rs/hr)	160.96	147.99	-8.06
$\dot{Z}_{tot}$ (Rs/hr)	571.76	568.98	-0.49
$\dot{Z}_{htg}$ (Rs/hr)	119.65	22.91	-80.85
$\dot{Z}_{ltg}$ (Rs/hr)	54.54	282.60	418.11
$\dot{Z}_c$ (Rs/hr)	120.36	66.23	-44.97
$\dot{Z}_e$ (Rs/hr)	104.91	96.39	-8.12
$\dot{Z}_a$ (Rs/hr)	115.98	66.31	-42.82
$\dot{Z}_p$ (Rs/hr)	9.67	6.89	-28.73
$\dot{Z}_{shx1}$ (Rs/hr)	29.25	19.95	-31.79
$\dot{Z}_{shx2}$ (Rs/hr)	14.82	5.12	-65.47

Table 3: Comparative results between the base case and the optimum case of the system

Table 3 represents a comparative study of the final cost optimal configuration with the Base Case. The overall thermoeconomic cost of the product (chilled water) is decreased by about 12.0 % and the corresponding decrease in the fuel costs is 17.2%. Also, the results show a significant reduction in the exergy destruction cost (about 21.5%) and exergy loss cost (about 8.1%). The corresponding increase and decrease in the investment costs of the components are also shown in the same table. The greater investment is mainly in the LTG. Incidentally, the overall investment cost of the system almost remains same. It is because increase in investment cost of some components is compensated by reductions in investment cost of some other components. The exergetic efficiency and the COP are both increased by about 20.7%.

In order to remain competitive, it is crucial for any system to be robust with respect to the uncertainty pertaining to frequently changing parameters with time. In general, the economic parameters, such as the fuel costs and the capital investments, are the

uncertain terms as they vary with time. Therefore, it is necessary to investigate their effect on the decision variables and the product costs of the optimal solution. In this work, the variation with respect to capital investment cost is not considered, as once installed the system components are not supposed to alter in response to change in their capital investment. Hence, only the fuel cost is considered. To study the robustness of the optimal solution, analysis is carried out for 20%, 40%, 60%, 80%, and 100% increase in the fuel cost for the operating decision variables and the product costs of the system. Figure 3 shows the variation of the product cost with respect to the increase in the fuel cost. The trend of this increase in the product cost is same as that of the fuel cost variation and Table 4 presents the percentage change in the decision variables with respect to the present optimum. It is seen that the change in the decision variables with respect to the change in the fuel cost is very small; in fact, it is well within ± 1.5%. Therefore, it can be concluded that the decision variables of the system are not very sensitive to the changes in the fuel cost (uncertainty) in the close vicinity of the optimal solution space.

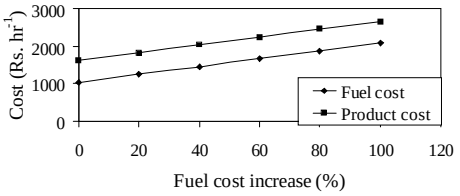

Figure 3: Sensitivity of the product cost (Rs. hr^{-1}) with respect to increased fuel cost (%)

		Changes in decision variables (%)							
		t_{htg}	t_{ltg}	t_c	t_e	t_a	χ_{shx1}	χ_{shx2}	η_p
Fuel cost increase (%)	20	0.00	0.00	0.00	0.00	0.00	0.41	-0.02	1.12
	40	0.00	0.00	0.00	-0.01	0.00	0.41	-0.09	0.81
	60	-0.31	-0.50	-1.23	-0.84	-1.39	0.41	-1.10	0.56
	80	0.00	0.00	0.00	0.00	0.00	0.24	0.01	-0.85
	100	0.00	0.00	-0.01	-0.04	-0.01	0.30	-0.41	-1.29

Table 4: Sensitivity of the decision variables with respect to increase in fuel cost (%)

CONCLUSIONS

The thermoeconomic optimization of the double-effect H_2O/LiBr VAR system, presented in this paper, provides one cost-effective design configuration. The results clearly show the performance improvement of the system with almost same investment cost to produce the cooling effect at a reduced cost. However, the application requires adequate attention to the following points:

- Proper definition of the productive structure of the system.
- Proper selection of local decision variables for various subsystems.
- Reliability of the cost information available.
- Proper engineering judgment to relate the costs with thermodynamic parameters.

APPENDIX-A

Calculations for the Investment Costs and Capital Recovery Factor

The investment cost of the double-effect system is taken the THERMAX Ltd., Pune, India [18]. For the purpose of analysis, the HTG, LTG, condenser, evaporator, absorber, SHX-1, and SHX-2 of the system are considered as simple heat exchangers. The costs of these heat exchangers are calculated based on their area-weighted average after duly deducting the investment costs of pump and motor and using the following relation [8]:

$$Z_k = Z_{R,k}.\left(\frac{A_k}{A_R}\right)^{0.6} \qquad \text{(A-1)}$$

where $k = htg, ltg, c, e, a, he1, he2$

The subscript 'R' represents the reference component of a particular type and size. The investment cost of the pump and the motor can be written respectively as [8,9]:

$$Z_p = Z_{R,p}\left(\frac{\dot{W}_P}{\dot{W}_{R,P}}\right)^{m_p}\left(\frac{1-\eta_{ip}}{\eta_{ip}}\right)^{n_p} \qquad \text{(A-2)}$$

$$Z_m = Z_{R,m}\left(\frac{\dot{W}_m}{\dot{W}_{R,m}}\right)^{m_m}\left(\frac{1-\eta_{im}}{\eta_{im}}\right) \qquad \text{(A-3)}$$

The cost of electric energy is taken as Rs. 5.0 per kWh, based on the commercial power tariffs in India (i.e. about $ 31.0 per GJ of energy). The capital recovery factor (ξ) is given by [8,15]:

$$\xi = \left(\frac{i_r.(1+i_r)^{N_y}}{(1+i_r)^{N_y}-1}\right) \text{ yr}^{-1} \qquad \text{(A-4)}$$

An interest rate of 8%, 20 years of life span and 1800 hours of operation per year are used in the analysis presented in this paper.

APPENDIX-B

Expression for investment cost as functions of exergetic product and local decision variable for Eq. (15)

In this work, since all the major components are heat exchangers, the decision variables are related to their areas. Thus, the effect of changing the decision variable can be registered not only in exergetic product of the component, but also in the investment cost of that component. Then by generating the investment cost data and corresponding exergetic product of a particular component for a range of x_k, Z_k of the component is expressed as

$$Z_k = a\left(\frac{A_{hx,k}}{A_{hx,tot}}\right)^b B_{P,k} \qquad \text{(B-1)}$$

By plotting the data between $\left(A_{hx,k}/A_{hx,tot}\right)$ and $\left(Z_k/B_{P,k}\right)$, the parameter '*a*' and the exponent '*b*' can be found out through curve fitting technique. For example, considering the case of HTG, the plot between $\left(A_{hx,htg}/A_{hx,tot}\right)$ and $\left(Z_{htg}/B_{P,htg}\right)$ for a given range of t_{htg} is presented in Fig. 4.

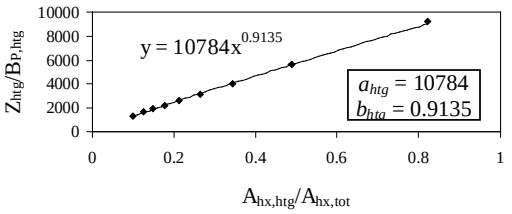

Figure 4: Plot of investment cost equation (Eq. 15) for the HTG ($148^0 \le t_{hta} < 160^0$C)

REFERENCES

[1] McMullan JT. *Refrigeration and the environment – issues and strategies for the future*. Int J Refrig. 2002;25(1):89-99.

[2] Lozano MA, Valero A. *Theory of the exergetic cost*. Energy 1993;18(9):939-960.

[3] Tsatsaronis G, Javier P. *Exergoeconomics evaluation and optimization of energy systems – application to the CGAM problem*. Energy 1994;19(3):287-321.

[4] Valero A, Lozano MA, Serra L, and Torres C. *Application of the exergetic cost theory to the CGAM problem*, Energy 1994;19(3):365-381.

[5] Valero A, Lozano MA. *An introduction of thermoeconomics*. In: Boehm, RF editor. Developments in the design of thermal systems, Cambridge University Press, New York, U.S.A., 1997.

[6] Frangopoulos CA. *Application of the thermoeconomic functional approach to the CGAM problem*. Energy 1994;19(3):323-342.

[7] von Spakovsky MR. *Application of engineering functional analysis to the analysis and optimization of the CGAM problem*. Energy 1994;19(3):343-364.

[8] d'Accadia MD, de Rossi F. *Thermoeconomic optimization of a refrigeration plant*. Int J Refrig. 1998;21(1):42-54.

[9] Wall G. *Optimization of refrigeration machinery*. Int J Refrig. 1991;14:336-340.

[10] Misra RD, Sahoo PK, Sahoo S, Gupta A. *Thermoeconomic optimization of a single effect water/LiBr vapour absorption refrigeration system*. Int J Refrig. 2003;26(1): 158-169.

[11] Misra RD, Sahoo PK, Gupta A. *Application of the exergetic cost theory to the LiBr/H_2O vapour absorption system*. Energy 2002; 27(11):1009-1025.

[12] Sahoo PK, Misra RD, Gupta A. *Exergoeconomic Optimization of an Aqua Ammonia Absorption Refrigeration System*. In: Proceedings of the First International Exergy, Energy, and Environment Symposium, Izmir, Turkey, 2003.

[13] Irvine TF, Liley PE. *Steam and gas tables with computer equations*. USA: Academic Press, 1984.

[14] Chua HT, Toh HK, Malek A, Ng KC, Srinivason K. *Improved thermodynamic property fields of LiBr-H_2O solution*. Int J of Refrig. 2000;23:412-29.

[15] Bejan A, Tsatsaronis G, Moran M. *Thermal design and optimization*. New York: John Wiley and Sons Inc., 1996.

[16] Ahrendts J. *Reference states*. Energy 1980;5: 667-677.

[17] Szargut J, Morris DR, Steward FR. *Exergy analysis of thermal, chemical, and metallurgical processes*. New York: Hemisphere Publishing Corporation, 1988.

[18] *Technical and Economical Data of THERMAX LTD., Absorption Cooling Division*, Industrial Area, Chinchwad, Pune – 411 019, India, (Personal Communication), http://www.thermaxindia. com/acd.

Proceedings of ECOS 2005
Trondheim, Norway
June 20–22, 2005

THERMOECONOMIC ANALYSIS OF A COGENERATION SYSTEM APPLIED TO A UNIVERSITY HOSPITAL

Raúl Gonzales Palomino
State University of Campinas
P.O. Box 6122, CEP:13083-970, Campinas, SP, Brazil
Email: rgpuni@fem.unicamp.br

Silvia A. Nebra*
State University of Campinas
P.O. Box 6122, CEP:13083-970, Campinas, SP, Brazil
Email: sanebra@fem.unicamp.br

ABSTRACT

A cogeneration system based on a reciprocating natural gas engine, a heat recovery steam generator (HRSG), an absorption refrigeration system (ARS) and a cooling tower (CT) is presented as an alternative to the current UNICAMP University Hospital (HC) utility plant. The objective of this work is to do a thermoeconomic analysis of a cogeneration system proposed for HC. Three thermoeconomic methodologies were applied to the cogeneration system. Three methodologies were based in the Theory of the Exergetic Cost, Functional Analysis and Functional Analysis using negentropy. The results show that there are differences in the costs of power, steam and refrigeration (cold) production which result from application of the methodologies.
Keywords: Cogeneration, thermoeconomics

NOMENCLATURE

E^*	Exergetic cost
k	Unit exergetic cost
E_x	Exergy (kW)
$E^*_{e,i}$	Exergetic cost of the input flows
$E^*_{s,j}$	Exergetic cost of the output flows
C	Monetary cost (US$/h)
c	Unit monetary cost (US$/MWh)
$C_{e,i}$	Monetary cost of the input flows (US$/h)
Z_k	Capital and maintenance cost (US$/h)
$C_{s,j}$	Monetary cost of the output flows (US$/h)
HRSG	Heat recovery steam generator
ARS	Absorption refrigeration system
CT	Cooling tower
HC	UNICAMP University Hospital

INTRODUCTION

The cogeneration is defined as the simultaneously production of electric (or mechanic) power and thermal energy, starting from a same primary energy source. It improves the use of the fuel energy minimizing the effects of the second law of thermodynamics, which foresees an obligatory loss in the transformation of energy from one form into another. The cogeneration has the main intention of to obtain a better use of the primary fuels; this is why it is considered a fundamental alternative in the energy rational use programs.

In the last years, a market tendency is perceived in the direction to the development and implantation of technologies and processes less aggressive to the environment, tendencies motivated, many times, by environmental protection laws. The cogeneration is an alternative to accomplish these laws, once it reduces the emissions of greenhouse effect gases and contributes to reach the objectives of the Kyoto Protocol.

In Brazil, the cogeneration is used in very specific cases, due to the availability and low cost of hydro-power. In cogeneration projects, the electricity

represents the revenue for the investor, while natural gas is a cost. The economic viability of natural gas-fired cogeneration in Brazil has as major barrier the value of electricity and natural gas price. The ratio of these two values is considered low to be viable some cogeneration projects. In this work a cogeneration system is designed to use natural gas as an alternative to the UNICAMP University Hospital (HC) and a thermoeconomic analysis is performed. The assessment of this system for the HC is part of the ECOGERA project, which is realized by the NIPE (Interdisciplinary Center of Energy Planning).

COGENERATION SYSTEM DESCRIPTION

In this work the cogeneration system is basically composed by an internal combustion engine, a heat recovery steam generator (HRSG), an absorption refrigeration system (ARS) and a cooling tower (CT). The details are shown in Figure 1.

The internal combustion engine is a Waukesha - VHP9500G, and has 1075 kW of nominal capacity. The fuel supplied to the engine is natural gas. The water used for cooling the jacket and auxiliary circuit of the engine will be used later as thermal energy source in the ARS. The engine exhaust gas has high quality of thermal energy; it will be used later in the HRSG.

The HRSG is of two pressure level, it takes advantage of the thermal energy contained in the exhaust gas of the engine. It has two pre-heaters, one of low pressure for heating of water that will go to the de-aerator, and the other of high pressure, after the exit of the feeding bomb. A part of the produced steam is injected later in the de-aerator.

The ARS uses as a work fluid, LiBr-H_2O; it is of single effect. The heat of the engine cooling water is used as energy source. The condenser and evaporator work in a temperature of 40ºC and 5ºC respectively. The condenser and absorber need to be cooling; a current of water is used for this.

The CT is used for cooling the water that was used to cool the absorber and condenser of the ARS. Due to the evaporative cooling of the CT, it needs replacement water to compensate the water that evaporates and goes to atmosphere with the dry air.

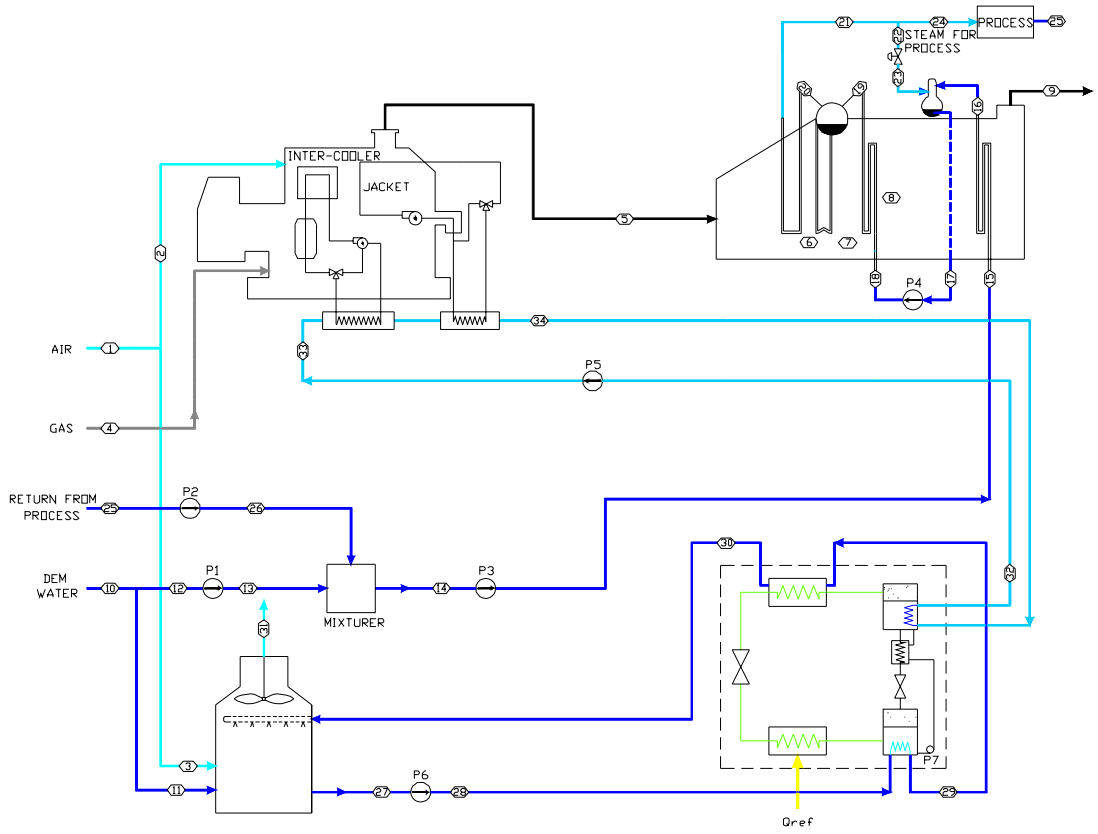

Figure 1: Sketch of proposed cogeneration system

ENERGETIC AND EXERGETIC ANALYSIS

Gonzales and Nebra [4] realized an energetic and exergetic analysis for the cogeneration system shows in Figure 1. The energetic analysis showed that at maximum load conditions, the cogeneration system produces 1052 kW of electricity, 1335 kg/h of process steam and 770 kW of refrigeration (cold production). Generally, the engine first law efficiency is 30% and the COP of the absorption refrigeration system is 0.7. The cogeneration system gets to save up to 28.5% of fuel in comparison with the separate production of heat and electricity. The Energy Utilization Factor reaches 88%. The exergetic analysis showed that the largest irreversibility happened in the system is due to the engine, this participates in the average with 78% of the total irreversibility. The other pieces of equipment that also contribute to the total irreversibility are the HRSG (13.5%), ARS (3%) and CT (4.7%). The optimization showed that the cogeneration system obtains its best performance with the smallest exhaust gas temperature of the HRSG (T9) and the maxim engine load percentage. The Table 1 presents the thermodynamic variable values at each system point (Figure 1), in the state for which the objective function presents a maximum.

THERMOECONOMIC ANALYSIS

Thermoeconomics combines exergy analysis and economic principles that provide information not available, but crucial to the design and operation of a cost-effective system [1].

The Exergeconomic methodology proposed by Tsatsaronis and Pisa [6], consists in the determination of the exergetic and energetic flows, capital and maintenance cost for each unit. An interesting concept introduced also by Tsatsaronis is that of the specific cost, where the cost of the addition of exergy to a current is determined and charged to the unit that make use of that exergy [2].

Cerqueira and Nebra [2] applied thermoeconomical analysis for gas turbine cogeneration problem. Besides, used four thermoeconomical methodologies, to compare the results of the power and heat cost, obtaining a significant difference of these costs for each applied methodology.

Flow	Composition	Temperature (ºC)	Pressure (kPa)	Mass flow (kg/s)
1	Air	25.00	101.30	33.1500
2	Air	25.00	101.30	1.3710
3	Air	25.00	101.30	31.7800
4	Natural gas	25.00	101.30	0.0878
5	Exhaust gases	645.00	121.60	1.4590
6	Exhaust gases	635.00	121.60	1.4590
7	Exhaust gases	180.40	121.60	1.4590
8	Exhaust gases	112.30	121.60	1.4590
9	Exhaust gases	90.00	121.60	1.4590
10	Water	25.00	101.30	0.7265
11	Water	25.00	101.30	0.6524
12	Water	25.00	101.30	0.0742
13	Water	25.02	200.00	0.0742
14	Water	61.02	200.00	0.3707
15	Water	61.06	350.00	0.3707
16	Water	84.03	350.00	0.3707
17	Water	100.00	350.00	0.3811
18	Water	100.10	800.00	0.3811
19	Water	167.40	800.00	0.3811
20	Steam	170.40	800.00	0.3811
21	Steam	190.40	800.00	0.3811
22	Steam	190.40	800.00	0.0104
23	Steam	178.00	350.00	0.0104
24	Steam	190.40	800.00	0.3707
25	Water	70.00	101.30	0.2966
26	Water	70.02	200.00	0.2966
27	Water	25.00	101.30	37.6100
28	Water	25.04	300.00	37.6100
29	Water	31.85	300.00	37.6100
30	Water	37.00	300.00	37.6100
31	Air (90%)	34.00	101.30	32.4300
32	Water	65	150	17.5500
33	Water	65.03	300	17.5500
34	Water	80	225	17.5500

Table 1: Thermodynamics states

In this work, three methodologies based in the Theory of the Exergetic Cost, Functional Analysis and Functional Analysis using negentropy were applied for the HC cogeneration system.

The exergetic cost is defined by the following equation:

$$E^{*} = k.E_{X} \quad (1)$$

The exergetic cost balance in a control volume is given by the following equation:

$$\sum E^*_{e,i} = \sum E^*_{s,j} \quad (2)$$

The monetary cost is defined by the following equation:

$$C = c.E_X \quad (3)$$

The monetary cost balance in a control volume is given by the following equation:

$$\sum C_{e,i} + Z_k = \sum C_{s,j} \quad (4)$$

The theory of the Exergetic Cost

The Theory of the Exergetic Cost (TEC) proposed by Lozano and Valero [5] consists of dividing appropriately the system into sub-systems, identifying the input and output exergetic flows, classifying them in fuels and products. Other authors have also worked with this methodology, proposing different approaches.

Following this methodology the system was separated in 9 control volumes: engine, HRSG (including the de-aerator and the pump 4), absorption refrigeration system and cooling tower (including the pump 6 and 7), mixer, process, pump 1, pump 2, pump 3 and pump 5. The Figure 2 shows the layout used for this evaluation. The fuels, products and losses of the control volumes are presented in the Table 2.

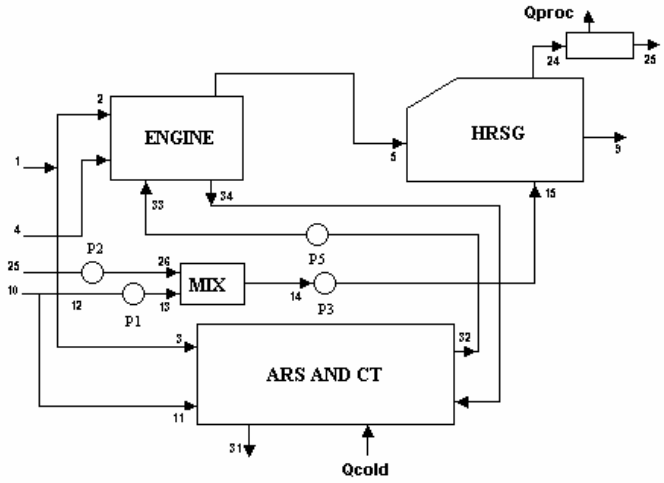

Figure 2: Layout for the Theory of the Exergetic Cost analysis

The exergetic and monetary cost balance in each control volume of the Figure 2 shows the following equations:

Engine

$$E^*_2 + E^*_4 + E^*_{33} = E^*_{em} + E^*_5 + E^*_{34} \quad (5)$$

$$C_2 + C_4 + C_{33} + Z_{motor} = C_{em} + C_5 + C_{34} \quad (6)$$

HRSG

$$E^*_5 + E^*_{15} + E^*_{B4} = E^*_{24} + E^*_9 \quad (7)$$

$$C_5 + C_{15} + C_{B4} + Z_{HRSG} = C_{24} + C_9 \quad (8)$$

ARS and CT

$$E^*_{34} + E^*_3 + E^*_{11} + E^*_{B6} + E^*_{B7} = E^*_{Qref} + E^*_{31} + E^*_{32} \quad (9)$$

$$C_{34} + C_3 + C_{11} + C_{B6} + C_{B7} + Z_{SRA+TER} = C_{Qref} + C_{31} + C_{32} \quad (10)$$

Control volume	Fuel	Product	Losses
Engine	$Ex_2+Ex_4-Ex_5-(Ex_{34}-Ex_{33})$	W_e	
HRSG	Ex_5+W_{B4}	$Ex_{24}-Ex_{15}$	Ex_9
ARS and CT	$(Ex_{34}-Ex_{32})+W_{B6}+W_{B7}+Ex_{11}+Ex_3$	Ex_{Qref}	Ex_{31}
Mixer	$Ex_{26}+Ex_{13}$	Ex_{14}	
Pump 1	W_{B1}	$(Ex_{13}-Ex_{12})$	
Pump 2	W_{B2}	$(Ex_{26}-Ex_{25})$	
Pump 3	W_{B3}	$(Ex_{15}-Ex_{14})$	
Pump 5	W_{B5}	$(Ex_{33}-Ex_{32})$	
Process	$(Ex_{24}-Ex_{25})$	$Ex_{Qprocesso}$	

Table 2: Fuels, products and losses for the Theory of the Exergetic Cost analysis

Process

$$E^*_{24} = E^*_{Qproc} + E^*_{25} \quad (11)$$

$$C_{24} + Z_{proc} = C_{Qproc} + C_{25} \quad (12)$$

Mixer

$$E^*_{13} + E^*_{26} = E^*_{14} \quad (13)$$

$$C_{13} + C_{26} + Z_{mist} = C_{14} \quad (14)$$

Pump 1

$$E^*_{B1} + E^*_{12} = E^*_{13} \quad (15)$$

$$C_{B1} + C_{12} + Z_{B1} = C_{13} \quad (16)$$

Pump 2

$$E^*_{B2} + E^*_{25} = E^*_{26} \quad (17)$$

$$C_{B2} + C_{25} + Z_{B2} = C_{26} \quad (18)$$

Pump 3

$$E^*_{B3} + E^*_{14} = E^*_{15} \quad (19)$$

$$C_{B3} + C_{14} + Z_{B3} = C_{15} \quad (20)$$

Pump 5

$$E^*_{B5} + E^*_{32} = E^*_{33} \quad (21)$$

$$C_{B5} + C_{32} + Z_{B5} = C_{33} \quad (22)$$

which Bi is used to indicate the bombs of the Figure 1.

These equations are not enough to determine all the exergetic and monetary costs. Then, to get a equation system with one solution is necessary to arbitrate the following equations:

For exergetic cost

$$k_1 = k_4 = k_{10} = 1 \quad (23)$$

$$k_9 = k_{31} = 0 \quad (24)$$

$$k_3 = k_2 = k_1 \quad (25)$$

$$k_{12} = k_{11} = k_{10} \quad (26)$$

$$k_{34} = k_5 = k_4 \quad (27)$$

$$k_{24} = k_{25} \quad (28)$$

$$k_{34} = k_{32} \quad (29)$$

For monetary cost

$$c_1 = c_9 = c_{31} = 0 \quad (30)$$

$$c_3 = c_2 = c_1 \quad (31)$$

$$c_{12} = c_{11} = c_{10} \quad (32)$$

$$c_{34} = c_{32} = c_4 \quad (33)$$

$$c_5 = c_4 \quad (34)$$

$$c_{24} = c_{25} \quad (35)$$

$$c_4 = 16{,}37854\ \text{US\$/MWh} \quad (36)$$

$$c_{10} = 1{,}5\ \text{US\$/MWh} \quad (37)$$

The results of this analysis are shown in the Table 3.

Flow	Composition	Exergetic cost		Monetary cost	
		k	E*	c US$/MWh	C US$/h
1	Air	1.000	28.080	0.00	0.00
2	Air	1.000	1.161	0.00	0.00
3	Air	1.000	26.910	0.00	0.00
4	Natural gas	1.000	3635.000	16.38	59.54
5	Exhaust gases	1.000	627.300	16.38	10.27
9	Exhaust gases	0.000	0.000	0.00	0.00
10	Water	1.000	36.330	1.50	0.05
11	Water	1.000	32.620	1.50	0.05
12	Water	1.000	3.707	1.50	0.01
13	Water	1.007	3.740	1.69	0.01
14	Water	2.005	43.500	34.46	0.75
15	Water	2.011	43.750	34.62	0.75
24	Steam	2.123	671.800	38.48	12.17
25	Water	2.123	39.630	38.48	0.72
26	Water	2.127	39.760	38.57	0.72
31	Air (90%)	0.000	0.000	0.00	0.00
32	Water	1.000	1059.000	16.38	17.34
33	Water	1.009	1071.000	16.58	17.61
34	Water	1.000	1212.000	16.38	19.85
Em	Engine electricity	2.668	2868	56.67	60.92
Qproc	Process heat	2.123	632.2	38.48	11.46
Qcold	Absorption heat	4.663	259.3	180.50	10.04
P1	Pump power	2.668	0.033	56.67	0.00
P2	Pump power	2.668	0.133	56.67	0.00
P3	Pump power	2.668	0.252	56.67	0.01
P5	Pump power	2.668	11.930	56.67	0.25

Table 3: Results with Theory of the Exergetic Cost analysis

Thermoeconomic Functional Analysis

The Thermoeconomic Functional Analysis in a complex thermal installation is understood as a system composed for connected units. Each unit has a unique function (or product) that determines its relation with the others units. This analysis was presented by Frangopoulos [3], it is based on the concept of junctions and distributors of exergy, and on the construction of the functional diagram.

The Figure 3 shows the functional diagram used to analyze the cogeneration system. In this analysis, the exergy hasn't been divided into pressure and thermal associated parts; it was taken as total exergy.

Following this methodology the system was separated in 15 control volumes: engine, HRSG (including the de-aerator and the pump 4), absorption refrigeration system and cooling tower (including the pump 6 and 7), mixer, pump 1, pump 2, pump 3 and pump 5, process, water distributor, air distributor, fuel distributor, electric power distributor, exergy junction and exergy distributor. Each unit generates a product through the consumption of a unique fuel; the fuels and products of the control volumes are presented in the Table 4.

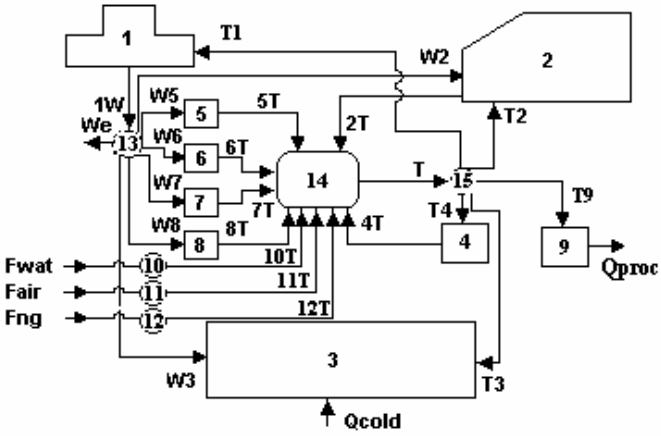

Figure 3 – Functional Diagram

Control volume	Fuels	Products
1. Engine	$T1=(Ex_2+Ex_4-Ex_5)-(Ex_{34}-Ex_{33})$	$1W=W_{engine}$
2. HRSG	$T2=Ex_5-Ex_9$; $W2=W_{B4}$	$2T=Ex_{24}-Ex_{15}$
3. ARS and CT	$T3=(Ex_{34}-Ex_{32})+(Ex_{11}+Ex_3-Ex_{31})$; $W3=W_{B6}+W_{B7}$	$E_{Qref}=Ex_{Qref}$
4. Mixer	$T4=Ex_{26}+Ex_{13}$	$4T=Ex_{14}$
5. Pump 1	$W5=W_{P1}$	$5T=(Ex_{13}-Ex_{12})$
6. Pump 2	$W6=W_{P2}$	$6T=(Ex_{26}-Ex_{25})$
7. Pump 3	$W7=W_{P3}$	$7T=(Ex_{15}-Ex_{14})$
8. Pump 5	$W8=W_{P5}$	$8T=(Ex_{33}-Ex_{32})$
9. Process	$T9=(Ex_{24}-Ex_{25})$	$E_{Qproc}=Ex_{Qprocess}$
10. Water distributor	$Fwat=Ex_{10}$	$10T=Ex_{10}$
11. Air distributor	$Fair=Ex_1$	$11T=Ex_1$
12. NG distributor	$Fng=Ex_4$	$12T=Ex_4$
13. Electric power allocation	1W	W2+W3+W5+W6+W7 +W8+We
14. Exergy junction	2T; 4T; 5T; 6T; 7T; 8T; 10T; 11T; 12T	T=2T+4T+5T+6T+7T+8T +10T+11T+12T
15. Exergy distributor	T	T1+T2+T3+T4+T9

Table 4 – Fuels and products for thermoeconomic functional analysis

The exergetic and monetary cost balance determines in each unit the fuels and products cost. The exergetic and monetary cost balance in each control volume of Figure 3 are performed through the following equations:

Engine

$$E^*_{T1} = E^*_{1W} \quad (38)$$

$$C_{T1} + Z_{engine} = C_{1W} \quad (39)$$

HRSG

$$E^*_{T2} + E^*_{W2} = E^*_{2T} \quad (40)$$

$$C_{T2} + C_{W2} + Z_{HRSG} = C_{2T} \quad (41)$$

ARS+CT

$$E^*_{T3} + E^*_{W3} = E^*_{Qcold} \quad (42)$$

$$C_{T3} + C_{W3} + Z_{ARS+CT} = C_{Qcold} \quad (43)$$

Mixer

$$E^*_{T4} = E^*_{4T} \quad (44)$$

$$C_{T4} + Z_{mixt} = C_{4T} \quad (45)$$

Pump 1

$$E^*_{W5} = E^*_{5T} \quad (46)$$

$$C_{W5} + Z_{P1} = C_{5T} \quad (47)$$

Pump 2

$$E^*_{W6} = E^*_{6T} \quad (48)$$

$$C_{W6} + Z_{P2} = C_{6T} \quad (49)$$

Pump 3

$$E^*_{W7} = E^*_{7T} \quad (50)$$

$$C_{W7} + Z_{P3} = C_{7T} \quad (51)$$

Pump 5

$$E^*_{W8} = E^*_{8T} \quad (52)$$

$$C_{W8} + Z_{P5} = C_{8T} \quad (53)$$

Process

$$E^*_{T9} = E^*_{Qproc} \quad (54)$$

$$C_{T9} + Z_{proc} = C_{Qproc} \quad (55)$$

Exergy Junction and distributor

$$E^*_{T1} + E^*_{T2} + E^*_{T3} + E^*_{T4} + E^*_{T9} = E^*_{2T} + E^*_{4T} + E^*_{5T} + E^*_{6T} + E^*_{7T} + E^*_{8T} + E^*_{Fng} + E^*_{Fair} + E^*_{Fwat} \quad (56)$$

$$C_{T1} + C_{T2} + C_{T3} + C_{T4} + C_{T9} = C_{2T} + C_{4T} + C_{5T} + C_{6T} + C_{7T} + C_{8T} + C_{Fng} + C_{Fair} + C_{Fwat} \quad (57)$$

These equations are not enough to determine all the exergetic and monetary costs. Then, to get an equation system with unique solution it is necessary to arbitrate the following equations:

For exergetic cost

$$k_{Fng} = k_{Fair} = k_{Fwat} = 1 \quad (58)$$

$$k_{T1} = k_{T2} \quad (59)$$

$$k_{T3} = k_{T4} \quad (60)$$

$$k_{T4} = k_{T9} \quad (61)$$

For monetary cost

$$c_{T1} = c_{T2} = c_{T3} = c_{T4} = c_{T9} \quad (62)$$

$$c_{Fng} = 16{,}37854 \text{ US\$/MWh} \quad (63)$$

$$c_{Fwat} = 1{,}5 \text{ US\$/MWh} \quad (64)$$

$$c_{Fair} = 0 \quad (65)$$

The Table 5 shows exergetic and monetary costs calculated for the cogeneration system using the Thermoeconomic Functional Analysis methodology. These results are different from that obtained with the Exergetic Cost Theory. With this methodology is keeping the trend in the unit exergetic cost of the products, however is observed that electricity unitary cost increased and the unitary costs of the steam and refrigeration (cold) production decreased.

Flow	Exergetic cost		Monetary cost	
	k	E*	c (US$/MWh)	C (US$/h)
Fwat	1.000	36.330	1.50	0.05
Fair	1.000	28.000	0.00	0.00
Fng	1.000	3635.000	16.38	59.54
2T	1.883	554.700	34.79	10.25
4T	1.164	25.250	20.08	0.44
5T	4.583	0.037	98.32	0.00
6T	4.983	0.150	106.90	0.00
7T	4.712	0.283	101.10	0.01
8T	4.469	13.410	95.90	0.29
T1	1.127	3222.000	18.53	52.97
T2	1.127	553.800	18.53	9.10
T3	1.127	156.000	18.53	2.57
T4	1.127	25.250	18.53	0.42
T9	1.127	335.600	18.53	5.52
1W	2.998	3222.000	62.21	66.87
W2	2.998	0.893	62.21	0.02
W3	2.998	52.900	62.21	1.10
W5	2.998	0.037	62.21	0.00
W6	2.998	0.150	62.21	0.00
W7	2.998	0.283	62.21	0.01
W8	2.998	13.410	62.21	0.28
We	2.998	3155.000	62.21	65.47
Qproc	1.127	335.600	18.53	5.52
Qcold	3.757	208.900	182.40	10.14

Table 5: Results with thermoeconomic functional analysis

Thermoeconomic Functional using negentropy

In the Exergetic Cost Theory the cost of the external irreversibility is load to the last unit product, being thus its cost overestimate. The negentropy was used for the external irreversibility evaluation by Frangopoulos. The objective of the negentropy is the costs redistribution: it gives credit or pain the process when it decreases or increases the entropy, respectively.

The negentropy is defined by:

$$S = \dot{m}.T_o.(s - s_o) \quad (66)$$

The negentropy flow for each control volume is give by:

$$N_i = S_i - S_{i-1} \quad (67)$$

"i-1" is the negentropy flow that input into control volume. The negentropy cost is defined by:

$$N_i^* = k_{n,i}.N_i \quad (68)$$

$k_{n,i}$ is the unit negentropy cost

The Figure 4 shows the functional diagram, considering negentropy, used to analyze the cogeneration system. The fuels and products of the control volumes are shows in the Table 6.

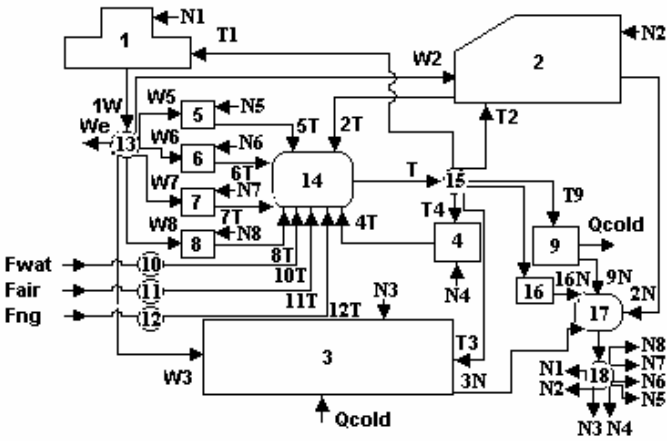

Figure 4: Functional diagram using negentropy for thermoeconomic analysis

Control volume	Fuel	Product
1. Engine	$T1=(Ex_2+Ex_4-Ex_5)-(Ex_{34}-Ex_{33})$ $N1=(S_5-S_4-S_2)+(S_{34}-S_{33})$	$1W=W_{engine}$
2. HRSG	$T2=Ex_5-Ex_9$; $W2=W_{B4}$ $N2=S_{24}-S_{15}$	$2T=Ex_{24}-Ex_{15}$ $2N=S_5-S_9$
3. ARS and CT	$T3=(Ex_{34}-Ex_{32})+(Ex_{11}+Ex_3-Ex_{31})$; $W3=W_{B6}+W_{B7}$ $N3=S_{31}-S_3-S_{11}$	$E_{Qcold}=Ex_{Qcold}$ $3N=S_{34}-S_{32}$
4. Mixturer	$T4=Ex_{26}+Ex_{13}$ $N4=S_{14}-S_{13}-S_{26}$	$4T=Ex_{14}$
5. Pump 1	$W5=W_{B1}$ $N5=S_{13}-S_{12}$	$5T=Ex_{13}-Ex_{12}$
6. Pump 2	$W6=W_{B2}$ $N6=S_{26}-S_{25}$	$6T=Ex_{26}-Ex_{25}$
7. Pump 3	$W7=W_{B3}$ $N7=S_{15}-S_{14}$	$7T=Ex_{15}-Ex_{14}$
8. Pump 5	$W8=W_{B5}$ $N8=S_{33}-S_{32}$	$8T=Ex_{33}-Ex_{32}$
9. Process	$T9=Ex_{24}-Ex_{25}$	$E_{Qproc}=Ex_{Qprocess}$ $9N=S_{24}-S_{25}$
10. Water distributor	$Fwat=Ex_{10}$	$10T=Ex_{10}$
11. Air distributor	$Fair=Ex_1$	$11T=Ex_1$
12. NG distributor	$Fng=Ex_4$	$12T=Ex_4$
13. Electric power allocation	1W	W2+W3+W5+W6+W7 +W8+We
14. Exergy junction	2T; 4T; 5T; 6T; 7T; 8T; 10T; 11T; 12T	T=2T+4T+5T+6T+7T+8T +10T+11T+12T
15. Exergy distributor	T	T1+T2+T3+T4+T9
16. Chimney	$T16=Ex_{31}+Ex_9$	$16N=S_{31}+S_9$
17. Negentropy junction	2N; 3N; 9N; 16N	N=2N+3N+9N+16N
18. Negentropy distributor	N	N1+N2+N3+N4+N5+N6+N7+N8

Table 6 – fuels and products for thermoeconomic functional analysis using negentropy

For this methodology three new virtual units had been added: the chimney, the junction and the negentropy distributor. The chimney produces negentropy, necessary to carry the humid air and exhaust gases that leave the cooling tower and HRSG, respectively, until the equilibrium conditions with the environment. The absorption refrigeration system produces negentropy, since it diminishes the entropy of the hot water used in the engine cooling. The HRSG consumes negentropy when the entropy of the water is increased to produce steam, and it produces negentropy when the entropy of the engine exhaust gases is decreased. The engine, the pumps, the mixturer and the cooling tower are pieces of equipment that consumes negentropy.

The exergetic and monetary cost balance determines in each unit the fuels and products cost. The exergetic and monetary cost balance in each control volume of the Figure 4 shows the following equations:

Engine

$$E^*_{T1} + E^*_{N1} = E^*_{1W} \quad (69)$$

$$C_{T1} + C_{N1} + Z_{engine} = C_{1W} \quad (70)$$

HRSG

$$E^*_{T2} + E^*_{N2} + E^*_{W2} = E^*_{2T} + E^*_{2N} \quad (71)$$

$$C_{T2} + C_{N2} + C_{W2} + Z_{HRSG} = C_{2T} + C_{2N} \quad (72)$$

ARS+CT

$$E^*_{T3} + E^*_{N3} + E^*_{W3} = E^*_{Qcold} + E^*_{3N} \quad (73)$$

$$C_{T3} + C_{N3} + C_{W3} + Z_{ARS+CT} = C_{Qcold} + C_{3N} \quad (74)$$

Mixer

$$E^*_{T4} + E^*_{N4} = E^*_{4T} \quad (75)$$

$$C_{T4} + C_{N4} + Z_{mixt} = C_{4T} \quad (76)$$

Pump 1

$$E^*_{W5} + E^*_{N5} = E^*_{5T} \quad (77)$$

$$C_{W5} + C_{N5} + Z_{P1} = C_{5T} \quad (78)$$

Pump 2

$$E^*_{W6} + E^*_{N6} = E^*_{6T} \quad (79)$$

$$C_{W6} + C_{N6} + Z_{P2} = C_{6T} \quad (80)$$

Pump 3

$$E^*_{W7} + E^*_{N7} = E^*_{7T} \quad (81)$$

$$C_{W7} + C_{N7} + Z_{P3} = C_{7T} \quad (82)$$

Pump 5

$$E^*_{W8} + E^*_{N8} = E^*_{8T} \quad (83)$$

$$C_{W8} + C_{N8} + Z_{P5} = C_{8T} \quad (84)$$

Process

$$E^*_{T9} = E^*_{Qproc} + E^*_{9N} \quad (85)$$

$$C_{T9} + Z_{proc} = C_{Qproc} + C_{9N} \quad (86)$$

Chimney

$$E^*_{T16} = E^*_{16N} \quad (87)$$

$$C_{T16} = C_{16N} \quad (88)$$

Exergy Junction and distributor

$$E^*_{2T} + E^*_{4T} + E^*_{5T} + E^*_{6T} + E^*_{7T} + E^*_{8T} + E^*_{Fng} + E^*_{Fair} + E^*_{Fwat} = E^*_{T1} + E^*_{T2} + E^*_{T3} + E^*_{T4} + E^*_{T9} + E^*_{T16} \quad (89)$$

$$C_{2T} + C_{4T} + C_{5T} + C_{6T} + C_{7T} + C_{8T} + C_{Fng} + C_{Fair} + C_{Fwat} = C_{T1} + C_{T2} + C_{T3} + C_{T4} + C_{T9} + C_{T16} \quad (90)$$

These equations are not enough to determine all the exergetic and monetary costs. Then, to get an equation system with unique solution it is necessary to arbitrate the following equations:

For exergetic cost

$$k_{Fng} = k_{Fair} = k_{Fwat} = 1 \quad (91)$$

$$k_{T1} = k_{T2} = k_{T3} = k_{T4} = k_{T9} = k_{T16} \quad (92)$$

$$k_{N1} = k_{N2} = k_{N3} = k_{N4} = k_{N5} = k_{N6} = k_{N7} = k_{N8} \quad (93)$$

$$k_{2N} = k_{3N} = k_{9N} = k_{16N} \quad (94)$$

For monetary cost

$$c_{T1} = c_{T2} = c_{T3} = c_{T4} = c_{T9} = c_{T16} \quad (95)$$

$$c_{N1} = c_{N2} = c_{N3} = c_{N4} = c_{N5} = c_{N6} = c_{N7} = c_{N8} \quad (96)$$

$$c_{2N} = c_{3N} = c_{9N} = c_{16N} \quad (97)$$

$$c_{Fng} = 16{,}37854 \text{ US\$/MWh} \quad (98)$$

$$c_{Fwat} = 1{,}5 \text{ US\$/MWh} \quad (99)$$

$$c_{Fair} = 0 \quad (100)$$

The Table 7 shows exergetic and monetary costs calculated for the cogeneration system with Functional Analysis using Negentropy methodology. These results are different to these gotten with the Exergetic Cost Theory and Functional Analysis. It is observed that electricity unitary cost increased and the unitary costs of the steam and refrigeration (cold) production decreased.

Flow	Exergetic cost		Monetary cost	
	K	E*	c (US$/MWh)	C (US$/h)
Fwat	1.000	36.330	1.50	0.05
Fair	1.000	28.000	0.00	0.00
Fng	1.000	3635.000	16.38	59.54
2T	1.942	572.100	35.77	10.54
4T	1.161	25.190	20.03	0.43
5T	4.874	0.039	103.10	0.00
6T	5.300	0.159	112.10	0.00
7T	4.996	0.300	105.80	0.01
8T	4.723	14.170	100.10	0.30
T1	1.121	3204.000	18.42	52.67
T2	1.121	550.600	18.42	9.05
T3	1.121	155.100	18.42	2.55
T4	1.121	25.110	18.42	0.41
T9	1.121	333.700	18.42	5.49
T16	1.121	42.910	18.42	0.71
1W	3.142	3377.000	64.58	69420.00
W2	3.142	0.936	64.58	0.02
W3	3.142	55.440	64.58	1.14
W5	3.142	0.038	64.58	0.00
W6	3.142	0.157	64.58	0.00
W7	3.142	0.296	64.58	0.01
W8	3.142	14.050	64.58	0.29
We	3.142	3306.000	64.58	67962.00
Qproc	0.866	257.800	14.23	4.24
Qcold	2.431	135.200	160.60	8.93
2N	0.116	55.260	1.90	0.91
3N	0.116	110.000	1.90	1.81
9N	0.116	75.920	1.90	1.25
16N	0.116	42.910	1.90	0.71
N1	0.116	173.500	1.90	2.85
N2	0.116	75.830	1.90	1.25
N3	0.116	34.630	1.90	0.57
N4	0.116	0.083	1.90	0.00
N5	0.116	0.001	1.90	0.00
N6	0.116	0.002	1.90	0.00
N7	0.116	0.003	1.90	0.00
N8	0.116	0.116	1.90	0.00

Table 7: Thermoeconomic functional analysis using negentropy

CONCLUSIONS

Three thermoeconomic methodologies were applied to a cogeneration system. There are differences in the costs of power, steam and refrigeration (cold) production which resulted from the application of the methodologies. The Theory of the Exergetic Cost showed that the unitary cost to produce refrigeration is more expensive than the electricity and the process heat. In the Functional Analysis the unit exergetic cost of the products have the same trends that with the Theory of the Exergetic Cost, however is observed that power unitary cost increased and the unitary costs of the steam and refrigeration (cold) production decreased. The difference between both methodologies is that in The Functional Analysis is not pain a unique piece of equipment (in ours case the exhaust gases of the HRSG and humid air that leaves the cooling tower) in the irreversibilities allocation. The exergy junction and distributor allow distributing the exergetic costs and irreversibility proportionally by the diverse piece of equipment. The Functional Analysis using Negentropy shows bigger differences in the costs allocation, because in this type of analysis the absorption refrigeration system would be acting as a condenser for engine cooling water.

ACKNOWLEDGMENTS

The authors would like to thank the Financer Bureau of Studies and Projects (FINEP) and the Research Council of Scientific and Technological Development (CNPq) by the financing offered.

REFERENCES

[1] Bejan, A., Tsatsaronis, G., Moran, M., 1996, Thermal design & optimization, John Wiley & Sons, 542 p.

[2] Cerqueira, S. and Nebra, S.A., 1999, Cost attribution methodologies in cogeneration systems, Energy Conversion and Management, v. 20, 1587-1597 p.

[3] Frangopoulos, C., 1994, Application of the thermoeconomic functional approach to the CGAM problem, Energy, v. 19, 322-342 p.

[4] Gonzales, R.P. and Nebra, S.A., 2004, Energetic, Exergetic and Exergetic Cost Analysis for a cogeneration system integrated by an internal combustion engine, HRSG and an absorption refrigeration system, ESDA2004-58052, July 19-22, Manchester, UK.

[5] Lozano, M.A. and Valero, A., 1993, Theory of the Exergetic Cost, Energy, vol. 18, No. 9, 939-960 p.

[6] Tsatsaronis, G. and Pisa, J., 1994, Exergoeconomic evaluation and optimization of energy systems – application to the CGAM problem, Energy, v.19, 287-321 p.

[7] Szargut et al., 1988, Exergy analysis of thermal and metallurgical processes, 332p.

Proceedings of ECOS 2005
Trondheim, Norway
June 20–22, 2005

SPECIFIC EXERGY COSTS AND REVENUES IN A TWO-PRESSURE COMBINED CYCLE PLANT

David Paulus[1]
Technical University of Berlin
Institute for Energy Engineering
Marchstrasse 18
10587 Berlin, Germany

Naroa Gonzales Zarraonandia
ESCP-EAP (European School of Management)
Arroyofresno 1
28035 Madrid, Spain

ABSTRACT

Paulus and Tsatsaronis presented a method with which specific exergy *revenues* can be calculated, as opposed to specific exergy *costs*. In this paper, specific exergy revenues and costs are calculated for a hypothetical two-pressure combined cycle power plant. First, the plant-internal specific exergy revenues and associated exergoeconomic variables are calculated for the case when the product revenues are equal to the product costs. The exergoeconomic, revenue-based variables are then compared to those resulting from the traditional, cost-based methods. The good agreement of the exergoeconomic variables calculated by both methods provides evidence of the validity of the proposed auxiliary equations for calculating revenues. Then, a parametric study with varying product revenues is performed. The resulting exergoeconomic variables show that, for a fixed fuel input, increased capital investment is desired as the products become more valuable.

Keywords: exergoeconomics, thermoeconomics, specific exergy revenue

NOMENCLATURE

c	specific exergy cost
$\dot{C}$	monetary flow
$\dot{E}$	exergy flow
f	f-factor
r	specific exergy revenue
$\dot{W}$	power
$\dot{Z}$	capital cost flow

Greek Variables

ε	exergetic efficiency

Subscripts

D	destruction
el	electric
F	fuel
i	component i
j	stream j
P	product

INTRODUCTION

Exergoeconomics is traditionally employed to find the specific cost of exergy associated with flows within a system, as well as the final product costs. In order to do this, monetary balances are written for each component, along with the appropriate auxiliary equations. When the cost of fuel is known, the resulting system of equations allows for the finding of the desired specific exergy costs, both within and at the boundaries of the system. The methodology for finding these auxiliary equations has been formulated by Lazzaretto and Tsatsaronis [1, 2, 3].

These costs can be used to calculate certain exergoeconomic variables, such as the f-factor. These variables are useful in the optimization of an energy system, when the goal is to minimize the total cost for a fixed output with the fuel and capi-

[1] corresponding author. e-mail: d.paulus@iet.tu-berlin.de

tal investment as the independent variables. (See, for example, [4])

There are times, however, when instead of specific exergy cost, it is desirable to find the specific revenue associated with the exergy flows of a system, and to calculate the other exergoeconomic variables therewith. As when calculating costs, monetary balances form part of the necessary set of equations to determine the revenues. However, the set of auxiliary equations will differ from that used for calculating costs, and the price of the products replaces the cost of the fuel as a boundary condition. Paulus and Tsatsaronis [5] developed a methodology for determining the auxiliary equations for finding specific exergy revenues, as well as explained the fundamental difference between specific exergy costs and revenues, and recommended when the latter should be used.

The purpose of this paper is to further examine the methodology given by Paulus and Tsatsaronis [5]. A comparison is made between exergoeconomic variables (cost rates of exergy destruction and f-factors) when calculated with costs and revenues for a hypothetical two-pressure combined cycle power plant (CCPP). When calculating specific exergy revenues, the specific revenue associated with electric power was set equal to its average cost. For this case, it was expected that the exergoeconomic variables should be in relatively good agreement when calculated from either revenue or cost data. It will be shown that, for most components, exergoeconomic variables calculated by both means have satisfactory agreement; the deviations will be elaborated upon.

One case where revenues are recommended for calculating exergoeconomic variables in lieu of costs is for the optimization of a system with a fixed fuel input. In this case, increased efficiency results in greater product revenue flow. In the optimization, capital costs are traded against the total product revenue flow. Therefore, components of the same system should show increased cost rates of exergy destruction with increasing product prices (specific revenue). The cost rate of exergy destruction here approximates the lost sales (lost product revenue) due to the exergy destruction in the component. As the cost rates of exergy destruction increase, the f-factors, which show the ratio of capital cost to total cost, decrease. A parametric study with varying product prices (revenues) has been performed on the sample CCPP, and it will be shown that the cost rates of exergy destruction and the f-factors behave as expected with varying product revenues.

THE AUXILIARY EQUATION RULES

Costs

The following two rules for formulating the auxiliary equations are valid when it is desired to find the specific costs of exergy associated with flows:

F-Principle: The total cost associated with the removal of exergy must be equal to the cost at which the removed exergy was supplied to the same stream in upstream components. [3]

P-Principle: Each exergy unit is supplied to any stream associated with the product at the same average cost. [3]

Revenues

The following two rules for formulating the auxiliary equations are valid when it is desired to find the specific revenues associated with exergy flows:

F-Principle (for revenues): Each exergy unit, of any type of exergy, which is supplied by any fuel stream to a device, has the same specific revenue associated with it. [5]

P-Principle (for revenues): The revenue associated with a unit of exergy, supplied to a stream, is the same as the revenue of a unit of exergy removed from the same stream in a downstream component. [5]

THE EXAMPLE SYSTEM

Description

The example system is a natural gas-fired, two-pressure CCPP, modeled in GateCycle. A system diagram is at the end of this article (Figure 2); the exergy flows are given in Table 1. Table 2 shows the capital costs for each component.

Fuel, Product and Efficiency Definitions

The definitions for the exergetic fuel and product are per Tsatsaronis et al. [1-3]. These definitions are independent of whether specific costs or revenues are being calculated.

Table 1: Exergy Flows

Stream	Exergy Flow [MW]	Stream	Exergy Flow [MW]
1	138.90	21	18.33
2	128.13	22	0.81
3	112.08	23	0.84
4	66.53	24	6.12
5	53.86	25	0.87
6	53.02	26	6.81
7	30.75	27	6.91
8	21.67	28	2.23
9	60.21	29	4.67
10	45.96	30	4.89
11	59.38	31	0.78
12	51.62	32	500.23
13	14.56	33	11.03
14	59.70	34	8.24
15	79.87	$\dot{W}_{el,\mathrm{GT1}}$	151.79
16	0.35	$\dot{W}_{el,\mathrm{ST1}}$	13.11
17	21.41	$\dot{W}_{el,\mathrm{ST2}}$	54.91
18	1.21	$\dot{W}_{el,\mathrm{PUMP1}}$	0.04
19	20.20	$\dot{W}_{el,\mathrm{PUMP2}}$	0.10
20	20.90	$\dot{W}_{el,\mathrm{PUMP3}}$	0.24

Auxiliary Equations

The auxiliary equations used for calculating both specific costs and revenues are given in Table 3. This table shows also the relevant rule used to formulate each auxiliary equation.

Boundary Conditions

Table 2 shows capital costs. Table 3 shows the fourteen auxiliary equations, which are used in conjunction with monetary balances on each component for the calculation of specific exergy costs. With forty unknown specific exergy costs, six boundary conditions are necessary to solve the resulting set of equations.

Table 2: Components, Capital Costs and Monetary Balances

Device	Capital Cost[2] [€/hr]	Device	Capital Cost[3] [€/hr]
CND1	16.2	PUMP2	6.0
DA1	1.6	PUMP3	12.3
ECON1	38.7	SP1	0
ECON2	42.6	SP2	0
EVAP1	125.3	SP3	0
EVAP2	258.8	SPHT1	38.9
GT1	1877.	SPHT2	64.7
M1	0	SPHT3	7.8
M2	0	ST1	296.6
PUMP1	2.6	ST2	712.6

The specific cost of the exergy of the natural gas is 5.539 €/GJ. The specific cost associated with both the intake air and the cooling water is zero. (The calculated exergy flow of this air is non-zero because Szargut's standard model [6] was used for chemical exergy, and the air was modeled with a chemical composition other than the reference state employed by the standard model.) The three remaining boundary conditions are given by setting the cost of electric power to the pumps equal to the average cost of power from the plant. For the calculation of revenues, there are again twenty balances and fourteen auxiliary equations; six boundary conditions are required. For the first calculation of specific revenues and exergoeconomic variables, the specific revenue associated with electric power was set equal to the average cost of the power:

$$r_{el} = \frac{c_{32}\dot{E}_{32} + \sum_j \dot{Z}_j}{\dot{W}_{el,net}} = 1.706\,€/\mathrm{MJ} \qquad (1)$$

Streams 8 and 33 are waste streams; they have zero revenue. Also, the revenue flow associated with the air at the gas turbine was set equal to zero.

[2] The capital costs associated with piping have been included with those of the primary components. Therefore, the capital costs of mixers and splitters are zero.

[3] The capital costs associated with piping have been included with those of the primary components. Therefore, the capital costs of mixers and splitters are zero.

For the parametric study, revenues and exergoeconomic values were additionally calculated at one half, three halves and twice the average cost of electric power:

$$r_{el} = (0.5, 1.0, 1.5, 2.0) \cdot 1.706\,€/\mathrm{MJ} \quad (2)$$

Table 3: Auxiliary Equations

Device	Cost Rule	Cost. Aux. Eq.	Rev. Rule	Revenue Aux. Eq,
CND1	F	$c_{21}=c_{22}$	P	$r_{24}=r_{33}$
DA1	-	-	P	$r_{24}=r_{26}$
ECON1	F	$c_4=c_5$	P	$r_{30}=r_{13}$
ECON2	F	$c_7=c_8$	P	$r_{23}=r_{24}$
EVAP1	F	$c_3=c_4$	P	$r_{13}=r_{12}$
EVAP2	F	$c_6=c_7$	P	$r_{28}=r_{17}$
GT1	P	$c_1=c_{el,GT1}$	-	-
M1	-	-	F	$r_{11}=r_{16}$
M2	-	-	F	$r_{14}=r_{20}$
PUMP1	-	-	P	$r_{22}=r_{23}$
PUMP2	-	-	P	$r_{26}=r_{27}$
PUMP3	-	-	P	$r_{29}=r_{30}$
SP1	F	$c_{18}=c_{16}$	-	-
SP2	F	$c_{17}=c_{18}$	-	-
SP3	F	$c_{27}=c_{28}$	-	-
SPHT1	F	$c_1=c_2$	P	$r_{10}=r_{11}$
SPHT2	F	$c_2=c_3$	P	$r_{12}=r_9$
SPHT3	F	$c_5=c_6$	P	$r_{19}=r_{20}$
ST1	F	$c_9=c_{10}$	-	-
ST2	F	$c_{15}=c_{21}$	-	-

Specific Costs (Revenues) Associated with the Exergetic Fuel or Product, Costs of Exergy Destruction and F-Factors

The specific cost of the exergetic fuel (or product) is found by dividing the cost flow associated with the fuel (or product) by its exergy flow. For example, for the heat exchanger SPHT1:

$$c_{F,\mathrm{SPHT1}} = \frac{\dot{C}_1 - \dot{C}_2}{\dot{E}_1 - \dot{E}_2} = \frac{c_1\dot{E}_1 - c_2\dot{E}_2}{\dot{E}_1 - \dot{E}_2} \quad (3)$$

$$c_{P,\mathrm{SPHT1}} = \frac{\dot{C}_9 - \dot{C}_{12}}{\dot{E}_9 - \dot{E}_{12}} = \frac{c_9\dot{E}_9 - c_{12}\dot{E}_{12}}{\dot{E}_9 - \dot{E}_{12}} \quad (4)$$

The same equations are used to calculate the specific revenue of the fuel or product, with "$\dot{R}$" substituted for "$\dot{C}$" and "r" for "c".

When working with costs, the cost rate of exergy destruction is defined with [4]:

$$\dot{C}_{D,i} = c_{F,i}\dot{E}_{D,i} \quad (5)$$

Alternatively, when working with revenues, the cost rate of exergy destruction is defined with [5]:

$$\dot{C}_{D,i} = r_{P,i}\dot{E}_{D,i} \quad (6)$$

Instead of approximating the additional cost to the system, Eq. (6) approximates the lost revenue to the plant due to the exergy destruction in component *i*.

The f-factor represents the ratio of the capital cost of a component to its total cost, the sum of capital cost and the cost of exergy destruction, as defined in Eqs. (5) and (6).

$$f_i = \frac{\dot{Z}_i}{\dot{Z}_j + \dot{C}_{D,i}} \quad (7)$$

RESULTS

Specific Costs and Revenues

The resulting specific costs and revenues associated with the exergy flows are reported in Table 4. (The revenues reported therein are for the case of the revenue associated with electricity set equal to its average cost.)

Exergoeconomic Variables

The cost of exergy destruction in each component, as well as the component's f-factor, are reported in Table 5. These values are shown as calculated from (1) the specific exergy costs and (2) the specific exergy revenue when calculated with the revenue associated with electricity set equal to its average cost.

Both methods of calculating the costs of exergy destruction and the f-factors for the steam turbines show excellent agreement. (The difference in the cost of exergy destruction is less than ten percent for both turbines; the difference in f-factor is less than two percent.) The values for the heat exchangers differ more, with the cost of exergy destruction averaging about eighteen percent higher than the corresponding revenue; the resultant f-factors average fourteen percent higher.

While the values for the steam turbines and heat exchangers are reasonably close, there is substan-

tial deviation in the exergy destruction cost and the f-factor of the gas turbine.

Table 4: Specific Costs and Revenues, $r_{el}=c_{el,avg}$

Stream	c [€/GJ]	r [€/GJ]
1	11.33	5.125
2	11.33	5.012
3	11.33	4.788
4	11.33	3.370
5	11.33	2.680
6	11.33	2.642
7	11.33	1.209
8	11.33	0.000
9	15.69	9.369
10	15.69	9.201
11	15.50	9.201
12	15.73	9.369
13	17.93	9.369
14	15.52	9.204
15	16.14	9.288
16	17.37	9.201
17	17.37	9.114
18	17.37	7.605
19	17.37	9.204
20	17.35	9.204
21	16.14	0.1652
22	16.14	9.286
23	17.08	9.286
24	21.09	9.286
25	17.37	6.966
26	21.20	9.286
27	21.38	9.286
28	21.38	9.114
29	21.38	9.369
30	21.85	9.369
31	0.00	0.000
32	5.539	5.557
33[4]	26.03	0.000
34	0.00	0.000
$\dot{W}_{el,\mathrm{GT1}}$	11.33	17.06
$\dot{W}_{el,\mathrm{ST1}}$	23.34	17.06
$\dot{W}_{el,\mathrm{ST2}}$	21.70	17.06
$\dot{W}_{el,\mathrm{PUMP1}}$	14.61	-12.60
$\dot{W}_{el,\mathrm{PUMP2}}$	14.61	-8.098
$\dot{W}_{el,\mathrm{PUMP3}}$	14.61	-5.737

[4] The condenser was not treated as a dissipative component in this paper.

Table 5: Exergoeconomic Variables as Calculated from Specific Costs and Revenues (with $r_{el}=c_{el,avg}$)

Device	C_D (from c_F) [€/hr]	f (from c_F)	C_D (from r_P) [€/hr]	f (from r_P)
DA1	8.9	0.152	4.7	0.254
ECON1	122.2	0.240	101.1	0.277
ECON2	155.0	0.216	127.1	0.251
EVAP1	346.2	0.266	286.4	0.304
EVAP2	126.1	0.672	101.5	0.718
GT1	4178.5	0.310	8567.5	0.180
PUMP1	0.4	0.867	0.3	0.911
PUMP2	0.5	0.923	0.3	0.950
PUMP3	1.3	0.902	0.9	0.935
SPHT1	88.9	0.304	73.5	0.346
SPHT2	106.9	0.377	86.8	0.427
SPHT3	6.0	0.567	4.8	0.617
ST1	64.6	0.821	70.2	0.809
ST2	385.5	0.649	407.5	0.636

Parametric Study

Table 6 shows the variation of the f-factor (as calculated with $\dot{C}_{D,i}=r_{P,i}\dot{E}_{D,i}$) with varying product revenue. For all components, the f-factor declines as the product revenue increases.

DISCUSSION

Exergoeconomic Variables

In the calculation of the specific costs and revenues, the combustion gas turbine was treated as a single component, as it is typically purchased as such. Therefore, it is not possible to calculate the specific exergy costs (or revenues) of the streams internal to the gas turbine. With this treatment of the gas turbine, there are two choices for auxiliary equations.

In the auxiliary equations used to calculate the specific exergy costs, the gas turbine was assumed to have two products, and the P-rule yields $c_1=c_{el,GT1}$. This results in the proportional assignment of gas turbine's capital costs to both the power output and the gas turbine's exhaust gas.

An alternative is to assume the gas turbine to have one product, electric power. With this assumption, all of the gas turbine's capital costs are assigned to the electricity, and the F-rule yields $c_1=c_{32}$. In

order to clarify why the f-factors of heat exchangers were consistently somewhat higher when calculated based on revenue data rather than cost data, the f-factors were recalculated. In this recalculation, the f-factors were calculated based on cost data with the assumption that the gas turbine had a single product.

Table 6: Variation of the F-Factor with Varying Product Price

	f-factor			
Device	$r_{el}=0.5 \cdot c_{el,avg}$	$r_{el}=1.0 \cdot c_{el,avg}$	$r_{el}=1.5 \cdot c_{el,avg}$	$r_{el}=2.0 \cdot c_{el,avg}$
DA1	0.503	0.254	0.169	0.127
ECON1	0.542	0.277	0.186	0.140
ECON2	0.500	0.251	0.168	0.126
EVAP1	0.575	0.304	0.207	0.157
EVAP2	0.876	0.718	0.609	0.528
GT1	0.336	0.180	0.123	0.093
PUMP1	0.968	0.911	0.860	0.815
PUMP2	0.983	0.950	0.919	0.890
PUMP3	0.978	0.935	0.896	0.860
SPHT1	0.621	0.346	0.240	0.184
SPHT2	0.673	0.427	0.313	0.247
SPHT3	0.817	0.617	0.496	0.414
ST1	0.894	0.809	0.738	0.679
ST2	0.778	0.636	0.538	0.467

When the f-factors of the heat exchangers, as calculated from revenue data, were compared to those from the recalculation, it was found that those calculated from revenue data were now somewhat lower than those calculated from cost data. That is, the f-factors of the heat exchangers, when calculated from revenue data, fell between the two sets of those calculated from costs. This is shown graphically in Figure 1. The lower calculated cost of exergy at stream 1 reduces the calculated costs of exergy destruction in the heat exchangers. This reduction results in higher calculated f-factors. (Not shown on the graph is the deaerator. Its f-factor, as calculated from revenue data, also falls between the f-factors from the two sets of cost data.)

If it were possible to split the combustion gas turbine into its components, the resulting specific exergy costs would fall between those calculated assuming (1) the gas turbine has one product and (2) the gas turbine has two products. This is because, when the gas turbine is split into components: (1) the generator's capital costs would be assigned entirely to the electric power, (2) the capital costs of the compressor and combustion chamber would be assigned proportionally to the exhaust gas and the electric power and (3) the expander's capital costs would be assigned directly to mechanical power; some of these costs (approximately half) flow back to the compressor, while the remainder are assigned to the electric power. As the *majority* of the capital costs would be assigned proportionally, the results would be expected to be closer to those from the assumption of two products. Because not *all* of the capital costs are assigned proportionally, the results must lay between those of the assumptions of one product and two products. Thus, if the gas turbine could be split into components, the authors would expect the f-factors calculated from both revenues and costs to match very closely.

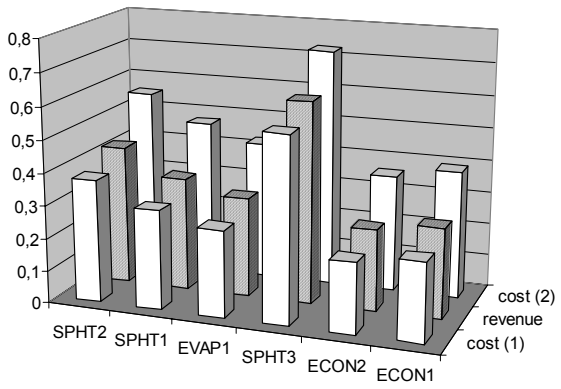

Figure 1: F-factors of the heat exchangers[5]

Calculations by the authors, estimating the internal parameters of the gas turbine, and estimating the capital costs as being equally split between the compressor, combustion chamber, turbine and generator, showed agreement in the f-factors of

[5] The set with the shaded bars was calculated from revenue data. The set cost(1) was calculated from cost data with $c_1=c_{el,GT1}$ and the set cost(2) with $c_1=c_{32}$.

these components within ten percent for all components except the combustion chamber (which had an f-factor of 0.15 and 0.092 calculated from costs and revenues, respectively).
This discussion reiterates that when a detailed cost breakdown of subassembly of an energy system is not available, even a rudimentary estimate of this breakdown may improve the accuracy of exergoeconomic calculations.

Parametric Study

The f-factor, representing the ratio of capital cost to total cost (capital cost and the cost of exergy destruction), is a tool useful in the iterative optimization of an energy system [4]. A very high f-factor is a sign that a reduction in efficiency should be accepted in order to reduce capital costs, and a very low value is a sign that additional capital should be invested in order to reduce exergy destruction. When calculated from cost data, the f-factor is in no way affected by the product price.
There are times, however, when it is desirable to have an f-factor that is influenced by price (the specific revenue associated with the product). Consider as an example a cogeneration system being designed for a company currently producing its own steam but purchasing all needed electricity. Assume that the plant will not completely meet the company's electric demand. Then, the specific revenue associated with the electricity is equal to the current purchase price of electricity for the company. Logically, if the fuel input to the plant is fixed (as it would be, for example, if the plant were fired by a gas turbine), the higher the purchase price of electricity, the more capital should be invested in the plant.
The results from the parametric study show that the f-factor, when calculated from revenue data, is strongly influenced by the product's specific revenue. As the specific revenue increases, the f-factors decrease, suggesting that more capital should be invested in each component. This is in agreement with logic and the expected behavior, and such behavior is nonexistent when the f-factors are calculated from cost data.
The authors suggest that when fuel input is fixed, exergoeconomic variables calculated from revenue data should be employed for any analysis.

CONCLUSION

Validity of the Auxiliary Equations for the Calculation of Specific Exergy Revenues

The generally good agreement between (1) the cost of exergy destruction in components and (2) the components' f-factors when calculated based on (a) costs and (b) revenues (the latter calculated with the revenue of electricity set to its average cost of production) provides evidence that the auxiliary equations for calculating the specific costs associated with exergy streams, as proposed by Paulus and Tsatsaronis [5], are valid. Although some discrepancies were initially noted, these were definitively attributed to the lumping of the individual components of the gas turbine.

Applicability of Revenues to Exergoeconomic Analysis

An exergoeconomic analysis in which specific exergy costs are used to calculate the exergoeconomic variables is unable to take into account product price information. For the case of a fixed system output, this is of no account to optimization. Minimizing product costs suffices as an optimization goal.
However, the design of some systems (including any system based on a commercially available combustion gas turbine) has the constraint of fixed fuel input. Then, capital costs are traded against additional output. In some cases (such as that of an additional power plant for a utility), minimizing the average costs likely suffices as an optimization goal. However, in other cases, such as the one where a proposed plant will offset the purchase of a currently commercially purchased commodity, it does not. In these latter cases, the economically optimal design of a plant will be strongly influenced by product price. Here, methods that take into account this price are necessary. The specific revenues associated with exergy flows should then be used to calculate exergoeconomic variables. This paper demonstrated that the use of revenues for these calculations provides price feedback to the exergoeconomic variables.

ACKNOWLEDGEMENT

The comments from Professor George Tsatsaronis are greatly appreciated.

REFERENCES

[1] Lazzaretto A, Tsatsaronis G. *A General Process-Based Methodology for Exergy Costing*. In: 1996 Proceedings of the ASME Advanced Energy Systems Division, AES-Vol. 36. New York: ASME p. 413-428.

[2] Lazzaretto A, Tsatsaronis G. *On the Quest for Objective Equations in Exergy Costing*. In: 1997 Proceedings of the ASME Advanced Energy Systems Division, AES-Vol. 37. New York: ASME p. 197-210.

[3] Lazzaretto A, Tsatsaronis G. *On the Calculation of Efficiencies and Costs in Thermal Systems*. In: 1999 Proceedings of the ASME Advanced Energy Systems Division, AES-Vol. 39. New York: ASME. p. 421-430

[4] Bejan A, Tsatsaronis G & Moran M. Thermal Design and Optimization. New York: John Wiley and Sons, 1996. Ch. 8

[5] Paulus, DM Jr.,Tsatsaronis G. *Auxiliary Equations for the Determination of Specific Exergy Revenues*. In: Proceedings of the 17th International Conference on Efficiency, Costs, Optimization, Simulation and Environmental Impact of Energy Systems, ECOS '04 (R. Rivero, L. Monroy, R. Pulido & G. Tsatsaronis, Editors), Guanajuato, México, July 7-9, 2004, p. 561-572

[6] Szargut J, Morris DR, Steward FR. *Exergy Analysis of Thermal, Chemical, and Metallurgical Processes*. New York: Hemisphere, 1988. p. 297-3

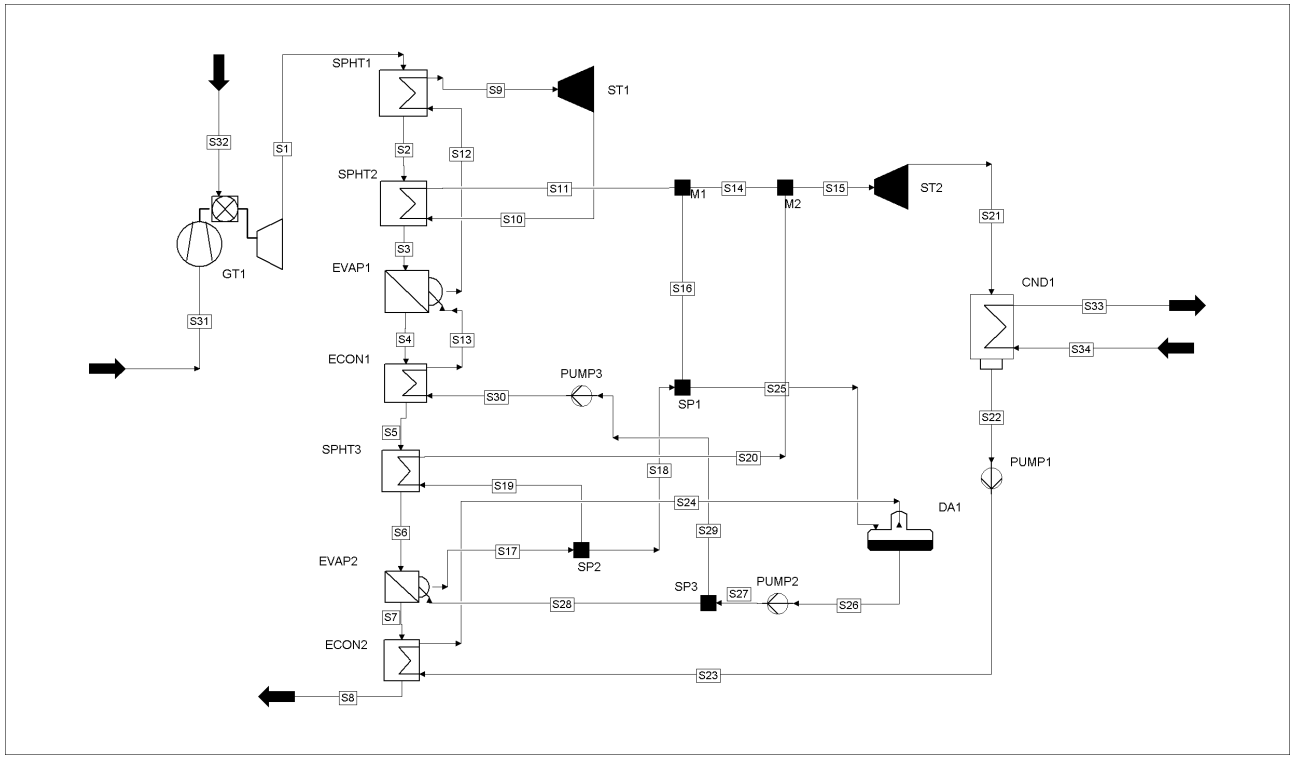

Figure 2: CCPP Flowchart

Proceedings of ECOS 2005
Trondheim, Norway
June 20–22, 2005

Thermal and economic evaluation of Heat Recovery Steam Generators (HRSG)

Sepehr Sanaye **Omid Hamidkhani**

Energy Systems Improvement Laboratory
Mechanical Engineering Department
Iran University of Science and Technology (IUST)
Tehran, Iran

Abstract
One of the efficient power producing technologies is the combined cycle which includes both Brayton (topping) and Rankine (bottoming) cycles. Due to this fact, an optimal design of heat recovery steam generator (HRSG) as an important part of this system is a subject of interest. In this paper a thermoeconomic analysis has been used to optimally design HRSGs in a combined cycle power plant. The applied method and the results of the performed sensitivity analysis are explained.

Keywords: Heat Recovery Steam Generator, Thermoeconomy, Capital Investment, Exergy destruction, Optimization

Nomenclature

$\dot{I}$	Exergy loss [kW]
$\dot{E}$	Exergy [kW]
C_T	Total cost [$/year]
a	Annual recovery factor [1/year]
$t_{op.}$	Operating period [hr/year]
C_E	Exergy unit price [$/kWh]
C_C	Capital cost [$]
C_p	Specific heat [kJ/kg K]
PP	Pinch temperature difference
P	Pressure [Mpa]
mr	Mass flow rate ratio
S	Entropy [kJ/kg K]
E_s	Exergy content of the produced steam [kW]
ex	exegetic
η	efficiency

Subscripts:

in	inlet
out	outlet
LP	Low pressure level
IP	Intermediate pressure level
HP	High pressure level
g	Gas side
s	steam
f	flue gas

Introduction

Heat recovery steam generator (HRSG) is an important part of a combined cycle power plant by which the energy of turbine exhaust gases is being recovered. These systems include three main groups of heat exchangers or elements named economizer, evaporator and superheater. An HRSG may contain up to three pressure levels, named low pressure (LP), intermediate pressure (IP) and high pressure (HP). Each pressure level has its own three mentioned heat transfer elements. When the turbine exhaust gases pass over HRSG elements, by the recovered energy, steam is produced inside tubes. This steam will be used for driving a steam turbine and generating shaft power. While water preheats in economizer and evaporates in evaporator, it will be separated from steam in drum. Water returns to down comers of evaporator and steam will be sent for superheating (figure 1).

The optimal design of such a thermal system is of primary interest specially due to extensive use of combined cycles as a preferred method of producing electricity. These systems are designed mainly based on the gas turbine exhaust mass flow rate and temperature. The

results of changing parameters such as ambient temperature, condenser type and pressure (or inlet water temperature to economizer) shows that these parameters have a neglecting effect on HRSG design parameters and performance. Therefore HRSGs may be optimized as a subsystem separated from other equipment in a combined cycle power plant.

Due to the energy or exergy crisis [1], this optimal design method provides a cost effective system [2] with the minimum total cost [3].

This fact resulted in choosing a target (60%) for thermal efficiency of combined cycle power plants by the manufacturers [4]. The optimal design of heat recovery has certainly important effects on overall cycle efficiency, power output, and cost of the system [5].

In this present work simulation and optimal design of HRSGs with up to three pressure levels is performed. An objective function, which is the total cost, per unit of steam produced exergy, is introduced. The total cost includes the capital cost, operational cost (in case of using duct burners in HRSG) and the cost of exergy or availability destruction for the system. The design parameters are selected when the system total cost per unit of steam exergy is minimized. A typical optimal design is performed and the output design parameters are reported for a two pressure level system.

Thermodynamic Analysis

To find the optimum physical and thermal design parameters of the system a simulation program was developed. Temperature profile, input and output exergy, exergetic efficiency, heat transfer surface are a of each element were estimated by study of heat recovery performance. The following assumptions have been considered in HRSG simulation program:

- The outlet stream from the evaporator and economizer assumed to be saturated vapor and saturated liquid respectively.
- The HRSG consists of up to three pressure levels and each level contains three components: Economizer, Evaporator, and Superheater.
- Dominant heat transfer mechanism is convection.
- Variation of the specific heat of the hot gas due to the temperature variations can be neglected.
- The inlet water streams are at ambient temperature.

The energy balance equations for various parts of the system (figure 1) are:

High-pressure Superheater

$$\dot{M}_g C_p (T_1 - T_2) = \dot{m}_{HP} (h_{20} - h_{19}) \quad (1)$$

High-pressure Evaporator

$$\dot{M}_g C_p (T_2 - T_3) = \dot{m}_{HP} (h_{19} - h_{18}) \quad (2)$$

High-pressure Economizer

$$\dot{M}_g C_p (T_3 - T_4) = \dot{m}_{HP} (h_{18} - h_{11'}) \quad (3)$$

Intermediate-pressure Superheater

$$\dot{M}_g C_p (T_4 - T_5) = \dot{m}_{IP} (h_{17} - h_{16}) \quad (4)$$

Intermediate-pressure Evaporator

$$\dot{M}_g C_p (T_5 - T_6) = \dot{m}_{IP} (h_{16} - h_{15}) \quad (5)$$

Intermediate-pressure Economizer

$$\dot{M}_g C_p (T_6 - T_7) = \dot{m}_{IP} (h_{15} - h_{11'}) \quad (6)$$

Low- pressure Superheater

$$\dot{M}_g C_p (T_7 - T_8) = \dot{m}_{LP} (h_{14} - h_{13}) \quad (7)$$

Low- pressure Evaporator

$$\dot{M}_g C_p (T_8 - T_9) = \dot{m}_{LP} (h_{13} - h_{12}) \quad (8)$$

Low- pressure Economizer

$$\dot{M}_g C_p (T_9 - T_{10}) = \dot{m}_{LP} (h_{12} - h_{11}) \quad (9)$$

These combinations of energy and mass balance equations were numerically solved and the temperature profile in the gas and water/steam side of HRSG were predicted.

From the system exergy balance, the exergy destruction in HRSG was computed using the following equation:

$$\dot{I} = \dot{E}_{in} - \dot{E}_{out} \quad (10)$$

The inlet exergy to the HRSG is the corresponding exergy of gas turbine exhaust. The exergy of the inlet water streams, which were assumed to be at ambient temperature (dead state), is zero.
The output exergy from HRSG is in two forms of steam generated in evaporator that then has been superheated in superheaters as well as the flue gas leaving the stack, thus:

$$\dot{I} = \dot{E}_g - \dot{E}_s - \dot{E}_f \quad (11)$$

Based on the definition of the exergy, the following equations can be derived:

Inlet Hot Gas Exergy

$$\dot{E}_g = \dot{M}_g \left[C_p (T_1 - T_a) - T_0 (S_1 - S_0)\right] \quad (12)$$

Steam Exergy

$$\dot{E}_S = \Sigma \dot{m}_i \left[(h_i - T_0) - T_0 (S_i - S_0)\right] \quad (13)$$

Flue Gas Exergy

$$\dot{E}_f = \dot{M}_g \left[C_p (T_{10} - T_a) - T_0 (S_{10} - S_0)\right] \quad (14)$$

The heat transfer surface areas can be obtained by solving the heat transfer equation in form of:

$$Q = U A \ \Delta T \quad (15)$$

Where the total heat transfer coefficient was obtained from the developed software program [6]. It is worth mentioning that the results of the developed software and simulation program were checked and found to be correct in compare to results reported in literature.

Economic Considerations

A key design parameter in each pressure level of HRSG is the pinch point, which is the temperature difference of steam leaving the drum and hot gases leaving the evaporator section. A bigger pinch point corresponds to a smaller exchanger heat transfer surface area and the relative lower capital cost of the recovery system for the same rate of energy exchange. A small pinch point corresponds to a larger heat transfer surface area and more costly system.

The average investment cost of the each component is calculated based on the following coefficients [7]:

Economizer

$$K_E = 34.9 \ \$/m^2 \quad (16)$$

Evaporator

$$K_V = 45.7 \ \$/m^2 \quad (17)$$

Superheater

$$K_S = 96.2 \ \$/m^2 \quad (18)$$

Thus the capital cost of the HRSG can be written as follows:

$$\begin{aligned} C_c = & (K_V A_V + K_E A_E + K_S A_S)_{LP} \\ & + (K_V A_V + K_E A_E + K_S A_S)_{IP} \\ & + (K_V A_V + K_E A_E + K_S A_S)_{HP} \end{aligned} \quad (19)$$

Optimization, objective function and Constraints

In this paper the total annualized cost per unit of steam produced exergy, (C_T / E_S) is selected as the objective function. The total annualized cost of the plant is obtained from:

$$C_T = t_{op.} C_E \dot{I} + a C_C \quad (20)$$

This function contains decision variables that their optimum values are the optimum system design parameters. These values minimize the total cost per unit of produced steam exergy, i.e., the objective function. There are some constraints for decision variables in minimization procedure. These constraints are ranges of variations or typical values of design parameters of an HRSG system which may be listed as below:

$5 < P_H < 22$ Mpa (21)

$1 < P_I < 10$ Mpa (22)

$0.01 < P_L < 3$ Mpa (23)

$8 < PP_H < 20$ K (24)

$8 < PP_I < 20$ K (25)

$8 < PP_L < 20$ K (26)

$$0.1 < mr_H < 0.9 \quad (27)$$

$$0.1 < mr_L < 0.9 \quad (28)$$

The decision variables in this problem are the pressure levels, pinch temperatures, and the mass flow rates of steam in each pressure level.
The lowest value of hot gas temperature was also a constraint. This temperature (dew point) specifies a lower limit to prevent the condensation of water vapor and corrosion.
Therefore the goal of the optimization process is to find a set of the decision variables to minimize the objective function (C_T), subject to constraints mentioned.

Computer program

A Visual Basic code is developed for simulation and optimization of HRSG system.
This code contains the following main modules:
Thermal analysis:

This part solves the thermodynamic model and computes the gas temperature variations along the heat recovery. Input and output exergy, exergy destruction, heat transfer surface areas and exergetic efficiency are among the output parameters. Pinch temperature differences, pressure levels and mass flow rates are the input data to this module.
Economic computations:

This part computes the total cost of HRSG. Temperature profile, heat transfer surface areas and exergy destruction of HRSG are input data to this module.
Using the economic parameters presented earlier, this module computes the capital cost of the heat transfer surface areas, the cost of the exergy destruction, and the total annualized cost of the system.
Optimization procedure:

This module links to the other modules and finds the optimum set of the decision variables subjected to the mentioned constraints using the search optimization method.
Besides these modules, a database containing the thermodynamic properties of the steam is linked to the code. This database was developed in Dynamic Library Link (DLL) format and has been generated in IUST Energy Systems Improvement Laboratory.
Through the relation of these modules the developed code solves the optimization problem and finds the optimum set of the decision variables as well as other important parameters of the system such as heat transfer surface areas, gas and water/steam side temperature profile along HRSG, steam turbine power output, log mean temperature differences and exergy destruction rate. The input and output data of the program are listed in table (1).

Results and Discussion

For the given input data (table 1), the obtained results from simulation and optimization programs (i.e., the system optimum design parameters) are listed in table (2) for various gas temperatures entering HRSG. As is shown from table (2) the lowest values of C_T / E_S, belongs to $700\,^{\circ}K$ turbine exhaust temperature.
The values of mr_l, mr_h (the fraction of the steam mass flow rates of two pressure levels), η_{ex} (the exergetic efficiency, a non-dimensional index which is defined as the ratio of the steam exergy produced to the inlet gas exergy) and pinch points are also listed.
The pinch points in LP level were lower than the corresponding values in HP level for this arrangement of heat transfer elements (arrangement A).

One of the most effective parameters that play a key role in thermoeconomic optimization is the exergy unit price that specifies the effect of exegetic efficiency on the total cost. The higher exergy unit prices, the better exergy efficiency gained. In this case the effect of the first term in equation (20) increases. Then for the minimizing the objective function (C_T / E_S), the decision variables (design parameters) will be computed with more attempt on decreasing the first term of C_T, which means decreasing the exergy destruction or increasing exgrgetic efficiency.
There are several methods for estimating exergy unit price [7]. One method considers the ratio of fuel cost divided by the plant efficiency (which in combined cycles is about 0.55 and is approximately used for heat recovery system) as exergy unit price. In another method the ratio of the fuel cost divided by the common plant

efficiencies is being used for the value of this parameter (typically of the order of 0.35 ~ 0.4). The average value of the selling price of electricity can be considered in the third method (the one has been used in this paper).
Table (3) shows the effects of changing C_E on optimum design parameters (pressure levels, pinch points and steam mass flow rates) at $800^\circ K$ for HRSG inlet gas temperature. For the case of C_E = 0.02 \$/kWh (nearly the electricity price in Iran), the pinch points are higher than the case in which C_E = 0.068 \$/kWh (nearly the electricity price in Italy) [7].

Figure (2) shows another arrangement for heat transfer elements in HRSG. The goal was finding whether the arrangement of elements changes the design parameters (decision variables), and C_T / E_S. Table (4) shows the outputs for arrangement B shown in figure (2) and C_E = 0.02 \$/kWh.

In most cases, the C_T / E_S values at each inlet gas temperature, was also lower in arrangement B in compare to the corresponding values in arrangement A. Furthermore η_{ex} values in arrangement B were also bigger than those in arrangement A.

In this case with the exception of $700^\circ K$, the pinch temperatures in HP level were less than the corresponding values in LP level.
Table (5) compares the outputs including mass flow rates, pinch points, and C_T / E_S for arrangements A and B for HP and LP levels. This parameter is lower in arrangement B when inlet gas temperature is above $700^\circ K$.

Conclusion

A thermoeconomic optimization method was applied to obtain the optimum values of design parameters in a heat recovery steam generator. The objective function introduced was the total cost per unit of steam produced exergy including the capital, operational (fuel cost in case of using duct burners) and exergy destruction costs.

The estimated exergy unit price and the arrangements of heat transfer elements also effects the design parameters. A sensitivity analysis carried out to examine the effect of exergy unit price on the results.
It was found that the arrangement of heat transfer elements also affects the design parameters as well as the total cost per unit of steam exergy produced.

References

[1] Rosen M. A. Energy crisis or exergy crisis? Exergy, 2002: 2: 125-127.

[2] Bejan A., Tsatsaronis G., Moran M. Thermal design and optimization. United States of America: John Wiley & Sons, Inc., 1996.

[3] Kotas TJ. The exergy method of thermal plants analysis. London: Krieger, 1995.

[4] Franco A., Casarosa C. On some perspectives for increasing the efficiency of the combined cycle power plants. Applied Thermal Engineering, 2002; 22: 1501-1518.

[5] Valdes M., Rapun J.L. Optimization of heat recovery steam generators for combined cycled gas turbine power plants. Applied Thermal Engineering, 2001; 21: 1149-1159.

[6] Sanaye S., Moradi A. Development of a new simulation program for combined cycle system. GT-2002-30467, ASME International Gas Turbine Conference, 2002.

[7] Casarosa C., Donatini F., Franco A. Thermoeconomic optimization of heat recovery steam generators operating parameters for combined plants. Energy, 2004; 29: 389-414.

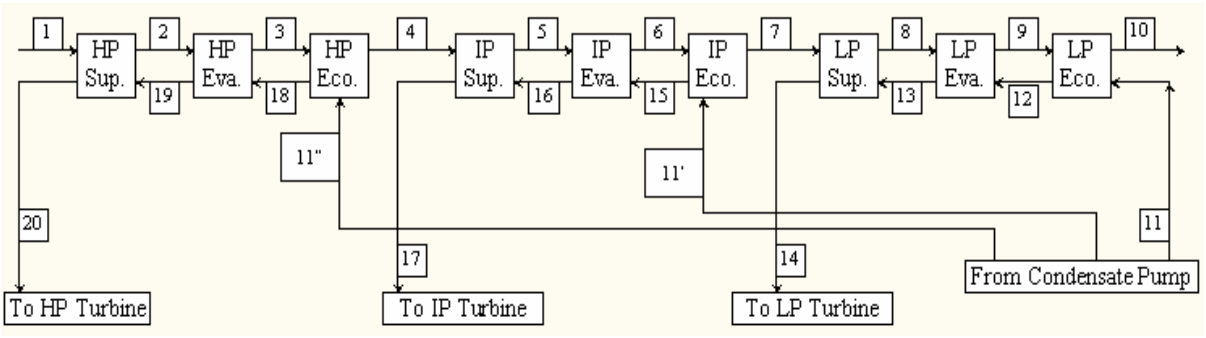

Figure 1: Schematic diagram of a typical two pressure level HRSG (arrangement A)

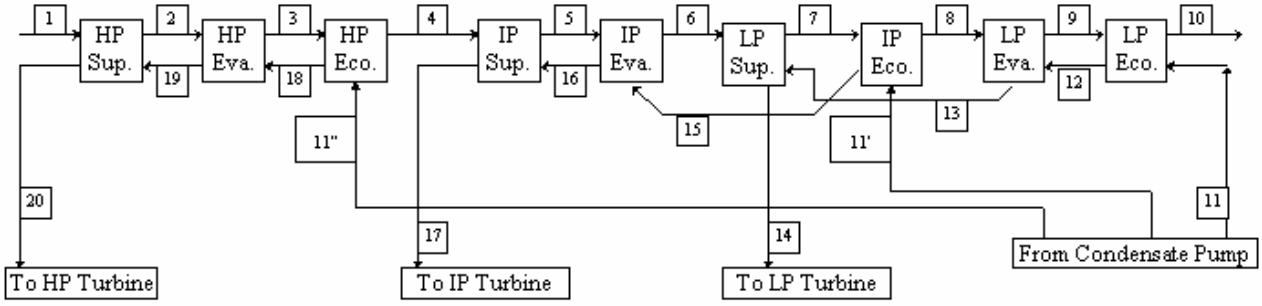

Figure 2: Schematic diagram of a typical two pressure level HRSG (Arrangement B)

Table 1: Inputs and outputs of the computer program

Input	Output
Inlet Gas Temperature	Optimum Decision Variables
Exergy Unit Price	Output Power
Inlet Water Temperature	Temperature Profile
Total Water Flow Rate	Total Annual Cost
Ambient Temperature	Total Exergy destruction
$\dot{m}_w$ = 50 kg/s	Exergetic Efficiency
$\dot{M}_g$ = 860 kg/s	
C_p = 1 kJ/kg K	
T_a = 293 K	

Table 2: Optimum design parameters for a dual pressure HRSG-(arrangement A) – C_E = 0.02 $/kWh

		High Pressure			Low Pressure			
T_g [K]	η_{ex}	P [bar]	PP [K]	mr_H	P [bar]	PP [K]	mr_L	C_T/E_s
700	77.32	214	18	0.9	3.5	8	0.1	25.29
725	79.62	219	14	0.9	2.5	8	0.1	27.85
750	79.62	219	14	0.9	2.5	8	0.1	27.12
775	79.62	219	14	0.9	2.5	8	0.1	26.85
800	80.67	216	18	0.9	3	10	0.1	27.26

Table 3: The effects of exergy unit price on optimum design parameters for arrangement A
HRSG inlet gas temp = 800 ° K

			High Pressure			Low Pressure		
C_E [$/kWh]	η_{ex} (%)	C_T/E_s	P [bar]	PP [K]	mr_H	P [bar]	PP [K]	mr_L
0.02	80.67	27.26	216	18	0.9	3	10	0.1
0.03	82.19	35.88	216	12	0.9	2.5	10	0.1
0.04	82.77	43.97	216	10	0.9	2.5	8	0.1
0.05	82.77	51.99	216	10	0.9	2.5	8	0.1
0.06	83.48	59.83	218	10	0.9	2	12	0.1

Table 4: Optimumdesign parameters for a dual pressure HRSG (arrangement B) – C_E = 0.02 $/kWh

		High Pressure			Low Pressure			
T_g [K]	η_{ex}	P [bar]	PP [K]	mr_H	P [bar]	PP [K]	mr_L	C_T/E_s
700	78.24	214	18	0.9	3.5	8	0.1	25.46
725	80.97	218	8	0.9	2	10	0.1	26.47
750	82.01	218	8	0.9	2	10	0.1	25.92
775	82.99	218	8	0.9	2	10	0.1	26.01
800	81.56	212	8	0.9	2	18	0.1	26.68

Table 5: The comparison of optimum design parameters for two arrangements A, and B for C_E = 0.02 $/kWh

			High Pressure			Low Pressure			
T_g [K]	Arrangement	$\eta_{ex.}$	P [bar]	PP [K]	mr_H	P [bar]	PP [K]	mr_L	C_T/E_s
700	A	77.32	214	18	0.9	3.5	8	0.1	25.29
	B	78.24	214	18	0.9	3.5	8	0.1	25.46
750	A	79.62	219	14	0.9	2.5	8	0.1	27.12
	B	82.01	218	8	0.9	2	10	0.1	25.92
800	A	80.67	216	18	0.9	3	10	0.1	27.26
	B	81.56	212	8	0.9	2	18	0.1	26.68

Proceedings of ECOS 2005
Trondheim, Norway
June 20–22, 2005

Thermal and Economic Evaluation of an Ice Thermal Storage System

Sepehr Sanaye[1] Abbasali Fardad[1] Hossein Babaie Touski[2]

Energy Systems Improvement Laboratory
Mechanical Engineering Department
Iran University of Science and Technology

Abstract
Gas turbine power output and efficiency, decrease with increasing the atmospheric temperature. This may be compensated by using compressor inlet cooling systems in forms of evaporative cooling, vapor compression and/or absorption, and thermal storage systems (TES). Thermal and economic evaluation of a latent TES system using ice storage is studied in this paper. The objective function is the capital and operational costs of the gas turbine plant with a vapor compression refrigeration system for producing ice in a storage tank. The system design parameters were obtained using the search method optimization technique.

Keywords: Thermal and Economic optimization, Inlet air cooling system, Thermal Storage System

Nomenclature:

$\dot{m}_a$	Air mass flow rate [kg/s]
$\dot{m}_g$	Turbine inlet mass flow rate [kg/s]
$\dot{m}_w$	Water mass flow rate [kg/s]
$\dot{m}_{fuel}$	Fuel mass flow rate [kg/s]
η_C	Compressor efficiency
η_T	Turbine efficiency
r_C	Compressor pressure ratio
r_T	Turbine pressure ratio
A_{AC}	Air cooler surface area [m^2]
A_{EV}	Evaporator surface area [m^2]
V_{ST}	Storage tank (Ice Bank) volume [m^3]
γ_g	Air specific heat ratio
γ_g	Gas specific heat ratio
Cp_a	Air specific heat at constant pressure [kJ/kg.K]
Cp_g	Gas specific heat at constant pressure [kJ/kg.K]
C_{fuel}	Cost per unit mass of fuel [$/Mj]
$\dot{W}_{net}$	Net power output [MW]
$\dot{W}_C$	Compressor power consumption [MW]
$\dot{W}_T$	Turbine power output [MW]
LHV	Lower heating value [kJ/kg]
Re_d	Inside tube flow Reynolds number
μ	Dynamic viscosity [$N.s/m^2$]
d	Pipe diameter [m]
h	Convection heat transfer coefficient [$W/m^2.K$]
U	Total heat transfer coefficient [$W/m^2.K$]
ΔT_{LMTD}	Mean logarithmic temperature difference [C]
NTU	Number of transfer units
i_{ph}	Melting latent heat [kJ/kg]
t_c	Charging time [sec]
t_h	Discharging time [sec]
$\dot{Q}_{AC}$	Air cooler heat rate [kW]
$\dot{Q}_{RC}$	Refrigeration heat rate [kW]
C_c	Cold water specific heat [kJ/kg.K]
Q_r	Reservoir available heat [kJ]
ρ_w	Density of water [kg/m^3]
C_r	Stored liquid specific heat [kJ/kg.K]

1- Assistant Professor
2- Researcher & M. Sc. Engineer

ΔT	The difference between the ambient temperature and liquid in thermal storage tank [$^\circ$C]
Z	Capital cost [$]
$\dot{Z}$	Capital cost rate [$/sec]
i	Interest rate [%]
n	Payback period [year]

Subscripts:

RC	Compression refrigeration system
AC	Air cooled heat exchanger
T	Turbine
C	Compressor
CC	Combustion chamber
EV	Evaporator
ST	Storage tank

Introduction

Gas turbine inlet air cooling by increasing the air density, increases the power output to about 20% of the nominal power and efficiency up to 6 percent. These systems satisfy the need for installing more gas turbines and therefore reduces capital and investment costs. The inlet cooling techniques include vapor or absorption refrigeration systems, evaporative cooling systems (inlet fogging, media and air washer), and thermal energy storage systems (TES).

In this paper the optimum design parameters of a TES system shown in figure (1) are predicted using a thermal and economic analysis and by minimizing the total cost as an objective function.

Thermal energy storage systems are in two major categories of sensible and latent heat types. In the first type, water and sand/stone are used to store the energy. The cost of the energy storage media (water or stone) is low in this case. In the second type, the phase of the energy storage media may change from solid to liquid when it receives energy and its phase shifts back to solid when it rejects energy. Considering the same volume, the latent type of energy storage systems can store more energy compared to the first type. In this paper thermal and economic optimization of ice storage tank is performed for gas turbines in 15 to 150 MW range of power output. By using ice storage tank and chilled water (25% Etylen Glycole and 75% water) the gas turbine inlet air temperature drops. This increases the inlet air density and gas turbine power output.

Consider a gas turbine (or combined cycle power plant) such as one shown in figure (1). The compressor inlet air cooling is performed by using a vapor compression refrigeration system to increase the power output. Inlet cooling might be necessary in time intervals with the maximum electricity consumption (on peak hours). On the other hand, running such a system consumes electricity (provided by the same or different power plant) in peak hours. This plan might not be economical since the electricity is the most expensive during peak hours. A better plan is to use the refrigeration system to make ice in off-peak hours in which the electricity consumption and its price is at the lowest values (usually after mid-night). Then the chilled water (25% Etylen Glycole and 75% water) inside tubes passes through the ice and will be pumped to an air cooler for cooling the inlet air and rejecting heat to the ice in storage tank in peak hours [1].

Thermal Analysis and Simulation of the System

The relations used for modeling the gas turbine sections such as compressor, combustion chamber and turbine are (figure 1):

$$r_T = p_3 / p_4 \tag{1}$$

$$T_2 = T_1 . \left[1 + \frac{r_C^{(\frac{\gamma_a - 1}{\gamma_a})} - 1}{\eta_C} \right] \tag{2}$$

$$T_4 = T_3 . \left[1 - \eta_T (1 - r_T^{(\frac{1-\gamma_g}{\gamma_g})}) \right] \tag{3}$$

$$\dot{W}_C = \dot{m}_a \, Cp_a \, (T_2 - T_1) \tag{4}$$

$$\dot{W}_T = \dot{m}_a \, Cp_a \, (T_2 - T_1) \tag{5}$$

For natural gas, the fuel lower heating value (LHV) was 45100 kJ/kg.

For cooling coil (air cooler) through which the chilled water (25% Ethylene Glycole and 75% water) passes, the following relations were used (figure1):

$$\dot{m}_W = \frac{\dot{m}_a\, Cp_a\, (T_0 - T_1)}{Cp_w\ (T_{h,i} - T_{h,o})} \quad (6)$$

$$Re_{d,i} = \frac{4\,\dot{m}_w}{10\,\pi\, d_i \mu_i} \quad (7)$$

$$(\Delta T_{LMTD})_{AC} = \frac{(T_1 - T_{h,i}) - (T_0 - T_{h,o})}{\ln[\frac{T_1 - T_{h,i}}{T_0 - T_{h,o}}]} \quad (8)$$

$$\dot{Q}_{AC} = \dot{m}\, Cp_a\, (T_0 - T_1) \quad (9)$$

$$A_{AC} = \frac{\dot{Q}_{AC}}{U\,(\Delta T_{LMTD})_{AC}} \quad (10)$$

The evaporator surface area of the refrigeration system and the ice storage tank volume are determined by [5]:

$$A_{EV} = \frac{(NTU)_c\, C_c}{U_{EV}} \quad (11)$$

$$Q_r = (\dot{Q}_{RC})\,(t_c) \quad (12)$$

$$V_{ST} = \frac{Q_r}{\rho_w\, C_r\, \Delta T + \rho_w\, i_{ph}} \quad (13)$$

Ten percent overestimation of the volume obtained from (13) was also considered due to expansion of water when it freezes in storage tank [8].

The Objective Function and Constraints

The objective function is the total cost including capital investment and operational costs in the form of:

$$\prod = \sum \dot{Z}_i\ (\$/s) + C_{fuel}\ (\$/Mj)\, LHV\, (Mj/kg)\, \dot{m}_{fuel}\, (kg/s) + Electricity\ cost\ rate\ (\$/s) \quad (14)$$

where the first term is the capital cost while the second and third terms are operational costs (including fuel and electricity). Due to the fact that the values of Z (capital cost) should be used in form of capital cost rate ($/sec), then:

$$\dot{Z} = Z \times \phi / 3600 \times 8000 \quad (15)$$

Where CRF is the capital recovery factor which is 18.2% in a 10 years period. ϕ is the operational and maintenance factor which was considered to be 1.06 [6].

The followings are the decision variables and the range of their variations. The mentioned ranges of values for variables are obtained based on the level of technologies present in the market.

$$273 \le T_1 \le T_0 \quad (16)$$

$$7 \le r_C \le 16 \quad (17)$$

(Pressure ratio of gas turbines for electricity production)

$$0.7 \le \eta_T \le 0.92 \quad (18)$$

$$0.7 \le \eta_C \le 0.9 \quad (19)$$

(The present level of technology in the market)

$$1000 \le T_3 \le 1550 \quad (20)$$

(Blade temperature limit)

$$0 \le t_c \le 86400 \quad (21)$$

(Seconds in a day)

$$273 \le T_2 \le T_4 \quad (22)$$

The followings are the system physical constraints:

$$T_4 \ge 400\ K \quad (23)$$

(To avoid water saturation and acid sulphoric formation)

$$T_{h,i} \ge T_{h,o} \quad (24)$$

$$T_3 \ge T_4 \quad (25)$$

$$(NTU)_c \ge 0 \quad (26)$$

$$\dot{Q}_{RC} \ge \dot{m}_w\, Cp_w\, (T_{h,i} - T_{h,o}) \quad (27)$$

The above objective function was minimized using search optimization method to get the design parameters (decision variables).

Economic Considerations

The capital cost of various components in the system (Z in equations (14) and (15)), are determined by equations (28) to (34) and

shown in figures (2) to (5) for gas turbine, inlet air cooler, refrigeration unit and TES system:
The capital cost equations for turbine, combustion chamber and compressor,are [4]:

$$Z_T = \frac{1094\,\dot{m}_g}{0.92-\eta_T}.\ln r_T \times\left[1+\exp(0.036\ T_3 - 54.4)\right] \quad (28)$$

$$Z_{CC} = \frac{102\,\dot{m}_g}{0.995-0.95}\times\left[1+\exp(0.018\ T_3 - 26.4)\right] \quad (29)$$

$$Z_C = \frac{16.53\,\dot{m}_g}{0.9-\eta_C}.r_C\ \log r_C \quad (30)$$

The capital cost equations for air cooler, refrigeration unit, evaporator and storage tank for the system operating conditions mentioned in this paper, were obtained in equation forms using graphical information provided in [3]:

$$Z_{AC} = 24202\ A_{AC}{}^{0.4162} \quad (31)$$

$$\begin{cases} Z_{RC} = 471.92(\dot{Q}_{RC}{}^{0.8198}) & (32) \\ Z_{EV} = 16648.3\ A_{EV}{}^{0.6123} & (33) \end{cases}$$

$$Z_{ST} = 5.7\times 10^{[2.9211\exp(0.1416\log V_{ST})]} \quad (34)$$

The electricity consumption of both compressor and condenser cooling water (cooling tower fan and cooling water pump) for vapor compression refrigeration system during the night and also the chilled water pumping during the peak hours were considered in the analysis. A simplified assumption uses 10% of the compressor electricity cost for all pumping services.
The electricity cost during the peak hours (TES discharging) was 0.08 $/kWh and during the off-peak hours (TES charging) was 0.05 $/kWh. C_{fuel} in relation (14) was 0.004 $/Mj [4]. It is apparent that these cost values may change in different locations and/or atmospheric conditions.

Discussion and Results

A computer program was developed to simulate and optimize the thermal system shown in figure (1). The inlet air temperature was changed from 280K to 320K for gas turbine nominal power outputs in range of 15 to 150 MW. The results are listed in tables (1) to (5). It is important to note that for gas turbine plants below 25 MW the use of thermal storage is logical only when the atmospheric temperature is higher than 320 K. For lower atmospheric temperatures, the results show that the use of thermal storage is not economical. This temperature limit decreases with increasing the gas turbine power output, i.e. for 25 MW at or more than 310 K, for 55MW at 290 K, and for 100 MW at 280 K ambient temperature.
It was found that for all inlet air temperatures, gas turbine power outputs, and decision variables such as r_C, η_C, η_T and T_3, the optimum charging period was about 40000 seconds (about 11 hours). The variations of this charging time with cost rate is shown in figure (6).
The payback period for thermal storage system has also been studied. If Ec is the capital cost of air cooler, refrigeration system and thermal energy storage (including operation and maintenance cost), the worth of this investment in n_{th} year later will be [7].

$$\begin{aligned} Ec_n &= (Ec)(1+i)^n \\ &= \left[Z_{AC}+Z_{RC}+Z_{EV}+Z_{ST}\right](1+i)^n \end{aligned} \quad (35)$$

Where i is the interest rate which was assumed to be equal to 0.1 (10%).
The payback period may be estimated for such a system by using the following formula:

$$\Delta EP_n = \left\{\begin{bmatrix}\text{Min cos t, without TES}\\ -\text{Min cos t, with TES}\end{bmatrix}\times 3600\times 24\times 365\right\} n \quad (36)$$
$$= Ec_n = (Ec)(1+i)^n$$

The payback period for a 25 MW gas turbine is about 2.5 years and this value decreases with increasing the gas turbine nominal power output (figure 7).
The percentage of increase in power output with the gas turbine nominal power when thermal energy storage and inlet cooling system are used is also shown in figure (8). The range of power output increase for 15 to 150 MW gas turbine nominal power is about 2.5 to 10 percent.

The variations of the cost rate with power output of a gas turbine power plant including thermal storage is also shown in figure (9). The cost rate changes from 0.0109 to 0.0091 $/Mj for 15 to 150 MW plants.

Conclusion

By performing thermal and economic assessment of an energy storage system, important physical or design parameters of the system were obtained at different ambient temperatures. Results show that the payback period and the cost rate per MW of using thermal storage system decrease with increasing the nominal power output. The net power increase shows a noticeable augmentation with increasing the power output.

References

[1] A.Ter-Gazarian, 1994, "Energy storage for power systems", Peter Peregrines Ltd.

[2] Birol Kilkis, Sadik Kakac, 1989, "Energy storage systems", Kluwer Academic Publishers series E: Applied Sciences, vol. 167.

[3] Bejan, A., Tsatsaronis, co., and Moran, M., 1996, "Thermal design and optimization", John Wiley and Sons.

[4] Jose C. F. Teixeira, Senhorinha F.C.F.Teixeira, Angela M. E. Silva, 2003 "Numerical optimization of a gas turbine cogeneration plant", proc., ASME, Georgia World Congress Center.

[5] Robert J. Krane, 1989, "Second law optimization of thermal energy storage systems, latent heat systems, Energy Storage Systems", Applied Sciences, vol. 167. pp 69-88.

[6] A. Valero, M. A. Lozano, L. Serra, C. Torres, 1993, "Application of the exegetic cost theory to the CGAM problem", Energy vol. 19, No.3, pp 365-381, 1994.

[7] K. K. Humpherys, S. Katell, 1981, "Basic Cost Engineering" Marcel Dekker, New York.

[8] ASHRAE, Handbook, 1999, Chapter 33, Thermal Storage.

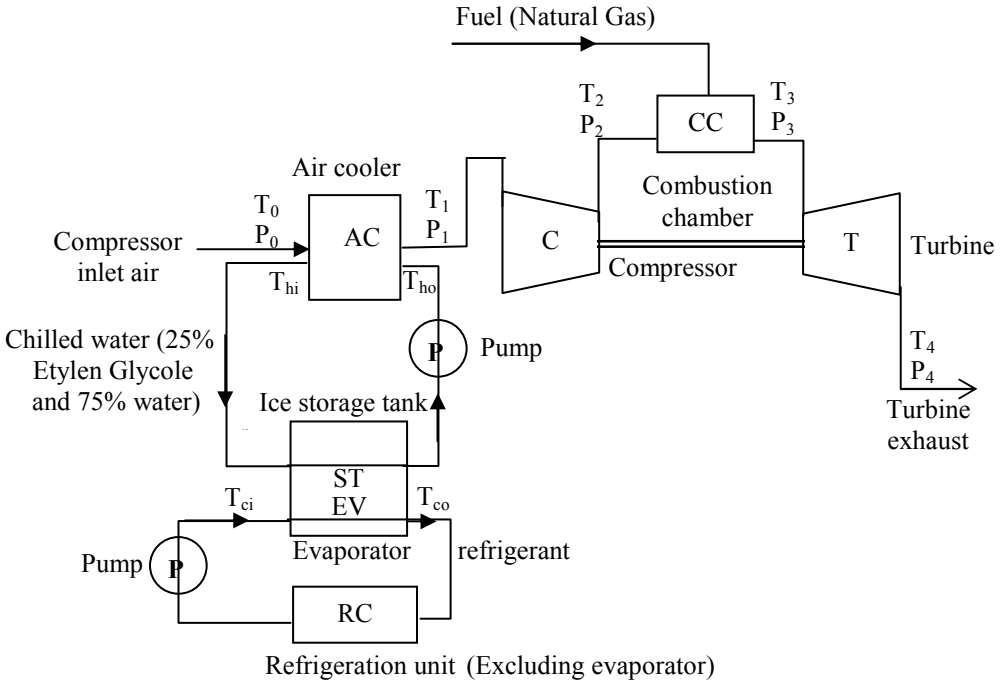

Fig. (1) : Schematic diagram of the modeled power plant with TES System

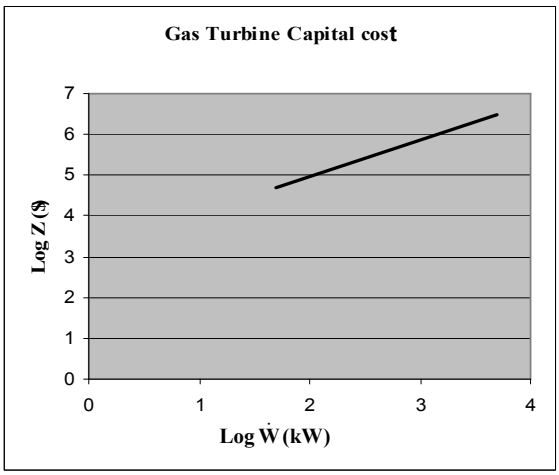

Fig. (2) : Variations of gas turbine capital cost with power output

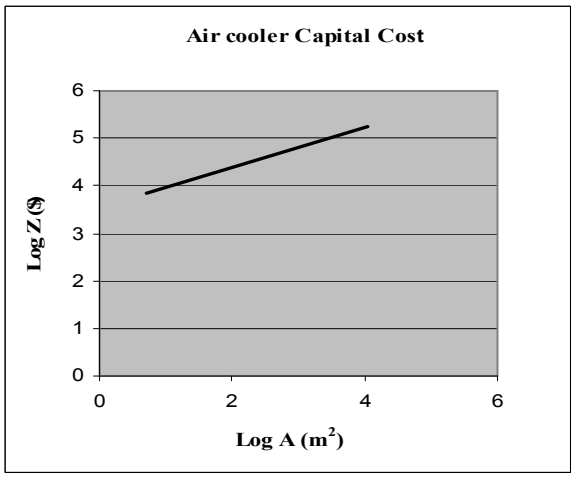

Fig. (3) : Variations of air cooler capital cost with heat transfer surface area

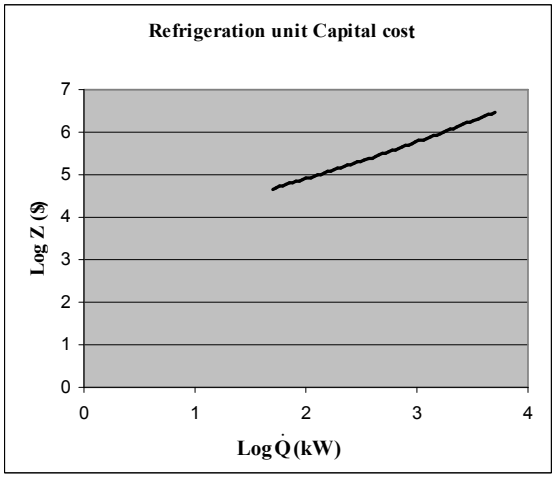

Fig. (4) : Variations of the capital cost of refrigeration unit with cooling capacity

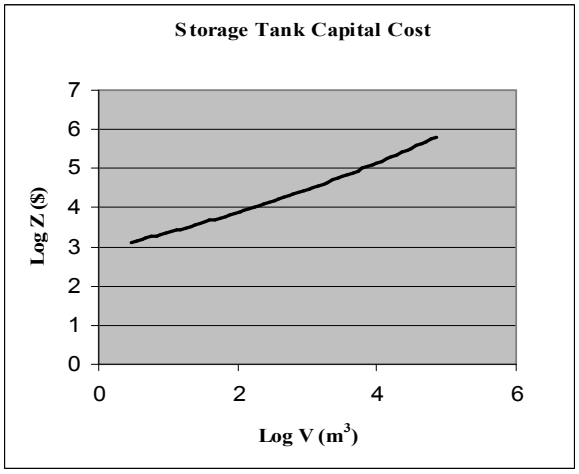

Fig. (5) : Variations of the capital cost of storage tank with volume

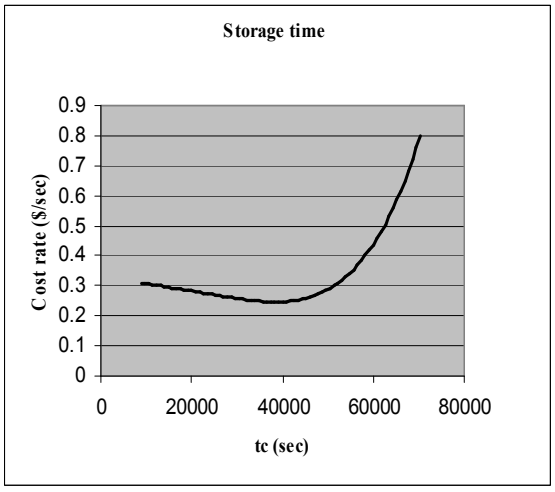

Fig. (6) : Variation of cost rate with charging time

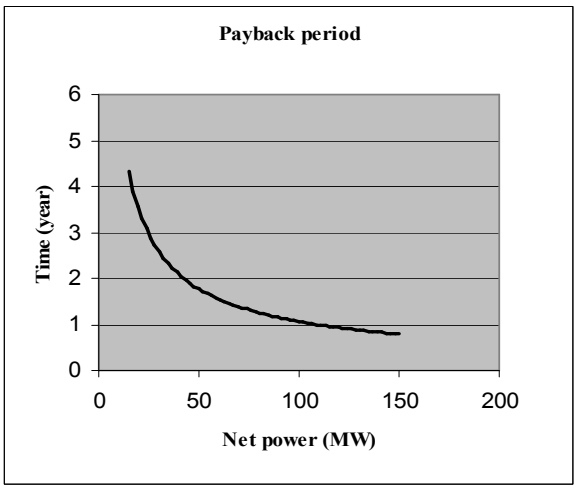

Fig. (7) : Variations of payback period with nominal power output (MW)

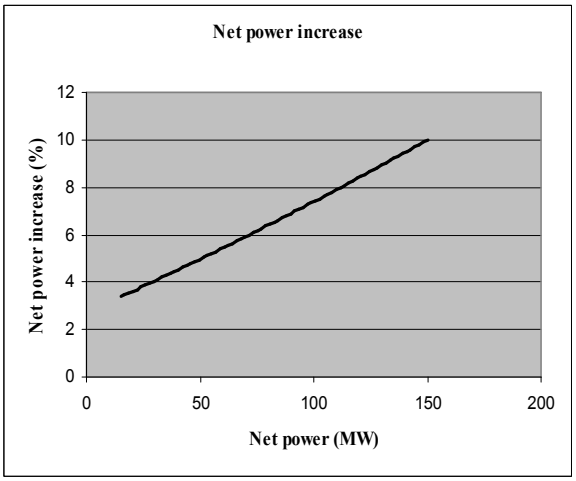

Fig. (8) : Variations of net power increase (percent) with power output (MW)

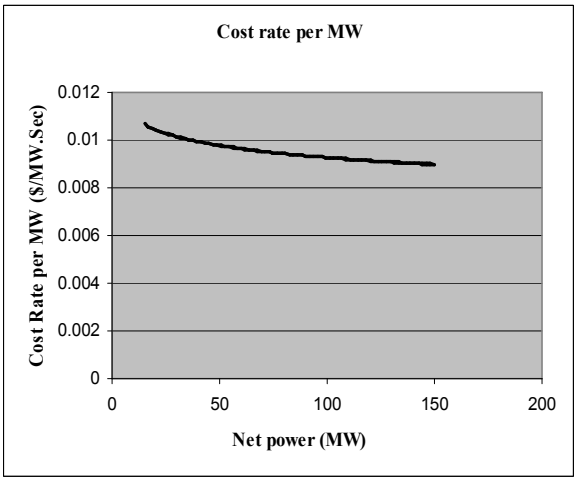

Fig. (9) : Variations of the cost rate per unit of net power production for different nominal net power outputs (MW)

Table (1) : The results of system optimization program for $p_0 = 101\,kPa, \dot{W}_{net} = 15\,MW$

T_0	280	290	300	310	320
T_1	280	290	300	310	280
T_3	1450	1450	1450	1450	1450
η_C	0.84	0.85	0.85	0.85	0.85
η_T	0.86	0.86	0.86	0.86	0.86
r_C	13	14	14	14	13
t_c	43200	43200	43200	43200	43200
Min cost	0.1623	0.1627	0.1633	0.1637	0.1642

Table (2) : The results of system optimization program for $p_0 = 101\,kPa, \dot{W}_{net} = 25\,MW$

T_0	280	290	300	310	320
T_1	280	290	300	280	280
T_3	1450	1450	1450	1450	1450
η_c	0.84	0.84	0.85	0.84	0.84
η_T	0.86	0.86	0.86	0.86	0.86
r_C	15	15	14	15	15
t_c	43200	43200	43200	43200	43200
Min cost	0.2521	0.2529	0.2537	0.2542	0.2546

Table (3) : The results of system optimization program for $p_0 = 101\text{kPa}, \dot{W}_{net} = 55\text{MW}$

T_0	280	290	300	310	320
T_1	280	280	280	280	280
T_3	1450	1450	1450	1450	1450
η_c	0.84	0.84	0.84	0.84	0.84
η_T	0.86	0.86	0.86	0.86	0.86
r_C	13	15	15	15	15
t_c	43200	43200	43200	43200	43200
Min cost	0.5230	0.5230	0.5239	0.5245	0.5251

Table (4) : The results of system optimization program for $p_0 = 101\text{kPa}, \dot{W}_{net} = 100\text{MW}$

T_0	280	290	300	310	320
T_1	280	280	280	280	280
T_3	1450	1450	1450	1450	1450
η_c	0.84	0.84	0.84	0.84	0.84
η_T	0.86	0.86	0.86	0.86	0.86
r_C	15	15	15	15	15
t_c	43200	43200	43200	43200	43200
Min cost	0.9249	0.9273	0.9285	0.9293	0.9302

Table (5) : The results of system optimization program for $p_0 = 101\text{kPa}, \dot{W}_{net} = 150\text{MW}$

T_0	280	290	300	310	320
T_1	280	280	280	280	280
T_3	1450	1450	1450	1450	1450
η_c	0.84	0.84	0.85	0.85	0.85
η_T	0.86	0.86	0.86	0.86	0.86
r_C	15	15	14	13	13
t_c	43200	43200	43200	43200	43200
Min cost	1.373	1.375	1.377	1.378	1.380

Proceedings of ECOS 2005
Trondheim, Norway
June 20–22, 2005

ECONOMICS OF A COAL-FIRED POWER PLANT – EXERGY APPROACH

Dejan Ziher*, M.Sc., Alojz Poredos, Ph.D.
Faculty of Mechanical Engineering
Askerceva 6, 1000 Ljubljana
Slovenia

Miran Zager
District heating and gas supply Velenje
Koroska cesta 37/B, 3320 Velenje
Slovenia

ABSTRACT

The paper presents a model for thermoeconomic analysis of the biggest thermal system in Slovenia in which electric power and heat energy are produced in five units all operated by steam turbines, the main fuel being lignite. The prices of heat and electric energy from the plant were calculated. The calculations and the ratio between electric energy price and district heating price were based on an exergy analysis that considers the economics of the system.
Keywords: coal-fired power plant, cogeneration systems, energy price, exergy analysis

NOMENCLATURE

c	specific cost	[€/kWh]
E, $\dot{E}$	exergy, exergy power	[kJ], [kW]
Δh	enthalpy difference	[kJ/kg]
p	pressure	[bar]
Q, $\dot{Q}$	heat, heat power	[kJ], [kW]
$\dot{q}$	mass flow	[kg/s]
T	temperature	[^{0}C]
$\dot{Z}$	specific investment cost	€/h
W	power	[kW]
ΔS	entropy change	[kJ/K]
η	efficiency	[/]
b	boiler	
e	electricity	
ex	exergetic	
f	fuel	
g	generator	
h	heat	
o	environment	
s	steam	
t	turbine	

* Corresponding author: Phone: + 386 1 4771 418 Fax: + 386 1 2518 567 E-mail: dejan.ziher@fs.uni-lj.si

INTRODUCTION

The biggest coal-fired power plant in Slovenia using lignite as fuel source consists of five units built over different periods of time. Each unit consists of a power plant run by a steam turbine. The main difference between units is in the power of each unit and in the temperature of steam used for district heating. Electric energy produced is sold to the public distribution system, while the heat energy is sold to a district heating company running two main heating substations. The first district heating substation is supplied from the first and second unit of the power plant and the second substation from the third, fourth and fifth unit. The goal of this study is to calculate prices of heat energy from each unit. On this basis it will be possible to determine in which time period it is best for one unit to produce heat and in this way optimize the system. Calculations of prices are based on an exergy analysis that considers the economics of the system. Calculations of this kind require the data on investment, maintenance and labor costs including depreciation. Incomes are from the electricity sold to the public electric energy distribution system where the price is determined by the government decree. So all other

costs have to be distributed on heat energy. This is the approach that is presently used. This study suggests recalculating the ratio between the electric energy and heat energy, considering also the incomes from the district heating. In the calculation the emphasis is on exergy approach.

Exergy analysis is based on the second law of thermodynamics. The second law states that, although energy cannot be created or destroyed, it can be degraded in quality. Exergy is the maximum work obtainable as a system comes to equilibrium with a reference environment or more simply, exergy is that part of energy which is available for performing useful tasks. While energy analysis is the conventional method of thermodynamic analysis, more recently exergy analysis has received a growing recognition. It gives engineers a tool for proper design and operation of such complex systems.

Exergy transfer associated with the transfer of energy of heat can be defined as [1]:

$$E_{12} = Q_{12} - T_o \cdot \int_1^2 \frac{dQ}{T} \quad (1)$$

Exergy losses at heat transfer can be defined as [1]:

$$E_{12} = T_o \cdot \sum \Delta S_i \quad (2)$$

According to the first law of thermodynamics, we can define energy efficiency of cogeneration system as [2]:

$$\eta_e = \frac{W_e + \dot{Q}_h}{\dot{Q}_f} \quad (3)$$

If we consider exergy as a measure of efficiency, equation 3 turns into [2]:

$$\eta_{ex} = \frac{W_e + \dot{E}_h}{\dot{E}_f} \quad (4)$$

Exergy as a measure of efficiency and further costs was applied to the biggest coal-fired power plant in Slovenia. Different levels of heat supply and the way this affects the heat price were identified. A comparison of energy prices from the coal-fired power plant was also done on the basis of energy and exergy.

DESCRIPTION OF THE COAL-FIRED POWER PLANT

The plant consists of five units each one producing electric energy and heat. The total installed power is 755 MW and an average yearly production is from 3.8 to 4.2 billion kWh of electric energy and 0.4 billion kWh of heat energy. For this production 4.4 million tons of lignite is spent.

The units of the power plant have been built gradually. The first three units produce electric energy heat being taken directly from boilers. In units 4 and 5 electric energy and heat are produced in cogeneration. The electric energy from all units is sold to the public network, while the heat is supplied to two main heat stations. The operation of each unit is adapted to current electric energy needs. The power production of units 1, 2 and 3 is changing on a daily basis, while the power production of unit 4 and 5 is regulated directly from the national power distributor. Heat production is therefore dependent on electricity production. The heat from heat stations is used for district heating, the temperature of feed water being 140 ^{0}C and of return water 90 ^{0}C. The objective was to find from which heat station, and consequently from which unit it is most appropriate to supply the heat stations. The analysis starts from the fuel source, which is in our case lignite, and concludes with the end product, which is electric power and heat. The first task is to find out the energy flow in the cogeneration system for each unit separately. Such analyses are mainly very complex and they demand numerical programming to optimize such a system.

Let us first present the energy production of each unit in the power station with simplified diagrams (Figures 1-4).

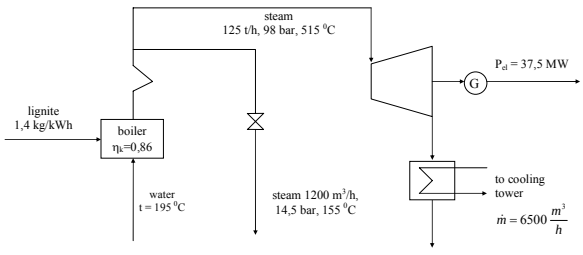

Figure 1: Simple schematic plan of unit 1 and 2

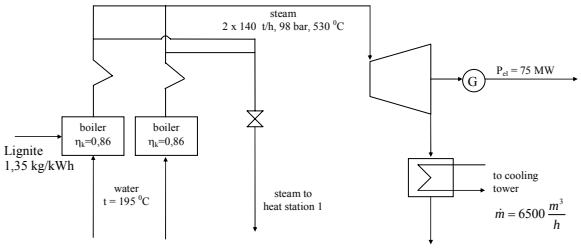

Figure 2: Simple schematic plan of unit 3

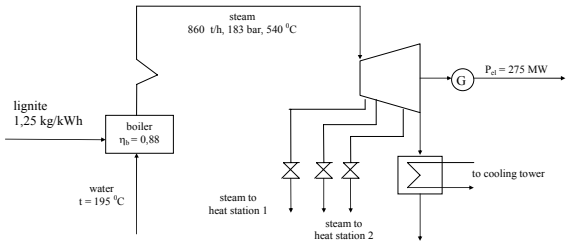

Figure 3: Simple schematic plan of unit 4

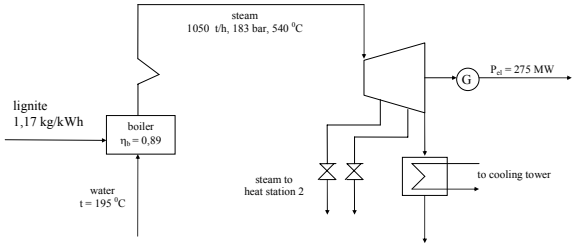

Figure 4: Simple schematic plan of unit 5

PRODUCTION OF HEAT ENERGY IN THE COAL-FIRED POWER PLANT

For district heating two heat stations are installed in the power plant. The first heat station located in unit 3 is supplied from units 1, 2, 3 and 4. The second heat station located in unit 5 is supplied from units 4 and 5 (Figure 5).

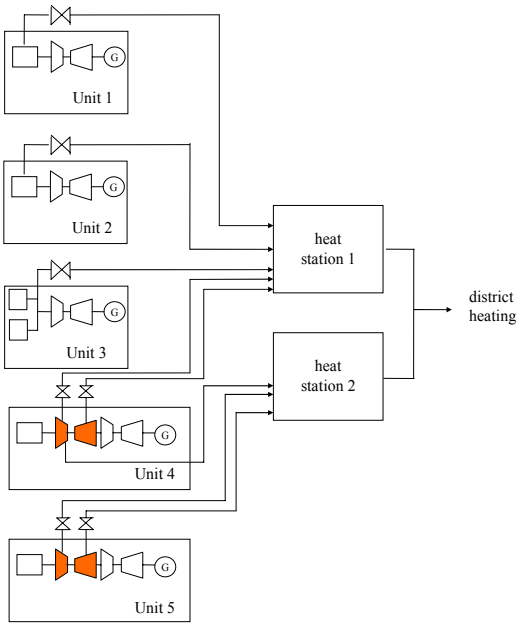

Figure 5: Supplies of heat from power plant to heat stations

Primary sources parameters for heat station 1 are presented in Tables 1-4.

	units	**parameters**	
		min.	**max.**
p	bar	98	98
T_s	°C	470	510
$\dot{q}$	kg/s	2,78	16,76
T_c	°C	92	150
Δh	kJ/kg	2923	2656,5
$\dot{Q}$	MW	8,12	44,27

Table 1: Primary source parameters for heat station 1 supplied from unit 1 and 2

	units	**parameters**	
		min.	**max.**
p	bar	98	98
T_s	°C	470	525
$\dot{q}$	kg/s	2,78	32,22
T_c	°C	92	150
Δh	kJ/kg	2923	2807,4
$\dot{Q}$	MW	8,12	90,45

Table 2: Primary source parameters for heat station 1 supplied from unit 3

Heat station 1 is supplied from two branches of unit 4 (Figure 5).

	units	parameters	
		min.	**max**.
p	bar	20	43,5
T_s	°C	320	343
$\dot{q}$	kg/s	13,88	13,88
T_c	°C	90	96,4
Δh	kJ/kg	2694	2680
$\dot{Q}$	MW	37,39	37,20

Table 3: Primary source parameters for heat station 1 supplied from unit 4 – branch 1

Branch 2 from unit 4 serves for supplying low temperature heat exchangers. Heat is taken from the steam line between the middle and lower part of the turbine.

	units	parameters	
		min.	**max**.
p	bar	2,0	4,6
T_s	°C	280	285
$\dot{q}$	kg/s	2,26	12,35
T_c	°C	90	96
Δh	kJ/kg	2654,7	2632,3
$\dot{Q}$	MW	6,0	32,5

Table 4: Primary source parameters for heat station 1 supplied from unit 4 – branch 2

Primary sources parameters for heat station 2 are presented in Tables 5-7.
To enable better heat supply from heat station 2 at standby of unit 5, a connection was later created between unit 4 and heat station 2. The steam is taken from the cold part of the steam line at intermediate overheating. The parameters of this supply source are given in Table 5.

	units	parameters	
		min.	**max**.
p	bar	20	43,5
T_s	°C	320	343
$\dot{q}$	kg/s	13,88	13,88
T_c	°C	90	96,4
Δh	kJ/kg	2694	2680
$\dot{Q}$	MW	37,39	37,20

Table 5: Primary source parameters for heat station 2 supplied from unit 4 – branch 3

From unit 5 (branch 1) the steam from cold overheating is supplied through pressure reduction to high temperature heat exchangers. The devices of the unit are planned so that in the whole operation part of the unit the second heat station fully ensures the heat power needed. The possible heat extraction from branch 1 - unit 5 is inversely proportional to the heat power of the unit, which is also seen from Table 6.

	units	parameters	
		min.	**max**.
p	bar	16	43,2
T_s	°C	268	333
$\dot{q}$	kg/s	17,78	3,69
T_c	°C	90	96,4
Δh	kJ/kg	2580	2631,1
$\dot{Q}$	MW	45,87	9,71

Table 6: Primary source parameters for heat station 2 supplied from unit 5 – branch 1

From unit 5 (branch 2) a connection steam line between the middle and lower part of the turbine creates a possibility of supplying low temperature heat exchangers. From Table 7 it is seen that this supply represents the basic supplier for heat station 2.

	units	parameters	
		min.	max.
p	bar	2,2	5,51
T_s	°C	270	274
$\dot{q}$	kg/s	14,4	31,1
T_c	°C	120,2	153
Δh	kJ/kg	2505,7	2364,7
$\dot{Q}$	MW	36,08	73,54

Table 7: Primary source parameters for heat station 2 supplied from unit 5 – branch 2

THERMOECONOMIC ANALYSIS

Thermoeconomics deals with exergy analysis in connection with economy. It gives us the information that cannot be obtained with a conventional energy/economic analysis. From the literature, different ways of establishing thermodynamic efficiencies of systems and exergy losses are known. To solve the problem for a particular power plant we need to know the values of these losses to improve the efficiency of the whole system and reduce the price of the product.
The steps in thermoeconomic analysis are:

- calculation of production costs for each product respectively,
- understanding development process of costs and cost flow in a system,
- optimization of certain variables in a particular component,
- optimization of the whole system.

A number of researcher have tried to apply thermoeconomic analysis to a combined production of energy with an exergy approach [3], [4], including a coal-fired power plant [5]. Some models and suggestions have also been done on concrete examples, but each power plant is different. To make a detailed thermoeconomic analysis, the first step is to do the cost balance. All the costs that occur in operation are needed to determine the cost flow through the plant and to determine the costs of the two energies produced. The cost of products (energies) c_p at constant operation consists of fuel costs c_f, investment costs c_i (yearly depreciation) and maintenance/operations costs c_m. It is often difficult to determine how big these costs are and even more difficult to determine what amount would go to electricity and what to heat. Our thermoenomic analysis based on exergy has shown how prices of heat energy could be determined according to heat supply from a specific unit. Heat taken away at higher temperatures would in such a way have a higher price than heat taken away at lower temperatures.
As the exergy method of costing is based on rational thermodynamic considerations, it encourages efficient production and is fair to consumers.
The cost is increasing in each next step of the system. The general balance equation would be [6]:

Cost input + cost generation – cost output = cost accumulation (5)

Cost generation corresponds to capital and all other maintenance costs.

In general in combined power plants four different methods for determining costs are known [2]. In the equality method, the generation of two products is considered to be equal. The prices of electric and heating energy would be in that case the same. In the extraction method, it is considered that production of power is the main purpose, and that every extraction of steam reduces the output power. Emphasis of costs is therefore given to electricity price. In the by-product work method, it is assumed that production of steam is essential, although no electricity is produced. A low pressure boiler is used and costs are mainly on steam production. This method is useful in some industrial facilities. And the last method is the by-product steam method where the main costs are on produced electricity.
However, none of these methods could be directly applied to our case. In the discussed coal-fired power plant electric power production is essential, but still the importance of steam production cannot be neglected. In the study an exergy analysis was done for the whole process of combined power production from the primary source (coal) to the end products (electricity and steam). Our main goal was to build a model that would serve as a basis for determining real prices of produced electricity and steam. Generally, we can say that input exergies must be equal to output exergies [2]:

$$\dot{E}_{in} \cdot c_{in} + (\dot{Z}_b + \dot{Z}_t + \dot{Z}_g) = \dot{E}_h \cdot c_h + \dot{W}_e \cdot c_e \quad (6)$$

This is just a general equation that does not consider exergy destructions through the process of combined production of the heat power process. The model that will also consider exergy destructions through the process is still being worked on.

A theoretical approach and basis for prediction of ratios between heat and electricity price is shown below. The exergy of electricity is 1, while the exergy of heat is calculated from equation 6 [6].

$$\dot{E}_h = \dot{Q}_h \cdot \left(\frac{T - T_0}{T} \right) \tag{7}$$

According to equation (6), we can calculate exergies of steam taken for each unit. Further we can compare prices of electricity and heat energy.

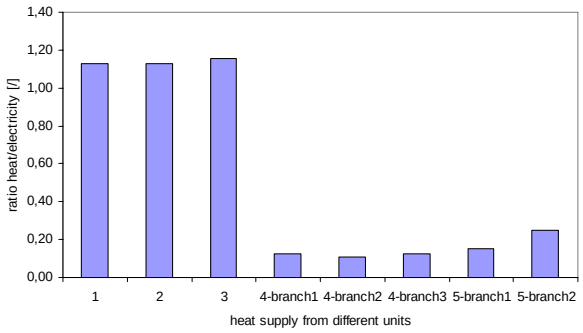

Figure 6: Ratio of heat to electricity prices regarding to heat supply

As we can see from Figure 6, heat from units 1, 2 and 3 should be even more expensive than electricity. The reason for this is the extraction of steam directly from the boiler and consecutively this steam does not produce mechanical work. The main exergy losses occur in this case at pressure reduction. The ratio of heat to electricity price for other units and branches ranges from 0.11 to 0.25. This means that the price from unit 4-branch 2 should be the cheapest. Regarding the different supplies of heat stations with heat (Figure 5) and considering different ratios of heat/electricity prices (Figure 6) we can calculate the ratio of heat/electricity prices for each station. The analysis has shown that this ratio is for the first station 0.25 and for the second 0.16. This means that the price of heating energy from heat station 1 and 2 should be respectively 4 and 6 times lower than the price of electricity.

CONCLUSIONS

In this paper we tried to identify prices of electricity and heat energy produced in a coal-fired power plant. Our main approach was exergy analysis. It is often difficult to get exact data for each step in the process of combined production of energies. One approach is to calculate exergy destruction in each part of the system, where energy (exergy) is changed. However, due to lack of exact data in the operation of the system and because of the complexity of the system, we have chosen a different approach. This approach is also based on exergy, because it considers different qualities of produced electricity and heating energy. Another difficulty was that we also could not set the exact prices of electricity and heating energy, because the operating devices are old and it was not possible to get the exact investment costs and the related depreciation. Our research was just aimed at defining which branch of heat supply is the optimal one to supply heating station 1 and heating station 2. It turned out as was expected that it was better to produce more electricity and to extract steam at lower temperatures for heating purposes. This is just a theoretical approach. However, it gives us a basis on which we can later calculate the exact price of heat from each unit. As it was mentioned in the paper, the coal-fired power plant was primarily set up for electricity production for Slovenian electricity network. Therefore the selling price of produced electricity from a coal power plant to public electricity network has already been determined by government decrees. Heat is in our case just a by- product and its price should be of course much lower.

The aim of the paper was to propose a method of determining the heating price from a coal-fired power plant. Units 1 and 2 have been planned to be replaced by new units, which will be based on a combined gas-steam process. It would be also interesting to see what in that case would be better to use for production of cooling energy: steam or electricity? An exergy approach would in this case certainly give interesting results.

REFERENCES

[1] Bejan A, Tsatsaronis G, Moran M. *Thermal Design & Optimization*, A Wiley- Interscience publication, 1996

[2] Kotas T. *The exergy method of thermal plant analysis*, Great Britain, 1985

[3] Verkhiver G P, Kosoy B V. *On the exergy analysis of power plants*. Energy Conversion & Management. Vol. 42, 2001, pp.2053-2059

[4] Tsatsaronis G, Moung-Ho Park: *On avoidable and unavoidable exergy destructions and investment costs in thermal systems*, Energy Conversion&Management, Vol. 43, 2002, pp. 1259-1270

[5] Rosen M A, Dincer I. *Thermoeconomic analysis of power plants: an application to a coal fired electrical generating station*. Energy Conversion & Management. Vol. 44, 2003. pp. 2743-2761

[6] Yehia M. El-Sayed: *The Thermoeconomics of energy conversions*, Elsevier, 2003

Optimisation

Proceedings of ECOS 2005
Trondheim, Norway
June 20–22, 2005

GENERAL MODEL OF REVERSED CYCLE CARNOT MACHINE WITH CONSTRAINTS AND NON-LINEAR HEAT TRANSFER LAWS

Michel Feidt*
University "Henri Poincaré" of Nancy 1
L.E.M.T.A., U.R.A. C.N.R.S. 7563
54504 Vandoeuvre-les-Nancy
France

Camelia Petre and **Monica Costea**
University "Politehnica" of Bucharest
Department of Engineering Thermodynamics
060042 Bucharest
Romania

Stoian Petrescu
Bucknell University
Department of Mechanical Engineering
Lewisburg, PA-17837
U.S.A.

ABSTRACT

A general model for the study and optimization of reversed cycle thermal machines with two heat reservoirs is presented. The mathematical model basically consists of the First and Second Laws of Thermodynamics applied to the cycle and machine, and the heat transfer equations at the source and sink considered non-linear laws, namely convective-like and radiative-like ones. The entropy generation terms consider internal and external irreversibilities of the cycle. Several constraints imposed to the system allow finding the optimum operating conditions, as well as the limited variation ranges of the system parameters. Some results generated by the model when applied to refrigeration machines are presented, pointing out two different operating regimes of the machine, namely maximum useful effect, respectively minimum dissipation. Some sensitive studies are also presented. These results are new and extensions of them we presently develop.
Keywords: Optimization, Irreversibilities, Non-linear heat transfer law, Operating regimes

NOMENCLATURE

COP	Coefficient of performance
c_p	Specific heat at constant pressure [J kg^{-1} K^{-1}]
K	Thermal conductance [W K^{-1}]
$\dot{m}$	Gas mass flow rate [kg s^{-1}]
n	Heat transfer law exponent
NTU	Number of heat transfer units
$\dot{Q}$	Heat flux [W]
$\tilde{\dot{q}}$	Dimensionless heat flux
$\dot{S}$	Entropy generation [W.K^{-1}]
$\tilde{\dot{s}}$	Dimensionless entropy generation
T	Temperature [K]
$\dot{W}$	Power consumption [W]
$\tilde{\dot{w}}$	Dimensionless power consumption
θ	Dimensionless temperature

Subscripts

H	Related to gas at the hot-end
L	Related to gas at the cold-end
gen	Generalized
i	Internal
max	Maximum
min	Minimum
SH	Source temperature
SL	Sink temperature
T	Total

* Corresponding author: Phone: +33 03 83595734 Fax: +33 03 83595551 E-mail: Michel.Feidt@ensem.inpl-nancy.fr

INTRODUCTION

During the 60s, a new direction in Thermodynamics appeared, namely the analysis of internally reversible heat engines considering finite heat transfer irreversibilities [1,2]. It was renewed during the 70s when an expression for the endoreversible efficiency at maximum power output was developed [3].

Since then, the so called Finite Time Thermodynamics has been developed for analyzing mostly endoreversible thermal engines, the main irreversibility considered being the heat transfer at finite temperature difference between the sources of the studied system and the working fluid [4,5]. Generally, the associated heat fluxes obeyed linear heat transfer laws (Newton's law of heat transfer) [5].

When applied to the study of heat pumps, the same method does not exhibit an optimum due to no theoretical limitation for gas temperature at the hot end [6]. Previously, an expression for the *COP* of a heat pump has been obtained corresponding to minimum power consumption for a required heating load [7]. Also, some complementary results have been obtained for a similar case, considering a given heat exchanger area to be allocated [8].

It followed an extensive study on the theory of irreversible heat transfer refrigeration systems [8]. Formulae for the *COP* and cooling rate of an endoreversible refrigerating machine were derived [9] and also for maximum specific cooling load [10]. All mentioned authors considered linear heat transfer laws.

A forward step was to introduce the internal irreversibilities, firstly represented by an irreversibility ratio [11], when maximum cooling load was determined for a required *COP*.

Recently, a review has been done [12] taking into account internal irreversibilities too, by introducing into the model the internal entropy generation term as parameter and also considering non-linear convective-like heat transfer laws, $\dot{Q} \sim (\Delta T)^n$. Two main non-linear heat transfer laws, convective and radiative-like ones ($\dot{Q} \sim (T_S^n - T^n)$), have further been explored extensively [13], the linear heat transfer law representing a particular case.

In the present paper we are analyzing general performance characteristics of an irreversible reversed cycle Carnot machine, applying the proposed model to such a refrigeration cycle.

We are considering a complete set of optimization procedures. The possible objective functions could be, not only maximum useful effect with imposed *COP*, but also minimum power consumption or minimum total dissipation. Also, the two main non-linear heat transfer laws stated above are analyzed, the convective-like one since in practice this case could represent natural convection or boiling, respectively the radiative-like one.

Internal and external irreversibilities of the cycle are taken into account too, by introducing two terms corresponding to internal and respectively, total entropy generation. The last mentioned one, which results by applying the Second Law of Thermodynamics to the whole system composed by the cycle and the two heat reservoirs, allows us to put emphasis on minimum dissipation operating regime. The entropy generation terms give the model a more general approach than the irreversibility ratio used in other papers [12,14,15]. More and more this approach concerning the entropic analysis of machines and processes [13,16-22] becomes an important tool for the design of real operating machines.

By applying this proposed model to a refrigeration cycle Carnot machine for which dimensional or performance constraints are imposed, one can notice the existence of different optimal operating regimes and also a limited range for the possible values of the system variables and parameters.

GENERAL MODEL MATHEMATICAL APPROACH FOR A REFRIGERATION CARNOT MACHINE

Machine Description

In Figure 1, the *T-S* diagram of an irreversible Carnot cycle machine is represented; therefore all processes are represented as irreversible ones. For the two adiabatic processes, the irreversibility is illustrated by entropy generation, while for the isothermal ones it is due to finite temperature heat transfer processes.

Generally, the internal irreversibility of the machine is represented by the corresponding internal entropy generation term, $\dot{S}_i$ as a model parameter. It takes into account the internal irreversibility generated on each cycle process, its value representing the sum of throttling losses, friction ones, etc. To this one an external irreversibility is added, being generated by finite

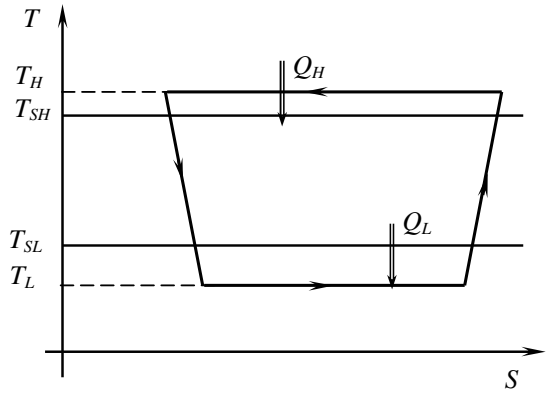

Figure 1: *T-S* diagram for an irreversible refrigeration Carnot cycle machine

temperature heat transfer process between the working fluid and the heat reservoirs. In this model, the two heat reservoirs are considered to be thermostats, of constant temperatures T_{SH} and T_{SL}, and also a steady state operating regime is considered.

Mathematical Equations

The proposed model is based on the most powerful and useful tools of Thermodynamics, namely the First and Second Laws of Thermodynamics, and also on the two heat transfer laws applied to the source and sink. For the considered hypotheses, the expression of the First Law of Thermodynamics is:

$$\dot{W} = \dot{Q}_H + \dot{Q}_L \tag{1}$$

The used sign convention is as follows: power consumption is considered negative and heat fluxes entering the cycle are considered positive, while leaving ones are negative.

The Second Law of Thermodynamics could be written in two different forms, function on the system to which it is applied. If it is applied to the endoirreversible machine, its expression is written taking into account the internal entropy generation term:

$$\frac{\dot{Q}_H}{T_H} + \frac{\dot{Q}_L}{T_L} + \dot{S}_i = 0 \tag{2}$$

If it is applied to the whole system (cycle and the two heat reservoirs), it is written taking into account the total entropy generation term:

$$\frac{\dot{Q}_H}{T_{SH}} + \frac{\dot{Q}_L}{T_{SL}} + \dot{S}_T = 0 \tag{3}$$

To these three above mentioned equations, the non-linear heat transfer laws between the heat reservoirs and working fluid are added:

$$\dot{Q}_H = K_{H,gen}\left(T_{SH} - T_H\right)^{n_H}\left(-1\right)^{n_H - 1} \text{ or}$$

$$\dot{Q}_H = K_{H,gen}\left(T_{SH}^{n_H} - T_H^{n_H}\right) \tag{4}$$

$$\dot{Q}_L = K_{L,gen}\left(T_{SL} - T_L\right)^{n_L} \text{ or}$$

$$\dot{Q}_L = K_{L,gen}\left(T_{SL}^{n_L} - T_L^{n_L}\right) \tag{5}$$

As in the present paper we apply the model to refrigeration machines, the expression of the corresponding coefficient of performance is:

$$COP = \frac{\dot{Q}_L}{\left|\dot{W}\right|} \tag{6}$$

Combining the two expressions of the Second Law, relations (2) and (3), we get:

$$\dot{S}_T = \dot{S}_i + \dot{Q}_H\left(\frac{1}{T_H} - \frac{1}{T_{SH}}\right) + \dot{Q}_L\left(\frac{1}{T_L} - \frac{1}{T_{SL}}\right) \tag{7}$$

One can notice that the total entropy generation is a sum of three positive terms each of them taking into account one type of irreversibility: the first term – internal, the last two ones – external irreversibilities due to finite temperature heat transfer processes between the heat reservoirs and working fluid.

Generally, it is difficult to establish a variation law for the internal entropy generation. We have chosen to consider the following approaches [23,24]:

a) constant: $\dot{S}_i = const$ (8a)

b) linear variation law with temperature:

$$\dot{S}_i = const \cdot \left(T_H - T_L\right) \tag{8b}$$

c) logarithmic variation law with temperature:

$$\dot{S}_i = const \cdot \ln\frac{T_H}{T_L} \tag{8c}$$

Dimensionless Model Equations

In order to avoid cumbersome computations and to make the model easy to apply to any machine, we preferred working non-dimensionally. Thus:

- dimensionless temperatures are expressed relative to the reference temperature T_{SH} which is the ambient temperature, too;
- dimensionless energy fluxes are expressed relative to the product $\dot{m}c_p T_{SH}$, where $\dot{m}c_p$ is the minimum heat rate capacity between those of the working gas and the heat reservoirs;
- non-linear thermal conductances are expressed relative to the product $\dot{m}c_p T_{SH}^{-(n-1)}$;

- entropy generation terms are expressed relative to the heat rate capacity, $\dot{m}c_p$.

According to a dimensionless constraint relative to a fixed heat exchanger area, we impose that:

$$NTU_T = NTU_H + NTU_L \quad (9)$$

which becomes a parameter of the model.

OPTIMISATION UNDER CONSTRAINTS

The dimensionless variables of the model are θ_L and NTU_L, while the considered parameters are: θ_{SL}, NTU_T, $\tilde{\dot{s}}_i$ and the imposed performance characteristics. In the present paper, we are studying the case when a certain value for *COP* is required. In this case, the objective functions could be: maximum refrigerating load, minimum power consumption or minimum total dissipation (minimum total entropy generation).

The analytical development for the optimization procedure is based on Lagrange Multipliers Method for which we wrote the Lagrangian function as:

$$L = FO + \lambda_1 C_1 + \lambda_2 C_2 \quad (10)$$

where: FO is one of the considered objective functions stated above; λ_1 and λ_2 are the corresponding Lagrange multipliers; C_1 and C_2 are the problem constraints represented by the First Law of Thermodynamics including the imposed performance characteristic restrictions and Second Law of Thermodynamics applied to the cycle including the internal entropy generation restriction.

After doing all necessary calculations, the above optimization procedure put in evidence the same system of non-linear equations no matter the considered objective function was.

It results that the optima of all objective functions (maxima and minima, respectively) correspond to the same values of the model variables.

GRAPHICAL RESULTS

By applying a numeric method for solving the system of non-linear equations for the present studied case (imposed *COP* and internal entropy generation), the proposed model put emphasis on two optimum operating regimes, namely maximum refrigerating load and minimum total dissipation.

No matter the variation law for internal entropy

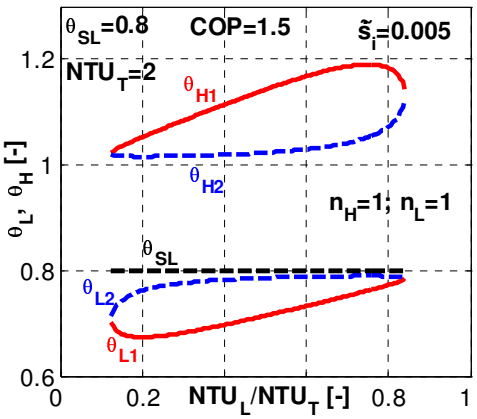

Figure 2: Variation of dimensionless temperatures θ_H and θ_L for the two solutions, function on NTU_L/NTU_T (linear heat transfer laws, $\tilde{\dot{s}}_i$=const)

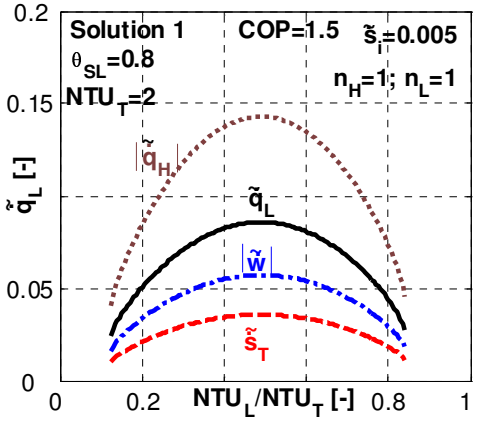

Figure 3: Variation of dimensionless energy fluxes for the maximum refrigerating load regime

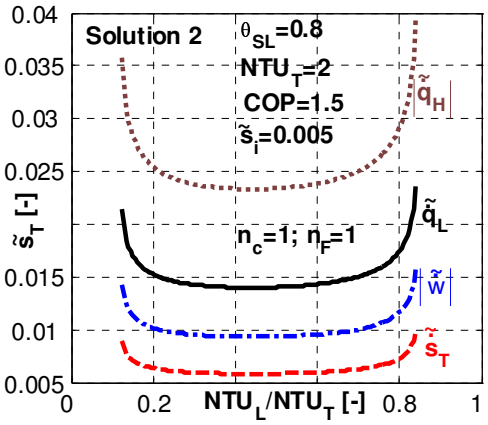

Figure 4: Variation of dimensionless energy fluxes for the minimum total dissipation regime

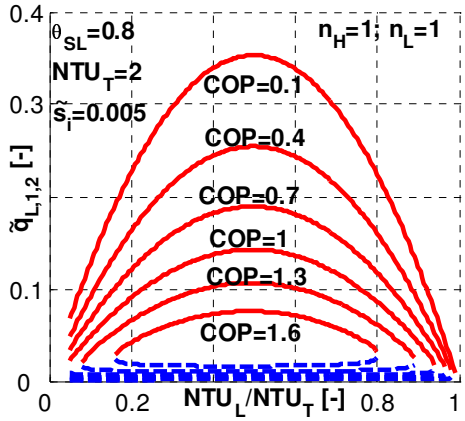

Figure 5: Sensitivity study of dimensionless refrigerating load with respect to *COP*

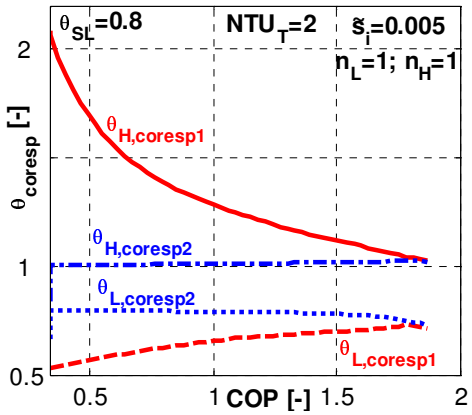

Figure 8: Optimal dimensionless gas temperatures for the two operating regimes

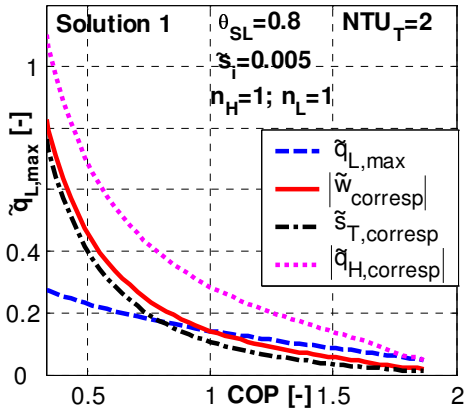

Figure 6: Sensitivity study of dimensionless energy fluxes with respect to *COP* for the maximum refrigerating load regime

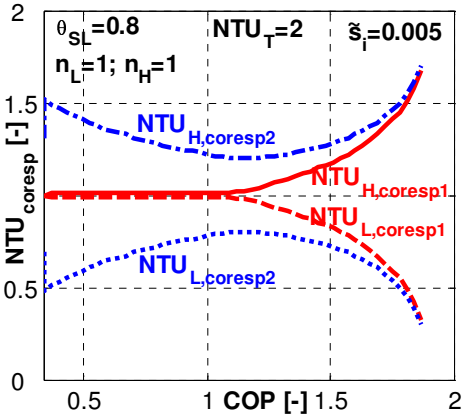

Figure 9: Optimal heat exchanger inventory distribution, for the two operating regimes

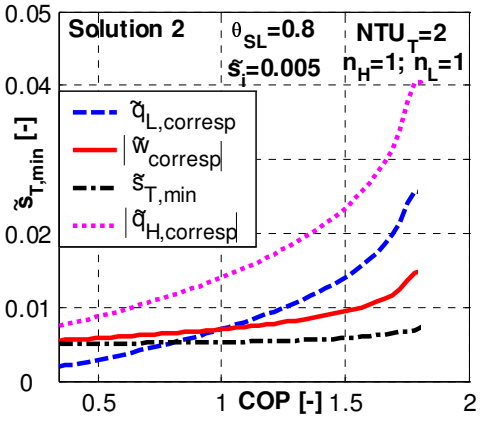

Figure 7: Sensitivity study of dimensionless energy fluxes with respect to *COP* for the minimum total dissipation regime

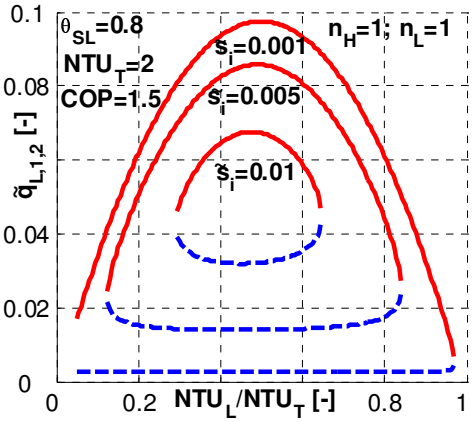

Figure 10: Sensitivity study of dimensionless refrigerating load with respect to internal entropy generation, for the two operating regimes

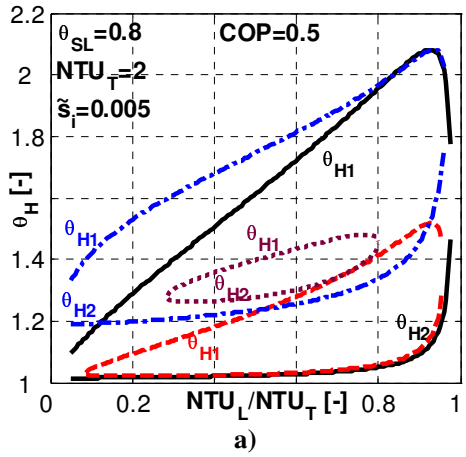

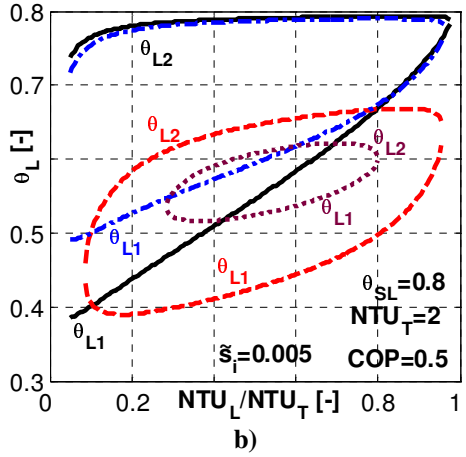

Figure 11: Variation of dimensionless temperatures θ_H (a) and θ_L (b) for the two solutions; sensitivity study with respect to the heat transfer law: ——— $n_H = n_L = 1.25$; - - - - $n_H = 1.25$, $n_L = 3$; — · — · $n_H = 3$, $n_L = 1.25$; ····· $n_H = 3$, $n_L = 3$

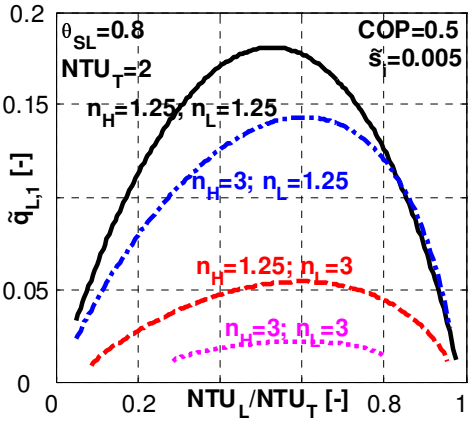

Figure 12: Dimensionless refrigerating load for the maximum refrigerating load regime; sensitivity study with respect to the heat transfer law

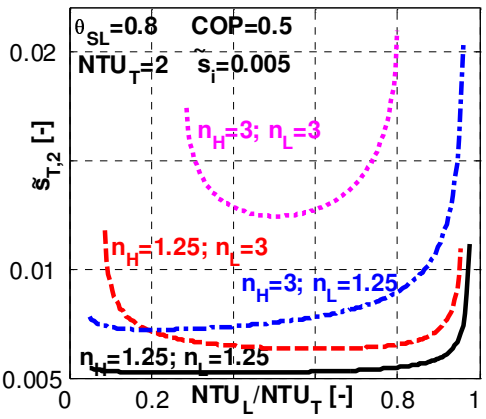

Figure 13: Dimensionless total entropy generation for the minimum total dissipation regime; sensitivity study with respect to the heat transfer law

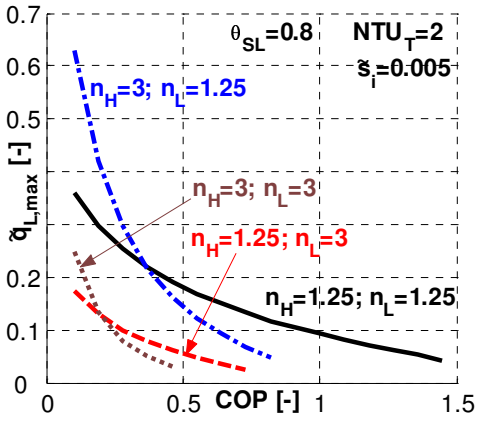

Figure 14: Maximum dimensionless refrigerating load; sensitivity studies with respect to the heat transfer law and *COP*

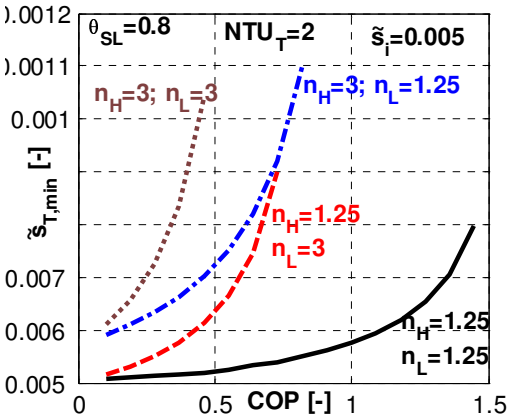

Figure 15: Minimum dimensionless total entropy generation; sensitivity studies with respect to the heat transfer law and *COP*

generation (relations (8)), the system of non-linear equations has two physical solutions corresponding to these two optimum regimes (Figure 2). This figure shows possible values for the model variables. It puts emphasis on the fact that for a chosen value of NTU_L (design stage), the machine can operate on two different regimes corresponding to solution 1 or 2, respectively. For reduced values of NTU_L (equivalent to a more important investment in the high temperature heat exchanger area), the heat transfer process is much better at the hot end, so is the temperature difference between the gas and the source (θ_H tends towards θ_{SH}=1). The opposite happens for high values of NTU_L.

The influence of these two solutions on the energy fluxes could be analyzed in Figure 3 for the first solution and Figure 4 for the second one. They also provide information about the optimal distribution of heat transfer areas between the two heat exchangers.

One can notice that the first solution corresponds to maximum refrigerating load regime, while the second one corresponds to minimum total dissipation regime. This is highlighted by the ordinate axis label, too. Once the machine parameters and desired operating regime are settled on, these two figures give us information about the future necessary distribution of total heat transfer area.

A sensitivity study with respect to *COP* values was made for the refrigerating load (Figure 5) and optimal energy fluxes corresponding to the above mentioned two operating regimes (Figures 6 and 7, respectively). We notice that an increase in *COP* value reduces the possible range values for the model variables (Figure 5). Also, higher required *COP* values determine simultaneously reductions in the refrigerating load and power consumption, for the maximum refrigerating load regime (Figure 6). For the minimum total dissipation regime (Figure 7), the higher *COP* is, the higher refrigerating load and power consumption are. This particular behavior of the system under the imposed constraints is explained by the gas temperature variation and heat exchanger inventory distribution, with respect to *COP* (Figures 8 and 9).

A second sensitivity study was made with respect to internal entropy generation values. In Figure 10, dimensionless refrigerating load for the two operating regimes in plotted for different values of imposed internal entropy generation. One can notice that higher values of $\tilde{\dot{s}}_i$ have a negative effect on the refrigerating load and also, the domain for possible values of the heat exchanger area (through NTU_L) is narrower. Of course, these limit values for the system variables depends, not only on $\tilde{\dot{s}}_i$, but also on the other imposed parameters (*COP*, θ_{SL} ,NTU_T, etc).

A third sensitivity study was made with respect to the nature of heat transfer laws at the source and sink (Figures 11-15), for which we have chosen symmetric and non-symmetric combinations of exponents (n_H and n_L).

When we compare the curves plotted in Figure 10 (representing dimensionless refrigerating load for the first operating regime), we notice different distributions of the heat transfer areas for maximum useful effect. The same conclusion is valid when comparing the curves in Figure 13. In this analysis, we have to take into account that the temperature difference between the two heat sources and the gas depends on the heat transfer law, too (Figure 11).

We also notice that the nature of the heat transfer law influences the domain for possible values of the system variables, especially the phase-change heat exchangers.

The sensitivity study with respect to *COP* and the nature of heat transfer laws (Figures 14-15) puts emphasis on the distribution of optimal values ($\tilde{\dot{q}}_{L,\max}$ and $\tilde{\dot{s}}_{T,\min}$) for the two operating regimes.

CONCLUSIONS AND PERSPECTIVES

In the present paper, we proposed a general model for the study and optimization of irreversible thermal machines, applied here to a Carnot refrigeration one.

The presented results confirm that this model is a very useful tool in spite of its simplicity. Also, they put emphasis on the limit ranges of model variables and parameters, optimal total surface distribution between the two heat exchangers of the studied machine and necessary conditions for achieving optimal operating regimes. Similar results were obtained when applying the model to the study and optimization of irreversible heat pumps.

Extension of this analysis to other cases of imposed parameters (e.g. refrigeration load and internal entropy generation, consumed mechanical

power and internal entropy generation) is under development. Also, in the near-by future, we are going to extend the model for the study of thermal machines with finite capacity heat reservoirs.

REFERENCES

[1] Chambadal P. *Évolution et applications du concept d'entropie.* Paris: Dunod, 1963.

[2] Novikov I. *The efficiency of atomic power stations*. Atommaya Energiya 1957;3:409.

[3] Curzon FL, Ahlborn B. *Efficiency of a Carnot Engine at Maximum Power Output*. American Journal of Physics 1975;43:22-24.

[4] De Vos A. *Efficiency of some heat engines at maximum power conditions.* American Journal of Physics 1985;53:570-573.

[5] Salamon P, Nitzan A. *Finite Time optimizations of a Newton's law Carnot cycle.* Journal of Chemical Physics 1981;74:3546-3560.

[6] Blanchard CH. *Coefficient of performance for finite speed heat pump.* Journal of Applied Physics 1980;51:2471-2472.

[7] Leff HS, Teeters WO. *EER, COP and second law efficiency for air conditioners.* American Journal of Physics 1978; 46: 19-22.

[8] Bejan A. *Theory of heat transfer irreversible refrigeration plant.* International Journal of Heat and Mass Transfer 1989; 32: 1631-1639.

[9] Agrawal DC, Menon VJ. Journal of Applied Physics 1993; 74: 2153.

[10] Wu C. Energy Conversion and Management 1995;36:7.

[11] Assad M. *Performance characteristics of an irreversible refrigerator.* In: Recent Advanced in Finite Time Thermodynamics, Nova Science Publishers, New York, 2000.

[12] Feidt M. *Advanced Thermodynamics of reverse cycle machine.* In: Low Temperature and Cryogenic Refrigeration, Kluwer Academic Publishers, 2003.

[13] Feidt M. *Thermodynamics and Optimization of Reverse Cycle Machines: Refrigeration, Heat Pumps, Air Conditioning, Cryogenics.* In: Thermodynamics Optimization of Complex Energy Systems, Kluwer Academic Publishers, 1999.

[14] Sieniutycz S, Salamon P. *Finite-Time Thermodynamics and Thermoeconomics.* New York: Taylor&Francis, 1990.

[15] Calvo Hernández A, Medina A, Roco JMM, Velasco S. *Comparison of Optimum Thermal Conductance Distribution for an Irreversible Carnot Cycle under Different Optimization Criteria*. In: Advances in Finite Time Thermodynamics, Analysis and Optimization, Nova Science Publishers, New York, 2004.

[16] Petrescu S, Feidt M, Harman C, Costea M. *Optimization of the Irreversible Carnot Cycle Engine for Maximum Efficiency and Maximum Power through Use of Finite Speed Thermodynamic Analysis.* In: Proceedings of. ECOS 2002 International Conference, Berlin, 2002.

[17] Feidt M, Petrescu S, Costea M. *From Carnot's Efficiency to the Finite Time Thermodynamics*, Proceedings of the Francophone Conference on Process Design, CFGP'2001, 83(15):125-131, Tech&Doc 2001.

[18] Bejan A. *Entropy Generation Minimization.* New York: Wiley & Sons, 1982.

[19] Feidt M. *Thermodynamique et optimisation énergétique des systèmes et procédés.* Paris: Tech & Doc, 1996.

[20] Bejan A. *Advanced Engineering Thermodynamics.* New York: Wiley & Sons, 1988.

[21] Petrescu S, Zaiser J, Petrescu V. *Lectures on Advanced Energy Conversion*. Lewisburg: Bucknell, 1996.

[22] Petrescu S, Costea M, Feidt M. *Les cycles des machines à froid et des pompes à chaleur à vitesse finie*. Entropie 2001; 32:51-56.

[23] Gordon JM, Ng KC. *Cool Thermodynamics*. Cambridge: Cambridge International Science Publishing, 2000.

[24] Wijeysundera NE. *Performance of three heat reservoirs absorption cycles with external and internal irreversibilities*. Applied Thermal Engineering 1997;17:1151-1161.

Proceedings of ECOS 2005
Trondheim, Norway
June 20–22, 2005

EFFECT OF GAS-PROPERTIES EVALUATION METHOD ON THE OPTIMUM POINT OF GAS TURBINE CYCLES

Christos A. Frangopoulos* and George G. Dimopoulos

National Technical University of Athens
Department of Naval Architecture and Marine Engineering
Heroon Polytechniou 9, 157 73 Zografou
Greece

ABSTRACT

Recent work has revealed that the assumption regarding the behavior of gases (perfect, ideal, real) and, consequently, the way their properties are evaluated may alter critically the picture obtained about the performance of gas turbine systems. This fact prompted an investigation of how the aforementioned assumption may affect the optimal design point of gas turbine systems. Three systems have been selected for study and three optimization problems have been formulated and solved for each system: two thermodynamic and one thermoeconomic. The results demonstrate that the method (assumption) used for the evaluation of properties of gases has a very significant effect on the optimal point of each system.

Keywords: Gas properties, Gas turbine cycles, Optimization, Thermoeconomics.

NOMENCLATURE

C_n	Capital cost of component n (installed)
c_f	Unit cost of fuel
c_p	Specific heat capacity at constant pressure
$\tilde{c}_p$	Molar heat capacity at constant pressure
c_v	Specific heat capacity at constant volume
$\tilde{c}_v$	Molar heat capacity at constant volume
FCR	fixed charge rate
f	fuel to air ratio: $f = \dot{m}_f / \dot{m}_a$
H_u	Lower heating value of the fuel
k	Specific heat ratio: $k = c_p / c_v$
$\dot{m}_a$	air mass flow rate
$\dot{m}_f$	fuel mass flow rate
$\dot{m}_g$	exhaust gas mass flow rate
P	Pressure
r	Pressure ratio
$\dot{Q}$	Useful heat rate of the cogeneration system (production of steam)
$\tilde{R}$	Universal gas constant
T	Absolute temperature $[K]$
T_1	Compressor inlet temperature
T_3	Turbine inlet temperature (simple cycle)
t	period of operation during a year
$\dot{W}$	Net power to the load
w	Specific work, as defined by Eq. (17)
x	set of independent variables for optimization
x_i	molar fraction of species i in a mixture
Z	Annualized cost rate of a system, in \$ (including capital as well as operation and maintenance expenses)

Greek letters

γ	$\gamma = (k-1)/k$
η	Efficiency
η_B	Efficiency of the combustor
η_C	Isentropic efficiency of the compressor

* Corresponding author: Phone: +30-210-7721108,
Fax: +30-210-7721117, E-mail: caf@naval.ntua.gr

η_J Efficiency of the Joule cycle
η_m Mechanical efficiency
η_T Isentropic efficiency of the turbine
τ_i Temperature ratio: $\tau_i = T_i / T_1$
ϕ Maintenance factor

Subscripts
A Air standard gas turbine cycle
a Air
B Combustor
C Compressor
f fuel
g exhaust gases
I Intercooler
T Turbine
R Exhaust gas boiler
X Air preheater
0 Standard conditions: 25°C, 1.01325 bar

Superscripts
* Optimum value

1. INTRODUCTION

It is common knowledge that the efficiency of a simple gas turbine cycle increases monotonically with the maximum cycle temperature for constant pressure ratio [1]. In order to be more specific, the efficiency of the air standard cycle (assumption of perfect gas with no change of mass flow rate due to fuel addition and no pressure losses in the ducts and the combustion chamber) is given by the equation

$$\eta_A = \frac{\eta_C \eta_T \eta_J \tau_3 - \left(r^k - 1\right)}{\eta_C \left(\tau_3 - 1\right) - \left(r^k - 1\right)} \qquad (1)$$

where

$$\eta_J = 1 - \frac{1}{r^k} \qquad (2)$$

is the Joule cycle efficiency, i.e. the ideal cycle with isentropic compression and expansion and no losses. Starting with Eq. (1) it is easily proved that, if the turbine temperature is increased, keeping the pressure ratio constant, the thermal efficiency of the air standard cycle increases continuously and asymptotically it reaches the limit:

$$\lim_{\tau_3 \to \infty} \eta_A = \eta_T \eta_J \qquad (3)$$

It was tacitly assumed that the general trend was the same even if a change of specific heat capacity or of the mass flow rate due to fuel addition were considered. Thus, it was a surprise to read in Ref. [2] that, if the assumption of a working substance of constant quality and quantity is relaxed, then the behavior changes drastically: for a constant pressure ratio, the efficiency initially increases with the turbine-inlet temperature, it reaches a maximum value and then it decreases. Detailed studies of these effects appear in Refs. [3]-[5]. This remark prompted the investigation reported here.
Many publications on optimization of gas turbine cycles, including Refs. [6]-[9], are based on the assumption of perfect gas with different values for the specific heats of air and exhaust gases, in order to decrease the inaccuracy. After the aforementioned, the question arises: "how is the optimum point affected if the properties of gases are evaluated with a higher accuracy?" An answer to this question is attempted in the following, using as examples three different system configurations.

2. EVALUATION OF GAS PROPERTIES

A clarification of terminology is useful at this point. The specific heat capacities of a *real gas* are functions of both temperature and pressure:

$$c_p = c_p(p, T), \qquad c_v = c_v(p, T) \qquad (4)$$

For an *ideal gas*, they are functions of the temperature only:

$$c_p = c_p(T), \qquad c_v = c_v(T) \qquad (5)$$

For a *perfect gas*, they are constant:

$$c_p = \text{const.}, \qquad c_v = \text{const.} \qquad (6)$$

This 'textbook material' is repeated here because it is often written in related publications that 'real-gas' effects are studied, while in fact the gases are considered ideal. Thus, the reader should be careful.
In the present work, it is considered that air consisting of N_2, O_2, CO_2 and H_2O is compressed and then it reacts with a fuel having the general composition $C_\alpha H_\beta$ in a complete combustion to produce exhaust gases consisting of N_2, O_2, CO_2 and H_2O. For simplicity, minor constituents (such as CO, NO_x, etc) due to additional reactions, dissociation, impurities or other reasons are not considered here. The properties of each species are evaluated by the following equations obtained

from Refs. [10] and [11]:

$$\frac{\tilde{c}_{p0}}{\tilde{R}} = a_1 \cdot T^{-2} + a_2 \cdot T^{-1} + a_3 + a_4 \cdot T + a_5 \cdot T^2 + a_6 \cdot T^3 + a_7 \cdot T^4 \quad (7)$$

$$\frac{\tilde{h}_0}{\tilde{R}} = -a_1 \cdot T^{-1} + a_2 \cdot \ln(T) + a_3 \cdot T + \frac{1}{2} a_4 \cdot T^2 + \frac{1}{3} a_5 \cdot T^3 + \frac{1}{4} a_6 \cdot T^4 + \frac{1}{5} a_7 \cdot T^5 + b_1 \quad (8)$$

$$\frac{\tilde{s}_0}{\tilde{R}} = -\frac{1}{2} \cdot a_1 \cdot T^{-2} - a_2 \cdot T^{-1} + a_3 \cdot \ln(T) + a_4 \cdot T + \frac{1}{2} \cdot a_5 \cdot T^2 + \frac{1}{3} \cdot a_6 \cdot T^3 + \frac{1}{4} \cdot a_7 \cdot T^4 + b_2 - \ln(P) \quad (9)$$

The numerical values of the parameters a_i depend on the species and the temperature range, and they are given in Ref. [11].
The properties of air and exhaust gases are evaluated with the assumption that they are ideal mixtures; for example the molar heat capacity is calculated by the equation

$$\tilde{c}_p = \sum_i x_i \tilde{c}_{pi} \quad (10)$$

Thus, the perfect gas assumption of previous works has been replaced here with the ideal gas assumption. The effect of pressure is still considered negligible for the pressure ranges used in the systems that are studied here, as justified by values obtained for the compressibility factor.

3. SYSTEMS STUDIED

3.1 Description of the Systems

Three systems have been selected in order to study the effect of the method used for property evaluation on the optimal design point.
System I consists of a simple, open-cycle gas turbine (Figure 1). An approach for its thermodynamic and thermoeconomic optimization based on the perfect gas assumption has been presented in Refs. [6] and [7].
System II is a cogeneration plant consisting of a regenerative gas turbine with an exhaust gas boiler producing saturated steam (Figure 2) of a given quality and quantity; it is the system of the CGAM problem [8,9].
System III is an inter-cooled, regenerative gas turbine with a twin spool gas generator and a power turbine (Figure 3).

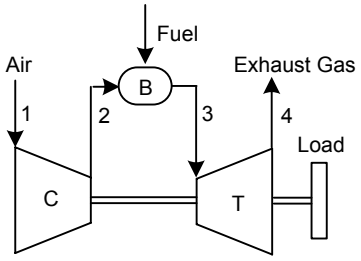

Figure 1: System I

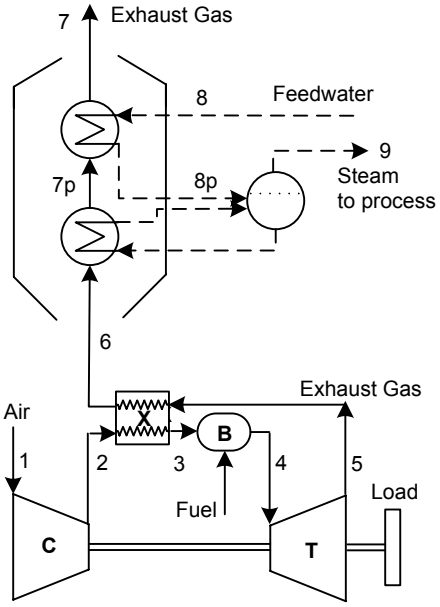

Figure 2: System II

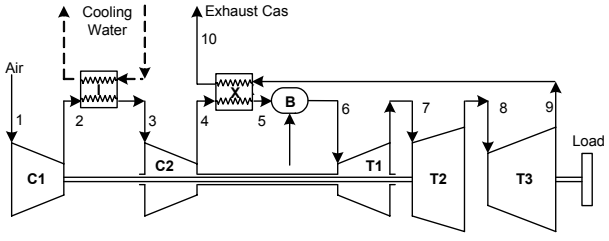

Figure 3: System III

3.2 Mathematical Models of the Systems

Thermodynamic model of System I

The air temperature at the exit of the compressor and the exhaust gas temperature at the exit of the turbine are evaluated by the equations

$$T_2 = T_1 \cdot \left[1 + \left(r_C^{\frac{k_{12}-1}{k_{12}}} - 1 \right) \cdot \frac{1}{\eta_C} \right] \qquad (11)$$

$$T_4 = T_3 \cdot \left[1 - \left(1 - r_T^{\frac{1-k_{34}}{k_{34}}} \right) \cdot \eta_T \right] \qquad (12)$$

where

$$k_{ij} = \frac{\tilde{c}_{pij}}{\tilde{c}_{pij} - \tilde{R}} \qquad (13)$$

$$\tilde{c}_{pij} = \frac{1}{T_j - T_i} \int_{T_i}^{T_j} \tilde{c}_p(T)\, dT \qquad (14)$$

Since k_{12} and k_{34} depend on the temperatures T_2 and T_4, respectively, Eqs. (11) and (12) are used in an iterative procedure in order to obtain the temperatures T_2 and T_4.

An energy balance in the combustion chamber gives the equation

$$f H_u \eta_B = (1+f)(h_3 - h_0) - (h_2 - h_0) \qquad (15)$$

which can be solved for f, if the temperature T_3 is given. The composition of the exhaust gases is determined by the reaction of combustion for any specified fuel. Since the temperature T_3 and the composition of exhaust gases are interrelated through the temperature-dependent properties of the constituents, an iterative procedure is applied also here.

The system efficiency is given by the equation

$$\eta_I = \frac{\dot{W}}{\dot{m}_f H_u} = \frac{(1+f)(h_3 - h_4) - (h_2 - h_1)}{f H_u} \qquad (16)$$

The specific work is also of interest:

$$w = \frac{\dot{W}}{\dot{m}_a} \qquad (17)$$

Thermodynamic model of System II

Equations (11)-(15) and (17) are valid for System II, with a proper adjustment of certain numerical indexes. The effectiveness of the air pre-heater is given by the equation

$$\varepsilon_X = \frac{h_3 - h_2}{h_{a5} - h_2} \qquad (18)$$

The subscript 'a5' is used in Eq. (18) in order to make it clear that h_{a5} is the enthalpy of air at temperature T_5. There is no ambiguity about h_2 and h_3. The following efficiencies are defined for this system.

Net shaft-power efficiency:

$$\eta_{II} = \frac{\dot{W}}{\dot{m}_f H_u} = \frac{(1+f)(h_4 - h_5) - (h_2 - h_1)}{f H_u} \qquad (19)$$

Efficiency of providing the useful heat:

$$\eta_{II,Q} = \frac{\dot{Q}}{\dot{m}_f H_u} = \frac{\dot{m}_s (h_9 - h_8)}{\dot{m}_f H_u} \qquad (20)$$

Total efficiency:

$$\eta_{II,tot} = \eta_{II} + \eta_{II,Q} = \frac{\dot{W} + \dot{Q}}{\dot{m}_f H_u} \qquad (21)$$

The model of System II consists of many more equations, which are given in Ref. [9], but they are not repeated here due to space limitations.

Thermodynamic model of System III

For the compression, combustion and expansion processes, equations similar to those of the System I are used. The effectiveness of the air pre-heater is given by an equation similar to Eq. (18), with proper adjustment of the numerical indexes. In addition, the following equalities are taken into consideration:

$$\dot{W}_{C1} = \dot{W}_{T2}, \qquad \dot{W}_{C2} = \dot{W}_{T1} \qquad (22)$$

The division of the pressure ratio between the low-pressure and high-pressure spool is determined by an iterative procedure so that Eqs. (22) are satisfied.

The system efficiency is given by the equation

$$\eta_{III} = \frac{\dot{W}}{\dot{m}_f H_u} = \frac{(1+f)(h_8 - h_9)}{f H_u} \qquad (23)$$

The specific work is given by Eq. (17).

Thermoeconomic models of the systems

The cost functions for Systems I and II appear in Refs. [6]-[9]. For System III, equations available for Systems I and II have been properly modified and used. Space limitations do not allow giving the complete set of equations here.

4. PERFORMANCE OF SYSTEMS WITH ALTERNATIVE METHODS FOR EVALUATION OF PROPERTIES

For the performance evaluation and for the optimization of the systems, certain values have been considered for the various parameters involved, which are given in Table 1.

System I	System II	System III
$r_B = 0.975$	$r_B = 0.975$	$r_{C1} = r_{C2}$
$\eta_B = 0.99$	$\eta_B = 0.99$	$r_I = 0.98$
$\eta_m = 0.99$	$r_{Xa} = 0.975$	$T_3 = T_1$
	$r_{Xg} = 0.965$	$r_B = 0.975$
Air	$\Delta T_{X\min} = 20\,K$	$\eta_B = 0.99$
N_2: 77.82%	$\eta_m = 0.99$	$r_{Xa} = 0.975$
O_2: 20.68%	$r_R = 0.95$	$r_{Xg} = 0.965$
CO_2: 0.03%	$\Delta T_{p\min} = 15\,K$	$\Delta T_{X\min} = 20\,K$
H_2O: 1.47%	$T_{7\min} = 373.15\,K$	$\eta_m = 0.99$
$T_{amb} = T_0$=25°C	$\dot{m}_{st} = 14\ kg/s$	$r_R = 0.95$
$P_{amb} = P_0$	$P_8 = 20\,bar$	
= 1.01325 bar	$T_8 = 298.15\,K$	
Fuel: CH_4	$T_{8P} = T_9 - 15\,K$	
$H_u = 50000 \frac{kJ}{kg}$	$P_9 = 20\,bar\,(sat.)$	

Table 1: Values of parameters

The first step in this investigation has been the study of the effect of properties evaluation on the simple cycle efficiency (System I). The results depicted in Figure 4 are revealing: the perfect gas assumption, as expected, gives an efficiency continuously increasing with the turbine inlet temperature. With the ideal gas assumption and properties evaluated by Eqs. (7)-(10), the efficiency exhibits a maximum at a temperature of about 1600 K (for the parameter values considered here). Thus, the related results of Ref. [5] are reproduced to a very close approximation (small differences are due to different values of parameters and to the different sources of equations for evaluation of gas properties).

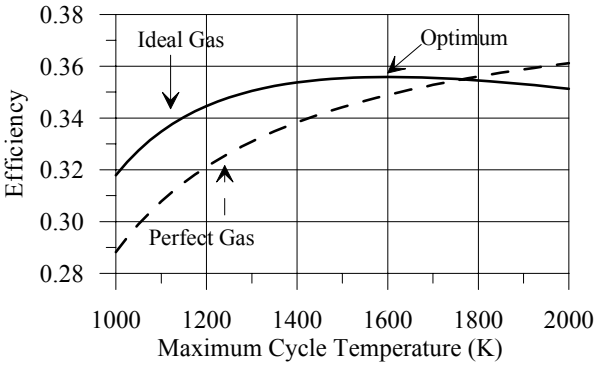

Figure 4: Efficiency of System I as a function of turbine inlet temperature with two gas models: perfect gas, ideal gas; η_C =0.90, η_T =0.92, r=10.

With the perfect gas model, the specific work increases continuously with turbine inlet temperature for a certain pressure ratio. This trend remains the same with the ideal gas model too.

In Figures 5 and 6, the effect of the gas model assumption on the system efficiency and specific work as functions of pressure ratio is shown. It is clarified that the graphs of Figures 5B and 6B correspond to the system of Figure 2 but without the exhaust gas boiler.

The coordinates of the optimum points in Figures 5 and 6 are given in Tables 2 and 3, respectively.

A change from perfect to ideal gas model changes the pressure ratio for maximum efficiency by +37.04%, –14.29% and –15.38% for the simple cycle, the regenerative cycle and the intercooled-regerenerative cycle, respectively. The optimum efficiency increases by 11.11%, 13.08% and 10.10%, respectively.

A change from perfect to ideal gas model increases the pressure ratio for maximum specific work by 16.67%, 28.57% and 50.00% for the simple cycle, the regenerative cycle and the intercooled-regerenerative cycle, respectively. The optimum specific work increases by 15.49%, 13.25% and 15.85%, respectively.

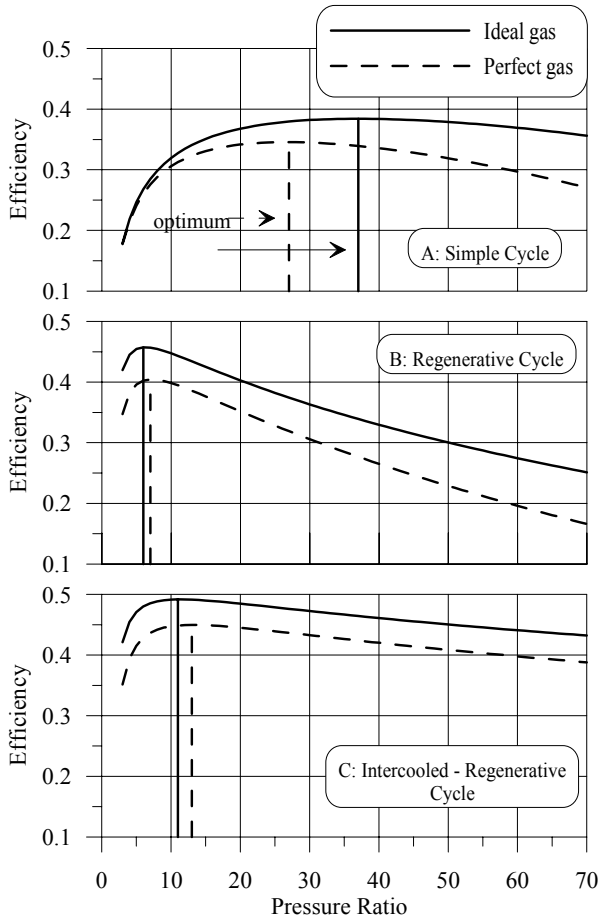

Figure 5: Efficiency as a function of pressure ratio with two gas models: perfect gas, ideal gas; η_C =0.85, η_T =0.88, τ_{max} =5.

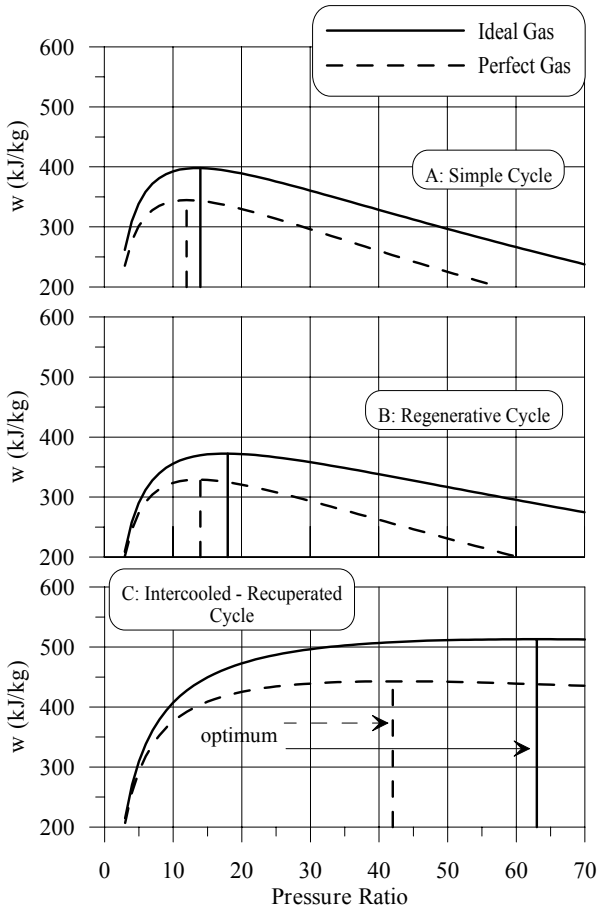

Figure 6: Specific work as a function of pressure ratio with two gas models: perfect gas, ideal gas; η_C =0.85, η_T =0.88, τ_{max} =5.

Cycle	Perfect gas		Ideal Gas	
	r*	η*	r*	η*
Simple	27	0.3457	37	0.3841
Regenerative	7	0.4045	6	0.4574
Intercooled Regenerative	13	0.4497	11	0.4918

Table 2: Coordinates of the optimum points of Figure 5.

Cycle	Perfect gas		Ideal Gas	
	r*	w*	r*	w*
Simple	12	344.64	14	398.04
Regenerative	14	328.93	18	372.50
Intercooled Regenerative	42	442.85	63	513.06

Table 3: Coordinates of the optimum points of Figure 6.

It is noted that for the Figures 5 and 6, component efficiencies more or less realistic have been used. For those values of efficiencies, the temperature of maximum cycle efficiency increases to an extremely unrealistic value. In order to keep the maximum point in a realistic temperature, we have considered more optimistic component efficiencies in Figure 4.

5. OPTIMIZATION OF SYSTEMS WITH ALTERNATIVE METHODS FOR EVALUATION OF PROPERTIES

Three distinct optimization problems have been formulated and solved for each system:

(a) Maximization of the cycle efficiency:

$$\max \eta_i , \qquad i = I, II, III \tag{24}$$

(b) Maximization of the specific work:

$$\max w_i, \qquad i = I, II, III \tag{25}$$

(c) Minimization of the annualized cost rate:

$$\min Z_i, \qquad i = I, II, III \tag{26}$$

$$Z = FCR \cdot \phi \cdot \sum_n C_n + c_f \cdot \dot{m}_f \cdot H_u \cdot t \qquad n = C, B, T, I, X, R \tag{27}$$

For the air standard cycle mentioned in the Introduction, the first two optimization problems have a well-known closed-form analytic solution [5-7]. Changing the model from constant to variable quantity and quality and simultaneously introducing pressure losses makes the analytic solution very difficult or impossible. An analytic solution for certain cases based on various simplifying assumptions has been attempted in Ref. [3] but, as mentioned in Ref. [5], the errors introduced by these assumptions may be critical. Therefore, the optimization problems are solved numerically here.

5.1 Optimization of System I

The following independent variables have been considered for the three optimization problems:

$$\mathbf{x}_{I,\eta} = (r), \quad \mathbf{x}_{I,w} = (r), \quad \mathbf{x}_{I,Z} = (\eta_C, r, \tau_3, \eta_T) \tag{28}$$

The problems (a) and (b) have been solved for the thermoeconomic optimum values of η_C^*, τ_3^*, and η_T^* obtained from the solution of problem (c). The results are given in Table 4, where the optimum values of the objective functions are written in bold numbers.

The most significant effects of the change from perfect to ideal gas are the following: The optimum pressure ratio for the problems (a), (b) and (c) increases by 34.48%, 9.69% and 21.05%, respectively. The optimum efficiency of problem (a) increases by 9.85%. The optimum specific work of problem (b) increases by 13.58%. The optimum annualised cost rate of problem (c) decreases by 7.78%.

5.2 Optimization of System II

The following independent variables have been considered for the three optimization problems:

$$\mathbf{x}_{II,\eta} = (r), \qquad \mathbf{x}_{II,w} = (r), \qquad \mathbf{x}_{II,Z} = (\eta_C, r, \tau_3, \eta_T, \varepsilon_X) \tag{29}$$

It is noted that the useful heat rate $\dot{Q}$ is fixed; consequently, maximization of η_{II} is equivalent to maximization of $\eta_{II,tot}$.

The problems (a) and (b) have been solved for the thermoeconomic optimum values of η_C^*, τ_3^*, η_T^* and ε_X^* obtained from the solution of problem (c). The results are given in Table 5.

The most significant effects of the change from perfect to ideal gas are the following: The optimum pressure ratio for the problems (a), (b) and (c) increases by 32.33%, 21.37% and 13.42%, respectively. The optimum efficiency of problem (a) increases by 3.72%. The optimum specific work of problem (b) increases by 12.41%. The optimum annualised cost rate of problem (c) decreases by 4.78%.

5.3 Optimization of System III

The following independent variables have been considered for the three optimization problems:

$$\mathbf{x}_{II,\eta} = (r, \varepsilon_X), \qquad \mathbf{x}_{II,w} = (r, \varepsilon_X), \qquad \mathbf{x}_{II,Z} = (\eta_C, r, \tau_6, \eta_T, \varepsilon_X) \tag{30}$$

The problems (a) and (b) have been solved for the thermoeconomic optimum values of η_C^*, τ_6^* and η_T^* obtained from the solution of problem (c).

The results are given in Table 6. The most significant effects of the change from perfect to ideal gas are the following: The optimum pressure ratio for the problems (a), (b) and (c) changes by –44.67%, +19.47% and –24.98%, respectively. The optimum efficiency of problem (a) increases by 12.24%. The optimum specific work of problem (b) increases by 15.89%. The optimum annualised cost rate of problem (c) decreases by 9.57%.

It is worth noting also that the maximization of the specific work results in elimination of the air pre-heater ($\varepsilon_X = 0$) in both cases (perfect and ideal gas).

5.4 Further remarks on system optimization

According to the analysis of Section 4, the optimization problem (a) of System I might be considered as having two independent variables:

	Perfect gas			Ideal gas		
	$\max \eta_I$	$\max w_I$	$\min Z_I$	$\max \eta_I$	$\max w_I$	$\min Z_I$
η_C^*	0.8445	0.8445	0.8445	0.8360	0.8360	0.8360
r*	29.0974	12.3112	18.9046	39.1313	13.5037	22.8845
τ_3^*	4.9924	4.9924	4.9924	4.9887	4.9887	4.9887
η_T^*	0.9047	0.9047	0.9047	0.9048	0.9048	0.9048
η_I	**0.3686**	0.3686	0.3686	**0.4049**	0.3582	0.3915
w_I	312.98	**356.44**	345.77	336.15	**404.84**	387.97
Z_I	$1.120 \cdot 10^7$	$1.110 \cdot 10^7$	$\mathbf{1.075 \cdot 10^7}$	$1.055 \cdot 10^7$	$1.037 \cdot 10^7$	$\mathbf{9.914 \cdot 10^6}$

Table 4: Optimization results for System I (simple cycle)

	Perfect gas			Ideal gas		
	$\max \eta_{II}$	$\max w_{II}$	$\min Z_{II}$	$\max \eta_{II}$	$\max w_{II}$	$\min Z_{II}$
η_C^*	0.8408	0.8408	0.8445	0.8323	0.8323	0.8323
r*	9.3053	13.4909	9.2207	12.3133	16.3740	10.4584
τ_4^*	5.0271	5.0271	5.0271	5.0292	5.0292	5.0292
η_T^*	0.8876	0.8876	0.8876	0.8864	0.8864	0.8864
ε_X	0.7675	0.7675	0.7675	0.6683	0.6683	0.6683
η_{II}	**0.3792**	0.3719	0.3791	**0.3972**	0.3933	0.3959
w_{II}	322.95	**330.79**	322.55	367.41	**371.84**	360.87
Z_{II}	$1.002 \cdot 10^7$	$1.029 \cdot 10^7$	$\mathbf{1.002 \cdot 10^7}$	$9.577 \cdot 10^6$	$9.734 \cdot 10^6$	$\mathbf{9.541 \cdot 10^6}$

Table 5: Optimization results for System II (cogeneration system)

	Perfect gas			Ideal gas		
	$\max \eta_{III}$	$\max w_{III}$	$\min Z_{III}$	$\max \eta_{III}$	$\max w_{III}$	$\min Z_{III}$
η_C^*	0.8579	0.8579	0.8579	0.8612	0.8612	0.8612
r*	9.8729	41.2845	8.5835	5.4628	49.3242	6.4390
τ_6^*	5.0213	5.0213	5.0213	5.0044	5.0044	5.0044
η_T^*	0.8919	0.8919	0.8919	0.8878	0.8878	0.8878
ε_X	0.9602	0.0	0.9630	0.9711	0.0	0.9691
η_{III}	**0.4729**	0.3813	0.4724	**0.5308**	0.4102	0.530
w_{III}	383.55	**458.00**	322.55	325.34	**530.79**	351.03
Z_{III}	$8.218 \cdot 10^6$	$1.116 \cdot 10^7$	$\mathbf{8.202 \cdot 10^6}$	$7.433 \cdot 10^6$	$1.077 \cdot 10^7$	$\mathbf{7.417 \cdot 10^6}$

Table 6: Optimization results for System II (intercooled regenerative cycle)

$$\mathbf{x}_{I,\eta} = (r, \tau_3) \quad (31)$$

The solution of this problem gives extremely and unrealistically high optimum values r* and τ_3^* for the values of η_C and η_T considered here. This is why only the pressure ratio has been considered as independent variable, while τ_3 is a parameter.

The effectiveness ε_X of the air pre-heater could be an independent variable for problems (a) and (b) of System II also. In such a case, maximization of the specific work would result in elimination of the air-pre-heater, changing the structure of the system. In order to keep the structure the same as in the CGAM problem, it was decided to treat ε_X as a fixed parameter for these problems.

It is interesting to note that, as we go from the simple cycle to the intercooled regenerative cycle, the optimum value of the annualized cost rate decreases by 25.22% (from $9.914 \cdot 10^6$\$ to $7.417 \cdot 10^6$\$), in spite of the fact that the system becomes more complex. The most important reasons for this decrease are the significant decrease of the pressure ratio (which decreases the capital cost of certain components) and the significant increase of the system efficiency (which decreases the fuel cost).

CONCLUSION

A preliminary performance evaluation followed by the solution of three optimization problems for each one of three different gas turbine system configurations has demonstrated that a change from the perfect gas to ideal gas model for evaluation of properties has a very significant effect on the results, which cannot be ignored. With the computing capabilities of today, the necessary calculations are conveniently performed.

REFERENCES

[1] Haywood R.W. *Analysis of engineering cycles.* 3rd ed. Oxford: Pergamon Press, 1987.

[2] Horlock J.H. *Advanced gas turbine cycles.* Amsterdam: Pergamon, 2003.

[3] Horlock J.H., Woods W.A. *Determination of the optimum performance of gas turbines.* Proceedings of the Institute of Mechanical Engineers, Part C: Journal of Mechanical Engineering Science 2000;214: 243-255.

[4] Horlock J.H. *Erratum* (for Ref. [2]). Proceedings of the Institute of Mechanical Engineers, Part C: Journal of Mechanical Engineering Science 2001;215: 1378.

[5] Guha A. *Effects of internal combustion and non-perfect gas properties on the optimum performance of gas turbines.* Proceedings of the Institute of Mechanical Engineers, Part C: Journal of Mechanical Engineering Science 2003; 217: 1085-1099.

[6] Frangopoulos C.A. *Optimal Design of a Gas Turbine Plant by a Thermoeconomic Approach.* In: 2nd International Symposium and Exposition on Turbo-machinery, Combined-Cycle Technolo-gies and Cogeneration, Montreaux, Switzerland, 1988.

[7] Frangopoulos C.A. *Thermoeconomic versus thermodynamic design optimization of a simple gas turbine plant. Part A′: Thermodynamic optimization. Part B′: Thermoeconomic optimization.* The International Journal of Mechanical Engineering Education 1992; 20(3):149–168.

[8] Valero A. et al. *CGAM Problem: Definition and conventional solution.* Energy 1994; 19(3): 279-286.

[9] Frangopoulos, C.A. *Application of the Thermoeconomic Functional Approach to the CGAM Problem.* Energy 1994;19(3): 323-342.

[10] Gordon S., McBride B.J. *Computer program for calculation of complex chemical equilibrium compositions and applications; I. Analysis.* NASA reference publication 1311, National Aeronautics and Space Administration, October 1994.

[11] McBride B.J., Zehe M.J., Gordon S. NASA Glenn coefficients for calculating thermodynamic properties of individual species. NASA/TP–2002-211556, National Aeronautics and Space Administration, September 2002.

Proceedings of ECOS 2005
Trondheim, Norway
June 20–22, 2005

ADDITIONAL FLOW RATE OF H_2 IN METHANOL PROCESS OPTIMIZATION USING NLP MODEL

Anita Kovač Kralj and Peter Glavič
Faculty of Chemistry and Chemical Engineering, University of Maribor,
2000 Maribor,
Slovenia

ABSTRACT

The opportunities for additional profit depend very much on the existing plant and energy system. Methanol plant was optimized using mathematical nonlinear programming (NLP) model by including an additional flow rate of hydrogen (H_2) in crude methanol recycle and increasing the methanol production by 2,5 %. The electricity can be generated in methanol recycle using gas turbine. The total additional profit is 2,5 MEUR/a.

Keywords: simultaneous optimisation, NLP, model, cogenerations, the product increase

NOMENCLATURE

A	area of heat exchanger [m^2]
C_{37}	cost of 37 bar steam [EUR/(kW a)]
C_{el}	cost of electricity [EUR/(kW a)]
C_{H2}	cost of H_2 purification [EUR/t]
C_M	cost of methanol [EUR/t]
C_m	molar heat capacity [J/(mol K)]
C_{tax}	taxes and costs of CO_2 emissions [EUR]
F	amount flow rate [mol/s]
G	Gibbs free energy [J]
K_r	equilibrium constant of reaction r
n	equilibrium composition [mol]
P	power [W]
r	payback multiplier [1]
T	temperature [K]
η_{tur}	thermodynamical efficiency of the medium pressure turbine [1]
η_{gen}	mehanical efficiency of the generator [1]
y	equilibrium composition [1]
w_r	equilibrium conversion [mol/s]
Φ	heat flow rate [W]

INTRODUCTION

Heat and power integration can be performed by thermodynamic (pinch analysis) or by mathematical methods (nonlinear programming, NLP).

Pinch analysis is guiding heat and power integration using extended grand composite curve [1]. The pinch analysis does not guarantee the global optimal solution because it cannot be used simultaneously with material balances but it quickly proposes good ideas for process heat and power integration of complex processes. Combined heat and power integration adds degrees of freedom to the optimisation method [2]. The graphical representations of gas turbine using pinch analysis help us to better understand the integration [3]. A step-wise methodology of gas turbine integration combined with heat and power cogeneration developed by Axelsson and coauthors [4] is based on pinch analysis.

The NLP algorithm [5], which is based on mathematical programming can be used for rigorous process and power integration. Although simultaneous, it is difficult to converge for complex and energy intensive processes because the number of variables increases with the number of combinations.

In this paper, we are concerned with simultaneous NLP mathematical optimization techniques after including increased production by additional flow rate of hydrogen in recycle system by cogeneration of electricity using gas turbine.

ADDITIONAL FLOW RATE OF THE RAW MATERIAL

The opportunities for increasing the production depend very much on the reaction conversion and reaction kinetics. Thermodynamic and kinetic properties of chemical reactions (r = 1, …, R) give a good predicted aspects about: flow rate and compositions of raw material, conversion efficiency of product and parameter conditions. The method based on minimization of Gibbs free energy (ΔG) is used for the calculations of chemical equilibrium composition (n, y) of components (s = 1, …, S) and equilibrium constant of reactions r (K_r):

$$\mathrm{d}n_s/y_s = \mathrm{d}\, w_r \qquad s = 1, \ldots, \mathrm{S} \quad r = 1, \ldots, \mathrm{R} \qquad (1)$$

$$K_r = \mathrm{e}^{(-\Delta Gr/RT)} \qquad r = 1, \ldots, \mathrm{R} \qquad (2)$$

GAS TURBINE

Many chemical products are produced at high pressure and temperature, followed separation at lower pressure and temperature follows. This pressure change can be used to drive a turbine conpled to an electricity generator. The reactor is acting as a combustion chamber of a gas turbine plant. The turbine uses process gas as a working fluid [6]. Gas turbine can be used in the plant with a steady flow rate.

The designed medium pressure of the turbine can be varied [7]. Its power (P_{tur}) is a function of the outlet ($T_{\mathrm{tur,\ out}}$) temperature, molar heat capacity (C_{m}) and amount flow rate (F; eq. 3). The inlet temperature ($T_{\mathrm{tur,\ in}}$) is constant:

$$P_{\mathrm{tur}} = C_{\mathrm{m}} \cdot (T_{\mathrm{tur,\ in}} - T_{\mathrm{tur,\ out}}) \cdot F \cdot \eta_{\mathrm{tur}} \cdot \eta_{\mathrm{gen}} \qquad (3)$$

The thermodynamical efficiency of the medium pressure turbine (η_{tur}) and mehanical efficiency of the generator (η_{gen}) are supposed to be 85 % each.

CO_2 EMISSIONS

CO_2 shall be separated from the process for the following reasons:

- it is forming H_2CO_3 and
- it is mitigating the global climate conditions.

The simultaneous mathematical optimization method NLP model is presented containing the decreased CO_2 emissions by including taxes and costs of CO_2 emissions. The emissions can be reduced at the source. The CO_2 flow rate depends on [8]:

- the raw material inlet amount flow rate,
- the separation and reactor system and
- the fraction of the recycle exhaust flow rate.

CASE STUDY

We tested this ideas using a complex process of low-pressure Lurgi methanol production (Fig. 1). The methanol is produced from synthesis gas obtained from natural gas and steam in reactor (REA-1). The exothermal methanol reactor (REA-2) with three main reactions (r = R1, R2, R3):

$$\mathrm{CO} + 2\mathrm{H_2} \rightarrow \mathrm{CH_3OH} \qquad (\mathrm{R1})$$

$$\mathrm{CO_2} + 3\mathrm{H_2} \rightarrow \mathrm{CH_3OH} + \mathrm{H_2O} \qquad (\mathrm{R2})$$

$$\mathrm{CO_2} + \mathrm{H_2} \rightarrow \mathrm{CO} + \mathrm{H_2O} \qquad (\mathrm{R3})$$

is operated at high pressure and unconverted gas is recycled. The reactor is to be operated at the existing parameters. The high recycle ratio and operating pressure of the reactor are exploited to produce electricity, using gas turbine (TUR) placed downstream the reactor. The turbine is using process gas as a working fluid. The inlet stream of the reactor is heated by a process stream (HEPR) or by high pressure steam (HEST) or combining both of them. The stream leaving the turbine is cooled using air (HEA) and water (HEW) heat exchangers before entering the flash (SEP). The liquid stream of the separation is the product and the recycled gas stream is compressed to 51 bar in a two stage compressor (COMP1, 2) with intermediate water cooling (HEW1).

The simultaneous mathematical optimization method using the NLP model for methanol plant is presenting the effects of the:

- additional flow rate of H_2,
- decreased raw material rate (the high pressure steam),
- decreased CO_2 emissions,
- increased product production depending on the raw material flow rate (H_2 and steam), the separation (SEP) and reactor system (REA-2),
- electricity cogeneration
- integration of heat flows and
- reduced exhaust flow rate (purge gas).

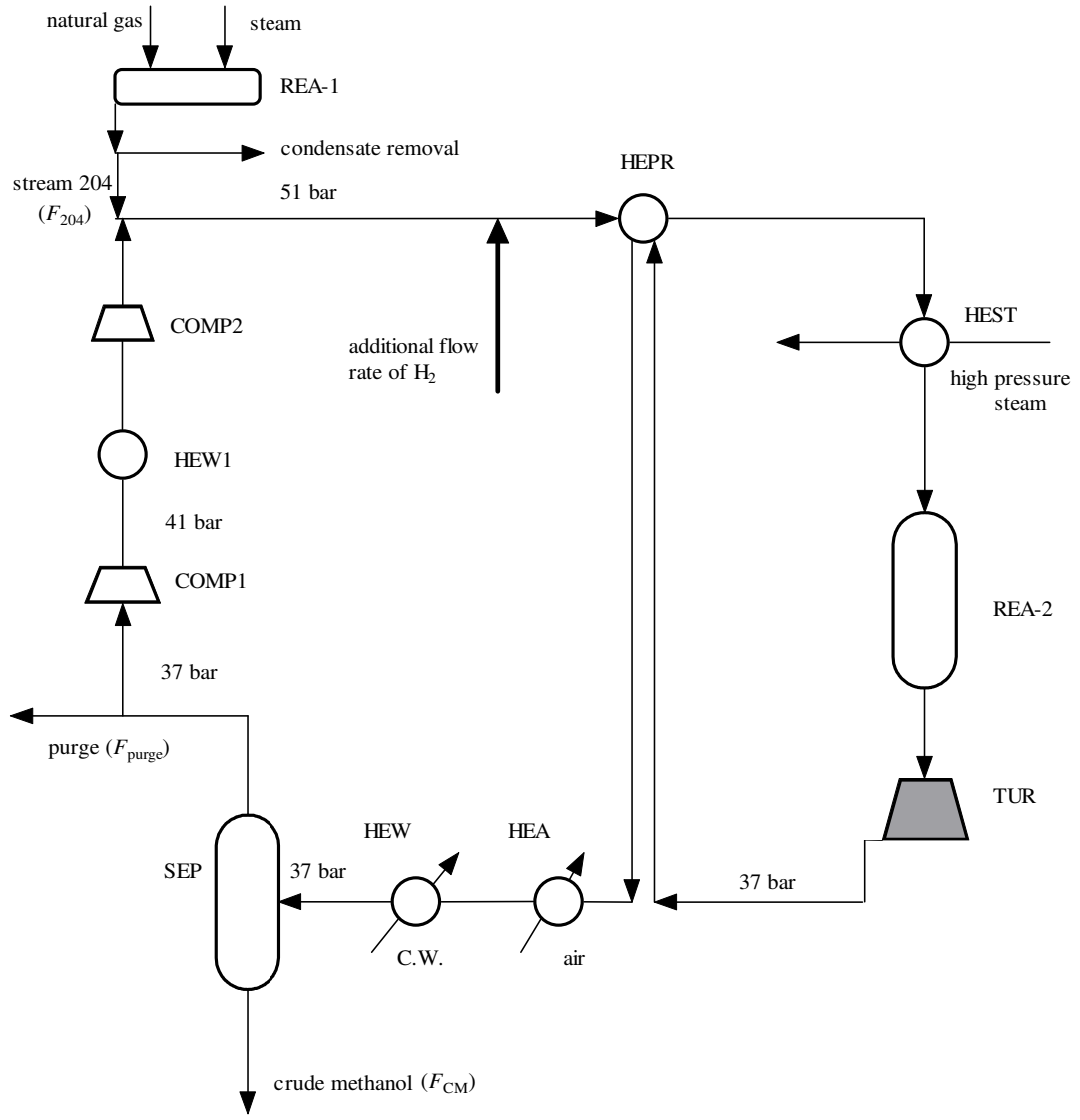

Figure 1: Simplified flow sheet of the methanol plant with gas turbine with additional H_2 flow rate.

Additional flow rate of H_2

Additional flow rate of hydrogen (H_2) in crude methanol recycle is increasing the methanol production. The methanol conversion is calculated with the equilibrium reaction system (eq. 1 and 2) depanding on raw material flow rate, the recycle flow rate and operating conditions.

H_2 shall be separated from the purge gas by an existing pressure swing adsorption (PSA) column. The purge gas is purified by the PSA column to

deliver hydrogen at the 90 % to 99,99 % level by removing N_2, CO, CO_2, CH_4 and H_2O. The pressure swing adsorption uses an adsorber packed with a molecular sieve adsorbent with 50 % efficiency. The PSA column is operated at the 26 bar pressure and the 35 ^oC temperature with maximal 488 kg/h capacity of H_2.

In the NLP model the additional flow rate of hydrogen in the reactor REA-2 can be varied from 0 kg/h to 488 kg/h (ΔF_H) and it can effect the optimal process structure and production rate. After start-up the PSA column will produce pure H_2 in 2 to 4 h. The purification system is competely automatic. The H_2 purification cost in the existing PSA column and inlet injection cost in recycle (with inlet parameters 51 bar and 60 ^oC) is 0,1 EUR/kg.

Synthesis gas is produced from natural gas using 33 100 kg/h of high pressure steam in the reactor (REA-1). The flow rate of high pressure steam (as the raw material) can be decreased to the lower operating bound constraint of 32 000 kg/h and the flow rate of the high pressure steam as reactant can be reduced by 9 192 t/a. All the other process units shall be operated at the existing parameters. The lower flow rate of high pressure steam influences the reaction equilibrium, as well as conversions in the synthesis gas and methanol synthesis reactors. The higher equilibrium conversion in the synthesis gas reactor is decreasing the flow rate of CO_2 and increasing the flow rate of CO. In the NLP model the flow rate of high pressure steam in the synthesis gas reactor can be varied from 0 t/a to 9 192 t/a (ΔF_{steam}) and with them the composition of stream 204 (F_{204}) is changing:

$$F_{204,\,i} = a_i + b_i\,\Delta F_{steam} \quad (4)$$

i = CO_2, CO, H_2, CH_4, N_2 and H_2O

$$F_{204} = \Sigma\, F_{204,\,i} \quad (5)$$

Decrease CO_2 emissions

The reduced flow rate of CO_2 is to decrease the corrosion of the gas turbine and the emissions.

Increase product production

Increased product production depends on the raw material flow rate (H_2 and steam), the separation (SEP), reactor system (REA-2) and exhaust flow rate.

Additional production of methanol can be calculated:

$$\Delta F_M = F_M - 138{,}97 \quad (6)$$

F_M being the optimized amount flow rate of methanol, and 138,97 mol/s the existing one.

Cogeneration of electricity in gas turbine

In methanol production the pressure drop can be used for electricity cogeneration.

Integration of heat flows

The model is including the heat integration between outlet and inlet streams.

Exhaust flow rate (purge gas)

The exhaust flow rate can be varied from 5,2 % to 5,9 %.

The equations for heat and mass balance of the process units shown in Fig. 1 were included [9]. The NLP model contains equations for structural and parametric optimisation. The goal of the optimization is to maximize additional annual income and minimize the additional annual depreciation (eq. 7). The additional annual income sums up:

- the additional cogeneration of electricity ($P_{tur} \cdot \eta_{tur} \cdot \eta_{gen}$),
- the additional production of methanol (ΔF_M) and
- saving obtained by decreasing the flow rate of high pressure steam (ΔF_{steam}) raw material.

The additional annual depreciation cost sums up (Table 1):

- the emission cost of outlet stream of crude methanol (F_{CM}),
- the gas turbine with power P_{tur},
- the compressors COMP1 and COMP2 and
- the enlarged and new areas of heat exchanger (A_{HE}).

The objective function is including:

- H_2 purification cost in existing PSA column and
- the buying the flow rate of high pressure steam in heat exchanger HEST.

Max. additional annual profit =

$$C_{el} \cdot P_{tur} \cdot \eta_{tur} \cdot \eta_{gen} + C_M \cdot \Delta F_M + C_{37} \cdot \Delta F_{steam} - C_{tax} \cdot F_{CM,CO2} - C_{37} \cdot \Phi_{HEST} - (22\,946 + 13{,}5 \cdot P_{tur}) \cdot 4 - [2\,605 \cdot P_{COMP1}^{0,82} - 2\,605 \cdot P_{COMP2}^{0,82} - \sum_{new} (8600 + 670 \cdot A_{HE,new}^{0,83}) \cdot 3{,}5 \cdot 2 - \sum_{add} 670 \cdot \Delta A_{HE,add}^{0,83} \cdot 3{,}5 \cdot 2] \cdot r - C_{H2} \cdot F_{H2} \quad (7)$$

new = HEST, HEW1
add = HEW, HEA, HEPR

Table 1: Cost items for example process.

Installed cost of heat exchanger*/EUR: $(8\,600 + 670\,A^{0,83}) \cdot 3{,}5 \cdot 2$ #
Cost of compressor, C_{com}&/EUR: $2\,605 \cdot P^{0,82}$
Cost of gas turbine, C_{tur}&/(EUR/a): $(22\,946 + 13{,}5\,P_{tur}) \cdot 4$ #
Cost of methanol $(C_M)^+$/(EUR/t): 115,0
Cost and taxes of CO_2 emissions $(C_{tax})^{++}$ /(EUR/t): 11,5
Cost of electricity $(C_{el})^{**}$/(EUR/(kW · a)): 435,4
Cost of H_2 purification in existing PSA column and inlet injection in recycle (C_{H2}) /(EUR/kg): 0,1
Cost of 37 bar steam $(C_{37})^{**}$/(EUR/(kW · a)): 106,3

* [11] A = area in m^2
** [12]
& [5] P = power in kW
++ [4]
\+ ten years average
\# the published cost equations for the equipment are adjusted to the real, higher industrial costs, by multiplier of 2 or 4.

The inlet stream of the reactor REA-2 can be heated by a process stream in heat exchanger (HEPR) or/and by high pressure steam (HEST) with varying heat flow rate.
In the model the existing areas can be used ($A_{HE,ex}$), enlarging them with additional areas ($\Delta A_{HE,add}$) if necessary. The additional annual depreciation of the enlarged and new areas ($A_{HE,new}$) of heat exchangers and compressors (Table 1) are multiplied by the payback multiplier (r = 0,216; [10]).

The simultaneous NLP of heat and power integration with 488 kg/h maximal additional flow rate of H_2 was selected with electricity generation using gas turbine pressure drop from 49,7 bar to 37 bar and outlet temperature, $T_{tur,out}$ = 110 °C. The existing PSA column for purification the H_2 can be used. The total additional annual methanol production (including all the effects of the additional flow rate of hydrogen, reduced the flow rate of steam and reaction kinetics) is 3,5 mol/s. The structure enables 17,5 MW of electricity to be generated. The steam exchanger (HEST) needs 22,85 MW of heat flow rate. The integrated process streams exchange 5,18 MW of heat flow rate in HEPR. The powers of the first and the second compressor are 2,9 MW and 4,0 MW, respectively. The HEW1 exchanges 3,0 MW. In the heat exchangers HEW and HEA 5,3 MW and 8 MW of heat flow rate are exchanged by cooling, respectively. The purge gas is decreasing outlet fraction flow rate from 5,9 % to 5,2 %.
The additional annual depreciation of the gas turbine, new heat exchangers (HEST, HEW1) having 730 m^2 and 324 m^2 area, respectively and the new two-stage compressor is 2,69 MEUR/a. The emission cost is 0,01 MEUR/a. The cost of high pressure steam used in HEST is 2,43 MEUR/a. The H_2 purification cost in the existing PSA column and inlet injection cost in recycle is 0,4 MEUR/a.
The annual income of the additional electricity produced is 7,6 MEUR/a and of the additional methanol produced 0,37 MEUR/a. The steam flow rate can be reduced to 9 192 t/a with

additional annual income of 0,06 MEUR/a. The additional profit of the process including cogeneration and additional methanol production is estimated to be 2,5 MEUR/a with 2,3 years of the payback time.
The NLP program is including 130 equations and 138 variables with computation time of 17 s on the VAX-3100 using the GAMS program.

CONCLUSIONS

The paper has presented efficient NLP model formulations for simultaneous cogeneration of electricity using gas turbine and process heat integration including additional equations for reaction conversion and the CO_2 emissions. The simultaneously optimized NLP model of low-pressure Lurgi methanol plant can include the effects of raw material flow rate (the additional flow rate of H_2 and reduced flow rate of steam as reactants), reactor conversion, temperature efficiency of flash, fraction of the exhaust flow rate and energy saving to decrease the CO_2 emissions in outlet stream of crude methanol by 900 t/a. The higher equilibrium conversion with all the effects in both reactors can increase the conversion of methanol by 2,5 %, producing 3 200 t/a of additional methanol. We have carried out simultaneous heat, power and emission optimization with a potential additional profit of 2,5 MEUR/a.

REFERENCE

[1] Glavič P. Complex integration of processes. The Canadian Journal of Chemical Engineering 79 (7), 2001. 643–654.

[2] Maréchal F. and Kalitventzeff B. Identify the optimal pressure levels in steam networks using integrated combined heat and power method. Comput. Engng Science 52/17, 1997. 2977–2989.

[3] Maréchal F. and Kalitventzeff B. Targeting the minimum cost of energy requirements: a new graphical technique for evaluating the integration of utility systems. Comput. chem. Engng 20, 1996. S225–S230.

[4] Axelsson H., Harvey S., Asblad A. and Berntsson T. Potential for greenhouse gas reduction in industry through increased heat recovery and/or integration of combined heat and power. Applied Thermal Engng 23, 2003. 65–87.

[5] Biegler L. T., Grossmann I. E. and Westerberg A. W. Systematic methods of chemical process design. Prentice Hall, Upper Saddle River, New Jersey. 1997.

[6] Greeff I. L., Visser J. A., Ptasinski K. J. and Janssen F. J. J. G. Utilisation of reactor heat in methanol synthesis to reduce compressor duty – application of power cycle principles and simulation tools. Applied Thermal Engng 22, 2002. 1549–1558.

[7] Kovač Kralj A. and Glavič P. Optimization of gas turbine using NLP model. FOCAPD 2004, 545–548.

[8] Kovač Kralj A. and Glavič P. Decreasing the flow rate of CO_2 in methanol process using NLP model, System engineering, CD, CHISA 2004. p. 1469.

[9] Kovač Kralj A., Glavič P. and Kravanja Z. Retrofit of complex and energy intensive processes II: stepwise simultaneous superstructural approach. Comput. chem. Engng 24/1, 2000. 125–138.

[10] Ahmad S. Heat exchanger networks: Cost tradeoffs in energy and capital. Ph. D. Thesis, University of Manchester, Manchester, 1985. 113 –306.

[11] Tjoe T. N. and Linnhoff B. Using pinch tehnology for process retrofit. Chem. Engng 28, 1986. 47–60.

[12] Swaney R. Thermal integration of processes with heat engines and heat pumps. AIChE Journal 35/6, 1989. p. 1010.

Proceedings of ECOS 2005
Trondheim, Norway
June 20–22, 2005

OPTIMUM PERFORMANCE ANALYSIS OF AN IRREVERSIBLE THREE-SOURCE CHEMICAL PUMP

Guoxing Lin[1, 2, *], Jincan Chen[2] and Ben Hua[1]

[1)] Chemical Engineering Research Institute, South China University of Technology, Guangzhou 510642, P. R. China

[2)] Department of Physics, Xiamen University, Xiamen 361005, P. R. China

ABSTRACT

The cyclic model of an irreversible three-source chemical pump is put forward, in which finite rate mass transfer and internal irreversibilities resulting from friction, eddy currents and other dissipation inside the cyclic working fluid are taken into account. The performance of the chemical pump is optimized by using the optimal control theory. The optimal relation between the coefficient of performance and the rate of energy pumping is derived. The bounds of some important performance parameters, such as the maximum rate of energy pumping and its corresponding coefficient of performance and so on, are obtained. The optimally operating region of the chemical pump is determined and evaluated. The optimal time distribution spent on the three mass transfer processes is also discussed. Moreover, the condition that the chemical pump has the maximum rate of energy pumping is analyzed in detail. The results obtained in the present paper can not only include some important conclusions relative to the endoreversible three-source chemical pump and the irreversible chemical engine which have been investigated in some literatures, but also provide some guidance for the optimal design and development of chemical pumps.

***Keywords*:** Three-source chemical pump; Irreversibility; Finite rate mass transfer; Optimization; Performance bound.

NOMENCLATURE

h	Coefficient of mass transfer
I	Internal irreversibility parameter
k	Boltzmann's constant
L	Lagrangian function
P	Power output
T	Temperature
t	Time of mass transfer
ΔN	Transferred mass
ΔU	Internal energy flow
μ	Chemical potential of the reservoirs or working fluid

*Corresponding author: Fax: +86-592-2189426; E-mail : gxlin@xmu.edu.cn

χ Coefficient of performance

Σ Rate of energy pumping

η Efficiency

τ Cyclic period

λ Lagrangian multiplier

INTRODUCTION

In the last decades, the investigation on the optimal performance of thermodynamic cyclic systems has been extended to the cyclic devices driven by mass fluid [1-14]. For example, the optimal analysis on the performance of chemical engines [4-9] and the two- and three-source chemical pumps [10-14] are some of the successful applications of the theory of optimum thermodynamics. The three-source chemical pump is one of the typical mass transfer systems, which is operated among three mass reservoirs and is analogous to a heat transformer [15,16], which has a potential advantage of saving energy and reducing environmental pollution. Lin *et al.* [11,12] analyzed the optimal performance of an endoreversible chemical potential transformer. By using the optimal control theory, they studied the influence of the finite rate mass transfer on the performance of the chemical potential transformer. However, for real thermodynamic system, there often exist other sources of irreversibility besides the finite rate mass transfer. In the present paper, a general cycle model of a three-source chemical pump affected by finite rate mass transfer and other irreversiblities resulting from the internal dissipation of the working fluid is established and used to analyze the optimal performance of the three-source chemical pump. In particular, the optimized expressions for two key performance parameters, the coefficient of performance and the rate of energy pumping, of the chemical pump are calculated and the optimal relation between them is derived. Furthermore, the other optimal performances of the chemical pump are analyzed and evaluated. The results obtained can play a significant reference role for the development and optimal design of mass exchangers, electro-chemical, photochemical and solid state devices related to mass transfer processes.

THE CYCLIC MODEL OF IRREVERSIBLE THREE-SOURCE CHEMICAL PUMP

We consider a class of chemical pumps operating among the three mass reservoirs whose chemical potentials are, respectively, μ_h, μ_p and μ_O, as shown schematically in figure 1, where $\mu_p > \mu_h > \mu_O$ and μ_1, μ_2 and μ_3 are, respectively, the chemical potentials of the cyclic working fluid in the three iso-chemical-potential processes. They are different from the chemical potentials of the three mass reservoirs, so that mass transfer is carried out under a finite chemical potential difference. It is assumed that mass exchange obeys the mass-transfer law of linearized irreversible thermodynamics [1-14], i.e.,

$$\Delta N_1 = h_1(\mu_h - \mu_1)t_1 \tag{1}$$

$$\Delta N_2 = h_2(\mu_2 - \mu_p)t_2 \tag{2}$$

$$\Delta N_3 = h_3(\mu_3 - \mu_O)t_3 \tag{3}$$

where ΔN_1, ΔN_2 and ΔN_3 are, respectively, the exchanged mass between the working fluid

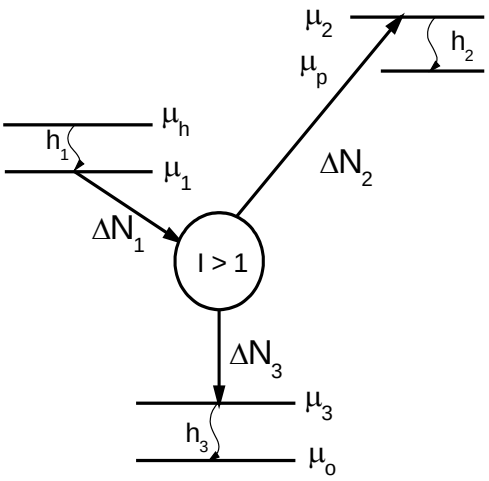

Figure 1: Schematic diagram of an irreversible three-source chemical pump cycle

and the three reservoirs at chemical potentials μ_h, μ_p and μ_O, h_1, h_2 and h_3 are, respectively, the coefficients of mass transfer between the working fluid and the three reservoirs, and t_1, t_2 and t_3 are the corresponding mass transfer times spent on the three mass transfer processes.

Except for three mass exchange branches between the working fluid and the three reservoirs, there exist other additional branches of the three-source chemical pump cycle that connect the three mass exchange branches. These branches may be regarded as instant because there is no mass exchange in these additional branches [6-14]. Therefore, the cyclic period τ of the chemical pump equals approximately the sum of t_1, t_2 and t_3, i.e.,

$$\tau = t_1 + t_2 + t_3 \qquad (4)$$

It should be pointed out that besides the mass-transfer irreversibility, the internal irreversibilities resulting from friction, eddy currents and other irreversible effects inside the cyclic working fluid are inevitable, such that the internal cycle of the chemical pump is irreversible. This implies that the sum of entropy flows flowing out from the iso-chemical-potential μ_2 and μ_3 processes are always larger than that flowing into the iso-chemical-potential μ_1 process. Therefore, according to the definition of entropy, one has

$$[(\Delta U_2 - \mu_2 \Delta N_2) + (\Delta U_3 - \mu_3 \Delta N_3)] - (\Delta U_1 - \mu_1 \Delta N_1) \geq 0 \qquad (5)$$

where ΔU_1 is the internal energy flow flowing into the iso-chemical-potential μ_1 process and $\Delta U_2, \Delta U_3$ are the internal energy flows flowing out from the iso-chemical-potential μ_2 , μ_3 processes, respectively. They satisfy $\Delta U_1 = \Delta U_2 + \Delta U_3$. According to above analysis, we have

$$\mu_1 \Delta N_1 - (\mu_2 \Delta N_2 + \mu_3 \Delta N_3) \geq 0 \qquad (6)$$

The equality in equations (5) and (6) is true only when the cycle is endoreversible.

Moreover, the consideration in this approach is limited to isothermal irreversible three- source chemical pump in order to isolate and more transparently illustrate results that are linked to the mechanism of mass transfer, rather than these effects combined with that of heat transfer across a temperature difference.

On the basis of equation (6), we can introduce an internal irreversibility parameter

$$I = \frac{\mu_1 \Delta N_1}{\mu_2 \Delta N_2 + \mu_3 \Delta N} \geq 1 \qquad (7)$$

to describe the internal irreversibilities resulting from friction, eddy currents and other irreversible effects inside the cyclic working fluid. The value of I is, in general, larger than 1. It is equal to 1 only when the internal irreversibility may be neglected. It is thus clear that the endoreversible cyclic model (I =1) of the three-source chemical pump [11,12] is just a special case of the cyclic model established in the present paper, so that the

optimal performance of an endoreversible three-source chemical pump can be directly derived from the results obtained in the present paper.

TWO KEY PERFORMANCE PARAMETERS AND THEIR OPTIMUM RELATION

According to the law of mass conservation and equation (7), one has

$$\Delta N_1 - \Delta N_2 - \Delta N_3 = 0 \tag{8}$$

$$\Delta N_1 \mu_1 - I(\Delta N_2 \mu_2 + \Delta N_3 \mu_3) = 0 \tag{9}$$

On the other hand, from the definitions of the coefficient of performance χ_{3P} and the rate of energy pumping Σ_{3P}, we have

$$\chi_{3P} = \Delta N_2 \mu_p / (\Delta N_1 \mu_h) \tag{10}$$

$$\Sigma_{3P} = \Delta N_2 \mu_p / \tau \tag{11}$$

Using equations (1)-(4), (8), (9), one can prove that the coefficient of performance and the rate of energy pumping are expresses as

$$\chi_{3P} = \mu_p(\mu_1 - I\mu_3)/[I\mu_h(\mu_2 - \mu_3)] \tag{12}$$

$$\Sigma_{3P} = \mu_p \left\{ \frac{I(\mu_2 - \mu_3)}{h_1(\mu_1 - I\mu_3)(\mu_h - \mu_1)} + \frac{1}{h_2(\mu_2 - \mu_p)} + \frac{I\mu_2 - \mu_1}{h_3(\mu_1 - I\mu_3)(\mu_3 - \mu_O)} \right\}^{-1} \tag{13}$$

For the optimal purpose, we introduce the Lagrangian function [2]

$$L = \chi_{3P} + \lambda \Sigma_{3P} = \frac{\mu_p(\mu_1 - I\mu_3)}{I\mu_h(\mu_2 - \mu_3)}$$

$$+\lambda\mu_p \left\{ \frac{I(\mu_2 - \mu_3)}{h_1(\mu_1 - I\mu_3)(\mu_h - \mu_1)} + \frac{1}{h_2(\mu_2 - \mu_p)} + \frac{I\mu_2 - \mu_1}{h_3(\mu_1 - I\mu_3)(\mu_3 - \mu_o)} \right\}^{-1} \tag{14}$$

where λ is the Lagrangian multiplier. From the Euler-Lagrange equations $\partial L/\partial \mu_1 = 0$, $\partial L/\partial \mu_2 = 0$ and $\partial L/\partial \mu_3 = 0$, we can find that when the chemical potentials of the cyclic working fluid in the three iso-chemical- potential processes

$$\mu_1 = \frac{(\sqrt{b_2} + \sqrt{Ib_1}\chi_{3P})\mu_h\mu_p - I(\sqrt{b_2} - 1)\mu_h^{\,2}\chi_{3P} - \sqrt{Ib_1}\chi_{3P}\mu_h\mu_o + \sqrt{Ib_1}\mu_p\mu_O}{(\sqrt{I^{-1}b_1} + \sqrt{b_2})\mu_p - (\sqrt{b_2} - 1)\mu_h\chi_{3P}} \tag{15}$$

$$\mu_2 = \frac{(\sqrt{b_1 I^{-1}} + \sqrt{b_2})\mu_p^{\,2} - \sqrt{b_2}\mu_h\mu_p\chi_{3P} + \mu_h\mu_o\chi_{3P} - \mu_p\mu_o + I^{-1}\mu_h\mu_p}{(\sqrt{b_1 I^{-1}} + \sqrt{b_2})\mu_p - (\sqrt{b_2} - 1)\mu_h\chi_{3P}} \tag{16}$$

and

$$\mu_3 = \frac{I^{-1}\sqrt{b_2}\mu_h\mu_p + \sqrt{I^{-1}b_1}\mu_p\mu_o + \mu_h\mu_o\chi_{3P} - \sqrt{b_2}\mu_h\mu_p\chi}{(\sqrt{I^{-1}b_1} + \sqrt{b_2})\mu_p - (\sqrt{b_2} - 1)\mu_h\chi_{3P}} \tag{17}$$

the relation between the optimal coefficient of performance χ_{3P} and the rate of energy pumping Σ_{3P} of the irreversible three-source chemical pump is given by

$$\Sigma_{3P} = H_I \chi_{3P} \frac{\mu_h^{\,2}\mu_p(\mu_p - \mu_o)[(\chi_{3P})_I - \chi_{3P}]}{(\mu_p - B_I\mu_h\chi_{3P})^2} \tag{18}$$

where $H_I = Ih_1h_3/(\sqrt{Ih_1} + \sqrt{h_3})^2$,

$B_I = (\sqrt{b_2} - 1)/(\sqrt{I^{-1}b_1} + \sqrt{b_2})$,

$(\chi_{3P})_I = \mu_p(\mu_h - I\mu_o)/(I\mu_h(\mu_p - \mu_o))$; and $b_1 = h_2/h_1$ and $b_2 = h_2/h_3$. Equation (18) is an important optimum relationship and the optimal performance of a class of three-source chemical pumps can be obtained from it.

SEVERAL IMPORTANT PERFORMANCE BOUNDS

It can be seen from equation (18) that when the coefficient of performance χ_{3P} equals some value, the rate of energy pumping Σ_{3P} has a maximum. Using equation (18) and the extreme condition $\partial\Sigma_{3P}/\partial\chi_{3P} = 0$, we can obtain the

maximum rate of energy pumping as

$$(\Sigma_{3P})_{\max} = \frac{H_I}{4} \frac{(I^{-1}\mu_h - \mu_o)^2 \mu_p}{[\mu_p - \mu_O - B_I(I^{-1}\mu_h - \mu_o)]} \quad (19)$$

with the corresponding coefficient of performance

$$\chi_{3P} = \frac{\mu_P(1 - I\mu_O/\mu_h)}{2(\mu_P - \mu_O) - B_I(I^{-1}\mu_h - \mu_O)} \equiv (\chi_{3P})_m \quad (20)$$

where $(\Sigma_{3P})_{\max}$ and $(\chi_{3P})_{\mathrm{m}}$ are two important performance bounds of the irreversible three-source chemical pump. In fact, the maximum rate of energy pumping $(\Sigma_{3P})_{\max}$ determines an upper bound for the rate of energy pumping, while the corresponding coefficient of performance $(\chi_{3P})_m$ determines the allowable value of the lower bound of the optimal coefficient of performance. Obviously, the optimal coefficient of performance should be located between $(\chi_{3P})_m$ and $(\chi_{3P})_I$.

It should be pointed out that there exists a maximum rate of energy pumping for the irreversible three-source chemical pump only when the following equation is satisfied, i.e.,

$$B_I < \frac{(\mu_P - \mu_O)}{I^{-1}\mu_h - \mu_O} \quad (21)$$

For example, when $\mu_h / \mu_O = 6, \mu_P / \mu_O = 10$, I = 1.1, the value of B_I should be less than 2.02 otherwise there doesn't exist a maximum rate of energy pumping. Notice that the value of B_I depends closely on the coefficients of mass transfer and the internal irreversibility parameter, and hence equation (21) determines the relation among the coefficients of mass transfer, the chemical potentials of the mass reservoirs and the

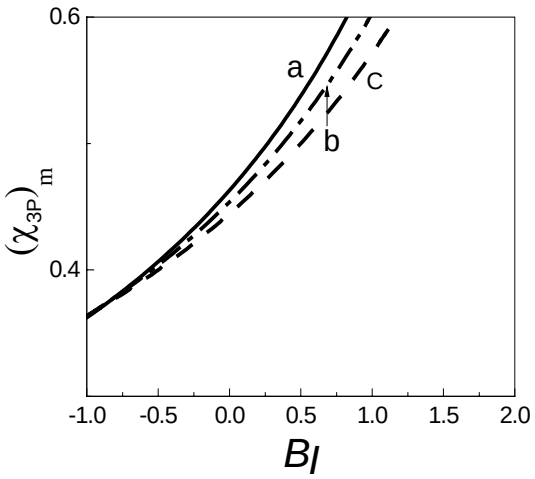

Figure 2: The $(\chi_{3P})_m$ versus B_I curves. Plots are presented for $\mu_h / \mu_O = 6, \mu_P / \mu_O = 10$. Curves *a*, *b* and *c* correspond to the case of *I*= 1, 1.1 and 1.2

internal irreversibility parameter. This indicates indirectly that the lower bound of the coefficient of performance depends closely on the internal irreversibility parameter besides the chemical potentials of the three reservoirs and the mass transfer coefficients.

It can be seen from equation (20) that when the internal irreversibility parameter I is given, the lower bound $(\chi_{3P})_{\mathrm{m}}$ of the coefficient of performance decreases as B_I decreases, as shown in figure 2. At the same time, it can be seen from figure 2 that the lower bound $(\chi_{3P})_{\mathrm{m}}$ of the coefficient of performance decreases as the internal irreversibility parameter I increases, especially when B_I is large. Therefore, we should

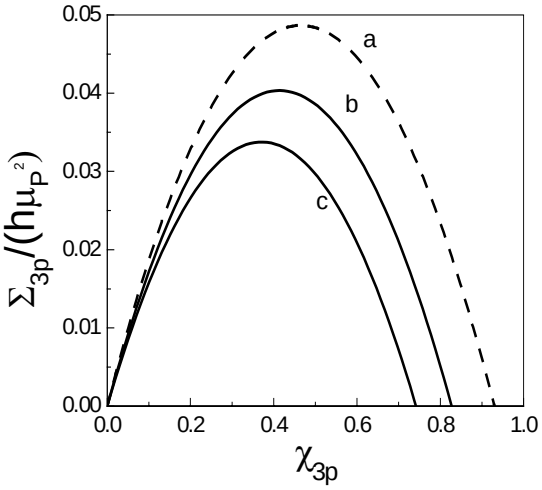

Figure 3: The Σ_{3P} versus χ_{3P} curves. Plots are presented for $\mu_h / \mu_O = 6, \mu_P / \mu_O = 10$ and $h_1 = h_2 = h_3$. Curves *a*, *b* and *c* correspond to the case of I = 1, 1.1 and 1.2

pay more attention to the internal irreversibility besides to the irreversibility of mass transfer in research into real chemical pumps and try to decrease the internal irreversibility as much as possible.

DISCUSSION

1) Using equation (18), we can easily generate the $\Sigma_{3P} \sim \chi_{3P}$ curves of the irreversible three-source chemical pump, as shown in figure 3, where $\mu_h / \mu_O = 6, \mu_P / \mu_O = 10$ and $h_1 = h_2 = h_3 = h$. From figure 3, we can see that as the internal irreversibility parameter I increases, the upper bound of the rate of energy pumping, $(\Sigma_{3P})_{\max}$, and the upper and lower bounds,

I	$(\chi_{3P})_m$	$(\chi_{3P})_I$	$(\Sigma_{3P})_{max}$*
1	0.467	0.929	0.049
1.1	0.416	0.822	0.040
1.2	0.373	0.736	0.034

Table 1: The value of $(\chi_{3P})_m$, $(\chi_{3P})_I$ and $(\Sigma_{3P})_{max}$* with different I

$(\chi_{3P})_I$ and $(\chi_{3P})_m$, of the coefficient of performance all decrease. Some values of the two important parameters with I =1、1.1 and 1.2 are listed in Table 1, where $h_1 = h_2 = h_3 = h$ and $(\Sigma_{3P})_{max}$* = $(\Sigma_{3P})_{max}/(h\ \mu_P^2)$ is the dimensionless maximum rate of energy pumping. Further analysis of equation (18) shows that when the other parameters are given, not only the lower bound $(\chi_{3P})_m$ but also the upper bound $(\chi_{3P})_I$ of the coefficient of performance decrease as μ_P increases; and $(\chi_{3P})_m$ decreases and $(\chi_{3P})_I$ is unchanged as B_I decreases, as shown in figure 4.

2）In order to make the chemical pump operate in the optimal states, the times of the mass transfer processes between the working fluid and the three mass reservoirs should satisfy certain conditions. From equations (1)-(3)，(4), (10), (11) and (18) , we can find that the optimal times spent on the three mass transfer processes are given by

$$t_1 = \frac{\sqrt{h_3}}{\sqrt{Ih_1} + \sqrt{h_3}} \frac{\mu_p}{(\mu_p - B_I \mu_h \chi_{3P})} \tau \qquad (22)$$

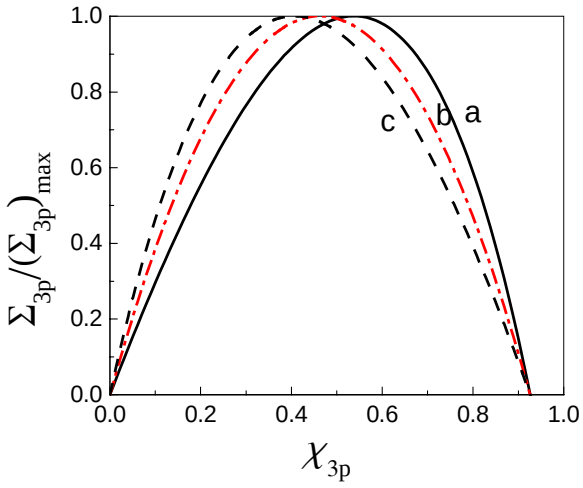

Figure 4: The rate of energy pumping versus the coefficient of performance curves. Plots are presented for $\mu_h/\mu_O = 6, \mu_P/\mu_O = 10$ and $I = 1$. Curves *a*, *b* and *c* correspond to the case of B_I = 0.5, 0 and -0.5

$$t_2 = \frac{\sqrt{Ih_1h_3}}{\sqrt{h_2}(\sqrt{Ih_1}+\sqrt{h_3})}\frac{\mu_h\chi_{3P}}{\mu_p - B_I\mu_h\chi_{3P}}\tau \qquad (23)$$

$$t_3 = \frac{\sqrt{Ih_1}}{\sqrt{Ih_1}+\sqrt{h_3}}\frac{\mu_p - \mu_h\chi_{3P}}{\mu_p - B_I\mu_h\chi_{3P}}\tau \qquad (24)$$

such that the optimal time distribution of the three mass transfer processes satisfies the following relation

$$\sqrt{Ih_1}t_1 = \sqrt{h_2}t_2 + \sqrt{h_3}t_3 \qquad (25)$$

For example, when $h_1 = h_2 = h_3$, equation (25) is simplified as $t_1 = (t_2 + t_3)/\sqrt{I}$。This implies that the mass transfer time t_1 decrease as the internal irreversibility parameter *I* increases. These results can play an instructive role for engineers to design the mass exchangers of real chemical pump.

3) When $\mu_P \to \infty$, equation (18) is simplified as

$$\Sigma_{3p} = \frac{Ih_1h_3}{(\sqrt{Ih_1}+\sqrt{h_3})^2}\mu_h{}^2\eta(\eta_I - \eta) \equiv P \qquad (26)$$

Equation (26) is just the optimal relation between the power output *P* and the efficiency η of the irreversible chemical engine [9], where h_1 and h_3 are the coefficients of mass transfer between the working fluid and the reservoirs μ_h and μ_O, respectively; and η_I is the maximum efficiency of the irreversible chemical engine. Furthermore, when *I* = 1, equations (15)、(17)、(19)、(22) become

$$\mu_1\Big|_{\eta=\eta_m^{ce}} = \mu_h - \frac{\mu_h - \mu_o}{2(1+\sqrt{h_1/h_3})} \qquad (27)$$

$$\mu_3\Big|_{\eta=\eta_m^{ce}} = \mu_o + \frac{\mu_h - \mu_o}{2(1+\sqrt{h_3/h_1})} \qquad (28)$$

$$(\Sigma_{3P})_{\max} = h_1\left(\frac{\mu_h - \mu_o}{2(1+\sqrt{h_1/h_3})}\right)^2 \equiv P_{\max} \qquad (29)$$

$$t_1 = \tau/(1+\sqrt{h_1/h_3}) \qquad (30)$$

where η_m^{ce} is the efficiency of the endoreversible chemical engine at the maximum power output $P_{max.}$ Equations (27)-(30) are just the important parameter equations of the endoreversible chemical engine. They are consistent with the related equations in the Ref. 6. This shows once again the results obtained in the present paper are more general and useful than those of the endoreversible three-source chemical pump, irreversible and endoreversible two-source chemical engines.

CONCLUSIONS

A cyclic model of a class of three-source chemical

pumps is set up, in which the external irreversibilities between the working fluid and the mass reservoirs and the internal irreversibilities inside the cyclic working fluid have been taken into account. Based on the optimal control theory, the fundamental optimal relation of the irreversible three-source chemical pump cycle is derived. The influence of finite rate mass transfer and the internal irreversibility on the cyclic performance of the chemical pump is revealed. Some new performance bounds are determined and evaluated. The results obtained here are more general and useful, and can not only play an instructive role for the optimal design and operation of a class of chemical pumps but also be directly used to derive the important results of some relevant cyclic models appeared in the existing literatures.

ACKNOWLEDGEMENTS

This work has been supported by the State Major Basic Research Development Program (G20000263) and the Scientific Research Foundation of South China University of Technology, People's Republic of China.

REFERENCES

[1] Wu C, Chen L, Chen J. *Recent advances in finite-time thermodynamics*, New York: Nova Science Publishers, Inc., 1999.

[2] Hoffmann K, et al. *Optimal process paths for endoreversible systems*, J. Non-Equilib Thermodyn., 2003, 28(3): 233-268

[3] Hoffmann K, et al. *Endoreversible Thermo-dynamics*, 1997, 22(4): 311-355

[4] De Vos A. *Endoreversible thermodynamics and chemical reaction.* J Phys. Chem. 1991; 95: 4534-4540

[5] De Vos A. *The endoreversible theory of solar energy conversion: a tutorial*. Solar Energy Materials and Solar Cells 1993; 31: 75-93

[6] Gordon J, Orlov V. *Performance characteristics of endoreversible chemical engines*. J. Appl. Phys. 1993; 74 (9): 5303-5309.

[7] Gordon J. *Maximum work from isothermal chemical engines* J Appl Phys 1993; 73: 8-11.

[8] Chen L, Sun F, Wu C. *Performance of chemical engines with mass leak*. J. Phys. D: Appl. Phys. 1998; 31(13): 1595-1600.

[9] Lin G, Chen J, Brück E. *Irreversible chemical-engines and their optimal performance analysis.* Applied Energy 2004; 78(2): 123-136

[10] Lin G, Chen J. *Optimal analysis on the cyclic performance of a class of chemical pump.* Appl. Energy 2001; 70(1): 35-47.

[11] Lin G, Chen J, Hua B. *General performance characteristics of an irreversible three source chemical pump*. Energy Convers. Mgmt. 2003; 44(10): 1719-1731

[12] Lin G, Chen J, Wu C. *The equivalent combined cycle of an irreversible chemical potential transformer and its optimal performance*. Exergy 2002; 2 (2): 119-124.

[13] Lin G, Chen J, Hua B. *Optimal analysis on the performance of a chemical engine-driven chemical pump*. Appl. Energy 2002; 72 (1): 359-370.

[14] Lin G, Chen J, Wu C, Hua B. *The equivalent combined cycle of an irreversible chemical pump and its performance analysis.* Int. J. of Ambient Energy 2002; 23(2): 97-102

[15] Chen J. *The influence of multi-irreversibilities on the performance of a heat transformer*. J. Phys. D: Appl. Phys. 1997; 30: 2953-2957.

[16] Iyoki S, Tanaka K, Uemura T. *Theoretical performance analysis of absorption refrigerating machine, absorption heat pump and absorption heat transformer using alcohol as working medium.* Int J. Refrigeration 1995; 17: 180-190.

Proceedings of ECOS 2005
Trondheim, Norway
June 20–22, 2005

ANALYSIS OF ALPINE HYDROPOWER WITH AN OPTIMISING ENERGY SYSTEM MODEL

D. Möst, W. Fichtner, O. Rentz
Institute for Industrial Production (IIP)
Universität Karlsruhe (TH)
Hertzstr. 16, D-76187 Karlsruhe, Germany
email: Dominik.Moest@wiwi.uni-karlsruhe.de
phone: +49 / 721 / 608-4689

M. Balmer
Centre for Energy Policy and Economics (CEPE)
ETH Zürich
CH-8092 Zürich, Switzerland

ABSTRACT

The general objective of the energy model described in this paper is to provide a powerful analysis tool to evaluate the market value of Swiss hydropower plants and to quantify the future value of hydropower on the background of a liberalised European electricity market considering various scenarios. The energy system analysis model PERSEUS-HYDRO is a technology-based modelling approach, employing linear programming algorithms with a focus on hydropower. Due to its detailed representation of the real energy supply system, including the specific techno-economic characteristics and constraints of this sector, the model permits an in-depth analysis of the interrelations between capacity development, power exchange volumes, plant dispatching, and price information. In order to assess the influence of alternative assumptions on future technological investment options, the model parameters include the projected techno-economic characteristic of future energy conversion technologies.
Keywords: Investment planning, energy system modelling, hydropower, electricity prices, power system reserve

INTRODUCTION

Investments in hydropower plants are characterised by high capital intensity and long project durations. In the liberalized energy markets, most independent power producers are not wiling to accept the risks connected with investments in hydropower plants. About one fourth of the prolongations of concessions (licenses) of hydropower plants in Switzerland are estimated not to be obviously cost-efficient. Thus, the long-term use of hydropower production is at risk [1]. On the other hand, hydropower plants are characterised by a high controllability for the provision of peak load and control energy and as a renewable energy carrier with good predictability, which can achieve high prices on liberalized energy markets.

Due to the high complexity of the real energy supply system, sophisticated analysis tools are required to support research and planning activities in order to evaluate the expected effects. Energy systems analysis models have been widely used in the past to support policy design or strategic planning issues within energy companies. Within this paper, the developed energy system model for a hydro-thermal generation system to analyse the long-range prospects for Swiss hydropower within the European electricity market will be presented.
The challenges faced to model hydropower will be shown too. With the developed model approach four questions are addressed: Will hydropower in the Alps be a competitive energy in the European energy system? What is the trend and absolute level of electricity prices in the next

three decades for base and peak load? Will hydropower in the Alps be a technological response to balance fluctuating wind energy (e.g. in Northern Germany) or are there other suitable responses? How will the interregional power exchange develop?

OBJECTIVES AND METHODOLOGY

The general objective for the development of the energy system model PERSEUS-HYDRO[1] was to provide an analysis tool to assess a hydro-thermal generation system with regard to the long-term competitiveness of alpine hydropower, electricity prices, technology choices, capacity development, and interregional power exchanges. In this long-term model approach for decision support related to investment planning also generation scheduling and dispatchability features are included[2]. PERSEUS-HYDRO is an energy and material flow model applying a multi-periodic mixed integer linear programming approach (MILP).

The modelling approach is based on a detailed representation of energy conversion technologies, including hydropower cascades and the interconnecting flows of energy and material (i. e. primary energy carriers, emissions of pollutants etc.). The structure of the model is equivalent to a directed graph: Energy and material flows represent the edges of the graph. Conversion technologies and their processes correspond to the nodes of the graph. The model follows a linear, mixed integer programming approach.

The target function is the minimization of all decision-relevant expenditures within the entire energy supply system. This basically comprises fuel supply and transport costs, transmission fees, fixed and variable costs of the physical assets (operation, maintenance, load variation costs etc.) and specific investments for new plants. The relevant techno-economic characteristics of the real supply system have been considered by implementing further equations covering technical, ecological (e.g. renewable energy targets) and political (e.g. nuclear phase out) restrictions. The most important technical restrictions are:

- *Physical energy balances*: Restrictions providing the balance of supply and demand taking into account the load curve of electricity demand.
- *Capacity restrictions*: transmission constraints, availability of installed capacities, hydro storage constraints, commissioning restrictions, technical lifetime of physical assets.
- *Plant operation*: maximal/minimal operating hours at full load, fuel options, cogeneration options, load variation restrictions.

The time horizon of the model is 30 years. As not every hour of a year can be optimized, so called characteristic days are used. Eight characteristic days represent one year - four seasons are considered, each characterised through a working day and a weekend day which are both represented by a simplified load curve of 6 (working day) respectively 3 time periods (weekend).

A detailed description of the basic modelling package can be found in [3]. Within this paper, we do not want to go more into detail on the general modelling approach, as similar approaches have been used in other energy models. We focus on the modelling of hydropower, power system reserve, the regional structure covering the alpine regions and neighbouring countries as well as the analysis options of the model.

POWER SYSTEMS RESERVE MODELLING

As electricity cannot be stored, the amounts of the electricity consumed and generated have to be in balance. The transmission system operator (TSO) is responsible for system balancing within a defined region and must guarantee to have enough excess reserve generation available for use at all times in order to ensure the reliable operation of the system. Reserve power and reserve energy have to be distinguished here. Reserve power (or reserve capacity) is necessary to balance unforeseen power fluctuation (e.g. station blackouts or fluctuating wind energy production) and load changes. Reserve energy is the energy

[1] **P**rogramme Package for **E**mission **R**eduction **S**trategies in **E**nergy **U**se and **S**upply – with focus on **Hydro**power;

[2] Within [2] is demonstrated that dispatchability features such as start-up costs and ramp rates are important for the economic profitability assessment of a project, especially in hydro-thermal systems.

effectively used for the balancing of the system. Depending on national and/or international regulations, different types of reserve have to be provided by the generators. In the UCTE, the following reserve qualities can be distinguished by the time horizon: primary reserve to be fully available within 30 seconds, secondary reserve replacing primary reserve within 5 minutes and tertiary reserve freeing secondary reserve within 15 minutes. In a simpler model, only spinning reserve (primary and secondary reserve) and non-spinning reserve (tertiary or minute reserve) is distinguished, the first being called automatically and the latter manually via rescheduling of generation.

Within the PERSEUS-HYDRO model several approaches to model power systems reserve are integrated.

Capacity reserve restriction (for spinning reserve): A capacity reserve factor is defined, guaranteeing that for each time interval the total installed capacity of one region plus a factor (1 + *capacity reserve factor*) exceeds the cumulated load of that particular region. The value of the capacity reserve factor can be calculated on the basis of the stipulated capacity reserve of the UCTE (first synchronous zone: 3000 MW [4]). In other words, this equation guarantees that the capacity used for production plus the reserve capacity exceeds the cumulated load in every time period of the model.

Energy reserve restriction (for non-spinning reserve): To ensure within the energy system model that also plants for (secondary and) tertiary reserve (e.g. hydropower plants and fast starting thermal plants like gas turbines) are needed within the generation portfolio, a reserve energy restriction is defined. This equation guarantees that the production of selected plants (hydropower plants and gas turbines) exceeds the necessary amount of energy for tertiary reserve. The energy for tertiary reserve is modelled as a share of the total energy demand.

The capacities and the energy supply by selected plants for the provision of reserve power are guaranteed with the two described equations. But as the model is deterministic, only the plant dispatch for the forecasted energy demand schedule is calculated within the optimization. This forecasted energy demand schedule is planned for the next day by the energy utility on the basis of the anticipated probable consumption of their consumers and can be traded at energy exchanges or arranged in bilateral contracts.

Simulation of the plant operation for tertiary reserve (energy reserve): To estimate the plant operation for tertiary reserve a second optimization is based on the results of the first optimization. For the provision of tertiary reserve all fast starting units are available because of their high flexibility. Consequently, only fast starting plants can provide tertiary energy within the second optimization of the model approach. Hence, a large part of variables are fixed namely these of the installed capacity and the plant dispatch of units, which can not provide tertiary reserve. Only the operation of fast starting units is optimized within the second optimization. Thus, a tertiary reserve energy demand has to be provided in the second optimisation step in order to be able to analyze the plant operation for tertiary reserve. This tertiary reserve energy demand is derived from forecast errors of the forecasted scheduled energy demand and the forecasted wind energy production.

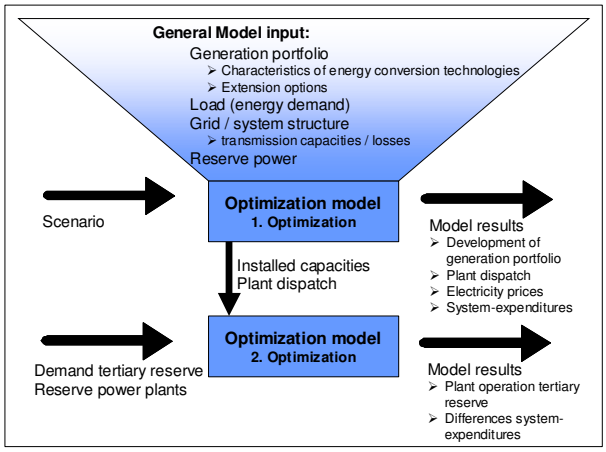

Figure 1: Model input and output

HYDROPOWER MODELLING

Beside thermal power plants, hydropower plants play a considerable role in many electric power systems. Three main types of hydropower plants can be classified:

Run-of-river plants do not have any storage possibilities and need to produce electricity

continuously depending on the water-flow of the river. They are used for base load production.

Hydro storage plants are able to store the water outflow of a catchments area in a reservoir. They can further be classified by the size of the storage in relation to the water inflow (day-, week or year-storage). Having the ability to store water allows shifting large parts of the average annual production into peak power times.

Pumped storage power plants have an additional capability to pump water from a lower reservoir to a higher one which means they can also consume energy. This designates pumped storage plants for providing ancillary services, especially (negative) balancing power.

Hydro storage plants are far more complicated to model than base-load producing run-of-river plants since through the storage, several time periods in the model are linked. This requires the introduction of nodes for storage purposes in the energy system model. The energy and material balance equation for storage nodes has to be extended to a storage equation and storage level variables have to be introduced. The storage equation is also used for the pumped storage plants where a second process (pump process) has to be integrated within the model too. In order to consider hydropower cascades, the cross linking of turbines has to be modelled. As the same hydro flow rate generates a different amount of electricity in each hydropower plant, the head of the turbines have to be taken into account. In particular, for the detailed modelling of individual hydropower plants the following data is crucial:

Hydro inflow (Pardé coefficient) to the reservoirs needs to be modelled to represent the seasonal variability of the hydropower energy production. For all reservoirs and run-of-river plants the seasonal inflow shares on monthly basis (Pardé coefficient) for an average hydrological year have been determined using data from [5], [6]. Due to the missing storage capacities the run-of-river plants are very sensitive to inflow variations and have usually a significantly higher energy production in summer. Even though storage and pumped storage plants are to some extent disconnected from the seasonal water inflow and try to collect water in summer to produce in winter they are still dependent on regional inflow characteristics. Modelling additional natural water inflow to lower reservoirs of hydropower cascade systems accounts for the flexibility of the lower plants to produce energy without using water from an upper reservoir. By multiplying the average annual energy production on half-year basis with the Pardé coefficients for every plant's reservoir, the monthly inflow can be expressed in energy units, which is necessary for modelling purposes.

Energy volumes of reservoirs have been calculated using both geographic information system data from the Swiss Federal Office of Water and Geology on reservoir area and perimeter as well as technical literature data on reservoir water volumes and maximum reservoir level fluctuations [7]. The energy volumes in relation to the average annual production give insight into the plants capability to shift potential energy from summer to winter or generally from base load to peak load times. Energy volumes of reservoirs are always calculated in relation to the maximal and minimal head of the turbine they feed, not over the whole cascade system. Further, the storage capacity at the reservoirs limits production and pumping possibilities of the plant as these depend strongly on the relation of water inflow, reservoir volume, and maximal turbine flow. By taking into account all three factors, an exact model of the hydropower plants can be constructed.

The head of the turbines have been looked up in the technical literature for all power plants in a thorough data collection and then used to express the water flow within cascade systems in energy units. Because the energy potential of the turbined water depends on the head of the connected plant, the energy inflows into a plant node are not the same as the outflows. To keep the energy balance in the system right the energy inflow to every plant node is multiplied by the ratio 'gross head of the lower plant / gross head of the upper plant' to obtain the energy outflow. This calculated outflow and the possibly joining natural inflow on that particular level of the cascade system sum up to the inflow of the following plant in the system.

Maximal installed power of every hydropower plant is the crucial variable used to integrate the plant into the model. Depending on the restrictions from water availability and storage

possibility this installed power can be used to cover part of the exogenously given load. On average, for run-of-river plants maximum installed power is available for about 4'000-8'000 hours a year depending on the ratio of the maximum turbine flow and the minimum flow of the river. In the case of storage plants in Switzerland it is about 2'500 hours a year. Pumped storage plants are usually stronger focused on peak load times and are producing power during about 1'500 hours.
Cross linking hydropower plants to cascade systems is crucial because the single power plants cannot in all cases be operated independently.

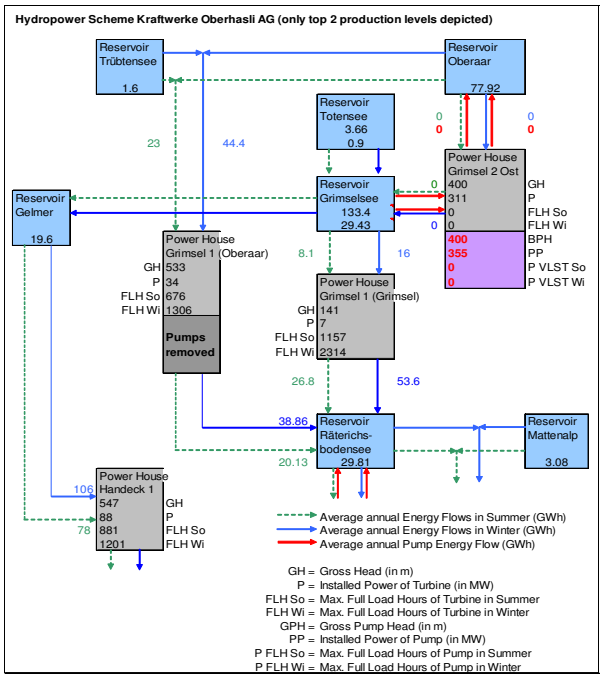

Figure 2: Cascade System with Energy Flows

All the larger storage hydropower plants in Switzerland are part of cascade systems where the classical scheme comprises two reservoirs and two plants. Based on the characteristics of the cascade system, the degree to which the lower plant can be operated independently from the upper one can vary a lot and needs to be considered in detail. Therefore, all cascade systems were analysed, their hydraulic schemes described and plotted with all relevant technical details including pumping possibilities. A simple example is depicted in Figure 2. A mathematical model description including equations for the hydropower modelling and the representation of reservoirs can be found in [8].
Within the PERSEUS-HYDRO model about 180 Swiss hydropower plants have been modelled in detail. Another 340 plants larger than 300 kW installed power are integrated on an aggregate basis divided into typical subgroups considering their production characteristics. Of course the 5 nuclear plants providing 40 % of the Swiss electricity production are contained in the model too.

APPLICATION AREA AND TRANSMISSION CAPACITIES

To analyse the Swiss energy system within a European context, the neighbouring countries Austria, France, Germany and Italy, as well as Belgium, Luxemburg, the Netherlands, and Slovenia are modelled on an aggregated level. All power generators within one region compete on a free market for the national electricity demand that has to be satisfied. However, at the same time there is also direct competition between the different regions given that neighbouring countries are connected by interconnection lines. The consideration of transmission capacities and losses as well as transmission fees ensures a realistic representation of the real power exchange characteristics within the model. The transmission capacities of the interconnection lines are modelled as upper limits of the energy flows. Figure 3 gives an overview about the modelled transmission capacities.
Interconnection lines between modelled and non-modelled countries, e.g. Germany - Poland, are modelled as fixed energy amounts with load flow characteristics.

IMPLEMENTATION OF THE MODEL

The model described above has been implemented as a PC version that can be run on commercial PCs. However, due to their high complexity and the resulting large problem size, they require state-of-the-art hardware components.
The PERSEUS models are equipped with an MS Access based data management system that permits easy data handling and a fully automated link to the mathematical module. The mathematical model is programmed in GAMS (c.p. [11]). In order to solve the problem,

commercial solvers like CPLEX can be applied. Formatted and structured results become available in MS Excel spreadsheets.

The resulting optimising model consists of roughly 610'000 continuous and 1'300 integer variables and about 410'000 restrictions with approximately 2'200'000 non-zero elements. Solving the model on a PC with Pentium 4 - 3 GHz and about 1.6 GB main memory results in calculation times of about 20 minutes to 4 hours with the commercial solver CPLEX 9.0.

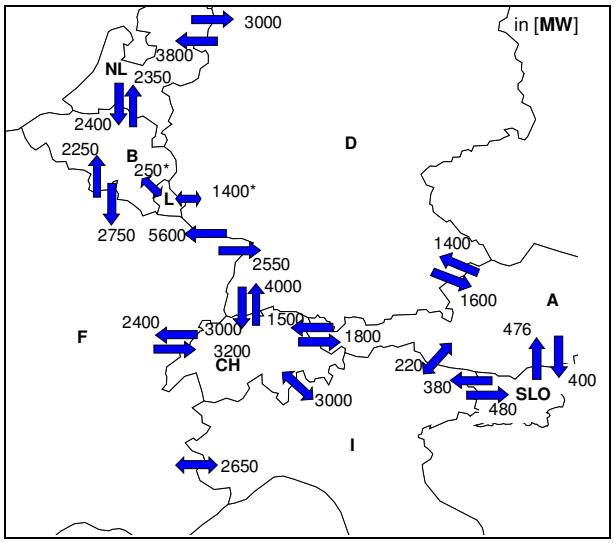

Figure 3: Transmission capacities of interconnection lines in the PERSEUS-HYDRO model (Source: Own calculations based on data of [9] and [10])

ANALYSIS OPTIONS

The PERSEUS-HYDRO model has been implemented within a project for a Swiss energy utility. At present, due to the confidential nature of results achieved, no quantitative results will be shown, instead the quantitative analysis options of the model will be presented. However, the results of the model give interesting insights on the interactions of investments in hydropower, investments in conventional power plants and electricity prices, and show similar tendencies as estimations of energy experts.

Electricity price projections: The basic idea of fundamental models, like the one constructed, is to explain electricity prices from the fundamental generation costs, which is based on the assumption that the market price of a homogeneous good in an open and fully competitive market is set by its marginal costs. We therefore use the marginal costs (shadow prices) of the mathematical model to indicate the resulting electricity prices that can be analysed for every time period of a day (as already mentioned before, a year is represented by eight characteristic days). Electricity prices can be derived on a national/regional level. The exact derivation of price information based on system-marginal-costs is described in more detail in [8].

Structural changes: Energy technologies show significant differences in their relevant parameters like cost structure, emission factors and load variation abilities. Plant dispatch depends on the merit-order of all available power plants established on cost categories. However, these decision-relevant costs and also the merit-order depend on fuel prices, possibly CO_2-certificate prices, and load profiles which all may vary over time. Given that the optimization algorithm used in this model results in a simultaneously optimized plant dispatch and (dis)investment strategy, expected structural adaptations of the entire system to external market conditions can be analysed in detail.

The most obvious structural changes are the shares different technologies cover within the total installed capacity and/or the total electricity generation. New investment options can be added or modified in order to study the impact of a modification within the plant characteristics (e.g. improved efficiency with consequently higher specific investment, or different fuel options) on the future market penetration of this technology.

Interregional power exchanges: Given that every regional supply system is characterised by a different set of available power generation technologies with varying cost characteristics and emission data, any modification of the generation structure from one region/player to another will directly affect power generation structures and/or power exchange characteristics between the two regions. Hence, the influence on the Swiss energy system by a massive growth of wind use in neighbouring countries or the phasing out of nuclear energy can be analysed.

Furthermore, planned projects of common interest

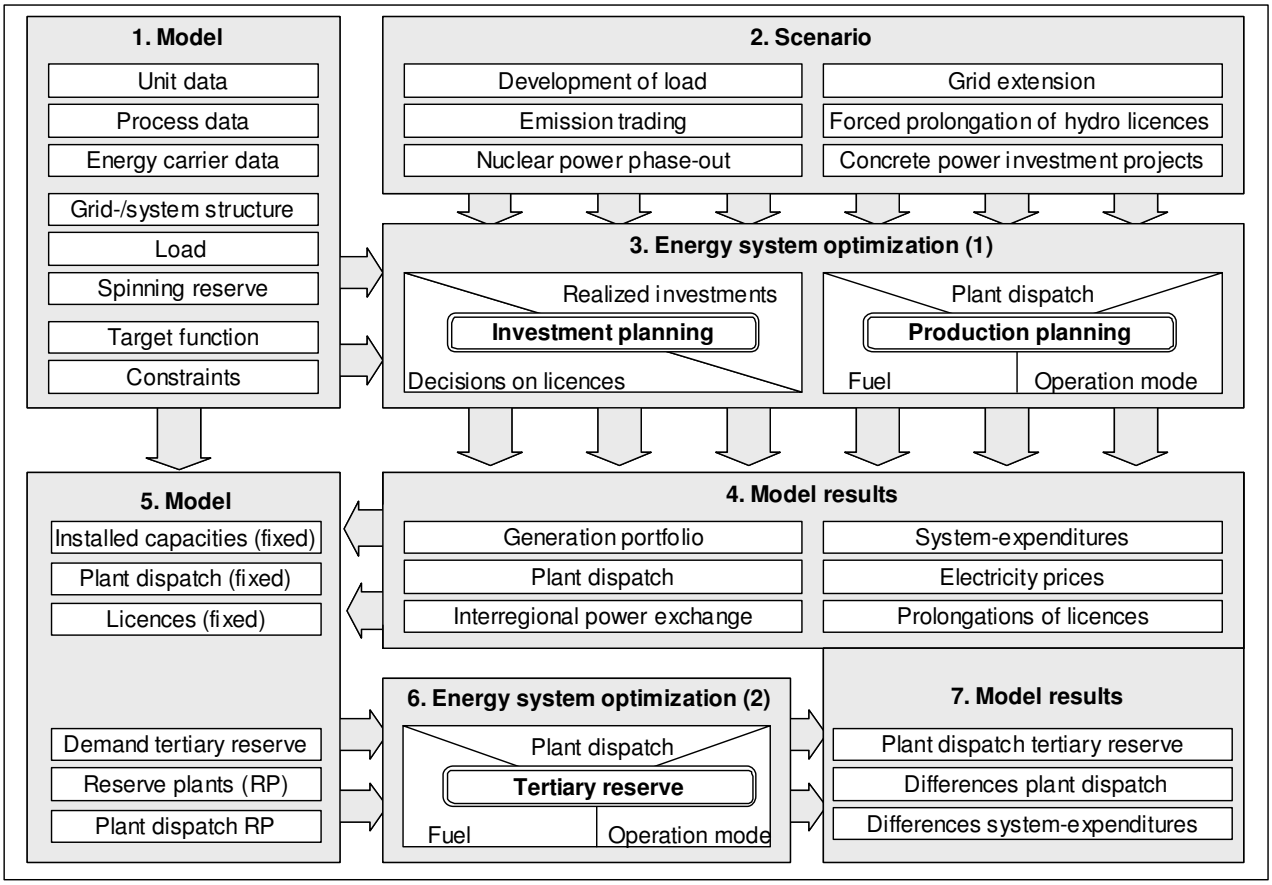

Figure 4: Steps of model-based scenario analysis

in the sector of the trans-European energy networks [12] and their influence on electricity prices and the interregional power exchanges can be quantified. For example, transmission capacities between Switzerland and Italy show a high utilization ratio. Within the model, the effects of an increase of transmission capacities can be used to analyse their influence on investment decisions and electricity prices.

Financial valuation of specific investment projects: Due to the detailed modelling of hydropower plants it is possible to valuate license and investment decisions for current hydropower projects. New investment options of concrete projects (e.g. license decisions of water power plants or (pumped) storage extensions) can be added, and their cash flow can be analysed taking interrelations within the European energy market into account. Hence, an added decision support can be given to strategic planners in energy utilities and to power plant operators.

Tertiary reserve energy: The plant operation for tertiary reserve is analysed within the second step of the optimization. With this approach, it is possible to quantify the value of selected plants for the generation portfolio. E.g. the influence of hydropower plants on the provision of tertiary reserve can be analysed by computing two scenarios: one with and one without the possibility to provide tertiary reserve.

In Figure 4 the steps of the model based scenario analysis are summarized. In a first step, the model has to be built up including modelling data, system structure and mathematical equations. Second, various scenario options have to be defined before the energy system is optimized. Model results are the plant dispatch, investment planning, development of generation portfolios, interregional power exchanges, electricity prices and the total system expenditures. The second optimization process is built up on the basis of these results (Step 5). Within the second

optimization, the plant operation for tertiary reserve is estimated and the results calculated are the plant dispatch for tertiary reserve and differences in the system-expenditures.

CONCLUSIONS

Energy system analysis models have been widely and successfully used in the past supporting energy system development projections under different external circumstances. Within this paper it has been shown how such an energy model can be amended in order to provide an analysis tool for a generation system with a high share of hydropower. The detailed modelling of hydropower plants is a crucial step in order to be able to evaluate the long-term competitiveness of hydropower and the re-licensing decisions of existing capacities in liberalised electricity markets. The model has been successfully tested for the Swiss energy system under non-flexible connections with neighbouring countries. Assessed dispatching results of the various hydropower plant types, especially of the pumped storage plants, show that the Swiss hydropower production is modelled accurately.
Furthermore, a novel approach to model power system reserve requirements within an energy system model has been developed and presented. The various analysis options of the presented model cover most relevant aspects that decision makers may need in order to get an indication on what are the most likely developments of the Swiss electricity park under different scenarios: price information, energy system structures, technology choice and power exchange characteristics.

ACKNOWLEDGEMENT

The development and application of the described model have been the topic of a research project together with the Centre for Energy Policy and Economics (CEPE) at the ETH Zürich, the BKW Energie AG, the Kraftwerke Oberhasli AG, and ETRANS. In this context we would like to thank our project partners for providing all the necessary data and for the fruitful discussions and meetings. Moreover, we would like to thank PSEL (Projekt- und Studienfonds der Elektrizitätsswirtschaft) and BKW Energie AG for financing.

REFERENCES

[1] Filippini, M.; Banfi, S.; Luchsinger, C.; Wild, J.: *Perspektiven für die Wasserkraftwerke in der Schweiz - Langfristige Wettbewerbsfähigkeit und mögliche Verbesserungspotentiale*, Studie im Auftrag des Bundesamtes für Energie, 2001.

[2] Kahn, E.; Marnay, C.; Berman, D.: *Evaluating dispatchability features in competitive bidding*, in: IEEE Transaction on Power Systems, 7 (1992), H. Nr. 3, S. 1259-1265.

[3] Fichtner, W.: *Strategische Optionen der Energieversorger zur CO2-Minderung: ein Energie-und Stoffflussmodell zur Entscheidungsunterstützung.* Berlin: Erich Schmidt, 1999.

[4] UCTE: *Policy 1: Load-Frequency Control and Performance*, UCTE - Union for the Co-ordination of Transmission of Electricity, 2004, www.ucte.org.

[5] Weingartner, R.; Aschwanden, H.: *Die Abflussregimes der Schweiz, Karte*, Geographisches Institut der Universität Bern, 1986.

[6] Swiss Federal Office of Water and Geology: *http://www.bwg.admin.ch/service/hydrolog/e/index.htm*, 2004.

[7] Link, H.: *Speicherseen der Alpen*, in: Sonderheft „Wasser- und Energiewirtschaft" Jg.62 (1970), H. 9.

[8] Möst, D.; Tietze- Stöckinger, I.; Fichtner, W.; Rentz, O.: *Optimising energy models for hydrothermal generation systems to derive electricity prices*, in: Operations Research Proceedings 2004. Berlin: Springer, 2004.

[9] etso (Hrsg): *Indicative values for Net Transfer Capacities (NTC) in Europe Winter 2002/2003, working day, peak hours (Non binding values).*

[10] UCTE: *Statistical Yearbook UCTE 2002*, 2004.

[11] Brooke, A.; Kendrick, D.; Meeraus, A.; Raman, R.: *GAMS - A User's Guide (Edition December 1998).* Washington: GAMS Development Corporation, 1998.

[12] European Commission: *Commission decision of 16 November 2000 defining the specifications of projects of common interest identified in the sector of the trans-European energy networks by Decision No 1254/96/EC of the European Parliament and of the Council*, in: Official Journal of the European Communities (2000), H. L305, S. 22-31.

Proceedings of ECOS 2005
Trondheim, Norway
June 20–22, 2005

OPTIMAL HEAT EXCHANGER AREA ALLOCATION FOR POWER AND REFRIGERATION

J.C. Ordonez[1]*, J.V.C. Vargas[2] and S. Chen[1]

[1]Department of Mechanical Engineering and Center for Advanced Power Systems
Florida State University, Tallahassee, Florida 32310

[2]Department of Mechanical Engineering, Federal University of Parana, Curitiba, Brazil

ABSTRACT

This paper summarizes a series of works on thermodynamic optimization of heat exchanger area allocation for power and refrigeration plants. It is shown that the thermodynamic optimum is pinpointed by an optimal distribution of the heat exchanger area inventory among the heat exchangers of the installation. Hot-stream-driven power producing devices, solar-driven refrigerators and a combined[1] power and refrigeration systems are discussed. The optimal allocation of heat exchanger area appears as a common result for all the installations.

Keywords: Heat exchangers, thermodynamic optimization, power plants, refrigerators

Nomenclature

A	heat transfer area, m^2
c_p	specific heat at constant pressure, $J/kg\ K$
C	thermal conductance, W/K
M	mass flow rate ratio
$\dot{m}$	mass flow rate, kg/s
$\dot{m}_h$	hot water mass flow rate, kg/s
N	number of heat transfer units
$\hat{N}$	conductance ratio
$\hat{q}_0, \hat{q}_L$	dimensionless heat transfer rates
$\dot{Q}$	heat transfer rate
r	absorbent mass flow rate fraction
R	relative refrigeration load, $\dot{Q}_L/\dot{W}$
$\dot{S}_{gen}$	entropy generation rate, W/K
T	temperature, K
$\dot{W}$	power, W
w	dimensionless power
x, y	allocation ratios

Greek Symbols

ε	heat exchanger effectiveness
μ_w	dimensionless collector's physical and operating parameter [8]
η_{II}	second law efficiency

*Corresponding author. Email:ordonez@eng.fsu.edu

τ dimensionless temperature

Subscripts

b boiling section

C reversible compartment

H high temperature

L low temperature

l liquid section

opt optimum value

r receiving stream

s superheating section

st collector stagnation temperature

w water

0 ambient temperature

1. Introduction

Thermodynamically, the maximum limit to the power that is available from a single-phase hot stream with mass flow rate $\dot{m}$ and initial temperature T_H is given by the flow exergy [1],

$$\dot{W}_{rev} = \dot{m} c_p T_0 \left(\frac{T_H}{T_0} - 1 - \ln \frac{T_H}{T_0} \right) \qquad (1)$$

Equation 1 is based on the assumption that the stream behaves as an ideal gas with nearly constant c_p and it is in contact only with the atmospheric temperature reservoir.

The maximum power is not reached in practice due to entropy generation. For example, the stream-to-stream temperature difference, the thermal mixing of the hot stream being discharged into the environment, and the pressure drop experienced by the hot stream constitute main sources of irreversibility and as such a departure from Equation (1).

The problem of optimizing heat transfer area allocation is relevant to power and refrigeration applications ([2], [3]). In the effort of minimizing the irreversibilities and maximizing power output or refrigeration capacity, it is possible to identify an optimal heat exchanger area allocation for a given heat exchanger inventory. In this paper some results that illustrate the existence of such optimum are summarized.

2. Power Extraction

2.1. Phase change in the collecting stream

Consider the system of Figure 1. The left side of Figure 1 illustrates the extraction of power from a hot exhaust, the right side illustrates the isolation of the irreversible component that receives the heat input. Given is the single-phase stream of hot exhaust, which has the mass flow rate $\dot{m}$ and the initial temperature T_H. This fluid behaves as an ideal gas with nearly constant c_p. The temperature of this stream decreases as it serves as heat input to a power plant. The objective is to maximize the power output $\dot{W}$, or to minimize the total rate of entropy generation of the plant subject to the area constraint,

$$A = constant \qquad (2)$$

The mass flow rate of the collecting stream, $\dot{m}_w$, is not fixed and represents a degree of freedom.

In [4], it was shown that when the collecting stream remains in a single phase, the power extracted from

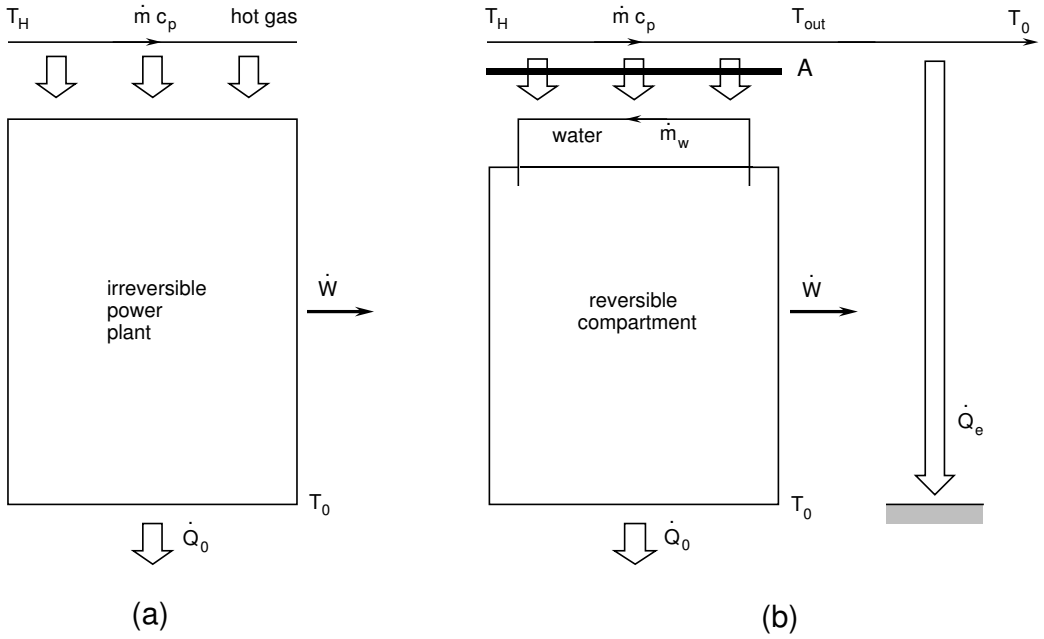

Figure 1: (a) Power extraction from a hot exhaust stream. (b) Isolation of the irreversible component that receives the heat input.

the hot stream, can be maximized by using a counterflow heat exchanger whose degree of imbalance can be determined from thermodynamic optimization.

The configuration shown in Figure 2 was studied in [5]. The counterflow configuration was selected following the results in [4]. The available heat transfer surface splits itself into three sections: a preheating region, a boiling region and a superheating region. It was pointed out the existence of an optimal mass flow rate ratio of the hot stream to the collecting stream. Figure 3 illustrates the allocation of heat exchanger inventory for different mass flow rate ratios ($M = \dot{m}_w/\dot{m}$). The mass flow rate ratio (indicated with dashed lines) maximizes the second law efficiency of the installation.

2.2. Phase change in contact with hottest gases

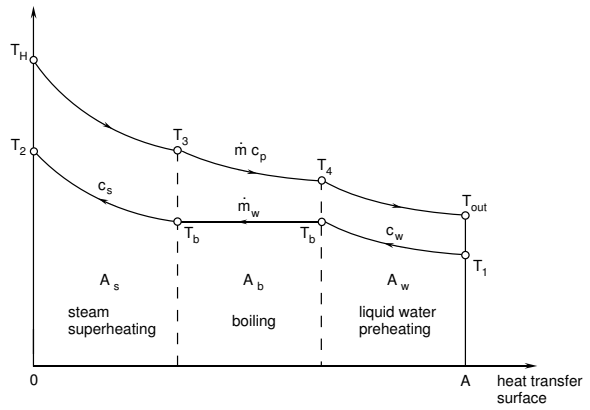

Figure 2: Temperature distribution for the counterflow configuration.

Limitations imposed by the materials used in the construction of the heat exchangers may require a departure from the configuration of Figure 2. Placing the boiling section in contact with the hottest

gases will prevent pipe overheating due to the higher heat transfer coefficient associated with phase change [6]. In [7] the best 'match' between $\dot{m}$ and $\dot{m}_w$, across A, when the boiling section is in contact with the highest temperature section of the hot stream was studied (Figure 4).

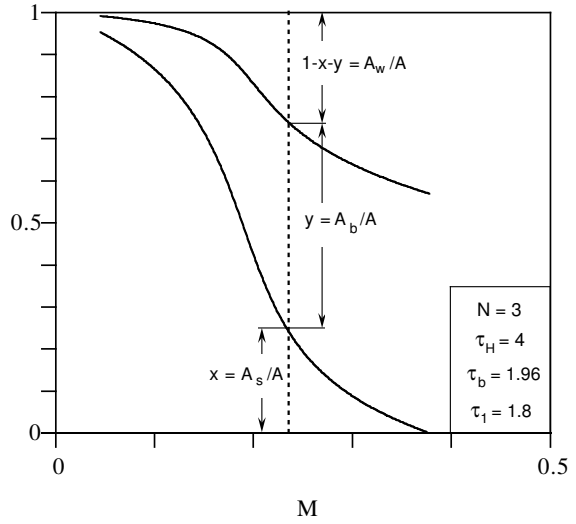

Figure 3: Optimal allocation of heat exchanger area for the counterflow configuration.

It can be anticipated that due to larger stream-to-stream temperature differences the maximum power that can be extracted using the configuration of Figure 4 would be smaller than the one that could be extracted using the optimal configuration of Figure 2. In spite of this, the former configuration is more commonly implemented in power plants, where the hot gases leaving the burners are placed in contact with the boiling section, then with the superheating and finally the pre-heating section.

Figure 5 illustrates, for this new configuration, the heat exchanger area allocation for different mass

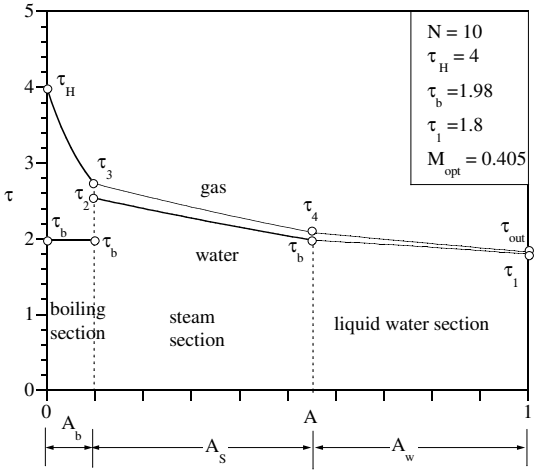

Figure 4: Temperature distribution for the configuration with the boiling section in contact with hottest gases.

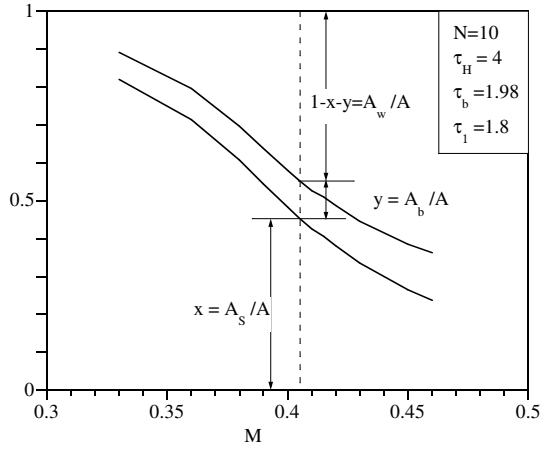

Figure 5: Optimal allocation of heat exchanger area for the system of Figure 2.

flow rate ratios of the collecting stream to the hot stream. Each vertical gap corresponds to an area allocation: the lower gap, x, represents the fraction of the total area, A, allocated to the superheating section, the middle gap, y, corresponds to the fraction of the total area allocated to the boiling section, and the upper gap, 1-x-y, corresponds to the fraction of the total area allocated to the preheating section. In [7], it was shown that there is a mass flow rate ratio $(M = \dot{m}_w/\dot{m})$ that maximizes the second law efficiency, η_{II} (and the power extraction from the hot stream). The optimal value of M is associated to an optimal heat exchanger area allocation (indicated with dashed lines in Figure 5).

3. Solar driven refrigerators

Figure 6 illustrates a solar-driven refrigerator [8]. The transfer of heat from the hot water to the solution stream occurs across a surface of area A, which is considered to be constrained. The solution refrigerant/absorbent experiences a change of phase, i.e., it vaporizes over an intermediate section of the heat exchanger, at constant temperature. Therefore, the temperature of the working fluid stream shows abrupt changes in slope.

With respect to the heat transfer surface A, on the water side the fluid is single-phase, and the heat transfer coefficient is well documented by the technical literature and fairly uniform along the surface. On the refrigerant side, however, the heat transfer coefficient differs considerably from one section to the next, i.e., surface A_l over which the liquid refrigerant is heated to the boiling point, surface A_b over which the refrigerant stream boils, and, surface A_s where the refrigerant is superheated.

The heat transfer surface constraint is expressed as

$$A = A_l + A_b + A_s \tag{3}$$

Each section is characterized by distinct overall heat transfer coefficients. The optimization problem focuses on determining the solution refrigerant/absorbent mass flow rate, an important operating parameter for the equipment, that maximizes the refrigeration rate. Just like in the power producing systems considered previously, there is an associated optimal heat exchanger area allocation.

Figure 7 shows the allocation of heat exchanger area and the corresponding to the thermodynamic optimum (M_{opt}).

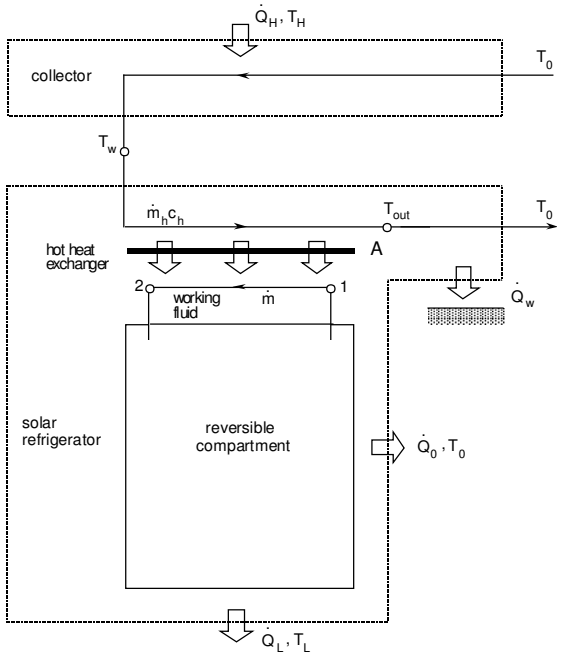

Figure 6: Sketch of a solar driven refrigerator

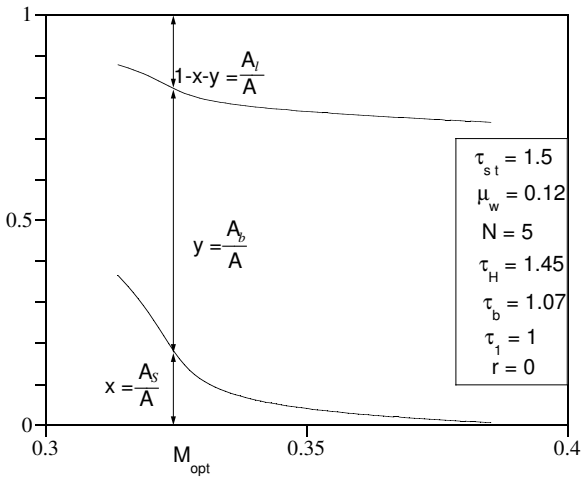

Figure 7: Allocation of heat exchanger area for the system of Figure 6.

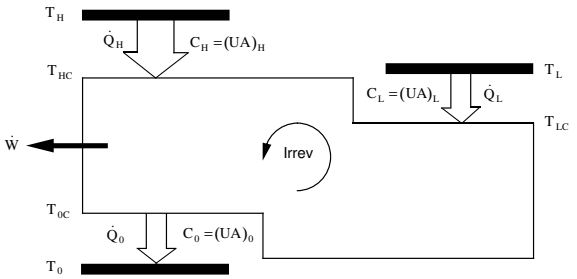

Figure 8: Model of combined power and refrigeration system with internal irreversibility.

4. Combined power and refrigeration

In the model of Figure 8 we propose to examine a combined power and refrigeration system with internal irreversibility. The generated power is used for generating the refrigeration effect Q_L, and the remaining fraction is delivered as net power $\dot{W}$ to an external user. The operation of the combined system may span the entire spectrum from pure refrigeration to pure power production, and its position on this scale is marked by the ratio $R = \dot{Q}_L/\dot{W}$.

The irreversibility of the system characterizes the interior of the power and refrigeration installation. This feature can be accounted for by means of the exergetic efficiency η_{II} of the system defined by the solid line in Figure 8. The specified parameter η_{II} is less than 1, and is defined as the ratio of the net exergy flow rate out of the system divided by the net flow of exergy into the system.

The heat input rate Q_H is a fixed (given) parameter. The region of lower temperature T_{HC} on the solid-line boundary receives the heat transfer interaction Q_H,

$$\dot{Q}_H = C_H(T_H - T_{HC}) \tag{4}$$

From the first and second laws of thermodynamics,

$$\dot{Q}_H + \dot{Q}_L - \dot{Q}_0 - \dot{W} = 0 \tag{5}$$

$$\dot{S}_{gen} = \frac{\dot{Q}_0}{T_{0C}} - \frac{\dot{Q}_L}{T_{LC}} - \frac{\dot{Q}_H}{T_{HC}} \geq 0 \tag{6}$$

The heat interactions with the environment and the low temperature space are modelled as

$$\dot{Q}_0 = C_0(T_{0C} - T_0) \tag{7}$$

$$\dot{Q}_L = C_L(T_L - T_{LC}) \tag{8}$$

For the nondimensionalization of these equations, T_0 was used as temperature scale, $\tau = T/T_0$, $C = C_H + C_L + C_0$, and

$$\hat{q}_0 = \frac{\dot{Q}_0}{\dot{Q}_H} \quad \hat{q}_L = \frac{\dot{Q}_L}{\dot{Q}_H} \quad w = \frac{\dot{W}}{\dot{Q}_H} \tag{9}$$

$$\left(\hat{N}_H, \hat{N}_0, \hat{N}_L, \hat{N}\right) = \frac{T_0}{\dot{Q}_H}\left(C_H, C_0, C_L, C\right) \tag{10}$$

$$x = \hat{N}_H/\hat{N} \quad y = \hat{N}_L/\hat{N} \quad 1-x-y = \hat{N}_0/\hat{N} \qquad (11)$$

In summary, the dimensionless equations that govern the functioning of the the model of Figure 8 are

$$1 - \hat{q}_L - \hat{q}_0 - w = 0 \qquad (12)$$

$$\eta_{II} = \frac{\hat{q}_0(1-\tau_{0C}^{-1}) + w}{1 - \tau_{HC}^{-1} + \hat{q}_L(1-\tau_{LC}^{-1})} \leq 1 \qquad (13)$$

$$1 = x\hat{N}(\tau_H - \tau_{HC}) \qquad (14)$$

$$\hat{q}_0 = (1-x-y)\hat{N}(\tau_{0C} - 1) \qquad (15)$$

$$\hat{q}_L = y\hat{N}(\tau_L - \tau_{LC}) \qquad (16)$$

$$\hat{q}_L = Rw \qquad (17)$$

where the second-law efficiency statement, Equation (13) accounts for the second law, Equation (6). The system of six equations (12) - (17) was solved numerically for the six unknowns: $w, \hat{q}_0, \hat{q}_L, \tau_{HC}, \tau_{0C}$, and τ_{LC}. These were developed numerically as function of the remaining parameters: x, y, $\tau_H, \hat{N}, \eta_{II}$ and R.

The specific work output with respect to the spatial distribution of heat exchanger inventory, x and y, was maximized. The impact of the internal irreversibility,(η_{II}), was also investigated.

Figure 9 shows how the distribution of heat exchanger equipment responds to changes in the internal second-law efficiency, when the operating mode ratio is set at $R = 1$. The sizes of the three heat exchangers are plotted in relative terms, so that the three sizes always add up to 1. The Figure shows that the size of the hot-end heat exchanger (x_{opt}) is relatively insensitive to changes in η_{II}. The other two heat exchangers respond together: the refrigeration-load heat exchanger decreases in size as η_{II} decreases, and vanishes entirely at approximately $\eta_{II} = 0.3$. The power output and refrigeration effect also vanish at this point, as shown by the corresponding dashed line in Fig. 10. This behavior has its source in the irreversibility of the combined system. When η_{II} is too low, all the exergy available based on Q_H [namely $Q_H(1 - T_0/T_H)$], is destroyed through the irreversibility of the power and refrigeration installation.

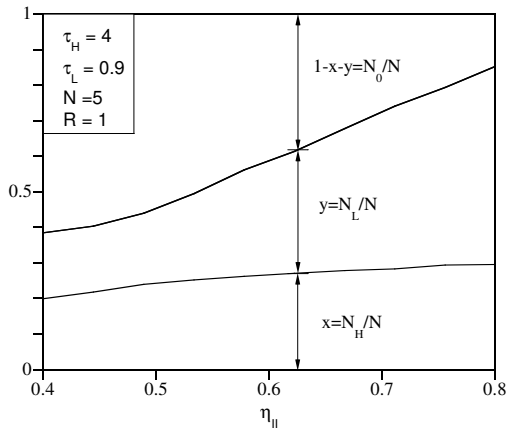

Figure 9: The optimal distribution of heat exchanger inventory, as a function of the second-law efficiency of the power and refrigeration system.

5.Concluding remarks

The existence of an optimal allocation of heat exchanger area resulting from maximization of the thermodynamic performance of both power and refrigeration systems has been documented. When the total heat transfer area available is given, the cases studied have shown two basic results: first, that in one heat exchanger where a hot stream transfers energy to a phase-changing working fluid, there

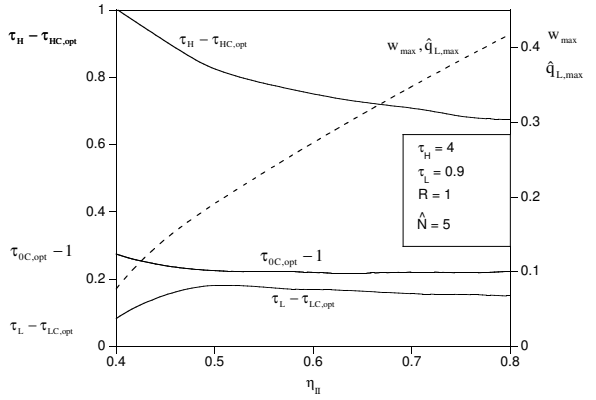

Figure 10: The maximized power and refrigeration, and the three temperature gaps that correspond to the system optimized in Figure. 9.

is an optimal heat transfer area splitting among the three sections (pre-heating, boiling and superheating). This has been documented for two configurations in the case of power generation (sections 2.1 and 2.2) and for solar-driven refrigerators (section 3); second, that when a combined power and refrigeration system is in contact with three temperature reservoirs by means of three heat exchangers, there is an optimal allocation of the total heat exchanger area available for the installation between the heat exchangers (section 4).

Finally, the results summarized in this paper came from thermodynamic optimization and should be complemented with a thermoeconomic analysis.

6. Acknowledgments

The authors acknowledge with gratitude the support from the Center for Advanced Power Systems at Florida State University.

REFERENCES

[1] Bejan A. *Advanced Engineering Thermodynamics. 2nd ed.* New York: Wiley, 1997.

[2] Chen CK, Su YF. *Exergetic efficiency optimization for an irreversible Brayton refrigeration cycle*. International Journal of Thermal Sciences 2005;44(3):303-310.

[3] Chen L, Sun F, Wu C. *Optimal allocation of heat-exchanger area for refrigeration and air-conditioning plants*. Applied Energy 2004; 77(3):339-354.

[4] Bejan A, Errera MR.*Maximum power from a hot stream*. International Journal of Heat Mass Transfer 1998; 41:2025-2036.

[5] Vargas JVC, Ordonez JC, Bejan A. *Power extraction from a hot stream in the presence of phase change.* International Journal of Heat Mass Transfer 2000;43: 191-201.

[6] Harman C. *Private communication to J.C. Ordonez*. Duke University, 2002.

[7] Ordonez JC, Cheng S. *Maximum power extraction from a hot stream in the presence of phase change under limiting collecting temperatures.* In:Proceedings of the 2004 ASME Heat Transfer/Fluids Engineering Summer Conference, Charlotte, NC, USA, July, 2004.

[8] Vargas JVC, Fleming JS, Parise JAR. *Maximum exergy input rate from a hot stream in solar-driven refrigerators*. International Journal of Energy Research 2001;25:751-767.

Proceedings of ECOS 2005
Trondheim, Norway
June 20–22, 2005

OPTIMIZATION AND ENTROPY GENERATION CALCULATION FOR THERMODYNAMIC CYCLES WITH IRREVERSIBILITY DUE TO FINITE SPEED

Stoian Petrescu
Bucknell University
Department of Mechanical Engineering
Lewisburg, PA-17837
U.S.A.

Charles Harman
Duke University
Department of Mechanical Engineering
Durham, NC-27706
U.S.A.

Monica Costea and Camelia Petre
Polytechnic University of Bucharest
Dept. of Engineering Thermodynamics
060042 Bucharest
Romania

Michel Feidt
University "Henri Poincaré" Nancy1
L.E.M.T.A., U.R.A. C.N.R.S. 7563
54504 Vandoeuvre-les-Nancy
France

ABSTRACT

A newly expanded expression of the First Law of Thermodynamics for Processes with Finite Speed is presented. This expression includes three principal sources of internal irreversibility. It is used to develop equations that relate properties for each of the five commonly encountered irreversible processes that may occur with finite speed. Using these equations applied to the particular process involved, equations are developed for calculating the heat and work of the system. This paper includes entropy generation calculations as a function of the finite speed of the process and other parameters. They can then be used to optimize any finite speed cycle. An example is presented to illustrate how the power and efficiency of any cycle can be optimized when the effects of both external and internal irreversibility due to finite speed are considered.
Keywords: Optimization, Finite speed processes, Irreversibilities, Entropy generation calculation

NOMENCLATURE

A	Area [m^2]
a	Coefficient
c	Average molecular speed [m s^{-1}]
c	Mass specific constant [J kg^{-1} K^{-1}]
D	Diameter [m]
g	Thickness [m]
h	Heat transfer coefficient [W m^{-2} K^{-1}]
L	Length [m]
m	Mass [kg]
P	Pressure [Pa]
Q	Heat [J]
$\dot{Q}$	Heat transfer rate [W]
R	Gas constant [J kg^{-1} K^{-1}]
S	Entropy [J K^{-1}]
T	Temperature [K]
U	Internal energy [J]
V	Volume [m^3]
W	Work [J]
w	Piston speed [m s^{-1}]
y	stroke [m]
z	Coefficient

Greek symbols

ε	Volumetric compression ratio
γ	Ratio of the specific heats
η	First law efficiency
λ	Conductivity
τ	Duration time of a process

Subscripts

ad	Adiabatic

av	Average
C	Carnot cycle
Cz	Curzon-Ahlborn
f	Friction
H	Related to the gas at the source
HS	Source, at the hot side of the engine
i	Internal
ins	Insulation
ir	Irreversible
L	Related to the gas at the sink
LS	Sink, at the cold side of the engine
T	Isothermal
t	Total
thr	Throttling
v	Constant volume

INTRODUCTION

A recently model for the optimization of a Carnot cycle engine based on the "Direct Method" and the First Law of Thermodynamics for processes with Finite Speed was developed [1-2]. In that model a closed system has been studied. Therefore, no internal irreversibilities generated by throttling process were involved. In the present paper we study an irreversible Carnot cycle executed in four separate machines (an isothermal expansion machine at T_H, an adiabatic expansion machine, an isothermal compression machine at T_L and an adiabatic compression machine) that are connected through tubes and valves. Another difference is that in the previously papers [1-2] we kept the compression ratio of the low temperature isothermal compression constant. Now we keep the expansion ratio during the isothermal expansion at the high temperature constant.

This "Direct Method" analytic model will now be extended to include the effect of the internal irreversibility generated by throttling processes through the valves and also the adiabatic irreversibility generated by finite speed, during the adiabatic compression and adiabatic expansion. As in paper [2], this analysis includes the temperature differences between the engine and both the heat source and sink that generate the heat losses. In addition, the method for optimizing the temperatures of the cycle gas with respect to the source and sink temperatures as a function of the speed of the piston [2] is used. The resulting optimization predicts different optimum speeds for maximum efficiency and for maximum output power, as expected from the results of the previous research [2].

Optimum cycle temperatures and the resulting efficiency and power are computed using both the "Direct Method" analysis [3-4] and the analysis of Chambadal [5] and Curzon-Ahlborn [6] and the results predicted by the two methods of analysis are compared. Under conditions corresponding to maximum engine power, the Curzon-Ahlborn optimization technique was found to predict results that were more favorable than those predicted by the "Direct Method" analysis presented here. Also, computations of Carnot cycle efficiency and entropy generation per cycle that are based on a "Finite Speed" analysis indicate that both the maximum efficiency and minimum entropy generation per cycle occur at the same optimal piston speed. At maximum engine power, however, the entropy generation per unit time (entropy source) is greater than when the engine operates at maximum efficiency.

There are other models for the study and optimization of the Carnot Cycle that take into account the speed of the cycle (as frequency or number of rotations per minute) [7-8] but in those papers only external irreversibility is included. The present model is much more general and closer to engineering applications because it takes into account the internal irreversibility generated by the finite speed of the pistons, in addition to the external irreversibility with finite speed.

There are some models that take into account internal irreversibilities that are not based on the finite speed of the processes in the cycle, but are based on certain assumptions regarding the internal entropy generation [9-10]. The present model has the advantage, in comparison with those models, that it correlates the efficiency and power directly with the internal and external losses generated by the same essential parameter, the finite speed. In addition it also makes possible to calculate the entropy generation as a function of speed and to correlate it with the efficiency or power. It is important to note that all of these correlations are made possible through use of the “Direct Method”, based on the First Law of Thermodynamics for processes with finite speed. This method is proven to be very powerful in the analyses and optimization of all irreversible cycles, not only Carnot cycles but also, for example, practical machines that work on the Stirling cycle [11] and it is useful in engineering applications such as design and optimization [11-13].

THERMODYNAMICS OF PROCESSES WITH FINITE SPEED APPLIED TO AN IRREVERSIBLE CARNOT CYCLE ACHIEVED WITH 4 MACHINES, USING "THE DIRECT METHOD"

The efficiency, output power, entropy generation per cycle and entropy generation per unit time for the Carnot engine with irreversible processes is computed using the First Law of Thermodynamics for processes with "Finite Speed" [13-14]. The various forms of irreversibility that occur in a Carnot cycle are considered and their effect on the performance of the cycle is presented.

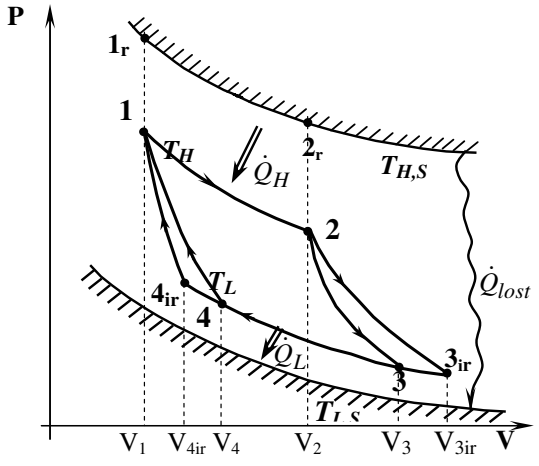

Figure 1: A comparison on p-V coordinates of the Carnot cycle with internal and external irreversibilities (1-2-3ir-4ir-1) with the Carnot cycle only with external irreversibilities (1-2-3-4-1)

The First Law of Thermodynamics for Processes with Finite Speed is [13-14]:

$$dU = \delta Q - p\left(1 \pm \frac{aw}{c} \pm \frac{\Delta p_f}{p} \pm \frac{\Delta p_{thr}}{p}\right) dV \quad (1)$$

where each term in parenthesis takes into account one type of irreversibility:

$\frac{aw}{c}$ = contribution of finite speed;

with $c = \sqrt{3RT}$; $a = \sqrt{3\gamma}$;

$\Delta p_f / p$ = contribution of mechanical friction between mechanical parts;

$\Delta p_{thr} / p$ = contribution of throttling processes (for example, through the valves).

The sign (+) is for compression and the sign (–) is for expansion.

The terms Δp_f and Δp_{thr} can be expressed as a function of speed and stroke based on experimental data [2]:

$$\Delta p_f = \left(0.97 + 0.45\frac{w}{100 \cdot y}\right) \cdot 10^5 \quad [\mathrm{N/m^2}] \quad (2)$$

$$\Delta p_{thr} = 0.45\left(\frac{w}{100 \cdot y}\right)^2 \cdot 10^5 \quad [\mathrm{N/m^2}] \quad (3)$$

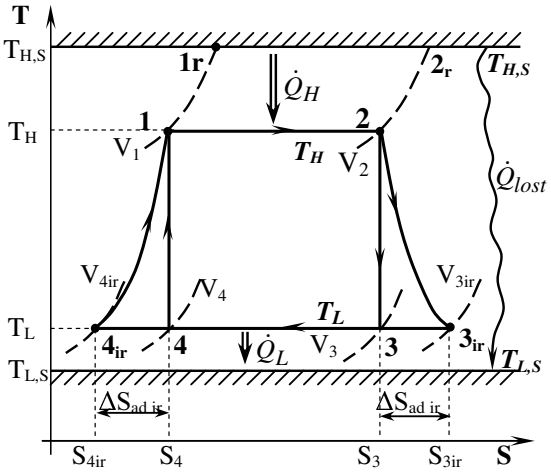

Figure 2: Representation of the irreversible Carnot cycles on T-S coordinates

Each process in the Carnot cycles shown in Figs. 1 and 2 occurs in a separate machine. The resulting four machines are assumed to be connected by tubes and valves as needed.

Note that the expression of the First Low for processes with finite speed has been derived taking into account the irreversibilities introduced by the Second Law of Thermodynamics, caused by finite speed, friction and throttling processes.

Equation (1) can be integrated for various processes with finite speed, to obtain the process equations and also the resulting expressions for the irreversible work and heat.

Adiabatic Process with Finite Speed

For an adiabatic compression or expansion of an ideal gas, we get from (1):

$$m c_v\, dT = -\frac{mRT}{V} \cdot z_{ad} \cdot dV \; ; \quad c_v = \frac{R}{\gamma - 1} \quad (4)$$

where:

$$z_{ad} = \left(1 \pm \frac{aw}{c} \pm \frac{\Delta p_f}{p} \pm \frac{\Delta p_{thr}}{p}\right) \quad (5)$$

By integrating eq. (4) we get the following expression for the adiabatic process with finite speed:

$$T_1\, V_1^{z_{ad}(\gamma-1)} = T_2\, V_2^{z_{ad}(\gamma-1)} \tag{6}$$

where:

$$z_{ad} = \left[1 \pm \frac{aw}{\sqrt{3R(T_1+T_2)/2}} \pm \frac{\Delta p_f}{(p_1+p_2)/2} \pm \frac{\Delta p_{thr}}{(p_1+p_2)/2}\right] \tag{7}$$

$$p_{12}{}_{av.ad} = \frac{p_1+p_2}{2} = \frac{p_1}{2}\left(1+\frac{p_2}{p_1}\right) = \frac{p_1}{2}\left[1+\left(\frac{T_2}{T_1}\right)^{\frac{\gamma}{\gamma-1}}\right] \tag{8}$$

Upon substitution of eq. (2). (3) and (8) in (7):

$$z_{ad} = \left[1 \pm \frac{w\sqrt{3k}}{\sqrt{3R(T_1+T_2)/2}} \pm \frac{2\left(0.97+\frac{0.45w}{100y}\right)\cdot 10^5}{p_1\left[1+(T_2/T_1)^{\gamma/(\gamma-1)}\right]} \pm \right.$$
$$\left. \pm \frac{0.9\left(\frac{w}{100y}\right)^2 \cdot 10^5}{p_1\left[1+(T_2/T_1)^{\gamma/(\gamma-1)}\right]}\right] \tag{9}$$

When eq. (9) is used with the two adiabatic processes in the irreversible Carnot cycle, (1-2-3_{ir}-4_{ir}-1), the result is:

$$z_{ad}{}_{2-3_{ir}} = \left[1 - \frac{w\sqrt{2\gamma}}{\sqrt{R(T_H+T_L)}} - \frac{(1.94+0.009w/y)\cdot 10^5}{p_2\left[1+(T_L/T_H)^{\gamma/(\gamma-1)}\right]} - \right.$$
$$\left. - \frac{(3w/y)^2}{p_2\left[1+(T_L/T_H)^{\gamma/(\gamma-1)}\right]}\right] \tag{10}$$

$$z_{ad}{}_{4_{ir}-1} = \left[1 + \frac{w\sqrt{2\gamma}}{\sqrt{R(T_H+T_L)}} + \frac{(1.94+0.009w/y)\cdot 10^5}{p_1\left[1+(T_L/T_H)^{\gamma/(\gamma-1)}\right]} + \right.$$
$$\left. + \frac{(3w/y)^2}{p_1\left[1+(T_L/T_H)^{\gamma/(\gamma-1)}\right]}\right] \tag{11}$$

Expressions for the pressures p_1 and p_2 are as follows:

$$p_{1r} V_1 = mRT_{HS} \quad \text{and} \quad p_1 V_1 = mRT_H$$

It results:

$$p_1 = p_{1r}\frac{T_H}{T_{HS}} \tag{12}$$

The value of p_{1r} is imposed by material resistance considerations. A high value of p_{1r} is not recommended.

$$p_2 = p_1/\varepsilon_H = \frac{p_{1r}}{\varepsilon_H}\frac{T_H}{T_{HS}} \tag{13}$$

where

$$\varepsilon_H = \frac{V_2}{V_1} \tag{14}$$

Upon using eq. (6), the irreversible adiabatic expansion with finite speed 2–3_{ir} becomes:

$$T_2\, V_2^{(\gamma-1)z_{ad,2-3_{ir}}} = T_{3_{ir}}\, V_{3_{ir}}^{(\gamma-1)z_{ad,2-3_{ir}}} \tag{15}$$

which upon solving for V_{3ir} becomes:

$$V_{3_{ir}} = V_2 \cdot \left(\frac{T_H}{T_L}\right)^{\frac{1}{(\gamma-1)z_{ad,2-3_{ir}}}} \tag{16}$$

Similarly, for the irreversible adiabatic compression with finite speed 4_{ir}–1, we get:

$$V_{4_{ir}} = V_1 \cdot \left(\frac{T_H}{T_L}\right)^{\frac{1}{(\gamma-1)z_{ad,4_{ir}-1}}} \tag{17}$$

The duration time of the isothermal processes is:

$$\tau_H = \frac{V_2 - V_1}{A_p \cdot w} = \frac{V_1}{A_p \cdot w}(\varepsilon_H - 1) \tag{18}$$

$$\tau_L = \frac{V_{3_{ir}} - V_{4_{ir}}}{A_p \cdot w} = \frac{V_{3_{ir}}}{A_p \cdot w}\left(1 - \frac{1}{\varepsilon_{L_{ir}}}\right) \tag{19}$$

where

$$\varepsilon_{L_{ir}} = \frac{V_{3_{ir}}}{V_{4_{ir}}} = \frac{V_2}{V_1}\cdot\left(\frac{T_H}{T_L}\right)^{\alpha} \tag{20}$$

and

$$\alpha = \frac{1}{\gamma-1}\left(\frac{1}{z_{ad,2-3_{ir}}} - \frac{1}{z_{ad,4_{ir}-1}}\right) \tag{21}$$

Upon substituting eq. (16) into eq. (19):

$$\tau_L = \frac{V_2}{A_p \cdot w}\cdot\left(\frac{T_H}{T_L}\right)^{\frac{1}{(\gamma-1)z_{ad,2-3_{ir}}}} \cdot \left(1 - \frac{1}{\varepsilon_{L,ir}}\right) \tag{22}$$

We denote:

$$\frac{T_H}{T_L} = t \qquad \frac{1}{(\gamma-1)z_{ad,2-3_{ir}}} = \beta \tag{23}$$

Upon substituting eqs. (14),(20),(23) into eq. (22):

$$\tau_L = \frac{V_2}{A_p \cdot w}\cdot t^{\beta}\cdot\left[1 - \frac{1}{\varepsilon_H \cdot t^{\alpha}}\right] \quad \text{with} \quad \frac{V_2}{A_p} = L_2 \tag{24}$$

The heat exchanger area of the hot and cold end of the machine respectively is expressed by:

$$A_H = \pi D \cdot \frac{V_2 - V_1}{A_p}\,; \quad A_L = \pi D \cdot \frac{V_{3_{ir}} - V_{4_{ir}}}{A_p} \tag{25}$$

Isothermal Processes with Finite Speed

The isothermal compression and the isothermal expansion process with finite speed of the Carnot cycle will be considered in the present section. From eq. (1), the expression for the heat exchange for an ideal gas in an isothermal process with finite speed is:

$$\delta Q = p\left(1 \pm \frac{aw}{c} \pm \frac{\Delta p_f}{p} \pm \frac{\Delta p_{thr}}{p}\right) dV \qquad (26)$$

Upon integrating eq. (26) for a isothermal irreversible process 1-2 with finite speed w,

$$W_{1-2,T,ir} = Q_{1-2,T,ir} = z_{T,1-2} \cdot m R T_1 \ln \frac{V_2}{V_1} \qquad (27)$$

is obtained, where:

$$z_{T,1-2} = 1 \pm \frac{aw}{\sqrt{3RT}} \pm \frac{2\Delta p_f}{p_1(1+p_2/p_1)} \pm \frac{2\Delta p_{thr}}{p_1(1+p_2/p_1)} \qquad (28)$$

with $\frac{P_2}{p_1} = \frac{V_1}{V_2} = \frac{1}{\varepsilon_e}$ (expansion) = ε_c (compression)

However, considering the isothermal processes:

$$\varepsilon_H = \frac{V_2}{V_1} \qquad \varepsilon_L = \frac{V_3}{V_4} \qquad (29)$$

Expressions for the isothermal work/heat result in:

$$W_H = W_{1-2,T,ir} = Q_{1-2,T,ir} = Q_H = z_{T,H} \cdot mRT_H \ln \varepsilon_H \quad (30)$$

When eq. (28) is used with the two isothermal processes in the irreversible Carnot cycle, (1 – 2 – 3_{ir} – 4_{ir} – 1), the result is:

$$z_{T,H} = 1 - \frac{w\sqrt{3\gamma}}{\sqrt{3RT_H}} - \frac{(1.94 + 0.009\, w/y)\cdot 10^5}{p_1(1+1/\varepsilon_H)} - \frac{(3w/y)^2}{p_1(1+1/\varepsilon_H)} \qquad (31)$$

$$z_{T,L} = 1 + \frac{w\sqrt{\gamma}}{\sqrt{RT_L}} + \frac{(1.94 + 0.009\, w/y)\cdot 10^5}{p_3(1+\varepsilon_L)} + \frac{(3w/y)^2}{p_3(1+\varepsilon_L)} \qquad (32)$$

where $$p_3 = p_2\left(\frac{T_3}{T_2}\right)^{\frac{\gamma}{\gamma-1}} = p_2\left(\frac{T_L}{T_H}\right)^{\frac{\gamma}{\gamma-1}} \qquad (33)$$

The isothermal heat transfer from the source, Q_H at temperature T_H, for a process at finite speed is:

$$Q_H = h_H \cdot A_H \cdot (T_{HS} - T_H) \cdot \tau_H \qquad (34)$$

where:

$$A_H \cdot \tau_H = \left(\pi D \cdot \frac{V_2 - V_1}{A_p}\right) \cdot \frac{V_2 - V_1}{A_p \cdot w} = \left(\frac{V_2 - V_1}{A_p}\right)^2 \frac{\pi D}{w} = \frac{V_1^2}{A_p^2}(\varepsilon_H - 1)^2 \cdot \frac{\pi D}{w} \quad \text{with } V_1 = A_p \cdot L \qquad (35)$$

Upon substituting eq. (35) into eq. (34):

$$Q_H = h_H \cdot L_1^2 \cdot (\varepsilon_H - 1)^2 \cdot \frac{\pi D}{w} \cdot (T_{HS} - T_H) \qquad (36)$$

The irreversible Carnot engine with finite speed operating in steady state must satisfy eqs. (36) and (30). Therefore:

$$z_{T,H} \cdot mRT_H \ln \varepsilon_H = h_H \cdot (A_H \cdot \tau_H) \cdot (T_{HS} - T_H) \qquad (37)$$

Upon solving the eq. (37) for T_H :

$$T_H = T_{HS}\left[1 + \frac{z_{T,H} \cdot mR \ln \varepsilon_H}{h_H \cdot (A_H \cdot \tau_H)}\right]^{-1} \qquad (38)$$

where $z_{T,H}$ is given by eq. (31) and ($A_H \cdot \tau_H$) by eq. (35).

The term $z_{T,H}$ contains T_H. Therefore the value of T_H results from an iterative calculation.

The isothermal heat transfer at the sink, Q_L at the sink temperature T_L, for a process at finite speed using eq. (27) for the process 3_{ir} –4_{ir} is:

$$|W_L| = |Q_L| = z_{T,L} \cdot mRT_L \ln \frac{V_{3_{ir}}}{V_{4_{ir}}} = z_{T,L} \cdot mRT_L \ln \varepsilon_L \qquad (39)$$

where $z_{T,L}$ is given by eq. (32).

The isothermal heat transfer from the sink, Q_L at temperature T_L for a process at finite speed is:

$$Q_L = h_L \cdot A_L \cdot (T_L - T_{LS}) \cdot \tau_L \qquad (40)$$

which in steady-state equals Q_L as expressed by eq. (39) for thermodynamics with finite speed:

$$h_L \cdot A_L \cdot (T_L - T_{LS}) \cdot \tau_L = z_{T,L} \cdot mRT_L \ln \varepsilon_L \qquad (41)$$

Upon solving eq. (41) for T_L :

$$T_L = T_{LS}\left[1 - \frac{z_{T,L} \cdot mR \ln \varepsilon_L}{h_L \cdot A_L \cdot \tau_L}\right]^{-1} \qquad (42)$$

Since the terms $z_{T,L}$, ε_L, A_L, and τ_L all depend on T_L, the solution requires iterative calculations. The iterated value of T_L that is sufficiently close to the value of the previous iteration is then used to calculate the efficiency, power, and entropy generations.

CALCULATION OF THE EFFICIENCY, POWER, ENTROPY GENERATION PER UNIT TIME AND ENTROPY GENERATION PER CYCLE

The efficiency of the Carnot cycle with internal

and external irreversibility is:

$$\eta_{C,ir} = 1 - \frac{Q_L}{Q_H} = 1 - \frac{z_{T,L} \cdot mR\,T_L \ln\varepsilon_L}{z_{T,H} \cdot mR\,T_H \ln\varepsilon_H} = 1 - \frac{z_{T,L} \cdot T_L \ln\varepsilon_L}{z_{T,H} \cdot T_H \ln\varepsilon_H} \quad (43)$$

The power output of the Carnot irreversible engine is:

$$Power = \frac{Q_H \cdot \eta_{C,ir}}{\tau_{cycle}} = \frac{Q_H - Q_L}{\tau_{cycle}} \quad (44)$$

The total entropy generation per cycle is:

$$S_t = -\frac{Q_H}{T_{HS}} + \frac{Q_L}{T_{LS}} = -\frac{z_{T,H} \cdot mR\,T_H \ln\varepsilon_H}{T_{HS}} + \frac{z_{T,L} \cdot mR\,T_L \ln\varepsilon_L}{T_{LS}} \quad (45)$$

The total entropy generation per unit time is:

$$\dot{S}_t = S_t / \tau_{cycle} \quad (46)$$

The internal entropy generation per cycle is:

$$S_i = -\frac{Q_H}{T_H} + \frac{Q_L}{T_L} = -\frac{z_{T,H} \cdot mR\,T_H \ln\varepsilon_H}{T_H} + \frac{z_{T,L} \cdot mR\,T_L \ln\varepsilon_L}{T_L}$$

$$S_i = m\,R\left(-z_{T,H} \cdot \ln\varepsilon_H + z_{T,L} \cdot \ln\varepsilon_L\right) \quad (47)$$

The internal entropy generation per unit time is:

$$\dot{S}_i = S_i / \tau_{cycle} \quad (48)$$

The effect on the Carnot Cycle of including the heat loss that could occur between the cycle and the heat reservoirs

The equations in the above section are changed when the external and internal losses are included in the analysis. An expression for the heat loss, between the cycle and the heat reservoirs, $\dot{Q}_{lost}$, is:

$$\dot{Q}_{lost\cdot} = \pi D\left(L_2 - L_1\right) \cdot \frac{\lambda_{ins}}{g_{ins}}\left(T_{HS} - T_{LS}\right) \quad (49)$$

$$Q_{lost\cdot} = \dot{Q}_{lost\cdot} \cdot \tau_{cycle} \quad (50)$$

The effect of the heat loss is to reduce the efficiency:

$$\eta_{C,lost} = 1 - \frac{Q_L + Q_{lost}}{Q_H + Q_{lost}} \quad (51)$$

The power output is not affected by the heat losses, as shown below:

$$Power = \frac{\left(Q_H + Q_{lost}\right) - \left(Q_L + Q_{lost}\right)}{\tau_{cycle}} = \frac{Q_H - Q_L}{\tau_{cycle}} \quad (52)$$

The total entropy generation per cycle with heat loss is:

$$S_t = -\frac{Q_H + Q_{lost}}{T_{HS}} + \frac{Q_L + Q_{lost}}{T_{LS}} \quad (53)$$

The total entropy generation per unit time is:

$$\dot{S}_t = S_t / \tau_{cycle} \quad (54)$$

The internal entropy remains the same.

DISCUSSION

A "Finite Speed" analysis of a Carnot cycle engine achieved in four machines was performed. Air modeled as an ideal gas with constant specific heat is the working gas in the cycle. Losses due to heat transfer between the cycle and the heat source and sink were included as was the effect of variation in the area for heat transfer and in the dwell time for heat transfer due to the movement of the piston during the isothermal expansion and compression processes. Irreversibility during the adiabatic compression and expansion with finite speed also has been taken into account. The results of these calculations are presented in Figs. 3 to 9.

Figures 3, 4, 5 and 6 illustrate the effect on the power output, the cycle efficiency, the entropy generation and the temperatures in the gas, as a function of piston speed for a Carnot engine with internal and external irreversibilities, generated by the Finite Speed of the pistons in each of the 4 machines, for $V_2/V_1 = 8$. Figures 3 and 4 illustrate the power output and cycle efficiency including all irreversibilities, respectively internal and external ones. Also the Curzon-Ahlborn efficiency is included in Figure 4. These results are based on the following fixed parameters: D = 0.1m; L_2 = 1 m; $\varepsilon = 8$; P_{1r} = 1 bar (pressure of the gas in state 1r); T_{HS} = 600 K; T_{LS} = 300 K; γ = 1.4; g_{ins} = 0.03 m; λ_{ins} = 0.04 W m^{-1}K^{-1}.

As illustrated in Fig. 4, the optimum piston speed for maximum efficiency is only 3 m/sec. At this speed the rate of entropy generation (per unit time) is a very low 0.25. However, the optimum piston speed for maximum power is 8.5 m/sec and the rate of entropy generation per unit time at this speed is significantly higher, 0.7. The expectation is that, the maximum power output and the efficiency would decrease, as would the optimum speed for maximum power if additional irreversibilities were included in the analysis.

The efficiency of the Carnot cycle as determined by the "Finite Speed" analysis for any piston speed is less than the efficiency based on the Chambadal-Curzon–Ahlborn analysis when both internal and external irreversibilities are included in the analysis, but it is close to the maximum efficiency.

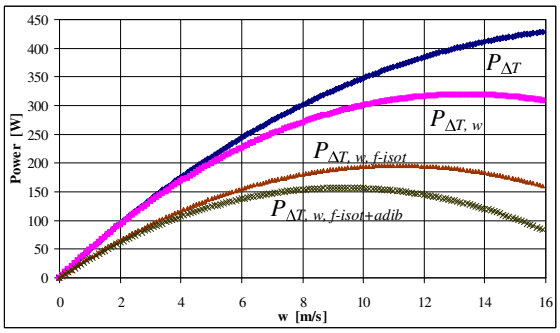

Figure 3: Power output versus the piston speed

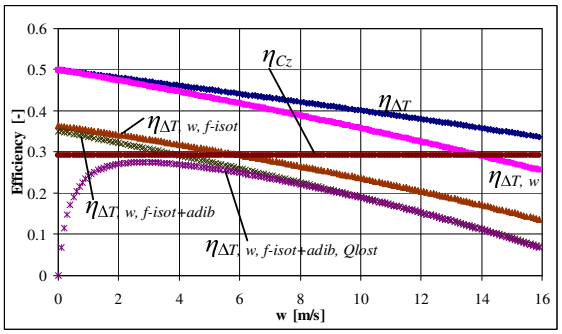

Figure 4: Cycle efficiency versus the piston speed

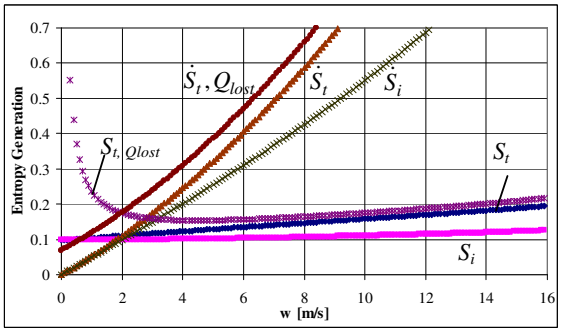

Figure 5: Entropy generation versus the piston speed

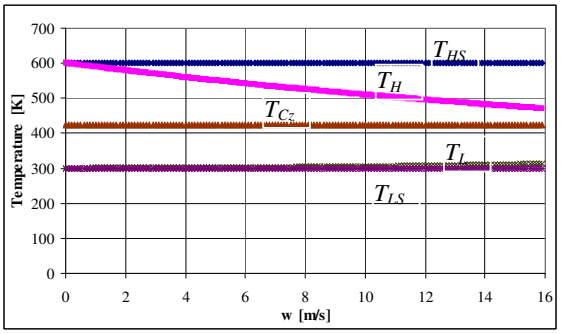

Figure 6: Temperature versus the piston speed

This difference is illustrated in Fig. 4. In addition, the efficiency of the Carnot cycle at maximum power as determined by the "Finite Speed" analysis is less than the efficiency based on the Curzon-Ahlborn analysis. The Carnot cycle efficiency based on a "Finite Speed" analysis, at the speed corresponding to Maximum Power, is 0.43, when only external irreversibilities are included and is 0.22, when both internal and external irreversibilities are included in the analysis.

The hot and cold heat reservoir temperatures, the hot and cold side engine gas temperatures, and the Chambadal-Curzon-Ahlborn optimized temperature are shown in Fig. 6 as a function of the piston speed. The hot side gas temperature optimized for maximum power is shown to be higher (530 K compared to 420 K), over the full range of piston speeds investigated, than the Chambadal–Curzon–Ahlborn optimized temperature. Also, the predicted temperature difference between the high and low gas temperature is shown to increase as the piston speed decreases and to be especially great at piston speeds less than the speed for maximum efficiency.

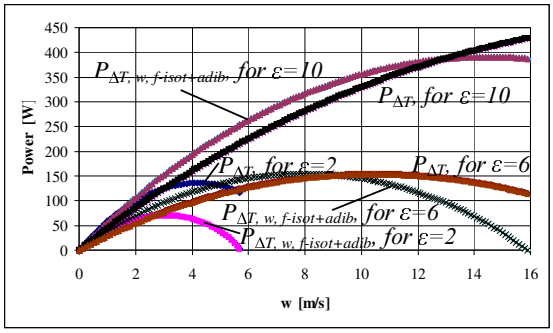

Figure 7: Sensitivity study of the power output with respect to the ε_H

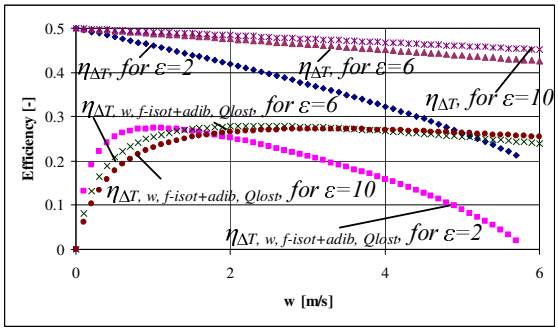

Figure 8: Sensitivity study of the cycle efficiency with respect to the ε_H

It is important to note, in Fig. 4, that the piston speed for maximum efficiency (3 m/s) is the same as the piston speed for the minimum entropy generation on a per cycle basis. As piston speeds decrease to the optimum speed (3 m/s) for maximum efficiency, the entropy generation on a per cycle basis continually decreases to a minimum. If the piston speed is decreased beyond that, the entropy generation per cycle will increase dramatically, because of heat losses between the heat sources. This implies that optimization of the piston speed for minimum entropy generation per cycle is equivalent to optimization the piston speed for maximum efficiency, when the isothermal expansion ratio V_2/V_1 is held constant.

It should be pointed out however that the time rate of entropy generation at maximum efficiency is much lower compared to the corresponding value at maximum power.

Figures 7 and 8 illustrate the same conclusions for values of V_2/V_1 of 10, 6 and 2. The shape of the curves for efficiency and power are very similar, but they shift with the maximum at lower speeds. Also the maximum power and the maximum efficiency will decrease as V_2/V_1 decreases.

CONCLUSION

Important performance parameters of a Carnot engine achieved in a 4 cylinders machine, based on a "Finite Speed" analysis have been presented. The optimum piston speed for maximum power and optimum speed for maximum efficiency has been found for a particular set of engine parameters and it has been shown that minimum entropy generation per cycle occurs at maximum efficiency. This study produces a more realistic model for the design of Carnot cycle engines since it includes many of the various internal and external irreversible processes that occur in the actual operation of these engines and correlates them with the finite speed of the piston.

Thermodynamic analysis based on the "Direct Method" and "Finite Speed" is shown to be especially effective for engineering optimizations since the efficiency and power can each be optimized based on gas temperatures and process speed. Based on these engineering optimizations, there is hope that industry soon will choose to build quasi-Carnot machines. To hasten that day it would be very useful to use this method to evaluate the optimum values for other parameters such as piston diameter, compression ratio, piston stroke.

REFERENCES

[1] Petrescu S, Costea M, Feidt M. *Optimization of a Carnot Cycle Engine using Finite Speed Thermodynamics and the Direct Method*. In: Proceedings of ECOS'2001 Conference, Istanbul, Turkey, 2001.

[2] Petrescu S, Feidt M, Harman C, Costea M. *Optimization of the Irreversible Carnot Cycle Engine for Maximum Efficiency and Maximum Power through Use of Finite Speed Thermodynamic Analysis*, In: Proceedings of the ECOS'2002 Conference, Berlin, Germany, 2002.

[3] Petrescu S, Stanescu G, Costea M. *The Study of the Optimization of the Carnot Cycle which Develops with Finite Speed*. In: Proceedings of ENSEC'93 Conference, Krakow, Poland, 1993.

[4] Petrescu, S. et al. *Application of the Direct Method to Irreversible Stirling Cycles with Finite Speed.* International Journal of Energy Research 2002;26:589-609.

[5] Chambadal P. *Évolution et applications du concept d'entropie*. Paris: Dunod, 1963.

[6] Curzon FL, Ahlborn B. *Efficiency of a Carnot Engine at Maximum Power Output*. American Journal of Physics 1975;43:22-24.

[7] Spence RD, Harrison MJ. *Speed dependence of efficiency of heat engines*. American Journal of Physics 1985;53(9).

[8] Rebhan E, Ahlborn B. *Frequency-dependent performance of a nonideal Carnot Engine*. American Journal of Physics 1987;55(5).

[9] Chen LG, Zhou JP, Sun FR, Wu C. *Ecological optimization for generalized irreversible Carnot engines*. Applied-Energy 2004;77(3):327-338.

[10] Hernández C, Medina A, Roco JMM, Velasco S. *Comparison of Optimum Thermal Conductance Distribution for an Irreversible Carnot Cycle under Different Optimization Criteria*, in Advances in Finite Time Thermodynamics, Analysis and Optimization. New York: Nova Science Publishers, 2004. p. 471-490.

[11] Petrescu S, Harman C, Costea M, Petre C, Florea T. *A Scheme of Computation, Analysis, Design and Optimization of Solar Stirling Engines*. In: Proceedings of ECOS'2003 Conference, Copenhagen, Denmark, 2003.

[12] Petrescu S, Harman C, Costea M, Feidt M. *Thermodynamics with Finite Speed versus Thermodynamics in Finite Time in the Optimization of Carnot Cycle*, In: Proceedings of The 6-th ASME-JSME Thermal Eng. Joint Conference, Hawaii, 2003.

[13] Petrescu S, Harman C, Costea M, Florea T, Petre C. *Advanced Energy Conversion.* Lewisburg: Bucknell University, 2005.

[14] Petrescu S, Harman C. *The Connection between the First and Second Law of Thermodynamics for Processes with Finite Speed. A Direct Method for Approaching and Optimization of Irreversible Processes*. Journal of The Heat Transfer of Society of Japan, 1994;33(128):60-67.

Proceedings of ECOS 2005
Trondheim, Norway
June 20–22, 2005

A SECOND LAW AID IN POWER PLANT REPOWERING IMPROVEMENT

Joseph EA Roy-Aikins
University of KwaZulu-Natal
School of Mechanical Engineering
Private Bag X54001
Durban 4000
South Africa

ABSTRACT

Exergy analysis is a technique that embodies the second law of thermodynamics, and when combined with costs analysis forms that branch of energy system analysis known as thermoeconomics. Thermoeconomics can be used to aid the design and analysis of power plants, with regard to costs, by giving either an optimised solution or an improved design.
With this in mind, an investigation was carried out to find out if it would be feasible to repower the steam turbine plants at a power station in South Africa. This was looked at with a view to adding capacity, in order to alleviate the shortfall in capacity that is about to be experienced. Parallel repowering was the repowering option chosen, as it was identified as the most appropriate, in view of the company's business strategy and in line with the national energy plan. A base case design was formulated and a thermoeconomic analysis was carried out to improve on the design. An improved design was arrived at, but the cost of the power was higher than what it was for the existing plant. It was concluded that in the light of the present power situation repowering of old steam turbine plants is an option that should be considered to help manage the capacity problem, in the short to medium term.
Keywords: combined cycle plants, exergy analysis, power plant design optimisation, repowering, second law analysis, thermoeconomics.

INTRODUCTION

The electric utility company Eskom generates about 92 percent of the electrical power produced in South Africa. Eskom is the fourth largest power company in the world, with regard to capacity, and has for a number of years been producing the lowest cost electricity in the world, as a result of the abundance of cheaply priced coal in the country, which has resulted in the coal-fired steam turbine being the primary power generation plant. Eskom has announced that it will run out of excess peaking capacity in 2007, and of excess baseload capacity in 2010.
Several options are being looked at to determine strategies that will enable the company meet the growth in power demand in the short to medium term. No new coal-fired power stations are being planned for construction during this time frame, as considerable time is required to get such large central power generation facilities up and running. The only type of power plant that is being considered, and which is for long-term application, is the Pebble Bed Modular Reactor, which is a nuclear plant operating on the closed-cycle gas turbine. Work on the development of the technology is at an advanced stage. The company has embarked on some demand-side management initiatives in all three sectors, i.e. industrial, commercial, and residential, to encourage consumers to reduce their electricity consumption and to be more energy efficient. However, more

needs to be done to manage the problem, and alternatives are to be investigated to find the correct mix of solutions.

The Integrated Energy Plan published by the government in 2004 for comments stipulates that energy supply will remain reliant on coal for the next two decades, and that energy supply should be diversified through increased use of gas and new and renewable energies. With natural gas arriving in the country in 2005 from Mozambican gas fields, new opportunities for the use of gas turbines in meeting the country's energy needs will arise.

One alternative that could provide a temporary fix of the problem of diminishing generation capacity is that of steam turbine repowering, where a gas turbine (and in some cases a heat recovery steam generator (HRSG) as well) is added as a topping plant to an existing steam turbine either to increase capacity or improve heat rate, or both. In some cases, the objective of repowering is to reduce emissions, and this could result in a loss of capacity [1]. Old power plants, especially those with boilers coming to the end of their useful lives, are good candidates for repowering. There are a few such plants in the arsenal of power stations owned by Eskom, and they present an opportunity for increasing generation capacity through repowering.

This paper investigates the thermoeconomic benefits of repowering the steam turbines at an Eskom power station. The repowering exercise is carried out in line with the company's business strategy in view of the national Integrated Energy Plan. An exergy analysis of the repowered cycle is carried out to obtain improvements to the design until the cost of plant output is minimised. The Arnot power station is taken as an example.

THE STEAM TURBINE PLANT

The Arnot power station consists of six steam turbine plants in base load application. The average age of the plants is 31 years. Each unit is fired on pulverised coal and operates on the reheat Rankine cycle with six stages of feed water heating. At the design point, the boiler generates 316.5 kg/s superheated steam at 167 bar and 516 ^{o}C. After expansion in the high pressure (HP) turbine the steam is reheated to the same temperature as the main steam before being fed to the intermediate pressure (IP) turbine, and upon leaving the IP turbine the steam is fed to a double-flow low pressure (LP) turbine that exhausts to a condenser pressure of 0.075 bar. The plant generates 350 MW at a heat rate of 9557 Btu/kWh, at the design point, based on a lower heating value of 21.353 MJ/kg for coal. A schematic of the plant is shown in Fig. 1, and the thermodynamic data at the major stations are shown in Tab. 1.

Station	Mass Flow (kg/s)	Pressure (bar)	Temp. (^{o}C)
1	316.5	167	516
2	274.9	41.7	320
3	274.9	39.6	516
4	228.1	7	171
5	200.2	0.075	40.3
6	247.8	0.075	40.3
7	247.8	7	45
8	247.8	7	66
9	247.8	7	115
10	316.5	7	165
11	316.5	187.4	171
12	316.5	187.4	194
13	316.5	187.4	220
14	316.5	187.4	251
15	19.7	41.7	320
16	19.7	0.1	46
17	21.9	41.7	320
18	21.9	40	220
19	14.2	20	422
20	36.1	20	200
21	10.9	15	386
22	47.0	15	172
23	21.7	7	171
24	8.2	0.3	69
25	27.4	0.3	46
26	19.2	3	139
27	19.2	3	70

Table 1: Steam turbine performance data

THE REPOWERED PLANT

As mentioned earlier, repowering of the steam turbine plants is to be carried out in line with the company's business strategy and in view of the national energy plan. Consequently, a number of practical issues are to be taken into consideration, which in turn impact technical matters. The main practical consideration is the use of coal as (primary) fuel. A direct impact of this on technical matters is the repowering option, i.e. full or

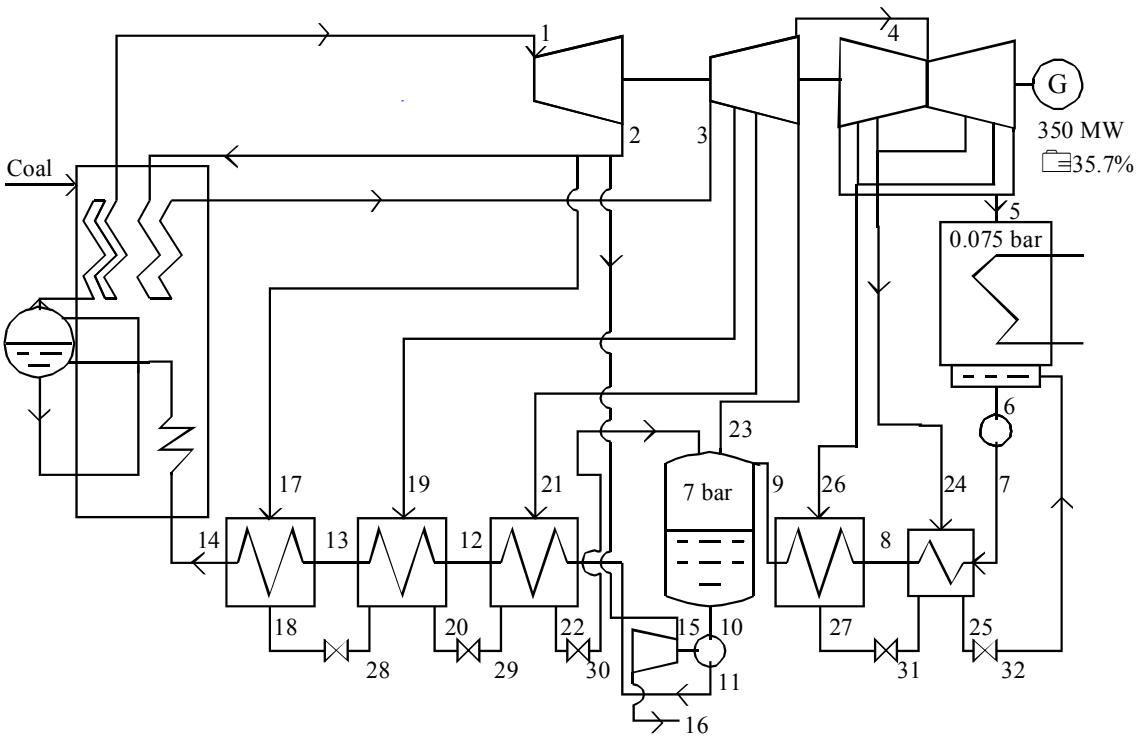

Fig.1 Schematic of the Steam Turbine Plant

parallel repowering. Joyce [2] describes these repowering options.

The first step in the repowering process is to determine the structure and performance of the repowered plant. As the preferred fuel for gas turbines is natural gas, and as coal is taken to be the dominant energy resource, it was decided to use both gas and fuel in the repowered plant. Consequently, parallel repowering was the repowering option that was chosen, and a decision must then be made on whether the topping or straight option is selected. In both options the existing boiler is kept and steam is raised independently of the operation of the gas turbine. However, in the former, the exhaust gas from the gas turbine is used as vitiated air in the boiler, whereas in the latter, an HRSG is incorporated, in addition.

Press. Ratio	TIT	EGT	Power	Heat Rate
	°C	°C	MW	Btu/kWh
11.0	1100	543	156	9977

Basis: ISO conditions, LHV = 50057 KJ/kg

Table 2: Gas turbine performance

Taking into consideration on the one hand technical issues [3], which include the capacity of the existing steam turbine, the matching of the HRSG and the steam turbine, and fuel handling, and on the other, financial issues, notably the need for low capital investment, the straight option was chosen. The gas turbine chosen for the topping cycle is the Siemens V94.2, whose performance at the design point is shown in Tab. 2, for an exhaust mass flow of 514 kg/s. In repowering the steam turbine with this gas turbine, the repowered plant has an output of 506 MW and a heat rate of 7921 Btu/kWh. The station output has increased by 45%, while the heat rate has improved by 17%. The basis of the re-design is that the existing steam turbine components are refurbished and kept. The computer software BRAKINE [4] was used to analyse the performance of the combined plant. Because of the age of the steam turbine, it is necessary to refurbish the boiler to extend its life. To avoid huge refurbishment costs, it was decided to de-rate the steam turbine. As a result, the superheater and reheater outputs were reduced to lower the steam turbine output to 280 MW, thereby reducing the output of the combined plant to 436

Throttle Conditions		Reheat Conditions		Output		Heat Rate
Pressure (bar)	Temp. (^oC)	Pressure (bar)	Temp. (^oC)	GT (MW)	ST (MW)	(Btu/kWh)
120	500	30	500	152	280	7935

$P_{deaerator}$ = 9.6 bar, $P_{condenser}$ = 0.08 bar

Table 3: Combined cycle performance

MW. Table 3 shows the performance of the repowered plant.

Bare Equipment Cost, $/kW	83.7
Shipping Cost, %	2.8
Construction Cost, %	11.5
Start-up Capital, %	5.5
Construction Time, years	1
Payment Schedule, %	100
Fixed Yearly Disbursements, %	2
Operation and Maintenance:**	
Fixed, $/kW	18.3
Incremental, mills/kWh	3.5
Fuel Cost, $/GJ:	
Coal	0.36
Natural Gas	5.02
Owner's Interest Rate,* %	10.7
Debt Interest Rate,* %	7.3
Owner's Income Tax Rate, %	0
Inflation Rate, %	5.1
Equity Fraction of Capital	0.44
Equipment Life, years	20
Salvage Value, $	0

* Inflation adjusted

** Subject to a real escalation rate of 1.4% and the inflation rate

Table 4: Project economic data

ECONOMIC EVALUATION

The next step in the analysis procedure is to carry out an economic analysis to determine the overall costs associated with owning and operating the plant. The investment made in the equipment must be recovered during the life of the plant, and an acceptable rate of return must be obtained. In addition, provision must be made to recoup the cost of the fuel and the operation and maintenance charge. To effect these calculations, costs and economic data, load duration curves and plant overall performance are required. The data used are shown in Tab. 4. The bare equipment cost includes the cost of refurbishing the steam turbine plant. The cost of the gas turbine was estimated with the aid of [5].

The economic analysis was carried out by using the computer program PEACES [6]. The levelised net present value was obtained as $34.2 million, and the levelised cost of electricity was 5.06 ¢/kWh.

THERMOECONOMIC ANALYSIS

As mentioned earlier, thermoeconomics is a technique that combines economic analysis with exergy analysis, to aid the design of thermal energy systems. Exergy analysis (or second law analysis) helps to pinpoint the sources of inefficiency in an energy system, and when combined with economic analysis has the potential to minimise or reduce costs. Hence, the objective of thermoeconomic analysis is to minimise the cost of the product of the plant. A few authors have proposed techniques for carrying out cost optimisation of thermal energy systems [7–10]. The method proposed by Tsatsaronis [11] is used here, because of the manner in which BRAKINE and PEACES work, which allows the method of Tsatsaronis to lend itself to easy adaptation. A computer program XAG [12] was developed to carry out thermoeconomic analyses of energy systems; it complements BRAKINE and PEACES. The three software were used to analyse the performance of the combined cycle plant, with a view to improving on the design.

Improving on the design of the repowered plant involves altering those decision variables that alter the overall performance of the plant. Hence, the third and final step of the design process is to determine the thermoeconomic variables that define the improvement process. Usually, each component of the plant is looked at and its thermodynamic and cost data examined to find out the impact of the performance of the component on the overall performance of the plant. The structure

of the plant could change during the improvement exercise, but in this case the structure of the plant is fixed, comprising of the gas turbine, the HRSG, and the steam turbine. The performance of the gas turbine is fixed and so nothing changes in this unit. The performance of the HRSG changes in line with the steam requirements of the steam turbine, hence improvement to the design of the combined plant comes primarily from improving the performance of the steam turbine cycle, by modifying the cycle performance variables.
The variables that determine the overall performance of the steam turbine plant are:

1. the main steam pressure and temperature
2. the reheat steam pressure and temperature
3. the condenser pressure
4. the deaerator pressure

The pressures of the bleed steam affect the overall performance of the plant as well, but to a lesser extent. These decision variables are all not completely independent, since the structure is fixed and since the existing components are not replaced. In general, the decision variables affect directly the thermodynamic performance of the plant and, indirectly, the sizes of the components. Component size affects the cost of the plant, which in turn affects the economic performance of the system. With regard to the above variables, the main and reheat steam temperatures are set the same, as the reheat steam is heated to the temperature of the main steam. The pressure of the reheat steam is controlled by the performance of the HP turbine.
The design improvement exercise requires the calculation of certain thermoeconomic variables for each component. Following the method of Tsatsaronis [11], these variables are the exergetic efficiency ε, rate of exergy destruction $\dot{E}_D$, exergy destruction ratio y_D, the cost rate of exergy destruction $\dot{C}_D$, capital investment and operating and maintenance cost rates, $\dot{Z}^{CI}$ and $\dot{Z}^{OM}$, and their sum $\dot{Z}$, the relative cost difference r, and the exergoeconomic factor f. The definitions and significance of these variables are explained by Bejan, Tsatsaronis, and Moran [13], and the authors also explain the thermoeconomic optimisation process in detail.
Briefly speaking, the design improvement exercise is carried out iteratively, wherein a cost balance is formulated for each component, to determine the cost of each exergy stream. The cost balance is affected by the performance of the component, which in turn is influenced by the value of one or more decision variables. Hence, by altering the values of the decision variables progressively, where necessary, a localised optimal solution representing an improved design can be arrived at.

RESULTS

The values of the decision variables for the base case design are given in Tab. 3, and the values of the critical variables required for the thermoeconomic analysis are shown in Tab. 5 for the base case design, and for the important plant components. The components are listed in decreasing order of $\dot{C}_D+\dot{Z}$ values.

To start off the iterative process, the values of the decision variables given in Tab. 3 are altered in a logical manner, and the whole process is repeated all over again by first analysing the thermodynamic performance of the plant, and then carrying out an economic analysis, and thereafter performing a thermoeconomic analysis.

Component	ε (%)	$\dot{C}_D + \dot{Z}$ ($/h)	r (%)	f (%)
Gas turbine	37.8	21637	261.6	12.1
Boiler	81.6	4899	27.1	9.2
HRSG	72.1	4082	85.5	41.6
IP Turbine	84.6	3144	39.1	83.3
LP Turbine	85.3	2980	38.6	81.4
HP Turbine	86.9	2449	28.0	87.3
Deaerator	85.8	1634	34.9	46.4

Overall product cost $\dot{C}_P$= 49031 $/h

Table 5: Base case thermoeconomic data

The analysis of the data in Tab. 5 was carried out by inspection and by applying logic. This is the shortfall in iterative thermoeconomic analysis that has not yet been addressed. It requires the attention of the experienced performance analyst. In [14], the author explained in detail how the thermoeconomic data presented for the case examined there was analysed to alter the decision variables until a cost optimal solution was reached. A similar process is followed here. After an analysis of the data in Tab. 5, the decision variables were changed to the following:

Superheater pressure = 110 bar

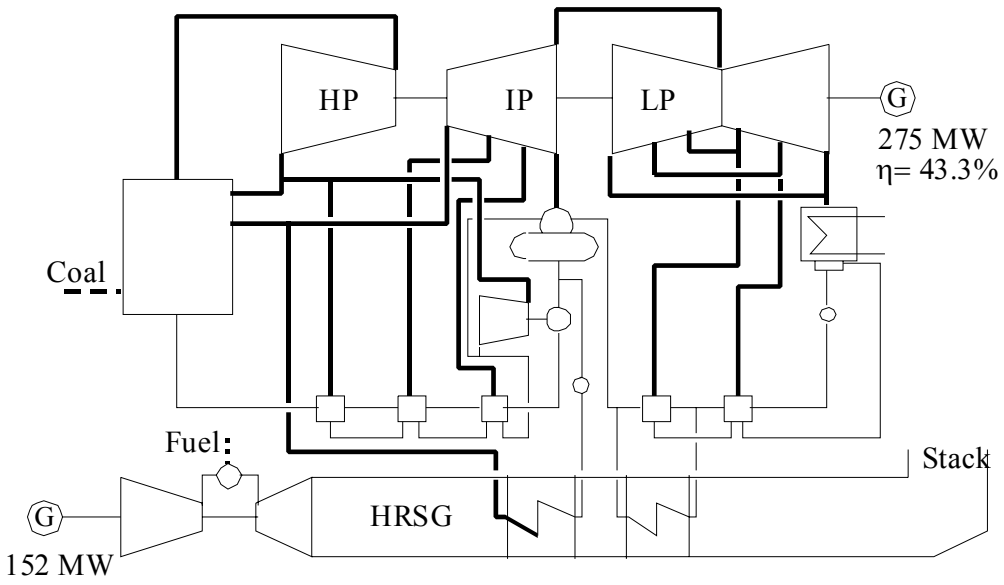

Fig. 6 Schematic of the Repowered plant

Superheater temperature = 480 °C
Reheat pressure = 25 bar
Deaerator pressure = 8 bar
Condenser Pressure = 0.078 bar

Component	ε (%)	$\dot{C}_D + \dot{Z}$ ($/h)	r (%)	f (%)
Gas turbine	37.7	21636	261.7	12.1
Boiler	81.4	4899	28.7	10.1
HRSG	72.9	4374	89.2	43.4
LP Turbine	85.6	2841	39.1	79.9
IP Turbine	84.2	2830	38.4	82.3
HP Turbine	86.7	2253	27.8	87.9
Deaerator	86.0	1552	35.8	48.0

Overall product cost $\dot{C}_P$= 45398 $/h

Table 6: Thermoeconomic data after Iteration 1

The thermoeconomic data after the first iteration is shown in Tab. 6. The iterative process continued, and after seven iterations it was believed that the cost optimal solution had been obtained. The thermoeconomic data at the cost-optimal point is shown in Tab. 7 and the performance of the plant at this point is shown in Tab. 8. The output of the plant is 427 MW at a heat rate of 7880 Btu/kWh, which was obtained at an overall product cost of 40046 $/h. The schematic of the plant is shown in Fig. 2.

Component	ε (%)	$\dot{C}_D + \dot{Z}$ ($/h)	r (%)	f (%)
Gas turbine	37.7	21635	261.7	12.1
Boiler	82.4	4213	25.4	8.6
HRSG	72.7	3981	92.5	46.0
LP Turbine	85.2	2047	35.2	70.1
IP Turbine	84.5	2042	32.4	68.9
HP Turbine	87.0	1559	22.9	72.6
Deaerator	86.0	1391	32.9	59.3

Overall product cost $\dot{C}_P$= 40046 $/h

Table 7: Cost-optimal data of repowered cycle

CONCLUSION

A steam turbine plant was repowered by adding a gas turbine and a HRSG as a topping cycle. A thermoeconomic analysis of the repowered cycle was carried out in an attempt to optimise the performance of the plant with regard to costs, i.e. to minimise the cost of the product of the plant. The analysis was restricted to the fixed structure obtained by combining a particular gas turbine with a given steam turbine. No changes could be

Throttle Conditions		Reheat Conditions		Output		Heat Rate
Pressure (bar)	Temp. (^oC)	Pressure (bar)	Temp. (^oC)	GT (MW)	ST (MW)	(Btu/kWh)
112	490	27	490	152	275	7880

$P_{deaerator}$ = 9 bar, $P_{condenser}$ = 0.08 bar

Table 8: Performance of the optimised repowered cycle

made to the decision variables that impact the performance of the gas turbine, as the gas turbine was employed to operate at its design point at the optimum performance point of the repowered cycle.

A very large portion of the investment cost went into purchasing the gas turbo set and HRSG equipment, leaving a small amount for refurbishing the steam turbine plant. As a result, the thermoeconomic optimisation process centered around reducing the cost of refurbishment of or the cost due to exergy destruction in the steam turbine components. The capacity of the repowered plant increased by 22% while the heat rate improved by 17.5%. An overall product cost of 40046 $/h was obtained for the plant, and the levellised cost of the electricity produced was obtained as 4.81 ¢/kWh, which is higher than the 2.99 ¢/kWh for that produced by the steam turbine plant. The higher cost is due primarily to the use of natural gas, in addition to coal, the sole fuel used in the existing plant. There are, however, environmental benefits to be gained by the use of natural gas, which benefit was not quantified in the analysis.

Repowering is feasible, and though the cost of electricity is increased, repowering of old steam turbine plants with gas turbines is a viable option that could be used to manage the looming capacity problem, in the short to medium term.

REFERENCES

[1] Termuehlen H. *Repowering, an effective way to reduce CO_2 discharge*. In: Proceedings of the 1998 International Joint Power Generation Conference, Baltimore, 1998.

[2] Joyce JS. *How gas turbines can improve the operating economy and environmental compatibility of new and old steam generating stations*. Siemens Power Journal 1992;1.

[3] Brander JA, Chase DL. *Repowering application considerations.* Journal of Engineering for Gas Turbines and Power 1992; 114: 643–652.

[4] Roy-Aikins JEA. *BRAKINE: a programming software for the performance simulation of Brayton and Rankine cycle plants*. Proc Instn Mech Engrs 1995; 209(A): 281–286.

[5] *2004 Gas Turbine World Handbook*, CT, Pequot Publishing Inc., 2004.

[6] Roy-Aikins JEA. *PEACES: a program for the economic analysis of combined energy systems*. ASME Paper No. 2000-GT-302, 45th International Gas Turbine and Aeroengine Congress and Exposition, Munich, 2000.

[7] Tsatsaronis G, Pisa J. *Exergoeconomic Evaluation and Optimization of Energy Systems – Application to the CGAM Problem*. Energy 1994; 19(3): 287–321.

[8] Frangopoulos CA. *Application of the Thermoeconomic Functional Approach to the CGAM Problem*. Energy 1994; 19(3): 323–342.

[9] von Spakovsky MR. *Application of Engineering Functional Analysis to the Analysis and Optimization of the CGAM Problem*. Energy 1994; 19(3): 343–364.

[10] Valero A, Lozano MA, Serra L, Torres C. *Application of the Exergetic Cost Theory to the CGAM Problem*. Energy 1994; 19(3): 365–381.

[11] Tsatsaronis G. *Design Optimization Using Exergoeconomics*. In: Bejan A, Mamut E, editors. Thermodynamic Optimization of Complex Energy Systems. Kluwer Academic Publishers, 1999. p. 101–115.

[12] Roy-Aikins JEA. *XAG: a tool in the design improvement of power plants*. Undergoing a review for publication in the Proceedings of the Institution of Mechanical Engineers.

[13] Bejan A, Tsatsaronis G, Moran MJ. *Thermal Design and Optimization*. New York: J. Wiley, 1995.

[14] Roy-Aikins JEA. *Thermoeconomic Optimisation of a Hybrid Microturbine and Fuel Cell*. In: Proceedings of the 15th International Conference on Efficiency, Costs, Optimization, Simulation and Environmental Impact of Energy Systems, Berlin, 2002.

Proceedings of ECOS 2005
Trondheim, Norway
June 20–22, 2005

MINIMIZING THE ENTROPY PRODUCTION IN A CHEMICAL PROCESS FOR DEHYDROGENATION OF PROPANE

A. Røsjorde[1,*], S. Kjelstrup[1], E. Johannessen[1] and R. Hansen[2]

[1] *Department of Chemistry, Norwegian University of Science and Technology, Trondheim, Norway*
[2] *Statoils Research Centre, Rotvoll, Norway*

Abstract

We minimize the total entropy production of a process designed for dehydrogenation of propane. The process consists of 21 units, including a plug-flow reactor, a partial condenser, two tray distillation columns and a handful of heat exchangers and compressors. The units were modeled in a manner that made them little sensitive to changes in the molar flow rates, to make the optimization more flexible. The operating conditions, and to some degree the design of selected units, which minimized the total entropy production of the process, were found. The most important variables were the amount of recycled propane and propylene, conversion and selectivity in the reactor, as well as the number of tubes in the reactor. The optimal conversion, selectivity and recycle flows were results of a very clear trade-off among the entropy produced in the reactor, the partial condenser and the two distillation columns. Although several simplifying assumptions were made for computational reasons, this shows for the first time that it is also meaningful to use the entropy production as an objective function in chemical engineering process optimization studies.

Keywords: Entropy production rate, propane dehydrogenation, optimization.

INTRODUCTION

Large amounts of high quality energy are spent in the chemical process industry to convert raw materials into desired products. The art of process design and optimization is continuously being developed [1, 2]. In this paper we study the energy efficiency of a chemical process, a topic that so far has received little attention.

We have previously studied the state of minimum entropy production in several process units [3, 4, 5, 6, 7]. These studies gave insight in the design of the particular units with more or less fixed boundary conditions. In a process, each unit has few or no boundary conditions; the boundary conditions are placed on the process itself. Optimization of a process, the topic of the present work, may thus likely give very different results from optimization of single units.

In a chemical process, the aim is to convert a feedstock into products of certain purities. Typically, this is done with a reactor(s) that transforms the raw materials, followed by a separation to obtain the desired purity. One particularly important question in such chemical processes is: How does the selectivity and conversion in the reactor affect the downstream separation section? We shall see that the composition and flow rate of the recycle streams, as well as the operation of reactors and separation equipment, will have a large influence on the overall energy efficiency of the process.

We study the production of a fixed amount and quality of propylene from propane. Propylene is mostly used for production of polypropylene, a polymer with numerous applications. An emerging technology is the dehydrogenation of propane, which presently accounts for a small share of the total propylene production in the World. This share is expected to increase due to higher demands for propylene and because the dehydrogenation process uses propane instead of higher alkanes as feed [8].

[*] Corresponding author. *E-mail address:* audunro@phys.chem.ntnu.no.

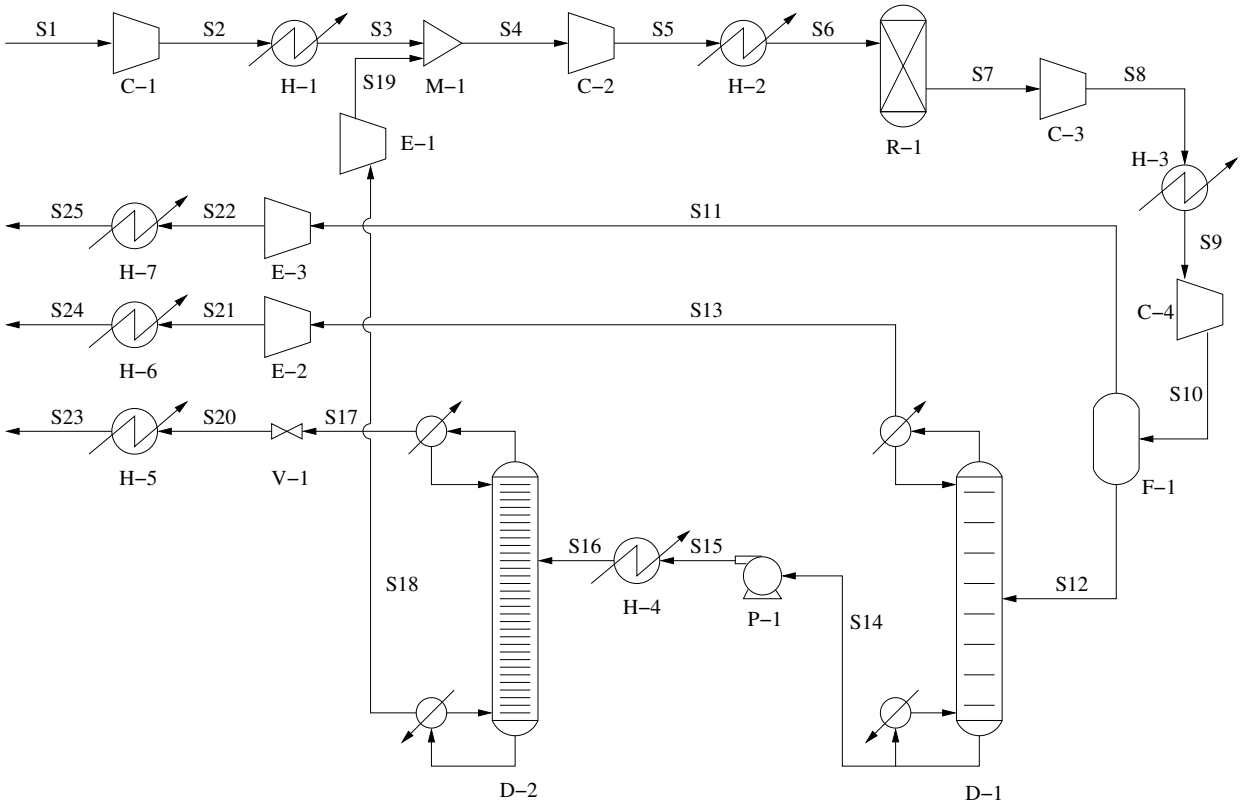

Figure 1: Flow sheet showing the propane dehydrogenation process. Symbols are explained in the text.

We have here chosen to minimize the entropy produced in the propane dehydrogenation process inspired by Linde's design [9]. The complete process consists of hundreds of units, but we study a simplified version where the main features are preserved. We concentrate our effort on finding the operating conditions of the process that give the least entropy production, without changing the structure of the process.

The most important result from this study is that there exists a meaningful trade-off in the energy efficiency among a handful of units, and that it may be found by minimizing the total entropy production of the process. The exact numerical values for operating conditions are of less importance, because of the assumptions that are used.

THE PROPANE DEHYDROGENATION PROCESS

The process we study in this work, is a simplified version of the propane dehydrogenation process designed by Linde [9]. One of the central process units is the dehydrogenation reactor in which the following two reactions are the dominating ones [10]:

$$C_3H_8 = C_3H_6 + H_2 \quad \text{(I)}$$

$$C_3H_8 = C_2H_4 + CH_4 \quad \text{(II)}$$

The expression for the reaction kinetics of reaction (I) was given by [11]. No expression that included the backward reaction of reaction (II) was found, so we guessed an expression [12].

According to the two reactions, the system contains five components: Hydrogen (H_2), methane (CH_4), ethylene (C_2H_4), propylene (C_3H_6) and propane (C_3H_8). We neglect other species that normally would be present in a real dehydrogenation process, among them water.

A flow sheet of the dehydrogenation process is shown in Fig. 1. The process consists of 21 units, and the chosen superstructure is an attempt to keep the main features of a real dehydrogenation process [13, 9, 8, 14]. Fresh feed enters the process and is mixed with a recycle stream before entering the reactor (R-1).

Equal amounts of hydrogen and propylene are formed in the reactor, along with some methane and ethylene. In order to separate the hydrogen from the main process stream, the pressure is increased and the temperature lowered before the stream enters a condenser (F-1), after which mostly hydrogen still is in the vapor phase. The remaining products are fed to two distillation columns in series (D-1 and D-2). The distillation column D-1 separates C_2-components from C_3-components. The distillate of the propane-propylene splitter (D-2) contains most of the propylene product, while the bottom stream is used as recycle to the reactor.

In at least three positions, heat exchangers must remove heat at cryogenic conditions (the temperature of the cooling fluid is then lower than the environmental temperature). First, the condenser (F-1) must operate under high pressure (15-25 atm), but also at very low temperatures (ca. 230 K) to ensure that a liquid phase of the heaviest components is present. Second, the top condenser in D-1 must work under quite similar conditions as those of F-1. Third, the required temperature of the cooling medium in the top condenser in D-2, may be below 298 K if the pressure is low. A refrigeration cycle consisting of four units is used to supply these cold heat exchanger fluids [13]. Using propane as the working fluid, temperatures no lower than 230 K could be obtained.

CALCULATIONS

We did two kinds of calculations: First, we found a set of initial operating conditions for the process by using a numerical solver. Second, we used this information as the initial guess in a minimization of the total entropy production, using a numerical optimization routine.

Every unit in the process under consideration had several design parameters that determined how that unit changed the process stream (for instance length of reactor, etc.). We chose to keep most of these parameters fixed during this study and did only allow to vary the *load* , or in a few cases other parameters, on each unit. With the load, we mean the amount of heat transferred in a heat exchanger, the work input to a compressor, the fractional recovery of a distillation column, etc. The values of the fixed unit parameters are given in Tab. 1.

Each unit were modeled according to widely used textbooks [17, 18].

Table 1: Process unit parameters. Reactor and catalyst parameters taken from [15] and compressor efficiency from [16].

Unit	Parameter	Value
Reactor	Length [m]	8.0
	Diameter [m]	0.2
	Heat transfer number [W/m^{2}K]	56.784
	Catalyst dens. [kg cat./m^3]	984.4
	Void of catalyst bed	0.45
	Catalyst particle diameter [m]	$4.572{\cdot}10^{-3}$
	Gas viscosity [kg/sm]	$3.7204{\cdot}10^{-5}$
	Residence time [s]	5
Heat ex.	Pinch, ΔT [K]	50
Comp./exp.	Efficiency, $\eta_{c/e}$	0.8
Dist. D-1	Number of trays, N	8
	Feed tray, N_F	6
	Light key, LK	3
	Heavy key, HK	4
Dist. D-2	Number of trays, N	100
	Distillate comp., $x_{D,LK}$	0.99

The following properties were chosen for the fresh feed stream to the process [13]: T_1 = 275 K, P_1 = 1 atm, F = [1, 1, 1, 1, 96] mol/s. The components in this vector are ranged from the lightest to the heaviest. We use this notation to describe the composition of the process stream from now on. The temperature and pressure of the three process streams exiting the process, were set to 310 K and 1 atm, respectively. The environmental temperature, T_0, was set to 298 K. All physical and thermodynamical properties were taken from [19] and [20]. The molar enthalpy, entropy and fugacity coefficients were derived from the Soave-Redlich-Kwong equation of state with the binary interaction parameters equal to 0 [21].

Modeling the process

For a given temperature, pressure and flow rates of the five components at the inlet of the process, we calculated sequentially the change each unit did to the process stream. All parameters in Tab. 2, except T_{19}, F_{19,C_3H_6} and F_{19,C_3H_8}, were fixed to a set of reasonable values. Initially, the state of the recycle stream was not known, and it was necessary to solve the following three equations to find the right values

of T_{19}, F_{19,C_3H_6} and F_{19,C_3H_8}:

$$\hat{T}_{19} - T_{19} = 0 \quad (1)$$

$$\hat{F}_{19,C_3H_6} - F_{19,C_3H_6} = 0 \quad (2)$$

$$\hat{F}_{19,C_3H_8} - F_{19,C_3H_8} = 0 \quad (3)$$

where the variables with a hat symbol represent the guessed values and those without represent the values found after calculating through the whole process. The numerical solver *fsolve* from the Optimization Toolbox in Matlab R13, MathWorks Inc. was used to find the solution to the above nonlinear problem.

With the correct values of the recycle stream (given in Tab. 2) we calculated all properties of the process like duties of heat exchangers, work of compressors, entropy production of each unit etc. The set of values for the properties given in Tab. 2 were used as initial guess in the optimization problem. We will therefore refer to this process as the *initial* process.

Optimizing the process

To find the state of minimum entropy production of the propane dehydrogenation process, we used the sum of the entropy produced by each of the 21 units as the objective function:

$$\left(\frac{dS}{dt}\right)^{\text{irr}}_{\text{process}} = \sum_{i=1}^{21} \left(\frac{dS}{dt}\right)^{\text{irr}}_{i} \quad (4)$$

where $(\frac{dS}{dt})^{\text{irr}}_i$ was the entropy production of unit i.

The variables we used in this optimization problem are listed in Tab. 2, along with their initial values. Table 2 gives also the fractional recovery, FR, of the two distillation columns, defined as [17]:

$$FR = \frac{Dx_{\text{D,LK}}}{Fx_{\text{F,LK}}} \quad (5)$$

where D and F are the molar flow rate of distillate and feed stream, respectively. Furthermore, $x_{\text{D,LK}}$ and $x_{\text{F,LK}}$ are the mole fractions of the light key component in the distillate and feed stream, respectively. The light (LK) and heavy (HK) key components are the components that we wish to separate in distillate and bottom product of the distillation column, respectively.

Upper and lower boundaries were set for the variables in order to avoid breakdown of the models (i.e negative pressures in reactor).

Table 2: Variables in the optimization: Initial and optimal values.

Unit	Variable	Init./opt.
Compressor (C-1)	P_2 / atm	3.0 / 2.3
Heat exchanger (H-1)	T_3 / K	500 / 494
Mixer (M-1)	T_{19} / K	261 / 250
	F_{19,C_3H_6} / mol/s	0.72 / 10.5
	F_{19,C_3H_8} / mol/s	99.4 / 27.9
Compressor (C-2)	P_5 / atm	5.0 / 2.0
Heat exchanger (H-2)	T_6 / K	1100 / 1099
PFR reactor (R-1)	T_a / K	1300 / 1343
Compressor (C-3)	P_8 / atm	10.0 / 25.0
Heat exchanger (H-3)	T_9 / K	500 / 460
Compressor (C-4)	P_{10} / atm	15.0 / 19.0
Condenser (F-1)	T_{12} / K	230 / 251
Distillation (D-1)	RR	10.0 / 9.8
	FR	0.99 / 0.986
Pump (P-1)	P_{15} / atm	15.0 / 18.0
Heat exchanger (H-4)	T_{16} / K	300 / 310
Distillation (D-2)	FR	0.99 / 0.87

As equality constraints we used the three Eqs. (1)-(3) in addition to the following demand on the production of propylene:

$$F^{\text{init}}_{17,C_3H_6} - F_{17,C_3H_6} = 0 \quad (6)$$

where $F^{\text{init}}_{17,C_3H_6}$ was the flow of propylene out of the propane-propylene splitter (and thus out of the process) in the initial process. A constant purity of the propylene product was ensured by always enforcing $x_{\text{D,LK}} = 0.99$ in D-2.

To find the minimum of Eq. (4) we used the function *fmincon* from the Optimization Toolbox in Matlab. This function solves numerically constrained nonlinear optimization problems by employing a sequential quadratic programming algorithm.

To reduce the required computational time needed to find the optimum, we made the additional assumption that the process stream entering the propane-propylene splitter (D-2) consisted of propylene and propane only. This means that traces of the three lightest components were technically removed before D-2, making it a binary distillation. Since any components that are lighter than propylene will almost exclusively end up in the distillate of D-2, we added the following inequality constraint on the content of C_2H_4 in the bottom stream from D-1 (and thus the feed stream to D-2):

$$F_{14,C_2H_4} - F^{\text{init}}_{14,C_2H_4} \leq 0 \quad (7)$$

By keeping the amount of ethylene at least as low as in the initial process, we reduced the error associated with the assumption of a binary distillation in D-2.
To further reduce the required computational time, we compiled a table with the entropy production, product temperatures etc., for different combinations of variables in D-2, before we did the process optimization. For four values of the feed mole fraction, fractional recovery, feed temperature and pressure, we carried out 256 simulations of D-2. We used this four-dimensional table instead of solving the distillation model itself when we optimized and modeled the process.

RESULTS

By solving Eqs. (1)-(3) we found the properties of the recycle stream that corresponded to the operating conditions chosen as in the initial process.
The residence time of 5 seconds was fulfilled with a number of tubes in the reactor equal to 72, giving a conversion of propane and selectivity toward propylene of 0.47 and 0.82, respectively.
The total entropy production of the initial process was 95.21 kW/K. Most of this entropy was produced in the reactor (R-1) and the three separation units (F-1, D-1, D-2). Around 24% of the total entropy production was due to the presence of cryogenic heat exchange in the three separation units. In Tab. 3 we have given the net work and heat added to the process.
By minimizing the entropy production as described in Calculations, we found a new set of operating conditions that gave the same product flow rate as the initial process (due to the constraints Eqs. (6) and (7)). The most important results can be summarized in three points:

- The amount of recycle was reduced from 100.1 mol/s to 38.4 mol/s.
- The conversion of propane increased from 0.47 to 0.74, while the selectivity toward propylene increased from 0.82 to 0.92.
- The pressure in the separation section attained the highest allowed value, thus reducing the need for cryogenic heat exchange.

The number of tubes in the reactor in the optimized process was calculated to be 124. A conversion and a selectivity of 0.74 and 0.92, respectively, was found in the reactor. Detailed values of the optimization variables are given in Tab.2.

The optimal process had an entropy production of 44.66 kW/K of which 12% was due to cryogenic heat transfer. The net work and heat added to the process is shown in Tab. 3.

As a consequence of the optimization, the total entropy production of the propane dehydrogenation process was reduced with 53%, or 50.6 kW/K. Six units produced the majority of the total entropy in both the initial and optimal process: H-2, R-1, C-3, F-1, D-1 and D-2. Each of these contributions, from both processes, is shown in Fig. 2.

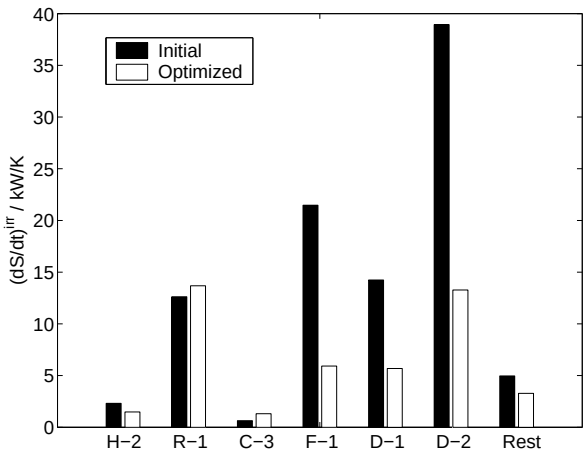

Figure 2: Entropy production in the 6 most significant units and the rest of the process, both in the initial and optimal process.

The entropy production due to the cryogenic process units, all of these located in the separation part (F-1, D-1 and D-2), decreased with 75% or 16.8 kW/K. This lead to a large reduction in the net work added, as shown in Tab. 3.

Table 3: Net work and heat added to the initial and optimal process.

	Net work [kW]	Net heat [kW]
Initial	21140	-11350
Optimal	13100	-2840
Change	-8040	8510

DISCUSSION

The most important result of this study is that we were able to formulate and solve an optimization problem using the entropy production of a chemical process as the objective function.

From the initial process, we know the variables that have the greatest impact on the entropy production of the process. There is little knowledge of whether the initial process is reasonable, however. The operating conditions of the initial process were not taken from a real, existing process, but were rather obtained through qualified guesses. The results from the optimization must be understood with this perspective in mind.

The great reduction of the total entropy production of the process, was due to the three major changes listed in the end of Results. It is apparent that the reduced recycle flow reduced the flow through most parts of the process with 30-40%. This translates almost directly into equivalent reductions in the entropy production. In other words: 55-75% of the demonstrated reduction in entropy production was caused by the reduced recycle flow. Furthermore, a simple estimate shows that the reduction in entropy production due to cryogenic heat exchange was partly due to the reduced process flow, but mainly due to higher temperatures for heat exchange. Approximately 20% of the decrease in total entropy production can be traced back to the increased heat exchange temperatures in F-1, D-1 and D-2. The last 5-25% of the reduction is likely to come from the increased selectivity toward propylene in the reactor, which lead to less work needed in the separation section.

The reduced entropy production translated into changes in the work and heat added to the process. When adding the work needed in all units, the results show that 8040 kW less work was needed to operate the optimal process. An approximately equal decrease in the released heat was found. As expected, the general tendency was that heat was supplied to the process at lower temperatures (except those with cryogenic conditions), while heat was released at higher temperatures.

To obtain further improvements in the entropy production, more variables could be added to the optimization (unit design), the process could be more integrated, and units could be upgraded. The design and operation of the heat exchanger network [22] may be included in the optimization. This requires, however, a very different mathematical treatment.

The reactor was modeled as a one-dimensional plug-flow reactor with side firing. Of the two reactions, only one reaction rate was founded on experimental results. The predictive ability of the reactor was thus probably low. The rate of the second reaction was chosen to never dominate the first reaction, since the purpose of including the second reaction was to introduce impurities.

Both distillation columns were modeled assuming equilibrium between the vapor and liquid that left each tray. This assumption gave a too high performance of the columns. No fluid dynamics were accounted for inside the columns and this also contributed to make the separation too efficient compared to a real column.

In general, most of the units were lacking the level of detail necessary to predict the detailed behavior of the real process. Some simplifications were done in order to make the optimization converge fast, while other, more critical assumptions were done due to lack of better models (i.e. the reaction rate expression). Most of the models of the units seem to have underestimated the entropy production. However, it was not the absolute value of the entropy production, but rather how it varied, that was of principal interest.

In order to find the solution of the optimization problem in a reasonable amount of time, several limitations and simplifications were introduced. This was partly due to the choice of numerical solver and partly due to a desire to use less than a few days of computational time to find the optimum. A fixed superstructure of the process was the most serious limitation in the optimization. To include the different interconnections and alternative units as variables gives a highly complex optimization problem. At the present stage in the method development this was not seen as necessary. We concentrated instead on the effect of finding the best operating conditions.

To develop the methodology based on minimization of the entropy production, it seems necessary to include both a heat exchanger network (see e.g. [22]) and allow the superstructure of the process to vary

(see e.g. [23]). Furthermore, a very interesting possibility is to perform entropy production minimizations with additional constraints on the operating or capital cost. Several of these optimizations would give valuable information of the additional cost associated with increasing the energy efficiency of a process, as recently demonstrated by [24].

To the authors' knowledge, this is the first time a minimization of the entropy production has been carried out for a chemical process. It is difficult to extract general knowledge from this kind of optimization but the questions answered is a classical chemical engineering question: How far does it pay to operate the reactor to avoid to pay in the separation section? It is interesting to see that there is a possibility for larger gains, to be found through optimization. This illustrates that there is a potential for similar optimizations to ensure high energy efficiency of chemical processes.

CONCLUSION

We have shown in this work that it is meaningful to use the entropy production in a chemical process as objective function in an optimization that aims to find the most energy efficient state of operation and, in some aspects, design. A process where propylene was produced in a dehydrogenation reactor from propane was studied. A plausible initial process was chosen as reference, inspired by Linde's design. The optimal process gave a large reduction in entropy production, for feasible new operating conditions. In both the initial and optimal process, the units with the largest entropy productions were the reactor, partial condenser and the two distillation columns. The results show that there was a large gain possible in the separation part of the process, by reducing the recycle stream. A higher conversion of propane and selectivity toward propylene in the reactor also contributed to reduce the entropy produced in the distillation column separating propylene from propane. Finally, we found that a higher operating pressure in parts of the process reduced the need for cryogenic heat exchange.

Assumptions and models, introduced to have reasonable computational times in the initial phase, can now be improved. Most important is to include water among the species in the process and implement the corresponding expressions for the reaction rates in the two reactions. To improve the energy efficiency of the process further, a reasonable strategy will be to include a heat exchanger network and a variable superstructure in the optimization. Future stages in the development of these procedures should include economic optimizations.

ACKNOWLEDGMENTS

Statoil's VISTA program is thanked for the financial support to Audun Røsjorde. The Norwegian Research Council is thanked for the financial support to Eivind Johannessen.

REFERENCES

[1] Smith R. *Chemical process design*. McGraw-Hill, 1995.

[2] Edgar TF, Himmelblau DM , Lasdon LS. *Optimization of chemical processes*. Singapore: McGraw-Hill, 2001.

[3] Johannessen E, Nummedal L, Kjelstrup S.. *Minimizing the entropy production in heat exchange*. Int. J. Heat Mass Transfer 2002; 45:2649–2654.

[4] Johannessen E, Kjelstrup S. *Minimum entropy production rate in plug flow reactors. An optimal control problem solved for SO_2 oxidation*. Energy 2004; 29(12-15):2403–2423.

[5] Nummedal L, Costea M, Kjelstrup S. *Minimizing the entropy production rate of an exothermic reactor with constant heat transfer coefficient: The ammonia reactor*. Ind. Chem. Eng. Res. 2003; 42:1044–1056.

[6] De Koeijer GM, Johannessen E, Kjelstrup S. *The second law optimal path of a four-bed SO_2 converter with five heat exchangers*. Energy 2004; 29(4):525–546.

[7] Røsjorde A, Kjelstrup S. *The second law optimal state of a diabatic binary tray distillation column*. Chem. Eng. Sci. 2005; 60:1199.

[8] Kirk-Othmer. *Encyclopedia of Industrial Chemistry*. Wiley, 1994.

[9] Rytter E, Bölt H. *An improved process for catalytic dehydrogenation of propane to propylene*. In: Proceedings of CatCon, Houston, USA, 2000.

[10] Sundaram KM, Froment G.F. *Modeling of thermal cracking kinetics - I*. Chem. Eng. Sci. 1977; 32:601–608.

[11] Loc LC, Gaidai NA, Kiperman SL, Thoang HS. *Kinetics of propane and n-butane dehydrogenation over platinum-alumina catalysts in the presence of hydrogen and water vapor*. Kinetics and Catalysis 1996; 37(6):851–857.

[12] Røsjorde A, Johannessen E, Kjelstrup S. *Minimizing the entropy production in two heat exchangers and a reactor*. In: Proceedings of Energy-Efficient, Cost-Effective and Environmentally-Sustainable Systems and Processes, Copenhagen, Denmark, 2003.

[13] Bohnet M, editor. *Ullmann's encyclopedia of industrial chemistry*. Wiley, 2003.

[14] Pujado PR, Vora BV. *Make C_3-C_4 olefins selectively*. Hydrocarbon processing 1990, March:65–70.

[15] Fogler HS. *Elements of Chemical Reaction Engineering*. New York: Prentice-Hall, 1992.

[16] Perry RH, Green DW. *Perry's Chemical Engineers Handbook*. New York: McGraw-Hill, 1997.

[17] McCabe W, Smith J, Harriot P. *Unit Operations of Chemical Engineering*. New York: McGraw-Hill, 1993.

[18] Seader WD, Seader JD, Lewin DR. *Process design principles: synthesis, analysis, and evaluation*. Wiley, 1999.

[19] Aylward G, Findlay T. *SI Chemical data*. Wiley, 1994.

[20] Daubert TE, Danner RP. *Physical and Thermodynamic Properties of Pure Chemicals. Data Compilation*. Washington: Hemisphere, 1992.

[21] Prausnitz JM, Lichtenthaler RN, de Azevedo EG. *Molecular thermodynamics of fluid-phase equlibria*. New Jersey: Prentice Hall PTR, 1999.

[22] Gundersen T, Naess L. *The synthesis of cost optimal heat exchanger networks*. Heat Recovery Systems & CHP 1990; 10:301–328.

[23] Grossmann IE, Daichendt MM. *New trends in optimization-based approaches to process synthesis*. Comput. Chem. Eng. 1996; 20:665–683.

[24] Toffolo A, Lazzaretto A. *Evolutionary algorithms for multi-objective energetic and economic optimization in thermal system design*. Energy 2002; 27:549–567.

Proceedings of ECOS 2005
Trondheim, Norway
June 20–22, 2005

OPTIMAL PERFORMANCE CHARACTERISTICS OF AN IRREVERSIBLE COMBINED CHEMICAL PUMP

Zhengrong Xia[a] ,Guoxing Lin[a,b,]*, Ben Hua[b]
[a)] Department of Physics, Xiamen University, Xiamen 361005, P R China

[b)] Chemical Engineering Research Institute, South China University of Technology, Guangzhou 510642, P R China

ABSTRACT

An irreversible cycle model of a combined chemical pump is set up, in which mass transfer irreversibility between the cyclic working fluid and the mass reservoirs and mass leak between the two mass reservoirs are taken into account. On the basis of the new cycle model, by using the optimal control theory method, the optimal relationship between the coefficient of performance and the rate of energy pumping is derived. Furthermore, the maximum coefficient of performance and the corresponding rate of energy pumping, the optimal chemical potentials in the iso-chemical-potential processes, the minimum power input and some other performance parameters are analyzed and discussed. The results obtained provide insight into the design of combined chemical pumps to achieve their optimum performance. The conclusions are of practical values to mass exchangers, chemical reactive devices, electrochemical, photochemical and solid state devices.

***Keywords*:** Chemical pump, Combined cycle, Irreversibility, Optimization

NOMENCLATURE

h	Coefficient of mass transfer
h_L	Coefficient of mass leak
P	Power input
W	Work input
t	Time of mass transfer
ΔN	Transferred mass
χ	Coefficient of performance
μ_H	Chemical potential of high chemical potential reservoir
μ_L	Chemical potential of low chemical potential reservoir
μ	Chemical potential of the working fluid
τ	Cycle period
Σ	Rate of energy pumping

---

*Corresponding author : Fax: +86-592-2189426; E-mail : gxlin@xmu.edu.cn

INTRODUCTION

In recent years, the theory of the optimum thermodynamics and the entropy generation minimization [1,2] have been extended to the chemical reaction, the chemical engine and chemical pump. De Vos [3], Gordon *et al*. [4,5], Chen *et al*. [6,7] and Lin *et al* [8] analyzed the

optimal performance characteristics of chemical engines. Lin *et al* [9-11] investigated the general performance characteristics of the two-source and three-source chemical pumps. Chen *et al* [6] explored the optimal cycle performance of the combined chemical engine. These works are of practical value for many chemical cycle devices and have provided us a good overview of possible developments and applications of chemical engines and chemical pumps. Similar to the combined heat pump [12,13], when the span of the chemical potentials of the two mass reservoirs is very large, a combined chemical pump is needed in order that we can upgrade some substance located in a low chemical potential region to a higher chemical potential region so that they can be more effectively utilized. So far the investigation on the cyclic performance of combined chemical pump has not been made. For this reason, it is a new and significant work to study the optimal performance characteristics of a combined chemical pump cycle. In the present paper, the general performance characteristics of the combined chemical pump cycle are studied and the influence of finite rate mass transfer and mass leak on the cyclic performance of the combined chemical pump is revealed. Furthermore, some important performance parameters are discussed and evaluated. The results obtained can provide some theoretical guidance for mass exchanger, electrochemical, photochemical and solid-state devices as well as development of some new type of chemical pumps.

A COMBINED CHEMICAL PUMP CYCLE MODEL

An irreversible combined chemical pump, which is operated between two mass reservoirs at

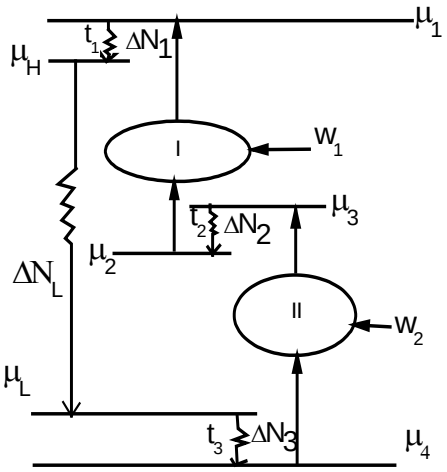

Figure 1: Schematic diagram of an irreversible combined chemical pump cycle

constant chemical potential μ_H and μ_L, consists of the chemical pumps I and II, as shown in figure 1, where μ_1, μ_2 and μ_3, μ_4 are, respectively, the chemical potentials of the working fluid in two iso-chemical-potential processes of chemical pump cycles I and II. It should be pointed out that the iso-chemical-potential processes result from linearized mass transfer law [4-11]. And, $\mu_1 > \mu_H > \mu_3 > \mu_2 > \mu_L > \mu_4$; W_1 and W_2 are the work input of chemical pump cycles I and II; ΔN_1 and ΔN_3 are the exchanged mass between the cyclic working fluid and the reservoirs μ_H and μ_L; t_1 and t_3 are the corresponding mass transfer times; Moreover, ΔN_2 is the exchanged mass between the two iso-chemical -potential processes μ_3 and μ_2 and the corresponding time of mass exchange is t_2. As the combined heat pump, t_2 in the combined chemical pump cycle is the public mass exchange time of chemical pumps I and II. Therefore, it is natural to assume $t_1 = t_3$ in order to make the combined chemical pump operate

normally [6,13,14].

In order to isolate and more transparently illustrate the results that are uniquely related to the process of mass transfer across a difference in chemical potentials, our consideration is restricted to an isothermal combined chemical pump. On the other hand, it is assumed that mass exchange obeys the mass transfer law of linearized irreversible thermodynamics [3-11], i.e.,

$$\Delta N_1 = h_1(\mu_1 - \mu_H)t_1 \qquad (1)$$

$$\Delta N_2 = h_2(\mu_3 - \mu_2)t_2 \qquad (2)$$

$$\Delta N_3 = h_3(\mu_L - \mu_4)t_3 \qquad (3)$$

where h_1, h_3 and h_2 are the mass transfer coefficients between the working fluid and the two reservoirs and between the iso-chemical-potential processes μ_3 and μ_2, respectively. In addition, it is inevitable that there exists mass leak in the combined chemical pump and it is assumed that the mass leak is proportional to the chemical potential difference of the two reservoirs, i.e.,

$$\Delta N_L = h_L(\mu_H - \mu_L)\tau \qquad (4)$$

where τ is the cycle period of the combined chemical pump. It should be pointed out that except for the mass exchange branches, there exist other additional branches of the cycle that connect the mass exchange branches. These branches may be regarded as instant**.** Although instantaneous change is clearly impossible in a real cyclic device, the time spent on the connecting branches without mass exchange is sufficiently short compared with the time spent on the mass exchange branches so that it can be treated as negligible for analytic purpose. Therefore, based on $t_1=t_3$ and above analysis, the cycle period of the combined chemical pump may be written as

$$\tau = t_1 + t_2 \qquad (5)$$

This implies that the processes of mass transfer between the working fluid and the two reservoirs is carried out synchronously [14].

THE FUNDAMENTAL OPTIMAL RELATIONSHIP

Based on figure 1, one has the total work input of the combined chemical pump cycle

$$W = W_1 + W_2 \qquad (6a)$$

where

$$W_1 = \Delta N_1(\mu_1 - \mu_2) \qquad (6b)$$

$$W_2 = \Delta N_2(\mu_3 - \mu_4) \qquad (6c)$$

From the law of mass conservation, it yields

$$\Delta N_1 = \Delta N_2 = \Delta N_3 \equiv \Delta N \qquad (7)$$

Thus, according to the definition of rate of energy pumping[9-11] , we have

$$\sum = \frac{\mu_H(\Delta N - \Delta N_L)}{\tau} \qquad (8)$$

Substituting equations (5), (6), (7) and (8) into the definition of coefficient of performance [9-11] yields

$$\chi = \frac{\Sigma}{W/\tau} = \frac{\mu_H(\Delta N - \Delta N_L)}{[(\mu_1 - \mu_2) + (\mu_3 - \mu_4)]\Delta N} \qquad (9)$$

By substituting equations (1)-(3) into equations (8) and (9), the rate of energy pumping and the coefficient of performance are expressed as

$$\Sigma = \frac{\mu_H(\beta - \mu_H\chi_r^{-1})}{\alpha} - h_L\mu_H^{\,2}\chi_r^{-1} \qquad (10)$$

$$\chi = \frac{\mu_H(\beta - \mu_H\chi_r^{-1}) - h_L\mu_H^{\,2}\chi_r^{-1}\alpha}{\beta(\beta - \mu_H\chi_r^{-1})} \qquad (11)$$

where $\alpha = (1+\lambda)/h_0 + (1+\lambda^{-1})/h$, $\lambda = t_2/t_1$ is a dimensionless parameter, $h_0 = h_1h_3/(h_1+h_3)$, $h = h_0h_2/(\sqrt{h_0}+\sqrt{h_2})^2$. $\chi_r = \mu_H/(\mu_H - \mu_L)$ is the coefficient of performance of the reversible two-source chemical pump [9] operating between

μ_H and μ_L and $\beta=\mu_1-\mu_2+\mu_3-\mu_4$. In view of equations (10) and (11), we can see that both the rate of energy pumping Σ and the coefficient of performance χ are functions of λ and β when other parameters are given. And our objective is to find out the maximum coefficient of performance for the combined chemical pump cycle. For this reason, by using the optimal control theory and the extreme condition $\partial\chi/\partial\lambda=0$ or $\partial\Sigma/\partial\lambda=0$, one can obtain when

$$\lambda=\sqrt{h_0/h_2} \quad , \tag{12}$$

the coefficient of performance χ attains its extremum. By substituting equation (12) into equations (10) and (11), the rate of energy pumping Σ and the coefficient of performance χ are rewritten as

$$\Sigma=h\mu_H(\beta-\mu_H/\chi_r)-h_L{\mu_H}^2/\chi_r \tag{13}$$

$$\chi=\frac{\mu_H(\beta-\mu_H/\chi_r)-h_L{\mu_H}^2/(h\chi_r)}{\beta(\beta-\mu_H/\chi_r)} \tag{14}$$

Furthermore, combining equations (13) with (14), one can obtain the relationship between the optimal coefficient of performance and the rate of energy pumping is given by

$$\chi=\frac{1}{[\Sigma/(h{\mu_H}^2)+(1+h_L/h)/\chi_r][1+h_L{\mu_H}^2/(\chi_r\Sigma)]} \tag{15}$$

Equation (15) is the optimal relationship between the rate of energy pumping and the coefficient of performance and also called as the fundamental optimal relationship of the irreversible combined chemical pump cycle. From it, the optimal performance characteristics of the combined chemical pump affected by the mass transfer irreversibility and mass leak can be revealed. Using equation (15), we can generate the Σ^*-χ characteristic curves, as shown in figure 2, where $\Sigma^*=\Sigma/(h_1{\mu_H}^2)$ is the dimensionless rate of energy pumping. Figure 2(a), 2(b) and 2(c) show, respectively, the coefficient of performance χ versus the rate of energy pumping Σ characteristics under different mass transfer coefficients ratio h_2/h_1, different mass leak coefficient h_L and different chemical potentials ratio μ_H/μ_L. Based on figure 2 and the above analysis, the optimal performance characteristics of the combined chemical pump will be discussed further in the following sections.

DISCUSSION

Maximum coefficient of performance

For the irreversible combined chemical pump, there exists a maximum coefficient of performance. In fact, substituting equation (15) into the extreme condition $\partial\chi/\partial\Sigma=0$, we can find that when

$$\Sigma=\Sigma_m={\mu_H}^2\chi_r^{-1}\sqrt{h_L(h_L+h)}\,, \tag{16}$$

the maximum coefficient of performance

$$\chi_{\max}=\{[1+\frac{h_L}{\sqrt{h_L(h_L+h)}}]\frac{1}{\chi_r}+[(h_L(h+h_L))^{1/4}+\frac{h_L}{[h_L(h+h_L)]^{1/4}}]^2\frac{1}{h\chi_r}\}^{-1} \tag{17}$$

Equations (16) and (17) determine the two important performance bounds. Σ_m is not only the rate of energy pumping at the condition of the maximum coefficient of performance but also the allowable values of the lower bounds of the optimum rate of energy pumping. $\chi_{\max}$ is the upper bound of the coefficient of performance. It is clear that these bounds are more realistic and useful than those of classical and endoreversible thermodynamics. As mentioned last section, the coefficient of performance versus the rate of energy pumping characteristics depends closely on

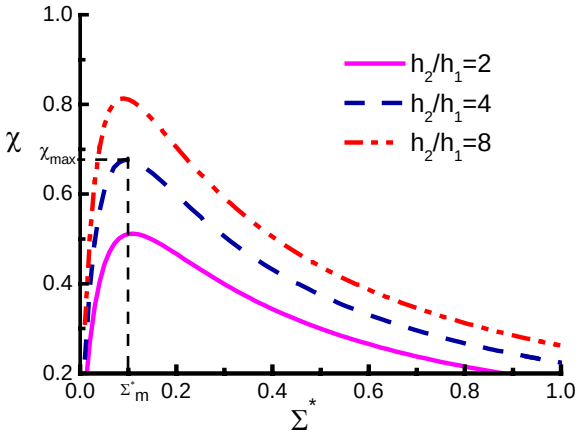

(a)

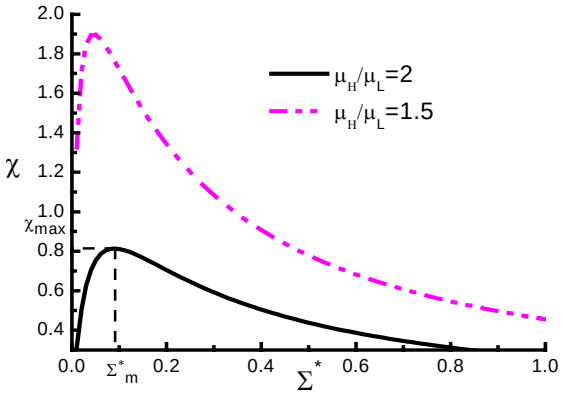

(c)

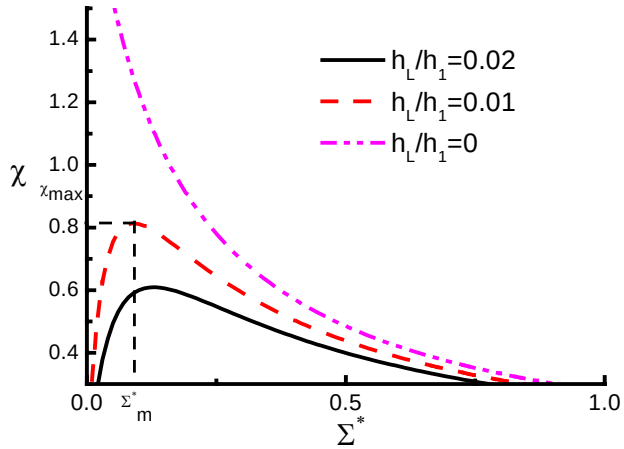

(b)

Figure 2: The coefficient of performance χ versus the dimensionless rate of energy pumping Σ^* curves. Plots are presented for $h_1 = h_3$ and (a) $\mu_H/\mu_L = 2$, h_L/h_1 =0.01 (b) $\mu_H/\mu_L = 2$, $h_2/h_1 = 8$ (c) $h_2/h_1 = 8$, h_L/h_1 =0.01

the mass transfer coefficients, the mass leak coefficient and the chemical potentials of the two reservoirs. Figure 2(a) shows clearly that the coefficient of performance χ increases as the value of h_2/h_1 increases. For example, when h_2/h_1=2, 4 and 8, χ_{max} =0.51, 0.68 and 0.82. It is clear that increasing h_2 or decreasing h_1 is beneficial to increase of the coefficient of performance. On the other hand, we can see from figure 2(b) that the influence of mass leak on the coefficient of performance is obvious. The larger the mass leak coefficient, the smaller the coefficient of performance becomes. For example, when h_L/h_1 = 0.01, χ_{max} =0.82; when h_L/h_1 = 0.02, χ_{max} =0.61. And when the mass leak coefficient, compared with the mass transfer coefficient h_1, is small enough that it can be ignored, there hardly exists any extremum of the coefficient of performance, as shown in figure 2(b). Moreover, the chemical potentials ratio μ_H/μ_L of the two mass reservoirs has also obvious effect on the optimal performance of the combined chemical pump, as shown in figure 2(c). In view of figure 2(c), we can see the coefficient of performance χ decreases as the value of μ_H/μ_L increases, whereas the rate of energy pumping Σ_m at the maximum coefficient of performance hardly changes. As an example, when μ_H/μ_L=2, χ_{max} =0.82, and when μ_H/μ_L=1.5, χ_{max} =1.91. It is clear because increasing the value of μ_H/μ_L will result in the increase of mass leak quantity.

Optimal chemical potentials

From equations (1), (2), (3), (12) and (15), one can obtain

$$\Delta N = (\beta - \mu_H \chi_r^{-1})\tau / h \qquad (18)$$

$$\beta - \mu_H \chi_r^{-1} = \frac{\mu_H (\chi^{-1} - \chi_r^{-1}) + \mu_H A}{2} \qquad (19)$$

When the combined chemical pump is operated in the optimal operating state, we can find the chemical potentials of iso-chemical-potential processes should satisfy

$$\mu_1 = \mu_H + \frac{\mu_H (\chi^{-1} - \chi_r^{-1}) + \mu_H A}{2h_3\sqrt{h_2}/[h(\sqrt{h_0} + \sqrt{h_2})}, \qquad (20)$$

$$\mu_3 - \mu_2 = \frac{\mu_H (\chi^{-1} - \chi_r^{-1}) + \mu_H A}{2h_2\sqrt{h_0}/[h(\sqrt{h_0} + \sqrt{h_2})]}, \qquad (21)$$

$$\mu_4 = \mu_L - \frac{\mu_H (\chi^{-1} - \chi_r^{-1}) + \mu_H A}{2h_1\sqrt{h_2}/[h(\sqrt{h_0} + \sqrt{h_2})]}, \qquad (22)$$

where $A = \sqrt{(\chi^{-1} - \chi_r^{-1})^2 - 4h_L(h\chi_r\chi)^{-1}}$. Obviously, when the coefficient of performance, the mass transfer coefficients and the chemical potentials of the reservoirs are given, as the mass leak coefficient increases, μ_1 and $\mu_3 - \mu_2$ should decrease, whereas μ_4 should increase, otherwise the combined chemical pump can't attain its expected optimum performance.

Minimum power input

For a combined chemical pump, when the rate of energy pumping is given, the minimum total power input is an important performance parameter. Substituting equations (6) into $P = W/\tau$, we find the minimum power input of the combined chemical pump affected by mass transfer irreversibility and mass leak may be expressed as

$$P = h\,\mu_H^{\,2}/4\{[\chi^{-1} + A]^2 - \chi_r^{-2}\} \qquad (23)$$

Then, the minimum power input versus the coefficient of performance curves are shown in figure 3, where $P^* = P/(h\mu_H^{\,2})$ is the dimensionless minimum power input. We can see from equation (23) and figure 3 that the minimum power input decrease with increasing coefficient of performance. As the mass leak coefficient increases, the minimum power input decreases under same coefficient of performance. In other words, as long as the coefficient of performance is same, the larger the mass leak coefficient, the smaller the minimum power input becomes. Because, for the combined chemical pump cycle, the larger the mass leak, the smaller the rate of energy pumping becomes, such that the minimum power input should decrease under same coefficient of performance. Of course, if we want the larger rate of energy pumping and the larger coefficient of performance, increasing the power input becomes necessary.

Optimization of mass transfer times

In order to make the combined chemical pump operate in the optimum operating states, the distribution of the mass transfer times should satisfy certain condition. By using equations (5) and (12), the optimal mass transfer times spent in the mass transfer processes are given by

$$t_1 = \tau/[1 + (h_0/h_2)^{1/2}] \qquad (24)$$

$$t_2 = \tau/[1 + (h_2/h_0)^{1/2}] \qquad (25)$$

In view of equations (24) and (25), we find the optimal distribution of the mass transfer times is

$$\sqrt{h_2}\,t_2 = \sqrt{h_1 h_3/(h_1 + h_3)}\,t_1 \qquad (26)$$

Especially, when $h_1 = h_3$, $t_2/t_1 = \sqrt{h_1/2h_2}$; Furthermore, when $h_2 = 2h_1$, $t_1 = 2t_2$; when $h_1 = 2h_2$, $t_1 = t_2$. These results provide some theoretical guidance for the optimal design of the mass exchanger in the combined chemical pump.

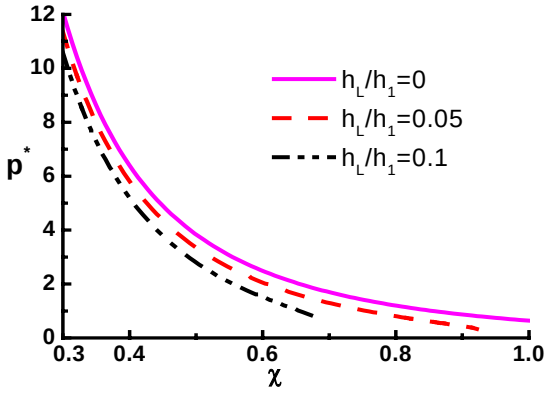

Figure 3: The dimensionless power input P^* versus the coefficient of performance χ curves of the combined chemical pump. Plots are presented for μ_H/μ_L=2, h_1=h_3 and h_2/h_1=8

Special cases

When the mass leak is small enough that it can be neglected, i.e., $h_L \to 0$, equation (15) is simplified as

$$\chi = \frac{1}{\Sigma(h\mu_H{}^2)^{-1} + \chi_r{}^{-1}} \qquad (27)$$

Equation (27) is the fundamental optimal equation of the endoreversible combined chemical pump in which only mass transfer irreversibilities between the working fluid and the two reservoirs and between the iso-chemical-potential processes μ_3 and μ_2 are taken into account. Moreover, if the mass transfer coefficient $h_2 \to \infty$, equation (27) is expressed as

$$\Sigma = \frac{h_1 h_3}{h_1 + h_3}\mu_H{}^2(\chi^{-1} - \chi_r{}^{-1}) \qquad (28)$$

Equation (28) is the optimal relationship between the rate of energy pumping and the coefficient of performance for the two-source endoreversible chemical pump, in which only the mass transfer irreversibility between the cyclic working fluid and the two reservoirs is taken into account.

CONCLUSIONS

A new cyclic model of irreversible combined chemical pump is established. Based on the model, the optimal relationship between the coefficient of performance and the rate of energy pumping is derived. Some important performance bounds are obtained and evaluated. The influence of finite rate mass transfer and the mass leak on the performance of the combined chemical pump cycle is revealed. The optimal chemical potentials in the iso-chemical-potential processes, the minimum power input and the optimal distribution of the mass transfer times are also analyzed and discussed. The results obtained are more general and useful than those of classical and endoreversible thermodynamics and can provide some instructions for the development and optimal design of a combined chemical pump.

ACKNOWLEDGEMENTS

This work has been supported by the State Major Basic Research Development Program (G20000263) and the Scientific Research Foundation of South China University of Technology, People's Republic of China.

REFERENCES

[1] Bejan A. *Advanced Engineering Thermodynamics*. New York: Wiley; 1998

[2] Wu C, Chen L, Chen J. *Recent advances in finite time thermodynamics*. Now York: Nova Science Publishers; 1999

[3] De Vos A. *Endoreversible thermodynamics and chemical reactions*. J. Phys. Chem. 1991,95 (11): 4534-4540

[4] Gordon J, Orlov V. *Performance charac-*

teristics of endoreversible chemical engines. J. Appl. Phys. 1993; 74(9): 5303- 5308

[5] Gordon J. *Maximum work from isothermal chemical engines.* J.Appl. Phys. 1993; 73(1): 8-11

[6] Chen L，Sun F, Wu C. *Maximum power of A-combined isothermal chemical engine,* Applied thermal Engineering 1997; 17(7): 629-637

[7] Chen L，Sun F, Wu C. *Performance of chemical engines with a mass leak.* J Phys. D: Appl Phys 1998; 31:1595- 1560

[8] Lin G, Chen J, Br ü ck E. *Irreversible chemical-engines and their optimal performance analysis.* Applied Energy 2004; 78: 123- 136

[9] Lin G, Chen J. *Optimal analysis on the cycle performance of a class of chemical pumps.* Applied Energy 2001; 70: 35-47

[10] Lin G, Chen J, *General performance characteristics of an irreversible three source chemical pump*. Energy Convers Mgmt. 2003; 44:1719-1731

[11] Lin G, Chen J, Hua B. *Optimal analysis on the performance of a chemical engine-driven chemical pump*. Applied Energy 2002; 72 (1): 359-370.

[12] Kaushik S, Kumer P, Jain S. *Performance evaluation of irreversible cascaded refrigeration and heat pump cycles*. Energy Convers. Mgmt. 2002; 43(17): 2405-2424

[13] Chen J, Wu C. *Performance of a cascade endo-reversible heat pump system.* Journal of the Institute of Energy, 1995; 68: 137-141

[14] Chen J, Yan Z. *Optimal performance of an endoreversible combined refrigeration cycle*. J. Appl. Phys. 1988; 63(10): 4795-4798

Proceedings of ECOS 2005
Trondheim, Norway
June 20–22, 2005

PREDICTION OF ENERGY DEMANDS USING NEURAL NETWORK BY A GLOBAL OPTIMIZATION METHOD

Ryohei Yokoyama*, Makoto Inui, and Koichi Ito
Osaka Prefecture University
Department of Mechanical Engineering
Sakai, Osaka, Japan

ABSTRACT

To operate energy supply systems optimally from the viewpoints of energy and cost savings, it is important to predict energy demands accurately as basic conditions. Several methods of predicting energy demands have been proposed, and one of them is to use multi-layered neural network models. Although gradient methods have conventionally been adopted in the back propagation procedure to identify the values of model parameters, they have the significant drawback that they can derive only local optimal solutions. In this paper, a global optimization method named "Modal Trimming Method" for nonlinear programming problems is adopted in the back propagation procedure to derive global quasi-optimal solutions. The multi-layered neural network model is applied to the prediction of the cooling demand in a building used for a bench mark test of a variety of prediction methods, and its validity and effectiveness are clarified.
Keywords: Prediction, Energy demands, Multi-layered neural network, System identification, Nonlinear programming, Global optimization, Gradient method, Newton-Raphson method, Chaos

NOMENCLATURE

$\hat{a}$	error between measured and predicted values of w or zero [kWh/h]
C	binomial coefficient
D	order of periodic difference
d	order of ordinary difference
F	function composed of objective function
f	objective function
g	function for neurons of hidden layer
h	function for neurons of output layer
I	number of neurons of input layer
J	number of neurons of hidden layer
K	number of neurons of output layer
L	number of sampling times for prediction
M	number of sampling times for measured energy demand
N	number of patterns
p	number of sampling times for values of $\hat{w}$ for prediction
q	number of sampling times for values of $\hat{a}$ for prediction
R	number of sampling times reduced for predicted values of w
s	number of sampling times for periodic differential operation
Δt	sampling time interval [h]
u	weights for neurons between input and hidden layers
v	weights for neurons between hidden and output layers
w	time series data after Dth order periodic differential operation on y [kWh/h]
$\hat{w}$	measured or predicted value of w [kWh/h]
X	input to and output from neurons of input layer
$\boldsymbol{x}$	vector for variables
Y	output from neurons of hidden layers
y	time series data after dth order ordinary differential operation on z [kWh/h]

*Corresponding author: Phone: +81-72-254-9232 Fax: +81-72-254-9904 E-mail: yokoyama@ese.me.osakafu-u.ac.jp

Z output from neurons of output layer
z time series data on energy demand [kWh/h]
α constant coefficient for h
β step width
γ decelerating parameter
η thresholds for neurons of hidden layer
θ thresholds for neurons of output layer
∇ ordinary differential operator
∇_s periodic differential operator
$\tilde{()}_{t'|t}$ value at sampling time t' predicted at sampling time t
$||\ ||_2$ Euclidean norm

Subscripts

i index for neurons of input layer
j index for neurons of hidden layer
k index for neurons of output layer
(m) number of renewal of values of variables
n index for patterns
t, l index for sampling times

Superscripts

T transposition
+ Moore-Penrose generalized inverse
–1 inverse
* tentative global quasi-optimal solution

INTRODUCTION

Distributed energy supply systems have conventionally been operated based on experiences and intuitions of operators for stable energy supply. However, energy and cost savings have recently been required to operators in addition to stable energy supply. Therefore, it has become difficult for operators to operate the systems properly in consideration of energy demands which change with season and time as well as corresponding energy consumptions and costs.

Under these situations, advisory systems which assist operators in operating energy supply systems in real-time manner are required. The basic functions for the advisory systems are to predict energy demands accurately as basic conditions for the operational planning, and to conduct the operational planning properly based on the predicted energy demands from the viewpoints of stable energy supply, and energy and cost savings.

Several methods of predicting energy demands have been proposed, and typical examples are time series analysis and neural network [1–3]. In addition, an optimal operational planning method for the real-time operation of energy supply systems has also been proposed [4], and case studies have been conducted on the operation based on predicted energy demands [5]. Moreover, an effort to coadunate the energy demand prediction and operational planning has been made [3].

In this paper, a multi-layered neural network model is adopted to predict energy demands [6]. The values of model parameters are identified in the back propagation procedure. Local optimization methods such as gradient methods have conventionally been adopted for this purpose. However, they have the significant drawback that they can derive only local optimal solutions. Some global optimization methods have also been proposed [7–9]. Here, a global optimization method named "Modal Trimming Method" is adopted, which has been proposed to derive global quasi-optimal solutions for constrained nonlinear programming problems [10]. The multi-layered neural network model is applied to the prediction of the cooling demand in a building used for a bench mark test of a variety of prediction methods. The results obtained by the global optimization method are compared with those by a conventional gradient method.

PREDICTION MODEL

Removal of trend and periodic change

Before the application of the multi-layered neural network model, the trend and periodic change are removed in time series data on energy demand. Especially, since the energy demand changes periodically with a period of 24 hours, the removal of the periodic change will improve the accuracy of the prediction. Here, the time series data on energy demand is designated by z_t $(t = 1, 2, \cdots)$ with a sampling time interval of Δt.

First, the ordinary differential operation is conducted to remove the trend, and the first order ordinary difference is obtained as follows:

$$\nabla z_t = z_t - z_{t-1} \tag{1}$$

where ∇ is the ordinary differential operator. By conducting this operation d times, the dth order ordinary difference y_t is obtained as follows:

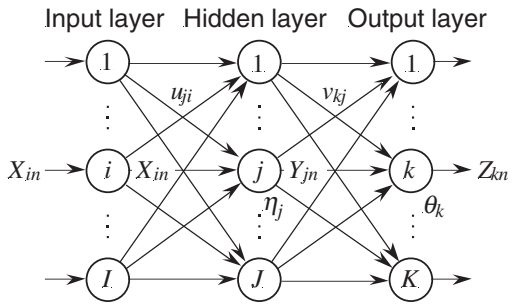

Figure 1: Three-layered neural network model

$$y_t = \nabla^d z_t = \begin{cases} z_t & (d=0) \\ \sum_{e=0}^{d} (-1)^e {}_dC_e z_{t-e} & (d \geq 1) \end{cases} \quad (2)$$

where ${}_dC_e$ is the binomial coefficient which expresses the number of combinations for selecting e elements among d ones.

Second, the periodic differential operation is conducted to remove the periodic change, and the first order periodic difference is obtained as follows:

$$\nabla_s y_t = y_t - y_{t-s} \quad (3)$$

where ∇_s is the periodic differential operator with a period of $s\Delta t$, and s is the number of sampling times for the periodic differential operation. By conducting this operation D times, the Dth order periodic difference w_t is obtained as follows:

$$w_t = \nabla_s^D y_t = \begin{cases} y_t & (D=0) \\ \sum_{e=0}^{D} (-1)^e {}_DC_e y_{t-es} & (D \geq 1) \end{cases} \quad (4)$$

Three-layered neural network model

As shown in Figure 1, a three-layered neural network model is considered. This neural network model is composed of I, J, and K neurons of the input, hidden, and output layers, respectively. To apply this model to the energy demand prediction, the number of neurons of the output layer is set at $K=1$.

Input and output. As output from the model, the value $\breve{w}_{t+l|t}$ at the sampling times $t+l$ ($l = 1, 2, \cdots, L$) predicted at the sampling time t is adopted, where $\breve{(\,)}_{t'|t}$ means the value at the sampling time t' predicted at the sampling time t. Here, it is assumed that $L \leq s$. As input to the model, the p measured or predicted values $\hat{w}_{t+l-1}$, $\hat{w}_{t+l-2}$, $\cdots$, $\hat{w}_{t+l-p}$ at the sampling times $t+l-1$, $t+l-2$, $\cdots$, $t+l-p$, respectively, are adopted. Here, $\hat{w}_{t'}$ is evaluated as the measured value $w_{t'}$ if it can be evaluated, otherwise as the predicted value $\breve{w}_{t'|t}$. Here, it is assumed that $p < s$. In addition, the q errors between the measured and predicted values $\hat{a}_{t+l-1}$, $\hat{a}_{t+l-2}$, $\cdots$, $\hat{a}_{t+l-q}$ at the sampling times $t+l-1$, $t+l-2$, $\cdots$, $t+l-q$, respectively, are adopted. Here, $\hat{a}_{t'}$ is evaluated as

$$\hat{a}_{t'} = w_{t'} - \breve{w}_{t'|t'-1} \quad (5)$$

if $w_{t'}$ can be evaluated, otherwise as zero. Here, it is assumed that $q < s$. This is similar to the autoregressive moving average model for time series analysis. Therefore, the number of the neurons of the input layer is $I=p+q$.

Input-output relationships. The input-output relationships for the jth neuron of the hidden layer and the kth neuron of the output layer are expressed as follows:

$$Y_{jn} = g\left(\sum_{i=1}^{I} u_{ji} X_{in} + \eta_j \right) \quad (n = 1, 2, \cdots, N; j = 1, 2, \cdots, J) \quad (6)$$

$$Z_{kn} = h\left(\sum_{j=1}^{J} v_{kj} Y_{jn} + \theta_k \right) \quad (n = 1, 2, \cdots, N; k = 1, 2, \cdots, K) \quad (7)$$

respectively. Here, X_{in} is the input to and output from the ith neuron of the input layer for the nth pattern, Y_{jn} is the output from the jth neuron of the hidden layer for the nth pattern, Z_{kn} is the output from the kth neuron of the output layer for the nth pattern, u_{ji} is the weight for the connection between the ith neuron of the input layer and the jth neuron of the hidden layer, η_j is the threshold for the jth neuron of the hidden layer, v_{kj} is the weight for the connection between the jth neuron of the hidden layer and the kth neuron of the output layer, and θ_k is the threshold for the kth neuron of the output layer.

In Eqs. (6) and (7), N is the number of patterns, which is equal to the number of the predicted values $\breve{w}_{t+l|t}$, or the number of the sets of the measured or predicted values $\hat{w}_{t+l-1}$, $\hat{w}_{t+l-2}$, $\cdots$, $\hat{w}_{t+l-p}$ and the errors between the measured and predicted values $\hat{a}_{t+l-1}$, $\hat{a}_{t+l-2}$, $\cdots$, $\hat{a}_{t+l-q}$.

In Eqs. (6) and (7), $g(x)$ and $h(x)$ are the functions which convert input into output in the neurons of the hidden and output layers, respectively. The sigmoid function has conventionally been adopted as these conversion functions. However, the predicted value $\breve{w}_{t+l|t}$ can be negative and

larger than unity in the problem under consideration. Therefore, the following functions are adopted here:

$$g(x) = \tanh x \tag{8}$$

$$h(x) = \alpha \tanh x \tag{9}$$

where α is a constant coefficient.

Conversion from output to energy demand

The relationship between the predicted values $\hat{w}_{t+l\,|\,t}$ and $\hat{y}_{t+l\,|\,t}$ is expressed as follows:

$$\hat{y}_{t+l\,|\,t} = \begin{cases} \hat{w}_{t+l\,|\,t} & (D = 0) \\ \hat{w}_{t+l\,|\,t} - \displaystyle\sum_{e=1}^{D} (-1)^e {}_D\mathrm{C}_e y_{t+l-es} & \\ & (D \geq 1) \end{cases}$$
$$(l = 1, 2, \cdots, L) \tag{10}$$

In addition, the relationship between the predicted values $\hat{y}_{t+l\,|\,t}$ and $\hat{z}_{t+l\,|\,t}$ is expressed as follows:

$$\hat{z}_{t+l\,|\,t} = \begin{cases} \hat{y}_{t+l\,|\,t} & (d = 0) \\ \hat{y}_{t+l\,|\,t} - \displaystyle\sum_{e=1}^{l-1} (-1)^e {}_d\mathrm{C}_e \hat{z}_{t+l-e\,|\,t} & \\ \quad - \displaystyle\sum_{e=l}^{d} (-1)^e {}_d\mathrm{C}_e z_{t+l-e} & \\ & (d \geq 1,\ l \leq d) \\ \hat{y}_{t+l\,|\,t} - \displaystyle\sum_{e=1}^{d} (-1)^e {}_d\mathrm{C}_e \hat{z}_{t+l-e\,|\,t} & \\ & (d \geq 1,\ l > d) \end{cases}$$
$$(l = 1, 2, \cdots, L) \tag{11}$$

MODEL IDENTIFICATION

Optimization problem for back propagation

Generally, the squared error between the output from the kth neuron of the output layer Z_{kn} and the corresponding teaching data is evaluated for the nth pattern, and its summation for the K outputs and N patterns is minimized as the objective function. In the problem under consideration, the output Z_{kn} and the corresponding teaching data are replaced by the predicted and measured energy demands, $\hat{z}_{t+l\,|\,t}$ and z_{t+l}, respectively. Therefore, the objective function is defined as follows:

$$f = \sum_{l=1}^{L} \sum_{t=R}^{M-l} (\hat{z}_{t+l\,|\,t} - z_{t+l})^2 \tag{12}$$

The number of patterns N is replaced by $L\{(M - R) - (L-1)/2\}$, where M is the number of sampling times for the measured energy demand, and R is the number of sampling times reduced for the predicted value $\hat{w}_{t+l\,|\,t}$ and is expressed as follows:

$$R = Ds + d + \max(p, q) \tag{13}$$

The variable vector composed of the weights and thresholds whose values are to be determined is defined as follows:

$$\boldsymbol{x} = \big(u_{11}, \cdots, u_{JI}, v_{11}, \cdots, v_{KJ}, \eta_1, \cdots, \eta_J, \theta_1, \cdots, \theta_K\big)^{\mathrm{T}} \tag{14}$$

where the superscript T means a transposition.

In the back propagation approach, the error function for each pattern in Eq. (12) is minimized sequentially. Here, to secure the local optimality of solutions and make the convergence faster, the total error function for all the patterns of Eq. (12) is minimized simultaneously.

Search for local optimal solutions

The search for local optimal solutions can be conducted by a gradient method for unconstrained nonlinear programming problems. For example, the simplest gradient method is the steepest descent one, and the renewal of the values of the variables $\boldsymbol{x}$ is expressed as follows:

$$\boldsymbol{x}_{(m+1)} = \boldsymbol{x}_{(m)} - \beta \big[\partial f(\boldsymbol{x}_{(m)}) / \partial \boldsymbol{x}\big]^{\mathrm{T}} \tag{15}$$

where the subscript (m) is the number of the renewal of the values of the variables $\boldsymbol{x}$, and β is the step width. However, the steepest descent method has the drawback of slow convergence. Therefore, the conjugate gradient and quasi-Newton methods with faster convergence are often adopted instead of the steepest descent method.

Nevertheless, as aforementioned, these methods have the significant drawback that they cannot derive global optimal solutions. Therefore, the modal trimming method is adopted as a global optimization one.

Global optimization by modal trimming method

Basic concept. The concept of the modal trimming method is shown in Figure 2. This method is composed of the following two procedures: A local optimal solution is searched to obtain a tentative global quasi-optimal one; A feasible solution with the value of the objective function equal to that for the tentative global quasi-

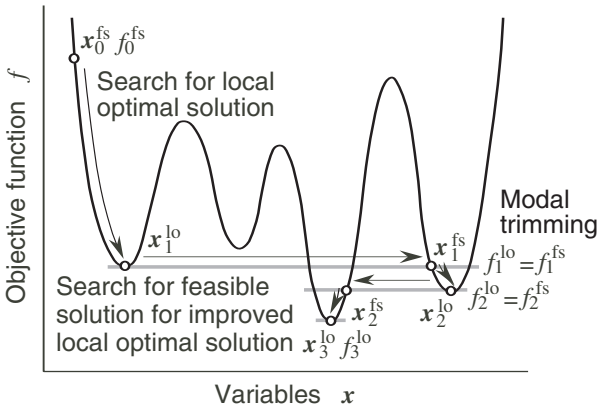

Figure 2: Concept of modal trimming method

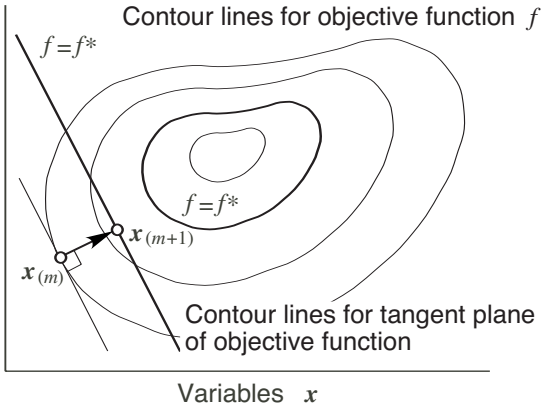

Figure 3: Renewal of values of variables

optimal one is searched to obtain an initial point for finding a better local optimal one. These procedures are repeated until a feasible solution with the value of the objective function equal to that for the tentative global quasi-optimal one cannot be found, and the tentative global quasi-optimal one is adopted as the global quasi-optimal one.

The aforementioned idea is similar to that of the tunneling algorithm, which has also been proposed to derive global quasi-optimal solutions [11]. In the tunneling algorithm, a feasible solution is searched by a conventional gradient method. However, in the modal trimming method, a feasible solution is searched by an extended Newton-Raphson method based on the Moore-Penrose generalized inverse of the Jacobi matrix of the objective function and constraints. The method can have a high possibility of deriving global optimal solutions, if it has the capability of global search for feasible ones.

Search for feasible solutions. An extended Newton-Raphson method is applied to search a feasible solution with the value of the objective function equal to that for the tentative global quasi-optimal one. Namely, the function composed of the objective function

$$F(\boldsymbol{x}) = f(\boldsymbol{x}) - f^* \tag{16}$$

is defined, and the values of the variables $\boldsymbol{x}$ are renewed to satisfy $F(\boldsymbol{x}) = 0$ by the following equation:

$$\boldsymbol{x}_{(m+1)} = \boldsymbol{x}_{(m)} - \gamma \left[\partial F(\boldsymbol{x}_{(m)}) / \partial \boldsymbol{x}\right]^+ F(\boldsymbol{x}_{(m)}) \tag{17}$$

In Eq. (16), f^* is the value of the objective function for the tentative global quasi-optimal solution. In Eq. (17), $[\ ]^+$ means the Moore-Penrose generalized inverse and is applied to the Jacobi matrix $\partial F(\boldsymbol{x}) / \partial \boldsymbol{x}$ of the function $F(\boldsymbol{x})$, and γ is the decelerating parameter whose value is between 0 and 1.

The application of the Moore-Penrose generalized inverse is because of the multiple variables $\boldsymbol{x}$ produce numerous solutions which satisfy $F(\boldsymbol{x}) = 0$. For the problem under consideration, the Moore-Penrose generalized inverse is reduced to the right inverse as follows:

$$\begin{aligned}\left[\partial F(\boldsymbol{x}_{(m)}) / \partial \boldsymbol{x}\right]^+ &= \left[\partial F(\boldsymbol{x}_{(m)}) / \partial \boldsymbol{x}\right]^{\mathrm{T}} \\ &\quad \times \left(\left[\partial F(\boldsymbol{x}_{(m)}) / \partial \boldsymbol{x}\right] \left[\partial F(\boldsymbol{x}_{(m)}) / \partial \boldsymbol{x}\right]^{\mathrm{T}} \right)^{-1} \\ &= \left[\partial f(\boldsymbol{x}_{(m)}) / \partial \boldsymbol{x}\right]^{\mathrm{T}} / \left\| \partial f(\boldsymbol{x}_{(m)}) / \partial \boldsymbol{x} \right\|_2^2 \end{aligned} \tag{18}$$

where $\| \ \|_2$ means the Euclidean norm of a vector. Therefore, Eq. (17) is reduced to

$$\begin{aligned}\boldsymbol{x}_{(m+1)} = \boldsymbol{x}_{(m)} &- \gamma \{ f(\boldsymbol{x}_{(m)}) - f^* \} \\ &\times \left[\partial f(\boldsymbol{x}_{(m)}) / \partial \boldsymbol{x}\right]^{\mathrm{T}} / \left\| \partial f(\boldsymbol{x}_{(m)}) / \partial \boldsymbol{x} \right\|_2^2 \end{aligned} \tag{19}$$

For example, in an unconstrained nonlinear programming problem with two variables, Eq. (19) means that the values of $\boldsymbol{x}_{(m+1)}$ are determined as the point where the line on the tangent of the objective function drawn from the point $\boldsymbol{x}_{(m)}$ toward the direction with the steepest descent gradient crosses the plane $f(\boldsymbol{x}) = f^*$, as shown in Fig. 3.

The renewal of the values of the variables $\boldsymbol{x}$ based on the extended Newton-Raphson method has the following features: In the region with a feasible solution, the renewal can have the convergence to it; In the region with no feasible solution, the renewal can create a chaotic behavior and has the capability of global search; In the region with no feasible solution, the renewal can also create a cyclically vibrating behavior and has the possibility of trap into a local optimal solution. To prevent

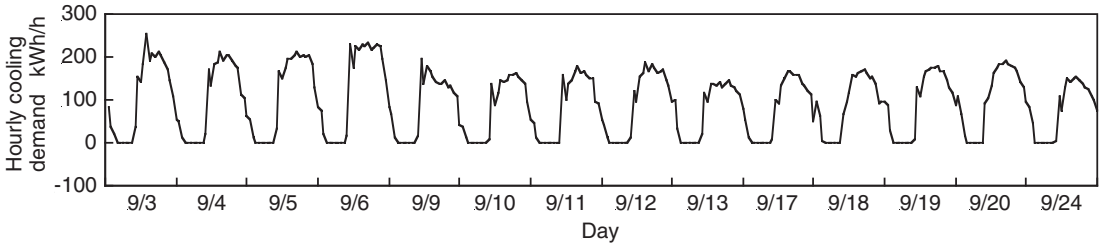

Figure 4: Measured cooling demand for identification

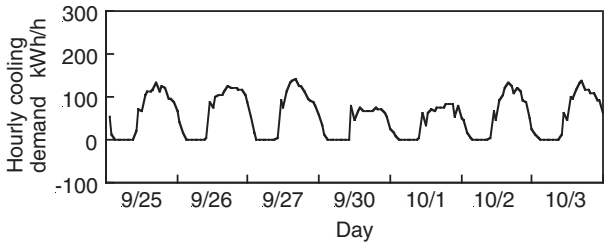

Figure 5: Measured cooling demand for prediction

the trap, the decelerating parameter γ is changed randomly in the range $0 < \gamma \leq 1$ at each renewal.

NUMERICAL STUDY

The aforementioned neural network model is applied to the prediction of the cooling demand in a building used for a bench mark test of a variety of prediction methods.

Calculation conditions

The cooling demand is for a commercial building with nine floors, a parking space on the first floor, and a total floor area of 5400 m^2.

The measured cooling demand on the 14 weekdays from Sept. 3 to Sept. 24, 1996 is used to identify the values of model parameters, or weights and thresholds. Figure 4 shows the measured cooling demand for identification. Here, a day is defined as the period from 22:00 on the previous day to 22:00 on the corresponding day. The sampling time interval is set at Δt = 1 h. Therefore, the number of sampling times for the measured cooling demand is $M = 14 \times 24 = 336$. The prediction of the cooling demand is conducted using the identified values of model parameters on the 7 weekdays from Sept. 25 to Oct. 3, 1996. Figure 5 shows the measured cooling demand for prediction.

The order of the ordinary difference is set at $d = 0$. On the other hand, the number of sampling times for the periodic differential operation and the order of the periodic difference are set at $s = 24$ and $D = 1$, respectively. The number of sampling times for prediction is set at $L = 3$. The numbers of measured or predicted values and errors are set at $p = 3$ and $q = 3$, respectively. Consequently, the number of sampling times reduced is $R = 27$.

From the aforementioned conditions, the number of patterns is $N = 924$. The number of neurons of the input layer is $I = p + q = 6$. On the other hand, the number of neurons of the hidden layer is set at $J = 6$. Therefore, the number of model parameters is $(I + 1)J + (J + 1)K = 49$. The constant coefficient α in Eq. (9) is set at 200.0 in consideration of the magnitude of the periodic difference of the cooling demand.

The quasi-Newton method is adopted as a conventional gradient method, and the Broyden-Fletcher-Goldfarb-Shanno (BFGS) formula is applied to express the inverse of the Hessian matrix approximately.

Basic study

First, the quasi-Newton method is applied to the identification of the values of model parameters. Figure 6 (a) compares the measured and predicted cooling demands. Here, the predicted cooling demand is based on the values of model parameters corresponding to a local optimal solution obtained by the quasi-Newton method. The predicted cooling demand fluctuates widely, and the errors between the measured and predicted cooling demands are too large. Therefore, this result cannot be validated.

Next, the modal trimming method is applied to the identification of the values of model parameters. Figure 6 (b) compares the measured and predicted cooling demands. Here, the predicted cooling demand is based on the values of model parameters corresponding to the global quasi-optimal solution obtained by the modal trimming method. This solution is obtained through some local optimal solutions. The measured and predicted cooling demands are in good agreement.

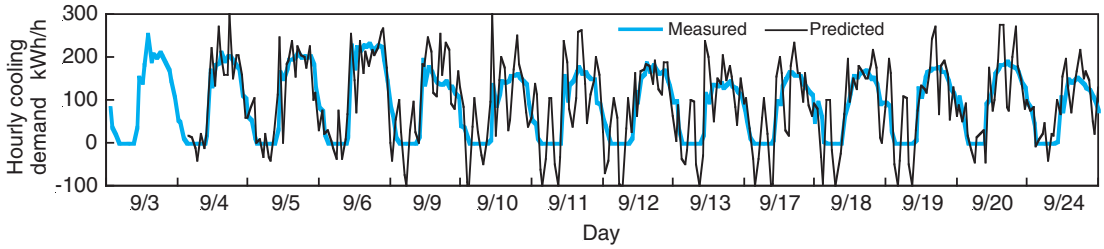

(a) Local optimal solution by quasi-Newton method

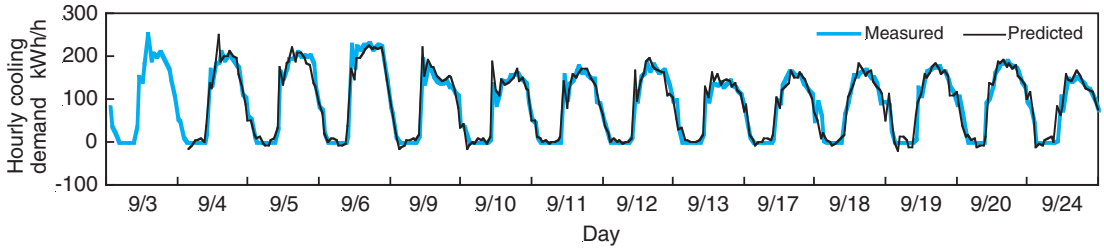

(b) Global quasi-optimal solution by modal trimming method

Figure 6: Comparison of measured and predicted cooling demands for identification

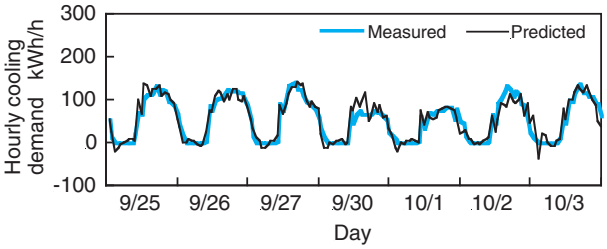

Figure 7: Comparison of measured and predicted cooling demands for prediction

Finally, the prediction is conducted using the values of model parameters corresponding to the global quasi-optimal solution obtained by the modal trimming method. Figure 7 compares the measured and predicted cooling demands. Although the cooling demand for prediction is smaller than that for identification, the measured and predicted cooling demands are also in good agreement.

These results show that the identification of the values of model parameters for the neural network model needs a global optimization method, and that the modal trimming method can find appropriate values as the global quasi-optimal solution.

Extended study

An extended study is conducted in consideration not only of the cooling demand but also of the air temperature as the inputs to the neural network model. In this study, a neuron is added to the input layer, and the air temperature is assigned to this neuron. Two types of air temperature are considered: One is the maximum air temperature of each day; The other is the hourly air temperature. As an initial study, the measured values are used in place of the predicted ones for all the air temperatures. Since the air temperature also changes periodically with a period of 24 hours, the 1st order periodic differential operation is conducted on the air temperature. In this case, the number of neurons of the input layer is $I = p + q + 1 = 7$, and the number of model parameters is $(I+1)J + (J+1)K = 55$.

Table 1: Average errors between measured and predicted cooling demands

(Unit: kWh/h)

Case	Identification	Prediction	Identification and prediction
A	18.09	17.60	17.90
B	17.59	16.91	17.35
C	16.51	16.27	16.43

Table 1 compares the average errors between the measured and predicted cooling demands in the following three cases:

Case A: without consideration of air temperature
Case B: in consideration of maximum air temperature
Case C: in consideration of hourly air temperature

It appears that the consideration of the air temperature, especially the hourly air temperature, can

improve the accuracy of the prediction. This is because the cooling demand is affected significantly by the air temperature.

CONCLUSIONS

A multi-layered neural network model has been adopted to predict energy demands. To identify the values of model parameters in the back propagation procedure, the modal trimming method has been applied as a global optimization one. The multi-layered neural network model has been applied to the prediction of the cooling demand in a building used for a bench mark test of a variety of prediction methods.

It has turned out that the identification of the values of model parameters needs a global optimization method, and that the modal trimming method can find appropriate values as the global quasi-optimal solution. It has also turned out that the consideration of the air temperature, especially the hourly air temperature, can improve the accuracy of the prediction.

ACKNOWLEDGMENT

This work was supported by the JSPS Grant-in-Aid for Scientific Research (C) No. 15560734.

REFERENCES

[1] Senjyu T, Takara H, Uezato K, Funabashi T. *One-hour-ahead load forecasting using neural network*. IEEE Transactions on Power Systems 2002; 17 (1): 113–118.

[2] Dodier RH, Henze GP. *Statistical analysis of neural networks as applied to building energy prediction*. Transactions of the ASME, Journal of Solar Energy Engineering 2004; 126 (1): 592–600.

[3] Yokoyama R, Kumashiro D, Ito K, Kamimura K, Matsuba T. *A method of predicting energy demands in consideration of minimizing variations in their predicted values*, Transactions of the JSME, Ser. C 2004; 70 (697): 2682–2690 (in Japanese).

[4] Yokoyama R, Ito K. *A combinatorial optimization approach to real-time equipment startup/shutdown scheduling for energy supply systems*. Proceedings of the International Symposium on Optimization and Innovative Design, paper no. 115. Tokyo, 1997.

[5] Yokoyama R, Ito K, Kamimura K, Miyasaka F. *Development and evaluation of an advisory system for optimal operation of a district heating and cooling plant*. Proceedings of the International Conference on Renewable and Advanced Energy Systems for the 21st Century, paper no. RAES99-7641. Lahaina, 1999.

[6] Rumelhart DE, McClelland JL, the PDP Research Group, *Parallel Distributed Processing*. MIT Press, 1986.

[7] Baba N. *A new approach for finding the global minimum of error function of neural networks*. Neural Networks 1989; 2: 367–373.

[8] Uchida O, Endo T. *Minimum search technology via chaotic steepest descent method and its application to back propagation*, ISICE Transactions, Ser. A 1995; J78-A (11): 1516–1518 (in Japanese).

[9] Yokoyama R, Ito K. *Global optimization for neural network back propagation by modal trimming method*. Proceedings of the Third China-Japan-Korea Joint Symposium on Optimization of Structural and Mechanical Systems, Kanazawa, 2004; 639–644.

[10] Yokoyama R, Ito K. *Modal trimming method for improving local optima of nonlinear programming problems*. Transactions of the JSME, Ser. C 2003; 69 (688): 3243–3250 (in Japanese).

[11] Levy AV, Montalvo A. *The tunneling algorithm for the global minimization of functions*, SIAM Journal of Scientific and Statistical Computing 1985; 6 (1): 15–29.

Proceedings of ECOS 2005
Trondheim, Norway
June 20–22, 2005

THE SECOND LAW OPTIMAL OPERATION OF A NEWSPRINT PAPER DRYING MACHINE

Anita Zvolinschi*, Eivind Johannessen and Signe Kjelstrup
Norwegian University of Science and Technology
Department of Chemistry
N-7491 Trondheim, Norway

Abstract

Paper drying is an exergy costly operation, so also a few percent saving may be of importance. The entropy production for the paper drying process was derived for the newsprint paper drying machine at Norske Skog ASA in Skogn, Norway. The machine has 51 cylinders grouped in three drying groups. The cylinders are heated from the inside by steam, unheated or operated under vacuum conditions. The inlet drying air is supplied with same parameters in all air-pockets of the machine. The entropy production of the total process was calculated for actual operating conditions (i.e. reference conditions) and then optimised subject to a defined outlet paper moisture content (i.e. 0.07 kg H_2O/ kg dry paper). Inlet air humidity and cylinder group conditions were varied. Optimum conditions were obtained for a range of inlet air humidities, and for different cylinder groupings. We found that it was very favorable to increase the inlet air humidity. The realisation of such a change is probably hampered by unwanted condensation. Other changes had a negligible effect on the entropy production. The results pointed to the need for a revision of the current model of heat and mass transfer, as the second law was violated at high air humidities with this model.
Keywords: Paper drying; Entropy production; Optimisation; Heat and mass transport

NOMENCLATURE

b	Paper width [m]
B	Basis weight of paper [kg/ m^2]
C_p	Heat capacity [J/ K kg]
D_{cyl}	Cylinder diameter [m]
h	Heat transfer coefficient [J/ K m^2 s]
$\Delta_{\text{vap}}H$	Vaporization enthalpy of free water [J/ kg]
$\Delta_{\text{sor}}H$	Sorption enthalpy of water to paper [J/ kg]
l	Paper length between two cylinders [m]
L	Total length of paper [m]
J	Mass flux of evaporated water [kg/ m^2 s]
J_q	Heat flux [J/ m^2 s]
M_{H_2O}	Molar weight of water [kg/ mol]
n	The drying mode-related coefficient [-]
$p^{\ominus}$	Standard pressure [bar]
p^*	Equilibrium vapour pressure [bar]
p^*_{p}	Equilibrium vapour pressure over paper [bar]
Pr	Prandtl number [-]
R	Gas constant [J/ K mol]
Re	Reynolds number [-]
$(dS/dt)_{\text{irr}}$	Total entropy production rate [J/ K s]
$\Delta_{\text{vap}}S$	Vaporization entropy of free water [J/ K kg]
$\Delta_{\text{sor}}S$	Sorption entropy of water to paper [J/ K kg]
T	Temperature [K]
X_{air}	Air humidity [kg H_2O/ kg dry air]
V	Machine speed [m/s]
w	Paper moisture content [kg H_2O/ kg dry paper]
β_1, β_2	Coefficients in Eq. (14)
Θ	Desorption isotherm function [-]
κ	Thermal conductivity [J/ K m s]
μ	Dynamic viscosity [kg/ m s]
ν	Kinematic viscosity [m^2/ s]
σ	Local entropy production [J/ K m s]
ω	Paper sheet wrap angle [$^{\text{o}}$]

Sub- and superscripts

cyl	cylinder
p	paper

*Corresponding author. Phone: +47 7359 1675. Fax: +47 7355 0877. E-mail:anitaz@phys.chem.ntnu.no

INTRODUCTION

All industrial paper drying techniques require high temperatures, high heat fluxes and large partial pressure differences. They are thus sources of considerable exergy loss. Significant losses occur not only in the drying machine itself, but also in the connected steam generation and heat recovery system. Therefore, when one discusses paper drying techniques it is not sufficient to evaluate the specific heat requirement, like literature proposes [1]. Also the exergy loss has to be considered. The exergy loss is defined as the entropy production in the process times the temperature of the surroundings.

The purpose of this paper is to formulate, calculate and optimise the entropy production of a multi-cylinder Valmet newsprint paper drying machine, which uses saturated steam as heating agent inside the cylinders. This machine dries paper as it travels over three drying groups of heated and un-heated cylinders, cf. Table 1. Additional cylinders are operated under vacuum. Although new paper drying techniques such as impingement and impulse drying have been introduced [2], the conventional steam-heated cylinder drying technique is still widely used in the paper industry, and can serve as a reference for the others.

The entropy production for the system shall be formulated. Then, a constrained optimization method shall be applied. The same method was used to minimize the entropy production in a chemical reactor [3]. In this study, the temperatures of the saturated steam supplied to each drying group shall be used as optimization variables, and the dryness of the paper sheet at the end of the machine as the constraint. A varying inlet air humidity and a re-grouping the drying groups shall also be studied. The outcome of the calculation is thus knowledge about the second-law optimal operation of the drying machine, and a recommendation for a more energy efficient process.

THE PAPER DRYING MACHINE

The machine that we study, the Valmet Paper Machine PM2 at Norske Skog, Skogn, Norway, manufactures newsprint (540 tonn paper/ day). It consists of 51 cylinders that are assembled in three drying groups, see Table 1.

There are two types of felt configuration in the machine; the single-felt configuration in the first group and the double-felt one in the last groups, see Fig. 1.

Table 1: Drying groups. Cylinders that are not mentioned, are operated under vacuum.

Drying Group	Un-heated cyl.	Heated cyl.
1st (1-8)	1	3,5,7
2nd (9-23)	16,18,20,22	9,11,13,15,17 19,21,23
3rd (24-51)	31,51	24-30,32-50

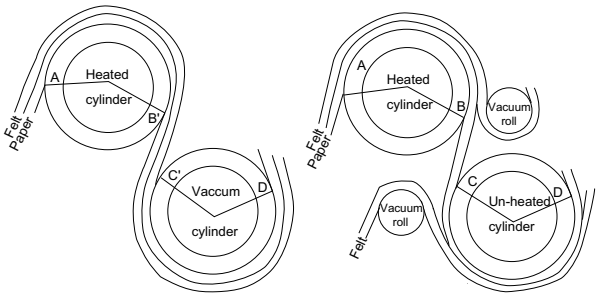

Figure 1: Drying modes with single- (*left*) and double-felt (*right*) configurations.

Table 2: Drying mode specifications. See also Fig. 1

Mode	Specification	n
A	Paper in contact with a heated cylinder surface on one side and felt on the other (A-B, B')	1
B	Paper in contact with air on both sides (B-C)	2
C	Paper in contact with an un-heated cylinder surface on one side and felt on the other (C-D)	1
D	Paper in contact with air on one side and felt on the other (B'-C')	2
E	Paper in contact with air and felt on a cylinder under vaccum (C'-D)	1

The machine has five types of drying modes; identified by the letters given in Table 2, (see also Fig. 1). The whole machine is a combination of 102 drying modes. Figure 1 (*left*) and (*right*) gives as examples the following combinations: **ADE** and **ABC**, respectively. This change of drying modes throughout the machine lead to a discontinuous variation in the paper temperature. Near heated cylinders, the

Table 3: Operating conditions. See Nomenclature for the symbols' dimensions

Parameter	Symbol	Value
Machine speed	V	20.83
Basis weight	B	0.045
Paper sheet width	b	6.65
Paper sheet wrap angle	ω	220
Cylinder diameter	D_{cyl}	1.50
Total length of paper	L	197.8
Paper length b. two cylinders	l	1.00
Total pressure	p	1.01
Paper inlet temperature	$T_{p,in}$	313
Paper inlet moisture content	w_{in}	1.20
Paper outlet moisure content	w_{out}	0.07
Air inlet temperature (dry-bulb temperature)	$T_{in,air}$	313
Air inlet humidity	$X_{in,air}$	0.026
Saturated steam temperature		
in 1st drying group	$T_{cyl,1}$	371
in 2nd drying group	$T_{cyl,2}$	384
in 3rd drying group	$T_{cyl,3}$	394

paper temperature is high, away from them it is low. Inlet and outlet conditions of the paper, air and steam, as well as other parameters of the machine, are given in Table 3.

CONSERVATION EQUATIONS

The paper travels from the wet to the dry-end of the paper drying machine; we defined this direction as the z-direction. We consider transport of mass and heat at a given moment in the direction normal to the paper sheet. Gradients within the paper are neglected. Conservation of mass gives:

$$\frac{dw}{dz} = -\frac{n}{V\,B}\,J \tag{1}$$

while conservation of internal energy gives

$$\frac{dT_p}{dz} = \frac{n}{V\,B\,Cp,p}\left(J_{q,cyl} + J_{q,air} - J\frac{\partial(w\Delta H)}{\partial w}\right) \tag{2}$$

Here J is the flux of water evaporating from the paper sheet, $J_{q,cyl}$ and $J_{q,air}$ are heat fluxes from cylinder to the paper sheet, and from the air to the paper sheet, respectively, and n equals 1 or 2 depending on the type of drying mode (see Table 2).

LOCAL ENTROPY PRODUCTION

The local entropy production, σ, was found from the entropy balance over a small element dz of the total length of paper sheet. The entropy balance gives

$$\sigma = nb\left(VB\frac{\partial s_p}{\partial z} - \frac{J_{q,cyl}}{T_{cyl}} - \frac{J_{q,air}}{T_{air}} + Js^{\text{in air}}_{H_2O}(T_{air})\right) \tag{3}$$

where s_p is the entropy of the paper, given by

$$s_p = s_{\text{dry-p}}(T_p) + ws^{\text{in paper}}_{H_2O}(T_p, w) \tag{4}$$

Derivation of Eq. (4) with respect to dz gives

$$\frac{\partial s_p}{\partial z} = \frac{C_{p,p}}{T_p}\frac{\partial T_p}{\partial z} - \frac{J}{VB}s^{\text{in air}}_{H_2O}(T_{air}) + \frac{J}{VB}\frac{\partial(w\Delta S)}{\partial w} \tag{5}$$

Introducing Eq. (5) into Eq. (3) gives

$$\sigma = nb\left[J_{q,cyl}\left(\frac{1}{T_p} - \frac{1}{T_{cyl}}\right) + J_{q,air}\left(\frac{1}{T_p} - \frac{1}{T_{air}}\right) + J\left(-\frac{1}{T_p}\frac{\partial(w\Delta H)}{\partial w} + \frac{\partial(w\Delta S)}{\partial w}\right)\right] \tag{6}$$

where ΔH and ΔS are the enthalpy and entropy change, respectively, for water between states in the paper sheet and the surrounding air (see the Appendix: *Thermodynamic relations*).

The first two terms on the right-hand side of Eq. (6) give the contributions from heat transport, while the last term gives the contribution from mass transport. Integration of Eq. (6) over the paper travelling through the whole machine, was the objective function:

$$\left(\frac{dS}{dt}\right)_{\text{irr}} = \int_0^L \sigma\,dz \tag{7}$$

As constraint in the optimisation, a defined outlet paper moisture content (w_{out}) was used, see Table 3.

Fluxes and forces

The heat and mass transport forces are defined by Eq. (6), where $\left(\frac{1}{T_p} - \frac{1}{T_{cyl}}\right)$ and $\left(\frac{1}{T_p} - \frac{1}{T_{air}}\right)$ are the forces for the heat transport, and $\left(-\frac{1}{T_p}\frac{\partial(w\Delta H)}{\partial w} + \frac{\partial(w\Delta S)}{\partial w}\right)$ is the force for the mass transport.

The literature [4, 5] gives the evaporation flux from the paper to the air as

$$J = \frac{1}{C_{p,dry-air} + X^*\,C_{p,H_2O}}h_{p-air}(X^* - X_{in,air}) \tag{8}$$

where h_{p-air} is the heat transfer coefficient between paper sheet and air, $C_{p,dry-air}$ and C_{p,H_2O} are the heat capacities of dry air and of vapour water, respectively, X^* is the saturation humidity above the paper, and $X_{in,air}$ is the inlet air humidity.
The heat flux from the cylinder to the paper is

$$J_{q,cyl} = h_{cyl-p}(T_{cyl} - T_p) \tag{9}$$

while that from the air to the paper is

$$J_{q,air} = h_{p-air}(T_{air} - T_p) \tag{10}$$

The heat transfer coefficients in Eqs. (9) and (10) were taken from literature [6] (see the Appendix: *Heat transfer coefficients*).
The evaporation flux equation, Eq. (8), shall be used here, despite the fact that the driving force in Eq. 8) it is not according to that defined by Eq. (6). We shall see that this mismatch leads to a violation of the second law for some conditions, which means that the Eq. (8) proposed in literature cannot correctly predict the evaporation flux for the entire range of operating conditions of the machine.

CALCULATIONS

We calculated first the reference system, i.e. the actual paper drying machine, which is the starting point of the analysis. The distribution of the paper moisture and temperature was found by numerical integration of Eq. (1) and (2), respectively, over the total length of the paper within the machine. The drying groups are given in Table 1, and the operating conditions in Table 3. Physical properties, heat capacities, and thermal conductivities of air and water vapour were taken from [7].
The optimization was performed numerically using the *Matlab® 6.1.0 (R12.1) Optimization Toolbox* function *fmincon*. This function uses a sequential quadratic programming method to find a minimum of the objective function [8]. The temperatures of the saturated steam supplied to the drying groups were the optimization variables, and the paper moisture content at the outlet of the machine was the constraint (w_{out}= 0.07 kg H_2O/ kg dry paper). The following lower and upper bounds were applied to the saturated steam temperature: 338 and 393 K in the 1st drying group, and 358 and 403 K in the 2nd drying group.
We studied the effect of different inlet air humidities and the effect of re-grouping of the drying groups on the optimal solution.

RESULTS AND DISCUSSION

The reference system

Figure 2 presents the variation in the paper temperature and moisture content in the reference system.
The temperature profile shows clearly the increase and decrease in temperature as the drying mode is changing; it has a *zig-zag* pattern. All temperature rises correspond to drying mode **A**. This is common for all drying groups. In the 1st drying group, the cooling effect is caused first by drying mode **D** then by **E**. The cooling of the paper sheet is about 7 °C in the 1st drying group, but it is 16 °C in the 2nd drying group. In the 3rd drying group, the presence of an un-heated cylinder is the reason for the big shift in the temperature profile at cylinder 36, at z = 139 m. The gradually increase in the heat required for the evaporation of sorbed water in the 3rd drying group, causes an overall decrease in paper temperature of about 13 °C until the paper sheet reaches cylinder 31. After this location, the paper sheet temperature increases with few degrees, and then it decreases to about 50 °C when the paper sheet reaches the end of the drying machine.

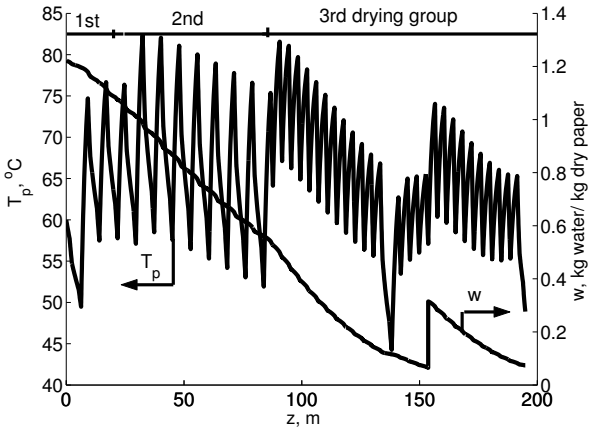

Figure 2: The temperature and moisture profile along the paper sheet in the reference system. The top line shows the three drying groups.

The paper moisture profile in Fig. 2 gives an approximately constant rate of paper drying in the 1st and 2nd drying groups. The falling drying rate regime

starts at the begining of the 3rd drying group. The presence of a moisture control device (i.e. steam box that shower the paper sheet) after cylinder 40, at z= 155 m, explains the jump in the paper moisture profile at this location in Fig. 2. This device controls the smoothness and moisture distribution of the paper surface in the width direction of the machine.

Entropy production in the reference system

The local entropy production along the machine is shown in Fig. 3. Its detailed contributions from the drying modes are given in Fig. 4, while the result of the integration is given in Table 4.
We see from Fig. 3 that σ reaches the largest values at the begining of each drying group. Similar to the paper temperature profile, σ has a *zig-zag* pattern. In the 3rd drying group, when the falling drying rate regime develops, the value of σ is falling steadily towards the end of the machine.

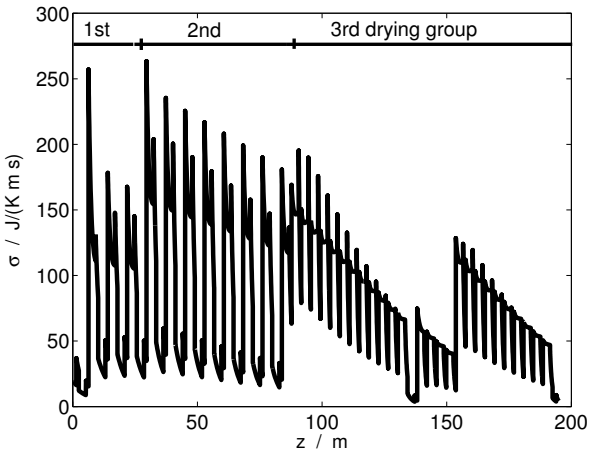

Figure 3: Local entropy production in the reference system. The top line shows the three drying groups.

Heat and mass transport contributions account almost equally to the entropy production in the paper drying process (see Table 4, first column).
The contributions from the drying modes to σ are also interesting, see Fig. 4. The highest driving force for heat and mass transport is found at the heated cylinders (mode **A**). We therefore find the highest values of the entropy production here. Un-heated cylinders (mode **C**) and cylinders operated under vacuum (mode **E**) have a smaller entropy production. When the paper travels between two cylinders (mode **B** and **D**), the contributions are among the lowest ones

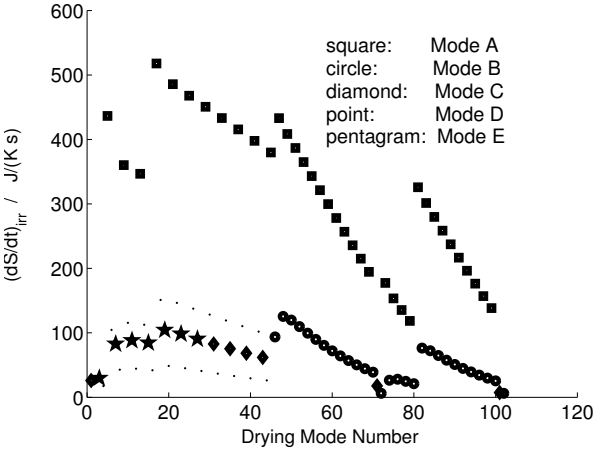

Figure 4: Entropy production per drying mode in the reference system.

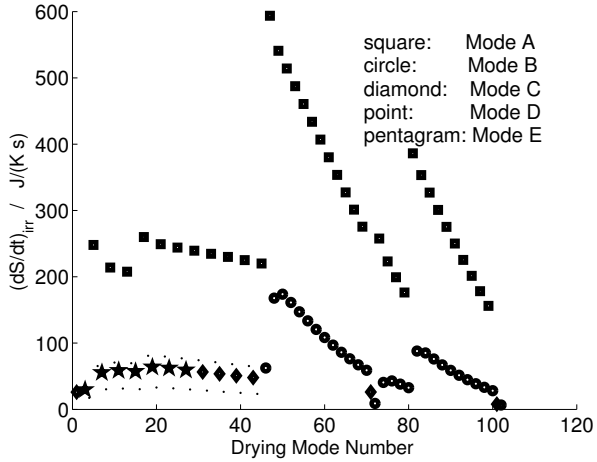

Figure 5: Entropy production per drying mode in the optimal system.

(point and filled circle symbols, respectively). There is still an evaporation taking place over the cylinders under vaccum (star symbols) and un-heated cylinders (diamond symbols), giving a positive contribution also at these locations.

The impact of cylinder temperatures

The results for the total entropy production and the optimal drying group temperatures are shown in Table 4 for three inlet air humidities. Figure 5 gives the entropy production per drying mode in the optimal system, for an inlet air humidity of 0.026 kg H_2O/ kg dry air. The corresponding results are summarized in the second column of Table 4.

Table 4: Total entropy production, $(dS/dt)_{irr}$, contributions from the heat and mass transport, and the saturated steam temperatures in the reference (*ref*) and optimal (*opt*) system for different inlet air humidities, $X_{in,air}$.

$X_{in,air}$, kg/kg	0.026	0.026	0.065	0.13
System	*ref*	*opt*	*opt*	*opt*
$\left(\frac{dS}{dt}\right)_{\text{irr}}$,$10^3$ J/ Ks	15.5	15.0	12.5	10.0
Contributions:				
Heat transport	7.9	7.5	7.7	6.8
Mass transport	7.6	7.5	4.7	3.2
Reduction, %	-	3	19	35
$T_{cyl,1}$, °C	98	84	88	94
$T_{cyl,2}$, °C	111	89	94	99
$T_{cyl,3}$, °C	121	126	131	133

The first optimization was done with an inlet air humidity of 0.026 kg H_2O/ kg dry air, to investigate the effect of the saturated steam temperature on the total entropy production. The reduction in entropy production from the reference state to the state of minimum entropy production was 3%. This improvement is achieved if the saturated steam temperature is reduced with 14 °C and with 22 °C in the 1st and 2nd drying group, respectively, while it is increased with 5 °C in the 3 rd drying group.

Figure 5 shows that the optimal solution occurs when entropy production of the modes **A** in the 1st and 2nd drying groups is halved compared with that in the reference solution. This happens as a response to the changes in the saturated steam temperature.

The impact of air conditions

Furthermore, the impact of changing the inlet air conditions was studied. Figure 6 shows the minimum entropy production as a function of inlet air humidity. The final paper moisture content was the same in all cases (w_{out}= 0.07 kg H_2O/ kg dry paper). The reference system is shown as the point (square symbol) in the Fig. 6. This point lies very near the curve for optimal solutions, according to the results described in the previous section.

Table 4 gives details of the optimal solution for the three selected inlet air humidities. The curve (Fig. 6) gives a clear message: It is possible to reduce the total entropy production up to 35 % by increasing the inlet air humidity, and changing the cylinder temperatures accordingly to the values given in the last column of Table 4. As the inlet air humidity sets out higher and higher, the cylinder temperatures in the 1st and 2nd drying groups get closer and closer to the corresponding values in the reference system. This results can be understood from the fact that the heat transport has almost the same contribution to the entropy production in all cases, while the mass transport contribution decreases when higher inlet air humidity is used.

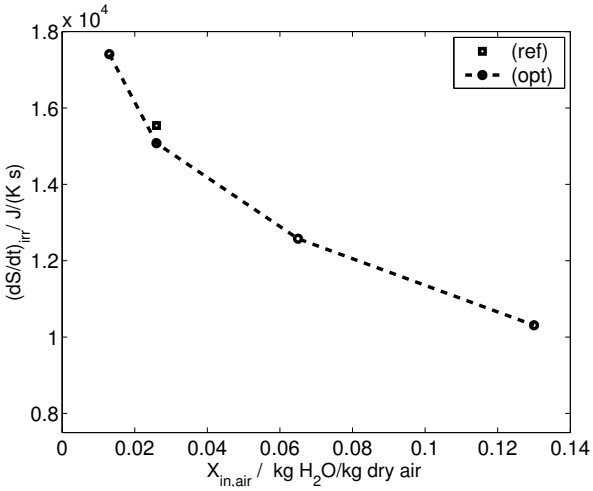

Figure 6: Total entropy production rate of the optimal (*opt*) systems vs different inlet air humidities, including the reference (*ref*) system.

The highest inlet air humidity shown in the Table 4 $X_{in,air}$= 0.13 kg H_2O/ kg dry air, is near to the saturation limit for the air in the machine's air-pockets. This means that it may be difficult to realise in practice. An high inlet air humidity means an increased likelihood for condensation, and condensation must be avoided everywhere in the machine's hood. A high humidity is, however, an advantage for the heat recovery process, which is located upstream of the paper drying process.

The curve in Fig. 6 was not drawn beyond the point given by $X_{in,air}$= 0.13 kg H_2O/ kg dry air. For higher values of inlet air humidity, the entropy production given by the mass transport contribution became negative in some points of the machine. This is of course an unphysical situation. It arose because the driving force for mass transport was not the thermodynamic one, compare Eq. (6) and Eq. (8). Another reason is that the coupling between mass and heat transport was not proper described as it is required

in the irreversible thermodynamics [13]. Therefore, whitout having a coupling effect taken into account, we can not admit entropy production to be negative. We conclude that there is a potential for an improved model at this point. This is a topic for the future, however.

The impact of drying groups conditions

A possible effect of opening the un-heatead cylinders and of re-grouping the drying groups was investigated, without any significant effect of the total entropy production. When the 2^{nd} drying group was extended from 15 to 17 cylinders, or it was contracted from 15 to 13 cylinders, the total entropy production was reduced by only 0.1% compared to the reference. A small gain was also obtained when less cylinders were used in the 1^{st} drying group, and when un-heated cylinders 1, 36 and 51 were set on.

CONCLUSION

We have analyzed a Valmet newsprint drying machine, and found that its total entropy production can be reduced with 3% when the conditions for the minimum entropy production are followed. These new operation conditions concern the temperature of the steam used in the drying groups. We found that low temperatures should be used in the first two drying groups, while high temperature should be used in the last group.

The total entropy production rate can be drastically reduced by increasing the inlet air humidity. How far it is possible to go in this direction remains to be studied. The physical model for the system should first be improved, to give possitive entropy production everywhere in the paper drying machine.

ACKNOWLEDGEMENTS

The Research Council of Norway funded this research. Norske Skog ASA, Skogn, made data available. We wish to thank Mr. Sadeghi for valuable suggestions.

REFERENCES

[1] Manninen J, Puumalainen T, Talja R, Perrersson H. *Energy aspects in paper mills utilizing future technology.* Appl. Thermal Eng. 2002; 22:929–937.

[2] De Beer J, Worrell E, Block K. *Long-term energy-efficiency improvements in the paper and boad industry.* Energy 1998;23:21–42.

[3] De Koeijer G, Johannessen E, Kjelstrup S. *The second law optimal path of a four-bed SO_2 converter with five heat exchangers.* Energy 2004;29:525–546.

[4] Soininen M. *Modeling of web drying* Drying Technology 1995;13:823–866.

[5] Yeo Y, Hwang K, Yi S, Kang H. *Modeling of the drying process in paper plants* Korean J. Chem. Eng. 2004; 21:761–766.

[6] Incropera F.P, De Witt D.P. *Fundamentals of heat and mass transfer.* John Wiley and Sons, 1985, p.319-321 and p.336.

[7] Pakowski Z, Bartczak Z, Strumillo C, Stenström S. *Evaluation of equations approximating thermodynamic and transport-properties of water, steam and air for use in cad of drying processes.* Drying Technology 1991;9:753–773.

[8] The Mathworks Inc. (2001) Matlab 6.1.0 (R12.1). http://www.mathworks.com.

[9] Prahl J.M. *Thermodynamics of paper fiber and water mixtures.* Ph.D. Thesis, Harvard University, USA, 1968.

[10] Karlsson M, Soininen M. *The influence of the hygroscopic properties of paper on the transient phenomena during contact drying of the paper webs.* in Ashworth, J.C. (Ed.), Proc. Third Int. Drying Symposium, vol. 1, 1982.

[11] Wilhelmsson B, Fagerholm L, Nilsson L, Stenström S. *An experimental study of contact coefficients in paper drying.* Tappi Journal 1994;77:159–168.

[12] Rhodius D., Gottsching L. *Paper and board drying process and its independence upon drying and paper technological parameters. 4. Drying in the multi-cylinder dryer section.* Papier 1979; 33:1-9.

[13] Førland K. S., Førland T. and Kjelstrup S. *Irreversible thermodynamics. Theory and applications.* Tappir Academic Press, Trondheim, 2001.

APPENDIX
Thermodynamic relations

The enthalpy change for water between states in the paper sheet and the surrounding air is

$$\Delta H = \Delta_{sor}H + \Delta_{vap}H + \int_{T_p}^{T_{air}} C_{p,H_2O}^{\text{in air}}\, dT \qquad (11)$$

where $\Delta_{sorp}H$ is the sorption enthalpy of water from the paper, and $\Delta_{vap}H$ is the vaporisation enthalpy of free water.
The entropy change for water between states in the paper sheet and the surrounding air is

$$\Delta S = -\frac{\Delta_{sor}H}{T_p} - \frac{R}{M_{H_2O}} ln\left(\Theta(w,T_p)\right) + \frac{\Delta_{vap}H}{T_p} - \frac{R}{M_{H_2O}} ln\left(\frac{p_{H_2O}^{\text{in air}}}{p^*}\right) + \int_{T_p}^{T_{air}} \frac{C_{p,H_2O}^{\text{in air}}}{T}\, dT \qquad (12)$$

The sorption enthalpy is derived from the desorption isotherm for liquid water to paper, $\Theta(w,T_p)$;

$$\Delta_{sor}H = -R\frac{\partial ln\Theta(w,T_p)}{\partial(1/T_p)} \qquad (13)$$

The desorption isotherm was measured by [9] as a function of temperature and water content

$$\Theta(w,T_p) = \frac{p_{\text{p}}^*}{p^*} = \exp(\beta_1 T_p - \beta_2) \qquad (14)$$

The coefficients β_1 and β_2 in Eq. (14) were determined by [10]

$$\beta_1 = \exp(-15.03w - 1.37\sqrt{w} - 3.14) \qquad (15)$$

$$\beta_2 = \exp(-13.53w - 2.90\sqrt{w} + 2.9) \qquad (16)$$

Using Clausius-Clapeyron's relation, we find $\Delta_{vap}H$ from the equilibrium vapour pressure (p^*), as

$$\Delta_{vap}H = -R\frac{\partial ln(p^*/p^{\ominus})}{\partial(1/T_p)} \qquad (17)$$

where $p^{\ominus}$ is the standard pressure. An empirical relation for the equilibrium vapour pressure was given by [7]:

$$p^*(T_p) = 0.133\times 10^3 \exp(18.303 - \frac{3816.44}{T_p - 46.13}) \qquad (18)$$

The heat capacity of paper, $C_{p,p}$, is estimated from

$$C_{p,p} = C_{p,dry-p} + wC_{p,H_2O} \qquad (19)$$

where $C_{p,dry-p}$ = 1256 J/ K kg for newsprint [11].

Heat transfer coefficients

The heat transfer coefficient between cylinder and paper at the contact side with cylinder was calculated by [12]

$$h_{cyl-p} = 1556.6w + 52.87 \qquad (20)$$

The heat transfer coefficient between paper and air at non-contact side with cylinder was calculated by [6]

$$h_{p-air} = \frac{\kappa}{D_{cyl}}\left\{ 0.3 + \frac{0.62Re_D^{1/2}Pr^{1/3}}{\left[1+\left(\frac{0.4}{Pr}\right)^{2/3}\right]^{1/4}} \left[1+\left(\frac{Re_D}{282000}\right)^{5/8}\right]^{4/5} \right\} \qquad (21)$$

The heat transfer coefficient between paper and air when the paper sheet travels between two cylinders was calculated by [6]

$$h_{p-air} = \frac{\kappa}{l}\left(0.664Re_l^{1/2}Pr^{1/3}\right) \qquad (22)$$

when $Re_l < 5\times 10^{\,5}$.

$$h_{p-air} = \frac{\kappa}{l}Pr^{1/3}\left(0.037Re_l^{4/5} - 871\right) \qquad (23)$$

when $Re_l > 5\times 10^5$.
The Reynolds (Eqs. (24) and (25)) and Prandtl (Eq. (26)) numbers were determined by

$$Re_D = \frac{V\, D_{cyl}}{\nu} \qquad (24)$$

$$Re_l = \frac{V\, l}{\nu} \qquad (25)$$

$$Pr = \frac{C_p\, \mu}{\kappa} \qquad (26)$$

All physical properties of the gas phase (C_p, κ, μ and ν) are calculated at the film temperature (average of T_{air} and T_p).

Simulation and modelling

Proceedings of ECOS 2005
Trondheim, Norway
June 20–22, 2005

SIMULATION OF INDUSTRIAL ENERGY SUPPLY SYSTEMS WITH INTEGRATED COST OPTIMIZATION

Eckardt Augenstein*, Stefan Herbergs*, Isabel Kuperjans*, Klaus Lucas*
***Chair of Technical Thermodynamics (LTT),**
Aachen University, Germany.
top-energy@ltt.rwth-aachen.de

ABSTRACT

Rational energy use in industry decreases costs, environmental pollution and depletion of resources. Since energy costs are often in the magnitude of the profit, a reduced energy use considerably affects the company-results. Yet, a systematic and profound analysis and optimization of the energetic processes is seldom conducted. In order to reduce the effort and increase the quality of energy system analysis, a computer aided method is being developed in a research project called TOP-Energy (Toolkit for Optimization of Industrial Energy Systems). The main goal of TOP-Energy is to support energy consultants in analyzing and optimizing industrial energy supply systems by supplying modules for documentation, simulation and evaluation of energy systems in respect to energetic, economic and environmental aspects. TOP-Energy consists of two major parts, a unifying framework and a set of modules: The former supplies the services of a modern GUI-application like module-sensitive dialogs and presentations, flow sheet editing and report generation. The latter are technical modules addressing particular aspects of energy system analysis like economical analysis or system simulation. An outstanding module of TOP-Energy is the supply system simulator called eSim, tailored to the consultant's needs. It evaluates energy supply concepts by means of historical or estimated demand data. In contrast to other simulator packages eSim supersedes costly modelling of control systems at an early stage of concept development by automatic optimization of component use. In order to model temperature sensitive components like chillers or heat pumps the conventional MILP-method was modified by employing evolutionary algorithms.
The article briefly presents the basic concepts of TOP-Energy including the framework's capabilities and then puts the focus on the simulator module, discussing its foundations and the solver numeric.
Keywords: Rational Energy Use, Energy System Simulation, Optimization, Engineering Framework, Object Model

NOMENCLATURE

Variables

A	Cross sectional area [m^2]
c_{il}	Specific heat capacity of ideal liquid [kJ/(kg K)]
$\dot{H}$	Enthalpy flow [kW]
$\dot{m}$	Mass flow [kg/s]
p	Pressure [Pa]
$\dot{Q}$	Heat flow [kW]
T	Thermodynamic Temperature [K]
λ	Pressure loss coefficient []
ρ	Density [kg/m^3]

Indices

i	Vertice index
j	Edge index
k	Cycle index
0	Reference

INTRODUCTION

Today, energy savings and efficient use of energy are important means of sustainable development. Particularly in industry, an appreciable amount of primary energy can be saved by enhancing the existing energy supply and transformation systems. Apart from the possibility of avoiding energy losses due to deteriorated equipment and insufficient system con-

trol, a considerable amount of primary energy can be saved by designing optimized energy systems on the basis of techniques such as cogeneration, heat pumps and heat integration. For cogeneration, for example, this has been surveyed in [1]. Unfortunately, methods and supporting tools to find such potentials, for example exergy analysis and system simulation, are well known in science but rarely used in practice.

Since the costs of energy are frequently of the same magnitude as the company's profits, reducing energy costs can lead to an appreciable effect on the profitability of the company. On the other hand, any investment in the energy system of a company competes against investments in new products or production equipment. It has to be profitable over a short payback period, even though it is a long term investment. Furthermore, the high costs of expert advice with the risk of uncertain results are usually avoided. This leads to a situation in which significant potentials for saving primary energy and money are not employed.

For these reasons, it is desirable to take steps to reduce the efforts and costs of an analysis and subsequent improvement of industrial energy systems. The use of computer aided methods seems favorable for this task, as an integrated tool can speed up work and offer effective methods for system analysis and optimization. In addition, aspects usually neglected in decision processes, like environmental protection can easily be incorporated by an automated evaluation of appropriate coefficients.

These considerations lead to the development of a new modular designed software called TOP-Energy (Toolkit for Optimization of Industrial Energy Systems), which is developed by a cooperation of several partners from universities and industry.

OBJECTIVES

The main objective of TOP-Energy is to provide an application that supports the process of energy system optimization for small- and middle-sized industrial sites. This work is usually done by smaller energy engineering companies that can not afford expensive custom developments. Contrary to numerous computational tools focusing on a specific technical problem, TOP-Energy integrates all steps of the typical work flow in one application, supplying a seamless flow of information from the first step of a project to the last. Apart from the support of computational methods like system simulation, special attention was paid to combining pure scientific methods with services such as comfortable user I/O and report generation. It is expected that this approach enhances working results by allocating appropriate computational methods, as well as reducing routine work by the automation of standard calculations and integrated project management.

BASIC CONCEPTS OF TOP-ENERGY

The approach taken for the design of TOP-Energy is outlined by the a number of basic concepts incorporated into the application. The main objective of these concepts is to supply an abstract description of the processes and elements involved in order to transform the multiplicity of engineering requirements to a consistent and coherent application. The most important of them are briefly described below.

Business Process Model

A business process model was defined in order to describe a standard work-flow for industrial energy system analysis and enhancement. It was derived from the German guideline, VDI 3922 (energy advisory for industry and trade) [2]. It describes a typical process for problem solution and is divided into three phases: problem analysis, solution development and decision. In accordance with this guideline a set of modules is defined each covering a major step in the work flow: A preliminary analysis module serves to give an overview of the energetic and energy-economic situation of the examined site.

This is followed by a detailed analysis where the goal is to document the energy supply system and identify its weak points in order to develop measures which enhance rational energy use.

In the solution development phase, a concept for an optimized system is found. For this purpose, TOP-Energy offers a system simulator designed for fast composition and simulation of energy supply system models. The result of the simulation contains various energetic, economic and ecological coefficients helping to evaluate the effects of the improvement measures planned.

Finally, to assist decision making, the developed variants are evaluated comparatively using one as a reference. For economical aspects, this is performed

by an economy module capable of computing a variety of key figures directly from the simulation results.

System Boundary Model

While VDI 3922 describes the engineer's workflow very well, it lacks a precise definition for system boundaries, especially the distinction between the energy supply system and energy utilizing systems. As this is vital for the interpretation of balance results and system coefficients, an appropriate definition is introduced in TOP-Energy. Basically, it distinguishes between four subsystems: First, the public energy market which represents the economic boundary conditions, supplying various forms of end energy to the examined site. Second, an environment based on the definition of a thermodynamical environment capable of exchanging energy and matter with the remaining two subsystems covering the examined site itself: The energy supply system and the systems of energy end users (usually the production site). The former converts the available forms of end energy into forms required by the end users. The latter employs the delivered energy in all kinds of technical processes, possibly rejecting waste heat or production residues to the energy supply system.

Framework Approach

Analyzing the basic use cases of the application, it became apparent that every technical module requires certain functionalities that are non-specific to the technical problem it addresses: Basically, these are the persistent data storage and data exchange, user interface functionality like I/O-dialogs and flow sheeting, managing projects and report generation. In case these services are outsourced to a generic framework which exposes appropriate interfaces, the development of a module is reduced to the implementation of its technical contents. On the one hand, the availability of such a framework simplifies the transfer of a scientific program code to an engineering application tremendously. On the other hand, cooperation on the level of technical contents between framework, modules and component models, makes high demands on interface specifications and the underlying object model.

Application Object Model

As the framework supplies services for persistent data storage and data manipulation on the user interface to the modules and model components, sophisticated interface specifications are needed. The foundation for these definitions is an object model describing the structure and semantics of data to be exchanged. Its central element – the component – is used to map real-world units, as well as to represent the usage of a module within the project tree.
A component can aggregate a set of different elements in order to store information about technical data, GUI appearance, network structures and report generation. First of all, components can contain other components and thus are able to build tree structures or collections. However, depending on the component sub-class, the aggregation of components is restricted. In order to map network structures like they occur in schematic representation of energy systems, components can contain connection points (*pins*) that can be connected to internal or external networks.
Components are not restricted to mapping real world objects to the data space, they may represent any configurable element of the application as long as it forms a complete and autonomous unit.

Content Database

Closely related to the object model, a content database was developed in order to support the development of technical data structures: Using well defined technical terms when requesting user input or presenting results is vital to the usefulness of the application. Furthermore, developing a set of cooperating modules and component models requires a method to guarantee identical semantic interpretation of data by all communicating elements.
This is achieved by setting up a global dictionary of technical terms. In order to set up component data structures based on this dictionary, every definition of a technical term is attached to a pre-defined basic data type (such as *number* or *characteristic diagram*) including appropriate template data like units and value boundaries. These atomic data units – called *primitives* – can then be assembled to tree like data structures and be imported to a component template and thereby defining its data space. The unique definition of technical terms allows the save

exchange of data between different modules even without exact knowledge of their data structures.

THE TOP-ENERGY FRAMEWORK

Based on the concepts described above, an application framework was implemented, using the Computer Aided Schematics Toolbox (CASTool) developed by the R&D Department for Graph-based Engineering Systems of the Society for the Promotion of Applied Informatics (GFaI), Berlin.

The framework supplies the services of a modern GUI-application like module-sensitive dialogs and presentations, flow sheet editing for creating energy system schemes and report generation. Further more, the system provides a special editor that supports the buildup of component templates. Modules can be integrated into the application via a plug-in mechanism that allows the call of module code as well as the insertion of module specific menus.

A detailed description of the developed object model, the framework architecture and its capabilities can be found in [3].

THE SYSTEM SIMULATION MODULE

TOP-Energy was designed to incorporate various computational methods implemented as plug-in modules. The most prominent one to be part of the first release of TOP-Energy is *eSim*, a module for simulation of energy supply systems. The main objective of this module is to determine a set of economic, energy-related and environmental key figures of an energy supply infrastructure for a term of usually one year. The boundary conditions of a system model are demand profiles for the different forms of energy as well as information about the environment.

Overwiev

Energy system simulation is well known in science today. Various different solutions are available [4] although only few meet the usability requirements of engineering applications. Depending on the specific objectives of a simulation system, different mathematical approaches are used. The most sophisticated models base on differential equations (either DAE or ODE), being able to forecast the dynamic behavior of an energy supply system [5]. This, of course, requires a detailed modeling of the feedback control systems. Apart from that, detailed design data is required to calculate a machine's time constants. In a more simple approach, the inertia of the system components is neglected due to the fact that the time resolution of boundary conditions usually is not better than one hour. These quasi-static models result in algebraic systems requiring less detailed design parameters of the system components. However, the problem remains that control rules must be supplied by the user.

An approach that supersedes the specification of any control rules is to determine the system state by means of operation optimization. These systems, usually based on mixed integer linear optimization (MILP) [6], are frequently used to determine optimal power plant schedules [7]. However, this approach is capable of evaluating the design of energy supply systems too [8]. One drawback of these optimizing systems is the fact, that, due to the limitations of the underlying MILP, their models regard media temperatures to be independent from the system state, i.e. constant, or must be estimated before the linear problem is solved.

Basic Concepts

eSim was designed to read network schemes created in the framework's scheme editor and stored in the format of the TOP-Energy object model. Figure 1 shows a simple scheme of an energy supply system created with the scheme editor.

While the component models are formulated using a modelling language designed to the specific numerical needs, the different network types are implemented in the simulator code. Currently these are electrical power lines, fuel distribution networks, hydraulic networks as well as nets modelling air and flue gas lines. Other network types e.g. for steam networks are currently under development. All network types except the electrical network are directed, each distinguishing input and output pins. Reverse flow in directed networks is not considered. As components may include other components in the object model, it is possible to design hierarchical simulation models. The lowest modelling level introduced defines a set of basic operations typical to the respective network type. These low level models can be thought as connectors between the network model and the modelling language. Examples are

sources, sinks, pressure change and heat exchanging in hydraulic or combustion for air and flue gas networks.

The set of equations and algorithms describing the complete system model are assembled from the model descriptions of the single components and equations derived from the structure analysis of the connecting networks. While the network model based on components, pins and nets is the appropriate means to assemble, display and store energy network schemes, the structure analysis and the generation of balance equations is better conducted on graphs. Therefore the network description is transformed into a set of graphs, each describing one single coherent network with the vertices representing balance nodes and the edges describing a state change of the flowing medium through a component. From these graphs, the equations describing the system can be derived. Besides the balances for mass and energy flows, a system of algebraic equations is generated in order to propagate constant parameters, e.g. medium properties, through the system.

Time Step Algorithm

As eSim is thought to be used in an early stage of planning, modelling a system should not be too time consuming and require only data available to the user. Therefore, the operating optimization approach as described above was chosen.

This implies that the problem of modelling dependencies between fluid temperatures and component efficiencies has to be solved: When modelling a conventional boiler, it can be assumed that its efficiency is independent from the inlet temperature at every state of operation. To describe a hydraulic system of a set of such components, it is sufficient to formulate temperature independent energy balances regarding the all heat suppliers and consumers attached to the network.

$$\sum \dot{Q}_{network} = 0 \tag{1}$$

Apart from that, it only has to be assured that the second law is not violated due to unappropriate temperature differences in the heat transferring components. However, assuming constant temperatures this constraint can be checked before the optimizing algorithm is carried out.

This is different if temperature sensitive technologies like condensing boilers, heat pumps or chillers are to be modelled. As the efficiency of such components depends on the inlet temperatures of their heat exchangers, temperatures cannot be assumed to be constant but must be considered as system variables. As a consequence, the equations of mass conservation have to be solved in addition to the energy balances. E.g. for a hydraulic network with no storage effects, this leads to equations 2 and 3 for each vertice and 4 and 5 for each edge in the network graph.

$$\sum \dot{m}_i = 0 \tag{2}$$

$$\sum \dot{H}_i \approx \sum \dot{m}_i c_{il} (T_i - T_0) = 0 \tag{3}$$

$$\dot{m}_{j,in} = -\dot{m}_{j,out} = \dot{m}_j \tag{4}$$

$$\dot{Q}_j = \dot{m}_j (h_{j,in} - h_{j,out}) \approx \dot{m}_j c_{il} (T_{j,in} - T_{j,out}) \tag{5}$$

In order to consider the pumping energy needed for operation of the hydraulic network using a simple pressure loss model, equations 6 and 7 occur for each edge and each cycle in the graph respectively.

$$\sum \Delta p_j = \frac{\lambda}{2\rho A^2} \dot{m}_j^2 \tag{6}$$

$$\sum \Delta p_k = 0 \tag{7}$$

Even under the assumption of an ideal liquid with constant heat capacity, products of two variables occur as well as squares of $\dot{m}$. Being part of the system to be optimized, the equations above introduce nonlinear constraints which cannot be treated with established algorithms like linear or even quadratic programming [6]. Being in need of a robust algorithm as well as integer variables for modelling switching events, ways had to be found to linearize these constraints. This would allow to treat the remaining problem using mixed integer linear programming (MILP) fulfilling the requirements stated. Two approaches for the separation of mass and energy equations were found in literature: Filter [9] discretizes the mass flow variable by creating ”mass flow quantums”. This allows the formulation of both balances in one MILP system for the price of a high number of integer variables, causing a huge branch an bound tree to be calculated. Hackländer [10] separates the variables of the product by a binomial transformation. The remaining squares are then approximated by piecewise linearization. Though beeing very elegant, this approach as well introduces a

huge number of integer variables in order to approximate three parabolas per linearized product. Moreover, the approximation leads to errors in the energy and mass balances depending on the quality of approximations.

In order to avoid a high number of integer variables in the MILP system, the approach proposed here separates the mass flow balances into a an additional system of linear equations and uses a special algorithm to coordinate the latter with the remaining MILP system. In the actual implementation, an optimizer based on evolutionary algorithms [11] was chosen, using the linearly independent mass flow variables as genome.

The principle of the algorithm is shown in figure 2. In order to create an individual of a generation, the optimizer chooses a set of linearly independent mass flow variables, either randomly at the beginning of the optimization run or by recombination and mutation from individuals of the parent generation. The set then is passed to a linear solver in order to calculate the dependent mass flow variables from the mass flow balances (eqn. 2 and 4). Finally, the complete set of mass flow variables is transferred to the MILP system, generated from the network energy balances and remaining constraints specified in the component models. As a result of the MILP solution, the target function value is returned to the optimizer in order to evaluate the relative quality of the individual compared to competing individuals.

As the mass flow variables are chosen stochastically by the optimizer, a relevant number of proposals will lead to a violation of constraints in the MILP system and therefore will end up without a solution. This occurs due to the fact that the vertice enthalpy balances (eq. 3) cannot be satisfied with the given set of mass flows. In order to return information about the proximity to a valid solution, a slack variable is introduced for each network graph vertice. Literally spoken, the slack variable represents a virtual enthalpy source or sink compensating the – otherwise invalid – enthalpy balance of the vertice. In order to let the slack variables converge towards zero during the optimization run, an accordant contribution is added to the target function, referred to as ”virtual target function” in figure 2.

Finally, the time step results including the energy and cost flows as well as the load of the components involved can be obtained from the MILP solution of the best individuum calculated.

In the basic implementation presented here, the calculation effort needed during a simulation is comparable to the algorithm proposed by Filter [9]. This can be ascribed to the fact that the mass flow values are chosen randomly by the optimizer and therefore a high number of linear systems has to be evaluated to find valid solutions of the energy balances. Though not implemented yet, a number of enhancements promise a relevant performance gain:

Evaluating the slack variables of the energy balances after a MILP run, information can be obtained about the local optimization direction in order to create better individuals. Passing this information back to the optimizer, a faster convergence of the time step algorithm can be expected.

As many load profiles show recurring patterns in practice, good starting individuals for the time step optimization can be obtained from previous time step solutions by a least square comparison of the respective system coefficients. This means is expected to speed up the time step calculation with increasing simulation time.

Example Simulation

Figure 3 shows the results of a 48 hour cost optimized simulation run of the system shown in figure 1. The upper diagram shows the split of the heat load between boiler and cogeneration unit, the lower the customer generated fraction of the power demand. The power supply tariff distinguishes two energy rates depending on the time of day, marked by LT (low tariff) and HT (high tariff) in figure 3.

It can be seen that the operation of the cogeneration unit is driven by the heat load in the low tariff hours, feeding superfluous power into the public grid (see 5 a.m. of the first day). During the high tariff time, the cogeneration unit is controlled by the internal electric power demand. In case spare heat is produced, it is released to the environment via the emergency cooler (see 6 p.m. of the first day).

The example shows the capability of the simulator to optimize the system operation depending on the physical and economical boundary conditions given.

CONCLUSIONS AND PERSPECTIVES

The main aim of TOP-Energy was the development of a software system to support the analysis and op-

timization of small to medium energy supply systems. Claiming cheap integration of additional computational methods and user-specific adaptability, a generic framework incorporating technical modules was developed.
In order to supply a simulation module for energy supply systems for the estimation of annual system efficiency and costs, a new algorithm was developed integrating the optimization of the component operation and therefore superseding the costly modelling of feedback control systems. Though the algorithm lacks of performance in the actual implementation, the feasibility of the approach could be proven.
Further development of the TOP-Energy framework will focus on the version control of component and module templates, an enhanced object model and report generation. Future development of the simulator will include the optimization of the actual implementation in terms of performance as well as the research on alternative coordination algorithms and additive network types and model components. Moreover, additional modules are under development, so a module for bench-marking energy demand and CO_2-emissions of industrial sites.
More information about TOP-Energy can be found on the project website at http://top-energy.ltt.rwth-aachen.de.

ACKNOWLEDGEMENTS

The authors would like to thank the following persons which are working in the TOP-Energy project team: Jan Feller, LTT, Aachen; Gregor Wrobel, Matthias Pleßow, Oliver Berndt, GFaI, Berlin; Jörg Meyer, EUtech GbR, Aachen; Rainer Küffmeier, BFT GmbH, Aachen. The authors are also grateful to the Bundesministerium für Wirtschaft und Technologie (BMWA) and the German Federation of Industrial Cooperative Research Associations "Otto von Guericke" (AIF) for the financial support of the project. The work was done from 01.01.2003 to 31.12.2004 under project code 92 ZBG / 1.

REFERENCES

[1] K. Lucas. On the thermodynamics of cogeneration. *Int. J. Therm. Sci.*, 39:1039–1046, 2000.

[2] Workgroup Energy Consulting. VDI 3922, energy consulting in industry and business. Technical report, VDI, 1998.

[3] E. Augenstein, G. Wrobel, I. Kuperjans, and M. Pleßow. TOP-Energy – computational support for energy system engineering processes. In *Proceedings of the 1rst IC-SCCE*, Athen, 2004.

[4] B. Elmegaard and N. Houbak. Software for the simulation of power plant processes, part A and B. In G. Tsatsaronis, M.J. Moran, F. Cziesla, and T. Bruckner, editors, *Proceedings of ECOS 2002*, pages 742–772, Berlin, 2002.

[5] S. Wischhusen, B. Lüdemann, and G. Schmitz. Economical analysis of complex heating an cooling systems with the simulation tool hksim. In Peter Fritzson, editor, *Proceedings of the third International Modelica Conference*, pages 259–268, November 2003.

[6] P.E. Gill, W. Murray, and M.H. Wright. *Practical Optimization*. Academic Press, 1982.

[7] K.-D. Maubach. *Mittelfristige Einsatzoptimierung in Versorungssystemen mit Kraft-Wärme-Kopplung*. PhD thesis, Bergische Universität-Gesamthoschschule Wuppertal, 1994.

[8] T. Bruckner. *Dynamische Energie- und Emissionsoptimierung regionaler Energiesysteme*. PhD thesis, Institut für theoretische Physik, Universität Würzburg, 1997.

[9] S. Filter. *Zur Modellgenauigkeit der mittelfristigen Einsatzoptimierung von Querverbundsystemen*. PhD thesis, RWTH, Aachen, 2001.

[10] P. Hackländer and J. Verstege. Optimierung der Betriebsplanung von Gasversorgungsunternehmen. In VDI Gesellschaft Energietechnik, editor, *Fortschrittliche Energiewandlung und -anwendung*, volume 1594 of *VDI-Berichte*, pages 605–614, 2001.

[11] Peter Roosen. Concept and application of the evolutionary parameter optimization toolbox EPO. In *1999 Proceedings of the ASME-Conference "Modeling and Simulation"*, 1999.

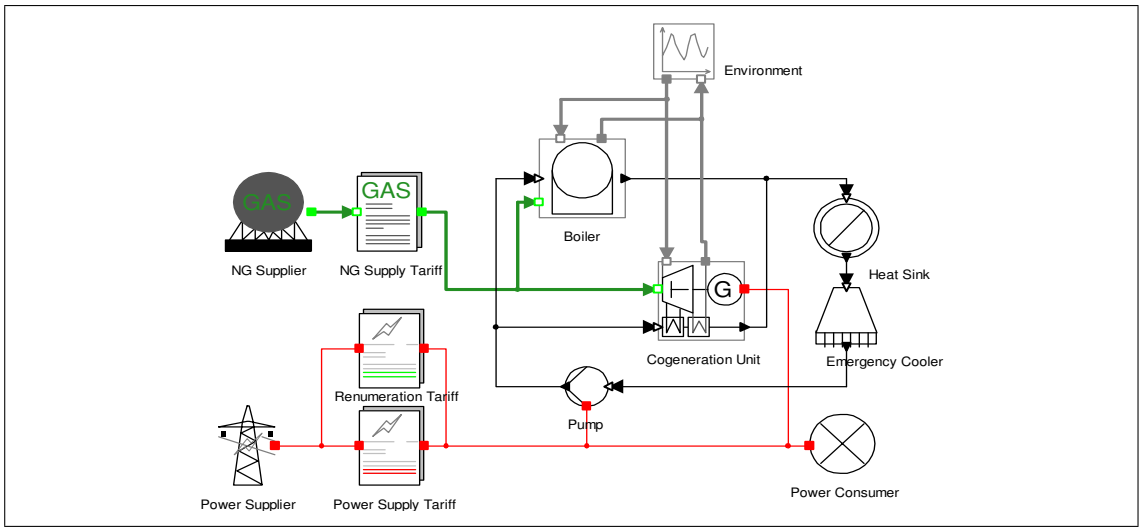

Figure 1: Example of a simple energy supply system scheme created with the scheme editor.

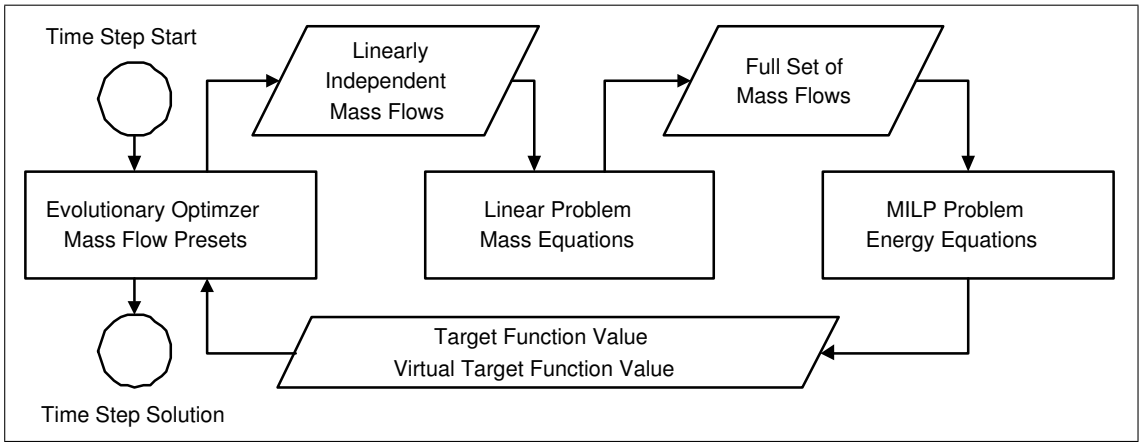

Figure 2: Principle of the proposed time step algorithm.

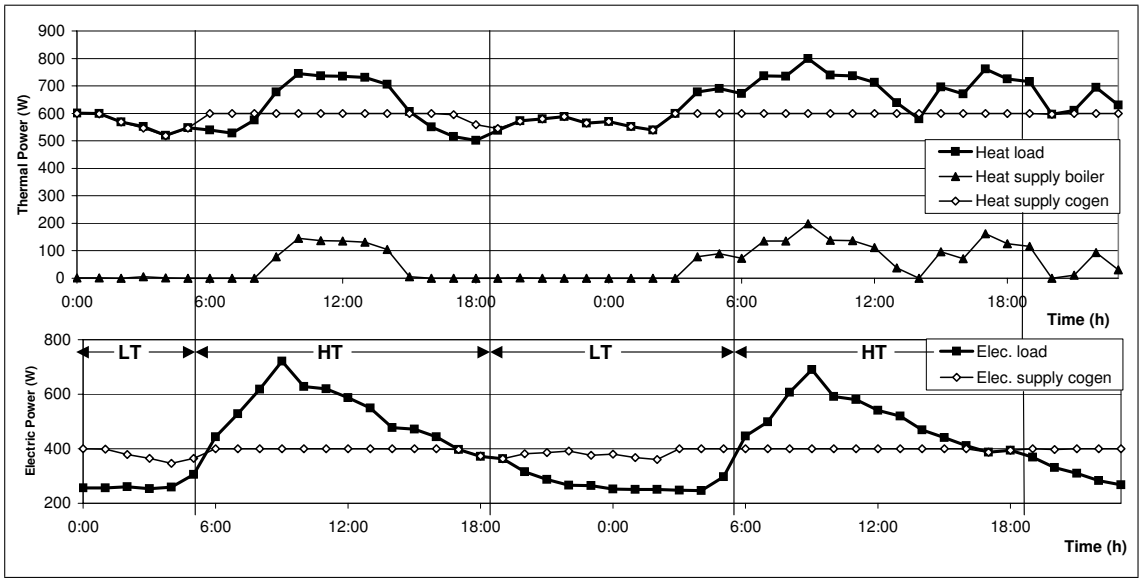

Figure 3: Results of a simulation run for the system shown in figure 1.

Proceedings of ECOS 2005
Trondheim, Norway
June 20–22, 2005

TRANSIENT ANALYSES OF CONJUGATE HEAT TRANSFER IN A THREE-DIMENSIONAL GAS TURBINE BLADE MODEL

Alfonso Campos-Amezcua [a,b], Armando Gallegos-Muñoz [a,*]
Zdzislaw Mazur-Cerwiec [b], Alejandro Zaleta-Aguilar [a]

[a] *Department of Mechanical Engineering, University of Guanajuato.*
Av. Tampico 912, Col. Bellavista, Salamanca, Gto., C.P. 36730.México.

[b] *Department of Turbomachinery, Mexican Electric Research Institute.*
Reforma No.113, Col Palmira, Cuernavaca, Mor. México

ABSTRACT

A conjugate numerical methodology was employed to predict the metal temperature of a three-dimensional gas turbine blade model under different operating conditions. The conjugate heat transfer approach allows the simultaneous solution of the external flow and conduction within the metal vane, eliminating the need for an uncertain additional boundary condition for decoupled solutions.

Taking into account the enormous computational load to deal with the whole processes in the start-up and the shut-down (transient analyses), a reduced model with standard wall function near-wall treatment was considered to simulate the actual blade.

The results obtained by a commercial code, on the basis of finite volume method are presented, where the maximum temperature gradients appear in the trailing edge (ΔT=270 K) followed by the leading edge and the region between cooling holes and suction side (ΔT=250 K).

Keywords: gas turbine, blades, CFD.

NOMENCLATURE

$C_{1\varepsilon}$	Model constant
$C_{2\varepsilon}$	Model constant
C_{μ}	Model constant
E	Total energy per unit mass [kJ/kg]
F_i	External body force
h	Enthalpy [kJ/kg]
$J_{j'}$	Diffusion flux of species j'
k	Thermal conductivity [W/m-K]
k_{eff}	Effective conductivity $(k + k_t)$ where $k_t = \mu_t / \mathrm{Pr}_t$
p	Static pressure [kN/m^2]
Pr_t	Turbulent Prandtl number
R	Auxiliary function
S	Modulus of the mean rate-of-strain tensor S_{ij}
S_h	Heat of volumetric heat source
S_m	Mass added from any user-defined sources
t	Time [s]
T	Temperature [K]

* Corresponding author: Phone: +52 464 80911 Fax: +52 464 72400 e-mail: gallegos@salamanca.ugto.mx

u_i Velocity [m/s]

w_i Relative velocity [m/s]

x_i Distances in radial coordinates [m]

α_ε Inverse effective Prandtl number for ε

α_κ Inverse effective Prandtl number for κ

β Model constant

ε Dissipation rate of turbulent kinetic energy [m^2/s^3]

η Strain rate

η_0 Initial strain rate

κ Turbulent kinetic energy [m^2/s^2]

μ Molecular viscosity [kg/m-s]

μ_{eff} Effective viscosity,

$$\mu_{eff} = \mu_{mol}\left[1+\sqrt{\frac{C_\mu}{\mu_{mol}}\frac{k}{\sqrt{\varepsilon}}}\right]^2$$

μ_t Turbulent viscosity

ρ Density of fluid [kg/m^3]

ρg_i Gravitational body force

T_{ij} Components of stress tensor [N/m^2]

Ω Rotation vector [rad/s]

INTRODUCTION

Turbine entry temperature has been increased from 1200 K in the 50's up to more than 2000 K at the present time [1], reason why the nozzles and blades made principally with superalloys have become critical elements. The cost of these components is raised, owing principally to the cost of the materials as well as to their manufacturing process, representing approximately 30 % of the cost of the turbine.

Due to the high cost of the blades and the safety at which they must operate, the useful life of the blades must be optimized. For this, it is necessary to have available tools that allow to predict the useful remaining life of the gas turbine blades to determine if the blades can continue operating, if they can be rehabilitated or if they must stop operating to avoid catastrophic faults.

Nowadays methods exist to estimate the useful life of components that work at high temperature, which consider the interaction of fatigue phenomena and thermofluence. Among the methods to predict the useful remaining life for thermofluence, there exist those which relate the time and temperature and extrapolate information of thermofluence. Nevertheless, these models present inaccuracies that are caused by: a) dispersion of the material properties; b) mistakes in the determination of the temperature and stress; c) effects caused by corrosion and coating; and d) degradation of the material during operation [2].

Recently several articles have been published applying the conjugate calculation technique to predict the metal temperature of a three-dimensional gas turbine vane [3, 4, 5]. However there are few works on transient analyses [6] due principally to high computational expense and the lack of experimental data to compare to the results.

The main objective of this study is to predict the transitory profile of temperature inside the first stage blade caused by the process of take-off of the turbine using CFD.

DESCRIPTION OF ANALYSIS

The numerical analysis was conducted by using the CFD commercial code Fluent 6.1 [7] on the basis of the finite volume method. User defined functions were used for creating the numerical conditions of the flow and heat transfer in each time step.

Governing equations

The Navier–Stokes equations for rotating flows are applied. The mass conservation equations or continuity equation derived from the RNG theory is:

$$\frac{\partial \rho}{\partial t}+\frac{\partial}{\partial x_i}\left(\rho w_i\right)=S_m \qquad (1)$$

The momentum conservation equation for flows in rotating domains is modelled by

$$\frac{\partial}{\partial t}\left(\rho\mu_i\right)+\frac{\partial}{\partial x_j}\left(\rho w_i u_j\right)=-\frac{\partial p}{\partial x_i}+\frac{\partial T_{ij}}{\partial x_j} \qquad (2)$$
$$-\varepsilon_{jki}\Omega_j\rho\mu_k+\rho g_i+F_i$$

The energy conservation equation for rotating flows is described by

$$\frac{\partial}{\partial t}(\rho E)+\frac{\partial}{\partial x_i}\left[w_i(\rho E+p)\right]= \frac{\partial}{\partial x_i}\left[k_{eff}\left(\frac{\partial T}{\partial x_i}\right)-\sum_{j'}h_{j'}J_{j'}+u_j\left(\tau_{ij}\right)_{eff}\right]+S_h \quad (3)$$

Energy equation in solid regions includes only the heat flux due to conduction within the solid:

$$\frac{\partial}{\partial t}(\rho E)=\frac{\partial}{\partial x_i}\left(k\frac{\partial T}{\partial x_i}\right) \quad (4)$$

Equation (4) is solved simultaneously with the energy conservation equation (3) in the flow regions to yield a fully coupled conduction-convection heat transfer prediction.

The turbulence model considers the transport equations for κ and ε, provided as

$$\frac{\partial}{\partial t}(\rho\kappa)+\frac{\partial}{\partial x_i}(\rho u_i\kappa)=\frac{\partial}{\partial x_i}\left(\alpha_\kappa\mu_{eff}\frac{\partial\kappa}{\partial x_i}\right) + \mu_t S^2-\rho\varepsilon \quad (5)$$

and

$$\frac{\partial}{\partial t}(\rho\varepsilon)+\frac{\partial}{\partial x_i}(\rho u_i\varepsilon)=\frac{\partial}{\partial x_i}\left(\alpha_\varepsilon\mu_{eff}\frac{\partial\varepsilon}{\partial x_i}\right) + C_{1\varepsilon}\frac{\varepsilon}{\kappa}\mu_t S^2-C_{2\varepsilon}\rho\frac{\varepsilon^2}{\kappa}-R \quad (6)$$

In the high-Reynolds limit $\alpha_k=\alpha_\varepsilon\approx 1.393$, S is the modulus of the mean rate-of-strain tensor, which is defined as

$$S\equiv\left(2S_{ij}S_{ij}\right)^{1/2} \quad (7)$$

R in the equation (6) is given by

$$R=\frac{C\mu\rho\eta^3\left(1-\eta/\eta_0\right)}{1+\beta\eta^3}\frac{\varepsilon^2}{\kappa} \quad (8)$$

where

$\eta=S\kappa/\varepsilon$, $\eta_0\approx 4.38$, $\beta=0.012$, $C_{1\varepsilon}=1.42$, and $C_{2\varepsilon}=1.68$

Finally, ideal gas law was used as the equation of state.

Numerical methods

The turbulence model used was the two equation model RNG (renormalization group) κ-ε [8]. Likewise, in turbulence scalar transport, an algebraic model derived from RNG theory was applied. The SIMPLE algorithm was used to solve the discretized equations with spatial second order accuracy. In the internal circular passages, heat balance was made, using a convective heat transfer coefficient obtained from a previous study [5]. A compressible analysis was developed and thermal properties were set up taking into account the dependency on temperature.

Computational domain and grid

The computational domain consists of a fluid region around the rotor blade and a region of solid material that composes the blade. Figure 1 shows the computational grid on the blade surface (solid) and on the gas surface (fluid).

Hexaedron cells were applied in both solid and fluid regions. The number of cells is 27,680 around the blade and 16,224 inside the blade. The regions of the cooling air were not modelled.

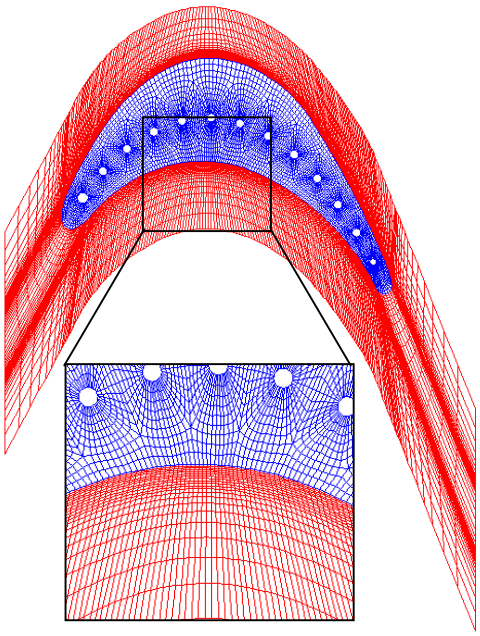

Figure 1: Grids on the gas and blade surfaces

Boundary conditions

The boundary conditions to the computational domain are presented in figure 2 and summarized in table 1. The variation of the gas and air temperature in space and time are presented in figure 3.

The heat transfer coefficient in the wall of the internal circular passages is taken from a study [5], where fully developed turbulent flow in the circular pipe is assumed. Inlet temperature was linearly related to the turbine inlet temperature and to the temperature of the air at the compressor outlet.

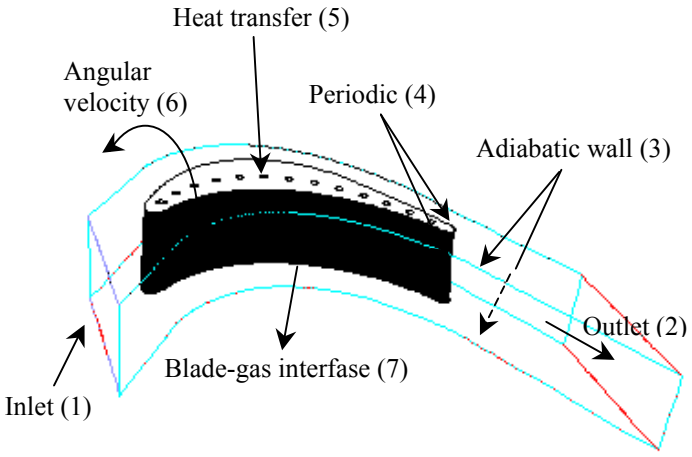

Figure 2: Location of the boundary conditions

Figure 3 shows time variations of inlet total temperature, both gases and air. These conditions were based on characteristic diagrams that simulate a hot start-up process of daily start operation of an actual gas turbine. The rest of the boundary conditions are fixed in time and space. The end walls were assumed adiabatic wall to consider a large blade where no changes occur in radial directions. Wall function [7] was used and the thermal conditions were computed to conjugate between inside and outside of the walls.

Time step for each transient calculation was set from 0.01 to 10, increasing as the time advanced.

No.	Boundary condition	Units	Value
0	Atmospheric pressure	kPa	97.7
1	Input gases: Mass flow rate Angle with regard to the axial axis Static Pressure Total Temperature Turbulence intensity Length scale	 Kg/s degrees kPa (man) K % m	 0.21 60.0 510.0 Fig. 3 5.0 0.006
2	Output gases: Static Pressure Turbulence intensity Length scale	 kPa (man) % m	 470.0 5.0 0.006
3	Heat flow rate	kJ/kg	0
4	Periodic		
5	Heat transfer: Air temperature Heat transfer coefficient	 K W/m^2-K	 Fig. 3
6	Angular velocity	rpm	5100
7	Coupled conduction convection heat transfer		

Table 1: Boundary conditions

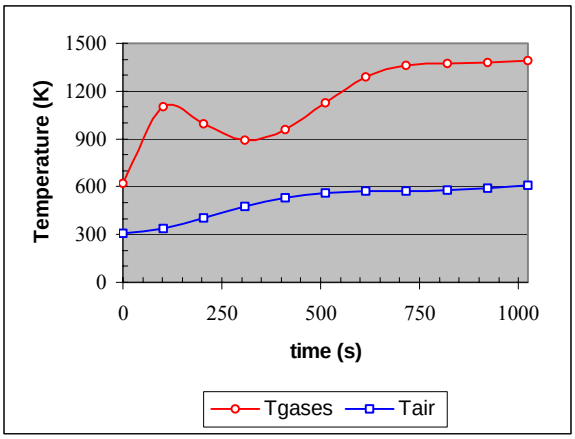

Figure 3: Variation of gases and air temperature

RESULTS AND DISCUSSION

Figure 4 shows the vectors of relative velocity distribution in the bucket passage at 50% vane height. The maximum flow velocity of 920 m/s is reached in the throat of passage, the local minimum is on the vane pressure side and the bucket leading edges.

Figure 5 to Figure 7 show time variations of total temperature. They illustrate the temperature

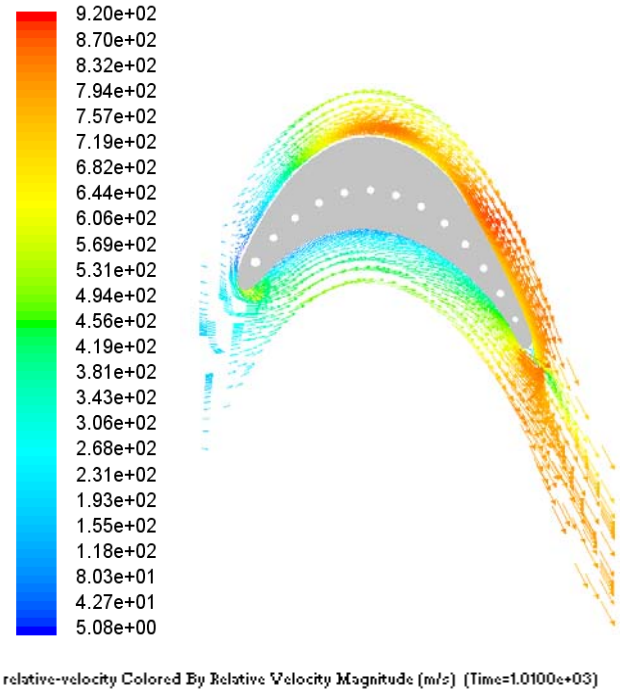

Figure 4: Vectors of relative velocity distribution

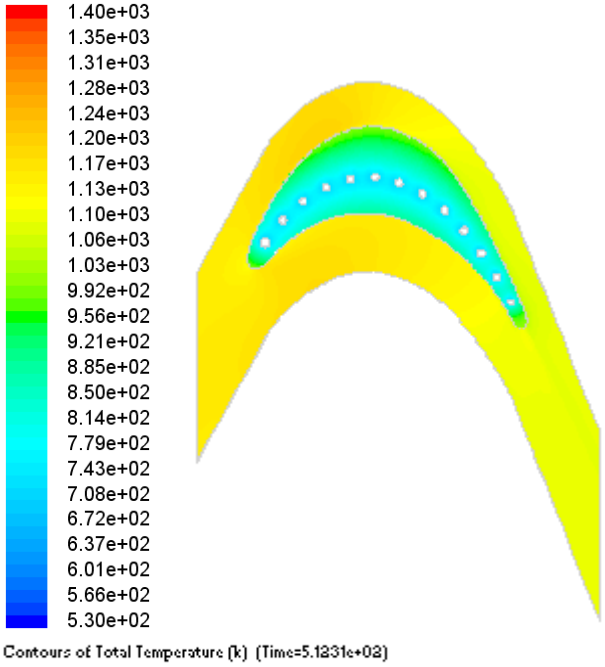

Figure 6: Total temperature contours in the bucket passage at 50% vane height (512 s).

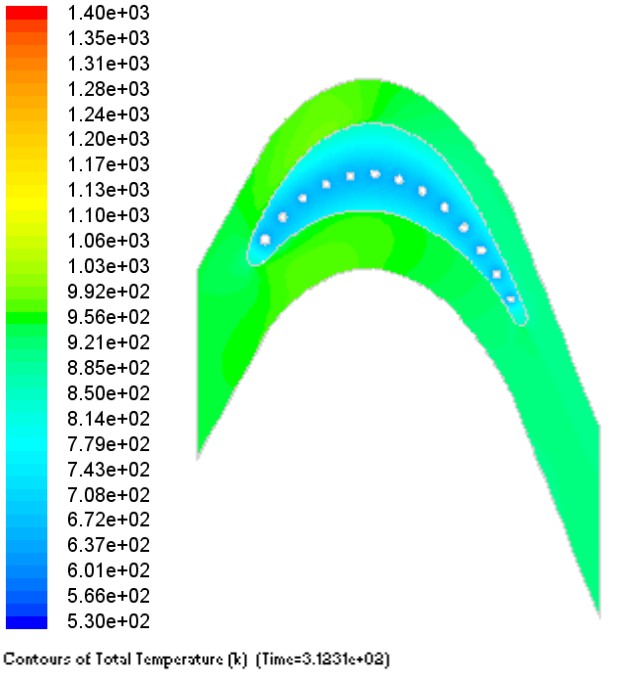

Figure 5: Total temperature contours in the bucket passage at 50% vane height (312 s).

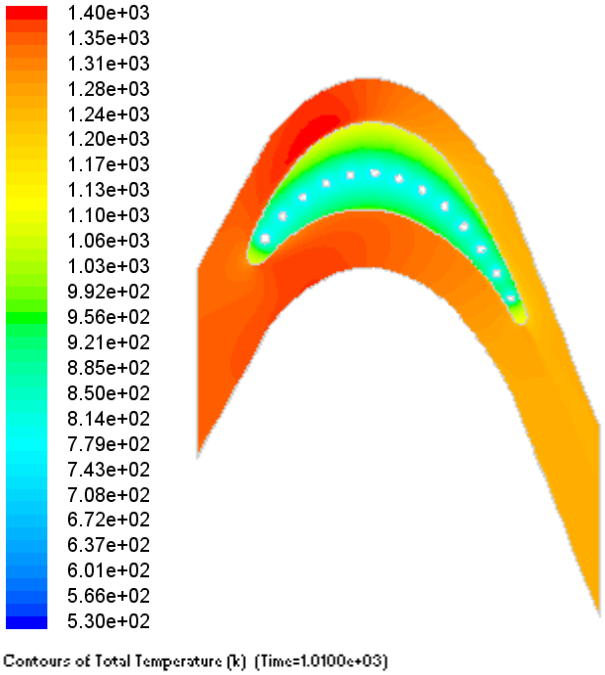

Figure 7: Total temperature contours in the bucket passage at 50% vane height (1010 s).

distribution in the external fluid (combustion gases) and bucket solid body. An asymmetric temperature field distribution can be appreciated in the solid body around the cooling passages due to bucket rotating effect.

The maximum temperature gradients appear in the trailing edge (ΔT=270 K) followed by the leading edge and the region between cooling holes and suction side (ΔT=250 K). These zones must to be taken into account in a succeeding thermal stress analysis, due to the severe gradient of the temperature.

It can be seen that temperature distribution in the blade is markedly influenced by unsteady conditions (Figure 3). The global temperature difference inside the blade increases as the difference of combustion gas and cooling air temperature increases, reaching roughly the value of 300 K. This is higher than temperature gradient presents in a steady-state analysis (220K).

On the other hand, if the initial conditions had been the corresponding ones to t=1010 s, without considering the variation of controlled temperatures, the steady-state would be reached in 180 seconds approximately, but the gradients of temperature would be very higher, affecting seriously the blade life through thermal fatigue.

CONCLUSIONS

The computations were able to simulate the heat transfer of the bucket during transient operation, being a contribution to transient analyses of conjugate heat transfer simulation in gas turbine blades. Temperature predictions were made in a reduced gas turbine blade model, considering time variations of total temperature both in the combustion gas and in the cooling air. However, definite conclusion in this regard may await more experimental data to compare to the results.

The maximum temperature gradients appear in the trailing edge followed by the leading edge. These severe gradients will seriously affect the blade life due to thermal fatigue.

In the future, work time variations of angular velocity and mass flow rate will be taken into account, as well as the whole blade model.

The present predictions will make it possible to estimate stress and creep strain loaded on the bucket and to assess the bucket remaining life based on the evaluation of the damage.

REFERENCES

[1] Han Je-Chin, Dutta Sandip, Ekkad Srinath. *Gas Turbine Heat Transfer and Cooling Technology*, Taylor & Francis, 2000.

[2] Viswanatan R. *Life Assessment Technology for Combustion Turbine Blades*, Electric Power Research Institute, Palo alto, Ca, Vol. 109, 1987.

[3] Takahashi T et al. *Thermal Conjugate Analysis of a First Stage Blade in a Gas Turbine*, International Gas Turbine & Aeroengine Congress & Exhibition, Munich, Germany, 2000.

[4] York W. and Leylek J. *Three-dimensional Conjugate Heat Transfer Simulation of an Internally-Cooled Gas Turbine Vane*, Proceedings of ASME Turbo Expo, Atlanta, USA, 2003.

[5] Mazur Z, Campos A, Campos R. *Steady-state analysis of conjugate heat transfer of a gas turbine first stage bucket*. 10th International Symposium on Transport Phenomena and Dynamics of Rotating Machinery 2004;023

[6] Toshihiko Takahashi, et. *Transient Analyses of Conjugate Heat Transfer of a First Stage Rotor Blade in Start-Up and Shut-Down.* International Gas Turbine & Aeroengine Congress & Exhibition, 2001

[7] FLUENT V6.1.22 User Guide, Fluent Inc., Canterra Resource Park, 10 Covendish Court, Lebanon NH03766, USA, 2003.

[8] Yakhot V, Orzag SA. Renormalization Group Analysis of Turbulence. I. Basic Theory, J. Sci. Comp 1986., 1: 3-51.

Proceedings of ECOS 2005
Trondheim, Norway
June 20–22, 2005

GAS TURBINE COOLING MODEL FOR EVALUATION OF NOVEL CYCLES

Maria Jonsson* **and Olav Bolland**
Norwegian University of Science and Technology
Department of Energy and Process Engineering
NO-7491 Trondheim, Norway

Dominikus Bücker
ALSTOM (Switzerland) Ltd
Segelhof 1, 5405 Baden-Dättwil
Switzerland

Mike Rost
Siemens AG, PG W8IN
P.O. Box 3220, 91050 Erlangen
Germany

ABSTRACT

Simulation and parameter variation of novel gas turbine-based cycles require a simple yet reliable cooled gas turbine model that is easy to implement. This study proposes a generic cooling model using open-loop cooling. The model has been tuned to represent modern heavy-duty gas turbines in cooperation with the gas turbine manufacturers involved in the ENCAP (Enhanced Capture of CO_2, EU 6th Framework Programme) project, of which this work is a part. Additionally, a commercial gas turbine simulation tool has verified the results of the model. Besides the conventional working fluid air, the model has been investigated for a CO_2/H_2O working fluid typical for a semi-closed oxygen-combustion gas turbine cycle, since the cooling model will be used for simulation of such cycles and pre-combustion cycles within the ENCAP project.
Keywords: gas turbine simulation, cooled turbine model, novel cycles

NOMENCLATURE

A_c	cross-section area for the hot gas [m^2]
air-GT	gas turbine with air as the working fluid
A_Q	area for heat transfer [m^2]
b	a cooling model parameter [-]
c_p	constant pressure specific heat capacity [kJ/(kg·K)]
h	specific enthalpy [kJ/kg]
h_T	heat transfer coefficient [W/(m^2·K)]
K	a cooling model parameter [-]
LHV	lower heating value [kJ/kg]
$\dot{m}$	mass flow rate [kg/s]
M	Mach number [-]
p	pressure [bar]
PR	compressor pressure ratio [-]
Q	heat transfer [W]
s	a cooling model parameter [-]
SCOC-GT	semi-closed oxygen-combustion gas turbine
St	Stanton number [-]
T	temperature [°C]
TIT	ISO turbine inlet temperature [°C]
u	velocity [m/s]
W	work [kW]
w_{spec}	specific work [kJ/kg]
y	mole fraction [mol/mol]
α	ratio between A_Q and A_c [-]
$\Delta\eta$	polytropic efficiency reduction due to cooling [%]
Δp	pressure drop due to cooling [bar]
ζ	cooling air mixing loss factor [-]
η	efficiency [%]
κ	specific heat capacity ratio [-]
λ	oxygen-fuel equivalence ratio [-]
ρ	density [kg/m^3]

* Corresponding author: Phone: +47 73 59 37 28
Fax: +47 73 59 83 90 E-mail: maria.jonsson@ntnu.no

Subscripts

b	blade
c	cooling fluid, cooling, cooled
cmb	combustion chamber
cmpr	compressor
cw	cooling water
g	combustion chamber exit gas
gen	generator
i	in, before the cooled blade
is	isentropic
mech	mechanical
o	out, after the cooled blade
p	polytropic
tbn	turbine
uc	uncooled

INTRODUCTION

Simulation of gas turbine-based power cycles requires accurate modelling of the turbine cooling. However, the cooling models available in the literature are not always easy to implement, especially for novel power cycles using non-conventional working fluids.

In this study, a cooled gas turbine model has been developed. The main reason for proposing this model is to have a simple and generic method for use in general process simulators. The work is part of the ENCAP (Enhanced Capture of CO_2) project, an integrated project within the 6th EU Framework Programme. ENCAP's objective is to develop new pre-combustion carbon dioxide (CO_2) capture technologies for power generation. Carbon capture can reduce the CO_2 emissions from power production, thus mitigating climate change. Included in this project is the investigation of novel gas turbine-based power cycles with oxygen combustion and pre-combustion CO_2 capture. In cycles where the fuel is combusted in a nitrogen-free atmosphere (oxygen-combustion), the exhaust gas contains mainly CO_2 and steam; thus, CO_2 can be separated by condensation of the steam. In pre-combustion capture cycles, the fuel is processed into mainly hydrogen and CO_2 and the CO_2 is separated before the hydrogen is burnt. Simulation of such novel cycles requires a simple cooled gas turbine model that can easily be implemented within in-house or commercial simulation tools.

This paper presents the theory of the proposed cooling model and calculation results for air and CO_2/H_2O working fluids. The model has been tuned to represent a generic, large, state-of-the-art F-Class gas turbine in cooperation with the gas turbine manufacturers participating in the ENCAP project, Alstom and Siemens. The model has been verified by comparison to the simulation tool Thermoflex [1].

BACKGROUND

Increased turbine inlet temperature, matched with an optimised pressure ratio, generally raises the gas turbine efficiency, as well as the specific work. However, material issues restrain the allowable temperatures. Thus, turbine cooling is necessary when using turbine inlet temperatures above what is acceptable for turbine blade materials. For a given level of cooling technology, a turbine inlet temperature raise results in augmented efficiency, up to a point where the gain from increased temperature is outbalanced by the losses caused by the cooling. The mixing of the hot gas and the cooling fluid results in losses due to:

1) reduced temperature of the gas expanding through the turbine, which decreases the turbine work
2) reduced momentum of the hot gas as the cooling fluid has to be accelerated to the speed and direction of the hot gas
3) disturbances to the flow profile around the blades, which increase the flow losses.

In most gas turbines, blade cooling is accomplished by air extracted from the compressor. In convective cooling, the air flows through the blades, cooling them by convection, then the air exits from the blades and mixes with the hot gas. Film cooling is used in some more advanced designs. Here, the air exits from the blades through a large number of small holes, forming a film that partially shields the blades from the hot gases. Recently, some large gas turbines, intended for combined cycles, using steam from the bottoming cycle as a coolant in a closed loop, have been introduced. The heated steam is led back to the steam cycle, improving the overall plant efficiency.

A detailed analysis of turbine cooling is complex, especially for film cooling. The analysis requires a stage-by-stage method with rigorous heat transfer calculation inside and outside the blade, as well as through the blade wall. Such a detailed analysis may produce information about blade surface temperature profiles. However, for cycle analysis aiming at efficiency prediction for novel cycles, a simplified procedure is needed to achieve a certain number of calculations for various cycle

configurations and parameter values. Most of the models presented in the literature are unsuitable for this purpose. Horlock et al. [2] give an overview of some models suggested in the literature. They divide these into models that consider:

1) the effect of continuous cooling on the turbine expansion line and the resulting changes in polytropic efficiency and reheat factor
2) stage-by-stage analysis of the effect of cooling on individual blade rows.

Horlock et al. [2] suggested a model belonging to the second group. This method estimates the cooling fluid flow rate for each blade row and the losses in stagnation temperature and pressure resulting from the mixing of the cooling fluid and the hot gas. The method applies to convective as well as film cooling.

Jordal et al. [3] presented three models, one belonging to the first group, originally presented by Bolland and Stadaas [4], and two belonging to the second group. The purpose of the paper was to investigate the behaviour of a specified cooled gas turbine when the working fluid was changed from air to CO_2/H_2O. It was found that a CO_2/H_2O gas turbine would need some re-design, due to the lower specific heat ratio for this working fluid compared with air. For a given pressure ratio, both the compression enthalpy increase and the expansion enthalpy drop are lower for CO_2/H_2O.

The model presented by Bolland and Stadaas [4], belonging to the first group, is based on one model of Elmasri [5]. In this model, the turbine is considered to be an expander where work is continuously extracted through the walls. The expansion process is divided into a large number of steps and in each step, three parts are calculated:

1) adiabatic expansion (work extraction)
2) mixing of cooling fluid and hot gas at constant pressure (loss of stagnation temperature)
3) mixing of cooling fluid and hot gas at constant enthalpy (loss of stagnation pressure).

THEORY OF THE MODEL

The layout of the proposed cooled gas turbine model is shown in Figure 1. In this model, the cooling fluid, taken from the compressor exit, is mixed with the hot combustion gas before the turbine inlet. The temperature at which the expansion begins is the ISO TIT[1] [6]. The

[1] The ISO TIT is the temperature resulting from mixing all cooling flows and the combustor exit flow in a single point.

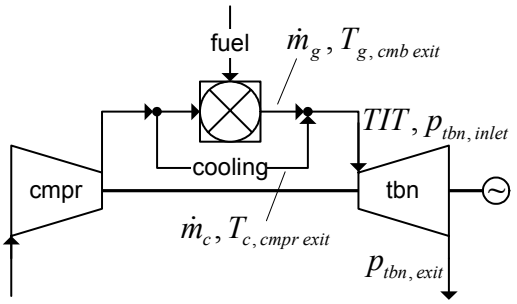

Figure 1: The generic cooled gas turbine model

expansion work is calculated using the sum of the combustor exit and cooling fluid flow rates. Three adjustable parameters (b, K and s) are tuned in order to represent a gas turbine at a given technology level. The cooling model calculates the required cooling fluid flow rate and the reduction of the turbine polytropic efficiency due to the cooling. Compared with models found in the literature, this model is simpler, using merely cooling fluid from the compressor exit and three parameters. The model has been developed for design-point calculations.

The cooling fluid mass flow rate is calculated with Equation (1). The derivation of this equation is described in the appendix.

$$\frac{\dot{m}_c c_{p,c}}{\dot{m}_g c_{p,g}} = b\left(\frac{T_{g,cmb\ exit} - T_b}{T_b - T_{c,cmpr\ exit}}\right)^s \qquad (1)$$

In this equation, b and s are adjustable parameters and T_b is the maximum sustainable blade surface metal temperature. Since the cooling model uses a lumped model approach, no turbine geometry is specified and the blade temperature T_b is a generic surface temperature that describes the ability of the blade material to withstand high gas temperatures. The specific heat capacities $c_{p,c}$ and $c_{p,g}$ are calculated (Equation (2)) as the average values between the blade temperature and the compressor exit and combustor exit temperatures, respectively. The blade enthalpy at compressor exit conditions ($h_{b,c}$) is calculated at the blade temperature and the compressor exit pressure and composition. The blade enthalpy at combustor exit conditions ($h_{b,g}$) is calculated at the same temperature, but using the combustor exit pressure and composition.

$$c_{p,c} = \frac{h_{b,c} - h_{c,cmpr\ exit}}{T_b - T_{c,cmpr\ exit}};\ c_{p,g} = \frac{h_{g,cmb\ exit} - h_{b,g}}{T_{g,cmb\ exit} - T_b} \qquad (2)$$

Mixing of the cooling fluid in the hot gas path reduces the momentum of the hot gas, as the

cooling fluid has to be accelerated to the speed and direction of the hot gas. This can be expressed as a pressure loss for the hot gas, calculated with Equation (3) [4], which is a momentum balance for the mixing. The pressure loss can be added to the combustor pressure loss, or it can be converted to a reduction of the turbine polytropic efficiency. Equation (4) relates the pressure drop to the loss of polytropic efficiency. Equation (5) defines the efficiency loss ($\Delta\eta$).

$$\frac{\Delta p}{p_{tbn,\,inlet}} = -\frac{\dot{m}_c}{\dot{m}_g}\kappa_g M_g{}^2 \zeta = -\frac{\dot{m}_c}{\dot{m}_g} K;\ \Delta p < 0 \quad (3)$$

$$\frac{\eta_{p,\,uc\,tbn} + \Delta\eta}{\eta_{p,\,uc\,tbn}} = \frac{\ln\left(p_{tbn,\,exit} \,/\, p_{tbn,\,inlet}\right)}{\ln\left(p_{tbn,\,exit} \,/\, \left(p_{tbn,\,inlet} + \Delta p\right)\right)} \quad (4)$$

$$\eta_{p,\,c\,tbn} = \eta_{p,\,uc\,tbn} - \Delta\eta;\ \Delta\eta > 0 \quad (5)$$

The mixing loss factor ζ accounts for the direction in which the cooling fluid is injected into the hot gas flow. If the injection is perpendicular to the hot gas flow, ζ is in principle equal to unity. The heat capacity ratio (κ_g), the Mach number (M_g) and ζ are summarized in the parameter K. For most air gas turbines, κ_g is about 1.3 and M_g is 0.6-0.8. A rough estimate gives ζ as 0.3-0.6. Hence, K should be in the range 0.15-0.5. It should be noted that $p_{tbn,\,exit}$ can be selected not only as the turbine exit pressure, but also as an intermediate pressure in the expansion path. When the expansion is divided into a cooled and an uncooled part, it can be convenient to select $p_{tbn,\,exit}$ as the cooled turbine exit pressure. Observe that a higher turbine exit pressure increases the efficiency correction, which depends on the turbine pressure ratio.

To calculate the compression and expansion end point states, the polytropic efficiencies are converted to isentropic efficiencies. The conversion follows the ASME method [7], [8]. For the turbine, the polytropic efficiency including the cooling loss ($\eta_{p,\,c\,tbn}$) is used. The gas turbine net efficiency is calculated with Equation (6), where the compressor work is defined as negative.

$$\eta_{net} = \eta_{mech}\eta_{gen}\left(W_{tbn} + W_{cmpr}\right)\Big/\left(\dot{m}_{fuel} LHV\right) \quad (6)$$

INPUT DATA AND PARAMETER TUNING

Data for a generic gas turbine (Table 1) were supplied by the ENCAP project partners Siemens and Alstom. These values represent well the technology level of large modern gas turbines, like Siemens' SGT5-4000F (formerly V94.3A) and Alstom's GT 26B. This technology level is comparable to that of other manufacturers' gas turbines, like GE's 9351F and Mitsubishi's 701F. The data were derived from actual gas turbine performance data provided by the manufacturers. However, since these data are confidential, the model was set up as a generic gas turbine model that resembles, but does not necessarily replicate, the performance of the aforesaid gas turbines.

Fixed values			
$\Delta p_{cmpr,\,inlet}$ & $\Delta p_{tbn,\,exit}$ [mbar]		10	
PR [-] (base case)		17	
$\eta_{p,\,cmpr}$ [%]	91.5	T_b [°C]	860
cmb heat loss [%]	0.2	η_{mech} [%]	99.6
Δp_{cmb} [%]	3	η_{gen} [%]	98.5
Target values			
η_{net}=38.50 % at $T_{cmb,\,exit}$=1425 °C			
TIT (ISO)=1230 °C at $T_{cmb,\,exit}$=1425 °C			
cooling fraction[2]=22 % at $T_{cmb,\,exit}$=1425 °C			
Maximum net efficiency at $T_{cmb,\,exit}$=1350 °C			
$\eta_{p,\,uc\,tbn}$ [%]		89	
Tuned parameters			
b [-]	0.1884	K [-]	0.237
$\eta_{p,\,uc\,tbn}$ [%]	87.94	s [-]	1

Table 1: Fixed values, target values and tuned parameters for the generic model

All calculations were performed in the simulation tool gPROMS [9]. Thermodynamic properties were calculated with Multiflash [10], with the advanced Redlich-Kwong-Soave equation of state. Complete combustion and no dissociation were assumed. The ambient air and natural gas specifications are shown in Table 3 in the appendix.

The values of b, K and s were found by tuning the model to the data in Table 1. The parameter s was set to 1 since this gave the most reasonable behaviour of the model. The parameters b and K were adjusted to yield a net efficiency of 38.50 % at a combustor exit temperature of 1425 °C with a cooling fraction of 22 %, at the same time as the maximum efficiency appeared at a combustor exit temperature of 1350 °C. To meet these requirements, the polytropic efficiency of the uncooled turbine had to be reduced from the original value of 89 %. The tuning resulted in the cooling model parameter values in Table 1. Results

[2] The cooling fraction is the cooling fluid mass flow rate divided by the compressor inlet mass flow rate.

	air-GT	*SCOC-GT*
$\eta_{is,\ cmpr}$ [%]	87.95	89.01
$T_{cmpr,\ exit}$ [°C]	410.69	289.15
$\dot{m}_{fuel}$ [kg/s][3]	2.2790	3.0810
$T_{cmb,\ exit}$ [°C]	1425	1425
cooling fraction [%]	22.00	20.45
$c_{p,\ c}$ [kJ/(kg·K)]	1130.92	1149.80
$c_{p,\ g}$ [kJ/(kg·K)]	1308.35	1331.81
TIT (ISO) [°C]	1229.42	1244.21
$\eta_{p,\ c\ tbn}$ [%]	85.77	86.25
$\eta_{is,\ c\ tbn}$ [%]	89.65	88.88
$T_{tbn,\ exit}$ [°C]	581.43	752.53
$w_{spec,\ cmpr}$ [kJ/kg]	410.97	251.60
$w_{spec,\ tbn}$ [kJ/kg]	808.42	637.88
$w_{spec,\ gas\ turbine}$ [kJ/kg][4]	415.88	482.97
η_{net} [%]	38.50	33.07
η_{net} [%] at $T_{cmb,\ exit}$=1350 °C	38.52	33.11

Table 2: Results for the base case (*PR*=17, $T_{cmb,\ exit}$=1425 °C) for the air gas turbine and the SCOC-GT cycle

from the gas turbine model for these parameters are shown in Table 2.

VERIFICATION

After tuning the generic model to manufacturer data, it was compared to a cooled gas turbine model in the simulation tool Thermoflex [1] as verification. The Thermoflex cooling model is more complex than the generic model in that it models the cooling of the stator and rotor of each stage [1], [11]. The Thermoflex model included a compressor, a combustor and three cooled turbine stages with cooling air taken from the compressor exit. Film cooling was used for the first stage; convective cooling for the second and third stages. The third stage required cooling only for combustor temperatures above 1700 °C for *PR*=17. The input data for the Thermoflex model was the same as for the generic model, except for the values in Table 4 in the appendix.

The Thermoflex model was tuned to give the same gross work output, fuel mass flow rate, turbine outlet temperature and cooling fraction as the generic model base case, see Table 5 in the appendix. The Thermoflex cooling model includes

[3] Based on a compressor inlet mass flow rate of 100 kg/s.
[4] The specific work is defined as the total gross work divided by the compressor inlet mass flow rate.

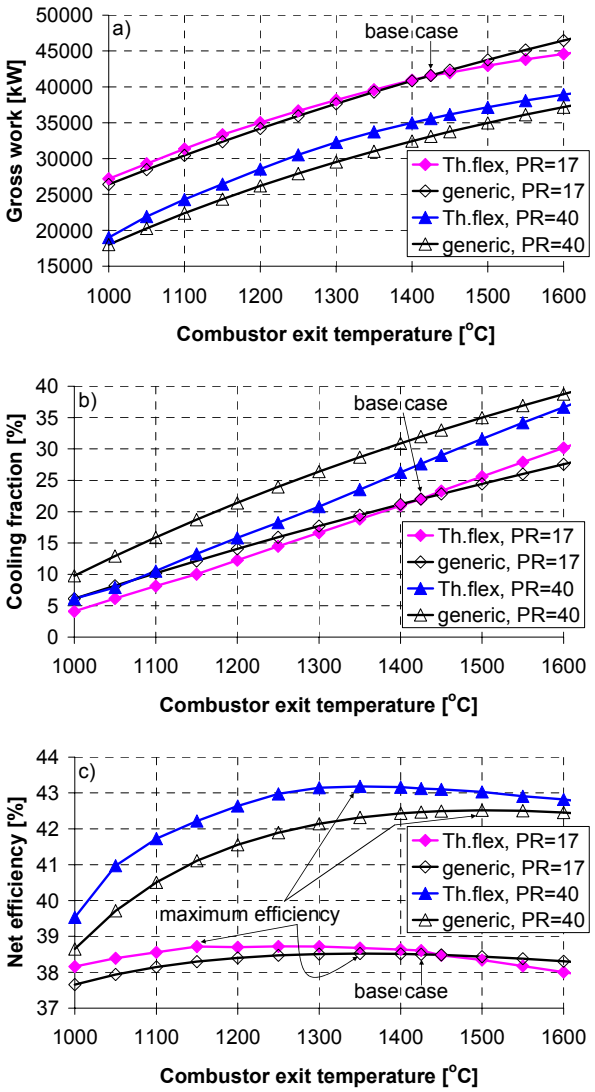

Figure 2: Comparisons of the generic and the Thermoflex models

the parameter *ARC* that corresponds to *b* in the generic model and the parameter *Y* that corresponds to *K*. To tune the Thermoflex model, *ARC* had to be increased to 2.075 times its default value and *Y* had to be decreased to 0.21 times its default value.

The generic model was compared with the Thermoflex model for the combustor exit temperatures 1000-1600 °C, for *PR*=17 and *PR*=40. For *PR*=40, the same *ARC* and *Y* values as for *PR*=17 were used. As can be seen in Figure 2a, the Thermoflex model has a lower work output than the generic model at high temperatures for *PR*=17. For *PR*=40, the Thermoflex model has a higher work output for all temperatures. Comparisons of the fuel mass flow rate and the

turbine exit temperature show the same trends as the work output comparison.

Figure 2b shows the comparison of the cooling fractions. It can be seen that the generic model depends more on the pressure ratio than the Thermoflex model. This is shown by the larger distance between the curves for *PR*=17 and *PR*=40 for the generic model than for the Thermoflex model. For *PR*=40, the generic model gives a significantly higher cooling fraction than the Thermoflex model, for example, at a combustor exit temperature of 1250 °C, the generic model calculates a 30 % higher cooling fraction than the Thermoflex model. However, the difference is smaller at higher combustor exit temperatures since the model was tuned at a combustor exit temperature of 1425 °C. Furthermore, the Thermoflex model is more dependent on the hot gas temperature, as the curves for this model have steeper slopes than the curves for the generic model. The Thermoflex cases with lower cooling fractions than the generic model have correspondingly higher power outputs and net efficiencies.

Figure 2c shows that the Thermoflex model locates the maximum net efficiency at lower combustor exit temperatures for both pressure ratios compared with the generic model. In total, the comparisons between the generic model and the Thermoflex model show that the two models behave similarly.

Another way of verifying the model is to compare the values of *b* and *K* resulting from the tuning with the theoretically estimated intervals for these parameters. The value of *b*, which is estimated in the appendix, depends on the cooling method: convective or film cooling. In this study, convective cooling is applied and the value of *s* is set to 1 (see the appendix). The value of *b* for two convectively cooled stages should be 0.2-0.7 with a conservative estimate of the cooling efficiency and 0.1-0.3 with a less conservative cooling efficiency estimate. The value of *b*=0.1884 falls within the interval estimated for a higher cooling efficiency. The value of *K*=0.237 falls within the range estimated in the theory section (0.15-0.5).

PARAMETER VARIATION

The behaviour of the generic cooled gas turbine model was investigated for different combustor exit temperatures (1000-1600 °C) and pressure ratios (10-40). The compressor inlet mass flow rate was 100 kg/s in all cases.

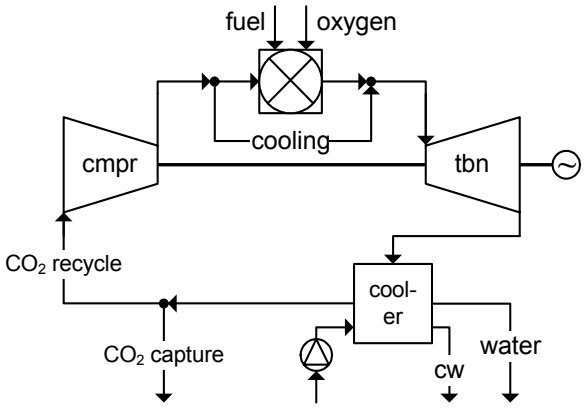

Figure 3: Semi-closed oxygen-combustion gas turbine (SCOC-GT) cycle

Figure 4a shows that for a specific pressure ratio, increasing the combustor exit temperature raises the net efficiency up to a point where the cooling fluid flow rate becomes so large that the losses caused by the cooling outbalance the benefits of the higher temperature. The maximum net efficiency is higher, and occurs at higher combustor exit temperatures, for higher pressure ratios.

Figure 4b and Figure 4c show that a higher pressure ratio for a specific combustor exit temperature results in a higher cooling fraction and thus a lower TIT. Figure 4d shows that the larger cooling fraction for higher pressure ratios reduces the turbine polytropic efficiency more, except for *PR*=10 and *PR*=20 that have approximately the same cooled turbine polytropic efficiencies.

SEMI-CLOSED OXYGEN-COMBUSTION GAS TURBINE CYCLE

The generic cooling model was used for simulation of a semi-closed oxygen-combustion gas turbine (SCOC-GT) cycle [12]. In the SCOC-GT, shown in Figure 3, the fuel is combusted with an oxygen-rich stream. Thus, the exhaust gas mainly contains CO_2 and steam, which can be separated by cooling the exhaust gas in the cooler shown in the figure. In the cooler, part of the steam condenses and is thereby removed. The cooler can be partially replaced by a heat recovery steam generator that generates steam for a steam bottoming cycle, augmenting the cycle efficiency. A steam cycle was not included in this study as the main purpose was to study the turbine cooling and not the cycle efficiency. A large part of the gaseous stream from the cooler is recycled to the compressor, to control the combustor temperature and provide a nitrogen-free working fluid. The remaining part of

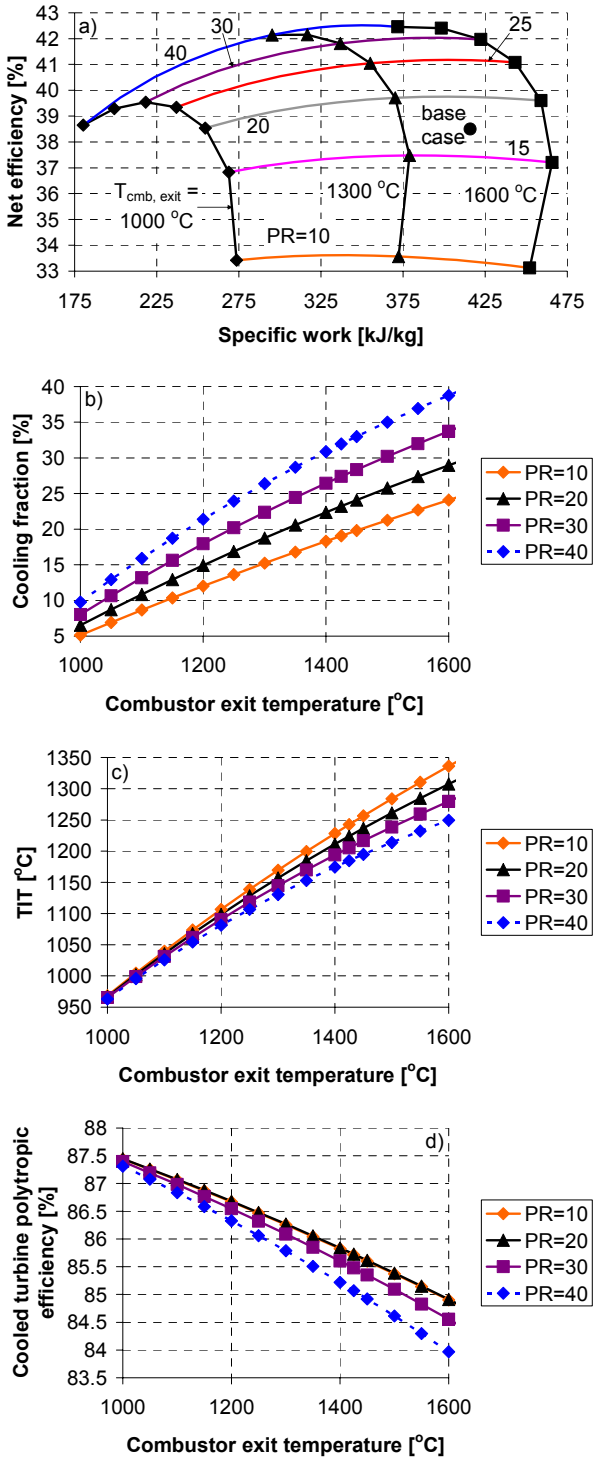

Figure 4: Results for the generic cooled gas turbine

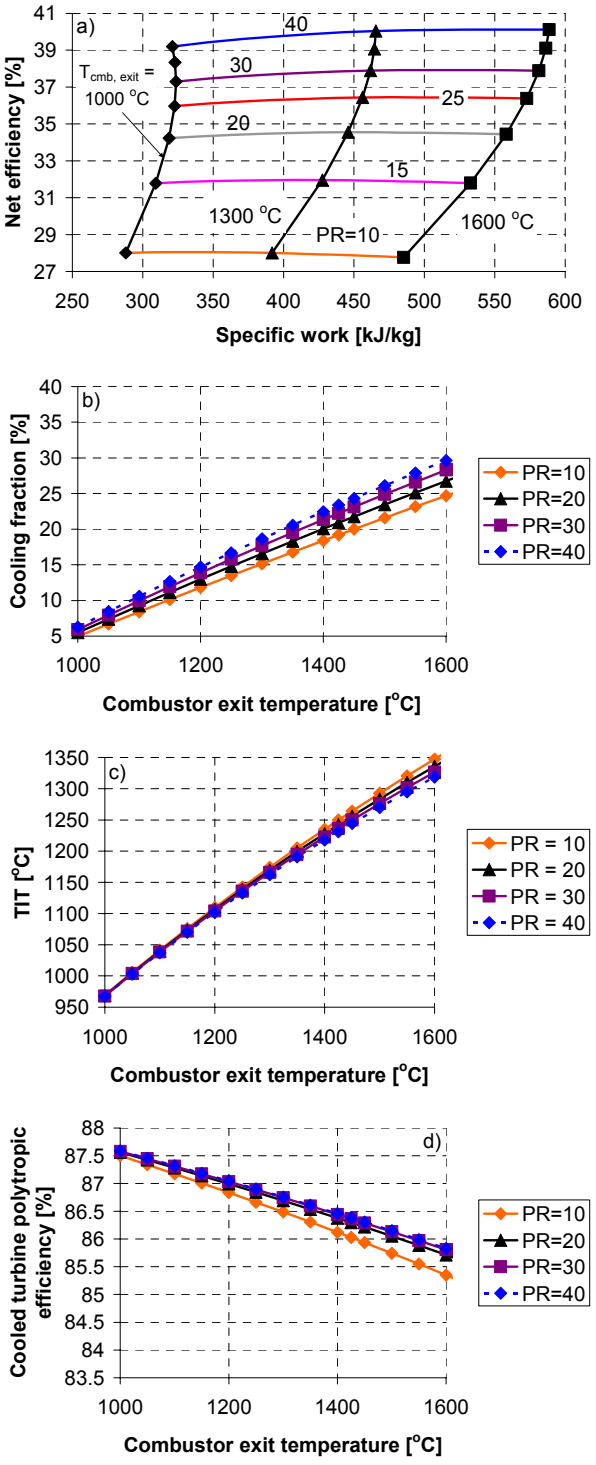

Figure 5: Results for the cooled SCOC-GT cycle

the gaseous stream can be compressed and sequestered.

The SCOC-GT was simulated with the same input data as the air gas turbine (air-GT), except for the data in Table 6 in the appendix. The work required generating the oxygen-rich stream by, for example, cryogenic distillation, the cooling water pump work and the CO_2 compression work were not included in the efficiency. The cooler was modelled as a counter-current heat exchanger and a flash chamber. The values of the parameters b, K, s and $\eta_{p,\ uc\ tbn}$ were the same as for the air-GT. The

cooling model considers the change of the cooling fluid and hot gas compositions by changed specific heat capacities. However, a CO_2/H_2O turbine with the same polytropic efficiency as the air turbine would require another design; this might necessitate other values for *b*, *K* and *s*. On the other hand, this supposition is countered by:

- *b* (see the appendix) depends on the Stanton number and the geometry. It is reasonable to assume that the Stanton number is about the same for both working fluids. A changed turbine design affects the geometry parameter, but it is impossible to quantify the change.
- *K* (see Equation [3]) depends on:
  - the heat capacity ratio, which is only slightly smaller for CO_2/H_2O than for air
  - the Mach number, which should be about the same for both turbines
  - the mixing loss factor, which can be assumed to be the about same for both working fluids.
- It is valid to assume that *s* has the same value for the CO_2/H_2O turbine as for the air turbine, since this parameter describes the type of cooling (convective or film).

Results for the SCOC-GT base case are shown in Table 2, and in Table 7 in the appendix. In addition, the behaviour of the SCOC-GT has been investigated for different combustor exit temperatures (1000-1600 °C) and pressure ratios (10-40).

Figure 5a shows that the SCOC-GT has lower net efficiency and higher specific work than the air-GT for all cases in the investigated pressure and temperature range. Since CO_2/H_2O has a lower specific heat ratio than air, both the compressor enthalpy increase and the turbine enthalpy decrease are lower in the SCOC-GT than in the air-GT for a specific pressure ratio. Although the SCOC-GT compressor work is lower than for the air-GT, the net efficiency is lower since the SCOC-GT turbine work is lower and the fuel flow rate is higher. However, as the compressor work reduction for the SCOC-GT is so large, the specific work is higher than for the air-GT.

Figure 5b shows that the SCOC-GT requires a smaller cooling fraction at a specified pressure ratio and combustor exit temperature than the air-GT, except for *PR*=10 where the required cooling fractions are about the same. The SCOC-GT has a lower compressor exit temperature and a higher cooling fluid heat capacity. According to Equation (1), this implies a lower cooling fraction. However, the SCOC-GT has higher hot gas heat capacity and combustor exit mass flow rate, which increase the cooling fraction. In total, the SCOC-GT has a lower cooling fraction than the air-GT above *PR*=10. Additionally, the impact of the pressure ratio on the cooling fraction is smaller for the SCOC-GT, since the compressor specific work and exit temperature increase less with raised pressure ratio for the SCOC-GT than for the air-GT. The smaller cooling fraction for the SCOC-GT compared with the air-GT results in higher TITs for all pressure ratios above 10, as shown in Figure 5c.

As a consequence of the lower cooling fractions, the reduction of the cooled turbine polytropic efficiency is smaller for the SCOC-GT (Figure 5d) than for the air-GT (Figure 4d). However, for the SCOC-GT, the reduction of the polytropic efficiency is largest for the lowest pressure ratio, while the highest pressure ratio has the lowest reduction. Tendencies of this behaviour can be seen for the air-GT in Figure 4d, where the efficiency reductions for *PR*=10 and *PR*=20 are the same, but for higher pressure ratios; a higher pressure ratio gives a larger reduction. The pressure drop due to the cooling calculated with Equation (3) is always larger for a situation with a larger cooling fraction. However, the conversion of the pressure drop to a polytropic efficiency reduction with Equation (4) will not always result in a larger efficiency reduction for a case with a larger cooling fraction.

DISCUSSION

A simple cooled gas turbine model will show deviations from the behaviour of a real gas turbine, which will increase with the distance from the operating point for which the model was tuned. Additionally, assuming a fixed cooling technology level for a broad range of pressure ratios and turbine inlet temperatures is a very simplified approach. However, including turbine cooling in the model gives more realistic results than using an uncooled model. A cooling model ensures that the efficiency has a maximum for a given pressure ratio and cannot be increased infinitely by raising the combustion temperature.

In the proposed cooling model, all of the cooling fluid is mixed with the combustor exit gas before the turbine inlet. Thus, the whole thermodynamic mixing loss is taken at the turbine inlet. As a result, the mixing losses are overestimated compared with a real turbine, where the mixing of the hot gas and

the coolant takes place at, on average, a smaller temperature difference. In a real gas turbine, the cooling air is extracted from the compressor at different pressure levels to be mixed with the hot gas at several locations in the turbine. When tuning the cooling model to real gas turbine data, the overestimated mixing loss at the turbine inlet is compensated for by reducing the value of the parameter *K*.

The cooled generic gas turbine model will be used for simulation of, for example, combined cycles, oxygen-combustion cycles and pre-combustion cycles. When optimising the efficiency of a gas turbine cycle where the energy in the gas turbine exhaust gas is recovered, it may benefit the overall cycle efficiency to operate at a point where the simple cycle gas turbine efficiency is not maximized. A high turbine exit enthalpy means that there is more energy to recover for a bottoming cycle of some kind.

CONCLUSIONS

This paper presents a simple, generic, cooled gas turbine model, which can be used for simulation and parameter variation of novel and conventional cycles. The model has been tuned to represent a generic large state-of-the-art F-Class gas turbine. The behaviour of the model has been verified as reasonable for such a gas turbine by the gas turbine manufacturers that participate in the ENCAP project, Siemens and Alstom. In addition, the model compares reasonably well with the cooled turbine model in the simulation tool Thermoflex.

In addition to a cooled air gas turbine, the cooling model was used to simulate a semi-closed oxygen-combustion gas turbine cycle, where the working fluid is mainly a mixture of CO_2 and steam. Parameter variations show that the behaviour of the cooled semi-closed cycle is represented reasonably well by the generic model.

ACKNOWLEDGMENTS

This work was sponsored by the 6th EU Framework Programme within the ENCAP (Enhanced Capture of CO_2) project.

REFERENCES

[1] *Thermoflex*, Thermoflow Inc., version 13.0.0.

[2] Horlock JH, Watson DT, Jones TV. *Limitations on Gas Turbine Performance Imposed by Large Turbine Cooling Flows*. J. of Engineering for Gas Turbines and Power 2001;123(July):487-494.

[3] Jordal J, Bolland O, Klang A. *Aspects of Cooled Gas Turbine Modeling for the Semi-Closed O_2/CO_2 Cycle With CO_2 Capture*. J. of Engineering for Gas Turbines and Power 2004;126(July):507-515.

[4] Bolland O, Stadaas JF. *Comparative Evaluation of Combined Cycles and Gas Turbine Systems with Water Injection, Steam Injection, and Recuperation*. J. of Engineering for Gas Turbines and Power 1995;117(January):138-145.

[5] Elmasri MA. *On Thermodynamics of Gas Turbine Cycles: Part 2 - A Model for Expansion in Cooled Turbines*. J. of Engineering for Gas Turbines and Power 1986;108:151-159.

[6] International Organization for Standardization. *Gas Turbines -- Acceptance Tests*. ISO 2314:1989. 1989.

[7] The American Society of Mechanical Engineers (ASME). *Performance Test Code on Compressors and Exhausters*. PTC 10-1997. 1998.

[8] Hyprotech, Aspen Technology, Inc. *Operations Guide HYSYS 3.1*. 2002.

[9] *gPROMS*, ModelBuilder version 2.3.1, Process Systems Enterprise Limited, 2004.

[10] *Multiflash*, version 3.1.31, Infochem Computer Services Ltd, 2001.

[11] Elmasri MA, Pourkey F. *Prediction of Cooling Flow Requirements for Advanced Utility Gas Turbines - Part 1: Analysis and Scaling of the Effectiveness Curve*. ASME Paper 86-WA/HT-43, 1986.

[12] Ulfsnes RE, Bolland O, Jordal K. *Modelling and Simulation of Transient Performance of the Semi-Closed O_2/CO_2 Gas Turbine Cycle for CO_2-Capture*. In: Proceedings of ASME Turbo Expo 2003, Atlanta, 2003, ASME Paper GT2003-38068.

[13] Louis JF, Hiraoka K, Elmasri MA. *A Comparative Study of the Influence of Different Means of Turbine Cooling on Gas Turbine Performance*. ASME Paper 83-GT-180, 1983.

[14] Horlock JH. *Advanced Gas Turbine Cycles*. Elsevier Science Ltd, 2003.

APPENDIX

p_{air} *[bar]*	1.01325	*T [°C]*	15
Rel. humidity [%]	60	$y_{O2,\ air}$	0.2074
$y_{N2,\ air}$	0.773	$y_{H2O,\ air}$	0.0101
$y_{Ar,\ air}$	0.00923	$y_{CO2,\ air}$	0.0003
$LHV_{nat.\ gas}$ *(at 25 °C) [kJ/kg]*		46503	
$p_{nat.\ gas}$ *[bar]*	70	$T_{nat.\ gas}$ *[°C]*	10
$y_{CH4,\ nat.\ gas}$	0.89	$y_{C5H12,\ nat.\ gas}$	0.00009
$y_{C2H6,\ nat.\ gas}$	0.07	$y_{C6H14,\ nat.\ gas}$	0.00001
$y_{C3H8,\ nat.\ gas}$	0.01	$y_{CO2,\ nat.\ gas}$	0.02
$y_{C4H10,\ nat.\ gas}$	0.001	$y_{N2,\ nat.\ gas}$	0.0089

Table 3: Ambient air and natural gas specifications

	PR=17	***PR=40***
$\eta_{is,\ uc\ tbn,\ stage\ 1}$ *[%]*	89.02	89.36
$\eta_{is,\ uc\ tbn,\ stage\ 2}$ *[%]*	89.05	89.43
$\eta_{is,\ uc\ tbn,\ stage\ 3}$ *[%]*	89.09	89.50

Table 4: Isentropic efficiencies for the Thermoflex model, calculated with three uncooled stages (generic model) with equal pressure ratios and $\eta_{p,\ tbn}$=87.94 %

	Gen. mod.	**Th. flex**	**Abs. diff.**	**Rel. diff. [%]**
W_{gross} *[kW]*	41588	41592	3.6	0.01
m_{fuel} *[kg/s]*	2.279	2.273	-0.01	-0.26
$T_{tbn,\ exit}$ *[°C]*	581.43	581.23	-0.20	-0.04
cool. frac. [%]	22.00	22.01	0.01	0.05
η_{net} *[%]*	38.50	38.60	0.10	0.27

Table 5: Tuning of the Thermoflex model to the generic model base case (*PR*=17, $T_{cmb,\ exit}$=1425 °C)

$p_{cmpr,\ in}$ *[bar]*	1.01325	$y_{Ar,\ oxygen}$	0.03
$p_{oxygen\ stream,\ in} = p_{cmpr,\ exit}$		$T_{cmpr,\ in}$ *[°C]*	20
$y_{O2,\ oxygen}$	0.95	$T_{oxygen,\ in}$ *[°C]*	15
$y_{N2,\ oxygen}$	0.02	$T_{cw,\ in}$ *[°C]*	15
$\Delta p_{cmpr,\ in}$ & $\Delta p_{tbn,\ exit}$ *[mbar]*	0	$T_{cw,\ out}$ *[°C]*	25
Δp_{cooler} *(hot, cold side) [%]*	1	λ *[-]*[5]	1.02

Table 6: Additional input data for the SCOC-GT

$m_{oxygen\ stream}$ *[kg/s]*		12.0768	
$y_{CO2,\ cmpr\ inlet}$	0.8772	$y_{CO2,\ tbn\ exit}$	0.7738
$y_{H2O,\ cmpr\ inlet}$	0.0232	$y_{H2O,\ tbn\ exit}$	0.1384
$y_{Ar,\ cmpr\ inlet}$	0.0534	$y_{Ar,\ tbn\ exit}$	0.0471
$y_{N2,\ cmpr\ inlet}$	0.0428	$y_{N2,\ tbn\ exit}$	0.0377
$y_{O2,\ cmpr\ inlet}$	0.0034	$y_{O2,\ tbn\ exit}$	0.0030

Table 7: Additional results for the base case SCOC-GT (*PR*=17, $T_{cmb,\ exit}$=1425 °C)

Derivation of Equation (1)

The heat transfer between the cooling fluid in the blade and the hot gas is given by Equation (7).

$$\begin{aligned} Q &= \dot{m}_c c_{p,c}\left(T_{c,o}-T_{c,i}\right) = \\ &= \dot{m}_g c_{p,g}\left(T_{g,i}-T_{g,o}\right) = h_{T,g} A_Q \left(T_{g,i}-T_b\right) \end{aligned} \quad (7)$$

The cooling efficiency, η_c, is defined for convective and film cooling in Equation (8).

$$\eta_c = \frac{T_{c,o}-T_{c,i}}{T_b-T_{c,i}}\ (convective);\ \eta_c = \frac{T_{c,o}-T_{c,i}}{T_{g,i}-T_{c,i}}\ (film) \quad (8)$$

[5] The amount of oxygen supplied (moles) divided by the amount of oxygen required for stoichiometric combustion.

The ratio α between the heat transfer area, A_Q, and the hot gas cross-section area, A_c, is assumed to be constant (Equation (9)). The cross-section area is found from the continuity equation.

$$\alpha = A_Q / A_c;\ A_c = \dot{m}_g / \left(\rho_g u_g\right) \quad (9)$$

The convective cooling efficiency is inserted in Equation (7) to remove the cooling fluid outlet temperature and Equation (9) is inserted to remove the heat transfer area. Equation (10) shows the resulting expression, note that this equation contains the Stanton number (Equation (11)).

$$\frac{\dot{m}_c c_{p,c}}{\dot{m}_g c_{p,g}} = \alpha \frac{h_{T,g}}{c_{p,g}\rho_g u_g} \frac{T_{g,i}-T_b}{\eta_c\left(T_b-T_{c,i}\right)} \quad (10)$$

$$\mathrm{St} = h_{T,g} / \left(c_{p,g}\rho_g u_g\right) \quad (11)$$

Convective cooling

For convective cooling, the cooling efficiency is not proportional to the hot gas inlet temperature. Thus, Equation (10) can be rewritten as Equation (12). The parameter b replaces the constant α, the St number and the cooling efficiency. The constant α is 10-20 for one cooled stage and 20-40 for two cooled stages. The St number is approximately 0.005 for blade cooling. Louis et al. [13] give the cooling efficiency as 0.3-0.5, Horlock [14] gives 0.6-0.8. Thus, with a conservative estimate of the cooling efficiency (0.3-0.5), b should be 0.1-0.3 for one cooled stage and 0.2-0.7 for two cooled stages. With a less conservative estimate of the cooling efficiency (0.6-0.8), b should be 0.1-0.2 for one cooled stage and 0.1-0.3 for two cooled stages. Equation (12) is the same as Equation (14) with s=1.

$$\frac{\dot{m}_c c_{p,c}}{\dot{m}_g c_{p,g}} = \frac{\alpha \mathrm{St}}{\eta_c}\left(\frac{T_{g,i}-T_b}{T_b-T_{c,i}}\right) = b\left(\frac{T_{g,i}-T_b}{T_b-T_{c,i}}\right) \quad (12)$$

Film cooling

For film cooling, the cooling efficiency is proportional to the inverse of hot gas inlet temperature, but the dependence is also influenced by the cooling fluid temperature. Consequently, Equation (10) can be rewritten as Equation (13).

$$\frac{\dot{m}_c c_{p,c}}{\dot{m}_g c_{p,g}} \propto \alpha \mathrm{St}\left(\frac{T_{g,i}-T_b}{T_b-T_{c,i}}\right) T_{g,i} \quad (13)$$

When $\alpha \cdot$St is replaced by b and the impact of the hot gas inlet temperature is included by the parameter s, Equation (14) results. s is in the range of 1 to 2, where 1 represents convective cooling. b should be 0.05-0.1 for one cooled stage and 0.1-0.2 for two cooled stages.

$$\frac{\dot{m}_c c_{p,c}}{\dot{m}_g c_{p,g}} = b\left(\frac{T_{g,i}-T_b}{T_b-T_{c,i}}\right)^s \quad (14)$$

Proceedings of ECOS 2005
Trondheim, Norway
June 20–22, 2005

MODELING OF AN IGCC PLANT BASED ON AN OXY-FUEL COMBUSTION COMBINED CYCLE

Philippe MATHIEU[1] and Frédéric VAN LOO
University of Liège
Department of Mechanical Engineering
Belgium

ABSTRACT

The objective of the paper is to show that a novel IGCC plant based on an oxy-fuel Matiant combined cycle is a possible alternative to a standard IGCC with pre-combustion capture from the performance viewpoint. From recent studies on new IGCC plants ranging in size from 350-800 MWe and using commercially available physical absorption systems, the average values of energy penalties are around 15% and of CO_2 capture rates within 80-90% per kWh generated. The FutureGen project recently developed in USA is designed to use a 275 MWe IGCC with pre-combustion capture with the objective to evaluate the performance and reduce substantially the costs of both electricity with capture and of hydrogen.
The proposed IGCC is a combination of an O_2/CO_2 gas turbine power cycle with reheat and a steam cycle with 2 pressure levels and a reheat in the heat recovery steam generator. Here a coal gasification unit with clean-up of the syngas is added upstream of the combustion chambers. The cleaned syngas $CO+H_2$ is feeding the oxy-fuel Matiant cycle. After combustion in pure oxygen, the reaction products CO_2 and water are nearly totally extracted out of the cycle by using a cooler/separator. The proposed IGCC takes advantage of the already existing air separation unit which has to be sized in order to produce the total amount of O_2 required.
All in all, the performance of the proposed IGCC cycle is similar to the one of an IGCC with pre-combustion capture but now the CO_2 retention rate is nearly 100% instead of 90%. However the turbo-machines operating on CO_2/water mixtures require a new design and are not commercially available today. In this paper, a sensitivity analysis on the basic parameters is carried out and the best configuration is derived from the discussion of the results.

NOMENCLATURE

η	efficiency (%)
ASU	Air Separation Unit
CC	Combined Cycle
GT	Gas Turbine
IGCC	Integrated Gasification Combined Cycle
LHV	Low Heating Value (MJ/kg)
NGCC	Natural Gas fired Combined Cycle
PC	Pulverized Coal fired power plant
ST	Steam Turbine
TIT ISO	Turbine Inlet Temperature taking the cooling of blades and vanes into account

INTRODUCTION

Deep reductions in CO_2 emissions are critically needed to meet the UNFCCC target of stabilising GreenHouse Gases "*at a level, which will prevent dangerous anthropogenic interference with the climate system*" but without indicating a figure for that level. For example, ensuring an "acceptable" level of 550ppmv in CO_2-equivalent concentration would imply a 80-90% reduction in carbon emissions by the end of the 21st century and by 50% from 2030, much beyond the modest 5% target for world emissions agreed in the 1997 Kyoto protocol [1]. If coal has to be used in this context, such a significant CO_2 emissions reduction is possible only if coal is converted efficiently and cleanly in energy, that means that

[1] Phone : +32-4-3669268 – E-mail : pmathieu@ulg.ac.be

old and low-efficient pulverized-coal-fired power plants be replaced by advanced IGCC plants. An extensive removal of CO_2 from flue gas (post-combustion de-carbonisation) and fuel gas (pre-combustion de-carbonisation) should play an important role but at the cost, however, of a significant loss of plant efficiency and power output [2]. On the other hand, if the world is evolving towards a carbon-free economy, Zero Emissions Technologies are further alternatives likely to play a role within this mix of technologies, as burning fossil fuels will remain a cheap option for a long time, especially in developing countries where huge reserves of coal are still to be exploited. The aim of the present paper is to introduce the technical principles underpinning a nearly zero emission IGCC and compare the performance to the same IGCC with pre-combustion capture.

THE NEARLY ZERO EMISSION IGCC

Pre-combustion systems process the primary fuel in a reactor to produce separate streams of CO_2 for storage and H_2 which is used as a fuel [3-8]. Oxy-fuel combustion uses oxygen instead of air for combustion, producing a flue gas that is mainly H_2O and CO_2 that is readily captured, and is an option still under development. The oxy-fuel combustion process eliminates thus nitrogen from the flue gas. According to the flue gas recycling rate, the flame temperature varies from about 1300°C with a large recycle flow to over 3500°C with no recycle and pure oxygen used for combustion.

In this work, the oxy-fuel combustion power cycle is an O_2/CO_2 cycle, called the MATIANT cycle in the literature [11-18]. In such a cycle, CO_2 is used as the cycle working fluid.Water is extracted from the flue gas, a mixture of water and CO_2, in a cooler/separator while the CO_2 generated in the combustion process is extracted from the recycled CO_2 by opening a valve, either before or after the GT compressor. The key advantage compared to traditional capture methods is the ability to capture 99.5%vol of the CO_2 generated in the combustion chamber as well as nearly all other pollutants, mainly NO_x. This benefit does however come with a cost : a penalty on performance due to production of nearly pure O_2 through cryogenic separation and

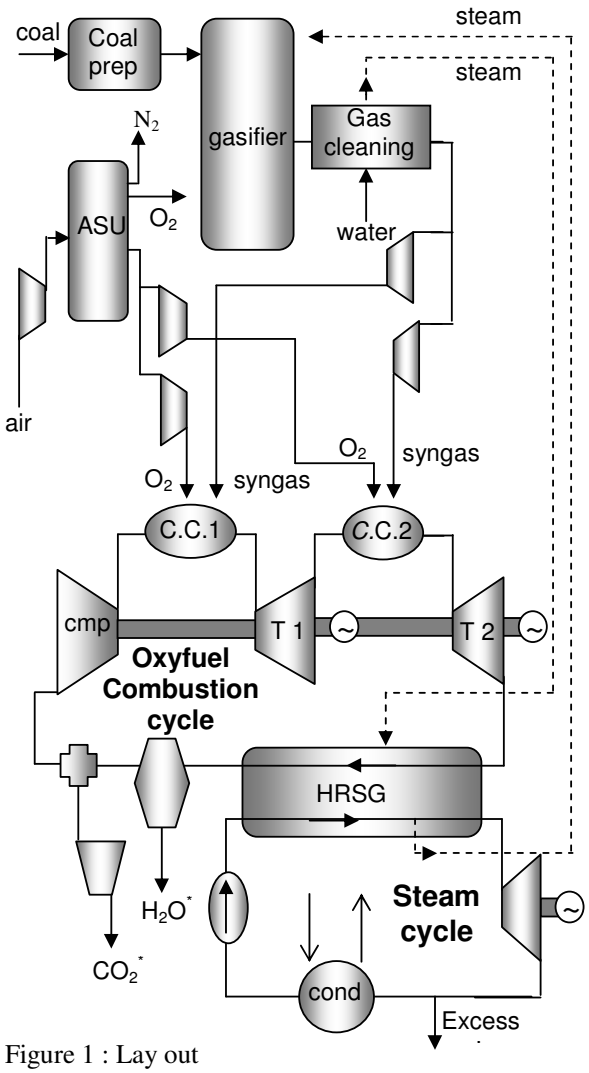

Figure 1 : Lay out

to the compression of CO_2 up to the required delivery pressure for transportation and storage (above 110 bar). However an ASU is already existing in a standard IGCC producing the needed oxygen in the gasification unit. Consequently if this latter feeds a Matiant cycle with a cleaned syngas, the O_2 required for its combustion in stoichiometric proportions may come from the existing ASU provided its production is adapted to the new need. On top, the power consumption of auxiliaries in a standard IGCC is not more than around 6% of the net power output. That is why the O_2 production in the proposed system should be much less penalizing than in an oxy-fuel combustion cycle alone. Figure 1 shows the law out of an IGCC plant based on the Matiant cycle used in a combined cycle configuration. It is

represented on figure 2 as a closed loop O_2/CO_2 Brayton gas cycle with an adiabatic compressor and a staged expansion, namely a reheat in a second combustion chamber, and with 2 near – isobaric processes, namely in the 2 combustion chambers and in the cooling of the flue gas down to the compressor inlet temperature. O_2 is produced in a cryogenic air separation unit (ASU) consuming a lot of electricity, i.e. 0.25kWh/kg O_2 at 1.7 bar, 15°C and a 95% purity (95% mol CO_2 and 5% mol Argon, the other impurities such as nitrogen being in negligible amounts) [19].

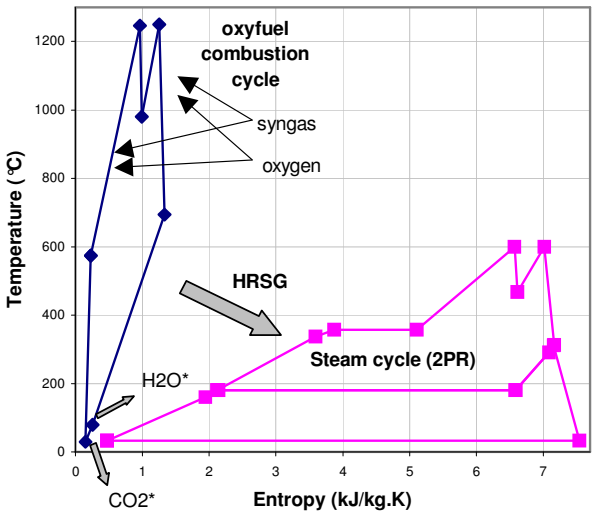

Figure 2: T-s diagram for the IGCC based on a MATIANT cycle

The upper cycle pressure is above the CO_2 critical pressure (73 bar ; 30 °C), 110 – 150 bar being the pressure required for CO_2 transportation under liquid or supercritical state. The heat of the expander exhaust gas is given up to a steam cycle within a heat recovery steam generator with 2 pressure levels and a reheat. In this modelling, the inlet HRSG temperature is limited at 700 °C for technological reasons. At the HRSG outlet, the flue gas is further cooled in a cooler/separator, cooled by an external water circuit. Water is then condensed out of the flue gas before the compressor while the excess CO_2 (produced in the combustion process) is extracted from the cycle either before the compressor at atmospheric pressure or behind the compressor at the upper cycle pressure, in supercritical state. After cooling down to the cold sink temperature (30°C), the extracted CO_2 is ready for a possible use (such as enhanced recovery of oil or methane) or for its long term storage. If necessary, the compressed CO_2 is dried and cleaned up from contaminants coming both from the fuel and the oxygen (N_2, excess O_2, Ar, NO_x) and an additional compressor may be needed to bring about the purified CO_2 flow up to required delivery pressure for transport. A small fraction of CO_2, typically 0.1%vol of the excess CO_2 flow, is however leaving the cycle with the extracted H_2O. This is the reason why the system is called "near zero emission" and not strictly "zero emission". Before its re-use or its storage, the extracted excess CO_2 may be partly cooled and recycled in the hot parts of the cycle for cooling of walls, vanes and blades at the upper cycle temperature. Taking account of the penalties due to this cooling of the hot parts , due to the ASU consumption, due to the compressions and due to the pressure losses, the net efficiency of a Matiant cycle in CC is around 58% when operating on natural gas and with 1300°C upper temperatures of the gas turbines (TIT ISO), compatible with the currently available materials.

In the IGCC configuration, coal is gasified with oxygen and steam and is transformed in a syngas $CO + H_2$ at high temperature (1400 °C). This latter as well as the gasifier walls are cooled. The sensible heat of the hot syngas is recovered in a recovery boiler and the syngas is purified at low temperature. Particles, sulfur and nitrogen are nearly totally removed from the syngas which is now the fuel used in the Matiant cycle together with pure oxygen in stoichiometric proportions. Saturated steam is bled from the HRSG for the syngas cooling, superheated in the recovery boiler and sent to the MP steam turbine.

The already existing ASU in a standard IGCC has here to be sized to supply O_2 to both the gasifier and the combustion chambers of the MATIANT cycle. The O_2 consumption is about 2.5 times higher. Here there is no more need to shift CO since the MATIANT cycle accepts this mixture as the fuel and is designed to extract nearly all the water and the excess CO_2 from the combustion. At the US DOE, a study was conducted on a MATIANT cycle fuelled with a syngas produced in an O_2-blown gasifier, the O_2 being obtained through an Ion Transport Membrane operating on a high temperature pressurized air stream (850°C, 12-20 bar). The efficiency is around 45% (some 4 – 5% points below the efficiency of the same IGCC operating on an air based CC) and the CO_2 retention rate goes up to 99.5% in contrast to the 90% in an IGCC with pre-combustion capture [20].

ENERGY ANALYSIS

Reference IGCC

IGCC is the best emerging technology regarding a high level of CO_2 capture. Using a water gas shift reactor system allows to convert the CO in the syngas into CO_2 and H_2 using H_2O. Sulfur compounds together with around 90 % of the CO_2 generated in the combustion process can then be removed, for instance using a solvent like Rectisol. Here the solvent regeneration is made by flashing the solution, which is much less energy consuming than for a regeneration by heating. For a given coal input and a given GT efficiency , the pre-combustion capture gives rise to a net efficiency penalty resulting first from a decrease in fuel heat input (H_2+N_2 instead of CO+H_2+N_2) in the GT combustion chamber and consequently a drop in the GT power output, second and increase of consumption of auxiliaries whose the ASU and CO_2 compressor and third an increase of the steam flow from the gasification and clean up sections to the HRSG and consequently an increase of the ST power output. In the best cases, the addition of a CO shift and a CO_2/H_2 separation units results in a net plant efficiency drop of about 11 to15% or to a loss of 5 to 7 % points [5;6;21;22;23].

The reference IGCC without capture is an advanced one with a 49% net efficiency in base load and has the following characteristics. The GT with a TIT ISO = 1250 °C and a pressure ratio of 16.6 has a power output of 267.4 MW and an efficiency of 49.2% in open cycle and 58.1% in CC. The Shell gasifier is an entrained fluidised bed fed with dry coal (LHV= 31.44 MJ/kg), O_2 and steam. The steam cycle comprises 3 optimized pressure levels and a reheat (3PR) at 200 bar/600°C/61 kg/s; 38 bar/249°C/50kg/s; 4 bar/389°C/13 kg/s and reheat at 33 bar/600 °C. In the integration of water/steam flows between the gasifier and raw gas coolers and the steam cycle, the IP drum is in the gasification island, receives 58 kg/s IP saturated water and delivers a throughput of 50 kg/s saturated steam at 38 bar to the superheater inlet of the second pressure level, the 8kg/s difference being injected in the fuel gas saturator. The steam turbine power output is 189.3 MW so that the total power is 456.7 MW. The steam cycle efficiency is then 35.7% [8;24;25].

In the energy flow, around 75% of the chemical energy of coal input is transferred to the syngas, the remaining 25% representing losses and steam produced in the cooling of the gasifier walls and of the raw syngas in heat recovery boilers. The heat in that steam represents some 17% of coal input and is converted in electricity with the steam cycle efficiency. The ASU consumes some 8.5% of coal input as electricity $_{for}$ the air compressor. These factors are mainly responsible of the loss of efficiency compared to the standard natural gas fired CC (around 8%points). The global efficiency of the IGCC plant amounts to 49% with a share of 62% for the GT and 38% for the ST with a ratio GT/ST = 1.6 instead of 2 in a standard NGCC that is due to the water/steam integration. When the pre-combustion capture is implemented, the LHV of the fuel decreases by some 30% resulting in a drop of the GT power while the ST power increases (GT/ST power ratio is 1.3) but the net power output decreases by some 11% and so does the net efficiency.

The oxy-fuel combustion IGCC plant

The cycle efficiency is calculated using the ASPEN+ and EES commercial codes. The boundary conditions such as the technical data are given in table 1 and meet technical limitations such as the HRSG inlet temperature at 700°C complying with the requirements of material resistance criteria.

The Shell gasifier consumes 0.61 kg coal and 0.49 oxygen per kg cleaned fuel. The syngas is delivered, after cooling and clean-up, at 22 bar and 315°C, with a composition of 62.7%mol CO, 29.7% hydrogen and 7.6% inert gases resulting in a LHV of 12.45 MJ/kg.

The ASU produces O_2 at 1.7 bar,15°C at a purity of 95%mol, the 5% remaining being Argon with an electricity consumption of 0.25 kWh/kg O_2 [19].

In the 2PR recovery boiler, the superheat and reheat temperatures are taken at 565°C, that is 135°C below the GT exhaust temperature. The results at the design point corresponding to the data mentioned in table 1 are shown on figure 3.

Excess CO_2 is extracted before the compressor and is compressed from 1 to 110 bar. All the figures are given for a unit of working fluid, namely for 1 kg/s CO_2 recycled to the combustion chamber. The calculated syngas mass flow rate is 0.119 kg/s or 0.119 kg syngas/kg CO_2 recycled.

GT cycle	
2de turbine exhaust pressure	1,05 bar
HRSG inlet temperature	700 °C
Excess of water extraction temperature	30°C
Combustion chambers pressure drop	3 %
HRSG pressure drop	5 %
Isentropic efficiency of Turbines Compressor	 90 % 88 %
HRSG and steam cycle : 2 PR	
Max superheat temperature	565,5 °C
Isentropic efficiency of Turbines Pump	 87 % 85 %
Condenser pressure	46,2 mbar
Approach temperature	20 °C
Pinch point	10 °C
Air Separation Unit	
Oxygen composition (molar)	95 % O_2 5% Ar
Electricity consumption	250 kWh / ton produced O_2
Oxygen pressure temperature	1,7 bar 15 °C
Gasifier – gas clean up system : Shell	
Coal HHV LHV	Illinois #6 27,14 MJ/kg 26,16 MJ / kg
Coal consumption	0,61 kg / kg clean gas
Coal preparation	6,4 k Wh / ton coal
Shell gasifier O_2 consumption	0,49 kg O_2 / kg clean gas
Gasifier O_2 compressor	189,85 kJ / kg O_2 supplied to the gasifier
Gas clean up system	16,7 kJ / kg clean syngas
Cleaned syngas Pressure Temperature Composition (molar) LHV HHV	21,9 bar 315,5 °C 62,7 % CO 29,7 % H_2 12,45 MJ/kg 12,91 MJ/kg

Table 1 : data

The total O_2 production is 1.26 kg/kg syngas or 0.15 kgO_2/kg CO_2 recycled split into 2 parts : 40% to the gasifier and 60% to the combustion chambers of the Matiant cycle. Now the need for O_2 is 2.5 times higher than for the gasifier alone in a standard IGCC. The electricity requirement for the ASU is hence 135 kW/ kg CO_2 recycled.
At the design point, taking a TIT of 1250°C and an upper cycle pressure of 120 bar, the net power output is 0.86 MWe/ kg CO_2 recycled (0.71 for the GT, 0.5 for the ST and 0.36 Mwe for the auxiliaries) while the coal input (LHV = 26.16 MJ/kg) in the plant is 1.91 MWth.

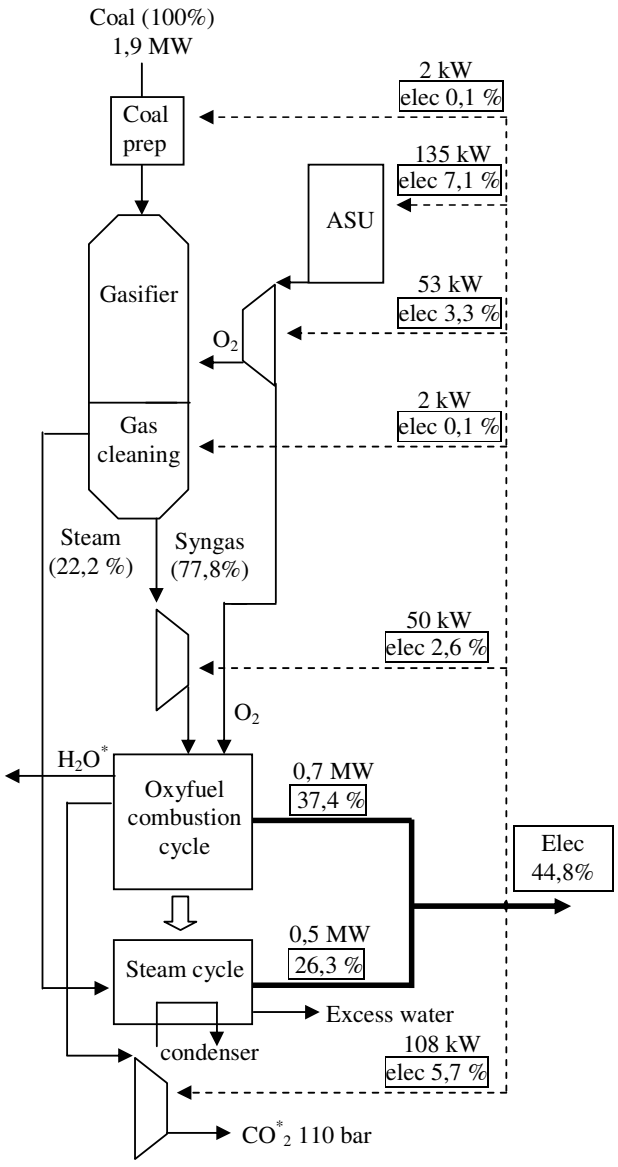

Figure 3 : Energy Cascade

The resulting net efficiency is 44.8%, all the losses being taken into account, including the losses due to CO_2 compression from 1 to 110 bar (13% of the net electricity production), to the ASU consumption (16% of the net electricity production) and to the cooling of the hot parts of the GTs using CO2 bled from the compressor since the TIT used in the calculations are the TIT ISO.
At the design point, in a configuration 2-2-1 with 2 GTs rated at 0.35 Mwe and 1 ST at 0.5 MWe, one of the GTs is used to provide approximately the electricity needed to the auxiliary systems while the ST generates approximately the power required by the GT compressors. Consequently the net plant power output is that of one GT and the ratio of power outputs of GTs and ST is 1.4 instead of 1.6 in the reference IGCC.
The energy cascade on figure 3 shows how the coal energy content is converted into electricity.
Note that the ASU consumes 16% of the net power output of the plant instead of 17.4% in the reference plant .

SENSITIVITY ANALYSIS

From the diagram efficiency against specific work on figure 4, it appears that both efficiency and specific work increase with the upper cycle pressure up to a maximum. The higher the TIT, the higher the maximal efficiency and the corresponding specific work. For a 1250°C TIT, the maximal efficiency (45%) and the maximal specific work (0.86 MJ/kg CO_2 recycled) are reached when the upper cycle pressure is 120 bar. This latter remains nearly constant above the optimal pressure. When the TIT goes up to 1300°C, the optimal pressure is 140 bar. The maximal efficiency increases only slightly by about 0.2 %point (45.2%) and again the specific work remains nearly constant above the optimal pressure. For a 1400°C TIT, the optimal pressure is very high, about 200 bar while the maximal efficiency is not more than 46%. Consequently increasing the TIT incurs indeed an increase of maximal efficiency only if the pressure is also increased. In this type of cycle however, it is not interesting to go on increasing the TIT in contrast to a standard IGCC since, when increasing the TIT from 1200 to 1400 °C, the efficiency climbs by only 2 % points provided the pressure strongly increases from 120 to 220 bar. Consequently it is better to bring about the effort on reducing the consumption for O_2 production than to increase the TIT.

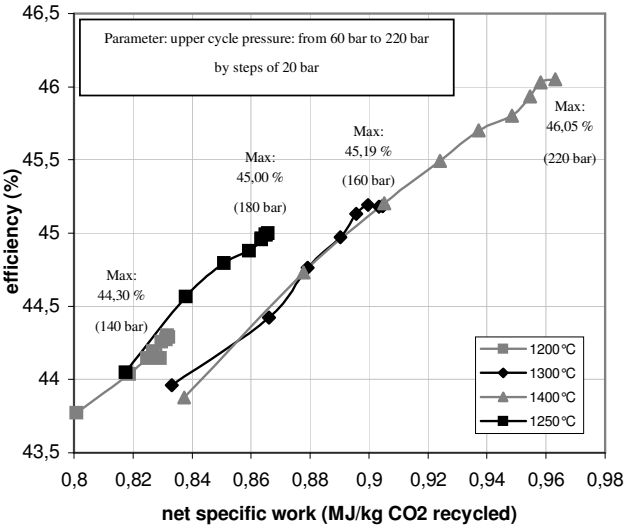

Figure 4 : efficiency against specific work for various TITs, the upper cycle pressure being the parameter

Regarding the consumption for O_2 production, the two most popular systems of O_2 separation are cryogenics and high t° conducting mixed oxide membranes. Both require a compression of the feeding air up to some 20 bar and this is the major part of the consumption in the two processes. Consequently the penalties are similar but on top of the compression, the air feeding the membranes must be heated up to some 900°C.

PURITY OF CO_2

The amounts of CO_2 and H_2O generated in the combustion are respectively 0.16 and 0.03 kg/ kg CO_2 recycled. With a solubility coefficient of 1.26 mg/kg water at 30 °C, the amount of CO_2 leaving the plant dissolved in the extracted water is only 0.1% of the water flow rate or 0.02% of the CO_2 generated in the combustion or about 0.1g/kWh. However, the extracted CO_2 and H_2O flows are not 100% pure CO2 and H_2O .The composition of the fluid extracted at the compressor inlet is 90.5 % CO_2, 4.25 % Ar, 1.4% H_2O and 3.84% unburned CH_4. This fluid needs to be dried and purified before transport to storage. Consequently the calculated amount of CO_2 leaving the cycle together with H_2O is only 0.001% of the CO_2 generated in the combustion or 5 mg CO_2 /kWh.

TECHNICAL ISSUES

Many technical issues have been raised in the development of the MATIANT cycles due to the nature of the working fluid, CO_2 or a mixture CO_2/H_2O. In particular, developments are required on cooled CO_2 expanders operating at high temperatures, on combustion in pure oxygen in a CO_2 atmosphere under pressure, on compressors and on condensers of mixtures of CO_2 and H_2O at low pressures.

As to the IGCC with pre-combustion capture, even if CO shift and CO_2 extraction from a mixture are proven, it still requires the development of H2 fuelled GTs. Such GTs are still appearing on the market today[25] .

CONCLUSIONS

Compared to a reference IGCC plant, the net efficiency of the oxy-fuel base IGCC is about 4 to 5% points lower while that of an IGCC with pre-combustion capture with 90% CO_2 retention rate is 7 to 9 % points lower, when the boundary conditions and the internal losses are the same in both plants and when the CC is optimised, but now the CO_2 emission is nearly zero. The production of oxygen is however now about 2.5 times higher than that of the reference IGCC but the shift of CO in the syngas using steam and the subsequent separation of CO_2 and H_2 using physical absorption are no longer needed. Consequently the proposed IGCC is an alternative to other capture options and more particularly to IGCC with pre-combustion capture, such as designed in the FutureGen project [26].

The main barrier for their implementation lies in their high cost resulting from the production of O_2 and from the need for new designs of the components operating on CO_2. This barrier is however likely to vanish if the value of environmental damages induced by fossil fuel combustion is adequately reflected within the costs (i.e. including externalities). Environmental market and political mechanisms (e.g. Kyoto protocol, carbon taxes, emissions trading market) could soon induce strong financial and regulatory incentives to adopt zero emission technologies and thereby provide a sound and cost-effective way to combat climate change.

REFERENCES

[1] IPCC, 2001a: Climate Change 2001 – Mitigation. The Third Assessment Report of the Intergovernmental Panel on Climate Change. B. Metz, O. Davidson, R. Swart, J. Pan (eds.). Cambridge University Press, Cambridge, UK

[2] IEA GHG R&D Programme , 2000, “Leading options for the capture of CO2 emissions at power stations", Report No. PH3/14 www.ieagreen.org.uk

[3] Chiesa P., S. Consonni, G. Lozza,1998, comparative analysis of IGCCs with CO_2 sequestration . 4th International conference on greenhouse gas control technologies, Interlaken, Switzerland .

[4] Doctor R.D., J.C.Molburg, P.R. Thimmapuramm. Oxygen blown gasification combined cycle : Carbon dioxide recovery, transport, and disposal. Energy Conversion. Management Vol 38, Suppl. Pp S575-S580 (1997). DOE report, Technology opportunities to reduce US greenhouse gas emissions. (1997a). DOE Report. Carbon Management. Assessment of fundamental Research Needs. (1997b). Enerpresse, 7498, Jan. 20, (2000).

[5] Simbeck,DR, 2002, CO_2 capture and storage, the essential bridge to hydrogen economy, 6th International conference on greenhouse gas control technologies GHGT-6, Kyoto, Japan .

[6] IEA GHG, 2003: Potential for Improvement in IGCC with CO2 Capture, report PH4/19, May 2003, IEA Greenhouse Gas R&D Programme, Cheltenham UK, 788 pp.

[7] Karg, J. and Hannemann, F., 2004, Karg, J. and Hannemann, F., .IGCC . Fuel-Flexible Technology for the Future., Presented at the Sixth European Gasificatin Confoerence, Brighton, UK May 2004. IGCC . Fuel-Flexible Technology for the Future., Sixth European Gasificatin Confoerence, Brighton, UK May 2004.

[8] Simbeck, D.R., 2001: .World Gasification Survey: Industrial Trends and Developments. Gasification Technology Conference, San Francisco, CA, USA, October.

[9] Bolland O., Boden J., Kvamsdal H.M.,2001, A thermodynamic comparison of the oxy-fuel power cycles: Water-Cycle, Graz-Cycle and Matiant-Cycle. International Conference on Power Generation and Sustainable Development, Liège, Belgium, 8-9 October 2001

[10] Bolland O. and Mathieu P.,1997, Comparison of two CO_2 removal options in combined cycle power plants, FLOWERS 97, Florence, Italy.

[11] Houyou, S., Nihart, R., Mathieu, P., Techno-economic comparison of different options of very low CO_2 emission technologies, Proc. *Fifth International Conference on Greenhouse Gas Control Technologies,* Cairns, Australia, 13-16 Aug. 2000.

[12] Mathieu, P. Presentation of an innovative zero-emission cycle for mitigating the global climate change. Int. J. of Applied Thermodynamics, Vol. 1, 1998.

[13] Mathieu, P., Nihart, R., 1999, Sensitivity analysis of the Matiant cycle, Energy Conversion and Management, vol 40, issues 15-16,pp 1687-1700

[14] Mathieu, P., Dubuisson, R., Houyou, S., Nihart, R. New Concept of CO_2 removal technologies in power generation, combined with fossil fuel recovery and long term CO_2 sequestration, ASME International Gas Turbine & Aeroengine Congress & Exhibition, Munich, Germany, May 8-11.2000.

[15] Mathieu, P. Mitigation of CO_2 emissions using low and near zero CO_2 emission power plants. Sixth International Conference on Technologies and Combustion for a Clean Environment, Porto, July 2001.

[16] Mathieu,P, 2003, Economics of Climate Change Mitigation using Zero Emission Technologies, International Conference on Technologies and Combustion for a Clean Environment, Lisbon ,to be published in Int Jl on Energy for a Clean Environment in 2005 .

[17] Mathieu,P, 2003, Zero Emission Technologies , an Option for Climate Change Mitigation, 3d Nordic Symposium on CO_2 capture and storage, Trondheim; to be published in " Jl of Green Energy" in 2005

[18] Mathieu,P, 2004, Towards the hydrogen economy using zero CO_2 emission energy systems, Energy-Int Journal, Elsevier, vol 29, issues 12-15,pp 1993-2002

[19] Allam R.J., Castle-Smith H., Smith A.R., Sorenson J.C. . Future direction of air separation design for gasification, IGCC and alternative fuel projects.. I Chem E Gasification conference Dresden 1998

[20] Ruether J, Le P, White C, Electricity generation from coal with CO_2 capture by means of a novel power cycle, 25th Int Technical Conf on Coal Utilization and fuel Systems, Clearwater,Florida, March 2000

[21] Chiesa, P., S. Consonni, T. Kreutz, and R. Williams, 2003: Co-production of hydrogen, electricity and CO2 from coal with commercially ready technology. Part A: Performance and emissions, International Journal of Hydrogen Energy

[22] IEA GHG (International Energy Agency Greenhouse Gas R&D Programme), 2003: Potential for improvements in gasification combined cycle power generation with CO2 Capture, report PH4/19, IEA GHG, Cheltenham, UK, 788 pp.

[23] Haupt,G, Zimmerman,G,Pruschek,R,Oeljeklaus,G, 2002, IGCC-The best choice for producing low CO_2 power, Green House Gas Technologies GHGT-6, Kyoto

[24] NETL-DOE (National Energy Technology Laboratory and the United States Department of Energy), 2002: Worldwide Gasification Database online, Pittsburgh, PA, USA. http://www.netl.doe.gov/coalpower/gasification/models/dtbs

[25] Todd DM; Battista RA "Demonstrated Applicability of Hydrogen Fuel for Gas Turbines", 4th European Gasification Conference 11-13th April 2001, Noordwijk Norway.

[26] Der V, US DOE, FutureGen : zero emission energy plant of the future, PowerGen conf , Barcelona, May 2004.

Proceedings of ECOS 2005
Trondheim, Norway
June 20–22, 2005

POLICY-ORIENTED ENERGY SYSTEM MODELING WITH *XEONA*

Robbie Morrison,* Tobias Wittmann, Jan Heise, and Thomas Bruckner
Technische Universität Berlin
Institute for Energy Engineering
D–10587 Berlin
Germany

ABSTRACT

Energy systems exist to provide industry, commerce, and households with fuels and energy-services. In addition to financial cost and reliability imperatives, these systems are now being asked to perform across a range of sustainability criteria. Most national systems fall well short on this second count and governments need to promote a suitable transition. Market liberalization over the last 20 years has made this task more challenging in public policy terms and yet could provide good incentives for innovation, reinvestment, and user responsiveness, given the right institutional measures. The development of suitable public policy may necessitate sophisticated simulation techniques, particularly considering the technical and commercial complexities involved, the multi-criteria nature of the policy problem, and the fact that most interventions will interact.

This paper presents *xeona* (extensible entity-oriented optimization-based network-mediated analysis), an object-oriented simulation environment designed for such use and currently under development. The modeling ethos is to represent important entities from the problem domain as elements within the simulation domain. Hence a *xeona* model is built from the ground up using the technical plant, controllers, markets, actors, and policy measures that exist in reality or are under consideration. The presence of actors allows low-stake commercial and domestic decision-making to be embedded within the model and thereby drive system evolution in response to commercial pressures and proposed policy interventions.

Model construction is one aspect, but the specifics of policy usage and interpretation are also important. To this end, a technology evaluation issue involving neighborhood fuel cell cogeneration in northern Europe is briefly illustrated with numerical results.

Keywords: complex systems, energy policy, entity-oriented modeling, network dynamics

INTRODUCTION

There is a growing interest by governments and the informed public alike in the role that proactive energy policy might play in promoting a transition to more sustainable energy systems. Energy policy formation is a complicated exercise involving institutional issues as diverse as international treaties, environmental law, market design and regulation, government support, mandatory standards, research funding, and the dynamics of technology innovation and uptake. Nowadays energy policy needs to be evaluated across multiple public interest criteria, including cost-competitiveness, carbon mitigation, energy security, system resilience, and any number of social factors. The underlying technical and commercial systems are now recognized as complex in nature. And the contexts in which such systems operate are increasingly volatile in both economic and environmental terms.

*Author for correspondence: Fax: ++49.30.314 21683 Email: morrison@iet.tu-berlin.de

Many of the established energy policy analysis methods are unable to perform in such circumstances and a number of new strategies are being developed to address some of the more evident shortfalls. One of these strategies makes use of highly disaggregated and relatively literal simulation techniques.

This paper reviews *xeona* and its underlying design. More specifically, *xeona* is a policy-oriented energy system modeling environment currently under development by the authors (however for convenience, the paper is written as though the software is complete). It is both *high resolution* and *bottom-up* in the sense that each plant, connection, actor, decision, and transaction can be depicted if deemed important to the problem at hand. *xeona* supports supply contract competition and nodal market pricing.

Simulations of this type fall under the complex adaptive systems (CAS) paradigm. In the case of *xeona*, a subset of this paradigm is used which might be best described as a dynamical networked systems approach with market and non-market coordination/control protocols and explicit endogenous *low-stake* decision-taking. Conversely, *high-stake* decision-making (for instance, commissioning a major power station) is left as an exogenous input for the modeler to specify prior to or during runtime — that is, as a *fixed* or *interactive* scenario, respectively.

xeona combines sophisticated actors with a rich technology depiction. These actors exhibit *bounded rationality* — which means that, for example, house owners take decisions in a natural way, consistent with their rationality type (related to temperament) and social milieu (related to social status and value orientation). The technology description is likewise based on a consideration of reality and incorporates *context-dependent technical performance* covering plant efficiency, capacity, and cost formation.

The term *actor* is used here to describe decision entities who interact relatively infrequently and warrant a sophisticated decision model. Whereas *agent* is reserved for entities which interact often and tend to make more spontaneous decisions. Hence the somewhat unusual term *actor-based modeling* is adopted.

xeona supports *numerical optimization* where it exists in practice or is under consideration. For instance, a facilities operator can assign unit (plant) commitment based on minimized short-run marginal cost (SRMC) or minimized direct CO_2-e (carbon dioxide equivalent) emissions. Nodal markets based on linear programming (LP) can be similarly included [1]. As will be seen later, *xeona* embraces the idea of *distributed management*.

This style of simulation has been called *entity-oriented* (EO) modeling due to the fact its underpinning ethos is for all relevant entities in the problem domain to be represented in the simulation domain in relatively concrete form — an approach made feasible by object-oriented programming [2, 3].

EO modeling is particularly suited to distributed systems operating in variable circumstances. In such arrangements, network dynamics tend to be a preeminent issue [4]. Briefly, *network dynamics* are the effects and externalities that arise from the capacitated nature of networks and the benefits of membership, respectively. These characteristics impose demands on network coordination and drive recruitment in ways that can be difficult to anticipate without numerical modeling.

The concept of an energy system is accorded a broad interpretation and is defined in terms of purpose. In all but a few specialist circumstances, the *purpose* of an energy system is to supply exergy-services.[1] *Exergy-services* are amenities that are either provided through exergy consumption *or* could have been supplied thus. Hence, the scope of such systems normally extends well beyond the boundaries encompassed by commercial transactions. Examples of exergy-services include: space and water heating, illumination, food and timber drying, and motive power applications.

xeona can be applied and interpreted in a variety of ways [5]. The most adventurous mode is evolutionary, whereby a given simulation is triggered and left to evolve under endogenous low-stake and exogenous high-stake decision-taking. Less ambitious application modes include non-evolutionary simulation and comparative analysis.

xeona itself does not directly prescribe a set of overarching policy goals. But concerns over *climate protection* [6] and *long-run energy security* are certainly

[1] Readers unfamiliar with the term *exergy* can substitute the word *energy* in its colloquial sense. Both indicate the potential of a resource to provide thermodynamic work, although energy tends to be restricted to recognized fuels.

topical, with the Kyoto Protocol having entered into force in early-2005 and the issue of *peak oil* [7] gaining attention. In addition, and given sufficient structural detail, local public interest issues, such as *air pollution load*, can be tallied for policy support — and even constrained or locally minimized. Moreover, *xeona* does not posit perfect markets and can provide a platform for examining *pricing regulation* and *market design* in the presence of strategic commercial behavior.

Some matters of usage conclude this introduction. The phrases *energy system* and *exergy-services supply system* (ESSS) are taken as synonymous. The term *plant* is used in its most general sense and, for instance, would include those features of a house which contribute to thermal comfort. The term *fuel* is also accorded a broad meaning and covers electric power, heating and cooling utility, and carbon dioxide sequestration. The term *intensity* refers to a quantity associated with a resource which remains independent of scale, examples might include: unit price, specific carbon content, and *flo* and *return* temperatures. A *graph* is mathematical structure suitable for depicting networks [8].

RELATED WORK

As indicated, *xeona* combines actor-based modeling and high resolution technical simulation.

Most of the policy-oriented actor/agent-based simulation projects to date have focused on the electricity industry, either to investigate industrial organization or market behavior and abuse. This research orientation is no doubt related to the economic importance of the sector and the fact that liberalization has thrown up a number of counter effects, such as: circular asset valuation (whereby pricing drives valuation and *vice versa*), zonal market power (where network saturation within nodal markets confers dominance), and strategic pricing (more particularly to defend incumbent grids from encroachment).

Actor/agent-based modeling has been used to investigate structural consolidation within the German electricity industry [9] and to scrutinize participant behavior within primary electricity markets in North America [10], Australia [11, 12, 13], and elsewhere.

High resolution technical simulation has played a very limited role in energy policy analysis thus far [4]. That said, European initiatives to better understand neighborhood cogeneration and district heating are starting to employ this approach [14].

The CAS paradigm — or, more precisely, its actor/agent-based and high resolution subsets — is not the only methodology being applied to support *energy policy formation* [15]. Other paradigms (with examples) include: planner-oriented structural optimization [16], system dynamics [17], econometric [18], general equilibrium [19], dynamic input/out [20], optimal growth [21], and climate policy integrated assessment [22] — with many now seeking to better represent technological change [23] and (as necessary) climate issues. Note that these different methodologies can be successfully mixed in some but not all cases. Work in Japan to combine energy system models with other policy models and projections through the AIM suite [24] warrants mention. Integrated analysis based on multi-level control is also emerging as a research theme [25]. More broadly, the notion of using actor/agent-based modeling for investigating social and economic systems is described in [26]. *xeona* also shares some similarities in approach and application with urban development microsimulation [27].

XEONA

xeona has been formulated to be more general than the electricity industry models indicated previously. Key publications include [4, 5, 28].

xeona builds on an earlier high resolution technical modeling environment called *deeco* [29] which was released in 1995 [30].[2] *deeco* remains in active use and development and is well suited to single operator jurisdictions where volatile operation and non-financial additionality considerations (such as carbon mitigation) also apply.

An early application of *deeco* found that sets of technical measures are likely to interact in an adverse way — meaning that the individual contributions are sub-additive. In such cases, the design task becomes one of identifying those configurations which give the least compromised outcome [31] — a result which also has implications for policy-makers [32].

xeona is built around three conceptual layers comprising primarily *actors*, *plant*, and *zones*. Actors

[2] See: `http://www.iet.tu-berlin.de/deeco`

are grouped by *legal entity* for the purposes of individual analysis and reporting. Likewise, plant are grouped by *control domain* for the purposes of single operator unit commitment *or* market clearing and dispatch. Each plant is associated with at least one actor. Zones supply *context information* to actors and plant, thus providing a backdrop covering the prevailing physical, commercial, and institutional conditions.

These ideas are broadly indicated in Figure 1, in a scheme that bears some resemblance to arrangements in New Zealand.[3] In practice, many of plant depicted would be composed of other plant. A low-stake investment option might be to extend the photovoltaic (PV) panel area, perhaps in response to some institutional incentive.

The *technical layer* is structured around the processing of resource stocks and flows, much as is discussed in [29]. Individual unit commitment is multi-dimensional for multiple fuel and/or product processes (including cogeneration). The resource flow conventions adopted for *xeona* are shown in Figure 2, with reverse (or negative) flow now supported. Mandatory and optional sinks and sources are represented by equality and inequality constraints, respectively.

Interconnected control domains are interfaced by *gateways* which pass across the required demand and intensity information. Each gateway is associated with one or more *legal contract*, covering, for instance, connection and supply (banded tariffs are supported) or market participation (through electronic auctioning). In this latter case, the market operator clears price and quantity using forward projections (two hours ahead, say), while the independent system operator (ISO) manages technical dispatch. In more basic models, these two functions can be treated as one in the same.

The control domains form a *control domain graph* (CDG) which is solved sequentially in topological sort order, as shown in Figure 3, for each interval. Hence, the CDG must be directed acyclic [8] in terms of demand transfer — rather than resource

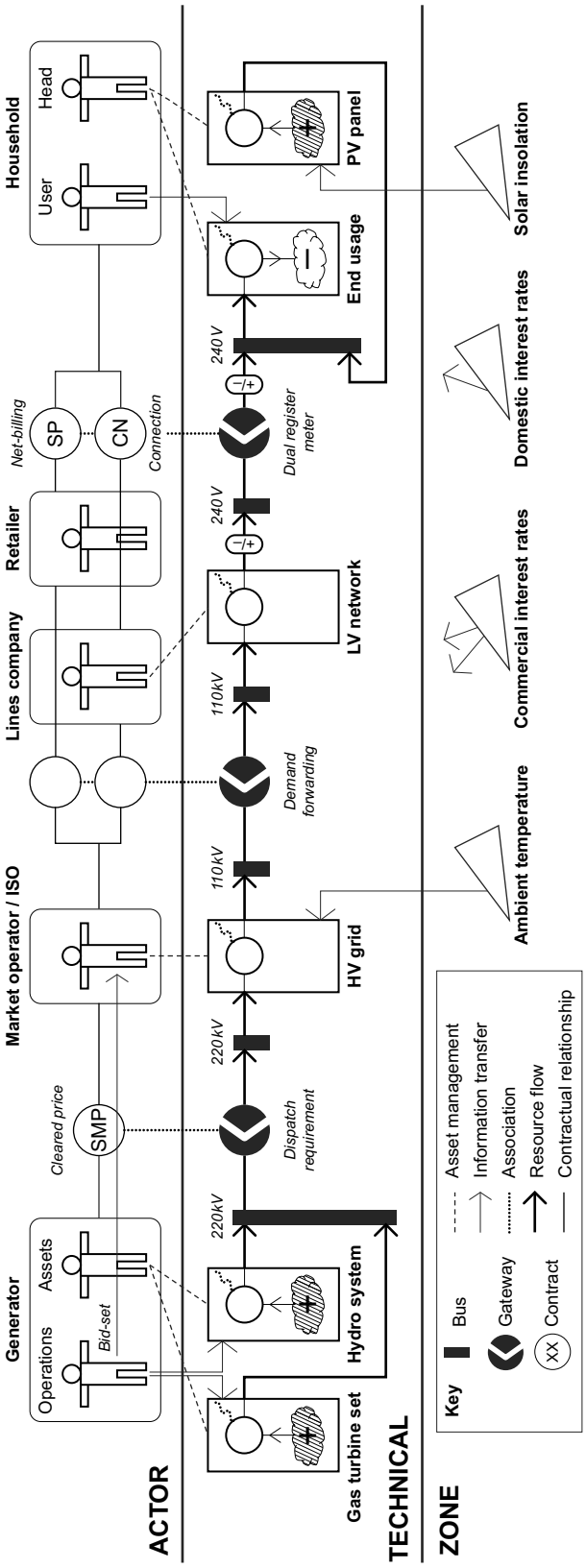

Figure 1: Three-layer diagram showing some of the key abstractions employed by *xeona*.

[3]New Zealand has a number of attributes that make it interesting in relation to the development of sustainable energy policy modeling techniques. These include: island status, an unparalleled renewable resource base, an institutional preference for deregulation, significant network characteristics, and pressing infrastructure renewal decisions.

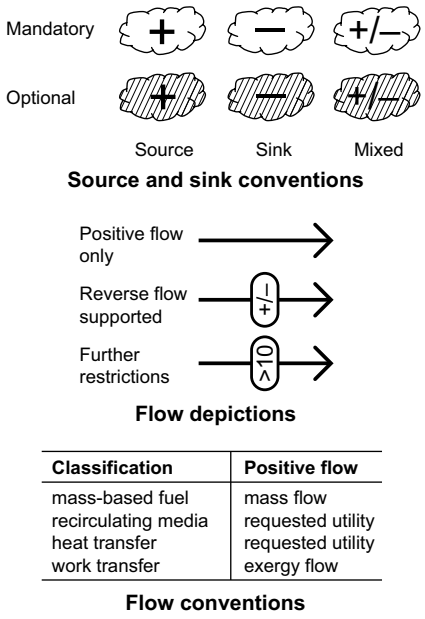

Figure 2: Resource flow conventions for *xeona*.

flow which cannot be guaranteed to be anti-parallel. Moreover, it is the demand for exergy-service and/or fuel provision that *drives* this model — a situation entirely consistent with the purpose of system definition introduced earlier.

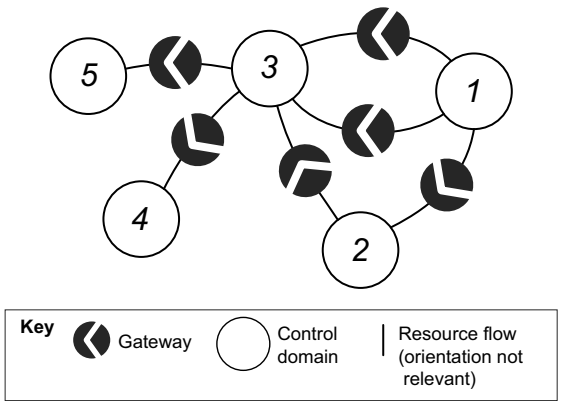

Figure 3: Control domain graph (CDG) with an acceptable solution order indicated.

The *actor layer* facilitates commercial interactions — as enabled by a particular scenario. Actors might therefore participate in nodal markets or purchase publicly posted supply contracts, technical equipment, and third-party services. Actors may also be placed in an *acquaintance network* (not shown) to facilitate bilateral negotiations.

The *zone layer* is where public policy interventions would normally be specified and where extreme external events can be defined. Given a sufficiently sophisticated model, *xeona* would be able to estimate the effects of anticipated climate change on existing and revised exergy-services supply systems.

xeona operates over various *timeframes*. Intervals typically span half or one hour, investment decisions might be revisited every three months or after key events, and scenario horizons may range from a year to a decade or more.

Space considerations meant the following design topics have either been skimmed over or omitted: exergy-services modeling (yielding fuel usage), logical flow and thermal intensity setting (including *flo* and *return* states), plant performance (including context-dependency), optimized shutdown-mode unit commitment (using mixed-integer linear programming), infeasible status responses (including relitigation and rationing), closing inventory matching (for comparative analysis), and the use of dynamic data structures and algorithms (to enable runtime intervention).

In terms of software licensing, both *xeona* and *deeco* are open-source.[4] This permits modelers the freedom to evaluate and develop the source code as they see best.

ACTOR DECISION-MAKING

Decision-making within *xeona* falls under several categories. *Operational* decisions cover unit commitment and market bid-set formulation, while *structural* decisions include plant investment and decommissioning. *Low-stake* decisions are taken within the model using context-specific algorithms, whereas *high-stake* decisions must be supplied externally, either as part of a fixed scenario or during runtime by including human subjects in the decision loop.

Low-stake structural decisions are based on the bounded rationality approach described in detail in [33]. Unit commitment is also low-stake, but relies on nominated protocols such as merit order and/or short-run optimization. Market bid-set formulation is low-stake as well, but has yet to be investigated in

[4]Both projects use the GNU GPL license together with requests to forward code changes to the principal authors and to not redistribute the codebase through anonymous download.

detail — there is, however, a growing literature on this topic [13, 34].

The term *bounded rationality* is used to describe actor decision-making which sidesteps the doctrines of (Bayesian) maximized subjective expected utility and discounted profit stream [35, 36]. And instead recognizes that actors, be they domestic or commercial, have limited knowledge, limited information gathering and processing abilities, and different preferences and perceptions as to future states of the world. Furthermore, actors may take decisions traversing only a subset of the information they hold. Researchers are currently attempting to understand this decision behavior and the particular environments in which it is exhibited. Their resultant models use simple search, stop, and decision rules. As an illustration, *satisfying* is a strategy in which one simply accepts the first decision option encountered that meets current aspiration levels.

POLICY SUPPORT

xeona supports energy policy formation from two distinct directions. First, the overall system performance is reported in terms of key public interest criteria — typically system financial cost, CO_2-e emissions, and depletable (fossil) resource use — thereby enabling informed policy decisions to follow. These results are normally presented using two and three dimensional *trade-off diagrams* [29]. And second, sets of specific policy measures can be embedded in particular scenarios and tested *in situ* against the aforementioned criteria. Such measures can range from: direct financial support, eco-taxation, feed-in laws, accelerated write-down, mandatory performance standards, and point-source air and thermal pollution discharge restrictions [5].

A key premise in this paper is that ESSS development trajectories can be affected by seemingly minor network dynamics in a manner comparable to the *butterfly effect* in long-range weather systems.

Providing insight into the way in which energy systems might be prompted to evolve from their present state is crucial when thinking about pathways to energy sustainability. It is necessary, but not sufficient, for analysts to identify socially beneficial transitions using, say, climate policy, dynamic general equilibrium, or system dynamics models. Such transitions will almost certainly need to be driven by specific policy measures — and their detailed evaluation provides a potential role for EO modeling. In short, both a roadmap and steerage are required.

This paper proposes two analytical roles for EO modeling — which can (and perhaps should) be dealt with jointly. One is examining the contribution that identified energy efficiency responses can make and how governments might best incentivize their uptake. And the other is studying the linkages between commercial strategic behavior, system evolution, and sustainability improvements.

EMBEDDED USE

There is a further reason for developing entity-oriented simulation techniques. It is likely that future energy systems will be strongly *status-awar*e in order to respond to changing circumstances in an intelligent way. This means that sections of the system (probably by control domain) may need to embed a suitable localized high resolution simulation which can cast forward hours and days to analyze and offer adaptive responses. One such action might be the online auctioning of demand deferral.

DISTRIBUTED TECHNOLOGY EXAMPLE

The following example from southern Germany shows how high resolution modeling can be used to assess the attractiveness (or otherwise) of distributed technology deployment from the point of view of both a new entrant *and* the wider public interest.

The study [4, 37] looks at the merits of installing 200 kW_e natural gas-fired PAFC (phosphoric acid) fuel cells, which supply — in parallel with peak-load boilers and other measures — heat and power to low-rise apartment blocks. These various schemes compete with district heat and electricity from the incumbent municipal utility. The study also considered potential network interactions with renewable energy opportunities, in this case, solar thermal systems with seasonal storage and local windfarms. Representative results are summarized in Figure 4. One conclusion is that the multi-criteria performance of technology groupings of this kind are strongly sensitive to the quality of local integration. Even so, in this particular situation and given

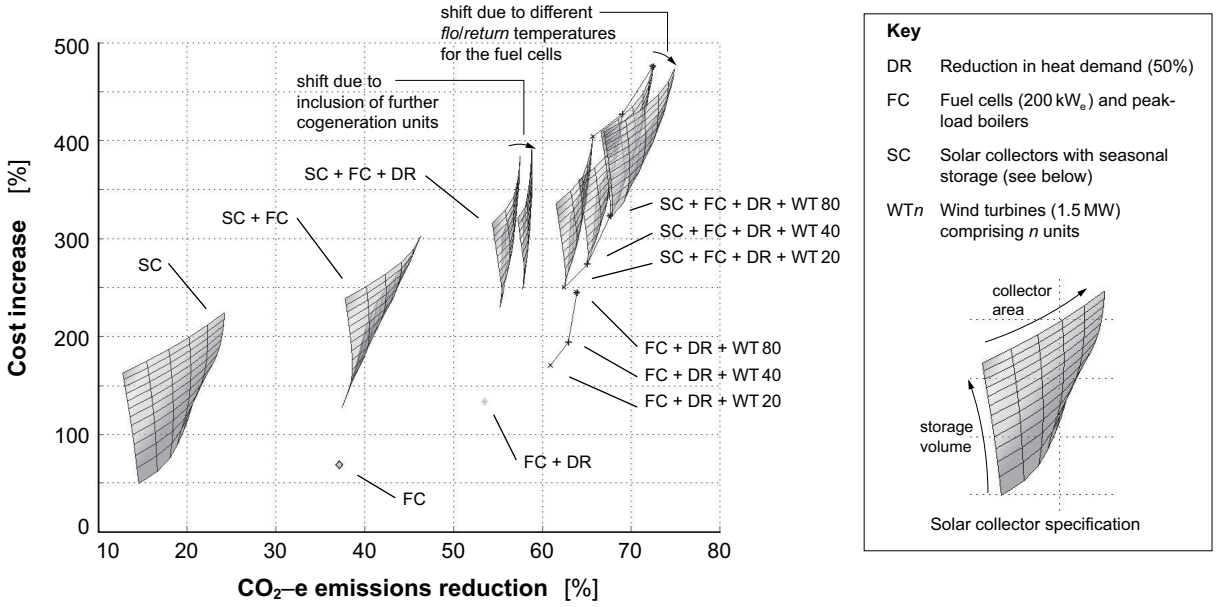

Figure 4: Relative carbon and financial additionalities for 200 kW_e neighborhood fuel cells operating in a range of configurations and control settings. The overall system performance, when combined with other local renewable energy and/or demand reduction opportunities, is also indicated. *Source*: [37, fig. 7.5]

the projected costs and other scenario assumptions, none of the options tested qualify as fully commercial propositions — despite positive social externalities. Hence, this form of modeling can provide a useful test-bed on which to evaluate policy measures designed to support low-carbon technologies.

DISCUSSION

Highly disaggregated and relatively literal energy system simulations — as exemplified by *xeona*— represent an emerging field. Many of the building blocks are still being sketched in and thus yet to be verified and accepted. However the tangible nature of these simulations lends confidence to this venture. And despite being detail intensive, entity-oriented (EO) models should not be fundamentally difficult to calibrate. Other model types, by contrast, often require abstract causalities to be estimated (for example, demand elasticity and feedback delay) and can be quite sensitive to inaccuracies.

EO models capture network dynamics naturally. This means that such models are particularly suited to system architectures and institutional arrangements where these dynamics are likely to develop. Most, if not all, energy efficiency propositions would fall into this category.

EO models maintain a clear separation between the private and public realms. This will avoid, for example, controversy over the choice of a single discount rate — because each actor, together with the public policy-maker, can be assigned an appropriate figure.

Financial cost-effectiveness should continue to be seen as a sustainability issue. This is because non-financial performance will invariably be traded off against financial cost, either explicitly or otherwise.

Such models also provides a useful qualitative description of energy systems and policy issues. This may not appear significant to the modeling community, but policy-makers and analysts often struggle to conceptualize complexity. Having access to a simplified but representative proxy model of the underlying system could assist in this regard.

Previously unreported work includes the concept of a control domain graph and the application of bounded rationality techniques to low-stake consumer and commercial energy efficiency investment decisions. The ability to include explicit decision-making in policy models appears to be a useful step. A number of current energy modeling initiatives attract criticism because they contain too little sociology — in many respects, *xeona* represents an attempt to rectify this shortcoming.

ACKNOWLEDGEMENTS

Robbie Morrison acknowledges support from New Zealand Government Bright Future Top-Achiever Doctoral Scholarship TAD 523. Tobias Wittmann acknowledges support from the Stiftung der Deutschen Wirtschaft, Germany.

REFERENCES

[1] Outhred HR, Kaye RJ. *Incorporating network effects in a competitive electricity industry : an Australian perspective*. In: Einhorn MA, Siddiqui R, editors. Electricity transmission pricing and technology, Kluwer Academic Publishers, 1996. p. 207–228. ISBN 0-7923-9643-X.

[2] Dattatri K. *C++ : effective object oriented software construction : concepts, principles, industrial strategies and practices — 2/e*. Prentice Hall PTR, 2002. ISBN 0-13-086769-1.

[3] Papazoglou MP, Saccapietra S, Tari Z, editors. *Advances in object-oriented data modeling*. The MIT Press, 2000. ISBN 0-262-16189-3.

[4] Bruckner T, Morrison R, Wittmann T. *Public policy modeling of distributed energy technologies : strategies, attributes, and challenges*. Ecological Economics (*forthcoming*).

[5] Morrison R, Wittmann T, Bruckner T. *Energy policy and distributed solutions : a model-based interpretation*. In: Proceedings of the Australia New Zealand Society for Ecological Economics (ANZSEE) Think Tank, Auckland, New Zealand, 2003.

[6] Hasselmann K, Latif M, Hooss G, Azar C, Edenhofer O, Jaeger CC, Johannessen OM, Kemfert C, Welp M, Wokaun A. *The challenge of long-term climate change*. Science 2003;302(5652):1923–1925.

[7] Campbell CJ, Laherrere JH. *The end of cheap oil*. Scientific American 1998;(Mar.):60–65.

[8] Gross J, Yellen J. *Graph theory and its applications*. CRC Press, 1999. ISBN 0-8493-3982-0.

[9] Bower J, Bunn DW, Wattendrup, C. *A model-based analysis of strategic consolidation in the German electricity industry*. Energy Policy 2001;29(12):987–1005.

[10] North M, Macal C, Cirillo R, Conzelmann G, Koritarov V, Thimmapuram P, Veselka T. *Multi-agent modeling of electricity markets*. In: Proceedings of the Social Agents : Ecology, Exchange, and Evolution Conference, Chicago, USA, 2002.

[11] Grozev GV. *Can we simulate Australia's National Electricity Market with the agent-based tool NEMCAS*. In: Proceedings of the International Conference on Optimization : Techniques and Applications (ICOTA), Ballarat, Australia, 2004.

[12] Veselka TD, Boyd G, Conzelmann G, Koritarov V, Macal C, North M, Schoepfle B, Thimmapuram P. *Simulating the behavior of electricity markets with an agent-based methodology : the Electric Market Complex Adaptive Systems (EMCAS) model*. Vancouver, Canada, 2002.

[13] Hu X. *Understanding generators' bidding strategies in Australia's National Electricity Market*. In: Proceedings of the International Conference on Optimization : Techniques and Applications (ICOTA), Ballarat, Australia, 2004.

[14] Grohnheit PE. *Energy policy responses to the climate change challenge : the consistency of European CHP, renewables, and energy efficiency policies — Report Risø-R-1147(EN)*. Risø National Laboratory, Roskilde, Denmark, 1999. ISBN 87-550-2626-5.

[15] Bunn DW, Larsen ER, editors. *Systems modelling for energy policy*. John Wiley and Sons, 1997. ISBN 0-471-95794-1.

[16] Seebregts AJ, Goldstein GA, Smekens KEL. *Energy/environmental modeling with the MARKAL family of models*. In: Proceedings of the International Conference on Operations Research (OR 2001), Duisburg, Germany, 2002. p. 75–82. ISBN 3-450-43344-9.

[17] Bunn DW, Dyner I. *Systems simulation to support integrated energy analysis and liberalised planning*. International Transactions in Operational Research 1996;3(2):105–115.

[18] Barker T. *Large-scale energy-environment-*

economy modelling of the European Union, In: Begg I, Henry SGB, editors. Applied economics and public policy. Cambridge University Press, 1998. p. 15–40. ISBN 0-521-62414-2.

[19] Kemfert C. *An integrated assessment model of economy-energy-climate : the model WIAGEM*. Integrated Assessment – An International Journal 2002;3(4):281–298.

[20] Kemfert C, Kuckshinrichs W. *MIS : a model-based macroeconomic information system for energy analysis in Germany* In: [15], 1997. p. 47–66.

[21] Popp D. *ENTICE : endogenous technological change in the DICE model of global warming*. Journal of Environmental Economics and Management 2004;48(1):742–768.

[22] Bruckner T, Petschel-Held G, Tóth FL, Füssel H-M, Helm C, Leimbach M, Schellnhuber H-J. *Climate change decision-support and the Tolerable Windows Approach*. Environmental Modeling and Assessment 1999;4(4):217–234.

[23] Kemfert C, Vollebergh HRJ. *The role of technological change for a sustainable development — Editorial*. Ecological Economics (*forthcoming*).

[24] Kainuma M, Matsuoka Y, Morita T. *Climate policy assessment : Asia-Pacific Integrated Modeling*. Springer Verlag, 2003. ISBN 4-431-70264-4.

[25] Tommy Mølbak. *Integrated model based optimisation of a power production system*. In: Proceedings of ECOS 2003 — 16th International Conference on Efficiency, Costs, Optimization, Simulation and Environmental Impact of Energy Systems, Copenhagen, Denmark, 2003.

[26] Epstein JM, Axtell RL. *Growing artificial societies : social science from the bottom up*. The MIT Press, 1996. ISBN 0-262-55025-3.

[27] Waddell P. *UrbanSim : modeling urban development for land use, transportation and environmental planning*. Journal of the American Planning Association 2002;68(3):297–314.

[28] Morrison R, Wittmann T, Bruckner T. *Energy sustainability through representative large-scale simulation : the logical and physical design of xeona*. In: Proceedings of the International Conference on Sustainability Engineering and Science (ICSES), Auckland, New Zealand, 2004.

[29] Bruckner T, Morrison R, Handley C, Patterson M. *High-resolution modeling of energy-services supply systems using deeco : overview and application to policy development*. Annals of Operations Research 2003;121(1–4): 151–180.

[30] Bruckner T. *Dynamische Energie- und Emissionsoptimierung regionaler Energiesysteme — Doktorarbeit*. Institut für Theoretische Physik, Universität Würzburg, Germany, 1997. [Dynamic energy and emissions optimization for regional energy systems — PhD thesis].

[31] Bruckner T, Groscurth H-M, Kümmel R. *Competition and synergy between energy technologies in municipal energy systems*. Energy–The International Journal 1997;22(10):1005–1014.

[32] Morrison R, Bruckner T. *High-resolution modeling of distributed energy resources using deeco: adverse interactions and potential policy conflicts*. In: Proceedings of the 3rd International Workshop : Advances in Energy Studies, Porto Venere, Italy, 2002. p. 97–107.

[33] Gigerenzer G, Selten R, editors. *Bounded rationality : the adaptive toolbox*. The MIT Press, 2001. ISBN 0-262-57164-1.

[34] Bunn DW, editor. *Modelling prices in competitive electricity markets*. John Wiley and Sons, 2004. ISBN 0-470-84860-X.

[35] Simon HA. *Models of man : social and rational*. John Wiley and Sons, 1957.

[36] Bettman JR, Luce MF, Payne JW. *Constructive consumer choice processes*. Journal of Consumer Research 1998;25(3):187–217.

[37] Heise J. *Emissions- und Kostenoptimierung von Energieversorgungssystemen mit Brennstoffzellen und Anlagen zur Nutzung erneuerbarer Energien — Diplomarbeit*. Institut für Energietechnik, Technische Universität Berlin, Germany, 2004. [Emissions and cost optimization of energy supply systems containing fuel cells and renewable energy technologies — Masters thesis]. □

Proceedings of ECOS 2005
Trondheim, Norway
June 20–22, 2005

CONTROL PROPERTIES OF BOTTOM FIRED MARINE BOILERS

Brian Solberg and Claus M. S. Karstensen
Aalborg Industries A/S
9100 Aalborg, Denmark
Palle Andersen
Dept. of Control Engineering, Aalborg University
9220 Aalborg Øst, Denmark

ABSTRACT

This paper focuses on model analysis of a dynamic model of a bottom fired one-pass smoke tube boiler. Linearised versions of the model are analysed to determine how gain, time constants and right half plane zeros (caused by the shrink-and-swell phenomenon) depend on the steam flow load. Furthermore the interactions in the system are inspected to analyse potential benefit from using a multivariable control strategy in favour of the current strategy based on single loop theory.
An analysis of the nonlinear model is carried out to further determine the nonlinear characteristics of the boiler system and to verify whether nonlinear control is needed.
Finally a controller based on single loop theory is used to analyse if input constraints become active when rejecting transient behaviour from the disturbance steam flow.
The model analysis shows large variations in system gains at steady state as function of load whereas gain variations at the crossover frequency are small. Furthermore the interactions in the system prove not to be negligible and a subsequent controller design should take this into account using either Multiple input Multiple output control or Single input Single output controllers supported by a dynamical decoupling.
The results indicate that input constraints will become active when the controller responds to transients in the steam flow disturbance. For this reason an MPC (model predictive control) strategy capable of handling constraints on states and control signals should be considered. Furthermore hard constraint on the level variations also supports the choice of this strategy.
Keywords: Marine boiler, Dynamic models, Load dependency, Interaction, RGA, RIM, Decentralised control, Model nonlinearities

NOMENCLATURE

Symbol	Description
d, $\mathbf{d}$	disturbance (scalar/vector)
D, $\mathbf{D}$	scaling factor (scalar/matrix)
e, $\mathbf{e}$	error (scalar/vector)
k	valve conductance $\left[\frac{\text{kg}}{\text{s}\sqrt{\text{Pa}}}\right]$
L	level [m]
$\dot{m}$	mass flow $\left[\frac{\text{kg}}{\text{s}}\right]$
P	pressure [Pa]
r	reference
T	temperature [°C]
u, $\mathbf{u}$	input (scalar/vector)
x, $\mathbf{x}$	state (scalar/vector)
y, $\mathbf{y}$	output (scalar/vector)
κ	RIM
$\mathbf{\Lambda}$	RGA
Subscripts	**Description**
b	bobbles
f	flue gas
fw	feed water
fu	fuel
m	metal
s	steam
w	water
Abbreviations	**Description**
MIMO	multiple input multiple output
MPC	model predictive control
ORG	origin
PI	proportional and integral
RGA	relative gain array
RHP	right half plane
RIM	Rijnsdorp interaction measure
SISO	single output single input

INTRODUCTION

During the years marine boilers have been controlled using classical SISO controllers. Lately focus has been put on optimising the boiler performance through a more comprehensive and coherent control

strategy. This includes model-based MIMO control to minimise variation in especially drum water level. With this parameter minimised it is possible to reduce the physical dimensions of the boiler which imply lower production costs and gives a more competitive product.
Prior to setting up a control strategy it is important to understand the process to be controlled and the model describing it. The boiler system is nicely described by means of first principles resulting in a model based on nonlinear differential equation, see e.g. [1] and [2]. This model has a MIMO structure meaning that all process inputs affect all the outputs. It is of interest to know how large the interactions in the MIMO system are and also the degree of nonlinearities in the model and if any of these properties will affect the controlled boiler system.
The model which is analysed in this paper is based on the bottom fired one-pass smoke tube boiler (MISSION^{TM} OB) from Aalborg Industries A/S product range. The largest of these has a maximum steam load of 3000 $\frac{\text{kg}}{\text{h}}$.
The paper starts by introducing the boiler model and deriving linear versions of this depending on the operating point. After that follows the analysis based on mostly linear system theory using the concept of decentralised control and decoupling to find interaction.

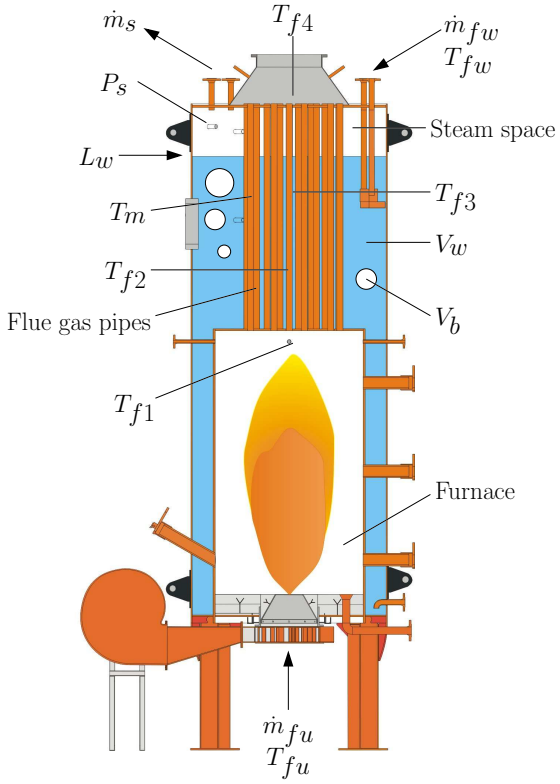

Figure 1: Drawing of the bottom fired one-pass smoke tube boiler.

BOILER MODEL

A drawing of the bottom fired one-pass smoke tube boiler is shown in figure 1 with model variables indicated. A model of this boiler was presented in [2]. The model has the structure:

$$\mathbf{F}(\mathbf{x})\dot{\mathbf{x}} = \mathbf{h}(\mathbf{x},\mathbf{u},\mathbf{d}) \quad (1)$$
$$\mathbf{y} = \mathbf{c}(\mathbf{x}) \quad (2)$$

where $\mathbf{u} = [\dot{m}_{fu}, \dot{m}_{fw}]^T$ (fuel flow and feed water flow), $\mathbf{y} = [P_s, L_w]^T$ (steam pressure and water level), $\mathbf{d} = [k, T_{fu}, T_{fw}]^T$ ("steam flow", fuel temperature and feed water temperature) and $\mathbf{x} = [T_{f1}, T_{f2}, T_{f3}, T_{f4}, T_m, P_s, V_w, V_b]^T$ (T_f being temperatures at four different levels in the furnace and convection parts, T_m is the temperature of the metal separating the heating part and the liquid part and V_w and V_b are volumes of water and steam bobbles under the surface in the drum).
It should be mentioned here that the disturbance k is related to the actual steam flow as $\dot{m}_s = k\sqrt{P_s - P_{atm}}$, and can be interpreted as an overall steam valve and pipe system conductance. k will also be referred to as the steam flow disturbance. P_{atm} is the atmospheric pressure at the pipe outlet.
A parameter estimation was made to find the critical parameters in the model in such a way that it reflects the physical boiler system as well as possible.

Linear Model

Linearised versions of the plant are introduced as most of the model analysis and controllers designed will be based on these. The linearisation is based on a first order Taylor series expansion. Scaling of the models is introduced (according to Skogestad and Postlethwaite [3]) as it makes both model analysis and controller design simpler.
Let the unscaled linear small signal valued plant model including tracking error in the Laplace domain be given as:

$$\check{\mathbf{y}}(s) = \check{\mathbf{G}}_u(s)\check{\mathbf{u}}(s) + \check{\mathbf{G}}_d(s)\check{\mathbf{d}}(s) \quad (3)$$
$$\check{\mathbf{e}}(s) = \check{\mathbf{r}}(s) - \check{\mathbf{y}}(s) \quad (4)$$

Introduce scaling factors put up from system demands; allowable control error, knowledge of disturbance variations and allowable input change e.g. due to valve opening constraints or maximal flow rate etc.:

$$D_{e,i} = \check{e}_{max,i}, \quad D_{u,j} = \check{u}_{max,j}, \quad D_{d,k} = \check{d}_{max,k}$$

where the subscripts i, j, k represent the different numbers of entries in the error, input and disturbance

vector respectively. The specific values are listed below:

	$\check{e}_{max}$	$\check{u}_{max}$	$\check{d}_{max}$
1	0.5 bar	160 $\frac{\text{kg}}{\text{g}}$	$6.0 \cdot 10^{-4}$ $\frac{\text{kg}}{\text{s}\sqrt{\text{Pa}}}$
2	0.1 m	4500 $\frac{\text{kg}}{\text{g}}$	5 °C
3			5 °C

The value of $\check{d}_{max,1} = k_{max}$ is determined from assuming a maximal steam flow of 3000 $\frac{\text{kg}}{\text{h}}$, a steam flow range of 40-100% and assuming that steps in the flow from maximum to minimum and the opposite can occur.
Using vector notation, putting the scaling element on the diagonal of a scaling matrix, the scaled output, input, disturbance and reference vectors are given as:

$$\mathbf{y} = \mathbf{D}_e^{-1}\check{\mathbf{y}}, \quad \mathbf{u} = \mathbf{D}_u^{-1}\check{\mathbf{u}}$$
$$\mathbf{d} = \mathbf{D}_d^{-1}\check{\mathbf{d}}, \quad \mathbf{r} = \mathbf{D}_e^{-1}\check{\mathbf{r}}$$

Substituting these scaled vector representations into equations 3 and 4 gives the scaled model:

$$\begin{aligned} \mathbf{y}(s) &= \mathbf{G}_u(s)\mathbf{u}(s) + \mathbf{G}_d(s)\mathbf{d}(s) \qquad (5) \\ \mathbf{e}(s) &= \mathbf{r}(s) - \mathbf{y}(s) \end{aligned}$$

where $\mathbf{G}_u(s) = \mathbf{D}_e^{-1}\check{\mathbf{G}}_u(s)\mathbf{D}_u$ and $\mathbf{G}_d(s) = \mathbf{D}_e^{-1}\check{\mathbf{G}}_d(s)\mathbf{D}_d$.
Now $\|\mathbf{d}(t)\|_\infty \leq 1$ and the objective is to keep $\|\mathbf{e}(t)\|_\infty \leq 1$ while obeying $\|\mathbf{u}(t)\|_\infty \leq 1$. If needed additional scaling can be applied to the references to keep $\|\mathbf{r}(t)\|_\infty \leq 1$ during reference changes.

Actuator Models

In the aforementioned boiler model the actuator dynamics were omitted. The actuators will enter in the closed loop strategy in a cascade configuration. The actuators used for both the fuel and feed water flow are valves with a pneumatic actuation. Measurements show that these have a rise time from control signal to flow of $t_r < 10$ s. It is assumed that cascade controllers linearising the actuator dynamics can be designed with a dynamic behaviour equal to or faster than the open loop actuator dynamics.
Models of the controlled actuators with reference flows as input and actual flows as output can be put in a matrix form as:

$$\mathbf{G}_a(s) = \begin{bmatrix} G_{a11}(s) & 0 \\ 0 & G_{a22}(s) \end{bmatrix}$$

Both controlled actuators are assumed to be well described by second order systems. Introducing this model in the total linear model gives a new transfer function from input to output: $\mathbf{G}(s) = \mathbf{G}_u(s)\mathbf{G}_a(s)$

MODEL ANALYSIS

During this analysis especially three operating points will be considered; minimum load: 40%, middle load: 70% and maximum load 100%. Expanding the notation of equation 5, including the actuator dynamics, illustrates the transfer functions of the model:

$$\begin{bmatrix} y_1 \\ y_2 \end{bmatrix} = \begin{bmatrix} G_{11} & G_{12} \\ G_{21} & G_{22} \end{bmatrix} \begin{bmatrix} u_1 \\ u_2 \end{bmatrix} + \\ + \begin{bmatrix} G_{d11} & G_{d12} & G_{d13} \\ G_{d21} & G_{d22} & G_{d23} \end{bmatrix} \begin{bmatrix} d_1 \\ d_2 \\ d_3 \end{bmatrix}$$

where the dependency of s is omitted. This will be done throughout the analysis, to simplify expressions, where this dependency is obvious. A block diagram illustration of the system is shown in figure 2. In

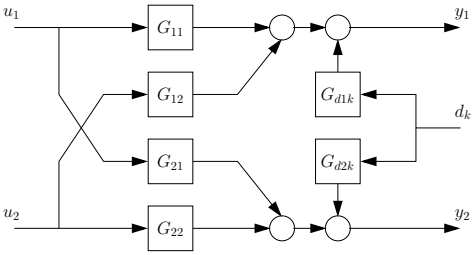

Figure 2: Block diagram of linear boiler model.

figure 3 a magnitude plot of the transfer functions of $\mathbf{G}(s)$ is presented for each of the three mentioned operating points.

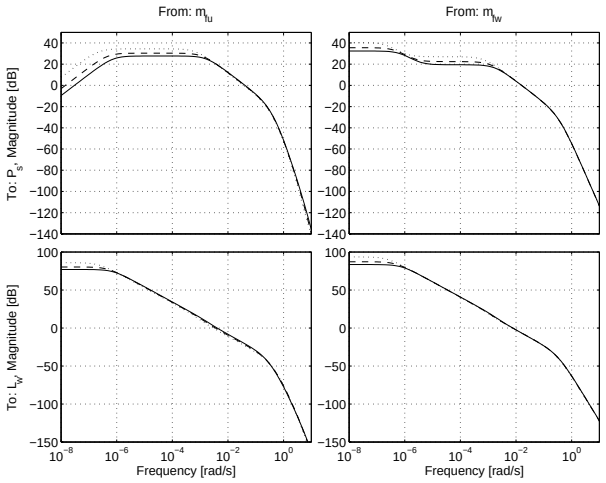

Figure 3: Magnitude plots of transfer functions in $\mathbf{G}(s)$ at three different loads; 100% solid, 70% dashed and 40% dotted.

The actual differences in model dynamics are not well visualised in these plots. In figure 4 magnitude plots

of $G_{ij,40}/G_{ij,100}$, the ratios between the transfer functions at 40% load and 100% load are shown.

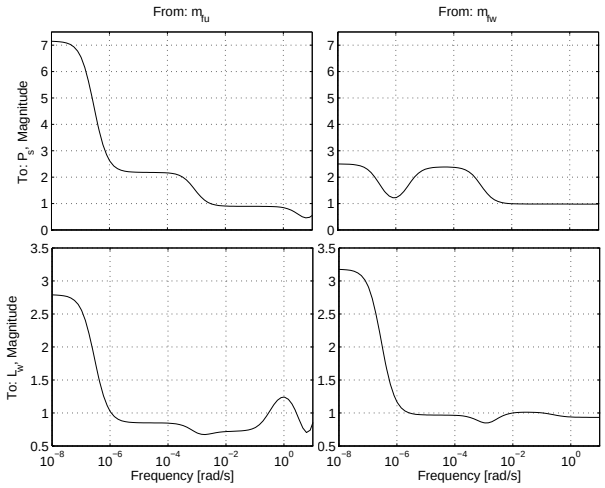

Figure 4: Magnitude plot of $G_{ij,40}/G_{ij,100}$.

From the plots it can be seen that the main differences between the model dynamics at the different operating points are at low frequencies where gain increases at lower load. On the other hand at frequencies above 10^{-3} rad/s for output one, P_s, and above 10^{-6} rad/s for output two, L_w, the behaviours are similar at least up to about 10 rad/s where the ratios associated with the fuel flow input break off. It is of interest to find out whether these differences have any practical implication in a controller design and furthermore whether interactions in the system should be handled by a MIMO control strategy.

It is obvious from the magnitude plots that they do not give any useful information regarding gains and time constants as both quantities are unreasonable high due to a pole in the left half plane close to the origin. Furthermore it can be seen that the steady state gain of $G_{11}(s)$ is zero indicating a zero in the origin.

Instead of looking at gains at steady state and at the usual definition of time constants another approach is taken. Focus is put at the crossover frequency ω_c. Assuming knowledge of this quantity at the operating point of 100% a suitable controller for this specific load can be designed. Now the system gain variations can be defined as the variations at the crossover frequency when the operating point is changed but the same controller is applied. Furthermore instead of considering the actual time constants the variations of the crossover frequency when the operating point is changed are investigated.

This approach gives insight to the stability properties of the nonlinear boiler system.

Decentralised Control

The controller designed is a simple decentralised controller using SISO PI controllers. An estimate of the bandwidth requirements without taking MIMO interaction into account are investigated from a plot of the magnitudes of the transfer functions from the disturbances to the output, $G_d(s)$, shown in figure 5.

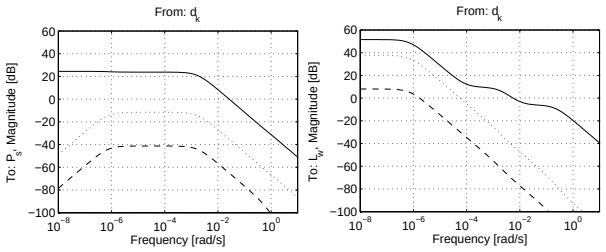

Figure 5: The left plot shows the magnitude plot from $\mathbf{d}$ to y_1 and the right plot the magnitude plot from $\mathbf{d}$ to y_2. The solid line is associated with d_1, the dashed line with d_2 and the dotted line with d_3.

Control is needed at frequencies where $|G_{dik}(j\omega)| > 1$, $|G_{dik}|$ being the disturbance gain from disturbance k to output i. From the plots it can be seen that for both the pressure, y_1 and water level, y_2, the worst disturbance is the change in the steam flow; disturbance d_1. The two temperature disturbances have proved to play a minor role in a closed loop configuration and will not be addressed further in this paper. G_{d11} cross the zero axis at $\omega_{b1} \approx 0.027$ rad/s and G_{d21} cross the zero axis at $\omega_{b2} \approx 0.006$ rad/s, setting an estimated bandwidth requirement for the pressure and level loop, respectively.

Stability conditions imposed by interaction

Of interest when performing model analysis and designing decentralised controllers are the stability conditions imposed by interactions in the MIMO model when using the diagonal controller.
Let $\mathbf{P}$ be a square $n \times n$ plant and let $\tilde{\mathbf{P}}$ ("nominal plant") be given as:

$$\tilde{\mathbf{P}} = \begin{bmatrix} P_{11} & 0 & \\ 0 & \ddots & 0 \\ & 0 & P_{nn} \end{bmatrix}$$

Then the closed loop system can be presented as in figure 6.
$\mathbf{K}$ is diagonal and $\mathbf{E}$ is an output multiplicative perturbation given as:

$$\mathbf{E} = (\mathbf{P} - \tilde{\mathbf{P}})\tilde{\mathbf{P}}^{-1}$$

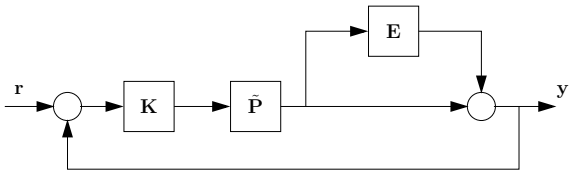

Figure 6: Block diagram of closed loop with $\mathbf{P}$ represented as the diagonal plant $\tilde{\mathbf{P}}$ and an output multiplicative perturbation $\mathbf{E}$.

By Skogestad [3] the overall output sensitivity function for this system can be factorised as:

$$\mathbf{S} = \tilde{\mathbf{S}}(\mathbf{I} + \mathbf{E}\tilde{\mathbf{T}})^{-1}$$

where $\tilde{\mathbf{S}} = (\mathbf{I} + \tilde{\mathbf{P}}\mathbf{K})^{-1}$ is the sensitivity function of the nominal system and $\tilde{\mathbf{T}} = \mathbf{I} - \tilde{\mathbf{S}}$.
Now assume that $\mathbf{P}$ is stable and furthermore that the individual loops are stable ($\tilde{\mathbf{S}}$ and $\tilde{\mathbf{T}}$ stable), then for stability of the overall system it suffices to look at

$$\det(\mathbf{I} + \mathbf{E}\tilde{\mathbf{T}}(s)) \tag{6}$$

as s traverses the Nyquist D-contour and make sure it does not encircle the origin. This follows from lemma A.5 in [3]. The spectral radius stability condition then yields stability of the overall system if:

$$\rho(\mathbf{E}\tilde{\mathbf{T}}(j\omega)) < 1 \ \forall\, \omega$$

2×2 **systems:** For these systems the condition becomes especially simple. This will be illustrated with the system addressed in this paper.

$$\mathbf{E} = \begin{bmatrix} 0 & \frac{G_{12}}{G_{22}} \\ \frac{G_{21}}{G_{11}} & 0 \end{bmatrix}, \quad \tilde{\mathbf{T}} = \begin{bmatrix} \tilde{T}_{11} & 0 \\ 0 & \tilde{T}_{22} \end{bmatrix}$$

The spectral radius of $\mathbf{E}\tilde{\mathbf{T}}(j\omega)$ is given by:

$$\rho(\mathbf{E}\tilde{\mathbf{T}}(j\omega)) = \left|\sqrt{\tilde{T}_{11}\tilde{T}_{22}\kappa(j\omega)}\right|$$

where $\kappa = \frac{G_{12}G_{21}}{G_{11}G_{22}}$ is the RIM (Rijnsdorp interaction measure) introduced by Rijnsdorp [4]. Now the sufficient condition for stability of the overall system is:

$$|\tilde{T}_{11}\tilde{T}_{22}(j\omega)| < \frac{1}{|\kappa(j\omega)|} \ \forall\, \omega$$

or the more conservative condition:

$$|\tilde{T}_{ii}(j\omega)| < \frac{1}{\sqrt{|\kappa(j\omega)|}} \ \forall\, \omega, i \in [1,2]$$

Bounds can be set on the sizes of $\tilde{T}_{11}(j\omega)$ and $\tilde{T}_{22}(j\omega)$ according to their resonant peaks which again are related to the stability margins of the individual loops. This gives the more conservative condition:

$$\|\tilde{T}_{ii}\|_\infty < \frac{1}{\sqrt{|\kappa(j\omega)|}} \ \forall\, \omega, i \in [1,2] \tag{7}$$

Hence to ensure stability of a system with offset-free tracking ($T_{ii}(0) = 1$) assuming no resonant peaks the condition becomes $1 < 1/|\kappa(j\omega)| \ \forall\, \omega$. From equation 7 it follows that the interactions in the system pose no limit on the achievable closed loop system bandwidth if $\kappa < 1$.
It is obvious that systems with $|\kappa(j\omega)| \ll 1 \ \forall\, \omega$ are preferable. One could interpret the degree to which $\kappa < 1$ as an insurance of a good stability margin. This also relates to another measure of interaction; the relative gain array (RGA), first introduced by Bristol [5], which is given as

$$\mathbf{\Lambda}(\mathbf{G}(s)) = \mathbf{G}(s) \circ (\mathbf{G}^{-1}(s))^T$$

where $\circ$ is the element wise product (also known as the Schur or Hadamard product). In the following shortened to $\mathbf{\Lambda}(\mathbf{s})$. An element of the RGA, $\Lambda_{ij}(s)$, is the ratio between the gain of G_{ij} assuming all other loops open and the gain of G_{ij} assuming all other loops closed by perfect control. Both the RIM and the RGA are independent of the particular plant input and output scaling. For 2×2 systems the RGA can be expressed as:

$$\mathbf{\Lambda}(s) = \begin{bmatrix} \frac{1}{1-\kappa(s)} & \frac{-\kappa(s)}{1-\kappa(s)} \\ \frac{-\kappa(s)}{1-\kappa(s)} & \frac{1}{1-\kappa(s)} \end{bmatrix}$$

In most cases for stability of the overall system using diagonal decentralised control it is sufficient to require $\mathbf{\Lambda}(j\omega_c) \approx \mathbf{I}$ at the crossover frequencies [3], which is the same as requiring $|\kappa(j\omega_c)| \ll 1$. $\mathbf{\Lambda}(j\omega_c) = \mathbf{I}$ imply that the individual loops are independent of the closing of the other loops meaning that the stability margins from the individual loops are preserved. Furthermore a unity RGA implies that there are zero or only one way interaction. One way interaction can be interpret and treated as a disturbance.
In figure 7 $1/|\kappa(j\omega)|$ for $\mathbf{G}$ is plotted.

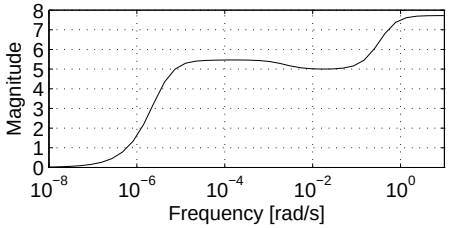

Figure 7: Plot of $1/|\kappa(j\omega)|$.

Now assume that $\tilde{T}_{ii}$ for all i is designed with no resonant peak such that $\|\tilde{T}_{ii}\|_\infty \leq 1$ given the sufficient

condition for stability: $1 < 1/|\kappa(j\omega)| \; \forall \omega$ then it is obvious from the figure 7 that stability is not ensured in the low frequency band. This is due to the zero in the origin of G_{11}. However the spectral radius stability condition is conservative meaning that this does not necessarily imply that the system is unstable.
To investigate whether the conditions in the low frequency band cause any stability problems for the overall loop again look at equation 6. Notice that at low frequencies $\tilde{\mathbf{T}} \approx \mathbf{I}$. This means that for overall stability it suffices to ensure that $\det(\mathbf{I} + \mathbf{E}(j\omega))$ behaves well at low frequencies (does not encircle the origin). Given this overall stability is ensured by (7) for $\|\tilde{T}_{ii}\|_\infty$ small enough. The Nyquist plot of $\det(\mathbf{I} + \mathbf{E}(j\omega))$ is shown in figure 8.

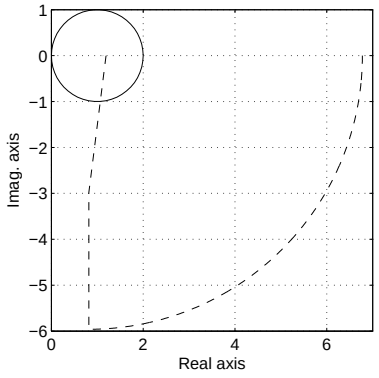

Figure 8: Nyquist plot of $\det(\mathbf{I} + \mathbf{E}(j\omega))$.

As can be seen the curve indeed behaves well at low frequencies and there are no encirclements of the origin. From the analysis it can be concluded looking at figure 7 (assuming $\tilde{\mathbf{T}}(j\omega) \approx \mathbf{I} \; \forall \omega < 10^{-5}$ for the previous analysis to hold) that to ensure stability of the overall system the condition is according to (7); $\|\tilde{T}_{ii}\|_\infty < \sqrt{5}$ that is a resonant peak less than $\sqrt{5}$. If $\tilde{T}_{ii}$ is assumed to have second order characteristics the resonant peak requirement can be related directly to the phase margins of $\tilde{T}_{ii}$ [6]. E.g. a resonant peak of $\sqrt{5}$ corresponds to a phase margin of approximately 26°.

Pairing

The RGA is often used as a measure for pairing control inputs to outputs as the structure of the RGA is dependent on this pairing. Recalling from the last section that to ensure stability one often requires that $\mathbf{\Lambda}(j\omega_c) \approx \mathbf{I}$, similar to requiring $1 \ll 1/|\kappa(j\omega_c)|$. From the discussion regarding the required bandwidth the crossover frequencies can be expected to be $\omega_{c1} > 0.027$ rad/s and $\omega_{c2} > 0.006$ rad/s. It can be seen from figure 7 that the current pairing (controlling pressure with fuel flow and water level with feed water flow) is the best choice, as would be expected. Intuitively pairing inputs and outputs for which $\Lambda_{ij} = 1$ also makes sense as this means that the gain seen from input j to output i is unaffected by the closing of the other loops.
However focusing on the low frequency range figure 7 shows that the chosen pairing results in small RGA elements indicating control problems if one loop breaks. The problem here is a zero in the origin of the transfer function $G_{11}(s)$ from fuel to pressure discussed below.

RHP-zeros

In SISO controller design and for process understanding it is of interest to determine possible non-minimum phase zeros in the process. Furthermore as discussed above zeros in the origin play a dominant role in the controller design.
A list of the transfer functions with either a RHP-zero or a zero in the origin (ORG-zero) is shown below.

RHP − zero	G_{12}	G_{21}	G_{d21}	G_{d22}	G_{d23}
ORG − zero	G_{11}	G_{d12}	G_{d13}		

In the following only the zeros most important to the analysis will be discussed.
The zero in the origin of $G_{11}(s)$ arises from the fact that with the boiler in steady state an increase in fuel input, keeping feed water flow constant, causes the steam flow to increase and the water level to drop. But as the water level drops efficiency drops. At some point the water level has dropped so much that the efficiency is so poor that the steam outlet is equal to the feed water input and a new equilibrium is found at the same pressure. In reality this new equilibrium will not appear due to the large system steady state gains meaning that the boiler will dry out. The zero may be removed by closing the water level loop. This means that if for some reason the level loop should break then difficulties in controlling the pressure could be expected. This was also the conclusion from the RGA analysis in the previous section.
Regarding the RHP-zeros the most interesting are the ones in the cross connections G_{12} and G_{21} and the one from steam flow to water level in G_{d21} which describes the shrink-and-swell phenomenon in the process. In fact the zero in G_{21} is closer to the origin than the zero in G_{d21} and furthermore it is associated with a larger gain.
Common for the RHP-zeros are that as the operating load drops the zeros move closer to the origin. Together with the increasing gain this makes the effect of these zeros most pronounced at low loads.
Seen from a control point of view the RHP-zeros do not pose any limits on performance as they are not present in $G_{11}(s)$ and $G_{22}(s)$. However it should

be mentioned that a RHP-zero was expected in the transfer function $G_{22}(s)$ from feed water to water level but so far no measurement have indicated this.

Loop Closing

As was noted previously the transfer function $G_{11}(s)$ has a zero in the origin, indicating that u_1, fuel flow, can not be used to control y_1, the pressure. However the RGA analysis showed a different result which calls for design via sequential loop closing. This technique also has the advantage of ensuring stability, though the performance of the inner loop might be disturbed when closing the outer loop [3].
PI controllers are used in both loops. These are designed to achieve the largest possible bandwidth in both loops having a phase margin of 45° well above the limit found previously.
First the level loop is closed using K_{22} as illustrated in figure 9. The new transfer function from u_1 to y_1 is given as:

$$y_1 = G_{11}\left(1 - \frac{\kappa}{\frac{1}{G_{22}K_{22}} + 1}\right) u_1 = G'_{11}u_1 \qquad (8)$$

Inspecting this equation it can be seen that at low frequencies: $G'_{11} \approx G_{11}(1-\kappa)$, as $G_{22}K_{22}$ is large at frequencies where feedback is effective. At high frequencies κ is small indicating that $G'_{11} \approx G_{11}$. As the controller design focuses on relatively high frequencies a design using G_{11} should be adequate though (8) is used to design K_{11}, due to slight phase differences between this and the approximation.

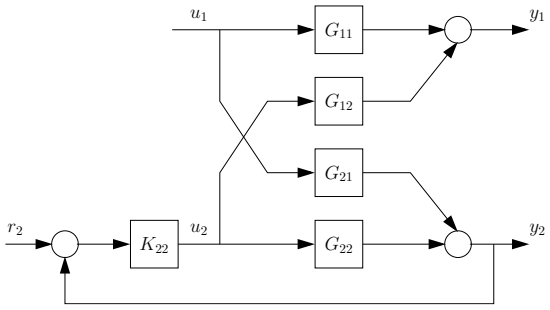

Figure 9: Level loop closed in the sequential design strategy.

Load dependency

Having determined two SISO controllers and thereby found the crossover frequency for both loops ($\omega_{c1} = 0.08$ rad/s $> \omega_{b1}$ and $\omega_{c2} = 0.13$ rad/s $> \omega_{b2}$) the load dependency of gains at the crossover frequencies and the variation of these crossover frequencies can be determined applying the controllers found for the 100% load at the remaining two operating points considered, 70% and 40%.
In the following it is assumed that the level loop is closed meaning that $G'_{11}(s)$ and not $G_{11}(s)$ is in focus. In figure 10 the mentioned variations as function of load are plotted. Included in the figure are also the variations of the stability margins.

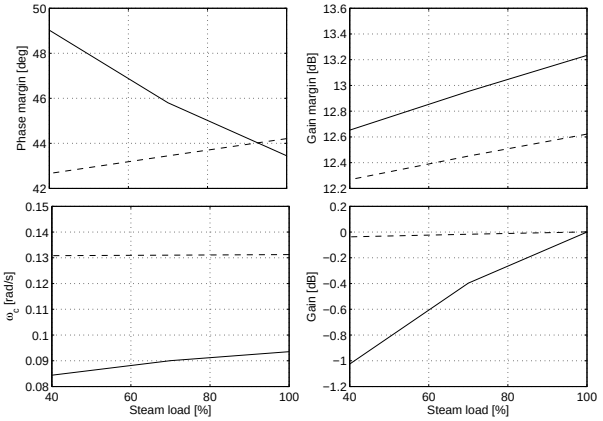

Figure 10: Plots of phase margin variations (top left), gain margin variations (top right), crossover frequency variations (bottom left) and variations of gain at the crossover frequencies for the loop at 100% load (bottom right) all as function of load. The solid line represents the loop associated with G'_{11} (pressure loop) and the dashed line the loop corresponding to G_{22} (level loop).

It is clear from the figure that nonlinearities in the model have most effect on the pressure loop. Nevertheless neither stability margins nor gains and crossover frequency vary remarkably over the load range considered.
To illustrate that the cross terms in the model do not cause the system to become unstable and to illustrate the little influence nonlinearities have on stability a Nyquist plot of $\det(\mathbf{I} - \mathbf{GK}(s))$ is shown in figure 11. The plot is shown for the three operating points under consideration given the same controller. From the right plot, focusing around the unit circle, it can be seen that stability is not effected by cross terms and nor by nonlinearities as the three curves cross the unit circle at the same point.

Model Nonlinearity

From figure 3 and the results above it is clear that the nonlinearities are mainly pronounced in the low frequency band as function of load. To investigate whether these low frequency variations should have any influence on the choice of control strategy (linear/nonlinear) the two SISO controllers developed in

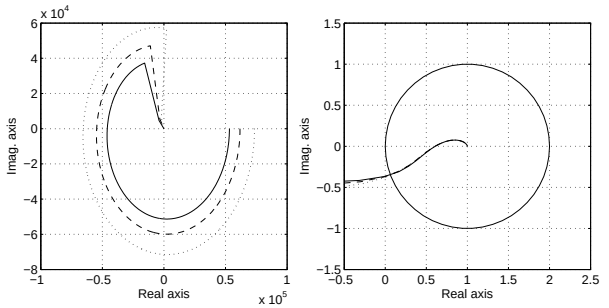

Figure 11: Nyquist plot of open loop system with controller base on sequential loop closing. Left: full plot, right: zoom around the unit circle. The solid line represents a linear model at 100% load, the dashed line a model at 70% load and the dotted line a model at 40% load.

the last section are simulated together with the nonlinear model. Steps in the steam flow disturbance, k, of different sizes are made starting from different operating points. To compare the responses the outputs are normed with the size of the disturbance step. The result is shown in figure 12.

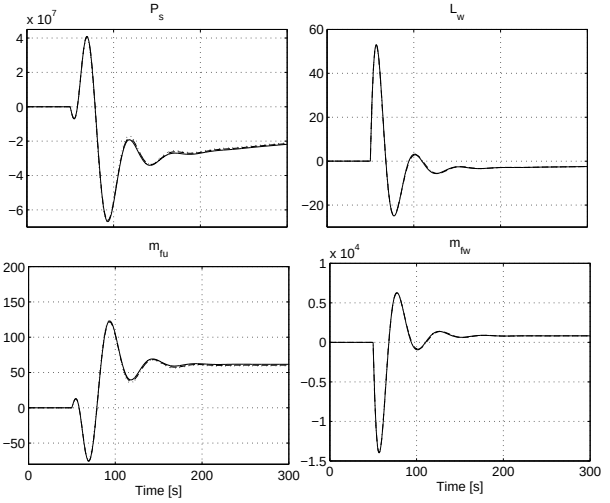

Figure 12: Closed loop response to step disturbance on nonlinear model. Three different step responses are shown; 50% → 75%, solid, 50% → 100%, dashed and 75% → 100%, dotted.

From the plots it can be seen that the transient behaviour for each step made is approximately the same. The largest differences in the plots are on pressure and fuel flow. This is illustrated in figure 13 where only the last 200 s of figure 12 is shown. Referring to figure 4 this makes sense as the largest gain variations over load are associated with the pressure.

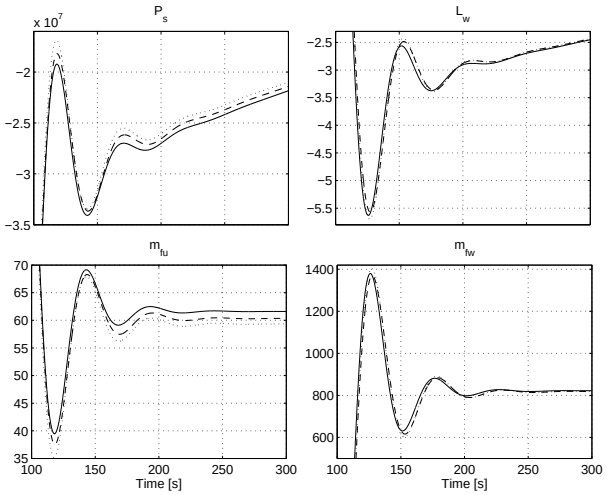

Figure 13: Figure 12 repeated with reduced axes.

Influence of interaction on performance

Having a MIMO system it is of interest to investigate the potential benefit from a MIMO controller design. This can be evaluated by inspecting the influence of the interactions in the model on the achievable controller performance, hereby meaning the ability of the controller to reject the disturbances.
The effect of the cross terms might be positive causing damping of the disturbances but amplification is also a possibility. To investigate this the performance of the previously designed controller will be compared to that of a controller designed after decoupling the interactions in the model. The decoupled system is illustrated in figure 14 assuming perfect decoupling.

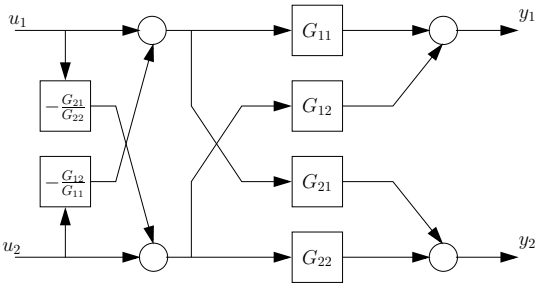

Figure 14: Decoupled system.

This system can be described as:

$$\mathbf{y} = \mathbf{G}^*\mathbf{u} = \mathbf{GWu}$$

where

$$\mathbf{W} = \begin{bmatrix} 1 & -\frac{G_{12}}{G_{11}} \\ -\frac{G_{21}}{G_{22}} & 1 \end{bmatrix}$$

giving the new system:

$$\begin{bmatrix} y_1 \\ y_2 \end{bmatrix} = \begin{bmatrix} G_{11}(1-\kappa) & 0 \\ 0 & G_{22}(1-\kappa) \end{bmatrix} \begin{bmatrix} u_1 \\ u_2 \end{bmatrix} \quad (9)$$

Note that at low frequencies the transfer function from fuel to pressure is approximately the same as when designing using sequential loop closing, see equation 8. Furthermore at high frequencies $\mathbf{G}^* \approx \text{diag}(G_{11}, G_{22})$.
In practice perfect decoupling is not possible due to model uncertainties. Decoupling controllers requires accurate process models and are sensitive to modelling errors, particularly when the RGA elements are large [3]. However theoretically the decoupling from u_1 (fuel flow) to y_2 (water level) can be assumed perfect. Regarding decoupling the other way problems arise in realizing $-\frac{G_{12}}{G_{11}}$ due to an improper system and the zero in the origin of G_{11}. In the frequency range of interest around the crossover frequency $-\frac{G_{12}}{G_{11}}$ is nearly constant with zero phase. For this reason $-\frac{G_{12}}{G_{11}}$ is substituted with a constant. The decoupled system is compared with the original system in the magnitude plot in figure 15.

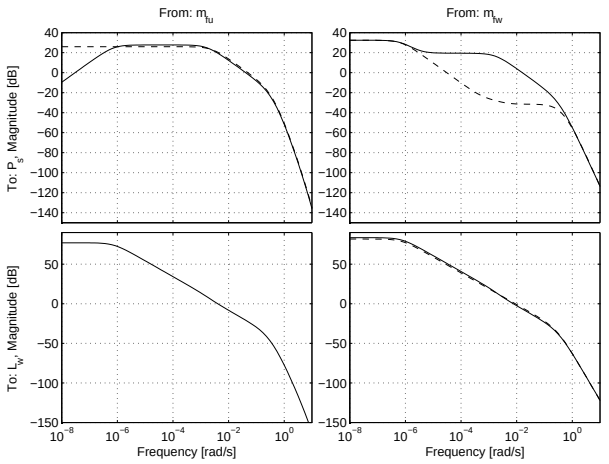

Figure 15: Comparison of open loop model without decoupling, $\mathbf{G}(s)$, solid and with decoupling, $\mathbf{G}^*(s)$, dashed.

From the figure it can be seen that for G_{11}^* the zero in the origin has disappeared. Furthermore the non perfect decoupling from u_2 to y_1 has damped the interaction at frequencies from well below the crossover frequency.
Now PI controllers are designed based on the diagonal elements in the new transfer matrix. Again these are designed to achieve the largest possible bandwidth in both loops having a phase margin of 45°. It should be mentioned that controllers with and without decoupling become very much alike, even though equation 9 is not valid, as the design focuses on the frequency band where figure 15 shows little difference between the graphs of the paired inputs and outputs. This also means that the only thing that influences whether a decoupling has any positive effect is whether the interaction amplifies the disturbance effect or not.
Bode plots of the output sensitivity functions achieved using the decoupling controller and that of the controller designed using sequential loop closing are compared in figure 16.

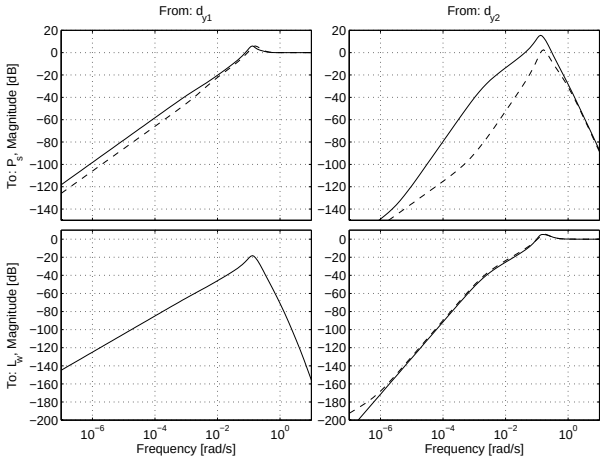

Figure 16: Comparison of sensitivity functions using sequential loop closing, solid, and decoupling design, dashed.

As the figure shows the individual sensitivities of the system based on decoupling are more damped than those based on sequential loop closing. The influence of the interactions can now be evaluated from evaluating the two controllers ability to reject disturbances on the output noting that from the specification of the normed system the objective of the controller is:

$$\|\mathbf{S}_o \mathbf{G}_{dk}\|_\infty \leq 1 \ \forall k$$

where $\mathbf{S}_o$ is the output sensitivity transfer matrix. $|\mathbf{S}_o \mathbf{G}_{d1}(j\omega)|$ is plotted in figure 17, that is only from the steam flow disturbance.
The plots show that decoupling has had a positive effect on the controller performance especially regarding the pressure loop. Here the resonant top using sequential loop closing is avoided at 10^{-1} rad/s and furthermore the controller actually complies with the demands.

Input Constraints

An important issue in controller design is whether input constraints cause any limit on the achievable performance. Constraints can be a problem when rejecting the transients in the disturbance.

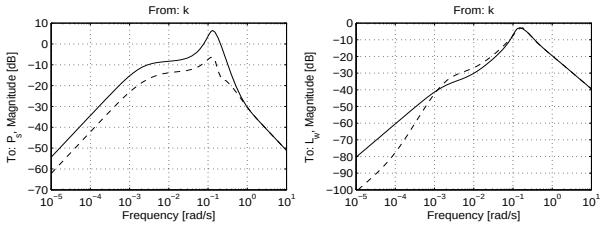

Figure 17: Illustration of effect of interaction. $|\mathbf{S}_o\mathbf{G}_{d1}(j\omega)|$ is plotted for two control strategies. Solid line is sequential loop closing and dashed line is design by decoupling.

Previous results showed that nonlinearities were concentrated in the low frequency band for which reason constraint problems as a consequence of rejecting transients in the disturbances can be carried out using linear model analysis.
This analysis can be carried out by introducing the control sensitivity $\mathbf{M} = (\mathbf{I} + \mathbf{GK})^{-1}\mathbf{K}$, describing the effect of the disturbances on the control signals. Checking whether the constraints become active can be seen from the inequality:

$$\|\mathbf{MG}_{dk}\|_\infty \leq 1 \ \forall\, k$$

If this inequality is violated there is not enough control signal to reject the disturbances. This reasoning of course requires a scaling of the inputs that reflects the constraints as was done previously. Again focus is limited to the steam flow disturbance. In figure 18 a plot of $|\mathbf{MG}_{d1}(j\omega)|$ is shown.

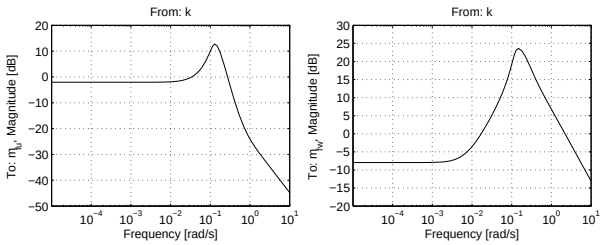

Figure 18: Plot of $|\mathbf{MG}_{d1}(j\omega)|$. The top plot represents the fuel flow and the bottom plot the feed water flow.

From this plot it is easy to see that input constraints become active for both the fuel and feed water supply.

CONCLUSIONS

This paper has shown that benefit of MIMO control can be achieved in a control strategy for the boiler system. This was a result of improved performance when decoupling the system prior to a SISO controller design.

The boiler model proved to have nonlinear behaviour mainly in the low frequency band below the crossover frequency. It was shown that one linear controller suffices leaving out gain scheduling or another nonlinear control strategy. This was manifested inspecting the performance of one linear controller to steps in the steam flow disturbance.
Input constraints showed to be a problem when controlling the boiler. This also means that the controller performance will be limited, however it is not a practical problem. The controller could be detuned to be less aggressive if the performance demands can be loosened.

Future Work

The fact that input constraints pose limitations on achievable performance, and that hard constraints for level variations are present, urge to include constraints in the controller design through an MPC strategy.
Furthermore it is of Aalborg Industries A/S' interest to introduce controllers for their boilers that do not require manual tuning and these controllers should work for a whole family of boilers. For this reason work remains in developing a strategy for making the control system self tuning. Also possible problems with model scaling should be investigated as the degree of nonlinearity and interactions in the model for scaled versions of the boiler concerned in this paper are not yet known.

REFERENCES

[1] K. Sørensen, C. M. S. Karstensen, T. Condra, N. Houbak, Optimizing the integrated design of boilers - simulation, ECOS 3 (2004) 1399–1410.

[2] B. Solberg, C. M. S. Karstensen, P. Andersen, T. S. Pedersen, P. U. Hvistendahl, Model-based control of a bottom fired marine boiler, IFAC (2005) .

[3] S. Skogestad, I. Postlethwaite, Multivariable Feedback Control: Analysis and Design, John Wiley & Sons, 1996.

[4] J. E. Rijnsdorp, Interaction in two-variable control systems for distillation columns-i, Automatica I (1965) 15–28.

[5] E. H. Bristol, On a new measure of interactions for multivariable process control, IEEE Transactions on Automatic Control AC-II (1966) 133–134.

[6] G. F. Franklin, A. Emami-Naeini, J. D. Powell, Feedback Control of Dynamic Systems, Addison Wesley Longman, 1993.

Proceedings of ECOS 2005
Trondheim, Norway
June 20–22, 2005

TURBULENT COMBUSTION SIMULATION IN A JET BURNER

Hirotatsu Watanabe[1], Yoshikazu Suwa[2], Yoshio Morozumi[1]
Hideyuki Aoki[1] and Takatoshi Miura[1]
[1]Department of Chemical Engineering, Tohoku University 6-6-07, Aoba, Aramaki, Aoba-ku, Sendai 980-8579 Japan

[2]SHI Mechanical & Equipment INC. Development & Process Group Engineering Department 1501, Imazaike, Saijyo, Ehime 799-1393, Japan

ABSTRACT

A turbulent combustion simulation to predict the fluid flow, temperature and chemical species concentrations in a jet burner that generates a jet of high temperature and high speed is carried out. Conservative equations of mass, momentum and energy in the turbulent flow field are solved in conjunction with a k-ε turbulence model. A radiative heat transfer model that considers the radiative properties of soot, water and CO_2 are included in the simulation. The validity of the numerical model is presented by comparing with the experimental data. The effect of soot on the combustion is also examined.

The calculated temperature without considering the soot is higher than the experimental data. However, with considering the soot, the differences between calculated and experimental results become small. The peak temperature is in good agreement with the experimental data. This is because that the soot greatly affects the radiative heat transfer in the burner.

Moreover, to improve combustion behavior in the jet burner, a numerical simulation considering a baffle plate that causes recirculation flows is also carried out. As a result, a suitable baffle plate shifts the high temperature region to upstream.

Keywords: turbulence, combustion simulation, jet burner

NOMENCLATURE

A	Pre-exponential factor of Rate constant	[$cm^3mol^{-1}s^{-1}K^{-1}$]
E	Activation energy	[$Jmol^{-1}$]
k	Turbulent kinetic energy	[m^2s^{-1}]
m_i	Mass fraction for species i	[-]
r	Stoichiometric oxygen weight required to burn 1kg fuel	[-]
S_ϕ	Source term for ϕ	
$S_{d\,\phi}$	Source term evaluated by PSI-CELL model	
U, V, W	Time mean velocity component	[m/s]
x, r, θ	Cylindrical coordinate	

Greek Symbols

Γ	Diffusion coefficient for ϕ	[$kgm^{-1}s^{-1}$]
ε	Eddy dissipation rate	[m^2s^{-3}]
μ	Viscosity	[$kgm^{-1}s^{-1}$]
ρ	Density	[kgm^{-3}]
ϕ	dependent variables	

Subscripts

Arr	Arrhenius
Eddy	Eddy diffusion
Fu	Fuel
Ox	Oxidant
S	Soot

INTRODUCTION

A jet burner, in which a fuel and an oxidizing agent burn under high-pressure conditions, generates a jet of high temperature and high speed, is mainly used for grinding and drying of processed products. The jet has the advantage that it can crush caking processed products and has a

[1] Corresponding author: Phone: +81-22-795-7251 Fax: +81-22-795-6165
E-mail: hiro@tranpo.che.tohoku.ac.jp

large heat transfer coefficient. In constructing a new jet burner efficiently, we need to understand the combustion behavior in the jet burner. Experiments are usually considered to be better for the prediction of combustion behavior, however, it is difficult to measure combustion characteristics such as temperature and chemical species concentrations. In addition, the data include unavoidable errors because the combustion characteristics are complicated under high-temperature conditions.

Thus, a numerical simulation of combustion behavior have attracted much attention for many years because it is easy and safe to understand combustion behavior in detail. In recent years, many researchers carried out a combustion simulation for gas turbine combustor[1], utility boiler[2] and spray combustion furnace[3]. However, combustion simulation is used as a complement of the experimental value because the reliability of calculated result is insufficient. Moreover, there is no research of the application of combustion simulation to the jet burner. To improve the reliability of combustion simulation, it is necessary to compare the calculated data with experiments and examine how individual factors in the simulation contribute to the combustion behavior. Especially, the radiation from soot is much stronger than that from combustion gas, and greatly contributes to the heat transfer in the burner. However, it is sometimes neglected in combustion simulation of practical combustion furnaces[1][3].

In this paper, we carry out a turbulent combustion simulation of the jet burner considering soot. The effect of soot on combustion and the validity of the numerical model are investigated. Then, we investigate combustion behavior with a baffle plate that is easy to equip the jet burner.

2. MATHEMATICAL MODEL

2.1. Governing equation

The standard k-ε turbulence model is widely used in turbulent combustion simulation[2][3]. So, in this simulation, this model is used to describe the turbulent flow. Transport equations used in this study can be expressed in cylindrical three-dimensional geometry is expressed as Eq. (1),

$$\frac{\partial}{\partial x}(\rho U\phi)+\frac{1}{r}\frac{\partial}{\partial r}(r\rho V\phi)+\frac{1}{r}\frac{\partial}{\partial \theta}(\rho W\phi) = \frac{\partial}{\partial x}\left(\Gamma_\phi\frac{\partial \phi}{\partial x}\right)+\frac{1}{r}\frac{\partial}{\partial r}\left(r\Gamma_\phi\frac{\partial \phi}{\partial r}\right)+\frac{1}{r}\frac{\partial}{\partial \theta}\left(\Gamma_\phi\frac{\partial \phi}{r\partial \theta}\right)+S_\phi+S_{d\phi}, \quad (1)$$

where ϕ represents the dependent variables, which denote mass (1), momentum (U, V, W), turbulence energy(k), dissipation rate of turbulence energy(ε), enthalpy (h) and mass fraction(m_i; i = $C_{12}H_{24}$, O_2, CO_2, H_2O, N_2, CO, H_2 and C(soot)), Γ_ϕ is the diffusion coefficient, S_ϕ is the source term in gas phase, $S_{d\phi}$ is the source term arising from droplet phase which is calculated by PSI-CELL model[4], ρ is the density and x, r, θ are axial, radial and tangential coordinates, respectively. This governing equations are solved using the original code(DRAGON) developed in our laboratory. Density is obtained from the equation of state. The gas flow characteristics at the wall boundary are estimated using the wall function model.

2.2. Reaction model

In this study, $C_{12}H_{24}$ is used to represent kerosene[5]. So, a four-step global reaction mechanism to express kerosene-air combustion reaction is used as

$$C_{12}H_{24} + 6O_2 \rightarrow 12\ CO + 12\ H_2,$$
$$CO + 1/2O_2 \rightarrow CO_2,$$
$$H_2 + 1/2O_2 \rightarrow H_2O,$$
$$CO + H_2O \Leftrightarrow CO_2 + H_2,$$

Reaction rate R_i is expressed by Eq. (2) considering both the eddy motion(EDC model, Eq. (3)) and the chemical reaction(Eq. 4),

$$R_i = -\min(R_{eddy}, R_{Arr}), \quad (2)$$

$$R_{eddy} = 4.0\frac{\varepsilon}{k}\min\left(\frac{m_{ox}}{r_{fu}}, m_{fu}\right), \quad (3)$$

$$R_{Arr} = A[fuel]^a[oxygen]^b \exp(-E/RT), \quad (4)$$

where r_{fu} is a stoichiometric oxidant requirement to burn 1 kg of fuel, A is a pre-exponential factor of rate constant, E is an activation energy and T is the temperature. The values of coefficients A, E, a and b are referred from Jones and Lindstedt[6] and Westbrook and Dryer[7].

The effect of soot on combustion is discussed in this study. Modeling of soot formation in practical combustion systems is an extremely challenging problem. Although some detailed

kinetic models of soot inception, growth and oxidation have been derived[8], it is still very difficult and time consuming to implement the detailed kinetic model to the simulations of multi-dimensional combustion systems. So, in this study, single step global reaction that produces soot directly from $C_{12}H_{24}$ and the oxidation of soot are used as follows

$$C_{12}H_{24} \rightarrow 12C(soot) + 12H_2,$$
$$C(soot) + 1/2O_2 \rightarrow CO,$$

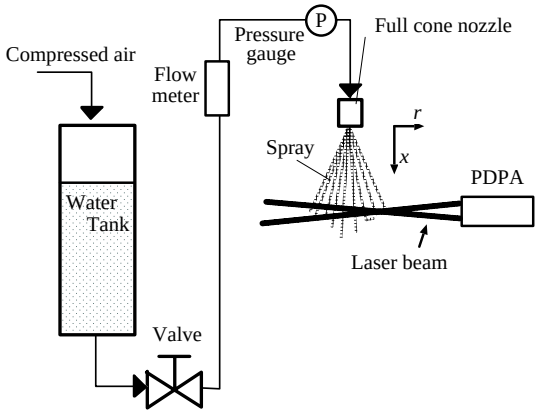

Fig. 1 Schematic diagram of experimental apparatus for examining spray properties

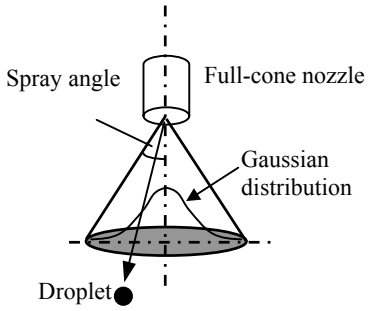

Fig. 2 Modeling of full-cone spray pattern

where pseudo-gas graphite carbon C(s) is used to represent soot. The formulation of the soot formation follows the previous study[9] where the soot formation is assumed to be a function of temperature, oxygen and soot building block concentration(Eq. (4)). In the oxidation model,

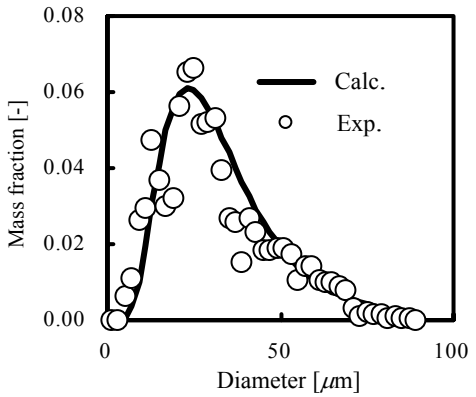

(a) Diameter distribution

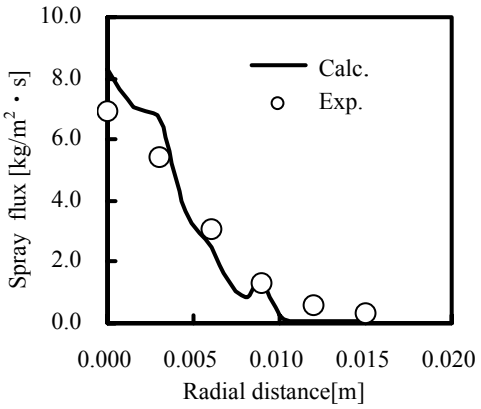

(b) Spray flux distribution

Fig. 3 Full-cone spray properties

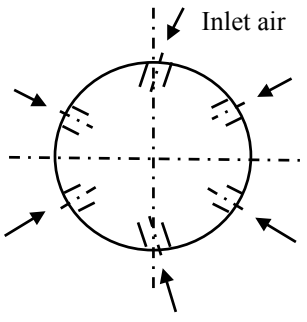

(a) r-θ plane(at inlet nozzle)

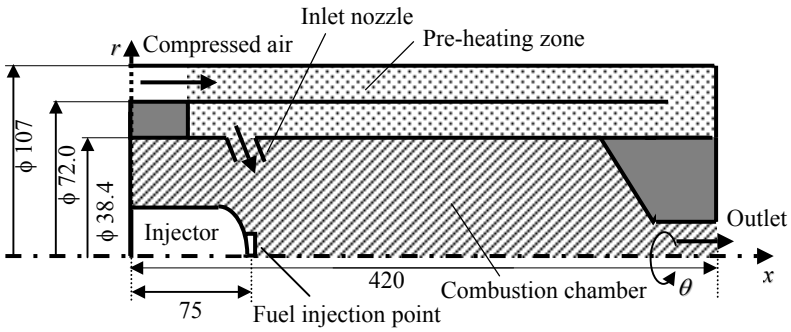

(b) x-r plane(at inlet nozzle)

Fig. 4 Schematic diagram of jet burner

$$R_{eddy,soot} = \min[4.0\, m_s \frac{\varepsilon}{k}, \frac{4.0\, m_{o_2}}{r_s} \frac{\varepsilon}{k} \frac{m_s r_s}{m_s r_s + m_f r_f}]. \quad (5)$$

considering both the eddy motion(Eq. (5)) and chemical reaction(Eq. (4)), the reaction rate is expressed as Eq. (2). The value of coefficients *A*, *E*, *a*, and *b* in the soot formation is referred from Wang[5] and those in the soot oxidation is referred from Nagle[10]

2.3. Radiation model

Radiative heat transfer is calculated using a 6-flux method coupled with a WSGGM(Weighted-Sum-of-Gray-Gases Model). Beer's model [11] is used when soot is considered in the simulation, whereas Smith's model [12] is used in case of gas radiation without soot.

2.4. Spray model

2.4.1 model

The motions of fuel droplets in the turbulent combustion flow field are calculated using a Lagrangian method. It is assumed that the fuel is injected into the combustor as a fully atomized spray which consists of spherical droplets with various size. The Lagrangian equations for the change of droplet velocity, mass and temperature are solved simultaneously. The effect of turbulence fluctuation of gas flow on the droplet motions is considered in the droplet velocity calculation.

2.4.2 Inlet condition

A schematic diagram of experimental setup for examining spray flow inlet conditions is shown in Fig. 1. At *x*=30mm, the diameter of the droplets and the spray flux distribution is measured with PDPA. Water is used as a working fluid, pressure drop defined as the difference between injection pressure and discharged back pressure is corresponds to the combustion operation condition.

In this simulation, the diameter distribution expressed as a log-normal distribution from 0 to 90μm is divided into 45 ranges and each range has 100 computational droplets. The injection angle of a droplet is chosen randomly from a Gaussian distribution to represent the full-cone spray pattern of the nozzle used in the jet burner (Fig. 2).

Table 1 Inlet condition

	AFR 3	AFR 2
Air flow rate[Nm^3/hr]	122	81.6
Fuel flow rate[kg/hr]	3.60	3.60

To obtain the initial average velocity of droplet and injection-angle, we carry out spray calculations as to agree with the measured data for the diameter distribution and spray flux [13].

Fig. 3 shows full-cone spray nozzle properties. Calculated data express a typical characteristic of a full-cone nozzle and is in good agreement with the experiments. So these parameters can reproduce the spray pattern of the full-cone nozzle.

3. NUMERICAL SOLUTION

The governing equations are discretized using a control volume method. The discretized governing equations are solved employing the SIMPLER algorithm. Bi-CGSTAB method is used for solving linear systems. A schematic diagram of the computational domain is shown in Fig. 4. The jet burner is composed of a burner and a preheating zone. The dimension of the burner is 38.4mm in inner diameter and 420mm in length. The inlet air nozzle diameter in the burner is ϕ8mm. The burner wall is cooled by air. In this calculation, the burner and the preheating zone are separately calculated. Considering only the heat transfer between wall surfaces of combustion chamber and pre-heating zone, calculation is carried out as follows;

Overall Solution procedure

1) The calculation in the burner is carried out until a convergence is reached without considering pre-heating zone.
2) The calculated inner wall temperature is set as boundary conditions, and the calculation in the pre-heating zone is carried out.
3) The calculated outer wall temperature is set as boundary conditions, the calculation in the burner is carried out again.
4) Steps 1 through 3 are repeated until the convergence is reached and wall temperature is fixed.

Numbers of computational grid in the axial, radial and tangential directions are 122×41×30 for the simulation of a 1/6 circumference of a jet

burner and 122 × 21 × 30 for that of the combustion chamber, respectively. It assures grid-independency of the solution. The convergence criterion is that normalized residuals in all conservation equations are less than 0.015. The inlet conditions are shown in Table 1.

4. RESULTS

4.1 Combustion behavior in the burner

In this section, we discuss the combustion behavior in the burner, the effect of soot on combustion and the validity of the numerical model. Inlet condition AFR 2 is preferable in the burner. However, the experimental data under AFR 2 is insufficient because of the high temperature. So, in this section, computations are carried out under the condition AFR 3.

Fig. 5 shows the time-mean velocity vectors of the combustion gas flow. The zero-axial velocity contour is plotted in Fig. 5. In Figs. 5(a) and 5(b), the flow fields have little differences, though the velocity of the gas flow without considering soot is higher than that with considering soot.

Fig. 6 shows the time-mean temperature distribution. High temperature region exists near the injector where fuel and air are well mixed. In Figs. 6(a) and 6(b), the high temperature region above 2200K in the case without considering soot is a little larger than that with considering soot,

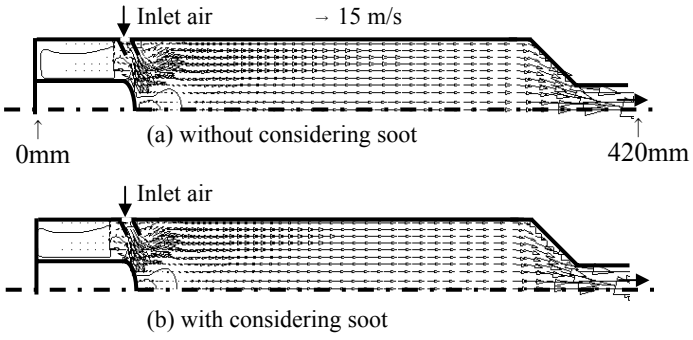

Fig. 5 Predicted combustion gas flow(AFR 3)

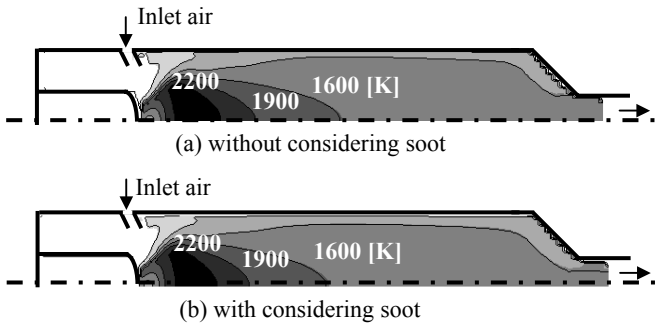

Fig. 6 Predicted temperature distribution(AFR 3)

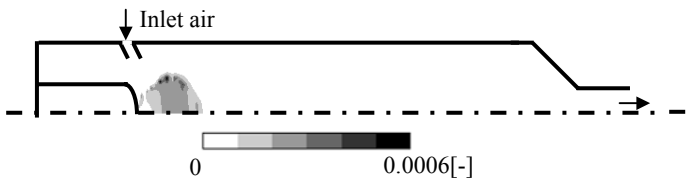

Fig. 7 Predicted soot mass fraction distribution

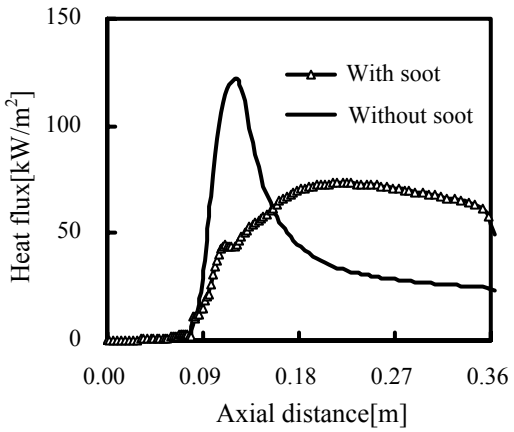

Fig. 8 Net radiative wall heat flux

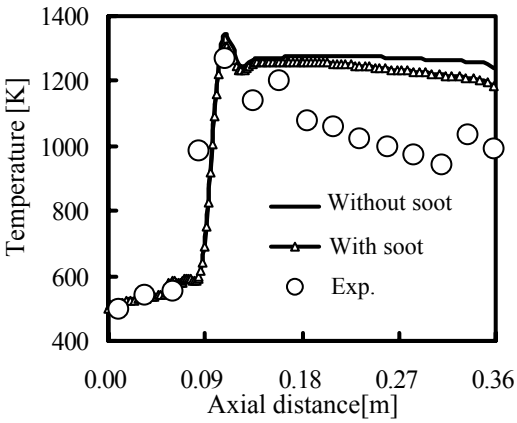

Fig. 9 Axial distribution of temperature (r=0.015m)

Fig. 10 Predicted temperature contour(AFR 2)

since the radiation intensity is increased by soot.

Fig. 7 shows the time-mean soot mass fraction distribution. In the high temperature region above 2000K, the soot is formed.

Fig. 8 shows the profile of the net radiative wall heat flux under different soot loadings. In the upstream region of the burner, net radiative wall heat flux without considering soot is higher than that with considering soot. Because of the radiation from soot, temperature of the upstream region decreases greatly. In the downstream region, the heat flux with considering soot is about twice as much as that without considering soot.

Fig. 9 shows the axial distribution of temperature at r=0.015m. The axial temperature profiles are measured with a thermocouple. The measured temperature is not accurated by the radiation loss to surrounding. So, the predicted temperatures are corrected. In the downstream region, the calculated temperature without considering soot is higher than the experimental data. With considering soot, the differences between the calculated and experimental results become small, and the peak temperature is in good agreement with the experimental data. However, the difference between measured and calculated temperature increases in the downstream, because, the thermocouple is inserted from upper part of that burner and is deviated from the correct position during the experiment. In addition, the thermocouple may be bended to the wall side by thermal stress, therefore the measured temperature is lower than the calculated one.

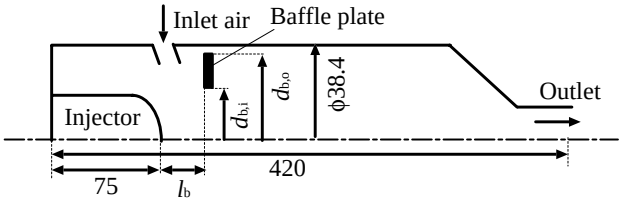

Fig. 11 Baffle plate position

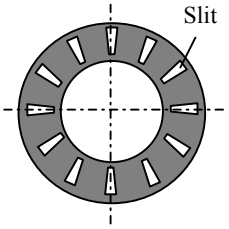

Fig. 12 Schematic diagram of baffle plate

Table 2 Baffle plate size and location

	l_b	$d_{b,i}$	$d_{b,o}$
Baffle plate A	2.0	13	22
Baffle plate B	2.0	28	36
Baffle plate C	12	28	36

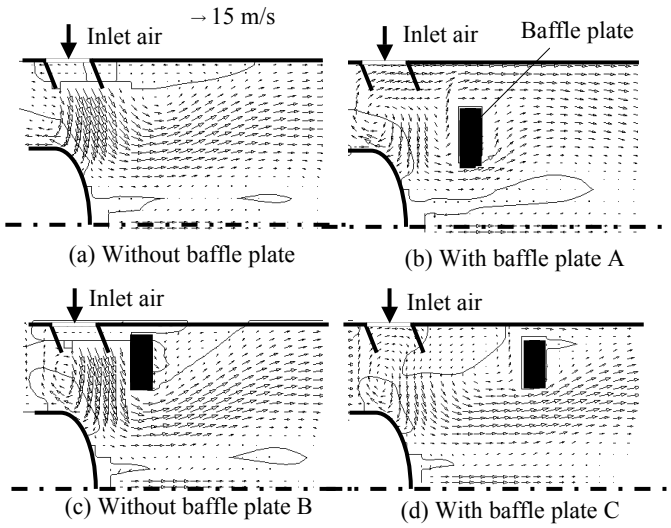

Fig. 13 Combustion gas flow near injector

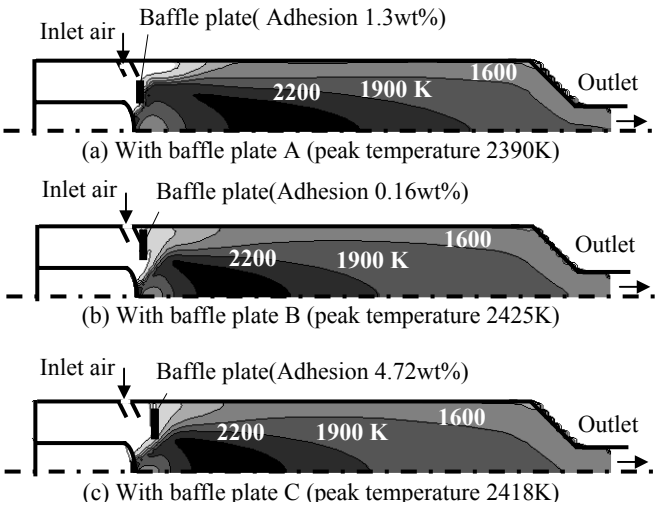

Fig. 14 Predicted temperature contour(AFR 2)

4.2 Development of the jet burner using baffle plate

Fig. 10 shows the predicted temperature distribution under AFR 2 with considering soot. In Fig. 6(b)(AFR 3) and Fig. 10(AFR2), the differences between the predicted temperature distributions are particularly noticeable. In AFR 3, a high temperature region near the injector is

small and the combustion reaction finishes in the upstream near the injector. However, under AFR 2, the high temperature region extends to downstream because the mixing of spray and air deteriorates. To shorten the flame length, a baffle plate is applied since it is easy and reasonable to equip that in the jet burner. Moreover, it does not require drastic changes of the burner shape. In this section, the effect of the baffle plate on combustion behavior is numerically investigated.

Combustion simulation is carried out under the different baffle plate size and location as shown in Fig. 11 and Table 2, where l_b is the distance between spray injector and baffle plate, $d_{b,i}$ and $d_{b,o}$ are the inside and outside diameter of baffle plate, respectively. The schematically baffle plate used in this study is shown in Fig. 12 schematically.

Fig. 13 shows the time-mean velocity vectors of the combustion gas flow near the baffle plate. The zero-axial velocity contour is also plotted in Fig. 13. The size and position of the baffle plate have a strong influence on the gas flow. Fig. 14 shows the predicted temperature contours and the ratio of the predicted adhesion of droplets to the baffle plate to the total amount of injected fuel. Fig. 15 shows predicted soot mass fraction.

Temperature and soot concentration distribution with baffle plate compare with those without baffle plate. When baffle plate A is set in the chamber, the high temperature region above 2200K is extended to downstream as shown in Fig. 14(a) compared with Fig. 10 and the soot mass fraction increases as shown in Fig. 15(b) compared with Fig. 15(a). This is because the distance between the spray injector and the baffle plate is too narrow to provide air sufficiently near the injector as shown in Fig. 13(b).

When the inner diameter of the baffle plate increases, the high temperature region becomes narrow and shifts toward the upstream as shown in Fig. 14(b) compared with Fig. 14(a), and the soot concentration decreases as shown in Fig. 15(b) compared with Fig. 15(a). This is because the mixing of spray and air is improved and the air is sufficiently supplied to the vicinity of the injector by increasing the inner diameter of baffle plate as shown in Fig. 13(c).

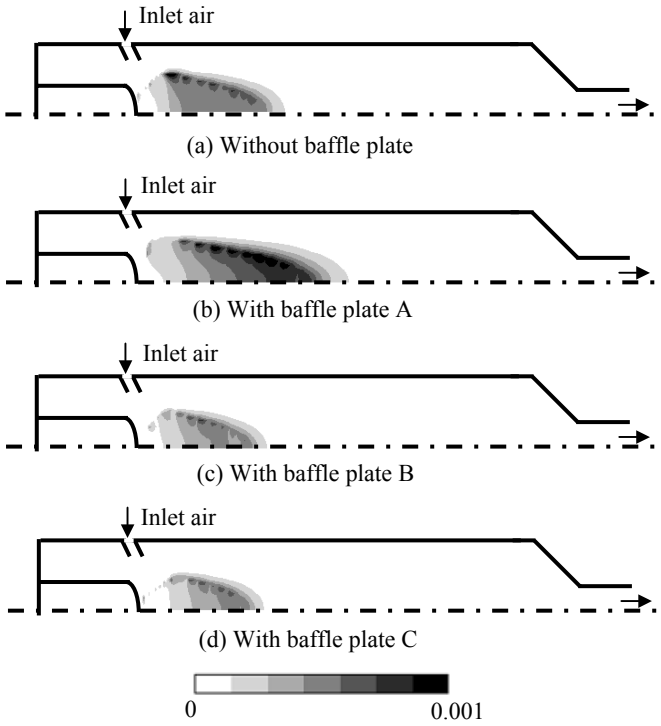

Fig. 15 Predicted soot mass fraction

When the distance between the spray injector and the baffle plate increases, temperature and soot concentration distribution have a little difference as shown in Fig. 14(b), (c) and Fig. 15(c), (d). However, adhesion of droplets to the baffle plate increases greatly.

In each case, the peak temperature is not so difference. So, NO_x formation is not so dependent on the peak temperature but dependent on high temperature region in this case. If the high temperature region becomes narrow and shifts toward upstream, NO_x reduction can be expected because of shortening of the residence time in the high temperature region. The more soot decreases, the more thermal efficiency increases. The more adhesion of droplets to baffle plate increase, the more it is difficult to carry out the stabilized continuous running to carbon deposit. Comparing the temperature distribution and the soot concentration without baffle plate (Fig. 10, Fig. 15(a)) with those with baffle plate B (Fig. 14(b), Fig. 15(c)), the combustion behavior is improved using baffle plate B. Consequently, baffle plate B has the better position of the baffle plate.

5. CONCLUSION

A turbulent combustion simulation in the jet burner is carried out. The effect of soot on the combustion behavior and the validity of the numerical model are investigated.

With considering soot, a high temperature region become small and then the prediction is improved. The soot greatly affects the heat transfer in the burner. So, it is important to develop a suitable soot formation model for practical combustion simulation.

A numerical combustion simulation with a baffle plate is also carried out. When using a baffle plate in the burner, the distance between the injector and baffle plate is important parameter. As a result, the high temperature region becomes narrow and shifts towards the upstream and soot in the burner decreases when the suitable baffle plate is used.

REFERENCE

[1] Mare, F. di, Jones, W. P. and Menzies, K. R., Large eddy simulation of a model gas turbine combustor. Combustion and Flame 2004;137: 278-294.

[2] Furuhata, T., Tanno, S., Miura, T., Ikeda, Y. and Nakajima, T., Performance of numerical spray combustion simulation. Energy Convers. Mgmt, 1997;38: 1111-1122

[3] Aoki, H., Tanno, S., Miura T. and Ohnishi S., Three dimensional spray combustion simulation in a practical boiler, JSME Int. J. 1992;35: 428-434

[4] Crowe, C. T., Sharma, M. P. and Stock, D. E., The Particle-Source-In Cell(PSI-CELL) Model for Gas-Droplet Flows. Trans. ASME J. Fluid Eng., 1977; 99: 325-332

[5] Ten-See Wang, Characterization of Kerosene Combustion Thermophysics. J. Thermophysics and Heat transfer, 2001;15; 140-147

[6] Jones, W. P. and Lindstedt, R. P., Global reaction schemes for hydrocarbon combustion. Combustion and Flame 1988:73; 233-249

[7] Westbrook, C. K. and Dryer, F. L., Simplified reaction mechanism for oxidation of hydrocarbon fuels in flames, Combust. Sci. Technol. 1981:27; 31-43

[8] Wen, Z., Yun, S., Thomsom, M. J. and Lightstone, M. F., Modeling soot formation in turbulent kerosene/air jet diffusion flames, Combustion and Flame 2003:135; 323-340

[9] Farmer, R. C., Edelman, R. B. and Wong, E., Modeling Soot Emissions in Combustion Systems, Particle Carbon Formation During Combustion, edited by D. C. Siegla and G. W. Smith, Plenum, New York, 1981, p. 299-320

[10] Nagle, J. and Strickland-Constable, R. F., Oxidation of Carbon between 1000-2000 ℃, Proceeding of Fifth Carbon Conference, Vol. 1, Pergamon, London, 1962, p. 151-164

[11] Beer, J. M., Heat Transfer in Flames, John Wilet & Sons, 1974. p. 30

[12] Smith, T. F., Shen, Z. F. and Friedman, J. N. Evaluation of coefficients for the weighted sum of gray gases model. Trans. ASME, 1982;104: 602-608

[13] Watanabe, H., Matsushita, Y., Morozumi Y., Aoki, H., Tanno, S. and Miura, T., Numerical analysis of Spray Flow by a Lagrangian Method Considering the Volume Fraction of Droplets, Kagaku Kogaku Ronbunsyu, 2004;30: 795-801

Proceedings of ECOS 2005
Trondheim, Norway
June 20–22, 2005

DYNAMIC MODELLING OF THE STEAM POWER PLANTS

Maryam Younessi-Sinaki[1], Siamak Farhad and M. Saffar-Avval
Amirkabir University of Technology
Mechanical Engineering Department
Iran

ABSTRACT

The operation of steam power plants varies from steady state to dynamic state by means of several factors; one of the most important of these factors is load variation. The practices used to control load, cause changes in working fluid properties in the cycle. Some of these properties have significant effects on the efficiency and appropriate operation of the cycle components; therefore, it is necessary to keep their variations in a suitable range. The controllers are used to perform this task and guaranty the correct operation of the steam power plant. The study of the dynamic behavior of the steam power plant is necessary for the selection and regulation of controllers.

In this paper, an object oriented and flexible simulator is presented which gives the ability to investigate the dynamic behavior of any steam power plant. The results of this simulator can be used to determine the type of controllers required in steam power plants and their regulating coefficients.

Keywords: Dynamic Simulation, Dynamic Modelling, Steam Power Plants

NOMENCLATURE

F	Constant coefficient [kPa.s^2/kg.m^3]
h	Specific enthalpy [kJ/kg]
k	Constant coefficient
N	Component number
p	Pressure [kPa]
$\dot{Q}$	Rate of heat transfer [kW]
T	Temperature [K]
t	Time [s]
u	Specific internal energy [kJ/kg]
V	Volume [m^3]
w	Flow rate [kg/s]
x	Defined state variable [kJ/m^3]
ρ	Density [kg/m^3]
σ	Stefan-Boltzmann constant [W/m^2.K^4]
Δt	Time step [s]

Subscripts

con	Convective
G	Furnace flue Gas
g	Flue gas or from flue gas
i	Inlet
o	Outlet
r	Risers
Rad	Radiative
s	Steam
t	Tube
w	Water or to water

INTRODUCTION

Many controllers are used in steam power plants; these devices apply changes in adjustable variables in order to guaranty the proper operation of a power plant during dynamic conditions and lead the plant toward steady state conditions. Load variation is one of the most probable reasons causing dynamic conditions in power plants and is investigated in this paper. In order to design and regulate the controllers, it is necessary to study the dynamic behavior of a plant, provided by changes in control variables. This investigation is performed by theoretical simulation instead of experiments, which are in general expensive,

[1] Tel.: +98-21-2228876; Fax: +98-21-2262468
E-mail address: mrmyou@yahoo.com

#

difficult, risky, and may prevent the normal operation of the plant.

The work of Chien et al [1] in 1958 on modelling a boiler is considered a pioneer work in the dynamic simulation of power plants. Since then, modelling power plant components have been discussed in several papers. Dynamic simulation may be used in designing plant components, training the operators and also designing and regulating controllers. In simulators applied in components design, like the RETRAN software [2], accurate models are necessary. A real time response is required in training simulators; where, simple mathematical models shall therefore be used. In simulators used in control field, the results shall reasonably represent the plant real behavior, but high accuracy is not necessary.

The purpose of the present simulation is to develop a modular and object-oriented simulator by using simple mathematical models of steam power plant components, which correctly represents the dynamic response of these plants when changes are applied to control variables.

MODELLING OF STEAM POWER PLANT COMPONENTS

In order to simulate the behavior of steam power plants, steam turbine, condenser, condensate and boiler feed pumps, feedwater heater and boiler are modeled using conservation laws and experimental heat transfer and thermodynamic equations. Assumptions are made to simplify these equations, with considering the purpose of simulation.

Boiler

Boilers have a significant effect on the dynamic behavior of power plants. In the boiler modeled in this paper, the flue gas in the furnace radiates heat to the risers and superheater tubes, passes through the superheater, reheater and economizer and leaves the boiler. In the water side, water supplied by the feedwater system is heated while passing through the economizer. It is then mixed with some saturated liquid in the drum and passes through the downcomers and risers with a constant volumetric flow rate regulated by a pump, changing into two-phase fluid. Saturated steam is separated from the saturated liquid in the drum and sent to the superheater, where it is heated. Then the steam leaves the boiler, and after passing the high-pressure turbine, enters the reheater and continues its course with a higher temperature.

The boiler is composed of different surface heat exchangers; to model the boiler, each of these heat exchangers is divided into two control volumes, the fluid inside the tubes and flue gas; the equations describing the behavior of these volumes are then derived. The fluid inside risers tubes is two-phase, while single phase fluid flows through reheater, superheater and economizer tubes; thus, both single and two phase fluid shall be modeled.

In order to simplify equations and solve partial differential equations in modelling one phase fluid (water or flue gas), the fluid volume is divided into segments in which fluid properties are considered lumped. For example, the furnace flue gas may be segmented to dimensionless, one-dimensional and three-dimensional models. In the dimensionless model, which is used in this simulation, flue gas properties are independent of the coordinate and are considered uniform all over the furnace [3]. In the one-dimensional model, the furnace is divided into horizontal layers, and several three-dimensional elements form the furnace in the three dimensional model. It is noted that the application of the three dimensional model is very complex and is only used in furnace design.

A dimensionless lumped parameter model is considered for the single-phase fluid in each heat exchanger, where the flue gas and single-phase water properties are respectively considered equal to the heater inlet gas and outlet water properties. It should be noticed that the tubes metal temperature of each heat exchanger is assumed uniform all over the heater. The lumped parameter model is only suitable in high velocities and may cause a considerable error in modelling the economizer. Considering the fact that the accuracy of the economizer model has a negligible effect on the simulation results at high loads, the application of the lumped parameter model is acceptable.

Homogeneous or quasi-homogeneous models are used to model two-phase fluid flow. In high-pressure flows, like the flow of water inside the risers, the slip velocity is negligible; thus, the homogeneous model is used, where the fluid is considered as a single-phase fluid which properties are calculated using the fluid quality. Other assumptions used to model the boiler are as follow:

- Flue gas flow rate is proportional to furnace pressure [4].
- Superheater and reheater steam are ideal gases with constant specific heats.
- Flow rate variation in the reheater is modeled with a first order lag [4].

- The pressure drop takes place at the inlet of the superheater and steam compressibility is negligible; therefore:

$$p_{si} - p_{so} = f_s \frac{w_{si}^2}{\rho_{si}} \qquad (1)\#$$

- Water pressure difference in the downcomers and risers path is about 1% of the drum absolute pressure, which can be neglected. Therefore, the fluid pressure over this path is considered equal to the drum pressure.
- Water inside drum, downcomers and risers is modeled using the following assumptions [5]:
  - Saturated liquid and vapor in the drum are in equilibrium.
  - There is no mass storage in the downcomers and risers tubes.
  - Heat is uniformly transferred to the risers.

The models used in this simulation lead to the following equations for calculating the rate of heat transfer in each heat exchanger.

- Rate of convective heat transfer from gas to tubes and from tubes to single-phase fluid inside tubes:

$$\dot{Q}_{cong} = k_{cong} w_g^{0.6} \left(T_g - T_t\right) \qquad (2)$$

$$\dot{Q}_{conw} = k_{conw} w_w^{0.8} \left(T_t - T_w\right) \qquad (3)$$

- Rate of heat transfer to boiling fluid and radiative heat transfer from furnace flue gas:

$$\dot{Q}_{rtw} = k_r \left(T_{rt} - T_{rw}\right)^3 \qquad (4)$$

$$\dot{Q}_{rad} = k_{rad} V_G \sigma T_G^4 \qquad (5)$$

It is noticed that k_{cong}, k_{conw}, k_{rad} and k_r are coefficients that are constant for each plant [3 , 6].

The law of energy conservation is presented in equation 6.

$$\frac{dx}{dt} = \frac{1}{V}\left(\dot{Q} + w_i h_i - w_o h_o\right) \qquad (6)$$

Where $x = \rho u$ is a state variable. It should be noticed that the flue gas response in dynamic state is faster than the water response; therefore, steady sate equations are used to model this gas, except in the furnace. Dynamic relations are only used when furnace pressure control or flame stability problems are to be studied.

Steam Turbine

In order to simplify the modelling of steam turbines in dynamic simulations, the turbine is divided into steady and dynamic sections [4]. A lumped parameter model is chosen for the dynamic section, where steam properties are set equal to the outlet fluid properties. The flow rate variation of the dynamic section is modeled with a first order lag. The steady state section is a simple turbine that expands steam in a polytropic process. The generated power is calculated considering the steady state section enthalpy change. Steam is assumed ideal gas with constant specific heat, and the low-pressure turbine outlet fluid is assumed saturated vapor. The efficiencies of all stages of a turbine are assumed equal and constant [7], except in the low-pressure turbine where the total efficiency is considered constant [8].

In governing control, the throttle steam pressure and flow rate are proportional [5]. The steam pressure and flow rate at the inlet of the reheater [7] and each turbine stage [9] are also proportional in this condition.

Condenser

A shell and tube condenser is modeled in this simulation. A very complex model shall be used when the inlet steam is superheated and some of the condensate remains inside the shell. To avoid this complexity, the fluid at the shell inlet and inside it are assumed saturated vapor, while the outlet condensate is considered saturated liquid.

Distributed and lumped parameter models can be applied to solve condenser differential equations. A lumped parameter model, which validity has been approved by experimental tests [10], is applied in this simulation. In this model, the cooling water is divided into several sections in the axial direction, and the properties of the shell, tubes, steam and cooling water in each section are assumed lumped.

Pump

Several pumps are used in a steam power plant but only condensate pump and boiler feed pump are considered in this paper. The condensate pump increases the water pressure to the deaerator pressure and the boiler feed pump provides the drum pressure and regulates the feedwater flow rate. The pressure of the water leaving condensate and boiler feed pumps are assumed equal to the deaerator and drum pressures respectively. Steady state equations are generally used when modelling pumps in dynamic behavior studies of power plants [7]. In this simulation, a variable speed

#

pump is modeled, which efficiency is assumed constant with regard to the range of variations investigated.

Feedwater Heaters

Models used to study the dynamic behavior of feedwater heaters are very complex. Studies have shown that it is not necessary to apply these complex models in simulations where the objective is to design, study or regulate main controllers of steam power plants. A model, in which the variations in properties of the fluid leaving the feedwater system and saturated liquid at the pressure of the steam entering the heater are estimated to be similar, is suitable in this simulation [7]. In modelling closed feedwater heaters, mass storage is ignored and the initial and terminal temperature differences are assumed constant. In modelling the deaerator, it is assumed that the liquid leaving this heater is saturated and that variation of water level is negligible.

CONTROL VARIABLES

Before developing the simulator, control variables causing the dynamic behavior of the plant, and variables affecting its proper operation shall be specified. In order to control the power output, the rate of boiler steam generation and throttle flow are regulated. The governing valve opening is used in regulating the throttle flow, and is therefore a control variable. The rate of steam generation is adjusted by applying changes to the fuel flow, burner tilt angle and air temperature; the fuel flow is considered a control variable while other mentioned factors are assumed constant. In order to perform a complete combustion, air flow must vary along with the fuel flow and is thus considered a control variable.

Fuel flow variations cause changes in throttle and reheat temperature. Decrease in these temperatures reduces the cycle efficiency, and increase of these values reduces components life; therefore, the temperature variations shall be controlled in a safe range which is about ±5˚C [11].

Drum water level is also affected by throttle flow variations. The decrease of this value causes the risers tube to overheat and its increase prevents the proper operation of the steam and liquid separator. The allowable range of variations of drum water level is about ±2.5 cm [11]. Feedwater flow is the control variable for the drum water level adjustment.

It is noticed that throttle and drum pressure shall also be maintained in a safe range, which for the throttle pressure is ±1 percent of the design pressure [11].

THE SIMULATION SOFTWARE

The aforementioned modelling was applied to develop a modular and object-oriented software with DELPHI, which can simulate the dynamic behavior of steam power plants due to step or ramp changes in air and fuel flow, feedwater flow and throttle valve opening. The software is executed in consecutive steps shown in figure 1 and the results are accessed and displayed in the form of plots and tables.

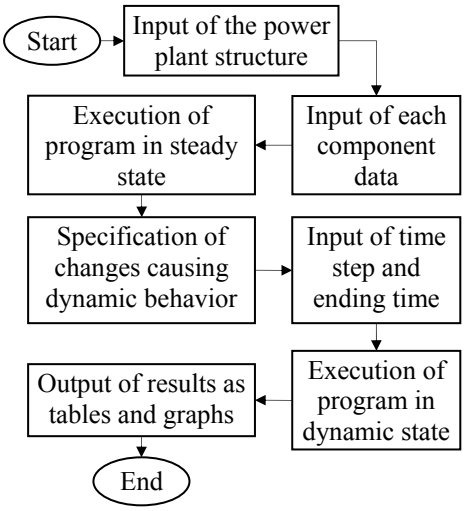

Figure 1: Consecutive steps in running the simulator

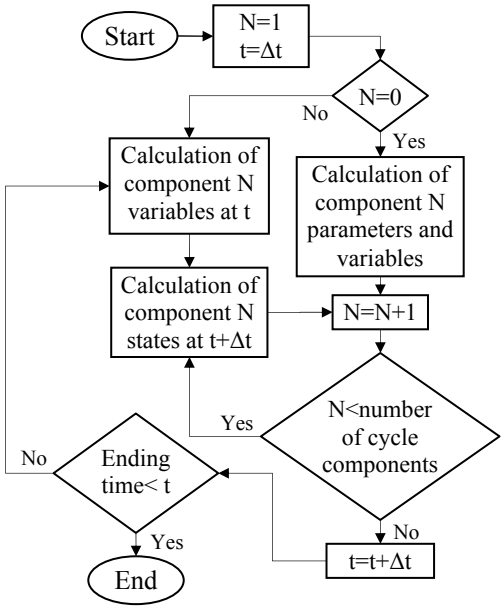

Figure 2: Calculation design of the software

The design of figure 1 shows that steady state calculations are performed before dynamic calculations, which purpose is to derive some parameters used in dynamic equations, like the constant coefficients of equations 2 to 5, and thus minimize the data entry. The dynamic and steady state calculations are realized as shown in figure 2. It should be noted that IFC experimental formulation [12] is used in calculating thermodynamic properties of water and the Euler's method is applied to solve differential equations.

VALIDATION

Before simulating a plant, the mathematical modelling used in the simulator shall be validated and the results must be shown to reasonably represent the plant response.

The steady state results of the simulator were validated using the manufacturer data of the Shahid Rajaei steam power plant. This plant has been commissioned in 1990 with 4×250 MWe steam units. The main steam pressure and temperature are 137.3 bar_g and 538 °C, while the condenser pressure is 0.19 bar_g. Each unit has a sub-critical single-reheat boiler with five close feedwater heaters and a deaerator included in the steam cycle. Tables 1 and 2 show the comparison of some actual quantities of the mentioned plant with simulation results at full load.

Component	Outlet fluid flow rate (kg/s)#		#Outlet fluid enthalpy (kcal/kg)		Extraction flow rate#(kg/s)#	
	actual	simulation	actual	simulation	actual	Simulation
Superheater#	773442#	773892#	819.3	819.3	-	-#
Reheater#	693604#	709432#	844.9	844.9	-#	-#
Turbine 1	693604#	709432#	740.6	740.6	62838	64459#
Turbine 2	657660#	665808#	794.8	794.8	42838#	43625#
Turbine 3	615136#	623530#	739.8	739.8	42524#	42277#
Turbine 4	602465#	602118#	689.7	689.7	21412#	21412#
Turbine 5	577979#	577752#	662.2	662.2	24486#	24366#
Turbine 6	555921#	555931#	629.8	634.1	22058#	21821#
Turbine 7	555921#	555931	593.5	593.5	0	0
Condensate pump	625660#	623530#	61.18	61.31	-	-
Boiler feed pump	773888#	773892#	171.6	171.32	-	-

Table 1: Comparison of steady state results in boiler, turbines and pumps

#

Component#	Drain flow rate (kg/s)		Drain enthalpy (kcal/kg)		Inside fluid pressure (kg/cm^2)		Outlet feedwater enthalpy (kcal/kg)	
	actual	simulation	actual	simulation	actual	simulation	actual	simulation
FWH 1	67975	67560	66.78	66.78	0.5992	0.5992	82.62	82.61
FWH 2	45898	45778	88.24	88.23	1.39	1.39	105.9	105.8
FWH 3	21412	21412	111.5	111.5	2.6	2.6	125.7	125.7
FWH 4	105700	108084	175.2	175.2	16.4	16.4	209	207.5
FWH 5	62838	64459	213.6	213.5	35.4	35.4	251.8	251.4
Deaerator	-	-#	-	-#	7.09	7.087	166.2	166.2

Table 2: Comparison of steady state results in feedwater heaters

Operational data needed for validation of the dynamic response of the simulator cannot be obtained by experiments because of the regular operation of power plant controllers. Thus, the dynamic response is validated by comparison of simulator results and data extracted from others' papers. Due to lack of information about power plants discussed in the papers, qualitative comparison is made between the simulation results of Shahid Rajaei steam power plant and these data.

In figure 3, the dynamic response of Jack McDonough power plant [5] is compared with the simulator results, due to a 2% step increase in throttle valve opening at full load. These plots validate throttle pressure, drum pressure and throttle flow variations obtained by the simulator. Comparison between the dynamic response of Fusina power plant [13] and the simulator results, due to a step increase in throttle valve opening is shown in figure 4. According to these plots, the trend of throttle temperature, drum water level and generated power variations obtained from the simulator are similar to the results of the mentioned paper, but the response of Shahid Rajaei steam power plant is approximately 10 times faster than Fusina. This can be explained by the differences in components properties of these plants. One of theses differences is the size of the

#

boiler and consequently the tubes metal mass of surface heat exchangers in the boiler. In order to show the effect of tubes metal mass on the dynamic response of the plant, the simulation of Shahid Rajaei steam power plant is performed while replacing the tubes mass of the boiler with the power plant studied by M.E. Flynn and M.J. O'Malley [14]. The trend of variations obtained by this simulation are similar to figure 4 plots, but the response is approximately 5 times slower than Shahid Rajaei simulation results, which shows the significant effect of heat exchangers tubes metal mass on the dynamic response. This can justify the difference in response times of figure 4, and the throttle temperature, generated power and drum water level variations obtained by the simulator are therefore validated. It can also be concluded that the temperature control system shall be faster in modern power plants with lighter boiler tubes.

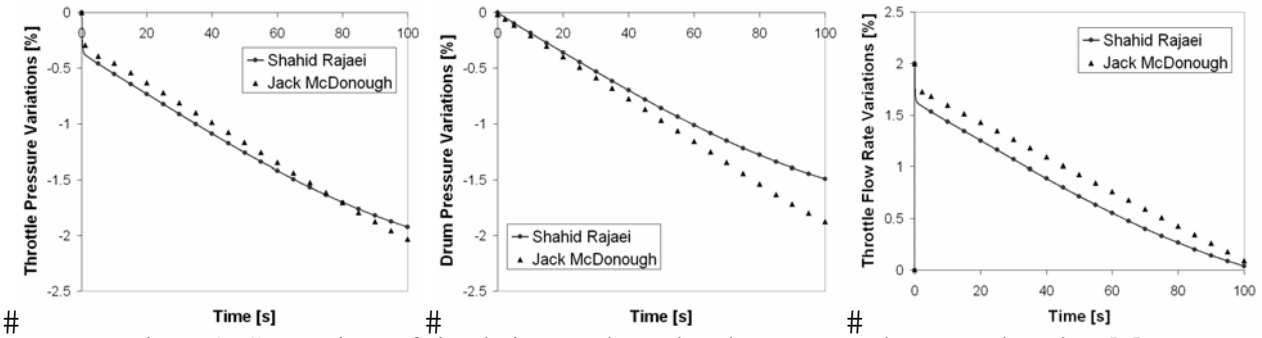

Figure 3: Comparison of simulation results and Jack McDonough power plant data [5].

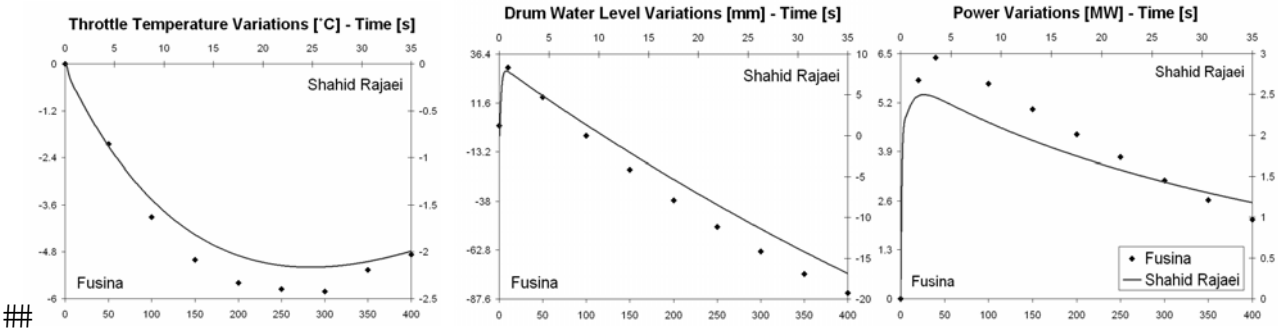

Figure 4: Comparison of simulation results (right and top axis), and Fusina power plant data (left and bottom axis) [13].

SIMULATION RESULTS

After verification of the models, the simulator is used to simulate the Shahid Rajaei steam power plant operating with natural gas at full load. The data needed to simulate this plant are obtained from the plant design documents.

At first, the effect of each control variable is separately investigated on Shahid Rajaei steam power plant. Figure 5 shows the dynamic response of this plant due to 2 percent ramp increase in feedwater flow, fuel and air flow and governing valve area, during 2 seconds. The following observations are made from these plots.

Increase of throttle valve opening - An increase in throttle flow results when the governing valve area increases. This change causes the drum pressure and consequently the throttle pressure to decrease. When the valve opening is constant, throttle flow rate is proportional to the throttle pressure; thus, the throttle flow rate decreases after 2 seconds, which leads to a decrease in generated power. The throttle pressure shall therefore be controlled while increasing governing valve opening in order to control generated power. It is also noticed that the change in valve opening has a considerable effect on drum water level, which shall be controlled.

Increase of fuel and air flow- Drum pressure, throttle pressure, throttle flow and generated power increase due to fuel and air flow raise. This change provides a raise in the flue gas temperature, therefore heat transfer to the superheater and reheater, and consequently steam temperature at the outlet of these heaters are increased; but after a short period, these temperatures fall due to the

increase in steam flow rate and temperature difference decrease. These temperature variations have the effect of reducing the rate of power variations.

The aforementioned variations are in accordance with simultaneous application of fuel and air flow and throttle valve opening in controlling the power output with turbine or boiler follow mode.

Increase of feedwater flow- The feedwater flow mainly affects the drum water level and has negligible effect on other values. It is therefore suitable for controlling the drum water level.

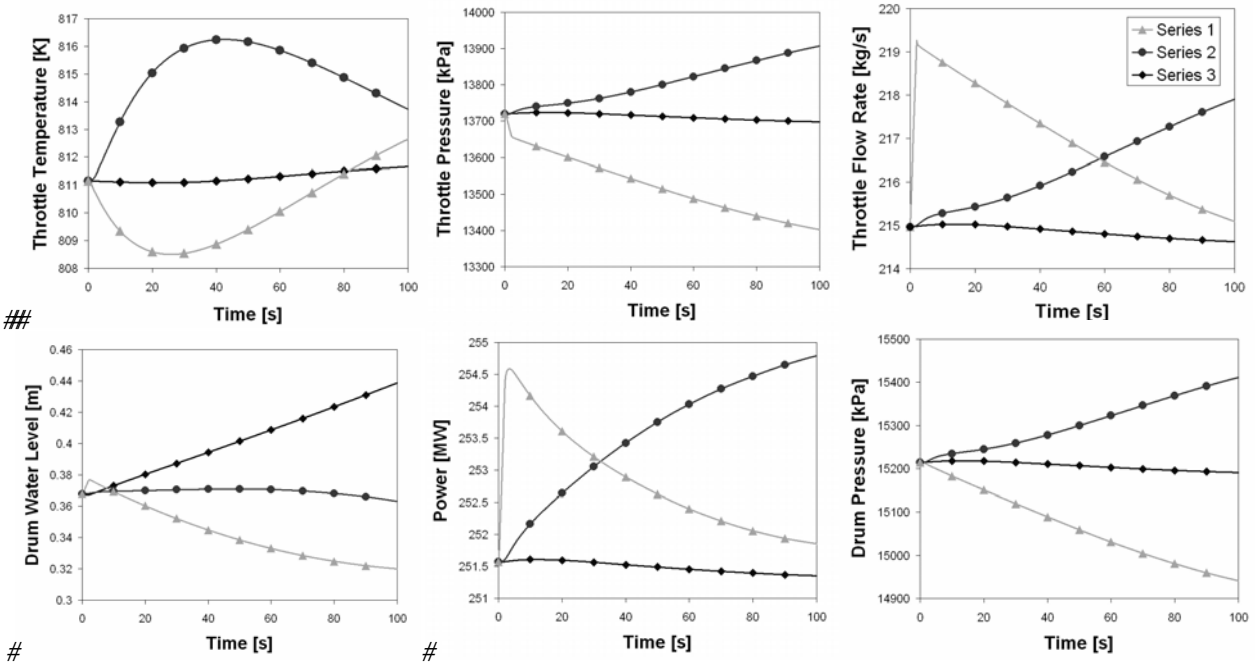

Figure 5: Simulation results of Shahid Rajaei steam power plant due to 2% ramp increase in throttle valve opening (Series1), air and fuel flow (Series 2), and feedwater flow (Series 3), during 2 seconds.

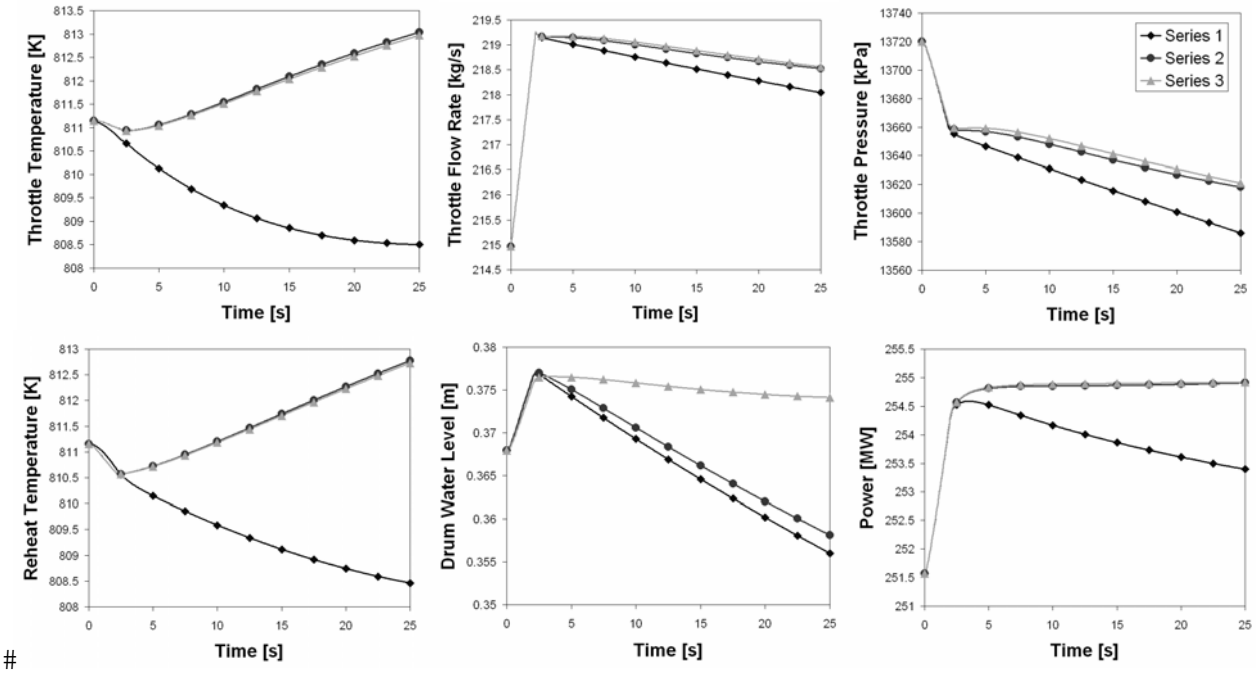

Figure 6: Simulation results of Shahid Rajaei steam power plant due to 2% ramp increase in throttle valve opening (Series1), air and fuel flow and throttle valve opening (Series 2), feedwater flow, and air and fuel flow and throttle valve opening (Series 3), during 2 seconds.

The next step in this study is to apply simultaneous changes to different control variables in the Shahid Rajaei steam power plant simulation. Therefore, the air and fuel flow are raised while the throttle valve opening increases, and the results are compared with the effect of throttle valve opening increase in figure 6. The effect of increasing all control variables simultaneously is also shown in this figure. All the changes are 2 percent ramp increase with 2 seconds durations. The following observations are made for each case.

Increase of air and fuel flow and throttle valve opening- The throttle flow rate, throttle temperature, throttle pressure and generated power variations are reduced when a raise in air and fuel is superposed to the throttle valve opening increase. In this case, the power variations are less than throttle flow variations, which is due to the temperature raise of the boiler outlet steam, that shall be controlled. The drum water level decreases considerably and shall be controlled either.

Increase of air and fuel flow, throttle valve opening and feedwater flow- This change has approximately the same effect as the previous case, but also reduces the drum water level variations. Figure 6 shows that the throttle and reheat temperature variations due to this change have considerable values and shall therefore be controlled. Variables used to control temperature are not considered in this study.

It should be emphasized that the purpose of this study is not to control the variables affecting proper function of the power plant, but is rather to show the ability of the models in representing the plant response when applying control variables separately or simultaneously.

CONCLUSION

Simple models were presented for steam power plant components and a flexible and object-oriented software was developed for multivariable control and dynamic studies. The simulator was validated in dynamic and steady state and applied to model the Shahid Rajaei steam power plant dynamic behavior due to changes in control variables. The control variables included in the simulation are air and fuel flow, feedwater flow and throttle valve opening.

The simulator displays variations of plant main variables due to changes in the aforementioned control variables, and thus can be applied to derive their beginning time, duration and rate, in order to guaranty the proper operation of the plant during change of load. These data are valuable in the design of generated power, throttle pressure and drum water level controllers.

REFERENCES

[1] Chien KL, Ergin EI, Ling C, Lee A. Dynamic Analysis of a Boiler. Trans. of the ASME, 1958.

[2] McFadden JH et al. . RETRAN-02 – A Program for Transient Thermal hydraulic Analysis of Complex Fluid Flow Systems. EPRI Report, CS/NP-2945, Palo Alto, 1983

[3] Clelland PJ, Kwanty HG. Modelling and Simulation of Gas Dynamics in a Fossil-Fuel Power Boiler. ISA-Proceeding of Advances in Instrumentation, 1983.

[4] Ordys AW, Pike AW, Johnson MA, Katebi RM. Modelling and Simulation of Power Generation Plants. Springer-Verlag, London, 1994.

[5] De Mello FP. Boiler Models for System Dynamic Performance Studies. IEEE Transaction on Power Systems, Vol.6, no.1, 1991.

[6] Lu S, Swidenbank E, Hogg BW. An Object-Oriented Power Plant Adaptive Control System Design Tool. IEEE Transaction on Energy Conversion, Vol. 10, 1995.

[7] Maffezzoni C. Issues in Modelling and Simulation of Power Plants. IFAC Symposium on Control of Power Plants and Power Systems, 1992.

[8] Chou QB, Luk JWK, Morrow LD. Simulation of a Condensing-Tandem-Compound Type Steam Turbine for Power Plant Training Simulator. #

[9] Li KW, Priddy AP. Power Plant System Design. John Wiley & Sons, 1985.

[10] Kapadia M, Wolgemuth CH. A Dynamic Model of a Condenser in a Closed Rankine Cycle Power Plant. Proceeding of American Control Conference, 1984.

[11] Liptak BG. Optimization of Industrial Unit Processes. CRC Press, 1999.

[12] The 1967 IFC Formulation for Industrial Use. *A*SME Steam Tables, Sixth Edition, ASME Press.

[13] Cori R, Maffezzoni C. Practical-Optimal Control of a Drum Boiler Power Plant. IFAC 8th Triennial World Congress, Japan, 1981. #

[14] Flynn ME, O'Malley MJ. A Drum Model for Long Term Power System Dynamic Simulation. IEEE Trans. on Power Systems, Vol. 14, 1999#

#

Proceedings of ECOS 2005
Trondheim, Norway
June 20–22, 2005

CO_2 capture and storage

Proceedings of ECOS 2005
Trondheim, Norway
June 20–22, 2005

A TEST TO CLARIFY INTERNAL FEATURES OF A FOSSIL SIMULATOR

Alexander S. Rubashkin, Vladimir A. Rubashkin,
"Power Plants Simulators", Russia, Moscow, Semenovsky per., 15, 224,
pps@edunet.ru, www.fpps.ru

ABSTRACT

Any simulator vendor always praises its simulators no matter how good they are. His past customer could praise its simulator too. It doesn't for sure mean that the simulator is really good – it could mean anything, for example that the customer just didn't see anything better. In the past when mainly black-and-white TV sets were available a lot of people who didn't see color TV sets were satisfied with black-and-white ones – they didn't see anything better.
How a potential customer could choose a vendor for his simulator development if he has no objective information he could rely upon? To give the objective information about our simulation technology we conducted on an our simulator a set of tests that could disclose for experts the internal features of our simulation technology. The paper presents one of such test.
Keywords: Fossil power unit, simulation, criteria heat exchange equations.

INTRODUCTION

At present an average price of an average simulator for a fossil power unit is a few times less then the price of an average simulator for a nuclear power unit. If so the fossil simulator vendors promote an idea that customers of fossil simulators ought to humble with numerous simulation simplifications that a lot of modern simulators have. All the simplifications lead to the fact that many modern simulators could be characterized with the following features:

- they are able to implement with an acceptable error margin a few static working modes of the simulated power unit only
- during simulation of complicated transient processes (start-ups, shut-downs and so on) the simulators implement for many important parameters a tendency only but not a full-fledged transient curve

The mentioned features of the simulators could be acceptable if such a simulator is going to be used to train people how to run the power unit in accordance with the operation instruction of the unit only.
But what to do if a trainee needs some more deep understanding of how a fossil power unit works? Let us assume that you are going to illustrate for high students in a university the fundamental principals of heat exchange or the fundamentals of once-through fossil power unit behavior. Or an engineer needs an information how the power unit is going to work as a result of the forethought reconstruction.
In such the cases a simulator with an advanced simulation technology needs to be used.
The paper illustrates some of the internal features of a simulation technology used by Russian company "Power plant simulators". The features allow the simulation technology to be publicly recognized as a very advanced one, and simulators developed on the base of the technology could be recognized as to be suitable to obtain the deep knowledge of fundamentals of fossil power units.
To illustrate the above mentioned internal features we made a number of tests on one of our simulator. The complete test results with colored pictures could be found on our web-site www.fpps.ru. In the paper we present a one test only.

WHICH SIMULATOR WAS TESTED?

For testing we used 200 MW oil fired drum boiler at a drum pressure of 14 MPa with natural circulation and at a pressure before the turbine of 13 Mpa.
The oil fuel is pumped into the boiler furnace through 16 burners. From the furnace the flue gases pass into the horizontal gas duct and first encounter the platen superheater. Then the gases pass the 1st stage convective superheater (CSS-1). After the

CSS-1 the flue gases pass into the 2nd stage convective superheater (CSS-2), which serves as an exit superheater of the live steam. After the CSS-2 along the gas duct the heating surfaces of the intermediate steam reheating, economizer and regenerative air heater (RAH) are situated.

UNIT TRIP, SAFEGUARDING AND START_UP

The objective of this test is to show how the gas route of the boiler is modeled. The parameters of the flue gases and metal in the CSS-1 were examined.
Plots display trends of the following variables:
BMAZSC – oil fuel flow to the boiler (kg/sec)
OXIG – oxygen content in the effluent gases (%)
FDI14M – live steam flow, leg A (ton/hour)
RA11T2 – temperature of live steam in the live steam pipeline after the boiler (°C)
TGMKH1 – gas temperature in the CSS-1 (°C)
KH1Tma – average temperature of the metal of heat exchangers in the CSS-1 area (°C)
TZMKH1 – average temperature at the soiled wall of heat exchangers in the CSS-1 area (°C)
WGKH1 – gas flow velocity in the CSS-1 (m/sec)
ALKKH1 – convective heat transfer coefficient from flue gases toward clean metal (kcal/(m^2·h·°C))
KH1Nu – kinematic viscosity coefficient of the gases in the CSS-1 ($\nu \cdot 10^6$, m^2/sec)
KH1Li – thermal conductivity coefficient for gases in the CSS-1 ($\lambda \cdot 10^2$, kcal/(m·h·°C)
KH1Pr – Prandtl criterion for gases in the CSS-1
BLKH1 – gas flow "blackness" degree in the CSS-1
ALLKH1 – coefficient of the heat irradiation toward the clean metal (kcal/(m^2·h·°C))
ALGKH1 – net heat transfer coefficient from the gases toward soiled metal (kcal/(m^2·h·°C))
The test was run as follows. Immediately after the beginning of the test a unit protection was activated. It stopped the boiler and the turbine. The operator ventilated the furnace after the shutdown, which took about 10 minutes. After this operation the unit was safeguarded in order to conserve heat for the subsequent start-up.
One hour after the shutting down the operator began the power unit start-up. At 1 hour 3 minutes the furnace ventilation before start-up was initiated. At 1 hour 20 minutes the boiler was ignited. The test took about four hours, although the plots show only the first three hours.
The results of the test are shown in three pairs of plots. Each plot contains five variables. The plots with the index a) show the evolution of the chosen variables during the first 90 minutes of the test. The plots with the index b) show the evolution of the same variables during the next 90 minutes.
What was the evolution of the chosen variables?

During the furnace ventilation after the shutdown (the first ten minutes) a relatively large amount of air necessary for the ventilation was passing through the boiler. The mass flow of air was even slightly more than the air flow in the nominal state. However, the gas flow velocity in the region of the CSS-1 (WGKH1) diminished considerably in comparison with the nominal value. During the furnace ventilation the gas flow velocity in the region of the CSS-1 (WGKH1) was about 2.6 m/sec (fig. 1-b), while the velocity was 8.8 m/sec for the nominal load of the boiler. This phenomenon is explained by the fact that gas temperature in the CSS-1 (TGMKH1) during ventilation was considerably lower than at the nominal loading.
At the same time the following was happening:

- the gases T in the CSS-1 (TGMKH1) dropped from the nominal value 1000°C to approximately 220°C and stabilized at this level (fig.1-a);
- the average metal T of the heat exchangers at the CSS-1 (KH1Tma) was dropping smoothly from the nominal value 490°C to 370°C (fig.2-a);
- the average temperature at the soiled wall of the heat exchangers (TZMKH1) was dropping as well and was all the time lower than the temperature of the clean metal (KH1Tma) – fig.2-a
- the kinematic viscosity coefficient of the gases at CSS-1 (KH1Nu) dropped from the nominal value 172.5 to 34 and stabilized at this value (fig.2-a);
- the thermal conductivity coefficient for gases at the CSS-1 (KH1Li) dropped from nominal value 9.6 to 3.6 and stabilized at this value (fig.3-a);
- the Prandtl criterion for gases at the CSS-1 (KH1Pr) increased from the nominal value 0.58 to the value 0.66 (fig.3-a);
- the convective heat transfer coefficient (ALKKH1) dropped from the nominal value 57 to the value 32;
- the gas flow "blackness" degree (BLKH1) dropped from the nominal value 0.14 to the value 0.06, which corresponds to the absence of combustion products at T 200-250°C (fig.3-a);
- the coefficient of the heat irradiation (ALLKH1) practically dropped to zero from the nominal value 33
- the net heat transfer coefficient from the gases toward soiled metal (ALGKH1) dropped from the nominal value 57 to the value 20 (fig.3-a)

The convective heat transfer coefficient linearly depends on the thermal conductivity coefficient and on the quotient of the gas velocity over the kinematic viscosity coefficient to the 0.65 power. The convective heat transfer coefficient depends on the Prandtl criterion to the 0.33 power.

Given our plots let us verify that in the tested simulator the convective heat transfer coefficient fulfils the formula:

$$\mathbf{Alfa = k\cdot\lambda\cdot(w/\nu)^{0.65}\cdot Pr^{0.33}}$$

where k – constant coefficient which depends on the structure of the gas duct at the CSS-1,

λ - thermal conductivity coefficient

w – gas velocity

ν - kinematic viscosity coefficient for gases

Pr - Prandtl criterion for gases

In the nominal state we have:

$$\mathbf{\lambda\cdot(w/\nu)^{0.65}\cdot Pr^{0.33}=9.6\cdot(8.8/172.5)^{0.65}\cdot 0.58^{0.33}=1.16}$$

The nominal value of the convective heat transfer coefficient (ALKKH1) is equal to 57. If our assumption is correct, then k=57/1.1593=49.2

So our assumption could be formulated like that: in the simulator under test the convective heat transfer coefficient is calculated according to the following formula:

$$\mathbf{Alfa = 49.2\cdot\lambda\cdot(w/\nu)^{0.65}\cdot Pr^{0.33}}$$

Given the data from the figures 1-3 we have the following for the moment of time seven minutes:

$$\mathbf{49.2\cdot\lambda\cdot(w/\nu)^{0.65}\cdot Pr^{0.33}=49.2\cdot 3.7\cdot(2.7/33)^{0.65}\cdot 0.665^{0.33}=31.3}$$

According to the plot 2-a the convective heat transfer coefficient (ALKKH1) for the moment of time seven minutes is approximately equal to 32. This means our assumption is fulfilled.

Let us continue to study the test.

An operator completed the ventilation and safeguarded the boiler in order to conserve heat for the subsequent start-up. The process of natural cooling down started.

The average temperature of the metal of the heat exchangers in the CSS-1 area (KH1Tma) began to drop very slowly (fig.1-a). The reason for this slow decrease in temperature is the fact that the region under consideration is situated inside the hermetically closed at the moment boiler. At the same time the temperature of live steam in the steam pipeline at the boiler outlet (RA11T2) was dropping much faster (fig.1-a). The reason for this process is the heat loss through the isolation in the pipeline.

Let us point out that at the same time average temperature at the soiled wall of the heat exchangers in CSS-1 (TZMKH1) evened up with the temperature of the metal itself (KH1Tma) (fig.2-a).

The gas flow velocity at the CSS-1 (WGKH1) dropped practically to zero (fig.1-a). As a result the convective heat transfer coefficient toward the clean metal (ALKKH1) dropped considerably as well (fig.2-a). The T of the gases (TGMKH1) rose to 345°C (fig.1-a) while the metal T (KH1Tma) reached 350°C (fig.2-a). You know that if there is no gas flow, the temperature of the gases has to reach the same value as the metal temperature.

The kinematic viscosity coefficient of the gases (KH1Nu) stabilized at a new value slightly less than 50. This corresponds also to the new gas T of 350°C. Following the increase in the temperature of the gases:

- the thermal conductivity coefficient for the gases (KH1Li) increased as well to the new value equal to 4.5 (fig.3-a);
- the Prandtl criterion (KH1Pr) dropped to 0.65 (fig.3-a)

One hour after the beginning of the test the operator began the power unit start-up.

In the period between 1 hour 5 minutes and 1 hour 15 minutes the boiler was ventilated before the ignition. This ventilation was performed with less air flow in comparison with the ventilation, which took place between the first and tenth minutes after the unit shutdown. As a result of this new ventilation:

- the gas flow velocity in CSS-1 (WGKH1) rose to 1.6 m/sec, while during the first ventilation it was 2.6 m/sec (fig.2-a);
- the T of the gases at CSS-1 (TGMKH1) dropped to 250°C. This value is higher than for the first ventilation because the air flow during the second ventilation was smaller (fig.1-a);
- the live steam T in the live steam pipeline (RA11T2) started a faster dropping. This was due to the fact that the process of natural cooling was coupled with the process of pressure dropping in the steam route as a result of the ventilation (fig.1-a);
- the CSS-1 metal T (KH1Tma) was dropping more actively due to the consumption of relatively cool air in the gas duct at the CSS-1 (fig.2-a);
- the average temperature at the soiled wall of the heat exchangers (TZMKH1) in the CSS-1 became lower than the temperature of the clean metal in the CSS-1 (KH1Tma) (fig.2-a);
- all other variables reacted realistically as well

At 1 hour 20 minutes the boiler was ignited. The oil fuel consumption to the furnace (BMAZSC) could be seen; the oxygen content (OXIG) reached 12 percent. A steam flow from the boiler appeared. Let us remember that, in the first part of the test, on one hand the ventilation of the furnace was performed twice, on the other hand, there was no steam flow from the boiler because it was sealed. As a result of these factors the metal inside the heated zones of the boiler cooled considerably more than the metal of the unheated steam headers and pipelines since the steam headers and pipelines cooled only due to a natural cooling. Therefore, before the ignition of the boiler the steam in the unheated steam headers and pipelines was considerably hotter than the steam inside the boiler. Thus, after the boiler ignition, as soon as the relatively cool steam started to flow into

the live steam pipeline, the temperature of the steam in the live steam pipeline dropped considerably. All these phenomena are shown in figure 2-a.
In addition, the following were happening:

- as a result of a fuel burning the T of the gases at CSS-1 (TGMKH1) rose till 600 °C (fig 2-b);
- as a consequence of the gas temperature rise as well as the increase in the quantity of gases the velocity of the gases (WGKH1) rose (fig 2-b);
- the convective heat transfer coefficient (ALKKH1) rose mainly due to the increase in the gas velocity (fig 2-b);
- the clean metal temperature (KH1Tma) was rising and the temperature at the soiled wall of the heat exchangers (TZMKH1) became bigger than the clean metal temperature (fig 2-b);
- the kinematic viscosity coefficient of the gases (KH1Nu) increased due to the gas T rise (fig 2-b);
- the gas flow "blackness" degree (BLKH1) changed due to the appearance of combustion products in the flue gases (fig.3-b);
- the coefficient of the heat irradiation (ALLKH1) increased mainly due to the rise of the gas temperature (TGMKH1) (fig.3-b);
- the thermal conductivity coefficient (KH1Li) and the Prandtl criterion (KH1Pr) for gases reacted adequately too (fig.3-b)

Let us by plots calculate the following expression for the moment of time 1 hour 30 minutes:

$$49.2 \cdot \lambda \cdot (w/\nu)^{0.65} \cdot Pr^{0.33} = 49.2 \cdot 6.4 \cdot (2.2/90)^{0.65} \cdot 0.61^{0.33} = 23.96$$

According to the plot in figure 2-b, for this moment of time the value of the convective heat transfer coefficient (ALKKH1) is equal about to 24. Thus, we can conclude that in the tested simulator the convective heat transfer coefficient from the gases to the metal under any conditions fulfils the formula:

$$k \cdot \lambda \cdot (w/\nu)^{0.65} \cdot Pr^{0.33}$$

It is worth mentioning that, while developing the simulator under test, the coefficient k was determined not from the observation of the real object but from the constructive parameters of the boiler. There is a special method for determining the coefficient k for a superheater of any type and for a boiler of any type. The Russian firm "Power Plants Simulators" masters this method.

CONCLUSIONS

The tested simulator has at least the following features:

- it simulates the heat flow from the flue gases to the metal based on the criteria heat exchange equations;
- in convective heaters it takes into account not convective heat exchange only but the radiant heat exchange too;
- it calculates independently heat transfer from gases to metal and from metal to steam/water but not the direct heat transfer from gases to steam
- the heated surfaces of the boiler and the unheated surfaces are simulated independently without merging them – parameters of the heat exchangers are taken from power unit construction data;
- the soiling of the metal by burning products is taken into consideration
- to achieve the precise implementation of transient curves the simulator has a deep fragmentation of gas and steam ducts along the spatial coordinate

A one could ask us why in your simulator do you take into account, for example, the soiling of the metal by burning products? Why don't you make it simple? In Russia there is a well-known method for static calculation of boilers on the base of constructive data. In the former Soviet Union all the boilers had to be calculated in accordance with the method. Numerous comparisons of parameters taken from real power unit with calculated ones had proved the method is very precise. We have applied the method for dynamic simulation of fossil power units in the frame of our simulation technology. The method includes not only equations that has to be used for calculation but in addition the comprehensive recommendations how to calculate numerous coefficients in the equations too. The method requires to take into consideration the soiling of the metal by burning products and we do it like that. As soon as we make any simplifications to the method we ought to change procedures for calculation of coefficients but we don't know how to do it. Just thanks to an implementation of the method in the frame of our simulation technology our simulators are really able to reproduce with a tiny error margin any static working mode of the simulated power unit.
The simulator allows to trace the details of the heat exchange in furnace, in all the convective gas ducts, in pipe lines, inside the turbine, in the regeneration system and so on during any complicated transient process of the simulated power unit. In the furnace the simulator takes into consideration air suctions both to lower and upper part of the furnace, the fuel description, recirculation of flue gases, steam for oil fuel atomization and so on.
All the mentioned features of the simulator really allow to obtain a deep understanding of power unit fundamentals.

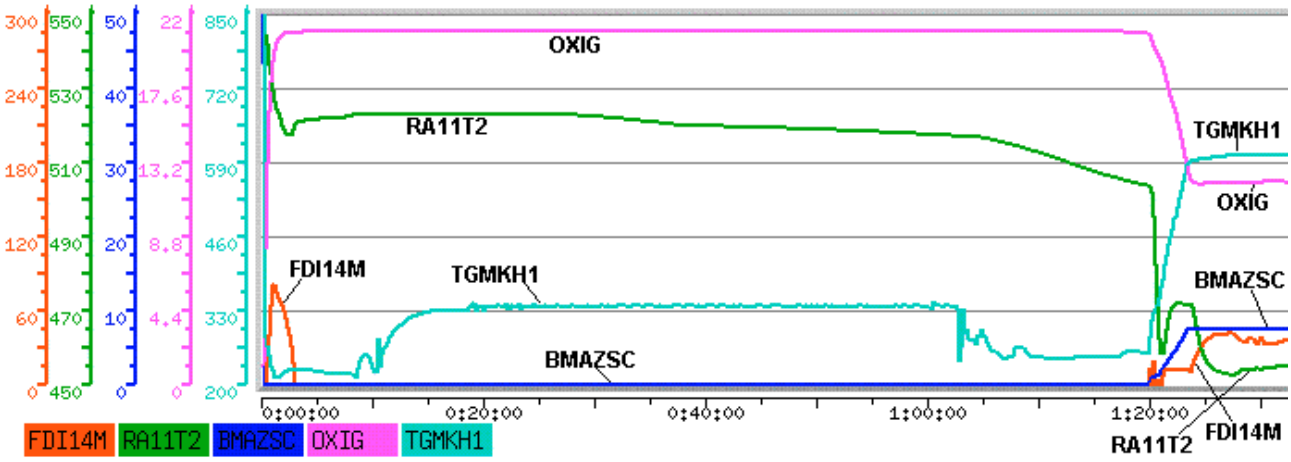

Picture 1-a

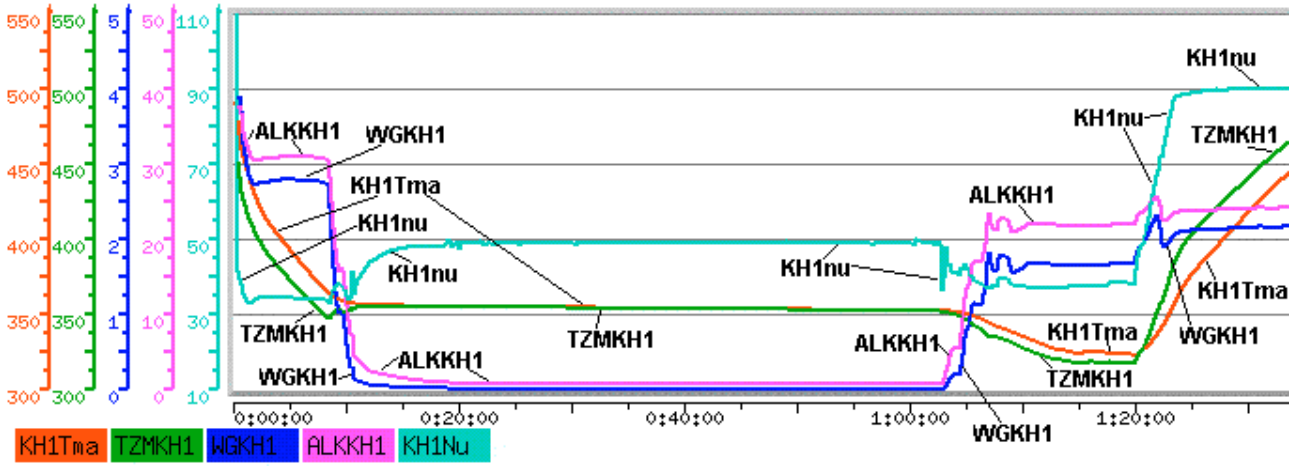

Picture 1-b

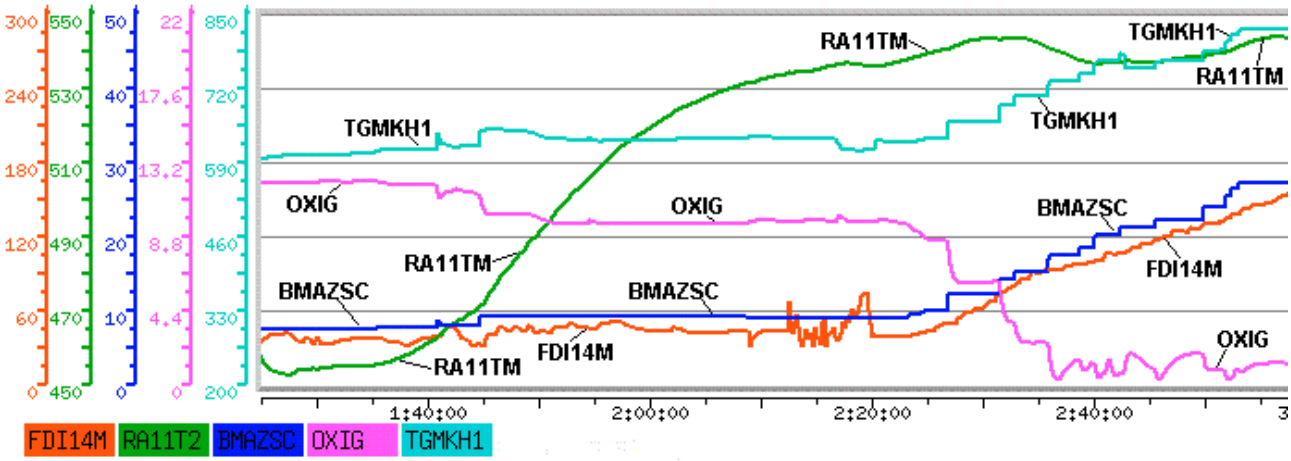

Picture 2-a

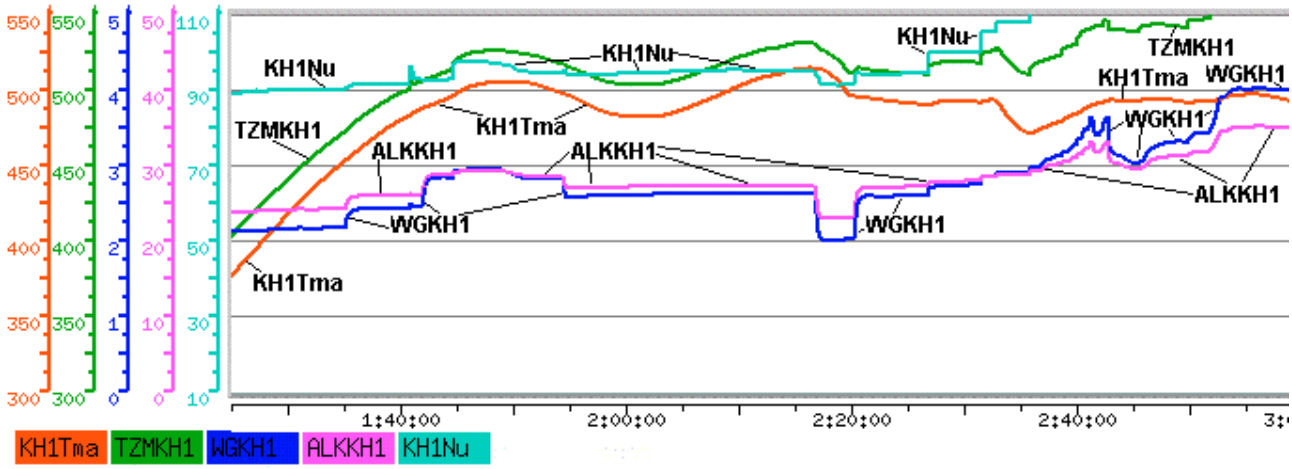

Picture 2-b

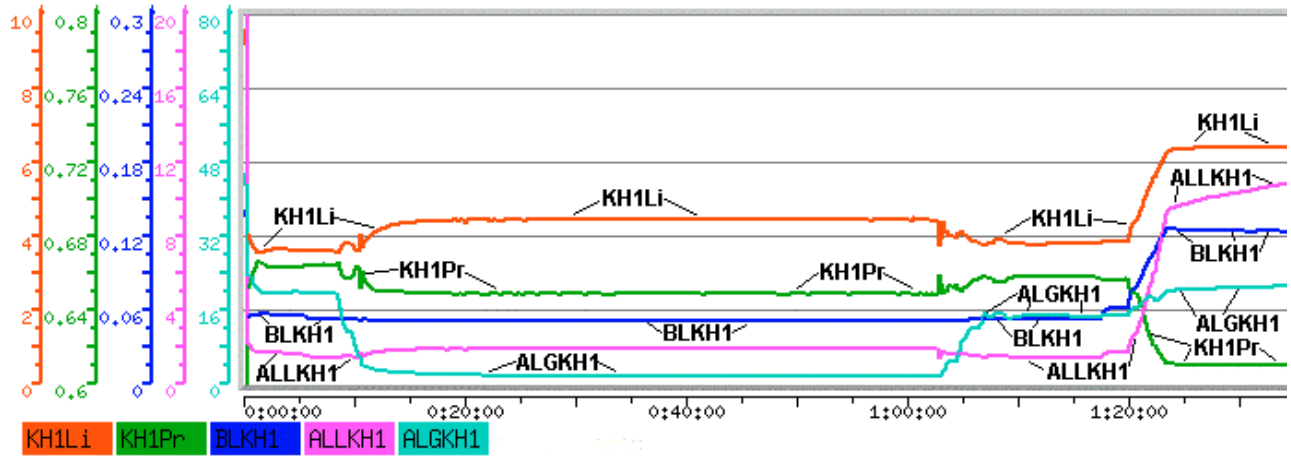

Picture 3-a

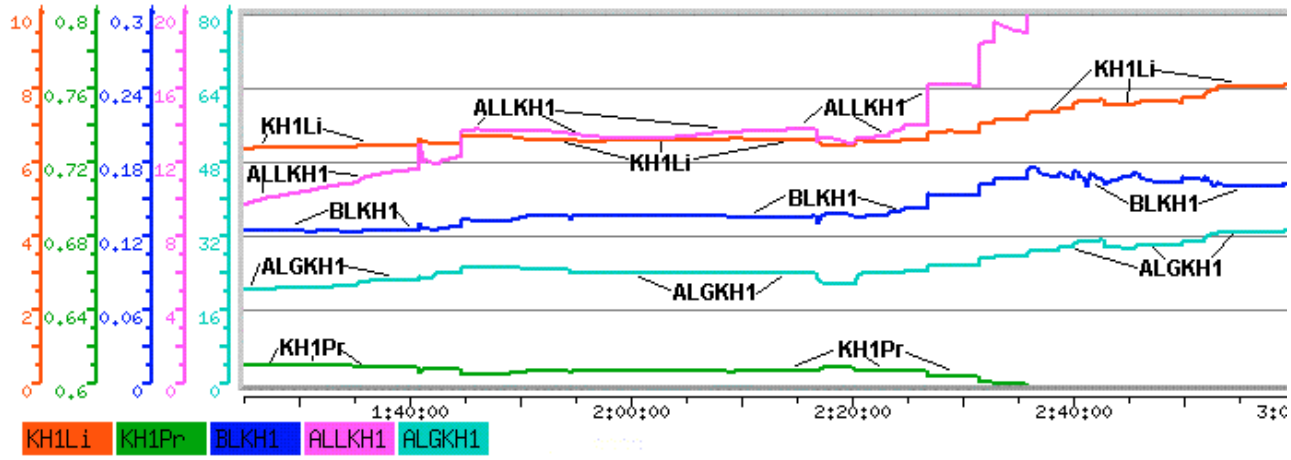

Picture 3-b

Proceedings of ECOS 2005
Trondheim, Norway
June 20–22, 2005

FEASIBILITY STUDY OF CO_2 REMOVAL FROM PRESSURIZED FLUE GAS IN A FULLY FIRED COMBINED CYCLE - THE SARGAS PROJECT

Mårten Bryngelsson[*] and Mats Westermark
KTH – Royal Institute of Technology
Dept. of Chemical Engineering and Technology
SE-100 44 Stockholm
Sweden

ABSTRACT

In this article a novel concept for CO_2 removal from power plants is discussed from a systems perspective. The main advantage of the process is that the investment cost and the power penalty for CO_2 removal can be substantially reduced compared to conventional combined cycles. The proposed technical solution comprises fully fired combined cycle, which minimizes the amount of flue gas. Furthermore, the CO_2 absorption is performed at pressurized conditions prior to the expansion, which further enhances the CO_2 removal. The modification of the power cycle and integration of absorption stages makes CO_2 removal equipment much more compact and allows the use of CO_2 absorbents with lower heat demand for the regeneration. The partial pressure of CO_2 is above atmospheric pressure and removal efficiencies above 95% can be obtained with potassium carbonate absorption (the Benfield process). The treated flue gas is then reheated and re-humidified before the expansion in the gas turbine.

A Norwegian consortium has developed the concept and feasibility studies have been performed for 100 MW and 400 MW power plants based on natural gas in Norway. The produced carbon dioxide is intended for storage in the Norwegian oil and gas fields in order to enhance the oil recovery. The suggested localizations of the power plants have been chosen accordingly. The design study is based on the same gas turbine and steam cycle as used in the commercial Pressurized Fluidized Bed Combustion (PFBC) cycle. PFBC plants are presently fired with coal but the fluid bed combustor for coal will be replaced by a gas combustor if natural gas is used. A key advantage is that the process can be built solely from commercially available components.

This report is an assessment of the features, capabilities, advantages and future possibilities of the suggested power cycle with integrated CO_2 removal. A power plant for 100 MW power output and based on natural gas is considered suitable as a first demonstration plant to be built in Hammerfest, Norway. A permit application has been turned in. For such a demonstration plant the process simulations have indicated that an efficiency of about 40 % can be obtained, including the penalties from CO_2 capture and compression. Further improvements, e.g. supercritical steam cycle or more advanced gas turbine increases the efficiency and for a 400 MW power cycle a net efficiency of about 44-48% has been simulated (including CO_2 capture and compression). The cycle may also be suitable for CO_2 removal from coal-fired plants.

Keywords: CO_2 capture, CO_2 removal, CO_2 storage, enhanced oil recovery, power plant, demonstration plant, Norway

NOMENCLATURE

COE	Cost of Electricity [Euro/kWh e]
E	CO_2 emissions [kg CO_2/kWh e]
MC	Mitigation Cost [Euro/kg CO_2]

INTRODUCTION

Norway has been blessed with an abundance of natural resources in the form of oil and gas. Ever since the 1980s Norway has harvested these resources, which has made them the seventh and eighth largest producer of oil and natural gas respectively in the world [1].

[*] Corresponding author: Phone: +46 8 7908285 Fax: +46 8 7230858 E-mail: mrtn@kth.se

Norway does not use the natural gas for power production, even though the building of natural gas fired power plants have been proposed for a long time. The question about power plants has become an important political question though, and more specifically the question of the CO_2 emissions, that among other things made the Prime Minister Bondevik step down from his post in 2000. Today however, the building of a gas-fired power plant in Norway seems closer to realization than ever before. Several concepts are competing to become the first one built. Sargas AS is one of the competing companies with a promising concept. In cooperation with the company Hammerfest Energi they have turned in a permit application for the building of a 100 MW natural gas fired power plant with CO_2 capture [2]. Their proposed novel process (patent no EP 037 567 64.1) is the topic of this paper.

The demand for CO_2 for enhanced oil recovery, as well as high CO_2 taxes in Norway are important driving forces that needs to be discussed in order to put this development into a systems perspective. As explained in the following section, these forces are tightly linked with Norway's declining oil production and climate change.

DRIVING FORCES

The global demand for oil increases rapidly. The consumption has now reached a stunning 78 million barrels (bbl) per day [3]. At the same time oil reserves are stagnating, not only in Norway, which affects the oil price and makes competition about existing oil fierce. At the present time price is over $50 per bbl. At this high oil price, oil companies consider using sophisticated methods such as Enhanced Oil Recovery (EOR) with CO_2 to increase oil production.

Enhanced oil recovery

When the rate of recovery declines in an oil field, there are several available methods for maintaining a high production rate. After primary production comes pressure maintenance and water flooding, but an even larger amount of oil can be recovered by using Enhanced Oil Recovery (EOR). The number of EOR projects has increased rapidly over the last few decades, and among them EOR projects based on CO_2, CO2-EOR.

CO_2 -EOR is an example of a miscible recovery method where CO_2 is injected into the oil field. The CO_2 mixes with the oil and displaces it, which increases the rate of production. One region that could have use for EOR to boost production in the near future is the North Sea and especially Norway. In the United States CO_2 has been injected into oil wells for around three decades, it is a common and well-understood practice. In the year 2000 they had 66 CO_2-EOR projects running producing 216 000 barrels per day (bpd), 4 % of US oil production [4].

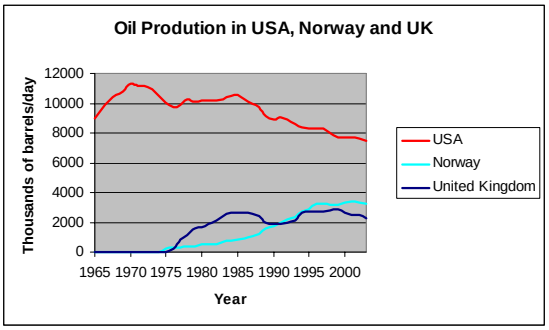

Figure 1: Oil production in the United States, Norway and the United Kingdom, 1960-2003 [3].

Figure 1 shows that the North Sea is entering its declining phase, similar to that which occurred in the United States around 1980. Previous studies of CO_2 -EOR have shown that an additional 6-15 % of the original oil in place (OOIP) can be recovered. This corresponds to a total of 10-30 % more oil for a given field [5]. For the North Sea region up to 2 billion barrels of incremental oil could be produced in a 25-year span [5].

There are alternatives for EOR, other than using CO_2-injection, which means that the availability of CO_2 and the cost of getting it to the injection site might become important factors for the future roll of CO_2-EOR in the North Sea. But if CO_2 might be hard to get at an affordable price, why not use other methods? The most appealing thing about CO_2-EOR is that it gives an opportunity to increase oil production while mitigating the effects of climate change, creating a win-win situation.

Climate change and CO2 storage

The United Nations Framework Convention on Climate Change [6] together with the later added Kyoto Protocol (KP) state that the Annex 1 countries to the protocol should reduce their overall emissions of greenhouse gasses by 5 % below 1990 level during the first commitment period 2008-2012. The KP has now entered into

force as Russia signed the protocol in late 2004. Carbon dioxide has been pointed out as the most significant greenhouse gas since it contributes to the largest radiative forcing, and three quarters of the CO_2 comes from the burning of fossil fuels [7].

Suggestions on how to mitigate the CO_2 emissions flourish. Efficiency improvement, fuel switch and the use of renewable energy are a few of them, but lately yet another one has been introduced, i.e. carbon capture and storage (CCS). The idea is to capture CO_2 from different point sources, ship it to storage sites where the CO_2 is compressed and injected into reservoirs such as oil wells (as discussed above) and sedimentary basins. If it works, CCS makes it possible to continue burning fossil fuel with minor effects on the climate. Oil wells are suitable storage sites, and the CO_2 will most likely be trapped indefinitely since oil has been trapped in there for millions of years.

One of the main problems with CCS is the efficiency penalty when capturing CO_2. In a power plant the penalty is expected to be in the order of 10 %, which makes the technology costly. In the long run however, CCS is expected to play an important roll since it can contribute a lot to the long term goal that e.g. EU has of a 70 % reduction in greenhouse gas emissions compared to 1990 levels [8]. Riahi et al predict that CCS might penetrate the market around 2040, and at the turn of the century all fossil fueled power plants could be equipped with CCS technology [9].

Whether CCS will become a reality on a global scale or not, does not only depend on cost, but also on the development of international policy. Today it is not even clear how CCS is going to be handled under the KP. However, CCS may still become a reality in the North Sea since the oil companies might need CO_2 for EOR, and the economical benefits of EOR may offset costs for CO_2 capture.

The economy of CO_2-EOR

When it comes to the economy of CO_2-EOR projects, three fundamental indicators have been identified [5]:

1. The value of the incremental oil
2. The price of delivered CO_2 at the oilfield.
3. The value of permanently stored CO_2 as a greenhouse gas.

The first two factors are connected so that a higher price of oil makes the oil companies willing to pay more for CO_2 delivered at the oilfield. Historically, the oil industry in the United States has paid \$10-\$15/t CO_2 delivered to an EOR site [10], but that figure might increase if the high oil price remains. The value of permanently stored CO_2 as a greenhouse gas sink might also become important. In the future CCS might get tradable credits, for example in trading systems like the recently adopted European Union Emissions Trading System (EU-ETS). The value of CO_2 under the EU-ETS is at the present time 15 euro per tonne. There is also a relevant tax relief in Norway when storing CO_2, which has been one of the major driving forces behind the SACS project [11].

So far most of the CO_2 used for EOR has come from natural CO_2 accumulations. In the future, and in the North Sea region however the CO_2 has to be extracted from anthropogenic industrial sources. Above all to contribute to the mitigation of climate change, but also because there are no natural CO_2 accumulations around the North Sea. CO_2 from industrial sources is more expensive though, and a lot of research is currently being done on the development of power plants with CCS. Both coal- and gas-fired power plants have been proposed, but in the case of Norway it seems logical to suggest a gas-fired plants. If a gas-fired power plant with CO_2 capture were built in Norway, it would hopefully be able to deliver CO_2 to oilfields at an acceptable cost for the oil companies. The power production, would also give a contribution to the Nordic electricity system. The plant proposed in this paper is introduced in the following section, and it is based on the PFBC-technology.

PROCESS DESCRIPTION

Pressurized Fluidized Bed Combustion (PFBC) is an advanced clean-coal power production system with low emissions of both sulphur dioxide (SO_2) and nitrogen oxides (NO_x). It has also fairly good efficiency, especially compared with conventional coal fired plants. The main part of the system consists of a pressurized fluidized bed where combustion takes place at 12-16 bars. At that pressure the combustion process is very efficient and requires very little residual oxygen. That means that the CO_2 in the flue gas is fairly concentrated. Apart from low emissions of SO_2 and NO_x, the PFBC plant has the advantage of being compact in size.

In this application the process is based on PFBC technology but the fluidized bed is replaced by a gas combustor. The process is called "Fully Fired Combined Cycle with CO_2 removal from pressurized flue gas" and is described below. An overview of the process is shown in figure 2.

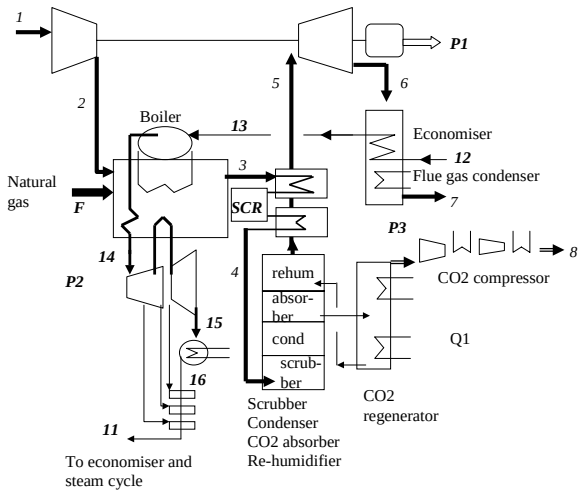

Figure 2: Process scheme. For further details see table 1.

First of all air is compressed in the compressor part of a gas turbine (1). The air is then fed to an external pressurized combustion system (2), a combination of a boiler and a gas heater where hot gas to drive the expander is produced. After the combustion the gas with a high partial pressure of CO_2 is cooled down to a temperature suitable for NO_x reduction and CO_2 capture.

Most of the NO_x is removed in a selective catalytic reduction unit, SCR. This is not only for environmental reasons but also to prevent the potassium carbonate from parasitic side reactions. The absorption of CO_2 is then performed by potassium carbonate, flowing counter current with the sour flue gas absorbing mainly CO_2 (4). CO_2 lean flue gas is then rehumidified, reheated and expanded, which produces power P1 (5, 6). Finally, the gas delivers heat to a heat recovery steam generator, HRSG (6, 7).

The CO_2 rich solution from the absorption column is fed to a regeneration column where CO_2 is released by desorption with steam. The CO_2 is then compressed using power P3 to a pressure suitable for transport (8). The regeneration process is driven by low-pressure steam taken from the steam turbine (Q1).

Steam is produced in a HRSG with the pressure vessel working as a super-heater (11,12, 13, 14). The steam is fed to a steam turbine that produces 80-85 % of the total power output P2 (14, 15). The table below displays the most important cycle data:

Table 1: Process data

No		Flow kg/s	Pressure bar	Temp ºC
1	Air inlet	400	1.0	15
2	Comp outlet	400	16.0	300
3	Flue gas	420	16.0	850
4	Cooled flue gas	420	15.5	200
5	CO_2 lean flue gas	380	14.6	837.5
6	Exp outlet	380	1.06	358
7	Exhaust	340	1.0	40
11	Preheated condensate	268	340	210
13	Boiler inlet water	268	330	280
14	Admission steam	268	300	600
15	Steam to condenser	193	0.03	25
16	Condensate	193	0.03	25
		MW		
P1	Power ; gas turbine	82		
P2	Power ; steam turbine	420		
P3	CO_2 compressor	20		
Q1	Regeneration heat	100		

Stream number 8 is 54 kg/s liquefied CO_2 stream from the process at 30°C and 100 bars. 98 % of the original CO_2 is captured.

Main process advantages

The main process advantages are the following:

- The investment cost for the removal plant and the power penalty for CO_2 removal can be substantially reduced compared to conventional combined cycles.
- The "fully firing" means low excess of combustion air, which minimizes the amount of flue gas.
- The CO_2 absorption is performed at pressurized conditions prior to the expansion, which further enhances the CO_2 removal. However, the decrease of flue gas volume due to CO_2 absorption will give some power loss in the turbine.
- The combination of fully firing and pressurized absorption makes CO_2 removal equipment much more compact and less expensive. As an example the volume flow is reduced by a factor of 40 if the air demand is reduced by a factor of 4 and the pressure is increased to 10 bars. The power demand to

overcome pressure losses are small due to the low volumetric flow of flue gas

- The Benfield process, which is a commercially available technology, can be used for the CO_2 absorption at high partial pressure of CO_2. This process uses potassium carbonate as an absorbent and is less sensitive to oxidation than amines. The CO_2 absorption in potassium carbonate can run at e.g. 90°C (the absorbent is not volatile) and still reach CO_2 removal efficiencies as high as 98%.
- High partial pressure of CO_2 will lower the heat demand for the regeneration.
- The reliability of the proposed power cycle is predicted to be better than for a conventional combined cycle. The gas turbine is a non-cooled machine and the steam cycle also has excellent reliability. The downtime is estimated to 2 %.

PROCESS PERFORMANCE

The calculations of the performance for a full-scale power plant have been simulated using the HYSYS Process (Aspentech) software. The efficiency of the process without CO_2 capture is around 47,5 %, which is lower than e.g. a conventional NGCC. Capture and compression of CO_2 then incur some efficiency penalties. The results from the simulations show that the total net efficiency after capturing CO_2 is 44 %

Performance of competing processes

Other proposed methods of capturing CO_2, have been compared e.g. by Göttlicher [12], Audus [13] and Bolland [14]. They show figures in the same range as the above 44 %, i.e. a thermal efficiency between 42 and 50 %. These processes are a) separation of CO_2 after combustion, b) oxy-fuel combustion, and c) separation before combustion.

Table 2: Process performance for three different CO_2 capture concepts

Technology	Göttlicher		Audus		Bolland	
	η_{th} [%]	ref. sys. [%]	η_{th} [%]	ref. sys. [%]	η_{th} [%]	ref. sys. [%]
a	50		47		49,6	
b	48	57,5	48	58	47,2	58
c	42		48		45,3	

The three types of processes are described in the following sections.

Separation of CO_2 after combustion

Technologies for separation of CO_2 from conventional gas turbines after combustion include the use of chemical absorption. The first step in a CO_2 capture plant is flue gas cooling and a booster fan to overcome the exhaust gas pressure drop in the CO_2 absorption. The next step is absorption of CO_2 by an absorbent (usually monoethanolamine, MEA) and steam stripping of CO_2 from the absorbent. Low-pressure steam extracted from the steam turbine in the CC is used to cover the heat demand in the stripping process. Finally, CO_2 compression is used to obtain liquid CO_2.

However, the integration of CO_2 removal with conventional gas turbines suffers from the low concentration of CO_2 in the flue gas (due to the high excess of air). Therefore, a powerful absorbent with strong binding to CO_2 must be used. The most suitable absorbent is MEA but the use of such a strong CO_2 absorbent increases the heat demand for regeneration.

Furthermore, MEA is rather volatile and the emission of MEA gives losses, at least above temperatures of 30-40 °C. Another problem is the oxidation of MEA by air, which also give losses of absorbent. Flue gas re-circulation has been suggested in order to obtain higher partial pressure of CO_2, which eases the absorption [13]. However, present gas turbines have to be modified before this method can be available.

Oxy-fuel combustion

The alternative is based on a combined cycle with a near stochiometric combustion using pure oxygen from an air separation unit (ASU) to oxidize the natural gas in an atmosphere of re-circulated flue gases. CO_2 and steam are produced in the combustion and the working medium in the gas turbine is mainly CO_2. The CO_2 can be concentrated by simply condensing the water [15]. Oxy-fuel combustion is not yet commercially available since it needs the development of new gas turbines adapted to compression of CO_2 and combustion in low excess of air. The gas turbine also has to be modified both in the compressor and the turbine due to different density for the working medium compared to existing gas turbines.

Separation before combustion

Separation before combustion is not yet commercially available for combined cycles since

it needs the development of new gas turbines that are modified for combustion of hydrogen. Separation before combustion includes steam reforming, partial oxidation or auto-thermal reforming plus a CO/H2 shift reactor and a high pressure CO_2 capture unit to produce a hydrogen rich (H2++) fuel gas. When using auto-thermal reforming some portion of the compressed air and steam are extracted from the combined cycle and used for the reforming. Some high-pressure steam is transferred back into the combined cycle [14]. The production of hydrogen is commercially available but new combustors must be developed for the combustion of hydrogen in the gas turbine.

Future technologies

One future technology is based on mixed conducting membranes (MCM). The basic principle is that MCM separates a part of the compressed air into oxygen and nitrogen. Fuel is then combusted in pure oxygen making the technology similar to oxy-fuel combustion discussed above. A process based on MCM called Advanced Zero Emission Power plant (AZEP) has been proposed to have an efficiency penalty of 2 % [16].

Chemical looping is yet another novel concept that uses metal-oxides instead of air for oxidizing fuel. Thus the combustion is performed in a nitrogen-free environment, leaving a flue gas consisting mainly of water vapor and CO_2 [17].

Future processes will hopefully be more efficient than today's due to technological progress and learning. However, climate change and the demand for enhanced oil recovery is a strong incentive to start CO_2 capture as soon as possible with present available technology.

DEVELOPMENT POTENTIAL

One improvement that would increase the thermal efficiency and CO_2 capture of the fully fired combined cycle is serial coupled gas turbines. The first turbine's exhaust is used in the steam cycle and then further cooled in a flue gas condenser before entering the process shown in figure 2. The net efficiency can be improved to about 48% (including CO_2 capture and compression).

PROCESS ECONOMY

The economical benefits with Sargas' proposed power plant is shown in this section by comparing it to a NGCC plant with post combustion CO_2 capture. The Sargas technology is not primarily advantageous because of higher thermal efficiency but for easier integration with CO_2 capture. Those reasons are underlined again and backed up by figures. First table 3 shows a comparison between the two concepts without CO_2 capture:

Table 3: Economical comparison between NGCC and Sargas technology without CO_2 capture

	NGCC	Sargas
Capital cost [Euro/kW e]	660	750
Operation and maintenance cost [Euro/MWh e]	2,6	1,5
Efficiency [%]	55	47,5
Down time [%]	8%	2%
Power [MWe]	400	400

Sargas can compete with lower operating costs and lower down time, but the technology without CO_2 capture has disadvantages when it comes to capital expenditure, which is higher, and a lower thermal efficiency. On the other hand, when the CO_2 capture plant is added, things look better, as seen in table 4.

Table 4: Economical comparison between NGCC and Sargas technology with CO_2 capture

	NGCC	Sargas
Capital cost [Euro/kW e]	1300	940
Operation and maintenance cost [Euro/MWh e]	5,0	2,1
Efficiency [%]	45%	44%
Down time [%]	10%	2%
CO_2 capture efficiency [%]	85%	98%
Power [MW e]	330	370

A more compact and efficient CO_2 capture plant leads to lower capital expenditure and lower efficiency penalties for Sargas.

An additional benefit is the higher CO_2 capture efficiency as shown below in table 5, which means lower emissions (lower emission factor) and as a result lower CO_2 tax costs. The NGCC plant emits 7,3 times more CO_2 per kWh than the Sargas process. Higher capture efficiency also means more CO_2 to e.g. CO_2-EOR projects, which improves income from selling CO_2.

Table 5: Emitted and captured CO_2.

	NGCC	Sargas
Emission factor [kg CO_2/kWh]	0,067	0,0092
CO_2 captured [kg/kWh e]	0,38	0,45

Cost of electricity and natural gas price
The cost of electricity is made up of the cost of capital, operating and maintenance cost and fuel cost. With a current high natural gas price, fuel cost is the largest expenditure.

The market for natural gas is not like the market for oil where the price is set on a global market. For natural gas the regional markets set the price, primarily because gas is expensive to transport. Sargas therefore seek to locate the power plant in Hammerfest, Norway, which improves the chance of getting a good price on gas. However, the market price is hard to predict, especially when considering the whole plant life cycle, and since regional price differences on the natural gas market are expected to converge within three decades [18].

In the following figure, cost of electricity for the two CO_2 capturing plants is calculated using different gas prices. The capital charge rate is 11% based on a 10% discount rate and a 25-year lifetime.

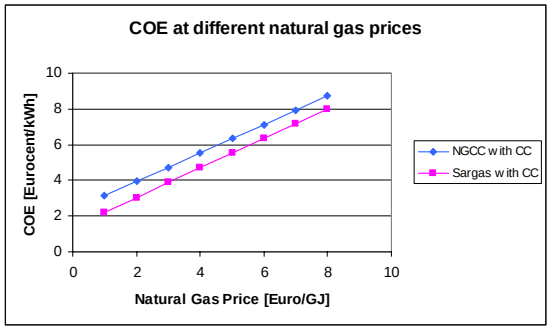

Figure 3: COE at different natural gas prices

The figure shows that Sargas has lower COE than NGCC when considering CO_2 capture. The steep slope of the COE underlines the importance of a low natural gas price that a plant location close to the source might help secure.

Mitigation cost
It has been shown earlier in this paper that both the emission factor and the cost of electricity is lower for the Sargas technology, and those are the factors that make up the mitigation cost (MC).

$$MC = \frac{COE_{cap} - COE_{ref}}{E_{ref} - E_{cap}} \qquad [19]$$

The MC for the two CO_2 capture concepts (cap) is in figure 4 calculated using the NGCC plant without CC as a reference (ref), again with a varying natural gas price.

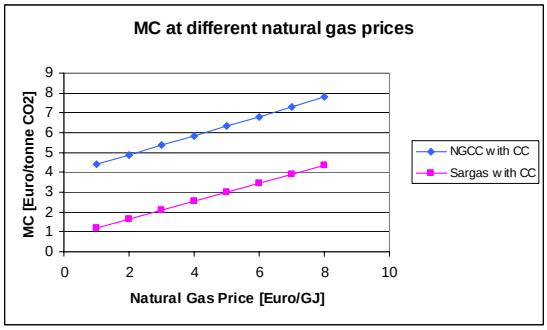

Figure 4: MC at different natural gas prices

Again we see that the Sargas process is predicted to be most cost effective with a MC of less than half of its' competitors.

CONCLUSIONS
The concept that Sargas AS has introduced has clear advantages. It is first of all based on commercial technology, which cannot be said about all previously proposed concepts. It also has a very efficient handling of flue gases under pressurized conditions that enables low penalties, compact capture plant and low capture cost.

Many studies focus primarily on comparing the thermal efficiencies of CO_2 capturing concepts, while this paper also tries to quantify other features. The thermal efficiency is not better for Sargas than for the competing NGCC with post combustion CO_2 capture. However, the Sargas process makes up by its' low emissions, low downtime, low capital cost for the capture plant and low operating and maintenance cost. With the input parameters used in this paper, the result is both lower cost of electricity and lower mitigation cost.

Because of technical difficulties realizing competing concepts, the Sargas process might be one of the better concepts for CCS that is feasible today. In combination with the high oil price and the increasing need for EOR in Norway, it might be commercially successful, and even more so if the capturing of CO_2 is somehow credited.

REFERENCES

[1] Key world energy statistics. Paris: OECD/IEA, 2004.

[2] Hammerfest Energi AS. Gasskraftverk med fjerning av CO_2 – konsesjonssøknad. Hammerfest: Hammerfest Energi AS, 2005. See also: http://www.hfel.no/CO2/Konsesjonssøknad%20.pdf

[3] BP statistical review of world energy. London: BP, 2004.

[4] Stevens S H, Kuuskraa V A and Gale J. Sequestration of CO_2 in depleted oil and gas fields: global capacity, costs and barriers. Proceedings of the 5th international conference on greenhouse gas control technologies, Cairns, Australia, 2000.

[5] Hustad, C W, editor. Large-scale CO_2 sequestration on the Norwegian Continental Shelf: a technical, economic, legal and institutional assessment. Oslo: Norwegian Research Council, 2004. See also: http://www.co2.no/files/files/co2/23.pdf

[6] United Nations framework convention on climate change. Bonn: UNFCCC, 1992. See also:http://unfccc.int/essential_background/convention/background/items/2853.php

[7] IPCC, Climate change 2001: The scientific basis. Cambridge: Cambridge University Press, 2001.

[8] EU. Directive 2003/87/EC of the European Parliament and of the Council of 13 October 2003 establishing a scheme for greenhouse gas emission allowance trading within the Community and amending Council Directive 96/61/EC. EU, 2003.

[9] Riahi K, Rubin E S, Taylor M R, Schrattenholzer L and Hounshell D. Technological learning for carbon capture and sequestration technologies. Energy Economics 2004;26(4):539-564.

[10] Kuuskraa V A and Pekot L J. Defining optimum CO_2 seqestration sites for power and industrial plants. Proceedings of the 6th international conference on greenhouse gas control technologies, Kyoto, Japan, 2002.

[11] Kongsjorden H, Kårstad O and Torp T A. Saline aquifer storage of carbon dioxide in the Sleipner project. Waste Management 1998;17(5-6);303-308.

[12] Göttlicher G and Pruschek R. Comparison of CO_2 removal systems for fossil-fuelled power plant processes. Energy Conversion and Management 1997;38:173-178.

[13] Audus H. Leading options for the capture of CO_2 at power stations. Proceedings of the fifth international conference on greenhouse gas control technologies, Cairns, Australia, 2000.

[14] Bolland O and Undrum H. A novel methodology for comparing CO_2 capture options for natural gas-fired combined cycle plants. Advances in environmental research 2003;7:901-911.

[15] Bolland O and Sæther S. New concepts for natural gas fired power plants which simplify the recovery of carbon dioxide. Energy Conversion Management and 1992;33(5-8);467-475.

[16] Sundqvist S-G. AZEP - Development of an integrated air separation membrane - gas turbine. Proceedings from the second Nordic minisymposium on carbon dioxide capture and storage, Gothenburg, Sweden, 2001. See also:http://www.entek.chalmers.se/~anly/symp/symp2001.html

[17] Ishida M and Jin H. CO_2 recovery in a power plant with chemical looping combustion. Energy Conversion and Management 1997;38:187-192.

[18] World Energy Outlook, 2002. Paris: OECD/IEA, 2002.

[19] David J and Herzog H. The cost of carbon capture. Proceedings of the fifth international conference on greenhouse gas control technologies, Cairns, Australia, 2000.

Proceedings of ECOS 2005
Trondheim, Norway
June 20–22, 2005

THE STRUCTURE OF MARINE PHAGE POPULATIONS

Karl Heinz Hoffmann
Physics Institute
Technical University of Chemnitz
Chemnitz, D-09107 Germany

Beltran Rodriguez-Brito, Mya Breitbart, David Bangor, Florent Angly,
Ben Felts, James Nulton, Forest Rohwer, Peter Salamon
Computational Sciences
San Diego State University
San Diego, CA 92182-7720
United States of America

ABSTRACT

Phage are the most abundant biological entities in the biosphere, with an estimated 10^{31} particles on the planet. They also play a major role in carbon cycling; at least 25% of fixed carbon passes through phage. Their roles as predators of bacteria have important implications for possible marine CO_2 sequestration. Metagenomic analyses show that the rank-abundance curve for marine phage communities follows a power law distribution. This distribution is consistent with a proposed, modified version of Lotka-Volterra predator-prey dynamics, where blooms of a specific microbial species lead to blooms of their corresponding phage and a subsequent decrease in abundance. The model predicts that the majority of phage genotypes in a population will be rare and it is unlikely that the most abundant phage genotype will be the same at different time points. The model is based on spatial-temporal heterogeneity and a power law phage decay, which are both supported by empirical data.

Keywords: CO2 sequestration, phage, viruses, diversity, rank-abundance, power law, distribution, model, Lotka-Volterra, kill the winner, neutral evolution, metagenomics

NOMENCLATURE

MMFW marine microbial food web
DOM dissolved organic matter
POM particulate organic matter
B bacterial concentration
Φ phage concentration
α, β, γ, and δ coefficients in dynamical equations for B and Φ.
LV Lotka-Volterra population model
GLV generalized Lotka-Volterra model
SP Scripps Pier population
MB Mission Bay population

INTRODUCTION

The marine microbial food web (MMFW) is the consortium of heterotrophic and autotrophic prokaryotes and their predators which inhabit the world oceans. The MMWF controls the transfer of nutrients and energy to higher trophic levels and thereby greatly influences global carbon cycling. Dissolved organic matter (DOM) and particulate organic matter (POM) are the largest biogenic sinks of carbon in the ocean. The concentration is so high that the bacterial populations feeding on them are controlled by predation rather than by nutrient availability. The two predator guilds that keep bacterial populations in check are protozoa and phages with about equal shares of the biomass passing through each guild. When bacteria are eaten by protozoa, their biomass can be transferred to higher trophic levels; when bacteria are eaten by phage, the biomass returns to the POM pool. How much of this POM sinks to the deep oceans for sequestration is largely dependent on whether bacterial growth digests these particles and

converts them to DOM. Understanding and controlling marine phage populations would therefore provide a route to increasing CO_2 sequestration. The paper below is a step in that direction.

A POWER LAW BEST DESCRIBES THE RANK-ABUNDANCE DISTRIBUTION OF MARINE PHAGE COMMUNITIES

Six different standard mathematical and ecological distributions (reviewed in [1]) were tested for their goodness of fit to marine phage metagenomic data described in Breitbart et al. [2]. An overlap between sequences from different clones of a shotgun library (i.e., a contig) means that the same phage genotype has been re-sampled. This information was used to predict the population structure of the phage communities based on a modified Lander-Waterman equation [3]. To determine which distribution best described the metagenomic data, the error between the predicted and the observed contig spectrum was used in a quasi-log-likelihood function using a weighted sum of squared errors (Table 1). In both marine phage populations, the data were best described by a power law distribution (error for Scripps Pier (SP) = 1.8 and Mission Bay (MB) = 2.1), followed by the lognormal distribution (error for SP = 1.9 and MB = 2.3). In contrast, classical niche-based ecological models like Broken Stick (error for SP = 11 and MB = 15) and Niche Preemption (error for SP = 12 and MB = 16) were a very poor fit to the data.

There was a major difference between the number of phage genotypes predicted by the different distributions. For example, the lognormal distribution predicted 3 to 5 times more phage genotypes in the samples than did the power law (Table 1). This is important because recent estimations of global microbial diversity have assumed lognormal distributions and may have significantly overestimated species richness [4].

Model	Error	Predicted # of Phage Genotypes
Scripps Pier (SP) [1021 17 2 0]		
Power Law	1.8	3400
Lognormal	1.9	13000
Logarithmic	2.5	1400
Broken Stick	11	1200
Exponential	12	10000
Niche Preemption	12	9100
Mission Bay (MB) [841 13 2 0]		
Power Law	2.1	7400
Lognormal	2.3	43000
Logarithmic	2.8	1600
Broken Stick	15	960
Exponential Law	16	7500
Niche Preemption	16	8200

Table 1. Goodness of fit for six different models to the observed contig spectra of two marine phage metagenomes. The error was calculated as the variance weighted sum squared deviation from predicted contig spectra, which gives the value of the log pseudo likelihood function as described in ref 2. The models are listed in order of increasing error for each sample. The observed contig spectra are shown in square brackets next to each of the samples, where a contig spectrum of [A, B, C, …] represents A one contigs, B two contigs, etc.. The exponential and logarithmic models were named according to their analytic form in the frequency-rank relationship, viz. frequency proportional exp(k*rank)) or frequency

A GENERALIZED VERSION OF LOTKA-VOLTERRA DYNAMICS PREDICTS THE POWER LAW DISTRIBUTION

Determining the population structure of marine phage communities also suggests ecological models to explain how phage and their microbial hosts interact. It is assumed that different hosts interact through competition for food. This interaction is very weak because food is not a limiting resource for microbes in the marine ecosystem [5, 6]. The second assumption is that there is a strong and specific interaction between a microbial host and its phage predators, where the most abundant microbes are killed. This relationship has been termed "kill the winner" and predicts that specific predator-prey pairs oscillate in time as blooms of a particular

microbe are followed closely by blooms of its phage predator [7]. Using these assumptions, the problem becomes a system of many non-interacting predator-prey systems. The simplest model matching the assumptions is classical Lotka-Volterra (LV; Equation 1):

$$\frac{dB}{dt} = \alpha B - \beta B\Phi$$
$$\frac{d\Phi}{dt} = -\gamma\Phi + \delta B\Phi \qquad (1)$$

where B denotes the size of the microbial population for a single genotype, Φ denotes the population size of the corresponding phage predator, and where α, β, γ, and δ are positive constants that describe microbial growth, microbial death, phage decay and phage production, respectively. For simplicity it was assumed that all phage-host pairs follow identical dynamics[1], but bloom at independent times (i.e., they are randomly distributed along a common cycle). Note that in order to match the observed population structure, blooms must alternate with comparatively long periods of "hiding out" at concentrations several orders of magnitude lower than the bloom titers (see Fig 4 in [8]). For a Lotka-Volterra model such cycles can be found by using initial states near the origin.

Figure 1a-d show the results of adopting Lotka-Volterra dynamics for a population of non-interacting phage-host pairs. Transformation of this data to a log-log plot (Fig 1d) shows a mediocre fit to the power law (R^2=0.83). The relatively poor fit occurs because the high abundance phage are over-represented on the log-log plot (i.e., too many ranks correspond to these values and destroy the linearity). The dynamics would fit the data much better if the blooms were shorter and more intense. Mathematically this can be accomplished by using a generalized version of Lotka-Volterra (GLV), where an exponent (n>1) is added to the predator populations to account for cooperativity [9]. A GLV model with an exponent of 2 produced an almost perfect fit to the power law distribution (R^2=0.99; Figure 1e-h).

$$\frac{dB}{dt} = \alpha B - \beta B\Phi^2$$
$$\frac{d\Phi}{dt} = -\gamma\Phi^2 + \delta B\Phi^2 \qquad (2)$$

We propose that in the marine environment, the cooperativity between phage in the lysis event ($\delta B\Phi^2$) and microbial death ($\beta B\Phi^2$) reflects spatial-temporal heterogeneity. The ocean is a gel made up of particles ranging from colloids to marine snow[10-12]. These particles represent higher, local concentrations of nutrients than are necessary for microbial growth [13]. Microbes are known to chemotax to these particles [14]. Phage lysis of microbes on particles would create locally high concentrations of both predators and prey (i.e., a local change in mass action). This would lead to an apparent cooperativity in the predation.

One consequence of adding the cooperativity function to the lysis event ($\delta B\Phi^2$) is that the decay exponent on Φ must match the exponent in the mass action terms to keep the populations oscillating (i.e., to maintain neutral stability of the orbits). This feature of the proposed model matches data on phage decay, which shows that phage particles display rapid initial decay rates, which then decrease over time [15,16]. Environmental factors such as local entanglement of phage particles in microbial debris would account for this observation.

The "kill the winner" hypothesis, as interpreted through the proposed model, predicts that typical phage-host cycles involve long periods of hiding from the predators at very low numbers alternating with brief spurts of dominance. Therefore, it is unlikely that the most abundant phage genotype will be the same at different time points and there should be several orders of magnitude difference in the numbers of a specific phage present at different times. Limit cycles traversing approximately the same orbit would make similar predictions and represent a viable alternative to the proposed model. In addition to making several predictions that match empirical data, the proposed model represents a new mechanism for how a system can display power-law behavior.

[1] This feature of the model is for simplicity alone – the real dynamics surely varies among the types. In this neutral evolution hypothesis, our hope is that the qualitative features are captured by replacing the full complexity of the problem by one "average" type. In fact, a comparable calculation using a distribution of parameter values also gives a close fit to the power law.

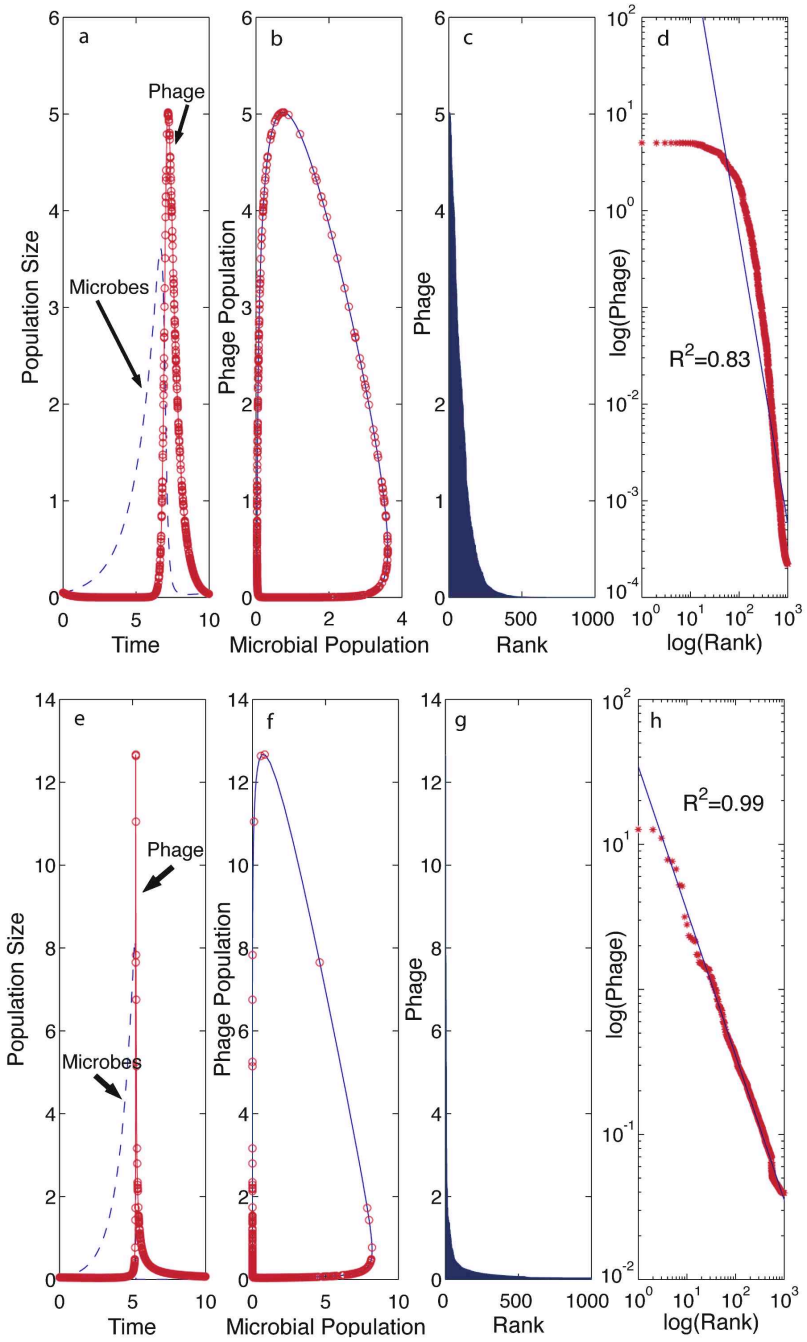

Figure 1. Comparison of phage population structure predicted by Classical Lotka-Volterra (a-d) and the proposed Generalized Lotka-Volterra (e-h) dynamics. All population sizes and time are in arbitrary units. a) Populations of microbes (dashed blue line) and phage (solid red line) as a function of time. Red circles show 1000 random samples along the cycle. b) The relationship between the sizes of the microbial and phage populations (solid blue line). Red circles show the same 1000 random samples along the cycle. c) Rank abundance plot of the 1000 random phage samples. d) Log-log version of panel c. The solid blue line is the least-squares fit to the ranked phage populations (red asterisks). Panels e-h show the same relationships for the Generalized Lotka-Volterra dynamics. The R^2 is the coefficient of determination

REFERENCES

[1] Magurran A. *Measuring Biological Diversity*. Malden, MA: Blackwell Publishing, 2004.

[2] Breitbart M, Salamon P, Andresen B, Mahaffy JM, Segall AM, Mead D, Azam F, Rohwer F. *Genomic analysis of uncultured marine viral communities*. Proc Natl Acad Sci USA 2002; 99: 14250-14255.

[3] Lander ES, Waterman MS. *Genomic mapping by fingerprinting random clones: a mathematical analysis*. Genomics 1988; 2: 231-239.

[4] Curtis T, Sloan W, Scannell J. *Estimating prokaryotic diversity and its limits*. Proc Natl Acad Sci USA 2002; 99: 10494-10499.

[5] Sano E, Carlson S, Wegley L, Rohwer F. *Movement of viruses between biomes*. Applied and Environmental Microbiology 2004; 70: 5842-5846.

[6] Wilcox RM, Fuhrman JA. *Bacterial viruses in coastal seawater: lytic rather than lysogenic production*. Mar Ecol Prog Ser 1994; 114: 35-45.

[7] Thingstad T. *Elements of a theory for the mechanisms controlling abundance, diversity, and biogeochemical role of lytic bacterial viruses in aquatic systems*. Limnol Oceanogr 2000; 45: 1320-1328.

[8] Suttle C, Chan A. *Dynamics and distribution of cyanophages and their effect on marine Synechococcus spp*. Applied and Environmental Microbiology 1994; 60: 3167-3174.

[9] Dancso A, Farkas H, Farkas M, Szabo G. *Investigations on a class of generalized two-dimensional Lotka-Volterra schemes*. Acta Applicandae Mathematica 1990; 23: 103-127.

[10] Azam F. *Microbial control of oceanic carbon flux: the plot thickens*. Science 1998; 280: 694-696.

[11] Chin WC, Orellana MV, Verdugo P. *Spontaneous assembly of marine dissolved organic matter into polymer gels*. Nature 1998; 391: 568-572.

[12] Alldredge AL, Cole JJ, Caron DA. *Production of heterotrophic bacteria inhabiting macroscopic organic aggregates (marine snow) from surface waters*. Limnol. Oceanogr. 1986; 31: 68-78.

[13] Martinez J, Smith DC, Steward GF, Azam F. *Variability in ectohydrolytic enzyme activities of pelagic marine bacteria and its significance for substrate processing in the sea*. Aquat. Microb. Ecol. 1996; 10: 223-230.

[14] Blackburn N, Fenchel T, Mitchell J. *Microscale nutrient patches in planktonic habitats shown by chemotactic bacteria*. Science 1998; 282: 2254-2256.

[15] Mathias C, Kirschner A, Velimirov B. *Seasonal variations of virus abundance and viral control of the bacterial production in a backwater system of the Danube river*. Applied and Environmental Microbiology 1994; 61: 3734-3740.

[16] Heldal M, Bratbak G. *Production and decay of viruses in aquatic environments*. Mar Ecol Prog Ser 1991; 72: 205-212.

Proceedings of ECOS 2005
Trondheim, Norway
June 20–22, 2005

EVALUATION OF CO2 MITIGATION RETROFIT OPTIONS FOR LOW-QUALITY COAL FIRED POWER PLANTS

E. Kakaras, A. Doukelis, D. Giannakopoulos, A. Koumanakos, Ch. Hatzilau
Laboratory of Steam Boilers and Thermal Plants
National Technical University of Athens
Heroon Polytecniou 9, 15780 Athens, Greece
Tel +30 210 772 3662, Fax +30 210 772 3663

ABSTRACT

The purpose of the work presented in this paper is to examine and evaluate the state of the art in technological concepts for the retrofit of low-quality coal-fired power plants for CO_2 capture and sequestration. The discussion will be based on the evaluation of the most promising options in technological and economical terms, taking into account the technical and operational requirements and characteristics of existing power plants. The work will be mainly focused on oxyfuel combustion and flue gases treatment by amine scrubbing. Results from thermodynamic simulations of the retrofit power plants will be used to demonstrate the potential for emissions reduction and evaluate the associated power output and efficiency penalties. These data, coupled with the investment costs, will provide an insight on the economics associated to CO_2 retrofit sequestration options and the viability of the power plants within the framework of the application of a CO_2 economic penalty, in an electricity generation system based on low-quality coal.

Keywords: CO_2 sequestration, low-quality brown coal, oxyfuel, amine scrubbing

NOMENCLATURE

ASU	: Air Separation Unit
CCT	: Clean Coal Technologies
CCS	: Carbon Capture and Storage
ENBIPRO	: Energie-Billanz-Program
HP	: High Pressure
IPCC	: Intergovernmental Panel on Climate Change
LP	: Low Pressure
MEA	: Monoethanolamine
MP	: Medium Pressure
NGCC	: Natural Gas Combined Cycle

*Corresponding author: Phone: +30 210 7722720
Fax: +30 210 7723663 E-mail: adoukel@central.ntua.gr

INTRODUCTION

In analysing measures for reducing CO_2 emissions, the Intergovernmental Panel on Climate Change (IPCC) [1] concludes that none of the following measures alone would be sufficient to stabilise atmospheric CO_2 concentrations: demand reductions and/or efficiency improvements; substitution among fossil fuels; switching to renewables or nuclear energy; CO_2 sequestration; or afforestation. Thus, in identifying strategies for climate change mitigation, combinations of multiple technologies in all sectors must be considered.

At present, fossil fuels are the dominant source of the global primary energy demand, and will likely remain so for the rest of the century. Fossil fuels supply over 85% of all primary energy; the rest is produced by nuclear, hydro-electricity and renewable energy (commercial

biomass, geothermal, wind and solar energy). Currently, renewable energy supplies less than 1% of the global energy demand. While great efforts and investments are made by many nations [1] to increase the share of renewable energy to the primary energy demand and to foster conservation and efficiency improvements of fossil fuel usage, addressing climate change concerns during the coming decades will likely require significant contributions from carbon sequestration in thermal power plants.

Carbon sequestration can be defined as the capture and secure storage of carbon that would otherwise be emitted to the atmosphere. This is called carbon capture and storage (CCS). The rationale for carbon capture and storage is to enable the use of fossil fuels while reducing the emissions of CO_2 into the atmosphere, and thereby mitigating global climate change. The commercial or under development CO_2 sequestration technologies for coal-fired power plants can be divided into three broad categories [2]:

- Separation of CO_2 from waste gas
- Combustion in O_2 instead of air
- Production of a carbon free fuel

A detailed presentation of these technologies has been provided in [3]. The present study focuses on the application of the oxyfuel process and the MEA scrubbing process which are applicable to all fossil fuelled power plants and are considered as the two most promising CO_2 sequestration technological options for the retrofit of low-quality coal fired power plants.

RETROFIT OF A TYPICAL POWER PLANT UTILISING GREEK LOW QUALITY COAL WITH CO_2 SEQUESTRATION

The present study has focused on the application of two CO_2 sequestration technological options based on the examination of operating characteristics of a typical low-quality coal fired power plant. The simulations of the power plant and the CO_2 sequestration retrofit options were performed with the thermodynamic cycle calculation software ENBIPRO (**EN**ergie-**BI**llanz-**PRO**gram) [4], a tool for heat and mass balance solving of complex thermodynamic circuits, calculation of efficiency and exergetic and exergoeconomic analysis of power plants. The software code models all pieces of equipment that usually appear in power plant installations for both full load and part load operation and can accurately calculate all thermodynamic properties (temperature, pressure, enthalpy) at each node of the thermodynamic circuit, power consumption of each component, flue gas composition etc. The code has proven its validity by accurately simulating a large number of power plants and through comparison of the results with other commercial software, such as IPSEPRO [5].

The 330 MW_{el} gross power output power plant under examination has a supercritical boiler, a HP-MP-LP steam turbine and 8 preheating stages and represents a typical Greek low-quality coal fired power plant with flue gas desulphurisation. Table 1 presents the basic operating data of the power plant under examination compared to the simulation data. The auxiliary power consumption used to calculate the net power output includes the consumptions of FD fan, ID fan, lignite mills, LUVO, water pumps and the desulphurization plant.

		Existing Plant	**Simu-lation**
Fuel input	MW_{th}	830	830
Flue gas temperature after air preheater	°C	152.0	149.5
Steam flow at HP ST inlet	kg/s	265.4	265.4
Steam pressure at HP ST inlet	bar a	235.4	235.4
Steam temperature at HP ST inlet	°C	540	540
Steam flow at IP ST inlet	kg/s	227.4	227.4
Steam pressure at IP ST inlet	bar a	38.2	38.2
Steam temperature at IP ST inlet	°C	539.7	539.7
Steam pressure at IP ST outlet	bar a	2.22	2.22
Water flow at the boiler inlet	kg/s	265.4	265.4
Pressure after feedwater pump	bar a	292.5	292.5
Flue gas CO_2 concentration	w. %	20.7	20.7
CO_2 emissions	kg/s	-	87.7
Specific CO_2 emissions	kg CO_2/ kWh	-	1.075
Net power output	MW	294.2	293.7
Net efficiency	%	35.4	35.38

Table 1: Basic operating data of the conventional power plant

In the examined retrofit test cases, the following general assumptions have been made:

- The fuel consumption remains the same
- The water/steam cycle remains as much as possible unchanged
- The final product (CO_2-rich stream) is compressed in a multi-stage compressor to 110 bar, in order to facilitate transportation and sequestration
- The final CO_2 stream purity is 98%

O_2/CO_2 recycle combustion (oxyfuel)

According to the oxyfuel concept, presented schematically in Fig. 1, combustion is achieved with high-purity oxygen. Cryogenic air separation by an Air Separation Unit (ASU) is the most efficient commercially available technique [6] and has been used in the current study. The oxygen purity chosen is 95%, the majority of the rest 5% being Argon, and all oxygen contained in the air is used. The air entering the ASU has a pressure of 5.5 bar and air compression occurs in four stages, with an isentropic efficiency of 0.83. After each compression step, the air is cooled to 20ºC in order to decrease the compression energy demand. The compression steps are 1.013-1.53 bar, 1.53-2.35 bar, 2.35- 3.6 bar and 3.6-5.5 bar [7].

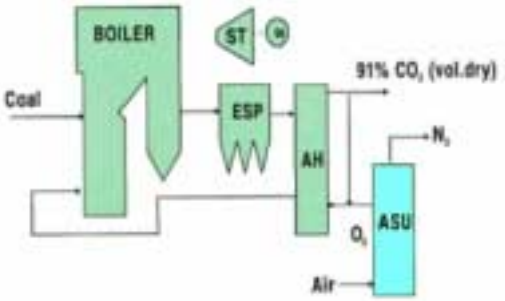

Figure 1: Oxyfuel process (IEA)

When applying the O_2/CO_2 recycle combustion concept in a coal-fired power plant, the air preheaters are not used. As a result, in the case studied, the flue gas exit temperature is increased to ca. 310 ºC. Another energy demanding process regarding air separation is air cleaning. Before air enters the distillation column, water vapour, CO_2 and any other impurities are removed, utilising adsorption with molecular sieves. For the regeneration of the molecular sieves, dry nitrogen that is produced from the ASU is used [7]. The temperature of the air nitrogen is about 180ºC and, consequently, heaters are required to heat the air nitrogen. In the current case study, the flue gases exiting the boiler at ca. 310ºC provide the heat required for nitrogen heating. Air leakage in the boiler as well as the oxygen purity play a significant role in the CO_2 concentration of the flue gases. Under the assumptions of 95% oxygen purity and 3% boiler air infiltration, the O_2/CO_2 recycle combustion process can capture 79% of the CO_2 that is produced from coal combustion [8], the rest being vented to the atmosphere during the purification process for removal of non-condensable gases. This is the value used in the current study, a lower CO_2 recovery rate compared to the recovery with the amine scrubbing process. It should, nevertheless, be mentioned that in a greenfield application, where improved sealing can be incorporated from the design and the air infiltration rate can be lower, the CO_2 recovery rate can be comparable to the amine scrubbing process.

Excess oxygen applied for the simulation is 1.5% [9]. On the other hand, the flue gas recirculation is chosen so as to maintain the flue gas flow and temperature inside the boiler at the same level as in the conventional power plant.

To conclude, the main energy requirements for the O_2/CO_2 recycle combustion are:

- Air compression for the ASU (5.5 bar)
- Compression of the final product for transportation and sequestration (110 bar)
- Cooling water pumps consumption for flue gas cooling and air inter-cooling at the ASU

Table 2 presents the simulation results of the power plant retrofit to oxyfuel operation, demonstrating the high efficiency and power output loss and the significant reduction in CO_2 emissions compared to the conventional power plant.

The current study focuses on the retrofit application of the oxyfuel process for CO_2 capture in an existing coal-fired power plant. However, considerations for a greenfield application include the optimisation of the water/ steam cycle through the integration of the heat produced during the air compression before the ASU and the compression of the CO_2, as well as the integration of the heat content of the flue gas at the boiler exit. The heat

of the above mentioned sources could partly replace some of the feedwater heating stages with steam extraction. Consequently, in a greenfield application of the oxyfuel technology, the net efficiency is expected to be increased compared to the net efficiency of the retrofit application.

Air mass flow in ASU	kg/s	315.6
O_2 mass flow	kg/s	72.78
Flue gas mass flow at boiler's exit	kg/s	416.5
Recirculated flue gas mass flow	kg/s	270.0
CO_2 concentration (wet) CO_2 concentration (dry)	w. %	58.84 96.97
ASU power consumption (n_{is}= 0.83)	MW	58.1
CO_2 compression power consumption (n_{is}= 0.85)	MW	22.4
Cooling water pumps, flue gas cooling and air inter-cooling at the ASU	MW	1.5
CO_2 emissions	kg/s	18.11
Specific CO_2 emissions	kg CO_2/ kWh	0.31
Net power output	MW	211.0
Net efficiency	%	25.42

Table 2: Oxyfuel power plant simulation results

Amine scrubbing

The present study has focused on the commercially available MEA process (Fig.2). In the amine gas processing operation, CO_2 is absorbed from the flue gas by the liquid solvent in an absorption tower, where the gas stream and the liquid solvent are contacted in counter-current flow. In the stripper (regeneration stage) the charged amine solution is heated with steam, in order to strip off the CO_2.The energy requirements of MEA scrubbing are:

- Heat consumption for regeneration of the reach solution: this low-grade heat is provided from the power plant in the form of low-pressure steam extraction at about 5 bars. The stripper column thermal consumption, according to the state of the art commercially available solutions, is about 3.25 MJ/kg of CO_2 removed, which equals to about 1.4 kg steam/kg CO_2.
- Electricity consumption: the most energy-consuming process is the flue gas blower, which is used for the flue gas pressure elevation in order to overcome the system pressure drop. This category also includes the energy required for the pumping of the amine solution and the pumping of the absorber wash water.
- Compression of the final product to 110 bar for transportation and sequestration.

The flue gases at the outlet of the boiler are cooled down to 40ºC in order to condense the water vapour and then compressed up to about 1.3 bar [10]. CO_2 recovery from the flue gases is assumed to be 90%. The heat required for regeneration of the rich solvent is provided by low-pressure steam, which is extracted from the low-pressure steam turbine at 5.96 bar and 285ºC. The steam provides its latent heat for the regeneration of the solvent and the condensate is compressed and returned to the feed-water tank.

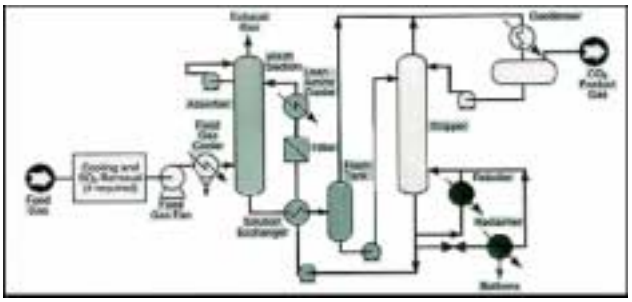

Figure 2: Amine flue gas processing operation (IEA)

Table 3 presents the simulation results of the power plant retrofit to amine scrubbing operation, demonstrating the high efficiency and power output loss, as well as the higher CO_2 emission reduction potential, compared to the conventional power plant. The loss in this case is higher than with the oxyfuel retrofit option.

Steam extraction	kg/s	109.6
Thermal consumption for solvent regeneration	MWth	256.5
CO_2 compression power consumption (n_{is}= 0.85)	MW	20.5
CO_2 absorption unit power consumption (flue gas fan, solution pumps)	MW	8.7
Cooling water pumps for flue gas cooling	MW	0.7
CO_2 emissions	kg/s	8.76
Specific CO_2 emissions	kg CO_2/ kWh	0.17
Net power output	MW	200.5
Net efficiency	%	24.16

Table 3: Power Plant with amine scrubbing simulation results

GLOBAL EMISSION REDUCTION POTENTIAL AND CO_2 CAPTURE COST

The simulations presented in the previous section have demonstrated the effect of two CO_2 sequestration retrofit options on the power output, efficiency and emissions of a typical coal fired power plant utilising low-quality brown coal. Both options demonstrate a significant reduction in the emitted CO_2, at the expense of reduced net power output and efficiency. This in its turn means that the actual emissions reduction achieved by application of a retrofit technology and the capture cost per ton CO_2 avoided, in the context of a power grid, can be assessed by making a global calculation of emissions, taking into account that the electricity generation deficit to the grid should be compensated by operation of another power plant. In the current study, three different options for covering the electricity generation deficit have been evaluated:

- operation of a conventional power plant of the same type as the retrofit plant
- operation of an advanced CCT 330 MWel low-quality brown coal fired power plant with an electric efficiency of 44%
- operation of a fourth-generation 400 MWel natural gas fired Combined Cycle with an efficiency of 56.5%.

In all cases, the power plant covering the electricity generation deficit of the retrofitted plant operates at base load for 7000 hours. The electricity generation cost has been calculated in all cases using literature data on capital costs [2], life of investment, fixed and variable operating and maintenance costs, inflation rate and company rate of return. The capital costs of the retrofit plants have been calculated on the basis of literature data.

Operating hours per year	Emissions (tons)
3000	947,183
4000	1,262,910
5000	1,578,638
6000	1,894,365
7000	2,210,093
8000	2,525,820
8760	2,765,773

Table 4: Reference CO_2 emissions of power plant

Table 4 presents the reference annual CO_2 emissions of the power plant under study, for varying annual operating hours. By applying the oxyfuel and amine retrofit technologies and covering the deficit electricity generation by each one of the three options mentioned above, the annual emissions are reduced considerably, as shown in Fig. 3. The largest emissions reduction potential is achieved when the deficit electricity generation is covered by a natural gas fired combined cycle, since this power plant type has the lowest specific CO_2 emissions.

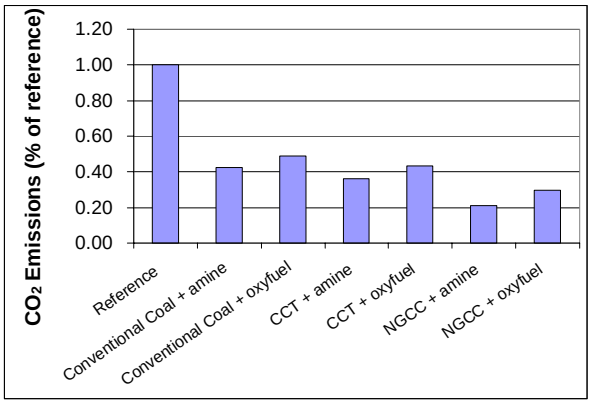

Figure 3: Global emissions from retrofit power plant and coverage of deficit electricity generation by additional power plant

Figures 4 and 5 present the overall grid CO_2 reduction cost per ton of CO_2 avoided, for two different fuel prices for low-quality coal. The transportation and storage costs are not included

here. As it is illustrated in figures 4 and 5, the CO_2 reduction cost for the amine retrofit case is always higher that the oxyfuel case, due to the increased efficiency penalty associated with this technology. In terms of global treatment of the cost, it can be seen that the CCT power plant can be competitive to the natural gas fired combined cycle for base load operation. Nevertheless, the emissions reduction is larger for the combined cycle, therefore the final decision should be taken by considering a multitude of factors such as the required cut in emissions, security of supply and economic considerations.

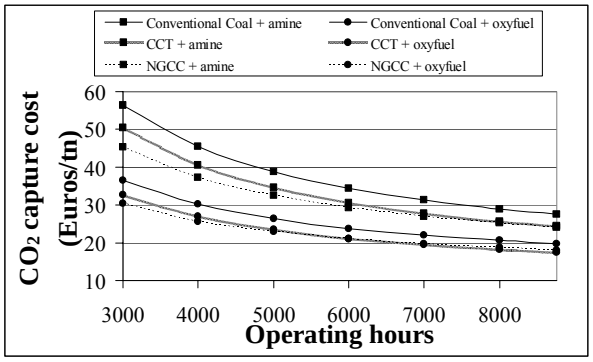

Figure 4: CO_2 reduction costs for different retrofit technologies and coverage of deficit electricity generation (coal cost: 1.8 Euros/GJ)

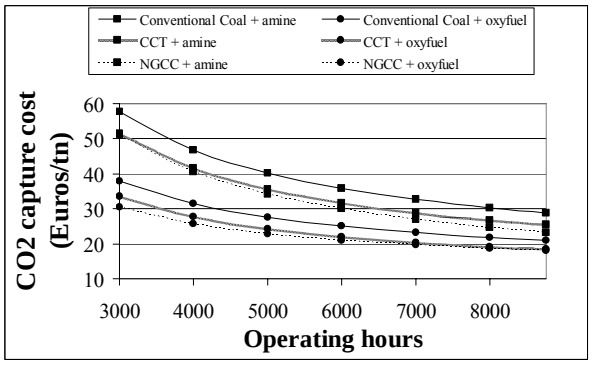

Figure 5: CO_2 reduction costs for different retrofit technologies and coverage of deficit electricity generation (coal cost: 2.4 Euros/GJ)

CONCLUSIONS

The purpose of the work presented in this paper was to examine and evaluate the state of the art in technological concepts for the retrofit of low-quality coal-fired power plants for CO_2 capture and sequestration. The present study focused on the application of the two most promising CO_2 sequestration technological options, namely the oxyfuel process and the MEA scrubbing process.

Results from thermodynamic simulations of the retrofit power plant were presented, demonstrating the potential for emissions reduction of 79% and 90% for the cases of oxyfuel and amine scrubbing respectively. The associated energy penalties are 82.7 MWel for the power output and 10 percentage points for efficiency concerning the oxyfuel retrofit and 93.2 MWel and 11.2 percentage points for the amine scrubbing option.

The case of supplementary energy supply by conventional, CCT or NGCC plants in order to cover the deficit electricity generation was examined and the overall CO_2 emissions and CO_2 reduction cost were assessed taking into account only CO_2 capture costs. The case of additional CCT use proves competitive to the NGCC option in the cases of oxyfuel or amine scrubbing retrofit power plant under base load operating conditions.

REFERENCES

[1] Intergovernmental Panel on Climate Change (IPCC): Climate change 2001: the scientific basis, Cambridge University press, 2001

[2] VGB Powertech: Separation and Sequestration of CO_2 from Power Plants - Literature Survey, VGB Project Group "CO_2 Separation and Sequestration", Essen, August 2002

[3] E. Kakaras, A. Doukelis, G. Giannakopoulos, A. Koumanakos: CO_2 Sequestration Options for Coal-Fired Power Plants, IFRF 14th Members' Conference - A Sustainable Energy Supply for Industry: A Challenge for the IFRF, Netherlands, 11-14 May 2004

[4] Stamatelopoulos G. N.: Calculation and optimisation of power plant thermodynamic cycles, VDI-Regulations, Series 6, Nr. 340. Braunchweig, Mechanical Engineering Department, 1996 (in German).

[5] Pogoreutz M., Giglmayr I., Nixdorf M.: Comparison of software for calculation of thermodynamic processes, report of VGB

research project Nr.177. VGB, 2000 (in German).

[6] Anderson K., H. Birkestad, P. Maksinen, F. Johnson, L. Strömberg and A. Lyngfeld: An 865 MW Lignite Fired CO_2 Free Power Plant - A Technical Feasibility Study, Sixth International Conference on Greenhouse Gas Control Technologies, Kyoto, October 1-4, 2002

[7] K. Andersson and P. Maksinen: Process evaluation of CO_2 free combustion in an O_2/CO_2 power plant, Master thesis, Chalmers University of Technology, Sweden, 2002

[8] D. Singh, E. Croiset, P.L. Douglas, M.A. Douglas: Techno-economic study of CO_2 capture from an existing coal-fired power plant: MEA scrubbing vs. O_2/CO_2 recycle combustion, Energy Conversion and Management, 44, pp. 3073-3091, 2003

[9] H. Birkestad: Separation and Compression of CO_2 in an O_2/CO_2-fired Power Plant, Master of Science degree thesis, Chalmers University of Technology, Sweden, 2002

[10] O. Bolland and P. Mathieu: Comparison of two CO_2 removal options in combined cycle power plants, Energy Conversion and Management 39, 16-18, pp. 1653-1663, 1998

Proceedings of ECOS 2005
Trondheim, Norway
June 20–22, 2005

COMPARATIVE ANALYSIS OF ENERGY REQUIREMENTS OF CO_2 REMOVAL FROM METALLURGICAL FUEL GASES

Krzysztof Lampert* and Andrzej Ziebik
Institute of Thermal Technology
Silesian University of Technology
Konarskiego 22, 44-101 Gliwice
Poland

ABSTRACT

The paper presents preliminary results of the analysis of CO_2 removal process, applied to metallurgical fuel gases: blast-furnace gas and Corex gas. The CO_2 removal is realized by the physical absorption process with the Selexol solvent as the absorbing liquid. The analysis is focused on the energy consumption in the case of such installations, when blast-furnace gas or Corex gas are supposed to be treated. The CO_2 removal from metallurgical gases can be attractive from both technological and environmental points of view. Decreased CO_2 content in the gases and increased LHV results in better conditions for its utilization e.g. in a gas turbine-based CHP plant or direct utilization within the process, e.g. as an auxiliary fuel or reducing gas in a blast furnace. As the composition, flow rate and LHV of the raw blast-furnace and Corex gases differ strongly, the physical absorption installation has different requirements and operation parameters in both cases. The optimisation leads to minimal energy consumption with the assumed CO_2 removal efficiency. The results indicate which technology of pig-iron production has greater potential in the field of mitigation of greenhouse gas emissions, with respect to the technological possibilities of utilisation the treated fuel gases.
Keywords: CO_2 removal, physical absorption, Corex process, blast furnace

NOMENCLATURE

BF	Blast furnace,
C	Compressor,
CL	Cooler,
DH	Dehydrator,
DRI	Direct Reduced Iron,
f	Fuel,
FD	Flash drum,
GC	Fuel gas compressor,
GCL	Fuel gas cooler,
GT	Gas Turbine,
LHV	Lower Heating Value, kJ/kg,
$\dot{m}$	Mass flow rate, kg/s,
M	Electric Motor,
N	Power, kW, MW,
RC	Recycle gas compressor,
RCL	Recycle gas cooler,
SCL	Solvent cooler,
SP	Specific power consumption, kJ/kg,
SR	Specific amount of removed CO_2,
STP	Standard temperature and pressure.

*Corresponding author: Phone: +48 32 237 2003, Fax: +48 32 237 2872, E-mail: lampert@itc.polsl.pl

INTRODUCTION

The best known technology of pig iron production is the blast-furnace process, commonly applied all over the world. Although some development has been made in blast-furnace technology, the process still has some important drawbacks, as the necessity of using coke and sinter, previously prepared in separate processes. In recent decades a few alternative processes of pig iron production have been developed. However, the Corex process is practically the only technology, which has been applied industrially.

Both blast-furnace and Corex processes are accompanied by the production of gaseous fuels, but the composition and LHV of these gases are different. However, both fuels contain large

amounts of CO (as the main combustible component) and CO_2. Therefore, the utilisation of such gases is connected with a relatively high CO_2 emission to the atmosphere, if compared with other hydrocarbon fuels, e.g. natural gas. CO_2 contained in the off-gas may be removed and sent for further utilisation or storage. The removal of CO_2 from the gas results in a wider range of possibilities of utilizing the purified gas. Some of the most often considered possibilities are also presented in the paper.

A number of technologies has been described in literature concerning CO_2 removal. These technologies base on different chemical and physical processes. However, special emphasis has been put on the power production sector – metallurgical processes have received little attention so far, although CO_2 removal processes are applied in a few installations, where reducing gas is needed, e.g. for iron ore reduction (DRI processes). Among different CO_2 removal technologies, physical absorption with the Selexol solvent has been chosen for this analysis as the most often considered solution for such an application, i.e. in the case of gas containing more than 10 % of CO_2 [4,6].

AN OUTLINE OF THE COREX PROCESS

The Corex process of obtaining pig iron is a modern technology, considered as more friendly for the natural environment than blast-furnace, because non-coking coal is used as a source of energy and reducing agents. In this way the harmful effects of cokeries are eliminated. The Corex installation realizes the blast-furnace function in two separate reactors (Fig. 1)[3]. The reduction of iron ore to sponge-iron takes place in a shaft furnace and the production of reducing gases and the melting of the sponge-iron are carried out in a smelting gasifier. Pig iron and slag obtained from the Corex process are nearly identical in their composition and properties to the blast-furnace technological products. In comparison with blast-furnace technology, the Corex process requires less energy due to the fact that coal is coked within the process. In this way the loss of energy due to cooling of the coke and heating it up again is eliminated. The Corex process eliminates also the consumption of energy for sintering and production of the hot blast. In this way the production of harmful substances is also eliminated.

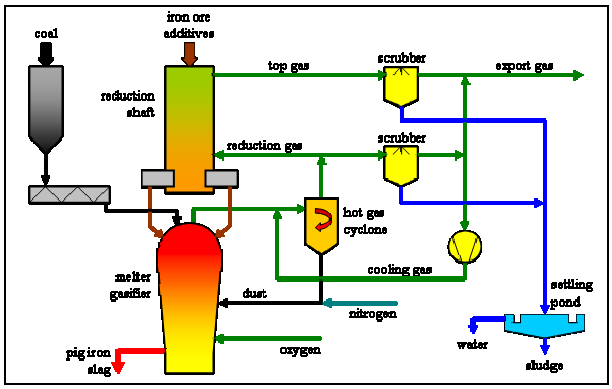

Fig. 1: Schematic diagram of the Corex process

Besides the production of pig iron, medium-LHV Corex gas is produced as the by-product. Its lower calorific value (LHV) is about two times greater than the LHV of blast-furnace gas (Table 1).

Property		Unit	Corex gas	Blast furnace gas
Gas comp. (molar)	CO	%	38 - 45	18 - 38
	CO_2	%	30 - 35	5 - 17
	H_2	%	15 - 23	1,4 - 7
	CH_4	%	1 - 2	0,1 - 1
	N_2	%	Balance	50 - 61
	H_2O, O_2	%	Balance	Balance
LHV		kJ/m^3 (STP)	7500 - 8000	3400 - 5300

Table 1: Typical analysis of the Corex export gas and blast-furnace gas [3,9,10]

The biggest difference in the off-gas composition appears when the content of nitrogen is taken into consideration. Blast-furnace gas contains at least 50% of N_2, as the process itself is supplied with a blast containing air only little enriched with oxygen. Such a ballast amount results in high costs of purification technologies. Relatively low LHV of the gas implies some difficulties with its utilization in a combustion chamber of the gas turbine, thus causing a significant decrease in the efficiency of a gas-turbine-based CHP plant. As the Corex process uses oxygen, the main ballast substance in the Corex gas is carbon dioxide.

The composition of both blast-furnace and Corex gases may be changed in specified limits. The injection of auxiliary fuels into the blast furnace influences the concentration of the main components in the blast-furnace gas. The Corex

process provides even more possibilities of changing the gas flow rate and composition, as the process is carried out in two separate reactors. A high flexibility in the Corex process is achieved by exceeding the amount of coal required for the smelting and reduction processes and increasing the amount of gas supplied directly from the gasifier to the scrubbers and for further utilization [1,8].

THE PHYSICAL ABSORPTION PROCESS

In the physical absorption process a non-reactive fluid is used as the absorbing liquid. The most frequently encountered solvent in CO_2 removal applications is Selexol, which is basically a dimethylether of polyethyleneglycol. Stripping of the solvent is realised only by pressure change and thus the process is more energy-effective than e.g. chemical absorption in many applications [6]. However, high pressure required in the absorption column leads to limited applications of the Selexol process. The necessity of compressing the gas is not a problem if the gas is supposed to be burnt in a gas turbine combustion chamber, but it is a barrier if the Selexol process should be considered in other cases, e.g. for flue gas purification.

A general flow sheet of the Selexol absorption process is shown in Fig. 2 [2]. The raw gas is compressed by means of a double-body compressor (GC1 and GC2) with an intercooler (GCL1). The compressed gas is afterwards cooled (GCL2), in order to keep the temperature in the absorber at a low level (30°C). The efficiency of the absorption process decreases with rising temperature. Therefore, cooling all the streams entering the absorber is recommended. Before entering the absorber, the raw gas is mixed with the recycling gas, coming from the first flash drum (after compressing and cooling).

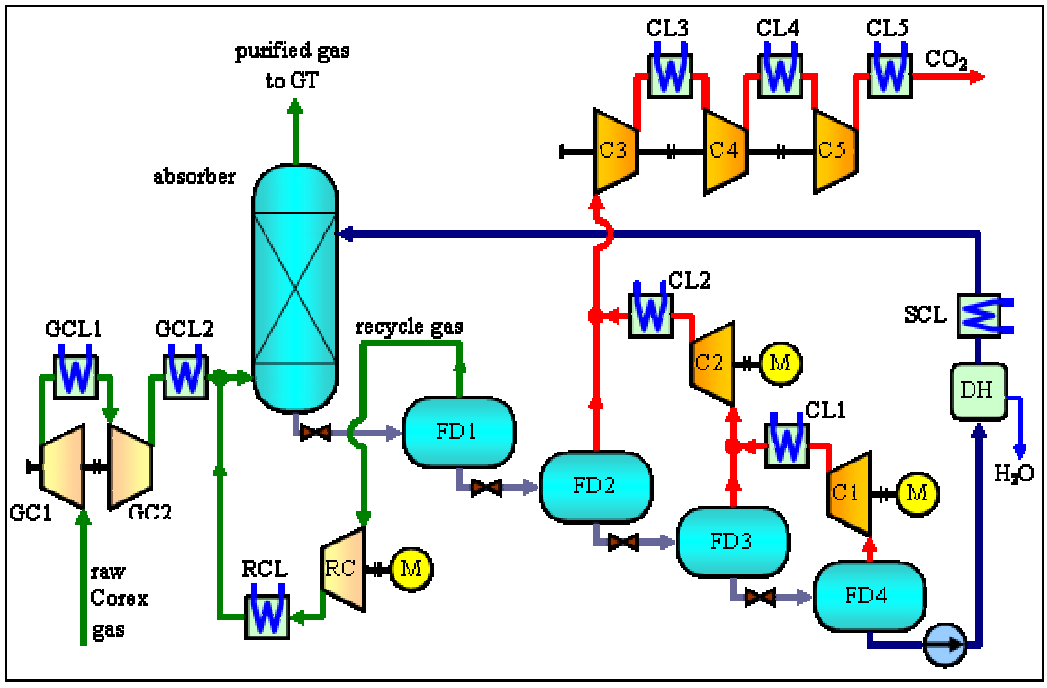

Fig. 2: Flow sheet of the analysed Selexol installation

Gas absorption is commonly realized in packed towers filled with an inert packing that provides a large interface area between the gas and the absorbing liquid. The gas rises through the tower, the solvent trickles counter-currently downward [4]. The flow rate of the Selexol solvent depends on the following parameters:

- the amount of carbon dioxide supposed to be removed from the gas (in this analysis the CO_2 removal efficiency is assumed as 90%, referred to the raw fuel gas composition),
- the CO_2 partial pressure in the gas, which depends on the overall gas pressure and composition,
- the absorption process temperature.

The purified gas leaves the absorber at the top. The carbon dioxide-rich solution leaves the absorber at the bottom and its pressure is then reduced to a value slightly lower than the solvent equilibrium pressure. Then the solvent enters the first flash drum (FD1). Apart from the absorbed CO_2, the solvent leaving the absorber contains also small amounts of CO, H_2 and water. In the first drum practically the whole amount of CO and H_2 absorbed by the solvent is released, together with some part of the CO_2. Therefore, the gas from the first flash drum is sent to the recycle gas compressor (RC), then cooled by a water cooler (RCL) and mixed with the raw gas. The solvent leaving the first flash drum is further depressurised and flows through the next flash drums (FD2…FD4), each one with a lower pressure level. Part of the carbon dioxide contained in the solvent is released at every stage of the stripping process. The CO_2 lean solvent leaving the last drum flows to the pump, where its pressure is raised to the value adequate to the pressure in the absorber. The carbon dioxide streams, previously released at different pressure levels in the flash drums (FD2, FD3, FD4), are delivered for final compression. The CO_2 delivery pressure is assumed as 8 MPa, which is higher than the critical pressure of carbon dioxide (7.39 MPa), so that CO_2 is obtained as a liquid [7].

The optimisation leads to the minimization of power consumption by the compressors, which is achieved by setting pressure levels in the flash drums and thus the pressure between the compressors.

RESULTS OF THE SIMULATION

Calculations concerning the physical absorption process have been carried out using the *EES* software [5]. The Corex unit C-2000 has been taken as reference. Such a unit is designed to produce 0.6 – 0.8 mln tons of pig iron per year (daily production 2000 tons). The average flow rate of the export gas is 50 kg/s [3]. In this analysis the average composition has been taken into consideration (Table 2) giving the LHV about 7600 kJ/m^3 (STP) (6000 kJ/kg). In the case of blast-furnace gas also the average composition has been assumed. Its LHV amounts to about 4000 kJ/m^3 (STP) (3000 kJ/kg). The following tables show the most important results obtained from the calculations.

Parameter		Unit	Raw gas		Gas entering the absorber (after mixing)		Recycle gas		Purified gas	
			COREX	BF	COREX	BF	COREX	BF	COREX	BF
Gas flow rate		kg/s	50	98,6	53,83	102,9	3,83	4,3	25,46	76,7
		kmol/s	1,75	3,35	1,85	3,47	0,10	0,12	1,18	2,84
Gas comp. (molar)	CO_2	%	35,0	16,0	37,0	17,8	70,9	71,0	5,2	1,9
	CO	%	42,0	27,0	40,8	26,8	19,9	19,8	62,2	31,9
	H_2	%	18,0	3,5	17,5	3,7	9,2	9,2	26,7	4,1
	CH_4	%	1,0	0,5	0,9	0,5	-	-	1,5	0,6
	N_2	%	2,0	51,0	1,9	49,3	-	-	3,0	60,3
	H_2O	%	2,0	2,0	1,9	1,9	-	-	1,5	1,2

Table 2: Parameters of gas in different stages of the process

To have a good comparison between both gases, it has been assumed that the flow rate of blast-furnace gas is such that it gives approximately the same flux of chemical energy delivered with the fuel as the Corex gas. The pressure level in the absorption column has been set at 1.8 MPa, allowing the direct utilization of the purified gas in the combustion chamber of a modern gas turbine.

As it is seen in Table 3, the LHV of both gases has risen because of removing 90% of carbon dioxide. However, this increase is higher in the case of Corex export gas, due to the higher CO_2 concentration in the raw gas. The higher CO_2

concentration (and thus partial pressure in the raw gas) affects also in higher pressure levels in the flash drums and a lower flow rate of the solvent (Table 4). Such a difference in the solvent flow rate obviously results in the energy demand of the solvent pump (1626 kW in the case of Corex gas and 3770 kW in the blast-furnace case). Also the size of all the equipment depends on the solvent flow rate, causing higher investment costs in the case of the blast-furnace gas.

The main power consumers in the analysed installation are the compressors, especially those for raw gas compression (Table 5). The overall power consumption concerning the raw gas compression and the whole absorption installation amounts to 26.3 MW in the case of Corex gas and 46.0 MW in the blast-furnace case. These values seem to be very high, however it must be mentioned that the major part of power is consumed to increase the fuel gas pressure, which would be realized anyway, if the gas is supposed to be the fuel for the gas-turbine-based CHP plant.

Parameter	Unit	COREX gas		BF gas	
		Raw gas	CO_2 lean gas	Raw gas	CO_2 lean gas
LHV	kJ/kg	5 960	11 700	3 020	3 880
	kJ/m^3 (STP)	7 600	11 260	3 960	4 680
	kJ/kmol	170 400	252 440	88 880	105 000
Density	kg/m^3 (STP)	1,28	0,96	1,31	1,21

Table 3: Changes of the fuel gas parameters

Parameter	Unit	COREX gas				BF gas			
		FD1	FD2	FD3	FD4	FD1	FD2	FD3	FD4
Pressure in the drum	MPa	0,60	0,42	0,23	0,10	0,29	0,24	0,16	0,10
Solvent flow rate at drum exit	kg/s	836,3	827,7	818,4	812,1	1905	1900	1891	1883
Released gas flow rate	kg/s	3,83	8,80	9,24	6,16	4,30	5,28	8,80	7,04
	kmol/s	0,10	0,20	0,21	0,14	0,12	0,12	0,20	0,16

Table 4: Parameters concerning operation of the flash drums

Parameter		Unit	GC1	GC2	RC	C1	C2	C3	C4	C5
Gas type		-	Raw gas	Raw gas	Recycle gas	CO_2	CO_2	CO_2	CO_2	CO_2
Gas flow rate	COREX	kg/s	50	50	3,83	6,16	9,24	24,2	24,2	24,2
	BF		98,6	98,6	4,30	7,04	8,80	21,2	21,2	21,2
Pressure at inlet	COREX	MPa	0,10	0,40	0,60	0,10	0,23	0,42	1,27	3,54
	BF		0,10	0,40	0,29	0,10	0,16	0,24	0,88	2,96
Pressure at outlet	COREX	MPa	0,40	1,80	1,80	0,23	0,42	1,27	3,54	8,00
	BF		0,40	1,80	1,80	0,16	0,24	0,88	2,96	8,00
Power consumption	COREX	kW	8789	9408	387	395	684	2035	1778	1200
	BF		17067	18209	793	251	452	2150	1924	1363

Table 5: Parameters of the compressors

In such a case the power consumption connected with the absorption process itself (omitting the energy demand of raw gas compressors) amounts to 8.1 MW in the case of Corex gas and 10.7 MW in the blast-furnace case. Based on these values, the following factors have been calculated:

- specific power consumption per kg of removed CO_2:

$$SP_{CO_2} = \frac{\Delta N}{\dot{m}_{CO_2}}, \text{ kJ/kg } CO_2 \qquad (1)$$

- specific amount of removed CO_2 per kg of the fuel gas:

$$SR_f = \frac{\dot{m}_{CO_2}}{\dot{m}_f}, \text{ kg } CO_2\text{/kg fuel} \qquad (2)$$

where: ΔN – power consumption in the absorption process, kW,

$\dot{m}_{CO_2}, \dot{m}_f$ - mass flow rate of the removed CO_2 and fuel gas, kg/s.

The calculated values are presented in Table 6. These values allow to estimate the consequences of applying the CO_2 removal for the treatment of metallurgical gases and to facilitate the comparison between gases with different compositions, like blast-furnace gas and Corex gas.

Parameter	Unit	COREX gas	BF gas
specific power consumption	kJ/kg CO_2	335	505
specific amount of removed CO_2	kg CO_2/kg$_{fuel}$	0,484	0,215

Table 6: Values of specific factors

The specific power consumption, as well as specific amount of removed CO_2 differ strongly, depending on the kind of gas. CO_2 removal from blast-furnace gas requires more energy due to the lower CO_2 content in the raw gas.

POSSIBILITIES OF IMPROVEMENTS

Combustion in the gas-turbine-based CHP plant is not the only way of utilization of metallurgical fuel gases. Therefore, the purified gas may have different requirements concerning its pressure. Specifically, there are many metallurgical processes, where it is enough to deliver the fuel at nearly atmospheric pressure. It concerns mostly blast-furnace gas, which is commonly used for firing hot-blast stoves, coke-ovens and metallurgical furnaces. However, also Corex gas may replace other fuels in many applications.

The removal of carbon dioxide from the blast-furnace or Corex gas provides another interesting option. As the purified gas has a relatively high content of reducing agents (carbon monoxide and hydrogen), it may be used as the reducing gas improving the blast-furnace process. Such an option brings many positive aspects from the environmental point of view, as the consumption of coke may be in this way limited.

Further analysis has been focused on the absorption process at different pressure levels. It is obvious that increasing the pressure in the absorber results in a higher power consumption by the raw gas compressors. Keeping a constant pressure of the raw gas coming from the metallurgical installation (here assumed as 0.1 MPa) it is recommended to have also a constant reference pressure level of the purified gas. This is achieved by adding an expansion turbine at the absorber outlet. The gas expands to about 0.1 MPa. As the gas leaving the absorber has a relatively low temperature (about 30°C) and contains a large amount of vapour, heating of the gas has been applied in order to limit the condensation of water inside the expansion turbine. Heating may be realized by the partial burning of the gas or in a separate heat exchanger. Here the second possibility has been taken into consideration. The purified gas transfers heat from the compressed raw gas. The following figures show the influence of absorption pressure on the main parameters of the process and overall power demand, including raw gas compressors and power recovery in the expansion turbine (with an isentropic efficiency of 80%).

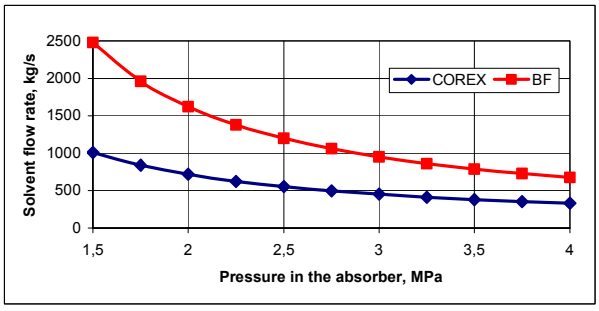

Fig. 3: Influence of pressure in the absorber on solvent flow rate

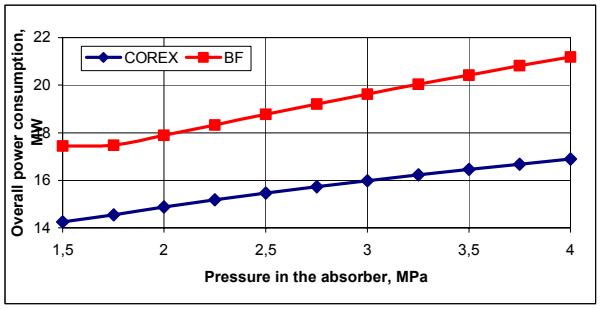

Fig. 4: Influence of pressure in the absorber on overall power consumption

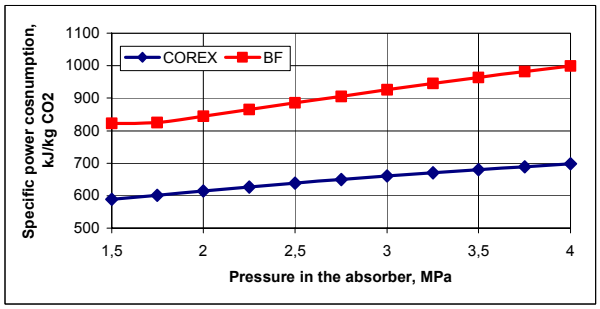

Fig. 5: Influence of pressure in the absorber on specific power consumption per kg of removed CO_2

CONCLUSIONS

The results of calculations indicate that the physical absorption process may be useful method of CO_2 removal from metallurgical fuel gases on a large industrial scale. However, such a process is always accompanied by a high power consumption. The optimisation of parameters concerning the absorption process is necessary to keep the energy demand at a minimum level.

Different CO_2 contents in Corex and blast-furnace gases result in a higher power consumption in the case of blast-furnace gas treatment. Changing the pressure level in the absorber is possible within specified limits; however this should be connected with an economical analysis which has not been applied in the paper.

A further increase of CO_2 removal effectiveness would require a shift reactor to convert some part of CO into CO_2 and simultaneously increase the H_2 content in the gas.

ACKNOWLEDGMENTS

The authors are grateful to Prof. Giampaolo Manfrida (University of Florence) for his cooperation within this project and numerous valuable suggestions.

REFERENCES

[1] Boehm C., Eberle A., Gould L., Kriechmair J., Woedlinger R.: *The Corex Revolution*. Steel Times, May 1995.

[2] Chiesa P.: *Private communication*, 2003.

[3] *Corex status report*. September 2000. VAI Voest Alpine Industrieanlagenbau.

[4] Cussler E. L.: *Diffusion. Mass Transfer in Fluid Systems*. Cambridge University Press, 1997.

[5] *Engineering Equation Solver* Academic Version 5.226. © 1992-2000 S.A. Klein and F.L. Alvarado.

[6] Gielen D.: *CO_2 Removal in the Iron and Steel Industry*. Energy Conversion and Management, vol. 44, Elsevier Science Ltd, 2003.

[7] Lampert K., Ziebik A., Manfrida G.: *Energy Analysis of CO_2 Removal in a CHP Plant Fired with COREX Export Gas*. Proceedings of ASME ESDA Conference, Manchester, July 2004.

[8] Lemperle M., Maschlanka W.: *Corex Today and Tomorrow*. Metallurgical Plant and Technology International, April 1993.

[9] Peacey J.G., Davenport W.,G.: *The Iron Blast Furnace. Theory and Practice*. Pergamon Press, 1979.

[10] Szargut J., Ziebik A.: *Fundamentals of Thermal Engineering* (in Polish). PWN Warsaw 2000.

Proceedings of ECOS 2005
Trondheim, Norway
June 20–22, 2005

A NEW MODIFICATION ON RK EOS FOR GASEOUS CARBON DIOXIDE

H. Li[1,*], X. Ji[1] and J. Yan[1,2]
1 Chemical Engineering and Technology /Energy Processes
Royal Institute of Technology
SE-100 44 Stockholm, Sweden

2 Department of Public Technology
Malardalen University
SE-721 23 Vastras, Sweden

ABSTRACT

Mitigation technologies including CO_2 capture and storage in various energy conversion systems have been intensively developed in recent years. However, it is of importance to develop an equation of state (EOS) with simple structure and reasonable accuracy for engineering application for both pure CO_2 and CO_2 mixtures. In this paper, Redlich-Kwong equation of state was modified for gaseous CO_2. In the new modification, parameter 'a' was correlated as a function of temperature and pressure from reliable experimental data in the range: 220K to 750K and 0.1MPa to 400MPa. To verify the accuracy of the new parameters, densities were calculated and compared with experimental data. The average error is 1.68 %. Other thermodynamic properties of CO_2, such as enthalpy and heat capacities, were also calculated; results fit experimental data well except critical region. This method can be further developed for CO_2 mixture systems.
Keyword: CO_2, Redlich-Kwong EOS, thermodynamic properties

NOMENCLATURE

Symbols:	Description:
a	Parameter in RK EOS
b	Parameter in RK EOS
m	Residual Properties
N	Number of Experiment Points
P	Pressure
R	Gas Constant
T	Temperature
v	Volume
Subscripts:	
c	Critical Point
cal	Calculation Value
exp	Experimental Value
Superscripts:	
ig	Ideal Gas

INTRODUCTION

Due to increased importance of climate change mitigation, R&D on capture and storage of CO_2 associated with cleaner fossil fuel plants have been intensively carried out worldwide.

However, thermodynamic properties of CO_2 and its mixtures play an important role in the development and design of the processes of CO_2 capture and storage. A reasonably accurate and easy-to-use equation of state (EOS) to calculate properties such as enthalpy and specific heat capacities of CO_2 and its mixtures which encountered in the related process is necessary. In this paper, it is first step to develop a suitable equation of state for gaseous CO_2.

There are many kinds of EOSs, which can be used to describe properties of CO_2. However, it is often that EOSs with simple structures result in poor

* Corresponding author: Email: hailong@ket.kth.se, Phone +46-8-7906527, Fax +46 8 7230858

calculation accuracy; and ones with good calculation accuracy are too complicated for engineering applications. From an engineering point of view, an EOS with simple structure and reasonable accuracy is preferable.

RK EOS [1] is a kind of cubic equation in molar volume, which has simple structure and can represent vapor and liquid behaviors relatively effectively. It was proposed in 1949 as:

$$P = \frac{RT}{v-b} - \frac{a}{v(v+b)T^{1/2}} \tag{1}$$

Where 'a' and 'b' are parameters. Parameter 'a' reflects intermolecular attraction, and parameters 'b' reflects molecular size (repulsive forces). For simple non-polar gases, they can be calculated from critical data.

$$a = \frac{0.42748R^2T_c^{2.5}}{P_c}$$
$$b = \frac{0.08664RT_c}{P_c} \tag{2}$$

RK EOS can get good results for many non-polar substances. But if both 'a' and 'b' with the consistent values calculated from Equation 2 even though in different conditions, RK EOS is not appropriate for the polar gases, such as CO_2.

Since 1980s, many new experiments (referring to Table 1) on gaseous CO_2 have been carried out, but little work on EOSs with simple structure for gaseous CO_2 was done. Therefore, new modification with the consideration of new experimental data for EOS is necessary. In this paper, based on more precisely measured PVT

Source	Year	No. of data	T (K)	P (MPa)	Uncertainty
Juza [2]	1965	82	323-748	70-400	P: ±2MPa; T: ±0.2K; V: ±0.3%
Holste et al [3]	1987	236	215-448	0.1-50.0	P: ±0.01%; T: ±0.01K; V: ±0.1%
Magee and Ely [4]	1988	10	250-330	5.8-27.1	P: ±0.01%; T: ±0.03K; V: ±0.1%
Ely [5]	1989	61	250-330	2.2-35.4	P: ±0.001%; T: ±0.001K; V: ±0.02%
Duschek [6]	1990	362	217-340	0.3-9.0	P: ±0.02%; T: ±0.003K; V: ±0.025%[a]
Gilgen et al [7]	1992	264	220-360	0.3-13.0	V: ±(0.015~0.04)%
Brachthuser [8]	1993	29	233-523	0.8-30.1	V: ±(0.02~0.04)%
Fenghour [9]	1995	119	329.82-697.81	3.032-34.203	P: ±0.02%; T: ±0.01K; V: ±0.1%
Klimeck et al [10]	2001	118	240-470	0.5-30	P: ±0.016%' T: ±0.004K[b]; V: |0.00012v+0.0015kg/m^3|

[a] T>=295K, uncertainty is 0.25%. [b] T=523K, uncertainty is 0.01K.

Table 1 Summary of the experimental data used for correlation

properties, RK EOS will be modified for better precision for gaseous CO_2.

MODIFICATION ON RK EOS

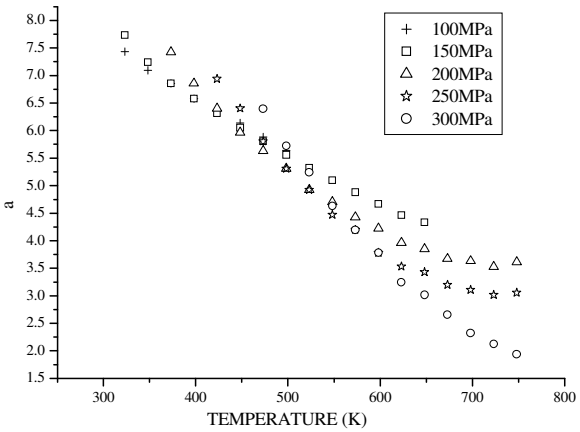

Fig. 1 Values of 'a' at different temperatures and certain pressures

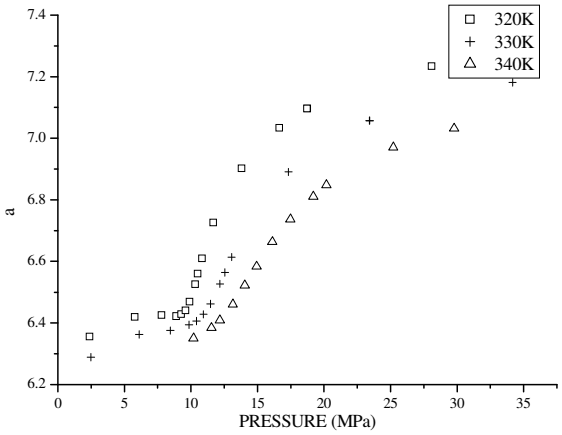

Fig. 2 Values of 'a' at different pressures and certain temperatures

It has been verified that if the parameters 'a' and 'b' in RK EOS were not constants, but functions, RK EOS can be used to describe properties of polar gases [11, 12]. Based on this conclusion, we studied the relationship between temperature and pressure and parameters 'a' and 'b'.

Compared with intermolecular attraction, repulsive forces impact gas's volume less. So here; 'b' is kept unchanged; and only 'a' will be correlated as a function. If parameter 'b' is still calculated from Equation 2, with PVT data, parameter 'a' can be calculated from Equation 1 for each point by the Newton method. Fig. 1 shows values of 'a' at different temperatures and certain pressures. Obviously, parameter 'a' depends on both temperature and pressure.

In former studies [11, 12, 13], for simplicity, 'a' was usually assumed to be dependent only on temperature; however from Fig. 2, which shows values of 'a' at different pressures and certain temperatures, it is easy to find that pressure has great effects on 'a' as well as temperature. So to get more accurate results, effects of pressure can't be ignored. With further inspection on Fig. 2, it can be found that at different temperatures, the curves 'a' versus pressure have similar trends. Thus, this may indicate that 'a' can be regressed as a function of temperature and pressure, a=(T, P).
Finally we derived Equation 3 to describe the temperature and pressure effects on 'a' for gaseous CO_2.

$$a = a_1 + a_2 P$$

$$a_1 = \frac{2.3457\times10^{5}}{T^{2}} - \frac{1.3612\times10^{3}}{T} - 4.8365\times10^{-3}T + 9.9191 \quad (3)$$

$$a_2 = \frac{1.9141\times10^{-2}}{T^{2}} - \frac{1.0132\times10^{-4}}{T} - 1.3654\times10^{-10}T + 0.1934\times10^{-6}$$

Chorng [14] pointed out that according to the temperature behavior of attractive force, 'a' should be finite and positive at any temperature. So Equation 3 can't be extrapolated to extremely high temperature cases.

RESULTS:

To verify the reliability of new correlation, density, enthalpy, and heat capacities were calculated and compared with measured values.

Calculation on density of gaseous CO_2

Fig. 3 shows the comparisons of the calculated densities of gaseous CO_2 at some temperatures and pressures with experimental data. Obviously, the calculated results in this paper agree well with experimental data throughout those comparison temperature and pressure ranges. In Fig. 4, calculated densities of gaseous CO_2 were compared with measured values in the whole experimental range. The maximum deviation is

97.52%, which occurs at the critical point; and the average deviation is 1.68%. Moreover at high pressures (400MPa) deviations are also large, up to 5-10%.

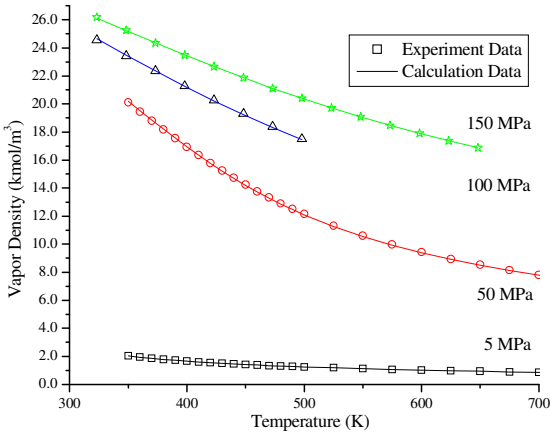

Fig. 3 Calculated densities of gaseous CO_2 at some temperatures and pressures

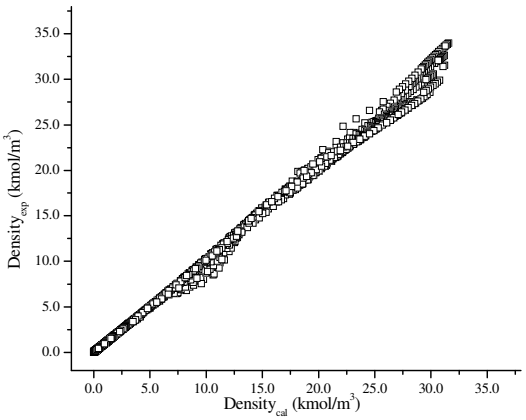

Fig. 4 Calculated densities of gaseous CO_2 versus experimental data in whole experiment range

Because the intermolecular potential energy function for CO_2, from which 'a' and 'b' should be derived, is not well understood; based on RK EOS, there are still some other empirical modifications. Santis et al [11] proposed that parameter 'a' should be a function of temperature. Later, Holloway [13], according to Santis's conclusion, regressed 'a' to a polynomial on temperature. However Bottinga et al [12] developed another set of expressions to describe the parameters 'a' and 'b', which are functions of volume. Moreover Kerrick et al [15] also regressed the parameters 'a' and 'b' as functions of volume, but they are more complex. In addition, Nakamura et al [16] proposed an EOS with simple structure in a new way to describe the properties of gaseous CO_2.

In this paper, all of these models were used to calculate molar densities and results were compared with the experimental data throughout the whole experimental data range except critical area. The comparison is listed in Table 2. The model with the parameter regressed in this paper is the best; both the standard and average errors are much lower than others. The models of Kerrick and Bottinga's are better than model proposed by de Santis and Holloway; which may be due to that functions of volume can be regarded as functions of temperature and pressure as well.

Model	STANDARD.Err*	AVERAGE.Err** %
New Model	1.031	1.6843
RK	1.433	6.1972
Holloway	1.518	5.2485
Bottinga	1.408	3.4154
Kerrick	1.291	2.9834
Nakamura	1.427	3.6527

Table 2 Comparison results of density among different models

$$^{*}STANDARD.Err = \left(\frac{\sum \left(v_{\exp} - v_{cal} \right)^2}{N} \right)^{1/2} \; kmol/m^3$$

$$^{**}AVERAGE.Err = \frac{\sum abs\left(\frac{v_{\exp} - v_{cal}}{v_{\exp}} \right)}{N}$$

Enthalpy and heat capacities

In this paper, residual method is used to calculate enthalpy, heat capacities and other properties.

As we know, residual properties can be calculated from the following equation:

$$\Delta m(T,P) = \int_0^P \left[\left(\frac{\partial m^{ig}}{\partial P} \right)_T - \left(\frac{\partial m}{\partial P} \right)_T \right] dP \qquad (4)$$

Thus enthalpy, and heat capacities can be calculated by:

$$m(T,P) = m^{ig} - \Delta m(T,P) \quad (5)$$

To solve the integration terms in Equation 4, numerical method can be employed. The rule of integration is like this: first we set an integration interval, thus the whole integration area can be divided into many segments. We regard these segments as trapeziums and calculate their areas until their values are less than 10^{-6}. Consequently, the sum of those segments' areas is the integration value.

Enthalpy

Möller [17] measured the enthalpy differences at two different temperatures. We also used RK EOS with the new correlated parameter to calculate enthalpy differences under the same conditions. Comparisons between them were shown in Fig. 5. From it, it is clear that the calculated results agree with experimental data.

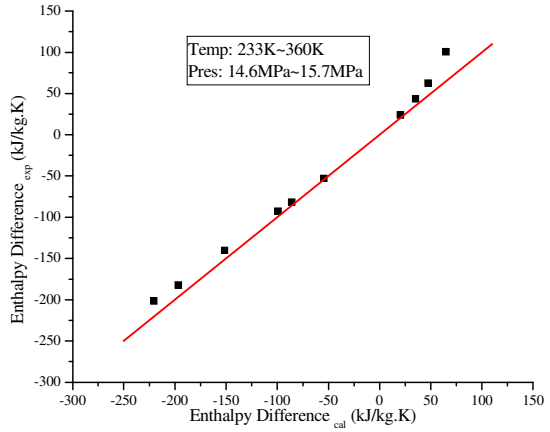

Fig. 5 Comparisons on enthalpy differences with experimental data

Heat capacities

Ernst et al [18, 19] have done a lot of work on isobaric heat capacity (C_p) measurement. Here we compared our calculated results with their experimental data on CO_2. In Fig. 6, scatters are experimental data and lines are calculation results. It is obvious that in the area close to critical point, calculation accuracy is poor; while in other areas, it is acceptable; disagreements are usually smaller than 5%.

Since only few experimental data on isochoric heat capacities are available, to test our model, we compared our results with Span's [20] in temperature range: 220K~1100K and pressure range: 0.1MPa~200MPa, which uncertainty is among ±2%. Results were shown in Fig. 7. It can be seen that at high pressure and low temperature (especially close to critical temperature), difference is big. Actually uncertainty of Span's data becomes bigger when pressure rises and temperature descends. Generally, our average deviation is less than 5%.

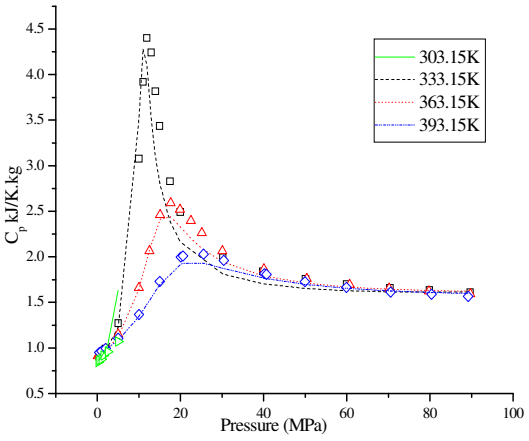

Fig. 6 Isobaric heat capacities at different temperatures and pressures

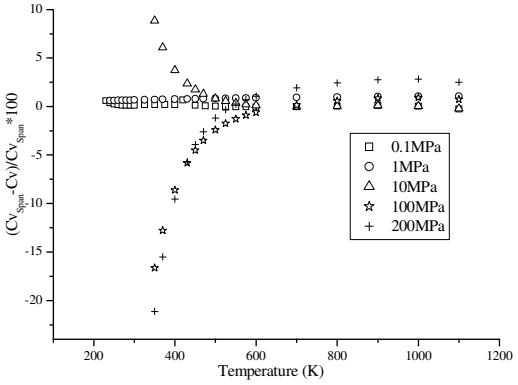

Fig. 7 Comparison on isochoric heat capacities with Span's calculation results

CONCLUSIONS

Based on some new updated experiments on CO_2, RK equation of state was modified. Compared with other EOSs, which have simple structures as well, the new model has better calculation accuracy on densities of gaseous CO_2 in temperature range: 220K~700K and pressure range: 0.1MPa~400MPa, except critical region 295~315 K and 6.5~9.5MPa. For other thermodynamic properties, such as enthalpy and

specific heat capacities, this model also predicts them well if the critical region is excluded.

ACKNOWLEDGEMENT

Financial supports from Swedish Energy Agency (STEM) and EU are gratefully acknowledged.

REFERENCE

[1] Redlich O., Kwong J. N. S., *On the thermodynamics of solutions,* Chem. Rev. 1949;44: 233-244.

[2] Juza J., Kmonicek V., Sifner O., *Measurements of the specific volume of carbon dioxide in the range of 700 to 4000 b and 50 to 475 °C*, Physica 1965;31: 1735-1344.

[3] Holste J. C., Hall K, R., Eubank P. T., Esper G., Watson, W. Warowny M. Q., Bailey D. M., Young J. G., Bellomy M. T., *Experimental (p, Vm, T) for pure CO_2 between 220 and 450K*, J. Chem. Thermodynamics 1987;87: 1233-1250.

[4] Magee W., Ely J. F., *Isochoric (p, v, T) measurements on CO_2 and (0.98 CO_2 + 0.02 CH_4) from 225 to 400 K and pressure to 35 MPa*, Int. J. Thermophysics 1988;9(4): 547-557.

[5] Ely J. F., Haynes, Magee W., Bain B. C., *Isochoric (p, Vm, T) measurements on CO_2 and on (0.982 CO_2 + 0.018 CH_4) from 250 to 330 K and pressure to 35 MPa*, J. Chem. Thermodynamics 1989;21: 879-894.

[6] Duschek W., Kleinrahm R., Wanger W., *Measurement and correlation of the (pressure, density, temperature) relation of carbon dioxide I. The homogeneous gas and liquid regions in the temperature range from 217 K to 340 K at pressures up to 9 MPa*, J. Chem. Thermodynamics 1990;22: 827-840.

[7] Gilgen R., Kleinrahm R., Wagner W., *Supplementary measurements of the (pressure, density temperature) relation of carbon dioxide in the homogeneous region at temperatures from 220K to 360K and pressures up to 13MPa*, J. Chem. Thermodynamics 1992;24: 1243-1250.

[8] Brachthäuser K., Kleinrahm R., Lösch H. W., Wagner W., *Entwicklung eines neuen Dichtemeßverfahrens und Aufbau einer Hochtemperatur-Hochdruck-Dichtemeßanlage, VDI-Verlag*, Düsseldorf 1993

[9] Fenghour A.; Wakeham W. A., Waston J. T. R., *Amount-of-substance density of CO_2 at temperatures from 329 K to 698 K and pressures up to 34MPa*, J. Chem. Thermodynamics 1995;27: 219-223

[10] Klimeck J., Kleinrahm R., Wagner W., *Measurements of the (p, ρ, T) relation of methane and carbon dioxide in the temperature range 240K to 520K at pressures up to 30MPa using a new accurate single-sinker densimeter*, J. Chem. Thermodynamics 2001;33: 251-267.

[11] de Santi R., Breedveld G. J. F., Prausnitz J. M., *Thermodynamic properties of aqueous gas mixture at advanced pressure*, Ind. Eng. Chem. Process Des. Develop. 1974;13(4): 374-377..

[12] Bottinga Y., Richet P., *High Pressure and Temperature Equation of State and Calculation of the Thermodynamic Properties of Gaseous Carbon Dioxide*, American Journal of Science 1981;281(5): 615-660.

[13] Holloway J. R., *Fugacity and activity coefficients of molecular species in fluids at high pressures and temperatures*, Carnegie Inst. Washington Year Book 75, 1976, 771-775.

[14] Chorng H. T, David B, John R. C, John E. C., *A cubic equation of state with a new alpha function and a new mixing rule*. Fluid Phase Equilibria 1991;69: 33-50.

[15] Kerrick D. M., Jacobs G. K., *A modified Redlich-Kwong equation for H_2O, CO_2 and H_2O-CO_2 mixtures at elevated pressures and temperatures*, American Hournal of Science 1981;281: 735-767

[16] Nakamura R., Breedveld G. J. F., Prausnitz J. M., *Thermodynamic properties of gas mixtures containing common polar and non-polar components,* Indus. Eng. Chemistry Process Devel. 1976;15: 557-565.

[17] Möller D., Gammon B. E., Marsh K. N., Hall K. R., Holste J. C., *Enthalpy-increment measurements from flow calorimetry of CO_2*

and of {xCO_2+(1-x)C_2H_6} from pressures of 15 MPa to 18 MPa between the temperatures 230 K and 350 K, J. Chem. Thermodynamics 1993;25: 1273-1279.

[18] Ernst G., Hochberg E. U., *Flow-calorimetric results for the specific heat capacity c_p of CO_2, of C_2H_6, and of (0.5CO_2 + 0.5C_2H_6) at high pressures*, J. Chem. Thermodynamics 1989;21: 407-414.

[19] Ernst G., Hochberg E. U., *Flow-calorimeter for the accurate determination of the isobaric heat capacity at high pressures; results for carbon dioxide*, J. Chem. Thermodynamics 1989;21: 53-65.

[20] Span R., Wagner W., *A New Equation of State for Carbon Dioxide Covering the Fluid Region from the Triple-Point Temperature to 1100 K at Pressures up to 800 MPa*, J. Phys. Chem. Ref. Data 1996;25(6): 1509-1596.

Proceedings of ECOS 2005
Trondheim, Norway
June 20–22, 2005

MODELING OF EQUILIBRIUM SOLUBILITY OF CARBON DIOXIDE IN AQUEOUS 30 MASS % 2–(2–AMINOETHYL–AMINO)ETHANOL SOLUTION

Sholeh Ma'mun[†], Jana P. Jakobsen, and Hallvard F. Svendsen[*]
Norwegian University of Science and Technology
Department of Chemical Engineering,
N–7491 Trondheim
Norway

Olav Juliussen
SINTEF Materials and Chemistry
N–7465 Trondheim
Norway

ABSTRACT

This work focuses on the experimental determination and thermodynamic modeling of the solubility of carbon dioxide (CO_2) in aqueous solution of 30 mass % AEEA, AEEA being a potentially new solvent for post–combustion CO_2 capture. The vapor–liquid equilibrium (VLE) experiments were performed over a range of temperatures from (40 to 120) °C and for partial pressures ranging from (0.01 to 220) kPa. The results obtained were then modeled by use of the Deshmukh–Mather thermodynamic model. The model provides a good representation of the experimental data over the whole temperature range. In addition to modeling the experimental VLE data, ^{1}H and ^{13}C 1D NMR spectra were acquired for species identification. Quantitative analysis of the speciation from NMR data was found to be in reasonable agreement with model predictions.

Keywords: AEEA, carbon dioxide, carbamate, absorption, equilibrium, NMR

NOMENCLATURE

a	activity, ionic size in eq. (18) [Å]
A_γ	Debye–Hückel limiting slope in eq. (18)
B	function of temperature and dielectric constant of solvent in eq. (18)
C	constant in eq. (20)
F	objective function
H	Henry's law constant [Pa]
I	ionic strength [mol.kg^{-1}]
K	equilibrium constant
m	molality [mol.kg^{-1}]
p	partial pressure [Pa]
P	total pressure [Pa]
P_s^o	saturation pressure of water [Pa]
R	universal gas constant [8.314 J.mol^{-1}.K^{-1}]
T	absolute temperature [K]
v	molar volume [m^3.mol^{-1}]
$\bar{v}_i^{\infty}$	partial molar volume at infinite dilution [m^3.mol^{-1}]
x	liquid–phase mole fraction
y	vapor–phase mole fraction
z_i	absolute charge of ith ionic species

Greek Symbols

β_{ij}	parameter for the interaction of species i with species j [kg.mol^{-1}]

[*] Corresponding author: Phone: +47-735 94100 Fax: +47-735 94080 Email: hallvard.svendsen@chemeng.ntnu.no
[†] Permanent address: Department of Chemical Engineering, Gadjah Mada University, Jl. Grafika 2 Kampus UGM Jogjakarta, Indonesia 55281

γ activity coefficient
ϕ fugacity coefficient

Subscripts

$AEEAH^+$	protonated AEEA
$^+HAEEAH^+$	diprotonated AEEA
$AEEACOO^-$	carbamate of AEEA
$^+HAEEACOO^-$	protonated carbamate of AEEA
$^-OOCAEEACOO^-$	dicarbamate of AEEA
p	primary
s	secondary, solvent
w	water

Superscripts

o	total in all forms
cal.	value calculated by model
exp.	experimentally measured value

INTRODUCTION

Removal of acidic gases, in particular CO_2, is an important industrial operation. Carbon dioxide is produced in large quantities by fossil–fuel–fired power plants, in steel production, in the production of petrochemicals, in cement production, and in natural gas purification. The global climate change, where CO_2 is found to be a major contributor, is one of the most important and challenging environmental issues facing the world community. This has motivated intensive research on CO_2 capture and storage.

Carbon Dioxide capture by absorption is the most common industrial technology today and recent economic studies show that the process will remain competitive also in the future. One of the key improvements that is under development is new, faster and more energy efficient absorbents. A chemical to be used as a commercial absorbent must have high net cyclic capacity, high reaction rate for CO_2, and good chemical stability. Alkanolamines, e.g. monoethanolamine ($H_2NCH_2CH_2OH$, MEA), are the most commonly used chemical absorbents for the removal of acidic gases today.

From previous work on screening tests for a large number of solvents [1], focusing on the absorption rate and capacity of the amines, it has been found that 2–(2–aminoethyl–amino)ethanol ($H_2N(CH_2)_2NH(CH_2)_2OH$, AEEA) as a diamine may be a potentially very good absorbent for capturing CO_2 from post–combustion exhaust gases. It offers high absorption rate combined with high net cyclic capacity. The net cyclic capacity of AEEA is significantly higher than that of MEA and it maintains its absorption power at higher loadings.

The objective of this work is experimental characterization and thermodynamic modeling of the absorbent, AEEA. It focuses on the experimental determination and thermodynamic modeling of the vapor–liquid equilibria (VLE) of CO_2 in aqueous solution of 30 mass % AEEA. Equilibrium experiments have been performed at temperatures ranging from (40 to 120) °C. The results obtained were modeled by use of the Deshmukh–Mather model [2]. In addition to the VLE experiments, NMR analyses have also been performed to determine the species existing in the liquid phase as function of CO_2 loading.

EXPERIMENTAL APPARATUSES AND PROCEDURES

The experimental apparatuses and procedures have been described by Ma'mun et al. [1, 3]. All the equilibrium measurements for AEEA were carried out in the VLE apparatuses designed for atmospheric and medium pressures, as shown in Figures 1 and 2.

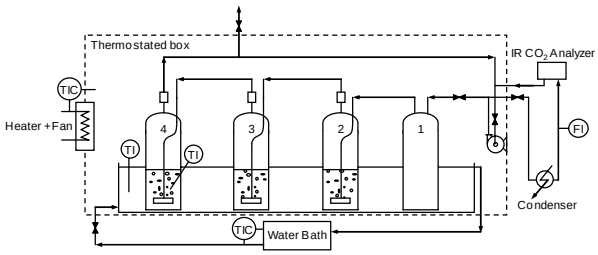

Figure 1: Vapor–liquid equilibrium apparatus for atmospheric pressure.

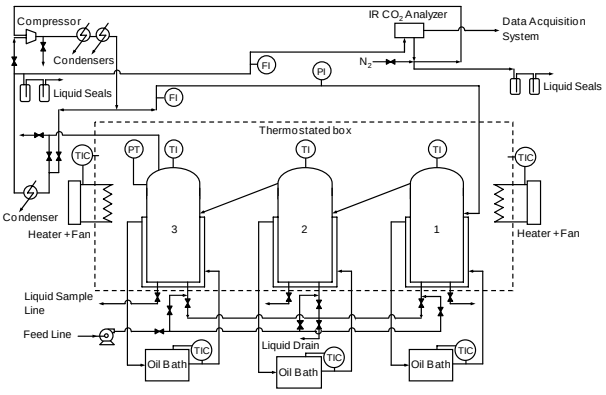

Figure 2: Vapor–liquid equilibrium apparatus for medium pressure.

The VLE apparatus for atmospheric pressure is designed to operate at temperatures up to 80 °C and consists of four 360–cm^3 glass flasks. A preloaded AEEA solution of 150 cm^3 was fed into flask 2. The same amount was also fed into flasks 3 and 4 while flask 1 was used as a gas stabilizer. The flasks were heated by water and placed in a thermostated box with temperature measured to within ±0.1 °C. The gas phase was circulated as the temperature reached the desired level and equilibrium was obtained when the analyzer showed a constant value. After the equilibrium reached in (30 to 60) min, a liquid sample was then withdrawn from the flask 4 to be analyzed.

In addition, the VLE apparatus for medium pressure consists of three 300 cm^3 stainless steel cylinders (the equilibrium cells 1, 2, and 3) designed to operate at pressures up to 700 kPa and temperatures up to 130 °C with recirculation of the gas phase. Before starting the experiment, N_2 was flushed through the apparatus to purge out the air within the cells. A 30 mass % AEEA solution of 200 cm^3, preloaded with CO_2, was then fed into the cell 1 while cells 2 and 3 held 150 cm^3 each of the same solution. The cells, placed in a thermostated box, were heated by individual oil baths and the temperatures were measured to within ±0.1 °C. Typically, temperature variations during an experiment would be within ±0.5 °C. To prevent boiling and vaporization of the solvent during the heating up, the minimum initial pressure in the cells was set to 300 kPa. As the temperature reached the desired value the compressor increased the pressure up to 700 kPa and circulated the vapor. A back-pressure valve was used to maintain the pressure at 700 kPa. Equilibrium was obtained when the temperature was established at a constant value and the CO_2 concentration in the vapor phase was constant. This took about (2 to 3) h including the heating–up period. After equilibrium was obtained, a liquid sample was withdrawn from cell 3 into a 75 cm^3 evacuated sampling cylinder such that the cylinder was completely filled by the liquid sample and then cooled to ambient temperature. The temperatures and pressures were automatically collected by the FieldPoint™ data acquisition system.

Liquid samples containing all bound CO_2 for both experiments were analyzed by the barium chloride ($BaCO_3$) method. The amount of hydrogen chloride (HCl) not used to dissolve $BaCO_3$ was titrated with 0.1 $mol.L^{-1}$ sodium hydroxide (NaOH) carried out with an automatic titrator (Metrohm 702 SM Titrino) with end point pH 5.2. Due to solvent losses during the process at high operating temperature, the AEEA concentrations were then determined by titration. A liquid sample of 0.5 cm^3 was diluted into deionized water of 75 cm^3 and titrated with 0.1 $mol.L^{-1}$ sulfuric acid (H_2SO_4) using Metrohm 702 SM Titrino. The end point was obtained at pH 4 to 5.

pKa measurements

Protonation constants (pKa) of AEEA were measured over a range of temperatures from (20 to 60) °C. An aqueous solution of 30 mass % AEEA, heated in a water bath, was neutralized by use of 5 M HCl solution. Due to the increase of temperature during titration, the HCl solution was discretely added in to the AEEA solution and the pH was measured by use of pH meter at a constant temperature.

PHASE AND CHEMICAL EQUILIBRIA

The AEEA–CO_2–H_2O system is very complex as AEEA is a diamine containing one secondary and one primary amine group. This gives rise to a large number of possible species and the following 14 species are considered to exist: AEEA, $AEEAH^+$, $^+HAEEAH^+$, $AEEACOO^-_p$, $AEEACOO^-_s$, $^+HAEEACOO^-_p$, $^+HAEEACOO^-_s$, $^-OOCAEEACOO^-$, CO_2, HCO_3^-, $CO_3^=$, H_2O, H_3O^+, and OH^- with the chemical equilibria written as follows:

Dissociation of water

$$2H_2O \rightleftharpoons H_3O^+ + OH^- \quad (1)$$

Dissociation of carbon dioxide

$$CO_2 + 2H_2O \rightleftharpoons HCO_3^- + H_3O^+ \quad (2)$$

Dissociation of bicarbonate ion:

$$HCO_3^- + H_2O \rightleftharpoons CO_3^= + H_3O^+ \quad (3)$$

Dissociation of protonated AEEA:

$$AEEAH^+ + H_2O \rightleftharpoons AEEA + H_3O^+ \quad (4)$$

Dissociation of diprotonated AEEA:

$$^+HAEEAH^+ + H_2O \rightleftharpoons AEEAH^+ + H_3O^+ \quad (5)$$

Formation of carbamates:

$$AEEA + CO_2 + H_2O \rightleftharpoons AEEACOO^-_p + H_3O^+ \quad (6)$$

$$AEEA + CO_2 + H_2O \rightleftharpoons AEEACOO^-_s + H_3O^+ \quad (7)$$

Dissociation of protonated carbamates:

$$^{+}\text{HAEEACOO}^{-}_{p} + \text{H}_2\text{O} \rightleftharpoons \text{AEEACOO}^{-}_{p} + \text{H}_3\text{O}^{+} \quad (8)$$

$$^{+}\text{HAEEACOO}^{-}_{s} + \text{H}_2\text{O} \rightleftharpoons \text{AEEACOO}^{-}_{s} + \text{H}_3\text{O}^{+} \quad (9)$$

Formation of dicarbamate:

$$\begin{aligned}&\text{AEEACOO}^{-}_{p} + \text{AEEACOO}^{-}_{s} + 2\text{CO}_2 \\ &+ 2\text{H}_2\text{O} \rightleftharpoons {}^{2-}\text{OOCAEEACOO}^{-} + 2\text{H}_3\text{O}^{+}\end{aligned} \quad (10)$$

The corresponding equilibrium constants are mathematically defined in term of activity coefficients γ_i and mole fractions x_i:

$$K = \prod_i a_i^{v_{ij}} = \prod_i \left(x_i \gamma_i\right)^{v_{ij}} \quad j = 1, 2, ..., R \quad (11)$$

where v_{ij} is the stoichiometric coefficient for component i in reaction j and R is the number of chemical reactions.

The balance equations for the reacting species include total mass balance expressed in term of mole fraction x,

$$\sum_i x_i = 1.0 \quad (12)$$

mass balance for AEEA,

$$\begin{aligned}x^{o}_{\text{AEEA}} = {} & x_{\text{AEEA}} + x_{\text{AEEAH}^+} + x_{{}^{+}\text{HAEEAH}^+} + x_{\text{AEEACOO}^-_p} \\ & + x_{\text{AEEACOO}^-_s} + x_{{}^{+}\text{HAEEACOO}^-_p} + x_{{}^{+}\text{HAEEACOO}^-_s} \\ & + x_{{}^{-}\text{OOCAEEACOO}^-}\end{aligned} \quad (13)$$

mass balance for carbon dioxide,

$$\begin{aligned}x^{o}_{\text{CO}_2} = {} & x_{\text{CO}_2} + x_{\text{HCO}^-_3} + x_{\text{CO}^{=}_3} + x_{\text{AEEACOO}^-_p} \\ & + x_{\text{AEEACOO}^-_s} + x_{{}^{+}\text{HAEEACOO}^-_p} + x_{{}^{+}\text{HAEEACOO}^-_s} \\ & + 2x_{{}^{-}\text{OOCAEEACOO}^-}\end{aligned} \quad (14)$$

and electroneutrality.

$$\begin{aligned}x_{\text{H}_3\text{O}^+} + x_{\text{AEEAH}^+} + 2x_{{}^{+}\text{HAEEAH}^+} = {} & x_{\text{OH}^-} + x_{\text{HCO}^-_3} \\ & + 2x_{\text{CO}^{=}_3} + x_{\text{AEEACOO}^-_p} + x_{\text{AEEACOO}^-_s} \\ & + 2x_{{}^{-}\text{OOCAEEACOO}^-}\end{aligned} \quad (15)$$

Equations 11–15 represent a system of 10 chemical equilibria for the reactions 1–10 together with 3 mass balances and the electroneutrality. These equations are solved simultaneously to determine the equilibrium composition of the liquid phase.

At equilibrium, the fugacities of each volatile component are equal in the vapor and liquid phase and the equilibrium is defined by

$$\phi_i y_i P = \gamma_i x_i H_i^{\infty} \exp\left\{\bar{v}_i^{\infty}\left(P - P_s^{o}\right)/RT\right\} \quad (16)$$

where H_i^{∞} and $\bar{v}_i^{\infty}$ are the Henry's law constant and partial molar volume for molecular solute i at infinite dilution in the solvent, respectively. The Henry's law constant for CO_2 at infinite dilution in water was taken from Chen et al. [4] and the partial molar volume of CO_2 was substituted by molar volume and taken form Brelvi and O'Connel [5].

For the volatile solvent (water), the vapor–liquid equilibrium is given by

$$\phi_s y_s P = \gamma_s x_s P_s^{o} \phi_s^{o} \exp\left\{v_s\left(P - P_s^{o}\right)/RT\right\} \quad (17)$$

The fugacity coefficients ϕ_i for all volatile components were calculated by the Peng–Robinson equation of state [6].

ACTIVITY COEFFICIENT MODEL

The data obtained in this work were correlated using an adaptation of the Deshmukh–Mather [2] model. This model has been chosen because it is more rigorous than the simple approaches e.g. Kent and Eisenberg [7] and is capable of producing reasonable species concentrations. Yet algebraically it is simple enough to be computationally efficient for column and plant calculations. More complex models like the electrolyte–NRTL and the MSA models are more expensive computationally [8] without seeming to offer any better fit to VLE data or species concentrations. In the Deshmukh–Mather model, the activity coefficients of the species in the liquid phase are calculated using the extended Debye–Hückel equation. The equation is described as:

$$\ln \gamma_i = \frac{-2.303 A_\gamma z_i^2 I^{1/2}}{1 + BaI^{1/2}} + 2\sum_j \beta_{ij} m_j \quad (18)$$

The first term of this equation represents the electrostatic forces and the second term represents the short–range van der Waals forces. A_γ (the Debye–Hückel limiting slope) and B are functions of temperature and the dielectric constant of the solvent. I is the ionic strength and is defined as function of the charge number on the ion z_j and molality.

$$I = \frac{1}{2}\sum_j m_j z_j^2 \quad (19)$$

The values for the quantity *a* represent the effective diameter of the ions and were taken from Weiland et al. [8] and treated as constants independent of the ionic strength. AEEA is considered a solute and the reference state is infinite dilution in water. The activity coefficients obtained by equation (18) are molality based and have to be transformed to the molar fraction concentration scale on which the equilibrium constants were defined.

Simplifications were made for the Deshmukh–Mather model in which the value of the Debye–Hückel limiting slope at 25 °C in water was used (A_γ = 0.509) and B was set equal to 1. In addition, the second term of the extended Debye–Hückel equation representing the short–range van der Waals forces was disregarded at this stage of the work. This implies that the activity coefficient model as used in this work does not contain any parameters for regression.

THERMODYNAMIC PARAMETERS

The thermodynamic parameters needed for the model are such as equilibrium constants for all chemical reactions, parameters in the activity coefficient model, and Henry's law constant for CO_2 in pure water.

The temperature dependency of the equilibrium constants and the Henry's law constant can be expressed in the form

$$\ln K = C_1 + C_2/T + C_3 \ln T + C_4 T \qquad (20)$$

Coefficients C_1–C_4 for reactions 6–10 were determined by regression of the VLE data with the model and are summarized in Table 1. The protonation constants for reaction 4 and 5 were determined from separate titration experiments. For reaction 1, the equilibrium constant of water is given by Olofsson [9], and for reactions 2 and 3, the equilibrium constants were taken from Edward et al. [10].

PARAMETER REGRESSION

The parameters regressed in this model are those contained in the equilibrium constants for reactions 6–10. The regression was performed by using Modfit, an in–house MATLAB computer program for parameter estimation. The regression method used was the Levenberg–Marquardt minimization with the normalized objective function as given by

$$F = \sum_{i=1}^{n} \left(\frac{100\left(p_{CO_2}^{exp.} - p_{CO_2}^{cal.} \right)}{p_{CO_2}^{exp.}} \right)^2 \qquad (21)$$

The criterion used was the relative error between the calculated and experimental values of the CO_2 partial pressures.

RESULTS AND DISCUSSION

The vapor–liquid equilibrium experiments were performed at temperatures ranging from (40 to 120) °C. The results are given in Figure 3 together with the predictions obtained by the model. As shown in the figure the representation of the data by the model agrees well with the experimental data. However, this should only be taken as a preliminary result. The only parameters fitted were the parameters involved in the temperature dependency of the chemical equilibrium constants. It is very unlikely that a model based only on equilibrium constants should be able to describe the complex AEEA–CO_2–H_2O system perfectly, especially with regard to the species distribution, as will be discussed later.

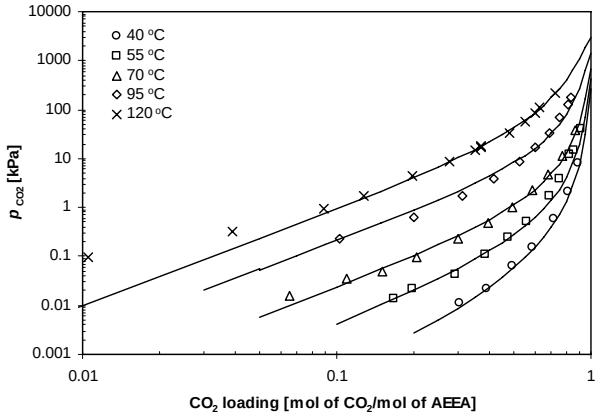

Figure 3: Equilibrium solubility of CO_2 in aqueous solution of 30 mass % AEEA. All data points were measured in this work. Curves were calculated by the VLE model.

A more advanced activity coefficient model will certainly be needed. Including the short range term of the Deshmukh–Mather model might make the model more flexible and regression of the interaction parameters might improve the fit. However we do not have enough experimental information on the system to be able to reliably determine both the equilibrium constant parameters and the parameters of the activity coefficient model. So in

reaction no.	parameter	C_1	C_2	C_3	C_4	temp. range, °C	source
2	K_{CO_2}	231.465	-12092.1	-36.7816	0.0	0-225	Edward et al. [10]
3	$K_{HCO_3^-}$	216.049	-12431.7	-35.4819	0.0	0-225	Edward et al. [10]
4	K_{AEEAH^+}	205.939	-23039.1	-20.8581	0.10920	20-60	This work
5	$K_{^+HAEEAH^+}$	165.806	-18888.3	-16.1336	0.08989	20-60	This work
6	$K_{AEEACOO^-_p}$	-33.169	8492.2	0.0	0.0	40-120	This work
7	$K_{AEEACOO^-_s}$	-10.049	-1393.9	0.0	0.0	40-120	This work
8	$K_{^+HAEEACOO^-_p}$	-20.654	-177.19	0.0	0.0	40-120	This work
9	$K_{^+HAEEACOO^-_s}$	16.64	-13040.0	0.0	0.0	40-120	This work
10	$K_{^-OOCAEEACOO^-}$	-97.992	25628.0	0.0	0.0	40-120	This work
	H_{CO_2}	170.7126	- 8477.711	- 21.95743	0.005781	0-100	Chen et al. [4]

Table 1: Temperature dependence of the equilibrium constants for reactions 2–10 and Henry's law constant for CO_2.

this work, the liquid phase non–idealities were lumped into the obtained equilibrium constant parameters. On the other hand, the done here regression was based on data that are typically used for such a procedure. Very often VLE data of the kind presented in this work are the only data available. The findings here thus also highlight the need for a variety of data for developing equilibrium models for complex absorption systems, and not only VLE data. As a first estimate, however, the regressed equilibrium constant parameters given in Table 1 should be satisfactory.

pKa determinations

Protonation constants of AEEA were measured over a range of temperatures from (20 to 60) °C. The results are given in Figure 4 and Table 2. AEEA is a diamine with one primary and one seconddary amine group and will therefore have two equilibrium points (EPs). In the first EP, the protons will associate with both the primary and secondary amine groups with a certain ratio which cannot be determined from the experiment, but probably 80–90% with the primary group. The first protonation constant (K_{AEEAH+}) is therefore the constant for the total of the first protonated AEEA ($AEEAH^+$) from both primary and secondary amine groups. In addition, dissociation of the second protonated AEEA ($^+HAEEAH^+$) will then form primary and secondary protonated AEEA ($AEEAH^+_p$ and $AEEAH^+_s$). The second protonation constant ($K_{+HAEEAH+}$) is therefore the constant for the total of the second protonated AEEA ($^+HAEEAH^+$). The temperature dependency of the protonation constants are given in Table 1.

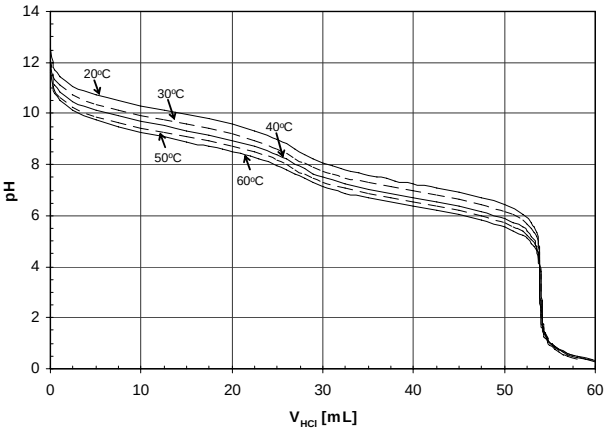

Figure 4: pH curves of aqueous solution of 30 mass % AEEA for several temperatures.

T/°C	pKa_1	pKa_2
20	10.05	7.21
30	9.70	6.94
40	9.44	6.67
50	9.20	6.49
60	9.00	6.31

Table 2: pKa values of aqueous solution of 30 mass % AEEA for several temperatures.

Speciation and NMR analysis data

In order to identify the species existing in the liquid phase in the AEEA–CO_2–H_2O system, an NMR study was performed. CO_2–loaded 30 mass % AEEA solutions were investigated at 20 °C and loadings of 0.20, 0.50, and 0.80 mol of CO_2/mol of AEEA, respectively. Both ^1H and ^{13}C 1D NMR

spectra were acquired. Three types of amine species were identified; amine, primary carbamate, and secondary carbamate and the peaks were assigned to particular proton/carbon types with help of 2D NMR spectra. The different types of proton/carbon atoms are shown for AEEA molecule in Figure 5. An example of a ^{13}C spectrum is given in Figure 6. There were observed 4×3 peaks representing the four carbon types for each of the three AEEA species in the spectra. On the spectrum in Figure 6, the peaks of highest intensity correspond to primary carbamate, the middle intensity peaks to AEEA, and the lowest intensity peaks to secondary carbamate.

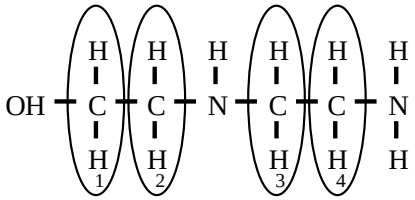

Figure 5: The four different carbon atoms in AEEA molecule.

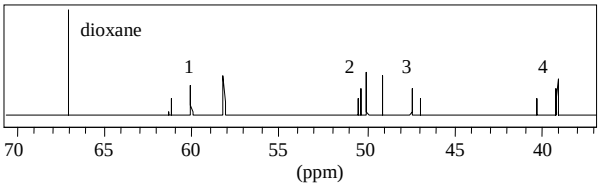

Figure 6: ^{13}C spectra of aqueous solution of 30 mass % AEEA at a loading of 0.80 mol of CO_2/mol of AEEA.

Since the peak intensities correspond to the species concentrations, the NMR spectra were also used for a quantitative investigation of the species distribution as function of CO_2 loading. The relative species concentrations were evaluated based on the area integrals. The detailed procedure can be found in Jakobsen et al. [11]. Because of the fast proton exchange with water, the data obtained actually represent the sum of the free and protonated AEEA, the sum of the primary and protonated primary carbamates, and the sum of the secondary and protonated secondary carbamates. In Figure 7, the NMR data are compared to the concentrations predicted by the model.

The VLE model was fitted to experimental data down to 40 °C and an extrapolation to 20 °C was deemed to be uncertain. Therefore 40 °C model data were compared to 20 °C data from the NMR experiments. This is the main reason for the discrepancies observed in Figure 7. Qualitatively, however, the model predictions are in good agreement with the NMR data. It should be noted that the given loadings are weighed in loadings and that these were not in total accordance with the material balances calculated from the NMR data.

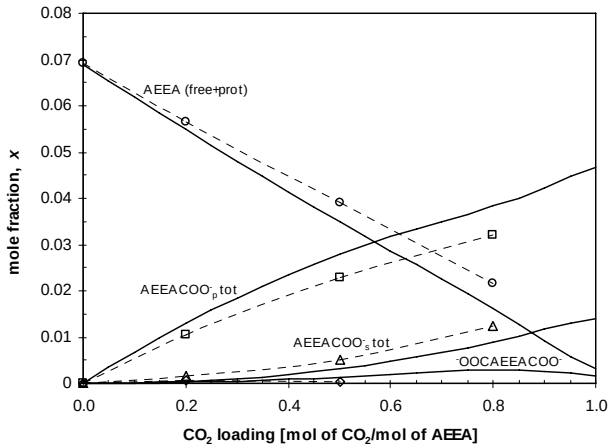

Figure 7: Liquid–phase concentrations of a CO_2–loaded 30 mass % AEEA at 40 °C in comparison to those analyzed using NMR at 20 °C. Solid lines are calculated by the model and points from NMR data. {AEEA (free+prot) = AEEA + $AEEAH^+$ + $^+HAEEAH^+$; $AEEACOO^-_p$ tot = $AEEACOO^-_p$ + $^+HAEEACOO^-_p$; $AEEACOO^-_s$ tot = $AEEACOO^-_s$ + $^+HAEEACOO^-_s$}.

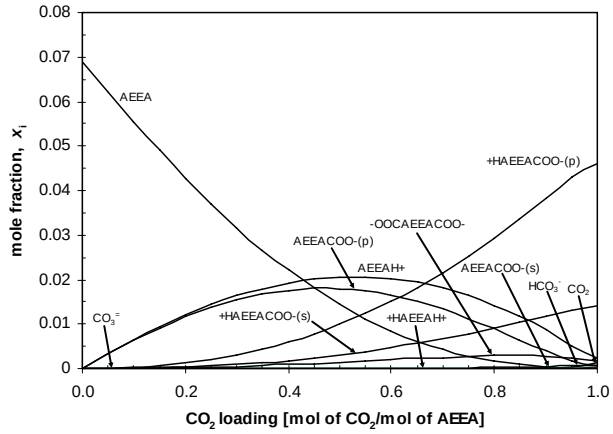

Figure 8: Distribution of species in aqueous solution of 30 mass % AEEA at 40 °C.

Figure 8 shows the distribution of species predicted by the model as a function of loading for 40 °C. As CO_2 is added to a fresh AEEA solution, the dominant product is the carbamate formed by the primary amine group ($AEEACOO^-_p$). At a loading of approximately 0.6 mol of CO_2/mol of AEEA, the

primary carbamate is progressively replaced by protonated primary carbamate ($^{+}HAEEACOO^{-}_{p}$). As the loading increases, pH decreases so that it is low enough to protonate the carbamates. In addition, secondary carbamate ($AEEACOO^{-}_{s}$) starts forming but still exists in very small amounts, approximately 0.03% of the primary carbamate. It is also clear that the dicarbamate only exists in small concentrations in the whole loading range. As expected, the formation of bicarbonate increases somewhat at high loadings, but the protonated carabamates are the main constituents in this region.

CONCLUSIONS

The vapor–liquid equilibrium data of CO_2 in aqueous solution of 30 mass % AEEA were measured over a range of temperatures from (40 to 120) °C for partial pressures ranging from (0.01 to 220) kPa. The Deshmukh–Mather model was fitted to the data and was shown to provide a good representation of the experimental points. ^{1}H and ^{13}C 1D NMR spectra were acquired for the system and used for identification of the system species. In addition, quantitative information on the species concentrations could be obtained and was shown to be in reasonable agreement with model predictions.

ACKNOWLEDGEMENT

This research was supported financially by the Norwegian Research Council "Klimatek Programme" through the SINTEF Project 661292.01.

REFERENCES

[1] Ma'mun S, Svendsen HF, Hoff KA, Juliussen O. *Selection of new absorbents for carbon dioxide capture*. Proceedings of the 7th International Conference on Greenhouse Gas Control Technologies (GHGT–7), refereed paper no. E3–2, Vancouver, 2004.

[2] Deshmukh RD, Mather AE. *A mathematical model for equilibrium solubility of hydrogen sulfide and carbon dioxide in aqueous alkanolamine solutions.* Chem. Eng. Sci. 1981; 36: 355–362.

[3] Ma'mun S, Nilsen R, Svendsen HF, Juliussen O. *Solubility of carbon dioxide in 30 mass % monoethanolamine and 50 mass % methyldiethanolamine solutions.* J. Chem. Eng. Data 2005; 50(2): 630–634.

[4] Chen CC, Britt HI, Boston JF, Evans LB. *Extension and application of the Pitzer equation for vapor–liquid equilibrium of aqueous electrolyte systems with molecular solutes.* AIChE J. 1979; 25(5): 820–831.

[5] Brelvi SW, O'Connell JP. *Corresponding state correlation for liquid compressibility and partial molal volumes of gases at infinite dilution in liquids.* AIChE J. 1972; 18(6): 1239–1243.

[6] Peng DY, Robinson DB. *A new two–constant equation of state.* Ind. Eng. Chem. Fundam. 1976; 5(1): 59–64.

[7] Kent RL, Eisenberg B. *Better data for amine treating.* Hydrocarbon Process. 1976; 55(2): 87–90.

[8] Weiland RH, Chakravarty T, Mather AE. *Solubility of carbon dioxide and hydrogen sulfide in aqueous alkanolamines.* Ind. Eng. Chem. Res. 1993; 32(7): 1419–1430.

[9] Olofsson G, Hepler LG. *Thermodynamics of ionization of water over wide ranges of temperatures and pressures.* J. Solution Chem. 1975; 4(2): 127–143.

[10] Edwards TJ, Maurer G, Newman J, Prausnitz JM. *Vapor–liquid equilibria in multicomponent aqueous solutions of volatile weak electrolytes.* AIChE J. 1978; 24(6): 966–976.

[11] Jakobsen JP, Krane J, Svendsen HF. *Liquid phase composition determination in CO_2–H_2O–alkanolamine systems, an NMR study.* Submitted to Ind. Eng. Chem. Res. Dec. 2004.

Proceedings of ECOS 2005
Trondheim, Norway
June 20–22, 2005

CO-UTILIZATION OF CO_2 AND CALCIUM SILICATE-RICH SLAGS FOR PRECIPITATED CALCIUM CARBONATE PRODUCTION (PART I)

Sebastian Teir[1], Sanni Eloneva and Ron Zevenhoven
Helsinki University of Technology
Laboratory for Energy Engineering and Environmental Protection
PO Box 4400, FIN-02015 Espoo
Finland

ABSTRACT

A promising option for long-term storage of CO_2 is to fixate carbon dioxide as carbonates in minerals. Slag from iron and steel works is a potential raw material for carbonation due to its high content of calcium silicates. Carbonation of calcium silicates produces calcium carbonate ($CaCO_3$), which is used as filler and coating materials in paper. Precipitated calcium carbonate (PCC) is currently produced by carbonating burned lime. If calcium silicate-rich slag materials are used instead of limestone for producing PCC, considerable energy savings and carbon dioxide emissions reductions could be achieved. A suitable process utilizing acetic acid for producing calcium carbonates from calcium silicates was identified. The option for fixating carbon dioxide with calcium silicate-rich slag using acetic acid as reaction intermediate and solvent was investigated using process modeling and laboratory-scale batch experiments. Using this process, 0.24 t of CO_2 could theoretically be captured and stored per ton of iron and steel slag products carbonated, while the world-wide CO_2 storage potential was estimated to be 62 – 83 Mt/a. The experiments showed that the calcium in iron and steel slags easily dissolve in acetic acid.
Keywords: mineral carbonation, CO_2 storage, CO_2 utilization, slag, calcium carbonate, calcium silicate

INTRODUCTION

The increasing carbon dioxide, CO_2, content in the atmosphere and its long-term effect on the climate has led to increasing interest and research in options for capture, utilization and long-term storage of carbon dioxide. Oil refineries, coal-fired power plants, iron and steel works, cement, lime and natural gas production are the largest producers of anthropogenic CO_2 emissions. However, the potential to reuse CO_2 in industry is limited, so the captured CO_2 has to be stored. Although CO_2 can be stored in aquifers and utilized in depleted oil and gas fields, the distances to the CO_2 producer site can be thousands of kilometers, which raise the storage cost significantly.

The disposal of CO_2 as solid carbonates is another potential option for long-term storage of CO_2. This method accelerates the natural weathering of silicate minerals, where these minerals react with CO_2 and form carbonate minerals and silica [1]. Suitable carbonates for storing CO_2 are magnesium- and calcium-based carbonates, since they are hard to dissolve in water. While magnesium- and calcium oxides and hydroxides carbonate faster, the availability of magnesium- and calcium silicates is much better [2]. Although calcium silicate has been successfully carbonated at temperatures and pressures relevant for industrial processes [3], natural calcium silicate resources are far too small and expensive to be of practical interest [2, 4]. Therefore, current research activities focus mostly on carbonation of magnesium silicates [5].

However, industrial by-products, such as iron and steel slags and cement-based materials, can have

[1] Corresponding author: Phone: +358 9 4513631 Fax: +358 9 4513418 E-mail: sebastian.teir@hut.fi

very high contents of calcium- and magnesium oxides, and could therefore be carbonated for CO_2 storage and hazardous waste neutralization [6, 7]. At the same time, calcium carbonate ($CaCO_3$) and precipitated calcium carbonate (PCC) has currently far more industrial uses than magnesium carbonate. Currently, PCC is manufactured by first calcinating limestone (natural calcium carbonate), and then carbonating the produced calcium oxide (CaO).
In this paper, we investigate the potential to use calcium silicate-rich slag products as raw material for PCC production, and explore the possibility to dissolve iron and steel slags in acetic acid for carbonation. A future paper will focus on the carbonation process step.

BACKGROUND

Precipitated calcium carbonate (PCC)

Calcium carbonate is mined and crushed to be mainly used as a concrete or bituminous aggregate and roadstone, as well as for manufacturing Portland cement. Lime (calcium oxide) is also calcinated from calcium carbonate for steelmaking, glassmaking, soil stabilization and neutralization, treating water, flue gas desulphurization, and PCC production. Ground and precipitated calcium carbonates are used as fillers in paints, rubbers, plastics and papers.
PCC is used as an alternative filler and coating material for changing physical and chemical properties of paper. It improves paper bulk, brightness, light scattering, fiber coverage and printability. In 2002, the world's PCC consumption was approximately 6 Mt, of which approximately 4 Mt was consumed by the paper industry [8], and approximately 425 kt produced in Finland [9].
Most PCC is currently produced from lime, which has been manufactured by calcining limestone in a lime kiln at temperatures over 900 °C:

$$CaCO_3 \rightarrow CaO + CO_2 \quad (1)$$

The lime is hydrated with water into a calcium hydroxide slurry:

$$CaO + H_2O \rightarrow Ca(OH)_2 \quad (2)$$

CO_2 is injected into the slurry, where it reacts with calcium hydroxide and forms calcium carbonate, which precipitates out:

$$Ca(OH)_2(aq) + CO_2 \rightarrow CaCO_3 \downarrow + H_2O \quad (3)$$

Although CO_2 is bound during the PCC production process, a larger amount of CO_2 is released from the lime production, due to the fuel combusted to provide heat to the endothermic calcination reaction (Equation 1).
According to Miner and Upton [10], almost all of the PCC in paper eventually ends up in landfills. Although significant amounts of inorganic carbon are removed from recovered paper in the recycling process, this material is disposed of in the landfills of recycled paper mills. In both cases, the carbon in PCC becomes eventually sequestered in landfills.
If PCC could be produced from a carbonate-free calcium mineral, such as calcium silicate, the calcination process could be abandoned and less CO_2 would be released. While the natural calcium silicate reserves are too few and too expensive to be used for manufacturing PCC [2, 4], the price, composition and availability of industrial slag products makes slag a more suitable material for carbonation.

Iron and steel slags

Slags are nonmetallic by-products of many metallurgical operations and consist primarily of calcium, magnesium, and aluminum silicates in various combinations. Iron and steel slags are co-products of iron and steel manufacturing.
Pig iron is produced by heating iron ore, coke and limestone in a blast furnace. Since silicon dioxide is a common impurity in iron ore and does not melt, limestone is needed. In the blast furnace, limestone calcinates to lime (CaO) (see Equation 1) and reacts with the silicon dioxide in the iron ore forming a molten calcium silicate slag:

$$CaO_x + (SiO_2)_y \rightarrow (CaO)_x \cdot (SiO_2)_y \quad (4)$$

The molten silicate slag is less dense than the molten iron and accumulates at the top of the reactor, where it can be drawn off. Different blast furnace slag types are produced depending on cooling technique used: air-cooled, expanded or foamed, granulated, or palletized slag.

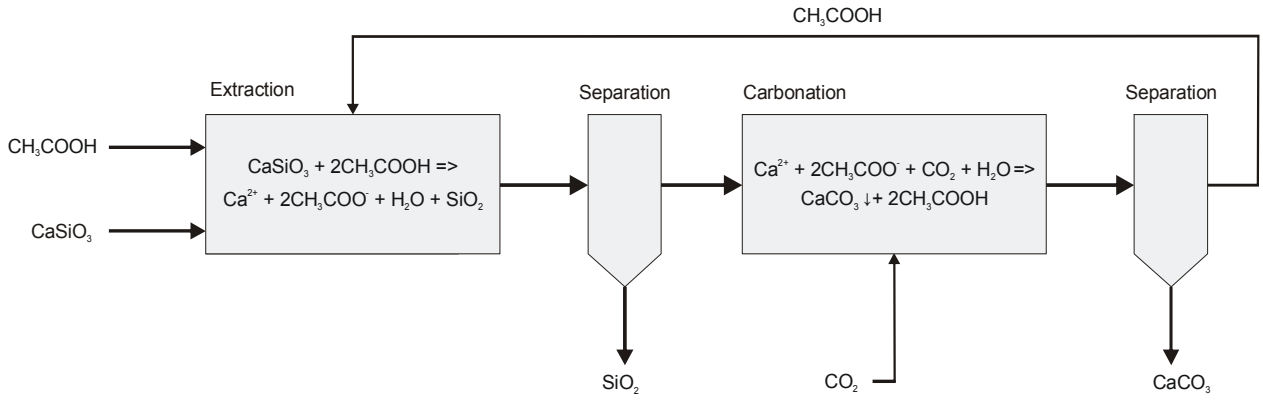

Figure 1: Acetic acid process

Element	Blast furnace slag	Steel slag
CaO	39.9 %	44.2 %
SiO_2	34.4 %	13.5 %
MgO	10.8 %	1.93 %
Al_2O_3	9.07 %	1.80 %
S	1.74 %	0.09 %
Fe	0.95 %	16.9 %
K_2O	0.71 %	0.12 %
Na_2O	0.50 %	-
Mn	0.35 %	2.35 %
P	0.002 %	0.33 %
Ti	-	0.50 %
Cr	-	0.21 %
Other	1.58 %	18.1%

Table 1: Annual average composition of slag products [12]

Steel slag is produced as lime reacts with molten iron ore, scrap metal, or other ingredients charged into the steel furnace. During this process, part of the liquid metal becomes entrapped in the slag.
This molten slag flows from the furnace into the pit area where it solidifies, after which it is transferred to cooling ponds and metals are removed by magnetic separation. Steel slags are highly variable with respect to their composition, even for the same plant and furnace.
The amount of slag produced is largely related to the overall chemistry of the raw material. For a blast furnace using high grade iron ore, about 0.25 – 0.30 t of blast furnace slag will be produced per ton of crude iron. Lower grade ores can yield as much as 1.0 – 1.2 t of slag per ton of crude iron. Steel slag output is also variable and depends on both the feed chemistry and the type of furnace used. Since 50 % of the molten steel slag is recycled inside the process, the slag remaining after entrained steel removal is usually equivalent to about 10 – 15 % of the crude steel output. It has been estimated that the world output was in 2003 160 – 200 Mt of iron slag and 96 – 145 Mt of steel slag [11]. Examples of the elemental composition of iron and steel slags can be found in Table 1.

Carbonation of calcium silicate

The most promising option for producing precipitated calcium carbonate from calcium silicates seems to be the acetic acid carbonation process suggested and studied by Kakizawa *et al.* [3]. The process consists of two main steps, where the reactions occur (Figure 1). First, calcium ions are extracted from a natural calcium silicate mineral by acetic acid (CH_3COOH):

$$CaSiO_3 + 2CH_3COOH \rightarrow Ca^{2+} + 2CH_3COO^- + H_2O + SiO_2 \quad (5)$$

After filtrating silica out of the solution, CO_2 is pumped into the solution, forming calcium carbonate that precipitates from the solution:

$$Ca^{2+} + 2CH_3COO^- + CO_2 + H_2O \rightarrow CaCO_3 \downarrow + 2CH_3COOH \quad (6)$$

Acetic acid is recovered in this step and recycled for use in the extraction step. According to Kakizawa *et al.*, the Gibbs free energy change of each step is negative, and should therefore not require large amounts of energy input. However,

the second step may require pressurized CO_2 in order to achieve a high carbonation efficiency.
The process was studied with batch experiments. Using an aqueous solution of acetic acid (27 % acid and 72 % water at 60 °C) to extract calcium ions from natural calcium silicate, an extraction ratio of 48 % was achieved in 250 min. Using CO_2 pressures of 5 – 50 bar and temperatures of 40 – 80 °C, a carbonation ratio of 20 % of a calcium acetate solution was achieved in approximately 1 h [3].

PROCESS COMPARISON

We have studied the feasibility of PCC production from calcium silicates using process modeling, and compared it with the current PCC production route from limestone [4]. The processes were modeled using Aspen Plus 12.1® and HSC 4.0 software. Both processes were modeled using a gas supply of 100 % CO_2 at room temperature, and at the pressure level needed for the process (assuming CO_2 is provided from a CO_2 capture facility).
The net CO_2 emissions from the current PCC production method were according to our model 0.21 kg CO_2/kg $CaCO_3$ produced, with the CO_2 bound in the carbonation process accounted for, and the energy need for the calcination facility included.
The PCC production from calcium silicates was modeled using an extraction efficiency of 100 % and 10 % carbonation ratio, in order to be comparable with available modeling results [3]. The model assumed that all acetic acid could be regenerated and recycled with the calcium ions that had not carbonated, so that the process has no other output streams than $CaCO_3$ and SiO_2. This model captures CO_2 and produces none, since the heat for the endothermic carbonation step was supplied by the exothermic extraction reactor. When the total power demand of the process was taken into account the fixation of CO_2 was calculated to be 0.34 kg/kg $CaCO_3$ produced [4]. If this process would replace existing PCC production facilities, the net reduction would be 0.55 kg CO_2/kg $CaCO_3$ produced.

Potential

According to our acetic acid process model, roughly 0.24 kg of CO_2 could be stored per kg of slag (with an average CaO content of 40 %) carbonated. The world-wide iron and steel slag carbonation potential can be estimated using these numbers at 62 – 83 Mt CO_2/a.
Production of PCC from carbonation of iron and steel slag could also be a profitable refining method for the slag products, if the purity required for commercial PCC could be achieved. In Finland, granulated blast furnace slag can be purchased for 10 €/t, which is approximately the same price as limestone lumps used for producing lime for PCC manufacturing (11 €/t), while the cheapest available PCC type has a price tag of 120 €/t [13].
For example, in 2003 Raahe steel works produced 2.80 Mt steel slabs, 899 kt slag products, and 4.84 Mt CO_2 emissions [14]. If all the slag products could be carbonated, 642 kt/a of PCC would be produced, reducing the CO_2 emissions of the plant with 218 kt/a (4.5 %), and possibly increasing the value of the slag product ten-fold. If this PCC produced from slag would replace conventional PCC manufactured from limestone on the filler market, an additional 135 kt/a of CO_2 emissions from lime kilns currently producing lime for PCC manufacture could be avoided. This would also annually save more than 642 kt of natural limestone mineral resources.
However, if the PCC purity specifications cannot be met, the carbonates could still possibly be used e.g. for soil neutralization and stabilization.

EXTRACTION EXPERIMENTS

In order to investigate the possibility to carbonate slag products instead of natural calcium silicates, the extraction of calcium ions from iron and steel slags in acetic acid was investigated using batch experiments.

Materials and methods

The iron and steel slags used in the experiment were provided by Ruukki Production, Co-products, from Raahe steel works in Finland. The experiment setup is displayed in Figure 2.
A solution of 200 g distilled water and 100 g acetic acid was heated to a specified temperature in a decanter glass. Depending on the temperature of the solution, its pH ranged from 0.74 to 1.7, prior to the addition of slag. The decanter glass was surrounded by a water bath, which was

heated using a magnetic stirrer with an integrated heater. Each slag was tested at solution temperatures of 30 °C, 50 °C and 70 °C. The solution was stirred at 650 min^{-1}. Nitrogen was continuously fed to the container at 6 l/min to prevent carbonation of atmospheric CO_2, and the container was sealed with a cork.

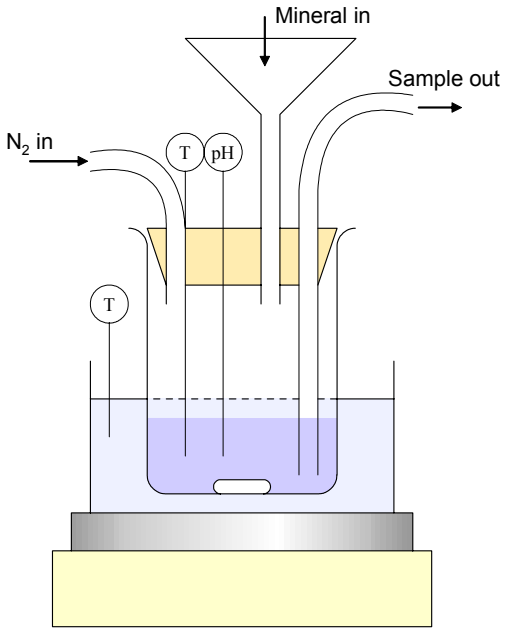

Figure 2: Experiment setup

When the temperature for the solution had stabilized after heat-up to the desired temperature, 5.0 g of slag, sieved to a particle size of 125 – 350 µm, was added to the solution. The temperature and pH of the solution were recorded with electrodes in real time, and were not regulated after the addition of the batch. The solution was stirred for 2 h, and four samples of 15 ml each were extracted during the course of the experiment using a syringe. The samples were immediately filtered through a syringe membrane filter of 0.45 µm pore size and stored for analysis. A few samples blocked the membrane filters immediately. These samples were filtered using other methods and are marked in the result figures. The Si, Fe, Al, Ca and Mg concentrations in the solution samples were measured after the tests using Inductively Coupled Plasma-Atomic Emission Spectrometry (ICP-AES) and Atomic Absorption Spectrophotometry (AAS), since these are the main species of the slag. The solution was assumed to be free from these species prior to the addition of the batch of slag, being prepared from only distilled water and pure acetic acid.

Results

The results from the AAS and ICP-AES analyses of the experiments made with steel slag are shown in Figure 3, Figure 4, and Figure 5. The corresponding results from the experiments with iron slag are shown in Figure 6, Figure 7 and Figure 8. Samples of the solution were extracted for each test at 15 min, 30 min, 1 h, and 2 h after the batch had been added, with one exception: sample extraction for the iron slag solution at 50 °C were performed at 15 min, 45 min, 1 h and 15 min, and 2 h after the addition of slag. Due to substantial weight loss at 50 °C and 70 °C as a result of solution evaporation, the concentration values have been corrected by assuming a constant evaporation rate, which was calculated using the initial mass of the container, the final mass of the container, sample volumes extracted and the time between measurements. The

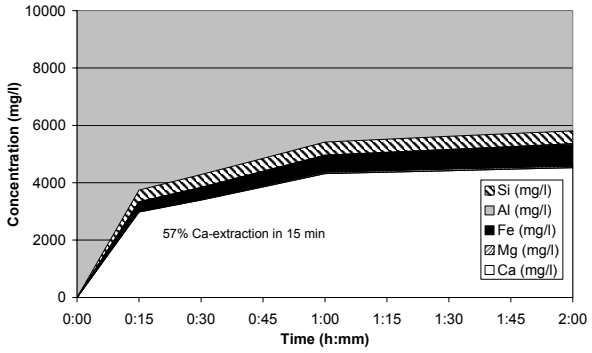

Figure 3: Steel slag in solution at 30 °C

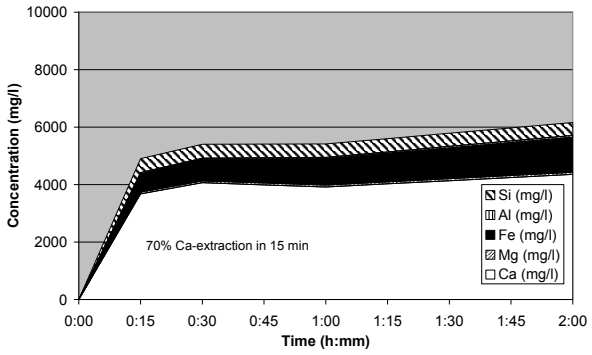

Figure 4: Steel slag in solution at 50 °C

mass/solution ratio was assumed not to be affected by the sample extraction, since the solution was continuously stirred.

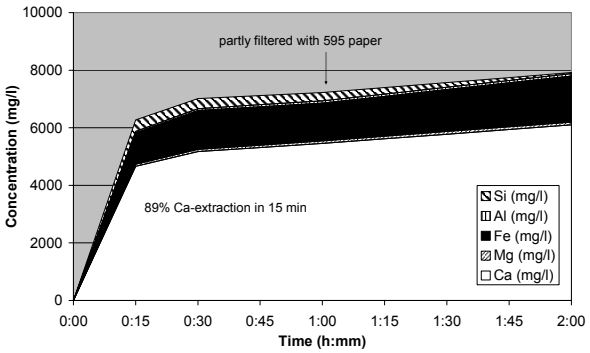

Figure 5: Steel slag in solution at 70 °C

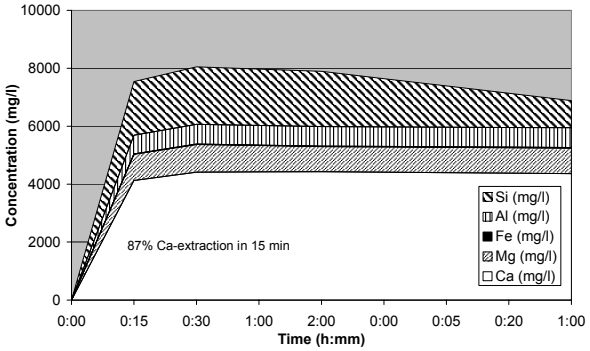

Figure 6: Iron slag in solution at 30 °C

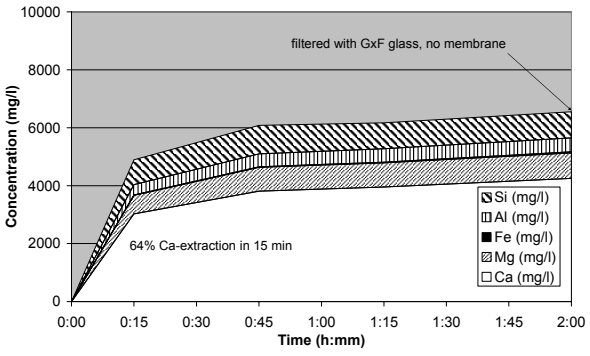

Figure 7: Iron slag in solution at 50 °C

In order to estimate the dissolution rate, the pH curve was plotted into the same graph as the Ca extraction rate, calculated from the Ca analyses (Figure 9 and Figure 10). The same scale was used for both experiments. Peaks in pH data have been filtered out, since the signal suffered from some interference in the data logger card. Only solutions at 30 °C were compared, since the evaporation loss made the comparison less reliable for solutions at higher temperatures.

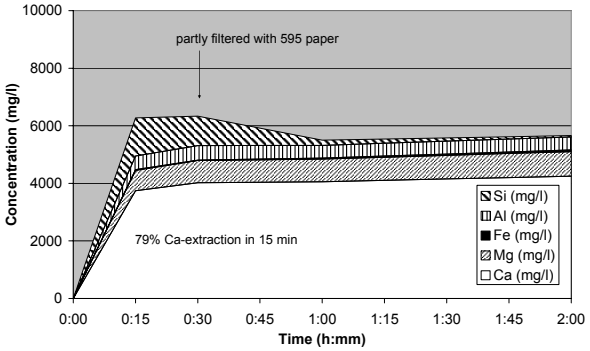

Figure 8: Iron slag in solution at 70 °C

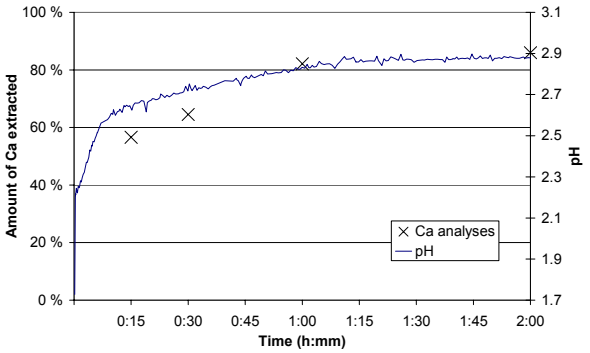

Figure 9: Steel slag in solution at 30 °C

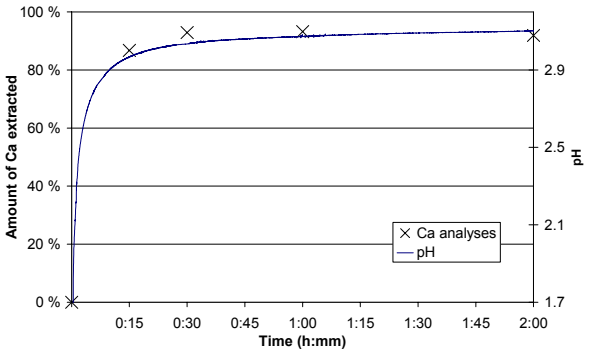

Figure 10: Iron slag in solution at 30 °C

Discussion

When the batch of slag was added to the solution, the solution temperature was raised immediately with a few degrees, verifying a reaction occurring and the exothermic nature of the reaction. The

results from the experiments (Figure 3 – Figure 8) show that Ca from iron and steel slag dissolves readily in acetic acid. While higher temperature allows more calcium to be dissolved from steel slag, temperature does not seem to have an effect on the calcium extraction from iron slag. In most experiments performed here, approximately 70 % of the calcium in the slag has been dissolved within 15 minutes. According to the estimates in Figure 9 and Figure 10, over 50 % was dissolved from both iron and steel slag within 5 minutes. This is much faster than the values reported by Kakizawa *et al.* The reason for this is still unclear, but indicates that calcium is much easier to extract from iron and steel slags than from natural calcium silicates. However, a much smaller batch load was used in the experiments presented here (16.7 g slag/kg acid, in comparison to 208 g calcium silicate/kg acid used by Kakizawa *et al.*). Since acid will continuously be regenerated in the subsequent carbonation process step, allowing more slag to dissolve, the achieved extraction ratio should be enough for a continuous process.

However, other elements of the slag, such as Si, dissolve as well. Extracting Ca from steel slag also dissolves Fe, while Ca extraction from iron slag dissolves Mg and Al. Both experiments performed at 70 °C show a gradual decline in dissolved Si content with residence time of the filtered samples. The filtration residue in both experiments was a gel, indicating that silica may be separated as a gel at temperatures > 70 °C using centrifugal separation technology. More research is needed to verify this.

FUTURE WORK

While the experimental work presented here only investigates the possibility to extract calcium from calcium silicate-rich slag, future work will investigate the carbonation of acetic acid solutions containing calcium. Experiments with precipitation of carbonate from these solutions will determine the purity of CO_2 required for carbonation, and the type of separation methods needed to eliminate impurities. The quality of the produced PCC will also be analyzed.

The extraction experiments will continue as well, by exploring the influence of higher solution temperatures, larger particle sizes, and the concentration of acetic acid on the extraction efficiency. The regeneration of acetic acid requires also investigation.

The results from that work will be submitted and hopefully accepted for presentation at ECOS 2006 as part II of this paper.

CONCLUSION

Carbonation of calcium silicate-rich slags is an interesting option for simultaneously reducing CO_2 emissions and refining by-products from the industry. If the produced calcium carbonate could reach the purity specifications of PCC, the processing of slags could increase its value ten-fold, while also reducing CO_2 emissions and preserving natural mineral resources. Although the global CO_2 storage potential by carbonating slags is low in comparison with other CO_2 storage options, it can reduce the annual CO_2 emissions for an individual steel plant with several hundreds of kilotons.

Using an acetic acid process 0.24 t of CO_2 could theoretically be captured and stored per ton of slag carbonated. The results from the experiments show that calcium ions can rapidly be extracted at an average 70 % efficiency from iron and steel slags in an acetic acid solution. However, filtration of the solution may be required to remove silica and other impurities.

ACKNOWLEDGEMENTS

We thank the people working at the Laboratory of Energy Engineering and Environmental Protection and the Laboratory of Applied Thermodynamics for facilitating this work. We also thank Hannu Revitzer at the Chemical Analysis Centre of the university for his technical support, and we thank the Nordic Energy Research, the National Technology Agency of Finland (TEKES) and the Finnish Recovery Boiler Committee for financial support. We also thank Prof. Mikhail Gasik for giving us the idea to investigate whether iron and steel slag could be carbonated.

REFERENCES

[1] Lackner KS. *A Guide to CO_2 Sequestration*. Science 2003;300:1677-1678.

[2] Lackner KS. *Carbonate Chemistry for Sequestering Fossil Carbon.* Annu. Rev. Energy Environ. 2002;27:193-232.

[3] Kakizawa M, Yamasaki A, Yanagisawa Y. *A new CO_2 disposal process via artificial weathering of calcium silicate accelerated by acetic acid.* Energy 2001;26:341-354.

[4] Teir JS, Eloneva SE, Zevenhoven R. *Production of precipitated calcium carbonate from calcium silicates and carbon dioxide.* In press, Energy Conversion and Management, 2005.

[5] Zevenhoven R, Kavaliauskaite I. *Mineral carbonation for long-term CO_2 storage: an exergy analysis.* In Proceedings of ECOS 2003, the 16th International Conference on Efficiency, Cost, Optimization, Simulation, and Environmental Impact of Energy Systems, Vol. I, Copenhagen, Denmark, June 30–July 2, 2003.

[6] Fernández Bertos M, Simons SJR, Hills CD, Carey PJ. *A review of accelerated carbonation technology in the treatment of cement-based materials and sequestration of CO_2.* Journal of Hazardous Materials 2004;B112:193-205.

[7] Stolaroff JK, Lowry GV, Keith DW. *Using CaO- and MgO-rich industrial waste streams for carbon sequestration.* Energy Conversion and Management 2005;46:687-699.

[8] Summary from the report "*The Economics of Precipitated Calcium Carbonate*". Roskill Metal and Mineral Reports, published 2003; January 12, 2005. See also: http://www.roskill.com/reports/precipitated

[9] *Industrial Minerals and Rocks.* Geological Survey of Finland. January 12, 2005. See also: http://www.gsf.fi/explor/eco_indust_frame.htm

[10] Miner R, Upton B. *Methods for estimating greenhouse gas emissions from lime kilns at kraft pulp mills.* Energy 2002;27:729-738.

[11] *Minerals yearbook, vol. I – Metals and minerals.* Published annually, data from 2002 – 2004 used. Reston (VA): United States Geological Survey; January 12, 2005. See also: http://minerals.usgs.gov/minerals/pubs/commodity/myb/.

[12] Annual average composition of slag products from Ruukki steel plant Raahe. Data supplied by Co-products, Ruukki Production, Autumn 2004.

[13] Price data supplied by Nordkalk Oy; June 2004, and Ruukki Productions, Co-products; September 2004.

[14] *Raahe Steel Works Environmental Statement 2003*. Rautaruukki, Raahe Steel Works. See also: http://www.ruukki.com/

Proceedings of ECOS 2005
Trondheim, Norway
June 20–22, 2005

EFFICIENCY OF CARBON STORAGE WITH LEAKAGE: PHYISCAL AND ECONOMICAL APPROACHES

Fei TENG[1,2,*] and Daniel TONDEUR[1]
[1]Laboratoire des Sciences du Génie Chimique-CNRS
ENSIC-INPL BP 451, 54001 Nancy Cedex
France
[2]Tsinghua University
Institute of Nuclear and New Energy Technology
100084 Beijing
China

ABSTRACT

In this paper, two methods are proposed to assess the efficiency of Carbon Capture and Sequestration schemes (CCS) involving back-leakage of CO2 from geological storage reservoirs to the atmosphere. In other words, we develop criteria to quantify the marginal benefit of non-permanent carbon storage. The first method is a physical approach based on radiative forcing. It leads to a criterion that assesses whether a given technology of CCS is physically beneficial compared to a reference technology without CCS. The second method is an economic approach based on the classical framework of Net Present Value. It leads to an economic feasibility condition that assesses whether a given CCS technology is economically beneficial compared to a reference technology. The two models are compared with respect to their parametric dependence. Under general assumptions, the economic criterion is stricter than the physical criterion when the leakage coefficient is small, and the opposite is true when the leakage coefficient is large.

Keywords: Carbon sequestration, Carbon dioxide, Efficiency assessment, leakage.

NOMENCLATURE

a_g	Radiative efficiency
CR	Capture rate of CCS technology
EF	Emission factor of fuel employed [tCO_2/GJ]
EF_C	Emission factor of generation in capture plant [tCO_2/kWhe]
EF_r	Emission factor of generation in reference plant [tCO_2/kWh]
$f^C(t)$	Time dependent decay function of CO_2
$f^g(t)$	Time dependent decay function of gas
GWP(η)	Global warming potential of carbon storage with a constant leakage coefficient η.
HR_c	Heat rate of captured plant [GJ/kWhe]
HR_r	Heat rate of reference plant [GJ/kWhe]
$L(t)$	Leakage rate [ton/year]
$l(t)$	Specific leakage rate [$year^{-1}$]
P_C	Carbon price at time 0 [$/$tCO_2$]
P_e	Electricity price in wholesale market [$/kWhe]
P_F	Fuel price at time 0 [$/GJ]
r	Discount rate
$S(t)$	Carbon stock in reservoir at time t [ton]
S_0	Amount of carbon sequestered at time 0 [ton]
β	Expectation of increase of carbon price
η	Leakage coefficient
λ	Energy penalty of Capture technology

INTRODUCTION

In line with the Kyoto Protocol [1], there is currently a great interest in carbon sequestration as a complemental option for carbon mitigation. The Intergovernmental Panel on Climate Change (IPCC) defines sequestration as an increase in carbon stock in some reservoir other than the atmosphere. Several kinds of reservoirs have been considered for carbon sequestration, such as bio-

*Corresponding author: Phone: +0033 383 17 5280
Fax:+0033 383 32 2975 Email: fei.teng@ensic.inpl-nancy.fr

logical carbon sinks including forests and soil; onshore geological reservoirs such as deep coal seams, depleted hydrocarbon reservoirs, deep saline aquifers; and deep ocean.

For geological reservoirs, greenhouse gas will be captured at the places of fossil fuel combustion and then transported and injected into these reservoirs. Such activities are often called CCS (Carbon Capture and Storage).

A particular feature of carbon sequestration is that the carbon sequestrated (stored in plantation or underground) is always at risk of leaking back to the atmosphere. In contrast, carbon mitigation caused by a reduction of fossil fuel consumption will result in a risk-free reduction in atmospheric CO_2 level. This is the issue of permanence which has been hotly debated in the literature [2, 3]. Existing approaches are mainly economical [4-6], and based on a Net Present Value (NPV) model. By contrast, the present paper firstly uses a physical approach, comparing the cumulative radiative forcing of the CCS plant with its reference plant. Then focusing on the economic efficiency, a more detailed NPV model is employed for the same comparison. At last, these two approaches are compared and conclusions are given.

BACKGROUND

The core problem of the permanence issue is the following: compared with carbon avoided from fossil fuel usage, what is the value of temporary sequestrated carbon? As Chomitz [7] suggested, two possible approaches can be used to address this issue: (1) To assess the environmental and economic benefit of commitments to limited-term sequestration agreements. (2) To devise mechanisms that provides reasonable assurance of indefinite sequestration. The first approach leads to researches for a numerical index comparing the contribution to global warming of temporary sequestration on one hand and permanent fossil fuel avoided on the other hand.

Radiative forcing or concentration are often used as proxy for climate change [8,9] because they can be specified with better accuracy, and most global carbon models (GCMs) suggest that global mean surface temperature response is related to radiative forcing by a linear relation.

Radiative forcing and global warming potential

The impact of GHGs upon the atmosphere is not only related to radiative properties, but also to their lifetime which controls the time-scale of their influence on the thermal budget. That means, the radiative property should be integrated over a selected time period to account for the cumulative effects of the gas during that period. Then, an absolute (rather than relative) global warming potential (AGWP) of a given GHG symbolized by "g" can be defined as:

$$AGWP(g) = \int_0^{TH} a_g f^g(t)dt, \qquad (1)$$

where *TH* is the time scale selected for the calculation[1], a_g is the radiative efficiency due to a unit increase in atmospheric abundance of the substance in question (i.e., $Wm^{-2}kg^{-1}$), $f^g(t)$ is the time-dependent decay function (sometimes called impulse response function). $f^g(t)$ is equal to the fraction of the initially added carbon at time t=0 which is still found in the atmosphere at any later time t. For the purpose of comparing various GHGs, a relative rather than absolute index is preferred, and CO2 is often selected as a reference gas. Then GWP can be defined as the ratio of the time-integrated radiative forcing from instantaneous release of 1 kg of a given GHG relative to that of 1 kg of CO2 (reference gas). This definition can be presented by the following formula:

$$GWP_C^g = \frac{AGWP(g)}{AGWP(CO_2)} = \frac{\int_0^{TH} a_g f^g(t)dt}{\int_0^{TH} a_C f^C(t)dt}, \qquad (2)$$

GWP of some typical GHGs are listed in Table 1.

	Radiative Efficiency ($Wm^{-2}ppb^{-1}$)	Global Warming Potential		
		20 years	100 years	500 years
CO_2	1.55×10^{-5}	1	1	1
CH_4	3.7×10^{-4}	62	23	7
N_2O	3.1×10^{-3}	275	296	156
SF_6	0.52	15100	22200	32400

Table 1: GWP of several typical GHGs.

Currently the best known CO_2 impulse response function is the function described in Bern's carbon cycle model [10]. In the literature, a simplified parameter version is often used [10], which doesn't take into account the concentration level, and is represented by equation (3):

$$f^C(t) = 0.30036 \bullet e^{-t/6.6993} + 0.34278 \bullet e^{-t/71.109} + 0.3568 \bullet e^{-t/815.727}, \qquad (3)$$

EFFICIENCY OF CCS

Based on the first approach suggested by Chomitz [7], two possible ways have been identified in the preceding context to evaluate the efficiency of temporary storage: one from an environmental point of view and the other from an economical point of view.

[1] The Kyoto Protocol uses 100 years as selected time scale, but it is based on a political negotiation rather than a scientific argument.

Radiative forcing efficiency of CCS

The impact of CO2 leakage from storage depends on volumes stored and leakage rate. However it is difficult to know how much carbon will be sequestered in the future because it will depend on the trade off among different mitigation options, and in addition there is still not sufficient experience to estimate leakage rate. To account for the first problem, we take a marginal point of view where only an additional unit of sequestered carbon is considered. To account for the second problem, we start from a conservation equation of CO_2 over the storage, assuming the leakage rate $L(t)$ is proportional to the stock.

$$L(t) = \frac{dS(t)}{dt} = -\eta \bullet S(t)\,, \tag{4}$$

where S is the carbon stock (ton) and the proportionality coefficient η (year^{-1}) is called the leakage coefficient and assumed constant in the following discussion. The product $L(t)=-\eta S(t)$ is the leakage rate with units of tons per year. Equation (4) is integrated over time into equation (5):

$$S(t) = S_0 e^{-\eta t}\,, \tag{5}$$

Where S_0 is the amount of carbon sequestered at time 0. Substituting equation (5) into equation (4) and dividing by the initial value S_0, we get:

$$l(t) = \frac{L(t)}{S_0} = \eta \bullet e^{-\eta t} \tag{6}$$

This "specific leakage rate" tells us that when one unit of CO_2 was sequestered at time 0, the amount $l(t)$ will have leaked from the stock at time t. This function is illustrated in Figure 1 for different leakage coefficients.

The leaked carbon will get into the atmosphere and the carbon cycle, so the cumulative decay function caused by the former leakage curve can be expressed from the following integral:

$$f^S(t) = \int_0^t f^C(t-\tau) l(\tau) d\tau\,, \tag{7}$$

that is illustrated in Figure 2.

If we treat sequestered carbon with leakage as a kind of "GHG", the corresponding "GWP" can be calculated from the above defined formulation, where the radiative efficiency is that of CO2. Hence the "GWP" of the sequestered carbon with leakage is calculated by the following formula:

$$GWP_{TH}^S = \frac{\int_0^{TH} a_C f^S(t) dt}{\int_0^{TH} a_C f^C(t) dt}\,, \tag{8}$$

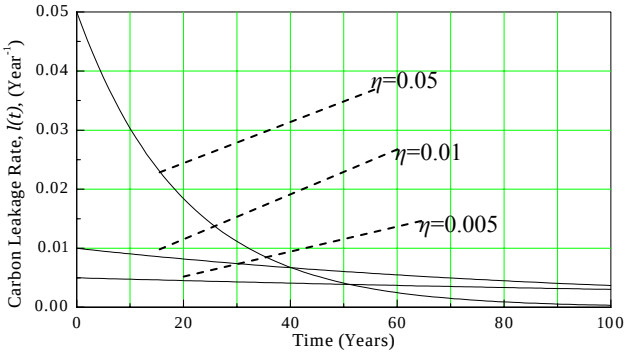

Figure 1: Leakage curve of carbon sequestration under different leakage coefficients

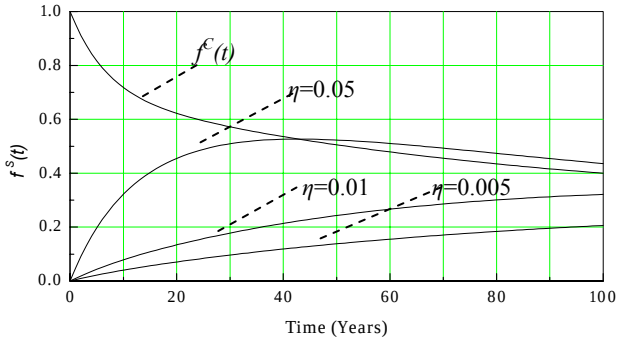

Figure 2: Decay function corresponding to different leakage coefficients

Assuming a constant radiative efficiency, we get a simplified version as follows:

$$GWP_{TH}^S = \frac{\int_0^{TH}\int_0^{TH} f^C(t-\tau) l(\tau) d\tau dt}{\int_0^{TH} f^C(t) dt}\,, \tag{9}$$

Given the leakage curve f^C of sequestrated carbon, its "GWP" compared with carbon avoided or with perfect sequestration can be calculated from the above formula using a numerical method. The following table gives some results for a series of constant leakage coefficients for the given time scale TH of 100 years.

Leakage coefficient (η)	0.001	0.005	0.01	0.02	0.05
GWP	0.054	0.237	0.404	0.613	0.839
Efficiency (1-GWP)	0.946	0.763	0.596	0.387	0.161

Table 2: "GWP" and efficiency factors of sequestered carbon under different leakage coefficient

The quantity of 1-GWP can be considered as an index of "efficiency" which translates one unit of temporary carbon storage into some unit of carbon reduction without leakage risk. For example, given η=0.01, one additional ton of carbon se-

questered has the same cumulated radiative forcing effect as 0.404 (Table 2) ton of carbon emitted at the same time (time 0). Thus it may be considered to be equivalent to 0.596 ton carbon avoided. Figure 3 illustrates the dependence of this efficiency on the leakage coefficient.

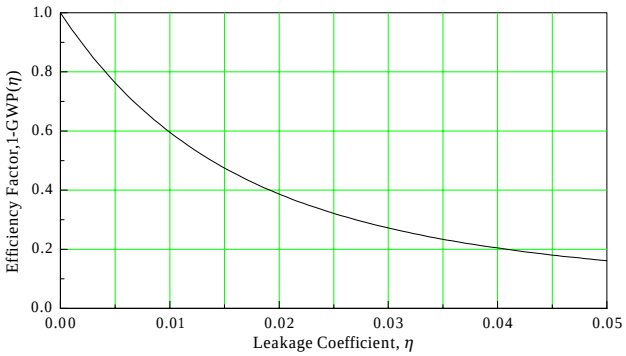

Figure 3: Function relationship between leakage coefficient and efficiency

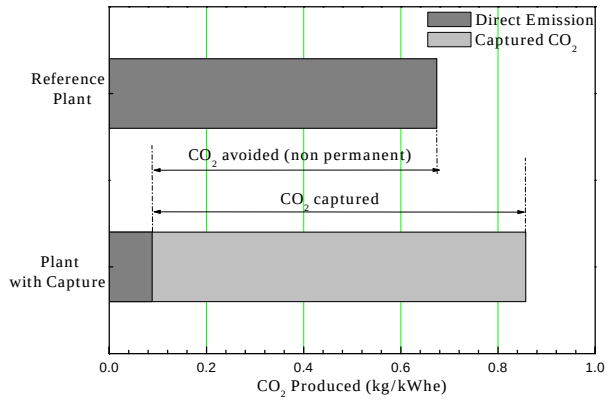

Figure 4: Difference between CO_2 "avoided" and CO_2 captured[2]

Energy penalty issue and carbon accounting

Even if there is no leak risk for carbon storage, it is still wrong to account all of the carbon captured and sequestered as carbon credits. We still have no idea how much carbon will be emitted into the atmosphere if carbon sequestration is not put into force. A benchmark needs to be defined for calculating how much carbon is offset compared with a business-as-usual scenario.

In the literature focused on CCS in power plants, a reference plant is often defined as a power plant without carbon capture facilities while other characteristics are the same as a plant with capture. Given this definition, a plant with capture will consume more fuel than a reference plant when generating the same output, because of the energy requirement for separating and compressing the carbon dioxide from the flue gas.[3] That is, not all of the carbon captured and sequestrated should be considered as a kind of carbon reduction, because the additional energy needed for carbon capture and compressing will also cause CO_2 emission but without contribution to energy output, and such emission should be removed from carbon credit. The difference between CO_2 captured and CO_2 non-permanent avoided is illustrated in Figure 4 [11].

Energy penalty λ is defined as the reduction in net power output of the capture plant compared to the reference plant for equal fuel inputs, thus:

$$\lambda = 1 - \frac{HR_r}{HR_C}, \qquad (10)$$

where HR is the so-called "heat rate", a measure of a power plant thermal efficiency.

For the reference plant, the CO_2 emission factor of electricity generation (in $kgCO_2/kWhe$) is:

$$EF_r = HR_r \cdot EF, \qquad (11)$$

while the emission factor of electricity generation in the plant with capture may be defined as :

$$EF_c = HR_c \cdot EF \cdot (1-CR) + HR_c \cdot EF \cdot CR \cdot GWP(\eta). \qquad (12)$$

The first term of equation (12) is related to direct emission of non-captured CO_2, and the second term is related to the captured and sequestered carbon with a leakage coefficient η. Recall that one unit of CO_2 stored is equivalent to GWP(η) unit of CO_2 emission based on cumulative radiative forcing. If we use equation(10) to rewrite equation(12), we get:

$$EF_c = [(1-CR) + CR \cdot GWP(\eta)] \cdot HR_r \cdot \frac{EF}{1-\lambda}. \qquad (13)$$

Comparing equation (11) and equation (13), we can establish the sufficient and necessary condition for the emission of the plant with capture to be smaller than that of the reference plant, that is $EF_c < EF_r$:

$$1-GWP(\eta) > \lambda/CR. \qquad (14)$$

This formulation means that carbon sequestration in a power plant MAY cause a LARGER global warming effect than in a reference plant, if the capture rate is too low, energy penalty is too high or leakage coefficient is too large. Generally speaking, if the criterion (14) is not satisfied, the CCS project should be rejected because it will increase cumulative radiative forcing instead of decreasing it. For this reason, equation(14) can be

[2] This figure and corresponding data came from Herzog [11] Figure 2.

[3] The energy used for carbon transportation and injection was not included here.

considered as an **efficiency criterion** for a carbon sequestration project in the power sector.

The ratio λ/CR can be looked at as an index representing characteristics of different capture technologies, while the characteristics of geological reservoir are represented by η. When given a specific λ/CR, we define a **maximum permissible leakage coefficient** η_m as the solution of the following equation:

$$1\text{-GWP}(\eta_m) = \lambda/\text{CR}. \qquad (15)$$

The equation (15) is illustrated in Figure 6 and shows the relationship between different capture technologies, characterized by their index λ/CR, and the corresponding maximum permissible leakage rate. Characteristics of different capture technologies are collected in Table 3; original data come from IEA [12].

Note that the graph of Figure 5 is identical to that of Figure 3, because of equation (15), but they have different interpretations.

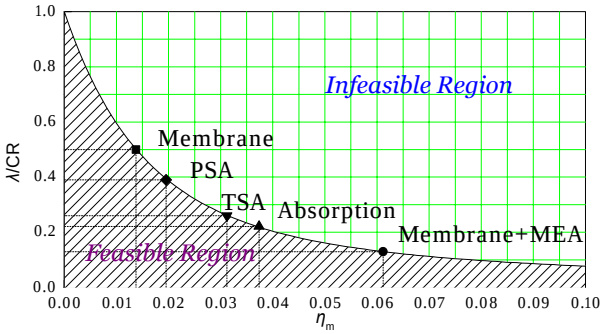

Figure 5: Different capture technologies and corresponding η_m.

	PC+FGD[1]	NGCC[2]	IGCC[3]	CO_2/O_2[4]	IGCC Selexol
Absorption	0.31	0.22	0.37	0.09	0.17
Adsorption (PSA)	0.32	0.39	0.40	0.13	----
Adsorption (TSA)	0.29	0.26	0.33	----	----
Cryogenic	----	----	0.16	0.21	----
Membranes	0.29	0.50	0.48	0.08	----
Membranes + MEA	0.31	0.13	0.30	0.11	----

1. Pulverised Coal Power Plant + Flue Gas Desulphurisation.
2. Natural Gas-fired Combined Cycle.
3. Integrated Gasification Combined Cycle.
4. Carbon Dioxide Recycle Power Plant.

Table 3:λ/CR of different capture technology with different reference plant

For example, a typical PC (Pulverized Coal) capture plant has an energy penalty λ of about 27%, while the capture ratio CR is assumed 90% for most research works [12]. According to condition(14), the efficiency of temporary carbon storage 1-GWP(η) should be larger than 0.30, which is equivalent to a leakage coefficient η smaller than 0.027. As another example, an energy penalty of 35% and a capture ratio of 80% require that the corresponding efficiency of temporary carbon storage be larger than 0.44, which is equivalent to a leakage coefficient smaller than 0.017.

The preceding simple analytical model shows that the trade-off between capture plant and non-capture plant is affected by two factors: (1) the capture technology characteristics defined as energy penalty divided by the capture ratio; (2) the leakage of stored carbon.

As a conclusion of the physical approach, it appears that CCS doesn't always prevent from global warming. Under certain conditions, for example high energy penalty and/or low capture ratio and/or high leakage, CCS can be ineffective and even worsen the warming effect.

ECONOMICS EFFICIENCY OF CCS

Differing from the above approach, some researchers suggested to treat emissions and removal separately [6], thus the sequestration will not be different from permanent carbon avoided. In other words, when one removes a ton of carbon, one gets credits for its removal; when the sequestered carbon leaks back to the atmosphere, one must buy credits from somewhere for offsetting its "emission", we call it "Pay When Leak". The essential feature of this approach is that sequestered carbon implies a permanent liability for the "owner". With this permanent liability, a potential investor in a sequestration project will face an investment decision problem based on a cash flow caused by leakage from reservoirs and carbon credits price in the future. The classical approach for such decision problems is based on the so-called Net Present Value (NPV), which calculates the discounted present value of project cash flow. It can be expressed as follows:

$$NPV = \int_0^\infty p(t)A(t)e^{-rt}dt\,. \qquad (16)$$

where t is the time, $p(t)$ is the carbon price or carbon tax at time t, $A(t)$ is the carbon credits acquired (positive) or needed (negative) at time t, r is the discount rate. This framework is widely employed for discussion of economic efficiency of sequestration [4-6]. But the definition of economic efficiency in literature is not consistent. Some researchers define it from a point of view of potential investors [4, 6], framing it as an industrial economics problem, while others define it on the basis of carbon tax path [5]. Such definition can give a more macroscopic measure for CCS

because carbon tax is often a shadow price of carbon emission coming from a complicated economy-environment model.

The difference between these two definitions is clear: the former is based on expectation about future carbon price and discount rate of specific investors, and can be used for explaining decision making of an individual; the latter is based on carbon tax path and social discount rate, and can be used for aggregation analysis. For the latter way, it can be considered as a partial equilibrium model if carbon tax path and social discount rate are exogenously given; it can also be integrated with some economy-environment model to make these variables endogenous, making it then a general equilibrium analysis.

As Keller et al [5] argued, in a simple NPV framework, the tradeoff between CO_2 abatement and CO_2 sequestration is affected by four factors: (1) energy penalty; (2) leakage rate; (3) future carbon tax path; (4) discount rate. We follow this simple analytical framework, from the view point of an investor, with the aim of determining whether or not CCS should be employed in a power plant. For linking this section and the former discussion, a fifth factor is added into this framework: the capture ratio.

For the reference plant, the marginal benefit for 1kWh electricity output is:

$$\text{Profit}_r = P_e - EF \cdot HR_r \cdot P_c - P_F \cdot HR_r. \quad (17)$$

While for the plant with capture, the marginal benefit for 1kWh electricity output is:

$$\text{Profit}_c = P_e - EF \cdot HR_c \cdot (1-CR) \cdot P_c - P_F \cdot HR_c - \int_0^\infty EF \cdot HR_C \cdot CR \cdot \eta e^{-\eta t} \cdot P_C \cdot e^{\beta t} \cdot e^{-rt} dt \quad (18)$$

The integral of the preceeding equation[4] can be calculated analytically, assuming $r+\eta-\beta>0$ [5] and the solution can be written as follows:

$$\text{Profit}_C = P_e - EF \cdot HR_c \cdot (1-CR) \cdot P_c - P_F \cdot HR_c - \frac{EF \cdot HR_C \cdot CR \cdot P_C \cdot \eta}{r+\eta-\beta}. \quad (19)$$

The criterion for the plant with capture to be preferred over a reference plant is $\text{Profit}_c > \text{Profit}_r$. Using equations(10), (17) and(19), this condition can be expressed as:

$$\left(1+\frac{P_F}{EF \cdot P_C}\right)\frac{\lambda}{CR} < 1 - \frac{\eta}{r+\eta-\beta}. \quad (20)$$

Letting

$$\alpha = \left(1+\frac{P_F}{EF \cdot P_C}\right)\frac{\lambda}{CR} \quad (21)$$

Equation 21 is equivalent to the following condition: [6]

$$\eta < \frac{(1-\alpha)(r-\beta)}{\alpha} \quad (22)$$

A necessary condition (but not sufficient) for formulation (22) is $\alpha<1$, otherwise the capture plant will be dominated by the reference plant no matter how small is the leakage rate, because it can't be negative. We call this condition **economical feasibility condition**.

When the economical feasibility condition stands, a **maximum permissible leakage coefficient** can be given by:

$$\eta_m = \frac{(1-\alpha)(r-\beta)}{\alpha}, \quad (23)$$

For illustration, the following parameters set are selected:

P_F=1.5\$/GJ[7], P_C=24\$/tCO_2[8], EF=90kg CO_2/GJ[9] for coal burning.

With the above parameter set for coal, the economic feasibility condition is: $\lambda/CR<0.59$, with a capture ratio of 90%; the above condition is equivalent to $\lambda<0.53$. Almost all of capture technologies listed in Table 3 are economically feasible.

COMPARISON AMONG DIFFERENT FACTORS

As we have discussed earlier, for a physical analysis based on a cumulative radiative forcing calculation, the maximum permissible leakage coefficient η_m^{I} is only related to the technological characteristics of capture technology, which is qualified as λ/CR. When we change to the economical viewpoint, η_m^{II} is affected not only by technological characteristics, but also by economical characteristics ($1+P_F/(EF \cdot P_C)$) and by the expectation term ($r-\beta$). The economical characteristics will determine whether or not a kind of capture technology is economically feasible (not considering the leakage issue), while the expectation term gives the individual expectation about future carbon price path and discount rate.

[4] For simplicity, we use an infinite time scale here instead of a finite one. This simplicity will not do harm to our subsequent conclusion because $\text{Profit}_C > \text{Profit}_r$ is a sufficient condition (but not necessary) for $\text{Profit}_C^{TH} > \text{Profit}_r$ with any given finite time scale.

[5] If this condition fails, the sum of (18) will be firmly negative so that the CCS project is financially unbeneficial.

[6] Note that $\alpha>0$ and $r+\eta-\beta>0$.

[7] Data came from World Energy Outlook [13].

[8] Data from [14], the carbon tax adopted by Norway government in 1999 for coal burning.

[9] Data came from Emission Factor Database ,http://www.ipcc-nggip.iges.or.jp/EFDB/main.php.

$$1\text{-GWP}(\eta_m^{\mathrm{I}}) = \lambda/\mathrm{CR}. \qquad (15)$$

$$\eta_m^{\mathrm{II}} = \frac{(1-\alpha)(r-\beta)}{\alpha}, \qquad (23)$$

Corresponding with criterion (14) coming from a radiative forcing approach, formulation (22) gives a criterion based on a financial analysis. If this latter criterion is not satisfied, a CCS project should be rejected economically, but it may still be acceptable physically, that means the criterion (14) still stands and vice versa. In other words, the radiative forcing criterion (15) is inconsistent with the economical one (23). In addition, the criterion based on radiative forcing is an objective criterion which doesn't change according to any subjective conclusion while the economical criterion will vary with different subjective expectation and economical characteristics.

These differences between radiative forcing criterion and economical criterion are illustrated in Figure 6 and Figure 7 under different expectation and different carbon price[10].

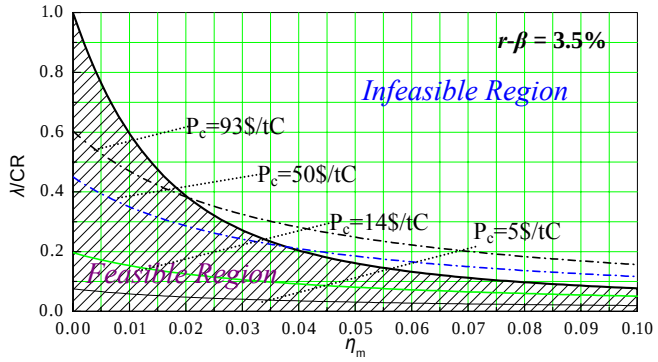

Figure 6: Physically and economically maximal permissible leakage rate under different carbon price.[11]

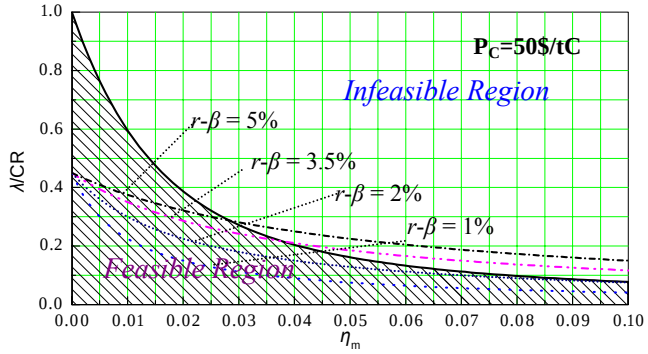

Figure 7: Physically and economically maximal permissible leakage rate under different future expectation.

The relationship between physical criterion and economic criterion is complex; none of them is simply dominated by the other. Generally speaking, for lower leakage coefficient, the economic criterion is stronger than the physical one while for higher leakage coefficient, it is just the opposite. As we discussed above, the economic criterion relaxes further and further when carbon price and/or expectation term become higher and higher, while the physical one doesn't vary. Under high carbon price and high expectation, some CCS technologies will be economically worthwhile but physically non-beneficial.

When using the economic approach, as Herzog argued [6], the potential investor of a sequestration project must make careful estimation about future carbon price and calculate the rate of return which will be compared with other alternatives. Once he decides to put such project into force, he must cover the leakage when it happens. But the "Pay When Leak" approach relies on individual expectation term (r-β), not on social aggregation one. If an individual investor underestimates the risk and uses a physically inefficient storage location, the whole society has to suffer because the permanent liability can't be really unlimited [15]: at one point the investor will chose bankruptcy to avoid further losses. Most important, if such risk are correlated, then they cannot be averaged through insurance mechanisms, then we have no way to average such risk, and the damage caused by such failure is difficult to be measured with monetary value. Just as Baer argued [15] "If we are to proceed with the use of sequestration, we need to regulate it in a way that establishes a precautionary limit on storage today based on the long-term rate of leakage and the plausible failure of liability".

When they underestimate the "expectation term", some physically feasible CCS project will be pending because of economical consideration, some other mitigation strategy with higher cost will be employed. There will be an efficiency loss.

CONCLUSION

This paper examined carbon capture and sequestration technology with leakage under different aspects: a physical aspect based on radiative forcing, and an economical aspect based on discounted net present value. The former approach can be interpreted as a systemic point of view, while the latter can be interpreted as a cost-benefit assessment from the viewpoint of individual investors.

The analysis based on the GWP concept confirms that a leakage coefficient of 0.001 is nearly the same as perfect storage, meaning storage without any leakage or carbon avoided. The same conclu-

[10] But the fuel price is assumed fixed here.
[11] (r-β)=3.5% is based on estimation of [5].

sion has been reached by several other researchers through different approaches [16]. A comparison analysis shows that for high leakage rates CCS may cause larger global warming effect than a reference plant, at least for CCS in power plants.

Although the economical approach is straightforward for CCS, it is strongly affected by "individual expectation" about the future, which is an expectation for future carbon price path. When the carbon price path is overestimated, it will lead to a "moral hazard" problem, and some high leakage reservoirs may be employed and cause higher radiative forcing in the future. When it is underestimated, some CCS project that ought to be good will be rejected, thus an efficiency loss.

Of course the radiative forcing approach also has some shortcomings. Firstly, it doesn't consider the economic terms and gives no idea on cost considerations and investors incentives. Secondly, the marginal treatment we used in this paper only gives an insight for comparative static analysis. But it is useful for being a benchmark case.

There is no simple relationship between the physical criterion and the economic criterion. Generally speaking, the economic criterion is more strict, more selective, than the physical one when the leakage coefficient of the reservoir is small, but it is just the opposite when this coefficient is large.

Finally, our models are based on a set of assumptions, some of which are strong and restrictive. The results should therefore be used carefully and checked under some more realistic assumptions. A fully comprehensive analysis requires more realistic numerical models to be developed in the future.

Acknowledgment

This work has been performed in the framework of the Sino-French center for Energy and Environment of Tsinghua University (CEFCEET).

REFERENCE

[1] United Nations Framework Convention on Climate Change, *Kyoto Protocol to the United Nations Framework Convention on Climate Change*. 1998.

[2] Marland G, Fruit K, Sedjo R. *Accounting for sequestered carbon: the question of permanence*. Environmental Science & Policy 2001**;** 4 (6): 259-268.

[3] IPCC. *Land Use, Land-Use Change, and Forestry: A Special Report of the IPCC*. Cambridge,UK: Cambridge University Press. 2000.

[4] Ha-Duong M, Keith DW. *Carbon Storage: the Economic Efficiency of Storing CO_2 in Leaky Reservoirs*. Clean Technologies and Environmental Policy 2003**;** 5 (3-4): 181-189.

[5] Keller K, Yang Z, Hall M, Bradford DF. *Carbon Dioxide Sequestration: When and How Much?* See also: http://www.princeton.edu/~ceps/workingpaper/94bradford.pdf

[6] Herzog H, Caldeira K, Reilly J. *An Issue of Permanence: Assessing the Effectiveness of Temporary Carbon Storage*. Climatic Change 2003**;** 59 (3): 293-310.

[7] Chomitz MK. *Evaluating Carbon Offsets from Forestry and Energy Projects: How do they compare?* report no. World Bank Policy Research Working Paper 2357. New York: World Bank, 2000.

[8] Smith SJ, Wigley ML. *Global Warming Potentials: 1. Climatic Implications of Emissions Reductions*. Climatic Change 2000**;** 44 (4): 445-457.

[9] Lashof DA, Ahuja DR. *Relative Contributions of Greenhouse Gas Emissions to Global Warming*. Nature 1990**;** 344: 529-531.

[10] Houghton JT, Meria Filho LG, Bruce J, Hoesung L, Callander BA, Haites E, Harris N, Maskell K. *Climate Change 1994: Radiative Forcing of Climate Change and an Evaluation of the IPCC 1992 IS92 Emission Scenario*. Cambridge, UK: Cambridge University Press. 1995.

[11] Herzog H. *The Economics of CO_2 Separation and Capture*. Technology 2000**;** 7: 13-23.

[12] IEA Greenhouse Gas R&D Programme. *Carbon Dioxide Capture from Power Stations*, report no. ISBN-1 898373 15 9. OECD,Paris: Februry, 1994.

[13] International Energy Agency(IEA). *World Energy Outlook*. Paris: IEA Publications. 2002.

[14] Bruvoll A, Larsen BM. *Greenhouse gas emissions in Norway: do carbon taxes work?* Energy Policy 2004**;** 32 (4): 493-505.

[15] Baer P. *An Issue of Scenarios: Carbon Sequestration as Investment and the Distribution of Risk*. Climatic Change 2003**;** 59 (3): 283-291.

[16] Hepple RP, Benson SM, *Implications of Surface Seepage on the Effectiveness of Geologic Storage of Carbon Dioxide as a Climate Change Mitigation Strategy*. In GHGT-6: Sixth International Conference on Greenhouse Gas Control Technologies, Kyoto, Japan, 2002.

Proceedings of ECOS 2005
Trondheim, Norway
June 20–22, 2005

MODELING OF THE REGENERATION UNITS FOR AMINE BASED CO_2 ABSORPTION PLANTS: INTRODUCTION OF AN ORGANIC STRIPPING MEDIUM

Finn Andrew Tobiesen and Hallvard F. Svendsen*
Norwegian University of Science and Technology
Department of Chemical Engineering,
N-7491 Trondheim
Norway

ABSTRACT

A computational model for the regeneration unit of a monoethanolamine (MEA) based absorption plant for CO_2 removal has been developed. The model simulates a three phase process in order to investigate the effects of adding an immiscible organic component to the units to control reboiler temperature. The results show that the desorption process using MEA is very sensitive to the reboiler temperature. There is a significant increase in reboiler duty as hydrocarbon is added to the system. However, the reboiler- and desorber column temperatures are reduced significantly. The driving force for desorption is lowered even though the acid gas is diluted throughout the column. This is due to the strong temperature dependency of the CO_2 partial pressure over the MEA.

Keywords: chemical desorption, energy consumption, desorption, absorption, MEA

NOMENCLATURE

i	chemical components
aq	aqueous phase
org	organic phase
x'	molar fraction; three-phase model
x	molar fraction; two-phase model
p	partial pressure
HC	hydrocarbon content

INTRODUCTION

The removal of carbon dioxide (CO_2) from gas streams, such as natural gas and flue gas, is an essential step in their purification process. This, as well as the desire to alleviate the problem of global warming has resulted in an increased emphasis towards designing more economically efficient technologies for removing CO_2 from natural- and industrial flue gases. Based on the technologies available today, post-combustion removal of CO_2 by use of absorption with chemical solvents is considered to be the most cost-effective and viable option. For CO_2 removal from natural gas and refinery gases, amine based absorption systems have been the most used alternative and is a well proven commercial technology [1, 2, 3]. Despite their extensive usage, the cost of removing CO_2 using traditional amino-compounds is still high, in particular when considering this as a cost penalty on electricity from the power producing industry. On the other hand, the earlier lack of incentive to really minimize the energy requirements in typical post-combustion situations with very large gas flows and low CO_2 partial pressures, does leave room for significant improvements to these processes

* Corresponding author: Phone: +47-735 94100, Fax: +47-735 94080
Email: hallvard.svendsen@chemeng.ntnu.no

For these reasons, there is a strong interest in new developments for both reducing the energy required and for improving the environmental impact of these processes.
In a typical post-combustion CO_2 removal process more than 90% of the energy requirement stems from regeneration of the loaded liquid in the desorber. This, in addition to solvent losses and financial costs, is a dominating contributor to the operational costs of the overall gas cleaning process.
Despite this, the available literature in the area of detailed desorber operation is relatively scarce as compared to the extensive work done on the absorption side.

The costs incurred are mainly due to the large amount of steam required by the indirectly heated desorber reboiler. This steam is needed mainly for three purposes:

1. To provide sufficient energy to reverse the exothermic amine-acid gas reaction.

2. For diluting the CO_2 gas throughout the desorber and thereby work as stripping gas.

3. To provide sufficient sensible heat to warm up the rich amine liquid feed.

The three above mentioned energy sinks are about equally important. This paper is mainly aimed at investigating the effects of providing an additional low cost stripping gas to the regeneration column, thereby reducing the second sink term in the list above. This is suggested done by introducing an organic solvent to the traditional aqueous MEA absorption process, providing a three-phase system, containing two liquid phases, one organic and one aqueous, as well as the vapor phase. The principle is that the organic stripping gas medium is immiscible with the aqueous phase. After being evaporated in the desorber reboiler, it dilutes the CO_2 in the regenerator and is subsequently fully recovered as an organic immiscible liquid in the condenser. The organic liquid is then separated from the condensed water and piped directly back to the reboiler while maintaining its full vapor pressure. Since the two liquid phases are immiscible, the organic phase is not a part of the lean solution and is thereby contained only in the regeneration part of the gas cleaning process and will not circulate to the absorber via the cross-flow heat exchanger.

PROCESS DESCRIPTION AND THEORY

The fundamental nature of adding a volatile organic immiscible component to the regeneration process is to increase the degrees of freedom and give room for an increased number of ways of operating the desorber.
Firstly it enables the aqueous phase components, mainly water and CO_2, as well as the volatile organic solvent, to be evaporated, and subsequently recovered, at a temperature substantially below that of the boiling point of the aqueous phase alone. Since there are two immiscible liquid phases present in the reboiler, each more or less unaffected by the presence of the other (as long as they are agitated so that the lighter liquid does not form an impenetrable layer over the heavier), they both vaporize to an extent determined only by their individual volatilities. The phases will behave as distinct entities and there will be no dependence on how much of each species is present as long as the amount to be vaporized is balanced by the reboiler steam input. Therefore, such a mixture always boils at a temperature lower than that of either constituent alone. In this way, by keeping the pressure constant, the reboiler temperature can be gradually decreased by adding more third component to the desorber cycle. Secondly, one may wish to operate the reboiler at a certain temperature. For instance since MEA is prone to corroding steel as well as degrading at elevated temperatures, it might be advantageous to keep an upper limit for the reboiler temperature. The reboiler temperature can be controlled by adding a certain amount of an organic component, while the total pressure is increased. The water/CO_2 ratio remains for all practical purposes unchanged, while the third component creates the pressure increase. Earlier studies show that an increased pressure in the regenerator system can have a positive effect on the desorber performance [4, 5], as well as decreasing possible recompression costs for CO_2 if this is to be recompressed for further piping and storage.
Finally, one may utilize a combination of the above two effects and increase both the reboiler temperature and pressure. If the CO_2 product pressure can be increased to about 6 bar, then one may do away with the compressor for recompression altogether and liquefy the CO_2 directly for storage.

MODEL DEVELOPMENT

Introduction of an organic immiscible stripping medium to the desorber cycle introduces some new complications in the process simulations.

An earlier developed two-phase model for CO_2 regeneration with MEA was modified to accommodate for three phases. The general code for the mass and energy transfer in the desorber column including reboiler, desorber and condenser, as well as the equilibrium and interfacial mass transfer models, were written in FORTRAN 90. The details of the complete two-phase model, including model assumptions, are addressed in a separate paper [5]. A discussion of the choice of interfacial mass transfer model and thermodynamic model for the aqueous phase is also found in this paper.

In order to minimize the complications associated with the introduction of a second liquid phase, the following simplifying assumptions were made:

- It is assumed that the two liquid phases are completely immiscible. An effect not accounted for in this study is the non-ideal nature of this aqueous-organic system.
- When present, the organic component is at its saturation point throughout the system.
- The aqueous phase yields its own equilibrium partial pressures given by an explicit activity coefficient based thermodynamic model.
- The organic phase yields its equilibrium partial pressure given by an Antoine relationship.
- Daltons law is applicable eg.; the total equilibrium partial pressure of the liquid phases is the sum of the vapor pressures of the two phases.
- For the liquid phase, in terms of mass and energy balances, the new component is included as an additional molar fraction in the overall sum of components. Therefore, the model does not separate the two liquid phases at the overall level in terms of balances. However, a separate phase will give, in terms of thermodynamics and gas phase driving forces, an organic phase with its full partial pressure obtained throughout the system, which is described for one organic component:

Aqueous phase components:

$$x'_{i,aq} = \frac{x_{i,aq}}{\sum(x_{i,aq}) - x_{1,org}}$$ where

$$\sum x_{i,aq} = 1 \text{ and } \sum x'_{i,aq} = 1$$

Organic phase component:

$$x'_{1,org} = 1$$

- The reboiler is calculated as two temperature-pressure (TP) flashes, one for each phase (aqueous and organic). A schematic diagram is shown in figure 1. Since there are three phases (one vapor and two liquids) and four components, the phase rule shows that the reboiler has three degrees of freedom. Therefore, an inner loop iteration is used to obtain the total partial pressures of each phase at an initial given temperature and total pressure, while the inlet stream is fully defined. To ensure that the vapor flow generated from the reboiler is stable for overall code stability, an outer loop can be used to iterate to a given reboiler vapor fraction using the reboiler temperature as the iteration variable.

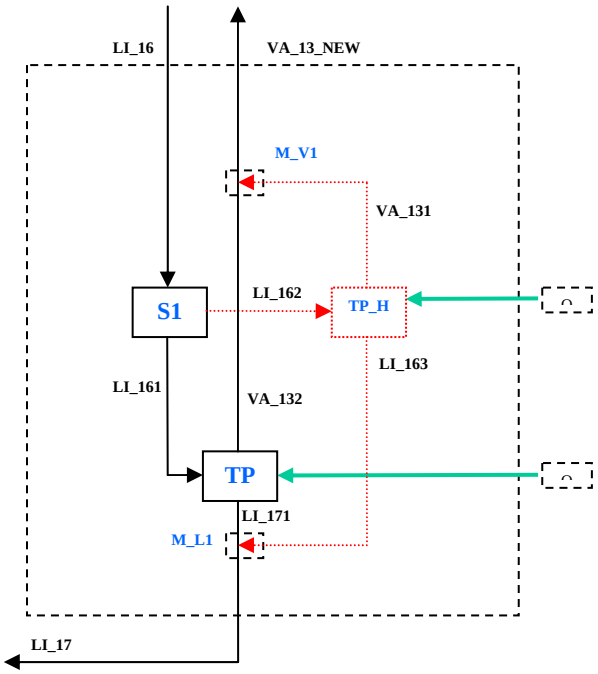

Figure 1: Schematic diagram of the three-phase reboiler model. Dotted lines indicate organic streams.

- The condenser is modelled in a similar manner but here the temperature is always fixed and an outer iteration loop is not necessary.
- The organic component is taken from the condenser and piped directly to the reboiler.
- Since the temperature in the reboiler is higher than the organic component boiling point, all of it will vaporize.

The overall flow sheet is shown in figure 2.

BASE CASE

The base case is a conceptual MEA pilot plant intended to recover CO_2 from flue gas at atmospheric pressure with parameters and dimensions identical to a pilot plant available in our laboratories. It should be noted that the regeneration unit does not necessarily depend on whether the absorption unit is for flue gas or natural gas since the units in both cases are usually operated at low pressure and elevated temperature.

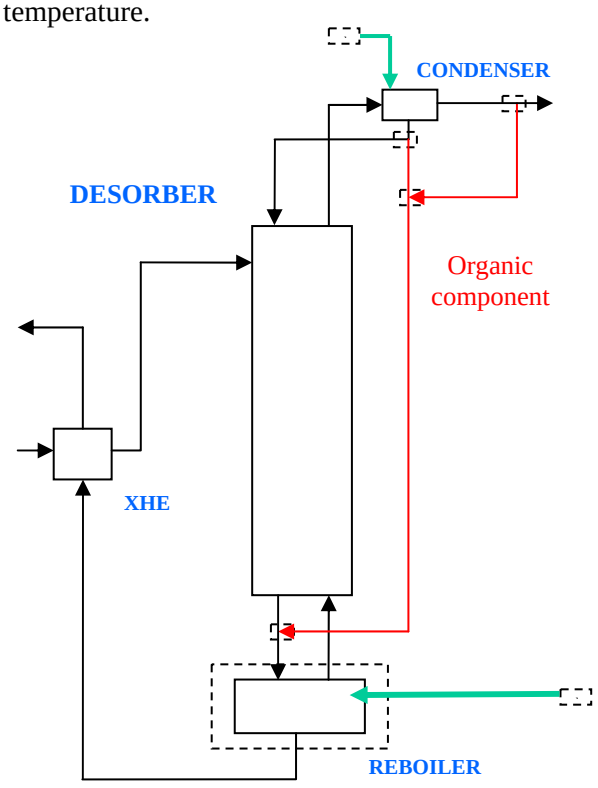

Figure 2. Schematic diagram of the modified flow sheet.

The MEA concentration has been set to 30wt% and initially there is no added organic component. This high MEA concentration is not uncommon today and standard for the Fluor Econamine Process [2]. With the higher amine concentration in the circulating liquid, including corrosion inhibitors, a higher CO_2 pickup is possible without the extensive corrosive effects normally associated with MEA solutions. For this to be applicable, however, the temperature must be closely controlled. The desorber column characteristics and the operating conditions used in the simulations are all given in table 1. All other details about the two-phase model are described elsewhere [6].

Table 1: Column characteristics and operational parameters for the base case

Column characteristics	Value
Column internal diameter (m)	0.10
Main packing height (m)	4.0
Wash section packing (m)	0
Desorber height (m)	4.0
Packing (Structured):	Sulzer Mellapak 250Y

Parameter:	Value
Liquid circulation rate (kmol/h)	12.0
MEA concentration wt% (15 C)	30.2
Rich solution loading (kmol CO_2/ kmol amine)	0.48
Lean solution loading (kmol/kmol)	0.16
Reboiler pressure (kPa)	200.0
Condenser temperature (C)	60.0
Percent to equilibrium reboiler* (%)	70.0

* Percentage reduction of the equilibrium value of CO_2 with the ideally mixed aqueous phase in the reboiler

SIMULATION RESULTS AND DISCUSSION

Base case

Results from the base cases without addition of hexane are given in table 2 and 3. A cyclic capacity of 0.32 mol CO_2/mol, using 0.48 mol CO_2/mol as rich loading and 0.16 mol CO_2/mol as lean amine loading, has been used for all simulations. It should be noted that in table 2 and 3 the column giving “loading after flash” is the actual loading of the solvent entering the desorber packing. For the base case at 180 kPa, which is a little lower than the more conventional 200-220 kPa, the simulation yields a steam consumption of 4.01 MJ/kg CO_2 removed. This number is very comparable to the numbers reported to be attainable in the industry today, 3.24-4.20 MJ/kg CO_2 [2, 3]. At 240 kPa the reboiler temperature is raised to 129^{o}C. It is evident that this has a significant positive effect on the steam consumption. The energy required for stripping decreases from 4.01 to 2.93 MJ/kg CO_2 recovered. This temperature is too high for the MEA process, but it does indicate the potential that lies in optimising the reboiler temperature.

The added bonus is the reduced recompression costs. It should be kept in mind that the recompression costs can be reduced significantly when going from 1.2 to 2.4 bar CO_2 condenser outlet pressure.
Although the heat duty figures given here are reasonable, they are not intended to be accurate as absolute optimized numbers. Ideally, by maximizing the loading obtainable from the absorber and at the same time avoiding the pinch region in the desorber during stripping, it is possible to lower steam usage substantially. Also, the model flow sheet does not consider split flow configurations. For the purpose of studying desorber performance characteristics for an MEA plant with given operating conditions, the specific steam consumption parameter should therefore be regarded as a relative number only, and the purpose of the present paper is to study variations in this.

Addition of Hexane to the regeneration unit

The organic component to serve as a stripper gas could basically be a fictitious compound. However, to have something to relate to, a real component has been chosen, in this case hexane. This does not imply that hexane is an ideal component. Hexane does not dissolve to any significant extent in the aqueous phase and it is significantly more volatile than water with a normal boiling point of 68.7 ºC, and a boiling point of 92.4 ºC at 200 kPa. This will ensure that the hexane is liquid phase in the condenser while it is evaporated after being piped to the reboiler.
Table 2 and 3 show the effects of increasing the amount of hexane in the reboiler at 180 kPa and 240 kPa respectively. In both cases the total pressure is kept constant. As more hexane is added to the reboiler providing more dilution agent to the column, a lower reboiler temperature results. From table 2 it is seen that at a 23 mole% hexane concentration in the vapour from the reboiler, the reboiler temperature is reduced with 8ºC compared to the base case. Conversely, the steam consumption increases significantly, from 4.05 to 6.49 MJ/kg CO_2 removed. The same trends are seen in table 3 where the pressure is increased to 240 kPa. The base case simulation at 240 kPa shows a reboiler temperature of 129 ºC, and an energy requirement of 3.27 MJ/kg CO_2 removed, while as the hexane is added to a molar fraction of 26%, the temperature is reduced to 120 ºC and the energy duty is raised to 5.7 MJ/kg CO_2 removed. The reboiler temperature in the last case is very close to the temperature of the base case for 180 kPa pressure. It is from this clear that one may not expect energy savings by only keeping the reboiler temperature constant and adding a third immiscible component to raise the pressure.

It is clear from the simulations that there are mainly two competing effects causing the significant change in reboiler heat duty as more hydrocarbons are added to the system. At constant total pressure, the partial pressure of CO_2 throughout the desorber decreases significantly due to the added dilution agent, thus providing a larger driving force for desorbption of CO_2. This should make the desorber more efficient. The second and counteracting effect is due to the reduced temperature in the reboiler which reduces both the water and CO_2 partial pressures. If the P_{CO2} / P_{Water} ratio increases with decreasing temperature, a possible positive effect of the reboiler temperature decrease would result. If the opposite is true, then the effect would be negative. The degree to which this second non-favorable effect affects the desorption process is governed by the thermodynamic properties of the amine and it is clear that for MEA this effect is negative and large.
Figure 3 shows the effects on the CO_2 content in the vapor and on the equilibrium partial pressures in the liquid throughout the tower as hexane is added. The dotted lines represent the liquid phase equilibrium pressure of CO_2 while the plain lines indicate the actual vapor CO_2 partial pressure. As more hydrocarbon is added, the driving force (area between the same color dotted and plain lines) decreases, which signifies that the temperature effect is greater than the CO_2 dilution effect for MEA.

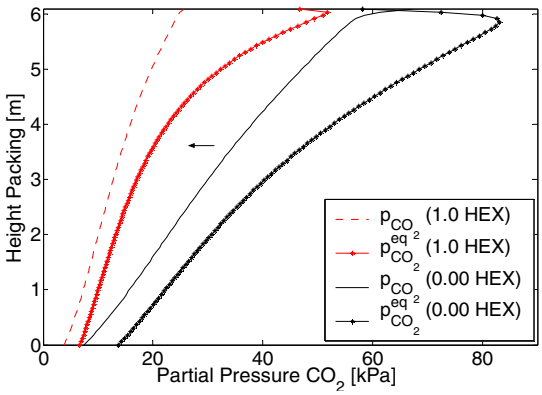

Figure 3: Partial pressures in the tower.
Rich loading, 0.48. Lean loading, 0.16. Reboiler temperature, 120 ºC.

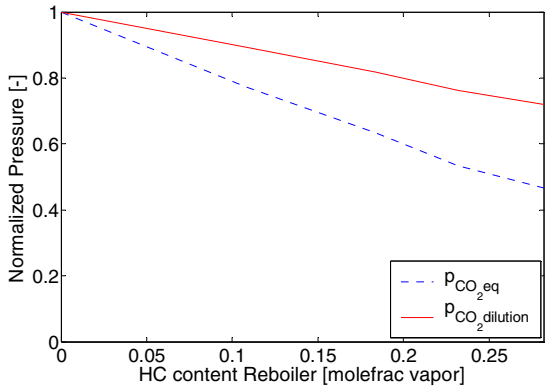

Figure 4: The CO_2 dilution vs. temperature effect.

These competing effects are more clearly shown in figure 4. The line named $P_{CO2\ dilution}$ is a function of the dilution effect from the added hydrocarbon, while the line named $P_{CO2\ eq}$ is a function solely of temperature and composition in the liquid phase. For a favourable steam consumption effect, $P_{CO2\ dilution}$ should change more rapidly than the $P_{CO2\ eq}$ line as hexane is added, or:

$$-\frac{dp_{CO_2}^{Dilution}}{dHC_{content}} \geq -\frac{dp_{CO_2}^{Eq.}}{dHC_{content}}$$

which is clearly not the case for MEA.

Increasing reboiler pressure at constant temperature

Table 4 shows simulations where the pressure is increased while the temperature is kept constant by adding hexane. The cost of recycling the added hexane causes the specific steam consumption ratio to increase significantly as pressure throughout the units increase. The favourable effects by increasing pressure found earlier [4, 5], is found to be almost exclusively due to the increased temperature in the reboiler/desorber. Increasing the pressure requires progressively larger amounts of hexane to maintain constant temperature, which in terms leads to more expenses associated with evaporation and to keep the organic solvent in circulation. The same can be seen in table 5, where the base temperature is 129 ºC. The raised temperature leads to a significant enhancement in desorber performance.

This suggests that the temperature should be maximized in the reboiler to yield a high liquid partial pressure of acid gas as the pressure effect caused by the dilution with hexane is less prominent compared to the temperature effect in the case for chemical desorption with MEA.

It should be noted that the rich amine entering the packing has the full rich amine loading of 0.48 mol CO_2/mol. At this pressure no stripping in the desorber feed lines will take place (see column "loading after flash" in figures 2 and 3) and no problems with two phase flow in the cross flow heat exchanger (XHE) will occur. One problem that may arise if the amine entering the desorber packing is stripped too low, e.g. by lowering the temperature approach of the XHE too much, or by operating the desorber at low pressure, is that absorption and not stripping takes place at the top of the packing. This occurs because the equilibrium partial pressure of the inlet feed is lower than the desorber section CO_2 partial pressure, which will yield a driving force for absorption at the top of the column. This absorption effect is more pronounced at lower feed pressures and will occur until enough sensible heat is provided from the steam for the liquid to reach equilibrium. A part of the upper packing might therefore not be utilized. This can easily happen and indicates an over-sizing of either desorber or XHE. It is therefore important to realize the combined interactions between these units and that their sizes should be chosen depending on the other unit's size and efficiency.

Cost of CO_2 compression

The usual parameters for transportation in pipelines are pressure of about 140 bar and ambient temperature. For liquefaction and transport in ships, the optimal pressure is 6 bar. In any case, if compression is required, increased pressure in the desorber will reduce compression work for subsequent transportation process. It can be omitted completely if pressure approaches 6 bar in the desorber and liquefaction is required. Table 6 shows an estimation of the energy requirement for a simple compressor. The ideal compressor work is calculated from the change in enthalpy of the stream, by holding the stream entropy constant. Here it is assumed that the outlet stream from the condenser contains pure CO_2. The values show that the compression work required

Table 2: Addition of hexane at a reboiler pressure of 180 kPa

Simulation	*Mol% HC reboiler steam*	*Loading after flash*	*Loading to reboiler*	*Temp reboiler*	*Reboiler heat duty*	*Steam boilup*	*HC boilup*	*Specific heat consumption*	*Reflux ratio*
	%	[-]	[-]	C	kW	kmol/h	kmol/h	MJ/kg CO_2	kmol/kmol
BASE_D_0	0	0.395	0.217	120.3	22.64	1.90	0.0	4.017	2.52
HEX_0_17	7.29	0.395	0.217	118.0	26.08	2.04	0.17	4.632	2.93
HEX_0_35	13.32	0.395	0.218	116.0	29.47	2.17	0.35	5.245	3.31
HEX_0_57	19.02	0.395	0.217	114.0	33.62	2.33	0.57	5.982	3.75
HEX_0_81	23.79	0.395	0.216	112.2	38.14	2.48	0.81	6.767	4.20

Reboiler pressure 180 kPa, pressure drop column 1 kPa, efficiency reboiler 70%

Table 3: Addition of hexane at a reboiler pressure of 240 kPa

Simulation	*Mol% HC reboiler steam*	*Loading after flash*	*Loading to reboiler*	*Temp reboiler*	*Reboiler heat duty*	*Steam boilup*	*HC boilup*	*Specific heat consumption*	*Reflux ratio*
	%	[-]	[-]	C	kW	kmol/h	kmol/h	MJ/kg CO_2	kmol/kmol
BASE_D_1	0	0.48	0.231	128.9	16.52	1.54	0.0	2.95	0.75
HEX_1_16	8.373	0.48	0.227	126.2	21.68	1.65	0.16	3.85	1.11
HEX_1_23	13.15	0.48	0.225	124.6	23.78	1.72	0.28	4.22	1.37
HEX_1_43	18.11	0.48	0.223	122.8	26.48	1.82	0.43	4.69	1.67
HEX_1_69	24.89	0.48	0.222	120.3	30.99	1.97	0.69	5.50	2.15

Reboiler pressure 240 kPa, pressure drop column 1 kPa, efficiency reboiler 70%.

Table 4: Temperature reboiler: 120.3 ºC

Simulation	*Pressure reboiler*	*Mol% HC reboiler steam*	*Loading after flash*	*Loading reboiler*	*Reboiler heat duty*	*Steam boilup*	*HC boilup*	*Specific heat consumption*	*Reflux ratio*
	kPa	%	[-]	[-]	kW	kmol/h	kmol/h	MJ/kg CO_2	kmol/kmol
BASE_D_0	180	0	0.395	0.217	22.64	1.90	0.0	4.017	2.52
HEX_0_200	200	9.90	0.480	0.221	26.12	1.98	0.23	4.627	2.08
HEX_0_220	220	18.07	0.480	0.222	28.50	1.97	0.46	5.056	2.10
HEX_0_240	240	24.89	0.480	0.222	30.99	1.97	0.69	5.500	2.15
HEX_0_260	260	30.62	0.480	0.223	33.26	1.96	0.91	5.918	2.19
HEX_0_340	340	46.93	0.480	0.223	43.05	1.95	1.82	7.663	2.35

Reboiler temperature 120.3 ºC, pressure drop column 1 kPa, efficiency reboiler 70%.

Table 5: Temperature reboiler: 128.9 ºC

Simulation	*Pressure reboiler*	*Mol% HC reboiler steam*	*Loading after flash*	*Loading reboiler*	*Reboiler heat duty*	*Steam boilup*	*HC boilup*	*Specific heat consumption*	*Reflux ratio*
	kPa	%	[-]	[-]	kW	kmol/h	kmol/h	MJ/kg CO_2	kmol/kmol
BASE_D_1	240	0	0.480	0.231	16.52	1.54	0.0	2.935	0.75
HEX_0_260	260	8.44	0.480	0.231	20.63	1.54	0.15	3.669	0.82
HEX_0_300	300	19.94	0.480	0.233	23.80	1.56	0.42	4.222	0.90
HEX_0_320	320	24.89	0.480	0.234	25.39	1.56	0.56	4.510	0.95
HEX_0_330	330	27.17	0.480	0.234	26.23	1.56	0.63	4.657	0.98

Reboiler temperature 128.9 ºC, pressure drop column 1 kPa, efficiency reboiler 70%.

is small for a pressure raise to 400 kPa. The gain by increasing pressure in the desorber in terms of compression work saved is therefore only marginal.

Table 6: Estimated compression work

Outlet stream pressure	*Outlet stream Temp*	*Post comp pressure*	*Post comp Temp*	*Comp work*
kPa	C	kPa	°C	***MJ/kg CO_2***
180	60	400	139	0.073
400	60	400	60	0
180	60	4000	417	0.36
400	60	4000	311	0.24
180	60	14000	604	0.57
400	60	14000	482	0.43

A comparison between the investigated method introducing a third immiscible component to the stripper, and the conventional stripper needs to be done where all effects are included. The following items should be considered in the overall evaluation, starting with the favourable effects

Possible advantages

- Reduced compression work, although only small gains.
- Reduced temperatures in reboiler, reduced steel corrosion, (lower quality steel can be used), less amine degradation.
- Larger driving forces for desorption at the same temperature.
- Decreased desorber diameter due to the pressure increase.
- If pressures increases up to 6 bar, the entire recompression prior to liquefaction might be avoided.

Disadvantages:

- Somewhat thicker steel to account for higher pressures.
- Added reboiler duties associated with the inclusion of the organic component. A factor that seems to be the decisive factor when using MEA.

In conclusion, the principle point that probably surpasses the advantageous points regarding the addition of an organic immiscible stripping medium, is that the incurred costs associated with the increased reboiler duty as more hydrocarbon is added to the reboiler, increase too rapidly when MEA solvent is used. Therefore, addition of hexane to the regeneration process is most probably not favourable using MEA, due to the strong temperature dependence of the equilibrium CO_2 pressure. A thorough cost investigation must be carried out. However, since this effect is specific for each amine there might be, and probably are, amines with more favourable properties. Also, there are certainly organic solvents that have better properties, lower heats of vaporization and lower heat capacities.

CONCLUSION

A computational model for the regeneration unit of a monoethanolamine (MEA) based absorption plant for CO_2 removal has been developed. The model simulates a three phase process in order to understand the effects of adding an immiscible organic component to the units to control reboiler temperature. The results show that the desorption process using MEA is very sensitive to the reboiler temperature. There is a significant increase in reboiler duty as hydrocarbon is added to the system. However, the reboiler- and desorber column temperatures are reduced significantly. The driving force for desorption is lowered even though the acid gas is diluted throughout the desorber tower. This is due to the strong temperature dependency of the CO_2 partial pressure over the MEA. It is thus probably not feasible to increase pressure in the desorber to the extent such that a CO_2 recompression unit can be avoided. The amount of hexane that must be added causes the reboiler duty to increase excessively. However, an increased desorber pressure can reduce compression costs.

If a reduction in reboiler temperature is required because of excessive corrosion or solvent degradation, the addition of an organic component can greatly reduce tower temperatures, however, at the expense of increased reboiler duties.

ACKNOWLEDGEMENT

This research was supported financially by the Norwegian Research Council “Klimatek Programme” through the SINTEF Project 661292.01.

REFERENCES

[1] St. Clair, J. H., Simister, W. F. *Process to recover CO_2 from flue gas gets first large scale tryout in Texas.* Oil and Gas Journal 1983;81:109-113.

[2] Reddy, S., Roberts, C. *Fluor's Econamine FG Plus^{SM} Technology: An enhanced Amine-Based CO_2 capture process.* In: Second national conference on carbon sequestration, Alexandria, USA, May 5-8. 2003.

[3] Sander, M.T., Mariz, C.L. *The Fluor Daniel ECONAMINE FG^{SM} Process: Past experience and present day focus*. Energy Convers. Mgmt.1992;33:341-348

[4] Desideri U., Paolucci A., *Performance Modelling of a CO_2 Removal System for Power Plants.* Energy Convers. Mgmt.1999; 40;1899-1915

[5] Finn Andrew Tobiesen, Hallvard F. Svendsen, Karl Anders Hoff, *Desorber energy consumption in amine based absorption plants*, Accepted in Int. J. of Green Energy, 2004.

[6] Finn Andrew Tobiesen, Hallvard F. Svendsen, Juliussen O. *Modeling and Experimental study of carbon dioxide desorption in a structured bed contactor.* To be published, 2005.

Proceedings of ECOS 2005
Trondheim, Norway
June 20–22, 2005

Combined cycle power plants

Proceedings of ECOS 2005
Trondheim, Norway
June 20–22, 2005

ADVANCED POWER PLANT DESIGN METHODOLOGY USING PROCESS INTEGRATION AND MULTI-OBJECTIVE THERMO-ECONOMIC OPTIMISATION

Raffaele Bolliger, Francois Maréchal*, Daniel Favrat
Laboratory for Industrial Energy Systems
École Polytechnique Fédérale de Lausanne
Switzerland - 1015 Lausanne

ABSTRACT

Thermo-economic modelling techniques are well known techniques to optimise power plant designs. These methods are usually based on the definition of a superstructure that includes the major options of the design. If this approach has proved to be appropriate for the optimisation of several conventional NGCC (Natural Gas Combined Cycles), it reveals some weaknesses when dealing with particularly complex systems where heat integration leads to a lot of possible heat exchange configuration. This is for example the case in advanced cycles in zero emission plants where numerous heat exchanges between the gas turbines, the steam network and the CO_2 capture units can be considered. In this situation, the superstructure approach is not anymore practical and new modelling techniques are needed. In this paper, we present a new modelling technique developed to be used in the context of a multi-objective optimisation framework. This method uses a thermodynamic model of the energy flows of the energy conversion units. The results of the model allow the calculation of the hot and cold streams to be considered in the heat exchanger network. A heat cascade model using the ΔT_{min} concept is used to compute the optimal integration of the heat exchange in order to maximise the energy conversion. In this model, a special steam cycle model has been developed to represent all the possible heat exchange interactions and to compute the optimal flowrates in the system with a minimum of structural information. The third part of the model is the thermo-economic estimation of the system cost to deduce the performances of the system. An optimisation method, based on a multi-objective evolutionary algorithm is then used to identify the most important system configurations. The method is illustrated on an AZEP (Advanced Zero Emission Plant) combined cycle design.

Keywords: process integration, heat cascade, multi-objective optimisation, thermo-economic, advanced power plants, AZEP

NOMENCLATURE

C_x	cost of equipment x
$C_{x,r}$	reference cost of equipment x
V	sizing variable
V_r	reference value for sizing
n	size factor
$f_{M\&S}$	Marshall & Swift actualisation factor
Π_x	Pressure ratio of x
$\dot{m}$	Mass flowrate
$\dot{\tilde{m}}$	Molar flowrate
T	Temperature (K)
A	Area (m^2)
P	Pressure (bar)
R	Universal gas constant (8.314 J/K mol)
$\dot{E}$	Power (kW)
AZEP	Advanced Zero Emission Plant
OTM	Oxygen Transfert Membrane
MER	Minimum Energy Requirement
GA	Genetic Algorithm
HRSG	Heat Recovery Steam Generator

*Corresponding author: Phone: +41 21693 3516 Fax: +41 21693 3502 E-mail: francois.marechal@epfl.ch

BACKGROUND

The conventional process simulation approach [8], [15] is based on the idea of scenario: a model is built according to a given structure, in order to meet mass and energy balance. All the elements of the process are connected together to form a superstructure. For each heat exchange, one has to choose between which units it is performed. From here the idea of scenario: each heat exchangers network design corresponds to a well defined structure. When the network is not trivial, i.e. when there is more than one way to exchange heat between units, it is necessary to build several scenarios in order to evaluate the performance of all the possible combinations. When modelling a very complex superstructure composed by several units, the possible scenarios for heat exchangers network become too large to be entirely taken into account. At this point, it is necessary to eliminate some possible solutions and to select only the most interesting ones. The major drawback of this approach is that, when handling with non-linear models, the optimal solution is not known a priori. So, eliminating some possible solutions could lead to the loss of some good solutions. The same topological problem is met when analysing several technological alternatives for a given process. For each unit it is necessary to create the streams and energy connections with the rest of the model, which means creating a scenario. The pinch technology [9] has been widely used in industrial processes to encompass the difficult task of the optimal heat exchanger network design. The method has been adapted to consider streams with unknown flowrates [10] and optimise the combined production of heat and power in a process. It has been demonstrated that the method may be adapted to tackle the optimal integration of steam cycles in power plants [11].

A NEW APPROACH FOR COMPLEX SYSTEMS

The approach developed combines the use of thermo-economic modelling and process integration concepts. In the first step, the process is divided into subunits according to the material flows. Each subunit of the process is modelled independently from the others using a thermo-modelling package. The heat exchanges between the units considered as hot or cold sources. In a second step, an energy integration is performed to model the heat exchange contribution to the final layout of the superstructure. By this way, all the units are correctly sized according to the thermodynamic of heat exchanges, as shown in Figure 1. With this approach the heat exchangers network is a part of the solution of the optimisation problem. The main advantage is that it is possible to build a model without taking care of the heat exchangers network layout, avoiding therefore the creation of scenarios. The same reasoning can be applied to the choice of process alternatives: in the process modelling all the alternatives are programmed; the energy integration will choose the one which best satisfies the objective functions. Alternatively, the use of integer variables allows the direct control of the alternatives during the optimisation. After the application of the energy flows and the process integration model, all the necessary data for computing the system cost estimation is available.

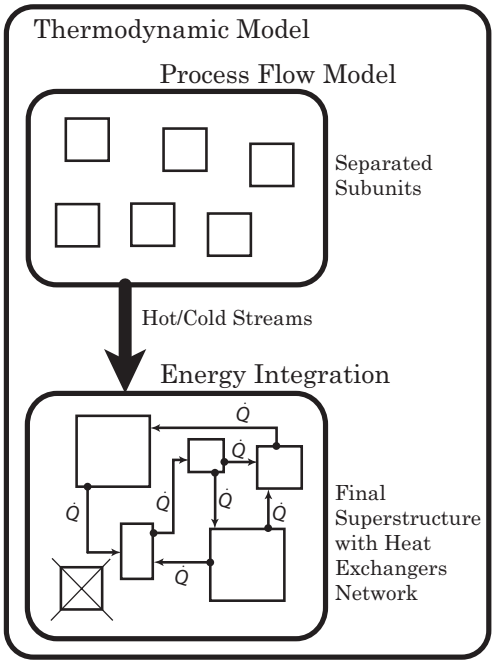

Figure 1: Detail of the thermodynamic model

HOW IT WORKS

The approach can be split into two parts: modelling and optimisation. As shown in figure 2, the optimiser sends the values of the decision variables to the model. Its performance is then evaluated and the values of the objective functions are returned to the optimiser. Decision variables can be sent to all

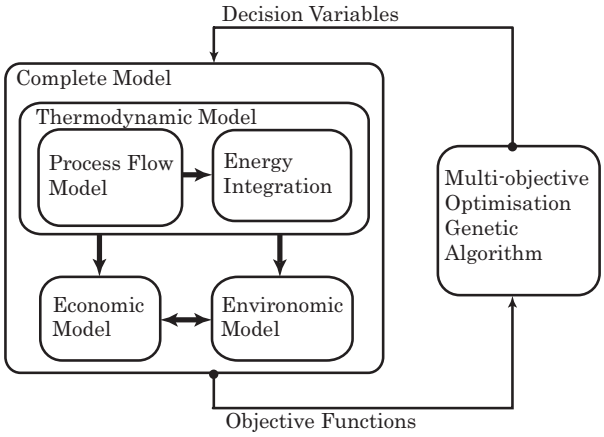

Figure 2: Schematic view of the process integration approach

subparts of the model, in particular, to the process flow, to the energy integration model, to the economic model, to the environomic model or to any sub-model developed for the simulation.

Integrating models

The Laboratoire d'Energétique Industrielle (LENI) is developing a MATLAB® routine called OSMOSE allowing to apply the approach presented in this paper. The details of the modelling and energy integration software called by OSMOSE can be found in [12]. The first sub-model to be run is the process flow. Here the thermodynamics of the material and energy transformation for each sub-unit in the process is computed. Then, the table of cold and hot streams is established. The list can be completed with some units which can be entirely defined in the energy integration model, like the steam network, described later. The process is then perfectly integrated and sized by solving the energy integration as an optimisation [10]. The information coming from the thermodynamic model are then passed to the thermo-economic performance evaluation model in order to compute the objective functions of the global optimisation. At this stage, the values of the objective functions are returned to the optimiser, and the cycle can restart.

Process Flow Model

The process flow model is built with a process modelling software, BELSIM [2]. Each sub-unit of the process is modelled as if it was energetically independent from the others. All the heat exchanges are performed between streams and imaginary sources, assumed to be available at the required temperature. Two types of units are defined: process units and utilities. First ones are the units with fixed flow, which will be used to compute the Minimum Energy Requirement (MER) of the process. Utilities are units with a well defined structure (temperature levels, pressures,...), but with unknown level of utilisation. They are built in the process flow model with a nominal size and the best size is defined to reach the optimal energy integration.

Energy integration - pinch technology

The list of the hot and cold streams of the process is built. Other units can be added to complete the model. The energy integration of the process allows to build the composite curves, in order to determine the MER and to integrate the utilities. The steam network model is embedded in the approach allowing the calculation of the optimal flows in the steam cycle that maximises the power production using the exergy delivered or required by in the process streams. Heat exchanges are computed according to the pinch technology [10], allowing the design of the heat exchangers network, which becomes a solution of the optimisation problem,

Thermo-economic model

Thermo-economic modelling allows predicting the cost of the units used in the process. The thermo-economic costing model used in this paper is using the concepts proposed by Turton [16]:

$$C_x = C_{x,r}(\frac{V}{V_{ref}})^n$$

where V is the sizing variable representing a technical characteristic of the process unit treated. It can be an area (typically for heat exchangers), a mechanical power, a pressure ratio or a temperature.

Hybrid Multi-objective optimisation method

The approach presented in this paper can use both genetic (GA) and conventional semi-Newton optimisation algorithms. GA's are very useful to explore an extremely large solution space, since they can

easily handle first degree discontinuities and multiple local minimums. Their weakness is that they ask a lot of computational time and they can't ensure convergence, since they don't compute objective function's first derivative. Conventional optimisation methods based on semi-Newton algorithm offer the guarantee of convergence (if there is one) with a limited number of iterations. Unfortunately, these algorithms are extremely sensitive to the slope of the objective and they are limited to the research of local minima.
Coupling GA with conventional optimisation allows reducing computational time and ensures convergence. In our work we used advanced GA developed at LENI (MOO) [7],[13] exploiting clustering and multi-objective functions. The usage of integer variables allows studying several technological alternatives leading to the creation of different solution's families. The optimisation of several objectives functions like exergetic efficiency, cost, environmental impacts, leads to the generation of a Pareto curve which is a powerful information support for decision making considering mature and new technologies. In the hybrid approach, the members of the Pareto curve are optimised along the two objectives (the other being considered as a constraint) so that the Pareto curve is pushed to its frontier.

CASE STUDY - ADVANCED NGCC WITH CO_2 CAPTURE

For demonstration purposes, we choose to study the performance of an advanced natural gas combined cycle based on the zero-emission gas turbine (AZEP) developed by Alstom [6]. This cycle combines a conventional 3-stage steam turbine with reheat and a modified gas turbine allowing CO_2 capture. Modifications concern the combustor: the conventional combustion chamber has been substituted with a system composed of two heat exchangers and an oxygen separation membrane (OTM) [6]. Figure 3 shows the concept. After compression, air is preheated to the membrane working temperature (between 800 and 900°C) and oxygen is partially captured. The remaining air is then heated and finally expanded in the turbine. Since depleted air does not participate in the combustion, there is no additional water in the flue gases and therefore it can be cooled down to the ambient temperature. The separated

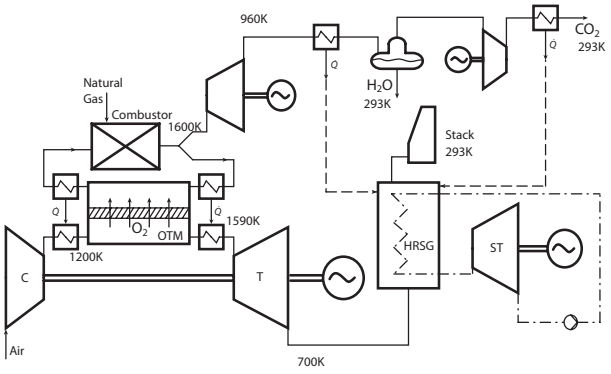

Figure 3: AZEP combined cycle layout

oxygen is recovered in a recirculation loop containing CO_2 and steam and burned with methane. The combustion in the absence of N_2 eliminates concerns about NO_x formation. Combustion gases are partially recycled in the loop and partially sent to the CO_2 capture system. The latter flow is expanded in a turbine down to ambient pressure and then cooled down in order to almost completely condense water. Since the gas phase is composed of CO_2 and water, it is possible to separate the CO_2 by condensation and recover it by pressurising it to about 100 bars and cooling it down to 25°C in order to be transported to its storage place [1].
This cycle is very interesting from the point of view of energy integration, because there are several hot streams that can be used to heat up steam in the heat recovery steam generator (HRSG). Since the network structure is not known a priori, energy integration allows creating the optimal one.

Advanced zero-emission power plant (AZEP) gas turbine

The AZEP gas turbine developed for this study is extremely simplified (Figure 3): the compressor has an isentropic efficiency of 88%, the turbine 93%, combustion is assumed complete, natural gas is composed by pure methane and air is 78%N_2 and 22%O_2. Heat exchangers have a global heat exchange coefficient of 1 kW/°C/m^2. The oxygen separation membrane is assumed ideal, i.e. it is possible to separate as much oxygen as needed; membrane area and cost are backward calculated. Stack temperature is fixed at 25°C. Heat exchanges performed in the membrane zone are directly computed in the process flow model, i.e they are not considered for

energy integration.

CO_2 capture system

Combustion gases which are not recycled are expanded in a turbine and then cooled down to 25°C in order to condense water, which is separated in a liquid/gas separator. The gas phase, composed by more than 99% of CO_2 is then pressurized with a compressor up to 100 bar, and then cooled down to 25°C in order to be liquified. Turbine efficiency is 90% and compressor efficiency is 80%.

Steam network

The steam network model is entirely developed in the energy integration model, using the technique explained in [11]. The concept is related to the definition of a superstructure made by combining Rankine cycles that define one hot stream, one cold stream, one mechanical power by steam expansion and one mechanical power consumption for liquid pumping. Both counter pressure and condensing pressure turbines are considered. Knowing the temperature and pressure levels, the thermodynamic state of the hot and cold streams are computed as well as the mechanical power productions and consumptions. There are two types of streams: steam production and steam condensation. The former can be represented as cold streams by choosing steam pressure and starting/ending temperature. the latter are modelled in the same way as headers, but they are hot streams, since they need to be cooled down. Finally, a steam network can be modelled in the energy integration software by using an assembly of three elements: steam headers (for collecting and distributing steam), extraction ports (to extract steam form the turbines) and one condensation level (representing the return to the deaerator), each one being associated with an integer variable. The superstructure being built to represent all the possible interconnections between the headers.
The main advantage of this way of modelling the steam network is that it is possible to build a very complex steam network by assembling the base elements and to let the software choose the optimal configuration. At each model evaluation, the software performs a MILP (Mixed Integer Linear Programming) optimisation over all the streams appearing in the process and will choose the configuration that best fits the objective function. In this way, the optimal flowrate of each stream of the steam network is computed and some of the headers or extraction ports will be turned off (flowrate equal to zero) and the complex initial configuration will be simplified. The mathematical modelling of the steam network is based on the definition of one or more steam headers and one or more condensate headers. Steam headers can receive steam from four different sources: from an external source (e.g. from the process), from a previous steam header (i.e. from an header with higher pressure), from a condensate header or from an expansion turbine placed between the actual header and a previous one. Symmetrically, a steam header can distribute steam to four kinds of outlets: the exterior of the steam network (e.g to the process), to one of the downstream steam headers, to one of the following condensate headers or to an expansion turbine. Since an header is defined by a pressure and a temperature, it is possible that an expansion from a header A to the pressure of a header B will not provide the corresponding temperature defined for the header B. In order to maintain consistency in the steam network model and to valorize the expansion (which allows extraction of mechanical power from the turbine), the temperature difference is compensated by injecting into header steam coming from either the previous steam header or the condensate header which follows. with this procedure the solution of the MILP optimisation consist in the choice of the headers to be used (integer variables) and their flowrates. The steam network developed for the model presented in this paper is composed by three steam headers, and five steam condensing levels. Steam can be extracted from one of the steam headers, superheated and re-injected in the steam network. This is equivalent to a reheat system. The corresponding steam turbine is a three-stage turbine with one reheat and four extractions. This is the most complex configuration that the energy integration software can select.

Thermo-economic model

The thermo-economic model is based on the investment cost functions of the following equipment: air compressor and turbine, combustion chamber, combustor heat exchangers, oxygen transport membrane, CO_2 compressor and turbine, HRGS heat exchangers and steam turbines system.

Compressors [14]:

$$C_C = \frac{f_{M\&S}}{1069.9}\frac{C_{C,r}}{0.95-\eta_C}\dot{m}_{C,r}\left(\frac{\dot{m}_C}{\dot{m}_{C,r}}\right)^{0.7}\pi_{C,r}\ln(\pi_C)$$

Turbines [14]:

$$C_T = \frac{f_{M\&S}}{1069.9}\frac{C_{T,r}}{0.94-\eta_T}\dot{m}_{T,r}\left(\frac{\dot{m}_T}{\dot{m}_{T,r}}\right)^{0.7} \cdot \ln(\pi_T)\left(1+e^{0.025(T_T-1570)}\right)$$

Combustion Chamber [14]:

$$C_{CC} = \frac{f_{M\&S}}{1069.9}\frac{C_{CC,r}}{|0.995-\pi_{CC}|}\dot{m}_{CC,r}\left(\frac{\dot{m}_{CC}}{\dot{m}_{CC,r}}\right)^{0.7} \cdot \left(1+e^{0.015(T_{CC}-1540)}\right)$$

Heat exchangers [3]:

$$C_{HX} = \frac{f_{M\&S}}{1069.9}\cdot C_{HX}(A_{HX})^{0.7948}$$

The energy integration of the process computes the overall area of the heat exchangers network and gives the minimum number of heat exchangers to respect the minimum energy requirements. With these two values it is possible to estimate the average area and the minimum number of the heat exchangers. The cost of the heat exchangers is then estimated by assuming identical heat exchangers.
Oxygen Transport Membrane [5],[4]:

$$C_{OTM} = \frac{C_{OTM,r}\cdot\dot{\tilde{m}}_{O_2}}{0.0022(P_{O_2})^{0.25}e^{-72000/RT}}$$

The membrane cost (c_{OTM}) is estimated on the basis of a guest future commercial price. For this reason $f_{M\&S}$ is not used.

Steam Turbine with alternator [14]:

$$C_{ST} = \frac{f_{M\&S}}{1069.9}1.15\dot{E}_{ST}\cdot C_{ST,r}\left(\frac{\dot{E}_{ST}}{\dot{E}_{ST,r}}\right)^{0.7}$$

Multi-objective optimisation

The optimiser used for this case study is MOO (Multi-objective Optimiser, [7], [13]), developed at LENI. Two objectives are defined for the problem: maximising the efficiency of the combined cycle and minimising the specific cost of the installation ($\$/kWe$). Twenty decision variables have been defined. They are resumed in Table 1.

Decision variable	Range
Gas turbine press. ratio	15 - 45
OTM inlet temp.[1]	1050 - 1200 K
Oxygen sep. ratio[2]	0.2 - 0.6
OTM outlet HX ΔT[3]	30 - 100 K
Combustor outlet temp.	1500 - 1600 K
Steam head. press.	1 - 100, 1 - 50
	100 - 160 bar
Steam head. superheating	0 - 400, 0 - 500
	100 - 400 K
Condensate head. press.	2x 1 - 10, 1x 1 - 100
	1x 0.020 - 0.025, 1x 0.020 - 1
ΔT multiplication factor[4]	1 - 3

[1] Inlet temperature of the air entering the OTM's heat exchanger

[2] Ratio of of oxygen molar flowrate captured by the OTM

[3] Temperature difference between air entering the OTM heat exchanger and recycling gases entering the combustor (See fig. 3)

[4] ΔT is defined for each stream depending on its thermodynamic state (liquid, gas,two-phase). The multiplication factor optimised here allows amplifying the ΔT_{min} defined by default.

Table 1: Definition of the decision variables and their range

Results

Pareto curve

The Pareto curve allows showing the relationship between the two objectives of the optimisation. It represents the frontier of the solution space, separating feasible and infeasible solutions. In the application, it defines the best specific cost for a given efficiency or, symmetrically, the best efficiency which can be obtained for a given specific cost. The Pareto curve obtained for the optimisation of the AZEP combined cycle is shown in Figure 4. Since clustering has been used to keep local minima alive, the different markers in Figure 4 represent the different families of solutions obtained. It is possible to see that the cluster represented by the square marker is performing a little bit worse in terms of efficiency than the other clusters.
The best performance that can be obtained with the AZEP combined cycle is about 62%, which puts the cycle in direct competition with the best conventional combined cycles and with the new CC's, like gas turbines with fuel cells.

Solutions analysis

Two solutions are detailed in Table 2 : solution A represents the lower specific cost configuration; solution B is the one which gives the best efficiency.

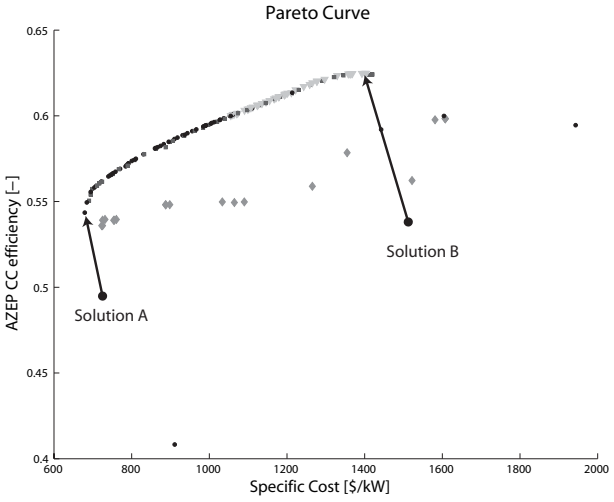

Figure 4: Pareto curve of the multi-objective optimisation

	Solution A	Solution B
Gas Turb. press. ratio	18	41
OTM inlet temp.	1200 K	1200 K
Oxygen sep. ratio	21.8%	31.2%
OTM outlet HX ΔT	100 K	97 K
Combustor out. temp.	1600 K	1600 K
Steam head. press.	101 bar	102 bar
	14 bar	13 bar
	2 bar	1 bar
Steam head. superh.	357 K	365 K
	311 K	214 K
	283 K	290 K
Condensate head. press.	0.021 bar	0.020 bar
ΔT multiplication factor	1	1
Specific Cost	690 US$/kW	1404 US$/kW
Efficiency	55.1%	62.5%

Table 2: Best solution of the optimisation

The layout of the two solutions is extremely similar. The only consistent difference is given by the gas turbine pressure ratio and the oxygen separation rate. Higher ratios lead to better performances but also to higher specific cost. A comparison between Table 1 and Table 2 shows that some variables (OTM inlet temperature, OTM outlet heat exchanger ΔT and combustor outlet temperature) are pushed to their upper bounds, which means that performances will increase when the ceramic technology will accept higher temperatures. The steam network resulting from the optimisation is very simple: 3-stage steam turbine. Reheat is not selected. Compared to conventional steam network, where several steam extractions and reheat are necessary to ensure a good performance, this simplified configuration allows money saving, which compensate the cost of the OTM. Figure 5 shows the integrated composite curve of the steam network. The slope change of process streams at high temperature (around 700 K) is due to the difference of temperature between the expanded CO_2-steam stream and the depleted air from the turbine (the first temperature is 260K higher). It is ideal to integrate steam superheating and to minimize exergy losses. Cooling down streams to 25°C ensures heat availability to preheat water and avoids low pressure steam extractions. From the figure, it can be seen that heat remains available from 75°C to 25°C for district heating, if necessary.

It should be noted that the excellent efficiencies obtained with our model can be partly explained with the following assumptions: the default ΔT_{min} defined for the HRSG (16K for gas-gas heat exchanges, 8K for liquid-gas and 4K for liquid-liquid) allows to increase the efficiency of the plant by 1-2%; the steam superheating of 365K for the high pressure steam header is also critical for conventional HRSG.

The method presented in this paper shows nevertheless that the integration of the hot streams of condensing water are extremely useful to improve the combined cycle performances: taking Solution B as reference, we obtain 62.5% of efficiency. If the temperature at stack is limited to 120°C, the performances are limited to 61.9%. If the heat recovery of the CO_2 separation system is limited to 120°C, the efficiency goes down to 60.9%, because it becomes necessary to introduce steam extraction in the cycle. Finally, if the CO_2 separation system is not integrated in the HRSG, performances fall to 56%. If the steam network is not implemented, the efficiency of the AZEP gas turbine plus the CO_2 system is 46%, and the efficiency of the AZEP gas turbine alone is 37%. The latter value is similar to the results published in [6], where the CO_2 capture system is not considered for power production.

CONCLUSIONS

The optimisation framework based on the coupling of process flow modelling and energy integration, is extremely useful to study complex superstructures and identify promising process configuration at early stage of design. The multi-objective optimisation performed with genetic algorithms combined

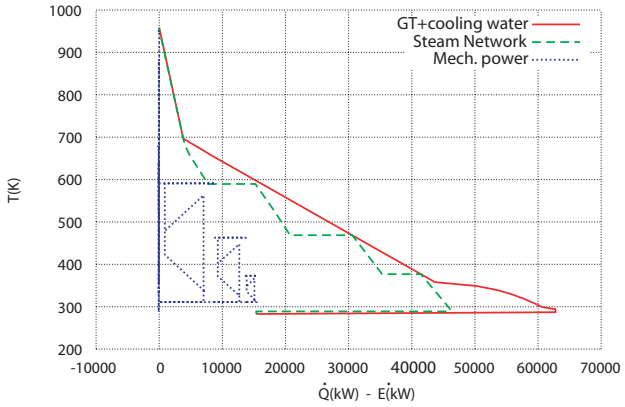

Figure 5: Optimal steam network for the AZEP combined cycle

with conventional optimisation method is ideal to handle multiple decision variables generating non-linear objective functions. Clustering techniques allow the simultaneous study of several promising solutions. The approach is very useful to explore new energy conversion technologies and combined cycles and to generate complex superstructures with unknown heat exchangers network. This is the case of fuel cells, thermal solar energy, organic Rankine cycles, biomass conversion or hydrogen production, to cite a few examples. In this approach, the heat exchangers network is a solution of the optimisation and its structure can be optimally designed thanks to energy integration when optimised configuration and operation of the other energy conversion units are decided.

In the application, the CO_2 capture, which represents a cost increase for conventional NGCC, becomes an interesting option for AZEP combined cycles: the availability of heat down to the ambient temperature allows an significant simplification of the steam network with an increase of performance of the combined cycle. When OTM technology will be mature enough to be commercially competitive, AZEP combined cycles will become a valid alternative in the energy conversion market.

REFERENCES

[1] S. Anderson and R. Newell. Prospects for carbon capture and storage technologies. *Annual Review of Environment and Resources*, 29:109–142, 2004.

[2] Belsim. http://www.belsim.com.

[3] R. Bolliger. Développement d'une méthodologie pour la conception et l'optimisatin thermo-économique de cycles thermodynamiques avancés. Master's thesis, Ecole Polytechnique Fédérale De Lausanne, 2004.

[4] H. Bouwmester and A. Burggraaf. *The CRC handbook of solid state electro-chemistry*, chapter Dense ceramic membranes for oxygen separation, pages 481–553. CRC, Boca Raton, 1997.

[5] R. Bredesen and J. Sogge. A technical and economic assessment of membrane reactors for hydrogen and syngas production. In *Seminar in the Ecological Applications of Innovative Membrane Technology in the Chemical Industry, Cetraro, Calabria (Italy)*, 1996.

[6] T. Girffin and et al. Advanced zero emission gas turbine power plant. In *ASME Turbo Expo*, June 2003.

[7] G. Leyland. *Multi-objective optimisation applied to industrial energy problems*. PhD thesis, Ecole Polytechnique Federale de Lausanne, 2002.

[8] H. T. Li, M. Burer, Z. P. Song, D. Favrat, and F. Marechal. Green heating system: characteristics and illustration with multi-criteria optimization of an integrated energy system. *Energy*, 29(2):225–244, 2004.

[9] B. Linnhoff, D. Townsend, and et al. A user guide on process integration for the efficient use of energy. *The Institution of Chemical Engineers*, 1982.

[10] F. Marechal and B. Kalitventzeff. Heat and power integration : a milp approach for optimal integration of utility systems. *Proceedings Proceedings of the 22nd Symposium of the working party on use of computers in chemical engineering, COPE'91 (Barcelona)*, 1991.

[11] F. Marechal and B. Kalitventzeff. Targeting the optimal integration of steam networks: Mathematical tools and methodology. *Computers and Chemical Engineering*, 23:S133–S136, 1999.

[12] F. Marechal, F. Palazzi, J. Godat, and D. Favrat. Thermo-economic modelling and optimisation of fuel cell systems. *Fuel Cells : From Fundamentals to Systems*, 2004. In Press.

[13] A. Molyneaux. *A practical evolutionary method for the multi-objective optimisation of complex integrated energy systems including vehicle drivetrains*. PhD thesis, École Polytechnique Fédérale de Lausanne, 2002.

[14] S. Pelster. *Environomic Modeling and Optimization of Advanced Combined Cycle Cogeneration Power Plants including CO_2 Separation options*. PhD thesis, École Polytechnique Fédérale de Lausanne, 1998.

[15] S. Pelster, M. von Spakovsky, and D. Favrat. The thermoeconomic and environomic modeling and optimization of the synthesis, design and operation of combined cycles with advanced options. *Journal of Engineering for Gas Turbines and Power, 2001.*, Vol.123(4):pp.717–726, 2001.

[16] R. Turton. *Analysis, Synthesis, and Design of Chemical Proceses*. Prentice Hall, 2003.

Proceedings of ECOS 2005
Trondheim, Norway
June 20–22, 2005

COMPARATIVE ANALYSIS OF NATURAL AND SYNTHETIC REFRIGERANTS IN APPLICATION TO LOW TEMPERATURE CLAUSIUS-RANKINE CYCLE

Aleksandra Borsukiewicz-Gozdur* and Władysław Nowak
Szczecin University of Technology
Faculty of Mechanical Engineering
Chair of Heat Engineering
al. Piastów 19, 70-310 Szczecin
Poland

ABSTRACT

In the paper are presented the results of calculations regarding effectiveness of operation of binary power station fed by low-temperature waste heat/geothermal water. Analysed are possibilities of application of various working media with a view of the most effective utilization of energy. Apart from fundamental thermophysical properties of a working medium such as temperature of thermal disintegration, normal boiling temperature, medium specific heat in liquid and vapour state, considered is the influence of properties such as critical temperature, latent heat of evaporation with a particular attention paid ecological indicators of assessment of low-boiling fluids.
Keywords: natural working fluid, power plant, low-temperature Rankine cycle, geothermal heat exhanger

INTRODUCTION

Electricity production based on a low temperature Clausius-Rankine cycle has been known for over 100 years now. First binary power plant producing electricity for a large industrial scale, which formed a part of Paratunsky Power Plant (Russia), with geothermal water as the upper heat reservoir, was built in the years 1965-67 [1]. At that time R-12 has been used as a working fluid. The Montreal Protocol, however, seriously postulates the issue of reduction of production and consumption of substances from the CFC and HCFC group, which are regarded as harmful to the ozone layer. Technologies of production of electricity using the geothermal waters or a low-temperature waste energy are continuously intensively developing, particularly in the direction of substitution of popular freons with natural or new synthetic fluids offered by the chemical industry. Due to the fact that geological conditions of existence of geothermal waters in Poland together with potential resources of contained there thermal energy form significant possibilities of its utilization in production of electricity the authors of the present work strive to search for optimal design for Polish conditions. On the territory of Poland there is approximately 6600 km^3 of geothermal waters with temperature ranging from 25°C to 150°C. The resources are more or less evenly distributed across Poland in specified geothermal basins and sub-basins belonging to selected provinces and geothermal periods [2].

A SYSTEM OF INSTALLATIONS UTILISING GEOTHERMAL ENERGY/ LOW-TEMPERATURE WASTE ENERGY IN PRODUCTION OF ELECTRICITY

Development of power plant installations practically is independent from the way in which energy is acquired, but temperature and properties of water or other medium being the heat carrier of geothermal/waste heat. In fig. 1 presented is a schema of binary power plant operating according to the Rankine cycle [3]. The working medium in such types of installations are low boiling point fluids, usually refrigerants.

*Corresponding author: Phone:+48 914494136
E-mail:aleksandra.borsukiewicz-gozdur@ps.pl

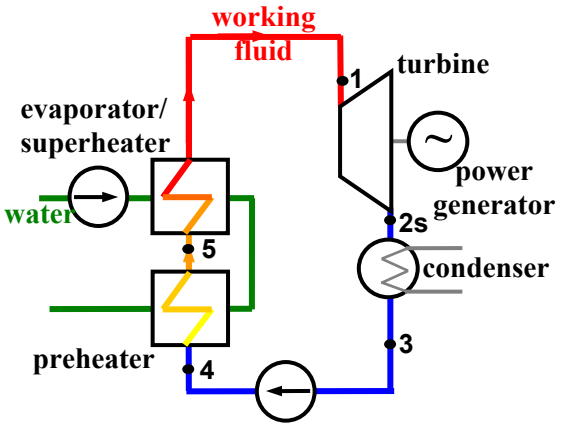

Figure 1: Schema of installation of binary power plant operating according to low temperature Rankine cycle

GENERAL CHARACTERISTIC OF LOW BOILING POINT FLUIDS WITH THE VIEW OF THEIR UTILISATION IN POWER CYCLES

The molecular mass, normal boiling temperature, critical temperature, latent heat of evaporation, specific heat in the liquid and vapour state belong to the fundamental thermophysical properties of working fluids. These quantities influence the shape of saturation curves. Due to the shape of saturation lines all low boiling point fluids can be divided into two groups (fig. 2 and 3). To the first group belong all these which feature the fact that the isentropic expansion starting on the saturated vapor line continues in the superheated vapour region. To the second group belong all these low boiling point fluids, which must be superheated before directing it into the turbine, if the decompression process in turbine must be realized in the region of superheated steam. Schematic diagram of geothermal power plant operating according to the above cycle of processes and the temperature field in heat exchangers have been presented in fig. 4. In the case of fluids from group I there is no necessity of using the superheater.

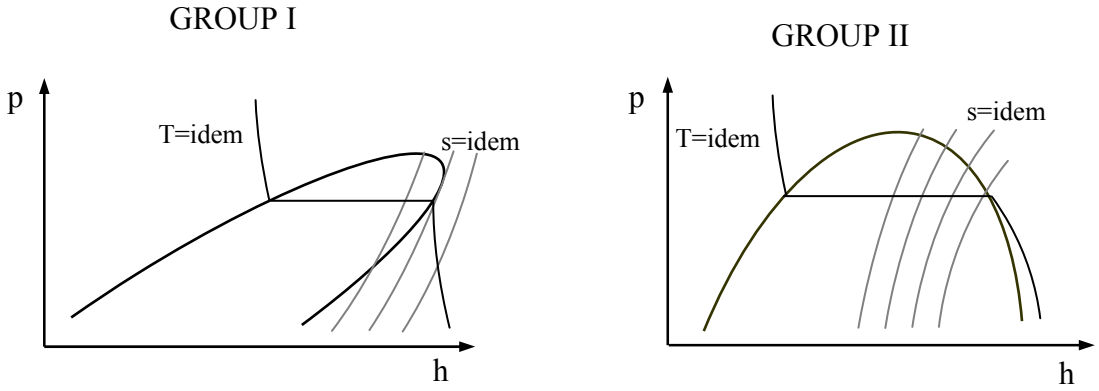

Figure 2: Shape of saturation curves in the pressure-enthalpy diagram

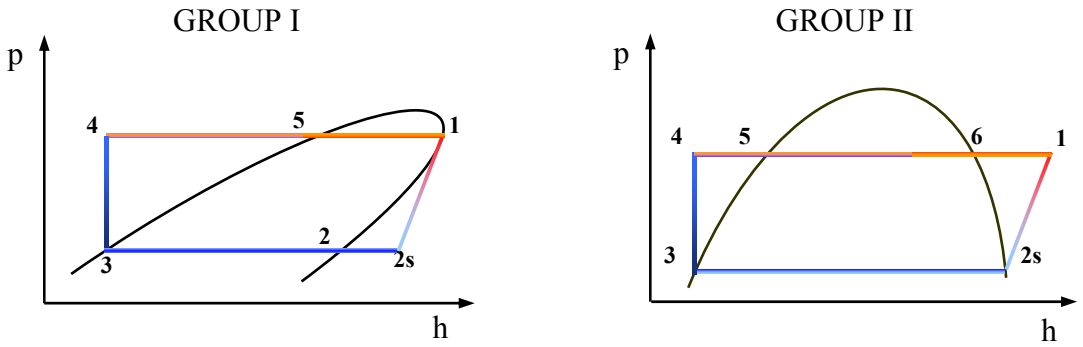

Figure 3: A cycle of thermodynamic processes of the working mediumk in the C-R cycle realised in the region of superheated vapour

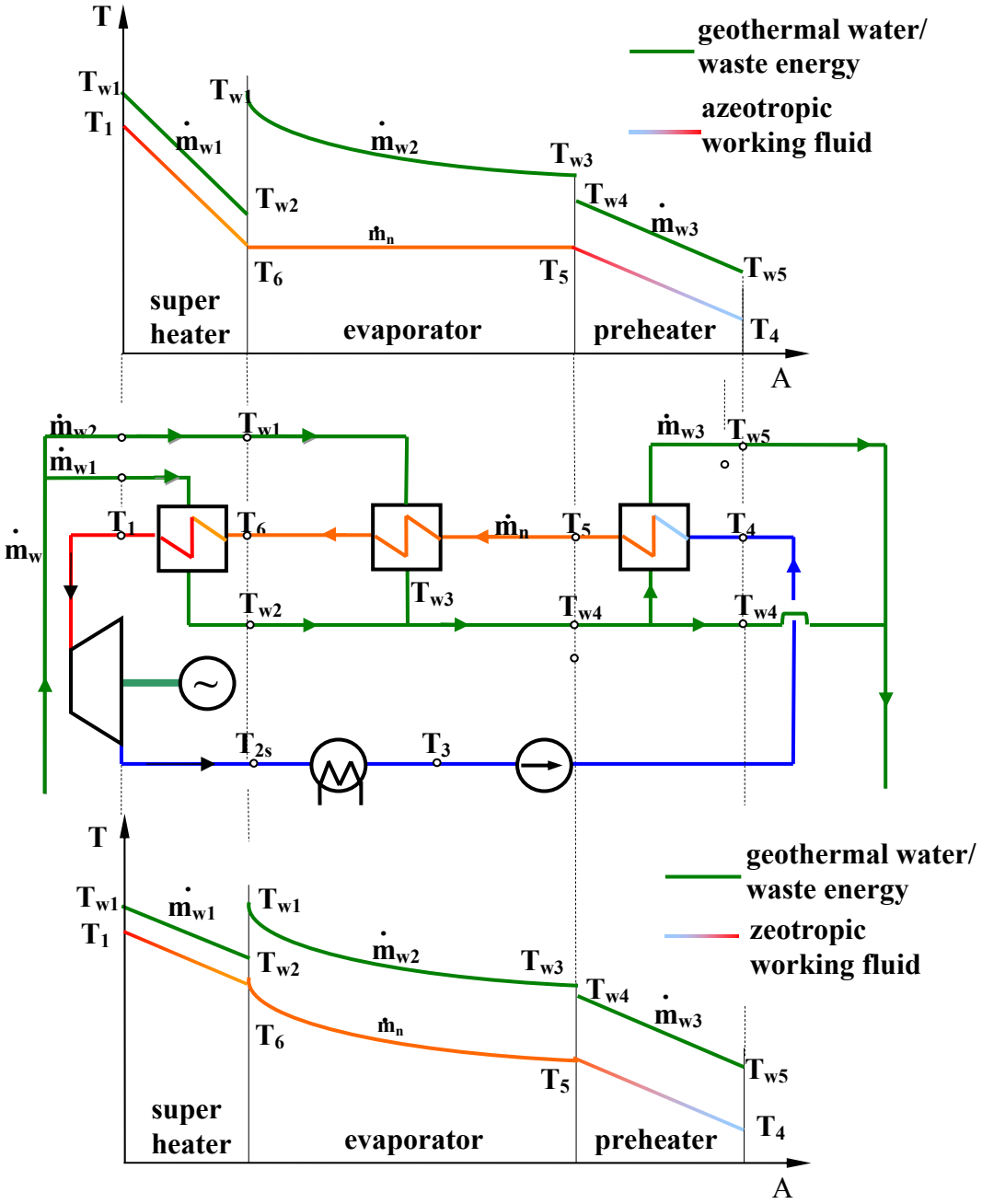

Figure 4: Schema of geothermal power plant operating according to the above cycle of processes and the temperature field in heat exchangers

CHARACTERISTICS OF ZEOTROPIC WORKING MEDIA

Transition of the two-component solution from one state of the matter to another takes place in a completely different way than in the case of single-component media [4]. Implementation of multi-component fluids in the Clausius-Rankine cycle requires knowledge of their behaviour during processes occurring in the evaporator and condenser [5]. In figure 5 presented have been thermodynamic processes of working fluid in the Clausius-Rankine cycle. On the other hand the schematic presenting the binary power station operating according to such cycle in the superheated vapor region together with the temperature field in the heat exchanger is shown in figure 6.

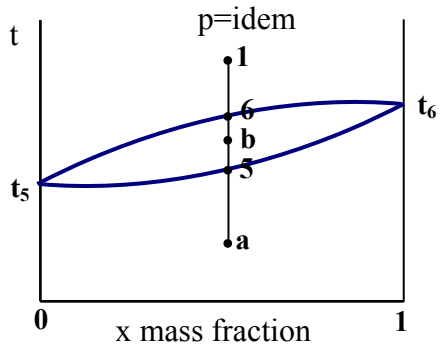

Figure: 5 Isobaric process of boiling of a real zeotropic solution

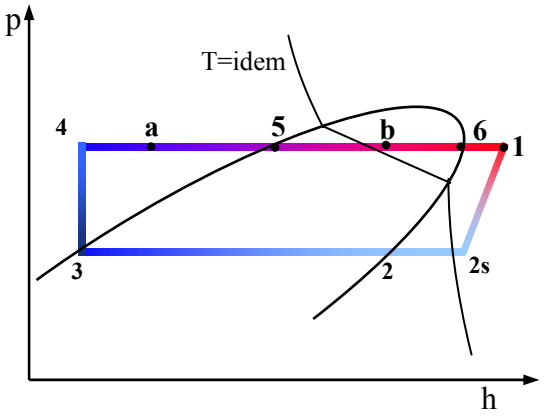

Figure 6: A cycle of thermodynamic processes of two-component working fluid in the Clausius-Rankine cycle

BASIC ASSUMPTIONS

In the paper presented are the results of calculations of the C-R cycle efficiency and turbine power in line with the fig. 4. Carried out have been calculations for the fluids presented in table 1. Thermodynamic parameters of fluids have been taken from the code Refprop 7.0 [6].
Assumptions:
- flowrate of water being the heat carrier of geothermal/waste heat $\dot{m}_w$ =30kg/s;
- temperature of water flowrate $\dot{m}_w$ T_{w1}=80-115°C;
- temperature of evaporation of single component fluids $T_5=T_6=T_{w1}$-15K, for zeotropic mixtures the mean arithmetic evaporation temperature in the beginning and final states $T_e=(T_5+T_6)/2=T_{w1}$-15K;
- temperature of condensation of working medium T_c=25°C, for zeotropic mixtures arithmetic mean of condensation temperatures in the beginning and final states $T_c=(T_2+T_3)/2$=25°C;
- process of isentropic expansion in turbine takes place in the superheated vapour region, which means that for the fluids from the second group considered have been additional energy required to superheat the fluid prior to the turbine (6-1).

Name of fluid	Critical temp. °C	Remarks
propylene	92,4	Single-component natural fluid
propane	96,7	Single-component natural fluid
ibutane	134,7	Single-component natural fluid
ethane	32,2	Single-component natural fluid
water	373,9	Single-component natural fluid
0.9 propane/ 0.1 ethane	90,7	Two-component zeotropic mixture (mass fraction)
0.8 propane/ 0.2 ethane	84,6	
0.7 propane/ 0.3 ethane	78,4	
0.6 propane/ 0.4 ethane	72,1	
0.5 propane/ 0.5 ethane	65,7	
R227ae	101,7	Single-component synthetic fluid
R236fa	124,9	Single-component synthetic fluid
RC 318	115,2	Single-component synthetic fluid
R407C	86,0	Zeotropic mixture of synthetic fluids

Table 1: Tabulation of fluids used in calculations

RESULTS OF CALCULATIONS

On the basis of obtained results of calculations constructed have been relevant diagrams illustrating the influence of temperature of geothermal water on efficiency and power of

binary geothermal power station for selected low boiling point fluids.

In fig. 7 compared have been values of thermal efficiency of the C-R cycle for different fluids, which have been obtained for water with temperature 90-115°C (upper heat reservoir) and condensation temperature of working fluid 25 °C.

In fig. 8 presented has been turbine internal power in the C-R cycle for different fluids, obtained for condensation temperature 25°C in function of feeding water temperature.

In fig. 9 and 10 presented has been enthalpy of fluid evaporation and flowrate of working fluid in the C-R cycle for different fluids, obtained for condensation temperature 25°C in function of feeding water temperature.

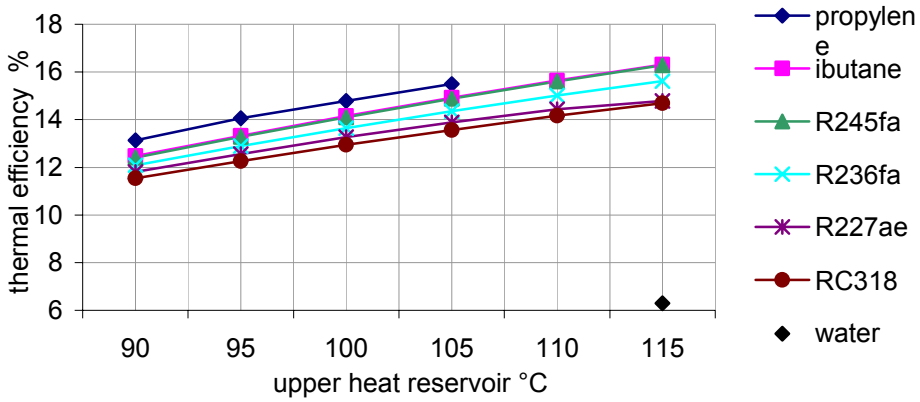

Figure 7: Efficiency of C-R cycle for different fluids obtained for the condensation temperature t_2=25°C

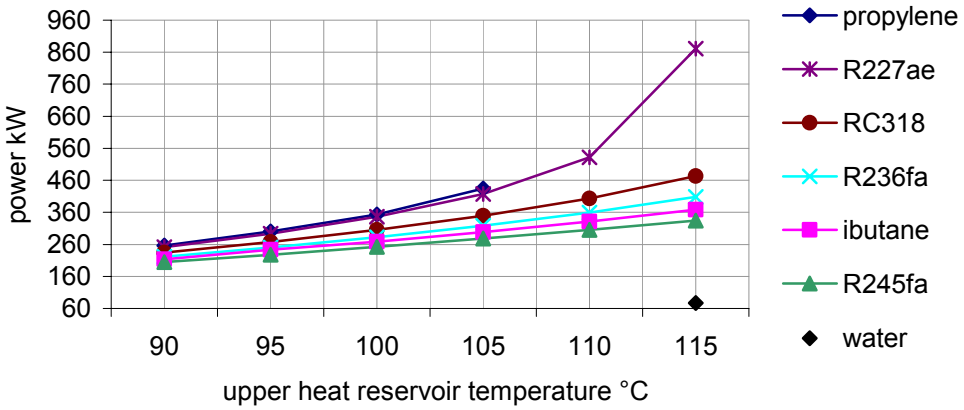

Figure 8: C-R cycle power (temperature of supply water t_1=80-100°C, flowrate of feeding water 100 m^3/h, fluid condensation temperature t_2=25°C

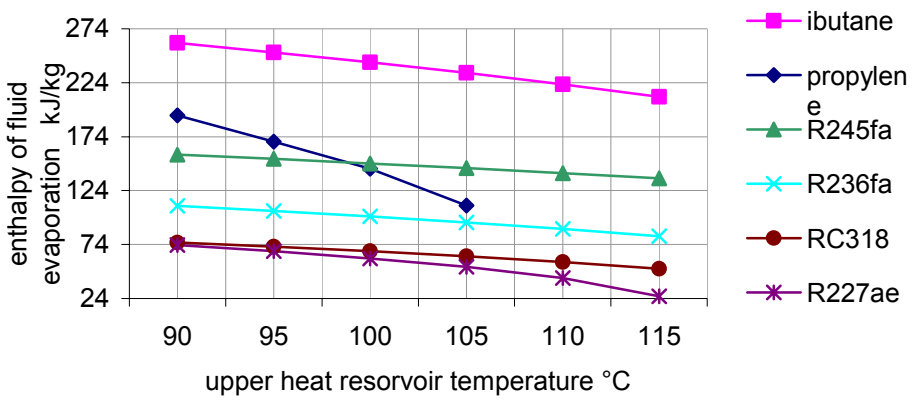

Figure 9: Enthalpy of fluid evaporation in function of feeding water temperature

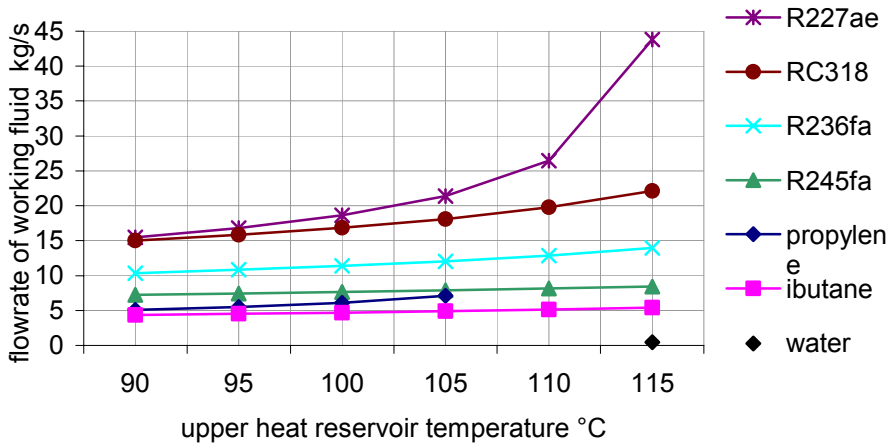

Figure 10: Flowrate of working fluid in function of feeding water temperature

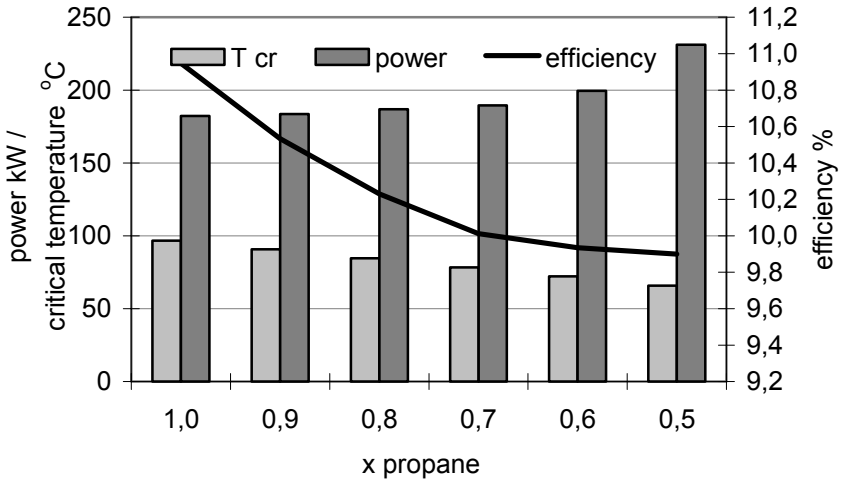

Fig. 11. Power of C-R cycle and thermal efficiency for the propane-ethane mixtur

In the figure 11 tabulated have been the results of calculations of efficiency and power of C-R cycle in the case of propane - ethane mixture (with five different mass fractions) obtained for the temperature of feeding water t_{w1}=80°C, feeding water flowrate 30 kg/s, fluids condensation temperature t_2=25°C. Propane-ethane form a zeotropic mixture (the temperature slip is present).
Analysing the above diagram it can be noticed that the highest cycle efficiency has been obtained for the pure propane and that it decreases with the increase of the share of ethane in the mixture. A different relation is observed when we focus our attention on the function of the cycle power in function of the working fluid composition. The highest value of power has been obtained in the case of a 50/50 propane/ethane mixture. A tendency of power increase with decrease of the critical fluid temperature has also been noticed. That can be explained due to the fact that the enthalpy of fluid evaporation decreases with increase of pressure (a temperature) to achieve a value of zero in the critical point. The lower the latent heat of evaporation the more of it can be introduced to the cycle at a constant flowrate of geothermal water (fig. 12 and 13).

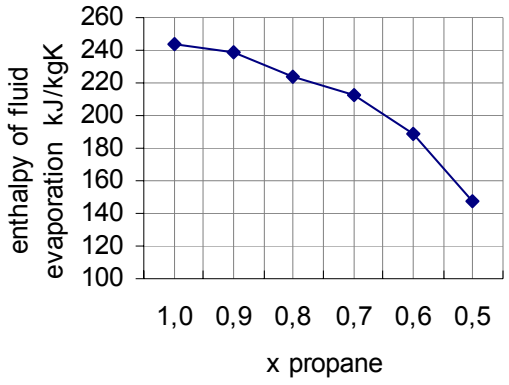

Figure 12: Enthalpy of fluid evaporation in function of composition of working fluid

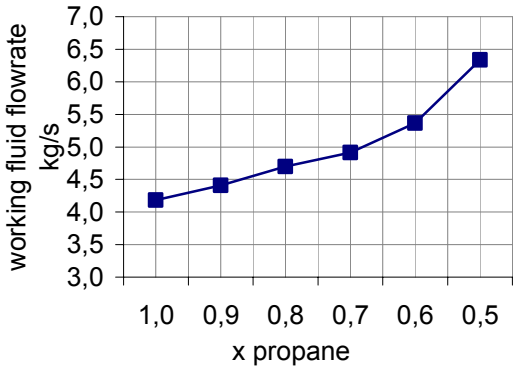

Figure 13: Cycle fluid flowrate in function of composition of working fluid

CONCLUSIONS

In the paper presented have been the results of calculation of theoretical efficiency and power of Clausius-Rankine cycle for different refrigerants and a zeotropic mixture propane-ethane of different mass composition.
On the basis of analysis of obtained results of calculations there can be formulated the following final conclusions:

- determination of efficiency of C-R cycle operating with the low boiling point fluid as a working fluid is insufficient in the energetical assessment of the fluid; for similar efficiencies for different fluids obtained have been different powers in both groups of fluids;
- highest values of power of C-R cycle are obtained for the fluid, which critical temperature is mostly approaching the temperature of the upper heat reservoir;
- usually low value of fluid evaporation enthalpy is desirable property in low-temperature Rankine cycle;
- highest values of power obtained have been for the natural working fluid – propylene and single-component synthetic fluid R227ae;
- highest values of efficiency obtained have been for the natural working fluid – propylene and single-component synthetic fluid R245fa;
- for similar efficiencies (10.9 - 9.9%) for different mass compositions of propane-ethane mixture obtained have been different values of power (182.3 - 231.2 kW).

Acknowledgements

The work has been carried out in the frame of the project 3T10B07527 financed by the Polish Ministry of Scientific Research and Information Technology.

REFERENCES

[1] Boyarski M Yu, Nikolski AI, Sapozhnikov MB, Shipkov AA. *Comperative performance of working fluids in low-temperature vapor-turbine cycle*, International Geothermal Workshop, Sochi, Russia 2003.

[2] Sokołowski J. *Methodology of assessment of geothermal resources and conditions of their presence in Poland*, Notes of the Polish Geothermal School, 3rd edition, PGA i CPPGSMiE PAN Publishers, Kraków-Stręszecin, 1997.

[3] Campbell RR. 1995. *Drafting a Geothermal Project for Funding*, World Geothermal Congress, Pre-congress Courses, Pisa, Italy.

[4] Angelino G, Colona di Paliano P. *Multcomonent Working Fluids for Organic Rankin Cycles*, Energy 1998; 23(6): 449-463.

[5] Czapp M. *Phase changes of fluids in coiled refrigeration heat exchangers*, Koszalin University of Technology Publisher, 2002.

[6] National Institute of Standards and Technology, 2002. Standard Reference Database 23, Reference Fluid Thermodynamic and Transport Properties - *Refprop 7.0*, US.

Proceedings of ECOS 2005
Trondheim, Norway
June 20–22, 2005

DEVELOPMENT OF A BIOMASS SLOW PYROLYSIS ROTARY KILN MODEL

D.Chiaramonti, M.Berti, D.Fiaschi
Department of Energy Engineering "S.Stecco"
University of Florence, Via S.Marta 3 I-50139 Florence
d.chiaramonti@ing.unifi.it

ABSTRACT

A model for the simulation of biomass slow pyrolysis in rotary kilns is necessary for preliminary sizing bioenergy plants based on this process. In order to develop this kind of model, the thermochemical conversion process as well as the solid motion within the reactor have to be modelled.
As regards the thermochemical process, the conversion of each component (cellulose, hemicellulose and lignin) has been considered, and literature data implemented. The impact of ash composition (inorganics) on product yields has been taken into account, together with other relevant parameters, such as reactor temperature and heating rate.
The analysis of the possible solid motion in the reactor identified the so-called "rolling motion" as the appropriate one for the process under study. The geometrical dimensioning model has then been coupled to the heat balance of the rotary kiln.
Pyrogas (tar and gases) is used as fuel in a boiler of a small scale steam power plant, while char is used to thermally sustain the slow pyrolysis process. In addition, assuming 9-10 % d.a.f. moisture content of the biomass input, only 10 % of the energy in the biomass fed to the reactor is needed to sustain the process: therefore, 70 % of the char yield can be used for additional energy production or for other uses (as a co-product). In this last case, the final energy efficiency of the plant is comparable to the values typical of small scale bioenergy plants.

NOMENCLATURE

$\dot{M}_B$	biomass flow rate, (kg/s, daf)
$\dot{M}_{TOT}$	mass flow rate (biomass+water+ash) (kg/s, daf)
d	mean particle diameter (mm)
D	cylinder diameter (m);
Fr	Froude number
g	acceleration due to gravity (m^2/s);
h_0	bed depth at kiln inlet (m)
h_{ex}	bed depth at kiln outlet (m)
L	reactor length (m)
MRT	mean residence time (min)
MVF	material volumetric flow (m^3/min)
n	kiln rotational speed (rpm)
PBR	Packed Bed Reactor
R, R_{Ti}, r	internal radius of kiln (m)
RC, f	fill ratio
TGA	Thermogravimetric analysis
X_a	initial silica-free ash fractional content (%wt daf)
X_C	initial fraction of cellulose (% wt daf)
X_l	initial fraction of lignin (%wt daf)
X_{si}	initial silica fraction (% wt daf)
$Y_{b,i}$	Y is the product yield (% wtdaf); subscript "b" denotes biomass, subscript "i" denotes char (c), liquid (l) or gas (g) accordingly.
Y_C	producted char yield (%wt daf)
α	kiln slope (deg)
β	bed slope (rad)
ε	filling angle: it corresponds to the half bed angle of the circular segment occupied with solids
ε_f	correctional coefficient (ε_f=1.03)
ε_t	correctional coefficient (ε_t=1.04)
θ, θ_d	dynamic angle of repose (deg)
μ_W	frictional coefficient of bed material – wall.
μ_{W,C_max}	maximum frictional coefficient of bed material – wall.
ρ_B	bulk density (kg/m^3)
ρ_C	char density (kg/m^3)
ω	kiln rotational speed (rad s^{-1})

INTRODUCTION

The development of a mathematical model able to preliminary design a small scale bioenergy plant based on slow pyrolysis in a rotary kiln reactor requires the simulation of several aspects of the energy conversion process, such as the kinetic of the pyrolysis process, the solid motion in the reactor, the exchange of the heat inside and outside the reactor.
The rotary kiln reactor is an interesting technology for bioenergy units, thanks to its ability to deal with heterogeneous materials (as regards particle

dimensions and characteristics), and process parameters can be modified in a relatively simple way to meet the process requirement.
Slow pyrolysis is a reliable and well know method for biomass conversion: products (char, gas and tar) can be used to generate electrical energy in steam cycle, and to provide the heat necessary to the process.
As regards pyrolysis-based plants, a wide number of researches and reviews have been published on the issue of biomass pyrolysis: modelling allows for the estimation of the interactions between process parameters and end-products. In fact, a biomass pyrolysis model should:

1. Estimate the link between process conditions (e.g. heat of pyrolysis, moisture content, biomass particle size, etc) and product yields
2. Allows for process optimisation by modifying the above mentioned process parameters
3. Represent a first instrument for preliminary reactor selection, sizing and dimensioning

KINETIC MODELLING

A large number of homogeneous and heterogeneous reactions occur during the biomass pyrolysis process, in a simultaneous as well in a consecutive way. Reactor conditions govern these reactions.
The attempt of kinetic modelling is therefore to simulate the process as a whole (by using Arrhenius type equations to model pyrolysis reaction rates), being individual reaction pathways very difficult to be described.
Di Blasi [1] reviewed modelling of biomass pyrolysis kinetics distinguishing among: (1) one step global reaction (which cannot predict the relationship between products yields and reaction conditions), where a constant ratio between volatiles and char is assumed; (2) multi-reaction models (which cannot be generalized, as they are based on different and distinct reactions that correlate specific experimental data); (3) semi-global models (kinetic pathways here consider primary and secondary reactions, and three main products – tar, gas and char –).
Semi-global models seem the most appropriate choice for developing engineering tools aimed at preliminary reactor design and optimisation, as they take into account competitive chemical pathways, estimate product yields on the basis of reactor conditions, but also limit the complexity of the model itself and the data needed for running the model, and allows for coupling chemistry and transport processes.
Most of the first semi-global models which have been developed were focused on pyrolysis of cellulose, while only few works examined hemicellulose and lignin pyrolysis.
Semi-global models considering the biomass degradation rate as the sum of cellulose, hemicellulose and lignin pyrolysis were then proposed: they represented a first rough attempt to describe the entire biomass pyrolysis process in a relatively simple way, as it is not possible to determine accurate correlations among the various components and process conditions which are valid on a general basis. This was probably due to the presence of inorganic matter in the biomass fuel: inorganics behave as a catalytic/inhibitor component, which therefore significantly modify the process of thermal degradation of raw biomass. Also the purity and the characteristics of cellulose play a role in this problem. It was then concluded that the specific biomass type has an influence on the pyrolysis process iself.
In the '90s Raveendran *et al* [2, 3, 4] carried out a number of studies and experimental works focused on the estimation of the impact of inorganic components contained in biomass ash on the pyrolysis process. Thirteen different biomass types have been investigated in a packed bed reactor (PBR) and in a TGA experiment: the TGA analysis examined a temperature range between the environment temperature and 1273 K, at a linear heating rate of 50 $Kmin^{-1}$, while the packed bed reactor was operated at a temperature of 773 K. These research activities developed correlations able to reasonably estimate the product yields (char, tar, gas) in slow pyrolysis processes (TGA or PBR) through the weighted sum of the partial contributions of biomass components.
In addition, correlations taking into account the impact of inorganic components on the thermal conversion process were developed and experimentally verified by the authors.

Among the correlations reported in the previously mentioned studies, the simplified overall correlation (valid for the PBR case) has been selected for the present work. The necessary input are the cellulose, lignin, silica-free ash and silica content in biomass.

$$Y_{b,i} = \left[A \left(\frac{X_c}{X_l} \right)^{n_1} X_a^{n_2} X_{Si}^{n_3} \right] \qquad \text{eq. 1}$$

A, n_1, n_2, n_3 are constant obtained by experimental analysis and different for char, tar and gas products (tab. 1).

Table 1 *Constant for eq. 1*

	A	n_1	n_2	n_3
char	49,9	-0,0258	0,258	-0,044
tar	102,86	0,7028	0,335	0,033
gas	13,93	-0,4168	-0,337	-0,002

Being the aim of this work the preliminary design of a bioenergy system based on slow pyrolysis of biomass, the use of the given above equation seemed reasonable because:

1. a Packed Bed Reactor is a good approximation for a rotating kiln slow pyrolyser of biomass. In fact, heating rates are rather similar, even if the PBR is operated in the batch mode and the rotating kiln in the continuous one.
2. the final process temperature adopted for the present work is very similar to the one used for the PBR case.

ROTARY KILN MODELLING

The use of rotary kiln systems as heterogeneous noncatalytic gas-solid reactors is very wide in some industrial sectors, as the metallurgical and the chemical ones. Among other uses, drying or heating of wet solids, mixing or grinding of powders, calcining of limestone, clinckering of cementitious materials, reducing of iron ore or ilmenite are well known applications: other recent applications are related to the thermochemical conversion of wastes. Even if new and more recent reactors (such as Fluidized Bed Reactors, FBRs) have been developed in the recent years and achieved commercial maturity, rotary kiln are still playing an important role.

Biomass pyrolysis can be efficiently implemented in rotary kilns: the slow rotational motion of the reactor, which can be varied in its inclination and speed, can be well coupled to slow pyrolysis processes, as it facilitates mixing of solids and can be well adopted with heterogeneous fuels, which are different not only in terms of biomass type, but also in terms of physical aspects. In fact, the production of biofuels of constant physico-chemical quality is a major issue in the bioenergy field, and the costs associated to this action can be significant for the whole process economy.

Even if a large number of studies have been published on the modelling and design of this type of thermochemical conversion technology, few of them describe the pyrolysis process keeping at the same time into consideration the simultaneous mass transfer and heat transfer in the reactor. These are instead essential elements of a model designed for this type of endothermic process.

The present work was therefore focused on coupling selected results from various research works [5] where the solid motion into the reactor is described and modelled, with other studies which examined the heat transfer process and, in particular, defined the heat exchange coefficients.

Possibile motions in a rotating kiln

Mellmann [6] reviewed the forms and the transition behavior of the transverse motion of free-flowing bed materials in rotantig cylinders. He distinguished among the following possible alternatives: sliding, surging, slumping, rolling, cascading, cataracting and centrifuging. All these motions have different and distinct mixing characteristics, and therefore different effects on the heat transfer in the bed of solids.

Boateng [7] observed that the heat transfer process in a rotary kiln is carried out in the same way as the PBR. Radiation and conduction occur between solid particles, and convection between solids and gas. There is also an advective component, which has the capability of regulating the overall process.

All these types of motion mainly depend on rotational speed, filling degree and rheology properties of solids, which has a deep influence on the bed rotational motion and therefore on mixing.

Also the roughness characteristics of the material used in the internal walls of the reactor are very important in dimensioning the system.

The most used motion type for these kind of technologies is the rolling motion, which allows for a fast transfer of solid particles between the upper and lower surfaces of the bed. The rolling motion is in fact characterised by two different regions, as regard the particle motion: the Active Layer, which is very thin and where most of the mass and heat transfer occur, and a larger part, the Plug Flow region, where the solid is pushed by the rotational motion towards the upper surface of the bed.

The best mixing, and therefore the most appropriate, heat transfer conditions are achieved through the rolling motion: Mellmann [6] provides the equation needed to identify the boundary conditions among different motion regimes. The parameters which play the most important roles in this process are the following:

1. The Froude number, Fr, i.e. the ratio between centrifugal forces and gravity:

$$Fr = \frac{\omega^2 * R}{g} \qquad \text{eq. 2}$$

In the case of rolling motion it has to stay in the range $10^{-4}<Fr<10^{-2}$;

2. The filling degree, which is the part of the transver section of the cylinder which is occupied by the solid bed:

$$f = \frac{(\varepsilon - \sin\varepsilon * \cos\varepsilon)}{\pi} \qquad \text{eq. 3}$$

It has to be in the range $0,1< f < 0,2$ in order to have a rolling motion regime;

3. The friction coefficient between inner wall of the reactor and solid bed. In the rolling motion it has to be greater than the maximum friction coefficient at wall, which can be expressed as a function of the dinamic angle of repose θ:

$$\mu_W > \mu_{W,C\_\max} = sen\theta \qquad \text{eq. 4}$$

4. The size of the solid particles, which in the rolling regime must be:

$$d > F_r * D \qquad \text{eq. 5}$$

fig. 1 Section of the reactor

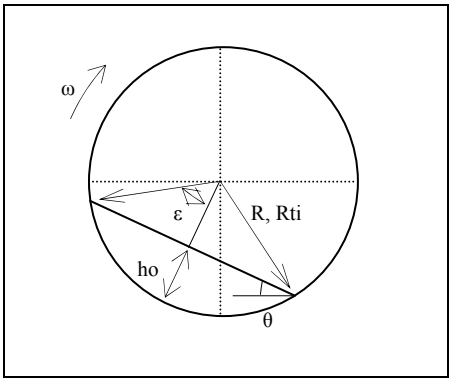

Geometrical dimensioning of the reactor

Given the conditions to establish a rolling motion regime in the reactor, a geometrical dimensioning model has been developed to define the geometry of the rotating kiln, in terms of both length and diameter. The fill ratio has been varied between 0.1-0.2, which correspond to a range of 93° - 121° of filling angle (2ε). Equations 2, 4 and 5 have been used for the verification of the rolling motion regime.

The system consists of two equations which links the residence time and the mass flowrate of solids with the geometrical characteristics of the rotating kiln reactor.

The equations are the following:

$$MRT = \varepsilon_t * \frac{L * \sin\theta_d}{2 * \pi * r * n * (\tan\alpha + \cos\theta_d * \tan\beta) * \cos^2\beta} \qquad \text{eq. 6}$$

$$MVF = \varepsilon_f * \frac{4}{3} * n * \pi * \cos^2\beta * \left(\frac{\tan\alpha}{\sin\theta_d} + \frac{\tan\beta}{\tan\theta_d}\right) \qquad \text{eq. 7}$$

$$* \left(2 * R * h_0 - h_0^2\right)^{3/2}$$

$$\tan\beta = \frac{h_0 - h_{ex}}{L} \qquad \text{eq. 8}$$

$$RC = \frac{1}{\pi}\cos^{-1}\left(\frac{R_{Ti} - h_0}{R_{Ti}}\right) - \frac{(R_{Ti} - h_0)\sqrt{\left(2R_{Ti}h_0 - h_0^2\right)}}{\pi R_{Ti}^2} \qquad \text{eq. 9}$$

where eq. 9 is the same as eq. 3 in different terms.

A further equation is needed, which links the initial and final height of the solid bed (h_0 and h_{ex}):

$$h_{ex} = \frac{\left(Y_C \frac{M_B}{\rho_C}\right) h_0}{\frac{M_{tot}}{\rho_B}} \qquad \text{eq. 10}$$

This equation is proportional to the amount of solids entering and leaving the rotary kiln: these are estimated on the basis of the previously mentioned pyrolysis model developed by Ravendran *et al* [2, 3, 4].

Thermal dimensioning of the reactor

Preliminary dimensioning in terms of heat exchange was developed considering the kiln as a heat exchanger: flue gases from char combustion heat the cylinder and therefore the biomass in that (fig.2).

The heat exchange process is therefore defined by:

- Convection, between flue gases from char combustion and external wall of the reactor;
- Conduction, between outer and inner wall of the cylinder;
- Conduction, between inner reactor wall and solid biomass/char;
- Convection, between inner reactor wall and pyrogas.

No heat sources are located in the internal part of the rotary kiln, being pyrolysis and endothermal process.

Heat exchange coefficient have been taken from literature [8].

Fig. 2 Scheme of the pyrolysis plant

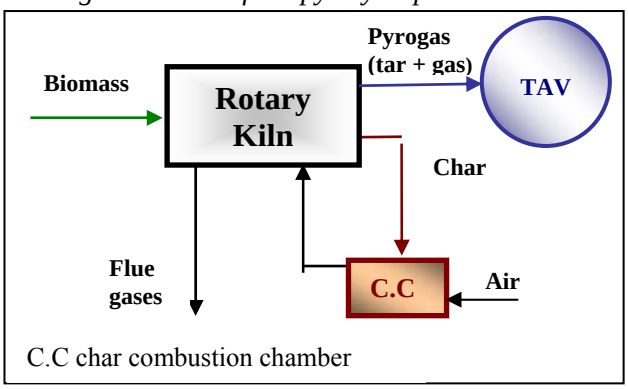

The model has been integrated with the thermodynamic analysis of the steam cycle for power generation and the balance in the char combustion chamber.
The initial biomass flowrate has been derived by considering the percentage distribution of pyrolysis products as a function of the pyrogas flow necessary to supply the heat to the steam boiler of a given steam power cycle.

Summarising, the overall model is structured as described in the following figure:

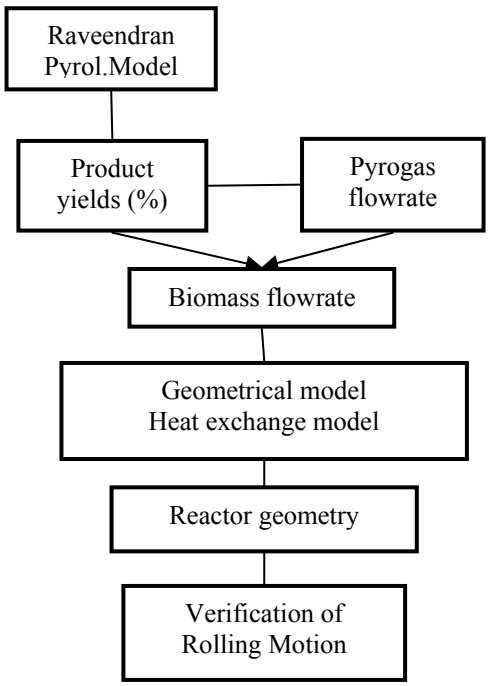

MODEL APPLICATION

The rotating kiln reactor model has been used to preliminary dimensioning of two small scale steam power plants, the first using a steam engine (155 kWe power output) and the second one a steam turbine (225 kWe).

Biomass pyrolysis product yields

The selected feedstock is straw biomass, which composition is given in tab.2. It has been derived from literature data on straw composition analysis [9, 2,10],

Table 2 Composition of straw (wt% daf)

Cell.	Hemicell.	Lign.	Extractt.	Ash	Si
33,56	31,80	18,05	14,75	10,05	3,48

By applying the pyrolysis model, this biomass is expected to generate the following distribution of pyrolysis products, expressed as percentage of the initial biomass amount:

- char: 28,2 % wt, daf;
- tar: 44,69 % wt daf;
- gas: 27,11 %wt daf.

These results, obtained by applying the Ravendran correlations, are in good agreement with other data available in literature for this type of process [10, 11, 12, 13].

155 kWe bioenergy plant

The plant has been preliminary dimensioned on the basis of the following main input:

- biomass flowrate: 0,297 kg/s;
- Pyrolysis temperature: 823 K;
- Reactor inclination: $\alpha = 2°$;
- Reactor rotational speed: n = 5 rpm;
- Dinamic angle of repose: $\theta = \theta_d = 48,5°$.

The calculation has been performed by changing the fill ratio RC (eq. 9) between 0,1 and 0,2:

Table 3 Results and verification of rolling motion conditions (155 kWe plant)

RC	MRT	L_T	R_{Ti}	Fr	d_p
	[min]	[m]	[m]		[mm]
0.1	11.54	12.1	0.8559	$3.8\ 10^{-3}$	6.5
0.11	11.9	12.24	0.8306	$3.7\ 10^{-3}$	6.1
0.12	12.23	12.36	0.8083	$3.6\ 10^{-3}$	5.8
0.13	12.53	12.47	0.7884	$3.5\ 10^{-3}$	5.5
0.14	12.81	12.57	0.7707	$3.4\ 10^{-3}$	5.3
0.15	13.05	12.66	0.7547	$3.37\ 10^{-3}$	5.1
0.16	13.27	12.74	0.7401	$3.3\ 10^{-3}$	4.9
0.17	13.48	12.81	0.7268	$3.25\ 10^{-3}$	4.7
0.18	13.66	12.87	0.7146	$3.19\ 10^{-3}$	4.5
0.19	13.82	12.93	0.7033	$3.14\ 10^{-3}$	4.4
0.2	13.96	12.98	0.6929	3.110^{-3}	4.2

The analysis of results given in Table 3 indicates that: (1) the solid residence time is in agreement with typical values of slow pyrolysis processes, which requires slow residence times in order to limit secondary reactions; (2) rolling motion conditions - being the Froude number in the specified range of $10^{-4}<Fr<10^{-2}$ - are met if biomass dimension at reactor inlet are above the values indicated in the table and in the case the material which constitutes the inner wall has roughness within the range that guarantee a friction coefficient above the critical-conditions friction coefficient ($\mu_{wc;max}$ = sen θ = 0,749).

The application of the model also shows that the thermal power required by the biomass pyrolysis process (in order to heat the biomass from 293 K to 823 K) is approximately 405 kW, assuming a 1156 kJ the necessary energy for pyrolysing 1 kg of biomass. This last figure is a slightly lower value than the one given by Jensen [14], 1359 kJ/kg, for a similar process but different biomass conditions at inlet: in fact, this difference is probably due to the feedstock moisture content, which is higher for Jensen than for the case studied in the present work.

255 kWe bioenergy plant

Similar calculations have also been performed for a different bioenergy plant, having a greater capaicity but still in the range of very small unit (255 kWe). The same critera have therefore been applied, the main difference being a lower biomass flowrate (0,136 kg/s), thanks to a greater efficiency of the steam turbine compared to steam engine at nominal conditions.

Results are shown in table 4:

Table 4 Results and verification of rolling motion conditions (255 kWe plant)

RC	MRT	L_T	R_{Ti}	Fr	d_p
	[min]	[m]	[m]	$exp10^{-3}$	[mm]
0.1	7.747	6.811	0.6334	2,8	3,6
0.11	7.982	6.888	0.6143	2,8	3,4
0.12	8.193	6.956	0.5975	2,7	3,2
0.13	8.383	7.016	0.5826	2,6	3,0
0.14	8.555	7.07	0.5692	2,5	2,9
0.15	8.71	7.119	0.5572	2,5	2,8
0.16	8.849	7.162	0.5462	2,4	2,7
0.17	8.974	7.2	0.5361	2,4	2,6
0.18	9.085	7.234	0.5269	2,4	2,5
0.19	9.183	7.263	0.5184	2,3	2,4
0.2	9.269	7.289	0.5106	2,3	2,3

Similar considerations apply to this case.

CONCLUSIONS

The goal of the present work was to develop a mathematical model simulating biomass slow pyrolysis process in a rotary kiln reactor: the overall scope of the model is to provide a useful tool for the design of pyrolysis-based bioenergy unit.

In order to achieve this objective, three different aspects have been considered, and the relative models coupled:

- Slow pyrolysis process;
- Reactor geometrical design;
- Thermal dimensioning of the reactor.

The model which has been developer has been applied to simulate two different biomass microgeneration unit, where pyrolysis products are used not only to generate power in a bottom steam cycle, but also to provide the necessary heat to the pyrolsysis process itself.

The considered biomass flowrates at the reactor inlet where 0,297 kg/s and 0,136 kg/s, for a power generation of 155 kWe and 255 kWe respectively.

Results are in agreement with those available in literature for similar plants

ACKNOWLEDGMENTS

Authors wish to acknowledge Prof. Colomba Di Blasi and Prof. Francesco Martelli for their scientific support to the present work.

REFERENCES

[1] Di Blasi C.: "*Comparison of semi-global mechanisms for primary pyrolysis of lignocellulosic fuels*", Journal of Analytical and Applied Pyrolysis, 47 (1998) 43-64.

[2] Raveendran K., Ganesh A. and Khilar K. C..: "*Influence of mineral matter on biomass pyrolysis characteristics*", Fuel, Volume 74, Issue 12, December 1995, Pages 1812-1822

[3] Raveendran K., Ganesh A. and Khilar K. C..: "*Pyrolysis characteristics of biomass and biomass components*", Fuel, Volume 75, Issue 8, June 1996, Pages 987-998;

[4] K. Raveendran et al.: "*Heating value of biomass and biomass pyrolysis product*", Fuel, Volume 75, Issue 15, November 1996, Pages 1715-1720;

[5] S. -Q. Li, J. -H. Yan, R. -D. Li, Y. Chi and K. -F. Cen.: "*Axial transport and residence time of MSW in rotary kilns: Part I. Experimental*", Powder Technology, Volume 126, Issue 3, 12 August 2002, Pages 217-227; "*Axial transport and residence time of MSW in rotary kilns: Part II. Theoretical and optimal analyses*", Powder Technology (2002).

[5a] S. -Q. Li, J. -H. Yan, R. -D. Li, Y. Chi and K. -F. Cen.: "*Axial transport and residence time of MSW in rotary kilns: Part II. Theoretical and optimal*

analyses", Powder Technology, Volume 126, Issue 3, 12 August 2002, Pages 228-240

[6] Mellmann J.: "*The transverse motion of solids in rotating cylinders – forms of motion and transition behaviour*", Powder Technology, Volume 118, Issue 3, 28 August 2001, Pages 251-270

[7] Boateng A.A., Barr P.V.: "*A thermal model for the rotary kiln including heat transfer within the bed*", International Journal of Heat and Mass Transfer, Volume 39, Issue 10, July 1996, Pages 2131-2143

[8] Martins M. A., Oliveira L.S., Franca A.S.: "*Modeling and simulation of petroleum coke calcination in rotary Kilns*", Fuel, Volume 80, Issue 11, September 2001, Pages 1611-1622

[9] Jensen P.A., Sander B., Dam-Johansen K.: "*Removal of K and Cl by leaching of straw and straw char*", Biomass and Bioenergy, Volume 20, Issue 6, June 2001, Pages 447-457

[10] Di Blasi C., Signorelli G., Di Russo C., Rea G.: "*Product distribution from pyrolysis of wood and agricultural residues*", Ing. Eng. Chem. Res.,38, (1999).

[11] Onay, Kockar: "*Slow, fast and flash pyrolysis of rapeseed*", Renewable Energy 28 (2003).

[12] Karaosmanoglu F., Tetik E. and Göllü E.: "*Biofuel production using slow pyrolysis of the straw and stalk of the rapeseed plant*", Fuel Processing Technology, Volume 59, Issue 1, April 1999, Pages 1-12

[13] Williams P.T., Besler S.: "*The influence of temperature and heating rate on the slow pyrolysis of biomass*", Renewable Energy, Volume 7, Issue 3, March 1996, Pages 233-250.

[14] P.A. Jensen, B.Sander, K.Dam-Johansen: "*Pretreatment of straw for power production by pyrolysis and char wash*", Biomass and Bioenergy 20 (2001) 431–446.

AN ENERGETIC, EXERGETIC AND THERMOECONOMIC ANALYSIS OF A GAS/STEAM COMBINED CYCLE COGENERATION PLANT

Can O. Colpan and Tülay Yeşin*
Middle East Technical University
Mechanical Engineering Department
06531 Ankara
TURKEY

ABSTRACT

This paper is a case study of thermodynamics and economics related analyses applied to an existing gas/steam combined cycle cogeneration plant. Basic thermodynamic properties of the plant are determined by energy analysis utilizing main operation conditions. Exergy destruction and losses within the plant are investigated to determine thermodynamic inefficiencies in the system and to assist for guiding future improvements in the plant. Cost balances are applied to several subsystems in the plant, hence, cost formation in the plant is observed. Besides, cost of each product of the system is calculated.

NOMENCLATURE

c	Cost per unit of exergy [$/GJ]
$\dot{C}$	Cost rate associated with exergy [$/h]
CC	Carying charges
CRF	Capital recovery factor
e	Specific exergy [kJ/kg]
$\dot{E}$	Exergy flow rate [kW]
EXC	Expenditure costs
FC	Fuel Costs
FUE	Fuel utilization efficiency
h	Enthalpy [kJ/kg]
hl	Heat loss
HP	High pressure
i_{eff}	Effective annual cost-of-money rate
IP	Intermediate pressure
LP	Low pressure
$\dot{m}$	Mass flow rate [kg/s]
OMC	Operating and maintenance costs
PEC	Purchased equipment costs
PHR	Power-to-heat ratio
$\overline{R}$	Universal gas constant [kJ/kmol-K]
RWC	Raw water costs
$\dot{Q}$	Heat rate [kW]
T	Temperature [°C]
x	Mol fraction
X	Value of a cost component [$]
$\dot{W}$	Power [kW]
y_D^*	Exergy destruction as a percentage of the total exergy destruction within the plant
y_D	Exergy destruction as a percentage of the total exergy supplied to the plant
$\dot{Z}^{CI}$	Cost rate associated with capital investment [$/h]
$\dot{Z}^{OM}$	Cost rate associated with operating and maintenance expenses [$/h]
$\dot{Z}$	Cost rate associated with the capital and operating and maintenance expenses [$/h]
ε	Exergetic Efficiency
τ	Total annual number of hours of system operation at full load. [h]
ϕ_o	Relative Humidity

Subscripts

ap	Approach
CV	Control volume
DEST	Destruction
e	Exit
eff	Effective
El	Electrical
EX	Expenditure

*Corresponding author: Phone +90-312-210 25 46 Fax: +90-312-210 1266 E-mail: yesin@metu.edu.tr

GT	Gas turbine
i	Inlet
L	Levelized
o	Environmental state
pp	Pinch point
ST	Steam turbine

INTRODUCTION

There is a range of technologies that can be applied to cogenerate electricity and heat. Among these technologies, gas/steam combined cycle cogeneration systems are currently in widespread use. These systems can be quite complex as there are different configurations that can be selected and optimized to provide the desired flexibility, reliability and rate of return for the owner [10]. Main configuration differences arise due to using different kinds of steam turbines (i.e. back pressure, condensing) and HRSG (differ in number of pressure levels, circulation type, supplementary firing). The configuration of the plant chosen in this study is explained in detail in the following sections.

Thermodynamic analysis and improvement of plants are meaningful via exergy analysis. There are many papers and books that explain the exergy analysis method and its importance [1,2,7]. Unlike energy analysis, this analysis takes into account the quality of the energy.

Thermoeconomic analysis combines exergy and economics principles. There are different approaches in literature. In this study, specific exergy costing method (SPECO method) [3] is used to analyze the plant.

DESCRIPTION OF THE PLANT

General Description

Bilkent combined cycle cogeneration plant is located in Bilkent University complex, Ankara, Turkey. The plant produces electrical energy and steam for the adjacent paper mill and the nearby Bilkent University complex; the electrical surplus is sold. Besides, there is also an old system next to this plant, consisting of a gas turbine and a waste heat recovery boiler which is used only to produce process steam. However, this system is not taken into account in this study.

The plant consists of a gas turbine package, a heat recovery steam generator (HRSG), a steam turbine with relevant generator and a main steam condenser. Furthermore, auxiliary systems common to the combined cycle are provided. The schematic drawing of the plant is shown in Figure 1. Besides, there is a dump steam condenser, which is needed during start-up and shut-down of the unit, or in case of steam turbine outage.

Fuel of the plant is natural gas supplied by local supplier Botaş. Natural gas is seperated from oil and humidity in dedicated seperators and compressed by the electrically driven natural gas compressors.

Raw water is supplied by municipality. It is used as the make-up of the condensate return from the process. Also, it is supplied to the cooling tower basin.

Steam export is either only steam from the intermediate pressure steam generator (in case of no extraction from the steam turbine) or a mixture of steam from the intermediate pressure steam generator and steam from the controlled extraction of the steam turbine.

Process Description and Operation Conditions

In this paper, the performance of the plant is investigated at ISO day condition (15°C, 101.325 kPa, 60% relative humidity). The conditions of natural gas supplied at plant battery limit are 16 bar and 15°C. It is compressed by the fuel compressor to 40 bar. After cooling to 35°C and throttling, it enters the combustion chamber.

The aeroderivative gas turbine consists of a gas generator, a power turbine and an electrical generator. The exhaust gas of the power turbine is used as the waste heat source of the HRSG which is an unfired, natural circulation, three pressure level type. The superheated high pressure steam is delivered to the steam turbine which produces power. Some of that steam is extracted to IP level according to the process steam demand and mixed with steam produced in IP steam drum, the remaining steam is diverted to the condenser. The return condensate from the paper mill has very low quality, hence it is sent to the old system. The return condensate from university (60°C) and raw water enters the demineralisation unit to be treated. It is accepted that approximately 70% of the steam export from combined cycle cogeneration plant returns as condensate. These streams are mixed with the condensate from condenser and the mixture enters the deaerator where it is heated up to the saturation temperature corresponding to the pressure of the LP steam drum and degassed by

means of the saturated steam produced in the LP evaporator. The heated feedwater in the LP drum is removed by the feedpumps and sent to relevant economizers.
In addition to the descriptions above, the plant data used in this study are given in Table 1.

Operation data at ISO ambient conditions	
Gas turbine	
Gas Generator[1]	
Exhaust Temperature	1006.75 K
Exhaust Pressure	359.21 kPa
Power Turbine Isentropic Eff.[2]	0.91
Electric Generator Efficiency	0.98
HRSG[3]	
HP Steam Drum Pressure	46 bar
IP Steam Drum Pressure	16 bar
LP Steam Drum Pressure	1.7 bar
HP Pinch Point	11 °C
HP Evaporator Approach Temp.	9 °C
IP Pinch Point	11 °C
IP Evaporator Approach Temp.	9 °C
Steam Turbine	
Inlet Temperature	450 °C
Isentropic Efficiency of Stages	0.70
Electric Generator Efficiency	0.98
Condenser Pressure	0.07 bar
Pumps Isentropic Efficiency [2]	0.80
Steam Export Pressure (Sat. Vap.)	13 bar
Raw Water Temperature	15 °C
Make-up Tank Outlet Temperature	32 °C

[1] Data is obtained from a performance test of the gas generator at ISO ambient conditions.
[2] The values that are assumed.
[3] Pressure drop across HRSG is assumed to be 5%, heat loss to environment is assumed to be 2% of heat absorbed and blow down requirements are not taken into account.

Table1: Operation data of the plant at ISO ambient conditions

ENERGY ANALYSIS

The aim of the energy analysis in this study is to determine the thermodynamic properties of the plant such as; electrical output of the plant, enthalpy difference of process, mass flow rate of steam generated at steam drums and stack gas temperature, etc. Besides, performance assessment parameters related to energy analysis are investigated for different steam demands.
For ideal gases, formulations in [1] is used which takes into account the variation of enthalpy and absolute entropy with temperature for various substances. For water, steam tables at [9] are used.
In this paper, gas generator is treated as a single unit. The exhaust gas composition is calculated by using the available data which gives mass flow rates at several points including the bleeding and cooling mass flow rates which are represented by the dashed lines in Figure 1 under the gas generator and using the combustion equation. Fuel (natural gas) is taken as methane in the combustion equation.
Ambient air molar analysis, considering relative humidity, is taken as: 78.18% N_2, 20.78% O_2, 1.01% $H_2O_{(g)}$, 0.03% CO_2. Exhaust gas composition of the gas turbine is found as: 75.85% N_2, 14.19% O_2, 6.95% $H_2O_{(g)}$, 3.01% CO_2.

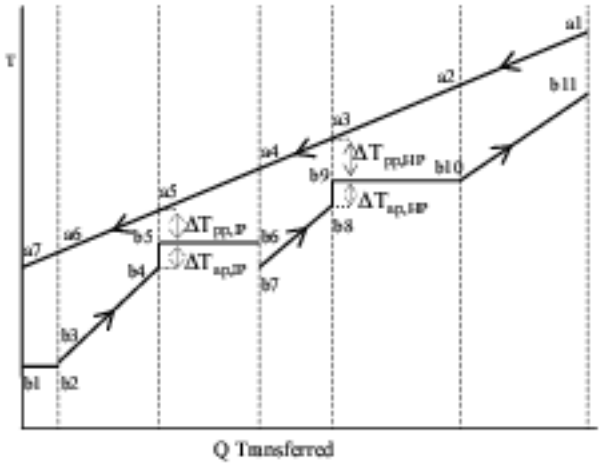

Figure 2: HRSG temperature profile

Mass flow rate of the steam generated at the HP steam drum is calculated by applying an energy balance around the HP evaporator and the HP superheater stages.

$$\dot{m}_1 = \dot{m}_E \cdot [(1-hl)\cdot(h_{a1}-h_{a3})/(h_{b11}-h_{b8})] \quad (1)$$

Mass flow rate of saturated steam generated at the IP steam drum is calculated by using an energy balance around the IP evaporator.

$$\dot{m}_6 = \dot{m}_E \cdot [(1-hl)\cdot(h_{a4}-h_{a5})/(h_{b6}-h_{b4})] \quad (2)$$

where h_{a4} is calculated from an energy balance around the HP 2nd economizer:

$$h_{a4} = h_{a3} - [\dot{m}_1 \cdot (h_{b8}-h_{b7})] / [(1-hl)\cdot \dot{m}_E] \quad (3)$$

Stack gas should be calculated due to corrosion considerations. From the energy balance in the LP evaporator, we have

$$h_{a7} = h_{a6} - \left[\dot{m}_{l5} \cdot (h_{b2} - h_{b1})\right] / \left[(1 - hl) \cdot \dot{m}_E\right] \quad (4)$$

where h_{a6} is calculated from the energy balance around the HP 1st economizer and the IP economizer, $\dot{m}_{l5}$ may be calculated from an energy balance around the deaerator as follows.

$$h_{a6} = h_{a5} - \left[(\dot{m}_1 + \dot{m}_6) \cdot (h_{b4} - h_{b3})\right] / \left[(1 - hl) \cdot \dot{m}_E\right] \quad (5)$$

and

$$\dot{m}_{l5} = \dot{m}_{l4} \cdot (h_{b1} - h_{l4}) / (h_{b2} - h_{b1}) \quad (6)$$

After calculating h_{a7}, T_{a7} is calculated by iteration. It should be checked whether stack gas temperature is greater than 400 K.

Electrical output of the plant may be given as

$$(\dot{W}_{el})_{plant} = (\dot{W}_{el})_{GT} + (\dot{W}_{el})_{ST} - (\dot{W}_{el})_{consum.} \quad (7)$$

Enthalpy difference of the process may be given as

$$\Delta\dot{H}_{process} = \dot{m}_9 \cdot h_9 - \dot{m}_{10} \cdot h_{10} - \dot{m}_{11} \cdot h_{11} \quad (8)$$

Performance assessment parameters for cogeneration systems are described in [6]. Among these parameters, fuel utilization efficiency is the most widely used one. However, power-to-heat-ratio and exergetic efficiency are the most useful parameters. Moreover, exergetic efficiency is the most meaningful and logical parameter which is discussed in the exergy analysis section.

Results of energy analysis

Although kinetic and potential energy effects are ignored and some assumptions are done, the results are compared with that of the monitoring system of the plant which gives mass flow rate, temperature, electrical output, etc. of some key points and it is found that the results are in good agreement. Stack temperature is about 130°C and this does not vary significantly with the steam demand. Also, this is a safe value when corrosion effects are considered. Other results are given in Figure 3 and Figure 4.

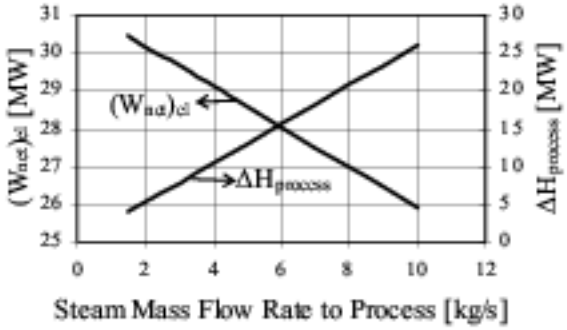

Figure 3 : Variation of outputs of the system with the process steam mass flow rate

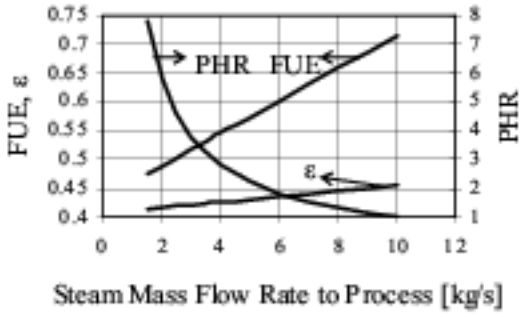

Figure 4 : Variation of system performance parameters with process steam mass flow rate

EXERGY ANALYSIS

For exergy analysis, a complex system is seperated into several subsystems. Exergy inflows and outflows to these subsystems, exergy destruction in these subsystems and exergy losses to the environment are calculated.

The steady state form of control volume exergy balance is

$$0 = \sum_j \left(1 - \frac{T_o}{T_j}\right) \cdot \dot{Q}_j - \dot{W}_{cv} + \sum_i \dot{m}_i \cdot e_i - \sum_e \dot{m}_e \cdot e_e - \dot{E}_{DEST} \quad (9)$$

Specific exergy consists of physical specific exergy and chemical specific exergy. Formulations of these terms may be found in [1,2].

Exergy balances applied to control volumes (subsystems) in this study are given in Table 6.

Exergetic efficiency of the plant may be given as

$$\varepsilon_{plant} = \frac{(\dot{W}_{net})_{el} + (\dot{E}_9 - \dot{E}_{10} - \dot{E}_{11})}{\dot{E}_A + \dot{E}_{11} + \dot{E}_{23}} \quad (10)$$

Results of exergy analysis

Exergy destructions in the subsystems shown in Table 6 are given in Table 2 for 15 t/h process steam. Exergy flow rates are given in Table 5. Process steam demand change does not affect significantly the exergy destruction ratios except steam turbine. To illustrate, y_D^* decreases from 7.8% to 2.7% as steam flow to process changes from 1.5 kg/s to 10 kg/s.

Exergy losses due to heat losses in the gas generator and the HRSG, and exergy losses due to the cooling tower and the natural gas cooler exit streams are considered as zero by taking the control volumes large enough so that the heat losses occur at the ambient temperature and the exit streams mix with the ambient air. Hence, the only exergy loss is due to the HRSG exit. It is found as 3054 kW which is 3.96% of the exergy supplied to the plant.

Control Volume#	$\dot{E}_{DEST}$ [kW]	y_D [%]	y_D^* [%]
1	307	0.40	0.75
2	30590	39.74	74.53
3	1394	1.81	3.40
4	3390	4.40	8.26
5	2574	3.34	6.27
6	2549	3.31	6.21
7	167	0.22	0.41
8	30	0.04	0.07
9	2	0.00	0.01
10	41	0.05	0.10

Table 2: Exergy destruction and relevant ratios at 15 t/h steam flow to process

It is seen from Table 2 that the largest portion of exergy destruction occurs in control volume 2 (gas generator), mainly because of combustion process. Exergy destructions in control volume 4 (HRSG); control volume 5 (steam turbine), control volume 6 (condenser + cooling tower + condensate pump), control volume 3 (power turbine) and others follow it, respectively.

From Figure 2, it can be observed that exergetic efficiency varies a little with the steam demand.

ECONOMIC ANALYSIS

The aim of economic analysis in this study is to provide necessary inputs to be used in the thermoeconomic analysis. These inputs are the levelized cost rates associated with capital and operation and maintenance expenses for components of the plant and the levelized cost rates of the expenditures (i.e. fuel costs, raw water costs) supplied to the overall system. Although fuel costs and raw water costs may be seen as a part of O&M costs, they should be treated seperately.

If money transactions occur at the end of each year within the plant economic life, for any cost component, X (i.e.carrying charges, fuel cost, etc.), levelized cost can be shown as [4]

$$X_L = CRF \cdot \sum_{j=1}^{n} \frac{X_j}{(1+i_{eff})^j} \qquad (11)$$

$$CRF = \frac{i_{eff} \cdot (1+i_{eff})^n}{(1+i_{eff})^n - 1} \qquad (12)$$

Cost rate associated with the capital and operation and maintenance expenses for the kth component:

$$\dot{Z}_k = \frac{CC_L}{\tau} \cdot \frac{PEC_k}{\sum_k PEC_k} + \frac{OMC_L}{\tau} \cdot \frac{PEC_k}{\sum_k PEC_k} \qquad (13)$$

The first term in (13) gives $\dot{Z}_k^{CI}$ and the second term gives $\dot{Z}_k^{OM}$.

Levelized cost rate of an expenditure (fuel, raw water) supplied to the overall system is

$$\dot{C}_{EX} = \frac{EXC_L}{\tau} \qquad (14)$$

The economical data needed to calculate cost rates are obtained from Bilenerji A.S., the company that operates the plant. The plant is started its commercial operation at the beginning of 2000. For its entire economic life, 25 years, year by year data for carrying charges prepared by the company is obtained. Operating and maintenance, fuel and raw water costs for the past years are obtained from company, local natural gas and raw water suppliers. For the future years; these expenditure costs are escalated using average nominal escalation rates of costs. In this study, these escalation rates of costs are taken as the estimated average general inflation within the plant economic life, which is 3% in U.S. Dollars. Besides, for operating and maintenance costs, there is an extra overhaul cost which is 0.85 M$ in the third year and 1.75 M$ in the sixth year of every six year periods. Effective annual cost-of-money rate is taken as 10%. Total number of hours of system operating at full load is taken as 8200 hours. Total capital investment of the plant is 27.8 M$.

Results of economic analysis

Levelized costs are calculated by using purchased equipment costs and year-by-year analysis. Results are given in Table 3 and Table 4, respectively.

Levelized Costs	CC_L	OMC_L	FC_L	RWC_L
$10^3 \times \$$	4139	2826	13362	1023

Table 3: Levelized costs of cost components

Component	PEC (M$)	$\dot{Z}_k^{CI}$ ($/h)	$\dot{Z}_k^{OM}$ ($/h)	$\dot{Z}_k$ ($/h)
Gas Turbine Sys	9.00	238	163	401
Steam Turbine	2.50	66	45	111
HRSG	1.85	49	33	82
Gas Compressor	0.85	23	15	38
Cooling Tower	0.75	20	14	33
Condenser	0.50	13	9	22
Demineral. Sys.	0.40	11	7	18
Circulat. Pump	0.35	9	6	16
Conden. Pump	0.20	5	4	9
HP BFW Pump	0.20	5	4	9
IP BFW Pump	0.10	3	2	4
IP Steam Desup.	0.10	3	2	4
Make-up Tank	0.10	3	2	4
Make-up Pump	0.05	1	1	2
Other Comp.	2.10	56	38	94

Table 4: Purchased equipment costs and levelized costs for the components of the plant.

Gas turbine system is sold as one unit, and prices of its subcomponents are not available. However, to obtain more accurate results from thermoeconomic analysis, gas generator and power turbine are considered seperately. Hence, it is assumed that power turbine and its electricity generator has a price of 2 M$ and gas generator 7 M$, respectively. Levelized costs are shared according to this assumption.

Levelized cost rate of fuel is calculated as 1629 $/h and that of raw water as 119 $/h.

THERMOECONOMIC ANALYSIS

The objective of the thermoeconomic analysis in this study is to understand the cost formation process and to calculate the cost of each product generated by the plant.

Aggregation level influences the accuracy of the results, hence it is taken low enough. Discussions on aggregation level may be found in [1,8].

Cost balance is applied to each subsystem. Auxiliary equations are applied by using fuel and product rules[3]. Hence, a set of linear equations are formed and solved.

The steady-state form of control volume cost balance is

$$\sum_{j=1}^{n} \dot{C}_{j,k,in} + \dot{Z}_k = \sum_{j=1}^{m} \dot{C}_{j,k,out} \qquad (15)$$

$$\dot{C}_j = c_j \cdot \dot{E}_j \qquad (16)$$

Results of thermoeconomic analysis

Cost formation in the plant for 15 t/h process steam flow is given in Table 5. It can be observed that the highest cost is achieved at state F, which is the exit of gas generator. Costs of states D, A, and others follow it, respectively. On the other hand, the highest cost per unit exergy is seen at state 5.

Cost rate of products, $\dot{C}_9$ and $\dot{C}_{Wast}$ are calculated by cost balances. Then, cost rate associated with other plant equipment and exergy loss in the plant should be apportioned between products as discussed in [1]. Figure 5 shows the final cost rates of products for different process steam flows.

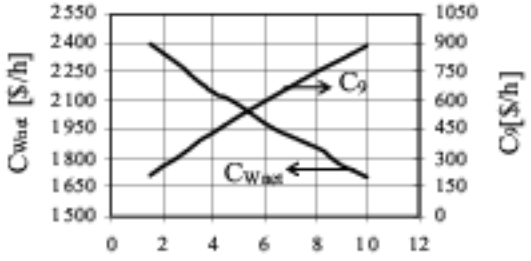

Fig. 5: Variation of cost rate of products with steam mass flow rate to process

CONCLUSIONS

This study points out the thermodynamic inefficiencies, cost formation and cost of products of the plant. The plant owner may maintain an opinion for future improvements of the plant and check the plant's economic policy. Besides, the methodology and results of this paper can be beneficial in the analysis and design of similar systems.

The results of the thermoeconomic analysis can be improved if seperate forms of total exergy of streams (e.g., physical and chemical exergies) are used. However; this increases the number of equations significantly and it is not very useful for the purpose of this study.
The results of the present study can be used as a basis for thermoeconomic optimization.

State	Substance	$\dot{E}$ (kW)	$\dot{C}$ ($/h)	c ($/GJ)
A	Natural Gas	76050	1629	5.95
B	Air	0	0	0.00
C	Air	0	0	0.00
D	Natural Gas	76250	1702	6.20
E	Air	0	0	0.00
F	Exhaust Gas	45660	2023	12.30
G	Exhaust Gas	20547	910	12.31
H	Exhaust Gas	3054	135	12.31
I	Air	0	0	0.00
J	Air	0	0	0.00
1	Water	13474	1129	23.28
2	Water	2827	237	23.28
3	Water	1779	149	23.28
4	Water	510	-	-
5	Water	511	366	199.27
6	Water	1402	132	26.13
7	Water	4297	-	-
8	Water	4210	-	-
9	Water	4107	387	26.19
10	Water	237	0	0.00
11	Water	85	11	35.39
12	Water	291	-	-
13	Water	292	-	-
14	Water	802	401	139.11
15	Water	1172	-	-
16	Water	1439	440	84.99
17	Water	221	68	84.99
18	Water	1217	372	84.99
19	Water	222	72	89.96
20	Water	45	14	89.96
21	Water	177	57	89.96
22	Water	1232	385	86.89
23	Water	849	108	35.39
24	Water	409	0	0.00
25	Water	414	0	0.00

Table 5: Exergy and cost flow rates for 15 t/h steam flow to process

ACKNOWLEDGEMENTS

The authors wish to express their gratitude to Bilenerji A.Ş. managers and engineers for their cooperation in supplying data for the plant and Professor Yalçın A. Göğüş for his important contributions to this study.

REFERENCES

[1] Bejan, A., Tsatsaronis G., Moran M., *Thermal design and optimization*, John Wiley and Sons Inc., U.S.A., 1996.

[2] Bejan, A., *Advanced engineering thermodynamics*, 2nd ed. New York: Wiley, 1998

[3] Lazzaretto, A., Tsatsaronis, G., *On the calculation of efficiencies and costs in thermal systems*, In: Proceedings of the ASME Advanced Energy Systems Division, AES-Vol.39, 1999.

[4] Tsatsaronis, G., Cziesta, F., *Thermoeconomics*, In: Optimisation of Energy Systems and Processes Summer School, Gliwice, Poland, 2003.

[5] Karthikeyan, R., Hussain, M.A., Reddy, B.V., Nag, P.K., *Performance simulation of heat recovery steam generators in a cogeneration system*. International Journal of Energy Research 1998; 22:399-410

[6] Huang, F.F., *Performance assessment parameters of a cogeneration system*, In: Proceedings of ECOS '96, Stockholm

[7] Dincer, I., Rosen, M.A., *Exergy as a driver for achieving sustainability*. International Journal of Green Energy 2004; 1(1):1-19

[8] Narin, B., Göğüş, Y.A., *Application of the method of exergy splitting to cost evaluation of a retrofitted J-79 engine as cogeneration unit*, In: Proceedings of ECOS 2002, Berlin, Germany..

[9] Çengel, Y.A., Boles, M.A., *Thermodynamics: an engineering approach*, 4th ed., Dubuque, Iowa: McGraw-Hill, 2002

[10] Tawney R., Ehman J., Brown M., *Selection of cycle configurations for combined cycle cogeneration power plants*, In: ASME Turbo Expo 2000, Munich, Germany

Control Volume	Exergy Balance	Cost Balance
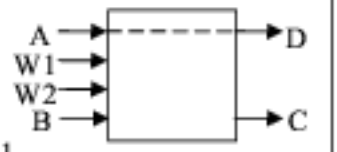 1	$\dot{E}_{DEST} = (\dot{E}_A - \dot{E}_D) + (\dot{E}_B - \dot{E}_C) + \dot{E}_{W1} + \dot{E}_{W2}$	$(\dot{C}_A - \dot{C}_D) + \dot{C}_{W1} + \dot{C}_{W2} + \dot{C}_B - \dot{C}_C + \dot{Z}_1 = 0$ $\dot{C}_B = \dot{C}_C = 0 \; (\dot{E}_B = \dot{E}_C = 0)$
 2	$\dot{E}_{DEST} = \dot{E}_E + \dot{E}_D - \dot{E}_F$	$\dot{C}_E + \dot{C}_D + \dot{Z}_2 = \dot{C}_F$
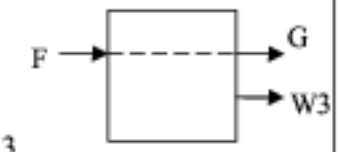 3	$\dot{E}_{DEST} = (\dot{E}_F - \dot{E}_G) - \dot{E}_{W3}$	$(\dot{C}_F - \dot{C}_G) + \dot{Z}_3 = \dot{C}_{W3}$ $\frac{\dot{C}_F}{\dot{E}_F} = \frac{\dot{C}_G}{\dot{E}_G}$ (F Rule)
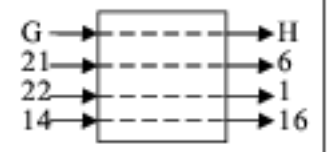 4	$\dot{E}_{DEST} = (\dot{E}_G - \dot{E}_H) + (\dot{E}_{21} - \dot{E}_6) + (\dot{E}_{22} - \dot{E}_1) + (\dot{E}_{14} - \dot{E}_{16})$	$(\dot{C}_G - \dot{C}_H) + (\dot{C}_{21} - \dot{C}_6) + (\dot{C}_{22} - \dot{C}_1) + (\dot{C}_{14} - \dot{C}_{16}) + \dot{Z}_4 = 0$ $\frac{\dot{C}_G}{\dot{E}_G} = \frac{\dot{C}_H}{\dot{E}_H}$ (F Rule) $\frac{\dot{C}_6 - \dot{C}_{21}}{\dot{E}_6 - \dot{E}_{21}} = \frac{\dot{C}_1 - \dot{C}_{22}}{\dot{E}_1 - \dot{E}_{22}} = \frac{\dot{C}_{16} - \dot{C}_{14}}{\dot{E}_{16} - \dot{E}_{14}}$ (P Rule)
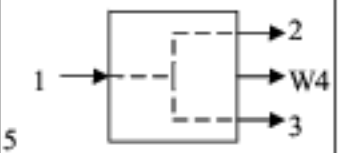 5	$\dot{E}_{DEST} = (\dot{E}_1 - \dot{E}_2 - \dot{E}_3) - \dot{E}_{W4}$	$(\dot{C}_1 - \dot{C}_2 - \dot{C}_3) + \dot{Z}_5 = \dot{C}_{W4}$ $\frac{\dot{C}_1}{\dot{E}_1} = \frac{\dot{C}_2}{\dot{E}_2} = \frac{\dot{C}_3}{\dot{E}_3}$ (F Rule)
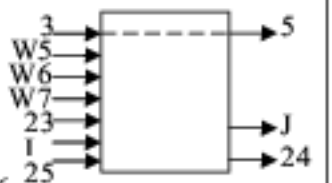 6	$\dot{E}_{DEST} = (\dot{E}_3 - \dot{E}_5) + \dot{E}_{W5} + \dot{E}_{W6} + \dot{E}_{W7} + \dot{E}_{23} + \dot{E}_1 + \dot{E}_{25} - \dot{E}_J - \dot{E}_{24}$	$(\dot{C}_3 - \dot{C}_5) + \dot{C}_{W5} + \dot{C}_{W6} + \dot{C}_{W7} + \dot{C}_{23} + \dot{C}_1 + \dot{C}_{25} + \dot{Z}_6 - \dot{C}_J - \dot{C}_{24} = 0$ $\dot{C}_{25} = 0$ (Assumption) $\dot{C}_1 = \dot{C}_J = 0 \; (\dot{E}_1 = \dot{E}_J = 0)$
 7	$\dot{E}_{DEST} = \dot{E}_2 + \dot{E}_6 + \dot{E}_{20} - \dot{E}_9$	$\dot{C}_2 + \dot{C}_6 + \dot{C}_{20} + \dot{Z}_7 = \dot{C}_9$
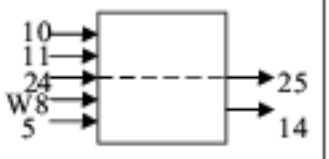 8	$\dot{E}_{DEST} = \dot{E}_{10} + \dot{E}_{11} + (\dot{E}_{24} - \dot{E}_{25}) + \dot{E}_{W8} + \dot{E}_5 - \dot{E}_{14}$	$\dot{C}_{10} + \dot{C}_{11} + (\dot{C}_{24} - \dot{C}_{25}) + \dot{C}_{W8} + \dot{C}_5 + \dot{Z}_8 = \dot{C}_{14}$ $\frac{\dot{C}_{24}}{\dot{E}_{24}} = \frac{\dot{C}_{25}}{\dot{E}_{25}}$ (F Rule) $\dot{C}_{10} = 0$ (Assumption)
 9	$\dot{E}_{DEST} = (\dot{E}_{17} - \dot{E}_{19}) + \dot{E}_{W9}$	$\dot{C}_{17} + \dot{C}_{W9} + \dot{Z}_9 = \dot{C}_{19}$
 10	$\dot{E}_{DEST} = (\dot{E}_{18} - \dot{E}_{22}) + \dot{E}_{W10}$	$\dot{C}_{18} + \dot{C}_{W10} + \dot{Z}_{10} = \dot{C}_{22}$

Table 6: Exergy and cost balances for the control volumes

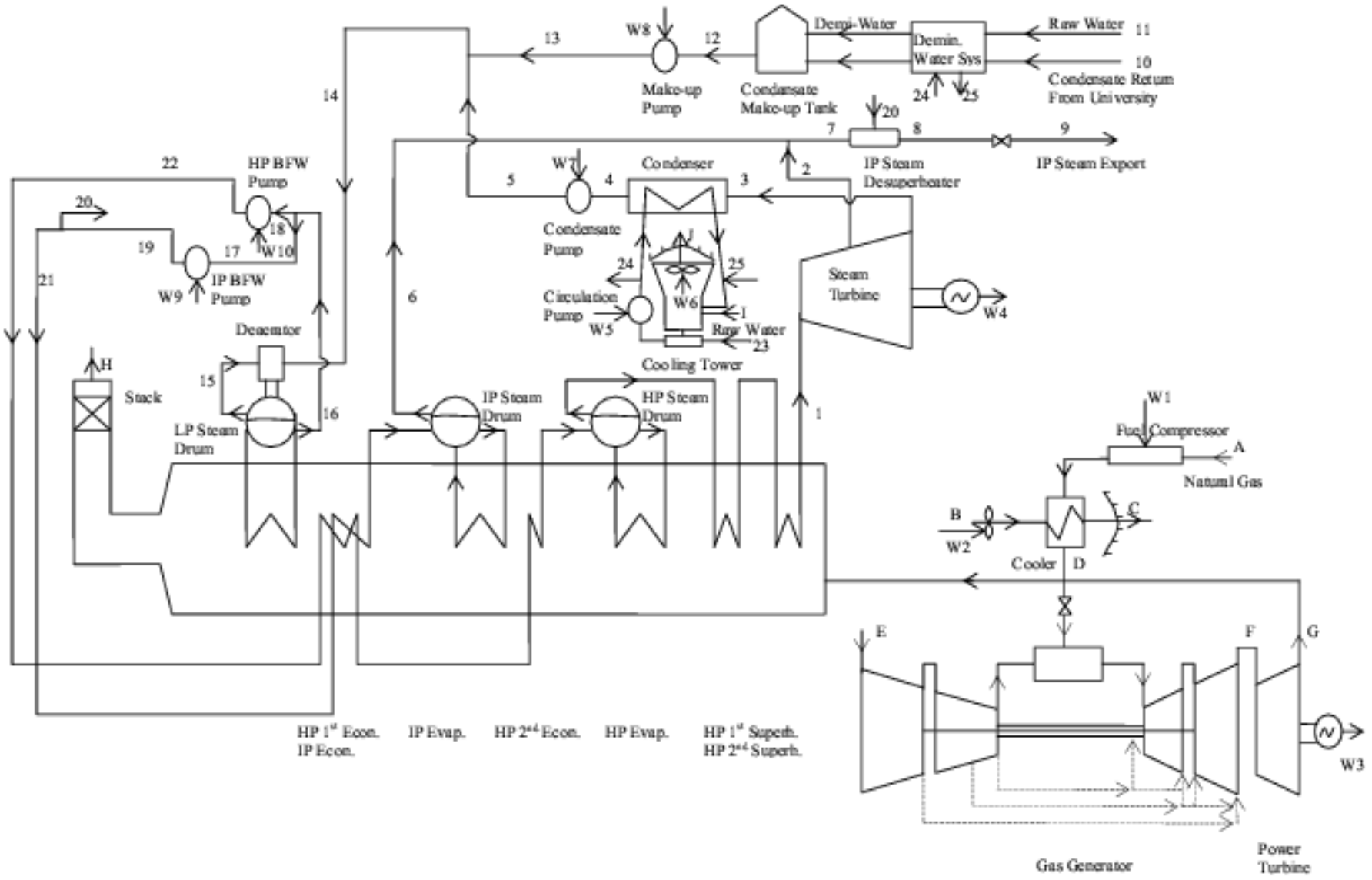

Figure 1: Schematic Drawing of Bilkent Combined Cycle Cogeneration Plant

Proceedings of ECOS 2005
Trondheim, Norway
June 20–22, 2005

ON THE OFF-DESIGN OF A NATURAL GAS-FIRED COMBINED CYCLE WITH CO_2 CAPTURE

Björn Fredriksson Möller*, Magnus Genrup, Mohsen Assadi
Lund Institute of Technology
Department of Heat and Power Engineering
P.O. Box 118, SE-221 00 Lund, SWEDEN

ABSTRACT

During the last 15 years cycles with CO_2 capture have been in focus, due to the growing concern over our climate. Often a natural-gas fired combined cycle with a chemical absorption plant for CO_2 capture from the flue gases have been used as a reference in comparisons between cycles. The integration of the steam production in the cycle to minimise the drop in efficiency have not been extensively studied. Neither have there been any studies on the off-design behaviour of such a plant if it should be built.

In this paper the integration of steam production for regeneration of the amines is modelled at design load and studied in off-design conditions for a combined cycle. Different ambient conditions and part-load strategies and their influence on the cycle performance are also examined. Of particular interest is a novel strategy with the possibility of longer life of gas turbine blading, with marginal loss in efficiency.

The off-design performance of the combined cycle is modelled in a rigorous way, using a gas turbine performance deck to calculate the performance of the gas turbine. The boiler is calculated using simplified correlations for off-design heat transfer and pressure drop. The steam turbine calculation is based on verified models for the flow – pressure – efficiency relations, whilst the steam condenser is based on the HEI (Heat Exchange Institute) method.

Keywords: CO_2 capture, combined cycles, off-design

NOMENCLATURE

a	constant or Baumann coefficient
A	area
b, c	constants
C_T	turbine constant
EGT	exhaust gas temperature
f	function of
h	enthalpy
HEI	Heat Exchange Institute
HP	high pressure
HRSG	heat recovery steam generator
IGV	inlet guide vanes
IP	intermediate pressure
K	combustor section pressure drop coefficient
LP	low pressure
$\dot{m}$	mass flow
MEA	monoethanolamine
p	pressure
SHT	steam superheating temperature
SOT	stator outlet temperature
T	temperature
u	blade speed
v	specific volume
VSV	variable stator vanes
W	work
$\overline{y}$	section mean moisture content
α	off-design pressure drop coefficient
δ, Δ	difference
η	efficiency
π	pressure ratio
ξ	blade stagger angle
X	Parson number

*Corresponding author: Phone: +46-46-222 4770 Fax: +46-46-222 4717 E-mail: bjorn.fredriksson@vok.lth.se

Subscripts

0	stagnation properties
act	actual
C	cold
cc	combustion chamber
CHIC	compressor characteristic
CO_2	carbon dioxide
des	design
H	hot or fundamental
i,j	indexes
IGV	inlet guide vane
in	inlet
out	outlet
rel	relative
s	isentropic
wet	expansion in wet zone

Superscripts

*	normalized to ISO conditions
dry	expansion in dry zone

INTRODUCTION

Fossil fuels are the dominant source of global energy demand and will most likely remain so for another century [1]. Recent statistics by International Energy Agency show that 87% of the worlds energy supply originates from fossil fuels [2]. The interest in combined cycles with high efficiency, especially those with CO_2 capture, is therefore understandable. Numerous studies and research projects are either ongoing or finished in the large research field of CO_2 capture [3], but still only small applications where the CO_2 is needed anyhow has been built. Few reports have been made on the integration of capture in the power plant, and there seem to be little to gain in terms of heat recovery from the capture plant to a combined cycle [4].

Part-load behaviour of these cycles have to the authors knowledge not been studied at all, but they are likely to behave like a normal combined cycle. These have been modelled in part-load with different control strategies by Kim [5], and dynamic studies have been performed by Shin et al. [6].

CYCLE LAYOUT

As a reference basis a combined cycle based on the gas turbine GE PG9351FA has been chosen. This will also simplify comparisons with other concepts as a benchmarking study has previously been performed by SINTEF/NTNU on different gas turbine cycles using this gas turbine [7]. The combined cycle is a triple-pressure reheat steam cycle with steam pressure levels chosen at 111/27/3.2 bar, where the lowest pressure corresponds to a condensation temperature of 135°C in the reboiler section of the CO_2 capture plant. Steam is extracted from the LP section of the steam turbine and returned to the high pressure feedwater circuit. A schematic process layout of the cycle with the MEA-based CO_2 capture system is shown in Figure 6. The post-combustion capture plant is based on the calculation model by Kohl and Nielsen [8] with the heat requirement for regeneration of MEA set to 4.9 MJ/kg CO_2, a figure representative for an optimised MEA plant with 3% CO_2 in the exhaust gas [9]. The CO_2 compressor work in kJ/kg is approximated by equation (1) [10].

$$W_{CO_2} = -120 \ln\left(p_{CO_2}\right) + 369 \qquad (1)$$

The design case input data can be seen in Table 1.

Parameter	Value	Unit
Steam turbine efficiency HP/IP	0.92	-
Steam turbine efficiency LP	0.89	-
Condenser pressure	0.04	bar
Deaerator pressure	1.2	bar
Fan pressure increase	0.06	bar
HRSG pressure drop	0.04	bar
Evaporator pinchpoint	10	°C
Economiser pinchpoint	20	°C
Approach point	5	°C
Steam superheating temperature (SHT)	560	°C
Steam reheat temperature	560	°C
Stator outlet temperature (SOT)	1328	°C
Pressure ratio	15.4	-
Air mass flow	611	kg/s
Exhaust gas temperarure (EGT)	617	°C
MEA heat demand	4.9	MJ/kg CO_2
Amine regeneration temperature	120	°C

Table 1: Design case input data

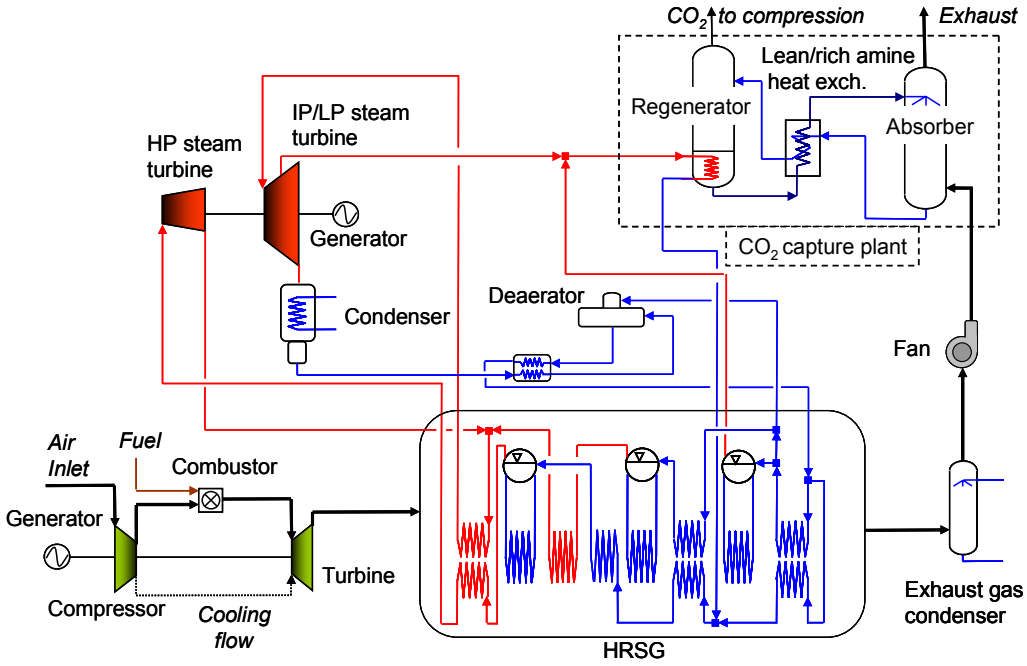

Figure 1: Process layout of the post-combustion CCGT plant

OFF DESIGN MODELLING

The basic off-design modeling of a combined cycle comprises three models. The first one is the gas turbine off-design model or "performance deck", the second one is the heat recovery steam generator (HRSG) and the third one is the steam turbine model. In this work, all three are combined into a single model. The used platform is the commercially available heat- & mass balance software IPSEpro. The basic "built in" models were changed to a set of models developed at Lund University [11] and [12]. In this paper, however, the models will be described separately for clarity.

Gas turbine

The gas turbine model or performance deck is based on component matching. The standard approach is to use component characteristics, and solve the matching equilibrium. The matching equilibrium is, loosely stated, when the operational point is fulfilling e.g. geometry, speed and work balance. The calculation is highly iterative and the necessary loops are numerous. Therefore, the use of a matrix type equation solver speeds up the solution procedure. The model contains additional advanced features like a bellmouth condensation model in connection to the bellmouth pressure drop.

The modeled gas turbine is the GE Power System PG9351FA. The model was adapted to open literature performance data and details regarding e.g. secondary air system and component performance, was estimated. The exact details of the unit are proprietary and not known to the authors. The estimates are, however, in the range that can be expected for a heavy frame unit of this size. The overall performance at design load is the one found in the open literature. One further limitation in the model is the use of a generic compressor and turbine characteristics.

The compressor is modeled with a non-dimensional compressor map. This approach gives the possibility to use the same compressor behavior regardless of compressor. Providing design levels parameterizes the map, where values of unity represent design values of: normalized flow, efficiency, pressure ratio and aerodynamic speed. Variable geometry (e.g. IGV and VSV's) is introduced by the use of influence coefficients.

$$\dot{m}^*_{rel} = \dot{m}^*_{rel,CHIC}\left(1+\frac{a_{IGV}}{100}\Delta\xi\right),\ a_{IGV} = \frac{\delta\left(\dot{m}^*_{rel}\right)}{\delta\left(\Delta\xi\right)} \qquad (2)$$

$$\pi_{rel} = \pi_{rel,CHIC}\left(1+\frac{b_{IGV}}{100}\Delta\xi\right),\ b_{IGV} = \frac{\delta\left(\pi_{rel}\right)}{\delta\left(\Delta\xi\right)} \qquad (3)$$

$$\eta_{rel} = \eta_{rel,CHIC}\left(1+\frac{c_{IGV}}{100}\left[\Delta\xi\right]^2\right),\ c_{IGV} = \frac{\delta(\eta_{rel})}{\left\{\delta(\Delta\xi)\right\}^2} \quad (4)$$

The used compressor characteristic (CHIC) is based on a published industrial compressor map [13]. The compressor bellmouth- and diffuser pressure drop is modeled as a standard fix geometry pressure drop:

$$\frac{\Delta p_0}{p_0} = \alpha \cdot \left(\frac{\dot{m}\sqrt{T_0}}{p_0}\right)^2 \quad (5)$$

A thermodynamic bellmouth condensation model is included into the model. Bellmouth condensation is due to the depression in the bellmouth and the normal ambient humidity. This model is based on a thermodynamic equilibrium, with an influence factor of one half. The effect of bellmouth condensation is release of latent heat and a corresponding increase in total temperature before the compressor. The loss in output is mainly due to lost flow, and to some extent increased work input to the first stage.

The combustor section is modeled with custom methods. The pressure drop is divided into a cold (friction and dump) and the hot or fundamental:

$$\frac{\Delta p_{0,cc}}{p_{0,in}} = \left(\frac{\dot{m}_{in}\sqrt{T_{0,in}}}{A_{cc}\ p_{0,in}}\right)^2 \left[K_C + K_H\left(\frac{T_{0,out}}{T_{0,in}} - 1\right)\right] \quad (6)$$

The combustor heat leak is assumed to be a fix fraction of the fired heat. This loss also includes heat leakage from all hot section. The reason for lumping all heat leaks into a single source is to simplify e.g. the turbine efficiency.

Heat recovery steam generator

The heat recovery steam generator (HRSG) is modelled in components rather than e.g. individual tubes in different boiler sections. This approach simplifies the HRSG calculation to: (a) convective heat transfer correlations for sections and (b) section pressure drop characteristics. The details of the methods are not presented here and the reader is referred to standard textbooks for further information [14].

Steam turbine

The steam turbine model is based on a part turbine methodology. In this approach, a number of turbine stages are lumped to a group or part turbine. Each of these turbines is principally described by two parameters: efficiency and swallowing capacity. The efficiency (isentropic) is defined as:

$$\eta_s = \frac{\Delta h_0}{\Delta h_{0,s}} = \frac{h_{0,in} - h_{0,out}}{h_{0,in} - h_{0,s,out}} \quad (7)$$

For a group of stages, the efficiency is normally correlated against the Parson number. The Parson number normally replaces the isentropic velocity ratio, used for single stages, when dealing with part turbines. The Parson number is normally defined as:

$$\mathrm{X} = \frac{\sum u^2}{\Delta h_s} \quad (8)$$

It is very convenient to correlate the relative efficiency versus relative Parson number [15]. A further simplification is then evident; the sum of the blade speeds squared cancels out, since the rotation speed is unchanged. This gives a correlation for turbine section dry efficiency[†] versus isentropic heat drop only:

$$\eta_{s,act}^{dry} = \eta_{s,des}^{dry} \cdot f\left(\frac{\Delta h_{s,des}}{\Delta h_{s,act}}\right) \quad (9)$$

A *caveat* is in order, the use of standard parabolic efficiency correlations, may result in erroneous results. One typical reason for this is supersonic flow in e.g. control stages below some 50 percent load. Normally, all part turbines, except for an eventual control stage (partial arc admission) and the last stage or last partial turbine, are operated with more or less the same isentropic heat drop.

The swallowing capacity or flow – pressure – relation is used to calculate the node pressures. The pressure at each node sets the heat drop distribution through the turbine train. The probably most widely used model is the one evolved from Stodola's "cone law":

$$\dot{m}_{i-j} = C_{T,i\to j}\sqrt{\frac{p_i^2 - p_j^2}{p_i\ v_i}} = C_{T,i\to j}\sqrt{\frac{p_i}{v_i}}\sqrt{1 - \frac{1}{\left(p_i/p_j\right)^2}} \quad (10)$$

The equation above shows that the flow is directly proportional to the pressure and inversely proportional to the temperature. The model derived from Stodola is, however, known to be quite

[†]Wet efficiency is calculated according to the standard Baumann approach: $\eta_{wet} = \eta_{dry}\left(1 - a\bar{y}\right)$

erroneous on choked highly loaded sections (e.g. control stages) [16]. Instead, in this work, the model by Beckmann is used. The Beckmann correlation is more intricate and the reader is referred to the original source [17] for comprehensive information. A comparison between the models is shown in Figures 2 and 3.

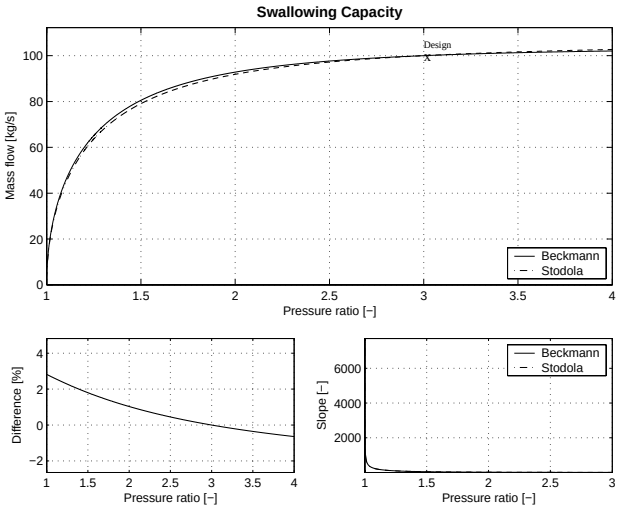

Figure 2: Comparison between the Stodola cone law and the more advanced Beckmann model for modest loaded blades (stage pressure ratio approx. 1.25)

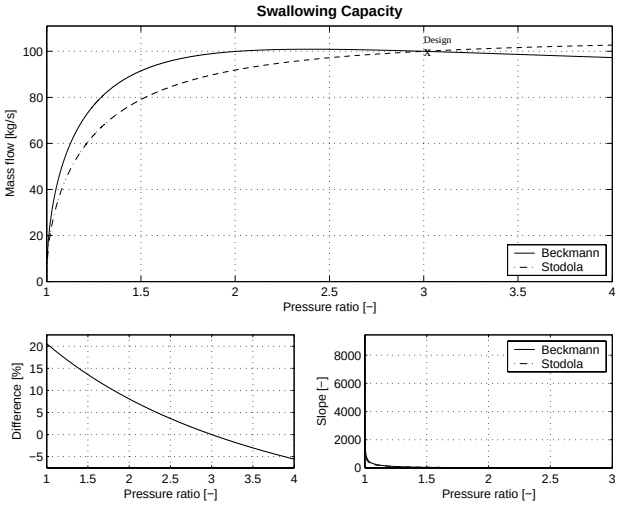

Figure 3: Comparison between the Stodola cone law and the more advanced Beckmann model for highly loaded blades (stage pressure ratio approx. 3)

This type of correlations results in a numerical problem, when transforming and using the Jacobi-matrix in the solving procedure. If one, assume constant inlet condition to the section, then the partial derivate of the expression above yields:

$$\dot{m} \propto \sqrt{1-\frac{1}{\pi^2}} \quad \rightarrow \quad \frac{d\dot{m}}{d\pi} \propto \frac{1}{\pi^2\sqrt{\pi^2-1}} \qquad (11)$$

Hence, a singularity when the pressure ratio is close to unity. This problem is solved by abandoning the equation from the system, when the section pressure ratio is below 1.001.

The exhaust loss is calculated according to the procedure in DIN 1943 [18].

The condenser performance/heat transfer coefficient is calculated according to the method developed by Heat Exchange Institute (HEI) [19].

The model has been evaluated against two real power plants and the results are well within the expectations. In both cases, the model has been calibrated against the full load cases (test code performance tests). The comparison has been done at part load cases [11]. Both plants were condensing units and the precision in calculation of e.g. the final feed water temperature was in the order of 1°C/2°F. Additional tests were carried out and the model was used to e.g. calculate the impact of removing the top heater out of service with its resulting decrease in admission flow.

CO_2 capture system

The part-load model of the CO_2 capture system is in this work limited to pressure drop correlations scaling the pressure drop to changes in massflow and velocity squared through the absorber and desorber, simulating constant geometry. The regeneration temperature and the MEA heat demand is kept constant (proportional to the moleflow of captured CO_2), while the amine overcirculation rate is varied.

OPERATIONAL STRATEGIES

Three different operational strategies have been tested for the cycle configuration. The first strategy includes a simple decrease in firing temperature which in the model corresponds to a decreasing Stator Outlet Temperature (SOT), called '*SOT decrease'* strategy. The second strategy, called '*High EGT'* strategy is a bit more complicated because it includes three different steps. In the first regime the Inlet Guide Vanes is closed with unchanged SOT. This proceeds until the Exhaust Gas Temperature (EGT) reaches 630°C, when the second regime starts. In the second regime the IGVs continue to close and the SOT is decreased with unchanged EGT. When the IGVs are fully

closed (-25°), a continued decrease in SOT also causes a decrease in EGT. Finally as a third strategy, a novel strategy called *'Constant SHT'* is introduced. Here the second regime is dictated by a constant steam superheating temperature (SHT) of maximum 565°C. This would avoid unnecessary temperature stress on the gas turbine blading and non-optimal spray cooling of steam in the superheater/reheater. The difference between the two last strategies can be seen in Figure 4 where the dotted area is cooled in the '*High EGT'* strategy.

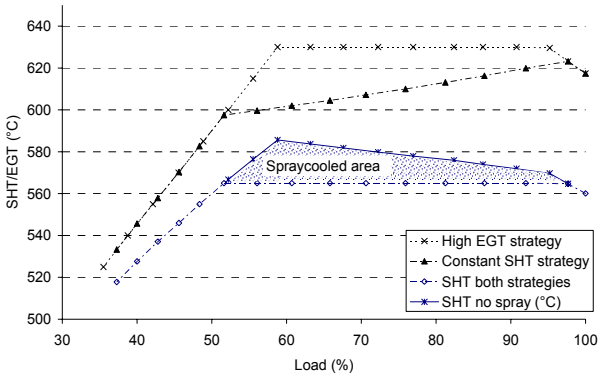

Figure 4: Difference between '*High EGT'* and '*Constant SHT'* strategies

The lowest steam pressure level is kept constant during part-load operation with variable guide vane stagger varying the swallowing capacity of that part turbine. The use of variable stagger is a powerful means to achieve a controlled extraction and one degree re-stagger typically results in five percent change in capacity. This is introduced to keep the temperature level in the regeneration part of the CO_2 capture plant high enough for efficient operation.

Two different ambient conditions have also been evaluated; a 'cold' condition with an ambient temperature set to -5°C and a 'hot' condition set to 35°C.

RESULTS AND DISCUSSION

Design case

The modelled cycle shows a design electrical efficiency of 48.6% and a gross power output of 346.5 MW, slightly higher than the SINTEF/ NTNU study which showed an efficiency of 48.1% [7]. The difference lies probably within the different assumptions for CO_2 compression and amine regeneration heat demand. Auxiliary power losses sum up to 19.2 MW in this study, more than half of it originating from the CO_2 compression.

If one wants to further improve the models using steam turbine data from GE, additional information is available in the excellent textbook by Ken Cotton "Evaluation and Improving Steam Turbine Performance" [20]. This source gives exhaustive information about General Electric's steam units. The presented material in this book is still valid with proper vintage corrections.

Part-load behaviour

The electrical efficiency resulting from the three different part-load strategies can be seen in Figure 5. The '*High EGT'* and *'Constant SHT'* show as expected the same efficiency in the first and third regime, both approximately three percentage point higher than the '*SOT decrease'* strategy below 50% load. However, the difference between the two high temperature strategies in the second regime is very small, at maximum 0.3 percentage points. It should be possible to avoid using the exergetically non-optimal spraying with only small losses in efficiency.

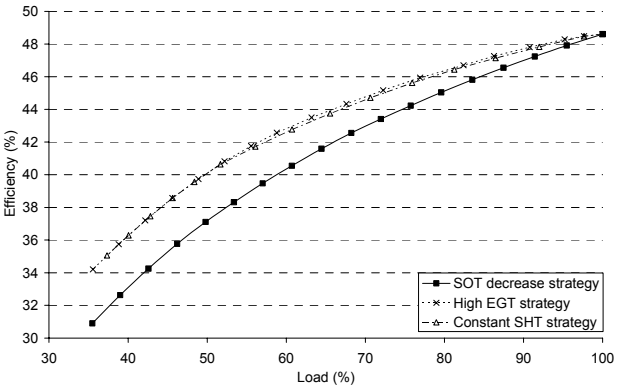

Figure 5: Electrical efficiency with different operational strategies at part-load

Furthermore, if looking into Figure 6 it is apparent that the decrease in SOT between the *'High EGT'* strategy and the *'Constant SHT'* strategy will result in longer life for the gas turbine blading.

The difference in SOT is about 20°C at 75% load and 30°C at 60% load which could be translated into terms of lifing by using the Larson-Miller parameter [21]. It is difficult to estimate the difference in lifing without details of the specific

gas turbine and its flow path. In order to get a better value it is nessecary to perform a detailed blade-to-blade analysis or 3-D CFD together with the blade cooling model [21]. However, with the use of the Larson-Miller parameter the mentioned reductions can be translated to more than a factor two in terms of lifing. This figure is conservative and a more exact evaluation should probably render in a higher figure.

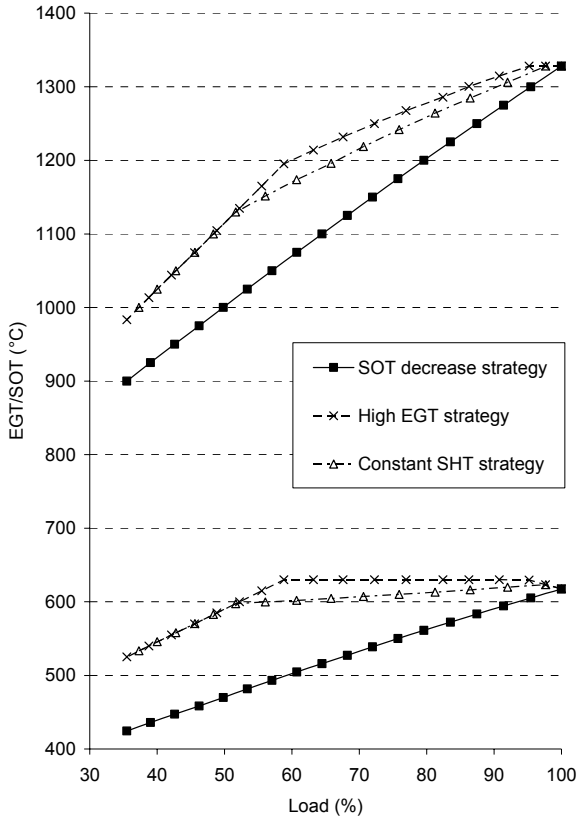

Figure 6: Difference in EGT and SOT with different operational strategies at part-load

Ambient conditions

The performance of the combined cycle at different ambient conditions behaves as expected, see Table 2. Cold ambient conditions are beneficial for power output and results in a modest increase in efficiency, whereas warmer conditions cause large decrease in both power output and efficiency. The two hot off-design strategies can be applied also to the warm ambient conditions, and in this case the '*Constant SHT'* strategy seems less attractive. The '*High EGT'* strategy shows both higher power output and efficiency at the given condition. This suggests that the novel '*Constant SHT*' strategy is more beneficial further away from the design point than close.

	'Cold'	'Hot'		Unit
Strategy		**High EGT**	**Constant SHT**	
Gross power	374.1	305.5	292.9	MW
Auxiliary power loss	20.9	17.1	16.7	MW
Net power	353.2	288.4	280.0	MW
Efficiency	48.59	47.87	47.28	%
EGT	604.3	630	618.6	°C
SOT	1328	1308	1283	°C
SHT	550.2	565	565	°C

Table 2: The influence of ambient conditions on cycle performance

CO_2 capture at off-design operation

With the assumed variable geometry in the low pressure section of the steam turbine no difficulties were experienced with the CO_2 capture plant model used. The lower CO_2 concentration in the exhaust gas flow was not reflected with higher energy demand in the capture plant, as probably would be the case [9]. This could possibly be out-weighed by changes in the heat transfer conditions in the reboiler section of the capture plant, with decreased pinchpoint etc. A more refined model of the CO_2 plant in off-design is probably needed to further evaluate this section of the power plant, and should be the subject of future work.

CONCLUSIONS

The off-design performance of a triple-pressure reheat combined cycle with post-combustion CO_2 capture has been evaluated. Three different strategies for part-load operation were tested, one of them being proposed by the authors as the '*Constant SHT*' strategy. All results presented are also relevant for a conventional combined cycle without CO_2 capture, although at a higher level of electrical efficiency.

The proposed strategy has a potential of significantly reducing the firing temperature with a marginal efficiency penalty. In order to make a "ball park" estimate, the Larson-Miller parameter can be used to give a quantitative estimation. The gain for a fix-speed unit with constant centrifugal loading is, with a conservative estimation, in the order of two. It should however be mentioned that

the discussed lifing is the first rotor creep and does not take into account e.g. oxidation of blades.

The results reveal no problem with the CO_2 capture system at part-load. During the calculations the low-pressure steam pressure was held constant, by means of a standard controlled extraction.

ACKNOWLEDGMENTS

The work presented in this paper is the result of many parallel research projects. The off-design model for gas turbines was developed as a general in-house calculation tool; the work was funded by Swedish Gas Center. Most of the actual programming was performed by Marco Lorentz. The steam cycle model was developed in the framework of the "GTX100 Helsingborg evaluation project." This work was also funded by Swedish Gas Center. The authors acknowledge Markus Truedsson for his work in programming and validation of the steam cycle models. The financial support from Sydkraft on CO_2 capture is also gratefully acknowledged.

REFERENCES

[1] Herzog H, Golomb D, *Carbon capture and storage from fossil fuel use,* Encyclopedia of Energy, Elsevier Science, 2004.

[2] International Energy Agency, *Key energy world statistics 2004,* from: `http://library.iea.org`, Jan 20, 2005.

[3] Smith D, *Does competition rule out CO_2 capture?* Modern Power Systems, November 2002, Wilmington Publishing.

[4] Roberts CA, Gibbins J, Panesar R, Kelsall G, *Potential for improvement in power generation with post-combustion capture of CO_2,* Seventh Int. Conf. on Greenhouse Gas Control Technologies, GHGT-7, Vancouver, Canada, 2004.

[5] Kim TS, *Comparative analysis on the part load performance of combined cycle plants considering design performance and power control strategies*, Energy 29 (2004), 71-85, Elsevier Science.

[6] Shin JY, Jeon YJ, Maeng DJ, Kim JS, Ro ST, *Analysis of the dynamic characteristics of a combined-cycle power plant*, Energy 27 (2002), 1085-1098, Elsevier Science.

[7] Kvamsdal HM, Maurstad O, Jordal K, Bolland O, *Benchmarking of gas-turbine cycles with CO_2 capture*, Seventh Int. Conf. on Greenhouse Gas Control Technologies, GHGT-7, Vancouver, Canada, 2004.

[8] Kohl AL, Nielsen RB, *Gas purification*, 5th ed., Gulf Publ., Houston, USA, 1997.

[9] Alie C, Backham L, Croiset E, Douglas PL, *Simulation of CO_2 capture using MEA scrubbing: a flowsheet decomposition method*, Energy Conversion Management, Vol.46 (2005), 475-487, Elsevier Science.

[10] Jordal K, Fredriksson Möller B, Bolland O, Torisson T, *Optimisation with genetic algorithms of a gas turbine cycle with H_2-separating membrane reactor for CO_2 capture*, accepted for publication in International Journal of Green Energy.

[11] Truedsson M, *Systemstudie av Västhamnsverket i Helsingborg*, MSc-thesis, Lund Inst of Tech., ISRN LUTMDN/ TMHP-04/5051-SE, ISSN 0282-1990.

[12] Lorentz M, *Modeling and Off Design Simulation of the Evaporative Gas Turbine*, MSc-thesis, Lund Inst of Tech., ISRN LUTMDN/TMHP-04/5039-SE, ISSN 0282-1990.

[13] Stevenson JD, Saravanamutto HIH, *Simulating Indirect Thrust Measurement Methods for High-Bypass Turbofans*, Journal of Engineering for Gas Turbines and Power, January 1995, Vol. 117, page 38.

[14] Stultz SC, Kitto JB, *Steam: Its Generation and Use*, 40th Ed., Babcock & Wilcox, ISBN 0-963-45700-4.

[15] Kostyuk A, Frolov V, *Steam and Gas Turbines*, English Version, Mir Publishers, Moscow, ISBN 5-03-000032-1.

[16] Cordes G, *Strömungstechnik der gasbeaufschlagen Axialturbine*, Springer Verlag, 1963.

[17] Beckmann G, *Eine allgemeine Theorie der Mengenddruckgleichung*, PhD-Thesis, Dresden, 1963.

[18] DIN 1943, *Thermal Acceptance Tests of Steam Turbines*, 1975.

[19] Heat Exchange Institute, *HEI Standards for Steam Surface Condensers,* 8th Ed. Cleveland, Ohio, 1984.

[20] Cotton KC, *Evaluating and Improving Steam Turbine Performance*, 2nd Ed., Cotton Fact Inc., 1998, ISBN 0-9639955-1-0.

[21] Moustapha H, Zelesky M, Baines N, Japikse D, *Axial and Radial Turbines*, Concepts NREC, 2003, ISBN 0-933283-12-0.

Proceedings of ECOS 2005
Trondheim, Norway
June 20–22, 2005

AZEP GAS TURBINE COMBINED CYCLE POWER PLANTS - THERMO-ECONOMIC ANALYSIS

Björn Fredriksson Möller*, Tord Torisson, Mohsen Assadi
Lund Institute of Technology, Department of Heat and Power Engineering
P.O. Box 118, SE-221 00 Lund, Sweden

Sven Gunnar Sundkvist, Mats Sjödin, Åke Klang
Siemens Industrial Turbomachinery AB, SE-612 83 Finspong, Sweden

Knut Ingvar Åsen, Kjersti Wilhelmsen
Norsk Hydro Oil & Energy Research Centre, NO-3908 Porsgrunn, Norway

ABSTRACT

Conventional power plants based on fossil fuel without CO_2 capture produce flue gas streams with concentrations of CO_2 between 3% and 15%, contributing to the threat of increasing global warming. Existing capture technologies such as post-combustion flue gas treatment using chemical absorption or pre-combustion carbon removal suffer from significant efficiency penalties as well as major increase in investment costs. Alternatively, combustion in O_2/CO_2 atmospheres also requires expensive and energy-consuming oxygen supplies.

A less energy intensive concept for oxygen production is a Mixed Conducting Membrane (MCM) reactor which produces pure oxygen from compressed air. The MCM reactor is best integrated into a conventional gas turbine combined cycle, called Advanced Zero Emissions Plant (AZEP), to provide an efficient and cost-effective power plant altogether.

In this paper the economic performance of four different combined cycle alternatives in two different gas turbine sizes are evaluated; a 50 MW_e size based on the Siemens SGT800 gas turbine and a 400 MW_e size based on the Siemens SGT5-4000F gas turbine. The evaluated combined cycles are one conventional combined cycle, one combined cycle with post-combustion CO_2 capture and two optimised AZEP cases from a previous thermodynamic study. One AZEP alternative provides 100% CO_2 capture and is thus a true zero emissions alternative, whereas the second alternative uses a sequential combustion system which enables 85% of the CO_2 to be captured, making a comparison with traditional post-combustion treatment easier. The results show that the AZEP concept presents a more competitive system in terms of efficiency and economy compared to traditional capture systems.

Keywords: CO_2 capture, zero emissions, combined cycles, thermo-economy

NOMENCLATURE

AZEP	Advanced Zero Emissions Plant
CCGT	Combined Cycle Gas Turbine
COT	Combustor Outlet Temperature
HP	High Pressure
HRSG	Heat Recovery Steam Generator
LP	Low Pressure
MCM	Mixed Conducting Membrane
MEA	Monoethanolamine
O&M	Operation and Maintenance

INTRODUCTION

Carbon dioxide has been identified as a major green house gas responsible for a large part of the enhancement of global warming. Combustion of fossil fuels for power generation is one of the main contributors to CO_2 emissions, where flue gas streams contain from 3% (natural gas fired combined cycle) to around 15% (conventional coal fired condensing plant) carbon dioxide by volume.

*Corresponding author: Phone: +46-46-222 4770 Fax: +46-46-222 4717 E-mail: bjorn.fredriksson@vok.lth.se

Capture of CO_2 can be done in several ways, often divided in three main groups as follows.

- The post-treatment of flue gases, which separates the carbon dioxide from the flue gas by means of chemical absorption (most common), membranes, distillation or other techniques [1], [2], [3], [4], [5].
- The second group includes pre-treatment of the fuel, most often seen in coal gasification plants where synthesis gas from the gasification is enriched in hydrogen through the shift reaction. The CO_2 is then removed by physical or chemical absorption [1], [6], [7].
- The third group involves nitrogen-free oxidation, also called oxy-fuel processes, as combustion with pure oxygen in semi-closed systems [8], chemical looping combustion [9], electrochemical reactions in fuel cells [10], [11], [12] or new concepts like AZEP [13], all able of producing an exhaust gas consisting of only water and CO_2.

In none of the groups above the capture is done without great effort. The post-combustion treatment, being the most mature technology, needs a significant part of the energy input to regenerate chemicals used in the process, while in pre-combustion treatment some of the fuel heating value is lost in the decarbonisation. Oxy-fuel processes are also very energy demanding if the oxygen comes from conventional air separation units.

THE AZEP CONCEPT

A less energy intensive proposition is the Mixed Conducting Membrane (MCM) which produces pure oxygen from air. The transport mechanism through the membrane is surface adsorption followed by decomposition into ions. Oxygen ions are then transported by occupying vacancies in the membrane structure. The driving force is partial pressure differences between the air and a sweep stream of recirculated exhaust gas, see Figure 1. Previous work [14] has indicated that the most efficient and cost-effective utilisation of the MCM reactor is its integration into a conventional gas turbine system to produce an Advanced Zero Emissions Power Plant, the AZEP concept.

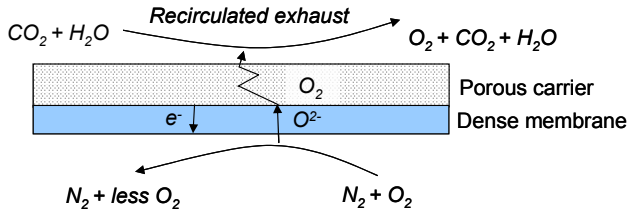

Figure 1: Schematic drawing of the MCM-membrane [14]

The combustion chamber in an ordinary gas turbine is here replaced by the MCM-reactor, which includes a combustor, sections with 'low' temperature heat exchanger (LTHX), MCM membrane and high temperature heat exchanger (HTHX) as well as a bleed gas heat exchanger, see Figure 2.

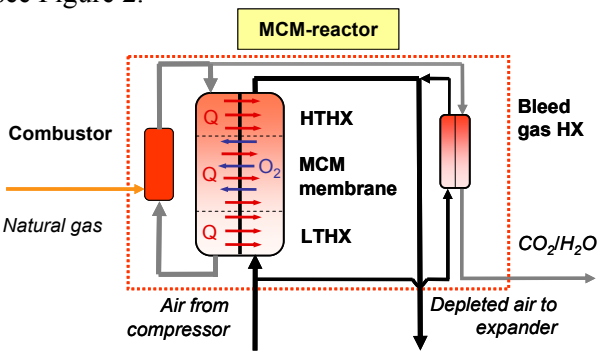

Figure 2: MCM-reactor build-up

SYSTEM BOUNDARIES

The scope of this study is to evaluate the optimal AZEP solutions [15] from a thermo-economic point of view and to compare them to alternative low emission solutions. The comparison must be as fair and transparent as possible, meaning that system boundaries should be identical in all cases. The product CO_2 will be delivered at liquid state at 100 bar for all the modelled cases. No district heating is considered from the different exhaust gas condensers present in some cases. The economic viewpoint is the CCGT plant supplier's, meaning that so called "owner's costs" are not included. Costs like these vary greatly from site to site and are difficult to model without knowledge of the specific site. For CO_2 there is not accounted for any transport or end storage cost, nor is any value assigned to the product CO_2, except the "value" of avoided CO_2 taxation.

SYSTEMS MODELLED

Two sizes of CCGT power plants are studied: a nominal 50 MW_e size based on a Siemens SGT800 (former GTX100) gas turbine and a nominal 400 MW_e size based on a Siemens SGT5-4000F (former V94.3A) gas turbine. The different systems are modelled in the commercial software IPSEpro [16], using model libraries developed within GTPOM; a European Community research project [17].

CCGT based on reference gas turbine

The first system design modelled is a reference system. As such a traditional CCGT power plant is chosen, see Figure 3. Data from such plants are in abundance, both in terms of thermo-dynamical performance used as a base in the modelling, and to some extent also cost data.

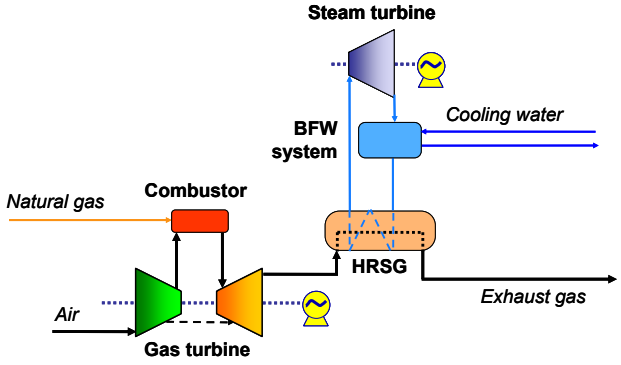

Figure 3: The reference CCGT cycle

The cost models can therefore be calibrated to Siemens CCGT power plant prices and from there extrapolated to all cases, making comparisons fair and objective. For the 50 MW_e case, a dual-pressure HSRG is chosen with live steam at 80 bar(a) and 510°C for the HP steam turbine and for the 400 MW_e case a triple-pressure cycle with reheat is chosen. In this case the live steam data is ~130/30/5 bar(a) and ~560/545/240°C.

The AZEP 100% case

This is a "traditional" type of combined cycle arrangement, but with an MCM-reactor system replacing the traditional combustion chamber. Air is compressed in the gas turbine and is then heated in the MCM-reactor. Due to MCM material and reactor design limitations the MCM-reactor outlet temperature has been restricted to 1200°C, which is considerably lower than the reference CCGT. A percentage of the oxygen contained in the air is transferred through the membrane and is carried along by the CO_2/H_2O sweep gas. The oxygen containing sweep gas is then reacted with natural gas to generate heat in a combustion chamber. A share of the sweep gas is bled off to keep the sweep gas mass flow constant in the MCM-reactor. The heat contained in the bleed gas is recovered in a separate CO_2/H_2O HRSG providing extra steam for the steam cycle and preheating of the natural gas fuel. The heat recovery has to be terminated at a higher temperature than in the ordinary HRSG due to the high water content in the bleed gas. After the HRSG the water is condensed and the remaining CO_2 is compressed from the MCM-reactor pressure at around 20 bar to delivery pressure at 100 bar. A layout of the AZEP 100% cycle is shown in Figure 4.

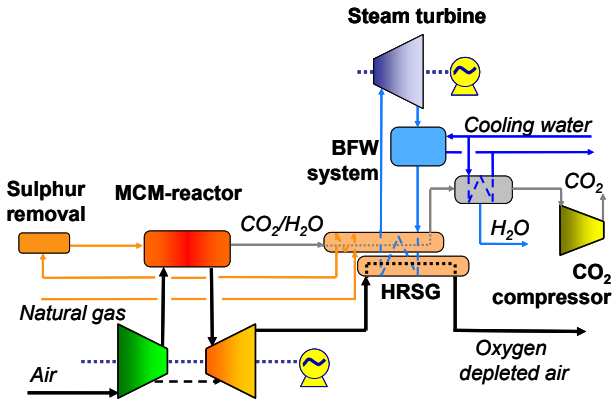

Figure 4: The AZEP 100% case

Compared to the reference system the power output is significantly reduced due to the lower turbine inlet temperature reducing gas turbine output, but also due to the lower exhaust gas temperature reducing steam production in the steam cycle. In the 400 MW_e case it is not feasible to sustain the triple-pressure reheat steam cycle from the reference case due to the low exhaust gas temperature. A dual-pressure steam cycle is therefore considered both for the 50 MW_e and the 400 MW_e case in the AZEP 100% case.

The AZEP 85% case

The third alternative, the AZEP 85% case, includes a sequential combustion chamber to increase the turbine inlet temperature. This is to improve the thermal performance of the MCM based power plant. Figure 5 shows a power plant including a sequential burner increasing the

turbine inlet temperature to 1327ºC on the air-side using natural gas as fuel.

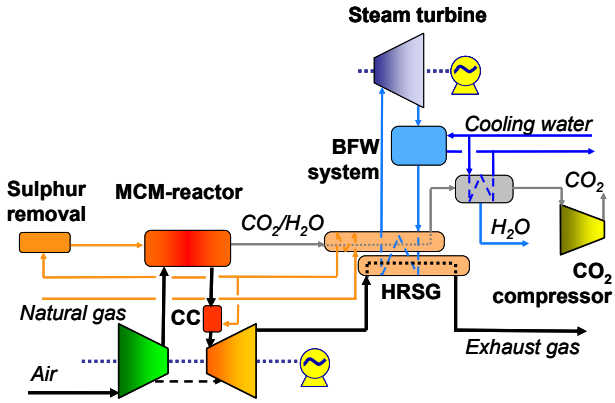

Figure 5: The AZEP 85% case

This concept is not a "pure" AZEP concept since the sequential burner will add CO_2 to the exhaust gas stream and thereby reduce the degree of CO_2 capture to 85%; a figure comparable to what is achievable in traditional amine-based CO_2 capture systems. Power plant efficiency and power output will however increase due to the higher temperature level. In this case the 50 MW_e case is modelled with a dual-pressure steam cycle with a HP steam temperature of ~500°C. The 400 MW_e alternative is modelled with a triple-pressure steam cycle with live steam data at ~130/30/5 bar(a) and ~510/485/240°C.

CCGT with CO_2 capture using MEA

The last system design modelled is the reference system with a traditional amine-based CO_2 capture system. In this case steam data is the same as for the reference system, although steam is extracted from the LP steam turbine to provide the energy needed to regenerate the amines. This steam is condensed in the reboiler section of the CO_2 capture plant and then pumped back to the steam cycle. A schematic process layout of the CCGT with an amine-based CO_2 capture system is shown in Figure 6, hereafter called the MEA 85% case. Assumptions for the CO_2 capture plant can be seen in Table 1.

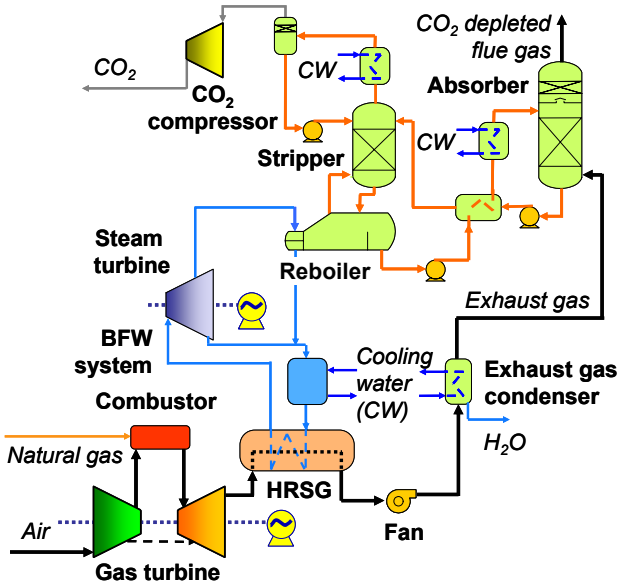

Figure 6: CCGT with post-combustion CO_2 capture

Parameter	Unit	Value
Regeneration temperature	°C	120
Regeneration heat consumtion	MJ/kg CO_2	4.5
Fan pressure increase	bar	0.06
Reboiler pinchpoint	°C	15

Table 1: Assumptions for the CO_2 capture

ECONOMIC ANALYSIS

A detailed economic model for an AZEP power plant delivery covering both main equipment, auxiliary equipment and engineering has been developed for one economic reference case; the AZEP 100% case in the 50 MW_e size. The scope is based on the vendor's scope of supply and does therefore not include the client's costs for preparing the site with connections to the main grid, to the fuel supply line etc. [18]. The scope is divided into different cost groups as follows:

- Gas turbine/genset
- Steam turbine including condenser and feed water system
- HSRG including drums, stack and ancillaries
- MEA/AZEP specific components and installation
- Buildings and civil works
- Auxiliary systems including electricals and instrumentation not included in the main component groups

- Project management, erection costs, commissioning, engineering, etc

The reference case, based on the experience of several delivery projects for CCGT plants using the SGT800 gas turbine, determines specific cost factors based on total capital cost for each of the three last groups. Auxiliary systems and project cost factors is for example considered to have approximately the same ***cost*** for an AZEP plant as for a CCGT plant of similar size (the specific AZEP equipment cost group includes both engineering and system costs), while the MEA case is considered to have a similar ***cost share*** for auxiliary systems and project costs as an AZEP plant. Buildings and civil works are treated in a special way, assuming they are based on HRSG cost, total plant power output and AZEP/MEA specific costs. The specific cost factors for project and auxiliary systems are tuned to match the reference case, while inhouse rules-of-thumb and literature data are used to determine AZEP/MEA specific costs, see Table 2. In a similar way the operation & maintenance (O&M) cost is divided into gas turbine, steam turbine, HRSG and AZEP/MEA O&M-costs. Cost of electricity for each of the cases can then be calculated as the sum of capital cost, fuel cost, O&M-costs and, if applicable, cost for CO_2 taxes.

	MEA/AZEP cases	**CCGT case**
Proj. cost 50MW_e	18%	23%
Aux. cost 50MW_e	11%	14%
Proj. cost 400MW_e	8%	10%
Aux. cost 400MW_e	9%	12%
MEA plant	6.25 k€/kg/s flue gas + 32.5 k€/kg/s CO_2	
CO_2 compressors	800 €/kW_e	
MCM reactor 50MW_e	54 k€/MW_{th} @ 1200°C[†]	
MCM reactor 400MW_e	45 k€/MW_{th} @ 1200°C[†]	

Table 2: Specific cost data used in the economic analysis [19]

[†] Includes reactor with pressure vessel and support structures

In order to determine the economic parameters having the greatest impact on the thermo-economic performance of the compared power plant concepts, a sensitivity study is performed. Apart from the ordinary parameters like discount rate and fuel price, the cost and life of the MCM reactor and CO_2-tax is also included, see Table 3.

Parameter	**Unit**	**Lower cost**	**Base case**	**Higher cost**
Discount rate	%	7.5	**10**	15
Fuel price	€/GJ	3	**4.5**	6
CO_2-tax	€/ton CO_2	-	**0**	40
MCM reactor cost	%	-25	**±0**	+25
MCM exchange period	years	2.5	**5**	7.5

Table 3: Sensitivity analysis parameters used in the study and their variation range

RESULTS AND DISCUSSION

Thermodynamic evaluation

The thermodynamic performance of the different concepts varies very little from the results presented in the preceding study [15], and is summarized in Table 4 and Table 5. Efficiencies decrease from less than 3 percentage points (AZEP 85%, 50MW_e) to over 8 percentage points (AZEP 100%, 400MW_e) in the low CO_2 emission alternatives, compared to the reference CCGT plants. Power output also decreases in all cases, most for the AZEP 100% case and least for the CCGT-MEA case, with the AZEP 85% case in between. For the AZEP cases the decrease in power output is less significant using the smaller gas turbine, due to smaller difference in COT between the unmodified gas turbine and the AZEP concept. The efficiency decrease for the MEA 85% case, around 7.5 percentage points, is at the lower end of the range previously found in literature [2],[20],[21].

Plant data 50 MW_e power plants	**CCGT**	**AZEP 100%**	**AZEP 85%**	**MEA 85%**
Net power output (MW)	63.8	46.2	53.8	55.0
Plant fired heat (MJ/s)	120.5	95.4	107.1	120.5
Net plant efficiency (LHV) (%)	**53.0**	**48.4**	**50.3**	**45.6**
CO_2 compression power (MW)	-	0.49	0.47	1.63
Plant total auxiliary power (MW)	0.7	1.1	1.1	4.0

Table 4: Process simulation results of the 50 MW_e cases

Plant data 400 MW_e power plants	CCGT	AZEP 100%	AZEP 85%	MEA 85%
Net power output (MW)	400.9	248.1	300.4	346.9
Plant fired heat (MJ/s)	692.4	500.5	562.5	692.4
Net plant efficiency (LHV) (%)	**57.9**	**49.6**	**53.4**	**50.1**
CO_2 compression power (MW)	-	2.95	2.85	9.2
Plant total auxiliary power (MW)	4.9	5.5	7.5	22.5

Table 5: Process simulation results of the 400 MW_e cases

Assumptions for the MEA case have on purpose been rather optimistic, due to the comparison between a MEA power plant, available more or less today, and AZEP power plants available some years into the future.

Thermo-economic evaluation

The results of the thermo-economic evaluation of the 50 MW_e system models are compared in Table 6. It can be seen that all of the CO_2 reduced cases suffer from large increases in cost of electricity. The lowest cost of electricity of the low CO_2 emission alternatives is shown by the AZEP 85% case with 20% increase in cost of electricity. Then comes the AZEP 100% case with 28% increase and worst is the MEA 85% case with an increase of 36% in cost of electricity. It can also be seen that the fuel price, apart from CO_2 taxation for the CCGT case, is the single variation factor that has the largest impact on the cost of electricity. Furthermore is the influence from MCM reactor cost and exchange period rather small. For all variations in MCM reactor cost and exchange period the AZEP 85% is clearly superior to the AZEP 100% which in turn is superior to the MEA 85% case.

If a CO_2-tax set to 40 €/ton is applied the results will be very different, with the AZEP 85% case showing the best economy followed by the AZEP 100% case and the reference case. The MEA 85% case is still the worst from an economic point of view. From Figure 7 a breakeven CO_2-tax can be expected at 31 €/ton for the AZEP 85% case and at 37 €/ton for the AZEP 100% case compared to the reference CCGT.

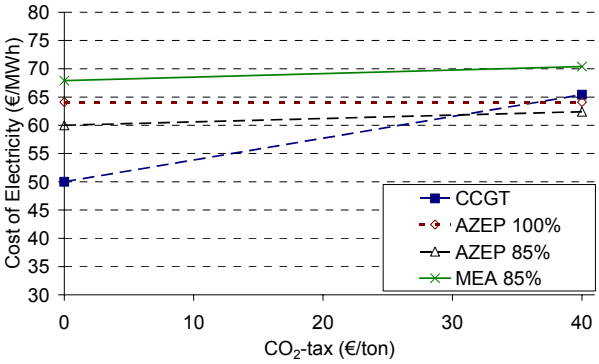

Figure 7: Influence of CO_2-tax on cost of electricity, 50 MW_e cases

The results of the thermo-economic evaluation of the 400 MW_e system models are compared in Table 7. As for the 50 MW_e cases, all of the CO_2 reduced cases suffer from large increases in cost of electricity. For the 400 MW_e systems it is again the AZEP 85% case showing the best results of the low CO_2 emission alternatives with 26% increase in cost of electricity.

Cost of Electricity (€/MWh)	CCGT	AZEP 100%	AZEP 85%	MEA 85%
Base Case	**50.0**	**64.1**	**60.0**	**67.9**
Discount rate – low	47.8	60.4	56.8	64.1
Discount rate – high	54.6	71.9	67.0	76.2
Fuel price – high	60.2	75.2	70.7	79.7
Fuel price – low	39.8	52.9	49.2	56.0
CO_2-tax – high	65.4	64.1	62.4	70.4
MCM reactor cost – high	-	65.1	60.8	-
MCM reactor cost – low	-	63.0	59.1	-
MCM exchange period – long	-	63.6	59.6	-
MCM exchange period – short	-	65.4	61.1	-

Table 6: Cost of electricity for the 50 MW_e cases

Cost of Electricity (€/MWh)	CCGT	AZEP 100%	AZEP 85%	MEA 85%
Base Case	**39.5**	**53.9**	**49.7**	**52.9**
Discount rate – low	38.4	51.6	47.7	50.6
Discount rate – high	41.9	59.1	54.1	57.8
Fuel price – high	48.8	64.8	59.8	63.7
Fuel price – low	30.2	43.0	39.6	42.1
CO_2-tax – high	51.7	53.9	52.1	55.2
MCM reactor cost – high	-	54.6	50.3	-
MCM reactor cost – low	-	53.2	49.1	-
MCM exchange period – long	-	53.5	49.3	-
MCM exchange period – short	-	55.3	51.0	-

Table 7: Cost of electricity for the 400 MW_e cases

The MEA 85% case and the AZEP 100% case show similar economic performance with the MEA case having a somewhat lower cost of electricity for all cases, except when a CO_2-tax is applied. The increase in COE for the base case is 34% for the MEA 85% case and 36% for the AZEP 100% case. Similar to the 50MW_e cases, it is the fuel price that is the single variation factor having the largest impact on the cost of electricity. The impact from uncertainties in the MCM reactor cost and exchange period is rather small also in the 400 MW_e cases. From Figure 8 a breakeven CO_2-tax can be expected at 40 €/ton for the AZEP 85% case. It can also be seen that the AZEP 100% case becomes more economical than the MEA 85% case at about 20 €/ton.

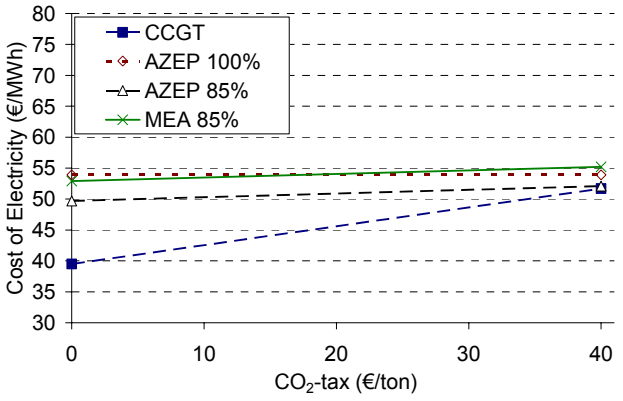

Figure 8: Influence of CO_2-tax on cost of electricity, 400 MW_e cases

CONCLUSIONS

With the economic assumptions made in this study it has been shown that the two optimal AZEP cycles (AZEP 85% and AZEP 100%) are more economical than one comparable alternative (MEA 85%) using a medium sized gas turbine, SGT800. Using a larger industrial gas turbine, SGT5-4000F, the AZEP 85% alternative is still more economical than the alternative (MEA 85%), while the AZEP 100% case needs support from CO_2 taxation to compensate for the lower emission level. With an assumed CO_2-tax of 40 €/ton the two AZEP alternatives show better economic performance than a conventional CCGT at the smaller size.

It has also been shown that uncertainties in MCM reactor cost and the life expectancy of MCM reactor ceramics do not have a big influence on the cost of electricity. It should be emphasized that the current study does not include so called "owner's costs", due to the inherent difficulties in modelling these. However, they could be expected to be bigger for a post-combustion capture plant due to the much larger footprint of that plant.

ACKNOWLEDGMENTS

The authors want to thank all partners in the AZEP project for their contributions to the results in the project. The AZEP project is partly funded by the European Commission in FP5, contract number ENK5-CT-2001-00514, and the Swiss Government (BBW 01.0054-1), the support of which is gratefully acknowledged.

REFERENCES

[1] Hendriks C, *Carbon-dioxide Removal from Coal-fired Power Plants*, Dissertation from University of Utrecht, Kluwer Academic Publishers, Netherlands, 1994.

[2] Bolland O, Undrum H, *A novel methodology for comparing CO_2 capture options for natural gas-fired combined cycle plants*, Advances in Environmental Research 7 (2003) 901-911, Elsevier Science.

[3] Chiesa P, Consonni S, *Natural gas fired combined cycles with low CO_2 emissions*, J. of Eng. for Gas Turbines and Power, Trans. of the ASME, Vol.122, pp. 429-436, 2000.

[4] Corti A, Lombardi L, Manfrida G, *Absorption of CO_2 with amines in a semiclosed GT cycle: Plant performance and operating costs*, Int. Gas Turbine & Aeroengine Congress & Exhibition, Stockholm, Sweden, 1998.

[5] Corti A, Beconi BM, Lombardi L, *Alkali Absorbing for CO_2 removal: Thermo-economic comparison between carbonate and sodium hydroxide based processes*, Italian Conf. on Chemical and Process Eng., Florence, Italy, 2001.

[6] Andersen T, Kvamsdal HM, Bolland O, *Gas turbine combined cycle with CO_2 capture using auto-thermal reforming of natural gas*, In: Proceedings of ASME Turbo Expo 2000, München, 2000.

[7] Chiesa P, Consonni S, *Shift reactors and physical absorption for low CO_2 emission IGCCs*, Int. Gas Turbine & Aeroengine Congress & Exhibition, Stockholm, Sweden, 1998.

[8] Chiesa P, Lozza G, *CO_2 emission abatement in IGCC power plants by semiclosed cycles. Part A: with oxygen-blown combustion*, Int. Gas Turbine & Aeroengine Congress & Exhibition, Stockholm, Sweden, 1998.

[9] Mattisson T, Lyngfeldt A, *Applications of chemical-looping combustion with capture of CO_2*, Second Nordic Minisymposium on Carbon Dioxide Capture and Storage", Gothenburg, Sweden, 2001.

[10] Dijkstra JW, Jansen D, *Novel concepts for CO_2 capture with SOFC*, Sixth Int. Conf. on Greenhouse Gas Control Technologies, GHGT-6, Kyoto, Japan, 2002

[11] Campanari S, Chiesa P, *Potential of solid oxides fuel cells (SOFC) based cycles in low-CO_2 emission power generation*, Fifth Int. Conf. on Greenhouse Gas Control Technologies, Cairns, GHGT-5, Australia, 2000.

[12] Riensche E, Achenbach E, Froning D, Haines MR, Heidug WK, Lokurlu A, von Andrian S, *Clean combined-cycle SOFC power plant – cell modelling and process analysis*, Journal of Power Sources 86 (2000), 404-410, Elsevier Science

[13] Sundqvist SG, Griffin T, Thorshaug NP, *AZEP - Development of an integrated air separation membrane – gas turbine*, Second Nordic Minisymposium on Carbon Dioxide Capture and Storage", Gothenburg, Sweden, 2001.

[14] Griffin T, Sundkvist SG, Åsen K, Bruun T, *Advanced zero emissions gas turbine power plant*, In: Proceedings of ASME Turbo Expo 2003, Atlanta, USA, 2003.

[15] Sundkvist SG, Klang Å, Sjödin M, Wilhelmsen K, Åsen K, Tintinelli A, McCahey S, Ye H, *AZEP gas turbine combined cycle power plants – thermal optimisation and LCA analysis*, Seventh Int. Conf. on Greenhouse Gas Control Technologies, GHGT-7, Vancouver, Canada, 2004.

[16] SimTech Simulation Technology, *IPSEpro User Documentation version 3.1.001*, 1991-2000.

[17] Knight R, Obana M, von Wovern C, Mitakakis A, Perz E, Assadi M, Fredriksson Möller B, Sen P, Potts I, Traverso A, Torbidoni L, *GTPOM: Thermo-Economic Optimization of Whole Gas Turbine Plant*. In: Proceedings of ASME Turbo Expo 2004, Vienna, Austria, 2004.

[18] Thorèn M, *AZEP project island preliminary scope of supply,* Internal Siemens document, Oct 2003.

[19] Simbeck DR, *CO_2 Mitigation Economics for Existing Coal-Fired Power Plants*. First National Conf. on Carbon Sequestration, Washington, DC, 2001.

[20] Rubin ES, Rao AB, Chen C, *Comparative assessments of fossil fuel power plants with CO_2 capture and storage,* Seventh Int. Conf. on Greenhouse Gas Control Technologies, GHGT-7, Vancouver, Canada, 2004.

[21] Kvamsdal HM, Maurstad O, Jordal K, Bolland O, *Benchmarking of gas-turbine cycles with CO_2 capture*, Seventh Int. Conf. on Greenhouse Gas Control Technologies, GHGT-7, Vancouver, Canada, 2004.

Proceedings of ECOS 2005
Trondheim, Norway
June 20–22, 2005

OFF-DESIGN EVALUATION OF A NATURAL GAS FIRED CHEMICAL LOOPING COMBUSTION COMBINED CYCLE WITH CO_2 CAPTURE

Rehan Naqvi* **and Olav Bolland**
Norwegian University of Science and Technology (NTNU)
Department of Energy and Process Engineering
NO-7491 Trondheim
Norway

Jens Wolf
Vattenfall Utveckling AB
SE-16287 Stockholm
Sweden

ABSTRACT
This paper presents off-design evaluation of a natural gas-fired Chemical Looping Combustion (CLC) Combined Cycle with CO_2 capture. The unconventional combined cycle employs an air-based gas turbine, a CO_2 turbine and a steam turbine cycle. The proposed combined cycle has a net plant efficiency of 52.15% at full-load. At 50 % load the efficiency drops by 3.6 %-points. The efficiency drop at part-load is higher when compared to a conventional combined cycle. The pressure in CLC-reduction and -oxidation reactors is balanced by airflow reduction, using a compressor equipped with variable guide vanes. A combination of control strategies are discussed for plant start-up and part-load below 56 % when airflow reduction is not practically possible with current generation of compressors.

Keywords: power generation, natural gas, CO_2 capture, circulating fluidised bed, solids internal recirculation, metal oxide reduction, metal oxidation, combined cycle, variable guide vanes.

NOMENCLATURE

A	Area	[m^2]	u	velocity	[m/s^2]
D	diameter	[m]	$\dot{W}$	power	[kW]
H	diameter	[m]	w	specific work	[kJ/kg]
C_D	drag coefficient				
d_p	particles diameter	[mm]	**Greek**		
I	solids internal recirculation ratio		ε	solids fraction	
M	solids hold-up	[kg]	η	efficiency	
$\dot{m}$	mass flowrate	[kg/s]	μ	kinematic viscosity	[Ns/m^2]
Ox	oxidation		ρ	density	[kg/m^3]
P	Pressure	[bar]	τ	residence time	[sec]
R	solids entrainment ratio				
Re	Reynolds number				
Red	reduction				

*Corresponding author: Phone: +47 73596894, Fax: +47 73598390, E-mail: rehan.naqvi@ntnu.no

INTRODUCTION

Carbon dioxide is the most prevalent of man-made emissions of greenhouse gases. Power plants combusting fossil fuels are a major source of CO_2 release. Natural gas is the cleanest of fossil fuels and combustion of natural gas in power plants results in CO_2 emissions per kWh electricity below half of that compared to coal combustion. This paper presents off-design evaluation of a natural gas fired combined cycle power plant with CO_2 capture. The plant is based on Chemical Looping Combustion instead of a conventional combustor.

Chemical Looping Combustion (CLC), proposed by Richter and Knoche[1] in 1983, is a novel concept of power production with inherent CO_2 capture. In CLC, unlike a conventional combustion process, combustion takes place without direct contact between air and fuel. Combustion is split up into intermediate oxidation and reduction reactions. This goal is achieved by introducing a certain metal oxide as oxygen carrier that circulates between the two reactors, as depicted in fig. (1).

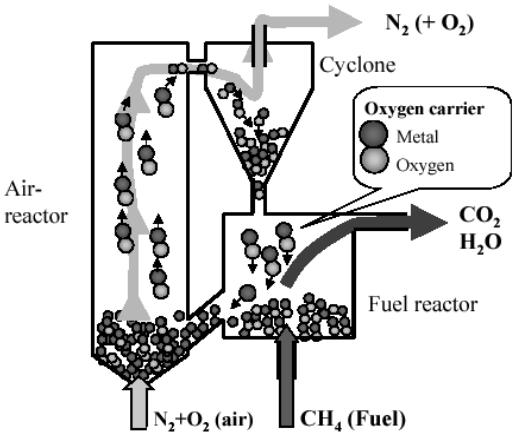

Fig. 1: The CLC Principle

In a reduction reactor, fuel reacts with oxygen in the metal oxide in a stoichiometric ratio thereby reducing the metal oxide.

The reduction reaction is given by eq. (1).

$$C_nH_{2n+2} + mMeO \rightarrow nCO_2 + [n+1]H_2O + mMe \quad (1)$$

The reduced metal oxide circulates to the oxidation reactor, carrying with it the chemical energy in the fuel. In the oxidation reactor, oxygen in the air oxidises the metal to metal oxide.

The oxidation reaction is given by eq. (2).

$$mMe + \left(\frac{m}{2}\right)O_2 \rightarrow mMeO \quad (2)$$

The metal oxide circulates back into the reduction reactor, transports oxygen to the fuel through reduction as well as provides heat for the endothermic reduction reaction. Equation (3) gives the net exothermic reaction.

$$C_nH_{2n+2} + [n+1]O_2 \rightarrow nCO_2 + [n+1]H_2O + Heat \quad (3)$$

In eq. (1), (2) and (3) MeO is metal oxide, Me is a reduced metal, C_nH_{2n+2} is a fuel (hydrocarbon), while n and m are stoichiometric factors.

The oxidation of the metal is exothermic and the oxygen depleted air is available at high temperature and pressure (in case of a pressurised reactor) and can be utilised for power production. The hot CO_2-rich exhaust stream can also be utilised for power generation, either by expansion or steam generation. The CO_2-rich exhaust stream can afterwards be condensed to separate water and CO_2 is compressed. In this way the energy penalty for CO_2 separation and compression is lower than a conventional power plant where CO_2 is diluted with other combustion products.

The metal oxide performance is vital to the process. The metal oxide should be mixed with an inert stabiliser to provide adequate mechanical stability and improved chemical reactivity. So far, investigations have been made for Iron Oxide[2] and various other metal oxides[3] (Ni, Cu, Mn, Co). Out of all, Nickel Oxide (NiO) exhibits the most promising properties[4] and the present work uses NiO supported on $NiAl_2O_4$ (60% NiO by mass).

CYCLE DESCRIPTION

Figure 2 presents the proposed CLC-combined cycle with CO_2 capture. The cycle has a unique feature that it operates two turbines on Brayton cycle i.e. an air-based gas turbine and a CO_2-turbine. The high temperature/pressure oxygen-depleted air at the air reactor (Ox) exit enters the air turbine where it mixes with the coolant bleed drawn from the compressor. The air turbine exhaust generates steam in a heat recovery steam generator. The CO_2-rich stream from the fuel reactor (Red) expands in the CO_2-turbine. The CO_2-turbine exhaust is used to pre-heat the fuel in the fuel recuperator. The exhaust is then fed to the CO_2 dehydration and recompression plant. The power plant is configured to give large power outputs (>300 MW) under varying conditions to achieve a reasonable thermodynamic design which can further be analysed under off-design mode. The computational assumptions used in the present work are given in appendix.

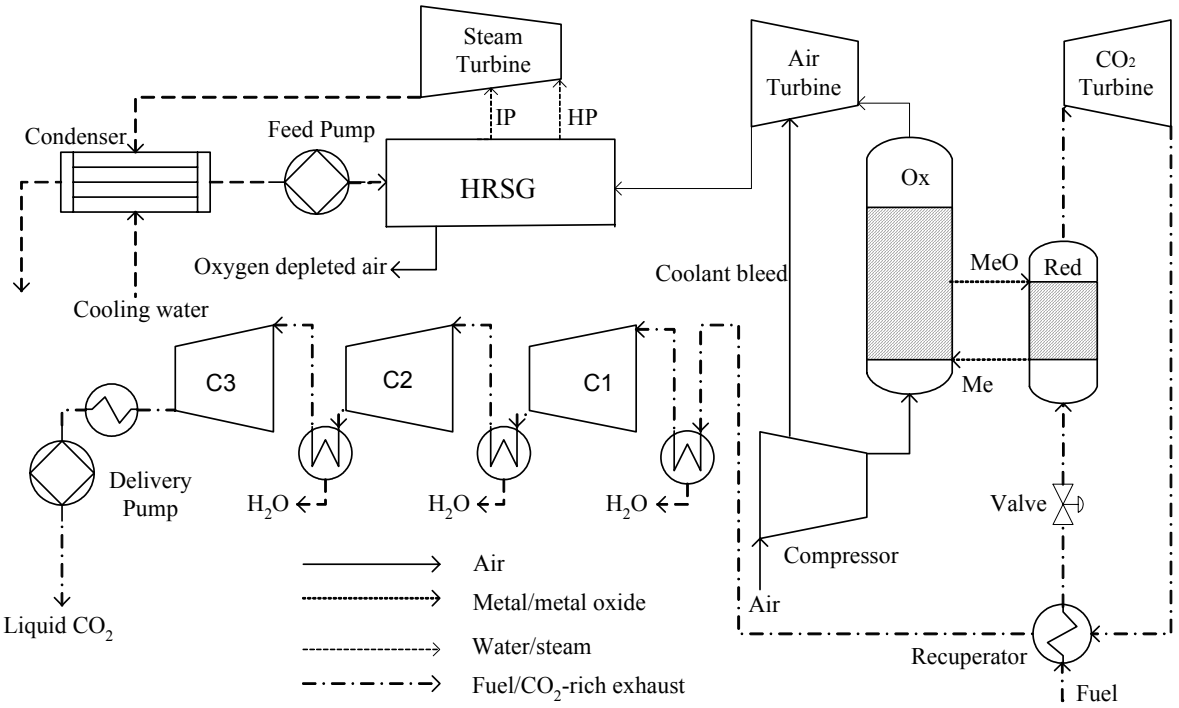

Fig. 2: Schematics of the proposed CLC-combined cycle with CO_2 capture

MODELLING BACKGROUND

The steady-state generic models of the air compressor, fuel recuperator, reactor system, air turbine and the CO_2-turbine were developed and implemented in the simulation tool gPROMS[5]. The cooling penalty for the air turbine was determined by incorporating a cooling model[6] into the air turbine model. The CO_2-turbine works at relatively lower temperatures and was assumed to be uncooled. The steam cycle was simulated in GTPRO/GTMASTER[7]. The CO_2 compression plant was simulated in PRO/II[8]. The reactor system model is based on two sub-models; a heat and mass balance model[9] and a model considering the hydrodynamic behaviour of the reactors by involving reactors geometry. In off-design mode, the compressor and the air turbine are assumed to operate according to the characteristic maps of a large axial compressor and a large axial turbine, respectively. The off-design behaviour of the CO_2-turbine is governed according to the standard choked nozzle equation.

Reactor System

The reactors should be capable of not only transporting the required amount of solids but also providing necessary solids conversion rate. The concept of circulating fluidised bed reactor (CFBR) was proposed by Lyngfelt[10] and the present work employs the same. Figure 3 presents the schematic sketch of the reactor system.

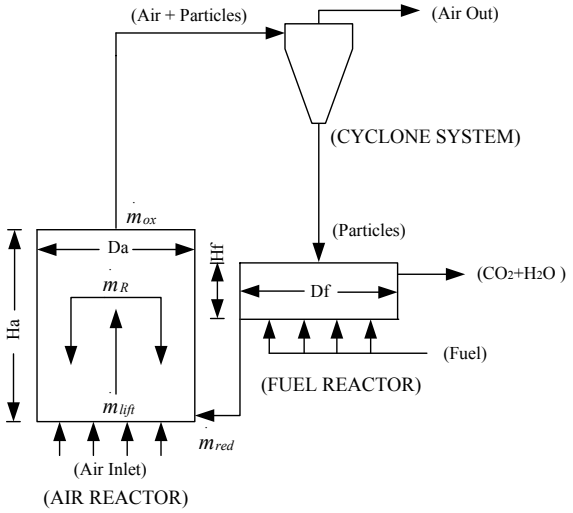

Fig. 3: Schematic sketch of CFBR System

In this work, the CLC-reactor system design is based on certain simplifications and assumptions yet sufficient details have been maintained to predict its behaviour under load-varying conditions. It is assumed that the solids leaving the air reactor are fully oxidised, homogenously mixed and in thermal equilibrium with the air leaving the reactor. The

solids at the fuel reactor exit are also in thermal equilibrium with the exhaust (CO_2/H_2O) stream. With a given air reactor diameter resulting in a certain superficial air velocity, flowrate of particles lifted from bottom of the air reactor can be calculated by eq. (4).

$$\dot{m}_{lift} = A_a \cdot \rho_s \cdot \varepsilon \cdot (u_0 - u_T) \quad (4)$$

In eq. (4) A_a is cross-sectional area of the air reactor, ρ_s is average density of particles and ε is average solids fraction in the air reactor. u_0 and u_T are superficial air velocity and terminal falling velocity of particles, respectively. Terminal falling velocity of particles is calculated as;

$$u_T = \left[\frac{4 \cdot g \cdot d_p}{3 \cdot C_D} \cdot \left(\frac{\rho_s}{\rho_{air}} - 1 \right) \right]^{1/2} \quad (5)$$

In eq. (5) g is acceleration due to gravity, d_P is average diameter of particles and C_D is drag coefficient, which is calculated by eq. (6).

$$C_D = \frac{a_1}{Re_T^{\,b}} \quad (6)$$

The constants a_1 and b were calculated according to Howard[11]. In eq. (6) Re_T is Reynolds Number of particles at terminal falling velocity given by eq. (7).

$$Re_T = \frac{u_T \cdot d_p \cdot \rho_{air}}{\mu} \quad (7)$$

In eq. (7), μ is kinematic viscosity of air. In the riser (air reactor), there is a certain internal recirculation of the solids. The internal recirculation ratio (I) is given by eq. (8).

$$I = 1 - R \quad (8)$$

In eq. (8) R is the entrainment ratio defined as:

$$R = \frac{\dot{m}_{ox}}{\dot{m}_{lift}} \quad (9)$$

From eq. (8) and (9) it can be seen that internal recirculation of particles increases with decrease in the entrainment of particles out of the reactor. Internal recirculation of particles results in an increased overall solid fraction (ε in eq. 4) in the air reactor. The overall solids fraction is calculated as:

$$\varepsilon = \frac{(2 - R) \cdot \varepsilon_{se}}{R} \quad (10)$$

In eq. (10), ε_{se} is solid fraction at exit of a pneumatic transport reactor. This is typically in the range of 0.001-0.003 and is assumed to be 0.0015. In eq. (9) $\dot{m}_{ox}$ is flowrate of fully oxidised solids (pure NiO) and inert stabiliser. According to eq. (9), at R=0, there is no particle entrainment and hence the reactor behaves as a steady-state fluidised bed. And when R=1, all the particles are entrained i.e. transported out of the reactor in a single pass and hence there is no internal recirculation of particles. The entrainment ratio, R is a function of the difference in superficial velocity and particles terminal velocity, say; $\Delta u = u_0 - u_T$. Entrainment ratio increases with an increase in superficial velocity until a threshold point is reached where all the particles are blown out of the reactor without any internal recirculation. The difference in the two velocities at the threshold point is denoted as Δu_{TH} and is assumed to be 2.5, which is fairly realistic for a pneumatic transport reactor. After the threshold point, an increase in superficial air velocity has no effect on internal recirculation and a continuous pneumatic transport prevails. This phenomenon is expressed in the form of eq. (11) and fig. 4.

$$R = \begin{cases} \dfrac{1}{\Delta u_{TH}} \cdot \Delta u & \Delta u - \Delta u_{TH} < 0 \\ 1 & \Delta u \geq \Delta u_{TH} \end{cases} \quad (11)$$

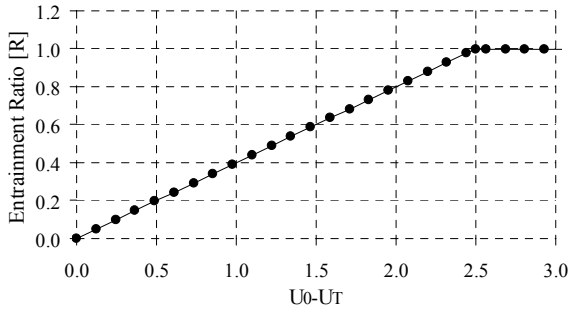

Fig. 4: Entrainment ratio vs. Δu

The air reactor hold up of solids is calculated as:

$$M_a = A_a \cdot H_a \cdot \rho_s \cdot \varepsilon \quad (12)$$

Mean residence time of the solids in the air reactor is then calculated by eq. (13).

$$\tau_a = \frac{M_a}{\dot{m}_{lift}} \quad (13)$$

Mean residence time of particles in the fuel reactor is calculated on the basis of average flowrate of particles, given by eq. (14).

$$\tau_f = \frac{2 \cdot M_f}{\dot{m}_{red} + \dot{m}_{ox}} \quad (14)$$

Where M_f is solids mass in fuel reactor given as:

$$M_f = A_f \cdot H_f \cdot \rho_s \cdot \varepsilon_f \quad (15)$$

In eq. (14) $\dot{m}_{red}$ is flowrate of solids leaving the fuel reactor and is calculated as:

$$\dot{m}_{red} = A_f \cdot \rho_s \cdot \varepsilon_f \cdot \left(u_{0,f} - u_{T,f}\right) \quad (16)$$

In eq. (15) and (16) ε_f is the solids fraction at the fuel reactor exit and is assumed to be 0.4 which is typical for a fluidised bed reactor. The present work is based on a constant ε_f under various load and flow conditions. Pressure drop in the air and fuel reactor is calculated by eq. (17).

$$\Delta P = \Delta P_B + \Delta P_D \quad (17)$$

ΔP_B and ΔP_D is pressure drop in the fluidised bed and pressure drop caused by gas distributors, respectively. The pressure drop over the fluidised bed (ΔP_B) is calculated by using eq. (18) which is derived from the hydrodynamics described by Carberry and Varma[12] & Kunii and Levenspiel[13].

$$\Delta P_B = 1.2 \cdot \frac{M \cdot g}{A} \quad (18)$$

In Equation (18), M is the hold up of the solids in air or fuel reactor, g is acceleration due to gravity and A is cross-sectional area of the reactor. Pressure drop due to the gas distributors is given as:

$$\Delta P_D = 0.4 \cdot \Delta P_B \quad (19)$$

The pressure drop in cyclones is assumed to be 20 mbar.

RESULTS AND DISCUSSION

Thermodynamic Analysis

In order to analyse a power cycle under off-design mode, it is essential to have a reasonable thermodynamic design. A sensitivity study of the key cycle parameters was carried out to thermodynamically analyse the combined cycle and a design point was established. Under the thermodynamic analysis, the reactor system was based on certain assumptions. Pressure drop in both the reactors was calculated in accordance with eq. (17) for oxidation temperature 1200 °C and compressor pressure ratio 18. The same pressure drop percentage was used during the thermodynamic analysis under all conditions. It was also assumed that the internal of both the reactors is well-mixed and the exiting solid streams are in thermal equilibrium with the corresponding exiting gaseous stream. It was assumed that 100 % of the solids entering the air reactor are converted (oxidised) while only 70 % of the solids entering the fuel reactor are converted (reduced). Experimental studies by Lyngfelt[5] show that the thermodynamic limit of NiO to convert fuel is 99.5 %. However, 100% fuel conversion was assumed for the present work. The net plant efficiency includes CO_2 compression penalty and losses (mechanical, generator, auxiliaries). The definitions of net plant efficiency and specific work used in the present work are given by eq. (20) and (21), respectively.

$$\eta_{net} = \frac{\left(\left(\dot{W}_{GT} + \dot{W}_{CO_2-T} + \dot{W}_{ST} - \dot{W}_{comp}\right) \cdot \eta_{m+g+aux}\right) - \dot{W}_{CO_2-comp}}{\dot{m}_{fuel} \cdot LHV} \quad (20)$$

$$w = \frac{\left(\left(\dot{W}_{GT} + \dot{W}_{CO_2-T} + \dot{W}_{ST} - \dot{W}_{comp}\right) \cdot \eta_{m+g+aux}\right) - \dot{W}_{CO_2-comp}}{\dot{m}_{air}} \quad (21)$$

Figure 5 presents the net plant efficiency as a function of specific work for different values of compressor pressure ratio (PR) and TIT values. The term TIT refers to the air reactor exit temperature.

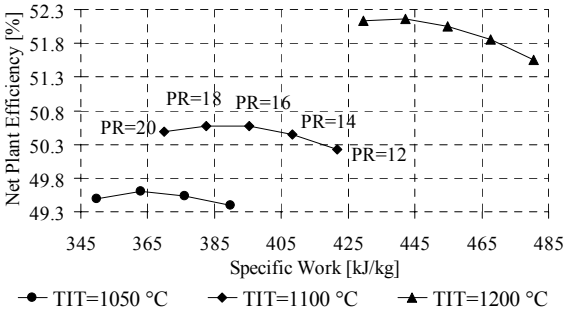

Fig. 5: Net plant Efficiency vs. specific work

The simulation results showed that the proposed CLC-combined cycle can achieve a net plant efficiency of 52.15 % at TIT=1200 °C and compressor pressure ratio (PR) of 18. The reactors were dimensioned for TIT=1200 °C and PR=18 for the full-load condition. The design is based on assumption that all the solids leaving the air reactor are fully oxidised. The air reactor (D=14m,

H=25m, ΔP=153 mbar, τ=47 s) supplies the required amount of pure NiO (and inert stabiliser) to the fuel reactor under all load conditions. At full-load, 74.6 % of the particles are internally recirculated. The fuel reactor (D=8m, H=2m, ΔP=316 mbar, τ=156 s) can convert 70 % of the NiO supplied to the fuel at full-load.

Off-design Strategy

In the off-design mode, the combined cycle was analysed under load-varying conditions. The air turbine is the key component in the cycle and drives the compressor. The compressor pressure ratio and inlet flow are determined from the choked air turbine at part load. Pressure in the fuel reactor is determined by the choked CO_2-turbine. The coolant fraction at different load conditions also varies. There are two major strategies for determining the coolant fraction (% of flow at compressor inlet). It can either be assumed as the same as at full-load; or it can be assumed that the coolant flow is choked. The latter approach has been adopted for the present work. The steam turbine work is dependent on the air turbine exhaust temperature and varies accordingly. The CO_2-turbine determines pressure at the fuel reactor entry and its work also varies at reduced fuel flowrate (part-load). The control strategy for the present work focuses on two major issues: fuel cut at part load in order to meet the load requirements; and use of variable guide vane angles at the compressor inlet (VGVs) in order to reduce the air flowrate, influencing the pressure through the system thereby achieving the same pressure at the two reactors exits.

Pressure at Reactors Exit

It is important to achieve the same pressure at the exit of both reactors. If there is a pressure difference between the two reactors, the gas from the reactor at higher pressure will tend to flow into the other reactor. With the proposed reactor system, the air reactor has a lower pressure drop than the fuel reactor. The power plant is configured such that the streams leaving the air and the fuel reactor are at the same pressure at full-load. As soon as the load is reduced, a pressure gradient occurs at the reactors exit because the two turbines require different inlet pressures. Under such a condition, an uncontrolled (in terms of pressure) system will result in a higher pressure at the air reactor exit. The consequence will be air entrapment into the fuel reactor, coming in direct contact with the fuel, thereby upsetting the stoichiometric reactions and resulting in undesired combustion products. The present work employs a compressor with variable inlet guide vanes to cope with this problem.

Part-load Performance

The presented part-load analysis uses the following definition of Load Factor (LF).

$$LF = \dot{W} / \dot{W}_0 \qquad (22)$$

In eq. (22) $\dot{W}$ and $\dot{W}_0$ are the net plant output at part-load and full-load, respectively. Figure 6 compares the relative net plant efficiency of the proposed cycle with two conventional combined cycles at various values of load factor. The part-load results for the conventional cycles were obtained by simulations in GTMASTER[7].

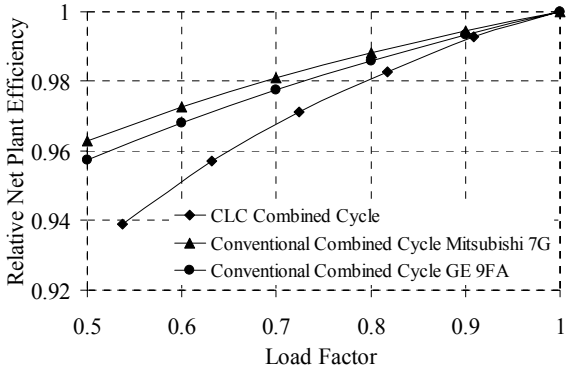

Fig. 6: Relative net plant efficiency at varying load

The results show that by reducing the load down to 50 % the net plant efficiency drops by 3.65 %-points. The relative net plant efficiency of CLC-combined cycle at part-load decreases more rapidly in comparison with a conventional combined cycle. This effect is a consequence of the presence of the CO_2-turbine. Under part-load, the plant is controlled by reducing the airflow at the compressor inlet which results in pressure reduction at the air turbine inlet. This strategy is adopted for controlling the plant in order to match with the lowest pressure occurring in the air and the fuel reactors. Therefore, the pressure at the air turbine inlet is controlled according to the pressure at the CO_2-turbine inlet which is the lower of the two. The pressure reduction results in a reduced pressure ratio across the air turbine. The net effect is an additional work reduction and efficiency drop at part-load compared to a conventional combined cycle. The airflow reduction at part-load, by means of variable guide vanes, is of interest as regards the plant control

strategy. Figure 7 presents airflow reduction as a function of varying load.

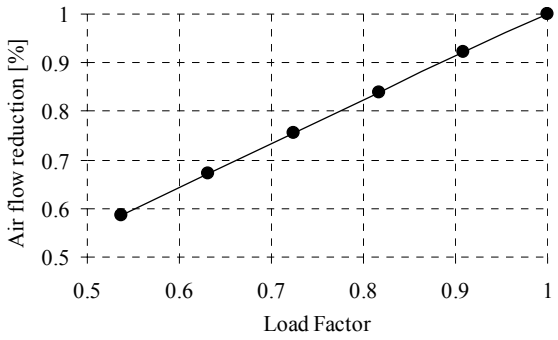

Fig. 7: Air flow reduction vs. Load Factor

It is seen in fig. 7 that decreasing the load down to 56 % results in 60 % air flow reduction. Modern compressors are equipped with VGVs that can reduce the flowrate from 100 % to typically 60 %. Therefore, according to fig. 7, the plant can not be controlled with the proposed control strategy under a load factor of 0.56 when air flow reduction is 60 %. This implies that this strategy is not valid for the plant start-up as well. This conclusion calls for the need to investigate the alternative control strategies. There is a range of diverse control strategies which can be employed in combination with one another at different load conditions. The system can also be controlled from the start-up to the 56 % load by using VGVs as well as taking extra bleeds from the compressor thereby reducing the flowrate through the air reactor and regulating the pressure. Another interesting scheme is to throttle the air after the compressor exit. While the major focus of the afore-mentioned schemes is controlling the air-side of the plant, there is certain degree of freedom to manipulate with the fuel/exhaust-side. Exhaust from the fuel reactor can be throttled and an innovative solution to the problem is to introduce VGVs at CO_2-turbine inlet.

The system can also be simplified by not employing any CO_2-turbine and generate steam in a condenser via heat recovery from the exhaust stream. This is beneficial in the terms that it is easier to control the pressure in a condenser as compared to that at turbine inlet. The system can also utilise the exhaust stream as air recuperator after the compressor prior to its entry into the air reactor.

The results concerning the reactor system behaviour at part-load are of interest. The results show that the solids conversion in the fuel reactor decreases by 20% at 50 % load compared to full-load. The internal recirculation of solids in the air reactor increases from 74.6% at full-load to 81 % at 50 % load. Residence time of particles in air reactor increases from 47 sec at full-load to 64 sec at 50 % load. In this work, the reduction rate (solids conversion) is a function of the fuel supplied and results show that despite an increase in the residence time, reduction rate decreases down to 50.6 % at 50 % load. Also, the fuel reactor is assumed to remain fluidised no matter what the load and eventually flow conditions may be. This is due to the assumption of a constant overall solids fraction. In reality, the solids fraction will change according to the flow conditions and must be accounted for the changes and determined at different conditions. This fact does imply that during the operation a condition may occur when the bed tends to defluidise. This means that the reactor will start behaving like a fixed bed and there will be no more transport of solids out of the reactor. In other words, the system will collapse. This problem can be dealt with by adopting control techniques at the fuel/exhaust side. The solids conversion in the reactors is in principle function of the solids residence time. In the air reactor with fixed geometry, air flowrate reduction results in lesser particles lifted by air. The consequence is an increased internal recirculation and decreased solids transport. This altogether has an effect of increased residence time of solids. The solids internal recirculation has been assumed to be a linear function of the relative velocity between the air and the solids. This should be determined on the basis of empirical formulations for a pressurised circulating fluidised bed system. There is, however, a different scenario in the fuel reactor. The solids conversion rates in air and fuel reactor need to be determined on the basis of residence times of particles. The solids fraction in the fuel reactor needs also to be determined by taking into account the fuel flowrate together with residence time of particles. Reactor system and oxygen carrier performance should be investigated experimentally for long-term operations at high pressure and temperature.

CONCLUSIONS

This work has been the very first attempt to analyse a CLC-combined cycle in off-design mode. At full-load the plant has an efficiency of 52.15% which is promising. The efficiency drops by 3.6 %-points when reducing the load down to 50 %. The efficiency reduction is higher at part-load as compared to a conventional combined cycle. This work suggests airflow reduction at compressor inlet

in order to balance reactors exit pressure at part-load. Other strategies have also been indicated when airflow reduction alone is not applicable under 56 % load. The results show that a CLC-combined cycle has promising efficiency at full-load yet it exhibits some operational problems at part-load which are indicated and solutions suggested.

ACKNOWLEDGEMENTS
This work has been sponsored by the Norwegian Research Council Klimatek Project.

REFERENCES

1. Richter, H. J., Knoche, K., **1983**, *Reversibility of combustion processes, Efficiency and Costing. Second Law Analysis of Processes,* ACS symposium Series 235, Washington D.C., pp. 71-85
2. Mattisson, T., Järdnäs, A. and Lyngfelt, A., **2003,** *Reactivity of Some Metal Oxides Supported on Alumina with Alternating Methane and Oxygen-Application for Chemical-Looping Combustion,* Energy and Fuels, vol. 17, pp. 643-651
3. Mattisson, T., Lyngfelt, A., Cho, P., **2001,** *The use of iron oxide as an oxygen carrier in chemical-looping combustion of methane with inherent separation of CO_2*, Fuel, vol. 80, pp.1953-1962.
4. Lyngfelt A., Kronberger B., Adánez J., Morin J.-X., Hurst P., **2004**, *The Grace Project. Development of oxygen carrier particles for Chemical-Looping Combustion. Design and operation of a 10kW Chemical-Looping Combustor,* Presented at GHG7, Vancouver, Canada, 5-9 September 2004
5. gPROMS® ModelBuilder 2.3.3, Copyright © 1997-2004 Process Systems Enterprise ltd
6. Bolland, O., Stadaas, J. F., **1995,** *Comparative evaluation of Combined Cycles and Gas Turbine Systems with Water Injection, Steam Injection and Recuperation, ASME Journal of Engineering for Gas Turbines and Power*, Vol. 28, Jan. 1995
7. GT PRO/GT MASTER, Version 11.0.2, Copyright ©1987-2004, Thermoflow Inc.
8. PRO/II 6.0, © 1994-2002 Simulation Sciences, Inc.
9. Naqvi, R., Bolland, O., Brandvoll, Ø. Ad Helle, K., **2004,** *Chemical Looping Combustion-Analysis of Natural Gas Fired Power Cycles With Inherent CO_2 Capture,* Proceedings of ASME Turbo Expo 2004, June 14-17, Vienna, Austria, ASME Paper No. GT2004-53359
10. Lyngfelt, A., Leckner, B., Mattisson, T., I., 2000, A fluidized-bed combustion process with inherent CO_2 separation-application of chemical- looping combustion, Chem. Eng. Sci. vol. 56, pp. 3101-3313
11. Howard, J.R., **1989,** Fluidized Bed Technology - Principles and Application, Adam Hilger, Bristol, UK.
12. Carberry, J. and Varma, A., **1986,** *Chemical Reaction and Reactor Engineering,* Dekker, New York, USA, ISBN: 0-8247-7543-0.
13. Kunii, D. and Levenspiel, O., **1991,** *Fluidization Engineering, 2nd Edition*, Butterworth-Heinemann, USA, ISBN 0-409-90233-0.

APPENDIX

Computational assumptions used in the present work are given below.

Ambient Air:
15 °C, 1.01325 bar, 60% Relative Humidity
Air Composition (Mole Percent): N_2 (77.3), O_2 (20.74), CO_2 (0.03), H_2O (1.01), Ar (0.92)

Fuel:
Natural Gas:
10 °C, 70 bar, LHV=46503 kJ/kg
Natural Gas Composition (Mole-%):
N_2 (0.89), CO_2 (0.2), CH_4 (89), C_2H_6 (9.4), C_3H_8 (4.7), C_4H_{10} (1.6), C_5H_{12} (0.7)

CLC- Reactors System:
Adiabatic reactors
Mean particle diameter: 150 μm

Gas Turbine Cycle:
Compressor:
Polytropic efficiency 91.5 %
Turbines: Polytropic efficiency: 86.17 %
Air turbine back pressure: 10 mbar
Efficiency $\eta_{m+g+aux}$ (Mech. + gen. + aux.): 96.634 %

Steam Cycle
HRSG: 2-Pressure levels: 60 bar, 5 bar
Hot side temperature difference: 20 °C
IP temperature: 260 °C, Pinch (HP, IP): 10 °C
Steam turbine isentropic efficiency: 92 %

CO_2 compression:
Polytropic efficiency (stage 1, 2, 3) (%): 85, 80, 75
Adiabatic efficiency Pump (%): 75
Compressor intercooler exit temperature: 30 °C
CO_2 delivery pressure: 200 bar

Proceedings of ECOS 2005
Trondheim, Norway
June 20–22, 2005

CO-UTILIZATION OF BIOMASS AND NATURAL GAS IN COMBINED CYCLES THROUGH PRIMARY STEAM REFORMING OF THE NATURAL GAS

J. De Ruyck*, F. Delattin, S. Bram
Vrije Universiteit Brussel,
Dept. of Mechanical Engineering
Pleinlaan 2, 1050 Brussels,
Belgium

*Corresponding author : tel +32 2 629 2393, fax +32 2 629 2865, email jdruyck@vub.ac.be

ABSTRACT

Power production from biomass can occur through external combustion (e.g. steam cycles, Organic Rankine Cycles, Stirling engines), or internal combustion after gasification or pyrolysis (e.g. gas engines, IGCC). External combustion has the disadvantage of delivering limited conversion efficiencies (max 30-35%). Internal combustion has the potential of high efficiencies, but it always needs a severe and mostly problematic gas cleaning.

The present article proposes an alternative route where advantages of external firing are combined with the potential high efficiency of combined cycles through co-utilization of natural gas and biomass. Biomass is burned to provide heat for partial reforming of the natural gas feed. In this way, biomass energy is converted into chemical energy contained in the produced syngas. Waste heat from the reformer and from the biomass combustor are recovered through a waste heat recovery system. It is shown that in this way biomass can replace up to 5% of the natural feed. It is also shown that in the case of combined cycles, this alternative route allows for external firing of biomass without important drop in cycle efficiency.

NOMENCLATURE

LHV	Lower heating value (J/kg)
$\dot{m}$	mass flow rate (kg/s)
$\dot{W}$	net power output (W)
η	LHV Efficiency
BBHRS	Black Box Heat Recovery System
HEN	Heat Exchanger Network
CC	Steam and Gas turbine combined cycles

KEYWORDS

Biomass, methane-steam reforming, Combined Cycle, high efficiency

INTRODUCTION

The system proposed in the present paper combines the advantages of external combustion (no gas cleaning) with the advantages of internal combustion (higher efficiencies). This is realised by using the heat from the external combustion of biomass for partial primary reforming of natural gas into mainly hydrogen and carbon monoxide (see Figure 1). In this way, the biomass energy is transferred into the syngas as chemical energy and the biomass exhaust gases are kept separate from the syngas and the internal parts of the gas turbine.

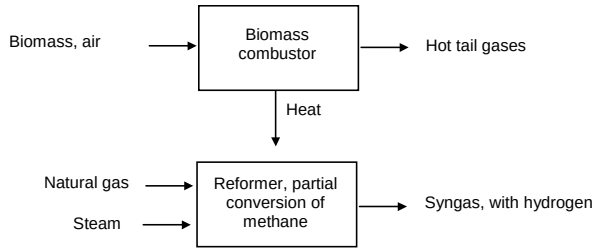

Figure 1 : Concept of steam reforming based on external combustion of biomass

The principles of combining the external biomass firing with a gas turbine cycle are further detailed in Figure 2, as follows:

- Biomass (1) is burnt in a furnace (3).
- The reforming reaction takes place in the tubes surrounding the furnace and containing the catalyst (7). The combustion air (2) needs to be preheated up to at least 600°C and the amount must yield +/- 6% O2 in the exhaust gases (4). Preheating will occur in a designated Heat Exchanger Network (HEN).
- The exhaust gases (4) with a temperature of 700°C, will feed the HEN.
- Natural gas, after desulphurisation, is mixed with steam (6) and preheated to +/- 650°C before entering the reformer (7). The required heat for natural gas and steam will be drawn from the HEN.
- Heat from the biomass furnace (3) feeds the reformer reactions (7):

$CH_4 + H_2O <\!\!\longrightarrow CO + 3H_2$ $\quad \Delta H^0_{298} = 206$ kJ.mol^{-1}

$CO + H_2O <\!\!\longrightarrow CO_2 + H_2$ $\quad \Delta H^0_{298} = -41$ kJ.mol^{-1}

Biomass energy is in this way partially converted into chemical energy in the syngas (10).
- To avoid coking in the reformer, a sufficient excess of steam is added. If appropriate, excess water is condensed and recycled (8) after the reformer.
- The obtained syngas (10) is cooled to a temperature specified by the gas turbine supplier (<300°C). The heat will be used in the HEN (9).
- The heat of the exhaust gases is recuperated in the HEN (11). This recuperation consists of the (existing) bottom cycle feed and a surplus to close the cycle energy balance.

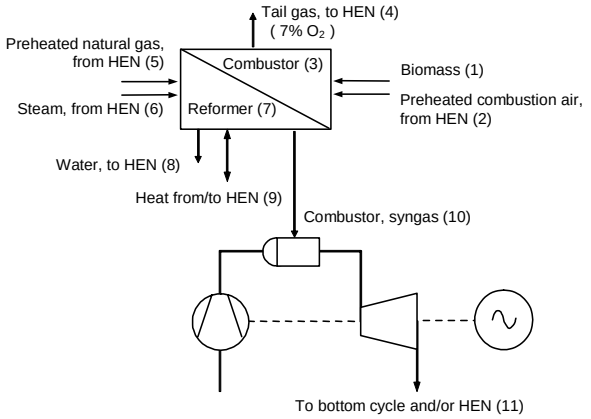

Figure 2 : Overall concept of the replacement of some natural gas by biomass through reforming (HEN = Heat Exchanger Network)

The idea of using methane-steam reforming in gas turbine cycles is not new. Two relevant papers describing the use of methane-steam reforming for heat recovery purposes are Adelman et al [1] and more recently Fiaschi et al [2]. Such 'Chemically Recuperated Cycles' use a methane-steam reformer in order to extract heat from the full gas turbine exhaust stream, and transform this heat into chemical energy in the syngas [1]. Temperatures in the gas turbine exhausts are however too low to achieve a high amount of reforming, and the obtained energy recovery is therefore too limited for practical application. Fiaschi et al [2] propose to overcome this problem by adding post-combustion of natural gas in the full exhaust of the gas turbine. They use the reforming not for purposes of heat recovery, but to capture CO2 from the fuel feed prior to the combustion process.

Another application of reforming is patented by Mittricker [3]. In this patent a reforming process is proposed to enrich fuels with low methane concentration with hydrogen. The syngas is dried in order to deliver a syngas suitable for use in gas turbines. The process integration is not further detailed.

APPLICATION TO COMBINED STEAM AND GAS TURBINE CYCLES

In the following it is shown that in the case of combined steam and gas cycles (CC) the cycle efficiency can remain unaffected when replacing a limited amount of natural gas by biomass through the proposed reforming. This proof is based on a 'black box' approach developed by the authors and applied successfully in the past [4-6]. The black box approach occurs in four steps as follows:

In a first step an adiabatic control volume is chosen around all the reference CC components, with exclusion of the compressor, the expander (Figure 3) and the steam turbine(s). The corresponding boundary conditions are given in Table 1. Assuming a Steam and Gas Turbine a certain amount of water is evaporated and preheated in the black box before feeding it to the external steam turbines. This amount is calculated from the adiabatic condition of the black box. The amount of fuel flow is adjusted to reach 1200°C at turbine inlet (turbine inlet temperature or TIT). Once the boundary conditions of the system are determined, the performance of the cycle is independent of what happens inside this 'black box heat recovery system' or BBHRS (principles of the first and second law of thermodynamics).

During the second step, the minimal amount of physical connections is made inside the BBHRS, and each connection between inlet and outlet is equipped with the necessary heaters and/or coolers. Figure 4 is drawn for the reference Steam and Gas Turbine case. The water is preheated, evaporated and superheated to 350°C before feeding it to the external steam turbine(s) (1). Methane is injected into the combustion chamber with a temperature of 150°C (2). The sole available heat source is the stack (3). Fuel and compressed air are injected in the combustor (4) where 1200°C is imposed as exit temperature.

In the third step, 'Composite Curves' of the BBHRS are drawn (Figure 5). Composite curves show at which temperatures heat is exchanged between components that require heat ('cold curve'), and components that provide heat ('hot curve'). Crossing hot and cold curves corresponds to a violation of the second law of thermodynamics. From Figure 5 it appears that the chosen boundary conditions do not lead to a second law violation. Boundary conditions can be adjusted to meet the optimal pinch point in the composite curves.

Eventually the BBHRS synthesis can be designed in the last step by means of a pinch analysis.

BASE CASE WITH REFORMING

The second to fourth steps can be repeated assuming a reforming reactor. The resulting cycle will be referred to as the 'adapted' cycle with 5% biomass input. Figure 6 shows the minimum physical connections to be made to achieve the proposed reforming step. Components 1 to 4 are as before. Part of the fuel and water is diverted and preheated (5,11). The diverted preheated fuel is then partially mixed in an isothermic way with enough water to reach a steam-methane ratio of 2 before entering the reforming reactor (8). The requested water is diverted from the steam cycle water supply, thus reducing the steam turbine flow rate (13). The residual diverted fuel is fed to the combustor (7) to deliver the required heat for the reforming process (8). For coherence in this proof, this fuel is assumed to be methane whereas in reality it has to be replaced by biomass. The comburant air is taken from the turbine exhaust gas (6). Its flow rate is adjusted to yield 6% of excess oxygen in the combustor. The heat in the combustion tail gas is to be used as a heat source in the black box (9). The syngas is cooled (10) down to the same temperature as the undiverted preheated fuel, a temperature suitable for the nozzle and combustion chamber. The amount of diverted fuel (e.g. biomass) is such that the biomass energy input into the cycle reaches 5%. According to the assumed reformer temperature, the syngas at exit of the reformer can be considered as in equilibrium : it contains 35.7% of hydrogen, 3.4% CO, 6.4% CO2, 12% methane and 42.5% water (in mole fraction).

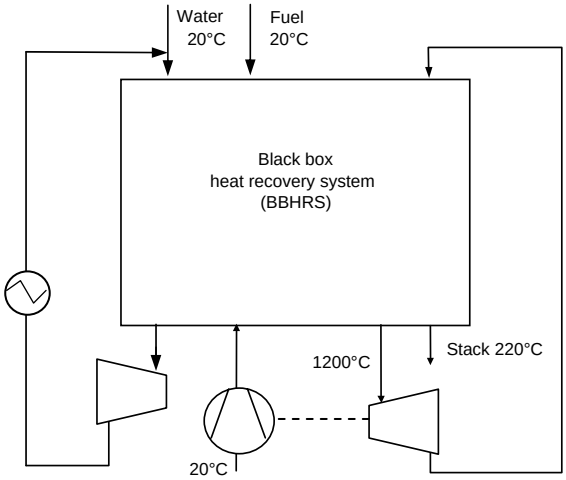

Figure 3: Black box heat recovery system(BBHRS)

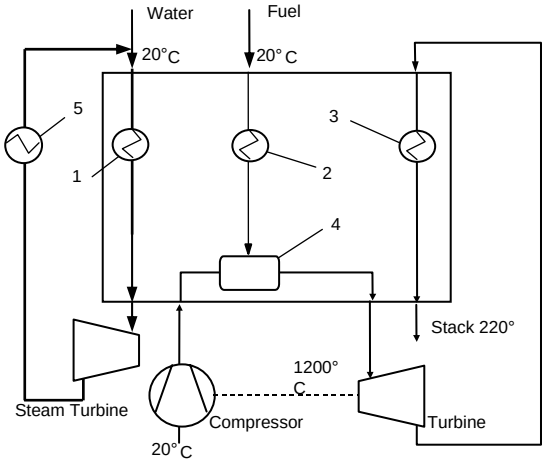

Figure 4: BBHRS with minimal amount of connections

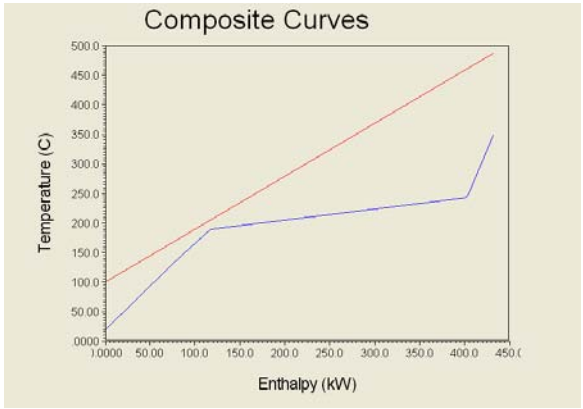

Figure 5: Composite curves of the 'original' CC cycle

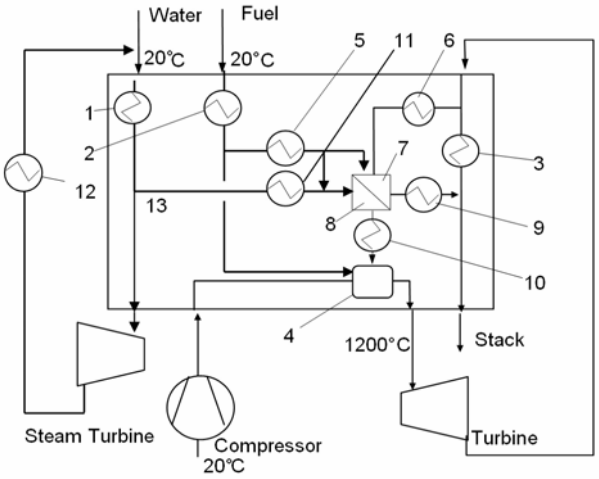

Figure 6: Minimal connections when introducing biomass through reforming

Table 1 summarises all the relevant boundary conditions of both systems, without and with reforming. Small differences are observed, due to

- the fact that part of the fuel is diverted to a different route through the combustor and next to the stack, without being expanded in the turbine.
- The diversion of part of the water from the steam cycle, lowering the flow rate of the steam turbine

The total water flow rate however, remains constant. After superheating an equal amount of steam, the residual heat must be rerouted inside the black box, where the sole appropriate heat sink is the syngas. The loss in mass flow and power in the steam turbine can thus be compensated by the increased mass flow through the main turbine and elevated methane and syngas injection temperatures. A marginal LHV efficiency of the diverted fuel η^{mar} can be defined as follows

$$\eta^{mar} = \frac{\dot{W} - \eta^{ref}\dot{m}^{meth}LHV^{ref}}{\dot{m}^{bio}\ LHV^{bio}} \qquad \eta^{ref} = \frac{\dot{W}^{ref}}{\dot{m}^{ref}LHV^{ref}}$$

In these formulas, $\dot{m}^{meth}$ stands for the remaining methane mass flow in the adapted gas turbine cycle and $\dot{m}^{bio}$ stands for the diverted 'biomass' fuel.

		Refcase	*5% Bio*
Air in	kg/s	1	1
	°C	444	444
	atm	20	20
Methane in	kg/s	0.017308	0.017607
	°C	20	20
	atm	20	20
Water in	kg/s	0.1323	0.1325
	°C	20	20
	atm	20	20
Turbine In	°C	1200	1200
	atm	19	19
Turbine Out	°C	490	490
	atm	1	1
Steam Turbine In	kg/s	0.1323	0.1164
	°C	350	350
	atm	20	20
Steam Turbine Out	°C	89	89
	atm	0.6	0.6
Stack out	kg/s	1.0173	1.0336
	°C	100	100
	atm	1	1

Table 1: Boundary conditions of the reference case (refcase) and base 5% biomass case

The reference LHV efficiency η^{ref} is determined for the original cycle in which all the energy input is methane. By means of η^{ref} , the remaining fossil fuel in the adapted cycle would provide a power output equal to $\eta^{ref}\dot{m}^{meth}LHV^{ref}$ and the surplus work can be attributed to the diverted methane (or biomass).

As indicated in Table 2a, the adiabatic condition of the black box needs the combustor injection temperature to be forced up to 470°C, delivering a marginal efficiency of over 60%. Although this may seem very interesting in theory, in practice such an injection temperatures is too high. If the residual heat is appointed to the bottom cycle to produce more superheated steam instead of heating the syngas, Table 2b shows a 20% drop in marginal efficiency compared to the reference cycle. This can be explained as follows: The amount of water rerouted to the reformer, is calculated to obtain a 100% surplus of water to methane in the reactor. After the reforming reactions, a lot of the unreformed water remains in the syngas and is injected into the combustion chamber further down the road. The unreformed water is therefore consumed according to the definition of a Steam-injection cycle, instead of the more efficient combined steam and gas cycle. In order to elevate the adapted cycle efficiency, a condenser is therefore needed to separate the unreformed water from the syngas and feed it to the bottom cycle.

REFORMING CYCLE WITH CONDENSER

When introducing a condenser in the BBHRS at a temperature of 50°C into the adapted cycle, the major part of the 42.5% water (mol fraction) can be recuperated and routed to in the bottom cycle at 20 atm. This condensation raises the marginal efficiency by ten percent and compensates half of the loss found when no condenser was used (Table 2c).

For the results shown in table 2c, all the residual heat was used in the bottom cycle, resulting in an increase in water flow rate from 0.1323 in the reference case to 0.137 in

		Reference	a	b	c	d
Main methane flow rate	kg/s	0.01731	0.01761	0.01854	0.0177	0.0174
Diverted methane rate	kg/s	0	0.00884	0.0093	0.00894	0.0071
Net power	kW	436.15	447.8	458.64	442.27	439.08
Combustor injection temperature	°C	150	470	150	150	350
Overall efficiency	%	50.4	50.9	49.5	49.99	50.46
'Biomass' marginal efficiency	%	na	60.2	31.2	41.8	51.75

Table 2a-d:

- *a) 5% biomass, constant water flow, no condenser or saturation tower*
- *b) 5% biomass, no constant water flow, all heat assigned to the bottom cycle, no condenser or saturation tower*
- *c) 5% biomass, constant water flow, addition of a condenser*
- *d) 5% biomass, constant water flow, condenser, addition of a saturation tower*

the adapted case. For comparison purposes however, it is better to keep the water flow rate constant as it is a boundary condition of the black box. After preheating, evaporating and superheating a 0.1323 kg/s water flow rate to 350°C, the remaining heat is used to increase the syngas injection temperature, making the box adiabatic. The resulting marginal efficiency surpasses the reference cycle efficiency and the injection temperature of 360 °C is more realistic for current injection nozzles (Table 2d).

Figure 7 shows the corresponding composite curves. The composite curves show that hot and cold are in balance in the adapted cycle. However at the level of evaporating water, a cross-pinch or second law violation occurs, rendering the BBHRS unfeasible. This problem can be solved by the more gradual evaporation within a saturation tower. This saturation tower mixes water and methane before entering the reforming reactor rather than evaporating water at a constant temperature in a conventional boiler.

REFORMING CYCLE WITH CONDENSER AND SATURATION TOWER

Figure 9 shows a final arrangement of the HEN, with inclusion of a saturation tower. Methane and liquid water are preheated and fed to the counter stream saturation tower, where water is evaporated at a variable temperature. In order to reach a steam-methane ratio of three, the inlet temperature of water and (to a lesser extent) methane must be sufficiently high so the desired amount of water is mixed into the methane. Before entering the reformer, the mixture is further preheated to 650°C.

Figure 8 shows the corresponding composite curves. Both curves are kept on a comfortable temperature difference from each other, in contrast to the curves without saturation tower in Figure 7.

Table 2d and table 3 confirm that while keeping the boundary conditions (nearly) constant, the adapted cycle is capable of maintaining and even surpassing the reference cycle efficiency. It is apparent that the unavoidable loss in efficiency due to the nature of biomass can be compensated by the increase in injection temperature of the syngas.

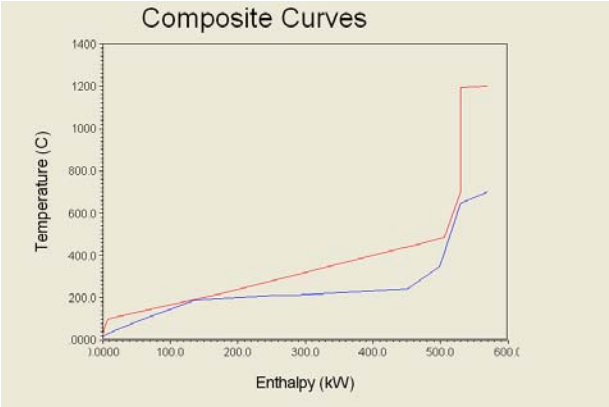

Figure 7: Composite Curves of the adapted case (5% biomass, condenser included)

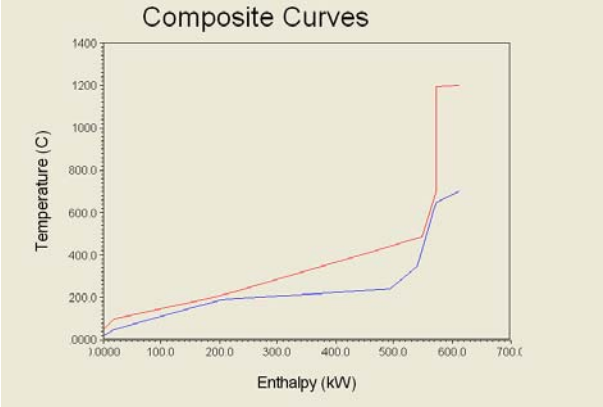

*Figure 8: Composite Curves of the adapted case **with** the introduction of a saturation tower*

To conclude the simulation, pinch analysis helped designing the BBHRS synthesis as shown in Figure 9.

The implementation of a saturation tower yields a second advantage, as the high quality requirements of the consumed water can also be reduced considerably and high priced purifications can be avoided: experimentally [6] salts and sulfur tend to lag behind in the recirculating surplus of water, ruling out expensive purification systems.

CONCLUSIONS

The present paper demonstrates that it is possible to combine the advantages of external and internal firing of biomass without a significant drop in efficiency by means of (partial) steam reforming of natural gas. In retrospect, the adapted cycle had to satisfy three conditions to be competitive with the reference cycle:

- While maintaining a constant stack temperature, all available heat must be appointed adequately
- After the reforming reactions take place, redundant water must be condensed and expanded in the bottom cycle
- A saturation tower is necessary to avoid a second law violation when keeping the water flow constant

		Refcase	5% Bio
Air in	kg/s	1	1
	°C	444	444
	atm	20	20
Methane in	kg/s	0.017308	0.017402
	°C	20	20
	atm	20	20
Water in	kg/s	0.1323	0.1326
	°C	20	20
	atm	20	20
Turbine In	°C	1200	1200
	atm	19	19
Turbine Out	°C	490	490
	atm	1	1
Steam Turbine In	kg/s	0.1323	0.1273
	°C	350	350
	atm	20	20
Steam Turbine Out	°C	89	89
	atm	0.6	0.6
Stack out	kg/s	1.0173	1.0227
	°C	100	100
	atm	1	1

Table 3: Boundary conditions of the reference case (refcase) and the adapted, 5% biomass case, saturation tower and condenser included

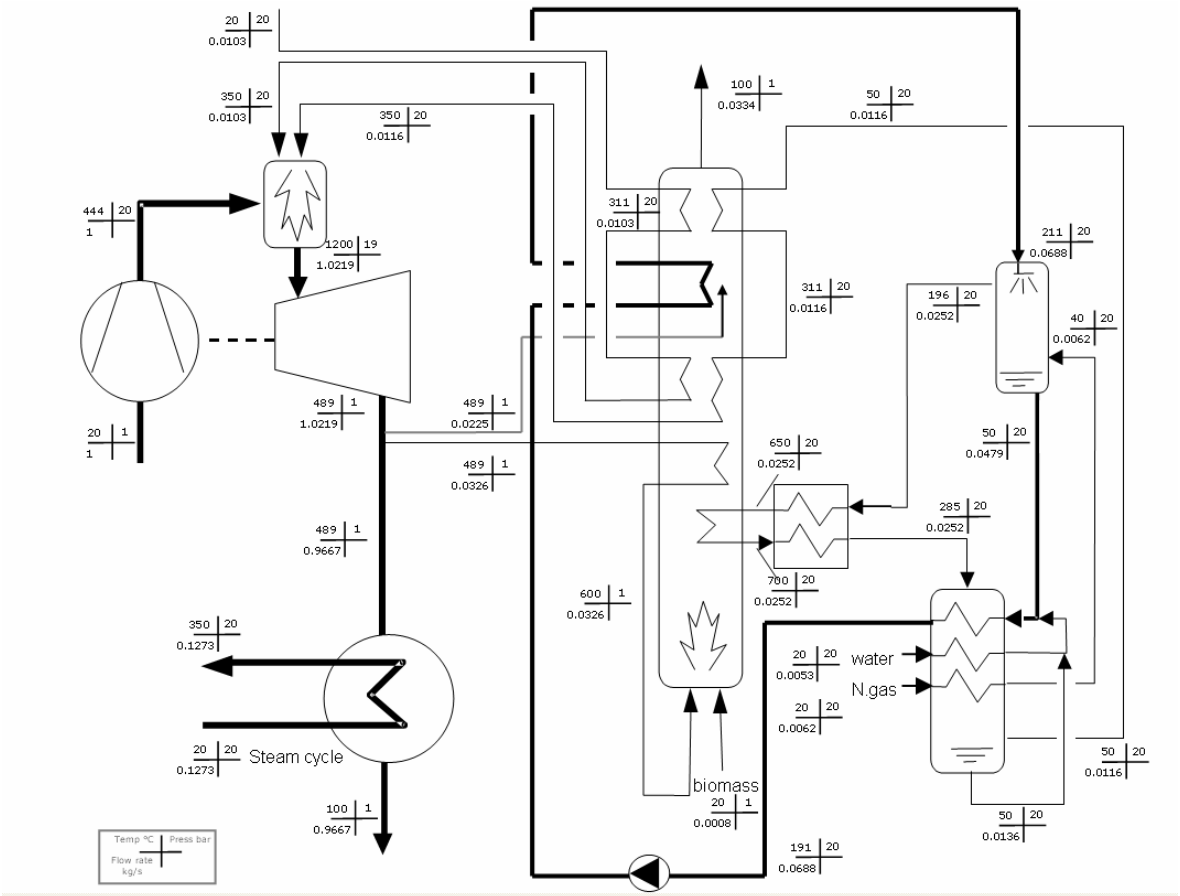

Figure 9: Synthesis of the reforming case including condenser and saturation tower (5% biomass)

The suggested alternative route has minimal interference with the reference cycle and allows a bio-input of 5% to result in a 51.7% cycle-efficiency compared to the reference cycle-efficiency of 50.4 %. In other words, biomass is converted at a marginal efficiency of 51.7%, which is a very high conversion efficiency for an external combustion route. Constant overall efficiencies can be obtained by routing some stack heat to the syngas, leading however to increased gas temperatures in the combustor nozzles. It is to be observed that the volume flow in the combustor nozzles is nearly doubled in the adapted case.

The next logical step will be the simulation of an existing power plant, with a comparison between the reference and the adapted cycle. This simulation will deliver the final theoretical proof of the capabilities of the suggested biomass process. If no significant drop in efficiency is noted for a 5% biomass energy input, this alternative route is worth to be tested in practice. In the current cycle, methane is used instead of natural gas and even though no problems are likely to turn up, this simplification needs to be validated.

ACKNOWLEDGMENTS

The present work is supported by the Belgian Power Utility Company ELECTRABEL.

REFERENCES

[1] Adelman S., Hoffman M., Baughn J., 1995, A Methane-Steam Reformer for a Basic Chemically recuperated Gas Turbine, ASME Journal of Engineering for Gas Turbines and Power, Vol 117, pp16-23

[2] Fiaschi D., Lombardi L., Tapinassi L., 2004, The Recuperative Auto Thermal Reforming Gas Turbine Power cycles with CO2 Removal-Part II, ASME Journal of Engineering for Gas Turbines and Power, Vol 126, pp62-68

[3] Mittricker F., 2001, Method for Utilizing Gas Reserves with Low Methane Concentrations for Fueling Gas Turbines, Patent WO 01/42636 A1

[4] Bram S., De Ruyck J., 1997, Exergy analysis tools for ASPEN applied to evaporative cycle design , Energy Conversion and Management 38 (15-17): 1613-1624

[5] De Ruyck J., Bram S., Allard G., 1997, REVAP : A new Evaporative cycle without saturation tower, ASME Journal of Eng. for Gas Turbines and Power, Vol 119, p893

[6] Bram S., The thermodynamic Potential of Evaporative Regeneration in Gas Turbine Cycles for Power Production, PhD Thesis, june 2002, VUB Faculty Applied Sciences, department of Thermodynamic

Refrigeration and air condition

Proceedings of ECOS 2005
Trondheim, Norway
June 20–22, 2005

VELOCITY DISTRIBUTION AND PRESSURE DROP CHARACTERISTICS OF COLD AIR CIRCULATION IN A REFRIGERATED SPACE

Md. Latiful Afaz*, Shigeki Kametani, and Toshihiko Fujita
Tokyo University of Marine Science and Technology
Department of Marine Electronics and Mechanical Engineering Tokyo, Japan
Yoshihiro ShimaokaToba National College of Maritime Technology Mie, Japan

ABSTRACT

Good air circulation within the storage room is essential to maintain proper product temperature and relative humidity. At present, the transportation of refrigerated cargo, by sea, land and air, is increasing rapidly due to economic growth. In addition to fruits, fresh vegetables, and marine products, semiconductors and precision instruments are also conveyed as constant temperature transportation products.

Little published data are available to predict supply air volumes for optimum cooling of the products. In order to improve and establish the storage and transportation technology, studies are necessary on the cold air circulation systems.

In this study, the velocity distributions of airflow and pressure drop in the loading space are measured at various supply air velocities under various geometrical conditions of clearance area, aperture area, packing factor and carton stage. The results of this study can be summarized as follows: Steep changes are observed in the air velocity and pressure drop with the change of clearance area of the aisle. The pressure drop increases with the decrease of aperture area. The effect of the packing factor on the pressure drop is comparatively small. The pressure loss coefficient is nearly proportional to the number of carton stage, but it increases a little with the decrease of airflow.

key words: airflow velocity, pressure drop, carton, packing factor

NOMENCLATURE

a length of test section [m]

A cross-sectional area of the test section [m^2]

b width of test section [m]

D hydraulic diameter [m], $D = 2A/(a+b)$

Q Total flow rate [m^3/s]

N number of piled carton(s)

Re Reynolds number [-], $Re = VD/\nu$

V airflow velocity [m/s], $V = Q/A$

α aperture factor [%]

$$\alpha = \frac{\text{Total area of bottom face holes}}{\text{Face area of carton}} \times 100\%$$

β packing factor [%]

$$\beta = \frac{\text{Total volume of balls}}{\text{Internal volume of carton}} \times 100\%$$

*Corresponding author: Phone & Fax: +81 3 5245 7411
E-mail: mlatiful@e.kaiyodai.ac.jp

γ clearance factor [%]

$$\gamma = 1 - \frac{\text{Cross-sectional area of carton}}{\text{Cross-sectional area of test section}} \times 100\%$$

ΔP pressure drop in cartons [kPa]

ζ pressure loss coefficient [-]

$$\zeta = \Delta P \Big/ \left(\frac{1}{2} \rho V^2 \right)$$

v dynamic viscosity of air [m^2/s]

ρ density of air [kg/m^3]

INTRODUCTION

The most popular refrigerated transportation systems at present are marine cargo containers and stores. As the mechanism of the systems is to maintain a controlled atmosphere around the products by circulating cold air, they are called "cold air circulation systems". In the case of the marine container, the cold air intake is located at the bottom of the container. So the cold air passes through the products from bottom to top of the container. Then it returns to the refrigeration unit from the ceiling duct and enters into the bottom intake again. In refrigerated transport, maintaining regular temperature throughout the cargo is essential to preserve quality, safety and shelf life of perishable foods. In the refrigerated enclosure, the control of temperature and temperature homogeneity is directly governed by airflow patterns [1]. A uniform cooling and cold storage of fresh produce are difficult to obtain in industrial cooling rooms because of an uneven distribution of the airflow [2,3].

It is considered that the cooling rate of this system is largely governed by the characteristics of airflow passing through the products and the airflow is affected by the geometrical conditions of the products and the loading space.

Recent investigation showed that little research on the characterization of air velocities has been performed. Van Gerwen et al. applied PHOENICS to simulate the velocity and temperature distribution in a refrigerated room. The validation was done for the airflow velocity, airflow patterns, static pressure and temperature of the air and the product. However, no data were given. Furthermore no information was reported about how the boundary conditions were applied [4,5]. More recently, Hoang et al. used the CFX CFD package code to predict the airflow pattern in empty and loaded cold stores [6].

In this study, the influences are examined experimentally of clearance factor, aperture factor, packing factor and carton stage (i.e., the number of piled cartons) on the velocity distribution and pressure drop.

EXPERIMENT

Experimental apparatus

A schematic view of the experimental apparatus is shown in Figure 1.

An inverter control fan (3.7kW) is used to supply air into the test section. In order to set the air volume, total and static pressures are measured with a composite Pitot tube sensor at a location between fan outlet and test section inlet [7]. To make airflow distribution as uniform as possible at both entering and leaving sides of the test sections, two wire nets of 30 meshes are fitted across the passage, 350 mm apart. A stainless steel honeycomb frame is also fitted to support the upper wire net.

Some boxes made of transparent acrylic resin panels of 5 mm thickness are used as model cartons. All faces of the boxes have holes of 10 mm inside

diameter with a square pitch of 15 mm. The dimension of the carton is $280^{L}\times180^{W}\times120^{H}$ mm and its cross-sectional area $A = 6.05\times10^{-3}$ m^2. The upper face of the carton can be opened, for it is fastened with bolts.

Plastic balls of 66.7 mm outside diameter are used as imitation loads. The packing factor is changed with the number of balls inside the carton, while the aperture factor is changed by sealing some holes [8]. The clearance factor is changed by filling partly or wholly the aisle open section between the carton and the test section sidewall with foamed polystyrene blocks.

Velocity and pressure drop measurement

Airflow velocities in the test section are measured with a three-dimensional ultrasonic anemometer and recorded in a personal computer. Figure 2 shows a block diagram of the anemometer.

In order to measure the air velocity distribution, whole cross-sectional area of the test section is divided into 6×4 meshes of 100 mm×100 mm square. The anemometer probe is moved to the center of each mesh to measure local air velocity.

Pressures are measured at each of the suction nozzle, the composite Pitot tube section, and the test section, under the various conditions of fan speed, clearance factor, aperture factor, packing factor and carton stage. Pressure drops in the test section are measured with digital vacuum manometers through the measuring holes on the test section sidewall.

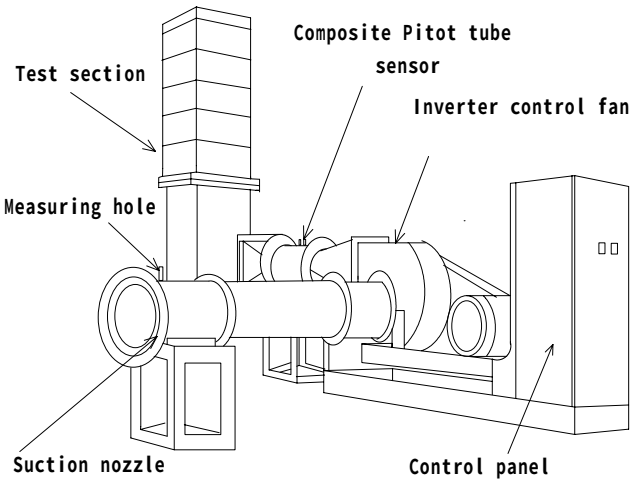

Figure 1: Schematic view of the experimental apparatus

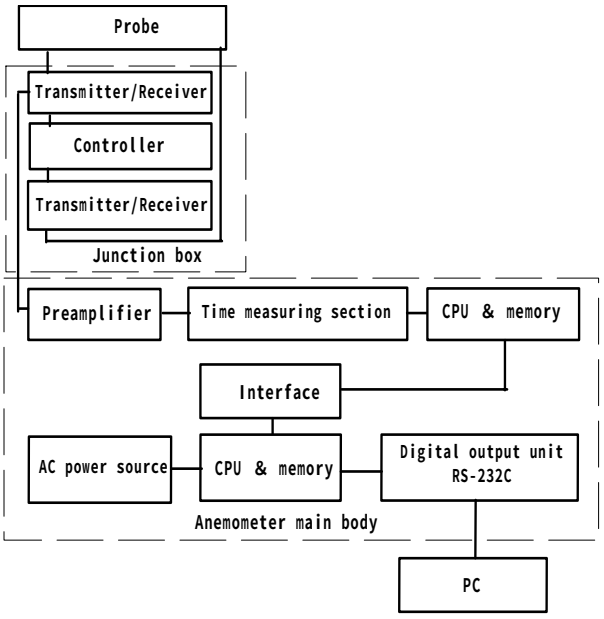

Figure 2: Block diagram of ultrasonic anemometer

DISCUSSION AND RESULTS

Figure 3 shows the relationship between the local mean air velocity and total flow rate Q in relation to clearance factor γ and the number of carton stage N, at an aperture factor α = 8.1% and a

packing factor β = 43.1%. Effect of clearance factor γ on velocity distribution is shown in Figure 3. In this figure, solid symbols represent the data for the aisle open section between carton and the sidewall, while the other symbols represent the data for the carton section. The total flow rate means the intake air volume per second.

Figure 4 shows the relationship between pressure loss coefficient ζ and Reynolds number *Re* in relation to clearance factor γ, for α = 8.1%, β = 43.1%, and the number of carton stage *N* =1 and 7. Figure 5 shows the relationship between the pressure loss coefficient ζ and clearance factor γ at *Re* = 50000. As is evident from these figures, a combination of the smallest clearance area, γ = 0, and the largest number of carton stage, *N* = 7, has the largest effect on the pressure loss coefficient ζ. In the case where γ = 0 and *N* = 7 the pressure loss coefficient ζ increases with the decrease of Reynolds number *Re*, while in the other cases the pressure loss coefficients ζ are far smaller and nearly constants.

In the same manner as Figure 3, Figure 6 shows the relationship between the arithmetic mean air velocity of 24 mesh points and total flow rate *Q* under the condition of no clearance, γ = 0. Needless to say, the air velocity and the flow rate are directly proportional regardless of aperture factor α and the number of carton stage *N*, for the air volume through the area other than carton section can be neglected.

Figure 7 and 8 show the effect of aperture factor α and the number of carton stage *N* on pressure loss coefficient ζ under the condition of no clearance, γ = 0. The aperture factor α has a significant effect on the pressure loss coefficient ζ especially in the case where *N* =7.

Figure 9 shows that the relationship between the mean air velocity and total flow rate is not affected by packing factor β in the case where γ = 0 for the same reason as above.

Figure 10 show the effect of packing factor β and the number of carton stage *N* on pressure loss coefficient ζ under the condition of no clearance, γ = 0, and the largest aperture factor α =16.2%.

Figure 11 shows the relationship between the mean air velocity and total flow rate for various number of carton stages, *N* =1 to 7, under the condition of no clearance, γ = 0.

Figure 12 shows that the pressure loss coefficient ζ increases with the increase of the number of carton stage *N* and is affected to some extent by Reynolds number *Re* and the number of carton stage *N* in the case of small *Re* and large *N*.

As shown in Figure 13, the pressure loss coefficient ζ is directly proportional to the number of carton stage in the case where γ = 0.

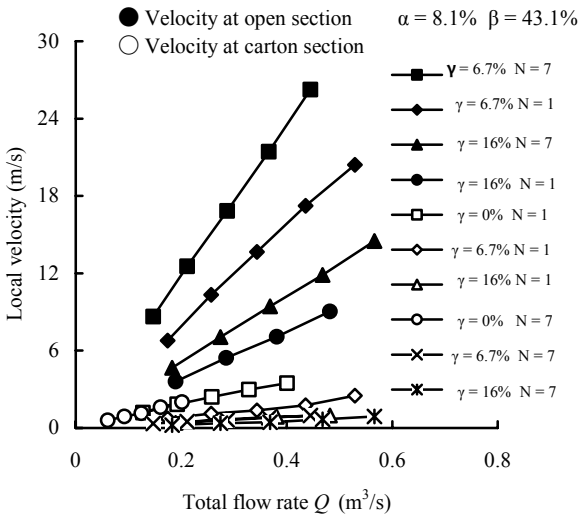

Figure 3: Relationship between local velocity and total flow rate *Q* for various clearance factor γ and number of carton stage *N* =1 and 7

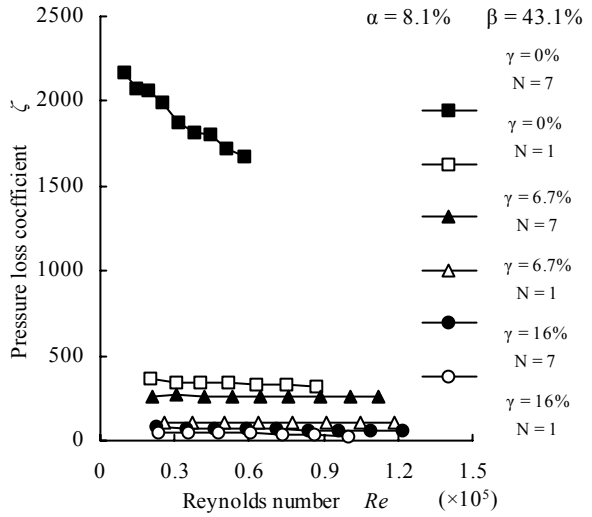

Figure 4: Relationship between pressure loss coefficient ζ and Reynolds number *Re* for various clearance factor *γ* and the number of carton stage *N* =1 and 7

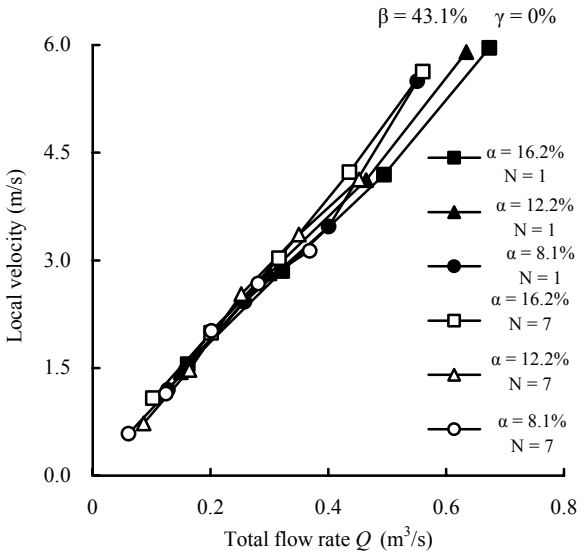

Figure 6: Relationship between the mean air velocity and total flow rate *Q* under the condition of no clearance, *γ* = 0, for various aperture factor *α* and the number of carton stage *N* =1 and 7

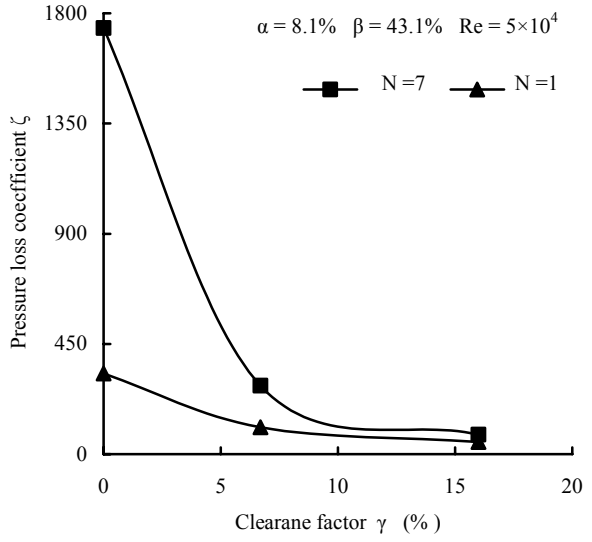

Figure 5: Effect of clearance factor *γ* on pressure loss coefficient *ζ*

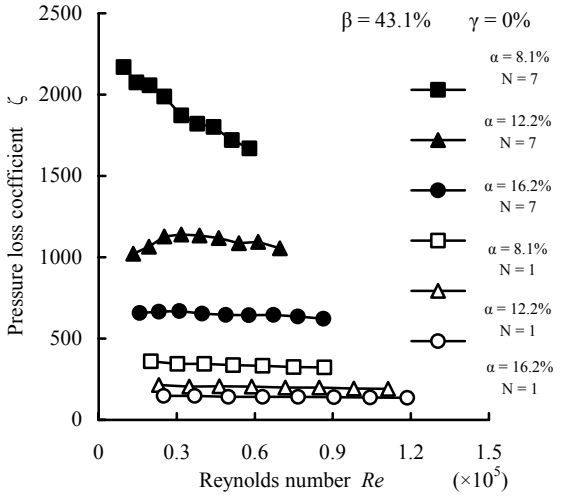

Figure 7: Relationship between pressure loss coefficient *ζ* and Reynolds number *Re* under the condition of no clearance, *γ* = 0, for various aperture factor *α* and the number of carton stage *N* =1 and 7

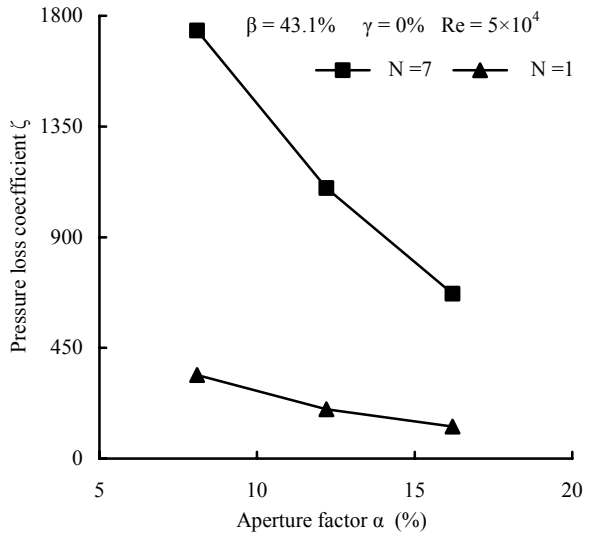

Figure 8: Effect of aperture factor α and the number of carton stage N on pressure loss coefficient ζ under the condition of no clearance, $\gamma = 0$

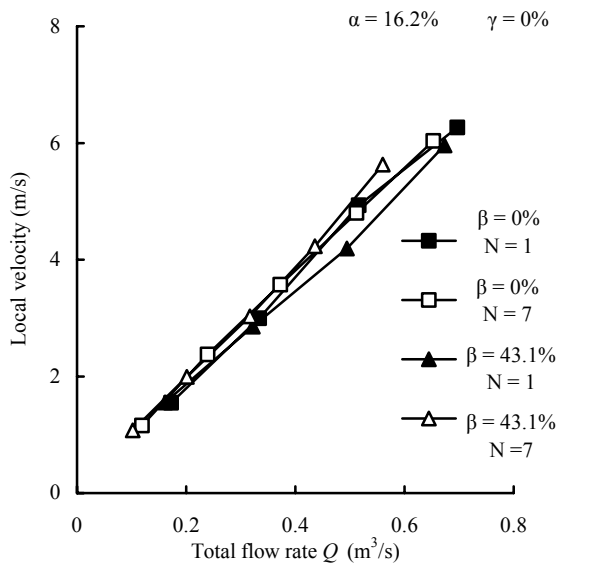

Figure 9: Relationship between the mean air velocity and total flow rate Q under the condition of no clearance, $\gamma = 0$, for packing factor $\beta = 0$ and 43.1% and the number of carton stage $N = 1$ and 7

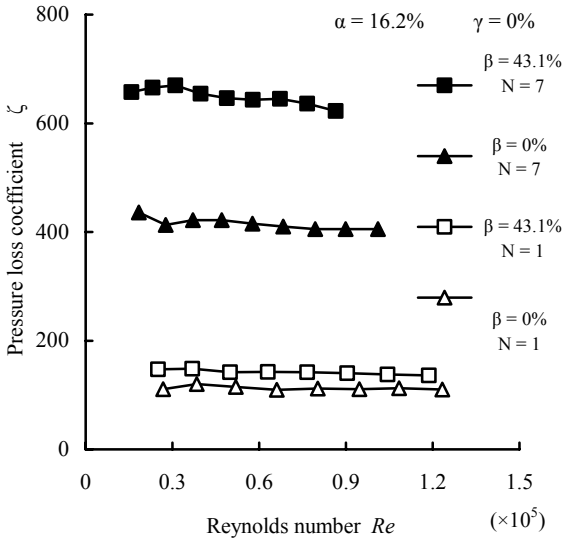

Figure 10: Relationship between pressure loss coefficient ζ and Reynolds number Re under the condition of no clearance, $\gamma = 0$, for packing factor $\beta = 0$ and 43.1% and the number of carton stage $N = 1$ and 7

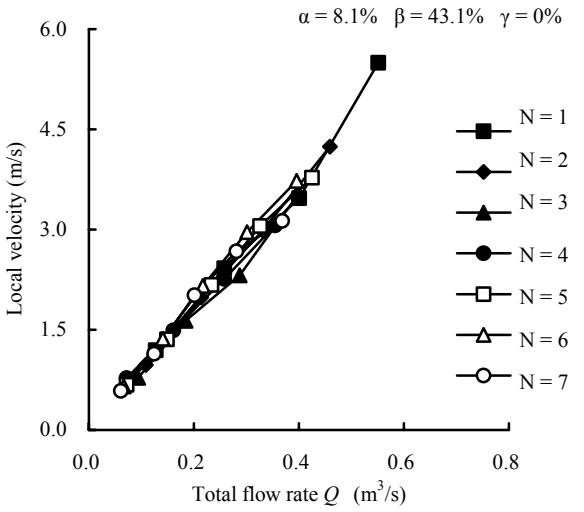

Figure 11: Relationship between the mean air velocity and total flow rate for various number of carton stages, $N = 1$ to 7, under the condition of no clearance, $\gamma = 0$

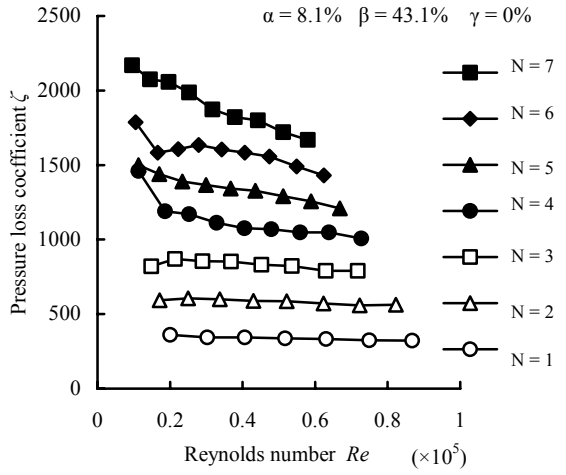

Figure 12: Relationship between pressure loss coefficient ζ and Reynolds number Re under the condition of no clearance, $\gamma = 0$, for various number of carton stage N =1 to 7

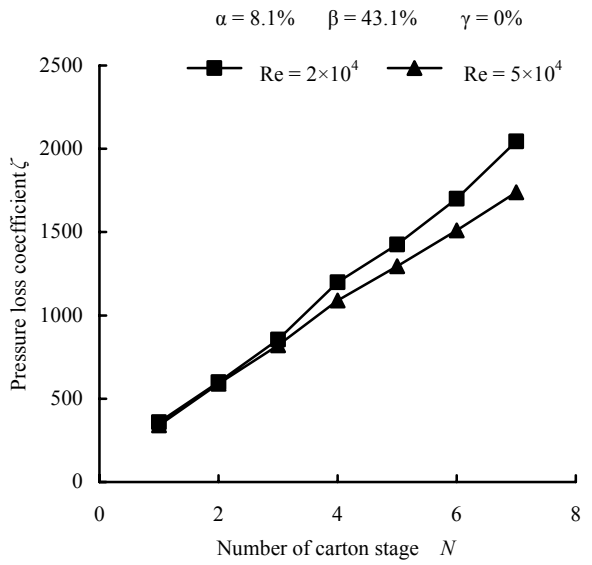

Figure 13: Effect of the number of carton stage N on pressure loss coefficient ζ under the condition of no clearance, $\gamma = 0$

CONCLUSIONS

From the experimental result on the velocity distribution of airflow and pressure drop in the model loading space, the following conclusions are obtained:

1) The velocity in the aisle, open section, becomes steeply higher with the decrease of clearance factor and the pressure loss coefficient suddenly increases near 0 clearance factor.
2) The pressure loss coefficient increases with the decrease of aperture factor and with the increase of packing factor and the number of carton stage.
3) The effect of packing factor on the pressure loss coefficient is relatively smaller than the other factors.
4) The pressure loss coefficient at 0 clearance factor is nearly proportional to the number of carton stage, although it increases a little with the decrease of Reynolds number.

REFERENCES

[1] J. Moureh, N. Menia, and D. Flick: *Numerical and experimental study of airflow in a typical refrigerated truck configuration loaded with pallets*. Computers and Electronics in Agriculture, 2002; 34: 25-42.

[2] PS. Mirade. *Contribution a l'amelioration des procedes de traitement des solides par l'air gace a la description et a la simulation de l'aeraulique. Application au refroidissement et au sechage des viands*, Ph. D. thesis, Universite de Poitiers, France, 1996.

[3] H. Wang H and S. Touber: *Distributed dynamic modeling of a refrigerated room*. International Journal of Refrigeration 1990; 13: 214-222.

[4] V. Gerwen RJM, and H. V. Oort: *The use of fluid dynamics simulation models in cold store design*. Proceedings I.I.F-I.I.R. Commission B2, Bristol, UK, 1989.
[5] V. Gerwen RJM, and H. V. Oort: *Optimization of cold store using fluid dynamics models*. Proceedings I.I.F-I.I.R. Commissions B2, C2, D1, D2/3, Dresden, Germany, 1989.
[6] M. L. Hoang, P. Verboven, J. De Baerdemaeker and B. M. Nicolai: *Analysis of the airflow in a cold store by means of computational fluid dynamics*. International Journal of Refrigeration, 2000; 23: 127-140.
[7] Ikui T: *Fan and Compressor*. Tokyo: Asakura Publication, 1969. p. 22-23, (in Japanese).
[8] Afaz ML, Shimaoka Y, Kametani S, and Fujita T: *Velocity distribution and pressure drop of the load during cold air circulation in a refrigerated space*. Proceedings of the 38th Japanese Joint conference on Air-conditioning and Refrigeration, Tokyo, 2004.

Proceedings of ECOS 2005
Trondheim, Norway
June 20–22, 2005

GEOMETRICAL ANALYSIS OF THREE-DIMENSIONAL NON-STEADY STEAM SUPERSONIC PRESSURE EXCHANGE EJECTORS

KHALED ALHUSSAN [1]
King Abdulaziz City for Science and Technology
Space Research Institute
Riyadh KSA

CHARLES GARRIS
The George Washington University
Washington DC, USA

ABSTRACT

The work to be presented herein is a Computational Fluid Dynamics investigation of the complex fluid mechanisms that occur inside a non-steady, three-dimensional, supersonic pressure exchange ejector, specifically with regard to the pressure exchange mechanisms and the induction processes between a primary fluid and a secondary fluid using steam as working fluid. It is the purpose of this research to study from the computational perspective the complex non-steady flow processes and induction mechanisms within a supersonic pressure-exchange ejector, how they relate to overall ejector performance, and to obtain geometrical parameters such as primary inlet area, rotor length, cone angle, and spin angle which would allow this technology to be utilized in many applications such as in ejector refrigeration systems. Results utilizing velocity vectors, contour plots of total enthalpy and static pressure showing the actual behavior of the steam supersonic pressure exchange ejector are presented. In this research, computational study is used to show how the aerodynamics flow is managed to provide the desirable flow induction characteristics of steam supersonic pressure exchange ejector. The geometry of this steam ejector is as follows: a 20-degree spin angle, 20-degree half angle cone, 1.80 inches rotor length and a 0.30 inlet area ratio. This research shows that the adiabatic efficiency is as high as 23% for this steam ejector.

If this new concept in ejector technology based on non-steady flow processes can be shown to be viable, the impact on refrigeration and air conditioning in the commercial, automotive, and residential sectors would be enormous and would enable environmentally benign refrigerants such as water to replace the harmful CFC's, and reduce the effluence of greenhouse gases by reducing fuel consumption through the use of waste heat and improved efficiency.

Keywords: Ejector, Pressure Exchange, Ejector Refrigeration, CFD.

NOMENCLATURE

P_s	Static pressure
P_e	Exit static pressure
P_{ts}	Total pressure of secondary fluid
P_{tp}	Total pressure of primary fluid
T_{ts}	Total temperature of secondary fluid
T_{tp}	Total temperature of primary fluid
$T_{\Re}$	Temperature ratio of the primary fluid to secondary fluid
μ	Mass flow ratio of secondary fluid to primary fluid
η_d	Adiabatic Efficiency

INTRODUCTION

All the attempts to improve the ejector performance have involved variations on the conventional design of the steady-flow ejector. The physical principle upon which this ejector operates is that of entrainment of a secondary

[1] Khaled alhussan: Phone +9661 481 4508 Fax +9661 481 3845 P.O. Box 6086 Riyadh 11442, KSA, alhussan@kacst.edu.sa

flow by an energetic primary flow by virtue of the work of turbulent shear stresses. Thus, the relatively low-energy secondary flow is dragged by the relatively high-energy primary flow through tangential shear stresses acting at the interface between the two contacting streams. These turbulent stresses are a result of mixing that occurs between primary and secondary streams and the consequent exchange of momentum.

While this mechanism is quite effective and has been widely adopted in many applications, an inherent characteristic of the mixing process is the dissipation of valuable mechanical energy. This results in a substantial entropy rise, which is intimately connected with ejector performance and consequently, refrigeration system performance [1-4].

On the other hand, the pressure-exchange ejector offers the possibility of attaining a breakthrough in the level of performance of ejectors by means of utilizing non-dissipative non-steady flow mechanisms [5-6].

Unlike the steady flow conventional ejector, the non-steady pressure exchange ejector is designed to utilize an entirely different physical principle, which is based on the pressure exchange phenomenon. Pressure exchange utilizes the reversible work of interface pressure forces, which exist only in non-steady flows. This mode of energy exchange is inherently non-dissipative. The utilization of this mode of energy-transfer is of interest, because of its potential to produce high efficiency [7-10]. The overarching goal is to create a flow induction machine which utilizes the work of interface pressure forces available in non-steady flows through direct contact of two fluids.

Pressure exchange is a designation applied to any process whereby contiguous fluid bodies or flows exchange mechanical energy through the work of mutually exerted pressure forces at their interfaces [11]. Pressure exchange cannot take place in steady flow, because no work is done by pressure forces acting on a stationary interface [12]. Therefore, pressure exchange is always a non-steady process.

An ejector is a direct contact flow induction device, which exchanges mechanical energy and momentum between a high-energy primary fluid and a relatively low-energy secondary fluid to produce a discharge of an intermediate specific energy level. The transfer of momentum gives rise to an increase in the stagnation enthalpy of the secondary fluid and enables the ejector to function as a compressor [13-15].

The work to be presented herein is a Computational Fluid Dynamics investigation of the complex fluid mechanisms that occur inside a non-steady, three-dimensional, supersonic pressure exchange ejector, specifically with regard to the pressure exchange mechanisms and the induction processes between primary fluid and secondary fluid [16-19].

This research is based upon utilizing a non-steady flow field resulting in the work of pressure forces acting at a fluid interface between primary fluid and secondary fluid. These interfaces are produced through the aerodynamic design of a flow field, non-steady in the laboratory frame of reference, consisting of rotating oblique shock waves and expansion fans. Minimizing the possible losses from the oblique shocks and boundary layers offer the potential of achieving adiabatic efficiencies approaching those of turbo-machines[5-6 and 16-20].

Study of the actual flow configuration inside the complex three dimensional supersonic pressure exchange ejector offers some insight into the complex flow phenomena that occur inside the ejector. This paper shows some geometrical parameters that produce the right environment for pressure exchange to take place, for the steam supersonic pressure exchange ejector that generates a high adiabatic efficiency about 23% [18]. Adiabatic efficiency is related to both the ratio of mass flow rate and the ratio of temperature of secondary fluid to primary fluid [2 & 21]. The efficiency of the energy exchange is increased if it is made to take place, at least in part, through the non-dissipative work of interface pressure forces.

COMPUTATIONAL FLUID DYNAMICS ANALYSIS

The flow induction in the supersonic pressure exchange ejector is so complex that there exist direct fluid-fluid interactions, oblique shock waves, expansion fans, slip surfaces, and shock wave interactions and reflections. The flow is

non-steady, viscous, compressible, and high-speed supersonic.

The governing equations are a set of coupled nonlinear, partial differential equations. In order to formulate or approximate a valid solution for these equations they must be solved using computational fluid dynamics techniques. To solve the equations numerically they must be discretized. That is, the continuous control volume equations must be applied to each discrete control volume that is formed by the computational grid. The integral equations are replaced with a set of linear algebraic equations solved at a discrete set of points.

CFX is used in the current research to model the flow in the supersonic pressure exchange ejector. The code uses block-structured, non-orthogonal grids with grid embedding and grid attaching to discretize the domain. CFX is a finite volume method, but is based on a finite element approach of representing the geometry. Thus, the method used here possesses much of the geometric flexibility of finite element methods as well as the important conservation properties of the finite volume method.

It should be possible to model the interaction of the shock waves and expansion fans around the rotating vanes and describe how the secondary flow is drawn into the interstices. It should be possible to study the mutual deflection and pressure exchange processes between primary and secondary flows using the CFD analysis [16].

A numerical analysis must start with breaking the computational domain into discrete sub-domains, which is the grid generation process. A grid must be provided in terms of the spatial coordinates of grid nodes distributed throughout the computational domain. At each node in the domain, the numerical analysis will determine values for all dependent variables such as pressure and velocity components.

Creating the grid is the first step in calculating a flow. A 180-deg sector was chosen to model the flow. The grid is refined near the surface of the vanes in order to model the large gradient in that region. For computation, a Mach number of 3.0 is used as the Nozzle Exit Mach number. Solution parameters and fluid properties are defined in the parameter file. For the steady-state solution, the time step is selected equal to 0.00001. The advection discretization scheme selected is the Modified Linear Profile Skew scheme with the Physical Correction. The convergence criterion is 10E+04 and the maximum number if iteration is 300. The maximum number of iteration is increased form 300 to 1000 to allow the solver to run until a converged solution is found.

A computational model that illustrates the physics of flow induction through non-steady shock waves and expansion fans was developed. This provides strong insight into the mechanisms through which the supersonic pressure exchange ejector operates.

Through this computational analysis, a better interpretation of the physical phenomenon of the non-steady pressure exchange ejector can be achieved. The results from the numerical analysis are used to study the flow structure inside the complex geometry of the pressure exchange ejector and to develop a design methodology so as to predict optimal ejector performance.

DISCUSSIONS

Water is an excellent refrigerant, which has a high latent heat of vaporization, a high specific heat, good heat transfer characteristics, non-corrosive, and is totally in harmony with the environment. However, for normal air conditioning applications, the specific volume of water vapor under operating conditions must be hundreds of times larger than that of a system using CFC's under comparable environmental conditions and design requirements. Water as a refrigerant, when used with a positive displacement type compressor, requires a much larger compressor displacement volume. The need for a much larger compressor, and the associated increased cost, has rendered water less desirable as a refrigerant for conventional air conditioning. However, this problem can be resolved by the use of an ejector, which is capable of transporting large volumes of vapor within a relatively small space and at a low cost [6].

It is an objective of this research to provide an ejector refrigeration system with a Coefficient of Performance considerably higher than that of the conventional steady flow ejector and approaching that of the ideal turbo-machinery standard. The

pressure-exchange ejector utilizes a non-steady flow principle to obtain higher adiabatic efficiencies than conventional ejector while retaining much of the simplicity of construction and the low manufacturing cost of a conventional ejector [5-8].

Advantages of the Pressure-Exchange Ejector in Refrigeration Systems:

1) The pressure-exchange ejector could benefit the environment by reducing pollutants at their source.
2) The pressure-exchange ejector retains much of the mechanical simplicity of conventional steady flow ejector.
3) The pressure-exchange ejector could be amenable to the utilization of environmentally benign refrigerants such as water instead of chlorofluorocarbons.
4) This ejector is capable of compressing high specific volume vaporized refrigerants with an ejector of reasonable size and cost.
5) Since this ejector refrigeration system uses a boiler, which could be energized by waste heat instead of a compressor, the emissions of undesirable greenhouse gases, i.e., carbon dioxide (CO_2), nitrous oxide (N_2O), methane (CH_4), etc., could be reduced considerably.

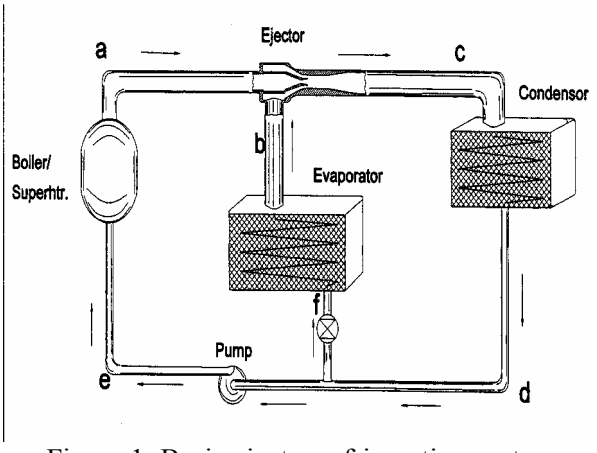

Figure 1: Basic ejector refrigeration system

A basic ejector refrigeration system is shown in figure 1. A pump discharges condensate to a boiler/superheater that releases energetic primary vapor to the ejector. The ejector draws secondary vapor from the evaporator and discharges it to the condenser. The condensate from the condenser is divided between the pump inlet and the expansion means that supplies cool vapor/liquid to the evaporator. A high-energy primary fluid compresses a lower energy secondary fluid through direct fluid-fluid momentum exchange.

It can be shown [1-2], that the COP for a basic ejector refrigeration system is given by:

$$COP = \mu \frac{h_b - h_f}{h_a - h_d} \qquad (1)$$

where COP is the Coefficient of Performance, the ratio of energy extracted from the evaporator to the energy provided in the boiler/superheater and the pump; μ is the ratio of secondary mass flow rate to primary mass flow rate; h_a, h_b, h_d, h_f are the specific enthalpies at points a, b, d, and f in the system as indicated in figure 1.

Equation 1 shows that with the system operating at prescribed evaporator, condenser, and superheater conditions the COP is directly proportional to the ratio of the ejector secondary mass flow rate to the ejector primary mass flow rate. This ratio is commonly known as a fundamental figure of merit for the flow induction efficiency of an ejector. Hence, the higher the ratio of secondary to primary mass flow rates, the higher the COP [22].

The performance of the ejector is a controlling factor in determining the performance of the refrigeration system. This has been recognized in the literature with many attempts at improving the ejector performance [6].

The efficiency of an ejector is closely connected with the entropy generation processes occurring within it. The operating principles of a conventional steady-flow ejector result in two major sources of entropy generation: turbulent mixing and strong normal shock waves. By means of the pressure-exchange ejector that utilizes physical mechanisms which produces modest entropy rises, a substantial improvement over conventional technology is possible.

The advantage of the pressure exchange process is that, even accounting for shock losses, the entropy rise can be small. Post-pressure-exchange mixing will incur a much smaller entropy rise than would have occurred with primary-secondary mixing in a conventional ejector, since the energy levels in the former are nearly equalized by pressure exchange.

It can be shown [2& 21] that the ejector efficiency is defined as:

$$\eta_d = \mu \frac{(T_{ts})}{(T_{tp})} \left[\frac{\left(\frac{p_e}{p_{ts}}\right)^{\frac{\gamma-1}{\gamma}} - 1}{1 - \left(\frac{p_e}{p_{tp}}\right)^{\frac{\gamma-1}{\gamma}}} \right] \qquad (2)$$

From this equation, one can see that increasing the mass flow ratio,μ, of the ejector will result in increasing the overall adiabatic efficiency η_d. Remember that increasing the ratio of the mass flow rate of the ejector also will result in increasing the COP of the refrigeration cycle. Thus one can conclude that the higher the adiabatic efficiency, the higher the COP.

RESULTS

The domain of interest is a complex, three-dimensional, bounded conical shape. The flow is non-steady and compressible. In this situation, one should expect oblique shock waves, expansion fans, shock wave interactions, and slip surface generation.

The previous discussion demonstrated that steam makes an excellent working fluid for the pressure exchange ejector. In this paper a numerical analysis was conducted to study the actual behavior of the steam supersonic pressure exchange ejector.

Figure 2 depicts the shape of the rotor vane. The geometry of this steam ejector is as follows: a 20-degree spin angle, 20-degree half angle cone, 1.80 inches rotor length and a 0.30 inlet area ratio. Inlet area ratio is defined as primary inlet area to the secondary inlet area. Figure 3 shows three-dimensional schematic view of the aerodynamic shroud surface.

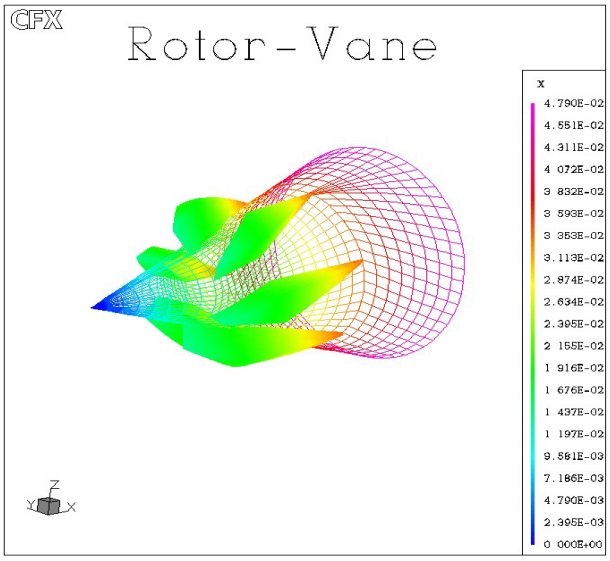

Figure 2: Partial sketch of the geometry for 20-degree spin angle, 20-degree cone half angle, steam ejector

The vane configuration plays a very important role in the design analysis of the supersonic pressure exchange ejector. The best vane configuration was chosen based on a previous study [20].

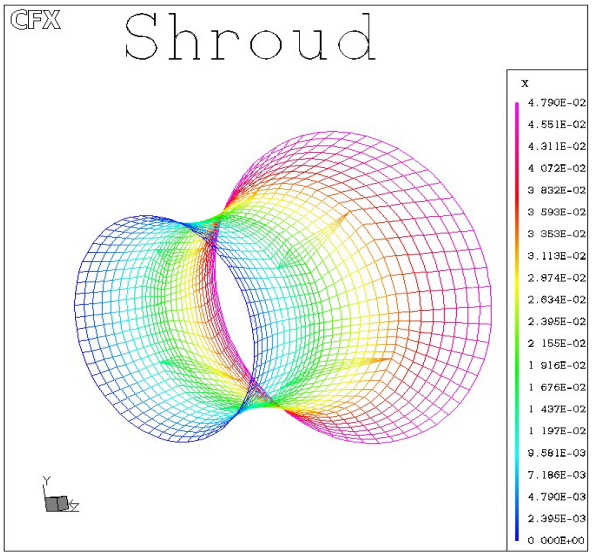

Figure 3: Partial sketch of the geometry (shroud) of steam ejector, 0.30 inlet area ratio, steam ejector

In order to see the flow pattern between the vanes and on the vanes, contour plots are shown projected on the surfaces defined in figure 4.

Figure 4 shows two surfaces, one surface is on the vanes and the other surface is between the vanes. Figure 4 shows a sketch of the planes that will be used in this analysis. In this figure one should notice that the planes over the vanes and between them are not simple colinear with the longitudinal axis. Rather they are a series of planes, which show the flow path through the vanes. The reason is to show the three-dimensionality of the problem and the construction of the grid.

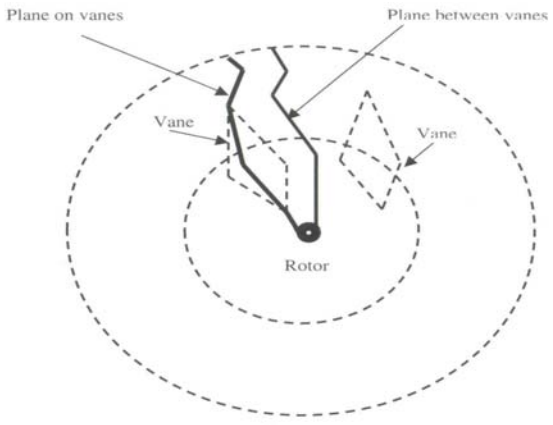

Figure 4: Sketch to show the surfaces of side view planes between and on the vanes

Figure 5 shows velocity vectors for steam ejector. By analyzing this figure, one can observe the existence of expansion fans over the vanes and the direction of the velocity vectors when they pass over the vanes. One can see the primary fluid expanding and pulling the secondary fluid with it. This is represented by the direction and the magnitude of the velocity vectors of the entrained secondary fluid. In the same figure, one can see that the velocity vectors of the secondary fluid are growing and curved in this steam ejector. Also, from figure 5, one can notice that at the surface of each vane, a three-dimensional expansion fan develops. This expansion draws secondary fluid down into the interstices of the primary flow behind the vanes and initiates the pressure-exchange process between the primary and secondary flows. One can also see the presence of the attached oblique shock wave at the apex of the cone. One can conclude from this figure that the primary fluid expands rapidly and the secondary fluid finds itself accelerating and is being drawn with the driving stream. The velocity vectors show the entrainment of the secondary fluid. From the same figure one sees the deflection of the secondary fluid near the expansion fan.

The velocity vectors in planes passing between the vanes are plotted in figure 6. In this figure one should only see the primary flow filling up the passage and this is accomplished for the design.

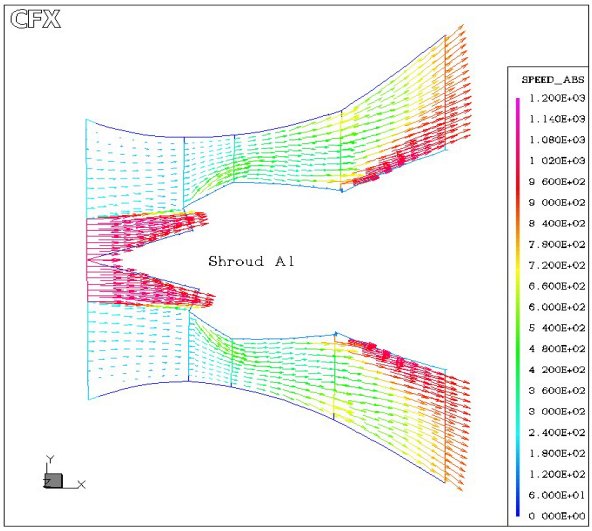

Figure 5: Velocity vectors, planes passing over the vanes, side view, steam ejector

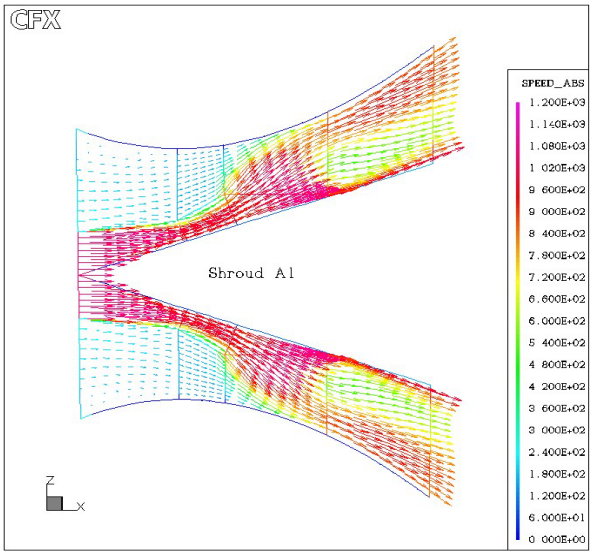

Figure 6: Velocity vectors, planes between the vanes, side view, steam ejector

Figure 7 shows the side view (see figure 4) of static pressure for of the entire ejector. Analyzing this figure, one should see that the expansion fan is causing the suction of the secondary fluid. Also this figure shows that the pressure exchange zone is indeed very short and that the compression is completed. Figure 7 also, shows the static pressure for steam as working fluid for planes passing over the vanes. In this figure one can notice the shape of the shock wave over the fore-body and in this figure the expansion fan is also clear. The oblique shock wave was designed to be a weak one that extends to touch the top surface of the leading edge of the vane. This is accomplished, as seen in figure 7.

In the pressure-exchange ejector system, the interaction of primary fluid and secondary fluid is completed in two consecutive processes: the deflection phase and the mixing phase. During this flow induction process, energy transfers from the primary flow to the secondary flow and the energy level of the secondary flow is increased [16]. The basic principle of the energy exchange between two fluids in the non-steady flow induction is that one should optimize the total enthalpy rise of the secondary fluid. This is shown in figure 8 where the total enthalpy for steam ejector is plotted. This figure shows the top view of the entire ejector near the shroud surface. This figure shows that indeed the total enthalpy of the secondary fluid is increased as it flows inside the ejector. This figure shows also the formation of the pseudo-blade and how this is related to the increase of the total enthalpy (in the absolute frame of reference) of the secondary fluid as it passes through these pseudo-blades. This can be seen, also, from the side view of the steam ejector, namely figure 9 the total enthalpy.

Figure 9 shows the total enthalpy in planes on the vanes. In this figure one can see that the primary fluid and the secondary fluid enter the ejector with different levels of energy. Then as they pass over the vanes the level of energy of the secondary fluid increases, and this is represented by the increase of the total enthalpy as seen from the absolute frame of reference.

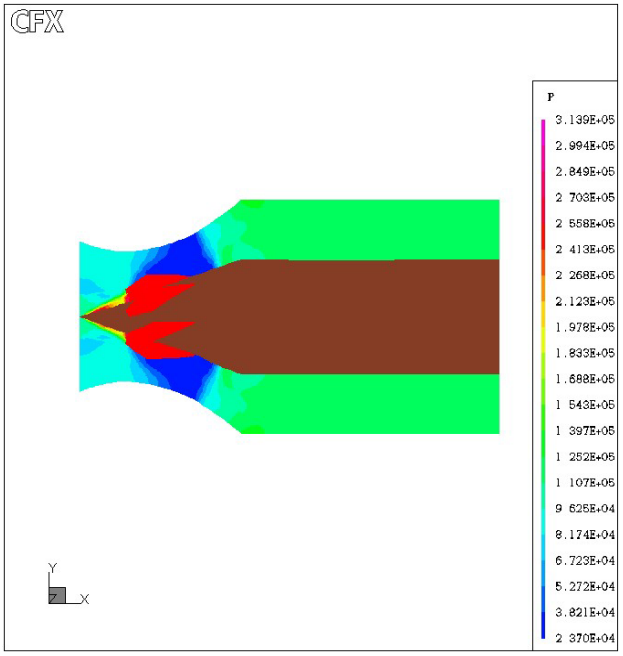

Figure 7 Contour plot of static pressure planes passing over the vanes, steam ejector

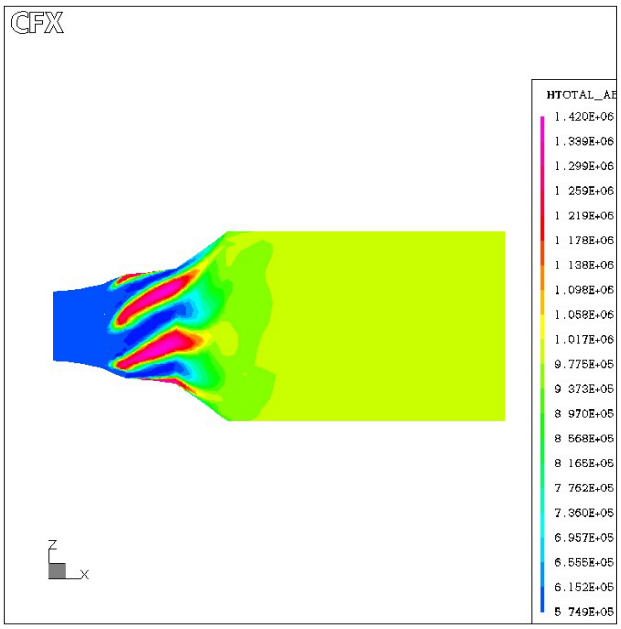

Figure 8: Contour plot of total enthalpy, absolute frame of reference, for steam ejector, top view, steam ejector

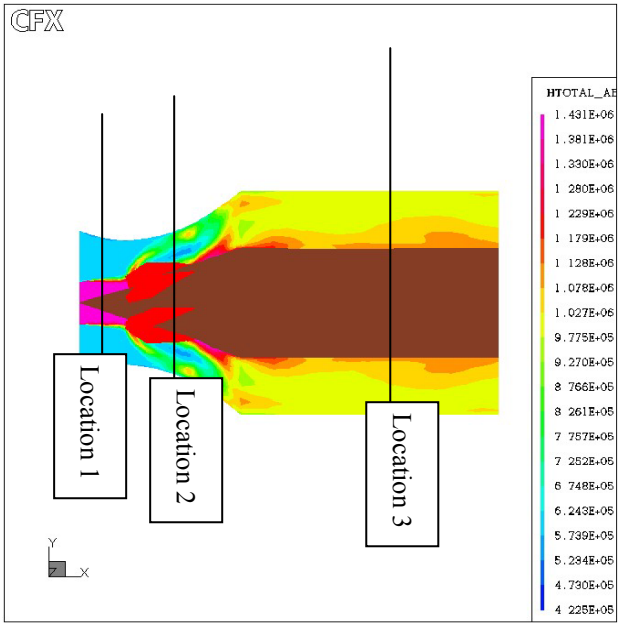

Figure 9: Contour plot of total enthalpy, absolute frame of reference, planes passing over the vanes, steam ejector

One should notice that at location 1, in figure 9, there are two fluids; namely, the primary represented by red color, and the secondary represented by blue color, and both have different total enthalpy. At location 2 the primary stream impinging on the canted-vanes causes the rotor to free spin. At location 2 one should observe the initiation of the expansion fan in between the vanes. From the same figure the secondary fluid is being drawn into the interstices of the primary flow where they are permitted to exchange their energy. At the same location, one should notice the structure of the flow where the secondary flow is co-rotating and the primary fluid is counter rotating. The exchange of pressure energy between the primary and the secondary fluids start in region 2. Finally at location 3, the total enthalpy of the secondary fluid is increased as it is shown in figure 9.

The adiabatic efficiency of the steam ejector is important, and this research shows that for $T_{\Re}$ of 1.125 the calculated adiabatic efficiency is as high as 23% and the mass flow ratio is 1.164. It should be noted that this adiabatic efficiency is calculated on the basis of the assumptions that perfect expansion in the primary nozzle is achieved, the total pressure at the exit as an average value over the flow cross section, and the ideal gas assumption is used. The main purpose of calculating this adiabatic efficiency is to use it in this analysis of determining the flow requirements of the supersonic pressure exchange ejectors [16-19].

The results suggest two points in regard to the calculation of the adiabatic efficiency: mass flow ratio and the temperature ratio. From analyzing the mass ratio one can conclude that the higher the mass flow ratio the lower the entropy production. The lower the entropy rise the higher the COP for the refrigeration system.

CONCLUSION

This research showed how to utilize the pressure exchange principle to overcome the shortcomings of conventional steady-flow ejectors. This pressure exchange ejector can be used in a refrigeration system. The ejector can utilize refrigerants such as water instead of environmentally harmful chlorofluorocarbons (CFCs) and can utilize waste heat as an energy source.

The results showed increase in total enthalpy. The increase in the total enthalpy confirmed the advantage in energy transfer by work of interface pressure forces in the non-steady ejector over the viscous shear forces in the steady flow ejector.

A high mass flow ratio was achieved. This parameter is an important characteristic of the steam ejector, since the higher the mass flow ratio the lower the entropy production. This results in a higher COP for the system.

The geometry of this steam ejector is as follows: a 20-degree spin angle, 20-degree half angle cone, 1.80 inches rotor length and a 0.30 inlet area ratio. The adiabatic efficiency was calculated for this ejector using steam as working fluid, and it was shown that the adiabatic efficiency is related to both the ratio of mass flow rate and the ratio of temperature. A high adiabatic efficiency of 23% of the steam ejector was calculated with this simulation.

This pressure-exchange ejector could positively contribute to the environment by reducing the production of hazardous effluents at the source.

ACKNOWLEDGEMENT
We gratefully acknowledge sponsorship of this research through grants from the National Science Foundation and the U.S. Environmental Protection Agency. We also, acknowledge the support of King Abdulaziz City for Science and Technology.

REFERENCES

[1] Hung, B.J., Jiang, C.B., Hu, F.L.: "Ejector Performance Characteristics and Design Analysis of Jet Refrigeration System", Journal of Engr. For Gas Turbine and Power: ASME, 1985; 107:792-802.

[2] Matsuo, K., Sasaguchi, K., Tasaki, K., Mochizuki, H.: "Investigation of Supersonic Air Ejectors: Part 2 effects of throat-area Ratio on Ejector Performance", Bulletin of the Japanese Society of Mechanical Engineers: JSME, 1982; 25:210.

[3] Addy, A. L., Dutton, J. C., Mikkelsen, C. D.: "Supersonic Ejector-Diffuser Theory and Experiments", Report No. UWU-ENG-824001, Department of Mechanical and Industrial Engineering, University of Illinois, Urbana, August 1981.

[4] Chow, W.L., Addy, A.L.: "Interaction between Primary and Secondary Streams of Supersonic Ejector Systems and Their Performance Characteristics" AIAA Journal, pp686-695, April, 1964.

[5] Garris, C. A.: "Pressure Exchanging Ejector and Method of Use", US Patent 6,138,456; July 15, 1997.

[6] Garris, C. A.: "Pressure Exchanging Ejector and Refrigeration Apparatus and Method", US Patent 5,647,221; July 15, 1997.

[7] Alhussan, K., Hong, W., Garris, C. A.: "Non-Steady Pressure-Exchange Ejector", Fluids Engineering Summer Conference Montreal, Canada, July 2002.

[8] Hong, W. J., Alhussan, K., Zhang, H., Garris, C. A.: "A novel Thermally Driven Rotor-Vane/Pressure-Exchange Ejector Refrigeration System with Environmental Benefits and Energy Efficiency", 15th International Conference on Efficiency, Cost, Optimization, Simulation and Environmental Impact of Energy Systems", Berlin Germany, July 2002.

[9] Hong, W. J., Alhussan, K., Zhang, H., Garris, C. A.: " A novel Thermally Driven Rotor-Vane/Pressure-Exchange Ejector Refrigeration System with Environmental Benefits and Energy Efficiency, Energy Journal, In Press.

[10] Alhussan, K., Garris, C. A.: "Non-Steady Three-Dimensional Flow Field Analysis in Supersonic Flow Induction", Fluids Engineering Summer Conference Montreal, Canada, Paper No. FEDSM2002-13088, July 2002.

[11] Foa, J. V.: "Method of Energy Exchange and Apparatus for Carrying Out the Same", US Patent 3,046,732, July 1962.

[12] Dean, R. C., Jr.: "On the Necessity of Nonsteady Flow in Fluid Machines", Trans.ASME, v81, Series D, No.1, pp.24-28, March 1959.

[13] Garris, C. A., Hong, W. J.: "A Radial-Flow Pressure-Exchange Ejector", Proceedings of the Third International Symposium on Pumping Machinery, Vancouver, Canada, ASME, June 1997.

[14] Garris, C. A., Hong, W. J., Mavriplis, C. M., Shipman, J.: "An Experimental and Numerical Study of the Pressure-Exchange Ejector; forum on Fluid Machinery, 1998 ASME Fluids Engineering Division Summer Meeting, Washington, D. C., June, 1998.

[15] Garris, C. A., Hong, W. J., Mavriplis, C. M., Shipman, J.: "The Pressure-Exchange Ejector Heat Pump", 1998 ASME International Mechanical Engineering Conference and Exposition, Anaheim, CA, November 15-20, 1998.

[16] Alhussan, K.: "Direct Fluid-Fluid Interaction in Three Dimensional Supersonic Non-steady Flow", The George Washington University, D.Sc. Dissertation, August 2002.

[17] Alhussan, K., Garris, C., " Comparison of Cylindrical and 3-D B-Spline Curve of Shroud-Diffuser for a Supersonic Pressure Exchange Ejector in 3-D, Non-

Steady, Viscous Flow" IASME Transactions Issue 3, Volume 1, pp 474-481, ISSN 1790-031X, July 2004.
[18] Alhussan, K., Garris, C., "Computational Study of Three- Dimensional Non-Steady Steam Supersonic Pressure Exchange Ejectors" IASME Transactions Issue 3, Volume 1, pp 504-512, ISSN 1790-031X, July 2004.
[19] Alhussan, K., Garris, C.:" Study the Effect of Changing Inlet Area Ratio of a Supersonic Pressure Exchange Ejector", 43rd AIAA Aerospace Science Meeting & Exhibit, Paper No. AIAA-2005-519, Reno, NV, January 2005.
[20] Hong, W. J., Alhussan, K., Garris, C. A.: "The Supersonic/Rotor-Vane/Pressure-Exchange Ejector", 39th AIAA Aerospace Science Meeting & Exhibit, Paper No. AIAA-2001-8058, Reno, NV, January 2001.
[21] Hedges, K.R. Hill, P.G.: "Compressible Flow Ejectors: Part 2- Flow field Measurements and Analysis", Journal of Fluids Engr.: ASME, Sept. 1974; 282-288.
[22] Rice, N. C.: "Environmental Control System" US Patent 3,259,176, July1966.

Proceedings of ECOS 2005
Trondheim, Norway
June 20–22, 2005

PROPOSED EXERGETIC BASED LEAK DETECTION AND DIAGNOSIS METHODOLOGY FOR AUTOMOTIVE CARBON DIOXIDE AIR CONDITIONING SYSTEMS

Erin Canfield, BS/MS Student
Rochester Institute of Technology
Department of Mechanical Engineering
Rochester, New York, USA
ekc1789@rit.edu

Margaret B. Bailey, Ph.D., P.E., Associate Professor
Rochester Institute of Technology
Department of Mechanical Engineering
Rochester, New York, USA
Margaret.Bailey@rit.edu

ABSTRACT

Due to the overwhelming concern of global warming and ozone depletion, the replacement of many currently used refrigerants is a pressing matter within all sectors of refrigeration. When deciding to replace a refrigerant worldwide, many factors are taken under consideration. The benefits and necessary changes that occur when using carbon dioxide (CO_2) as the working fluid are explored. One important aspect of using CO_2 as a replacement refrigerant in automotive air conditioning (AC) systems lies in diagnosing refrigerant leakage within a faulty system. A reliable refrigerant leakage detection and diagnosis system is a necessity for the automotive industry. In current research at Rochester Institute of Technology (RIT), advanced thermodynamics is being used to develop a detailed simulation model as well as a fault detection and diagnosis system specifically for the future CO_2 automotive AC systems.
Keywords: Carbon Dioxide, Automotive, Air Conditioning Systems, Exergy, Leak Detection

NOMENCLATURE

e	exergy [kJ/kg]
De	change in exergy [kJ/kg]
h	enthalpy [kJ/kg]
m	mass flow rate [kg/min]
P	pressure [kPa]
Q	heat flux [kW]
s	entropy [kJ/kg-K]
T	temperature [K]
W	mechanical work rate [kW]
1, 2, 3…	cycle path designations
x	exergetic efficiency

Subscripts

0	environmental or dead state

INTRODUCTION

Refrigeration systems are a common technology in today's world, being used in everyday activities, such as food preservation and air conditioning (AC) applications. Presently, the hydroflourocarbon HFC-134a, the working fluid of automotive air conditioning systems, greatly contributes to global warming. Natural refrigerants have gained worldwide attention as the logical replacement for HFCs. Carbon dioxide (CO_2) is the natural refrigerant receiving the most attention due to its abundance in nature.

In order to better understand the operation of an automotive AC system which utilizes CO_2 as its working fluid, a simulation model is created by the authors using the software program Engineering Equation Solver (EES) [www.fchart.com]. The model simulates normal operation as well as faulty operation due to refrigerant loss within an automotive AC system using CO_2. The First and Second Laws of Thermodynamics are used to verify normal operational data and performance parameters obtained from past experimental and analytical work described within this paper. Using the EES model, refrigerant losses are simulated throughout the system one at a time at locations prone to leaks and the model produces a faulty operating data library. Analyzing the simulated fault data for possible trends or patterns is done in order to detect future system faults and to diagnose the faults accordingly.

Each of the different types of refrigeration systems can be modeled thermodynamically in order to find the system's overall efficiency. Both a first law based (energetic) efficiency as well as a second law based (exergetic) efficiency can be found in order to evaluate the system's performance. The concept exergy comes from using the Second Law of Thermodynamics in conjunction with the conservation of energy laws. The idea of exergy better enables the examiner to further understand the location, types, and true magnitudes of waste and loss. An exergy loss or destruction can reflect an inefficient use of fuel or a location of major irreversibilities within the system. With exergetic efficiency, the examiner can gauge the potential for improvement in the performance of a system [1].

Throughout the history of refrigeration, the working fluid (refrigerant) used for applications has changed based on economical, safety and environmental reasons. Major contributors to the evolution of refrigerants are system efficiency as well as emission issues. Balancing the amount of hazardous emissions released to the atmosphere with the financial burden of increasing the system's efficiency is essential in designing an automotive air conditioning system.

The Montreal Protocol, an international treaty that controls the production of ozone-depleting substances, disallowed the production of chlorofluorocarbons (CFCs), such as R-12, by the year 1996. R-22, a hydrochloroflourocarbon (HCFC), is to cease production by 2030 [2]. In addition, HFC-134a will not be produced in Europe after 2017. On October 14, 2004, the Environment Ministers of the European Union agreed that a ban will apply to all new vehicles being produced beginning in 2011. By 2017, every new vehicle produced must utilize a refrigerant that has a global warming potential (GWP) of less than 150 [4]. Thus, new environmental regulations have lead to an increased interest from the AC automotive industry to explore the use of CO_2 as a refrigerant.

Carbon dioxide as a refrigerant has been used in past air conditioning systems. It was originally used for cold storage refrigerators in food markets and for comfort cooling in motion picture theaters in the 1900s [3]. Within automotive applications, more investigations are necessary to design an automatic or manual leak detection and diagnosis system for use during troubleshooting and maintenance. All CO_2 cycles are transcritical, which means they move between sub and supercritical pressures during the cycle, due to a low critical temperature of 31.1°C. Also, segments of the system are under extremely large pressures which can contribute to refrigerant loss.

RESEARCH OBJECTIVE

The objective of research currently underway at Rochester Institute of Technology (RIT) is to effectively detect and diagnose leaks for automotive carbon dioxide air conditioning (AC) systems using a technique that incorporates exergetic analysis. Before designing the experimental setup which will be used to validate the proposed technique, a computer simulation of a CO_2 automotive AC system is developed. First, a normal operating AC system is simulated in order to better understand the operating condition of a normal system. When the experimental setup is completed it will be utilized to verify the accuracy of the EES simulation model under normal operating conditions.

Developing a simulation model for refrigerant loss is enhanced through the identification of probable leak locations within the system. Based on the fleet of prototype vehicles in Europe that currently use CO_2 AC systems, leaks typically occur around

the compressor and between connections of hoses and lines. A major change that must be made to a current air conditioning system is that the lines of the system are no longer hoses, but a combination of metal lines and hoses. Metal lines are incorporated because the CO_2 cycle is transcritical and therefore the CO_2 remains as a superheated vapor or liquid-vapor mixture throughout the cycle. The metal lines include hoses in order to dampen the vibrations that would occur otherwise. The connections between the metal lines and the hoses are considered one probable area for refrigerant loss. Any time there is a connection made between components, the chance for leakage increases. Another probable location for leaks is within the compressor. The compressor used in most automotive CO_2 AC systems is non-hermetically sealed. It incorporates an open configuration with a sealed rotating shaft which is a significant contributor to potential leakage.

Using an EES refrigerant loss simulation model, the typical fault areas are reproduced by inflicting mass flow rate losses upon the system in order to replicate refrigerant losses. Losses must be varied in order to accurately replicate an actual leak. Some leaks can be slow if they are steady and constant, but some leaks may be large if a seal erratically breaks open. The refrigerant loss simulation model will be validated using the experimental setup. Currently, the refrigerant loss simulation model provides insights into locations and types of sensors required to detect and diagnose CO_2 losses within the system.

Within this paper, a more detailed description of the EES simulation model and proposed sensor locations is provided. The objective of this ongoing research is to develop an inexpensive, effective, and automatic leak detection and diagnosis methodology for automotive CO_2 AC systems. The work is performed in conjunction with industry in order to add to its relevance and to ease potential market transfer in the future.

CURRENT LEAK DETECTION METHODS

Technically, every system has leaks, because all equipment leaks to some degree. According to Tomczyk [5], a leak is "a physical path or hole, usually of irregular dimensions, that may be the tail end of a well fracture, a speck of dirt on a gasket, or a micro-groove between fittings." Leaks can be classified by a number of factors: pressure dependent, temperature dependent, vibration dependent, etc. Reducing the likelihood and detecting leaks is a significant challenge in developing refrigeration systems.

Within many research, development, and testing facilities, gas analysis is used in order to detect leaks within HFC-134a AC systems. This method is used for experimental purposes in order to identify faulty equipment before it is used in manufacturing. Components (all or some) of an air conditioning system are placed inside a closed test chamber of a known volume. This test chamber is calibrated using a correlation factor determined through a known leakage rate of refrigerant. The components are placed in the chamber and operated, allowing for refrigerant to leak. The HFC-134a gas concentration is determined by measuring the level of sound created by the expansion of the gas following absorption of infrared light at a specific wavelength. Gas sensitivity is achieved using optical filters capable of detecting concentrations in the parts per billion (ppb) range. To ensure the accuracy of the equipment, the analyzer compensates for temperature, pressure, and water vapor interference.

For on-sight maintenance, automotive repair technicians utilize a refrigerant detecting gun like the one shown in Figure 1 [6]. On-sight maintenance refers to testing components which have been installed on the vehicle. The refrigerant detection gun can detect leaks only as small as 500 parts per million (ppm), which is highly ineffective for smaller leaks.

Figure 1: Example Leak Detection Gun

CARBON DIOXIDE AS A REFRIGERANT

In the past, research has been conducted in using carbon dioxide as the refrigerant for many different types of refrigeration cycles. More recently, automotive air conditioning applications that utilize CO_2 are investigated as well. Currently, HFC-134a is used as the automotive AC working fluid. As compared with carbon dioxide, it has a much higher GWP. The GWP for a substance is calculated as the ratio of the radiative forcing impact that results from the emissions of one kilogram of the substance to that from emissions of one kilogram of carbon dioxide over a period of time (usually 100 years) [7].

The GWP of HFC-134a is approximately 1300; therefore it has 1300 times the GWP of CO_2. If one unit of HFC-134a is released into the atmosphere, it will take 1300 units of CO_2 to create the same amount of damage. Table 1 [7] shows how the GWP value for HFC-134a has been adjusted by scientists since 1990 due to improved understanding of effects on global warming. An increase in the adjustments regarding the GWP value is anticipated to continue into the future.

	Year	
Refrigerant	**1990**	**1996**
CO_2	1	1
R-134a	1200	1300
R-22	1400	1400
R-12	7300	7300

Table 1: Global Warming Potential (GWP) of Various Refrigerants in 1990 and 1996

Carbon dioxide appears to be a logical replacement for chemical based refrigerants because of its natural occurrence in the atmosphere. Also it is non-flammable and involves a high operational pressure for effective performance which results in a reduction in required compressor size. The required compressor volume is inversely proportional to the suction pressure. The volumetric capacity of carbon dioxide is eight times higher than conventional refrigerants, which allows for a smaller compressor compared to conventional ones [8]. A major disadvantage of CO_2 as a refrigerant is that it is not self-alarming and therefore leak detection is difficult. This is a major concern for system manufacturers. The term 'self-alarming' means that one cannot detect (smell or taste) small amounts of CO_2 in the air.

The basic design of an AC system is typically affected by its refrigerant selection. Fartaj et al. [8] used a CO_2 AC system developed by Lorentzen and Pettersen [9] that incorporates a few changes to the typical AC system configuration (shown in Figure 2) to take the transcritical properties of the CO_2 refrigerant into account. The condensation process within the CO_2 AC cycle is changed. The purpose of the condenser is to transfer heat from the refrigerant to the cooler surroundings. Because the critical temperature of carbon dioxide is so low (of 31.1°C), it is normally below the typical ambient temperature. The condenser is replaced with a gas cooler and the condensation process is further enhanced with an internal heat exchanger as shown in Figure 3.

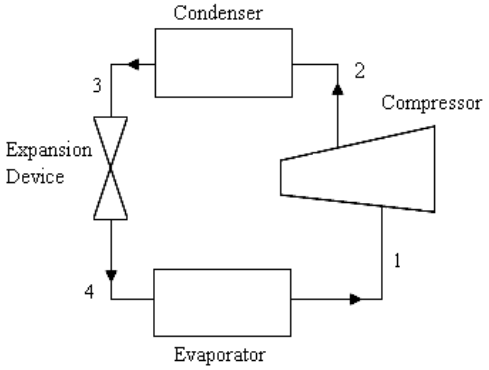

Figure 2: Basic HFC-134a Refrigeration System Schematic

Figure 4 is the representation of the temperature-entropy diagram for a CO_2 refrigeration cycle superimposed on the vapor dome for this substance [8]. High temperature supercritical CO_2 exiting the compressor (state point 2 in Figures 3 and 4) is cooled in the gas cooler to a lower temperature (state point 3) and then enters the internal heat exchanger where the high pressure refrigerant is further cooled by the low pressure CO_2 coming off of the evaporator (state point 6). This cooled carbon dioxide (state point 4) passes through an expansion valve where it is throttled to a lower pressure and temperature (state point 5). Finally, the refrigerant absorbs heat from the air within the car's interior while flowing through the evaporator and exiting as a high quality mixture (state point 6). The AC system's evaporator is the part of the system attached near the inside of the vehicle.

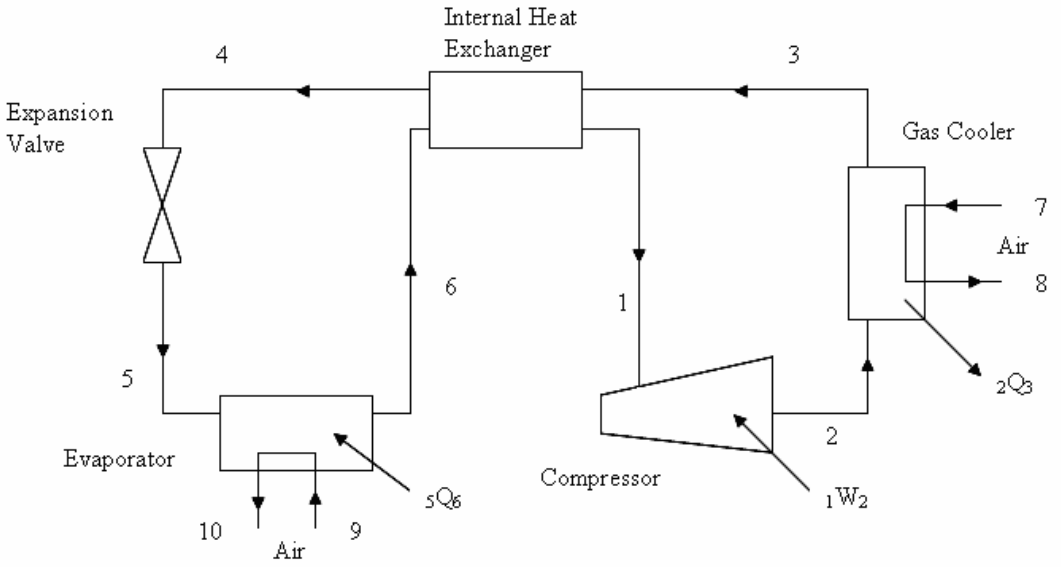

Figure 3: CO_2 Refrigeration System Schematic

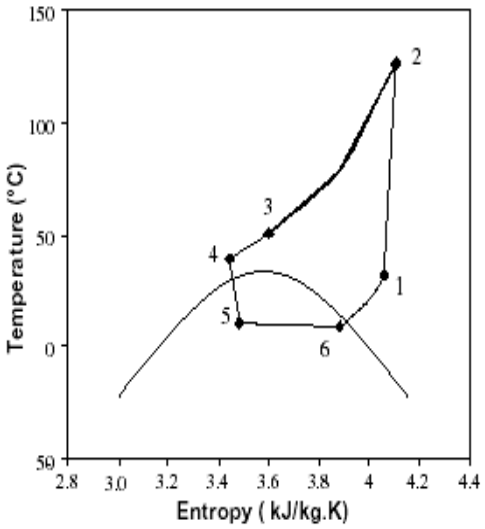

Figure 4: Temperature vs. Entropy Diagram for CO_2 Refrigeration Cycle

SIMULATION MODEL DEVELOPMENT

The EES simulation model developed considers the CO_2 AC system shown in Figure 3. The simulation model assumes steady state operation and thus transient operation such as at initial start up of the system is neglected. This assumption is made to reflect the data provided by Fartaj et al [8]. The heat exchangers, expansion device and compressor are considered adiabatic. Constant pressure drops across the system's heat exchangers are assumed and based on past published experimental work. In addition, the isentropic efficiency of the compressor and heat exchanger effectiveness are assumed to remain constant during both normal and refrigerant loss scenarios. When modeling refrigerant loss, three potential refrigerant loss areas are investigated, however simultaneous losses at more than one location are not considered. Compressor power consumption during loss scenarios is also considered constant.

The simulation program provides pressure, temperature, enthalpy, and internal energy of state points around the system. It uses these values to also determine exergetic efficiency of system components. Exergy can be defined as the maximum theoretical work obtainable as a system and its reference environment interact to equilibrium [1]. The use of exergy in thermodynamic analysis provides more meaningful results that simply using the first law of thermodynamics. An exergy analysis can

determine where and how losses occur in the system so that energy can be used more effectively and efficiently.

The exergy of a pure substance is given by Equation 1.

$$e = (h - h_0) - T_0(s - s_0) \quad (1)$$

where the enthalpy (h) and entropy (s) of the given state is compared to the reference, or dead state (depicted by subscripts of '0'). An environment is assumed to be a simple compressible system that is large in extent and uniform in both temperature and pressure. This reference state is typically the ambient temperature and pressure for the system, such as 298 K and 101.325 kPa, respectively. The exergy loss (Δe) is calculated using Equation 2 [1].

$$\Delta e = \text{exergy supplied} - \text{exergy recovered} \quad (2)$$

By calculating the exergy loss, components of the system can be ranked based upon their contribution to the overall exergy destruction of the system. An energy balance and an exergy balance are done around every component of the system (gas cooler, compressor, evaporator, internal heat exchanger, and expansion valve). The energy balances produce the total coefficient of performance for the system, and the exergy balances produce the corresponding exergetic efficiency of each component of the system. The exergetic efficiency of each component is given by Equation 3 [1].

$$x = \textit{exergy recovered / exergy supplied} \quad (3)$$

With the knowledge of the locations prone to leaking, mass flow rate losses are applied across the compressor and across the evaporator. The mass flow rate loss across the compressor is applied after the compressor (state 2 in Figure 3), because if leaking is to occur, it would do so across the seal of the compressor. Both the mass flow entering and leaving the evaporator are adjusted to simulate joint leaks between metal tubing and hoses. The refrigerant flowing into and out of the evaporator (states 5 and 6) is the portion of the cycle that is subcritical, which means the refrigerant is a liquid-vapor mixture. With this mixture, manufacturers can place the hoses in between metal lines and components in order to reduce vibrations. Also, the evaporator is the portion of the system closest to the passengers, which is where vibrations need to be dampened the most.

Vargaftik [10] provides a detailed table of carbon dioxide properties based on temperature and pressure. Fartaj et al [8] used these tables in order to calculate the corresponding exergy losses for each component. The developed simulation model verifies this published normal operation data. EES utilizes a set of databases that have been organized by various published works for properties of a substance.

Table 2 is a list of the temperatures and pressures for each state point used in analyzing the AC system assuming a constant mass flow rate of 2.64 kg/min thus under normal operation (no leakage).

State	T (K)	P (kPa)
1	305.05	4259
2	399.75	11410
3	323.55	11279
4	312.55	11129
5	283.45	4540
6	282.35	4409

Table 2: Properties of State Points in the Normal Mode CO_2 Refrigeration System

Using the normal operation simulation model, mass flow rate loss is incorporated in the locations described earlier. For each of the leaks experienced by the system, a loss of 0.005 kg/min is applied at the location of the leak and at each subsequent state point. Only discrete values of the mass flow rate are considered.

For each loss, a new simulation is performed around the cycle in order to calculate the new state points based on the new mass flow rates. State points 7 through 10 remain constant with every leak scenario, by assuming that the vehicle is under constant load and is operating under steady state conditions. The mass flow rate of the air through the evaporator and gas cooler are also held constant. The initial refrigerant loss is considered after the available charge in the receiver (at State 4) is emptied and the system is operating at normal conditions with the minimum amount of charge (~500g). In order to calculate the new temperatures and pressures along the system,

multiple assumptions are made as discussed previously. The gas cooler and the evaporator are modeled as non-mixing cross flow heat exchangers and the internal heat exchanger includes a counter flow configuration. Table 3 compares exergy loss across each component under normal operation and during a refrigerant loss where the three probable leak locations are considered. It also shows the differences of the exergetic efficiency of each component in the system. For simplicity, only one change of mass flow rate is applied and reported in Table 3.

PROPOSED CO_2 LEAK DETECTION METHODOLOGY AND FUTURE WORK

As shown in the development of the simulation model under normal and refrigerant loss scenarios, if the temperature and pressure is known at each point in the cycle, the performance of the cycle can be determined based on both the first and second laws of thermodynamics. When comparing the results of the normal and leakage models based on exergy losses, differences can be seen. When a leak is applied to the compressor (state 2), the exergy loss of the expansion device and heat exchanger decreases. On the other hand, the exergy loss for the compressor and gas cooler increases.

For the leak applied before the evaporator (state 5), the heat exchanger, compressor, and expansion device decrease in exergy loss, while the gas cooler experiences an increase in exergy destroyed. For the leak applied after the evaporator (State 6), the heat exchanger's exergy destroyed increases while the other comparisons remain the same.

When looking at the efficiency differences between normal operation and leakage conditions, one can see an opposite change compared to the exergy loss. By looking at Table 3, the efficiency decreases when the exergy loss increases across the gas cooler. The opposite occurs for the evaporator; the exergy loss decreases and therefore the exergetic efficiency increases. The correlation between exergy loss and efficiency is expected. If a component has greater exergy destroyed, the efficiency should go down, because the component is not functioning to its maximum capability.

The premise behind the proposed leak detection system is that these differences will be used to detect a refrigerant loss within the system. Data collected from sensors embedded within the system will be used to determine system performance characteristics. An on-board system will collect the data and periodically determined the system's performance profile. This will occur during steady state operation of the system. Over time, if the system develops a refrigerant leak, deviations in performance characteristics will be determined by the on-board system and a fault condition will be detected.

	Normal Operation		**Leak at State 2**		**Leak at State 5**		**Leak at State 6**	
Component	**Exergy Loss (kW)**	x (%)	**Exergy Loss (kW)**	x (%)	**Exergy Loss (kW)**	x (%)	**Exergy Loss (kW)**	x (%)
Compressor	0.5572	81.11	0.5598	81.02	0.5058	82.85	0.5243	82.23
Gas Cooler	0.5579	67.85	0.5780	67.84	0.6089	66.70	0.5951	67.20
Heat Exchanger	0.2646	20.22	0.2533	23.57	0.2533	24.83	0.2689	23.59
Expansion Valve	0.6054	--	0.4875	--	0.5090	--	0.4892	--

Table 3: Exergy Loss and Exergetic Efficiency for the CO_2 Refrigeration System

Ongoing and future research includes developing an experimental carbon dioxide air conditioning system which will be used to verify the simulation models described within this paper. In addition, the experimental setup will be used to validate the feasibility and viability of the proposed leak detection methodology based on operational and economical consideration.

CONCLUSIONS

An EES simulation model of a carbon dioxide air conditioning refrigeration system is developed. The simulation is based upon the Second Law of Thermodynamics or exergetic analysis of the system. Refrigerant leaks simulated as mass flow rate losses are applied to three areas prone to leaking in the system. From the simulations, it is concluded that differences exist in exergetic efficiencies and exergy destroyed within each component during the different operating scenarios. Future work includes developing an experimental set-up to validate the simulation model. In addition, a fault detection and diagnosis system will be developed which will use differences in thermodynamic behavior to classify the system's operation.

ACKNOWLEDGEMENTS

The authors extend their gratitude to Mr. Prasad Kadle and Edward Wolfe from Delphi-Harris Corporation for their guidance and continuing support of this ongoing research. In addition, to the Gleason Foundation and Rochester Institute of Technology for the financial support required to conduct this research.

REFERENCES

[1] Moran, MJ and Shapiro, HN. *Fundamentals of Engineering Thermodynamics*. New York: John Wiley and Sons, Inc., 2000.

[2] ASHRAE, 2001, *2001 ASHRAE Handbook: Fundamentals*, Atlanta: American Society of Heating, Refrigerating, and Air Conditioning Engineers, Inc.

[3] Bodinus, WS. *The Rise and Fall Of Carbon Dioxide Systems*. ASHRAE Journal; 41 (4): 37-42.

[4] *EurActive*. An online forum of EU News, Policy Positions and EU Actors. January 2005. http://www.euractiv.com/Article?tcmuri=tcm:29-130988-16&type=PolicyNews

[5] Tomczyk, J, *Troubleshooting and Servicing Modern Air Conditioning and Refrigeration Systems*. Illinois: ESCO Press, 1995

[6] *Network Tool Warehouse*. A catalog of various air conditioning maintenance tools. January 2005. http://www.ntxtools.com/airconditioning/actools/

[7] *US Emissions Inventory 2004*. A yearly inventory of green house gas emissions. Environmental Protection Agency. January 2005. http://yosemite.epa.gov/OAR/globalwarming.nsf

[8] Fartaj, A and Ting, DSK and Yang, WW. 2004, "Second law analysis of the transcritical CO_2 refrigeration cycle", *Energy Conversion & Management*, Vol. 45, pp. 2269-2281.

[9] Lorentzen, G and Pettersen, J. 1993, "A new, efficient and environmentally benign system for car air conditioning", International Journal of Refrigeration, Vol. 16, pp. 4-12.

[10] Vargaftik, NB, *Tables on the thermophysical properties of liquids and gases: in normal and disocciated states*. London: Hemisphere Publishing Company, 1975.

Proceedings of ECOS 2005
Trondheim, Norway
June 20–22, 2005

SYNTHESIS AND CHARACTERIZATION OF METAL DOPED MESOPOROUS SILICA AS AN ENERGY STORAGE MATERIAL

Satoko Fujisaki, Yuki Inagi, Akira Endo*, Takuji Yamamoto, Takao Ohmori, Masaru Nakaiwa
National Institute of Advanced Industrial Science and Technology (AIST), 1-1-1, Higashi, Tsukuba, Ibaraki 305-8565, Japan

ABSTRACT

Energy-efficient adsorption systems which utilize water as a working fluid, such as adsorption heat pump, desiccant cooling, humidity control system, thermal energy storage etc., have attracted much attention, because they have an advantage of energy saving and environmental acceptance. Since the water adsorption properties required to such system depend on the temperature level of generation, environment and recovery, it is necessary to design and synthesize new adsorbent which have large heat storage capacity for each systems. Zeolites are one of the most commonly used adsorbents; however, the adsorption of water by zeolite saturates at low relative pressures because of its small pore size of around 1 nm and its strong affinity with water molecules, making them unsuitable as a heat storage material for the low-temperature recovery. It has been reported metal doped mesoporous silicas show a suitable water adsorption properties (a steep increase of adsorption amount at a certain relative humidity) for the low-temperature recovery and enough stability toward water vapor. However, there are no systematic studies on the mesoporous silica as useful adsorbents for energy-efficient adsorption systems. In this work, we synthesized metal doped mesoporous silica by a solvent evaporation method and examined their water adsorption properties. In the synthesis, hexadecyl trimethyl ammonium chloride was used as a structure directing agent and $ZrO(NO_3)_2$, $Al(NO_3)_3$, titanium diisopropoxide bisacetylacetonate and $Fe(NO_3)_3$ was used as the metal source. The possibility/applicability of them for various energy-efficient adsorption systems are also discussed.

Keywords: Energy-efficient adsorption system, Metal doped mesoporous silica, Solvent evaporation, Water vapor stability

INTRODUCTION

Thermal energy conversion systems, such as adsorption heat pumps, desiccant cooling systems, humidity control systems, thermal energy storage devices, etc., are increasingly expected to function as decentralized energy systems for reducing energy consumption based on their ability to utilize low temperature exhaust heat. When porous materials are used for water adsorption in these systems, the primary performance of these systems is dictated by the capacity and the rate of water vapor adsorption/desorption under the relative humidity conditions specific to their practical operation. Since the water adsorption properties required by these systems depend on the temperature level of generation, environment and recovery, the design and synthesis of new adsorbents that have large heat storage capacities is an ongoing process.

Silica gel and zeolite are commonly used adsorbents in the systems listed above. Silica gel has a low adsorption/desorption capacity in the specific relative humidity regions of these systems due to its disordered porous structure. Although zeolites have ordered porous structures, zeolites saturate with water at low relative humidities because of their small pore size

*Corresponding author. Phone: +81-29-861-4653 Fax: +81-29-861-4660 E-mail: endo-akira@aist.go.jp

(around 1 nm) and their strong affinity with water, making them unsuitable as heat storage materials for low-temperature utilization.

The synthesis of ordered mesoporous silicas (MPSs) with pore diameters of 2 ~ 3 nm, e.g. MCM-41 [1, 2] and FSM-16 [3], have potential applications in many various fields, including as adsorbents of water vapor. MPSs posses a large adsorption/desorption capacity in a range of specific relative humidities due to the capillary condensation of water in the mesopores, making them potentially applicable as new adsorbents that can be recovered by low temperature exhaust heat. After MPSs were discovered in the early 90's, studies were conducted on the water vapor adsorption properties of MPSs from the viewpoint of stability in the presence of water vapor and humidity. Initially, MPSs did poorly as adsorbents of water vapor, as the pore structure of MPSs was easily destroyed by humidity, directly resulting in a decreased adsorption capacity [4]. The introduction of metallic elements into the silica network was performed in order to modify the silica surface, and to introduce catalytic activity onto the surfaces [5]. These metal-doped mesoporous silicas have been reported to have higher stabilities compared with non-doped MPSs. For example, Ohashi *et al.* reported the synthesis of a Ti-doped mesoporous silica prepared under hydrothermal conditions [4]. The stability of this material towards water vapor increased, and a potential application as a humidity control material was demonstrated. Park *et al.* reported the synthesis of a zirconium-doped MCM with a high alkaline resistance [6]. Specifically, Zr-MCM-41 and Zr-MCM-48 showed a high structural stability in alkaline solutions of pH 10-11.5. The structures of pure silica samples were destroyed in the solution of pH 10. Yano *et al.* reported a super-microporous aluminosilicate having a water vapor adsorption capacity of 0.2 ml/g at a relative vapor pressure of 0.2 [7]. They suggested that if were to be utilized as an adsorbent for an adsorption heat pump, it would be possible to produce a coolant with a lower temperature than could be produced with an adsorbent that does not incorporate Al. Aika *et al.* published a study of the water sorption/desorption behavior $CaCl_2$-doped materials [8]. This study reported that the heat storage capacity of FSM-16 with 33 wt% $CaCl_2$ (1200 MJm^{-3}) was higher than that of zeolite (Na-Y, 345 MJm^{-3}) and FSM-16 (731 MJm^{-3}). Based on this, $CaCl_2$-doped materials are more suitable as chemical heat storage media for water adsorption than zeolite. These studies suggest metal-doped mesoporous silicas do have a sufficient stability towards humidity and water vapor to be applied in this way. Though it has been reported that metal-doped mesoporous silicas have been applied to adsorption heat pumps, desiccant cooling systems, humidity control systems, thermal energy storage devices, etc. as described above, there are no systematic studies focused on the specific metal elements that increase the stability of these materials towards water vapor and their potential applicability as energy-efficient adsorbents. The focus of this study is the synthesis and properties of four ordered, metal-doped mesoporous silicas and pure silica using a solvent evaporation method. The water adsorption properties and stability in steam of these silicas, as well as the energy storage capacity of these materials, are reported.

EXPERIMENTAL

Synthesis

Metal-doped mesoporous silicas and pure silica were prepared according to Endo's procedure [9]. Hexadecyltrimethylammonium chloride (C_{16}TAC) was used as a structure-directing agent. For the introduction of metal, salts of zirconium, aluminum, iron and titanium were chosen and used at a fixed quantity of 5 mol% relative to the silica source.

Zirconium oxynitrate dihydrate [$ZrO(NO_3)_2$ $2H_2O$], aluminum nitrate nonahydrate [$Al(NO_3)_3$ $9H_2O$], titanium diisopropoxide bisacetyl acetonate and iron(III) nitrate enneahydrate [$Fe(NO_3)_3$ $9H_2O$] were used as the metal sources. The starting solution, a mixture of

tetraethylorthosilicate (TEOS) as a silica source, the metal source, C_{16}TAC, hydrochloric acid, water and ethanol, was stirred for 1 hour at room temperature. The typical molar ratio of the starting solution was 1 TEOS : 1 metal source : 0.2 C_{16}TAC : 10 EtOH : 1.8×10^{-4} HCl : 10 H_2O. The reaction mixture was then transferred to a round-bottom flask and evaporated using a vacuum rotary evaporator for 1 hour. The base temperature was kept at 298 K during the solvent evaporation. After the solution reached a paste-like consistency, the pressure was reduced and the solvent was again evaporated for 2 hours. This resulted in the viscous, paste-like liquid changing to a wet solid with some bubbling. The temperature was then increased to 333 K to evaporate the remaining solvent. 1 hour later, the obtained silica-surfactant composite was calcined at 873 K for 5 hours in air to remove the surfactant, resulting in a porous solid. It should be noted that the total synthetic time was almost the same for all of the metal sources except Al-doped MPS. (The solvent evaporation in the synthesis of Al-doped MPS was longer than for the others.)

Characterization

XRD and nitrogen adsorption/desorption measurements were carried out for the characterization of the metal-doped mesoporous silicas. XRD measurements were performed using a Rigaku Miniflex diffractometer (Cu/Ka radiation, operated at 40 kV and 30 mA). The nitrogen adsorption isotherm was measured using Belsorp-mini, fully automatic adsorption isotherm measuring equipment (manufactured by BEL Japan, Inc.). The measurements were carried out at 77 K. The pre-treatment was carried out at 573 K for 5 hours under a nitrogen atmosphere.

Water vapor adsorption properties

The water adsorption isotherms were measured using a Belsorp 18 plus and a Belsorp 18-3, both of which are fully automatic adsorption isotherm measurement instruments (manufactured by BEL Japan, Inc.). The measurements were carried out at 298 K. The pre-treatment was carried out at 573 K for the first measurement and 413 K for the second measurement for 8 hours under a pressure of 2 Pa. The stability of pure silica and the obtained metal-doped mesoporous silica samples towards water vapor was evaluated based on the nitrogen and water adsorption/desorption measurements before and after steam treatments at 373 K for 24 hours.

RESULTS AND DISCUSSION

Synthesis

The metal source is very important when metal is introduced into a silica network. Metal alkoxides are generally used in the synthesis of metal-doped mesoporous silicas. However, the reactivity of metal alkoxides is much higher in comparison with silica alkoxides, namely TEOS. Metal alkoxides are easily hydrolyzed by atmospheric moisture, leading to polymerization. For this reason it was necessary to select a metal salt with a low reactivity. In terms of the metal sources described in the experimental section, all of the starting solutions were transparent and precipitation was not observed.

The synthesis was completed in two days, including the calcination. This synthetic method that makes use of a vacuum rotary evaporator is very simple compared with conventional methods, such as a hydrothermal synthesis or a sol-gel synthesis. It can be performed in a relatively short time and is suitable for large-scale synthesis.

The pH was measured after the hydrolysis reaction, and the metal-doped mesoporous silica products were much more acidic than pure silica, as shown in Table 1.

The yields of the calcined samples, defined here as the proportion of the obtained silica to the supplied TEOS and metal source, were over 95% for all of the syntheses, indicating that only the ethanol and water were removed during the vacuum evaporation. The obtained metal-doped mesoporous silicas are herein referred to as Zr-MPS, Al-MPS, Ti-MPS and Fe-MPS.

X-ray diffraction

Figure 1 shows the X-ray diffraction patterns of (a) pure silica, (b) Zr-MPS, (c) Al-MPS, (d) Ti-MPS and (e) Fe-MPS after calcination. The XRD data of the metallic-MPSs (b-e) had a characteristic peak of mesoporous silicas, also present in (a) pure silica. As a result of the introduction of the metals into the silica network, the peak intensity of d_{100} in (b) Zr-MPS, (d) Ti-MPS and (e) Fe-MPS was reduced, whereas the intensity of (c) Al-MPS increased and sharpened, even more so than (a) pure silica. With regard to the d_{100} peak position, it shifted a greater distance as a result of metal doping in all of the samples (Table 1).

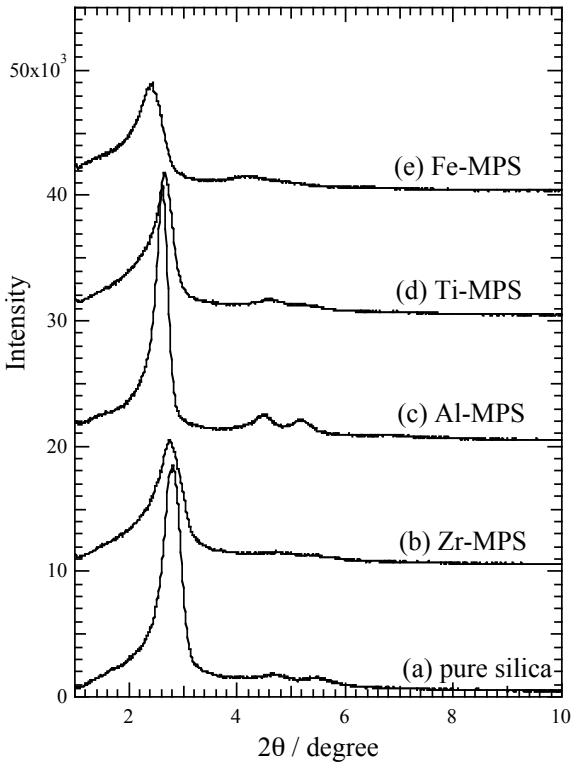

Figure 1: XRD patterns of pure silica and metal doped mesoporous silicas

N_2 adsorption/desorption isotherms

The porous structure of the obtained metal-doped mesoporous silicas was evaluated by nitrogen adsorption measurements at 77 K. The adsorption/desorption isotherms are shown in Figure 2. The porous properties obtained from these experiments are summarized in Table 1. The isotherms were similar to type IV in terms of an IUPAC classification, clearly indicating a mesoporous structure. The pore size distribution curves (PSD) were calculated using the Broekhoff and de Boer equation [10] with the D-H algorithm. The amount of adsorbed nitrogen at $P/P_0=1$, which is almost identical to the total pore volume, was higher with the introducing of a metal with the exception Zr-MPS. The most common pore size for the metal-doped mesoporous silicas was larger than that of pure silica, again with the exception of Zr-MPS. It was reported that the pore size of mesoporous silicas could be decreased by incorporating aluminum into the skeleton of the silica [7, 11-13]. The results of these experiments, however, indicated a pore size of 2.95 nm for Al-MPS, which is clearly larger than that of pure silica. The thickness of the silica wall did not depend on the metal used, remaining around 1 nm for all of the samples.

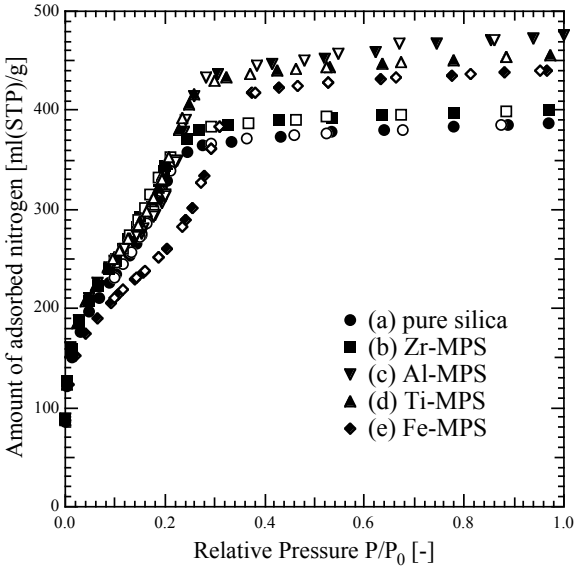

Figure 2: Adsorption isotherms of nitrogen on (a) pure silica, (b) Zr-MPS, (c) Al-MPS, (d) Ti-MPS and (e) Fe-MPS.

Table 1: Characterized porous properties of the obtained pure silica and the metal-doped mesoporous silicas.

Sample	pH	d_{100} [nm]	d_P [nm]	d_W [nm]	V_P [ml/g]	S_{BET} [m^2/g]
Pure silica	3.43	3.12	2.66	0.94	0.60	1155
Zr-MPS	1.44	3.14	2.63	1.00	0.62	1238
Al-MPS	1.77	3.36	2.95	0.92	0.73	1098
Ti-MPS	2.61	3.31	2.76	1.06	0.70	1168
Fe-MPS	1.87	3.63	3.28	0.92	0.68	935

Water vapor adsorption properties

The water vapor adsorption/desorption isotherm of pure silica is shown in Figure 3(a), and those of the metal-doped mesoporous silicas are shown in Figure 4(b-e). The amount of water vapor adsorbed increased with the introducing of all of the metals in this study. The absorbed amount in low relative humidity (P/P_0<~0.3) increased such that the hydrophilicity of the pore surface of the silica increased after the first measurement due to the rehydrorization of water molecules on the pore surface. The position of the steep increase in the water vapor adsorption isotherm shifts to the lower relative pressure side in the second measurement (Figures 3 and 4). In terms of the four metal-doped mesoporous silicas, the lowest amount of saturated adsorption was observed in Zr-MPS (Figure 4(b)), but there was little change in the capillary condensation position or in the amount of saturated adsorption between the first and second measurement.

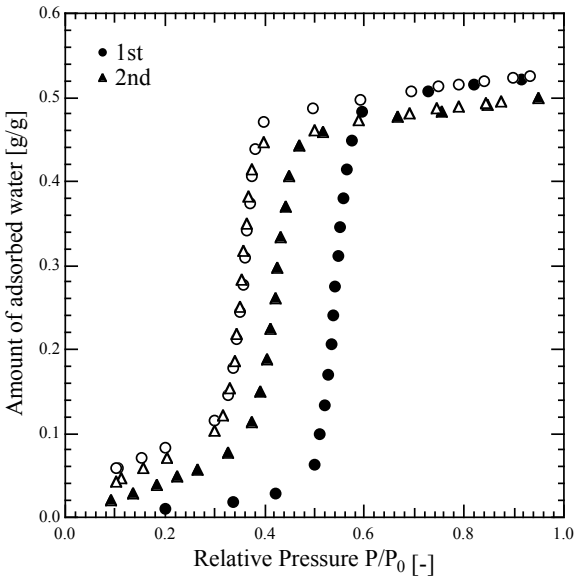

Figure 3: Adsorption isotherms of water vapor on (a) pure silica at 298 K. The pre-treatment temperature was 573 K for the first measurement and 413 K for the second measurement for 8 hr in vacuum.

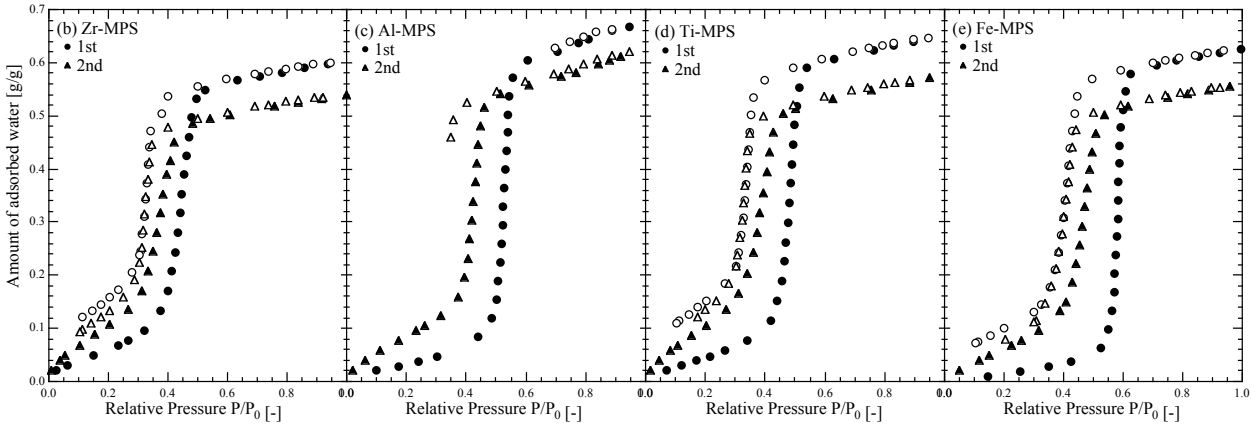

Figure 4: Adsorption isotherms of water vapor on (b) Zr-MPS, (c) Al-MPS, (d) Ti-MPS and (e) Fe-MPS at 298 K. The pre-treatment temperature was 573 K for the first measurement and 413 K for the second measurement for 8 hr in vacuum.

Water vapor stability

Figure 5 shows the nitrogen adsorption/desorption isotherms, and the porous properties obtained from these experiments are shown in Table 2. The water adsorption/desorption isotherms before and after the steam treatment are shown in Figure 6 and 7, respectively. The pore structure of pure silica (Figure 6(a)) collapsed during the steam treatment, decreasing the BET surface area. The capillary condensation previously observed disappeared (Figure 6). On the other hand, no significant change was observed in the shape of adsorption isotherms of the metal-doped mesoporous silicas after the steam treatment, indicating an increase in the stability of these materials in the presence of water vapor. In particular, (b) Zr-MPS and (e) Fe-MPS showed the highest stability.

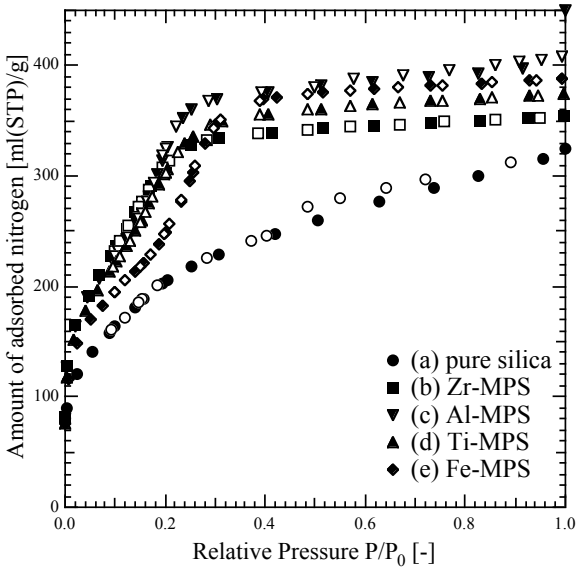

Figure 5: The nitrogen adsorption isotherms of (a) pure silica, (b) Zr-MPS, (c) Al-MPS, (d) Ti-MPS and (e) Fe-MPS after the steam treatment.

Table 2: Characterized porous properties of (a) pure silica, (b) Zr-MPS, (c) Al-MPS, (d) Ti-MPS and (e) Fe-MPS after the steam treatment.

Sample	d_P [nm]	V_P [ml/g]	S_{BET} [m^2/g]
Pure silica	2.45	0.48	764
Zr-MPS	2.45	0.55	1140
Al-MPS	2.67	0.63	1035
Ti-MPS	2.56	0.58	1023
Fe-MPS	3.04	0.60	869

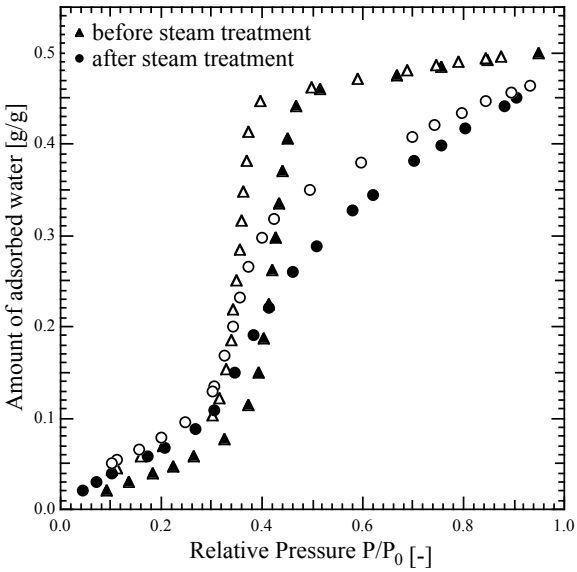

Figure 6: The water adsorption isotherm of (a) pure silica before and after the steam treatment.

CONCLUSION

Highly ordered, metal-doped mesoporous silicas, Zr-MPS, Al-MPS, Ti-MPS and Fe-MPS, were synthesized by a rapid solvent evaporation method using a vacuum rotary evaporator. In this synthesis, $ZrO(NO_3)_2$, $Al(NO_3)_3$, titanium diisopropoxide bisacetylacetonate and $Fe(NO_3)_3$ were used as metal sources based on their lower reactivity. The introduction of these metals into silica network effectively enhanced the water vapor stability. The water vapor stability of (b) Zr-MPS, (c) Al-MPS and (e) Fe-MPS was enhanced based on the results of the nitrogen and water vapor adsorption/desorption isotherms

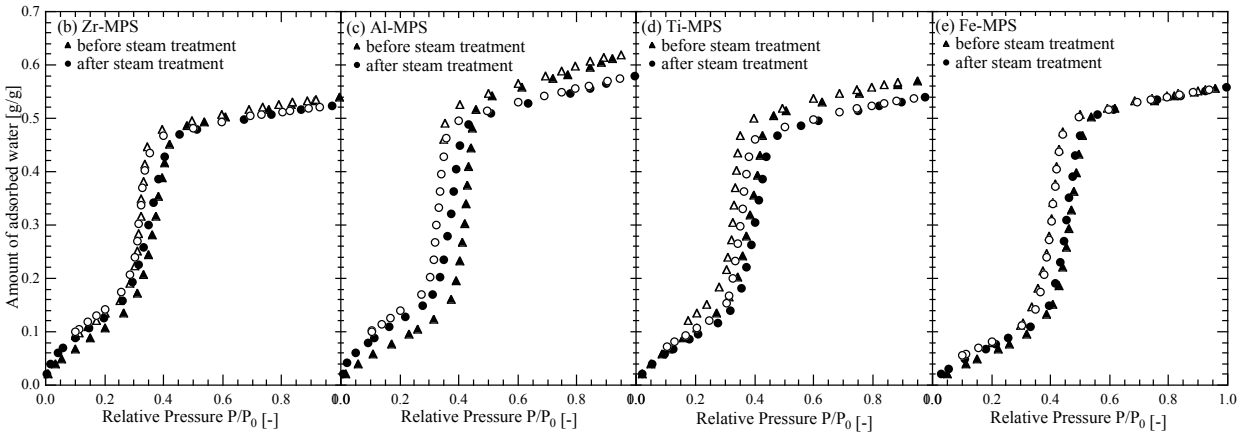

Figure 7: The water adsorption isotherms of the metal-doped mesoporous silicas (b-e) before and after the steam treatment.

before and after the steam treatment. In terms of the practicality of the syntheses of these materials, it took a longer time to synthesize Al-MPS uniformly compared with the synthesis of pure silica, making it unsuitable for large-scale synthesis. This was not the case for Zr-MPS and Fe-MPS, making them more suitable adsorbents for energy-efficent adsorption systems from the vewpoint of practial demands such as stability and mass productivity.

REFERENCES

[1] Kresge C. T, Leonowicz M. E, Roth W. J, Vartuli J. C. and Beck J. S. *Ordered mesoporous molecular sieves synthesized by a liquid-crystal template mechanism.* Nature1992;359:710-712.

[2] Beck J. S, Vartuli J. C, Roth W. J, Leonowicz M. E, Kresge C. T, Schmitt K. D, Chu C. T-W, Sheppard E. W, McCullen S. B, Higgins J. B. and Schlenker J. L. *A new family of mesoporous molecular sieves prepared with liquid crystal templates.* 1992;114:10834-10843.

[3] Yanagisawa T, Shimizu T, Kuroda K. and Kato C. *The preparation of alkyltrimethyl ammonium-kanemite complexes and their conversion to microporous materials.* Bull. Chem. Soc. Jpn., 1990;63(4):988-992.

[4] Ohashi F, Maeda M, Suzuki M, Tomura S, Okazaki M. and Toroyama K. *Water vapor adsorption properties of Ti-containing mesoporous silica.* J. Ceramic. Soc. Jpn., 1999;107(9):844-849.

[5] Ogawa M. *Preparation of inorganic-organic mesostructured materials by using surfactant aggregantes.* Hyomen 1997;35(11):563-588.

[6] Park D. H, Matsuda M, Nishiyama N, Egashira Y. and Ueyama K. *Zirconium-containing mesoporous silica with high alkaline resistance.* J. Chem. Eng. Jpn., 2001;34(10):1321-1324.

[7] Yano K. and Fukushima Y. *Synthesis of super microporous aluminosilicate having excellent water vapor adsorption property as an adsorbent for an adsorption heat-pump.* J. Porous Mater., 2003;10:223-229.

[8] Liu C. Y, Morofuji K, Tamura K. and Aika K. *Water sorption of $CaCl_2$-containing materials as heat storage media.* Chemistry Letters 2004;33(3):292-293.

[9] Endo A, Inagi Y, Fujisaki S, Yamamoto T, Ohmori T. and Nakaiwa M. *A simple and rapid synthesis of ordered mesoporous silicas using vacuum-assisted solvent evaporation.* Submitted to AIChE Journal.

[10] Broekhoff J. C. P. and de Boer J. H. *Studies on pore systems in catalysts : XIII. Pore distributions from the desorption branch of*

a nitrogen sorption isotherm in the case of cylindrical pores B. applications. J. Catal., 1968;10:377.

[11] Mokaya R. *Al content dependent hydrothermal stability of directly synthesized aluminosilicate MCM-41*. J. Phys. Chem. B 2000;104:8279-8286.

[12] Kawi S and Shen S.-C. *Effects of structural and non-structural Al species on the stability of MCM-41 materials in boiling water.* Materials Letters 2000;42:108-112.

[13] Aguado J, Serrano D. P. and Escola J. M. *A sol-gel approach for the room temperature synthesis of Al-containing micelle-templated silica.* Microporous and Mesoporous Materials 2000;34:43-54.

Proceedings of ECOS 2005
Trondheim, Norway
June 20–22, 2005

WATER VAPOR ADSORPTION PROPERTIES OF Zr-DOPED MESOPOROUS SILICA FOR DESICCANT COOLING SYSTEMS

Yuki Inagi, Satoko Fujisaki, Akira Endo*, Takuji Yamamoto, Takao Ohmori, Masaru Nakaiwa
National Institute of Advanced Industrial Science and Technology (AIST),
1-1-1, Higashi, Tsukuba, Ibaraki 305-8565, Japan
Fumio Matsuoka
Mitsubishi Electric Corporation,
5-1-1 Ofuna, Kamakura, Kanagawa 247-8501, Japan

ABSTRACT

Desiccant cooling is one of the most attractive air-conditioning systems, not only owing to their high energy efficiency but also due to environmental acceptance. A typical adsorptive desiccant cooling process is an open heat driven cycle consisting of a rotary dehumidifier and a sensible heat exchanger and the most popular adsorbents are zeolite and silica-gel. A desiccant (adsorbent) removes moisture from the air, and then the adsorbed water removed using thermal energy supplied by electricity, waste heat or solar heat. From the perspective of energy saving, the recovery of adsorbents should be carried out at low temperature, which can utilize the waste heat. Ordered mesoporous silica (MPS) templated by self-assembly of surfactant molecules is one of the most prominent adsorbent because of their characteristic adsorption properties as reported in many literatures. The water adsorption isotherm of MPS shows steep increase at a certain relative humidity region, depending on the pore size thus it is possible to reproduce at low temperature as low as 50-80℃. In particular, metal-doped MPSs have high stability toward water vapor, making it suitable as an adsorbent for desiccant cooling systems.

In this work, we report the water adsorption/desorption properties and stability toward water vapor of Zr-doped MPS. The synthesis of MPS was carried out by a solvent evaporation method. The preparation of honeycomb rotary dehumidifier using Zr-doped MPS and their performance is also discussed.

Keywords: desiccant cooling, mesoporous silica, adsorption, water vapor

INTRODUCTION

Energy efficient adsorption systems such as desiccant cooling systems, heat pumps, humidity control systems, etc. using low temperature exhaust heat have attracted recent attention due to the increasing interest in the global environmental problems. The desiccant cooling process is based on an open heat driven cycle consisting of a combination of a dehumidifier and sensible heat exchanger.

*Corresponding author. Phone: +81-29-861-4653 Fax: +81-29-861-4660 E-mail: endo-akira@aist.go.jp

Desiccants are materials that adsorb moisture and can be dried, and thus regenerated, by adding heat supplied by waste heat. In most systems, a turning rotor that contains a desiccant picks up humidity from incoming air and discharges that humidity outdoors. The most popular adsorbents for these systems are zeolites and silica gels [1, 2]. These materials have been used because of their low cost and ease of acquisition, although their adsorption/desorption properties regarding water vapor are not optimal from the viewpoint of system performance.

Zeolites are microporous materials with pores

smaller than 1.5 nm with a water vapor adsorption isotherm typical of Type I in IUPAC classification. A relatively high temperature (as high as 473 K in most cases) is necessary for their recovery. Silica gels have a disordered pore structure from the microporous to the mesoporous or macroporous region. Their adsorption capacity increases gradually with increasing relative humidity.

In recent years, highly ordered mesoporous silicas templated by surfactant micelles, such as MCM-41, FSM-16, etc. formed by a hydrothermal synthesis or a sol-gel based synthesis has attracted increased attention. These ordered mesoporous materials have potential applications in catalysis, adsorbents, membranes, sensors, etc., based on their orderly and uniform mesopores, large specific surface area and pore volume. Moreover, it is possible to control the pore diameter of these materials by changing the alkyl chain length of the surfactant. In considering the application of highly ordered MPSs as adsorbents of water vapor, control of the pore size is very important for effective adsorption. That is, materials that have a high adsorption capacity at the humidity present during practical operation are preferable as heat storage materials for desiccant cooling that exploit low temperature exhaust heat [3].

Unfortunately, MPS materials tend to dissolve in water and alkaline solutions, which decreases the possibility of their practical use as adsorbents of water vapor. Recently, some researchers have reported a porous glass containing zirconium with a high resistance to water and alkaline solutions [4]. Furthermore, an additional study reported that while the structures of pure silica samples were destroyed in a solution of pH 10, zirconium-doped MCM-41 and MCM-48 had a high structural stability in alkaline solutions ranging from pH 10 to pH 11.5 [5].

In the present study, zirconium-doped MPSs with hexagonal arrays of cylindrical pores were synthesized using a solvent evaporation method, and their water adsorption/desorption properties and stability in the presence of water vapor were investigated. Blocks of zirconium doped MPS were ground up into a fine powder for the preparation of a honeycomb rotary dehumidifier, of which the performance is also reported.

EXPERIMENTAL PROCEDURES

Tetraethoxysilane (TEOS), HCl aqueous solution (10^{-3}M), $ZrO(NO_3)_2$ and C_nTAC (n = 10 - 18) were added into ethanol, where n represents the number of carbon atoms composing the alkyl chain of alkyltrimethylammonium chloride (C_nTAC). The starting solution was stirred at room temperature for 1 hour to hydrolyze the TEOS. The typical molar ratio of the starting solution was 1 - 0.95 TEOS : 0 - 0.05 $ZrO(NO_3)_2$: 0.2 C_nTAC : 10 EtOH : 1.8×10^{-4} HCl : 10 H_2O. The solvent was then transferred to a round-bottom flask and evaporated using a vacuum rotary evaporator at 70 hPa. After the solution reached a paste-like consistency, the pressure was reduced to 20 hPa. After the paste-like liquid changed to a white solid, the temperature was increased to 333 K to evaporate the remaining solvent. The resulting solid, a silica-surfactant composite, was calcined at 873 K for 5 hours to remove the surfactant.

The powder X-ray diffraction measurements for the obtained solids were carried out using a Rigaku MiniFlex (CuK α, 40 kV, 30 mA).

The nitrogen adsorption isotherms were measured to investigate the pore structure of the obtained MPSs using a BELSORP-mini instrument (BEL Japan, Inc.) after outgassing the samples at 573 K for 5 h. The BET surface areas of the MPSs were calculated, and the pore size distributions (PSD) were calculated using the

BdB method with the DH algorithm [6]. The water vapor adsorption isotherms were measured using a BELSORP 18PLUS instrument.

For evaluating the durability of the samples, the synthesized silicas were not exposed to water directly, but rather were exposed to water vapor in an autoclave at 373 K for 24 hours. After this water vapor treatment, the adsorption characteristics of the samples were examined.

The obtained zirconium-doped MPS solid was ground to a fine powder. The honeycomb rotor dehumidifier used in this study was designed to have a thin wall of zirconium-doped MPS-based sheet adsorbent.

RESULTS AND DISCUSSION

Characterization of MPSs

Figure 1 and 2 show XRD patterns of pure silica and zirconium-doped mesoporous silicas. The XRD patterns for the synthesized silicas exhibit a strong (100) reflection peak with two small peaks in the higher 2 θ region. The diffraction peaks indicate that the samples have a periodic mesostructure in a hexagonal array.

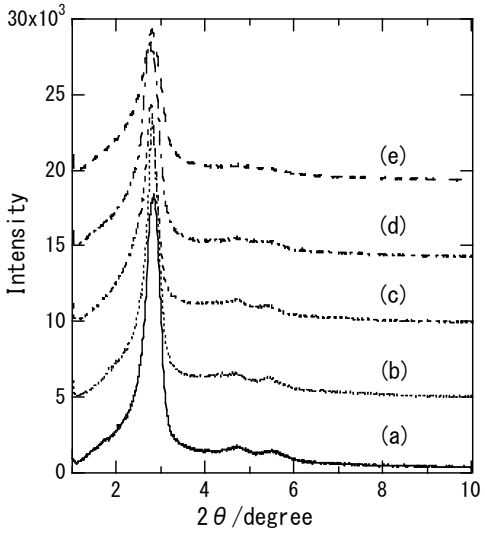

Figure 1: XRD patterns of pure silica and zirconium-doped silica; (a) pure silica, (b) 0.5% Zr-doped silica, (c) 1% Zr-doped silica, (d) 3% Zr-doped silica, (e) 5% Zr-doped silica

The XRD patterns of silicas with varying quantities of zirconium are shown in Figure 1 (b) - (d). The peak intensity of the (100) peak decreased as the zirconium content increased.

Figure 2 shows the XRD pattern of the zirconium-doped C_{10} - C_{18}TAC templated silicas. These MPSs have a different (100) peak. As the alkyl chain length of the template increases, the (100) peak shifts to a lower angle.

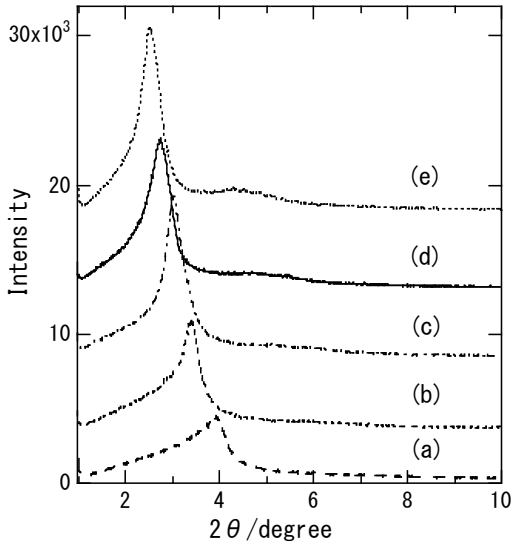

Figure 2: XRD patterns of zirconium-doped silica; (a) C_{10} TAC templated silica, (b) C_{12} TAC templated silica, (c) C_{14} TAC templated silica, (d) C_{16} TAC templ ated silica, (e) C_{18}TAC templated silica

The nitrogen adsorption isotherms measured at 77 K are shown in Figures 3 and 4. In the zirconium-doped samples, the absorption quantity and pore size were generally higher than in the pure silica. However, the pore characteristics of the 5% zirconium-doped MPS were almost equal the same as those of pure silica.

Table 1 lists the structural parameters of the samples. The pore diameters of the 0.5 - 3% zirconium-doped samples were 2.76 - 2.77 nm, whereas the 5% zirconium-doped sample was 2.66 nm, which is the same as that of the pure

silica. A similar result was observed in the pore volume values. The BET surface areas of the zirconium-doped MPSs were all higher than that of the pure silica.

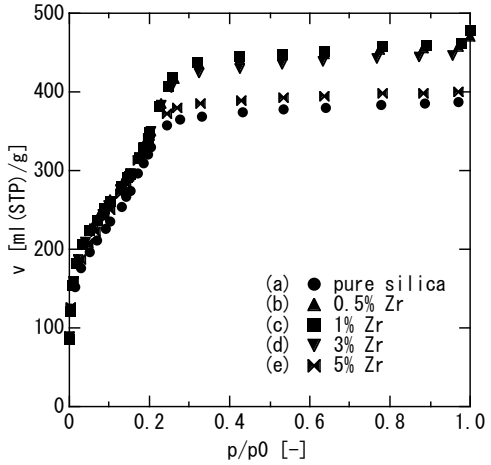

Figure 3: Adsorption isotherm of nitrogen; (a) pure silica, (b) 0.5% Zr-doped silica, (c) 1% Zr-doped silica, (d) 3% Zr-doped silica, (e) 5% Zr-doped silica

Table 1: Pore diameter, pore volume and surface area of pure silica and Zr-doped silicas

Sample	**d_{100} [nm]**	**d_p [nm]**	**d_w [nm]**	**V_p [ml/g]**	**S_{BET} [m^2/g]**
Pure silica	3.12	2.66	0.94	0.60	1155
0.5%Zr	3.18	2.76	0.91	0.71	1201
1%Zr	3.20	2.77	0.92	0.71	1196
3%Zr	3.23	2.77	0.96	0.69	1202
5%Zr	3.19	2.66	1.02	0.61	1220

Figure 4 shows the nitrogen adsorption isotherms of the zirconium-doped C_{10} - C_{18}TAC templated silicas. All of the samples had a small pore size distribution, from 1.6 nm to 3.0 nm, due to the differences in the template surfactant. As the *n* value of the template decreased, the adsorption isotherms changed from Type IV to Type I in the IUPAC classification due to the decrease in the pore size.

Table 2 lists the pore structural parameters of the zirconium-doped C_{10} - C_{18}TAC templated silicas.

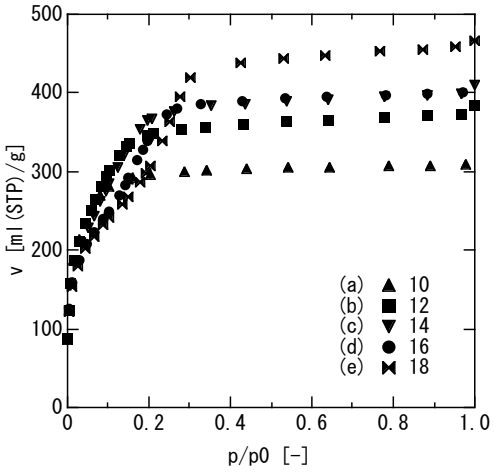

Figure 4: Adsorption isotherm of nitrogen; (a) C_{10} TAC templated silica, (b) C_{12} TAC templated silica, (c) C_{14} TAC templated silica, (d) C_{16} TAC templ ated silica, (e) C_{18}TAC templated silica

Table 2: Pore diameter, pore volume and surface area of Zr-doped silicas with variable *n* values

Sample C_nTAC	**d_{100} [nm]**	**d_p [nm]**	**d_w [nm]**	**V_p [ml/g]**	**S_{BET} [m^2/g]**
n=10	2.24	1.63	0.96	0.48	1103
n=12	2.57	2.06	0.91	0.58	1401
n=14	2.90	2.30	1.05	0.61	1447
n=16	3.19	2.66	1.02	0.61	1220
n=18	3.50	3.00	1.04	0.71	1078

Water vapor adsorption properties of MPSs

Figures 5 and 6 show the second water vapor adsorption/desorption isotherms at 298 K for the zirconium-doped silicas. After the first measurement, the surfaces of the silica walls were rehydrorized, and the isotherms for later measurements were shifted to a lower relative pressure region. The shapes of the isotherms indicated a class of Type V with a hysteresis loop.

Figure 5 shows the water vapor adsorption isotherms of pure silica and the zirconium doped silicas. The zirconium-doped samples adsorbed more water and the relative pressure where the steep increase in the amount of adsorbed water

occurred was shifted to a lower region. This indicates the zirconium doped samples posses a stronger hydrophilic nature than the pure silica.

Figure 6 shows the adsorption isotherms of the zirconium-doped samples with different pore sizes (different *n* values). The relative humidity where the steep increase in the adsorption occurred for all of the samples was shifted to a lower relative humidity with decreasing pore diameter.

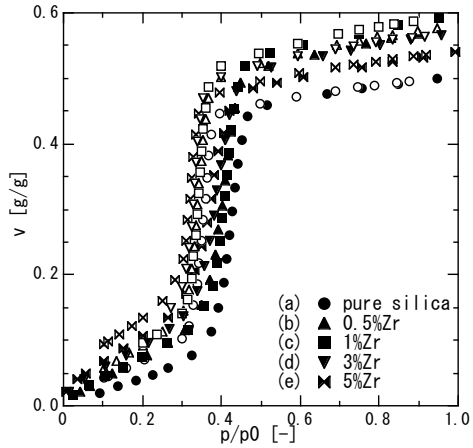

Figure 5: The second adsorption isotherm of water vapor (a) pure silica, (b) 0.5% Zr-doped silica, (c) 1% Zr-doped silica, (d) 3% Zr-doped silica, (e) 5% Zr-doped silica

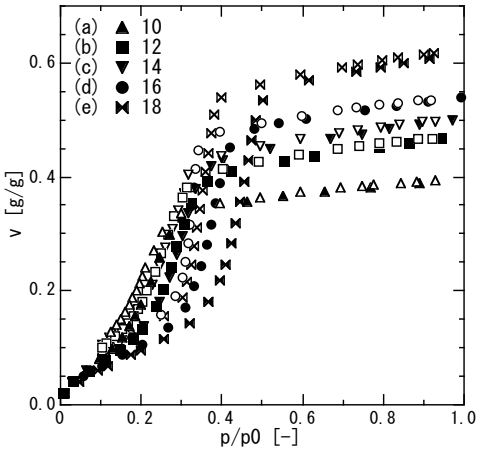

Figure 6: The second adsorption isotherm of water vapor (a) C_{10} TAC templated silica, (b) C_{12} TAC templated silica, (c) C_{14} TAC templated silica, (d) C_{16} TAC templ ated silica, (e) C_{18}TAC templated silica

For ordered mesoporous materials such as MCM-41 and FSM-16, in which the pore size is between about 3 nm and 10 nm, the adsorption of water vapor occurs at a relative humidity of over 40% [7, 8]. These MPSs can be used as adsorbents in humidity control systems in a relatively high humidity region. The adsorption of water vapor on zeolite, however, saturates at a low relative humidity because of its small pore size (less than 1.5 nm) and strong interaction with water molecules. The amount of adsorption and desorption in the operating pressure region is very small, and the recovery temperature for zeolite is higher than 473K [9]. Thus, zeolite can be used for systems that tolerate high temperatures, or for systems that require the humidity to be controlled at a very low level.

As shown in Figure 6, the second adsorption of the variable pore sized MPSs showed a steep increase in adsorption in the relative pressure region of 0.1 - 0.4, which is the intermediate between the zeolites and conventional MPSs (namely, MCM-41 and FSM-16 etc.).

Stability of MPS in the presence of water vapor

Figure 7 shows the water vapor adsorption isotherms.

In the case of the pure silica, the adsorbed amount of water vapor greatly decreased after the steam treatment, indicating the porous structure was considerably collapsed. The results of the isotherms of the zirconium-doped samples, however, showed only a slight decrease, indicating the structure was maintained. This suggests the durability of these samples was increased by the addition of zirconium. From the water vapor isotherms, it is clear that an increase in durability can be achieved from as little as the addition of 0.5% zirconium.

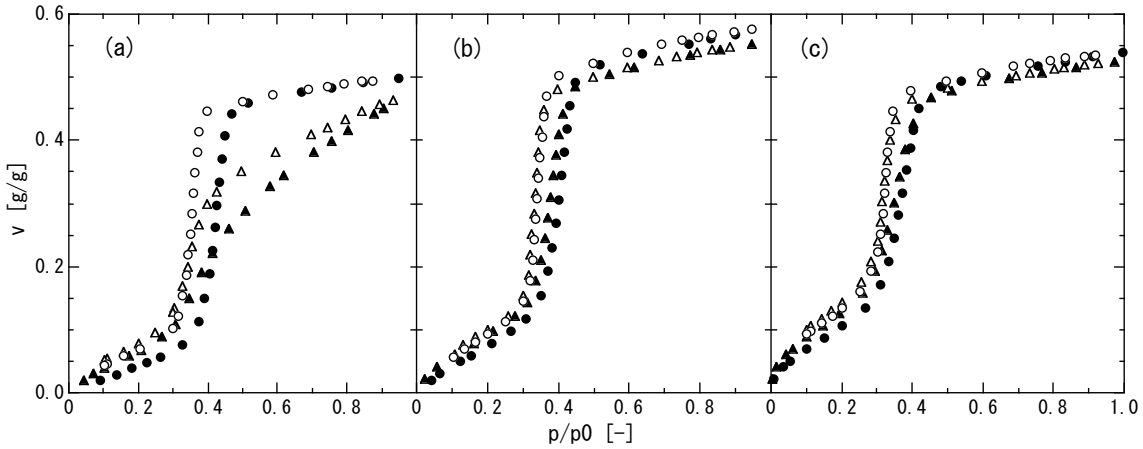

Figure 7: Adsorption isotherm of water vapor (a) pure silica, (b) 0.5% Zr-doped silica, (c) 5% Zr-doped silica; ● original (2nd ads.), ▲ after the water vapor treatment

These results suggest that the introduction of zirconium into the silica structure does not deteriorate the porous properties and maintains the quality of the ordered structure.

As an application, the synthesized zirconium doped MPSs were ground up into a fine powder, and a honeycomb rotary dehumidifier was manufactured with a slurrying sample. The adsorption/desorption capacity of this rotor was investigated, and it was confirmed that the primary properties of the zirconium-doped MPS were maintained after this preparation. This honeycomb rotor adsorber could be used as part of a high-efficiency desiccant cooling process driven by lower temperature (as low as 323 K) waste heat.

CONCLUSION

Ordered, zirconium-doped mesoporous silicas were synthesized through a solvent evaporation method with controllable pore diameters in the region from 1.6 nm to 3.0 nm. This synthetic method can easily introduce metals into silica materials such as these, in comparison with a hydrothermal synthesis, and can be scaled-up as required. These zirconium-doped MPSs have a large adsorption capacity than conventional materials at a relative humidity between 0.2 and 0.4, which is suitable as adsorbents for desiccant cooling systems.

The zirconium-doped samples possess a high structural stability in the presence of water vapor compared with pure silica. The introduction of only a small amount of zirconium into MPSs effectively enhances water vapor resistance, showing the potential possibility for their practical use in energy-efficient adsorption systems.

REFERENCES

[1] Srivastava NC, Eames IW, *A review of adsorbents and adsorbates in solid-vapour adsorption heat pump systems*. Appl. Therm. Eng., 1998;18:707-714.

[2] Moise JC, Bellat JP, Methivier A, *Adsorption of water vapor on X and Y zeolites exchanged with barium*. Microporous and Mesoporous Mater., 2001;43:91-101

[3] Endo A. Design and synthesis of nanoporous materials for energy efficient adsorption systems. In: Thermally Powered

Sorption Technology, Proceedings of the International seminar on thermally powered sorption technology, Fukuoka, 2003

[4] Ohashi F, maeda M, Inukai K, Suzuki M, Tomura S. *Study on intelligent humidity control materials: Water vapor adsorption properties of mesostructured silica derived from amorphous fumed silica.* J. Mater. Sci., 1999;34(6):1341-1346

[5] Park DH, Matsuda M, Nishiyama N, Egashira Y, Ueyama K. *Zirconium- containing mesoporous silica with high alkaline resistance.* J. Chem. Eng. Jpn. 2001;34(10): 1321-1324.

[6] Miyata T, Endo A, Ohmori T, Akiya T, Nakaiwa M. *Evaluation of pore size distribution in boundary region of micropore and mesopore using gas adsorption method.* J. Colloid and Inter. Sci., 2003;262:116-125

[7] Llewellyn PL, Schuth F, Grillet Y, Rouquerol F, Rouquerol J, Unger KK. *Water sorption on mesoporous alminosilicate MCM-41*. Langmuir, 1995;11:574-577

[8] Matsumoto A, Sasaki T, Nishimiya N, Tsutsumi K. *Evaluation of the hydrophobic properties of mesoporous FSM-16 by means of adsorption calorimetry.* Langmuir, 2001; 17: 47-51

[9] Kanamori M, Hiramatsu M, Shibata T, Watanabe F, Matsuda H, Hasatani M. *Experimental study of adsorption equilibrium of water on zeolite and adsorption heat storage under low relative vapor pressure*. kagaku kougaku ronbunshu, 1998; 24: 243-247

Proceedings of ECOS 2005
Trondheim, Norway
June 20–22, 2005

Quantitative evaluations on available models for calculating thermodynamic properties of humid air

H. Li[*, 1], X. Ji[1] and J. Yan[1,2,]
1 Department of Chemical Engineering and Technology /Energy Processes
Royal Institute of Technology
SE-100 44 Stockholm, Sweden

2. Department of Public Technology
Malardalen University
SE-721 23 Vastras, Sweden

ABSTRACT

Engineering calculation of the thermodynamic properties for cycle simulation and design requires simple but reliable models. This has been proved to be of importance for the research and development on humidified gas turbines, such as humid air turbine (HAT) cycles and compressed air energy storage (CAES). This paper has made a comprehensive review and comparison among different models for calculating thermodynamic properties of the humid air mixtures, including ideal gas model (IG), ideal mixing model (IM), and real gas model (RG); and based on temperature and pressure range, gave quantitative evaluations on saturated water vapor composition and enthalpy. Based on performance conditions of an HAT cycle, several suggestions were given for the use of the today's available models for engineering cycle calculations, which can provide accurate results for cycle performance analysis and design while keeping the methods straightforward.

Keyword: thermodynamic properties, EOS, humid air

NOMENCLATURE:

Symbols:	Description:
H	Specific enthalpy,
P	Pressure, bar
R	Gas Constant
S	Specific entropy
T	Temperature
y	Mole fraction in the vapor phase
Subscripts:	
a	Air
w	Water vapor
Superscripts:	
0	Reference status
E	The excess part of a property
S	Saturated
Abbreviations:	
DEV	Deviation
EOS	Equation of state
EvGT	Evaporative gas turbine
HAT	Humid air gas turbine
IG	Ideal gas model
IM	Ideal mixing model
RG	Real gas model
RK	Redlich-Kwong
SA	Saturated Humid Air
SH	Superheated Humid Air

INTRODUCTION:

The basic idea of gas turbine humidification is that the injected water or steam increases the mass flow rate through the turbine. This augments the specific power output, since the compressor work remains constant (i.e., if water is injected after the compressor) and much less work is required to increase the pressure of a liquid than a gas. When energy in the gas turbine exhaust is recovered by preheating water or generating steam for injection

* Corresponding author: Email: hailong@ket.kth.se, Phone +46-8-7906527, Fax +46 8 7230858

or preheating the combustion air in a recuperator, the cycle efficiency is raised. An additional advantage of humidifying the gas turbine working fluid is a reduced formation of NO_x in the combustion process [1, 2]. Advanced gas turbines integrated with humidification have been comprehensively reviewed by Jonsson and Yan [3]. The options for water or steam addition to a gas turbine are shown schematically in Figure 1.

The technology of water or steam addition can also be used in the process of compressed air energy storage (CAES) [4], including the recuperated adiabatic process, and the adiabatic process with humidification. Figure 2 illustrates schematically the adiabatic CAES process.

The addition of water or steam to the air changes the thermophysical properties (i.e., thermodynamic properties and transport properties) of the working fluid. So far several models are available to calculate the properties of air-water mixtures. It has been verified in our previous paper [5] that to model the processes for cycle performance estimations and component sizing and design reliably, the impact of the changes of thermodynamic properties on simulation should not be ignored. In this paper, we made further quantitative evaluations on different models for the difference of thermodynamic properties including density and enthalpy. Moreover we discussed the impacts on cycle performance analysis due to the choices of calculation methods; several suggestions were given at the end.

SUMMARY OF DIFFERENT MODELS

In this paper, three types of models, which are used to calculate thermodynamic properties for the air-water mixtures, have been included for the comparison. They are ideal gas model, ideal mixing model and real gas model.

Ideal gas model (IG)

An easy approximation for the air-water mixture is the assumption that it is a mixture of the ideal air and ideal water vapour. The calculation of property m (heat capacity, enthalpy and molar volume) except entropy s is:

$$m = y_a m_a^0 + y_w m_w^0 = (1 - y_w) m_a^0 + y_w m_w^0 \qquad (1)$$

where m^0 is the properties in the ideal-gas state at temperature T and standard pressure P^0.

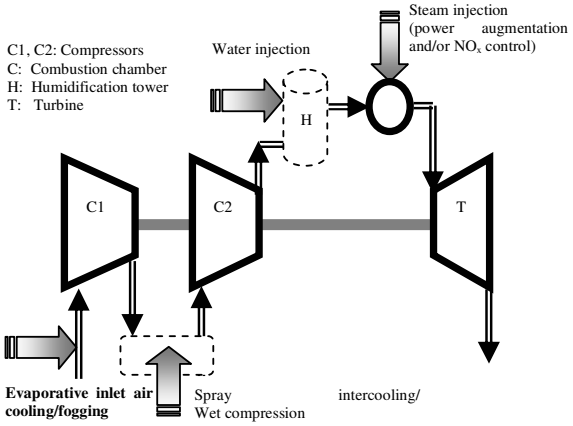

Figure 1. Options for water or steam addition in simple cycle gas turbines

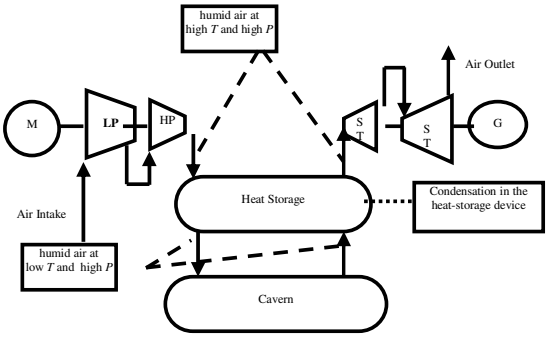

Figure 2. Adiabatic CAES process

The calculation of the property entropy s in the ideal gas model is:

$$s = (1 - y_w) s_a^0(T, P^0) + y_w s_w^0(T, P^0) - R \ln\left(\frac{P}{P^0}\right) - R[(1 - y_w)\ln y_a + y_w \ln y_w] \qquad (2)$$

The saturated composition is related to the temperature in the ideal gas model and is calculated with the following equation.

$$y_{ws} = \frac{P_w^s(T)}{P} \qquad (3)$$

where P_w^s is the saturation pressure of water at the corresponding temperature T, and P is the system pressure.

Ideal mixing model (IM)

The properties of water vapour and the dry air have been studied extensively [6, 7]. In engineering calculations, it is often assumed that each property of the air-water mixture is an ideal mixture of the properties of real gaseous air and water vapour [6]. The calculation of property *m* (heat capacity, enthalpy and molar volume) except entropy *s* is:

$$m = (1 - y_w) m_a(T, P) + y_w m_w(T, P) \quad (4)$$

where *m* is the properties of a real gas at temperature *T* and pressure *P*.

The calculation of the property entropy *s* is:

$$s = (1 - y_w) s_a(T, P) + y_w s_w(T, P) - R[(1 - y_w) \ln y_a + y_w \ln y_w] \quad (5)$$

The calculation of the saturated composition wasn't described in previous studies [8]. In this paper, y_{ws} can be calculated with two methods. In method one y_{ws} is estimated with Equation (3) (noted as IMG model). In method two, y_{ws} is calculated from the real gas model (real gas model 2) (noted as IMR)

.

Real gas model (RG)

Both the ideal gas model and ideal mixing model are suitable at low pressures. The calculation of the properties for the humid air at high pressures is performed with real gas models. The calculation of property *m* (heat capacity, enthalpy, molar volume) except entropy *s* is:

$$m = (1 - y_w) m_a^0(T, P) + y_w m_w^0(T, P) + m^E(T, P) \quad (6)$$

The calculation of the property entropy *s* is:

$$s = (1 - y_w) s_a^0(T, P^0) + y_w s_w^0(T, P^0) - R \ln(P / P^0) + s^E(T, P) \quad (7)$$

The saturated composition is calculated from phase equilibrium.

In this paper, two real gas models were included for comparison, one is the model proposed by Hyland and Wexler [9, 10] (real gas model 1); the other is the model proposed in our previous paper (real gas model 2). Real gas model 1 is based on the virial equation of state (EOS) with the assumption that the dry air is a homogeneous pure component. The reliable application range is stated to be 273.15-372.15 K and up to 50 bar. Their calculated results have been collected in the handbook as standard data [11]. Recently, the commercial software, MOISTAIR TAB [12], was developed based on this model, and the calculation was extended to 473.15 K and 50 bar. Real gas model 2 proposed in our previous papers [13-15] is based on the modified Redlich-Kwong (RK) EOS. The dissolved gas in the liquid phase follows Henry's law in order to calculate the saturated composition. The dry air was assumed to be the mixture of nitrogen and oxygen with a fixed mole ratio. It is stated that the application range can be up to 573 K and 200 bar for the humid nitrogen, oxygen, air and the nitrogen-oxygen mixture. This model is mainly used to calculate the saturated vapour composition in our previous work.

COMPARISON OF MODELS

The comparison of different models with experimental data

Experimental data for the air-water mixture in the vapor phase have been determined [16-20] and all of them are related to enhancement factors, from which saturated vapor composition in humid air can be derived. The PvT experimental data and excess enthalpy are not available in the literature. Therefore, the comparison of the calculated results of different models with the available experimental data can only be performed in composition under saturated conditions.

Among the available experimental data, several groups were determined at the pressure higher than 1atm [16, 18-20]. However, Hyland and Wexler [18] stated that the experimental data of Pollitzer and Strebel [16] were not accurately enough. In our previous work [15], it is found that the experimental data of Hyland [19] were not consistent with others. It is likely that best available experimental data are those of Hyland and Wexler [18] and Wylie and Fisher [20], which have been used for comparing with the calculated results of each model. Part of comparison is shown in Figure 3.

It is clear that the calculated results of these two real gas models are accurate, and the average deviation from the experimental data is less than 0.4% in the whole experimental temperature and pressure ranges. While for the ideal gas model and IMG model, the calculations of the saturated vapor composition are the same; and the deviations are

much larger than those of two real gas models. The highest deviation is up to 34%; and the lower the temperature and the higher the pressure, the lager the deviation. We may conclude that real gas models are more suitable for calculating saturated vapor composition than ideal gas model and IMG model in the experiment range.

Moreover Figure 3 also indicates real gas model 2 can be used in much wider pressure range (up to 140 bar) than real gas model 1 (up to 50 bar).

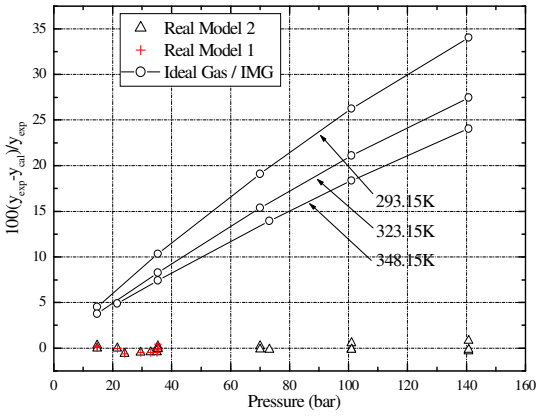

Figure 3 Comparison on saturated vapor composition of different models with experimental data

Comparison among different models

In this section, calculated results of real gas model 2 were used as reference; and deviation was defined as:

$$Deviation = \frac{Calculation_{RG2} - Calculation}{Calculation_{RG2}} \times 100\% \qquad (8)$$

Saturated properties

Water vapor composition, enthalpy and entropy of saturated humid air were calculated with different models from 273.15 to 623.15 K and 5 to 200 bar for comparison.

To calculate saturated vapor composition, three models, i.e. ideal gas model, real gas model 1, and real gas model 2, are available. The comparison between ideal gas model and real gas model 2 was shown in Figure 4. The largest deviation is up to 48.6% at 273.15 K and 200 bar; and the average deviation is 16.32%. It is clear that at the same temperature, deviations increase with pressure; and at the same pressure, deviations decrease with temperature. It can be concluded that the lower the temperature and the higher the pressure, the larger the deviation. Figure 5 shows the distribution of deviations of the saturated water vapor composition calculated by the ideal gas model. It indicates that ideal gas model is not suitable for calculating saturated water vapor composition in those cases above the line illustrated in Figure 5.

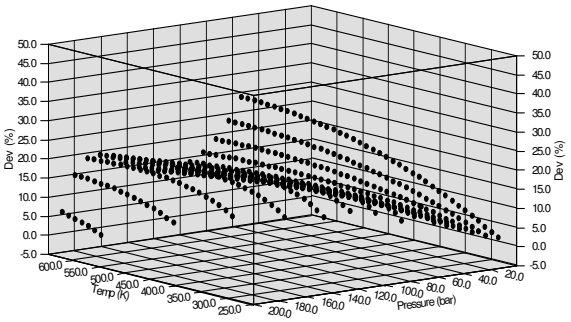

Figure 4 Comparison of the saturated water vapor composition calculated by the ideal gas model, and real gas model 2 from 273.15 to 623.15 K and 5 to 200 bar

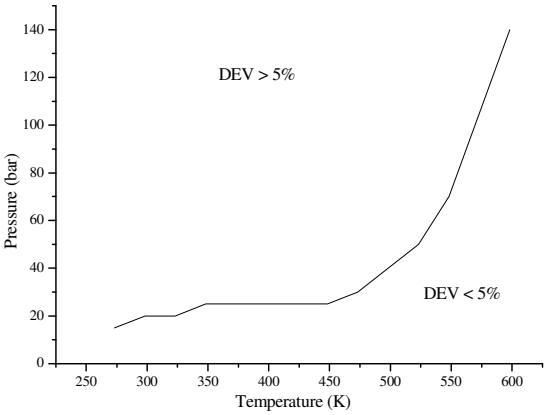

Figure 5 Distribution of deviations of the saturated water vapor composition calculated by the ideal gas model.

In Figure 6, two real gas models were compared. They agree well with each other except in the temperature range close to 473.15 K. The reason might be that the original model of Hyland and Wexler was applied only up to temperature 373.15 K. It may be questionable, when it is extrapolated to 473.15 K. However the calculation range of real gas model 2 is much wider in pressure than that of real gas model 1, so real gas model 2 is better than real gas model 2

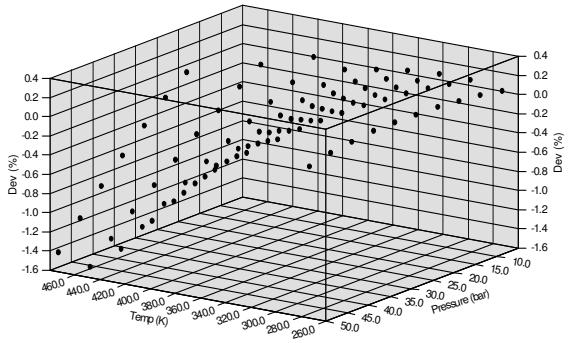

Figure 6. Comparison of the saturated water vapor composition calculated by the real gas model 1 and real gas model 2 from 273.15 to 473.15 K and 5 to 50 bar.

The deviation in the compositions calculated by various models may result in even larger differences in other saturated properties, e.g. enthalpy and entropy. However for enthalpy, the calculated results of ideal mixing model are closed to those of real gas model 2 when the temperature is low (<423.15 K), even though the saturated water vapor composition is far away from those of real gas model 2. This may be explained that in this temperature range, water composition in the vapor phase is so low so that the composition of water vapor has little impacts on enthalpies of moist air. The comparison of entropy is not the same as that of enthalpy. If temperature is lower than 550 K, average deviations among different models are always larger than 5%.

Properties in temperature range 273.15-1773.15 K and pressure range up to 200 bar

Superheated properties and properties at supercritical temperature of water were also calculated and compared among different models. The considered range in this paper is 273.15-1773.15 K and up to 200 bar. Because the only difference between IMG and IMR model is how to calculate y_{water}, if enthalpy and entropy are calculated at given temperature, pressure, and y_{water}; they have the same results. Therefore in the following discussion, only ideal gas model, IM model, real gas model 1 and real gas model 2 are compared. In the area out of the application range of real gas model 1, the comparison was performed between the ideal gas model, ideal mixing model and real gas model 2.

In Figure 7, comparison results of enthalpy between IM and real gas model 2 are comprehensively illustrated with information of deviations under considered pressure and temperature. From Figure 7, it is easy to see that at low temperature, temperature close to water's critical point, and high pressure, deviations are large. The deviations of enthalpy between ideal gas model and real gas model 2 in the temperature range less than 647 K were shown in Figure 8. The maximum deviation is up to 500%, and the average deviation is 73.5%; and the deviations decrease with temperature and increase with pressure. As to the part in the temperature range higher than 647 K, because in this range the deviations between IG and IM are less than 1%, ideal gas model can be regarded having the same accuracy as IM model. Thus the right part of Figure 7 can be used to illustrate IG model as well. Moreover the deviations between real gas model 1 and real gas model 2, in 273.15-473.15 K and 0-50 bar are less than 1%. This figure can be divided into two parts by temperature 647 K which is water's critical temperature.

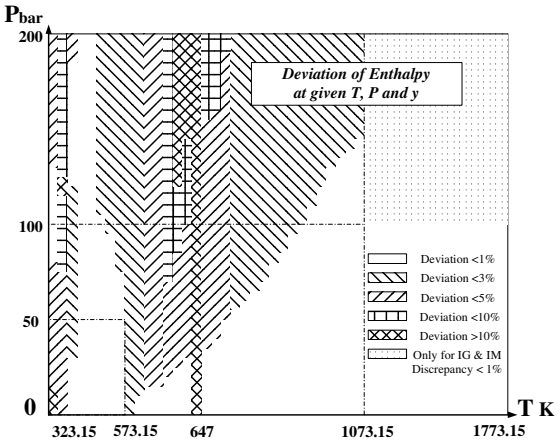

Figure 7 Comparison on enthalpy among ID, IM and real model 2 at given T, P and y_{water}

With Figure 7 and 8, generally we can get such results that when temperature is lower than 623.15 K, if not at very low temperature and high pressure, ideal mixing model is suitable to calculate enthalpy of humid air with an average error less than 3%; while when temperature is higher than 673.15, ideal gas model can be used.

Calculated results of entropy with different models were compared in Figure 9. It shows that deviations of entropy among those models are very

large and much more complicated than deviations of enthalpy. Only when temperature is higher than 1073.15 K they become less than 50%. So it is difficult to evaluate different models. In practical application, choosing a model should depend on other properties.

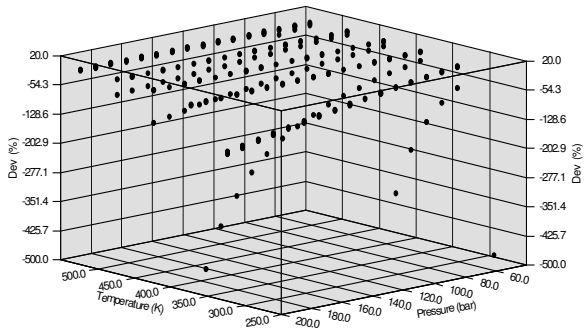

Figure 8 Comparison on enthalpy between ID and real model 2 at given T (T<647 K), P and y_{water}

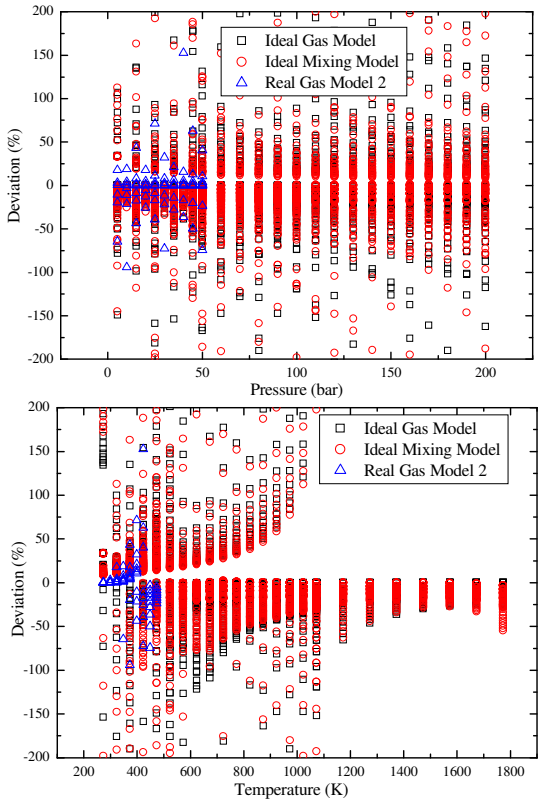

Figure 9 Comparison on entropy among ID, IM and real model 2 at given T, P and y_{water}

IMPACTS ON HAT CYCLE

Component	Saturated humid air		Superheated humid air	
	T (K)	P (bar)	T (K)	P (bar)
Heat exchanger	432.9	35.3	505.1	35.3
Compressor	288.2	1.01	-	-
Humidificati on tower	373.2-393.2	35.3	505.1 -720	35.3

Table 1 Parameters in a HAT cycle [20, 21]

Advanced humidified gas turbines have been studied and developed in the past [3]. For example, Ågren and Westermark [21, 22] simulated an HAT cycle. Some parameters of several main components in their simulation, such as heat exchanger, compressor, and humidification tower, were summarized in Table 1. Based on these parameters, we can analyze the impacts of different models on every component.

Referring to Figure 5 and 7, it is clear that to these components, different models have large discrepancies on calculated results of saturated water vapor composition, especially in humidification tower, up to 7% (both IG and IMG model). Moreover, discrepancies of different models on enthalpy are comparatively small, usually less than 3%. Therefore we have such suggestions that real gas models are preferred to calculate saturated water vapor composition; after getting $y_{s,w}$, ideal gas model might be applied to calculate enthalpy at given temperature, pressure in this HAT cycle.

CONCLUSIONS

In this paper different models were used to calculate thermodynamic properties of humid air to investigate their impacts on the simulation results of wet cycles. The comparison results of the saturated water vapor composition of different models with the reliable experimental data show that the deviations of the ideal model and ideal mixing model are larger, especially at low temperature and high pressure; and the highest deviation is up to 34 % at 293.15 K and 140 bar.

The comparison of other properties (enthalpy and entropy) up to 1773.15 K and 200 bar of different models reveals that at given temperature, pressure and y_{water}, discrepancies of enthalpy may be large at low temperature, while small at high temperature; and discrepancies of entropy always exist among different models. Finally we have such a conclusion that to calculate saturated water vapor composition, real gas model should be chosen except at low pressure or high temperature; to calculate enthalpy from given temperature, pressure and y_{water}, if T<623.15 K, except very low temperature and high pressure, ideal mixing model can be used with an average discrepancy less than 3% compared with real gas model, if T>673.15 K, ideal gas model is available and its average discrepancy with other model is less than 3%; to calculate entropy from given temperature, pressure and y_{water}, real gas models may be preferred according to their accuracy on other properties.

Moreover based on running conditions of an HAT cycle, today's available models for engineering cycle calculations were analyzed. We recommend using real models to calculate saturated water vapor composition, then using ideal gas model to calculate enthalpy.

ACKNOLEGEMENT

Financial supports from Swedish Energy Agency (STEM) and EU are gratefully acknowledged.

REFERENCES

[1] Mori, Y., Nakamura, H., Takahashi, T., and Yamamoto, K., *A Highly Efficient Regenerative Gas Turbine System by New Method of Heat Recovery with Water Injection*, In: Tokyo International Gas Turbine Congress, Tokyo, 1983

[2] Tuzson, J., *Status of Steam-Injected Gas Turbines*, Journal of Engineering for Gas Turbines and Power, 1992;114: 682-686.

[3] Jonsson M., Yan J., *Humidified Gas Turbine – A Review of Proposed and Implemented Cycles*, Energy, 2005;30: 1013–1078.

[4] Walk, K. Jr., *Advanced thermodynamics for engineers*, New York, McGraw-Hill, 1995.

[5] Yan J. Ji X. Jonsson M., *Thermodynamic property models for the simulation of advanced wet cycles,* In Proceeding of ASME Turbo Expo, Georgia, 2003

[6] Wagner, W. and Kruse, A., *Properties of water and steam*, Berlin, Springer, 1998.

[7] Lemmon, E. W., Jacobsen R. T., Penoncello S. G. and Friend, D. G., *Thermodynamic properties of air and mixture of nitrogen, argon and oxygen from 60 to 2000 K at pressures to 2000 Mpa*, J. Phys. Chem. Ref. Data, 2000;29(3): 331-385

[8] Perry, R. H., and Green, D. W., *Perry's chemical engineering handbook*, 7th edition, McGraw-Hill, 1997.

[9] Hyland, R. W. and Wexler, A., *Formulations for the thermodynamic properties of the saturated phases of H_2O from 173.15 K to 473.15 K*, ASHRAE Transactions, 1983;89(2A): 500-519.

[10] Hyland, R. W. and Wexler, A., *Formulations for the thermodynamic properties of dry air from 173.15 K to 473.15 K, and of saturated moist air from 173.15K to 372.15K, at pressures to 5Mpa,* ASHRAE Transactions, 1983;89(2A): 520-535.

[11] ASHRAE, *Fundamentals Handbook*; Atlanta, GA, ASHRAE, 1993.

[12] See also: http://www.chemicalogic.com/moistairtab/default.htm

[13] Ji, X., Lu, X. and Yan. J. *Saturated humidity, entropy and enthalpy for the nitrogen-water system at elevated temperature and pressure*, Int. J. Thermophysics, 2003;24(6): 1681-1698

[14] Ji, X., Lu, X. and Yan. J. *Phase equilibria for the oxygen-water system at elevated temperatures and pressures*, Fluid Phase Equilibria, 2004: 39-47.

[15] Ji, X and Yan, J., *Saturated thermodynamic properties for the air-water system at elevated temperature and pressure*, Chemical Engineering Science, 2003;58(22): 5069-5077

[16] Pollitzer, F., and Strebel, E., *Über der Einfluss indifferenter Gas auf die Sättigungsdampfkonzen-tration von Flussigkeiten, Zeit*. Fur Phys. Chemie, 1924;110: 768-785.

[17] Goff, J. A., and Bates, A. C., *ASHVE Research Report No. 1186 — The interaction constant for moist Air*, ASHVE Transactions, 1941;47: 373-390.

[18] Hyland, R. W. and Wexler, A. *The enhancement of water vapor in carbon dioxide – free air at 30, 40 and 50 °C*, J. Res. NBS., 1973;77A: 115-131.

[19] Hyland, R. W., *Correlation for the second interaction virial coefficients and enhancement factors for moist air*, J. Res. NBS., 1975; 79A: 551-560.

[20] Wylie, R. G. and Fisher, R. S., *Molecular Interaction of water vapor and air*, J. Chem. Eng. Data. 1996;41: 133-142.

[21] Ågren, N. D., and Westermark, M. O., *Design Study of Part Flow Evaporative Gas Turbine Cycle: Performance and Equipment Sizing, Part 1*, In: ASME International Gas Turbine and Aeroengine Congress and Exhibition, New Orleans, Louisiana, USA, 2001.

[22] Ågren, N. D., and Westermark, M. O., *Design Study of Part Flow Evaporative Gas Turbine Cycle: Performance and Equipment Sizing, Part 2*, In: Industrial Core, Proc., International Gas Turbine and Aeroengine Congress and Exhibition, New Orleans, Louisiana, USA, 2001.

Proceedings of ECOS 2005
Trondheim, Norway
June 20–22, 2005

EXPERIMENTAL STUDY OF FORCED CONVECTIVE BOILING HEAT TRANSFER FOR REFRIGERANTS IN A HORIZONTAL, SPIRALLY GROOVED STEEL TUBE

Satoru Momoki* and Shinya Higashiiue
Nagasaki University
Department of Materials Science
1-14 Bunkyo-machi Nagasaki 852-8521
Japan

Toru Shigechi and Tomohiko Yamaguchi
Nagasaki University
Department of Mechanical Systems Engineering
Japan

Hideo Mori
Kyushu University
Department of Mechanical Engineering Science
Japan

ABSTRACT

The experiments on the flow boiling heat transfer of HCFC22 and HCFC123 were performed using a horizontal spirally grooved STB-340-S-C steel tube with 12mm in average inner diameter. The test tube was developed as a evaporator tube of an air-conditioner using an ammonia refrigerant. The circumferentially averaged heat transfer coefficients and wall temperature distributions were presented and discussed by comparison with the predicted values by available correlations for ordinary grooved copper tubes. The empirical correlation was proposed for the heat transfer coefficients in the region where the wall surface is completely covered by liquid.
Keywords: Spirally Grooved Steel Tube, Flow Boiling, Heat Transfer Coefficient, Refrigerant

NOMENCLATURE

Cp	isobaric specific heat [J/(kg·K)]
d_i	mean inner diameter [m]
G	mass velocity [kg/(m^2·s)]
P	Pressure [MPa]
Pr	Prandtl number [-]
q	heat flux [W/m^2]
T	temperature [K]
T_{wo}	average temperature at outer surface [K]
T_{sat}	saturated temperature [K]
x	vapor quality [-]
α	heat transfer coefficient [W/(m^2·K)]
λ	thermal conductivity [W/(m·K)]
μ	viscosity [Pa·s]
ρ	density [kg/m^3]
σ	surface tension [N/m]

Subscript

b	lower half of tube
t	upper half of tube
l	liquid
v	vapor

*Corresponding author: Phone +81-95-819-2528 Fax: +81 95-819-2534 E-mail: momoki@net.nagasaki-u.ac.jp

INTRODUCTION

Internally spirally grooved tubes have been widely used as heat transfer enhancement tubes for evaporator/condenser of heat pumps, refrigerators and air-conditioners. Many researches have been performed on the forced convective boiling heat transfer inside these grooved tubes, and so far some correlation equations have been proposed[e.g. 1-5]. Most of these tubes are made of copper which may be the best material for fluorocarbon refrigerants, and

can not be applied to an ammonia refrigerant due to its corrosion behavior against copper. Ammonia has attracted the attention again as a working fluid of refrigerators owing to its extremely small GWP(Global Warming Potential). The internally spirally grooved tube used in the present study was made of STB-340-S-C steel and originally developed as a heat transfer enhancement tube for air conditioning applications using an ammonia refrigerant. Most of above mentioned correlations for the flow boiling heat transfer have been obtained with the experimental results for ordinary grooved copper tubes. The present STB-340-S-C steel tube has much different surface roughness and groove configuration from those of ordinary copper tubes, mainly due to the difference of hardness. These parameters are expected to affect on the flow boiling heat transfer. In order to investigate the difference of heat transfer characteristics between the present steel tube and ordinary copper tubes the experimental investigation were carried out on the flow boiling heat transfer inside this steel tube using two fluorocarbon refrigerants HCFC22 and HCFC123, which makes experiments easier than ammonia.

EXPERIMENTAL APPARATUS AND PROCEDURE

The experimental apparatus is made up of a closed refrigerant loop and a brine loop to supply cooling fluid to condensers. The refrigerant loop mainly consists of a magnet drive gear pump, three preheaters, a test evaporator and two condensers. The pump was used for the circulation of refrigerant in order to exclude an effect of compressor lubricating oil, which is required in practical vapor compression refrigeration systems.

Figure 1 indicates the scheme of the test evaporator and the arrangements of the sensors. The refrigerant flowing inside the tube is heated directly by alternative current and the supplied heat rate was obtained by measuring the electric power input. The wall temperatures of the tube were measured at three locations of 1350, 2150 and 2950mm apart from the inlet with six T-type thermocouples, which were soldered on the outer surface at every 60° point in circumferential direction from the top of the tube. The pressure at the outlet of the test section and the pressure drop for the whole of the test tube were measured with an absolute pressure transducer and differential pressure transducer, respectively.

The internally grooved tube used in the present study is made of STB-340-S-C steel and configured by 3.5m in length, 15mm in outside diameter, 12mm in average inside diameter, 32 in number of fins, 0.4mm in fin height, 15 degree in helix angle, and 1.34 in area expansion ratio. The expanded cross sectional drawings are shown in the Figure 2 for the test tube and internal fins.

The average heat flux, the wall temperature and the refrigerant temperature required to calculate the axially local heat transfer coefficient(circumferentially averaged), α, are defined as follows, respectively. (1)The heat flux, q, is defined based on the average inner diameter, (2)the circumferentially averaged inner surface temperature, T_{wi}, is computed by using the one dimensional heat conduction equation in radial direction with internal heat source and the circumferentially averaged value of the measured outer surface temperatures, and (3)the saturation temperature corresponding to the measured pressure is used as the refrigerant temperature, T_{b}. The uncertainity in heat flux due to errors in power meter is estimated at most 4%. The error in wall temperature measurement is 0.1 K judged from the calibration of thermocouples. The uncertainity in the saturation temperature depends on the accuracy of the absolute pressure measurement, the pressure drop estimation and the thermophysical tables, and those are estimated to be 0.2 to 0.3 K. From these uncertainities the accuracies of the heat transfer coefficients are determined to be 10 to 24%.

A series of experiments listed in the table 1 were carried out with HCFC22 and HCFC123. All data were

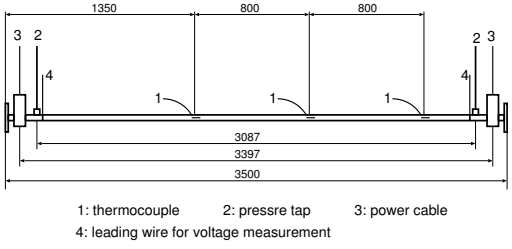

Figure 1: Scheme of test section

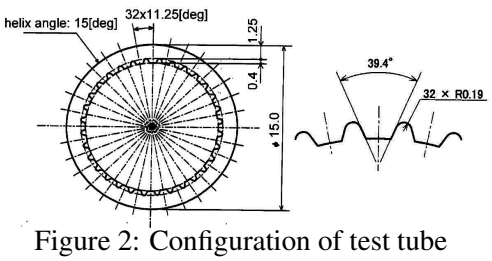

Figure 2: Configuration of test tube

Table 1: Experimental range

Fluid	HCFC123	HCFC22
Pressure, P [MPa]	0.2, 0.3	1.1
Mass velocity, G [kg/(m^{2}s)]	100 ~ 300	
Heat flux, q [kW/(m^2)]	5 ~ 25	
Vapor quality, x [-]	0.2 ~ 0.8	

taken under steady state conditions. The present experimental conditions are different from those of ordinary ammonia refrigerator and similar to those of the dataset which were used in the developing process of some available correlations for ordinary grooved copper tubes, in order to investigate the effect of larger inner grooves and surface roughness by comparing with these correlations.

EXPERIMENTAL RESULTS

The heat transfer characteristics of the evaporating refrigerant inside the present steel tube would be discussed here using the Figures 3 and 4, which indicates the measured heat transfer coefficients and the temperature differences, ΔT, between the saturated refrigerant and the arithmetic mean of the measured values at the outer surface for the upper and lower halves of the tube, against the vapor qualities. These two temperature differences are plotted in order to estimate the condition of the liquid film on the inner surface of the tube, which affects strongly on the flow boiling heat transfer.

The present steel tube has much larger surface roughness and groove depth and pitch than those of ordinary spirally grooved copper tubes widely used for fluorocarbon refrigerants, and somewhat different flow regimes are supposed to be appeared. Thus, in order to investigate the peculiarity of the present steel tube about the flow boiling heat transfer against ordinary grooved copper tubes, the predicted values by the two available correlations, Mori *et al.*[5] and Murata[1] equations, are plotted in the figures as the estimated values for an ordinary grooved copper tube under the same experimental conditions. The Mori *et al.* correlation is one of the most recommendable equation in Japan for ordinary grooved copper tubes, which was developed using a large dataset of experimental results. Mori *et al.* also showed that all of Murata, Kandlikar-Raykoff[2], Thome *et al.*[3], Cavallini *et al.*[4] correlations gave nearly same accuracies in about 30 to 35% mean deviation against their dataset. The Murata correlation was chosen because this equation showed better agreement with the present result than other correlations assessed in our research so far. It should be noted that the inner diameter of the tube used in developing the Murata correlation is 10.7mm and nearly equal to 12.5mm of the present tube, and also that its experimental conditions are similar to those for HCFC123 in the present study.

Heat transfer at low heat flux condition

Figure 3 shows the heat transfer coefficients and wall temperatures at the upper and lower part of the tube against vapor qualities at the low heat flux condition, q=5kW/m^2, where the contribution of nucleate boiling is supposed to be relatively small.

Figures 3(a)-1 to (a)-3 present the results for the refrigerant HCFC123 in the condition of mass velocity, G= 100, 200 and 250 kg/(m^{2}s), respectively. The pressure range of the data shown in these figures is 0.2 to 0.3MPa. Except for the high quality region with G=100kg/(m^{2}s) the measured heat transfer coefficients of HCFC123 agree well in the low heat flux condition with the estimated values by the Murata[1] correlation.

In the case of low mass velocity, G=100kg/(m^{2}s), the heat transfer coefficient is nearly constant when the vapor quality is less than about 0.6 as shown in the Figure 3(a)-1. In this region of $x < 0.6$ the wall temperatures at the upper half are about 1 to 1.5K lower than those at the lower half. The difference in wall temperatures and the constant heat transfer coefficient suggest the separated flow regime where the most of liquid flows in the lower part of the tube. Also, from the lower wall temperatures at the upper half the wall surface of the upper part is considered to be covered by the thin liquid meniscus which has fine heat transfer characters. On the other hand, the typical trends of the annular flow on the flow boiling heat transfer inside a tube, increasing heat transfer coefficients with larger vapor quality and circumferentially constant wall temperatures, are observed in the region where the vapor quality is larger than about 0.6. Nevertheless the both Mori *et al.*[5] and Murata[1] correlations estimate the flow pattern to be a separated flow in this region of $x > 0.6$ and underpredict the heat transfer coefficient for the present steel tube. It is to be noted that the equations for the angle of the wetted perimeter used in these two correlations were developed based on the same equation, the Yoshida *et al.*[6] correlation.

Similar trends to the case of G=100kg/(m^{2}s) were

obtained for the case of 200 and 250 kg/(m^{2}s), except for the vapor quality at the transition point between the separated and annular flow regimes, as shown in the Figures 3(a)-2 and (a)-3. The qualities at the transition point are about 0.3 and 0.15 for the case of G=200 and 250kg/(m^{2}s), respectively, and much smaller than that of 100kg/(m^{2}s), 0.6. While this transition point is not correlated by the either Mori *et al.*[5] or Murata[1] equation in the low mass velocity condition, G=100kg/(m^{2}s), the both equations predict well in the higher mass velocity conditions, G=200 and 250kg/(m^{2}s).

Figures 3(b)-1 to (b)-3 indicate the results for the refrigerant HCFC22. The pressure of these data is 1.1MPa that is more than five times higher than 0.2MPa of the results for HCFC123 shown in the Figures 3(a). Therefore the velocity of HCFC22 is much slower than that of HCFC123, and the contribution of nucleate boiling on flow boiling heat transfer is supposed to be much larger as a result of this higher pressure.

The heat transfer coefficient of HCFC22 with mass velocity, G=100kg/(m^{2}s), shown in the Figure 3(b)-1 increases moderately with larger vapor quality in the region of $x < 0.4$, rises abruptly near the point with the vapor quality, x=0.5, and keeps a quite high value at $0.6 < x < 0.8$. The degrees of the wall superheat at the upper half of the tube are rather smaller than those at the lower half in the region of $x < 0.4$. This trend of wall temperatures and the nearly constant heat transfer coefficient against vapor quality suggest that the flow pattern is a sep-

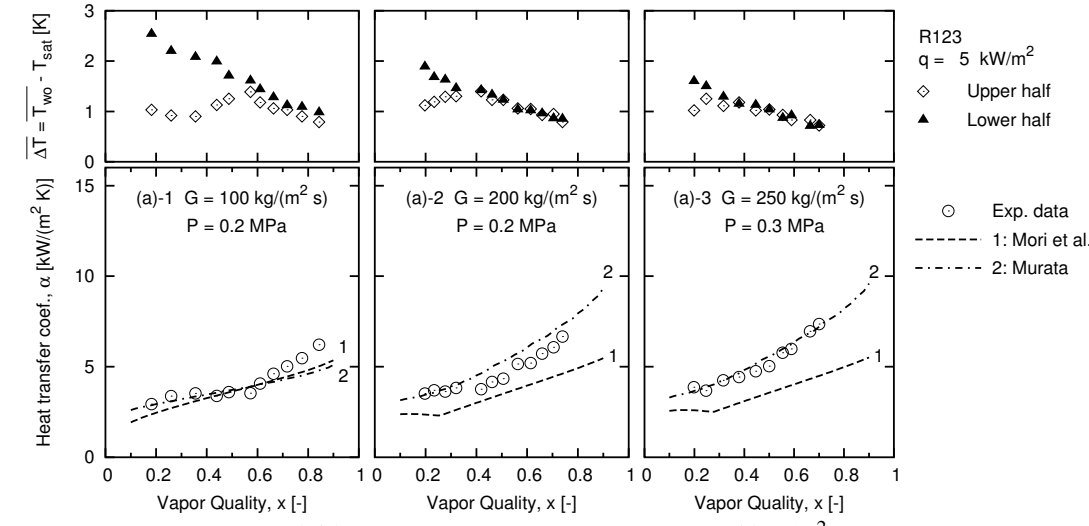

(a) Fluid: HCFC123, P = 0.2 – 0.3 MPa, q = 5 kW/m^2

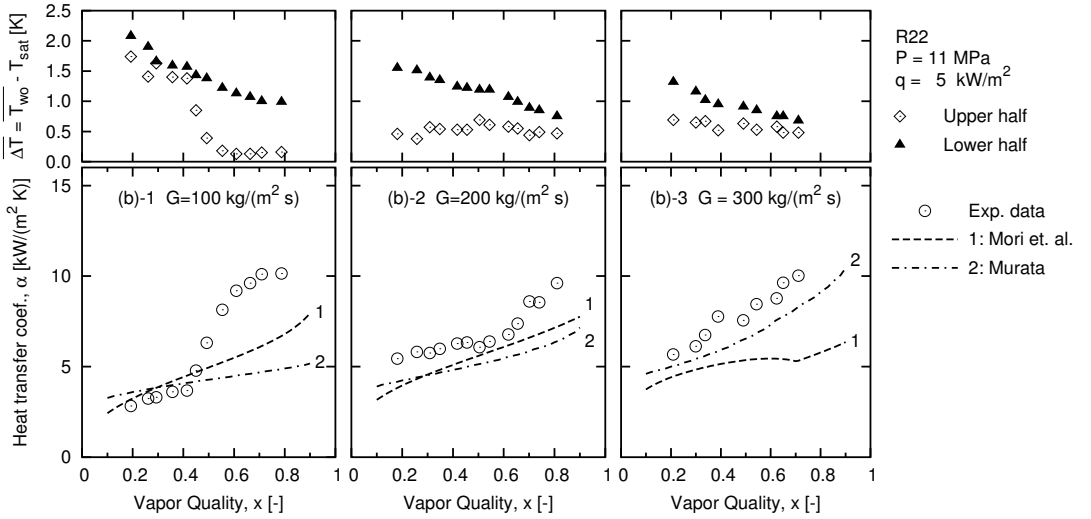

(b) Fluid: HCFC22, P = 1.1 MPa, q = 5 kW/m^2

Figure 3: Heat transfer coefficient vs. vapor quality at low heat flux condition, q = 5 kW/m^2

arated flow at $x < 0.4$. Compared with the result of HCFC123 in the low quality region plotted in the Figure 3(a)-1, the wall temperatures at the lower half are almost same, and those at the upper half are about two times higher. From this higher wall temperature at the upper half, small area near the top of the tube are supposed to be dried, where the heat transfer coefficient is extremely smaller. The liquid film on the tube surface usually rises toward the top with increasing the vapor quality, and the dried area around the top may become covered by the liquid meniscus at $x \approx 0.5$. Therefore the cause of the rapid increasing of heat transfer coefficients and decreasing of wall temperatures at the upper half at $x \approx 0.5$ is considered to be this covering of the extremely thin liquid meniscus, which has excellent heat transfer characters.

In the Figures3(b)-2 and (b)-3, which presents the experimental results for HCFC22 with the mass velocity, G=200 and 300kg/(m^{2}s), respectively, the lower temperatures at the upper half and the gradually increasing of the heat transfer coefficient are observed in the whole region of the vapor quality. These trends agree with the typical characteristics of the separated flow expect for the rather steep gradient of heat transfer coefficients in the high quality region, which might be caused by the relatively high vapor velocity. The measured heat transfer coefficients of HCFC22 are about 20% higher than the predicted values by the Murata[1] correlation that predicts those of HCFC123 in the low heat flux condition with enough accuracy. The heat transfer coefficients at the lower half, $q/\overline{\Delta T}$, agree well to the predicted value by the relevant term in the Murata correlation(not shown). So the discrepancy of the circumferentially average heat transfer coefficient may be caused by the thinner liquid meniscus around the top of the tube generated by the relatively large inner diameter and groove width of the present tube.

Heat transfer at high heat flux condition

Figure 4 indicates the heat transfer coefficients and wall temperatures at the upper and lower halves of the tube at the high heat flux condition, q=15kW/m^2, in the same manner with the Figure 3. The combination of the higher heat flux and large surface roughness of the present tube usually produce the much larger ratio of the nucleate boiling contribution against the whole heat transfer than that in the low heat flux condition.

Figures 4(a)-1 to (a)-3 present the experimental results for HCFC123. The measured heat transfer coefficients are higher than predicted values by the Murata[1] correlation in the high vapor quality region with G=100kg/(m^{2}s) and the low vapor quality region with G=200 or 250kg/(m^{2}s), where the contribution of nucleate boiling is supposed to be dominant. The low quality region with G=100kg/(m^{2}s) is the domain where the contribution of the nucleate boiling should be largest. However, in this region the some area around the top of the tube seems to be dried out because of the too high heat flux and heat transfer coefficient against the expected thin liquid film, and this dry area reduces the circumferential average heat transfer coefficient.

The trend of the wall temperature at the lower half in the case of HCFC123 with G=100kg/(m^{2}s), shown in the Figure 4(a)-1, is almost same in the low quality region with that shown in the Figure 3(a)-1 for the low heat flux condition. In the high quality region the wall temperatures at the lower half are nearly constant against the vapor quality and identical to those at the upper half. Thus, the flow condition in the high quality region is considered to be an annular flow with a relatively large contribution of nucleate boiling due to the high heat flux.

For the case of G=200 and 250kg/(m^{2}s), the Figures 4(a)-2 and (a)-3 indicate the similar trends of wall temperatures against the vapor qualities to those in the low heat flux condition plotted in the Figures 3(a)-2 and (a)-3, except for the the wall temperatures at the upper half near x=0.4. In this region the temperatures at the upper half are slightly lower than those at the lower half, and the temperature difference between the upper and lower halves is smaller than those in the low heat flux condition. The small area near the top of the tube may be covered by the very thin liquid meniscus that is thinned by the higher heat flux in this case, and the cause of the lower temperatures at the upper part is considered to be the higher heat transfer coefficient of this thin liquid meniscus.

The Figures 4(b)-1 to (b)-3 show the experimental results for HCFC22 with the pressure, P=1.1MPa. The wall temperatures of the upper and lower halves are different each other in most of the present data for HCFC22. So the flow pattern of these data is considered to be a separated flow. The dominance

of the separated flow is caused by the relatively large inner diameter and the low velocity as a result of the high pressure condition of HCFC22.

The wall surface at the upper part of the tube is completely dry in the most case of HCFC22 with the mass velocity, G=100kg/(m^{2}s), judging from much higher temperatures at upper half than those at lower half, as shown in the Figure 4(b)-1. The heat transfer coefficients of the data with dry surface are extremely low. It should be noted that for ordinary grooved copper tubes the wall surface near the top of the tube is covered by the thin liquid meniscus and that the largest heat transfer enhancement performance by the grooves of the tube is usually obtained in the case of $G \approx$ 100kg/(m^{2}s).

On the other hand, the relatively low wall temperatures at the upper half are indicated in the Figures 4(b)-2 and (b)-3 for the HCFC22 with G=200 and 300kg/(m^{2}s). The low temperatures signify the excellent heat transfer at the upper half and suggest that the heat transfer surface is covered by the very thin liquid meniscus. The average heat transfer coefficients, $q/\overline{\Delta T}$, at the upper half in the high heat flux condition are slightly larger than those in the low heat flux condition, which is shown in the Figures 3(b)-2 and (b)-3. The heat transfer coefficients at the lower half are smaller than those at the upper half, but still fine compared with the results in other experimental conditions in the present work. The present steel tube has much rougher surface than ordinary copper tube as above mentioned. Therefore this fine heat transfer coefficients at the lower

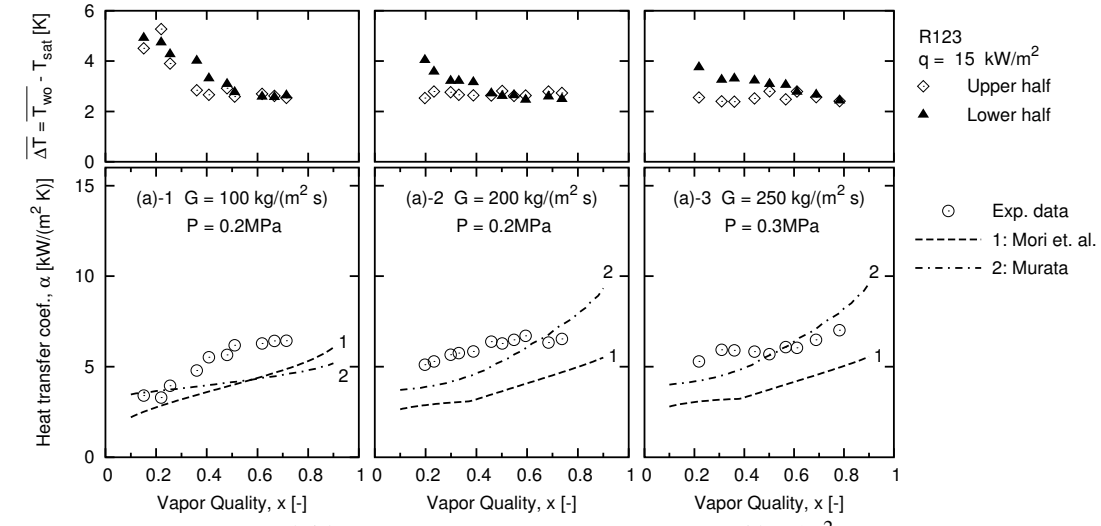

(a) Fluid: HCFC123, P = 0.2 – 0.3 MPa, q = 15 kW/m^2

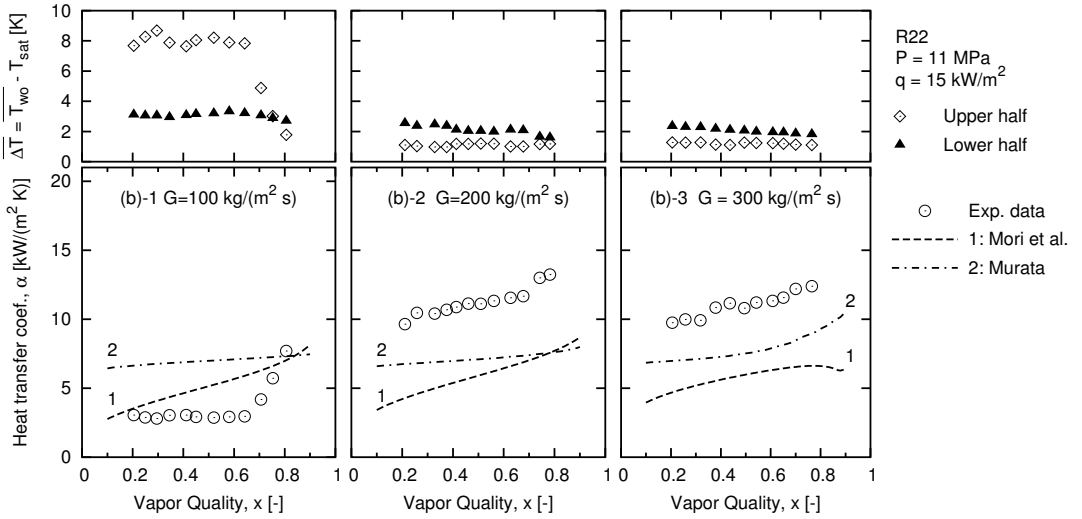

(b) Fluid: HCFC22, P = 1.1 MPa, q = 15 kW/m^2

Figure 4: Heat transfer coefficient vs. vapor quality at high heat flux condition, q = 15 kW/m^2

half are caused by the excellent nucleate boiling heat transfer due to the high heat flux and pressure.

CORRELATION FOR HEAT TRANSFER COEFFICIENT

The correlation for the heat transfer coefficient is obtained for the region where the wall surface is completely covered by liquid (film or thin meniscus) in the present study. Circumferentially averaged heat transfer coefficient is expressed using the three correlation equations for the heat transfer coefficient at the well-wetted wall surface, α_{ww}, and at the surface covered by the thin liquid meniscus, α_{tl}, and the degree of the well-wetted perimeter, ϕ_s.

Heat transfer coefficient at the well-wetted surface, α_{ww}

Based on the Takamatsu *et al.*[7] correlation for the heat transfer coefficient inside a smooth tube in the annular flow regime, the following equations are obtained for the heat transfer coefficient at the well-wetted surface, α_{ww}.

$$\alpha_{ww} = \alpha_{cv} + \alpha_{nb} \tag{1}$$

where

$$\alpha_{cv} = 0.040\,F\cdot Re_{lo}^{0.8}\,Pr_l^{0.4} \tag{2}$$

$$Re_{lo} = G(1-x)d_i/\mu_l \tag{3}$$

$$F = 1+2.0X_{tt}^{-0.8}+0.13X_{tt}^{-1.6} \tag{4}$$

$$X_{tt} = \{(1-x)/x\}^{0.9}(\rho_v/\rho_l)^{0.5}(\mu_l/\mu_v)^{0.1} \tag{5}$$

$$\alpha_{nb} = K^{0.745}\cdot S\cdot\alpha_{pb} \tag{6}$$

$$K = (1+0.768\eta+0.351\eta^2 +0.347\eta^3+0.131\eta^4)^{\frac{-1}{0.745}} \tag{7}$$

$$\eta = \alpha_{cv}/(\alpha_{pb}S) \tag{8}$$

$$\alpha_{pb} = 1.6\,\alpha_{SA} \tag{9}$$

$$\alpha_{SA} = 246(\lambda_l/La)^{0.255}(q/T_{sat})^{0.745} \times(\rho_v/\rho_l)^{0.581}\,Pr_l^{0.533} \tag{10}$$

$$S = (1-e^{-\xi})/\xi \tag{11}$$

$$\xi = 1.2\times10^{-5}\,Ja^{*1.25}\,La\,\alpha_{cv}/\lambda_l \tag{12}$$

$$Ja^* = (\rho_l/\rho_v)(Cp_l T_{sat})/h_{fg} \tag{13}$$

$$La = \sqrt{2\sigma/\{g(\rho_l-\rho_v)\}}. \tag{14}$$

In this correlation the total heat transfer coefficient is expressed as the sum of the forced convective and nucleate boiling heat transfer coefficients, and the nucleate boiling heat transfer coefficient based on the degree of wall superheat is obtained using the total heat flux q and the parameter $K \equiv q_{nb}/q$. The detail of the physical base of this correlation is stated in the reference [7], and therefore omitted here. Empirical constants in the present equations are 0.040 in the equation(2), all constants in the equation(4), 1.6 in the equation(9), and 1.2×10^{-5} in the equation(12). These were determined through the assesment with assumed values, whose parameter ranges had been arbitrary settled refereeing to the Takamatsu *et al.* correlation. It is to be noted that the equation (7) for K was modified to become more suitable to the model used in the developing process of the Takamatsu *et al.* correlation.

Heat transfer coefficient at the surface covered by the thin liquid meniscus, α_{tl}

Using the boiling number, Bo, Froude number, Fr, and the Reynolds number of the vapor, Re_v, The α_{tl} is correlated empirically by the following equation.

$$\alpha_{tl} = 5.62\times10^3\,(Re_{vo}\times10^{-4})^{0.16}(Bo\times10^4)^{0.45} \times Fr^{0.8}\,(\rho_v/\rho_l)^{0.85}\,\lambda_l/d_i\,. \tag{15}$$

The definitions of Re_{vo}, Bo and Fr are $Re_{vo}=G\,x\,d_i/\mu_v$, $Bo = q/(G\,\Delta h_{fg})$ and $Fr = G/\sqrt{g\,d_i\rho_v(\rho_l-\rho_v)}$, respectively.

Degree of well-wetted perimeter, ϕ_s

Assuming that the boundary between the well-wetted surface and the area covered by the thin liquid meniscus is almost equal to the boundary between the wetted and dried surfaces in the flow boiling inside a smooth tube, the following Mori *et al.*[8] correlation for the degree of the wetted perimeter in a smooth tube is applied for the degree of well-wetted perimeter, ϕ_s.

$$\frac{\phi_s}{\phi_0} = 1+0.75\left[\frac{x}{1-x}\left(\frac{\rho_l}{\rho_v}\right)^{0.5}\right]^n e^{1.06-23.8\left(\frac{\rho_l}{\rho_v}\right)}, \tag{16}$$

where

$$n = 0.26\,Fr^{0.84}\,(Bo\times10^4)^{-0.16} \tag{17}$$

$$\frac{1}{1+\{(1-x)/x\}(\rho_v/\rho_l)} = 1-\frac{\phi_0-\sin\phi_0\cos\phi_0}{\pi} \tag{18}$$

Comparison with measured values

The circumferentially averaged heat transfer coefficient is estimated in the present correlation by solving the one dimensional heat conduction problem in circumferential direction assuming that the temperature difference between the outer and inner surfaces of the tube can be neglected. The method to solve this problem is not explained here due to the limited space, and the detail of the procedure may be referred, for example, to the appendix B of the reference [6]. It is noted that the circumferential distribu-

Table 2: Percentage deviations of the present correlation in the region where the wall surface is completely covered by liquid

Heat flux	HCFC22			HCFC123		
[kW/m^2]	N	AD	MD	N	AD	MD
5	49	-11.8	14.2	33	-20.9	21.7
15	39	-8.0	10.6	30	-23.6	24.0
25	24	-8.8	9.6	21	-31.3	31.3

tion of the temperature difference between the inner and outer surfaces can be considered smaller than the circumferential temperature distribution due to the small ratio of thickness and circumference of the tube. Therefore, the circumferencial heat conduction was treated as a dominant factor in this problem even though the temperature difference in the radial direction of the steel tube may not be neglected.

Table 2 lists the comparison result on the measured and predicted circumferentially averaged heat transfer coefficients. The N, AD and MD in the table are the number of the data and the average and mean deviations between the measured and predicted values, respectively, and the definitions of AD and MD are $AD=\sum(\alpha_{\mathrm{cal}}/\alpha_{\mathrm{exp}}-1)/N\times 100[\%]$ and $MD=\sum\left|\alpha_{\mathrm{cal}}/\alpha_{\mathrm{exp}}-1\right|/N\times 100[\%]$. The present correlation predicts the experimental data with good accuracy, about 10 to 15% for HCFC22 and 20 to 30% for HCFC123 in mean deviations. However, the experimental data with the dry surface, such as shown in the Figure 4(b)-1, were eliminated in the comparison because the present correlation is applicable only to the region in which the wall surface is completely covered by liquid. In order to extend the applicable region of the present correlation, the prediction method is to be established for the border of this dry surface.

CONCLUSION

The experiment was carried out on the flow boiling heat transfer of refrigerants HCFC22 and HCFC123 inside a horizontal, spirally grooved steel tube with the 12mm average inner diameter. The conclusions are as follows:

1. In the case of HCFC123 with P=0.2MPa the annular flow seems to be formed even in the low mass velocity, G=100kg/(m^{2}s), condition.
2. In the case of HCFC22 with P=11MPa the wall surface at the upper part of the tube appears to be completely dry in the low mass velocity, G=100kg/(m^{2}s), condition with the high heat flux, 15kW/m^2.
3. The measured heat transfer coefficients at high heat flux condition, q=15kW/m^2, are higher than the predicted values by both Murata and Mori *et al.*[5] correlations except for the case with some dry area around the top of the tube.
4. A set of correlation equations is proposed for circumferentially averaged heat transfer coefficients in the region where the wall surface is completely covered by liquid.

REFERENCES

[1] Murata K. *A Correlation for Forced Convictive Boiling Heat Transfer of Binary Refrigerant Mixture.* Trans. of JSME. 1996;62(599):2723-2728 (in Japanese).

[2] Kandlikar SG, Raykoff T. *Predicting Flow Boiling Heat Transfer of Refrigerants in Microfin Tubes.* Enhanced Heat Transfer. 1997;4:257-268.

[3] Thome JR, Kattan N, Favrat D. *Evaporation in Microfin Tubes: A Generalized Prediction Model.* Proc. Convective Flow and Pool Boiling Conf., Kloster Iress. 1997;VII-4:239-244

[4] Cavallini A, Del Col D, Doretti L, Longo GA, Rossetto L. *Refrigerant Vaporization Inside Enhanced Tubes: A Heat Transfer Model.* Heat Transfer in Condensation and Evaporation:Application to Industrial and Environmental Processes, Proc. of Eurotherm Seminar 62, Grenoble-France. 1998.p.222-231

[5] Mori H, Yoshida S, Koyama S, Miyara A, Momoki S. *Prediction of Heat Transfer Coefficients for Refrigerants Flowing in Horizontal, Spirally Grooved Evaporatior Tubes.* Proc. of 2002 JSRAE Annual Conference, Okayama Japan. 2002.p.547-550 (in Japanesse).

[6] Yoshida S, Mori H, Hong H, Matsunaga T. *Prediction of Heat Transfer Coefficient for Refrigerants Flowing in Horizontal Evaporator.* Trans. of JSRAE 1994;11(1):67-78 (in Japanese).

[7] Takamtsu H, Momok S, Fujii T. *A Correlation for Forced Convective Boiling Heat Transfer of Pure Refrigerants in a Horizontal Smooth Tube.* Int. J. Heat Mass Transfer. 1993;26(14):3351-3360

[8] Mori H. Yoshida S. Kakimoto Y. Ohishi K. *Reform of the Correlation for the Prediction of Heat Transfer Coefficient for Refrigerants Flowing in Horizontal Evaporator.* Trans. of JSRAE 1999:16(2)177-187 (in Japanese).

Proceedings of ECOS 2005
Trondheim, Norway
June 20–22, 2005

Performance analysis of dehumidification utilizing the thermo-sensitive adsorbent in desiccant air conditioning system

Yoshio Nakano
Tokyo Institute of Technology, Japan

Mitsuteru Ogawa, Mutsuhiro Ito, Tatsuya Asano and Hitoshi Higo
Fuji Silysia Chemical Ltd., Japan

ABSTRACT

The desiccant cooling system coupled with low temperature sources less than 323K has been attracted from the view point of effective energy utilization. It has been desired to enhance the performance of the adsorber containing the adsorbent in commercial and industrial uses. We have developed a thermo-sensitive gel - silica gel composite adsorbent bed column equipped with the recycle flow system for increasing the capacity of adsorbing water vapor and regenerating the thermo-sensitive gel-silica gel composite adsorbent quickly at low temperatures. The numerical study on heat and mass transfer (water vapor) in the thermo-sensitive adsorbent packed within a bed column was carried out. A part of dehumidified air was recycled through a heat exchanger into the entrance of the packed bed column. The rise of temperature within the packed bed column during adsorption of water vapor was reduced by introducing the recycle process, so that the amount of adsorbed water vapor increased remarkably. The adsorption – desorption cycle operation was simulated to investigate the regeneration property of the thermo-sensitive adsorbent. The thermo-sensitive adsorbent packed within the bed column was almost regenerated at low temperature of 323K. This is why the thermo-sensitive adsorbent changes in hydrophobic state when it is heated at somewhat higher temperatures than a specific one which is called phase transition temperature of the thermo-sensitive adsorbent. The desorption of adsorbed water took place quickly. As a result, the thermo-sensitive adsorbent was regenerated reversibly at such low temperatures. The performance of the desiccant cooling system can be improved by the introduction of both the recycle flow system and the use of the thermo-sensitive gel – silica gel composite adsorbent

Keywords: Desiccant air conditioning, thermosensitive adsorbent, numerical simulation

NOMENCLATURE

Cp_{ads} heat capacity of adsorbent [J kg-ads^{-1} K^{-1}]
Cp_{gas} heat capacity of air [J kg-air^{-1} K^{-1}]
Cp_{w} heat capacity of water [J kg-H_2O^{-1} K^{-1}]
D_P intraparticle diffusion [m^2 s^{-1}]
H absolute humidity [kg-H_2O kg-air^{-1}]
h overall heat transfer coefficient [W m^{-2} K^{-1}]
k_e heat conductivity of adsorbent [W m^{-1} K^{-1}]
M_{H2O} molecular weight of water [kg mol^{-1}]
q amount of adsorbed water vapor [mol kg-ads^{-1}]
R recycle ratio [-]
S area for heat transfer [m^2 m^{-3}]
T_{gas} temperature in air [K]
T_{ads} temperature in adsorbent [K]
t time [s]
u superficial gas velocity [m s^{-1}]
ΔH heat of adsorption [J mol^{-1}]
ε porosity of adsorbent bed [-]
ρ_{gas} density of air [kg-air m^{-3}]
ρ_{ads} density of adsorbent [kg-ads m^{-3}]

INTRODUCTION

Desiccant air conditioning system has been paid much attention to an energy saving cooling method, which can utilize effectively the waste heat sources at temperatures less than 333K. For enhancement of the efficiency of desiccant air conditioning system, it will be an important item

to improve both the ad-and desorption properties of water vapor adsorbent and heat transfer during ad-and desorption.

The performance of adsorbents is mainly governed by their surface properties and sizes. Silica gel and zeolite have been commonly used as the water vapor adsorbents for open-cycle desiccant cooling system [1-4]. Zeolite has a large capacity for water vapor adsorption at low relative vapor pressure. However, for regeneration, the high temperature heat source is required. On the other hand, silica gel is a favorable material for regeneration because the heat of adsorption of water vapor is equivalent to the heat of condensation of water. To improve the regeneration property of the water vapor adsorbent, thermo-sensitive gel was immobilized onto the silica gel [5-9]. Thermo-sensitive gel shows the changes of its physical property (hydrophobic-hydrophilic balance) depending on surrounding temperature. We tried to evaluate the isotherms of thermo-sensitive water vapor adsorbent using an adsorption apparatus.

For using the thermo-sensitive water vapor adsorbent effectively, the adsorption process should be modified for reducing a rise in temperature accompanied by adsorption of water vapor below the phase transition temperature of the thermo-sensitive water vapor adsorbent. A part of the dehumidified air is introduced into the adsorbent bed unit after removing the heat of adsorption through a heat exchanger unit, so that a temperature rise within the unit is reduced to increase the capacity of adsorbing water vapor.

The aim of our investigation is to evaluate the dehumidified and regenerated properties of silica gel adsorbent and the thermo-sensitive gel - silica gel adsorbent by a numerical calculation of simultaneous water vapor mass transfer and heat transfer in the adsorbent bed unit equipped with the recycle flow system.

MATHEMATICAL MODEL

Figure 1 shows a schematic diagram of the desiccant cooling system. This system is composed of an adsorbent bed unit, a recycle flow path of a dehumidified air and a heat exchanger unit. The heat generated with adsorption in the adsorbent bed unit is transferred to the dehumidified air that is recycled through the heat exchanger. To predict this system by mathematical modeling, it is assumed that

(1) Adsorption of water vapor is performed under an adiabatic condition.
(2) Adsorption equilibrium exists at the surface of the adsorbent.
(3) The temperature distribution inside the adsorbent particle is uniform
(4) The dehumidified air exhausted from the adsorbent bed is immediately cooled to a room temperature by heat exchanger.

A set of equations describing the mathematical model of the combined water vapor mass transfer and heat transfer in the adsorbent bed unit can be written as follows:

(Water vapor mass transfer balance)

Mass transfer in the packed bed

$$\frac{\partial H}{\partial t} = -\frac{u}{\varepsilon}\frac{\partial H}{\partial z} - \frac{(1-\varepsilon)\rho_{ads} M_{H2O}}{\varepsilon \rho_{gas}}\frac{\partial q}{\partial t} \quad (1)$$

Mass transfer in a silica gel adsorbent particle

$$\frac{\partial q}{\partial t} = D_P\left(\frac{\partial^2 q}{\partial r^2} + \frac{2}{r}\frac{\partial q}{\partial r}\right) \quad (2)$$

(Heat transfer balance)

Heat transfer in the gas phase

$$\frac{\partial T_{gas}}{\partial t} = -\frac{u}{\varepsilon}\frac{\partial T_{gas}}{\partial z} + \frac{(1-\varepsilon)hS}{\varepsilon \rho_{gas} Cp_{gas}}(T_{ads} - T_{gas}) \quad (3)$$

Heat transfer in the adsorbent phase

$$\frac{\partial T_{ads}}{\partial t} = \frac{k_e}{\rho_{ads}(Cp_{ads} + qM_{H2O}Cp_w)}\frac{\partial^2 T_{ads}}{\partial z^2} - \frac{\varepsilon hS}{(1-\varepsilon)\rho_{ads}(Cp_{ads} + qM_{H2O}Cp_w)}(T_{ads} - T_{gas}) + \frac{\Delta H}{Cp_{ads} + qM_{H2O}Cp_w}\frac{\partial q}{\partial t} \quad (4)$$

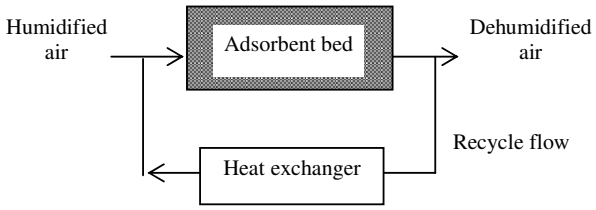

Fig. 1 Schematic diagram of the adsorbent bed unit equipped with recycle flow system

The calculation is performed for the particle radius of 2.0×10^{-3} m and for D_P of 5.0×10^{-10} m^2 s^{-1}. To investigate the effect of the recycle flow on the water vapor adsorption, the recycle ratio, R, is defined as:

$$R = \frac{G_{re}}{G} = \frac{G_{re}}{G_{re} + G_{exh}} \quad (5)$$

where G_{re} is the mass flow circulated in the desiccant system, and G_{exh} is the mass flow of dehumidified air exhausted from the desiccant system. The value of G_{exh} (=0.503 kg s^{-1}) is fixed in this study. Therefore, for R = 0.5, the mass flow rate in the adsorbent bed unit, G, is twice the mass flow rate of G_{exh}.

THERMO-SENSITIVE ADSORBENT

N-isoprolylacrilamide gel (NIPA gel) is known as a thermo-sensitive polymer. This polymer shows the changes of its physical property (hydrophobic-hydrophilic balance) depending on surrounding temperature. NIPA gel was immobilized onto silica gel particles. In Figure 2, the adsorption amount of water vapor on the thermo-NIPA-silica gel adsorbent is shown as a function of relative vapor pressure. The isotherm of water vapor onto the NIPA-silica gel adsorbent depended on the adsorption temperature. NIPA-silica gel shows the hydrophobic property above 306K in the NIPA-water system. As a result, the amount of water adsorbed onto the NIPA-silica gel adsorbent was reduced drastically at high temperature (308K) [5-8]. On the basis of the adsorption isotherms of water vapor for the NIPA-silica gel adsorbent, the numerical study on heat and mass transfer (water vapor) within the adsorbent bed unit packed with the thermo-sensitive NIPA-silica gel particles was carried out, as described in the following section.

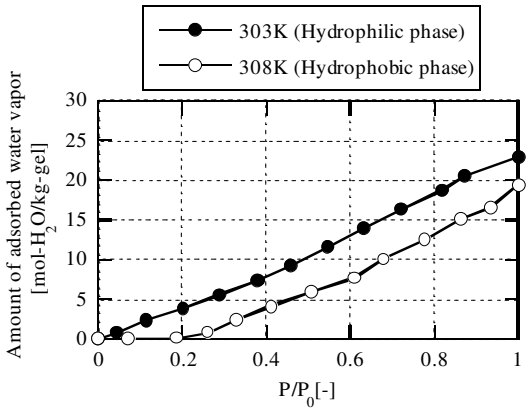

Fig.2 Adsorption isotherms of the thermo-sensitive NIPA-silicagel adsorbent for water vapor

RESULTS AND DISCUSSION

Adsorption

In the adsorption process, only silica gel was used as a water vapor adsorbent whose adsorption isotherm was almost the same as that of NIPA-silica gel adsorbent at 303K. The time history of the absolute humidity of humidified air and the temperature were calculated numerically using Eqs.1-4. The height of the adsorbent bed is 5cm. The mass flow rate of the dehumidified air exhausted from the adsorbent bed unit is 0.503kg s^{-1}. The absolute humidity of humidified air supplied into the unit is 0.012 kg-H_2O/kg-air. Figure 3 shows the temperature rise of dehumidified air at the exit of adsorbed bed unit packed with silica gel adsorbent. For R=0, the temperature reached 318K. On the other hand, the temperature rise decreased by introducing the mixture of humidified air and part of dehumidified air through recycle process. When R was 0.8, the maximum temperature at the exit of the unit was 306K which was lower 12K than that of R=0.

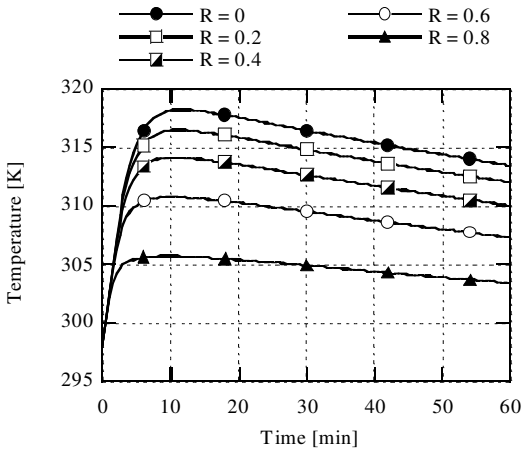

Fig.3 Effect of the recycle ratio on temperature rise of defumidified air at the exit of adsorbent bed unit

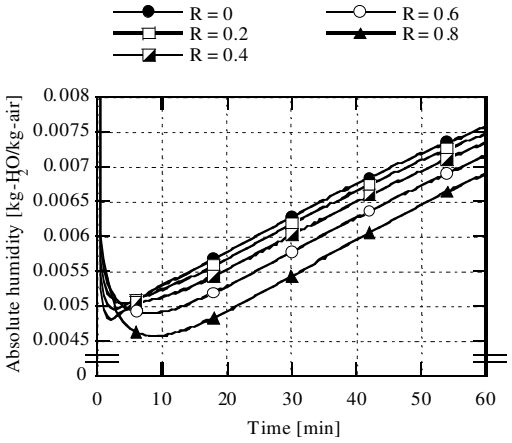

Fig.4 Effect of the recycle ratio on absolute humidity of dehumidified air at the exit of adsorbent unit

Figure 4 shows the time history of the absolute humidity of dehumidified air at the exit of adsorbent bed unit. The absolute humidity was lowered with increasing the recycle ratio. Although the mass flow rate of the humidified air passing through the unit increased with increasing the recycle ratio so that the residence time became short, adsorptivity of water vapor adsorbent became high due to the reduction of temperature rise within the adsorbent bed. As a result, the volume of dehumidified air which was treated less than 0.0055, 0.006 or 0.007 kg-H_2O/kg-air increased with an increase in recycle ratio, as shown in Fig.5.

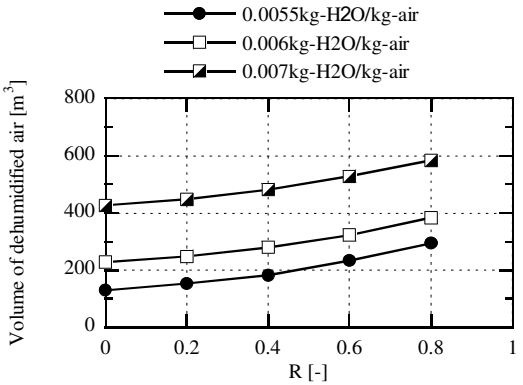

Fig.5 Relationship between the volume of defumidified air treated less than 0.0055, 0.006 or 0.007 kg-H2O/kg-air and the recycle ratio, R

Regeneration

To investigate the regeneration property of the NIPA-silica gel adsorbent bed, the adsorption-desorption cycle operation was simulated. Following the adsorption operation for 60 min, the regeneration operation was performed for 300 min. The humidified air heated at 323 or 353K (AH=0.012 kg-H_2O/kg-air) was used as the regeneration gas.

Figure 6(A) shows the time history of the amount of water vapor adsorbed onto the NIPA-silica gel adsorbent during the adsorption and desorption cycle. When the regeneration temperature was as high as 353K, the NIPA-silica gel adsorbent was regenerated quickly and completely, while the silica gel adsorbent was not regenerated completely. The regeneration property of the NIPA-silica gel adsorbent at a lower temperature level (323K) is shown in Fig. 6(B). Although the silica gel adsorbent was not regenerated at 323K, the NIPA-silica gel adsorbent was almost regenerated completely. This elucidates that the NIPA-silica gel became hydrophobic because the regeneration temperature was higher than the phase transition temperature (306K) of the NIPA-silica gel. So, the amount of water vapor adsorbed onto the NIPA-silica gel adsorbent dropped drastically, as shown in Fig.6(B). It was found that NIPA-silica gel adsorbent can be regenerated easily at even a lower temperature level. Although the thermo-sensitive gel - silica gel that has a somewhat lower phase transition temperature is used in this simulation, it can be said that the water vapor adsorbents with such thermo-sensitive properties

are extremely useful for developing a new desiccant air conditioning system.

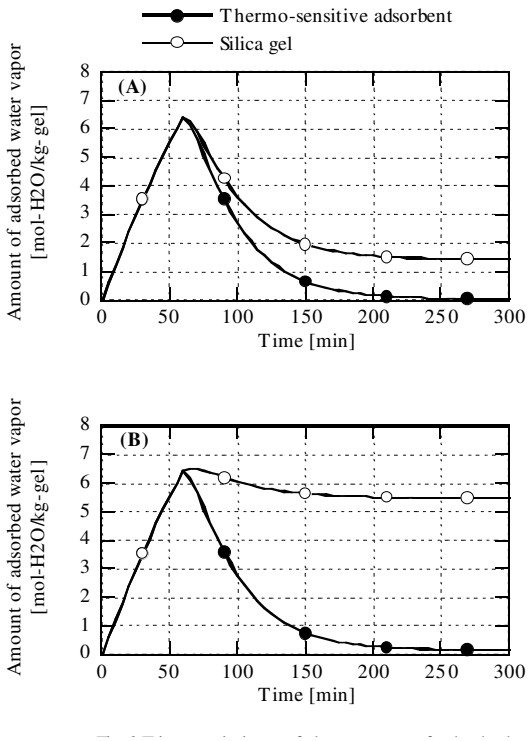

Fig.6 Time histories of the amounts of adsorbed water vapor onto the thermo-sensitive water vapor adsorbent and silica gel adsorbent
(A) Regeneration temperature: 353K
(B) Regeneration temperature: 323K

CONCLUSION

The dehumidified and regeneration properties of the thermo-sensitive gel – silica gel adsorbent were investigated by the numerical calculation of simultaneous heat and water vapor transfer in the adsorbent bed unit equipped with the recycle flow system. In the adsorption process, the recycle flow of the dehumidified air was effective to increase adsorptivity of water vapor adsorption by reducing the temperature rise of the adsorbent bed and the dehumidified air. In the regeneration process, the thermo-sensitive gel - silica gel adsorbent was regenerated quickly and reversibly by heating beyond the phase transition temperature of the immobilized thermo-sensitive gel. The performance of the desiccant cooling system can be improved by the introduction of the recycle flow system and by the use of the thermo-sensitive gel - silica gel adsorbent.

REFERENCES

[1] Kuma, T., T. Hirose, M. Goto and A. Kodama *Thermally regenerative monolithic rotor dehumidifier for adsorption cooling system.* ASME Journal of Solar Energy and Engineering 1988;120: 45-50.

[2] Kodama A., M. Goto, T. Hirose and T. Kuma *Experimental study of the optimal operation or a honeycomb adsorber operated with thermal swing*. Journal of Chemical Engineering of Japan 1993;26: 530-535.

[3] Srivastava, N. C. and I. W. Eames *A review of adsorbents and adsorbates in solid-vapour adsorption heat pump systems* Applied Thermal Engineering 1998;18:707-714.

[4] Kanoğlu M., M. Ö. Çarpınlıoğlu, M. Yıldırım *Energy and exergy analyses of an experimental open-cycle desiccant cooling system.* Applied Thermal Engineering 2004;24:919-932.

[5] Nakano, Y., K. Kuwano, T. Asano and M. Itoh *Proc. 15th Japan adsorption society research meeting*, 2001 .p.15.

[6] Nakano, Y., K. Kuwano, M. Ogawa, M. Ito and T. Asano *Thermosenstive polymer gel / silica gel adsorbents in desiccant cooling system: Proc. 67th Annual Meeting of Chem. Eng.* Chem. Eng. Soc. Japan, 2002a. G216.

[7] Nakano, Y., M. Ogawa, K. Kuwano, M. Ito and T. Asano *Desiccant air conditioning using thermosensitive water vapor adsorbent: Proc. 67th Annual Meeting of Chem. Eng.* Chem. Eng. Soc. Japan 2002b. G217.

[8] Nakano, Y., T. Asano and M. Ito *Performance of a thermosensitive polymer gel – silica gel / water vapor cooling system* Proceedings of 2002 JSRAE Annual Conference 2002c; 581–584.

[9] Nakano, Y., M. Ogawa, M. Ito, T. Asano and H. Higo *Desiccant air conditioning system using the packed bed unit equipped with recycle flow: Proc. 69th Annual Meeting of Chem. Eng*. Chem. Eng. Soc. Japan, 2004. D120.

Proceedings of ECOS 2005
Trondheim, Norway
June 20–22, 2005

THERMAL COMFORT AND ENERGY USE

A. Stegou-Sagia*, K. A. Antonopoulos, C. Angelopoulou
National Technical University of Athens
School of Mechanical Engineering
Department of Thermal Engineering
9 Iroon Polytechniou Str., Zografou 15780, Athens, Greece

ABSTRACT

In the present paper, an attempt has been made to estimate the energy consumption in Greek buildings. This is a subject of great interest due to the upcoming building certification that will take place in Greece after the application of the European directive concerning the energy performance of buildings. Our purpose is to examine the energy consumption throughout Greece by simulating the thermal behaviour of typical buildings. In order to achieve this we are founded on the philosophy of the computer programme EnerWin. Information with sketches of buildings showing the thermal zones, Greek climatic data, properties of the various construction assemblies, type of heating and cooling systems, the occupancy of the building in question, as well as hot water, lighting and ventilation profiles are fully outlined in the code.

The annual energy needs of a Greek residential and an office building, as well as the breakdown of energy use are presented. The results of such a simulation can give us a first indication on which end uses are the most energy consuming, the "weaknesses" of a building and thus urge the owner or engineer to take conservation energy measures.

The article focuses on the thermal comfort conditions of the occupants. Thermal comfort is an important issue which should not be overlooked. In the present article we will attempt to examine whether comfort conditions in typical Greek buildings comply with international standards and discuss the particularities of Greek people as far as thermal comfort, energy use and behaviour is concerned.

Keywords: Energy consumption, thermal comfort

NOMENCLATURE

SHGC Solar Heat Gain Coefficient
U Thermal transmittance [W/m^{2}K]
α Solar absorptivity
ε Emissivity
τ Daylight transmissivity

INTRODUCTION

In Greece the building sector accounts for the 36% of the country's total energy consumption [1]. Given the importance of buildings on the country's energy balance, an attempt has been made to study their energy behaviour and thermal comfort in three Greek cities, namely, Athens, Thessaloniki and Heraklion. Our primary purpose is to provide an estimation of the buildings' energy consumption and examine how this affects the comfort conditions. We cannot underestimate the value of

* Corresponding author: Phone: +30 210 7721255 Fax: +31 210 7723976 Email: asagia@central.ntua.gr

real measurements and observations of the buildings' energy systems, but such data are not always available.
The use of a computer programme, such as EnerWin, can offer an indication of the building's performance. EnerWin is a simulation tool, which consists of the user interface and the computer code. After the user has inserted the input data describing the building, the program can perform the thermal simulation.

METHODOLOGY

Two types of buildings were simulated, a residential and a commercial building. On the one hand residencies dominate as a building type in Greece (75% of the total number of buildings are residencies [2]). On the other hand, office buildings consume large amounts of energy within the commercial sector and as they have specific and homogeneous energy needs, it is easier to study and apply conservation measures.
Real building layouts were used.

Residential building

A typical Greek urban building is defined. Buildings used as residencies in the Athens area and the rest of the big cities in Greece have 4 to 6 floors with 1 to 5 apartments on each floor [3,4]. The building that was simulated has 4 floors with 2 apartments on each floor. The area of each floor is 172m^2, with the ground floor being a garage.

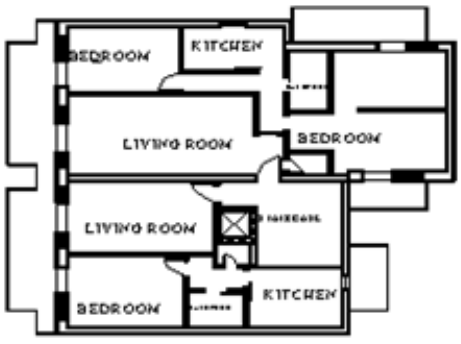

Figure 1: Layout of typical floor, Residential building

Office building

The building has three floors; the area of each is 390m^2. Window openings represent 20% of the total wall area.

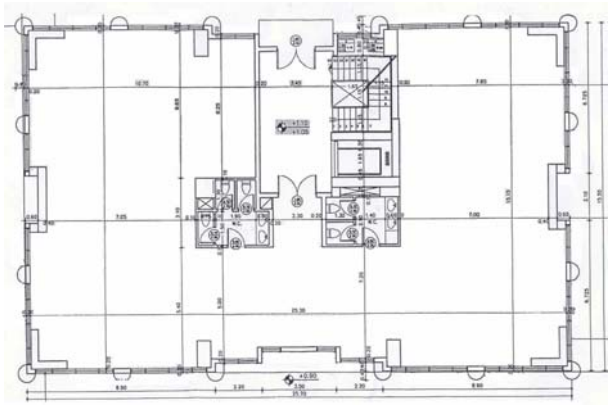

Figure 2: Layout of ground floor, Office building

The basic parameters to be inserted in order to conduct the thermal simulation are:

- The climatic data of the region. They include ambient temperatures, solar radiation data as well as wind speed [5-8].
- Geometry and building orientation. Zones are specified, that is spaces where similar conditions dominate.
- Wall, floor and roof materials and properties. The typical external wall of a Greek multi-storey building is 26cm thick and has the following properties: thermal transmittance U=0.66 W/m^{2}C, solar absorptivity α=0.75 [3,4]. Accordingly, the roof has U=0.397 W/m^{2}K, α=0.80 and the floor U=0.568 W/m^{2}K, α=0 [8].
- External shading. The effect of balconies, which is a very common feature in Greek residential buildings, is taken into consideration.
- Window properties. As far as the residential building is concerned, windows are double-glazed (25mm), transparent with U=2.839 W/m^{2}K, solar heating gain coefficient SHGC=0.75, emissivity ε=0.60, daylight transmissivity τ=0.77. The office building has grey tinted double-glazed windows, with properties U=2.839 W/m^{2}K, SHGC=0.47, ε=0.84, τ=0.39 [8,9]. It is noted that the SHGC is the percentage of the incident

solar radiation which turns into heat gain inside the space and is defined as $SHGC = \tau + \sum_{k=1}^{n} N_k a_k$, with N being the inward-flowing fraction of absorbed radiation in the k*th* layer.

- Heating system. Both the residential as well as the office building are assumed to use central heating system with oil as fuel. This is very common in Greek multi-storey buildings. The efficiency of the heating system is 85% [10].
- Air conditioning system. Residencies usually have direct expansion split units for air conditioning purposes. The coefficient of performance is 2.50, but its value is adjusted, according to the ambient temperature and humidity. It is noted that according to the philosophy of the program, all the spaces of the building are air conditioned. In reality, there is only a limited number of cooling units, usually in bedrooms or sitting rooms. The office building has a central VAV (Variable Air Volume) air conditioning system. Its coefficient of performance is 2.60.
- The maximum number of people expected to occupy the zone, as well as the occupancy profile of the zone. Each profile contains 24 hourly values that describe the average daily occupancy pattern.

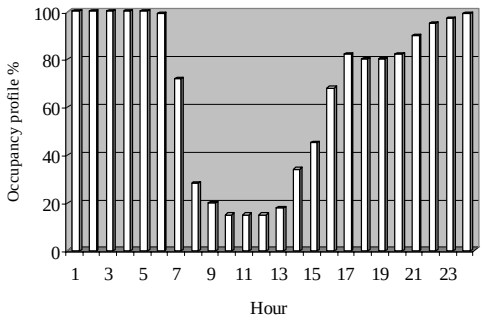

(a)

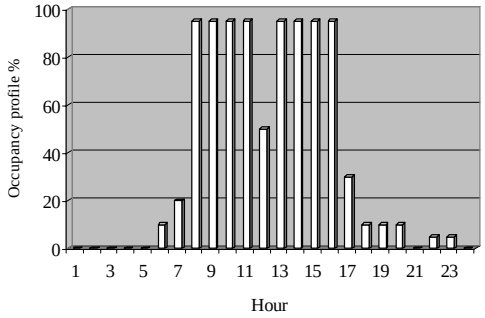

(b)

Figure 3: Occupancy profiles (%) for (a) the residential [11] and (b) office building [8].

The profiles have resulted after processing the available data [8,11]. The residential building is assumed to be occupied by four member families, while for the office building an estimation has been made according to the guide of the Greek Technical Chamber [13]. The guide indicates an occupancy of 10 persons/100 m^2 for an office building.

- The average number of volume units of hot water used per person per occupied day, which is 35 lt/day/person for the residential and 3.8 lt/day/person for the office building. The hot water profiles that describe the use by the occupants are a product of process of the available data [8,12]. Values represent the hourly percentage of total daily use.

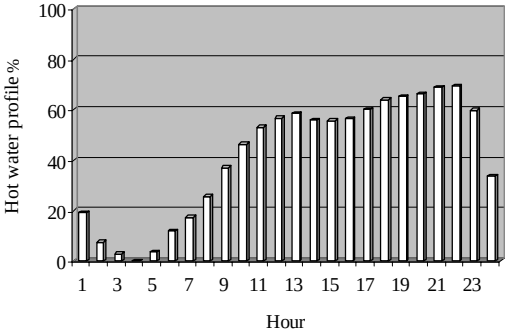

(a)

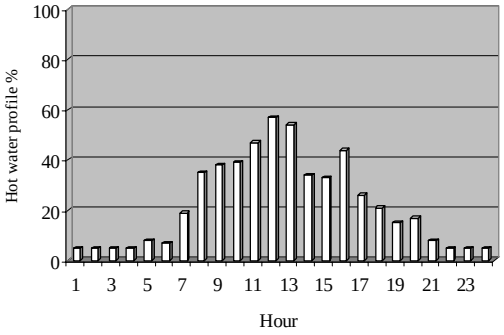

(b)

Figure 4: Hot water profiles (%) for (a) the residential [12] and (b) office building [8].

- Natural ventilation. This parameter simulates the opening of windows from the occupants, when the space is too warm. While this is common practice in residencies, natural ventilation is not assumed for the office building.
- Lighting and electrical equipment [8,14]. In the residence incandescent lamps are used, while in the office building fluorescent lighting sources are assumed. The equipment refers to any kind of electrical device, for example refrigerators, television sets, computers but no space conditioning equipment is included here.
- Space temperature. Temperature is allowed to float between set limits. Temperatures are those that exist in a building and are nor the desired ones neither the design temperatures. This is for simulating the real situation, and allows seeing what the comfort conditions are. The temperature range is set to be 20 to 29^{o}C.

It is stressed that the program sizes both the heating and cooling systems according to the existing load, the thermostat settings and the system efficiency. By setting the temperature to float in a range representing the real temperatures in the interior [16] we can estimate the actual energy consumption and examine what comfort conditions are achieved.

RESULTS

Three Greek cities were selected, in order to examine the effect of the climate on the building's energy consumption. The cities are representative of the three climatic zones in which the country is divided [9].
The results obtained for the two types of buildings are:

Residential building

	Total annual energy consumption
Athens	586.2 MJ/m^2
Thessaloniki	614.5 MJ/m^2
Heraklion	530.4 MJ/m^2

Table 1: Total annual energy consumption; Residential building

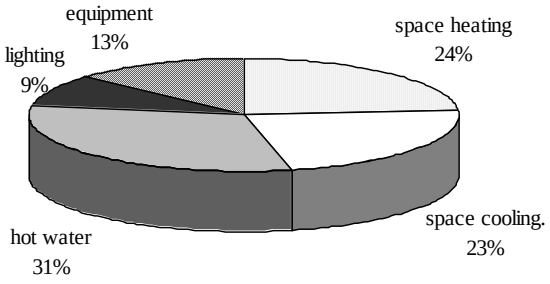

(a)

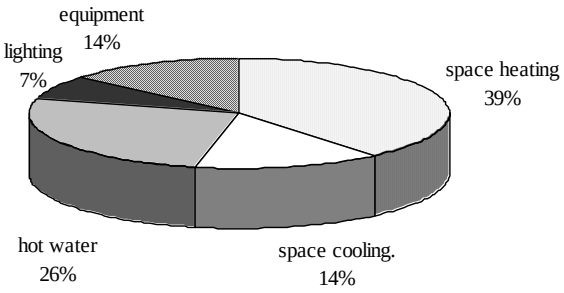

(b)

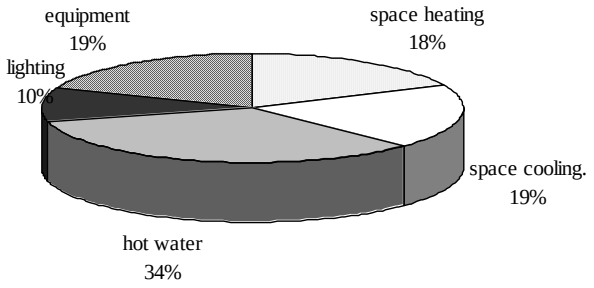

(c)

Figure 5: Breakdown of energy to end uses for the residential building in (a) Athens, (b) Thessaloniki and (c) Heraklion

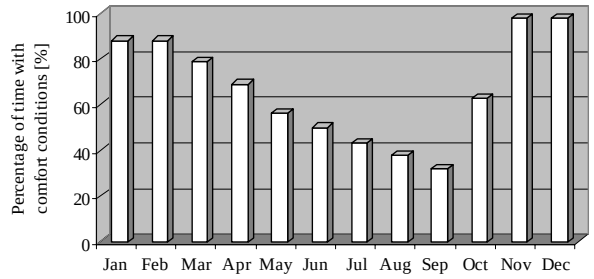

(a)

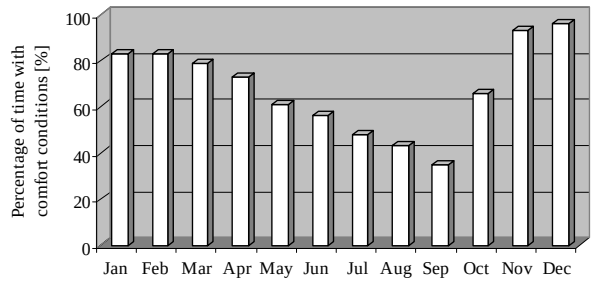

(b)

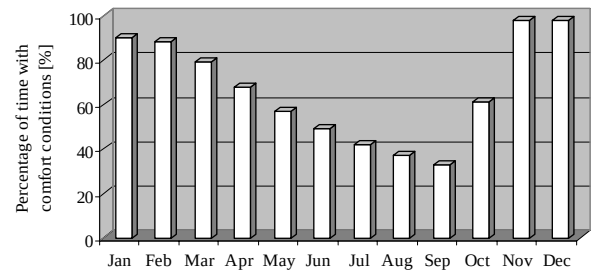

(c)

Figure 6: Percentage of time with comfort conditions inside the residence; (a) Athens, (b) Thessaloniki, (c) Heraklion

Office building

	Total annual energy consumption
Athens	1714.5 MJ/m^2
Thessaloniki	1741.8 MJ/m^2
Heraklion	1735.2 MJ/m^2

Table 2: Total annual energy consumption; Office building

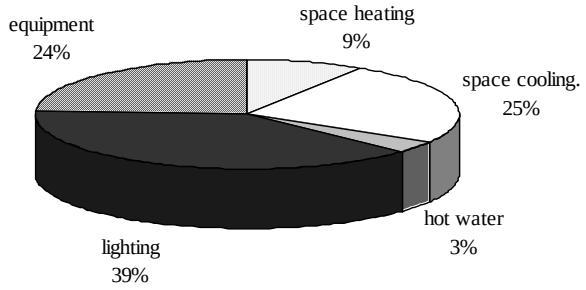

(a)

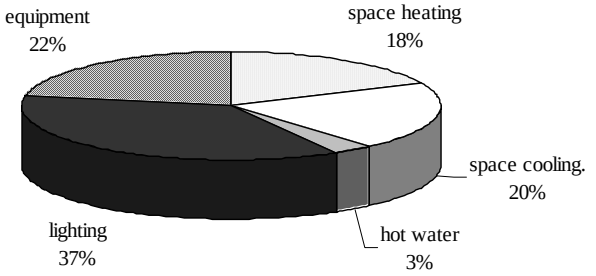

(b)

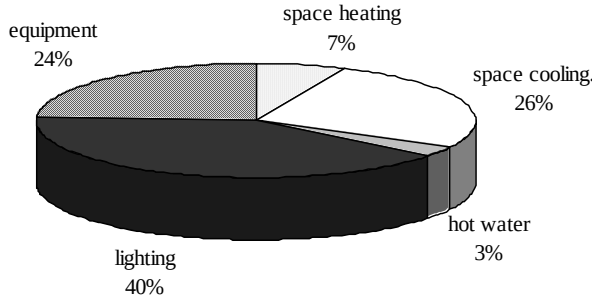

(c)

Figure 7: Breakdown of energy to end uses; Office building in (a) Athens, (b) Thessaloniki and (c) Heraklion

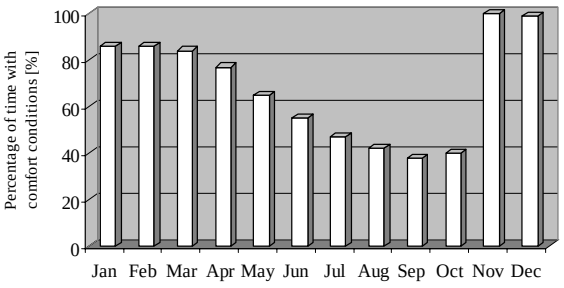

(a)

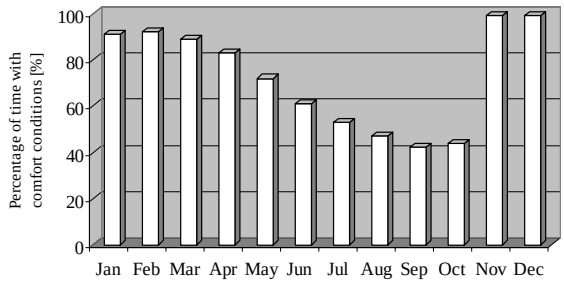

(b)

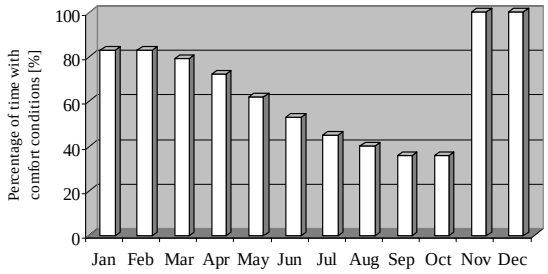

(c)

Figure 8: Percentage of time with comfort conditions inside the office building in (a) Athens, (b) Thessaloniki and (c) Heraklion

CONCLUSIONS

Energy consumption

End uses differ with the building type. Space heating and hot water heating are the most important end uses for the residential building, whereas lighting and space cooling for the office building.

Although an attempt was made to estimate the needs of a typical building, the results indicate a relative small demand in heating energy in comparison to common experience. This is because there is a great number of existing buildings with little or no insulation and single glazed windows. The building used, has on the contrary, double-glazed windows and good insulation, as the Greek regulation (1979) indicates [9].

It is important to stress that the energy behaviour of the occupants has been considered as a parameter. Occupancy and hot water use profiles have been used. Moreover, the use of natural ventilation is allowed, as means of controlling indoor climate.

The effect of the climate on both energy consumption and breakdown is decisive. This is to be taken into consideration in the case of application of energy conservation measures. In northern climate (Thessaloniki) it is clear that heating energy is the most energy consuming sector. Nevertheless, it is harder to achieve thermal comfort during the winter months in comparison with the other two cities.

The fact that the urban climate has specialties must not be overlooked. Temperatures in densely populated cities are higher than in the surrounding areas. This mostly affects the cooling load, thus the electricity demand.

Thermal comfort

The conditions proposed from ASHRAE have been used as the comfort zone [15]. The problem of thermal discomfort is concentrated on the summer months, as it is observed even up to 70% of the occupancy time. During winter months the problem is not so intense.

International comfort standards are based on energy balance models (static models). ASHRAE defines that the comfort conditions in terms of operative temperature values range from 20 to 27^{o}C.

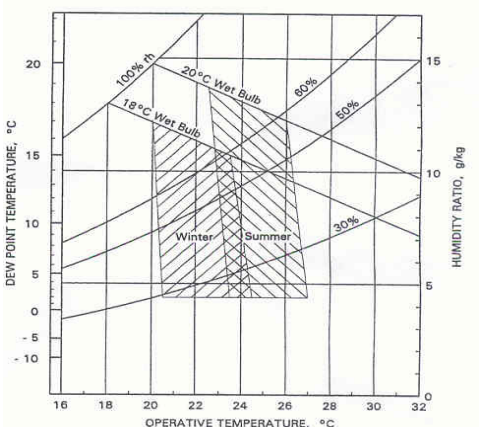

Figure 9: ASHRAE Comfort Zone

According to the standards, it seems that for a large percentage of time on yearly basis, there is discomfort inside Greek buildings. This is only partially true. On the one hand, there is room for better use of energy as well as improvement of thermal comfort in Greek residencies. On the other hand, a number of factors concerning the occupants' behaviour [17] indicate that the results regarding thermal comfort are overestimated:

- In various cases there may exist the possibility of improving comfort, but reasons such as financial, cause the occupant to take measures other than using available control mechanisms. It is very common for example to adjust clothing according indoor conditions so as to avoid turning on a heating or cooling apparatus.
- The thermal sensation is subjective. This consists of an important factor which can affect energy consumption, but cannot be easily measured or taken into consideration in case of thermal simulation, designing, etc. International standards can act as guiding lines, cannot, however, be approached globally. Especially in the case of the Mediterranean climate, the tolerance in higher temperatures is given. While, for example the standard indicates that 28^{o}C are outside the comfort zone, a resident in Greece would find the conditions acceptable.
- When it comes to residential buildings, an important factor influencing thermal comfort is the long stay in a space, which causes the adaptation of settings of the physiological thermoregulation system. In other words, the occupant is acclimatized and responds to expected conditions.
- Another parameter has to do with perceived control of the occupants. That is, in cases when a person has, or think (s/)he has some control over the indoor environment, the person is more tolerant against climatic changes.

Energy use and thermal comfort interact, and with careful designing comfort can be provided using rational amounts of energy.

In Greece the problem of comfort is focused on summertime, mostly due to the climate, but also because the majority of building designers do not lay importance on cooling. Moreover, there are no regulations concerning air-conditioning or cooling, as there are for heating systems. In all, action has to be taken so that both comfort and energy conservation is achieved.

REFERENCES

[1] Iatridis M. *Energy Efficiency in Greece*, Report, Centre for Renewable Energy Sources, SAVE Project, 2003.

[2] *Statistical Yearbook of Greece 1996*, National Statistical Service of Greece, 1997.

[3] Koronaki EP. *Dynamic thermal characteristics of buildings*, Doctoral Thesis, National Technical University of Athens, 2000.

[4] Antonopoulos KA, Tzivanidis C. *Time constant of Greek buildings*. Energy 1995; 20:789-802.

[5] Kouremenos DA, Antonopoulos KA, Domazakis ES. *Solar radiation correlations for the Athens, Greece, area*. Solar Energy 1985;35:259-269.

[6] Kouremenos DA, Antonopoulos KA. *Numerical determination of relative humidity and dry bulb temperature in Greece from meteorological observations*. Proceedings of the 4th International Conference on Numerical Methods in Laminar and Turbulent flow, Swansea, UK, 1985.

[7] Kouremenos DA, Antonopoulos KA. *A daily variation model for the outdoor temperature and relative humidity in Athens/Greece*. Proceedings of the International ASME Conference on Modelling and Simulation, Sorrento, Italy, 1986.

[8] Degelman LO. *Ener-Win 97.2000, User's Manual*, 2002.

[9] Presidential decree: *On the approval of thermal insulation for buildings*, The Government Gazette, Issue 4, no. 362, 4/7/1979.

[10] Presidential decree no. 335: *Demands in efficiency for new hot water boilers supplied with liquid or air fuel, in compliance with the directive*

of the Council of the European Community 92/42/EEC of the 21st May 1992 (L167/92), The Government Gazette, Issue 1, no. 143, 2/9/1993.

[11] Papakostas KT, Sotiropoulos BA. *Occupational and energy behaviour patterns in Greek residences*. Energy and Buildings 1997;26:207-213.

[12] Papakostas KT, Papageorgiou NE, Sotiropoulos BA. *Residential hot water use patterns in Greece*. Solar Energy 1995;54:369-374.

[13] Technical Chamber of Greece. *Elements for calculating cooling loads in buildings*, Technical Guide no. 2425/86, 2002.

[14] CIBSE. *Energy use in offices*, Energy Consumption Guide 19, 2000.

[15] ASHRAE. *Fundamentals Handbook*, 1997.

[16] Tsilingiridis G, Sotiropoulos V. *Three-year measurements of ambient and indoor air temperatures in Solar Village-3, Athens, Greece*. Energy and Buildings 1998;28:127-136.

[17] Brager GS, de Dear RJ. *Thermal adaptation in the built environment: a literature review*. Energy and Buildings 1998;27: 83-96.

Proceedings of ECOS 2005
Trondheim, Norway
June 20–22, 2005

POWER SAVING OF PACKAGED AIR CONDITIONING SYSTEM BY AUTOMATIC SWITCHING TECHNIQUE

S N Tay
Centre for Green Building Technologies
School of Mechanical & Aerospace Engineering
Nanyang Technological University
50 Nanyang Avenue, Singapore 639798
Email: msntay@ntu.edu.sg

K J Phua
Facilities Planning and Management
Nanyang Technological University, Singapore

Satoshi Uetsugu
Toyo Standard Asia Pte Ltd
Singapore

ABSTRACT

This paper reports an energy conservation project implemented on a packaged air cooled air conditioning (PAC) system at an office within Nanyang Technological University campus. The PAC system is serving an office with a built up floor area of 1,664 m^2. Before the implementation of the project, the average monthly energy consumption of the PAC system was 10,236 kWh with average operating time of 60 hours per week. After the implementation of the BeONE automatic switching control system for 6 months, average saving on power consumption recorded was 956.7 kWh per month. Based on the prevailing electricity cost of S$0.1354/kWh, a payback period of 19.3 months is achieved for installing the BeONE system. Similar application of BeONE controller in a manufacturing plant with 24-hours operation of PAC achieved a much shorter pay back period of 6 months. With the large number of PAC systems installed in offices, retail and commercial properties in Singapore, the wide spread use of such automatic switching control systems will have significant contribution to building energy saving.
Keywords: Energy conservation, air conditioning, compressor switching control

INTRODUCTION

Electricity used for air conditioning accounts for a significant portion of total electricity consumption in tropical cities. In Singapore, this portion is relatively high at 24% according to a study done by Energy Market Authority of Singapore [1].The results were based on a series of survey done during the period from late eighties to early nineties. There are reasons to believe that this figure is much higher at around 30% now. Packaged air cooled air conditioning units are popular with small and medium sized commercial properties. The low cooling load prohibits the use

of higher capacity and more efficient central air conditioning systems. PAC systems are easy to install and lower in initial investment. However, PAC systems suffer from inefficient cut in/cut off of compressor using thermostat temperature set point control.

A project to investigate the effectiveness of an automatic programmed switching controller BeONE developed by Toyo Standard Co., Ltd of Japan was jointly under taken by Nanyang Technological University (NTU) and Toyo Standard Asia Pte Ltd. Two sites employing PAC systems for their air conditioning need were selected concurrently for the study; one at an office of 1,664 m^2 built up floor area at NTU Campus and the other a manufacturing plant of Matsushita Electronic components of Singapore.

The objectives of the study were to quantify energy saving, obtain field data on thermal comfort and evaluate payback of installing the controller under various operating conditions. It is hoped that the study will establish some useful criteria to help building owners in decision making of using such controllers.

PAC AIR CONDITIONING SYSTEM

The PAC air conditioning system in NTU Office of Facilities Planning and Management is a Daikin system consists of one indoor unit and two outdoor units. The indoor unit model FRJ1120P as shown in Figure 1 consists of two compressors and two evaporators arranged in parallel with rated cooling capacity of 107.6kW. The refrigerant used is R22 with compressor operating at suction pressure of 0.5 MPa and discharge pressure of 1.55 MPa. The outdoor unit is an air cooled condenser model CRJ560 (Figure 2). Thermostat temperature settings are used to switch on/off of compressors at 23.5^{o}C ON and 22^{o}C OFF based on return air. Fan motors are controlled by main switch which will be on whenever the PAC system is switched on.

Figure 1 Indoor unit of PAC

Figure 2 Outdoor unit of PAC

During a typical working day operation, the PAC system is switched on at about 07:30 and switched off at 18:00. For a typical 5½-day work week, total operating hours of the PAC system is about 60 hours. The average power consumption of the indoor unit (compressors and circulating fans) was measured to be 40.77 kW over a four days period in June 2004. Power by compressors alone was measured to be 33.76 kW.

BeONE COMPRESSOR SWITCHING CONTROLLER

The BeONE controller was developed by Toyo Standard of Japan. The heart of the system consists of a power monitoring device (Figure 3) and an automatic switching control system (Figure 4) which can be programmed to switch on and off of the refrigerant compressor and its driving motor. The system differs from other demand controllers with a patented compressor protection system which can automatically protect the compressor from excessive and inappropriate switching. Another unique feature is the time-zoning capability available with the system such that day and night periods can be programmed by the time-zoning system.

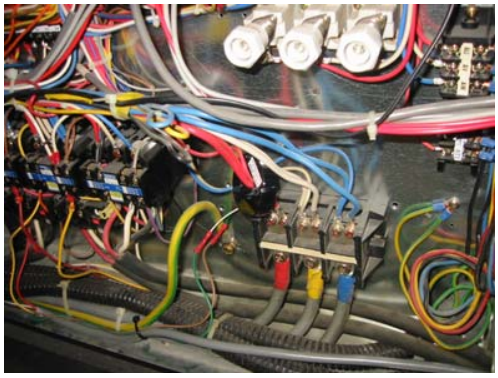

Figure 3 Power monitored by CT connection

Figure 4 BeONE controller

The controller uses a 30-minute interval as a standard session for switching control. Users only need to key in the seconds that users want to stop and save (between 10%/180s to 50%/900s) and the built-in program of the controller will do the rest. A 10% control means that the compressor will cut off for 3 minutes over a 30-minute session. Figure 5 explains the basic functions of the cut out/cut in control of a single unit at 15% and 20% control and a multi-unit PAC at 15% control. The fundamental strategy of BeONE controller is based on the assumption that PAC system with traditional thermostat control can be further exploited for energy saving by switching off the compressor for a few minutes in a 30-minute interval. With the circulating fan remains working, indoor air conditions should still maintain at comfort level.

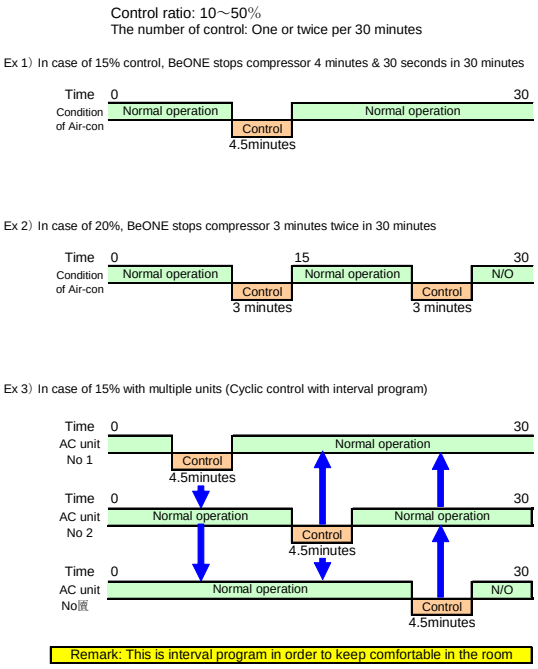

Figure 5 Basic function of BeONE control

The BeONE controller incorporate a built-in timer and program such that compressors being controlled are protected from excessive cut out when working together with thermostat controller.

TEST PROGRAM AT NTU

The objectives of the test program at NTU is to use the PAC air conditioning system at the Office of Facilities Planning and Management to quantify the power saving, evaluate the effect on indoor comfort level and to perform the cost/benefit analysis of installing the BeONE controller.

The BeONE controller was installed on 15 June 2004 but did not activate the control function. The power consumption and indoor air temperature and relative humidity data were collected for the one week under the usual thermostat control. The control function was then activated for 15% control but some part of the office had recorded temperature higher than 25^{o}C. Control level was set to 10% on 23 June 2004 and the power consumption, room temperature and humidity were monitored continuously at hourly interval. The temperature and humidity monitoring stopped on 2 July 2004 but the BeONE controller continues to operate at 10% control level to monitor the long term power saving.

TEST RESULTS OF NTU PROGRAM

Power Saving

The hourly electrical power consumption of the PAC system using the usual thermostat control and BeONE is shown in Figure 6. The data displayed cover the period from 15 June to 30 June. Average hourly electricity consumption reduces from 40.77 kWh with thermostat control to 36.56 kWh, a saving of 10.3%. At an independent test conducted by a certifying agency in Singapore, the saving in compressor power alone for a single 30-min period was 8.83% [2]. The daily power consumed and controlled for the month of July 2004 is shown in Figure 7. The total electrical power saved for the month is 935.8 kWh which represents 8.6 % of saving. For the six months period from July 2004 to December 2004, monthly saving in electricity is shown in Table 1 with average saving of 956.7 kWh/month. It is believed that the saving can be further exploited if the time-zoning option is used.

Month	**Jul04**	**Aug04**	**Sep04**
Power Saved (kWh)	935.8	962.8	1000.2
Month	**Oct04**	**Nov04**	**Dec04**
Power Saved (kWh)	991.2	863.0	987.2

Table 1 Monthly power saved from BeONE control

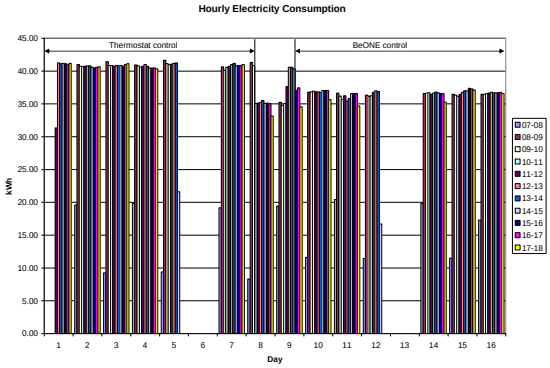

Figure 6 Hourly electrical power consumption

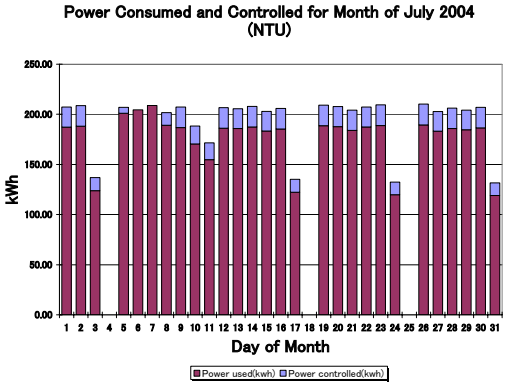

Figure 7 Daily power consumed and controlled for one compressor

Thermal Comfort

Energy saving devices used for air conditioning system must be evaluated against the effects on

thermal comfort of the indoor environment. The present study monitors the indoor air temperature and relative humidity before and after using the BeONE control. Figure 8 shows the upper and lower room temperatures and relative humidity of the office served by the PAC system before and after the use of BeONE controller. It is obvious that no noticeable effects can be observed with the activation of BeONE controller when control level was set to 10%. However when the control level was originally set to 15%, the upper temperature reaches 25^{o}C with complaint from occupants and the controller was re-set to 10% control level.

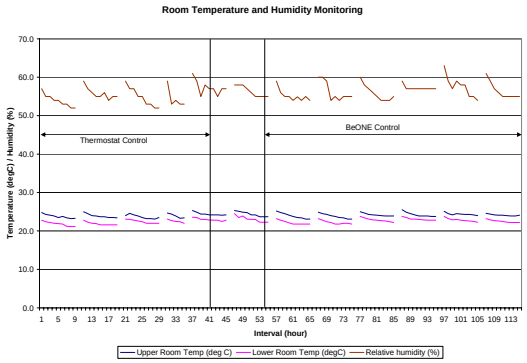

Figure 8 Temperature and relative humidity

The closer comparison of the average room temperatures with the usual thermostat control and BeONE control is shown in Figure 9. The use of BeONE control did not adversely affect the room temperature over the operating hours.

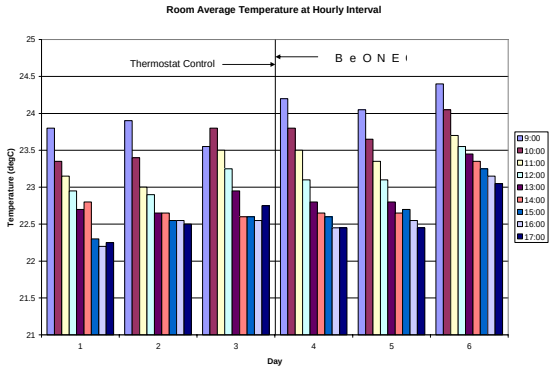

Figure 9 Average room temperature with thermostat and BeONE control

Cost and Benefit Analysis

Any energy saving device must be evaluated for its economic viability. As energy conservation projects are competing for financial resources of organization with other project, a short pay back period can ensure its acceptance to decision makers. The application of the BeONE controller to a typical office PAC system like the one at NTU Facilities Office is of representative significance. Based on the average monthly saving of 956.7 kWh for the six months tested and the prevailing electricity tariff of S$0.1354/kWh, saving per month is S$129.50. With the cost of BeONE system at S$2,500.00, the pay back period is 19.3 months or 1.6 years. The following simplified method of analysis can be applied to other PAC systems for first order evaluation.

Analysis of NTU PAC system using BeONE controller

- PAC usual compressor power consumption = *33.76 kW*
- Usual operating hours per week = *60 h/week*
- Annual power consumption without BeONE control = *33.76x60x52 =105,331 kWh/yea*r
- Control level = *10%*
- Annual electricity saving = *0.1x105331 = 10533 kWh*
- Electricity Tariff = *S$0.1354/kWh*
- Annual cost saving = *0.1354x10533 = S$1426/year*
- Cost of BeONE controller = *S$2500*
- Simple pay back period = *2500/1426 = 1.75 years.*

The pay back period of 1.75 years from the analysis is close to the actual pay back period of 1.6 years based on 6 months data.

It is observed that the most important parameters affecting the payback of installing BeONE controller or similar energy saving devices are:

Compressor power (kW)
Average weekly operating hours

Control level (%)
Local electricity tariff

BeONE CONTROLLER APPLIED TO MANUFACTURING PLANT

Air conditioning systems installed at manufacturing plants operate for longer hours. Many electronics plants are running continuously for 24 hours a day. Such plants provide good opportunities for installing energy saving devices like BeONE controller.

A case study on a BeONE controller installed at Matsushita Electronic Components in Singapore delivered the following results:

- PAC model: Hitachi/RP60-WSY
- Motor capacity: 60 HP
- Operating hours: 24 hours/day
- Control level: 20%/360s
- Power consumption without controller in December 2004 = 32,403 kWh
- Power saved in December 2004 = 6434 kWh
- Electricity tariff = S$0.1354/kWh
- Cost saved in December 2004 = S$671
- Cost of BeONE controller = S$2500
- Payback period using December 2004 as average monthly cost saving = 2.87 months.

The daily power consumed and controlled for December 2004 is shown in Figure 10. With a bigger PAC system running at longer hours in a factory environment, the pay back period is shortened to less than 3 months. As December is usually a rainy month with lower ambient temperature, power consumption in air conditioning is lower than other months. It is therefore safe to use December consumption as the average monthly consumption.

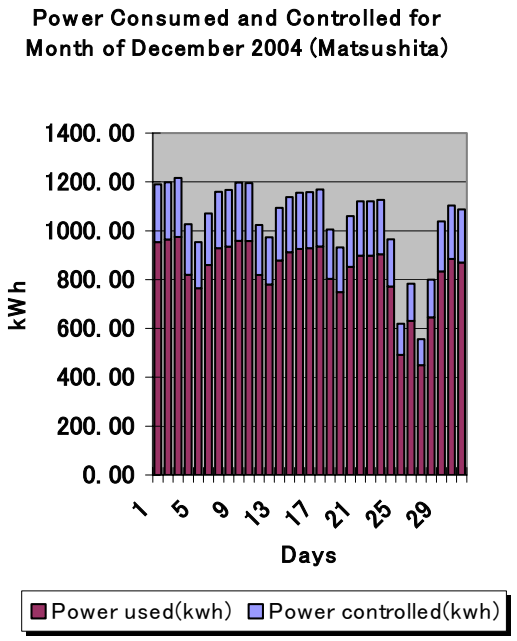

Figure 10 Daily power consumed and controlled for Matsushita PAC plant

MONITORING OF PAC SYSTEM

As half-hourly loading and unloading of compressors were recorded within the controller's memory system, any malfunction of compressor and its motor can be detected when data is downloaded to a computer for examination. It is also an added advantage that the BeONE controller can be doubled up as an equipment surveillance system for fault diagnosis and human malpractice.

CONCLUSIONS

In conclusion, the projects on saving power consumptions of packaged air cooled air conditioning systems have proven to be successful. Typical pay back period for medium sized office space of 1700 m^2 with power capacity of 40-kW is less than 2 years. In manufacturing plants where air conditioning is needed for 24 hours, pack back period will be shortened to a few months.

No damage on compressors or motors was observed for 6 months test running. The room temperature and humidity were maintained at the comfort zone for its occupants.

ACKNOWLEDGEMENTS

The authors are grateful to the supports of Nanyang Technological University, Office of Facilities Planning and Management; Toya Standard Co., Ltd. of Japan; Toya Standard (Asia) Pte Ltd and Matsushita Electronic Components (s) Pte Ltd. in this project.

REFERENCES

[1] Ganesh L R, *Initiatives and Schemes on Energy Management Undertaken by Public Sector*, Seminar on Efficient Energy Management, Singapore, September, 2000.

[2] PSB Corporation, *On Site Performance Test of Energy Saving Device, Report No 55S050076/GT/YCI*, PSB Corporation, Singapore, January 2005.

Proceedings of ECOS 2005
Trondheim, Norway
June 20–22, 2005

MODELLING OF LOW ENERGY COOLING STRATEGIES FOR UNDERGROUND RAILWAYS

Thompson J.A.[1], Maidment G.G., Karayiannis T.G. and Missenden J.F.
Department of Engineering Systems, London South Bank University,
103 Borough Road, London SE1 0AA

ABSTRACT

Underground railways often experience high temperatures during the summer months. It is not practical to install conventional cooling systems on the older underground systems because of increased heat rejection. Sustainable and low energy cooling systems have been developed for use in conventional building services applications but have not been used on underground railways because of an inability to effectively model them in this type of environment. This paper introduces a novel mathematical model, which has been used to investigate low energy cooling strategies on underground railways.

Keywords: Sustainable Cooling, Underground Railways, Mathematical Modeling

NOMENCLATURE

A	Frontal train area [m^2]
a	Interior of concrete liner radius [m]
b	Far field radius [m]
C_d	Drag coefficient
C_p	Specific heat of dry air in train [kJ/kg K]
D	Depth of pipe [m]
e	Traction motor efficiency
F	Mechanical resistance force [N]
g	Humidity ratio [kg/kg]
h_{fg}	Latent heat of evaporation, water [kJ/kg]
K_{earth}	Thermal conductivity of earth [W/mK]
KE	Kinetic energy [J]
L_{stop}	Stopping distance of train, max speed [m]
L	Length of section [m]
$\dot{m}_{air}$	Mass flow rate of ambient air [kg/s]
$\dot{m}_{tuair}$	Mass flow rate of tunnel air [kg /s]
N	Number of carriages to train
N_{Pass}	Number of passengers
n	Train frequency [trains/hour]
Q_{aero}	Heat gain from aerodynamic drag [W]
Q_f	Heat gain through train floor [W]
Q_g	Heat gain through train glass [W]
Q_{gr}	Heat load through the ground [W]
Q_{lat}	Latent heat gain from the train [W]
Q_{mech}	Mechanical heat losses [W]
Q_{pl}	Heat gain from passengers, latent [W]
Q_{ps}	Heat gain from passengers, sensible [W]
Q_{res}	Resistor heat losses [W]
Q_{sens}	Sensible heat gain for the train [W]
Q_{tl}	Heat gain from train lighting [W]
Q_{tlat}	Latent heat gain in the tunnel [W]
Q_{tul}	Heat gain from tunnel lighting [W]
Q_{tsen}	Sensible heat gains in the tunnel [W]
Q_w	Heat gain through train walls [W]
R	Exterior of concrete liner radius [m]
R_{total}	Total thermal resistance [m^2K/W]
T	Temperature [°C]
U	Thermal transmittance [W/m^2 K]
UA	UA value [W/K]
V_{ave}	Average train velocity [m/s]
W_e	Weight including rotational inertia [kg]
ρ	Air density [kg/m^3]

subscripts

amb	Ambient
t	Tunnel
tr	Train
FFR	Far Field Radius
s	Surface

[1] Corresponding author: Phone + 44 20 7815 7634
email thompsje@lsbu.ac.uk

INTRODUCTION

Underground railway systems can generate enough heat from their operations to raise tunnel and station temperatures as much as 8 to 12 K above outdoor temperatures, the greatest differences being at night and in the early morning hours [1]. Passenger discomfort will result in warm weather conditions if the underground railway environment is not cooled.

Ventilating techniques for an underground railway environment in which there is to be heavy traffic of electrically propelled rapid transit trains differ from those normally encountered in air-conditioning work. The heat generated by the train motors and electric lighting, together with body heat from passengers, is so great that excessive temperatures would prevail in the summer when limited cooling is available [1]. The installation of in car air-conditioning units adds another major heat source in the tunnel. This heat must be rejected to make in car air-conditioning units worthwhile.

The need in modern society to provide sustainable and low energy solutions to engineering problems is recognised through national and international legislation, [2]. This has produced an expansion in the use of low energy cooling strategies in buildings. Low energy is defined for the purposes of this paper as solutions, which provide substantial cooling power with minimal net energy input required. This could involve the use of ground cooling, thermal storage, nighttime and seasonal ventilation and phase change materials [3][4].

However, few low energy strategies have been used on an operational underground railway. This is largely due to the lack of a dedicated mathematical model to simulate their application in the thermal environment of underground railways, [1]. The mathematical models that are designed for use in underground railways do not currently take proper account of the capacitance, storage and heat sink issues which are associated with low energy cooling systems and are used for assessing peak summertime conditions in systems employing conventional technology, [1].

An initial proposal by Maidment and Missenden [5], suggested the use of a groundwater based cooling system to operate on an underground railway. The work included a mathematical model, which was used to evaluate the system. The model did not use fully crowded loading of passengers and as such was not investigating a worst-case scenario. This could lead to incorrect sizing of the system. The model also did not deal with the tunnel geometry and conditions in detail. The model was developed under steady state conditions and as such cannot model time varying effects. The preliminary work of [5] was continued by Ampofo et al. in [6]. This model corrected the passenger loading section to be under maximum crush loading. The model also extended the analysis to include the tunnel and provide it with specific geometry. It specifies a value of the far field radius taken from the earlier work [7]. The value given there though contains little justification of distance given as the far field radius. Also the concept of far field radius is still poorly reported in the literature.

This paper builds on the work of Maidment, Missenden and Ampofo et al. [5], [6] and describes the mathematical model that has been designed to provide an overview of the thermal environment of underground railways. The model uses steady state theory to show the inter-relationship between the various heat loads present in an underground railway. Whilst the model is unable to simulate the exact nature of the time dependence of low energy systems it can be used to provide an initial sizing of these systems. This model forms the basis of a transient simulation, which is being developed and will be published later.

OVERVIEW OF THE MODEL

The mathematical model has been written in EES (Engineering Equation Solver) created by f-Chart software [8]. This package was used for development of the model because EES will automatically determine the correct order to solve the equations entered. It allows each section of the model to be individually packaged without interdependence problems. EES allows easy parametric analysis for all variables in the system. Also EES has built in psychometric functions, which allows the easy calculation of humidity and thermal comfort for both the train and tunnel.

The model solves 143 equations iteratively to reach the solution. It has been designed to operate on a generic deep line underground railway tunnel section. The model uses the geometric and thermofluid properties of the railway under

investigation to determine its solutions. It predicts temperatures, humidities and thermal comfort parameters under summer worst-case scenario steady state conditions. It uses average peak loads and normal train running conditions. While the model has been constructed to be very general in nature the investigations were all performed using London Underground data and as such certain material and geometric constraints were modeled for the London system.

The tunnel is considered to be a control volume with the following loads considered and analysed.

- Internal heat generation
  - Train carriage heat loads
  - Heat generated by the braking mechanism
  - Heat generated by the tunnel lighting
- Ground heat sink load
- Ventilation heat due to air entering through the ventilation shafts

The tunnel is assumed to be cylindrical in cross-section having an internal diameter equal to 2R. The tunnel is formed from a hollow concrete lining which is also cylindrical. The final boundary is located at the far field radius (FFR). This is the distance away from the tunnel where there is no longer heat transfer occurring. While this point is theoretically located at infinity, for the purposes of this model the FFR has been varied to investigate the effect that this parameter has on the temperature of the system. If this variable is to be fixed then the value chosen was taken from the work of Cockram and Birnie [7] as 6.825 m. This is shown as distance b in Figure 1.

Internal Heat Load

Train Carriage load

The train carriage load is the heat load that is generated within the train carriage. The latent and sensible gains as a result of the passengers and operation of the train carriage are included in this section. The various loads are shown in Figure 2.

The solution is calculated by balancing the energy and mass transfer between the various components and the global system. The two global equations for latent and sensible heat gain are given in equations (1) and (2).

$$Q_{sen} = Q_r + Q_w + Q_g + Q_f + Q_{ps} + Q_{tl} \quad (1)$$

$$Q_{lat} = Q_{pl} \quad (2)$$

The train carriage construction for the roof, walls and floor are assumed to be made with an external and internal skin with mineral wool insulation in between. The external heat transfer coefficient was assumed to be mainly convective and to depend on the velocity of the surrounding air. The internal surface heat transfer coefficient was assumed to be constant. The heat transfer for the roof, walls and floor are all evaluated using the following conductive equation.

$$Q = UA(T_t - T_{tr}) \quad (3)$$

Where

$$UA = \sum AR_i^{-1} \quad (4)$$

Which is summed across all surfaces.

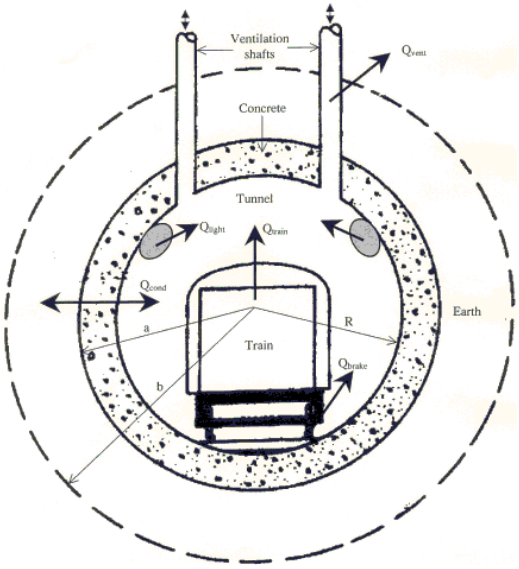

Figure 1 – Model representation of the tunnel control volume

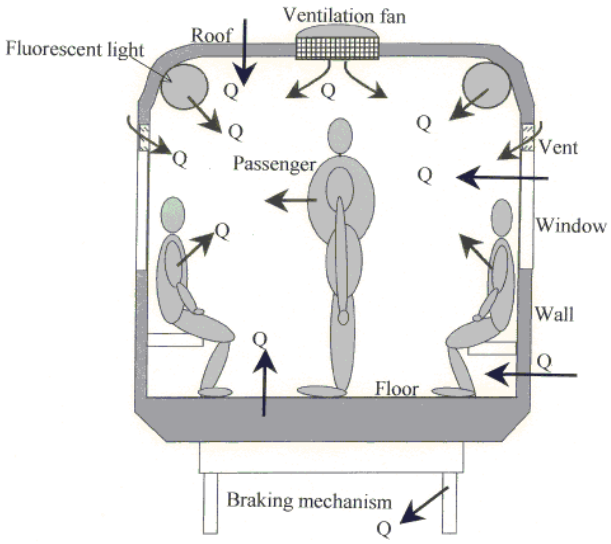

Figure 2 – Heat Loads in the train

The passenger load was assumed to be 90 people per carriage. This is a realistic average that could be expected on the London underground system during rush hour conditions in the center of London. The latent and sensible passenger heat gains were calculated according to equations (5) and (6).

$$Q_{ps} = -3.6517 \cdot T_{tr} + 168.15 \quad (5)$$

$$Q_{pl} = 3.6517 \cdot T_{tr} - 28.146 \quad (6)$$

Equations (5) and (6) were obtained by fitting trend lines to heat emission data for occupants involved in light activity, [9]. The train lighting was assumed to be 1400W per carriage.

The latent and sensible loads for the carriage can now be balanced with that produced from the ventilation air. The latent and sensible loads produced in this way are given in equations (7) and (8).

$$Q_{sens} = \dot{m}_{tuair} C_p \left(T_{tr} - T_t\right) \quad (7)$$

$$Q_{lat} = \dot{m}_{tuair} h_{evap} \left(g_{tr} - g_t\right) \quad (8)$$

Braking Mechanism

The heat load developed by the traction motor can be broken into three parts. The aerodynamic drag due to airflow generated within the tunnel; the mechanical friction losses due to the wheel, flange and other moving parts and the resistor losses due to electrical energy produced by the generators, [6]. The aerodynamic drag resistance is defined in equation (9).

$$Q_{aero} = \tfrac{1}{2} \rho V_{ave}^2 A C_D \cdot L_{stop} \cdot n \quad (9)$$

The mechanical friction is defined using equation (10). The weight in this equation is the equivalent weight taken from the combined weight of the train, the passengers and the rotational inertia.

$$Q_{mech} = F L_{stop} W_e N n \quad (10)$$

$$F = 0.0058 + \frac{516}{W_e} + 0.00045 \cdot V_{ave} \quad (11)$$

The final heat load in this section is the load due to the resistor losses. This parameter is defined in equation (12).

$$Q_{res} = \frac{KE}{e} \quad (12)$$

Here the kinetic energy is calculated with respect to the mass and velocity of the train as a whole.

Tunnel Lighting

The tunnel is assumed to have 100 fluorescent tubes per km each of which have an output of 50W. The lighting is assumed to be on at all times, although some subway systems only use tunnel lighting during 'engineering hours'.

Ventilation Heat Loads

The sensible and latent heat gains to the tunnel are in balance with the sensible and latent heat loads produced by the ventilation air entering the tunnel through the ventilation shafts. The heat gains to the tunnel are in equations (13) and (14).

$$Q_{tsen} = Q_{sens} + Q_{aero} + Q_{mech} + Q_{res} + Q_{tul} + Q_{gr} \quad (13)$$

$$Q_{tlat} = Q_{lat} \quad (14)$$

These heat loads are then balanced with equations (15) and (16).

$$Q_{tsen} = \dot{m}_{air} C_p \left(T_t - T_{amb}\right) \quad (15)$$

$$Q_{tlat} = \dot{m}_{air} h_{fg} \left(g_t - g_{amb}\right) \quad (16)$$

It should be noted that both C_p and h_{fg} both vary with changes in temperature. These two values are then not constant and are calculated by EES using the inbuilt psychometric functions.

Energy Balance

The heat loads in the system are then balanced using the following logic; In the summer, a cold air stream is continuously flowing into the tunnel through the ventilation shafts. Warmer air of the same mass flow rate is also flowing out of the ventilation shafts. The tunnel (control volume) is losing heat to the surrounding soil while the train, braking mechanism and tunnel lighting are heating the tunnel air. The conservation of energy principle is then applied to the underground railway system in the model.

Ground Heat Transfer

The heat transfer in the ground involves both steady and transient functions. Previous models had purely considered the steady state without considering the implications of the transient effects of heat. This investigation considers the implications of this on system performance.

The ground heat transfer load is the heat conducted through the tunnel walls and surrounding earth. Soil is a poor conductor and at depths beyond 5m the temperature is approximately constant. This temperature is the mean annual temperature and therefore during the summer months heat is

transferred from the tunnel to the surrounding soil. The simplest steady state theory for the calculation is that based on the thermal resistances. However CIBSE buried pipe equations could also be applicable in this situation, [10]. This coupled with the imprecise location of the FFR mean that this area of the model was investigated extensively. The two approaches are shown respectively in equations (17) and (18).

$$Q_{gr} = \frac{-(T_t - T_{FFR})}{R_{total}} \quad (17)$$

Where R_{total} is defined as the total thermal resistance to heat. In this case this comprises of three parts, resistance to heat in the tunnel, thermal resistance to heat through the tunnel walls and the thermal resistance to heat through the earth beyond the tunnel walls.

$$Q_{gr} = \pi 2RU(T_{surface} - T_{FFR})L_{tunnel} \quad (18)$$

Where U is the overall thermal transmittance and is given as

$$U = \frac{1}{R_{in} + R_{earth}} \quad (19)$$

R_{in} is the thermal resistance due to the tunnel liner and R_{earth} is given by equation (20), [10]

$$R_{earth} = \frac{a}{K_{Earth}} \ln\left[\frac{2D}{2R}\left(1+\left(1-\left(\frac{2R}{2D}\right)^2\right)^{0.5}\right)\right] \quad (20)$$

The results of the comparison of these models are shown in figures 3, 4 and 5. From figure 3 it can be seen that the train and tunnel temperature is approximately 2 K higher when using simple resistance theory than using the CIBSE buried pipe equations. The gradients using both solution methods are similar. Figure 4 shows that the simple resistance approach is strongly dependent on the position of the FFR. This figure shows the temperatures within the tunnel and trains against different FFR values for both the simple resistance and the CIBSE models for a given ambient temperature. It can be clearly seen that the CIBSE buried pipe model does not depend on far field radius but only on the depth of the pipe or in this case the tunnel. The depth of the tunnel is a known factor for an underground railway and therefore the CIBSE equations require only known information. In contrast the far field radius is not strongly reported and must be found either experimentally or by assumption.

Figure 5 shows the temperature variation through the tunnel lining and surrounding ground for the CIBSE model and the simple resistance model with a range of FFR values. The models have been using a given ambient temperature and have been compared against real data taken from Cockram

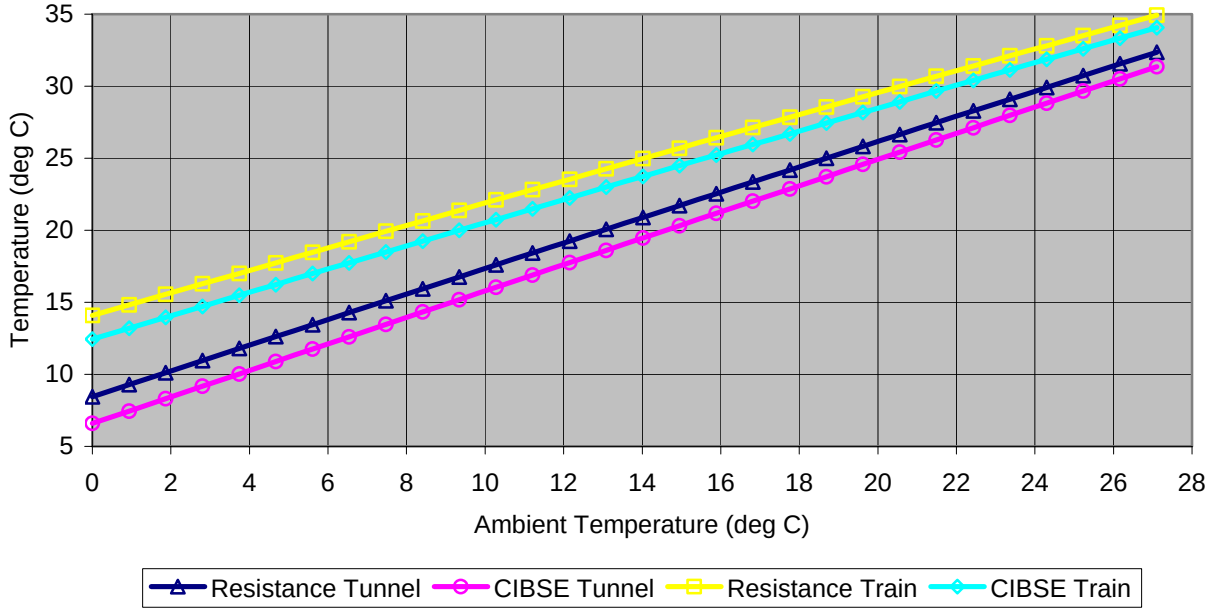

Figure 3 – Comparison of CIBSE buried pipe theory with thermal resistance theory

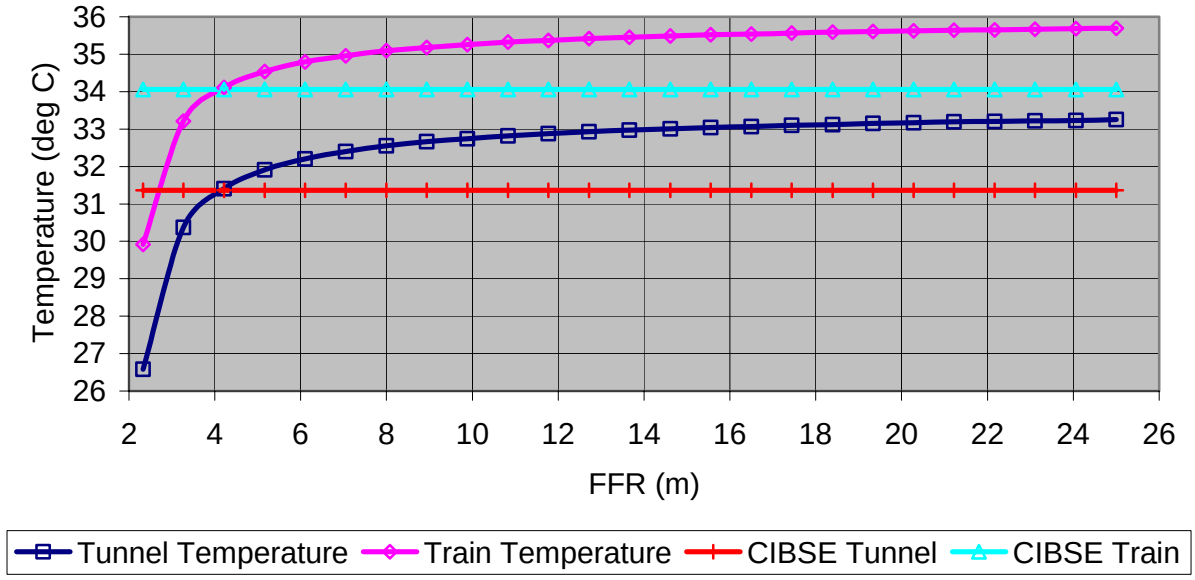

Figure 4 – Variation of FFR and its effect on temperature

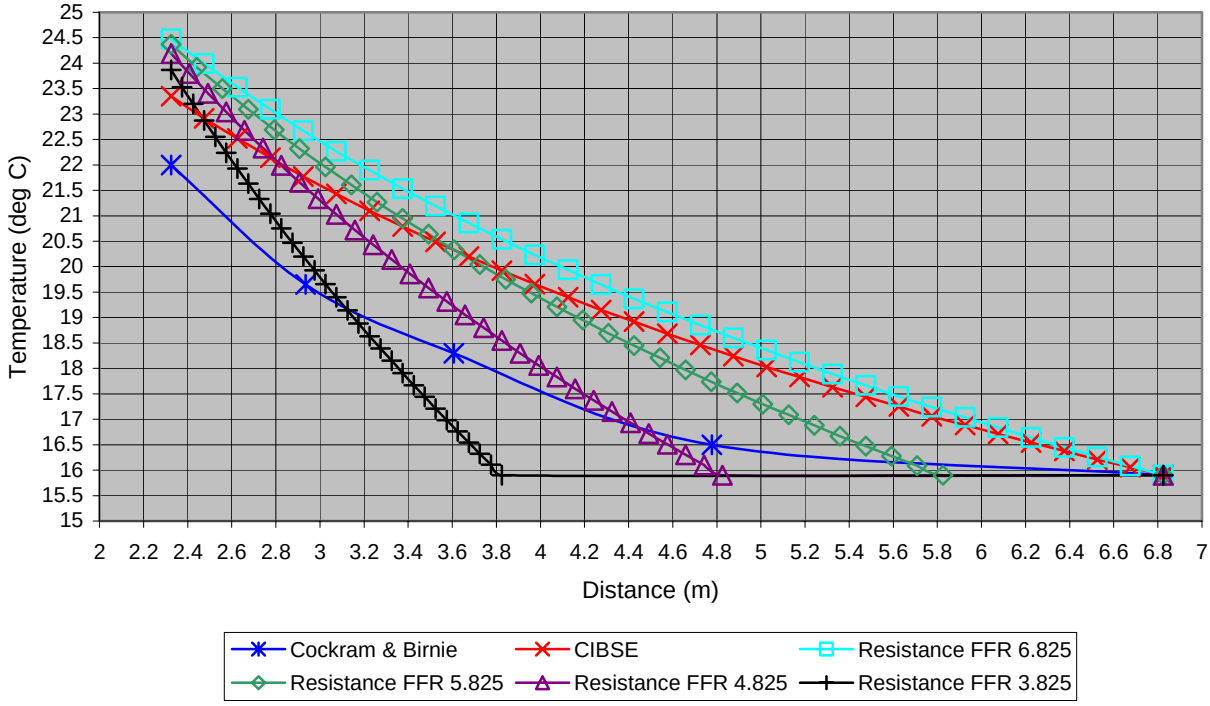

Figure 5 – Variation of temperature in the ground surrounding a railway tunnel

and Birnie [7]. From the results in Figure 5 it can be seen that all approaches produce similar temperature profiles to the Cockram and Birnie data. The main difference is that the surface and ground temperatures are colder than those predicted by the models. This is probably due to capacitance effects partly because the Birnie and Cockram data was obtained soon after the Victoria line was opened and partly due to diurnal variations.

Tunnel Wall Surface Temperature

It is assumed that there is no variation in temperature around the surface of the tunnel wall. Surface temperature can therefore be calculated at one point only and extended around the surface. It

was calculated using the surface finite differences equation taken from [11].

It can be observed that with all models the temperature of the bulk air is very close to the tunnel lining surface temperature. For both calculation methods the difference is very small and is approximately 0.15 K. This implies that the ground controls the heat transfer. The results also clearly show that whilst a FFR of 6.825 m is needed to simulate the deep ground temperature distribution accurately, the FFR value has much less of an effect on the lining surface temperature. The first 3 meters of tunnel lining therefore appear to control heat transfer.

Validation of the Mathematical Model

The model was shown to respond similarly to experimental data obtained from the London Underground. The experiment measured the train and tunnel temperature concurrently. The relative humidity of the train was also measured together with passenger loading and train position. As can be seen in Figure 6 the model has a similar gradient but is shifted to higher train temperatures. This is a consequence of trying to model a constantly transient system using steady state theory. Figure 7 shows the capacitance issues and coupling between train and tunnel temperatures. The variation in tunnel temperature is very large compared to the temperature variation in the train. Also the two temperatures do not peak at the same time. This shows that for complete understanding the ground heat transfer should be modeled using full transient analysis methods.

CONCLUSIONS

Current thermal modeling of underground railways does not allow for the successful modeling of sustainable cooling systems. This is because of poor modeling of the heat sink effect, thermal storage and other capacitance issues. This has led to a need to improve the modeling of these effects under the complex environment of an underground railway tunnel.

This paper has presented a mathematical model that provides an initial overview of the heat transfer in an underground railway. This model is used to provide an overview of the thermal environment and focus the research on the areas that require full transient modeling. The model now needs revising to allow for transient effects to be evaluated in conjunction with the sustainable cooling schemes.

The ground heat sink effect will require full transient modeling because of the potential for heat transfer both to and from the ground depending on how the remainder of the environment reacts to the heat loads in the system. This will enable the full use of geothermal cooling in underground railway systems.

ACKNOWLEGMENTS

London Underground has supplied both data and documentation to assist with this project. They have also allowed the authors to conduct experiments on the underground railway. This PhD is funded by the Engineering and Physical Sciences Research Council and their support is gratefully acknowledged.

REFERENCES

[1] Thompson J.A., Maidment G.G., Karayiannis T.G., Missenden J.F. and Ampofo F, *Low Energy Cooling Strategies on Underground Railways*, 3rd Int. Conf. Heat Powered Cycles, Cyprus, 2004.

[2] Rybach L., *Geothermal energy: sustainability and the environment*, Geothermics, 2003, 32 pp 463 – 470

[3] Ampofo F., Maidment G.G. and Missenden J.F., *Underground railway environment in the UK Part 3: Methods of delivering cooling*, Applied Thermal Engineering, 2004, 24 pp 647 – 659

[4] Seaman A., Martin A. and Sands J., *HVAC Thermal Storage: Practical application and performance issues*, BSRIA Application guide AG 11/2000, 2000

[5] Maidment G.G. and Missenden J.F., *Evaluation of an underground railway carriage operating with a sustainable groundwater cooling system,* Int. Jour. Refrigeration, 2002, 25 pp 569 – 574

[6] Ampofo F., Maidment G.G. and Missenden J.F., *Underground railway environment in the UK Part 2: Investigation of heat load*, Applied Thermal Engineering, 2004, 24 pp 633 – 645

[7] Cockram I.J. and Birnie G.R., *The Ventilation of London's Underground Railways*, 2nd Int.

Symp. on the Aerodynamics and Ventilation of Vehicle Tunnels, Cambridge, 1976
[8] F-Chart Software, http://www.fchart.com/, 2004
[9] CIBSE, *Section A Design Data*,CIBSE, pp A7-3, 1986
[10] CIBSE, *Section C Reference Data*, CIBSE, 1986
[11] Fundamentals of Heat and Mass Transfer, Incropera, F.P. and DeWitt, D.P., John Wiley 5th Edition, 2002

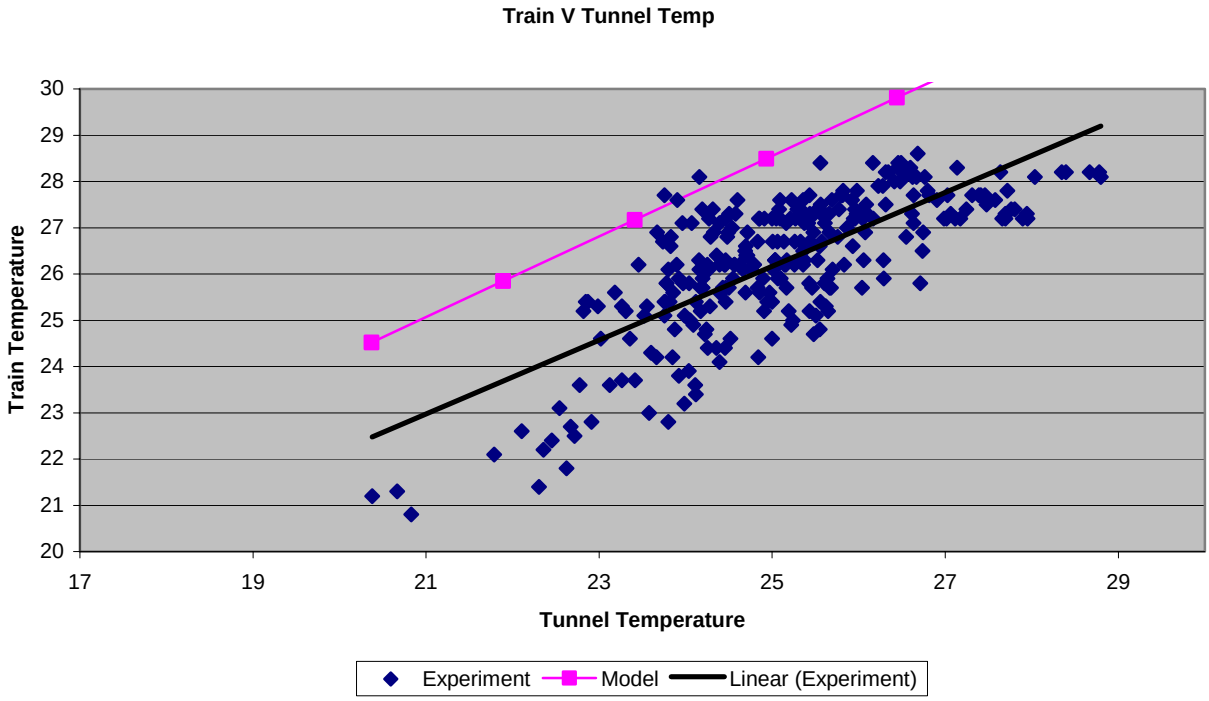

Figure 6 – Comparison of Model with Experiment

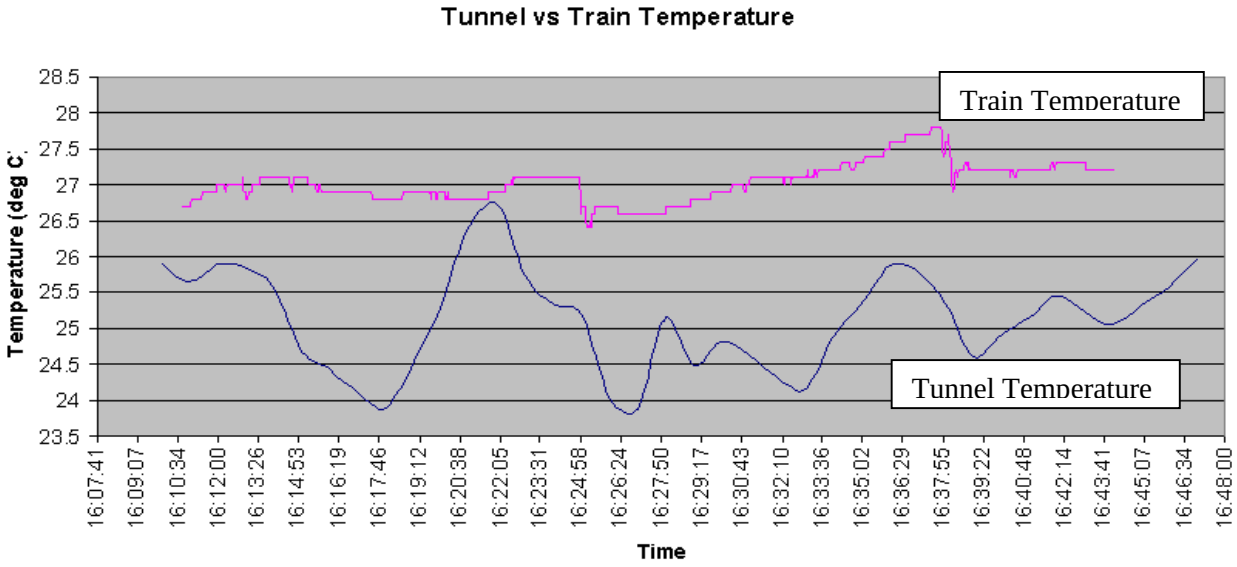

Figure 7 – Temperature variation over time on the Victoria Line, London Underground.

Proceedings of ECOS 2005
Trondheim, Norway
June 20–22, 2005

THERMOECONOMIC EVALUATION AND OPTIMIZATION OF AN WATER-AMMONIA VAPOUR-ABSORPTION REFRIGERATION SYSTEM USING EVOLUTIONARY PROGRAMMING

P. K. Sahoo*
Mechanical & Industrial Engineering Department
Indian Institute of Technology Roorkee, Roorkee - 247 667 (India)
R. D. Misra
Mechanical Engineering Department
National Institute of Technology Silchar, Silchar – 788 010 (India)

ABSTRACT
The main obstacles of the aqua-ammonia vapour-absorption refrigeration (VAR) systems for getting the market acceptance are their higher investment cost and lower first law efficiency when driven by high exergy input. In this paper, the thermoeconomic concept is applied to the optimization of an aqua-ammonia VAR system—aimed at minimizing its overall product cost. Thermoeconomic concept based simplified cost minimization methodology calculates the economic costs of all the internal flows and products of the system by formulating thermoeconomic cost balances. The system is then thermoeconomically evaluated to identify the effects of design variables on costs and thereby enables to suggest values of design variables that would make the overall system cost-effective. Finally, the optimization of the system is carried out using evolutionary programming. The optimized result shows that the performance of the system can be improved significantly without any additional capital investment.

Keywords: thermoeconomic analysis; aqua-ammonia; exergy; optimization.

NOMENCLATURE

c = Cost per exergy unit (Rs kJ^{-1})
COP = Coefficient of performance
$\dot{C}$ = Cost flow rate (Rs hr^{-1})
e = Specific exergy (kJ kg^{-1})
$\dot{E}$ = Exergy flow rate (kW)
f = Thermoeconomic factor (%)
h = Specific enthalpy (kJ kg^{-1})
i_r = interest rate (Rs yr^{-1})
$\dot{m}$ = Mass flow rate (kg s^{-1})
N_y = years
r = Relative cost difference (%)
s = Specific entropy (kJ kg^{-1} K^{-1})
t = Temperature on Centigrade scale (C)
T = Temperature on Kelvin scale (K)
Y = Ratio of exergy destruction (or loss) to total exergy supplied to the system
z = Concentration
Z =Investment cost of the system components (Rs)
$\dot{Z}$ = Levelized (annual) investment cost of the system components (Rs s^{-1})

Greek letters

c = Effectiveness of the heat exchangers
e = Exergetic efficiency (%)
h = Isentropic or mechanical efficiency
t = Annual number of hours of system operations
x = Capital recovery factor

Superscripts

Ch = Chemical component
Ph = Physical component

Subscripts

0 = Environmental state
1,2,3,....i,...17,18 = System state points
a = Absorber
c = Condenser
D = Exergy destruction
e = Evaporator
ea = Evaporator assembly
ex = Expansion valve
F = Fuel
g = Generator
H_2O = Water
i = The ith stream

in = Entering streams
k = The k^{th} component of the system
L = Exergy losses
m = Electric motor
NH_3 = Ammonia
out = Exiting streams
p = Pump
P = Product
r = Rectifier
rhx = Refrigerant heat exchanger
shx = Solution heat exchanger
tot = Total system

Vector & Matrices

$[A]$ = Matrix containing the unknowns
$[X]$ = Vector of unknown variables
$[Y]$ = Vector of known variable

INTRODUCTION

Ammonia absorption refrigeration is one of the oldest known refrigeration technologies. The vapour-compression technology invented later almost ousted the absorption systems because of poor efficiency and higher cost of absorption systems. Vapour-compression systems use electricity, which has poor conversion efficiency. Presently, the energy and environmental norms regarding the ozone layer depletion and global warming are becoming more and more stringent in almost all countries [1]. In this challenging scenario, the binary mixture of ammonia and water has once again become a research topic in the past few years. The natural character of this mixture and its excellent thermodynamic properties equal out its negative aspects.

The oil embargoes of the 1970s focused attention on the efficient use of energy. Attention refocused on the concept of exergy, because it allows a uniform basis to compare between disparate processes. Since the exergy analysis (i.e. the second law analysis) gives a clear picture about the losses of a system quantitatively as well as qualitatively, the use of exergy in the thermodynamic analysis and optimization becomes obvious choice [2]. However, the thermodynamic optimization, which aims at achieving the maximum thermodynamic efficiency, does not guarantee a cost-effective design. It is because the cost of a component/system generally increases with the increase in its efficiency. This calls for multi-disciplinary analysis and optimization. In this respect, the thermoeconomic concept has emerged to be a better tool as it addresses this multi-disciplinary analysis by blending the exergy analysis with economic analysis. The most significant advantage of the thermoeconomic optimization method lies in its capacity to solve complex practical problems without using sophisticated numerical analysis.

The recent developments by Tsatsaronis and his coworkers [3], Valero and his coworkers [4,5], Frangopoulos [6], von Spakovsky [7], d'Accadia and de Rossi [8] adequately represent the different directions of development. The major fields of application of these developments are mainly in the field of large cogeneration and combined power plants, chemical plants, etc. [3-7], whereas the domains of refrigeration and air-conditioning are still limited. Application of thermoeconomics to refrigeration systems can be found in references [8-11]. It is because the industrial utilities are probably considered with great interest, as they are capital intensive. Refrigeration systems, particularly absorption systems, require improvement in theirs performance to be competitive with conventional vapour compression systems.

In this work, a heat-operated aqua-ammonia VAR system is analyzed using thermoeconomic principles and optimized using evolutionary programming.

ASSUMPTIONS USED IN THE ANALYSIS

Figure 1 shows the schematic diagram of an aqua-ammonia VAR system, which uses ammonia as refrigerant and water as absorbent. For the purpose of analysis the following assumptions are made:

- The system is in steady state.
- The temperatures of the condenser, evaporator, absorber, generator, and rectifier are constant and uniform throughout the components.
- The condenser and evaporator pressures are the equilibrium pressures corresponding to the temperatures and concentrations in the condenser and evaporator respectively.
- The pressure loss in pipes between the rectifier and the condenser, and between the RHE and the absorber, respectively, are taken as $\Delta p/p_{out}$ =0.05 and $\Delta p/p_{out}$ =0.05 [12].
- Strong solution leaving the absorber and the weak solution leaving the generator are in equilibrium at their respective temperature and pressure.
- The refrigerant vapour concentration at the rectifier exit is equal to 0.999 [12].

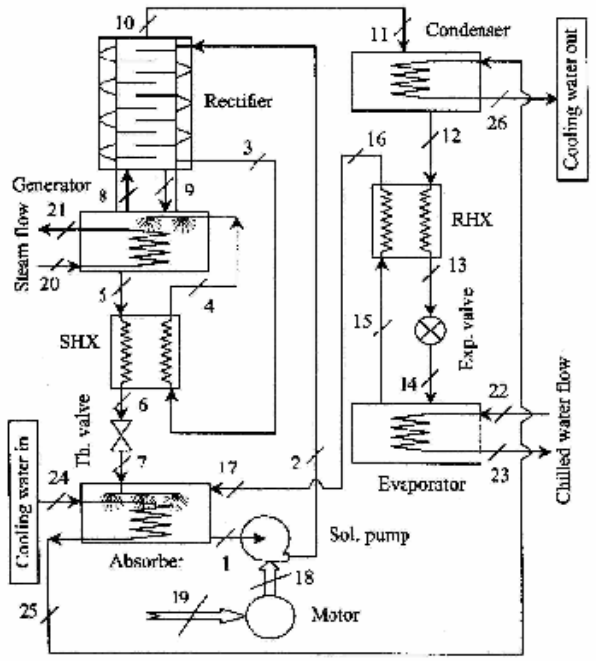

Figure 1. Schematic diagram of the Aqua-ammonia vapour absorption system.

- The generator temperature and pressure determine the vapour concentration at State 8, while the rectifier temperature and pressure determine liquid concentration at State 9.
- Refrigerant vapour at the rectifier and evaporator exit is equivalent to the vapour state at their respective temperature and pressure, while refrigerant liquid at the condenser exit is equivalent to the liquid state at the condenser temperature and pressure.
- The rectifier temperature is equal to the average temperature between the generator and the condenser temperature.
- The reference environmental state for the system is water at an environment temperature (T_0) of 25^0C and 1 atmospheric pressure(p_0).
- The system uses high-pressure steam to drive the generator.
- Cooling water first enters the absorber at 27^0C, then is passed through the condenser, and finally is rejected by the system at 35^0C.
- The chilled water enters the evaporator at 20^0C and leaves at 10^0C.

Based on these assumptions, a workable initial design, referred to as the base case, is conceptualized for the VAR system shown in Fig. 1 with the following data: t_g = 150^0C, t_c = 40.3^0C, t_e = -10^0C, t_a = 39.4^0C, c_{rhx} = 60 %, c_{shx} = 60 %, h_p = 75%, h_m = 90%, t_{21} = 170^0C, t_{22} = 170^0C. Thermodynamic properties of the aqua-ammonia mixture in liquid and gas phase are taken from the work of Ziegler and Trepp [13]. The property data for the water/steam are taken from the correlations provided by Irvine and Liley[14].

EXERGY ANALYSIS

The second law analysis, i.e. the exergy analysis, calculates the system performance based on exergy, which is defined as the maximum possible reversible work obtainable in bringing the state of the system to equilibrium with that of environment [2]. In the absence of magnetic, electrical, nuclear, surface tension effects, and considering the system is at rest relative to the environment, the total exergy of a system can be divided into two components: physical exergy and chemical exergy;

$$\dot{E} = \dot{E}^{Ph} + \dot{E}^{Ch} \quad (1)$$

The physical exergy component is calculated using the following relation:

$$\dot{E}^{Ph} = \dot{m}\left[(h - h_0) - T_0(s - s_0)\right] \quad (2)$$

The calculation procedure of the chemical exergy of various substances based on standard chemical exergy values of respective species is widely discussed by Bejan et al. [2], Ahrendts [15], and Szargut et al. [16]. Chemical exergy of the flows is calculated using the following equation:

$$\dot{E}_i^{CH} = \dot{m}_i\left[\left(\frac{z_i}{M_{NH_3}}\right)e^0_{CH,NH_3} + \left(\frac{1-z_i}{M_{H_2O}}\right)e^0_{CH,H_2O}\right] \quad (3)$$

where, e^0_{Ch,NH_3} and e^0_{Ch,H_2O} are the standard chemical exergy of ammonia and water, respectively, and their values are taken from Ahrendts [15].

A detailed exergy analysis includes calculation of exergy destruction, exergy loss, exergetic efficiency, exergy destruction ratio, and exergy loss ratio in each component of the system along with the overall system. Mathematically, these are expressed as follows [2]:

$$\dot{E}_{D,k} = \dot{E}_{F,k} - \dot{E}_{P,k} - \dot{E}_{L,k} \quad (4)$$

$$e_k = \dot{E}_{P,k} / \dot{E}_{F,k} = 1 - \left[\left(\dot{E}_{D,k} + \dot{E}_{L,k}\right) / \dot{E}_{F,k}\right] \quad (5)$$

$$Y_{D,k} = \dot{E}_{D,k} / \dot{E}_{F,total} \quad (6)$$

$$Y_{L,k} = \dot{E}_{L,k} / \dot{E}_{in,tot} \quad (7)$$

The exergy analysis of the system and its components are carried out using fuel-product relationships and Eqs. (4-7). The results are

summarized in Table 1. Low exergetic efficiency of the system suggests the designer to find means for the improvement of the overall exergetic efficiency to maximum possible value. However, the thermodynamic optimum, so obtained, does not guarantee a cost-optimal design. A cost-optimal design can be obtained through thermoeconomic analysis and optimization of the system, which is discussed in the following sections.

Table 1. Exergy analysis of the system - base case.

Compo-nents	$E_{F,k}$ (kW)	$E_{P,k}$ (kW)	$E_{D,k}$ (kW)	$E_{L,k}$ (kW)	$Y_{D,k}$ (%)	$Y_{L,k}$ (%)	e_k (%)
Generator	75.1	57.6	17.6	0.00	23.2	0.00	76.6
Rectifier	6.79	2.30	4.50	0.00	5.92	0.00	33.8
Evaporator assembly	46.2	3.49	36.3	6.42	47.7	8.45	7.56
RHX	0.46	0.16	0.30	0.00	0.40	0.00	34.4
Solution pump	0.83	0.47	0.37	0.00	0.48	0.00	56.0
SHX	17.3	10.6	6.73	0.00	8.85	0.00	61.2
Overall system	76.0	3.49	66.1	6.42	87.0	8.45	4.59

THERMOECONOMIC ANALYSIS

The prerequisite for the thermoeconomic analysis is a proper 'Fuel-Product-Loss' definition of the system to show the real production purpose of its subsystems by attributing a well defined role, i.e. fuel, product or loss, to each physical flow entering or leaving them [2]. In the case of aqua-ammonia system, this is quite easy for the generator, rectifier, evaporator, pump, solution heat exchanger (SHX), and refrigerant heat exchanger (RHX), where exergy of the product stream is increased. However, in the case of heat dissipative devices, e.g. the condenser, expansion valve, absorber, and the throttling valve, the product cannot be readily defined. Therefore, they are considered as a single virtual component, named as evaporator assembly, together with the component(s) they serve, i.e. the evaporator in this case. The 'Fuel-Product-Loss' (F-P-L) structure of the system is shown in Fig. 2. Thus, the system can be considered to be composed of six productive components, namely, generator, rectifier, evaporator assembly, solution pump, RHX, and SHX.

The thermoeconomic costs of all the flows that appear in the system's F-P-L definition are

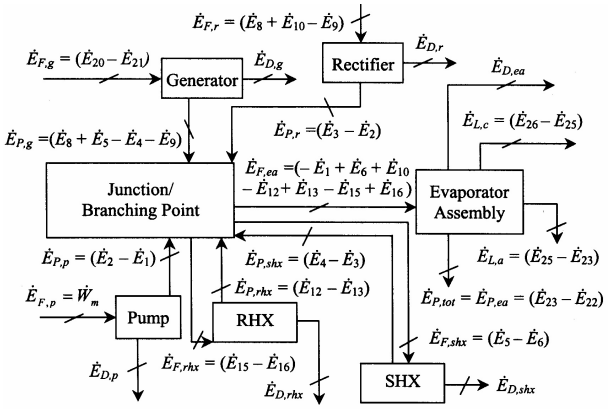

Figure 2. Fuel-Product-Loss structure of the system

obtained through exergy costing principles, discussed by Bejan et al. [2]. Exergy costing involves formulation of cost balances for each component. One can write six equations for the six subsystems shown in the productive structure. The number of unknowns is more than the number of subsystems and one needs auxiliary equations to have a close form solution. The cost balance equations along with auxiliary equations for each of the subsystems are given below:

Generator: The purpose of the generator is to provide a stream of ammonia vapour (stream 8) and a weak solution of refrigerant (stream 5). This purpose is achieved by supplying the exergy of steam to it. Hence, streams 8 and 5 are charged with all costs associated with owning and operating the generator. Thus, the following equations are developed:

$$\dot{C}_H + \dot{C}_4 - \dot{C}_5 - \dot{C}_8 + \dot{C}_9 = -\dot{Z}_g \tag{8}$$

$$\frac{\dot{m}_8(c_8 e_8 - c_4 e_4)}{\dot{m}_8(e_8 - c_4)} = \frac{\dot{m}_5(c_5 e_5 - c_4 e_4)}{\dot{m}_5(e_5 - c_4)}$$

$$\Rightarrow \frac{(e_8 - e_5)\dot{C}_4}{\dot{m}_4(e_8 - e_4)(e_5 - e_4)} - \frac{\dot{C}_5}{\dot{m}_5(e_5 - e_4)} + \frac{\dot{C}_8}{\dot{m}_8(e_8 - e_4)} = 0 \tag{9}$$

$$\frac{\dot{m}_8(c_8 e_8 - c_9 e_9)}{\dot{m}_8(e_8 - c_9)} = \frac{\dot{m}_5(c_5 e_5 - c_9 e_9)}{\dot{m}_5(e_5 - c_9)}$$

$$\Rightarrow -\frac{\dot{C}_5}{\dot{m}_5(e_5 - e_9)} + \frac{\dot{C}_8}{\dot{m}_8(e_8 - e_9)} + \frac{(e_8 - e_5)\dot{C}_9}{\dot{m}_9(e_8 - e_9)(e_5 - e_9)} = 0 \tag{10}$$

Rectifier: The purpose of the rectifier is to drag the possible amount of unwanted water vapour from the ammonia vapour leaving the generator (stream 10) by cooling it. The condensed water is returned to the generator (stream 9). The cooling is done by the strong solution leaving the pump. Hence, streams 10 and 9 are charged with all costs associated with owning and operating the generator. Thus, the following equations are developed:

$$\dot{C}_2 - \dot{C}_3 + \dot{C}_8 - \dot{C}_9 - \dot{C}_{10} = -\dot{Z}_r \tag{11}$$

$$\frac{\dot{m}_9(c_9 e_9 - c_8 e_8)}{\dot{m}_9(e_9 - c_8)} = \frac{\dot{m}_{10}(c_{10} e_{10} - c_8 e_8)}{\dot{m}_{10}(e_{10} - c_8)}$$

$$\Rightarrow \frac{(e_{10} - e_9)\dot{C}_8}{\dot{m}_8(e_9 - e_8)(e_{10} - e_8)} - \frac{\dot{C}_9}{\dot{m}_9(e_9 - e_8)} + \frac{\dot{C}_{10}}{\dot{m}_{10}(e_{10} - e_8)} = 0 \tag{12}$$

RHX: The purpose of the RHX is to subcool the liquid refrigerant leaving the condenser (stream 12) by the refrigerant vapour (stream 15) leaving the evaporator. Therefore, stream 13 is charged with all costs associated with owning and operating the RHX. Accordingly, the cost equations become,

$$\dot{C}_{12} - \dot{C}_{13} + \dot{C}_{15} - \dot{C}_{16} = -\dot{Z}_{rhx} \tag{13}$$

$$\dot{C}_{15} - (\dot{E}_{15}/\dot{E}_{16})\dot{C}_{16} = 0 \tag{14}$$

Solution pump: The purpose of the pump is to raise the pressure of the strong solution leaving the absorber (stream 2) to the generator pressure with the help of external work. Thus, stream 2 is charged with all costs associated with purchasing and operating the pump (with motor). Accordingly, the cost equation becomes

$$\dot{C}_m + \dot{C}_1 - \dot{C}_2 = -(\dot{Z}_p + \dot{Z}_m) \tag{15}$$

SHX: The purpose of SHX is to transfer the exergy of weak solution (stream 5) coming from the generator to the strong solution moving towards the generator (stream 4). Therefore, stream 4 is charged with all costs associated with owning and operating the SHX. Accordingly, the cost equations become

$$\dot{C}_3 - \dot{C}_4 + \dot{C}_5 - \dot{C}_6 = -\dot{Z}_{shx} \tag{16}$$

$$\dot{C}_5 - (\dot{E}_5/\dot{E}_6)\dot{C}_6 = 0 \tag{17}$$

Evaporator assembly: The evaporator and heat dissipative components—condenser, expansion valve, absorber, and throttling valve—are combined in the evaporator assembly. The cost rates associated with the capital investment for these components and the cost rates associated with the exergy losses are charged to the final product. The cost rates associated with the exergy losses in condenser and absorber are given by the following two equations

$$\dot{C}_{11} - \dot{C}_{12} - \dot{C}_{L,c} = -\dot{Z}_c \tag{18}$$

$$-\dot{C}_1 + \dot{C}_7 + \dot{C}_{17} - \dot{C}_{L,a} = -\dot{Z}_a \tag{19}$$

For the dissipative components and the evaporator, following auxiliary equations are developed:

$$\dot{C}_6 - (\dot{E}_6/\dot{E}_7)\dot{C}_7 = 0 \tag{20}$$

$$\dot{C}_{10} - (\dot{E}_{10}/\dot{E}_{11})\dot{C}_{11} = 0 \tag{21}$$

$$\dot{C}_{11} - (\dot{E}_{11}/\dot{E}_{12})\dot{C}_{12} = 0 \tag{22}$$

$$\dot{C}_{13} - (\dot{E}_{13}/\dot{E}_{14})\dot{C}_{14} = 0 \tag{23}$$

$$\dot{C}_{14} - (\dot{E}_{14}/\dot{E}_{15})\dot{C}_{15} = 0 \tag{24}$$

$$\frac{\dot{C}_1}{\dot{E}_1} - \frac{\dot{C}_7 + \dot{C}_{17}}{\dot{E}_7 + \dot{E}_{17}} = 0 \tag{25}$$

$$\dot{C}_{16} - (\dot{E}_{16}/\dot{E}_{17})\dot{C}_{17} = 0 \tag{26}$$

Since the purpose of the evaporator is to transfer exergy from stream 14 to the product stream 23, therefore, all costs associated with the owning and operation of the evaporator is charged to stream 23. Considering all these points the following cost equations are developed:

$$-\dot{C}_1 + \dot{C}_6 + \dot{C}_{10} - \dot{C}_{12} + \dot{C}_{13} - \dot{C}_{15} + \dot{C}_{16} - \dot{C}_{L,c} - \dot{C}_{P,tot} - \dot{C}_{L,a} = -(\dot{Z}_c + \dot{Z}_{ex} + \dot{Z}_e + \dot{Z}_a + \dot{Z}_v) \tag{27}$$

In the above formulations cost of equipment are calculated using relations provided in references [17,18]. The cost per exergy unit of the product of the system is given by,

$$c_{P,tot} = \frac{\dot{C}_{P,tot}}{\dot{E}_{P,tot}} = \frac{\dot{C}_{23} - \dot{C}_{22}}{\dot{E}_{23} - \dot{E}_{22}} \tag{28}$$

Out of these 22 variables used for system analysis $[X] = \{\dot{C}_1, ..., \dot{C}_{17}, \dot{C}_{L,c}, \dot{C}_{L,a}, \dot{C}_{P,tot}, \dot{C}_H, \text{and } \dot{C}_m\}$, the last two are known parameters. They are the costs of steam used to energize the generator $(\dot{C}_H)$ and the electrical energy input to the solution pump through the motor $(\dot{C}_m)$, and their values are Rs. 300.0 per 1000 kg of steam and Rs. 5.00/kWh espectively. These are the existing market price in

India. The remaining 20 unknowns are calculated by solving the linear system of equations ($[A][X]=[Y]$), where the coefficient matrix $[A]$ contains the terms on the LHS and $[Y]$ contains the terms on the RHS of Eqs. (8-27).

THERMOECONOMIC EVALUATION

In this section, the system is evaluated with the help of the following thermoeconomic variables, namely, the average unit cost of fuel ($c_{F,k}$), the average unit cost of product ($c_{P,k}$), the cost rate of exergy destruction ($\dot{C}_{D,k}$), the cost rate of exergy loss ($\dot{C}_{L,k}$), and the thermoeconomic factor (f_k). These are calculated using the following relations [2]:

$$c_{F,k} = \dot{C}_{F,k} / \dot{E}_{F,k} \quad (29)$$

$$c_{P,k} = \dot{C}_{P,k} / \dot{E}_{P,k} \quad (30)$$

$$\dot{C}_{D,k} = c_{F,k} \dot{E}_{D,k} \quad (\dot{E}_{P,k} \text{ is constant}) \quad (31)$$

$$\dot{C}_{L,k} = c_{F,k} \dot{E}_{L,k} \quad (\dot{E}_{P,k} \text{ is constant}) \quad (32)$$

$$f_k = \frac{\dot{Z}_k}{\dot{Z}_k + \left(\dot{C}_{D,k} + \dot{C}_{L,k}\right)} \quad (33)$$

The guidelines for the thermoeconomic evaluation are presented in details by Bejan et al. [2]. The thermoeconomic analysis results for the base case operating conditions of the system are presented in Table 2. It is seen that the evaporator assembly has the maximum value of $(\dot{C}_{D,k} + \dot{C}_{L,k} + \dot{Z}_k)$ with higher value of r_k and a lower value of f_k. Therefore, improvement of the exergetic efficiency of this unit should be considered at the cost of capital investment. The generator has the second largest value of $(\dot{C}_{D,k} + \dot{C}_{L,k} + \dot{Z}_k)$ with slightly lower values of f_k, suggesting the possibility of increasing the generator temperature. The third next component in that order is the SHX, where the lower value of f_k suggests improvement in exergetic efficiency through increase in its effectiveness. Next comes the rectifier, where there is no direct decision variable controlling the exergetic efficiency or the investment cost for this component, rather it is controlled mainly by the generator and condenser temperatures. Therefore, the effect of these two variables on rectifier is seen globally. As far as RHX is concerned, there is a slight scope for improvement in the exergetic efficiency of the system by increasing its effectiveness. The solution pump, on the other hand, shows a very high value of thermoeconomic factor f_k. The logical conclusion would be to try to decrease the investment cost of pump at the cost of its exergetic efficiency. This information for each component is extremely helpful to the designer for the improvement of the system.

Table 2. Results of the thermoeconomic analysis of the system – Base Case

Compo-nents	$c_{F,k}$ (Rs./GJ)	$c_{P,k}$ (Rs./GJ)	$C_{D,k}$ (Rs./hr)	$C_{L,k}$ (Rs./hr)	Z_k (Rs./hr)	$C_{D,k}+C_{L,k}+Z_k$ (Rs./hr)	f (%)
Gen.	447.48	722.83	28.34	0.00	28.7	57.05	50.3
Rect.	722.83	2471.8	11.71	0.00	2.8	14.46	19.0
Evap. Assem.	1023.7	5365.4	133.6	23.7	106.5	263.82	40.4
RHX	883.73	5365.1	0.96	0.00	1.6	2.55	62.3
Sol. pump	1395.0	6532.4	1.85	0.00	6.8	8.63	78.6
SHX	1610.6	2765.8	39.0	0.00	5.1	44.10	11.6
Overall system	457.89	5365.4	108.9	10.58	302.9	422.37	71.7

OPTIMIZATION OF THE SYSTEM USING EVOLUTIONARY PROGRAMMING

Theoretically, the system optimization requires a compromise between two conflicting objectives; one is the increase in the exergetic efficiency and the other is a decrease in the product cost. The first objective is governed by thermodynamic requirements and the second by economic constraints. The maximization of exergetic efficiency means minimization of exergy destruction costs and exergy loss costs. Thus, the objective function becomes a minimization problem. Cammarata et al. [19] demonstrated the use of this technique in optimizing district heating networks using GA. The objective function for this problem is defined as to minimize a total cost function $\dot{C}_S$, which can be modeled as:

$$\dot{C}_S = \dot{C}_{P,total} + \dot{C}_{L,total} \quad (34)$$

$$\text{where, } \dot{C}_{P,total} = \dot{C}_{F,total} + x\, Z_{total} \quad (35)$$

The cost of exergy destruction is a hidden cost and is charged to the product cost. The capital recovery

factor x is calculated using the following relation

$$x = \left(\frac{i_r.(1+i_r)^{N_y}}{(1+i_r)^{N_y}-1} \right) \text{ yr}^{-1} \qquad (36)$$

The system is subject to the following constraints:

- minimum approach temperature for the condenser and absorber $\geq 2^0$C
- minimum approach temperature for the evaporator $\geq 2.5^0$C
- minimum approach temperature for the generator $\geq 10^0$C
- $70 \leq h_p \leq 90$ %
- $50 \leq c_{rhx} \leq 90$ %
- $50 \leq c_{shx} \leq 90$ %

The main steps of the optimization procedure are as follows:

Initialization: The i[th] trial vector that represents the decision variables of this system to be optimized can be written as $\overline{p}_i = [t_{g,i}, t_{c,i}, t_{e,i}, t_{a,i}, c_{rhx,i}, c_{shx,i}, h_{p,i}]$. Selecting each decision variable randomly from their allowable range creates each trial vector. For each trial, the objective function is evaluated through the thermoeconomic formulations after satisfying the constraints mentioned above.

***Fitness Evaluation*:** As shown in Fig.3, in the first part, the program evaluates fitness of the parent individuals (N_p) capable for producing offspring from a randomly generated large population. The value of the objective function, $\dot{C}_S$, is used as the fitness function for evaluating the fitness value of the total available individuals and the first N_p populations are selected by sorting the population generated in ascending order of the $\dot{C}_S$ values. These populations are allowed for producing offspring through mutation.

Mutation: Each of the decision variables $\overline{p}_i = [t_{g,i}, t_{c,i}, t_{e,i}, t_{a,i}, c_{rhx,i}, c_{shx,i}, h_{p,i}]$ of the i[th] parent individual is mutated to a new variable $\overline{p}_i^{/} = [t_{g,i}^{/}, t_{c,i}^{/}, t_{e,i}^{/}, t_{a,i}^{/}, c_{rhx,i}^{/}, c_{shx,i}^{/}, h_{p,i}^{/}]$, by adding a Gaussian random variable with zero mean and a standard deviation to each of them as, i.e., the generator temperature is evaluated as

$$t_{g,i}^{/} = t_{g,i} + N(0, s_{i,g}^{2}) \qquad (37)$$

In the above equations, N is a Gaussian distribution with zero mean and standard deviation of s. The standard deviations for the generator temperature is

$$s_{i,g}^{2} = f \times \frac{\dot{C}_{S,i}}{(\dot{C}_S)_{\min,p}} (t_{g,i,\max} - t_{g,i,\min}) \qquad (38)$$

where f is the scaling factor, $\dot{C}_{S,i}$ is the cost function of the i[th] parent going for producing offspring and $(\dot{C}_S)_{\min,p}$ is the minimum value of the cost function of the population selected for offspring production. In this work, the value for the scaling factor, f, is taken as 0.01. The other variables are similarly modified.

Competition & Selection: The offspring produced and the parent individuals, thus, form a set of $2\times Np$ populations. As shown in Fig. 3, they are placed in a competition pool, where a stochastic competition for survival of these individuals is carried out by assigning appropriate score to each of them. The score for each trial vector after a stochastic competition is calculated by the following relation given by Yang et al.[20].

$$w_{pi} = \sum_{t=1}^{N_p} w_t \qquad (39)$$

where, $w_t = 1, \quad \text{if } u_1 > \dfrac{f(p_i)}{f(p_r)+f(p_i)}$

$= 0, \quad \text{otherwise}$

where the competitor p_r is selected at random from among the $2N_p$ trial solutions based on $r = [2\ N_p u_2 + 1]$ and u_1 and u_2 are the random numbers ranging over [0,1].

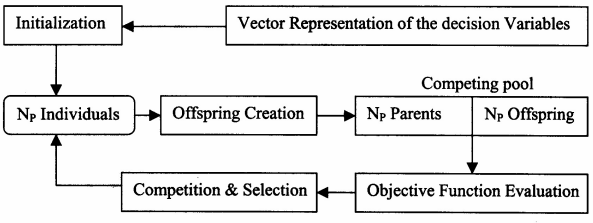

Figure 3. Schematic diagram of the evolutionary programming algorithm

After the competition, the $2\times N_p$ individuals are arranged in descending order of the score obtained by them. The first *Np* trial solutions are considered to be the survivors, and are transcribed along with their objective function value and other related values into a new survivor set of individuals. Thus,

they become the parent individuals for the next generation. For a particular iteration, the individual (trial solution) that gives the minimum value of the objective function is the best individual in that lot.

Termination/Stopping Rule: The above-mentioned process of generating offspring and competition for survival, i.e. iterations, continues till the solution converses within a predefined tolerance limit or a predefined maximum number of iteration is reached.

RESULTS AND DISCUSSIONS

The following admissible range of the decision variables, which form the trial vectors, are considered for both industrial steam and natural gas driven systems:

$140 \le t_g \le 160^0$C, $33 \le t_c \le 45^0$C,

$-15 \le t_e \le 7.5^0$C, $33 \le t_a \le 42^0$C,

$50 \le c_{rhx} \le 90\%$, $50 \le c_{shx} \le 90\%$,

$50 \le h_P \le 90\%$.

The fitness (objective function of the best trial vector in a given population) curve against the number of iterations is shown in Fig. 4, which clearly shows the rapid convergence of the objective function. It is seen that after about 65 iterations the objective function stabilizes to the value of Rs. 385.2 hr^{-1}. The optimized variables of the system are as follows: t_g = 157.55^{0}C, t_c = 37.65^{0}C, t_e = 7.4^{0}C, t_a = 34.2^{0}C, c_{rhx} = 77 %, c_{shx} = 90%, h_P = 69%.

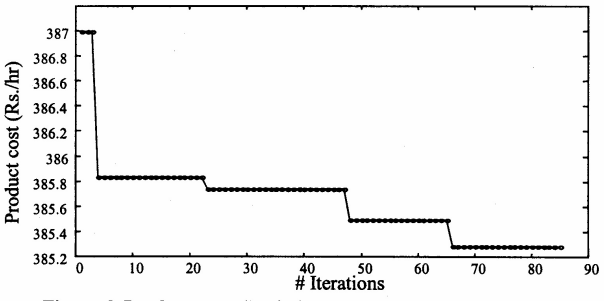

Figure 4. Product cost (Rs./hr) versus iterations for optimization of the aqua-ammonia system

The final results of the optimized system are summarized in Table 3. The value of the objective function, i.e. the product cost is reduced by 10.0% and the fuel cost is reduced by 29.9%. The exergy destruction cost and the exergy loss cost also are decreased by 32.4% and 20.7% respectively. The exergetic efficiency and the COP of the system are increased by 42.7% and 42.2% respectively. Incidentally, the overall investment cost of the system is decreased by 1.5% in comparison to the Base Case. This is because, on one hand the investment costs of the evaporator assembly and the RHX are increased by about 17.6%, and 61.5% respectively, on the other hand the investment costs of the generator, the rectifier, and the SHX are decreased by about 58.4%, 66.4%, and 22.4% respectively.

Table 3. Comparative results between the Base Case and the Optimum Case of the system.

Properties	Base Case	Optimum Case	%-Variation
OBF ($C_{P,tot}$ Rs./hr)	428.12	385.20	-10.03
$E_{F,tot}$ (kW)	75.97	53.23	-29.93
$E_{P,tot}$ (kW)	3.49	3.49	--
$E_{D,tot}$ (kW)	66.06	44.65	-32.41
$E_{L,tot}$ (kW)	6.42	5.09	-20.73
e_{tot} (%)	4.59	6.56	42.71
COP	0.43	0.62	42.24
$C_{F,tot}$ (Rs./hr)	125.24	87.03	-30.50
$C_{D,tot}$ (Rs./hr)	108.90	73.01	-32.96
$C_{L,tot}$ (Rs./hr)	10.58	8.32	-21.37
Z_{tot} (Rs./hr)	302.89	298.17	-1.56
Z_g (Rs./hr)	28.71	11.95	-58.38
Z_r (Rs./hr)	2.75	0.92	-66.38
Z_{ea} (Rs./hr)	106.51	125.26	17.60
Z_{rhx} (Rs./hr)	1.59	2.56	61.48
Z_p (Rs./hr)	6.79	4.43	-34.76
Z_{shx} (Rs./hr)	5.10	3.96	-22.38

CONCLUSIONS

The thermoeconomic optimization using EP is found to be a powerful and systematic tool in optimizing the design of thermal systems. However, the designer should pay adequate attention to the following points:

- Proper definition of fuel-product-loss of the system.
- Proper selection of local decision variables for various subsystems.
- Reliability of the cost information available and how to relate these with thermodynamic parameters

REFERENCES

[1] McMullan, J. T. Refrigeration and the environment – issues and strategies for the future. Int J Refrigeration 2002; 25(1):89-99.

[2] Bejan A, Tsatsaronis G, Moran M. Thermal design and optimization. New York: John Wiley and Sons Inc., 1996.

[3] Tsatsaronis G, Javier P. Exergoeconomics evaluation and optimization of energy systems – application to the CGAM problem. Energy 1994; 19(3):287-321.

[4] Lozano MA, Valero A. Theory of the exergetic cost. Energy 1993; 18(9):939-60.

[5] Valero A, Lozano, MA, Serra, L, and Torres, C. Application of the exergetic cost theory to the CGAM problem. Energy 1994; 19(3):365-81.

[6] Frangopoulos CA. Application of the thermoeconomic functional approach to the CGAM problem. Energy 1994; 19(3):323-42.

[7] von Spakovsky MR. Application of engineering functional analysis to the analysis and optimization of the CGAM problem. Energy 1994; 19(3):343-64.

[8] d'Accadia MD, de Rossi F. Thermoeconomic optimization of a refrigeration plant. Int J Refrigeration 1998; 21(1):42-54.

[9] Wall G. Optimization of refrigeration machinery. Int J Refrigeration 1991; 14:336-40.

[10] Misra RD, Sahoo PK, Sahoo S, and Gupta A. Thermoeconomic optimization of a single effect water/LiBr vapour absorption refrigeration system. Int J Refrigeration 2003; 26(1):158-69.

[11] Misra RD, Sahoo PK, Gupta A. Application of the exergetic cost theory to the LiBr/H_2O vapour absorption system. Energy 2002; 27(11):1009-25.

[12] Ataer, ÖE, Gögüs, Y. Comparative study of irreversibilities in an aqua-ammonia absorption refrigeration system", Int J Refrigeration 1991; 14(2):86-92.

[13] Ziegler, B, Trepp, Ch. Equation of state for ammonia-water mixtures", Int J Refrigeration 1984; 7(2):101-6.

[14] Irvine TF, Liley PE. Steam and gas tables with computer equations. USA: Academic Press, 1984.

[15] Ahrendts, J. Reference states. Energy 1980; 5: 667-77.

[16] Szargut J, Morris DR, Steward FR. Exergy analysis of thermal, chemical, and metallurgical processes. New York: Hemisphere Publishing Corporation, 1988.

[17] Boehm RF. Design analysis of thermal systems. New York: John Wiley and Sons Inc., 1987.

[18] Economic indicators. Chemical Engineering 2000; August:745-63.

[19] Cammarata, A. Fichera, and L. Marletta, "Using Genetic Algorithm and the Exergoeconomic Approach to Optimize District-Heating Network" *ASME J. Energy Resources Technology* 1998 120: 241-246.

[20] H. T. Yang, P. C. Yang, and C. L. Huang, "Evolutionary Programming Based Economic Dispatch for Units with Non-Smooth Fuel Cost Functions", *IEEE Transactions on Power Systems*, 1996; 11:112-118.

Proceedings of ECOS 2005
Trondheim, Norway
June 20–22, 2005

OPTIMAL PERFORMANCE ANALYSIS OF A SMALL-SIZE GAS-FIRED AIR-COOLED AIR CONDITIONER

L. Wang*, G.M. Chen and Q. Wang,
Zhejiang University
Institute of Refrigeration and Cryogenics
Hangzhou 310027
P. R. China

ABSTRACT

Absorption refrigeration cycle using lithium bromide-water solutions as a working fluid has been increasingly considered one of the most desirable alternatives for electricity-powered compression refrigeration cycle in China. A small size gas-fired air-cooled air-conditioner is developed. The system has two new features of waste heat recovery of condensed water from high-pressure generator and an adiabatic absorber with an air cooler. It helps solve the problems, for example, boost of pressure, temperature and concentration in the generators, increase of risk of crystallization and acceleration of corrosion occurring in the conventional air-cooled falling film absorption refrigeration system. Optimal performance of the device is simulated. The results indicated that the system conserved energy. And COP with heat recovery was 0.058 higher than that without heat recovery. Optimal solution distribution ratio into HG made it achieve the maximum COP.

Keywords: adiabatic absorption; heat recovery; heat transfer; mass transfer; COP

1. INTRODUCTION

The problems of power supply and potential environmental destruction have become momentums of developing air-cooled gas fired air conditioner using lithium bromide-water solutions as a working fluid. In the last ten years, rapid expansion in the use of electricity-powered air conditioning system in Chinese big cities partially has caused occurrence of electricity demand peaks in the summer and winter seasons. Chinese government has done something to change the adverse situation by encouraging customers into using heat-driven absorption refrigeration devices. It is promising in China. Firstly, it uses natural working fluids and helps to protect environment. Secondly, there are plentiful natural gas resources in China. In addition, the Project of the Western Natural Gas Transported Into the East Area has been fulfilled. It is popular that water-cooled absorption heat pumps supply cooling and heat for large buildings, but it is advisable to develop air-cooled absorption refrigeration systems for small building such as villa. The

*Corresponding author: Phone: +86 571 87931782 Fax: +86 571 87954624 Email:wanglinsichuan@163.com

air-cooled absorption refrigeration has great advantages such as low construction, installation and operation cost, outdoor installation, no special machine rooms, increased ease of handing and enhanced level of reliability [1]. On the other hands, the advantages in human health and application in areas lack of water source are remarkable. However, the higher temperature in the condenser and absorber causes boost of pressure, temperature and concentration in the generators, increase of risk of crystallization and acceleration of corrosion [2]. In order to solve these problems, some theoretical or experimental studies are devoted to invention of new cycle modes, selection of new working fluids and enhancement of heat and mass transfer process in the absorber [3-6]. In view of the facts that the above questions caused by the traditional air-cooled falling film absorption aren't really solved in terms of practical application, in this paper, based on previous works, an air-cooled adiabatic absorption refrigeration air conditioner are developed. To ensure the optimal control and reliability of operation in extremely hot climates, in this study, its operation performance is evaluated.

2. DEVELOPMENT OF AIR CONDITIONER

Fig.1 shows schematically the gas-fired air-cooled double-effect absorption refrigeration device with an adiabatic absorber. The system has two generators. The refrigerant vapor generated from the high-pressure generator (HG) supplies heat energy for the low-pressure generator (LG) to increase the efficiency of the cycle. It uses outdoor air as a cooling source for an air-cooler and a condenser. The weak solution leaving the absorber is split into two parts that flow in parallel. One part flows into the high-pressure generator (HG) after passing through the high temperature heat exchanger (HX), and the other one flows into the low-pressure generator (LG) after passing through the low temperature heat exchanger (LX). When weak solution flowing into the high-pressure generator (HG) is concentrated into the strong solution, the strong solution passes back through the high temperature heat exchanger (HX) and its heat is transferred to the weak solution stream going to the high-pressure generator (HG). Similarly, when weak solution flowing into the low-pressure generator (LG) is concentrated into the strong solution, the strong solution passes back through the low temperature heat exchanger (LX) and its heat is transferred to the weak solution stream going to the low-pressure generator (LG). Finally, the two parts of strong solutions are mixed and return to the absorber.

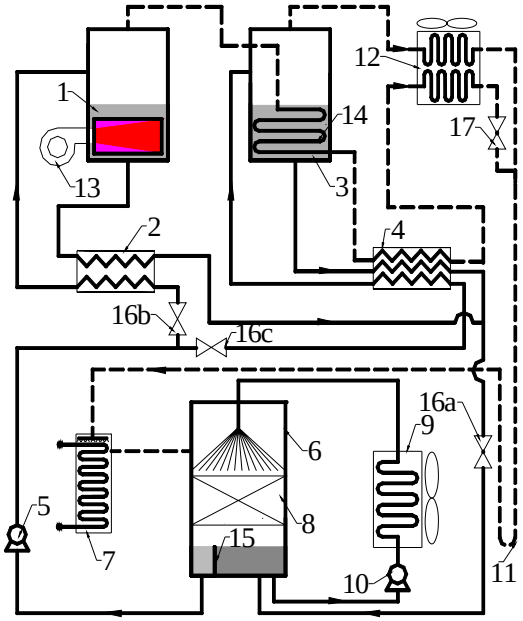

1－HG 2－HX 3－LG 4－LX 5－solution pump 6－adiabatic absorber 7－evaporator 8－packed bed 9－air-cooler 10－circulation pump 11－U-type throttle tube 12－condenser13－gas-fired heater 14－solution heat exchanger 15－throttle valve 16a(b, c)－regulation valve 17－nozzle

Fig.1: Schematic diagram of a small size air-cooled air-conditioner

The system has two new features of waste heat recovery of condensed water from generator and an adiabatic absorber with an air cooler, and contributes to solving the problems occurring in

the conventional air-cooled absorption refrigeration system Owing to different mechanics of heat and mass transfer, it is difficult to enhance heat and mass transfer in air-cooled falling film absorber simultaneously. However, Heat and mass transfer process is separated in adiabatic absorber with an air-cooler. In this way, heat is rejected effectively in an air-cooler while the mass transfer occurs subsequently in an adiabatic absorber. There is a packed bed to enhance the mass transfer in adiabatic absorber. The pack bed augments interface between vapor and spray solution, and provides enough space and time for mass transfer process.

2. SIMULATION MODEL

The simulation models involves mathematical model of governing equations for each component making up the cycle system. The governing equations are developed based on conversation of mass and conversation of energy. For the purpose of simplification of the models and steady state simulation, the following assumptions are made:

1. After the superheated vapor from the high-pressure generator supplies heat for low pressure generator, the coolant leaving the low pressure generator is in the saturated water state.
2. Thermophysical properties of subcooled water are treated as that of saturated water at the same temperature conditions. Subcooled water temperature from the low temperature heat exchanger is 15 ℃ higher than weak solution temperature leaving the absorber.
3. After the superheated vapor from the low-pressure generator is condensed in the condenser, the coolant leaving the condenser is in the saturated water state.
4. The pressure drop in the absorber is considered.
5. Flow in the heat exchangers is regarded as the counterflow.
6. Heat loss to the environment is negligible, and pressure drop in the system except the absorber is neglected.
7. Thermophysical properties of air are constant.

According to conversion of mass, total mass balance equation and solution mass balance equation is shown as follows respectively

$$\sum G_i - \sum G_o = 0 \qquad (1)$$

$$\sum G_i X_i - \sum G_o X_o = 0 \qquad (2)$$

where G_i, G_o is mass flow rate of solution (or refrigerant) flowing into and leaving each component respectively, kg/s; X_i, X_o is concentration of solution flowing into and leaving each component respectively, %(wt).

According to conversion of energy, energy balance equation for each component is written as follows

$$Q + \sum G_i h_i - \sum G_o h_o = 0 \qquad (3)$$

where Q is heat capacity, W, and it is equal to zero, for the other component except high pressure generator; h_i, h_o is enthalpy of solution (or refrigerant) flowing into and leaving each component respectively, J/kg.

Coefficient of preference (*COP*) is defined as ratio of the cooling capacity output from the system to the sum of heat input from the gas-fired heater and power input from pump, fan and other electric component, which is shown as follows:

$$COP = Q_{EV} / (Q_{HG} + P) \qquad (4)$$

To solve the set of governing equations, several specific model details incorporated into the model for each component must be addressed. The model details involve the empirical relations and the thermophysical properties of lithium bromide-water solutions, water and steam. The nucleate boiling heat transfer coefficient of lithium bromide-water solutions is derived from Charters' correlations [7]. The convection heat transfer coefficient of water is evaluated according to the equation given by Dittius and Bolter [8]. The

evaporation heat transfer coefficient outside horizontal tubes is calculated using the correlation by Lorenz et al [9]. The convective condensation heat transfer in tubes is obtained from the correlation employed by Sarma et al [10]. Thermophysical property values of lithium bromide-water solution, water and steam required by the model in solving the governing equations were evaluated from Reference [11-16]. Based on the thermodynamic property and transport property equations in the literatures, a subroutine is made. Thermophysical properties values are calculated when the subroutine is called from the main program.

In addition, the model involves heat transfer area of each component. According to optimization design results, Solution distribution ratio (SDR) into HG is 0.483, which is defined as the ratio of the solution mass flow rate into the high pressure generator to total solution mass flow rate leaving the absorber, and power input from pump, and fan and other component is equal to 1.486 kW. Table 1 shows the optimization design results of heat transfer surface area for LG, HX, LX, air-cooler, condenser and evaporator.

Component	Area (m^2)
Coolant side of LG	1.189
Strong solution side of HX	8.842
Strong solution side of LX	7.939
Coolant side of LX	0.249
Air side of air cooler	118.202
Air side of condenser	48.099
Water-cooled side of evaporator	1.949

Tab1: Results of heat transfer area obtained from optimization design for the normal system

4. RESULTS AND DISCUSSION

The influences of SDR into HG, outdoor air temperature and cooled water inlet temperature to evaporator on cycle performances are investigated.

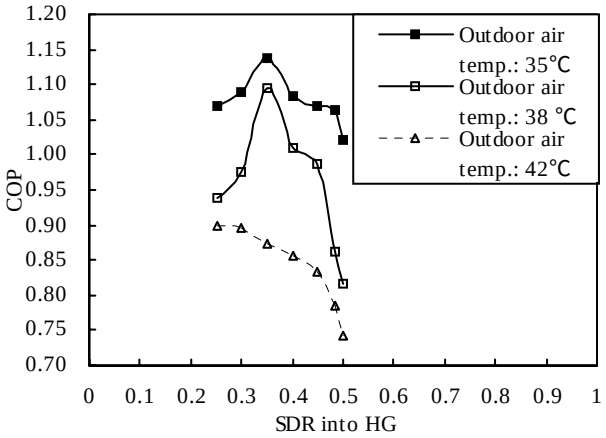

Fig.2: Effects of SDR into HG on COP

Fig.2 shows the effects of SDR into HG on COP at outdoor air temperature of 35℃, 38℃ and 42℃. It is seen that the maximum of COP appears as SDR into HG varies. So at different outdoor air temperature, optimal SDR into HG makes the cycle the most efficient.

SDR	Solution crystal-zation temp	Outdoor air temp. with crystallization
0.25	55.2	39.0
0.30	51.8	36.0
0.35	47.7	32.0
0.40	43.2	28.0

Tab.2 Solution crystallization temp in HX and outdoor air temp with crystallization

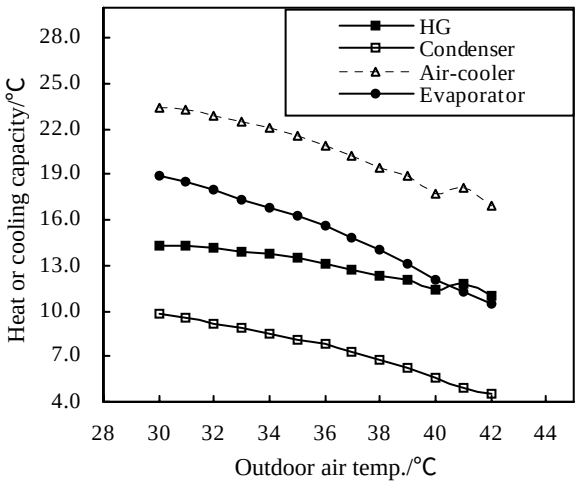

Fig.3: Effects of outdoor air temp. on heat or cooling capacity

Tab.2 illustrates both solution crystallization temperature in HX and outdoor air temperature with crystallization decrease with SDR into HG rise. It results from the increase of solution leaving the HG as SDR decreases.

Fig.3 shows the influences of outdoor air temperature on heat capacity of three components (HG, condenser and air-cooler) and cooing capacity of evaporator. It is seen that both heat capacity and cooling capacity decrease in steps with air temperature increase. However, the slope of heat input into HG is the smallest of all.

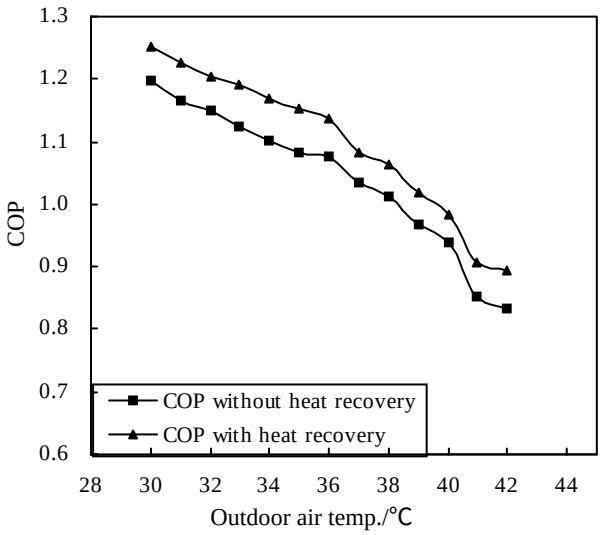

Fig.4: Effects of outdoor air temp on COP

Fig.4 shows the trends of variation of COP with outdoor air temperature increase when SDR into HG is 0.35. It is seen that COP decreases as air temperature rises. Especially at extremely hot climates, when air temperature reaches 43℃, COP reduces significantly 1. At the same air temperature, COP with heat recovery is higher than that without heat recovery. On the average, COP with heat recovery increases 0.058.

Fig.5 shows the effects of cooled water inlet temperature to evaporator on COP and cooling capacity at SDR of 0.483. It is seen that COP and cooling capacity increases linearly with cooled water inlet temperature rise. It indicates that, at the extremely hot climates, cooled water inlet temperature to evaporator is properly boosted so as to improve COP and cooling capacity.

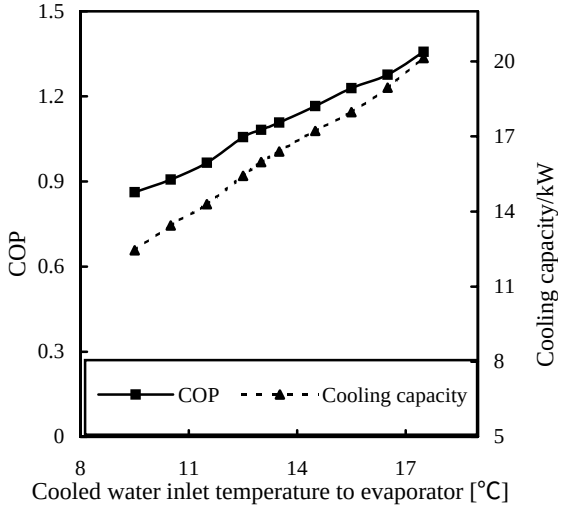

Fig.5: Effects of cooled water inlet temperature to evaporator on COP and cooling capacity

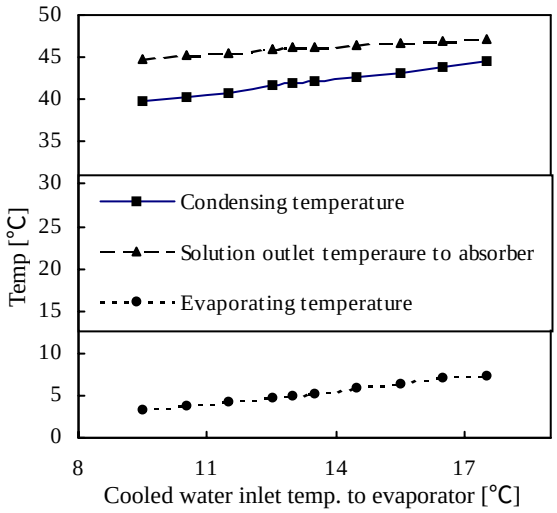

Fig.6: Effects of cooled water inlet temp to evaporator on solution outlet temp to absorber, condensing temp and evaporating temp

Fig.6 shows the effects of cooled water inlet temperature to evaporator on solution outlet temperature to absorber, condensing temperature and evaporating temperature at SDR of 0.483. As cooled water inlet temperature to evaporator rises, condensing temperature, evaporating temperature and solution outlet temperature to absorber increase in steps. However, the rate of increase of solution outlet temperature to absorber is not obvious. When cooled water inlet temperature to

evaporator varies between 9.5 ℃and 17.5℃, solution outlet temperature to absorber ranges from 44.8 ℃ to 47.2 ℃, but condensing temperature ranges from 39.7 ℃ to 44.5℃ and evaporating temperature from 3.3 ℃ to 7.4 ℃.

Fig.7 shows the effects of cooled water inlet temperature to evaporator on circulation solution flowrate, recirculation solution flowrate, subcooling of spray solution, which is defined as temperature difference between solution from absorber and spray solution from air cooler, at SDR of 0.483. It is seen that, recirculation solution flowrate linearly rises as cooled water inlet temperature to evaporator, but circulation solution flowrate decreases in steps. Recirculation solution flowrate has a strong effect on power input from circulation pump, but circulation solution flowrate has a small effect on power input from solution pump because circulation solution flowrate is too small compared with recirculation solution flowrate. The figure illustrates that subcooling temperature has small variations when cooled water inlet temperature to evaporator varies. Although Subcooling is almost kept constant, absorption effects of solution are still enhanced owing to increase of evaporating pressure.

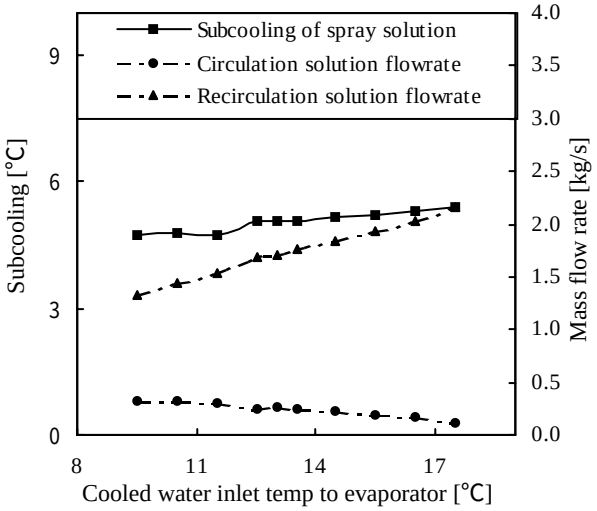

Fig.7 Effects of cooled water inlet temp to evaporator on subcooling of spray solution, circulation flowrate and recirculation flowrate

4. CONCLUSIONS

Small size gas-fired air-cooled adiabatic absorption air conditioner is developed. Heat is recovered from coolant-saturated water in the low temperature heat exchanger. It contributes to energy-conservation and COP boost. Adiabatic absorber with air-cooler separates mass transfer process with heat transfer process. It is feasible to enhance mass transfer in adiabatic absorber and heat transfer in air cooler effectively. Based on performance simulation and characteristic analysis, the optimal control and mode of reliable operation in extremely hot climates are obtained. It indicated that the device resolved some problems occurring in air-cooled falling film absorption refrigeration systems and helped save energy. At extremely hot climates, boost of cooled water inlet temperature to evaporator contributes to increase of cooling capacity and COP, but it causes increase of condensing temperature. Solution outlet temperature to absorber is insensitive to cooled water inlet temperature to evaporator.

ACKNOWLEGEMENT

The authors would like to express the appreciation to Air conditioner Technology Research Institute, Air Conditioning Company, Changhong Electric Co., Ltd., who gives the support to the research work of this paper.

REFERENCE

[1] Jung-in Yoon, Oh-Kyung Kwon. Cycle analysis of air-cooled absorption chiller using a new working solution. Energy, 1999(24): 795-809

[2] S. Kurosawa, S. Fujimaki. Development of air-cooled double-effect gas-fired absorption water chiller-heater. ASHRAE Trans, 1989, 95(1): 318-325

[3] N. Velazquez, R. Best. Methodology for the energy analysis of an air cooled GAX

absorption heat pump operated by natural gas and solar energy. Applied Thermal Engineering, 2002(22): 1089-1103

[4] Huen Lee, K.K. Koo S. Jeong, J.S. Kim, H. Lee. Thermodynamic design data and performance evaluation of the water +lithium bromide+ lithium iodide +lithium nitrate +lithium chloride system for absorption chiller. Applied Thermal Engineering, 2000(20): 707-720

[5] Franz Summerer, Peter Riesch, Felix Ziegler, Georg Alefeld. Hydroxide absorption heat pumps with spray absorber. ASHRAE Trans, 1996(102): 1010-1016

[6] G. M. Chen, Y. J. He. Study on lithium bromide aqueous solution air precooled adiabatic absorption process. Acta Energiae Solaris Sinica, 2002(23): 166-170

[7] W. W .S. Charters, V. R. Megler, W. D. Chen and Y. F. Wang. Atmospheric and sub-atmospheric boiling of H_2O and $LiBr/H_2O$ solutions. International Journal of Refrigeration, 1982(5): 107-114

[8] J. P. Holman. Heat transfer. 9th edition, international edition. New York, McGraw-Hill, 2002

[9] J.J. Lorenz, D. Yung. A note on combined boiling and evaporation liquid films outside horizontal tubes. Transactions ASME of Journal of heat transfer, 1979(101):178-180

[10] R. K. SARMA, C.V.N. Sastry, V.V. Rao, Sadik Kakac, Hongton Liu. Convective condensation heat transfer in a horizontal condenser tube. International Journal of Thermal Science, 2002(41): 295-301

[11] McNeely L.A. Thermodynamic properties of aqueous solutions of lithium bromide. ASHRAE Transactions, 1979(85): 413-434

[12] Y. Kaita. Thermodynamic properties of lithium bromide-water solutions at high temperatures. International of Journal Refrigeration, 2001(24): 374-390

[13] R. J. Lee, R.M. DiGuilio, S.M. Jeter, A. S. Teja. Properties of lithium bromide-water solutions at high temperatures and concentrations I: Thermal Conductivity. ASHRAE Trans, 1992(98): 702-708

[14] R. J. Lee, R.M. DiGuilio, S.M. Jeter, A. S. Teja. Properties of lithium bromide-water solutions at high temperatures and concentrations II: Density and Viscosity. ASHRAE Trans, 1992(98): 709-714

[15] R. W. Hyland, A. Wexier. Formulations for the thermodynamic properties of the saturated phases of H_2O from 173.15 K to 473.15K. ASHRAE Trans, 1983(89): 500-514

[16] A. Malhotra, D. M. R. Panda. Thermodynamic properties of superheated and supercritical steam. Applied Energy, 2001(68): 387-393

Proceedings of ECOS 2005
Trondheim, Norway
June 20–22, 2005

CONFIGURATION SELECTION METHODOLOGY FOR COMBINED POWER/REFRIGERATION GENERATION AMMONIA-WATER CYCLES

Na Zhang*
Institute of Engineering Thermophysics, Chinese Academy of Sciences
Beijing 100080, P. R. China

Noam Lior
Department of Mechanical Engineering and Applied Mechanics
University of Pennsylvania
Philadelphia, PA 19104-6315, USA

ABSTRACT

In this paper, ammonia-water systems are analyzed for the cogeneration of refrigeration and power. Some general principles for the system integration are summarized, for better recovery of both the external and internal heat and pressure exergy, and reduction of the exergy destruction in the condensation process. Based on these principles, three ammonia-water systems are proposed and analyzed. The plants operate in combined cycle mode with ammonia-water Rankine cycle(s) and an ammonia refrigeration cycle, interconnected by absorption, separation and heat transfer processes. It is found that the cogeneration systems have good thermal performances, with energy and exergy efficiencies of ~28% and 55~60%, respectively, for the base-case studied (at maximum heat input temperature of 450°C). That efficiency is, by itself, excellent for cycles using heat sources at these temperatures, and comparable to that of nuclear power plants. When using the waste heat from topping gas turbine power plants, the total plant energy efficiency can rise to the remarkable value of about 57%. The hardware proposed for use is conventional and commercially available, no hardware additional to that needed in conventional power and absorption cycles is needed.

Keywords: power/refrigeration cogeneration, configuration, ammonia-water

NOMENCLATURE

E	Exergy [kW]
h	Specific enthalpy [kJ/kg]
m	Mass flow rate [kg/s]
P	Pressure
Q	Heat duty [kW]
R	Refrigeration/power ratio
RR	Rectifier molar reflux ratio
SF	Split fraction
s	Specific entropy [kJ/kg·K]
T	Temperature [K]
t	Temperature [°C]
W	Power output [kW]
ΔT_P	Pinch point temperature difference [K]
η_1	Energy efficiency [%]
η_2	Exergy efficiency [%]

Subscripts

a	Ambient state
EVA	Evaporator
hs	Heat source fluid
in	Input
i	Inlet
1, 2, … 29	States on the cycle flow sheet

* Corresponding author: Tel. 86-10-62561887; Fax. 86-10-62575913; E-mail. zhangna@mail.etp.ac.cn

1. INTRODUCTION

An approach to reduce the exergy loss in the heat transfer process from a variable temperature heat source is to concurrently also vary the temperature of the heat sink and thus make the temperature difference between the heat source and sink more uniform along the heat exchanger (cf. [1]). This can be accomplished in a number of ways, one is using binary-component working fluids that exhibit a variable boiling temperature during the boiling process. The ammonia/water mixture is one of the most widely used working fluids in refrigeration

machines. Maloney and Robertson [2] proposed the use of an ammonia/water mixture as the working fluid in an absorption power cycle. In the combined power cycle proposed by Kalina [3], an ammonia/water mixture was employed as the working fluid in the bottoming cycle. Both systems have power as their only usable output. Refrigeration, however, is also a very valuable product in many circumstances.

Cogeneration is a highly efficient energy utilization method [4]. Goswami et al [5] proposed a combined power/refrigeration cycle using mixed working fluids and investigated its performance [6, 7]. In their system, the ammonia rich vapor from a rectifier unit, which is about 20% of the total mass flow, first expands in a turbine to generate power and then the cold turbine exhaust provides cooling by transferring only sensible heat to the chilled water. The amount of produced cooling is relatively small, and none would be produced for high turbine inlet temperature; hence the system was mainly intended to be operated with low temperature heat sources including geothermal or solar. Zheng et al [8] also proposed an absorption power and cooling (APC) combined cycle based on the Kalina cycle. To produce almost pure ammonia, a rectifier was used to replace the flash tank in the Kalina cycle. The outflow from the top of the rectifier is throttled by a valve and then produces refrigeration before mixing with the main stream. An energy efficiency of 24.2% and an exergy efficiency of 37.3% were reported with the turbine inlet parameters of 350°C/50bar.

In integrated refrigeration/power combined cycles, driven by the same external heat source, such as the one proposed and analyzed here, the integration can be accomplished via several configurations. Such configurations are studied and compared here, with an attempt to also develop and demonstrate a basic general methodology for the system integration.

2. THE MAIN PRINCIPLES FOR SYSTEM INTEGRATION

The power and refrigeration cycles generally operate in different temperature regions. They are complementary to each other in some way: for example, in the power cycle, there are some middle/low temperature waste heats, which are impractical for generating additional power because of their low temperatures, but might be a suitable heat source for an absorption refrigeration cycle. Similarly, in the cooling cycle, some cooling capacity may exist that is not cold enough for refrigeration, but could be an appropriate heat sink to the power cycle. Their integration thus has the potential for becoming a new combined cycle or cogeneration system that may have a higher efficiency.

In the cogeneration systems proposed in this paper, there are two sub-cycles: a Rankine power cycle and an absorption refrigeration cycle, interconnected by the absorption, separation, and heat transfer processes. They use the same working fluid, a mixture of ammonia and water, but with different concentrations, and they are supplied with heat by one external heating fluid. The energy input to the system is via several heat exchangers, and to obtain high efficiency they should be arranged in a cascade according to their temperature level. Within each heat exchanger, small temperature difference should be maintained to allow for a good thermal match between the hot and cold streams.

Binary component mixtures exhibit a boiling temperature that varies during the boiling process, and their employment as working fluids thus allows maintenance of a more constant temperature difference between them and variable temperature heat sources, and consequently reduces exergy losses in the heat addition process. To have an increasing temperature during the evaporation process, the working fluid concentration should be neither too high nor too low, to be able to produce the necessary glide.

To produce more power, the turbine back-pressure should be as low as possible. Condensation of the binary working fluid is a temperature varying process too. To attain complete condensation, the fluid bubble point temperature should be higher than the cooling water inlet temperature by at least the minimal heat transfer temperature difference that allows use of practical heat exchanger sizes. Since ammonia has a lower saturation temperature than water for a given pressure, completing the condensation of ammonia/ water mixtures at the same temperature results in a higher pressure than that for pure water. A binary working fluid in the power turbine must thus expand to a higher back-pressure, which is unfavorable for power generation. In the Kalina cycle, this problem is addressed by an absorption condensation process, in which a weaker stream from the bottom of the flash tank dilutes the turbine exhaust so that the latter can be condensed at a lower pressure [3].

For better efficiency, the physical exergy of any pressure differences in the system, needed for the process, should also be recovered properly.

3. THE EFFICIENCIES AND MAIN ASSUMPTIONS

This analyzed system has two useful outputs: power and refrigeration. In this paper, the heat source fluid

is chosen to be air (79% N_2 and 21% O_2 by volume), entering at the hot end of the Boiler.

The most commonly used energy efficiency and exergy efficiency definitions are adopted for the system performance evaluation. Since the heating fluid is finally exhausted to the environment, the calculation of the efficiencies is based on its initial state. The energy efficiency is defined as:

$$\eta_1 = (W + Q_{EVA}) / Q_{in} \quad (1)$$

where $$Q_{in} = m_{hs} \cdot (h_{hs,i} - h_{hs,a}) \quad (2)$$

Since the energy efficiency weighs the power and refrigeration outputs, as well as the heat input, equally, even though the quality of these energies is rather different, exergy efficiency is a more proper evaluation criterion in this case, and in the evaluation of cogeneration systems with more than one kind of energy output or input in general.

The exergy efficiency is defined as the exergy output divided by the exergy input to the cycle:

$$\eta_2 = (W + E_{EVA}) / E_{in} \quad (3)$$

where the exergy of the heating fluid, E_{in}, is given as:

$$E_{in} = m_{hs} \cdot [(h_{hs,i} - h_{hs,a}) - T_a (s_{hs,i} - s_{hs,a})] \quad (4)$$

The exergy of refrigeration, E_{EVA}, is calculated as the working fluid exergy difference across the evaporator *EVA*.

Table 1. Main assumptions for the calculation

Evaporator *EVA*	Pressure p_{EVA} [bar]	1.6
	Pressure loss [%]	3.0
	Outlet temperature [°C]	-15
(High pressure) Absorber $ABS_{(H)}$	Absorption pressure [bar]	1.55
	Pressure loss [%]	3.0
	Outflow vapor fraction	0
Ambient state	Temperature t_a [°C]	25.0
	Pressure p_a [bar]	1.013
Turbine *T*	Inlet temperature t_7 [°C]	450.0
	Isentropic efficiency [%]	87
Rectifier *REC*	Theoretical stage number	6
	Molar reflux ratio *RR*	0.3
	Operation pressure p_{REC} [bar]	14
	Pressure loss [%]	3.0
	Feed stream vapor fraction	0
Reboiler *REB*	Outlet temperature t_{REB} [°C]	165
Heat exchangers (*B*, *REB*, *HEX*, *CON*, *C*, *ABS*)	Pinch point temperature difference ΔT_P [K]*	5 or 15
	Pressure loss [%]	1.0~3.0
Pumps *P*	Efficiency [%]	75

*ΔT_P is 15 K when one side is air

It is assumed that the system operates at steady state. The simulations were carried out using the commercial Aspen Plus [9] code, with the thermal property method of the Electrolyte NRTL model or the SR-Polar model for high temperatures (>246°C) and pressures (>100 bar) application.

The proposed cogeneration systems could be used as a bottom cycle in a combined cycle system, with a gas turbine as the topping cycle. Since the flue gas temperature of common gas turbines of small size or middle size is about 500°C, the binary turbine inlet temperature is chosen to be 450°C in this study, because ammonia starts dissociating at higher temperatures to nitrogen and hydrogen, although some past studies (cf. [3]) have assumed its use in power cycles up to 532°C. In the condensers *CON* and the absorbers *ABS*, the working fluid is cooled by 30°C water.

Three cogeneration cycle configurations are studied below.

4. THE PARALLEL POWER/REFRIGERATION COMBINED CYCLE

This plant combines an ammonia-water Rankine cycle and an ammonia refrigeration cycle in parallel, as shown in Fig. 1. The power cycle can be identified as 6-7-8-9-10-11-1 and the refrigeration cycle as 14-15-16-17-18-1. They connect together in the process 1-2-3-4/12-…6/14. Correspondingly, the working fluid has 3 primary concentration levels: the basic concentration solution in the process 1-2-3; the weak concentration solution in the power cycle 6-7-8-9-10-11, and the high concentration solution in the refrigeration cycle 14-15-16-17-18. The combined cycle also has 4 pressure levels.

The main motivation in the development of this cycle was the recognition that proper operation of the absorption cooling cycle requires the generator to be at a significantly higher pressure than the absorber (here the pressure ratio is ~9), and that the weak solution flow (which is about 80% of total work fluid mass flow rate) from the generator to the absorber is just throttled for creating this pressure drop, with the accompanying large exergy destruction. Introduction of a steam-driven power generation system in lieu of the throttling valve, with heat addition to vaporize the weak solution, allows generation of power alongside with the refrigeration produced by the absorption system.

The calculations are based on a unit mass flow rate (1.0 kg/s) of the basic working fluid fed to the rectifier. The system performances are reported in Table 2; good performance is obtained with the energy efficiency and exergy efficiency being 28 and 56%, respectively. Incidentally, the exergy efficiency is much higher than the energy efficiency because the

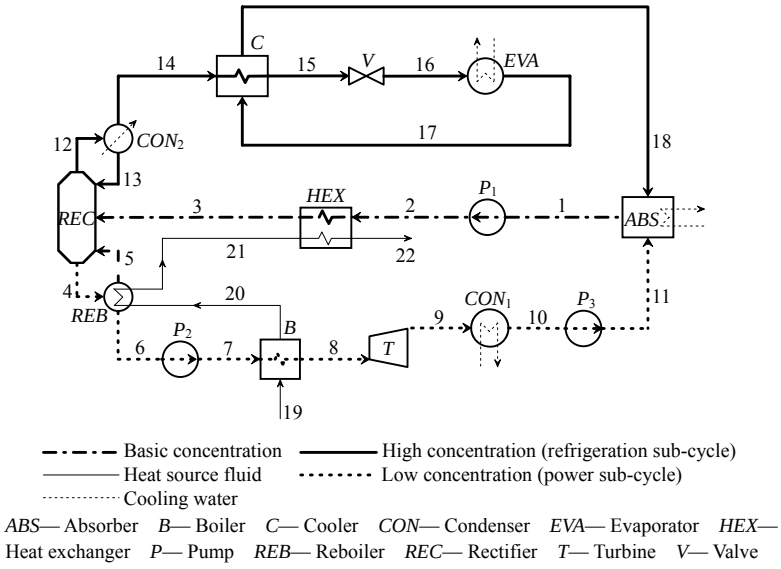

ABS— Absorber *B*— Boiler *C*— Cooler *CON*— Condenser *EVA*— Evaporator *HEX*— Heat exchanger *P*— Pump *REB*— Reboiler *REC*— Rectifier *T*— Turbine *V*— Valve

Fig. 1 The flow sheet of the combined power/cooling cycle

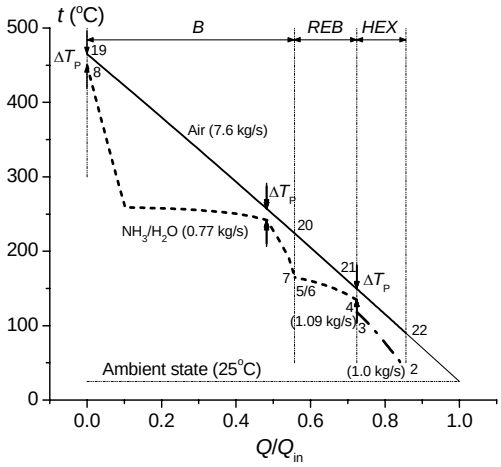

Fig. 2 the heat exchange *t*-*Q* diagram in the parallel cogeneration system

external heat source fluid is at a relatively low temperature and its exergy content is hence much lower than its energy content.

Table 2. The performance summary for the parallel cogeneration system

Turbine *T* work [kW]		726.9
Pump work [KW]	P_1	2.2
	P_2	5.6
	P_3	0.15
Refrigeration output Q_{EVA} [kW]		266.2
Condenser CON_1 load [kW]		1732.7
Rectifier condenser CON_2 load [kW]		381.0
Cooler *C* load [kW]		59.4
Absorber *ABS* heat load [kW]		427.9
Boiler *B* heat input [kW]		1947.1
Reboiler *REB* heat input [kW]		585.4
Heat exchanger *HEX* heat input [kW]		462.11
Net power output *W* [kW]		719.0
Refrigeration/power ratio *R*		0.37
Heat input Q_{in} [kW]		3496.0
Exergy input E_{in} [kW]		1379.6
Energy efficiency η_1 [%]		28.2
Exergy efficiency η_2 [%]		55.8

Figure 2 is the *t*-*Q* diagrams of the cycle heat addition process. The heat duty *Q* is normalized by the cycle energy input Q_{in} (eq. 2), to show more clearly the fraction of heating fluid energy utilized in the system. To get a better temperature match with the heat source fluid, the positions of the boiler *B*, the reboiler *REB*, and the heat exchanger *HEX*, are arranged (cascaded) in the plant according to their temperature levels.

In this cycle, the working fluid in the power sub-cycle is a weak solution from the reboiler; its physical exergy of pressure is recovered for power generation. The working fluid has a low ammonia concentration (0.098) in both the heat addition and condensation processes; this has both advantages and disadvantages. The power turbine has a relatively low back-pressure, but the temperature in the evaporation process does not change very much, leading to a poor match with the heating fluid variable temperature in the evaporation process.

5. THE SERIES-CONNECTED COGENERATION CYCLE

In the parallel system, the working fluid in the refrigeration sub-cycle has the highest concentration, and in the power sub-cycle the lowest. Consequently, the desired temperature glide in the power sub-cycle boiling process does not occur. In the series-connected system proposed in this Section, the power sub-cycle is downstream of the refrigeration cycle, thus allowing the use of a relatively strong solution, with a consequent desirable temperature glide, in its heat addition process. At the same time there are also some impairments: the working fluid is brought into the power cycle at a lower temperature and pressure than in the parallel cycle, and it is hard to lower the turbine backpressure because of the relatively high working fluid concentration.

The cycle layout is shown in Fig. 3. The refrigeration cycle can be identified as 15-16-17-18-19, followed by the power cycle: 20-21-22-23-24. 1-2-3-4-5/13-…7/15 is the preheat and rectification process. The weak solution from the reboiler is split into two streams in the splitter *SP*: one stream merges with stream 19 to accomplish the absorption process in the high pressure absorber ABS_H and form the

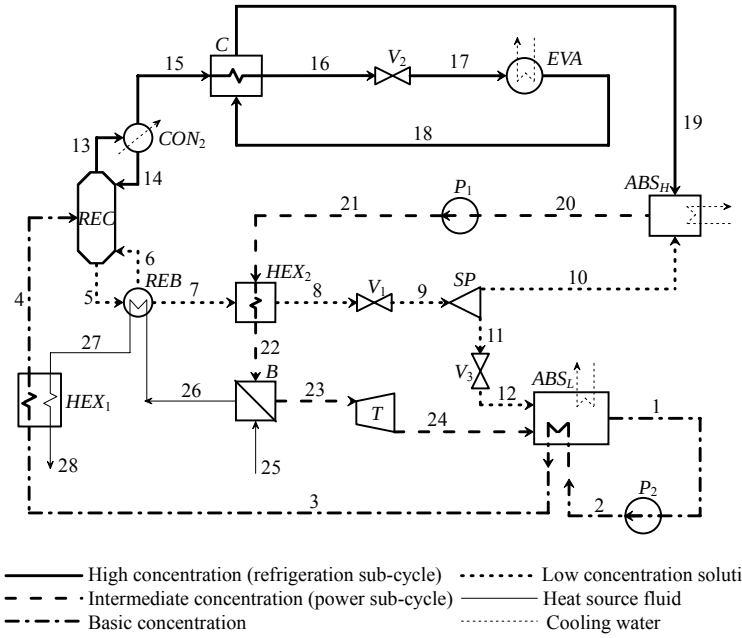

Fig. 3 The flow sheet of the series connected power/refrigeration cycle

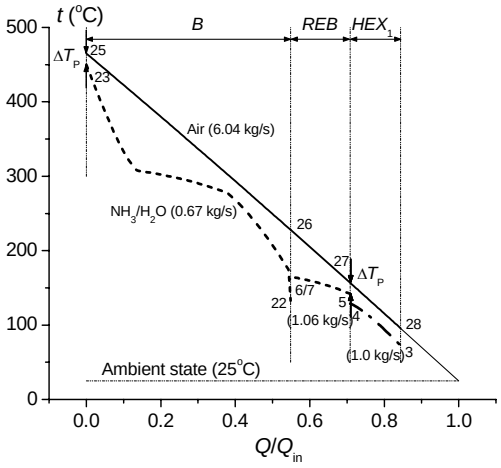

Fig. 4 the heat exchange *t*-*Q* diagram in the series-connected cogeneration system

turbine working fluid with the intermediate concentration; and the remainder is sent to the power sub-cycle and mixes with the turbine exhaust in the low pressure absorber ABS_L. This has two advantages: (1) the working fluid concentration in the power cycle boiling process can be adjusted to match the variable temperature heat source fluid, and (2) the turbine exhaust fluid is diluted in the low pressure absorber ABS_L by a part of the weak solution (12), bringing its concentration back to the basic value (1), thus reducing the condensation pressure somewhat and increasing the turbine power output. Consequently, the working fluid has 4 ammonia concentration levels and also has 4 main pressure levels. The heating fluid follows the path of 25-26-27-28. The calculation was based on 1 kg/s basic working fluid feed to the rectifier. The computed cycle performance is reported in Table 3.

The *SP* split fraction SF_1 (= m_{11} / m_9) is a key parameter to the cycle performance. When the split fraction is 0, the low-pressure absorber ABS_L is eliminated, replaced by a common condenser. As the split fraction increases, more of the dilute working fluid bypasses the high-pressure absorber and the turbine and is sent to the low-pressure absorber (ABS_L) directly. On the one hand, this raises the concentration of turbine working fluid, but on the other hand, the turbine inlet working fluid mass flow rate decreases, and leads to less power generation, but the boiler *B* heat demand decreases too. It is found that there exist values of SF_1, which maximize the thermal or exergy efficiencies.

Figure 4 is the *t*-*Q* diagram of the cycle heat addition process for SF_1=0.4, the tubine inlet pressure is 153 bar. The amount of heat needed in the evaporation process is only a small portion of the total heat demand, leading to a better thermal match in the boiler heat transfer process.

Table 3. Cycle performance summary for the series-connected cogeneration system

Split Fraction SF_1		**0.4**
Basic solution concentration		0.25
Intermediated solution concentration		0.32
Turbine working fluid mass flow rate [kg/s]		0.67
Turbine inlet pressure [bar]		152.5
Turbine backpressure [bar]		0.85
Turbine power output [kW]		581.0
Pump work [KW]	P_1	2.2
	P_2	17.2
Cycle input [kW]	Reboiler	443.9
	Boiler	1522.4
	Heat exchanger HEX_1	376.2
Cycle output [kW]	Cooling capacity Q_{EVA}	171.8
	Net power output *W*	561.6
Refrigeration/power ratio *R*		0.31
Heat source fluid	mass fluid rate [kg/s]	6.04
	Inlet temperature [°C]	465.0
Energy input Q_{in} [kW]		2776.24
Exergy input E_{in} [kW]		1095.55
Energy efficiency η_1 [%]		26.42
Exergy efficiency η_2 [%]		54.12

The efficiencies are somewhat lower than those of the parallel cycle despite the higher turbine inlet pressure. The variation of SF_1 has no effect on the turbine backpressure. The turbine backpressure (0.853 bar) is much higher than that in the previous parallel congeneration system. The comparatively big exergy loss in the condensation process is the cause for the modest efficiencies of this cycle.

6. THE COMPOUND COGENERATION CYCLE

In the parallel system, the working fluid in the power sub-cycle has a fairly low concentration, so it is hard to achieve the best temperature glide and consequent thermal match in the boiling process with the heating fluid, but, on the other hand, the turbine may have a desirable low backpressure. The opposite happens in the series-connected cycle. The ideal system should have low exergy losses in both the heat addition and condensation processes. To address an improvement in this direction, we now propose and analyze, a more complex cycle configuration, based on the parallel cogeneration cycle of Section 4. The major difference is the addition of another power route 5-14-15-16 as shown in Fig. 5, to reduce the irreversibility in the cycle heat addition process.

Now the working fluid with the basic ammonia concentration (3) is divided by the splitter *SP* into two streams (4) and (5). Stream 5 is directly brought into one power cycle by being pumped and heated, and then expands in turbine T_2, so it is possible to have a stronger solution at least in this power cycle heat addition process. The other (stream 4) is sent to the rectifier *REC*, where it is separated into ammonia-rich vapor (19) and ammonia weak solution (6). The weak solution is further weakened to state (8) in the reboiler by boiling off ammonia-rich vapor (7), and then is sent to the boiler *B* and a second turbine T_1, for power generation.

There are two power routes in this system: 8-9-10-11-12-13 and 5-14-15-16. The ammonia concentrations of the two turbine working fluids are also different. The exhausts of the two turbines merge in the low pressure absorber ABS_L to form an intermediate concentration solution (17). In that way the stream 16 is diluted and therefore turbine T_2 may have a lower backpressure.

It adopts the Kalina cycle concept of varying working fluid concentration to reduce the turbine backpressure. The working fluid (8) in the first power route is not only used for power generation, but also as the absorbent in the low pressure absorber, therefore the condensation process for the second power route is eliminated and replaced with a absorption process.

The cycle performance is calculated and the results are reported in Table 4. Similar to the former sections, the calculation was based on 1 kg/s basic working fluid feed to the rectifier.

In addition to the advantages of the absorption condensation, it is found that the heat transfer process in the boiler is improved too.

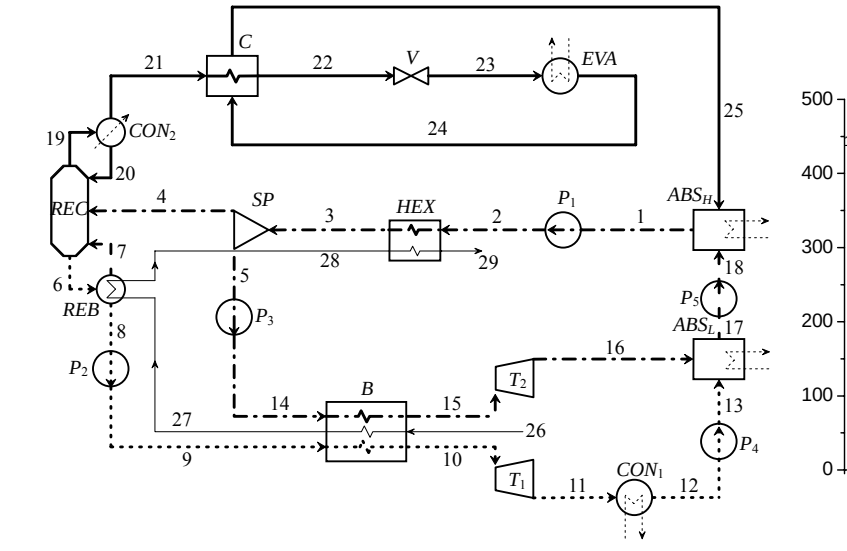

Fig. 5 The flow sheet of the combined power/cooling cycle

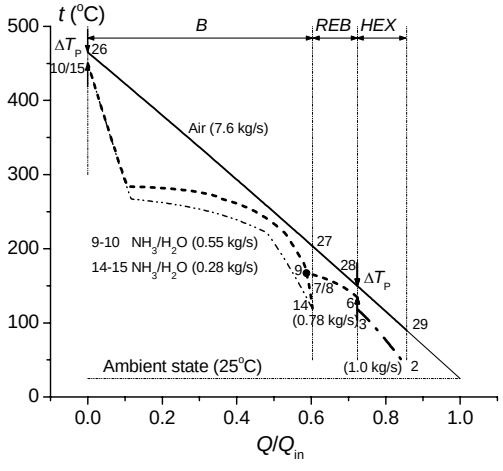

Fig. 6 the heat exchange *t*-*Q* diagram in the compound cogeneration system

Figure 6 shows the *t*-*Q* diagram of the heat addition process. The two cold streams in the boiler have concentrations of 0.3 and 0.098 respectively; they neither have high ammonia concentrations nor high pressures. The thinner dash-dot-dot line shows a temperature curve of a single cold stream with the ammonia mass fraction of 0.3, heated by the same heating fluid. It can be seen that the combination of the two cold streams has a much better temperature match with the heating fluid, thus reducing the irreversibility of the heat transfer process.

Table 4. Cycle performance summary for compound cogeneration cycle

Split Fraction SF_2		**0.72**
Turbine *T* work [kW]	T_1	540.78
	T_2	255.61
Pump work [KW]	P_1	2.18
	P_2	6.74
	P_3	3.56
	P_4	0.017
	P_5	0.15
Refrigeration output Q_{EVA} [kW]		191.66
Condenser CON_1 load [kW]		1209.28
Rectifier condenser CON_2 load [kW]		274.37
Cooler *C* load [kW]		42.75
Absorber heat load [kW]	ABS_H	628.85
	ABS_L	287.6
Boiler *B* heat input [kW]		2108.64
Reboiler *REB* heat input [kW]		421.43
Heat exchanger *HEX* heat input [kW]		462.12
Net power output *W* [kW]		783.75
Refrigeration/power ratio *R*		0.245
Heat input Q_{in} [kW]		3493.26
Exergy input E_{in} [kW]		1378.51
Energy efficiency η_1 [%]		27.92
Exergy efficiency η_2 [%]		59.5

Similar to the series-connected system, the split ratio in the splitter, defined as $SF_2 = G_4/G_3$, is also a key parameter for this cycle. It is easy to see that when SF_2=1 the cycle becomes the parallel one described in Section 4.

As SF_2 increases, more basic concentration working solution is sent to the rectifier, leading to the increase of the refrigeration output. When SF_2 increases, the concentration of the mixture (state 17) at the two turbine exhausts decreases, leading to the decrease of the backpressure of turbine T_2. It is found that there are SF_2 that maximizes the exergy efficiency and the energy efficiency.

The base case compound cogeneration cycle has very good thermal performance with the energy efficiency and exergy efficiency of 28% and near 60% respectively, as reported in Table 4. The good thermal match in the boiler is obtained by the arrangement of two cold streams with different low ammonia concentrations, rather than one high concentration cold stream; and the backpressures of both turbines can be maintained at a lower level because of the low ammonia concentration and the adoption of absorption condensation. The irreversibility in both the power cycle heat addition process and condensation process can thereby be reduced.

We note that all three analyzed systems have power as the main output, the parallel one has the highest refrigeration/power ratio *R* of 0.37, and the compound one has the lowest *R* of 0.25. For the same heating fluid mass flow rate, the compound cycle can produce 9% and 11% more power and 28% and 11% less refrigeration, respectively, than the parallel and series-connected systems. Its exergy efficiency is 4 and 5 percentage points higher, respectively, than those of the parallel and series connected systems.

7. CONCLUDING REMARKS

This paper shows the implementation of some general principles for power and refrigeration cogeneration system design and synthesis, with ammonia/water mixture as the working fluid. The well-known principles, and the way they were implemented in this development, are:

1) Both the external heat input and heat exchanged within the cycle components should be used/recovered properly and thoroughly: an important way for that is to cascade the heat exchange according to the temperature of both hot and cold streams.

This principle was followed here by creating a component configuration cascaded, heat source to sink, by their temperatures. To generate more power, the turbine working fluid needs to be heated to as high a temperature as possible in the boiler. The reboiler at the bottom of the rectifier needs mid-temperature heat to boil off the ammonia-rich vapor. Therefore, to match with the heating fluid, the boiler was placed at the highest temperature region, followed by the reboiler. Lower in the cascade, the heating fluid at the outlet of the reboiler was used to preheat the working fluid feed to the rectifier, helping to reduce the reboiler load.

2) To obtain a good temperature match with the sensible heat source, the working fluid must exhibit an appropriate temperature glide in the boiler, that was accomplished here by ensuring that its concentration in the evaporation process is neither too high nor too low.

3) The turbine backpressure should be as low as

possible to generate more power output and reduce as much as possible the exergy loss in the condensation process.

Principles 2 and 3 are not always easy to satisfy at the same time in the ammonia/water system. For example, in the evaporation process, accomplishment of a working fluid temperature glide that produces a good thermal match with the sensible heat source requires an ammonia concentration of about 50%. That, however, creates a high turbine backpressure and thus reduces power production if this solution is used as the turbine working fluid. The ideal system should have low exergy losses in both the heat addition and condensation processes, which requires that different ammonia concentration be maintained in these processes.

To accomplish that, a splitting and absorption unit is employed to adjust some stream mass flow rates and thus maintain the desired ammonia concentrations in both the heat addition process and the absorption process, in the series-connected and the compound cogeneration systems. That unit brings a stronger solution into the power sub-cycle heat addition process, thus making a better temperature match with the heating fluid. It also dilutes at the same time the turbine exhaust in the absorption-condensation process, leading to a drop of the turbine back-pressure and improvement of the temperature match in the condensation process.

4) The exergy loss associated with pressure drops needed for the process should be minimized, for example by substituting a throttling process with a power generation one.

That was accomplished in the parallel and compound systems by recovering the pressure exergy of the reboiler weak outflow, by introduction of a steam-driven power generation system instead of the throttling valve. This increased the power output significantly. Other means for pressure exergy recovery are under investigation.

In the three cycle configurations analyzed, the energy and exergy efficiencies were found to be 26~28% and 55~60%, respectively, in the base case when the top heat input temperature is 450°C. That efficiency is, by itself, excellent for cycles using heat sources of ≤450ºC, and comparable to that of nuclear power plants. When using the waste heat from topping gas turbine power plants, which, if used independently, typically have efficiencies of about 40%, the total plant energy efficiency rises to the remarkable value of about 57%. The hardware used is conventional and commercially available, no hardware additional to that needed in conventional power and absorption cycles is needed, and the use of mixtures results in a smaller total required heat exchanger area than the conventional separate cycles.

It is of course of interest to compare the performance and capital investment of the proposed cogeneration system with separate conventional steam Rankine power cycles and absorption refrigeration cycles that produce the same power and refrigeration outputs. Such comparison was made by the authors [10], where it was demonstrated that a somewhat similar cogeneration system operates at better efficiency than the separate cycles, with no penalty in capital equipment.

ACKNOWLEDGEMENT

The authors gratefully acknowledge the support of the Chinese Natural Science Foundation Project (No. 90210032) and K. C. Wong Education Foundation, Hong Kong.

REFERENCES

[1] J. H. Horlock, 2003, Advanced gas turbine cycles, Pergamon, Oxford.

[2] J. D. Maloney, R. C. Robertson, 1953, Thermodynamic Study of Ammonia-Water Heat Power Cycles, ORNL Report CF-53-8-43, Oak Ridge, TN.

[3] A. I. Kalina, 1984, Combined-Cycle System with Novel Bottoming Cycle, ASME Journal of Engineering for Gas Turbines and Power, Vol. 106, pp. 737-742.

[4] J. H. Horlock, 1987, Cogeneration-Combined Heat and Power (CHP) -Thermodynamics and Fluid Mechanics Series, Pergamon, Oxford.

[5] D. Y. Goswami, 1998, Solar Thermal Technology: Present Status and Ideas for the Future, Energy Sources, Vol. 20, pp. 137-145.

[6] D. Y. Goswami and F. Xu, 1999, Analysis of a New Thermodynamic Cycle for Combined Power and Cooling Using Low and Mid Temperature Solar Collectors, Journal of Solar Energy Engineering, Vol. 121, pp. 91-97.

[7] S. Lu and D. Y. Goswami, 2003, Optimization of a Novel Combined Power/Refrigeration Thermodynamic Cycle, ASME Journal of Solar Energy Engineering, Vol. 125, pp. 212-217.

[8] D. Zheng, B. Chen and Y. Qi, 2002, Thermodynamic Analysis of A Novel Absorption Power/Cooling Combined Cycle, Proceedings of ISHPC'02, pp. 204-209.

[9] Aspen Plus®, Aspen Technology, Inc., version 11.1, http://www.aspentech.com/.

[10] Na Zhang, Ruixian Cai, Noam Lior, 2004, A Novel Ammonia-Water Cycle for Power and Refrigeration Cogeneration, ASME paper IMECE2004-60692, Anaheim, CA, ASME, N.Y..

Proceedings of ECOS 2005
Trondheim, Norway
June 20–22, 2005

EVAPORATION OF REFRIGERANTS IN A SMOOTH HORIZONTAL TUBE: PREDICTION OF R407C HEAT TRANSFER COEFFICIENTS AND PRESSURE DROPS

Filippo de Rossi and Simonetta Tino
Dipartimento di Ingegneria, Università degli Studi del Sannio
Piazza Roma, 21, 82100 Benevento, Italy

Alfonso William Mauro*
DETEC, Facoltà di Ingegneria, Università degli Studi di Napoli, Federico II
Piazzale Tecchio, 80, 80125 Napoli, Italy

ABSTRACT

This paper presents experimental local heat transfer coefficient and pressure drop results obtained during the evaporation of the zeotropic mixture R407C (R32-R125-R134a, 23/25/52 % in weight). The test section was a smooth, horizontal, stainless steel tube (6 mm ID, 6 m length) uniformly heated by Joule effect. The effects of mass flux, heat flux and evaporating pressure on the heat transfer coefficients have been investigated. The experimental tests have been performed with a refrigerant mass flux of 200 and 355 kg/m^{2}s varying the heat flux within the range 8.0-16.9 kW/m^2 and the evaporating pressure from 3.5 up to 10.0 bar.
Keywords: R407C, heat transfer coefficient, pressure drop, experimental results, convective boiling.

NOMENCLATURE

A	heat-transfer area of the tube [m^2]
G	mass flux [kg/m^{2}s]
h	heat-transfer coefficient [W/m^{2}K]
$\dot{m}$	mass flow rate [kg/s]
p	pressure [Pa]
q	heat flux [W/m^2]
$\dot{Q}$	heat transfer rate [W]
T	temperature [°C]
x	quality
Δp	pressure drop [Pa]

Subscripts

bulk	referred to bulk properties
ev	evaporative
in	inlet
sat	saturation
tot	total
w	wall

INTRODUCTION

Following global climate changes, the environmental impact of technology systems need to be investigated. Refrigeration systems contribute to both global warming and ozone layer depletion. As known a new family of substances harmless towards the ozone layer is hydro-fluorocarbons, HFCs. Nevertheless, these fluids are greenhouse gases and may be subjected to limitations on their use in the future. The refrigerant fluids with long atmospheric lifetimes and high numbers of carbon-fluorine bonds have been identified as greenhouse gases (direct contribution).
The vapour compression air conditioners, heat pumps and refrigeration plants that use refrigerants also use energy. Therefore they contribute to global warming both by release of refrigerants and by emission of carbon dioxide and other greenhouse gases, in powering the devices

*Corresponding author: Tel.: +39-81-768-2303; Fax: +39-81-768-2964;
E-mail address: wmauro@unina.it

(indirect contribution). If the proposed replacements for CFCs and HCFCs are characterized by a lower performance coefficient, higher amounts of electrical energy must be supplied to the machine. In turn, this implies higher amounts of primary fossil energy and higher carbon dioxide emissions.

Therefore the choice of vapour compression machine operating fluids must be governed by both the absence of chlorine and bromine atoms in the molecule and a low direct and indirect contribution to the greenhouse effect.

Experimental tests carried out with these new refrigerants have pointed out a reduction of the energetic performances of the systems that means a larger environmental impact in terms of green house effect. Accurate investigations highlighted how these performances are influenced from the functioning of the heat exchangers (evaporator and condenser). For this reason the knowledge of two-phase characteristics is of prime importance to design heat exchangers for refrigeration and air-conditioning applications. In this paper the results about the experimental evaluation of heat transfer coefficients and pressure drops for the zeotropic mixture R407C (R32-R125-R134a, 23/25/52% in weight) are presented.

EXPERIMENTAL APPARATUS

An experimental apparatus schematic view is provided in Fig.1. It consists of different loops: the main loop and two auxiliary ones. The main loop is not a classic compression vapour plant to keep the refrigerant free by lubricant. Along the main loop a gear pump drives the liquid refrigerant coming from a boiler and by means of a hydrodynamic speed variator allows the refrigerant to flow at different flow rates. The mass flux can be varied continuously within the range 200–1100 kg/m^{2}s.

At the test section inlet, saturated liquid conditions are ensured by a thermally controlled electric ribbon wound around the tube upstream from the test section.

The test section is a 6 m stainless steel horizontal

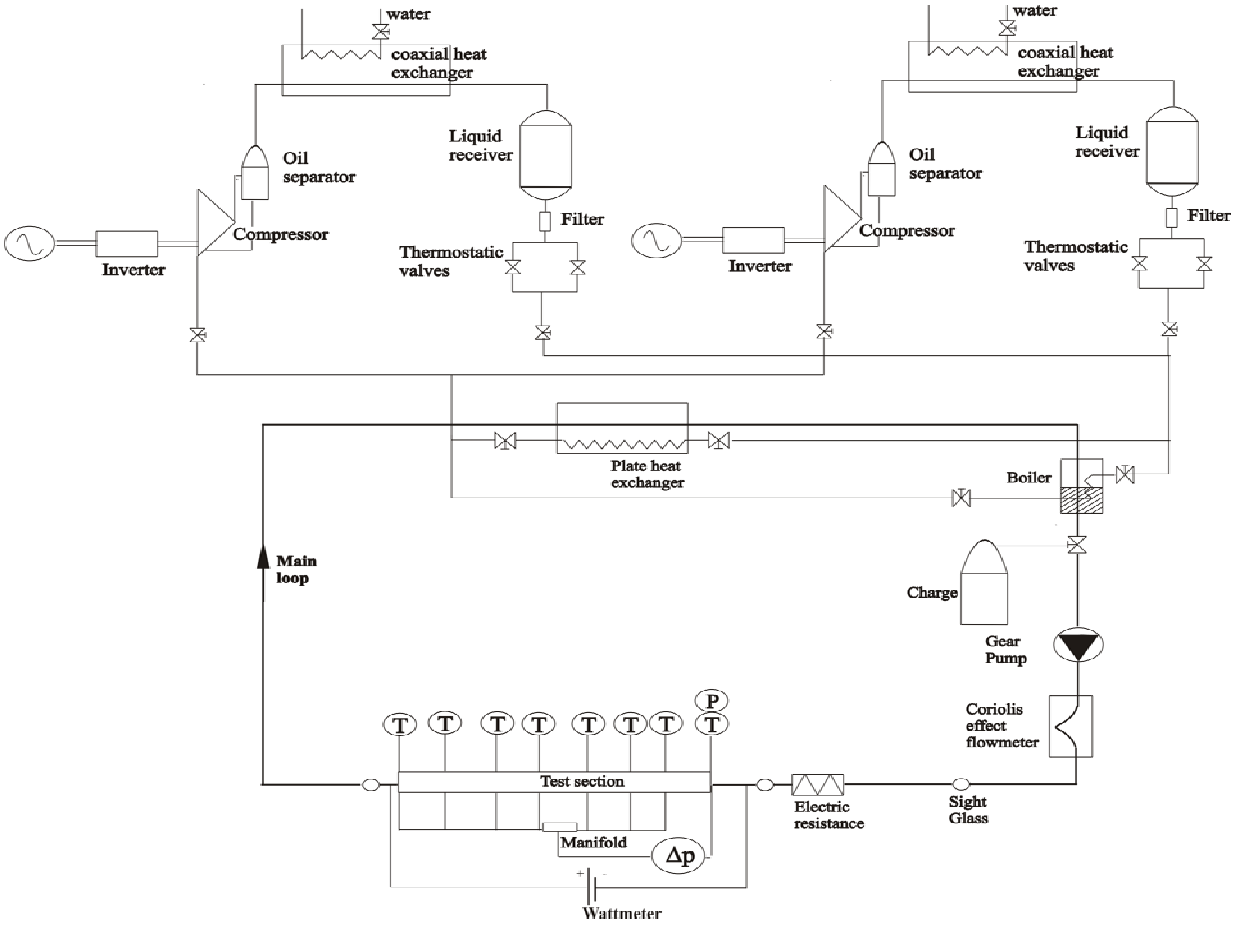

Fig. 1 Experimental apparatus

tube with inside diameter 6 mm and wall thickness 1 mm in which the refrigerant evaporates. The tube is electrically heated by Joule effect and insulated by means of PFA connections at its headers. A direct electrical current supplied by a feed current device circulates on the surface of the tube. Varying the direct electrical current, it is possible to have heat fluxes within the range of 8–70 kW/m^2.The heat flux supplied along the tube can be safely considered constant. Two sight glasses are installed at the inlet and outlet of the test section to check the refrigerant flow patterns. The refrigerant condenses in a plate heat exchanger. This heat exchanger may be the evaporator of two different vapour compression plants, alternately working as auxiliary. R507a is the working fluid for each auxiliary loop, which is composed by a semi-hermetic bi-cylindrical compressor, a coaxial condenser, two thermostatic valves and a plate evaporator.

In order to separately analyse the influence of several operating parameters on the evaporating heat transfer characteristics, the experimental apparatus has to be able to carry out tests in which it is possible to control independently the evaporating temperature, the mass flow rate of the circuiting refrigerant and the heat flux in the test section. To this aim a vapour compression plant with a classic design cannot be utilized, otherwise only one evaporating temperature corresponds to an evaporating power.

For this reason the components of the two auxiliary loops are sized differently, in particular one is sized to work at higher evaporating temperature and the other one to work at lower evaporating temperature. Moreover the compressor of each loop is connected to an inverter, which enables to vary its revolution speed, and each loop has two thermostatic expansion valves to permit a correct lamination in different operating conditions. Using all systems it can be varied the evaporating temperature within the range of -30°C to 20 °C.

Finally the test apparatus has been heavily insulated with a 32 mm layer of cellular insulate for the heat exchangers and with a coaxial tube of armflex insulate for tubes and tube fittings.

MEASUREMENTS AND DATA REDUCTION

Locations of sensors in the test section are shown in Fig.1.

Since the test section is thermally insulated the heat transferred to the refrigerant can be evaluated as the electric power supplied by the feed current device. The voltage and the current are monitored by means of a voltmeter and an amperometer. The voltmeter has an accuracy of ±0.2% in the range 0-30 V and the amperometer has an accuracy of ±0.2% in the range of 0-220 A.

A four wire 100 Ω platinum resistance thermometers are inserted in the refrigerant flow stream at the inlet of the test section. Such type of resistance thermometers is located in other key-points of the test circuit.

Along the tube there are eight test stations. Each test station is placed according to the qualitative diagram relating the evaporative heat transfer coefficient to vapour quality. For each station there are four four-wire 100 Ω platinum resistance thermometers. These thermometers are located on the top, bottom and both sides of the outside tube wall. All the resistance thermometers are calibrated in the proper operating range and they have an accuracy of ±0.03°C.

An absolute piezoelectric pressure transducer measures the pressure at the inlet of the test section. It has an accuracy of 0.1% F.S. in the range 0-14 bar. Pressure drops between the inlet and each test station are directly measured. In fact each station is shunted one by one to a manifold and by means of a pressure gauge the pressure drop between the inlet and the manifold can be measured. This piezoelectric pressure gauge has an accuracy of 0.1% F.S. in the range 0-1 bar.

Refrigerant mass flow-rate is measured by a Coriolis effect mass flow-meter, inserted after the gear pump, where sub-cooled liquid conditions have been achieved. This device has an accuracy of ±0.2% in the range 0-2 kg/min. Since the measurement could be affected by mechanical vibrations, it has been mounted on a 5 kg steel plate separated from plant.

In each station the heat transfer coefficient is calculated four times for the four wall temperature measurements by the following equation:

$$h_{ev} = \frac{\dot{Q}}{A_{tot}\left(T_w - T_{bulk}\right)} \qquad (1)$$

where $\dot{Q}$ is the power supplied to the refrigerant, A_{tot} the total area of the tube, T_w the temperature of the inner wall, T_{bulk} the fluid bulk temperature. Than their mean value is held and stored as the local heat transfer for that station.

According to the previous equation also the fluid bulk and the inner wall temperatures have to be known. The bulk fluid temperature along the tube

is calculated rather than measured directly, because an in-stream thermometer considerably perturbs the two phase flow pattern. Since R407C is a zeotropic mixture, to evaluate the fluid bulk temperature (i.e. saturation temperature, during evaporation) the local pressure and the local specific enthalpy must be known. The local pressure is derived from the inlet pressure and the pressure drop between the inlet and each test station.

The local specific enthalpy is derived from an energy balance between the generic test station and the inlet:

$$h = h_{in} + \frac{\dot{q} A}{\dot{m}} \qquad (2)$$

where h_{in} the enthalpy at the inlet section, $\dot{q}$ is the heat flux along the test section, A is the inner tube area between the generic test station and the inlet and $\dot{m}$ is the mass flow rate. By measuring the inlet pressure and the inlet temperature the specific enthalpy at the inlet is known.

All the thermodynamic properties of the refrigerant fluid are evaluated using a computer program [1].

The inner wall temperature along the test section is estimated from the measured outside wall temperature by applying the one-dimensional, radial, steady-state heat conduction equation for a hollow cylinder assuming uniform heat generation within the tube wall and an adiabatic condition on the outside of the tube.

DATA ACQUISITION AND UNCERTEAINTIES ESTIMATION

The data acquisition starts when steady-state conditions have been achieved. A personal computer connected to a data-acquisition system, consisting in a controller, a 48-channel scanner and a multimeter, performs data collection. To control the achievement of the steady-state conditions temperature and pressure values in key points of the plant are continuously monitored. Preliminarily it is fixed a deviation value and the steady-state conditions are assumed to hold when the deviations of the controlled variables from their corresponding mean value are lower than the fixed deviation.

If steady-state conditions have been achieved, the test starts and the data logging with a 1 Hz sampling rate is performed on all channels for 1000 s. For the channels corresponding to the gauges of the test section, the 1000 samples recorded are averaged. Each sample is checked against the corresponding mean value and it is rejected if it does not lay within the fixed range. If more than 5% of the samples are rejected, the whole test is discharged.

Uncertainties in the experimental data are calculated using the analysis suggested by Moffat [2]. The uncertainty of each measured quantity consists mainly of uncertainties of the measurement device and of the data-acquisition system.

For the heat transfer coefficient the error analysis is carried out with the following equation:

$$\frac{\partial h_{ev}}{h_{ev}} = \sqrt{\left(\frac{\partial \dot{Q}}{\dot{Q}}\right)^2 + \left(\frac{\partial A}{A}\right)^2 + \left(\frac{\partial T_w}{T_w - T_{sat}}\right)^2 + \left(\frac{\partial T_{sat}}{T_w - T_{sat}}\right)^2} \qquad (3)$$

The total error depends on the uncertainties in measurements and on the operating conditions. Under the employed operating conditions for the zeotropic mixture R407C the inaccuracy of the heat transfer coefficients are ranged between 1.8% and 8.5%.

EXPERIMENTAL RESULTS AND DISCUSSION

The flow boiling tests in the present paper are carried out for the zeotropic mixture R407C (R32-R125-R134a, 23/25/52 % in weight).

In the present paper the heat transfer coefficients and pressure drops are measured varying the evaporating pressure, keeping the refrigerant mass flux almost constant.

The test conditions are performed in the refrigerant mass flux range 200-355 kg/m^{2}s, varying the heat flux between 8.0-16.9 kW/m^2 and the evaporating pressure within the range 3.5-10.0 bar.

The experimental conditions are summarized in Table 1. Refrigerant mass-flux, evaporating pressure at the inlet of the test section, the corresponding saturation temperature, and heat flux are specified for each test.

Because the heat-transfer process depends on the flow regime, first the flow patterns have to be identified in order to calculate the heat transfer coefficients and pressure drops. Numerous flow pattern maps have been proposed over the years for the prediction of two-phase flow regime transitions in horizontal tubes. In this paper, the latest version of the Kattan-Thome-Favrat map [3, 4] is used. An intermittent flow pattern is observed from the inlet

G [kg/m^{2}s]	P_{ev} [bar]	T_{ev} [°C]	q [kW/m^2]
196	3.50	-14.0	7.96
211	6.00	1.7	7.96
207	7.88	10.4	9.19
200	9.97	18.6	10.4
351	3.80	-11.8	9.42
353	4.80	-5.1	11.9
354	5.90	1.2	12.3
356	6.90	6.1	15.5
361	7.90	10.6	15.5
355	9.02	15.1	15.5
352	9.84	18.1	16.8

Table 1 The operating conditions

section to the part of the test section with vapor qualities between 30 – 40 %, depending on the test conditions. The intermittent flow covers both plug and slug flow regimes (it is essentially a stratified–wavy flow pattern with large amplitude waves that wash the tube top). With increasing vapor qualities, an annular flow is achieved. At higher vapor qualities (>76 % in dependence of the heat flux values) the liquid film in the upper part of the tube disappears and the flow became annular with a partial dry-out.

The experimental heat transfer coefficients obtained during the evaporation of R407C are depicted in Fig. 2 as a function of vapour quality obtained by varying the evaporation pressure at the almost constant refrigerant mass flux of 200 kg/m^{2}s.

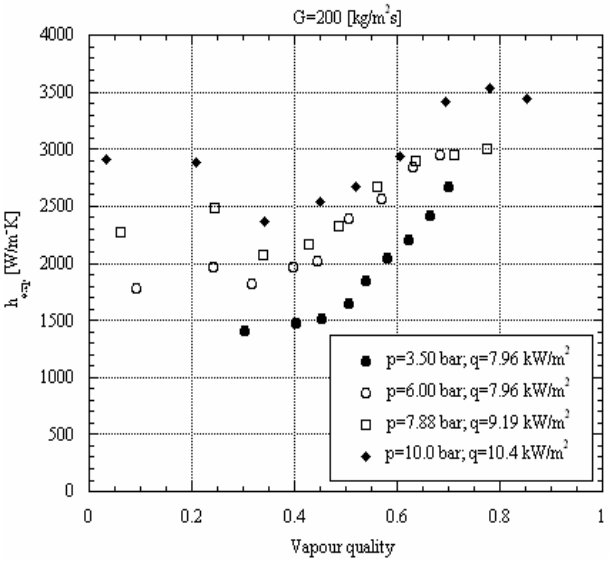

Fig.2 Local heat transfer coefficients as a function of the vapor quality at a fixed refrigerant mass flux varying the evaporating pressure.

The heat transfer coefficients present distinct behavior depending upon the quality range. The heat transfer coefficients first decrease with increasing vapor quality and then increases again. The local minimum corresponds to the transition from intermittent flow to the annular flow regime. The experimental test corresponding to the evaporating pressure of 3.5 bar does not present this local minimum, though the transition quality occurs outside the range considered in the present study (x < 30%).

In the experimental tests reported in this figure, corresponding to low mass velocities, there were observed two distinct heat transfer regions during evaporation. In the first one, occurred at low vapour qualities, nucleate boiling (characterized by the formation of bubbles on the heated wall of the tube) was dominant. In this region, the heat-transfer coefficients decreased as the effect of nucleate boiling diminished. Indeed, with increasing vapor qualities, the wall-to-interface temperature difference needed to drive the heat flux was reduced.

The decrease in the wall superheat reduced the number of active nucleation sites for bubble formation. Furthermore, in flow boiling the wall shear stress causes the bubbles to depart early from the wall, and reduce the bubble size compared with pool boiling. This effect leads to a reduction in the nucleate boiling component with increasing shear stress. Both effects lead to a reduction in the effectiveness of nucleate boiling with increasing vapour quality. The second region corresponded to convective evaporation. It is characterized by the

increase of the heat transfer coefficients with increasing vapour qualities. In an annular regime, heat-transfer is dominated by evaporation at the interface between the liquid (located at the wall) and the vapour (in the tube core). As vaporization proceeds, the thickness of the liquid film on the tube wall decreases together with its thermal resistance thereby enhancing the heat-transfer effectiveness. The ensuing increase of the heat transfer coefficient proceeds until the liquid film disappears, leaving the tube-wall partially or totally dry. In this region, the heat transfer coefficient decreases because of the low thermal conductivity of the vapour.

It is clearly highlighted from the experimental results that the heat transfer coefficients increase together with the pressure and the heat flux.

With increasing pressure, the nucleate boiling contribution to the heat transfer coefficients increased mainly due to the corresponding decrease in the bubble radius for a given wall superheat. Assuming spherical nuclei, the required bubble radius at which the bubble is in equilibrium with the liquid follows from the well-known equilibrium conditions for a small bubble (Thomson equation) and the linearized Clausius-Clapeyron equation and it depends on physical properties (surface tension, enthalpy of vaporization, vapour-phase density). With increasing pressure the vapour density strongly increases and the surface tension decreases.

The decrease of the average departure diameter of vapour bubbles with increasing pressure implies the activation of the additional new small cavities on the heated surface, and therefore the increase of the nucleate boiling contribution to the heat transfer coefficient. For lower values of the refrigerant mass-fluxes, the dependence of the heat-transfer coefficients from pressure was stronger, since nucleate boiling contribution became increasingly more important and there is no bubble suppression in the whole quality range.

The experimental heat transfer coefficients of R407C are depicted in Fig. 3 as a function of vapour quality obtained by varying the evaporation pressure at the almost constant refrigerant mass flux of 355 kg/m^{2}s.

The experimental tests reported in this figure correspond to higher mass velocities and the convective contribution to heat-transfer predominates in the whole quality range. Indeed, as the flow proceeds downstream and vaporization takes place, the void fraction increases, thus

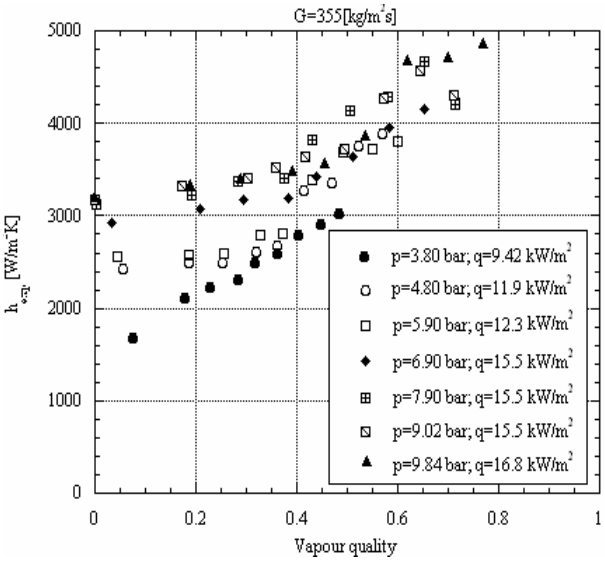

Fig.3 Local heat transfer coefficients as a function of the vapor quality at a fixed refrigerant mass flux varying the evaporating pressure.

decreasing the density of the liquid-vapour mixture. As a result, the flow accelerates enhancing convective transport from the heated wall of the tube.

For these higher refrigerant mass fluxes, the convective contribution was predominant and therefore the dependence on the evaporating pressure became weaker. The heat transfer coefficients increased with pressure, but only for low vapour qualities. For higher qualities, the effect of the evaporating temperature became weaker and the heat-transfer coefficients merged together.

The local pressure drops of R407C as a function of the vapour quality varying the evaporative pressure at the almost constant refrigerant mass fluxes of 200 and 350 kg/m^{2}s are reported in Fig.4 and 5, respectively. The pressure drop is evaluated as the pressure drop per unit length between the pressure taps. As seen in both the figures, the pressure drop increases with the quality. The total pressure drop is mainly caused by the frictional pressure drop. It involves not only the transfer of momentum between fluid and wall, but also the transfer of momentum between the individual phases. This contribution increases with the vapour quality to a maximum between 70-90% and then decreases to the pressure drop of the vapour flow. Indeed, increasing the vapour quality, the void fraction increases, thus decreasing the density of the liquid-vapour mixture. As a result, the flow accelerates increasing the frictional pressure drop.

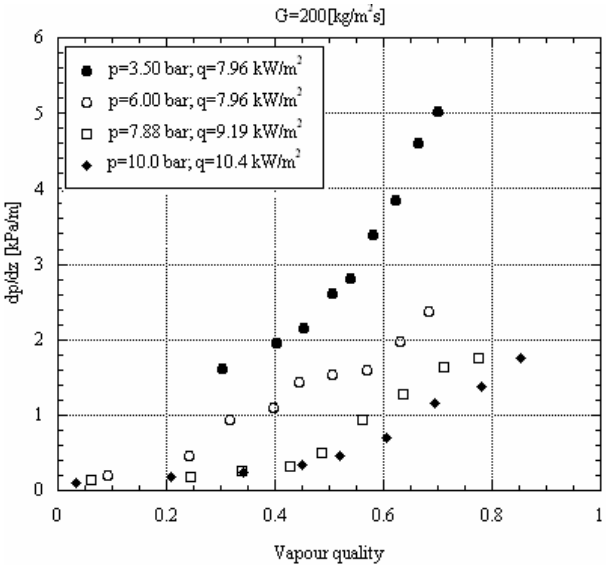

Fig.4 Local pressure drops as a function of the vapor quality at a fixed refrigerant mass flux varying the evaporating pressure.

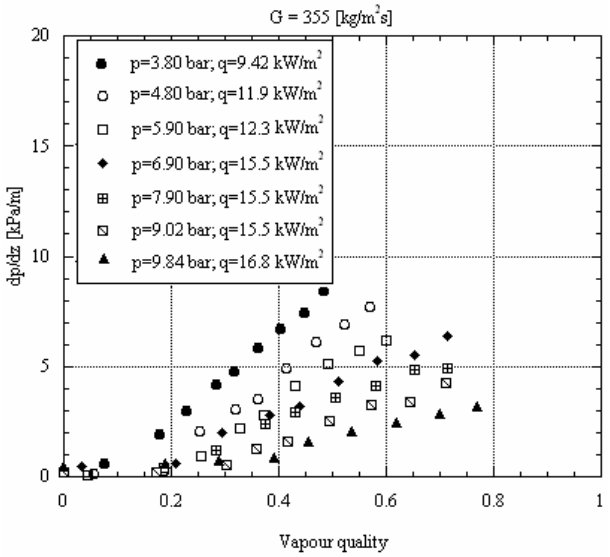

Fig.5 Local pressure drops as a function of the vapor quality at a fixed refrigerant mass flux varying the evaporating pressure.

The pressure drop decreases strongly with the increase of the evaporating pressure. Indeed, as the evaporating temperature increases, the decrease of the liquid viscosity and of the specific volume of the vaporized refrigerant leads to the decrease of refrigerant velocity and pressure drop.

CONCLUSIONS

An experimental apparatus has been set up at the University of Naples for evaluating the heat transfer characteristics of pure and mixed refrigerants. This paper presents the experimental results for evaluating the local heat transfer coefficients and the pressure drops for the zeotropic mixture R407C (R32-R125-R134a, 23/25/52 % in weight) during convective boiling in a horizontal tube. The experimental tests have been performed with a refrigerant mass flux of 200 and 355 kg/m^{2}s varying the heat flux within the range 8.0-16.9 kW/m^2 and the evaporating pressure from 3.5 up to 10.0 bar.

It is highlighted from the experimental results that the heat transfer coefficients increase with increasing the saturation pressure for a constant refrigerant mass flux. With increasing pressure, the nucleate boiling contribution to the heat transfer coefficients increases mainly due to the corresponding decrease in the bubble radius for a given wall superheat. For the higher refrigerant mass flux, the convective contribution is predominant and the dependence on the evaporating pressure becomes weaker.

The total pressure drop is mainly caused by the frictional pressure drop. The pressure drop decreases strongly with the increase of the evaporating pressure.

REFERENCES

[1] M. Mc Linden, et al., *NIST Standard Reference Database 23: Refprop 6.1, computer software*, U.S. Department of Commerce, Technology Administration, National Institute of Standard and Technology, Gaithersburg, 1998.

[2] Moffat R.J., *Describing uncertainties in experimental results*, Experimental Thermal Fluid Science 1988, 1: 3-17.

[3] Kattan N., J.R. Thome, Favrat D., *Flow boiling in horizontal tubes: Part I – Development of adiabatic two phase flow pattern map,* Transaction of ASME 1998 (120): 140-147.

[4] J.R. Thome, J. El Hajal, *Two-phase flow pattern map for evaporation in horizontal tubes: latest version.* In: Proceedings of International Conference HEFAT, Kruger Park, South Africa, 2002.

Proceedings of ECOS 2005
Trondheim, Norway
June 20–22, 2005

Combined heat and power plants, district heating

Proceedings of ECOS 2005
Trondheim, Norway
June 20–22, 2005

NATURAL GAS HEATING BOILERS EMISSIONS A RESIDENTIAL BUILDING STUDY

C. Balocco, A. Gagliardi, G. Grazzini[1], M. Sarti
Università di Firenze
Dipartimento di Energetica "S. Stecco"
Via Santa Marta 3 - 50139 Firenze
Italy

ABSTRACT

This work shows evaluation of emissions from natural gas heating systems applied to a residential building and its flats located in Firenze. Two building designs have been considered: the reference residential house proposed as standard by the AICARR and its flats, and the same but with higher insulation. The operating response of different boilers due to the hourly heating power demand of building has been studied. The CO and NO_X emissions have been evaluated during the heating season and also for each month. Results show that the centralized boiler is more suitable to the building heating demand and it has lower emissions impact.
Key words: domestic burner; natural gas combustion; emissions; control.

NOMENCLATURE

C	heat capacity [MJ/K]
E	daily emission [mg/day]
I	global solar radiation [W/m^2]
N	users number Eq.(1)
P	boiler's power [W]
R^2	regression coefficient
T	temperature [°C]
ΔT	temperature difference [°C]
W	water demand [l/d]
w	average wind speed [m/s]
φ	relative humidity
τ	time [s]

Subscripts

CO	carbon monoxides emission
H_2O	water
NO	nitrogen oxides emission
O	horizontal
off	not working boiler
on	working boiler
tot	total
v	vertical surface

INTRODUCTION

High ozone levels, summer smog in cities, forest depletion and the threat of irreversible changes in climate provide the only answer of drastic reduction of air pollution. The White Paper [1] has introduced emissions standards in the European Communities Countries focusing high attention on the fact that a third of our energy consumption and the resulting emissions can be ascribed to domestic heating and hot water production. The Kyoto Protocol for greenhouse gases and the introduction of emission standards rouse several studies, researches and technologies for low NO_X emission of small-scale combustion equipment.

There are many measures adopted in building design and there are also many laws in each European Country about energy saving and integrated energy use with particular attention to sustainable development and environmental pollution [2,3,4,5,6]. So recent developments in materials and technologies for the energy conservation, have opened new possibilities for reducing the total energy consumption in

[1] Correspondig author: Phone +390554796242 Fax:+390554796342 E-mail:ggrazzini@ing.unifi.it

residential buildings and for lowering the NO_X and CO_X emissions, while maintaining acceptable comfort levels.
There are many certification schemes to identify products with different degrees of energy efficiency. Some are specifically oriented to environmental effects taking into account emissions from the use of appliances and the life-cycle sustainability of the product. There is abundant literature [7,8,9,10,11,12,13,14,15,16, 17] concerning greenhouse gas emissions reduction, but not so ample [18,19,20,21] on the emissions from domestic heating systems for different buildings.
The introduction of new gas burner technology by using the V-shaped flame stabilised at the centre of the burner blade [3,20,21,23,24], the modulating fan powered premixed low NO_X burners [16,24], and the new catalytic combustion technology for different applications for condensing boilers and water heaters [25], needs a flexible and critical approach. Looking at the many existing heating old systems in buildings, not all of them are able to meet these new combustion techniques. The V-shaped flame technique bases on an extended bladed combustion front with low mean temperatures and low NO_X, CO_X, HC emissions [17,06]; fully aerated premixed burner technology provides the lowest NO_X emission values and low CO_X and other air borne pollutants [3,19]; flameless catalytic combustion applied to domestic heating systems, then catalytically stabilised and completely catalytic radiation boiler are recently studied but not so adopted and diffuse in the real plant systems [22,23,25].
In particular there are not studies in transient conditions of domestic and centralised natural gas boiler applications.
The aim of this work is to investigate the performances in transient conditions of different gas heating systems for a typical residential building.
CO_X and NO_X emissions related to the heating systems working hours at different load have been analysed for the heating season by using experimental data and the climatic data of the standard year in Firenze.

THE METHOD

Building and its plant for heating and domestic hot water production have been considered as an integrated system. Three kinds of heating boilers and different regulations of gas burners have been considered:

- a wall mounted boiler with room sealed, 25 kW nominal power and modulating low NO_X burner with drawing up fan;
- a base boiler with open chamber, low NO_X burner with on-off regulation and 35 kW nominal power;
- a wall mounted boiler with conventional burner, on-off regulation and 25 kW nominal power.

Experimental results from direct measurements of CO, CO_2 and NO_X emissions for the considered boilers, reported by Sarti [26, 27], have been used. The studied building is the residential house proposed as standard by the AICARR (Italian Air Conditioning Association) in the '60's. Four similar flats located on two levels compose it. To evaluate the heating needs for the whole building and for each flat, the Italian Standard UNI EN832 and UNI EN ISO13789 have been used [28,29,30]. An appropriate computational tool was built by using interactive spreadsheets. The method is based on a steady state energy balance for each zone with an allowance for external temperature variation, and an utilisation factor taking into account the effect of thermal internal and solar gains. The hourly climatic data have been used [31].
The gain utilisation factor is evaluated as a function of the gain to load ratio and of a thermal inertia parameter expressed by the time constant of the zones for each flat. The same was made for the building. Each flat and the whole building have been evaluated separately because of different heating systems and related to different burners considered. Heating energy need for the building agrees to the imposed value due to DPR 412/93 Italian Standard [28], considering a fixed internal temperature value of 20 °C with a tolerance of ± 2 °C.
To compare the performances of the studied boilers, working with modulating or intermittent regulation, also the same building, with higher

insulated envelope, has been considered. New building data and comparison between the two thermal peak load are shown in table 1.

Thermal transmittance [W/m^2 K]	**Reference**	**High insulated**
Glass wall	2.9	2.3
Opaque wall	1.22	0.5
Roof	1.52	0.51
Floor	1.4	0.34
Nominal peak load [kW]		
Building	30.49	19.85
Flat	7.94	4.78

Table 1: Thermal characteristics of reference and high insulated building.

The nominal power of the studied boilers is higher than the maximum thermal load calculated for building and flats. On the other hand, only transient condition emissions of these boilers are available.
Hot water demand has been calculated separately from heating demand. A correlation equation that relates the water needs per day W has been built with reference data [32,33,34,35] as a function of users N:

$$W = 0.0639\ N + 65.995 \ ; \ R^2 = 0.1129 \qquad (1)$$

R is the R-squared value used to evaluate the reliability of the regression line.
Regression equations reported in some reference models [36,37] are comparable to the above calculated. The hourly typical domestic hot water trend, for a 3 persons average family, built by experimental data [32,33,34,35], is reported in figure 1.
Considering for each flat that a tap opening duration of about six minutes, hot water demand controls the power supply. For a water mass flow of 0.2 kg/s with a rise temperature of 30 °C, the requested power is 25 kW, which meets the boiler's one. Total hot water consumption evaluated considering same taps opening, is greater than that shown in figure 1.

The 35 kW boiler alone doesn't satisfy hot water power demand for the whole building; then a water storage tank has been considered. By taking four delivering taps for each flat, results a

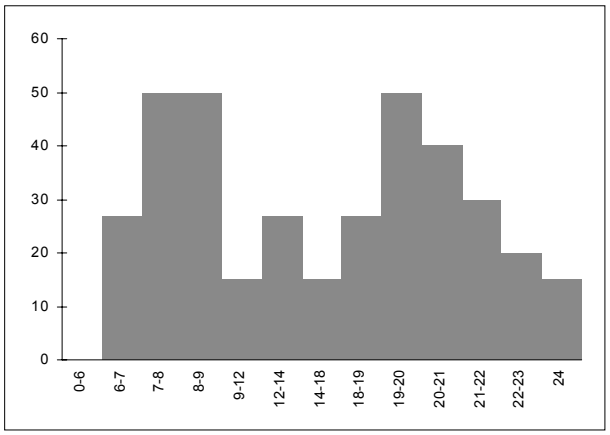

Fig.1: Typical domestic hot water load - 3 persons average family.

contemporary factor of 30% [38]. In table 2 the considered water flow rates for the different sanitary equipments are given.

Sanitary equipments	**Flow rate [l/s]**
1 bath sink	0.10
1 bidet	0.10
1 kitchen sink	0.20
1 shower	0.15

Table 2: Sanitary equipments flow rate for a flat.

In these conditions a 300 litres hot water storage tank is sufficient for the whole building.
The 35 kW boiler can easily provide the needed water also with a 50 °C rise temperature.
For an on-off burner regulation, the heat capacity of the building has been calculated for a temperature variation of 4 K, to estimate the working and turning off period of the boiler, as a function of temperature difference. Those periods are given by:

$$\tau_{on} = (C\ \Delta T) / (P - H_{tot}) \qquad (2)$$

$$\tau_{off} = (C\ \Delta T) / H_{tot} \qquad (3)$$

Daily emissions due to heating and to hot water demand have been evaluated by:

$$E_{tot\,CO} = \sum E_{CO}\ \varepsilon\, P\, \tau_{on} + \sum E_{CO}\ P\, \tau_{H_2O} \qquad (4)$$

$$E_{tot\,NO_X} = \sum E_{NO_X} \varepsilon\, P\, \tau_{on} + \sum E_{NO_X}\ P\, \tau_{H_2O} \qquad (5)$$

where E concerns the daily CO and NO_X emissions due to heating and hot water demand; P is the boiler's power; ε is the percentage of the nominal power, always 1 for the on-off boiler. The experimental results [26, 27] have been used to evaluate CO and NO_X emissions of different boilers for domestic hot water production and heating. This calculus has been done during the legal heating season in Firenze and from 6 a.m. to 10 p.m. of each day.

RESULTS

Hourly heating load and hourly hot water demand have been calculated for flats and building. Results have been obtained for each month of the heating season. Firenze heating season is 151 days long (starting from 15 November). Heating and hot water CO and NO_X emissions for the six months have been evaluated for the low NO_X burner with on-off regulation on 35 kW nominal power boiler, for the 25 kW boiler with modulating low NO_X burner, and for the 25 kW boiler with on-off regulation conventional burner (Bunsen flame). The 35 kW nominal power boiler has been used for the building; the last two kinds of boiler have been used for each flat. Building and flats have been also considered with high-insulated envelope and the new emissions results have been compared.

The 35 kW boiler considered for the insulated building produces lower CO and NO_X emissions values, for all the heating season and also for each month, than the corresponding values calculated for the other two kinds of boiler considered for the four insulated flats (figg.2,3). Comparing monthly and seasonal CO and NO_X emissions obtained for the reference building and four flats, with the corresponding values obtained for insulated building and flats (figg.4,5), the 35 kW boiler always provides lower values than the 25 kW on-off and modulating ones. Moreover, the same

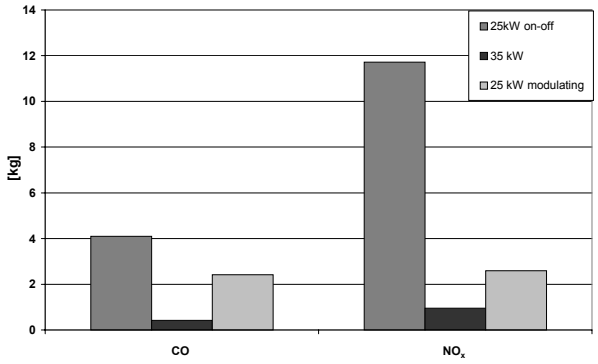

Fig.2: CO and NO_X emissions for the heating season – Building and four high insulated flats.

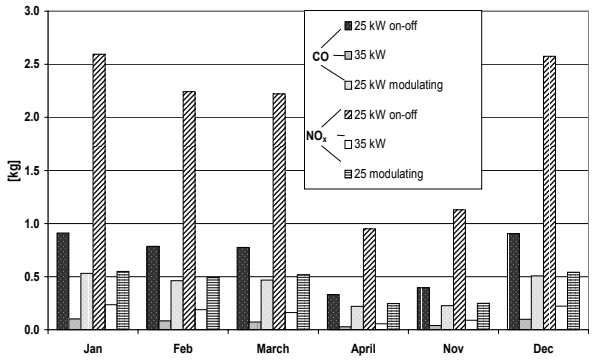

Fig.3: Monthly CO and NO_X emissions – Building and four high insulated flats.

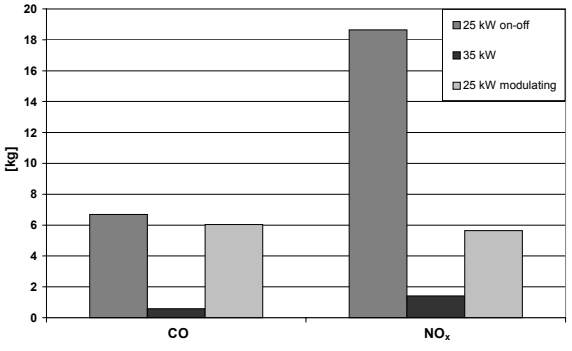

Fig.4: CO and NO_X emissions for the heating season – Reference building and four flats.

comparison between 25 kW on-off boiler with the modulating one shows that the CO and NO_X

monthly and seasonal emissions for this last kind of boiler are lower than the first one.

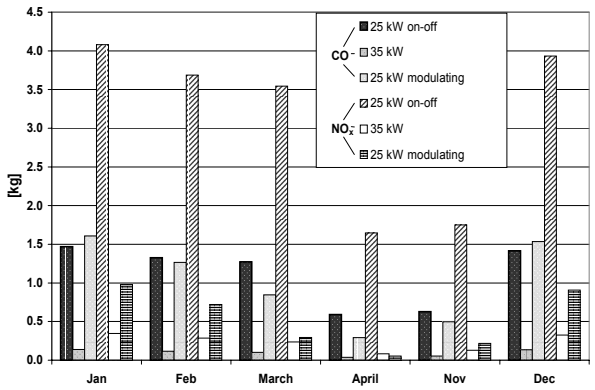

Fig.5: Monthly CO and NO_X emissions – Reference building and four flats.

A day of the whole season, when the outside air temperature value is 0°C, that is the 13th January, corresponding to the design building peak load due to the difference between inside and outside temperature of 20°C, has been considered as an example of this analysis. Figure 6 shows that modulating boiler for the reference flat works at about 30% nominal load from 6 a.m. to 22 p.m. If the insulated flat is considered, it modulates on 20% nominal load only from 6 a.m. to 12 a.m..

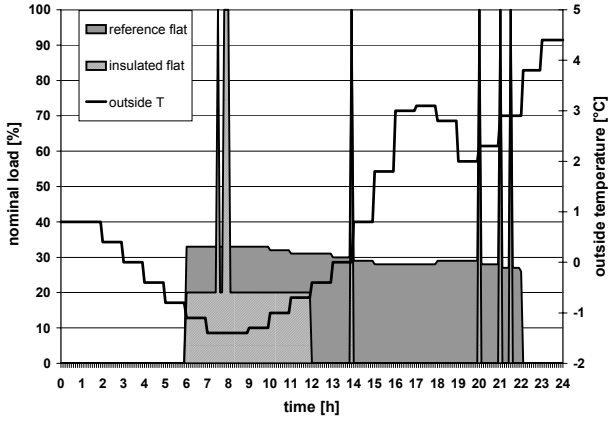

Fig.6: Rate of nominal load for the modulating boiler – Insulated and reference flat – 13th January.

In fact each flat has a boiler with a power higher than heating peak demand due to instant sanitary hot water power demand. Load peaks on the graph are due to hot water demand.

As it can be seen by comparisons at specific climatic conditions and in presence of high insulated building, it can be more convenient by energy, economic and also environmental impact point of view to use the centralised base boilers with low NO_X burner. From this study, centralised base boiler results indicated for high-insulated buildings' applications compared to modulating boilers single flats' applications.

By comparison, it can be deduced that our 35 kW nominal power base boiler provides lower emissions for all the heating season and for each month.

Transient condition emissions data for a condensing boiler of the same power and with modulating gas burner are not available, but the Authors believe they'll be lower.

CONCLUSIONS

Natural gas domestic boilers with different burners have been compared for building and household applications. In particular a reference building and its flats with two different envelope insulations, supplied by different boilers, have been considered. CO and NO_X emissions for the heating season and for each month have been calculated using experimental transient conditions results [26]. The more reliable domestic boiler application depends on the local climatic conditions and the connected building heating energy demand, but also on its operating conditions during defined daily heating time. Existing and new centralised base boilers are more suitable for buildings energy retrofitting especially if they are connected to the actual gas and temperature sensors [12]. The analysis was limited to data available to the Authors, so a centralised modulating boiler was not considered.

REFERENCES

[1] White Paper - *Una politica energetica per l'Unione Europea*. COM(95) 682, IT-ver., December 1995.

[2] Jacoby, H., Prinn R., Schmalensee R., Needed: *A Realistic Strategy for Global Warming.* MIT Joint Program on the Science and Policy of Global Change, Report n. 21, August 1997.

[3] Joynt B., Wu S., *Nitrogen Oxides Emissions Standards for Domestic Gas Appliances - Background Study*. Environment Australia Report, February 2000.

[4] Van Eck H., *Market transformation: water heaters.* SAVE Conf., 8-10 Nov.1999, Graz, Austria; Vol. I-I-9.

[5] Vekemans G., *Boiler inspection in the EU: achievements and challenges for the future.* SAVE Conf., 8-10 Nov.1999, Graz, Austria, Vol. I-I-10.

[6] Ybema J.R. et al., *Scenarios for Western Europe on long term abatement of CO_2 emissions.* ECN-C--97-051, 2000.

[7] Börjesson P., Gustavsson L., Christersson L. and Linder S., *Future Production and Utilisation of Biomass in Sweden: Potentials and CO_2 Mitigation.* Biomass and Bioenergy, 1997;13 (6); 399-412.

[8] Commission of the European Communities, *Simulation of thermal systems A modular program with interactive pre-processor EMGP3*. Kluwer Academic Publisher, London 1991.

[9] Gustavsson L, *District heating systems and energy conservation-part I.* Energy, 1994; 19 (1); 81-91.

[10] Hamelinck C.N., *Potential for CO_2 sequestration and enhanced coalbed methane production in the Netherlands*. NOVEM, Utrecht, the Netherlands. NWS-E-2001- 07.

[11] Herman H., *Residential heat pump system and controls.* IEA HPC News Letter, 1997; 15(2).

[12] Hoefer U., Frank J., Fleischer M., *High temperature Ga_2O_3-gas sensors and SnO_2-gas sensors: a comparison. Sensors and Actuators* B Chemical, 2001; (78); 6-11.

[13] IEA Statistics, *CO_2 Emissions from fuel combustion* 1971-1999. Int. En. Agency Edition 2001.

[14] Jacob L., Norris J., *Domestic water heating in UK*. European Renewable Energy Magazine, Sun at work in Europe, 1996; 11(2); June.

[15] Marion J., Nsakala ya N., Griffin T., Bill A., *Controlling power plant CO_2 emissions: a long-range view.* DOE Publication, 2001.

[16] Seebregts A.J. et al., *Endogenous technological learning: experiments with MARKAL.* Contribution to Task 2.3 of the EU-TEEM project, ECN-C--98-064, Petten, 1998.

[17] Toqan, M., Nicholson J., Briggs O., Borio R., Beér J., *Low NO_X Burners for Boilers and Furnaces: Design and Application.* Power-Gen. Europe 97 Conf., Madrid, Spain, June 17-19, 1997.

[18] Butola V., Muhic S., *Impact of burner cycle time in liquid fuel pressure burners on the thermal efficiency of heating appliances*, Energy 2001;26: 299-306

[19] Foster T., Dupont V., Pourkashanian M., Williams A., *Low-NOx Domestic Water Heating Appliances.* The J. Inst. of Energy, 1994; 472:101-108.

[20] Ritter H., Benke G., *Natural gas for domestic appliances in Austria*. SAVE-Conference: Energy Efficiency in Household Appliances and Lighting, Naples, Italy, 27-29 Sept. 2000.

[21] Twist T.H., Hargreaves K.J.A., *Emissions control and its implications on the domestic gas burner manufacturer.* The Inst. of Energy's II Intern. Conf. on Combustion and Emissions Control, 4-5 Dec. 1995, London, UK; pp. 29-38.

[22] Miller F., *Heating without polluting: the flameless burner*. Fraunhofer Inst. for Solar Energy Systems, Friburg 5 February 1997.

[23] Moallemi F. Batley G. A., Dupont V., Williams A., *Experimental and Modelling Studies of Catalytic Burners.* Eurotherm Sem. N. 54, Compact Fired Heating Units, 11-12 Dec. 1997, Leuven, Belgium.

[24] Solero G., Beghi M., *Experimental fluid dynamic characterization of a premixed natural gas burner for domestic and semi-industrial applications.* The Inst. of Energy's II Intern. Conf. on Combustion and Emissions Control, 4-5 Dec. 1995, London, UK; pp. 39-48.

[25] Vaillant S. Ro, Gastec A.S., *Catalytic combustion in a domestic natural gas burner*. Catalysis Today, 1999; 47:415-420.

[26] Sarti M., *Emissioni da impianti civili termici di bassa potenza*, Thesis (In Italian), University of Firenze, Italy, 2001.
[27] Grazzini G., Balocco C., Sarti M., *Transient Conditions Emissions From Low-Power Gas Heating Systems,* accepted at XXIII Congr. Nazionale UIT , 20-22 June 2005, Parma, Italy.
[28] UNI 10344, *Riscaldamento degli edifici. Calcolo del fabbisogno di energia*. CTI, Novembre, 1993.
[29] UNI EN ISO 13789, *Prestazione termica degli edifici - Coefficiente di perdita di calore per trasmissione. Metodo di calcolo*. Marzo 2001.
[30] UNI EN832, *Prestazione termica dell'edificio. Calcolo del fabbisogno energetico per il riscaldamento degli edifici residenziali*. Giugno 2001.
[31] Alabisio M., Sidri R. *Gestione archivio anno tipo*. ENEL CRTN, Milano, 1995
[32] AAB, *Vandbesparende foranstaltninger.* Miljøudvalget, February 1993
[33] Kvisgaard B., Hadvig S., *Varmetab fra fjernvarmeledninger.* Teknisk Forlag, 1980.
[34] Mazin M., Maleki M., *Optimering af varmt brugsvandssystem,* Ekasamensprojekt Hovedrapport. Laboratoriet for Varmeisolering, DTU DK, July 1995.
[35] Yang L., *District heating house stations with hot water storage. Simulation and evaluation of dynamic performance*. Centre for district heating technology, Lab. HAC, DTU-DK, 1995.
[36] Lawaetz H., Bøhm B., *Varmeforsyningsalæg-Matematiske modeller for produktionion distribution og varmebehov*. Tekn. Inst., October 1984.
[37] Gustavsson L., *District Heating and Energy Conservation.* Energy, Vol. 1, 1994, London UK, pp 81-91.
[38] Riva F., *Guida agli impianti tecnici-Impianti idrosanitari: criteri di dimensionamento ed installazione*. PEG, Milano, 1985.

Proceedings of ECOS 2005
Trondheim, Norway
June 20–22, 2005

CLUSTERS OF MODULAR CHP PLANTS

Gian Luigi Berta[1]
Industrial Engineering Department
University of Parma, Italy

Alessandro Pini Prato, Francesco Ferretti, Luca Garbarino, Matteo Repetto
Department of Heat Machines, Energy Systems & Transportation
University of Genoa, Italy

ABSTRACT

"On site power production" is dealt with, namely based on small size co-generative (CHP) plants. The best results can be achieved with highly standardised units, suited to be grouped in batteries, preferably coupling units of different size (e.g. a CHP plant could reach 600kW with 2x100kW and 2x200kW modules).
A convenient control logic is developed, that pursues technical-economical optima: a case study of a modular system applied to CHP plant for hospitals is presented, and the suitability is demonstrated by comparing cascaded to uniformly shared load control.

Keywords: CHP, cogeneration, DER, distributed energy resources

NOMENCLATURE

CF	cash flow	[€]
CHP	combined heat and power	
DER	distributed energy resources	
f	present worth factor	
F	fuel energy	[GJ]
$\dot{F}$	fuel energy rate	[kW]
$FESR$	fuel energy saving ratio [2]	
GT	gas turbine	
IRR	internal rate of return [2]	
M	annual fuel costs	[€]
NPV	net present value[2]	[€]
Q	utilised heat	[GJ]
$\dot{Q}$	utilised heat per unit of time	[kW]
SWH	space & water heating	
t	time	[d]
TET	turbine entry temperature	[K]
W	work produced	[GJ]
$\dot{W}$	work rate (electric power)	[kW]
Y	price of energy unit	[€/MJ]
z	dimensionless position of controls	
ΔC	extra capital cost	[€]
η	efficiency	
λ	heat/work ratio	

Subscripts

$=$	evenly shared load
$\neq$	unevenly shared load
A,B	units in a cluster
ap	annuity present
b	boiler
CHP	combined heat and power
c	conventional
f	fuel
i	interest or discount rate
N	years period
n	rated at $z = 0$
o	overall
th	thermal
u	useful heat
w	work
1	pertinent to a single unit

Superscripts

N	years period
*	assigned load

[1] Corresponding author: ph.: +39 010 353 2705 or …2458; Fax: +39 010 353 2700; email: gianluigi.berta@unipr.it

INTRODUCTION

This paper deals with "on site power production", namely based on small size co-generative (CHP) plants.
Distributed electricity generation allows to catch many more opportunities of energy savings, arising from the use of heat released by mechanical work producing processes [3,4,6].
Main issues are control flexibility, investment cost containment, and the pursuit of lower operation and maintenance costs [9].
Distributed generation means producing energy on site, where it is required, thus reducing electric power flowing along transmission lines. In order to be competitive with the electricity produced by larger plants, which is available from the mains, it will be required to control "clusters" of small plants, large enough (in terms of both number of units and total installed power) to be economic [8]. Any single small plant, so far as it works independently (though connected to the electrical grid), produces more costly energy: scale economy can be recovered by means of a great number of small units rather than of a restricted number of large plants.
The best results can be achieved with highly standardised units, suited to be grouped in batteries, preferably coupling units of different size (e.g. a CHP plant could reach 600kW with 2x100kW and 2x200kW modules).
Suitable control logics will allow to reach the best thermodynamic efficiency in any load condition, as well as to yield to renewable energy units whenever they are available, thus balancing undesired effects of small size [7,10].
The presence of a large number of small units gives rise to the question as to whether all the units should better be modulated their load together, or should advantages be obtained by cascading, i.e. starting the units in sequence on increasing load, while keeping running plants mostly at a steady state.
The problem was set down quite early in the history of CHP plants (see e.g. [1]), but outcomes were fairly against cascading, the main issue being the slow start up of steam units, the only kind of prime movers suitable for cogeneration at that time.
In this work a convenient control logic is developed, that pursues technical-economical optima: a case study of a modular system applied to a CHP plant for hospitals is presented, and the suitability is demonstrated by comparing cascaded to uniformly shared load control. The same electric and heat loads vs. time (functions extracted from real cases) are imposed on both cases, for which the price sensitivity among energy vectors (fuels, electricity, biomass, etc.) is given parametrically [9].

UNEVENLY SHARED LOADS

In order to find out suitable conditions as to whether the load must be shared in equal or different amounts among plants in a cluster, the simplest cluster is analysed, i.e. a plant consisting of two equal units.

Power plants

Let a case where only work production is present be first considered. The Willans (or consumption) line ($\dot{F}$ vs. $\dot{W}$) for one unit is plotted in fig. 1.

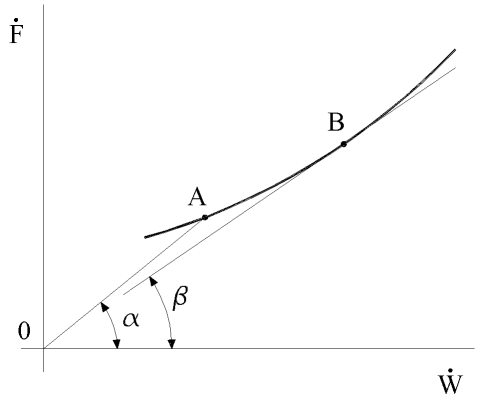

Fig. 1: Properties of Willans line

For any given point on the curve, A, the slope of the straight line ($\tan\alpha$) connecting to the origin O, represents the heat rate, while the efficiency is

$$\eta = \frac{\dot{W}}{\dot{F}} = \operatorname{cotg}\alpha$$

The best efficiency is easily found, and it is remarked that, where the projecting straight ($\overline{OB}$) is tangent to the Willans line, efficiency may show an optimum ($\operatorname{cotg}\beta$) at a lower than maximum load.

Passing to the set of two units (fig. 2), the Willans line is plotted for one unit, which is also representative of the behaviour of the set, provided that values are read on the scales ($2\dot{W}_1$,$2\dot{F}_1$), as far as the load is evenly shared between the units.

A given load $\dot{W}^*$ (scale $2\dot{W}_1$) can be either satisfied by running both sets at E, or by running one at a lower (G) and the other at a higher (H) than E power output, the only condition being

$$\dot{W}_A + \dot{W}_B = \dot{W}^*$$

that, passing from ($\dot{W}_1$,$\dot{F}_1$) to ($2\dot{W}_1$,$2\dot{F}_1$) scales, is represented by point K, i.e. the arithmetic average on the graph for both work and fuel energy rate.

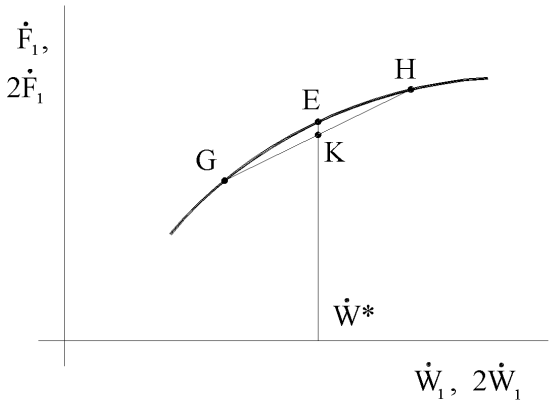

Fig. 2: Conditions for uneven load sharing

Point K yields a lower or higher value of $\dot{F}$ than point E depending on the curvature of the Willans line, thus determining a condition for uneven load sharing to be convenient from an energy saving viewpoint. If the consumption line is convex upward, then K lies beneath E, and fuel energy saved is given by

$$\Delta(2\dot{F}_1) = \dot{F}_{=} - \dot{F}_{\neq} = 2(\overline{KE})$$

In this case the best efficiency is sought by so choosing G and H as to maximise $\overline{KE}$. Of course benefits from cascading can be expected in terms of fuel savings, in the circumstances outlined for the convenience of non uniform load sharing.

CHP plants

When a CHP plant is considered, conditions can be identified in which electrical (work) and heat loads can be conveniently split, in a similar way as described above. Lines analogous to Willans' can be drawn, namely ($\dot{F}$,$\dot{W}$) at $\dot{Q}$ = const, ($\dot{F}$,$\dot{Q}$) at $\dot{W}$ = const, where, of course, the energy input $\dot{F}$ represents the whole fuel consumption of the CHP unit.

When plant features include the possibility to supply heat independently - to a certain extent - of work, at least one control device exists which determines how much of energy is diverted from work to heat production (e.g. a by-pass flap in a GT exhaust duct). Let z be the position of this control device, such as to have maximum heat yield for z = 1, minimum at z = 0. It is sometimes easier to plot ($\dot{F}$,$\dot{W}$) and ($\dot{F}$,$\dot{Q}$) lines at z = const.

Limiting the number of devices controlling λ in any single unit to one, for a CHP plant consisting of two units, called to match assigned electrical $\dot{W}^*$ and thermal $\dot{Q}^*$ loads, four are the control variables, namely $\dot{F}_A$, $\dot{F}_B$, z_A, z_B ; therefore, assuming no energy storage, i.e. loads are met at any time, there are two degrees of freedom in plant control. There may be chances for optimisation, if an objective function is identified, suitably dependent on the parameters remaining free.

In the following an energy conservation criterion is assumed, as to minimise fuel cost, on the basis of a quasi-steady approximation.

In the more general case of a cluster made of many CHP plants, each comprising several units for a total number N of units, as far as the couple ($\dot{W}^*$,$\dot{Q}^*$) can be considered assigned to the whole cluster, the degrees of freedom are easily recognised to be (2 N – 2). The problem becomes hard to solve on a rational basis.

Hence a simple case will be analysed, in order to throw some light on the subject.

APPLICATION TO A SAMPLE CASE

A sample case is introduced, which consists of two small co-generative gas turbine units (350 kW rated electrical power), grouped into a CHP plant.

Brief description of the unit

The unit is a regenerative GT, compressor and expander are radial, single stage machines, the regenerative heat exchanger (RHX) is of the plate-fin type. A co-generative heat exchanger (QHX) is installed downstream RHX; a diverter allows

part of the exhaust gas flow rate to bypass RHX, thus increasing $\dot{Q}$ through QHX. In this application only hot water (possibly superheated) is produced by QHX.
The flap diverter is the device in charge of controlling λ, so that z represents its position in a dimensionless fashion.

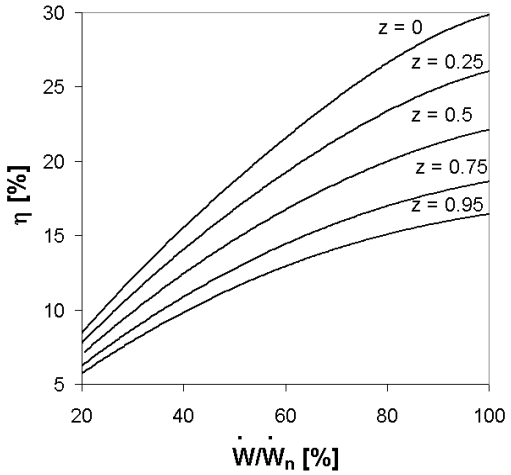

Fig 3: Electric efficiency of the GT unit

The performance of the GT unit, in its standard, regenerative setup, and the effect of the RHX bypass are shown in fig. 3, in terms of overall efficiency vs. electrical load.

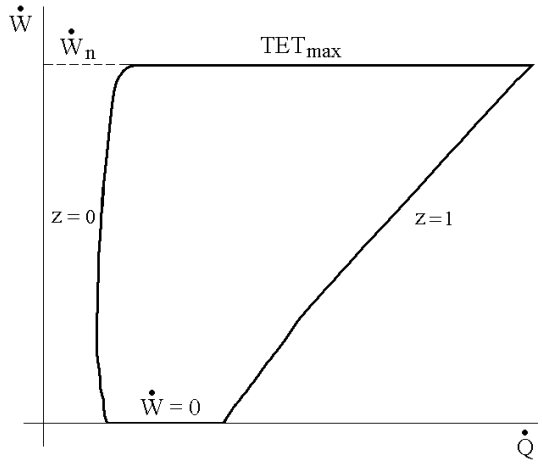

Fig 4: CHP unit operating range

The operating range of this CHP unit is shown in fig. 4 [7], where the boundaries are determined (clockwise, starting from the bottom) by:

- idling ($\dot{W} = 0$)
- bypass closed ($z = 0$)
- maximum *TET*
- bypass fully open ($z = 1$)

Constant z lines are significant, at least because they fix the left and right ends of the working field, and also:

- $z = 0$ means minimum (in the example) $\dot{Q}$ and describes how the unit behaves in its non-CHP set-up
- $z = 1$ shows what can be done in case heat is supplied at the highest possible rate.

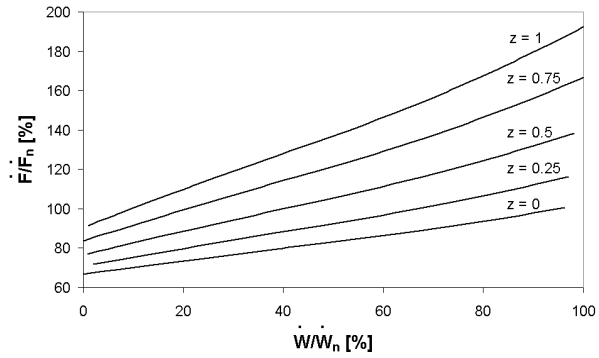

Fig 5: constant z lines, fuel consumption vs. electric power

In fig. 5 fuel energy rate is reported against electric power at z = const: the lower is a true Willans line, the others are akin. The curvature (slightly convex downward) of the $z = 0$ line, demonstrates that this kind of GT unit, when used in a non-CHP mode, should not experience energy savings from a cascaded control. This holds only in steady operating conditions.

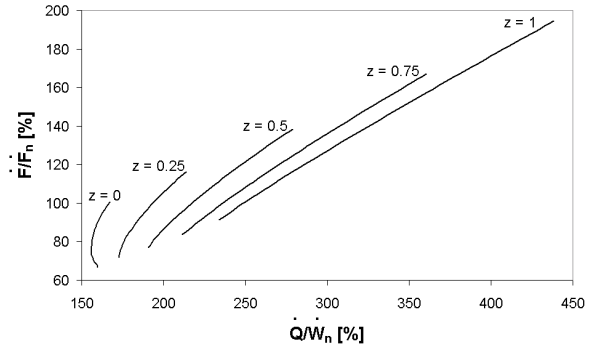

Fig. 6: constant z lines, fuel consumption vs. heat load

Fig. 6 reports fuel energy versus heat (rate terms) at constant bypass flap position. It is remarkable that also at $z = 0$ a significant rate of useful heat can be supplied. This is because the exhaust gas temperature at RHX exit is well above compressor

outlet temperature, i.e. enough to transfer heat to hot water (probably a worse result would be obtained if steam generation were required).

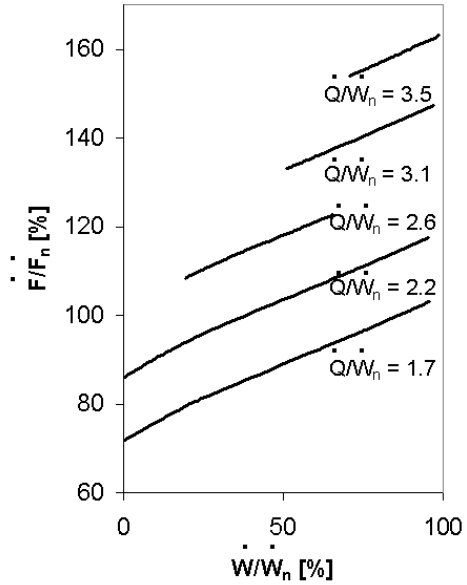

Fig. 7: constant heat load lines

The curvature of z = const lines suggests that uneven heat load sharing is convenient, at least in the lower range of thermal output.

For assessment purposes constant $\dot{Q}$ (fig. 7) and constant $\dot{W}$ (fig. 8) lines are introduced.

In fig. 7 a range is recognized where

$$\left.\frac{\partial^2 \dot{F}}{\partial \dot{W}^2}\right|_{QQ} < 0$$

while in fig. 8 it is found that

$$\left.\frac{\partial^2 \dot{F}}{\partial \dot{Q}^2}\right|_{WW} \cong 0$$

actually throughout the operating field.

Hence conditions exist for electric load cascading to be beneficial: uneven distributions of thermal load might also be found consequently necessary, because of the shape of the operating range. It is noteworthy that by introducing heat exploitation, what was not convenient beforehand, has now become beneficial.

It is necessary to further investigate on the suitability of cascaded control by means of simulation [10], bearing in mind that both conclusions hitherto, and results from the next point, are valid for the particular CHP arrangement considered [7].

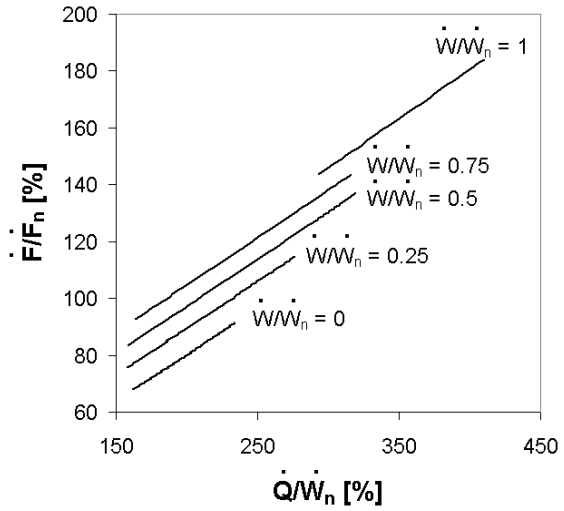

Fig. 8: constant electrical power lines

Method of analysis

To find the optimum combination of parameters (sharing heat and electrical load between the two plants) a numerical procedure has been employed, consisting of a minimum search algorithm linked to a GT and heat exchangers thermodynamic model. The objective function was the total fuel consumption in steady conditions.

An algorithm was first tested, based upon the aforementioned criterion of the second derivatives of fuel flow rate.

Later a different criterion prevailed, that requires the same model to be used for optimising both design and control/management during operation: for this reason a thorough search throughout the operating field is adopted, which permits deterioration of performance to be taken into account, when coupled to a self-learning monitoring system.

Results highlighted that the best conditions are obtained with uneven load distribution, one unit being called to supply both more work and more heat than the other.

Simulation results

A simulation has been carried out throughout one year [10], starting from meteorological records for heat request, and from typical load courses for the particular application: figs. 9 and 10 show control parameters vs. time, for part of the simulated time.

Two control modes are compared, load cascading and even sharing. In both modes a control system

is envisaged, performing functions that a dispatcher will be committed in a larger cluster.

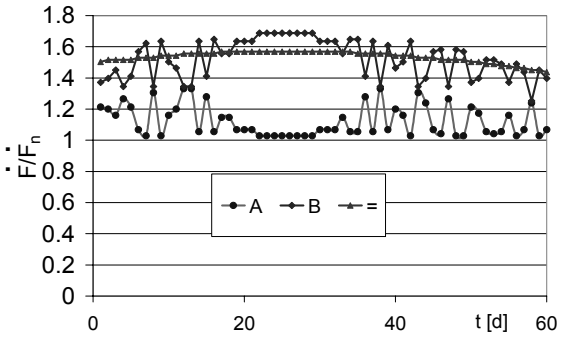

Fig. 9: simulated fuel energy rate vs. time

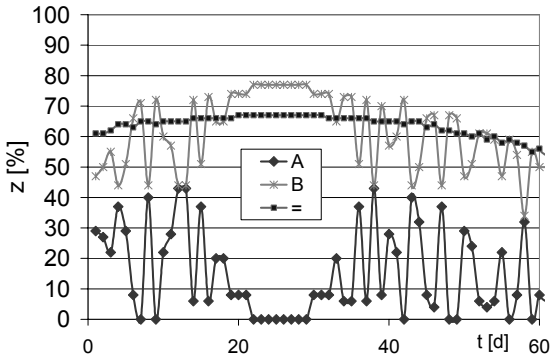

Fig. 10: simulated diverter flap position vs. time

This device automatically forces the total heat produced by the plant to match heat users' requests, while the electrical power is so controlled as to maximise cash flow, mismatches to internal requests being compensated by the mains. In this process the dispatcher-controller utilises predictive-self learning algorithms [8,10] committed to assure the target *FESR* value to be reached on an annual basis, which entitles the plant to be granted CHP benefits.

In order to give an idea of how cascaded control affects the operating points of the two units in the simulated plant, in fig. 11 an outlook at typical load unevenness is given through a couple of samples, each representing an instant situation: a high total electrical and a high total thermal load case are reported.

Economic analysis

The results of the thermo-economic analysis[2] are summarised in tab.1, in terms of *FESR* and of *NPV* per unit installed electrical power, $\dot{W}_n$. During simulations the same electric and heat loads vs. time are assigned to both cases, and the price sensitivity among energy vectors is given parametrically [9]. *NPV* is evaluated for a 10 years lifetime.

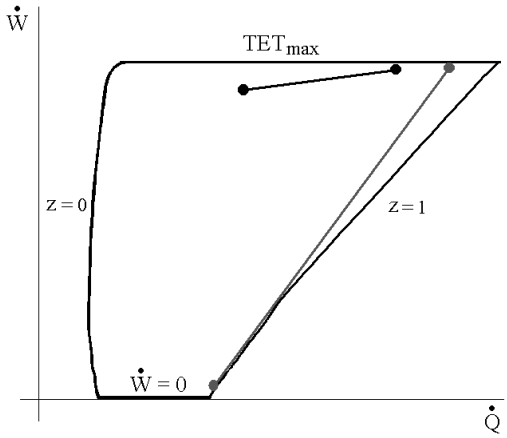

Fig. 11: split operating points for cascaded control

Operation has been simulated by applying both control/monitoring strategies to the same request for electric and thermal load, e.g. a given hospital unit in the same climate conditions.

Steady state performance of the cogeneration unit, as a function of control parameters and of environmental conditions, has been represented by matrices, obtained from mass and energy balances, matching of GT components and heat exchangers, on design as well as off-design conditions of the CHP plant.

The data supplied by the model (fig. 12, *FESR* map as a function of $\dot{Q}$ and $\dot{W}$) highlight an increasing irreversibility as *z* increases, just like what happens in "duct burner" plants when raising the afterburning ratio; because in both cases the energy of added fuel is utilised at similar, fairly low temperature values.(250 – 650°C).

For low *z* values, the above solution is however more efficient than afterburning and it looks sim-

[2] See Appendix for definitions of economic and performance criteria

pler and more compact: it is obviously more effective than the utilization of donkey boilers.

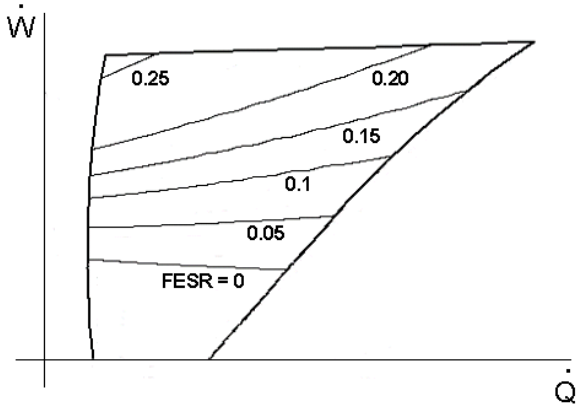

Fig. 12: *FESR* map of the single unit

The model was obtained by using Matlab-Simulink and validated through comparison with data supplied by the manufacturer in full regenerated as well as in many by-pass conditions. *FESR* was calculated by reference – for separate generation – to the average efficiency of Italian thermoelectric power plants (i.e. 0.38) and to the reference efficiency of civil boilers (taken as 0.8) according to the Italian rules in force. Start up, load connection and stop transients, which cannot be represented by the steady state model, have been assessed by the simulator according to suitable algorithms. The same tariffs for natural gas and electric energy (taken in or supplied by the plant) has been used to assess the cash-flow while taking the same operation and maintenance costs into account, although "even" and "uneven" control modes may cause small, but hardly to assess, differences.

The investment profitability for is assumed 5% net of the inflation drift of electric/gas energy carriers and present costs.

Parameterization in this simulation model of elasticity between fuel cost and electric energy value (Y_f/Y_w) is possible and shows in all cases an improvement of economic as well as of thermodynamic results when this ratio is reduced.

This and further aspects cannot be discussed in this Paper because of lacking space.

Improvements from uneven load sharing exist, but they are tiny comparatively to the complexity of cascaded dispatching, which is significantly increasing with the number of units in a cluster.

The results strictly depend on the particular type of GT employed and on CHP arrangement. It is believed that different kinds of prime movers showing more suitable features to cascaded control may give better figures: it is therefore worthwhile to account for possible benefits of uneven load sharing.

		load sharing	
		even	uneven
FESR		0.151	0.159
$NPV/\dot{W}_n$	[€/kW]	210	350

Tab.1 Thermo-economic results

Anyhow considerations other than energy based, e.g. transient behaviour of both GTs and heat exchangers, thermal stresses, components ageing, maintenance, suggest to minimise the number of units following load variations, while taking advantage of the quick start time of small GTs.

In a cluster any single module will be shifted his function periodically, from base to peak load supplier and vice versa.

Environmental issues

From the environmental point of view, CO_2 savings can be achieved through converting to cogeneration a number of heat users that otherwise produce heat (either SWH or process) separately. Passing to DER, which is cheaper thanks to a modular approach, makes the range larger of applications for which CHP plants are cost effective. This corresponds to the exploitation of *heat quarries*, i.e. thermal users not yet converted to cogeneration, as explained in [9].

CONCLUSIONS

A modular arrangement of CHP plants belonging to an independently controlled DER cluster allows to better follow instant loads, and to increase the fraction of electricity produced through cogeneration.

Modules can easily be standardised, thus improving reliability and availability, and reducing operation costs.

In this scenario, while the load is shared among several modules, units work out to be better utilised if a cascaded control is applied. Appropriate dispatcher logics, together with a suitable choice of components, can lead to energy savings, by seeking at any time the best set of control parameters.

REFERENCES

[1] Lyle O. *The efficient use of steam* HMSO, London 1947

[2] Horlock J.H. *Cogeneration, combined heat and power* Krieger, Malabar FL 1997

[3] Payne F.W. *Cogeneration management reference guide* Prentice Hall, Lilburn GA 1997

[4] Boyce M.P. *Handbook for cogeneration and combined cycle power plants* ASME press, New York 2002

[5] Lindsley D. *Power plant control and instrumentation* IEE, London 2000

[6] Chambers A., Schnoor B., Hamilton S. *Distributed generation a non technical guide* Pennwell, Tulsa OK 2001

[7] Bonello P. et alii *Microturbina rigenerata per il minigrid cogenerativo del Campus Universitario di Savona*, ATI Conference, Genoa 2004

[8] Berta G. L., Garbarino L., Pini Prato A. *Riflessioni sul potenziale della cogenerazione diffusa* ATI Conference, Padova 2003

[9] Berta G.L., Pini Prato A., Garbarino L. *Design criteria for distribuited cogeneration plants* ECOS 2003, Copenaghen 2003

[10] Berta G.L., Pini Prato A. *Conceptual design and operator's guide a sound, common basis for quite faraway engineering applications* ATI S.Stecco conference, Genova 2001

[11] Berta G.L., Pini Prato *About Cost Sharing in Combined Plants* ECOS'96, Stockholm 1996.

APPENDIX

The parameters described in this appendix comply with the criteria assumed in [2].

FESR is a performance criterion developed for CHP plants, that involves comparison between the fuel required to meet the given electricity and heat loads with that required in separate conventional plants to meet the same loads, say in a conventional electric power station of overall efficiency $(\eta_0)_c$ and a "heat only" boiler of efficiency $(\eta_b)_{th}$. Then the fuel energy saved is

$$\Delta F = \frac{Q_u}{(\eta_b)_{th}} + \frac{W}{(\eta_o)_c} - F,$$

and the fuel energy saving ratio is defined as the ratio of the saving (ΔF) to the fuel energy required in the conventional plant

$$FESR = \frac{\Delta F}{\left(\frac{Q_u}{(\eta_b)_{th}} + \frac{W}{(\eta_o)_c}\right)} = 1 - \frac{(\eta_o)_c / (\eta_o)_{CHP}}{\left[1 + \left(\lambda_{CHP}(\eta_o)_c / (\eta_b)_{th}\right)\right]}$$

where $\lambda_{CHP} = \frac{Q_u}{W}$ is the useful heat to work ratio of the CHP plant, and $(\eta_o)_{CHP}$ is its overall efficiency.

The net present value derived from a change type of analysis (from an existing conventional scheme to a new CHP scheme), balances extra capital cost (ΔC) against the rate of savings which arises (ΔM), mainly from the reduced use of fuel.

If the extra capital ΔC invested at time zero leads to immediate annual money saving ΔM in the first year, and this money is invested at the end of that year, subsequent years lead to identical savings and investment. These savings may be discounted back to time zero and lead to a net present value of

$$(NPV)_{(i)} = \frac{\Delta M}{({}_N f_{AP})} - \Delta C$$

where $({}_N f_{AP})$ is the annuity present worth factor, for an interest rate i over a period of N years, i.e. the life of the project,

$$({}_N f_{AP}) = \frac{i(1+i)^N}{\left[(1+i)^N - 1\right]}$$

The interest rate (*i*) can be chosen to make (*NPV*) zero after a chosen number of years, N. This value of *i*, given by

$$NPV = \sum_{K=1}^{n} \frac{CF}{(1+i)^k} = 0$$

is known as the internal rate return (*IRR*)

Proceedings of ECOS 2005
Trondheim, Norway
June 20–22, 2005

OPTIMAL OPERATION OF BOILER PLANT WITH THERMAL STORAGE

Jiacong CAO[1] and Muwen CAO[2]

1 College of Environmental Science and Engineering, 2 College of Basic Sciences
Donghua University, 1882 West-yan'an Road, Shanghai 200051, China

ABSTRACT

Industrial boiler plants play an important role in energy conservation, for there is huge amount of energy consumed by a great number of industrial boilers. Optimal operation of an industrial boiler plant through optimal load assignment to boilers in the boiler plant is one of the major effective methods to improve the real efficiency of the plant. It is especially convenient for industrial boiler plants to carry out optimal load assignment in practice when the boiler plants are assisted by thermal energy storage (TES) that stabilizes the load levels of boiler plants. To accomplish this, accurate load forecast is a prerequisite. Based on the analysis of recorded load data the error back propagation (BP) neural networks are used to perform the forecast of daily load curves. Combined with the segmentation of the daily load curve, the minimum-departure model (MDM) that is newly developed is used to optimally assign the plant load, which is invariant due to TES during a time segment, to various boilers in the plant, so that the boiler plant can achieve the minimum daily fuel cost. A computer program was completed and used in an example. The results show that the fuel costs of the boiler plant are reduced.

Keywords: Optimal operation, boiler plant, thermal energy storage, load forecast, load assignment

NOMENCLATURE

A	lower limit of the departure of boiler load rate
B	upper limit of the departure of boiler load rate
C	fuel cost, kg/hr
d	date
E	error function
k	ordinal number of network training epoch
L	load of boiler plant, MW
n	maximum number of time segments of a day, or boiler number in a boiler plant
n	day(s)
m	hour(s)
Q	capacity of a TES, or thermal energy stored in TES, MJ
q	output rate of a boiler, MW
R	load rate vector
R	coefficient of correlation
r	load rate of a boiler
s	length of a time segment, hr
T	vector of beginning or end time of a segment
t	time, hr
W	connection weight vector
X	vector of departure of load rates from economical load rates
x	input to neural network, or departure of load rate from economical load rate
Y	expected output of neural network in training
y	output of neural network in training
α	momentum term
Δ	incremental
η	learning rate of neural network
$\boldsymbol{\theta}$	bias vector
τ	time (o'clock), or beginning or end time pitches of a segment
¥	Chinese monetary unit

SUBSCRIPT

0	initial, or beginning of a segment, or no-load
AV	average
d	day
f	fuel
k	ordinal number of network training epoch
M	maximum
m	economical load condition
n	maximum number of time segments of a day, or boiler number in a boiler plant
rt	rated condition
w	times of load recording per hour

INTRODUCTION

When boiler plants adopt thermal energy storage (TES), usually their real energetic efficiencies increase because of stabilized load levels for the boilers in the plants. However, for a boiler plant having 2 or more boilers there is still a task to guarantee the plant to perform best in efficiency. The task is to guarantee every boiler working at its appropriate load rate so as to enable the

plant as a whole to perform best. Compared with the cases without TES, the boiler plants in question here are easier to achieve this goal thanks to the function of TES in stabilizing plant loads. Usually, boiler plants equipped with TES often adopt an operation mode of segmenting a whole workday into several time intervals (segments) with different lengths, and work at different stable load levels during the various intervals. This is helpful for the controls of a boiler plant to assign the plant loads to separate boilers in the plant optimally so that the boiler plant works with the efficiencies as high as possible, consuming the least amount of fuel. To accomplish the segmentation of a whole day, the precondition is just the accurate forecast of the load curve of that day.

In the paper a new method of optimal load assignment to working boilers is developed and combined with optimal segmentation of a workday to carry out the optimal operation of the boiler plant with TES based on the forecast of load curve of the plant.

FORECAST OF LOAD CURVE OF A BOILER PANT USING ARTIFICIAL NEURAL NETWORKS

There are load forecast techniques for industrial boiler plants[1,2], e.g., the method using cascaded neural networks (CNN) can perform load forecasts with the average errors of lower than 3%[1]. However when a boiler plant is equipped with TES, it allows the forecast error to increase to some extent. It is because when the forecasted load curve is averaged for a period by TES the positive and negative errors cancel out each other, and then the error of the averaged load level is actually much smaller than those of the forecasted load curve. For this reason, the relatively simple BP network (see Fig.1) instead of CNN, which usually forecasts the loads for boiler plants with errors smaller than that BP network does, can be applied in this paper to forecast the load curves of the boiler plants. Relatively simple algorithm for BP network results in shorter computer time, and it makes sense for operation control of boiler plants.

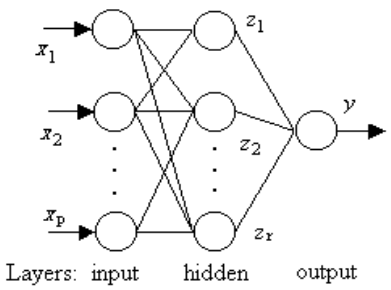

Fig.1 Structure of BP network

Usually, there are only historical load data available as a data bank for load forecasting by neural networks. For BP networks, proper preprocess of the data bank is necessary for the improvement of load forecast in accuracy. Ref.1 introduced an effective data procession by estimating the coefficients of correlation between the data in data set according to three correlation directions of "vertical", "horizontal" and "oblique" in the matrix of the data set (see Fig.2). Then select input data among the data set as the input pattern according to the coefficients of correlation that are higher enough.

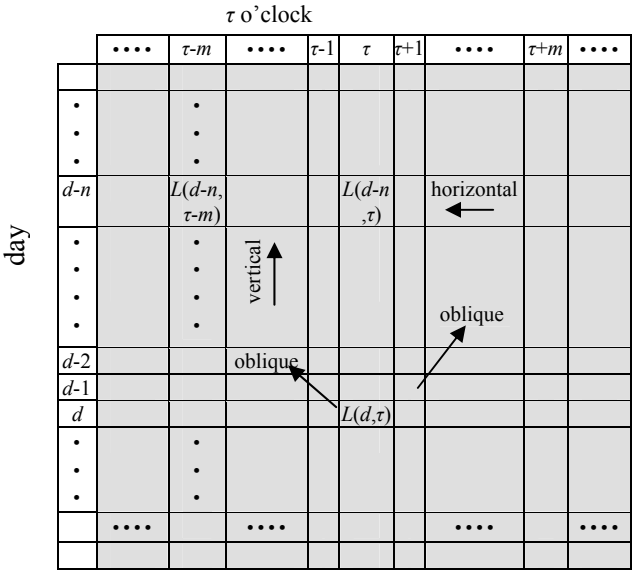

Fig.2 Matrix of data bank of hourly thermal load

A row of the data matrix that constitutes the training set for the BP network contains the load records in a whole day. As a computation example, a series of hourly load data of successive 28 workdays (excluding the weekends) from March 19 to April 27, 2004 is plotted against time as shown in Fig.3, which was recorded by a steam plant in Shanghai and now constitutes the data bank for use.

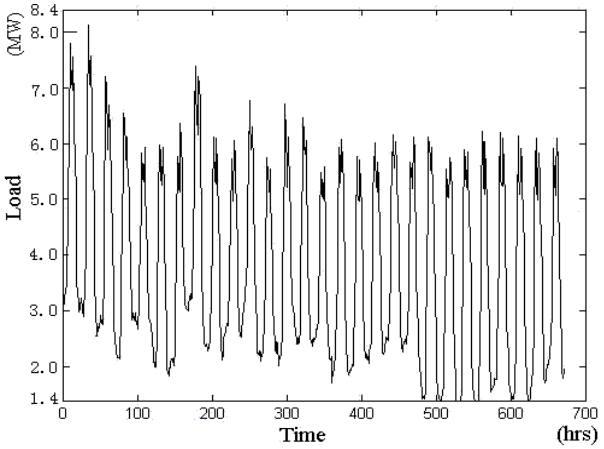

Fig.3 Data bank containing load records of 28 workdays

Similar to the method introduced in Ref.1, if $L(d,\tau)$ denotes the hourly load of the boiler plant at τ o'clock on the day of d, coefficient of correlation $R_d(n)$, which is called "vertical" (Fig.2), represents the relationship of the loads $L(d,\tau)$ on the day of d to the loads $L(d\text{-}n,\tau)$ (n=1,2,⋯ [days]) that are n days ahead of the day of d. Then $R_{d,\mathrm{AV}}(n)$ (see Table 1), representing the mean coefficient of correlation of all such $R_d(n)$s, can be easily calculated. Coefficient of correlation $R_\tau(m)$, which is called "horizontal" (Fig.2), represents the relationship of the loads $L(d,\tau)$ at τ o'clock to the loads $L(d,\tau\text{-}m)$ (m=1,2,⋯ [hours]) that are of m hours before τ o'clock. Thus $R_{\tau,\mathrm{AV}}(m)$ (see Table 1), representing the mean coefficient of correlation of all such $R_\tau(m)$s, can be calculated in a similar way horizontally.

Table 1: Mean vertical and horizontal coefficients of correlation for different n and m

Vertical		Horizontal	
n [days]	$R_{d,\mathrm{AV}}(n)$	m [hours]	$R_{\tau,\mathrm{AV}}(m)$
1	0.9739	1	0.9230
2	0.9675	2	0.8252
3	0.9730	3	0.7410
4	0.9683	4	0.6754
5	0.9668	5	0.6190
6	0.9575		
7	0.9649		

The "oblique" correlation of a load to other loads that are of the previous days and are not in vertical or horizontal directions in the data bank (Fig.2) may be useful to see if there is close relationship between them. In other words, the oblique coefficient of correlation $R_{d\tau}(n,m)$ represents the correlation of the load $L(d,\tau)$ to the load $L(d\text{-}n,\tau\text{+}m)$ (n=1,2,⋯; m=±1, ±2,⋯) and can be calculated in an analogous way. Therefore, the mean oblique coefficient of correlation $R_{d\tau,\mathrm{AV}}(n,m)$ is obtained in the same way (see Table 2)

Table 2 Mean oblique correlation coefficients for n=1 and different m

m [hours]	$R_{d\tau,\mathrm{AV}}(n,m)$
-2	0.4655
-1	0.4912
+1	0.4887
+2	0.4599

Obviously, it is reasonable that the load data with higher correlation to the future loads that are to be tested in training or to be forecasted could be selected as the input to the BP network. According to this principle, two kinds of 3-layer BP networks have been constructed, and correspondingly there are two groups of the networks including totally 24 BP networks, each serving a single hourly load of a day to be tested in training or to be forecasted. For the first group of networks, the input layer has 10 neurons for the input of 4 "vertical" records (n=1,2,⋯,4), 4 "horizontal" records (m=1,2,⋯,4), and 2 "oblique" records (n=1, m=±1), and the hidden layer has 7 neurons, which has been determined through trial-and-error method. The second group including 8 networks is used for testing or forecasting the loads of 7-10 o'clock and 20-23 o'clock, to which the coefficients of horizontal correlation are lower than average values. Therefore the number of "horizontal" records as the input to the network of the 2nd group should decrease to 2 and some other factors should be considered as the input so that the forecast errors do not increase at all. As a result of many calculation trials, the input layer of the network of the 2nd group can have 11 neurons for the input of 4 "vertical" records (n=1,2,⋯4), 2 "horizontal" records (m=1,2), 2 "oblique" records (n=1, m=±1), and the records of the average, maximum and minimum loads of the day before the day to be tested in training or to be forecasted. The hidden layer of the 2nd group has 9 neurons also determined by trial-and-error method. The output layer of the network in both groups has only one neuron for output. In brief, the BP network structures can be expressed as 10-7-1 and 11-9-1 for the 2 network groups respectively.

A total of 648 records (from March 19 to April 26) were used as the training set. After the data in the training set had been normalized[1] totally (from then on all the load records $L(d,\tau)$ represented the normalized ones), the BP networks could be trained in the following way. Take the load records of the first 5 days as the first data group for the first training epoch. For the τ-th network of the 1st network group, use 10 records in "vertical", "horizontal", and "oblique" directions to the load of τ o'clock on the 5-th day as the input to the network (see Table 3). Then the iteration of training through the network could be carried out according to the epoch sequence in Table 3 and was repeated from the beginning of Table 3. The iteration did not stop until any stop condition reached. The 16 networks of the 1st network group could be trained in the same way. The 8 networks of the 2nd group could be trained similarly, while the difference was only in the different input sets, which was mentioned in previous paragraph.

Table 3 Scheme for training the 1st network group

Epoch No.	Day ordinal in the sample: d	Input (x_i) of BP network
1	5	$L(1,\tau)$,⋯,$L(4,\tau)$; $L(5,\tau\text{-}1)$,⋯,$L(5,\tau\text{-}4)$; $L(4,\tau\text{-}1)$,$L(4,\tau\text{+}1)$*
2	6	$L(2,\tau)$,⋯,$L(5,\tau)$; $L(6,\tau\text{-}1)$,⋯,$L(6,\tau\text{-}4)$; $L(5,\tau\text{-}1)$,$L(5,\tau\text{+}1)$*
⋮	⋮	⋮
25	29	$L(25,\tau)$,⋯,$L(28,\tau)$; $L(29,\tau\text{-}1)$,⋯, $L(29,\tau\text{-}4)$; $L(28,\tau\text{-}1)$,$L(28,\tau\text{+}1)$*

*If $\tau\text{-}n \le 0$, $\tau\text{-}n$ should be substituted by $24 - (\tau\text{-}n)$. If $\tau\text{+}n \ge 24$, $\tau\text{+}n$ should be substituted by $\tau\text{+}n\text{-}24$.

In the training, the error function E, the weight vector $\mathbf{W}$, and the bias vector $\boldsymbol{\theta}$ are calculated by the BP networks. The adaptive variable learning rate method with momentum terms is adopted to improve the learning efficiency and calculation convergence of networks. The incremental vectors $\Delta\mathbf{W}$ and $\Delta\boldsymbol{\theta}$ are introduced for updating the weights and biases. Equations 1 to 5 describe the calculation of what mentioned above.

$$E = \frac{1}{2}\sum_{k}(y_k - Y_k)^2 \tag{1}$$

$$\mathbf{W}(k+1) = \mathbf{W}(k) + \eta(k)\frac{\partial \mathbf{E}}{\partial \mathbf{W}(k)} + \alpha\Delta\mathbf{W}(k) \tag{2}$$

$$\boldsymbol{\theta}(k+1) = \boldsymbol{\theta}(k) + \eta(k)\frac{\partial \mathbf{E}}{\partial \boldsymbol{\theta}(k)} + \alpha\Delta\boldsymbol{\theta}(k) \tag{3}$$

$$\Delta\mathbf{W}(k) = \mathbf{W}(k) - \mathbf{W}(k-1) \tag{4}$$

$$\Delta\boldsymbol{\theta}(k) = \boldsymbol{\theta}(k) - \boldsymbol{\theta}(k-1) \tag{5}$$

where Y_k denotes the expected outputs in training, viz., the corresponding load records in the data sample, and y_k denotes the forecasted outputs in training, viz., the outputs produced by the network calculation. k is the ordinal number of network training epoch. η is the learning rate and α the momentum term.

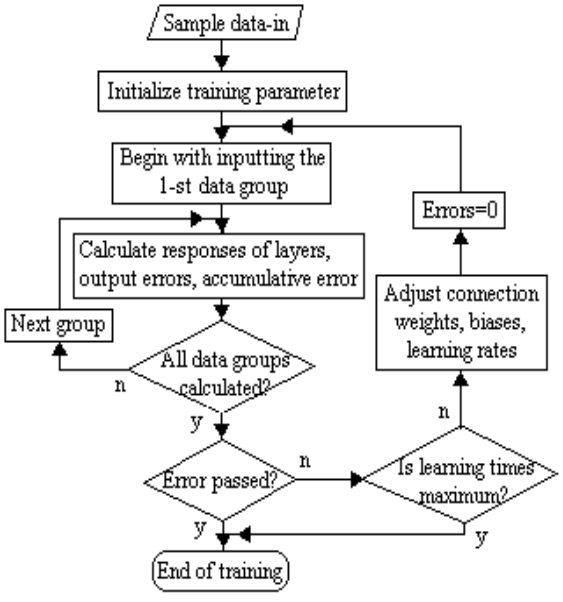

Fig.4 Flow chart of network training

For the training and later for the forecasting, values should be set to some factors as follows. The momentum term α = 0.90, and the learning rates: the initial η_0 was set 0.01, while the increasing rate of η was set 1.05 and the decreasing rate of η was set 0.70. Finally, 0.01 was set to the training errors, which was one of the stop conditions of training.

Fig.4 shows the process of the BP network training. When the training finished, use 120 load records (from April 20 to April 26, 2004 excluding the weekend April 24 and 25) in the data bank as the testing set. The trained BP networks gave the testing results as shown in Fig.5 and Fig.6. The mean relative error of the hourly tested loads on April 26 was 6.07%. The properly trained BP networks could be used to perform the load forecast through computer simulation for the boiler plant. Fig.7 shows the forecasted hourly loads on April 28 and the corresponding relative errors are plotted out versus time on Fig.8. The mean relative error was 7.28%.

In fact there are a number of other types of neural networks can forecast the load curves with higher accuracies. It is on purpose, however, to use BP network here to prove later in the text that BP network is applicable in the case when TES exists in boiler plants.

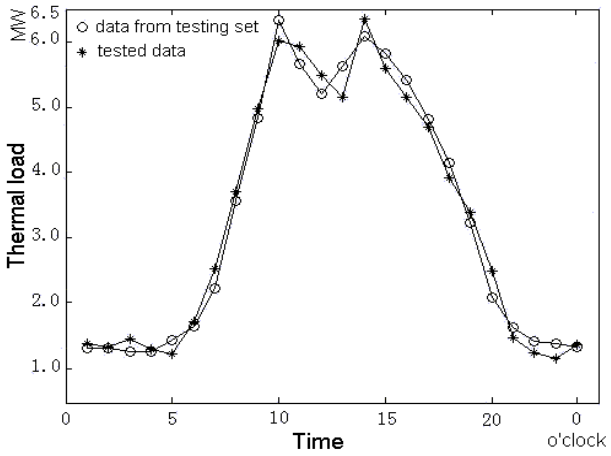

Fig.5 Load curve in testing for April 26

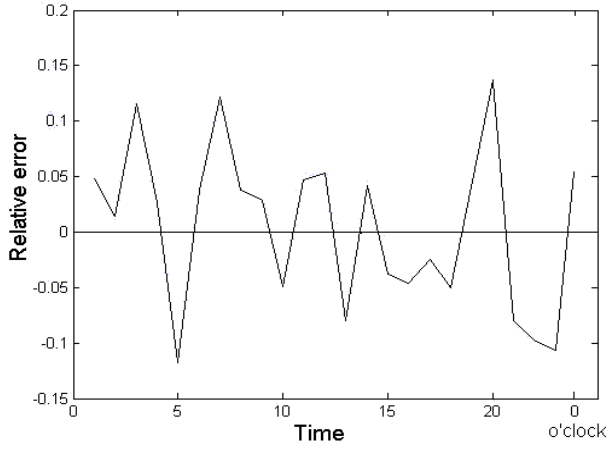

Fig.6 Tested relative errors on April 26

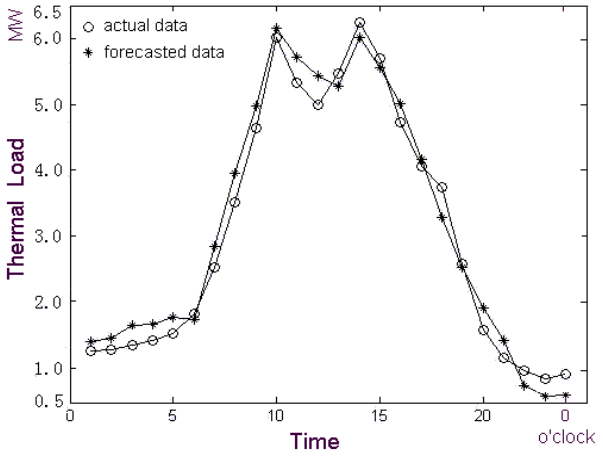

Fig.7 Forecasted load curve on April 28

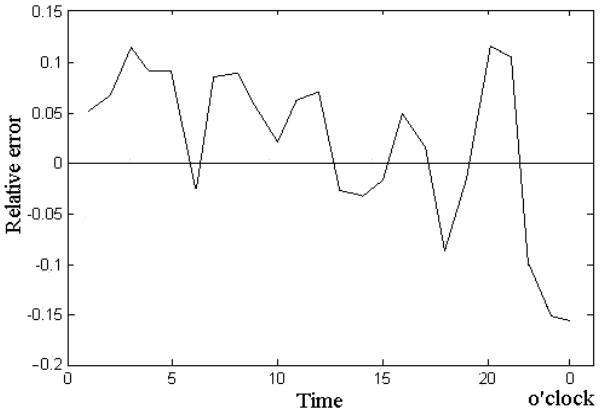

Fig.8 Relative errors of the load forecast for April 28

SEGMENTATION PATTERN OF A WORKDAY FOR THE OPERATION OF TES

When a boiler plant is assisted by TES, it works at stabled load levels in several segments in a workday. The number, the lengths and the starting moments of the segments depend upon the daily load curve. In other words, the segmentation of a day should satisfy the daily load curve. Suppose a thermal storage tank has a storage capacity of Q (MJ) and the daily load curve of the boiler house is denoted by $Q'= f(t)$. A segmentation pattern could be described as the following. A whole day is divided into n time intervals (segments). The i-th interval is from moment t_{0i} to moment t_i, s_i denoting the length of the i-th segment. The average load, Q_{AVi}, during the i-th segment is expressed below.

$$Q_{AVi} = \frac{\int_{t_{01}}^{ti} f(t)dt}{s_i} \qquad (6)$$

Equation 7 defines the average load function, Q_{AV}, when $t \in [t_{01}, t_n]$. In fact, t_n is just t_{01} after 24 hours.

$$Q_{AV} = Q_{AVi} \qquad t \in [t_{01}, t_n],\ i = 1,2,\cdots,n \qquad (7)$$

The thermal energy stored in the storage tank at moment t could be calculated by the integral of the difference of Q_{AV}–Q' against t between the limits of t_{01} and t.

$$Q_i(t, \mathbf{T}_0, \mathbf{T}) = \int_{t_{01}}^{t} (Q_{AV} - Q')dt$$

$$i=1,2,\cdots,n; \quad t \in [t_{01}, t_n] \qquad (8)$$

where

$$\mathbf{T}_0 = (t_{01}, t_{02}, \cdots, t_{0n})^T, \qquad \mathbf{T} = (t_1, t_2, \cdots, t_n)^T \qquad (9)$$

The difference between the values at the highest point and the lowest point of the integral curve, viz. $Q_i(t,\mathbf{T}_0,\mathbf{T})$, is the maximum amount of thermal energy Q_M that need be stored in the storage tank. The segmentation pattern can satisfy the load curve if Q_M does not surpass the storage capacity Q. It follows that

$$Q_M = \max Q_i(t,\mathbf{T}_0,\mathbf{T}) - \min Q_i(t,\mathbf{T}_0,\mathbf{T}) \le Q \qquad (10)$$

It is obvious that because the starting moment of a segment is just the ending moment of the previous segment, a set of n and $\mathbf{T}_0$ determines a segmentation pattern and Q_M as well. Generally speaking, there may be a lot of segmentation patterns can meet Eq.10 and they as a whole constitute a feasible domain of segmentation patterns.

Take a segmentation pattern arbitrarily from the domain. There are n segments and each has an averaged load on which the boiler plant works. By using MDM method of optimal load assignment that is going to be introduced in next section of the paper, the average load in every segment can be assigned to separate working boilers in the plant optimally. Then an optimized operation mode for the boiler plant is obtained corresponding to the segmentation pattern and the daily total fuel costs can be easily calculated for the operation mode. This calculation continues until the whole domain is covered. The calculations constitute a set of daily total fuel costs, among which the segmentation pattern called optimal segmentation with the least daily total fuel costs could be picked out by comparing the values of the total fuel costs.

In order to be convenient for computer programming Eq.8 can be descretized as Eq.11 (see Ref.[3] for detail).

$$Q_i(j, \tau_{0i}, \tau_i) = \frac{1}{w}\left[\frac{j-\tau_{0i}+1}{\tau_i-\tau_{0i}+1}\sum_{j=\tau 0i}^{\tau i} f(j) - \sum_{j=\tau 0i}^{j} f(j)\right]$$

$$i = 1,2,\cdots,n \qquad j = 1,2,\cdots,24w \qquad (11)$$

OPTIMAL OPERATION OF BOILER PLANTS

Model of optimization of load assignment

Almost all the sections or accessories of a boiler plant system involve with the optimization of plant operation. However, optimal assignment of plant load to various boilers is one of the most effective approaches to the optimal operation of boiler plants.

The optimization of load assignment among different units in a public utility system has been a long-lasted subject since the middle of the 20-th century when E.E. George, H.W. Page, and J.B. Ward raised the principle of coordination of incremental fuel costs[4] and L.K. Kirchmayer contributed to the complete of it[5]. From then on, this principle has been cited in a lot of papers. It is noticed that recently there were still authors who applied the method of coordination of incremental fuel costs to solve the problem of optimal load assignment for boiler plants[6]. However, for all practical purposes, the coordination of incremental fuel costs could take effect mainly in principle because of complexity in many real cases. As it is, optimal load assignment for boiler plants is even more difficult than for public utility systems in a way, for industrial boiler plants are much smaller in size than utility systems and their load fluctuation is usually more vigorous. This is one of the major reasons why there are quite a few reports on successful work on optimal load assignment to boilers in a boiler plant. Establishing stable load levels in several segments, TES makes it easier to perform load assignment in a boiler plant. In this section the method of minimum-departure model (MDM) is developed for this task. The method of MDM, as an applicable method to boiler plant practice, takes some considerations into account, such as the allowable limits of load rate for each boiler, the strategy of determining in advance how many and which boilers going to work, etc.

As a matter of fact, almost all the existed methods of optimal load assignment reported so far rely on fuel cost curves of boilers. It is well known that fuel cost curves of industrial boilers present a form of polynomial, and in most cases they can be considered as quadratic curves (Eq.12).

$$C_{\mathrm{f}} = a_0 + a_1 r + a_2 r^2 \tag{12}$$

$$r = \frac{q}{q_{rt}} \tag{13}$$

where C_{f} is the fuel cost per hour, q denotes boiler output rate and q_{rt} the rated output of the boiler.

However, for most industrial boiler plants, it is not easy and is expensive to obtain accurately the complete fuel cost curves for every boiler through tests on the spot, especially for coal-fired boilers. It is well worth pointing out that the method of MDM is such a one that needs, instead of complete fuel cost curves, only a few data that are originally available or ready-made and accurate.

From Eq.12 it is easy to find out following relationships (see Eq.14) through simple development if special behavior of the first derivative of the equation is considered at the economical load rate r_{m}.

$$a_1 = \frac{C_{\mathrm{f\,m}} - 2C_{\mathrm{f}\,0}}{r_{\mathrm{m}}}, \qquad a_2 = \frac{C_{\mathrm{f}\,0}}{r_{\mathrm{m}}^2} \tag{14}$$

where subscripts 0 denotes no-load conditions. Since the data on such two typical load conditions can be easily obtained from daily records of boiler operation or from the master data manufacturer supplied and thus are more accurate than the data on other non-typical load conditions, coefficients a_1 and a_2 are relatively reliable.

The development of MDM can be explained in brief as follows.

The objective function of optimal load assignment takes the form as the following (Eq.15) in the case that there are n working boilers in the industrial boiler plant under consideration.

$$\min\ C(\mathbf{R}) = \sum_{i=1}^{\mathrm{n}} C_{\mathrm{f}i}\ , \quad \mathbf{R} \in \mathbf{E}^{\mathrm{n}} \tag{15}$$

where $$\mathbf{R} = (r_1, r_2, \cdots, r_{\mathrm{n}})^{\mathrm{T}} \tag{16}$$

Equation 15 can be transformed equivalently into Eq.17.

$$\min\ \Delta C = C(\mathbf{R}) - C(\mathbf{R}_{\mathrm{m}}), \quad \mathbf{R} \in \mathbf{E}^{\mathrm{n}} \tag{17}$$

where $\mathbf{R}_{\mathrm{m}}$ is the condition on which every boiler in the boiler plant works at its economical load rate $r_{\mathrm{m}i}$. Namely,

$$\mathbf{R}_{\mathrm{m}} = (r_{\mathrm{m}1}, r_{\mathrm{m}2}, \cdots, r_{\mathrm{mn}})^{\mathrm{T}} \tag{18}$$

Expand $C(\mathbf{R})$ around $\mathbf{R}_{\mathrm{m}}$ into Taylor series, while considering the fact that $C(\mathbf{R})$ is a quadratic function and therefore the n-th nablaes of $C(\mathbf{R})$ equal zero when $\mathrm{n} \geqslant 3$. Therefore $C(\mathbf{R})$ becomes Eq.19 accurately.

$$\begin{aligned} C(\mathbf{R}) &= C(\mathbf{R}_{\mathrm{m}}) + [\nabla C(\mathbf{R}_{\mathrm{m}})]^{\mathrm{T}} (\mathbf{R} - \mathbf{R}_{\mathrm{m}}) \\ &\quad + \frac{1}{2} (\mathbf{R} - \mathbf{R}_{\mathrm{m}})^{\mathrm{T}} \mathbf{H}_{\mathrm{m}} (\mathbf{R} - \mathbf{R}_{\mathrm{m}}) \end{aligned} \tag{19}$$

The terms in the right hand of Eq.19 are developed as Eqs.20 to 24.

$$\begin{aligned} [\nabla C(\mathbf{R}_{\mathrm{m}})]^{\mathrm{T}} (\mathbf{R} - \mathbf{R}_{\mathrm{m}}) &= \sum_{i=1}^{\mathrm{n}} (a_{1i} + 2a_{2i})(r_i - r_{\mathrm{m}i}) \\ &= \sum_{i=1}^{\mathrm{n}} (a_{1i} + 2a_{2i}) x_i = \sum_{i=1}^{\mathrm{n}} \frac{C_{\mathrm{fm}i}}{r_{\mathrm{m}i}} x_i \end{aligned} \tag{20}$$

where $x_i = r_i - r_{mi}$ (21)

or $\mathbf{X} = \mathbf{R} - \mathbf{R}_m = (r_1 - r_{m1}, r_2 - r_{m2}, \cdots, r_n - r_{mn})^T$ (22)

As to Hessian matrix $\mathbf{H}_m$,

$$\mathbf{H}_m = \begin{pmatrix} \frac{\partial^2 C}{\partial r_1^2}, \frac{\partial^2 C}{\partial r_1 \partial r_2}, \cdots, \frac{\partial^2 C}{\partial r_1 \partial r_n} \\ \frac{\partial^2 C}{\partial r_2 \partial r_1}, \frac{\partial^2 C}{\partial r_2^2}, \cdots, \frac{\partial^2 C}{\partial r_2 \partial r_n} \\ \cdots \quad \cdots \\ \frac{\partial^2 C}{\partial r_n \partial r_1}, \frac{\partial^2 C}{\partial r_n \partial r_2}, \cdots, \frac{\partial^2 C}{\partial r_n^2} \end{pmatrix} = 2 \begin{pmatrix} a_{21} & & & \\ & a_{22} & & \\ & & \cdots\cdots & \\ & & & a_{2n} \end{pmatrix} \quad (23)$$

It follows that

$$\frac{1}{2}\mathbf{X}^T \mathbf{H}_m \mathbf{X} = \sum_{i=1}^{n} a_{2i} x_i^2 = \sum_{i=1}^{n} \frac{C_{f0i}}{r_{mi}^2} x_i^2 \quad (24)$$

In combination of Eqs.17, 19, 20 and 24, the objective function of MDM for load assignment of industrial boiler plants can be expressed as Eq.25, while Eq.26 is the constraint conditions of the problem.

$$\min \Delta C = \sum_{i=1}^{n} \left(\frac{C_{fmi}}{r_{mi}} x_i + \frac{C_{f0i}}{r_{mi}^2} x_i^2 \right), \quad i = 1, 2, \cdots, n \quad (25)$$

subject to

$$h(\mathbf{X}) = \sum_{i=1}^{n} q_{rt,i} (x_i + r_{mi}) - L = 0 \quad i = 1, 2, \cdots, n \quad (26)$$
$$-A_i \le x_i \le B_i$$

Equations 25 and 26 constitute the model referred to as minimum-departure model (MDM), which needs only the fuel cost data at two typical load rates: no-load and economical load rates instead of complete fuel cost curves, and thus this model is more accurate than other models.

Two steps for the algorithm of MDM

So far the first phase, i.e., to determine in advance how many and which boilers are going to work, has not yet been discussed. In performing the task, set 0 and 1.2 to A_i and B_i in Eq.26 respectively, and then run the computer program to solve the problem equations (Eqs.25 and 26). According to the solutions in this phase, if there were a boiler assigned with a load rate less than a preset critical value, say 0.2, it would be assigned automatically a zero load rate or even rejected from use. Computation trials proved that the boilers to be rejected from use tend to have the worst characteristic curves.

Then comes the 2nd phase—to solve the problem equations (Eqs.25 and 26) again, while the values of A_i and B_i are re-assigned according to the actual requirements of working boilers, to which the load of the boiler plant is going to be assigned. The computer program proves robust enough, for it is almost impossible for the fuel cost curves of industrial boilers in the form of quadratic functions to be ill-conditioned when iteration is going on.

Programming of optimal operation of boiler plants with TES

On the basis of 3 major modules, i.e., Module 1: the forecast of a daily load curve by BP neural networks, Module 2: the optimal segmentation of the curve, and Module 3: the optimal assignment of loads to boilers in a boiler plant, the modeling of a comprehensive program can be accomplished. The program is finished based on the platform of MATLAB6.5.

AN EXAMPLE

As an example, the load data (see Fig.3) that were used in the section of "Forecast of load curve of a boiler pant using artificial neural networks" are to be used again. The related boiler plant is equipped with a TES, a steam (latent heat) accumulator of 130 m^3, and some original data of the boiler plant are listed in Table 4.

A sub-program for selecting working boilers, which determines in advance how many and which boilers in the boiler plant to work at a particular load level, is added as the first phase in Module 3, this also helps the load assignment by MDM to be more preferable than by other reported models.

Table 4 Some data of the boilers in the boiler plant

Boiler No.	Rated capacity, q_{rt} [MW]	Economic capacity, q_m [MW]	Fuel consumption, C_{f0} on no-load, [kg/hr]	Fuel consumption, C_{fm} at economical load rate, [kg/hr]
1	2.2	1.0	10.2	110.1
2	6.63	3.4	45.7	365.6
3	2.2	1.0	10.2	110.1

Table 5 Optimal operation condition on April 28 based on forecasted load curve

Segmentation pattern	Load level [MW]	Assigned load rate		
		Boiler 1	Boiler 2	Boiler 3
8:00~12:00	5.281	0.4336	0.5092	0.4344
13:00~16:00	5.462	0.4523	0.5244	0.4524
17:00~7:00	2.515	0	0.3795	0

Table 6 Optimal operation condition on April 28 based on actually recorded load curve

Segmentation pattern	Load level [MW]	Assigned load rate		
		Boiler 1	Boiler 2	Boiler 3
8:00~12:00	4.998	0.4045	0.4855	0.4064
13:00~16:00	5.520	0.4581	0.5292	0.4582
17:00~7:00	2.510	0	0.3784	0

It took several minutes for the computer to complete calculation of the load curves forecasted on April 27 and 28, the optimal segmentation patterns for the operation of the 2 whole days, the preferable schemes of working boilers, and the calculated least fuel costs of the boiler plant of the two days respectively. The major computation results are listed in Table 5, which were resulted from the forecasted load curves. Based on the actually recorded load curve of the boiler plant, instead of the forecasted load curve, on April 28, similar results are listed in Table 6. Comparing Table 5 with Table 6, one can see that there is trivial difference in optimal segmentation patterns and the preferable schemes of working boilers between the two cases. This proves that BP network can meet the requirement of optimal segmentation in the case when TES exists in boiler plants, though the forecast accuracy using BP network is somewhat lower than those using some other types of neural networks. Table 7 gives the comparison in daily fuel cost of the boiler plant between the cases with and without optimal load assignment. The difference between the two cases means savings about ¥4.4×10^5 (5.3×10^4 USD) per year, which sometimes makes sense for an industrial boiler plant that is often not big in size. The difference may be much bigger if there is not optimization of segmentation (thanks to the successful load forecast) for daily operation of the boiler plant.

Table 7 Daily fuel costs with and without optimization of load assignment

Date	Fuel cost with optimization of load assignment, [kg]	Fuel cost without optimization of load assignment, [kg]
April 27	9198.715	9459.543
April 28	9579.968	9827.254

CONCLUSIONS

- The method of optimal operation of industrial boiler plants introduced in the paper is effective on saving energy in the case of the assistance of TES.
- When boiler plants are equipped with TES, the forecast carried out simply by BP networks is accurate enough for optimal load assignment to boilers in an industrial boiler plant.
- The minimum-departure model (MDM) is more practicable to use in optimal load assignment for boiler plants than most existing methods.
- The method and the computer program can be applied to the online control of optimal operation of boiler plants with TES.

References

[1] Cao, Jiacong; Cao, Shuanghua. Study of load forecasting using cascaded neural networks for industrial boiler plants. Proc. the 16th int. conference ECOS2003, ed. Niels Houbak, et.al., vol.2, 555-562, Copenhagen, Denmark. June, 2003.

[2] Cao, Jiacong; Sheng, Kaitai. Study of load forecasting and optimal operation of boiler plant with thermal storage. Proc. int. conference ICEE2003, Shanghai, China. Dec. 2003. ed. Kangmin Chen, et.al., vol.2, 1075-1080.

[3] Cao, Jiacong. Optimization of thermal storage based on load graph of thermal energy system. Int.J. Applied Thermodynamics, 2000, 3(2):.91-97.

[4] George, E.E.; Page, H.W.; Ward, J.B. Coordination of fuel costs and transmission loss by use of the network analyzer to determine plant loading schedules. AIEE Trans, 1949; 68(Part II): 1152-1163.

[5] Kirchmayer, L.K. Economic operation of power systems, John Wiley &Sons, Inc. New York, 1958, 9-46.

[6] Gao, Yan; Liang, Tailong. Optimization of load assignment among boilers running in parallel. Journal of Beijing University of Science and Engineering, 2002, 22 (3): 318-320 (in Chinese).

Proceedings of ECOS 2005
Trondheim, Norway
June 20–22, 2005

A THERMOECONOMIC MODEL FOR OPTIMAL DESIGN AND OPERATION OF TRIGENERATION PLANTS WITH HEAT STORAGE SYSTEMS.

G. Chiummo, A. Di Nardo, G. Langella[1], C. Noviello
University "Federico II"
Department of Mechanical Engineering and Energetics
Naples - ITALY

ABSTRACT

A useful numerical code for energetic design of a co-generation system and its economic optimal operation is presented. In the planning phase, the numerical model allows to match different configurations of the system, finding the best one in the econimic point of view. The plant scheme is as general as possibile, in fact is possible to choice among the following elements: gas turbine, steam turbine, diesel engine, absorption heat pump and electrical and mechanical heat pumps, boilers and storage system of thermal energy, heat recovery steam generators with in-duct burners system. Once assigned the electrical and thermal demand, the code examines alternative solutions from the general scheme, with respect to the traditional one (boilers, electrical and mechanical heat pumps and electricity national distributor). Aim of the numerical code is finding all the maximum energetic power of the elements and, hour per hour, the optimal operation conditions. In the usual situation of contemporary demand of hot and/or cold thermal and electric energy, priority is given to the energy with higher cost, considering the energetic rates, hour per hour, meanwhile the satisfaction of the demands would have however to happen with not cogenerative systems. In the numerical code is considered the possibility to sell the electric energy surplus and to storage the thermal one.

In particolar the benefit of using a thermal storage unit has been highlighted in this paper, by reporting results of numerical simulation carried out varying electrical and thermal load of CHP plant.

Keywords: heat storage, optimisation

INTRODUCTION

The rising diffusion of CHP plants has been led to develop design and operation models able to indicate, in every single case, which is the best plant configuration among all possible, giving the lowest cost for the best performances.

Such a model has been built up in this work, searching for the optimum operation parameters of a tri-generation plant, for any assigned electrical, thermal and cooling load. The numerical model which has been developed by authors is quite general and has two specific application phases: the design phase ant the operation one.

In the first type of approach (the design one) the model indicates the best plant solution for a given

[1] corresponding author: giulange@unina.it

energy demand, making a comparison among all technologically available and choosing the most efficient in terms of cost/benefit ratio.
The chance to cheaply and fast foresee economic performance of such a plant , which is often a big plant, has led to a very detailed numerical model, comprehensive of all technological solutions
A very important reliability characteristic of the model is the capability to foresee the plant performances not only in steady regime but also in transitory phases according with thermal and electrical demand fluctuation.

THE MODEL

For given daily curves of thermal, cooling and electric demand, both for holiday and working days, summer and winter, the numerical code computes the optimum load curve (from a money saving point of view), hour per hour, of the single components of the plant (main engine, integrative boilers, post combustion systems, absorbption chillers etc), varying engine load within the allowed range
In order to keep the model as general as possible, it is possible to evaluate the advantage of the contemporary installation of different engines, such as steam turbines, gas turbines, internal combustion engines, specifying their performances depending on weather condition and load variation.
For example, the variation of electrical efficiency of a gas turbine has been taken into account, depending on environment temperature.
The model takes into account the different heat recovery systems of above mentioned engines according with temperature levels required for thermal vectors: in case of gas turbine, for example, heat is recovered only at high temperature, while internal combustion engines allows two different temperature levels of recovery (heat from lubricating and jackets cooling systems and heat from exhaust gas); for steam turbines besides, heat recovery has temperature constrains coming from backpressure circuit. Another comparison can be made about post combustion: for gas turbines it is easy to install such a system downstream the machine, for ICE instead it is possible to do it only when they work in very lean condition, for environmental demands, and installation and operation are more complex.
A basic requirement of a CHP system is the chance of using heat recovery in summer: in this case the energetic recovery index is higher than traditional or electrical heat pump cooling systems: for this reason the use of absorbption chillers is strongly recommended, even if these machines appear less efficient than traditional.
The model takes into account also the situation of underproduction and overproduction of electricity with respect to the instantaneous demand: the economic evaluation of such situation is carried out on the basis of national rates and their variability hour per hour.
The model is structured in order to estimate the influence of delay between heat recovery from the plant and thermal demand within the day, considering the chance to storage surplus thermal energy.
The generalized scheme of the whole plant is sketched in fig.1.
As remarked, the thermoeconomic model can be easily used both in design and in operation phase.
In design phase it matches the layout which gives the best economic and energetic performances, with respects to energy demands. In operation phase, for the given layout, it determines the load level of the components, according with energy demands, hour per hour, and giving the best efficiency.
Economic analysis is based on comparison between the investment costs and the money saving feedback, during plant lifetime. Discounted Pay-Back period (DPB), Internal Rate of Return and Net Present Value methods have been adopted.
The concept the model is based on is the comparison of the different money value of energy available in a given point of the plant, depending on destination to electric, thermal or cooling demand, in the case that this energy can be utilized by different components of the system.

In a preliminary phase plant layout is defined, specifying machines with their efficiency, load limits, regulation facilities, possible absorbption system and relative COP, post-combustion burners and heat storage systems with their maximum capacities.

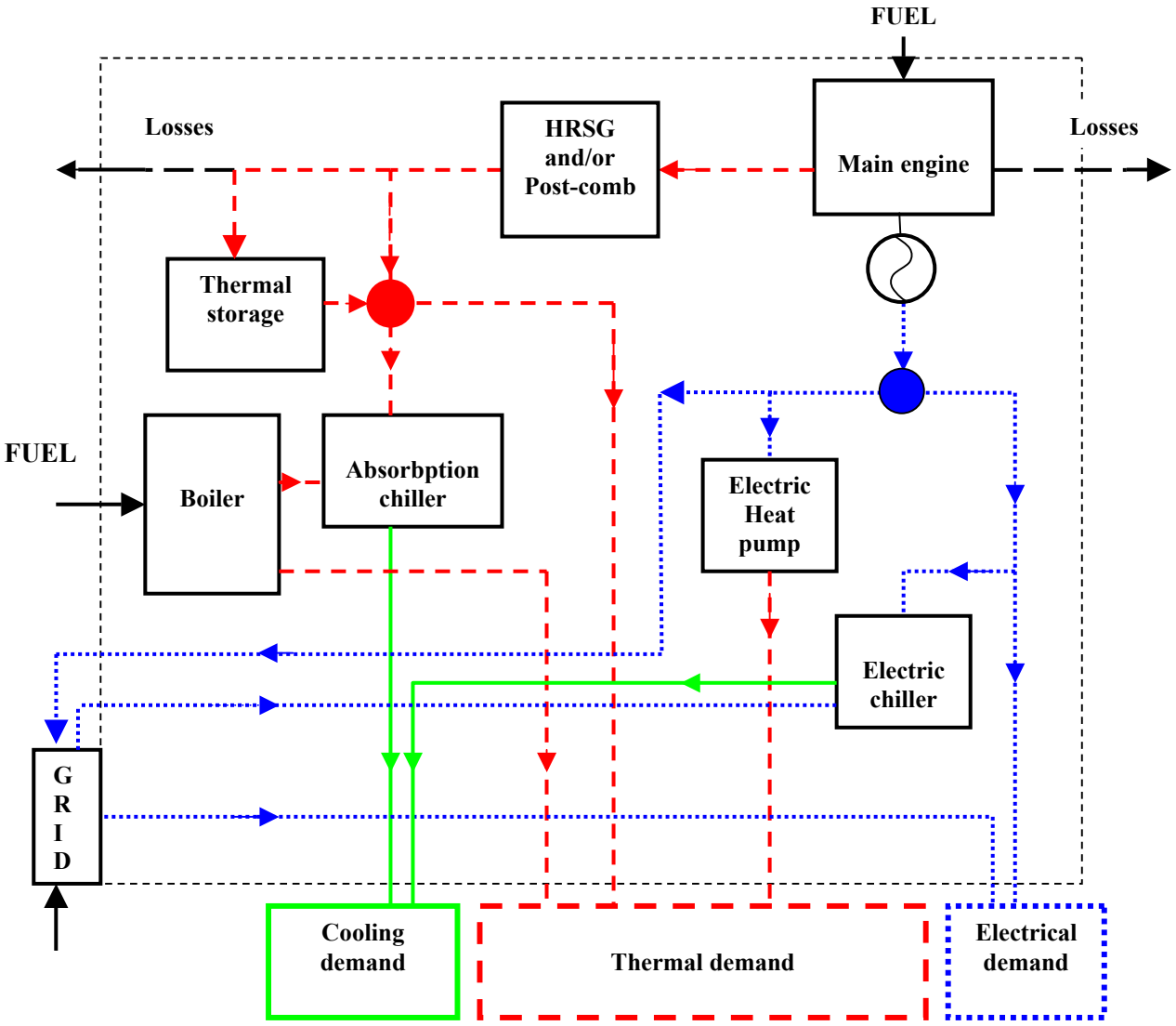

Fig.1: generalised scheme of the plant

Within the economic parameters, fuel rates, electricity tariffs, machine costs, production taxes, possible tax discount, maintenance costs are the most relevant.

After computation, the routine gives the economic indexes, optimum load curve of the components along the day, load curves for integrative systems, the electricity given to the grid and the thermal energy stored. At this point, calculation are repeated for different layout configuration, evaluating the most convenient one.

The general scheme of the plant is made of different sections of energy production:

1. mechanical-electric energy production
2. thermal energy production

3. cooling energy production

In section 1 it's possible to insert one or more different engines, depending on energy user requirement, in terms of size, electric load variability and temperature of heat recovery.
In section 2 heat recovery steam generator is positioned, together with post-combustion system, when possible, heat storage system and integrative boilers.
In section 3 absorbption chillers and/or heat pumps or electrically driven chillers are considered; the first ones can be fed by heat recovered and/or by integrative boilers and /or by post combustion system, while the second ones can be fed by electricity produced by the plant or taken from the grid.
In section 2 the maximum size of each component can be assigned, together with efficiency variation diagram vs partial load; in a different way the size of the component can be considered as a variable parameter to be computed by the model as optimum value together with the number of components, depending on the minimum and the maximum power given to the user by the single component.
The whole plant, sketched in fig.2, can be considered as a number of energy transformers, closed in control volumes, crossed by energy fluxes, changing from primary energy to end user energy with some energy loss, related to the specific process.
For a given plant configuration, the best and cheapest path for energy fluxes can be identified, when different choices are available. The analysis is performing making a comparison with traditional energy solutions like grid supply , boilers and electrical cooling systems. By simple and rational consideration based on specific efficiencies and standard tariffs for electricity and gas, the best configuration can be identified.
By the fig. 1 it can be highlighted that a generic energy flux can be transferred directly to the end user or to another "energy box" downstream it. We indicate as "joints" these intersection points.

SIMULATIONS

The characteristics and potentialities of the code have been already described in previous works [1]. The parameters and functions the code is based on are the following:

- daily curves of electrical, thermal and cooling demand for holyday and working, summer and winter days
- electrical efficiency of main engine varying the engine typology, load level and weather condition
- thermal efficiency of boilers, Heat Recovery Steam Generators (HRSG), post-combustion systems and heat pumps and their dependence on load level
- cooling efficiency of absorbption systems and electrical chillers and their dependence on load level
- heat storage capacity
- electricity tariffs also for selling case
- fuel costs
- maintenance costs
- cost for engine and auxiliary installation

In this paper the benefit of installing a heat storage system, when electrical and thermal load have specific characteristics is analysed. In a special way it's very interesting when thermal and electrical demand are not coherent and shifted from each other during the day, or when thermal load arises and decreases continuously with respect to a mean value.
In the first case, the absence of a thermal storage unit, should lead to switch off the engine when only thermal energy is required: but in this case we should have a less operation time in a year and a longer pay-back period. In the second case, it should be necessary to operate the engine at partial load when heat recovery should be greater than demand and to integrate with auxiliary boilers when recovery is less than demand: partial load operation reduces system efficiency and money saving.
Thermal storage modules allow to separate load curves from demand ones , for a better and more convenient technical management of the plant.

Obviously, thermal storage capacity must be optimised with demand characteristics: this can be better understood by a simulation on a case study.
Let's consider a factory user with daily electrical and thermal demand as shown in fig 2-3.
Let's search for the optimal set up when a 3 MWe gas turbine is installed with a heat recovery steam generator, without heat storage system. Italian tariffs for gas and electricity have been considered for simulation.
Two cases have been analysed:

1. operation load electrical demand-dependent
2. operation load thermal demand-dependent

The first case is reported in fig. 4-5 by diagrams of electrical end thermal output of the system.
The second case is reported in fig 7-8.by similar diagrams.
In the first case gas turbine runs continuously at maximum load: this causes thermal recovery not to be utilized for a certain number of hours along the day, as shown in fig.6.
In the second case, referring to thermal demand, the gas turbine runs for a number of hours at partial load, needing an integration from electrical national grid.

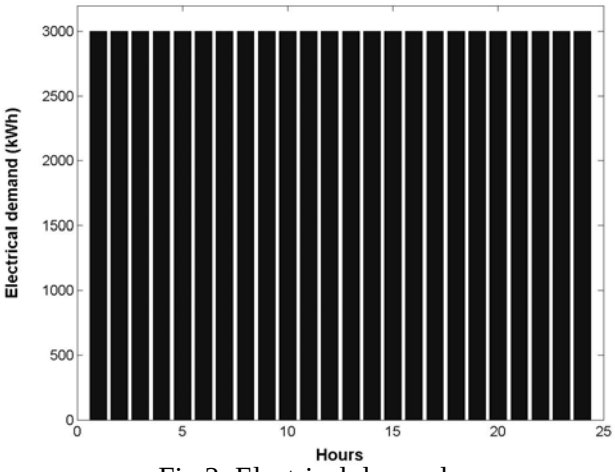

Fig.2: Electrical demand

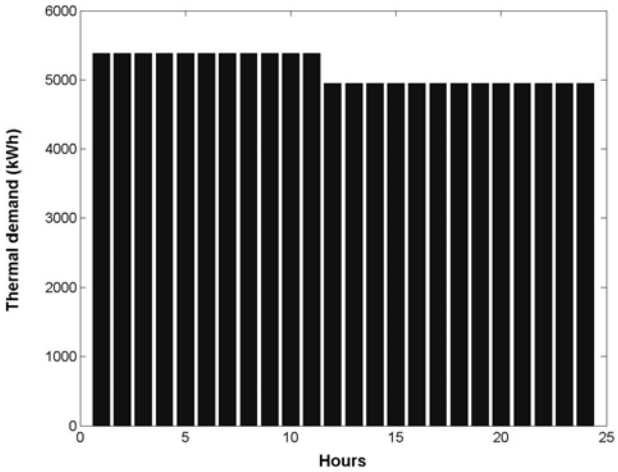

Fig.3: Thermal demand

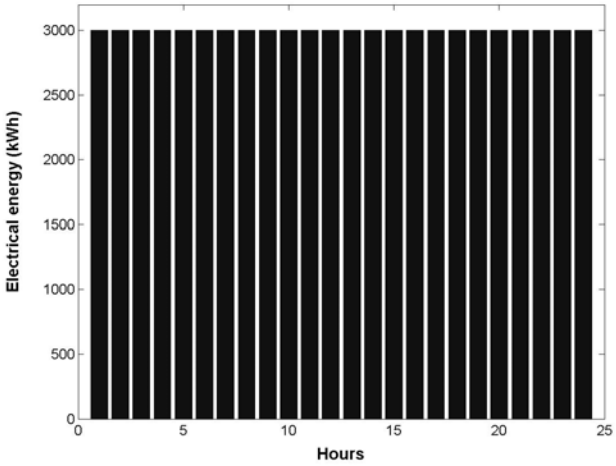

Fig.4: Electric output (case 1)

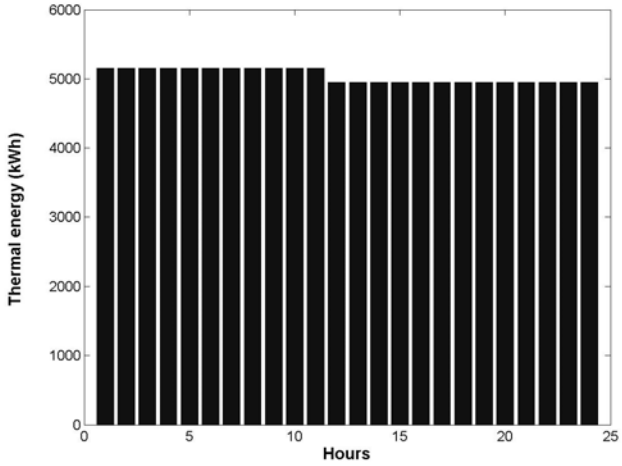

Fig.5: Thermal output (case 1)

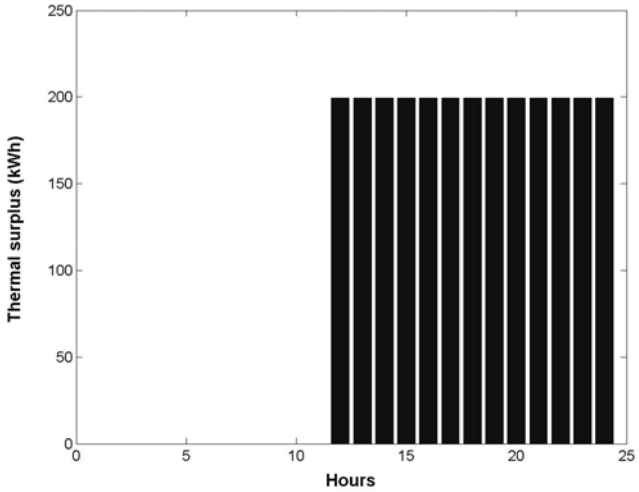

Fig.6: Thermal surplus (case 1)

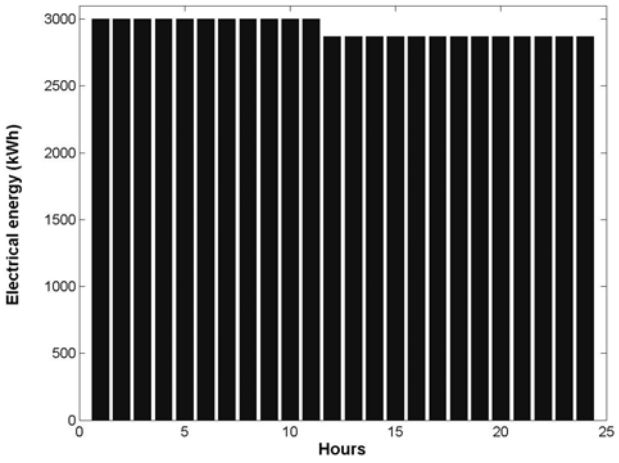

Fig.7: Electric output (case 2)

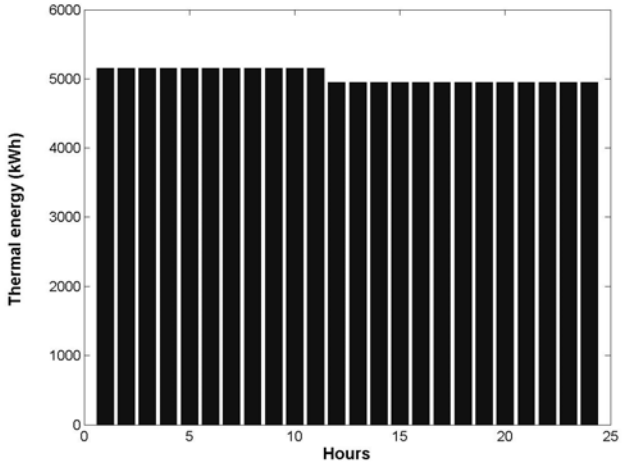

Fig. 8. Thermal output (case 2).

Let's consider now the same situation but with a thermal storage unit (case 3): this facility allows to storage hot water at 130 °C, with a return temperature of water at 80 °C. According with these values, an optimum capacity for storage tank should be 50 m^3 .

Energetic losses have been neglected, also because energy is stored for a few hours. The storage system allows to store all thermal surplus, which is given to the users at first hours of the day, when demand is higher than thermal output of the system (fig.9).

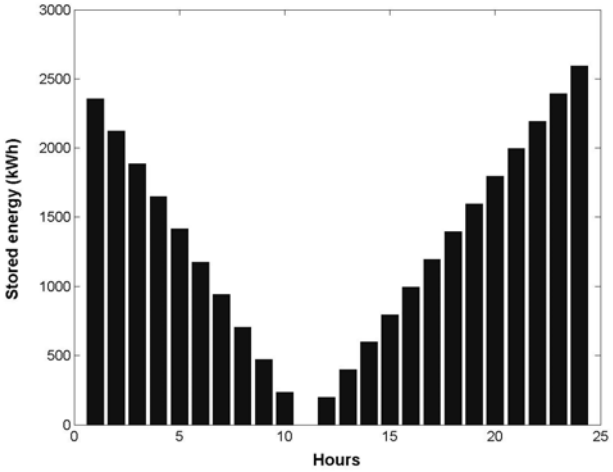

Fig.9 : stored energy per hour (case 3)

Finally the heat given to the end user by thermal storage is represented in fig.10

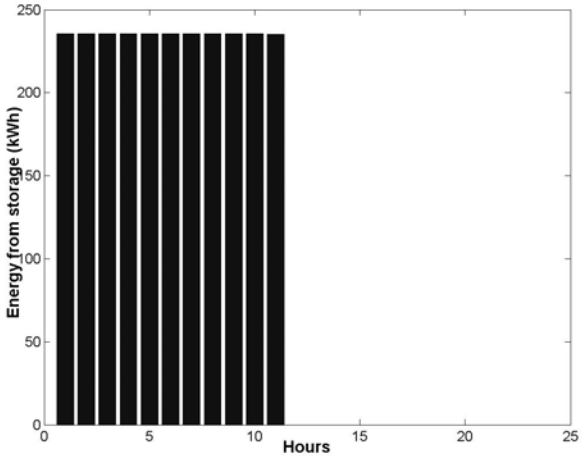

Fig.10: heat from storage (case 3)

Allowed benefits of such a system can be easily understood in the following table

Case	Money saving €/y	Electric **η**	Thermal **η**	Exergetic **η**
1	1.067.400	30.27	50.87	44.51
2	1.048.700	30.19	51.96	44.73
3	1.107.900	30.27	51.96	44.82

Tab 1: Comparison datasheet

η is the symbol adopted for efficiency.
Money saving is calculated with respect to a traditional plant which has the following energetic characteristic:

- Electricity from the grid
- Heat from gas fired boilers
- Cooling from electric chillers

The storage system increases money saving with respect to the traditional situation, allowing to save 40.000 € more (2% of the costs in a year) in the first case and 60.000 € more (3%) in the second. Considering the cost of a storage system with auxiliary equipment, it can be recovered in a couple of years.

CONCLUSIONS

The model built up by authors is quite general and the simulation reported in this paper is only a single application of it.
In design phase for example it can be very useful for the sizing of the main engine or other components of the plant, starting from daily energetic demands for all the year and from their efficiency at the different load levels.
The capacity oh thermal storage system can be optimised too.
From the operation point of view, it can be investigated the best regime from the main engine, if is better to follow the electric demand or to run the machine at constant load, taking benefit from thermal storage and from a constant load set on best efficiency level.
The convenience of selling electricity can be also evaluated, depending on the different tariffs of different electricity providers in the free electric market.
The operation with thermal storage can be integrated with weather forecast, storing more heat when a very cold day is going to come, for example.
The adoption of a heat storage system gives a big management flexibility of the plant. The chance to run the main engine at full load also when thermal demand is lower than production allows best efficiencies to be reached for the system. Money saving is often very interesting and justifies the investment with a short pay-back period.

REFERENCES

[1] Langella G., Amoresano A., Noviello C., *Heat Storage Optimization in the Primary Pipe Ring of a District Heating and Cooling (DHC) System*, ECOS 2003, Copenhagen, Denmark, June 30 – July 2, 2003.
[2] Beckmann, Gilli P.V.: *Thermal energy storage*. Springer – Verlag, Wien.
[3] Bejan .A., Tsatsaronis G., Moran M.: *Thermal design and optimisation*. A Wiley and Sons, INC., New York, 1996
[4] A. Ziebik, J. Zuwala, *The application of heat storage tanks in CHP plants in polish conditions*, ECOS 2002, Berlin, Germany.
[5] Szargut J., Ziebik A., *Fundamentals of Thermal Engeneering*. PWN, Warszawa, 1998.
[6] El Sayed Y.and Gogus Y., *Demand variability and mismatches in the cogeneration of power and process heat,* Int. J. Of Appl. Thermodynamics, Vol.3, pp 199-208, December 2000.
[7] D. Lindenberger, R.Kummel, *Thermodynamics and economics: energy-dependent production functions and the optimization model PRISE of price-induced sectoral evolution*, ECOS 2002, Berlin, Germany.

Proceedings of ECOS 2005
Trondheim, Norway
June 20–22, 2005

SIMULATION OF EXERGETIC PARAMETERS OF A DIESEL COGENERATION SYSTEM UNDER DISCRETE VARIABLE LOAD

Ricardo Wilson Cruz[1]
Superior School of Technology – State University of Amazon
Av. Getúlio Vargas, 361/402, CEP 69020-010, Manaus, AM,
Brazil

Silvia Azucena Nebra[2]
State University of Campinas
Mechanical Engineering Faculty – Energy Department
P.O. Box 6122, CEP 13083-970, Campinas, SP,
Brazil

ABSTRACT

This paper reports a research of behavior of second law performance parameters of a 1 MW Diesel plant cogeneration system under variable power load. An engine simulation model is used as well as a cogeneration cycle simulation model which permits to foresee the system performance with varying load. The adoption of second law viewpoint allows to perform the analysis according to a more realistic physical nature than first law analysis does, as heat and work have different qualities in heat-to-work conversions. For such a case, plus than enthalpy, heat and work, flux exergies are taking into account. The second law performance parameters used in this paper are the second law efficiency, and the relative irreversibility ratio. These factors are plotted in function of the engine power load.
Key-words: Exergy, simulation, cogeneration, Diesel engine, Second law, thermal analysis.

NOMENCLATURE

AF	Air-to-fuel ratio
$\dot{B}$	Exergy flux [kW]
b	Mass specific exergies [kJ/kg]
$\tilde{b}$	Molar specific exergy [kJ/mol]
bsfc	Brake specific fuel consumption [kg/kJ]
$\dot{F}$	Subunit fuel flux [kW]
H/C	Fuel hydrogen to carbon ratio
h	Specific enthalpy [kJ/kg]
$\dot{I}$	Subunit irreversibility flux [kW]
M	Molar mass [kg/kmol]
$\dot{m}$	Mass flux [kg/s]
m	Number of subunits
$\dot{L}$	Subunit lost exergy flux [kW]
$\dot{P}$	Subunit product flux [kW]
p	Pressure [kPa]
p	Number of Energy flows
Q	Fuel heating value [kJ/kg]
q	Power load [%]
$\tilde{R}$	Gases constant (8.314 [kJ/kmol.K])
s	Specific entropy [kJ/kg.K]
T	Temperature [K]
X	Mass fraction
Y	Molar fraction (in general)

[1] Corresponding author Phone: +55 92 8804 5758. E-mail: rcruz@uea.edu.br
[2] E-mail: sanebra@fem.unicamp.br
[5] The dry air standard pressure is 99.31 [kPa] (0.9 [atm]).

y Molar fraction of a substance in the reference environment

Subscripts and Superscripts

atmosf. Atmosphere
B Exergetic
BC1 Water pump
BC2 Engine cooling fluid pump
BR Refrigeration fluid pump
DO Diesel oil
e, i, j Indexes
fís. Physical
GG Electric generator
LHV Low heating value
Q Heat
lq Power load set point
quím. Chemical
RAA Absorption refrigeration subunits (1,2)
RCG Recovered heat from combustion gases
refr. Engine cooling fluid
rio River cooling water
W Work
0 Reference state
00 At the reference environment dead state

INTRODUCTION

Northern Brazilian power grid has a huge potential for cogeneration, due to that the electric generation is made through the use of Diesel engine in a decentralized grid. The uniquely generation of electric energy by the system is the cause of its unprofitable economic performance.
An advantageous way to perform the analysis of such cogeneration system is by searching how its second law efficiencies respond to the variation of the load of its power engine. For the daily engineering purposes, it is not easy to get such an engine simulation, but it can easily be done on Diesel engines through their performance parameters.

EXERGETIC PARAMETERS

The first parameter is the *rational efficiency*, for what the cogeneration system is divided into its subunits creating a *productive structure* as in Figure 3. The rational efficiency is defined as:

$$\eta_i^B \equiv \frac{\dot{P}_i}{\dot{F}_i} \quad (i = 1, ..., m) \qquad (1)$$

In this definition, by fuel we consider not only the inlet flux exergy but the net inflow of exergy to the subunit. As a consequence, product is the exergy outflow from the subunit (Table 3). An implicit result in Equation (1) is that $\dot{F}_i > \dot{P}_i$, as the exergy balances is expressed by:

$$\dot{F}_i = \dot{P}_i + (\dot{I}_i + \dot{L}_i) \quad (i = 1, ..., m) \qquad (2)$$

in which $\dot{I}_i$ are losses inside the bulk control volume evolving the whole plant, but $\dot{L}_i$ are losses in the form of fluxes that go outside the plant. Part of the summation inside parenthesis in Equation (2), usually denoted as *destroyed exergy* ([1], [2]), can be recovered by the cogeneration system, e.g. the combustion products and the heat loss to cooling fluid of Diesel engine. Figure 1 illustrates the whole idea behind Equation (2).

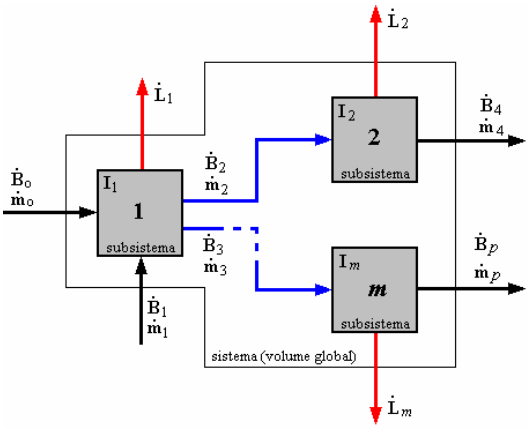

Figure 1: A general productive structure.

Besides the rational efficiencies of the subunits, one can define the *relative irreversibility* of each subunit as:

$$\zeta_i \equiv \frac{\dot{I}_i}{\sum \dot{I}_i} \quad (i = 1, ..., m) \qquad (3)$$

In general, any exergy flow of the plant may be calculated by:

$$\dot{B}_j = \dot{m}_j \left(b_j^{\text{fís.}} + b_j^{\text{quím.}} \right) \quad (4)$$

where the physical part of exergy is:

$$b_j^{\text{fís.}} = \left(h_j - h_{0.j} \right) - T_0 \left(s_j - s_{0.j} \right) \quad (5)$$

$$s_j = \sum_e X_e s(T_j, Y_e p_j) \quad (6)$$

$$h_j = \sum_e X_e h(T_j) \ (e = CO_2, H_2O, O_2, N_2) \quad (7)$$

In (6) and (7), s_j, h_j and h_0 are given by the JANAF tables, at $T_0 = 298.15\,[\text{K}]$ (25 [C]) and $p_0 = 101.325\,[\text{kPa}]$ (1 [atm]).
And for the chemical term of Equation (4):

$$b_j^{\text{quím.}} = \tilde{R} T_0 \sum_e \left(\frac{Y_e}{M_e} \right) \ln \left(\frac{y_{0.e}^j}{y_{00.e}} \right) \quad (8)$$

Usually for the heat flux exergies we do:

$$\dot{B}_j^Q \equiv \dot{Q}_j \left(1 - \frac{T_0}{T_j} \right) = \dot{Q}_j \eta_{C\,j} \quad (9)$$

where $\eta_{C,i} \equiv 1 - (T_0 / T_i)$ (i = 1, ..., *m*) is the *Carnot efficiency*.
For power/work exergy:

$$\dot{B}_j^W = \dot{W}_j \quad (10)$$

In all these equations, j = 1, ..., *p*. For water as a working fluid it is assumed the Szargut, Morris and Steward [3] standard environment, for what these authors define the concept of *standard chemical exergy*. For water in liquid phase [3], $\tilde{b}_{H_2O}^{\text{quím.}} = 0.9$ [kJ/mol]; and for the Diesel oil, the following correlation is enough [3]:

$$b_{DO}^{\text{quím.}} = Q_{LHV} \left[1.046 + 0.0144 (H/C) \right] \quad (10)$$

For the gases composing the combustion products mixture, Table 1 shows the molar fractions considering the Szargut, Morris and Steward [3] standard environment.

Substance	$y_{00.e}$ **(in dry air)**	**Standard pressure[5] [kPa]**
CO_2	0.000 345	0.033 5
H_2O_{gas}	—	2.2
O_2	0.209 9	20.39
$N_{2atmosf.}$[6]	0.7898	76.705

Table 1: Fractions of some gases in the standard atmosphere [3].

SYSTEM CONCEPTION

In this section we show the conceived cogeneration system intended to produce electric energy, low temperature cooling flux for food conservation (RAA-1 at -25 [C]) and ice for fishing conservation (RAA-2 at -3 [C]), as shown in Figure 2. On Figure 3 we show the productive structure defined for the system of Figure 2.
The most important characteristic of the plant in Figure 2 is that we defined the low temperature cooling flux as being generated by the high temperature energy of the exhausted gases of the Diesel engine, and the production of ice being generated by the low temperature energy contained in the cooling water of the Diesel engine. We assume that the absorption systems belonging to the refrigeration units may be properly designed to get these purposes.

[6] It is considered the gas N_2 plus the rest of the gases and the dust which compose the actual atmosphere, except O_2.

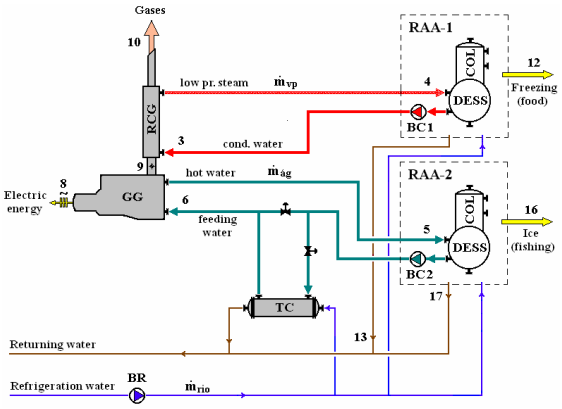

Figure 2: Cogeneration system conceived [4].

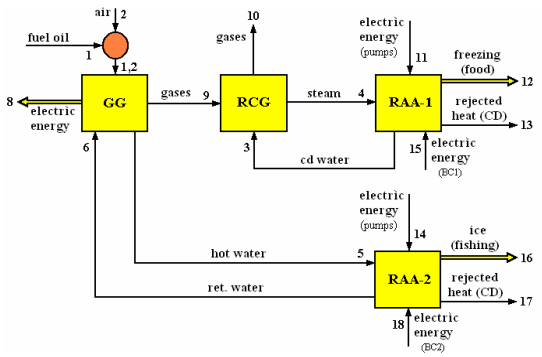

Figure 3: Structural diagram for the system of Figure 2 [4].

Technical Characteristics of the System

The RAA-1 and RAA-2 subunits are the 'clients' of the cogeneration system. These subunits adopt the aqua-ammonia absorption refrigeration cycle. The heat to RAA-1 is furnished by low pressure steam and the heat to RAA-2 is transported by hot water, which main data are shown on Table 1, assumed constant with the varying power load. This assumption does not imply that the cogeneration system must supply constant heat, but determined electric power, defined as mandatory.

The electric generator is powered by a commercial supercharged Diesel engine which main technical data are reported in Table 3 [5] at four discrete power loads ($q \equiv \dot{W}_{lq} / \dot{W}_{l100}$).

Stations	T [K] (C)	p [kPa]
3 (sat. liq.)	403.15 (130)	—
4 (sat. st)	403.15 (130)	270
5 (comp. liq.)	363.15 (90)	250
6 (comp. liq.)	348.15 (75)	—

Table 2: Water properties at cycle points.

q	10^{-8} *bsfc*	AF
25	6 841	89.92
50	6 034	50.97
75	5 688	36.05
100	5 592	27.50

Table 3: Main Diesel engine data [5].

A simple simulation model of the energy balance of the Diesel engine may be found in Reference [4], or on a related paper submitted to ECOS 2005, from the authors of this work. Figure 4 shows the results of the simulated energy balance of the Diesel engine of Table 3 obtained by that model [4].

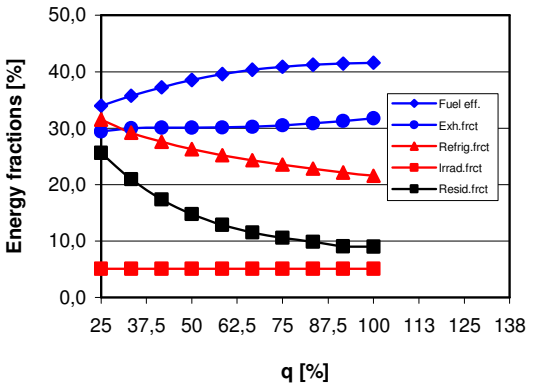

Figure 4: Simulated energy fractions for the Diesel engine [4].

Exergy Balances for the Subunits

On Table 4 we show the exergy balances for the subunits of Figure 3, written in obedience to Equation (2). In this sense, we firstly had to

discuss the philosophy to follow for the F-P-L structure of the cogeneration plant under analysis.

Subunit	Flow	Balance
GG	F	$\dot{B}_1 - \dot{B}_9 - (\dot{B}_5 - \dot{B}_6)$
	P	$\dot{B}_8$
	L	—
RCG	F	$\dot{B}_9$
	P	$(\dot{B}_4 - \dot{B}_3)$
	L	$\dot{B}_{10}$
RAA-1	F	$(\dot{B}_4 - \dot{B}_3) + \dot{B}_{11} + \dot{B}_{15}$
	P	$\dot{B}_{12}$ (freezing)
	L	$\dot{B}_{13}$ (heat rejection)
RAA-2	F	$(\dot{B}_5 - \dot{B}_6) + \dot{B}_{14} + \dot{B}_{18}$
	P	$\dot{B}_{16}$ (ice)
	L	$\dot{B}_{17}$ (heat rejection)

Table 4: Exergy balances of the subunits [4].

So, when defining the F-P-L structure for the structural diagram of Figure 3 we took into account:

1. RAA-1 and RAA-2 are closed control volumes for what only the bulk losses will be computed.
2. Flow $\dot{B}_8$ (electric power) is considered the unique product of the Diesel power generator (GG). This assumption was adopted by various authors, see for instance, Frangopoulos [6], Lozano and Valero [7], Silveira and Nogueira [8]. Nevertheless we decided to adopt this criterion by analyzing the hypothesis of taking as GG products also the flows $(\dot{B}_5 - \dot{B}_6)$ (Diesel engine cooling water) and $\dot{B}_9$ (combustion gases). In this last case the GG irreversibilities should be equally partitioned among these three products, as done by Tozer and Capilla [9][7]. However, it has no sense considering that the engine irreversibilities must be equally "loaded" to the principal product, e.g. electric energy, and the fluids that transport the thermal rejects.
3. The RCG recover is assumed as a subunit apart from the subunit GG. In this way, the flow $\dot{B}_9$ (combustion products exiting GG) and $(\dot{B}_5 - \dot{B}_6)$ (hot water feeding RAA-1) result to be by products of the subunit GG.

[7] In this case the working fluid is the exhaust gases from a gas turbine.

SIMULATION RESULTS

Figure 5 shows the rational efficiency and the relative irreversibility of the subunits varying discretely, at the power load values of 25 [%], 50 [%], 75 [%] and 100 [%]. Intending to furnish more information, we detached figures from Figure 5 for the η_i^B and the ζ_i, as shown on Table 5, at the power load values of 25 [%] and 100 [%].

As one can see both on Figure 5 and Table 5, the power generator GG is the major producer of irreversibility of whole cogeneration system. This subunit is the most rationally efficient too, closely followed by RAA-1 efficiency and by the efficiency of whole system.

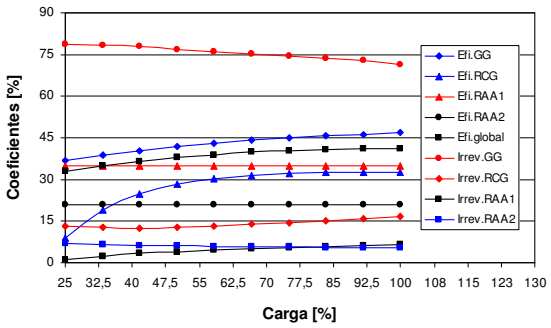

Figure 5: Second law parameters for the cogeneration system [4].

It is interesting to mention that the irreversibilities generated by the heat transfer between the combustion products and the steam and the exhaust gas flux are 'loaded' to heat recover RCG and not to the RAA-1 aqua-ammonia refrigeration subunit, as it would be if the heat fed to RAA-1 were carried directly by the combustion products (in a system without the RCG). Despite its low rational efficiency performance, RCG subunit

irreversibility diminishes with increasing load, what reflects the part that subunit plays in lowering the system entropy generation.

Subunit	25 [%]		100 [%]	
	η_i^B	ζ_i	η_i^B	ζ_i
GG	36.7	78.9	46.9	71.5
RCG	8.9	13.2	32.7	16.7
RAA-1	35.0	1.0	35.0	6.5
RAA-2	21.0	6.8	21.0	5.3
Bulk	32.9	—	41.3	—

Table 5: Second law parameters for the cogeneration system [4].

Figure 5 and Table 5 show that the refrigeration subunits RAA-1 and RAA-2 perform constant values in the 'efficiency game' of the cogeneration system. This result was already expected, as the heats fed to these subunits keep a constant relation to the heat transferred by the Diesel engine on its combustion products and water refrigeration, what can be seen on the balance of Figure 4.

CONCLUSIONS

The present methodology shows to be useful for application on the analysis of energy planning of cogeneration systems; however, it depends on the performance simulation method for the energy balance of the system power engine. In particular, that adopted on this paper shows no difficulties for the daily engineering.

On Figure 5 and Table 5, we could see that the GG subunit is which generates the greatest irreversibility. An important result should be detached from those figures, which is the fact that the refrigeration subunits RAA-1 and RAA-2 perform constant efficiencies all over the power load range.

Figure 5 and Table 5 show too the important part the RCG subunit play on lowering the entropy generated in the combustion process performed in the Diesel engine. That is why the efficiency of the RAA-1 subunit is quite close to that of the GG subunit.

ACKNOWLEDGEMENTS

The authors wish to thank Cummins do Brasil S.A. for the kind permission for utilization of their engine data sheets information; as well as FUCAPI Foundation in Amazon, State University of Amazon (UEA) and National Bureau for Scientific and Technologic Development (CNPq), for their financial support.

REFERENCES

[1] Valero A., Lozano M., Muñoz M. *A general theory of exergy saving. II. On the thermoeconomic cost.* In: AES - Computer-Aided Engineering and Energy Systems. Vol. 3, Second Law analysis and Modelling, ASME Book No. H0341C, Atlanta, 1986.

[2] Renobales L. M. S. Exergoeconomic Optimization of Termal Systems (in Spanish) *Doctoral Thesis*, University of Zaragoza, Zaragoza, Spain, 1994.

[3] Szargut J., Morris D. R., Steward F. R. *Exergy Analysis of Thermal, Chemical, and Metallurgical Processes*. New York: Hemisphere Publishing Corporation, 1988.

[4] Cruz Ricardo. Cruz Ricardo. *Evaluation of the Introduction of Cogeneration in the isolated electric generation System of the Amazonian State.* (in Portuguese) Doctoral Thesis. Mechanical Engineering Faculty, State University of Campinas, 2004.

[5] Cummins Co. Inc. *Engine performance report FR-6250. Data sheet DS-6250*. Columbus, Ohio, 2000.

[6] Frangopoulos C. A. *Thermoeconomic Functional Analysis: A Method for Optimal Design or Improvement of Complex Thermal Systems*. PhD Dissertation. Georgia: Georgia Institute of Technology, 1983.

[7] Lozano M. A., Valero A. *Thermoeconomic analysis of gas turbine cogeneration systems.* In: Thermodynamic and the Design, Analysis, and the Improvement of Energy Systems, AES-Vol. 30, ASME Book No. H00874, Atlanta, 1993.

[8] Silveira J. L., Nogueira L. H. *Thermoeconomic functional analysis applied in cogeneration systems associated to cellulose plants.* In: International Symposium on Efficiency, Costs, Optimization and Simulation of Energy systems (ECOS '92), Zaragosa, 1992.

[9] Tozer R., S. M. A. L., Capilla A. V., James R. *Thermoeconomics applied to an air conditioning system with cogeneration.* In: Proc. CIBSE Building Serv. Res. Technol., 17(1), UK, 1996.

Proceedings of ECOS 2005
Trondheim, Norway
June 20–22, 2005

SIMULATION OF FIRST LAW PARAMETERS OF A DIESEL PLANT COGENERATION SYSTEM UNDER DISCRETE VARIABLE LOAD

Ricardo Wilson Cruz[1]
Superior School of Technology – State University of Amazon
Av. Getúlio Vargas, 361/402, CEP 69020-010, Manaus, AM,
Brazil

Silvia Azucena Nebra[2]
State University of Campinas
Mechanical Engineering Faculty – Energy Department
P.O. Box 6122, CEP 13083-970, Campinas, SP,
Brazil

Elizabeth Ferreira Cartaxo[3]
Technology Faculty – Federal University of Amazon
Av. Rodrigo Otávio, 3000, CEP 69000-000, Manaus, AM,
Brazil

ABSTRACT

The first law parameters are commonly used in cogeneration system analysis, mainly because of their practical meaning despite the fact that those factors neglect any considerations about energy quality (availability) during heat-to-work conversions. In this paper, the first law efficiency of each subunit of the plant, the heat to power ratio, the fuel utilization factor, the fuel saving factor, and the artificial efficiency factor are the first law parameters that are used to characterize a Diesel plant cogeneration system performance under variable power load.
Key-words: Simulation, Diesel plant cogeneration, First law parameters for cogeneration systems.

NOMENCLATURE

AF	Air-to-fuel ratio
bsfc	Brake specific fuel consumption [kg/kJ]
$\dot{E}$	Energy liberated by time unit [kW]
$\dot{F}$	Fuel flux to the subunit [kW]
h	Specific enthalpy [kJ/kg]
$\dot{m}$	Mass flux [kg/s]
m	Counter for the number of subunits
$\dot{P}$	Product flux from the subunit [kW]
p	Pressure [kPa]
p	Counter to the energy flows
Q	Fuel heating value [kJ/kg]
q	Power load [%]
X	Mass fraction
η	Efficiency

Subscripts and Superscripts

art.	Artificial
BC1	Condensed steam pump
BC2	Engine cooling fluid pump
BR	Refrigeration fluid pump

[1] Corresponding author Phone: +55 92 8804 5758. E-mail: rcruz@uea.edu.br
[2] E-mail: sanebra@fem.unicamp.br
[3] E-mail: ecartaxo@ufam.edu.br

BS	H_2O-NH_3 solution pump
coger.	Cogeneration
comb.	Engine Diesel oil
E	Energetic
el.	Electric
exaus.	Exhaust
e, i, j	Counter indexes
GG	Electric generator
LHV	Low heating value
Q	Heat
lq	Discrete power charge set point
RAA	Absorption refrigeration subunits (1,2)
RCG	Heat recovered from gases
refr.	Refrigeration
rio	River cooling water
W	Work
0	Reference state

INTRODUCTION

The methodology developed by the authors in this paper is intended to be used in energy planning studies for autonomous power stations being upgraded towards cogeneration. Northern Brazilian power grid is such a case, in which the power stations presently generate only electricity on an unprofitable basis.

FIRST LAW PARAMETERS

First law analyses usually consider the system embodied in a closed control volume. Such an approach is suitable for a plant producing even more than just electric energy, as in cogeneration systems.

However, first law analysis is allowable too for analyzing systems divided into subunits, what generates a *productive structure* as in Figure 3.

Given a disaggregated plant the *first law efficiencies* of its subunits may be defined as:

$$\eta_i^E \equiv \frac{\dot{P}_i}{\dot{F}_i} \qquad (i = 1, ..., m) \qquad (1)$$

It should be noted that the fuel is not the inlet energy flow but the net energy inflow to the subunit, and the product is a net energy outflow (see Table 3).

For the bulk control volume Horlock [1] gives suitable coefficients. The *heat-to-power ratio* measures the magnitude of one product of the plant relative to the other, for what Silvia Nebra [2] and Lozano Serrano [3] suggest values ranging from 2 to 0.5. So:

$$RCP \equiv \frac{\dot{E}_{coger.}}{\dot{W}_{el.}} \qquad (2)$$

The *energy utilization factor* is an extension of the common bulk first law efficiency of the system:

$$FUE \equiv \frac{\dot{E}_{coger.} + \dot{W}_{el.}}{\dot{E}_{comb.}} \qquad (3)$$

Another way to visualize the whole system is by the *fuel saving factor*, defined as:

$$IPE \equiv \frac{\left(\frac{\dot{E}_{coger.}}{\eta_Q} + \frac{\dot{W}_{el.}}{\eta_W}\right) - \dot{E}_{comb.}}{\left(\frac{\dot{E}_{coger.}}{\eta_Q} + \frac{\dot{W}_{el.}}{\eta_W}\right)} \qquad (4)$$

IPE demands previous definition of the two *reference virtual efficiencies* η_W and η_Q, showed in Figure 1, in which the cogeneration is 'substituted' by a virtual system consisting of a thermo machine and a heater.

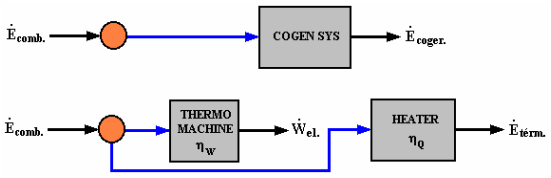

Figure 1: Cogeneration system and its virtual references [4].

Finally, the *artificial mechanical efficiency* is a trial to measure the fraction of the fuel inflow to the plant that attempts the mechanical product of the plant:

$$\eta_{art.} \equiv \frac{\dot{W}_{el.}}{\dot{E}_{comb.} - \left(\frac{\dot{E}_{coger.}}{\eta_Q} \right)} \qquad (5)$$

Any energy flow of the plant may be given by:

$$\dot{E}_j = \dot{m}_j \left(h_j - h_0 \right) \quad (j = 1, ..., p) \qquad (6)$$

For gas mixtures, the following equation should be accessed as well:

$$h_j = \sum_e X_e h(T_j) \quad (e = CO_2, H_2O, N_2, O_2) \; (7)$$

In these equations h_j and h_o are given by the JANAF tables at $T_0 = 298.15$ [K] (25 [C]) and $p_0 = 101.325$ [kPa] (1 [atm]).

SYSTEM CONCEPTION

In this section we show the conceived cogeneration system intended to produce electric energy, low temperature freezing for food conservation (at -25 [C]) and ice for fishing conservation (at -3 [C]), as shown in Figure 2.

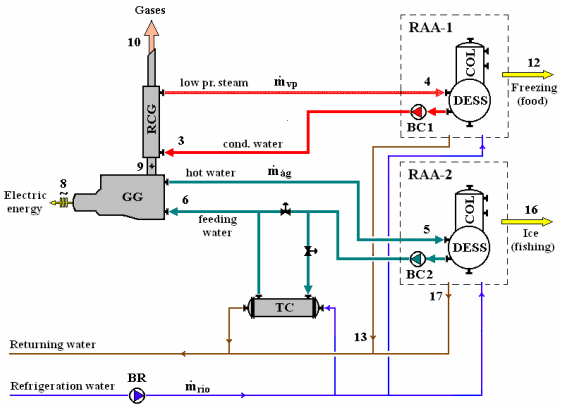

Figure 2: Cogeneration system conceived [4].

The system in Figure 2 has a productive structure associated to it, as shown in Fig. 3.

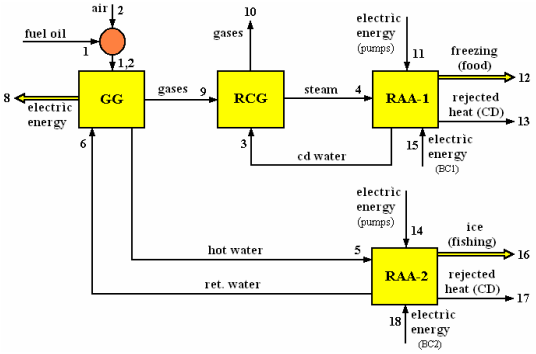

Figure 3: Structural diagram for the system of Figure 2 [4].

Technical Characteristics of the System

The RAA-1 and RAA-2 subunits are the 'clients' of the cogeneration system, which adopt the aqua-ammonia absorption refrigeration cycle, and for what the data shown on Table 1 are chosen assuming water properties constant with the varying power load.

The assumption for constant thermodynamic states for water at the cycle points of Table 1 does not imply that the cogeneration system must supply constant heat, but instead, determined electric power defined as mandatory.

Stations	T [K] (C)	p [kPa]
3 (sat. liq.)	403.15 (130)	—
4 (sat. steam)	403.15 (130)	270
5 (comp. liq.)	363.15 (90)	250
6 (comp. liq.)	348.15 (75)	—

Table 1: Water at the stations of the system.

In order to attempt to the heat surplus, the electric generator is powered by a supercharged Diesel engine which main technical data is reported on Table 2 [5] at four discrete power loads ($q \equiv \dot{W}_{lq} / \dot{W}_{l100}$).

A simulation model attempting to the energy balance of the Diesel engine under its variable power charge may be found in Reference [4], or on a related paper submitted to ECOS 2005, from the authors of this work. On Figure 4, one can find the simulated energy balance varying with

the power load of the Diesel engine of Table 2, obtained by the mentioned model ([4]).

q	10^{-8} *bsfc*	AF
25	6 841	89.92
50	6 034	50.97
75	5 688	36.05
100	5 592	27.50

Table 2: Main Diesel engine data [5].

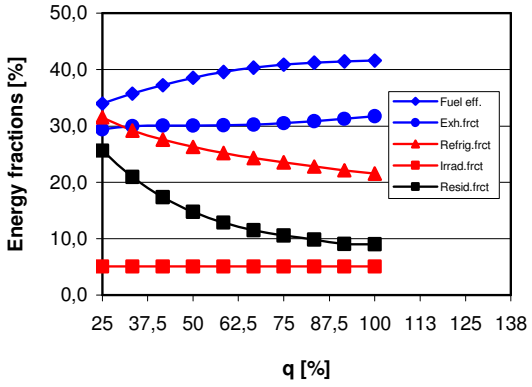

Figure 4: Simulated balance of energy fractions for the Diesel engine.

Energy Balances for the Subunits

Equations given on Table 3 compile the balances of energy flows through the subunits of Figure 3.

Subunit	Flow	Balance
GG	F	$\dot{E}_{1,2}$
	P	$\dot{E}_8 + \dot{E}_9 + (\dot{E}_5 - \dot{E}_6)$
RCG	F	$\dot{E}_9$
	P	$(\dot{E}_4 - \dot{E}_3)$
RAA-1	F	$(\dot{E}_4 - \dot{E}_3) + \dot{E}_{11} + \dot{E}_{15}$
	P	$\dot{E}_{12}$ (freezing)
RAA-2	F	$(\dot{E}_5 - \dot{E}_6) + \dot{E}_{14} + \dot{E}_{18}$
	P	$\dot{E}_{16}$ (ice)

Table 3: Energy balances of the subunits.

And for those equations on Table 3, the following equations show their correlative energy terms:

$$\dot{E}_{1,2} = \dot{m}_{comb.} Q_{LHV} \equiv \dot{E}_{comb.} \quad (8)$$

$$(\dot{E}_5 - \dot{E}_6) \equiv \dot{E}_{refr.} \quad (9)$$

$$\dot{E}_8 \equiv \dot{W}_{el} \quad (10)$$

$$\dot{E}_9 = \dot{m}_{exaus.}(h_9 - h_o) \equiv \dot{E}_{exaus.} \quad (11)$$

$$(\dot{E}_4 - \dot{E}_3) + (\dot{E}_5 - \dot{E}_6) \equiv \dot{E}_{coger.} \quad (12)$$

$$\dot{E}_x \equiv \eta_{BR} \lambda_z \dot{W}_{BR} + \eta_{BS} \dot{W}_{BS} \quad (13)$$

$$\dot{E}_y \equiv \eta_{BC} \dot{W}_{BC} \quad (14)$$

$$\lambda_z = \frac{\dot{m}_z}{\dot{m}_{rio}} \quad (15)$$

The subscripts x, y and z on these equations are referred to the stations as follow: x, to 11 and 14; y, to 15 and 18; and z, to 13 and 17.

As a consequence of the previous balances, it may be determined the first law parameters given by equations (1) to (5). By the way, it may be noted that if neglected the electric power demanded by water and solution pumps of the system, the first law efficiencies η^E_{RAA-1} and η^E_{RAA-2} equal the *performance coefficients* of the RAA-1 and RAA-2 subunits. Particularly, the bulk Horlock's coefficients [1] may be written as:

$$RCP = \frac{(\dot{E}_4 - \dot{E}_3) + (\dot{E}_5 - \dot{E}_6)}{\dot{E}_8} \quad (16)$$

$$FUE = \frac{(\dot{E}_4 - \dot{E}_3) + (\dot{E}_5 - \dot{E}_6) + \dot{E}_8}{\dot{E}_{1,2}} \quad (17)$$

$$IPE = 1 - \left\{ \frac{\eta_Q \eta_W \dot{E}_{1,2}}{\eta_W [(\dot{E}_4 - \dot{E}_3) + (\dot{E}_5 - \dot{E}_6)] + \eta_Q \dot{E}_8} \right\} \quad (18)$$

$$\eta_{art.} = \frac{\eta_Q \dot{E}_8}{\eta_Q \dot{E}_{1,2} - \left[(\dot{E}_4 - \dot{E}_3) + (\dot{E}_5 - \dot{E}_6)\right]} \quad (19)$$

For IPE and $\eta_{art.}$, we defined the constant values for the reference virtual efficiencies, η_Q = 0.95 and η_W = 0.40, which are usual figures for steam generators and Diesel engines [2], [3].

SIMULATION RESULTS

It can be seen on Figures 5 the plots of the simulation of the first law parameters. We have plotted on Figure 5 an efficiency curve for the power generator producing only electric energy $\eta_{el.}$ (power plant without cogeneration), to suit comparisons. It was accomplished by permuting the term relative to thermal energy at the numerator of the above FUE equation by Equation (10); i.e. the unique product is $\dot{W}_{el}$.

For the purpose of conciseness, the constant first law efficiencies η^E_{RAA-1} = 37.1 % and η^E_{RAA-2} = 36.2 % were not plotted on Figure 5, as their curves over-plot another ones. It should be emphasized that these efficiencies are constant by the reasons discussed after Table 1.

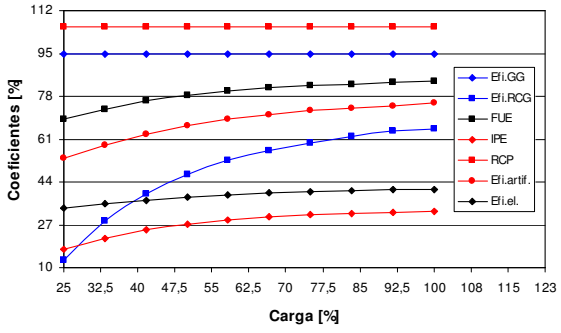

Figure 5: Simulated first law parameters.

On Figure 5, η^E_{GG} is constant and high (94.9%) for every value of the power load. This high figure denotes the enormous energy losses rescued by cogeneration. That can be seen noticing on Figure 5 that the low electric power generator efficiency ranges from $\eta_{el.}$ = 33.5 % (q = 25 [%]) to $\eta_{el.}$ = 41.0 % (q = 100 [%]).

The reason for the behavior of η^E_{GG} can be explained by noticing on Table 3 that η^E_{GG} is the summation of the *fuel conversion efficiency*, $\eta_f = 1/(bsfc\, Q_{LHV})$, the *energy fraction of the exhaust gases* $f_{exaus.} = \dot{E}_{exaus.lq} / (\dot{m}_f Q_{LHV})$ an the *energy fraction of the refrigerant* $f_{refr.} = \dot{E}_{refr.lq} / (\dot{m}_f Q_{LHV})$, where both fractions are related to the energy of the Diesel oil fuelled to the engine. As so, one can see on Figure 4, η_f grows, while $f_{refr.lq}$ decreases and $f_{exaus.lq}$ is kept quite constant.

Another constant parameter on figure 5 is RCP, set on 105.5, a value that rests in the range recommended by Silvia Nebra [2] and Lozano Serrano [3]. That behavior can be justified by noticing on Equation (2) that $\dot{W}_{el}$ (Equation (10)) responds quite faster than $\dot{E}_{coger.}$ (Equation (12)) to the power charge increases.

The rest of the first law parameters on Figure 5, i.e. FUE, $\eta_{art.}$, η^E_{RCG}, and IPE, present a general growth that is related to the behavior of the energetic terms by which these first law parameters are defined. It may be noticed that most of those energetic terms show their behavior relative to the variable power load on Figure 4.

It is import to emphasize that IPE and $\eta_{art.}$ were determined under the hypothesis of constant values for the reference virtual efficiencies η_Q and η_W, as it is difficult to find figures for these coefficients varying with the power load on the literature.

However, for the purpose of analysis, we issued a sensitivity analysis of IPE and $\eta_{art.}$ to η_Q and η_W, while these efficiencies vary ±2.5 % and ±5.0 % around their assumed values. By the plot on Figure 6, we show that IPE senses the variations of η_Q and η_W on a quite higher basis than $\eta_{art.}$ in the previously defined range of variation. Nevertheless, it can be seen that both IPE and $\eta_{art.}$ do not vary so highly as η_Q and

η_W vary from -5% to +5%, what gives confidence to the assumption of constant value for these reference efficiencies.

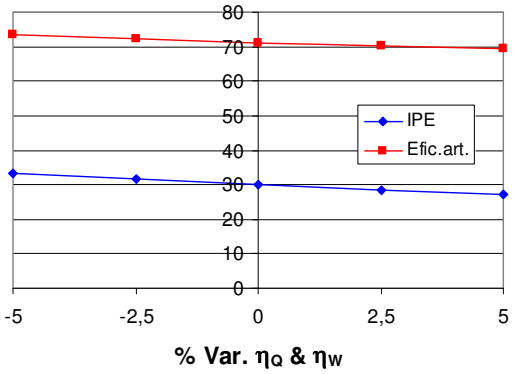

Figure 6: Sensitivity of IPE and $\eta_{art.}$.

CONCLUSIONS

The methodology presented in this work is suitable and reliable for energy analysis on a structural basis, despite it is not usual to perform such an analysis in energy planning studies. The effectiveness of the methodology, however, depends on the method for the simulation of the energy balance of the engine.

The simulation showed that the two most important first law efficiency parameters are constant along the range of the power load, to say, η_{GG}^{E} and RCP.

It is a very interesting result, as these parameters assume an important row on the definition of the part work and heat share in the performance of a cogeneration plant. In other words, work and heat shall ride side by side in terms of their relative magnitudes in the cogeneration system behavior. It means that the only effort a designer has to perform in his project is on defining the *share* of work and heat, as it depends mainly on the purpose of the cogeneration plant.

ACKNOWLEDGEMENTS

The authors wish to thank Cummins do Brasil S.A. for the kind permission for utilization of their engine data sheets and costs information; as well as FUCAPI Foundation in Amazon, State University of Amazon (UEA), National Bureau for Scientific and Technological Development (CNPq) and Federal University of Amazon (UFAM), for their financial support.

REFERENCES

[1] Horlock J. H. *Cogeneration – Combined Heat and Power (CHP).* Oxford: Pergamon Press, 1987.

[2] Nebra Silvia A. *Cogeneration Systems: Evaluation Methods,* (In Portuguese) Invited Speech, Brazilian Congress of Mechanical Engineering , Campina Grande, Paraíba, Brazil, 2002.

[3] Serrano Lozano M. A. *Cogeneration* (in Spanish) , Edited by the University of Zaragoza,. Zaragoza, Spain, 179 p, 1998.

[4] Cruz Ricardo. *Evaluation of the Introduction of Cogeneration in the isolated electric generation System of the Amazon State.* (in Portuguese) Doctoral thesis. Mechanical Engineering Faculty, State University of Campinas, 2004.

[5] Cummins Co. Inc. Engine performance report FR-6250. Data sheet DS-6250. Columbus, Ohio, 2000.

Proceedings of ECOS 2005
Trondheim, Norway
June 20–22, 2005

THERMOECONOMIC COSTS OF A DIESEL PLANT COGENERATION SYSTEM UNDER DISCRETE VARIABLE LOAD

Ricardo Wilson Cruz[1]
Superior School of Technology – State University of Amazon
Av. Getúlio Vargas, 361/402, CEP 69020-010, Manaus, AM,
Brazil

Silvia Azucena Nebra[2]
State University of Campinas
Mechanical Engineering Faculty – Energy Department
P.O. Box 6122, CEP 13083-970, Campinas, SP,
Brazil

ABSTRACT

A simulation of a cogeneration system was performed. The systems consisted of a Diesel engine with two different refrigeration system, one of which working with steam generated using the engine exhaust gases and the other working with the engine cooling water. The first one produced cold water and the other one, ice. Afterwards, a thermoeconomic structure was defined for the system to perform a thermoeconomic costs analysis which gave information about every system flow on a monetary basis. The methodology used was the Exergetic Cost Theory (ECT). The costs obtained differed from that from got the first law point of view, by the fact that the later loses information about the quality of energy, which is taken into account in a second law approach. Unit costs and exergetic and exergoeconomic costs are plotted as the engine power load varies.
Key-words: thermoeconomics, costs, cogeneration, Diesel power plant, variable load.

NOMENCLATURE

$\mathbf{A}$	Leontieff's incidence matrix
$\dot{\mathbf{B}}^*$	Flow exergetic cost vector
$\dot{\mathbf{B}}$	Exergy flux vector
$\dot{\mathrm{B}}$	Exergy flux [kW]
bsfc	Brake specific fuel consumption [kg/kJ]
$\dot{\mathbf{C}}$	Exergoeconomic cost time-rate vector
$\dot{\mathrm{C}}$	Exergoeconomic cost time-rate [US$/s]
C	Capital cost of a subunit [US$]
$\dot{\mathrm{F}}^*$	Exergoeconomic cost of fuel [US$/s]
$\dot{\mathrm{F}}$	Fuel flux to a subunit [kW]
FA	Amortization factor
FK	Capitalization factor
k	Flows number
f_{IS}	Auxiliary additive factor
$f_{\mathrm{O\&M}}$	O&M factor
f_{RP}	Diesel power set refurbishment factor
$\dot{\mathrm{I}}$	Irreversibility time-rate of a subunit [kW]
i	Discount rate [%]
$\dot{\mathrm{L}}$	Exergy loss flux of a subunit [kW]
m	Number of subunits
$\dot{\mathrm{P}}^*$	Exergoeconomic product cost vector [US$/s]
$\dot{\mathrm{P}}$	Product flux of a subunit [kW]
p	Energy flow number
p	Price [US$/kW]
q	Power load [%]

[1] Corresponding author Phone: +55 92 8804 5758. E-mail: rcruz@uea.edu.br
[2] E-mail: sanebra@fem.unicamp.br

$(\mathbf{Y})$	Vector of external exergetic assessments
$(\mathbf{Z})$	Vector of external monetary assessments
$\dot{Z}$	Capital cost time-rate of a subunit [US$/s]
η	Efficiency
τ	Yearly operation time of Diesel engine [s]

Subscripts and Superscripts

B	Exergetic
C	Carnot
DO	Diesel oil
e, i, j,p	Indexes
F	fuel
GG	Electric generator
P	Product
Q	Heat
lq	Discrete power load set point
RAA	Absorption refrigeration subunits (1,2)
RCG	Heat recoverer from combustion products
t	Diesel power set useful life; transpose vector
W	Work
0	Reference state

INTRODUCTION

The potential to upgrade the Northern Brazilian power grid up to cogeneration is determined by both its high social importance and poor profitability. The electric energy generation by autonomous Diesel power plants, under a great number of logistic and maintenance problems, is particularly trouble-some in Brazilian Amazon. This was the motivation to perform simulations and then extract thermoeconomic costs for a Diesel cogeneration plant under varying power load. A simple engineering method, explained in other paper presented at this congress, was used to simulate Diesel engines.

THERMOECONOMIC MODELING

Exergetic Costs Balance

To any productive structure, as the one illustrated on Figure 1, it can be assigned a *F-P-L structure*, what defines the exergy balance [1]:

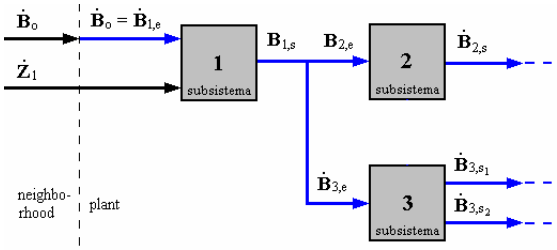

Figure 1: Exergy flows through a productive structure [3].

$$\dot{F}_i = \dot{P}_i + \left(\dot{I}_i + \dot{L}_i\right) \leq \dot{P}_i \quad (\mathrm{i} = 1, ..., m) \qquad (1)$$

In general, for the defined productive structure, the following matrix exergetic cost balance can be written:

$$\mathbf{A}\,\dot{\mathbf{B}}^{*} = \mathbf{A}\left(\mathbf{k}\,\dot{\mathbf{B}}\right) = \mathbf{0} \qquad (2)$$

in which $\dot{\mathbf{B}}^{*}$ and $\dot{\mathbf{B}}$ are $m \times 1$ column-vectors, $\mathbf{A}$ is a $m \times k$ matrix (which elements are +1 to inflows and -1 to outflows), and $\mathbf{k}$ is the vector of the *unit exergetic costs*, which are defined as [1], [2]:

$$k_j \equiv \frac{\dot{B}_j^{*}}{\dot{B}_j} \quad (j = 0, 1, ..., p) \qquad (3)$$

For the flow exergies in Equation (3), we took into account its physic and chemic parts. Detailed description about the formulation for those figures can be found in [3]. Moreover, it was considered, for work and heat:

$$\dot{B}_j^{Q} \equiv \dot{Q}_j \left(1 - \frac{T_0}{T_j}\right) = \dot{Q}_j\,\eta_{Cj} \qquad (4)$$

$$\dot{B}_j^{W} = \dot{W}_j \qquad (5)$$

As an extension of Equation (3), for the fuel and the product of any subunit, it is possible to define unit exergetic costs to fuel and product of each subunit as well:

$$k_{F,i} \equiv \frac{\dot{F}_i^{*}}{\dot{F}_i} \qquad (6)$$

$$k_{P.i} \equiv \frac{\dot{P}_i^*}{\dot{P}_i} \qquad (7)$$

In Equations (6) and (7), i = 1, ..., *m*.
Once Equation (2) is written for the system, it can easily be seen that it demands $k - m$ additional equations for the matrix system to be solved, while $k > m$. One set of additional equations can be satisfactorily defined by the propositions postulated by Valero et al.[1]. So the whole matrix exergetic cost balance plus the additional equations can be written as:

$$[\mathbf{A} \ \vdots \ \mathbf{a}]^t \dot{\mathbf{B}}^* = (\mathbf{0} \ \vdots \ \mathbf{w})^t \qquad (8)$$

Or, in a more concise form, as:

$$[\boldsymbol{A}]\dot{\mathbf{B}}^* = (\mathbf{Y}) \qquad (9)$$

In Equation (9), matrix $[\boldsymbol{A}]$ contains matrix **A** and vectors **a** and **w**, which respectively contain the first member and the second member of the Valero et al. [1] propositions.

Exergoeconomic Cost Balance

Defining *unit exergoeconomic costs* similarly to the exergetic unit costs, Equation (3), as:

$$c_j \equiv \frac{\dot{C}_j}{\dot{B}_j} \quad (j = 0, 1, ..., p) \qquad (10)$$

And taking into account the same discussion issued to write Equation (8), a matrix exergoeconomic cost balance results too:

$$[\boldsymbol{A}]\dot{\mathbf{C}} = (\boldsymbol{Z}) \qquad (11)$$

Equation (11) requires information about the flow of capital cost to the subunits of the plant, embodied in vector $(\boldsymbol{Z})$. Each element in this vector may be obtained by:

$$\dot{Z}_i = \frac{C_i\left(f_{O\&M} + FK \cdot FA\right)}{\tau} \qquad (12)$$

for what i = 1, ..., *m*. The factor $FK = 1 + f_{IS} + f_{RP}\sum_{j=1}^{p}(1+i)^{-3j}$ contemplates the cost of the generator set and its maintenance. The $FA = i(1+i)^t\left[(1+i)^t - 1\right]^{-1}$ isthe cost of auxiliary equipment.. These figures can be found in [3].

SYSTEM CONCEPTION AND THE COSTS STRUCTURE

The cogeneration Diesel plant is rated as 1 [MW] electric power, planned to generate electric energy, low temperature freezing for food conservation and ice for fishing conservation, as shown in Figure 2. Detached from Figure 2, on Figure 3 we show the productive structure defined to guide the thermoeconomic discussion.
On Figure 2, subunit RAA-1 is powered by the high temperature exhaust gases from the Diesel engine. And subunit RAA-2 is powered by the low temperature cooling water from the Diesel engine. Both units are aqua-ammonia absorption systems.
Thermoeconomic costs are appropriate monetary expressions for cogeneration plants. The exergetic costs and the exergoeconomic costs are interpreted as *average costs* in economy, i.e. costs developed by the economic system, 'measured' after a time period has past. Similarly, the *marginal cost*, defined in economy as the addition to the unit cost a growth of the production factor imputes to the product (it is the derivative of a production function relative to its productive factors), has its correlative in thermoeconomics. This approach was not taken into account in our analysis.

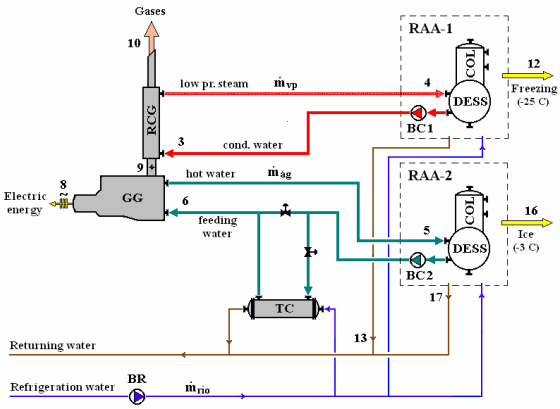

Figure 2: Cogeneration system conceived [3].

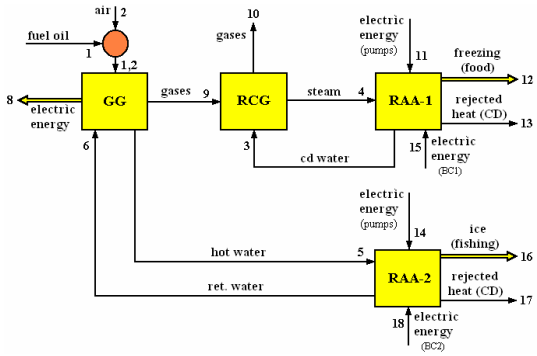

Figure 3: Structural diagram for the system of Figure 2 [3].

Technical Characteristics of the System

Heat for RAA-1 is furnished by low pressure steam, and for RAA-2 it is done by hot water. For the water data in Table 1 we assumed constant temperature and pressure while the engine power load varies, noticing that this assumption does not imply a constant heat supplement by the cogeneration system. This results from the fact that the plant generates primarily electric energy, which is the product that must be privileged.
The electric generator of the plant is powered by a supercharged Diesel engine from an international manufacturer, which main technical data are shown in Table 3, at four discrete power loads ($q \equiv \dot{W}_{lq} / \dot{W}_{l100}$).

System Points	T [K] (C)	p [kPa]
3 (sat. liq.)	403.15 (130)	—
4 (sat. st)	403.15 (130)	270
5 (comp. liq.)	363.15 (90)	250
6 (comp. liq.)	348.15 (75)	—

Table 2: Water at the system points.

q	10^{-8} *bsfc*	AF
25	6 841	89.92
50	6 034	50.97
75	5 688	36.05
100	5 592	27.50

Table 3: Main Diesel engine data [4].

In accordance to the purposes exposed in previous sections, a simple simulation model of the engine energy balance is mandatory, in order to allow the thermoeconomic analysis of the autonomous Diesel cogeneration plant at the actual economic, social and technical conditions of Amazon. Defeating sophisticated modeling procedures, simple simulations can be done by means of *performance parameters* of internal combustion engines, as that one found in [3] for discrete simulation, or on a related paper submitted to ECOS 2005, from the authors of this work.
Adopting such a simple model [3], we obtained Figure 4, as illustration of the simulated energy balance of the Diesel engine of Table 3.

F-P-L Structure for the Cogeneration Plant

It was assumed that flow $\dot{B}_8$ (electric power) is the unique product of the Diesel power generator (GG), as referred on [5], [6], [7]. We considered subunit RCG apart from GG. Table 4 shows the exergy balances written with the aid of Equation (1). As a consequence, flows $\dot{B}_5$ (hot water input to RAA-2), $\dot{B}_6$ (hot water exiting RAA-2) and $\dot{B}_9$ (gases exiting GG) are *sub products* of GG.

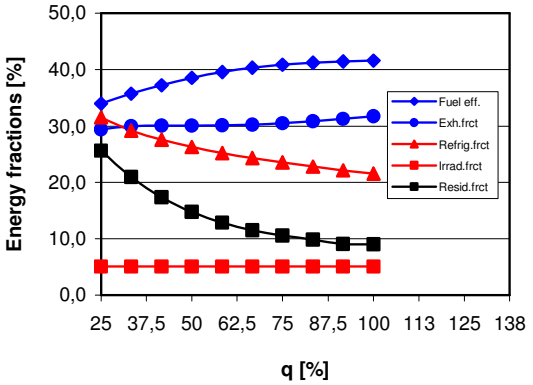

Figure 4: Simulated energy fractions for the Diesel engine [3].

Subunit	Flow	Balance
GG	F	$\dot{B}_1 - \dot{B}_9 - (\dot{B}_5 - \dot{B}_6)$
	P	$\dot{B}_8$
	L	—
RCG	F	$\dot{B}_9$
	P	$(\dot{B}_4 - \dot{B}_3)$
	L	$\dot{B}_{10}$
RAA-1	F	$(\dot{B}_4 - \dot{B}_3) + \dot{B}_{11} + \dot{B}_{15}$
	P	$\dot{B}_{12}$ (freezing)
	L	$\dot{B}_{13}$ (heat rejection)
RAA-2	F	$(\dot{B}_5 - \dot{B}_6) + \dot{B}_{14} + \dot{B}_{18}$
	P	$\dot{B}_{16}$ (ice)
	L	$\dot{B}_{17}$ (heat rejection)

Table 4: Exergy balances of the subunits [3].

The Cost Equations of the Cogeneration Plant

When the matrix exergetic cost Equation (9) is written for the plant, it generates a set of 4 linear equations, one for each subunit. Then, as for the productive structure of Figure 3 there are 17 unknown exergetic cost flows, so 13 additional equations must be defined to the system to be solved, what can be done with the aid of the propositions of Valero et al. [1]. On Table 5, additional equations were listed, written in terms of unit costs, and following the previous discussion about the parts that flows $\dot{B}_5$, $\dot{B}_6$, $\dot{B}_8$ and $\dot{B}_9$ play as sub products.

$k_1 = 1$	$k_{11} = k_8$
$k_2 = 0$	$k_{13} = 0$
$k_3 = k_4$	$k_{14} = k_8$
$k_5 = k_6$	$k_{15} = k_8$
$k_6 = k_9 = k_1$	$k_{17} = 0$
$k_{10} = 0$	$k_{18} = k_8$

Table 5: Set of additional equations for the solution of the exergetic cost equation.

Equation (11) can be written to obtain the exergoeconomic costs $\dot{C}_j = c_j \dot{B}_j$ (j = 0, 1, ..., *p*), in this case also additional equations are required. Such additional equations are those in Table 5, however on a monetary basis, i.e. written as unit exergoeconomic costs. For flow 1 (Diesel oil feeding the plant), the unit cost equals the price of Diesel oil per exergy unit.

Analyzing the Cost Formation of the Two Products of the Cogeneration Plant

Besides proceeding to the solution of the exergetic and exergoeconomic equations, it seems interesting to go deeper into the analysis of how the unit costs c_8 (electric energy) and c_4 (low pressure steam) of the cogeneration system become formed. It must be noticed that both the unit costs related to the engine cooling hot water flows (c_5 and c_6) are equal to the Diesel fuel oil price, in such a way these flows are not 'charged' with any cost relative to the Diesel engine.
The analysis was performed by extracting from the matrix equations written for the productive structure of Figure 3 the following equations; i.e. from the exergoeconomic cost equation obtained from Equation (11) and the exergetic equation obtained from Equation (9):

• GG:
$$c_1\dot{B}_1 + c_6\dot{B}_6 - c_5\dot{B}_5 - c_8\dot{B}_8 - c_9\dot{B}_9 + \dot{Z}_{GG} = 0 \quad (13)$$

$$\dot{B}_1 + \dot{B}_6 - (\dot{B}_5 + \dot{B}_8 + \dot{B}_9) - \dot{I}_{GG} = 0 \quad (14)$$

• RCG:
$$c_3\dot{B}_3 + c_9\dot{B}_9 - c_4\dot{B}_4 + \dot{Z}_{RCG} = 0 \quad (15)$$

$$\dot{B}_3 + \dot{B}_9 - \dot{B}_{10} - \dot{B}_4 - \dot{I}_{RCG} = 0 \quad (16)$$

Equation (13), aided by the additional equation $c_1 = p_{DO}$, can be solved for the unit cost of the cogeneration electric energy:

$$c_8 = \frac{p_{DO}[\dot{B}_1 - (\dot{B}_9 + \dot{B}_5 - \dot{B}_6)] + \dot{Z}_{GG}}{\dot{B}_8} \quad (17)$$

This solution shows the expected result that the unit cost of the electric energy partly derives from the cost of the Diesel fuel oil associated to the exergetic fuel to the subunit GG (see Table 4), and partly from the capital cost of the plant

(Diesel power set plus building, and equipments, etc.). Another form of viewing unit cost c_8 is by changing the term $\left(\dot{B}_9 + \dot{B}_5 - \dot{B}_6\right)$ in Equation (17) for its correlative term obtained from Equation (14), resulting:

$$c_8 = \frac{p_{DO}\left(\dot{B}_8 + \dot{I}_{GG}\right) + \dot{Z}_{GG}}{\dot{B}_8} \qquad (18)$$

What corroborates the previous hypothesis that the irreversibilities of the Diesel power set GG are 'carried' by the cost flow $\dot{B}_8^*$; fact that, by its turn, justifies the hypothesis of considering subunit RCG apart from subunit GG.

Besides, it can be noticed that in the case the plant generates only electricity (without cogeneration), the term $\left(\dot{B}_9 + \dot{B}_5 - \dot{B}_6\right)$ in Equation (17) equals zero, as this term of 'sub products' (in the cogeneration case) turns into lost exergies. In such a case, Equation (18) simplifies to $c_{8,WC} = \left(p_{DO}\dot{B}_1 + \dot{Z}_{GG}\right)/\dot{B}_8$, expression which reflects the fact that as the electricity becomes the unique product, it 'charges' all the costs, Diesel fuel oil and capital cost. Finally, we can say: $c_{8,WC} < c_8$, which means that cogeneration works towards contributing to lower the cost of the generation of electric energy.

Solving Equation (15), the cost of the product of the subunit RCG is obtained:

$$c_4 = \frac{p_{DO}\dot{B}_9 + \dot{Z}_{RCG}}{(\dot{B}_4 - \dot{B}_3)} \qquad (19)$$

As done for the unit cost c_8, we changed $\dot{B}_9$ in Equation (19) by its expression gotten from Equation (16):

$$c_4 = p_{DO} + \frac{p_{DO}\left(\dot{I}_{RCG} + \dot{B}_{10}\right)}{(\dot{B}_4 - \dot{B}_3)} + \frac{\dot{Z}_{RCG}}{(\dot{B}_4 - \dot{B}_3)} =$$

$$= p_{DO} + \frac{p_{DO}\dot{D}_{RCG}}{(\dot{B}_4 - \dot{B}_3)} + \frac{\dot{Z}_{RCG}}{(\dot{B}_4 - \dot{B}_3)} \qquad (20)$$

In other words, the unit cost of the low pressure steam is generated by the price of the Diesel fuel oil, adding the cost of the exergy destroyed by the subunit RCG and the capital cost.

SIMULATION RESULTS

The equations and simulations were solved with the aid of the software EES®, whose property data bank for many substances suffices.

Exergetic Costs Results

Figures 5 and 6 show the results of the unit exergetic costs and the exergetic costs, respectively, along the engine power load range.

It is interesting to discuss the two distinct behaviors presented in Figure 5.

On the one hand, flows 12 (freezing from RAA-1), 4 (low pressure steam) and 3 (condensed steam) have decreasing unit exergetic cost as the power load increases, what in economy is visualized as the *scale effect* of the production factor (its 'elasticity' is positive). At a load of 37.5 [%] the curves diminish notably its slope, denoting the increasing temperature of the exhaust gases, while its energy is kept quite constant; while the power load decreases (see Figure 4) – i.e. as the quality of the energy fed decreases, the unit cost of subunit RAA-1 increases.

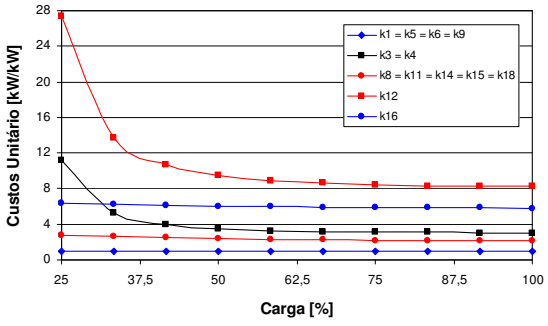

Figure 5: Unit exergetic costs of the flows of the cogeneration system [3].

On the other hand, the rest of the flows do not present a scale effect, meaning that their unit costs are constant (called 'economically inelastic').

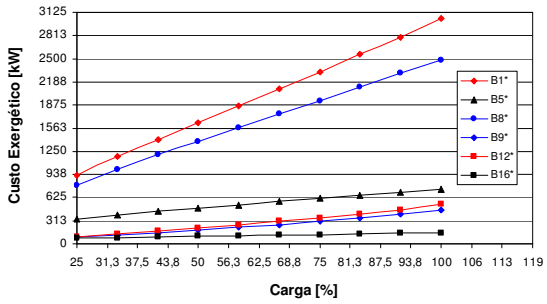

Figure 6: Exergetic Costs of the flows of the cogeneration system [3].

In Figure 7, the total exergetic cost of the *fuel* (F) of each subunit was plotted in function of the engine load. It may be noted that the figures in Figure 7 are the same for the total exergetic costs of the *product* (P) of each subunit, in accordance to what Valero et al. [1] have shown. It does not mean that the unit exergetic costs of fuels and products are the same, as each product carries the irreversibilities generated into the subunit from which it comes from. Figure 7 denotes also the importance of the subunit GG ('Grupo-gerador'), by both its departure from the other lines to a higher cost level, and by its bigger slope meaning higher fuel consumption. Figure 7 shows that the total exergetic costs of subunits RCG and RAA-1 are quite coincident and increasing along the power load range.

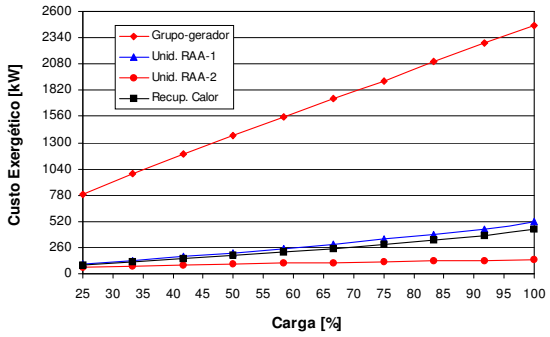

Figure 7: Total Fuel and Product Exergetic costs in the cogeneration plant [3].

Simulations of the Exergoeconomic Costs

Comparing Equation (9) to Equation (11), it can be noticed that the exergetic costs and the exergoeconomic costs of the flows behave in the same way. So we restricted our analysis to the exergoeconomic costs of the products of the 'economic' subunits, e.g. GG, RAA-1 and RAA-2, plotted at Figures 8 and 9.

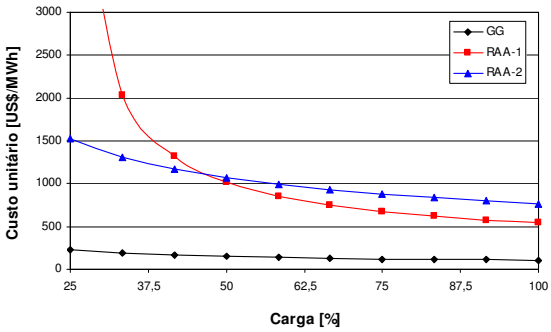

Figure 8: Exergoeconomic unit costs of the three principal products of the cogeneration plant [3].

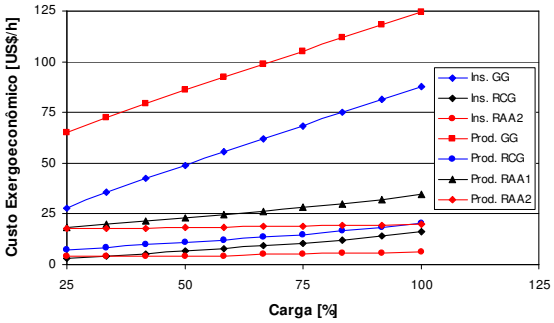

Figure 9: Exergoeconomic costs of F and P of the subunits of the cogeneration plant [3].

It can be seen, on Figure 8, that subunit RAA-1 has the highest cogeneration unit cost at a power load of 25 [%], and drops fast from that point. Such behavior denotes that the cost of its fuel – heat flux exergy – is inversely dependent of its 'quality' (temperature), particularly for power load bellow 50 [%].

By the exergoeconomic costs side, Figure 9 shows the quick answer of subunit GG to the power load, while the rest of the subunits do not.
The total exergetic and the exergoeconomic costs of fuel and product of the subunits behave similarly, but despite the exergetic cost of F and P are equal, the exergoeconomic are not, as can be seen at Figures 7 and 9.

CONCLUSIONS

The analysis performed in this work is useful for deepening energy planning studies about Diesel cogeneration systems, which, so, may go beyond the usual engineering practice. Some subsidiary analysis could be performed, but the main goal of simulating the behavior of the thermoeconomic costs of the plant, as its power load varies, was achieved.
On emphasizing a special result from all the conclusions we got, we would like to emphasize the corresponding established between the engineering thermoeconomics and the economy points of view, once we found that the economic scale effect explains the relationship among the unit costs and the engine power load. The importance this result embodies is the fact that it adds well to the behavior of the 'quality' of the heat flux fueled by the cogeneration system, i.e. it grows when the Diesel engine power load goes toward its maximum, as it was expected to be.

ACKNOWLEDGEMENTS

The authors wish to thank Cummins do Brasil S.A. for the kind permission for utilization of their engine data sheets and costs information; as well as FUCAPI Foundation in Amazon, State University of Amazon (UEA) and National Bureau for Scientific and Technologic Development (CNPq), for their financial support.

REFERENCES

[1] Valero A., Lozano M., Muñoz M. *A general theory of exergy saving. II. On the thermoeconomic cost.* In: AES - Computer-Aided Engineering and Energy Systems. Vol. 3, Second Law analysis and Modelling, ASME Book No. H0341C, Atlanta, 1986.

[2] Tsatsaronis G., Pisa J. *Exergoeconomic evaluation and optimization of energy systems – Application to the CGAM problem*. Energy, Vol. 19, No. 3, UK, 1994.

[3] Cruz Ricardo. *Evaluation of the Introduction of Cogeneration in the Isolated Electric Generation System of the Amazon State.* (in Portuguese) Doctoral thesis. Mechanical Engineering Faculty, State University of Campinas, Brazil, 2004.

[4] Cummins Co. Inc. *Engine performance report FR-6250. Data sheet DS-6250*. Columbus, Ohio, 2000.

[5] Frangopoulos C. A. *Thermoeconomic Functional Analysis: A Method for Optimal Design or Improvement of Complex Thermal Systems*. PhD Dissertation. Georgia: Georgia Institute of Technology, 1983.

[6] Lozano M. A., Valero A. *Thermoeconomic analysis of gas turbine cogeneration systems.* In: Thermodynamic and the Design, Analysis, and the Improvement of Energy Systems, AES-Vol. 30, ASME Book No. H00874, Atlanta, 1993.

[7] Silveira J. L., Nogueira L. H. *Thermoeconomic functional analysis applied in cogeneration systems associated to cellulose plants.* In: International Symposium on Efficiency, Costs, Optimization and Simulation of Energy systems (ECOS '92), Zaragosa, 1992.

Proceedings of ECOS 2005
Trondheim, Norway
June 20–22, 2005

TECHNICAL AND ECONOMIC PERFORMANCE ANALYSIS FOR A MICROTURBINE IN COMBINED HEAT AND POWER GENERATION

Juha Kaikko [1] and Jari Backman
Lappeenranta University of Technology
Department of Energy and Environmental Technology
PB 20, FIN-53851 Lappeenranta
Finland

ABSTRACT

This paper focuses on the single-shaft microturbine in combined heat and power generation. In the application, the microturbine is operated by the heat demand and it replaces purchased electricity and produced heat in an existing boiler. The objective of the study is to analyze the effect of recuperation and different load control methods on the overall economy of the operation. The control parameters include the turbine inlet temperature and the rotational speed of the shaft. As a basis for the analysis, a steady state performance model using realistic component descriptions has been constructed for the microturbine. The operating values of the microturbine are obtained by solving the system of non-linear equations formed by the governing relations. The economy of the operation is determined by combining the performance model with the economy model developed for the engine. The economy model uses the present value of the gain from investing in the microturbine as a criterion. As a result, the conditions are determined for the cost-effective operation of the engine. In addition to the analysis of general validity, the developed models are applied to a case with given profiles for heat and power demand. The size range with the highest economic potential is determined for the microturbine options. For the selected size, the maximum costs are determined that can be allowed for the investment. Apart from the microturbine specifications and case-specific heat and power demand, the results are strongly dependent on the economic parameters. Sensitivity analysis is presented for the main affecting factors.
Keywords: gas turbine, mathematical models, combined heat and power

NOMENCLATURE

a	Factor of present value of periodic payment [-]
C	Cost [EUR]
c	Specific cost [EUR/MWh]
e	Energy price [EUR/MWh]
N	Rotational speed [1/s]
P	Power [W]
p	Pressure [Pa]
q_m	Mass flow rate [kg/s]
r	Ratio of annual maintenance cost to investment cost [-]
T	Temperature [K]
E	Term for efficiency [-]
ε	Effectiveness [-]
η	Efficiency [-]
μ	Dynamic viscosity [Ns/m^2]
Π	Term for pressure ratio [-]
π	Pressure ratio [-]
Φ	Term for rotational speed [-]
	Heat flow rate [W]
X	Term for mass flow [-]

Subscripts

0	Reference conditions
av	Avoided
b	Boiler
e	Electric

[1] Corresponding author. Phone: +358 5 621 2704 Fax: +358 5 621 2799 E-mail: juha.kaikko@lut.fi

f	Fuel
h	Heat
inv	Investment
ma	Operation and maintenance
mt	Microturbine
s	Isentropic
sur	Surplus
α,β	Inlet
γ,δ	Outlet

INTRODUCTION

Microturbines are small gas turbines (25 - 250 kWe) with high potential for future energy systems. They are expected to have steady growth especially in distributed generation, for instance in hospitals, supermarkets, and in small industry [1]. Additional value in distributed generation is gained when the thermal energy from the exhaust gases is recovered to supply local heat.

The turbine inlet temperatures of microturbines are low (800 - 1000°C) to keep the material costs at a reasonable level. The resulting power generation efficiency is quite low, but it can be counteracted by using recuperation. As a result, microturbines typically apply a recuperated cycle and achieve power generation efficiencies as high as 30 % [2]. The use of recuperation always increases the investment costs and needs to be justified economically.

In combined heat and power (CHP) generation, the overall efficiencies of the microturbines are in the range 75 - 85 %. The total investment costs for microturbine-based CHP applications are estimated to vary from 1000 to 1700 EUR/kWe [3].

Microturbines are typically single-shaft engines. The microturbine and the generator have a common shaft that rotates at high speed. The high-frequency current from the generator is converted to grid frequency with an inverter, which enables variable-speed operation.

This paper focuses on a single-shaft microturbine in CHP use. The study includes recuperated and non-recuperated configurations and two alternative load control methods: 1) using the turbine inlet temperature as the only control parameter, and 2) using the rotational speed of the shaft together with the turbine inlet temperature. The objective of the study is to investigate the effect of different configurations and control methods on the technical and economic performance of the specified microturbine. In the analysis, the conditions for profitable operation are determined. Furthermore, the most promising size range and the maximum allowed investment costs are determined for the microturbine in a selected CHP application. The sensitivity of the results against the energy prices is studied.

CHP SYSTEM

The studied CHP system has the maximum electric power demand of 220 kW, and the heat power demand of 728 kW as hot water at 80 °C. The annual energy demand for electricity is 824 MWh and for heat 2378 MWh. Figure 1a presents the annual load profiles for heat and power, and Figure 1b the load duration curves for the case.

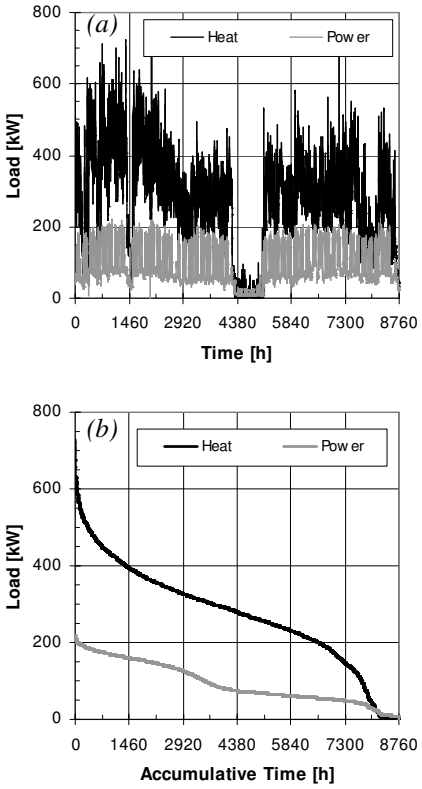

Figure 1: Load profiles *(a)* and duration curves *(b)* for heat and power demand.

In the studied case, the power and heat from the microturbine replaces purchased electricity from the network and produced heat in an existing natural gas-fired boiler. The load level of the microturbine is controlled – within the control range – by the heat demand of the system. If the demand is lower than the minimum heat output

from the microturbine, the excess heat remains unutilized. If the electric power demand is lower than the actual power output from the microturbine during the operation, the exceeding amount is exported. The microturbine is operated only when it is economical, compared to the alternative case where all the required electricity is purchased and the heat produced in the boiler.

GAS TURBINE MODEL

Model Composition

For the performance analysis, a steady state one-dimensional model has been constructed for the operation of single-shaft recuperated gas turbines at the design point and outside design conditions. The model is composed of 1) mass and heat balances, 2) process equations, for instance for compression and expansion, 3) general correlations, such as ellipse law for the mass flow through the turbine, and 4) component-specific maps. While the mass and heat balances and process equations set the universal model base to determine engine performance at reference (design) conditions, correlations and component-specific maps determine the variation of some parameters (mass flows, pressure ratios and pressure losses, for instance) in the system and, together with the other relationships, the overall operation outside design conditions. Figure 2 demonstrates the computational relationships between the equations setting the model base (DES) and the additional equations outside design-point operation (OD).

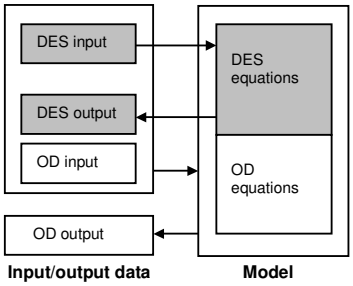

Figure 2: Computational relationships in the gas turbine model.

In the model, the assumption of perfect gas has been applied for the fluids in the cycle: fuel, air and combustion gases. The computation of the fluid properties utilizes polynomial functions for the specific heat capacities of gaseous components and the viscosity of air, a table for combustion reactions, and molecular heating values for the reactions.

The variation of the mass flow and the isentropic efficiency of the compressor outside design conditions is modeled using component-specific maps adapted from in-house design software for radial turbomachinery. For the turbine, the variation of isentropic efficiency is modeled using a map adapted from [4]. The maps are shown in Figures 3 and 4. The map parameters Π, Φ, X, and E for pressure ratio π, rotational speed N, mass flow q_m, and isentropic efficiency η_s are presented in generalized form, which makes the maps valid also outside the reference conditions (denoted with subscript 0). The inlet and outlet states for the components are referred to with subscripts α and β.

$$\Pi = \frac{\pi - 1}{\pi_0 - 1} \tag{1}$$

$$\Phi = \frac{N}{N_0}\sqrt{\frac{T_{\alpha 0}}{T_\alpha}} \tag{2}$$

$$X = \frac{q_m}{q_{m0}}\sqrt{\frac{T_\alpha}{T_{\alpha 0}}}\frac{p_{\alpha 0}}{p_\alpha} \tag{3}$$

$$E = \frac{\eta_s}{\eta_{s0}} \tag{4}$$

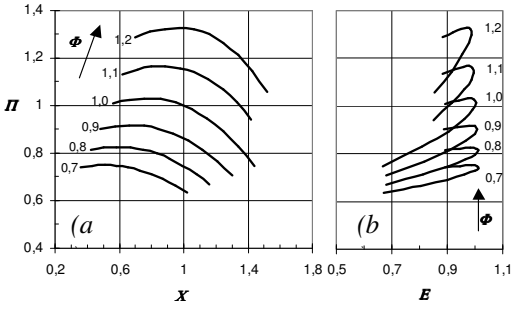

Figure 3: Compressor mass flow *(a)* and efficiency *(b)* maps.

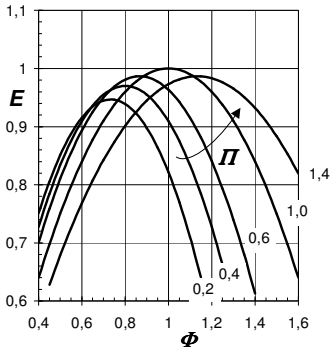

Figure 4: Turbine efficiency map.

The variation of the turbine mass flow outside design conditions is approximated using the ellipse law.

$$\frac{q_m}{q_{m0}} = \frac{p_\alpha}{p_{\alpha 0}} \sqrt{\frac{T_{\alpha 0}}{T_\alpha}} \sqrt{\frac{1-\left(\frac{p_\beta}{p_\alpha}\right)^{\frac{2.3}{1.3}}}{1-\left(\frac{p_{\beta 0}}{p_{\alpha 0}}\right)^{\frac{2.3}{1.3}}}} \tag{5}$$

For recuperator effectiveness ε, the variation is assumed to follow an equation suggested in [5] for a plate-fin recuperator of the counterflow type. In the equation, the inlet and outlet states on the airside and, correspondingly, on the combustion gas side are denoted with subscripts α, β, γ, and δ. Dynamic viscosity is referred to with μ.

$$\frac{\varepsilon}{\varepsilon_0} = \frac{q_{m0}}{q_m} \frac{\bar{\mu}_{\alpha,\beta}}{\bar{\mu}_{\alpha,\beta\,0}} \frac{T_\delta - T_\alpha + T_\gamma - T_\beta}{T_{\delta 0} - T_{\alpha 0} + T_{\gamma 0} - T_{\beta 0}} \frac{T_{\gamma 0} - T_{\alpha 0}}{T_\gamma - T_\alpha} \tag{6}$$

The variation of the mechanical losses outside design conditions is determined as proportional to the square of the rotational speed. The variation of the pressure losses Δp is given by a correlation derived from the model for tubular flows. In the correlation, constant factors for friction and minor losses are assumed.

$$\frac{\Delta p}{\Delta p_0} = \left(\frac{q_m}{q_{m0}}\right)^2 \frac{p_{\alpha 0}}{p_\alpha} \frac{T_\alpha}{T_{\alpha 0}} \tag{7}$$

Electromechanical losses for the generator and the inverter are determined on the basis of the curve presented in Figure 5. The values are presented relative to the corresponding design-point values.

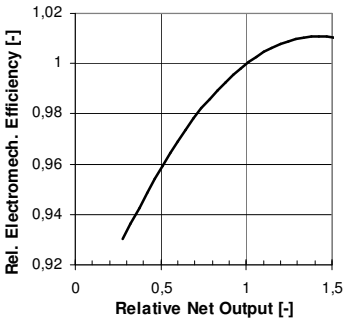

Figure 5: Electromechanical efficiency of the generator and the inverter against net power output.

The calculations are based on the ISO operating conditions (15°C, 101.325 kPa, 60 %), using Russian-type natural gas as fuel. The main components of the fuel are as follows: methane (97.9 %-vol), nitrogen (0.96 %-vol), ethane (0.82 %-vol), and propane (0.23 %-vol).

The turbine inlet temperature is 900°C, a typical value in the microturbine scale that allows the use of standard materials without cooling the hot gas-path components. The compressor pressure ratio is selected to yield the maximum net electric efficiency for the given specifications. However, the upper limit 4 is applied in the optimization. This is considered the highest possible value for a single-stage centrifugal compressor when using lower cost aluminum material [6]. The specifications for the component efficiencies and losses have been selected to reflect the typical values for the microturbine scale. The specifications are presented in Table 1.

The fuel is virtually sulfur-free, and therefore the amount of heat that can be recovered from the combustion gases is not limited by the condensation risk of sulfuric acids. The heat output is determined at design-point operation as well as outside design conditions by assuming the combustion gases to be cooled down to 70°C in the heat recovery boiler.

Compressor polytropic efficiency	84 %
Turbine polytropic efficiency	83 %
Recuperator effectiveness	90 %
Mechanical efficiency of the shaft	98 %
Electromechanical efficiency (generator and inverter)	90 %
Inlet pressure loss	1 %
Recuperator air-side pressure loss (if fitted)	3 %
Combustion chamber pressure loss	3 %
Recuperator exhaust gas-side pressure loss (if fitted)	3 %
Outlet pressure loss	1 %
Pressure loss in the heat recovery boiler	3 %

Table 1: Design-point specifications for the calculations. All pressure losses are given relative to the corresponding inlet pressure.

Computational basis

The relations defining the operation of the gas turbine form a set of non-linear equations, as shown schematically in Figure 2. This set of equations is solved to obtain the operating values for the gas turbine [5]. The selected solution method applies a modification of Newton's method to increase the convergence properties of the basic Newton method. The method requires the calculation of the Jacobian matrix, composed of partial derivatives. The derivatives are approximated using forward differences. Errors arising in finite-precision computing have been reduced by applying double precision arithmetic. The basis for the method and the source codes for the implementation have been presented in [7].

When using deterministic methods, such as Newton's method as the basis, a necessary precondition for convergence is that the starting point is sufficiently close to the root. Newton-based methods also require the Jacobian matrix to be non-singular and the partial derivatives in the matrix to be continuous [8].

For the gas turbine model, the determination of the above-mentioned starting point for the design and off-design calculations is based on simplifications in the model, so that sequential computation can be applied to the equations that set the model base.

The performance maps of the compressor and turbine have been modeled by approximating the constant parameter curves with appropriate polynomial fits and using basic bivariate interpolation schemes [9]. For any value of the curve parameter, the surrounding curves on the map are then transferred to approximate the curve that corresponds to this value, obtaining the result by a linear interpolation of these curves. Although the method does not ensure continuity of the first derivatives as the interpolating point crosses the surrounding curves, the solutions were found without exceptions.

ECONOMIC MODEL

The economic analysis is based on determining the present value C of the gain from investing in microturbine-based CHP. It uses the performance data for the microturbine options and the variation of the heat and power loads. In the analysis, the following costs are taken into account: the investment costs C_{inv} for the microturbine and the associated components, the present value C_f of the fuel costs from using it, the present value C_{ma} of the operation and maintenance costs, the present value C_{av} of the avoided costs, and the present value C_{sur} of the income from selling the surplus electricity to the network.

$$C = C_{av} + C_{sur} - C_{inv} - C_f - C_{ma} \quad (8)$$

In addition to the microturbine itself, the investment costs for the microturbine-based CHP include the heat recovery boiler, the electrical system, as well as the building and installation.

When in operation, the heat output $\Phi_{h,mt}$ from the microturbine is set to follow the heat load $\Phi_{h,load}$. If the load remains below the control range, the engine is operated at the minimum heat output level. The electric power output $P_{e,mt}$ and fuel power $\Phi_{f,mt}$ that correspond to the actual heat output are gained from the performance characteristics, determined for each configuration and control method. If the electric power demand $P_{e,load}$ remains below the actual power output from the microturbine, the exceeding amount is sold to the network.

Denoting the energy prices of purchased and sold electricity with $e_{e,buy}$ and $e_{e,sell}$, the fuel price with e_f, and the boiler efficiency with η_b, the present value of the avoided costs is given by

$$C_{av} = a \int_0^{8760h} \left[P_{e,av}(t)\, e_{e,buy} + \frac{\Phi_{h,av}(t)}{\eta_b}\, e_f \right] dt \quad (9)$$

where

$$P_{e,av}(t) = \min\left(P_{e,load}(t), P_{e,mt}(t)\right) \quad (10)$$

and

$$\Phi_{h,av}(t) = \min\left(\Phi_{h,load}(t), \Phi_{h,mt}(t)\right) \quad (11)$$

In the equation, a is the factor of the present value of periodic payments. The operation and maintenance costs of the boiler are assumed to be constant and thus have no effect on the avoided costs.

The present value of selling the excess electricity to the network is determined from

$$C_{sur} = a \int_0^{8760h} P_{e,sur}(t)\, e_{e,sell}\, dt \quad (12)$$

where

$$P_{e,sur}(t) = \max\left(0, P_{e,mt}(t) - P_{e,load}(t)\right) \quad (13)$$

The constant part of the annual operation and maintenance costs of the microturbine is determined as a fraction r of the investment costs and the variable part as relative to the produced eletricity, using the factor c_{ma} for the specific costs.

$$C_{ma} = a \left(r\, C_{inv} + \int_0^{8760h} P_{e,mt}(t)\, c_{ma}\, dt \right) \quad (14)$$

The present value of the fuel costs is determined from

$$C_f = a \int_0^{8760h} \Phi_{f,mt}(t)\, e_f\, dt \quad (15)$$

At low power levels, the use of the microturbine may not be economical when compared to the alternative case where all the required electricity is purchased and the heat produced in the boiler. On an hourly basis, a criterion for the operation of the microturbine is obtained by requiring that the energy-related total gain flow (EUR/h) from using it be positive. The gain flow includes the avoided costs from using the microturbine to generate power and heat, the income from selling any surplus electricity, the fuel costs, as well as variable maintenance costs for the microturbine. For the calculation, the gain flow is formed from the integrands in equations (9) to (15).

The maximum investment cost that can be allowed for the microturbine-based CHP to be an economically feasible investment has been determined by using the criterion for profitable operation, taking into account equations (8) to (15), and setting the present value C of the gain to equal zero. In the calculation, the integrals have been approximated numerically using discrete data points. The values for the parameters in the calculation are presented in Table 2. The price for the purchased electricity includes transmission costs, and all energy prices include taxes (excluding value added tax), fiscal charges and fees [10].

$e_{e,buy}$	[EUR/MWh]	60
$e_{e,sell}$	[EUR/MWh]	40
e_f	[EUR/MWh]	20
η_b	[%]	90
a	[-]	7.722 *)
r	[-]	0.02
c_{ma}	[EUR/MWhe]	10

*) Interest rate 5 %, operating time 10 years

Table 2: Parameter values in the economic analysis.

RESULTS

The pressure ratio that maximizes the net electric efficiency at design point operation is very close to 4 for the recuperated (Rec) configuration, while for the non-recuperated (No Rec) cycle the optimum would lie well above the limiting value 4, applicable for the selected compressor type. Consequently, the pressure ratio of 4 was selected for both configurations. The corresponding performance is presented in Table 3. The table certifies the established impact of the recuperator: an increase in the electric efficiency and a decrease in the heat output. In this case the electric efficiency of the non-recuperated cycle is further penalized by the limitations in the pressure ratio.

As a result of heat regeneration in the cycle, the ratio of unusable (exhaust) heat to incoming (fuel) heat is increased, which decreases the overall efficiency.

		No Rec	Rec
Power-to-heat ratio	[-]	0.220	0.659
Net electric efficiency	[%]	16.4	32.0
Overall efficiency	[%]	90.8	80.6

Table 3: Performance data for the microturbine options at design point operation.

Figure 6 presents the part load characteristics for the recuperated and non-recuperated microturbine configurations and for both control methods used in the study. The parameters are presented as relative to their design-point values. To produce the curves for the turbine inlet temperature (TIT) control, the temperature has been reduced with 25°C steps. For the combined rotational speed and turbine inlet temperature (Sp and TIT) control, first the relative speed of the shaft has been reduced with 0.05 steps until the limiting value 0.70, set by the compressor map, has been achieved. After this, the turbine inlet temperature has been reduced again with 25°C steps while the speed has remained unchanged.

The use of combined speed and turbine inlet temperature control has a strong increasing impact on the electric efficiency of the recuperated cycle, but also a strong decreasing impact on the heat output when compared to using the turbine inlet temperature as the only control method. For the non-recuperated configuration, the difference between the control methods is smaller. The variation of the overall efficiency relative to its design value is fairly small and similar in the studied microturbine options.

For the recuperated configuration, the heat output does not determine the operating point unambiguously when altering the turbine inlet temperature after the speed control. Therefore, only speed control is considered for the recuperated cycle instead of combined speed and turbine inlet temperature control.

To evaluate the economic potential of the selected microturbine options, Figure 7 presents the effect of the varying heat and power demand on the gain flow from the microturbine. The parameters in the figure are divided by the performance parameters of the microturbine at design-point operation. The load levels that exceed the design heat and power output of the microturbine have no effect on the gain flow, and hence are not shown in the figure. As a result, the presentation depends on the energy prices, but is independent of the microturbine size and the size of the CHP system.

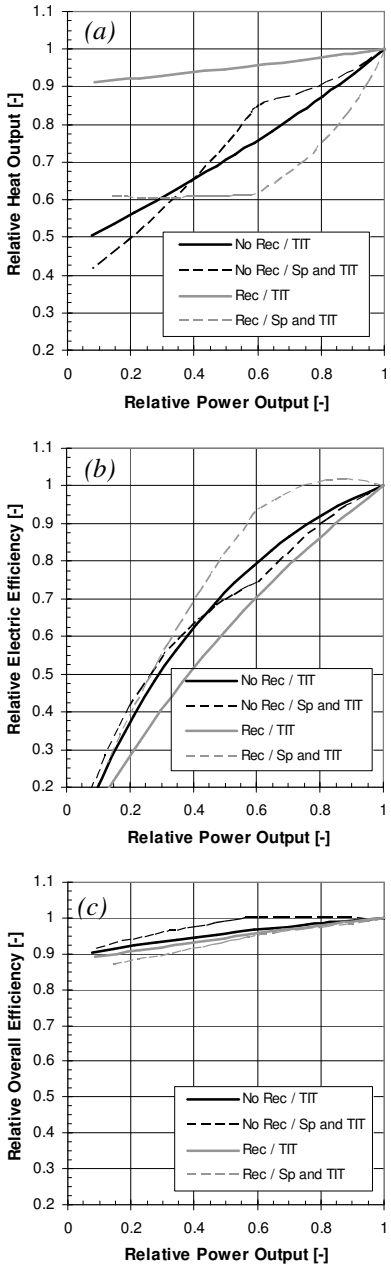

Figure 6: Heat output *(a)*, net electric efficiency *(b)*, and overall efficiency *(c)* during part-load operation for the selected microturbine options.

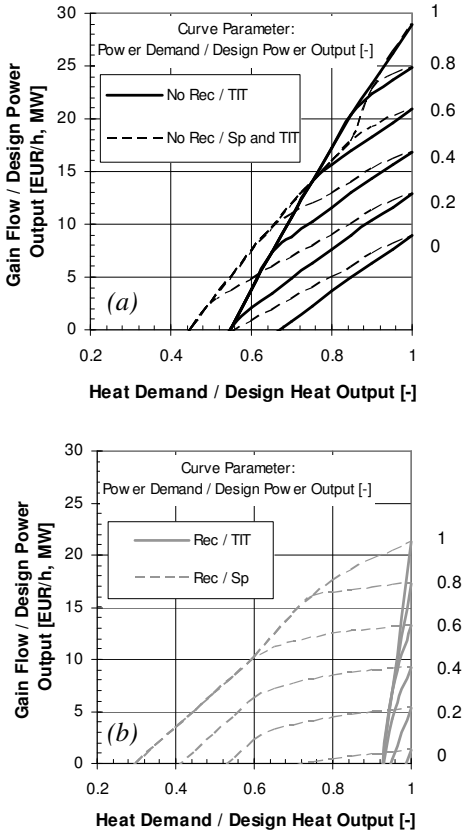

Figure 7: The gain flow from using the microturbine options at varying heat and power demand. Non-recuperated *(a)* and recuperated *(b)* configuration.

Compared to the recuperated configuration, the non-recuperated cycle has a higher maximum gain flow for a given microturbine size. Due to the high cost of the recuperator, the non-recuperated configuration is also less expensive, despite the increased size of the heat recovery boiler. As a result, the non-recuperated cycle has higher potential for feasibility at design point operation. It must be noted that in order to realize this potential, significantly higher heat load levels are required for a given power level than with the recuperated cycle. The recuperated configuration with turbine inlet temperature control suffers from a very narrow margin for profitable operation when the heat demand is decreased. The implementation of the speed control expands the range significantly. For the non-recuperated configuration, the control methods have a lesser impact on the economy of operation.

As a result of the economic analysis using the heat and power profiles from Figure 1a, Figure 8 presents the effect of the electric power output (engine size) on the maximum investment costs that can be allowed for the microturbine-based CHP. As a general rule, increase in power output increases the investment costs of the engine. Therefore, the best economy for the investment can be expected at the increasing part of the curves. Since the recuperated configurations are more expensive than the non-recuperated cycles of the same power output, the non-recuperated configurations gain the highest potential for feasibility at lower power levels while for the recuperated cycles the optimum power levels are higher.

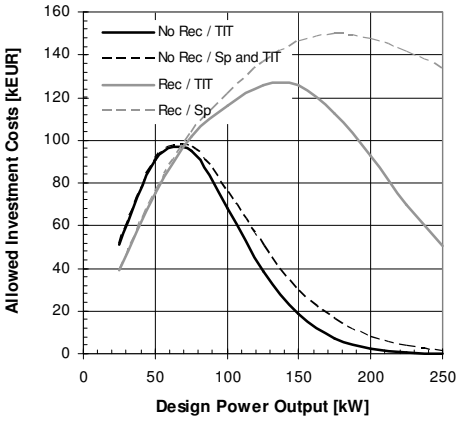

Figure 8: The effect of the engine size on the maximum investment costs that can be allowed for the microturbine-based CHP.

For further analysis, the electric power output of the recuperated configuration was selected to be 100 kW at design-point operation, and one third of this was chosen for the non-recuperated cycle. As a result of the selection, the heat output levels of the configurations are close to each other at design-point operation. Table 4 summarizes the selected sizes for the configurations.

		No Rec	Rec
Power output	[kW]	33.3	100.0
Heat output	[kW]	151.3	151.7
Air mass flow	[kg/s]	0.241	0.825

Table 4: The selected microturbine size at design point operation.

Table 5 presents the annual operating hours and the maximum specific investment costs [EUR/kWe] that can be allowed for the microturbine options of the selected size when supplying the heat and power demand from Figure 1a.

	Operating hours	Allowed specific investment costs
	[h/a]	[EUR/kWe]
No Rec / TIT	7808	2006
No Rec / Sp and TIT	7899	2007
Rec / TIT	7364	1162
Rec / Sp	7887	1218

Table 5: The annual operating hours and the maximum specific investment costs that can be allowed for the selected microturbine size.

With the selected energy prices and load profiles, the allowed specific investment costs are significantly higher for the non-recuperated cycle than for the recuperated one. However, the difference must be weighted against the different size of the engines: smaller size is typically featured with higher specific investment costs. The specific investment costs for the microturbine-based CHP applications are typically in the range of 1000 - 1700 EUR/kWe, and hence, the investment may be feasible in all the studied options.

Compared to the turbine inlet temperature control, the use of a more expensive combined turbine inlet temperature and speed control has no effect on the allowed investment costs, and is hence not justified with the non-recuperated configuration. This is also indicated in Figure 8. For the recuperated cycle, the use of speed control instead of turbine inlet temperature control yields an increase in the allowed investment costs, which may make the speed control a feasible choice.

Figure 9 presents the sensitivity of the allowed specific investment costs against energy prices. Increase in the price for the purchased electricity and decrease in the fuel price have a similar contribution for both non-recuperated and recuperated cycles. Compared to these, the price of sold electricity has a lesser effect on the recuperated cycle and no effect on the non-recuperated one.

The energy prices have only a small effect on the difference between the control methods for the recuperated cycle. For the non-recuperated cycle, the difference remains negligible.

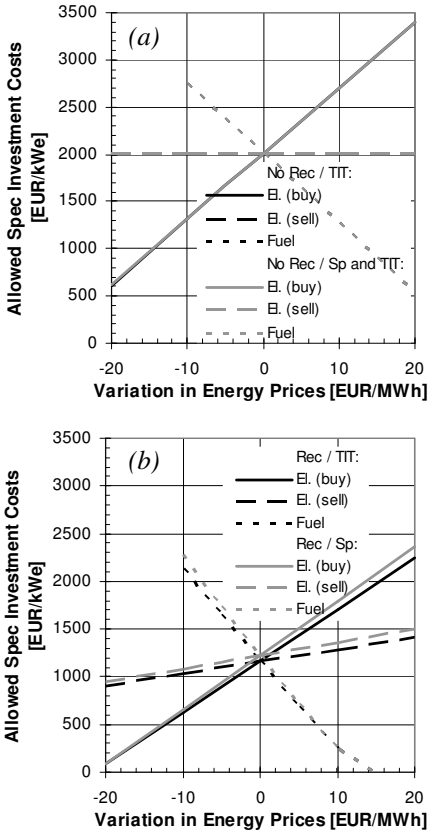

Figure 9: The sensitivity of the allowed specific investment costs against energy prices. Non-recuperated *(a)* and recuperated *(b)* configuration.

The allowed costs given in Table 5 and Figure 9 are based on the selected interest rate 5% and the operating time 10 years, the factor a of the present value of periodic payments during the operating time being 7.722. The costs are directly proportional to the factor of $a/(1+ra)$ where r is the ratio of the annual maintenance costs to the investment costs.

DISCUSSION

The use of a recuperator has a strong effect on the design-point performance of the microturbine by increasing the electric efficiency, but decreasing the heat output when compared to the non-

recuperated cycle of the same power output. This phenomenon affects the sizing of the microturbine as well.

At part load, the implementation of variable speed operation maintains the electric efficiency of the recuperated cycle significantly better than with turbine inlet temperature as the only control parameter. Again, benefits in electric efficiency are gained at the cost of reduced heat output. For the non-recuperated configuration, variable speed operation has a lesser effect on the part load characteristics.

With the selected energy prices, higher gain flows can be attained by using the non-recuperated cycle instead of the recuperated one. However, essentially higher heat demand for given power demand is required to realize this potential. The use of speed control increases significantly the economically feasible operating range of the recuperated configuration. As a result, the recuperated cycle with speed control is especially suitable for applications with a high power-to-heat ratio, and with largely varying heat and power loads.

For the selected CHP application, the engine size range has been found for each configuration where it is expected to have the highest potential for feasibility. The results for the selected microturbine sizes suggest that the investment may be feasible for all the studied microturbine options. Consequently, a non-recuperated microturbine of smaller power output and with simple turbine inlet temperature control may offer a feasible alternative to a larger recuperated cycle. However, the overall economy of the microturbine options must be thoroughly investigated using accurate cost data before any further decisions.

High prices for purchased electricity or low fuel prices contribute strongly to the economy of the microturbine-based CHP.

This study has focused on a case where the microturbine is installed parallel to an existing boiler. In case both the microturbine and the boiler are obtained simultaneously, the boiler size could be reduced compared to the stand-alone alternative. This would further increase the feasibility of the microturbine investment.

REFERENCES

[1] Opdyke DE, Franus DJ. *Gas Turbine Industry Set to Rebound*. Turbomachinery International Handbook 2004, Vol. 44, No. 6. Connecticut, USA: Business Journals Inc., 2004.

[2] Hamilton SL. *The Handbook of Microturbine Generators*. Tulsa, USA: PennWell Corporation, 2003, ISBN 0-87814-853-1.

[3] Vartiainen E, Luoma P, Hiltunen J, Vanhanen J. *Distributed Generation: Technology, Fuels, Markets and CO2 Emissions* (in Finnish). Helsinki, Finland: Gaia Group Oy, 2002, ISBN 952-91-4465-2.

[4] Traupel W. *Thermische Turbomaschinen*, Vol. 1, 2nd ed. Berlin: Springer-Verlag, 1966.

[5] Kaikko J. *Performance Prediction of Gas Turbines by Solving a System of Non-Linear Equations* (dissertation), Research Papers 68. Lappeenranta, Finland: Lappeenranta University of Technology, 1998, ISBN 951-764-142-7.

[6] Cohen H, Rogers GFC, Saravanamuttoo HIH, *Gas Turbine Theory*, 4th ed. Harlow, England: Longman Group Limited, 1996, ISBN 0-582-23632-0.

[7] Press WH, Flannery BP, Teukolsky SA, Vetterling WT. *Numerical Recipes in FORTRAN: The Art of Scientific Computing*, 2nd ed. Cambridge, Great Britain: Cambridge University Press, 1992, ISBN 0-521-43064-X.

[8] Dennis JE Jr., Schnabel RB. *Numerical Methods for Unconstrained Optimization and Nonlinear Equations*. Englewood Cliffs, USA: Prentice-Hall, 1983, ISBN 0-13-627216-9.

[9] Münzberg HG, Kurzke J. *Gasturbinen - Betriebsverhalten und Optimierung*. Berlin: Springer-Verlag, 1977, ISBN 3-540-08032-5.

[10] Energy Market Authority. Electricity prices in Finland 1.1.2005. January 2005, http://www.energiamarkkinavirasto.fi.

Proceedings of ECOS 2005
Trondheim, Norway
June 20–22, 2005

CASCADING AND RADIATOR FLOW OPTIMIZATION IN DISTRICT HEATING SUBSTATIONS AND ADVANCED CUSTOMER ACCOUNTING – IN PURSUIT OF IMPROVED COOLING

Patrick Ljunggren* and Janusz Wollerstrand
Lund Institute of Technology
Department of Heat and Power Engineering
P.O. Box 118, SE-221 00 Lund
Sweden

ABSTRACT

This paper deals with various methods of improved cooling of primary water in district heating (DH) substations and evaluates the benefit of an improved cooling from the perspective of the construction of an appropriate customer accounting method. The general benefit of an improved cooling is well-known: Less thermal stresses in pipelines, lowered heat and pumping losses and increased capacity in the network, improved efficiency of combined heat and power plants and other types of generating plants using heat pumps, waste heat and flue gas condensation.

To stimulate improved cooling in customer owned DH substations, some Swedish DH companies apply a method of customer accounting based not only on heat energy consumption but also on primary water usage and mean water cooling. This benefits customers with thermodynamically well-functioning substations, i.e. a proper cooling, at the expense of customers with less well-functioning substations. The extension of 'flow accounting' has been mapped and found to be applied for a majority of the delivered heat. It represents an important incentive for proper cooling in substations. The study has found that the size of the flow accounting generally very well reflects the benefits for the DH company from an improved cooling.

The amount of cooling of DH primary water achieved in DH substations depends on the employed connecting scheme. In a recent study, we demonstrated that adopting three-stage cascading could achieve significant improvements in this respect. The economical aspects on this subject are here further mapped out based on the results from the study of flow accounting. Optimized and properly functioning substation and secondary systems are, from an economical perspective, of at least equal interest as the choice of connection scheme. Especially if there is an existing oversizing of the radiators, considerably larger savings can be made if optimized control of the radiator circuit is employed.

Keywords: District heating, substations, cascading, customer accounting, radiator circuit

INTRODUCTION

District heating (DH) is a system connecting many buildings to one or more large heat producing plants via a network with hot water as heat-carrier. The large-scale heat production provides efficient use of primary energy and possibility to use waste heat from nearby industries or from electricity production, so-called combined heat and power (CHP) production. Figure 1 shows a schematic overview of a DH network.

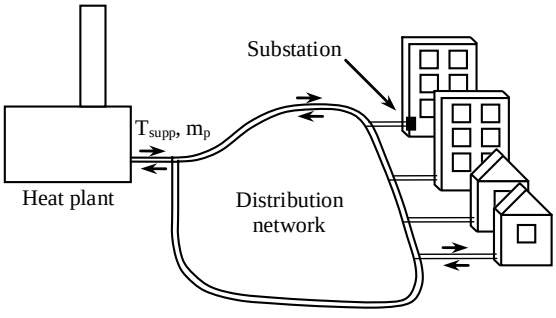

Figure 1: DH network. T_{supp} and m_p denotes supply temperature and primary mass flow respectively.

*Corresponding author: Phone +46 46 222 92 73 Fax: + 46 46 222 4717 E-mail: Patrick.Ljunggren@vok.lth.se

The substation is marked out in the figure, i.e. the equipment that transfers heat from the network to the consumer installations. The essential components of the substation are heat exchangers, temperature sensors, controller, control valves and heat meter.

A central concept concerning district heating is the thermal efficiency of consumer installations, which especially applies to cooling of primary water in substations. It is a well-known fact that low temperatures in the DH networks are beneficial. Heat losses and thermal stresses in pipes will decrease, the required flow will be smaller due to the improved cooling and will thereby require less pumping energy and increase the capacity of the network. There are also advantages for the heat plant from lower temperature levels such as improved efficiency for CHP production and other types of heat plants using heat pumps, waste heat and flue gas condensation.

This paper evaluates the economical benefits of an improved cooling, from the customer's as well as the DH company's perspective. The condition for a possible profit for a customer is, however, that an accounting based on primary water usage, so called 'flow accounting', is employed by the DH company. The paper presents an inquiry concerning the use of such an accounting.

Efforts in pursuit to improve the cooling, such as cascading in substations and certain optimizations of the hydronic system, will be evaluated using the most common flow accounting models.

THE CONCEPT OF CASCADING

In a recent study [1] we dealt with the concept of cascading in DH substations. A short summary of that work is presented here to give the reader some background.

Differences in temperature level in building side thermal requirements (space heating and hot service water) entails that cascading, i.e. dividing the cooling of DH water into two or more stages, can reduce the return temperature, i.e. improve the cooling. This is usually performed by using a two-stage connection instead of the simple parallel connection. However, in Sweden today there is a trend away from cascading mainly because most investigations so far have shown marginal return temperature gains and that the parallel connection is simpler and slightly cheaper. The first argument, however, deserves a closer examination. We have used an English translation of the Swedish nomenclature for the different connection schemes shown in figure 2:

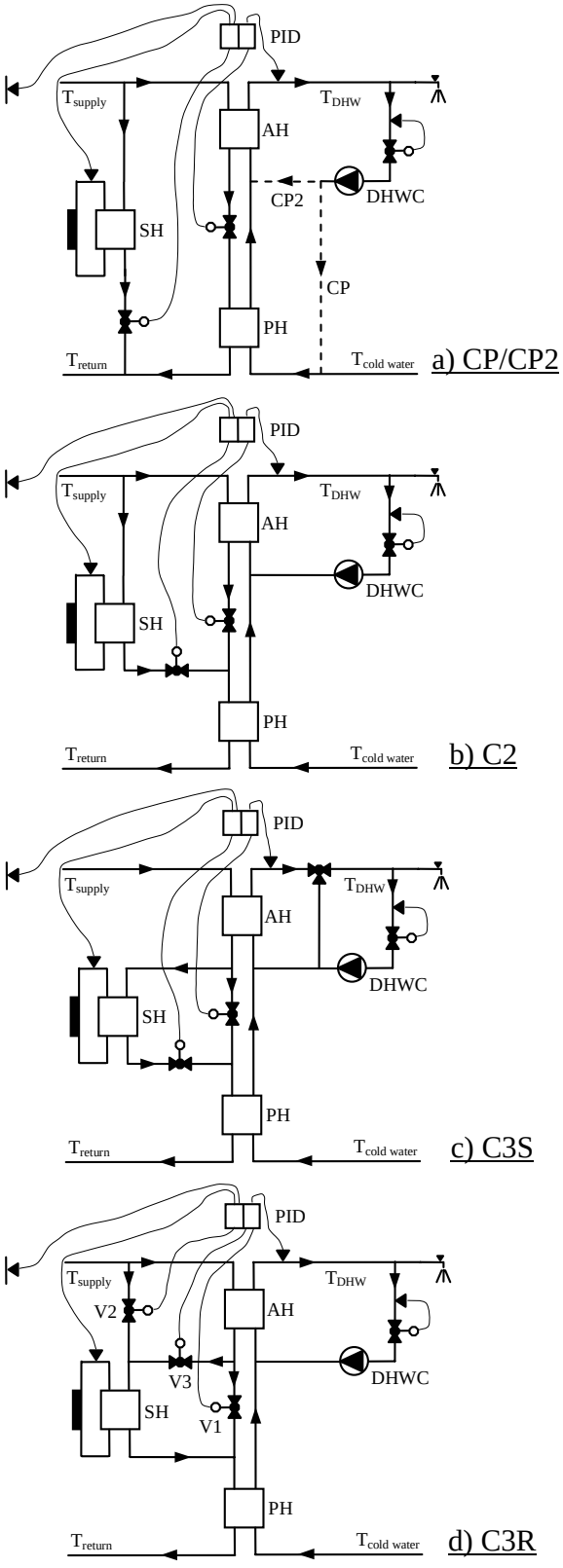

Figure 2: Various substation connection schemes

The abbreviations in figure 2 represent the following cases:

- CP is a simple parallel connection with two heat exchangers only
- CP2 is a parallel connection, where hot water heating has been split on two heat exchangers
- C2 is an example of what is termed a two-stage connection scheme
- C3S is an example of what is termed a three-stage connection scheme
- C3R is an example of another type of three-stage connection scheme

All of them, except the last one can be found in various editions of recommendations [2] issued by the Swedish DH association. Case C3R resembles a scheme found in old Russian DH literature [3]. The 'R' in the designation stands for 'Russian'.

The parallel connection scheme can be designed in two ways, illustrated by the dashed lines in figure 2a. CP is the simpler one where the re-circulated hot service water is connected to incoming cold water. This is the type usually shown by the Swedish DH association. Re-circulation is generally used in larger buildings to prevent bacterial growth (especially legionella) and to maintain a proper hot tap water comfort.

It is in fact rather obvious that when a tapping occurs, mixing incoming cold water with much warmer re-circulated hot water results in a substantial thermodynamical loss. Instead, as long as there is re-circulation, provision of hot service water should be divided in two stages with mixing of re-circulated water between them. This is done in all connection schemes except for CP.

C3S has been abandoned in Sweden due to the risk of scaling of the heat exchanger. Since all primary flow has to pass the afterheater (AH), a high space heating load may cause the hot service water to be overheated.

The Russian type of three-stage connection does not suffer from this drawback because of the use of a third valve, see figure 2d. If there is no space heating load, only valve V1 will be open. If then some space heating is demanded, valve V3 will open to a degree that will result in the required supply temperature of the radiator circuit and the valve V1 will tend to close. When V3 reaches its fully opened position, and further increase of primary water flow for space heating is required, then valve V2 will open, to supply water directly from the incoming primary supply line. At high hot water loads, when a great flowrate needs to be passed through the after-heater, the valve V1 opens again and leads the appropriate amount of flow in bypass of the radiator heat exchanger preventing overheating of water in the radiator circuit.

The dynamic simulation of the different connection schemes were performed for a number of cases, a building with 20 and 100 apartments respectively, and supply/return temperatures in the hydronic system of 60/40 ºC and 80/60 ºC respectively. Figure 3 shows an example of a simulation of one case:

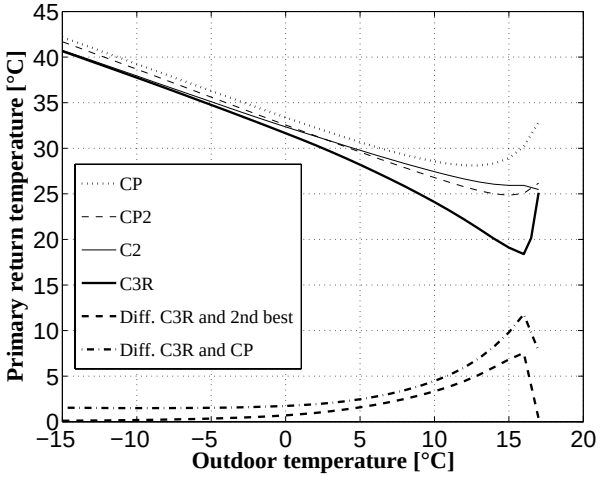

Figure 3: Building with 20 apartments, 60/40 °C space heating system design.

An average return temperature for a whole year was calculated for each case, with respect to outdoor temperature duration and the magnitude of the primary flow, see table 1:

Connection scheme/ case:	**A**	**B**	**C**	**D**
CP	32.5°	41.8°	32.8°	42.1°
CP2	31.1°	41.1°	30.8°	40.9°
C2	31.0°	40.6°	31.0°	40.5°
C3R	29.7°	40.1°	29.5°	39.9°
Gain: C3R compared with second best alternative	1.24°	0.52°	1.05°	0.56°
Gain: C3R compared with worst alternative	2.80°	1.79°	3.30°	2.13°

A: 20 apartments, 60/40 °C space heating system
B: 20 apartments, 80/60 °C space heating system
C: 100 apartments, 60/40 °C space heating system
D: 100 apartments, 80/60 °C space heating system

Table 1: Average return temperature [°C] for various connection schemes.

As can be seen from the results connection scheme C3R can produce substantial gain, especially at modest heat loads. The opinions differ weather a

parallel or two-stage connection is to prefer. The average return temperature for CP2 and C2 is about the same, although slightly better for C2 in the case with higher temperatures in the hydronic system. The simpler parallel variant, CP, which often is claimed to be comparable to C2, shows significantly worse performance in terms of cooling.

RADIATOR FLOW OPTIMIZATION

In Sweden, up to 90 per cent of the annual heat energy demand in residential buildings is due to space heating (SH). For this reason, the cooling of DH water in properly sized and correctly operating DH substations depends mostly on the working parameters of the radiator circuit, which in turn depends on the sizing of the circuit and on how the heat output is controlled. A traditional way of controlling the heat output from the circuit is to keep the flow rate of the circulating water constant and to vary the supply temperature, depending on the outdoor temperature and on the thermal characteristics of the radiators used. As a consequence of constant flow rate the temperature drop in radiators is proportional to its heat output and has a largest value at maximum load operating point. A principal scheme of SH circuit connected to a DH network is given in Figure 4.

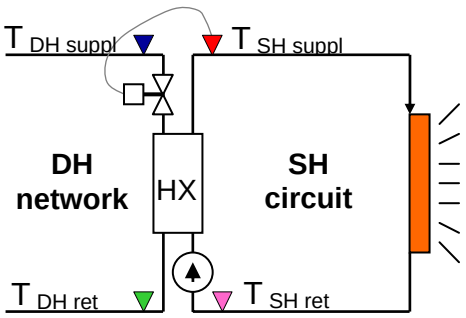

Figure 4: SH circuit in the DH substation

Given some supply and return temperatures of radiator water at sizing conditions, the space heating heat exchanger (HX) in the DH substation can be sized in such a way that least temperature difference (LTD) between DH and radiator water return respectively will fulfil the design rules [2]. Now, the DH water cooling will be optimal at full load operating point. However, this does not guarantee that the cooling will be optimal at part load. Frederiksen et al [4] proved that, to maximize DH water cooling in space heating heat exchanger at part load, the radiator water flow rate should be decreased while the radiator supply temperature should be increased until minimum LTD was achieved.

The phenomenon is exemplified in figure 5, where the calculated temperatures in HX with outdoor temperature are shown. The radiators are intended to operate at 80 °C supply and 60 °C return temperature at full load. The continuous and bold lines show the condition at constant radiator flow rate, while the dot stretched lines shows the optimal condition. The black dot stretched line at the bottom of the diagram shows how the optimum flow rate decreases with decreasing load. We can see that flow rate optimization alone does not result in large gain of DH water cooling compared to results in figure 3. However, the situation changes if we consider that both radiators and HX often are oversized.

Figure 6 shows results when the radiators sized as in previous example are in fact 100 per cent oversized (not an unusual situation until the 70's in Sweden). As we can see here, the oversized radiators are able to operate as if they were sized for about 60–40 °C at full load, and at reduced LTD, which results in substantial increase of DH water cooling (compare the green lines in figure 5 and 6 respectively). This leads to the conclusion that in practice, it is important that flow rate optimization should take possible oversizing of heat transfer areas in space heating circuit into account.

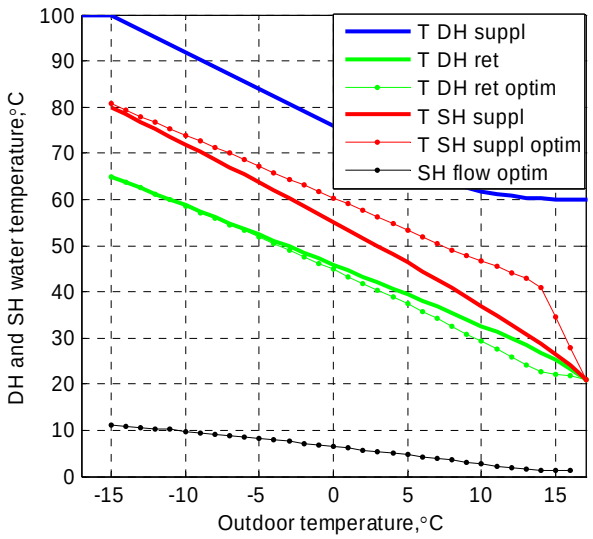

Figure 5: SH supply temperature and circulation flow rate optimisation in space heating circuit sized for 80–60 °C.

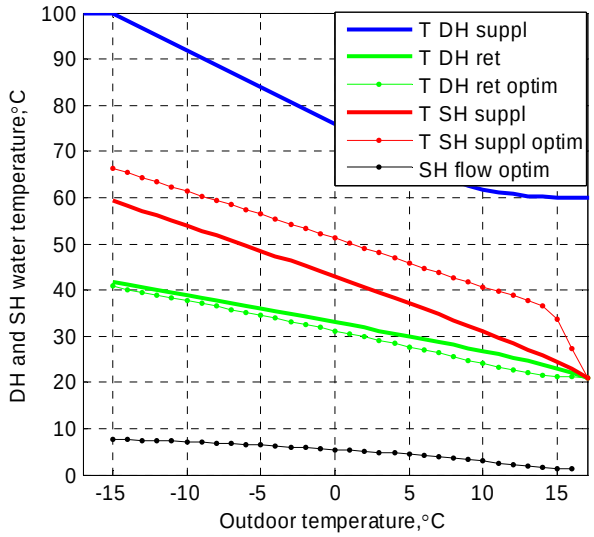

Figure 6: Optimisation as in figure 5 if the SH radiators are in fact 100 per cent oversized.

THE BENEFIT OF AN IMPROVED COOLING

Flow accounting

A DH substation will always transfer the same amount of heat energy for a specific heat load, no matter how well or poorly it is operating. This is a difference from for instance a furnace that will consume less fuel if the efficiency is better. The substation will however consume less primary water if the cooling of the flow is better. This means that with a traditional customer accounting where the customer only pays for consumed heat energy, the thermodynamical performance of the substation will not be of interest. On the other hand, if the accounting model also is based on the amount of primary flow that is used, there will be an incentive for maintaining a proper performance of the substation.

Some of the Swedish DH companies apply a customer accounting model that takes the usage of primary flow into account. Still, many companies just charge the customer for consumed heat energy. A number of questions regarding the various accounting models may be aroused, such as how common this type of accounting model is, i.e. how many of the DH companies that charge the customers for flow consumption and how much of the total amount of delivered heat that these companies correspond to. It is also essential to evaluate how much a *customer* can gain from an improved cooling.

To be able to map out the various accounting models, information was collected, mainly through the DH companies' homepages but also by telephone and email contact. However, there is a large number of companies and in order to limit the effort, the goal has been to cover most of the total delivered energy. Therefore, not all existing DH companies have been included in the survey. The objective with this work has been to create an overall picture of the extent of accounting models with flow accounting and how they are designed.

The annual delivery of DH in Sweden amounts to about 47 TWh[1]. The Swedish DH association has about 150 members, which corresponds to 99 per cent of the delivered DH. [5] The accounting models of 115 of these companies, corresponding to at least 90 per cent of the total amount of delivered heat, have been examined. A majority of the companies (62 per cent) proved to be charging the customers for heat energy only, i.e. not at all for primary flow usage. However, the companies in this category tend to be smaller than the ones charging also for flow usage. Therefore, it turned out that a majority of the delivered heat (61 per cent) corresponds to companies with some kind of flow component in their accounting model. A reservation should be made for the statement that the companies applying flow accounting are larger. Not all companies were included in the investigation and there are a quite large number of smaller companies among these.

Additional differences between the companies that apply flow accounting and those who do not, was attempted to be found. Therefore, the composition of the heat generation plants was mapped out according to the fact that, as mentioned in the beginning, certain types of heat generation are more favoured by a lower return temperature. The result was compared with statistics from the Swedish DH association [6], embracing the total average heat generation composition, see table 2. For the companies applying flow accounting the composition is presented both as an average value and as an average weighted with respect to the size of the networks.

[1] 1 Wh = 3 600 Ws = 3 600 J = 3.6 kJ

Energy source	All	Flow accounting	Flow accounting (weighted)
Bio fuels	55	64	52
Fossil fuels	16	18	23
Waste heat	12	10	7
Heat pumps	13	4	10
Electricity	2	2	6
Other	2	3	2

Table 2: Energy sources for heat generation. Comparison between all DH networks and those who apply flow accounting. All data expressed in per cent.

The conclusion from the results in table 2 is that a significant connection between the energy sources used in a DH network and the use of flow accounting in the same network does not seem to exist.

The customer's perspective

A typical accounting model consists of a number of components such as a fixed component (often based on the size of the substation), a component based on the demand for power, a flexible component based on the heat consumption and finally a possible flow component. It is not unusual that one of the first two components is omitted.

The flow component is usually designed as a cost per consumed cubic metre of primary water. Some companies use a more refined component where the customer's use of primary flow in relation to the heat consumption (which corresponds to the cooling) is compared to the average relation for the whole network. Such a variant entails a flow component that works as a charge if the customer's cooling is worse than the average for the network, or as a bonus if the cooling is better.

Many companies use flow accounting only during the colder half of the year, i.e. when the load in the network is higher and additional, more expensive heat production has to be utilized.

Price information have been collected from the companies applying flow accounting in order to evaluate an improved cooling from the customer's perspective. An average cost for a building with 20 and 100 apartments respectively could then be calculated for a number of different degrees of cooling, see figure 7. The two lines in the diagram are parallel, a fact that is rather obvious since a change in cooling only affects the flow component of the price. The offset between the lines is, however, due to the fixed price in the various accounting models, which entails a lower price per kWh for the building with 100 apartments.

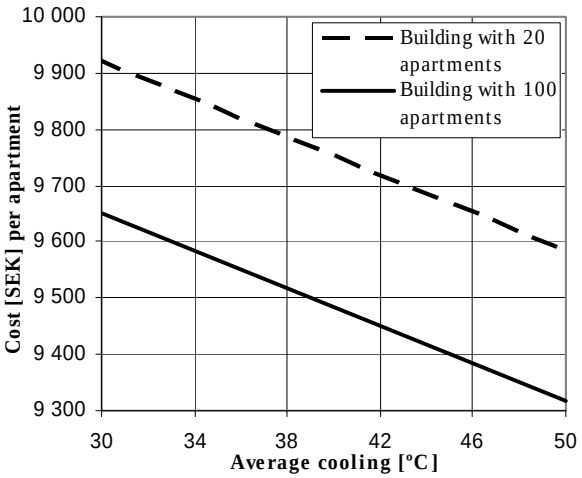

Figure 7: Annual cost for building with 20 or 100 apartments respectively depending on the cooling of primary water flow.[2]

The next diagram, figure 8, shows how much that can be gained from a certain number of degrees improved cooling.

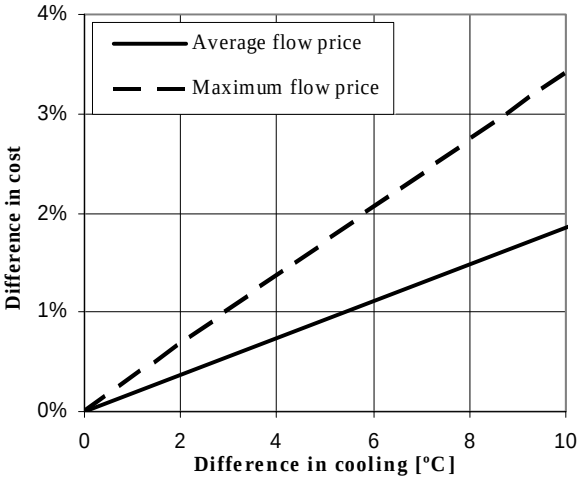

Figure 8 The difference in cost for a customer for a change in cooling, either with average flow accounting level or the maximum found.

The results from the simulations of various connection schemes, as presented in table 1, has been economically evaluated from the perspective of a customer being charged with flow accounting, see table 3. As can be seen, the economical gain from a change in connection scheme must be considered rather small. However, for a larger building, i.e.

[2] 1 SEK is equivalent to 0.1109 EUR (2005-01-19)

100 apartments or more, installing a substation of type C3R instead of the simpler substation CP, which often is the case, could be economically defensible.

Connection scheme/ case:	A	B	C	D
CP	194 652	198 357	945 728	964 298
CP2	194 410	198 112	944 238	961 587
C2	194 384	197 878	944 079	962 637
C3R	194 054	197 636	942 522	960 365
Gain: C3R compared with second best alternative	242 (0.12 %)	245 (0.12 %)	1 490 (0.16 %)	1 661 (0.17 %)
Gain: C3R compared with worst alternative	598 (0.31 %)	721 (0.36 %)	3 206 (0.34 %)	3 932 (0.41 %)

A: 20 apartments, 60/40 °C space heating system
B: 20 apartments, 80/60 °C space heating system
C: 100 apartments, 60/40 °C space heating system
D: 100 apartments, 80/60 °C space heating system

Table 3: Average cost and gain [SEK] for different connection schemes.

The possibility to utilize a possible oversizing in the space heating system can also be evaluated. As shown in the previous chapter this could, at the best, correspond to a shift from an 80/60 ºC to a 60/40 ºC space heating system design. Under these circumstances, the comparison will be made horizontally in table 3, from columns B to A and D to C respectively. The former one corresponds to a saving of about 3 600 SEK (1.8 per cent) and the latter to 18 000 SEK (1.8 per cent), thus substantially more than when comparing just connection schemes.

The district heating company's perspective

The gains from low temperature levels in a DH network are well-known. It is, however, a rather complex task to evaluate how much an improvement is worth due to the characteristics of every specific network. Still, it would be interesting to compare the benefits of an improved cooling for the customer with the benefit for the DH company. In order to accomplish this task a calculation program, accessible from the Swedish DH association's homepage has been used. The program gives the opportunity to specify numerous parameters regarding a DH network and to evaluate a specific change in supply and/or return temperature with reference to both the heat generation plant as well as the network, i.e. heat losses and pumping work. Another factor of importance for a DH company that was found in the study is the existence of bottlenecks, which, however, is not included in the program. Still, these can also be reduced by an improved cooling and produce substantial gain.

Three different cases of heat production composition were tested with the program:

a) 80 per cent bio or fossil fuel (the difference is negligible) and 20 per cent flue gas condensation
b) The same composition as the average network applying flow accounting, cf. table 2
c) 95 per cent waste heat or heat pump (the difference is negligible) and 5 per cent electricity (used as peak load)

Here it must be emphasized that default values in the program has been used regarding the production data. For instance, changing the efficiency of the flue gas condenser or the temperature levels for the waste heat or heat pump can cause large variations in the result. However, the number of possible combinations is infinite and the purpose here has been to show some demonstrative examples of how much that can be gained.

It turned out that case a) produced the smallest gain from a lowered return temperature. Case c) produced the largest gain and consequently case b) was found in between. The resulting gain from the lowered return temperature was distributed on one apartment, see figure 9.

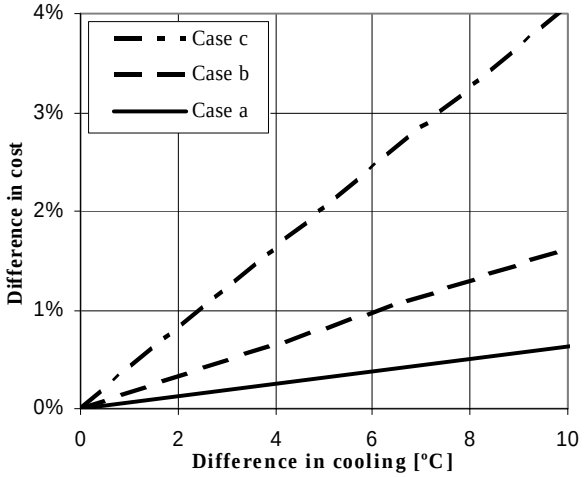

Figure 9: The difference in cost for a company for a change in cooling, distributed among the customers, either with average flow accounting level or the maximum found.

If one compare figure 9 with figure 8 it can be found that the flow accounting in general seems to reflect the size of the earnings for the DH company in case of an improved cooling.

Reflections on flow accounting

The dominating apprehension among DH companies applying flow accounting is that the flow accounting method is functioning very well. However, some companies claim that the flow accounting, although it did have effect when it was introduced, now hardly makes any difference. The companies *not* applying flow accounting are of the opinion that the customers do not understand the use of flow accounting and find it complicated. Instead they mean that a customer with extremely poor cooling is taken care of individually.

The annual Swedish survey "Nils Holgersson" [7], performed by a number of Swedish tenants' associations, examines various charges regarding DH, electricity, water, drain and waste for multi-family houses in Swedish municipalities. The DH accounting is claimed to be complicated with too many components. A simpler model, preferably with only *one* component, is inquired.

It should be pointed out that flow accounting is not applied for single-family houses. For this category, the flow accounting can be considered as complicated. In addition, single-family houses represent a very small part of the total DH.

For larger buildings, it is our opinion that flow accounting entails an important incentive for proper thermodynamical operation of substations. This especially applies when the DH company does not own the substations, which generally is the case in Sweden.

Another issue regarding flow accounting is that the supply temperature in the DH network varies, i.e. it is decreasing with increasing distance from the generating plant. With a lower supply temperature, a substation will use more primary water flow. The flow accounting is by that not entirely fair. However, if this should be considered as a problem, the flow accounting component could be adjusted depending on where in the network a customer is situated.

CONCLUSIONS

Swedish DH companies rather commonly apply flow accounting, preferably the larger ones. In general, it is considered to be functioning well. This study has found that the size of the flow accounting generally very well reflects the benefits for the DH company from an improved cooling. Still, an improved cooling in a substation in the order of a couple degrees C does not result in any larger savings. Of at least equal interest as the choice of connection scheme is, from an economical perspective, optimized and properly functioning secondary systems and substation. However, considerably larger savings could be made if there is an existing oversizing of the radiators and an optimized control of the radiator circuit is employed.

No matter how much that can be gained from an improved cooling, flow accounting is an important incentive to stimulate proper thermodynamical operation of DH substations.

REFERENCES

[1] Ljunggren, Patrick – Wollerstrand, Janusz & Frederiksen, Svend: Cascading in District Heating Substations – in Pursuit of Low Return Temperatures. Proceedings of the 9th International Symposium on District Heating and Cooling, Espoo, 2004. Energy Engineering and Environmental Protection Publications.

[2] Swedish District Heating Association: District Heating Substations (in Swedish), Publications 1996:13, 1997:13 & 2004:3, Stockholm, Sweden.

[3] Sokolov, E.: Heat Supply and District Heating Networks (in Russian). 5th Edition. Published by 'Energoizdat', Moscow, 1982.

[4] Frederiksen, S. & Wollerstrand, J.: Performance of District Heating House Stations in Altered Operational Modes. Paper to the UNICHAL-Congress 17-19.6.1987 in Berlin.

[5] Swedish District Heating Association: Statistics, *http://www.svenskfjarrvarme.se/indexphp3?-use=publisher&id=286&lang=1*

[6] Swedish District Heating Association, calculation program: Värderingsmetod.xls, *http://-www.svenskfjarrvarme.se/index.php?use=publisher&id=260&lang=1*

[7] *http://www.nilsholgersson.nu/*

Proceedings of ECOS 2005
Trondheim, Norway
June 20–22, 2005

Thermo-Dynamic Analysis of CHCP Microturbines

Marco Milanese, Antonio Ficarella, Domenico Laforgia
University of Lecce
Department of Engineering for Innovation
73100 Lecce (Italy)

ABSTRACT

The CHCP (combined heating, cooling and power) microturbines allow a large operational flexibility at sites with demand for energy in the form of electricity, heating and cooling. These systems are particularly relevant in those countries, where air-conditioning is a must and a variety of factories require process cooling.

An investigation on the several trigeneration systems, based on CHCP microturbines, was carried out, developing a software, called "Trigen 1.0". Trigen 1.0 analyzes the fluid-dynamic parameters, as pressure, temperature, enthalpy, and entropy, in every point of the trigeneration system; assesses the machine efficiency and the power generated in terms of electricity, heating and cooling.

The comparison between commercial CHCP microturbines has allowed to evaluate the performances of these systems under different conditions, as atmospheric air temperature, temperature of gas turbine and compression/expansion ratio. Further calculations were carried out to develop a model to evaluate the break-even point of the microturbines, under several conditions.

Keywords: Microturbine, CHCP, Mathematical model

NOMENCLATURE

a	Coefficient [-]
b	Coefficient [-]
C	Coefficient [-]
A_i	Coefficient [-]
BEP	Break even point [y]
C_{ener}	Cost of the energy on the market [EUR]
C_m	microturbine cost[EUR]
COP_{hp}	Heat pump average COP [%]
C_{SPE}	Cost of the energy self-produced [EUR]
F_{cons}	Fuel consumption [m^3/h]
FUI	Fuel utilization index [%]
$Hair$	Enthalpy of air [kJ/kg K]
ΔH_{burner}	Enthalpy on the burner [kJ/kg K]
ΔH_c	Enthalpy on the compressor [kJ/kg K]
$Hgas_i$	Enthalpy of a gas [kJ/kg K]
ΔH_t	Enthalpy on the turbine [kJ/kg K]
ΔH_{term}	Enthalpy on the heat recovery system [kJ/kg K]
IS	Investment saving [EUR]
$\dot{m}$	Mass flow [kg/s]

n_i	Moles of gas [n. of moles]
P_{cool}	Average price of cooling energy [EUR]
P_{el}	Average price of electric energy [EUR]
P_{fuel}	Average price of fuel [EUR]
P_i	Power index [kW]
P_{th}	Average price of thermal energy [EUR]
Q	Heat [kW]
SHC	Specific heat capacity of fuel [J/kg]
T	Temperature [K]
UCM	Annual utilization coefficient of microturbine [%]
$\dot{W}_c$	Compressor power [kW]
$\dot{W}_{cool}$	Cooling power [kW]
$\dot{W}_{el}$	Electric power [kW]
$\dot{W}_t$	Turbine power [kW]
$\dot{W}_{th}$	Thermal power [kW]
η_{burner}	Burner efficiency [%]
η_{el}	Electric efficiency [%]
η_{gen}	Generator efficiency [%]

INTRODUCTION

In many industrial processes (food industry [1], cold storage and ice production industry [2], chemical and petrochemical industry, pharmaceutical industry [3-4]) there is a simultaneous need for electric power and refrigeration at low temperatures. In these cases, a trigeneration plant, that produces electric energy and converts the waste heat a cogeneration plant would have wasted into useful energy in the form of chilled water, is a viable and, under certain circumstances, economical option [5].

The major improvements in the economic, operational, and environmental performance of microturbines have been achieved through decades of intensive research; nowadays microturbines operate with fuels with low NOx emissions, higher reliability and energy efficiency [6, 7].

Onsite trigeneration plants are much more efficient, economically-sound and environmentally-friendly than typical (central) power plants. Because of this, their demand is growing.

There are several reasons why the market for microturbine is growing: firstly, they are less polluting than other forms of power generating devices. Secondly, thanks to the environmental legislation, the availability of gas as a fuel is possible for smaller scale industrial and cogeneration applications. Thirdly, a small microturbine is quick to install, easy to maintain and has a short payback period.

This paper presents a numerical benchmark of 5 trigeneration systems available on the market.

The performances of these systems have been examined varying their working conditions: atmospheric air temperature, temperature of gas turbine and compression/expansion ratio.

Further calculations were carried out to evaluate the break even point of the microturbines, varying the annual utilization coefficient of the microturbine and other parameters, as performances, energy price, etc.

SYSTEM DESCRIPTION

A trigeneration or combined heat, cooling and power (CHCP) system is a thermal system, often involving a turbine, in which fuel is burnt to produce hot gases to power a turbine coupled to an electric generator. The heat/thermal energy from the exhaust gases, before being discharged to the environment, is recovered to produce hot water and steam and/or to power an absorption chiller

The trigeneration systems presented in this paper comprise 4 subsystems:

1) fuel supply;
2) microturbine;
3) heat recovery system;
4) absorption chiller.

Figure 1 shows a typical scheme of the microturbine trigeneration system analyzed [6]. Exhaust gases from the microturbine were directed into a recuperator, to recover the heat from the turbine, and then in a heat recovery system coupled to an absorption chiller, that produces heat and cold, respectively.

Table 1 shows the main characteristics of the commercial microturbine analyzed in this work.

N.	Microturbine	Power (kW)	Type of lubrification	Type of recuperator	Turbine speed (rpm)	Further notes
Turbine 1	Turbec T100	100	Oil	External	70000	Only cogeneration
Turbine 2	Bowman TG80CG	80	Oil	External	68000	Trigeneration
Turbine 3	IR PowerWorks	70	Oil	External	44000	Trigeneration
Turbine 4	Capstone C30	30	Pneumatic	Internal	96000	Trigeration
Turbine 5	Elliott TA-80R	80	Pneumatic	Internal	70000	Trigeration

Table 1. Commercial microturbines analyzed

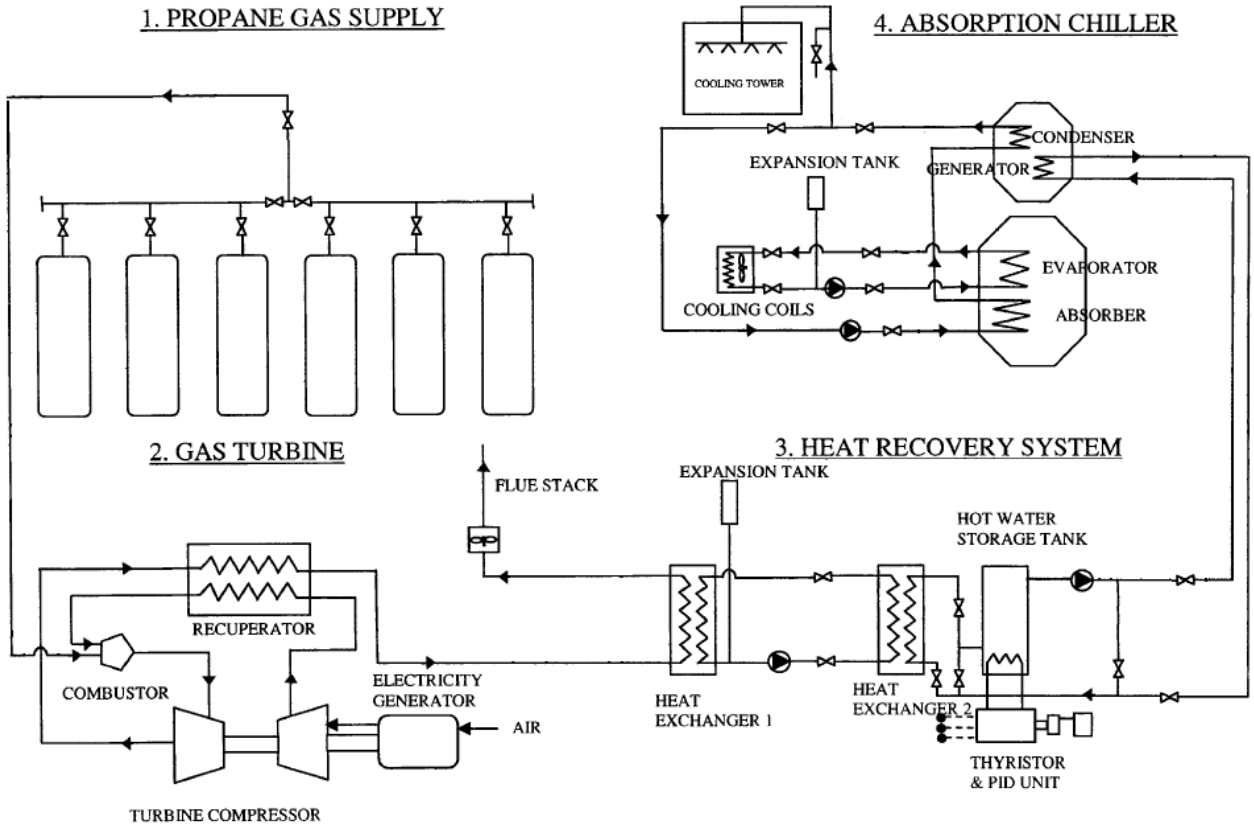

Figure 1: Schematic diagram of a typical trigeneration system

MATHEMATICAL MODEL

To investigate the commercial trigeneration systems, analyzed in this paper (see Table 1), a software, named TRIGEN 1.0, was developed. The software input parameters were the following:

- air pressure inlet;
- compression ratio;
- expansion ratio;
- air temperature inlet;
- air mass flow;
- adiabatic efficiency of the compressor;
- adiabatic efficiency of the turbine;
- generator efficiency;
- temperature of gas turbine;
- flow resistance of the recuperator;
- flow resistance of the heat exchanger;
- NTU recuperator;
- NTU heat exchanger;
- water temperature inlet in the heat recovery system;
- water mass flow inlet in the heat recovery system;
- COP refrigerator;
- net heat value of methane;
- net heat value of oil.

The software allows to calculate electric power, thermal power, cooling power, fuel consumption, electric efficiency, fuel utilization coefficient, etc, and in each point of the system, as Figure 2 shows, pressure, temperature, enthalpy, entropy, volume and density of the gas.

Mathematical model determines the compressor power, the turbine power and the electric power respectively by Equations 1, 2 and 3.

$$\dot{W}_c = \dot{m}\Delta H_c \quad (1)$$

$$\dot{W}_t = \dot{m}\Delta H_t \quad (2)$$

$$\dot{W}_{el} = \left(\dot{W}_c + \dot{W}_t\right)\eta_{gen} \quad (3)$$

To calculate air enthalpy (*Hair*) in every point of the system, the mathematical model considers the air as mixture of 8 gases (Ar, N_2, O_2, CO, CO_2, H_2O, NO, SO_2), and for each gas it calculates the enthalpy as indicated in the equations 4 and 5.

$$Hgas_i(T) = n_i\left(A_1T + A_2T^2 + ... + A_nT^n\right) \quad (4)$$

$$Hair(T) = \sum_i Hgas_i(T) \quad (5)$$

Electric efficiency, fuel utilization index, and fuel consumption were determined by equations 6, 7 and 8.

$$\eta_{el} = \frac{\dot{W}_{el}}{Q} \quad (6)$$

$$FUI = \frac{\dot{m}\Delta H_{term} + \dot{W}_{el}}{Q} \quad (7)$$

$$F_{cons} = \frac{\dot{m}\Delta H_{burner}}{SHC_{fuel}} \quad (8)$$

In Figure 2 the interface of the software Trigen 1.0 is shown.

In the second part of this work, to evaluate the break even point of the systems under investigation, several parameters were considered and calculated.

According to Campanari [8], the cost of the microturbines was calculated by Equation 9.

$$C_m = \dot{W}_{el}\left[44000\left(\frac{\dot{W}_{el}}{75}\right)^{0.66}\right] + 10000 \quad (9)$$

The break even point was evaluated as ratio between the cost of the microturbine and the investment saving (difference between the cost of the energy bought on the market and the cost of the energy self-produced) (Eq. 10, 11, 12 and 13)

$$BEP = \frac{C_m}{IS} \quad (10)$$

where:

$$IS = C_{Ener} - C_{SPE} \quad (11)$$

$$C_{Ener} = 8760UCM\left(\dot{W}_{el}P_{el} + \dot{W}_{th}P_{th} + \dot{W}_{cool}P_{cool}\right) \quad (12)$$

$$C_{SPE} = 8760F_{cons}P_{fuel}UCM \quad (13)$$

In Equations 12 and 13 the annual utilization coefficient of the microturbine (UCM) is defined as a part of the year when the microturbine is on.

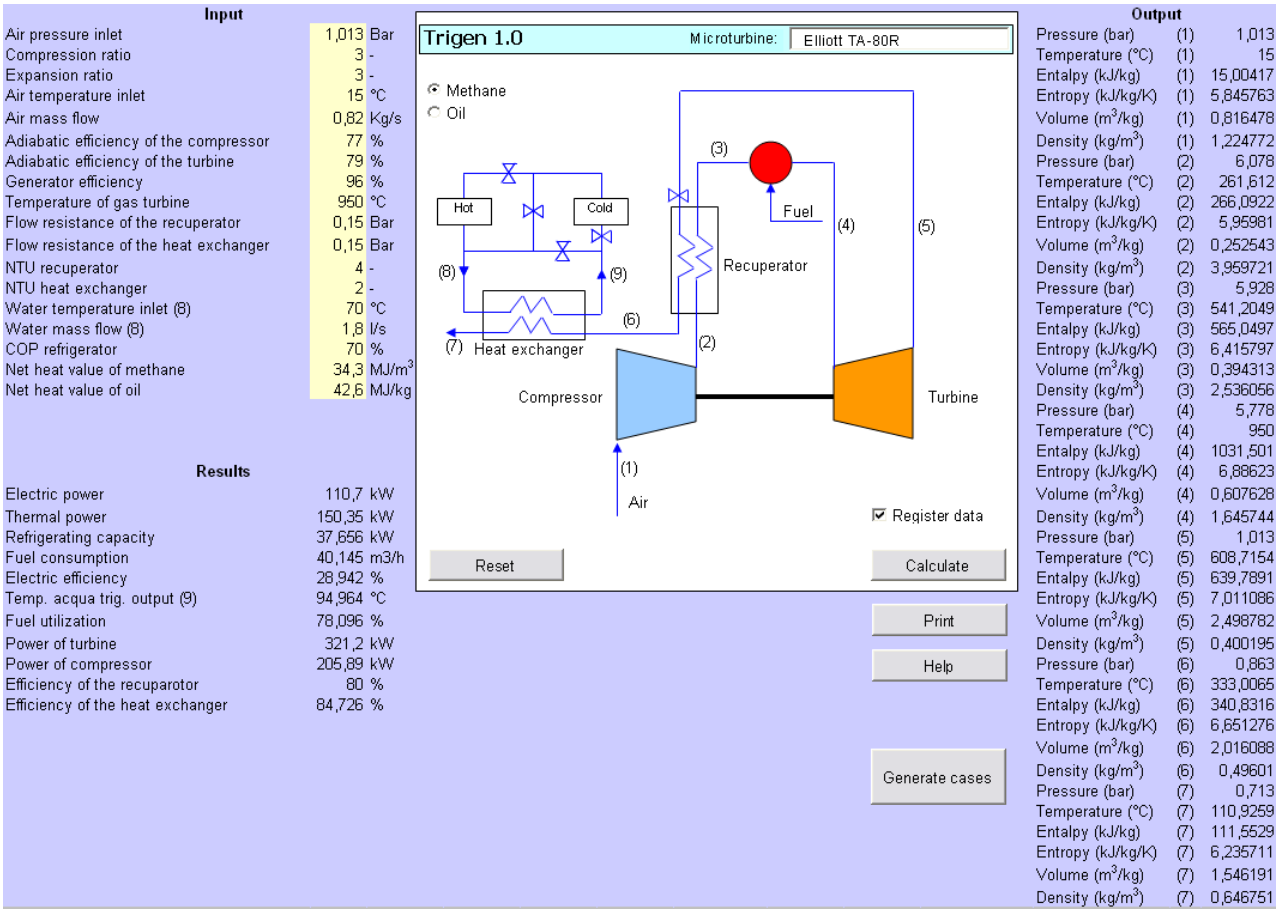

Figure 2: Software Trigen 1.0

PERFORMED SIMULATIONS

Several numerical simulations were carried out varying some parameters (air temperature inlet, compression and expansion ratio, temperature of gas turbine) to calculate possible variation in the microturbine performances (electric power, electric efficiency and fuel utilization).

Table 2 shows the cases under investigation in the present work.

In the calculations, the air pressure inlet and the air temperature inlet were varied in order to investigate the influence of the atmospheric parameters on the microturbine performances.

Air temperature inlet (K)	Compression and expansion ratio (-)	Temperature of gas turbine (K)
273	1.5	873
278	2	923
283	2.5	973
288	3	1023
293	3.5	1073
298	4	1123
303	4.5	1173
308	5	1223
313	5.5	1273
318	6	1323
323		1373

Table 2: Variation of air temperature inlet, compression/expansion ratio and temperature of gas turbine in the cases under investigation

Further simulations were carried out to examine the variation of the electric power, electric efficiency and fuel utilization of the microturbines, adapting both the compression/expansion ratio and the temperature of gas turbine.

DISCUSSION OF RESULTS

Microturbine electric power and microturbine electric efficiency are strongly influenced by atmospheric air temperature, as Figures 3 and 4 show. In particular, low atmospheric temperature is preferable than high temperature: between 0 °C and 50 °C all microturbines present an electric efficiency decrease equal to 5÷6%.

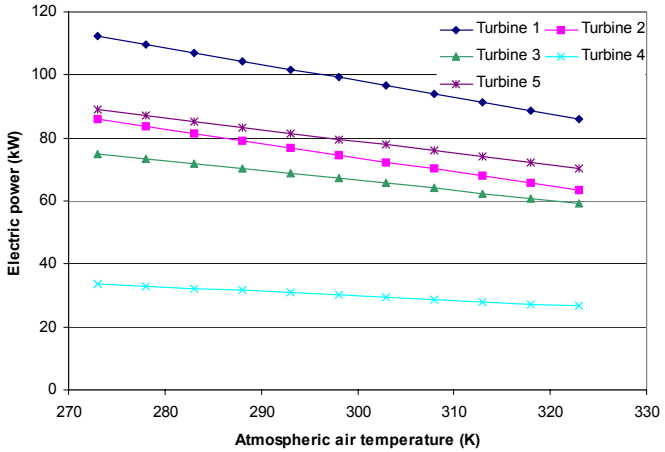

Figure 3: Electric power as a function of atmospheric air temperature

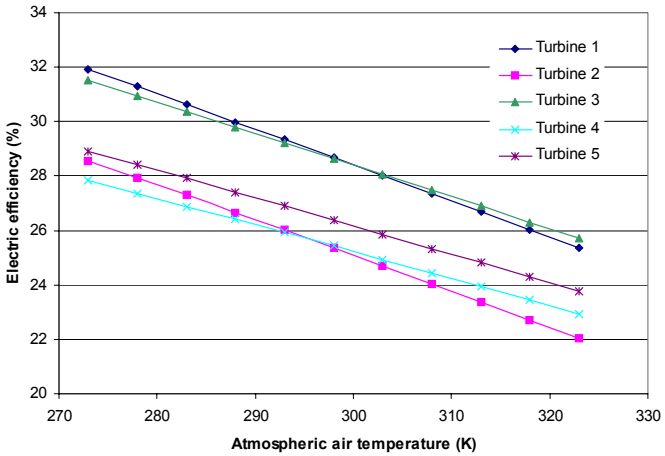

Figure 4: Electric efficiency as a function of atmospheric air temperature

The gas turbine temperature and the compression/expansion ratio are important parameters to improve the peak efficiency of a microturbine, as Figures 5, 6, 7 and 8 show.

For all microturbines, electric efficiency and generated power is almost directly proportional to the temperature of gas turbine. While, the compression/expansion ratio is a very negative working parameter at low values and in all cases a good range is equal to 3÷4.

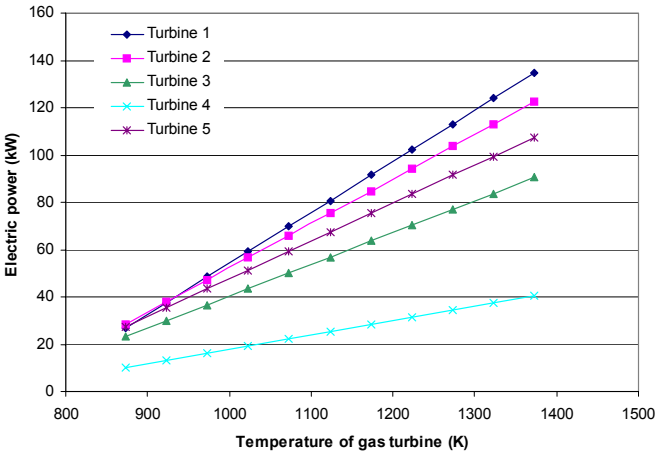

Figure 5: Electric power as a function of temperature of gas turbine

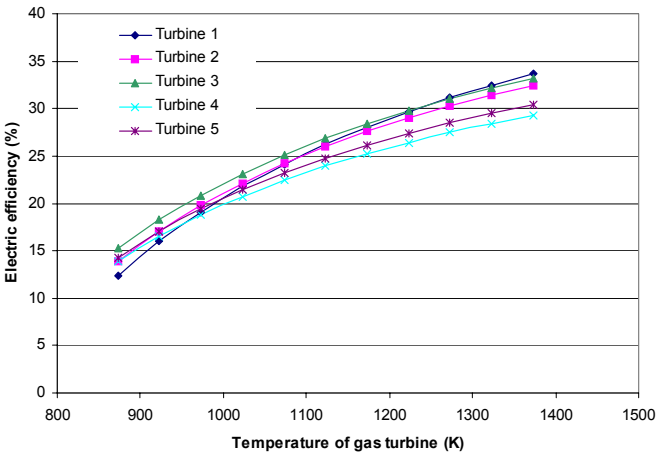

Figure 6: Electric efficiency as a function of temperature gas turbine

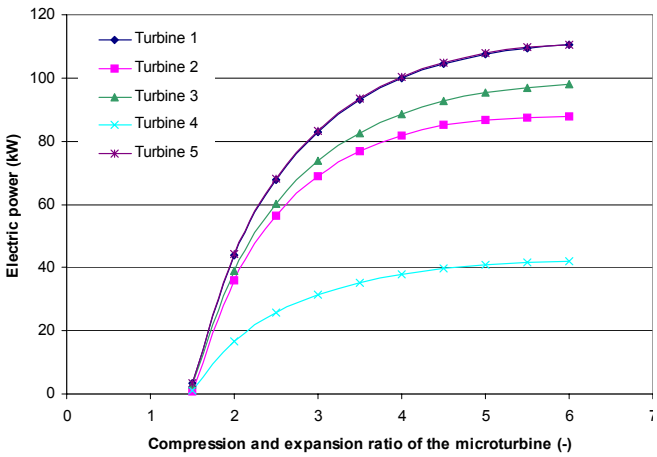

Figure 7: Electric power as a function of compression and expansion ratio of microturbine

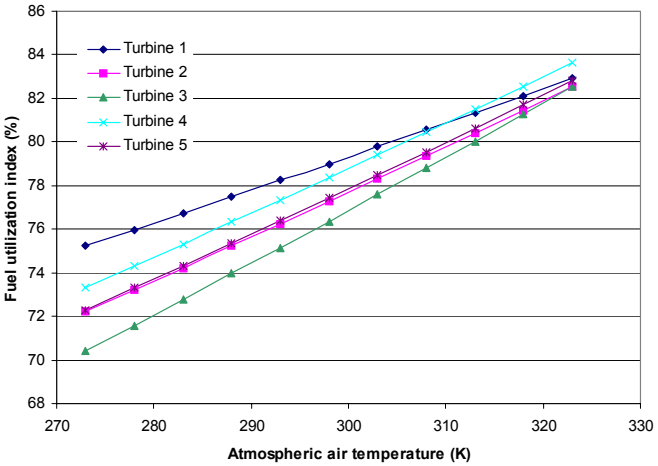

Figure 9: Fuel utilization as a function of atmospheric air temperature

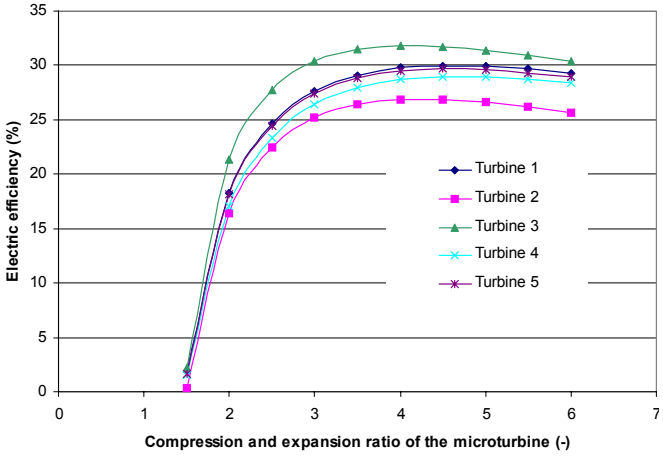

Figure 8: Electric efficiency as a function of compression and expansion ratio of microturbine

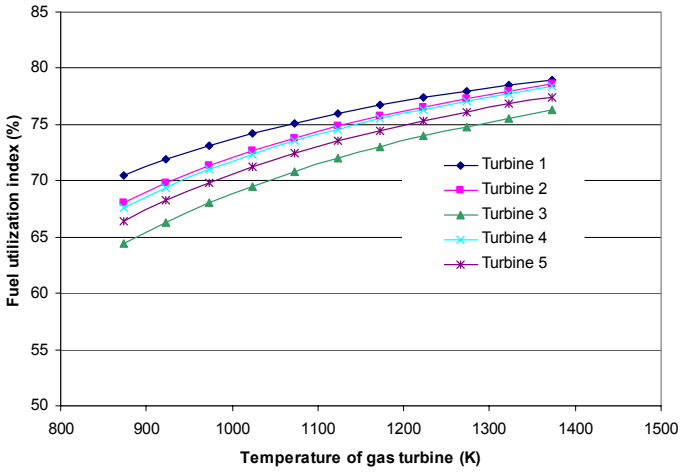

Figure 10: Fuel utilization as a function of temperature of gas turbine

Fuel utilization is a parameter used to estimate the global efficiency of the trigeneration systems, because it takes into account both electric and thermal (and/or cooling) power.

As Figure 9 shows, fuel utilization is influenced by atmospheric air temperature, but the variation of the global microturbine performances is contrary with respect to the previously examined cases: the rise of air temperature causes the increase of the total fuel utilization.

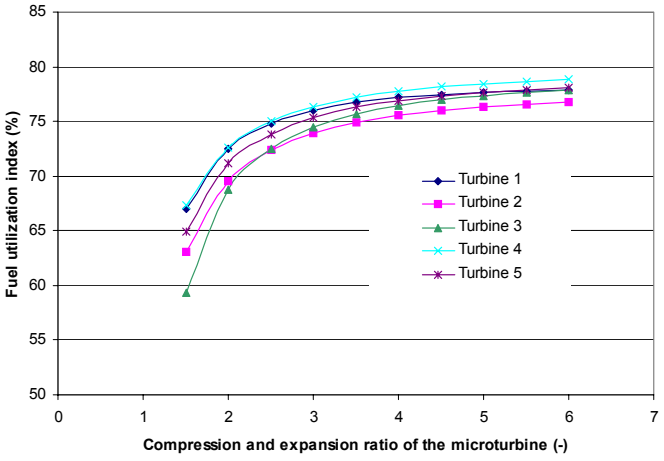

Figure 11: Fuel utilization as a function of compression and expansion ratio of microturbine

Figures 10 and 11 show the variation of the fuel utilization as a function of the gas turbine temperature and the compression/expansion ratio of the microturbine. The influence of these parameters on the microturbine fuel utilization is less important than the previously examined cases.

Considering the previous results together with the manufacturers' official data, the microturbine performances were calculated by means of TRIGEN 1.0. Figure 12 shows the results.

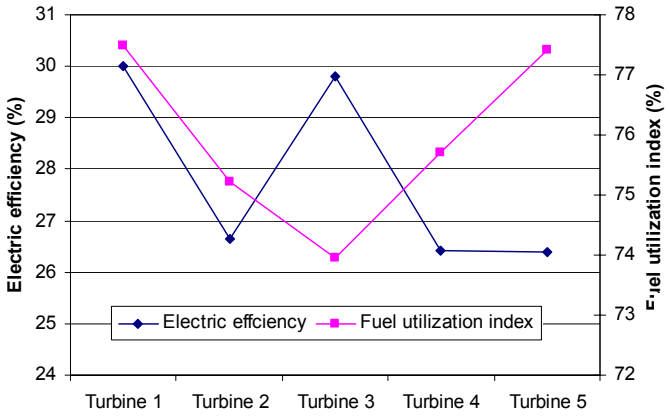

Figure 12: Performance of the microturbines

Turbine 1 is a very efficient system because it provides high electric efficiency and high fuel utilization index.

The other microturbines seem less efficient than the first one, as they show a lower electric efficiency or a lower fuel utilization coefficient.

It is important to note that the quality of a microturbine does not depend on electricity efficient and fuel utilization index only. Other features (as technical life, maintenance charges, reliability of a system, etc, not considered in this paper) are as much important as the considered parameters.

To develop this study, several parameters were considered, as the annual utilization coefficient of the microturbine, the average price of the electric, thermal and cooling energy on the market and the average price of the fuel.

The average price of the thermal and cooling energy can be expressed as a function of P_{fuel} as Equations 14 and 15 show.

$$P_{th} = \frac{P_{fuel}}{\eta_{burner} SHC_{fuel}} \quad (14)$$

$$P_{cool} = \frac{P_{th}}{COP_{hp}} \quad (15)$$

Where η_{burner}, SHC_{fuel} and COP_{hp} can be considered constants.

Taking into account Eq. 11, 12 and 13, *IS* results:

$$IS = UCM \cdot f\left(P_{el}, P_{fuel}, \dot{W}_{el}, \dot{W}_{th}, \dot{W}_{cool}\right) \quad (16)$$

As Figure 13 shows (case of turbine 1, other cases are similar) Eq. 16 can be written as Eq. 17.

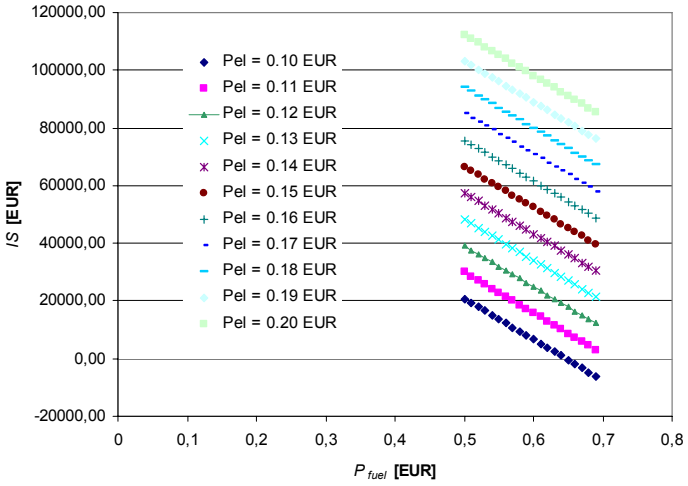

Figure 13: Investment saving (case of turbine 1)

$$IS = UCM\left[aP_{fuel} + b\right] \quad (17)$$

where:

$$a = f\left(\dot{W}_{el}, \dot{W}_{th}, \dot{W}_{cool}\right) \quad (18)$$

$$b = f\left(P_{el}, \dot{W}_{el}, \dot{W}_{th}, \dot{W}_{cool}\right) \quad (19)$$

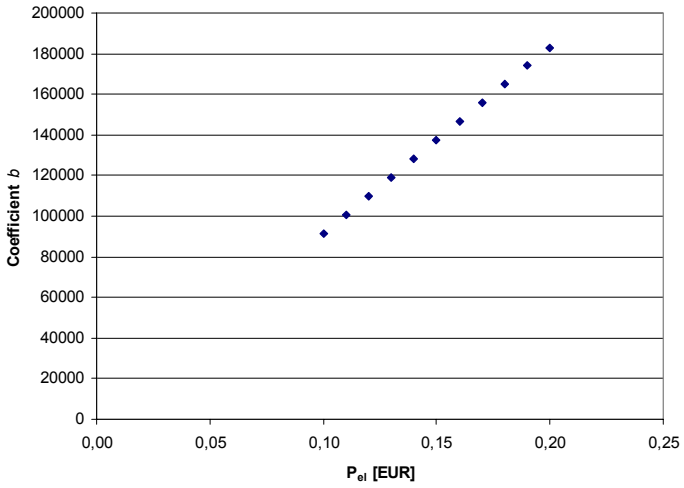

Figure 14: Coefficient *b* (case of turbine 1)

In similar manner, Figure 14 shows that Eq. 19 can be written as follows:

$$b = cP_{el} \tag{20}$$

where:

$$c = f\left(\dot{W}_{el}, \dot{W}_{th}, \dot{W}_{cool}\right) \tag{21}$$

and so:

$$IS = UCM\left[aP_{fuel} + cP_{el}\right] \tag{22}$$

Defined the power index as:

$$P_i = \dot{W}_{el}\eta_{el} + \left(\dot{W}_{el} + \dot{W}_{th} + \dot{W}_{cool}\right)FUI \tag{23}$$

the relationship between *a*, *c* and P_i is shown in the Figure 15.

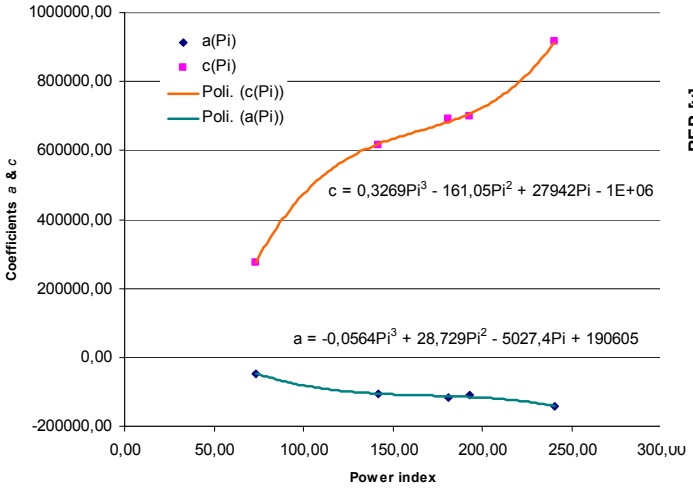

Figure 15: Coefficient *a* and *b* as a function of power index

Applying a third order polynomial regression to the coefficients *a* and *c*, Equations 24 and 25 were solved.

$$a = -0.0564P_i^3 + 28.729P_i^2 - \ldots \\ \ldots - 5027.4P_i + 190605 \tag{24}$$

$$c = 0.3269P_i^3 - 161.05P_i^2 + \ldots \\ \ldots - 27942P_i - 1037258 \tag{25}$$

Equations 10 and 22 allow to assume Equation 26.

$$BEP = \frac{C_m}{UCM\left[aP_{fuel} + cP_{el}\right]} \tag{26}$$

This mathematical model allows to calculate in a very simple way the microturbines' BEP, knowing the cost of the system (*CCA*), the efficiency of the microturbine (taking into account by coefficients *a* and *b*), the annual utilization coefficient of the microturbine (UCM), the fuel and electricity price on the market.

As example, Figure 16 shows the break even point in the case of the microturbine 1, supposing the UCM factor equal to 100% (BEP over 20 years is not shown).

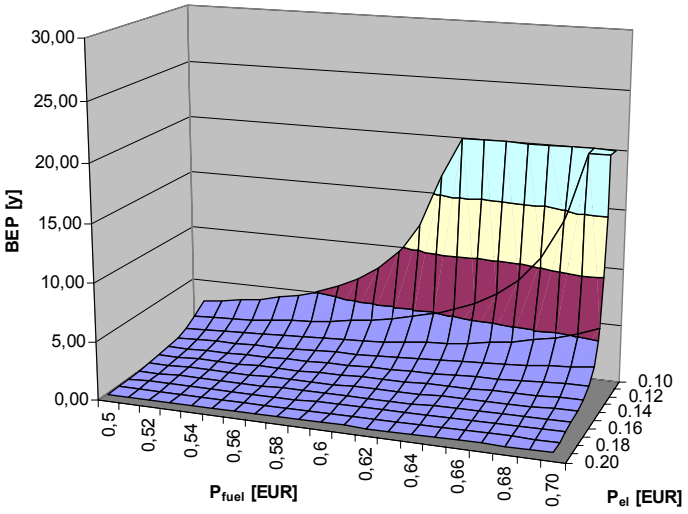

Figure 16: Break even point (case of turbine 1, UCM = 100%, BEP over 20 years is not shown)

CONCLUSIONS

A study of five commercial trigeneration systems that meet electrical, thermal and cooling demands has been carried out, examining their performance varying some working conditions, as atmospheric air temperature, temperature of gas turbine and compression and expansion ratio of microturbine.

The numerical simulations, performed by a software called TRIGEN 1.0, shown that the microturbine electric efficiency and fuel utilization are influenced in opposite manner by the atmospheric air temperature.

To improve the peak efficiency of a microturbine, temperature of gas turbine and compression/expansion ratio are parameters very important: in fact, for all examined microturbines, electric efficiency and generated power are almost directly proportional to the temperature of the gas turbine. Whereas, the compression/expansion ratio can have a very negative impact on the working parameter at low values.

As well, in the second part of this work a mathematical model was developed. This model allows to calculate in a very simple way the microturbines' BEP, knowing the cost of the system (*CCA*), the efficiency of the microturbine (taking into account by coefficients *a* and *b*), the annual utilization coefficient of the microturbine (UCM), the fuel and electricity price on the market.

The model is an efficient tool to decide, as first approach, if the CHCP Microturbines is a valid alternative respect to a more traditional solutions.

REFERENCES

[1] Bassols, J. Kuckelkorn, B., Langreck, J., Schneider, R., Veelken, H. *Trigeneration in the food industry*, Applied Thermal Engineering 2002; 22: 595–602.

[2] Apte, A. *Efficient and economical cold storages driven by ARP*, web site, 1999.

[3] Dorgan, C.B., Leight, S.P., Dorgan, C.E. *Application Guide for Absorption Cooling/Refrigeration Using Recovered Heat, American Society of Heating, Refrigerating and Air-conditioning Engineers* (ASHRAE), 1995.

[4] Bruno, J., Miquel, J., Castells, F. *Modeling of ammonia absorption chillers integration in energy systems of process plants*, Applied Thermal Engineering 1999; 19: 1297–1328.

[5] Colonna, P., Gabrielli, S. *Industrial trigeneration using ammonia–water absorption refrigeration systems (AAR)* Applied Thermal Engineering 2003; 23: 381–396.

[6] Ho, J.C., Chua, K.J., Chou, S.K. *Performance study of a microturbine system for cogeneration application*. Renewable Energy 2004; 29:1121–1133.

[7] Zhu, Y, Tomsovic, K. *Development of models for analyzing the load-following performance of microturbines and fuel cells*. Electric Power System Research 2002; 62:1–11.

[8] Campanari, S, Lozza, G., Bedogni S. *Microturbine a gas e pompe di calore*. Power Technology 2002; 30–39.

Proceedings of ECOS 2005
Trondheim, Norway
June 20–22, 2005

FIELD STUDIES OF DOMESTIC HOT WATER COMFORT IN SEMI-DETACHED HOUSES DURING SUMMERTIME

Tommy Persson* and Janusz Wollerstrand
Lund Institute of Technology
Department of Heat and Power Engineering
P.O. Box 118, SE-221 00 Lund
Sweden

ABSTRACT

The paper describes measurements performed in three district heating (DH) substations in semi-detached houses. In all these houses more than 40 % of the domestic hot water (DHW) tappings turned out to be shorter than 10 s. The fraction of total energy used to heat this water varied between 2.4 % and 10.2 %, indicating a large influence of households' daily habits. For 60-78 % of tappings, the total amount of supplied DH water volume was below 2.5 litres, which underlines the importance of using small volume pulses for the energy metering. When analysing the off-load behaviour of the DH substations it was established that radiator circuit control valves for the most part of the studied period were working on/off. During periods when there was no radiator load, the primary supply temperature was typically 50-60 °C, which was higher than expected. The differences in supply temperature level between the substations might be caused by leaking valves or by differences in off-load set point temperature of DHW control valves. Furthermore, the measurements indicate large differences among DHW controllers regarding the characteristics of the feed-forward control. In more than 80 % of the tappings with duration of more than 10 s, an outgoing DHW temperature of at least 40 °C was obtained within a maximum of 10 s. However, depending on the house studied, in 17-55 % of those tappings the monitored DHW temperature did not reach the level of at least 50 °C, as required by the Swedish District Heating Association.

Keywords: Domestic hot water, district heating, low-heat density areas, semi-detached houses

NOMENCLATURE

Abbreviations

CW	Cold water
DH	District heating
DHW	Domestic hot water
HEX	Heat exchanger
q	Flow, [l/s] or [m^3/h]
Primary	Referring to the DH system
Secondary	Referring to the house internal system
T	Temperature, [°C]
τ	Time, [s] or [h]

Subscripts

outdoor	Outdoor conditions
ret	Return pipe
prim	Primary
sup	Supply pipe
tap	Quantity referring to a tapping

INTRODUCTION

Due to heat losses the temperature will decrease in the supply pipes of a DH system. As a consequence of the lower heat load during summertime the supply temperature in peripheral parts of the system may become so low that an acceptable DHW comfort cannot be maintained. This especially is a problem in low-heat density areas, such as single-family house areas. Of special interest is how DHW controllers in DH substations behave during off-load. In order to investigate these issues measurements were performed in three semi-detached houses. The paper is a follow-up on previous theoretical work by the authors on DHW comfort in detached houses, [1,2].

*Corresponding author: Phone: +46 46 22 29273; Fax: +46 46 22 24717; E-mail: Tommy.Persson@vok.lth.se

DESCRIPTION OF THE STUDIED DH SUBSTATIONS AND MEASUREMENTS

Measurements were performed during summertime in the DH substations of three semi-detached houses connected to the DH system of the town Malmö in the southern Sweden. All of the studied DH substations are furnished with instantaneous DHW heaters equipped with self-acting, proportional and flow-compensated DHW controllers termed 'AVTQ' (manufactured by Danfoss A/S). AVTQ is the most commonly used DHW controller in single-family houses connected to Swedish DH systems. A detailed description of the AVTQ controller can be found in [2].

The three houses studied are labelled "House 1", "House 2" and "House 3". The households comprise two adults two children, two adults, and one adult, respectively. The houses are located in the DH system as shown in Figure 1. With respect to DH supply temperature House 2 and House 3 are better located than House 1, which is found at the end of a branch of the network.

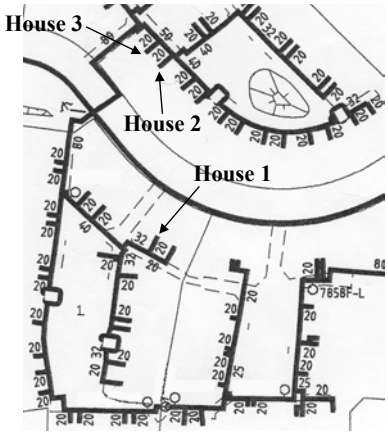

Figure 1 Location of investigated houses in the DH system

Analysed measurements were performed during months June-October of year 2004. The parameters monitored were: DH and DHW flows, DH supply and return temperatures, as well as cold water (CW) and DHW temperatures. The DH flow was measured using the existing flow meter already in place on the primary side, used for billing heat consumption. Since the measurements were performed during summertime and the study focuses on the DHW load, one flow meter on the secondary side was considered sufficient. The measurement set up is shown in Figure 2.

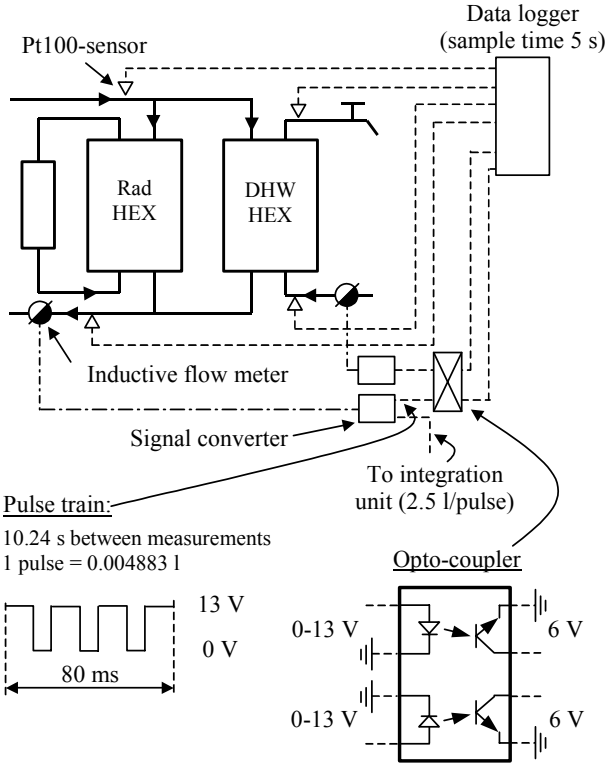

Figure 2 Measurement set up

All temperatures were measured with paired Pt100-sensors of the clamp-on type that were placed identically in all the DH substations. The DHW temperature was measured on the outside of the HEX outlet in which the AVTQ temperature sensor is installed. The Pt100-sensor was placed only a few centimetres from the HEX but not within its insulation. Both the primary side flow meter already in place and the supplementary flow meter were of the inductive type, which was found suitable for monitoring flow rates. Specifications for the flow meters are given in Table 1.

Table 1 Specifications for inductive flow meter, [3]

Property	**Value**
Start flow, q_{start}	0.003 m^3/h
Minimum flow, q_{min}	0.030 $m^3/h \pm 5$ %
Nominal flow, q_n	1.5 m^3/h
Maximum flow, q_{max}	3 m^3/h

The signal converter interprets the signal from the flow meter and sends a pulse to the integration unit at a resolution of 2.5 litres of flow volume. There is also a test pulse output that sends a pulse train every 10.24 s. Each pulse in the pulse train represents a volume of 0.004883 litres. This signal

was sent to the data logger using an opto-coupler interface. The latter provided galvanic insulation between the signal converter and the data logger, which minimised the risk of measurements causing disturbance to the signal used for energy metering.

All data were logged with a sample time of 5 s. This sample time was selected to be appropriate in relation to the response time of the temperature sensors and the limited data storage capacity. However, due to the sample time of the flow meters used, the effective sample time for the flow measurements is only 10.24 s. This relatively long sample time will introduce uncertainties when determining tapping lengths and flows. A typical result from a flow measurement during a tapping is displayed in Figure 3.

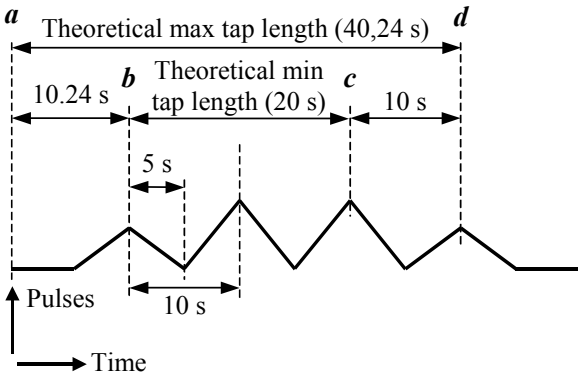

Figure 3 Illustration of typical result from a flow measurement during a tapping

To simplify the analysis the assumption was made that when two subsequent registered volumes are approximately of the same size, the flow has been constant during the studied period. Considering typical human behaviour and various aspects of system performance, such as the moderate pressure fluctuations in the CW system, the simplifying assumption made is considered to be acceptable.

For the case shown in Figure 3 it is known that no water has been drawn off prior to time ***b*** and after time ***d***. However, the tapping may have started anytime in the time interval ***a-b*** and may have ended within the time interval ***c-d***. Assuming that water is drawn off continuously during the period under consideration, the theoretical minimum and maximum tapping length can be expressed as:

$$\tau_{tap,min} = (N-2)\cdot 10 \text{ [s]}$$

$$\tau_{tap,max} = (N-2)\cdot 10 + 20.24 \text{ [s]}$$

Where: N = Number of registered values > 0 pulses

In order to limit the error caused by the sample time of the flow meter the tapping length in this work is estimated as the mean value of $\tau_{tap,min}$ and $\tau_{tap,max}$.

MEASUREMENT RESULTS

During the period studied almost 30 million data points were registered. Obviously, it is impossible to account completely for all data in the paper. In this section results derived from the measurements are analysed and discussed. The displayed results are examples of representative consumer behaviour as observed in the studied DH substations. When studying the results the reader should keep in mind how the measurements were carried out (as described in the previous section). Especially the sample times of the flow meters have a significant influence on the results.

Variation in domestic hot water consumption depending on social factors

The houses studied comprise three households with quite different composition. Consequently, it appears be of interest to investigate if there are any distinct differences between them concerning DHW use. In Figure 4 information about the DHW use in the three houses are shown.

The bars in the figure show how large part of the tappings during the studied period that are within the specified tapping lengths. Above each bar is accounted for how large part of the total energy usage these tappings represent. It should be noted that the last category contains all tappings longer than 125 s. The upper boundary for this category is determined by the longest tapping in each house. This value varies between 11-23 minutes. The DHW volume specified in Figure 4 is the water volume heated up at the DH substation. This water is mixed with fresh water at the taps and thus the volume of heated water leaving the taps will be greater than the specified DHW volume.

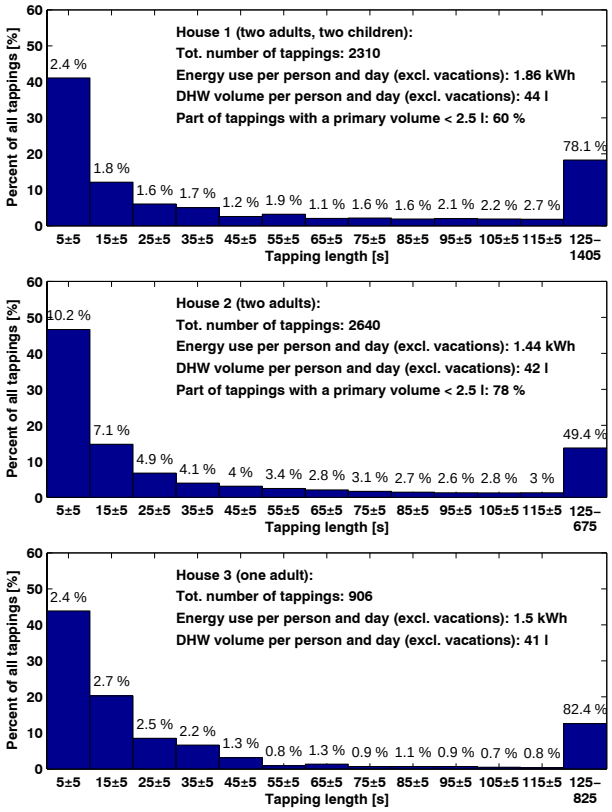

Figure 4 Characteristics for domestic hot water use in three houses

In the studied houses 41-47 % of all tappings are shorter than 10 s. In Houses 1 and 3 the part of the total energy required to heat this water is only 2.4 % while it is 10.2 % in House 2. For tappings longer than 125 s the situation is the opposite. While about 80 % of the total energy is required to heat the water at these tapping lengths in House 1 and 3, the corresponding value for House 2 is only 49 %. A possible explanation for is that on average more water is drawn off at tappings shorter than 10 s in House 2 than in the other houses (0.69 litres compared to 0.52 and 0.34 litres). This deviation may be caused by differences in habits between the households or by faucets with a larger capacity in House 2. Another possible explanation of the difference is that House 2 is only equipped with a shower while the other houses have a bathtub. This may increase the part of the energy used in long tappings since the energy required to fill up a warm bath is normally larger than the energy used when someone is taking a shower.

Excluding days when all members of a household were on vacation (= no DHW used) the energy use per person and day is greatest in House 1 (1.86 kWh) while it is approximately equal in Houses 2 and 3 (1.44 and 1.50 kWh, respectively). This could be caused by different habits and by the fact that there are children in House 1. A third possible explanation can be found by comparing the DHW volume prepared at the DH substation.

The energy used to heat each litre DHW is significantly larger in House 1 than in the other houses. This could be explained by the fact that the DHW temperature is generally higher in the substation in House 1 than in the other substations (see Figure 9). Thus, since the temperature of the fresh water entering the substations is about the same in all houses, either the household members of House 1 have a preference for warmer water than the persons in the other houses and/or they use larger amounts of hot water (note that the DHW is mixed with fresh water at the taps).

Finally, a comment should also be made regarding the accuracy of the energy metering used for billing purposes. In Houses 1 and 2 the primary flows were measured (but not in House 3). According to the measurements the total primary water volume passed during a tapping was below 2.5 litres, which is the pulse value sent to the integration unit (see Figure 2), in 60 % of the cases in House 1 and in 78 % in House 2. The energy used in these tappings corresponds to 6 % and 33 %, respectively, of the total energy used to prepare DHW in the two houses. Based on this it is obvious that the accuracy in the energy metering can be rather poor during summertime unless pulse volumes significantly smaller than 2.5 litres are used.

Domestic hot water controller behaviour during off-load

In Sweden, the heat load in residential areas with semi-detached houses, during summertime, is mainly caused by DHW preparation. If the DHW control valves only open when there is a DHW load, the DH flow in parts of the system will be very small from time to time, resulting in a low DH supply temperature. In consequence, waiting times until the DHW reaches an acceptable temperature during tappings might be long. For this reason the off-load behaviour of the DHW controller is of interest. According to the manufacturer's specification the AVTQ valve functions as a thermostatic valve with a set point

temperature of approximately 40 °C when there is no DHW load, [4].

In Figure 5 off-load behaviour in the studied sub-stations during the 14th of July is shown. All the households were on vacation on this day.

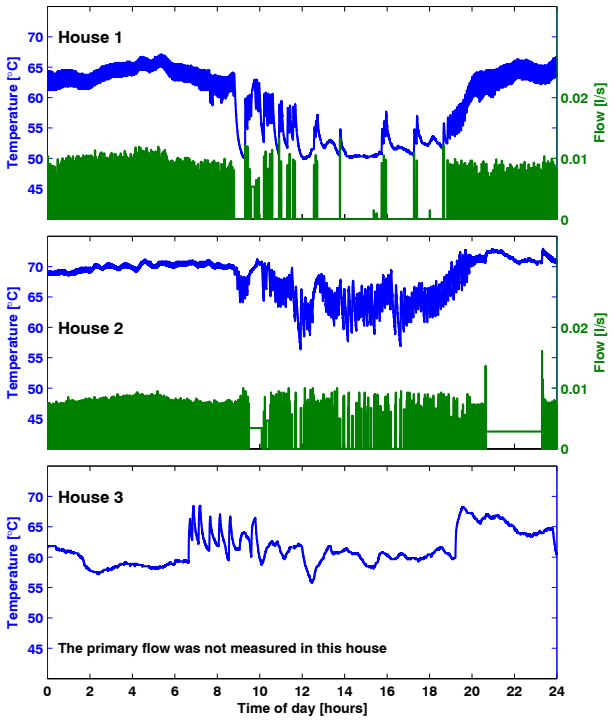

Figure 5 Off-load behaviour in three DH substations, the 14th of July. DH water supply temperature and flow are shown.

A DH supply temperature slightly above the off-load set point of 40 °C for the AVTQ should be expected. However, when studying Figure 5, three quite surprising phenomena can be observed:

1. The supply temperature is high compared to the off-load set point for the AVTQ.
2. In Houses 1 and 2 the supply temperature is 5-15 °C higher during the night than during daytime.
3. During most of the day the primary flows in Houses 1 and 2 show on-off behaviour with a rather high frequency (2-4 minute periods). When looking at the entire range of measurements, it becomes apparent that day-time flow fluctuations begin and end approxi-mately at the same time in both houses.

The explanation to these load behaviours can be found by studying the primary supply and return temperatures, and DHW and CW temperatures together with the outdoor temperature, Figure 6.

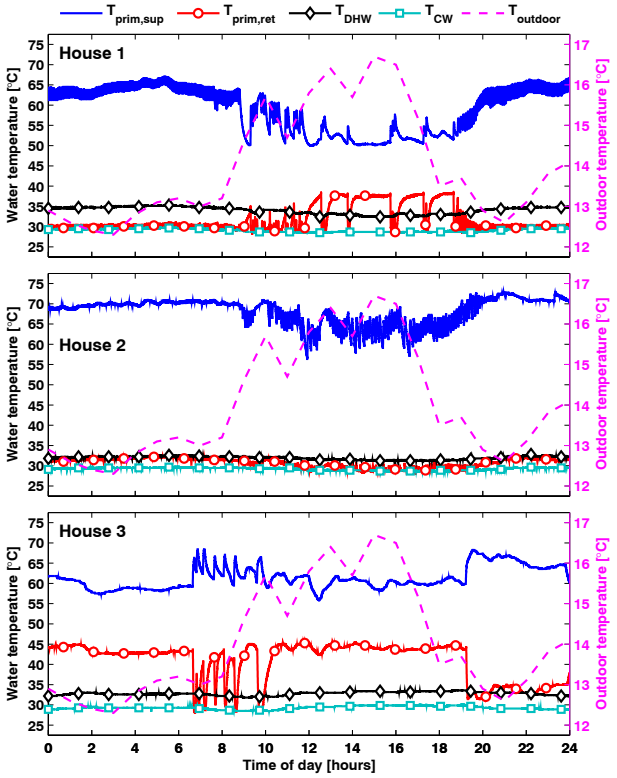

Figure 6 Outdoor temperature and primary and secondary temperatures corresponding to Figure 5

The frequency of the primary flow fluctuations in Houses 1 and 2 decreases between 9 a.m. to 7 p.m. when the outdoor temperature rises. Between 11.30 a.m. and 6.30 p.m. there is almost no primary flow at all in House 1 and the DH water supply temperature decreases, while there is still some DH flow present in House 2. According to Figure 6 these flow changes are closely correlated to changes in outdoor temperature. It is a general trend that the primary flow ceases at slightly lower outdoor temperatures in House 1 than in House 2.

Furthermore, during periods when a primary water flow is registered it is typically cooled off 35-40 °C as it passes through the substation. This is to be compared to a cooling of 10-15 °C when there is no registered flow. Apparently there is a flow in some of the secondary circuits that cools the primary water. However, the measured DHW temperature is only marginally influenced by the large changes in primary temperatures. In other words, the primary water does not pass through the DHW HEX.

The conclusion from this is that it is actually the space heating circuit that causes the observed primary flows. Unfortunately the primary flow was not measured in House 3 but the temperature variations indicate a similar behaviour in this house. Notice for instance in Figure 6 the temperature changes between 7 and 10 a.m. and the step-like temperature change at 19 p.m. in the bottom diagram. The primary temperatures also indicate that nighttime temperature set-back between 0 and 6.30 a.m. is employed in House 3.

The characteristic of the flow variations in Houses 1 and 2 proves that the radiator valves are working on/off. This causes wear of the valves and is therefore highly undesirable. The primary temperature variations in House 3 suggest that this valve to a much less degree is working on/off.

In Figure 7 off-load behaviour in the studied houses during the night between the 15th and 16th of August is shown. The outdoor temperature varied between 17 and 18 °C. During the studied period no primary or DHW flows were registered.

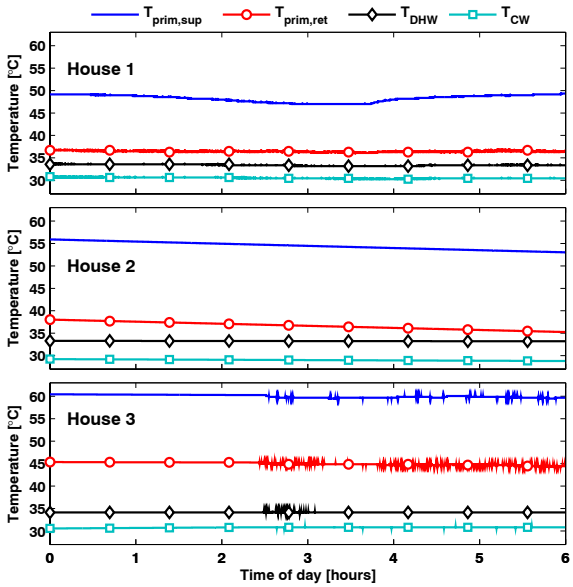

Figure 7 Off-load behaviour in House 1 and 3, the night between the 15th and 16th of August

Considering the high outdoor temperature, low supply temperatures, 47-60 °C, and a primary water cooling of 12-17 °C it can be stated that there is no space-heating load in the houses (compare with Figure 6). Notice the large differences in supply temperatures between the houses. A keyword in this context is that no primary flows were *registered*, which does not necessarily mean that there were no flows. According to Table 1 the flow meters used start to register flow at q_{start}=0.003 m^3/h. An estimation of the heat loss from new service supply pipes confirms that a primary flow lower than q_{start} can actually uphold the observed DH supply temperatures.

The registered DHW and CW temperatures only differ a few degrees among the various houses. Since there is no DHW flow the influence of the ambient temperature on the measured secondary temperatures will be large. The registered CW temperatures indicate that the air temperatures within the DH substations are approximately 30 °C. The registered DHW temperature is somewhat higher than the air temperature due to the fact that the temperature sensor is attached close to the AVTQ temperature sensor in the DHW HEX. However, due to heat losses both the AVTQ temperature sensor and the Pt100-sensor will register a DHW temperature that is lower than the temperature inside the HEX.

The real off-load set point temperatures can be estimated to be somewhere between $T_{sup,prim}$ and $T_{ret,prim}$. The differences in supply temperatures between the substations might be caused by differences in off-load set point temperatures or by leaking control valves.

Domestic hot water controller behaviour during tappings

Next, the controller behaviour during tappings will be studied. Due to the relatively large sample times of the flow meters used some details of the controller behaviours are lost. Still, some principal differences between the controllers in the studied houses can be observed. The flows have been reconstructed based on registered volumes.

Some representative controller behaviour patterns during tappings are shown in Figure 8. The temperatures before the tappings occur are seen to depend on the previously studied off-load behaviour of the controllers. Note that the uncertainty of when a tapping actually starts can introduce some obviously incorrect reconstructed flows. One example of this is that the primary flow starts 5 s before the first tapping in House 2 in Figure 8.

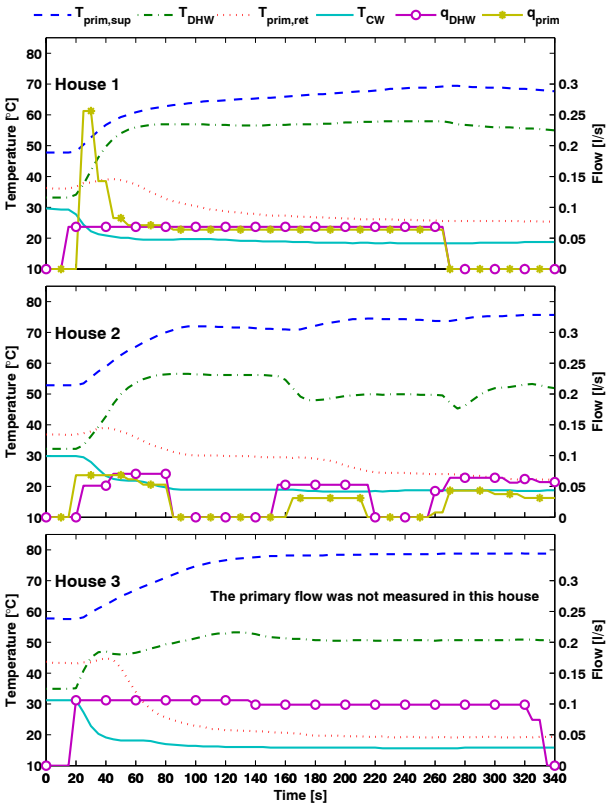

Figure 8 DHW controller behaviours during tappings, the 5th of August

In House 1 it can clearly be observed that the feed-forward control gives rise to an initially large valve opening, resulting in a large primary flow. As the DHW temperature increases the thermostatic part of the controller decreases the valve opening. In House 2 the influence of the feed-forward control cannot be noticed, and the initial primary flow is significantly lower than in House 1. This difference in controller behaviour can be observed during the whole measurement period. For instance the maximum tapping flow is 0.27 l/s in both houses while the maximum primary flow is 0.35 l/s in House 1 and only 0.17 l/s in House 2. A typical initial primary flow at a tapping is above 0.2 l/s in House 1 and below 0.1 l/s in House 2. Thus, the measurements indicate a relatively large variation in controller characteristics. This phenomenon has also been observed in laboratory testing of DH substations, [1].

According to Figure 1 it holds that Houses 2 and 3 are advantageously located in the DH system compared to House 1 with regard to supply temperature. The influence of this can be observed in Figure 8. Although the studied tapping in House 1 is 4 minutes long the supply temperature does not reach 70 °C while it in House 3 is nearly 80 °C.

It is hard to draw any definite conclusions regarding the set point of the AVTQ:s based on Figure 8. For this to become possible, the average DHW temperature at the end of tappings for the whole measurement period must be studied. The temperature partly depends on the tapping length and this has to be taken into consideration in order to make a fair comparison between the houses. In Figure 9 is shown the mean DHW temperature at the end of tappings with different lengths.

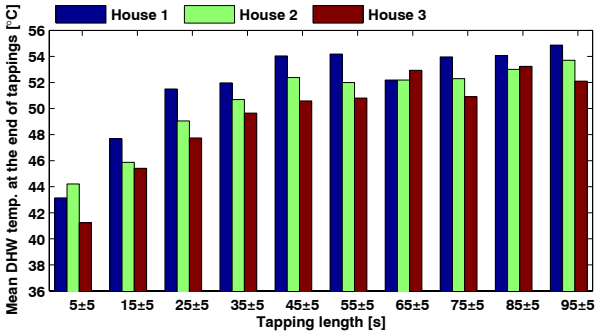

Figure 9 Average final DHW temperatures at different tapping lengths

Based on the information in Figure 9 it seems likely that the AVTQ set point is highest in House 1 and lowest in House 3.

Domestic hot water temperature at the district heating substation and DHW comfort

When opening a tap one expects water of sufficient quantity and temperature to be delivered. The purpose of the DHW controller is to secure that an acceptable temperature is obtained. Swedish authorities stipulate that the temperature at the tap in single-family houses should be above 50 °C (to secure a good DHW comfort and to avoid bacterial growth) and below 65 °C (to avoid scalds), [5]. If only temperature comfort is regarded most people find a water temperature of 40-45 °C to be sufficient, [6].

In Figure 10 is studied how long the delay is between the point when the tap is opened and when the DHW temperature at the DH substations reaches 40 °C, 45 °C and 50 °C, respectively. Note that only the temperatures at the substations, and not at the taps, are studied. Depending on the

distance between the heat source and the tap, the total time delay for the warm water to reach the tap can be significantly longer. This holds for any heat source and is not a problem related to DH. For short tappings it seems realistic to assume that the demand for a high DHW temperature is low. For this reason tappings shorter than 10 s are disregarded in the analysis in Figure 10.

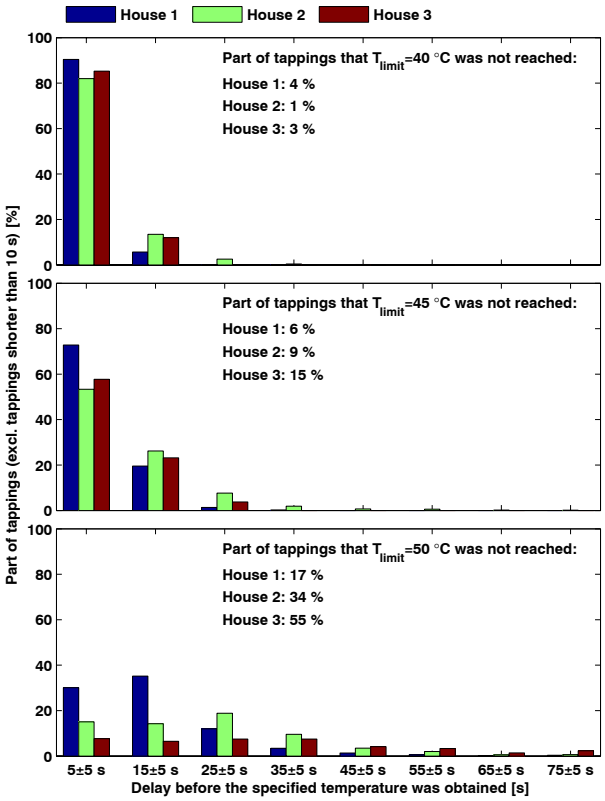

Figure 10 Waiting times before the specified DHW temperature is obtained at the substation

Considering the off-load primary supply temperatures shown in Figure 7 it is not surprising that a DHW temperature of 40 °C is obtained within 10 s in almost all tappings (the upper part of Figure 10). A DHW temperature of 45 °C is typically reached within 20 s, while the situation is considerably worse if the prescribed temperature of 50 °C is studied. This observation corresponds well to results from a theoretical investigation, [1]. In House 1 the DHW temperature reaches 50 °C within 30 s in 77 % of all tappings longer than 10 s, while in House 3 the corresponding figure is only 21 %. Furthermore, 50 °C is not at all reached in 17-55 % (depending on which house is regarded) of the studied tappings.

Next, let's study if the tappings when 50 °C is not reached have something in common that clearly distinguish them from other tappings. One possible explanation is that the DH system in itself causes the low DHW temperatures. For instance the DH parameters during some parts of the studied period may be disadvantageous considering the DHW control. A low supply temperature could potentially be the result of the low load during nighttime, causing long delays before warm primary water reaches the DH substation. However, when studying the distribution of the 'deficit' tappings in time, they do not clearly differ from other tappings.

Another explanation is that it is the characteristics of the tappings themselves that causes that 50 °C is not obtained. In Table 2 the 'deficit' tappings are compared to the average tappings regarding tapping length and volume.

Table 2 Information about tappings where 50 °C was not reached

House number	τ_{tap} = 10-20 s	Tapping vol. / Mean tapping vol.
1	84 %	0.86 l / 6.13 l
2	80 %	1.78 l / 2.55 l
3	81 %	1.16 l / 3.91 l

From Table 2 it is clear that most of the tappings have in common that they are short (shorter than 20 s) and that small volumes are drawn off. Due to this the warmer water in the DH mains simply do not reach the substation before the tapping has ended.

Finally, also the characteristics of the DHW controllers must be considered. With the large capacity of the DHW control valve in House 1 into consideration (see Figure 8) it is not surprising that the waiting times are shortest in this house despite its disadvantageous location in the system. This clearly shows the benefit with a feed-forward control that has a large influence on the initial position of the valve. The lower primary flows in House 2 causes longer waiting times. The relatively high off-load primary supply temperature in House 3 secures short waiting times if 40 °C and 45 °C are considered. However, the

low DHW controller set point (see Figure 9) causes a poor DHW comfort if 50 °C is considered.

CONCLUSIONS

The measurements proved that a large part (approximately 40 %) of all tappings are shorter than 10 s. The part of the total energy used to heat this water varied between 2.4 % and 10.2 %, indicating a large influence of the households' habits etc. The primary water volume consumed was below 2.5 litres in 60-78 % of the tappings, which illustrates the importance of using energy metering volume pulses that are significantly smaller than this value. The volume pulses in old flow meters, still installed in DH systems, are therefore often too large, resulting in inaccurate energy measurements. During periods with no DHW load, it was observed that the radiator control valves for the most part of the studied period were working on/off. This behaviour is undesirable considering wear of the valves and the increased temperature level in the return service pipe. The latter fact will result in unnecessarily high heat losses from the DH system during summertime. During periods when there was neither a DHW load nor a radiator load, the primary supply temperature was typically 50-60 °C, which is higher than expected. The differences in supply temperature might be caused by leakage or differences in off-load set point temperature of the DHW control valves. Large differences in feed-forward control behaviour were observed. For instance, at tappings the initial primary flow in the substation with the largest flow was about twice as large as in the substation with the smallest flow. The waiting time before a specified temperature is reached was typically shorter in the substation with a distinct influence of the feed-forward. This indicates that manufacturing tolerances of the valve might be improved. In general, however, feed-forward control works well when implemented in a DHW controller. When DHW is drawn off a temperature of 40 °C is typically obtained within 10 s in more than 80 % of all tappings longer than 10 s. Depending on which house that is studied, the temperature prescribed by Swedish authorities (50 °C) was not reached in 17-55 % of the tappings longer than 10 s.

ACKNOWLEDGMENTS

The authors would like to thank Mr Anders Lövdahl at Sydkraft AB who mediated the contact with the households in which the measurements were performed. Mr Lövdahl also installed the flow meters and temperature sensors. Our colleagues Peter Matsson and Per-Olof Johansson at the Department of Heat and Power Engineering assisted at the installation of the measurement equipment. The study was funded by the official Swedish district heating programme, which is cosponsored by the Swedish State and the Swedish District Heating Association.

REFERENCES

[1] Persson T, *District heating for residential areas with single-family housing -With special emphasis on domestic hot water comfort*, PhD thesis to be defended in June 2005, Department of Heat and Power Engineering, Lund Institute of Technology, Sweden, 2005

[2] Persson, T., *Tappvarmvattenreglering i fjärrvärmecentraler för småhus [Domestic hot water control in district heating substation for single family houses]*, Licentiate thesis, Department of Heat and Power Engineering, Lund Institute of Technology, Sweden, 2002

[3] Product information from HG International, inductive flow meter SVMI1

[4] Danfoss A/S, product catalogue for AVTQ, *http://www.danfoss.com*

[5] *Fjärrvärmecentralen -Utförande och installation [The district heating substation -Design and installation]*, Svenska Fjärrvärmeföreningen, FVF F:101, Svenska Fjärrvärmeföreningens Service AB, 101 53 Stockholm

[6] Wollerstrand J, *Tappvarmvattensystem - egenskaper, dimensionering och komfort [Domestic hot tap water systems - characteristics, sizing and comfort],* FoU 2002:75, Svenska Fjärrvärmeföreningens Service AB, 2002

Proceedings of ECOS 2005
Trondheim, Norway
June 20–22, 2005

ENERGY AND COST ASSESSMENT OF MICRO-CHP PLANTS IN HIGH-PERFORMANCE RESIDENTIAL BUILDINGS

Benoit Sicre[1] and Andreas Bühring
Fraunhofer-Institut für Solare Energiesysteme ISE
Heidenhofstr. 2
79110 Freiburg, Germany

Bernd Platzer
Technische Universität Chemnitz
Fakultät für Maschinenbau
Professur Technische Thermodynamik
09107 Chemnitz, Germany

Karl Heinz Hoffmann
Technische Universität Chemnitz
Institut für Physik
Theoretical Physics especially Computational Physics
09107 Chemnitz, Germany

ABSTRACT

Recently, efforts have been made to scale down some types of Combined Heat and Power (CHP) plant technology, such as fuel cells, gas turbines, Stirling engines or organic Rankine cycles, in order to adapt them for residential applications. The driving force for this is the high overall thermal efficiency and the low associated GHG emissions. Beside this, distributed power generation is expected to alleviate partially the issue related to the general rise in electricity demand. However, as micro-CHP have only modest electrical conversion efficiencies, the effective exploitation of the thermal output is critical to realising high levels of energy efficiency and the associated environmental benefits. The heat-to-power ratio of currently available micro-CHP units (in the best case approx. 2 to 1) compares poorly with the heat-to-power ratio of high-performance buildings (on average 1 to 1 according to recent construction practice).
The present paper considers the building and the heating, ventilating, and air-conditioning (HVAC) system (including the micro-CHP) and the resident's heat and power patterns as a whole, taking into account their inherent interactions. First, it describes new simulation tools which were developed to balance the production and the consumption of both heat and electricity in terms of both energy and costs. Computations based on Solid Oxide Fuel Cells (SOFC) and Stirling engines are discussed. Second, these technologies are compared in terms of primary energy consumption and costs to competing technologies such as condensing gas boilers. Third, the role of the appropriate level of thermal insulation for the building as a compromise between building heat losses and overall primary energy efficiency, including electricity supply, is discussed.
Keywords: micro CHP, building, fuel cell, stirling engine, primary energy, retail costs

[1] Corresponding author: Phone: +49 761 4588 5291 Fax: +49 761 4588 9000 E-mail: sicre@ise.fraunhofer.de

INTRODUCTION

Local and global environmental issues, the steady rise in costs for crude oil and natural gas, people's expectation of comfort, cosiness and automation and the changes in the commercial and political framework lead to the need to conceive cost-effective buildings with highly reliable, low-energy building services.

In Europe, on average, one third of the end energy is consumed in the building sector, especially for space heating. The first step taken to address this form of energy usage was to reduce the specific heating load of buildings by increasing their thermal insulation and by rendering the building envelop more air-tight to reduce heat losses by natural ventilation (due to wind pressure and cracks in the wall). New high-efficiency construction standards arose, such as the 3-litre house (3LH) with a heating load ceiling at 30 kWh/(m² a). The passive-house (PH) standard is even stricter with a ceiling at 15 kWh/(m² a). This kind of housing typically requires low-temperature heat that can be supplied in an efficient way by a compact heat pump. Heat pumps are high-performance heat suppliers because they take heat from the environment and transfer it to the house, but they generally require electric power to do their job (compression heat pumps). Therefore, running the heat pump will add to the domestic electric bill and will put even more strain on the local electric grid.

The second step was to develop supply systems able to meet energy loads of all kinds in the building. These are basically electricity, heat and, to a lesser extent, cooling. Micro-Combined Heat and Power (mCHP) systems arose from the scaling-down of reliable CHP technologies such as fuel cells, Stirling engines, reciprocating engines and micro-turbines. However, as mCHP systems have only modest electrical conversion efficiencies, effective exploitation of the thermal output is critical to realising high levels of energy efficiency and the associated environmental benefits. Designing and operating a building-integrated cogeneration system that delivers useful thermal output, however, is a complex task due to the strong coupling between the cogeneration unit, other HVAC components, and the building's thermal and electrical demands. The volume and thermal characteristics of the storage tank, the occupant's electrical usage patterns, the house's thermal characteristics, and the prevailing weather, all influence whether this thermal energy will be exploited or wasted.

This paper intends to assess the feasibility of coupling high-performance residential buildings with mCHP systems in terms of energy conservation and of costs. The scope of the work is restricted to single-family buildings and mCHP systems with an electrical output power of less than 5 kW. First, the energy requirements and load patterns of high-performance buildings will be described. Second, the specifications of mCHP for residential applications will be explained. Third, models for fuel-cell mCHP and Stirling mCHP will be detailed briefly and the results gained from whole-year simulation will be presented. Performance of mCHP will be compared to conventional heaters like condensing gas boilers (cGB) within a benchmark analysis. Finally, the issue of building thermal performance versus energy conversion technology will be addressed with regard to the simulation results.

Nomenclature

E	Expense
M	Amount
n	Primary energy conversion factor
P	Primary energy
SUBSCRIPT	
el	Electricity
NG	Natural gas
SUPERSCRIPT	
Exp	Export
FC	Fuel cell
GB	Auxiliary gas burner
Imp	Import

HIGH-PERFORMANCE BUILDINGS

A new trend in construction practice arose from concerns about fuel scarcity and environmental protection: Buildings must guarantee comfort with as little energy as possible even during cold winters. This demand can be met by enhancing the thermal performance of the building envelope and by smarter usage of solar input through the windows. Heat losses through the envelope arise

when heat flows through the external walls and cold outdoor air enters the house due to wind pressure. The first issue can be alleviated by making the thermal insulation layer of the external walls thicker, while the second issue is counteracted by rendering the walls air-tight. The passive-house construction standard arose from the offset between the benefits due to lower energy bills and the additional costs due to extra thermal insulation. The optimum is found for a specific heat load of approx. 15 kWh/(m² a). Below this value, there is no longer any need for room-based heating equipment such as radiators, as the heat can be distributed by using hot air that is circulated by the central mechanical ventilation system with heat recovery (more details in [1]). The heat recovery considerably decreases the energy demand for heating. However, it adds strongly to the overall investment costs of the house and significantly prolongs the payback time of the additional equipment. In addition to this, the HVAC system requires a heat supplier with extra-low power output (the total thermal output for an average free-standing house does not exceed 1.5 kW), which prohibits the use of low-cost gas boilers. Instead, expensive small-scale exhaust air heat pumps, that are not mass products, have become a standard [2].
As a result of this dilemma, the 3-litre house construction standard, that draws on the concept of higher energy costs but lower capital costs, has become established on the marketplace. This standard puts a ceiling at a heat load of 30 kWh/(m² a). In this case, radiators or floor radiation systems are necessary, but low-cost exhaust air ventilators replace the expensive ventilation system with heat recovery. Heat is preferably provided by low-priced boilers, but compact heat pumps can also be used.

MICRO-CHP SYSTEMS FOR RESIDENTIAL APPLICATIONS

Benefits and sales expectation

In the meantime, new systems with similar output power, producing not only heat but also electricity from the same fuel, are emerging on the market place. These are known as micro-Combined Heat and Power. The concurrent production of electricity and heat from a single fuel source can reduce primary energy consumption and associated GHG emissions. Reductions in combustion by-products such as nitrogen oxides and hydrocarbons are also a possibility. The distributed generation nature of the technology also has the potential to reduce electric transmission inefficiency (the European Commission estimates that transmission and distribution losses amount to an average of 6% of the electricity transported in the EU [3]). Since the device can partly meet the power demand of the household [4], mCHP may be able to alleviate utility peak demand problems and the need for grid reinforcement caused by the general rise in electricity demand. 40 million homes in 15 countries of Europe are said to be suitable for mCHP systems [5]. Sigma Elektroteknisk of Norway estimates a yearly market potential for mCHP of some 800,000 units per annum only in Europe [6]. Leading contenders for building cogeneration include fuel cells, Stirling engines, reciprocating engines and micro-turbines.

System sizes

As a result of a statistical survey carried out in England, stating that the power consumption of an average household amounts to approx. 1 kW as a daily average, two different output power categories have become established on the marketplace so far. These are units with a nominal output power of around 1 kW for usage in free-standing houses and 5 kW output power for medium-density housing with central heating. Since the specific internal consumption of the balance-of-plant components diminishes significantly with the size of the plant, larger units ought to display better efficiency. However, issues related to heat storage and distribution may annihilate the benefits of size. One can observe that the nominal power-to-heat ratio currently varies from 1 to 10 (i.e. steam engine systems) up to approx. 1 to 2 (fuel cell system) depending upon the core technology of the mCHP plant. Since effective usage of the heat released is critical to achieving high levels of energy efficiency, the plant should be chosen judiciously to match the heat load of the building well,

bearing in mind that system costs depend strongly on the core technology inside.

Marketplace

Moreover, mCHP must compete against more traditional types of technology such as cGB, wood/oil furnaces, district heat, distributed electricity and renewable energy converters such as solar thermal energy, photovoltaics and small-scale wind mills. If mCHP wants to gain a share of the marketplace, it must show proven economical and environmental benefits. There are three main reasons why now is the right moment for mCHP. First, new commercial possibilities are arising simultaneously with the liberalisation of the European energy markets, which are stimulating radical changes to the thinking about energy production. Second, environmental pressures to minimise CO_2 emissions are mounting, accompanied by governmental financial incentives. Third, the technology is becoming available. All over Europe, energy distribution and supply companies have expressed interest in mCHP, as a way to gain new customers or retain previously captive customers. Furthermore, mCHP can be used not only in new buildings but also in old buildings that have been retrofitted according to current building thermal standards.
As a conclusion, designing and optimising a mCHP system with regard to energy and overall costs is a complex task, that requires dedicated computational tools.

SYSTEM MODELLING

The SOFC-mCHP

The SOFC generally operates between 800 and 1000 °C and belongs to the category of high-temperature fuel cells. At this temperature, the solid ceramic electrolyte is able to conduct ionised oxygen molecules. At the same time, hydrogen is oxidised at the anode, liberating electrons which flow via an external circuit to the cathode. When fuelled with natural gas, hydrogen is gained from reforming the hydrocarbons with steam. While electricity can be obtained at the cell's poles, useful heat is produced from cooling down the flue gas of the cell.
This study has been carried out by using characteristic curves presented in [7]. Dynamic features gained from the detailed model can be found in [8]. Parameters of the model are given in Table 1. Efficiency hypotheses were taken from [9]. It has been assumed that the SOFC system can be modulated in the range between 20 and 100% of the nominal electric power. Below 20%, the SOFC is led to the hot-standby mode where it produces neither electricity nor useful heat. The fuel consumption in hot standby is dictated by the heat losses of the stack at around 1000 °C. These amount to approx. 200 W fuel (lower heating value LHV).
An additional gas burner backs up the SOFC when the heat load is large.

Nominal net power output	1000 W
Warm-up time for the stack initially at room temperature	8 hr
Thermal losses of the thermal jacket of the stack	0.16 W/K
Maximal load variation rate	55 W / min
Electrical efficiency at nominal power (LHV)	29.5%
Thermal efficiency at nominal power (LHV)	50.5%

Table 1: : Parameters of SOFC characteristic-curve model

The Stirling mCHP

Stirling engines operate according to the principle that when heat is provided to a gas, it expands and when heat is removed, the gas contracts. Cyclic supply and removal of heat can put a piston into motion. The piston rod is connected to a crankshaft that drives a power generator.
The Stirling mCHP system has been described using a dynamic characteristic curve. The data intends to describe a commercial system that could be available by 2010 on the German market. The mCHP system is considered as a package with a 1 kW_{el} Stirling engine and an additional gas burner. With the German market in mind, a machine with a rather high electrical efficiency

was suggested (about 25%). The parameters used in the simulations are presented in [10]. These characteristics assume that the mCHP unit is equipped with an exhaust gas/cooling medium heat exchanger, where steam contained in the flue gas condenses. The flue gas is expected to exit the CHP unit at a temperature around 50 °C. The overall thermal efficiency was assumed to be 95%. The electrical and thermal response time at 63% of the set value is approx. 60 seconds for electrical power and 100 seconds for thermal power.

HVAC system and building model

The HVAC system consists essentially of a pressurised water heating system. It is illustrated in Fig. 1. In order to optimise the operation cycle of the mCHP, a large heat storage tank of 750 liters has been foreseen. Domestic hot water is produced from a flat-plate heat exchanger. The temperature setting is 45 °C. The seasonal variation of water inlet temperature is taken into account. The quantity for hourly consumed domestic hot water (DHW) has been derived from a statistical study. Depending on the thermal insulation of the building, hot air (PH) or radiators (3LH) have been used for heat redistribution in the room (heating loop). The setting for the room temperature is 20 °C.

The space heating load is computed using a multiple-zone building model describing the thermal behaviour of an free-standing house. Details can be found in [11]. The building is located in the Frankfurt area. Parameters of the model can be found in Table 2.

The mCHP unit is thermally controlled. If the temperature in the storage tank is below a set value, then the mCHP will be operated until the temperature rises above an offset value. When the heating load has been met, case A: the SOFC is switched to the hot stand-by mode or case B: the Stirling engine is switched off. When it is operated, the mCHP concurrently produces electricity that is intended to cover the household electricity load. At some time of the day, the mCHP may produce more electricity than consumed by the household. The surplus is sold to the grid utility. When self-generation is not enough to cover the needs, electricity can be bought from the utility.

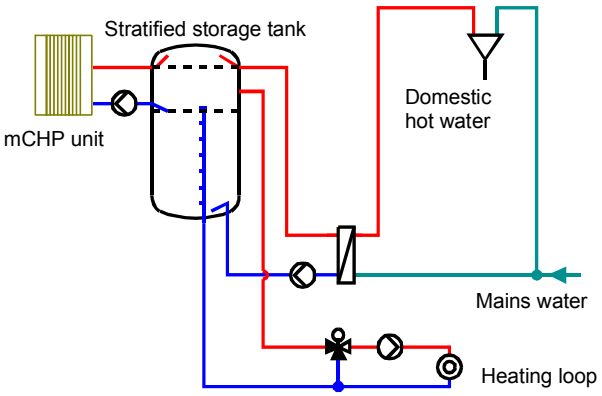

Fig. 1: Schematic diagram of the HVAC system

A two-way metering system enables separate billing according to the rates of Table 3. Costs are recovered and profit is generated by a mCHP through the electricity exported. However, electricity reaches its highest monetary value when it is used directly in the house (substituting the electricity that would have been bought from the grid) since resale of the electricity produced is at a lower price (about 8 c€/kWhe in Germany). The latter price consists of a bonus (5.11 c€/kWh$_{el}$, defined in a law) plus the price of the electricity traded on the wholesale market.

Building type		3LH	PH
Space heating load	KWh/(m²a)	29	11
Floor area	m²	118	118
Household electricity	MWh/a	5.5	5.5
Water heating	MWh/a	2.6	2.6

Table 2: Annual energy comsumption of different building services

Energy	Pricing
Natural gas	3.8 c€/kWh (LHV)
Electricity from the grid	13 c€/kWh
Electricity exported to the grid	8 c€/kWh

Table 3: Pricing of energy according to [9] (without VAT)

SIMULATION RESULTS AND PERFORMANCE BENCHMARK

In order to handle electricity and natural gas on the same basis, the consumed energy amounts have been transformed into their corresponding amount of primary energy. For natural gas, the primary energy factor equals 1.1 and for grid electricity 3 (both referring to the national average for Germany). Equation 1 illustrates the primary energy balance of the building. The total primary energy expenditure equals the sum of primary energy in the form of natural gas for the prime mover and for the auxiliary burner of the mCHP, and in the form of electricity that is imported from or exported to the grid .

$$\begin{aligned} P_{total} &= P_{NG}^{FC} + P_{NG}^{GB} + P_{el}^{Imp} - P_{el}^{Exp} \\ &= n_{NG}\left(M^{FC} + M^{GB}\right) + n_{el}\left(M_{el}^{Imp} - M_{el}^{Exp}\right) \end{aligned} \quad (1)$$

A similar balance can be established for monetary costs for energy supply to the building (see equation 2).

$$E_{total} = E_{NG}^{FC} + E_{NG}^{GB} + E_{el}^{Imp} - E_{el}^{Exp} \quad (2)$$

Whole-year simulations have been run for the 3LH and PH building with the same boundary conditions (DHW load, electricity load, geographic location). First, it turns out that the thermal power output of both mCHP systems is enough to cover the thermal needs of the building. The auxiliary gas burner has only safety-of-supply function and could easily be replaced by a low-cost electric heating element in the storage tank. Second, due to the low heating load of the building, the operation time of the mCHP's does not exceed 3000 hr/a. Therefore, a large proportion of the household electricity must be bought from the utility grid. This adds strongly to the primary energy balance and to the costs.
In order to assess the financial viability of mCHP in high-performance buildings, a conventional cGB with 7 kW thermal output and 100% overall thermal efficiency was chosen as the baseline product, while electricity is bought completely from the utility. In a further step, the cGB was coupled to solar thermal collectors with 5 m² absorber area in order to reduce the natural gas consumption without reducing comfort. Fig. 2 shows the results of the benchmark analysis in terms of primary energy expenditure.

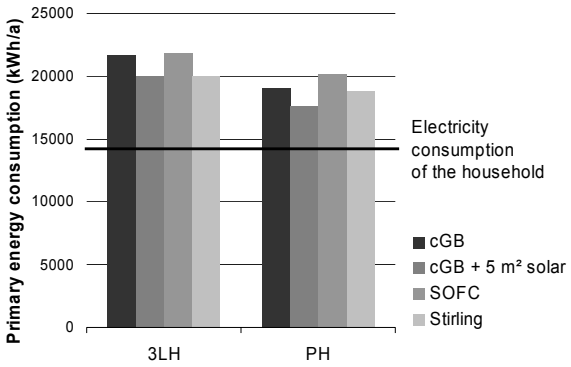

Fig. 2 : Primary energy consumption of the building vs. the thermal insulation standard and the energy conversion system

The electricity consumption of the household accounts for the major part of the energy consumption. DHW production and room heating account approx. for ¼ of the total. Fig. 2 illustrates as a result that even if the space heating load of the 3LH is more than twice as high as that of the PH, its overall primary energy consumption increases only by 10% on average.
In the case of 3LH, the lowest primary energy consumption is achieved by both the pair cGB + solar collector and by the Stirling- mCHP. The Stirling yields better results than the SOFC because it features higher thermal efficiency and no hot-standby consumption.
In the case of PH, the pair cGB + solar performs the best. The reason why the Stirling can not perform better is the lack of heat demand (i.e. short operating time). The Stirling engine is not able to compensate its comparatively poorer efficiency with electricity export to the grid. The SOFC performs worst mainly because of the hot-standby consumption.

Financial aspect

Operation and investment costs are the major issues affecting commercial success and wide market uptake of mCHP. Since mCHP technologies are in an early phase of development,

retail prices are not known yet. For most mCHP manufacturers, the allowable retail price for their product is a major concern. The allowable price is defined as the upper limit at which the mCHP can be offered in order that the customer gets the same benefit as if he used the baseline technology. The income drawn from electricity export or household electricity substitution plays the major role and helps to offset the additional costs due to the more complex technology. As shown in Fig. 3, the allowable retail price for the mCHP device is derived from the accumulated difference of annual total costs over a period of 15 years (expected lifetime of the mCHP).

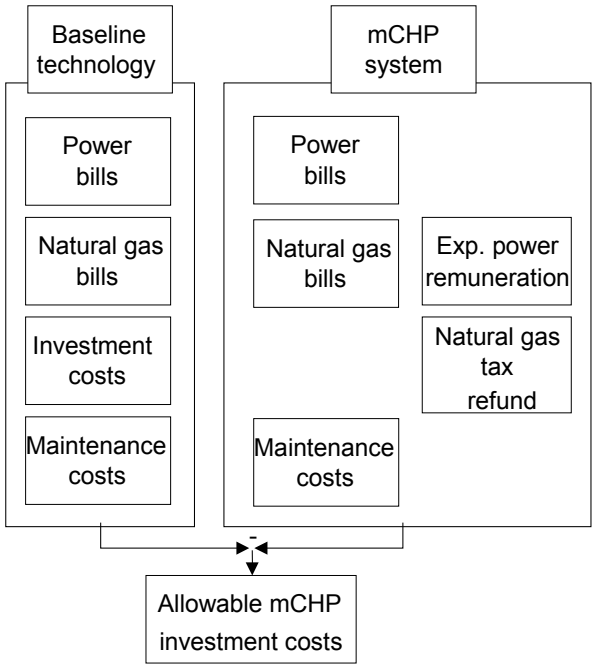

Fig. 3: The annual allowable investment costs for the mCHP are derived from the difference between the annual total costs of the baseline system and the mCHP

Simulation results such as fuel consumption, running time of the mCHP and the amount of exported or imported electricity serve as input for the operation costs. The retail price basically depends upon the technology employed and upon the specification of the building. The final computation results are found in Table 4. The computation details are documented in [4].

Considering the investment costs for a conventional cGB (on average, 3100 EUR on the German market), it makes no sense to propose SOFC-mCHP products for high-performance houses, since the allowable retail price is much too low. SOFC-mCHP units fit much better in non-refurbished houses. In the case of the Stirling-mCHP, the sales margin depends strongly on the actual production costs, especially the manufacturing costs of the complex and heavy Stirling engine unit.

	3LH	PH
SOFC-mCHP	2372	1956
Stirling-mCHP	4536	3901

Table 4: Allowable retail prices (in EUR) in comparison to the currently standard option (a split supply consisting of power taken from the local grid and heat from a condensing boiler). The higher the allowable cost, the bigger the margin for the manufacturer, while the customer's benefit remains the same.

Thermal insulation vs. overall primary energy consumption

It is straightforward to conclude that mCHP units better suit poorly insulated buildings, since more electricity can be generated. However, one should bear in mind that the primary energy bonus obtained when exporting CHP electricity to the grid depends strongly upon the local efficiency of the grid. Subsequent investigations [4] have shown that approaches like building refurbishment and use of solar-assisted cGB may lead to greater energy conservation than use of mCHP in non-refurbished building stock houses (this is even true for countries with relatively little solar radiation). Both facts, steadily rising crude oil and natural gas prices and mass production, are expected to cause a rise in the cost-effectiveness of solar thermal systems, so that they can further compete on the marketplace.

CONCLUSION

The paper presents a method to assess energy supply systems for buildings in terms of energy

conservation and monetary costs. The method was illustrated by handling the case of two innovative micro-CHP technologies together with high-performance buildings. Based on whole-year simulations involving dedicated mCHP models and a multiple-zone building model, the energy benefits have been evaluated via a benchmark analysis. Since mCHP technologies are in an early phase of development, retail prices are presently not known. The allowable retail price gives the manufacturer an indication of how expensive his product may be, in order that the customer gets the same benefit as if he used conventional technology.

Computation results indicate that mCHP roughly achieves the same degree of energy conservation as modern high-efficiency technologies such as condensing boiler and electricity taken from the modern public grid. However, the low heat load leads to reduced operating time and therefore to little generation of electricity. As a result, the allowable retail prices turn out to be rather low or even prohibitive.

In order to access the market of high-performance buildings, manufacturers must definitely improve the electrical performance of their units. One way to do this is to significantly lower the parasitic power consumption of the balance of plant. This can be achieved when the mCHP is judiciously integrated into HVAC systems especially developed for high-performance houses. Fraunhofer ISE is presently delving into that topic.

REFERENCES

[1] Badescu V, Sicre B. *Time-Dependent modelling of the heating demand for three-zone passive houses*. In: Proceedings ECOS Conference:560-568; Berlin, 2002

[2] Buehring A. *Development and measurements of compact heating and ventilation devices with integrated exhaust air heat pump for high performance houses*. In: Proceedings 8th IEA Heat Pump Conference, Las Vegas, 2005

[3] Cogen Europe. *An introduction to Micro-Cogeneration; Briefing 8*, 1999. See also http://www.cogen.org/Downloadables/Publications/Briefing%20MicroCHP.pdf (Last visited: 25/01/04)

[4] Sicre B. *Sustainable energy supply to very-low-energy buildings by means of CHP technologies and solar thermal energy*; PhD thesis at the Chemnitz University of Technology, In German, 2004

[5] Future cogen *The future of CHP in the European Market; Final report of the European Cogeneration study*, 2001 See also http://tecs.energyprojects.net/ (Last visited: 25/01/04)

[6] Kolin S. *The Stirling engine in micro cogeneration - Some crucial application and market issues*. In: Proceedings of the 10th international Stirling Engine conference 2001, Osnabrück, September 2001.

[7] Sicre B, Ullah S, Buehring A. *An Energy economic Assessment of Solid Oxide Fuel Cell Applications in Residential Buildings.* In: Proceedings of the TRNSYS Usertag 2004; Stuttgart; 2004

[8] Sicre B. *Development of a model for small-scale SOFC cogeneration plants for heat and power supply in residential buildings*. In: Proceedings of the TRNSYS Usertag 2003; Stuttgart; 2003

[9] Krewitt W, Pehnt M, Fischdick M, Temming H(Editors). *Brennstoffzellen in der Kraft-Wärme-Kopplung - Ökobilanzen, Szenarien, Marktpotenziale*. Stuttgart: Erich Schmidt Verlag, In German, 2004

[10] Sicre B, Henckes L. *Environmental impact and economical potentials of small-scale Stirling-CHP units for distributed heat and power supply to residential buildings*. In: Proceedings of the international Stirling engines conference ISEC, p. 185-195, Rom; 2003

[11] Ullah S. *Integration of a Solid Oxide Fuel Cell System into a Compact Ventilation System for supplying Heat and Power to Passive Houses*. Master's Thesis at the University of Applied Sciences, Offenburg, 2004

Proceedings of ECOS 2005
Trondheim, Norway
June 20–22, 2005

CONTROL OF SUPPLY TEMPERATURE IN DISTRICT HEATING SYSTEMS WITH MULTIPLE SUPPLY POINTS

Torben Skov Nielsen* **and Henrik Madsen**
Technical University of Denmark,
Informatics and Mathematical Modelling,
DK-2800 Lyngby
Denmark

Lars Gottlieb
Seven Technologies A/S
Bregnerødvej 94
DK-3460
Denmark

Abstract

The paper describes a new concept for controlling the supply temperature in district heating systems using stochastic modelling, prediction and control combined with physical modelling. The method is well suited for district heating systems with more than one supply point and possibly with different production costs. The new controller minimises the heating and pumping costs under the restriction that the consumer requirements to inlet temperature are fulfilled and that the flow rate in the system is kept within acceptable limits. The controller closely resembles the Model Predictive Control scheme allowing the restrictions to be incorporated directly into the control problem. At each time-step a linearisation of the system around the current operating point is derived using a physical network model to simulate the system response to changes in the supply temperatures. Based on the linearised system the optimal control sequence is then found by solving a linear programming problem defined such that the probability of violating the restrictions is fixed and small. Simulation results are presented showing that around the current operating point the system is well approximated by a linearisation as well as demonstrating the control scheme for a realistic case study.

Keywords: District Heating, Model Predictive Control, Deterministic Modelling, Stochastic Modelling.

INTRODUCTION

District heating plays an important part in covering the heating demands in the Nordic countries, hence the subject of optimal operation of district heating systems has a huge economical potential. This is by no means a trivial subject though, as district heating systems are inherently non-linear and non-stationary, and the issue is further complicated by the fact that district heating systems are very diverse with respect to production facilities, operational requirements and so forth.

A district heating system can be seen as consisting of three primary parts: one or more central heat producing units, a distribution network and finally the consumer installations for space heating and hot tap water production. The task of identifying a cost function for the operation of an entire district heating system with multiple heating plants and following that finding a feasible solution to the posed minimisation problem will in most cases be very difficult due to the size of the problem. The problem is subject to continued research though. In [1] an op-

*email: tsn@imm.dtu.dk

timisation scheme based on fairly detailed physical models of the heat production units and the distribution network is proposed, where the unit commitment problem is solved by a fuzzy logic approach. Under certain simplifications a pseudo optimal control strategy is derived for the district heating system of Malmö, but as the simplifications include disregarding power production, heat accumulators and flow restrictions the control strategy is not considered operational.

In order to make the solution of the optimisation problem feasible it is suggested to separate the optimisation of the entire system into a scheduling between the different heat (and power) producing units (long planning horizon) followed by a control problem for the distribution network (considerably shorter control horizon). The potential gains by optimal scheduling between several production units will typically eclipse the potential gains by optimal operation of the distribution network by a considerable margin. Hence it makes sense to let the operation of the distribution network be subordinate to the scheduling even at the cost of a (slightly) suboptimal solution compared to an optimisation which encompass the entire district heating system. Furthermore the heat production units and the distribution network are often owned by different utilities, hence it makes economic sense from a company point of view to optimise the operation of heat production units and distribution network separately.

This paper considers optimal operation of the distribution network. At the distribution level the controllable variable is supply temperature as the load balancing between the production units done at the plant optimisation level has determined the flow control strategy. Traditionally the supply temperature in a district heating system is determined centrally as a function of the current ambient air temperature. Thus the supply temperature control is in fact a open loop control without any feedback from the distribution network, and consequently the control curve has to be determined conservatively to ensure a sufficiently high temperature in the district heating network at all times. The proposed control scheme has two objectives. First of all it optimises the operation of the distribution network with respect to operational costs. Secondly it brings the supply temperature control into a closed loop context thereby making the control a more objective matter compared to the traditional ad hoc approach.

[8] presents a method for controlling supply temperature in district heating systems with one supply point based on stochastic models of the distribution network and an extension of the Generalised Predictive Control scheme proposed by [2]. For more complex systems with multiple supply points the stochastic black box models used in [8] will be difficult to identify reliably. A different approach is to use detailed deterministic models to describe the distribution network[1]. The computational requirements for this type of models prevents direct use in numerical optimisation algorithms, but deterministic network models can serve as a mean for deriving a linearisation of the system response around the current operation point by imposing the model a predetermined input signal for each input variable. The optimisation is then carried out using the linearised model. This is the approach which will be pursued in the following.

CONTROL PROBLEM

The objectives of the present section is to identify the main conditions under which an operational optimisation of a district heating distribution system is carried out. Optimal operation of the distribution system is here assumed to be achieved by minimising the productions cost to the extent, that it can be achieved without compromising the safe operation of the system, adversely affecting the maintenance cost of the system, or sacrificing consumer satisfaction. The operational costs are separated into heating and distribution costs.

For a time interval, $]t-1,t]$ indexed t, the integrated energy balance for the distribution network can be formulated as

$$E_t^h = E_t^l + E_t^c + \bigtriangledown E_t^n \qquad (1)$$

where E_t^h is the energy feed into the network at the supply points, E_t^l is the energy loss in the network, E_t^c is the energy delivered to the consumers, and $\bigtriangledown E_t^n$ is the energy accumulated in the network. The use of an external energy storage – a heat accumulator – is not included in (1) as heat accumulators typically are part of the production system.

[1] These models are widely used to validate the daily operation and are therefore often already available at the district heating systems utilities.

Following (1) the accumulated heating costs C^{heat} over a period T can be written as

$$C^h = \sum_T (E_t^l + E_t^c + \bigtriangledown E_t^n) * P_t^h \qquad (2)$$

where P_t^h is the cost per unit energy during time interval t. In (2) E_t^c is given whereas E_t^l and $\bigtriangledown E_t^n$ are controllable. The heat loss in the network is a (complex) function of the supply temperature, but experience shows that down to a certain limit a decrease in supply temperature implies a lower temperature in the network in general and consequently a decrease in the heat loss from the network. Below the limit the return temperature will increase with decreasing supply temperature. The energy storage in the distribution network can be useful for redistribution of heat load, e.g. smoothing of peak loads, but does normally not allow larger rescheduling of heat load. P_t^h will for some systems be fixed, but for other systems increasing levels for supply and return temperature and peak load will imply a higher price per unit energy. In systems with different production costs for the production units P_t^h will depend on the load distribution between production units.

The distribution costs are dominated by the cost of the electricity consumption by the pumps at the supply points. The supply temperature has direct impact on the pumping costs as flow rate and thus pumping costs will increase with decreasing supply temperature. For most district heating utilities in Denmark the pumping costs are an order of magnitude less than the energy costs associated with the heat loss in the distribution network.

The optimisation of production cost is carried out under restrictions imposed by the distribution network and consumer installations. The restrictions are mainly due to maximum limits on the flow rates as well as requirements to a minimum inlet temperature at the consumer installations. Both sets of restrictions can be fulfilled by maintaining a sufficiently high supply temperature.

The operation of a district heating utility has a direct impact on the maintenance costs for the network. Large and frequent variations in supply temperature will increase the maintenance costs compared to a more steady operation, hence large and frequent fluctuations in the supply temperature should be avoided. It is often a requirement from the utilities that hard restrictions are placed on rate of change as well as the absolute range for supply temperature.

Based on the above considerations the operation of the distribution network can be optimised using supply temperatures as control variables by minimising the heating and pumping costs subject to the restriction that flow rates, consumer inlet temperatures as well as range and rate of change for supply temperatures are kept within acceptable bounds.

CONTROLLER IMPLEMENTATION

Following the optimisation criteria outlined above minimisation of production costs at the distribution level requires that models describing the dynamic relationship between cost variables (heat and pumping costs), restricted variables (flow rates and consumer inlet temperatures) and the control variable (supply temperatures) are available. One possible solution could be to extend the statistical models presented in [8]. However for more complex systems this type of models will be difficult to identify reliably as many of the input variables will exhibit little variation or be closely correlated. A different approach is to use a detailed deterministic model to describe the distribution network. In the following a control scheme for minimising production costs at the distribution level based on a deterministic network model will be derived.

Costs and flow rates at the supply points of the district heating network are well defined whereas consumer inlet temperature is a distributed measure. The consumer inlet temperature requirements are therefore monitored by introducing a set of *critical points* in the distribution network. The critical points are selected so that if the temperature requirements for the critical points are satisfied then the temperature requirements for all consumers are satisfied.

Flow rates and net-point temperatures exhibit different response characteristics on changes in supply temperature with an immediate but slow dying response in flow rate[2] and a delayed but fast response in the net-point temperatures. The primary factor controlling the dynamic relationships between cost and restricted variables and supply temperatures are the time-varying heat load in the system. The heat load exhibits a diurnal as well as an annual variation caused by the diurnal cycle in consumer behaviour

[2] A change in supply temperature will affect the flow rate from the time where the introduced temperature gradient reaches the first consumers and until it has reached the most distant consumers.

and the annual cycle in climate. The optimisation must be able to handle the different time scales in the responses as well as the diurnal cycle in the responses.

An approach capable of handling these requirements is to pose the control problem as a constrained minimisation problem with receding horizon. This formulation has close resemblance to Model Predictive Control (MPC), c.f. [6], but with a non-quadratic cost function.

Prediction models relating future values of cost and restricted variables to past and future values of supply temperature have to take the future heat load into account, i.e. they will depend on heat load predictions. Introducing the vector notation

$$\mathbf{T}^{s,i}_{t+k} = (T^{s,i}_{t+1}, \ldots, T^{s,i}_{t+k})^T$$

the future heat (E^h) and pump (E^p) loads, flow rates (Q) and net-point temperatures (T^{np}) can be written as

$$\begin{aligned} E^{h,i}_{t+k} &= E^{h,i}(\mathbf{I}_t, \mathbf{T}^{s,1..r}_{t+k}, E^c_{t+k}) + \varepsilon^{E^{h,i}}_{t+k} \\ E^{p,i}_{t+k} &= E^{p,i}(\mathbf{I}_t, \mathbf{T}^{s,1..r}_{t+k}, E^c_{t+k}) + \varepsilon^{E^{p,i}}_{t+k} \\ T^{np,j}_{t+k} &= F^{T,j}(\mathbf{I}_t, \mathbf{T}^{s,1..r}_{t+k}, E^c_{t+k}) + \varepsilon^{F^{T,j}}_{t+k} \\ Q^i_{t+k} &= F^{Q,i}(\mathbf{I}_t, \mathbf{T}^{s,1..r}_{t+k}, E^c_{t+k}) + \varepsilon^{F^{Q,i}}_{t+k} \end{aligned} \quad (3)$$

where E^c_{t+k} is the future consumer load, $i \in [1;r]$ is the set of supply points, $j \in [1;s]$ is the set of critical net points, $\mathbf{I}_t$ is the information set with respect to the distribution system at time t, ε^* are independent identically distributed (iid.) white noise sequences, and $\mathbf{T}^{s,1..r}_{t+k}$ is the set of future supply temperature vectors covering all supply points.

For prediction horizons more than a few hours ahead in time the future weather situation must be taken into account when predicting the consumer heat load E^c. [7] and [1] identifies stochastic prediction models for consumer load using numerical weather predictions (NWP) from a meteorological service as input to the load predictions. The consumer heat load predictions can be written as

$$\hat{E^c}_{t+k|t} = \hat{E}^c(\mathbf{I}_t, \mathbf{W}^{NWP}_{t+k|t}, h^{24}) \quad (4)$$

where $\mathbf{W}^{NWP}_{t+k|t}$ is a set of NWP variables describing the future climate, h^{24} is time of day and $\hat{E}^c(\cdot)$ is a function to be estimated.

Substituting (4) into (3) gives

$$\begin{aligned} E^{h,i}_{t+k} &= E^{h,i}(\mathbf{I}_t, \mathbf{T}^{s,1..r}_{t+k}, \hat{E}^c_{t+k|t}) + e^{E^{h,i}}_{t+k} \\ E^{p,i}_{t+k} &= E^{p,i}(\mathbf{I}_t, \mathbf{T}^{s,1..r}_{t+k}, \hat{E}^c_{t+k|t}) + e^{E^{p,i}}_{t+k} \\ T^{np,j}_{t+k} &= F^{T,j}(\mathbf{I}_t, \mathbf{T}^{s,1..r}_{t+k}, \hat{E}^c_{t+k|t}) + e^{F^{T,j}}_{t+k} \\ Q^i_{t+k} &= F^{Q,i}(\mathbf{I}_t, \mathbf{T}^{s,1..r}_{t+k}, \hat{E}^c_{t+k|t}) + e^{F^{Q,i}}_{t+k} \end{aligned} \quad (5)$$

Following [4],[3] which considers model estimation in the presence of errors in the regressors, bias in the noise sequences e^* for the models (5) must be expected due to the inevitable errors in the predictions of consumer load. Consequently the predictions given by (5) should be filtered through a prediction error model, see [5], to obtain unbiased predictions $\hat{E}^{h,i}_{t+k|t}$, $\hat{E}^{p,i}_{t+k|t}$, $\hat{T}^{np,j}_{t+k|t}$ and $\hat{Q}^i_{t+k|t}$ of the system response.

The optimisation problem may now be formulated in more mathematical terms as

$$\min_{\mathbf{T}^{s,1..r}_{t+N_p}} \sum_{i=1}^{r} \sum_{k=1}^{N_p} \hat{E}^{h,i}_{t+k|t} \cdot P^{h,i}_{t+k} + \hat{E}^{p,i}_{t+k|t} \cdot P^{p,i}_{t+k} \quad (6)$$

subject to

$$\begin{aligned} \hat{T}^{np,j}_{t+k} &\geq T^{np,j}_{min,t+k} \\ \hat{Q}^i_{t+k} &\leq Q^i_{max,t+k} \\ T^{s,i}_{t+k} &\leq T^{s,i}_{max} \\ \bigtriangledown T^{s,i}_{t+k} &\leq \begin{cases} \bigtriangledown T^{s,i}_{max} & , k <= N_u \\ 0 & , k > N_u \end{cases} \\ \forall \quad i \in [1;r], j \in [1;s], k \in [1;N_p] \end{aligned}$$

where N_p is the prediction horizon, N_u the control horizon, $T^{np,j}_{min,t+k}$ are the minimum net-point temperatures at the critical net-points, $Q^i_{max,t+k}$ are the maximum flow rates at the supply points, and $P^{h,i}_{t+k}$ and $P^{p,i}_{t+k}$ are the price per unit energy for heat and power, respectively. $P^{h,i}_{t+k}$ and $P^{p,i}_{t+k}$ are assumed to be independent of the control actions within the prediction horizon. The subject of determining appropriate limits for the restricted model output values are referred to the following section.

In (6) it assumed that the network return temperature is not adversely affected by the optimisation

[3] In [4] it is found, that in the presence of errors in the regressors a dedicated prediction model should be estimated as use of the true system for prediction will not result in the best possible predictions.

and the return temperature is not monitored explicitly. However if necessary an additional restriction on the return temperature similar to the restrictions in flow rate and net-point temperature could easily be added.

The high level supply temperature control will typically run in an hourly cycle, hence the problem (6) needs solving once every hour. The calculation time (in the order of minutes on a 1.8 GHz PC for a medium size district heating system) prohibits direct use of a detailed deterministic network model in a numeric solution of (6). Instead it is proposed to linearise the deterministic model around its current operating point by identifying a step response model and apply the supply temperature optimisation on the linearised model.

For a MIMO system a step response model is easily derived as follows

- For each output j the system response v_t^j is recorded while maintaining the control variables at their current value.
- For each input output pair (i, j) the system response $\delta_t^{i,j}$ is recorded when applying an additional unit step at time $t+1$ for input i and maintaining the remaining input variables at their current value. The step response is calculated as $s_t^{i,j} = \delta_t^{i,j} - v_t^j$. This is repeated for each time step $t+2$ to $t+k$ to allow for the time-varying dynamics in the system.

The linearised k-step prediction for output j is given as

$$\hat{y}^j_{t+k|t} = \sum_i \sum_{l=1}^{k} s^{i,j}_{t,t+l} \bigtriangledown u^i_{t+l} + v^j_{t,t+k} \qquad (7)$$

Using matrix notation the output predictions (7) for horizons between 1 and N_p is written as

$$\hat{\mathbf{y}}^j_t = \sum_i \mathbf{S}^{i,j}_t \bigtriangledown \mathbf{u}^i_t + \mathbf{v}^j_t \qquad (8)$$

where

$$\begin{aligned}
\hat{\mathbf{y}}^j_t &= (\hat{y}^j_{t+1|t}, \ldots, \hat{y}^j_{t+N_p|t})^T \\
\bigtriangledown \mathbf{u}^i_t &= (\bigtriangledown u^i_{t+1}, \ldots, \bigtriangledown u^i_{t+N_p})^T \\
\mathbf{v}^j_t &= (v^j_{t,t+1}, \ldots, v^j_{t,t+N_p})^T \\
\mathbf{S}^{i,j}_t &= \begin{pmatrix} s^{i,j}_{t,t+1} & 0 & \cdots & 0 \\ s^{i,j}_{t,t+2} & s^{i,j}_{t+1,t+2} & \cdots & 0 \\ \vdots & \vdots & & \vdots \\ s^{i,j}_{t,t+N_p} & s^{i,j}_{t+1,t+N_p} & \cdots & s^{i,j}_{t+N_p,t+N_p} \end{pmatrix}
\end{aligned}$$

Approximating the system response functions (5) for heat and pump load, flow rate and net-point temperature by step response functions (8), i.e.

$$\begin{aligned}
\hat{\mathbf{E}}^{h,i}_t &\approx \sum_{l=1}^{r} \mathbf{S}^{E^{h,l,i}}_t \bigtriangledown \mathbf{T}^{s,l}_t + \mathbf{v}^{E^{h,i}}_t \\
\hat{\mathbf{E}}^{p,i}_t &\approx \sum_{l=1}^{r} \mathbf{S}^{E^{p,l,i}}_t \bigtriangledown \mathbf{T}^{s,l}_t + \mathbf{v}^{E^{p,i}}_t \\
\hat{\mathbf{T}}^{np,j}_t &\approx \sum_{l=1}^{r} \mathbf{S}^{F^{T,l,j}}_t \bigtriangledown \mathbf{T}^{s,l}_t + \mathbf{v}^{F^{T,j}}_t \\
\hat{\mathbf{Q}}^{i}_t &\approx \sum_{l=1}^{r} \mathbf{S}^{F^{Q,l,i}}_t \bigtriangledown \mathbf{T}^{s,l}_t + \mathbf{v}^{F^{Q,i}}_t
\end{aligned}$$

and inserting in (6) leads to

$$\min_{\mathbf{T}^{s,1..r}_t} \sum_{i=1}^{r} \left[\mathbf{P}^{h,i}_t \sum_{l=1}^{r} \mathbf{S}^{E^{h,l,i}}_t + \mathbf{P}^{p,i}_t \sum_{l=1}^{r} \mathbf{S}^{E^{p,l,i}}_t \right] \bigtriangledown \mathbf{T}^{s,l}_t + const \qquad (9)$$

subject to

$$\begin{aligned}
\sum_{l=1}^{r} \mathbf{S}^{F^{T,l,j}}_t \bigtriangledown \mathbf{T}^{s,l}_t + \mathbf{v}^{F^{T,j}}_t &\geq \mathbf{T}^{np,j}_{min,t} \\
\sum_{l=1}^{r} \mathbf{S}^{F^{Q,l,i}}_t \bigtriangledown \mathbf{T}^{s,l}_t + \mathbf{v}^{F^{Q,i}}_t &\leq \mathbf{Q}^{i}_{max,t} \\
\mathbf{T}^{s,i}_t &\leq T^{s,i}_{max} \\
\bigtriangledown \mathbf{T}^{s,i}_t &\leq \bigtriangledown \mathbf{T}^{s,i}_{max} \\
\forall \quad i \in [1;r]\,, j \in [1;s]\,,
\end{aligned}$$

where

$$\begin{aligned}
\mathbf{P}^{h,i}_t &= (P^{h,i}_{t+1}, \ldots, P^{h,i}_{t+N_p}) \\
\mathbf{P}^{p,i}_t &= (P^{p,i}_{t+1}, \ldots, P^{p,i}_{t+N_p}) \\
\mathbf{T}^{np,j}_{min,t} &= (T^{np,j}_{min,t+1}, \ldots, T^{np,j}_{min,t+N_p}) \\
\mathbf{Q}^{i}_{max,t} &= (Q^{i}_{max,t+1}, \ldots, Q^{i}_{max,t+N_p}) \\
\bigtriangledown \mathbf{T}^{s,i}_{max} &= (\underbrace{\bigtriangledown T^{s,i}_{max}}_{1 \ldots N_u}, \ldots, \underbrace{0}_{N_u+1 \ldots N_p})
\end{aligned}$$

Cost function and restrictions in (9) are linear functions of the control variables $\mathbf{T}^{s,1..r}_{t+N_p}$, hence (9) is readily solved by applying standard Linear Programming techniques.

LIMITS IN OUTPUT RESTRICTIONS

The optimisation problem (6) requires, that future output restrictions are specified. The limiting value in the restrictions may be constant over time or given

as a function of one or more explanatory variables, but in any case uncertainty in predicting system outputs and explanatory variable(s) must be taken into account, when the output limit values are determined. In the following a method for determining the output limits so that the probability of future observations violating the limit is fixed (and small) is outlined using the net-point temperature restriction as an example.

In [3] the inlet temperature requirements are investigated for a number of existing buildings and a dependency on ambient air temperature as illustraited in Figure 1 is identified. The minimum net-point temperature should to be governed by a similar function. The increasing net-point temperature with decreasing air temperature reflects the limited capacity in the consumers room heating installations, whereas the minimum is determined by the hot tap water installations.

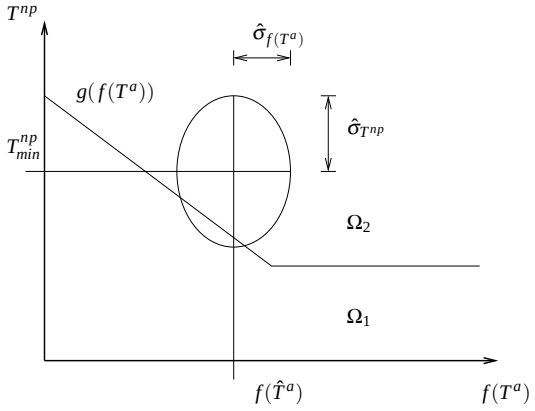

Figure 1: Minimum net-point temperature curve. The minimum curve determines the required net-point temperature as a function of the low pass filtered air temperature, $f(T^a)$.

The heat capacity of the thermal mass of the buildings acts as a low pass filter on the influence of air temperature on heat demand, hence the required net-point temperature is determined as a function of filtered air temperature. The relationship between heat demand and ambient air temperature is investigated in [7], where a physically motivated first-order filter for the ambient air temperature is proposed

$$f(T^a_t) = \frac{1-c}{1-cq^{-1}} T^a_t \ , \qquad (10)$$

and the required net-point temperature must be expected to exhibit a similar dependency on ambient air temperature. For hourly observations [7] identifies an optimal value $c = 0.94$.

Figure 1 establishes the "legal" area Ω_2 as the area above $g(f(T^a))$ as well as the "illegal" area Ω_1 below $g(f(T^a))$, where in the latter case the consumer inlet temperature restriction is violated. The minimum net-point temperature $T^{np}_{min,t+j|t}$ is determined so that

$$\begin{aligned} Prob\{\ (\ f(T^a_{t+j}), T^{np}_{t+j}\ ) \in \Omega_2 \mid \mathbf{I}_t\} &= \pi\ ,\ j>0 \\ \{(f(T^a_t), T^{np}_t) \mid T^{np}_t \geq g(f(T^a_t))\} &= \Omega_2 \qquad (11) \end{aligned}$$

where $f(T^a_{t+j})$ and T^{np}_{t+j} are future values of filtered air temperature and net-point temperature, respectively, $1-\pi$ is the probability of violating the restriction, and $\mathbf{I}_t$ is the information set at time t. Given the distribution of the prediction errors for $f(T^a_{t+j})$ and T^{np}_{t+j} and inserting

$$\begin{aligned} f(T^a_{t+j}) &= f(\hat{T}^a_{t+j|t}) + e^{f(T^a)}_{t+j|t} \\ T^{np}_{t+j} &= T^{np}_{min,t+j|t} + e^{T^{np}}_{t+j|t} \end{aligned}$$

into (11) the resulting equation is readily solved with respect to $T^{np}_{min,t+j|t}$ by numerical methods.

A PHYSICAL DISTRICT HEATING MODEL

The deterministic district heating model used is the TERMIS model of Seven Technologies. TERMIS simulates the hydraulic and thermal state of district heating systems using the fundamental physical laws as basis for modelling the various types of equipment, which constitutes a district heating system. The simulations are performed either as steady-state simulations or as dynamic simulations, where temperature tracking and heat storage are included.

One important feature of TERMIS in this context is the capability of operating in real-time mode. In real-time mode simulations of the current hydraulic and thermal state in the network are performed at a fixed frequency. The simulations are to the greatest possible extent driven by actual measurements of process variables and state indicators, which are provided via the SCADA system. In real-time mode TERMIS may also perform state forecasts, which are simulations of the future hydraulic and thermal state in the network driven by forecasts of the boundary conditions, e.g. consumer heat loads, supply temperatures or load distribution between supply points. The step responses used in the linearisation of the system are calculated as state forecasts.

SIMULATION STUDY

A feasibility study for the proposed supply temperature controller has been carried out using a TERMIS model of Randers District Heating Utility[4] – see Figure 2.

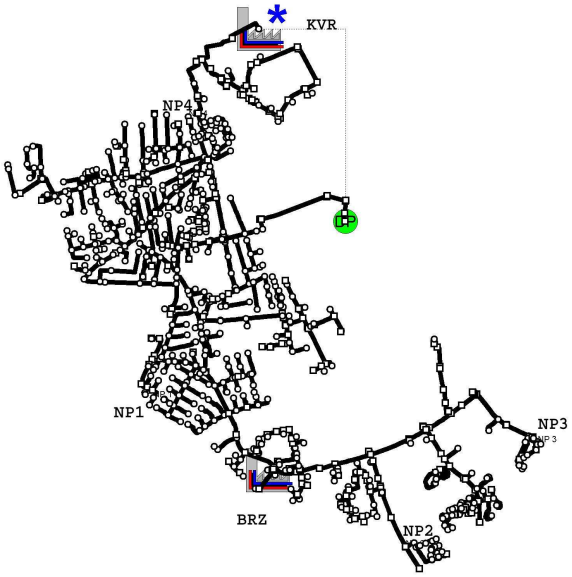

Figure 2: The case study used in the simulations. The network has two supply points (KVR and BRZ), where KVR is main station and BRZ sub-station. Four critical net-points have been identified in the network (NP1 to NP4).

The non-linearities in a district heating network are mainly related to the varying flow rate in the system, but also the different operational modes give raise to non-linearities e.g. variations in the relative flow rate between production units or differences in consumption patterns for the various types of consumers. In the following simulations the flow rate from the BRZ sub-station has been fixed at $30\frac{kg}{s}$ whereas the flow rate from the KVR main station is allowed to vary freely.

The flow rate exhibits a strong diurnal variation and as can be seen from Figure 3 diurnal differences between maximum and minimum flow of up to 40-50% of diurnal mean flow is quite common. The effect of varying the flow rate is investigated in Figure 4. From the figure it is seen that the system step responses strongly depend on flow rate. The "strange" response at NP1 is caused by the supply

[4]Randers is a mid size Danish town located in the northern part of Jutland.

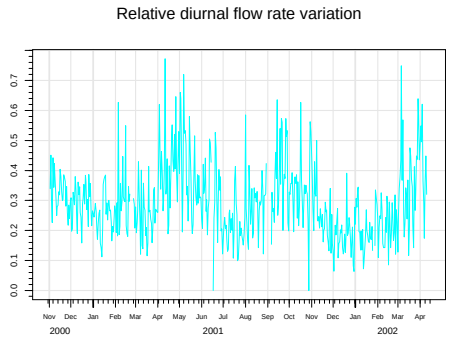

Figure 3: Observed diurnal variation in flow rate relative to diurnal mean flow for a district heating system.

of the point shifting from BRZ at low flow rates to KVR at high flow rates.

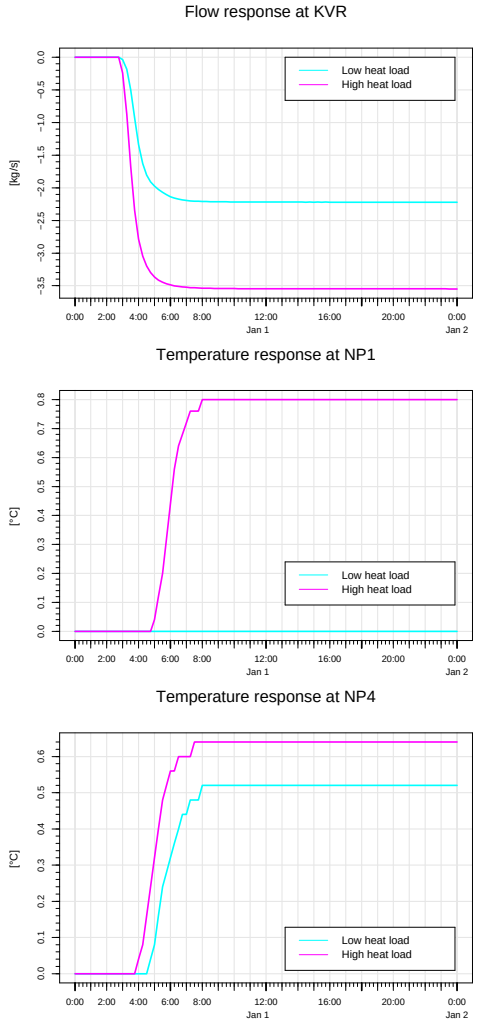

Figure 4: System responses on a unit step in supply temperature at 03:00 for the KVR main station. High and low heat load correspond to KVR flow rates of $179\frac{kg}{s}$ and $112\frac{kg}{s}$, respectively.

The validity of the linearity assumption – $F(c^1 u_t^1 +$

$c^2 u_t^2) = c^1 F(u_t^1) + c^2 F(u_t^2)$ – is investigated for a fixed heat load in Figure 5 and 6, respectively.

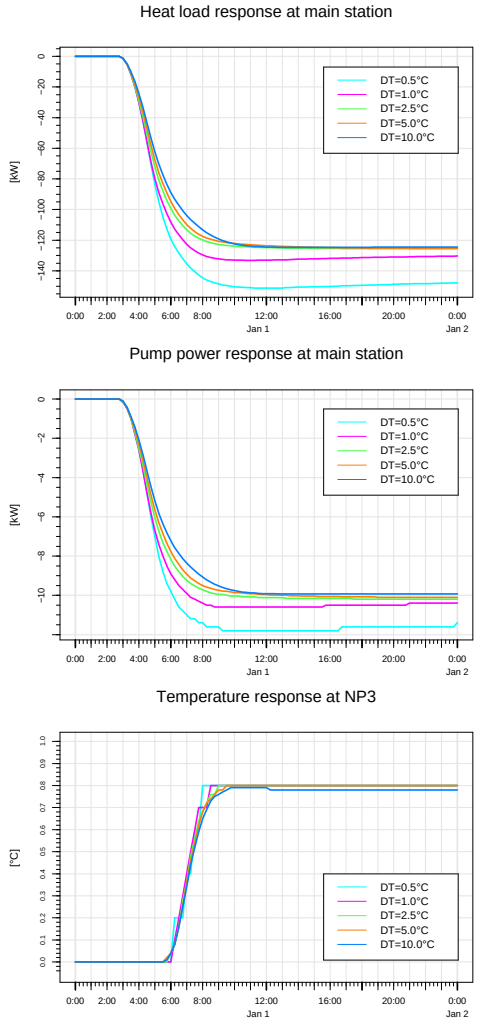

Figure 5: Normalised system response on a step in supply temperature at 03:00 for the BRZ sub-station. The response normalised with step height is shown for five different step heights ranging from 0.5 °C to 10 °C. The initial flow rate is 179 $\frac{kg}{s}$ at KVR.

The response plots indicate that for a fixed consumer load the true system as given by the TERMIS model is well approximated by a linearisation. The deviations found in Figure 5 for the pump and heat load responses to small steps in supply temperature is down to the resulting model responses being close to the modelling accuracy of the TERMIS model.

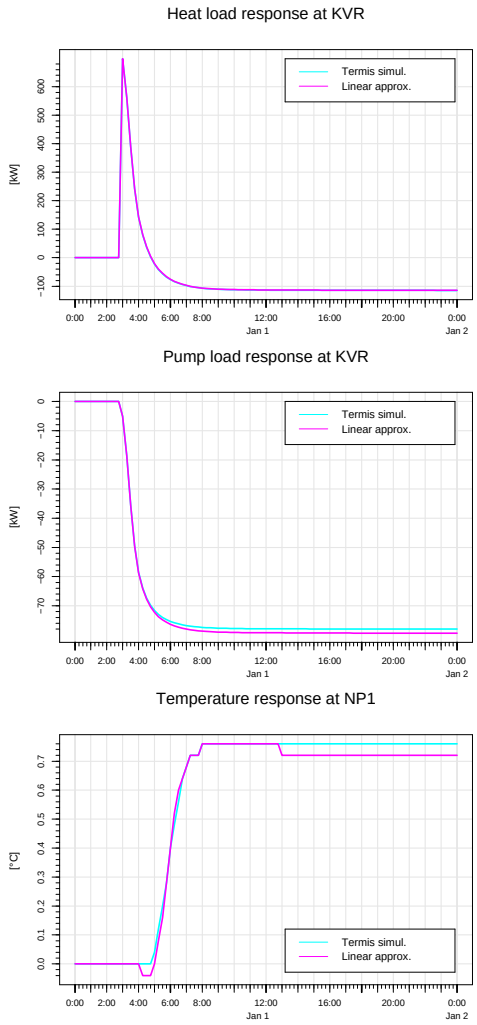

Figure 6: System response on a step response in supply temperature at 03:00 for both stations. "Linear approx." is the calculated response using the linearised step response model and "Termis simul." is the simulated response from the TERMIS model. The initial flow rate is 179 $\frac{kg}{s}$ at KVR.

The supply temperature control (9) is applied to the case study using the following conditions in the optimisation:

Heat costs:	$P^{h,KVR}$=0.3 $\frac{dkk}{kWh}$	$P^{h,BRZ}$=0.4 $\frac{dkk}{kWh}$
Pumping costs:	$P^{p,*}$=0.6 $\frac{dkk}{kWh}$	
Input restric.:	$T_{max}^{s,*}$=105 °C	$C_{max}^{\nabla T^s,*}$=1.5 °C
Output restrict.:	Q_{max}^{KVR}=150 $\frac{kg}{s}$	$T_{min}^{np,*}$=75 °C
Horizons:	N_p=24h	N_u=12h

The optimal solution w.r.t. supply temperature and corresponding system response is found in Figure 7. The changes in supply temperature over the control horizon are large and for BRZ much larger than what would happen if the system has been governed by the controller for some period. Nevertheless the sys-

tem response in Figure 7 indicates that the TERMIS model is well approximated by a linearisation over the control horizon.

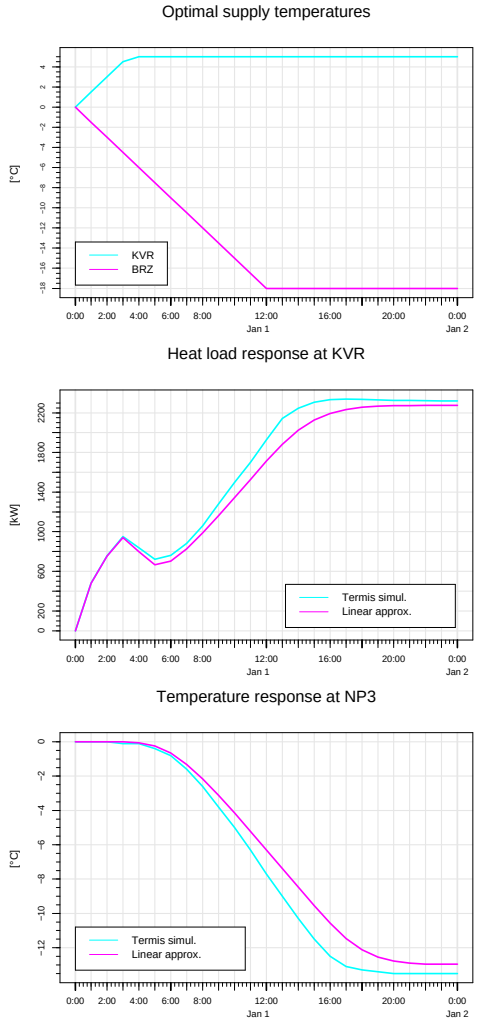

Figure 7: The optimal supply temperature trajectory and the resulting system responses. "Linear approx." is the response from the step response model and "Termis simul." is the response from the TERMIS model. The initial flow rate is $112\frac{kg}{s}$ at KVR.

The controller actions imply that heat load is moved from the BRZ sub-station to the less expensive KVR main station. As an indication of the savings potential available when optimising the operation of a district heating system it is remarked that the saving obtained in the optimisation example corresponds to an annual saving of 2.3 million ddk in steady state.

CONCLUSION

A new concept for controlling the supply temperature in a district heating system based on linearisation of readily available detailed physical system models has been presented. The control problem has been formulated as an optimisation problem with restrictions. The controller minimises the operational costs for the distribution network without compromising safety of supply or consumers temperature requirements.

Promising simulations results have been presented using a realistic case study as an example. However further work remains w.r.t. proving the controller for a longer period with simulations driven by measured data.

Eventually the controller is expected to be implemented on-line at a district heating utility.

REFERENCES

[1] L. Arvastson. *Stochastic Modelling and Operational Optimization in District Heating Systems*. PhD thesis, LU - MS, Lund, Sweden, 2001.

[2] D. W. Clarke, C. Mohtadi, and P. S. Tuffs. Generalized predictive control – part I. The basic algorithm. *Automatica*, 23:137–148, 1987.

[3] K. K. Hansen and B. Bøhm. Required supply temperature for existing district heating consumer installations. Technical report, DTU - ES, Lyngby, Denmark, 1996. In Danish.

[4] B. Jonsson. Prediction with a linear regression model and errors in a regressor. *International Journal of Forecasting*, 10:549–555, 1994.

[5] L. Ljung. *System Identification, Theory for the User*. Prentice-Hall, Englewood Cliffs, NJ, 1987.

[6] D. Q. Mayne, J. B. Rawlings, C. V. Rao, and P. O. M. Scokaert. Constrained model predictive control: Stability and optimality. *Automatica*, 36:789–814, 2000.

[7] H. Aa. Nielsen and H. Madsen. Predicting the heat consumption in district heating systems using meteorological forecasts. Technical report, DTU - IMM, Lyngby, Denmark, 2000.

[8] T. S. Nielsen and H. Madsen. Control of supply temperature in district heating systems. In *Proceedings of the 8th International Symposium on District heating and Cooling*, Trondheim, Norway, 2002.

Proceedings of ECOS 2005
Trondheim, Norway
June 20–22, 2005

USE OF LOCAL THERMAL STORAGE SYSTEMS IN DISTRICT HEATING NETWORKS.

Vittorio VERDA*, Michele Calì, Federica Mussa
Department of Energy Engineering
Politecnico di Torino
ITALY

ABSTRACT

District Heating is an efficient way to provide heat to residential, tertiary and industrial users. It involves the substitution of small boilers with systems such as cogenerative (CHP) plants and larger boilers. In particular, CPH plants are usually designed to provide the base thermal load (40-50% if the maximum load) while boilers provide the rest. This choice is made on the basis of economic criteria, in fact the investment cost of a CHP plant is higher than the cost of boiler, thus its use is convenient when it operates for a large number of hours.

The use of storage tanks would permit to increase the annual operating hours of CHP: heat can be produced when the request is low (for instance during the night), stored and then used when the request is high. The use of boilers results partially reduced, thus the thermal load diagram is flattered.

In this paper, the use of local storage systems, positioned in some of the buildings connected to the district heating systems, is examined. The optimal economic volume of the tanks is first calculated. A simple thermal fluid dynamic model of the tanks is considered in order to calculate the amount of energy actually provided, taking the real operating conditions into account. These considerations are applied to the Turin district heating system; the effect on the global thermal load diagram and the economic impact are determined.

Keywords: District heating network, Thermal storage, load diagram.

NOMENCLATURE

A	annuity [€/year];
c	specific heat [kJ/kg];
c_H	unit cost of heat [€/kJ];
C	cost [€];
f	factor accounting for the installation, the piping and the control system;
hh	number of heating hours per day [h/day];
K	global heat transfer coefficient [W/(m^2·K)];
Q_{DR}	thermal request per day [kJ/day];
Q_{DP}	actual amount of heat per day provided to the users by the storage tank [kJ/day];
Q_{DS}	maximum amount of heat per day that can be provided by the storage tank [kJ/day];
Q_l	heat loss per day [kJ/day];
r	heat transfer coefficient per unit volume of building [W/(m^{3}K)];
S	cross section [m^2];
T	temperature [°C];
u	velocity [m/s];
U	daily internal energy [kJ/day];
V	building volume [m^3];
V_S	storage tank volume [m^3].

Greek

α	convective heat transfer coefficient [W/(m^2·K)]
η_S	storage tank efficiency;
λ	conductivity [W/(m·K)];
ρ	density [kg/m^3];
Ω	perimeter [m].

Subscripts

c	cold flow entering the storage tank (discharge);
D	daytime;
h	hot flow entering the storage tank (charge);

* Corresponding author: Phone (+39) 011 564 44 78, Fax. (+39) 011 564 44 99, e-mail: vittorio.verda@polito.it

i	i-th period in the heating season;
int	internal;
is	insulating;
ext	external;
m	metal;
N	nighttime;
o	hot flow at the users
S	storage system.

1. INTRODUCTION

District Heating is a rational way to provide heat to users localized in a sufficiently dense urbanization, since heat is produced by means of large, more efficient, thermal systems. These systems can be CHP units, biomass boilers, waste heat recuperators (e.g. recuperators of industrial processes) and boilers.

The thermal plant design is performed on the basis of the maximum total request. The shape of the thermal load curve is also considered. As explained hereafter, this is necessary to properly consider the economic impact of the system design. Figure 1 shows the thermal load of an urban area (the total volume of connected buildings is almost $20 \cdot 10^6$ m^3) in a typical day of January [1].

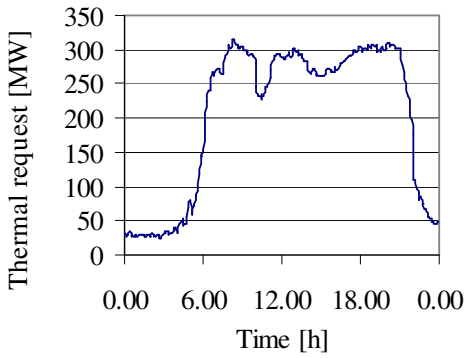

Figure 1 – Thermal request in a day of January.

This area is located in Turin and it is actually heated through a district system. The thermal plant is constituted by two cogeneration systems able to generate 167 + 63 MW. The first system is a steam turbine plant; the cogeneration is performed by condensing steam extracted from the middle pressure turbine. The second system is a gas turbine plant. A combined cycle will start operating next year in order to replace the old groups and satisfy the increasing heat demand due to the network enlargement. Some additional boilers complete the system. These boilers are mainly used for backup purpose as well as for covering pick loads.

In winter, the cogeneration systems operate at their maximum power during the day. Some of the boilers must also operate. In springs the CHPs generally operate at reduced thermal load, in particular, less steam is extracted from the MP turbine, which allows the obtainment of a larger amount of electricity. [2]

During the night, the thermal load is very low and almost constant along the year.

The use of thermal storage systems would determine a large utilization of the cogeneration plant and a consequent reduction in the use of boilers. In fact, a quote of the thermal energy could be produced during the night, stored and then used during the day. This is expected to produce some economic benefits since heat produce through a CHP generally costs less than heat produced through boilers.

In spring there are additional benefits if cogeneration is performed through steam extraction (steam power plants or combined cycles): the displacement of part of the heat production from day to night determines an increase of the electricity production during the day, when electricity has higher price. This concept is particularly important when the system is operating in the free electricity market.

In addition, thermal storage could allow one to reduce the total power installed in the thermal plant; for instance a boiler can be dismissed.

In this paper, the use of thermal storage within a district heating network is investigated by considering technical constraints as well as economic and energy impacts. In particular, local thermal storage systems, positioned in the buildings (i.e. directly at the user's side of the hydraulic circuit) are considered. Non-pressurized tanks are used. Such devices reduce the safety issues for the users, but the maximum temperature is limited to less than 100 °C in order to avoid the water evaporation.

The optimal volume of the storage tank is calculated as the function of the volume of the building where it is installed. Finally, after a discussion on the possible constraints, the impact on the thermal load diagram produced by using storage systems is determined.

A schematic of the thermal storage system is shown in figure 2.

Valve 1 controls the mass flow rate at the heat exchanger, which is a function of the ambient

temperature. The by-pass duct is used when the thermal request of the user changes. When tank charge is operated, water flows through the HE and ducts A, B, C, D. Valves 2 and 3 are closed in the verse towards the user. When tank discharge is operated, water flows to the users through ducts B, E, H and it returns to the storage tank through ducts I, F, C.
Temperature of the water flowing to the users (T_0) is controlled by mixing in valve 3 the mass flow rate extracted from the tank with some cold water flowing back from the users (duct G).

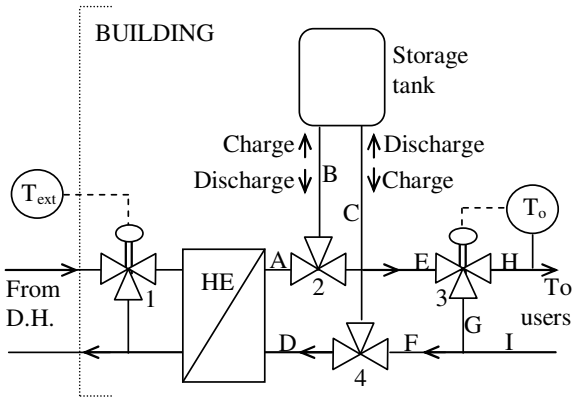

Figure 2 – Schematic of the storage tank installation

2. CHOICE OF THE STORAGE TANK VOLUME

The main design parameter for the storage system is represented by the tank volume. The optimization problem is strongly affected by some variables that are only roughly predictable, in particular the thermal request during the year. For this reason the heating season is considered as composed for the examined case, by 7 periods, each characterized by a particular value of the average ambient temperature. This means that in each period the external temperature and the daily thermal request are considered as constant.
The daily thermal request of a user can be calculated as

$$Q_{DR,i} = r \cdot V \cdot (T_{int} - T_{ext,i}) \cdot hh \cdot 3.6 \qquad (1)$$

where r is a heat transfer coefficient per unit volume of building (assumed 0.85 W/(m^{3}K) on the basis of measures conducted on several buildings), V is the total heated volume of the building, hh is the number of heating hours per day (14 h/day), T_{int} the internal temperature (20 °C) and $T_{ext,i}$ the external temperature in the i-th period. The external temperatures for the considered case are shown in Table 1.

Month	Days	T_{ext}	T_o	T_c
October	15	16	38.4	21.7
November	30	10	48	30
December	31	6	54.4	36.5
January	31	3	59.2	40
February	28	5	56	38.1
March	31	12	44.8	27
April	15	16	38.4	21.7

Table 1 – Data for the heating season.

The maximum amount of heat provided daily by the storage tank to the users Q_{DS} can be calculated:

$$Q_{DS,i} - Q_{l,i} = \Delta U_i = \rho \cdot V_S \cdot c \cdot (T_h - T_{c,i}) \qquad (2)$$

where Q_l is the heat lost during the complete process (charge and discharge of the tank), V_S is the tank volume, T_h is the temperature at which water is stored in the tank (95 °C) and T_c is the temperature of the cold water returning at the storage tank from the heating system. In table 1 the temperature T_o of the mass flow supplied to the users is also indicated.
Equation (2) is valid for an ideal tank, characterized by a volume at temperature T_h and the remaining volume at temperature T_c. The hypothesis of absence of heat conduction inside the tank is overcome by considering an efficiency η_S, defined as the ratio between the heat provided to the users and the thermal energy stored in the tank. The efficiency also accounts for the heat losses:

$$Q_{DS,i} = \eta_S \cdot \rho \cdot V_S \cdot c \cdot (T_h - T_{c,i}) \qquad (3)$$

This efficiency is calculated by using the model described in the next paragraph and it is assumed as independent on the tank volume. The average annual value is η_S=0.868.
The actual heat provided to the users Q_{DP} is the minimum between Q_{DS} and Q_{DR}.
The optimal volume for the storage tank can be calculated by using an economic criterion and by considering all the technical constraints. These constraints limit the maximum storage tank volume because of the available room and because of the time required for a complete charge. This time has been considered 7 hours, since the charge process is operated only nighttime.

The optimal volume is found by minimizing the overall annual cost for the users. The annuity includes the cost for the storage system and for heat supplied to the building by the district heating network. The unit cost of heat nighttime or daytime is different. During the night only the CHP plant is used because of the lower request while during the day also the boilers are used.
The annual cost can be calculated:

$$A = \sum_{i=1}^{7} Q_{DP,i} \cdot c_{HN} + \sum_{i=1}^{7} \left(Q_{DR,i} - Q_{DP,i}\right) \cdot c_{HD} + A_S \quad (4)$$

where c_{HN} is the unit cost of heat required during the night (3.66 €/GJ) and c_{HD} is the unit cost of heat required during the day (14.14 €/GJ) [1].
The cost of the storage tank C_S is expressed as the function of its volume [3]:

$$C_S = f \cdot C_{S,0} \cdot \left(\frac{V_S}{V_{S,0}}\right)^{0.3} \quad (5)$$

where $C_{S,0}$ is a reference cost (1356 €) for a storage tank characterized by the volume $V_{S,0}$ (0.2 m^3) and f is a factor accounting for the installation (including the insulation), piping and control system. This factor is assumed 4.33.
The annuity A_S is calculated as:

$$A_S = C_S \cdot \frac{i \cdot (1+i)^n}{(1+i)^n - 1} \quad (6)$$

where *i* is the rate of return, assumed 6% and n the expected lifetime. Alternative formulation for determining the total cost of the storage system, including owning, maintaining and operating costs can be found in [4].
Figure 3 shows the unit cost of heat to the user as the function of the storage tank volume, for two different volumes of building.

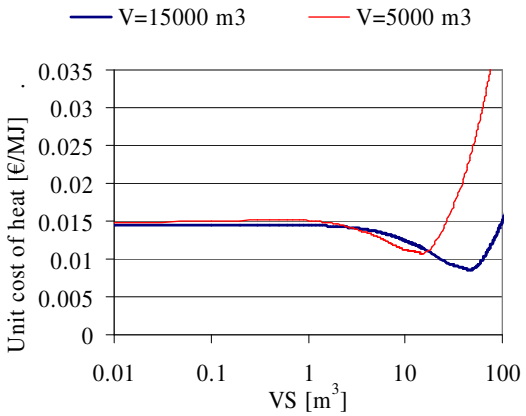

Figure 3 – Unit cost of heat as the function of the storage tank volume [€/MJ].

For small volumes of the storage tank (V_S < 2.8 m^3) the unit cost of heat is higher than the cost of heat bought daytime, thus the thermal storage does not produce any advantage. For higher volumes the unit storage system becomes convenient; the optimal volume is 14.8 m^3 in the case of a building of 5000 m^3 and 47 m^3 in the case of a building of 15000 m^3. The corresponding unit cost of heat is 10.73 €/GJ and 8.59 €/GJ, respectively. The unit cost increases for higher volumes, because the amount of heat Q_{DS} is higher than the thermal request of the users in some days.
Up to now, the constraints have not been still introduced.
The first constraint is represented by the maximum room available for the storage tank in the building. This calculation has been performed by considering existing buildings. When the building is connected to the district heating network, the old boiler is substituted by an heat exchanger. The available room for the storage tank can be evaluated by considering the boiler base surface plus an additional area for maintenance and safety reasons (assumed 1 m times the boiler perimeter). The surface required for installing the heat exchanger is subtracted; an additional area required for maintenance is subtracted as well (this area is assumed 1 m times the HE length). The available area has been assumed as squared.
The average height of a technical room is assumed 3 m, but the tank has been limited to 2 m. In table 2, the data for determining the available area for three different volumes of the buildings are shown. Nevertheless, it is expected that in most buildings the available room is larger than the limiting value determined here.

V [m^3]	5000	10000	15000
Φ[kW]	125	250	375
S_B [m^2]	3.35	3.91	4.47
S_{HE} [m^2]	0.52	0.52	0.52
V_S [m^3]	5.3	6.1	7.0

Table 2 – Data for calculating the volume constraints.

The second constraint is represented by the minimum time required for the complete charge of the tank. This time is calculated through the model presented in the next section and by considering that the initial temperature of the water is equal to T_c. This calculation is performed by considering data referred to April, which is the month

characterized by the lowest value of T_c.
The simulation of the tank charge requires to model the heat exchanger connected to the district heating network. The effectiveness-NTU method has been considered for this purpose. The water in the district heating network is available at 120 °C; the heat transfer coefficient is assumed 285 W/m^{2}K.
The charge process is stopped when the average temperature is 95 °C.
In figure 4 the time required for the complete charge of the storage tank is shown as the function of the tank volume. In the graph two cases are considered for two different values of the building volume.

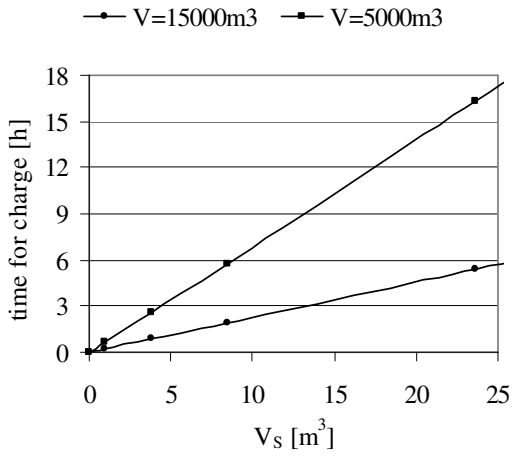

Figure 4 – Time required for the storage tank charge.

The limit for the storage tank is almost 11 m^3 for a building volume of 5000 m^3 and 27 m^3 for a building volume of 15000 m^3.
Further calculations have been performed by considering a volume for the storage tank equal to 5 m^3. Actually in most buildings in Turin there is room enough for the installation of the storage systems.

3. STORAGE SYSTEM MODEL

Numerous numerical models of storage systems are available in the literature. 2D and 3D models are mainly suitable for the design of such systems. In particular, they allows one to properly consider the hydrodynamic effects at the inlet and outlet ports, together with the fluid dynamics inside the tank [5-9].

One dimensional models are more suitable for the analysis of storage systems operation; the use of more complex model in this case involves large computational efforts. Some of the available 1D models are listed in [10, 11] and their features are presented.
A schematic of the tank is shown in Figure 5. The volume is divided into cylindrical elements, whose section is also shown.

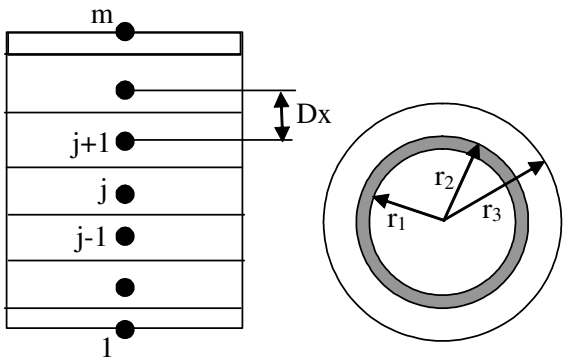

Figure 5 – Schematic of the storage tank

The energy equation applied to the general volume can be written:

$$\lambda \frac{\partial^2 T}{\partial x^2} - K \frac{\Omega}{S}\left(T - T_{int}\right) = \rho \cdot c \cdot \frac{\partial T}{\partial t} + \rho \cdot c \cdot u \cdot \frac{\partial T}{\partial x} \quad (7)$$

where the global heat transfer coefficient accounts for convective internal and external heat transfer and conductive heat transfer through the wall:

$$K = \frac{1}{\frac{1}{\alpha_i} + \frac{r_1}{\lambda_m} \cdot ln\frac{r_2}{r_1} + \frac{r_1}{\lambda_{is}} \cdot ln\frac{r_3}{r_2} + \frac{r_1}{\alpha_e \cdot r_3}} \quad (8)$$

The following assumptions have been made:
1) fluid flow in the tank is laminar (low Reynolds number; actual value is Re~50);
2) a baffle plate has been considered as located close to the inlet section in order to allow a better stratification [12]. No inlet mixing effects have been considered, which corresponds to a low Froude number [5].
The partial differential equation has been solved through a crank Nicholson finite difference scheme which allows one to rewrite it as:

$$\rho \cdot c \cdot \frac{T_j^{n+1} - T_j^n}{\Delta t} = \lambda \cdot \frac{T_{j+1}^{n+1} - 2 \cdot T_j^{n+1} + T_{j-1}^{n+1}}{\Delta x^2} - c \cdot \rho \cdot u \cdot \frac{T_{j+1}^{n+1} - T_{j-1}^{n+1}}{2 \cdot \Delta x} - K \frac{\Omega}{S}\left(T_j^{n+1} - T_{int}\right) \quad (9)$$

where n is the actual instant (all the variables are known at n-th instant) and Δt is the integration time step. The number of cylindrical elements and the integration time step must be chosen in order to avoid numerical instabilities. For further details see [13].
In the first element the boundary condition is imposed, while for the m-th element the thermal balance is written.
This model is used in order to determine the internal temperature during charge and discharge processes and, consequently, to determine the amounts of energy required for the charge and provided through the discharge.
As an example, in figure 5 the temperature profile corresponding to a possible utilization in a day of January of the storage tank in a building of 5000 m^3 is shown. The initial temperature in the tank is assumed 40 °C. The complete charge requires almost 2 hours and 30 minutes. After this time, the average temperature of 95 °C is reached. The tank is not used for 1 hour; then it covers the entire thermal request of the building. The tank utilization is stopped when the temperature of water supplied to the users becomes equal to T_0 (59.2 °C). Thermal stratification in the tank allows one to use it also if the average temperature is lower than this temperature; in particular the average temperature corresponding to this condition is about 44 °C in the specific case here considered.

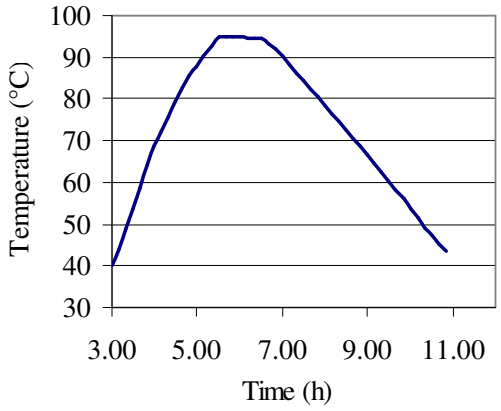

Figure 6 – Temperature profile of the storage tank during a complete process

4. USE OF THE STORAGE TANKS IN COMBINATION WITH DH.

In this section, the effect on the overall district heating system produced through massive utilization of storage tanks is determined.
For this purpose, a total volume of about $7.5 \cdot 10^6$ m^3 (almost 1/3 of the total volume of buildings connected to the D.H.) of buildings are supposed making use of storage systems. This scenario is technically feasible in the actual network configuration.

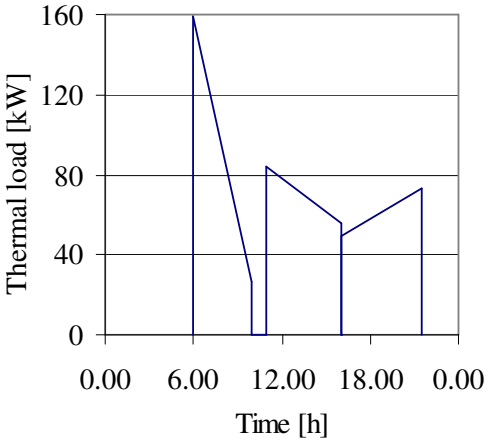

Figure 7 – Three adopted profiles for the utilization of the thermal storage systems in March

Three different utilization profiles are considered: morning (6:00-10:00), afternoon (11:00-16:00) and evening (16:00-21:30) utilization. This means that there are buildings where the storage system is used in the morning, others in the afternoon and finally others in the evening. The number of buildings for each profile is set in the model in order to determine the most effective impact on the thermal load curve. The assumed profiles are ramps. These ramps can be modified each month depending on the shape of the total load curve. As an example, Figure 7 shows three possible curves for the case of March.
For all the storage tanks the charge process has been considered as spread over a period of time of 7 hours.
In Figures 8 and 9 the comparison between the global thermal load of the D.H. network with or without storage systems is shown for two different days, one in January and one in March.
In both cases the storage systems determine a reduction in the difference between nighttime and daytime thermal load as well as a reduction in the maximum load. In January, this difference is reduced from about 250 MW to about 150 MW. The maximum load is reduced of about 30 MW.

These results suggest that a wider use of storage systems is possible.

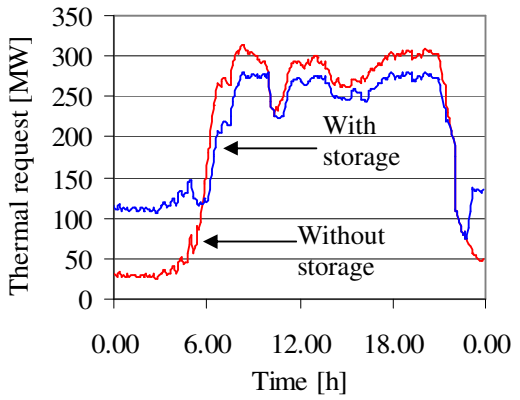

Figure 8 – Thermal load in a day of January [MW].

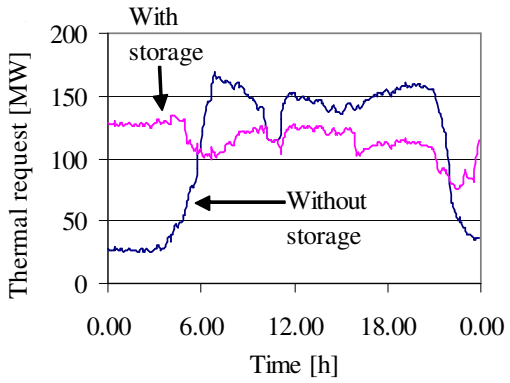

Figure 9 – Thermal load in a day of March [MW].

In March, the difference between the obtained daytime and nighttime loads becomes slightly negative. This has positive benefits since the electric production daytime can increase.
Finally the effect on the annual thermal load curve is analyzed. This curve is a typical tool for dimensioning CHP systems, since it shows the number of hours that the thermal load is over a defined value. If a CHP is dimensioned at the maximum load, it would be used for very few hours at 100%, while it would operate most of the time at partial load. Instead, if the plant it is designed in order to operate between 40-50% of the maximum load, it operates most of the time at 100%. Figure 10 shows the effects of a wide utilization of storage tanks on this curve.

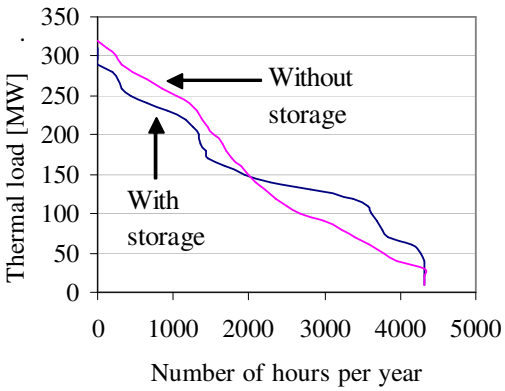

Figure 11 – Cumulate curve of the thermal load.

The use of storage tanks determines a reduction in the maximum request, as well as shift of a part of the energy request from hours characterized by a high total load to hours characterized by low total load. The diagram changes its shape, highlighting a larger utilization of the CHP system. In the case of the actual plant this benefit is not the main one, since the thermal load that can be produced in cogeneration is 230 MW. The amount of heat produced in cogeneration passes from 92.4% to 94.5%, as shown in figure 12. This last value only considers the useful energy provided to the users, i.e. it takes into account the efficiency of the storage system.
In this case, the most effective benefit is constituted by the possibility of increasing the electricity production in hours when electricity is paid more by reducing the thermal load produced in these hours.
Instead, if a CHP plant characterized by nominal thermal power of 150 MW were considered, the advantage of using storage systems would be more evident. In this case the annual amount of heat produced through the CHP plant would be 78.7%, instead of 73% obtained without storage systems.

CONCLUSION

In this paper, the effects of a wide use of storage tanks located in buildings connected to a DH system are analyzed. The economical feasibility of this system is closely related to the thermal plant configuration. If the plant is constituted by a CHP and one or more additional boilers, the use of storage systems makes increase the annual amount of heat produced through the CHP plant.

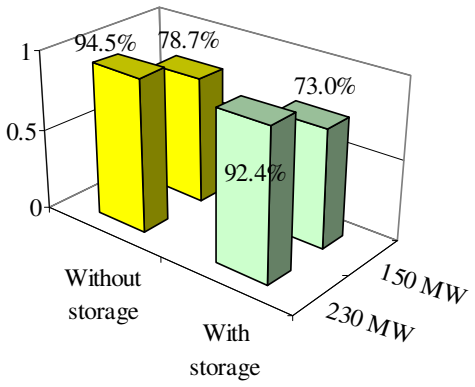

Figure 11 – Annual amount of heat produced through CHP with or without storage systems

In this way, the daily load curve results more flat.
The optimal number of local storage systems that can be usefully installed depends on the shape of the thermal load cumulate curve. The installation of any number of storage systems less or equal to this optimal number produces benefits, provided that the storage tank volume is properly chosen.
In the present paper the number of installed devices has been assumed. The optimization problem will be presented in a future paper.

BIBLIOGRAPHY

[1] AES Torino (2004). *The Turin District Heating Network*. www.aes.torino.it. In Italian.

[2] Verda V. (2001) *Thermoeconomic Diagnosis of an Urban District Heating System based on Cogenerative Steam and Gas Turbines*. Ph.D. Thesis. Turin, Italy: Politecnico di Torino and University of Zaragoza.

[3] Bejan A., Tsatsaronis G., Moran M. (1996). *Thermal Design and Optimization*. Wiley. New York.

[4] Domanski R., Fellah G. (1998). *Thermoeconomic Analysis of Sensible Heat, Thermal Energy Storage Systems*. Applied Thermal Engineering, Vol. 18, No. 8, pp. 693-704.

[5] Shin M.S. Kim H.S., Jang D.S., Lee S.N., Lee Y.S., Yoon H.G. (2003). *Numerical and Experimental Study on the Design of a Stratified Thermal Storage System*. Applied Thermal Energy. Vol. 24. pp. 17-27.

[6] Consul R., Rodriguez I., Perez-Segarra C.D., Soria M. (2004). *Virtual prototyping of storage tanks by means of three-dimensional CFD and heat transfer numerical simulations*. Solar Energy, 77, pp. 179-191.

[7] Al-Najem N.M., Al-Marafie A.M., Ezuddin K.Y. (1993). *Analytical and Experimental Investigation of Thermal Stratification in Storage Tanks*. Int. J. of Energy Research. Vol. 17. pp. 77-88.

[8] Ghajar A.J., Zurigat Y.H. (1991). *Numerical Study of the Effect of Inlet Geometry on Stratification in Thermal Storage*. Numerical Heat Transfer, Part A. Vol. 19. pp. 65-83.

[9] Lightstone M.F., Raithby G.D., Hollands K.G.T. (1989). *Numerical Simulation of the Charging of Liquid Storage Tanks: Comparison with Experiment*. Journal of Solar Energy Engineering. Vol. 111. pp. 225-231.

[10] Al-Najem N.M., El-Refaee M.M. (1997). *A Numerical Study for the Prediction of Turbulent Mixing Factor in Thermal Storage Tanks*. Applied Thermal Engineering. Vol. 17. No. 12. pp. 1173-1181.

[11] Zurigat Y.H., Maloney K.J., Ghajar A.J. (1989). *A Comparison Study of One-Dimensional Models for Stratified Thermal Storage Tanks*. Journal of Solar Energy Engineering. Vol. 111. pp. 204-210.

[12] Li Z.F., Sumathy K. (2002). *Performance study pf a partitioned thermally stratified storage tank in a solar powered absorption air conditioning system*. Applied Thermal Engineering, 22, pp. 1207-1216.

[13] Shyu R.J., Lin J.Y., Fang L.J. (1989). *Thermal Analysis of Stratified Storage Tanks*. Journal of Solar Energy Engineering. Vol. 111. pp. 54-61.

[] Badescu V. (2004). *Optimal operation of thermal energy storage units based on stratified and fully mixed water tank*. Applied Thermal Engineering, 24, pp. 2101-2116.

Proceedings of ECOS 2005
Trondheim, Norway
June 20–22, 2005

DIMENSIONING ASPECTS OF CHP SYSTEMS IN THE DOMESTIC ENERGY SUPPLY

Claudia Werner* and Gerd Walter
Freiberg University of Mining and Technology
Subdepartment of Thermodynamics and Heat Engineering
Germany

Dagmar Hentschel
Leipzig University of Applied Sciences
Department of Mechanical and Energy Engineering
Germany

ABSTRACT

Based on the latest developments of combined heat and power systems (CHP) in the range of performance of up to 30 kW electric power chosen natural gas-powered gasoline engine and Stirling engine units are discussed by means of the specific ecological and economic properties.
Detailed simulation processes for the domestic energy supply of defined model housing estates implicate the dimensioning aspects of these CHP units and the resulting ecological and economic parameters. For this purpose, different variants of dimensioning concerning the thermal CHP rate, the mode of operation and the load control are taken into consideration.
The evaluation of the CHP application in the model housing estates is realised in comparison with conventional domestic energy supply systems. Concerning the simulation results of primary energy demand and CO_2-, CO- and NO_x-emissions, the gasoline engine and the Stirling engine may be an advisable ecological option to the conventional domestic energy supply. More critical are the economic parameters of both investigated CHP units in comparison to the conventional domestic energy supply.
Keywords: cogeneration, gasoline engine, Stirling engine, domestic energy supply

NOMENCLATURE

P_{el}	electric load [kW]
P_f	fuel power [kW]
P_{th}	thermal load [kW]
α	heat yield [%]
β	electricity yield [%]
ω	fuel efficiency factor [%]

Subscripts

n	nominal

* Corresponding author:
Phone: +49 3731 39 3141
Fax: +49 3731 39 3655
E-mail: clwerner@merkur.hrz.tu-freiberg.de

INTRODUCTION

At the present time the German gross power generation is characterised by a CHP contribution of some 11 %. Concurrently CHP technologies are involved in the satisfaction of the thermal heat and the hot water demand (about 6 %) as well as the thermal demand of industrial processes below 500 °C (about 30 %) [1].
The main focus of current CHP applications within the distributed energy supply is ascertainable in industrial and communal areas. Until 2010 essential developments of the actual German CHP stock are estimated in the area of the peripheral thermal energy supply of housing estates and industrial estates [2]. In this range of application CHP units of up to 30 kW electric power such as gasoline

		gasoline engine	Stirling engine
performance data and energy ratios			
electric load P_{el}	kW	16.8	8.5
thermal load P_{th}	kW	36.9	26.4
fuel power P_f	kW	54.7	37.2
electricity yield β	%	30.7	22.8
heat yield α	%	67.5	71.0
fuel efficiency factor ω	%	98.2	93.8
emission values			
carbon dioxide CO_2	kg/kWh	0.2	0.2
carbon monoxide CO	mg/kWh	59.1	84.3
nitrogen oxide NO_x	mg/kWh	186.5	71.0
economic parameters			
specific investment costs	EUR/kW	1820	2915
specific maintenance costs	ct/kWh	2.6	1.2
life cycle	h	80000	80000

Table 1: Properties of CHP units related to the nominal load operating state [3], [4], [5].

engines or Stirling engines seem to be an interesting option over the medium term.
In the following different variants of dimensioning these CHP systems will be investigated in the domestic energy supply of model housing estates. Depending on the dimensioning variants ecological and economic consequences of CHP applications will be described.

GASOLINE ENGINE AND STIRLING ENGINE UNITS

These analyses are based on experimental investigations of natural gas-powered gasoline engine and Stirling engine units as mentioned in table 1. The steady state performance data of the CHP systems in table 1 are related to a consistent return temperature of 50 °C in the downstream heating system. At this operating state the utilisation of condensing technique of both CHP systems has been registered within the scope of the experimental investigations. The energy ratios heat yield α and fuel efficiency factor ω, calculated according to the definition of VDI 4661 [12], document this result explicitly.

The following sections describe the emission values and the economic parameters of the gasoline engine and Stirling engine unit.

Emission values

The emission values according to table 1 signify the direct release of pollutants during the steady nominal load operating state. The deviation from the steady nominal load operating state regarding the CO- and NO_x-emissions is illustrated in figure 1 (gasoline engine) and figure 2 (Stirling engine).

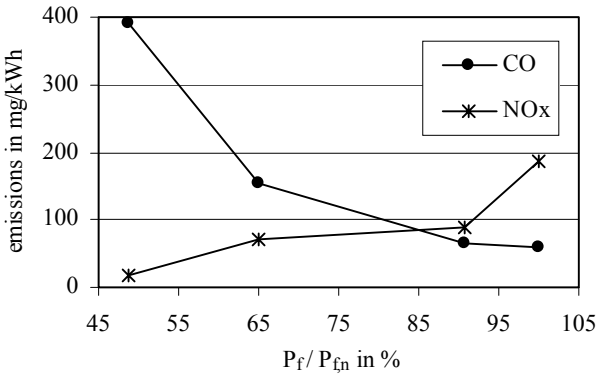

Figure 1: Gasoline engine: emission values [3].

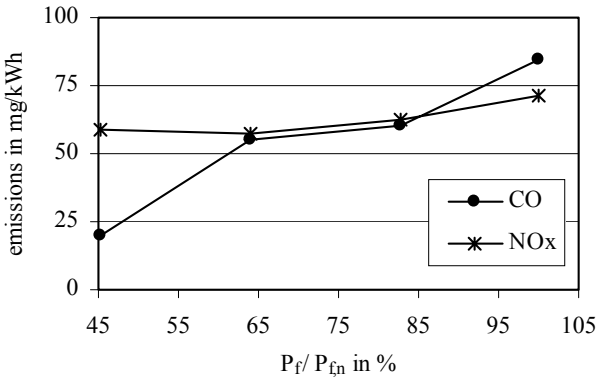

Figure 2: Stirling engine: emission values.

		low-temperature boiler	steam and gas power station
performance data and energy ratios			
performance data	MW	≤ 0.3 (P_{th})	660 (P_{el})
energy ratios	%	92.2 (α)	58.0 (β)
emission values			
carbon dioxide CO_2	kg/kWh	0.2	0.2
carbon monoxide CO	mg/kWh	100	98.2
nitrogen oxide NO_x	mg/kWh	200	343.6
economic parameters			
energy producing costs	ct/kWh	2.5 - 3.2 (net)	3.6 (net)

Table 2: Conventional systems [6], [7], [8].

Regarding to figure 1 and 2 the development of the CO-emissions of the gasoline engine is especially influenced as a result of the steady part load operating state.
A connection with the resulting CO_2-emissions in reliance on the level of load was not ascertained within the experimental investigations of the gasoline engine and the Stirling engine unit.

Comment: According to the reduction of emission values, the gasoline engine operated with a stoichiometric combustion and a three-way catalytic converter [3]. The operation of the Stirling engine was effected by means of external combustion on the basis of a FLOX-burner.

Economic parameters

Table 1 contains fundamental aspects to describe economic coherences of a CHP application.
Furthermore the following economic parameters were considered:

delivery costs (natural gas): 2.3 ct/kWh (net),
credit items (electric power): 3.6 ct/kWh (net),
interest rate: 0.08 1/a.

Thus the thermal energy producing costs k of CHP units are ascertainable concerning the definition of VDI 2067-7 [13].
Figure 3 shows the thermal energy producing costs k of the gasoline engine and the Stirling engine system with regard to the level of load, on the basis of the annual utilisation period of 4500 h/a.

Consistent tendencies of both CHP systems are certifiable with respect to the developments of the thermal energy producing costs k at a variable level of load.
Leaving taxes, subsidies, etc. out of considerations, the situation of the CHP application is represented from the point of view of political economics.

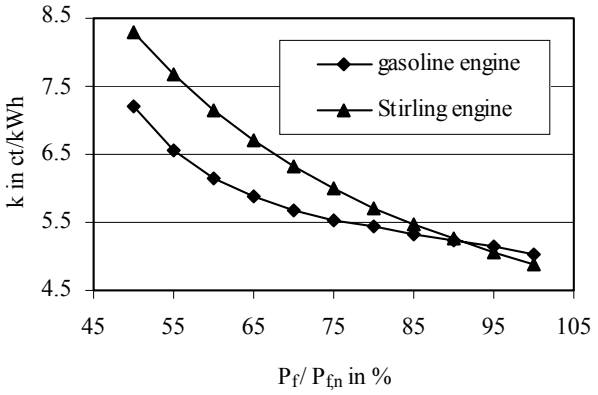

Figure 3: Example of thermal energy producing costs k of CHP systems.

The following simulation analyses the CHP integration into the domestic energy supply of the model housing estates based on these specific properties of the gasoline engine and the Stirling engine unit.
For the evaluation of the energy supply with CHP systems a comparison with the conventional energy supply is carried out. The conventional energy supply method will be considered by a natural gas-powered low-temperature boiler and a steam and gas power station according to table 2.

		model housing estate (gasoline engine)	model housing estate (Stirling engine)
annual demand (electric energy)	MWh	316.1	226.3
annual demand (thermal energy)	MWh	613.4	439.1
peak load (electric power)	kW	84.1	60.2
peak load (thermal power)	kW	184.2	131.9

Table 3: Definition of the model housing estates (example: thermal CHP rate: 20 %).

DIMENSIONING ASPECTS OF CHP SYSTEMS

The integration of cogeneration units requires a previous definition of dimensioning aspects, such as the thermal CHP rate of the objects to be supplied (model housing estates), the mode of operation or the load control of the CHP systems.

Thermal CHP rate

The thermal CHP rate describes the proportion of the nominal thermal load of the CHP unit and the maximal thermal demand of the supplied object.
At present, thermal CHP rates of up to 50 % are realised depending on the energy demand structures of the objects to be supplied [9]. Thermal CHP rates around 20 % are characteristic in domestic energy supply applications in the Federal Republic of Germany [10]. Therewith CHP systems are an essential part in the base load supply of housing estates. The remaining quota of the thermal and electric energy demand ought to be covered by the conventional energy supply.

Within the scope of the simulation processes the thermal CHP rate in the model housing estates will be analysed between 10 % and 50 %.

Mode of operation of the CHP systems

As for supply requirements, the heat oriented and electricity oriented mode of CHP operation is distinguished.
Within the heat oriented mode of operation the application of the CHP system is defined by the thermal load curves of the objects to be supplied.
On the other hand, a cogeneration unit operating in an electricity oriented mode is controlled by the electric load curves of the supplied objects.

The impact of these modes of operation to the CHP application will be verified by means of the simulation analyses.

Load control of the CHP systems

The regulations to the level of load result in the following variants of load control:

- modulating operation: The adaptation to the temporal variable demand of energy is achievable by the control of the level of load of the CHP units. A part load operation of cogeneration systems ought to be limited to 50 % of the nominal load because of the resulting economic values (thermal energy producing costs k) [11].

- intermittent operation: This kind of load control excludes any part load operation of the cogeneration systems. The adaptation to the thermal energy demand of the objects to be supplied is realised by the number of clock cycles.

By means of the simulation processes the variants of a modulating and intermittent operation of the CHP units will be discussed. The modulating operation of the cogeneration systems will be analysed with regard to different values of the lower load.

MODEL HOUSING ESTATES

The subsequent application of the gasoline engine and Stirling engine unit refer to the domestic energy supply of defined model housing estates.
These model housing estates are characterised by thermal and electric energy demand structures and values.
The modelling of the annual energy demand structures of the model housing estates results from the diurnal load characteristics of the VDI 2067-7 records. Within the scope of the following simulation processes these diurnal load characteristics were adapted to the defined model housing estates.
The description of the energy demand values in table 3 decisively factors in parameters like the nominal load data of the CHP units, the defined thermal CHP rate and the energy demand structures according to the VDI 2067-7 [13].

RESULTS OF SIMULATION ANALYSES

The present mathematical simulation of the CHP application connect the specific properties of the CHP systems, in particular the gasoline engine and the Stirling engine units, the different dimensioning aspects as well as parameters of the domestic energy supply of model housing estates.
The evaluation of the CHP application in the model housing estates is based on a relative comparison with the conventional domestic energy supply systems. The primary energy demand, the emission components CO_2, CO, NO_x and the resulting total costs describe the evaluation criteria of the energy supply variants discussed.

Analyses of the thermal CHP rate of the model housing estates

Figure 4a-e compares the simulation results with respect to the defined thermal CHP rates of the model housing estates.

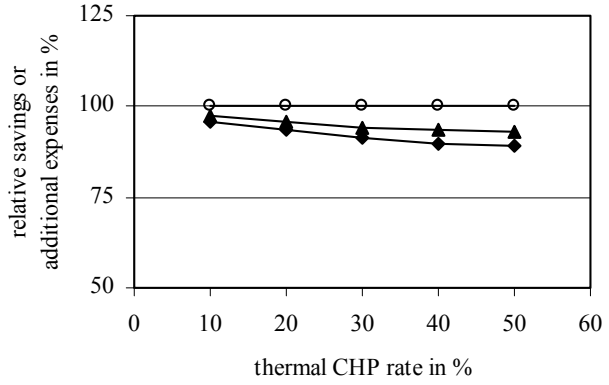

Figure 4a: Primary energy demand.

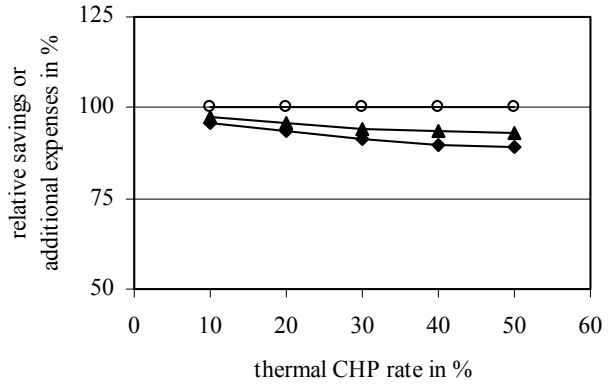

Figure 4b: Carbon dioxide.

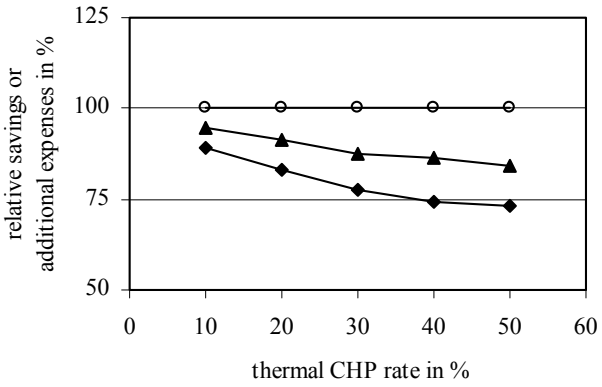

Figure 4c: Carbon monoxide.

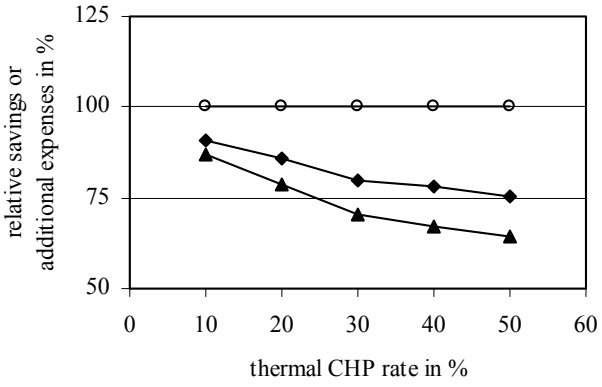

Figure 4d: Nitrogen oxide.

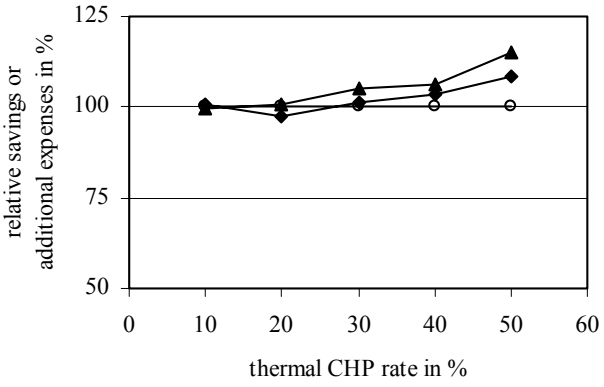

Figure 4e: Resulting total costs.

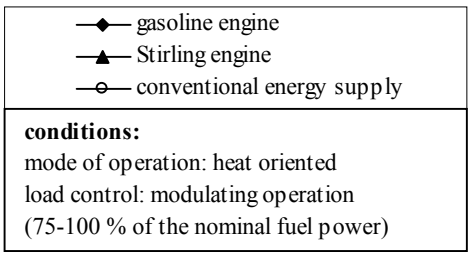

Figure 4a-e: CHP application: variation of the thermal CHP rate.

Figure 4a-e describes the following connection regarding the energy supply including CHP units: The higher the defined CHP rate of the model housing estates, the higher the achievable primary energy savings and the reduction of CO_2, CO and NO_x in comparison with the conventional energy supply. But the higher the defined CHP rate of the model housing estates, the higher the additional expenses of the resulting total costs of the energy supply based on the gasoline engine and Stirling engine unit.

Analyses of the mode of operation of the CHP systems

Figure 5a-e sums up the simulation results of the heat oriented and electricity oriented mode of operation of the gasoline engine and Stirling engine system.

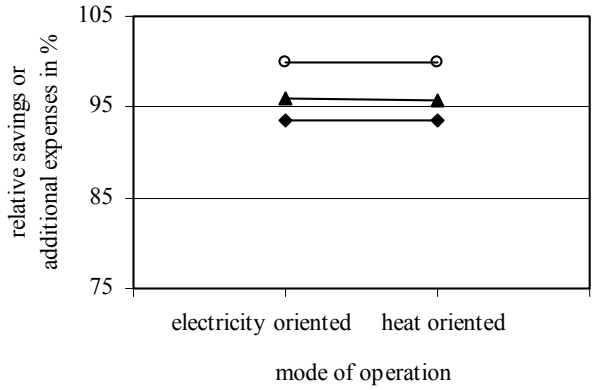

Figure 5a: Primary energy demand.

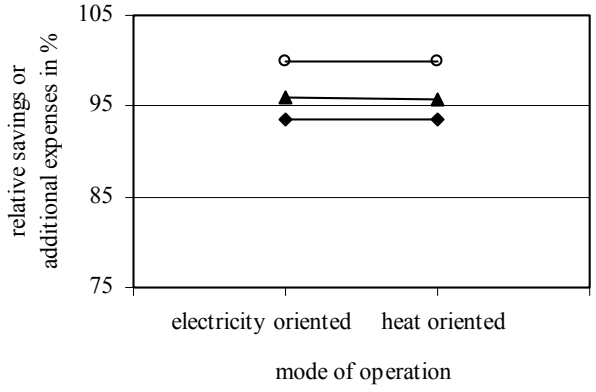

Figure 5b: Carbon dioxide.

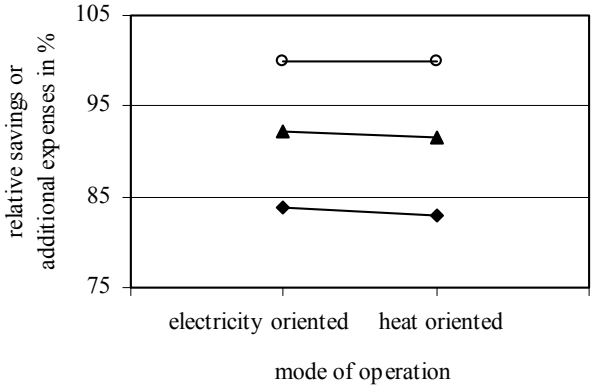

Figure 5c: Carbon monoxide.

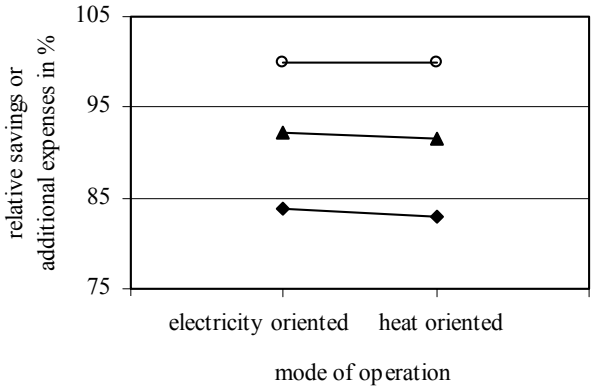

Figure 5d: Nitrogen oxide.

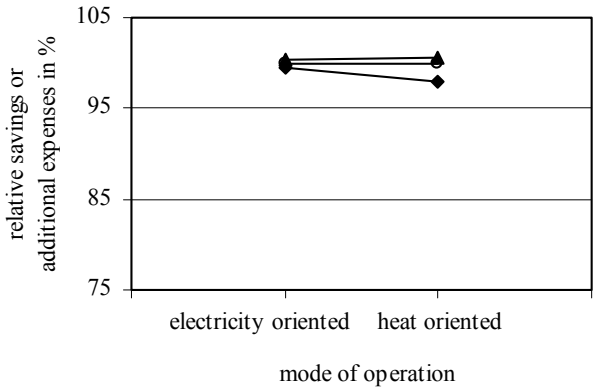

Figure 5e: Resulting total costs.

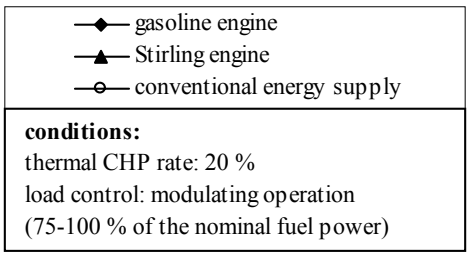

Figure 5a-e: CHP application: variation of the mode of operation.

In accordance with figure 5a-e there are no significant differences of the primary energy demand and the CO_2-emission rates regarding these modes of operation of the CHP systems discussed. Relating to the resulting CO- and NO_x-emissions and the total costs of the domestic energy supply by gasoline engine and Stirling engine units, the consideration of the mode of operation is necessary.

Analyses of the load control of the CHP systems

Figure 6a-e summarises the simulation results of the analysed variants of the load control of the gasoline engine and Stirling engine within the domestic energy supply of the model housing estates.

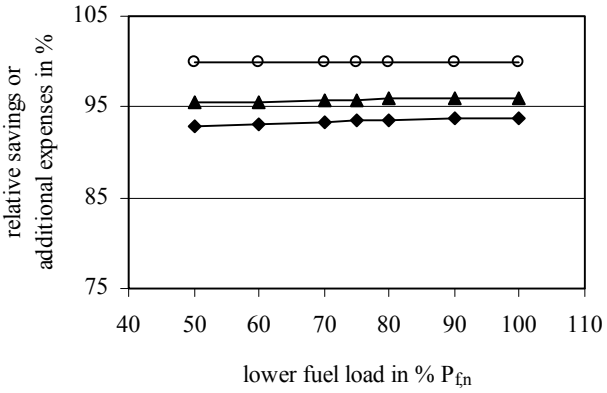

Figure 6a: Primary energy demand.

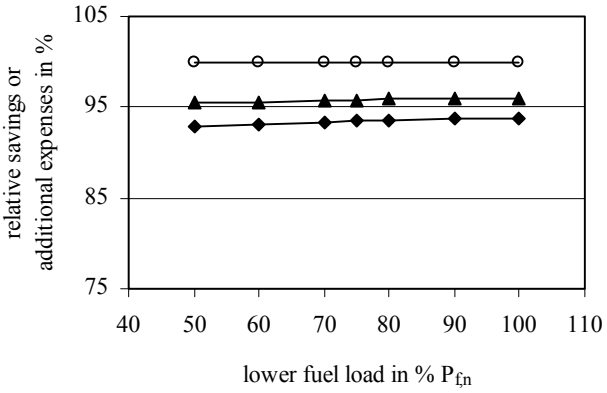

Figure 6b: Carbon dioxide.

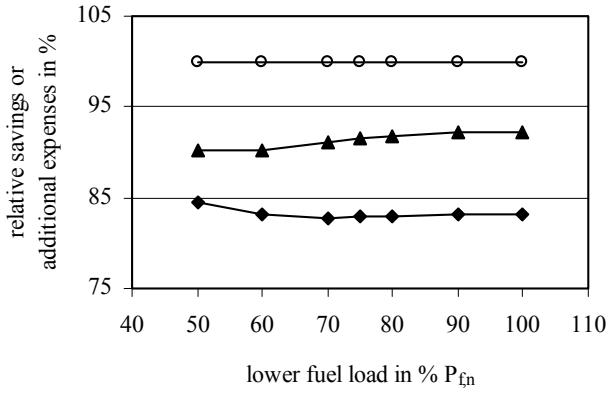

Figure 6c: Carbon monoxide.

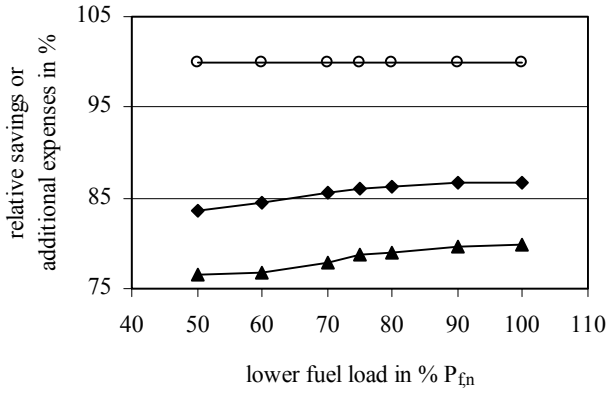

Figure 6d: Nitrogen oxide.

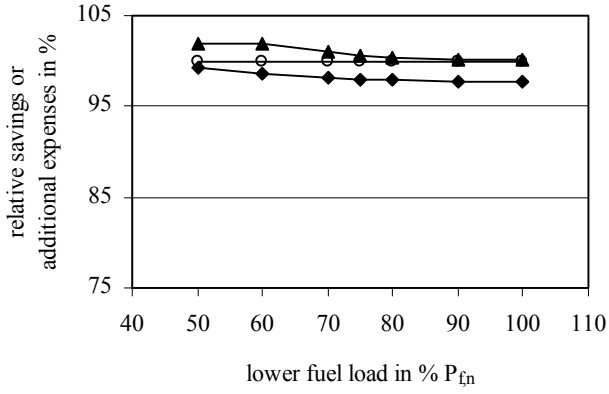

Figure 6e: Resulting total costs.

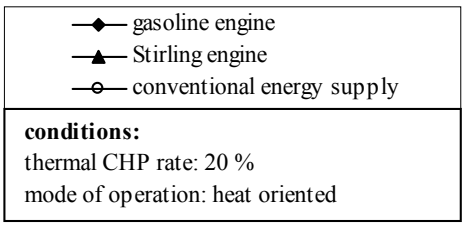

Figure 6a-e: CHP application: variation of the load control.

According to tendency, the better results of the primary energy demand and the CO_2-, CO- and NO_x- emissions in the domestic energy supply are available in a modulating operation of the gasoline engine and the Stirling engine system. But the resulting total costs of the domestic energy supply indicate the interest in an intermittent operation or an operation near the nominal load of cogeneration systems, respectively.

CONCLUSION

The focus of the preceding analyses is natural gas cogeneration systems on the basis of gasoline engine and Stirling engine units, which have been enhanced to domestic energy supply applications because of their present market potential.
The specific properties of these CHP systems, different dimensioning aspects and parameters of defined model housing estates are summarised in a mathematical simulation.
The results of the simulation analyses document the positive influence of both CHP systems on the primary energy savings and CO_2-, CO- and NO_x-reduction compared to the conventional energy supply of the model housing estates. At the same time the simulation results point out that there is no eminent economic advantage of CHP application under these terms in comparison with the conventional energy supply at present.
The simulation analyses illustrate the requirement of a system-compatible and user-specific dimensioning of cogeneration systems in objects to be supplied in order to satisfy ecological and economic demands.

For further studies referring to the application of CHP systems in the range of performance of up to 30 kW electric power the following should be mentioned:

- Based on the present simulation process of gasoline engine and Stirling engine application, fuels cells, micro turbines or steam engines need to be taken into consideration.

- The simulation processes may be enhanced by non steady state performance data while starting or load change processes of CHP systems.

- The options of further developments of the simulation processes regarding optimisation of the CHP application may be achieved.

- Considering the appropriate energy demand structures and energy demand values the simulation processes may be advanced for trigeneration applications.

REFERENCES

[1] Pehnt, M. *Ganzheitliche Bilanzierung von Brennstoffzellen in der Energie- und Verkehrstechnik*. In: Fortschritt-Berichte VDI Reihe 6 Nr. 476, Düsseldorf: VDI-Verlag, 2002.

[2] Gailfuß, M. *Zukünftige industrielle und kommunale BHKW-Potentiale*. In: GAS-WÄRME International, 3/1998, p.176-180.

[3] Einax, M. *Bestimmung der thermischen und elektrischen Wirkungsgrade eines Klein-Blockheizkraftwerkes bei verschiedenen Laststufen*. FH Hannover, 1999.

[4] ASUE. *BHKW-Kenndaten 2001 – Module, Anbieter, Kosten*. Kaiserslautern: Verlag Rationeller Erdgaseinsatz, 2001.

[5] *Personal information*. SOLO Stirling GmbH, 2003.

[6] Kaltschmitt, M., Wiese, A. *Erneuerbare Energien - Systemvergleich, Wirtschaftlichkeit, Umweltaspekte.* Berlin, Heidelberg: Springer-Verlag, 1997, p. 30-41.

[7] Buderus Heiztechnik GmbH. *Heiztechnik 1/2 – Preise und Technik*. Wetzlar, 2001.

[8] Buderus Heiztechnik GmbH. *Handbuch für Heizungstechnik*. Berlin, Wien, Zürich: Beuth-Verlag GmbH, 1994.

[9] Schramek, E.-R. *Taschenbuch für Heizung und Klimatechnik*. München: R. Oldenbourg Verlag GmbH, 1995.

[10] Vogelsang, H. *Optimale Auslegung von Blockheizkraftwerken*. In: BWK, 10/1998, p. 24-29.

[11] ASUE. *BHKW-Grundlagen*. Kaiserslautern: Verlag Rationeller Erdgaseinsatz, 1999.

[12] Verein Deutscher Ingenieure e.V. (VDI): *VDI 4661: Energiekenngrößen – Definitionen - Begriffe - Methodik*, 2003.

[13] Verein Deutscher Ingenieure e.V. (VDI): *VDI 2067-7: Berechnung der Kosten von Wärmeerzeugungsanlagen – Blockheizkraftwerke*, 1988.

Proceedings of ECOS 2005
Trondheim, Norway
June 20–22, 2005

INFLUENCE OF AMBIENT TEMPERATURES ON PERFORMANCE OF A CO_2 HEAT PUMP WATER HEATING SYSTEM

Ryohei Yokoyama*, Takeshi Shimizu, and Koichi Ito
Osaka Prefecture University
Department of Mechanical Engineering
Sakai, Osaka, Japan

Kazuhisa Takemura
The Kansai Electric Power Co., Inc.
Research and Development Department
Amagasaki, Hyogo, Japan

ABSTRACT

In the residential application, a CO_2 heat pump is used in combination with a hot water storage tank, and the performance of this system is affected significantly not only by instantaneous air and feed water temperatures but also by hourly changes of hot water consumption and temperature distribution in the hot water storage tank. In this paper, the performance of a CO_2 heat pump water heating system is analyzed by numerical simulation. A simulation model is created based on thermodynamic equations, and the values of model parameters are estimated based on measured data on existing devices. The performance calculated is compared with that measured, and the simulation model is validated. The system performance is clarified in consideration of seasonal changes of air and feed water temperatures.
Keywords: Heat pump, Thermal storage, System performance, Thermodynamics, Cycle analysis, Numerical simulation

INTRODUCTION

Heat pumps using CO_2 as a natural refrigerant have been developed and commercialized. They are expected to contribute to energy saving in hot water supply [1].

Many theoretical and experimental studies have been conducted for the performance analysis only on CO_2 heat pumps [2–10]. However, in the residential application, a CO_2 heat pump is used in combination with a hot water storage tank. Therefore, the performance of this system is affected significantly not only by instantaneous air and feed water temperatures but also by hourly changes of hot water consumption and temperature distribution in the hot water storage tank. It takes much time to analyze the performance by experiment, and it is expected that numerical simulation enables one to analyze the performance efficiently.

The objective of this paper is to analyze the performance of a CO_2 heat pump water heating system by numerical simulation. A simulation model of the system is created based on thermodynamic equations, and the values of model parameters are estimated based on measured data on existing devices. The model results in a set of nonlinear differential algebraic equations, and it is solved by a hierarchical combination of the Runge-Kutta and Newton-Raphson methods. The performance calculated is compared with that measured, and the validity of the simulation model is investigated. In addition, the performance is analyzed in consideration of seasonal changes of air and feed water temperatures, and the influence of these ambient tem-

*Corresponding author: Phone: +81-72-254-9232 Fax: +81-72-254-9904 E-mail: yokoyama@ese.me.osakafu-u.ac.jp

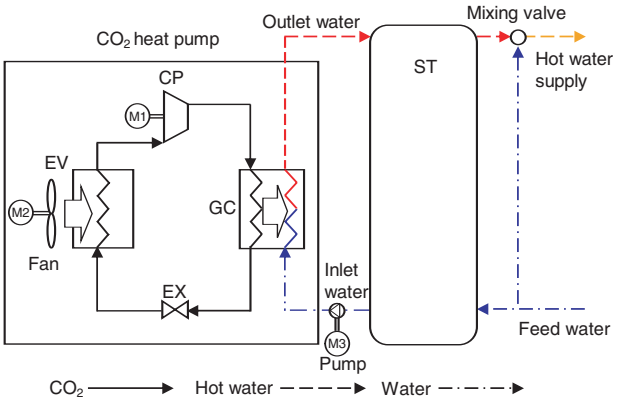

Figure 1: CO_2 heat pump water heating system

peratures on performance criteria is investigated.

CO_2 HEAT PUMP WATER HEATING SYSTEM

Figure 1 shows the configuration of the CO_2 heat pump water heating system investigated in this paper. This system is composed of a CO_2 heat pump and a hot water storage tank (ST). The CO_2 heat pump is composed of a compressor (CP), a gas cooler (GC), an expansion valve (EX), and an evaporator (EV). The system is equipped with a fan, a pump, and motors (M1~3) as auxiliary machinery. The system heats water using the refrigeration cycle of the CO_2 heat pump, stores hot water in the hot water storage tank, and supplies it to a user.

NUMERICAL SIMULATION

Summary of modeling

For each component of the system, the mass flow rates of CO_2 and water, the pressure of CO_2, and the temperatures of CO_2 and water are adopted as variables whose values are to be determined. In addition, the mass, pressure, and energy balance relationships are adopted as basic thermodynamic equations to be satisfied. If necessary, other relationships are adopted. The characteristics of the CO_2 heat pump are expressed by static equations, while those of the hot water storage tank are expressed by dynamic ones. The values of model parameters included in the equations are estimated based on measured data on existing devices commercialized initially. At the connection points between the adjacent components, connection conditions for the variables are considered. At the boundaries of the system, boundary conditions for the variables are considered. If necessary, ambient conditions are considered.

Component models

The following features are incorporated into the model of each component.

Compressor. The ideal characteristics of the compressor are expressed by an isentropic change. In addition, the adiabatic efficiency is introduced to express the real characteristics in comparison with the ideal ones. Here, the adiabatic efficiency is expressed as a function with respect to the pressure ratio.

Gas cooler. The gas cooler is regarded as a counter-flow heat exchanger. Here, it is necessary to consider a strong nonlinearity in the function of the specific enthalpy with respect to the pressure and temperature for the real CO_2 gas. For this purpose, the gas cooler is divided into multiple control volumes, in each of which the specific heat of the real CO_2 gas is assumed to be constant, and the rate of heat transfer between CO_2 and water is expressed as the product of the overall heat transfer coefficient, heat exchange area, and log-mean temperature difference. The pressure of CO_2 is assumed to be constant throughout the gas cooler.

Expansion valve. At the inlet to the expansion valve, CO_2 has only the gas phase. However, at the outlet from the expansion valve, CO_2 has both the gas and liquid phases. To express the specific enthalpy at the outlet, the quality is used instead of the temperature.

Evaporator. At the inlet to the evaporator, CO_2 has both the gas and liquid phases. However, at the outlet from the evaporator, CO_2 has only the gas phase. To evaluate the rate of heat transfer between air and CO_2, it is necessary to change equations for the two states and find the location of their boundary. Here, it is assumed that the overall heat transfer coefficient is common to the two states. In addition, the heat exchange area is divided into the ones for the two states, and they are considered as variables whose values are to be determined. For each state, the rate of heat transfer between air and CO_2 is expressed as the product of the overall heat transfer coefficient, heat exchange area, and log-mean temperature difference. Here, the air temperature is assumed to be constant. The pressure of CO_2 is assumed to be

constant throughout the evaporator.

Hot water storage tank. To consider the dynamic characteristics of temperature distribution in the hot water storage tank, the tank volume is divided into many control volumes, in each of which, the temperature is assumed to be constant. In the energy balance relationship, the heat transfer by water flow and heat conduction as well as the heat loss from the tank surface are considered. It is assumed that the temperature distribution keeps monotonic, and the mixing loss is neglected.

Control conditions

In addition to the aforementioned equations for the components, control conditions must be considered. For example, they are for the revolution of the compressor, the opening of the expansion valve, and the revolution of the pump. However, it is difficult to obtain these control conditions on existing devices. In place of the control conditions, the following equations are considered in this paper: The temperature of CO_2 at the outlet from the compressor is related with that of water at the outlet from the gas cooler; The pressure of CO_2 at the outlet from the expansion valve is related with the air temperature; The mass flow rate of CO_2 is also related with the air temperature; The mass flow rate of water is related with the temperature of water at the outlet from the gas cooler.

Ambient and boundary conditions

The air temperature is considered as the ambient condition. In analyzing the performance of the CO_2 heat pump, the temperatures of water at the inlet to and the outlet from the gas cooler are considered as the boundary conditions. In analyzing the performance of the CO_2 heat pump water heating system, the feed water temperature at the inlet to and the mass flow rate of hot water at the outlet from the hot water storage tank are considered as the boundary conditions.

Solution method

The aforementioned modeling for the performance analysis by numerical simulation is conducted by a building block approach as follows: The component models for the compressor, gas cooler, expansion valve, evaporator, and hot water storage tank, and the substance models for CO_2 and water are defined independently; The system model is composed of the component and substance models as well as the control, connection, ambient, and boundary conditions. The equations for the compressor, gas cooler, expansion valve, evaporator are static, while those for the hot water storage tank are dynamic. Therefore, the modeling results in a set of nonlinear differential algebraic equations. It is solved by the hierarchical combination of the Runge-Kutta and Newton-Raphson methods.

To calculate the properties of the real CO_2, REFPROP Ver. 7.0 is adopted [11]. However, it takes much time to calculate the properties in the iterations of the Runge-Kutta and Newton-Raphson methods. Here, the properties for each combination of many discrete values of pressure and temperature or quality are calculated in advance, and those for the combination of any values of pressure and temperature or quality are calculated by interpolation in the iterations of the Runge-Kutta and Newton-Raphson methods.

Table 1: Ambient and boundary conditions I

(Unit: ˚C)

Season	Air	Inlet water	Outlet water
Summer	25.0	24.4	65.0
Mid-season	16.1	17.5	65.0
Winter	7.0	9.7	85.0

COMPARISON OF NUMERICAL SIMULATION AND EXPERIMENT

To investigate the validity of the aforementioned model, the numerical simulation and experiment are conducted for the CO_2 heat pump and overall water heating system under the same conditions, and their results are compared with each other. All the studies are conducted for a system commercialized initially. In the following, relative values are used for system performance criteria, because the system performance has been improved. The capacities of the CO_2 heat pump and hot water storage tank are set at 4.5 kW and 0.30 m^3, respectively.

CO_2 heat pump

The properties of CO_2 and water in the CO_2 heat pump are investigated. Table 1 shows the ambient and boundary conditions which correspond to summer, mid-season, and winter. Figures 2 (a) to (c) show the *T-s* diagrams with the measured and calculated values of the properties of

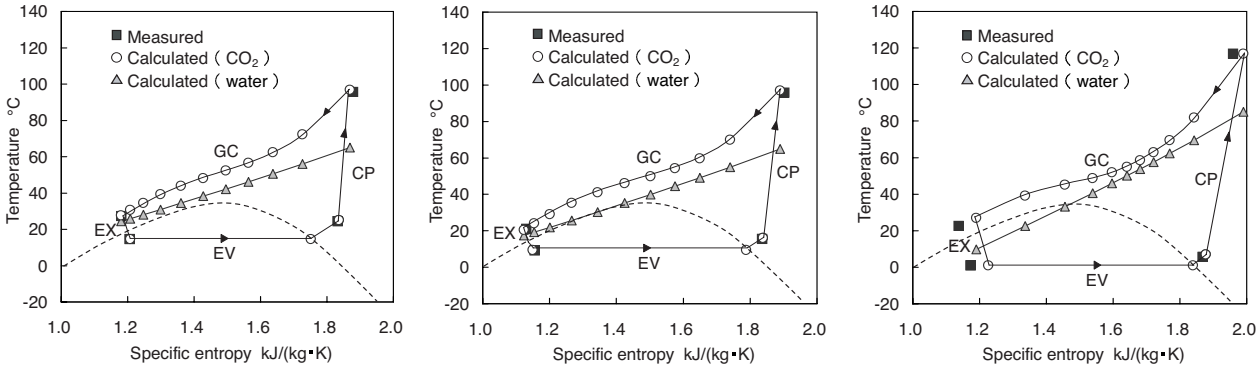

(a) Summer (b) Mid-season (c) Winter

Figure 2: Measured and calculated values of properties

Table 2: Ambient and boundary conditions II

(Unit: ˚C)

Case	Air	Outlet water
1	35.0	75.0
2	20.0	80.0
3	10.0	85.0

CO_2 at the inlet to and the outlet from the components for these seasons. They also show the calculated values of the properties of CO_2 and water for each control volume in the gas cooler, as well as the properties of CO_2 on the boundary between the two states of the gas and liquid phases, and the gas phase in the evaporator. According to these figures, the measured and calculated values are in good agreement. The temperature distributions of CO_2 and water in the gas cooler show some features in each season. In addition, the properties of CO_2 in the evaporator are determined rationally.

The values of heat pump COP are investigated. Table 2 shows the ambient and boundary conditions in the cases investigated. Figure 3 compares the measured and calculated values in the relationship between the inlet water temperature and heat pump COP for these cases. Here, the ratio of heat pump COP is relative to its measured value for the air, inlet water, and outlet water temperatures of 20, 15, and 85 ˚C, respectively. Figure 3 shows that the measured and calculated values are in good agreement.

From these results, it turns out that the simulation model is valid for the CO_2 heat pump.

Overall water heating system

The numerical simulation and experiment for the overall water heating system with the CO_2 heat pump are conducted for four days. This is because

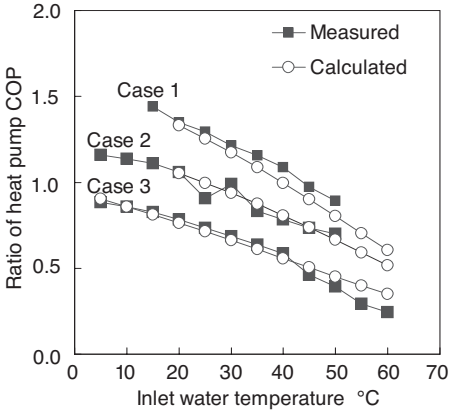

Figure 3: Measured and calculated values of relative heat pump COP

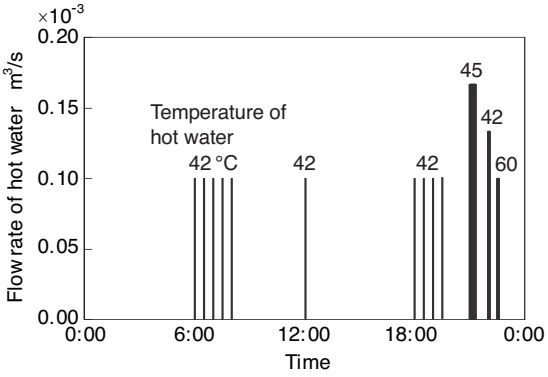

Figure 4: Hourly change of hot water demand

the results on the 4th day are similar to those on the 3rd day, and the periodic steady state appears.

As the ambient and boundary conditions, the air and feed water temperatures are set at 16 and 15 ˚C, respectively. The hourly change of hot water demand is given on each day as shown in Figure 4. As the initial condition, the temperature of water in the hot water storage tank is set at 15 ˚C.

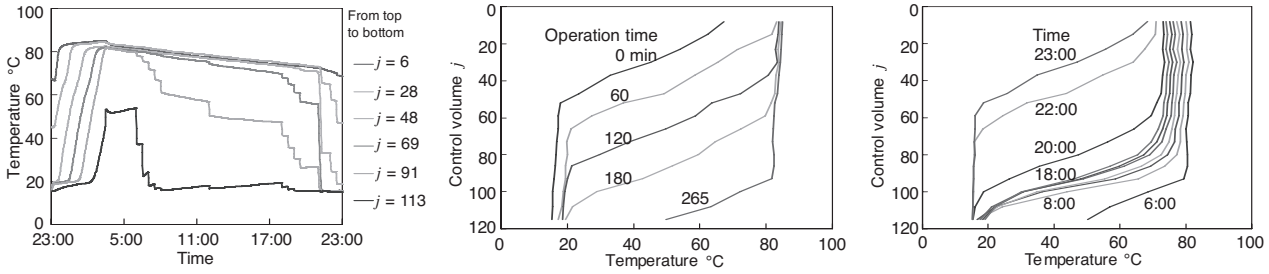

(a) Hourly changes (b) Distributions in charging (c) Distributions in discharging

Figure 5: Measured values of temperatures in hot water storage tank (4th day)

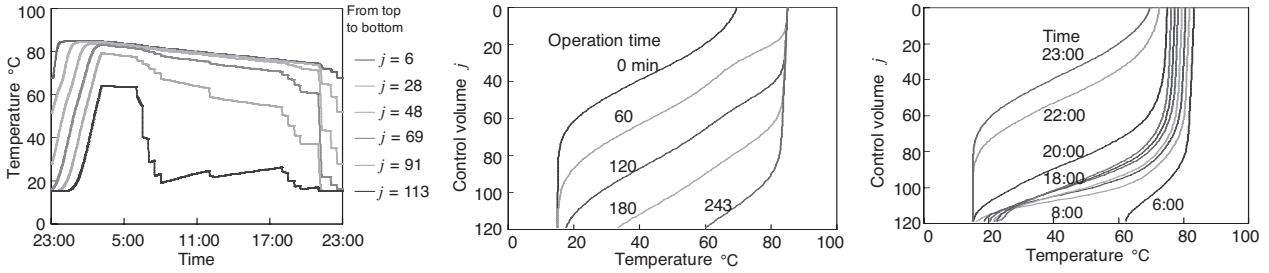

(a) Hourly changes (b) Distributions in charging (c) Distributions in discharging

Figure 6: Calculated values of temperatures in hot water storage tank (4th day)

The CO_2 heat pump is operated only during the nighttime. The CO_2 heat pump is shut down with a shutdown condition satisfied at an appropriate time before 6:00, and it is started up at an appropriate time of night correspondingly. The shutdown condition is that the inlet water temperature attains 60 ˚C. In addition, the outlet water temperature is set at 85 ˚C, which is based on a standard operation mode of an existing CO_2 heat pump.

Figures 5 and 6 show the measured and calculated values of temperatures in the hot water storage tank on the 4th day, respectively. Figure (a) shows the hourly changes of temperatures at several representative positions. Figure (b) shows the temperature distributions at representative operation times in charging the hot water storage tank. Figure (c) shows the temperature distributions at representative times in discharging the hot water storage tank. Here, *j* means the vertical position of 120 control volumes of the hot water storage tank. According to these figures, the measured and calculated values are in good agreement.

Figure 7 compares the measured and calculated values of the hourly change of the heat pump COP on the 4th day. Here, the ratio of heat pump COP is relative to its calculated value for the air, inlet water, and outlet water temperatures of 16, 15, and 85 ˚C, respectively. As time passes, the heat pump COP decreases with an increase in the

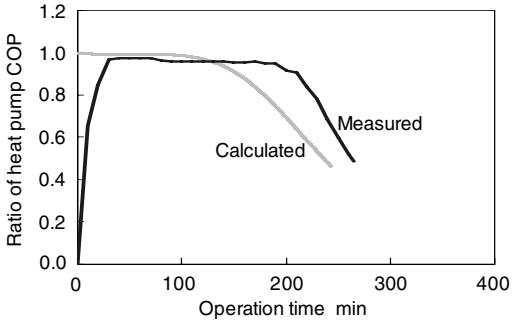

Figure 7: Measured and calculated values of hourly change of relative heat pump COP (4th day)

inlet water temperature in both the numerical simulation and experiment. In the experiment, the heat pump COP increases drastically soon after the CO_2 heat pump is started up. In the numerical simulation, however, the dynamic characteristics of the CO_2 heat pump for its startup is not considered, and the operation time is shorter than that in the experiment.

Figure 8 compares the measured and calculated values of the daily changes of the heat pump COP, and storage and system efficiencies. Here, the storage efficiency is defined as the ratio of heat output for hot water supply to heat input by the CO_2 heat pump, and the system efficiency is defined as the ratio of heat output for hot water

suppy to electric power consumption by the system. In addition, the ratio of each performance criteria is relative to its measured value on the 1st day. The daily changes in the numerical simulation and experiment are in good agreement. The errors are 0.2 to 2.1 %, –3.5 to 6.7 %, and –2.4 to 7.3 % for the heat pump COP, and storage and system efficiencies, respectively.

From these results, it turns out that the simulation model is valid not only for the CO_2 heat pump but also for the hot water storage tank. In addition, the computation time necessary to conduct the numerical simulation for four days on an AlphaStation ES47 with a CPU of 1.0 GHz is only about 1.3 hours, and the numerical simulation enables one to analyze the performance efficiently, as compared with the experiment.

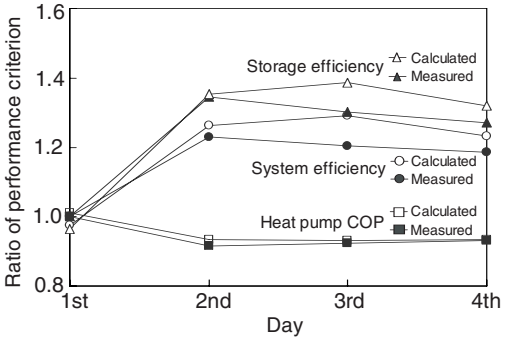

Figure 8: Measured and calculated values of daily changes of relative system performance criteria

INFLUENCE OF AMBIENT TEMPERATURES ON PERFORMANCE

The numerical simulation for the overall water heating system is conducted for four days in each month of a typical year.

As the ambient condition, the hourly change of air temperature in each month is based on its monthly average observed in Osaka, Japan [12]. As the boundary condition, the feed water temperature is assumed to be constant in each month, and it is calculated from the monthly average of the differences between daily average air and feed water temperatures [13]. The hourly change of hot water demand shown in Figure 4 is adopted. As the initial condition, the temperature of water in the hot water storage tank is assumed to be equal to the instantaneous feed water temperature.

The CO_2 heat pump is started up and shut down as described previously. In addition, the outlet water temperature is set at 85, 80, and 75 ˚C for the air temperature lower than 23 ˚C, between 23 and 30 ˚C, and higher than 30 ˚C, respectively, which is based on a standard operation mode of an existing CO_2 heat pump.

Figures 9 to 11 show the calculated values of

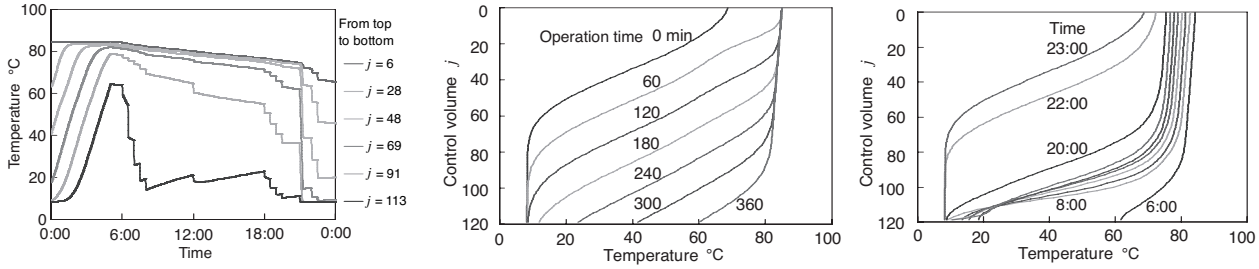

(a) Hourly changes (b) Distributions in charging (c) Distributions in discharging

Figure 9: Calculated values of temperatures in hot water storage tank (January, 4th day)

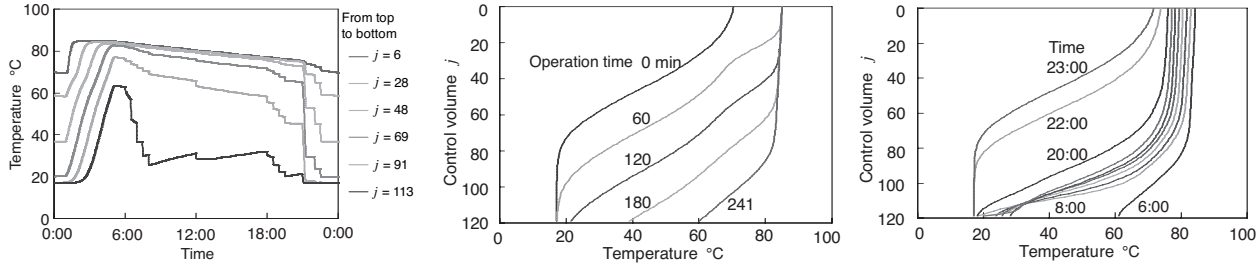

(a) Hourly changes (b) Distributions in charging (c) Distributions in discharging

Figure 10: Calculated values of temperatures in hot water storage tank (April, 4th day)

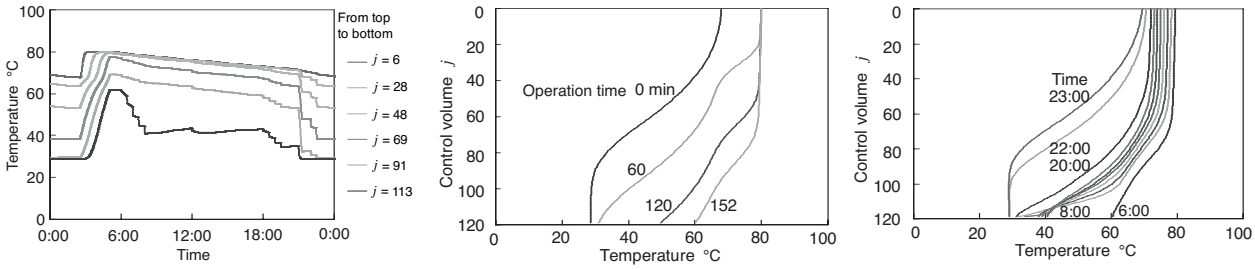

(a) Hourly changes (b) Distributions in charging (c) Distributions in discharging

Figure 11: Calculated values of temperatures in hot water storage tank (August, 4th day)

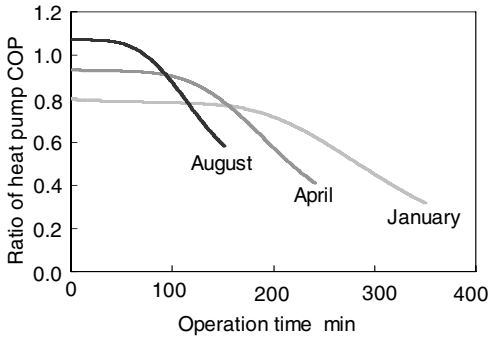

Figure 12: Calculated values of hourly change of relative heat pump COP in each month (4th day)

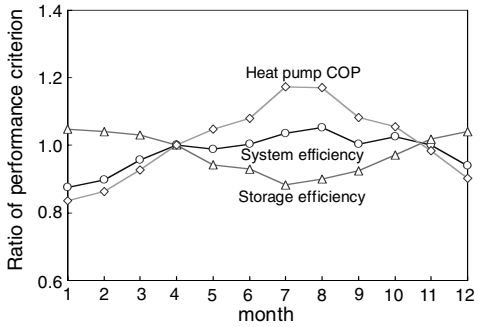

(a) Heat pump COP, and storage and system efficiencies

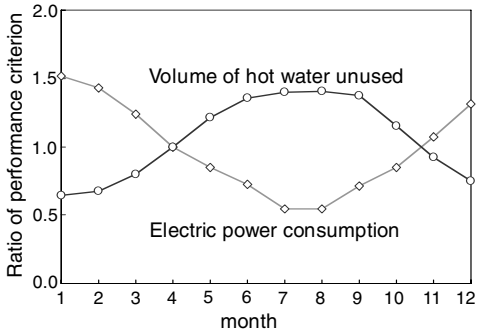

(b) Electric power consumption and volume of hot water unused

Figure 13: Calculated values of monthly changes of relative system performance criteria (4th day)

temperatures in the hot water storage tank on the 4th day in January, April, and August, respectively. Figures (a) to (c) are similar to those in Figure 6. Since the air and feed water temperatures in April are similar to those for the case corresponding to Figure 6, the calculated values in April are similar to those shown in Figure 6. In January, since a larger amount of hot water produced by the CO_2 heat pump is used for hot water supply, the volume of hot water unused is smaller. As a result, the gradients of the temperature distributions are larger, and the volume of hot water with middle temperatures is smaller. In August, however, since a smaller amount of hot water produced by the CO_2 heat pump is used for hot water supply, the volume of hot water unused is larger. As a result, the gradients of the temperature distributions are smaller, and the volume of hot water with middle temperatures is larger.

Figure 12 shows the calculated values of the hourly change of the heat pump COP in January, April, and August. Here, the ratio of heat pump COP is relative to its calculated value for the air, inlet water, and outlet water temperatures of 16, 15, and 85 ˚C, respectively. The operation time of the CO_2 heat pump becomes shorter with increases in the air and feed water temperatures. However, the time when the heat pump COP decreases becomes relatively longer to the operation time. This is because of the aforementioned smaller gradients of the temperature distributions in the hot water storage tank.

Figure 13 shows the calculated values of the monthly changes of the heat pump COP, storage and system efficiencies, electric power consumption, and volume of hot water unused. Here, the ratio of each performance criteria is relative to its value in April. With increases in the air and feed

water temperatures, the heat pump COP increases, but the storage efficiency decreases. This is because although the heat loss from the hot water storage tank decreases, its ratio to the heat produced by the CO_2 heat pump increases. As a result, the system efficiency does not necessarily increase with the air and feed water temperatures in summer.

CONCLUSIONS

The performance of a CO_2 heat pump water heating system has been analyzed by numerical simulation. A simulation model of the system has been created based on thermodynamic equations, and the values of model parameters have been estimated based on measured data on existing devices. The model has resulted in a set of nonlinear differential algebraic equations, and it has been solved by a hierarchical combination of the Runge-Kutta and Newton-Raphson methods.

First, the performance of the CO_2 heat pump calculated has been compared with that measured. The measured and calculated values have been in good agreement. Second, the performance of the overall water heating system calculated has been compared with that measured. The measured and calculated values have also been in good agreement. As a result, it has turned out that the simulation model has been valid. In addition, it has turned out that the numerical simulation enables one to analyze the performance efficiently, as compared with the experiment. Finally, the performance of the system has been analyzed in consideration of seasonal changes of air and feed water temperatures. The influence of these ambient temperatures on several performance criteria has been clarified quantitatively.

REFERENCES

[1] Saikawa M, Hashimoto K, Kobayakawa T, Kusakari K, Itoh M, Sakakibara H. *Development of CO_2 heat pump water heater for residential use—development and performance evaluation of the prototype system*. Transactions of the JSRAE 2001; 18 (3): 225–232 (in Japanese).

[2] Hwang Y, Radermacher R. *Theoretical evaluation of carbon dioxide refrigeration cycle*. International Journal of Heating, Ventilating, Air-Conditioning and Refrigerating Research 1998; 4 (3): 1–20.

[3] Nekså P, Rekstad H, Zakeri R, Schiefloe PA. *CO_2-heat pump water heater: characteristics, system design and experimental results*. International Journal of Refrigeration 1998; 21 (3): 172–179.

[4] Saikawa M, Hashimoto K, Hasegawa H, Iwatsubo T. *Study on efficiency and control method of CO_2 heat pump*, report no. W98004. CRIEPI, 1999 (in Japanese).

[5] Hihara E. *Performance of heat pump systems operated with natural working fluids*. Transactions of the JSRAE 2000; 17 (1): 85–97 (in Japanese).

[6] Saikawa M, Hashimoto K. *Evaluation on efficiency of CO_2 heat pump cycle for hot water supply—evaluation on theoretical efficiency and characteristics*. Transactions of the JSRAE 2001; 18 (3): 217–223 (in Japanese).

[7] Nekså P. *CO_2 heat pump systems*. International Journal of Refrigeration 2002; 25 (4): 421–427.

[8] White SD, Yarrall MG, Cleland DJ, Hedley RA. *Modelling the performance of a transcritical CO_2 heat pump for high temperature heating*. International Journal of Refrigeration 2002; 25 (4): 479–486.

[9] Skaugen G, Nekså P, Pettersen J. *Simulation of trans-critical CO_2 vapour compression systems*. Proceedings of the 5th IIR-Gustav Lorentzen Conference on Natural Working Fluids, Guangzhou, 2002; 82–89.

[10] Richter MR, Song SM, Yin JM, Kim MH, Bullard CW, Hrnjak PS. *Experimental results of transcritical CO_2 heat pump for residential application*. Energy 2003; 28 (10): 1005–1019.

[11] Lemmon EW, McLinden MO, Huber ML. *NIST reference fluid thermodynamic and transport properties—REFPROP version 7.0 users' guide*. U.S. Secretary of Commerce, 2002.

[12] *Japan Meteorological Agency annual report 2001*. Japan Meteorological Agency, 2002 (in Japanese).

[13] *Heat pump water heaters using carbon dioxide refrigerant*, standard no. JRA 4050: 2001. Japan Refrigeration and Air Conditioning Industry Association, 2001 (in Japanese).

Proceedings of ECOS 2005
Trondheim, Norway
June 20–22, 2005

COMPARATIVE EVALUATION OF NATURAL GAS AND SUGAR CANE BAGASSE BASED COGENERATION SYSTEM

Leonardo Moneci Zamboni[1], Luiz Felipe Pellegrini, Silvio de Oliveira Jr. and Arlindo Tribess
Polytechnic School – University of São Paulo
Department of Mechanical Engineering
Brazil

ABSTRACT

Co-firing systems consist in burning two different fuels in the same system in order to produce power and/or heat. Following this concept, two combined cycles burning natural gas and sugar cane bagasse are proposed and evaluated, as an option for electricity generation in sugarcane mills. One system consists in Brayton cycle burning natural gas and the exhaust gases are used in burning bagasse in a Rankine Cycle. In the other, bagasse gasification is introduced and the produced gas is used together with natural gas in a Brayton cycle and the exhaust gases used in a HRSG (Heat Recovery Steam Generator). The thermoeconomic analysis developed for the systems evaluates the exergy efficiency and the production costs of steam and electricity for each system. A parametric study on the natural gas consumption is performed in order to evaluate the impacts of this fuel on costs.

Keywords: Co-firing, sugar cane bagasse, natural gas and cogeneration.

NOMENCLATURE

C	Specific cost [US$/MWh]
$\dot{C}$	Annual cost rate [US$/s]
C_a	Levelized cost [US$/year]
ex	Specific exergy [kJ/kg]
$\dot{E}x$	Exergy rate [MW]
F	Factor [%]
FC	Load factor [%]
H	Specific enthalpy [kJ/kg]
I	Investment [US$]
N	Period [years]
P	Pressure [Pa]
R	Annual rate of interest [%]
S	Specific entropy [kJ/(kg K)]
T	Temperature [ºC]
T_o	Plant operation period [h]
$\dot{W}$	Power [kW or MW]
η	Efficiency

Subscripts

0-2	Thermodynamic states
B	Sugar cane bagasse
E1	Electricity generated by gas turbine
E2	Electricity generated by steam turbine
EQ	Equipment
ex	Exergetic
I	Input
NG	Natural gas
omf	Annual fixed cost of operation and maintenance
omv	Annual variable cost of operation and maintenance
P	Pump; product
PS	Process steam
RS	Return process steam
W	make-up water

[1] Corresponding author: Phone: +55 11 9856-6225
E-mail: Leonardo.zamboni@poli.usp.br

INTRODUCTION

The sugar and alcohol industry uses the sugar cane bagasse, by-product from the milling process, as fuel in boilers for steam production. This steam is responsible for the production of electro-mechanical energy, used in plant equipment (mills, pumps, turbo generators, etc.), and for heat supplied to the production of sugar and alcohol.

With regard to the largest efficiency and the economical and environmental advantages, gasification of sugar cane bagasse and usage of the produced gas in gas turbines may become a promising possibility for this industry. The surplus of electricity generated can be sold to the grid, thus contributing to the expansion of the Brazilian generation park [1].

Unfortunately, the generation of electricity using sugar cane bagasse is only made during the harvest (on-season), which lasts approximately seven months. Therefore, it would not be feasible to operate a thermoelectric plant that works only part of the year.

The purpose of this study is to analyze cogeneration plants that work not only with sugar cane bagasse, but also with natural gas (available the whole year), as a complement.

In this paper a comparative evaluation of two cogeneration plants based on configurations that use natural gas and sugar cane bagasse is carried out. The first configuration is a Biomass Integrated Gasification/Combined Cycle (BIG/CC) [3 and 4] and the second is a Combined Cycle with Injection of Biomass in the Boiler (CC/IB) [5].

NATURAL GAS

Natural gas is considered a clean fuel presenting the smallest indexes of pollutant emission in the atmosphere. The gas methane, containing 75% of carbon in mass, produces 2.77 kg of CO_2 and generates 55,950 kJ per kilogram of methane burned. One kilogram of a liquid hydrocarbon with 10 atoms of carbon produces 3.15 kg of $CO_2$and generates only 45,780 kJ/kg [6].

The Bolivian natural gas is composed practically by methane (CH_4) – 92% - and ethane (C_2H_6) – 6%. Its composition can be visualized in Table 1. The lower heating value of the Bolivian natural gas is 41,665 kJ/Nm^3.

Component	% molar fraction	
	Bolivian natural gas	Produced gas
C_2H_2	6.00	-
C_2H_4	6.00	-
C_2H_6	4.00	-
CH_4	80.61	3.24
CO	-	11.33
CO_2	0.52	18.38
H_2	1.00	25.09
H_2O	0.07	3.13
N_2	1.80	-
N_2	-	38.84

Table 1 – Composition of the Bolivian natural gas and the produced gas [3, 8].

SUGAR CANE BAGASSE

After the crop, sugar cane is prepared and fed to mills, where raw juice is extracted and sent to the process. From this milling process is obtained as a by-product in a proportion of 25% in weight. So, a sugar cane ton produces 250 kg sugar cane bagasse on average with 50% of humidity and lower heating value of ~7,350kJ/kg [9].

The sugar cane bagasse in excess can provide storage problems. During off-season periods (no harvest) this excess can generate expenses, even though these costs can be reduced with constant handling outdoors storage [1]. In Figure 1 surplus of sugar cane bagasse generated by a Sugar and Alcohol Mill, located in the state of São Paulo, Brazil is shown.

Figure 1 – Surplus of sugar cane bagasse generated by a sugar and alcohol mill.

Over the last years, the electricity generated by Brazilian sugar and alcohol mills has been gradually increasing.

GASIFICATION OF SUGAR CANE BAGASSE

Gasification is a thermo-chemical process in which a fuel, solid or liquid, is fragmented with the use of heat, in an oxidizer atmosphere, for the generation of a gas (mixture of gases) with low/medium heating value. This process is an alternative to the combustion of solid and liquids fuels.

The great advantage of this process is the use of the exhaust gas produced in power cycles with gas turbines, with superior efficiencies compared to the conventional Steam cycles with direct burn [3].

This work uses data generated by the model developed by Pellegrini and Oliveira [8] for biomass gasification. The model is based on the establishment of a chemical equilibrium among the main products of the gasification (CH4, CO, H2, H2O, CO2, N2, C(s)) – not considering the formation of pollutant and larger hydrocarbons. The model also makes use of correlations for the production of CH4 and C(s), as proposed by Li et al [10].

The composition of the produced gas used in this work is shown in Table 1.

THERMOECONOMY

Exergy

In the cogeneration plants, with simultaneous production of electro-mechanic energy and useful heat, there are two products whose generation costs must be calculated. In this case, it might be used thermoeconomic analysis in exergetic basis to calculate those costs.

According to Kotas [11], the exergy is a standard of the quality of the energy, that is equal to the maximum useful work that can be obtained from a given "form of energy ", using the environmental parameters (pressure, temperature, and chemical potential) as reference state.

For the purposes of this work exergy is divided in two parts: the physical exergy and the chemical exergy. The change in physical exergy can be given by the following expression:

$$ex_{ph1} - ex_{ph2} = (h_1 - h_2) - T_0(s_1 - s_2) \quad (1)$$

The chemical exergy can be obtained as a function of the heating values of the fuels [12].

Cost balance

The cost balance of a system can be given by the following expression:

$$\sum \dot{C}_P = \sum \dot{C}_I + \dot{C}_{EQ} \quad (2)$$

where:

$$\dot{C} = c \cdot \dot{E}x \quad (3)$$

COGENERATION SYSTEMS

A cogeneration system corresponds to the simultaneous production of different forms of useful energy, as electric-mechanical and thermal energies, to supply the needs of a process unit, in an industrial, agricultural or tertiary sector or an isolated system, starting from the same primary source of energy [13].

For simultaneous production of electricity and steam, a backpressure turbine or a condensing-extraction turbine, in the called process CEST - Condensing Extraction Steam Turbine - can be used. In this process, a part of the steam is extracted from the turbine in an intermediate pressure, to be used in the process; the remaining

steam expands in the turbine until the pressure of the condenser, condenses and returns to the boiler together with the condensed of the process [8].

Combined cycles based systems, composed by a gas turbine, a heat recovery steam generator and a condensation-extraction steam turbine, are used to increase the cogeneration systems efficiency.

In this paper two-cogeneration systems that use natural gas and sugar cane bagasse as inputs are studied:

1. CC/IB [5] - A Combined Cycle with Injection of Biomass in the Boiler, composed by a Gas Turbine that uses only the natural gas as input, and a Steam cycle where, in the heat recovery steam generator, bagasse is burned with the exhaust gases of the gas turbine, as represented in Figure 3.

2. BIG/CC [3] – Biomass Integrated Gasification/Combined Cycle, similar to the first cogeneration system with the differences that no bagasse is burned in the heat recovery steam generator, but is now gasified and fed to a gas turbine mixed with natural gas, as shown in Figure 4.

For the comparative evaluation of these two-cogeneration systems using natural gas and sugar cane bagasse, part of steam is extracted from the steam turbine to attend a heat demand.

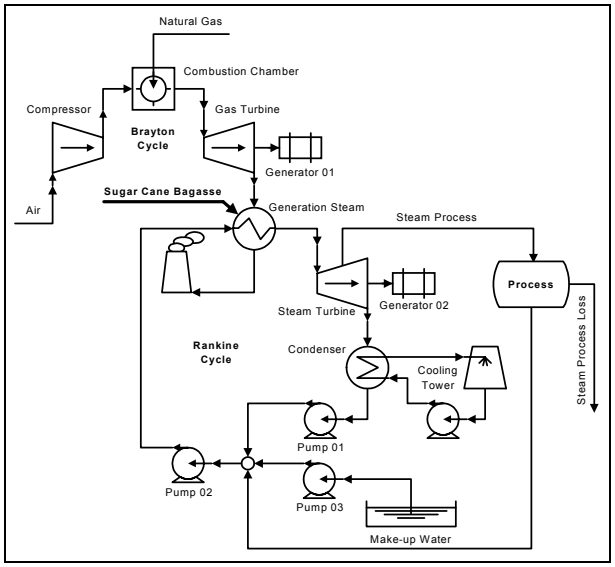

Figure 3 - Combined Cycle with Injection of Biomass in the Boiler (CC/IB).

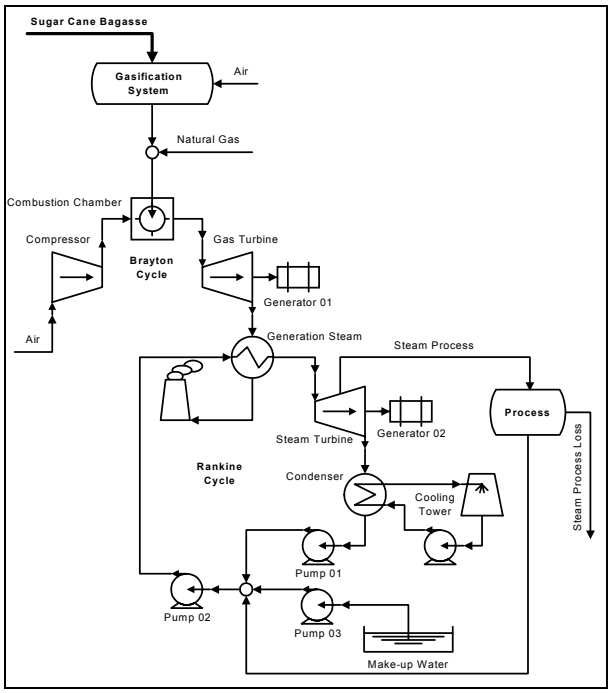

Figure 4 - Biomass Integrated Gasification/ Combined Cycle (BIG/CC).

Operational conditions

The operational conditions shown in Table 2 were adopted in the simulations. Thermodynamic properties, mass and energy rates were performed using the computational program Cycle Tempo [14].

Brayton Cycle	
Pressure ratio	16 bar
Temperature of the combustion chamber exhaust gases	1200ºC
Compressor isentropic efficiency	83%
Gas turbine isentropic efficiency	87%
Generator efficiency	95%
Produced gas mass flow rate	75.5 kg/s
Rankine Cycle	
Temperature of the steam generated	520ºC
Boiler pressure	70 bar
Temperature of the exhaust gases of the gas turbine	140ºC
Sugar cane bagasse mass flow	62 kg/s
Steam turbine isentropic efficiency	90%
Generator efficiency	95%
Pressure of the condenser	0.1 bar

Table 2 – Operational conditions.

The operational conditions regarding the steam extraction for process were:

- 77% of the turbine entrance steam mass flow is extracted for the cogeneration process at a pressure of 0.25 MPa;
- 35% of the process flow is lost in the steam form and condensed contaminated;
- Make-up water comes from an external source with environment temperature;
- The cost of the make-upt water is 0.40 US$/t.

Thermoeconomic evaluation

For the calculation of the equipment costs (I_{EQ}), the following equation was used:

$$I_{EQ} = I_r \left(\frac{S}{S_r} \right)^m \quad [US\$] \tag{4}$$

where the values of the terms of the equation are shown in Table 3.

Equip.	m	I_r	S_r	S	Ref.
Boiler	0.78	768	1	$\dot{Q}$ [kW]	[15]
Steam turbine	0.68	17082	1	$\dot{W}$ [kW]	[15]
Gas turbine	1.00	400	1	$\dot{W}$ [kW]	[1]
Condenser	0.55	3000	10	5-10[5] [kW][2]	[16]
Pumps	0.39	2500	1	1-23 [kW]	[16]

Table 3 – Values of the terms of equation (4)

It was considered a US$ 50 million cost for the gasification system.

The annual cost of the equipment (levelized), is a function of the levelized factor, f_a, annual fixed cost of operation and maintenance, f_{omf} (9%), annual variable cost of operation and maintenance. f_{omv} (1%), and of the load factor, FC (75%), is given by the following equation:

$$C_{a_{EQ}} = I_{EQ}\left(f_a + f_{omf} + FC \cdot f_{omv}\right) \left[\frac{US\$}{year} \right] \tag{5}$$

And the levelized factor f_a is given by:

$$f_a = \frac{r}{1-(1+r)^{-n}} \tag{6}$$

where *r* is the annual rate of interests (12%) and *n* is the equipment levelized period in years (20 years).

The cost of the equipment can be given by the following expression:

$$\dot{C}_{EQ} = \frac{C_{a_{EQ}}}{T_o \cdot 3\,600} \left[\frac{US\$}{s} \right] \tag{7}$$

where $C_{a_{EQ}}$ is the annual levelized equipment cost, T_0 (7000 h) is the annual operation period of the plant[h].

The cost of the natural gas is 143 US$/t and that of bagasse considered 10 US$/t.

Exergy efficiency

The exergetic efficiency of the cogeneration plants is given by:

$$\eta_{ex} = \frac{\dot{W}_{E1} + \dot{W}_{E2} - \dot{W}_P + \dot{E}x_{PS} - \dot{E}x_{RS}}{\dot{E}x_{NG} + \dot{E}x_B + \dot{E}x_W} \ [\%] \tag{8}$$

RESULTS

The simulation results can be depicted in the following graphs. The first graph (Figure 5) presents the electricity generation power by the two turbines (gas and steam) as a function of the natural gas mass flow.

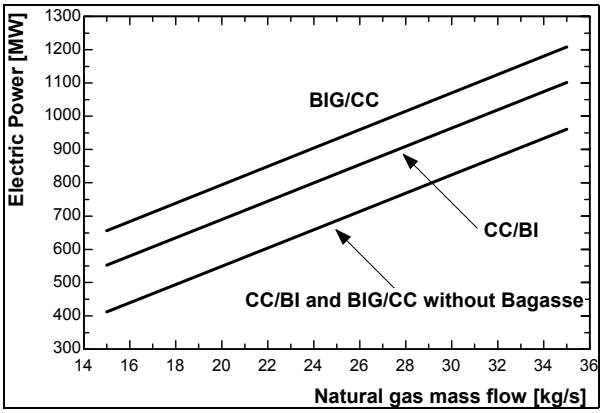

Figure 5 – Electricity generation power vs. natural gas mass flow

2 Value regarding the thermoelectric plant power.

Analyzing the results presented in Figure 5, it can be observed that the system BIG/CC, working in the sugar cane harvest, presents larger electricity generation power compared to the system CC/BI and also when the two systems work in the time between harvests (only with natural gas).

On the other hand, both systems working only with natural gas (between harvests) present the best exergetic efficiency, as shown in Figure 6. It is due to the abscenceof exergy destruction either in the gasification process (BIG/CC system) or by the temperature increasing in the HRSG - Heat Recovery Steam Generator (CC/BI system).

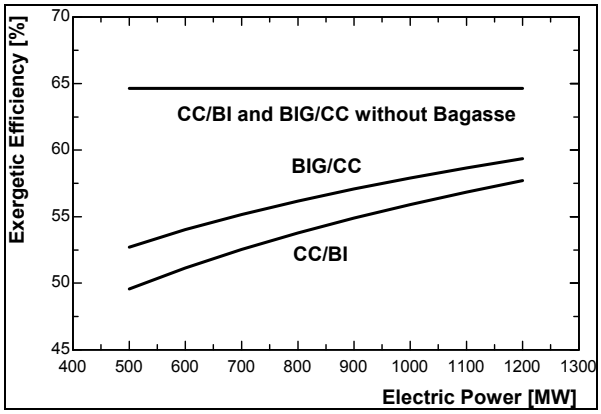

Figure 6 – Exergetic efficiency vs. electricity generation power.

In Figure 7 the average cost of electricity generated is presented. the average cost of electricity generation by the system CC/BI is smaller than the system BIG/CC. Although the BIG/CC system has higher exergetic efficiency, one of the reasons of the higher electricity generation cost is the high cost associated to the gasification system.

It can also be observed that the more natural gas is added, the lesser will be the cost of electricity generated in both cogeneration systems (Figure 7), and that the tendency of the exergetic efficiency is to be around 65% (Figure 6), corresponding to no use of sugar cane bagasse.

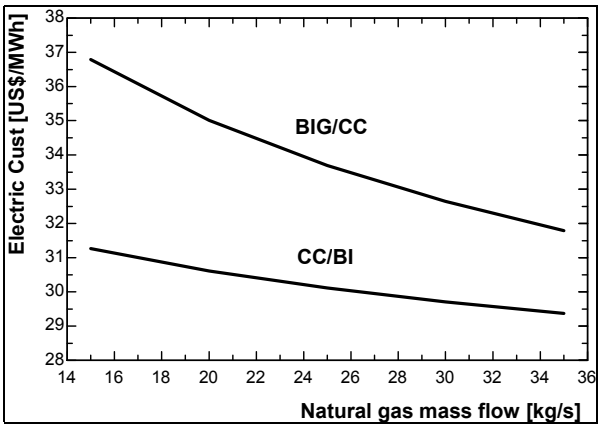

Figure 7 – Average cost of electricity generation vs. natural gas mass flow.

In Figure 8 are shown the results relative to the mass flow rate extracted for the cogeneration process (77% of the turbine inlet steam mass flow) as a function of the natural gas mass flow. the system CC/BI presents significant higher steam mass flow rates for process.

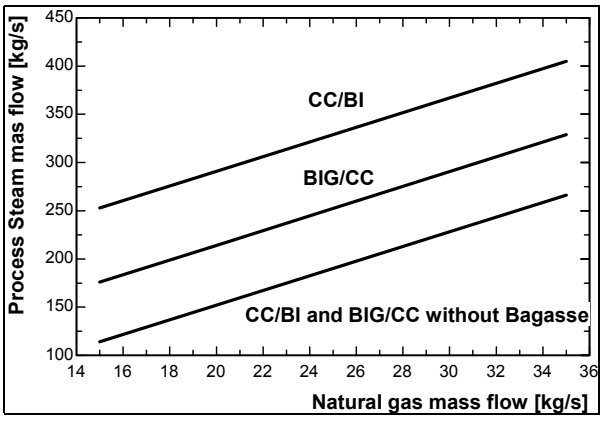

Figure 8 – Mass flow extracted for the process as a function of the natural gas mass flow.

Finally, the average cost of the steam extracted for process is shown in Figure 9. It can be observed that the average cost of the steam generated by system CC/BI is cheaper than the cycle BIG/CC. Once more, it happens due to the high cost of the gasification system.

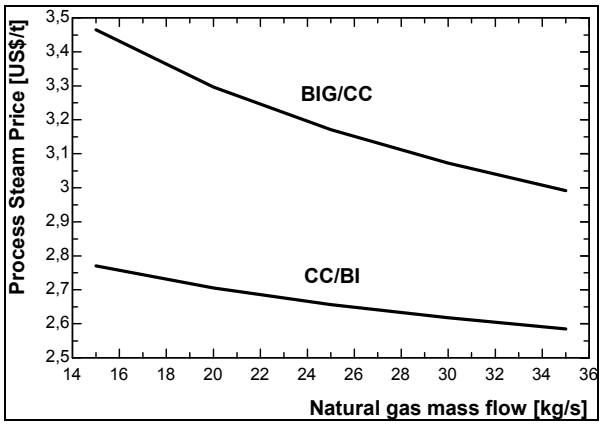

Figure 9 – Steam generation cost vs. natural gas mass flow.

CONCLUDING REMARKS

The comparative evaluation of natural gas and sugar cane bagasse based cogeneration system show that the Combined Cycle with Injection of Biomass in the Boiler (CC/IB) presents lower costs of electricity and steam generation than the Biomass Integrated Gasification/Combined Cycle (BIG/CC).

Even though these results indicate that system CC/IB is better than the BIG/CC, a closer look into the fixed costs involved (equipment costs) could bring about another idea. While the BIG/CC attains higher exergetic efficiencies, the high cost related to the gasification system more than offsets this advantage. So, gasification based cycles are still very dependent on research efforts in order to decrease its costs.

ACKNOWLEDGMENT

Leonardo Moneci Zamboni and Arlindo Tribess wish to acknowledge CNPq (Brazilian National Research Council) and Luiz Felipe Pellegrini and Silvio de Oliveira Jr. wish to acknowledge FAPESP (São Paulo State Foundation for Research Support) for the financial support received. The authors also wish to acknowledge Usina Iracema (Brazilian Sugar and Alcohol Mill) for their technical support and data.

REFERENCES

[1] Leite C. P. *Selecting thermoelectric plants using natural gas and sugar cane bagasse.* M.Sc. Thesis, Polytechnic School of the University of São Paulo, 148 pp. São Paulo, 2003. (in Portuguese).

[2] CATI - *Coordenadoria de Assitência Técnica Integral - Órgão da Secretaria de Agricultura e Abastecimento do Estado de São Paulo*. Dezembro 20, 2004. See also: http://www.cati.sp.gov.br.

[3] Rodrigues M.; Walter A.; Faaij A. *Co-firing of natural gas and biomass gas in biomass integrate gasification/combined cycle systems*. Energy 2003; 28: 1115-1131.

[4] Rodrigues M.; Faaij A.; Walter A. *Techno-economic analysis of co-fired biomass integrated gasification/combined cycle systems with inclusion of economies of scale*. Energy 2003; 28:1229-1258.

[5] Zamboni L. M.; Oliveira Jr S. Tribess A. Performance optimization of natural gas and sugar cane bagasse based cogeneration system. Proceedings of ECOS 2004, p. 1171-1178, México, 2004.

[6] Ieno G. O. Natural gas as Mercosul integration factor, PhD Thesis, Institute of Electrotechnic and Energy/Polytechnic School of the University of São Paulo, 2000 (in Portuguese).

[7] CESP – Comissão de Serviços Públicos de Energia. São Paulo. May 12, 2004. See also: http://www.cspe.sp.gov.br

[8] Pellegrini L. F., Oliveira S. *Exergy Analysis of Sugarcane Bagasse Gasification*. ECOS 2005.

[9] Coelho S. T. *Evaluation of cogeneration of electricity starting from sugar cane bagasse in gasifier/gas turbine systems.* Institute of Electrotechnic and Energy/Polytechnic School of the University of São Paulo, 1992 *(in Portuguese)*.

[10] Li, X. T. et al. *Biomass Gasification in a Circulating Fluidized Bed*. Biomass and Bioenergy, 2004; 26:171-193.

[11] Kotas T. J. *The exergy method of thermal plant analysis. Boston:* Krieger Publishing Company, 1995.

[12] Szargut, J.; Morris, D.R; Stewart, F. R., *Exergy analisys of thermal, chemical and metallurgical processes*, Hemisphere, New York, 1988.

[13] Balestieri, J. A. P. *Cogeneration – Generation of electricity and heat* (in Portuguese). Editora da UFSC, Florianópolis, 2002.

[14] *Cycle Tempo. Release 4.0.* Netherlands: TNO, 1999. See also: http://www.cycle-tempo.nl.

[15] Garagatti A. D. W. *Tri and tetra combined systems of cogeneration: Exergetic and thermoeconomic evaluation*, M.Sc. Thesis, Polytechnic School of the University of São Paulo, São Paulo, Brazil, 2000 (in Portuguese).

[16] Boehm R. F. *Design analysis of thermal systems.* New York: John Wiley & Sons Inc,

Proceedings of ECOS 2005
Trondheim, Norway
June 20–22, 2005

SIMULATION OF INTERNAL COMBUSTION ENGINES COGENERATION SYSTEMS: FOUR DIFFERENT ENGINES SIZES WITH HOT WATER ABSORPTION CHILLER

Denilson Boschiero do Espirito Santo
Mechanical Engineering Faculty - Energy Department
State University of Campinas-SP-Brazil
denilson@fem.unicamp.br

ABSTRACT

Cogeneration systems proved to be a good option for decentralized power generation in sites of coincident electrical and thermal loads. Site electrical and thermal loads demands can vary in a large range that makes cogeneration systems achieve high energy utilization factor (EUF) at hours of coincident high demands and low EUF at hours of small coincident demands. Energy availability of the prime mover must be compared with energy demands turning possible to evaluate and compare different options. Simulation of thermal systems is a powerful tool to well design power plants, helping designers evaluate several possibilities trying to turn economically feasible the cogeneration system.

INTRODUCTION

Environmental impacts, scarce and limited natural resources and a competitive electrical market are factors that turn vital the design of cogeneration systems with high energy utilization factor and that replaces costs of electricity and thermal loads at a form that turns the system economically feasible.

Evaluation of cogeneration systems involves several variables, turning the evaluation analysis a time spending process developed by an experienced engineering professional team. Energy balances, load profiles, equipments performances, operational strategies, legislation knowledge, operational costs, investment costs, environmental aspects, etc are some of the fields that must be studied.

Computational evaluation can reveal important information about the match of the loads by the system under analysis. Designing cogeneration systems sometimes lead to systems that doesn't meet all energy demands of the site, auxiliary equipments must meet particular loads and complement equipments must meet peak loads (i.e. electricity : grid). Legal aspects and tariffs structures have direct influence in the size of the cogeneration system, conducting to design of systems that attend the total electricity demand or the base of the electricity demand. Design of cogeneration systems permits several sizes for the prime mover and many systems conceptions.

CASE STUDY: HOSPITAL

To demonstrate the use of computational algorithms for the evaluation of internal combustion engines cogeneration systems, we will consider typical loads of a hospital.

The profiles weren't measured but through the analysis of electricity and gas bills and the installed equipments (chillers, boilers, water heaters, etc), it was possible to construct expected profiles for the main energy demands in the hospital. An energy monitoring system is planned to be installed.

Figure 1 shows a typical electricity demand profile. The figure was constructed with data of consumption at peak and out of peak hours, during the whole year of 2003. Figure 2 shows a typical demand profile of hot water for sanitary purpose (50^{o} C) and saturated steam demand at 6 bar. It was estimated based on the existing equipment and the gas bill. Figure 3 shows the cooling load (air conditioning) profile, based on characteristics of existing equipment, activity of the hospital and typical cooling load profiles for summer at south hemisphere. At figure 4 we can see a typical summer weather profile.

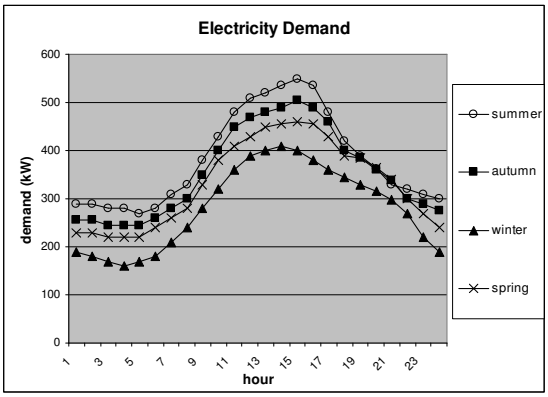

Figure 1 – Electricity demand

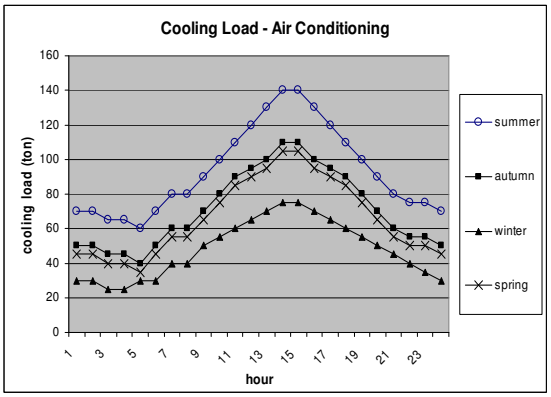

Figure 3 – Cooling load

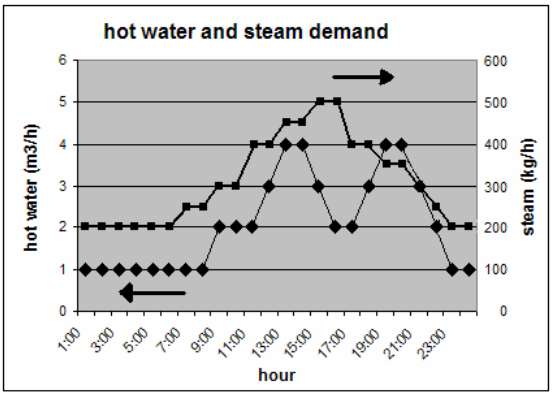

Figure 2 – Hot water and steam demand

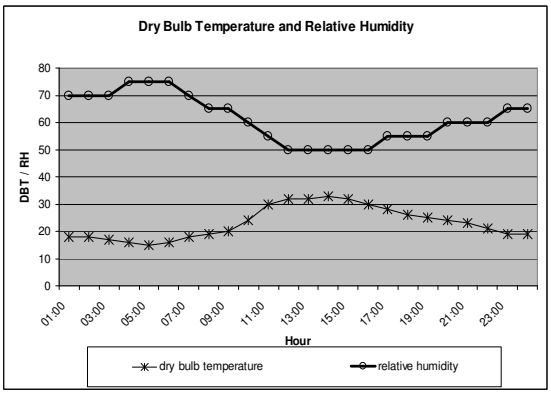

Figure 4 – local weather profiles

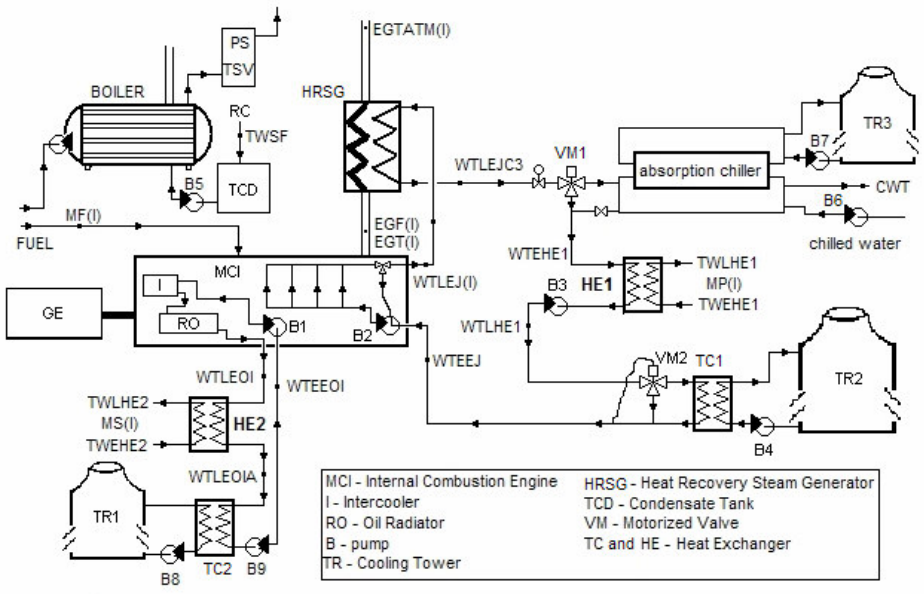

Engine + Exhaust gases heat exchanger + Hot water Absorption chiller + auxiliar heat exchangers

Figure 5 – Cogeneration Scheme

COGENERATION CONCEPTION

Figure 5 shows the cogeneration conception that will be simulated. It's composed by an internal combustion engine, primary and secondary water circuits, an exhaust gases heat exchanger, an absorption chiller and auxiliary equipments (pumps, cooling towers, heat exchangers).

Primary circuit recovery energy from the engine jacket and from the exhaust gases through an exhaust gases heat exchanger. The energy of the primary circuit is used at the absorption chiller and to warm water for sanitary purpose (after recovery at secondary circuit). Secondary circuit recovery energy from the oil radiator of the engine and utilize it to warm water for sanitary purpose.

Figure 6 reveals the energy balance of the engine at full and partial loads and figure 7 reveals the exhaust gases flow and temperature as a function of engine load. Maximum engine efficiency occur at load near 0,8 and correspond to 33%. Corrections for atmospheric pressure and dry bulb temperature are considered. No excess electricity will be sold to the grid, the engine will follow the electricity demand (electrical dispatch).

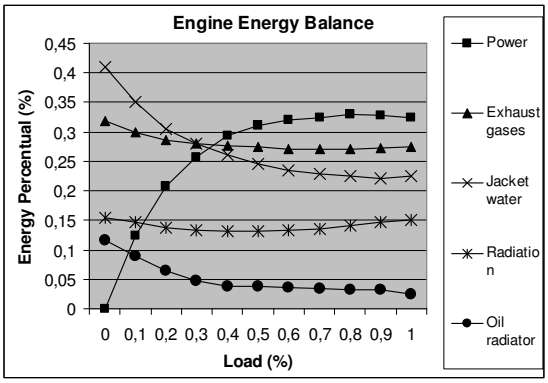

Figure 6 – Engine Energy Balance

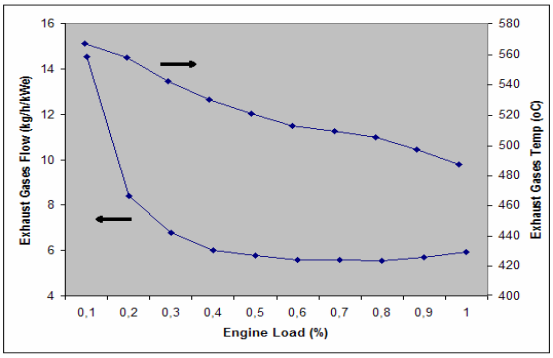

Figure 7 – Exhaust gases flow and temperature

DESIGN PARAMETERS

To compare different sizes of engines to meet the energy loads exposed, we will imagine a family of engine that has the same energy balance (figure 6) and exhaust gases flow and temperature (figure 7).

Four sizes of engines will be evaluated: 200 kW (solution 1), 300 kW (solution 2), 400 kW (solution 3) and 500 kW (solution 4).

At design condition (full load) water (primary circuit) should enter the engine (jacket) at 75° C and leave it at 95° C. After leaving engine hot water enters the exhaust gases heat exchanger.

Exhaust gases heat exchanger was designed to achieve an approach temperature of 11,1° C, with engine at full load. Approach point considers temperature difference between the gases discharged to atmosphere and hot water entering the exhaust gases heat exchanger. Exhaust gases composition are fixed and properties is calculated at mean temperature. Heat loss is equal to 1%.

At design condition water (secondary circuit) enter the engine at 35° C and leave the engine at 50° C. Water flows at primary and secondary circuit are designed considering the energy at the circuit and the design temperature difference.

Heat exchanger HE2 utilized to recovery energy from the secondary circuit (hot water for sanitary purpose) was designed to achieve an approach point of 2° C with the engine at full load.

Heat exchanger HE1 utilized to reheat the hot water for sanitary purpose was designed to achieve an approach point of 5,5°C with engine at full load.

Cooling towers and auxiliary heat exchangers are responsible to reject energy not utilized, preventing engine to operate under unsafe condition. Design of these equipments will not be developed.

Absorption chiller was designed to operate with hot water. Hot water temperature entering absorption chiller is a function of water flow at primary circuit and available energy in the exhaust gases. Absorption chiller was designed considering that hot water should leave it 8,3° C higher then the design temperature of water entering the engine. For solution 1, 2, 3 and 4 an absorption chiller of 70, 112, 148 and 200 tons was selected, respectively (nominal capacity under ARI 560). A drop of 1°C between engine and chiller is considered. Absorption chiller produce chilled water at 7°C with temperature difference of 5,5oC. Cooling water enter condenser at 29,5°C.

Total electricity produced is 3% higher then liquid engine power, taking into account the use of electricity in auxiliary equipments.

The avoided electricity due to the use of an absorption is evaluated at a rate of 1,2 kW/ton.

TECHNICAL RESULTS

Electricity

Simulating the operation of the four cogeneration systems, we have at figures 8, 9, 10 and 11 the electrical profile of the systems.

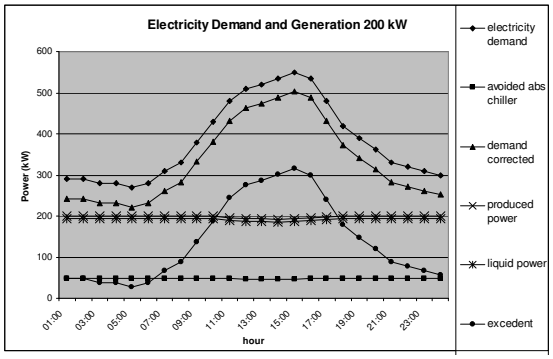

Fig. 8 – electricity demand / generation (200 kW)

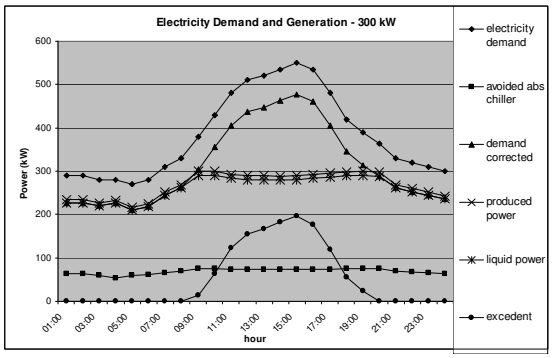

Fig. 9 – electricity demand / generation (300 kW)

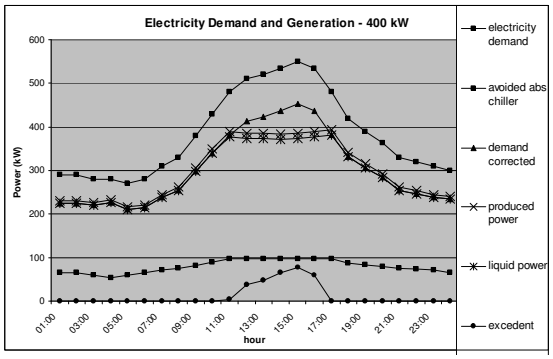

Fig. 10 – electricity demand / generation (400 kW)

Figures shows electricity demand, electricity demand with absorption chiller, total engine power, liquid available power, complement electricity (bought from the grid) and avoided electricity due to cooling load be met by the absorption chiller.

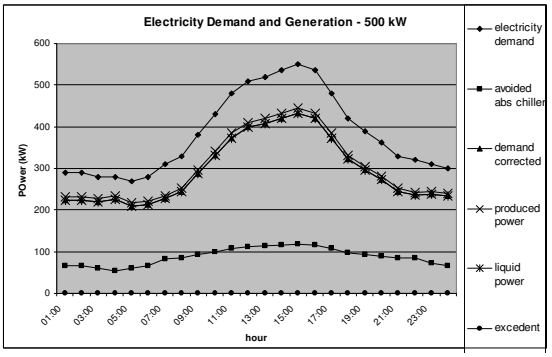

Fig. 11 – electricity demand / generation (500 kW)

It can be seen that at solution 1 the engine will operate at full load all the time, making absorption chiller produce constant capacity. At solution 2 and 3 the engine is expected to operate at full load only at electricity peak hours. At solution 4 the engine is expected to met electricity peak loads.

It's interesting to note the real capacity of the absorption chillers as a function of engine load and the surplus electricity bought from the grid as a function of engine and absorption chiller sizes. At solution 1 absorption chiller produces 40 tons and it's necessary to buy 3414,6 kWh daily. At solution 2 absorption chiller capacity ranges from 45 to 62 tons while total surplus electricity is 1277 kWh daily. For solutions 3 and 4 maximum absorption chiller capacity reaches 82 and 98 tons, respectively, while surplus electricity is equal to 293 kWh daily for solution 3.

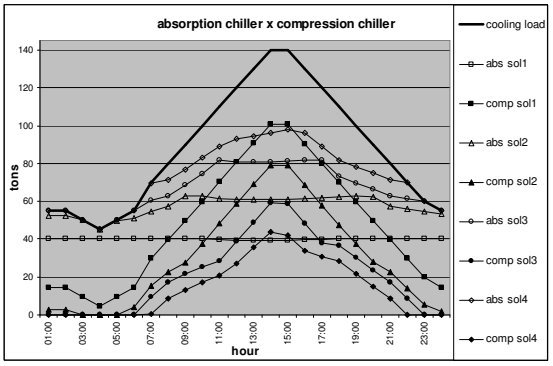

Fig. 12 – absorption and compression chiller loads

Cooling Load / Absorption Chiller

At figure 12 we see the cooling load of the hospital and the real capacity of the absorption

chiller for each solution. At solution 1 the absorption chiller operates at full load during all day. At solution 2 the absorption chiller operates at full load at all day except at hours 3 and 4 where the real capacity of the selected absorption chiller is higher then cooling load. Adopting solution 3 the absorption chiller operates at partial loads during the hours 1 to 6, 23 and 24, at the remaining hours it operates at full load. At solution 4 the absorption chiller will operate at full load between hours 7 and 21. Additional cooling load is met by a compression chiller that is expected to operate following the corresponding curve shown at figure 12.

Figure 13 shows the temperature of hot water entering the absorption chiller, the temperature of hot water leaving the absorption chiller (full load) and the hot water temperature difference at absorption chiller. Engine part load operation produces lower hot water temperature entering absorption chiller and consequent lower hot water temperature leaving absorption chiller. With engine at full load a higher difference of hot water temperature is verified, revealing a higher relation between real and nominal capacity of the absorption chiller.

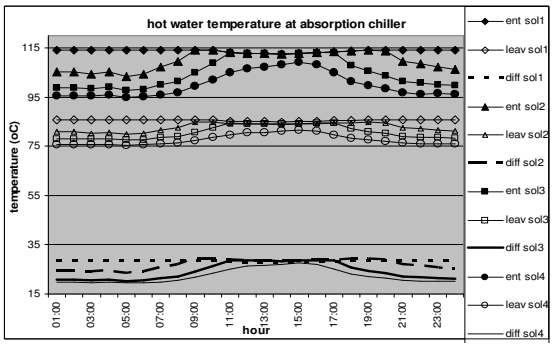

Fig 13 – hot water temperature at absorption chiller

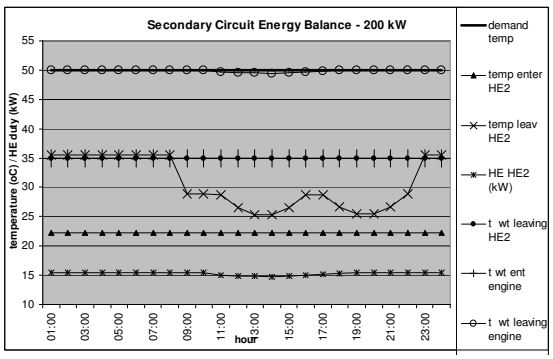

Fig 14 – Secondary circuit energy balance-200 kW

Engine Secondary Circuit (SC)

For the engine here evaluated, the secondary circuit recover energy from oil radiator. The energy at the secondary circuit is used to warm water for sanitary purpose. It can be noted that all hot water demand flow pass through heat exchanger 2 (HE2 – figure 5). Demanded hot water enter HE2 at 22° C (fixed) independent of day hour, and the demanded temperature for hot water is 50° C.

Secondary circuit hot water enter engine at 35° C (fixed) and leave engine at 50° C (full load).

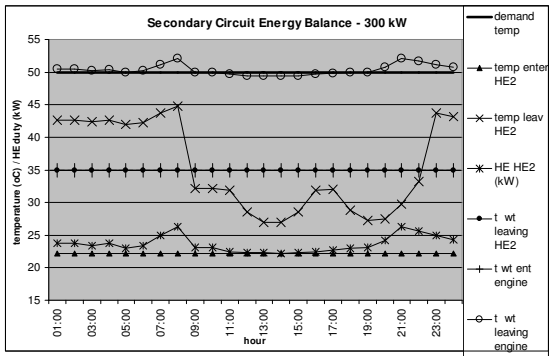

Fig 15 – Secondary circuit energy balance–300 kW

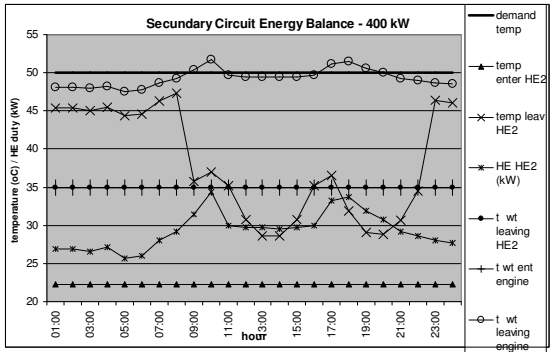

Fig 16 – Secondary circuit energy balance–400 kW

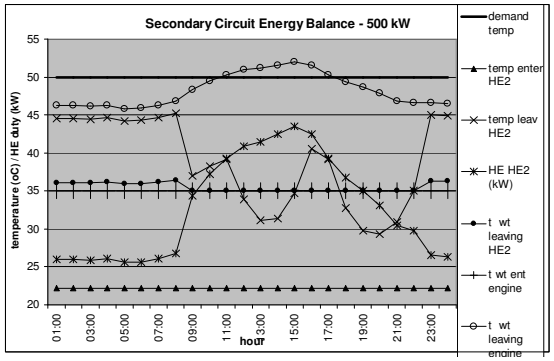

Fig 17 – Secondary circuit energy balance–500 kW

Figure 14 reveals the energy balance for SC adopting solution 1. We can note that hot water for sanitary purpose is warmed to a little more then 35° C when demand is 1 m^3/h. When hot water demand is 2, 3 and 4 m^3/h the water is warmed near to 28, 26 and 25° C, respectively.

Solutions 2, 3 and 4 have similar data, but we note that hot water temperature for sanitary purposes leaving HE2 rises as engine sizes rises.

Variation on temperature of water at secondary circuit leaving the engine is due to engine load variations for solutions 2, 3 and 4. Due to a quick rise of energy percentage at oil radiator for loads between 90 and 100%, the temperature of the water leaving engine is expected to be higher then at design condition.

All the energy of SC is used to warm hot water for sanitary purposes at solutions 1, 2 and 3 (SC hot water leaving HE2 is equal to design SC hot water entering engine). At solution 4, figure 17 reveals that not all the SC energy is used to warm water for sanitary purpose (hours 0-8 and 23-24). Design HE2 approach point is a limit for heat transfer.

Heat transferred at HE2 for all solutions are illustrated at the corresponding figures.

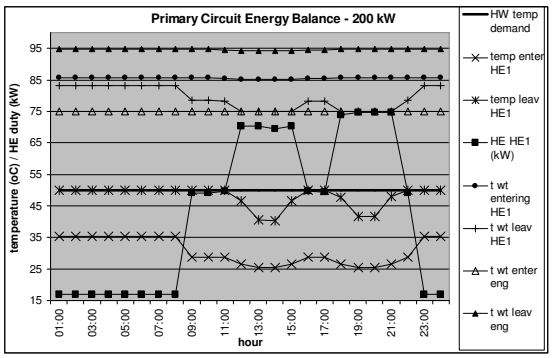

Fig 18 – Primary circuit energy balance–200 kW

Engine Primary Circuit (PC)

PC is responsible by recover energy of engine jacket and energy of the exhaust gases at exhaust gases heat exchanger (EGHE).

After leave the absorption chiller, water of the primary circuit enter HE1 that is responsible to warm hot water for sanitary purpose.

Hot water for sanitary purpose entering HE1 is at the temperature it leaves HE2. It can be seen that for solution 1 the base demand of hot water for sanitary purpose is met, while peak loads should be met by auxiliary equipments. At solutions 2, 3 and 4 a higher part of peak hot water for sanitary demand are met. Solution 3 needs less additional energy to met sanitary water demand at hours 19 to 21 than solution 4, due to part load operation of engine 4.

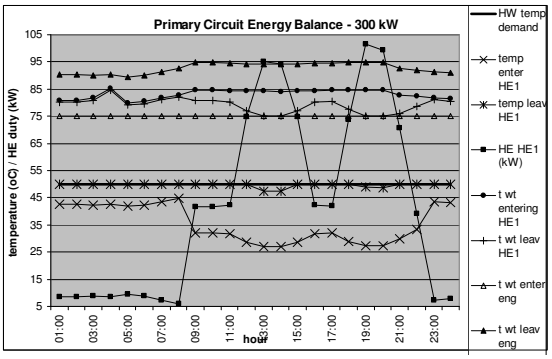

Fig 19 – Primary circuit energy balance–300 kW

Temperature of water leaving HE1 is another variable of interest, since the energy not utilized at HE1 are rejected, to return to engine at 75° C.

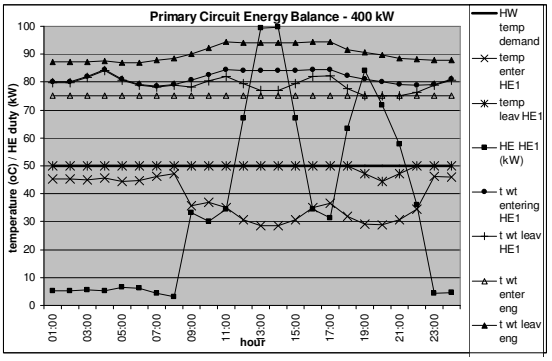

Fig 20 – Primary circuit energy balance–400 kW

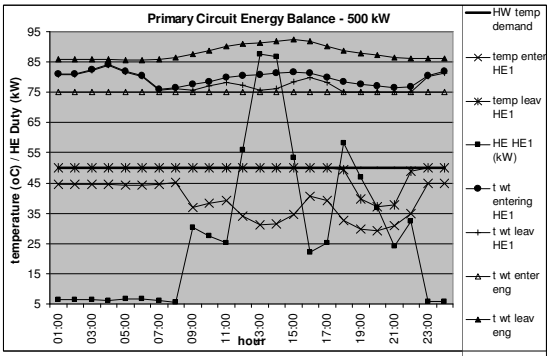

Fig 21 - Primary circuit energy balance–500 kW

It's interesting to note in figures 19, 20 and 21, that for hours 3, 4 and 5, the primary circuit water

temperature leaving absorption is higher then showed at figure 13 as a result of absorption chiller part load operation.

Exhaust Gases Heat Exchanger

Exhaust gases heat exchanger is responsible to recover energy from engine exhaust gases. Figure 22 reveals exhaust gases flow and temperature and the energy exchanged at EGHE for each solution.

Figure 23 reveals PC water temperature entering and leaving EGHE and exhaust gases temperature leaving EGHE (discharge to atmosphere).

For solution 1 PC water temperature entering and leaving EGHE remains almost constant and equal to 95 and 115°C respectively. Exhaust gases leaves EGHE near 106°C, revealing design approach temperature utilized at EGHE (11,1°C), with engine at full load this is also true for others solutions.

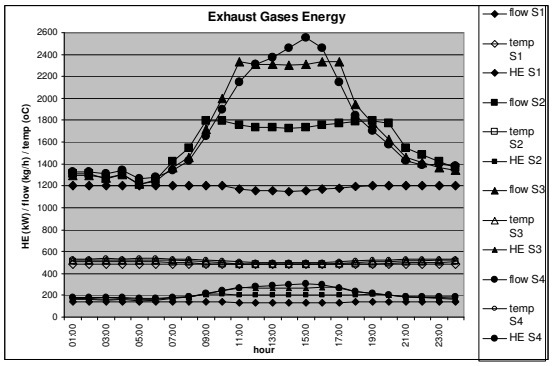

Fig 22 – Exhaust gases flow, temperature and HE.

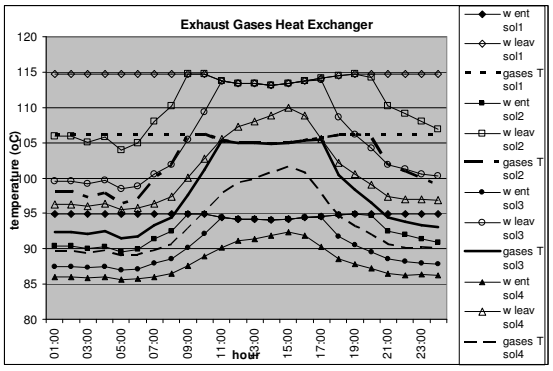

Figure 23 – Exhaust gases heat exchanger

Engine Load and Energy Utilization Factor

Figure 24 shows engines loads and figure 25 the energy utilization factor achieved on the hourly profile analysis.

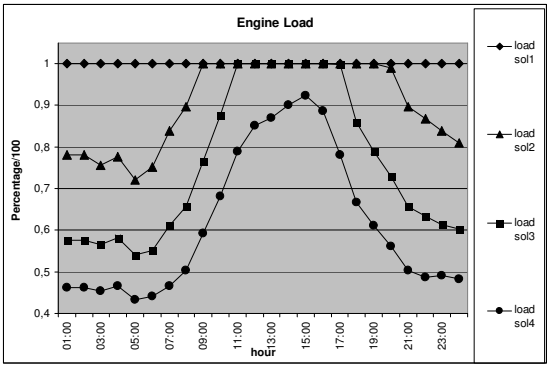

Figure 24 – Engine load

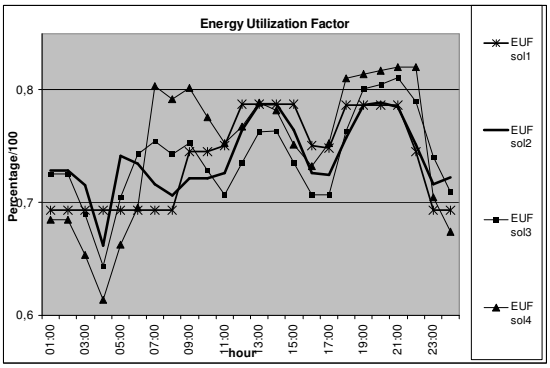

Figure 25 – Energy utilization factor

At solution 1 the engine operates at full load all the time, while for solutions 2 and 3 the engine is expected to follow electricity demand, operating at full load at high electricity demand hours. At solution 4 the engine is expected to operate with loads between 0,43 and 0,92.

Energy utilization factor is defined as the energy of the engine that is utilized by other system as a result of demands requirements, then the energy utilized at absorption chiller is computed and not the energy produced.

Energy utilization factor is a function of engine electrical efficiency (load), energy distribution at primary and secondary circuits and energy demands (electricity, cooling load and hot water).

At solution 1 EUF remains constant until hour 8, when it raises following hot water for sanitary purposes demand profile. Returning to figure 18 we can see the primary circuit water temperature leaving HE1, and justify it as the responsible by EUF rise. A medium EUF of 0,738 was found.

At solution 2 we see a quick decrease in EUF due to the operation of the absorption chiller at part load in hours 3 and 4. A medium EUF of 0,74 was found.

At solution 3 absorption chiller operate at partial load until hour 6, while the engine operate at partial loads until hour 11. A medium EUF of 0,739 was found. At solution 4 the engine operates at partial load all the time. Absorption chiller operates at full load between hours 7 and 21. Instantaneous high EUF is found at hour 22 (0.82). A medium EUF of 0,748 was found. Figure 26 reveals solution 4 engine energy balance.

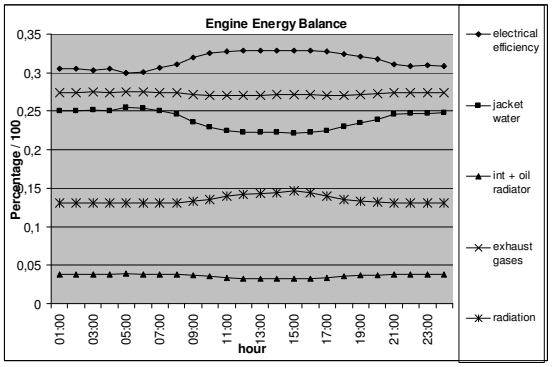

Figure 26 - 500 kW engine energy balance

CONCLUSIONS

Results here exposed were obtained through a program developed in Fortran with Delphi interface. The program is formed by one main program and more then twenty subroutines. Main program controls entrance data, report results and control all the procedures calculations. Several iterative procedures are involved, conducting results as a function of thermal loads, engine energy balance, design parameters, etc, to a converged point where all the individual equipments are expected to be in operation as a unique system.

Each solution has different nominal capacity of absorption chiller selected accordingly with design parameters and available nominal capacity on the market. Each solution has a different relation of nominal tonnage per engine nominal power.

Analysis of demand and availability can help decide to recover or not energy from secondary circuit.

High energy utilization factor was achieved for all solutions evaluated. Coincident loads profile (peak load of electricity, cooling load and hot water) contributes for these results. There is not a direct relation to evaluate EUF since we must evaluate and compare engine load, cooling load and absorption chiller load, heat exchangers simulations and hot water demand. Evaluate the variation on EUF for all the equipments individually help understand fig 25.

For the engine under evaluation radiation has a high participation on energy balance, limiting EUF for some hours.

Solution 1 has the best load factor for all the equipments involved. Justifying equipments cost acquisition, and probably a short payback period.

Considering a natural gas with low heating value of 45460 kJ/kg engines 1, 2, 3 and 4 have a daily consumption of 1159,2 kg, 1564,5 kg, 1758 kg and 1813,7 kg respectively. Solutions 1, 2, 3 and 4 produces 4756,6 kWh, 6447,1 kWh, 7187,9 kWh and 7285,7 kWh of electricity per day, respectively.

Results are particular for the engines under evaluation and are not conclusive about all possibilities. Economic analysis can reveal the better option considering costs and legal aspects.

REFERENCES

[1] Ganapathy, V. Waste Heat Boiler Deskbook. Fairmont Press, Lilburn:1991.

[2] ARI - Air Conditioning & Refrigeration Institute. Standard 560-92: Standard for absorption water chilling and water heating packages. N.York:1992.

[3] Hu, SD. Cogeneration. Reston Publishing House, Reston:1985.

[4] Orlando, J. A. Cogeneration Planners Handbook. Fairmont Press, Lilburn:1991.

[5] Dorgan, CB, Leight, SP, Dorgan, CE. Application Guide for Absorption Cooling / Refrigeration Using Recovered Heat. ASHRAE Publication. Atlanta:1995.

[6] Manufacturers Technical Catalogs (Jenbacher, Trane, Waukesha, York, Guascor, etc).

[7] Espirito Santo, D. B. and Gallo W. L., "Predicting Performance of a Gas Turbine Cogeneration System with Inlet Air Cooling". Ecos'2000, Twente, Netherlands, 2000.

[8] Espirito Santo, D. B. and Gallo W. L."Evaluating a Dual Pressure Combined Cycle Power Plant". Ecos'2001, Istanbul, Turkey, 2001.

[9] Espirito Santo, D. B. "Exergetic and Energetic Evaluation of a Triple Pressure Heat Recovery Steam Generator with Reheat", Ecos'2003, Copenhagen, Denmark, 2003.

ACKNOWLEDGEMENTS

We wish to thank the financial support given by FAPESP (São Paulo State Research Foundation).

Proceedings of ECOS 2005
Trondheim, Norway
June 20–22, 2005

Fuel cells and hydrogen systems

Proceedings of ECOS 2005
Trondheim, Norway
June 20–22, 2005

EXERGOECONOMIC STUDY OF HYDROGEN PRODUCTION FROM STEAM REFORMING OF NATURAL GAS

Lourenço Gobira Alves[1*]

Silvia Azucena Nebra[2]

[1,2] Energy Department, Mechanical Engineering Faculty, State University of Campinas.

DE/FEM/UNICAMP, P.O. BOX: 6122, CEP 13083-970 - Campinas – SP, Brazil

ABSTRACT

Steam Reforming of Natural Gas is, at the moment, the most economical process for producing hydrogen. This work performs an exergetic and exergoeconomic study of this process. The main steps in hydrogen production from steam reforming are the reforming reaction, the shift reaction and the hydrogen purification. The final hydrogen has purity of about 99,999% (wt) and can be used in fuel cells. Synthesis Gas containing H_2, H_2O, CO_2, CO and residual CH_4 is formed inside the reformer; its composition depends on the Steam-CH_4 ratio and the temperature-pressure conditions. Equilibrium conditions in the synthesis gas components are considered at reformer exit. After reforming, shift reaction converts CO and H_2O into CO_2 and H_2. Absorption in diethanolamine is used to separate CO_2 from the gas stream. CO_2 can be collected and sold as a by-product. Fixed adsorption beds are used to purify the hydrogen, eliminating H_2O, CO_2 and CO and CH_4 residuals. An exergy analysis was performed in this process identifying the main sources of irreversibility. The exergy flows are disaggregated into chemical and physical exergies. The theory of exergetic cost is applied to analyse the internal cost distribution. The results are discussed.

Keywords :exergy, exergoeconomy, hydrogen production, steam reforming.

NOMENCLATURE

K - Equilibrium constant
k - Unitary exergetic cost
P - Exergetic product [kW]
F - Exergetic fuel [kW]
I - Exergetic irreversibility [kW]
Ex - Exergy
ε - Exergetic efficiency *F-P* method
ζ - Exergetic efficiency input-output method
α - Chemical coefficients of reactants
β - Chemical coefficient of products

INTRODUCTION

Light hydrocarbons, especially methane, are the main source of hydrogen because they have a low production cost associated to large reserves all over the world [1]. Reforming of natural gas is the most economical way to produce hydrogen [2]. The process is described in three main steps: reforming, a highly endothermic reaction between H_2O and CH_4, shift reaction, an exothermic reaction between CO and H_2O producing H_2, and purification of hydrogen, where highly pure H_2 is separated.

[*] Corresponding author: phone: +55-19-37883285; fax: +55-19 32893722; email: lourenco@fem.unicamp.br

During purification, a large amount of CO_2 is produced as by product. In the simulation, natural gas was assumed as simply methane.
Some authors studied this process analysing energetic ([3],[4]) and exergetic consumption ([5], [6]).
During reforming, natural gas and steam react over nickel catalyst producing H_2, CO and CO_2, synthesis gas. Some of steam and methane persist in the synthesis gas. This reaction is highly endothermic and needs a source of heat, which is, generally, the same natural gas.
Hydrogen purification is performed through absorption in amine, followed by adsorption. During absorption large amount of CO_2 is produced as by product. Adsorption is the last step of purification process.
The H_2 production process was based on Rosen proposal [5] modified to incorporate an adsorption unit to produce highly pure H_2. In the adsorption unit, gas stream passes through an adsorbent bed and exits purified. Purity up to 99,999 % H_2, (in weight), is achieved [7].

STEAM METHANE REFORMING

The global reforming reaction between methane and steam can be represented generally as Equation (1), and the partial reactions as Equation (2) and (3):

$$\alpha_1 CH_4 + \alpha_2 H_2O \rightarrow \beta_1 CH_4 + \beta_2 CO + \beta_3 CO_2 + \beta_4 H_2 + \beta_5 H_2O \quad (1)$$

$$CH_4 + H_2O \rightarrow CO + 3\,H_2 \quad (2)$$

$$CO + H_2O \rightarrow CO_2 + H_2 \quad (3)$$

Starting from inputs α_1 moles of methane and α_2 moles of steam, the β coefficients in Equation (1) are determined based upon chemical equilibrium hypothesis of (2) and (3) reactions and element balances. The SMR was performed using sthoichiometric steam to methane ratio 2:1. Figure 1 shows a scheme of the process.
The process needs material inputs, methane (30 bar) and water (101.3 bar and 25ºC), and power inputs to water pump and absorption unit.

Process description

Water enters at environmental pressure and temperature and is compressed up to 3 MPa, heated and evaporated in a boiler, HR2, and is mixed with methane previously heated in a heat exchanger, HR3. (See Figure 1).
The mixture of steam and methane go to heat recovery HR1 and to reformer, where synthesis gas is produced. Methane is burnt in the combustion chamber to provide heat to reforming that occurs over nickel catalyst at 950ºC.
Inside reformer, synthesis gas rich in H_2 and CO is formed. Synthesis gas passes through shift reactors to reduce CO producing H_2, and goes to purification.

Reforming

The reforming step is composed of a heat recovery, HR1, the reformer and a boiler, HR2. HR1 heats the methane and steam mixture before reformer. HR2 produces superheated steam. The reformer is composed of a fixed bed with nickel catalyst.

Shift Reaction

The shift reaction is a reaction between CO and H_2O to reduce CO and produce H_2. To be more efficient, this reaction occurs in two steps: high temperature shift reaction, HTSR and low temperature shift reaction, LTSR, both occur in a fixed bed with catalyst. Shift reaction is exothermic, and after each shift reactor a heat recovery is used to heat methane and air that go to combustion chamber. After HTSR, gas stream is at 238 °C and after LTSR is 182 °C. Shift reduces the amount of CO from 15,1 % to 1,7 % in the HTSR and to 0,8 % in the LTSR.

Absorption Unit

CO_2 is separated in absorption unit and sold as a by-product. In this unit, CO_2 molar ratio is reduced from 18% (71.81 % wt) to 0.62 % (6.82 % wt). After absorption unit H_2 mol ratio is of 89%.
A solution of Diethanolamine in water at 30% was used as absorbent. Absorption of CO_2 in amine is of chemical absorption type. Amine is alkaline and CO_2 is an acid gas.
Absorption was modelled based on [8] and [9]. The absorption unit was idealised based on Ruthven description[10]. Figure 2 has a scheme of the absorption unit. The phenomenon is described as:

$$RNH_3 \overset{K_1}{\longleftrightarrow} H^+ + RNH_2 \quad (4)$$

$$RNHCOO^- + H_2O \overset{K_2}{\longleftrightarrow} RNH_2 + HCO_3 \quad (5)$$

$$CO_2 + H_2O \overset{K_3}{\longleftrightarrow} H^+ + HCO_3^- \quad (6)$$

$$HCO_3^- \overset{K_4}{\longleftrightarrow} H^+ + CO_3^{2-} \quad (7)$$

$$H_2O \overset{K_5}{\longleftrightarrow} H^+ + OH^- \quad (8)$$

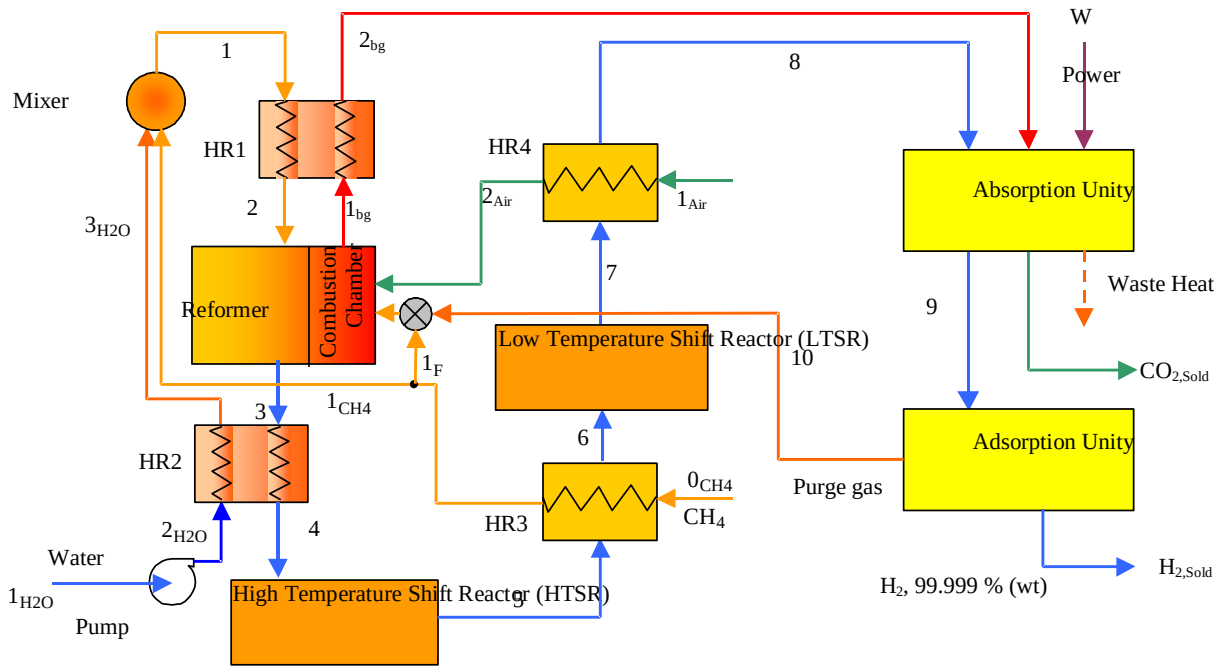

Figure 1 - Schematic of SMR process.

The equilibrium constants are:

$$K_1 = \frac{[RNH_2][H^+]}{[RNH_3^+]} \quad (9)$$

$$K_2 = \frac{[RNH_2][HCO_3^-]}{[RNHCOO^-]} \quad (10)$$

$$K_3 = \frac{[H^+][HCO_3^-]}{[CO_2]} \quad (11)$$

$$K_4 = \frac{[H^+][CO_3^{2-}]}{[HCO_3^-]} \quad (12)$$

$$K_5 = [H^+][OH^-] \quad (13)$$

Before pass through absorption column, the gas is cooled until 40ºC to promote better absorption. The absorbent and the gas flow in counter current along the absorption column, the CO_2 is carried out by the absorbent. To promote stripping, the absorbent is heated to 70 ºC and the pressure is reduced to 40 kPa.

As higher heating is, as better desorption is. The heating limit is the bubble point temperature of solution. To heat the absorbent solution, the unit has two heat exchangers

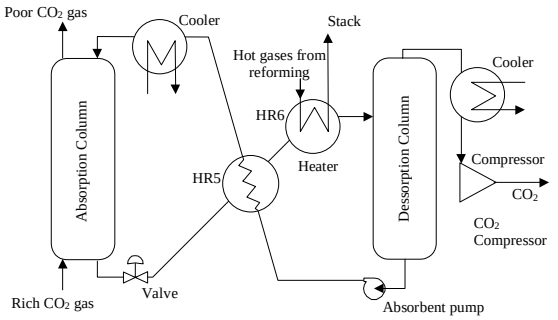

Figure 2 - Scheme of DEA absorption unit.

Adsorption unit

Adsorption is the last step in H_2 production. Its role is purifying H_2 up to 99.999 % (wt). This high purity is due to the elevated selectivity of hydrogen in the adsorbent bed related to CO_2, CO, N_2, CH4 and H_2O. Silica gel, activated carbon and zeolites compose the beds [7].

In this unit, a system of valves improves adsorption and regeneration of beds in a Pressure Swing Adsorption - PSA. At least four beds are required to improve PSA in order to establish the process near to steady state, while one bed is adsorbing, the others are regenerating, more details can be seeing at [7] and [11]. Steady state was assumed in adsorption process.

This system divides gas stream into two flows: pure hydrogen and purge gas. Purge gas is burnt in the combustion chamber. For this purge gas a Low Heat Value of 25400 kJ/kg was calculated. The purge stream saves 82 % of methane.
Due to PSA system, hydrogen exits at high pressure while purge gas at atmospheric pressure.
Recuperation factor, understood as amount of hydrogen present in the stream that is separated after adsorption cycle, was assumed as 82%. This value was based on [7] and [12].
Although adsorption process is an exothermic one it can be approximated as an isothermal process. This hypothesis is applied to cyclic process with short duration adsorption phase ([7], [11]).

EXERGETIC ANALYSIS

In order to improve exergetic analysis, the process was divided into several control volumes CV and each performance relative to its function.was determined. Some considerations were assumed:

- Environmental standard temperature and pressure conditions T0=25ºC and P0=101,3 kPa to exergy calculus. The composition was assumed as that proposed by [13].
- Efficiencies determined according to *Fuel* F, *Product* P and *Irreversibility* I concept [14], ε, or input output method, ζ, for dissipative control volumes. These efficiencies are defined as:

$$\varepsilon = \frac{P}{F} \quad (14)$$

$$I = P - F \quad (15)$$

$$\zeta = \frac{Ex_{in}}{Ex_{out}} \quad (16)$$

$$\zeta = Ex_{in} - Ex_{out} \quad (17)$$

Where Ex_{in} e Ex_{out}, are total exergies that enter and exit from CV respectively.
The exergy of a gas mixture is calculated as sum of each mixture component exergy plus the reversible isothermal work to compress (or decompress) from its partial pressure P_k to $P_{\infty,k}$ of the component in the environment [14] So, chemical exergy is calculated as:

$$\bar{e}x_{ch} = \sum_k x_k \bar{e}x_{ch,k} + RT_0 \sum_k x_k \ln(x_k) \quad (18)$$

Applying previous considerations to each CV according to figure 1:

Water pump:

$$F = \dot{W}_{pump} \quad (19)$$

$$P = Ex_{2,H_2O} - Ex_{1,H_2O} \quad (20)$$

Heat Exchanger 1 (HR1):

$$F = Ex_{1,bg} - Ex_{2,bg} \quad (21)$$

$$P = Ex_2 - Ex_1 \quad (22)$$

Heat Exchanger 2 (HR2):

$$F = Ex_3 - Ex_4 \quad (23)$$

$$P = Ex_{3;H2O} - Ex_{2;H2O} \quad (24)$$

Heat Exchanger 3 (HR3):

$$F = Ex_5 - Ex_6 \quad (25)$$

$$P = (Ex_{1;CH4} + Ex_{1;F}) - Ex_{0;CH4} \quad (26)$$

Heat Exchanger 4 (HR4):

$$F = Ex_7 - Ex_8 \quad (27)$$

$$P = Ex_{2;Ar} - Ex_{1;Ar} \quad (28)$$

Reformer:

$$F = (Ex_{1;F} + Ex_{11}) - Ex_{1,bg} \quad (29)$$

$$P = Ex_3 - Ex_2 \quad (30)$$

High Temperature Shift Reactor (HTSR):

$$F = Ex_{ch,4} - Ex_{ch,5} \quad (31)$$

$$P = Ex_{ph,5} - Ex_{ph,4} \quad (32)$$

Low Temperature Shift Reactor (LTSR):

$$F = Ex_{ch,6} - Ex_{ch,7} \quad (33)$$

$$P = Ex_{ph,5} - Ex_{ph,6} \quad (34)$$

For dissipative CV:
Mixer

$$Ex_{in} = Ex_{3,H2O} + Ex_{1,CH4} \quad (35)$$

$$Ex_{out} = Ex_1 \quad (36)$$

Absorption Unit

$$Ex_{in} = Ex_8 + Ex_{2,b} + \dot{W}_{ABS,pump} + \dot{W}_{CO2,Comp} \quad (37)$$

$$Ex_{out} = Ex_9 + Ex_{CO2,Sold} \quad (38)$$

Adsorption Unit

$$Ex_{in} = Ex_9 \quad (39)$$

$$Ex_{out} = Ex_{10} + Ex_{H2,Sold} \quad (40)$$

Where $\dot{W}_{pump}$ and $\dot{W}_{ABS,pump}$ are the power required by water and absorbent solution pumps, respectively, $\dot{W}_{CO2,Comp}$ is the power required by vacuum pump at stripping column; $Ex_{CO2,Sold}$ and $Ex_{H2,Sold}$ are the product exergies, CO_2 and H_2.
All these parameters were calculated related to 1 kmol/s of methane that enters in the reformer. These parameters are shown in Table 1.

Flow	T (K)	P (kPa)	$\dot{N}$ (kmol/s)
1_{H2O}	298.2	101.3	2
2_{H2O}	298.3	3300	2
3_{H2O}	1016	3000	2
0_{CH4}	298.2	3000	1.1034
1_{CH4}	490.6	3000	1
1_{bg}	1273	101.3	4.843
2_{bg}	877.5	101.3	4.843
1_{F}	490.6	3000	0.1034
1_{ar}	298.2	101.3	4.001
2_{ar}	445.8	101.3	4.001
1	803.4	2867	3
2	1253	2581	3
3	1223	2323	4.78
4	338.3	2206	4.78
5	510.6	2140	4.78
6	455.1	2076	4.78
7	465.8	2014	4.78
8	352.2	1953	4.78
9	313	1856	3.958
10	313	101.3	1.072
$CO_{2.Sold}$	458.7	101.3	0.8219
$H_{2.Sold}$	313	1670	2.886

Table 1: SMR operational parameters

The molar fractions of main flows are shown in Table 2. The exergetic efficiency of all CV are shown in Table 3 and exergies total, physical and chemical of flows are shown in Table 4.

Flow	CH_4	CO	CO_2	H_2	H_2O
1	0,333				0,667
3	0,0230	0,151	0,0348	0,593	0,197
5	0,0230	0,0170	0,169	0,728	0,0631
7	0,0230	0,00848	0,178	0,736	0,0545
10	0,0278	0,0103	0,00618	0,890	0,0659
11	0,103	0,0379	0,0229	0,593	0,244

Table 2: Molar ratio in main flows of SMR process

CV	ε	ζ
Water pump	0,8501	—
HR1	0,9684	—
HR2	0,739	—
HR3	0,5572	—
HR4	0,6534	—
HTSR	0,473	—
LTSR	0,3514	—
Reformer	0,4851	—
Mixer	—	0,9898
Absorption unit	—	0,9422
Adsorption unit	—	0,9936

Table 3: Exergetic Efficiency of CV

The exergetic balance identifying irreversibility along the cycle is made based on these previous values. Table 5 shows irreversibility of each CV.
It can be observed that the main source of irreversibility is the reformer (combustion chamber comprised), 52.7% of net irreversibility. This characteristic is due combustion, according discussed in [15].

EXERGOECONOMIC ANALYSIS

It was adopted the Exergetic Cost Theory proposed by [16] to perform exergoeconomic analyse of the process.
In order to apply this theory some considerations were made:

1) Input flows have unitary exergetic cost equal to one:

$k_{0,CH4} = 1$

$k_{1,H2O} = 1$

$k_{1,Ar} = 1$

$k_P = 1$

Where k_P is the power cost.

Flow	Ex_{ph} (kW)	Ex_{ch} (kW)	Ex (kW)
1_{H2O}	0	18980	18980
2_{H2O}	115,5	18980	19096
3_{H2O}	115183	18980	79249
0_{CH4}	9270	917936	927207
1_{CH4}	10239	831650	841889
1_F	1062	86286	87349
1_{ar}	0	0	0
2_{ar}	3259	0	3259
1_{bg}	103194	10355	102915
2_{bg}	52133	10355	51993
1	65872	845896	911768
2	115183	845896	961079
3	118270	959221	1077491
4	36867	959221	996088
5	44120	943885	988005
6	40474	943885	984359
7	40702	943236	983938
8	35714	943236	978950
9	28571	932042	960614
10	11,89	252273	252284
$CO_{2,Sold}$	1089	16331	17419
$H_{2,Sold}$	20078	681388	701466

Table 4: Flow exergies related to 1 kmol/s of inlet methane.

2) Streams that are fuel have same unitary exergetic cost.

$k_4 = k_5$

$k_7 = k_6$

$k_9 = k_8$

$k_{1,b} = k_{CC,In}$

$k_{1,b} = k_{2,b}$

Where $K_{CC,In}$ is the unitary exergetic cost of total exergy that enters combustion chamber and is determined as:

$$K_{CC,In} = \frac{Ex^*_{1F} + Ex^*_{13} + Ex^*_{2,Ar}}{Ex_{1F} + Ex_{13} + Ex_{2,Ar}} \qquad (41)$$

VC	**I (KW)**	**I (%)**
HR1	1611	0,687
HR2	21250	9,061
HR3	1615	0,688
HR4	1729	0,737
Pump	20,37	0,009
Mixer	9370	3,996
Reformer	123566	52,690
HTSR	8083	3,447
LTSR	420,9	0,179
Absorption Unit	59981	25,580
Adsorption Unit	6863	2,927
TOTAL	234508	100

Table 5 - Irreversibility in each control volume

3) Flow division, the streams have same unitary exergetic cost:

$k_{1,CH4}=k_{1,F}$

4) Main utility of CV:

CO_2 is a by-product of a hydrogen production plant. If this concept is applied to the absorption unit, whose main objective is to concentrate H_2, the unitary exergetic cost of CO_2 separated would be the same of inlet stream in the CV. Another possible interpretation is that the main objective of the absorption unit is to produce CO_2 , in this case, the exergetic cost of the CO2 separated would be different from the inlet stream, carrying the irreversibility cost generated in the unit. In this paper, the first concept is applied. This option penalises the final cost of hydrogen.

$k_8 = k_{CO2}$

Doing analogous consideration to adsorption unit, stream of purge gas does not change the unitary exergetic cost related to stream 9.

$k_9 = k_{10}$

Based on previous considerations, exergetic cost equations can be written, whose numerical results are expressed in Table 6.

Flow	Ex	Ex^*	k
1_{H2O}	18980	18980	1
2_{H2O}	19096	19116	1,001
3_{H2O}	79249	119174	1,504
0_{CH4}	927207	927207	1
1_{CH4}	841889	844142	1,003
1_F	87349	87583	1,003
1_{air}	0	0	1
2_{air}	3259	6184	1,897
1_{bg}	102915	127752	1,241
2_{bg}	51993	64540	1,241
1	911768	963316	1,057
2	961079	1026528	1,068
3	1077491	1324420	1,229
4	996088	1224362	1,229
5	988005	1224362	1,239
6	984359	1219843	1,239
7	983938	1219843	1,24
8	978950	1213659	1,24
9	960614	1263675	1,315
10	252284	331877	1,315
$CO_{2,Sold}$	17419	21596	1,24
$H_{2,Sold}$	701466	931798	1,328

Table 6 - Exergetic cost of flows.

Water pump:

$$Ex^*_{1,H2O} + \dot{W}_{Pump} = Ex^*_{2,H2O} \quad (42)$$

HR1: $$Ex^*_3 - Ex^*_2 = Ex^*_{1,b} - Ex^*_{2,b} \quad (43)$$

HR2: $$Ex^*_4 - Ex^*_5 = Ex^*_{3,H2O} - Ex^*_{2,H2O} \quad (44)$$

HR3: $$Ex^*_6 - Ex^*_7 = (Ex^*_{1,CH4} + Ex^*_F) - Ex^*_{0,CH4} \quad (45)$$

HR4: $$Ex^*_8 - Ex^*_9 = Ex^*_{2,Air} - Ex^*_{1,Air} \quad (46)$$

HTSR: $$Ex^*_5 = Ex^*_6 \quad (47)$$

LTSR: $$Ex^*_7 = Ex^*_8 \quad (48)$$

Mixer: $$Ex^*_{1,CH4} + Ex^*_{3,H2O} = Ex^*_2 \quad (49)$$

Reformer:

$$Ex^*_4 - Ex^*_3 = Ex^*_F + Ex^*_{13} + Ex^*_{2,Air} - Ex^*_{1,b} \quad (50)$$

Reformer combustion chamber:

$$Ex^*_{CC,In} = Ex^*_F + Ex^*_{2,Ar} + Ex^*_{13} \quad (51)$$

Absorption unit:

$$Ex^*CO2 + Ex^*11 = \dot{W}_{ABS,Pump} + \dot{W}_{CO_2,Comp} + Ex^*9 + Ex^*2,bg \quad (52)$$

Adsorption unit:

$$Ex^*_{H2} = Ex^*_{11} - Ex^*_{13} \quad (53)$$

CONCLUSIONS

This work simulated SMR hydrogen production in order to apply exergoeconomic tools, the method chosen was Unitary Exergetic Cost Theory.

Some important considerations were assumed to perform the simulation: temperature of reformer, 950 ºC; recuperation factor of hydrogen in the adsorption unit as 82 %; ideal gas mixture in the flows.

The reference environment was adopted as that proposed in [13] as well as the methodology to determine chemical exergy.

Exergetic analysis showed that the main source of irreversibility is the combustion inside combustion chamber of reformer. Irreversibility of reformer is 53 % the greatest along the process. This result is according to expected. Reform methane is the main step in hydrogen production; the simulation showed that 80% of hydrogen produced along the process is in the reforming step and 20% in shift reaction.

The second biggest source of irreversibility was the absorption unit, 26 % of total irreversibility. This result is due to the heat consumption, power to absorbent and CO_2 compressor and many heat exchangers wasting exergy to improve separation of CO_2 in this unit.

Adsorption unit produces only 3 % of total irreversibility. This low irreversibility generation has some reasons: isothermal process in ideal gases, in this condition, enthalpy of ideal gas remains unchanged; so, no heat and power consumption appear in this unit. The biggest reduction of pressure, source of irreversibility,

happens in the purge gas that has lower exergy than hydrogen flow.

Considering the exergies of H_2 and CO_2 products, the net process efficiency was 75.4 %. If CO_2 can not be used, its exergy must be neglected; in this case the net efficiency diminishes to 73.6 %.

The biggest unitary exergetic cost appeared in Nr. 2_{air} flow. This flow is heated in HR4 by 7 -8 flow.

The high unitary exergetic cost of this flow is due that it carries all the irreversibilities in the balance of HR4 and also to its low total exergy,

The second biggest unitary exergetic cost was in Nr. 3_{H2O}.flow. The situation is similar to the previous case, when the exergetic cost balance is applied to heat exchanger HR2. This CV accumulates two functions: evaporating and superheating the steam flow. The high irreversibility is due to high temperature difference between hot and cold side.

The exergoeconomic analysis assumes hydrogen as the main product and CO_2 as a by-product. The exergetic cost of H_2 is not the biggest exergetic cost because the regenerating process of adsorbent beds necessitates 18% of H_2 separated to perform regeneration.

Possibilities of variations of the exergoeconomic analysis that lead to different result are:

1. Adopt CO_2 as a product of process. The plant produces H_2 as well as CO_2 to sell. This analysis makes sense only if the process has a near consumer. Even if it is possible, the noblesse of hydrogen is always superior to that of dioxide carbon.
2. Adopt CO_2 as a flow without commercial utility. In this case the cost of CO_2 flow must be zero making H_2 more expensive.

REFERENCES

[1] Armor, J. N., "The Multiple Roles for Catalysis in the Production of H_2", Applied Catalysis A: General 176, pp. 159-176, 1999.

[2] Kothari, R., Buddhi, D. e Sawhney, R. L., "Sources and technology for hydrogen production: a review", International Journal of Global Energy, 2004, 21, (1-2), pp. 154-178.

[3] Choudhary, T. V. and Goodman D. W., "CO-Free Production of Hydrogen via Stepwise Steam Reforming of Methane", Journal of Catalysis, 192, pp. 316-321, 2000.

[4] Anderson, J.R. e Boudart, M., (editores); Catalysis – Science and Technology, V. 1, Edit. Springer-Verlag, Berlin, 1981.

[5] Rosen, M. A.; "The Development and Application of Process Analysis Methodology and Code Based on Exergy, Cost, Energy and Mass. PhD. Diss. Dept. of Mechanical Engineering, Univ. of Toronto, Toronto, 1986.

[6] Rosen, M. A., "Thermodynamic Investigation of Hydrogen Production by Steam-Methane Reforming", International Journal of Hydrogen Energy, v. 16, nº3, pp. 207-217, 1991.

[7] Yang, R. T., "Gas Separation by Adsorption Process" Series on chemical processes, Imperial College Press, 1997.

[8] Kent, R. and Eisenberg, B., "Better data for amine treating". Hydrocarbon Processing. v. 55, pp. 87-90, fev. 1976.

[9] Park, S. H., Lee, K. B., Hyun, J. C. and Kim, S. H., "Correlation and Prediction of the Solubility of Carbon Dioxide in Aqueous Alkanolamine and Mixed Alkanolamine Solutions". Industrial Engineer Chemical Research, v. 41, pp. 1658-1665, 2002.

[10] Perry, R. H., Grenn, D. W., "Perry's Chemical Engineers' Handbook, Mc Graw Hill Co., 1999.

[11] Ruthven, D. M. "Principles of Adsorption and Adsorption Processes" A Wiley-Interscience publication, 1984.

[12] Sircar S.; Waldron W. E.; Rao M. B. e Anand M., "Hydrogen production by hybrid SMR–PSA–SSF membrane system", Separation and Purification Technology, vol. 17, pp. 11–20, 1999.

[13] Szargut, J., Morris, D., R. and Steward, F., R., "Exergy Analysis of Thermal, Chemical, and Metallurgical Processes". Hemisphere Publishing Corporation, 1988.

[14] Kotas, T. J., "The exergy Method of Thermal Plant Analysis". Anchor Brandon LTD, Tiptree, Essex. Great Britain, 1985.

[15] Alves, L. G. e Nebra, S. A., "Thermoeconomic Evaluation of a Basic Optimized Chemically Recuperated Gas Turbine Cycle", International Journal of Thermodynamics, Vol.6 (No.1), pp.13-22, March-2003.

[16] Lozano, M.A. and Valero, A.;"Theory of the Exergetic Cost", Energy, v. 18, No. 9, pp. 939-960, 1993a.

Proceedings of ECOS 2005
Trondheim, Norway
June 20–22, 2005

COMPARISON OF PULP-MILL INTEGRATED HYDROGEN PRODUCTION FROM GASIFIED BLACK LIQUOR WITH STAND-ALONE PRODUCTION FROM GASIFIED BIOMASS

E. Andersson* and S. Harvey
Chalmers
Department of Energy and Environment
Sweden

ABSTRACT

When gasified black liquor is used for hydrogen production at a pulp mill site, significant amounts of biomass must be imported. This paper compares two alternative options for producing hydrogen from biomass: (A) pulp mill integrated hydrogen production from gasified back liquor; and (B) stand-alone production of hydrogen from gasified biomass. The comparison assumes that the same amount of biomass that is imported in alternative A is supplied to a stand-alone hydrogen production plant and that the gasified black liquor in alternative B is used in a BLGCC (Black Liquor Gasification Combined Cycle) CHP unit. The comparison is based upon equal amounts of black liquor fed to the gasifier, and identical steam and power requirements for the pulp mill. The potential for delivering low temperature excess heat to a district heating system is considered. The two systems are compared on the basis of total CO_2 emission consequences, based upon different assumptions for the reference energy system that reflect different societal CO_2 emissions reduction target levels. If the reference energy system includes electricity production in coal-fired power plants without CO_2 sequestration and car engines that are 30% more efficient than today's , the best alternative is to use the biomass in a stand-alone hydrogen production unit. However, if electricity production has lower CO_2 emissions , hydrogen produced with gasified black liquor integrated in the pulp mill can achieve the largest CO_2 emissions reduction.

Keywords: black liquor gasification, hydrogen production, CO_2 emissions, pulp mill

NOMENCLATURE

ADt	Air dried tonnes
BIGCC	Biomass Integrated Gasification Combined Cycle
BIOH2	Biomass gasification with Hydrogen production
BLGCC	Black Liquor Gasification Combined Cycle
BLGH2	Black Liquor Gasification Hydrogen production
DHS	District Heating System
KAM2	Kretsloppsanpassad massafabrik (Eco-Cyclic Pulp Mill)
LHV	Lower Heating Value
NG	Natural Gas
NGCC	Natural Gas Combined Cycle

*Corresponding author. Tel.: +46 31 7723018, Fax: +46 31 821928.E-mail: eva.andersson@chemeng.chalmers.se

INTRODUCTION

Background

Efforts to reduce greenhouse gas emissions favor the use of renewable energy sources. Biomass is an important renewable energy resource. Assuming that only a limited supply will be available in the future, it is essential to use biomass as efficiently as possible.

EU has set a target for renewable fuel usage in the transportation sector of 5.75% by 2010 [1]. With an expanding transportation sector, this is a challenging target. Furthermore, the target is probably quite modest compared to the anticipated need for CO_2 reduction in order to meet expected demanding targets for greenhouse gas emission reduction. Another motivation for finding renewable transportation fuels to replace

oil-based fuels is to secure the supply for a sector that will be even more dependent on imported fuels in the near future. This means that there could be a large demand for locally produced, renewable transportation fuels in the future. Other important options for the transportation sector include reducing the need for transportation, enhancing public transportation and using more fuel-efficient cars.

According to Azar el al [2], conventional oil-based fuels will remain dominant for transportation for the next 50 years. Hydrogen is expected to be the preferred choice when alternative fuels are introduced. Hydrogen will be particularly attractive if CO_2 separation and sequestration becomes an available technology.

In a future Hydrogen society, fuel cell vehicles are expected to be used since they use fuel more efficiently than cars with internal combustion engines. The advantages of using locally produced hydrogen in fuel cell vehicles have been discussed by Ogden et al [3], who conclude that the hydrogen fuel cell car has the lowest projected life-cycle costs if mass-produced and if a high value for external costs is considered. External costs include costs associated with air pollution, climate change and oil supply insecurity. Ogden's calculations are based on hydrogen produced from natural gas with CO_2 sequestration.

In the industrial sector, future pulp mills are expected to have a surplus of energy [4]. Most of the energy surplus is in the black liquor, the remaining fraction of the wood after extracting fibers for papermaking. The energy content of black liquor is currently recovered through combustion in a recovery boiler. Gasification is an alternative option, producing a syngas containing H_2, CO and CO_2 that can be used to produce electricity or upgraded biofuels, such as DME, methanol or hydrogen. A third option to use the excess energy in future pulp mills is to extract lignin from the black liquor and export it as biomass fuel, as discussed in [5]. This option was however not investigated in this study.

Previous studies have evaluated energy and net CO_2 emissions consequences of integration of hydrogen production from gasified black liquor in a chemical pulp mill and compared it with other uses of black liquor, including gasification and firing in a gas turbine combined cycle CHP unit (BLGCC) [6].

Objective

When hydrogen is produced from gasified black liquor, pulp mill steam must be generated in a biofuel boiler using imported biomass fuel. This study evaluates whether production of H_2 from black liquor is advantageous, with respect to CO_2 emissions reduction, or if the same amount of biomass should rather be used for H_2 production from gasified biomass in a stand-alone unit.

Method and assumptions

The methods used are described in the next three sections. The first section defines the compared systems, the second section provides input data background and the third section explains the methodology for CO_2 emissions calculations.

Important assumptions for the evaluation are:

- biomass is CO_2 neutral
- biomass is a limited resource
- demand for electricity, heat or transportation fuel is constant
- biomass is used to a great extent in DHS. If excess heat from a process can be delivered to DHS, biomass will be released for possible use in other applications.

HYDROGEN PRODUCTION SYSTEMS

The two hydrogen production systems are defined below. The expanded systems both produce the same amounts of electricity [MJ], transportation service [km] and heat [MJ]. They both include a pulp mill with the same input of wood and the same output of pulp, black liquor and biomass (bark), and with the same electricity and heat demand.

Hydrogen production units contain process streams with high CO_2 concentrations. This facilitates CO_2 separation. This option was not however included in this study.

Systems description

System A involves hydrogen production from black liquor integrated in a pulp mill, shown by the inner circle in Figure 1. Inputs to System A are wood, biomass and electricity and the products are pulp, hydrogen and heat.

System B produces hydrogen from gasified biomass. The objective is to compare the CO_2 emissions from the two hydrogen production

systems, based on the same input of biomass. Since input of wood to the pulp mill is part of the biomass input to System A, the system boundary for System B includes a pulp mill and associated energy flows. System B is the inner circle in Figure 2. The inputs to System B are wood and biomass and the outputs are pulp, hydrogen, electricity and heat.
The pulp mills in Systems A and B are identical, with the same pulp and black liquor flows, the same biomass (bark) surplus and the same steam and power demand.

Expanded systems

To calculate the CO_2 emissions, Systems A and B are expanded to include the reference energy system, where the output of electricity, transportation service, heat service and case-dependent energy service from the systems are identical.

Fossil fuel use for production of electricity and transportation fuel is increased or decreased to maintain a constant total production of electricity and transportation services. Biomass input for hydrogen production is the same in Systems A and B (underlined). If excess process heat can be delivered to the DHS, more biomass will be available for other uses (as defined in the reference energy cases). The net amount of available biomass is assumed to be constant.
Changes of biofuel usage in Systems A and B therefore lead to changes in amounts of biomass available for the reference use (Case dependent). The amount of case-dependent energy service delivered by the expanded system is constant, which also leads to variations in amounts of fossil fuel usage and CO_2 emissions.

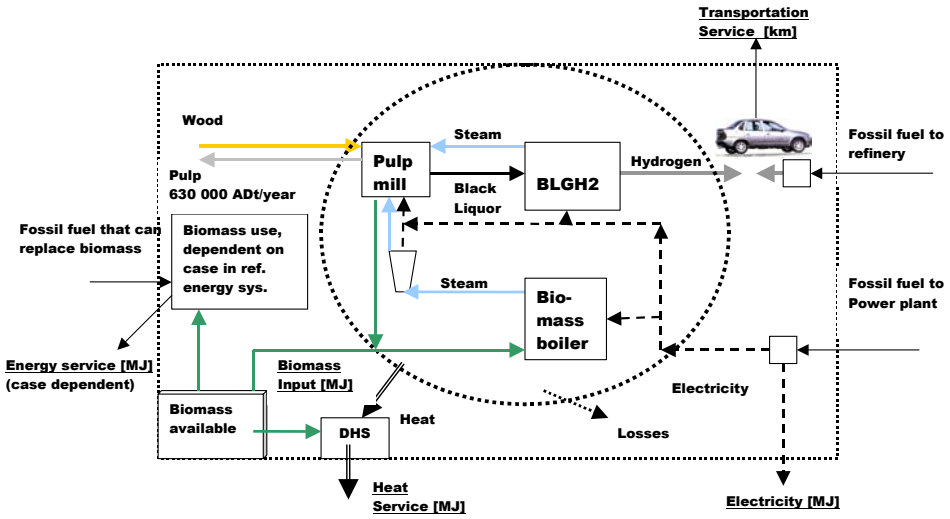

Figure 1 System A: H_2 production from gasified black liquor. The expanded system includes the reference energy system.

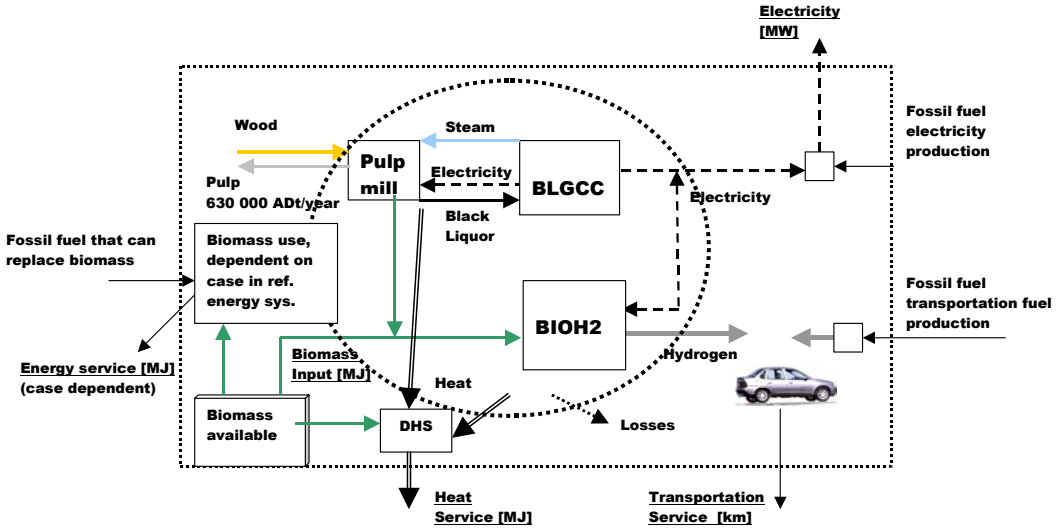

Figure 2 System B: H_2 production from gasified biomass and BLGCC. The expanded system includes the reference energy system.

INPUT DATA

Pulp Mill

The pulp mill energy flows used in the calculations are based upon results from the KAM 2 reference mill project developed within the Swedish research program KAM (Kretslopps Anpassad Massafabrik) [4]. The mill is assumed to incorporate the best available technology built and commercially used in the Swedish and Finnish pulp industry today. The pulp production is 630 000 ADt/year.

Hydrogen from gasified black liquor

The gasifier assumed for the calculations in this work has not been operated comercially, but is based on technology that has been developed since 1960. No pulp mill has yet fully replaced Tomlinson boiler technology with a black liquor gasification recovery system, but gasification plants have been introduced as booster units in parallel with existing recovery boilers to increase the plant's throughput. In these applications the performance of the gasification plant has been validated [7].

In System A, hydrogen is produced according to the process described in [8]. The possibility to deliver excess heat as district heating was evaluated and included in the energy balances for this study. Excess heat is available at the pulp mill and the hydrogen production unit. The heat is exported to a DHS, leading to biofuel savings.

Hydrogen from gasified biomass

In System B, hydrogen is produced from gasified biomass in a stand-alone production unit. The system includes a black liquor gasification combined cycle (BLGCC) unit for electricity production. The reason for selecting BLGCC is that previous studies have shown that BLGCC is an interesting alternative to a recovery boiler from a technical, economical and environmental perspective [6,9,10,11]. The excess biomass from the pulp mill is used for hydrogen production in the stand-alone facility.

Energy balances for the BLGCC plant are based on results presented in [10], in which electricity is assumed to be produced in a condensing steam turbine unit. In this paper we also evaluate the plant's energy balance assuming a back-pressure steam turbine unit delivering heat for district heating. In addition, excess heat is also available from the pulp mill.

Hydrogen production from gasified biomass has not been operated commercially. Estimated conversion efficiencies presented in the literature vary from 0.55 to 0.75 [12,13,14]. The data for a stand-alone hydrogen production unit adopted in

this work is based on the results of Hamelinck and Faaij [12], who report conversion efficiencies in the interval 0.6-0.66, which is a good average of other published studies. In addition, Hamelinck and Faaij present detailed energy balance calculations for different process configurations that produce hydrogen and electricity in different proportions with the same input of biomass. With a back-pressure turbine, excess heat can be delivered for district heating from the biomass gasification unit. To select the stand-alone facility configuration, the different configurations were assessed using the same evaluation method that was used for the final results later on (see "Evaluation of total CO_2 emissions using reference energy systems"). The configuration with the largest reduction of CO_2 emissions in each reference energy system case is retained for the stand-alone hydrogen production unit.

Limitations

CO_2 emissions associated with extraction of wood or production of chemicals used in the pulp production process are allocated to the pulp product and are not included. CO_2 emissions from construction of equipment for included processes or transportation vehicles are not included.

EVALUATION OF TOTAL CO_2 EMISSIONS USING REFERENCE ENERGY SYSTEMS

The CO_2 emissions from the expanded systems are based upon emissions associated with additional fossil fuel provided to the systems or avoided fossil fuel use. Fossil fuel is used for production of electricity and transportation fuel or to provide the same energy service that is provided by the reference use of biomass.
CO_2 emissions will depend on the technology used and the expected use of biomass. For this evaluation we assume different reference energy systems , Cases I-IVb, based on results presented by Ådahl [15]. The reference systems reflect the expected energy production technologies with increasing CO_2 emissions constraints in society. The numbers used include predictions for the future, based on qualified analysis of results from large-scale energy market models. The reference systems have been extended to also include the transportation system, see
Table 1. The alternative use of biofuel is specified for the different reference energy system cases. In Case I it is assumed to replace oil in e.g. heating applications, leading to a CO_2 emissions reduction.

Table 1 Reference energy systems with increasing CO_2 emissions reduction targets

	I	II	III	IVa	IVb
CO_2 emissions reduction target [%]	-5	-5	-25	-50	-50
Electric power production[1] (g CO_2 /MJ)	Coal (224)	Advanced coal (209)	NGCC (102)	Adv. coal with CO_2–sep (32)	Adv. coal with CO_2–sep (32)
Transportation[2] [16] (g CO_2/km)	Gasoline in today's cars (196)	Gasoline in a hybrid vehicle (140)	Gasoline in a hybrid vehicle (140)	NG-hydrogen in fuel cell vehicles (83)	NG-hydrogen in fuel cell vehicles (83)
Biomass use[1] (g CO_2 /MJ biomass)	Oil substitution (68)	Oil substitution (68)	Co-firing in coal power plant (91)	BIGCC (12)	Transporta-tion fuel (44)

[1] CO_2 emissions from extraction and transportation of biomass, coal and NG are included [17].

[2] The produced hydrogen is assumed to be used in fuel cell cars and will replace transportation fuel used for the technology described in the different cases. The functional unit when comparing transportation fuel is distance traveled. CO_2 emissions from extraction of raw materials, conversion to fuel, delivery to tank and combustion in the car engine are included in the calculations for transportation fuel.

RESULTS

Selection of stand-alone plant

As mentioned earlier, the stand-alone biomass-to-hydrogen plants presented by Hamelinck and Faaij were evaluated with the same criteria as when comparing systems A and B. The choice of stand-alone unit configuration is based on the largest reduction of CO_2 emissions. Since the different reference energy system cases yield different results for the configurations considered, the stand-alone production will vary in the different cases. Results are presented in Table 2. With reference energy system Cases I and II a stand-alone unit producing hydrogen, power and delivering heat is the best. With reference energy system Cases III, IVa and IVb, a stand-alone unit producing more hydrogen, but no power or heat gives a larger CO_2 reduction.

Table 2 Energy output from selected stand-alone hydrogen production plants [MW]

	DHS	H_2 (LHV)	Power	Heat
Case I and II	No	54	30	0
Case I and II	Yes	54	26	27
Case III, IVa, IVb	No	92	-7.9	0
Case III, IVa, IVb	Yes	92	-7.9	0[1]

[1]No excess heat available in this configuration

CO_2 emissions from extended Systems A and B

Table 3 shows the resulting energy input and output of System A and System B.

Table 3 Energy input and output from the hydrogen production units in Systems A and B. Losses are not included. See Figures 1 and 2 for definition of streams.

[MW]	Heat to DHS		No heat to DHS	
System	A	B	A	B
(Wood input – pulp output)	602	602	602	602
Biomass input	124	124	124	124
Power output[1]	-57	$108^2/74^3$	-57	$117^2/79^3$
Hydrogen output	261	$54^2/92^3$	261	$54^2/92^3$
Heat output	50	$73^2/45^3$	0	0

[1]A negative sign indicates input to system
[2] Used in Cases I and II
[3] Used in Cases III-IV

With the results in Table 3, the production (or avoided production if negative) of energy services that must be produced from fossil fuels in order to achieve a constant output from the expanded systems can be calculated. The results are shown in Table 4.

Table 4 Energy services that must be covered by fossil fuel usage to maintain constant output from the expanded systems. Operating time 315 days/year.

	Heat to DHS		No district heating	
System	A	B	A	B
Electricity[1] [PJ/year]	1.5	$-2.9^2/-2.0^3$	1.5	$-3.2^2/-2.1^3$
Transportation service [Tm/year]	-6.9	$-1.4^2/-2.4^3$	-6.9	$-1.4^2/-2.4^3$
Energy service[4] [PJ/year]	1.8	$1.2^2/2.0^3$	3.4	3.4

[1]A negative sign indicates avoided production
[2] Used in Cases I and II
[3] Used in Cases III-IV
[4] Case dependent

Using the values listed in Table 4, the CO_2 emissions are calculated based on the CO_2 emission factors from the reference energy system cases listed in. If heat can be delivered to a DHS, the reduction of CO_2 emissions will be as shown in Figure 3.

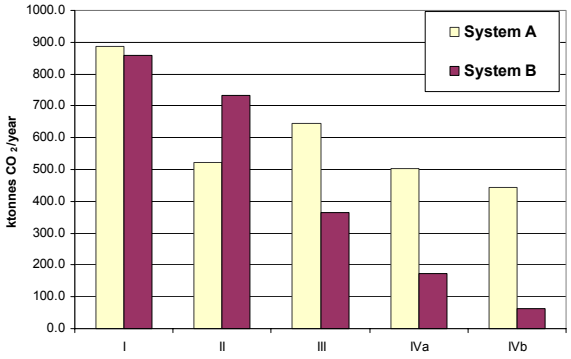

Figure 3 Reduction of CO_2 emissions for the two extended systems. Results shown for five different reference energy systems. Excess heat is used in DHS.

If heat cannot be delivered to a DHS, the total reduction of CO_2 will be less in both systems, Figure 4.

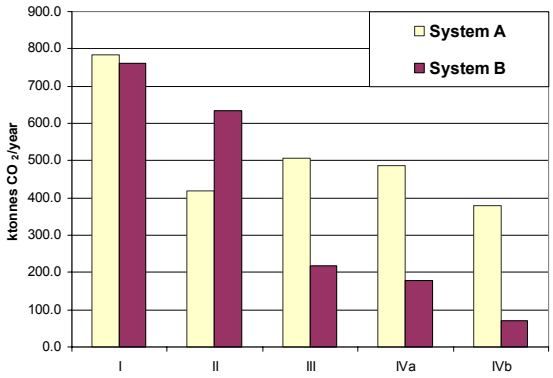

Figure 4 Reduction of CO_2 emissions for the two extended systems if excess heat cannot be used for district heating.

CONCLUSIONS

The objective was to compare hydrogen production from gasified black liquor (System A) with production in a stand-alone biomass gasification unit (System B) with respect to CO_2 emissions reduction, accounting for system consequences with an expanded system boundary. The total reduction potential is shown to be approximately the same for Systems A and B assuming reference energy system Case I. With Case II, where electricity is produced in a coal fired power plant and the reference transportation service is achieved with gasoline cars with a 30% better efficiency than today's cars, the reduction would be larger for expanded System B. In Case I, the reference transportation service is produced with gasoline in today's cars. Since the technology of fuel cell vehicles and hydrogen distribution is not widely available today, the calculated reduction would be hard to achieve in practice. In this respect, Case II probably provides a better description of the near term future.

In Cases III-IV, where reduction targets of 25 to 50 % are assumed, hydrogen from gasified black liquor achieves the largest CO_2 emissions reduction.

It is obvious that the CO_2 emissions reduction resulting from selection of a given process is very dependent on how the replaced or required energy is produced in the fossil fuel based reference energy system. The CO_2 reduction will be largest in the cases with less stringent CO_2 reduction targets.

The result show that introduction of black liquor gasification at pulp mills has benefits also when CO_2 emissions reduction targets are tougher.

Since the hydrogen production in Systems A and B is based on biomass, which is assumed to be CO_2 neutral, the reduction of CO_2 is achieved at other plants, where electricity and transportation fuel are produced. If more stringent CO_2 emission targets are adopted, this will lead to higher energy market prices. Price information for the reference energy systems must be included to evaluate the economic performance of the two hydrogen production systems.

ACKNOWLEDGEMENTS

We would like to thank Prof. Thore Berntsson for valuable comments. The work has been carried out under the auspices of The Energy Systems Programme, which is financed by the Swedish Energy Agency.

REFERENCES

[1] EU, *Directive 2003/30/EG*. 8 May 2003

[2] Azar C, Lindgren K, Andersson B A. *Global energy scenarios meeting stringent CO_2 constraints - cost-effective fuel choices in the transportation sector*. Energy Policy 31(2003) 961-971

[3] Ogden J M, Williams R H, Larson E D. *Societal lifecycle costs of cars with alternative fuls/engines*. Energy Policy 32(2004)7-27

[4] KAM-rapport nr A42, *KAM2 – programmets referensfabrik version 2000*. Sweden: STFi, February 2001.

[5] Eriksson H, Harvey S. *Black liquor gasification - consequences for both industry and society*. Energy (2004) 29(4): 581-612.

[6] Andersson E, Harvey S. *Pulp-mill integrated biorefineries: a framework for assessing net CO2 emission consequences.,* Paper presented at AIChE 2004 Fall Annual Meeting, Nov 7-12, 2004

[7] Ekbom T, Lindblom M, Berglin N, Ahlvik P. *Appendix 1 Final report BLGMF*. Stockholm Dec 2003

[8] Andersson E, Harvey S. *System Analysis of Hydrogen Production from Gasified Black Liquor*. ECOS2004, Guanajuato, Mexico, July 2004

[9] Larson E, Consonni S, Katofsky R. A. *Cost-Benefit Assessment of Biomass Gasification Power Generation in the Pulp and Paper Industry, Final Report*. Navigant Consulting, Inc., Princeton University and Politecnico di Milano. 8 October 2003.

[10] Berglin N, Lindblom M, Ekbom T. *Preliminary Economics of Black Liquor Gasification with Motor Fuel Production.* Paper at Colloquium on Black Liquor Combustion and Gasification, Park City, Utah, May 13-16, 2003

[11]Rehnström C. *LCA of two chemical recovery processes in the pulp industry- a case study*. Nordic Pulp and Paper Research Journal Vol 18 no.3 2003

[12]Hamelinck C N, Faaij A. *Future prospects for production of methanol and hydrogen from biomass.* Journal of Power Sources 2002 111(1): 1-22.

[13]Mann M K. *Technical and Economic Assessment of Producing Hydrogen by Reforming Syngas from the Battelle Indirectly Heated Biomass Gasifier*. August 1995 NREL

[14]Williams R H, Larson E D, Katofsky R E, Chen J. *Methanol and hydrogen form biomassfor transportation.* Energy for Sustainable Development, Vol 1 no 5 Jan 1995

[15]Ådahl A. *Process industry energy projects in a climate change conscious economy*. PhD Thesis, Chalmers Institute of Technology, Göteborg, Sweden 2004

[16]Well to Wheels Report Version 1, European Commission Directorate General Joint Research Centre, November 2003

[17]IVL Swedish Environmental Research Institute Ltd., *Miljöfaktabok för bränslen (Environmental facts about fuels)*. IVL report B 1334-2B

Proceedings of ECOS 2005
Trondheim, Norway
June 20–22, 2005

CONTROL-RELEVANT SOFC MODELING AND MODEL EVALUATION

Rambabu Kandepu[*], Lars Imsland[*], Bjarne A. Foss[*]
Department of Engineering Cybernetics

Christoph Stiller[†], Bjørn Thorud[†] and Olav Bolland[†]
Department of Process Engineering

Norwegian University of Science and Technology
7491 Trondheim, Norway

ABSTRACT

In this paper, a dynamic, lumped model of a Solide Oxide Fuel Cell (SOFC) is described, as a step towards developing control relevant models for a SOFC integrated in a gas turbine process. Several such lumped models can be aggregated to approximate the distributed nature of important variables of the SOFC. The model is evaluated against a distributed dynamic tubular SOFC model. The simulation results confirm that the simple model is able to capture the important dynamics of the SOFC. It is concluded that the simple model can be used for control and operability studies of the hybrid system.
Keywords: SOFC, control relevant, fuel cells, modeling

INTRODUCTION

Solid Oxide Fuel Cells (SOFC) integrated in Gas Turbine (GT) cycles (often denoted hybrid systems) is a promising concept for production of efficient and low-polluting electrical power. The SOFC can produce electric power at an electrical efficiency of about 55%, and when it is combined with a GT, studies show that the net electrical efficiency can be increased up to 70% [8]. The hybrid system uses natural gas as fuel and the percentage of pollutant flue gases is low compared to conventional power production from fossil fuels.

Due to the tight integration between the SOFC and the GT in a hybrid system, dynamic operability (and hence control) of the process is a challenge. It is important not only to design a good control system, but also to choose a process design that together with the appropriate control structure allows satisfying disturbance rejection and part load operation. Such a design procedure is usually called a integrated process design, see eg. van Schijndel [15]. To be able to design control structures and analyze dynamic behavior, it is very beneficial to have low complexity models of the components of the hybrid system. Such models are also valuable for online optimization. The aim of this article is to develop a low complexity mechanistic SOFC dynamic model which includes the relevant dynamics for operation in a hybrid system. There are several dynamic, distributed models reported in the literature. For example, Achenbach [1] developed a three dimensional, dynamic, distributed model for a planar SOFC stack. Chan et al. [4, 3], Thorud et al. [14], Stiller et al. [12] and Magistri et al. [10] all developed distributed, dynamic tubular SOFC models for designs similar to that of Siemens Westinghouse, for use in hybrid systems. In this paper, a simple, lumped, dynamic model of the SOFC based on mass and energy balances, with methane as fuel, is developed. The modeling approach proposed by Padulles et al. [11] for use in power systems simulation has some similarities with the approach described in this paper, however, therein hydrogen is used as fuel and only mass balances are considered.

The paper is outlined as follows: First a simple control relevant SOFC model is described with no regard to the geometric layout (tubular or planar). Extension of the simple lumped model towards capturing the distributed nature of the process by aggregating single volumes is explained next. Both SOFC models are evaluated against a distributed tubular SOFC model [14] with a considerably higher complexity. The two models are simulated for different realistic scenarios and the corresponding simulation results are presented. Applicability and shortcom-

[*] {Rambabu.Kandepu,Lars.Imsland,Bjarne.A.Foss}@itk.ntnu.no
[†] {Christoph.Stiller,Bjorn.Thorud,Olav.Bolland}@ntnu.no

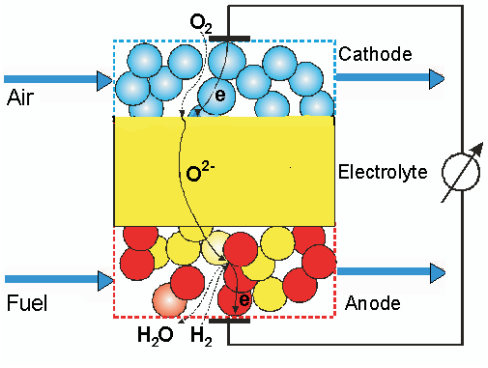

Figure 1: SOFC operation

Table 1: Reactions at anode and cathode

At anode	
Reaction	Reaction rate (r_j^{an})
$H_2+O^{2-} \rightarrow H_2O+2e^-$	r_1^{an}
$CH_4+H_2O \Leftrightarrow CO+3H_2$	r_2^{an}
$CO+H_2O \Leftrightarrow CO_2+H_2$	r_3^{an}
$CH_4+2H_2O \Leftrightarrow CO_2+4H_2$	r_4^{an}
At cathode	
Reaction	Reaction rate (r_j^{an})
$\frac{1}{2}O_2+2e^- \rightarrow O^{2-}$	r_1^{ca}

ings of the low complexity model are discussed. A nomenclature can be found at the end of the paper.

PROCESS DESCRIPTION

The Solid Oxide Fuel Cell (SOFC) is a device which converts chemical energy of a fuel directly into electrical energy [7]. The basic components of the SOFC are anode, cathode and electrolyte (conceptually illustrated in Figure 1). The electrolyte material is zirconia stabilized with the addition of a small percentage of yttria (Y_2O_3). The anode material is a zirconia cermet. The most common cathode material is strontium-doped lanthanum manganite. Fuel is supplied to the anode and air is supplied to the cathode. At the cathode-electrolyte interface, oxygen molecules accept electrons coming from the external circuit to form oxide ions, see Table 1 for reactions. The electrolyte layer allows only oxide ions to pass through and at the anode-electrolyte interface, hydrogen molecules present in the fuel react with oxide ions to form steam and electrons get released. These electrons pass through the external circuit and reach the cathode-electrolyte layer, and thus the circuit is closed. To increase the amount of power generated, a number of cells can be connected in series/parallel. This is known as stacking of cells. Also, there are mainly two types of SOFCs depending on the geometry; tubular and planar. The operating pressure can be from one bar to 15 bars. It is found that SOFCs show enhanced performance with increasing cell pressure [7]. The operating temperature of the SOFC is around 800-1000$^\circ C$. The high temperature and pressure operating conditions of the SOFC make it advantageous to combine the SOFC with a gas turbine (GT) to get a hybrid system with an high efficiency [8]. Due to the high operating temperature, an advantage is that several types of fuels can be used. In this paper methane is used as fuel. Because of the electrochemical reactions, there is a production of steam, and partial recirculation of this steam is used to reform methane into hydrogen. Typically, one third of the fuel is reformed (for example, in a pre-reformer) before it enters the SOFC and the remaining part is reformed within the SOFC. Table 1 gives the list of reactions that take place at anode and cathode and the corresponding reaction rates notation.

MODELING

The dynamic model of a single SOFC is developed using two mass balances; one for anode volume and the other for cathode volume, and one overall energy balance. In all of the streams from/to the SOFC, the following components can be present; Nitrogen (N_2), Oxygen (O_2), Hydrogen (H_2), Methane (CH_4), Steam (H_2O), Carbonmonoxide (CO), and Carbondioxide (CO_2). A number is assigned to each of these components to simplify the notation:

i	1	2	3	4	5	6	7
comp.	N_2	O_2	H_2	CH_4	H_2O	CO	CO_2

Model assumptions

The following main assumptions are made in developing the model.

1. All the physical variables are assumed to be uniform over the SOFC, resulting in a lumped model.

2. There is sufficient turbulence and diffusion within the anode and the cathode for perfect mixing to occur (CSTR).

3. The gas temperatures within the SOFC are assumed to be the same as the solid; i.e. the thermal inertia of the gases is neglected.

4. For the energy balance, pressure changes within the SOFC are neglected.

5. All gases are assumed to be ideal.

Mass balances

Two mass balances; one for the anode volume and one for the cathode volume are used:

$$\frac{dN_i^{an}}{dt} = \dot{N}_i^{in,an} - \dot{N}_i^{out,an} + \sum_{j=1}^{n_{rx}^{an}} a_{ij}^{an} r_j^{an}, \qquad (1)$$
$$i = 1,...,7, \;\; n_{rx}^{an} = 4$$

$$\frac{dN_i^{ca}}{dt} = \dot{N}_i^{in,ca} - \dot{N}_i^{out,ca} + \sum_{j=1}^{n_{rx}^{ca}} a_{ij}^{ca} r_j^{ca}, \qquad (2)$$
$$i = 1,...,7, \;\; n_{rx}^{ca} = 1$$

The reaction rates corresponding to the electrochemical reactions (r_1^{ca}, r_1^{an}) are directly related by the current,

$$r_1^{an} = I/(2F) = r_1^{ca} \qquad (3)$$

and the reaction rates corresponding to the reforming reactions are calculated as proposed by Xu [16]

$$r_2^{an} = \frac{k_2}{p_{H_2}^{an^2.5}} \left(p_{CH_4}^{an} p_{H_2O}^{an} - \frac{p_{H_2}^{an^3} p_{CO}^{an}}{K_2} \right) / (DEN)^2$$
$$r_3^{an} = \frac{k_3}{p_{H_2}^{an}} \left(p_{CO}^{an} p_{H_2O}^{an} - \frac{p_{H_2}^{an} p_{CO_2}^{an}}{K_3} \right) / (DEN)^2 \qquad (4)$$
$$r_4^{an} = \frac{k_4}{p_{H_2}^{an^3.5}} \left(p_{CH_4}^{an} p_{H_2O}^{an^2} - \frac{p_{H_2}^{an^4} p_{CO_2}^{an}}{K_4} \right) / (DEN)^2$$

In (4), DEN is given by

$$DEN = 1 + K_{CO}^{ads} p_{CO}^{an} + K_{H_2}^{ads} p_{H_2}^{an} + K_{CH_4}^{ads} p_{CH_4}^{an} \qquad (5)$$
$$+ K_{H_2O}^{ads} p_{H_2O}^{an} / p_{H_2}^{an}$$

and k_2, k_3 and k_4, the rate coefficients for the reforming reactions, are calculated by

$$k_j = A_{kj} \exp(\frac{-E_j}{RT}), \quad j = 2,3,4 \qquad (6)$$

The equilibrium constants for the reforming reactions K_2, K_3 and K_4 are given by

$$K_2 = \exp(-26830/T + 30.114) \quad [bar^2]$$
$$K_3 = \exp(4400/T - 4.036 \quad [-] \qquad (7)$$
$$K_4 = \exp(-22430/T + 26.078) \quad [bar^2]$$

In (5), $K_{CO}^{ads}, K_{H_2}^{ads}, K_{CH_4}^{ads}$ and $K_{H_2O}^{ads}$ are the adsorption constants, which are calculated by

$$K_i^{ads} = A_{K^{ads}i} \exp(\frac{-\Delta\overline{h}_i^{ads}}{RT}), \quad i = H_2, CH_4, H_2O, CO \qquad (8)$$

It is assumed that the exhaust flows at the anode and cathode outlets can be described by the choked exhaust flow equation. This means that the mass flow rate of the exhaust flow at the anode (cathode) depends on the pressure difference between the pressure inside the anode (cathode) and the pressure at the outlet [11]:

$$\dot{m}_{out,an} = \sqrt{k_{an}(p_{an} - p_{out,an})} \qquad (9)$$
$$\dot{m}_{out,ca} = \sqrt{k_{ca}(p_{ca} - p_{out,ca})}$$

The partial pressures, volume, and temperature are assumed to be related by the ideal gas equation, for instance at the anode,

$$p_i^{an} V_{an} = N_i^{an} RT \qquad (10)$$

Energy balance

The energy balance accounts for the whole SOFC volume, and is given by [13, 9]:

$$C^s \frac{dT}{dt} = \sum_{i=1}^{N} \dot{N}_i^{in,an} (\Delta\overline{h}_i^{in,an} - \Delta\overline{h}_i)$$
$$+ \sum_{i=1}^{N} (\dot{N}_i^{in,ca} (\Delta\overline{h}_i^{in,ca} - \Delta\overline{h}_i) \qquad (11)$$
$$- \sum_{j=1}^{M} \Delta\overline{h}_j^{rx} r_j^{an} - P_{DC} - P_{rad} - P_{cond}$$

In this equation, the temperature changes of gases are neglected as they are fast compared to the temperature changes of the solid and by assuming that these fast changes of gas temperatures do not influence the dynamics of the overall process. Hence the energy balance gives a dynamic equation for the temperature changes of the SOFC solid.
In (11), P_{DC} represents the amount of DC power produced by the SOFC, P_{cond} represents the conduction heat loss from SOFC to the surroundings and P_{rad} represents the amount of radiation heat given from the SOFC. As the SOFC operating temperature is higher than that of the surroundings, there is always some loss due to radiation. It can be calculated by [6]

$$P_{rad} = A\delta\varepsilon\sigma(T^4 - T_{sur}^4) \qquad (12)$$

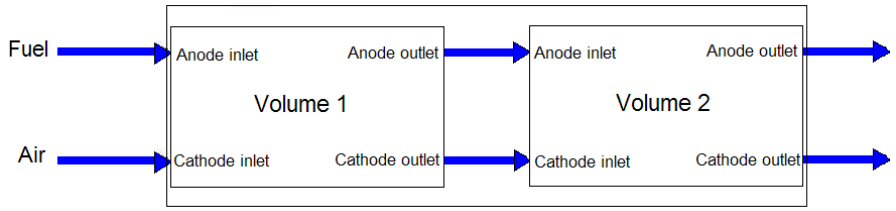

Figure 2: Aggregation mechanically

In (12), A is the surface area, δ is shaping factor, T_{sur} represents the surroundings temperature, ε is the emissivity of the SOFC surface and σ is the *Stefan-Boltzmann constant* ($\sigma = 5.67 \times 10^{-8}\text{W/(m}^2\text{.K}^4)$). The amount of DC power from the SOFC is given by

$$P_{DC} = VI \tag{13}$$

Voltage

The operating cell voltage is given by

$$V = E^{OCV} - V_{loss} \tag{14}$$

where the open circuit voltage of the cell is given by the *Nernst equation* [7],

$$E^{OCV} = E^o + \frac{RT}{2F} \ln \left(\frac{p_{H_2}^{an} p_{O_2}^{an^{0.5}}}{p_{H_2O}^{an}} \right) \tag{15}$$

where E^o is the EMF at standard pressure. V_{loss} is the voltage loss, as explained below.

Voltage loss

When the cell is operated, there are voltage losses coming from different sources; activation losses, concentration losses and ohmic losses [7]. Activation losses are caused by the limited reaction rate on the surface of the electrodes. Ohmic losses are due to the electrical resistance of the electrode material and the various interconnections, as well as the resistance of the electrolyte. The ohmic losses are responsible for the largest part of the voltage losses. The concentration losses result from the change in concentration of the reactants at the surface of the electrodes as the fuel is used. Stiller et al. [12], Thorud et al. [14], Campanari et al. [2], and Magistri et al. [10] used rather complex empirical functions to calculate the ohmic and activation losses. In this simple model the total voltage loss is approximated by a first order function of cell temperature and current. This function is obtained by curve fitting the simulated data obtained from a distributed model [14], where an active area of 834cm^2 is used to calculate the different voltage losses. Thus total voltage loss is calculated by

$$V_{loss} = f(I,T) \tag{16}$$

MODEL AGGREGATION

In a real SOFC, temperature and pressure vary over the SOFC volume. The distributed nature cannot be represented by using the ”one volume” model. By connecting many volumes in a sequential manner it is possible to approximate the distributed nature of the variables. The whole structure with all the volumes represent a single cell. So, if many volumes are connected, each volume can be represented by a scaled-down model. In principle, it is possible to connect any number of volumes, but for simplification, an example is considered where a single SOFC model is obtained by connecting two scaled-down models as shown in Figure 2. The two volumes are selected such that the first volume is represented by a scaled-down model by scaling down the ”one volume” model volume and heat capacity constants by 1/3. The second volume is represented by a scaled-down model obtained by scaling down the ”one volume” model constants by 2/3. Electrically, the two scaled-down models are connected in parallel (Figure 3). Ideally, the voltage across each of the volumes should be the same and the total current is divided between the two volumes. Then probably, most of the current will be produced from the second volume, as mainly reforming reactions take place in the first volume. In the present work it is assumed that the first volume supplies 1/3rd of the total current and the second volume supplies the remaining current. With this assumption, there is a small voltage difference between the two volumes. Developing a strategy for dividing the currents among the volumes when a SOFC is represented by many volumes is a part of further work. The basic point is

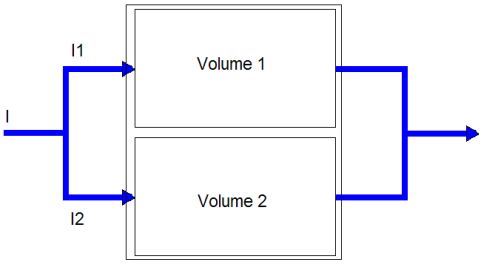

Figure 3: Electrical aggregation

to show that it is possible to approximate the distributed nature of the variables by aggregating the scaled-down models.

MODEL EVALUATION

As no experimental data is available to the authors for evaluating the simple model, the model is evaluated with an available detailed model. The detailed model [14] is a quasi two-dimensional dynamic model of a SOFC tube, similar to that of Siemens Westinghouse. It is a discretized model where gas flows are treated as 1D plug flows. The solid structures are modeled by a 2D discretization scheme in the axial and radial direction, neglecting effects in the circumferential direction. Both the simple and the detailed models are developed using gPROMS [5]. For solving the detailed model gPROMS uses about 1300 differential equations, where as for the simple model it uses 15 differential equations.

Figure 4 shows the comparison set up used for the simulation. Here the main aim is to evaluate the simple model against the detailed model [14]. The simulations are performed in such a way that the same input conditions are applied to the two SOFC models. Fuel is supplied to the pre-reformer which reforms about 30% of methane. The pre-reformer outlet gas is supplied to the anode inlet and air is supplied to the cathode inlet. Some part of the anode flue gas is recycled back to the pre-reformer to supply steam required by the reforming reactions. The other part of the anode flue gas and the cathode flue gas are supplied to a combustor where the remaining fuel is burnt and the resultant gas mixture will be the exhaust gas. The SOFC and pre-reformer are thermally connected by radiation. The details of the models of the other components used in the process shown in Figure 4 are not discussed here. The values of important parameters of the simple model are given in Table 2. The values of important variables at steady state are given in Table 3. Table 4 shows

Table 2: Model parameters

Anode volume	$1.032\times10^{-5}\mathrm{m}^3$
Cathode volume	$4.3\times10^{-5}\mathrm{m}^3$
C^s	800J/K
k_{an}	$1.9\times10^{-3}\mathrm{kg}^2\mathrm{s}^{-2}\mathrm{Pa}^{-1}$
k_{ca}	$4.2\times10^{-3}\mathrm{kg}^2\mathrm{s}^{-2}\mathrm{Pa}^{-1}$

Table 3: Steady state values

methane flow rate	4.50×10^{-4}kg/s
methane inlet temperature	950K
Air flow rate	1.44×10^{-2}kg/s
Air inlet temperature	950K
Current	250A
Anode pressure	3bar
Cathode pressure	3bar
Cell voltage	0.56V
Cell power	141W
Cell temperature	1113K
air utilization	0.21
fuel utilization	0.7

the simulation scenarios used for comparing the dynamic behavior of the two models.

SIMULATION RESULTS

Simulations are made for two comparison schemes; first, the simple SOFC model with one volume is compared to the distributed tubular SOFC model [14], and second, the simple SOFC with two volumes is compared to the distributed tubular SOFC model. SOFC mean solid temperature, cell voltage and cell power of the simple model and the detailed model are compared in each comparison scheme. Figures 5-7 show simulation results of the first comparison scheme and Figures 8-9 show simulation results of the second comparison scheme.

Table 4: Simulation details

Time(min)	Disturbance
90	fuel flow is decreased by 20%
180	fuel flow is increased back to 100%
270	air flow is decreased by 20%
360	air flow is increased back to 100%
450	current is decreased by 20%
540	current is increased back to 100%

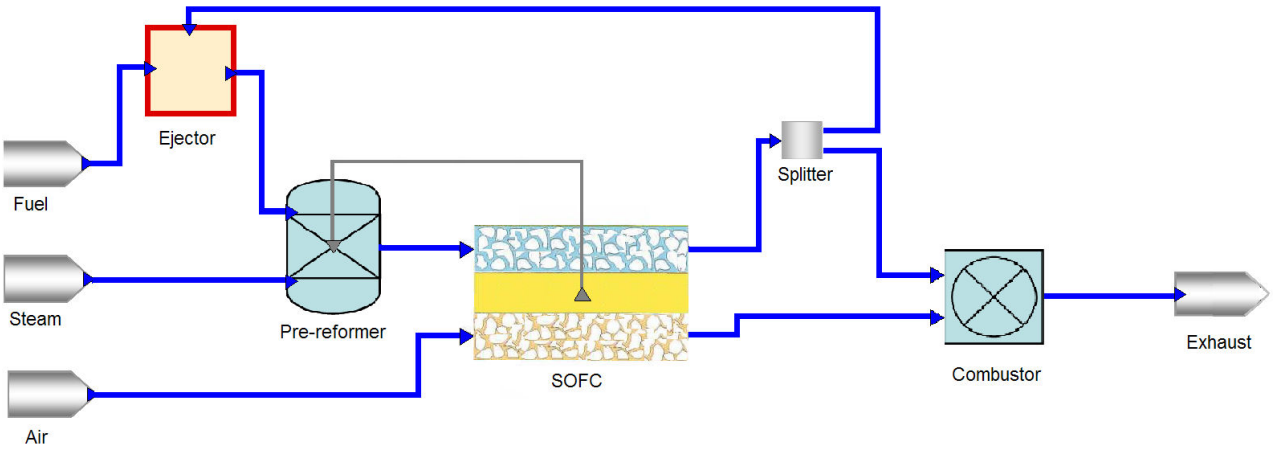

Figure 4: SOFC system

DISCUSSION

One volume SOFC model

Figure 5 shows the mean temperatures of the simple and the detailed SOFC models. At nominal steady state there is a temperature difference of about 120K between the two mean SOFC temperatures. This can be explained as follows. For both SOFC models, since inlet massflows and current are the same, the energy balance should ensure that the energy in the outlet massflow (and hence outlet temperature) is approximately[1] the same for both models. In a SOFC, the maximum temperature region is at the outlets of the anode and the cathode. Since the simple model is a bulk model, the exit temperature is equal to the mean temperature. For the detailed model, SOFC temperature is a distributed variable and the mean temperature is certainly less than the exit temperature. It is verified that the maximum temperature of the detailed model at the nominal steady state is approximately equal to the mean temperature of the simple SOFC model. From Figure 5, it is clear that both the models exhibit similar dynamics for the disturbances applied during the simulation. Figure 6 shows the voltages of the two models during the simulation. Here also both models show the same dynamic changes in the voltages for all the disturbances applied. Here the simple model has higher voltage than the detailed model which is also mainly because of the higher mean solid temperature of the simple SOFC model. Refering to (16), when temperature increases the voltage loss decreases. Hence the simple SOFC voltage given

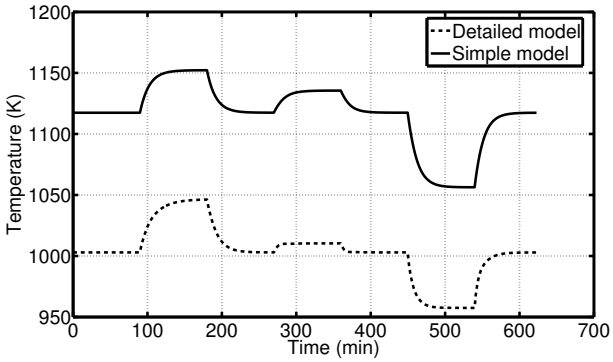

Figure 5: Comparison of mean solid temperatures of the simple model with one volume and the detailed model for different disturbances

by (14) is higher than that of the detailed SOFC model at the nominal steady state. Figure 7 shows a comparison of power production of the two models during the simulation. Since the voltage of the simple SOFC model is higher than that of the detailed model and the current is the same in both models, the power produced by the simple SOFC model is higher.

Two volume SOFC model

Figure 8 shows the comparison of the mean temperatures of the two SOFC models. Now, the simple SOFC is represented by aggregation of two volumes. The simple SOFC solid mean temperature is given by the average of the temperatures of the two volumes. The difference between the two mean temperatures at the nominal steady state is reduced to 51K as supposed to 120K. The dynamics of the two

[1] A slight difference in voltage and hence produced DC power gives a small temperature difference.

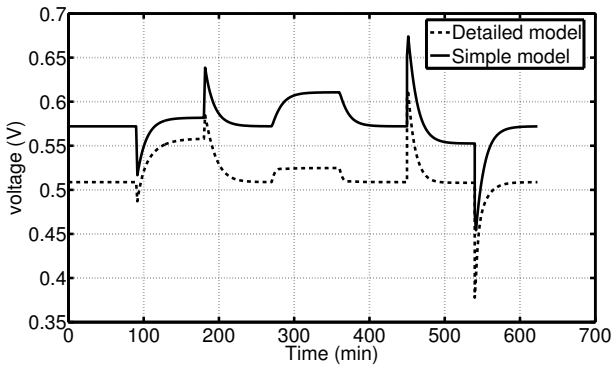

Figure 6: Comparison of voltages of the simple model with one volume and the detailed model for different disturbances

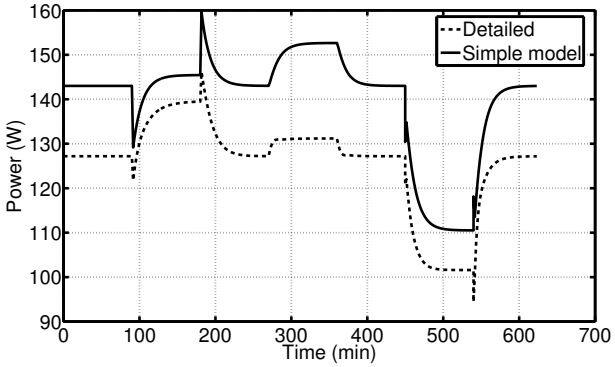

Figure 7: Comparison of power production of the simple model with one volume and the detailed model for different disturbances

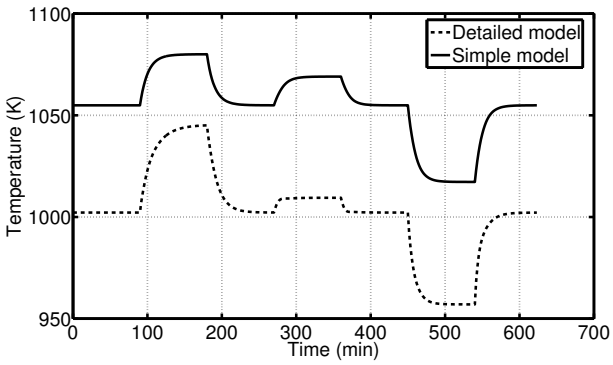

Figure 8: Comparison of mean solid temperatures of the simple model with two volumes and the detailed model for different disturbances

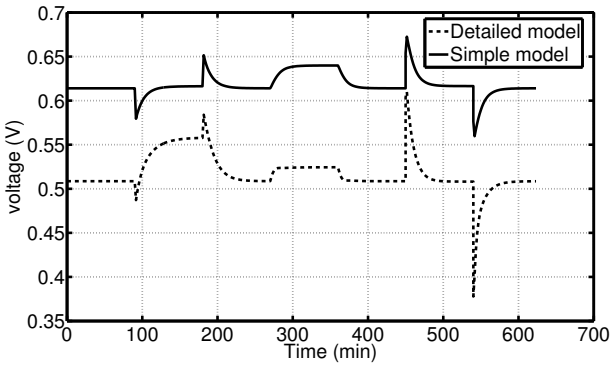

Figure 9: Comparison of voltages of the simple model with two volumes and the detailed model for different disturbances

volume model is similar to that the dynamics of the one volume model for all the disturbances. Figure 9 shows the comparison of the voltages of the two models, for the two volume model the average voltage is plotted. There is a small voltage difference of 0.1V between the two volumes and this is caused by the somewhat crude approximate distribution of currents between the two volumes. Developing a strategy for a more accurate distribution of currents between two or more volumes is a topic for future work.

CONCLUSION AND FURTHER WORK

From the simulation results, it is quite clear that even though there is some steady state offset, important variables of the simple and the detailed models show similar dynamic behavior during the simulations. It can therefore be concluded that the simple model is able to capture the overall dynamics of the SOFC. This model will hence be used for further studies on control and operability of the hybrid system, i.e. an SOFC integrated in a GT cycle.

If the one volume model is too crude, it is possible to aggregate a number of volumes. The results herein however indicate that a one volume model may suffice in many cases.

Further work includes developing the simple models of the other components in the SOFC-GT hybrid system, looking at how different design decisions affect controllability and developing an optimizing control structure for safe and part load operation.

Acknowledgments

Financial support from The Gas Technology Center, NTNU-SINTEF is acknowledged.

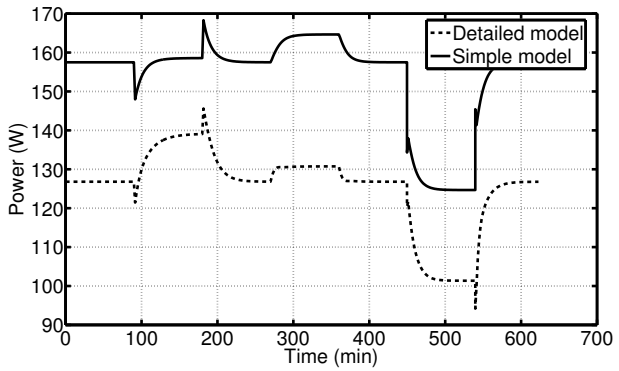

Figure 10: Comparison of powers of the simple model with two volumes and the detailed model for different disturbances

NOMENCLATURE

a_{ij}	stoichiometric matrix
A	SOFC surface area
A_{k_i}, $A_{K^{ads}}$	pre-exp. factors for k_i
C^s	solid heat capacity
DEN	denominator
E	activation energy
E^o	EMF at standard temperature and pressure
E^{OCV}	open circuit voltage
F	Faraday's constant
I	current
k_2, k_3, k_4	rate coefficients for reforming reactions
k_{an}, k_{ca}	choked flow constants
K_j	equilibrium constant for reaction j
K_i^{ads}	adsorption constant for component i
$\dot{m}$	mass flow rate
n_{rx}	number of reactions
N	number of moles
p	pressure
P	power
r_j	reaction rate of reaction j
R	universal gas constant
T	temperature
V_{an}, V_{ca}	volumes
V	voltage
$\Delta\overline{h}$	molar specific enthalpy
$\Delta\overline{h}^{rx}$	molar specific enthalpy change of reaction
$\Delta\overline{h}^{ads}$	enthalpy change of adsorption
δ	shaping factor

Subscripts and superscripts

i	chemical component
j	reaction
an	anode
ca	cathode
in	inlet
out	outlet
rad	radiation
$cond$	conduction

REFERENCES

[1] E. Achenbach. Three-dimensional and time-dependent simulation of a planar solid oxide fuel cell stack. *Journal of Power Sources*, 1994.

[2] S. Campanari. Thermodynamic model and parametric analysis of a tubular sofc module. *Journal of Power Sources*, 2004.

[3] S.H. Chan, H.K. Ho, and Y. Tian. Modelling of a simple hybrid solid oxide fuel cell and gas turbine power plant. *Journal of Power Sources*, 2002.

[4] S.H. Chan, H.K. Ho, and Y. Tian. Multi-level modeling of sofc-gas turbine hybrid system. *International Journal of Hydrogen Energy*, 2003.

[5] gPROMS (2004). gPROMS introductory user guide. *Process Systems Enterprise Ltd.*, 2004.

[6] F. P. Incropera and D. P. De Witt. *Fundamentals of Heat and Mass Transfer*. Wiley, USA, 2002.

[7] J. Larminie and A. Dicks. *Fuel Cell Systems Explained*. Wiley, England, 2003.

[8] J. Pålsson, A. Selimovic, and L. Sjunnesson. Combined solid oxide fuel cell and gas turbine systems for efficient power and heat generation. *Journal of Power Sources*, 2000.

[9] M. D. Lukas, K. Y. Lee, and H. Ghezel-Ayagh. An explicit dynamic model for direct reforming carbonate fuel cell stack. *IEEE Transactions on Energy Conversion*, 16(3), September 2001.

[10] L. Magistri, F. Trasino, and P. Costamagna. Transient analysis of a solid oxide fuel cell hybrids part a: fuel cell models. *Journal of Power Sources*, 2004.

[11] J. Padulles, G.W. Ault, and J. R. McDonald. An integrated sofc dynamic model power systems simulation. *Journal of Power sources*, pages 495–500, 2000.

[12] C. Stiller, B. Thorud, S. Seljebø, Ø. Mathisen, H. Karoliussen, and O. Bolland. Finite-volume modeling and hybrid-cycle performance of planar and tubular solid oxide fuel cells. *Journal of Power Sources*, 141:227–240, 2005.

[13] P. Thomas. *Simulation of Industrial Processes For Control Engineers*. Butterworth-Heinemann, Wobourn, MA, USA, 1999.

[14] B. Thorud, C. Stiller, T. Weydahl, O. Bolland, and H. Karoliussen. Part-load and load change simulation of tubular sofc systems. *Fuel Cell Forum, Lucerne, 28 June-2 July 2004*, 2004.

[15] J. van Schijndel and E. N. Pistikopoulos. Towards the integration of process design, process control, and process operability: Current status and future trends. *In the proceedings of FOCAPD '99, Breckenridge, Colorado, USA*, 1999.

[16] J. Xu and G. F. Froment. Methane steam reforming, methanation and water-gas shift: I. intrinsic kinetics. *AIChE Journal*, 1989.

Proceedings of ECOS 2005
Trondheim, Norway
June 20–22, 2005

POLYMER ELECTROLYTE FUEL CELLS BASED ON PHOSPHORIC ACID DOPED POLYBENZIMIDAZOLE (PBI) MEMBRANES

O.E. Kongstein,* F. Seland, B. Børresen and R. Tunold
Department of Materials Technology, Group of Electrochemistry
NTNU, 7491 Trondheim, Norway
T. Berning
Adam Opel AG, International Technical Development Center,
D-65423 Rüsselsheim, Germany

ABSTRACT

The development of high temperature polymer fuel cell systems has gained great interest among manufacturers of automotive and combined heat and power systems due to the carbon monoxide (CO) tolerance, enhanced heat management and better mass transfer. One of the promising high temperature polymer systems is based on polybenzimidazole polymer impregnated with phosphoric acid. In order to make fuel cells with high power density the structure and morphology for the three dimensional gas diffusion electrodes (GDE) are very important. In general the electrodes consist of three layers: i) backing material, ii) micro porous layer and iii) catalytic layer. Different preparation techniques yield GDEs with very different properties. Teflon treatment of the backing material is found to be beneficial for the performance of the electrodes. In general the open circuit voltage (OCV) with PBI-based cells is very low. The performance of the fuel cells is found to increase with increasing temperature, with a typical power output of 0.3-0.4 W cm^{-2} at 0.6 V and 175 °C.
*Keywords:*Fuel Cell, PBI, Gas diffusion electrodes, performance.

INTRODUCTION

Most membranes used as electrolyte for polymer electrolyte fuel cells, such as Nafion, relies on liquid water for protonic conductivity. Therefore, the operation temperature is limited by the boiling point of water. Cathode flooding caused by liquid water formed in the cathode is a common problem for low temperature fuel cells. This problem is not existent at higher temperatures where only water vapour can exist

Hydrogen gas produced from hydrocarbons in a reformer, for instance methanol, ethanol or diesel, will contain some CO. Fuel cell catalysts are very sensitive to CO. The CO is adsorbed on the Pt catalyst surface blocking the desired reaction. By increasing the operation temperature CO poisoning becomes much less pronounced. PBI based fuel cells operated at temperatures above 185 °C can tolerate up to 3 % CO [1, 2]. Li et al. [1] reported a CO tolerance of only 0.1 % at 125 °C, indicating a strong temperature dependence. Therefore, hydrogen produced by reforming of hydrocarbons can be used without CO removal. The membrane represents a significant cost in a fuel cell system. Compared to Nafion, PBI is considerably cheaper. The permeability of oxygen, hydrogen and methanol is very low.

At higher temperatures, the kinetics for both electrode reactions will be enhanced [3]. Operating the fuel cell at a high temperature also makes waste heat utilization more efficient. This heat can be supplied to for example a methanol reformer in order to produce hydrogen. The heat can also be utilized for desorption of hydrogen stored in metal hydrides. At temperatures below 80 °C the storage capacity in hydrides is usually limited to 1-2 wt.%. In $NaAlH_4$ at 150 °C 4-5 wt.% hydrogen can be stored more or less reversibly [3].

In addition the higher temperature results in better heat distribution within a fuel cell stack, and a smaller and cheaper cooling system is demanded.

*Corresponding author: Phone: +47 735 94116 Fax: +47 735 94083 E-mail:ole.edvard.kongstein@material.ntnu.no

A disadvantage by increasing the temperature, however, is longer start up time for the fuel cell.

Great efforts have recently been made to develop proton conductive membranes for fuel cell use above 100 °C. The work includes modification of perfluorosulfonic acid (PFSA), alternative sulphonated polymers and acid-base polymer membranes. The research in this field has lately been reviewed by Li et al. [4], Rozière and Jones [5] and Schuster and Meyer [6]. One of the most promising new membranes for operation above the boiling point of water is PBI doped with phosphoric acid for proton conductivity.

PBI was developed by Celanese as a fire resistant fibre for use in fire fighters clothing. PBI is an amorphous basic polymer with high thermal stability. In the pure state the conductivity is very low, about 10-12 S cm^{-1} [7, 8]. The conductivity can be substantially increased by addition of different acids. PBI has been doped with for example sulphuric acid, phosphoric acid, perchloric acid, nitric acid and hydrochloric acid [9], whereas phosphoric acid is the most promising because of its high boiling point, high thermal stability and high protonic conductivity even in anhydrous form. The idea to use phosphoric acid doped PBI as the electrolyte in fuel cells was first introduced by Wainright et al. [10].

The conductivity of phosphoric acid doped PBI increases with increasing doping level, temperature and humidification [11, 12, 13, 14, 15]. At room temperature the conductivity is unsatisfactory for normal fuel cell operations. The conductivity increase with increasing temperature following an Arrhenius equation [12].

The doping level is usually given as the mol percent of phosphoric acid per repeating unit of the polymer. Li et al. [14] suggested that two molecules of phosphoric acid per repeating unit of PBI is strongly bound to the nitrogen atoms in the imidazole ring. Exceeding the amount phosphoric acid in the membrane above two H_3PO_4 per repeating unit leads to the presence of "free acid", which contribute significantly to the ionic conductivity of doped PBI membrane. The mechanical strength of the PBI is decreasing with increasing temperature and increased level of doping. The doping level used in a fuel cell membrane is therefore a trade-off between operation temperature, membrane thickness and doping level. Li et al. [3] suggested an optimum doping level around 5 molecules of H_3PO_4 per repeating unit polymer.

The influence of the humidification of PBI is much less than for Nafion membranes. However an increase in relative humidity (RH) increase the conductivity for phosphoric acid doped PBI, especially at high temperature. This can be explained by interaction of water with excess acid [14]. For a doping level of 560 mol% a conductivity of 6.8 10^{-2} S cm^{-1} at 200 °C and 5 % RH was measured for PBI by He et al. [13]. This conductivity is close to the conductivity measured for Nafion membranes at 80 °C and 95 % RH.

For Nafion the electroosmotic drag coefficient for water has been determined to vary between 0.9 and 3.2 at room temperature. For PBI doped with phosphoric acid, an electroosmotic drag coefficient close to zero has been measured [1,15]. This may indicate that a PBI based fuel cell can be operated without any humidification, although some humidification is an advantage.

Material choice for fuel cells operating close to 200 °C with the presence of phosphoric acid, is a challenging task. For example is amorphous carbon known to be oxidized at the cathode at high voltages (low current densities). This probably indicates that traditionally used amorphous carbon can not be used as catalyst carrier in long term fuel cell operation [3].

A few works has been published about preparation of gas diffusion electrodes for PBI fuel cells. Savodogo and Xing [16] made electrodes with extremely good performance, at a cell voltage of 0.6 V the current density was 1.6 A cm^{-2} at 185 °C. Wang et al. [17] made gas diffusion electrodes in three different ways with a maximum current density at 0.2 A cm^{-2} at a cell voltage of 0.6 V and 150 °C. Li et al. [3] obtained a current density of 0.7 A cm^{-2} at 0.6 V and 200 °C.

In order to make fuel cells with high power density, gas diffusion electrodes with a large three phase area (catalyst-PBI-gas) with high electrical conductivity and high accessibility for reactants, are very important. The manufacturing of a desirable three dimensional structure is a challenging task. Many input parameters influence the performance of the final electrode. Because of the cost of the precious metals used for fuel cell catalysts, usually platinum, it is important to keep the catalyst loading low. The ob-

jective of this work has been to optimize the composition and structure of such gas diffusion electrodes.

EXPERIMENTAL

Gas diffusion electrodes (GDEs) were prepared with carbon fibre paper from Toray (TGP-H-120) as a backing material. The carbon paper was treated with PTFE(Polytetrafluoroethylene, Teflon) by immersing the electrodes into an aqueous dispersion of PTFE, and then let the electrodes dry in air, before heat treatment at 360 °C for 30 minutes.

Both the micro porous layer (MPL) and the catalyst layer were sprayed manually with an airbrush. This method allows uniform thickness of the different layers and accurate determination of the catalyst loading. Prior to the catalyst layer a MPL based on carbon black (Vulcan XC-72) was applied to the backing.

The catalytic layer was sprayed from a dispersion of platinum on carbon in PBI containing dimethylacetamide (DMAc). The electrocatalysts, 20 wt.%, 40 wt.% and 50 wt.% platinum on carbon (Pt/C) were purchased from Johnsson & Matthey. After spraying of the catalyst, the electrodes were heated at 190 °C for three hours to evaporate the remaining DMAc. In order to dope the PBI in the catalytic layer, the electrodes were sprayed with 10 wt.% phosphoric acid solution.

PBI foils with a thickness of 40 μm after hot pressing were supplied by the Department of Chemistry, Technical University of Denmark (DTU). The PBI membranes were saturated with 65 wt.% phosphoric acid before use, resulting in a doping level of approx. 560 mol%. The gas diffusion electrodes were hot pressed onto both sides of the membrane at approx. 250 N cm^{-2} at 130 °C for 25 minutes. The finished MEA was then cured for a few weeks.

The finished MEAs with an active area of 2×2 cm^2 were tested in a commercial fuel cell test rig (ElectroChem, Inc), with double serpentine flow field. The MEAs were tested in terms of their performance by recording polarization curves using pure oxygen and hydrogen at atmospheric pressure. After the MEAs were electrochemically tested, the cross section was examined in scanning electron microscope (SEM).

RESULTS AND DISCUSSION

Micro Porous Layer

The MPL was prepared in order to obtain a good electrical contact between the backing and the catalysts and prevent catalyst to penetrate into the carbon paper. The purpose of the MPL was also to provide good transport of reactants and product gases and to obtain a smooth and uniform surface for the catalytic layer. Reproducible results were first obtained after extensive study of the preparation steps involved.

Treatment in a 20 % PTFE dispersion led to reduced carbon penetration into the carbon paper during the preparation of the subsequent micro porous layer (MPL), resulting in an increase in the total porosity. It is unlikely that liquid water is present during cell operation at 175 °C, so a direct influence of PTFE on the cell performance was observed to be insignificant. The adhesion of carbon onto the carbon fibre was however found to be improved by PTFE treatment.

The properties of the MPL are strongly dependent upon the solvent used for carbon particles dispersion. During this work it was found that the drying time had a big impact on the MPL properties. By spraying carbon particles dispersed in a solution with low boiling point on a heated carbon paper, good adhesion was obtained, but the surface became uneven. Consequently, carbon particles dispersed in a solvent with a higher boiling point was sprayed on top of the layer described above. This led to a mud cracked structure with large islands and thin crevices, shown in Figure 1, due to the lengthening of the drying time.

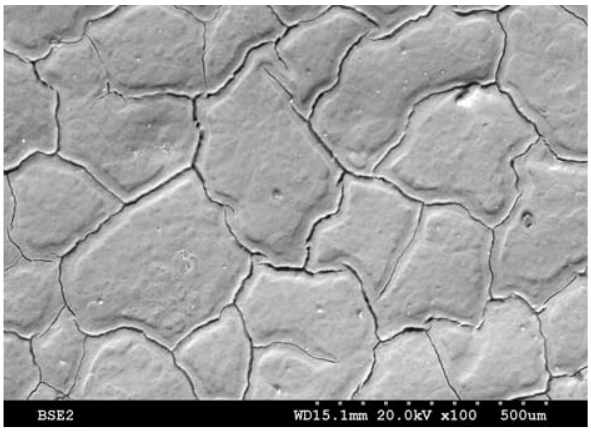

Figure 1: SEM micrograph of a complete electrode visualizing the mud cracked structure.

The catalyst eventually ending up in the crevice is far from the membrane and has a poor performance; this illustrates the importance of minimizing the total crevice volume in the support layer. A total amount of 2 mg cm^{-2} of carbon black was found to be sufficient to produce the MPL shown in Figure 1.

Catalyst Layer

The catalyst layer is a key element in a fuel cell. Because of its three-dimensional structure it can be very difficult to manufacture this layer with the desired properties. Many preparation methods for the catalytic layer have been tested. The best performing electrodes were sprayed from a dispersion of catalyst in DMAc containing PBI in solution.
The total loading on both anode and cathode was normally 1 mg Pt cm^{-2}. The overpotential for oxygen reduction is higher than for hydrogen oxidation. The performance improved when the anode loading was 0.4 mg Pt cm^{-2} and the cathode loading was 0.6 mg Pt cm^{-2} compared to a loading of 0.5 mg Pt cm^{-2} on both electrodes. SEM images of the electrodes are showing a very uniform catalytic layer made by spraying. Theoretical simulations of PEM fuel cells have shown that most of the catalytic reaction takes place within approx. 10 μm from the electrolyte membrane [18], which means that a high fraction of the catalyst in a thick layer will be inactive. In order to achieve as large three phase area as possible within the reaction zone close to the membrane 50 wt.% Pt/C was used. The best performance was obtained by first spraying a layer of 20 wt.% Pt/C and thereafter a thin layer of 50 wt.% Pt/C. This was observed both for the anode and the cathode. A cross section of a MEA is shown in Figure 2, where the different layers may easily be observed. Heavy compounds like Pt shines up in SEM backscatter mode. A polarization curve for the MEA in Figure 2 is shown in Figure 4.
The PBI loading was found to be very important. Too much PBI in the catalytic layer probably led to an electrical insulating coating around the catalytic particles. On the other hand too little PBI led to lower ionic conductivity and smaller three phase area in the catalytic layer. The experimental investigation indicates that a PBI loading in the range of 0.2 to 0.4 mg PBI cm^{-2} gave the best performing gas diffusion electrodes. Seland et al. [19] has studied this in more details.

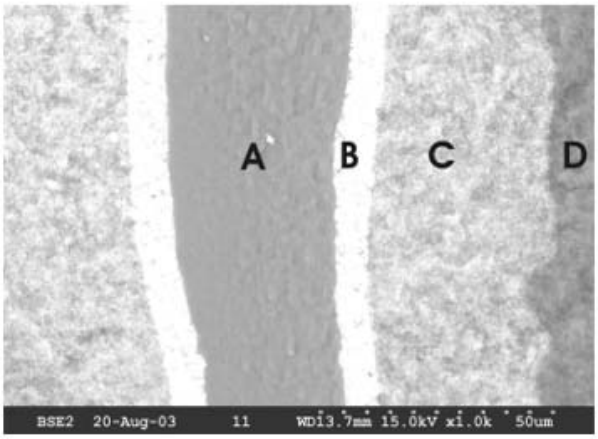

Figure 2: SEM micrograph of a cross section of an MEA, A: Membrane, B: Catalyst layer (50 wt.% Pt/C) C: Catalyst layer (20 wt.% Pt/C) and MPL. The image is taken in backscatter mode.

Open Circuit Voltage

The open circuit voltage (OCV) is the cell voltage at zero current. Commonly the OCV for fuel cells is not equal to the value calculated from thermodynamic data. This can mainly be explained by the very slow kinetics for the oxygen reduction reaction, which can easily be influenced by other parallel reactions, for instance corrosion of platinum. The thermodynamic voltage for an O2/H2 fuel cell is 1.23 V at 25 °C. The corresponding value at 175 °C is 1.10 V. The most frequently reported OCV for a Nafion based fuel cell is around 1.0 V. In this study the open circuit voltage at 175 °C varied from one MEA to another, but was typically around 0.9 V. The OCV increased with temperature above 100 °C. The variation in OCV may be explained by variation of the catalytic activity of the platinum and variations in the crossover rate caused by small variation in the membrane thickness. Carbon can be oxidized at a slow rate to carbon dioxide at high anodic voltages ($C + 2H_2O \rightarrow CO_2 + 4H^+ + 4e^-$) [20]. This may also tend to lower the OCV. The adsorption of phosphate ions on the catalyst surface may also affect the OCV value.

Testing of Single Membrane Electrode Assemblies

Figure 3 shows polarization curves as a function of temperature. In the figure the corresponding power density curves are also given. The Pt loading on the cathode was 0.6 mg cm^{-2} and 0.4 mg cm^{-2} on the anode. The PBI membrane was doped with 580 mol % phosphoric acid.

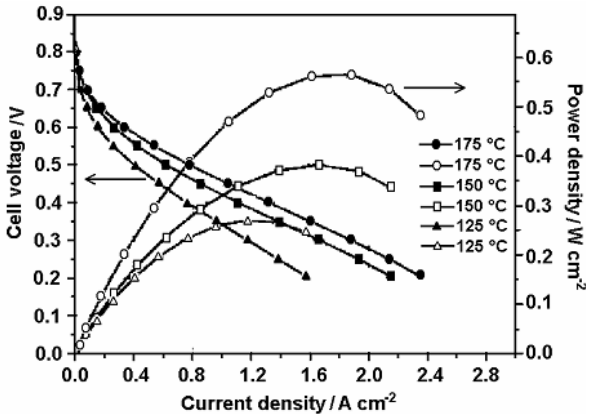

Figure 3: Cell voltage versus current density and corresponding power density versus current density for three temperatures. The cell was fed with pure H_2 and O_2 under atmospheric pressure.

Significant increase in performance by increasing the temperature was observed. This can mainly be explained by the increased membrane conductivity and enhanced reaction kinetics at elevated temperatures. When the temperature was raised above 175 °C, membrane puncturing was a common problem caused by reduced mechanical strength of the membranes. Membrane puncturing was usually observed at the edge of the GDEs.

As can be seen from Figure 4, a good MEAs prepared in house yielded a current density of 0.6 A cm^{-2} at 0.6 V. A maximum power density of 0.83 W cm^{-2} at 0.40 V was obtained for this MEA. This performance is considerably lower than the performance achieved for Nafion based fuel cells at 80 °C. This is mainly due to a lower proton conductivity of the phosphoric acid doped PBI membrane, and lower reversible voltage at high temperatures. Other explanations can also be slower reaction kinetics caused by strong adsorption of phosphate at the catalyst surface, and a substantially lower oxygen solubility in the phosphoric acid doped PBI than

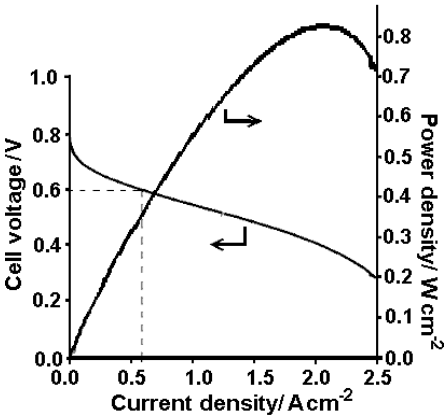

Figure 4: Cell voltage and power density versus current density at 175 °C. The cell was fed with H_2 and O_2 under atmospheric pressure.

in Nafion. This means that such fuel cells are not beneficial for pure hydrogen feed, but are superior to Nafion based cells above a certain CO level in the gas feed. Further electrode development is needed to enhance the MEA performance for the PBI based fuel cells

CONCLUSION

The well developed PEMFC is based on Nafion membranes operating at a typical temperature of 80 °C. Fuel cells operation at temperatures above 150 °C are desired for fast electrode kinetics, high CO tolerance, facilitated thermal, mass and water management and heat utilization. PBI based fuel cells are among the most promising candidates for operating at higher temperatures. Good performing MEAs have been demonstrated, but further optimization is needed both for higher performance and long term stability.

ACKNOWLEDGMENT

This work was funded by the European Commission in the 5^{th} Framework Programme (Contract no. ENK5-CT-2000-00323). The Department of Chemistry, DTU is greatly acknowledged for supplying the PBI membranes as a partner in this EU project.

REFERENCES

[1] Q. Li, H. Hjuler, N. Bjerrum, J. Appl. Electrochem. 31 (2001) 773.

[2] J. Holladay, J. Wainright, E. Jones, S. R. Gano, J. Power Sources 130 (2004) 111.

[3] Q. Li, R. He, J. Jensen, N. Bjerrum, Fuel Cells 4 (2004) 147.

[4] Q. Li, R. He, J. Jensen, N. J. Bjerrum, Chem. Mater. 15 (2003) 4896.

[5] J. Rozière, D. Jones, Annu. Rev. Mater. Res. 33 (2003) 503.

[6] Schuster, W. Meyer, Annu. Rev. Mater. Res. 33 (2003) 233.

[7] H. Poul, R. Chartoff, J. Polym. Sci., Part A 2 (1964) 2787.

[8] S. Aharoni, R. Signorelli, J. Appl. Polym. Sci. 23 (1979) 2653.

[9] B. Xing, O. Savadogo, J. of New Mat. Electrochem. Systems 2 (1999) 95.

[10] J. S. Wainright, J.-T. Wang, D. Weng, R. F. Savinell, M. Litt, J. Electrochem. Soc. 142 (1995) L121.

[11] J. A. Asensio, S. Borrós, P. Gómez-Romero, J. Electrochem. Soc. 151 (2004) A302.

[12] J. S. Wainright, M. H. Litt, R. F. Savinell, in: A. L. W. Vielstich, H. A. Gasteiger (Eds.), Handbook of Fuel Cells, Vol. 3, John Wiley & Sons Ltd., 2003, pp. 436–446.

[13] R. He, Q. Li, G. Xiao, N. J. Bjerrum, J. of Membr. Sci. 226 (2003) 169.

[14] Q. Li, R. He, R. Berg, H. A. Hjuler, N. J. Bjerrum, Solid State Ionics 168 (2004) 177.

[15] D. Weng, J. S. Wainright, U. Landau, R. Savinell, J. Electrochem. Soc. 143 (1996) 1260.

[16] O. Savadogo, B. Xing, J. of New Mat. Electrochem. Systems 3 (2000) 343.

[17] J.-T. Wang, R. Savinell, J. Wainright, M. Litt, H. Yu, Electrochim. Acta 41 (1996) 193.

[18] D. Bevers, M. Wohr, K. Yasuda, K. Oguro, J. Appl. Electrochem. 27 (11) (1997) 1254.

[19] F. Seland, T. Berning, B. Børresen, R. Tunold, Submittet to J. Power Sources Jan. 2005.

[20] D. Landsman, F. Luczak, in: A. L. W. Vielstich, H. A. Gasteiger (Eds.), Handbook of Fuel Cell, Vol. 4, John Wiley & Sons Ltd., 2003, pp. 811–831.

Proceedings of ECOS 2005
Trondheim, Norway
June 20–22, 2005

OPERATION LIMITATIONS FROM STUDIES OF AN AMBIENT PRESSURE PEM FUEL CELL STACK FOR PORTABLE APPLICATIONS

Torstein Lange[1] and Steffen Møller-Holst
SINTEF [2] - Materials and chemistry, Dept. of Energy Conversion and Materials
N-7465 Trondheim
Norway

Axel Baumann Ofstad
NTNU [3] - Dept. of Materials Technology
N-7491 Trondheim
Norway

ABSTRACT

A small 10-cell proton exchange membrane fuel cell (PEMFC) stack for demonstrational purposes was designed and tested. The stack was operated on pure hydrogen and ambient air without inlet gas humidification or external heating. Polarization curves for individual cells were obtained up to a current density of 0.40 A/cm^2 with a corresponding stack peak power of 41 W. The temperature distribution in the air channels of the stack was mapped showing temperature gradients of up to 10 ^{o}C. Polarization curves show very similar single cell performances despite these substantial temperature gradients. The simplicity of the PEMFC system limits the operation to low power densities. With the reactant air as the only means of stack cooling, long term operation at higher power densities was not possible due to stack overheating with subsequent risk of membrane failure.

Keywords: PEM fuel cell, polarization curves, heat distribution, water management

NOMENCLATURE

A	Geometric active cell area [cm^2]
F	Faraday constant [C/mol]
i	Current density [A/cm^2]
$p_{sat,T}^{H_2O}$	Saturation vapour pressure of water at temperature T [bar]
p_{tot}	Total system pressure [bar]
γ	Gas utilization factor
λ	Air stoichiometry

INTRODUCTION

Hydrogen based energy supply systems such as fuel cells are believed to play an important role in the future. Fuel cells are efficient devices for converting chemical energy into electricity, and will be able to provide energy for a broad range of applications. For automobile and portable applications the proton exchange membrane fuel cell (PEMFC) is considered the most promising candidate, due to its high power density, fast start-up capability and excellent dynamics [1, 2].

[1] Corresponding author: Phone: +47 98230451
Fax: +47 73591105 E-mail: torstein.lange@sintef.no
[2] The Foundation for Scientific and Industrial Research
[3] The Norwegian University of Science and Technology

Fast start-up is facilitated by the low operating temperature and stable operation conditions are typically reached within minutes.

High power density has historically been assured by pressurised PEMFC operation [3]. However, pressurised operation requires a number of auxiliary components leading to system complexity. System complexity again leads to reduced system reliability. Furthermore, pressurised PEMFC systems typically spend 20% of stack power output for air compression [4], giving negative impact on system efficiency.

The PEMFC stack itself exhibit very fast dynamics [2], but auxiliary components (e.g., compressors, reformers etc.) typically make the system response dramatically slower. To compensate for slower system response, various buffer systems can be introduced, but these again add severely to system complexity.

Requirements for lower cost, higher PEMFC efficiency and improved reliability have, therefore, lately shifted focus on simpler PEMFC systems operating at atmospheric or close to atmospheric conditions.

However, for simpler systems with minimal use of auxiliary components, the degrees of freedom available for system control during operation are dramatically reduced. The close interrelation between the thermal- and water management is particularly challenging for PEMFC systems, and limits the possibility to control these individually.

Prototype testing of fuel cells in the laboratory is essential for identification of operation limitations and provides valuable input to improved cell and stack design.

This work focuses on identifying the operation limitations for a small 10-cell PEMFC for portable applications with an air supply fan as the only moving part. For this system, where the reactant air also is utilised for cell cooling, the air flow-rate represents the only degree of freedom for thermal as well as water management. Cell temperature constitutes the most critical factors for assuring stable and efficient system operation. Therefore, detailed exploration of the temperature distribution constitutes the main objective of this work.

THEORETICAL ASPECTS

Water management

A major disadvantage of the PTFE based membranes used in PEMFCs is that their proton conductivity depends strongly on their water content, thus making the water management one of the critical parameters during operation [5]. A key factor when controlling the water balance of a fuel cell is the temperature. Controlling the temperature is a desirable way to assure a proper water balance because it does generally not result in an increased parasitic loss in the system.

The amount of water the gases can contain ($p_{sat,T}^{H_2O}$) is exponential to the temperature. Therefore, a minor change in temperature may have a substantially influence on the membrane hydration and, hence, the ohmic resistance in the cell. A simple relationship for the water balance of a hydrogen/air fuel cell has been deduced (Eq. 1) assuming no net water transport through the membrane.

$$\text{Water excess} = \frac{iA}{2F} - \frac{iA}{4F}\left(\frac{\lambda}{0,21} - 1\right)\frac{p_{sat,T}^{H_2O}}{p_{tot}} \quad (1)$$

The first term in Equation 1 represents the water produced in the cell reaction and the latter the water leaving the cell, assuming dry gases at air inlet and water vapour saturated air exhaust gas. Back diffusion and electro-osmotic drag effects also influence the overall water balance of the fuel cell system. However, for thinner membranes, these effects counter-balance such that the overall water transport is close to zero. This assumption is in agreement with the findings reported by Mosdale et al. [6]. The water balance for a low current density system is illustrated in Figure 1 below.

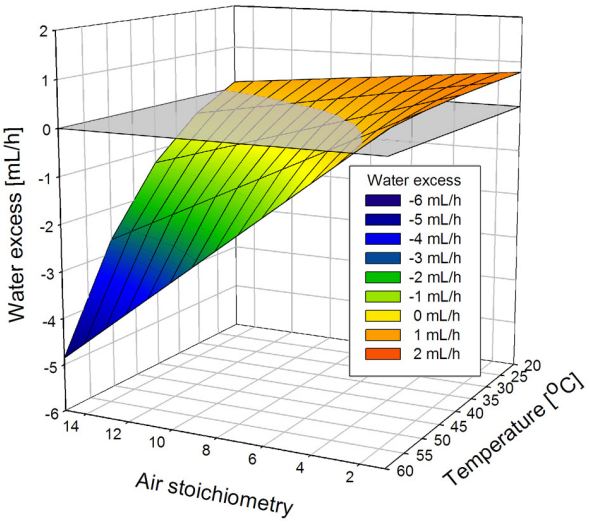

Figure 1: Simplified picture of the water balance (using Eq. 1) of a single fuel cell with a geometric area of 24 cm^2 operating at a current density of 0.10 A/cm^2, assuming atmospheric operation, no reactant gas humidification, no net membrane water transport and water vapour saturated air exhaust gas.

As expected, the water excess varies linearly with the air stoichiometry, and exponentially with respect to temperature (Figure 1). Water neutrality is indicated by the horizontal plane and its interception with the coloured surface. As can be seen from Figure 1, there is a surplus of water and hence risk of flooding at ambient stack operation temperatures for stoichiometries shown. At elevated temperatures, however, there is a water deficiency for almost any realistic set of operation conditions. For stable operation at 50 ^oC the air stoichiometry should be approximately 3.5 under these assumptions.

The simplified relationship illustrated in Figure 1 should be used with care and only serve as a guideline for water management during PEMFC operation.

Thermal management

The PEMFC is considered to be an efficient system, but still about 40-50% of the energy produced is typically dissipated as heat [6]. Heat production is mainly due to the activation overpotential of the cathode reaction, the ohmic losses and the concentration overvoltage in the fuel cell. Heat has to be removed from the fuel cell stack to prevent overheating during operation. This is usually done by means of water cooling for larger and pressurised stacks and air-cooling for smaller stacks. Active external cooling of the stack is supplemented by internal processes like water evaporation and condensation. An internal cooling effect is experienced at the cathode side where produced water is evaporated and subsequently transported out of the fuel cell by the air exhaust. Such an evaporative cooling principle has successfully been demonstrated in PEMFC stacks [4].

EXPERIMENTAL APPARATUS

The 10-cell PEMFC stack discussed in this paper is shown in Figure 2. Air was supplied by a CPU fan (Sunon) powered by an external power supply. Air flows from the transparent plastic manifold at the top and downwards through 34 straight channels (Figure 2). The four transparent 1/8 inch inlet/outlet tubes allow for counter- as well as parallel flow of hydrogen through the double serpentine anode flow field. Stack power was extracted by cables attached to gold plated copper current collectors sandwiched between graphite cell plates and aluminium end-plates. Individual cell voltages were monitored during operation.

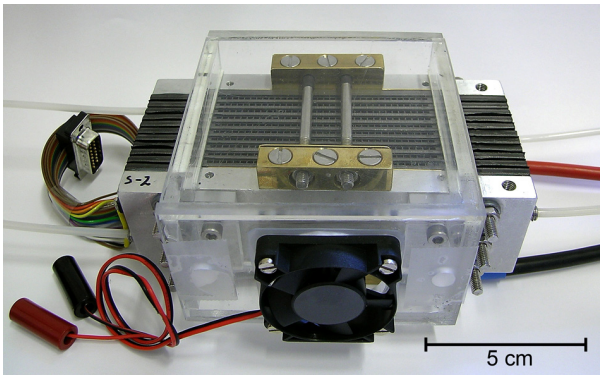

Figure 2: The PEMFC stack developed and characterized in this project.

The PEMFC stack consists of tailor made epoxy/graphite bipolar plates and commercial membrane electrode assemblies (MEAs) and gas diffusion layers (GDLs). The single cells were identical and had an individual geometric active cell area of 24 cm^2.

The MEAs were Gore Primea™ MEA Cleo Series 58 with a thickness of 18 µm, especially developed for operation with dry reactant gases. The catalyst loading was 0.4 mg Pt/cm^2 on both sides of the membrane. The GDL material used was ETEK V2 Double Sided Electrode Carbon Only with a thickness of 400 µm. The epoxy/graphite bipolar plate material was provided by SGL Carbon Group, Germany (SGL SIGRACET®, BMA5). The gas flow fields were designed and manufactured in-house using a CNC-machine. The gaskets were made from 0.5 mm silicone rubber.

The testing of the PEMFC stack was carried out at the group's test facilities with accurate control of the hydrogen gas-flow rate and logging of current, individual cell voltages and temperatures. During operation, individual cell temperature mapping was carried out by means of an array of small K-type thermocouples (Chromega/Alomega) from Omega Engineering, Inc. inserted into the air channels. The thermocouples were located at three different distances from the air outlet; bottom, middle and top position resulting in three measurement planes as indicated in Figure 3.

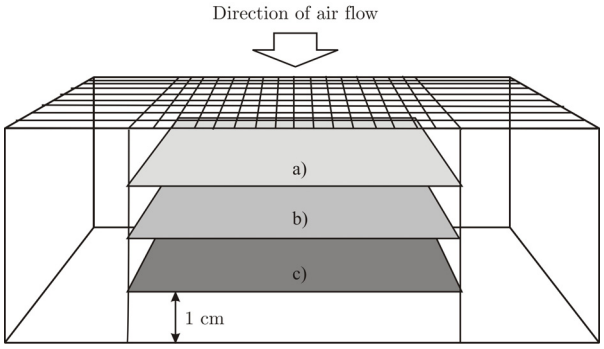

Figure 3: Sketch of the 10-cell PEMFC stack (end-plates not shown) and the three different planes a), b) and c) where the temperatures were measured by insertion of thermocouples into the air channels. Corresponding temperature contours are shown in Figure 4.

Polarization curves were obtained in a constant current mode by increasing current density from 0 to 0.40 A/cm^2 in steps of 0.05 A/cm^2.

RESULTS AND DISCUSSION

Cell performance results were obtained by generating polarization curves. Stable performance was obtained at 0.10 A/cm^2 over a period of 4 hours with less than 3 mV/h loss in single cell voltages. This small voltage decay is probably due to reversible effects such as platinum oxide formation and should not be interpreted as permanent degradation. Stack operation was limited to current densities below 0.40 A/cm^2, primarily due to uncontrollable internal temperature increase and potential risk of creating hot-spots and consequently pinholes in the membrane.

A semi-3-dimensional temperature distribution for the stack was obtained at steady state conditions. The temperature distribution (based on 300 measurement-points) is shown in Figure 4, at a current density of 0.10 A/cm^2.

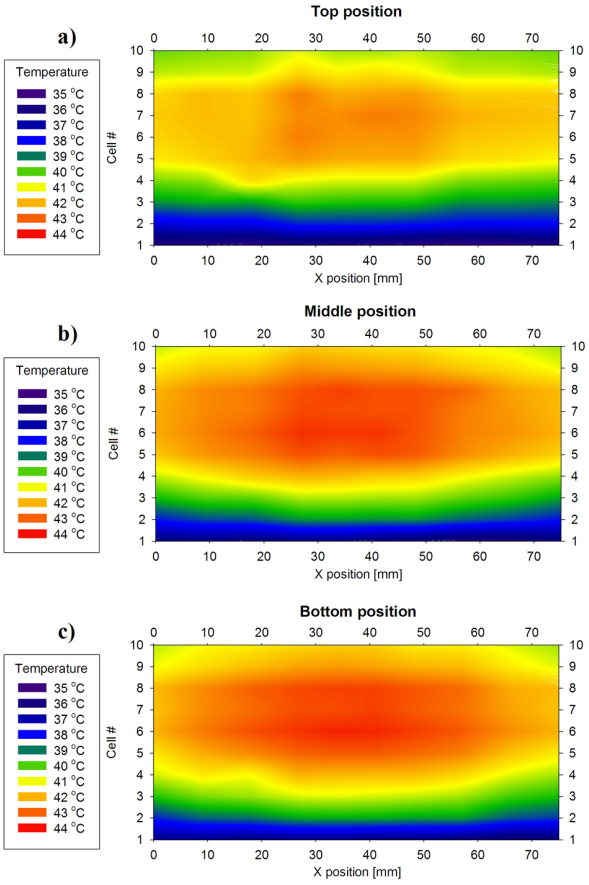

Figure 4: Temperature distribution in the air channels of the PEMFC stack at 0.10 A/cm^2, a) Top, close to air inlet, b) Middle of stack and c) Bottom, close to air outlet. H_2- and air-flow rates were 0.3 and approximately 20 L/min, respectively.

Under these operation conditions (Figure 4), the air stoichiometry is approximately 45. This high stoichiometry was chosen to keep cell temperature at approximately 40 °C. From Equation 1 it can be calculated that this corresponds to a water deficiency of approximately 5 mL/h per cell. Theoretically the cell should have dried out under these conditions. Four hours of stable operation indicates that the assumptions behind Equation 1 are not valid, and that the materials in use (MEAs and GDLs) exhibit pronounced water retention properties. Small pores in the GDLs may contribute to capillary forces and lower the water equilibrium pressure. From these results it can be concluded that the air exhaust leaving the PEMFC stack is not saturated with water vapour.

As can be seen from Figure 4, significant temperature gradients of up to 10 °C are encountered during operation. The air fan was located blowing towards one aluminium end plate to obtain a stagnant small overpressure in the air inlet manifold and a, hence, uniform air flow through all air channels. As can be seen, this contributes to substantial cooling of cells 1-3 which could have been avoided by placing the fan directly in front of the air channels. However, this may create "dead"-zones underneath the fan shaft and turbulence effects resulting in reduced stack performance.

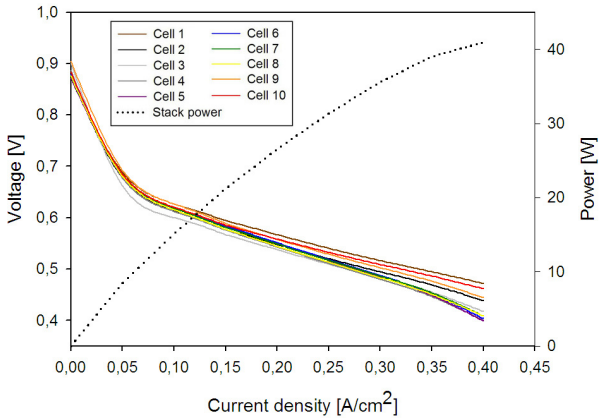

Figure 5: Cell voltages vs. current density for individual cells of the PEMFC stack up to a current density of 0.40 A/cm^2. Stack power is shown on the secondary Y-axis.

The substantial temperature gradients shown in Figure 4 may influence performance, but from Figure 5 it can be seen that all 10 cells show very similar polarization curves. However, the 2 outer most cells facing each end plate (cells 1 and 2 as well as 9 and 10) experiencing the lower operation temperatures show better performance than those closer to the middle at high current densities. This indicates that these outer most cells operate at more favourable conditions. Quantitatively, this is in agreement with the assumptions behind Equation 1 and Figure 1. The closer to water neutrality the cell operates, the better the performance. It may be concluded that although these new generation membranes which are optimised for dry reactant gases show good performance, proper water management is still of a certain importance for assuring high efficiency.

The electrical peak power output from the fuel cell stack was 41 W at 0.40 A/cm^2. Long term operation at this power density was, however, not possible due to uncontrollable temperature increase causing stack overheating with subsequent risk of membrane failure (pinholes).

Open circuit voltage (OCV) values obtained in this work were slightly lower (around 0.9 V) than OCVs measured in our laboratory for PEMFCs utilising Nafion 117 membranes (typically 0.92 to 0.98 V). This is probably due to thinner membranes (18 µm) applied in this study causing increased fuel crossover and hence a somewhat lower OCV.

The electrical efficiency, based on the lower heating value (LHV) when operating at 0.10 A/cm^2 assuming a hydrogen conversion rate of 90% ($\gamma = 0.9$), has been calculated to be 44% for the fuel cell stack and 41% for the PEMFC system, the difference due to the power consumption of the air fan.

CONCLUSIONS

An ambient pressure, self humidifying and air-cooled PEMFC stack has been designed and tested and operation limitations have been identified. Stable operation was realised at low current densities, despite temperature gradients of up to 10 ^{o}C. The stack operates well under dry conditions and provided a peak power of 41 W over short time intervals. Thermal management for this system has proven to be especially challenging and limits operation to low current densities. At high current densities, air cooling is not sufficient and the stack overheats. The water balance may be attained by proper thermal management.

Low OCV is assumed to be related to fuel crossover, typical for PEMFCs with thin MEAs. An overall electrical system efficiency (LHV) for the stack of 41% was achieved at 0.10 A/cm^2.

FURTHER WORK

A solution for more uniform cooling of the fuel cell stack is desirable. This may be obtained by placing the air-/cooling fan directly in front of the cathode air channels. However, the risk of "dead"-zones underneath the fan shaft and turbulence effects should be evaluated first. Alternatively the endplates of the stack can be thermally insulated, or dedicated cooling fans can be mounted on the stack as reported by Qi and Kaufmann [7]. However, additional fans will increase the parasitic losses in the system, and hence reduce the total efficiency of the system.

Further, since the membrane resistance gives valuable information about the humidity of the membrane, it could be interesting modifying the test facilities for online monitoring of individual cell resistivities by means of the current interrupt technique.

Recycling of hydrogen is a prerequisite for obtaining high fuel utilization and overall system efficiencies. Hence, the possibility to incorporate a pump to recycle the hydrogen should also be looked into. Even though this will add to the complexity of the system, this may increase total system efficiency.

ACKNOWLEDGEMENTS

This work was supported by The Research Council of Norway and SINTEF. IAESTE-student Feng Liu is acknowledged for carrying out the temperature measurements.

REFERENCES

[1] P. Costamagna, S. Srinivasan. *Quantum jumps in the PEMFC science and technology from the 1960s to the year 2000: Part II. Engineering, technology development and application aspects.* J. of Power Sources 102, 253-269 2001

[2] S. Kim, S. Shimpalee, J.W.Van Zee, *The effect of stoichiometry on dynamic behaviour of a proton exchange membrane fuel cell (PEMFC) during load change*, J. Power Sources, vol.135, 2004, pp110-121.

[3] J.T. Pukrushpan, H. Peng, A. G. Stefanopoulou, *Simulation and analysis of transient fuel cell system performance based on a dynamic reactant flow model*, Proceedings of 2002 ASME International Mechanical Engineering Congress and Exposition, November 17-22, 2002, New Orleans, Louisiana, USA

[4] M. S. Wilson, S. Møller-Holst, C. Zawodzinski, *Efficient Fuel Cell Systems*, Transportation Fuel Cell Power Systems, 2000 Annual Progress Report, U.S. Department of Energy 2000;88-90, URL: http://www.eere.energy.gov/hydrogenandfuelcells/pdfs/12.pdf

[5] *Ullmann's Encyclopedia of Industrial Chemistry*, 6th edition, vol.15, New York: John Wiley and Sons Inc., 2003.

[6] R. Mosdale, S. Srinivasan, *Analysis of performance and of water and thermal management in proton exchange membrane fuel cells*, Electrochemica Acta, vol.40 no.4, 1995, pp413-421.

[7] Z. Qi, A. Kaufman, *PEM fuel cell stacks operated under dry-reactant conditions*, Journal of Power Sources, 2002 109 pp469-476.

Proceedings of ECOS 2005
Trondheim, Norway
June 20–22, 2005

HEAT MANAGEMENT FOR HYDROGEN PRODUCTION BY HIGH TEMPERATURE STEAM ELECTROLYSIS

Christine Mansilla*
CEA / DEN / DM2S and Laboratoire de Génie Industriel de l'Ecole Centrale Paris
France

Jon Sigurvinsson
CEA / DEN / DM2S

André Bontemps
Université Joseph Fourier and CEA / DRT / DSEN

Alain Maréchal
CEA / DRT / DSEN

François Werkoff
CEA / DEN / DM2S

ABSTRACT

Many research and development projects throughout the world are devoted to sustainable hydrogen production processes. Low temperature electrolysis, when consuming electricity produced without greenhouse gas emissions, is a sustainable process, though having a limited efficiency.
It is possible to improve the performance of electrolysis processes by functioning at high temperature (High Temperature Electrolysis, HTE). This leads to a reduction in energy consumption but requires a part of the energy necessary for the dissociation of water to be in the form of thermal energy, and to be able to recover a part of the heat contained in the outlet products of the electrolysis. Heat would be brought by coupling the process either to a High Temperature Reactor (HTR) or to a geothermal source.
A technoeconomic optimisation of the upper heat exchanger network in the HTE process is carried out. The method we choose is the optimisation using genetic algorithms. The heat exchanger networks appear to be different depending on the heat source which is used.
Keywords: Technoeconomic optimisation, Heat exchanger, Hydrogen production, High temperature electrolysis, Genetic algorithms

NOMENCLATURE

B : heat exchanger plate width [m]
C_e : cost of thermal energy consumption [€/yr]
C_i : investment cost [€]
c_i : unit investment cost [€/m^2]
$c_{kWh_{th}}$: unit cost of thermal energy [€/kWh$_{th}$]
c_{kWh_e} : unit cost of electricity [€/kWh$_e$]
c_{Wh_e} : unit cost of electricity [€/Wh$_e$]
C_o : operating cost [€/yr]
C_{pomp} : pumping cost [€/yr]
D_h : hydraulic diameter [m]
h : heat transfer coefficient [W/m^2 °C]
L : heat exchanger plate length [m]
M : molar mass [kg/mol]
$\dot{m}$: mass flow rate [kg/s]
N : number of heat exchangers
Nu : Nusselt number
P : pressure [Pa]
Pd : heat production [kWh/yr]

* Corresponding author: Phone: +33 1 69 08 93 54
Fax: +33 1 69 08 29 77 Email: christine.mansilla@cea.fr

Pr : Prandtl number
Q : transferred heat [kW]
r : recycling ratio
Re : Reynolds number
S : heat exchange area [m^2]
T : temperature [°C]
TC : discounted total unit production cost [€/kWh]
T_e : number of operating years [yr]
t_e : annual operating time (number of seconds during which the system is running through one year) [s/yr]
T_i : number of years for the initial investment [yr]
U : overall heat transfer coefficient [kW/m^2 °C]
x : dividing factor
Δ : difference
$\Delta T_{\log\ mean}$: logarithmic mean temperature difference [°C]
ε : heat exchanger effectiveness
η : heat exchanger efficiency
η_{pomp} : pumping efficiency
λ : thermal conductivity [W/m.°C]
μ : viscosity [Pa.s]
ρ : density [kg/m^3]
τ : discount rate

Subscripts

1 : hot side
2 : cold side
e : electrical
geo : geothermal
H_2 : relative to hydrogen
H2 : relative to the H_2/H_2O heat exchanger
H_2O : relative to water
HT : high temperature
in : inlet
LT : low temperature
MT : medium temperature
n : heat exchanger number
O_2 : relative to oxygen
O2 : relative to the O_2/H_2O heat exchanger
out : outlet
t : year number
th : thermal

INTRODUCTION

The use of hydrogen as a substitute to hydrocarbons, is currently the object of many research and development tasks throughout the world. To be sustainable, a hydrogen production process must be carried out without consumption of raw materials other than water and driven by energies which are produced without greenhouse gas emissions. Low temperature electrolysis carried out using sustainably produced electricity satisfies these constraints and is currently used to produce hydrogen. However, today, it is more expensive than the process of producing hydrogen by steam reforming of natural gas, which presents a double disadvantage since it consumes natural gas and rejects carbon dioxide. In the long term, methane costs should significantly increase and greenhouse gas emissions may be taxed. Therefore alternative processes should become competitive.

From a thermodynamical point of view, it is possible to improve the performance of electrolysis by functioning at high temperature (HTE). That makes it possible to reduce consumption but requires a part of the energy necessary for the dissociation of water to be in the form of thermal energy.

Recent HTE research programs have profited from new financings, mainly within the Generation IV International Forum framework for developing long term nuclear reactors [1]. The forum considers the possibilities of using nuclear energy, particularly high temperature helium cooled reactors (HTR) which include the possibility of producing hydrogen.

An interest for HTE is also expressed by a European collaboration that aims at studying and then validating the possibilities of producing hydrogen with HTE coupled with a geothermal source. One objective is the production of hydrogen by HTE coupled with a geothermal source in the Icelandic context. The goal is to build a 5 kWe prototype on the site of Nesjavellir, which is 20 km from Reykjavik [2]. The economically harnessable geothermal energy in Iceland has been estimated at approximately 200 TWh/year, of which only 1% has been harnessed up to now. Assuming the same technology as the one used in Iceland today to produce electricity from geothermal steam, the 200 TWh/year could be used for the production of 20 TWh/year of electricity, or 17 TWh/year of hydrogen.

Firstly, the communication will be devoted to the influence of the heat source temperature (HTR or geothermics) and the corresponding energy costs for both heat and electricity. Then, a technoeconomic optimisation approach will be presented in order to optimise the balance between operating costs and investment. Finally we will

detail the heat exchanger networks refering to a HTR or an Icelandic geothermal heat source [3].

HEAT SOURCES AND ENERGY COSTS

High Temperature Electrolysis (HTE) differs from the conventional electrolysis process because some of the energy required to dissociate the water is provided as heat instead of electricity, thus reducing the overall energy required and improving the process efficiency (cf. Figure 1). Because the conversion efficiency of heat to electricity is low compared to using the heat directly, the energy efficiency can be improved by providing the energy to the system in the form of heat rather than electricity.

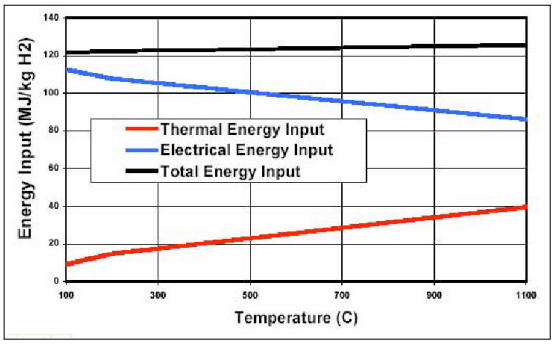

Figure 1: Thermal and electricity supply to the electrolyser

Then the economic interest of HTE will depend on both electricity and heat costs.
In Iceland the cost of extracting thermal energy from a geothermal source is only about 10% of the cost of electricity.

$$c_{kWh_{th}\,geo} = 0.1 \times c_{kWh_e\,geo} \quad (1)$$

With HTR the expected efficiency of electricity production is 50%. Hence we can assume that the price of thermal energy for HTR is 50% of the price of electricity.

$$c_{kWh_{th}\,HTR} = 0.5 \times c_{kWh_e\,HTR} \quad (2)$$

Thermal energy from a geothermal source is very inexpensive compared to thermal energy from a HTR.

In the Icelandic context steam could be supplied at 200°C. According to [3] only 3.8 kWh_e/Nm^3H_2 is needed with a thermal input of 200°C, compared with about 4.5 kWh_e/Nm^3H_2 in conventional electrolysers. Electricity price to industry in Iceland is approximately 0.014 €/kWh compared to 0.0284 €/kWh [4] for middle term electricity produced by nuclear reactors in France (cf. Table 1). The difference between producing hydrogen by HTE in Iceland or in France appears to be obvious, when regarding the cost of vaporising and heating water to the operating temperature of the electrolyser (cf. Figure 2).

c_{kWh_e} Iceland	0.014 €/kWh_e
c_{kWh_e} France	0.0284 €/kWh_e
$c_{kWh_{th}}$ Iceland	0.0013 €/kWh_{th}
$c_{kWh_{th}}$ France	0.0142 €/kWh_{th}

Table 1: Energy prices, geothermics / HTR

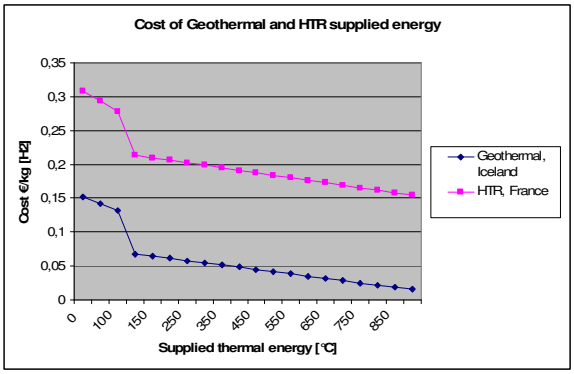

Figure 2: Cost of vaporising and heating water to the required temperature for the electrolyser

Although only 200°C of thermal output is possible today in Iceland, it could change. Recent research performed by Landsvirkjun on deep drilling in Iceland show a possibility of extracting 500-600°C steam at a depth of 4-5 km [5]. At this time deep drilling is purely experimental but could become a possibility within the next ten years. An increase of the exit temperature of the drilling well would significantly improve the economic interest of coupling HTE with a geothermal heat source.

A TECHNOECONOMIC OPTIMISATION FOR UPPER HEAT EXCHANGERS

The technoeconomic model

Method.

The technoeconomic approach we selected presupposes a heat exchanger network, also called a flow sheet. The optimisation procedure consists in minimising an objective function which takes into account operating as well as investment costs.

In the current context of sustainable development, advanced systems are being studied. These systems involve either high pressures, high temperatures, or corrosive products; sometimes several of these severe conditions. In all these cases investment costs can increase by one to two orders of magnitude when compared to classical alternative systems and consequently the interest for the technoeconomic approach should grow.

The heat exchanger network.

There are three possible operating modes for HTE depending on the energy balance at the electrolyser level: endothermal, isothermal and exothermal [6].

Endothermal. The temperature of the steam decreases from the input of the electrolyser to the output. This corresponds to the best energy efficiency but worst production cost because an endothermal electrolyser is much more expensive than an exothermal one.

Isothermal. The temperature of the steam is the same at the input as at the output. The energy efficiency is better than in the exothermal case but the electrolyser cost still outweighs better efficiency.

Exothermal. The temperature of the steam increases from the input of the electrolyser to the output. When coupling to a HTR, this corresponds to the worst energy efficiency but the best production cost because an exothermal electrolyser investment cost is the lowest of the three possibilities [6]. The exothermal mode is the only one to be considered for the geothermal context since the input temperature is only 200°C.

The heat exchanger network we optimised is the upper heat exchanger network involved in the HTE exothermal process (after the boiler, cf. Figure 3). The water entering these heat exchangers is already vaporised.

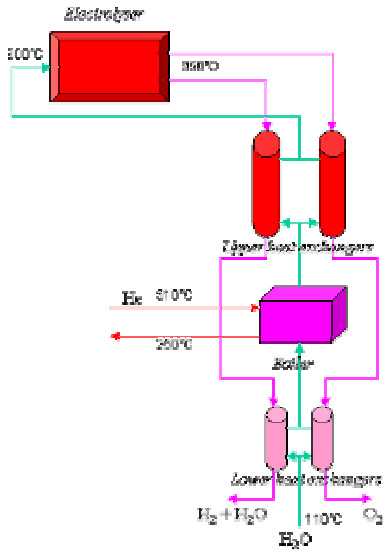

Figure 3: Heat exchanger network coupled with a HTR thermal source

The heat exchangers are supposed to be counter-current flow ones. They consist of a stack of corrugated plates. The heat exchangers characteristics are gathered in Table 2.

D_h	6.10^{-3} m
L	1 m
B	1 m

Table 2: Heat exchangers characteristics

Since we have a wide range of temperatures, we need different heat exchangers:

Low temperature (LT): < 650°C

Medium temperature (MT): 650°C < T < 850°C

High temperature (HT): > 850 °C

According to the heat source and the temperatures at the inlet and outlet of the electrolyser, either one, two or three temperature levels are involved.

The output of the electrolyser is firstly oxygen and secondly a mixture of hydrogen and water. This mixture is dependent on the recycling ratio *r*. Not all the water is electrolysed and the number *r* indicates the ratio of unelectrolysed water. The mixture of water and hydrogen is defined as follows:

$$\dot{m}_{1,H2} = (1-r)\cdot \dot{m}_{H_2 0}\cdot \frac{M_{H_2}}{M_{H_2O}} + r\cdot \dot{m}_{H_2O} \quad (3)$$

$$\dot{m}_{1,O2} = \frac{(1-r)}{2} \cdot \dot{m}_{H_2O} \cdot \frac{M_{O_2}}{M_{H_2O}} \quad (4)$$

The water flow rate used in the previous equations is the total one. This flow rate is split between the H_2/H_2O side and the O_2/H_2O side (cf. Eq. 5 et 6).

$$\dot{m}_{2,H2} = x \cdot \dot{m}_{H_20} \quad (5)$$

$$\dot{m}_{2,O2} = (1-x) \cdot \dot{m}_{H_2O} \quad (6)$$

Inlet temperatures and water outlet temperatures are fixed. Their numerical values depend on the kind of heat source and the temperatures at the inlet and outlet of the electrolyser (cf. Table 3).

The network is detailed in the Figure 4.

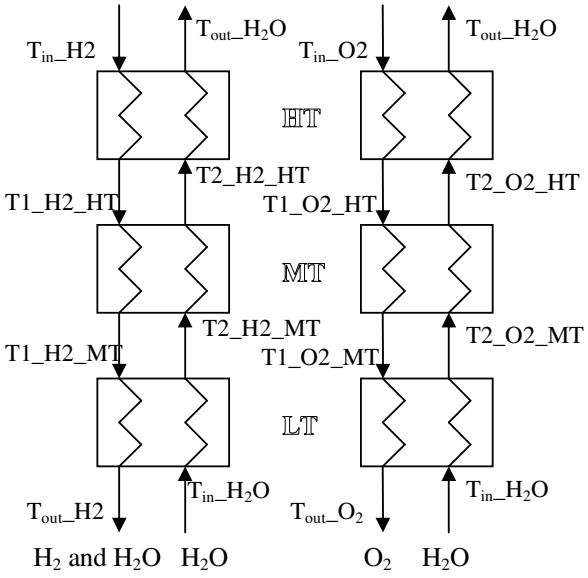

Figure 4: Upper heat exchanger network scheme

T_{in}_H2	950°C
T_{in}_O2	950°C
T_{out}_H_2O	900°C
T_{in}_H_2O (geothermics)	230°C
T_{in}_H_2O (HTR)	470°C
Pressure (geothermics)	1.5 MPa
Pressure (HTR)	3 MPa

Table 3: Fixed temperatures and pressures

The objective function.

It is the optimisation criterion, the function which is to be minimised. The objective function we chose is the discounted total unit production cost. (cf. Eq. (12)). The formula is similar to the one used in [1].

The total cost includes two parts: the investment costs (cf. Eq. (7)) and the operating costs.

$$C_i = c_i \cdot S \quad (7)$$

Investment can be done over several years (T_i). c_i depends on the heat exchanger type, materials, operating parameters. S is calculated using Equation (8).

$$S = \frac{Q}{U.\Delta T_{\log\ mean}} \quad (8)$$

The operating costs can be divided into two parts (cf. Eq. (9)): the cost of thermal energy consumption (cf. Eq. (10)) and the pumping costs (consumption of electricity, cf. Eq. (11))

$$C_o = C_e + C_{pomp} \quad (9)$$

$$C_e = c_{kWh_{th}} \frac{Q}{\eta} t_e \quad (10)$$

$$C_{pomp} = \frac{c_{Wh_e}}{\eta_{pomp}} \frac{\dot{m} \Delta P}{\rho} t_e \quad (11)$$

The discounted total unit production cost is obtained by dividing the discounted total production cost by the discounted production:

$$TC = \frac{\sum_{t=1}^{T_i+T_e} \left[\left(\sum_{n=1}^{N} (C_i)_{n,t} + \sum_{n=1}^{N} (C_o)_{n,t} \right) \cdot (1+\tau)^{-t} \right]}{\sum_{t=1}^{T_i+T_e} \left[\left(\sum_{n=1}^{N} (Pd)_{n,t} \right) \cdot (1+\tau)^{-t} \right]} \quad (12)$$

$$Pd = Q \cdot t_e \quad (13)$$

Table 4 gathers the values of the different parameters of the model.

T_i	3 yrs
T_e	30 yrs
Operating factor	80%
τ	6%
c_i	400 €/m^2 (LT) 800 €/m^2 (MT) 4000 €/m^2 (HT)
$c_{kWh_{th}}$ c_{kWh_e}	Cf. Table 1
η_{pomp}	0.80

Table 4: Model parameters

Assuming that plate heat exchangers with primary surfaces are used to insure high effectivenesses, the overall heat transfer coefficient can be derived as follows, neglecting the conduction thermal resistance:

$$U = \frac{1}{\frac{1}{h_1} + \frac{1}{h_2}} \quad (14)$$

where h_1 and h_2 are the heat transfer coefficients for the hot (*1*) and cold (*2*) side respectively.

$$h_i = \frac{Nu_i \cdot \lambda_i}{D_h}, \; i = 1, 2 \quad (15)$$

Nu_i is the Nusselt number which can be calculated for specific plates by:

$$Nu_i = 0.254 \, \mathrm{Re}_i^{0.638} \, \mathrm{Pr}_i^{1/3} \quad (16)$$

Pr_i being the Prandtl number and Re_i being the Reynolds number calculated from:

$$\mathrm{Re}_i = \frac{2 \dot{m}_i}{\mu_i \, B} \quad (17)$$

Variables and constraints.

The total mass flow rate of water $\dot{m}_{H20}$, the dividing factor x and the temperatures are the optimisation variables.

Several inequality constraints are taken into account:

- the temperatures of water are lower than the ones of the products of electrolysis;
- the velocity of the streams must not exceed 30m/s;
- the heat exchangers effectiveness must not exceed 0.9.

The optimisation software: based on genetic algorithms

The technoeconomic model was implemented in a software devoted to optimisation, called *Vizir*, which is based on genetic algorithms [7]. This software is developed at the CEA.

Genetic algorithms are a stochastic method of optimisation laying on an analogy with the Darwinist theory. They work with the same process, that is to say the evolution of a population using mutations and crossovers. The selected individuals are the ones who are adapted according to the objective function, which means for our study that the chosen values for the operating parameters are those corresponding to lower total costs.

This method has many advantages. The objective function does not need to be continuous or verify any other property. It is only needed to be able to evaluate it. Moreover, when a local optimum is found, the algorithm does not stop. Finally they are robust algorithms that allow complex systems to be studied.

HEAT EXCHANGER NETWORKS ACCORDING TO THE HEAT SOURCE: HTR OR ICELANDIC GEOTHERMICS

Icelandic geothermal heat source

The results of the optimisation are presented in Table 5, Figure 5, and Table 6.

TC	0.0033 €/kWh
Investment part	17.5 %
Part of thermal energy consumption cost	71.3 %
Part of pumping cost	11.2 %

Table 5: Cost of the heat recovered within the system

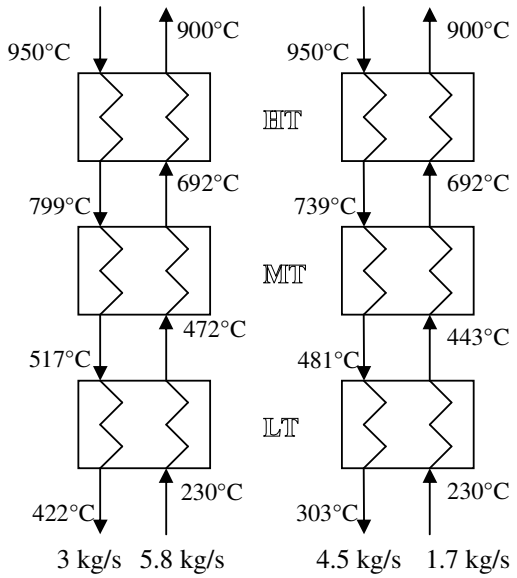

Figure 5: Heat exchanger network (Icelandic geothermics)

Q H2 HT (kW)	2870
Q O2 HT (kW)	850
Q H2 MT (kW)	2930
Q O2 MT (kW)	980
Q H2 LT (kW)	3030
Q O2 LT (kW)	790
S H2 HT (m^2)	74
S O2 HT (m^2)	28
S H2 MT (m^2)	121
S O2 MT (m^2)	77
S H2 LT (m^2)	85
S O2 LT (m^2)	36
ε H2 HT	0.81
ε O2 HT	0.81
ε H2 MT	0.67
ε O2 MT	0.84
ε H2 LT	0.84
ε O2 LT	0.85
$0.64 < Pr < 9.86$	
$2390 < Re < 11640$	
0.30 kW/m^2 °C $< U < 0.60$ kW/m^2 °C	

Table 6: Heat exchangers characteristics

As expected, the significant parts of investment and pumping costs can be noticed.

HTR heat source

When coupling the high temperature electrolysis system with a HTR, the Low Temperature level of the network is no longer needed because of the orders of magnitude of outlet temperatures.
The results are presented in Table 7, Figure 6 and Table 8.

TC	0.0262 €/kWh
Investment part	2.4 %
Part of thermal energy consumption cost	95.8 %
Part of pumping cost	1.8 %

Table 7: Cost of the heat recovered within the system

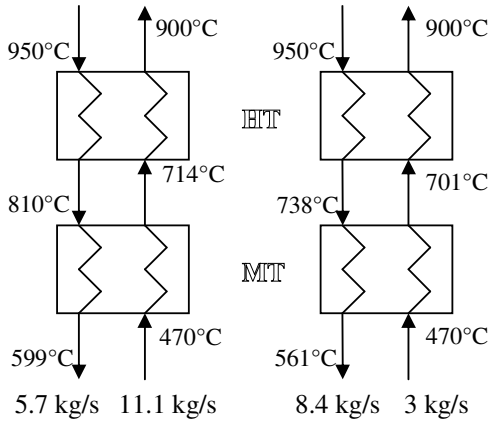

Figure 6: Heat exchanger network (HTR)

Q H2 HT (kW)	5037
Q O2 HT (kW)	1460
Q H2 MT (kW)	6273
Q O2 MT (kW)	1608
S H2 HT (m^2)	128
S O2 HT (m^2)	57
S H2 MT (m^2)	94
S O2 MT (m^2)	40
ε H2 HT	0.79
ε O2 HT	0.80
ε H2 MT	0.72
ε O2 MT	0.86
$0.64 < Pr < 9.03$	
$4690 < Re < 16540$	
0.55 kW/m^2 °C $< U < 0.65$ kW/m^2 °C	

Table 8: Heat exchangers characteristics

The dominant part is the thermal energy consumption cost.

CONCLUSION

First we can point out that genetic algorithms proved to be very effective to solve the problem of the optimisation of upper heat exchangers.

The results of the optimisation show that the heat exchanger networks strongly depend on the heat source. The investment part is very different for each case. When coupling the HTE to a HTR, the cost of thermal energy consumption clearly predominates.
Moreover, in this study, the electrolyser is supposed to work between 900°C and 950°C. Other ranges of temperature are possible. Indeed, research and development works are heading for lower ranges of temperature. This would lead to different networks, since the High Temperature level could no longer be needed.

The design of the networks for high temperature electrolysis processes will depend on the evolutions and progresses to come. In particular, in heat exchanger technology, many researches are in progress concerning materials and component assembling. It is also the case for electrolysers. It will also strongly depend on the evolutions of both heat and electricity costs.

REFERENCES

[1] GENERATION IV. *Generation IV Roadmap Crosscutting Economics R&D Scope Report.* GIF-007-00. December2002. See also: http://gif.inel.gov/roadmap/pdfs/007_crosscutting_economics_r-d_scope_report.pdf

[2] GEYSER. *High temperature electrolysis at CEA and comparison with other hydrogen production technologies*. In: Proceedings of the IEA Workshop on high temperature electrolysis, San Antonio, 2004.

[3] Arnason B, Sigfusson T.I. *Iceland as a future Hydrogen Economy.* International Journal for Hydrogen Energy 2000; 25: 389-394.

[4] DGEMP-DIDEME. *Coûts de référence de la production électrique*. 2003.

[5] Sigfusson T.I. *Private communication.* 2004

[6] Werkoff F, Maréchal A, Pra F. *Technoeconomic study on the production of hydrogen by high temperature steam electrolysis.* In: Proceedings of the 1st European Hydrogen Energy Conference, Grenoble, 2003.

[7] Perrin E, Mandrille A, Oumoun M, Fonteix C, Marc I, *Optimisation globale par stratégie d'évolution, technique utilisant la génétique des individus diploïdes.* Recherche opérationnelle / Operations Research 1997; 31(2): 161-201.

ACKNOWLEDGEMENTS

A part of this work was carried out for preparing a PhD. We would like to thank Professor J.-C. Bocquet, the scientific director of the thesis and head of the LGI (Laboratoire de Génie Industriel de l'Ecole Centrale de Paris).

Proceedings of ECOS 2005
Trondheim, Norway
June 20–22, 2005

HYDROGEN PRODUCTION BY ADVANCED PEM WATER ELECTROLYSERS - REDUCED ENERGY CONSUMPTION BY IMPROVED ELECTROCATALYSIS

A. Marshall*, B. Børresen, G. Hagen†, M. Tsypkin, R. Tunold
Department of Materials Technology, Group of Electrochemistry
NTNU, 7491 Trondheim, Norway

ABSTRACT

PEM water electrolysis systems offers several advantages over traditional technologies including greater energy efficency, higher production rates, and more compact design. Normally in these systems, the anode has the largest overpotential at typical operating current densities. By development of the electrocatalytic material used for the oxygen evolving electrode, great improvements in efficency can be made. We find that using cyclic voltammetry and steady state polarisation analysis, enables us to separate the effects of true specific electrocatalytic activity and active surface area. Understanding these two factors is critical in developing better electrocatalytic materials in order to further improve the performance of PEM water electrolysis cells. The high current performance of a PEM water electrolysis cell using these oxides as the anode electrocatalyst has also been examined by steady state polarisation measurements and electrochemical impedance spectroscopy. Overall the best cell voltage obtained is 1.567 V at 1 A cm^{-2} and 80 °C was achieved when using Nafion 115 as the electrolyte membrane.

*Keywords:*Electrocatalysis, Hydrogen Production, PEM water electrolysis

NOMENCLATURE

b	Tafel slope	[mV dec^{-1}]
E_{cell}	Total cell voltage	[V]
$E_{0.02AC^{-1}}$	Electrocatalytic activity^{-1}	[A C^{-1}]
$E_{1mAcm^{-2}}$	η_{anode} at 1 mA cm^{-2}	[V]
$E_{1Acm^{-2}}$	Cell voltage at 1 A cm^{-2}	[V]
I	Current density	[A cm^{-2}]
R	Cell resistance	[Ω cm^2]
$\varepsilon_{\Delta G}$	Cell efficiency ΔG basis	[%]
$\varepsilon_{\Delta H}$	Cell efficiency ΔH basis	[%]
η_{anode}	Anodic overpotential	[V]
$\eta_{cathode}$	Cathodic overpotential	[V]

INTRODUCTION

Carbon free hydrogen can be produced using water electrolysis. PEM water electrolysis systems offers several advantages over traditional technologies including greater energy efficency, higher production rates, and more compact design [1]. This method of hydrogen production is envisioned in a future hydrogen society whereby hydrogen as the energy carrier is incorporated in an idealised "energy cycle". In this cycle, electricity from renewable energy sources, is used to electrochemically split water into hydrogen and oxygen. The only input to this cycle is the clean renewable energy and the only output is electric power.

A basic schematic of a PEM water electrolysis cell is shown in Figure 1. The PEM water electrolysis cell consists primarily of a proton exchange membrane on which the anode and cathode are bonded. These electrodes are normally a composite of electrocatalytic particles and electrolyte polymer. Normally different electrocatalysts are utilised for the anode (eg. IrO_2) and cathode (eg. Pt). When the electrode layers are bonded to membrane, it is known as the membrane electrode assembly (MEA). The electrical contact and mechanical support is established

*Corresponding author: Phone: +47 735 94021 Fax: +47 735 94083 E-mail:aaron.marshall@material.ntnu.no

with porous backings like metallic meshes or sinters. In a PEM water electrolyser hydrogen is produced by supplying water to the anode where it is decomposed into oxygen, protons, and electrons (Equation 1). The protons are transported through the proton conductive membrane to the cathode. The electrons exit the cell via the external circuit, which supplies the driving force (i.e. cell potential) for the reaction. At the cathode the electrons and protons recombined to give hydrogen gas (Equation 2).

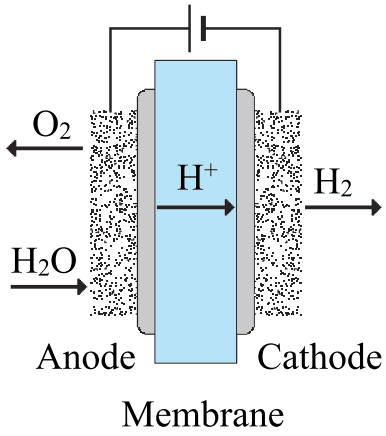

Figure 1: PEM water electrolyser schematic

$$H_2O \rightarrow \frac{1}{2}O_2 + 2H^+ + 2e^- \qquad (Anode) \qquad (1)$$

$$2H^+ + 2e^- \rightarrow H_2 \qquad (Cathode) \qquad (2)$$

$$H_2O \rightarrow \frac{1}{2}O_2 + H_2 \qquad (Cell) \qquad (3)$$

Presently there is no large scale use of PEM water electrolysis systems, with only a very few commercial systems available [2]. The restricting aspects of these systems is the high cost of the materials such as the electrolyte membrane and noble metal based electrocatalysts, as well as the complex system components to ensure safe and reliable operation.

Normally in these systems, the anode has the largest overpotential at typical operating current densities (normally around 10 kA m^{-2}) [3] with the total cell voltage required to split water given by equation 4. This is easily seen in a typical polarisation curve of a PEM water electrolysis cell (Figure 2). For this reason this work has concentrated on the anode electrocatalyst development. Recently $Ir_xSn_{1-x}O_2$ [4–7], $Ir_xRu_{0.5-x}Sn_{0.5}O_2$ [8] and $Ir_xRu_yTa_zO_2$ powders have been investigated as oxygen evolution electrocatalysts in our group.

$$E_{cell} = E^{rev} + \eta_{anode} - \eta_{cathode} + IR \qquad (4)$$

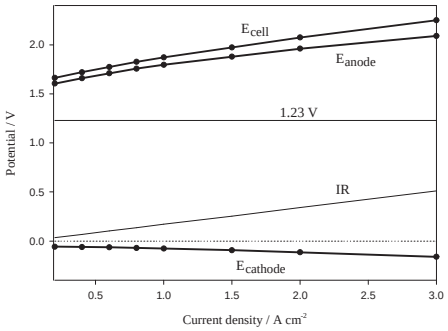

Figure 2: Polarisation curve for a PEM water electrolyser at 25 °C, IrO_2/N-105/40% Pt/C

Noble metal oxides as electrocatalysts are well established in many industrial electrochemical processes in the form of dimensionally stable anodes (DSA) as developed by Beer [9]. Ruthenium is known as the most active oxide for anodic oxygen evolution [10], however it suffers from instability and therefore should be stablised with another oxide such as IrO_2 [11] or SnO_2 [12]. Tantalum is a well known addition to DSA electrodes, and Ir-Ta oxides have been suggested as the most efficient electrocatalysts for oxygen evolution in acidic electrolytes due to the high activity and corrosion stability [13]. Although very comprehensive studies of the structural and electrochemical properties of DSA oxides have been carried out, little is known regarding the structure and electrocatalytic properties of oxide powders. This is mainly due to the prevalence of DSA electrodes in industrial processes compared with the same oxide compositions in particle form. In addition, it is well known that the a wide range of preparation conditions affect the formation and properties of DSA type oxide layers [14] as will the presence of Ti originating from the substrate (see [15]), and therefore analysis of powder based oxides gives an insight to the specific nature of noble metal oxides as electrocatalysts while providing a possible use in PEM water electrolysis applications.

In the following, we will use a range of recent results from our work to highlight the success we have had

using a muli-disciplined approach to electrocatalyst development.

EXPERIMENTAL

Electrochemical characterisation of the various electrocatalytic powders was conducted in 0.5 M H_2SO_4 (Merck, p.a) electrolyte at room temperature, by supporting the powders on titanium plates using a spraying technique. The electrocatalytic layer consisted of 95 wt% electrocatalyst and 5 wt% Nafion ionomer[1], with a total loading of 1 mg cm^{-2}. Cyclic voltammetry and polarisation measurements were performed using an IM6e electrochemical workstation from ZAHNER-elektrik GmbH & Co. KG. All potentials are quoted versus the reversible hydrogen electrode in the same electrolyte. Cyclic voltammetry is often used in DSA literature to compare the active area or number of active points of a noble metal oxide layer. This is carried out by measuring the charge (the number of electrons transferred) as a function of sweep rate. The charging / adsorption process for iridium oxide is given by the following equation [16]:

$$IrO_a(OH)_b \rightleftharpoons IrO_{a+\delta}(OH)_{b-\delta} + \delta H^+ + \delta e^- \quad (5)$$

This charging reaction allows the active surface area of the oxides to be compared assuming that the charging reaction is proportional to the total number of active sites at the oxide–electrolyte interface [17]. The outer charge represents the active area which is easily accessible, whereas the total charge includes active points within the particle structure, to which the electrolyte must diffuse, in order to be included in the electrode response.

A PEM water electrolysis cell was also used to evaluate the performance of the electrocatalysts under real conditions, by applying the oxides as the anode and 20% Pt/C[2] as the cathode. Details of the cell can be found elsewhere [6]. The membrane electrode assembly (MEA) was prepared by spraying the ink containing the electrocatalyst and Nafion ionomer directly to Nafion 115 membranes[3] at 90 °C using a custom built automated spray system. The MEA was mounted into the cell between two porous titanium sinters[4], and preheated deionised water was supplied to both the anode and cathode compartments at 5 l min^{-1}. Total cell polarisation curves were recorded by stepping the current between 1 and 2000 mA cm^{-2}, and the cell impedance was recorded at 20 mA cm^{-2} using frequencies ranging from 100 kHz to 100 mHz with an AC amplitude of 5 mV.

RESULTS AND DISCUSSION

Electrochemical Active Surface Area

In the system $Ir_xSn_{1-x}O_2$ we find that the active area is proportional to the iridium content of the oxide [6]. This is because the tin present in the oxide lattice does not contribute to the charging reaction. Small additions of tin (up to 20-30 mol%) may be considered reasonable as the total available area only decreases by 10-15% which probably results in a overall cost benefit considering the relative price of iridium and tin. Addition of ruthenium to the $Ir_xSn_{1-x}O_2$ system in order to replace the more expensive and less active iridium component with ruthenium results in a significant reduction in active surface area [8](Figure 3). The decrease is even more dramatic if the decrease in total tin content of the material and therefore higher noble metal loading on the electrode is considered. As said above mixtures of iridium and ruthenium oxide often give rise to a maximum in anodic charge at intermediate compositions [18, 19], however here we have found based on XPS and XRD results that the reduction in active surface area is explained by the shape decrease in the concentration of noble metal elements at the surface of the particles [8]. This is largely due to the synthesis method of the oxide, in which the ruthenium component clusters strongly together resulting in a heterogenous particle structure with active noble metal elements larger confined to the inner core of the particle. Since the majority of electrochemical processes occur at the surface, this noble metal core does not play a role in the charging reaction.

Similar results were obtained for the $Ir_xRu_yTa_zO_2$ system For the Ir-Ru oxides there is a slight maximum around 40 mol% Ru, whereas for the ternary

[1] Dupont 1100 EW 5% Nafion solution, Ion Power Inc.

[2] 20% Pt on Vulcan XC-72R, E-TEK Inc.

[3] N-115, Ion Power Inc.

[4] Applied Porous Technologies Inc, diameter 30mm, thickness 1.5mm, 50 % porosity

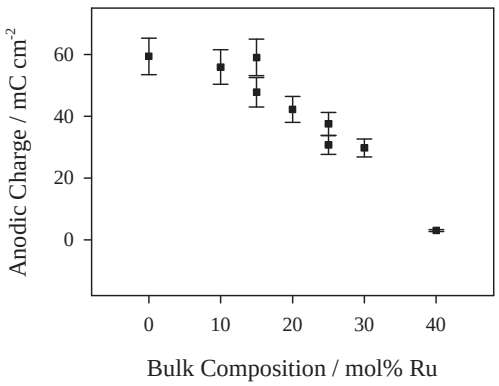

Figure 3: Outer anodic charge of $Ir_xRu_{0.5-x}Sn_{0.5}O_2$ in 0.5 M H_2SO_4

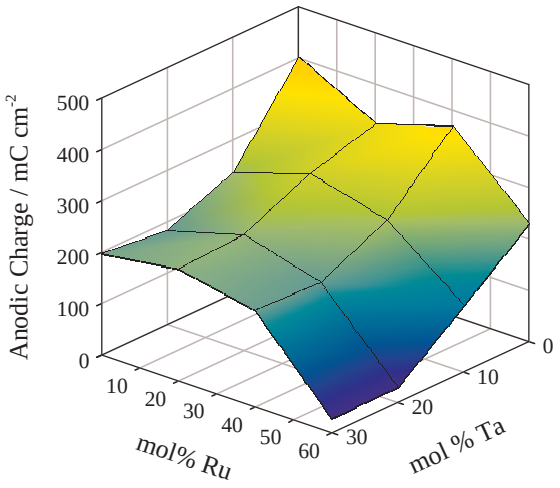

Figure 4: Total anodic charge of $Ir_xRu_yTa_zO_2$ in 0.5 M H_2SO_4

electrodes the maximums are found around 20 mol% Ru (Figure 4). The lower charge for the electrodes containing high levels of Ru, is due to the effect ruthenium has on the oxide crystallinity. Using XRD and EXAFS analysis showed that increasing the ruthenium content resulted in more ordered oxide structures which presumably have less roughness and defects. As tantalum will not take part in the charging process directly the results show the expected results with the total charge decreasing as tantalum content increases. Assuming that the charging process is similar, normally it should be expected that ruthenium oxide electrodes will have a larger anodic charge, as by weight, ruthenium oxide contains around 70 % more atoms than iridium oxide.

The choice of electrocatalyst at this stage of analysis is not straightforward. Although we know that the active area is a function of synthesis parameters and composition, we also know that specific activity, stability and cost will be effected, and thus much more analysis is required.

Steady state polarisation analysis

Low current steady state polarisation analysis is one clear method of determining an electrocatalysts ability to lower the overpotential and thus improve the efficiency the water electrolyser. A secondary result of this analysis is the ability to distinguish between various reaction mechanisms and rate determining steps for the oxygen evolution reaction [20]. Several low current polarisation curves in 0.5 M H_2SO_4 are shown in Figure 5. Data for the $Ir_xRu_{0.5-x}Sn_{0.5}O_2$ and $Ir_xRu_yTa_zO_2$ systems are shown in Table 1 and Figure 6 respectively.

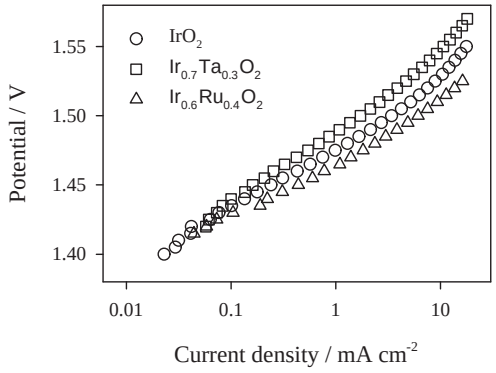

Figure 5: Polarisation curves of $Ir_xRu_yTa_zO_2$ in 0.5 M H_2SO_4

Based on this analysis and with comparison to the active area measurements, we can conclude that active surface area is not solely responsible for the electrocatalytic performance of these oxides. This is clearly due to the fact that oxide composition, particularly the type of noble metal used, effect the specific electrochemical activity, a property which is unaffected by surface area[5].

[5]This is generally true except when dealing with "nano"

Table 1: Summary of polarisation measurements of $Ir_xRu_{0.5-x}Sn_{0.5}O_2$ in 0.5 M H_2SO_4

x	b mV/dec	$E_{1mAcm^{-2}}$ V vs. RHE
0.5	35.5	1.522
0.4	43.0	1.500
0.35	45.3	1.496
0.3	45.2	1.496
0.25	43.9	1.493
0.2	43.4	1.500
0.1	83	—-

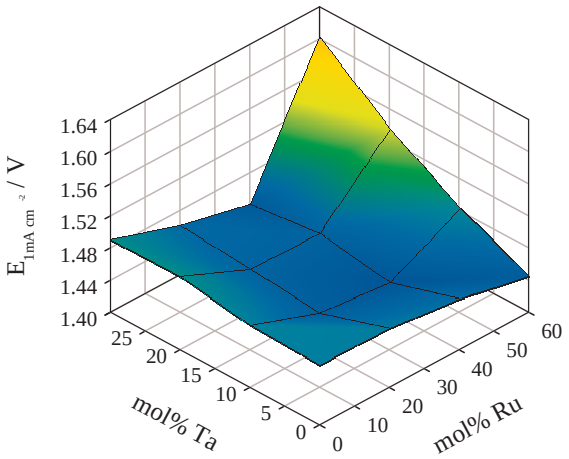

Figure 6: Potential at 1 mA cm^{-2} for $Ir_xRu_yTa_zO_2$ in 0.5 M H_2SO_4

Specific Electrocatalytic activity

In our work we have found that combining the active surface area measurements with the total electrocatalytic performance at low current densities can yield very useful information regarding the specific electrocatalytic activity, which is free from surface area effects [6, 8]. This best found by dividing the current density by the outer anodic charge found by the cyclic voltammetry measurements. The potentials at a normalised current density of 0.02 mA mC^{-1} can then be used to compare the materials (Figure 7). It is very clear that the specific electrocatalytic activity increases (i.e. $E_{0.02mAmC^{-1}}$ decreases) almost linearly with the ruthenium content. This is also true for $Ir_xRu_yTa_zO_2$ electrocatalysts, with tantalum having no effect of the specific activity of the material. In systems such as $Ir_xSn_{1-x}O_2$ where there is only one active element (assuming that the activity of SnO_2 is many times less than IrO_2) we find that the specific activity is constant. Therefore is systems containing multiple active elements we suggest that there is an optimum in the electrocatalytic performance of these materials, based on the active area and the specific activity. Although this finding does not directly result in any performance improvements it is important for electrocatalyst development. By carefully manipulating the synthesis procedure, it should be possible to prepare an oxide with high specific activity and high surface area, resulting in considerably increased performance.

Electrical conductivity measurements

The electrical conductivity of the active layer in a PEM water electrolyser cell is very important and contributes directly to the efficiency of the electrolyser as shown in Equation 4. This is even more critical when one considers that a main advantage of PEM water electrolysers in comparison with traditional systems is the high operating current densities which can be achieved. Due to this high operating current density, the cell (and therefore the layer) must have a low resistivity. Electrical conductivity of DSA type oxide layers has had some attention in literature [14], and as discussed in this review, the conductivity of the oxides rarely causes a signifi-

based materials, in which the small size of the particles may induce changes in the chemical and electronic properties of the material itself

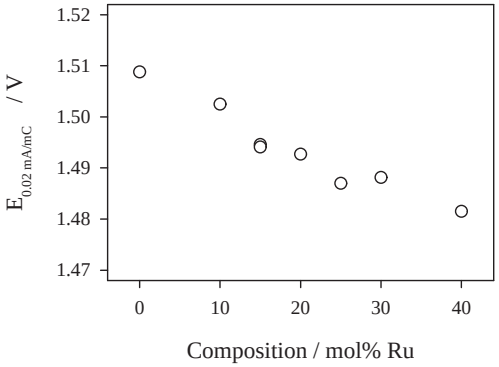

Figure 7: Specific activity of $Ir_xRu_{0.5-x}Sn_{0.5}O_2$ in 0.5 M H_2SO_4

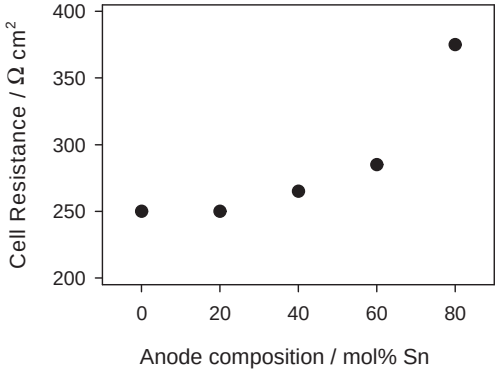

Figure 8: PEM water electrolysis cell resistance as a function of anode composition

cant performance loss as the highest resistivity reported is on the order of 10^{-2} Ω cm. Resistivities are around 3-6 x10^{-5} and 3-5 x10^{-5} Ω cm for crystalline IrO_2 and RuO_2 respectively [21]. The mechanism or cause of the resistivity is also suggested to occur primarily from the intergrain regions, and that the conductivity occurs with a "hopping" mechanism. Clearly in a layer consisting of particles, the resistance will be increased due to the large number of grain and particle boundaries. The contribution of the oxide layers resistivity to performance loss in PEM water electrolysers has been discussed previously [3, 6]. The resistivity in the MEA layer can be obtained directly by electrochemical impedance spectroscopy. From the previous work based on pressed powder measurements it was expected that the resistivity difference between the low tin and high tin content oxides should correspond to 50-100 mV at 1 A cm^{-2} [5]. The results from full cell impedance measurements show that there is an increase in the full cell resistance as the anode composition is varied (Figure 8). The maximum difference corresponds to 125 mV at 1 A cm^{-2} which is similar to that predicted by the pressed powder measurements. Clearly increasing the tin content to above 60 mol% causes unacceptable performance losses due to considerably increased ohmic resistance.

PEM water electrolysis performance

The performance of the various anode electrocatalysts were evaluated in a single PEM water electrolysis cell up to current densities of 2 A cm^{-2} with the total (anode + cathode) noble metal loadings less than 2 mg cm^{-2}. Typical polarisation curves at 80 °C are shown in Figure 9 (Anode composition indicated on Figure). The potential at 1 mA cm^{-2} is used to show the performance of the anode electrocatalysts without the influence of ohmic resistivity and high bubble formation, whereas the potential at 1 A cm^{-2} ($E_{1Acm^{-2}}$) will be affected by ohmic resistivity and bubble formation and thus gives a measure of the performance under real operating conditions.

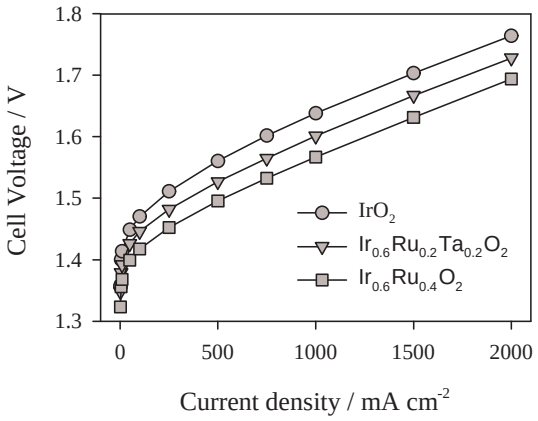

Figure 9: Polarisation curve of PEM water electrolysis cell at 80 °C

It is found that the overpotentials in 0.5 M H_2SO_4 and in the PEM environment at low current density

are highly correlated. The measurements in 0.5 M H_2SO_4 are therefore very useful in screening materials for their electrocatalytic properties. At high current densities, the relationship between the trends in low current density overpotential and high current overpotentials are complex. This is due to the influence of mass transport and electrical/ionic resistivity on the high current overpotential. Therefore using the differences between low and high current densities can yield information regarding the importance of structural aspects of the particles and catalytic layer.

Overall, by using a multi-disciplined approach to develop and characterise electrocatalysts, we have achieved significant improvements to the performance and efficency of a PEM water electrolysis cell. The best result was obtained with an $Ir_{0.6}Ru_{0.4}O_2$ anode and 20 wt% Pt/C cathode, with a cell voltage of 1.567 V at 1 A cm^{-2} and 80 °C when using Nafion 115 as the electrolyte membrane. This represents a cell efficiency based on minimum chemical work of 76 % ($\varepsilon_{\Delta G}$) and 94.4 % based on the higher heating value ($\varepsilon_{\Delta H}$), equating to an energy consumption of 3.75 kWh Nm^{-3} H_2 at 1 A cm^{-2}.

CONCLUSIONS

Hydrogen will be a part of future energy systems. By using PEM water electrolysis, this hydrogen can be produced efficiently without environmental impact if renewable energy is used as the power source. Improvements to the performance and efficiency of PEM water electrolysis cells has been studied by using electrocatalysis. Various aspects of electrocatalysis has been reviewed and it has been found that not one property should be used for characterising and understanding the electrocatalysis process. Active surface area, specific activity, electronic resistance and particle/layer structure are all important properties which need to be optimised in order to achieved high efficiency and performance. In the PEM water electrolysis, very high performance was obtained when using electrocatalysts developed following these guidelines. The best result was obtained with an $Ir_{0.6}Ru_{0.4}O_2$ anode and 20 wt% Pt/C cathode, with a cell voltage of 1.567 V at 1 A cm^{-2} and 80 °C when using Nafion 115 as the electrolyte membrane. This equates to a cell efficiency of 94.4 % ($\varepsilon_{\Delta H}$) and an energy consumption of 3.75 kWh Nm^{-3} H_2 at 1 A cm^{-2}.

ACKNOWLEDGMENTS

The authors would like to acknowledge the financial support from the Norwegian Research Council and Norsk Hydro ASA.

REFERENCES

[1] R. Oberlin, M. Fischer., in: T. Veziroglu, N. Getoff, P. Weinzierl (Eds.), Hydrogen Energy Progress VI, Proceedings of the 6th World Hydrogen Energy Conference, Pergamon Press, 1986, pp. 333–340.

[2] J. Divisek, Electrochemical Hydrogen Technologies, Elsevier Publishing Company, Amsterdam, 1990.

[3] E. Rasten, Electrocatalysis in water electrolysis with solid polymer electrolyte, Ph.D. thesis, NTNU, Trondheim, Norway (2001).

[4] A. Marshall, B. Børresen, G. Hagen, M. Tsypkin, R. Tunold, Journal of New materials for Electrochemical systems 7 (2004) 197–204.

[5] A. Marshall, B. Børresen, G. Hagen, M. Tsypkin, R. Tunold, Submitted to Mat. Chem. Phys., Jan 2005.

[6] A. Marshall, B. Børresen, G. Hagen, M. Tsypkin, R. Tunold, Submitted to Electrochim. Acta., Feb 2005.

[7] A. Marshall, B. Børresen, G. Hagen, M. Tsypkin, R. Tunold, Keynote Lecture 55th ISE meeting, 19-24 Sept. Thessaloniki, Greece (2004) 732.

[8] A. Marshall, B. Børresen, G. Hagen, M. Tsypkin, R. Tunold, To be Submitted.

[9] H. Beer, Improvements in or relating to electrodes for electrolysis, British Patent 1,147,442.

[10] S. Trasatti, Electrochimica Acta 29 (1984) 1503–1512.

[11] R. Kötz, S. Stucki, Electrochimica Acta 31 (1986) 1311–1316.

[12] R. Hutchings, K. Müller, S. Stucki, Journal of Materials Science 19 (1984) 3987–3994.

[13] Y. Roginskaya, O. Morozova, E. Loubnin, A. Popov, Y. Ulitina, V. Zhurov, S. Ivanov, S. Trasatti, Journal of the Chemical Society, Faraday Transactions 89 (1993) 1707–1715.

[14] S. Trasatti, Electrochimica Acta 36 (1991) 225–241.

[15] A. D. Battisti, R. Brina, G. Gavelli, A. Benedetti, G. Fagherazzi, Journal of Electroanalytical Chemistry 200 (1985) 93–104.

[16] D. Michell, D. Rand, R. Woods 89 (1978) 11–27.

[17] S. Ardizzone, G. Fregonara, S. Trasatti, Electrochimica Acta 35 (1990) 263–267.

[18] F. Mattos-Costa, P. de Lima-Neto, S. Machado, L. Avaca, Electrochimica Acta 44 (1998) 1515–1523.

[19] C. Angelinetta, L. Atanasoska, R. Atanasoski, S. Trasatti, Journal of Electroanalytical Chemistry 214 (1986) 535–546.

[20] J. Bockris, Journal of Chemical Physics 24 (1956) 817–827.

[21] S. Trasatti, G. Lodi, Electrodes of Conductive Metallic Oxides, Elsevier scientific publishing company, 1980, Ch. Properties of Conductive Transition Metal Oxides with Rutile-Type Structure, pp. 301–358.

Proceedings of ECOS 2005
Trondheim, Norway
June 20–22, 2005

DEVELOPMENT OF A ZERO-DIMENSIONAL MODEL OF A 2ND GENERATION PLANAR SOFC WITH EMPIRICAL CALIBRATION OF ELECTROCHEMICAL PARAMETERS

Thomas Frank Petersen *
Risø National Laboratory, Materials Research Department, Frederiksborgvej 399, P.O. 49, DK-4000 Roskilde.
Niels Houbak and Brian Elmegaard
Technical University of Denmark, Department of Mechanical Engineering, DK-2800 Lyngby

ABSTRACT

This paper presents a zero-dimensional mathematical model of a planar 2^{nd} generation Solid Oxide Fuel Cell (SOFC) suitable for simulation of hybrid power systems. The model accounts for methane reforming and the water-gas shift reaction in addition to the electrochemical oxidation of hydrogen. The most novel and important part of the model is the detailed electrochemical sub-model, which is phenomenological and based on the most recent research on SOFCs. Empirical current-voltage data was obtained and used to calibrate the activation and concentration polarization parameters of the electrochemical model. This approach gives good accuracy when compared to the original data. The SOFC model was implemented in the Dynamic Network Analysis (DNA) simulation software. The result is an accurate and flexible tool suitable for simulation of SOFC-based hybrid power systems.
Keywords: Solid Oxide Fuel Cells, SOFC, Mathematical modelling

NOMENCLATURE

Greek letters	Name	Unit
α	charge transfer coefficient	[-]
ρ	density	[kg/m^3]
σ	conductivity	[S/m]
τ	tortuosity	[-]
θ	temperature	[°C]

Sub/super script	Name
a	air
act	activation
bin	binary
an	anode
ca	cathode
conc	concentration
eff	Effective
el	electrolyte
f	fuel
i	inlet
Nernst	Nernst potential
o	outlet
offset	offset polarization
Ohm	Ohmic polarization
ref	reforming reaction
wgs	water-gas shift reaction

*Corresponding author. Phone:+4546775814, Fax:+4546775758, E-mail: thomas.frank.petersen@risoe.dk

Symbol	Name	Unit
A	cell area	$[m^2]$
B	Constant	[-]
D	diffusion coefficient	$[cm^2/s]$
D_h	hydraulic diameter	[m]
F	Faraday's constant	[C/mol]
f	Friction factor	[-]
E	Electric potential	[V]
$\Delta\bar{G}$	Gibbs energy	[kJ/mol]
ΔV	Polarization	[V]
i_d	current density	$[A/cm^2]$
i_0	exchange current density	$[A/cm^2]$
K	Pressure loss constant	[-]
L	SOFC length	[m]
l	length/thickness	[m]
$\dot{n}$	molar flow	[mol/s]
P	pressure	[bar]
P_{ref}	1.013	[bar]
p	partial pressure	[-]
$\dot{r}$	molar reaction rate	[mol/s]
T	Temperature	[K]
T_{ref}	1023	[K]
V	porosity	[-]
v	velocity	[m/s]
$\dot{W}$	Electrical power	[kW]
R	Universal gas constant	[kJ/(kmolK)]
U	utilization	[-]

INTRODUCTION

The high temperature Solid Oxide Fuel Cell (SOFC) is one of the most promising types of fuel cells. Because of its high operating temperature, SOFCs can use hydrocarbons like methane and natural gas directly as fuels. In addition, the high temperature makes SOFCs usable in small stationary hybrid power systems, where the high quality heat produced in the SOFC, can be utilized in heat engines. These hybrid power systems are often complex and a flexible simulation tool is necessary to analyze the systems in detail. This paper presents a zero-dimensional mathematical model of a planar SOFC suitable for this purpose. The model accounts for methane steam-reforming and the water-gas shift reaction in addition to the electrochemical oxidation of hydrogen. This type of SOFC model is not new, however previous models were mostly based on the tubular type of SOFC with a very different geometry and thermal characteristics, see eg. (Costamagna et al 2000, [1]) or (Massardo and Lubelli 2001, [2]). Furthermore, the electrochemical model used in those models was first presented over 10 years ago and does not account for all sources of electrical polarization in the SOFC (Achenbach 1994, [3]). The model presented here offers an improvement, as it uses recent research on 2^{nd} generation SOFC electrochemistry. To facilitate the objective of hybrid power system simulation, the SOFC model has been implemented in the open source simulation software "Dynamic Network Analysis" (DNA).

THE DNA SIMULATION TOOL

DNA is a component-based simulation tool designed for both static and dynamic simulation of power plants and other energy systems (Elmegaard 1999, [11]). It is developed at the Department of Mechanical Engineering at the Technical University of Denmark and its available for download from:
`http://www.et.dtu.dk/software/dna`
DNA features:

- An extensive component library of common energy system components such as compressors, turbines, heat exchangers etc.
- Built-in routines for thermodynamic, transport and radiative properties.
- Automatic satisfaction of mass and energy conservation for all system components.
- Automatic calculation of all gas compositions.
- Warning for simulations that do not fulfil the 2^{nd} law.

By implementing the developed model in DNA, the user can utilize the existing component library which reduce the work required to develop subsequent hybrid power system simulation models.

DESCRIPTION OF THE SOFC

The SOFC is a chemical reactor that electrochemically oxidizes hydrogen into water, thereby releasing energy in the form of electrical power and heat:

$$H_2 + \frac{1}{2} \cdot O_2 \rightarrow H_2O \qquad (1)$$

A SOFC consists of three main parts, the anode, the cathode and the electrolyte. Hydrogen is supplied

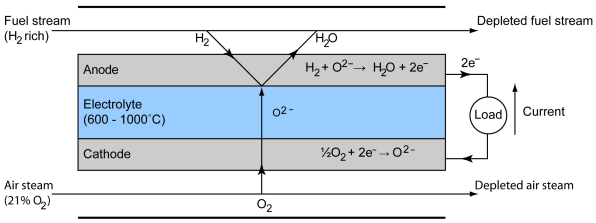

Figure 1: Solid Oxide Fuel Cell schematic (Petersen 2004, [4])

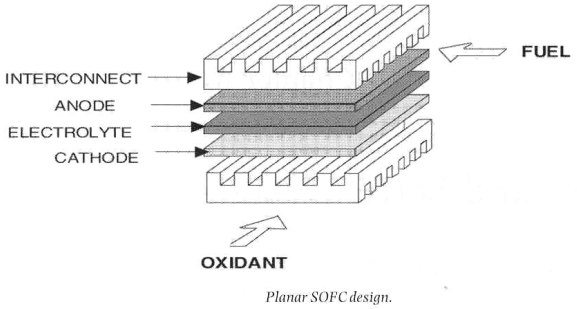

Figure 2: Planar SOFC design (Singhal and Kendall 2004, [7])

to the anode side of the SOFC, and oxygen (in air) is supplied to the cathode. A schematic of SOFC is illustrated in figure 1. The electrochemical oxidation is facilitated by the following part-reactions: Hydrogen is transported through the anode to the anode/electrolyte interface by diffusion, where it reacts with oxide ions (O^{2-}) suspended in the electrolyte. This produces water and releases two electrons:

$$H_2 + O^{2-} \rightarrow H_2O + 2e^- \tag{2}$$

The electrons are transported through an external electrical circuit to the cathode. At the cathode oxygen is transported to the cathode/electrolyte interface by diffusion, where it reacts with the electrons to produce new oxide ions:

$$\frac{1}{2} \cdot O_2 + 2e^- \rightarrow O^{2-} \tag{3}$$

The oxide ions are transported through the electrolyte to the anode, by ionic conduction, thus closing the circuit. Power is produced by inserting a load in the external circuit. The electrolyte is made from Yttria Stabilized Zirconia (YSZ), which only becomes an efficient conductor of oxide ions above approx. 650$^\circ C$. Because of this, SOFCs must operate at high temperatures (Larminie and Dicks 2003, [6]). The anode is made as a composite of metallic nickel and YSZ and is highly porous to allow for good mass transport of reagent and product gasses. The use of nickel gives the anode good electrical conductivity and it also acts as a current collector. In 2nd generation SOFCs the anode is many times thicker than the other parts as it provides mechanical strength to the entire cell. The cathode is most commonly made from Strontium-doped Lanthanum Manganite (LSM) and like the anode has a porous structure (Larminie and Dicks 2003, [6]). Interconnects are placed on both sides of the SOFC, to act as current collectors and provide effective electrical connections between the cells as illustrated in figure 2. The interconnects also provide hydrogen to the anode and oxygen to the cathode through a number of parallel channels. Interconnects are made from a stainless steel/chromium alloy provided the operating temperature is below 900$^\circ C$. The voltage of a single SOFC is in practice below one volt and to obtain higher voltages SOFCs are connected in electrical series in a SOFC stack where the number of cells depends on the required voltage. Multiple SOFC stacks can be connected in parallel in a SOFC module to provide the required power at a given voltage. Because of the high operating temperature, methane can be used directly as fuel using internal steam reforming (Larminie and Dicks 2003, [6]):

$$CH_4 + H_2O \leftrightarrow 3H_2 + CO \tag{4}$$

In addition to the reforming reaction hydrogen is produced by the water-gas shift reaction:

$$CO + H_2O \leftrightarrow H_2 + CO_2 \tag{5}$$

To avoid carbon build-up on the anode which can destroy the SOFC, more steam is supplied than required for stoichiometry. This leads to the definition of the Steam-To-Carbon-Ratio (STCR) which is the ratio between steam and combustible species (Braun 2002, [8]):

$$STCR = \frac{[H_2O]}{[CH_4] + [CO]} \tag{6}$$

The STCR is normally kept above 2 to avoid carbon deposition (Braun 2002, [8]). The reforming and the water-gas shift reactions can both be assumed to reach equilibrium because the nickel in the anode

acts as a catalyst (Larminie and Dicks 2003, [6]). Furthermore, the reforming reaction is assumed to reach completion because the high temperature and the water content result in a high equilibrium constant (Petersen 2004, [4]). Therefore, no methane is present at the SOFC outlet. There must be positive partial pressures of the reactants over the total fuel cell surface in order to generate a usable voltage. Thus, there must be un-reacted fuel and oxygen present at the exit of the fuel cell. This results in the definition of the fuel utilization which is the ratio of hydrogen consumed to hydrogen supplied, (Braun 2002, [8]). For a fuel consisting of a mixture of carbon monoxide, hydrogen and methane, fuel utilization is defined as:

$$U_f = \frac{\dot{r}_{H_2}}{4\dot{n}_{CH_4,in} + \dot{n}_{CO,in} + \dot{n}_{H_2,in}} \tag{7}$$

In eq. 7, methane and carbon monoxide are expressed as hydrogen equivalents; each methane molecule equals four hydrogen equivalents (one from reforming reaction and one from water-gas shift reaction) and each carbon monoxide is equal to one hydrogen equivalent (from the water-gas shift reaction). Air is used to supply oxygen to the reactions of the SOFC, but also to act as coolant for the SOFC. Thus the amount of oxygen supplied to the SOFC will be greater than what is required for stoichiometry. The oxygen utilization is defined as:

$$U_a = \frac{\frac{1}{2} \cdot \dot{r}_{H_2}}{\dot{n}_{O_2}} \tag{8}$$

THE ZERO-DIMENSIONAL SOFC MODEL

The approach used to model the SOFC is to split the governing equations in two categories: the conservation equations for mass, energy and momentum and the constitutive equations. The conservation equations are formulated for a control volume on a molar basis. Momentum conservation is formulated as two pressure balances; one for the anode side, and one for the cathode side (Braun 2002, [8]). The constitutive equations model the chemical and electrochemical reactions, occurring inside the SOFC. Only the constitutive equations are described in detail here, for further details see (Petersen 2004, [4]) In order to develop a simple but accurate model, a number of additional assumptions are made:

- Only steady state operation is considered.

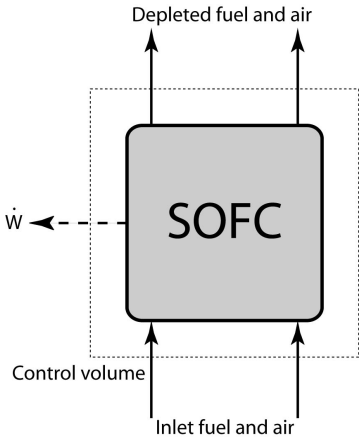

Figure 3: Control volume for the zero-dimensional SOFC model.

- Kinetic and potential energy is neglected.
- Adiabatic operating conditions.
- Outlet temperatures of air and fuel are equal to the operating temperature of the cell.
- Electrochemical oxidation, steam reforming of methane and the water-gas shift reaction are the only chemical reactions.
- Air only consists of N_2 and O_2. Fuel only consists of CH_4, CO, CO_2, H_2, H_2O and N_2. All are considered to be ideal gasses.
- There is enough water vapor present in the fuel stream to reform all the methane.
- The reforming reaction reaches completion and the water-gas shift reaction reaches equilibrium.
- Single cell performance is extrapolated to all the SOFC stacks (Braun 2002, [8]).

The control volume of the SOFC model is illustrated on figure 3, table 1 lists the user-specified inputs to the model.

The constitutive equations

The constitutive equations are split into three submodels: the first model the chemical reactions of the SOFC, the second model the cell's electrochemical behavior and the third model the pressure losses in the SOFC.

Inputs to the SOFC model
Temperature and pressure of inlet fuel and air
Chemical composition of inlet fuel and air
Fuel and air utilization
Fuel mass/molar flow
Number of cells per stack and total number of stacks

Table 1: Inputs to the SOFC model, which must be supplied by the user

Chemical reaction model

This chemical reaction model sub-model evaluates the composition fuel and air exiting the SOFC. The chemical model is based on conservation of species and chemical equilibrium, and is very commonly used in SOFC modelling (Braun 2002, [8]). The equations for conservation of species are formulated for the reactions in eq. 1, 4 and 5, and separately for the anode and cathode species:

$$\dot{n}^o_{CH_4} = \dot{n}^i_{CH_4} - \dot{r}_{ref} \tag{9}$$

$$\dot{n}^o_{CO} = \dot{n}^i_{CO} + \dot{r}_{ref} + \Delta\dot{n}^{wgs}_{CO} \tag{10}$$

$$\dot{n}^o_{CO_2} = \dot{n}^i_{CO_2} + \Delta\dot{n}^{wgs}_{CO_2} \tag{11}$$

$$\dot{n}^o_{H_2} = \dot{n}^i_{H_2} + 3\cdot\dot{r}_{ref} - \dot{r}_{H_2} + \Delta\dot{n}^{wgs}_{H_2} \tag{12}$$

$$\dot{n}^o_{H_2O} = \dot{n}^i_{H_2O} + \dot{r}_{H_2} - \dot{r}_{ref} + \Delta\dot{n}^{wgs}_{H_2O} \tag{13}$$

$$\dot{n}^o_{N_2} = \dot{n}^i_{N_2} \tag{14}$$

In the above equations $\dot{r}_{H_2}$ is the amount of hydrogen that is oxidized into water, $\dot{r}_{ref}$ is the amount of methane that is reformed, and $\Delta\dot{n}^{wgs}_i$ is the amount of species i that is consumed or produced in the water-gas shift reaction. The total molar flow of depleted fuel out of the SOFC is the sum of the individual fuel outlet flows:

$$\dot{n}^o_{tot} = \dot{n}^i_{tot} + 2\cdot\dot{r}_{ref} \tag{15}$$

The above reaction balances result in six equations with nine unknown. However, since a zero-dimensional model only describes what enters or exits the SOFC, simplifications can be made. First, the total amount of reacting hydrogen is known from eq. 7. Secondly, there is no methane present in the outlet fuel flow so $\dot{r}_{ref}$ is zero. Finally, the species involved in the water-gas shift reaction must fulfil the condition of chemical equilibrium, thus $\Delta\dot{n}^{wgs}_i$ can be determined for each species. The equilibrium constant is evaluated using the outlet temperature.
Conservation of the cathode species is expressed as:

$$\dot{n}^o_{N_2} = \dot{n}^i_{N_2} \tag{16}$$

$$\dot{n}^o_{O_2} = \dot{n}^i_{O_2} - \frac{1}{2}\cdot\dot{r}_{H_2} \tag{17}$$

As air is also used for cooling the air utilization is used to determine the total inlet flow of oxygen which, can be determined by assuming that air consists of 21% O_2 and 79% N_2.

$$\dot{n}^i_{air} = \frac{\dot{n}^i_{O_2}}{0.21} \tag{18}$$

The choice of air utilization depends on the required outlet temperature of the SOFC and is normally in the range of 15% - 25%.

Electrochemical model

The electrochemical sub-model evaluates the current density, voltage and electrical power of the SOFC. The electrochemical behavior of a given SOFC will depend on its manufacture and the materials used. The electrochemical model presented here is based on current research on 2^{nd} generation anode supported SOFCs and based on general phenomenological equations. These theoretical expressions are calibrated using empirical electrochemical data from a specific SOFC (Chick et al, 2002 [9]). In this section the general model is presented and the calibration is presented in the next section. The current density (current per unit area) through the SOFC is directly proportional to the amount of reacting hydrogen according to Faraday's law:

$$i_d = \frac{\dot{r}_{H_2}\cdot 2\cdot F}{A} \tag{19}$$

The ideal, reversible potential between the anode and cathode is determined by the Nernst equation:

$$E_{Nernst} = -\frac{\Delta G^0}{2F} - \frac{RT}{2F}\cdot ln\left(\frac{p_{H_2O}}{p_{H_2}\sqrt{p_{O_2}}}\right) \tag{20}$$

When current and power is drawn from the SOFC the reactions in the fuel cell occur irreversibly. The result is polarizations (losses) which reduce the reversible Nernst voltage to the operating voltage of the SOFC (Singhal and Kendall 2004, [7]). There are three major forms of polarizations: activation, Ohmic and concentration. A minor constant offset

polarization also contributes to the total polarization, and is the result of contact resistance, internal current and leaks. The operating voltage is found as the Nernst voltage minus the sum of the polarizations:

$$E_{fc} = E_{Nernst} - \Delta V_{act} - \Delta V_{Ohm} - \Delta V_{conc} - \Delta V_{offset} \quad (21)$$

Activation polarization is caused by that the electrodes require energy to activate and the transfer of electrons to and from the electrodes. Activation polarization is non-linear and dominates at low current densities; it can be evaluated from an approximation of the Butler-Volmer equation (Keegan 2002, [10]):

$$\Delta V_{act} = \frac{RT}{\alpha F} \sinh^{-1}\left(\frac{i_d}{2i_0}\right) \quad (22)$$

The charge transfer coefficient, α, and the exchange current density, i_0, are unknown parameters determined later.

Ohmic polarization can be described by Ohm's law and depends on the electrical conductivity of the electrodes and the ionic conductivity of the electrolyte. The contribution of the metallic interconnects is neglected since its conductivity is far greater than that of the other parts.

$$\Delta V_{Ohm} = \left(\frac{l_{an}}{\sigma_{an}} + \frac{l_{el}}{\sigma_{el}} + \frac{l_{ca}}{\sigma_{ca}}\right) \cdot i_d \quad (23)$$

The conductivity of the anode, cathode and electrolyte is evaluated from expressions previously developed for 2^{nd} generation SOFC materials, (Chick et al, 2002 [9]), presented in the following. The conductivity of a Nickel-cermets anode is assumed constant.

$$\sigma_{an} = 10^5 \quad (24)$$

The conductivity of a LSM cathode can be calculated from the following Arrhenius-type expression:

$$\sigma_{ca} = \frac{A_{ca}}{T} \cdot \exp\left(\frac{-E_{a,ca}}{k_{ca}T}\right) \quad (25)$$

The conductivity of both the anode and cathode is corrected to account for porosity:

$$\sigma_{porous} = \sigma_{solid} \cdot (1 - 1.8 \cdot \bar{V}) \quad (26)$$

The conductivity of the YSZ electrolyte is evaluated from a third-order polynomial:

$$\sigma_{el} = A_{el} \cdot \theta^3 + B_{el} \cdot \theta^2 + C_{el} \cdot \theta + D_{el} \quad (27)$$

Cathode	Electrolyte
$A_{ca} = 5.760 \cdot 10^7$	$A_{el} = 8.588 \cdot 10^{-8}$
$E_{a,ca} = 0.117$	$B_{el} = -1.101 \cdot 10^{-4}$
$k_{ca} = 8.617 \cdot 10^{-5}$	$C_{el} = 4.679 \cdot 10^{-2}$
-	$D_{el} = -6.54$

Table 2: Constants used to calculated the conductivity of the cathode and the electrolyte. Data from (Chick et al, 2002 [9])

Where θ is the SOFC outlet temperature in Celsius. Table 2 lists the constants used in eqs. 25 - 27. The concentration polarization is the result of mass transport of products and reactants to and from the interface between electrode and anode/cathode. The mass transport is accomplished by diffusion, which is associated with a resistance and thus a loss. Additionally, as the fuel is depleted, there is a decrease in the hydrogen partial pressure at the anode and in the oxygen partial pressure at the cathode. The magnitude of the depletion depends on the current density. At high current densities an insufficient amount of reactants will be transported to the electrodes and the voltage is reduced to near zero (Singhal and Kendall 2004, [7]). The current densities at which this occurs are called the anode and cathode limiting currents. Concentration polarization is therefore dominant at high current density and exhibits a non-linear behavior in the SOFC; it can be evaluated from the following equations:

$$\Delta V_{conc} = B \cdot \left(-\ln\left(1 - \frac{i_d}{i_{as}}\right) + \ln\left(1 + \frac{p_{H_2} i_d}{p_{H_2O} i_{as}}\right)\right) \quad (28)$$

In eq. 28 the cathode contribution to the concentration polarization has been neglected (Braun 2002, [8]). The anode limiting current is evaluated as:

$$i_{as} = \frac{2F p_{H_2} D_{an,(eff)}}{RT l_{an}} \qquad D_{an,(eff)} = \frac{D_{an,(bin)} \bar{V}_{an}}{\tau_{an}} \quad (29)$$

Both B and the diffusion coefficient are unknown parameters determined later.

Both the Nernst potential and the polarizations is evaluated using the outlet conditions from the SOFC. This is because the cell cannot support a voltage gradient and the lowest potential, which is found at the outlet, will dominate the entire cell (Braun 2002, [8]).

Pressure loss model

The flow in the interconnect channels can be assumed laminar and fully developed (Braun 2002, [8]). The pressure losses are mainly due to the friction between the fluid and the interconnect channels and from the fluid entering and exiting the interconnect channels (Fox 1994, [12]). The total pressure loss can be found as (Petersen 2004, [4]):

$$\Delta P = \rho \cdot f\left(\frac{L}{D_h} + 2K\right)\frac{v^2}{2} \tag{30}$$

Where f is the Blasius friction factor for laminar flow, and K is equal to 0.5 for a square edged inlets/outlet, (Fox 1994, [12]). Since the interconnect channels have a non-circular geometry the hydraulic diameter is used and the geometry of the channels and the number of interconnect channels must be known. The average of the density between inlet and outlet is used.

Calibration of of the electrochemical model

The offset polarization, the charge transfer coefficient, the exchange current density, the B parameter and the anode limiting current are unknown parameters which depend on the manufacture of a given SOFC. These parameters are normally regarded as constants and determined from reference. In this paper the above parameters are determined from experimental measurements, and nine empirical current-voltage curves were obtained for this purpose. The experimental data came from two experiments performed by the Pacific Northwest National Laboratory (PNNL) (Chick et al. 2002, [9]). The first experiments were performed with a constant fuel composition, of 7% hydrogen and 3% water vapor from 650°C to 800°C. The second experiment was performed at a constant temperature of 750°C, with a fuel composition containing from 10% to 97% hydrogen concentration, 3% water vapor concentration and nitrogen as the remainder. In both experiments the flow of fuel was 200 standard cubic centimeters per minute (sccm) and the flow of air was 300 sccm. The fuel flow was high with a low fuel utilization to keep the operating conditions almost constant over the entire cell. The performed experiments are summarized in table 3. The physical data of the anode, cathode and electrolyte used in the experiments are shown in table 4. The electroactive area of the empirical cell is 3.8cm^2, but the parameters determined in this section are assumed area independent.

T/[H_2]	10%	24%	49%	73%	97%
650°C	-	-	-	-	+
700°C	-	-	-	-	+
750°C	+	+	+	+	+
800°C	-	-	-	-	+

Table 3: : Temperature and hydrogen concentration ranges for the PNNL experiments, and a (+) denotes a performed experiment.

Part	Material	Thickness [μm]
Anode	Ni/YSZ 60	600
Cathode	LSF-20	50
Electrolyte	YSZ	10
Part	Porosity [%]	Tortuosity
Anode	30	2.5
Cathode	30	2.5
Electrolyte	-	-

Table 4: Physical characteristics of the SOFC used in the PNNL experiments

Calibration of the offset polarization

At zero current density all polarizations are zero, except for the offset polarization. It is evaluated as the difference between the measured cell voltage and the Nernst potential. This approach is used on all the current-voltage curves to determine the offset polarization for each curve. A single value of the offset polarization is then found as the average of the nine different offset polarizations, shown in eq. 31:

$$\Delta V_{offset} = 0.06 \tag{31}$$

Calibration of the activation polarization

To calibrate activation polarization, the current-voltage curves from the first experiments are used. Due to the high hydrogen concentration it can be assumed that concentration polarization is negligible (Larminie and Dicks 2003, [6]). All contributions to the total polarization are either Ohmic, activation or offset polarization. The offset polarization has been determined previously and the Ohmic polarization can be determined from eqs. 24 - 27. The activation polarization is isolated from the total polarization,

and curve fitted to eq. 22 where α and i_0 are the unknown parameters. This results in four values of α and i_0 which are expressed as functions of the temperature. The function for α is shown in equation 32, and the function for i_0 is shown in equation 33:

$$\alpha = 1.698 \cdot 10^{-3} \cdot T - 1.254 \quad (32)$$

$$i_0 = 13.087 \cdot T - 1.096 \cdot 10^4 \quad (33)$$

Calibration of the concentration polarization

To calibrate concentration polarization the current-voltage curves from the second experiment at constant temperature is used. First the concentration polarization is isolated from the total polarization using the previously developed expressions for the activation, Ohmic and offset polarization. This results in four different concentration polarization curves. These curves are fitted to eq. 28, where B and $D_{an,(bin)}$ are the only unknowns. This yields four values of the parameter B and the binary diffusion coefficient, which are expressed as functions of the hydrogen concentration. The B parameter is an inverse linear function of the hydrogen concentration. The function is modified to account for temperature, by assuming a linear dependence on temperature (Larminie and Dicks 2003, [6]). The final function is shown in eq. 34:

$$B = (8.039 \cdot 10^{-3} \cdot X_{H_2}^{-1} - 7.272 \cdot 10^{-3}) \cdot \frac{T}{T_{ref}} \quad (34)$$

Since the binary diffusion coefficient depends on both temperature and pressure, an empirical expression are used to make the fitted function pressure and temperature dependant, (Todd and Young 2002, [11]). The final function for the binary diffusion coefficient is given in eq. 35:

$$D_{a,(bin)} = (-4.107 \cdot 10^{-5} \cdot X_{H_2} + 8.704 \cdot 10^{-5}) \cdot \left(\frac{T}{T_{ref}}\right)^{1.75} \cdot \frac{P_{ref}}{P} \quad (35)$$

The calibration functions are only valid from 650°C to 800°C where supported by empirical data.

Validation of the electrochemical model

The calibrated electrochemical sub-model is validated by comparing the model's current-voltage curves to the original empirical curves used for the calibration. The comparison between model and empirical data of the first experiments are shown in figure 4. The comparison shows a good agreement

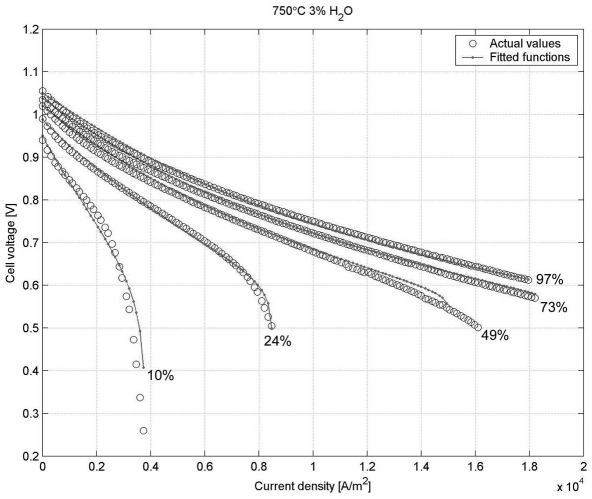

Figure 4: Comparison of empirical and model current voltage-curves from the first experiment. The line is the model results and the circles are the empirical values.

between the two sets of current-voltage curves. The maximum error between the model and the experiment set of curves is 1.05% root mean square error (rmse) at 650°C. The comparisons for the second experiments are shown on figure 5. Again the

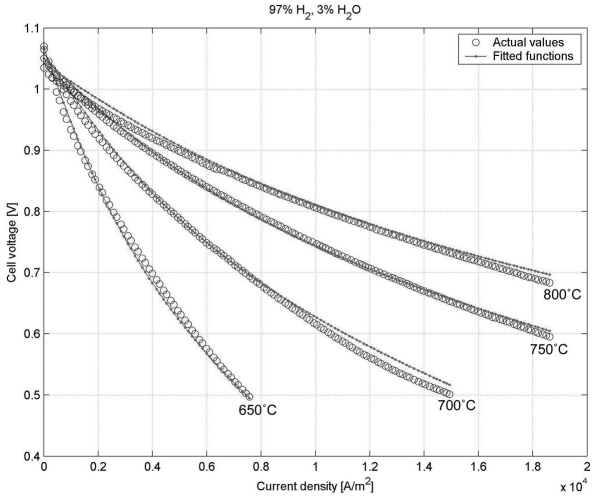

Figure 5: Comparison of empirical and model current-voltage curves from the second experiment. The line is the model results and the circles are the empirical values.

current-voltage curves show a good agreement between the two sets of current-voltage curves. The only exception is at 10% hydrogen concentration, which have the largest error of 5.21% rmse. The current-voltage curves at lower hydrogen concentrations, on figure 5, show a characteristic "tail" where the voltage is rapidly reduced at increasing current densities. This signifies the onset and the dominance of the concentration polarization, which is also the source of the greatest error. This is caused by the fact that concentration polarization dominates almost completely, which is hard to model theoretically, and eq. 28 only partly describes the concentration polarization (Larminie and Dicks 2003, [6]). This is a source of error in the SOFC model, since cell voltage is often determined at low hydrogen concentrations because of a high fuel utilization.

IMPLEMENTATION IN DNA

The SOFC model is added to the in existing DNA component library by implementing it in FORTRAN77 using a standard template for new DNA components. The additional data for the SOFC shown table 5 are used in the implementation, (Braun 2002, [8]). Note that the SOFC cell area used

Parameter	Value
Total cell area	144cm^2
Number of interconnect channels	24
Channel width	3mm
Channel height	1mm

Table 5: Physical data for the SOFC and interconnect used in the implementation of the model

in the implementation is different from the $3.8cm^2$ used in the calibration. This is because that area was for an experimental SOFC for test purposes. The area of future commercial SOFC will be as large as possible as this results in greater power. The implemented DNA SOFC model was tested thoroughly, and has subsequently been used to simulate a number of different hybrid systems. During this the model has proved robust and stable.

DISCUSSION

The chemical sub-model of the SOFC can simulate both hydrogen fuelled and methane fuelled SOFCs. However, the electrochemical sub-model is only valid for a hydrogen fuelled SOFCs because the polarization curves for a methane fuelled SOFC will be different from those of a hydrogen fuelled. This is due to the different partial pressures as well as different binary diffusion coefficients. But research has shown that the difference in diffusion coefficients are relative small, (Barfod 2004, [13]). Since the electrochemical sub-model accounts for the changes in partial pressures, the SOFC model is assumed valid for both hydrogen and methane. Calibration of general, theoretical polarization expressions was an accurate approach for the electrochemical sub-model. This was expected since in essence, a fitted function is compared to the data used for the fitting. The calibration reduces the generality of the electrochemical sub-model which cannot be expected to model any other type of SOFC accurately, since it is ”bound” to the performance a specific cell. However, the used approach is general and apply for all SOFC. The only parameters specific to the model presented here, are the charge transfer coefficient, the exchange current density, the B parameter and binary diffusion constant. When the voltage and electrical power of the SOFC are evaluated an average current density is used. But the current density varies over the cell and is lowest at the outlet (Sorrentino et al 2004, [14]). So the operating voltage is underestimated since the polarizations increases with the current density, which results in an error in the evaluated electrical power. The magnitude of this error is not clear, but assumed negligible.

CONCLUSION

A zero-dimensional model of a SOFC was developed for hybrid power system simulation. The model accounts for the oxidation of hydrogen, the reforming of methane, and the water-gas shift reaction, in a simplified but accurate manner. The electrochemical sub-model is phenomenological, and accounts for offset, activation, Ohmic and concentration polarization. It was calibrated using empirical data, and this approach has resulted in a good agreement with the original empirical data. The SOFC model can be used to obtain reliable results, for SOFC behavior within the temperature range from $650°C$ to $800°C$ where it is supported by empirical data. The model was implemented in the DNA software, which is developed specifically for energy system simulation.

ACKNOWLEDGEMENTS

The authors would like to thank Prof. Michael J. Moran from Ohio State University, Jens Paalsson and Jens Nielsen from Haldor Topsøe A/S and Rasmus Barfod from Risø National Laboratory for their invaluable help and time.

REFERENCES

[1] Massardo A.F. and Lubelli F., *Internal Reforming Solid Oxide Fuel Cell-Gas Turbine Combined Cycles (IRSOFC-GT): Part A - Cell model and Cycle Thermodynamic Analysis*, Journal of Engineering for Gas Turbines and Power number 122, 2000

[2] Costamagna P., Magistri L. and Massardo A.F., *Design and part-load performance of a hybrid system based on a solid oxide fuel cell reactor and a micro gas turbine.*, Journal of Power Sources, number 96 p. 352-368, 2001.

[3] Achenbach E., *Three-dimensional and time-dependant simulation of a planar solid oxide fuel cell stack*, Journal of Power Sources, number 49 p. 333-348, 1994.

[4] Petersen T.F., *Mathematical Model of a Solid Oxide Fuel Cell and Simulations of Hybrid Power Plants*, Master Thesis, partment of Mechanical Engineering, Technical University of Denmark, 2004

[5] Elmegaard B., *SIMULATION OF BOILER DYNAMICS - Development, Evaluation and Application of a General Energy System Simulation Tool*, Report number ET–PhD 99–02, Ph.D. Thesis, Department of Mechanical Engineering, Technical University of Denmark, 1999

[6] Larminie J. and Dicks A., *Fuel Cell Systems Explained Second Edition*, John Wiley & Sons Inc., 2004

[7] Singhal S. C. and Kendall K. (editors), *High Temperature Solid Oxide Fuel Cells - Fundamental, Design and Applications*, Elsevier Ltd., 2003

[8] Braun R. *Optimal Design and Operation of Solid Oxide Fuel cell Systems for Small-scale Stationary Applications*. Ph.D from University of Wisconsin-Madison, 2002, `http://www.ecw.org/prod/214-1.pdf`

[9] Chick, L.A., Williford R.E., Stevenson J.W., C.F. Windisch Jr C.F. and S.P. Simner, *Experimentally-Calibrated, Spreadsheet-based SOFC Unit-Cell Performance Model*, Pacific Northwest National Laboratory, 2002, Paper inlcuding Excel spread sheet obtained during visit to Haldor Topsøe A/S in 2003

[10] Keegan K., M. Khaleel M., Chick L.A., Recknagle K., Simner S., and Deibler J., *Analysis of a Planar Solid Oxide Fuel Cell Based Automotive Auxiliary Power Unit*, SAE Technical Paper Series No. 2002-01-0413, 2002

[11] Todd B. and Young J.B., *Thermodynamic and transport properties of gases for use in solid oxide fuel cell modelling*, Journal of Power Sources number 110 p. 186–200, 2002

[12] Fox R. W. and McDonald A. T., *Introduction to Fluid Mechanics 4th ed.*, John Wiley & Sons Inc.,1994

[13] Personal correspondance with Rasmus Barfod from Risø National Laboratories, Roskilde, Denmark, spring 2004.

[14] M. Sorrentino M., Mandourah A., Petersen T. F.,Guezennec Y. G. , Moran M. J. and Rizzoni G., *A 1-D MODEL FOR THE SIMULATION OF PLANAR SOLID OXIDE FUEL CELLS*, Proceedings of the 2004 International Mechanical Engineering Congress and R & D Expo November 13-19, 2004, Anaheim, California, USA

Proceedings of ECOS 2005
Trondheim, Norway
June 20–22, 2005

WELL-TO-WHEEL STUDY OF TRANSPORTATION CHAINS IN THE NORWEGIAN ENERGY SYSTEM

Ann Mari Svensson[*] and Steffen Møller Holst
SINTEF Materials and Chemistry
7465 Trondheim
Norway

Ronny Glöckner
Institute for Energy Technology
2027 Kjeller
Norway

Ola Maurstad
SINTEF Energy Research
7465 Trondheim
Norway

ABSTRACT

For the evaluation of potential routes for production and application of hydrogen in a future energy system, well-to-wheel methodologies provide a means of comparing overall impacts of technologies in a consistent and transparent manner. Such analysis provides important background information for decision makers when implementing political incentives for the conversion to environmentally more friendly energy production and consumption. In this study, a well-to-wheel (WtW) approach was applied in order to evaluate the energetic and environmental impacts of introducing hydrogen in the transportation sector, in terms of energy efficiency and emissions of CO_2 and NO_x, under conditions relevant for the Norwegian energy system. The hydrogen chains were compared to reference chains with conventional fuels.
Keywords: Hydrogen, transportation, well-to-wheel

NOMENCLATURE

CNG	Compressed natural gas
ICE	Internal combustion engine
PEMFC	Proton exchange membrane fuel cell
NG	Natural gas
TtW	Tank-to-wheel
WtT	Well-to-tank
WtW	Well-to-wheel

INTRODUCTION

It is commonly believed that hydrogen will be an important energy carrier in a future energy system based on sustainable energy conversion technologies. Hydrogen may be produced from various energy sources, and applied in a wide range of end-use technologies, and an evaluation of the environmental benefits of introducing hydrogen for certain segments thus depends on the emissions related to transport

[*] Corresponding author: Phone: +47 98230450 Fax: +47 73594083, Email: ann.m.svensson@sintef.no

and conversion of energy sources, as well as transport of hydrogen. An extensive well-to-wheel study has been conducted for the European transportation sector, comparing a wide range of technologies [1], clearly illustrating that a tank-to-wheel (TtW) analysis is not sufficient to draw conclusions of the energetic and environmental impacts on the various end-use technologies, and that WtW analysis must be applied. Another example of WtW analysis including transportation end-use, where several production technologies for hydrogen has been included, is provided in Ref. [2]. Still, WtW analysis is limited to the operational mode. For a full assessment of energy consumption and environmental impact including also production and disposal of materials and components, a LCA (life-cycle assessment) analysis is required.

A great potential for reduction of emissions in the Norwegian energy system can clearly be found in the transportation sector. Focus for this study has therefore been the possible routes for introduction of hydrogen as an energy carrier for transportation, putting emphasis on the uniqueness of the Norwegian energy system in terms of the predominantly renewable electricity production, but also on the relatively long transportation distances for the operation of filling stations.

SELECTED END-USE TECHNOLOGIES AND ENERGY CHAINS FOR PERSONAL CARS

Overviews of the chains evaluated in this study are given in Figure 1 and Table 1. The time perspective is relatively short (2010), and therefore, only electrolysis and natural gas reforming have been considered for hydrogen production, as these are the technologies considered to have reached a pre-commercial stage [3]. As hydrogen production from biomass has not reached the same state of development, biomass was not included in this study, although biofuels for combustion engines is a viable option for the future. The most promising technologies for utilization of hydrogen in private cars are fuel cells and the hydrogen combustion engine. In addition, electric cars are included for comparison, even if the application of electric vehicles at present is somewhat restricted w.r.t. range. Included are also hybridized petrol cars, i.e. cars combining a combustion engine and an electric motor.

The evaluation of the chains presented in Table 1 is based on the following assumptions:

- Efficiencies are based on lower heating value (LHV).
- Fossil fuels are assumed to be transported by trucks of ca 50 tons, with a capacity of 34 tons/40 m3, at an average distance of 50 km to the filling station. Natural gas is assumed to be transported as LNG.
- Well-to-tank efficiencies are assumed to be: 83% for refining of crude oil to petrol, 88 % for refining of crude oil to diesel, 95 % for liquefaction of natural gas, 98 % for shipping of natural gas (i.e. from north of Norway to the south)
- A loss of 6% is assumed for extraction, processing and pipeline transport of natural gas, as estimated in Ref. [1] for Norwegian gas production. No further refining of the gas is included.
- Hydrogen produced in central reformers is assumed to be stored/transported in compressed form at 700 bars. Average transportation distance is assumed to be 150 km (one way). Return of empty trucks is assumed.
- Electrolysers are assumed to deliver hydrogen at 30 bar. Additional energy loss for compression to 700 bar is included.
- An additional loss of 3% is assumed for removal of CO from hydrogen produced by reforming of NG, when PEMFC is the end-use technology.
- Efficiencies of renewable energy sources (wind, hydropower, solar energy) are not included; neither are possible efficiency reductions of electrolysers connected to the strongly fluctuating power from wind mills.
- The efficiency of gas turbines (CCGT) is assumed to be 58% wo/CO_2 cap, and 50% w/CO_2 cap.
- Efficiency of electricity transfer in the grid is assumed to be 93% for transfer from central power production units (i.e.

exergy efficiency). No losses are taken into account for distributed power generation.

- Average European electricity mixture contains: 17.4% from coal, 7.4% from natural gas, 16.4% from hydropower, 7.8% from lignite, 40.3% nuclear power, 10.7% from oil [4]. The corresponding CO_2 and NO_x emissions are: 0.428 kg/kWh and 0.92 g/kWh [4]. Average efficiency is 35% [1].
- Small scale reformers (natural gas to hydrogen) were assumed to emit the same amount of NO_x per kWh as large scale reformer (i.e. 76 % wo/CO_2 cap., and 73 % w/CO_2 cap). The efficiency of electrolysers is assumed to be 74 %.
- Catalytic removal of NO_x is assumed for the ICE H_2.
- The tank-to-wheel efficiency is assumed to be 32% for hybrid petrol vehicles, 20% for ICE H_2, 40% for PEMFC, 50% for hybrid PEMFC, 16% for ICE petrol, 17% for ICE CNG, 19% for ICE diesel, and 80% for electric cars.
- Standard European drive cycle (ECE [5]), relevant for city driving, is assumed for all the evaluated chains [5].

RESULTS AND DISCUSSION

Results for well-to wheel efficiencies and emissions for private cars (70 kW) are shown in Figures 2 and 4 for conditions typical for the Norwegian energy system (i.e. renewable energy production). Electric vehicles are therefore superior both in terms of efficiency and emissions. However, the application of electric vehicles is still limited due to their short driving range and long charging times.

On a longer time scale, utilization of hydrogen as a fuel will provide an option for eliminating emissions in the transportation sector, but this requires that the hydrogen is produced by electrolysis from renewable energy sources, or from hydrocarbon with carbon sequestration included. Fuel cell technology has a potential for high energy efficiencies, but is only expected to be commercially available in cars after the year 2010. For city driving, it is interesting to notice that hybridized petrol cars have higher efficiencies than fuel cell driven cars, regardless of how the hydrogen is produced. Similar results have been obtained in Refs. [1] and [6] This result would be different for evaluations based on highway drive cycles, as there is little benefit of hybridization at high speed. It should be noticed that both hybrid petrol cars and fuel cell driven cars have significant potentials for improvement, as opposed to engines driven by conventional liquid fuels.

It is interesting to notice that electric cars charged by electricity produced in gas turbines (NG) have efficiencies around two times higher than ICE NG cars, which is related to the fact that combustion processes have low efficiencies at part load. Similarly, the high efficiency of the hybridized petrol car is achieved because [6]: i) the engine is smaller, thus operating at higher load ii) power can be used to charge the batteries during part load operation iii) the battery can feed the electric motor for sole vehicle propulsion in urban traffic iv) energy can be recovered while braking.

There are no environmental benefits of internal combustion engines with H_2 as fuel if H_2 is produced by reforming of natural gas without CO_2 capture (for example on-board reforming, or distributed small scale reforming). The technology might, however, have the potential for creating early markets, as it is more mature than the fuel cell technology. In terms of energy efficiency, however, the fuel cell technology is superior (more than twice as efficient), and on a longer time scale, hybridization of fuel cell vehicles, or ICE H_2 could also be an interesting option for zero emission vehicles. The effect of hybridization of fuel cell vehicles is shown in Figures 3 and 5, where results for the hybridized PEMFC vehicles are included for all the chains with PEMFC as end use (5a, 7a, 9a, 12a, 15a). Although the relative improvement of efficiency is less with hybridization of fuel cell vehicles , the potential of obtaining high overall efficiencies is clearly illustrated.

From Figures 2 and 4 fuel cell driven vehicles appears to exhibit lower emissions of CO_2 and NO_x, and be more efficient than conventional ICE petrol/diesel/CNG cars, even when the

hydrogen is produced by local reforming of natural gas without CO_2 sequestration. In Ref. 7, a comparison of fuel cell cars and conventional ICE cars was made in a full LCA analysis, including both manufacturing and distribution of the vehicles. In this study, the estimated life-cycle energy consumption, as well as the life-cycle green house gas emissions are of similar magnitude for ICE vehicles and fuel cell vehicles, when the hydrogen is produced from hydrocarbons without CO_2 sequestration. The assumed drive-cycle in Ref. 7 was a mixture of urban (55 %) and highway (45 %) drive cycles.

The superiority of electric vehicles, both in terms of emissions and energy efficiency, is clearly related to the fact that the Norwegian energy system is almost entirely based on hydro power. Results for the corresponding WtW analysis based on the average European electricity mix (EU mix) are shown in Figure 3 and 5. Local/distributed power (chains 15 to 17) is assumed to be based on some kind of renewable power generation, and thus resembles the chains in Figure 2 and 3. Figure 5 clearly illustrates that hydrogen production based on electrolysis has no environmental benefits when electricity production is based on the European electricity mix. Even electric vehicles exhibit larger emissions of NO_x than petrol and CNG ICE in this case. This is related to the fact that the average European power production units emit a significant amount of NO_x per kWh. The CO_2 emissions of the electric vehicles are, however, relatively low in comparison. This is related to the large fraction of nuclear power in Europe.

It should be noticed that here, emissions are focused on CO_2 and NO_x, which are species harmful on a global and regional level. Other pollutants, such as particulate materials, hydrocarbons etc., which are released from vehicles driven on conventional liquid fuels, is a serious concern in terms of local pollution problems, which need to be solved either by a change to gaseous fuels, or by on-board cleaning of exhaust.

CONCLUSIONS

In a renewable energy system, electric vehicles are superior in terms of energy efficiency and emissions, but their application might be restricted due to the low range and high charging times.

For city driving, significant improvements of energetic and environmental impacts can be achieved by hybridization of ICE engines, and the technology is commercially available. Although the fuel cell technology is likely to exhibit even higher efficiencies and zero emissions at end-use, the WtW analysis shows that the hydrogen must be produced from renewable sources or from natural gas including CO_2 sequestration, for the fuel cell cars to be superior to the hybridized petrol/diesel cars in terms of energy consumption and emissions.

REFERENCES

[1] R. Choudhury et al. *ANNEX: Full Background Report – Methodology, Assumptions, Descriptions, Calculations, Results to the GM Well-to-Wheel Analysis of Energy Use and Greenhouse Gas Emissions of Advanced Fuel/Vehicle Systems – A European Study*, 2002, http://www.lbst.de/gm-wtw

[2] F. Kreith and R. West, *Fallacies of a Hydrogen Economy: A critical Analysis of Hydrogen Production and Utilization*, Journal of Energy Resources Technology – ASME, **126** (2004) p249

[3] M. Altmann, P. Schmidt, R. Wurster, M. Zerta, W. Zittel, *Potential for Hydrogen as a Fuel for Transport in the Long Term (2020-2030) –Full Background Report*, EUR 21090 EN, March 2004

[4] Buwal. *Evaluation of life cycle inventories for packaging, part I and II*, 2nd improved edition. SAEL, Switzerland, (1998).

[5] ECE standards Euro3/Euro4, http://www.dieselnet.com/standards/eu/ld.html

[6] U. Winter and H. Weidner, *Hydrogen for the Mobility of the Future Results of GM/Opel's Well-to-Wheel Studies in North America and Europe*, FUEL CELLS 2003, No3, Wiley-VCH Verlag GmbH & Co

[7] M.A. Weiss, J.B. Heywood, E. M. Drake, A. Schafer, F.F. and V.K. Natarajan, *Comparative Assessment of Fuel Cell Cars,* Report # MIT LFEE 2003-001 RP, Laboratory for Energy and the Environment, Massachusetts Institute of Technology, February 2003

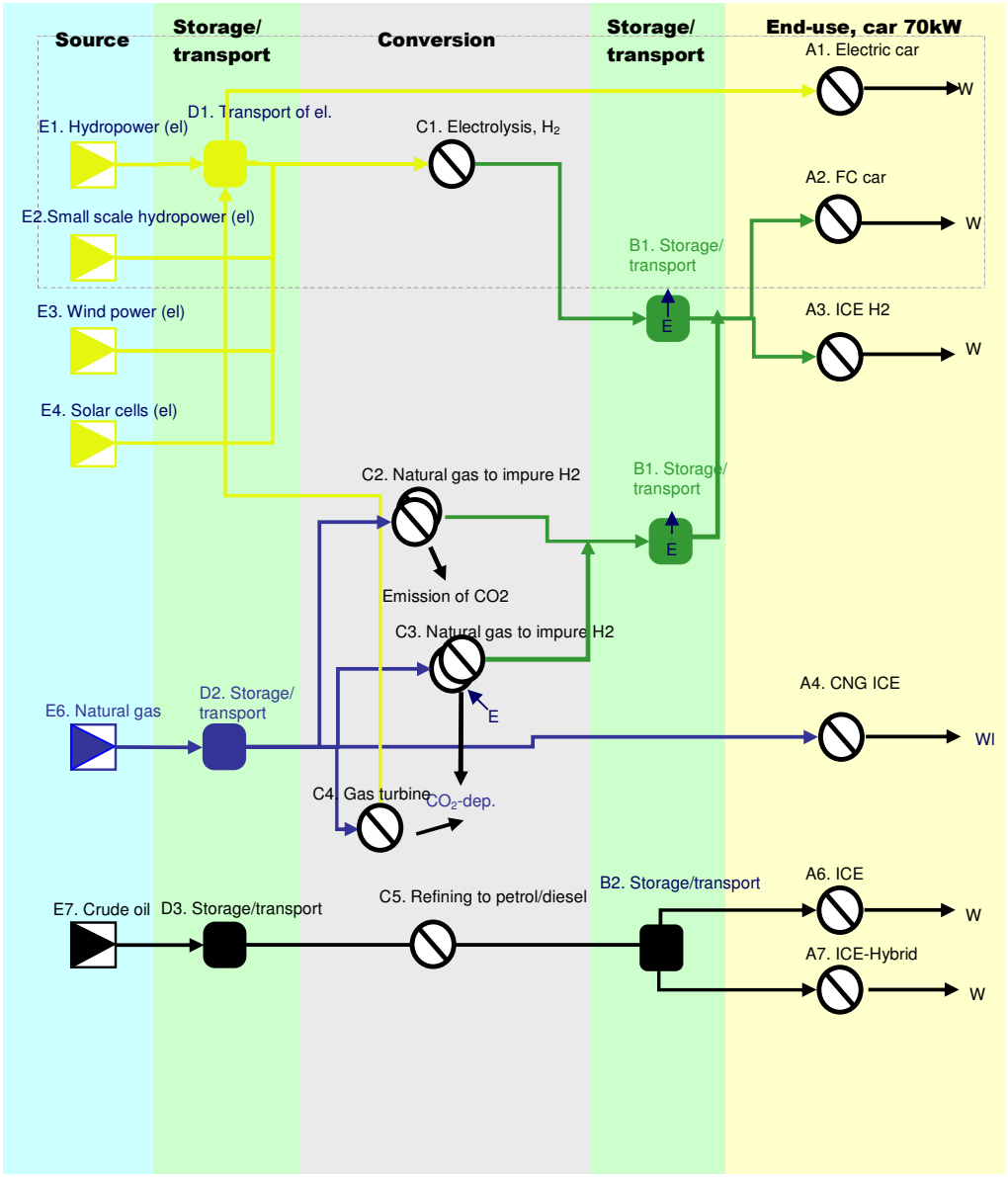

Figure 1. Schematic overview of the nodes and the WtW-chains they form when combined.

Table 1: Overview of all WtW-chains, including reference to nodes in Figure 1. Chains P1 to P4 are the reference chains based on conventional technologies

Chain no	*Source*	*Conversion*	*Storage/ transport*	*End-use*	*Nodes*
P1 (ref.)	Crude Oil	Refining to petrol	Transport of petrol	ICE petrol	E7-D3-C5-B2-A6
P2 (ref.)	Crude Oil	Refining to petrol	Transport of petrol	Hybrid propulsion, petrol	E7-D3-C5-B2-A7
P3 (ref.)	Crude Oil	Refining to diesel	Transport of diesel	ICE diesel	E7-D3-C5-B2-A6
P4 (ref.)	Natural gas	-	Transport of NG	ICE NG	E6-D2-A4
P5	Natural gas	Central reforming w/CO_2 cap.	Purification and transport of H_2 by truck	PEMFC	E6-D2-C3-A2
P6	Natural gas	Central reforming w/CO_2 cap.	Transport of H_2 by truck	ICE H_2	E6-D2-C3-A3
P7.	Natural gas	Local reforming wo/CO_2 cap.	Purification and transport of H_2 by truck	PEMFC	E6-D2-C2-A2
P8.	Natural gas	Local reforming wo/CO_2 cap	Transport of H_2 by truck	ICE H_2	E6-D2-C2-A2
P9.	Natural gas	Gas Turbine w/CO_2 cap.+ Electrolysis	Transport of H_2 by truck	PEMFC	E6-D2-C4-C1-B1-A2
P10.	Natural gas	Gas Turbine w/CO_2 cap.+ Electrolysis	Transport of H_2 by truck	ICE H_2	E6-D2-C4-C1-B1-A3
P11.	Natural gas	Gas Turbine w/CO_2 cap.+ Electrolysis	-	Electric car	E6-D2-C4-D1-A1
P12.	Hydro-power	Electrolysis	Compression of H_2	PEMFC	E1-D1-C1-A2
P13.	Hydro-power	Electrolysis	Compression of H_2	ICE H_2	E1-D1-C1-A3
P14.	Hydro-power	-	-	Electric car	E1-D1-A1
P15.	Local, renew. power	Electrolysis	Compression of H_2	PEMFC	E2-D1-C1-A2
P16.	Local, renew. power	Electrolysis	Compression of H_2	ICE H_2	E2-D1-C1-A3
P17.	Local, renew. power	-	-	Electric car	E2-D1-A1

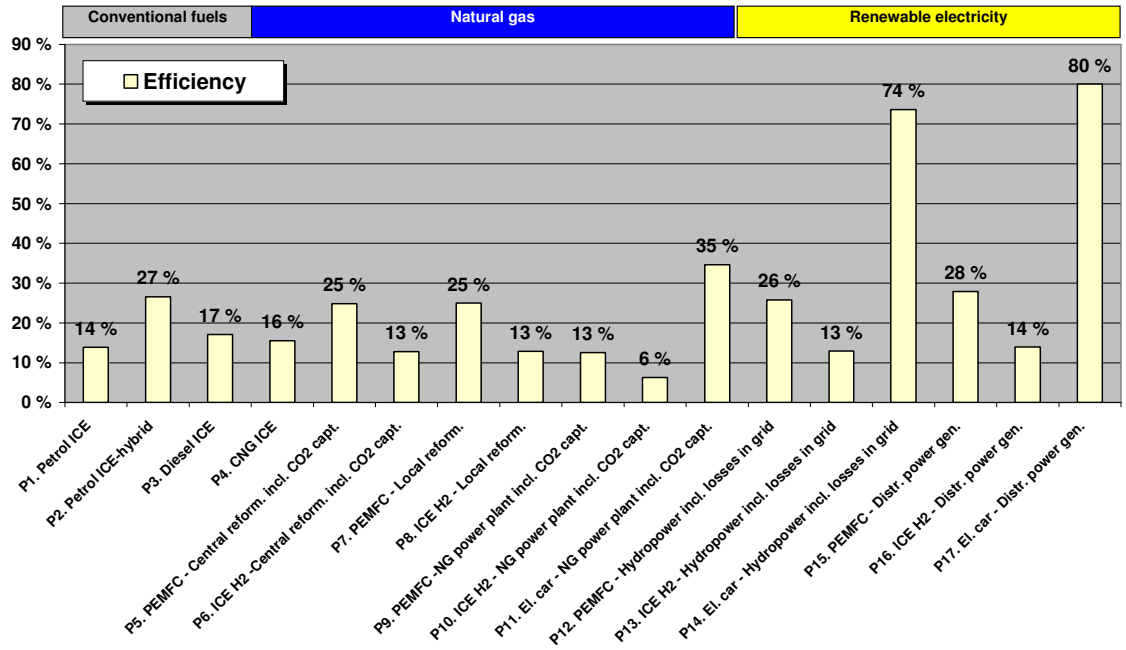

Figure 2: Energy efficiencies for the WtW-chains (see Table 1) with private cars as end-users.

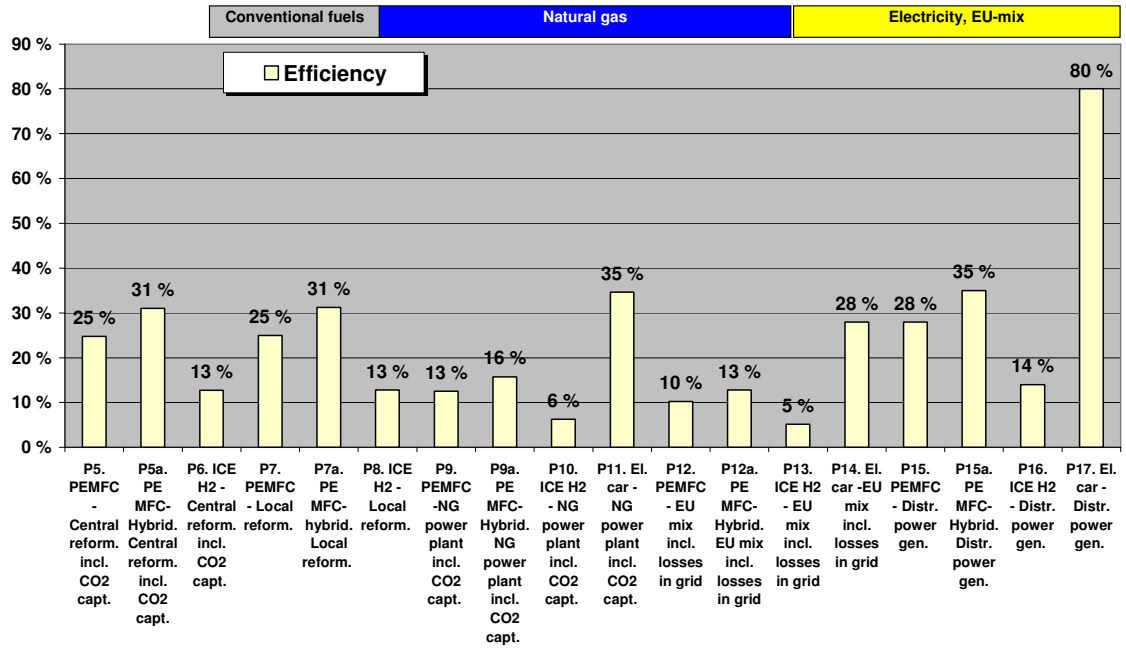

Figure 3: Energy efficiencies for the WtW-chains P5-P17 with hydropower in the chains P12, P13, P14 replaced by average European electricity production (EU mix). For chains 5, 7, 9, 12 and 15, effect of hybridization of PEMFC vehicles is included for comparison. Distributed power generation chains P15, P16 and P17 are still assumed to be based on renewables.

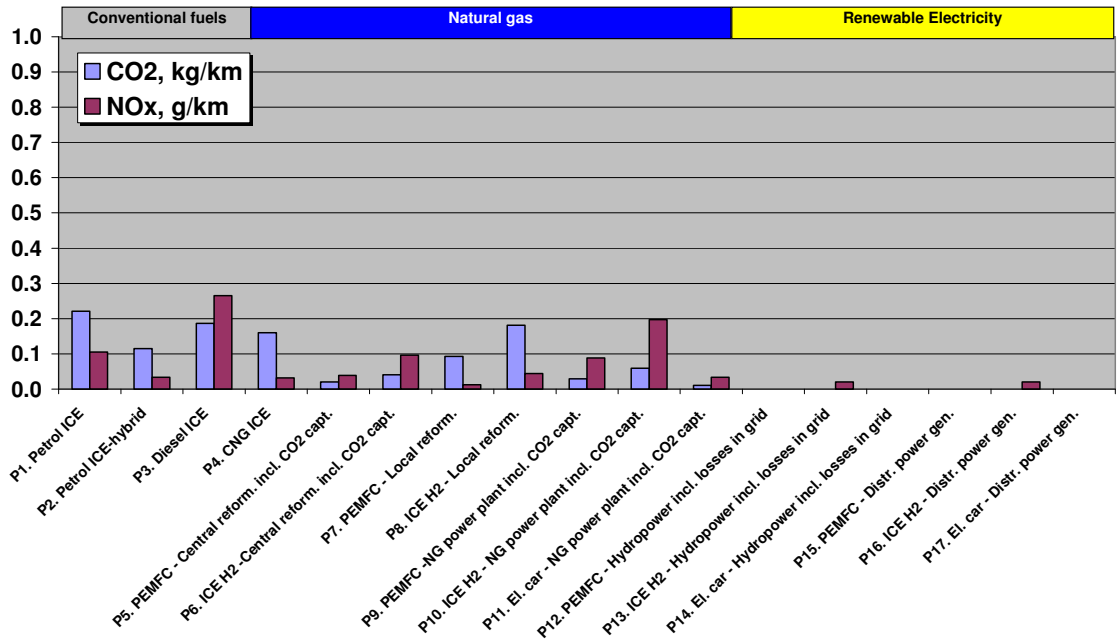

Figure 4: Emissions of CO_2 and NO_x for the WtW-chains P1-P17.

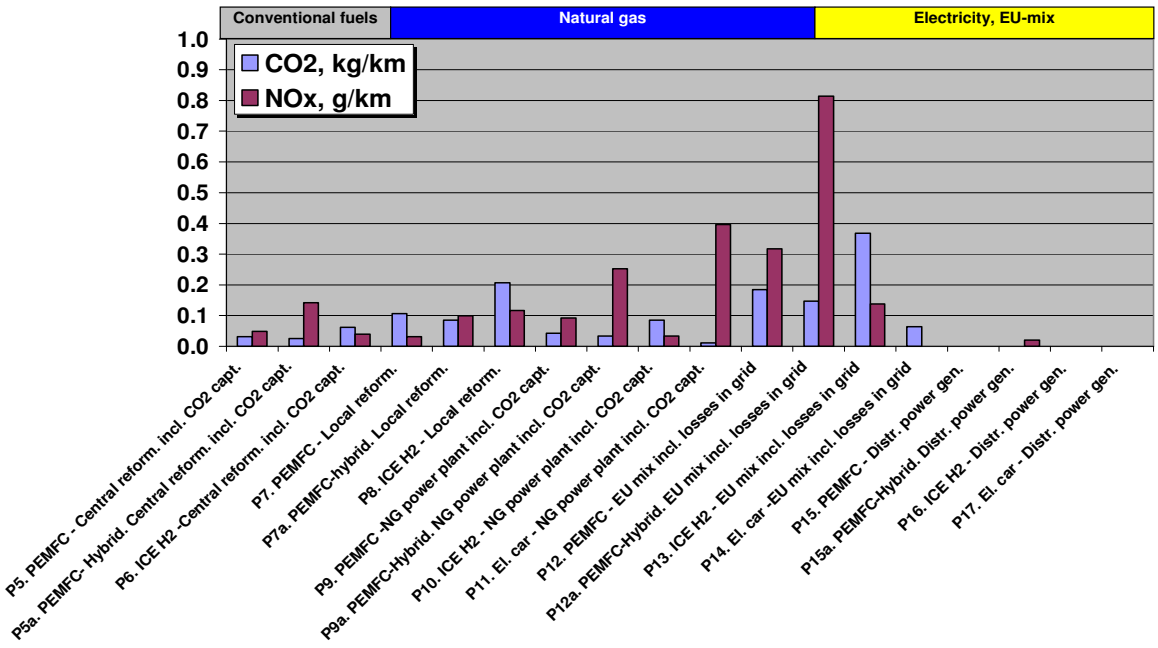

Figure 5: Emissions corresponding to Figure 4, with electricity production in accordance with average European electricity production.

Proceedings of ECOS 2005
Trondheim, Norway
June 20–22, 2005

Development of a Detailed Planar SOFC CFD Model for Analyzing Cell Performance Degradation

Vittorio Verda[†,*] Michael R. von Spakovsky[††], and Nathan Siegel[†††]

[†] Department of Energy Engineering, Politecnico di Torino, c.so Duca degli Abruzzi 24, 10129 Torino, ITALY
vittorio.verda@polito.it

[††] Center for Energy Systems Research, Department of Mechanical Engineering, Virginia Polytechnic Institute and State University, Blacksburg, VA 24061
vonspako@vt.edu

[†††] Sandia National Laboratories, PO Box 5800, MS-0753, Albuquerque, NM 87185
npsiege@sandia.gov

ABSTRACT

Solid Oxide Fuel Cells are a promising technology for distributed electricity generation and cogeneration. Numerous papers have been published in the last several years proposing mathematical / computational fluid dynamics (CFD) models for predicting the transient and steady state performance of such cells. In this paper, a detailed steady state CFD model of a planar anode supported SOFC is proposed, which accounts for mass, thermal, and charge transport as well as electrochemistry and the chemistry of internal fuel reforming. Its main characteristics include the use of a continuous model for the electrochemistry, allowing one to examine different three-phase boundary geometries. This is an improvement over the typical model reported in the literature, which utilizes an equivalent resistive circuit approach or a homogeneous distribution of three-phase boundaries.

The model proposed here is used to simulate the degradation of anode, cathode, and electrolyte due to instabilities (e.g., anode oxidation due to fuel depletion) or to the delamination of the electrodes from the electrolyte. Such degradations result in a drop in cell performance but are difficult to predict without the use of models which can be helpful for diagnosis. The model is applied to experimental data available in the literature both for the non-degraded and degraded cases.

Keywords: solid oxide fuel cells, computational fluid dynamics, cell performance degradation

Nomenclature

A	active surface area per unit volume [m^2/m^3];
AD	gas channel at anode side;
A_R	catalyst surface area per unit volume [m^2/m^3];
CD	gas channel at cathode side;
D_φ	general diffusion coefficient;
E	electrolyte;
E_a	activation energy [J/mol];
F	Faraday's constant [C/mol];
G	Gibbs free energy [J/mol];
i_0	exchange current density [A/m^2];
k	effective conductivity [$1/(\Omega \cdot m)$];
k_0	pre-exponential factor [$mol/(s \cdot m^2 \cdot Pa)$];
k_{TPB}	equivalent conductivity of the TPB [$1/(\Omega \cdot m)$];
K	permeability [m^2];
K	equilibrium constant;
M	molar mass [kg/kmol];
NP	number of products;
NR	number of reactants;
n	number of electrons exchanged;
p	pressure [Pa];
PA	porous anode;
PC	porous cathode;
r	rate of reaction [$mol/(s \cdot m^2)$];
R	universal gas constant [$J/(mol \cdot K)$];

[*] Corresponding author: Phone (+39) 011 564 44 78, Fax. (+39) 011 564 44 99, e-mail: vittorio.verda@polito.it

S_A mass source term for species A due to chemical or electrochemical reactions [kg/(m^3·s)];
$\mathbf{S_d}$ source term in the momentum equation [kg/(m^2·s^2)];
S_i source term in the current conservation equation [A/m^3]
S_φ general source term;
t layer thickness [mm];
T temperature [K];
u velocity [m/s];
V_{cell} cell potential [V];
V_{Nernst} Nernst potential [V]
V_Δ ohmic and activation overpotential [V];
y molar fraction;

Greek

α charge transfer coefficient;
β_1 conductivity term in equation (44) [1/(Ω·m)];
β_2 temperature term in equation (44) [K];
δ coefficient that activates terms in the momentum equation;
ε porosity;
φ general transport property;
ϕ_V heat flux generated per unit volume [W/m^3]
η_{conc} concentration overpotential [V];
l conductivity [W/(m·K)]
μ dynamic viscosity [kg/(m·s)];
ν stoichiometric coefficient;
ρ density [kg/m^3];
ρ resistivity [Ω·m];
ξ tortuosity;
Σv diffusion volumes;
Γ variable expressed by equation (21);
Ω variable expressed by equation (22);

Subscripts

B backward reaction;
D diagonal term;
el electronic;
F forward reaction;
io ionic;
k Knudsen diffusion mechanism;
ND non-diagonal term;
m gas mixture;
o ordinary mechanism of diffusion;
R steam reforming reaction;
S water-gas shift reaction;

Introduction

Solid Oxide Fuel Cells are a promising technology for decentralized power generation and cogeneration [1]. Some of the main advantages are the high efficiency, the low NO_x production, the possibility of directly using methane through internal reforming, and the possibility of using SOFCs in combination with bottoming cycles.

Important conditions for a large market penetration of such systems are sufficiently long operating lifetimes and minimal performance degradation. This paper deals with the problem of performance degradation and, in particular, presents a CFD model able to simulate the behavior of a SOFC under conditions of reduced efficiency. Such a model can help guide plant operations by providing information on degraded conditions in cells and stacks. Moreover, it can provide reliable information for developing diagnosis routines.

The fuel cell representation

The investigation of planar SOFC behavior is performed using a CFD model. The complete equation set is presented in this section, while its use for a 2D geometry is presented in the sections which follow. A schematic of the anode supported planar SOFC is depicted in Figure 1 where five layers are represented: the anodic and cathodic distribution channels (AD and CD), the porous anode and porous cathode, and the electrolyte.

CFD models typically rely on the hypothesis of the material within each layer being homogeneous, which is not the case for SOFC layer morphologies. In particular, the electrochemical reactions occur at the so-called triple-phase boundary (TPB), which is a surface where the ionic conductor, the electronic conductor, and the pores are simultaneously present. On this surface, the electrochemical conversion between ionic and electronic current (or vice-versa) takes place.

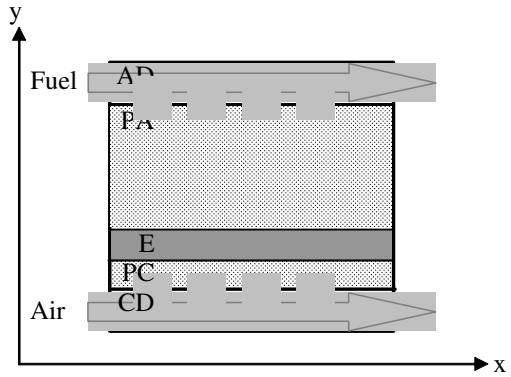

Figure 1. 2D schematic of a single cell of a planar SOFC.

The active sites where the reactions take place constitute a region which separates the ionic current thresholds and electronic current thresholds. The shape of this region generally is not regular, i.e. it is not homogeneously distributed within the electrodes. Information on this shape can come from a micro-structural analysis obtained through scanning or transmission electron microscopy. An example of a cathode reacting layer is shown in Figure 2. Larger particles are the ionic conductor, while smaller particles are the electronic conductor. The whole structure is porous so that gas can pass through.

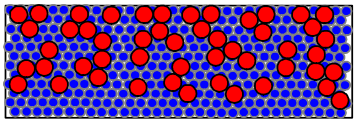

Figure 2. Example of cathode reacting layer.

Figure 3 shows the corresponding triple-phase boundary and the two regions where electronic current (areas in white) and ionic current (areas in grey) are transmitted. Two things must be highlighted: 1) the TPB is not a continuous surface, but it is interrupted by portions where only two phases are in contact. In these portions, the TPB is represented as a continuous line, but the active area is assumed zero; 2) in both regions there are non-conductive particles: ionic conductive particles within the electronic conductive region and electronic conductive particles within the ionic conductive region. These particles (areas in black) reduce drastically the conductivity in the regions since ionic conductive particles have very low electronic conductivity and vice-versa.

In addition, the area available for the electrochemical reaction at some of the active sites can decrease with time due to electrode degradation. Since the objective of the model presented here consists of simulating degraded operating conditions, the model must account for a non-homogeneous distribution of the active area.

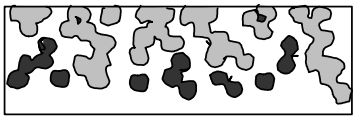

Figure 3. Shape of the triple-phase boundary.

The electrochemical reaction is a surface phenomenon but is treated in this model as if it would occur in a small volume. The domain is discretized into small cells as shown in Figure 4. For each cell, the active area per unit volume is considered. The different cells are characterized by a value of the conductivity, which is equal to the ionic conductivity for the cells in the gray region and to the electronic conductivity for the cells in the white region. The cells at the boundary are also characterized by a value of the active area, which is zero in the case of contact between just two phases. Finally, the cells in the black areas are characterized by very low values of the conductivity. This assumption is used in order to properly account for the effects of modifications in the TPB due to electrode degradation, as is explained further below.

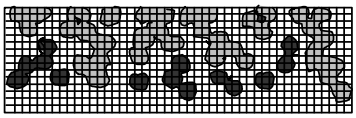

Figure 4. Example of the discretization of the region where the electrochemical reactions occur.

The fuel cell model

The fuel cell model has been developed, taking into account the following phenomena:

- fluid dynamics;
- heat transfer;
- chemical reactions;
- electrochemical reactions.

The model consists of a set of eight partial differential equations and some constitutive equations in order to model the different phenomena. The partial differential equations are: the continuity equation for the gas mixture, the momentum equation (2 components in a 2D geometry and 3 components in a 3D geometry), energy conservation, the conservation of species written for all components of the gas mixture minus one, and current conservation.

The hypotheses of steady-state conditions and incompressible fluid have been used. The partial differential equations have been solved by using a finite element code called CFDesign™ [2] modified with the help of researchers at Virginia Tech [3,4] to accommodate detailed fuel cell modeling. The general differential equation is written in the form:

$$\rho\mathbf{u}\cdot\nabla\varphi=\nabla\cdot\left(D_{\varphi}\nabla\varphi\right)+S_{\varphi} \tag{1}$$

where φ is any general transport property. The source term can be written by considering a diagonal term $S_{D\varphi}$ and a non-diagonal term $S_{ND\varphi}$, i.e.

$$S_{\varphi}=-S_{D\varphi}\cdot\varphi+S_{ND\varphi} \tag{2}$$

The general expression for the momentum equation is given by

$$\delta_1\mathbf{u}\cdot\nabla\cdot\left(\rho\mathbf{u}\right)=-\nabla p+\delta_2\mu\nabla^2\mathbf{u}+\mathbf{S_d} \tag{3}$$

where δ_1 and δ_2 are set equal to 1 in the gas channels and 0 in the porous media. For the latter case, equation (3) leads to the Darcy equation or to the Darcy-Forchheimer equation, depending on the expression assumed for the source term. Alternatively, δ_2 can be assumed to be the ratio between an effective viscosity and the fluid viscosity, namely,

$$\delta_2=\frac{\bar{\mu}}{\mu} \tag{4}$$

in order to provide Brinkman's extension to the Darcy formulation (see for example [5]).

The calculations in this paper have been performed by considering the Darcy expression in the porous media, which is obtained by writing the source term as

$$\mathbf{S_d}=\frac{\mu}{K}\cdot\mathbf{u} \tag{5}$$

where K is the permeability. The source term is null in the distribution channels.

The continuity equation is written as

$$\nabla\cdot\left(\rho\mathbf{u}\right)=S \tag{6}$$

where S is a source/sink term which accounts for the change in mass due to the electrochemical reactions.

This term is positive on the anode side and negative on the cathode side.

The conservation of species is written by considering two phases: the gas species and the mixture of gases. The species equation for the generic species A is then written as

$$\nabla \cdot (\rho \mathbf{u} w_A) = \nabla \cdot (D_A \rho \nabla w_A) + S_A \quad (7)$$

where w_A is the mass fraction of component A, D_A is the diffusion coefficient of species A in the mixture, and S_A is the source term of the species due to chemical and electrochemical reactions.

Equation (7) can be rewritten in the same form as equation (1), i.e.

$$\rho \mathbf{u} \cdot \nabla (w_A) = \nabla \cdot (D_A \rho \nabla w_A) + S_A - w_A \nabla \cdot (\rho \mathbf{u}) \quad (8)$$

so that the source term of equation (1) is given by

$$S_{wA} = S_A - w_A \nabla \cdot (\rho \mathbf{u}) \quad (9)$$

The diffusivity coefficient in this equation is calculated by considering both ordinary and Knudsen diffusion [6], the first accounting for molecular transport in the pores characterized by a large diameter in comparison to that of the mean free path, and the second for molecular transport in the pores characterized by a small diameter. For the generic species A in the gas mixture, the diffusion coefficient is expressed through the Bosanquet formula, multiplied by a term accounting for the pore characteristics [7], Thus,

$$D_A = \frac{1}{\frac{1}{D_{A,o}} + \frac{1}{D_{A,k}}} \cdot \frac{\varepsilon}{\xi} \quad (10)$$

where

$D_{A,o}$ is the ordinary diffusion coefficient
$D_{A,k}$ is the Knudsen diffusion coefficient
ε is the volume fraction of pores
ξ is the tortuosity.

The ordinary diffusion coefficient is calculated by considering the diffusivity of the species in the gas mixture, namely,

$$D_{A,o} = \frac{D_{A-m}}{1 - \alpha_{Am} \cdot y_A} \quad (11)$$

where y_A is the molar fraction of component A and

$$\alpha_{A-m} = 1 - \left(\frac{M_A}{M_m} \right)^{0.5} \quad (12)$$

In this last expression, M_A is the molar weight of species A and M_m the average mixture molar weight. The diffusivity coefficient in the mixture is calculated using the diffusion coefficient of species A in each binary system constituted by A and the other mixture contituents. A possible model is the one developed by Stefan-Maxwell which expresses this mixture diffusivity as (see for example [8])

$$D_{A-m} = \frac{1 - y_A}{\sum_{i \neq A} \frac{y_i}{D_{A-i}}} \quad (13)$$

where D_{A-i} is the diffusion coefficient for the specie A in a binary mixture constituted by the species A and i. This diffusion coefficient can be calculated by using an empirical as opposed to theoretical relation (see for example the application to a SOFC proposed by Yakabe et al. [9]). A reliable one is that suggested by Fuller, Schettler and Giddings [10]. For a mixture constituted by species A and B, the diffusion coefficient D_{A-i} is expressed as

$$D_{A-B} = \frac{101.325 \cdot T^{1.75} \cdot \sqrt{\frac{M_A + M_B}{M_A \cdot M_B}}}{p \cdot \left[\left(\sum v \right)_A^{1/3} + \left(\sum v \right)_B^{1/3} \right]^2} \quad (14)$$

where the terms Σv are the diffusion volumes. Some values of this quantity are Σv (H_2) = 7.07; Σv (N_2) 17.9; Σv (O_2) = 16.6; Σv (CO) = 18.9; Σv (CO_2) = 26.9; Σv (H_2O) = 12.7.

In case of a binary mixture, the mass concentration of species B is calculated as

$$w_B = 1.0 - w_A \quad (15)$$

When a multi-component gas mixture is considered, equation (8) must be written for n-1 species. In this case the mass fraction of the n^{th} species is calculated as

$$w_n = 1.0 - \sum_{i=1}^{n-1} w_i \quad (16)$$

The energy equation is written in the form

$$\rho \mathbf{u} \cdot \nabla T = \nabla \cdot (\lambda \nabla T) + \phi_V \quad (17)$$

where λ is the global thermal conductivity and ϕ_V the heat generated per unit volume due to chemical and electrochemical reactions. In equation (17) the hypothesis of thermal equilibrium between the porous structure and the gas is assumed so that a unique local temperature is considered.

Finally, the conservation of current equation is written as

$$k \cdot \nabla^2 V_\Delta = S_i \quad (18)$$

where k is the layer general electronic or ionic conductivity, V_Δ is the overpotential, and S_i is the current source. V_Δ accounts for the ohmic and the activation overpotentials. Other losses, such as the concentration overpotential, are considered through the boundary conditions as discussed below.

Two different approaches can be selected in order to write the resistivity (conductivity) and the source term. The choice depends mainly on the boundary conditions which one can assume for the problem. When a single electrode is considered, it is possible to treat the conversion between ionic and electronic current through a source term representing the local current density transformation. In this case, the source term assumes the form of the Butler-Volmer equation, namely,

$$S_i = A \cdot i_0 \cdot \left(e^{\frac{\alpha \cdot n \cdot F}{R \cdot T} V_\Delta} - e^{-\frac{(1-\alpha) \cdot n \cdot F}{R \cdot T} V_\Delta} \right) \quad (19)$$

This approach is used for example in [11] and [12]. The boundary conditions are imposed at the electrode surfaces, which allows one to guarantee the complete transformation of ionic current into electronic current or vice-versa, depending on the electrode analyzed.

A second approach can be used in order to avoid the need of boundary conditions at the electrode surfaces. In this case, the activation overpotential is modelled through the diffusive term, while the source term is absent. This also means that the electrochemical reaction is modelled as a volume reaction instead of a surface reaction.

The first of these approaches is used here. Furthermore, the expression for the total conductivity obtained from a one-dimensional calculation of an electrode is adopted for the model of the TPB [12]. This model is used here only for the TPB elements. These elements are described through a value of the active area in the normal direction with respect to current propagation. The conductivity (diffusive term) is:

$$k_{TPB} = \frac{\Gamma \cdot sinh(\Gamma)}{(\rho_{el} + \rho_{io})(cosh(\Gamma) + \Omega \cdot [2 + \Gamma \cdot sinh(\Gamma) - 2cosh(\Gamma)])} \quad (20)$$

where the expressions for the two dimensionless variables Γ and Ω are given by

$$\Gamma^2 = \frac{i_0 \cdot A \cdot F \cdot (\rho_{el} + \rho_{io}) \cdot a^2}{R \cdot T} \quad (21)$$

$$\Omega = \frac{\rho_{el} \cdot \rho_{io}}{(\rho_{el} + \rho_{io})^2} \quad (22)$$

All the necessary steps for deriving equation (20) are available in the reference cited. An important difference is that in the present paper, the variable a is a characteristic thickness assigned to the TPB in the normal direction with respect to the active surface available in the cell. This corresponds to the assumption of a progressive transformation between electronic and ionic currents in the element. Coherent with this assumption is A as the active area per unit volume. Note that equation (20) has been obtained by considering a linearized expression of the Butler-Volmer equation. Different approaches can be found in the literature (e.g., [13] and [14]).

The model is completed by means of a set of constitutive equations which are detailed as follow:

1) The gas mixture density is calculated through the ideal gas law. Specific heats are assumed to be dependent on the gas temperature.

2) The internal reforming is modelled by considering the methane reforming and the water-gas shift reactions only:

$$CH_4 + H_2O \leftrightarrow 3H_2 + CO \quad (23)$$

$$H_2O + CO \leftrightarrow H_2 + CO_2 \quad (24)$$

The water-gas shift reaction is usually assumed to be in equilibrium. The reaction rate depends on the gas temperature (see for example [15]). Thus,

$$K_S = \frac{K_{SF}}{K_{SB}} = \frac{y_{H_2} \cdot y_{CO_2}}{y_{H_2O} \cdot y_{CO}} \quad (25)$$

$$K_S = e^{-0.2935 \cdot z^3 + 0.6351 \cdot z^2 + 4.1788 \cdot z + 0.3169} \quad (26)$$

where

$$z = \frac{1000}{T} - 1 \quad (27)$$

The term expressing the generation of hydrogen in the water-gas shift reaction is dimensionally coherent with the conservation of species equation source term and is calculated as

$$S_S = K_{SF} \left(p_{H_2O} \cdot p_{CO} - \frac{p_{H_2} \cdot p_{CO_2}}{K_S} \right) \cdot M_{H_2} \quad (28)$$

where the forward reaction rate constant is determine by

$$K_{SF} = 0.0171 \cdot e^{-\frac{103191}{RT}} \quad (29)$$

The approach for the steam reforming is more complex. All the different approaches can be classified into two groups: a) empirical correlations and b) formal kinetic models such as the Langmuir-Hinshelwood model [16]. All the proposed relations can be implemented in the model. However, the calculations proposed in this paper have been performed using the formulation proposed by Achenback and Riensche [17], i.e.

$$r_R = k_0 \cdot p_{CH_4} \cdot \left(1 - \frac{p_{CO} \cdot {p_{H_2}}^3}{p_{CH_4} \cdot p_{H_2O} \cdot K_R} \right) \cdot e^{-\frac{E_a}{RT}} \quad (30)$$

where
$k_0 = 0.04274$ mol/(s m^2 Pa);
$E_a = 82000$ J/mol.

As to the source term in the conservation of species CH_4 equation (as reported in equation (7)), it is expressed as

$$S_{CH_4} = -r_R \cdot A_R \cdot M_{CH_4} \quad (31)$$

In the proposed calculations, the catalyst surface area A_R per unit volume has been assumed to be 0.01 m^2/m^3.

All of the other source terms for the conservation of species equations can be obtained based on reactions (23) and (24). Thus,

$$S_{H_2} = -3 \cdot S_{CH_4} \cdot \frac{M_{H_2}}{M_{CH_4}} + S_S \quad (32)$$

$$S_{CO} = -S_{CH_4} \frac{M_{CO}}{M_{CH_4}} - S_S \quad (33)$$

$$S_{CO_2} = S_S \tag{34}$$

3) The internal reforming introduces a source term in the energy equation, since the demethanization reaction (23) is endothermic (206 kJ/mol at 0 °C) while the water-gas shift reaction (24) is exothermic (-41.1 kJ/mol at 0 °C).

4) The species participating in the electrochemical reactions are CO and H_2 at the anode and O_2 at the cathode, i.e.

$$H_2 + O^{2-} \rightarrow H_2O + 2e^- \tag{35}$$

$$CO + O^{2-} \rightarrow CO_2 + 2e^- \tag{36}$$

$$\frac{1}{2}O_2 + 2e^- \rightarrow O^{2-} \tag{37}$$

A free variable in this model is the ratio between CO and H_2 participating in the electrochemical reactions. In some of the models proposed in the literature, this ratio is assumed to be 0 ([15] and [18]). Here the ratio is assumed to be dependent on the molar fraction of the two species at the TPB (see equation (42) below).

5) The relation between the local current density and the consumption of hydrogen, oxygen, and carbon monoxide as well as the generation of carbon dioxide is expressed through Faraday's law. This means that at the TPB, the source terms in the conservation of species equations are given by

$$S_{H_2} = -\frac{i_{H_2}}{a \cdot 2 \cdot F} M_{H_2} \tag{38}$$

$$S_{CO} = -\frac{i_{CO}}{a \cdot 2 \cdot F} M_{CO} \tag{39}$$

$$S_{O_2} = \frac{i}{a \cdot 4 \cdot F} M_{O_2} \tag{40}$$

where i_{H2} and i_{CO} are the current densities obtained from the two electrochemical reactions on the anode side. These currents can be obtained from the following relations:

$$i_{H_2} + i_{CO} = i \tag{41}$$

$$\frac{i_{CO}}{i_{H_2}} = \frac{y_{CO}}{y_{H_2}} \tag{42}$$

The generation of water is taken into account in the continuity equation, whose source term is written as

$$S = S_{H_2} \cdot \left(1 - \frac{M_{H_2O}}{M_{H_2}}\right) \tag{43}$$

6) The ionic and electronic resistivity are assumed to be dependent on the temperature such that

$$\rho = \frac{1}{\beta_1 \cdot e^{-\frac{\beta_2}{T}}} \tag{44}$$

The values of the selected parameters are indicated in the next section [19].

Application of the model to a 2D planar SOFC

In this section, an application of the proposed model is presented. In particular, the geometric characteristics and the boundary conditions are discussed.

A 2D model is considered for the anode supported planar SOFC shown in figure 1 above. The cell length is 20 mm. The main data are shown in table 1.

Table 1. Parameters adopted in the model.

	AD	PA	E	PC	CD
t [mm]	1	2	0.05	0.05	1
ε	-	0.45	-	0.45	-
ξ	-	4.5	-	4.5	-
β_1 [1/Ωm]	5000	7800	20500	12820	33770
β_2 [1/Ωm]	0	1290	9030	0	1130

In figure 5, the boundary conditions for the model are indicated. The values assumed in the application presented in this paper are given in table 2.

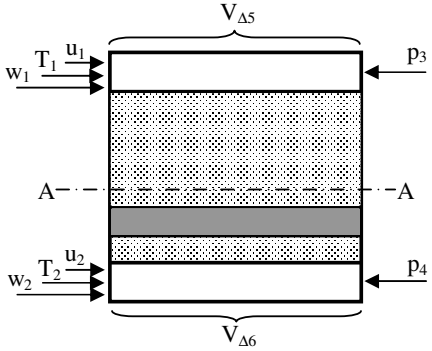

Figure 5. Boundary conditions imposed on the model.

Table 2. Values of the boundary conditions imposed in the model.

T_1	800 °C	T_2	800 °C
u_1	1.922 m/s	u_2	3.264 m/s
$w_1(CH_4)$	0.184	$w_2(CH_4)$	0
$w_1(H_2)$	0.036	$w_2(H_2)$	0
$w_1(CO)$	0.054	$w_2(CO)$	0
$w_1(CO_2)$	0.130	$w_2(CO_2)$	0
$w_1(O_2)$	0	$w_2(O_2)$	0.200
p_3	101000 Pa	p_4	101000 Pa
$V_{\Delta 5}$	Variable	$V_{\Delta 6}$	0

The boundary condition for the current conservation equation deserves a detailed explanation. As the boundary condition, the overpotential due to ohmic and activation losses is imposed in this work. Usually, the cell potential is assumed as the boundary

condition instead, especially when equivalent resistance models are adopted (see for example [20]). In the model proposed here, the cell potential could be imposed as the boundary condition provided that the other overpotentials, such as the concentration polarization, can be neglected or can be expressed through an equivalent resistivity similar to that for the activation overpotential. However, in our approach here, the cell potential is calculated once the calculation has been completed, namely,

$$V_{cell} = V_{Nernst} - (V_{\Delta 5} - V_{\Delta 6}) - \eta_{conc} \qquad (45)$$

The term $V_{Nernst} - \eta_{conc}$ can be directly calculated using

$$V_{Nernst} - \eta_{conc} = -\frac{\Delta G^0}{n \cdot F} - \frac{R \cdot T}{n \cdot F} ln\left(\frac{\prod_{i=1,NP}(p_i)^{\upsilon_i}}{\prod_{i=1,NR}(p_i)^{\upsilon_i}}\right) \qquad (46)$$

Results

The model just presented is now applied to a first case (Case 1), namely, where the TPB is homogeneously distributed at the interface between the electrodes and the electrolyte. The polarization curve is shown in figure 6.

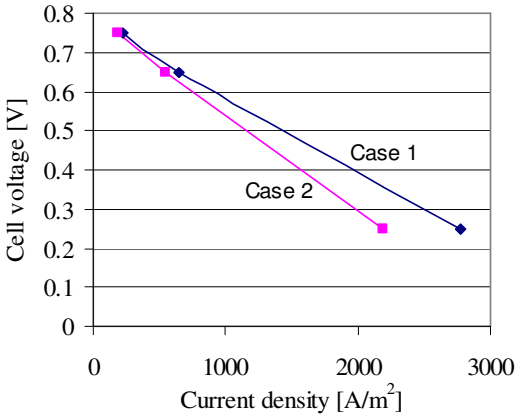

Figure 6. Polarization curves for Cases 1 and 2.

The model is then used to investigate the cell behavior when possible anomalies take place. Possible factors that determine degradation in SOFC performance are: 1) a delamination (decrease in the contact area) between the electrodes and the electrolyte, 2) an increase in the contact resistance between the electrodes and the current collector, and 3) chemical reactions between the materials constituting the electrodes, electrolyte, and interconnections [21].

The first simulation (Case 2) is performed by considering anode delamination, causing a 10% reduction in the anode active area due to a gap formed between the anode and electrolyte. This value has been assumed on the basis of some experiments conducted on a SOFC after almost 1000 h operation and available in the literature [22]. Data about the extension of the area subjected to delamination can be obtained through SEM [20].

This phenomenon has been simulated through considerable reduction of the active area for x<2.5 mm. The simulation of such an anomaly requires the use of a model able to take into consideration the shape of the TPB. The two polarization curves are shown in figure 6.

The results in figure 6 show an increase in the overvoltage. In figure 7, the current density distribution along cross-section AA in figure 5 is shown. It is evident that the reduction in the active surface area causes a significant drop in the current on the anode side of the cell.

The effects of a second anomaly (Case 3), the increase in contact resistance, are also presented in this paper. This increase in resistance was simulated by adding an electric resistance (8 mΩ·cm^2) between the cathode and gas channel, where the interconnections are located [23]. The corresponding polarization curve is shown in Figure 8.

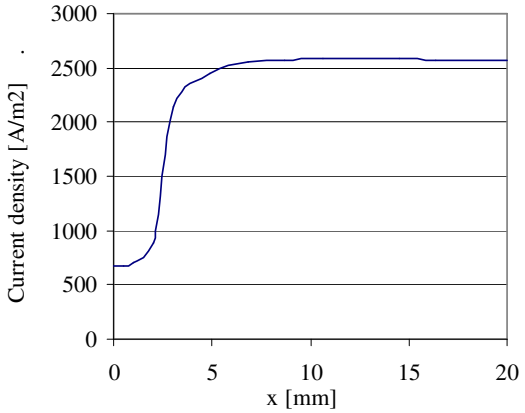

Figure 7. Current density distribution in the anode in the case of delamination (Case 2).

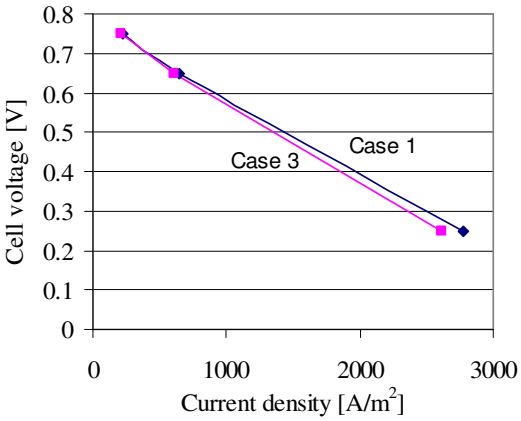

Figure 8. Polarization curves for Cases 1 and 3.

The last anomaly (Case 4) simulated in this work consists of an increase in the resistance between cathode and electrolyte due to formation of $LaZrO_7$ [21], i.e. anode oxidation. Resistance has been increased three orders of magnitude in the layer where both LSM (cathode material) and YSZ (electrolyte material) are present. The polarization curve results are not shown since they are close to those obtained for Case 3. Figure 9 shows the current density distribution in a cross section of the anode for Cases 3 and 4. As can be seen from this cross-section, the percentage difference in effect on the current density between the two cases is not great. Thus, performance in terms of the polarization curve for each case is essentially identical between the two. This also means that the effect of these two anomalies cannot be distinguished on the basis of the polarization curve only.

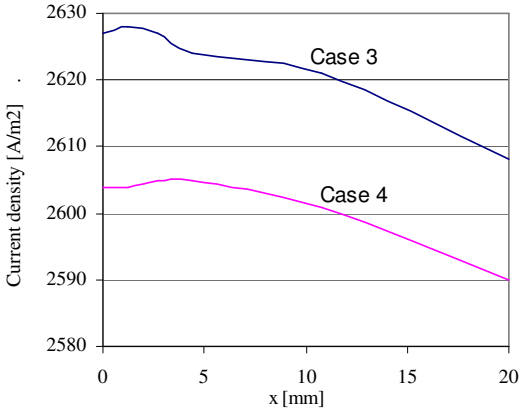

Figure 9. Current density distribution in the anode for the case of increased contact resistance.

Conclusions

In this paper a new CFD model is introduced for the analysis of SOFCs. The model was purposely developed in order to simulate possible anomalies in these devices, since it allows one to consider modifications in the shape of the TPB as well as variations in the ionic and electronic conductivity.

The model was tested by using data obtained from the literature, which deal with typical causes of performance degradation: electrode and electrolyte delamination (Case 2), increase in contact resistance (Case 3), and the formation of oxides (Case 4).

References

[1] Singhal S.C. (2000). *Advances in solid oxide fuel cell technology*. Solid State Ionics, 135, pp. 305–313.

[2] Blue Ridge Numerics Inc., (2004). CFDesign™, Charlottesville, VA.

[3] Siegel, N.P., Ellis, M.W., Nelson, D.J., von Spakovsky, M.R. (2004). *A Two-Dimensional Computational Model of a PEMFC with Liquid Water Transport*, Journal of Power Sources, vol. 128, issue 2, pp. 173-184.

[4] Siegel, N.P., Ellis, M.W., Nelson, D.J., von Spakovsky, M.R. (2003). *Single Domain PEMFC Model Based on Agglomerate Catalyst Geometry*, Journal of Power Sources, vol. 115/1, pp. 81 - 89.

[5] Nield D.A., Bejan A. (1999). *Convection in porous media*. Springer. New York.

[6] Suwanwarangkul R., Croiset E., Fowler M.W., Douglas P.L., Entchev E., Douglas M.A. (2003). *Performance comparison of Fick's, dusty-gas and Stefan–Maxwell models to predict the concentration overpotential of a SOFC anode*. Journal of Power Sources, 122, pp. 9–18.

[7] Veldsink J.W., van Damme R.M.J., Versteeg G.F., van Swaaij W.P.M. (1995). *The use of the dusty-gas model for the description of mass transport with chemical reaction in porous media*. Chemical Engineering Journal, 57. pp. 115-125. Krishna R., Wesselingh J. A. (1997). *The Maxwell-Stefan approach to mass transfer*. Chemical Engineering Science, Vol. 52, No. 6, pp. 861-911.

[8] Yakabe H., Hishinuma M., Uratani M., Matsuzaki Y., Yasuda I. (2000). *Evaluation and modeling of performance of anode-supported solid oxide fuel cell*. Journal of Power Sources, 86, pp. 423–431

[9] Fuller E.N., Schettler P.D., Giddings J.C. (1966). *A new method for prediction of binary gas-phase diffusion coefficients*. Industrial and Engineering Chemistry, Vol. 58, No. 5, pp. 18-27.

[10] Sun Y.P., Scott K. (2004). *An analysis of the influence of mass transfer on porous electrode performance*. Chemical Engineering Journal 102, pp. 83–91.

[11] Costamagna P., Costa P., Antonucci V. (1998). *Micro-modelling of solid oxide fuel cell electrodes*. Electrochimica Acta, Vol. 43, No 3-4. pp. 375-394.

[12] Tanner C.W., Fung K, Virkar A.V. (1997). *The effect of Porous Composite Electrode Structure on Solide Oxide Fuel Cell Performance*. Journal of Electrochemical Society, Vol. 144, No.1, pp. 21-30.

[13] Virkar A.V., Chen J., Tanner C.W., Kim J. (2000). *The role of electrode microstructure on activation and concentration polarizations in solid oxide fuel cells*. Solid State Ionics, 131, pp. 189–198

[14] Haberman B.A., Young J.B. (2004). *Three-dimensional simulation of chemically reacting gas flows in the porous support structure of an integrated-planar solid oxide fuel cell*. International Journal of Heat and Mass Transfer, 47, pp. 3617–3629.

[15] Satterfield C.N. (1996). *Heterogeneous Catalysis in Industrial Practice*. Krieger. Malabar, Florida. U.S.

[16] Achenbach E., Riensche E. (1994). *Methane/steam reforming kinetics for solid oxide fuel cells*. Journal of Power Sources, 52, pp 283-288.
[17] Campanari S., Iora P. (2004). *Definition and sensitivity analysis of a finite volume SOFC model for a tubular cell geometry*. Journal of Power Sources, 132, pp. 113–126.
[18] Lin Y., Beale S. (2003). *Performance Prediction in Solide Oxide Fuel Cells*. 3rd International Conference on CFD in the Minerals and Process Industry. CSIRO. Melbourne. Australia. 10-12 December.
[19] Li P., Chyu M.K. (2003). *Simulation of the chemical/electrochemical reactions and heat/mass transfer for a tubular SOFC in a stack*. Journal of Power Sources, 124, pp. 487–498
[20] Hsiao Y.C. , Selman J.R. (1997). *The degradation of SOFC electrodes*. Solid State Ionics, 98, pp. 33–38.
[21] Weber A., Sauer B., Muller A.C., Herbstritt D., Ivers-Tiffée E. (2002). *Oxidation of H2, CO and methane in SOFCs with Ni/YSZ-cermet anodes*. Solid State Ionics, 152–153, pp. 543– 550.
[22] Tu H., Stimming U. (2004). *Advances, aging mechanisms and lifetime in solid-oxide fuel cells*. Journal of Power Sources, 127, pp. 284–293.

Proceedings of ECOS 2005
Trondheim, Norway
June 20–22, 2005

DYNAMIC MODELLING AND CONTROL OF POLYBENZIMIDAZOLE FUEL CELLS

Federico Zenith,* Sigurd Skogestad
Norwegian University of Science and Technology
Department of Chemical Engineering
7491 Trondheim, Norway

ABSTRACT

A dynamic fuel-cell model for high-temperature PEM fuel cells with PBI membranes has been developed in Simulink. In such models it is common to use the current density as input variable, but this model uses a different approach. The current density is regarded as an unrealistic control variable, since it cannot be controlled directly. Instead, it is possible to simulate the effect of changing the characteristic of the external circuit, a more realistic manipulated variable, with resistances or MOSFET transistors. Experimental runs have been executed to confirm the theoretical development. To measure the parameters needed for the model, impedance tests on the fuel cell are considered an effective way to extract parameters by means of parameter regression: the model has therefore been extended and reimplemented to produce simulated impedance plots, that show good agreement with experimental measurements on fuel cells.

INTRODUCTION

Research in fuel cells has shown a rapid growth. The relatively minor interest for their dynamics has recently increased as a topic in its own merit and as a prerequisite for control analysis and controller design. However, many models provided in the literature [1, 2, 3, 4, 5] were not intended for control studies, and in that context they are often "flawed" because they consider *current density* as an input to the system. This is unrealistic from a process-control perspective, because in reality the current is determined by the characteristics of the fuel cell and of its external load, and is not set directly by the control system.

Currently, most PEM fuel cells are based on electrolytes that rely on liquid water for protonic conduction, binding them to an operating temperature below 100 °C (unless pressurized). In polybenzimidazole (PBI)-based fuel cells, water is produced in gaseous form, and since the membrane relies on phosphoric acid to function, the water management issue is removed. Finally, high-temperature PEM fuel cells based on PBI electrolyte exhibit a high tolerance to carbon monoxide [6].

*Corresponding author: zenith@chemeng.ntnu.no

The parameters used in the model need to be measured appropriately. Impedance tests are measurement of the impedance of the fuel cell at various frequencies. By applying the proposed model structure to calculate the impedance of the fuel cell, a plot of clear resemblance to experimental results is obtained. The fundamental theory about impedance spectroscopy can be found in many textbooks, for example in Macdonald [7].

The objective of this paper is to show the development of a model using the external circuit's characteristic as an input, and how this model is able to explain experimental results observed on a PBI fuel cell. Another objective is making the point that dynamic models for control-design purposes should make use of proper manipulated input variables, instead of using either voltage or current as an input. Furthermore, the usefulness of impedance measurements in determining the model parameters will be demonstrated.

EXPERIMENTAL METHODS

Experiments were carried out on a PBI fuel cell, previously assembled in the laboratory of the Depart-

ment of Materials Technology at NTNU, to determine the transient response of the cell to a variable load. The load itself was assembled as a variable-resistance board, with two resistances in parallel; in series with one of these resistances, a switch could be opened and closed manually. The PBI fuel cell was kept at a constant temperature of 150 °C by an external electric heater. The fuel cell ran on industrial-grade hydrogen and oxygen at atmospheric pressure.

EXPERIMENTAL RESULTS

The results obtained switching from an initial resistance to a smaller one and back are shown in figure 1. It can be seen how the operating point moves from a resistance's characteristic to the other along parallel lines. As a reference, the steady-state polarization curve is plotted as well. Since some hysteresis was experienced in its measurement, the polarization curve is not an entirely precise reference.

Looking carefully at figure 1, it is clear that in the descent to steady-state some transients are faster than others; this can be seen by the number of markers on the trajectory in the *V*-*I* plane. It appears that the electrochemical transient to 12.88 Ω is slower than the one to 5.47 Ω, which is in turn slower than the one to 2.85 Ω.

There is therefore an indication that the electrochemical transient can have *different time constants* depending on both the start and the end point. This behavior could be related to the one observed in a Master's thesis written at NTNU [8], where the same proportional controller, applied on a PBI fuel cell, performed too aggressively in some operating ranges and too mildly in others.

MODELLING

To model the behaviour presented in the previous sections and in figure 1, we actually only need to consider a simple differential equation referred to the cathode of the cell: it is basically a charge balance of a capacitor (3). This capacitor represents what is known in electrochemistry as the *charge double layer*, but also other electrically charged species. At this point we are neglecting the anodic overvoltage and concentrating instead on the cathodic one, but this assumes we do not have any catalyst poison (as CO) on the anode side. Butler-Volmer's equation (1) is implemented with an iterative loop to find the value of the overvoltage, using Tafel's approximation as an initial value for the iterative algorithm[1]. A scheme of the model is provided in figure 2.

A preliminary analysis was run to establish the influence of diffusion transients on the response of fuel cells. The results indicated diffusion transients in the order of 0.01–0.1 seconds, which is faster than the control bandwidth of interest[2]. Furthermore, the gas concentration at the reaction sites has a significant effect only when near to the mass-transfer limit, where oxygen cannot diffuse fast enough from bulk to the reaction surface. Because of these considerations, the model will assume that diffusion transients settle instantaneously, and also that all partial-pressure profiles are linear from bulk to reaction site. The model has later been extended to incorporate the simulation of the anodic overvoltage, but this will be useful only when a reliable simulation of the dynamics of CO poisoning in PBI fuel cells has been developed; without CO poisoning, the anodic overvoltage is negligible for most practical purposes.

The activation overvoltage η of an electrode can be calculated for a given reaction current density i_r and an exchange current density i_0, according to the Butler-Volmer equation:

$$i_r = i_0 \left(\mathrm{e}^{\alpha \frac{nF}{RT} \eta} - \mathrm{e}^{-(1-\alpha) \frac{nF}{RT} \eta} \right) \qquad (1)$$

The reversible potential E^{rev} can be found with well-known thermodynamic data, and the ohmic loss is $r_{cell}\, i$. The cell voltage is then found as:

$$V = E^{rev} - \eta - r_{cell}\, i \qquad (2)$$

During transients, the reaction current density i_r is different from the current density i, which we calculate dividing the current in the circuit by the fuel cell's area. Looking at the following differential equation [1], it is obvious to see that the difference $i - i_r$ is actually the driving force of the transient behaviour of the activation overvoltage:

$$\dot{\eta} = \frac{i - i_r}{C} \qquad (3)$$

[1] Using Tafel as an initial approximation accelerates the algorithm signifi cantly.

[2] We are assuming that the bandwidth of interests begins from time constants of 0.2 seconds, as is typical for automotive applications [9].

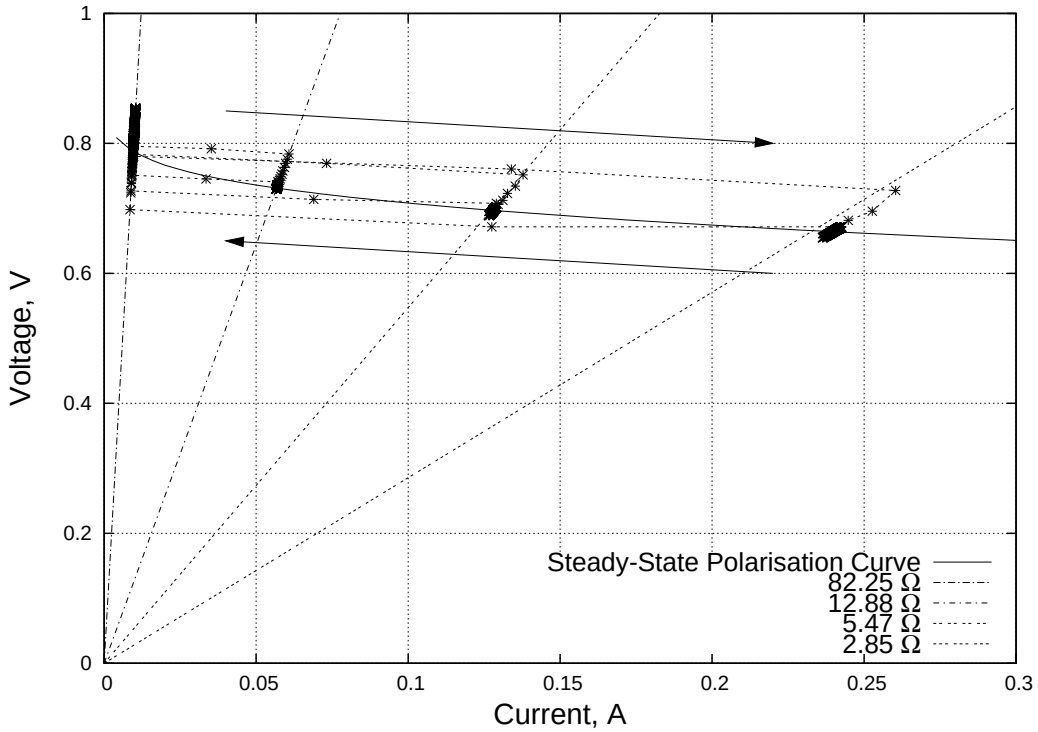

Figure 1: Operating points' path in the V-I diagram after step changes in the external circuit's resistance, starting from 82.25 Ω and switching back. The arrows indicate the path in the I-V plan.

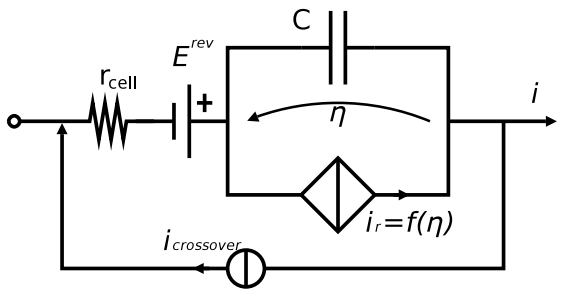

Figure 2: Diagram of the cathode-only fuel-cell model.

This is the only differential equation that we will be considering in order to compute the transient of the fuel cell. The cell's load in the model is generally allowed to vary with time, and is described by a function in the form $I = f(V,t)$.

The model can be expressed in an electrical-circuit diagram, as shown in figure 2. There, one can see the internal resistance r_{cell}, the reversible potential E^{rev}, the capacitor C and its voltage η. The bipole in parallel with the capacitor is a nonlinear voltage-controlled current generator, that enforces the Butler-Volmer law, and imposes a current i_r as a function of η (and many other parameters). This last bipole is often also modelled as a nonlinear resistance [10], or a linearized value in an area of interest. Incidentally, the ideal generator E^{rev} and the resistance r_{cell} in series with it can be viewed as a Thevenin equivalent circuit. Finally, a crossover current density (representing either electronic conductivity of the membrane or permeation of hydrogen molecules) is modelled with a current generator, and given a constant value; PBI fuel cells usually have small values for crossover current density, and a typical value is 5 A/m^2.

The actual integration of differential equation 3 is not very simple, since i_r is a function of many parameters, and also of η itself, through the Butler-Volmer equation (1). An iterative loop is therefore necessary to calculate i_r at all integration steps, and this is the major computational cost of the simulation. The resulting layout for the fuel-cell model in Simulink is shown in figure 3.

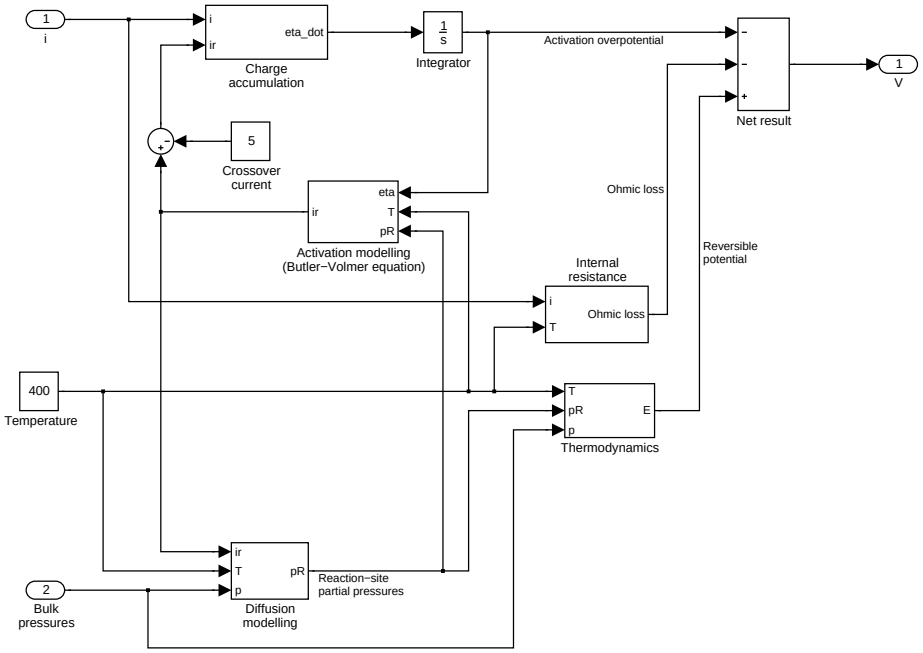

Figure 3: The Simulink implementation of the fuel-cell model, with only the cathode overvoltage being modeled.

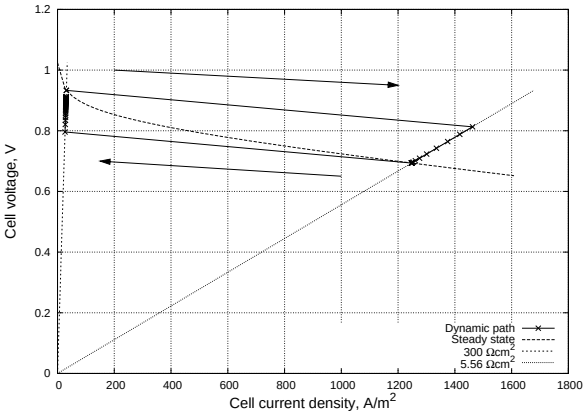

Figure 4: A typical output of the model: a simulation of a transient from a steady-state operating point to a new value of the external resistance, and back. Assumed temperature is 150 °C. The markers are spaced by 0.01 s.

MODEL RESULTS AND INSIGHTS

The cause of the sudden "kick" in the dynamic path diagram, as can be seen in the simulation in figure 4 and in experimental results in figure 1, is caused by the simple fact that the operating point *must* always lie on the load's characteristic, when the load is purely resistive. It is possible to determine to *which coordinates* on the load's characteristic the operating point will jump, considering that the activation overvoltage η varies *continuously* with time; when a step change in the outer load happens at time t_0, η will therefore be the same for times t_0^+ and t_0^-.

Using the load characteristic as the model's input has allowed to simulate real laboratory results, and has given the possibility of simulating the implementation of MOSFETs as manipulated variables in control of fuel cells. Pulse-width modulation (PWM) has also been implemented.

Looking at figure 4, it is clear that the drawn part of the polarization curve is closer to the characteristic of the higher resistance, when distance is measured along the i axis. Since $\dot{\eta}$ is proportional to the distance between the intersections of the instantaneous characteristic with the polarization curve and the external resistance along the i axis, i.e. $i - i_r$, it follows that the transient to the lower resistance will be faster than the one coming back, because of the higher val-

ues of $i - i_r$ along that path; this is confirmed by the experimental measurement shown in figure 1.

An analytic expression for the time constants has been found. Assuming that C and r_{cell} are constant, and that functions $V = \Psi(i)$ (the external load's characteristic) and $\eta(i_r, \ldots)$ are given, the time "constant" τ depends essentially on i and i_r:

$$\tau(i, i_r) = \frac{C}{\left(r_{cell} + \frac{\mathrm{d}\Psi}{\mathrm{d}i}\Big|_i\right)^{-1} + \left(\frac{\mathrm{d}\eta}{\mathrm{d}i_r}\Big|_{i_r}\right)^{-1}} \quad (4)$$

Considering the basic expression of the voltage of a fuel cell (2), and looking at figure 4, it is evident that the instantaneous characteristic at a given steady-state point stays at higher voltages than the polarization curve when moving to higher values of current density, and, conversely, at lower voltages for lower values of current density; in other words, a step change in the external resistance always results in some overshoot. Under these assumptions, a perfect step change in power output can in theory be obtained if the controller manages to steer the fuel cell properly.

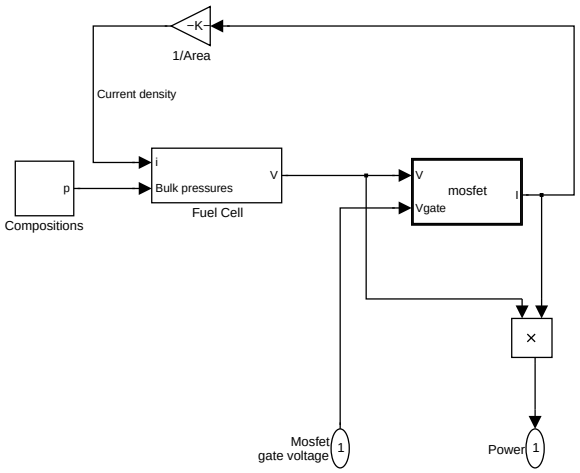

Figure 5: The structure of the fuel cell-MOSFET system in Simulink. The control input is the MOSFET's gate voltage, while the output is the power produced by the cell.

PID CONTROL

Using Skogestad's PID-tuning rules [11], a simple PI controller was devised to operate a fuel cell so that its power output would match the power necessary for an appropriately-scaled standard driving cycle. The control system operates by manipulating the gate voltage of a MOSFET transistor, which acts like a "valve" for the cell's power output. Measuring the error in watts, and using the parameters of a IRF1404 MOSFET by International Rectifier Inc., the parameters of the controller were found to be $k = 0.191$ and $\tau_I = 0.4\,\mathrm{s}$.

Several driving cycles were implemented, and in figure 6 the results for the European Urban Driving Cycle (ECE 15) are shown. It can be seen that the cell is definitely slower at following the reference signal at low power values, which correspond to high voltages and low activation overvoltages. This is consistent with the formula for time constants (4) that was found previously.

It should be remarked that this synthesis has not yet accounted for disturbances, since a satisfactory model for the main disturbance in the process, CO poisoning, is not yet available; it would therefore be

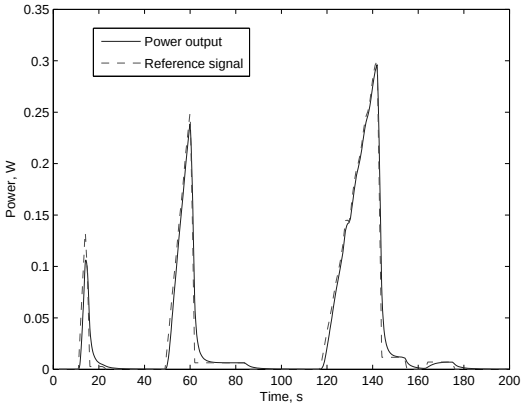

Figure 6: Simulation of a feedback-controlled fuel cell trying to deliver the power required by the ECE 15 standard driving cycle.

possible to make the cell model follow the reference almost perfectly if the proportionality constant in the controller were set to $k = \infty$. Of course this would just be a simulation trick. A more thorough synthesis will be possible when the effect of disturbances will have been estimated.

IMPEDANCE MEASUREMENTS

Given the model developed above, it is important to obtain values for its parameters. Impedance measurements are a good way to achieve this, allowing visual assessment as well as more precise techniques as nonlinear regression to estimate, among other things, the internal resistance, the overvoltages and the capacitances of both cathode and anode.

Using measurements obtained directly by logging data from transients when changing the load in a certain way is not always a good idea, since these measurements are often clouded by other transients, such as temperature variations at the reaction sites due to the different reaction rate; this is especially true for PBI fuel cells.

Impedance tests are performed by keeping the fuel cell in a known condition of voltage, temperature, partial pressures in the inlet gases, and eventually other relevant state variables, and measuring its impedance at various frequencies. The impedance values can then be plotted in a Bode diagram or, more commonly, in a Nyquist diagram[3].

Model layout

In order to estimate the model parameters, it was necessary to reformulate the model in a way that would present the user a function $Z = f(\mathbf{X}, \Theta)$, where Z is the impedance (in general a complex number), $\mathbf{X}$ is the vector of states, and Θ is the vector of parameters. The model was reimplemented in C++, and an interface function to allow its use in OCTAVE was written[4].

This time, the model was a steady-state model, but included also the anode in the description of the fuel cell. Since most impedance measurements show a "tail" at the highest frequencies, an inductance has been added in series with the fuel cell, and can be considered a parameter of the model. The model scheme is shown in figure 7.

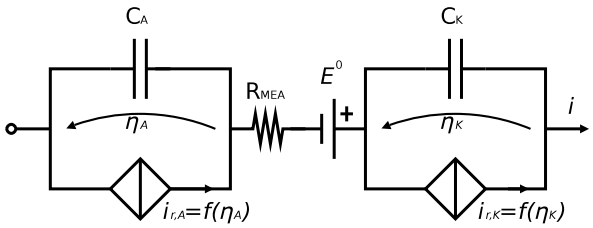

Figure 7: Diagram of the fuel-cell model used for impedance simulations.

Given this model, it is possible to develop the following formula for the impedance of the fuel cell:

$$\begin{aligned} \mathrm{Re}(Z) &= R_{cell} + \frac{R_a}{1+\omega^2 R_a^2 C_a^2} + \frac{R_c}{1+\omega^2 R_c^2 C_c^2} \\ \mathrm{Im}(Z) &= \omega L_{ext} - \frac{\omega R_a^2 C_a}{1+\omega^2 R_a^2 C_a^2} - \frac{\omega R_c^2 C_c}{1+\omega^2 R_c^2 C_c^2} \end{aligned}$$

where we have set, for ease of notation, $R_{\{a,c\}} = \eta_{\{a,c\}}/i_{r,\{a,c\}}$.

The compiled function showed excellent performance, calculating up to 4,000 values of impedance per second on a 2.4 GHz computer. Some values calculated by the function are shown in figure 8.

Assuming these equations are valid, an impedance plot can used to easily estimate some properties just by eye inspection. For instance, it is obvious that, for $\omega \to 0$, $\mathrm{Im}(Z) = 0$ and $\mathrm{Re}(Z) = R_{cell} + R_a + R_c$. When, instead, $\omega \to \infty$, $\mathrm{Re}(Z) = R_{cell}$. Fuel cells often show a similar pattern in impedance plots, with a large semicircle that represents the cathode, and a smaller one to represent the anode. The diameter of these semicircles is respectively R_c and R_a. Since we have defined these quantities to be the overvoltage divided by the reaction current at cathode and anode, and since the overvoltage has a very nonlinear dependence on the reaction current, it follows that these semicircles will vary greatly with the fuel cell's voltage. The presence of a crossover current will also be very influent, as it will cause overvoltage to be present even if there is no current moving through the outer circuit. In this latter case of open-circuit condition, the impedance plot degenerates into a vertical line (or, equivalently, a circle of infinite radius), with equations:

[3] It is common, for such Nyquist diagrams, to use an inverted ordinate axis.

[4] Writing a similar interface function to MATLAB is also possible.

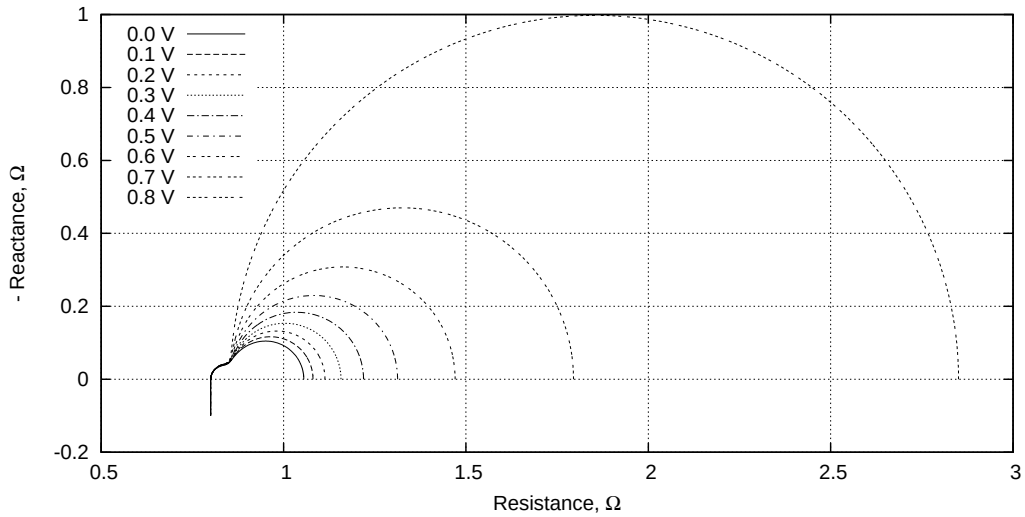

Figure 8: Nyquist plot of the impedance of a fuel cell at various voltages; the operating conditions and parameters are $p_{H_2} = 75\,\mathrm{kPa}$, $p_{O_2} = 21\,\mathrm{kPa}$, $C_a = 100\,\mathrm{F/m^2}$, $C_c = 500\,\mathrm{F/m^2}$, $T = 150\,^\circ C$, $L_{ext} = 1\,\mu\mathrm{H}$, crossover current $i_C = 300\mathrm{A/m^2}$.

$$\mathrm{Re}(Z) = R_{cell} \quad (5)$$

$$\mathrm{Im}(Z) = \omega L_{ext} - \frac{1}{\omega C_a} - \frac{1}{\omega C_c} \quad (6)$$

It should be noted that *Warburg impedance*, caused by diffusion phenomena, cannot be simulated by the model, since it was assumed for simplicity that the diffusion transient was infinitely fast. In experimental results, the Warburg impedance usually appears in the form of a small "tail" in the Nyquist plot in the lower range of frequencies, and more clearly so at high currents.

Finally, it can be demonstrated, by calculating the derivative, that the summit of the semicircles (assuming they can be isolated with reasonable precision) satisfies the equation:

$$\omega_{summit,\{a,c\}} = \frac{1}{R_{\{a,c\}} C_{\{a,c\}}} \quad (7)$$

RC has the dimensions of time, and is therefore often written τ in he literature.

These observations can be used to estimate the value of some parameters, in order to provide a more precise starting guess for a nonlinear regression algorithm for experimental values, which will be subject of further work.

Nyquist plots are also commonly used in control theory; in that context, the impedance can be viewed as the *transfer function* between current and voltage.

CONCLUSION

By using the characteristic of the circuit connected to a fuel cell as an input to a dynamic model, instead of more common inputs as current or voltage, it was possible to explain the shape of transients observed in a laboratory fuel cell, and to estimate their time constants. A simple PI controller has been synthesised, and it was observed that its performance was dependent on the power output of the fuel cell. In order to estimate the parameters of the dynamic model, the model was reimplemented in parametric form. The reimplemented model currently shows acceptable stability and good performance, and will soon be applied to data analysis.

ACKNOWLEDGEMENTS

Thanks to Helge Weydahl, Reidar Tunold, Børre Børresen and Frode Seland from the Department of Materials Technology of NTNU for construction of the fuel cell and of the resistance board, collaboration, suggestions and patience.

This work has received financial support from the Norwegian Research Council and Statoil AS.

REFERENCES

[1] M. Ceraolo, C. Miulli, A. Pozio, Modelling static and dynamic behaviour of proton exchange membrane fuel cells on the basis of electro-chemical description, Journal of Power Sources 113 (2003) 131–144.

[2] B. S. Kang, J.-H. Koh, H. C. Lim, Experimental study on the dynamic characteristic of kW-scale molten-carbonate fuel cell-systems, Journal of Power Sources 94 (2001) 51–62.

[3] C. N. Maxoulis, D. N. Tsinoglou, G. C. Koltsakis, Modeling of automotive fuel cell operation in driving cycles, Energy conversion and management 45 (2004) 559–573.

[4] K. Sundmacher, T. Schultz, S. Zhou, K. Scott, M. Ginkel, E. D. Gilles, Dynamics of the direct methanol fuel cell (DMFC): experiments and model-based analysis, Chemical Engineering Science 56 (2001) 333–341.

[5] S. Yerramalla, A. Davari, A. Feliachi, T. Biswas, Modeling and simulation of the dynamic behaviour of a polymer electrolyte membrane fuel cell, Journal of Power Sources 124 (2003) 104–113.

[6] Q. Li, R. He, J.-A. Gao, J. O. Jensen, N. J. Bjerrum, The CO poisoning effect in PEMFCs operational at temperatures up to 200 °C, Journal of the Electrochemical Society 150 (12) (2004) A1599–A1605.

[7] J. R. Macdonald (Ed.), Impedance Spectroscopy, emphasizing solid materials and systems, Wiley, 1987.

[8] R. L. Johansen, Fuel cells in vehicles, Master's thesis, Norwegian University of Science and Technology (2003).

[9] M. Soroush, Y. A. Elabd, Process systems engineering challenges in fuel cell technology for automobiles, in: AIChE Annual Meeting, 2004.

[10] P. R. Pathapati, X. Xue, J. Tang, A new dynamic model for predicting transient phenomena in a PEM fuel cell system, Renewable energy 30 (2005) 1–22.

[11] S. Skogestad, Simple analytic rules for model reduction and PID controller tuning, Journal of process control 13 (2003) 291–309.

Proceedings of ECOS 2005
Trondheim, Norway
June 20–22, 2005

Single-Level Strategy for the Optimal Synthesis/Design of a Hybrid SOFC-GT Power Plant

Francesco Calise and Massimo Dentice d' Accadia
DETEC-Università degli Studi di Napoli Federico II
P.le Tecchio 80- 80125 Naples . ITALY
frcalise@unina.it;dentice@unina.it

Laura Vanoli[1]
Dipartimento di Scienza degli Alimenti -Università degli Studi di Napoli Federico II
Via Università 100 - 80055 Portici (NA). ITALY
laura.vanoli@unina.it

Michael R. von Spakovsky
Center for Energy Systems Research - Department of Mechanical Engineering 0238
Virginia Polytechnic Institute and State University
Blacksburg. VA 24061. U.S.A.
vonspako@vt.edu

ABSTRACT

The detailed synthesis/design optimization of a hybrid Solid Oxide Fuel Cell - Gas Turbine (SOFC-GT) power plant is presented in this paper. The plant layout consists of the following principal components: an internal reforming SOFC, a steam-methane pre-reformer, a catalytic burner, a radial gas turbine, a centrifugal air compressor, a centrifugal fuel compressor, plate-fin heat exchangers, counter-flow shell and tube heat exchangers, and mixers. In the first part of the paper, the bulk-flow model used to simulate the plant is discussed. The off-design performance of the centrifugal compressors and radial turbine is determined using maps, properly scaled in order to match required mass flow rate and pressure ratio values. Compact heat exchangers are simulated using Colburn and friction factor correlations while for the SOFC, the cell voltage versus current density curves (i.e. polarization curves) are generated on the basis of the Nernst potential and overvoltages due to activation, Ohmic, and concentration losses using the Butler-Volmer, resistivity, and limiting current density equations, respectively. A SOFC configuration with internal reforming through anode re-circulation is chosen in order to avoid the use of an external heat recovery steam generator. Validation of the SOFC polarization curves is accomplished with data available from Siemens-Westinghouse. Both the steam-methane pre-reforming and internal reforming processes are modeled assuming the water-gas shift reaction to be equilibrium controlled and the de-methanization reactions to be kinetically controlled. Finally, a thermoeconmic plant and component model is developed by introducing capital cost functions for each plant component.

The whole plant is first simulated for a fixed configuration of the most important synthesis/design parameters in order to establish a reference design configuration. Next a synthesis/design optimization of the plant is carried out using a traditional single-level approach. These results and those for the synthesis/design optimization of the plant in general are presented in this paper.

1. Introduction

Solid Oxide Fuel Cells (SOFC) are considered one of the most promising technologies for power production in stationary applications [1]. Hybrid power plants based on SOFCs are expected to reach values of net electrical efficiencies higher than 70% [2-5]. As a consequence, much research in recent years on the analysis and design optimization of such systems has shown that the best way to use a SOFC in a hybrid power plant is to introduce the cell into a traditional Brayton cycle based on the gas turbine (GT) technology [6-10]. In fact, the usual temperature of streams exiting a SOFC is perfectly suitable for the Turbine Inlet Temperature (TIT) required by state-of-the-art-turbomachinery [4]. A great number of possible

[1] Corresponding author: Phone (+39) 081 253 93 32. Fax. (+39) 081 775 49 42. e-mail: laura.vanoli@unina.it

layouts for hybrid SOFC - GT plants have been proposed in the literature [1-10], which include combinations of SOFC stacks, heat exchangers, compressors, gas turbines, pre-reformers, mixers, heat recovery steam generators, and combustors in different arrangements. The performance of these plants have been investigated using a number of different techniques [11-17]. In this paper, mathematical optimization in what is called a single-level approach (e.g., see [18-20]) is used to determine the optimal synthesis/design of the configuration considered here. Detailed cost models are introduced for all components in order to establish a relationship between fuel and capital costs and the synthesis/design of the system and its components. Simulation of the system (plant), needed in order to evaluate the performance of the system and its components for given values of the synthesis/design variables, is based on a model previously developed by some of the authors [15-17]. However, a few of the simplifying assumptions used with respect to the original model are not employed here as is discussed in the following sections.

2. System Layout

Nowadays, at least four different types of SOFC are available (tubular, tubular "high power density", planar, and micro-tubular) [1-4]. In spite of the fact that such systems have been studied since the 1970s [1], until now only few prototypes have been developed and tested [1]. Siemens Westinghouse is probably one of the most important companies involved in the design and commercialization of hybrid SOFC-GT power plants [21]. This company has installed a 220 kWe hybrid tubular SOFC-GT system at the National Fuel Cell Research Center in California [1,21]. Results of a campaign of performance measurements indicate values of the design-point net electrical efficiency to be somewhat lower than the target (52% versus 57%) [1]. Furthermore, this particular system demonstrates the huge difficulties encountered in integrating a SOFC with a GT. As a result, much additional development is still required to develop this system further. Thus, an improvement of the coupling between traditional and innovative devices is not only mandatory but appears not to be necessarily straightforward [1-4]. In particular, the most stringent issue is to find a gas turbine suitable for this application [1]. On the basis of this experience, Siemens is now designing new hybrid plants in the range from 250 kWe to 1 MWe [1,21] since it is clear that the bigger the size of the plant is, the easier it is to find a GT suitable for the application [22].

In this paper, a 1.5 MWe hybrid power plant is investigated, based on an internal reforming tubular SOFC with an anode re-circulation tubular arrangement [1,2,4,10,17,22-25]. This configuration allows one to avoid the use of an expensive external heat recovery steam generator. In the present paper, the system is only analyzed at the design point. Thus, all components required for start-up and partial-load operation are not considered. Future work will also take into account partial-load operation by introducing time-dependent load curves.

The layout proposed for the hybrid plant is shown in Figure 1. It consists of a centrifugal air compressor (AC); a centrifugal fuel compressor (FC); a plate-fin, air-GT exhaust heat exchanger (HE); a plate-fin, fuel-GT exhaust heat exchanger (HE); a radial gas turbine (GT); mixers (M) for anode re-circulation, air by-pass, and pre-reforming bypass streams; a catalytic burner (C); an Internal Reforming Solid Oxide Fuel Cell (IRSOFC) Stack; a pre-reformer (PR); a counterflow air-SOFC exhaust heat exchanger (HRC); by-pass valves; an electrical generator; an inverter; and two water-exhaust gases, plate-fin heat exchangers (HE). The plant layout includes 31 streams or state points and 14 components.

The principle of operation can be summarized as follows:

- Air is compressed by the air compressor up to the fuel cell operating pressure. The air is then preheated in the plate-fin heat exchanger and brought to the cathode inlet of the SOFC stack (state point 18).
- Similarly, the fuel - natural gas - is compressed by the fuel compressor, preheated in the fuel-exhaust gas, plate-fin heat exchanger and then brought to the anode compartment of the stack (state point 1).
- Both fuel and air can by-pass the fuel cell, i.e. a certain amount of fuel flow can be brought directly to the combustor by-passing the electrochemical reaction occurring within the stack (state point 23), while excess air can be brought to the GT (state point 20).
- At the stack, fuel (state point 24) is mixed with the anode re-circulation stream (state point 5) in order to support the steam reforming reaction in the pre-reformer and in the anode compartment of the fuel cell. The mixture at state point 25 consists of methane and steam. Thus, in the pre-reformer the first step in the fuel reforming process occurs. The energy required to support the pre-reforming reaction

is derived from the hot stream at state point 26. The unreacted fuel at state point 2 is involved in the internal reforming reaction within the anode compartment of the SOFC stack. Here it is converted into the hydrogen that participates in the electrochemical reaction.

- On the cathode side, air is first preheated by a virtual counter-flow heat exchanger and then brought into the annulus (air pipe) of the SOFC where, at the three-phase boundary, the cathode electrochemical reaction occurs [1-4].
- The electrochemical reactions, occurring in the fuel cell, produce DC electrical and thermal energy [1-4]. The first of these is converted into AC current by the inverter; the latter is used by the internal reforming reaction and to heat-up the fuel cell stack.
- Anode and cathode outlet streams meet on the top of the fuel cell, entering the combustor. Un-reacted fuel and depleted air participate in the combustion reaction within the catalytic burner.
- The high energy flow rate at state point 8 is first used to preheat air in the counter-flow heat exchanger and then to supply energy to the pre-reforming reaction. This stream at state point 21 enters the gas turbine.
- The expansion in the GT supplies mechanical power and then electric power. The GT outlet stream (state point 10) energy flow rate can be used to preheat both fuel and air flows. Any residual thermal energy left over is available for cogeneration purposes, using two water-gas, plate-fin heat exchangers.

3. Plant Model

The model used to simulate the behavior of the system is a typical lumped-parameter model based on the following assumptions: one-dimensional flow; steady state; no gas leakage; negligible heat losses to the environment; negligible kinetic and gravitational terms. The model is implemented in a computer code developed by the authors and described in detail in [15-17]. However, as indicated previously, a few of the simplifying assumptions with respect to the original version are no longer employed here, and cost models are added for thermoeconomic evaluations. Finally, a genetic algorithm (GA) [26] is used for optimization purposes.

The code, including 50 subroutines, was written in MATLAB and is based on a number of built-in functions, tools and externally-developed subroutines [27-28]. When possible, equations are solved sequentially, avoiding large non-linear algebraic systems. However, in many cases, the solution of a non-linear system is necessary and is accomplished using the STRSCNE tool [24].

In the version developed for thermoeconomic optimization purposes, the model includes 19 fixed parameters (see Table 1) and 48 synthesis /design (S/D) decision variables (see Table 2). Fixed parameters, such as the net electric power production, remain constant during the optimization. The S/D decision variables can vary in a given range (usually ±30% of the starting value, or "initial" value) and represent the independent variables in the synthesis/design optimization of the system. Obviously, only some of the possible sets of values for the S/D decision variables correspond to actual feasible syntheses/designs. The others are automatically rejected by the code. For any acceptable synthesis/design, the model calculates all energy, entropy, and exergy flow rates entering and leaving each component and the capital cost of each device. In the following, the most significant aspects of the model will be described briefly as will the improvements introduced with respect to the first version of the simulation code found in [15-17].

3.1 Electrochemical Model

The modeling of the electrochemical phenomena is based on the model described in [15-17] and validated with data provided by Siemens Westinghouse [29]. The model is implemented with a number of routines for calculating the open circuit reversible voltage and activation, ohmic and concentration losses. As to the later, the model has been improved by introducing average diffusion coefficients and experimental formuli to calculate the limiting current density [30]. In order to validate the model, the polarization curves generated by the code are compared with experimental ones for different values of operating pressure, temperature, and chemical composition of the inlet streams. Results show that the lumped-parameter model achieves errors lower than 5%.

3.2. Calculation of Thermophysical and Transport Properties

As previously stated, natural gas is assumed as the input fuel with a typical Italian composition [15]. Air is assumed as the oxidant while reforming and combustion reactions occurring within several components of the plant generate four additional substances: CO, CO_2, H_2O, and

H_2. Calculation of the enthalpies, entropies, and physical and chemical exergies is based on the assumption of ideal gas, temperature-dependent specific heats and IAPWS-IF97 equations [31]. In order to calculate pressure drops, values of viscosity, conductivity, and density values are needed too. The viscosities and conductivities of each pure substance are calculated through empirical relationships [32]. Values for mixtures are calculated on the basis of Wilke's law and the inter-collision factor. Values for specific heat and density are calculated on the basis of the ideal gas model and Dalton's law.

3.3. Turbomachinery Model

Three turbomachines are included in the plant under study: an air compressor, fuel compressor, and gas turbine. These devices have been investigated in detail in order to match their requirements with those coming from the fuel cells [33]. Maps, available from the archives of the GSP software and Gasturb, are used, to describe the mass flow rate versus pressure ratio curves for different values of rotor speed. Since no map matches the values of mass flow rate and pressure ratios required by the components of the plant under investigation, all the maps are properly scaled. In particular, a centrifugal compressor (based on an ASME 95-GT-79 map) and a radial turbine (based on a NASA-CR-174646 map) are selected. Such devices show large ranges for both mass flow rate and pressure ratios so that a large number of operating points fall within the feasible region of these maps. Axial turbines, for example, can work only very close to the design mass flow rate so that it is very difficult to find a real operating point in case of a partial load.

Map scaling factors are considered as design decision variables and the code dynamically scales all the maps for each iteration of the optimization procedure. Each map is corrected on the basis of the values of inlet temperature and pressure [22,24,32]. In case of the air or fuel compressor, the inlet condition corresponds to the environmental one whereas the temperature and pressure of the GT inlet stream can vary considerably as a consequence of a change in the design and operating parameters. Consequently, once the GT corrected map is fixed, the un-corrected changes at each iteration of the procedure are updated.

The air compressor and gas turbine are assumed to be coupled on a single shaft. As a consequence they must have the same rotor speed. The speed of the fuel compressor can vary independently. The maps are used to calculate isentropic efficiencies and pressure ratios as a function of mass flow rates, rotor speed, and inlet conditions. Thus, the outlet conditions of the components are calculated as well as energy, entropy, and exergy balances. The use of maps dramatically restricts the feasible operating region of the plant. Thus, whenever the operating point of a turbomachine falls outside a map or the GT outlet pressure calculated is lower than the environmental one, the solution is rejected.

3.4. Heat Exchanger Model

In order to simulate the heat transfer between the air flowing through the fuel cell air tube and the stream coming from inside the stack (state point 8), a virtual counterflow tube-in-tube heat exchanger is implemented in the stack [1-4, 10,17,22-25]. This heat exchange is modeled on the basis of previous models [15,16], improved to take into account the dependence of thermophysical and transport properties on temperature and pressure drop models.

In general, heat exchanger (HE) performance is modeled using the ε – NTU [34,35] method, taking into account that specific heats, global heat transfer coefficients, and outlet pressures depend on temperature. The geometric model for the heat exchangers is derived from [36,37]. Pressure drops and overall heat exchange coefficients are calculated on the basis of experimental relations given for Colburn and friction factors [36]. In this calculation outlet temperatures and pressures must be calculated iteratively by embedded loops and calls to a number of routines for the evaluation of thermophysical and transport properties. As a consequence, this calculation is very time-consuming.

3.5. Pre-Reformer Model

In theory. SOFCs can be directly fed with natural gas, since the reforming process can be supported inside the stack [1-4, 10,14-17,22-25]. In practice, a pre-reforming process is always required. Two things in particular must be taken into account, namely, that i) the natural gas includes a small fraction of complex hydrocarbons that must be cracked before entering the cell; and ii) if the cell is fed directly with methane, the bottom of the SOFC tube would not be able to produce any voltage, since there would be no hydrogen available for the electrochemical reaction. A goal of the study presented here is that

of quantifying the optimum percentage of pre-reformed fuel particularly since there is a lack of clarity on this issue in literature, varying from 30% to 60%, depending on the author.

The pre-reformer unit consists of a number of tubes located inside a shell and filled with a particular catalyst [38,39]. The reformate gas flows inside these tubes. Hot gases, coming from the combustor, flow externally, supplying the thermal energy needed to support the process. In fact, the energy provided by the exothermic shift reaction is not sufficient for the endothermic demethanization or reforming process [38,39].

In order to simulate this component, the heat-exchange problem must be solved and the chemical composition of the outlet flows must be evaluated as well, taking into account both equilibrium and kinetics [40-42]. The heat-exchange problem cannot be solved with conventional techniques (log-mean or ε – NTU), since chemical reactions occur within the cold fluid. Therefore, an appropriate model is developed based on the differential form of the energy balance equation, integrated along the reformer tubes to calculate the outlet temperatures starting from a set of inlet ones and taking into account the rate at which both the reforming and shift reactions occur in the cold stream. For the shift reaction, it is assumed that chemical equilibrium is controlling whereas for the reforming reaction both equilibrium and kinetic calculations are performed in order to ascertain the actual state of the reaction[2]. The calculation of the demethanization rate is based on equations available in the literature [38-42] and can be directly related to the geometric and thermodynamic parameters of the pre-reformer [38,39]. Once the demethanization rate within the pre-reformer is known, the diameter and length of the pre-reformer tubes are calculated to match this rate. Average temperatures are used to calculate all pre-reformer kinetic and equilibrium properties.

These last set of calculations are usually very complex and time consuming, since a number of nonlinear systems of equations must be solved at each iteration. However, it can be simplified by assuming that the demethanization reaction is only ruled by the kinetics. At usual pre-reforming operating temperatures, the methane rate reaction is higher than 90%. In the present work, this value is assumed to range between 20% and 60%: in such a range, the process is ruled by kinetics [1-4].

[2] In fact in subsequent work, the authors have handled this more straightforwardly by using rate modified expressions for both reactions which incorporate the equilibrium constraints directly into the rate expressions (see [43-45]).

3.6. Internal Reforming Model

Reformate gas, coming from the pre-reformer, is rich in methane but also consists of hydrogen, carbon monoxide, carbon dioxide, some nitrogen, and steam. Usually, the CO concentration is relatively high, since the conversion rate of the shift reaction is very small and even sometimes negative. As a consequence, it is mandatory to design the fuel cell anode compartment to support both the demethanization and shift reactions within the fuel cell. To do this, it must be equipped with a proper catalyst in the same region of the SOFC stack where the anode electrochemical reaction takes place. As a consequence, three chemical reaction processes (demethanization, shift, and electrochemical) must be taken into account simultaneously. The unknowns are the methane, carbon monoxide, and hydrogen conversion rates. These variables are calculated on the basis of the shift equilibrium, kinetic/equilibrium, and electrochemical kinetics. From the solution of this strongly non-linear algebraic system of three equations, chemical compositions at both the anode and cathode outlet can be calculated. All properties and constants are evaluated at the SOFC outlet equilibrium temperature. It is assumed that temperature gradients along the cell radius are negligible as a consequence of the high conductivity and low thickness of materials used in SOFC technology [15, 16].

3.7. Combustor, Mixers, Inverter, and Electrical Generator Models

Mixers were modeled on the basis of simple energy and mass balances while the combustor reactions are assumed to be driven to completion within the catalytic burner [15, 16]. Its outlet chemical composition and energy rates are calculated by using mole, mass and energy balances. Empirical functions were introduced in order to simulate the efficiency of the inverter and the electrical generator as a function of their operational parameters.

3.8. Solution Approach

Due to the complexity of the models developed here and implemented in MATLAB™, the calculation of a single operating point is usually a very involved and time-consuming task.

Furthermore, whatever optimization approach is used, the search for an optimum set of synthesis/design decision variable values requires the calculation of a very high number of possible syntheses/designs for the plant. Thus, a great deal of effort has been spent by the authors to speed-up the calculation procedure by lightening the number of sub-functions, replacing the graphic interface, and introducing more efficient algorithms than available in MATLAB™ for the solution of integrals and non-linear systems of equations. This effort has resulted in a reduction by a factor of 4 of the computational time.

In addition, since the code is written in MATLAB™, which is not designed for the solution of strongly non-linear systems, the code has been written to the greatest extent possible using a sequential logic, which avoids having to solve a system or a set of systems of equations simultaneously. Nonetheless, in certain cases this is unavoidable and an iterative procedure is needed for some sub-systems of the plant. In particular, four main nested loops are introduced, respectively, to calculate: i) the chemical composition at state point 3; ii) the pressure and temperature at the outlet of the SOFC stack; iii) the temperature, pressure, and chemical composition at the outlet of the GT; and iv) the fuel flow rate. Since the solutions of the pre-reformer and stack subsystems require knowledge of all inputs, including the chemical composition at state point 3 and the latter depends on the characteristics and operating conditions of the stack and the GT, a guess value for chemical composition at state point 3 is fixed, starting from the value of the mass flow rate at state point 5. In other words, the re-circulation ratio is calculated in order to match the value of the steam-to-carbon ratio required to avoid carbon deposition in the anode compartment of the fuel cell. The mixer, pre-reformer, and stack are then solved followed by the anode outlet chemical composition. This is then compared with the initial guess and the iteration proceeds until the convergence criterion on the partial pressures of all the chemical constituents is satisfied.

The preceding iterative calculation requires the temperature of the stack, which must be iteratively calculated by the second loop mentioned above. Furthermore, both the preheating heat exchangers require the chemical composition, temperature, and pressure at state point 10. These can be calculated iteratively, by means of the third loop mentioned above. Finally, the fuel flow rate is iteratively calculated until the required net electrical power is achieved.

4. Cost Model

For any given set of values for the synthesis/design decision variables, corresponding to a feasible operating point of the plant, the estimated investment cost is calculated as the sum of the costs of all components provided by proper cost models. For the turbomachinery, the capital cost (C_{GT}, US$) is usually evaluated on the basis of the maximum power (P_{GT}, kW) produced. In particular, for the gas turbine, the cost function proposed by [46] is used such that

$$C_{GT} = \left(-98.328 \ln\left(P_{GT}\right) + 1318.5\right) \cdot P_{GT} \tag{1}$$

For the centrifugal compressors, the capital costs ($C_{compressor}$, US$) are calculated by interpolating data from manufacturers as a function of the maximum power ($P_{compressor}$, kW) required and using information provided in recent papers [47,48]. On this basis, the following function is employed:

$$C_{compressor} = 91562 \cdot \left(\frac{P_{compressor}}{445}\right)^{0.67} \tag{2}$$

The estimated capital costs of the compact heat exchangers (C_{HE}, US$) is related to their mass (m_{HE}, kg) [36] as described by

$$C_{HE} = 111.6\left(m_{HE}\right)^{0.95} \tag{3}$$

For the counterflow heat exchanger, the capital cost is determined on the basis of literature data [49] such that

$$C_{HEC} = 130\left(\frac{A_{HE}}{0.093}\right)^{0.78} \tag{4}$$

The cost of the SOFC stack is not calculated at present market values, since the technology is still sometime away from full commercialization. Thus, the cost is estimated with reference to market studies in which the expected cost for the case of a significant increase in production volumes is assumed. A detailed work performed by [50] relates the SOFC capital cost to the active area and the operating temperature (T_{cell}. °C). Furthermore, the electric energy produced by the SOFC must be filtered by an inverter, whose cost is not negligible and should, therefore, be taken into account. This cost depends primarily on the net power production (P_{cell}, kW) of the stack. Thus, for both of these costs, the following expressions are used:

$$C_{SOFC} = \left(n_{cells}\pi D_{cell} L_{cell}\right)\cdot\left(2{,}96\cdot t_{cell} - 1907\right) \quad (5)$$

$$C_{inverter} = 100000\cdot\left(\frac{P_{cell}}{500}\right)^{0.70} \quad (6)$$

The SOFC system also consists of a pre-reformer, whose cost is calculated on the basis of its catalyst volume (V_{PR}, m^3) and the finned exchange area ($A_{PR,fin}$, m^2) [38,39,49] which is related the number, diameter, and length of tubes. Thus, based on these references and updating the functions with literature data, the following cost functions are used.

$$C_{PR} = 130\left(\frac{A_{PR,fin}}{0.093}\right)^{0.78} + 3240\left(V_{PR}\right)^{0.4} + 21280.5\, V_{PR} \quad (7)$$

Finally, the capital costs for auxiliary devices such as combustors, mixers, and bypass valves are calculated as a fixed percentage (10%) of the stack cost. The counter-flow heat exchanger cost is given by [50].

$$C_{aux,SOFC} = 0.10 C_{SOFC} \quad (8)$$

The overall life cycle cost for owning and operating the plant is assumed as the objective function to be minimized. It is defined as the sum of the fuel and capital costs evaluated on a yearly base. The following assumptions are made: 10 year lifetime; an amortization rate of 5%; and 8760 operating hours per year. The cost avoided through the use of waste heat is also considered, assuming a reference efficiency for conventional furnaces of 90%. Thus, the objective function to be minimized is as follows:

$$f = \frac{\sum_{i}^{components} C_i}{7.72} + c_{fuel}\dot{V}_{fuel}(8760) - \frac{c_{fuel}\dot{Q}_{rec}(8760)}{9.59\,(0.90)} \quad (9)$$

5. Optimization Strategy

The optimization of the hybrid plant investigated is a very complex problem due to the non-linearity of the models, the high degree of coupling between components, the high number of synthesis/design decision variables, and the continuous and discrete nature of these variables. Furthermore, the performance maps for the compressors and turbine, introduced to develop a more realistic model, dramatically restrict the region of feasible solutions, leading to a large number of simulations with infeasible operating points. To more effectively deal with these difficulties, a Genetic Algorithm (GA) is used [26]. However, such an approach is very calculation intensive and, unlike with a gradient-based approach, is unable to mathematically establish a Kuhn-Tucker point, since it is a heuristic method. However, this can be circumvented by coupling the two types of optimization approaches together as is done in [18,20,36-38,44,45], with the former doing the general search of the optimization solution space and the latter helping narrow the search to a particular Kuhn-Tucker point or boundary. This is not done here due to software integration issues which have yet to be addressed. Nonetheless, the GA in and of itself is a very powerful tool to handle strongly non-linear, non-continuous, mixed integer optimization problems and is, thus used here.

Finally, the initial population for the GA is set at four times the number of decision variables while the number of generations is set to a very high value (700). The GA is stopped when no improvements of the objective function for a number of generations is observed.

6. Case Study: Results and Discussion

This single-level optimization strategy (i.e. as opposed to a multi-level decomposition optimization strategy) was run on PIV 3.2 GHz. 1Gb RAM and required more than a month of continuous execution to arrive at an optimum solution[3]. More than 200 generations were required to get close to the optimum design configuration.

As mentioned above, the values for the fixed parameters in this case study are summarized in Table 1 while Table 2 lists the synthesis/design decision variables, their initial guesses, their optimum values, and their ranges. In addition, Tables 3 and 4 summarize the most important thermodynamic information about plant performance for the initial and optimum syntheses/designs, respectively. By comparing the optimum and initial syntheses/designs, it can be seen that the initial configuration has been dramatically modified by the optimizer, resulting in an improvement of the objective function of about 21% (see Figure 2). This is a very remarkable result, if one takes into account how small the region of feasible solutions investigated actually is.

[3] Note that the term "optimum" is used here in an engineering sense and not a strictly mathematical sense since as already indicated the GA is unable to indicate whether or not the final point found is indeed a Kuhn-Tucker point. Nonetheless, it is the "best" or "optimum" that is found after an exhaustive search of the solution space and tens of thousands of cycle calculations.

The optimization made some important adjustments to the heat exchanger and turbomachinery syntheses/designs. The latter, in particular, is due to the complex relationship, which exists, between the turbomachinery and the fuel cell stack. Initial maps of turbomachinery are dramatically scaled, since the optimum scaling factors are found to be close to the boundary of the optimal search region. In fact, a special adjustment is made to the fuel compressor map, since a non-optimal design of this component could result in remarkable inefficiencies due to the lamination of the fuel before entering the stack. Conversely, the optimizer does not significantly change the value initially assumed for the rotor speed. This result depends on the shape of turbomachinery maps, since their design point is set very close to the minimum rotor speed. For higher rotor speeds, the code produces unfeasible points or very low values of the isentropic efficiency.

Table 2 also shows that both optimum by-pass mass flow rates are very close to the initial values. This implies that the optimum configuration corresponds to by-pass valves (state points 23 and 31) almost completely closed. Obviously, during part-load operation the management of such by-pass valves will be very useful for controlling both stack and GT inlet temperatures.

SOFC geometric parameters are also remarkably changed. The initial synthesis/design corresponds to a very low value of the current density at the design point. This allows the stack to achieve a very high potential but results in higher capital costs, since a higher number of tubes with greater length and diameters are required. The optimization procedure dramatically reduces the cell active area by decreasing the number, diameter, and length of tubes.

The optimum demethanization rate in the pre-reformer is also very low. High values of the demethanization rates are not useful, since the cell can support almost the entire reforming process internally. Higher values of the area and volume used for pre-reforming imply higher costs, which can be avoided because the same process can be realized within the fuel cell stack.

Table 2 also shows the optimum value of geometric variables of compact heat exchangers. Since no useful data in the literature for initial guesses for these variables was available, a number of values were simply picked. As can be seen from the table, the values selected are very far from the optimum. Furthermore the optimum value of the first design variable listed in Table 2 is very close to 1, as would be expected. In fact, the nominal mass flow rate was set in order to have both pre-heaters "balanced".

Finally, the optimum value of the pre-reformer demethanization rate is greater than 57% while the optimal efficiency of the plant at the design point is 67.5%, with a plant investment cost of 1.36×10^6 US$. The same plant, at the initial design point achieves a slightly greater 67.9% net electrical efficiency. However, the capital cost is 2.5×10^6 US$, which means that the optimum plant represents a 46% improvement in cost.

Figures 3, 4, and 5, respectively, show component costs, exergy destruction rates, and energy flows determined for the initial synthesis/design. For this case, the capital cost is mainly due to the fuel cell stack, as expected. The costs of the turbomachinery are much higher than those for the heat exchangers, especially for the GT. The exergy destruction rate is primarily due to the combustor, the SOFC, the GT, and the HEWA. The inefficiency of the turbomachinery (GT and compressors) is mainly caused by a non-ideal coupling so that at the initial design point, the turbomachinery does not achieve its highest values of isentropic efficiency. Finally, a very significant irreversibility is due to the heat exchange within the gas to water heat exchangers, caused by very high temperature differences.

After optimization (see Figures 6, 7, and 8), the role of the stack is reduced, since there is a greater share of the power required and produced by the turbomachinery. As a consequence, the SOFC capital cost decreases and that of the turbomachinery increases. Furthermore, in reducing the active area of the cell, its inefficiency increases remarkably. This loss in efficiency is compensated by a lower investment cost, leading to a better value of the system level objective.

8. Conclusions

The optimization described in this paper shows that the design of a hybrid SOFC-GT power plant must focus an all its components, paying special attention to their coupling. The typical mistake of optimizing only the stack as an isolated device should be avoided, since inefficiencies in the turbomachinery and in the balance of plant can be significant. Furthermore, the perspective of a full commercialization of Solid Oxide Fuel Cells is expected to lower their capital costs so that this component will not necessarily be the most expensive in the plant. This increases the importance of investigating the

plant as a whole by analyzing its behaviour at both design and part-load operation.

As a further development of this work, a decomposition strategy (multi-level optimization approach) is also being applied to this same system. It is based on the ILGO/DILGO methods proposed by Munoz and von Spakovsky [38, 39], Rancruel [44], and Rancruel and von Spakovsky [45] and is being applied in order to compare results, accuracy, and computational times to those obtained with the single-level approach used here. Results for these optimizations will be discussed in future papers.

References

[1] Singhal, S.C., Kendall, K., 2003, *High temperature Solid Oxide Fuel Cells*, Elsevier.

[2] Larminie, J., Dicks, A., 2004*, Fuel cell system explained*, John Wiley & sons LTD.

[3] Benjamin, T. G., Camera, E. H., Marianowski, L. G., 1995, *Handbook of fuel cell performance*, Institute of Gas Technology.

[4] *Fuel cell handbook (sixth edition)*, 2002, U.S. Departement of Energy.

[5] *Fuel cell technology handbook*, 2002, Gregors Hoogers, editor.

[6] Palsson, J., Selimovic, A., Sjunnesson, L., 2000, "Combined solid oxide fuel cell and gas turbine systems for efficient power and heat generation", *Journal of Power Sources* vol. 86, pp. 442-448.

[7] Kimijima, S., Kasagi, N., 2002, "Performance evaluation of gas turbine – fuel cell hybrid micro generation system", *Proceedings of ASMETURBO EXPO 2002*, June 3-6, Amsterdam, The Netherlands.

[8] Bae, B. H., Sohn., J. L., Ro, S. T,. 2003, "Thermodynamic modeling and performance analysis of a power generation system based on the solid oxide fuel cell", *Proceedings of ASME* Conference on *Fuel Cell Science, Engineering and Technology*, April 21-23, Rochester. New York. USA.

[9] Inui, Y. , Yanagisawa, S., Ispida, T., 2003, "Proposal of high performance SOFC combined power generation system with carbon dioxide recovery", *Energy Conversion and Management*, vol. 44, pp. 597–609.

[10] Campanari, S., 1998, "Power plants based on Solid Oxide Fuel Cells combined with gas turbine cycles," Ph.D. dissertation, Politecnico di Milano, Milano.

[11] Bedringas, K. W., Ertesvag, I. S., 1997, "Exergy analysis of solid oxide fuel cell systems". *Energy: The International Journal*, vol. 22, 403-412.

[12] Dunbar, W. R., Lior N. ,Gaggioli R., 1991, "Combining fuel cells with fuel-fired power plants for improved exergy efficiency". *Energy: The International Journal*, vol. 16, 10, pp. 1259-1274.

[13] Dunbar, W. R., Lior, N., Gaggioli., R., 1993, "The effect of the fuel-cell unit size on the efficiency of a fuel-cell-topped Rankine Cycle". *ASME J. Energy Resources Technology*, vol. 115, pp. 105-107.

[14] Chan, S. H., Low, C. F. , Ding, O. L., 2002, "Energy and exergy analysis of a simple solid – oxide fuel cell power system.", *Journal of Power Sources*, vol. 103, pp.188-200.

[15] Calise F. , Dentice d'Accadia M.,. Palombo A., Vanoli, L , 2004, "Simulation and exergy analysis of a hybrid SOFC – Gas Turbine System. part I: description of the model", *17th International Conference on Efficiency. Costs. Optimization. Simulation and Environmental Impact of Energy and Process Systems*, Gunajuato, Mexico, 7-9 July.

[16] Calise F., Dentice d'Accadia M., Palombo A., Vanoli, L., 2004, "Simulation and exergy analysis of a hybrid SOFC – Gas Turbine System, part II: Results and Discussion," *17th International Conference on Efficiency. Costs. Optimization. Simulation and Environmental Impact of Energy and Process Systems*, Gunajuato. Mexico 7-9 July.

[17] Calise F. , Dentice d'Accadia M.,. Palombo A., Vanoli, L., Vanoli, R., 2004, "Modelling, simulation and exergy analysis of a hybrid SOFC - Gas Turbine System". *3rd International Symposium Energy and environment 2004*, Sorrento, 30th September to 2nd October.

[18] Muñoz, J. R., von Spakovsky, M. R., 2001, "A The Use of Decomposition Approach for the Large Scale Synthesis/Design Optimization of Highly Coupled, Highly Dynamic Energy Systems," *International Journal of Applied Thermodynamics*, March, vol. 4, no. 1.

[19] Frangopoulos, C.A., von Spakovsky, M. R., Sciubba, E., 2002, "A Brief Review of Methods for the Design and Synthesis Optimization of Energy Systems," *International Journal of Applied Thermody-*

namics, ICAT, Istanbul, Turkey, December, vol. 5, no. 4.

[20] Rancruel, D. F., von Spakovsky, M. R., 2003, "Decomposition with Thermoeconomic Isolation Applied to the Optimal Synthesis/Design of an Advanced Fighter Aircraft System," *International Journal of Thermodynamics*, ICAT, Istanbul, Turkey, September, vol. 6, no. 3.

[21] www.fuelcells.org

[22] Costamagna, P., Magistri, L., Massardo, A. F., 2001," Design and part-load performance of a hybrid system based on a solid oxide fuel cell reactor and a micro gas turbine", *Journal of Power Sources*, vol. 96, pp. 352-368.

[23] Campanari, S., 2002, "Carbon dioxide separation from high temperature power plants", *Journal of Power Sources*, vol. 112, pp. 273-289.

[24] Campanari, S., 2001, "Full load and part load performance prediction for integrated sofc and microturbine systems", *Journal of Power Sources*, vol. 96, pp. 352-368.

[25] Campanari, S., 2001, "Thermodynamic model and parametric analysis of a tubular SOFC module", *Journal of Power Sources*, vol. 92, pp. 26-34.

[26] MOOLENI genetic algorithm software, 2004, LENI, Ecole Polytechnique Fédérale de Lausanne, Lausanne, Switzerland.

[27] Bellavia, S., Macconi, M., Morini, B., 2002, "An affine scaling trust region method approach to bound-constrained nonlinear systems," *Applied Numerical Mathematics*, accepted for publication.

[28] Bellavia, S., Macconi, M., Morini, B., 2002, "STRSCNE: A Scaled Trust Region Solver for Constrained Nonlinear Equations". Technical Report.

[29] Singhal, S. C., 1997, "Recent progress in Tubular Solid Oxide Fuel Cell Technology," *Fifth International Symposium on Solide Oxide Fuel Cells*.

[30] Marechal, F., Favrat, D., Palazzi, F., Godat, J., 2004, "Thermoeconomic modeling and optimization of fuel cell systems," *Fuel Cell Research Symposium*, ETH Zürich, March.

[31] http://www.iapws.org/newform.htm

[32] *Chemical Properties Handbook*, 1999, McGraw Hill, pp. 531-556.

[33] Chan, S. H., Ho, H. K., Tian, Y., 2003, "Modeling for part load operation of solid oxide fuel cell-gas turbine hybrid power plant", *Journal of Power Sources*, vol. 114, pp. 213-227.

[34] Kakac, S., Liu, H., 1998, *Heat Exchanger Selection, Rating, And Thermal Design*, CRC Press, Boca Raton, Florida

[35] Kays, W. M., London, A. L., 1998, *Compact Heat Exchangers*, Krieger Publishing Company, Florida, 3rd edition.

[36] Rancruel, D. F., 2003, "A decomposition strategy based on thermoeconomic isolation applied to the optimal synthesis/design and operation of an advanced fighter aircraft system," M.S. thesis, advisor: M. R. von Spakovsky, Virginia Polytechnic Institute and State University, Blacksburg, VA.

[37] Muñoz, J. R., 2000, "Optimization strategies for the synthesis/design of highly coupled. highly dynamic energy systems," Ph.D. dissertation, advisor: M. R. von Spakovsky, Virginia Polytechnic Institute and State University, Blacksburg, VA.

[38] Georgopoulos, N., 2001, "Application of a decomposition strategy to the optimal synthesis/design and operation of a fuel cell based total energy system," M.S. thesis, advisor: M. R. von Spakovsky, Virginia Polytechnic Institute and State University, Blacksburg, VA.

[39] Oyarzabal, B., 2001, "Application of a decomposition strategy to the optimal synthesis/design of a fuel cell sub-system," M.S. thesis, advisor: M. R. von Spakovsky, Virginia Polytechnic Institute and State University, Blacksburg, VA.

[40] Zanfir, M., Gavrilidis, A., 2003, "Catalytic combustion assisted methane steam reforming in a catalytic plate reactor". *Chemical Engineering Science*, vol. 58, pp. 3947 – 3960.

[41] Gallucci, F., Paturzo, L. , Basile, A. , 2004, "A simulation study of the steam reforming of methane in a dense tubular membrane reactor", *International Journal of Hydrogen Energy*, vol. 29, pp. 611 – 617.

[42] Xu, J., Froment, G. F., 1989, "Methanes-steam reforming: methanation and water-gas shift: I. Intrinsic kinetics", *AlXhE Journal*.

[43] Rancruel, D. F., von Spakovsky, M. R., 2004, "Investigation of the control strategy development using an integrated model of a SOFC based APU under transient conditions," *International Mechanical Engineering Congress and Exposition – IMECE'2004*, ASME Paper No. 62372, N.Y., N.Y., November.

[44] Rancruel, D. F., 2005, "Dynamic synthesis/ design and operational/control optimization approach applied to a solid oxide fuel cell

based auxiliary power unit under transient conditions," Ph.D. dissertation, advisor: M. R. von Spakovsky, Virginia Polytechnic Institute and State University, Blacksburg, VA.

[45] Rancruel, D. F., von Spakovsky, M. R., 2005, "Development and application of a dynamic decomposition strategy for the optimal synthesis/design and operational/ control of a SOFC based APU under transient conditions," *International Mechanical Engineering Congress and Exposition – IMECE'2005*, ASME, N.Y., N.Y., November, in preparation.

[46] Traverso, A., Massardo, A., Logorio, G., Cazzola, W., 2004, "WIDGET-TEMP: a novel web-based approach for thermoeconomic analysis and optimization of conventional and innovative cycles", ASME paper 2004-GT-54115, N.Y., N.Y.

[47] Chiesa, P., Consonni, S., Kreutz, T. G., Williams, R. H., 2003, "Co-production of Hydrogen. Electricity and CO_2 from Coal using Commercially-Ready Technology", *Second Annual Conference on Carbon Sequestration*, Washington. May 5-8.

[48] www.matche.com

[49] Bohem, R. F., 1987, *Design Analysis of Thermal Systems*, John Wiley and Sons.

[50] Chen, T.P., Wright, J.D., Krist, K., "SOFC system analysis", GRI study.

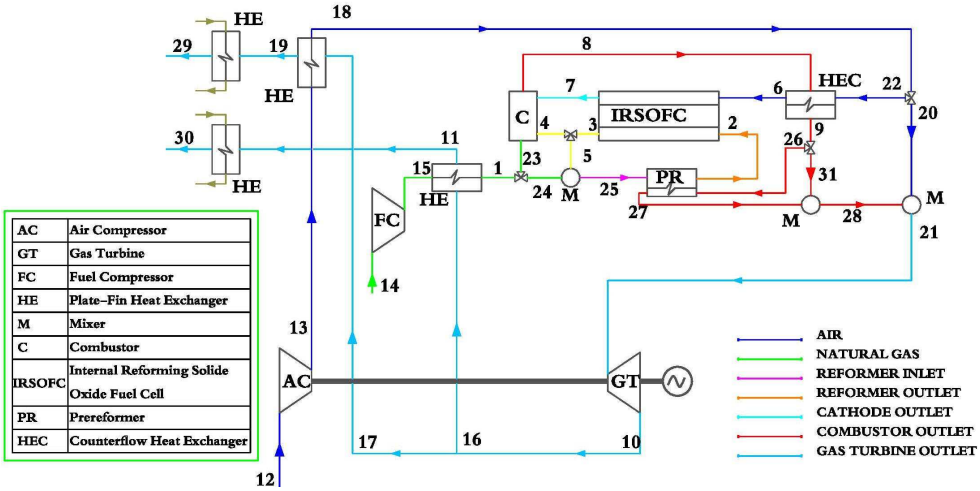

Figure 1. Plant layout.

Table 1. Fixed parameters and their values.

n	*Description*	*Unit*	*Guess Value*
1	Net electric power production	MW	1.5
2	Steam to Carbon Ratio	/	2.0
3	Fuel Utilization factor	/	0.85
4	Max SOFC pressure gradient	bar	0.6
5	Max SOFC temperature gradient	℃	60
6	Pre.reformer tube thickness	m	0.0001
7	Max TIT	℃	1250
8	Combustor efficiency	/	0.98
9	Fuel Cost	US$/Nm3	0.20
10	Plate fin Exchange area density	m2/m3	1204
11	HE Fin Conductivity	W/m K	35
12	HE wall-Fin Conductivity	W/m K	35
13	HE Fin Thickness	m	0.000152
14	Water inlet temperature	° C	60
15	Water outlet temperature	° C	80
16	Anode thicknes	cm	0.01
17	Cathode thickness	cm	0.22
18	Electrolite thickness	cm	0.004
19	Interconnections thickness	cm	0.0085

Table 2. Synthesis/design (S/D) decision variables and their values.

n	*Description*	*Unit*	*Guess Value*	*Min Value*	*Max Value*	*Opt. Value*
1	Ratio of actual to nominal mass flow rate at point 16	-	1.00E+00	0.00E+00	1.00E+00	*1.00E+00*
2	Fuel Compressor rotor speed	rpm	4.00E+04	3.80E+04	4.50E+04	*4.07E+04*
3	Mass flow rate scaling factor fuel compressor	-	0.00E+00	-2.00E-01	2.00E-01	*1.58E-01*
4	Pressure ratio scaling factor fuel compressor	-	0.00E+00	-2.00E-01	2.00E-01	*6.85E-02*
5	Cold-side length air-gas HE	m	1.50E+00	1.05E+00	1.95E+00	*1.05E+00*
6	Hot-side length air-gas HE	m	1.50E+00	1.05E+00	1.95E+00	*1.07E+00*
7	Cold-side plate spacing air-gas HE	m	6.35E-03	4.45E-03	8.26E-03	*4.59E-03*
8	Hot-side plate spacing air-gas HE	m	6.35E-03	4.45E-03	8.26E-03	*4.45E-03*
9	Number of plates air-gas HE	-	2.50E+02	1.75E+02	3.25E+02	*1.75E+02*
10	Cold-side fin spacing air-gas HE	m	6.35E-03	4.45E-03	8.26E-03	*8.04E-03*
11	Hot-side fin spacing air-gas HE	m	4.00E-03	2.80E-03	5.20E-03	*2.84E-03*
12	Cold-side length fuel-gas HE	m	5.00E-01	3.50E-01	6.50E-01	*4.75E-01*
13	Hot-side length fuel-gas HE	m	5.00E-01	3.50E-01	6.50E-01	*3.60E-01*
14	Cold-side plate spacing fuel-gas HE	m	6.35E-03	4.45E-03	8.26E-03	*4.98E-03*
15	Hot-side plate spacing fuel-gas HE	m	6.35E-03	4.45E-03	8.26E-03	*7.82E-03*
16	Number of plates fuel-gas HE	-	9.00E+00	6.30E+00	1.17E+01	*9.00E+00*
17	Cold-side fin spacing fuel-gas HE	m	6.35E-03	4.45E-03	8.26E-03	*7.72E-03*
18	Hot-side fin spacing fuel-gas HE	m	4.00E-03	2.80E-03	5.20E-03	*4.23E-03*
19	Cold-side length water-gas(air) HE	m	6.00E-01	4.20E-01	7.80E-01	*7.70E-01*
20	Hot-side length water-gas(air) HE	m	6.00E-01	4.20E-01	7.80E-01	*7.76E-01*
21	Cold-side plate spacing water-gas (air) HE	m	6.35E-03	4.45E-03	8.26E-03	*4.54E-03*
22	Hot-side plate spacing water-gas (air) HE	m	6.35E-03	4.45E-03	8.26E-03	*4.90E-03*
23	Rotor speed air compressor- GT	rpm	4.00E+04	3.80E+04	4.50E+04	*3.90E+04*
24	Number of plates water-gas (air) HE	-	1.00E+02	7.00E+01	1.30E+02	*1.30E+02*
25	Cold-side fin spacing water-gas (air) HE	m	6.35E-03	4.45E-03	8.26E-03	*4.61E-03*
26	Hot-side fin spacing water-gas (air) HE	m	4.00E-03	2.80E-03	5.20E-03	*2.94E-03*
27	Cold-side length water-gas (fuel) HE	m	3.00E-01	2.10E-01	3.90E-01	*2.85E-01*
28	Hot-side length water-gas (fuel) HE	m	3.00E-01	2.10E-01	3.90E-01	*2.77E-01*
29	Cold-side plate spacing water-gas (fuel) HE	m	6.35E-03	4.45E-03	8.26E-03	*6.50E-03*
30	Hot-side plate spacing water-gas (fuel) HE	m	6.35E-03	4.45E-03	8.26E-03	*4.60E-03*
31	Number of plates water-gas (fuel) HE	-	1.00E+01	7.00E+00	1.30E+01	*7.00E+00*
32	Cold-side fin spacing water-gas (fuel) HE	m	6.35E-03	4.45E-03	8.26E-03	*4.54E-03*
33	Hot-side fin spacing water-gas (fuel) HE	m	4.00E-03	2.80E-03	5.20E-03	*2.93E-03*
34	SOFC air injection tube diameter	m	7.00E-03	4.90E-03	9.10E-03	*4.91E-03*
35	SOFC air injection tube length	m	1.00E-01	7.00E-02	1.30E-01	*9.46E-02*
36	Pre-reformer tube length	m	2.20E-01	1.54E-01	2.86E-01	*1.67E-01*
37	pre-reformer demethanization factor	-	3.50E-01	2.50E-01	6.00E-01	*2.75E-01*
38	SOFC tube diameter	m	1.56E-02	1.09E-02	2.03E-02	*1.09E-02*
39	SOFC tube length	m	1.50E+00	1.05E+00	1.95E+00	*1.05E+00*
40	SOFC number of tubes	-	1.50E+04	1.05E+04	1.95E+04	*1.05E+04*
41	Mass flow rate ratio (point 20 versus point 18)	-	0.00E+00	0.00E+00	5.00E-01	*0.00E+00*
42	Mass flow rate ratio (point 23 versus point 1)	-	0.00E+00	0.00E+00	5.00E-01	*4.89E-04*
43	Pre-reformer tube diameter	m	1.56E-02	1.09E-02	2.03E-02	*1.33E-02*
44	Mass flow rate scaling factor air compressor	-	0.00E+00	-2.00E-01	2.00E-01	*-1.86E-01*
45	Pressure ratio scaling factor air compressor	-	0.00E+00	-2.00E-01	2.00E-01	*9.24E-02*
46	Mass flow rate scaling factor GT	-	0.00E+00	-2.00E-01	2.00E-01	*-1.73E-01*
47	Pressure ratio scaling factor GT	-	0.00E+00	-2.00E-01	2.00E-01	*1.40E-01*
48	Air mass flow rate	kg/s	1.76E+00	1.23E+00	2.28E+00	*1.87E+00*

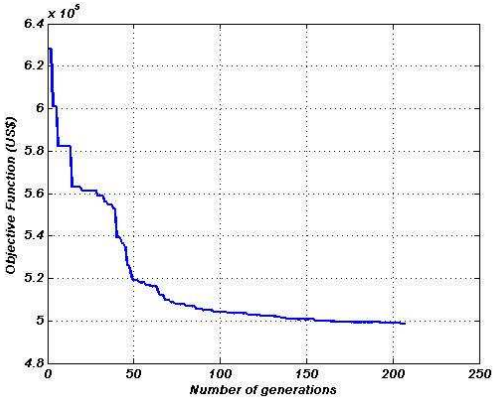

Figure 2. Genetic algorithm optimization process.

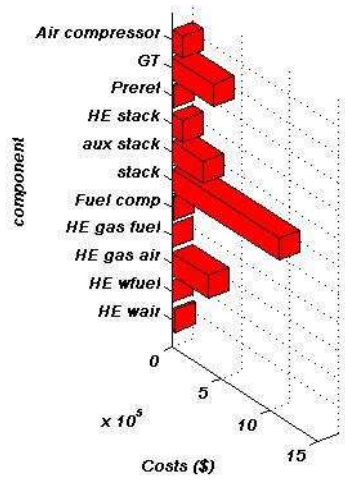

Figure 3. Costs of the components for the initial synthesis/design.

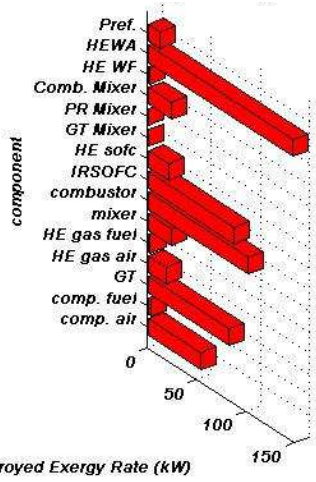

Figure 4. Exergy destruction rate for the initial synthesis/design.

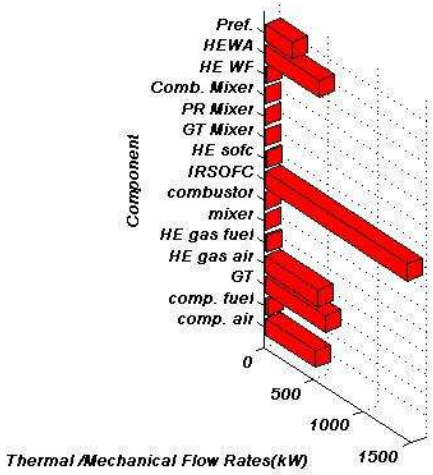

Figure 5. Mechanical and thermal flow rates for the initial synthesis/design.

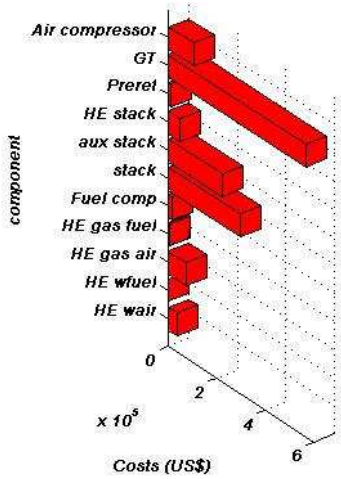

Figure 6. Costs of the components for the optimum synthesis/design.

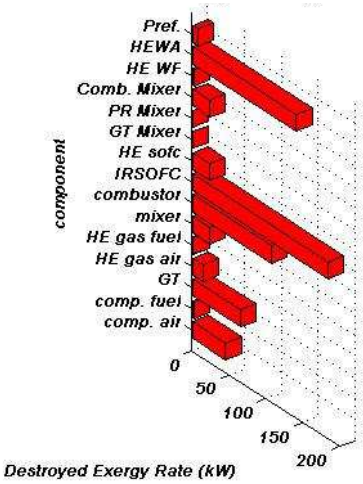

Figure 7. Exergy destruction rates for the optimum synthesis/design.

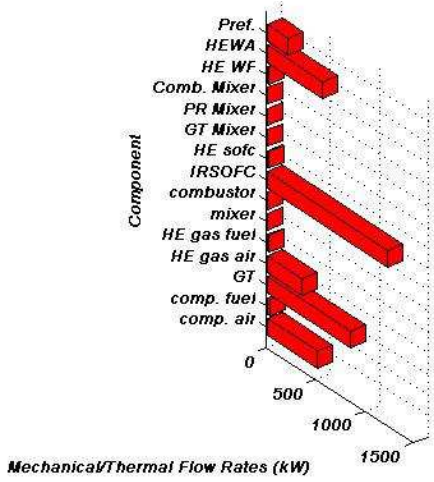

Figure 8. Mechanical and thermal flow rates for the optimum synthesis/design.

Table 3. Thermodynamic properties at various state points for the initial synthesis/design.

Key-point	Temp. (℃)	Press.(bar)	Enthalpy Flow Rate (kW)	Entropy Flow Rate (kW)	Physical Exergy Flow Rate (kW)	Chemical Exergy Flow Rate (kW)	Molar Flow Rate (kmol/s)	Mass Flow Rate (kg/s)	H_2O molar fraction	CO molar fraction	H_2 molar fraction	O_2 molar fraction	N_2 molar fraction	CO_2 molar fraction	CH_4 molar fraction
1	327.63	8.37	40	0.04588	27	2312.4	0.0028216	0.045942	0	0	0	0	0.02	0	0.98
2	827.99	8.37	464.19	0.68516	314.86	2856.3	0.014095	0.28282	0.34286	0.09639	0.22323	0	0.008678	0.18665	0.14219
3	907.99	8.37	650.97	0.8586	444.73	857.53	0.018103	0.43962	0.56663	0.054784	0.095535	0	0.0067564	0.2763	2.96E-06
4	907.99	8.37	300.18	0.39593	205.08	395.44	0.0083481	0.20273	0.56663	0.054784	0.095535	0	0.0067564	0.2763	2.96E-06
5	907.99	8.37	350.78	0.46267	239.65	462.1	0.0097553	0.2369	0.56663	0.054784	0.095535	0	0.0067564	0.2763	2.96E-06
6	546.84	7.76	1076.4	1	767	8	0.064677	2	0	0	0	0.21	0.79	0	0
7	907.99	7.76	1693.4	2	1198.1	10	0.059777	2	0	0	0	0.14524	0.85476	0	0
8	1045.7	7.76	2317	3	1646.6	56	0.067499	2	0.081935	0	0	0.11929	0.75781	0.040968	0
9	981.37	7.76	2162.1	3	1527.6	56	0.067499	2	0.081935	0	0	0.11929	0.75781	0.040968	0
10	515.12	1.08	1087.5	3	441.21	56	0.067499	2	0.081951	0	0	0.11928	0.75779	0.040976	0
11	293.01	1.08	15	0.046599	4	1	0.0016501	0.046739	0.081951	0	0	0.11928	0.75779	0.040976	0
12	25	1.00	47	0.44096	0	8	0.064677	2	0	0	0	0.21	0.79	0	0
13	297.74	7.77	574.1	0.59149	482.2	8	0.064677	2	0	0	0	0.21	0.79	0	0
14	25	1.00	2	0.010729	0	2312.4	0.0028216	0.045942	0	0	0	0	0.02	0	0.98
15	243.97	8.37	28	0.024628	22	2312.4	0.0028216	0.045942	0	0	0	0	0.02	0	0.98
16	516.97	1.08	27	0.064276	11	1	0.0016501	0.046739	0.081951	0	0	0.11928	0.75779	0.040976	0
17	516.97	1.08	1064.9	3	432.8	54.171	0.065849	2	0.081951	0	0	0.11928	0.75779	0.040976	0
18	470.99	7.76	921.4	1	671.14	8	0.064677	2	0	0	0	0.21	0.79	0	0
19	354.02	1.07	717.67	2	230.42	54.171	0.065849	2	0.081951	0	0	0.11928	0.75779	0.040976	0
20	470.99	7.76	0	0	0	0	0	0	0	0	0	0	0	0	0
21	891.34	7.75	1948.2	2	1366.5	56	0.067499	2	0.081935	0	0	0.11929	0.75781	0.040968	0
22	470.99	7.76	921.4	1	671.14	8	0.064677	2	0	0	0	0.21	0.79	0	0
23	327.63	8.37	0.019566	2.25E-05	0.013259	1	1.38E-06	2.25E-05	0	0	0	0	0.02	0	0.98
24	327.63	8.37	40	0.045858	27	2311.3	0.0028202	0.045919	0	0	0	0	0.02	0	0.98
25	738.71	8.37	390.74	0.58792	259.43	2757	0.012576	0.28282	0.43955	0.042498	0.07411	0	0.0097264	0.21433	0.21978
26	981.37	7.76	2162.1	3	1527.6	56	0.067499	2	0.081935	0	0	0.11929	0.75781	0.040968	0
27	891.34	7.75	1948.2	2	1366.1	56	0.067499	2	0.081935	0	0	0.11929	0.75781	0.040968	0
28	891.34	7.75	1948.2	2	1366.1	56	0.067499	2	0.081935	0	0	0.11929	0.75781	0.040968	0
29	63	1.04	124.52	0.82372	12	54.171	0.065849	2	0.081951	0	0	0.11928	0.75779	0.040976	0
30	114.28	1.06	6	0.027506	1	1	0.0016501	0.046739	0.081951	0	0	0.11928	0.75779	0.040976	0
31	981.37	7.76	0	0	0	0	0	0	0	0	0	0	0	0	0

Table 4. Thermodynamic properties at various state points for the optimum synthesis/design.

Key-point	Temperature (℃)	Pressure (bar)	Entalpy Flow Rate (kW)	Entropy Flow Rate (kW)	Physical Exergy Flow Rate (kW)	Chemical Exergy Flow Rate (kW)	Molar Flow Rate (kmol/s)	Mass Flow Rate (kg/s)	H_2O molar fraction	CO molar fraction	H_2 molar fraction	O_2 molar fraction	N_2 molar fraction	CO_2 molar fraction	CH_4 molar fraction
1	352.18	8.2808	44.256	0.052838	29.305	2343.9	0.00286	0.046568	0	0	0	0	0.02	0	0.98
2	827.42	8.2808	470.29	0.69589	318.82	2896.7	0.014347	0.28627	0.33926	0.099779	0.22927	0	0.0086291	0.18449	0.13857
3	907.42	8.2807	658.43	0.87019	449.33	867.65	0.018323	0.44498	0.56662	0.054714	0.095539	0	0.0067564	0.27637	2.93E-06
4	907.42	8.2807	303.62	0.40127	207.2	400.09	0.0084493	0.20519	0.56662	0.054714	0.095539	0	0.0067564	0.27637	2.93E-06
5	907.42	8.2807	354.81	0.46893	242.14	467.56	0.0098741	0.23979	0.56662	0.054714	0.095539	0	0.0067564	0.27637	2.93E-06
6	558.62	7.6786	1161.6	1.4313	823.97	8.8128	0.068259	1.9693	0	0	0	0.21	0.79	0	0
7	907.42	7.6786	1792.3	1.9918	1266.3	10.268	0.063299	1.8106	0	0	0	0.1481	0.8519	0	0
8	1041.2	7.6786	2426.4	2.8397	1722	55.628	0.071119	2.0159	0.07882	0	0	0.12274	0.75903	0.03941	0
9	961.64	7.6786	2225.4	2.682	1568.1	55.628	0.071119	2.0159	0.07882	0	0	0.12274	0.75903	0.03941	0
10	513.01	1.0629	1139.6	2.7609	458.78	55.63	0.071119	2.0159	0.078824	0	0	0.12273	0.75903	0.039412	0
11	307.95	1.0616	20.188	0.062357	5.8823	1.6753	0.0021417	0.060707	0.078824	0	0	0.12273	0.75903	0.039412	0
12	25	1	49.63	0.46538	0	8.8128	0.068259	1.9693	0	0	0	0.21	0.79	0	0
13	296.2	7.6811	602.69	0.62485	505.52	8.8128	0.068259	1.9693	0	0	0	0.21	0.79	0	0
14	25	1	2.4402	0.010875	0	2343.9	0.00286	0.046568	0	0	0	0	0.02	0	0.98
15	256.01	8.2811	30.155	0.028387	22.494	2343.9	0.00286	0.046568	0	0	0	0	0.02	0	0.98
16	513.01	1.0629	34.319	0.083143	13.816	1.6753	0.0021417	0.060707	0.078824	0	0	0.12273	0.75903	0.039412	0
17	513.01	1.0629	1105.3	2.6778	444.97	53.955	0.068978	1.9552	0.078824	0	0	0.12273	0.75903	0.039412	0
18	465.41	7.6786	960.45	1.1749	699.29	8.8128	0.068259	1.9693	0	0	0	0.21	0.79	0	0
19	352.47	1.0583	747.59	2.1716	238.18	53.955	0.068978	1.9552	0.078824	0	0	0.12273	0.75903	0.039412	0
20	465.41	7.6786	0	0	0	0	0	0	0	0	0	0	0	0	0
21	872.68	7.6652	2003.8	2.4967	1402	55.628	0.071119	2.0159	0.07882	0	0	0.12274	0.75903	0.03941	0
22	465.41	7.6786	960.45	1.1749	699.29	8.8128	0.068259	1.9693	0	0	0	0.21	0.79	0	0
23	352.18	8.2808	0.085214	0.00010174	0.056426	4.5132	5.51E-06	8.97E-05	0	0	0	0	0.02	0	0.98
24	352.18	8.2808	44.171	0.052736	29.248	2339.4	0.0028545	0.046478	0	0	0	0	0.02	0	0.98
25	744.26	8.2808	398.99	0.59958	264.73	2790.4	0.012729	0.28627	0.43955	0.042444	0.074114	0	0.0097264	0.21439	0.21978
26	961.64	7.6786	2225.4	2.682	1568.1	55.628	0.071119	2.0159	0.07882	0	0	0.12274	0.75903	0.03941	0
27	872.68	7.6652	2003.8	2.4967	1401.7	55.628	0.071119	2.0159	0.07882	0	0	0.12274	0.75903	0.03941	0
28	872.68	7.6652	2003.8	2.4967	1401.7	55.628	0.071119	2.0159	0.07882	0	0	0.12274	0.75903	0.03941	0
29	66.103	1.0371	135.79	0.87961	11.582	53.968	0.068978	1.9552	0.07884	0	0	0.12273	0.75901	0.03942	0
30	146.58	1.0403	9.442	0.041074	1.4819	1.6757	0.0021417	0.060707	0.07884	0	0	0.12273	0.75901	0.03942	0
31	961.64	7.6786	0	0	0	0	0	0	0	0	0	0	0	0	0

Proceedings of ECOS 2005
Trondheim, Norway
June 20–22, 2005

Process design; thermal and chemical systems

Proceedings of ECOS 2005
Trondheim, Norway
June 20–22, 2005

Modular simulation and Thermoeconomic Analysis of a Multi-Effect Distillation desalination plant

P. Fiorini[1], E. Sciubba
Mechanical and Aeronautical Engineering Department
University of Roma 1 "La Sapienza"

ABSTRACT
A model for the thermodynamic and thermoeconomic simulation of a MED desalination plant has been developed. As the code is embedded in a modular simulator, CAMEL©, it is relatively easy to use it for analyses of different plant configurations. CAMEL itself had been developed by the Mechanical and Aeronautical Engineering department of the University of Roma1, "La Sapienza". In the course of the present project, a model for the MED stage was included in the code library: this allows for a stage level description of the MED plant and for a more correct detailed identification of the plant losses and inefficiencies. The model can simulate all different MED configurations: here, only the parallel flow case was investigated. The thermodynamic model of each component is based on mass and energy balance criteria, and the results have been judiciously compared with literature data. Particular attention was devoted to the development of the thermoeconomic MED stage model: due to the presence of multiple products, the cost allocation is not trivial, and its degree of arbitrariness is even more dependent on the Designer's choices than it is usually in thermoeconomic analysis. A model for cost allocation across product and by-products has been proposed. The model allows individuating different strategies for plant design and optimisation. Applications of the model are exposed referring to a possible plant solution and design constrains.

Symbol		*Description*	**Units**
A	=	Heat exchange area	m^2
BPE	=	Boiling Point Elevation	K
D	=	Tube diameter	m
e	=	Specific exergy	kJ/kg
GOR	=	Gain output ratio (dimensionless)	-
h	=	Specific enthalpy	(kJ/kg)
Kl	=	Thermal conductivity	(kW/m/K)
m	=	Mass flow rate	(kg/s)
n	=	Revolutions per minutes	-
NEA	=	Non Equilibrium Allowance	(K)
LMTD	=	Logarithmic medium temperature difference	(K)
p	=	Pressure	(kPa)
PST	=	Function correlating the water saturation temperature with the liquid pressure	
PL	=	Pressure losses	(kPa)
Pr	=	Prandlt Number	
Q	=	Heat flow	(kW)
Re	=	Reynolds Number	
s	=	Brine salt concentration	(g/kg)
TBT	=	Top brine temperature	(K)
U	=	Overall heat exchange coefficient	(kW/m2/K)

[1] Corresponding Author: vox: +39 06 3048 6854; fax: +39 06 3048 4811; e-mail: paolo.fiorini@casaccia.enea.it

x	=	Mass steam quality	kg/kg
φ	=	Orifice contraction coefficient	-
η	=	Efficiency	-
η_m	=	Mechanical efficiency	-
μ	=	Viscosity	N/(sm)

1.INTRODUCTION

The interdependence between cost and efficiency has always been recognized qualitatively. It can be quantified by correctly correlating plant investment and primary resource consumption. Basing this correlation on exergy criteria, it is possible to determine the cost of the exergy unit of the final product. This methodology commonly recognized as “thermoeconomy" accounts both for the exergy destruction of the process, which is an index of the plant efficiency, and plant capital cost. The interest in formulating this interaction quantitatively with regard to seawater distillation applications dates back to the sixties [1,2,3,4]. In the last twenty years the usefulness of this concept was acknowledged by a large number of scholars and the development is still continuing today. Thermoeconomy is able to pinpoint and quantify energy inefficiencies, the possibility of systematically generating insight towards improvement, and the ease of its application in automated optimal searches.

Such an analysis is ideally suited for the concept of a modular code: on this basis, CAMEL has been provided of proper subroutines for the thermoeconomic analysis of thermal processes. A thermoeconomic model of each component has been constructed in addition to the thermodynamic one, and the flow exergy cost has been introduced as a flow parameters.

Even if exergo-economic analysis has been originally proposed to analyze desalination plant, mainly in their combination to power plant (cogenerative configuration), it is not uniformly applied at industrial level for plant optimization, and current cost analysis procedures are based on conventional technical analyses, which do not account for the energy quality. Exergy criteria overtake this problem.

In this paper, a thermoeconomic analysis of the MED desalination process is proposed and applied to a cogenerating power plant in which the topping part is a combined cycle and the bottoming a MED desalination plant.

A sensitivity calculation was performed to assess the dependence of the desalted water cost on both the temperature and the exergy content of the feed stream of a MED desalination plant.

2. THERMO-ECONOMIC MODEL DESCRIPTION

The component library of CAMEL™ includes the elements required for the simulation of a MED desalination plant (MED stage, Pump, Heat Exchanger). The thermodynamic model is reported in the Appendix.

In this section we discuss the thermoeconomic model proposed for the MED stage. It is characterized by four inlet flows (the feed brine, the feed steam, the recycled brine and the recycle coming from the upstream stage) and 3 outlet flows (the steam produced, the recycle brine, the condensate) (fig. 1). To formulate a correct thermoeconomic model of such complex unit, it is necessary to break down the process in elementary sub-processes, which can be directly referred to elementary models [5]. With reference to fig. 1, the component has been divided into three sub-units: 1) an evaporator, 2) a flashing chamber fed by the recycle brine, 3) a flashing chamber fed by the condensate. The common objective of all the three sections is to produce steam. The stage costs can be split across component sub-units: Z1, Z2, Z3 are respectively the costs of sub-unit1 1, sub-unit 2, sub-unit 3.

Considering sub-unit 1 in isolation, the feed steam (a) is assumed as a fuel, the steam produced (c) as product, and the outlet brine (e) as by-product. The cost balance equation of this section is:

$$m_a * e_a * c_a + m_d * e_d * c_d + Z_1 = m_c * e_c * c_c + m_e * e_e * c_e + m_b * e_b * c_b \quad (1)$$

Two auxiliary equations are needed to close the system and they can be derived as follow:

1) since stream “a” is a “fuel” [5], the exergy costs of flows (a) and (b) can be assumed the same:

$$c_a = c_b \quad (2)$$

2) cost of stream (e) depends on the exergy addition it receives during the process. The increase of the exergy
cost of flow (e) must be the same of flow (c).
So that the second is:

$$\frac{(e_e * c_e - e_d * c_d)}{(e_e - e_d)} = \frac{(e_c * c_c - e_d * c_d)}{(e_c - e_d)} \qquad (3)$$

This model attributes the whole cost of sub-unit 1 to the steam produced (c).
Considering sub-unit 2, we see that it behaves as a flashing chamber [6]. There are two feed streams: the recycle brine coming from the upstream stage (f), and brine flowing downstream the evaporator section (e). There is only one product, the flashing steam (h) that has to account for the cost of section 2.
The overall cost balance of this section is:

$$m_f * e_f * c_f + m_e * e_e * c_e + Z_2 = m_h * e_h * c_h + m_g * e_g * c_g \qquad (4)$$

To determine the cost of flow (g), current thermoeconomic criteria suggest to apply the following auxiliary equation:

$$\frac{m_f * c_f * e_f + m_e * c_e * e_c}{m_e * e_c + m_f * e_f} = c_g \qquad (5)$$

In a common flashing chamber, where only one feed flow is present, the exhaust brine cost is assumed to be the same of the inlet one. When several feed streams are present, in our case (e, f), it is reasonable to assume the cost of the outlet brine, flow (g), as the weighted average of exergy cost of flow (e) and (f) (equation 5).
The thermodynamic process of sub-unit 2 characterizes also sub-unit 3 as well as the thermoeconomic model:

$$m_j * e_j * c_j + m_b * e_b * c_b + Z_3 = m_l * e_l * c_l + m_m * e_m * c_m \qquad (6)$$

$$\frac{m_j * c_j * e_j + m_b * c_b * e_b}{m_j * e_j + m_b * e_b} = c_m \qquad (7)$$

The three steam flows produced in each sub-unit are mixed in one (S_o): it is the final product of the MED stage:

$$m_{So} * e_{So} * c_{So} = m_c * e_c * c_c + m_m * e_m * c_m + m_h * e_h * c_h \qquad (8)$$

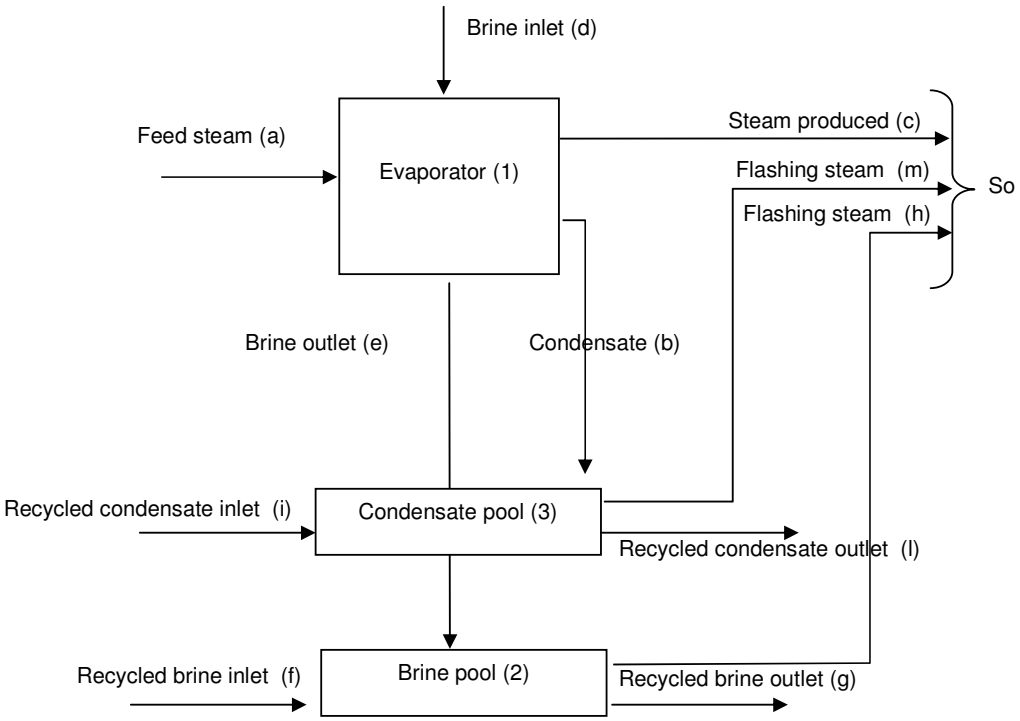

Fig. 1: MED stage scheme

The model proposed divides the MED stage in "thermoeconomic elementary units". It individuates as the main product the steam produced by the MED stage. The cost of the steam produced accounts for the cost of the exergy destroyed in the whole stage and its capital cost.

3. DESCRIPTION OF THE PROCESS CONFIGURATION TO WHICH THE MODEL WAS APPLIED

The plant chosen as benchmark of the thermoeconomic model described in section 2 consists of (fig. 2):

- A combined power plant: the bottoming section is a backpressure steam turbine. The steam extracted from plant feeds a MED desalination plant [7].
  - GT plant operates at 15 bars and 1300°C as TIT (Turbine Inlet Temperature)
  - Compressor and turbine efficiencies have been assumed respectively 85% and 88%
  - The steam power plant is characterized by a top pressure of 170 bars and throttle steam temperature of 550°C.
- A MED desalination plant: it is composed of two units. Each of them produces 15,000 m^3/day

Each unit produces 15,500 m^3/day. The plant efficiency is 9 (GOR). Table 1 displays the plant main parameters.

Tab. 1

MED Plant Parameters	
Number of Stages	14
Feed Steam Temperature (K)	348
Feed Steam Mass flow rate (kg/s)	18
Production (kg/s)	166.3247
Feed Brine (kg/s)	332.64933
Total heat exchanger (m^2)	59346
Cost (k$)	19857.7
Capital cost per m^3 of distillate ($/($m^3$d))	1.52

A thermoeconomic analysis is likely to derive a relatively low exergy cost for the steam extracted from the backpressure turbine. We would expect the distillate cost be affected more by the capital- than by the operative cost. If a different process, for example a boiler, determines a higher cost of the feed steam, we would also expect the distillate cost be more influenced by the operative than by the capital cost. These "feelings", conventionally

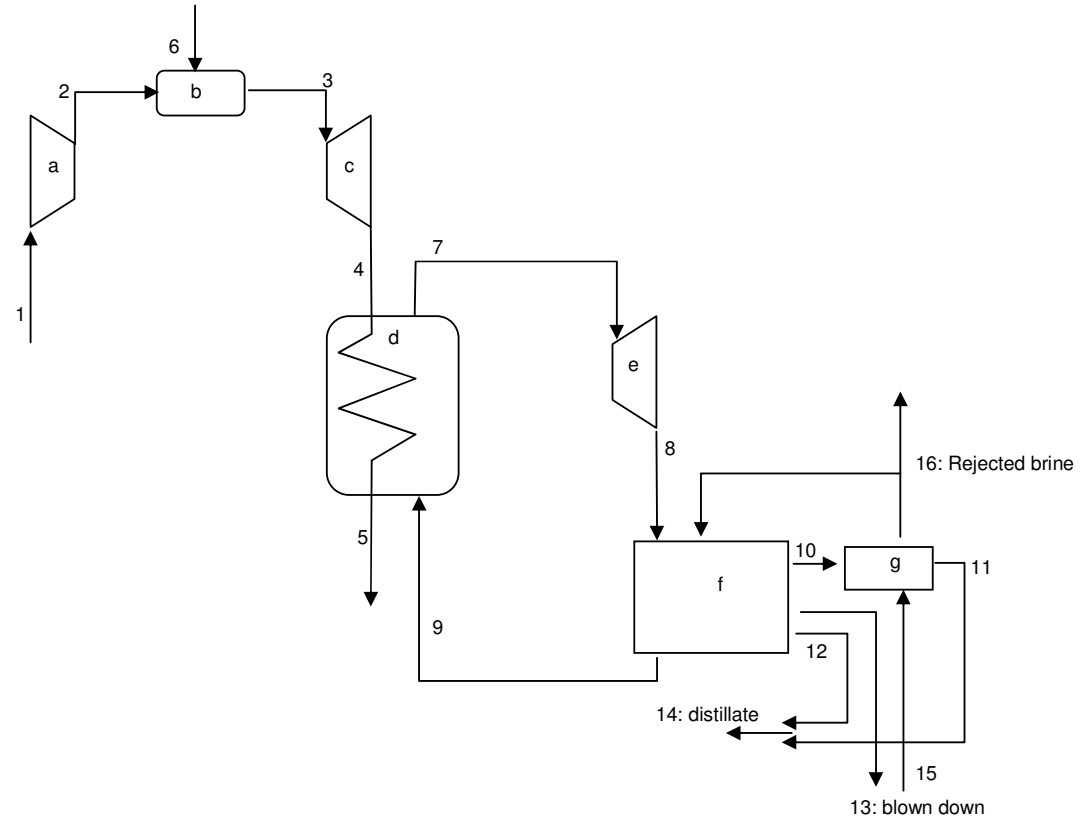

Figure 2: Scheme of the combined cogenerative power plant with MED bottoming

called "qualitative knowledge", can be now validated by a detailed thermoeconomic analysis of the process described in figure 2: it is clear from the above that the best way to proceed is to perform a sensitivity analysis to the unit cost of the steam exergy. In order to perform a thermoeconomic analysis, cost data of the plant component are required.

4.THE ANALYSIS PROCEDURE

The analysis has been divided in three separated-tasks:

1) Calculation the cost of the steam feeding the MED plant: the component cost of the topping plant have been determined using the cost function developed by El-Sayed [8]. In order to calculate the distillate cost under different operative conditions, the steam cost has been identified according to different temperature (and pressure) of the exhaust steam outgoing from the steam turbine (368 K & 348 K).

Tab 2: capital cost of MED plant configuration

Number of effects	**7**	**9**	**11**	**14**
Total production (kg/s)	**-**	**-**	**-**	166.00
Stage heat exchange surface (m^2)	8478	6594	5395	4239
Total heat exchange surface (m^2)	59346	59346	59346	59346
Brine heater heat exchange surface (m^2)	6123	6123	6123	6123
Capital cost per production capacity (k$/m3)	**-**	**-**	**-**	**1.52**
Total cost (k$)	14495.66	16492.02	18086.07	19857.78
MED stage cost (k$)	1805.49	1626.09	1475.35	1285.76
Brine heater cost (k$)	1857.20	1857.20	1857.20	1857.20

All configurations have the same total heat exchange area. As the plant cost depends on both total heat exchanger area and number of stages,

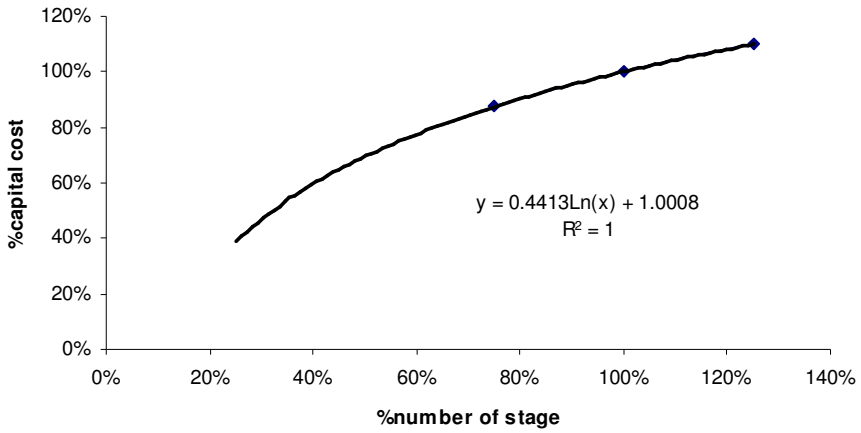

Fig. 3: Capital cost variation (%) vs. Number of stage variation (%)
Plant has supposed to have the same total heat exchange area.

2) Thermoeconomic analysis of MED desalination plant by comparing product cost vs. plant production.
3) Thermoeconomic comparison of several MED plant configurations. Each of them is characterized by a different number of stages (7, 9, 11, 14 stages, see tab. 2).

the configurations have different capital cost. Adopting an appropriate correction of the cost functions developed by El Sayed [8,10] for MSF stages, the impact of number of stage on total plant cost has been evaluated (fig. 3 and tab.3.3)
Since the number of stages affects the plant production range (the higher the number of stages, the lower the production range), the comparison has been performed considering the production rate vs. product cost.

The thermoeconomic analysis includes two sensitivity studies: the first by varying the feed steam temperature, the second by varying the feed steam mass flow rate.

5. Results

A first result has been obtained referring to the seven stages configuration and to 348 K as steam temperature. Fig 4 and 5 show the results. The procedure proposed for the MED stage thermoeconomic analysis, allows determining both the cost of product and by products. Since by-product exergy content is associated to exergy losses related to the process, by-product costs can be assumed as cost of process inefficiency. By increasing the feed steam mass flow rate, the specific exergy request of the plant increases (energy per m^3 of distillate produced). The process is less efficient and the amount of wasted exergy (and economical resources) rises up.

The main part of process cost is charged to the distillate production (fig 3). Minor costs are associated to other by-products: the main source of exergy losses is related to blow down brine flow.

Comparing MED plant configurations the whole cost of water production has to be accounted ($/$m^3$). Fig. 6 compares the water cost of different plant configurations vs. production rate. Due to thermodynamic reasons [9], different plant configurations have different production rates. High number of stages determines a high plant capital cost and high production efficiency. The configuration characterized by 14 stages has both higher capital cost and higher efficiency. Due to the high efficiency, plant-operating cost is low: if high production rates are required, the saving in operating cost balance the high investment (fig. 5).

Figure 6 shows a comparison of distillate costs according to plant configurations and distillate production rates, when the feed steam is available at 348K. Configurations characterized by a higher number of stages are convenient for higher production rates.

If the feed steam is available at higher temperature, the plant operative cost increase and the less capital intensive configuration is not the

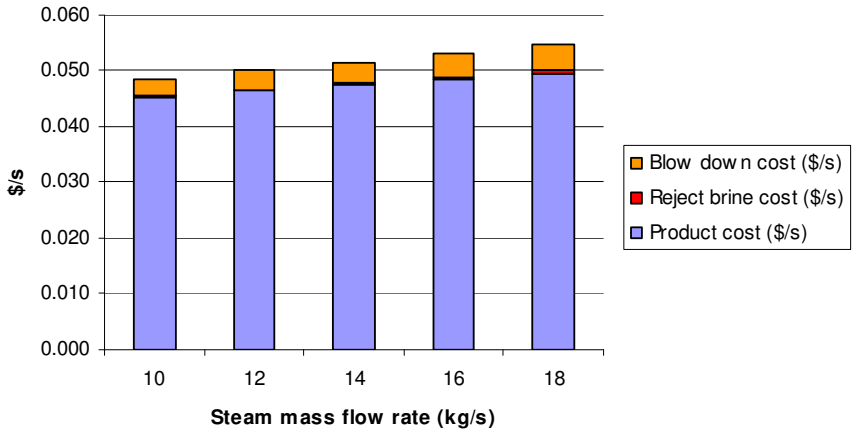

Fig. 4

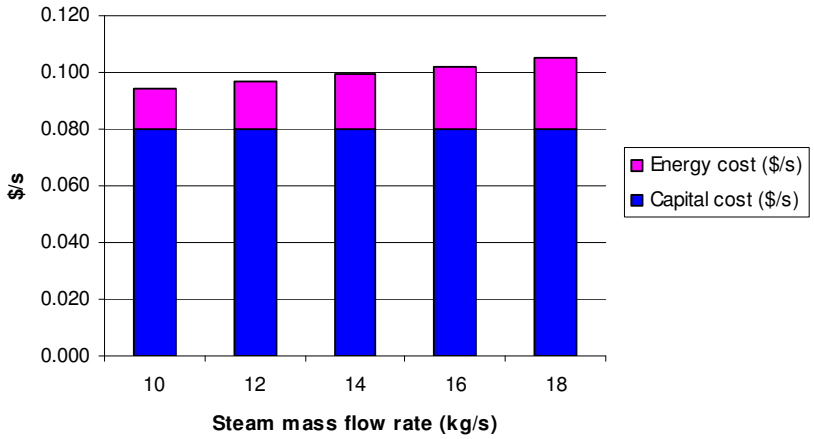

Fig. 5: inputs cost rate

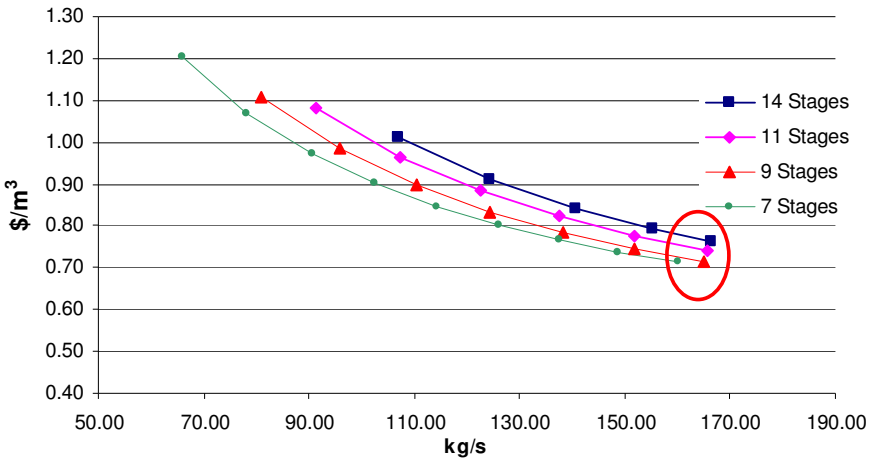

Fig. 6: Distillate cost vs. plant production for the four configurations analysed here. Feed steam temperature = 348 K

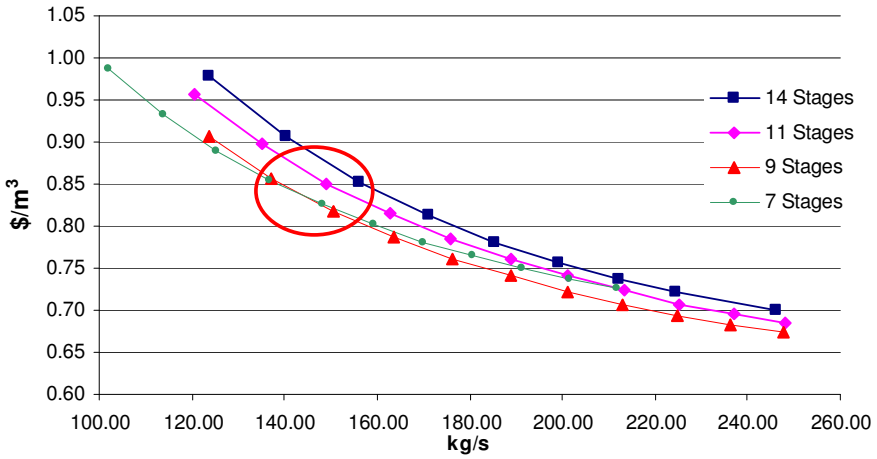

Fig. 7: Distillate cost vs. plant production Feed steam temperature = 368 K

most convenient (fig. 7). In this situation it is also possible to notice that configurations characterized by a low capital cost are convenient up to a well defined value of the production rate. Using thermoeconomic criteria, it is thus possible to optimise the plant configuration according to the plant operative conditions obtaining the lowest possible cost for the distillate. The correct number of stage that satisfies the production request and better suits the topping plant can be identified.

6. CONCLUSION

The thermoeconomic model proposed for the analysis of MED desalination processes allows both comparing and analysing different plant configurations.

Assuming a 14 stages configuration as the base case, a thermoeconomic analysis was performed considering a certain feed steam temperature (348 K). Several plant configurations, characterized by the same overall heat exchange area of the base case, but by a different number of stages, have been also investigated and compared. The feed steam is generated in a combined cycle power plant, and its cost has been assumed to be known from a previous thermoeconomic analysis. Distillate cost has been identified according to the cost of the feed steam, plant capital cost, and the plant production rate. Configurations characterized by high productions and low efficiencies values are preferable if feed steam is available at a relative low cost. If steam is available at higher cost, configurations characterized by higher capital cost (#stages) and higher efficiency values are more valuable.

According to feed steam cost, the analyses show as there are specific ranges of both distillate production where a certain configuration

(identified by a certain number of stages) is economically more convenient than another.

References

[1] T. H. Fehring, R.A.Gaggioli: *Economic of feed-water heater replacement*, Trans. Of the ASME, J. Eng. for Power, July 1977

[2] R. A. Gaggioli (Editor): *Thermodynamics and Costing*, ACS Symposium Series 122, 1983.

[3] Y. El-Sayed, R. Evans: *Thermo-economics and the Design of Heat systems*, J. Eng. for Power, Jan. 1970, pp 27-35.

[4] M. Tribus, R.L.Evans: *Thermoeconomics of Seawater Conversion*, UCLA TR 62-63, Aug. 1962

[5] A. Bejan, G. Tsatsaronis, M. Moran: *Thermal design and optimisation*, J. Wiley, 1997.

[6] P. Fiorini, E. Sciubba, "*Thermoeconomic analysis of a MSF desalination plant"*, **Submitted to:** Desalination And Environment, La Spezia, Italy, May 2005.

[7] Al Taweelah, A1 Desalination plant.

[8] Y. M. El-Sayed, *"The Thermoeconomics of Energy Conversion"*, Elsevier, California, USA, 2003

[9] P. Fiorini, *Comparative Exergy and Thermoeconomic Analyses of Innovative Power Plant and Thermal desalination processes*, PhD Thesis, 2004, University of Roma1 "La Sapienza".

[10] C. Sommariva, *Desalination Management and Economics*, Faversham House Group, 2004.

Appendix

In developing the MED thermodynamic model, we accounted that the first stage of the plant differs from others. In fig. 7, is represented a scheme for he first stage.

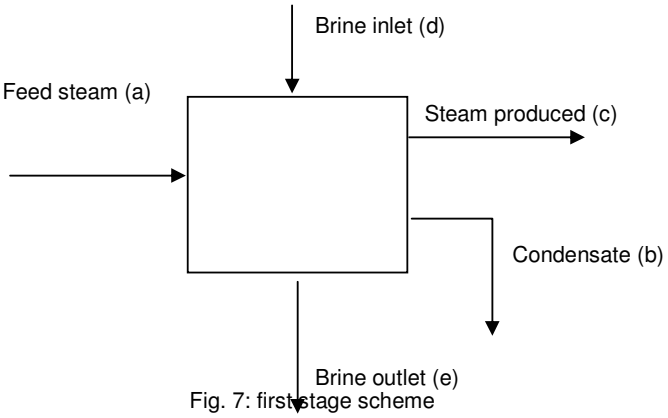

Fig. 7: first stage scheme

It is essentially a heat exchanger in which the feed steam condenses and the inlet brine is heated to the saturation temperature and evaporates. Applying the mass and energy balance equations:

$$m_a = m_b \quad (2.26)$$

$$m_d * s_d = m_e * s_e \quad (2.27)$$

$$m_d = m_e + m_c \quad (2.28)$$

$$m_a * h_a - m_b * h_b = m_e * h_e + m_c * h_c - m_d * h_d \quad (2.29)$$

The brine outlet and the steam produced have the same pressure:

$$p_c = p_e \quad (2.30)$$

The relation between the saturation pressure and temperature calculates the steam pressure:

$$p_c = PSL(T_c) \quad (2.31)$$

Brine and steam temperatures differ for the irreversibility associated with the process (NEA) [8] and the boiling point elevation (BPE) due to the brine salt concentration:

$$T_e = T_d + BPE + NEA \quad (2.32)$$

The heat exchange process takes into account the hardware characteristics, like the heat exchange area and the material properties, and the operative conditions, as required to determine the heat transfer coefficient and the temperature difference between the cold and hot side:

$$Q = U * A * LMTD \quad (2.33)$$

$$LMTD = \frac{(T_b - T_d) - (T_a - T_e)}{\ln(\frac{(T_b - T_d)}{(T_a - T_e)})} \quad (2.34)$$

The overall heat exchange coefficient depends on both the heat exchange coefficients on the steam and brine sides:

$$\frac{1}{U} = \frac{1}{U_{br}} + \frac{1}{U_{st}} + \frac{1}{U_{fouling}} + \frac{k_l}{s} \quad (2.35)$$

where the heat exchange coefficient on the brine and steam side are determined by appropriate functions. $U_{fouoling}$ is assigned as an hardware characteristics.

The model imposes the complete condensation of the inlet steam:

$$q_b = 0 \quad (2.36)$$

This assumption assumes that the component is behaving correctly. If it is not respected, energy losses are associated with the uncondensed steam. As direct consequence of this assumption;

$$T_b = TSL(p_b) \quad (2.37)$$

$$p_b = p_a - PL \quad (2.38)$$

where TSL is the steam saturation temperature as function of the pressure.

Also an option has been introduced to calculate the inlet brine mass flow rate. The heat absorbed by the inlet brine is split between the sensible heat, required to heat the brine up to the saturation temperature, and the latent heat absorbed for the steam production. The higher the stage performance, the higher the steam production, thus the inlet brine rate has to be the lowest thermodynamically allowed. The ideal optimum is obtained if all the brine evaporates. This is not possible due to scaling problems. In deep, the salt concentration cannot be higher than the maximum concentration allowed by the brine temperature inside the stage. As an option of the user, the model can automatically determine the optimal inlet brine mass flow rate by imposing the relation:

$$s_e = s_{\max} \quad (2.39)$$

s_{max} is an input defined by the user according with the stage temperature.
The model proposed for the other MED stage, is similar to that one described above, but more complex and it involves additional phenomena in order to allow the user to simulate the cross flow configuration. Figure 8 shows the scheme for the whole MED stage.

The steam produced and the outlet recycle brine have the same stage pressure imposed by the process in section 1:

$$p_b = p_l = p_m \quad (2.42)$$

Temperature are determined by the following relation:

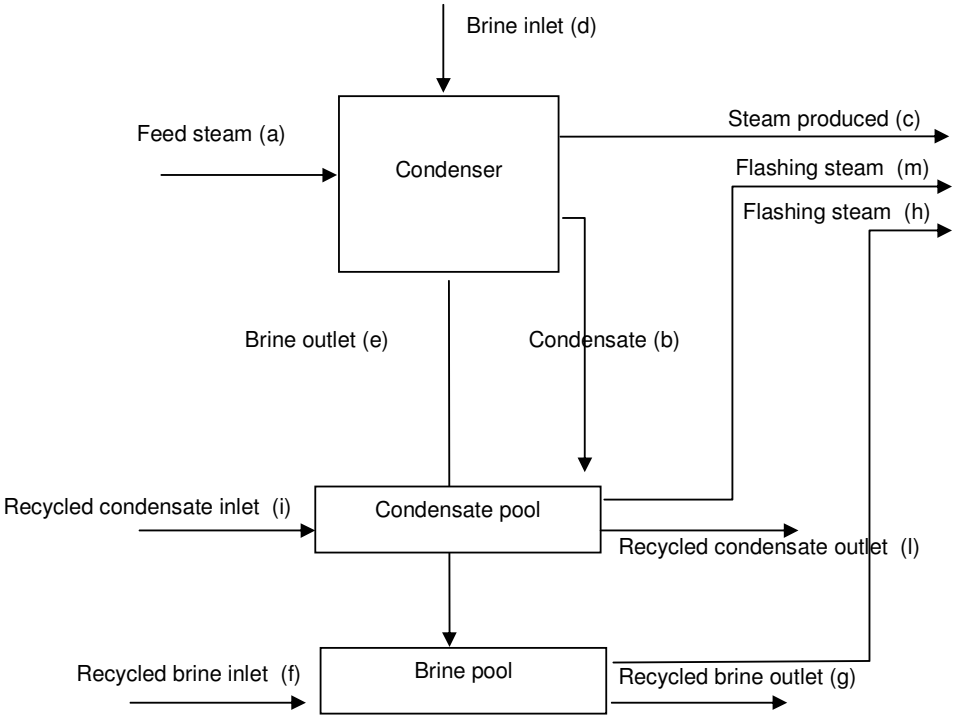

Fig. 2.9: MED stage scheme

The component is supposed to be divided in 3 main section: 1) the condenser, it heat the brine inlet producing the main fraction of the steam produced in the whole stage; 2) and 3) respectively the condensate and the brine pool, they produce additional steam by flashing the condensate and the hot brine coming from the previous stage.
Equations 26-39 describe "the condenser section". Additional equations have to be added in order to simulate the brine and condensate sections. Applying the mass and energy balances to section 2):

$$m_i + m_b = m_l + m_m \quad (2.40)$$

$$m_i * h_i + m_b * h_b = m_l * h_l + m_m * h_m \quad (2.41)$$

$$T_c = T_l = T_m + NEA \quad (43)$$

The temperature of flow *l* lowly differs from temperature of flow b. The gap is due to the different value of NEA associated to the different thermodynamic process of section 1 and 2.
In the whole stage, the main constrain is the pressure of the steam: it is imposed by section 1 and it has to be the same for both the steams produced in section 2 and 3. Section 3 is described almost by the same set of equation of section 2.
Applying mass and energy balances:

$$m_f + m_e = m_g + m_h \quad (2.44)$$

$$m_f * s_f + m_e * s_e = m_g * s_g \quad (2.45)$$

$$m_f * h_f + m_e * h_e = m_h * h_h + m_g * h_g \quad (2.46)$$

From the thermodynamic of the process, it is possible to determine pressure and temperature value.

$$p_g = p_e = p_h \quad (2.47)$$

$$T_g = T_h + BPE + NEA \quad (2.48)$$

The model proposed is able to describe all the processes that may take place inside the MED stage. Depending on the stage pressure and the brine temperature, stream "d" can firstly flash and then evaporate: equation 29 takes into account for this phenomenon.

The model completely fit the idea of a modular code: simulating all the possible plant configurations, included the MVC (MED with a vapor compressor), is possible by opportunely connecting the component flows. If a flow is not present (considering the parallel flow configuration where the recycle brine is not sent to the next stage), it is sufficient to consider the inlet recycle mass flow rate equal to zero and the flow is automatically excluded from the stage energy and mass balances.
Even this model, as the user requires, is able to calculate the inlet brine mass flow rate, imposing a value for the maximum salt concentration.

$$s_g = s_{\max}$$

Proceedings of ECOS 2005
Trondheim, Norway
June 20–22, 2005

The concept of the Gas Turbine-based Hybrid Vehicle: System, Design and Configuration Issues

R.Capata*, E.Cioffarelli, A.Coccia, M.Lora, E.Sciubba
Dept. of Mechanical & Aeronautical Engineering
University of Roma 1 "La Sapienza"
Roma, Italy

* corresponding author: Tel. +390644585271; Fax: +39064881749
E-mail address: roberto.capata@uniroma1.it

ABSTRACT

The paper presents the results of a theoretical and experimental study of a new hybrid propulsion system for a passenger sedan in which the thermal engine is a small turbogas. Some preliminary results on the possibility of employing a turbogas directly in lieu of the reciprocating engine were presented and discussed in a series of papers published in the last 3 years by the same Research Group. This study presents a summary of the results of the project and constitutes an attempt to put things in a proper engineering perspective: the technical feasibility of the project is assessed via a calculation of the required mission loads, a preliminary design of the most important elements of the propulsive system and the choice of the mission control strategy. The results allow for a direct comparison between a GT-hybrid vehicle and a modern diesel car, and indicate that the GT-hybrid may actually be a successful competitor also for the FC-powered vehicle concept. Our "optimal" configuration is a combination of a 100 kg bipolar Pb-acid battery pack and two 15 kW micro turbines for urban missions and highway drives. Using commercially available data for the components, the preliminary design of a road prototype is described and briefly discussed. For practical reasons the first prototype is likely to be equipped with a sub-optimal propulsion system: the differences and their implications are discussed as well.

Keywords:

Nomenclature

AC/DC	AC/DC inverter	m	weight [kg]
b	width [m]	M	electric motor
B	battery	n	angular speed [rpm]
BC	battery charger	P	power [W]
C	compressor	p	pressure [MPa]
c	fuel consumption [g/kWh]	Q	flow rate [kg/s]
CC	combustion chamber	r	radius [mm]
c_x	aerodynamic drag coefficient	R	wheel rolling radius [m]
f_r	tire rolling friction coefficient	RD	degree of regeneration
G	electric generator	RE	regenerator
h	blades height [mm]	S	net area [m^2]
H	height [m]	SOC	battery state of charge
HV	Hybrid Vehicle	T	temperature [K]
T	turbine	t	time [s]
U_{max}	impeller maximum tip velocity [m/s]	VMU	vehicle management unit
V	voltage [V]	z	number of blades
		z_k	number of compressor blades

z_{pt}	number of rotor blades
α	area ratio
δ	blade blockage coefficient
β	compression ratio
η	efficiency
η_{GT}	GT efficiency
τ	maximum allowable shaft torsional stress [MPa]
Γ_i	lower heating value [kJ/(kg °C)]
χ	hub-to-tip ratio
ρ	density [kg/m^3]

Subscripts

1	inlet
2	compressor delivery pressure
c	compressor
d	diffuser
e	equivalent
fuel	fuel
m	mechanical
n	turbine nozzle
nom	nominal
pc	polytropic compressor
pt	polytropic turbine
sp	specific
stage	stage
t	turbine

1. Principles of operation of a Turbogas-powered HV with an all-electric traction

A series-hybrid configuration, in which a turbogas is coupled to a high speed electrical generator, represents an interesting proposal under many points of view [1,3]. A high rotational speed turbogas coupled with a battery package is a feasible hybrid vehicle configuration: the vehicle can work in only electric mode, if requested, especially during urban missions. In our hybrid vehicle scheme the electronic VMU, vehicle management unit, controls ignition and switching off operations under a Load Following logic. The VMU determines how much energy produced by the turbogas reaches the batteries package or the electric engine directly. During the hybrid mode, the batteries provide the difference between electric engine power need and power produced by the turbogas: the current flow to- and from the batteries is controlled and maintained within a fixed range. In addition, the electric motors can also act as brakes, recovering much of the energy that is otherwise lost in braking.

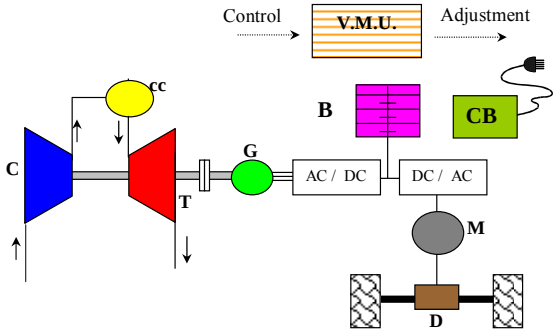

Figure 1: A scheme of the GT-hybrid propulsion system

Purpose of this study is to demonstrate the technical feasibility of the configuration in spite of some practical problems (which will briefly discussed in section 3 and 4), to identify and quantify the power requirements, to define the correct procedure for the selection of the appropriate turbogas set and to choose the most convenient energy flow control mode. In the HV scheme proposed here, a Vehicle Management Unit VMU controls the GT operating point in a *Load Following* mode: this mode has emerged as the most convenient from a series of simulations performed on a number of different configurations. The fact is, for passengers vehicles, subject to highly variable load requirements, the *On-Off* and the *Fixed Power* GT functioning modes are unsuitable (see section 2). The VMU, on the basis of a certain number of instantaneous mission parameters, determines what portion of the electrical energy generated by the GT-driven alternator ought to go -respectively- to the batteries or to the electric motor coupled with the wheels: the batteries may thus provide or absorb the difference between the energy requirements of the vehicle and the GT energy production. The generator acts as a starter for the GT as well. A continuous GT regulation is obtained via fuel flow control coupled with a variable geometry GT. Since GT power modulation is affected by a substantial efficiency penalty, the fuel flow control is coupled with a variable-stator turbine and IGV blades for the compressor: this solution is a very important aid to an effective energy flow control and regulation

strategy [9].
In the course of this study, two basic missions were analyzed: the first consisting of 10 consecutive urban cycles ECE15* (figure 2.a) and the second a "complex driving mission" (figure 2.b) composed of 4 consecutive extra-urban cycles EUDC* and 72 minutes of continuous highway drive at 120 km/hr.

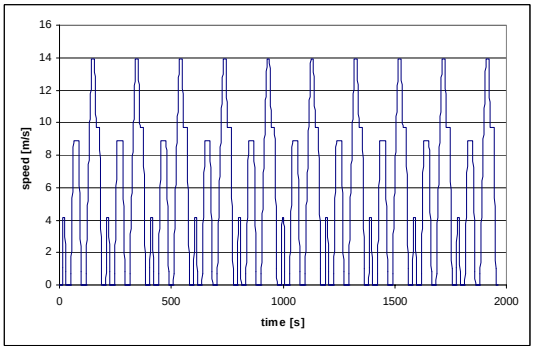

Figure 2.a: The basic mission composed of 10 consecutive ECE15 cycles.

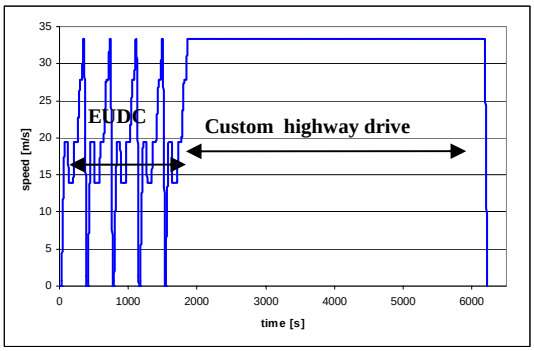

Figure 2.b: "Complex driving mission" composed of 4 consecutive extra-urban cycles EUDC and 72 minutes of continuous highway drive at 120 km/hr.

The vehicle design specifications are the same as those imposed in our previous papers [2, 4] and are reported in Table 1.

Table 1: GTHV Design Specifications

Wheel rolling radius	R = 0.265 m
Vehicle width	b = 1.7 m
Vehicle height	H = 1.4 m
Net front area	$S_f = 2.142\ m^2$
Area ratio (S_f/S_{tot})	$\alpha = 0.9$
Aerodynamic drag	$c_x = 0.25$
Tire rolling friction coefficient	$f_r = 0.015$
Vehicle mass	m = 1550 kg
Equivalent mass	$m_e = 1600$ kg
Air density	$\rho = 1.18\ kg/m^3$
Air intake temperature	T = 300 K
Minimum SOC	0.6
Maximum SOC	0.9

2. The power management protocol

There are three possible "logics" for the power management of a hybrid vehicle in a series configuration:

- I.c.e operating in a fixed mode: the GT runs constantly at its design conditions;
- I.c.e operating in a On-Off mode: the GT is alternatively run at idle ("Off ") and at its design conditions (" On ");
- I.c.e operating in a Load Following mode: the GT output is modulated conditionally between 70% and 110% of its design conditions;

In our final model, described here, we chose to adopt the load following operation mode [2]. Such a choice brings two significant advantages with respect to a simple on/off GT-management:

a) it maintains the GT within a sufficiently flat portion of the efficiency/load diagram (0.7-0.95, figure 3)
b) it allows for a "gentler" modulation of the charging and discharging of the battery, decreasing the steepness of the current/time charging curve and increasing battery life.

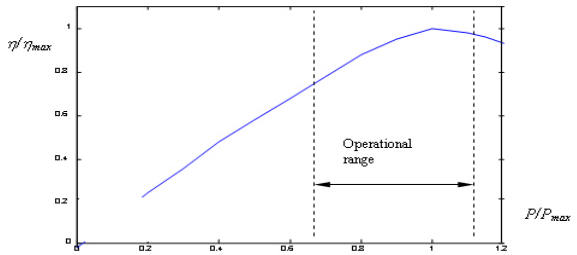

Figure 3: Efficiency/load diagram

* The EEC Directive 90/C81/01 consist of a series of Regulations that prescribes both the emissions limits (adjusted every year) and the methods for testing and certificating both passenger and commercial vehicles.

The logic of this "load following" GT management can be described as follows: The energy flows (GT-to-battery; brake-to-battery; battery-to-motor; GT-to-motor) must be exactly balanced at each instant in time;

1) The battery SOC is allowed to vary only between 0.6 (below which the GT is turned on to recharge the battery, whatever the vehicle power demand is) and 0.9 (above which the GT is turned off, whatever the vehicle power demand is).
2) In the SOC range from 0.6 and 0.9, the GT tries to provide the battery with the exact amount of instantaneous power extracted from the battery by the motor.

The logical decision matrix is shown in Table 2:

Table 2: Truth table for the GT "load following" mode

Soc, %	$(P_v - P_{bt})/P_{GTnom}$	GT load factor, % (= P_{GT}/P_{GTnom})
< 0.6	∀	100
> 0.9	∀	0
0.6 ≤ SOC ≤ 0.9	< 0 $0 \le (P_v - P_{bt})/P_{GTnom} \le 0.7$ $0.7 \le (P_v - P_{bt})/P_{GTnom} \le 1.1$ $(P_v - P_{bt})/P_{GTN} > 1.1$	0 0.7 $(P_v - P_{bt})/P_{GTnom}$ 1.1

3. Model, simulation protocol and results

The simulation program is based on an input-output model for the energy fluxes through the system, and it was implemented as an aid for configuration design. As mentioned above, the GT set is switched on when the SOC is lower than a prefixed level (0,6), and it is set to idling or to a partial load mode when the SOC reaches the maximum allowable level (0,9). Naturally, in real operation, a manual override must also be provided, but this was not considered in our calculations. In hybrid-mode operation, the batteries supply or absorb the difference between the net power demanded by the vehicle and the net power supplied by the GT. The simulation quantitatively enforced such a protocol, calculating the instantaneous power demand as a function of the assigned speed and acceleration values [2, 4]. As stated above, we have analyzed two different mission profiles: a first one consisting of 10 consecutive ECE15 cycles, and a second one composed by 4 consecutive EUDC cycles and 72 minutes of highway at a constant velocity of 120 km/h. The GT load management protocol is based on the realisation that a GT set can operate, without substantial efficiency derangements, between 70% and 110% of its nominal power. The need to compare the GT-HV with a commercial diesel sedan led us to verify several combinations of GT and batteries, to find the "optimal one": our final choice is a configuration with two 15 kW GT sets (compression ratio, inlet air conditions, TIT and rotational speed equal to those of the Elliott TA-45), and one 15 kW_e battery package .The overall constraint throughout the entire operational field (mission profile) was that of maintaining the GT Load Following operation mode while limiting the SOC variation between 0.6 and 0.9 for Pb-acid batteries (between 0,3 and 0,9 for a 41 kg Ni-Cd batteries package, considered a feasible alternate configuration). The choice of a GT-hybrid propulsion system is a heuristic balance between the relative advantages and drawbacks of the following parameters:

- A small number of moving parts;
- Compact size with the potential to be mounted within strict space limitations in the engine compartment of a sedan
- Light-weight of the micro turbines and electric engine
- Lower energy costs
- Lower emissions with multi-fuel capability
- Improved overall vehicle design due to weight and size savings
- High reliability
- Total gross weight of the battery package
- SOC trend during the mission
- Number of GT ignitions during the mission
- Instantaneous verification of the total demand power of the vehicle.

In Table 3 we report some of the considered combinations:

Table 3: GTHV configuration definition

Type	**A**		**B**	
Simulated mission profile	ECE 15	n.a.	ECE 15	EUDC + custom mission
P_{GT}	**P_{GT1}**	**P_{GT2}**	**P_{GT1}**	**P_{GT2}**
	5	0	10	25
P_{batt}	15		15	
Type	**C**		**D**	
Simulated mission profile	ECE 15	EUDC+ custom mission	ECE 15	EUDC+ custom mission
P_{GT}	**P_{GT1}**	**P_{GT2}**	**P_{GT1}**	**P_{GT2}**
	10	25	15	15
P_{batt}	25		15	

Design alternatives have to always abide the correct ratio of GT and batteries installed power, with respect to the vehicle type and missions profiles.
It turns out, that this constraint is a significant one, and limits in practice the number and type of possible configurations.
The turbogas could work at high efficiency conditions only for a low degree of hybridization (low P_{GT} , "always on" operation), but this implies a heavy battery package and leads to obvious disadvantages.
The choice of operating in a Load Following mode is in fact dictated by the need of striking a balance between a low installed battery power and a low specific fuel consumption (high average η_{GT}). We found that a small GT, operating between 70 and 110 % of its rated power, does not display a severe efficiency penalty.
Another problem is given by the fact that our simulations have shown that a 15 kW battery package and a 5 kW turbogas are suitable for urban missions, but not for high speed extra-urban missions, because the total installed power does not cover the higher vehicle power demand.
To make both urban and extra urban missions possible, the 15 kW batteries package had to be coupled with two turbogas set of 10 and 25 kW respectively: but in this case the load on the batteries (steepness of the SOC curve) increases, and the 25 kW GT is subject to an excessive number of ignitions.
Increasing batteries power up to 25 kW smooths the SOC curve and reduces the number of the ignitions, but does so at the cost of a substantial weight penalty.
The adoption of two 15 kW turbogas sets and a 15 kW battery package make both urban and extra-urban missions possible and does not seem to excessively tax either the battery and the GT life. Notice that, if Ni-Cd batteries could be used instead of the Pb-acid considered here, the same P_{GT} could be installed with a weight of the battery package of only 41 Kg.
.

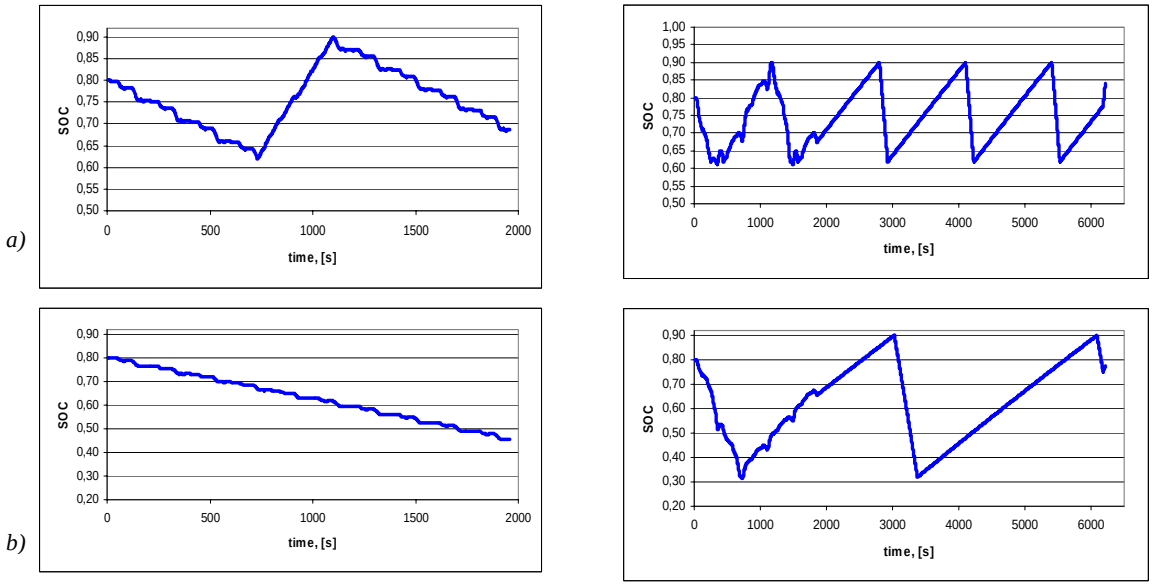

Figure 4: SOC profiles for configuration "D": a) ECE15 and "complex mission" SOC respectively with 100 kg Pb-acid battery pack b). ECE15 and "complex mission" SOC respectively with 41 kg Ni-Cd battery pack.

Table 4: Results of configuration "D"

10ECE15	GT1 "On" [s]	GT2 "On" [s]	Fuel cons.[g/km]	Km/l
Pb-acid	369	15	54	16,2
Ni-Cd	0	0	0	n.a.

Complex mission	GT1 "On" [s]	GT2 "On" [s]	Fuel cons.[g/km]	Km/l
Pb-acid	5158	4312	76,2	11,54
Ni-Cd	5045	4188	74,3	11,83

We considered the possibility of using Ni-Cd batteries because, in addition to their higher power-to-weight ratio, the operating characteristics are better suitable, for our purpose, than the usual Pb-acid batteries. Considering for example a purely urban mission, we see (figure 4.b) that the car can be propelled uniquely in an electric mode. In an extra-urban mission, the "turbine on time" is always lower with these batteries (they have a higher power density) and this implies of course less GT modulation and a lower fuel consumption. Thus, these is a double advantage in installing a Ni-Cd battery pack: first, the better specific energy density and lower weight (48% reduction w.r.t. Pb-acid) bear a direct influence on the design of the system, and lead to significant reduction of the vehicle overall dimensions and gross weight; furthermore, the improved electric characteristics (wider SOC range rechargebility from 0,3 to 0,9 and higher overload resistance) allow for the adoption of a more convenient system configuration and of a more flexible control logic. Unfortunately this kind of battery will be withdrawn from commercialisation in 2006, due to Cd related pollution problems. For future prototypes, we are thus considering the possibility of using Li-ion or Li-Mh batteries.

To obtain an experimental validation of our simulation, and to collect additional operational data, an experimental campaign was performed on an Elliott TA-45 turbine. The tests were conducted at the ENEA Casaccia Research Center: the Elliot is a 45 kW GT operating at partial load conditions (10 kW), with a rotational speed of 116.000 rpm and a cycle pressure ratio of 4.3. It appears that the system overall efficiency is quite low (≈16÷17 %): this confirms the need for an optimization of the GT operating point and control strategy.

4. Thermo-fluidodynamic optimization of the turbogas set

A simplified thermo-fluid dynamic study of the turbogas confirmed the possibility of using a one stage compressor, but indicated that a good overall efficiency requires substituting the single radial turbine stage with three-stage axial machine.

Table 5 Design Specifications for the15 kW-Turbogas Engine

Rotational speed, n	116000 rpm
Nameplate power, P	15 kW
Maximum tip velocity, U_{max}	500 m/s
Fuel Lower Heating Value, LHV	42900 kJ/kg
Inlet pressure, p_1	1 bar
Compressor delivery pressure, p_2	4.3 bar
Inlet temperature, T_1	288 °K
Maximum allowable TIT	1300 °K
Degree of regeneration, RD	0.5
Maximum allowable shaft torsion stress, τ	40 MPa
Turbine polytropic efficiency, η_{pc}	0.9
Compressor polytropic efficiency, η_{pc}	0.85
Mechanical efficiency, η_m	0.9

Figure 3 shows the final proposed turbogas configuration and the relevant thermodynamic and design data. The optimization has been carried out using the optimal n_s criterion**.** A zero-order fluid-dynamic study of the GT has confirmed the possibility of using a single stage radial compressor, but to achieve a good efficiency of the turbine set, with the imposed expansion ratio of about 4.3, the minimal number of stages of the turbine, necessarily axial, is equal to three (two in the limit). The sizing of the radial compressor has been performed by means of a quasi-one-dimensional energy balance at hub and tip, assuming a fixed law of variation of the tangential speed V_t with the radius and imposing a subsonic Mach number at the inlet (relative) and outlet (absolute) sections. The preliminary sizing of the axial turbine has been performed by the same method, but in this case the problem of the sonic phenomena is less serious except for the possible choking caused by a shock wave at the outlet rotor section (which is unlikely anyhow, since the nozzle exit is near chocking at design conditions).

The constructive outline and the calculated dimensions are shown here below.

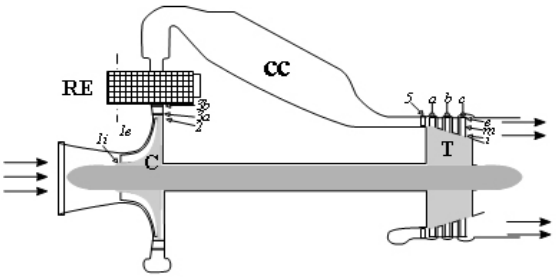

Figure 5: GT set section drawing

Table 6: Constructive scheme and relevant design values

P (kW)	β_{compr}	r_{shaft}	r_{1i}	r_{1e}	r_2	r_{3a}	r_{3b}
		mm	mm	mm	mm	mm	mm
15	4,3	5,3	8,3	16,7	41,2	45,3	53,4
r_{5e}	h_a	h_b	h_c	z_k	z_{pt1}	z_{pt2}	z_{pt3}
mm	mm	mm	mm				
41,2	3,13	4,77	8,04	15	56	50	46

We must remark that -from a thermodynamic point of view- the optimal value of β is approximately 8 and therefore the "thermodynamically optimal" TG cycle efficiency even without regeneration and intercooling results much greater than the calculated one; however we would have larger overall dimensions. In fact, the usual design procedure suggests in this case a three-stage compressor and a three-stage turbine: it is clear that the addition of an intercooler and of the regenerator lead a substantial increase of the size of the thermal power unit. Further investigations are underway to determine whether this "larger" GT set can be packaged in the trunk of a commercial passenger car.

P (kW)	β_{compr}	r_{shaft}	r_{1i}	r_{1e}	r_2
		mm	mm	mm	mm
15	8,3	6,9	9,8	20	43
r_{3a}	r_{3b}	r_{5e}	h_a	h_b	h_c
mm	mm	mm	mm	mm	mm
47	55	42	8,4	13	14

Since our main emphasis was on the possibility of assembling a working prototype using commercial existing units, we decided to adopt as a basic GT-set the supercharger of large Diesel engines, which is readily available on the market at accessible prices and has a proven record of feasibility.

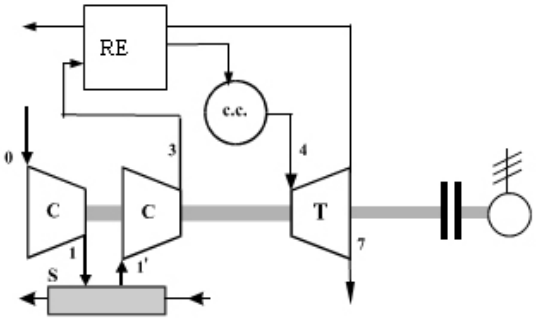

Figure. 6: Intercooled and regenerated turbogas constructive scheme

The introduction of the intercooler, even in such a simplified configuration, obviously increases turbogas efficiency, as shown in Table 7.

Table 7: Intercooled and regenerated performance values

Intercooled	β_{compr}	m_{air}	m_{fuel}	*fuel cons.*	*km/l*	η_{GT}
		g/s	*g/s*	*g/kWh*		
	4,3	0,1761	0,0029	310	18,06	0,243
Intercooled & Regenerated	β_{compr}	m_{air}	m_{fuel}	*fuel cons.*	*km/l*	η_{GT}
		g/s	*g/s*	*g/kWh*		
	4,3	0,086	0,0018	276	19,78	0,304

The constructive complexity and the higher installation costs caused by the intercooler are compensated by a real benefit obtained in terms of the specific fuel consumption. This reduced fuel consumption has a beneficial effect on another important feasibility parameter: it lowers the exhaust emissions.

7. Conclusions

Some of the most relevant issues that affect the technical feasibility of a GT-based hybrid passenger car have been discussed. Tests have confirmed that a single-stage radial-radial configuration (like the Elliott TA-45 examined here, but the results may be extended without loss of generality to other similar configurations), even if very convenient from the point of view of the installation cost, displays a rather poor efficiency. This prompted us to examine the technical feasibility of a different turbogas

configuration: a 2-stage intercooled radial CT coupled with a 2-or 3-stage axial GT. The GTHV system must be carefully designed for what the installed GT power is concerned, and the battery pack must be co-optimized with the turbogas, because the operating conditions are continuously varying. This leads to the necessity of installing a proper turbogas control unit: in simple words, the GT must operate in a "*load following"* mode, so as to maintain sufficiently high efficiency even at partial load conditions. In turn, this requires the installation of a continuous fuel flow control system, of variable turbine nozzle blades and of IGV blades at compressor inlet. We tested (i.e., simulated) several different combinations of P_{GT} and P_{BAT}. The constraints consisted in fixing the SOC variation and in "closing" the energy balance between GT, battery and wheels at $\Delta E = 0$ at each instant in time.The procedure is not yet fully systematic, but since the solution space is not connected (commercial GT sets are available only for certain power levels, i.e. 15, 30, 45 or 100 kW), such a heuristic approach was deemed convenient. Our conclusion is that, under the assumptions outlined in this paper, the "optimal" vehicle is equipped with a combination of a 100 kg Pb-acid battery pack and two turbogas sets, each rated 15 kW, to be used for both urban and highway missions drives.

Installing a Ni-Cd battery pack we could maintain the same optimal outline for urban missions or "complex missions" but we can reduce the total vehicle weight, or, conversely, increase the vehicle electric autonomy with the same weight of the battery pack (the difference between the two configurations is due to the lower specific power of Ni-Cd with respect the Pb-acid).In conclusion our preliminary results indicate that the turbogas option ought not to be discounted though: it is based on already mature technology, offers real multi-fuel characteristic, produces very low emissions and has the advantage of an extremely low installation cost.

References

[1] S.G.Berenyi et al.: *Hybrid vehicle turbine engine technology support,* ASME Paper 98-GT-451, 1998.

[2] R. Capata et al.: *A Gas Turbine-Based Hybrid Vehicle-Part II: technological and configuration issues*, JERT , V. 125 n. 2, july 2003, pag 777-782

[3] E. Cioffarelli, E Sciubba: *A new type of gas turbine based-hybrid propulsion system. part 1: concept development, definition of mission parameters and preliminary sizing*., Proc. AES/ASME Winter Meeting, Orlando, FL, USA, 2000.

[4] E. Cioffarelli, *Modelling of a Gas Turbine Driven Hybrid Propulsion System for a Commercial Passenger Car,* Ph.D. Thesis, U.of Roma 1.

[5] R.Gabrielsson, G.Holmqvist: *Progress on the European Gas Turbine Program AGATA*, J of Eng. for GT and Power, V.120, n.1, January 1998.

[6] N.Nakazawa et al.: *Radial Turbine in Automotive Development for the 100 kW Automotive Ceramic Gas Turbine*, J. Eng. for GT and Power, V.120, n.1, January 1998.

[7] G. Pede,: *Personal Communication*, 2003.

[8] M.Rautenberg, M.Malobabic: *On Turbochargers with Variable Geometry*, ASME PAPER N° 85-GT-149, 1985.

[9] M.Rautenberg et al.: *Improvement in Compressor Performance of a Small Turbocharger by using Ceramic Insulation between Turbine and Compressor,* Proc. Fifth Int. Conf. for Mech. Power Engineering, Cairo, October 1984.

[10] G.Willis, R.Radtke : *Hybrid vehicle systems analysis*, SAE paper 850225, 1985.

Proceedings of ECOS 2005
Trondheim, Norway
June 20–22, 2005

DISTILLERY C_3-C_5 ALCOHOLS RESIDUES REMOVAL BY SUPERCRITICAL WATER OXIDATION

Elena Daniela Lavric* **and Jacques De Ruyck**
Department of Mechanical Engineering
Vrije Universiteit Brussel
Pleinlaan 2, 1050 Brussels
Belgium

Herman Weyten
Vlaamse Instelling vor Technologisch Onderzoek
Boeretang 200, B-2400 Mol
Belgium

Valentin Pleşu and Vasile Lavric
Department of Chemical Engineering
University Politehnica of Bucharest
RO-011061 Polizu 1-7, Bucharest
Romania

ABSTRACT

As the quality of life increases and thus the demands for clean water, ensuring water purity and conservation became increasingly important. Water quality rules are more stringent, complex, and costly, to curb the tendency to use it irrationally. As a result, most companies have to clean their water both before and after they use it, since the harmful impact of waste streams of all types on the environment is hard to overstate. Supercritical water oxidation (SCWO) has been confirmed as a suitable technology to destroy the superior alcohols (common wastes from distilleries, especially C_3-C_5) before releasing the water to the environment. SCWO is an environmentally acceptable technology which produces disposable clean water and gases. SCWO is a process in which aqueous organic waste is rapidly oxidized at temperatures and pressures above water's critical point (647 K, 22.1 MPa). The process has conversions of about 99.999 %.

For the investigated test case, a flow-rate of about 0.8 m^3/h wastewater (containing 8% wt C_3-C_5 alcohols) from a distillery producing alcohol by fermentation is considered. Because the process is highly exothermic, the wastewater is diluted prior to entering the plug flow reactor to about 3.8 % wt, ensuring an exit reaction temperature of about 650 ^{0}C. The SCWO process was modelled using ASPEN Plus® process simulator. The thermal and energetic self-sufficiency of the process was proven, using thermal integration and power production with an Organic Rankine Cycle, using different working fluids.

Keywords: Supercritical water oxidation, heat and power integration, organic Rankine cycle, wastewater treatment

* Corresponding author: Phone: +32 2 629 2324
Fax +32 2 629 28 65 E-mail: dlavric@vub.ac.be

NOMENCLATURE

G	mass flow rate [kg/s]
h	specific enthalpy [J/kg]
I	irreversibility rate [W]
P	pressure [MPa]
$\dot{Q}_{condenser}$	heat transferred in the condenser [W]
r_W	work ratio, -
s	specific entropy [J/kg·K]
$SCWO$	supercritical water oxidation;
T	temperature, K;
w	specific work output [J/kg]
W	electric power [W]
Δ	finite change in quantity;
η	cycle efficiency, %

Subscripts

c	critic
t	turbine
w	clean water

INTRODUCTION

The distillery industry, which manufactures rectified spirit (plain undenatured spirit) for use both as industrial alcohol and for human consumption, is considered to be one of the most polluting industries, generating an average of 8–15 L effluent ("spentwash") per litter of alcohol produced [1, 2]. Fresh water is consumed at various stages of the alcohol manufacturing process namely yeast preparation, molasses dilution, bottle washing, adjusting the alcohol to the required strength for potable purpose and occasionally, dilution of the treated effluent, prior to discharge.

Raw spentwash (wastewater), generated from distillation of fermenter wash, is deep brown in colour, acidic in nature (low pH) with high concentrations of organic material and suspended solid. It cannot be directly discharged into rivers or on land without treatment due to its deleterious effect on human health and the environment [2].

Consequently, extensive treatment is required before the treated wastewater can meet the stipulated environmental norms.

In this context, improved water use in distilleries can contribute to:

- better operational efficiency;
- improved economic competitiveness through reduced water demand combined with savings in water and wastewater treatment costs;
- low environmental impact due to decrease in surface and subsurface withdrawals as well as less groundwater contaminant intrusion; also, such measures will mitigate the effects of water stress [1].

Monitoring of water use in industries is gaining importance due to increasing competition and stringent environment norms. Water is no longer perceived as a free commodity; further, innovative technologies, along with modification of the existing ones are commercially available to reduce process water consumption. In general, reduction in industrial wastewater can be achieved through one or a combination of the following measures:

- process modification or change in raw materials to reduce water consumption;
- direct reuse of wastewater;
- in-plant reuse of reclaimed wastewater;
- use of treated wastewater for non-industrial purposes.

The final choice of the measures adopted is dictated by the availability of substitute raw materials and technologies, nature of pollutants, purity requirement of water for reuse, competing water demands and overall treatment cost [1].

Before being disposed off or recycled, the waste water should be treated in order to decrease its pollutant content to levels that meet the increasingly stringent regulations. To reach this objective, several possible strategies may conceivably be used including concentration/ incineration, anaerobic digestion with bio-methane recovery, non-catalytic wet oxidation with steam generation followed by aerobic polishing and catalytic wet oxidation (*CWO*) using either homogeneous catalysts such as dissolved transition metal cations or solid catalysts such as supported noble metals and various metal oxides [2, 3].

In this context, supercritical water oxidation (*SCWO*) could be a solution, because appropriate water streams can be partially substituted for fresh water.

SCWO is an efficient and versatile oxidation process for the ultimate destruction of varied recalcitrant, xenobiotic or non-degradable organic wastes generating clean liquid (pure water), clean solid (metal oxides, salts), clean gas (CO_2, N_2) [4, 5, 6].

SCWO involves bringing together organic waste, water and an oxidant (such as air, oxygen, hydrogen peroxide, NO_3, etc.) to temperatures and pressures above the critical point of water. Supercritical water serves both as a reactant and as a reaction medium. In supercritical conditions, water acts as a

non-polar dense gas, and its solvation properties resemble to those of a low-polarity organic compound; as a consequence, organic compounds are soluble in supercritical water and inorganic salts are practically insoluble [4-7]. Because of the absence of mass transfer limitations due to the lack of phase-boundaries, the process rates are very high, large destruction rates being obtained inside small volumes of self contained systems.

The *SCWO* process requires temperatures higher than 400 ^{0}C and pressures above 23 MPa. During the oxidation process heteroatoms such as chlorine or other halogens, sulphur and phosphorus form acids. Because of low temperatures and low oxygen concentrations, nitrogen compounds produce mainly nitrogen gas, together with small amounts of nitrous oxides or ammonia. Organic bounded nitrogen predominately forms N_2 and small amounts of N_2O [6].

The *SCWO* process has some drawbacks related to the chemical corrosion caused by the acids formed during the oxidation and to the erosive action of the insoluble salts (which stick sometimes on the walls) already contained or formed during the neutralization process of the acids. Different reactor types and materials where proposed in order to solve the corrosion problem [4-7]. Generally, the maximum allowable temperature is 650 ^{0}C [6]. Concerning the presence of salts, this could be managed through an appropriate separation before and after the reactor, using hydrocyclone or cross microfiltration [5].

From the energetic point of view, *SCWO* is an exothermic reaction that could make the process autothermal, the heat of reaction released in the oxidation being enough to preheat the feed to operational conditions and to produce energy for the feed pump and the air compressor [5, 6]. For energy production, few solutions were proposed, namely the use of: a turbine, a Brayton Cycle or an Organic Rankine Cycle (*ORC*) [5, 6].

The use of a turbine – where a part of the reactor's effluent produces electricity is still a theoretical solution, since the extreme conditions and the presence of the salts make it hard to be practically realized, at least at this moment [6] (the turbine should be a two stage centripetal-axial engine running at speeds of 100.000 rpm – such engines are not readily available, but are technically feasible).

The Brayton Cycle is characterized by low thermal efficiencies. Because its working fluid is a gas, the presence of a compressor into the Brayton Cycle is mandatory, lowering even more its overall efficiency. Thus, the use of Brayton Cycle was disregarded, so much the more as the Brayton cycle is commercially almost unavailable.

The Organic Rankine Cycle, which works with organic vapours, is capable to recover low grade waste heat.

The *ORC* was chosen due to its advantages [6]:

- high ability in recovering waste heat at low to medium temperature;
- high (second law) cycle efficiency;
- high turbine efficiency (up to 85 %);
- low mechanical stress of the turbine, due to the low peripheral speed;
- no erosion of blades, due to the absence of moisture in the vapour nozzles;
- simple, reliable and easy operability;
- quiet operation;
- robustness (long service life, low maintenance costs).

The working fluid should have good thermodynamic properties, low toxicity, explosion and controllable flammability characteristics, and should be non-corrosive, thermally stable and cheap.

SUPERCITICAL WATER OXIDATION FOR WASTEWATER TREATMENT

The polluted water (flow rate of about 0.8 m^3/h) leaving a distillation column where the alcohols were recovered contains 8% wt C_3-C_5 alcohols (9.1% isopropyl, 19.2% isobutyl, 0.3% n-butyl, 19% amyl and 52.4% isoamyl). If the inlet feed concentration is too high for complete oxidation of the organic material to occur in one step without exceeding the reactor's design temperature, one solution may be the waste oxidization in two (or more) stages. Between stages quench water is added with the oxygen. The water cools the effluent from the previous stage enough to allow the additional oxygen to continue the oxidation reaction without exceeding the temperature limit [8].

The authors propose another solution, which uses water obtained from the *SCWO* process itself to dilute the polluted water up to 3.8 % wt. This concentration ensures that the temperature after the oxidation is as high as 647.25 ^{0}C (920.4 K), close to the limit temperature. After dilution, the flow rate of polluted water becomes about 2 m^3/h.

The simulation of a *SCWO* plant with a treatment capacity of 2 m^3/h of wastewater has been carried out using Aspen Plus© of Aspen Technology, Inc. The basic flowsheet is presented in Figure 1. For

the simulation, Peng-Robinson equation of state with modified Huron-Vidal mixing rules was used. The installation contains four parts: feedstream conditioning, reaction, effluent conditioning and heat integration.

In the first one, the polluted water is mixed with the purified one, the alcohols' concentration dropping down from 8 % to 3.8 % wt, then pumped to the operational pressure of 25 MPa and pre-heated up to 400 ^{0}C by the reactor effluent.

Oxygen, in an excess of about 6 % of the stoichiometric ratio, is compressed up to 25 MPa by a four stage compressor and has 213.55 ^{0}C at the exit, since the refrigeration is removed after the last stage. Wastewater and the oxygen are mixed and enter the plug flow reactor at 390.2 ^{0}C. Reactions take place, the pollutants' conversion being as high as 99.99 %. The kinetic used for the oxidation process was based on acetic acid as refractory compound [6]. The effluent, consisting of H_2O, CO_2 and O_2 leaves the reactor at 25 MPa (the pressure drop was neglected) and 647.25 ^{0}C.

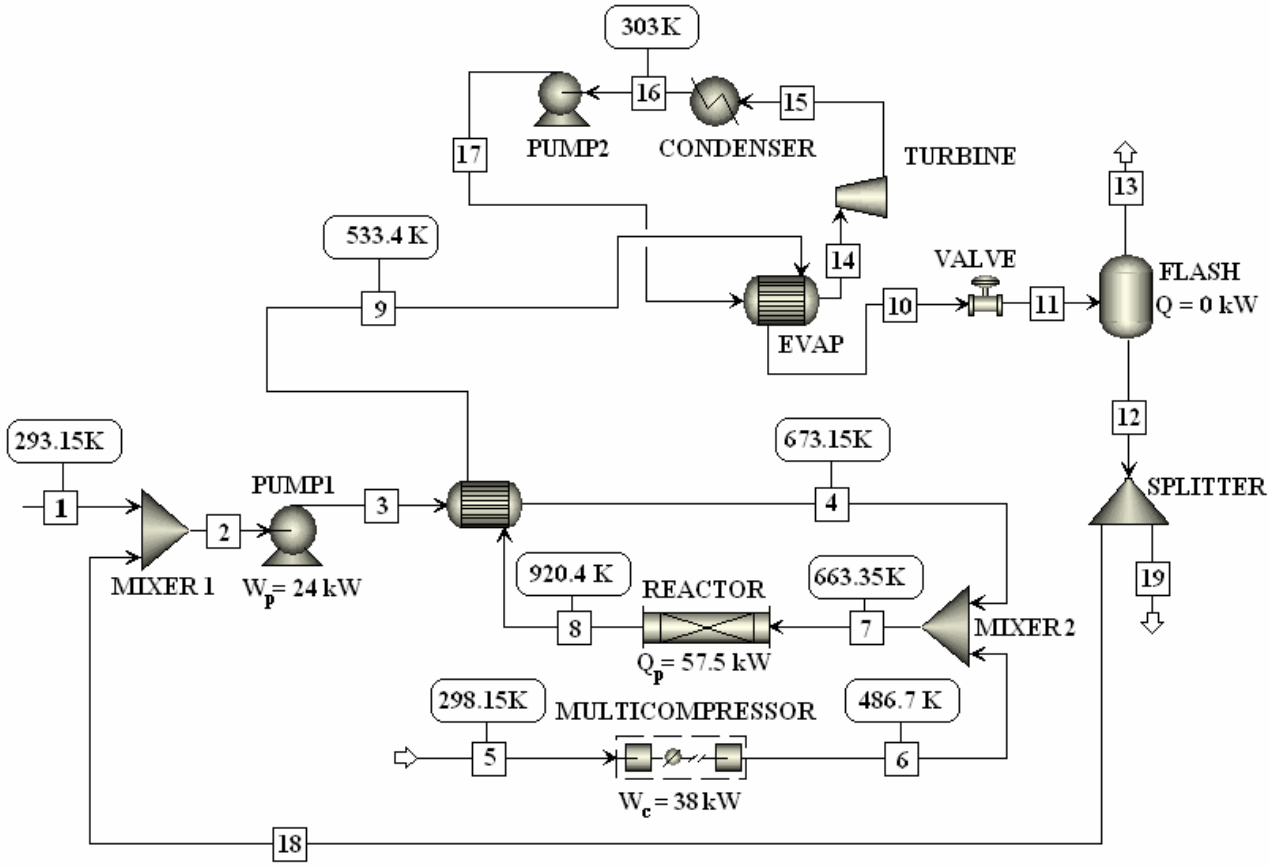

Figure 1. The flowsheet of the SCWO process for diluted wastewater treatment, with *ORC*.

The aim of the process heat integration is to achieve an autothermal operation. The energy released in the reaction is, firstly, used to preheat the liquid raw materials entering the reactor and then, the remained heat is recovered in an *ORC*, where power is produced to compensate that consumed by the pump and the oxygen compressor, ensuring, this way, at least the energetic self sufficiency of the *SCWO* process.

Several fluids were found to be able to provide the necessary electric power to cover the consumption for both pumps and the compressor. The power of the turbine is positively influenced by both higher ratios of pressures and higher inlet turbine temperatures. This is why the pressure of the organic fluids was chosen near the critical one (a little bit less than 2 MPa) and the vapours were superheated. The vapours' temperature and the flow rate were obtained after several trials and errors for different combinations, the set giving the maximum value for the turbine's power being picked up.

The turbine expands the vapours up to the condenser pressure corresponding to a saturation

temperature as high as 303 K. The organic liquid obtained in the condenser is pumped up to the working pressure, vaporized in EVAP using the heat of the purified water and the cycle repeated (see Figure 1).

The distinction between different working fluids could be done using the main performance parameters of the cycle [9]:

- the *specific work output*, *w*:

$$w = (h_{14} - h_{15}) - (h_{17} - h_{16}),\ \text{J/kg} \quad (1)$$

- the *work ratio*, r_W, defined as the ratio between the net work output and the gross work output:

$$r_W = \frac{\text{net work output}}{\text{gross work output}} = \frac{w}{h_{14} - h_{15}} \quad (2)$$

- the *cycle efficiency*, η_I, expresses the proportion of the heat transferred to the working fluid which is converted into mechanical work:

$$\eta_I = \frac{\text{heat converted into mechanical work}}{\text{heat transferred to the working fluid}} = 1 - \frac{h_{15} - h_{16}}{h_{14} - h_{17}} \quad (3)$$

- the *second law efficiency*, η_{II}, a ratio of the actual work generated and the maximum possible work:

$$\eta_{II} = \frac{\text{actual generated work}}{\text{maximum possible work}} = \frac{W_{net}}{W_{net} + I} = \frac{W_t - W_{pump2}}{W_{net} + I} \quad (4)$$

- the *irreversibility* of the *ORC* process, *I*, given by (for steady state conditions):

$$I = T_0 \cdot G_w \cdot (s_{10} - s_9) + \dot{Q}_{condenser} \quad (5)$$

The irreversibilities, as given by (5), were calculated considering the temperature of the surroundings, T_0, as high as 293 K.

The operational parameters for the *ORC*s with the working fluids used are given in Table 1, together with their enthalpies and entropies, specific to each fluid. The obtained main performance parameters are presented in Table 2.

As can be seen, all the considered working fluids used in an *ORC* produce more electrical power than that consumed in the *SCWO* process designed for the abovementioned working conditions, which is as high as 62 kW.

Regarding the performance parameters, the best of them seems to be the refrigerant R123, followed by ammonia, i-pentane and R 600.

Working fluid (T_c [K];P_c [bar])	***G*, kg/s**	**P_{14} = P_{17}, bar**	**P_{15} = P_{16}, bar**	**$h_{14}\cdot10^{-5}$, J/kg (T_{14}, K)**	**$h_{15}\cdot10^{-5}$, J/kg (T_{15}, K)**	**$h_{16}\cdot10^{-5}$, J/kg (T_{16}, K)**	**$h_{17}\cdot10^{-5}$, J/kg (T_{17}, K)**	**s_9, J/kg·K (T_{wi}, K)**	**s_{10}, J/kg·K (T_{we}, K)**	**$\dot{Q}_{condenser}$, kW**
NH_3 (405.4; 113)	0.325	111	15	-23.8 (510)	-26.5 (341.2)	-39.1 (303)	-38.8 (308.5)	-6031.86 (533.4)	-8352.5 (307)	409.6
i-butene (417.88; 40)	0.69	38	4	0.6 (510)	-0.5 (438.6)	-6.7 (303)	-6.6 (306.3)	-6031.86 (533.4)	-8378.3 (305)	422.8
i-pentane (461; 33.8)	0.8	31	1.1	-18.4 (475)	-19.5 (393.9)	-24.7 (303)	-24.6 (305.4)	-6031.86 (533.4)	-8417.1 (302)	413.2
R123 (CCl_2HCF_3) (456.96; 36.75)	1.875	34	1.4	-47.65 (475)	-48.12 (373.5)	-50.33 (303)	-50.29 (305.6)	-6031.86 (533.4)	-8417.1 (302)	414.3
R114 (CCl2FCF3) (419.0; 32.61)	2.33	30	2.6	-53.3 (450)	-53.6 (380.6)	-55.5 (303)	-55.45 (305.6)	-6031.86 (533.4)	-8417.1 (302)	425.7
R600(n-butane) (425.2; 37.96)	0.755	35	3	-18.61 (475)	-19.65 (404.2)	-25.24 (303)	-25.15 (306)	-6031.86 (533.4)	-8404.2 (303)	421.8

Table 1 Working parameters of the *ORC*s

Working fluid	η_I, %	η_{II}, %	w, kJ/kg	r_W	W_{net} kW	W_{excess}, kW	I, kW
NH_3	14.3	56.9	234	0.88	71.8	10.6	54.3
i-butene	13.0	50.9	101.1	0.91	66	4.8	63.6
i-pentane	15.2	54.8	103	0.93	78	16.8	64.3
R123	15.2	61.3	43.9	0.92	77.8	16.6	49.1
R114	12.7	51.8	29.6	0.90	65.2	4	60.6
R600	13.3	53.7	95.4	0.91	68.1	6.9	58.6

Table 2 Main performance parameters of the *ORC*s

CONCLUSIONS

Supercritical water oxidation was considered for the purification of the polluted water obtained in a distillery, containing C_3-C_5 alcohols as organic residue. The installation, used for the treatment of approximately 2 m^3/h polluted water with about 3.8% wt alcohols was modelled using ASPEN Plus®. After ensuring the thermal sufficiency – autothermal regime – the energetic sustainability of the process was investigated, for rather conservative conditions: high heat losses (of about 10% for the reactor and 3% for the heat exchangers) and low enough efficiencies (0.6 for the pumps and compressor and 0.75 for the turbine).

The Organic Rankine Cycle was the solution proposed to recover the low grade waste heat contained by the effluent of the reactor after heating the wastewater and to produce green electricity.

Six working fluids were tested and found suitable to be used in the analyzed case, the best, in terms of the main performance parameters of the *ORC*, being the refrigerant R123.

This Organic Rankine Cycle solution makes the *SCWO* process thermal and power self-sustained, being an example of efficient conversion of the reaction heat to electricity.

The power self-sufficiency implies a reduction of the power use from conventional resources, which should be associated with a lower consumption of fossil fuels and with the decreasing of the pollutant emissions.

ACKNOWLEDGEMENTS

The present paper is the result of a joint research of VITO, VUB and UPB-CTTIP developed under the auspices of the bilateral agreement between the Flemish and Romanian governments, BIL 031326 - *Application of chemical pinch technology in process industries*.

REFERENCES

[1] Saha, N.K., Balakrishnan, M., Batra, V.S. *Improving industrial water use: case study for an Indian distillery*. Resources, Conservation and Recycling 2005; 43(2): 163–174.

[2] Nandy, T., Shastry, S., Kaul, S.N. *Wastewater management in a cane molasses distillery involving bioresource recovery*. Journal of Environmental Management 2002; 65(1): 25-38.

[3] Belkacemi, K., Larachi, F., Sayari, A. *Catalytic wet oxidation of high-strength alcohol-distillery liquors*, Applied Catalysis A: General 2000; 199(2): 199-209.

[4] Goto, M., Nada, T., Ogata, A., Kodama, A., Hirose, T. *Supercritical water oxidation for the destruction of municipal excess sludge and alcohol distillery wastewater of molasses*. Journal of Supercritical Fluids 1998; 13(1-3): 277-282.

[5] Cocero, M.J., Sancez, E.A., Fernàndez-Polanco, F. *Supercritical water oxidation of wastewater and sludges - design considerations*, Eng. Life Sci. 2002; 2(7): 195-200.

[6] Lavric, E.D., Weyten, H., De Ruyck, J., Pleşu, V., Lavric, V. *Delocalized Organic Pollutant Destruction through a Self-sustaining Supercritical Water Oxidation Process*, Energy Conversion and Management, *to be published*.

[7] Baur, S., Schmidt, H., Krämer, A., Gerber, J. *The destruction of industrial aqueous waste containing biocides in supercritical water — development of the SUWOX process for the technical application*, J. of Supercritical Fluids 2005; 33(3): 149–157.

[8] Gidner, A., Stenmark, L. *Oxidation of deinking sludge in supercritical water*, Presented at Workshop, *Managing Pulp and Paper Process Residues*, 30-31 May, Barcelona, Spain 2002. See also www.chematur.se/sok/supercrit_scwo.

[9] Rogers, G., Mayhew, Y. *Engineering thermodynamics, work and heat transfer*. 4th ed. New York: John Wiley & Sons, Inc. 1994.

Proceedings of ECOS 2005
Trondheim, Norway
June 20–22, 2005

EFFECTS OF ROTARY AIR PREHEATER LEAKAGE ON STEAM POWER PLANTS PERFORMANCE

S. Farhad*, M. Younessi-Sinaki and M. Saffar-Avval
Amirkabir University of Technology
Mechanical Engineering Department,
Tehran, Iran

ABSTRACT

The effects of air leakage in the rotary air preheater on performance of steam power plants, such as fuel and power consumption, is an interesting subject in economical maintenance planning. In this paper, the analytical equations to determine the air leakage effects on the fuel consumption and consumed power of forced and induced draft fans in the steam power plants are developed. To show the rotary air preheater leakage effects, four units of 1000 MW Shahid Rajaei steam power plant were tested based on ASME PTC 4.1 and 4.3. The results show that, the air leakages average in these units have increased to 24.7% and 28.0% for natural gas and heavy oil fired fuels, respectively. According to the developed analytical equations, the fuel and power consumption increased to 850 ton/month, and 1078 kW for heavy oil and negligible variation of fuel consumption, and 834 kW for natural gas fuels firing, respectively. Therefore, higher fuel and power conservation can be obtained by proper planning to maintain the rotary air preheaters in suitable conditions.

Keywords: Rotary Air Preheater, Leakage, Steam Power Plant, Maintenance Planning, Energy Optimization

NOMENCLATURE

a	FDF constant coefficient [1/kg^2]
b	FDF constant coefficient [1/kg]
B	Total heat credits [kJ/kg]
c	FDF constant coefficient
C	Defined dimensionless number
c_{pA}	Specific heat of air at const. press. [kJ/kg°C]
c_{pG}	Specific heat of dry flue gas const. press. [kJ/kg°C]
c_{ps}	Specific heat of steam at const. press. [kJ/kg°C]
D	Defined dimensionless number
d	Differential sign
E	Defined dimensionless number
f	IDF constant coefficient [1/kg^2]
g	IDF constant coefficient [1/kg]
h	IDF constant coefficient
H_{fp}	Fuel heating value at const. press. [kJ/kg]
h	Enthalpy [kJ/kg]
K	Defined dimensionless number
kW	Electrical energy [kW]
L	kg of air leakage / kg of "as fired" fuel
Leak	Air Leakage [%]
Loss	Total heat loss [kJ/kg]
T_A	Temperature of air [°C]
T_G	Temperature of flue gas [°C]
W_A	kg of moisture air / kg of "as fired" fuel
$W_{G'}$	kg of dry flue gas / kg of "as fired" fuel
W_{fe}	Rate of "as fired" fuel [kg/s]
W_{mG}	kg of flue gas moisture/kg of fired fuel
X_1	Defined dimensionless number
X_2	Defined dimensionless number
η_b	Boiler Efficiency
η_{FDF}	Forced draft fan efficiency
η_{IDF}	Induced draft fan efficiency
η_T	Turbine efficiency

SUBSCRIPT

i	Isentropic process
in	Steam air heater inlet conditions
cond	Condenser exit conditions
out	Steam air heater outlet conditions

*Corresponding author: Phone: +98 21 2201599, Fax: +98 21 2262468, E-mail: siamak_farhad@yahoo.com

INTRODUCTION

Efficient operation of the steam power plants in order to minimize the operation costs is very attractive subject for the plant managers. Performing periodic performance tests on different parts of the power plants are useful effort to prepare maintenance planning in order to keep energy consumption and equipments life at economic conditions [1]. One of these important equipments is the rotary air preheater for determination of the air leakage. According to the Howden Company experience in a 200 MW unit of steam power plant in Hungary, deterioration of the sealing system in the rotary air preheaters has resulted in very high levels of air leakage into the flue gas. In this plant, increasing the air leakage from 4.7% to 24%, has incurred 1.9% decrease in boiler efficiency [2]. It shows that, the air preheater leakage has important effects on the steam power plants fuel and power consumption. Therefore, diagnosing the appropriate time to repair the rotary air preheater is an economical attempt to minimize the costs. In this paper, the analytical equations to determine the air leakage effects on the steam power plants are developed. Using these equations and regarding the economical analysis, the suitable maintenance planning would be obtained for the rotary air preheaters. Figure 1, which is shown a part of steam-generating unit, can be applied as a key to numerical subscripts employed throughout this paper.

ROTARY AIR PREHEATERS

The rotary air preheater is a compact heat exchanger which was invented by Dr. Ljungstrom from Sweden. These heaters are very popular in modern steam generators. Using the air preheater improves not only the boiler efficiency by lowering the stack temperature, but also the combustion conditions by raising the combustion air temperature. The location of the air preheater in steam-generators is shown in figure 1.

The rotary air preheaters are divided into two groups concerning the arrangement of their rotors, Vertical (V) types and Horizontal (H) types. These heaters contain baskets, as extended heat transfer surfaces, which are attached to the rotor which rotates at 2 to 4 rpm. The baskets are placed in three hot-end, intermediate and cold-end zones, where the gas inlet and air outlet section is called hot-end side and the gas outlet and air inlet section is called cold-end side. In these heaters, the flue gas flows though the baskets to rise their temperature and then air is passed through the same baskets to absorb the heat, while the baskets rotate continuously. Because the pressure of the air is higher than the flue gas pressure, a high amount of air could leak into the flue gas. To limit the total air leakage under 8% of weight of exit flue gas flow, the proper seals must be used in these heaters [3]. The air leakage Percentage depends on the pressure difference between the gas and air ducts on the seals.

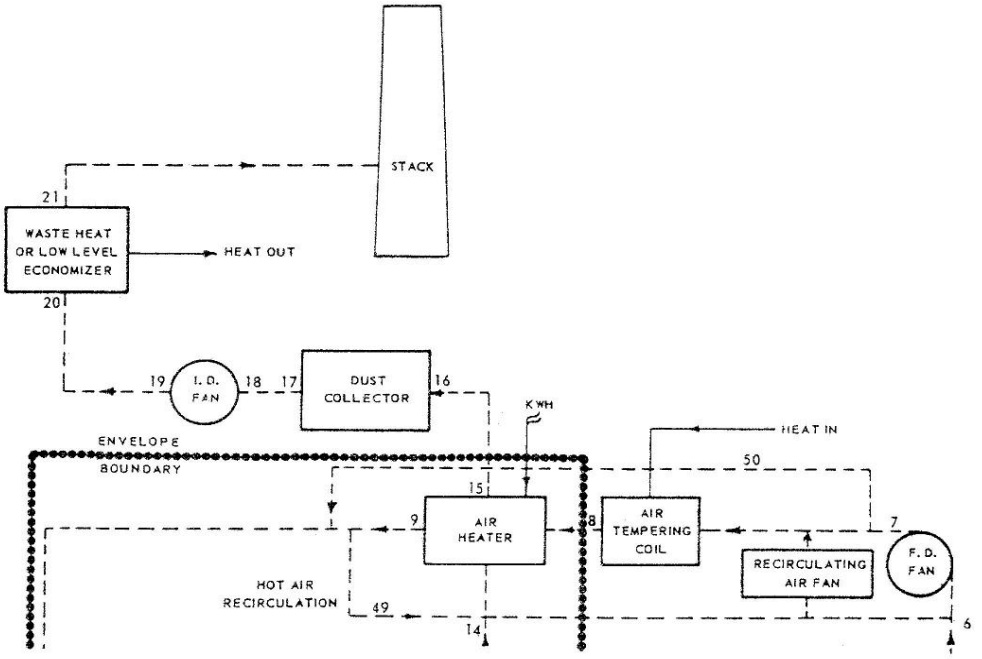

Figure 1: Steam-generating unit diagram [4]

The majority of the leakage occurs on the cold-end side, where the corrosion due to the relatively low air and gas temperatures result the larger clearances between the sealing surfaces. The amount of the air leakage per kg of as fired fuel and the air leakage percent are obtained from the equations 1 and 2, respectively [4, 5].

$$L = W_{G'15} - W_{G'14} \quad (1)$$

$$\%Leak = \frac{(W_{G'15} - W_{G'14})}{(W_{G'14} - W_{mG})} \times 100 \quad (2)$$

Whenever the metal temperature of air preheater falls bellow the dew point temperature of the flue gas, the corrosion of the metal caused by sulfuric acid is occurred. The sulfur content of the fuel and the type of firing has an important bearing on the flue gas dew point temperature. Because in most boilers the flue gas temperature decreases with boiler load, corrosion is more severe at part loads. Increasing heat transfer surfaces temperature is less possibility to cause condensation of acids from the flue gas stream. The design and operation of the air preheater control system is based on maintaining the **A**verage **C**old-**E**nd **S**ide **T**emperature (ACEST) of the rotary air preheaters in suitable limits. The ACEST is defined as equation 3 [1]:

$$ACEST = \frac{T_{G15} + T_{A8}}{2} \quad (3)$$

The air leakages can be reduced by repairing or replacing the damaged rotary air preheater baskets and seals in cold-end side of the preheater. Because this side of the rotary air preheaters is exposed to the sulfuric acid corrosion, the cold-ends zone of these heaters is designed so that the metal elements can be removed easily.

FORCED AND INDUCED DRAFT FANS

When the stack is not able to produce sufficient draft to overcome the pressure losses, the forced and induced draft fans are used. The force draft fan is required to supply sufficient static pressure to overcome the air resistance and the induced draft fan is used to overcome the flue gas resistance. It is necessary to mention that, having both forced and induced draft fans are not essential. For instance, in the pressurized steam generators, a forced draft fan overcomes all the resistances in the air and flue gas passages from the fan to the stack entrance. In this case, the furnace is under pressure and no induced draft fans are used [3]. Figure 1 shows the forced and induced draft fan locations in steam-generators.

The fans are divided into centrifugal, axial and mixed types which each one has particular advantages to another. Also the fans can be divided into straight, forward and backward blade curves. The forced draft fans ordinary use backward type and the forward or straight blades are used for induced draft fans. For any kind of the fans, the fan efficiency has similar mathematical trends in its characteristics curves. Therefore the fan efficiency can be estimated as parabolic equation versus the mass flow rate passing through the fan at constant density. In this paper, the equations 4 and 5 are applied to obtain forced and induced draft fan efficiencies, respectively.

$$\eta_{FDF} = \frac{T_{A7i} - T_{A6}}{T_{A7} - T_{A6}} = a \times [(W_A + L) \times W_{fe}]^2 + b \times [(W_A + L) \times W_{fe}] + c \quad (4)$$

$$\eta_{IDF} = \frac{T_{G16i} - T_{G15}}{T_{G16} - T_{G15}} = f \times [(W_{G'14} + W_{mG} + L) \times W_{fe}]^2 + g \times [(W_{G'14} + W_{mG} + L) \times W_{fe}] + h \quad (5)$$

QUANTIFYING THE EFFECTS OF AIR PREHEATER LEAKAGE ON STEAM POWER PLANTS

It was mentioned earlier that the leakage reduction of the rotary air preheater has an effective influence on energy consumption of steam power plants. Reduction of air leakage lead to reduce the flue gas temperature entering the stack and changes the capacity and exit temperature of the forced and induced draft fans, in the manner that the consumed power of forced and induced draft fans are decreased.

As shown in figure 1, usually three methods are used for increasing the cold-end zone metal temperature of air preheaters [3]:

1- Using the steam-air heater to increase the inlet air temperature, which is installed up-stream of the air preheater.
2- Recirculating some of the hot air from the air preheater outlet back to the inlet air, for increasing the preheater inlet temperature.
3- By-passing part of the air from the air preheater.

In the first method, the steam-air heater controls the ACEST to prevent corrosion of the rotary air preheater by increasing the air temperature at

entrance of the air preheater. In this paper, it is supposed that, the control of ACEST is performed by this method.

To show the effects of the rotary air preheater leakage on the steam power plants, the analytical equations are developed. According to PTC4.1, the energy conservation equation for steam-generators can be considered as equation 6.

$$HV\times W_{fe}+B\times W_{fe}=(BoilerOutput)+Loss\times W_{fe} \qquad (6)$$

To achieve the equation which obtains the fired fuel variations with respect to the air leakage percent, both sides of equation 6 will be differentiated. It is obvious that the differential conditions are different regarding the operating status of the steam air heater, forced and induced draft fans. These different conditions are presented in table 1. Equation 7 states the fuel consumption variation with respect to the air leakage percent for any condition of the steam air heater, forced and induced draft fans operations. Table 1 is guide key for equation 7. Notice that the dimensionless numbers of C, D, E, K, X_1, and X_2 in this equation are defined in table 2. Also the concept of the parentheses which are similar to the less than and more than sign, are specified in table 1. The variations of the forced and induced draft fan powers and the steam air heater steam consumption can be obtained with respect to the air leakage percent, from the equations 8 to 10, respectively. Also the variation of the exit flue gas temperature from the rotary air preheater which is affected from the rotary air preheater leakage can be obtained from the equation 11.

If $x \geq 1$ Then <x> =1 Else <x> =0		
If (FDF Exist) and (Effective on boiler fuel consumption)	Then $\alpha_1=1$	else $\alpha_1=0$
If (FDF Exist) and (Ineffective on boiler fuel consumption)	Then $\alpha_1'=1$	else $\alpha_1'=0$
If (IDF Exist) and (Effective on boiler fuel consumption)	Then $\alpha_2=1$	else $\alpha_2=0$
If (IDF Exist) and (Ineffective on boiler fuel consumption)	Then $\alpha_2'=1$	else $\alpha_2'=0$
If (SAH Exist) and (In service) and (Effective on boiler fuel consumption)	Then $\alpha_3=1$	else $\alpha_3=0$
If (SAH Exist) and (In service) and (Ineffective on boiler fuel consumption)	Then $\alpha_3'=1$	else $\alpha_3'=0$

Table 1: Guide key to use the developed equations.

$$\begin{aligned}
\frac{dW_{fe}}{W_{fe}} &= \{[1+\frac{<\alpha_3>}{E}\times\frac{(W_A+L)}{C}](T_{G15}-T_{A8})+\frac{<\alpha_3>}{E}[T_{A8}-T_{A7}-<\alpha_1+\alpha_1'>X_1(W_A+L)(T_{A7}-T_{A6})] \\
&-<\alpha_3+\alpha_3'>\frac{(W_A+L)}{C}(T_{G15}-T_{A8})+\frac{<\alpha_1>}{\eta_T}[1+X_1(W_A+L)](T_{A7}-T_{A6})+\frac{<\alpha_2>}{\eta_T}(1+X_2K)(T_{G16}-T_{G15}) \\
&-<\alpha_1+\alpha_1'><1-\alpha_3-\alpha_3'>(W_A+L)X_1(T_{A7}-T_{A6})-(1+\frac{<\alpha_2>}{\eta_T\eta_{IDF}})K\frac{<\alpha_1+\alpha_1'+\alpha_3+\alpha_3'>}{<\alpha_3+\alpha_3'>(C+D)-D}(T_{G15}-T_{A8}) \\
&-(1+\frac{<\alpha_2>}{\eta_T\eta_{IDF}})<1-\alpha_3-\alpha_3'>(T_{G15}-T_{A8})\}\times\frac{(W_{G'14}+W_{mG})}{100}/\{\frac{\eta_b}{cpA}(H_{fp}+B)-\frac{<\alpha_3>}{E}(W_A+L) \\
&\times[T_{A8}-T_{A7}-<\alpha_1+\alpha_1'>X_1(W_A+L)(T_{A7}-T_{A6})]-\frac{<\alpha_1>}{\eta_T}(W_A+L)[1+X_1(W_A+L)](T_{A7}-T_{A6}) \\
&-\frac{<\alpha_2>}{\eta_T}K\times[1+X_2(W_{G'14}+W_{mG}+L)](T_{G16}-T_{G15})+<\alpha_1+\alpha_1'><1-\alpha_3-\alpha_3'>(W_A+L)^2X_1(T_{A7}-T_{A6}) \\
&-(1+\frac{<\alpha_2>}{\eta_T\eta_{IDF}})K\frac{<\alpha_1+\alpha_1'><1-\alpha_3-\alpha_3'>}{D}(W_A+L)(T_{G15}-T_{A8})\}\times d(\%Leak)
\end{aligned} \qquad (7)$$

$$d(kW_{FDF})=W_{fe}\{c_{PA}[1+X_1(W_A+L)](T_{A7}-T_{A6})\frac{(W_{G'14}+W_{mG})}{100}d(\%Leak)+c_{PA}(W_A+L)[1+X_1(W_A+L)](T_{A7}-T_{A6})\frac{dW_{fe}}{W_{fe}}\}\# \qquad (8)$$

$$d(kW_{IDF})=W_{fe}\{c_{PA}(1+X_2K)\frac{(W_{G'14}+W_{mG})}{100}(T_{G16}-T_{G15})d(\%Leak)+c_{PA}K[1+X_2(W_{G'14}+W_{mG}+L)](T_{G16}-T_{G15})\frac{dW_{fe}}{W_{fe}}-\frac{c_{PA}K}{\eta_{IDF}}dT_{G15}\}\# \qquad (9)$$

$$d\dot{m}_S = W_{fe}\{\frac{<\alpha_3+\alpha_3'>}{h_{in}-h_{out}}c_{PA}\frac{(W_{G'14}+W_{mG})}{100}[T_{A8}-T_{A7}+\frac{(W_A+L)}{C}(T_{G15}-T_{A8})-<\alpha_1+\alpha_1'>(W_A+L)X_1(T_{A7}-T_{A6})]\ \#$$
$$\times d(\%Leak)+\frac{<\alpha_3+\alpha_3'>}{h_{in}-h_{out}}c_{PA}(W_A+L)[T_{A8}-T_{A7}-<\alpha_1+\alpha_1'>X_1(W_A+L)(T_{A7}-T_{A6})]\times\frac{dW_{fe}}{W_{fe}}\} \quad (10)$$

$$dT_{G15} = -[\frac{<\alpha_1+\alpha_1'+\alpha_3+\alpha_3'>}{<\alpha_3+\alpha_3'>(C+D)-D}+\frac{<1-\alpha_3-\alpha_3'>}{K}]\times\frac{(W_{G'14}+W_{mG})}{100}(T_{G15}-T_{A8})\times d(\%\,Leak)\ \#$$
$$+\frac{<\alpha_1+\alpha_1'><1-\alpha_3-\alpha_3'>}{D}(W_A+L)(T_{G15}-T_{A8})\frac{dW_{fe}}{W_{fe}} \quad (11)$$

#

$C = K + L + W_A\frac{(T_{A9}-T_{A8})}{(T_{G14}-T_{A8})}$
$D = \frac{K(T_{G15}-T_{A8})}{X_1[L+W_A\frac{(T_{A9}-T_{A8})}{(T_{G14}-T_{A8})}](T_{A7}-T_{A6})}$
$E = \frac{h_{in}-h_{out}}{h_{in}-h_{cond}}$
$K = W_{G'14}\frac{c_{PG}}{c_{PA}}+W_{mG}\frac{c_{PS}}{c_{PA}}+L$ #
$X_1 = \frac{W_{fe}}{-\eta_{FDF}}[2aW_{fe}(W_A+L)+b]$ #
$X_2 = \frac{W_{fe}}{-\eta_{IDF}}[2fW_{fe}(W_{G'14}+W_{mG}+L)+g]$ #

Table 2: Dimensionless numbers in equation 7

EFFECT OF THE AIR LEAKAGE IN TYPICAL STEAM POWER PLANT

To show the effects of the rotary air preheater leakage, Shahid Rajaei steam power plant is selected. This plant, which is placed in Iran, has four 250 MW units and was built in 1993. This plant operates at 3 loads of 250, 187.5 and 125 MW and has two types of burner for natural gas and heavy oil fuels firing. The rotary air preheater of this plant is the V type and the materials of its baskets are corrosion-resistant low-alloy steel for the cold-end, and cold-rolled steel for the intermediate and hot-ends zones. According to the design guideline considerations, the minimum ACEST is recommended 110°C for residual oil firing, when the excess air and fuel sulfur content are up to 5% and 2%, respectively, and 97°C, for other conditions; and this value is recommended 63°C for natural gas fuel firing, which is controlled by steam air heaters. The boilers of this plant are pressurized; therefore, the induced draft fan is not applicable in this plant. In fact, two forced draft fans and the 220 m stack are able to overcome all flow resistances. The forced draft fan efficiency of this plant can be obtained by equation 12. The other plant specifications are presented in tables 3 and 4. As presented in tables 3, the ACESTs of Shahid Rajaei's rotary air preheaters are more than the recommended temperature for the natural gas fuel firing; therefore it is not necessary to use the steam air heater to control the ACEST, while according to table 4, using this control system is essential when the heavy oil is consumed.

$$\eta_{FDF} = -1.95\times10^{-5}[(W_A+L)\times W_{fe}]^2 + 8.12\times10^{-3}[(W_A+L)\times W_{fe}] \quad (12)$$

Item	Unit	Natural Gas		
		250	**187.5**	**125**
T_{G14}	°C	353	310	278
T_{A8}	°C	38	34	32
T_{G15}	°C	120.19	101.75	87.69
T_{A7}	°C	38	34	32
W_A	-	17.45	17.62	18.62
W_{G14}	-	16.55	16.7	17.22
W_{mG}	-	2.074	2.074	2.074
L	-	1.3	1.45	2.24
Leak	%	7.0	7.7	11.6
W_{fe}	kg/hr	12.869	9.547	6.406
ΔT_{FDF}	°C	8.8	5.0	3.5
Boiler Eff.	-	0.955	0.960	0.962
Turbine Eff.	-	0.420	0.42	0.420
(H_{fp}+B)	kJ/kg	48580	48580	48580
E	-	0.914	0.914	0.914

Table3: Specification of the Shahid Rajaei steam power plant, natural gas firing

Item	Unit	Residual Oil		
		250	**187.5**	**125**
T_{G14}	°C	357	321	290
T_{A8}	°C	78	85	91
T_{G15}	°C	143.2	136.7	130.1
T_{A7}	°C	38	34	32
W_A	-	14.65	14.79	15.21
W_{G14}	-	14.71	15.28	14.85
W_{mG}	-	1.073	1.073	1.073
L	-	1.1	1.22	1.85
Leak	%	7.0	7.5	11.6
W_{fe}	kg/hr	15.006	11.161	7.494
ΔT_{FDF}	°C	8.7	5.0	3.6
Boiler Eff.	-	0.948	0.949	0.948
Turbine Eff.	-	0.423	0.427	0.425
$(H_{fp}+B)$	kJ/kg	41433	41433	41433
E	-	0.914	0.914	0.914

Table4: Specification of the Shahid Rajaei steam power plant, heavy oil firing

It is necessary to note that the steam which is used to control the ACEST is provided from the last stage of the intermediate turbine extraction line.
In this study, the air heaters of four units of Shahid Rajaei steam power plant (two per boiler) were tested based on ASME PTC 4.1 and 4.3 in 2002. The obtained experimental results are shown in figure 2 [1]. The results show that the air leakage average in this plant have increased to 24.7% and 28.0%, for natural gas and heavy oil fired fuel, respectively. It must be mentioned that the Shahid Rajaei steam power plant's air preheaters had not been repaired or replaced until the tests were performed.

Regarding the test results, the effects of the air preheater leakage on the fuel and forced draft fan power consumptions can be obtained from equations 7 and 8. It is necessary to mention that, to obtain the results, the coefficients of the equations 7 and 8 are assumed constant with respect to the air leakage variations. Regarding to this assumption, the mentioned differential equations can be integrated. Although such simple approximate is quick estimate, but the studies show that the error of this assumption is less than 3.5% per each 15% of air leakage on fuel consumption. Also this assumption does not have significant error on fans power consumption. Therefore, this approximation can be accepted in the present study, while these errors can be eliminated by using the iterative methods to solve these equations.
Increasing the fuel and power consumptions of four units of Shahid Rajaei steam power plant are presented in table 5. It is obvious that repairing or replacing the damaged seals and baskets of the rotary air preheaters can decrease the additional fuel and power consumptions.

Unit No.	Natural gas firing		Heavy oil firing	
	Fuel consumption (ton/month)	FDF Power (kW)	Fuel consumption (ton/month)	FDF Power (kW)
1	-0.1	259	258	307
2	-0.3	314	314	394
3	-0.1	154	125	179
4	-0.1	107	153	198
Total	**-0.6**	**834**	**850**	**1078**

Table 5: Improving potential of fuel and power consumptions in Shahid Rajaei steam power plant

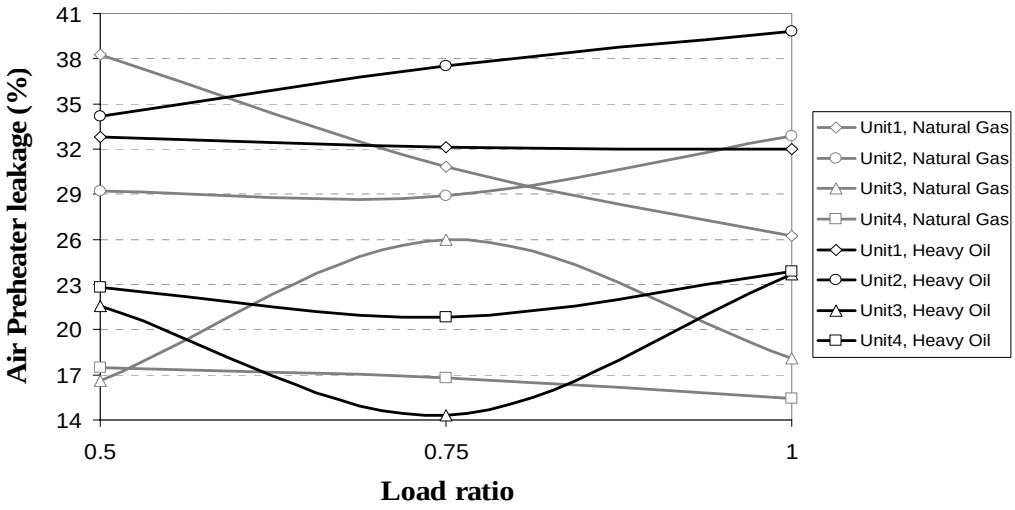

Figure 2: Air preheater leakage percent versus load ratio in Shahid Rajaei steam power plant [1]

To perform the economical analysis to determine the best planning to repair the rotary air preheaters, the additional fuel and power consumptions should be estimated with respect to the air leakage. The fuel and power consumption curves for three operating loads of Shahid Rajaei steam power plant are presented in figures 3a and 4, respectively. Because the steam-air heater is not applicable for natural gas fuel firing in Shahid Rajaei steam power plant, the variations of natural fuel consumption are negligible. By transforming the vertical axis of these graphs to the cost variations, and specifying the rotary air preheater repairing costs and detriments due to stopping the unit, the optimum rotary air preheater leakage for any steam power plants can be determined. Remember that, the optimum leakage depends on the fuel and electrical fuel prices and the repairing costs, which are different for any power plants. Thus the optimum leakage is different for any steam power plant and it is necessary to find this optimum value for each plant.

The variation of flue gas temperature with respect to the air leakage is important to estimate the ducts temperature after the air preheaters. As shown in figure 5, the air preheater flue gas exit temperature in Shahid Rajaei steam power plant reduced rapidly by increasing the air leakage. This leakage can cause the corrosion in any flue gas passage ducts after the rotary air preheater.

The variation of the consumed steam of the Shahid Rajaei's steam-air heaters with respect to the air leakage is shown in figure 3b. It seems that the air leakage has considerable influence on steam-air heater steam consumption and its influence is added by decreasing the operating load.

CONCLUSION

Generally, increasing the fuel and power consumption of operating steam power plants might be caused by various reasons like the increasing air-fuel ratio, malfunction of equipments and control devices, increasing the condenser pressure, increasing the rotary air preheater leakage, etc. Determining the effect of each item on fuel and power consumption provides a suitable opportunity to optimum maintenance planning. Obtaining the additional fuel and power consumption with respect to the rotary air preheater leakage leads to the optimum air leakage in steam power plants. This paper was intended to present the suitable analytical relations which could predict the effects of the rotary air preheater leakage on fuel and power consumption based on the plant design data in steam power plants. The results of the present study show that the increasing of fuel and power consumption due to increasing air leakage in rotary air preheaters is considerable. As shown in table 5, the fuel and power consumption of Shahid Rajaei steam power plant increased to 850 ton/month, and 1078 kW for heavy oil and, negligible fuel consumption variations, and 834 kW for natural gas fuel firing, due to the 24.7% and 28.0% air leakage average for natural gas and heavy oil fired fuel, respectively. Hence, the operation costs of this plant can save by repairing or replacing the damaged seals and baskets of rotary air preheaters.

ACKNOWLEDGMENT

The authors would like to express their appreciation to the Shahid Rajaei power plant director, and technical engineering staff.

REFERENCES

[1] Saffar-Avval M, Farhad S, Younessi-Sinaki M. Reduction in fuel consumption in Iran's thermal power plants, Nation project, Report 8, Amirkabir university of technology, Department of mechanical engineering, Tehran, Iran, 2002.

[2] Howden Company, UK, www.Howden power.com/ library/case_studies.htm.

[3] Potter P G. Power plant theory and design, reprinted by Krieger, 1989

[4] Performance teats on steam-Generating Units, ASME, PTC 4.1, Reapproved 1998

[5] Performance teats on air heaters, ASME, PTC 4.3, 1979.

[6] Black, Veatch. Power plant engineering, CBS Publishers, 2001.

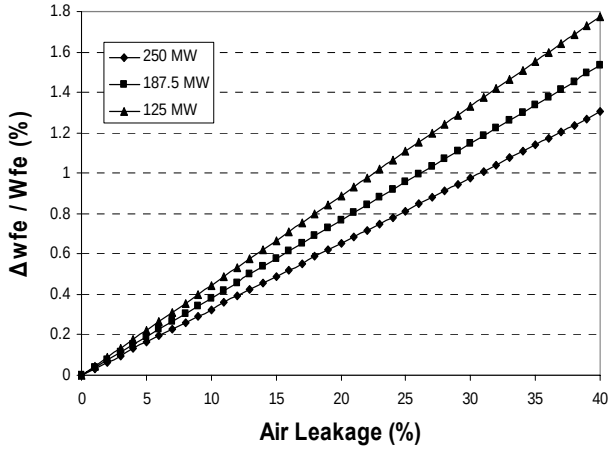

a) Fuel consumption ratio-Heavy Oil Firing

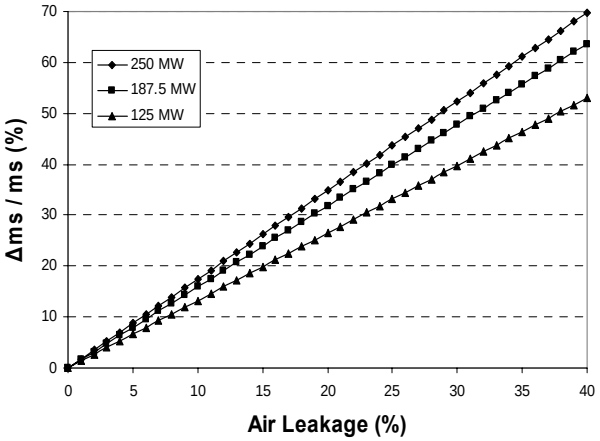

b) Steam consumption ratio-Heavy Oil Firing

Figure 3: Fuel and steam-air preheater steam consumption ratio versus air preheater leakage in Shahid Rajaei Steam power plant

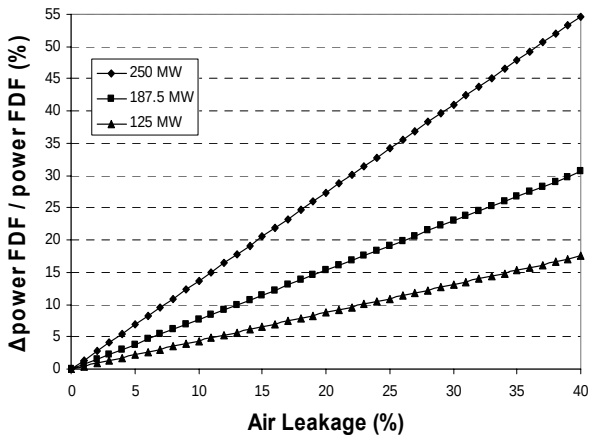

a) Natural Gas Firing

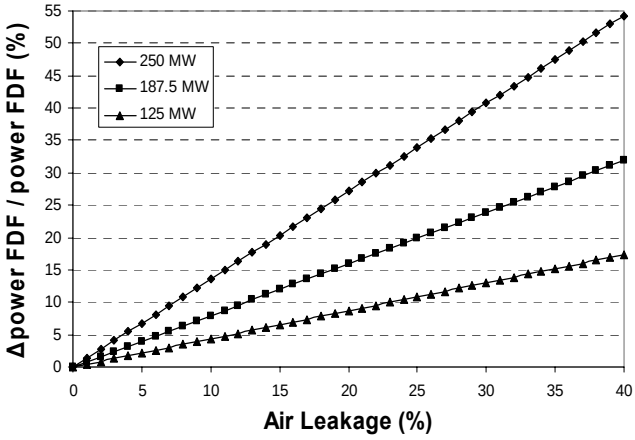

b) Heavy Oil Firing

Figure 4: FDF power consumption ratio versus air preheater leakage in Shahid Rajaei Steam power plant

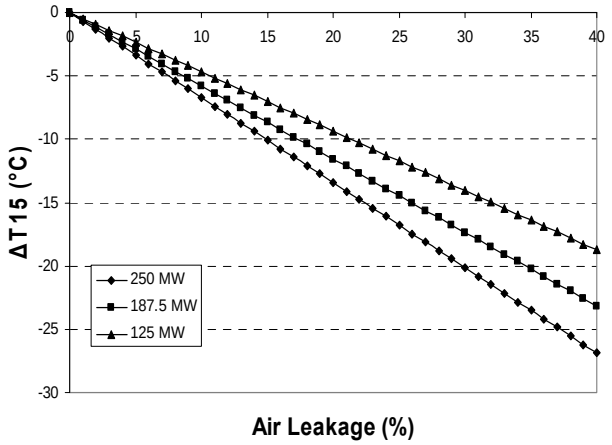

a) Natural Gas Firing

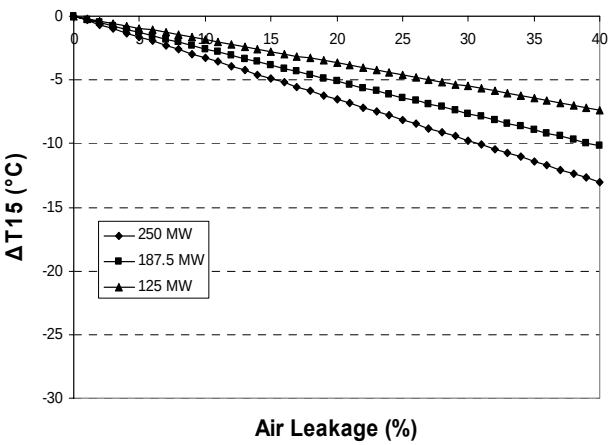

b) Heavy Oil Firing

Figure 5: Air preheater exit flue gas temperature versus air preheater leakage in Shahid Rajaei power plant

Proceedings of ECOS 2005
Trondheim, Norway
June 20–22, 2005

SUPERSONIC TECHNOLOGIES OF NATURAL GAS COMPONENTS SEPARATION

Salavat Imayev*, Vadim Alfyorov, Lev Bagirov,
Leonard Dmitriev, Vladimir Feygin, John Lacey
TRANSLANG TECHNOLOGIES LTD.
Canada

ABSTRACT

Over the last ten years the TransLang Technologies Ltd Company and its main partners have undertaken considerable efforts to carry out investigations and developments and to continuously improve a new approach to the technology of natural gas conditioning and the separation of natural gas components under the general name Super Sonic Separation ("3S"). The advancement of this technology is based on the application of results achieved in aerodynamics related to aerospace engineering. Based on these developments, facilities for separation of natural gas components have been developed which have passed successful laboratory and pilot testing in Russia and Canada.
Keywords: natural gas, LPG, low temperature separation, ECOS2005

NOMENCLATURE

a - sound velocity in gas [m/s]
m - mass fraction of condensate in flow [%]
M=V/a - Mach number
P - static pressure [bar]
T - static temperature [^{0}C]
V - gas velocity [m/s]
α_0 - initial (at the facility entry) mole concentrations of components C_{3+} [%, mol.]
$\alpha_к$ - final (at the facility exit) mole concentrations of components C_{3+} [%, mol.]
$\Delta\alpha=\alpha_0-\alpha_К$ - separation effectiveness [%, mol.]

INTRODUCTION

In this presentation we will report on the overall "3S-technology" without separating it between the various variants of types of devices within this group.

* corresponding author: Phone/Fax: +7 095 1351019
E-mail: imaevsalavat@netscape.net

The 3S technology is a modern technology intended to extract target components from natural gases. The technology is based on the cooling of natural gas in a supersonic swirling gas flow. The supersonic flow is created using a convergent-divergent Laval nozzle. In such a nozzle, gas is accelerated up to velocities exceeding the sound propagation velocity in gas. Due to transformation of a part of the potential energy of flow to kinetic energy the gas is cooled to a high degree.

As an example, Figure 1 shows variations in the main flow parameters when natural gas expands in the supersonic Laval nozzle. The natural gas composition is taken to be as follows: CH4 - 80%, C2H6 – 10%, C3H8 – 6%, C4H10 – 4%. The gas pressure and temperature at the nozzle entry are assumed to be 60 bar and 5 ^{0}C, respectively. These curves are plotted proceeding from the quasi-one-dimensional isentropic approximation of gas motion in the nozzle. The vapor-liquid equilibrium is calculated by the Peng-Robinson equation. As is obvious from these curves, the natural gas expansion even up to moderate supersonic Mach numbers (M ~1.5 – 2.0) allows the gas to be cooled to temperatures sufficient for the condensation of not

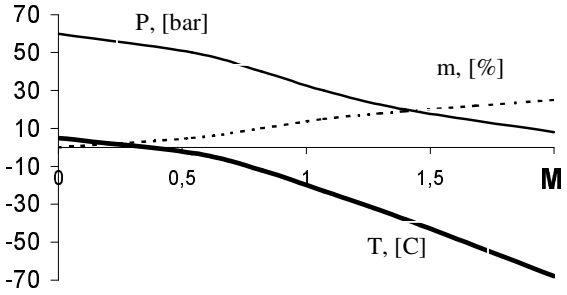

Figure 1: Main parameters of gas flow in supersonic nozzle vs Mach number

only components which are heavier than propane but also ethane. In this case, no additional cold sources, such as coolers, turboexpanders etc., are required to reach the relevant cryogenic temperatures of natural gases.

If condensed drops consisting mainly of heavy components, C3+, are separated from the gas flow in the supersonic nozzle, then the gas at the nozzle exit will primarily consist of light components, such as methane, ethane etc.

Using 3S technology, separation of condensate drops containing target components condensed in the supersonic nozzle occurs under the action of centrifugal forces. The field of centrifugal forces is created by means of flow swirling at the supersonic nozzle entry.

A schematic of the facility (hereinafter the 3S-separator) with the implemented 3S-technology is presented as Figure 2. The 3S-separator includes: 1 – swirling device, 2 – supersonic nozzle, 3 – working section, 4 – a device for the extraction of the gas-liquid mixture, 5 – diffuser.

The application of the diffuser at the 3S-separator working section exit makes it possible to transform a part of kinetic energy of the flow to potential energy to obtain the gas pressure at the diffuser exit larger than the static gas pressure in the supersonic nozzle.

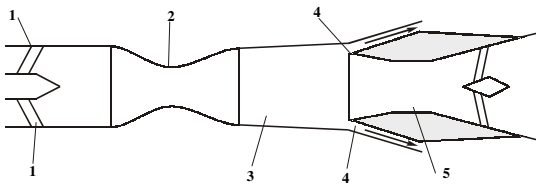

Figure 2: Schematic of 3S-separator

The international patents for the 3S-technology and the 3S-separators are the property of TransLang Technologies Ltd ([1,2] and others).

LABORATORY AND PILOT PRODUCTION TESTS OF THE 3S-TECHNOLOGY

To improve the technology and develop its commercial applications, TransLang Technologies Ltd. has developed a number of facilities. By now, the "3S"– type facilities developed are as follows:

- The test complex (Figures 3-4) at Didsbury (Calgary, Canada). The facility provides a gas flow rate of up to 12 kg/s at an initial gas pressure of 50 – 70 bar and an outlet gas pressure of not below 40 bar. The facility is designed to investigate extraction of the components C5+ from natural gas. The test facility is designed for long period tests and

Figure 3: Test bench at Didsbury

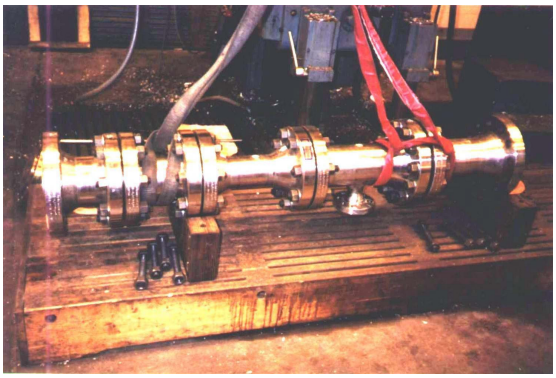

Figure 4: 3S–separator installed on the bench at Didsbury

equipped with a measuring complex to measure pressure, temperature and component concentrations in the 3S-separator elements.

- The experimental bench with the "3S"-type facility (Figure 5) in Moscow region (Russian Federation) provides a gas flow rate of 1.5 – 2.5 kg/s and

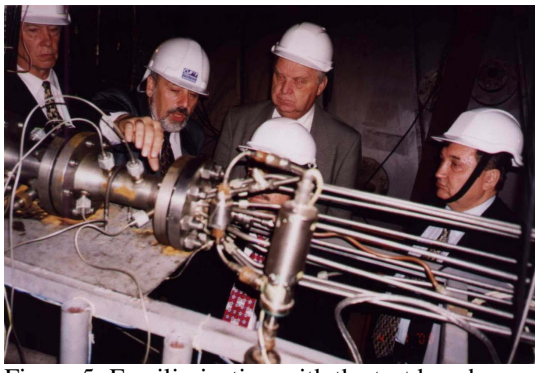

Figure 5: Familiarization with the test bench (Moscow region)

working pressures up to 150 bar. The initial temperature can be varied from –60 ^{0}C to +20 ^{0}C. The bench is equipped with special devices to specify required hydrocarbon gas mixture compositions at the 3S-separator entry.

- The pilot production facility in Western Siberia (Figure 6). In September, 2004, a complex consisting of two "3S" facilities with a capacity of above 400 mmscm per year each was successfully put into pilot production operation at one of the gas treatment plants in Western Siberia as a part of the

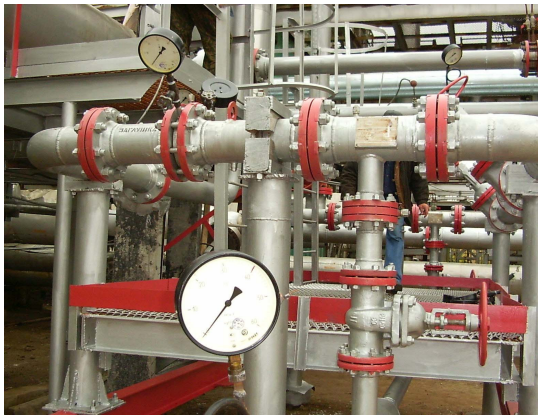

Figure 6: General view of the 3S-facility in Western Siberia

LPG complex. The initial gas pressure at the 3S-separator entry is 32 bar, the initial gas temperature is –30 ^{0}C. The 3S-separator provides extraction of components C3+ in the complex of LPG recovery.

- To investigate various fundamental physical aspects of applying the "3S" technology, two laboratory facilities are used in Moscow region. In one of them the working gas is air, while in the other the mixture of nitrogen and propane–butanes is used.

Over the last five years, more than 400 tests of "3S"-type facilities have been carried out at different temperatures, pressures and gas mixture compositions. Subsonic, transonic and supersonic separation modes have been tested. Optimal 3S-separator structures were designed to provide extraction of components C3+, C5+ from natural gas.

A range of experimental investigations were conducted under conditions up to those approaching industrial applications. Experiments confirmed the main results and conclusions made in the laboratory test facility, in particular the conclusion regarding the high level of effectiveness of the 3S-separator.

Relying on the data obtained from these test facilities, specific software was developed to calculate the 3S-separator physical components under various operating conditions.

The diagram in Figure 7 clearly demonstrates the results of a series of test runs with 3S-separator and their comparison with corresponding results for a *JT- valve*.

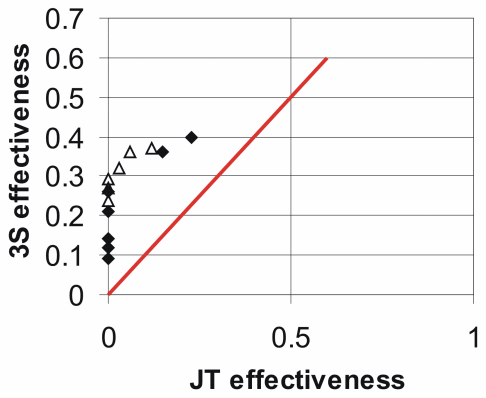

Figure 7: Comparison of 3S and JT effectiveness

Each point on the diagram corresponds to a specific experimentally achieved result. The extraction effectiveness for heavier components of natural gas (pentane, butanes+propane) in the 3S-separator is plotted on the vertical axis of the diagram and the effectiveness calculated for the facility with the JT valve for the same condition (at the same dif-

ferential pressure) is shown on the horizontal axis. The separation effectiveness is measured by $\Delta\alpha=\alpha_0-\alpha_к$, where α_0, $\alpha_к$ are the initial and final (at the facility exit) mole concentrations of components C_{3+}.

It is clear from these data that there exists a range of conditions, (especially where small initial concentrations of heavier hydrocarbons are present) when it is possible to extract such liquid components using the 3S-separator while it would be impossible if a JT valve were to be used.

In the tests, the results of which are presented on the above diagram, the initial concentrations of components, gas pressure and temperature at the 3S-separator entry, differential pressure through the facility and gas dynamic flow condition were varied. The results were obtained for conditions at Mach Number M<1.5 in the 3S-separator working section.

Comparison of the 3S-technology with *turboexpanders* shows that there exist schemes in which the 3S-technology provides better extraction of target components when compared with the schemes in which only the turboexpander is used. In some cases the 3S-separators provide extraction of target components for operating parameters when the operation of turboexpanders is impossible (see below).

ADVANTAGES OF THE 3S-TECHNOLOGY

Some advantages of the 3S-technology as compared with traditional technologies of hydrocarbons separation from natural gas are as follows:

- small size and therefore reduced space requirements, greater portability and reduced handling and installation costs,
- low capital and operating costs,
- no adverse environmental impact,
- the absence of moving parts,
- no requirement for routine maintenance,
- conservation of reservoir energy,
- superior performance capabilities compared to conventional separation equipment and configurations.

There are a wide range of potential applications for 3S-separators to solve the following problems of gas industry:

- gas conditioning (dehydration and extraction of heavy hydrocarbons);
- separation of propane-butanes (LPG);
- extraction of ethane
- production of LNG.

The calculations based on the experimental data for particular fields reveal that the application of the 3S-technology could result in an increased recovery of heavier gas components by more than 30% for the same power of requirements.

The application of 3S-separators instead of *JT-valves* on existing gas processing and extraction plants makes it possible, utilizing the same compressor power, to increase the LPG extraction by 10 – 20%. Similarly, if satisfied with the current extraction level, it would be possible to decrease the required compressor power by 10 – 20%.

At gas processing plants for LPG extraction equipped with *turboexpanders* and coolers (high LPG extraction), the application of 3S-extractors could lead to reduction in the required compressor power by 15 – 20% at the same extraction level.

These examples offer the possibility of increasing the profitability of gas processing plants by means of an inexpensive reconstruction.

APPLICATION OF THE 3S-TECHNOLOGY TO FACILITIES OF GAS CONDITIONING (HYDROCARBON DEWPOINTING)

Relying on the results of pilot production tests of the 3S-separator obtained, in particular, on the test bench at Didsbury, it is easy to show the advantages of using the 3S-technology under conditions of natural gas preparation for transportation.

The main aim of these facilities is to extract heavy components C5+ (C3+) from natural gas and to provide a required dew-point level for hydrocarbons in natural gas at the facility exit.

The process of natural gas dehydration is conducted either upstream of such a facility or water extraction is performed simultaneously with heavy components C5+ (C3+) extraction. If separation of components C5+ (C3+) and water is performed simultaneously, inhibitors of hydrate-formation, for example, ethylene glycol, are added to natural gas.

The functional diagram of the commercial facility of gas conditioning using the JT-valve is given in Figure 8. This diagram with similar parameters is typical, in particular, for various fields in Alberta (Canada).

Let us consider the operational parameters of the facility for one of the fields.

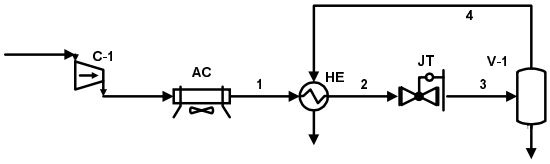

Figure 8: JT-valve LTS Process

Flow	1	2	3	4
Pressure, bar	76.3	75.6	58.8	58.8
Temperature, ^{0}C	48	-6	-15	-15
Content of Components C5+, % mass.	2.27	2.27	2.27	1.43

Table 1: Parameters of main flows for JT- valve LTS Process

Natural gas is delivered to the facility at pressure of 18.9 bar. In the compressor C-1 it is compressed up to 76.3 bar, as a result the gas temperature increases up to 140 ^{0}C. Then gas is cooled in the air cooler down to 48 ^{0}C and delivered to the recuperative heat exchanger. In the heat exchanger, gas is cooled down to -6 ^{0}C and supplied to the JT-valve entry. When the gas pressure in the JT-valve is reduced from 75.6 bar to 58.8 bar, gas is cooled down to -15 ^{0}C and there occurs condensation of heavy gas components. The condensed liquid fraction is then extracted in the three-phase separator V-1. After the separator, the gas fraction is supplied to the recuperative heat-exchanger and then to the gas main. The liquid fraction after the separator is supplied to the stabilization facility and then to the storage for condensate.

The mole composition of natural gas at the facility entry is as follows:

N2 – 1.65%, CO2 – 0.44%, CH4 – 87.49%, C2H6 – 7.00%, C3H8 – 2.07%, i – C4H10 – 0.35%, n-C4H10 – 0.46%, i – C5H12 – 0.17%, n – C5H12 – 0.14%, C6+ - 0.23%.

The parameters of main flows for Figure 8 are summarized in Table 1.

For the above process the extent of extraction of C_{5+} from natural gas flow is 38%, the dew-point for hydrocarbons being –15 ^{0}C (at gas pressure of 58 bar).

Figure 9 shows the diagram of the facility of gas conditioning using the 3S-separator. In this scheme the 3S-separator is installed instead of the JT-valve. The gas-liquid flow from the 3S-separator is delivered to the same three-phase separator V-1. Gas from the three-phase separator is mixed with purified gas from the 3S-separator and supplied to the recuperative heat exchanger.

The calculated parameters of main flows for Figure 9 are summarized in Table 2.

The calculation of the natural gas purification effectiveness in the 3S-separator is based on the results of its tests on the bench at Didsbury. For the scheme in Figure 7 the extent of extraction of C_{5+}

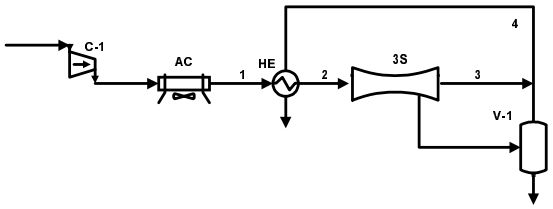

Figure 9: 3S-separator LTS Process

Flow	1	2	3	4
Pressure, bar	76.3	75.6	58.8	58.8
Temperature, ^{0}C	48	16.8	11.3	9.93
Content of Components C5+, % mass.	2.27	2.27	0.71	1.15

Table 2: Parameters of main flows for 3S-separator LTS Process

from natural gas flow at given parameters of the 3S-separator operation is 50%, while the mass fraction of gas-liquid flow delivered to the secondary gas-liquid separator from the 3S-separator is 20 – 30 % of the total flow supplied to the 3S-separator entry. Thus, simple replacement of the valve with the 3S-separator in the LTS facility of gas conditioning makes it possible to improve the C5+ extraction by a factor of 1.32. This is equivalent to reduction in the dew-point of the output gas by 4 ^{0}C.

Some modification of the scheme of using the 3S-separator, in particular, introduction of an additional recuperative heat exchanger allows the differential pressure through the facility to be decreased considerably. During the tests carried out at Didsbury it is shown that for gas pressure after

the compressor of 66.3 bar the extent of extraction of C_{5+} in the case under consideration can be 49%. Thus, with significant reduction in the compressor compression ratio and, respectively, with reduction in the compressor unit power by ~12% the application of the 3S-technology allows increase in extraction of components C5+ from natural gas by a factor of 1.3. In this case, the compressor power required for extraction of target components is halved.

APPLICATION OF THE 3S-TECHNOLOGY FOR OFFSHORE AND SUBSEA PROCESSING

Offshore Processing

It is believed that the advantages of 3S-technology listed above make the application of 3S-technology especially promising for fields in offshore locations.

The application of 3S-technology for subsea processing of gas from the fields located at sea bed is especially effective.

At the present time, the main scheme of natural gas conditioning on off-shore fields at medium and high field pressure is the scheme of low-temperature gas separation (LTS).

The purpose of such gas preparation can be provision for both the dew-point for hydrocarbons and water and, in some particular cases, achievement of required level of HV (Heat Value) of the prepared gas.

At the initial stage of operating the fields, only the Joule-Thomson effect is used in the LTS schemes for gas cooling. This effect is realized by reducing the gas pressure in the JT-valve. When the field pressure decreases with time, turboexpanders are generally used in which gas cooling is attained not only due to the Joule-Thomson effect but also due to additional work performed by the gas.

The model LTS schemes which use the JT-valve and the turboexpander are given in Figures 10 and 11.

Natural gas is cooled in the heat-exchanger by sea water or in the air cooler AC and the recuperative heat-exchanger HE and supplied to the primary separator V-1 in which the liquid fraction (water and heavy hydrocarbons) is separated from gas. Then the gas phase from the separator V-1 is delivered to the JT-valve or to the turboexpander TE. The cooled gas from the JT-valve or the turboexpander turbine is supplied to the secondary low-

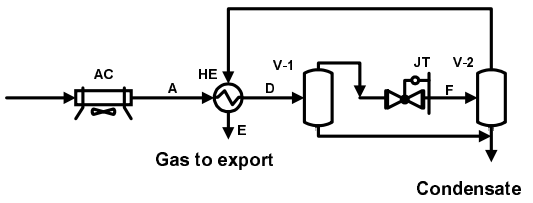

Figure 10: JT-valve LTS Process

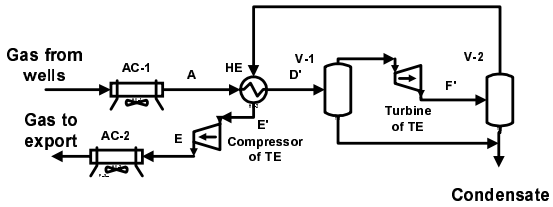

Figure 11: Turboexpander Process

temperature separator V-2, in which condensed components are separated, and then to the heat exchanger HE. Downstream of the heat exchanger gas is supplied to the gas main according to the scheme in Figure 10, but according to the scheme in Figure 11 gas is compressed in the turboexpander compressor, cooled in the air cooler and also supplied to the gas main.

The application of the 3S-separators developed by TransLang Technologies Ltd makes it possible to improve the operation of the considered schemes of gas processing.

The advantages of the 3S-separator as compared with the JT-valve are demonstrated in detail in the previous Section. Here are considered the cases when the 3S-technology offers advantages as compared with the schemes in which the turboexpander is used.

In this connection, of most interest is the case of using the 3S-technology in fields when it is necessary to maintain the pressure of the prepared gas at

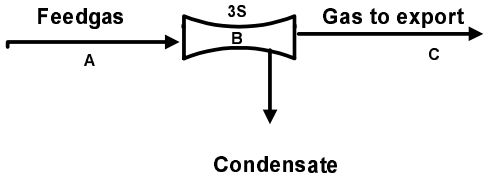

Figure 12: 3S-separator

the gas preparation facility exit at the level of ~100 bar and more. The high gas pressure level at the facility exit can be dictated by the necessity of gas transportation for long distances. This is of particular importance for versions when the prepared gas must be transported through the subsea pipe-line to the shore and then, without additional treatment, to the customer. In most cases, it is impossible to provide the natural gas conditioning using the JT-valve or the turboexpander. The reason is that in standard schemes the condensation of target components at high gas pressures is not feasible.

Figure 13 shows the phase envelope of natural gas in the "temperature –pressure" coordinates. Inside the phase envelope, natural gas represents a two-

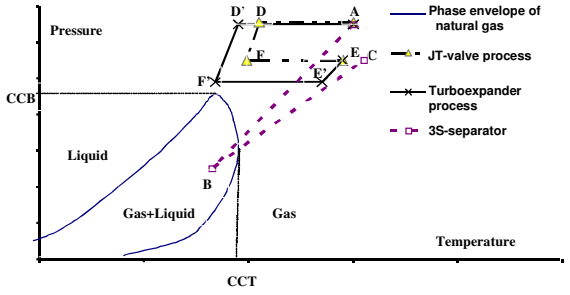

Figure 13: Diagrams of different processes of natural gas processing for high gas pressure at the facility exit

phase gas- liquid mixture. For natural gas components to be separated in the low-temperature process, it is necessary that natural gas at any process point should be in the two-phase state. At the same time, for any natural gas there are pressure Cricondenbar (CCB) and temperature Cricondentherm (CCT) above which the formation of liquid phase is impossible. For natural gases, Criconcenbar often does not exceed 100 bar, that is why at pressures above 100 bar the condensation and separation of natural gas components in the standard low-temperature processes prove to be unrealisable.

Figure 13 represents the diagrams of variations in the thermodynamic state when natural gas successively passes through different facility sections the schemes of which are shown in Figures 10–12.

The P-T diagram A-D-F-E corresponds to the scheme of the facility with the JT-valve given in Figure 10, the diagram A-D'-F'-E'-E refers to the scheme with the turboexpander (Figure 11), and the diagram A-B-C relates to the 3S-separator scheme (Figure 12). The segments A-D, A-D' and F-E, F'-E' show the gas passage through the cooling and heating channels of the recuperative heat exchanger HE, the segment D-F concerns the gas throttling in the JT-valve, the segment D'-F' reflects the gas passage through the turbine of the turboexpander TE, and the segment E'-E relates to the gas compression in the compressor of the turboexpander TE.

The diagram A-B-C corresponds to the gas passage through the 3S-separator (Figure 12). The segment A-B refers to the natural gas expansion in the 3S-separator nozzle accompanied by gas cooling, condensation of target components and separation of condensed drops of condensate, the segment B-C shows the gas compression in the 3S-separator diffuser.

In cases presented in Figure 13, neither the LTS process with the JT-valve nor the Turboexpander process provide condensation of gas components and, hence, separation of target components. While due to gas expansion up to supersonic velocities in the nozzle channel of the 3S-separator it is possible to cool gas to a sufficiently great extent and provide separation of heavy components.

Thus, the application of the 3S-technology opens up new capabilities for gas processing in offshore gas fields.

Subsea Processing

On most gas production platforms the gas pressure is limited to 100 bar. from considerations of platform and personnel safety. The gas pressure at the well-head often exceeds this by a considerable margin. This results in the necessity of installing a JT-valve at the well-head to reduce the gas pressure on the platform.

Replacement of the JT-valve with the 3S-separator will allow simultaneous solution of several problems: pressure reduction, gas dehydration, condensate (LPG) extraction together with dew-point control.

A possible scheme utilizing 3S-separator for condensate (LPG) extraction in Subsea Processing is shown in Figures 14, 15.

In these Figures, the following designations are used: 1 - Well , 2 - Well head, 3 - Condensate extraction facility, 4 - 3S-separator, 5 - Gas-liquid separator, 6 - Heat-exchanger, 7, 11 - Pipeline for condensate transportation, 8 - Gas pipeline for purified gas, 9 – offshore platform, 10 - Facility

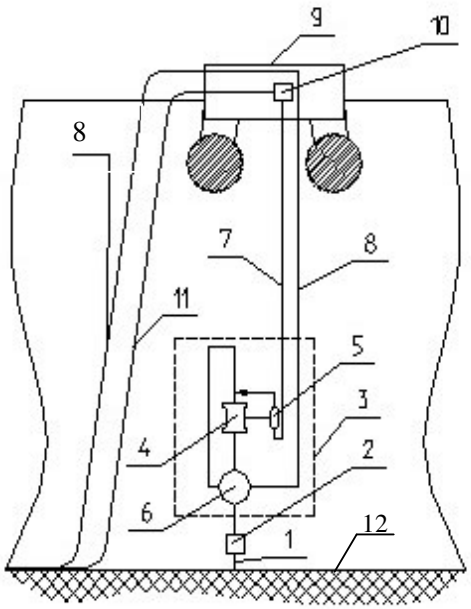

Figure 14: Application of the 3S-technology subsea

for preparing condensate for transportation, 12 – Sea land.

Gas from the well, after passing the well-head, is delivered to the processing facility with the 3S-separator mounted near the well-head located at the subsea. The facility consists of a recuperative heat-exchanger, a 3S-separator and a secondary separator for separation of the gas-liquid flow coming from the 3S-separator. The liquid mixture of hydrocarbons and water separated from the natural gas in the facility are supplied along pipelines to the platform facility to prepare condensate (LPG) for transportation.

A very important application of the 3S-separator is in a full subsea scheme. The scheme of gas preparation for transportation for this case is given in Figure 15.

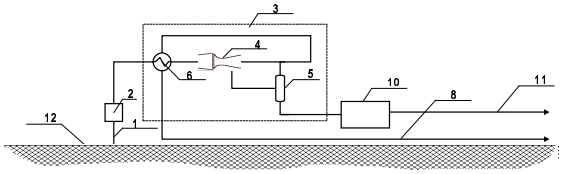

Figure 15: Fully subsea application of the 3S-technology

CONCLUSIONS

A new technology has been developed for the separation and processing of natural gas components based on the adiabatic cooling of swirling gas flow in a supersonic nozzle.

New, highly efficient, technological schemes for gas processing with 3S-separators have been designed and tested in test facilities.

There are a wide range of potential applications for 3S-separators in facilities for natural gas processing such as:

- facilities for gas conditioning;
- facilities for LPG extraction (shallow cut and deep cut);
- offshore gas separation and treatment facilities etc;
- many others (CO_2 extraction, Ethane recovery and LNG) are under extensive investigation.

In all cases considered, the technology supplied using 3S-separators makes it possible to provide a cost effective and highly efficient extraction process for C_{3+} gas components combined with a potential reduction in energy consumption.

REFERENCES

1. European Patent № 1131588.
2. United States Patent № 6372019.

Proceedings of ECOS 2005
Trondheim, Norway
June 20–22, 2005

DIABATIC TRAY DISTILLATION: EOEP AS AN APPROXIMATION TO THE STATE OF MINIMUM ENTROPY PRODUCTION

Eivind Johannessen* **and Audun Røsjorde**
Norwegian University of Science and Technology
Department of Chemistry
N-7491 Trondheim
Norway

Abstract

We show that the theorem of equipartition of entropy production is important for the understanding of the state of minimum entropy production in diabatic distillation. The theorem is not valid in a strictly mathematical sense. We explain why, when and in what sense this theorem is a good approximation to the optimal state in diabatic distillation. In order to make these predictions, we use a hypothesis for the state of minimum entropy production of an optimally controlled system, which was formulated on the basis of results of entropy production minimisation in chemical reactors. The hypothesis says that the state of minimum entropy production is characterised by approximately constant local entropy production and thermodynamic forces, given that there is sufficient freedom in the system. We present numerical results which are in agreement with the predictions. The results show that a column with constant tray entropy production in the stripping section and in the rectifying section is a good approximation to the optimal column, except when the total heat transfer area is low. The agreement between the two columns becomes better and better as the total heat transfer area and the number of trays increase. The fact that the predictions and the numerical results agree very well gives support to the validity of the hypothesis.

Keywords: Diabatic distillation, entropy production minimisation, equipartition of entropy production

NOMENCLATURE

A	Heat transfer area [m^2]
B	Bottom flow [mol / s]
C_p	Heat capacity [J / K mol]
D	Distillate [mol / s]
F	Feed flow [mol / s]
H	Enthalpy [J / mol]
L	Liquid flow [mol / s]
N	Number of trays
n	Tray number
P	Pressure [Pa]
Q	Heat [J / s]
q	Fraction of liquid in the feed
S	Entropy [J / K mol]
$\left(\frac{dS}{dt}\right)_{\text{irr}}$	Total entropy production [J / K s]
T	Temperature [K]
x	Liquid mole fraction (light component)
X	Average heat exchange force [1 / K]
y	Vapour mole fraction (light component)
V	Vapour flow [mol / s]
δ	Film thickness [m]
λ	Heat conductivity [J / s m K]

Super- and subscripts

B	Bottom
D	Distillate
F	Feed
L	Liquid
n	Tray number
V	Vapour

*Corresponding author. Phone: +47 7359 4183. Fax: +47 7355 0877. E-mail:eivindj@phys.chem.ntnu.no

INTRODUCTION

One way to increase the energy efficiency in traditional, adiabatic distillation is to add heat exchangers on all trays in the distillation column. This is called diabatic distillation [1]. It has been known for thirty years that diabatic distillation has a higher energy efficiency than adiabatic distillation [2, 3]. During the last ten years, minimisation of the entropy production of diabatic distillation columns has been studied extensively [4, 5, 6, 7, 8, 9, 10, 11, 12]. By minimising the entropy production of the column, the second law efficiency is maximised. The studies have shown that the potential savings of diabatic distillation are often large.

In this paper, we test a hypothesis for the state of minimum entropy production in an optimally controlled system. Based on results from entropy production minimisation in plug flow reactors, the following hypothesis was formulated [13]: "The theorem of equipartition of entropy production (EoEP, see for instance [14]), but also the theorem of equipartition of forces (EoF, see for instance [15]) are good approximations to the state of minimum entropy production in the parts of an optimally controlled system that have sufficient freedom." We want to check if the predictions contained in this hypothesis fit with the optimal state in diabatic distillation. We shall explain what the hypothesis means in diabatic distillation and test the predictions numerically.

We focus on EoEP as an approximation to the optimal state. EoEP (and EoF) was derived for models with a detailed local description of the irreversible phenomena taking place in the system [13, 14, 16]. The model which has been used in studies of entropy production minimisation in diabatic distillation does not contain such local information however (see for instance [8]). We shall therefore explain why, when and in what sense EoEP is a good approximation to the optimal state. Based on this explanation we define the "EoEP column". We shall present numerical results which show that the EoEP column is indeed a very good approximation to the optimal column, except when the total heat transfer area is low. This is in agreement with the hypothesis stated above.

Figure 1 shows a diabatic distillation column. The column has N plates, for instance sieve plates, which bring a rising stream of vapour in close contact with a descending stream of liquid. The feed stream, F, enters close to the middle of the column. The section of trays above the feed point is called the rectifying section, and the section of trays below the feed point is called the stripping section. Material leaves the column as a bottom stream, B, and as distillate, D. We consider binary distillation. The bottom stream contains thus mainly the high-boiling component and the distillate contains mainly the low-boiling component. In adiabatic distillation, heat is only added in a reboiler and only withdrawn in a condenser. In diabatic distillation, heat may also be added/withdrawn by means of heat exchangers on every tray.

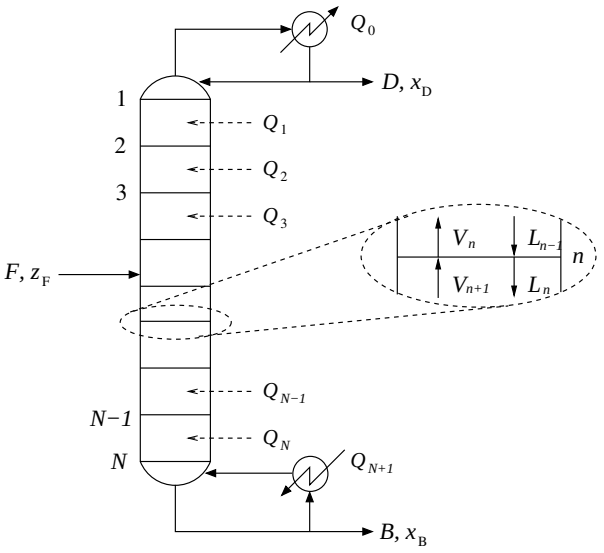

Figure 1: A diabatic tray distillation column

The studies of entropy production minimisation in diabatic distillation have focused on the optimal heating/cooling strategy along the column [4, 5, 6, 7, 8, 9, 10, 11, 12]. This strategy is represented by the heat exchanged on each tray, Q_n, in Fig. 1. In addition, the distribution of a fixed total heat transfer area, A_{total}, between all heat exchangers, has been optimised [7, 8, 12]. The optimal column with infinite heat transfer area, $A_{\text{total}} = \infty$, has been compared to the predictions of equal thermodynamic distance (ETD, see for instance [9, 10, 11]) and EoF (see for instance [4, 5]). The agreement with the true optimum was reasonably good, especially for ETD in long columns [11]. The agreement between the optimal column and EoEP has not been investigated in detail earlier, but some results suggest that parts of the optimal column have a constant entropy produc-

tion [12].

EOEP IN DIABATIC DISTILLATION

The proofs of EoEP [14, 16, 13] and EoF [15, 13], were given for processes where the total entropy production can be written as

$$\left(\frac{dS}{dt}\right)_{\text{irr}} = \int \sigma \, dz = \int \sum_i \Gamma_i J_i X_i \, dz \qquad (1)$$

Here, z is a spatial direction[1], σ is the local entropy production, Γ_i is a geometrical factor, J_i is a flux, and X_i is a thermodynamic driving force. The two most important assumptions in the proofs are that all the forces can be controlled independently and that the flux-force relations are linear (see [13] for a discussion of the assumptions needed to prove EoEP and EoF).

The model which has been used in studies of entropy production minimisation in diabatic distillation, contains very little local information, and the total entropy production can not be written in the same form as in Eq. (1), see Table 1. We shall therefore use a packed column instead of the tray column in order to explain the role of EoEP in diabatic distillation. In a packed column, condensation/evaporation at the liquid-vapour interface and heat exchange in the heat exchanger take place continuously along the rectifying and the stripping sections. At the feed point there is a mixer where the feed stream is mixed with the internal streams of the column. In addition, a condenser and a reboiler are placed at the top and at the bottom, respectively, just like in a tray column. The total entropy production of such a column can be written as

$$\left(\frac{dS}{dt}\right)_{\text{irr}} = \left(\frac{dS}{dt}\right)_{\text{irr}}^{\text{Condens.}} + \left(\frac{dS}{dt}\right)_{\text{irr}}^{\text{Reboil.}} + \left(\frac{dS}{dt}\right)_{\text{irr}}^{\text{Mix.}} + \int_0^{Z_{\text{Rectifier}}} \sigma \, dz + \int_0^{Z_{\text{Stripper}}} \sigma \, dz \qquad (2)$$

The three first terms on the right hand side of this equation are the contributions from the condenser, the reboiler and the mixer, respectively. We shall not discuss these terms in detail, but focus on the two last terms on the right. These terms give the entropy production of the rectifying and the stripping sections, respectively, and they have the same form as Eq. (1). The local entropy production, σ, has the standard form $\sum_i \Gamma_i J_i X_i$ when the local details of the processes taking place are described using irreversible thermodynamics [17]. There are four thermodynamic forces in the continuous column. Condensation/evaporation at the liquid-vapour interface involves three thermodynamic forces; the differences in chemical potential of both components across the interface and the difference in inverse temperature across the interface [18]. In addition, there is a temperature difference in the heat exchanger.

The total entropy production of the continuous column can be minimised in the following way: We fix the boundary conditions on both ends of the rectifying and the stripping sections. We then minimise the entropy production of the two sections, the condenser, the reboiler and the mixer, separately. In an outer loop, we optimise the boundary conditions on both ends of the two sections. This gives a reformulation of the optimisation problem as a combination of smaller optimisation problems. The sub-problems for the two sections are the kind of problems for which EoEP and EoF have been proved. EoEP and EoF were proved for the case when all forces in the system can be controlled independently, meaning that there are at least as many control variables as there are forces [13]. There are four forces in the column, as explain above. The controls are the heat duty along the column and the distribution of a fixed total heat transfer area. There are thus four forces and two control variables, meaning that one of the important assumptions leading to EoEP and EoF is not fulfilled [13]. This means that EoEP and EoF do not apply to the state of minimum entropy production in diabatic distillation in a strictly mathematical sense.

In order to proceed, we use the hypothesis formulated by [13]. The hypothesis says that the system will adjust to EoEP (and EoF) given that there is sufficient freedom to do so, even when there are too few control variables available. This hypothesis applies to the two sections of the distillation column, but not to the condenser, the reboiler and the mixer. The value of the local entropy production in a section of the column reflects the separation duty which is dedicated to that section. In general, the separa-

[1] Time can be used as the coordinate of the system instead of a spatial direction.

tion duty of the rectifying section and the stripping section differ, and the local entropy production will therefore be different from one section to another.

The same irreversible phenomena (condensation/evaporation and heat transfer) take place in the tray column and the packed column. The characteristics of the state of minimum entropy production in the two columns should therefore be comparable. We expect that EoEP is a good approximation to the state of minimum entropy production, also in the tray column. Based on this, we define the "EoEP column": The EoEP column is the diabatic tray column with minimum total entropy production given that the entropy production is the same on all trays in each section of the column. The condenser ($n = 0$), the reboiler ($n = N + 1$) and the tray(s) where the feed stream is mixed with the internal streams of the column, are left out in the equipartitioning[2]. The hypothesis now predicts that *the EoEP column is a good approximation to the true optimum when there is sufficient freedom in the problem*. There are many ways to change the freedom in a diabatic distillation column. In the result section, we shall discuss the effect of varying the total heat transfer area and the number of trays. The system is most free to adjust when the area and the number of trays are large. The freedom is reduced as both values decrease. The hypothesis predicts therefore that EoEP approximates the optimum best for large heat transfer areas and/or a large number of trays.

MODEL OF DIABATIC TRAY DISTILLATION

We use the standard tray distillation model that can be found in elementary textbooks on distillation (see for instance [19]). This model was also used in earlier studies of entropy production minimisation in diabatic distillation [8]. The model consists of two independent mole balances and a balance equation for the internal energy on each tray. Furthermore, the pressure drop is neglected and equilibrium is assumed between streams leaving a tray. For instance, the vapour stream V_n and the liquid stream L_n in the small frame in Fig. 1 are assumed to be in equilibrium with each other. Some minor modifications of the standard model are done in order to account for the heat exchange on each tray: A model of the heat exchangers is added and the heat added/withdrawn on each tray is taken into account in the balance equation for the internal energy. The model equations are summarised in Table 1. See [8] for details.

Table 1: Equations for binary tray distillation

Total mole balance:

$$V_{n+1} - L_n = \begin{cases} D, & n \in [0, N_\mathrm{F} - 2] \\ D - (1-q)F, & n = N_\mathrm{F} - 1 \\ D - F, & n \in [N_\mathrm{F}, N+1] \end{cases}$$

Mole balance for the light component:

$$V_{n+1} y_{n+1} - L_n x_n = D\,\kappa$$

$$\text{where } \kappa = \begin{cases} x_\mathrm{D}, & n \in [0, N_\mathrm{F} - 2] \\ x_\mathrm{D} - (1-q)F z_\mathrm{F}, & n = N_\mathrm{F} - 1, \\ x_\mathrm{D} - F z_\mathrm{F}, & n \in [N_\mathrm{F}, N+1]. \end{cases}$$

Balance equation for the internal energy:

$$Q_n = V_n H_n^\mathrm{V} + L_n H_n^\mathrm{L} - V_{n+1} H_{n+1}^\mathrm{V} - L_{n+1} H_{n+1}^\mathrm{L} - \gamma$$

$$\text{where } \gamma = \begin{cases} (1-q)\,F\,H_\mathrm{F}^\mathrm{V}, & n = N_\mathrm{F} - 1, \\ q F\,H_\mathrm{F}^\mathrm{L}, & n = N_\mathrm{F}, \\ 0, & \text{otherwise.} \end{cases}$$

Average heat exchange force:

$$X_n = \left(\delta / \lambda_n\, T_n^2\right)\, (Q_n / A_n)$$

The total entropy production:

$$\left(\tfrac{dS}{dt}\right)_\mathrm{irr} = B S^\mathrm{B} + D S^\mathrm{D} - F S^\mathrm{F} + \sum_{n=0}^{N+1} \left(Q_n X_n - \tfrac{Q_n}{T_n} \right)$$

CALCULATIONS

We have studied three tray columns: The adiabatic column, the optimal column, and the EoEP column. The results for these columns are marked with "Adiab", "Diab. opt." and "Diab. EoEP", respectively, in Figs. 2 to 9.

The adiabatic column and the optimal column were found as described by [8]. The EoEP column was found using sequential quadratic programming with the *Matlab® 6* function *fmincon*. As the initial guess of the solution, we used the optimal column.

[2]The tray(s) on which the feed is mixed with the internal streams, depends on whether the feed is a liquid ($n = N_\mathrm{F}$), a vapour ($n = N_\mathrm{F} - 1$) or a mixture of both ($n = N_\mathrm{F}$ and $N_\mathrm{F} - 1$). See the equations in Table 1.

Table 2: Parameters

P / atm	1
F / (mol/s)	1
Feed temperature / K	360
z_F	0.5
x_D	0.95
x_B	0.05
δ / m	10^{-5}

We used the parameter values in Table 2 in all calculations. The feed temperature and the feed composition in the table correspond to a liquid feed ($q = 1$). The number of the feed tray, N_F, the number of trays, N, and the total heat transfer area, A_{total}, varied. The numbers of the feed trays in the adiabatic, optimal and EoEP columns were chosen such that the entropy productions of the columns were minimised. We studied the effects of varying the number of trays between 14 and 40 and the total heat transfer area between 2 and 20 m^2.

Table 3: Thermodynamic properties

Component	1	2
T_{boil}/K	351.45	373.15
$C_p^V/(J/K\,mol)$	65.6	33.60
$C_p^L/(J/K\,mol)$	112.3	75.35
$\Delta_f H^{\ominus,L}/(kJ/mol)$	-277.6	-285.830
$\Delta_f H^{\ominus,V}/(kJ/mol)$	-234.8	-241.826
$S^{\ominus,L}/(J/K\,mol)$	161.0	69.95
$S^{\ominus,V}/(J/K\,mol)$[a]	283.3	188.836

[a] These entropies were adjusted so that $\Delta_{vap}G = 0$ at T_{boil} for each component.

We assumed that the liquid is an ideal mixture, and that the vapour is an ideal gas. We used pure component thermodynamic data for ethanol (component 1) and water (component 2), given in Table 3 [20]. The enthalpies and entropies in Table 3 are the values at 1 atm and 298 K. Enthalpies and entropies at other temperatures were found by integration of C_p and C_p/T, respectively, from 298 K to the temperature in question.

RESULTS AND DISCUSSION

We compare the EoEP column to the other columns. The focus shall be on how good the EoEP column approximates the optimal column. The adiabatic column is added as a reference. First, we discuss the total entropy production. Then, we discuss the characteristics of the columns.

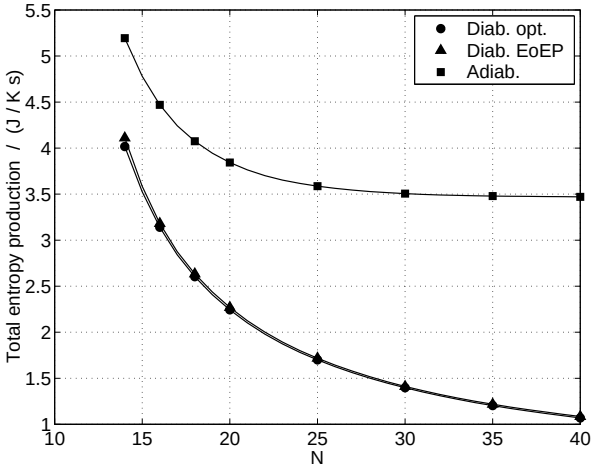

Figure 2: The total entropy production vs. the number of trays when the total heat transfer area is $20\,m^2$.

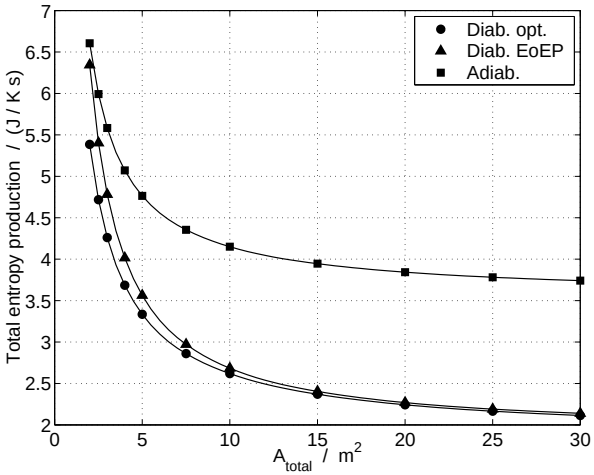

Figure 3: The total entropy production vs. the total heat transfer area when there is 20 trays.

The effects of varying the number of trays and the total heat transfer area on the total entropy production of the adiabatic, optimal and EoEP columns are shown in Figs. 2 and 3, respectively. The figures show, as expected, that the total entropy production increases when the number of trays and/or the total heat transfer area decrease. The adiabatic column has the highest entropy production, and the optimal column has the lowest entropy production. The EoEP column has approximately the same en-

tropy production as the optimal column, except for low heat transfer areas. For low heat transfer areas, the entropy production of the EoEP column is significantly higher than the entropy production of the optimal column. The agreement between the optimal and the EoEP column gets better and better as both the number of trays and/or the total heat transfer area increase.

The characteristics of the adiabatic, the optimal and the EoEP columns are presented in Figs. 4 - 9. In all the figures, tray 0 is the condenser, and tray 21 is the reboiler.

Figures 4 - 6 present the characteristics of column A. This is a column with 20 trays and a heat transfer area of 20 m^2. For this column, the total entropy production of the optimal and the EoEP columns are approximately the same (cf. Fig. 3).

The vapour flows and the heat duties on each tray in column A are shown in Figs. 4 and 5, respectively. The characteristics of the adiabatic and the optimal columns are the same as discussed earlier [7, 8, 11, 12]. The important point here is that the agreement between the optimal column and the EoEP column is very good. The vapour flow on each tray in the EoEP column is shifted slightly down in the rectifying section and slightly up in the stripping section compared the optimal column, but the differences are not substantial. The differences in the heat duties are barely visible, except on trays 8 and 20. Even smaller differences exist between the temperature profiles of the two columns (not shown). The liquid flows on each tray (not shown) differ approximately as much as the vapour flows do, see Fig. 4.

Figure 6 shows the entropy production on each tray in column A. This figure shows small differences between the optimal and the EoEP columns. The entropy production on each tray in the optimal column varies slightly in the rectifying and the stripping sections. In the EoEP columns, the entropy production is as required constant in each section.

Figures 7 - 9 present the characteristics of column B. This is a column with 20 trays and a heat transfer area of 2 m^2. For this column, the total entropy production of the optimal and the EoEP columns are significantly different (cf. Fig. 3).

The differences between the optimal column B and the EoEP column B are thus also significant. This is visible in Figs. 7 - 9. Figure 7 shows that the vapour flow is too low to be optimal in most of the EoEP

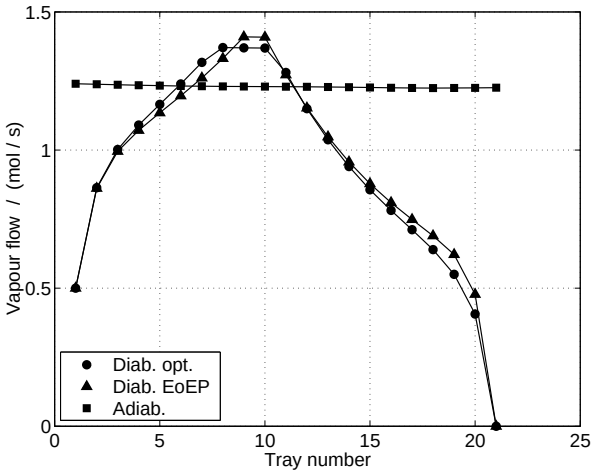

Figure 4: The vapour flow on each tray in column A.

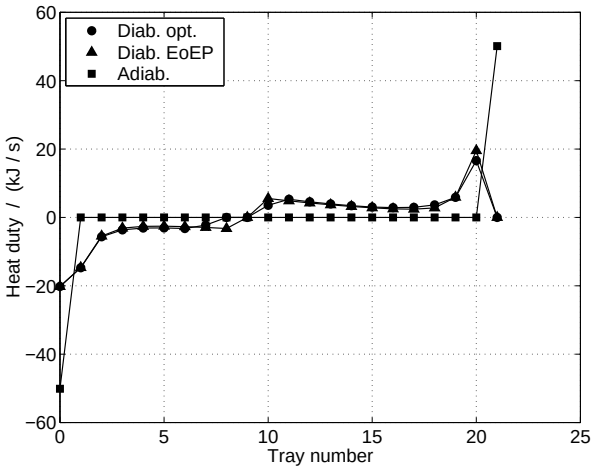

Figure 5: The heat duty on each tray in column A.

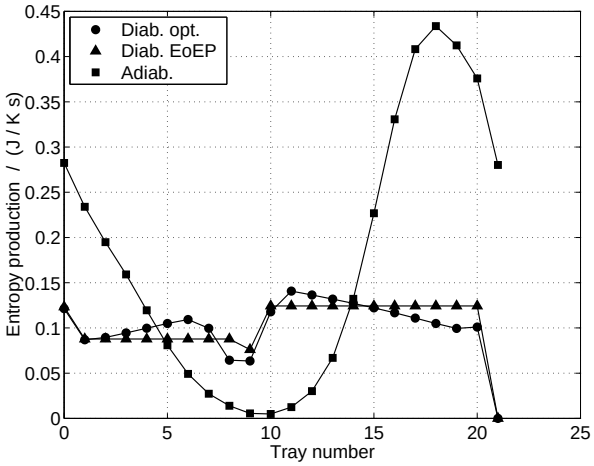

Figure 6: The entropy production on each tray in column A.

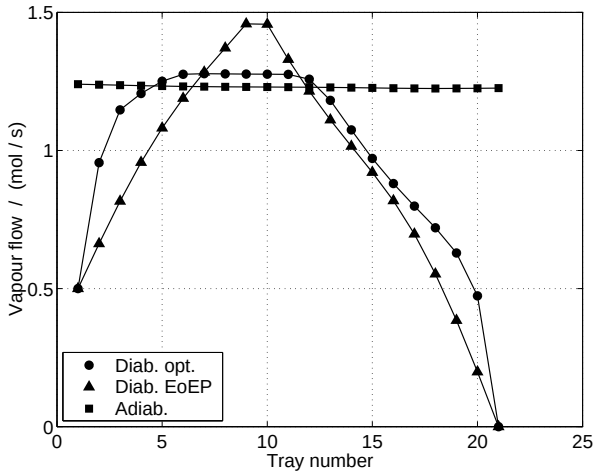

Figure 7: The vapour flow on each tray in column B.

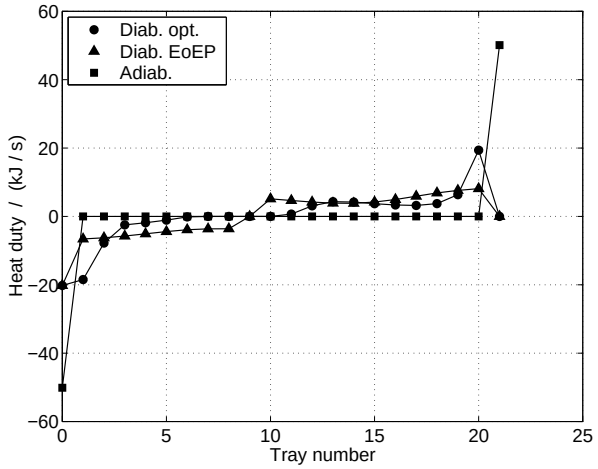

Figure 8: The heat duty on each tray in column B.

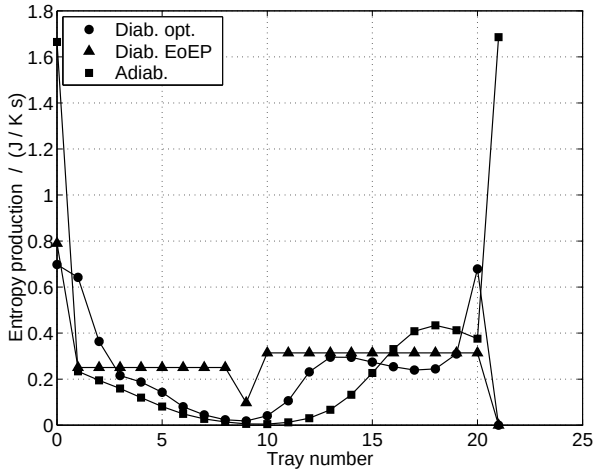

Figure 9: The entropy production on each tray in column B.

column, except close to the feed tray ($n = 9$) where it is too high. The heat duty on each tray in the EoEP column is higher than in the optimal column, especially in the rectifying section (cf. Fig. 8). The differences between the optimal column and the EoEP column, are also visible in the entropy production on each tray (cf. Fig. 9). The entropy production in the optimal column is far from constant in the rectifying section. The difference between the two columns is smaller in the stripping section.

The results show that the EoEP column is a good approximation to the optimal column, except when the heat transfer area is low. Moreover, the EoEP column approximates the optimal column best for long columns with a large heat transfer area. These results support the hypothesis put forward by [13]. Using column A and column B as examples, it is clear that there is sufficient freedom to adjust in column A, but not in column B. The fact that the total heat transfer area in column B is one tenth of that in column A, restricts the system's freedom to adjust.

As discussed earlier, the model of distillation that we have used in this paper, is not consistent with the kind of model for which EoEP (and EoF) has been derived. We therefore had to use the properties of a continuous distillation model to explain why EoEP is a good approximation to the optimum in diabatic distillation. In order to be completely sure that "EoEP, but also EoF are good approximations to the state of minimum entropy production in the parts of an optimally controlled system that has sufficient freedom" [13], we need to study continuous distillation in more detail. This is therefore an important next topic.

CONCLUSION

We have studied EoEP as an approximation to the state of minimum entropy production in diabatic tray distillation. A column with constant tray entropy production in the rectifying section and in the stripping section was a good approximation to the optimal column, except when the total heat transfer area was low. The agreement between the two columns became better and better as the total heat transfer area and the number of trays increased. The condenser, the reboiler and the tray(s) where the feed stream is mixed with the internal streams were left out in the equipartitioning.

We predicted these results using the hypothesis formulated by [13] on a continuous diabatic distillation

column. We explained why, when and in what sense EoEP applies. The properties of the optimal state in the tray column were deduced from the similarities with the continuous column. The numerical results supported the validity of the hypothesis, since the agreement with the predictions was very good.

ACKNOWLEDGEMENTS

We thank Signe Kjelstrup for suggestions and the Research Council of Norway for their funding.

REFERENCES

[1] Rivero R. *L'Analyse d'Exergie: Application à la Distillation Diabatique et aux Pompes à Chaleur à Absorption*. PhD thesis, Institut National Polytechnique de Lorraine, Nancy, France, 1993.

[2] Fonyo Z. *Thermodynamic analysis of rectification I. Reversible model of rectification.* Int. Chem. Eng. 1974;14:18–27.

[3] Fonyo Z. *Thermodynamic analysis of rectification II. Finite cascade models.* Int. Chem. Eng. 1974;14:203–210.

[4] Sauar E, Kjelstrup S, Lien KM. *Equipartition of forces - extensions to chemical reactors.* Comput. Chem. Eng. 1997;21:s29–s34.

[5] Sauar E, Siragusa G, Andresen B. *Equal thermodynamic distance and equipartition of forces principles applied to binary distillation.* J. Phys. Chem. A 2001;105:2312–2320.

[6] de Koeijer GM, Kjelstrup S, Salamon P, Siragusa G, Schaller M, Hoffmann KH. *Comparison of entropy production rate minimization methods for binary diabatic tray distillation.* Ind. Eng. Chem. Res. 2002;41:5826–5834.

[7] de Koeijer GM, Røsjorde A, Kjelstrup S. *Distribution of heat exchange in optimum diabatic distillation columns.* Energy 2004;29:2425–2440.

[8] Røsjorde A, Kjelstrup S. *The second law optimal state of a diabatic binary tray distillation column.* Chem. Eng. Sci., 2005;60:1199-1210.

[9] Salamon P, Nulton JD. *The geometry of separation processes: A horse-carrot theorem for steady flow systems.* Europhys. Lett. 1998;42:571–576.

[10] Andresen B, Salamon P. *Optimal distillation using thermodynamic geometry*. In: Sieniutycz S, De Vos A, editors. Thermodynamics of Energy Conversion and Transport. New York: Springer, 2000. p. 319–331.

[11] Schaller M, Hoffmann KH, Siragusa G, Salamon P, Andresen B. Numerically optimized performance of diabatic distillation columns. Comput. Chem. Eng. 2001;25:1537–1548.

[12] Schaller M, Hoffmann KH, Rivero R, Andresen B, Salamon P. *The influence of heat transfer irreversibilities on the optimal performance of diabatic distillation columns.* J. Non-Equilib. Thermodyn. 2002;27:257–269.

[13] Johannessen E, Kjelstrup S. *A highway in state space for reactors with minimum entropy production.* Chem. Eng. Sci., 2005;60:3347–3361.

[14] Tondeur D, Kvaalen E. *Equipartition of Entropy Production. An Optimality Criterion for Transfer and Separation Processes.* Ind. Eng. Chem. Res. 1987;26:50–56.

[15] Sauar E, Kjelstrup S, Lien KM. *Equipartition of Forces. A New Principle for Process Design and Operation.* Ind. Eng. Chem. Res. 1996;35:4147–4153.

[16] Spirkl W, Ries H. *Optimal finite-time endoreversible processes.* Phys. Rev. E 1995;52:3485–3489.

[17] de Groot SR, Mazur P. *Non-Equilibrium Thermodynamics*. London: Dover, 1984.

[18] Bedeaux D, Kjelstrup S. *Irreversible thermodynamics - a tool to describe phase transitions far from global equilibrium.* Chem. Eng. Sci. 2004;59:109–118.

[19] McCabe W, Smith J, Harriot P. *Unit Operations of Chemical Engineering*. 5th edition. New York: McGraw-Hill, 1993.

[20] Dean JA. *Lange's handbook of chemistry*. 15th edition. New York: McGraw-Hill, 1999.

Proceedings of ECOS 2005
Trondheim, Norway
June 20–22, 2005

EXTERNAL HEAT INTEGRATION FOR TERNARY MIXTURE SEPARATION

M. Nakaiwa*, K. Huang, K. Iwakabe, A. Endo, T. Ohmori, and T. Yamamoto
National Institute of Advanced Industrial Science and Technology (AIST)
Research Institute for Innovation in Sustainable Chemistry, Tsukuba, Japan

ABSTRACT

Although internal heat integration within a distillation column can be effective in reducing energy consumption, it needs generally much more expenditure on capital investment due to the necessity of an expensive compressor and the diminishing of mass transfer driving force. A novel method for intensification of distillation processes through external heat integration is proposed in this paper. The external heat integration signifies heat integration between a rectifying section and a stripping section of different distillation columns here. It can work as an alternative means for reducing not only energy consumption, but also capital investment through accommodation of the relevant distillation columns within one shell. Through examination on a distillation system separating a hypothetical ternary mixture, the advantages of external heat integration are demonstrated thoroughly. Sensitivity analysis is also conducted with respect to feed composition and product specifications. The results obtained indicate the inherent characteristics of the design procedure proposed. However, it must be pointed out that external heat integration can present negative effect to process dynamics and process operation and it is therefore necessary to exercise a careful trade-off between process economics and process operation during process development.

Keywords: Process intensification, distillation column, heat integration, process design, operating cost, capital investment

NOMENCLATURE

A	component
A_{vp}	vapor pressure constant
B	component
B_{vp}	vapor pressure constant
C	component
D	column diameter [m]
f	detuning parameter
F	feed flow rate [kmol/s]
ΔH_V	heat of vaporization [kJ/kmol]
L	liquid flow rate [kmol/s]
NT	number of stages
P	pressure [Pa]
P^s	saturation pressure [Pa]
q	feed thermal condition
R	ideal gas law constant [kJ/kmol K]
S	area, [m^2]
T	temperature [K]
U	overall heat transfer coefficient [kJ/m^2K]
V	vapor flow rate [kmol/s]
x	liquid composition
y	vapor composition
z	feed composition

Greek Letters

α	relative volatility

Superscripts/Subscripts

C	condenser
R	reboiler

Abbreviations

TAC	total annual cost
DSC	direct sequence of columns
IDSC	direct sequence of columns with external heat integration
ISC	direct sequence of columns
IISC	indirect sequence of columns with external heat integration

* Correspondence author: Phone: +81-29-861-4696
Fax: +81-29-861-4660; E-mail: nakaiwa-m@aist.go.jp

INTRODUCTION

Process intensification has now gained increasingly importance in the chemical and petrochemical process industries, for instance, the development of membrane reactor and reactive distillation columns, etc. The major driving force behind this tendency is the dramatic reduction in not only energy consumption but also the capital investment (Stankiewicz and Moulijn, 2000, 2002, 2003; Luyben and Hendershot, 2004). Other benefit includes, for example, the reduction of plant size and the improvement of risk management. For the intensification of distillation processes, the progress is rather unsatisfactory. Although reactive distillation offers an effective alterative for process intensification, its applications are quite limited due to the strict requirement on the match of reaction and separation operating conditions (Stankiewicz, 2003). As distillation process still represents the major means of separation operation currently, it appears therefore imperative to develop an effective way for the intensification of distillation processes.

Distillation columns have been well known for their low energy efficiency. For effecting a separation heat has to be given at a high temperature in the reboiler and simply drawn off at a low temperature in the condenser. For dealing with this deficiency, a considerable amount of research has been conducted and the earliest work can even be dated back to the beginning of 1920s, where the studies were concentrated primarily on the low-temperature air separation. Since then, heat pump principle has frequently been used in improving distillation efficiency. Freshwater (1961) ones proposed a very rough idea for pumping heat from a stage in the rectifying section and then apply it to a stage in the stripping section for multi-component distillation columns. Petlyuk and his coworkers (1965) developed a method for the design of multi-component distillation columns with intermediate condensers and/or reboilers through minimization of entropy production. The potential drawback, however, is the exceedingly complexities in problem formulations and their solutions, especially when highly non-ideal systems have been considered. Later, Fonyo (1974) derived in more detail a reversible model for multi-component distillation columns and displayed the necessity of simultaneously withdrawing heat from the rectifying section and supplying heat to the stripping section in order to achieve a more efficient process operation. Mah and his coworkers (1980) evolved a different process configuration, which was later called by them the secondary reflux and vaporization (SRV) distillation column. Instead of the heat integration between a pair of stages, SRV distillation column actually included internal heat integration between part of the rectifying and part of the stripping sections. Our research laboratory has been continuing the research work on this subject both theoretically and experimentally since 1980 and confirmed for the first time by large-scale pilot-plant evaluations the high advantages of internal heat integration to the separation of binary close-boiling mixtures (Nakaiwa et al., 2003). One of our principal contributions is the exploit of full degree of heat integration between the whole rectifying and whole stripping sections of a distillation column, by which a more perfect way can be realized to approximate the reversible distillation operation. Recently, our studies demonstrated that through internal heat integration between the whole rectifying and whole stripping sections, considerable reduction in energy consumption could also be achieved for some multi-component systems (Iwakabe et al., 2004).

However, it should be pointed out here that large investment has to be expensed for the internal heat integration due to, for instance, the necessity of an expensive compressor and the resultant very large distillation column (cf. Figure 1). These factors pose certainly severe constraints on the application of internal heat integration to distillation processes. The purpose of the present work is therefore to explore the feasibility of intensifying distillation columns through external heat integration between different distillation columns. The current work is organized as follows: The comparison of internal heat integration and external heat integration is conducted in the next section, followed by the description of a new method for intensification of distillation processes. The design method is then evaluated through separation a hypothetical ternary mixture. Comparative studies are conducted in both steady and dynamic states between distillation columns with and without external heat integration. Some concluding remarks on the intensification of distillation processes are given in the last section of

the paper.

INTERNAL HEAT INTEGRATION VS EXTERNAL HEAT INTEGRATION

Although internal heat integration within a distillation column can be effective in reducing energy consumption, it needs generally much more expenditure on capital investment due to the necessity of an expensive compressor and the diminishing of mass transfer driving force. Figure 1 shows a schematic of an internally heat-integrated distillation column. As can be seen, a compressor must be incorporated to realize the temperature rise between rectifying section and stripping section. Moreover, two column shells are needed for one distillation column, worsening further the process economics. To avoid these negative factors of internal heat integration, external heat integration appears to be an effective way to realize intensification of distillation processes. In Figure 2 the principle of external heat integration is illustrated between two distillation columns. It is not difficult to understand that external heat integration needs no expensive compressors and offers the possibility of reduction in capital investment by arrangement of two distillation columns in one shell.

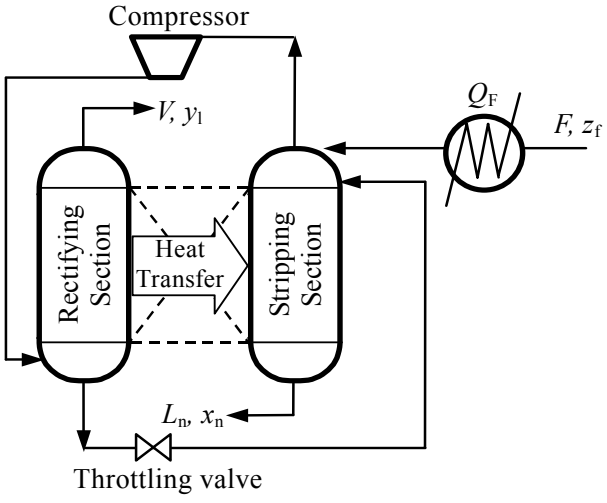

Figure 1: The schematic of an internal heat integrated distillation column

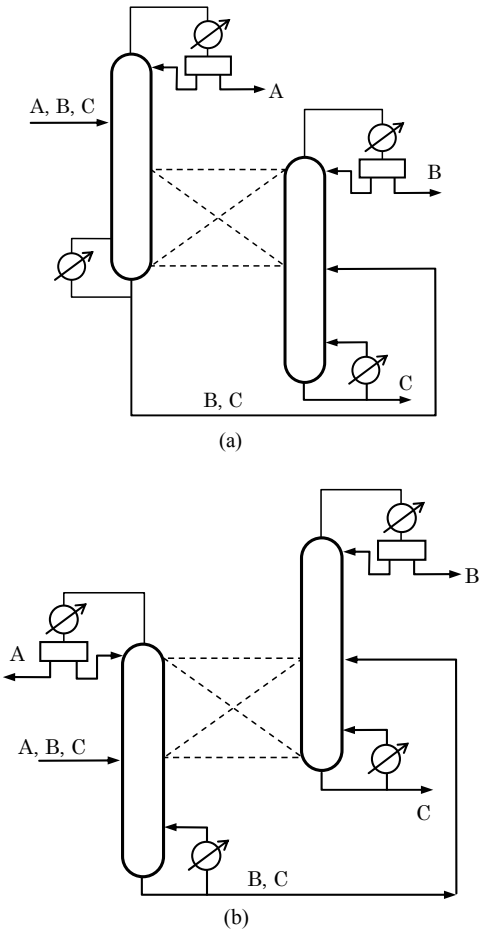

Figure 2: The direct sequence of distillation columns with external heat integration

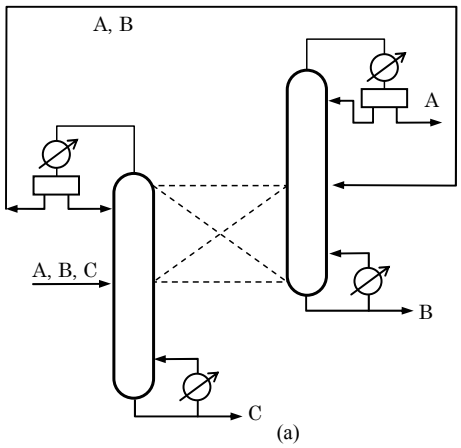

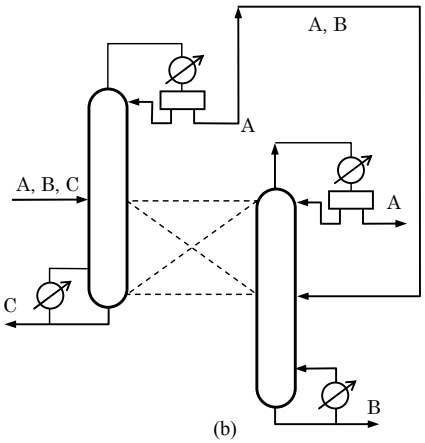

Figure 3: The indirect sequence of distillation columns with external heat integration

INTENSIFICATION OF DISTILLATION PROCESSES BY EXTERNAL HEAT INTGRATION

Although the distribution of heating and cooling sections are very complicated especially for multi-component distillation columns, it is reasonable to simply take the rectifying section as cooling section and stripping section a heating section in most cases. With this interpretation, the external heat integration can be exploited for any pair of distillation columns, provided the economical feasibility can be justified. Figure 2 illustrates the two schemes for the intensification of the direct sequence (DCS) of distillation systems separating a ternary mixture. The two schemes differ mainly in the magnitudes of pressure elevation between the two heat integrated distillation columns. Depending upon the detailed operating conditions, each of them can be effective for intensification of distillation processes. However, scheme (a) is generally superior to scheme (b), because relative small elevation of pressure is needed. Analogously, the two possible schemes for the intensification of indirect sequence (ICS) of distillation systems are illustrated in Figure 3. In this work, the process schemes of (a) in Figures 2 and 3 are mainly examined, because they represent the potentials of external heat integration.

It should be reminded here that external heat integration narrows also the driving forces in mass transfer within the two distillation columns and it is therefore still necessary to compensate these losses in the process development by adding additional stages in the corresponding sections of the two distillation columns.

AN ILLUSTRATIVE EXAMPLE: SEPARATION OF AN HYPOTHETICAL TERNARY MIXTURE

The Example System

A distillation system has been selected for the evaluation of the proposed design method of intensifying distillation processes by means of external heat integration. Table 1 tabulates the specification of process design, which includes the separation of an ideal liquid saturated ternary mixture into 0.9 pure products. For simplification, constant relative volatility and constant latent heat is assumed for the mixture to be separated.

Process Design for Distillation Processes with External Heat Integration

A general procedure for the design of distillation systems with external heat integration is presented in Appendix II and Table 2 shows the economical basis of the process design. The minimization of total annual cost (TAC) is taken as the design objective. Figure 4 shows the relationship between TAC and total stage numbers of distillation columns. The comparison against conventional distillation trains has been tabulated in Table 3 for the case of the direct sequence of distillation columns and Table 4 for the indirect sequence of distillation columns. As can be seen, external heat integration leads to a reduction of capital investment by 3.47% for the direct sequence of columns, and by 3.33% for the indirect sequence of columns. In the meanwhile, external heat integration gives also rise of reduction of operating cost by 11.43% for the direct sequence of distillation columns, and by 16.22% for the indirect sequence of distillation columns. These results are very striking; confirming that even without additional capital investment, the improvement of system performance can still be obtained. They also demonstrate that external heat integration can work as an alternative way for the intensification of distillation trains.

Items		Values
Pressure of the lower pressure column (atm)		1
Heat transfer area (m^2/stage)		5
Feed flow rate (kmol/s)		100
Feed concentration z_A: z_B: z_C (mol%)		1/3: 1/3: 1/3
Feed thermal condition		1.0
Relative volatility α_A: α_B: α_C		4: 2: 1
Latent heat of vaporization (kcal/kmol)		6944
Product specification A, B, C		0.9
Vapor pressure constants	A (Avp/Bvp)	13.04 / 4634.4
	B (Avp/Bvp)	12.34 / 4634.4
	C (Avp/Bvp)	11.64 / 4634.4

Table 1: Steady-state design conditions of the hypothetical distillation system

	Parameters	Units	Value
Reboiler	Heat transfer coefficient	kJ/(s·K·m^2)	0.568
	Temperature difference	K	34.8
Condenser	Heat transfer coefficient	kJ/(s·K·m^2)	0.852
	Temperature difference	K	13.9
	energy cost	\$/10^6 kJ	4.7
	Payback period	Year	3

Table 2: Sizing and economic basis

	Capital cost (\$ 10^6)	Operating cost (\$$10^6$/year)	TAC (\$$10^6$/year)
DSC	1.44	0.35	0.83
IDSC	1.39	0.31	0.77
Comparison	96.53%	88.57%	92.77%

Table 3: Comparisons of direct sequence of columns with and without heat integration

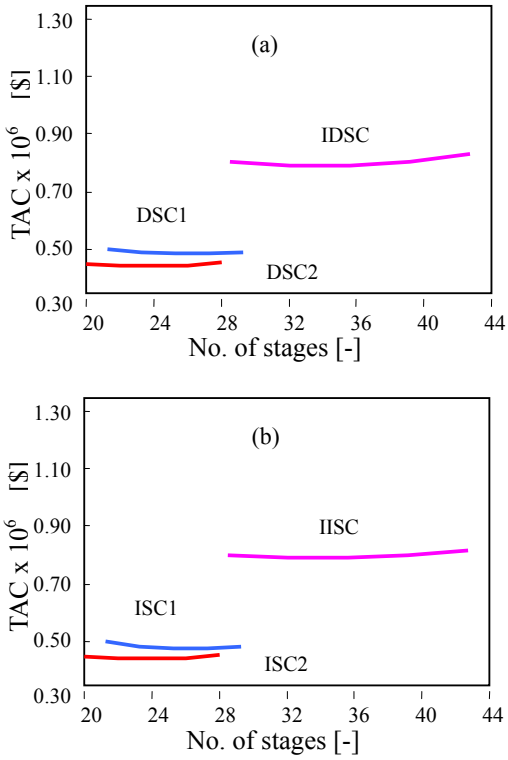

Figure 4: The relationship between TAC and the total number of stages

	Capital cost (\$ 10^6)	Operating cost (\$$10^6$/year)	TAC (\$$10^6$/year)
ISC	1.50	0.37	0.87
IISC	1.45	0.31	0.79
Comparison	96.67%	83.78%	90.81%

Table 4: Comparisons of indirect sequence of columns with and without heat integration

Sensitivity Analysis

Sensitivity analysis is conducted with respect to changes in feed composition. Tables 5 and 6 compare the performance of direct and indirect sequence of distillation columns with and without external heat integration for three feed compositions. It has been found that external heat integration appears to be relative insensitive to operating condition changes. In comparison with conventional process design, it can secure a

reduction of energy consumption from 9.09**%** to 15.38% for the direct sequence of columns and from 12.5% to 20% for the indirect sequence of columns.

Sensitivity analysis is also conducted with respect to changes in product specifications. Figure 5 illustrates the changing tendency of the effectiveness of external heat integration against the product specifications. As can be seen, the higher the product specifications are, the more effectiveness of the external heat integration. The phenomenon is due to the fact that high reflux ratio is needed to achieve high degree of separation. A similar observation can also been observed for the case of the indirect sequence of columns.

Feed compositions		4/9:1/9:4/9	1/3:1/3:1/3	2/9:5/9:2/9
Operating cost (10^6/year)	DSC	0.33	0.35	0.39
	IDSC	0.30	0.31	0.35
	Comparison	90.91%	88.57%	84.62%

Table 5: Comparisons between direct sequence of columns with and without external heat integration

Feed compositions		4/9:1/9:4/9	1/3:1/3:1/3	2/9:5/9:2/9
Operating cost (10^6/year)	DSC	0.32	0.37	0.40
	IDSC	0.28	0.31	0.32
	Comparison	87.5%	83.78%	80.00%

Table 6: Comparisons between direct sequence of columns with and without external heat integration

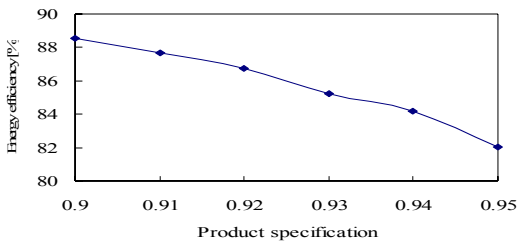

Figure 5: The effectiveness of external heat integration vs product specifications

Controllability Analysis

One of the major concerns in external heat integration of distillation columns is the influence to the process dynamics and process operation. The regulatory responses are illustrated in Figure 6 when the processes have been disturbed by a +10% step change, respectively, in feed flow rate of DSC and IDSC. Here, the levels of reflux drums and reboilers are controlled by the manipulation of top and bottom product flow rates and the purity of top and bottom products is controlled by the manipulation of reflux flow rates and boilup rates. It is readily to see that IDSC displays larger deviations and longer setting time than DSC. These realities indicates that external heat integration strengthens the interaction between the two distillation columns involved and thus poses additional difficulties to process operation.

Likewise, the regulatory responses are illustrated in Figure 7 when the processes have been disturbed by a -10% step change, respectively, in feed flow rate of ISC and IISC. Again, it can be found that external heat integration presents negative effects to the process dynamics and process operation.

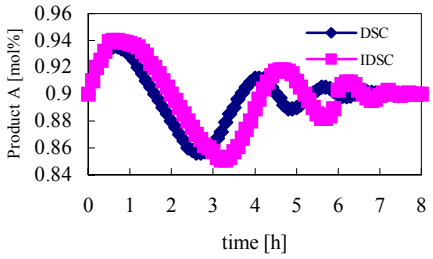

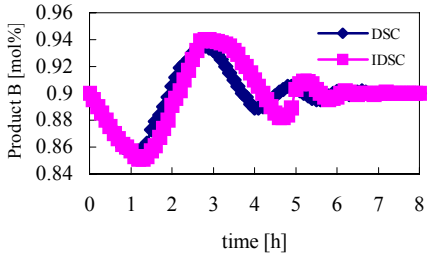

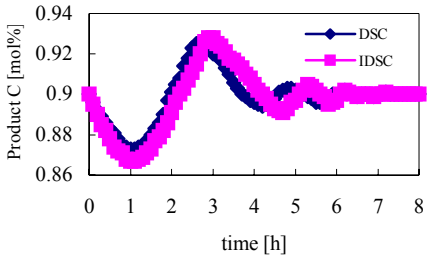

Figure 6: The comparison of dynamic performance between DSC and IDSC

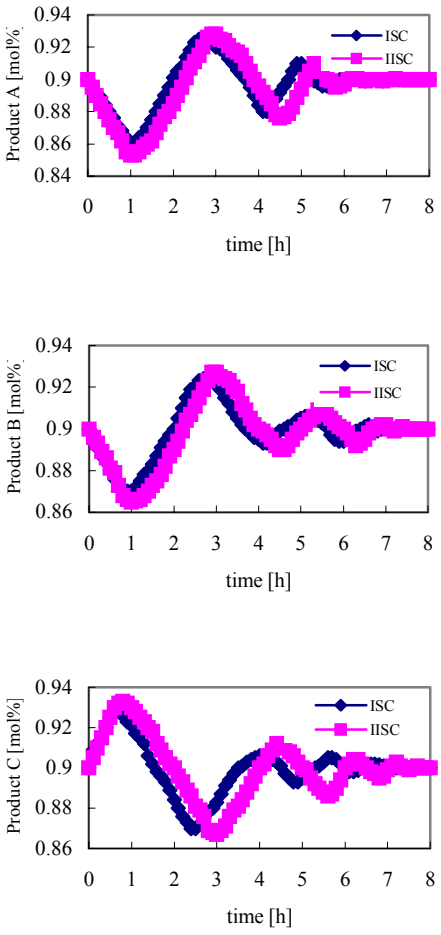

Figure 7: The comparison of dynamic performance between ISC and IISC

DISCUSSIONS

It is worth mentioning here that external heat integration offers more freedoms in process design than internal heat integration for the reduction of energy consumption of distillation systems. Provided it is economically feasible, it can be applied to any pair of distillation columns, which may even belong to different process systems. Internal heat integration can, however, only be used within the one distillation column. In addition to its high investment requirement, whether it can be used or not depends heavily on the mixture to be separated, for instance, the relative volatility, thereby limiting severely its application opportunities.

On the other hand, external heat integration has frequently been found to worsen process dynamics and introduce extra difficulties to process operation. It is thus of great significance to make a careful balance between process economics and process operation during process development.

CONCLUSIONS

In terms of the principle of external heat integration, a novel method for intensification of distillation processes is proposed in this paper. In contrast to internal heat integration, it includes heat integration between two different distillation columns and can allow accommodation of these two distillation columns within one shell. These characteristics permit it to work as an alternative way to reducing not only energy consumption, but also capital investment in the same time. Simulation studies are conducted for the separation of a hypothetical ternary mixture. Through comparison with conventional distillation schemes, the effectiveness of the external heat integration has been ascertained. It has also been found that external heat integration appears not so sensitive to changes in feed composition and product specifications.

However, it must be pointed out that external heat integration can strongly influence process dynamics and give additional difficulties to process operation. It is therefore necessary to make a careful balance between process economics and process operation during process development.

REFERENCES

[1] Flower J. R., and Jackson, R., 1964, Energy requirement in the separation of mixtures by distillation. *Trans. of Inst. Chem. Eng.*, 42: 249-258.

[2] Fonyo, Z., 1974, Thermodynamic analysis of rectification:1-reversible model of rectification. *Intern Chem. Eng.*, 14: 18-27.

[3] Petlyuk, F. B., Platonov, V. M., and Girsanov, L. V., 1965, The design of optimal rectification cascades. *Internl. Chem. Eng.*, 5: 309-317.
[3] Luyben, W. L., Hendershot, D. C., 2004, Dynamic disadvantages of intensification in inherently safer process design. *Ind. Eng. Chem. Res.*, 43: 384-396.
[4] Mah, R.S.H., Nicholas J. J. and Wodnik, R. B., 1977, Distillation with secondary reflux and vaporization: a comparative evaluation, *AIChE J*, 23: 651-658.
[5] Naito, K., Nakaiwa, M., Huang, K., Endo, A., Aso, K., Nakanishi, T., Nakamura, H., Noda H. and Takamatsu, T., 2000, Operation of a bench-scale ideal heat-integrated distillation column (HIDiC): an experimental study, *Computers Chem. Eng.*, 24: 495-499.
[6] Nakaiwa, M., Huang, K., Endo, T., Ohmori, T., Akiya T. and Takamatsu, T., 2003, Internally heat-integrated distillation column: a review," *Trans. IChemE*, 81: 162-177.
[7] Stankiewicz, A. and Moulijn J. A., 2000, Process intensification: transforming chemical engineering, *Chem. Eng. Progress*, 96: 22-34.
[8] Stankiewicz, A. and Moulijn J. A., 2002, Process intensification, *Ind. Eng. Chem. Res.*, 41: 1920-1924.
[9] Stankiewicz, A. and Moulijn J. A., 2003, Process intensification---has its time finally come? *Chem. Eng. Progress*, 99: 50-55.
[10] Stankiewicz, A., 2003, Reactive separation for process intensification: an industrial perspective, *Chem. Eng. Processing*, 42: 137-144.

ACKNOWLEDGMENT

The authors are grateful to the financial support from the Japan Science and Technology (JST) Corporation under the frame of Core Research and Evolutional Science and Technology (CREST).

Appendix I: Sizing and Economic Basis

The capital costs of distillation columns and the energy cost are estimated using the following equations

$$\text{Column cost} = 17640 D_C^{1.066} L_C^{0.802}$$
$$\text{Tray cost} = 229 D_C^{1.55} N_T$$
$$\text{Heat exchanger cost} = 7296 S_R^{0.65} + 7296 S_C^{0.65}$$
$$\text{Energy cost} = 0.6206\, \Delta H_V^{0.65} V_S$$

Assuming an F factor of 1 in engineering units, the diameter of the column is calculated from the equation

$$D_C = 173.5 (M_W T/P)^{0.25} V_{NT}^{0.5}$$

The column height is calculated assuming a 0.61-m (2 ft) tray spacing and allowing 20% more height for base level volume.

$$L_C = 0.73152\, N_T$$

The heat-transfer areas of the reboiler and condenser are calculated using the steady-state vapor flow rates and the heat of vaporization.

$$S_R = 0.0042 \Delta H_V^{0.65} V_S/(U_R T_R)$$
$$S_C = 0.0042 \Delta H_V^{0.65} V_S/(U_C T_C)$$

Appendix II: The Procedures for Design of Distillation Systems Separating a Ternary Mixture

The following rule of thumb method is used in the process design of ternary distillation systems. They include direct sequence of column (DSC), indirect sequence of column (ISC), direct sequence of column with external heat integration (IDSC), and indirect sequence of column with external heat integration (IDSC).

[1] Set the pressures of each column and determine the pressure difference at the same time.

[2] Given the recovery of the first distillation column.

[3] In each column, the reflux ratio is 1.2 times the minimum reflux ratio, which is calculated via the Underwood equations.

[4] In each column, the number of stage is twice the minimum number of stages, which is calculated via the Fenske equations.

[5] Kirkbride`s method is used to find the optimal feed location, N_F.

[6] Determine the number of stages that is heat integrated.

[7] Using these data, calculate the total annual cost (TAC) by combining the energy cost with the annual capital cost, using a payback period given.

[8] Vary the value of the recovery of the first distillation column and repeat steps iii–vi. Select the minimum in the TAC as the economically optimum steady state design for the given process.

Proceedings of ECOS 2005
Trondheim, Norway
June 20–22, 2005

DISTILLATION OPTIMIZATION USING IRREVERSIBLE THERMODYNAMICS

J.P. Schmal, H.J. van der Kooi, Ž. Olujić and P.J. Jansens
Laboratory for Process Equipment, TU Delft
Leeghwaterstraat 44, 2628 CA Delft, The Netherlands

ABSTRACT

In this paper a procedure is described to come to an optimal (in economic and exergetic sense) fluid based separation device and configuration. It consists of two steps: first the best device is determined with the help of a design tool and secondly for heat integrated distillation column (HIDiC) the optimal configuration is determined (for other devices this is known). To test this approach, rigorous models of conventional distillation (CD), vapor recompression (VR) and HIDiC have been built and the PP-splitter was used as case study. The design tool used in the first step predicted operational costs and exergetic losses within an error of 10 % for the PP-case. The HIDiC configuration has been optimized and the results have been explained with a force-flow analysis. HIDiC is shown to be more advantageous than VR both economically and exergetically for the PP-splitter case.
Keywords: HIDiC, design tool, force-flow analysis

NOMENCLATURE

The dimensionless numbers are given on the next page.

A	heat exchange area	m^2
B	bottom flow	kmole/s
Cp	heat capacity	kJ/kmole/K
D	distillate flow	kmole/s
Ex	exergy	MW
F	flow	kmole/s
H	enthalpy	kJ/mole
J	thermodynamic flow	
L	phenomenological coefficients	
N	number of trays	-
P	pressure	Pa
PR	pressure ratio	Pa/Pa
Q	heat duty	MW
R	gas constant	kJ/mole/K
S	entropy	kJ/mole/K
T	temperature	K
V	vapor flow	kmole/s
$\hat{V}$	molar volume	$m^3/kmole$
W	power	MW
x	mole fraction	mole/mole
X	thermodynamic force	
Z	compressibility	-

Greek:

α	defined by equation 1	
θ	local entropy production	MW/K
Θ	total entropy production	MW/K
η	efficiency	-

Super- and subscript:

a	holds for both top and bottom
aa	holds for both VR and HIDiC
b	normal boiling point
bot	bottom
c	critical
cd	conventional distillation
$comp$	compressor
$cond$	condensor
$feed$	feed
hid	HIDiC
htx	heat exchange (reboiler or condensor)
$loss$	loss
reb	reboiler
ref	reference
s	entropy
top	top
vap	vaporization
vr	Vapor recompression

Abbreviations:

CD	conventional distillation
HIDiC	heat integrated distillation column
MINLP	mixed integer non-linear program
VR	vapor recompression

INTRODUCTION

The increasing importance of sustainability and stronger competition has caused a renewed interest in improving the distillation processes. At present a number of alternatives exist for separating components in a fluid state. Of the many configurations [3] we will focus on a conventional distillation column (CD), the vapor recompression (VR) and the heat-integrated distillation column (HIDiC).

Other alternatives such as the diabatic column have been studied by among others Rivero and Le Goff [12], Rivero [11] and experimentally by de Koeijer and Rivero [4]. In particular recent efforts of Jimenez et al. [2] where only two independent heat exchange streams are used, are promising from an exergetic point of view. A disadvantage of the diabatic column besides the increased capital investment is the heat exchange fluid: if only sensible heat is used large flows are needed, if latent heat is used finding the appropriate mixture is difficult. In HIDiC it is the process fluid that is used for heat-exchange.

HIDiC has first been suggested by Mah and Wodnik [5] (introduced as secondary reflux vaporization) to improve the energy efficiency of distillation. HIDiC has a rectifying section at elevated pressure inside the stripping section as to allow for internal heat transfer (from the rectifying to the stripping section). A good overview of the results that can be achieved with HIDiC can be found in Nakaiwa et al. [6]. Olujić et al. [7] describe the conceptual design of HIDiC and Pritchard et al. [8] a continuation approach to get from CD to HIDiC.

In this paper we will use exergy as a sustainability indicator and annualized cost as competitiveness indicator. To get to optimal exergetic and economic operation we can divide the problem in two: 1) screen the different devices to see which is most optimal. Since conventional distillation can be considered a special case of HIDiC (mathematically by no heat-transfer area and no compressor duty), we only need to consider VR and HIDiC. 2) optimize the configuration of the device.

First we develop a design tool that allows us to quickly screen the devices. The optimization of the configuration is discussed next and the theory of irreversible thermodynamics is used to explain the optimization results. To test the design tool and the proposed optimization approach we explore the propylene propane splitter as a case study.

DESIGN TOOL

The design tool should allow us to choose the most optimal device HIDiC (CD is special case of HIDiC) or VR without having to model both devices rigorously. The approach we have used consists of investigating the changes from CD to either VR or HIDiC, since the conceptual design of CD has been well developed.

At present the design tool uses the following assumptions (always looking from the perspective of CD):

- same top and feed flow, i.e. T, P, x, F are the same (T_{bot}, P_{bot} different)
- Redlich-Kwong equation of state
- total condensor only
- Raoult's law (activity coefficients neglected in present version)

We would like to stress that constant molar overflow is **not** assumed in the design tool calculations. The tool needs information on:

- physical properties: $T_c, P_c, V_c, Cp(l), T_b$
- design variables:
  - purities: $x_{top}, x_{feed}, x_{bot}$
  - reflux rate
  - flows: top, feed and bottom
- Standard values: $T_{ref}, \Delta T_{htx}, \Delta T_{vr}, \Delta T_{hid}$
- cost data: electricity, steam and cooling water

A dimensional analysis of the differences in exergy loss (see appendix for derivation difference exergy loss) resulted in the following set of dimensionless variables:

$$PH_{aa} = \frac{\int \hat{V} dP}{\eta_{comp} \Delta H_{vap}^{reb}} \qquad VF = \frac{V_{feed}}{V_{bot}} \qquad \Delta T_{ho} = \frac{\Delta T_{htx}}{T_{ref}}$$

$$\Delta Ex_{i-j} = \frac{Ex_{loss}^{i} - Ex_{loss}^{j}}{V_{bot} \Delta H_{vap}^{reb}} \qquad T_{ro} = \frac{T_{reb}}{T_{ref}} \qquad \Delta H_{ft} = \frac{\Delta H_{vap}^{feed}}{\Delta H_{vap}^{top}}$$

$$DV = \frac{D}{V_{bot}} \qquad T_{co} = \frac{T_{cond}}{T_{ref}} \qquad \Delta H_{rt} = \frac{\Delta H_{vap}^{reb}}{\Delta H_{vap}^{top}}$$

$$BV = \frac{B}{V_{bot}} \qquad \Delta T_{vo} = \frac{\Delta T_{vr}}{T_{ref}} \qquad CH_a = \frac{Cp_a T_{ref}}{\Delta H_{vap}^{reb}}$$

It is interesting to see that all variables can best be scaled by the energy needed to generate the vapor boil-up (in CD) rather than the more intuitive reflux rate. The vapor boil-up is the "driving" engine in

CD, which makes the result understandable. Furthermore we introduce for reasons of brevity:

$$\alpha = \left(1 - \frac{1}{T_{co} - \Delta T_{ho}}\right) \tag{1}$$

The differences in exergy loss of VR and HIDiC with respect to CD in dimensionless variables is given by:

$$\begin{aligned}
\Delta Ex_{hid-cd} &= BV(T_{ro} - T_{co})CH_{bot}(1 - \frac{1}{T_{ro}}) \\
+(\frac{\Delta H_{rt}}{\Delta H_{ft}} &+ VF)PH + (VF\frac{\Delta H_{ft}}{\Delta H_{rt}} - \frac{DV}{\Delta H_{rt}})\alpha \\
&+ \left(\frac{1}{T_{ro} + \Delta T_{ho}} - \frac{1}{T_{co} - \Delta T_{ho}}\right) \qquad (2) \\
\Delta Ex_{vr-cd} &= \left(\frac{1}{T_{ro} + \Delta T_{ho}} - \frac{1}{T_{co} - \Delta T_{ho}}\right) \\
&+ \left(\frac{\Delta H_{rt}}{\Delta H_{ft}} + VF\right)PH_{vr} \\
-(\Delta H_{rt} &+ VF\Delta H_{ft})CH_{top}(T_{ro} + \Delta T_{vo} - T_{co})\alpha \qquad (3) \\
\Delta Ex_{hid-vr} &= BV(T_{ro} - T_{co})CH_{bot}(1 - \frac{1}{T_{ro}}) \\
&+ \left(VF\frac{\Delta H_{ft}}{\Delta H_{rt}} - \frac{DV}{\Delta H_{rt}}\right)\left(1 - \frac{1}{T_{co} - \Delta T_{ho}}\right) \\
+(\Delta H_{rt} &+ VF\Delta H_{ft})CH_{top}(T_{ro} + \Delta T_{vo} - T_{co})\alpha \\
&- (1 + \frac{\Delta H_{ft}}{\Delta H_{rt}}VF)\frac{\Delta T_{vo}}{T_{ro}} \qquad (4)
\end{aligned}$$

Some of the terms are generally in a certain range. For example in the first term in equation 2, BV usually increases when relative volatility gets closer to one, but in general $(T_{ro} - T_{co})$ reduces, changing ΔEx_{hid-cd} possibly only slightly. The relative heat of vaporization, $(\frac{\Delta H_{rt}}{\Delta H_{ft}})$, decreases when the relative volatility gets closer to one, reducing ΔEx_{hid-cd}, but the last term in equation 2 decreases, increasing ΔEx_{hid-cd} (last term is always smaller than zero).

These effects can be understood if one realizes that if the separation gets more easy less reflux and vaporboilup is needed (reducing flows) on the one hand, but the difference in quality of energy needed in reboiler and extracted from the condensor increases. Since exergy is flow times the quality of energy it is in principle not easy to say what happens. Finally, we would like to stress that in general we are interested in both the exergy flow as well as the exergy density (a large exergy flow at low exergy density is not that valuable).

CONFIGURATION OPTIMIZATION

The configuration can be optimized with respect to construction materials (amount, type and its actual geometrical lay-out) as well as its internal flows (e.g. by means of utility streams). To optimize the geometrical layout a very detailed model would be needed (e.g. CFD [10]). Since optimal configurations of both CD and VR have been reported abundantly (e.g. [3]), we will focus on optimization of HIDiC.

Internal flows could also be optimized by means of CFD calculations, but here we assume we have a model that has no spatial dependencies. We focus on two variables that are specific to HIDiC: the heat exchange area, A, and the pressure ratio over the compressor, PR. The optimization problem can now be stated as:

$$\begin{aligned}
\min_{A,PR} \quad & EC \\
s.t. \quad : \quad & f(y;PR,A) = 0 \qquad (5) \\
& g(y;PR,A) \leq 0
\end{aligned}$$

The function f is the model that will be described briefly in the next section, y are the model variables and g are all inequality constraints.

The objective, EC, can either be 1) economic: annualized costs (operation + capital) or exergetic: exergy loss. The heat-exchange area, A, can be considered in many ways:

- one total area: area is evenly distributed over all heat-exchange trays
- a distribution of area: a function is used to describe the form of the area distribution over the trays
- every area: every area on each heat-exchange tray is an optimization variable

In fact we have another degree of freedom: which tray exchanges heat with which other tray? Including this degree of freedom in the optimization would make it a MINLP. Let us designate trays in the rectifying section by Ri and in the stripping section by Si (counting from top to bottom). In that case R1 is located next to S1, or Ri is located next to Si. Now physically (from a construction and temperature profile point of view) it would be unwise to have a coupling like: R1-S8, R2-S1, R3-S12, etc.

Although it is possible to achieve this, it seems unlikely this would yield an optimum solution.
For analysis we use the theory of irreversible thermodynamics [1]:

$$J_i = \sum_j L_{ij} X_j \quad (6)$$

$$\theta = \sum_i J_i X_i = \sum_i \sum_j L_{ij} X_j X_i \quad (7)$$

In particular we will do a flow-force analysis [15, 14]. The heat exchange area's will be part of the L_{ih} (i being components and h is the heat flow at that tray trough the wall). Furthermore, PR has a direct influence on the $X's$. So we can rewrite the optimization problem (5) in irreversible theory as:

$$\begin{aligned} \min_{X,L} \quad & EC \\ s.t. \quad : \quad & f_s(J,X,L) = 0 \\ & g_s(J,X,L) \leq 0 \end{aligned} \quad (8)$$

The internal entropy production part of EC is now given by:

$$EC = \Theta = \sum_{k=1}^{N} \sum_i \sum_j L_{ij}^k X_j^k X_i^k \quad (9)$$

(X_j^k means force j on tray k) PR and A both influences both L and X, hence L and X cannot be varied independently. It is therefore to be expected that the principle of equipartition of forces will not hold in this case.

CASE STUDY

In this paper the PP-splitter is taken as a case study. A feed of 52 mole% propylene (110 ton/hr) is purified to 99.5 mole% in the top and 1.1 mol% in the bottom. The column consisted of 211 theoretical trays, 154 of which where in the rectifying section, i.e. 57 trays of the stripping section are connected with an equivalent number of trays in the upper part of the rectifying section [7].
Models of a conventional distillation, vapor recompression and HIDiC column were built in gPROMS, an equation oriented software package [9]. The model contains mass, energy and momentum balances as well as economic, exergetic and design (tray and column) equations. Main assumptions concern:

Table 1: Results design tool

	VR		HIDiC	
	Rig.	Des.	Rig.	Des.
Wcomp(MW)	7.55	7.80	6.87	6.20
Qreb (MW)	4.06	4.80	0.02	0
Qcond (MW)	14.45	14.99	8.63	8.37
Oper. cost(M$/yr)	7.4	7.7	5.9	5.35

Table 2: Comparison of exergy loss

	Abs. (MW)		Rel. (%)	
Exergy loss	Rig.	Des.	Rig.	Des.
CD-HIDiC	10.14	9.34	60	60
VR-HIDiC	1.80	1.24	21	17

- equilibrium tray
- Peng-Robinson EOS and Wilson activity model
- Constant heat transfer coefficient (800 $W/m^2/K$, has been verified by experimental data in a HIDiC column to be a safe estimate)

The results could be confirmed by literature data (equilibrium and saturation pressure data) and actual plant data from the Borealis group. The results agreed well with both literature and plant data.
The model size in combination with the MINLP size for theoretically 211 trays results in a problem that at present cannot be handled on a conventional PC. gPROMS was used for the numerical optimization of HIDiC. We started by optimizing the total area, next we optimized a (linear) function, which was increased in complexity. The optimization turned out to move to its maximum area for a large part of the column. Therefore in the last optimization we optimized a linear function describing the area profile of the bottom 45 heat-exchanging trays and simultaneously the top 12 area's were optimized. The following constraints were used in the optimization (function g in equation 5): 1) Maximum area on a stage : 500 m^2 and 2)A flow of 0.1 kmole/s is needed for proper operation.

RESULTS AND DISCUSSION

Design tool

First we look at the results of the design tool in comparison with the rigorous model. The results can be

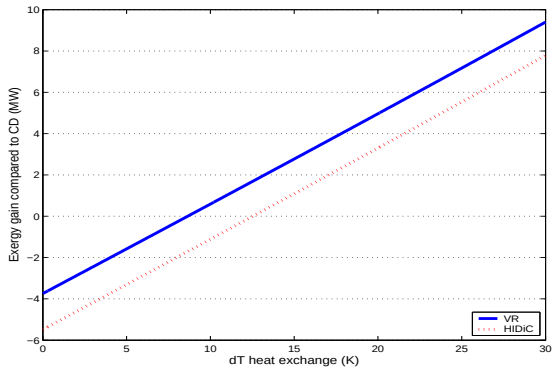

Figure 1: Exergy loss difference compared to CD

found in tables 1 and 2. The design tool correctly predicts that HIDiC is more favourable from an exergetic and operational cost point of view. Given the fact that the rigorous calculations contained in the order of 100.000 equations and the design tool in the order of 100, while the relative error found is below 10% means the tool is quite effective.

It has to be stressed that the choice of the device is sensitive to the used temperature difference for heating and cooling, ΔT_{htx} (figure 1). The break-even point for HIDiC lies at a temperature difference of 8 K and for VR at 16 K, i.e. CD is exergetically competitive with VR and HIDiC at those points.

Configuration optimization

The optimization results can be found in table 3. For the case study we verified that HIDiC was more optimal than VR. The fixed area means that during the optimization every tray had the same area and the optimized area means all areas were optimized as described in the case-study. An annual cost reduction of 0.67 M$ per year and 0.49 MW less exergy loss could be achieved within HIDiC if the tray area profile was optimized in comparison to the optimized case where every tray had the same area.

An idea of the objective surface for the fixed area case is given in figure 2. The lines are contours indicating the same exergy loss, the gray area is physically infeasible. The point Area=0 and Pressure ratio ≈ 1 corresponds to the CD case. From figure 2 we see that (as was remarked by [13]) the optimum is not flat which means two things: 1) we need to choose the area and pressure ratio smartly and 2) we can reduce the exergy loss substantially.

Table 3: HIDiC configuration optimization results

	VR	HIDiC fixed area	opt. Area
Wcomp (MW)	7.55	6.60	6.87
Qcond (MW)	-14.45	-12.64	-8.63
Qreb (MW)	4.06	4.22	0.02
Annual (M$/yr)	11.73	10.86	10.19
Capital (M$/yr)	4.33	4.28	4.30
Oper. (M$/yr)	7.40	6.58	5.90
Exloss (MW)	8.46	7.15	6.66

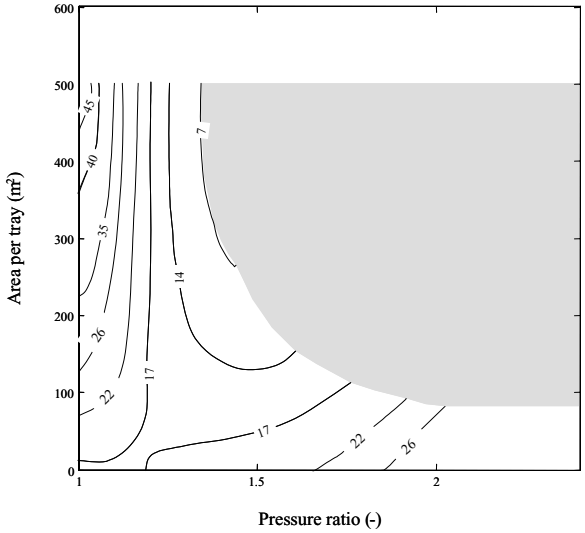

Figure 2: Exergy loss contours (MW)

Force-flow analysis

Now we will use the theory of irreversible thermodynamics to explain the results. In figure 3 we compare the local entropy production profiles in the column for VR and HIDiC (note that since HIDiC is heat integrated it is locally possible to have negative entropy production). Entropy production at the ends of the column is reduced (smaller flows) and at the same time entropy production is more concentrated around the feed.

To understand the profile we will analyze the thermodynamic flows and forces (figure 4 and 5). From the figures it is clear that the chemical forces are increased in the rectifying section and reduced in the stripping section for HIDiC compared to VR. The first is in contrast with a reduction in exergy loss (see equation 7).

If we look at the flows (figure 5) and local entropy

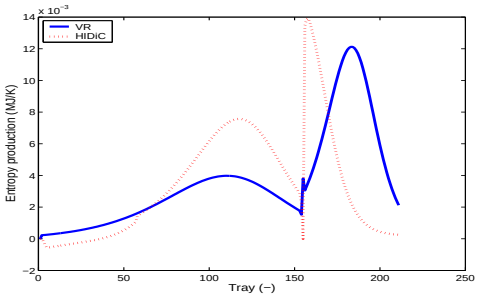

Figure 3: Local entropy production profile

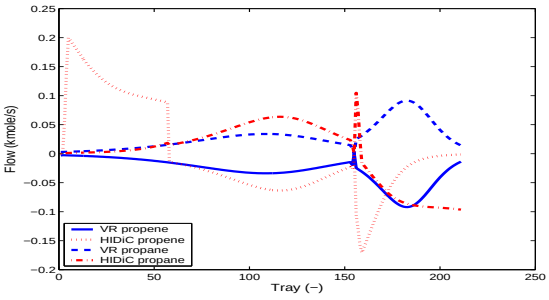

Figure 5: Flow overview

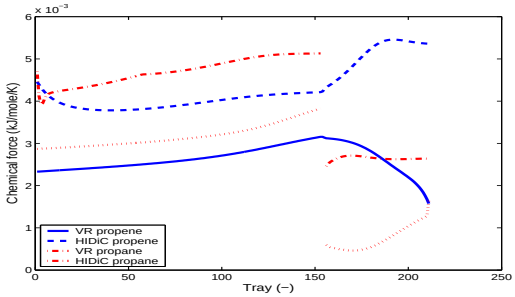

Figure 4: Chemical force overview

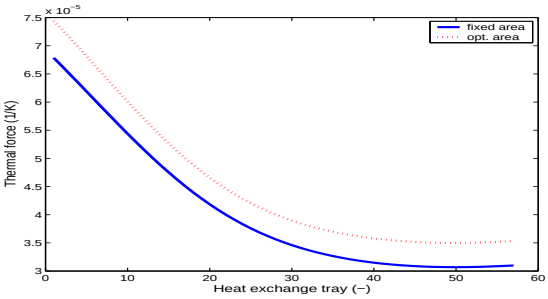

Figure 6: Thermal force heat integration

production (figure 3) however, we see that apparently it is beneficial to increase the entropy production at some points, which eventually results in a lower overall entropy production. A clear clue is given by the propylene flow in HIDiC (figure 5) compared to VR, here we see the influence of heat transfer through the wall, implying that L_{1h} (1 for propylene and h for heat through wall) plays a dominant role (as expected).

Another interesting phenomenon could be observed by looking at the differences in the optimization results for HIDiC for fixed area and optimized (=variable) area. The exergy loss, as shown in table 3, can be reduced by an increase in the thermal force as shown in figure 6. At the same time in figure 7 we see that the flow is also increased over the largest part of the column (increasing the internally generated reflux and vapor boil-up flows).

However, the flow is reduced at the place where the force is highest. This is caused by manipulation of the L's via the heat transfer area (see figure 8). Physically this can be understood since the reboiler and condensor duties do not cancel out (there is some remaining condensor duty, see table 3). This means that the at the top an "external" reflux already enters the column, reducing the need for an internally generated reflux. Also note that the area is increased gradually, i.e. not from a minimum to a maximum from one tray to the next.

CONCLUSIONS

We have developed a framework that helps to find the best (in economic and exergetic sense) device (CD, VR or HIDiC) and configuration for fluid based separation. It consists of two steps: 1) a screening tool that determines which device (HIDiC, CD or VR) is optimal and 2) numerical optimization to find the optimal configuration of HIDiC. We did not consider diabatic columns in this paper, because of the disadvantages mentioned in the introduction.

The theory of irreversible thermodynamics, in particular the flow-force analysis, was used to explain the results. Optimization was shown not just to be a matter of reducing all the forces, the complete picture has to be taken into account. The force-flow analysis helped to uncover the complex behavior and helped to explain what happened.

For the pp-splitter used in the case study HIDiC was correctly indicated to be the best device by the de-

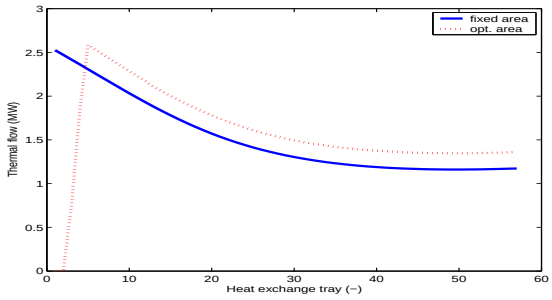

Figure 7: Thermal flow heat integration

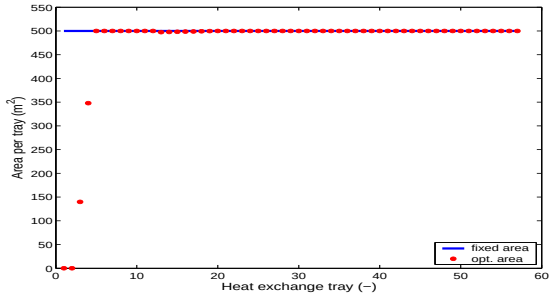

Figure 8: Heat exchange area profile

sign tool, which was verified by rigorous simulations. Optimization of HIDiC resulted in a reduction of exergy loss of 1.8 MW and a reduction in annualized cost of 1.5 M$ compared to state of the art VR.

From these results it is clear that particularly in devices where phenomena are coupled, like in HIDiC, optimization needs to be done globally, since local entropy production may well increase at some place while the over-all entropy production is reduced.

It is expected that the accuracy and overall usability of the design tool will improve if we: 1) improve estimate of Z, 2) possibly incorporate activity coefficients 3) incorporate a temperature profile matching check to assure no reversed heat-flow occurs, 4) incorporate capital cost and 5) incorporate tray efficiencies.

ACKNOWLEDGEMENT

This work was part of an EET project (EETK01025) with ECN, ABB-Lummus, Akzo Nobel, BP, DSM, Shell GS and Sulzer Chemtech. We are grateful to Ir. R. Cousaert from the BOREALIS Group (Antwerp) for providing actual plant data used in this work.

APPENDIX
DESIGN TOOL EQUATIONS

We start with (feed and distillate flow HIDiC is identical to CD in this derivation and assuming $Q_{reb} > Q_{cond}$ to keep equations clear):

$$\begin{aligned} & Ex^{hid}_{loss} - Ex^{cd}_{loss} = -B\left(H^{hid}_{bot} - T_{ref}S^{hid}_{bot}\right) \\ + \quad & B\left(H^{cd}_{bot} - T_{ref}S^{cd}_{bot}\right) + W_{comp} \\ + \quad & Q_{cond}\left(1 - \frac{T_{ref}}{T_{cond} - \Delta T_{htx}}\right) - Q_{reb}\left(1 - \frac{T_{ref}}{T_{reb} + \Delta T_{htx}}\right) \\ - \quad & Q^{hid}_{cond}\left(1 - \frac{T_{ref}}{T_{cond} - \Delta T_{htx}}\right) \end{aligned} \tag{10}$$

In which ΔT_{htx} represents the temperature difference used for heat transfer. Now if CD is a bottom temperature of T_{bot} and a pressure P_{bot} than HIDiC has a "bottom" temperature $T_{bot} - \Delta T$ and a pressure $p_{bot} - \Delta p$. In that case we may write:

$$H^{hid}_{bot} = H_{bot}(p_{bot} - \Delta p, T_{bot} - \Delta T) \tag{11}$$

$$S^{hid}_{bot} = S_{bot}(p_{bot} - \Delta p, T_{bot} - \Delta T) \tag{12}$$

Since pressure dependence of a liquid enthalpy is limited we may write (assuming Cp is constant over ΔT):

$$\begin{aligned} - \quad & B \quad \left(H^{hid}_{bot} - T_{ref}S^{hid}_{bot}\right) + B\left(H^{cd}_{bot} - T_{ref}S^{cd}_{bot}\right) \\ = - \quad & B \quad \left[-Cp_{bot}\Delta T - T_{ref}Cp_{bot}\ln\left(\frac{T_{bot} - \Delta T}{T_{bot}}\right)\right] \end{aligned} \tag{13}$$

Now since $\Delta T << T_{bot}$ we have:

$$\ln\left(1 - \frac{\Delta T}{T_{bot}}\right) \approx -\frac{\Delta T}{T_{bot}} \tag{14}$$

Assuming we may use the ideal mixing rule for the heat of vaporization of a mixture we can write:

$$V_{bot} = \frac{Q_{reb}}{\Delta H^{reb}_{vap}} \tag{15}$$

$$V_{top} = \frac{V_{bot}\Delta H^{reb}_{vap}}{\Delta H^{cond}_{vap}} + \frac{V_{feed}\Delta H^{feed}_{vap}}{\Delta H^{cond}_{vap}} \tag{16}$$

$$V_{comp} = \frac{V_{bot}\Delta H^{reb}_{vap}}{\Delta H^{feed}_{vap}} + V_{feed} \tag{17}$$

Using 13 and equations 14 in equation 10 gives us ($Q^{Hid}_{cond} = \frac{D}{V_{top}}Q_{cond}$):

$$\begin{aligned} Ex^{hid}_{loss} \quad & -Ex^{cd}_{loss} = B\Delta TCp_{bot}\left(1 - \frac{T_{ref}}{T_{bot}}\right) \\ + \quad & \frac{V_{top} - D}{V_{top}}Q_{cond}\left(1 - \frac{T_{ref}}{T_{cond} - \Delta T_h}\right) \\ - \quad & Q_{reb}\left(1 - \frac{T_{ref}}{T_{reb} + \Delta T_{htx}}\right) + W_{comp} \end{aligned} \tag{18}$$

If we now assume that $W_{comp} = V_{comp} \int \hat{V} dP / \eta_{comp}$ ($\hat{V}$ is the molar volume, V_{comp} is the flow at the location of the compressor in CD column), we can write ($Q_{cond} = \Delta H_{vap}^{top} V_{top}$):

$$\begin{aligned} Ex_{loss}^{hid} &- Ex_{loss}^{cd} = B\Delta T C p_{bot} \left(1 - \frac{T_{ref}}{T_{bot}}\right) \\ +(V_{top} &- D)\Delta H_{vap}^{top} \left(1 - \frac{T_{ref}}{T_{cond} - \Delta T_{htx}}\right) \\ -V_{bot}\Delta H_{vap}^{reb}(1 &- \frac{T_{ref}}{T_{reb} + \Delta T_{htx}}) + \frac{V_{comp} \int \hat{V} dP}{\eta_{comp}} \end{aligned} \quad (19)$$

Looking at the temperature profile we can see that ΔT above is close to the temperature difference in reboiler and condensor (as a safe guess).
Similar derivations can be made for CD compared to VR. The simplest way to find the difference between HIDiC compared to VR is than to subtract the results of the other differences ((HIDiC-CD) - (VR-CD)= (HIDiC-VR)).

REFERENCES

[1] S. R. de Groot and P. Mazur. *Non-equilibrium thermodynamics*. Dover Publications, 1984.

[2] E. S. Jimenez, P. Salamon, R. Rivero, C. Rendon, K. H. Hoffmann, M. Schaller, and B. Andresen. Optimization of a diabatic column with sequential heat exchangers. *Ind. Eng. Chem. Res.*, 43:7566–7571, 2004.

[3] C. J. King. *Separation processes*. McGraw-Hill, 2nd edition, 1980.

[4] G. de Koeijer and R. Rivero. Entropy production and exergy loss in experimental distillation columns. *Chem. Eng. Sci.*, 58:1587–1597, 2003.

[5] R. S. H. Mah and R. B. Wodnik. Distillation with reflux and vaporization: a comperative evaluation. *AIChE J*, 23(5):651–658, 1977.

[6] M. Nakaiwa, K. Huang, A. Endo, T. Ohmori, T. Akiya, and T. Takamatsu. Internally heat-integrated distillation columns: a review. *Trans IChemE*, 81(A):162–177, 2003.

[7] Ž. Olujić, L. Sun, A. de Rijke, and P. J. Jansens. Conceptual design of an energy efficient propylene splitter. In R. Rivero, L. Monroy, and G. Tsatsaronis, editors, *Cost-Effective, and Environmentally-Sustainable Systems and Processes (ECOS)*, pages 61–77, 2004.

[8] C. I. Pritchard, T. Caldwell, and W. Morton. Retrofitting internal heat integration to a distillation column. In R. Rivero, L. Monroy, and G. Tsatsaronis, editors, *Cost-Effective, and Environmentally-Sustainable Systems and Processes (ECOS)*, pages 127–135, 2004.

[9] Process Systems Enterprise Ltd. *gPROMS introductory user guide*, 2.2 edition, 2003.

[10] R. Pulido, Y. Dai, L. Monroy, and R. Rivero. Process and cfd simulations of a section of a pilot plant distillation tower. In R. Rivero, L. Monroy, and G. Tsatsaronis, editors, *Cost-Effective, and Environmentally-Sustainable Systems and Processes (ECOS)*, pages 13–23, 2004.

[11] R. Rivero. Exergy simulation and optimisation of adiabatic and diabatic binary distillation. *Energy*, 26:561–593, 2001.

[12] R. Rivero and P. Le Goff. Pompes à chaleur à distillation diabatique. *Int J Refrig*, 23:26–30, 2000 (French).

[13] A. Røsjorde, M. Nakaiwa, K. Huang, K. Iwakabe, and S. Kjelstrup. Second law analysis of an internal heat-integrated distillation column. In R. Rivero, L. Monroy, and G. Tsatsaronis, editors, *Cost-Effective, and Environmentally-Sustainable Systems and Processes (ECOS)*, pages 107–115, 2004.

[14] E. Sauer, S. Kjelstrup Ratkje, and K. M. Lien. Equipartition of forces: a new principle for process design and optimization. *Ind. Eng. Chem. Res*, 35(11):4147–4153, 1996.

[15] D. Tondeur and E. Kvaalen. Equipartition of entropy production - an optimality criterion for transfer and separation processes. *Ind. Eng. Chem. Res.*, 26(1):50–56, 1987.

Proceedings of ECOS 2005
Trondheim, Norway
June 20–22, 2005

Separation Profile of Binary Component in Conventional and Feed Splitting Distillation Column by Simulator HYSYS

Ruchira Taprap*
Faculty of Agro Industry
King Mongkut`s Institute of Technology Ladkrabang, Bangkok Thailand 10520
Phone: 662 326 4092, Fax: 662 326 4092
E-mail address: ktruchir@kmitl.ac.th

Junjiro Kawasaki and Hiroaki Habaki
Department of Chemical Engineering
Tokyo Institute of Technology, 2-12-1 O-okayama, Meguro-ku, Tokyo 152-8552 Japan
Telephone, Fax: 81-3-5734-3285

ABSTRACT

The separation performances of ideal mixture (n-hexane and n-heptane) were evaluated by using the commercial software simulator called HYSYS in the conventional distillation column and the feed splitting column. The optimum conditions of stage number and reflux ratio can be pointed out from the simulation results. To obtain a better separation performance, the stage number should be increased while having a low reflux or vice versa. From the result of conventional column, the condition of minimum reflux ratio was visualized. Moreover, the composition profiles of those two columns were performed with the variations of stage number, reflux ratio and the second feed location in feed splitting column in order to find the proper criteria.

Keywords: Binary Distillation, HYSYS, Simulation, Feed splitting column

INTRODUCTION

Distillation has been one of the most popular separation units being applied in many engineering fields. Since it is a major energy consuming, a lot of efforts to reduce energy consumption in distillation have been evolved throughout the world. One of the efforts is to introduce the intermediate heater/cooler to the column in order to reduce the amount of heat duty at the reboiler as well as at condenser [1, 2, 3]. Some studies have emphasized on the use of waste heat as a heat source to preheat and partially vaporize the feed before entering the column [4, 5]. Other approaches for energy saving or optimization in distillation unit are exergy analysis and entropy production of the column [6, 7, 8]. Although, the above mentioned efforts were done and still have been under investigated even it was proclaimed to be a dead end as mentioned by Soave and Feliu [4]. Nevertheless, calculation of distillation by using commercial software will be another approach for studying the performance of column [8].

In the operating problem, the separation of the mixture by distillation depends on the difference of volatility between components. The greater the relative volatility is, the easier the separation will be. For binary component, the profile of separation can be represented as the mole fraction of one component (usually light component in distillate) or as its equilibrium temperature of the column. Nowadays, some commercial simulators such as ASPEN PLUS and HYSYS are available and

become popular as the tool for process simulation. In some circumstance, those simulators can be used as the tool to study process control since they are rather reliable and less-time consuming [9, 10].

In this study, binary component of n-hexane and n-heptane will be selected as a case study and using commercial software HYSYS to simulate the conventional column and feed-splitting column in order to visualize the separation performance. Some conditions such as different reflux ratio, different feed location were investigated in this study as well.

CASE STUDY WITH SIMULATOR: HYSYS

Scheme of distillation column

Figure 1 (a) shows the schematic of conventional column. In binary component distillation, the McCabe-Thiele diagram can be used as a tool in design problem. By assuming the equimolal flow and equimolal latent heat both in the rectifying section and the stripping section, the operating lines of these two sections can be drawn as straight line on xy diagram. Then, the number of stages can be achieved by drawing the steps between the equilibrium line and the operating line. If the two operating lines intersect with the equilibrium curve, the minimum reflux condition will be reached as shown in Figure 1(b). At this intersect point, the number of stage will be infinity or in other word, there is no separation. Similar manner can be found in multicomponent as well by having the constant component concentration along the column [11]. In practical, the column should not be operated at this condition. It should be at the condition in between the minimum reflux and the total reflux. In the case of total reflux condition, the operating line will be shifted to the diagonal line. Figure 1 (c) shows the schematic of feed splitting column. The F2-feed is called the second feed whereas the F1-feed is the first feed. If the second feed is fed in the rectifying section and its temperature is lower than the first one, there will be two lines of feed making three operating lines of column because of the second feed as shown in Figure 1 (d). In this study, we would like to look at the separation profile of two type columns.

Separation performance of conventional distillation column

The HYSYS simulator was used to examine several operation cases of binary distillation column. The ideal mixture of n - hexane and n - heptane was selected for this study. The feed mixture of 50 % of each component was fed at stage number 10 with the flow rate 100 kmol/hr. The total number of stage in the column is 22 including total condenser and reboiler. The hypothesis UNIQUAC is used in this case. The column is operated at the atmospheric pressure. The simulator is run at steady state. Firstly, we will examine the case of conventional distillation column with manipulating reflux ratio. Secondly, the variation of thermal condition of feed will be examined. The column stage is fixed and distillate flow rate is 50 kmol/hr while the reflux ratio is varied. Figure 2 shows the composition profile of n-hexane with different reflux ratios. The ordinate is mole fraction of n-hexane along the column while the abscissa is the stage number of the column. When the reflux ratio is decreased, the obtained component in the distillate is decreased as well. Here, the smallest of reflux ratio is 0.5 whereas the highest is 1.4. It reveals that when the reflux ratio becomes large, the separation performance is improved and the composition profile is changed drastically along the column. When the reflux ratio is decreased, the profile is changed abruptly in the rectifying section. Similar manner can be seen also in the stripping section. The composition profile in the middle of column becomes constant when the small reflux is performed. It means the minimum condition of reflux is reached. Theoretically, the minimum reflux ratio can be observed from the composition profile along the column, if the composition appears constantly [11]. In binary component, this condition will appear at around feed stage as seen in Figure 2. Figure 3 shows the result of the temperature profile along the column which is the mirror image of the mole fraction. When we examine further if the thermal condition of feed is varied but keeping the reflux ratio fixed at 0.8. The other conditions of the column are kept the same. Figure 4 shows the temperature profile at each stage at the different feed condition. The higher temperature of feed is, the poorer of separation

performance is. This result supports the theory saying that when the feed temperature is low, it gives the internal reflux to encourage more condensation of the component resulting in having a better separation. However, having a low temperature of feed will enhance the heat duty at reboiler as shown in Figure 5.

Figure 6 shows the simulation result of the conventional column. When the reflux ratio is varied, the number of stages in the column will be varied as well. The y-axis is mole fraction of n-hexane in the distillate (X_{Hx}) and the x-axis is the number of stage in the column (excluding reboiler and condenser). At the stage number 11, the separation performance is poor at each value of reflux ratio comparing with the higher amount of stage number. The separation performance of n-hexane is improved by increasing the reflux ratio. At the stage number 20 with reflux ratio 2.5, the separation performance is about the same with the stage number 30 and reflux ratio at 1.5. The result of HYSYS program will give us a choice to obtain the suitable value of stage number or adjusted reflux ratio. We can say that the requirement of stage number is essential around 30-40 and reflux ratio 1.45-1.55 in order to obtain 100% separation of this mixture.

Separation performance of feed-splitting distillation column

In Figure 1(c), the feed will be split into two streams but keeping the same composition. The first feed is fed at the middle of column while the second is at different stage in the rectifying section. By doing that, the operating line of this column will be three lines since the internal flow is changed due to the second feed condition.

Figure 7 (a) shows the simulation result when the column has the feed splitting at ratio 10/90. The 10% of feed (the second feed) is fed at some certain stage (at stage 3, 5 and 7) while the 90 % (the first feed) is unchanged and fed at the middle of the column (at stage 10). It shows that the case with the second feed at stage 3 gives rather poor separation whereas the second feed at stage 5 and 7 give the insignificant result. Figure 7(b) shows the result when the stage number is 30 and the first feed is fed at stage 15 and the second feed is at stage 7, 9 and 12. The separation performances of each case are about the same but the profile of hexane can reach 100 % at reflux around 2. When we check the stage number from 40 up to 60 shown in Figure 7 (c)-(e), the separations show the same result. It implies that when the amount of stage increases up to 40 or more, it is not necessary to have such a huge number. Figure 7 (f) shows the result of separation of this feed splitting column. When the feed is split into 50/50 and fed at different stage similar to previous case. We observed that the separation performance of this splitting case gives the significant result as shown in Figure 8. Note that when the feed splitting ratio is great, the separation performance is affected at the small value of reflux ratio.

CONCLUSION

Commercial simulation program HYSYS has been used in this study to visualize the separation performance of n-hexane and n-heptane mixture. The conventional distillation column has given the better separation when the feed has a lower temperature. However, the heat duty at the reboiler will be increased as a consequence. Regarding the feed splitting column, the separation performance is partly affected at high value of reflux ratio.

Acknowledgement

One author (R.Taprap) was fully supported by The Hitachi Scholarship Foundation at Department of Chemical Engineering, Tokyo Institute of Technology, Japan.

Nomenclature

B: bottom flow rate, kmol/hr
D: distillate flow rate, kmol/hr
F: feed flow rate, kmol/hr
F_1, F_2: the first and the second feed rate, kmol/hr
L, L', L": liquid flow in rectifying, intermediate and in stripping section, kmol/hr
R or r: reflux ratio, L/D
V, V', V": vapor flow in rectifying, intermediate and in stripping section, kmol/hr

REFERENCES

[1] Y. Naka, M. Terashita, S. Hayashiguchi, T.

Takamatsu, An Intermediate heating and cooling method for a distillation column, J. Chem. Eng. Jpn. 13 (1980) 123.
[2] R. Agrawal and Z. T. Fidkowski, On the use of Intermediate reboilers in the rectifying section and condensers in the stripping section of a distillation column, Ind. Eng. Chem. Res. 35 (1996), 2801-2807.
[3] G. M. Koeijer, S. Kjelstrup, H. J. Kooi, B. Gorp, K. F. Knoche, T. R. Anderson, Positioning heat exchangers in binary tray distillation using isoforce operation, Energy Conversion and Management, 43 (9-12) (2002) 1571-1581.
[4] G. Soave and J.A. Feliu, saving energy in distillation towers by feed splitting, Applied Thermal Engineering, 22 (8) (2002), 889-896.
[5] P. C. Wankat and D. P. Kessler, Two-feed distillation: Same-composition feeds with different enthalpies, Ind. Eng. Chem. Res. 32 (1993), 3061-3067.
[6] R. Taprap and M. Ishida , Graphic exergy analysis of processes in distillation column by energy-utilization diagram. *AIChE J.* 42 (1996), 1633.
[7] S.K. Ratkje, E. Sauar, E.M. Hansen, K.M. Lien and B. Hafskjold , Analysis of entropy production rates for design of distillation columns, *Ind. Eng. Chem. Res.* 34 (1995), 3001.
[8] Q. Smejkel and M. Soos, Comparison of computer simulation of reactive distillation using Aspen Plus and Hysys software, Chemical Engineering and Processing, 41 (2002), 413-418.
[9] Santanu Bandyopadhyay, Effect of feed on optimal thermodynamic performance of a distillation column. Chem. Eng. Journal, 88 (1-3) (2002), 175-186.
[10] R. Agrawal and D. M. Herron, Optimal Thermodynamic feed conditions for distillation of ideal binary mixtures, AIChE J., 43 (11) (1997), 2984-2996.
[11] C. J. King, Separation processes, 2nd ed, New York, McGraw-Hill, 1980.

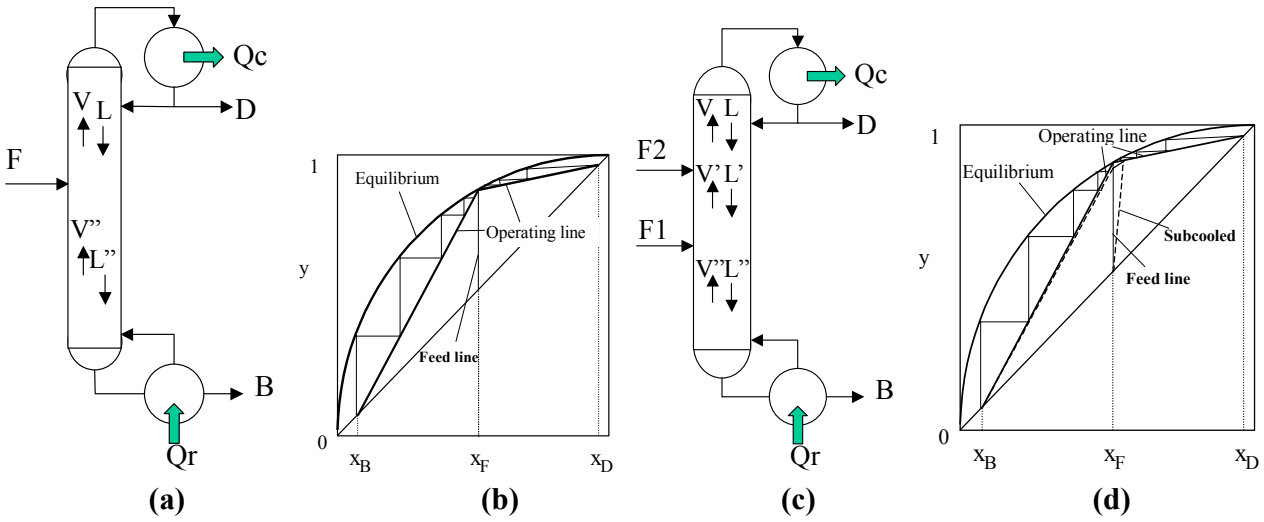

Figure 1 Schematic diagram of distillation columns
(a) conventional distillation column, (b) McCabe-Thiele diagram of conventional column
(c) feed splitting distillation column, (d) McCabe-Thiele diagram of feed splitting column

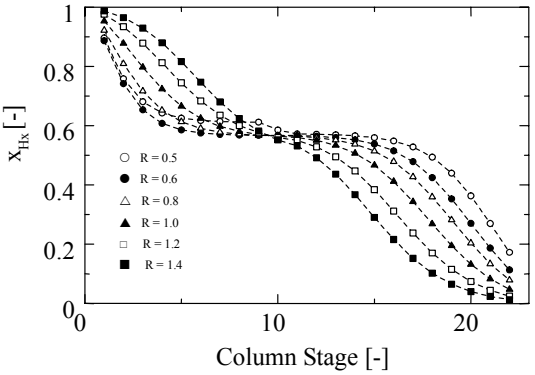

Figure 2 Composition profile of n-hexane at the top of conventional column

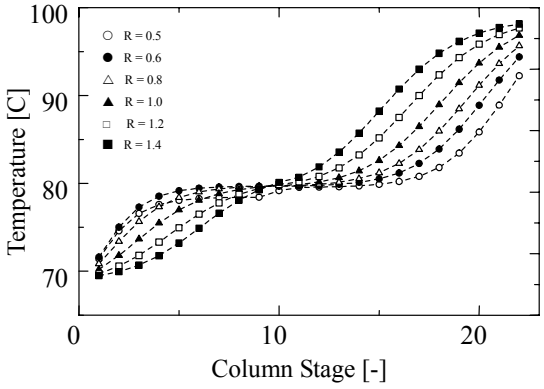

Figure 3 Temperature profile of conventional column

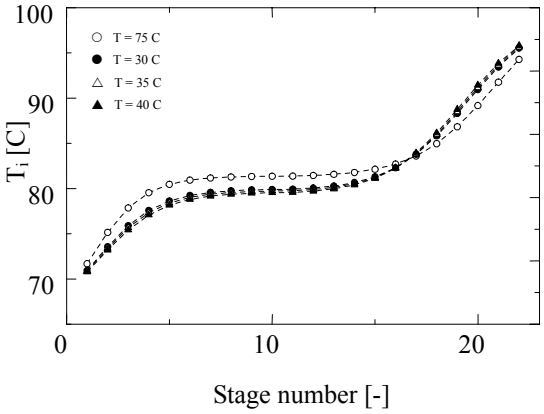

Figure 4 Temperature profile when feed at stage 10 and reflux ratio at 0.8

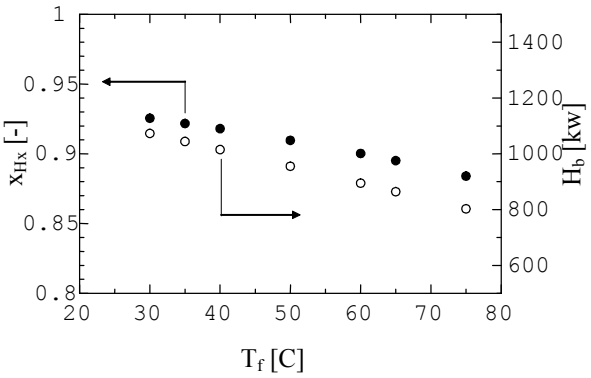

Figure 5 Separation performance and heat duty at reboiler when different feed condition

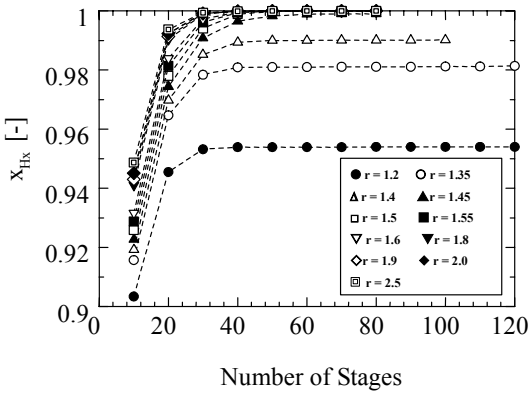

Figure 6 Separation performance at different reflux ratios

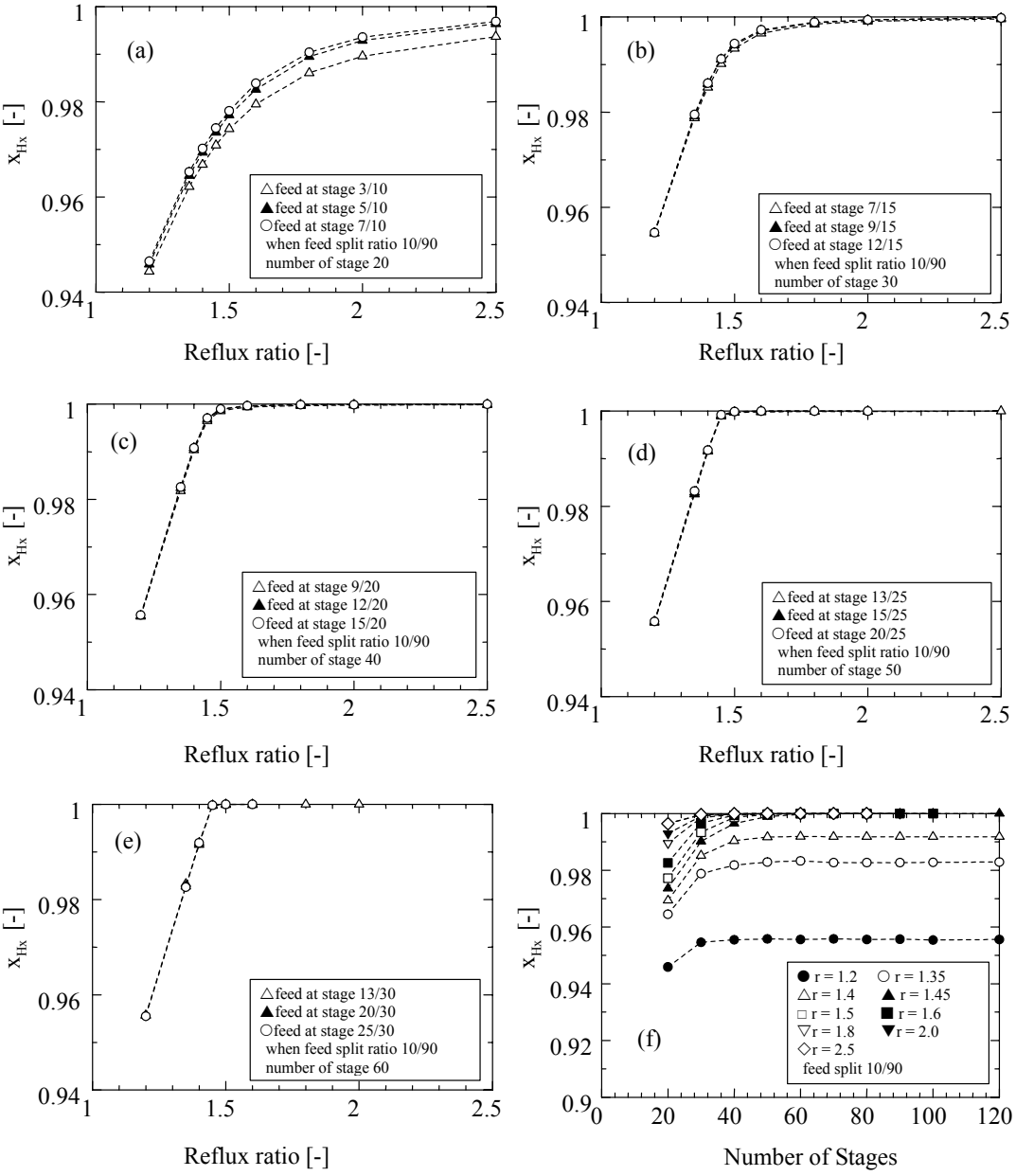

Figure 7 Separation performance when feed splitting at 10/90

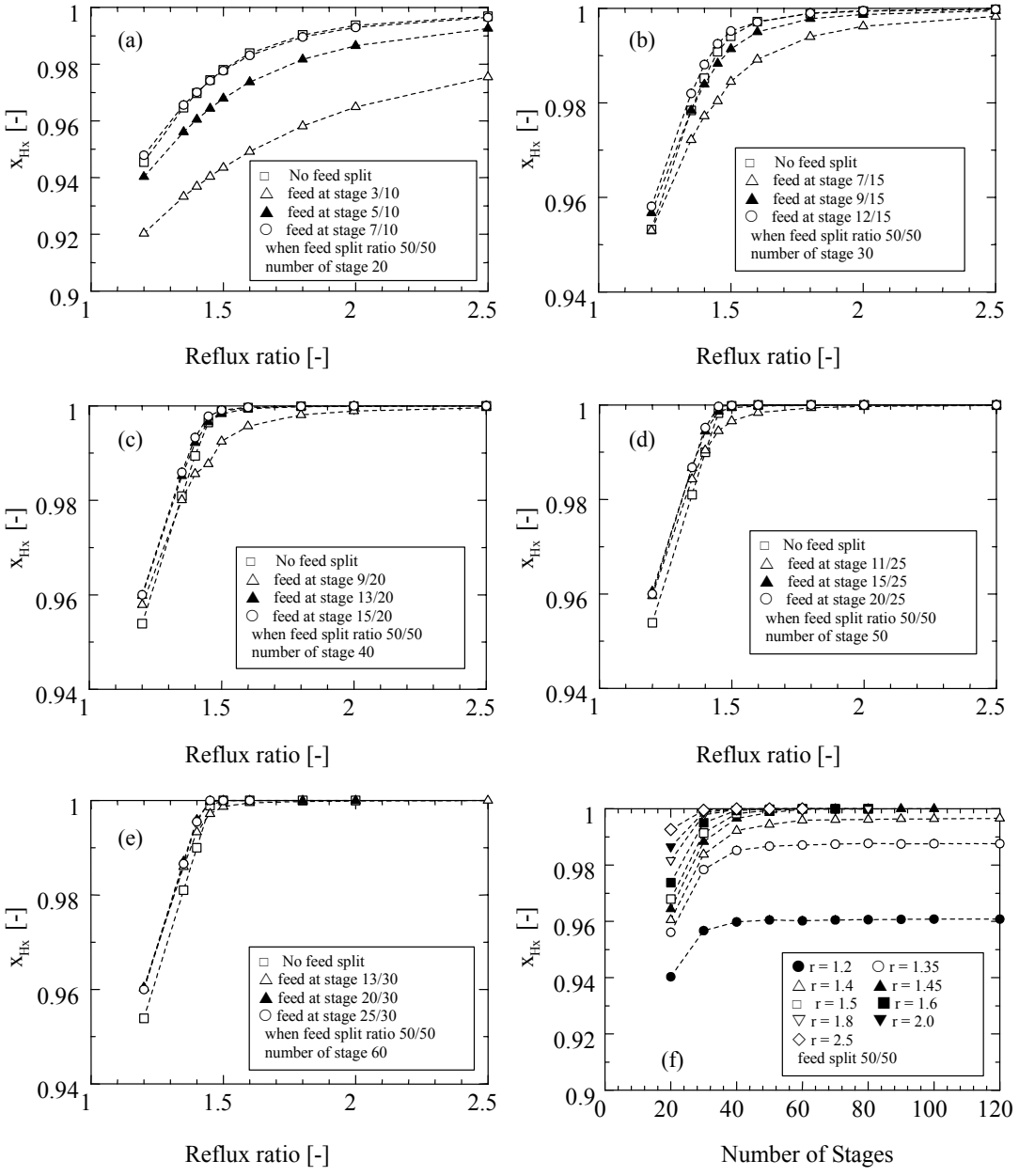

Figure 8 Separation performance when feed splitting at 50/50

Proceedings of ECOS 2005
Trondheim, Norway
June 20–22, 2005

The Investigation of Cooling Tower Packing in Various Arrangements

Goshayshi H R, BEng (Hons) MSc
Missenden J F, BSc PhD CEng MCIBSE FRSA
School of Engineering Systems & Design
South Bank University, London SE1 0AA, England

Abstract

The effect of form with corrugated packing on mass transfer and pressure drop characteristics in atmospheric cooling towers has been studied experimentally. The results showed that the mass transfer coefficient decreased with increase in packing pitch and increase in the ratio of rib pitch to rib height. Friction factors were expressed by a dimensional equation which included pitch and distance between the packings, for both smooth and rough surface. From these results, the relationship between packing mass transfer coefficient and pressure drop was deduced. The correlations were verified with additional experimental data taken with $1.1< P/D <1.70$ and $1 \leq p/e \leq 5$. This provides a useful semi experimental relation, in the area generally lacking in design and performance data.

Symbol

a	Pack density (surface area per unit volume)	m^{-1}
D	Distance between the cooling tower packing (rib)	mm
e	Height of roughness element,	mm
G	Flow rate (air),	kg/s
G'	Mass flux (air),	kg/m^2s
E	Height of corrugation,	mm
L	Flow rate (water),	kg/s
L'	Mass flux (water),	kg/m^2s
k	Mass transfer coefficient,	kg/m^2s
Nu	Nusselt Number	dimensionless
p	Distance between repeated ribs,	mm
P	Pitch of packing, (see Figures 3 & 4)	mm
Pr	Prandtl Number,	dimensionless
Z	Packed height,	m
Δp	Pressure drop,	Pa
Re_w	Water Reynolds number = $2L'D/\mu_w$	dimensionless
ρ_a	Air density,	kg/m^3
u_a	Air velocity inside the packing,	m/s
u_w	Water velocity inside the packing,	m/s
θ	Angle of inclination of cross ribbing with the horizontal,	°

Introduction

In general, the design of an efficient, compact mass transfer pack for gas/liquid applications is based on the optimisation of the passage diameter and passage length. Also from a number of recent studies it is apparent that the choice of material plays a major role in packing design, the ideal material being highly formable in order to provide a high specific surface area.(Egberongbe 1990). Heat and mass transfer between a falling liquid film along a vertical wall and upward flowing air contacting directly with the film is an important and interesting phenomenon in industrial apparatus such as cooling towers. While 96% of the cooling towers use PVC packing with smooth and cross ribbing, no data on the flow of liquid over a flat vertical wall with cross ribbing have been published. Only some of the features of their operation in contact heat exchangers have been investigated. (Bukowski 1995, Nabhan 1994, Kranc 1993, Marselle 1991). Major aspects that remain to be studied include: the geometry and layout of the main corrugation with and without the cross ribbings, the pattern of flow of the liquid film and interaction between phases. In this paper the mass transfer and pressure drop characteristics of many types of corrugated packing, including smooth and rough surface corrugated packings, are investigated, and the relationship between packing mass transfer coefficients and pressure drops are discussed. Mass transfer performance of rough corrugated packing is increased by 1.5 to 2.5 times the smooth packing values, but the pressure drop of packings also increases with the increase in heat transfer performance.

Experimental Apparatus and Procedure

The experimental apparatus for the heat transfer experiments, consisted of a counterflow forced draft cooling tower, as shown in Fig. 1. Water stored in a tank at the base was pumped into the spray nozzles. The supply water velocity was regulated by a valve. The cross sectional test area was A= 0.15 x 0.15 m. Inlet and outlet air and water temperatures were measured by mercury in glass thermometers with a range of 0-50°C and an accuracy of 0.2 K. Packing pressure drop was measured by an APM 2000 (0 to 2000 Pa) micromanometer with an accuracy of ±1% FSD (i. e. maximum of 1.2 Pa error in our measurements). Measurements of mass transfer and pressure drop were carried out in the steady state. The mass transfer coefficients and pressure drops were measured for a range of L/A (L') from 0.45 to 2.22 kg/m^{2}s and G/A (G') 0.20 to 1.50 kg/m^{2}s. A series of perimeter deflector plates as shown in Fig 1 was installed around the inner perimeter of the column, made in the laboratory of clear Poly Carbonate plastic to allow observation of the water flow. These deflector plates removed the water film from the wall of the tower's column and redistributed the water in the packing zone. As a result of deflection, most of the water was transferred to the packing surface from the outer wall, forming descending thin films, while air was blown vertically upward, counter current to the water by a fan at the base.

The packings tested were of two types, smooth and ribbed, both of PVC. The smooth packing had horizontal corrugations and the ribbed had horizontal corrugations with ribbing set at an angle to the main corrugations. The cross ribs were separated by distance p, ranging from 2 mm to 10 mm, for the six sample packings, and the height e of the ribs ranged from 1 mm to 3 mm. The main corrugation pitch, P, ranged from 30 mm to 70 mm. The thickness of packing was negligible. The forms of corrugated packings used in the experiments are listed in Table 1, and typical shapes are shown in Figs. 3 and 4. The column packed height, Z, was 160 cm and the water level in the sump was about 1.2 m below the top of the packing. Water inlet and outlet temperatures were 37 °C and 27 °C respectively.

Table 1: shapes of corrugated packing used for experiments

Test Group	Type of corrugation	Surface area per unit volume (m^{-1})	Pitch (mm)	Spacing (mm)	P/D	Type of surface	p/e	θ deg)
C1	sinusoidal	200	70	50	1.40	rough	1	45
C2	sinusoidal	250	65	40	1.65	rough	3	0
C3	triangular	300	45	40	1.13	smooth	-	-
C4	triangular	350	50	35	1.43	rough	4	0
C5	hexagonal	470	40	25	1.32	rough	5	0
C6	sinusoidal	500	30	20	1.50	rough	4	45
C7	triangular	500	30	20	1.50	rough	5	0

* All corrugations are parallel to each other and normal to the flow direction.

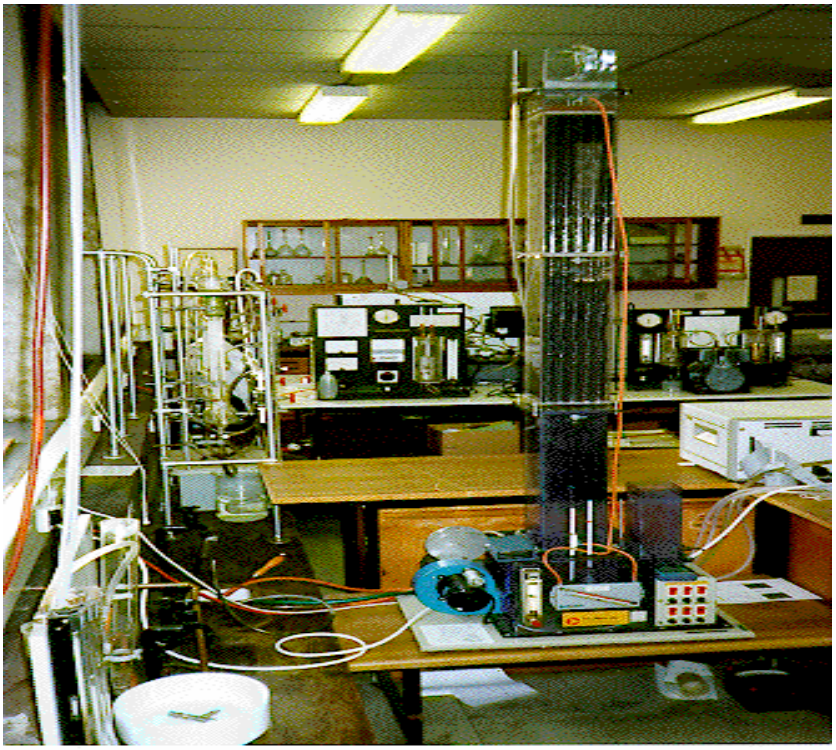

Fig. 1 Outside view of forced draft cooling tower in transport phenomena laboratory.

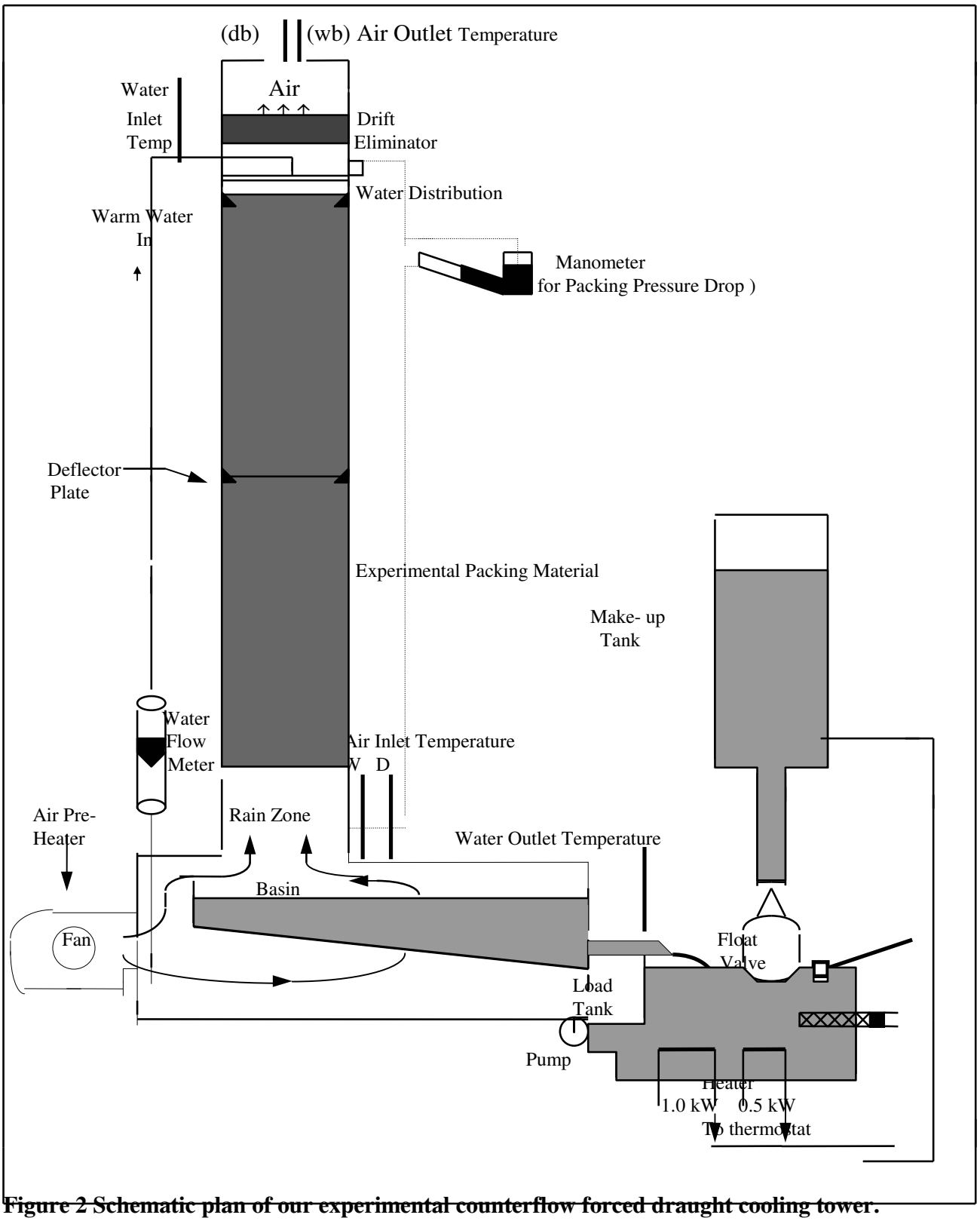

Figure 2 Schematic plan of our experimental counterflow forced draught cooling tower.

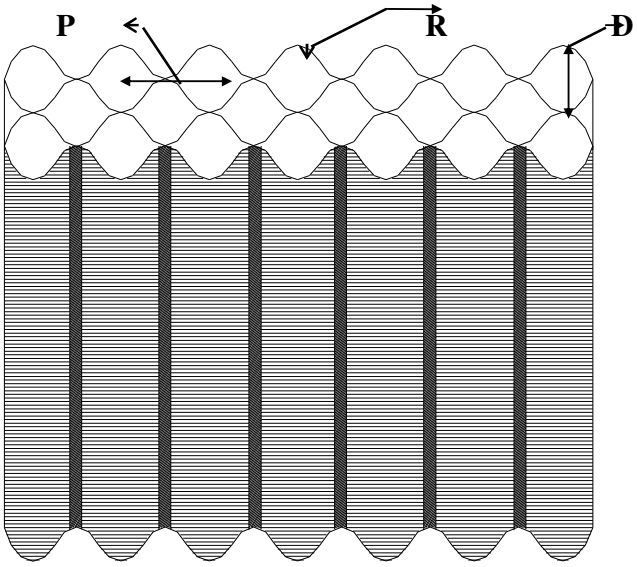

Fig. 3 Typical shape of smooth corrugated packing used in our experiment

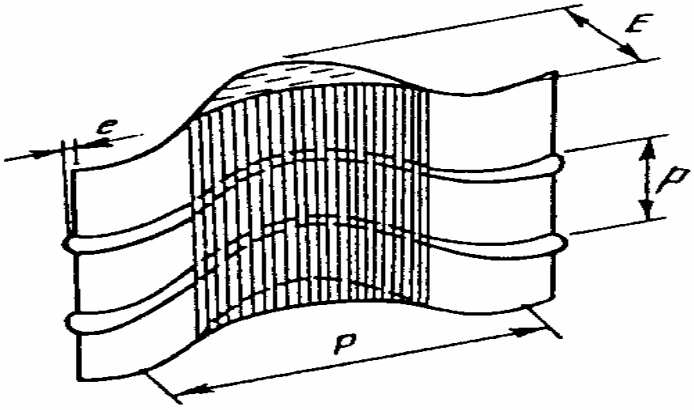

Fig. 4 Single cross ribbed sheet

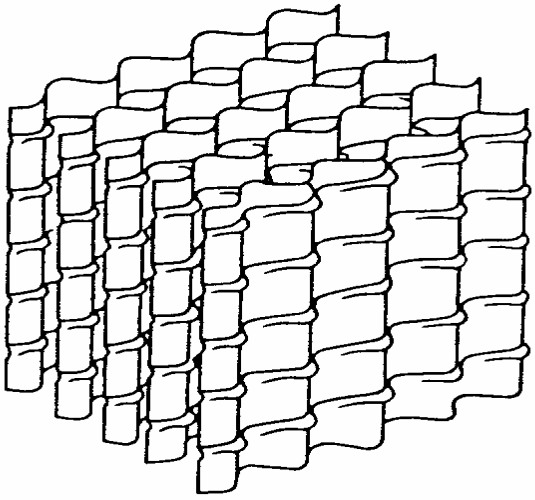

Fig. 5 Typical shape of rough corrugated packing used in our experiment.

Experimental Results

Heat Transfer Characteristics

Cooling tower packings typically have quite complex surface geometries, for which the mass transfer co-efficient, k, cannot be analytically predicted. Because manufacturers treat such data as proprietary, the k relation should be derived from test data, specific to the packing geometry.

Fig. 6 shows values of measured mass transfer coefficient k, plotted against the ratio of water flow rate to air flow rate (L/G) for existing packings. The values of k for corrugated packing were 1.5 to 2.5 times higher than comparable smooth packing k values when the water to air ratio was 1.0. The k values for rough and smooth corrugated packings decreased with the increase in pitch, and had a maximum value when P/D = 1.5 and the ratio of distance between repeated ribs to height of rib was 4, and the angle, θ, 45°. (Packing C6)

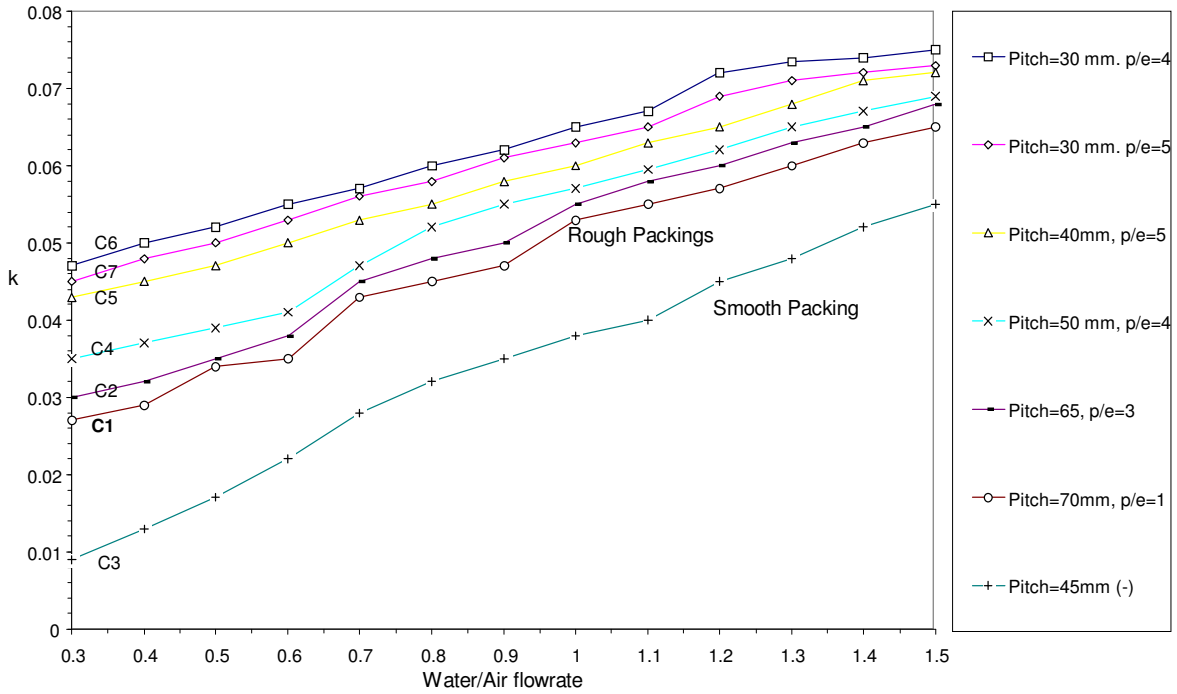

Fig. 6 Heat transfer characteristic of packing with different spacing and surface roughness.

As it can be seen from Fig. 6, k increases with

(i) decrease of the spacing between the sheets, all other parameters being constant.
(ii) increase in the value of L', for G' = constant.
(iii) increase in the ratio of the pitch of the corrugation to the of the spacing. P/D should be of the order of 1.5 and p/e should be of the order 5 to have maximum heat transfer.
(iv) decrease of the ratio of distance between repeated ribs and height of the rib.
(v) decrease in θ.

It can see that mass transfer increases with the decrease in spacing, but higher mass transfer in packing C6 compared with C7 and C5 is likely to be due mainly to the difference in the effect of the packing wall roughness[factors (iv and v) above].

The volumetric overall mass transfer coefficient based on enthalpy difference, which expresses the thermodynamic performance of a cooling tower, changes not only with the mass flow rate of air and water and temperature conditions but also with the dimensions, shape and arrangement of the cooling tower packing. Since the air and water flow in a cooling tower is complicated, the relationships between k, G and L have been found only by individual experiments for each cooling tower.
The resultant correlation k of the Nos 1 to 7 was determined from these experiments with the

most susceptible to error of ±4% by;

$$\mathbf{k = c_1 (L')^{0.45} (G')^{0.6}} \qquad \mathbf{(1)}$$

c_1 is an experimental constant. The constant for type No. 3, (smooth surface), is 1.20 while for type Nos 1, 2, 4, 5, 6, 7 the constant is 1.75, 1.83, 190, 1.98, 2.20, 2.10 respectively. Using the smooth sample, No 3 as reference, the relative increases due to ribbing were, for No. 1 = 1.45, for No. 2 = 1.52, for No. 4 = 1.58, for No. 5 = 1.65, for No. 6 = 1.83, and for No. 7 = 1.75 respectively.
Convective heat transfer data are usually correlated by an equation of the Dittus Boelter type; (Grigule 1969)

$$\mathbf{Nu_w = A\, Re_w^{\,m}\, Pr_w^{\,n}} \qquad \mathbf{(2)}$$

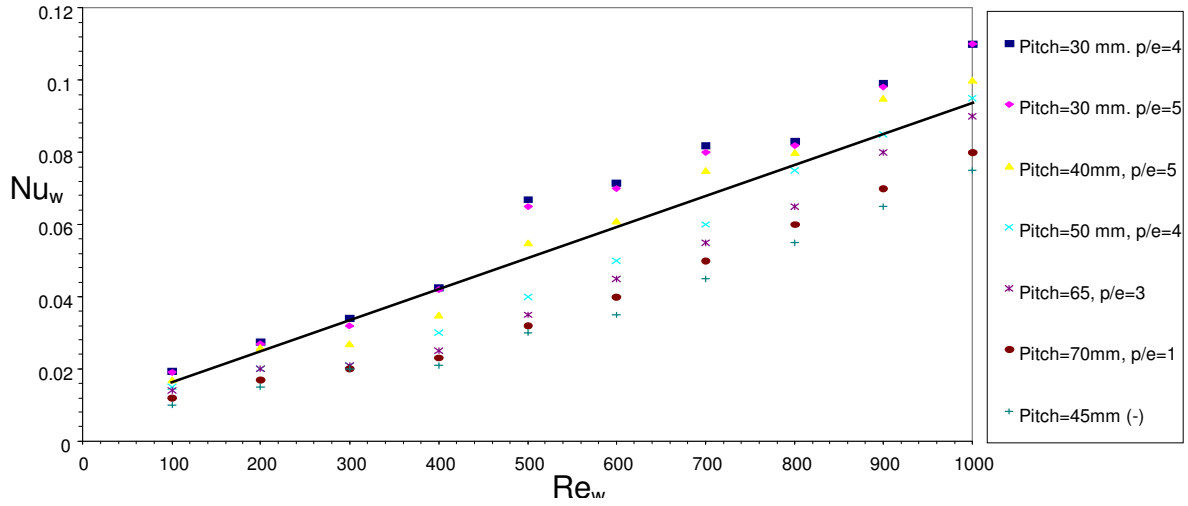

Fig. 7 Correlation of liquid phase heat transfer data.

The value of Nu_w can be evaluated based on empirical correlations found in the literature. In this paper, the value of Nu_w is evaluated using the Dittus - Boelter equation.(Bernier 1995)
Thereafter the dimensionless correlation of data is shown in Fig. 7, where a solid line gives approximations to Nu_w.

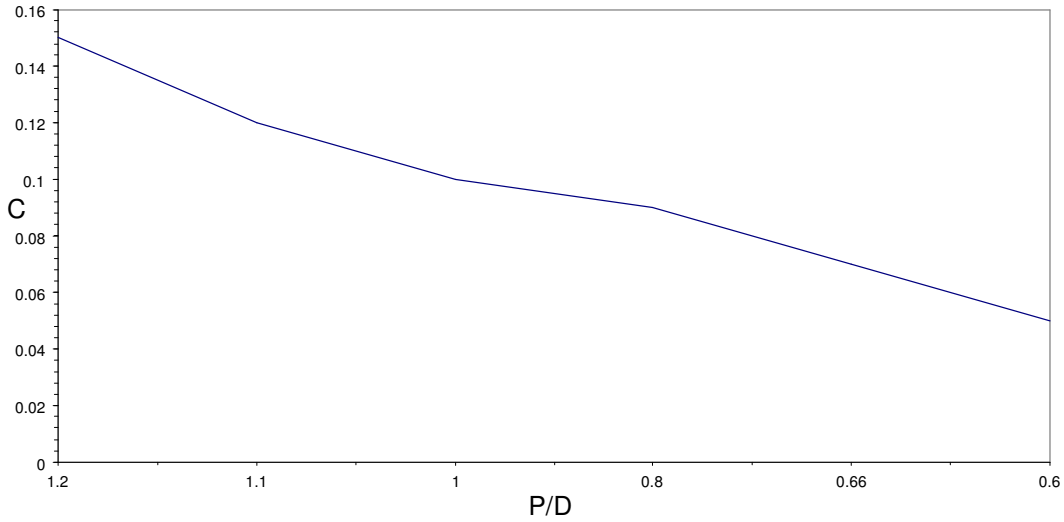

Fig. 8 Plots of C against the ratio of pitch to diameter.

From Fig.7 and 8 packing heat transfer coefficients were finally expressed as follows;

$$\mathbf{Nu_w = C\,(P/D)^{-0.15}\,Re_w^{0.8}\,Pr_w^{0.4}} \qquad \mathbf{(3)}$$

The constant C is a function of surface roughness and varies with ratio of distance between repeated ribs and height of roughness element.

Pressure drop characteristics

Another aspect of the investigation of the performance of packings concerned pressure drop characteristics.
As it can be seen from Fig. 9 ΔP increases with
(i) decrease in spacing between the sheets when all the other parameters being constant.
(ii) increase in L', for G' = constant.
(iii) increase of the ratio of distance between repeated ribs and height of rib.
(iv) decrease in θ.
The resultant of pressure drop for the packing No. 1 to No.7 is expressed with the most susceptible to error of ±3% by;

$$\mathbf{\Delta P = c_2\,(L')^{0.35}\,(G')^{0.55}} \qquad \mathbf{(4)}$$

c_2 is an experimental constant. The constant for type No. 3 having a smooth surface is 17.7 while those for types Nos. 1, 2, 4, 5, 6, 7, are 20.5, 22.6, 25.6, 27.8, 30.7, 32.5, 35.2, respectively.
The result in figure 9 shows that the pressure drop of packing C7 is about 70% higher than that of C1. This difference appears to be caused by difference in the height of the corrugations and the different surface created by the ribs.
The only exception is for C6 of the present investigation (spacing of 20 mm). The pressure drop is lower by about 15% than the pressure drop for the C7 (spacing of 20mm). This difference can be attributed to the difference of the turbulent flow condition caused by the wall roughness of the packing created by the lower distance between the plates.

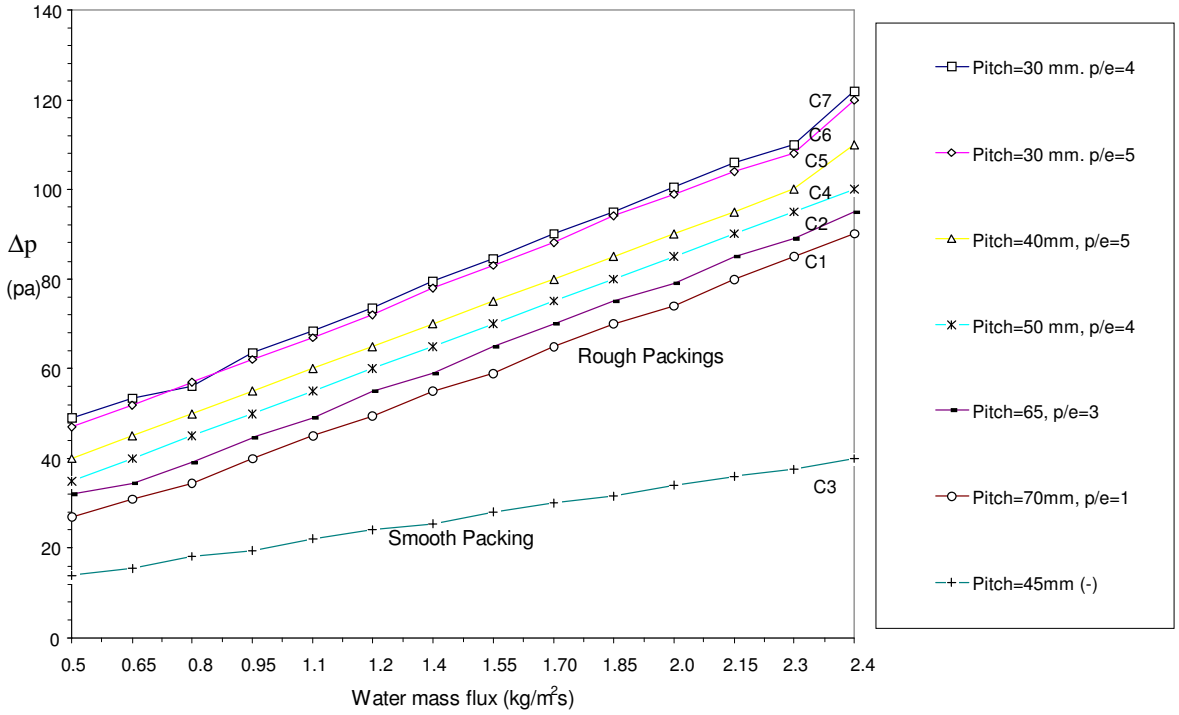

Fig. 9 Pressure drop characteristic with different spacing and surface roughness.

Friction factor f was derived using the following equation (Tezuka 1980)

$$f = \frac{1}{4}\,\frac{D}{Z}\,\frac{\Delta P}{\rho_a \left(\frac{u_a + u_w}{2}\right)^2} \qquad (5)$$

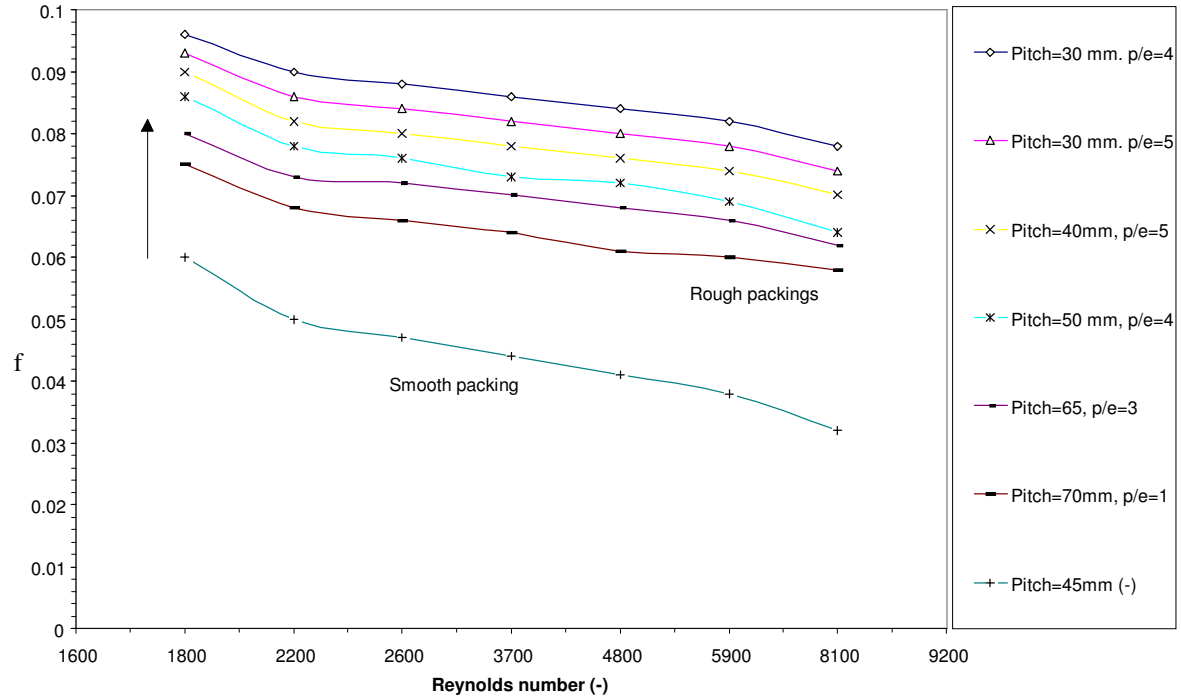

Fig. 10 Typical friction factor

Fig. 10 shows typical plots of friction factor f against the Reynolds Number Re. As it can seen from the graph, the friction factor of corrugated packing was affected by pitch, depth and also surface roughness.
The friction factor curve for packing C3 investigated in the present test, lies below the curves for packing C1 to C7. This can be expected because the height of the corrugation and the condition of the surface are dominating, the mean overall height of corrugations for packing C3 is 2.0 cm.

Therefore friction factors f was expressed by the following equation for the smooth packing;

$$f_{smooth} = C_f (P/D)^m \qquad (6)$$

And friction factor for the rough packings were expressed by the following equation;

$$f_{rough} = C_f (P/D)^m (p/e)^n \qquad (7)$$

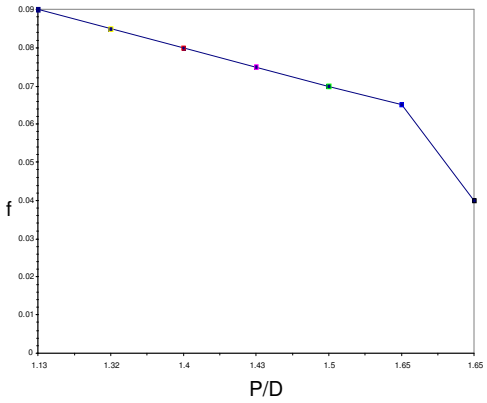

Fig. 11 Friction factor against P/D

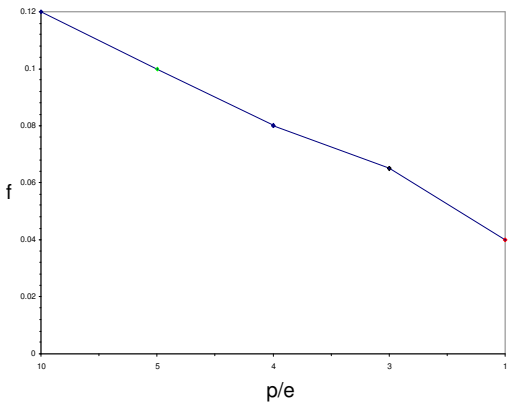

Fig. 12 Friction Factor against p/e

Fig 11 and 12 show plots of friction factor of packing against P/D and p/e respectively. From these figures the exponents m and n were obtained and friction factors of smooth and rough packings were expressed by the following equations;

$$f_{smooth} = C_f (P/D)^{-1.32} \qquad (8)$$

&

$$f_{rough} = C_f (P/D)^{-1.52} (p/e)^{-0.94} \qquad (9)$$

As an example, if m = -1.52 and n = -0.94, $C_f = 1.48$ is obtained for P = 30mm and D = 35 mm.

Discussion

When a fluid flows through a channel containing a solid system, various resistances to fluid flow (or friction factors) occur, according to the shape of the solid system. The conditions, which result in high friction factors, produce strong eddies in the fluid and thereby increase the rate at which heat may be transmitted from the fluid to the solid system. In other words, the friction and heat transfer properties of the system are correlated, so that it is generally impossible to achieve high heat transfer properties with low friction factor.

In relatively wide packings, the fluid stream is almost completely separated from the walls, and a large proportion of the packing is filled with recirculating fluid. (e.g. Packing C1)

In relatively narrow, corrugated packings flow separation takes place near the ridge of every corrugation, and flow re-attachment takes place upstream of the next ridge in the flow directions. The troughs of the corrugations are partly filled with re-circulating fluid. It was found that a packing of particular interest was the packing C6, which has a vertical main corrugation with the cross ribbing making an angle of 45°. Flow separation enhances the turbulence of the flow (compared with corresponding flow between smooth, straight wall) and thereby increases mass transfer rate and pressure drop. (e.g. Packing C6)

A packing with high turbulence in combination with a relatively low fluid velocity is more economic than a fairly smooth and straight packing in combination with a high fluid velocity. The results showed that mass transfer performance of the corrugated packing is increased by up to 1.5 to 2.5 times compared to the smooth packing, C3. In order to have the maximum mass transfer, the ratio of the pitch to spacing of the corrugation, P/D should be of the order of 1.36 to 1.50.

In this study packing mass transfer coefficients, k, of corrugated packings were expressed by Eq. (1). It was found that, for the effect of pitch on the Nusselt number, the value C was approximated to by $(P/D)^{-0.15}$. In fact the value C decreased with increase in P/D. Eq (3).

Finally, in order to compare the mass transfer performance of smooth packing with that of rough corrugated packing, the packing mass transfer coefficient (k) was correlated to pressure drop per unit length (ΔP/L) from experimental results (see Fig 13). It was found that at a given pressure drop, the maximum mass transfer coefficient for the corrugated packing can be obtained when $\frac{P}{D}$ = 1.5 and $\frac{p}{e}$ = 4 with an angle of 45° to the horizontal. For all corrugated packings, (ΔP/L) and k were correlated by the following equation;

$$\mathbf{k \propto (\Delta P/L)^{0.41}} \qquad \mathbf{(10)}$$

It has been found that mass transfer coefficients of rough corrugated packing are in proportion to the pressure drop raised to the power 0.41. This value of 0.41 is smaller than the value for smooth packing, 0.46.

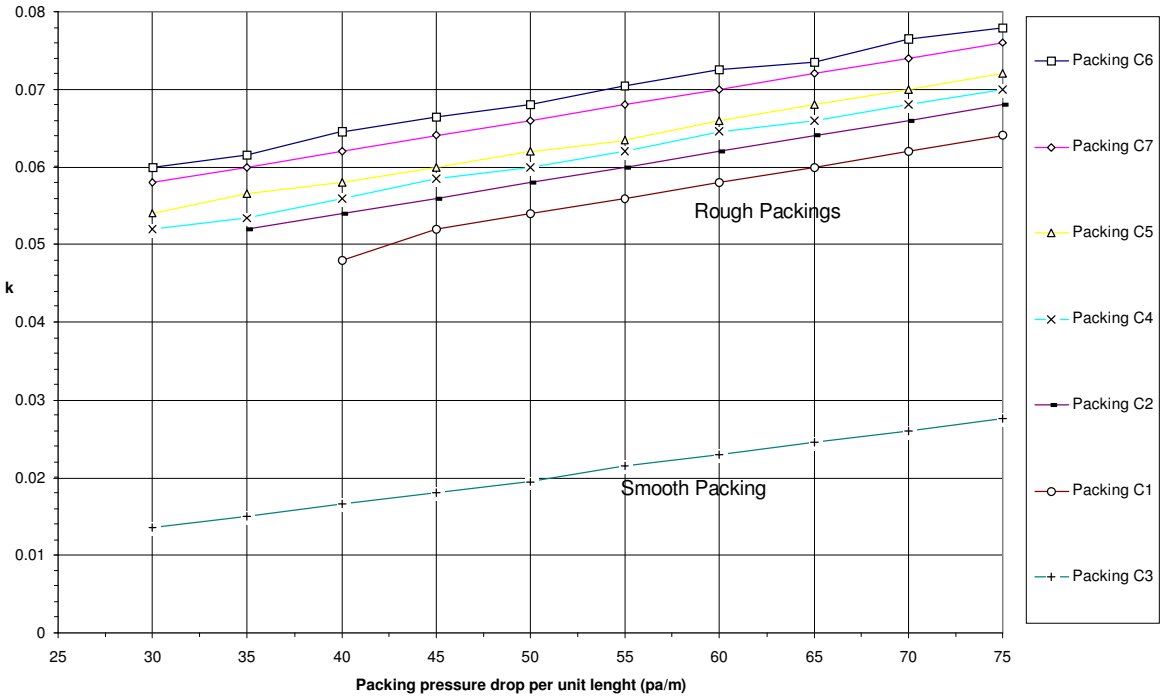

Fig. 13 Relation between packing mass transfer and pressure drop per unit length

Conclusions

Experiments were conducted to investigate the effect of the spacing and surface roughness on the mass transfer and pressure drop in PVC packing for which no comprehensive investigations had previously been reported. The experiments were carried out for comparative types of packing in a counterflow cooling tower. From the experimental results and discussion on the performance characteristic of seven vertical parallel packings arrangement in forced draft counterflow cooling tower the following conclusions may be drawn;

(1) Overall mass transfer coefficients and pressure drops of ribbed corrugated packings increase considerably compared with smooth packing and are affected by spacing of the packing and the distance between the ribs.

(2) It was found that the shape and configuration of the roughness projections are as important as the height of those projections in determining their effect on Fanning friction factor and mass transfer coefficient. It was found that a packing of particular interest was the packing C6 , which had maximum mass transfer value at P/D = 1.5 and the ratio 4 for the ratio of distance between repeated ribs to height of rib with the cross ribbing making an angle of 45°.

(3) Packing mass transfer coefficients vary in proportion to $(P/D)^{-0.15}$ and C the value decreased with increase in P/D.

(4) Friction factors of corrugated packings vary in proportion to $(P/D)^{-0.94}$ and $(p/e)^{-1.52}$.

(5) Mass transfer coefficients of corrugated packing vary in proportion to the 0.41 power of pressure drop per unit height. This value of 0.41 is smaller than smooth packing value 0.46.

References

Bernier, M. A (1995) 'Thermal performance of cooling towers' ASHRAE Journal. Vol 4. pp26 - 31.

Bukowski, J (1995) 'Taking the heat off industrial processes' Consulting Specifying Engineer. Vol 10. pp32 - 38.

Egberongbe, S. A (1990) 'How to design compact mass transfer packing for maximum efficiency' Process Engineering. Vol 9. pp5-11.

Griguil, U and Hahne, E (1969) 'Progress in Heat and Mass Transfer.' pp 56 - 62.

Kranc, S. C (1993) 'Performance of counterflow cooling towers with structured packings and maldistributed water flow' Numerical Heat Transfer. Vol 23. pp 15 - 23.

Nabhan, B. W and Anabtawi, M (1994) 'An investigation into a falling film type cooling tower' International Journal of Refrigeration. Vol 18. No: 8. pp 19 - 25.

Tezukas, S and Fusita, T et al (1980)'Performance of an induced draft cooling tower packed with parallel plates' Proceeding 15th International Congress of Refrigeration. pp 361-389.

Webb, R. L and Blanco, H (1986) 'Enhancement of combined heat and mass transfer in vertical tube and mass exchanger' Transactions of the ASME Journal of Heat Transfer. Vol 108. No: 2. pp 22 - 28.

Proceedings of ECOS 2005
Trondheim, Norway
June 20–22, 2005

ECONOMICS OF TRIGENERATION IN A PULP MILL FOR ENHANCED ENERGY EFFICIENCY AND REDUCED GHG EMISSIONS

Andrea Costa[1], Jean Paris
École Polytechnique Montréal
Chemical Department
Montréal, Québec
Canada

Michael Towers
Pulp and Paper Research Institute of Canada
Prince George, British Columbia
Canada

Thomas Browne
Pulp and Paper Research Institute of Canada
Pointe-Claire, Québec
Canada

ABSTRACT

The potential to liberate steam production capacity for power generation has been assessed using actual energy consumption data and the recorded seasonal consumption fluctuations for a kraft pulp mill. The revenues from power production are compared with possible energy savings, achieved through enhancement of the process efficiency using an absorption heat pump (AHP). Bunker oil, wood bark and black liquor, the fuels used, have very different costs and heating values. The net present value was used with a simple pay back time for the comparison of three cases, i) power production from liberated steam capacity using a cogeneration unit, ii) maximized energy savings using an AHP and iii) power production combined with heat upgrading and cold production using a trigeneration unit. The results show economic viability of all options investigated. The stand alone AHP achieves the shortest simple pay back time, whereas the trigeneration option reaches the highest net present value and therefore the best overall economics.
Keywords: absorption, heat pump, cogeneration, trigeneration, green power, heat recovery, pinch analysis, greenhouse gas emissions, kraft pulping, economic assessment.

INTRODUCTION

The pulp and paper industry is very energy intensive. Major advances have been made in the last two decades towards lower energy costs in the Canadian pulp and paper industry. However, enhanced energy efficiency measures implemented in pulp and paper mills have been mostly limited to low-investment, high-return projects, except for the revamping and up-grading of boilers [1]. Advanced engineering techniques, such as pinch analysis® [2], are now routinely used and with success to maximise internal heat recovery [3-4]. Process integration combining several approaches such as water system closure, production of power by cogeneration and heat exchange networks optimisation has paved the way for new and

[1] Corresponding author: Phone: +1 514 3404711
Fax +1 514 3405795 E-mail andrea.costa@polymtl.ca

innovative solutions [5-7]. These efforts have been induced by steadily increasing energy prices and the drive for energy savings on a large scale in the framework of the Kyoto protocol. It is becoming evident that low-investment measures will not suffice to meet these more ambitious goals. The perspective for future action is changing.

This work considers a new promising approach which combines waste heat upgrading and power production. Waste heat upgrading with simultaneous cooling of the waste heat stream can be achieved by absorption heat pumps (AHP) [8]; power production can be achieved by cogeneration. The coupling of both technologies is usually referred to as trigeneration [9]. The objective of the work was to perform a preliminary economic assessment of the retrofit implementation of AHP-based trigeneration in the pulp and paper industry.

The energy consumption pattern is studied and three cases are compared: a cogeneration unit, a stand-alone absorption heat pump and a trigeneration unit. The energy savings and CO_2 emission reduction are compared. The economics of the options are analysed in terms of simple pay back time and present net value to assess both the investment risk and the overall return on the retrofit installation of the required equipment.

THE PULP MILL

A kraft pulp mill can be seen for the purpose of this work as an energy producing facility delivering steam from different energy carriers. These are bunker oil, bark (a waste product of the lumber industry) which is bought by other industries as a low cost biomass fuel and black liquor (a by-product of the chemical digesting process which transforms wood chips into pulp). Black liquor is burned in specially designed recovery boilers after having been concentrated. Bark is burned in separate furnaces with an overall efficiency of about 67%. Oil is burned in conventional back-up boilers with about 80 % efficiency to cover steam demand fluctuations. An exhaustive description of the kraft process is given in [10]. Figure 1 shows the high pressure steam demand and the relative consumption of the two purchased fuels (oil and bark) for the year 2003 in an actual Canadian mill. Figure 1 clearly shows that whereas steam production and bark consumption are relatively constant throughout the year, the oil consumption varies by a factor of

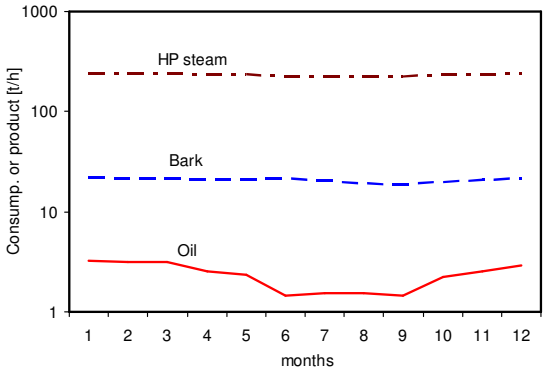

Figure 1: Yearly consumption patterns of purchased fuels and steam production.

nearly 2 between summer and winter periods. This is related to process independent parameters like temperature of make-up water and of ambient air. The yearly mill operational time has been divided in three equal periods – winter, summer and intermediate seasons – in order to analyse the technical and economic impacts of turbine and heat pumps under representative conditions. In the reference mill high pressure (HP) steam is produced at 3034 kPa (3160 kJ/kg). Roughly 20 % of it is used directly, 20 % is throttled down to medium pressure (MP) at 965 kPa (2779 kJ/kg) and 50 % to low pressure (LP) at 345 kPa (2743 kJ/kg).

ASSUMPTIONS

It was assumed that in all cases analysed the process had already been pre-optimised from the stand point of internal recovery using a state-of-the-art engineering approach. Based on previous experience in the P&P industry it has been assumed that this optimisation would achieve 5 % energy savings with a simple return on investment of 1 year [11]. This cost-efficient pre-optimization reduces the size of the new equipment to be installed and increases the economic profitability of the process changes. The energy savings cannot be entirely achieved through reduced consumption of bunker oil, which is always needed to ensure efficient combustion in the boilers. Therefore a ratio of 80/20 for the oil/bark savings was assumed. Moreover, a minimal hourly oil consumption of 25 GJ was set as baseline for the same reasons. Furthermore, the savings were assumed to be made on MP and LP steam, as this is more likely to be achieved with heat exchanger network optimization than HP steam savings.

These measures have been set as a baseline in all options analysed.

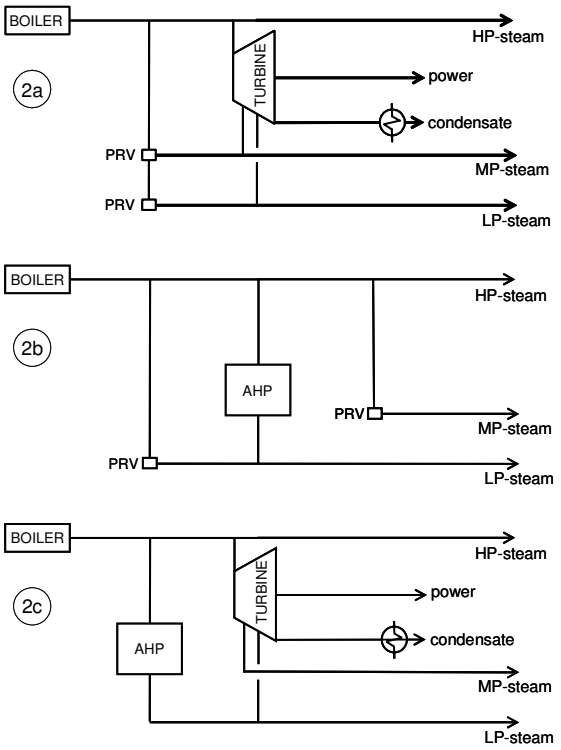

Figure 2: Schematic of the three options. 2a) Extraction and condensing turbine. 2b) Stand alone absorption heat pump. 2c) Combined turbine and heat pump.

THE THREE OPTIONS

Three options have been envisaged to enhance the process thermal efficiency beyond the maximum achievable by internal heat recovery. Two of them aim at liberating steam from the process allowing its use in a condensation turbine for power production. The third option targets a maximal reduction of the energy consumption without power production, for comparison.

Option I: cogeneration

This option consists of a steam turbine and a condensing unit installed as shown on figure 2a. The retrofit implementation of cogeneration in pulp and paper mills is not new, though not yet common practice in Canada. The turbine is normally fed by HP steam and delivers MP and LP steam (extraction operation mode) or condensate (condensing mode). Pressure retention valves (PRV) are situated on parallel lines balancing the steam production to follow demand fluctuations. The efficiencies were realistically set at 10 % for extraction and 30 % for condensation; condensation increases the turbine output considerably and consequently the power production. However, this operation is only economically feasible when steam is produced by bark combustion, assuming a mean bark price of 0.60 CAN$/GJ and a market price of 50 $/MWh for the power sold. In contrast, oil with an average price of 8 $/GJ would require a resale price of at least 120 $/MWh to be profitable (assuming efficiencies of 80 % for the burner and 30 % for the turbine) [11]. For these reasons a two-step strategy was considered in which the oil consumption is first minimised and subsequently surplus bark is burned for power production in a condensing turbine.

Option II: absorption heat pump

In this second option an absorption heat pump driven by heat from the HP steam delivers LP steam (figure 2b) [8]. Depending on the process temperatures a single effect cycle using water/lithium-bromide or ammonia/water as working pairs could be implemented. The coefficient of performance (COP) for heating would be between 1.4 and 1.8 [12]; a COP of 1.7 was used. It must be noted that a single heat pump would probably not be a practicable solution because of the very large capacity required to meet the needs of the whole process; smaller heat pumps distributed in the process are a more realistic option. However, in the context of a preliminary assessment without the benefit of detailed process data, this hypothetical case can provide a reliable benchmark. Since the steam pressure levels do not change between manifold and process, the thermodynamic properties and consequently the economic results of peripheral devices would not change, compared to a centrally installed device. It must be noted that the heat pump also delivers a cooling capacity that in this case is released at 80 to 90 °C. This could find advantageous uses in the process. Cooling possibilities were not taken into account in this work. The operation of the heat pump has been computed as a function of the percentage of the total LP steam required by the process which is supplied by the heat pump. For example, 40 %

Table 1: Production parameters and achieved savings

Power production with cogeneration

		Winter	Mid-season	Summer
Base case	Steam production	772 GJ/h	747 GJ/h	709 GJ/h
	Steam from oil	105 GJ/h	81 GJ/h	50 GJ/h
Pre-optimisation savings	Steam savings	39 GJ/h	37 GJ/h	35 GJ/h
	HP demand	150 GJ/h	145 GJ/h	138 GJ/h
	MP demand	225 GJ/h	218 GJ/h	207 GJ/h
	LP demand	358 GJ/h	346 GJ/h	329 GJ/h
	Oil saved	39 GJ/h	37 GJ/h	35 GJ/h
	Steam from bark savings for power produ	8 GJ/h	7 GJ/h	7 GJ/h
Cogeneration	HP to turbine	591 GJ/h	572 GJ/h	543 GJ/h
	steam extraction for MP and LP	583 GJ/h	564 GJ/h	536 GJ/h
	condensation (from bark)	8 GJ/h	7 GJ/h	7 GJ/h
	Turbine output	17 MW, el	16 MW, el	15 MW, el
	Seasonal oil savings	26 GWh,th	25 GWh,th	24 GWh,th
	Seasonal power produced	41 GWh, el	40 GWh, el	38 GWh, el
	Seasonal CO2 savings	6107 t	5909 t	5608 t

Maximized energy savings with absortion heat pump

		Winter						Mid-season						Summer					
Share covered by AHP	%	0	20	40	60	80	100	0	20	40	60	80	100	0	20	40	60	80	100
Heating capacity AHP	MW, th	0.0	19.9	39.8	59.7	79.5	99.4	0.0	19.2	38.5	57.7	77.0	96.2	0.0	18.3	36.5	54.8	73.0	91.3
Output AHP for LP	GJ/h	0	72	143	215	286	358	0	69	139	208	277	346	0	66	131	197	263	329
Savings heat pumps	GJ/h	0	29	59	88	118	147	0	29	57	86	114	143	0	27	54	81	108	135
Oil saved by AHP implementation	GJ/h	0	37	67	67	67	67	0	36	39	39	39	39	0	3	3	3	3	3
Bark saved by AHP implementatic	GJ/h	0	0	8	52	96	140	0	0	38	81	123	166	0	37	78	118	159	199
Seasonal savings pre-optimis.	GWh,	26	26	26	26	26	26	25	25	25	25	25	25	24	24	24	24	24	24
Seasonal savings heat pumps	GWh,	0	20	40	60	80	100	0	19	39	58	77	96	0	18	37	55	73	91
Seasonal CO2 savings	t	6107	11935	16761	16761	16761	16761	5909	11547	12143	12143	12143	12143	5608	6013	6013	6013	6013	6013

Power production with trigeneration

		Winter						Mid-season						Summer					
Share covered by AHP	%	0	20	40	60	80	100	0	20	40	60	80	100	0	20	40	60	80	100
Heating capacity AHP	MW, th	0.0	19.9	39.8	59.7	79.5	99.4	0.0	19.2	38.5	57.7	77.0	96.2	0.0	18.3	36.5	54.8	73.0	91.3
Output AHP for LP	GJ/h	0	72	143	215	286	358	0	69	139	208	277	346	0	66	131	197	263	329
Savings AHP	GJ/h	0	29	59	88	118	147	0	29	57	86	114	143	0	27	54	81	108	135
Oil saved by AHP implementation	GJ/h	0	37	67	67	67	67	0	36	39	39	39	39	0	3	3	3	3	3
HP to turbine	GJ/h	591	519	453	411	369	327	572	503	459	418	377	337	543	502	463	425	386	347
steam extraction	GJ/h	583	512	440	369	297	225	564	495	426	357	287	218	536	470	404	338	273	207
condensation	GJ/h	8	8	13	42	72	101	7	7	33	61	90	119	7	32	59	86	113	140
Turbine output	MW, e	16.8	14.9	13.3	13.8	14.2	14.7	16.3	14.4	14.6	15.0	15.5	15.9	15.5	15.7	16.2	16.6	17.0	17.4
Seasonal savings pre-optimis.	GWh,	26	26	26	26	26	26	25	25	25	25	25	25	24	24	24	24	24	24
Seasonal savings heat pumps	GWh,	0	20	40	60	80	100	0	19	39	58	77	96	0	18	37	55	73	91
Seasonal power produced	GWh,	41	36	32	33	35	36	40	35	35	37	38	39	38	38	39	40	41	42
Seasonal CO2 savings	t	6107	11935	16761	16761	16761	16761	5909	11547	12143	12143	12143	12143	5608	6013	6013	6013	6013	6013

heat pump coverage means that 40 % of the LP steam load is delivered by the heat pump output, while the remaining 60 % is supplied by PRV-depressurised steam. The threshold for profitability is given by the heat pump capacity leading to maximum oil savings. Beyond that point, savings of bark would not justify the high equipment investment.

Option III: trigeneration

The third option is the combination of a steam turbine and an absorption heat pump in parallel, as shown in figure 2c. The turbine delivers, by extraction, the total MP steam load and the fraction of LP steam not produced by the heat pump. The condensing mode is assumed. The parallel arrangement chosen reduces the HP steam available for the turbine; therefore, the load of the turbine is decreased while the heat pump capacity is increased. This drawback could be avoided by installing the heat pump in series with the turbine on the MP steam line. In this manner all the HP steam would become available for the turbine. However, the driving force for the heat pump would be lower and require the use of a double lift instead of a single effect cycle. The increased power output of the turbine would not compensate for the increased cost and lower efficiency of a double lift device. Therefore this last arrangement is not advantageous for this application; however, it could be under other steam pressure conditions.

ANALYSIS

The oil and bark savings exceeding the heat recovery benchmark were estimated for the three periods of the year defined earlier. The results are shown for the three strategies in table 1. It must be noted that savings of 5 % of the total steam

consumption through internal heat recovery, used in the computations constitute the threshold for an even yearly distribution of the oil savings. However, higher heat recovery savings would result in increased bark savings in the summer months, which in turn could be converted in higher condensing capacity and higher turbine output in the summer months. Thus, this should be targeted especially to old mills with high savings potential by heat exchanger network optimisation.

Option II has been analysed for six different heat pump coverage capacities of the LP steam demand ranging from 0 to 100 %. The results are shown in figure 3. The full lines represent winter, the dotted lines intermediate and the dashed lines summer operation. Since the periods of the year significantly affect oil consumption, the impact of the heat pump varies broadly with the seasons (figure 3a). The oil savings reach a plateau between 0 and 40 % of heat pump coverage, while bark savings on the contrary start to increase at that point. Whereas in the winter oil savings would steadily increase up to a heat pump output of about 40 MW (40 %), in the intermediate seasons they would stop growing at a heat pump coverage of 20 %. In summertime the heat pump contribution to oil savings would be almost zero. The implementation of heat pump capacities higher than 40 MW would result in wood bark savings, which have no energetic or economic advantage.

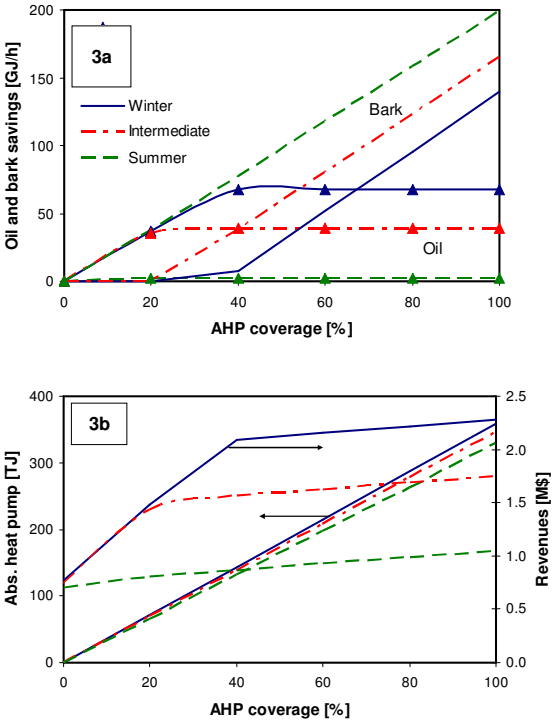

Figure 3. Effects of heat pump coverage. 3a) Oil (triangles) and bark savings. 3b) Heat pump savings and revenues.

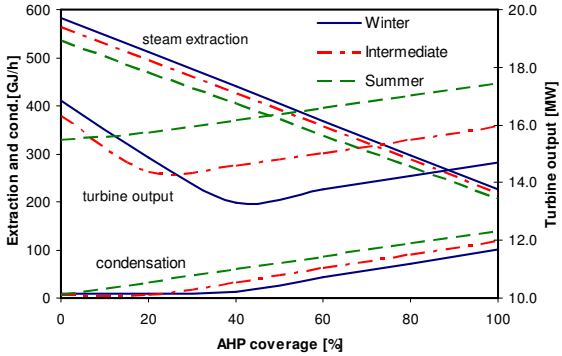

Figure 4: Extraction, condensing mode and turbine output.

Figure 3b shows how absorption heat pump savings increase steadily with increasing heat pump coverage whereas the revenues come to a plateau for high capacities. The CO_2 emission reductions which are dependant of oil consumption also do not increase proportionally to the size of the heat pump. The contribution of the heat pump could become substantial in summer if a seasonal application is found, for example for process or building cooling where electrical chillers or other equipment could be replaced. However, this application would require equipment capable of switching from heating to cooling modes.

The third option, trigeneration, is the combination of the two previous ones. Two main effects characterize this system: the trend of the oil savings and the performance of the turbine with increasing heat pump capacities. Increased process efficiency due to heat pump use lowers the oil consumption down to the baseline as in the first option. This affects the turbine operation in two ways: as oil is increasingly saved, the input to the boilers steadily decreases and so does the turbine output. Figure 4 shows the trends for the three periods. At the point where steam from bark is no longer needed in the process, thus becoming available for condensation, the net output of the turbine starts to increase steadily, despite the continuously decreasing output in the extraction

Table 2: Seasonal and yearly economics

Power production with cogeneration

	Winter	Mid-season	Summer
Seasonal revenue pre-optimisation	0.8 M$	0.7 M$	0.7 M$
Seasonal revenue turbine	2.0 M$	2.0 M$	1.9 M$
Seasonal revenue	2.8 M$	2.7 M$	2.6 M$

Overall yearly economics

Yearly revenue pre-opt. (retrofit cost for ROI = 1	2.2 M$
Yearly revenue turbine	5.9 M$
Total yearly revenue	8.1 M$
Retrofit cost for improvement from pre-opt.	2.2 M$
Turbine cost	16.8 M$
Total investment	19.1 M$

Maximized energy savings with absortion heat pump

	Winter						Mid-season						Summer					
Share covered by AHP [%]	0	20	40	60	80	100	0	20	40	60	80	100	0	20	40	60	80	100
Seasonal revenue [M$]	0.8	1.5	2.1	2.2	2.2	2.3	0.7	1.4	1.6	1.6	1.7	1.8	0.7	0.8	0.9	0.9	1.0	1.0

Overall yearly economics

Share covered by AHP	%	0	20	40	60	80	100
Total yearly revenue	M$	2.2	3.7	4.5	4.7	4.9	5.1
Retrofit costs for improvement from pre-optimisation	M$	2.2	2.2	2.2	2.2	2.2	2.2
Cost AHP	M$	0	3.3	6.5	9.8	13.0	16.3
Total investment	M$	2.2	5.5	8.7	12.0	15.3	18.5

Power production with trigeneration

		Winter						Mid-season						Summer					
Share covered by AHP	%	0	20	40	60	80	100	0	20	40	60	80	100	0	20	40	60	80	100
Seasonal revenue from savings	M$	0.8	1.5	2.1	2.1	2.1	2.1	0.7	1.4	1.5	1.5	1.5	1.5	0.7	0.7	0.7	0.7	0.7	0.7
Seasonal revenue turbine	M$	2.0	1.8	1.6	1.7	1.7	1.8	2.0	1.7	1.8	1.8	1.9	1.9	1.9	1.9	2.0	2.0	2.1	2.1
Seasonal revenue	M$	2.8	3.3	3.7	3.7	3.8	3.9	2.7	3.2	3.3	3.3	3.4	3.4	2.6	2.7	2.7	2.8	2.8	2.9

Overall yearly economics

Share covered by AHP	%	0	20	40	60	80	100
Yearly revenue from savings	M$	2.2	3.6	4.3	4.3	4.3	4.3
Yearly revenue turbine	M$	5.9	5.5	5.4	5.5	5.7	5.8
Total yearly revenue	M$	8.1	9.1	9.7	9.8	10.0	10.1
Retrofit costs for improvement from pre-optimisation	M$	2.2	2.2	2.2	2.2	2.2	2.2
Cost AHP	M$	0.0	3.3	6.5	9.8	13.0	16.3
Turbine cost	M$	16.8	15.7	16.2	16.6	17.0	17.4
Total investment	M$	19.1	21.2	24.9	28.6	32.3	36.0

mode. This is especially pronounced in winter with a threshold for 40 % of heat pump coverage. Accordingly, a heat pump of about 40 MW (40 %) achieves the highest oil savings possible as shown in Table 1 (67 GJ/h, 39 GJ/h and 3 GJ/h in winter, intermediate and summer, respectively). On the other hand with this heat pump coverage the turbine is being operated at part load in winter compared to summer conditions (13.3 MW vs. 16.2 MW). Hence, 20 % heat pump coverage is probably the best economic choice, since the oil savings are still 50 % of the maximum achievable in winter (37 GJ/h out of 67 GJ/h) and they reach 100 % during intermediate seasons and summer, while the turbine utilisation ratio (14.4 MW vs. 15.7 MW) is more even than at 40 % coverage.

ECONOMIC COMPARISON

Two indicators of economic performance have been used, the simple payback time (SPB) and the net present value (NPV). It must be noted that this study considered only the incremental cost of the system. Therefore the investment only consists of the retrofit cost of internal heat recovery measures, a new heat pump and a turbine. Revenues are the sold power and the oil saved, even if oil savings are in reality expenses not incurred rather than received revenue. For the purpose of this work, the installed capacities of the equipment were determined for maximum impact on energy consumption and CO_2 emissions achievable in the course of a year. Accordingly, these equipments operate at partial load during important periods. An economic optimised design would be based on minimal required capacities, which could not be determined with the data available.

Simple payback time

The economic calculation was performed on the basis of the yearly revenues during the aggregate of the three seasonal periods. The results are summarised in Table 2 and presented graphically on figure 5. All financial information is given in Canadian dollars. The oil savings achieved by heat

recovery pre-optimisation are evenly distributed and account for M$ 0.7 per season. The cogeneration option is characterised by an even utilisation of the turbine throughout the year with average revenue of M$ 2 per period. The total revenues add up to 8.1 M$/a. The total investment for the optimisation of the heat exchanger network and the installation of a new turbine (1000 $/kW) amounts to M$ 19.1. The simple payback time is 2.4 years.

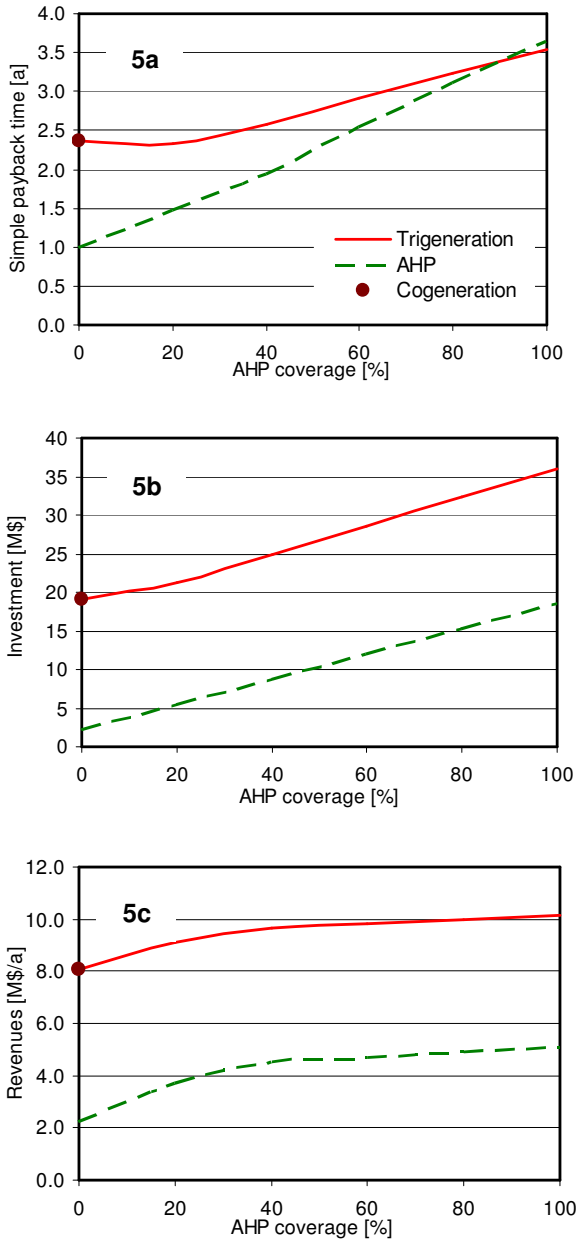

Figure 5: Profitability of three options as a function of the AHP coverage. a) Simple pay back time. b) Investment. c) Revenues.

The heat pump option has a less even pattern, especially for high coverage percentages. From 40 % coverage upwards the summer revenues become less than half that for the rest of the year (Table 2). Moreover, at high coverage the revenues do not increase proportionally to the investment necessary for the heat pump (165 $/kW heating) producing higher pay back times. Since the CO_2 emission reductions do not decrease either over 40 % coverage, the threshold for both economic viability and maximum environmental benefits is between 20 % and 40 % coverage.

Finally, the trigeneration option shows opposite trends for heat pump and turbine, which lead to a plateau of the SPB between 0 % and 40 % coverage. This is caused by the increasing revenues from oil savings which largely offset the loss in power produced, both in winter and intermediate season (Table 2). After 40 % heat pump coverage the increase in total revenues is very flat and does not compensate for the steady increase of the heat pump cost, with a resulting linear growth of the SPB.

Net present value

For this analysis an operational time of 20 years has been set for all equipment. An internal yearly interest rate of 7 %, which is usual for energy projects, and a yearly escalation rate of 4 % for fuel and power prices have been used [13]. The stand alone heat pump and trigeneration options were first analysed to determine the optimum percentage of heat pump coverage. The results are presented on figure 6. There is a maximum at 40 % coverage because of the non-linear relationship between revenue and investment. This value was used in the subsequent comparative analysis. Figure 6b shows the evolution of the NPV over 20 years. The abscissa shows the time elapsed from the date of investment. The cut through $0-value shows the time required by the projects to become cost-effective. The initial investment for the heat pump option has a clear advantage. Nevertheless the systems with high yearly outputs perform best in long-term comparison, even if the initial investment is higher. After 4 to 5 years the co- and tri-generation options become more advantageous than the stand alone heat pump. Trigeneration has 16 % higher initial revenue than cogeneration (M$ 9.7 against M$ 8.1) for a comparable investment burden

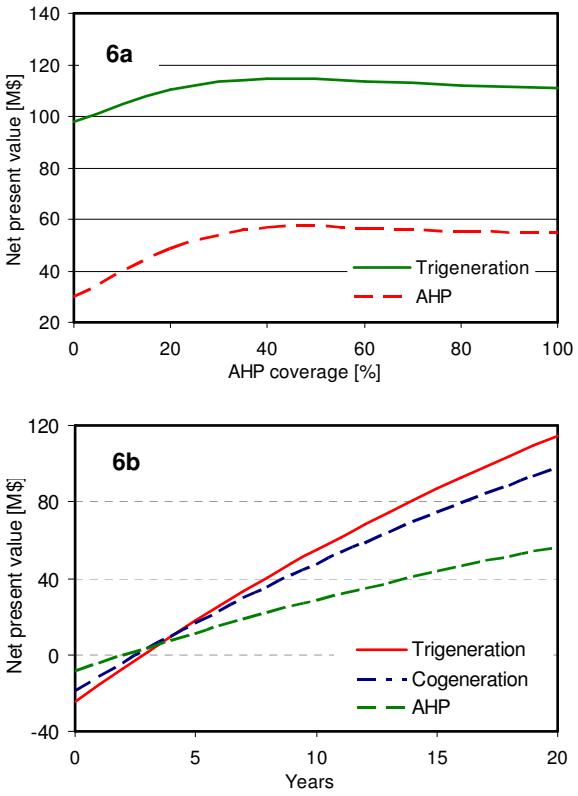

Figure 6: Net present value. a) Optimum NPV as function of AHP coverage. b) Overall NPV evolution.

(M$ 24.9 against M$ 19.1). This explains its better performance in the long term.

CONCLUSION

The energetic and economic incremental impacts of the retrofit implementation of three technological options, cogeneration, absorption heat pump and, trigeneration, have been analysed. The simple pay back time and the net present value of the options have been calculated. The results show an economic viability for all options investigated. Their simple pay back time ranges between 1 year for a single heat pump and 2.5 years for a trigeneration system including a heat pump covering 40 % of the low-pressure steam demand in the process. Moreover, the net present value is in all cases positive, which indicates that the equipment is viable. The options with high yearly revenues coming from power sales show the highest net present values, between M$ 100 and M$ 120. This supports the feasibility of the envisaged technologies.

REFERENCES

[1] Browne T., Francis D., Towers M. *Energy cost reduction in the pulp and paper industry: An overview - Increased energy efficiency can lead to improved competitive advantage*. Pulp and Paper Canada. 2001, v. 102, n. 2, p. 26, 5 p.

[2] Linnhoff B, Flower J. *Synthesis of Heat Exchanger Networks I: Systematic Generation of Energy Optimal Networks*. AIChE J. 1978; 24(4): 633-642.

[3] Dylke E., Folkestad C., Retsina T., Savvakis I. *Steam - Thermal optimization study at Prince George.* Pulp and Paper Canada. 2003, v. 104, n. 9, p. 24, 3 p.

[4] Sarimveis H., Angelou A., Retsina T., Rutherford S., Bafas G. *Optimal energy management in pulp and paper mills*. Energy Conversion and Management. 2003, v. 44, n. 10, p. 1707, 12 p.

[5] Labidi J, Noel G., Perrier M., Paris J. *Process analysis and energetic optimization*. In: Browne T, editor. Energy cost reduction in the pulp and paper industry. Montreal: PAPTAC, 1999. p. 29-64.

[6] Wising, U., Berntsson T., Stuart P. *The potential for energy savings when reducing the water consumption in a Kraft Pulp Mill.* Applied Thermal Engineering. 2005, v. 25, n. 7, p. 1057, 10 p.

[7] Brown D., Marechal F., Paris J. *A dual representation for targeting process retrofit, application to a pulp and paper process.* Applied Thermal Engineering. 2005, v. 25, n. 7, p. 1067, 16 p.

[8] Costa A., Vaillancourt J., Neuhann V., Paris J. *Applications of Absorption Heat Pumps in the Pulp and Paper Industry for Increased Efficiency and Reduction of Greenhouse Gas Emissions.* In: Proc. PaperWeek International, Montréal, Canada, 2004.

[9] Dharmadhikari S. *Consider trigeneration techniques for process plants - An enhancement to cogeneration, this technology produces heat, power and refrigeration.* Hydrocarbon Processing - Section 1. 1997, v. 76, n. 7, p. 91, 10 p.

[10] Smook G.A. *Handbook for pulp & paper technologists.* Vancouver: Angus Wild Publications, 1997.

[11] Personal communication Paprican, 2005.

[12] Ziegler F. *Recent developments and future prospects of sorption heat pump systems.* Int. J. Therm. Sci. 1999; 38: 191-208.

[13] Burer M., Tanaka K., Favrat D., Yamada K. *Multi-criteria optimisation of a district coge-neration plant integrating a solid oxide fuel cell-gas turbine combined cycle, heat pumps and chillers.* Energy - the International Journal. 2003, v. 28, n. 6, p. 497, 22 p.

Proceedings of ECOS 2005
Trondheim, Norway
June 20–22, 2005

SYSTEM ANALYSIS OF THE ENERGY MANAGEMENT OF A CHEMICAL PLANT

Part I - Methodology

Andrzej ZIĘBIK*
Silesian University of Technology
Institute of Thermal Technology
Konarskiego 22, 44-100 Gliwice
Poland

Stanisław GAŁUS
Nitrogen Plant PUŁAWY
Poland

ABSTRACT

Energy carriers needed for chemical technologies are produced in a network of mutually connected energy processes. Some part of these connections is of feedback character. A change in the balance of one energy carrier affects the production processes in all the other energy carriers. Hence, it becomes necessary to apply the system approach in the energy, exergy and ecological analysis of the energy management of a chemical plant. The mathematical model of the energy management of a chemical plant is based on the *input-output analysis*. Besides already known applications of the mathematical model in the system analysis of the balances of direct energy consumption, algorithms have been suggested for the calculation of the indices of cumulative energy consumption and the cumulative emission of noxious substances. This paper presents merely the fundamentals of methodology. An example of its application in nitrogen plant is foreseen to be presented at the next ECOS'06.
Keywords: energy management, system analysis, mathematical modeling, input-output analysis

NOMENCLATURE

$a_{ij,}\ \overline{a_{ik}}$ - coefficients of the direct consumption of energy carriers concerning energy processes and chemical processes, respectively,

$\hat{a}_{kl}$ - coefficient of the direct consumption of technological product or raw material in the technological subsystem,

$\mathbf{A},\ \overline{\mathbf{A}}$ - matrices of the coefficients of the direct consumption of energy carriers concerning the energy and technological subsystem, respectively,

$\hat{\mathbf{A}}$ - matrix of the coefficients of the direct consumption of technological semiproducts and raw materials,

$D_{ij,}\ \overline{D_k}$ - external supplies of energy carriers and technological raw materials or semiproducts,

* Corresponding author: Phone +48 32 237 16 61 Fax: +48 32 237 28 72 E-mail: ziebik@itc.polsl.pl

$\mathbf{D}, \overline{\mathbf{D}}$ - vectors of external supplies of energy carriers and technological raw materials or semiproducts, respectively,

e_i^* - index of cumulative energy consumption,

$\mathbf{e}^*$ - vector of indices of cumulative energy consumption,

$\mathbf{E}$ - unit matrix,

$f_{ij,} \overline{f_{ik}}$ - coefficients of the by-production of energy carriers in energy processes and chemical processes, respectively,

$\mathbf{F}, \overline{\mathbf{F}}$ - matrices of the coefficients of the by-production of energy carriers concerning energy and technological subsystem, respectively,

$\mathbf{G}$ - peak part of the main production of energy carriers in the case of the existence of a peak and basic installation; otherwise global main production of energy carriers,

$K_i, \overline{K_k}$ - sale of energy carrier and chemical products, respectively,

$\mathbf{K}, \overline{\mathbf{K}}$ - vectors of sale of energy carriers and chemical products, respectively,

P_i - basic part of the main production of energy carrier,

$\mathbf{P}$ - vector of the basic part of the main production of energy carriers,

Y_{ij}, Y_{ik} - consumption of energy carriers for general needs concerning energy and technological processes, respectively,

$\mathbf{Y}$ - matrix of general needs of energy carriers,

$\varepsilon_{si}, \varepsilon_{sk}$ - index of direct harmful emission concerning an energy process and chemical process, respectively,

$\boldsymbol{\varepsilon}_s$ - matrix of indices of direct harmful emissions,

ε_{si}^* - index of cumulative harmful emissions,

$\boldsymbol{\varepsilon}_s^*$ - matrix of indices of cumulative harmful emissions.

Subscripts and superscripts

d - diagonal matrix,

D - external supply,

E - energy carrier,

F - by-product,

G - peak part of the main production,

GD - external supply and peak part of production,

GG - peak part of production and peak installation,

i,j - current number of the energy carrier (energy branch),

k,l - current number of the chemical product (technological branch),

m - number of energy carriers,

n - number of energy carriers produced in chemical plant,

P - basic part of main production,

PD - external supply and basic part of production,

PP - basic part of production and basic installation,

p - number of chemical (technological) products,

r - number of chemical products and raw materials,

R - raw materials,

s - harmful emission of s-th kind,

T - transpose of a matrix,

t - technological (chemical) product.

1. SYSTEM APPROACH TO THE ENERGY ANALYSIS OF A CHEMICAL PLANT

System production of a chemical plant can be divided into two subsystems: the technological subsystem – a set of chemical processes (chemical branches) and the energy subsystem (energy management – a set of energy processes). The production of energy carriers is intended, first of all, to cover the needs of the chemical processes and partially also to cover the own consumption in the energy subsystem. Some part of the energy carrier production can be sold to external consumers (e.g. heat for district heating). The complex of connections between energy and chemical processes, as well as the interdependences between the energy processes cause that the energy management of a chemical plant is a system defined as a set of energy processes and internal relations between them and the external relations between energy management and the environment. Due to these relations the energy management of a chemical plant, treated as a complex, has attributes which its respective parts

(the particular energy processes considered separately) do not possess [1,2].
No energy process operates separately but is an element of a comprehensive energy system. The production and consumption of energy carriers take place within the network of interconnected energy processes. Therefore, both the direct consumption of energy carriers in the investigated process and the indirect consumption occurring in other processes must be analysed if we want to know the overall consumption of primary energy burdening the production of final energy carrier in a chemical plant. The same concerns the final chemical products which are also formed within the network of interconnected chemical processes.

Thus, energy is consumed not only in the last stage of production, but also in the preceding stages. Therefore the total energy consumption must be taken into consideration. In both cases, energy carriers and chemical products, the energy analysis should be based on system approach [4,5,6]. A convenient mathematical tool proved in this case to be *input-output analysis* [3].

2. LINEAR MATHEMATICAL MODEL OF THE ENERGY MANAGEMENT OF A CHEMICAL PLANT

The set of equations resulting from the balances of energy carriers is a mathematical model of the energy management of a chemical plant. This model comprises a network of interdependences existing in a real chemical plant between the technological and energy subsystems and inner relations between the respective energy processes. The algorithm of this model is a development of the *input-output analysis* applied to the energy management of a chemical plant [7,8]. In this method of analysis the production system is divided into branches (chemical and energy processes), and the set of balance equations is treated as a whole.

The chemical or energy process existing in the considered plant (e.g. nitrogen plant) is characterized by the production of one main product, as well as an optional number of by-products. If there are more than one source of the energy carrier produced as the main product, the production must be divided into its basic part and peak part (e.g. process steam from the co-generation system and steam from the pressure reducing valve). In some cases the own production of energy carriers must be supplemented by external supply (e.g. electricity). Some energy carriers are only provided from outside (mainly fuels). If a given energy carrier is the main product in one process and the by-product in another, it should be considered as a whole in one balance equation. Sometimes a part of the production of energy carriers is sold to external consumers (e.g. municipal district heating). Table 1 presents a set of equations of energy balance in compliance with "input-output analysis".

Table 1 " Input – output" balance table of energy carriers

Input part

Energy carrier	Main production		By-production		External supply
	Peak part	Basic part	Energy subsystem	Technological subsystem	
1	...	...	...	...	...
...					
i	G_i	P_i	$\sum_{j=1}^{n}(f_{ij}^{G}G_j + f_{ij}^{P}P_j)$	$\sum_{k=1}^{p}\overline{f}_{ik}\overline{G_k}$	D_{Gi}
...					
n	...	...	...	...	...
n+1	...	...	...	...	...
...					
i	*0*	*0*	*0*	*0*	D_{Di}
...					
m	...	...	...	...	...

Output part

Energy carrier	Interbranch flows		General needs	Sale
	Energy subsystem	Technological subsystem		
1	...	...	...	...
...				
i	$\sum_{j=1}^{n}(a_{ij}^{G}G_j + a_{ij}^{P}P_j)$	$\sum_{k=1}^{p}\overline{a}_{ik}^{G}\ \overline{G_k}$	$\sum_{j=1}^{n}\left(Y_{ij}^{GD} + Y_{ij}^{PD}\right) + \sum_{k=1}^{p}\overline{Y}_{ik}^{G}$	K_i
...				
n	...	...	...	...
n+1	...	...	...	...
...				
i	$\sum_{j=1}^{n}(a_{ij}^{GD}G_j + a_{ij}^{PD}P_j)$	$\sum_{k=1}^{p}\overline{a}_{ik}^{D}\ \overline{G_k}$	$\sum_{j=1}^{n}\left(Y_{ij}^{GD} + Y_{ij}^{PD}\right) + \sum_{k=1}^{p}\overline{Y}_{ik}^{D}$	*0*
...				
m	...	...	...	...

First part of equations concern energy carriers produced in chemical plant *(i,j=1, ..., n).* Second part deals with energy carriers supplied only from outside *(i =n+1, ..., m).*

Subset of balance equations concerning energy carriers produced in the energy subsystem of a chemical plant is as follows:

$$\mathbf{G} + \mathbf{P} + \mathbf{F}_{\mathbf{G}}\mathbf{G} + \mathbf{F}_{\mathbf{P}}\mathbf{P} + \overline{\mathbf{F}}\,\overline{\mathbf{G}} + \mathbf{D}_{\mathbf{G}} = \mathbf{A}_{\mathbf{GG}}\mathbf{G} + \mathbf{A}_{\mathbf{PP}}\mathbf{P} + \overline{\mathbf{A}}_{\mathbf{G}}\mathbf{G} + \mathbf{Y}_{\mathbf{GG}} + \mathbf{Y}_{\mathbf{PP}} + \overline{\mathbf{Y}}_{\mathbf{G}} + \mathbf{K} \qquad (1)$$

where the additional indices G or P denote submatrices concerning the by-production and consumption of energy carriers produced in the energy subsystem of chemical plant.

Equation (1 is usually employed to compute the elements of the vector **G**:

$$\mathbf{G} = \left(\mathbf{E} - \mathbf{A}_{\mathbf{GG}} + \mathbf{F}_{\mathbf{G}}\right)^{-1}\left[\left(\mathbf{A}_{\mathbf{PP}} - \mathbf{F}_{\mathbf{P}} - \mathbf{E}\right)\mathbf{P} + \left(\overline{\mathbf{A}}_{\mathbf{G}} - \overline{\mathbf{F}}\right)\overline{\mathbf{G}} + \mathbf{Y}_{\mathbf{GG}} + \mathbf{Y}_{\mathbf{PP}} + \overline{\mathbf{Y}_{\mathbf{G}}} + \mathbf{K} - \mathbf{D}_{\mathbf{G}}\right] \qquad (2)$$

The inverse matrix facilitates calculations particularly in the case of feedback character connections. Relation (2 is supplemented by a subset of balance equations concerning energy carriers only supplied from outside (mainly fuels):

$$\mathbf{D}_{\mathbf{D}} = \mathbf{A}_{\mathbf{GD}}\mathbf{G} + \mathbf{A}_{\mathbf{PD}}\mathbf{P} + \overline{\mathbf{A}}_{\mathbf{D}}\,\overline{\mathbf{G}} + \mathbf{Y}_{\mathbf{GD}} + \mathbf{Y}_{\mathbf{PD}} + \overline{\mathbf{Y}_{\mathbf{D}}} \qquad (3)$$

where the index D denotes submatrices concerning the consumption of energy carriers only brought from outside.

Eqs. (2) and (3) describe the simulation mathematical model of the energy management of a chemical plant. As input data there are given first of all: $\mathbf{A}_{\mathbf{G}}, \mathbf{A}_{\mathbf{P}}, \mathbf{F}_{\mathbf{G}}, \mathbf{F}_{\mathbf{P}}, \overline{\mathbf{A}}, \overline{\mathbf{F}}, \mathbf{Y}, \overline{\mathbf{G}}$. In the simulation model the vectors $\mathbf{P}, \mathbf{D}$ and $\mathbf{K}$ are given a priori, too. In the case of an optimization model these vectors are treated as decision values [8]. Yet, the presented model can be used only to analyse the direct energy consumption.

3. MATHEMATICAL MODEL OF CUMULATIVE ENERGY CONSUMPTION

The analysis of direct energy consumption is not a sufficient tool for the evaluation of the energy utilization effectiveness, because the consumption of energy in previous production and transportation processes leading to a given final energy carrier is not included. The same remark can refer to products of chemical processes. It is not enough to analyse only the direct consumption of energy, but

more important is the analysis both the direct and indirect energy consumption, that means cumulative energy consumption.

In order to determine the relation describing the indices of cumulative energy consumption, the balances of cumulative energy consumption were applied according to the balance equations of a linear mathematical model of the energy management of the chemical plant. In general, an energy carrier may be produced as the main product (basic and peak production) or be by-product of the energy or technological subsystem. It can also be an energy carrier from outside (external supply). Therefore the average index of cumulative energy consumption concerning the given i-th energy carrier ought to be taken into account:

$$e_{Ei}^{*} = \frac{G_i e_{Gi}^{*} + P_i e_{Pi}^{*} + F_i e_{Fi}^{*} + D_i e_{Di}^{*}}{G_i + P_i + F_i + D_i} \tag{4}$$

and

$$F_i = \sum_{j=1}^{n} \left(f_{ij}^{G} G_j + f_{ij}^{P} P_j \right) + \sum_{k=1}^{p} \overline{f}_{ik} \overline{G}_k \tag{5}$$

Vector $\mathbf{e}_{\mathbf{E}}^{*}$ of the average indices of cumulative energy consumption takes the following form:

$$\mathbf{e}_{\mathbf{E}}^{*} = \mathbf{H}^{-1} \left(\mathbf{G}^{\mathbf{d}} \mathbf{e}_{\mathbf{G}}^{*} + \mathbf{P}^{\mathbf{d}} \mathbf{e}_{\mathbf{P}}^{*} + \mathbf{L}^{\mathbf{d}} \mathbf{e}_{\mathbf{F}}^{*} + \mathbf{D}^{\mathbf{d}} \mathbf{e}_{\mathbf{D}}^{*} \right) \tag{6}$$

and

$$\mathbf{L} = \mathbf{F}_{\mathbf{G}} \mathbf{G} + \mathbf{F}_{\mathbf{P}} \mathbf{P} + \overline{\mathbf{F}}\,\overline{\mathbf{G}} \tag{7}$$

$$\mathbf{H} = \mathbf{G}^{\mathbf{d}} + \mathbf{P}^{\mathbf{d}} + \mathbf{L}^{\mathbf{d}} + \mathbf{D}^{\mathbf{d}} \tag{8}$$

where the index **d** denotes the diagonal matrix after the transformation column vector.

The indices of cumulative energy cunsumption e_{Gi}^{*} and e_{Pi}^{*} are determined basing on the cumulative energy balances. Fig. 1 presents a calculation scheme concerning the j-th energy branch in the general case when the basic and the peak part of main production are taken into account. Basing on this scheme the balance equations of the cumulative energy consumption can be set up for the peak part and basis part of the main production.

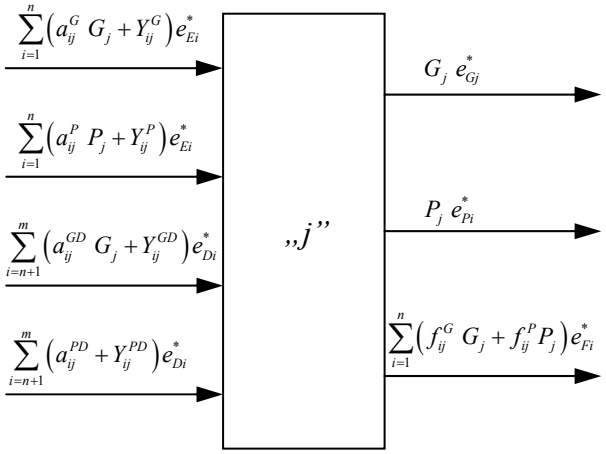

Fig. 1. Calculation scheme of cumulative energy balance of energy branch

$$\left[\mathbf{A}_{\mathbf{G}}^{\mathbf{T}} + \left(\mathbf{G}^{\mathbf{d}} \right)^{-1} \mathbf{Y}_{\mathbf{GG}}^{\mathbf{T}} \right] \mathbf{e}_{\mathbf{E}}^{*} + \left[\mathbf{A}_{\mathbf{GD}}^{\mathbf{T}} + \left(\mathbf{G}^{\mathbf{d}} \right)^{-1} \mathbf{Y}_{\mathbf{GD}}^{\mathbf{T}} \right] \mathbf{e}_{\mathbf{D}}^{*} = \mathbf{e}_{\mathbf{G}}^{*} + \mathbf{F}_{\mathbf{G}}^{\mathbf{T}} \mathbf{e}_{\mathbf{F}}^{*} \tag{9}$$

$$\left[\mathbf{A}_{\mathbf{P}}^{\mathbf{T}} + \left(\mathbf{P}^{\mathbf{d}} \right)^{-1} \mathbf{Y}_{\mathbf{P}}^{\mathbf{T}} \right] \mathbf{e}_{\mathbf{E}}^{*} + \left[\mathbf{A}_{\mathbf{PD}}^{\mathbf{T}} + \left(\mathbf{G}^{\mathbf{d}} \right)^{-1} \mathbf{Y}_{\mathbf{PD}}^{\mathbf{T}} \right] \mathbf{e}_{\mathbf{D}}^{*} = \mathbf{e}_{\mathbf{P}}^{*} + \mathbf{F}_{\mathbf{P}}^{\mathbf{T}} \mathbf{e}_{\mathbf{F}}^{*} \tag{10}$$

In the Eqs. (9) and (10) the vector of indices of cumulative energy consumption burdening the energy carriers supplied from outside $\mathbf{e}_{\mathbf{D}}^{*}$ is given a priori. These are average values of the indices of cumulative energy consumption concerning mainly fuels. The aforesaid equations contain also the vector $\mathbf{e}_{\mathbf{F}}^{*}$ concerning the indices of cumulative energy consumption burdening the by-products. Apparently it is an additional set of unknown values. In such a case, however, the principle of avoided energy expenditures should be applied (similarly as the principle of avoided costs). This means, that the by-products should be burdened by such a cumulative energy consumption as in the case of the specialistic (single-aimed) process which is substituted by the by-production of energy carrier [6]. For instance, in the heat and power co-generation process the electricity (by-product) should be assigned by the index of

cumulative energy consumption like in the power plants.

4. MATRIX METHOD OF CALCULATING THE INDICES OF CUMULATIVE ENERGY CONSUMPTION OF CHEMICAL PRODUCTS

From the point of view of investigating the energy consumption in chemical processes the system method of calculating the indices of cumulative energy consumption is still more interesting than previous application concerning energy carriers They are determined similarly as presented before basing on the set equations of the balances of cumulative energy consumption. The balance of technological subsystem can be also described by means of the *input-output table*. The balance equations concerning k-th technological products and technological raw material or semi-products have the following form:

$$\overline{G}_k = \sum_{l=1}^{p} \hat{a}_{kl}^{G}\, \overline{G}_k + \overline{K}_k \tag{11}$$

$$\overline{D}_k = \sum_{l=1}^{p} \hat{a}_{kl}^{D}\, \overline{G}_K \tag{12}$$

The set of balance equations of technological products, as well as raw materials and semiproducts in matrix notation have the following forms:

$$\overline{\mathbf{G}} = \hat{\mathbf{A}}_{\mathbf{G}}\overline{\mathbf{G}} + \overline{\mathbf{K}} \tag{13}$$

or

$$\overline{\mathbf{G}} = \left(\mathbf{E} - \hat{\mathbf{A}}_{\mathbf{G}}\right)^{-1}\overline{\mathbf{K}} \tag{14}$$

and

$$\overline{\mathbf{D}} = \hat{\mathbf{A}}_{\mathbf{D}}\overline{\mathbf{G}} \tag{15}$$

Fig. 2 presents a calculation scheme concerning the k-th chemical process (technological branch). Basing on this scheme a balance equation of the cumulated energy consumption can be set up.

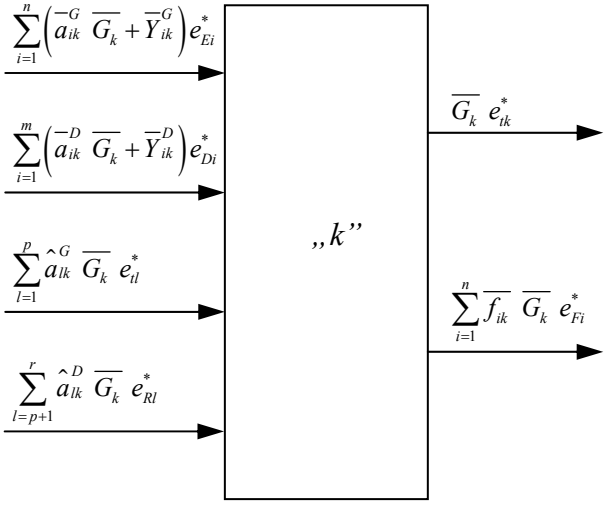

Fig. 2. Calculation scheme of cumulative energy balance of chemical process

The set of equations of the cumulative energy balance concerning the technological subsystem takes the following form:

$$\left[\overline{\mathbf{A}}_G^T + \left(\overline{\mathbf{G}}^d\right)^{-1}\mathbf{Y}_G^T\right]\mathbf{e}_E^* + \left[\overline{\mathbf{A}}_D^T + \left(\overline{\mathbf{G}}^d\right)^{-1}\overline{\mathbf{Y}}_D^T\right]\mathbf{e}_D^* + \hat{\mathbf{A}}_G^T\,\mathbf{e}_t^* + \hat{\mathbf{A}}_D^T\,\mathbf{e}_R^* = \mathbf{e}_t^* + \overline{\mathbf{F}}^T\,\mathbf{e}_F^* \tag{16}$$

In the algorithm of calculating the indices of cumulative energy consumption burdening the chemical products the input data comprise column vector $\overline{\mathbf{e}}_{\mathbf{R}}^{*}$ determining the average indices of cumulative energy consumption burdening chemical raw materials and semiproducts, as well as the previously determined vector $\mathbf{e}_{\mathbf{E}}^{*}$ (described in the previous chapter). Similarly as in chapter 3 the vector $\mathbf{e}_{\mathbf{F}}^{*}$ is determined basing on the principle of avoided energy expenditures.

5. SYSTEM ANALYSIS OF ECOLOGICAL INDICES

The production of energy carriers and chemical products is accompanied by the emission of noxious gaseous, liquid and solid substances, as well as surplus heat passed into the environment. The direct consumption of energy carriers (mainly fuels), as well as raw materials and technological semiproducts leads to the direct emission related to the production of the given carrier or chemical

product. The energy carriers, raw materials and technological semiproducts are, however, already burdened with harmful emissions resulting from earlier production and transporting processes. Similarly as in the case of the analysis of cumulative energy consumption this is the result of the production energy carriers and chemical products within the interconnected processes. The ecological burden of energy carriers or chemical products do not depend on the direct noxious emissions but on the global emission including also the indirect negative ecological effects occurring in previous stages of the network of energy and chemical processes. Thus, similarly as in the case of cumulative energy consumption we must take into account the indices of the cumulative harmful emissions burdening the production of energy carriers and chemical products.

In the case of energy carriers we must apply the average emission for the i-th energy carrier, because it can be obtain in basic or peak installations and can also be a by-product and external supply. Analogically to eg. (4) we can express the average index of cumulative harmful emissions concerning the i-th energy carrier as follows;

$$\varepsilon^*_{sEi} = \frac{G_i \varepsilon^*_{sGi} + P_i \varepsilon^*_{sPi} + F_i \varepsilon^*_{stui} + D_i \varepsilon^*_{sDi}}{G_i + P_i + F_i + D_i} \tag{17}$$

Similarly as in the case of cumulative energy consumption the vector $\boldsymbol{\varepsilon}^*_{\mathbf{sE}}$ of the average indices of cumulative harmful emissions takes the following form:

$$\boldsymbol{\varepsilon}^*_{\mathbf{sE}} = \mathbf{H}^{-1}\left(\mathbf{G}^{\mathbf{d}}\boldsymbol{\varepsilon}^*_{s\mathbf{G}} + \mathbf{P}^{\mathbf{d}}\boldsymbol{\varepsilon}^*_{s\mathbf{P}} + \mathbf{L}^{\mathbf{d}}\boldsymbol{\varepsilon}^*_{s\mathbf{F}} + \mathbf{D}^{\mathbf{d}}\boldsymbol{\varepsilon}^*_{s\mathbf{D}}\right) \tag{18}$$

The indices of the cumulative emission $\boldsymbol{\varepsilon}^*_{\mathbf{sGi}}$ and $\boldsymbol{\varepsilon}^*_{\mathbf{sPi}}$ are determined basing on the cumulative balance of emissions. Fig. 3 presents a calculation scheme concerning the j-th energy branch. Basing on this scheme we can express the set of balance equations used to calculate the indices of the s0th cumulative emission burdening the production of energy carriers:

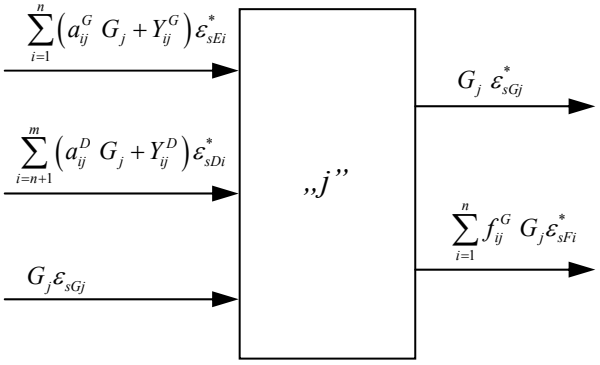

Fig. 3. Calculation scheme of cumulative emission of energy process

$$\left[\mathbf{A}_{\mathbf{G}}^{\mathbf{T}} + \left(\mathbf{G}^{\mathbf{d}}\right)^{-1}\mathbf{Y}_{\mathbf{G}}^{\mathbf{T}}\right]\boldsymbol{\varepsilon}^*_{\mathbf{sE}} + \left[\mathbf{A}_{\mathbf{GD}}^{\mathbf{T}} + \left(\mathbf{G}^{\mathbf{d}}\right)^{-1}\mathbf{Y}_{\mathbf{GD}}^{\mathbf{T}}\right]\boldsymbol{\varepsilon}^*_{\mathbf{sD}} + \boldsymbol{\varepsilon}_{\mathbf{sG}} = \boldsymbol{\varepsilon}^*_{\mathbf{sG}} + \mathbf{F}_{\mathbf{G}}^{\mathbf{T}}\boldsymbol{\varepsilon}^*_{\mathbf{sF}} \tag{19}$$

In Eq. 19 the unknown value is the vector $\boldsymbol{\varepsilon}^*_{\mathbf{sG}}$ of the cumulative emission burdening the peak part of the main production of energy carriers. The vector $\boldsymbol{\varepsilon}^*_{\mathbf{sE}}$ of the average emission of the s-th noxiouses substance being determined by means of Eq. (10). The analogical equation as (19) we can write in the case of basic part of main production of energy carriers. The input data (known a priori) are the vectors $\boldsymbol{\varepsilon}^*_{\mathbf{sD}}$ and $\boldsymbol{\varepsilon}_{\mathbf{sG}}$, the former of which denotes the indices of cumulative s-th harmful emission burdening the supply of energy carriers from outside. The latter one determines the direct s-th harmful emission resulting from the peak part production. The vector $\boldsymbol{\varepsilon}^*_{\mathbf{sF}}$ concerning the cumulative emission burdening the by-production of energy carriers is determined basing on the principle of avoided harmful emissions. That means that the by-product should be burned by such a cumulative harmful emission as in the case of a specialistic process, which is substituted by the by-production of energy carrier.

An analogical approach ought to be applied in calculations of the indices of cumulative harmful emissions concerning chemical products. The scheme of calculations is similar to that presented in Figs. 2 and 3.The set of equations applied in calculations of the indices of cumulative harmful emissions burdening chemical products takes the form:

$$\left[\overline{\mathbf{A}}_{\mathbf{G}}^{\mathbf{T}}+\left(\overline{\mathbf{G}}^{\mathbf{d}}\right)^{-1}\overline{\mathbf{Y}}_{\mathbf{G}}^{\mathbf{T}}\right]\boldsymbol{\varepsilon}_{\mathbf{sE}}^{*}+\left[\overline{\mathbf{A}}_{\mathbf{D}}^{\mathbf{T}}+\left(\overline{\mathbf{G}}^{\mathbf{d}}\right)^{-1}\overline{\mathbf{Y}}_{\mathbf{D}}^{\mathbf{T}}\right]\boldsymbol{\varepsilon}_{\mathbf{sD}}^{*}$$
$$+\widehat{\mathbf{A}}_{\mathbf{G}}^{\mathbf{T}}\,\boldsymbol{\varepsilon}_{\mathbf{st}}^{*}+\widehat{\mathbf{A}}_{\mathbf{D}}^{\mathbf{T}}\,\boldsymbol{\varepsilon}_{\mathbf{sR}}^{*}+\boldsymbol{\varepsilon}_{\mathbf{st}}=\boldsymbol{\varepsilon}_{\mathbf{st}}^{*}+\overline{\mathbf{F}}^{\mathbf{T}}\boldsymbol{\varepsilon}_{\mathbf{sF}}^{*} \qquad (20)$$

In the algorithm of calculating the indices of cumulative harmful emissions burdening the chemical products the input data comprise the vector $\boldsymbol{\varepsilon}_{\mathbf{sR}}^{*}$ determining the average indices of cumulative harmful emissions burdening chemical raw materials and semiproducts, the vector $\boldsymbol{\varepsilon}_{\mathbf{sD}}^{*}$ and the vector $\boldsymbol{\varepsilon}_{\mathbf{st}}$ determining the direct s-th harmful emission resulting from the chemical processes. The vector $\boldsymbol{\varepsilon}_{\mathbf{sE}}^{*}$ is previously determined basing on Eqs. 18 and 19 and vector $\boldsymbol{\varepsilon}_{\mathbf{sF}}^{*}$ results from the principle of avoided harmful emissions.

6. CONCLUSIONS

The system of production in a chemical plant consists of two subsystems, namely the energy and technological one. In the former subsystems energy carriers are produced, mainly for the needs of the technological subsystem. They are produced in networks of mutually connected processes. Some of them are of feedback character, which complicates the reconciliation of the balances of energy carriers by means of the traditional method applying partial balances.

The technological subsystem is also a network of interconnected chemical processes, additionally connected with the energy subsystem. In a modern chemical plant the technological subsystem is not only the consumer of energy carriers but also produces some energy carriers (e.g. steam and hot water from waste-heat boilers, technological fuel gases) by means of waste energy recovery.

Therefore, it is quite obvious that both energy and chemical processes realized in a chemical plant cannot be considered separately from each other because of the relations existing between them. For this reason the system approach is inevitable. In this paper a system approach to the energy management of a chemical plant by means of the *input-output analysis* has been applied.

Basing on the linear mathematical model of energy management in chemical plants algorithms have been suggested to be used in calculations of the indices of cumulative energy consumption, concerning both energy carriers and chemical products. Such a procedure was applied to construct a model for the calculation of the indices of cumulative emissions of harmful substances burdening energy carriers and chemical products.

The models presented in this paper are being implemented in practical calculations in one of the Polish chemical plant. The results of these investigations will be presented at the next ECOS'06.

REFERENCES

[1] Bertalanffy L. *General system theory. Foundations, development, applications.* Reviewed ed. New York: George Braziler: 1973.

[2] Klir G.J. (ed.) *Trends in general system theory.* New York: John Wiley and Sons, 1972.

[3] Leontief W.W. *The structure of American economy 1919-1939.* New York: Oxford University Press, 1951.

[4] Rettaroli M, Sciubba E. *"MASAI": A code for the symbolic calculation of thermal plants*. In: Proceedings of the 1994 Engineering Systems Design and Analysis Conference ESDA, ASME 1994.

[5] Sciubba E., Melli R. *Artificial intelligence in thermal systems. Design, concepts and applications.* Commack (New York): Nova Science Publishers, 1998.

[6] Szargut J. Ziębik A., *Fundamental of thermal engineering (in Polish)* . PWN, Warszawa 2000.

[7] Ziębik A. *Process and system analysis in thermal engineering.* Energy 2001: 26: 1145-1157.

[8] ZiębikA. *Mathematical modeling of energy management system in industrial plants,* Ossolineum, Wrocław 1990.

Proceedings of ECOS 2005
Trondheim, Norway
June 20–22, 2005

Engines, Combustion, Heat Exchange

Proceedings of ECOS 2005
Trondheim, Norway
June 20–22, 2005

ENGINE CHARACTERISTICS OF EMISSIONS AND PERFORMANCE USING MIXTURES OF NATURAL GAS AND HYDROGEN

Marie Bysveen
Department of Energy and Process Technology
Faculty of Engineering and Technology
Norwegian University of Science and Techniology (NTNU)
Norway

ABSTRACT

An evaluation was performed on the efficiency and emissions from an engine fuelled with CNG and a mixture of natural gas and hydrogen, respectively. The mixtures of CNG and hydrogen were named HCNG.
Two different mixtures were investigated; pure compressed natural gas (CNG), and 29 vol% H_2 in CNG (named HCNG). For each mixture, four engine speeds were tested under full load conditions, namely 1300 rpm, 1500 rpm, 1800 rpm and 2200 rpm. For each mixture and each engine speed four different excess air ratios (λ [-]) were chosen, in the range of λ= 1.1– 2.0 [-]. It is very important to note that the spark advance chosen for each of the mixtures is a major test parameter in this kind of study where hydrogen is involved, as the flame speed of hydrogen is much higher than the flame speed for CNG. This implies that the spark advance resulting in the maximum break mean effective pressure ($BMEP_{max}$) is closer to top dead centre (TDC) for the HCNG than for the pure CNG. This is taken into consideration in these tests, so the spark advance is optimized for each of the mixtures tested.
The full load curves (P_e=f(Engine speed)) for the two mixtures at different excess air ratio coincide at λ=1.4 [-] and λ=1.6 [-]. When the mixtures are leaned out to λ=1.8 [-] the HCNG gives more power than the equivalent CNG. The explanation for this is that the CNG is approaching the limit where the engine starts to misfire, i.e. it is too close to the limit on the lean side. This is also seen on the emissions of unburned hydrocarbons.
The emissions of total unburned hydrocarbons (in g/kWh) were also measured. From the plots of HC emissions as a function of lambda, one may see that at a certain excess air ratio, the emissions of unburned hydrocarbons start to increase considerably. This indicates that the lean limit is approached. The lean limit for the pure CNG tested in this engine is approximately λ=1.8[-], and the lean limit for the HCNG is even leaner, i.e. at about λ=2.0 [-]. This is as expected, and in accordance with the literature. It is also important to note that the level of the unburned hydrocarbons emitted at certain excess air ratio are considerably lower for the HCNG than for the pure CNG. On the other hand, comparing the emissions of nitrogen oxides, the HCNG is emitting more than the CNG at the same excess air ratio. This difference is decreasing as the λ increases from 1.4 [-] to 2.0 [-], where the level of NO_x are equal for the two mixtures investigated. However, it is important to note that the NO_x emissions is significantly reduced by increasing the excess air ratio, and by using HCNG this leaning out is easily achieved without any substantial HC penalty.
Considering the total emissions of unburned hydrocarbons and nitrogen oxides, it is easily seen that the positive effect of adding hydrogen to the CNG increases as a function of lambda. The results also indicate that the amount of hydrogen addition to the CNG needs to be varied as a function of engine load, in order to optimise engine efficiency and power.

Key words: Hydrogen, natural gas, SI Engine, emissions, performance.

NOMENCLATURE

BTDC	Before Top Dead Center [°]
CNG	Compressed Natural Gas
H_2	Hydrogen
HC	Unburned Hydrocarbons
HCNG	Hydrogen Enriched Compressed Natural Gas
IC Engine	Internal Combustion Engine
l	Excess air ratio [-]
LHV_{H_2}	Lower heating value of H_2 [$119{,}9 \cdot 10^3$ kJ/kg]
LHV_{CNG}	Lower heating value of CH_4 [$49{,}5 \cdot 10^3$ kJ/kg]
M	Torque [Nm]
m	Fuel mass flow rate [g/s]
MBT	Maximum Brake Torque
n	Engine speed [rpm]
NO_x	Nitrogen oxides
$h_{\text{th,brake}}$	Brake thermal efficiency [-]
SI Engine	Spark Ignition Engine
x_{H2}	Mass fraction for H_2 in the fuel [-]

INTRODUCTION

Global warming and the need for a stable energy market world wide have resulted in an increased focus on hydrogen as an energy source. A transition solution to the use of pure hydrogen may be the use of mixtures of hydrogen and hydrocarbons, based on both the availability and low cost of petroleum supply within the next decades. For comparison, most IC engines running on gasoline operate with a spark advance of approximately 35 degrees BTDC, while a CNG engine would require approximately 50 degrees BTDC. This slower burn rate results in reduced thermal efficiency and poor lean burn characteristics.

The reason for the increasing interest in the use of internal combustion engines operating on alternative gaseous fuels, is mainly the demand for reduced exhaust emissions combined with improvements in efficiency. The lean burn approach with addition of hydrogen offers a number of positive features that makes it attractive. Lean mixtures in general may provide both high thermal efficiency, reduced tendency of knocking, reduced emissions (especially NO_x) and less heat transfer.

On this background, the use of hydrogen as an additive to hydrocarbon fuels is interesting for many reasons, such as extended lean limit. The reactivity and diffusivity of hydrogen are responsible for potential explosions hazards due to either slow leakage or puncturing of the storage tank. In order to reveal the behaviour of CNG-H_2 mixtures, both fundamental and more applied research have been conducted on the combustion characteristics of hydrocarbon-air mixtures with hydrogen addition ([1], [2], [3]).

The addition of hydrogen to methane-air mixtures in SI engines will move the lean limit to leaner mixtures, increasing the combustion speed and the combustion temperatures. An increase in the combustion temperatures may result in increased NO_x emissions compared to pure natural gas (CNG) at the same excess air ratio.

Law and Kwon ([1]) have investigated the substitution of hydrogen with hydrocarbons up to C3 in hydrogen-air flames. Their results indicate that these hydrocarbons are all capable of reducing the temperatures and burning velocities of hydrogen-air flames significantly. A reduction of the flame temperature would most probably lead to a lower NO_x formation rate, although a slower burning rate could promote it. When it comes to knocking, the increased energy density of the fuel could obviate the need for supercharging, which promotes knocking, but the slower burning rate on the other hand favours knocking through auto-ignition.

An optimised combustion chamber design is an important parameter when CNG-hydrogen blends are considered. The reason for this is the fact that hydrogen will have most impact on the combustion process in a “slow” combustion chamber, and the potential for a simultaneous reduction of NO_x and HC is therefore highest for such a combustion chamber geometry.

Karim et al. ([3]) have reviewed the effects of some hydrogen addition to methane on the main combustion characteristics of the fuel for engine applications. Some of the parameters tested were flame propagation rate, optimum spark timing and average combustion duration.

Raman et al. ([4]) performed a comprehensive study on HCNG in lean burn SI engines, using 0, 5, 15 and 30 vol% H_2 on a GM 5.7l, V8 engine. With 15 and 30 vol% H_2 substantial reductions in NO_x with some HC penalty were observed as a result of very lean combustion. Above λ=1.4 [-] the BMEP was increased due to improvements in the lean combustion characteristics.

In the studies reported by Hoekstra et al. ([5] and [6]), experiments were employed with up to 50 vol% H_2 in CNG on a 4.6 l SI V8. Using 20-30 vol% hydrogen, the NO_x emissions were reduced below 0.5 g/kWh, but increasing the H_2 addition above 30 vol% did not result in a further NO_x benefit.

Fotache et al. ([7]) found that the hydrogen has a catalyzing effect in the ignition of hydrocarbons with only a few percent addition of hydrogen by volume.

The objectives of this work are to compare compressed natural gas (CNG) and HCNG under various steady-state conditions in order to supplement the research performed to date (see the reference list).

EXPERIMENTAL SET- UP

Two fuel gas mixtures were investigated in this work, namely Compressed Natural Gas (CNG), (which in this work consisted of about 99,5 vol % CH_4), and a mixture of 29 vol% hydrogen in this CNG/methane (HCNG).

The engine used for the experiments was three-cylinder, single spark plug, 2.7l Zetor Z4901 originally used for stationary applications. It was rebuilt for natural gas use, reducing the compression ratio form 17:1 [-] down to 11:1 [-]. The most important engine data is presented in Table 1.

Engine:	Zetor Z4901 (D)
Displaced volume:	2,7 dm^3
Bore:	102 mm
Stroke:	110 mm
Original compression ratio:	17:1
Compression ratio after rebuilding:	11:1
Power at 2200 rpm:	32,4 kW
Torque at 1500 rpm:	150 Nm
Brake specific fuel consumption BSFC [g/kWh]:	245 +/- 10%

Table 1: Engine data

The test engine was equipped with K-type thermo elements in the intake manifold, in the cooling water system and in the exhaust. A hydraulic water brake was employed in the engine set-up, and a coriolis device measured the mass rate of fuel entering the engine. The spark timing needed to be adjusted manually during the tests, based on MBT (Maximum Brake Torque) timings found in preliminary investigations. The sensitivity in spark timings for the fuels and the engine were studied in the range of 5-25 degrees BTDC.

The control and data logging system for the engine was written using National Instruments program LabView. It is also important to note that the HCNG mixture used in these tests was premixed outside the intake manifold, and not mixed within the manifold. But there is no reason to believe that this layout should be of any significant influence on the results obtained.

In order to design the experimental matrix for comparison of CNG and HCNG, operating values for engine speed, engine load, excess air ratio (λ [-]) and spark timing were chosen. The HCNG calibration included operation at retarded spark timings.

An experimental matrix comprised of these two fuel mixtures (CNG and HCNG), four different engine speeds and five excess air ratios. This test matrix is presented in Table 2.

As a result of practical considerations concerning the engine control system, lower values of air-fuel ratio for the HCNG tests were not performed.

The spark advance chosen for each of the mixtures is a major test parameter in this kind of study where hydrogen is involved, as the flame speed of hydrogen is much higher than the flame speed for CNG. This implies that the spark advance resulting in the maximum break mean effective pressure ($BMEP_{max}$) is closer to top dead centre (TDC) for the HCNG than for the pure CNG. This is taken into consideration in these tests, so the spark advance is optimized for each of the mixtures tested.

	EXCESS AIR RATIO λ **[-]**	
Engine speed [rpm]	**HCNG*** **(29 vol % H_2)**	**CNG****
1300 rpm	1.4	1.1
	1.6	1.4
	1.8	1.6
	2.0	1.8
1500 rpm	1.4	1.1
	1.6	1.4
	1.8	1.6
	2.0	1.8
1800 rpm	1.4	1.1
	1.6	1.4
	1.8	1.6
	2.0	1.8
2200 rpm	1.4	1.1
	1.6	1.4
	1.8	1.6
	2.0	1.8

*) HCNG = Hydrogen enriched Natural Gas;
In this case; 29 vol% H_2, 71 vol% CH_4
**) CNG = Compressed Natural Gas
In this case - 99,5vol CH_4 and 0,3 vol % C_2H_6

Table 2 : Experimental test matrix

The following spark advance timings were used for the various test points, see Table 3.

	SPARK ADVANCE [° BTDC]	
Engine speed [rpm]	**CNG**	**HCNG (29 vol % H_2)**
750	**5**	**2.5**
1300	**15**	**10**
1500	17.2	12.2
1800	20.5	15.5
2200	**25**	**20**

Table 3: Spark advance employed for the test points used

The experimental uncertainty in the spark timing is assumed to be about ± 2°.

RESULTS

Brake thermal efficiency is a measure of how much available power that is produced with respect to the chemical input rate. The brake thermal efficiency $\eta_{th,brake}$ is calculated for all the test points in the test matrix, with the efficiency defined as follows:

$\eta_{th,brake}$ = ENGINE POWER/ FUEL ENERGY =

$$= \frac{2p}{60} \frac{n \cdot M}{m \cdot \left(LHV_{H_2} \cdot x_{H_2} + LHV_{CNG} \left(1 - x_{H_2}\right)\right)} \quad (1)$$

Figure 1 shows the brake thermal efficiency versus engine power for tests with constant engine speed. For a given engine power, the brake thermal efficiency $\eta_{th,brake}$ is considerably higher using HCNG than using pure NG. This effect is most pronounced for the highest engine speeds.

In Figure 2 the engine power is plotted as a function of engine speed with each iso-line representing constant excess air ratio. It is important to note that the NG-air blends range from λ=1.1 – 1.8 [-], but the HCNG blends range form λ=1.4 – 2.0 [-] in this test series.

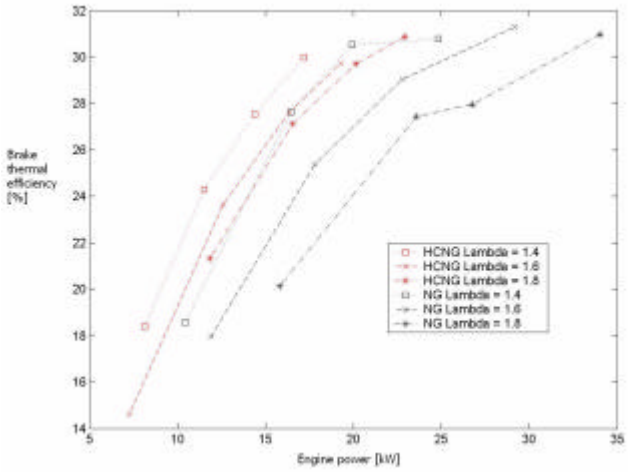

Figure 1: Brake thermal efficiency $\eta_{th,brake}$ as a function of engine power for test points with constant engine speed

Nagalingam et al. ([8]) noted that the power of HCNG compared to CNG was reduced due to the lower heating value of H_2 compared to methane. However, since the flame speed of hydrogen is so much higher than that of CNG, less spark advance is required to produce MBT (Maximum Brake Torque).

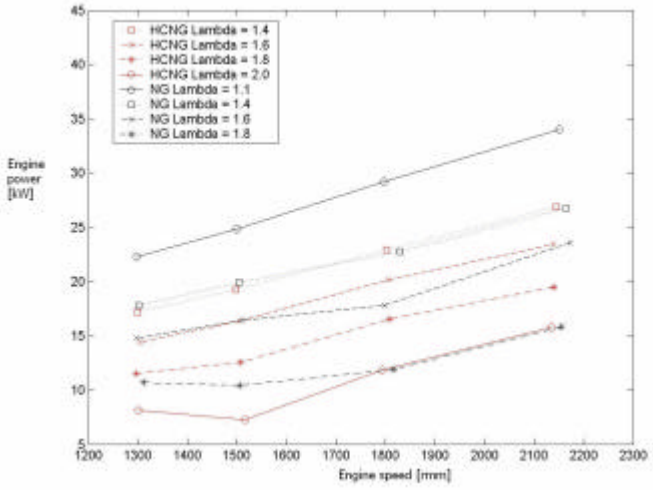

Figure 2: Engine power as a function of engine speed for constant excess air ratios λ [-]

The differences in engine power between CNG and HCNG increases while leaning out the excess air mixture, as expected. The difference is minor for λ=1.4 [-] and λ=1.6 [-], but a further increase in λ to λ=1.8 [-] results in a considerable deviation in the engine power using CNG and HCNG, respectively. This is the same effect that was seen in [9] when the lean limit is approached; that the positive effect of adding hydrogen to the methane-air mixture is most pronounced close to the lean limit.

The engine-out emissions of unburned hydrocarbons HC are plotted in Figure **3** and as a function of excess air ratio λ [-]. In general, the production of unburned hydrocarbons seem to be reduced when adding hydrogen to the CNG for a given excess air ratio. This is in accordance with the literature ([10], [11], [12], [13] and [14]), and the fact that the lean limit for pure methane-air mixtures is much richer then the lean limit for hydrogen-enriched methane-air mixtures. With H_2 addition, a smaller quenching zone results, enabling the flame to propagate closer to the walls, in addition to a reduction in the partial burning in the case of HCNG compared to CNG. For the CNG-air blends, the HC emissions increase considerably when increasing the lambda from 1.6 [-] to 1.8 [-]. On the other hand, the HC emissions form the HCNG blends experience the same trend when leaning out form λ=1.8 [-] to 2.0 [-].

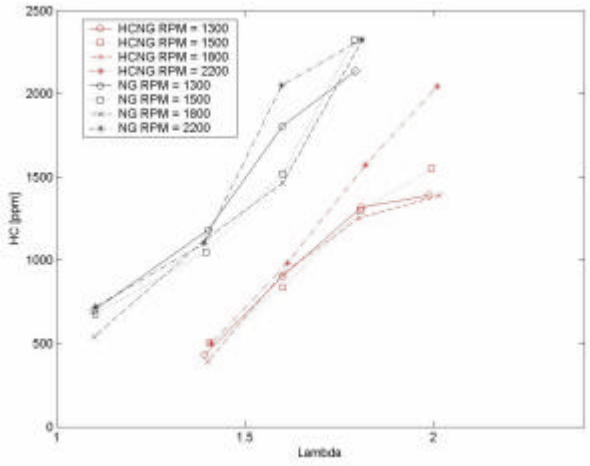

Figure 3: Emissions of unburned hydrocarbons (HC) ([ppm]) versus the excess air ratio λ [-]

In Figure 4 the specific concentrations of HC (g/kWh) for both the NG and the HCNG blends are shown as a function of λ.

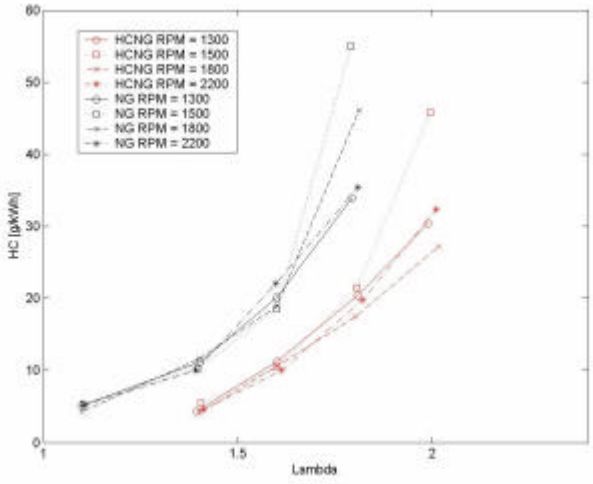

Figure 4: Specific HC emissions [g/kWh] as a function of excess air ratio λ [-]

In Figure 5 and Figure 6 the NO_x concentrations in the engine-out exhaust are shown as a function of the excess air ratio for all the air-fuel blends investigated. The addition of hydrogen to methane-air mixtures will increase the combustion speed

and the combustion temperatures, leading to increased NOx emissions compared to pure natural gas (CNG) at the same excess air ratio. This is as stated in [11], [17], [15], [12], [13] and [14].

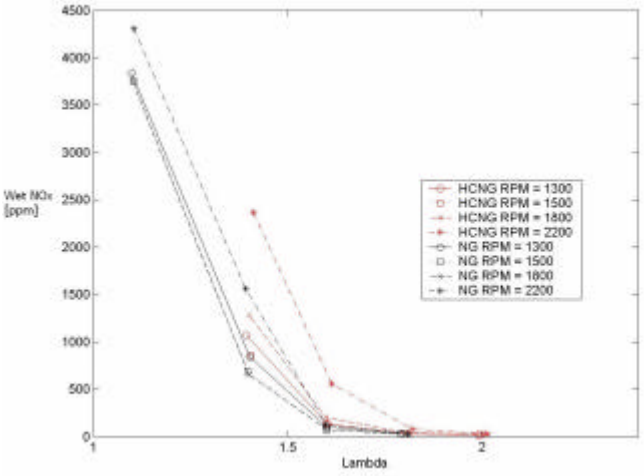

Figure 5: Emissions of nitrogen oxides NO_x ([ppm]) versus the excess air ratio λ [-]

Figure 7 presents both the NO_x and HC emissions (in ppm) for the CNG tests, while Figure 8 shows the corresponding results for all the HCNG tests.

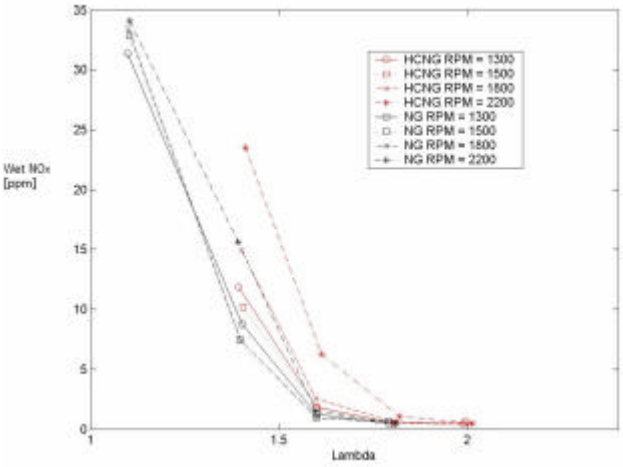

Figure 6: Specific NO_x emissions (wet) [g/kWh] as a function of excess air ratio λ [-]

The most obvious difference in the NOx emissions in these two figures is the higher NO_x emissions at the highest engine speed for HCNG for a given excess air ratio. This is as expected taking into consideration the deviations in laminar flame speeds between CNG and HCNG, which affect the flame temperatures most at higher engine speeds where the time available for reaching these temperatures is the shortest. Concerning the emissions of unburned hydrocarbons, these are higher for the pure CNG case compared to the HCNG cases for given excess air ratios, as expected. The measured engine out concentrations of HC is comparable between the CNG cases for λ=1.1 [-] with the HCNG cases for λ=1.4 [-], for the CNG cases with λ=1.4 [-] with the HCNG cases for λ=1.6 [-], and finally – for CNG cases with λ=1.6 [-] with the HCNG cases for λ=1.8 [-]. It is important to note the main trend in these NO_x results, that the NO_x emissions is significantly reduced by increasing the excess air ratio, and that the use of hydrogen addition to the CNG this leaning out may easily be achieved without any substantial HC penalty.

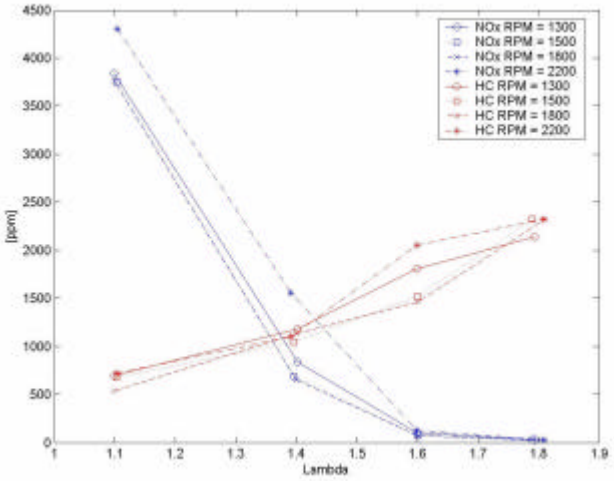

Figure 7: Emissions of nitrogen oxides (NO_x) and unburned hydrocarbons (HC) ([ppm]) versus the excess air ratio λ [-] for the pure natural gas (CNG) tests

Figure **3** – Figure 8 illustrate the fact that it is possible to reduce the emissions of both NO_x and HC by combustion of HCNG by leaning out the air-fuel mixture. This will be a trade-off against engine power and efficiency. In order to illustrate this fact, results form experiments using a constant engine speed of 1800 rpm will be used as an example in the following figures.

Figure 9 is another example of the trends discussed earlier when it comes to the effect of adding hydrogen to methane-air mixtures for spark ignition engines. The HC emissions increase rapidly as the lean limit is approached, and it is obvious that CNG at λ=1.8 [-] is very close to its

lean limit, and that by extrapolating the results for HCNG one may assume that the lean limit for the HCNG mixture is somewhat leaner than λ=2.0 [-].

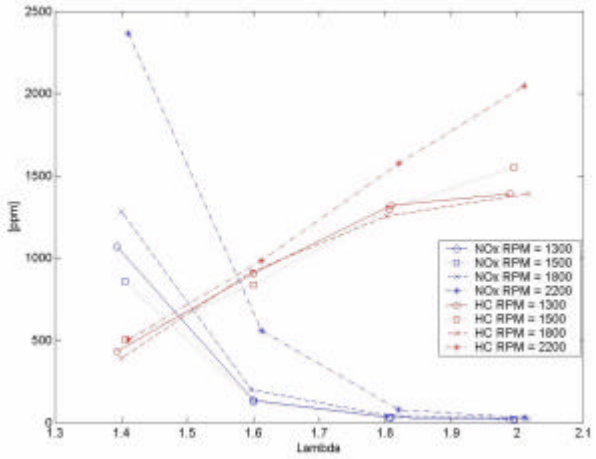

Figure 8: Emissions of nitrogen oxides (NO_x) and unburned hydrocarbons (HC) in [ppm] versus the excess air ratio λ [-] for the hydrogen enriched natural gas (HCNG) tests

As a result of the increase in flame speed and flame temperature, the NO_x emissions from the HCNG is higher than the CNG, and the CNG experiences a major increase in NO_x emissions for λ=1.1 [-]. It is a well known fact from the literature that the maximum NO_x emissions will be produced slightly lean of stoichiometric.

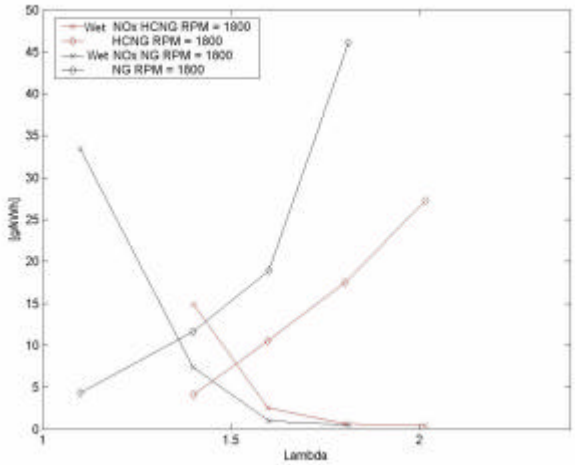

Figure 9: Specific HC and NO_x emissions [g/kWh] as a function of excess air ratio λ [-] at an engine speed of 1800 rpm

Figure 10 shows a typical trend in engine power as a function of excess air ratio for the CNG and the HCNG mixture. It is obvious from this figure that by adding hydrogen, an increase in power will result in the λ range investigated.

Figure 11 shows that the brake thermal efficiency $\eta_{th,brake}$ will decrease significantly with increasing excess air ratio as the lean limit is approached for both CNG and HCNG. This is in agreement with [14], [15] and [16]. The reason for this is the fact that addition of hydrogen to lean-burning methane-air mixtures solves the challenge of slower flame speed of lean methane-air mixtures, less complete combustion and increased cyclic variability ([9] and [16]).

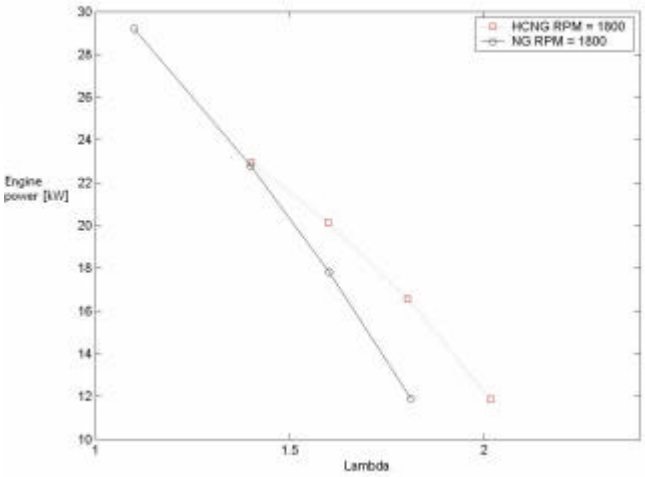

Figure 10: Engine power as a function of engine speed for tests at constant air-fuel ratio λ [-] at an engine speed of 1800 rpm

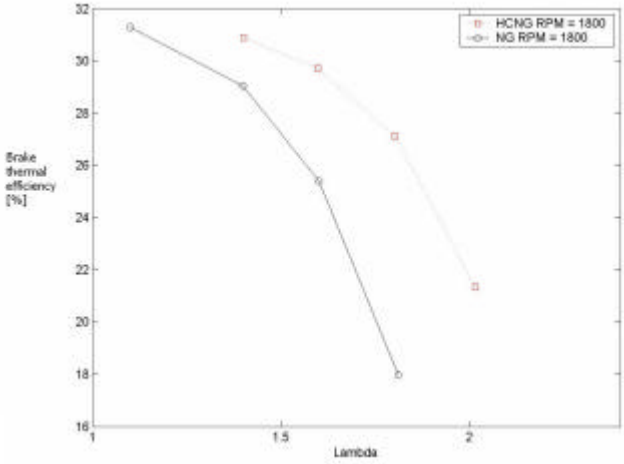

Figure 11: Brake thermal efficiency $\eta_{th,brake}$ as a function of excess air ratio λ [-] at an engine speed of 1800 rpm

The efficiency for HCNG is greater than for NG for the same λ, and the difference in $\eta_{th, brake}$ between HCNG and CNG for the same λ increases with increasing excess air ratio. In [16] an optimum in $\eta_{th,brake}$ was found around λ=1.3 [-] for CNG, and at λ=1.4 [-] for HCNG. In [12] it is found that the engine efficiency depends more on the excess air ratio than on the composition of the hydrogen-methane mixture.

The cylinder pressure development for the pure natural gas blends is presented in Figure 12. A reduction in the maximum combustion pressure developed results as the mixture is leaned out. For λ=1.8 [-] the combustion is very poor, and a very low efficiency results, as seen in Figure 10.

The accumulated Rate-Of-Heat-Release (ROHR) for the CNG blends is presented in Figure 13. The results in this figure correspond to the cylinder pressure curves in Figure 12.

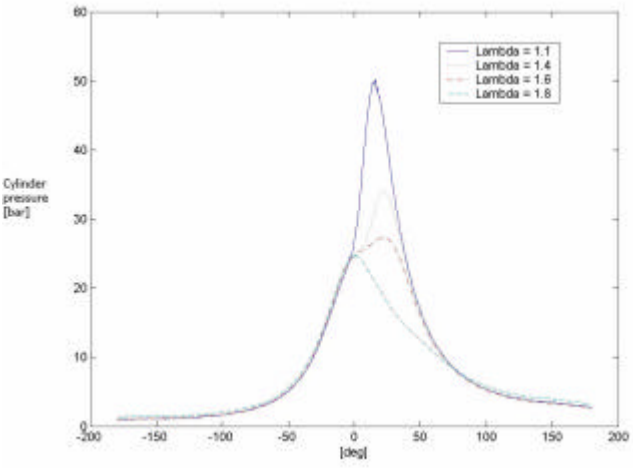

Figure 12: Cylinder pressure development using pure natural gas (CNG) at 1800 rpm

In Figure 14 the cylinder pressure curves for the HCNG blends are presented. The same trend as for CNG, a reduction in the maximum combustion pressure, occurs when the λ is increased. Comparing with the results in Figure 12, a higher p_{max} is measured at a certain excess air ratio for HCNG than for CNG. A shorter ignition delay is also found for HCNG than for the CNG blends.

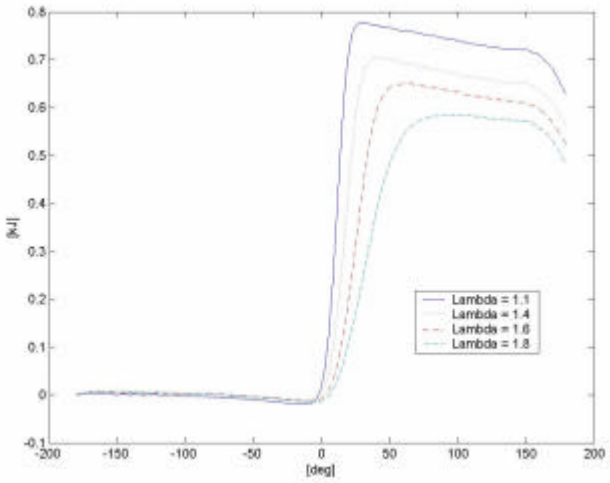

Figure 13: Accumulated Rate Of Heat Release (ROHR) using pure natural gas (CNG) at an engine speed of 1800 rpm

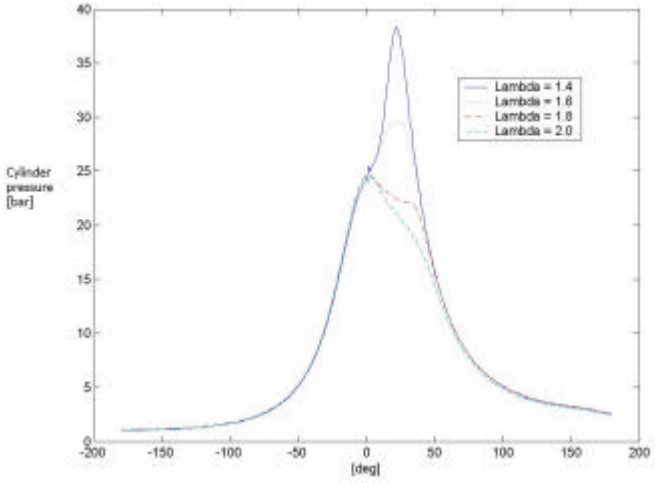

Figure 14: Cylinder pressure development of hydrogen enriched natural gas (HCNG) at an engine speed of 1800 rpm

The accumulated Rate-Of-Heat-Release for the HCNG blends is presented in Figure 15 . The results in this figure correspond to the cylinder pressure curves in Figure 14.

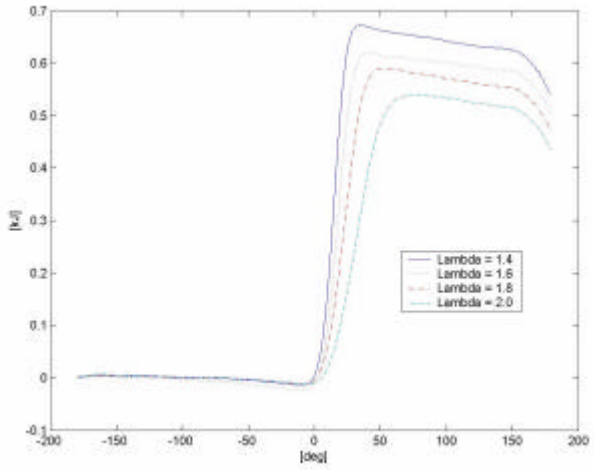

Figure 15: Accumulated Rate Of Heat Release (ROHR) using hydrogen enriched natural gas (HCNG)

CONCLUSIONS

The addition of hydrogen to Compressed Natural Gas (CNG) as a fuel in a SI engine has a significant, positive impact on the efficiency, especially close to the lean limit.

Pure compressed natural cas (CNG) and 29 vol% H_2 in CNG (named HCNG) were investigated at four engine speeds under full load conditions, namely 1300 rpm, 1500 rpm, 1800 rpm and 2200 rpm. For each mixture and each engine speed four different excess air ratios (λ) were chosen, in the range of λ= 1.1. – 2.0 [-].

Addition of H_2 to CNG makes it possible to run the engine leaner, resulting in lower emissions of CO_2, CO and HC at a certain λ [-], and higher NO_x emissions at constant excess air ratio. However, it is very important to note the fact that increasing the excess air ratio reduces NO_x significantly, and that the use of HCNG results in a major extension of the lean limit.

The full load curves (P_e=f(Engine speed)) for the two mixtures at different excess air ratio is coincides at λ=1.4 [-] and λ=1.6 [-]. When the mixtures are leaned out to λ=1.8 [-] the HCNG gives more power than the equivalent CNG. The explanation for this is that CNG approaches the limit where the engine starts to misfire, i.e. it is too close to the limit on the lean side. This is also seen on the emissions of unburned hydrocarbons.

The emissions of total unburned hydrocarbons were also measured. From the plots of HC–emissions as a function of lambda, one may see that at a certain excess air ratio, the emissions of unburned hydrocarbons start to increase considerably. This indicates that the lean limit is approached. The lean limit for the pure CNG tested in this engine is approximately λ=1.8[-], and the lean limit for the HCNG is even leaner, i.e. at about λ=2.0 [-]. This is as expected, and in accordance with the literature. It is also important to note, that the level of the unburned hydrocarbons emitted at certain air-fuel ratio is considerably lower for the HCNG than for the pure CNG.

at an engine s

On the other hand, comparing the emissions of nitrogen oxides, the HCNG is emitting more than the CNG at the same excess air ratio. This difference decreases as the λ increases from 1.4 [-] to 2.0 [-], where the level of NO_x is equal for the two mixtures investigated.

Considering the total emissions of unburned hydrocarbons and nitrogen oxides, it is easily seen that the positive effect of adding hydrogen to the CNG increases as a function of lambda.

ACKNOWLEDGMENTS

The financial assistance of Statkraft, Norway and the contributions of Eivind Fredriksen [18], Daniel Stanghelle, Ola Storrø (NTNU, Norway) in addition to Ingebrigt Valberg and Stein Inge Lien (Marintek, Norway) to this work are gratefully appreciated.

REFERENCES

[1] Law, C.K,. Kwon, O.C., *"Effects of hydrocarbon substitution on atmospheric hydrogen-air flame propagation"*. Int. J. of Hydrogen Energy 29 (876-879), Pergamont, 2004.

[2] Yu, G., Law, C.K., Wu, C.K., *"Laminar flame speeds of hydrocarbon + air mixtures with*

hydrogen addition". Combustion and flame 63:339-347, 1986.

[3] Karim, G.A., Wierzba, I., Al-Alousi, Y., *„Methane-hydrogen mixtures as fuels"*. Int. J. Hydrogen Energy, Vol.21, pp.625-631, 1996.

[4] Raman, V., Hansel, J., Fulton, J., Lynch, F., Bruderly, D. *"Hythane – an ultraclean transportation fuel"*. Proceedings 10th World Hydrogen Energy Conference, Vol 3, 1994.

[5] Hoekstra, R.L., Collier, K., Mulligan, N., *"Demonstration of hydrogen mixed gas vehicles"*. Proceedings 10th World Hydrogen Energy Conference, Vol 3, 1994.

[6] Hoekstra, R.L., Collier, K., Mulligan, N., Chew, L., *"Experimental study of a clean burning vehicle fuel"*. Int. J. Hydrogen Energy, Vol. 20, No.9, pp.737-745, 1995.

[7] Fotache C.G., Kreutz T.G., Law C.K.," *Ignition of hydrogen-enriched methane by heated air"*.
Combustion and Flame; 110:429-40. 1997.

[8] Nagalingam, B., Duebel, F., Schmillen, K., *„Performance study using natural gas, hydrogen-supplemented natural gas and hydrogen in AVL research engine"*. Int. J. Hydrogen Energy, Vol. 8, pp.715-720, 1983.

[9] Weinrotter, M., Kopecek, H., Tesch, M., Wintner, E., Lackner, M., Winter, F., *„Laser ignition of ultra-lean methane/hydrogen/air mixtures at high temperature and pressure"*. Experimental Thermal and Fluid Science, Elsevier, 2004

[10] Munshi, S. R., Nedelcu, C., Harris, J., Edwards, T., Williams, J., Lynch, F., Frailey, M., Dixon, G., Wayne, S., Nine, R. *"Hydrogen blended natural gas operation of a heavy duty turbocharged lean burn spark ignition engine"*. SAE Technical paper 2004-01-2956, 2004.

[11] Wallace, J. S., Cattelan, A. I., *"Hythane and CNG fuelled engine exhaust emission comparison"*. Proceedings 10Th World Hydrogen Energy Conference, 1994.

[12] Bauer, C.G., Forest, T.W., *"Effect of hydrogen addition on the performance of methane-fueled vehicles. Part I: Effect on S.I. engine performance"*. Int. J. Hydrogen Energy, Vol 26, pp 55-70, 2001.

[13] Bauer, C.G., Forest, T.W., *"Effect of hydrogen addition on the performance of methane-fueled vehicles. Part II: driving cycle simulations"*. Int. J. Hydrogen Energy, Vol 26, pp 71-90, 2001.

[14] Swain, M.R., Yusuf, M.J., Dulger, Z., Swain, M.N., *"The effects of hydrogen addition on natural gas engine operation"*. SAE Technical paper 932775, 1993.

[15] Sierens, R., Rosseel, E., *"Variable composition hydrogen/natural gas mixtures for increased engine efficiency and decreased emissions"*. Journal of Eng. For Gas Turbines and Power, Vol. 122, p.135-140, 2000.

[16] Yusuf, M.J., Swain M.R., Dulger, Z., *"An approach to lean burn natural gas fuelled engine through hydrogen addition"*. Int. J. Hydrogen Energy (p.485-491). 1997.

[17] IEA, USA, *"Reduction of CO2 emissions by adding hydrogen to natural gas"*. IEA Greenhouse gas R&D programme, report number PH4/24, 2003.

[18] Fredriksen, E. T, Jensen, M. *"HCNG – teknologi, prosjekter og mulige markeder" 2003"*. MSc thesis, IMT, IVT, NTNU, Norway, 2003.

CONTACTS

Post Doc Marie Bysveen
EPT, IVT, NTNU
marie.bysveen@marin.ntnu.no
Otto Nielsen vei 10
7491 Trondheim
NORWAY

Proceedings of ECOS 2005
Trondheim, Norway
June 20–22, 2005

METHODOLOGY FOR ANALYSIS AND MANAGEMENT OF HOT WATER GENERATION FOR INDUSTRIAL UTILIZATION

Gabriela Batista Pinto Coelho
ACESITA

Elizabeth Marques Duarte Pereira and José Ricardo Sodré*
Pontifical Catholic University of Minas Gerais
Department of Mechanical Engineering
30535-610, Belo Horizonte, MG
Brazil

ABSTRACT

This work shows a methodology for analysis and management of hot water generation for industrial utilization from solar energy and cogeneration, the latter involving usage of a gas turbine or a natural gas fuelled engine. The methodology presented uses criteria that allow for evaluation of the power/heat ratio in the project of a water heating system. A computer program was developed to furnish a complete analysis of the energy system. A case study in an automotive industry is presented. The results show that solar energy and cogeneration using a natural gas fuelled engine are the most economic options.

Keywords: cogeneration, internal combustion engines, solar energy, gas turbines, natural gas

NOMENCLATURE

A_{col}	solar plate area [m^2]
c_p	constant pressure specific heat of water [kJ/kg ^oC]
c_{pcomb}	fuel specific heat [kJ/kg ^oC]
c_{pg}	constant pressure specific heat of combustion gases [kJ/kg ^oC]
E_{mes}	monthly energy [kWh/day]
FC_j	cash flow values of the order j = 1,2,3,...,n
FC_0	initial cash flow [dimensionless]
F_u	shower utilization factor [dimensionless]
H_2	hydrogen concentration in the fuel [%]
h_{ar}	water enthalpy [kJ/kg]
h_d	outlet steam enthalpy [kJ/kg]
h_{gs}	boiler outlet steam enthalpy [kJ/kg]
h_s	boiler inlet water enthalpy [kJ/kg]
h_v	steam enthalpy [kJ/kg]
LHV	fuel low heating value [kJ/kg_{comb}]
$\dot{m}_c$	burned fuel mass flow rate [kg_{comb}/s]
$\dot{m}_d$	outlet steam mass flow rate [kg/s]
$\dot{m}_f$	cold water mass flow rate [kg/s]
$\dot{m}_g$	gas mass flow rate [kg/s]
$\dot{m}_{gs}$	dry gas mass flow rate [kg/s]
$\dot{m}_q$	hot water mass flow rate [kg/s]
$\dot{m}_v$	steam mass flow rate [kg/s]
N	number of daily equipment utilization [dimensionless]
Nb	number of daily showers [dimensionless]
P_{gs}	thermal loss through the dry gas [dimensionless]
P_{H2O}	thermal loss due to water formation in the fuel [dimensionless]
P_i	power of equipment i [kW]
P_{nm}	non-measured losses [dimensionless]
P_r	thermal loss by radiation [dimensionless]
P_u	loss associated to fuel humidity [dimensionless]
Q	total heat energy consumed [kWh/day]

*Corresponding author: Phone/Fax +55-31-3319-4910
E-mail ricardo@pucminas.br

$\dot{Q}_{cc}$	combustion heat transfer rate [kW]
Q_i	energy required for water heating in equipment i [kWh/day]
Q^*_{real}	energy given by Eq. [12] [kW]
$\dot{Q}_{th}$	thermal energy [kW]
r	loss by radiation [kJ/kg]
T	Thermal viability [dimensionless]
T_{ar}	air temperature [ºC]
T_{ef}	cold fluid inlet temperature [ºC]
T_{eq}	hot fluid inlet temperature [ºC]
T_{gs}	dry gas temperature [ºC]
$T_{máx}$	maximum water temperature [ºC]
$T_{mín}$	minimum water temperature [ºC]
T_{rede}	feed water temperature [ºC]
T_s	exhaust gas outlet temperature [ºC]
T_{sf}	cold fluid outlet temperature [ºC]
t	interest rate [dimensionless]
u	fuel humidity [%]
V_{ch}	changing room hot water consumption [liter/day]
V_i	hot water consumption in equipment i [liter/day]
vv_{ch}	shower volumetric flow rate [dimensionless]
vv_i	hot water consumption in each equipment per operation [liter/day]
x	unmeasured loss [kJ/kg]
ΔTi	temperature difference between water in equipment i and feed water [^oC]
h_e	exhaust thermal efficiency [dimensionless]
η_{eq}	equipment efficiency [dimensionless]
h_{hrsg}	recovery boiler efficiency [dimensionless]
η_{tc}	heat exchanger effectiveness [dimensionless]
$h_{tg}\|_{cog}$	overall thermal efficiency of cogeneration system with gas turbine [dimensionless]
θ	shower average time [dimensionless]
ρ	water density [kg/m^3]

INTRODUCTION

The Brazilian energy system, predominantly based on hydroelectric power plants, has been evaluated under the light of economic and ambient impact, and the need to diversify the energy source. The increase on natural gas availability will probably alter the present situation in the near future. To guarantee continuous economic growth, it is necessary to increase the energy efficiency of industrial processes, to reduce the environmental impact, and to guarantee energy delivery. In this case, utilization of cogeneration turns to be a very attractive option. Its use in Brazil is still low, being concentrated in some areas like sugar, alcohol, steel, paper and cellulose industries.

This work presents a methodology of energy analysis and management, with emphasis on hot water generation. The alternatives evaluated were natural gas-fuelled engines and gas turbines, and solar heating. A case study was applied to an automotive industry, which shows a daily demand of 250 m^3 of hot water to feed its refectories and changing rooms, with the need of 10% reduction of specific energy consumption under a strict environment control.

LITERATURE REVIEW

The growing energy demand and the potential use of cogeneration in Brazil have been evaluated by Janson *et al* [1], Nascimento *et al* [2] and Coelho *et al* [3], among others.

Hilbert *et al* [4] studied combined cycles, typical fuels and costs, and concluded that this alternative is economically attractive to be applied in Brazil.

Barreto *et al* [5] proposed a minimum agenda for critical evaluation of viability studies of thermal energy generation in combined cycles.

El-Masri [6], Torres and Gallo [7], and Tuma *et al* [8] evaluated the combined cycle under the first and second laws of thermodynamics. System losses and internal irreversibilities were identified, including reduction of the net power produced due to use of the thermal energy in the cogeneration process.

Feng *et al* [9] described a simple methodology that allows for evaluation of costs of implementation of cogeneration systems.

Bicalho [10] developed a study on the utilization of gas turbines in the Brazilian energy system, emphasizing the role of natural gas for energy generation and the technological challenges, based on energy systems worldwide.

Céspedes and Júnior [11] performed an exergy and thermal-economy analysis of cogeneration application in the tertiary sector. The authors pointed out utilization of natural gas in cogeneration processes applying gas turbines or internal combustion engines as an answer for the growing energy demand in the expanding sectors.

Ramalho [12] evaluated the payment of exceeding energy production by sugar and alcohol industries, and discussed the modification occurred in the national energy system.

Fernandes Filho [13] evaluated the application of cogeneration in steel industries, using the exhaust

gas from the high oven and integrating systems with the air blower or the steam generator. Among the advantages, the authors mentioned costs reduction between 15 to 25%.

Muniz and Andrade [14] evaluated the potentiality of cogeneration application to paper and cellulose industries. Implementation of gas turbines and boiler for heat recovery of combustion gases was studied, with a forecast of cogeneration use in case of substitution of conventional boilers.

López *et al* [15] discussed the application of cogeneration to paper and cellulose industries, emphasizing economic issues.

Methodologies for thermal-economy applied to cogeneration systems, according to studies by Cerqueira and Nebra [16] and Monteiro [17], showed the economic viability of self generation and cogeneration for several configurations of heat and electric power production.

METHODOLOGY OF ANALYSIS

Hot Water and Energy Demands

For determination of the daily hot water demand one must consider the industry working periods, the number of employees and daily showers, the number of meals served and hot water need in the industrial processes, with typical flow rates and temperatures. In the case of operating industries, measurements in the field are recommended. Hot water flow rate and temperature data are required. For changing rooms, hot water consumption is given by:

$$V_{ch} = Fu \cdot Nb \cdot q \cdot vv_{ch} \quad (1)$$

In the case of industrial kitchens and refectories, the number of daily utilization and hot water consumption must be measured or estimated for each equipment i. The volume of hot water consumed is given by:

$$V_i = N_i \cdot vv_i \quad (2)$$

The total consumption is given by the sum of Eqs. (1) and (2). For new plants, typical values are estimated from standards and catalogues. The estimated hot water consumption in industrial changing rooms and refectories in this wok were based on the ABNT – NBR 7198 standard [18]. The total energy consumed is the sum of the daily consumption, given by:

$$Q = \sum_i Q_i = \sum_i \frac{r.V_{i.}c_p \cdot \Delta T_i}{3{,}6} \quad (3)$$

Thermal Efficiency of the Equipment

In the case study of this work, water heating is provided through heat exchangers, which hot fluid is vapor originated from a gas boiler. Thus, calculation of thermal efficiency in this section will be restricted to this equipment. Incropera [19] shows a complete discussion on the effectiveness of heat exchangers, which can be written as:

$$h_{tc} = \frac{[\dot{m}_f \cdot c_p \cdot (T_{sf} - T_{ef})]}{[(\dot{m}_q \cdot c_p \cdot (T_{eq} - T_e f)]} \quad (4)$$

The efficiency of a steam generator is defined by the ratio between the heat transferred to the water during the process, $\dot{Q}_{útil}$, and the heat liberated by combustion, $\dot{Q}_{cc}$. Two different methods are used to calculate the boiler efficiency, one direct and one indirect. Dukelow [20] evaluates that the indirect method, also called method of losses, gives more precise results; however, the direct method is the most used due to ease of use, higher speed and lower costs. The efficiency calculated by the direct method is given by:

$$h_{DIR} = 100 \cdot \frac{\dot{m}_v (h_v - h_s) + \dot{m}_d (h_d - h_s)}{\dot{m}_c \cdot LHV} \quad (5)$$

Dukelow [20] emphasizes that, as this method uses three distinctive mass flow rates, a more precise evaluation requires utilization of measuring devices with maximum uncertainties between 1 and 2%. The uncertainty of industrial sensors have been estimated between 3 to 5%, being a major limitation to the application of this method, together with the uncertainty associated to the determination of the fuel heating value. The thermal efficiency calculated by the indirect method is given by [20]:

$$h_{IND} = 100 - (P_{gs} + P_u + P_{H_2O} + P_r + P_{nm}) \quad (6)$$

Calculation of the thermal losses must obey the procedures established by ASME PTC 4.1a and 4.1b standard [21]. The thermal loss through the dry gas is given by:

$$P_{gs} = \frac{\dot{m}_{gs} \cdot cp_{comb} \cdot (T_{gs} - T_{ar}) \cdot 100}{LHV} \quad (7)$$

The thermal loss due to fuel humidity is so calculated:

$$P_u = \frac{u \cdot (h_{gs} - h_{ar})}{LHV} \quad (8)$$

The loss due to H_2O formation from the fuel is calculated by:

$$P_{H_2O} = \frac{9 \cdot H_2 \cdot (h_{gs} - h_{ar})}{LHV} \quad (9)$$

The loss by radiation is thus calculated:

$$P_r = \frac{100 \cdot r}{LHV} \quad (10)$$

Finally, the non-measurable losses are evaluated:

$$P_{nm} = \frac{100 \cdot x}{LHV} \quad (11)$$

The calculation procedure described was developed considering only the losses related to utilization of natural gas as fuel.

Energy Consumption

The energy released by the natural gas associated to water heating is calculated as a function of the thermal efficiency of the equipment:

$$Q_{real} = \frac{Q}{\prod \cdot h_i} \quad (12)$$

The denominator represents the product of the efficiencies of all equipments used. The daily consumption of natural gas is given by:

$$NGC = \frac{3600 \cdot Q_{real}}{LHV} \quad (13)$$

where the LHV value is 61.500 kJ/kg_{comb} [18].

System Selection

- Solar Heating System

To define the solar system, the solar plate area is first calculated:

$$A_{col} = \frac{30 \cdot Q}{E_{mês}} \quad (14)$$

The hot water volume to be stored is the sum of the volume of each equipment i, multiplied by a safety factor f_{saf}:

$$V_{RT} = f_{saf} \cdot \sum_i V_i \quad (15)$$

It is also necessary to establish the local geographic coordinates, weather conditions and the presence of shadows for installation of the solar plates. The energy required by the equipment is calculated by Eq. (3), where $\Delta T_i = T_{máx} - T_{rede}$.

- Cogeneration Systems

To attend the hot water demand, small cogeneration systems using natural gas-fuelled internal combustion engines and gas turbines are considered. The cogeneration is defined by adjusting the thermal load. The heat transfer rate required for water heating is calculated by:

$$\dot{Q}_{cc} = \frac{P_i}{h_{eq}} \quad (16)$$

The energy released through the exhaust gas is so given:

$$\dot{Q}_{rec} = \dot{m}_g \cdot c_{pg} \cdot (T_s - 150) \quad (17)$$

The minimum boiler outlet temperature is set to 150 ºC, to avoid acid formation and corrosion [18]. Natural gas consumption for the new water heating configuration is calculated as:

$$NGC_i = \frac{3600 \cdot \dot{Q}_{cc}}{LHV} [kg\,NG/h] \quad (18)$$

The efficiency of the exhaust gases is calculated as a function of the power, number of equipments and the energy produced in the combustion chamber:

$$h_e = 1 - \frac{P_i + Q^*_{real}}{\dot{Q}_{cc}} \quad (19)$$

For an internal combustion engine in cogeneration systems, the power/heat ratio is calculated by:

$$PHR = \frac{h_{eq}}{h_e \cdot h_{hrsg}} \quad (20)$$

The equipment is thermally viable when:

$$T = P_i / PHR > (Q_{real} \cdot h_{cald}) \quad (21)$$

For gas turbines the calculation is analogous as for internal combustion engines, considering the typical losses in the equipment.

- Economical Analysis

The economical analysis of a project is done through the net present value (NPV) and internal return tax (IRT) methods. These methods are based on comparison of the sum of values in each future cash flow (payments and incomes) with the value of initial cash flow (income and payment) in the current period.
The cash flow analysis technique (NPV) is based on calculation of the present value of a series of equal or different payments at a known tax, discarding the initial flow value, which can be from borrowing, financing or investment:

$$NPV = \sum_{j=1}^{n} \frac{FC_j}{(1+t)^j} - FC_0 = \frac{FC_1}{(1+t)^1} + \ldots + \frac{FC_n}{(1+t)^n} - FC_0 \quad (22)$$

The internal return tax, IRT, equalizes the present value of one or more equipment (cash outcome) to the value of one or more income (cash income):

$$FC_0 - \sum_{j=1}^{n} \frac{FC_j}{(1+t)^j} = 0 \quad (23)$$

The net present value (NPV) and the internal return tax (IRT) are used for decision making between alternatives. A project is considered economically viable if NPV is, at least, equal to zero. As higher is NPV, as more attractive is the project. Besides, the internal return tax (IRT) turns a project attractive if it is higher than the minimum acceptable investment return tax.
The invested amount differs for each alternative, being necessary the knowledge of the equipment cost. In the construction period, the time for implementation of a project and the expenditure chronogram are considered. During the working period, operation and maintenance costs and the depreciation factor are considered. In this work, the annual depreciation factor presented by ANEEL resolution 044/99 [24] was considered. The income of the energy generated or saved must also be taken into account.

RESULTS - CASE STUDY

For the industry studied in this work, Table 1 shows the main data for the refectory and Table 2 shows the data for the changing room. Data for the efficiency of the equipment and the energy released are shown in Table 3.

Table 1 – Main data for the refectory.

PARAMETER	VALUE
Hot water temperature	70 ºC
Daily hot water consumption	117.6 m^3
Ambient temperature	21.7 ºC
Energy consumption	6595 kWh/day

Table 2 – Main data for the changing room.

PARAMETER	VALUE
Hot water temperature	45 ºC
Daily hot water consumption	122.4 m^3
Ambient temperature	21.7 ºC
Energy consumption	3311 kWh/day

Table 3 – Data of efficiency and released energy.

PARAMETER	VALUE
Thermal efficiency of heat exchanger	0.8
Thermal efficiency of boiler	0.8
Energy released (Eq. (12))	15479 kWh/day
Natural gas consumption	906 kg/day

Due to the dimensions and temperature requirements of this project, the solar heating system was divided into two parts, one for the refectory and the other for the changing room. The thermal reservoir for each system was subdivided into eight tanks of 15 m^3. For the system simulation, the minimum and the maximum average temperature were considered to be 18.9 ºC and 23.9 ºC, respectively, according to DNMET [25]. The efficiency of the simulated solar plate was 49.7%, with area of 1.99 m^2, and an average monthly energy production of 66.37 kWh/m^2. Tables 4 and 5 show the simulated results for the refectory and changing room, respectively. For the changing room two configurations were proposed.
Tables 6 and 7 present results for seven gas engine models and with the recovery boiler efficiency of 80%. The parameters Q_{cc}, Q_{rec}, NGC_i, η_e, PHR, and T were calculated through Eqs. (16) to (21), respectively. This simulation considered engine efficiencies of 35% (Tab. 6) and 45% (Tab. 7). From Tables 6 and 7, it is observed that the power-to-heat ratio is inversely proportional to the engine efficiency. As the engine efficiency is increased, PHR decreases, reaching, for the engines of 318

and 400 kW of power (Tabs. 6 and 7) and for the engine of 636 kW of power (Tab. 7), values that indicate the project to be thermally inadequate, as the parameter T (Eq. (21)) turns to be lower than Q_{th}.

Table 4 – Simulated results for the refectory.

PARAMETER	VALUE
Maximum hot water temperature	70 ºC
Minimum hot water temperature	65 ºC
Feed water temperature	20 ºC
Daily hot water consumption	117.6 m^3
Number of reservoirs	8
Reservoir capacity	15 m^3
Number of solar plates	1490
Total solar plate area	2965.1 m^2
Solar fraction	70%
Auxiliary heating	30%
Volume-to-area ratio	0.0413 m

Table 5 – Simulated results for the changing room.

PARAMETER	CONF. 1	CONF. 2
Maximum hot water temperature	50 ºC	50 ºC
Minimum hot water temperature	45 ºC	45 ºC
Feed water temperature	20 ºC	20 ºC
Daily hot water consumption	122.4 m^3	122.4 m^3
Number of solar plates	1496	820
Total solar plate area	2977 m^2	1631.8 m^2
Solar fraction	89.8%	68.8%
Auxiliary heating	10.2%	31.2%
Volume-to-area ratio	0.0411 m	0.0750 m

Table 6 – Simulated results for gas engines (η_{eq} = 35%, Q_{th}= 516 kW).

P [kW]	Q_{cc} [kW]	Q_{rec} [kW]	NGCi [kg/h]	η_e	PHR	T
400	1142	112	84	0,56	0,78	512
318	908	137	66	0,51	0,86	369
636	1817	279	133	0,51	0,86	738
748	2137	298	156	0,53	0,83	904
776[1]	2217	305	162	0,53	0,82	947
776[2]	2217	323	162	0,53	0,82	947
912	2605	395	191	0,55	0,79	1149

Simulation of gas turbines involved eight models (Tab. 8). Analysis of the results shows that the PHR parameter behaves in a similar way as for gas engines. Gas turbines allows for higher energy recovery than internal combustion engines due to higher exhaust gas temperature and mass flow rate. Thus, it is necessary to use a higher number of engines to furnish the thermal energy required for water heating, Q_{th}. The thermal viability was verified for all models, as $T > Q_{th}$.

Table 7 - Simulated results for gas engines (η_{eq} = 45%, Q_{th}= 516 kW).

P [kW]	Q_{cc} [kW]	Q_{rec} [kW]	NGCi [kg/h]	η_e	PHR	T
400	889	112	65	0,43	1,30	309
318	707	137	52	0,37	1,53	207
636	1413	279	103	0,37	1,53	415
748	1662	298	122	0,40	1,42	525
776[1]	1724	305	126	0,40	1,41	552
776[2]	1724	323	126	0,40	1,41	552
912	2027	395	148	0,42	1,33	686

Engine speed 1500 rev/min[1] and 1800 rev/min[2].

Table 8 – Simulated results for gas turbines (Q_{th}= 516 kW).

P [kW]	η_{eq}	Q_{cc} [kW]	Q_{rec} [kW]	NGCi [kg/h]	η_e	PHR	T
420	0,23	1818	1276	133	0,49	0,59	712
508	0,23	2170	1278	159	0,53	0,55	920
548	0,22	2480	1643	181	0,57	0,49	1131
585	0,24	2489	1677	182	0,56	0,53	1115
646	0,24	2749	1895	201	0,58	0,51	1276
678	0,25	2744	1644	201	0,57	0,54	1252
715	0,25	2837	1903	201	0,57	0,55	1293
848	0,26	3261	1903	239	0,58	0,56	1513

Economy Analysis

For the economy analysis of the three alternatives presented, electric power and natural gas were considered to have the same adjustment rate. The economy analysis for the solar energy considered two configurations: the first with the solar plate area of 5942.1 m^2 and auxiliary heating of 20.1%; the second with the solar plate area of 4596.9 m^2 and 30.8% of auxiliary heating. From Fig. 1 it can be observed that the first configuration requires a higher initial investment, but lower operational costs due to less dependence on auxiliary heating. This way, the net present value in the period of twenty years is higher for the first configuration with respect to the second one to the order of US$ 250000. The investment return for the first and the second configuration were after 40 and 41 months, respectively.

For the economy analysis of the cogeneration system using internal combustion engines, 8760

working hours per year, installation costs of 3% of the investment, operation and maintenance costs of 2% a year, and major maintenance costs at each five years of 4% of the investment were considered. From Fig. 1 it is noticed that the engine of 776 kW of power, simulated at an attractiveness rate of 1%, shows an investment return period of 49 months at the efficiency of 0.35, against 40 months when its efficiency is 0.45. The same initial investment was considered in both cases. Comparing the cogeneration system with internal combustion engines to the solar configurations proposed at the same attractiveness rate, the first option is the most economically attractive, accumulating higher incomes throughout an estimated thirty years lifetime.

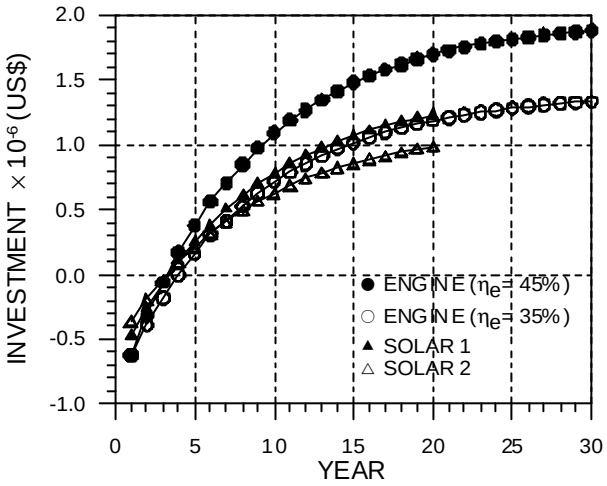

Figure 1 – Economy analysis of the 776 kW gas engine versus solar energy.

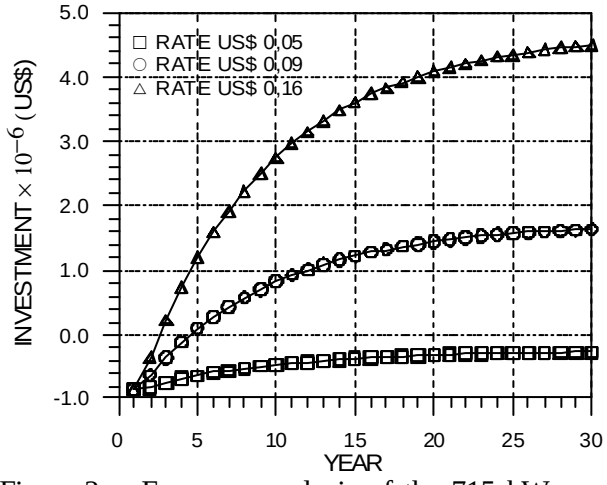

Figure 2 – Economy analysis of the 715 kW gas turbine.

For the economy analysis of the cogeneration system with gas turbine, 8760 working hours per year, installation cost of 3% of the investment, operation and maintenance costs of 1% a year and major maintenance costs of 2% of the investment were considered. Figure 2 shows that the gas turbine turns to be economically attractive only if the electric power rate is higher than US$ 0.09/kWh. If the electric power rate is the same as the natural gas, of US$ 0.16/kWh, the period for return of the investment would be 32 months and, after a lifetime of 30 years, would accumulate a total income of about US$ 4500000.

CONCLUSIONS

- A methodology of energy analysis and management was developed.
- The methodology was applied to an automotive industry for hot water generation using solar energy and cogeneration using gas turbines or internal combustion engines with a recovery boiler.
- The investment return period for two different solar energy systems, of distinct solar fraction and plate area, varied between 40 to 41 months.
- A cogeneration system with the internal combustion engine efficiency of 35% or 45% was simulated, for which the higher the system efficiency, the lower the power-to-heat ratio, and the investment return periods were 49 and 40 months, respectively.
- The cogeneration system with internal combustion engines showed higher income throughout a 30-year lifetime than the solar energy system, which lifetime is 20 years.
- The cogeneration system using gas turbine showed higher energy recovery, comparable to that produced by a higher number of engines to attend the thermal energy requirements for hot water generation.
- The cogeneration system with a 715 kW gas turbine showed economic disadvantages, being estimated an investment return period of up to 55 months, against lower investment return periods estimated for the solar heating system and for the cogeneration system using natural gas-fuelled 776 kW engines.

REFERENCES

[1] Janson, W.J., Wit, L.R., and Kema, W.B., 1997, “Aumentar a demanda de eletricidade para economizar”, *Revista Eletricidade Moderna*, jan., pp. 76-82. (In Portuguese)

[2] Nascimento, J.G.A., Rennó, I.V.C., Salomon, L.B.R., and Amaral, C.A., 1997, “A co-geração no Brasil: situação atual e

possibilidades futuras", *Revista Eletricidade Moderna*, jan., pp. 84-95. (In Portuguese)

[3] Coelho, S.T., Ieno, G.O., and Zylbersztajn, D., 1995, "Impactos da inserção da co-geração na matriz energética brasileira", *Revista Eletricidade Moderna*, jun., pp. 70-76. (In Portuguese)

[4] Hilbert, V.R., Lueska, C.A.D., and Klein, V.S., 1995, "Ciclo Combinado: estado da arte, combustíveis, custos e viabilidade econômica", *Revista Eletricidade Moderna*, jan., pp. 48-56. (In Portuguese)

[5] Barreto, B.C., Amaral, J.A.R., and Azola, E.P., 1999, "Estudos de viabilidade para termelétricas em ciclo combinado", *Revista Eletricidade Moderna*, jul., pp. 150-154. (In Portuguese)

[6] El-Masri, M.A., 1987, "Exergy Analisis of combined cycles: Part 1- Air Cooled Brayton-Cycle Gas Turbines", ASME Transactions, *Journal of Engineering for Gas Turbines and Power*, apr., vol. 109, pp. 228-236.

[7] Torres, E.A., and Gallo, W.L.R., 1998, "Exergetic evaluation of a cogeneration system in a petrochemical complex", Pergamon, *Energy Conversion & Management*, vol. 39, pp. 1845-1852.

[8] Tuma, M., Oman, J., and Sekavenik, M., 1999, "Efficiency of a combined gas-steam process", Pergamon, *Energy Conversion & Management*, v.40, pp. 1163-1175.

[9] Feng, X., Cai, Y., and Quian, L., 1998, "A new performance criterion for cogeneration system", Pergamon, *Energy Conversion & Management Strategy*, v.40, pp. 1163-1175.

[10] Bicalho, R., 2001, "Turbinas a gás: oportunidades e desafios para o sistema elétrico brasileiro", *Revista Eletricidade Moderna*, fev., pp. 44-64. (In Portuguese)

[11] Céspedes, J.F.P., and Oliveira Júnior, S., 1995, "Análise exergética e termoeconnômica da cogeração no setor terciário", *Revista Eletricidade Moderna*, dez., pp. 125-136. (In Portuguese)

[12] Ramalho, E.D., 1999, "A remuneração dos excedentes de autoprodução do setor sucroalcooleiro", *Revista Eletricidade Moderna*, oct., pp. 218-227. (In Portuguese)

[13] Fernandes Filho, G.E.F., 2000, As novas regras para consumidores livres e cativos", *Revista Eletricidade Moderna*, dec., pp. 104-112. (In Portuguese)

[14] Muniz, A.L., and Andrade, J.F.M., 2000, "Potencial presente e futuro da co-geração no setor de papel e celulose", *Revista Eletricidade Moderna*, apr., pp. 156-164. (In Portuguese)

[15] López, A., Calle, J., and Fontes, M., 2000, "Aplicações da cogeração no setor de papel e celulose", *Revista Eletricidade Moderna*, dec., pp. 94-102. (In Portuguese)

[16] Cerqueira, S.A.A.G., and Nebra, S.A., 1999, "Cost attribution methodologies in cogeneration systems", Pergamon, *Energy Conversion & Management*, v.40, pp. 1587-1597.

[17] Monteiro, M.A.G., 2001, "Estudos de viabilidade econômica para geração própria e co-geração", *Revista Eletricidade Moderna*, feb., pp. 140-156. (In Portuguese)

[18] United Nations, 2000, *Guidebook on Cogeneration as a means of Pollution Control and Energy Efficiency in Asia*, Economic And Social Commission for Asia and The Pacific.

[19] Duffie, J. A., and Beckman W. A., 1991, *Solar Engineering of Thermal Processes*, 2ª ed., John Wyley & Sons, Inc., USA.

[20] ABNT, *Norma Brasileira de Instalação Predial de Água Quente* – NBR 7198. (In Portuguese)

[21] Incropera, F.P., and Witt, D.P., 1992, *Fundamentals Heat and Mass Transfer*, 3 ed., Rio de Janeiro, LTC.

[22] Dukelow, S.G,1991, *The control of Boilers*, 2 ed., Instrument Society of America.

[23] ASME, 1964, *Fired Steam Generators*, PTC 4.1a e 4.1b.

[24] ANEEL, 1999, Anexo a resolução nº 044/99. (In Portuguese)

[25] DNMET, 2000 Ministério da Agricultura, Normas Climatológicas. (In Portuguese)

ACKNOWLEDGEMENTS

The authors wish to thank CNPq, CAPES and FAPEMIG for the financial support to this project.

Proceedings of ECOS 2005
Trondheim, Norway
June 20–22, 2005

A SIMPLE SIMULATION TECHNIQUE FOR ENERGY BALANCE OF INTERNAL COMBUSTION ENGINES UNDER VARIABLE LOAD

Ricardo Wilson Cruz[1]
Superior School of Technology – State University of Amazon
Av. Getúlio Vargas, 361/402, CEP 69020-010, Manaus, AM,
Brazil

Silvia Azucena Nebra[2]
State University of Campinas
Mechanical Engineering Faculty – Energy Department
P.O. Box 6122, CEP 13083-970, Campinas, SP,
Brazil

Elizabeth Ferreira Cartaxo[3]
Technology Faculty – Federal University of Amazon
Av. Rodrigo Otávio, 3000, CEP 69000-000, Manaus, AM,
Brazil

ABSTRACT

This paper reports a simple technique to perform simulations of Diesel engines, taking into account the discrete variation of engine power load under constant speed. This simulation technique was developed to be used in cogeneration systems simulation. To perform the model, some assumptions were made: the combustion reaction was supposed to have only four combustion products and the heat loss were treated through a bulk simple modeling. Some technical information introduced was taken from manufacturer's data spreadsheet.
Key-words: Engine simulation, Diesel engines, partial load.

NOMENCLATURE

AF	Air-to-fuel ratio
bsfc	Brake specific fuel consumption [kg/kW.s]
$\dot{E}$	Energy liberated by time unit [kW]
h, $\tilde{h}$	Specific enthalpy, [kJ/kg], [kJ/kmol]
$\dot{m}$, $\dot{n}$	Mass flux [kg/s], molar flux [kmol/s]
$\dot{Q}$	Heat flux [kW]
Q	Fuel heating value [kJ/kg]
q	Engine power load ratio [%]
T	Temperature [K]
$\dot{W}$	Power [kW]
η	Efficiency
ν	Stoichiometric coeficients [kmol/kmol-fuel]
ς	Irradiated heat / fuel energy ratio
ξ , α	Alcock et al. equation coefficients

Subscripts and Superscripts

air	air
b	Brake
exh.	Exhaust
f	Fuel, formation
gas	gas

[1] Corresponding author Phone: +55 92 8804 5758. E-mail: rcruz@uea.edu.br
[2] E-mail: sanebra@fem.unicamp.br
[3] E-mail: ecartaxo@ufam.edu.br

H_2O Water
irrad. Irradiated
i, j Counter indexes (related to P and R)
LHV Low heating value
lubr. Lubricating
net Net value
P, R Products, reactants
|q Load set point
refr. Refrigerant
resid. Residual
0 Reference state (1 [atm], 298.15 [K])

INTRODUCTION

Power generation by internal combustion engines is particularly dependent on fuel consumption level, by environmental or economical reasons, as it influences operational costs and gas emissions. In the context of the present lack of fossil energy resources, internal combustion engines are evolving towards the reduction of this parameter.
In the Amazon region, Diesel engines are responsible for power generation at villages and towns. The fuel cost, including transportation, is a very important factor. With these conditions, the analysis should attempt to the additional problem of the variation of engine power as a response to the electric power demand, which usually happens in autonomous power grids. A simple methodology to simulate the engine performance is helpful for energy generation planning and also to simulate cogeneration systems. To get these objectives, in this paper is presented a simple engine modeling under variable load.

ENGINE BALANCES

To perform the energy and mass balances under permanent conditions, a control volume surrounding the engine and its admission system and exhaust system is defined, see Figure 1:

$$(\dot{m}_f h_f)+(\dot{m}_{air} h_{air})-[\dot{W}_b+\dot{Q}_{irrad.}+(\dot{m}_{exh.} h_{exh.})+$$

$$+(\dot{m}_{refr.}\Delta h_{refr.})+(\dot{m}_{lubr.}\Delta h_{lubr.})]=0 \quad (1)$$

$$\dot{m}_{exh.}=\dot{m}_{air}+\dot{m}_f \quad (2)$$

Manufacturers give data spreadsheets for brake power upon load discrete values, usually set at 25 [%], 50 [%], 75 [%] and 100 [%]. The heat loss to lubricant $(\dot{m}_{lubr.}\Delta h_{lubr.})$ is small ([1], [2], [3], [4]), so it can be summed up to that of the cooling fluid $(\dot{m}_{refr.}\Delta h_{refr.})$.

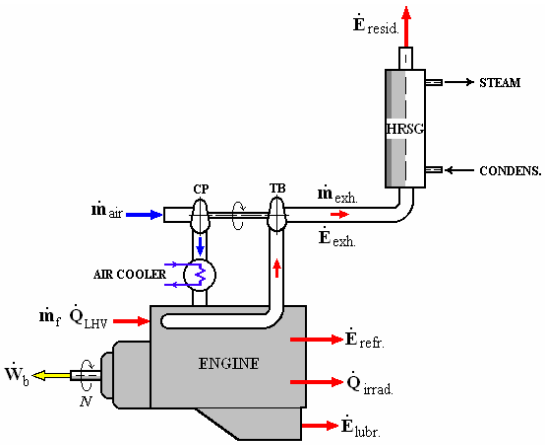

Figure 1: Engine energy balance

The above mentioned energy balance terms are related to the variable load, which is herein defined by the relation:

$$q \equiv \frac{\dot{W}_{b|q}}{\dot{W}_{b|100}} \quad (3)$$

Energy from Fuel under Variable Load

In Equation (1) the sum $(\dot{m}_f h_f)+(\dot{m}_{air} h_{air})$ is the fuel energy furnished by unit time $\dot{E}_f$. Taking into account a reaction balance where only the four main combustion products, enough for energy balance purpose, H_2O, CO_2, N_2 and O_2, are considered. The above mentioned sum may be written as:

$$\dot{E}_f=\dot{n}_f\left[\sum_P \nu_i\left(\tilde{h}^o_{f,i}+\Delta\tilde{h}_i\right)-\sum_R \nu_j\left(\tilde{h}^o_{f,j}+\Delta\tilde{h}_j\right)\right]=$$

$$=\dot{m}_f Q_{LHV} \quad (4)$$

where $\Delta\tilde{h}=\tilde{h}(T)-\tilde{h}(T_0)$ is the sensible enthalpy above the reference temperature (T_0 = 298.15 [K]) of reactants (fuel and air) at T_R and products at T_P.

And then the fuel conversion efficiency may be determined as:

$$\eta_f = \frac{1}{bsfc\, Q_{LHV}} \quad (5)$$

Where the brake specific fuel consumption is defined as:

$$bsfc \equiv \frac{\dot{m}_f}{\dot{W}_b} \quad (6)$$

The exhausted gas flux may be evaluated from the air-to-fuel ratio:

$$AF \equiv \frac{\dot{m}_{air}}{\dot{m}_f} = \frac{\dot{m}_{air}}{bsfc\, \dot{W}_b} \quad (7)$$

In general, AF is given by the manufacturers' spreadsheets, frequently only at 100 [%] load. Assuming the engine running at its nominal speed and that in fuel injected engines the air mass flux remains constant as load varies (full throttle), for discrete loads ranging from, say, 25 [%] to 100 [%], other air-to-fuel ratios may be inferred by:

$$\frac{AF_{|q}}{AF_{|100}} = \frac{\dot{m}_{air|q} / \dot{m}_{f|q}}{\dot{m}_{air|100} / \dot{m}_{f|100}} = \frac{\dot{m}_{f|100}}{\dot{m}_{f|q}} \quad (8)$$

Radiation Heat Loss under Variable Load

This effect is a markedly small part of the energy balance. The manufacturers provide data for 100 [%] load. Ferguson [4] reports values from 7% to 9% of $\dot{E}_f$, for every engine load for medium speed engines at constant speed. So it may be assumed that the relation $\varsigma \equiv \dot{Q}_{irrad.|100} / \dot{E}_{f|100}$ remains constant for every engine load. It can be avaluated from manufacturer's data spreadsheet. For loads others than 100 [%], the radiation heat loss can be inferred by:

$$\dot{Q}_{irrad.|q} = \varsigma \dot{E}_{f|q} \quad (9)$$

Cooling Fluid Heat Loss under Variable Load

The reciprocating nature of the internal combustion engines makes evaluating the heat loss to the cooling fluid and lubricant extremely difficult, by any practical method. In general, as reported by Ramos [5], even modern zero to multidimensional simulation methods demand empirical and not precise regressions for space averaged heat loss, such as proposed by Annand and Whoschnnis. In late fifties, Taylor [2] established one of the first methods for estimating the average bulk cylinder heat loss, to perform that, the author collected data from a wide range of engine types, speeds and conceptions, relating empirical parameters. Taylor's method at least explains this complex phenomenon. However, Taylor's methodology does not approach satisfactorily the behavior of Diesel engines under variable load.

A simpler method is reported by Stone [1], as a correlation developed by Alcock et al. based on extensive experiments, established as a exponential correlation between the cylinder bulk heat loss and the mass fuel consumption, which is:

$$\dot{E}_{refr.|q} = \xi \left(\dot{m}_{f|q} \right)^{\alpha} \quad (10)$$

It is obvious that this model should be viewed as a curve regression, where the coefficients ξ and α must be searched for any particular engine, as these are dependent upon engine's fuel injection conception, pressure, velocity, geometric parameters, etc. Stone [1] reports also that Alcock et al. got the value $\alpha = 0.6$ for a direct injected 1.8 litter Diesel engine. Equation (17) is Equation (10) applied to the practical example of this paper.

Energy and Temperature of the Gases under Variable Load

The heat rate exhausted by the combustion gases is given by solving the balance Equation (1). The exhausted gases energy must attempt to the following equation:

$$\dot{E}_{exh.|q} = \dot{m}_{gas|q} \left(h_{exh.} - h_0 \right) \quad (11)$$

The solution of Equation (11), joined to the energy balance, returns the exhaust gas temperature $T_{exh.|q}(h_{exh.|q})$. Many algorithms may solve such an iterative calculation which takes into account that the gas enthalpy data may be adjusted to polynomials, such as $h = B_6 T^6 + B_5 T^5 + ... + B_0$.

The available *residual energy* can be calculated from the date of allowable minimum exhaustion

temperature, which is established in order to avoid the formation of liquid sulfuric acid by Diesel oil. See equation (12).

$$\dot{E}_{residlq} = \dot{m}_{gaslq}\left(h_{resid.} - h_0\right) \qquad (12)$$

It is usually assumed for this minimum temperature, under Amazon weather conditions, the value $T_{resid.} = 413.15$ [K] (140 [C]). In such a case, the available energy of the exhaust gases is:

$$\dot{E}_{netlq} = \dot{m}_{gaslq}\left(h_{exh.} - h_{resid.}\right) \qquad (13)$$

A PRACTICAL EXAMPLE

The equations were applied to a supercharged Diesel engine of a national manufacturer working on continuous basis, whose most important technical data are related on the table bellow, Table 1.

q	**10^{-8} *bsfc*** [6]	**AF** [6]
25	6 841	89.92
50	6 034	50.97
75	5 688	36.05
100	5 592	27.50
Performance at rated speed		
Brake power [6]	1 200 [kW]	
Heat rejected to cooling fluid and lubricant [6]	618 [kW]	
Environment Radiation Loss [6]	150 [kW]	
Engine speed [6]	1 800 [rpm]	
Diesel oil Q_{LHV} [7]	40 270 [kJ/kg]	
Diesel oil molecular mass [7]	198,10 [kmol/kg]	
Diesel oil density [7]	850,0 [kg/m³]	
Average Diesel oil molecular composition [4]	$C_{14,4}H_{24,9}$	

Table 1: Diesel engine data.

For the above mentioned *bsfc* and AF data, the following polynomial regressions, equations (14) and (15), can be obtained. In both cases, the statistic parameters R^2 are 100%:

$$bsfc_{lq} = 8{,}320\,8\cdot10^{-5} - 7{,}545\,7\cdot10^{-7}\,q + 7{,}071\,7\cdot10^{-9}\,q^2 - 2{,}254\,7\cdot10^{-11}\,q^3 \qquad (14)$$

$$AF_{lq} = 1{,}705\,2\cdot10^{2} - 4{,}292\,9\,q + 4{,}744\,6\cdot10^{-2}\,q^2 - 1{,}882\,0\cdot10^{-4}\,q^3 \qquad (15)$$

In particular for the Diesel engine of the example, Equations (9) and (10) were adjusted to the values presented in equations (16) and (17):

$$\dot{Q}_{irradlq} = \dot{E}_{flq}\left(\frac{150}{\dot{E}_{fll00}}\right) \qquad (16)$$

$$\dot{E}_{refr.lq} = 3\,871\left(\dot{m}_{flq}\right)^{0,68} \qquad (17)$$

In Equation (17), ξ and α were found by equaling Equation (10) to 'environment radiation loss', see value on Table 1.

Figure 2 shows the energy balance. Figure 3 shows the energy balance ratios $\dot{E}/\dot{E}_f$. Figure 4 reports the combustion products exhaust temperature, obtained by solving Equation (11) as explained above. All of them are in function of the engine load. The solutions were obtained by solving the precedent equations with the aid of the software EES® [8].

For the purpose of comparison from the simulated results to actual data, in Figure 5, statistical data from ASHRAE [10] are reported, compiled from many types and sizes of supercharged Diesel engines. Note how similar Figures 3 and 5 are, despite the obvious statistical differences on each discrete power load points.

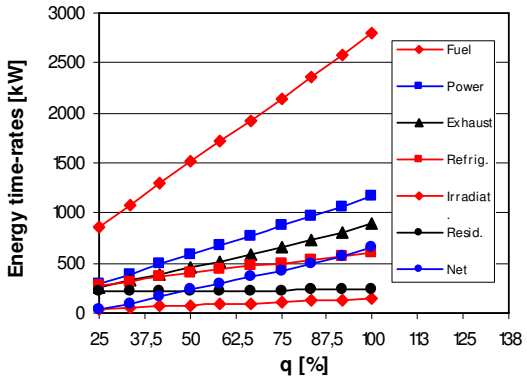

Figure 2: Simulated energy balance for the Diesel engine of the example [9].

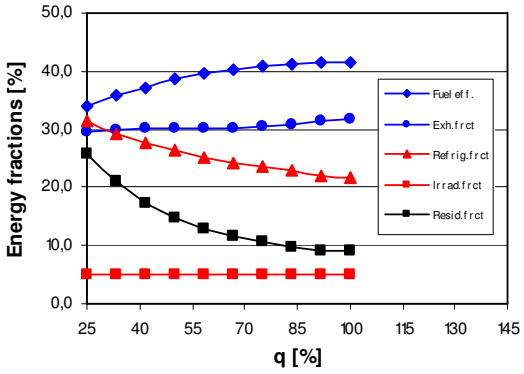

Figure 3: Simulated energy balance fractions for the Diesel engine of the example [9].

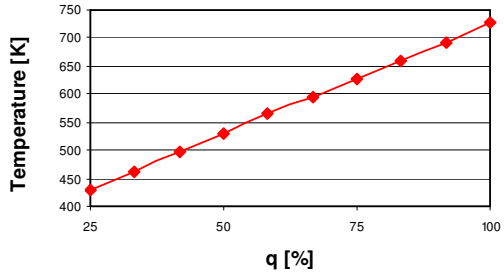

Figure 4: Simulated temperature of the exhausted gases for the Diesel engine of the example [9].

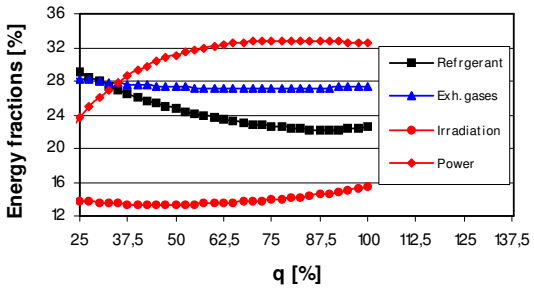

Figure 5: Supercharged Diesel engines energy fractions from ASHRAE [10]).

Figure 2 shows that the exhaust gases available energy increases with the load, at a higher rate than the cooling fluid available energy. Considering the energy fractions, both, Figure 3 and 5, show that the available heat fraction of the exhaust gases remain almost constant as the power load enhances.. Moreover, despite of its higher energy content, at low power loads, the combustion products do not support high temperature levels at that point, as shown in Figure 4. As the cooling fluid temperature do not vary as extensively as gases do, with the power load variation; it should be noted that most of rejected heat at low loads is concerning to the cooling fluid. At low power loads, cogeneration cycles should attempt to the low temperature of the combustion products.

CONCLUSIONS

The problem of simulating the performance of internal combustion engines under variable load is satisfactorily attempted by the simple procedure presented in this paper. If it is taken into account that most of the theoretical simulation procedures are difficult, to not say unpractical, to be implemented by daily engineering, the main calculation difficulties related to the present procedure may be promptly attained nowadays. These difficulties are mainly to obtaining performance data from engine manufacturers, thermo-physical data for gases, fuel and water. To facilitate the calculation, it is recommended the use of a computer software package as, for instance, EES® [8], whose thermo-physical data bank and equations solving algorithm can fully satisfy the computational efforts demanded.

ACKNOWLEDGEMENTS

The authors wish to thank Cummins do Brasil S.A. for the kind permission for utilization of their engine data sheets; as well as FUCAPI Foundation in Amazon, State University of Amazon (UEA), Federal University of Amazon (UFAM) and National Bureau for Scientific and Technologic Development (CNPq), for their financial support.

REFERENCES

[1] Stone Richard. *Introduction to Internal Combustion Engine*. Warrendale: Society of Automotive Engineers, Inc., 1999.

[2] Taylor C. F. *Análise dos Motores de Comb. Interna*. São Paulo: Ed. Edgard Blücher, 1988.

[3] Heywood J. B. *Internal Combustion Engine Fundamentals*. New York: McGraw-Hill, 1988.

[4] Ferguson C. R. *Internal Combustion Engines. Applied Thermosciences*. New York: John Wiley & Sons, 1986.

[5] Ramos J. I. *Mathematical Models of Diesel Engines*. In: Markatos N. C., Editor. Comp. Simul. for Fluid Flow, Heat and Mass Transfer, and Combustion in Reciprocating Engine Prococess of the International Centre for Heat and Mass Transfer, Hemisphere Publishing Co., New York, 1989.

[6] Cummins Co. Inc. *Engine performance report FR-6250. Data sheet DS-6250*. Columbus, Ohio, 2000.

[7] Petróleo Brasileiro S.A. (PETROBRÁS). Diesel Oil - Specifications Brochure (in Portuguese) Rio de Janeiro: Lanna Gráficos, 2000.

[8] F-Chart Software. *Engineering Equation Solver* (*EES*®). USA; January, 26, 2004. See also: http://www.fchart.com/.

[9] Cruz Ricardo. Evaluation of the Introduction of Cogeneration in the isolated electric generation System of the Amazon State. (in Portuguese) Doctoral thesis. Mechanical Engineering Faculty, State University of Campinas, 2004.

[10] American Society of Heating, Refrigeration and Air Conditioning (ASHRAE). *Cogeneration Systems and Engine and Turbine Drives*. In: Handbook for Heating, Ventilating and Air-Conditioning Systems and Equipment. SI Edition, Atlanta, 2000.

Proceedings of ECOS 2005
Trondheim, Norway
June 20–22, 2005

OXY-FUEL COMBUSTION SIMULATION IN A SUPERCRITICAL COAL-FIRED POWER PLANT

Franco Donatini, Gianluca Gigliucci , Massimo Schiavetti and Juri Riccardi*
Enel Produzione - Ricerca, Via Andrea Pisano 120, 56126 Pisa, Italy
Roberto Gabbrielli
Università di Pisa, Dipartimento di Energetica, Via Diotisalvi 2, 56126 Pisa, Italy

ABSTRACT

The purpose of this work is the evaluation of the feasibility of an Oxy-Fuel retrofit on a 660 MWe coal-fired boiler in order to obtain CO_2-rich flue gases and avoid post combustion CO_2 capture technologies. In order to achieve this goal, a GateCycle ® simulation model of a typical existing ENEL power station has been developed in detail and tested under normal operating conditions. Then, off-design conditions using pure O_2 and CO_2-rich flue gas recirculation have been explored. In particular, four plant configurations have been evaluated, both from the performance and plant complexity points of view. Some interesting results have been obtained, especially for what concerns parameters and configuration quantitative influence to the boiler performances.
keyword: Oxy-Fuel, coal fired boiler, simulation, zero emissions, oxygen combustion, flue gas re-circulation

NOMENCLATURE

ASU	Air Separation Unit
C	Condenser for separing CO_2 and H_2O
D	Deaereator
ECO	Economiser
HP	High Pressure turbine stage
LJ	Ljungstrom
LP	Low Pressure turbine stage
MEA	Monoethanolamine
MP	Middle Pressure turbine stage
RC1	Oxy-fuel re-circulation
RC2	Flue gas re-circulation to the boiler bottom
RH	Re-Heater
SH	Super-Heather

INTRODUCTION

Carbon dioxide (CO_2) is emitted into the atmosphere mainly through fossil fuel combustion in power plants, automotive engines and for heating purposes. The CO_2 emissions are the major contribution to the greenhouse effect resulting in a global warming of the earth's surface. Moreover, the world energy demand is increasing strongly and the fossil fuel use for energy supply will continue for a long time [1]-[2]. At present in the energy sector the main options in order to reduce the CO_2 emissions from fossil fuels are the following [1]-[3]:

- Increasing the fuel conversion efficiency;
- Increasing the use of fuels with a lower fossil carbon content and of renewable energies;
- Capturing and storing the CO_2 emitted in the fossil fuel fired power plants;

On the market today the use of renewable energies is available but limited to small scale energy production. Moreover, the cost to avoid CO_2 emissions using the renewable energies is very high. As discussed in [3], it is reasonable to think that only in the very long period the large scale energy production based on renewable and/or sustainable energy will have an important development. Therefore, in the middle and near period the study of innovative combustion technologies of fossil fuels (mainly bituminous coal and lignite) in large steam boiler power plants will have a strong development to reduce the CO_2 emissions and the greenhouse effect [2]-[7]. The most promising technologies use systems for the CO_2 capture from the flue gas together with its

*Corresponding author: Phone +39 050 6185971, Fax +39 050 6185585, E-mail juri.riccardi@enel.it

re-circulation to the boiler [1]-[7]. As well known, it is difficult to remove CO_2 efficiently because the CO_2 concentration in the flue gases exiting from a conventional fossil fuel power plant is only between 10 to 15% by volume. An efficient way to make the CO_2 capture easier is to increase the CO_2 concentration in the flue gas up to 95% using high purity oxygen rather than air as oxidant. In this case the flue gas consists mainly of CO_2 ad H_2O, from which CO_2 is easily separated, for example, by H_2O condensation, without the use of extra devices, like MEA scrubber, reducing strongly both the energy consumption and the plant cost. Then a fraction of the flue gas, after addition with a nearly stoichiometric amount of pure O_2, is re-circulated into the boiler. Oxy-fuel combustion is not a new concept because is already routinely employed in metallurgical and glass industries [2]-[3]. This technology for the capture and subsequent storage of the CO_2 is potentially attractive because the resulting mixture O_2/CO_2 provides a high flexibility for the temperature and flow rate control inside the boiler. Nevertheless the number of scientific papers concerning the applications of the oxy-fuel combustion in large conventional retrofit coal power plant is still small. Some limited research activities on the specific field have been mainly carried out in Japan, Canada and Sweden, especially at the Chalmers University of Technology [8]-[9].

The main goal of this paper is hence to investigate intensively the feasibility of the oxy-fuel combustion on a retrofit conventional 660 MWe coal fired boiler power station. Off-design conditions of the retrofit boiler have been studied using four possible plant engineering configurations, both from the performance variations and plant complexity point of view. The simulations has been carried out using Gate Cycle Version 5.2 commercial code.

The outline of this paper is as follows. In Section I the main characteristics of the reference boiler are described. The development of simulation model of the power station together with the its validation is also discussed. In section II the performance analysis of four oxy-fired boiler power plants in off-design conditions is described. At the end, some conclusions are reported.

I SIMULATION MODEL OF THE REFERENCE PLANT

Description of the ENEL's reference 660 MWe coal fired steam power plant

The ENEL's reference 660 MWe pulverised coal fired power station is constituted by a typical supercritical boiler and the main characteristics are reported in Table 1. The steam-cycle of the boiler is shown in Figure 1. The steam produced in the superheater (SH) is fed to the high pressure stage of the steam turbine (HP). Then, the steam goes through the re-heater (RH) and expands in middle pressure stage (MP) of the steam turbine. At the end, the MP outlet is connected to low pressure stage (LP) of the steam turbine. Six regenerative steam bleedings, from 77.4 bar to 1.2 bar of pressure, and a further auxiliary steam bleeding at 0.6 bar, are applied to the steam turbine (Figure 1). The mass flow of the regenerative steam bleedings varies in the range from 218 t/h to 56 t/h, while the mass flow of the auxiliary steam bleeding is about 121 t/h.

Reference 660 MWe Pulverised Coal Fired Boiler	
Height (m)	*61.5*
Width (m)	*15.5*
Depth (m)	*20.1*
RH Total Heating Surface (m^2)	*13045*
SH Total Heating Surface (m^2)	*12798*
Wing Wall Surface (m^2)	*2360*
Nominal Gross Power Output (MWe)	*660*
Gross Efficiency (-)	*0.427*
Superheat Steam Production (t/h)	*2091*
Re-heat Steam Production (t/h)	*1657*
Re-circulated Flue Gases Mass Flow (t/h)	*20.8*
SH1 Outlet Steam Temperature (°C)	*469*
SH2 Outlet Steam Temperature (°C)	*540*
RH Outlet Steam Temperature (°C)	*540*
ECO Inlet Water temperature (°C)	*290*
ECO Outlet Water temperature (°C)	*321*
HP Turbine Stage Inlet Steam Pressure (bar)	*242*
MP Turbine Stage Inlet Steam Pressure (bar)	*39*

Table 1: Main characteristics of the 660 MWe reference boiler.

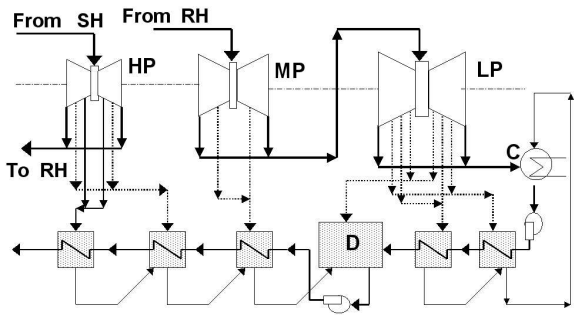

Figure 1: Scheme of the steam-cycle.

Modeling of the boiler and steam-cycle

The simulation model of the whole power station (boiler + steam-cycle) has been made using Gate Cycle Version 5.2 commercial code. In order to simplify the complexity of the real equipments that constitute the boiler and the steam-cycle, the following assumptions have been adopted:

1. the boiler has been divided in three independent sections: evaporative section, superheating section (SH) and re-heating section (RH). The SH section has been further subdivided in two subsections: SH1 and SH2, respectively. While SH2 subsection is undergoes to the convective and radiative heat transfer, for SH1 subsection the main contribution to heat transfer with the flue gases is due to convective processes. The SH2 outlet is connected to HP. The pressure loss between SH and HP has been included in the simulation model. Also RH section has been subdivide in two subsections: RH1 and RH2, respectively. Both these subsections are submitted to only convective heat transfer. Inside the boiler, the RH2 subsection is located between SH2 and SH1 subsection and the RH2 outlet is connected to MP. The pressure loss between RH and MP has been included in the model, too;

2. the economizer (ECO) has been simulated using a heat exchanger outside the boiler;

3. the Coal Lower Heating Value (LHV) has been assumed equal to 26.3 MJ/kg, corresponding to that of a typical Indonesian coal with the following chemical composition (as received): C=67.2%, H=5.9%, N=1.2%, S=0.6% and O=11.6% (by difference). Moreover, the coal moisture and ash contents have been assumed equal to 6.1% and 7,5%, respectively. The coal mass flow inside the boiler has been fixed equal to 212.2 t/h;

4. the excess of comburent air has been fixed equal to 17% with respect to the stoichiometric value. The air preheating takes place first in a steam exchanger using the auxiliary steam extraction and after in the Ljungstrom (LJ). The latter has been simulated using a general heat exchanger; for the heat transfer coefficient has been used a typical value of a heat exchanger gas/gas [10];

5. the steam turbine has been subdivided in three independent sections, as shown in Figure 1. For each sections a reasonable values for the isoentropic expansion coefficients, which have calculated using plant's nominal thermal data have been assumed. During the simulations, the values of these coefficients have been lightly adjusted in order to assure a good and a rapid convergence of the simulator to the plant working effective conditions. The steam leakages inside the turbines due to, for example, the steam seals, have been also taken into account in the model;

6. the heat regenerative exchangers (feedwater heaters) have been supposed adiabatic and composed by three independent sections: desuperheating section, condensing section and bleeding section. For each section a reasonable value for the heat transfer coefficient [10] has been defined;

7. the pressure of the condenser and the temperature of the cooling water have been fixed equal to 0.05 bar and 15^{o}C, respectively. Moreover, the inlet water mass flow has been established imposing on it a thermal increase equal to 10^{o}C;

In the simulation model the following aspects have been also included:

- the fans for the circulation of the comburent air and of the combustion gases;

- the condensated extraction pump and the feed-water pump (Figure 1).

On the basis of the assumptions reported above, the simulation model has been realized and the convergence has been checked by a detailed comparison between the simulation results and the nominal operating conditions of the plant (reference case). The main results of this comparison are reported in Table 2. The agreement between the simulation results and the nominal conditions of the reference case is good.

	Reference Case	Reference Case Simulation
Nominal Gross Power Output (MWe)	660	662
Gross Efficiency (-)	0.427	0.427
Superheat Steam Production (t/h)	2091	2091
Re-heat Steam Production (t/h)	1657	1655
ECO Inlet Water Mass Flow (t/h)	2005	2005
Re-circulated Flue Gases Mass Flow (t/h)	20.8	20.8
SH1 Inlet Steam Temperature (°C)	433	433
SH1 Outlet Steam Temperature (°C)	469	469
SH2 Inlet Steam Temperature (°C)	452	453
SH2 Outlet Steam Temperature (°C)	540	540
RH Outlet Steam Temperature (°C)	540	540
ECO Inlet Water Temperature (°C)	290	290
ECO Outlet Water Temperature (°C)	321	319
SH1 Inlet Flue Gas Temperature (°C)	694	700
SH1 Oulet Flue Gas Temperature (°C)	563	565
SH2 Inlet Flue Gas Temperature (°C)	1154	1154
SH2 Outlet Flue Gas Temperature (°C)	949	935
RH Inlet Flue Gas Temperature (°C)	942	935
RH Outlet Flue Gas Temperature (°C)	459	458
ECO Inlet Pressure (bar)	293	293
ECO Outlet Pressure (bar)	288	288
SH1 Outlet Steam Pressure (bar)	266	266
SH2 Outlet Steam Pressure (bar)	255	255
RH Outlet Steam Pressure (bar)	41	40
HP Turbine Stage Inlet Steam Pressure (bar)	242	242
MP Turbine Stage Inlet Steam Pressure (bar)	39	37.7

Table 2: Comparison between simulation results and nominal conditions of the reference case.

II OXY-FUEL COMBUSTION

Modeling of the oxy-fuel combustion

The off-design conditions of the developed simulation model have been explored in order to study pure O_2 and CO_2 enriched flue gases re-circulation. Four plant engineering configurations have been evaluated, both from performance variations and retrofit plant complexity points of view. In every simulation the SH1 inlet steam temperature has been fixed equal to 433^oC, according to the reference case. This choice allows an effective control of the heat exchanged inside the RH and SH sections. The following retrofit plant configurations have been examined:

Plant engineering configuration A

In this plant configuration (Figure 2), pure oxygen, produced in an air separation unit (ASU), is pre-heated in the LJ via flue gases cooling. The mixing and re-recirculation of a part of the flue gas (mainly constituted by CO_2 and H_2O) with pure oxygen take place downstream the ECO outlet. In the condenser C the remaining part of flue gas is cooled down to the water condensation in order to make it possible the CO_2 separation.

Plant engineering configuration B

As shown in Figure 3 the pure oxygen is preheated in the LJ and the mixing and re-recirculation of a part of the flue gases with the oxygen take place downstream the LJ.

Plant engineering configuration C

In this configuration (Figure 4) the pure O_2 is added to a part of the CO_2 separated in the condenser C. The mixture O_2/CO_2 is then preheated in the LJ via the flue gas cooling.

Plant engineering configuration D

As shown in Figure 5, this plant solution is very similar to the configuration C. The O_2/CO_2 mixture O_2/CO_2 is, at first, preheated in an adjunctive heat exchanger and then in the LJ via the flue gas cooling. The adjunctive heat exchanger (AUX) allows to improve the thermal exchange overall efficiency between flue gas and CO_2/O_2 mixture. The AUX thermal exchange surface has been calculated using a heat transfer coefficient of about 30 $W/m^2/K$, obtaining a value of about 150000 m^2, which is about

1.5 times the LJ's one.

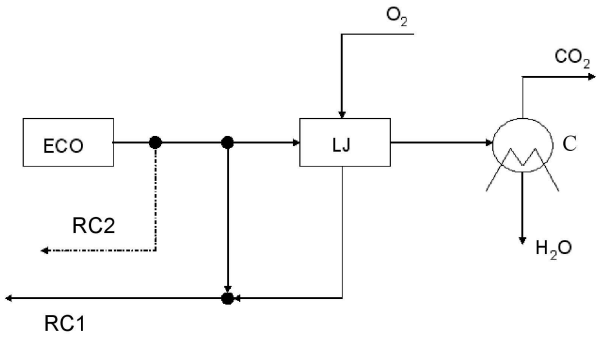

Figure 2: Plant engineering configuration A.

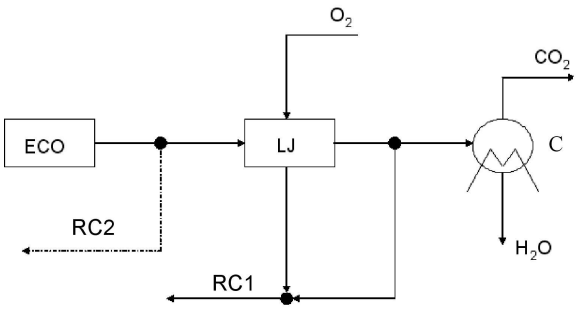

Figure 3: Plant engineering configuration B.

For each configuration a specific simulation model has been realised, tuning the reference model described in section I in order to take into account both the adjunctive equipments introduced and the modification to piping systems. Moreover, it has been supposed to use pure oxygen in order to emphasised the main effect of the oxy-fuel combustion. The excess of O_2 has been fixed equal to 10% of the stoichiometric value. In the simulations the coal mass flow has been fixed equal to 212.2 t/h, according to the reference case. The condenser H_2O/CO_2 has been simulated using a Flash Tank apparatus, fixing equal to 30^{o}C the water outlet temperature.

Oxy-fuel combustion simulation results

The simulation results for the configurations A, B, C and D are summarised in Table 3, where the symbol named Δ represents the percentage variation of the

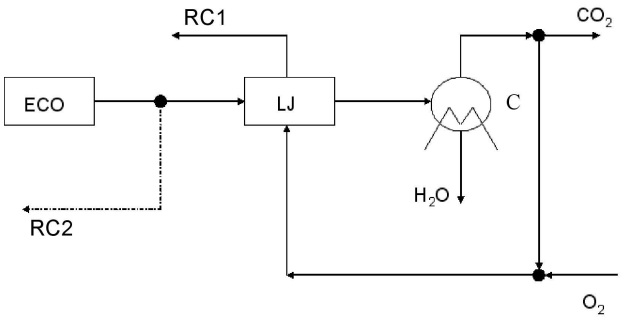

Figure 4: Plant engineering configuration C.

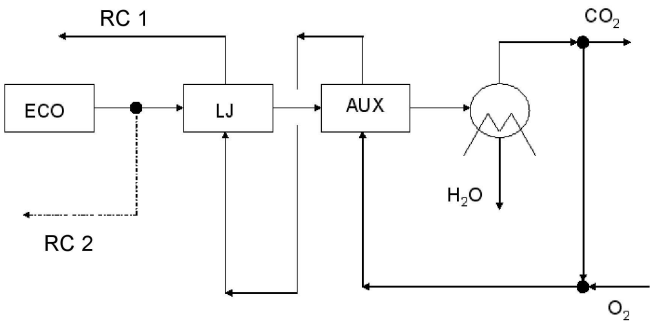

Figure 5: Plant engineering configuration D.

	Plant Engineering Configurations							
	A	**Δ%**	**B**	**Δ%**	**C**	**Δ%**	**D**	**Δ %**
Power Output (MWe)	675.6	2.0	663.5	0.2	662.2	0.1	672.0	1.5
Gross Efficiency (%)	43.51	2.0	42.73	0.2	42.65	0.1	43.29	1.5
Superheat steam production (t/h)	2109	0.9	2068	-1.1	2070	-0.9	2106	0.7
HP turbine stage inlet steam pressure (bar)	244.0	0.8	239.5	-1.0	240.7	-0.5	244.1	0.9
MP turbine stage inlet steam pressure (bar)	38.4	1.8	37.6	-0.3	37.5	-0.5	38.1	1.1
SH2 outlet steam temperature (°C)	540.4	0.1	540.2	0.0	542.3	0.4	542.3	0.4
RH2 outlet steam temperature (°C)	552.0	2.2	554.7	2.7	546.8	1.3	545.1	0.9
HP turbine stage inlet steam temperature (°C)	538.4	0.1	538.2	0.0	540.3	0.4	540.3	0.4
MP turbine stage inlet steam temperature (°C)	546.6	2.2	549.0	2.6	541.3	1.2	539.7	0.9
SH2 inlet flue gases temperature (°C)	1021.4	-1.3	1011.7	-2.3	1022.7	-1.2	1029.6	-5.0
ECO outlet flue gases temperature (°C)	380.2	7.5	379.9	7.4	362.3	2.4	362.5	25.0
Boiler inlet O_2+CO_2 temperature (°C)	377.8	26.3	341.1	13.7	314.0	5.6	348.9	16.6

Table 3: Summary of the main simulation results.

plant operating conditions with respect to the reference case. Using the data of Table 3 it is possible to point out the following considerations:

- only the configurations A and D make it possible to obtain consistent increases both of the plant power output and of the plant efficiency. This result is mainly due to the increase of the steam production with the same coal thermal power input;

- although the simulation results for the configuration A and D are very similar, it should be stressed that the latter requires the adjunctive heat exchanger with the increase of the plant cost;

- in the configuration A, the production of superheated steam reaches the maximum value;

- for the configurations B and C, the power plant output is slightly greater of that of the reference case, while it decreases the steam production. For these configurations the power output increase is mainly due to the simultaneous increment of the HP and MP steam temperature;

- the temperature of the O_2/CO_2 mixture recirculated to the boiler reaches the highest value in the configuration A (about 380^oC against 300^oC for the reference case). This fact allows to obtain the highest value of the gross plant efficiency.

In Table 4 the values of the thermal power recovered in the condenser C during the separation process of the flue gases, together with the condensed water mass flow, are also reported. Figures 6 and 7 show the temperature-exchanged heat diagram for the steam/water and flue gas inside RH1, RH2, SH1, SH2 and ECO in reference case and configuration A, respectively. The same diagram for the LJ is shown in Figure 8. From the comparison of Figure 6 with Figure 7 it is evident that flue gas temperature is higher in the configuration A with respect to the reference case; this fact is due to an increase of the flue gas thermal capacity. Moreover, it is possible to affirm that every plant pressure and temperature values calculated by the simulations are within the technological constraints.
Finally, a preliminary estimate of the power consumption for O_2 production is reported in Table 5, assuming to use a cryogenic air separation unit

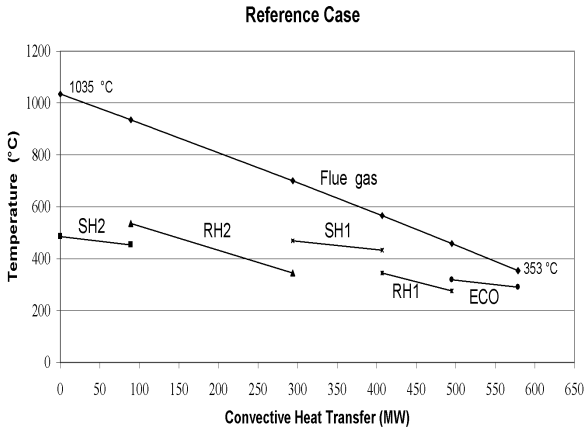

Figure 6: Temperature-exchanged heat diagram for steam/water and flue gas inside RH1, RH2, SH1, SH2 and ECO in the reference case.

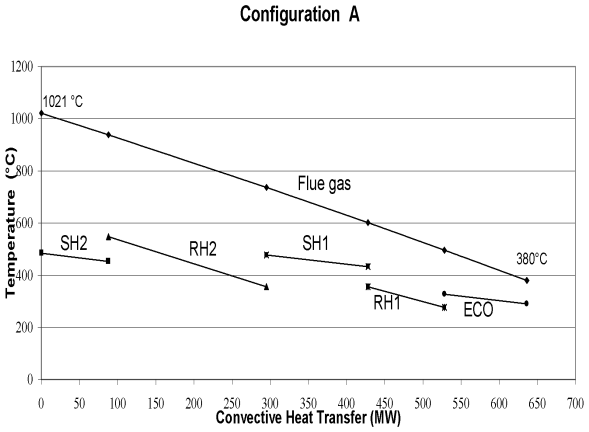

Figure 7: Temperature-exchanged heat diagram for steam/water and flue gas inside RH1, RH2, SH1, SH2 and ECO in the configuration A.

(cryo-ASU). At present, the O_2 production by cryo-ASU is the only available large scale technology for oxygen separation from air [2], [4], [6], although membranes and chemical looping technologies are sometime mentioned as possibile alternative to cryogenic air separation. According to Ref [11], it has been assumed that oxygen is produced (atmospheric pressure) at 0,25 kWh/kgO_2. Moreover, in Table 5 the plant net efficiency, which has been calculated assuming that the gross power output is partly consumed in the cryo-ASU is also reported: the plant auxiliary energy consumptions (fans, feedwater, pumps, etc.) and the thermal power recovered in the condenser C (see Table 4) are not included in the plant net efficiency calculation. It is evident from Table 5's data that the Cryo-ASU energy consumption severely penalizes the plant net efficiency.

Plant Configuration	Thermal Power *MWt*	H_2O Mass Flow t/h
A	111	113
B	139	112
C	139	114
D	118	114

Table 4: Thermal power recovered in the CO_2/H_2O separation process and condensed water mass flow.

	O_2 Mass Flow	ASU Power Consumption	Gross Power Output	Net Power Output	Gross Plant Efficiency	Net Plant Efficiency
	t / h	MWe	MWe	MWe	%	%
A	580	113	676	562	43.51	36.20
B	580	113	664	550	42.73	35.42
C	580	113	662	520	42.65	35.39
D	580	113	672	559	43.29	35.98

Table 5: Power consumption due to the O_2 production in the Cryo-ASU.

CONCLUDING REMARKS

A feasibility study of an Oxy-Fuel combustion in a 660 MWe pulverized coal fired steam power station has been carried out on four possible plant configurations. These have been evaluated both from the point of view of the performance variations and of the plant complexity. Some interesting results have been obtained, especially for what concerns parameters and configuration quantitative influence to boiler performances. In particular, in the configuration A the increase of power output and plant efficiency (about 2%) with respect to the base case assumes the highest value. It should be stressed that the overall evaluation of the simulation results is still in progress. In particular the energetic consumptions of the entire auxiliary equipments used to retrofit the reference plant for oxy-fuel combustion application will be analyzed in depth. From point of view of the energetic consumptions the air separation unit constitute certainly the most critical aspects. For the

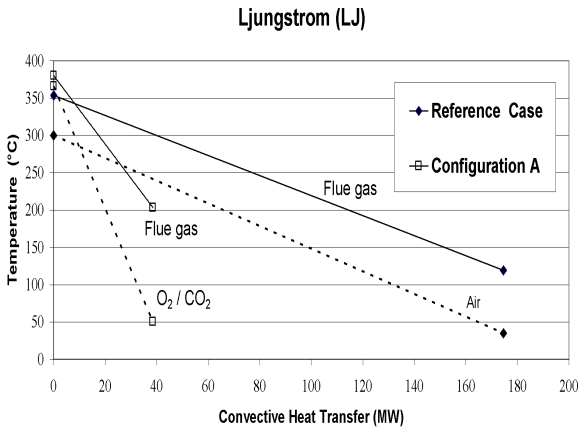

Figure 8: Temperature-exchanged heat diagram in the LJ for the reference case and the configurations A, respecively.

purposes of this paper, the power consumed in the cryo-ASU has been estimated in about 113 MWe, and the gross plant efficiency undergoes un decreasing of about 6-7 point per cent.

REFERENCES

[1] Chui EH, Douglas MA, Tan Y. *Modeling of oxy-fuel combustion for a western Canadian sub-bitominous coal.* Fuel 2003; 82:1201-1210.

[2] Simmonds M, Miracca I, Gerdes K. *Oxy-fuel technologies for CO_2 capture: a techno-economic overview.* Proceedings of the 7^{th} International Conference on Greenhouse Gas Control Technologies, Vancouver, 5-9 September 2004.

[3] Jordal K, Anheden M, Yan J, Strömborg S. *Oxyfuel technologies for coal-fired power generation with CO_2 capture-opportunities and Challenges.* Proceedings of the 7^{th} International Conference on Greenhouse Gas Control Technologies, Vancouver, 5-9 September 2004.

[4] Varagani R, Châtel-Pélage F, Pranda P. *Oxy-combustion in pulverized coal-fired boiler: a promising technology for CO_2 capture.* Proceedings of the 3^{rd} Annual Conference on Carbon Sequestration, Alexandria, 3-6 May 2004.

[5] Shao Y, Golomb D. *Power plants CO_2 capture using integrated air separation and flue gas reycicling.* Energy Convers. Mgmt 1996; 37(6-8):903-908.

[6] Liu H, Okazaki K. *Simultaneous easy CO_2 recovery and drastic reduction of SOx and NOx in O_2/CO_2 coal combustion with heat recirculation.* Fuel 2003; 82:1427-1436.

[7] Bolland O, Mathieu P. *Comparison of two CO_2 removal plant options in combined cycle power plants.* Energy Convers. Mgmt 1998; 39(16-18):1653-1663.

[8] Andersson K, Maksinen P. *Process evaluation of CO_2 free combustion in an O_2/CO_2 power plant*. Göteborg, Sweden: Chalmers University of Technology, 2002.

[9] Birkestad H. *Separation and compression of CO_2 in an O_2/CO_2 fired power plant.* Göteborg, Sweden: Chalmers University of Technology, 2002.

[10] Coulson J.M., Richardson J.F. *Chemical Engineering, Volume I*. Oxford: Pergamon Press, 1990.

[11] Mathieu P. *Toward a world based on near zero CO_2 emission fossil fuels power plants*, Liègi Belgium: University of Liègi, 2002.

Proceedings of ECOS 2005
Trondheim, Norway
June 20–22, 2005

PREDICTION OF S.I. ENGINE PERFORMANCE IN STEADY AND TRANSIENT CONDITIONS

Giancarlo Ferrari*, Angelo Onorati
Dipartimento di Energetica - Politecnico di Milano
20133 Milano
Italy

ABSTRACT

The 1D thermo-fluid dynamic code GASDYN has been used to optimize the new configuration of a Fiat Fire 1.4 L automotive s.i. engine. The complete system formed by the engine together with its intake and exhaust groups have been modeled to predict its main performance parameters not only in steady state conditions, but also during the first transient part of the ECE cycle. Meanwhile the same quantities were measured in a test room to check the predictive ability of the code. The satisfactory agreement found between predictions and measurements proved the good accuracy of the code in predicting the gas composition at the exhaust valves. Relevant are the results given by the code modeling the complete engine system during the during the first 90 seconds of the new European driving cycle, to predict the effects of both engine parameters as well as catalyst geometry and position on the pollutant conversion efficiency.

Keywords: fluid-dynamic modeling, internal combustion engines, pollutant emission control.

INTRODUCTION

To-day the development and optimization procedure of the main components of a new I.C. engine requires a good synergy between experimental techniques and computational models, so that the actual engine testing may begin from a prototype close to its optimum design. In fact, computer models [1-10] are now able to simulate in a satisfactory way the main characteristics of the technical components introduced in the current generation of engines (i.e. variable valve timing, internal and external EGR, secondary air injection, advanced catalytic converters, etc..). So, once the numerical codes have been sufficiently validated by comparison with experimental measurements, they can be used as predictive tools in the optimization processes of main design variables of the whole engine system. Moreover, among numerical codes of different complexity, the 1D fluid dynamic models are generally the most widely used for evident reasons of times and costs.

Also the authors during last decades have continuously developed a 1D fluid dynamic model, called GASDYN, to simulate the whole system: engine plus intake and exhaust groups. In fact, the computer code has been continuously improved in its ability to predict the unsteady flows with the transport of reacting chemical species through more and more complex components of intake and exhaust systems [7-10]. At first comparing predicted results with experimental data accurately validated each part of the model. Then the authors have used GASDYN to predict the performance of complete different engines and to optimize the main components of the hole system, as well as manifold, silencer and catalytic converter shapes and locations.

In order to show the main features and the accuracy level reached by the code at the moment, this paper reports some results of an optimization work recently carried out on a Fiat Fire 1.4 L S.I. engine. In particular they will be discussed some

* Corresponding author: Phone +39 2 23998515, Fax +39 2 23993940, E-mail: giancarlo.ferrari@polimi.it

meaningful comparison between predicted and measured engine parameters, suitable to describe the in-cylinder combustion process, the related pollutant formation and the evolution of the unsteady reacting flows in the manifolds during steady and transient engine operating conditions.

ENGINE CHARACTERISTICS

The simulated engine is the new Fiat Fire 1.4 L automotive engine, installed on the Fiat "Punto" vehicle and complying with Euro IV limits. The main geometric and performance parameters, as well as reference valve timings and lifts, are reported in Table I.

Engine type	4 strokes, S.I., 16 valves
Swept vol., compr. ratio	1368 cm^3; 11.0
Bore, stroke	72 mm; 84 mm
Max. power	72 kW at 6000 rpm
Max. torque	127 Nm at 4000 rpm
Ref.Int.valve AVO/AVC	16° BTDC / 64° ABDC
Ref.Exh.valve EVO/EVC	55° BBDC / 19° ATDC
Intake / exhaust valve lift	8.0 mm; 6.5 mm

Table I – Main data of the simulated Fiat Fire 1.4 L automotive engine.

Peculiarity of this engine is an hydraulic device which allows the rotation of the camshaft relatively to the driving mechanism. This results in a typical variation of the intake and exhaust valve timings, which can retard both the intake and exhaust valve openings and closings from 0°(no delay) to 50°(maximum delay) of crank angles. This retard is useful to achieve significant internal EGR rates at partial load, because of the late exhaust valve closing, whereas the late intake valve closing determines a partial back flow of fresh charge during the initial part of the compression stroke. At partial load, both effects causes a reduction of pumping losses, while the high internal EGR rates gives an important reduction of NO_x emissions.
Moreover the two intake valves are fed by ducts of different shapes and functions. One of them directs the flow straight toward the cylinder with low fluid dynamic resistance, resulting in a tumble port able to give high air mass flow at full load and high rpm. The second one has a strong helical shape, resulting in a tangential port suitable to impose an effective swirl on the flow, even with small mass flow rates. A moving slider closes the tumble port at low engine loads, forcing all the air to go trough the tangential port and notably increasing the turbulence intensity in the combustion chamber. Therefore this port-deactivation system greatly helps in sustaining the burning speed, when the engine is fed by high EGR rates at partial load running condition.
The engine exhaust after-treatment system is characterized by a compact design of the exhaust manifold and a close-coupled catalyst. Recently the complete system formed by this engine together with its intake and exhaust groups (shown schematically in Figure 1) have been modeled by GASDYN, to predict its main performance parameters in steady and transient (first 90 seconds of the ECE cycle) running conditions.

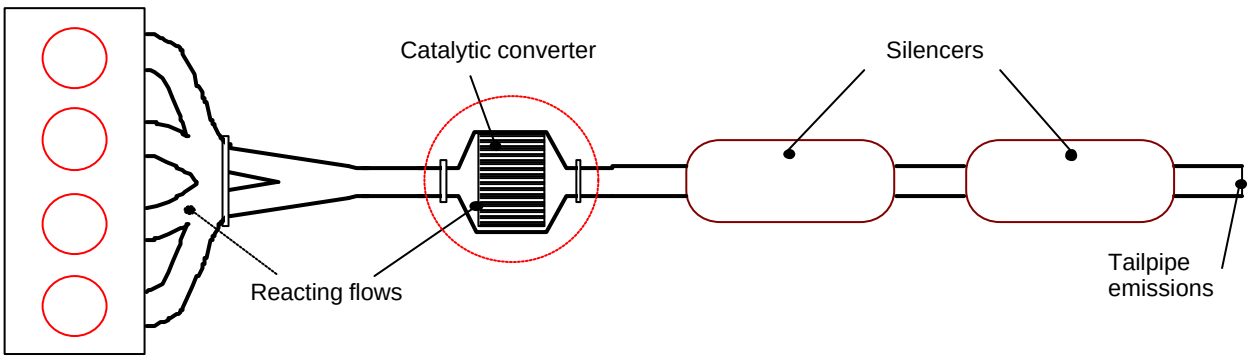

Figure 1 - Sketch of the four-cylinder spark ignition automotive engine simulated by GASDYN, in steady and transient (first 90 seconds of the ECE cycle) running conditions.

To validate the computer predictions with detailed experimental measurements, an extensive experimental work has been carried out on the engine test bench in ELASIS , in order to get a large set of measured data concerning: cylinder pollutant emissions, tailpipe emissions, gas and wall temperatures both in steady state engine running conditions and in transient conditions during the NEDC driving cycle. In particular, the attention has been focused on the first 90 seconds of the ECE cycle, which are quite critical during the global pollutant emission test.

STEADY CONDITION TESTS

First of all we recall that the initial composition of the exhaust gas discharged by the cylinders in the GASDYN code are predicted by means of a multi-zone thermodynamic combustion model, which includes dedicated kinetic emission sub-models described in detail in [9]. In fact the propagation of the flame front is calculated by means of an advanced fractal model [9-12] and an equilibrium approach is followed to evaluate the concentrations of the major species (H2O, H, H2, CO, CO2, O, O2, OH, N2, NO). However, CO, NO and HC cannot be satisfactorily calculated on the basis of the equilibrium assumption, but they have to be more properly evaluated by kinetic sub-models.

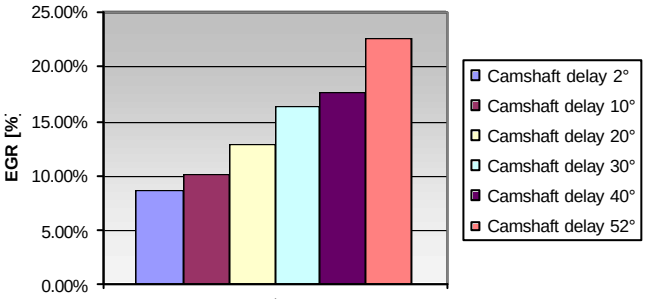

Figure 2 – Mass fraction of burned gases, trapped into the cylinder from the previous cycle, for different camshaft delays (engine conditions: n = 3000 rmp, bmep = 3 bar; slider closed).

The classical six-reaction extended Zeldovich model can be used for the calculation of NO, but also the super-extended Zeldovich model, based on 67 reactions, can be applied [13]. The CO concentration is evaluated on the basis of a kinetically controlled formation process [9]. Unburned HC are predicted by a dedicated sub-model, considering the different contributions due to crevices, to oil film layer and to incomplete combustion (partial burning and misfire) [14-18].
First of all the fractal combustion model, implemented within the thermo-fluid dynamic code GSDYN, can be tuned for the specific engine, to get a practical superposition of predicted and measured in-cylinder pressure history versus crank angle. In fact a good prediction of in-cylinder pressure is fundamental to correctly describe the physical action of the variable valve timing device and the wave actions in the intake and exhaust systems.

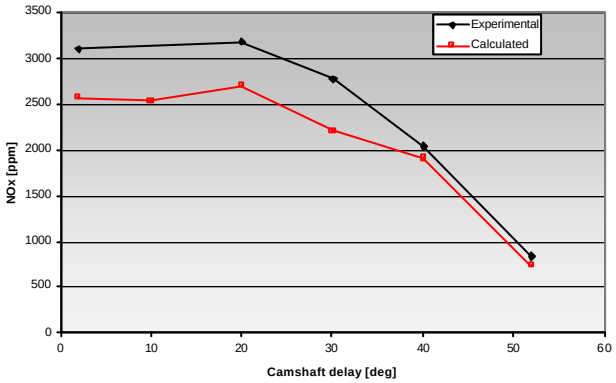

Figure 3 – Variation of NO_x concentration in gases exhausted by the cylinder, versus different camshaft delays (engine conditions: n = 3000 rmp, bmep = 3 bar; slider closed).

The model allows to follow in details the movement of different masses trough the valves and into the inlet and exhaust ducts, giving an important help in optimizing the effective valve timings. Finally it is possible to predict the total mass fraction of burned gases, trapped into the cylinder from the previous cycle (Figure 2), that is the internal EGR.
The burned gases act as a diluent in the new cylinder charge, reducing the combustion rate and the temperature reached after combustion. To keep the combustion rate at an acceptable level, in this engine the turbulence intensity is increased, closing the tumble port and forcing all the charge to flow trough the tangential port. On the other hand, because of the strong dependence of NO_x formation rate on the maximum temperature value

reached during combustion, the internal EGR effectively reduces NO_x emission levels.
The data in Figure 3 prove that the kinetic sub-model used to predict NO_x emissions from the cylinder, correctly catch the primary effect of EGR on NO_x formation process, given by a reduction of flame temperatures because of the increased heat capacity of cylinder charge, per unit mass of fuel burnt.

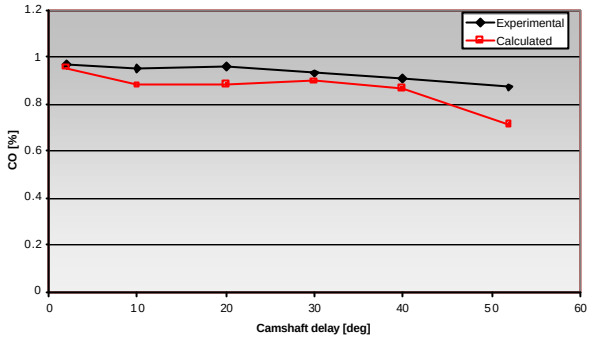

Figure 4 – Variation of CO concentration in gases exhausted by the cylinder, versus different camshaft delays (engine conditions: n = 3000 rmp, bmep = 3 bar; slider closed).

In fact the satisfactory agreement between predicted and measured values is the result of a correct simulation of both chemical and fluid dynamic processes.
Finally Figures 4 and 5 show that also the kinetic controlled sub-models for prediction of CO and HC emissions are strong enough, to be able to properly predict CO and HC concentration variation at the exhaust valves, with increasing camshaft delays and consequent masses of exhaust gas recycled.
Then, the main original feature of GSDYN is given by its ability in following the evolution of the gas composition along the exhaust ducts, taking account of possible chemical reactions that can occur node by node of the simulated system. In fact in the upper part of the exhaust system, where temperature is still high for many engine running condition, unburned HC and CO can be further oxidize, specially if secondary air is injected near the exhaust valve [10]. In any case the burned gases, whit their detailed chemical composition, are transported by the model through unsteady and reacting flows, until to the catalyst substrate, where catalytic reactions occur.

The prediction of the conversion characteristics of the catalysts is carried out on the basis of a specific sub-model that take into account in an integrated way the fluid dynamic, chemical and thermal processes typical of a catalytic converter [7,9]. A 1D approach is used to simulate the unsteady, laminar flow in the channels of the substrate. In this case only a single thin pipe, representing one channel, is considered for the simulation of the unsteady, reacting laminar flow in the monolith. The overall number of channels is important for the calculation of the substrate boundary conditions, i.e. the junctions (of several pipes) between the inlet/outlet cones and the monolith.
From the thermal point of view, in the converter is considered the heat released in solid phase by exothermic reactions and the thermal gradients due to the layer of insulating material. The multi-layer structure of the converter is taken into account, considering heat conduction in the system in the radial and axial direction. In this way the axial heat conduction from the metallic shell to the adjacent divergent and convergent ducts (and so to the rest of the exhaust system) can be calculated.

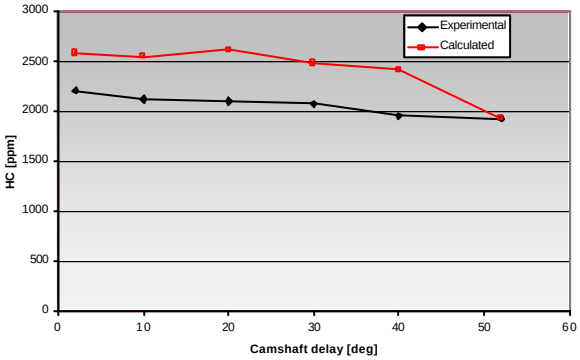

Figure 5 – Variation of HC concentration in gases exhausted by the cylinder, versus different camshaft delays (engine conditions: n = 3000 rmp, bmep = 3 bar; slider closed).

The main chemical reactions (oxidation of CO, C_3H_6, C_3H_8, H_2 and reduction of NO) occurring in the solid phase, within the wash-coat, are considered, by mean of appropriate kinetic expressions for the evaluation of the reaction rates on the basis of the catalyst temperature and species concentration in solid phase [19,20].

Moreover, the endothermic steam reforming reactions of the fast and slow oxidizing hydrocarbons have been introduced, which probably have a significant role in the conversion of HC for rich mixtures, providing some CO useful for the NO reduction. The water-gas shift reaction of CO with H_2O has been included, which is influenced by the oxidation state of Rhodium active sites. Finally an oxygen storage sub-model has been added to the chemical scheme, to describe the transient behavior of the system. The oxidation and processes of Cerium oxides are useful to store and release oxygen when the converter is fed with an oscillating gas composition. Typical mass transfer between gas and solid phase is taken into account. The predicted reaction rates are used to determine the specie source terms to be included in the fluid dynamic conservation equations, to allow for the modeling of chemical specie transport with reactions in the unsteady flow. The heat released by the exothermic reactions is accounted for as a source term in the heat transfer equations, to calculate the thermal transient of the catalyst and the consequent wall and gas temperature.

Comparisons between predicted and measured pollutant emissions at the catalyst inlet and outlet prove that a satisfactory modeling of the catalytic converter behavior can be achieved after an initial calibration of the kinetic constants which are needed to calculate the reaction rates, depending on the catalyst formulation. With an appropriate set of kinetic parameters the chemical model is able to properly catch the influence of the main operating parameters, in agreement with the experimental measurements.

TRANSIENT CONDITION TESTS

Moreover recently the code has been used to simulate the behavior of the complete engine system during the during the first part (first 90 seconds) of the new European driving cycle, to study the emission production related to the successive engine operating points (in transient conditions) and the consequent downstream action of the catalytic converter and to predict the effects of both engine parameters and catalyst geometry and position on the conversion efficiency.

In order to simulate the ECE driving cycle, coupling the engine to the vehicle, a simple one degree of freedom model has been developed, to evaluate the torque required by the vehicle to follow the prescribed velocity trend. A closed-loop control algorithm has been introduced in the simulation model to control the throttle valve opening angle and regulate the engine torque, in order to match the required vehicle torque. Moreover, a simplified modeling of the engine thermal transient from cold start has been considered, since the temperature of piston, cylinder head, cylinder liner, coolant have a significant influence on the production of unburned HC, originated from the crevices and the oil film layer. Similarly, possible partial burn and misfire during the combustion process of the first engine cycles have been taken into account. The variation of A/F ratio, spark timing, valve timing during the first 90 seconds of the ECE driving cycle have been considered as input data, assigned every second (or less) on the basis of the known engine operating points.

The simulation of the first part of the NEDC cycle, including the engine combustion, the vehicle, the transport of reacting species along the ducts and the catalyst conversion process, certainly requires a significant computational effort, since about a thousand of engine thermodynamic cycles must be calculated. On a Pentium IV 2 GHz PC the simulation requires about six hours, but the results provided are certainly important to investigate the key-issues of the engine + exhaust + vehicle system optimization, aiming at a reduction of pollutant emissions during the first seconds after the cold start.

Figure 6 shows the calculated emissions downstream of the engine, after the four-into-one manifold junction, and downstream of the catalytic converter, during the first 90 seconds of the ECE cycle. The predicted results are compared with the experimental measurements of NO, HC (as hexane, C_6H_{14}), CO and CO_2. These data prove that, with an appropriate set of kinetic parameters, the catalyst model can satisfactorily predict the conversion efficiency of the system as a function of the A/F values and other main engine parameters.

It can be noted that the overall agreement between predicted and measured emissions in Figure 6 is rather good in every case, both upstream and downstream of the catalyst, quantitatively and

qualitatively. In Figure 6(a) it is evident that the two peaks of emitted NO are related to the increase of load during the ECE cycle, corresponding to the accelerations of the vehicle.
Both of them are well predicted by the model. With regard to the unburned HC, the predicted trend is satisfactory, thanks to the sub-models embedded in the simulation code which take into account the different contributions due to the crevices, the oil film layer, the partial burn and some misfire during the engine cold running .

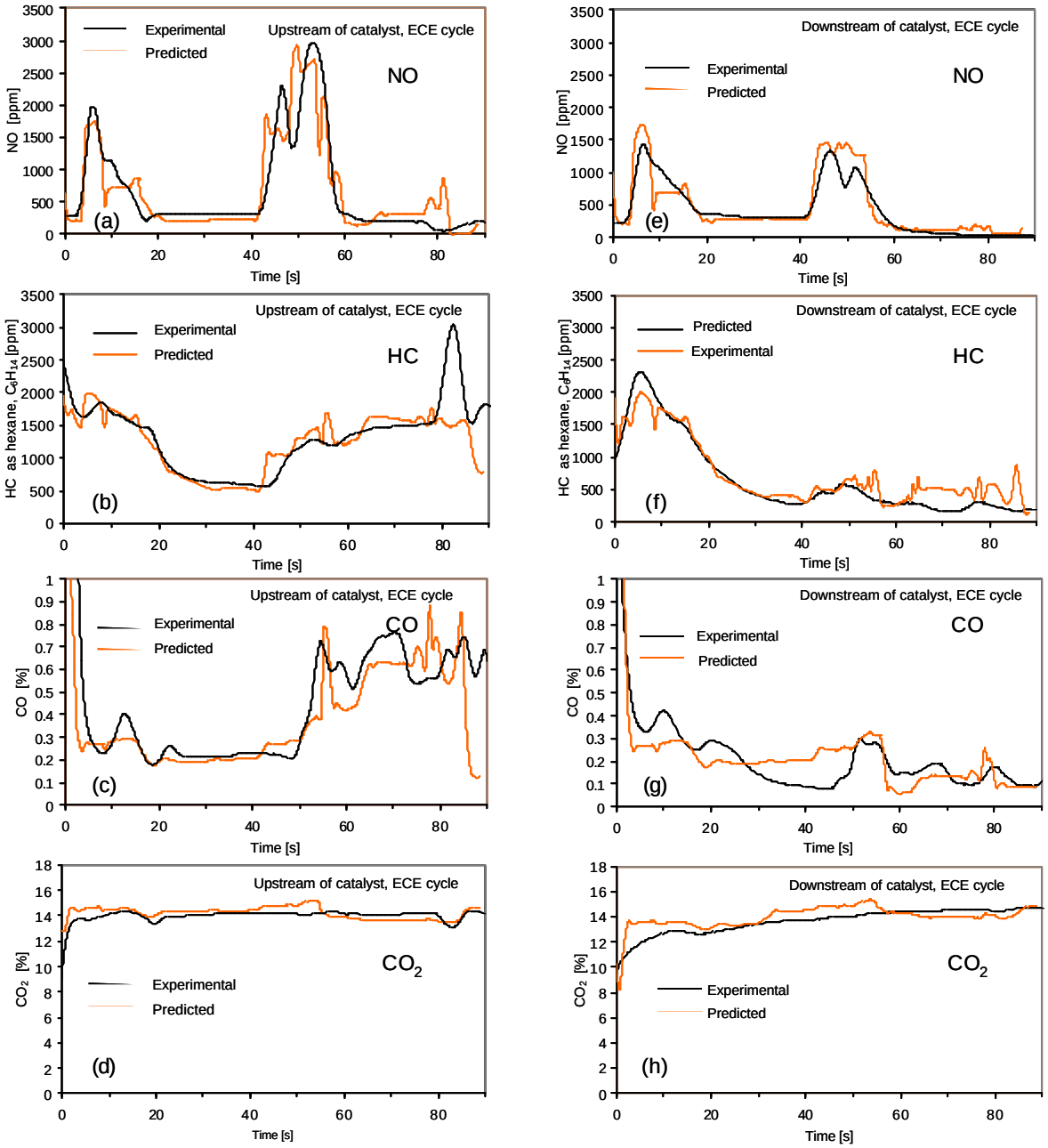

Figure 6 – Comparison between predicted and measured emissions upstream and downstream of the close-coupled catalyst, during the first 90 seconds of the ECE European cycle. Figures 6 (a), (b), (c), (d) refer to NO, HC, CO, CO_2 calculated and measured upstream of the catalyst, just downstream the exhaust manifold junction, while Figures 6 (e), (f), (g), (h) refer to NO, HC, CO, CO_2 calculated and measured downstream of the catalyst.

Also the agreement between predicted and measured CO and CO2 is fairly good, depending mostly on the A/F ratio values of the mixture fed to the engine during the ECE cycle. Some discrepancies can be noted in each diagram, which can be due both to some approximations in the modeling of engine emissions formation or of catalyst behaviour, as well as to inaccuracies in the experimental measurements.

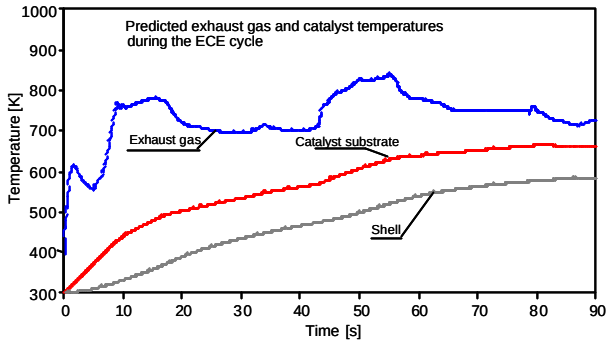

Figure 7 – Predicted exhaust gas temperature (upstream of the catalyst), catalyst substrate and shell temperatures during the first 90 s of the ECE cycle.

Figure 7 shows the predicted results concerning the exhaust gas temperature at the catalyst inlet (just downstream of the four-into one junction), the catalyst monolith temperature and shell temperature during the first 90 seconds of the ECE cycle. Two exhaust gas temperature peaks can be noted, related to the two vehicle accelerations (and consequent engine load increases) in this part of the ECE cycle. Moreover, the warm-up of the catalyst substrate (and consequently of the catalyst shell) is evident, starting from the ambient temperature of 300 K. The calculation points out a gradual heat-up from 300 K to about 650 K in 90 seconds.

CONCLUSIONS

The results achieved by the authors, using the GASDYN code to optimize different engine configurations, and particularly the Fiat Fire 1.4 L automotive s.i. engine presented in this paper, allow to draw the following conclusions:

- the code is able to simulate the fluid dynamic, thermal and chemical interactions between the engine and each intake and exhaust system component, predicting the exhaust gas composition from the cylinder to the tailpipe outlet and taking into account the effects of chemical reactions in the exhaust ducts and catalytic converters;
- the comparison between the simulation results and experimental measurements carried out on a new configuration of a Fiat Fire 1.4 L automotive S.I. engine, has pointed out that GASDYN can be used to calculate the behavior of the exhaust after-treatment system coupled to the engine not only in steady state conditions, but also during the real engine working conditions of the ECE cycle, considering the vehicle dynamics and the corresponding thermal transient of the system;
- therefore the influence of the engine parameters (A/F ratio, spark timing, valve timing, port-deactivation) and of the exhaust system design (geometry and position of the catalytic converter, monolith precious metal loading, etc..) can be usefully investigated during an important part of the effective test conditions, with a fundamental help in optimizing the manifold geometry as well as the silencers and converters shapes and locations.

REFERENCES

[1] D. E. Winterbone, R. J. Pearson, *Design Techniques for Engine Manifolds*, Professional Engineering Publishing, London, 1999.

[2] D. E. Winterbone, R. J. Pearson , *Theory of Engine Manifolds Design*, Professional Engineering Publishing, London, 2000.

[3] G. P. Blair, *Design And Simulation Of Four Stroke Engines*, SAE, R-186 Isbn 0-7680-0440-3, 1999.

[4] T. Morel, R. Keribar, A. Leonard, *"Virtual Engine/Powertrain/Vehicle" Simulation Tool Solves Complex Interacting System Issues*, SAE Int. Congress & Exp. (Detroit, Michigan) 2003, paper 2003-01-0372, March 2003.

[5] F. Bozza, E. Torella, *The Employment of a 1D Simulation Model for A/F Ratio Control in a VVT Engine,* SAE Int. Congress & Exp. (Detroit, Michigan) 2003, Paper 2003-01-0027, March 2003.

[6] Millo, C.V. Ferraro, F. Mallamo, *Numerical Simulation to Improve Engine Control During Tip-In Manoeuvres,* SAE Int. Congress & Exp. (Detroit, Michigan) 2003, paper 2003-01-0374, March 2003.

[7] Onorati, G. Ferrari, G. D'errico, *1D Unsteady Flows with Chemical Reactions in the Exhaust Duct-System of S.I. Engines: Predictions and Experiments*, SAE Int. Congress & Exp. (Detroit, Michigan), paper n. 2001-01-0939, 2001, SAE Transactions, Journal of Fuel and Lubricants, 2002.

[8] Onorati, G. Ferrari, G. D'errico, G. Montenegro, *The Prediction of 1D Unsteady Flows in the Exhaust System of a S.I. Engine Including Chemical Reactions in the Gas and Solid Phase*. SAE Int. Congress & Exp. (Detroit, Michigan), paper n. 2002-01-0003, 2002, SAE Transactions, Journal of Engines, 2003.

[9] D'errico, G. Ferrari, A. Onorati, T. Cerri, *Modeling the Pollutant Emissions from a S.I. Engine*, SAE Int. Congress & Exp. (Detroit, Michigan), paper n. 2002-01-0006, 2002, SAE Transactions, Journal of Fuel and Lubricants, 2003.

[10] Onorati, G. Ferrari, G. D'errico, *Secondary Air Injection in the Exhaust After Treatment System of S.I. Engines: 1D Fluid Dynamic Modeling and Experimental Investigation,* SAE Int. Congress & Exp. (Detroit, Michigan), paper n. 2003-01-0366, 2003.

[11] D. Liou, G.L. North, D.A. Santavicca, *A Fractal Model of Turbulent Flame Kernel Growth*, SAE paper 900024, 1990.F. Bozza, A.. Gimelli, A. Senatore, A. Caraceni, *A Theoretical Comparison of Various VVA Systems for Performance and Emission Improvements of SI-Engines*, SAE paper 2001-01-0670, March 2001.

[12] R. Miller, G. Davis, G. Lavoie, C. Newman, T. Gardner, *A Super-Extended Zel'dovich Mechanism for NOx Modeling and Engine Calibration,* SAE paper 980781, 1998.

[13] J. Schramm, S. C. Sorenson, *A Model for Hydrocarbon Emission from S.I. Engines,* SAE paper 902169, 1990.

[14] F. H. Trinker, J. Cheng, G.C. Davis, *A Feedgas HC Emission Model for SI Engines Including Partial Burn Effects,* SAE paper 932705, 1993.

[15] G. Lavoie, A.A. Adamczyk, E.W. Kaiser, J.W. Cooper, W.G. Rothschild, *Engine HC Emissions Modeling: Partial Burn Effects,* Combustion Science and Technology, Vol. 9, pp 99-105,1986.

[16] K. Frolund, J. Schramm, B. Noordzij, T. Tian, V. Wong, *An Investigation of the Cylinder Wall Oil Film Development During Warm-up of a S.I. Engine Using Laser Induced Fluorescence,* SAE paper 971699, 1997.

[17] D. Sandoval, J. B. Heywood, *An Improved Friction Model for Spark-Ignition Engines,* SAE paper n. 2003-01-0725, 2003.

[18] G.C. Koltsakis, A.M. Stamatelos, *Modeling dynamic phenomena in 3-way catalytic converters*, Chem. Eng. Sci., Vol. 54, pp. 4567-4578, 1999.

[19] S.H. Chang, D.L. Hoang, *Modeling of Catalytic Conversion of CO/HC in Gasoline Exhaust at Engine Cold-Start,* SAE paper n. 1999-01-0452, 1999.

Proceedings of ECOS 2005
Trondheim, Norway
June 20–22, 2005

SIMULATION ANALYSIS OF A CFB COMBUSTOR AND COMPARISON WITH EXPERIMENTAL RESULTS

Afsin Gungor[*] and Nurdil Eskin
İstanbul Technical University
Mechanical Engineering Faculty
34439 İstanbul
Turkey

ABSTRACT

It is important to determine the effect of operational parameters in CFB combustors via a simulation study instead of expensive and time consuming experimental studies. From this point of view, in this study a model for a CFB combustor, which can be employed to simulate under a wide range of operating conditions, has been developed. The developed model includes coal volatilization, attrition and combustion of a char particle. In the modeling, the combustor riser is analyzed in two regions: bottom zone considering as a bubbling fluidized bed and upper zone core-annulus solids flow structure is established. In the model, solids return cycle has been considered. Simulation model calculates the axial and radial distribution of voidage, velocity, particle size, pressure drop, gas emissions and temperature at each time interval for gas and solid phases. The simulation results are compared with test results obtained from various CFBC test rigs at different size and developed model has been validated.

***Keywords*:** Modeling CFB, combustion, pressure distribution, temperature distribution, velocity distribution, voidage distribution.

NOMENCLATURE

AFR	Air to fuel ratio [-]
C	Gas concentration [kmol/m^3]
C_D	Drag coefficient [-]
c_v	Specific heat of gas [kj/kmol K]
d_p	Mean particle diameter [m]
d_{pi}	Particle dimension interval [m]
E	Emissivity [-]
D	Riser diameter [m]
D_g	Diffusion coefficient for oxygen [m^2/s]
G	Mass flux [kg/m^{2}s]
$G(\varepsilon)$	Solids stress modulus [N/m^2]
H	Riser height [m]
h_t	Overall heat transfer coefficient [W/m^{2}K]
$\dot{J}$	Mass transfer rate via density difference per unit volume [kmol/ m^{3}s]
k_a	Attrition constant [-]
k_c	Char combustion reaction rate [kg/s]
k_{cr}	Kinetic rate [1/s]
k_{cd}	Diffusion rate [1/s]
k_L	Reaction rate [1/s]
P	Pressure [kPa]
R	Radius of riser [m]
R_a	Particle attrition rate [kg/s]
R_u	Universal gas constant [kJ/kmol K]
R'''	Total heat generated/consumed per unit volume [W/m^3]
$\dot{R}$	Mass flow rate generated/consumed from chemical processes per unit volume [kmol/ m^{3}s]
Re	Reynolds number [-]
T	Temperature [K]
U_0	Superficial gas velocity [m/s]
u	Gas velocity [m/s]
u_b	Absolute rise velocity of bubble [m/s]
v	Particle velocity [m/s]
W_b	Mass of particle in the furnace [kg]
X_k	Char weight fraction [-]
x_i	Weight fractions of particles [-]
z	Distance from top of the riser [m]
z_i	Height of inflection point [m]
Z_0	Bed characteristic height [m]

[*] Corresponding author: Phone: +905055044902 Fax: +90212450795 Email: afsingungor@yahoo.com

Sub indices

B	Bed
I	Core/annulus
J	Gas species
mf	Minimum fluidization
p	Particle

Greek Letters

β	Gas-solid friction coefficient [-]
ε	Void fraction [-]
ρ	Suspension/particle density [kg/m^3]
ρ_c	Char density [kg/m^3]
μ	Viscosity [Pa s.]
δ	Thickness of the annulus [m]
σ	Stefan-Boltzman constant [W/m^2 K^4]
τ	Shear stress [N/m^2]

1. INTRODUCTION

Increasing energy requirements and necessity of saving environment, Circulating Fluidized Bed Combustors (CFBC) are gaining importance when compared to other solid-fuel fired combustors. The advantages of CFBCs are; the ability to burn a wide variety of solid fuels with low pollutant emissions, high combustion efficiency, having smaller combustor cross section, fewer feed points, good turndown and load capability.

Modeling of coal combustion in the CFB is rather difficult. The fluid dynamics of this gas-solid two-phase flow is very complex and strongly dominated by particle to particle interactions. Furthermore, the numerous homogeneous and heterogeneous catalytic gas-phase reactions and their kinetics for the description of the combustion phenomena and the emission formation and destruction are not completely known. Therefore, it is necessary to develop simplified modeling approaches, which can describe both the gas-solid flow structure and the combustion process with sufficient accuracy. The main goal of the modeling of CFBCs is to constitute a system that maximizes combustion efficiency, and minimizes operating and investment costs and air pollutant emissions. It is also important to determine the effects of operational parameters in CFB combustors via simulation study instead of expensive and time-consuming experimental studies.

The publications in the literature about the CFB modeling may be subdivided into those that consider the hydrodynamic behavior [1-7,10,13-16], and others that investigate the combustion phenomena [1,2,17,18]. Although published models, have a similar structure, significant differences are found in the sub-models.

In the present study, a dynamic two dimensional CFBC model is developed. The model is applicable to different applications of CFBCs. The scheme of the combustor used in the model is shown in Fig.1. Simulation model calculates the axial and radial distribution of voidage, velocity, particle size, pressure drop, gas emissions and temperature at each time interval for gas and solid phase. The simulation results are compared with test results obtained from various CFBC test rigs at different size in the literature [6-10] and developed model has been validated.

2. CFB COMBUSTOR MODEL

This model includes the following constraints:

a) Although the physical and chemical processes occurring in the combustor are described, they include empirical correlations for less identified processes. b) The model should be flexible enough in order to be used in different applications of CFBCs. c) The computer code should be modular to allow users to update component modules easily as new findings become available.

Hydrodynamic Model: The flow structure of CFBs is known to exhibit axial nonuniformities [11,16]. In order to characterize this behavior, the riser is subdivided vertically into zones with different properties. According to Schoenfelder et.al.[12], four axial zones, bottom zone, splash zone, upper dilute zone and exit zone, are sufficient to give a reasonable description of the CFB flow structure.

According to the axial solid volume concentration profile, the riser is axially divided into two different zones: The bottom zone including splash zone and the upper zone including exit zone.

Bottom Zone: Experimental evidence has been reported by Svensson et.al. [13] and Werther and Wein [14] that, the fluid-dynamical behavior of the bottom zone is similar to that of bubbling fluidized beds. In generally lumped formulation is used for this zone in the literature. In this model, the bottom zone is simulated as a bubbling fluidized bed in fast bubbling fluidization regime. The flow domain is subdivided into a suspension phase and a bubble phase. The bubble rise velocity, the bubble size, the bubble volume fraction and the suspension porosity were calculated by extrapolating the Eskin [15] bubbling-bed model to the high gas velocities

used in the CFB. A single-phase back-flow cell model is used to represent the solid mixing in the bottom zone. Solids exchange, between the bubble phase and the suspension phase is a function of the bubble diameter and varies along the axis of the riser. The flow direction in the gas phase is considered upward; back mixing of gas is neglected.

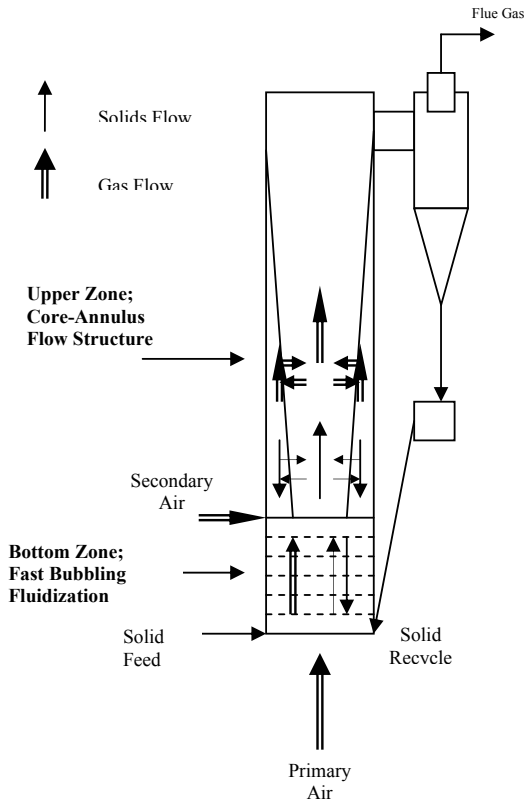

Figure 1. The scheme of the CFBC.

Upper Zone: Between the bottom zone and the riser exit the upper zone is located. Usually, most of the riser height is occupied by this zone, which is characterized by countercurrent-flow situation of dense clusters of particles (dense phase) moving downwards and upflowing lean suspension (lean phase) [1]. In this study, on the basis of the previous researchers [2,3,5], core-annulus flow structure in a CFBC is used. Particles move upward in the core and downward in the annulus. Thickness of the annulus varies according to the combustor height h. δ is given by Werther [14] as,

$$\frac{\delta}{D} = 0.55 \cdot \mathrm{Re}^{-0.22} \left(\frac{H}{D}\right)^{0.21} \left(\frac{H-h}{H}\right)^{0.73} \qquad (1)$$

Smolders et. al. [4] proposed a model in which the bed density was described as an exponential function of the bed height. In this paper, the model proposed by was used:

$$\frac{\varepsilon - \varepsilon_{mf}}{1-\varepsilon} = \exp\left(\frac{z - z_i}{Z_0}\right) \qquad (2)$$

In a conventional fluidized bed, the pressure drop through the bed is just equal to the weight of the solids in the bed. In the model, pressure drop in the riser consider as follows:

$$\nabla P = \rho g \nabla\left(z\left(1-\varepsilon\right)\right) + \frac{1}{2}\rho \nabla\left(v^2\left(1-\varepsilon\right)\right) \qquad (3)$$

where, the first term on the right hand side is pressure drop due to hydrostatic head of solids and second term is pressure drop due to solids acceleration.

In the fluidized beds, particle attrition takes place by surface abrasion, i.e. particles of a much smaller break away from the original particle. The upper limit size of the fines produced is in the range 50-100 μm [2,11,16]. The attrition rate is given as follows [2];

$$R_a = k_a \left(U_0 - u_{mf}\right) \frac{W_b}{d_p} \qquad (4)$$

For the upper zone, attrition rate is used as follows;

$$R_a = k_a \left(u - v\right) \frac{W_b}{d_p} \qquad (5)$$

Particles in the model are divided into n size groups in the model and mean particle diameter of different-sized particles considers as follows:

$$d_p = \frac{1}{\sum_{i=1}^{n}\left(x_i / d_{pi}\right)} \qquad (6)$$

Kinetic Model: While moving in the combustor, the char particle burns and undergoes attrition. The bed material in the combustor consists of coal, inert particles and limestone. Volatiles are entering the combustor with the fed coal particles. It is assumed that the volatiles are released in the bottom region of the CFB only. Volatiles are released at a rate proportional to the solid mixing rate. Volatile nitrogen and sulfur increases a function of bed temperature. The combustor model takes into account, the devolatilization of coal, subsequent combustion of volatiles followed by residual char, sulfur dioxide capture by limestone particles, reduction of NO_x by the char in the combustor.

Coal particles' behavior during the gas-solid reaction is assumed to be described in terms of shrinking core with attiring shell i.e. the dual shrinking-core model. Therefore the changes in particle diameter are taken into consideration in the model. The rate at which particles of size r_i shrink as follows;

$$r(r_i) = -\frac{dr_i}{dr} = \frac{12C_{O_2}}{\rho_c X_k (1/k_c + d_p / ShD_g)} \quad (7)$$

where D_g is the diffusion coefficient for oxygen, X_k is the char weight fraction.

The char combustion at each control volume is considered according to the reaction.

$$C + \frac{1}{\Phi} O_2 \rightarrow \left(2 - \frac{2}{\Phi}\right) CO + \left(\frac{2}{\Phi} - 1\right) CO_2 \quad (8)$$

and the combustion rate is calculated as follows:

$$r_c = \pi d_c^{\,2} k_c C_{O_2} \quad (9)$$

where k_c combustion reaction rate;

$$k_c = \frac{R_u T_b}{\frac{1}{k_{cr}} + \frac{1}{k_{cd}}} \quad (10)$$

During coal combustion, the sulphur compounds are oxidized and resultant sulphur dioxide is reduced by calcium oxide particles (produced by the limestone calcinations), forming calcium sulfate according to the reaction:

$$CaO + SO_2 + \tfrac{1}{2} O_2 \rightarrow CaSO_4 \quad (11)$$

The reaction rate of a limestone particle can be expressed as [19]:

$$k_L = \frac{\pi}{6} d_s^3 k_{vL} C_{SO_2} \quad (12)$$

where, k_{vL} presents the overall volumetric reaction rate constant and C_{SO_2} is the SO_2 concentration in the combustion gases.

Heat Transfer: Heat transfer model based on cluster renewal process[2]. The dilute phase is comprised of a continuous upflowing gas phase with thinly dispersed solids and relatively denser phase moving downward along the wall. Therefore some parts of the wall come in contact with the clusters and the dilute phase. If ε_{cl} is the average fraction of the wall area covered by the clusters, the time-averaged overall heat transfer coefficient, h_t, may be written as the sum of convective and radiative heat transfer coefficients,

$$h_t = \varepsilon_d h_{cl} + (1-\varepsilon_{cl}) h_d + \varepsilon_{cl} h_r + (1-\varepsilon_{cl}) h_{rd} \quad (13)$$

where h_{cl} and h_d are the convective heat transfer coefficient for the cluster and the dispersed phase respectively. Similarly h_r and h_{rd} stand for the radiative heat transfer coefficient for the cluster or the dispersed phase respectively. The radiative component is determined from the following equation:

$$h_r = \frac{\sigma \left(T_p^4 - T_b^4\right)}{\left\{\left(e_p^{-1} - e_b^{-1}\right) - 1\right\} \left(T_p - T_b\right)} \quad (14)$$

for gray particles. It is fairly accurate to estimate the bed emissivity from the particle emissivity.

$$e_b = 0.5\left(1 + e_p\right) \quad (15)$$

The external heat transfer coefficient h_o is calculated to be 17 W/m^{2}K, which is consistent with surface temperature measurements and experimental heat balances [9].

3. NUMERICAL SOLUTION

Table 1. shows the conservation of mass, momentum and energy equations for each phase and the constitutive relations used for the model. The calculation domain is divided into $m \times n$ grid nodes, in the radial and the axial directions respectively. With the cylindrical system of coordinates, a symmetry boundary condition is assumed at the column axis. The set of differential equations governing mass and momentum are solved using the Gauss-Seidel iteration method. At the walls, a partial slip condition is assumed for the solid and the gas phases. Then, the simulated results are obtained by using a combined Relaxation Newton-Raphson method.

4. RESULTS AND DISCUSSION

The developed simulation model is used for the simulation of the CFBC. In order to validate the developed model, simulation results are compared with the experimental data obtained from various CFBC test rigs at different size in the literature [6-10]. The information of experimental data used for comparison is shown in Table 2.

Continuity Equation

$$\frac{d\left(C_j\varepsilon_i\right)}{dt}=\sum_{\text{in}}\dot{C}_j\varepsilon_i-\sum_{\text{out}}\dot{C}_j\varepsilon_i+\dot{R}_j+\dot{J}_j$$

$$\left(j=O_2,CO,CO_2,NO,N_2O,N_2,HCN,CNO,NH_3,H_2O,SO_2,CH_4\right)$$

Momentum Equation

Radial direction

$$\frac{\partial\left(Cu\varepsilon_i\right)}{\partial t}+\frac{\partial\left(Cu\varepsilon_i u\right)}{\partial r}=-\frac{\partial\left(\tau_{rr}\varepsilon_i\right)}{\partial r}-\frac{\partial\left(\tau_{rz}\varepsilon_i\right)}{\partial z}-\beta\left(u-v\right)$$

Axial direction

$$\frac{\partial\left(Cu\varepsilon_i\right)}{\partial t}+\frac{\partial\left(Cu\varepsilon_i u\right)}{\partial z}=-\frac{\partial\left(\tau_{zz}\varepsilon_i\right)}{\partial z}-\frac{\partial\left(\tau_{zr}\varepsilon_i\right)}{\partial r}-\beta\left(u-v\right)$$

$$\tau_{rr}=2\mu\frac{\partial u}{\partial r}-\frac{2}{3}\mu\left(\frac{\partial u}{\partial r}+\frac{\partial u}{\partial z}\right)$$

$$\tau_{zz}=2\mu\frac{\partial u}{\partial z}-\frac{2}{3}\mu\left(\frac{\partial u}{\partial z}+\frac{\partial u}{\partial r}\right)$$

$$\tau_{rz}=\tau_{zr}=\mu\left(\frac{\partial u}{\partial z}+\frac{\partial u}{\partial r}\right)$$

Gas-solid friction coefficient [18];

$$\beta=\frac{3}{4}C_D\frac{C\varepsilon_i\left(1-\varepsilon_i\right)}{\varepsilon_i^{2.65}}\frac{1}{d_p}\left|u-v\right|$$

$$C_D=\frac{24}{\mathrm{Re}_p}\left(1+0.15\mathrm{Re}_p^{\,0.687}\right)\qquad \mathrm{Re_p}<1000$$

$$C_D=0.44\qquad \mathrm{Re_p}\geq 1000$$

İdeal gas equation

$$C=\frac{1}{R_u}\frac{P}{T_b}$$

Solids stress modulus

$$G\left(\varepsilon\right)=\frac{\partial\tau}{\partial\left(1-\varepsilon_i\right)}=10^{-8.76\cdot\varepsilon_i+5.43}$$

Energy Equation

$$C\varepsilon_i c_v\frac{\partial T_b}{\partial t}-uC\varepsilon_i c_v\frac{\partial T_b}{\partial x}-uC\varepsilon_i c_v\frac{\partial T_b}{\partial y}=R'''+\mu\varepsilon_i\left\{2\left[\left(\frac{\partial u}{\partial x}\right)^2+\left(\frac{\partial u}{\partial y}\right)^2\right]+\frac{1}{3}\left(\frac{\partial u}{\partial x}+\frac{\partial u}{\partial y}\right)^2\right\}$$

Table 1. The conservation of mass, momentum and energy equations for each phase and the constitutive relations for gas phase.

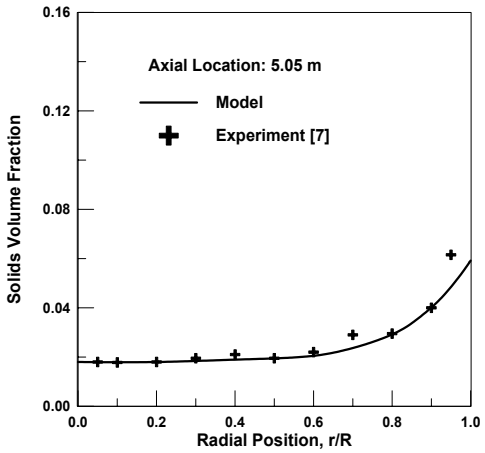

Figure 3. Comparison of model solids volume fraction values with Zheng et.al.[7]'s experimental data.

The solids particles are entrained up the column, against gravity, by the upflowing gas flow. The comparison of the radial profiles of local solids volume fraction with model predictions and experimental results are shown in Fig.3-4.

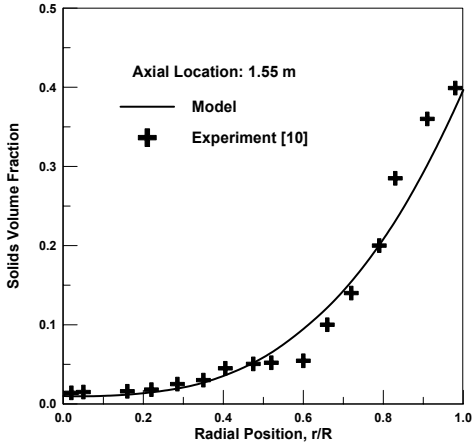

Figure 4. Comparison of model solids volume fraction values with Malcus and Pugsley[10]'s experimental data.

	Bed Temp. T(℃)	*Bed Diameter D(m)*	*Bed Height H(m)*	*Superficial Velocity U_0(m/s)*	*Particle Diameter d_p(μm)*	*Density ρ_p(kg/m^3)*	*Mass Flux G_p(kg/m^{2}s)*
Pugsley and Berruti [6]	25	0.05	5	8.5	208	2580	240
Zheng et.al.[7]	25	0.418	18	2.52	77	1398	-
Zhang et.al.[8]	25	0.1	15.1	5.5	67	1500	108
Topal[9]	850	0.125	1.8	3-9.28	400-1380	1740-2400	-
Malcus and Pugsley [10]	25	0.14	7	4.7	89	1740	264

Table 2. Data comparing model results.

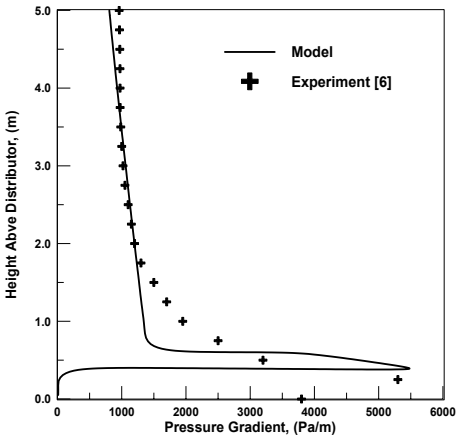

Figure 5. Comparison of model pressure gradient and Pugsley and Berruti [6]'s experimental data along the bed.

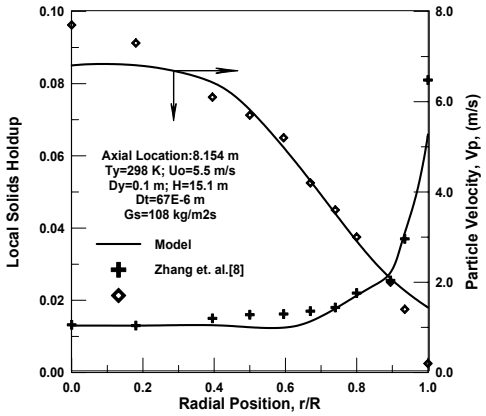

Figure 6.a. Comparison of model solids volume fraction and particle velocity values with Zhang et.al.[8]'s experimental data.

Generally, the change in the pressure gradient with height in CFBC is small. Figure 5 shows the axial profiles of pressure gradient predicted and obtained from experimental data. In the riser, the pressure gradient is always negative because the gas phase losses pressure head to accelerate and to suspend the particles. The absolute values of pressure gradient decrease monotonically with increasing distance from the riser entrance and then gradually approach a constant value.

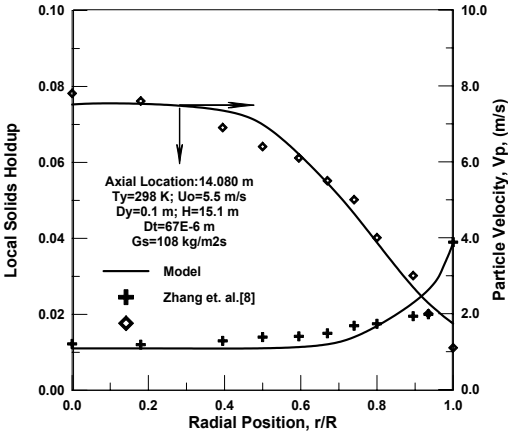

Figure 6.b. Comparison of model solids volume fraction and particle velocity values with Zhang et.al.[8]'s experimental data.

The overall radial structure generally shows a nonuniform solids volume fraction distribution with a dilute core and a dense annulus.

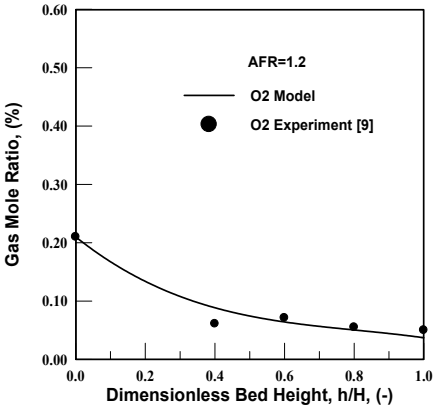

Figure 7. Comparison of model oxigen mol ratio with Topal[9]'s experimental data.

The radial profile is relatively flat in the core and solids volume fraction increases sharply toward the wall in the annulus with the highest solids volume

fraction right at the wall. The same trends above are observed in Fig.6 a-b. at two different bed heights corresponding to solids volume fraction profiles for test rig [8] which has smaller combustor diameter.

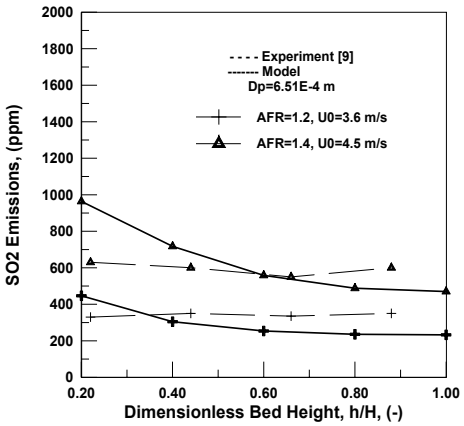

Figure 8. Comparison of model SO_2 emissions with Topal[9]'s experimental data.

To validate the hot bed model presented in this study, the molar ratio of oxygen, nitrogen oxide and sulfur dioxide emissions along the combustor height was obtained for the pilot CFBC using the same test data as the simulation program input Figs 7-9.

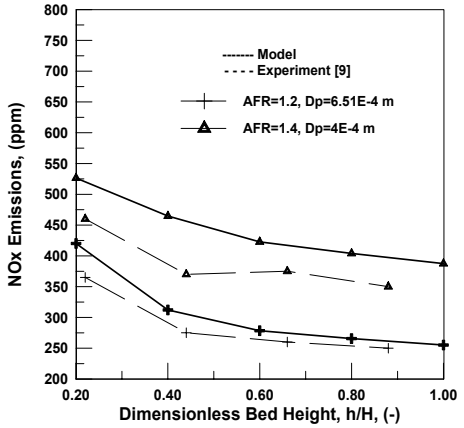

Figure 9. Comparison of model NO_x emissions with Topal[9]'s experimental data.

Mole ratio of oxygen along the combustor height in suspension phase in the bottom zone and dense phase in the upper zone is reasonably predicted by the model as shown in Fig. 7. As it is shown from the Figs.8-9., the simulated results are in good agreement with experimental ones.

The maximum deviation is about 5% for SO_2 and NO_x emissions at the bed height of 20 cm, which is at the coal feed point. This is due to the assumption that the great amount of the volatile matters is released at the feed point in the combustor.

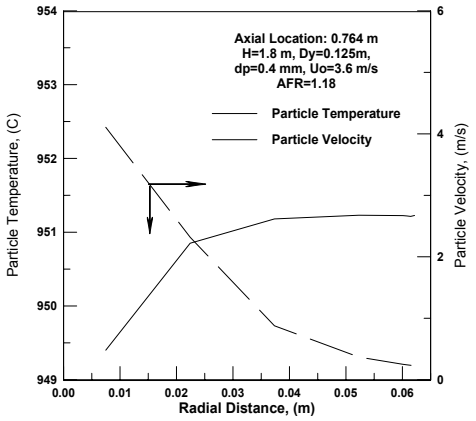

Figure 10. Radial profiles of bed temperature and particle velocity according to Topal[9]'s conditions.

Hot bed model results are shown in Figs.10-11. Particle temperature is increasing with increasing solids volume fraction toward the wall. Pressure gradient has an increasing trend along the radial distance as solids volume fraction increases and particle velocity decreases.

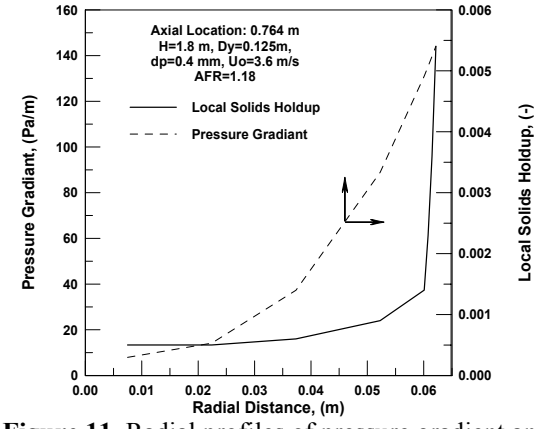

Figure 11. Radial profiles of pressure gradient and local solids hold up according to Topal[9]'s conditions.

5. CONCLUSION

In this study a dynamic two dimensional model for a CFB combustor is developed. The model is applicable to different applications of CFBCs. The

developed model includes coal volatilization, attrition and combustion of a char particle. In the modeling, the combustor riser is analyzed in two regions: bottom zone considering as a bubbling fluidized bed and upper zone core-annulus solids flow structure is established. In the model, solids return cycle has been considered. Simulation model calculates the axial and radial distribution of voidage, velocity, particle size, pressure drop, gas emissions and temperature at each time interval for gas and solid phase. The simulation results are compared with test results obtained from various CFBC test rigs at different size and developed model has been validated.

REFERENCES

[1] Knoebig T., Luecke K., Werther J., *Mixing and Reaction in the Circulating Fluidized Bed – A Three-Dimensional Combustor Model*, Chemical Engineering Science 1999; **54**: 2151-2160.

[2] Wang Q., Luo Z., Li X., Fang M., Ni M., Cen K., *A Mathematical Model for a Circulating Fluidized Bed (CFB) Boiler* 1999; Energy; **24**: 633-653.

[3] Wang W. and Li Y., *Hydrodynamic Simulation of Fluidization by Using a Modified Kinetic Theory*, Ind. Eng. Chem. Res. 2001; **40**: 5066-5073.

[4] Smolders, K. and Baeyens, J. *Hydrodynamic Modelling of the Axial Density Profile in the Riser of a Low-Density Circulating Fluidized Bed*, The Canadian Journal of Chemical Engineering 2001; **79:** 422-429.

[5] Hyre M.R., Glicksman L.R., *Axial and Lateral Solids Distribution Modelling in the Upper Region of Circulating Fluidized Beds,* Powder Technology 2000, **110:** 98-109.

[6] Pugsley T., Berruti F., *A Predictive Hydrodynamic Model for Circulating Fluidized Bed Risers*, Powder Technology 1996; **89**: 57-69.

[7] Zheng Y., Wan X., Qian Z., Wei F., Jin Y., *Numerical Simulation of the Gas-Particle Turbulent Flow in Riser Reactor Based on* $k-\varepsilon-k_p-\varepsilon_p-\Theta$ *Two Fluid Model*, Chemical Engineering Science 2001; **56:** 6813-6822.

[8] Zhang, H., Huang, W. X., Zhu, J., *Gas-Solids Flow Behavior: CFB Riser vs. Downer*, *A.I.Ch.E. Journal* 2001; **47(9):** 2000-2011.

[9] H. Topal, *Experimental Investigation of the Hydrodynamic, Combustion and Emission Properties of a Circulating Fluidized Bed*, PhD. Thesis of Gazi University Institute of Science and Technology, Ankara, Turkey, 1999.

[10] Malcus S. and Pugsley T., *Lateral Flux and Velocity of FCC Particles in a CFB Riser*, The Canadian Journal of Chemical Engineering 2001; **79:** 548-556.

[11] Huilin L., Gidaspow D., *Hydrodynamics of Binary Fluidization in a Riser: CFD Simulation Using Two Granular Temperatures,* Chemical Engineering Science. 2003; **58**: 3777-3792.

[12] Schoenfelder H., Werther J., Hinderer J. and Keil F., *A Multi-Stage Model for the Circulating Fluidized Bed Reactor*, A.I.ChE Symp. Ser. 1994; **301(90)**: 92-104,

[13] Svensson A., Johnsson F. and Leckner B., *Fluid-dynamics of the Bottom Bed of Circulating Fluidized Bed Boilers*, Proc. XII. International Conference on Fluidized Bed Combustion, San Diego, CA. 1993; 887-897.

[14] Werther J. and Wein J., *Expansion Behavior of Gas Fluidized Beds in the Turbulent Regime*, A.I.ChE Symp. Ser. 1994; **301(90):** 31-44.

[15] Eskin N. and Kılıç A., *Calculation of Steady-State Operation Characteristics of Fluidized Bed Coal Combustors*, Bulletin of Istanbul Technical University 1995; **48:** 11-36.

[16] Xu G., Sun G., Gao S., *Estimating Radial Voidage Profiles for All Regimes in Circulating Fluidized Bed Risers*, Powder Technology 2004, **139:** 186-192.

[17] Adanez J., Gayan P., Diego L.F., Armesto L., Cabanillas A., *Circulating Fluidized Bed Combustion in the Turbulent Regime: Modeling of Carbon Combustion Efficiency and Sulfur Retention,* Fuel 2001; **80:** 1405-1414.

[18] Huilin L., Guangbo Z., Rushan B., Yongjin C., Gidaspow D., *A Coal Combustion Model for Circulating Fluidized Bed Boilers*, Fuel 2000; **79:** 165-172.

[19] Adanez J., Diego L.F., Gayan P., Armesto L., Cabanillas A.,*: Modeling of Sulfur Retention in Circulating Fluidized Bed Combustors,* Fuel 1996; **75(3):** 262-270.

Proceedings of ECOS 2005
Trondheim, Norway
June 20–22, 2005

EFFECT OF ALCOHOLS ADDITION ON THE PERFORMANCE AND EMISSION CHARACTERISTICS OF AN ANIMAL FAT EMULSION FUELLED DIESEL ENGINE

A. Kerihuel, M. Senthil Kumar, J. Bellettre and M. Tazerout

Ecole des mines de Nantes
Department of Environment and Energy Engineering
BP 20722 – 4, rue Alfred Kastler - 44307 Nantes cedex 3
France

ABSTRACT

In this work, the effect of alcohol addition on the performance and emissions of a diesel engine fuelled with animal fat emulsions is studied. A single cylinder air-cooled, direct injection diesel engine is used. Tests are conducted using animal fat emulsions with water and alcohols. Methanol and ethanol are used to improve the physical properties of emulsions. Results show significant improvement in performance and emissions with animal fat emulsions as compared to neat animal fat. Smoke levels are drastically reduced with both the emulsions. Ethanol animal fat emulsion shows more reduction in smoke levels than methanol emulsion. No significant difference in NO emission is noted between the two emulsions. However, the values are very low as compared to neat fat and neat diesel. Hydrocarbon and carbon monoxide emissions are found as higher with ethanol emulsions as compared to methanol. However, these emissions are still lower than neat fat and neat diesel. On the whole it is concluded that animal fat emulsions with methanol and ethanol can be used as fuel in a compression ignition engine with improved performance as compared to neat animal fat.

Keywords: Diesel engine, Alternatives fuels, Alcohols, Animal fat, Emulsions, Emissions.

INTRODUCTION

The fast depletion of fossil reserve causes a renewal interest in renewable energy like biofuels based on vegetable oil or animal fat. In addition, since the European order dated on 14th November 2000 forbids to use animal fat in animal foods, the European feedstock has not found new applications. From its creation in 1909, compression ignition engines can run with vegetable oils as fuel. Studies of Elsbett's group on engine research very well proved that diesel engines can be directly run with vegetable oils as fuel [1,2]. Animal fats and vegetable oils are potential alternatives biofuels for diesel engines because their Lower Heating Value (LHV) and cetane number are close to standard diesel [3,4]. Moreover, animal fats and vegetable oils are composed of great molecules which are rich in oxygen as compared to standard diesel (cf. table 1). Contrary to fossil fuels, animal fats and vegetable oils are free from sulphur and heavy metals. But animal fat and vegetable oils have high viscosity and cause some injection problems if they are used without modifications in a compression ignition engine [5,6]. Transesterification is considered as one of the effective methods of improving the performance and reducing emissions of diesel engines using vegetable oils and fats as fuel. However, transesterification is a complex and time consuming process. It also produces certain products like glycerine and fatty acids which can not be used as fuel. The other effective solution to improve the combustion of heavy fuel is by

making stable emulsion with a water fraction [7,8]. Combustion of this kind of fuel leads to the well known “microexplosion” phenomenon [9,10].

Microexplosion occurs when a liquid droplet is trapped in an other liquid droplet with different volatility property. With temperature influence, the trapped droplet enters in a metastable state as far as homogeneous nucleation occurs violently. The resulting expansion causes the explosion of the second droplet leading to its fine atomisation. But in case of viscous liquid as emulsion formation increases the initial viscosity, the resulting emulsion is too viscous to be use in a C.I engine. The emulsion viscosity can be improved by the addition of alcohols with the animal fat while preparing the emulsions. Alcohols can also act as co-surfactants and improve emulsions stability. It has been reported that the animal fat emulsions with water and alcohol (ethanol and methanol) showed enhancement in physical properties of the emulsions and resulted in reduced emissions and improved performance of a diesel engine [11,12]. However, methanol has limited miscibility with diesel and heavy fuels. Contrary to methanol, ethanol is entirely miscible with animal fat. These alcohols are renewable fuels which can be obtained by fermenting agricultural waste containing sugar (ethanol) or by gasification of wood and coal (methanol) [13].

Properties	Diesel	Animal fat	Vegetable oil
Density (kg/m^3)	840	918	904
LHV (kJ/kg)	42490	39774	37000
Viscosity (cst)	4.59	49.93	40
Cetane number	45-55	40-45	35-40
Flash Point (°C)	75	96	120
Carbon (%w)	84-87	73	77.6
Hydrogen (%w)	33-16	12.3	11.6
Oxygen (%w)	0	12.5	10.8
Sulphur (%w)	0.29	0	0

Table 1 : Properties of Diesel, Animal fat and Vegetable oil [3-5]

In this study, the use of methanol and ethanol in making stable animal fat emulsion are compared. Performances and emissions with the two alcohols are studied and confront with base data obtained by using neat animal fat and standard diesel in compression ignition engine. The tested emulsions are the optima (cf. Table 3) from previous studies regarding in one hand: stability, fluidity and economical aspects [14,15], and in the second hand: performance and emission [3,11,13,16]. Experiments are conducted on a single cylinder diesel engine at the rated speed of 1500 rev/min with variable load conditions. Performance parameters like specific energy consumption, exhaust gas temperature and emission parameters like smoke, unburned hydrocarbon, carbon monoxide and nitric oxide emissions are evaluated. Finally, the efficiency of the added alcohol is discussed.

Best Emulsion	Water fraction	Animal fat fraction	Alcohol fraction
Methanol emulsion	10 %	80 %	10 %
Ethanol emulsion	10 %	50 %	36 %

Table 2 : Formulations of best animal fat emulsions with alcohol addition.

EXPERIMENTAL DETAILS

Emulsion process

An emulsion is obtained by mixing two immiscible liquids in presence of a stabiliser often called surfactant. The surfactant permits the emulsion to be well stable even if it is composed of a dispersed (the water) and a continuous (the fat) phase. The surfactant reduces the interfacial tension of the fat and allows the water droplets to be formed. The choice of surfactant is very important because it influences the emulsion stability and its nature. Referring to the bancroft law [17] , to make an indirect (water-in-oil) emulsion, the emulsifier must be more lipophilic than hydrophilic. Consequently the non-ionic surfactant SPAN 83 is used to stabilise the mixture because it has a HLB (Hydrophilic-Lipophilic-Balance) number equal to 3.7 [18]. According to the Davies’ scale, this emulsifier is appropriate for making water-in-oil

emulsions. Specified amounts of animal fat, water, alcohol and surfactant are taken in a container. The mixture is stirred vigorously since the fat and water are immiscible until a homogeneous phase is obtained. The emulsions are prepared by using a stirrer (Janker and Kunkel model RW 20 DZN) which rotates at maximum 2000 rpm. Since the fat is in solid form at temperatures lower than 60°C, a heater is used to give enough heat to maintain its liquid state. The heat energy is also used to enhance mixing rate and the emulsion formation. The animal fat container is kept in water bath and the emulsification process is carried out at a constant temperature of 30°C during mixing. This method has resulted in very stable emulsions. When the emulsion is ready, the heater is stopped and the emulsion can be used at ambient temperature (more than 20 °C).

Engine Set-up

A Single cylinder 4-Stroke air-cooled, direct injection open combustion chamber (bowl in piston) diesel engine developing a power output of 2.8 kW is used. Engine details are given in Table 3.

Make	LISTER – PETTER TS1
General Details	4-S, CI, Air cooled, DI, open chamber, NA, Single cylinder engine
Bore & Stroke	95.3 mm ×88.9 mm
Compression Ratio	18:1
Rated power output	2.8 kW at 1500 rev/min
Injector opening Pressure	250 bar
Displacement Volume	633 cc
Connecting rod length	165.3 mm
Fuel Injection Timing	20° BTDC

Table 3 : Engine Details

The Schematic of the experimental set up is shown in Fig.1. An electrical dynamometer is used for loading the engine. An orifice meter connected to a large tank is attached to the engine to make air flow measurements. An optical shaft position encoder is used to give signals at TDC. The fuel flow rate is measured on the volumetric basis using a burette. Chromel alumel thermocouple in conjunction with a slow speed digital data acquisition system is used for measuring the exhaust gas temperature. An infrared exhaust analyser is used for measuring HC/CO emissions. NO in the exhaust is measured by using a Beckman chemiluminascence analyser. Black carbon smoke levels are obtained by using a standard Hartridge smoke meter which works on light absorption technique (passing a light beam through the exhaust sample and the fraction of light is absorbed by the exhaust gas). Standard SAE J1667 procedure is followed for the measurement of smoke [19]. Light extinction coefficient K is used as the measure of smoke density per meter. It uses the following relationship:

$$K = (-1/L) * \ln (1-N/100),$$

Where, K = Smoke density (m^{-1}),
L = Optical path length of the smoke measurement (m) and
N = Smoke Opacity (%).

During the entire investigation the injection timing is optimized and set at 20^{o} before TDC. The engine is thermally stabilized before taking all measurements. Readings for engine speed, fuel flow, air flow, exhaust gas temperature etc. are recorded for obtaining performance parameters. Exhaust gas analyzers are calibrated before making measurements. Observations are made for smoke, NO, HC and CO to analyze the emission characteristics. Uncertainty analysis may be found in previous papers [3,12].

OBSERVATIONS AND RESULTS

As the quality of the fat vary according to the period, the results are influenced by its quality.

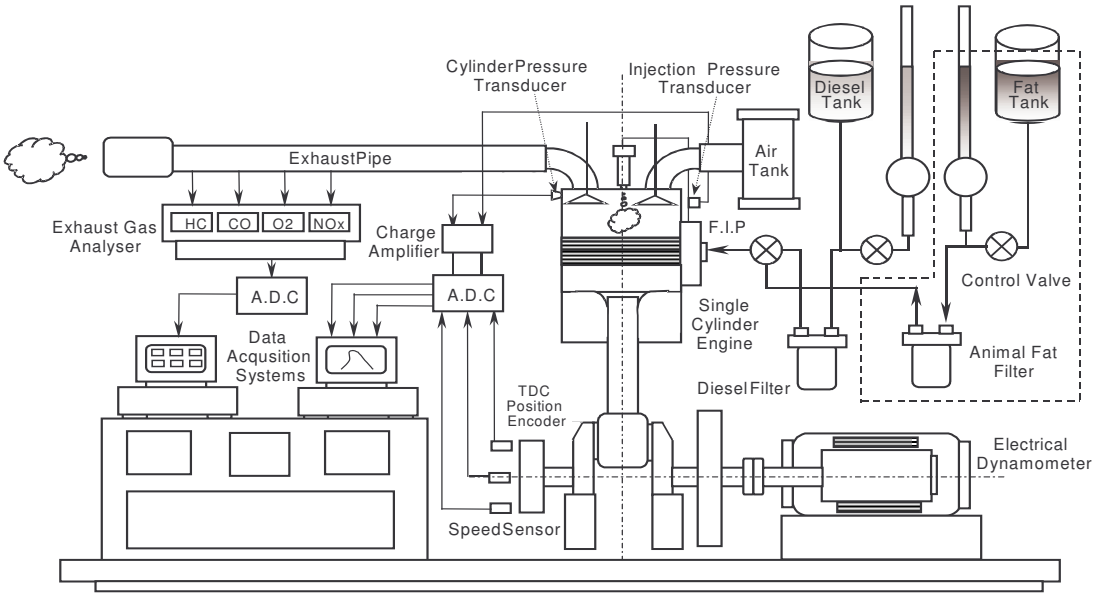

Figure 1 :Experimental setup

Thus on the obtained graphs neat fat results are represented by an interval drawn in dot lines instead of unique value.

Performance Parameters

The performance parameters are important because they permit to know the fuel ability to be used in a C.I engine. As shown in Fig. 2, Specific Energy Consumption (SEC) is estimated for neat diesel, neat fat and the best emulsions using methanol and ethanol at maximum power output.

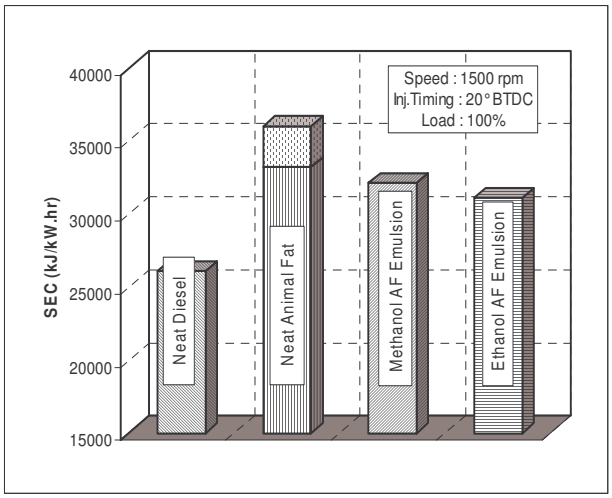

Figure 2 : Specific energy consumption estimated for the tested fuels(P =2.8 kW)

As compared to neat diesel, neat fat results in higher SEC that is due to its high viscosity. Viscous fuels suffer from bad atomisation which causes an increase in the SEC. In fact, mechanical efficiency is reduced as compared to standard diesel. As noted in Fig 2, emulsification of animal fat permits to reduce the SEC by decreasing the

mean diameter of injected fuel caused by the second atomisation (micro-explosion). In addition, the presence of surface agent in emulsions contributes to better atomisation characteristics of the fuel on leaving the injection nozzle. Ethanol emulsion reaches the minimum SEC of the emulsified fuels because ethanol is more miscible with animal fat than methanol that results in a lower viscosity.

The effects of substituting emulsified fuels for diesel oil on the exhaust temperature of the engine are shown in the Fig. 3.

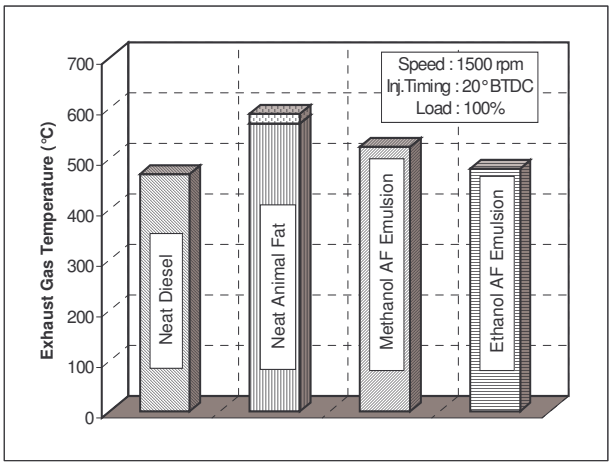

Figure 3 : Exhaust gas temperature measured for the tested fuels (P =2.8 kW)

The exhaust gas temperature in case of neat animal fat is higher than neat diesel. This result finds explanations in the facts that neat animal fat has longer ignition delay than standard diesel and is atomised in coarse droplets that take longer time to be entirely burned. Thus it is understandable that emulsified animal fat leads to a reduction of this temperature caused by a better atomisation. This result is the consequence of the microexplosion phenomenon. Ethanol animal fat emulsion yields to the minimum exhaust gas temperature as compared to methanol one. The obtained temperature is close to the temperature reached with neat diesel. Ethanol animal fat emulsion results in lower exhaust gas temperature as compared to methanol one due to the bigger quantity of high latent heat of vaporisation (alcohol + water) introduced in the fat (46 % by volume).

Emission Parameters

As shown in Fig. 4a and 4b, Carbon monoxide emission is measured for the different tested fuels at peak power output. Neat animal fat combustion yields to higher values as compared to neat diesel (cf. Fig. 4a).

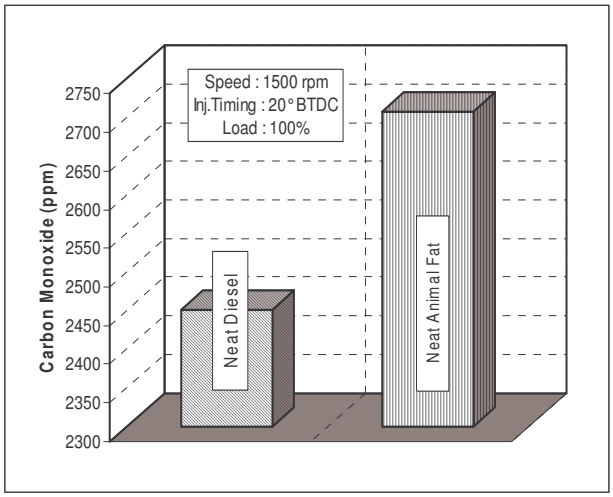

Figure 4a : Carbon monoxide emission measured for neat diesel and neat animal fat (P =2.8 kW)

The high viscosity of neat animal fat resulting in lean mixture can explain this value because this pollutant is mainly controlled by fuel/air ratio. However, animal fat emulsions drastically reduce this emission by improving the fuel/air mixture (cf. Fig. 4b). The two emulsions results in closed reduction but the methanol animal fat shows lower reduction than ethanol one.

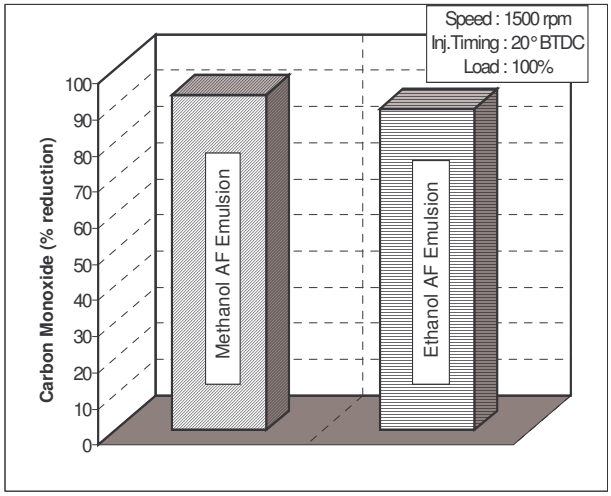

Figure 4b : Percentage reduction of carbon monoxide emission with animal fat emulsification (P =2.8 kW)

Figure 5a shows the measured unburned hydrocarbons at full power for standard diesel and neat animal fat. As unburned hydrocarbons are present in the exhaust gas for mainly the same reason than carbon monoxide, the same trend is observed.

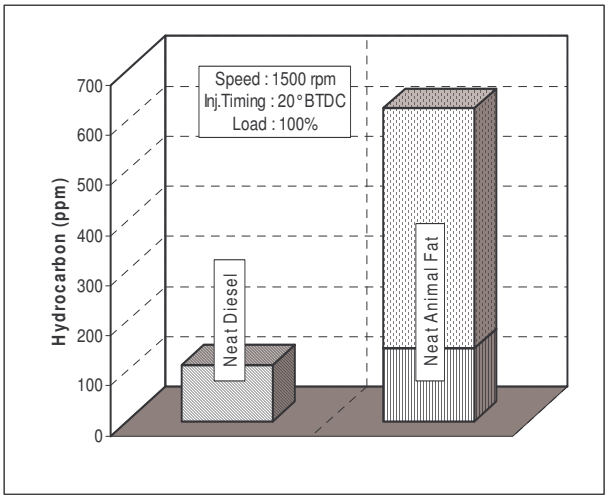

Figure 5a : Hydrocarbon emission measured for neat diesel and neat animal fat (P =2.8 kW)

Neat animal fat combustion yields to higher emission than standard diesel and its emulsification leads to a drastic reduction (cf. Fig 5b). Nevertheless ethanol animal fat emulsion results in lower reduction as compared to methanol one. This phenomenon find explanation in the bigger alcohol quantities in case of ethanol animal fat emulsion.

Thus the temperature of combustion is lower with ethanol than methanol and leads to partial combustion.

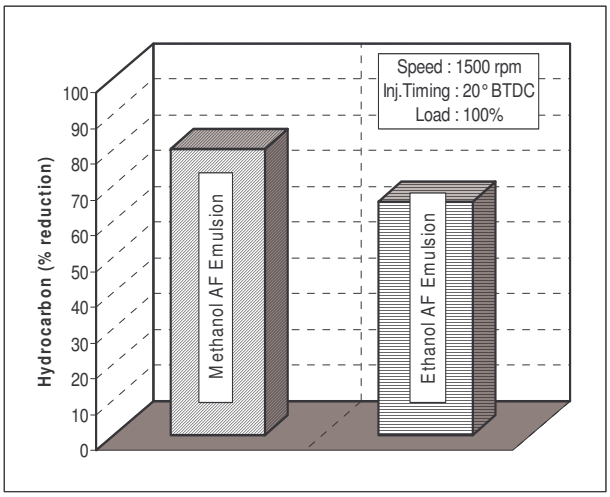

Figure 5b : Percentage reduction of hydrocarbon emission with animal fat emulsification (P =2.8 kW)

Nitric oxide emission is measured at peak power for the different tested fuels. The formation of NO is principally governed by high temperature and availability of oxygen. Neat animal fat yields to lower NO emission than standard diesel (cf. Fig. 6a). As previously noticed, neat animal fat is not well vaporised in the cylinder due to its high viscosity. Thus the resulting cylinder temperature is low. Emulsions further reduce NO emission because their alcohol + water content considerably decrease the flame temperature. Emulsions results are similar (cf. Fig. 6b).

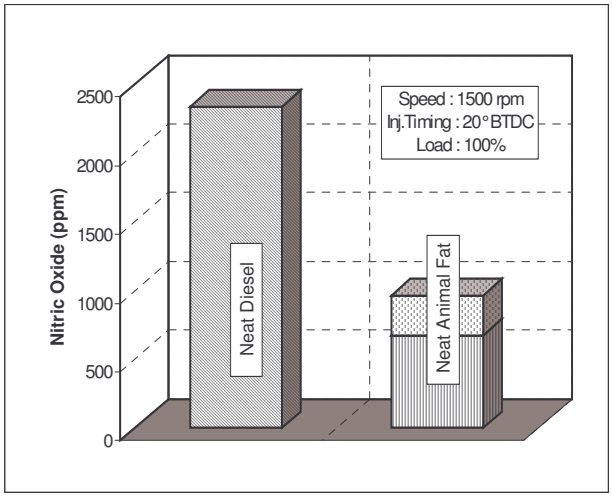

Figure 6a : Nitric oxide emission measured for neat diesel and neat animal fat (P =2.8 kW)

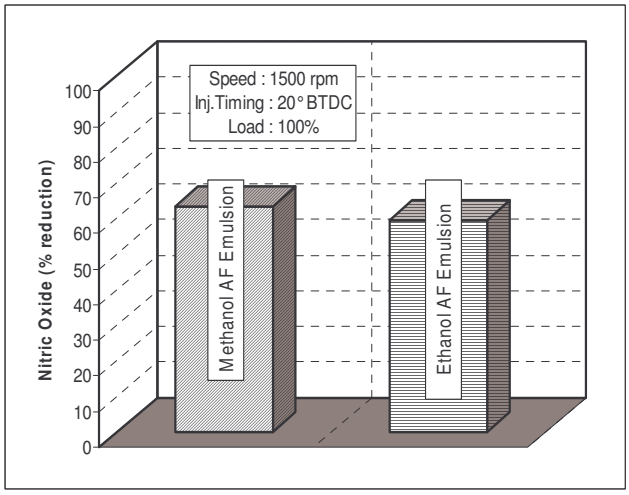

Figure 6b : Percentage reduction of nitric oxide emission with animal fat emulsification (P =2.8 kW)

Figure 7a illustrates the estimations of carbonaceous materials emission at full power output for standard diesel and neat animal fat. Neat animal fat results in lower smoke density than standard diesel. The high oxygen content of animal fat (cf. Tab. 1) permits to improve soot oxidation and to reduce its concentration in the exhaust gas.

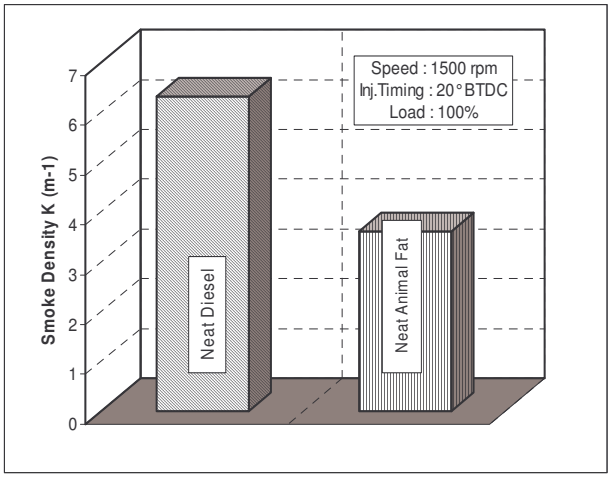

Figure 7a : Smoke density emission measured for neat diesel and neat animal fat(P =2.8 kW)

The emulsification of animal fat further promotes this reduction due to alcohol content which are well known oxidizers (cf. Fig 7b). In addition, the appearance of microexplosion that leads to a second atomisation permits to obtain a better fuel/air mixture. Hence smoke density reaches very low values with animal fat emulsions. The combustion of ethanol animal fat emulsion

produces the minimum soot emission because this emulsion has a higher alcohol content as compared to methanol one.

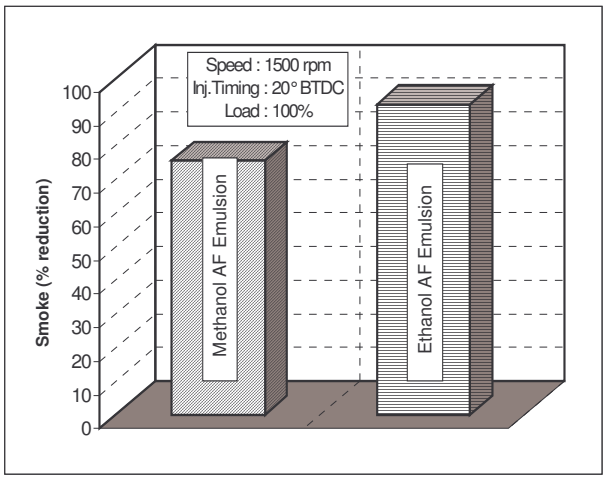

Figure 7b : Percentage reduction of smoke density emission with animal fat emulsification (P =2.8 kW)

Figure 8 shows the reduction percentage as compared to neat fat of pollutants emission at peak power output for animal fat emulsions. Emulsification of animal fat is a very efficient process to drastically reduce pollutants emission.

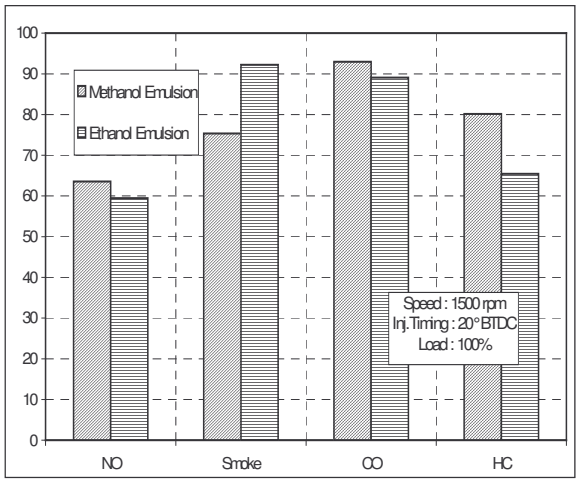

Figure 8 : Effect of the different animal fat emulsions on pollutants emission(P =2.8 kW)

As previously noticed, methanol and ethanol emulsions leads to similar results. Pollutants emission are reduced to more than 50 % and the reduction can reach 90 % for smoke or CO emission.

CONCLUSIONS

The use of animal fat in a compression ignition engine was achieved in this study. Neat animal fat and its emulsification with water via methanol and ethanol addition were tested. Performances and exhaust emission was analysed for this three different fuels and for standard diesel. From this experimental investigation several conclusions can be done :

- Engine performance by observing SEC and Exhaust gas temperature is lower with neat animal fat and its emulsions as compared to neat diesel. However, animal fat emulsions improve the performance as compared to neat fat. Ethanol animal fat results in best performance.
- Animal fat as a fuel yields to high emissions of hydrocarbons and carbon monoxides because of its high viscosity. Thus the fuel/air mixing is not well done. Nevertheless animal fat emulsions drastically reduce these emissions.
- Nitric oxide emission with animal fat is considerably decreased as compared to standard diesel. This phenomenon is amplified by its emulsification with methanol and ethanol which lead to closed values.
- Combustion of neat animal fat results in a decreased of smoke density as compared to standard diesel. In case of animal fat emulsions this emission is further reduced.

On the whole the percentage reduction of pollutant emission with animal fat emulsions are similar with the two alcohol added at peak load. This study can be extend by a partial load comparison.

REFERENCES

[1] Ludwig Elsbett, Glaxnter Elsbett, Klaus Elsbett and Michael Behrens, **"***Alternative Fuels on a Small High Speed Turbocharged D.I. Diesel Engine***"**. Society of Automotive Engineers, SAE 830556, 1983.

[2] Klaus Elsbett, Ludwig Elsbett, Glaxnter Elsbett and Michael Behrens, **"***The Duothermic*

*Combustion for D.I. Diesel Engines***"**, Society of Automotive Engineers, SAE 860310, 1986.

[3] A. Kerihuel, M. Senthil Kumar, J. Bellettre and M. Tazerout. "*Investigations On a CI Engine Using Animal Fat And Its Emulsions with Water and Methanol as Fuel*", Society of Automotive Engineers, SAE 2005-01-1729 (SP–1978), 2005.

[4] John W. Goodrum, Daniel P. Geller, Thomas T. Adams. *"Rheological Characterization of Animal Fats and Their Mixtures with # 2 Fuel Oil",* Biomass and Bioenergy, vol. 24, pp. 249-256, 2003.

[5] M. Senthil Kumar, A. Kerihuel, J. Bellettre and M. Tazerout. *"Investigations on the Use of Preheated Animal Fat as Fuel in a Diesel Engine"*, Renewable Energy, vol 30, 9, 1443-1456, 2005.

[6] A. W. Schwab, M. O. Bagby and B. Freedman. "*Preparationand Properties of Diesel Fuels from Vegetable Oils",* Fuel, vol. 66, pp. 1372-1378, 1987.

[7] Y. Yoshimoto, M. Onodera and H. Tamaki. *"Reduction of NO_x, Smoke and BSFC in a Diesel Engine Fueled by Biodiesel Emulsion with Used Frying Oil",* SAE Paper, No. 99013598, 1998.

[8] R. J. Crookes, Fariborz Kiannejad and M. A. A. Nazha. *"Systematic Assessment of Combustion Characteristics of Bio Fuels and Emulsions with Water for Use as Diesel Engine Fuels",* Energy Conversion and Management, Vol. 38, pp. 1785-1795, 1997.

[9] C. H. Wang, X. Q. Liu and C. K. Law. *"Combustion and Microexplosion of Freely Falling Multicomponent Droplets"*, Combustion and Flame, Vol. 56, pp. 175-197, 1984.

[10] K. C. Tsao and C. L. Wang. *"Puffing and Micro-Explosion Phenomena of Water Emulsion Fuels",* SAE Paper, No. 860304, 1986.

[11] A. Kerihuel, M. Senthil Kumar, J. Bellettre and M. Tazerout. "*Experimental study on the Use of Animal Fat as a CI Engine Fuel by transforming into* its Emulsion with Water and Ethanol", International Congress in the Renewable Energy and the Environment, 2005, TUNISIA.

[12] M. Senthil Kumar, A. Kerihuel, J. Bellettre and M. Tazerout. *"Effect of Water and Methanol Fractions on the Performance of a CI Engine Using Animal Fat Emulsions as Fuel"*, Journal of the Institute of Mechanical Engineers (Accepted), 2005.

[13] J. C. Guibet. *"Carburants et Moteurs"*, Publication of French Petroleum Institute (Paris), Vol. 2, 1987.

[14] A. Kerihuel, M. Senthil Kumar, J. Bellettre and M. Tazerout. *"Use of Animal Fats as CI Engine fuel by Making Stable Emulsions with Water and Methanol"*, Fuel (In press), 2005.

[15] A. Kerihuel, M. Senthil Kumar, J. Bellettre and M. Tazerout. *"Ethanol Animal Fat Emulsions as a Diesel Engine Fuel – part 1 : Formulations and Influential Parameters",* Fuel (Under review), 2005.

[16] M. Senthil Kumar, A. Kerihuel, , J. Bellettre and M. Tazerout." *Ethanol Animal Fat Emulsions as a Diesel Engine Fuel – part 2 :Engine Tests Analysis",* Fuel (Under review), 2005.

[17] W. D. Bancroft. *"The Theory of Emulsification"*, Journal of Physical Chemistry, Vol. 5, pp. 501, 1913.

[18] W. C. Griffin. *"Classification of Surface Agents by HLB"*, Journal of The Society of Cosmetic Chemists, Vol. 5, pp. 249-256.

[19] SAE J1667. *"Recommended Practice for Snap Acceleration Smoke Test Procedure for Heavy-Duty Powered Vehicles"*, SAE report 1996-02.

Proceedings of ECOS 2005
Trondheim, Norway
June 20–22, 2005

SIMULATION OF IN-CYLINDER PROCESSES AND EMISSION FORMATION IN INTERNAL COMBUSTION ENGINES

Ugur Kesgin and Aykut Safa*
Yildiz Technical University
Department of Naval Architecture
TR 34 349 Besiktas – ISTANBUL

ABSTRACT

In order to obtain the effects of design and operational parameters on the engine performance and exhaust gas emissions, i.e. NO_x and HC, in-cylinder processes are modeled and evaluated using one-, two- and three zone combustion models for the high pressure part of the engine process and filling and emptying model for the gas exchange part of the engine process. The results are evaluated and compared to the experimental data of a gas engine operating on natural gas displays agreement. The effects of charge pressure and temperature, excess air ratio, start of combustion, combustion duration and form of combustion on the engine performance and on the emissions are investigated and optimum fields of the engine operation regarding engine efficiency and emissions are investigated.

Keywords: Emission formation mechanisms, in-cylinder combustion models, engine parameters.

NOMENCLATURE

h enthalpy
m mass of the cylinder charge, mass
p pressure
Q heat transfer between gas and cylinder wall
R gas constant
T temperature
u internal energy
V cylinder volume
v specific volume
W piston work
x mass-burned fraction
θ crank angle
ω angular velocity of the crankshaft
α heat transfer coefficient
λ excess air ratio

Indices

b burned
c crevice
e exhaust
f fuel
i inlet
u unburned
w wall

Corresponding Author: Phone: +90 212 259 70 70,
Fax: +90 212 236 41 65, E-mail: safa@yildiz.edu.tr

INTRODUCTION

The goal in development of engines is to optimize engine performance within the reduced emission levels. Studies on NO and HC formation mechanisms for internal combustion engines using one-, two-, and three- zone models are widely available in the literature [1-12]. NO_x emissions are composed of NO and NO_2 emissions. In cylinder NO_x emissions are, in particular, NO gases. Atmospheric nitrogen is the main NO emission source. The other sources of NO emission are oxidation of molecular nitrogen and behind the flame front, NO formation in the flame front and oxidation of fuel bound nitrogen. HC emission formation processes in SI engines are: quenching of flame on the cylinder wall, crevice based HC emission formation, absorbed HCs by oil layer on the cylinder wall and lean combustion [13]. In this study, in cylinder processes are modeled and engine performance is analyzed, considering emissions released.

IN-CYLINDER PROCESS MODELING

In cylinder processes are modeled using zero dimensional process models in a computer program. In cylinder combustion models, one-, two- and three zone models are explained in Figure 1. The assumptions and the main equations of these models and the differences of the models can be seen from this Figure. The main difference between one-zone and multi-zone model is that the multi-zone models require dividing the combustion chamber in unburned and burned zones. In two zone model, combustion chamber consists of burned and unburned zones. In three zone model, the combustion chamber is divided into two zones, namely, burned and unburned zones, and an additional crevice volume. The crevice volume surrounded by cylinder liner, piston and piston ring is considered as the third zone, all the crevices are modeled as a single crevice with a volume equal to the total crevice volume. In three-zone model temperature of gas leaving crevice volume is equal to the liner temperature.

The heat is transferred through surfaces of the piston, cylinder head and cylinder liner. For the heat transfer areas of the unburned and burned zones some empirical relationships considering mass-burned fraction can be used [15]. By using this acceptation the heat transfer from the unburned and burned zones can be represented as follows:

$$\frac{dQ_u}{d\theta} = (1 - x^{1/2}) \sum_{i=1}^{3} A_i \alpha_u (T_u - T_{w_i})$$

$$\frac{dQ_b}{d\theta} = x^{1/2} \sum_{i=1}^{3} A_i \alpha_b (T_b - T_{w_i})$$

i=1 piston, *i=2* cylinder head, *i=3* cylinder liner

Detailed information about the two zone combustion model can be found in Pischinger [14] and Ferguson [15]. The combustion is modelled by using a VIBE function, which is defined by the start of combustion, the combustion duration, a shape parameter m, also called the form factor [14].

CALCULATION of NO_x and HC EMISSIONS

For the calculation of the NO_x and HC formation in internal combustion engines a computational program was developed. The NO_x model is based on a reaction-kinetic model developed by Pattas and Haefner [16] and calculates the NO_x formation with the input of engine speed and fuel data as well as the following: zero dimensionally determined pressure, temperature, air excess ratio, volume and mass depending on time in the burned zone. The latter is necessary because the theory for NO_x formation is based on the dissociation of N_2 and O_2 molecules following the high temperature of the gas in the front of flame. The reactions used for the calculation of the NO_x formation are represented in Table 1 [16]. The calculation of the NO_x formation is begun at the combustion start. In this reaction kinetic model the chemical equilibrium of 19 different concentrations is used, which are calculated with the help of a program developed at the Institute for Internal Combustion Engines and Thermodynamics of Technical University of Graz [56]. These concentrations are: CO_2, O_2, H_2O, N_2, Ar, CO, CH_4, C, O, O_3, OH, H, H_2, N, NO, NO_2, NH_3, HNO_3, HCN. During the calculation it was also necessary to calculate the concentration of N_2O. This is computed with the help of the statically averaged equilibrium constants, as partial pressure relation, obtained as follows [16].

$$\frac{N_2O}{N_2\sqrt{O_2}} = 1.1802.10^{-6}.T_1^{0.6125}.\exp\left[\frac{-18.71}{R.T}\right]$$

Table 1: Reactions for NO_x formation

$$N_2 + O \leftrightarrow NO + N$$
$$O_2 + N \leftrightarrow NO + O$$
$$OH + N \leftrightarrow NO + H$$
$$N_2O + O \leftrightarrow NO + NO$$
$$O_2 + N_2 \leftrightarrow N_2O + O$$
$$OH + N_2 \leftrightarrow N_2O + H$$

The HC formation mechanism for hydrocarbon fuels is so complex that it is usually not feasible to consider all the chemically reacting species and their reaction rates when analysing practical combustion systems. To simplify the chemistry it is useful to use a global reaction scheme. Therefore, to calculate the HC formation a post-flame oxidation with a one-step global reaction in cylinder is used. The Arrhenius equation for methane is taken from Borman and Ragland [17].

$$\frac{d[CH_4]}{dt} = -8.3 \cdot 10^5 \exp\left(\frac{-15098}{T}\right)[CH_4]^{-0.3}[O_2]^{1.3}$$

Post-flame oxidation in the cylinder is assumed to occur in a boundary layer near the cylinder wall, where the temperature is equal to the average of

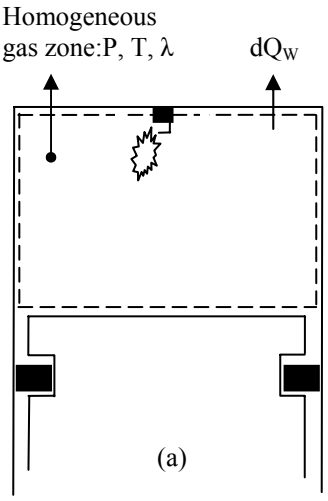

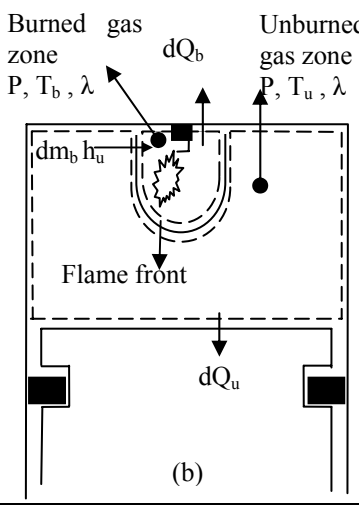

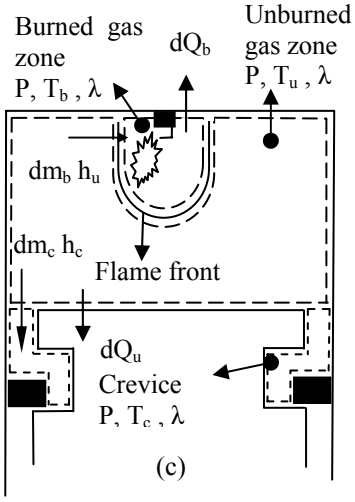

ASSUMPTIONS

1) The pressure in the combustion chamber is uniform at any instant of time.
2) Blow-by does not occur.
3) The mixture of residual gas, fuel and air is perfect.

EQUATIONS

Mass balance:

$$\frac{dm}{d\theta}=\frac{dm_i}{d\theta}+\frac{dm_f}{d\theta}-\frac{dm_e}{d\theta}$$

Energy equation:

$$\frac{d(mu)}{d\theta}=-p\frac{dV}{d\theta}+\frac{dQ_f}{d\theta}-\sum\frac{dQ_W}{d\theta}+\sum\frac{dm_i}{d\theta}h_i-\sum\frac{dm_e}{d\theta}h_e$$

$\frac{d(mu)}{d\theta}$ change of the internal energy in the cylinder

$-p\frac{dV}{d\theta}$ piston work

$\frac{dQ_f}{d\theta}$ fuel heat input

$\sum\frac{dQ_W}{d\theta}$ wall heat losses,

$\sum\frac{dm_i}{d\theta}h_i$ energy input into the cylinder through inlet valve,

$\sum\frac{dm_e}{d\theta}h_e$ energy output from the cylinder through exhaust valve

ASSUMPTIONS

Assumptions 1-3 from one-zone model:
4) No heat transfer between zones.
5) The flame front between the burned and the unburned zones is very thin.
6) Each zone is assumed to be in thermodynamically and chemically equilibrium.
7) For the compression the cylinder contents occupy only the unburned zone. The burned zone forms after combustion starts.

EQUATIONS

Total mass in cylinder:

$$m=m_u+m_b$$

$$\frac{dm_u}{d\theta}+\frac{dm_b}{d\theta}=0$$

Energy equation

$$m\frac{du}{d\theta}+u\frac{dm}{d\theta}=-p\frac{dV}{d\theta}+\frac{dQ_f}{d\theta}-\frac{dQ_W}{d\theta}+\sum\frac{dm_i}{d\theta}h_i-\sum\frac{dm_e}{d\theta}h_e$$

$p\frac{dV}{d\theta}$ = the piston work = W

Cylinder volume

$$V=V_u+V_b$$

V=f (Cylinder geometry, crank angle)

Energy of the cylinder content

$$u=\frac{U}{m}=xu_b+(1-x)u_u$$

Specific volume of the system

$$v=\frac{V}{m}=xv_b+(1-x)v_u$$

ASSUMPTIONS

Assumptions 1-6 from two-zone model:
4) The crevices in the combustion chamber are modelled as one crevice, which's volume is equal to the total volume of all crevices.
5) The temperature of the gas discharged from the crevices is the same as the cylinder liner temperature.
6) For the compression the cylinder contents occupy two zones, namely unburned zone and crevice zone, and each zone is spatially homogenous. The burned zone exists first after combustion start.

EQUATIONS

Total mass in cylinder:

$$m=m_u+m_b+m_c$$

$$\frac{dm_u}{d\theta}+\frac{dm_b}{d\theta}+\frac{dm_c}{d\theta}=0$$

The mass in the crevice volume:

$$m_c=\frac{pV_c}{RT_c},\quad \frac{dm_c}{d\theta}=\frac{V_c}{RT_c}\frac{dp}{d\theta}$$

The differentiation of the mass in the unburned zone:

$$\frac{dm_u}{d\theta}=-m_b\frac{dx}{d\theta}-\frac{V_c}{RT_c}\frac{dp}{d\theta}$$

Energy equation:

$$m\frac{du}{d\theta}+u\frac{dm}{d\theta}=-p\frac{dV}{d\theta}+\frac{dQ_f}{d\theta}-\frac{dQ_W}{d\theta}-h_c\frac{dm_c}{d\theta}+\sum\frac{dm_i}{d\theta}h_i-\sum\frac{dm_e}{d\theta}h_e$$

The enthalpy of the mass transferred between the cylinder and the crevice volume:

$$h_c=h_c(p,T_c),\quad \frac{dm_c}{d\theta}<0$$

$$h_c=h_u(p,T_u),\quad \frac{dm_c}{d\theta}>0$$

Figure 1: (a) One-, (b) two- and (c) three-zone models.

the wall and burned gas temperature in cylinder. This assumption is used also by Dent and Lakshminarayanan [18] and Schramm and Sorenson [19].

MODEL VERIFICATION

By adapting the calculation of combustion models to different engine operating conditions, the three-zone model presented here allows the prediction of the change in NO emission as well as HC emissions depending on engine load, engine speed, charge air pressure, charge air temperature, humidity of the combustion air, fuel type, combustion characteristics (start, duration and form of combustion). In the Figures 2 and 3, data measured on the test engine and computed values are shown. Test engine is a turbocharged lean burn gas engine working on natural gas. Its specifications are stroke/bore ratio of 220/190 mm/mm, engine speed of 1500 rpm, excess air ratio of over 1.7 and compression ratio of 11. The pressure data, measured and computed, shows a remarkably well agreement (Figure 2a). The changes in mass of three zones during combustion period can be seen in Figure 2b. Before the combustion starts, burned zone has not evolved, but unburned zone and crevice volume exist. With the start of combustion, burned gas region develops. As the combustion starts, burned gases prevail in the cylinder. However, the change in crevice volume mass is very small. Since the zones are fictitious, mass data are computed. Under eight different conditions of excess air ratio, charge pressure, ignition timing for the test engine, measured and calculated emissions data are shown in Figure 3. The results show a good proximity.

EFFECT OF ENGINE DESIGN AND OPERATION PARAMETERS ON ENGINE EFFICIENCY AND EMISSIONS

One of the primary optimisation targets in engine development is maximisation of the efficiency while, at the same time, producing minimum NO_x and HC emissions. The effects of combustion-start and duration, excess air ratio, charge temperature, charge pressure and crevice volume were investigated by using the three-zone combustion model described above. The results of these investigations are summarised in Table 2.

Effect of Combustion- Start and Duration

In order to execute parametric studies and to examine basic relations, application of the zero dimensional process calculation is particularly helpful and efficient. Thus, under the specification of the VIBE form factors derived by using heat release calculated from the three dimensional combustion model, variation calculations were also executed for different combustion starts and combustion durations. The results are represented via isolines for constant indicated efficiency and for constant emissions (Figure 4). From these results, basic information about the efficiency and emissions of the respective concepts can be determined immediately.

Table 2: Effect of excess air ratio, charge temperature and pressure and crevice volume

Engine Parameter	Change in the Parameter	Change in		
		Efficiency [%]	NO_x [%]	HC [%]
Excess Air Ratio	+ 0.1	+ 0.3	- 55	- 0.5
Charge Temperature	- 10 K	+ 0.6	- 14	- 1
Charge Pressure	+ 0.1 bar	+ 0.08	1	0
Crevice Volume	- % 50	+ 0.05	+ (5-8)	- 47 %

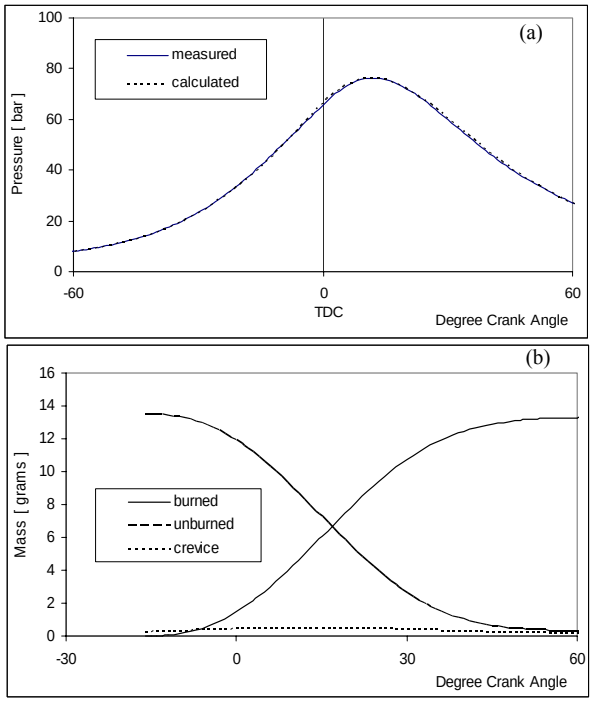

Figure 2: Comparison of computed and measured in cylinder pressure data (a) and of computed burned, unburned and crevice mass data (b) on crank angle basis.

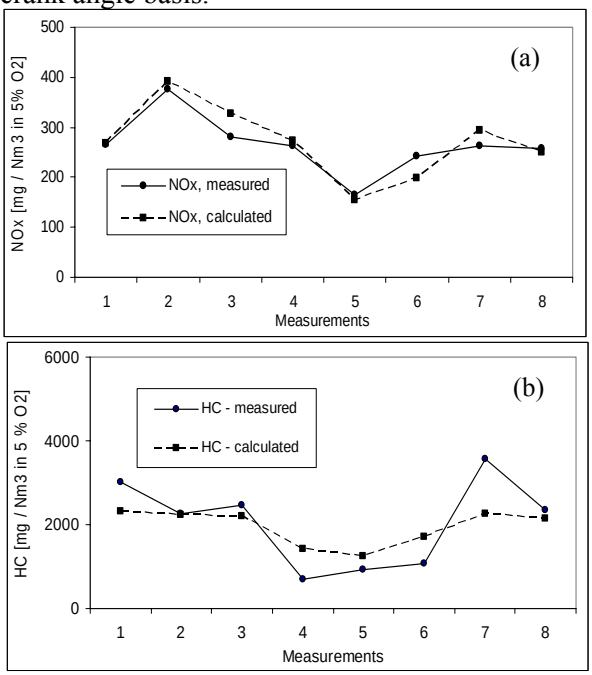

Figure 3: A Comparison of emissions from calculation and measurement
(a) NO_x emission, (b) HC emission

Spark timing significantly affects NO and HC emissions levels. Advancing the timing so that combustion occurs earlier in the cycle increases the peak cylinder pressure (because more fuel is burned before top dead centre (TDC) and the peak pressure moves closer to TDC where cylinder volume is smaller), while retarding the timing decreases the peak cylinder pressure (because more of the fuel burns after TDC). Higher peak cylinder pressures result in higher peak burned gas temperatures and, hence, higher NO formation rates. For lower peak cylinder pressures, lower NO formation results [20]. Naturally, the highest efficiency occurs at the maximum brake torque, hence retarding the timing moves away from this point and increases the specific fuel consumption. [17].

The same effects mentioned above for combustion start on the rate of NO_x emissions and on the engine efficiency for these engine concepts can be determined from Fig. 4a. As it can be seen from these Figures, the longer combustion durations result in a lower amount of NO_x emissions. Also as it can be seen from Fig. 4b, the same effect of combustion- start and duration on HC emission occurs as it is on NO_x emission.

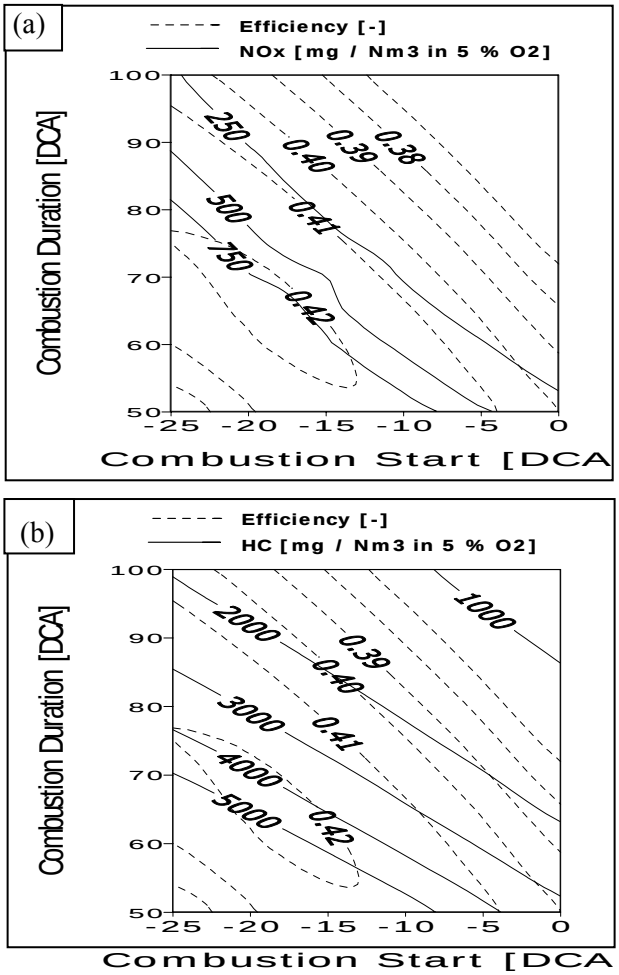

Figure 4: (a) Efficiency – NO_x Trade-Off,
(b)Efficiency –HC Trade-Off

Effect of Excess Air Ratio

The effect of excess air ratio and also leaner operation of the base engine, on emissions is shown in Fig. 5. The excess air ratio was varied from 1.5 to 2. Reduction of the fuel–air ratio to leaner and leaner conditions reduces CO and HC emissions as long as the flame speed and ignitability do not become a problem. Lean operation needs extra air. This results in greater cooling of the cylinder charge. Lower flame temperatures are produced during the cylinder processes, which reduce the NO formation. Not only are emissions reduced, but also fuel economy is improved by lean operation. However, lower flame speed creates drivability problems and, in the limit, partial burning of the charge. The partial burning takes place because the slow moving

flame burns during the rapid expansion stroke of the piston, which causes a lowering of the temperature to a point where the flame will no longer propagate. A second effect of lean operation is to lower the exhaust gas temperature, which is very important for the efficiency of the catalyst, if it exists [17].

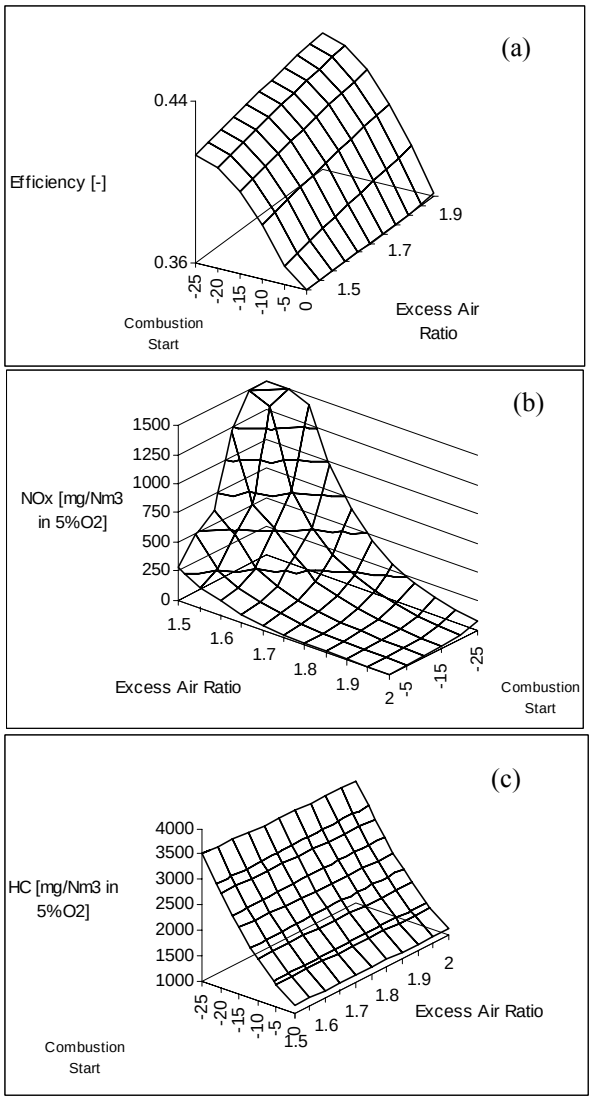

Figure 5: Effect of excess air ratio and combustion start on (a) Efficiency (b) NO_x (c) HC Emissions

Effect of Charge Temperature

The NO_x and HC emission production is very sensitive to the temperature of the charge. In order to clarify the effect of charge temperature on emissions, the temperature at the time of inlet valve closing was varied from 320 to 370 K, which is in the temperature range for stationary natural gas engines. Fig. 6 shows the effect of charge temperature on the engine efficiency and NO_x and HC formation for various excess air ratios. Because the reactions are slow, the amount of NO and HC produced is controlled by the rate of reaction. Thus, lower temperatures, which greatly reduce the reaction rate, lower the amount of NO produced before expansion lowers the temperature to about 800 K, where the reactions freeze [17].

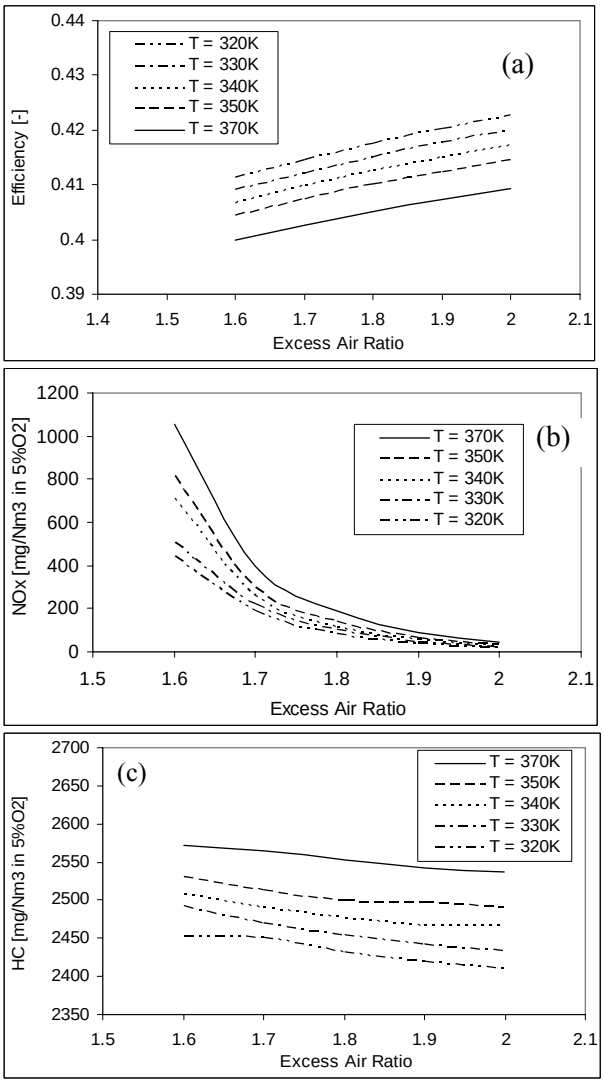

Figure 6: Effect of excess air ratio and charge temperature on (a) Efficiency (b) NO_x (c) HC Emissions

Effect of Crevice Volume

Many studies are being made about the influence of the crevice volume on HC emissions [21-23]. Reducing the crevice volume has a significant effect on the amount of HC returning to the combustion chamber [24]. Their investigations showed also that the crevice gas flow represents a significant power and efficiency loss. Depending

on the degree and rate of in-cylinder oxidation, and design and operating details, these losses are at least 2 to 7 percent.
In order to obtain the effect of crevice volume on the engine performance and emissions for the natural gas engine optimised here, the crevice volume is varied from 4.5 cm^3 to 22.5 cm^3.

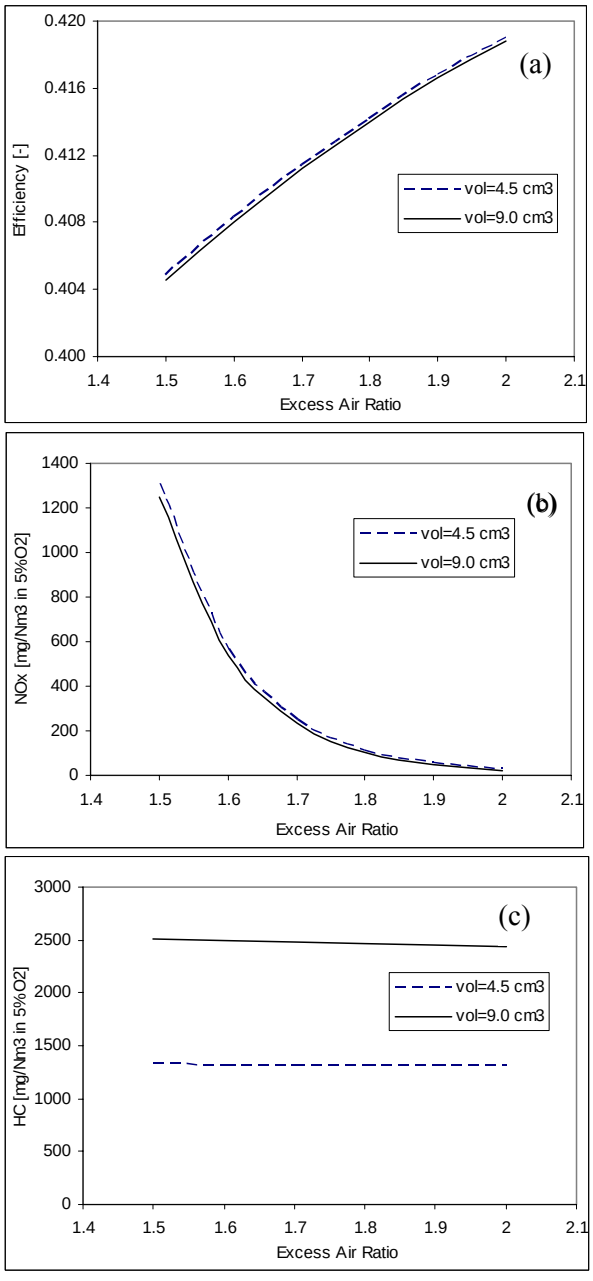

Figure 7: Effect of crevice volume on (a) Efficiency (b) NO_x (c) HC Emissions

As it can be seen from Figure 7 the engine efficiency and emissions decrease with decreasing of the crevice volume. The engine efficiency and NO_x emission increase with decreasing of the crevice volume. A reduction in crevice volume of 50% results in HC emissions of 48% because less unburned fuel-air mixture is stored within crevice volume during compression stroke and in the early stage of combustion. These results are comparable to that previous investigations mentioned above.

CONCLUSIONS

A computer program to calculate the engine process and the amount of NO_x and HC emissions based on a reaction kinetic model was developed. The model uses six reactions for NO_x formation and a global reaction scheme for HC formation. To do this totally 19 species are utilised. It calculates the NO_x and HC emissions with the input of engine speed and fuel data as well as the following data: zero dimensionally determined pressure, temperature, excess air ratio, volume and mass depending on time in the burned zone, resulting from a two zone engine cycle simulation program.

The validity of the program presented here was verified by measurements from a turbocharged, leanburn, natural gas engine. The results are represented via isolines for constant indicated engine efficiency and for constant emissions. From this, basic information about the efficiency and emissions of the respective concepts can be readily determined. Further, the effects of engine parameters were investigated. The results show a wide improvement potential from an emission point of view and are very useful for developing new engines, which must fulfil stricter emission limitations.
The following important conclusions can be drawn from the results of this study:
• The characteristics of the combustion have great influence on NO formation. The combustion- start and duration highly affect the level of NO and HC emissions. The natural gas engines investigated here produce very little NO emissions with a combustion start after TDC, but operating the engines with a combustion start after TDC is not realistic from an efficiency point of view.
• As expected, an increase in the excess air ratio causes a significant decrease in NO emissions.
• The effect of the pressure and temperature of the cylinder charge shows a wide potential from an emission point of view. Especially charge temperature highly affects the level of NO emissions, as expected. By reducing the charge temperature, the amount of emissions can be

decreased to a level sufficient to meet standards determined by international, national or other societies.

• The volume of crevices has a significant effect on the engine efficiency and emissions. A smaller crevice volume results in a decrease of HC emissions and an increase of the engine efficiency as well as NO_x emissions.

REFERENCES

[1] Guazennec YG and Hamama W, *Two-zone heat release analysis of combustion data and calibration of heat transfer correlation in an IC Engine*, SAE Paper 1999-01-0218, 1999.

[2] Eyzat P and Guibet JC, *A new look at nitrogen oxides formation in internal combustion engines*, SAE Paper, 680124, 1968.

[3] Heider G, Woschni G, Zeilinger K, *Two-zone calculation model for the prediction of NO emissions from DI Diesel engines (in German)*, Motortech Zeits 1998; 59:770–5.

[4] Mansour C, Bounif A, Aris A, Gaillard F, *Gas–Diesel (dual-fuel) modelling in Diesel engine environment*, Int J Therm Sci 2001;40:409–24.

[5] Merker GP, Hohlbaum B, Rauscher M, *Two-zone model for calculation of nitrogen-oxide formulation in direct injection Diesel engines*, SAE Paper 982454, 1998.

[6] Miller R, Davis G, Lavoie G, Newman C, Gardner T, *A super-extended Zel'dovich mechanism for NO_x modelling and engine calibration*, SAE Paper 980781, 1998.

[7] Weisser G and Boulouchos K, *NOEMI–A tool for the pre-calculation of nitric oxide emissions of DI Diesel engines*, 5 Tagung: der Arbeitsprozess des Verbrennungsmotors. Austria: TU Graz; Austria: Graz; 1995. p. 23–50.

[8] Dodge LG et. al., *Modeling NO_x Emissions from Lean-Burn Natural Gas Engines*, SAE Paper 981389, 1998.

[9] Caton JA, *Effects of Burn Rate Parameters on Nitric Oxide Emissions for a Spark Ignition Engine: Results from a Three-Zone, Thermodynamic Simulation*, SAE Paper 2003-01-0720, 2003.

[10] Alkidas AC, *Combustion-chamber crevices: the major source of engine-out hydrocarbon emissions under fully warmed conditions*, Progress in Energy and Combustion Science 25, 253-273, 1999.

[11] Bazari, Z., *Diesel Exhaust Emission Prediction under Transient Operating Conditions*, SAE paper 940666, 1994, pp. 29-43.

[12] Kesgin, U., *Study on prediction of the effects of design and operating parameters on NO_x emissions from a lean burn natural gas engine*, Energy Conversion and Management 44 (2003) 907–921.

[13] Heywood, J. B., *Internal Combustion Engine Fundamentals*, McGraw-Hill Inc., 1988.

[14] Pischinger R. et al. *Thermodynamik der Verbrennungskraftmaschine*. Berlin: Springer; 1989

[15] Ferguson, C. R., *Internal Combustion Engines*, John Wiley & Sons Inc., 1986.

[16] Pattas, K, Haefner, G., *Stickoxidbildung bei der ottomotorischen Verbrennung*, MTZ 1973, 34(12): 397–404.

[17] Borman G, Ragland KW. *Combustion engineering*. New York: McGraw Hill; 1998.

[18] Dent JC and Lakshminarayanan PA, *A Model for Absorption and Desorption of Fuel Vapor by Cylinder Lubricating Oil Film and its Contribution to Hydrocarbon Emissions*, SAE Paper 830652, 1983

[19] Jensen TK and Schramm J, *A Three-Zone Heat Release Model for Combustion Analysis in a Natural Gas SI Engine. Effects of Crevices and Cyclic Variations on UHC Emissions*, SAE Paper 2000-01-2802, 2000

[20] Silva LLC and Nigro FEB, *Modelling of Hydrocarbons Formation and Emission in Gas Engines*, SAE Paper 2000-01-2038, 2000

[21] Lavoie GA, Larusso JA and Adamczyk AA, *Hydrocarbon emission modelling for Spark Ignition Engines*, Combustion Modelling in Reciprocating Engines, 409-445, 1980

[22] Alkidas AC, *Combustion-chamber crevices: the major source of engine-out hydrocarbon emissions under fully warmed conditions*, Progress in Energy and Combustion Science 25, 253-273, 1999

[23] Cheng WK et al., *An Overview of Hydrocarbon Emissions Mechanisms in Spark-Ignition Engines*, SAE Paper 932708, 1993

[24] Namazian M and Heywood JB, *Flow in the Piston-Cylinder-Ring Crevices of a Spark-Ignition Engine: Effect on Hydrocarbon Emissions, Efficiency and Power*, SAE Paper 820088, 1982.

Proceedings of ECOS 2005
Trondheim, Norway
June 20–22, 2005

NUMERICAL PREDICTION OF THE THERMO-HYDRAULIC PERFORMANCE OF SECONDARY SURFACES FOR COMPACT HEAT EXCHANGERS

M. Picón Núñez[1]
Institute for Scientific Research
Cerro de la Venada S/N, Marfil, Gto.
University of Guanajuato, Mexico.

I. D. López Pérez and A. Gallegos Muñoz
Department of Mechanical Engineering
Av. Tampico 912, Salamanca, Gto.
University of Guanajuato, Mexico.

ABSTRACT

This work presents a numerical analysis of the thermo-hydraulic performance of secondary surfaces for compact heat exchangers of the plate and fin type. The study resulted in the determination of the film heat transfer coefficient and its variation with the distance from the exchanger inlet. The numerical results obtained provide a thorough description of the performance of the flow inside the exchanger and the heat transfer coefficient shows a similar behaviour compared with analytical models.

Keywords: compact heat exchangers, heat transfer coefficient, CFD

NOMENCLATURE

A	Total heat transfer surface area (m^2)
a	Coefficient in heat transfer correlation
b	Exponent in heat transfer correlation
Cp	Heat capacity (J/Kg°C)
d_h	Hydraulic diameter (m)
F	Log mean temperature difference correction factor
f	Friction factor
Gz	Graetz number
h	Heat transfer coefficient ($W/m^2°C$)
I	turbulence intensity
j	Colburn factor
K_h	Constant in heat transfer coefficient equation (thermo-hydraulic model)
K_p	Constant in pressure drop equation (thermo-hydraulic model)
l	Length (m)
m	Mass flow rate (kg/s)
Nu	Nusselt number
P	Pressure (Pa)
Pr	Prandtl number
ΔP	Pressure drop (Pa)
Q	Heat duty (W)
q	Heat flux (W)
R	Fouling resistance ($m^2°C/W$)
St	Stanton number
T	Temperature
ΔT_{LM}	Log mean temperature difference
Re	Reynolds number
U	Overall heat transfer coefficient ($W/m^2°C$)

[1] Corresponding author: phone +45 473 7327 555 Fax: +45 473 7326 252
E-mail: picon@quijote.ugto.mx

V_T Total exchanger volume (m^3)
v Velocity (m/s)
x Coefficient in friction factor correlation
y Exponent in friction factor correlation

Greek letters

α Ratio of total surface area of one side of the exchanger to the total exchanger volume (m^2/m^3)
η Fin efficiency
κ Fin thermal conductivity (W/m°C)
μ Viscosity (kg/ms)
ρ Density (kg/m3)

Subscripts

T Total
1 Side 1 of heat exchanger
2 Side 2 of heat exchanger
i Transition
lam Laminar flow
turb Turbulent flow
Ref Reference
W Wall

INTRODUCTION

A fundamental aspect in the design of compact heat exchangers of the plate and fin type is the prediction of the heat transfer coefficients and friction factor as a function of the Reynolds number. This information is available as experimental data for a number of surfaces or fins in Kays and London [1]. A number of researchers have used this information in the form of fitted potential expressions as a function of the Reynolds number and the resulting equations have been extensively used to develop design methodologies for this type of exchangers [2-6].

The data presented by Kays and London [1], assumes average values on the axial direction of the exchanger, this means that the heat transfer coefficient is not a function of the distance along the length of the unit in the flow direction. In a recent work, Polley and Abu-Khader [7], have developed a generalised model to predict the variation of the heat transfer coefficient as a function of the fluid velocity and the distance for rectangular plain fin surfaces. These findings lead us to conclude that current sizing methods must be modified to account for the variation of the heat transfer coefficient with the distance.

One way of predicting the thermo-hydraulic performance of secondary surfaces is through the simultaneous solution of the fundamental equations of mass, momentum and energy between two fluids separated by a solid surface. This system of equations can be solved using CFD software (Computational Fluid Dynamics). In this work, Fluent ® is used to determine the thermo-hydraulic performance of two plain fin surfaces. The methodology applied is as follows: 1.- A counter-current plate fin heat exchanger is designed using the approach presented by Picon et al. [6]; 2.- The heat transfer coefficient is determined using the generalised expressions introduced by Polley and Abu-Khader [7]; 3.- The thermal performance of the heat exchanger is simulated using CFD software and the heat transfer coefficient along the length of the exchanger is determined.

EXCHANGER DESIGN

One way of sizing a plate and fin heat exchanger is through the concept of full pressure drop utilization. This leads to the development of a thermo-hydraulic model that aids in achieving this objective [6]. The model relates the allowable pressure drop with the exchanger volume and the heat transfer coefficient.

The heat transfer performance for a number of compact surfaces can be expressed in terms of the Reynolds number in the following way:

$$j = aRe^{-b} \quad (1)$$

Where the term *j* represents the Colburn factor which is defined as:

$$j = StPr^{2/3} \quad (2)$$

Where *Pr* is the Prandtl number and *St* is the Stanton number.

The equation for the design of heat exchangers,

$$Q = UAF\Delta T_{LM} \quad (3)$$

can be combined with the expression that defines the overall heat transfer coefficient to give:

$$A_1 = \frac{Q}{F\Delta T_{LM}}\left[\frac{1}{\eta_1}\left(\frac{1}{h_1}+R_1\right)+\frac{1}{\eta_2}\left(\frac{A_1}{A_2}\frac{1}{h_2}+R_2\right)\right] \quad (4)$$

The terms A_1 and A_2 are the heat transfer area on sides 1 and 2 respectively. The exchanger volume and the surface area of one side are related through:

$$A_1 = \alpha_1 V_T \quad (5)$$

After substitution of A for sides 1 and 2 and rearranging we obtain:

$$V_T = \frac{Q}{F\Delta T_{LM}}\left[\frac{1}{\eta_1\alpha_1}\left(\frac{1}{h_1}+R_1\right)+\frac{1}{\eta_2\alpha_2}\left(\frac{1}{h_2}+R_2\right)\right] \quad (6)$$

Equation (6) represents the total exchanger volume as a function of the heat load, the heat transfer surfaces y the heat transfer coefficients. In this design method the heat transfer coefficient is assumed to be constant along the length of the exchanger for a given Reynolds number.

The total exchanger volume, heat transfer coefficient and pressure are related by:

$$\Delta P = \left(\frac{K_p}{K_h}\right)^{\frac{3-y}{1-b}} V_T h^2 \quad (7)$$

Where K_p and K_h are respectively:

$$K_p = \frac{xm^{2-y}\mu\alpha}{2\rho d_h^y} \quad (8)$$

and

$$K_h = \frac{am^{1-b}\mu^b C_p}{d_h^b \,\mathrm{Pr}^{2/3}} \quad (9)$$

Equation (7) represents the thermo-hydraulic model that relates the pressure drop with the exchanger volume and the heat transfer coefficient.

ANALYTICAL MODEL

Polley and Abu-Khader [7] present a generalised model to predict the variation of the heat transfer along the length of the exchanger based on the expression proposed by Churchill [8]. The equation for the heat transfer performance is:

$$\mathrm{Nu} = \left(\mathrm{Nu}_{\mathrm{lam}}^{10} + \left(\frac{1}{\mathrm{Nu}_{\mathrm{i}}^2}+\frac{1}{\mathrm{Nu}_{\mathrm{turb}}^2}\right)^{-5}\right)^{0.1} \quad (10)$$

Where the heat transfer for laminar flow under thermally developing conditions as well as fully developed flow can be estimated from [7]:

$$\mathrm{Nu}_{\mathrm{lam}} = \left[3.66^3 + 0.7^3 + \left(1.77\mathrm{Gz}^{1/3} - 0.7\right)^3\right]^{1/3} \quad (11)$$

and the Grazt number is given by

$$\mathrm{Gz} = \mathrm{RePr}\left(\frac{\mathrm{d_h}}{\mathrm{l}}\right) \quad (12)$$

The heat transfer rate for the turbulent region can be expressed by [9]:

$$\mathrm{Nu}_{\mathrm{turb}} = \frac{\left(\frac{\mathrm{f}}{2}\right)\mathrm{RePr}}{\left(1.07+12.7\left(\frac{\mathrm{f}}{2}\right)^{1/2}\left(\mathrm{Pr}^{2/3}-1\right)\right)} \quad (13)$$

In the above equations the tube diameter has been replaced by the surface hydraulic diameter.

Now, the term $\mathrm{Nu_i}$ can be calculated as:

$$\mathrm{Nu_i} = \mathrm{Nu}_{\mathrm{lam,Re_{critical}}}\exp\left(\frac{\mathrm{Re}-\mathrm{Re_{critical}}}{730}\right) \quad (14)$$

In the following case study a plate and fin exchanger is sized and the thermo-hydraulic performance of the geometry is simulated in Fluent®. The numerical performance is compared with the results obtained using the generalised model proposed by Polley and Abu-Khader [7].

CASE STUDY

A plate fin heat exchanger is designed using the following surfaces according to the nomenclature introduced by Kays and London [1]: Plain plate-fin surface 5.3 and Plain plate-fin surface 6.2. The operating conditions and fluid data for the problem are shown in Table 1. Using the design method presented above, the geometry of the exchanger is determined and the results are given in Table 2.

Table 1: Operating conditions and fluid physical properties for case study.

	Plain -fin surface 6.2 Gas side	**Plain -fin surface 5.3 Air side**
Inlet temperature [°C]	430	175
Outlet temperature [°C]	338.5	270.5
Mass flow rate [kg/s]	2.466	2.43
Pressure drop [kPa]	0.672	0.0477
Fin thermal conductivity[W/m°C]	20.8	20.8
Density [kg/m³]	0.58	5.7
Heat capacity [J/kg k]	1040	1050
Viscosity [kg/m s]	0.0000302	0.0000285
Fluid thermal conductivity [W/m °C]	0.047	0.044

Table 2: Geometry of the exchanger.

Exchanger volume	0.137 m^3
Length	0.38 m
Width	0.603 m
Height	0.599 m
No. of passages per stream	26
Air side heat transfer coefficient	94.72 W/m^2 °C
Gas side heat transfer coefficient	80.27 W/m^2 °C
Air side pressure drop	47.77 Pa
Gas side pressure drop	671.96 Pa
Reynolds number on gas side	2,952
Reynolds number on air side	3,024

The numerical study of the flow inside the passages of the exchanger requires the mathematical representation of the movement of the fluid. This representation is summarised by a set of equations of mass, momentum and energy conservation together with the equation that describes the turbulence phenomenon present.
A single passage of the exchanger was used to simulate the whole unit. It is assumed that the heat transfer coefficient varies only in the direction of the flow and that the flow distribution among the passages is uniform. Figure 1 shows the geometry of the passages and Figure 2 the control volume chosen for the simulation.

The whole exchanger length was simulated in sections of 0.05 m each until the total length of 0.38 m was covered.

The turbulent condition was modelled using the standard k-epsilon model. As for the boundary conditions, periodic conditions were chosen on the left and right walls; on the upper and lower planes, symmetrical conditions were chosen. The inlet and outlet conditions for the fluids are given in Table 3.

From the numerical results, the heat transfer coefficient is calculated as:

$$h = \frac{q}{T_{wall} - T_{ref}} \qquad (15)$$

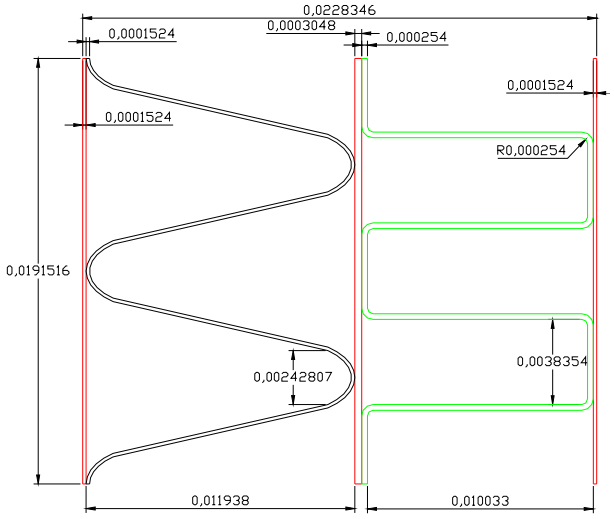

Figure 1: Cross sectional view of the hot and cold passages.

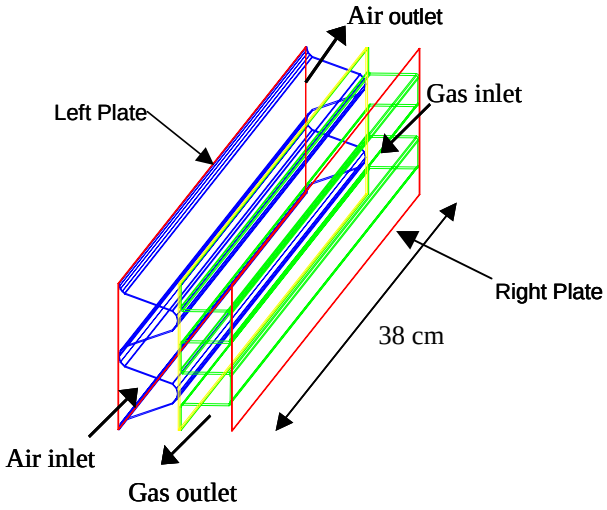

Figure 2: Control volume.

Table 3: Inlet and outlet conditions for hot and cold fluids.

Inlet	Outlet
Air side (Plain-fin surface 5.3)	
d_h = 0.006147 m	d_h = 0.006147 m
I = 6%	I = 6 %
v = 2.2929 m/s	P = 161 Pa
T = 175°C	
Gas side (Plain -fin surface 6.2)	
d_h = 0.00554 m	d_h = 0.00554 m
I = 6%	I = 6 %
v = 26.5384 m/s	P= 1453 Pa
T = 430°C	

Where q is the local heat flux; T_{wall} is the temperature of the wall and T_{ref} is the reference temperature. In this work the reference temperature is calculated in two ways:

1.- Fixed temperature. This can either be a fixed value or an average between the inlet and outlet temperature of the fluid.
2.- Variable temperature. Average fluid temperatures are calculated locally along the exchanger and are considered the reference value. Readings of temperature can be taken as nodal points or average values per cell.

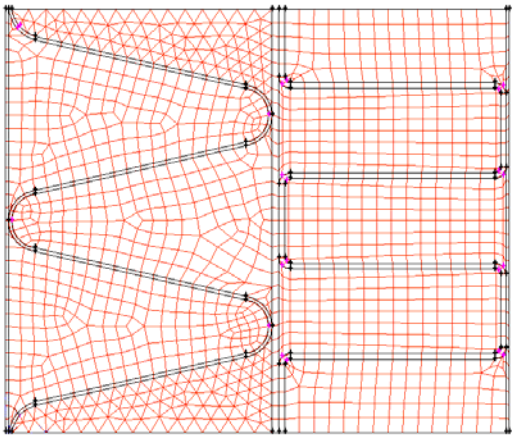

Figure 3: Computational domain.

RESULTS

The computational domain and mesh distribution for the numerical analysis of the exchanger are shown in Figure 3. The mesh size is of 0.7x0.7 mm.

Temperature readings were taken on various points as shown in Figure 4. The points close to the wall are separated 0.0001 m from it. For the inlet and outlet temperatures on the air side, a line was drawn between point a_4 and a_2 whereas for the gas side, a line was drawn between g_2 and g_5.

Figure 5 shows the outlet temperatures on the air side on positions a_1, a_2, a_4 and Figure 7 the outlet temperatures for the gas side on positions g_1, g_2, g_7, g_{10}, g_{11}, g_{12} and g_{19}. The temperatures along the exchanger on the same positions for the air and gas side are shown in Figures 6 and 8 respectively.

The temperatures calculated numerically (Figures 5 and 7) and the temperatures calculated along the exchanger (Figures 6 and 8) are consistent and close to the ones calculated with the analytical model. Similar consistent results are obtained for the case of the pressure drop as shown in Figures 9 and 10.

The average heat transfer coefficient between points a_1, a_2 and a_3 for the air side and between g_1, g_2 and g_3 for the gas side are calculated in three different ways: 1.- using the average fluid temperature as reference value, 2.- using fixed temperature as a reference value and 3.- using a variable reference temperature. The numerical results are compared to the analytical results in Figures 11 and 12 for the gas and air side respectively. Both results are consistent and show the same behaviour: larger heat transfer coefficients are found in the region near the exchanger inlet and tend to asymptotic values as the flow regime develops. The asymptotic value being close to the one predicted with the traditional fully developed flow model which is constant throughout the exchanger.

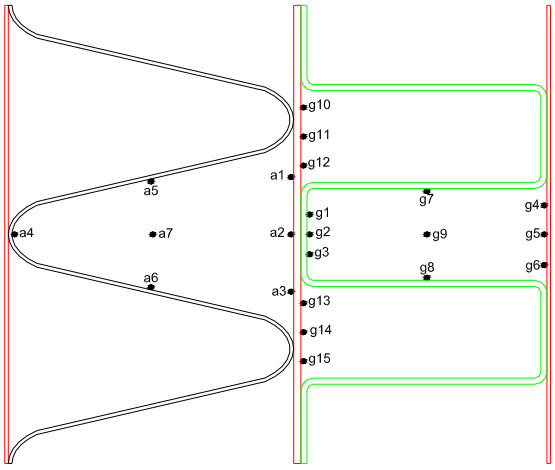

Figure 4: Reading points for local temperature.

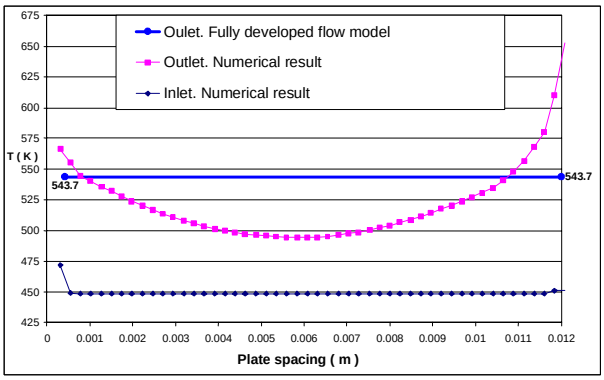

Figure 5: Inlet and outlet temperature on air side across the plate spacing.

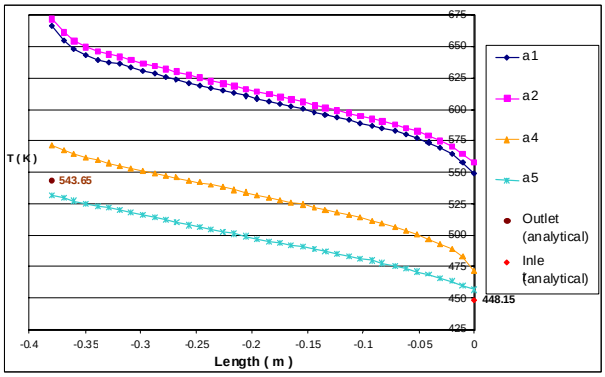

Figure 6: Temperatures along the exchanger on air side.

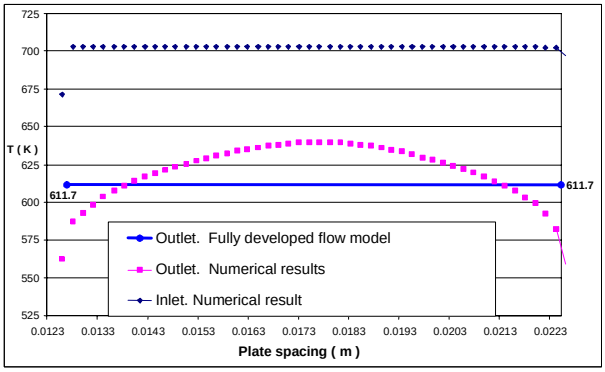

Figure 7: Inlet and outlet temperatures on gas side.

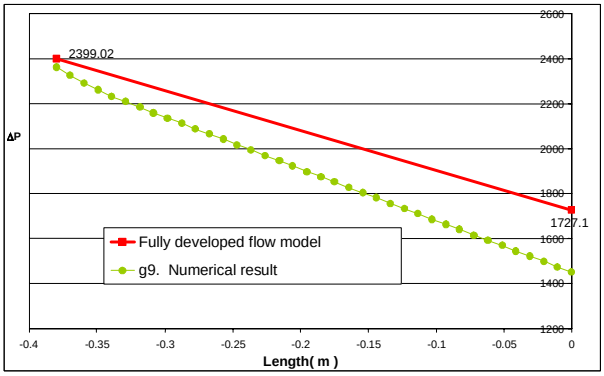

Figure 10: Pressure drop along the exchanger on the gas side.

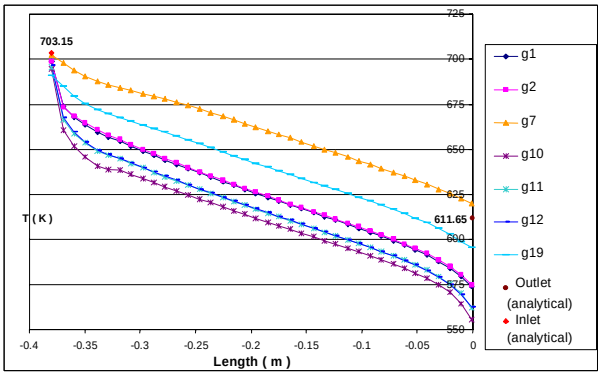

Figure 8: Temperatures along the exchanger on gas side.

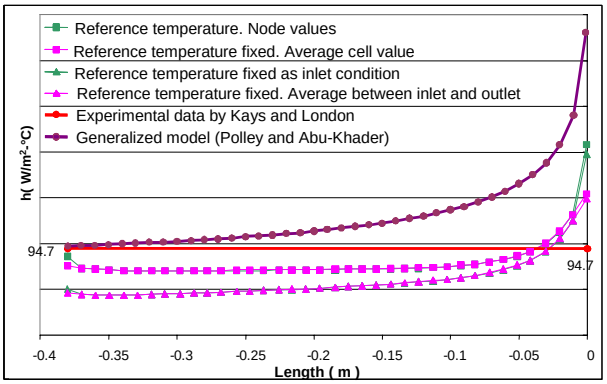

Figure 11: Heat transfer coefficient on air side.

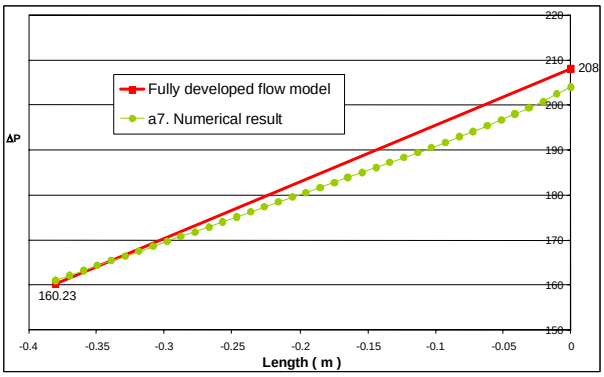

Figure 9: Pressure drop along the exchanger on the air side.

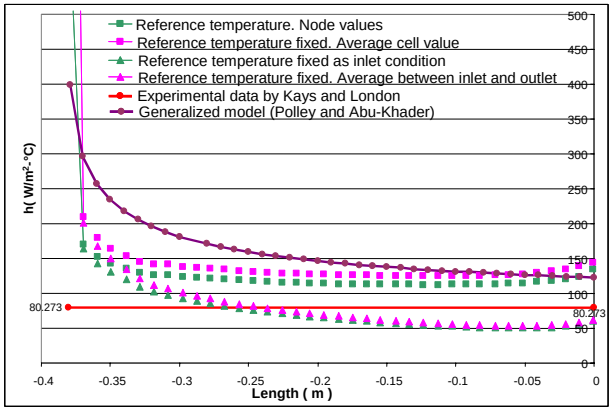

Figure 12: Heat transfer coefficient on gas side.

CONCLUSIONS

The experimental data for heat transfer performance of plain fin surfaces have been reported for conditions of non developed flow. In this region, values are greater than the ones found in the fully developed flow region. One of the most critical parameters for the numerical determination of heat transfer coefficients is the specification of the reference temperature. From the various ways of determining it, the condition where this temperature corresponds to the stream inlet temperature gives results which are closer to the values reported experimentally.

In this work, a model has been developed for the analysis of plain fins. The model can be applied to other geometries to predict the heat transfer coefficient as a function of the distance and the Reynolds number. In the case of new surfaces where the thermo-hydraulic performance is normally obtained experimentally, the model can be used to numerically determine their performance thus saving the long time required to produce the experimental data.

REFERENCES

[1] Kays W. M. & London A. L. *Compact Heat Exchangers*, 3rd Ed., McGraw-Hill Inc., 1984.

[2] Prasad, B.S.V. and Gurukul, S.M.K.A. *Passage arrangement in plate-fin heat exchangers.* Cryogenics 1987; 27(5): 257-262.

[3] Prasad, B.S.V. and Gurukul, S.M.K.A., *Differential methods for the performance prediction of multi-stream plate-fin heat exchangers.* Journal of Heat Transfer 1992; 14: 41-49.

[4] Prasad, B.S.V. *The sizing and passage arrangement of multi-stream plate-fin heat exchangers*. Heat Transfer Engineering 1996;17(3):35-43.

[5] Smith, E.M. *Direct thermal sizing of plate-fin heat exchangers*. Proceedings of the tenth International Heat Transfer Conference 1994; Brighton, U.K.:55-66.

[6] Picon Nuñez M., Polley, G. T., Reyes Torres E., Gallegos Muñoz A. *Surface selection and design of plate-fin heat exchanger*. Applied Thermal Engineering 1999;19:917-931.

[7] Polley, G.T. and Abu-Khader, M., *Interpreting and Experimental Data for Plate-Fin Surfaces*. Heat Transfer Engineering 2005, To be published.

[8] Churchill W. S. *Comprehensive correlating equations for heat, mass and momentum transfer in fully developed flow in smooth tubes*. Ind.Eng.Chem.Fundam. 1977;16(1):109-116.

[9] Petukov B. S. *Heat transfer and Friction in turbulent pipe flow with variable physical properties*. Advances in Heat Transfer, Academia Press 1970;6:503-564.

Proceedings of ECOS 2005
Trondheim, Norway
June 20–22, 2005

SINGLE-COMPONENT OPTIMAL HEAT EXCHANGER EFFECTIVENESS USING SPECIFIC EXERGY COSTS AND REVENUES

David Paulus[1]
Technical University of Berlin
Institute for Energy Engineering
Marchstrasse 18
10587 Berlin, Germany

ABSTRACT

It has been observed that in a heat recovery steam generator of a combined cycle power plant (CCPP) optimized to minimize its cost of electricity, the ratios of capital costs rates to the total cost rate (capital costs plus the cost rate of exergy destruction) of downstream (with reference to the hot gas) components often are greater than those of upstream components. In order to understand this relationship, the economic optimum design of a heat exchanger considered as a single component is explored. Expressions for time rates of profit are written using specific exergy revenues and costs. These expressions are non-dimensionalized, and their derivatives are taken to find the optimum heat exchanger effectiveness. This optimum is shown to be a function of several dimensionless groups. Three of the variables contained within these groups are both of the stream inlet temperatures and the reference temperature. Results of numeric optimization of heat exchangers confirm the validity of the dimensionless groups.
Keywords: exergoeconomics, specific exergy revenue, heat exchanger optimization

NOMENCLATURE

c	specific exergy cost
c_A	average heat exchange area cost
C	heat capacity of a stream
C_{min}	heat capacity of the stream with the smaller heat capacity
C_r	heat capacity ratio
$\dot{C}_D$	cost rate of exergy destruction
$\dot{E}$	rate of exergy flow/destruction
f	f-factor
NTU	number of transfer units
$\dot{P}$	profit per unit time
$\dot{Q}$	heat transfer rate
r	specific exergy revenue
$\dot{S}_\pi$	rate of entropy production
T	temperature
U	overall heat transfer coefficient
$\dot{Z}$	capital cost per unit time

Greek Variables

χ_A	dimensionless specific cost of area
χ_F	fuel cost/product revenue ratio
ε	heat exchanger effectiveness
Π	dimensionless profit
σ	dimensionless entropy production
θ	dimensionless temperature difference
τ	inlet temperature ratio

Subscripts

0	reference
c	cold
F	fuel
h	hot
i	in
ii	out
opt	optimal
P	product

[1] e-mail: d.paulus@iet.tu-berlin.de

INTRODUCTION

The f-factor is defined as

$$f = \frac{\dot{Z}}{\dot{Z} + \dot{C}_D} \quad (1)$$

It expresses the ratio of the capital cost rate of the component to its total cost, the sum of its capital cost rate and its cost rate of exergy destruction [1]. The capital cost rate is found by amortizing the component's capital cost, for example through the use of a capital recovery factor or by proportionally assigning the carrying charges calculated through the revenue-required method [1]. The f-factor can serve as a tool during iterative optimization by helping to judge whether it is desirable to reduce exergy destruction at the expense of additional capital, or to save capital at the expense of increased exergy destruction.

A complication to the use of the f-factor in the optimization of a heat exchanger network , such as a heat recovery steam generator (HRSG), was observed by Paulus and Tsatsaronis [2]. The capital costs in order to achieve a given heat exchanger efficiency tend to increase as hot stream temperatures decrease. For example, in a HRSG, the f-values of the heat exchangers in a CCPP optimized for minimal product costs often noticeably rise as the hot stream temperatures decrease (assuming that the hot stream is the fuel stream). This temperature dependency can make it very difficult to judge if an f-factor shows a good balance between capital and total costs, i.e. if the relative capital investment in the heat exchanger is correct for the system. For example, the author has encountered instances where the product costs of a two-pressure CCPP were decreased by lowering the pinch temperature (and *increasing* the capital investment) of the low pressure evaporator, although the f-factor of this component was judged quite high (which would suggest *decreasing* the capital investment). The author has similarly observed the opposite behavior with respect to the high-pressure evaporator.

The following work originated as an attempt to quantify the influence of temperatures on the f-factors in a HRSG. Initially, a heat exchanger, specifically an evaporator in a HRSG, was numerically optimized as a single component, with the goal of maximizing the time rate of profit (for that single component), as defined by[2]:

$$\dot{P} = r_P \dot{E}_P - c_F \dot{E}_F - \dot{Z} \quad (2)$$

Observation of the f-factors at the optimal single-component efficiency showed temperature influences, but the exact relationship was not readily quantifiable. Therefore, the expression for profit was rewritten as a function of the inlet stream temperatures and mass flows, along with the cost of heat exchanger area. As the resulting expression was a function of many variables, it was non-dimensionalized. This was done for an evaporator, where it was assumed that the exergy increase in the cold stream was the product, and for a heat exchanger without a phase change, again with the cold stream as the product. All calculations assumed a constant overall heat transfer coefficient, constant stream heat capacities and no occurrence of pressure drop in either stream.

NONDIMENSIONAL PROFIT FOR AN EVAPORATOR

If the product of an evaporator (see Figure 1) is the exergy increase of the cold stream, and it is assumed that no pressure drop occurs in the hot stream, the exergetic fuel can be expressed as

$$\dot{E}_F = C_h \left(T_{hi} - T_{hii}\right) - T_0 C_h \ln\left(T_{hi}/T_{hii}\right) \quad (3)$$

The term $C_h \left(T_{hi} - T_{hii}\right)$ is equal to the duty of the heat exchanger, $\dot{Q}$. The duty, in turn, is equal to the effectiveness times the maximum possible heat transfer with the given inlet conditions, $\dot{Q}_{max} = C_h \left(T_{hi} - T_{sat}\right)$. Equation (3) can thus be rewritten as

$$\dot{E}_F = \varepsilon \dot{Q}_{max} - T_0 C_h \ln\left(\frac{T_{hi}}{T_{hi} - \varepsilon \dot{Q}_{max}/C_h}\right) \quad (4)$$

If the cold stream enters as a saturated liquid, and leaves in a saturated state at the pressure with which it enters, the exergetic product is

$$\dot{E}_P = \left(1 - T_0/T_{sat}\right)\dot{Q} = \left(1 - T_0/T_{sat}\right)\varepsilon \dot{Q}_{max} \quad (5)$$

[2] See [2] for the methodology of calculation of specific exergy revenue. Lazzaretto and Tsatsaronis [3] provide an comprehensive reference on the definitions of exergetic fuel and product, as well as the calculation of specific exergy costs.

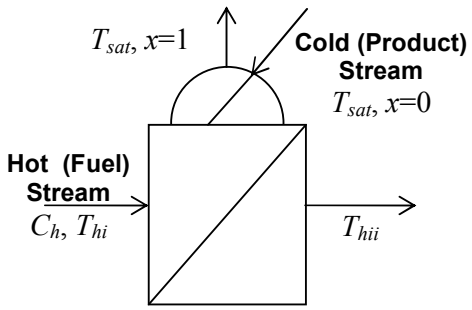

Figure 1: An evaporator

With the assumption that the cost of the heat exchanger varies linearly with its area (or that the average cost per unit area is known), the capital cost of the heat exchanger is given by

$$\dot{Z} = c_A A \tag{6}$$

From the definition[3] of *NTU*, $A = NTU \cdot C_h / U$ and $NTU = -\ln(1-\varepsilon)$. Equation (6) may be expressed as

$$\dot{Z} = -c_A \frac{C_h}{U} \ln(1-\varepsilon) \tag{7}$$

With the given assumptions, Eq. (2), after manipulation, can be rewritten as

$$\frac{\dot{P}}{r_P T_0 C_h} = \varepsilon\left[\left(\frac{T_{hi}-T_{sat}}{T_0}\right) - \left(\frac{T_{hi}}{T_{sat}} - 1\right)\right] - \frac{c_F}{r_P}\left[\varepsilon\left(\frac{T_{hi}-T_{sat}}{T_0}\right) + \ln\left(1+\varepsilon\left(\frac{T_{sat}}{T_{hi}}+1\right)\right)\right] + \frac{c_A}{r_P U T_0}\ln(1-\varepsilon) \tag{8}$$

Inspection of Eq. (8) shows that all of the variable groups are now dimensionless, and the following dimensionless variables may be defined[4]:

Dimensionless profit:

$$\Pi = \dot{P} / r_P T_0 C_h \tag{9}$$

Fuel cost-product revenue ratio:

$$\chi_F = c_F / r_P \tag{10}$$

Dimensionless entrance temperature difference:

$$\theta = (T_{hi} - T_{sat}) / T_0 \tag{11}$$

Entrance temperature ratio:

$$\tau = T_{hi} / T_{sat} \tag{12}$$

Dimensionless heat exchanger area cost:

$$\chi_A = c_A / r_P U T_0 \tag{13}$$

Equation (8) becomes

$$\Pi = \varepsilon[\theta - (\tau - 1)] - \chi_F\left[\varepsilon\theta + \ln\left(1+\varepsilon\left(1/\tau - 1\right)\right)\right] + \chi_A \ln(1-\varepsilon) \tag{14}$$

and the profit is now a function of four variables instead of nine.

The first derivative of Eq. (14) with respect to effectiveness is

$$\frac{\partial \Pi}{\partial \varepsilon} = \theta - (\tau - 1) - \chi_F\left(\theta + \frac{1/\tau - 1}{1+\varepsilon\left(1/\tau - 1\right)}\right) - \frac{\chi_A}{1-\varepsilon} \tag{15}$$

Equation (15), when solved for effectiveness when set equal to zero may have no solution, or it may yield either a local or global maximum in the range from ε=0 to 1. Figure 2 illustrates this with plots of Π as a function of ε at several values of θ. When it yields a global maximum, Eq. (15) allows the optimal effectiveness to be expressed as a function of four variables instead of eight.

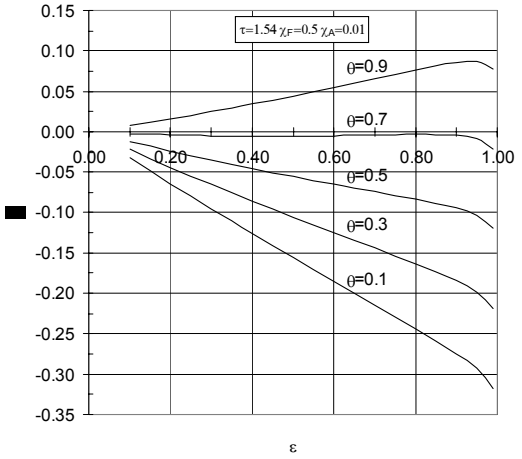

Figure 2: Nondimensional profit Π as a function of effectiveness and the nondimensionless temperature difference θ

[3] See [4] as a reference on the effectiveness-NTU method.

[4] It is worth noting that the ratio τ also appears in the equations for dimensionless entropy production in heat exchangers as defined by Sekulic [5]. The dimensionless entropy production is given the symbol σ and is equal to $\dot{S}_\pi / C_{min}$.

Figure 3 shows the effect of dimensionless variables containing temperature on the optimal effectiveness for one set of χ_A and χ_F. Interestingly, while a greater inlet temperature *ratio* favors a smaller heat exchanger, a greater inlet temperature *difference* favors a larger. (Not shown in the figures is that the optimal effectiveness decreases linearly with increasing χ_A and decreases approximately parabolically with increasing χ_F.)

Equation (1), after substitution of appropriate expressions for the capital cost and heat exchanger area, becomes

$$f = \frac{-c_A \dfrac{C_h}{U} \ln(1-\varepsilon)}{-c_A \dfrac{C_h}{U} \ln(1-\varepsilon) + r_P \dot{E}_D} \tag{16}$$

The exergy destruction can be found with $\dot{E}_F - \dot{E}_P$, and with Eqs. (4) and (5) is found to be

$$\dot{E}_D = \varepsilon \dot{Q}_{max} - T_0 C_h \ln\left(\frac{T_{hi}}{T_{hi} - \varepsilon \dot{Q}_{max}/C_h}\right) - \left(1 - T_0/T_{sat}\right)\varepsilon \dot{Q}_{max} \tag{17}$$

Equation (17) may then be substituted into Eq. (16). The resulting expression can be written in terms of the non-dimensional groups above:

$$f = \frac{-\chi_A \ln(1-\varepsilon)}{-\chi_A \ln(1-\varepsilon) + \ln\left[1 + \varepsilon\left(\dfrac{1}{\tau} - 1\right)\right] - \varepsilon(1-\tau)} \tag{18}$$

This is equivalent to

$$f = \frac{\chi_A NTU}{\chi_A NTU + \sigma} \tag{19}$$

where σ is the dimensionless entropy production, $\dot{S}_\pi / C_{min}$.

The f-factor itself is thus a function of NTU, dimensionless heat exchanger area cost and dimensionless entropy production (itself also a function of the inlet temperature ratio and effectiveness). Because the optimal effectiveness of an evaporator is a function of χ_A, χ_F, θ and τ, and the f-factor is a function of χ_A, effectiveness and τ, it follows that the optimal f-factor is dependent on the same dimensionless groups upon which the optimal effectiveness is dependent. Thus, it would be expected that the f-factors in a good design would vary with temperature along the gas path of the hot stream through the HRSG. Figure 4 shows the f-factor at optimal effectiveness for various τ and θ differences at fixed values of χ_A and χ_F. The inlet temperature ratio shows a decided effect on the f-factor at the optimal single-component effectiveness; the dimensionless inlet temperature difference has a much smaller effect.

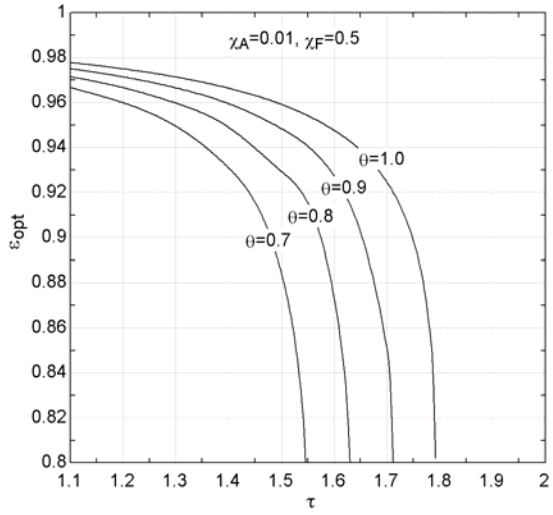

Figure 3: Influence of τ and θ on optimal effectiveness for an evaporator, constant χ_A and χ_F

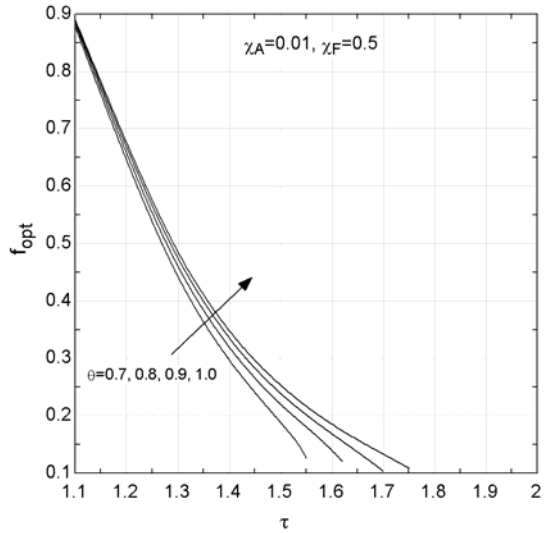

Figure 4: Influence of τ and θ on the f-factor at optimal effectiveness for an evaporator, constant χ_A and χ_F

NONDIMENSIONAL PROFIT FOR A HEAT EXCHANGER WITH NO PHASE CHANGE

For an economizer or a superheater (see Figure 5), Eq. (5) does not describe the exergetic product. This is instead given by

$$\dot{E}_P = C_C\left(T_{cii} - T_{ci}\right) - T_0 C_C \ln\left(\frac{T_{cii}}{T_{ci}}\right) \tag{20}$$

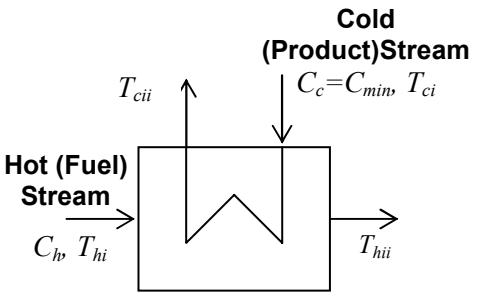

Figure 5: A heat exchanger

The introduction of the effectiveness and maximum heat transfer, $\dot{Q}_{max} = C_C\left(T_{hi} - T_{ci}\right)$, yields:

$$\dot{E}_P = \varepsilon\dot{Q}_{\max} - T_0 \ln\left(\left(T_{ci} + \frac{\varepsilon\dot{Q}_{\max}}{C_c}\right)\Big/ T_{ci}\right) \tag{21}$$

In order to express the maximum heat transfer as a function of the entrance temperatures, it is necessary to specify which stream has the smaller heat capacity, C_{min}. In a HRSG, the cold stream commonly has the lower heat capacity (when no phase change is present), so this derivation will proceed from this assumption. Moreover, in order to express it, it is necessary to specify the geometry of the heat exchanger. Because of the many tube passes in one of the HRSG's superheaters or economizers, counterflow geometry will be assumed. With these two assumptions, and using $NTU = UA/C_{min}$ along with the appropriate effectiveness-NTU relation for a counterflow heat exchanger, $NTU = \ln\left(\frac{\varepsilon - 1}{\varepsilon C_r - 1}\right)\Big/\left(C_r - 1\right)$, the heat exchange area may be expressed as

$$A = \frac{C_c \ln\left(\frac{\varepsilon - 1}{\varepsilon C_r - 1}\right)}{U\left(C_r - 1\right)} \tag{22}$$

where, for this case, $C_r = C_c/C_h$.

Now, Eq. (2) may be rewritten as

$$\dot{P} = r_P\left[\varepsilon\dot{Q}_{\max} - T_0 \ln\left(\frac{T_{ci} + \frac{\varepsilon\dot{Q}_{\max}}{C_c}}{T_{ci}}\right)\right] - c_F\left[\varepsilon\dot{Q}_{max} - T_0 C_h \ln\left(\frac{T_{hi}}{T_{hi} - \varepsilon\dot{Q}_{max}/C_h}\right)\right] - c_A\frac{C_c \ln\left(\frac{\varepsilon - 1}{\varepsilon C_r - 1}\right)}{U\left(C_r - 1\right)} \tag{23}$$

with $\dot{Q}_{\max} = C_c\left(T_{hi} - T_{ci}\right)$. This can be nondimensionalized, reducing an expression with ten independent variables to one with six:

$$\Pi = \left(1 - \chi_F\right)\varepsilon C_r\theta - \chi_F \ln\left[1 - \varepsilon C_r\left(1 - \frac{1}{\tau}\right)\right] - C_r \ln\left[1 + \varepsilon\left(\tau - 1\right)\right] - \chi_A\frac{C_r \ln\left(\frac{\varepsilon - 1}{\varepsilon C_r - 1}\right)}{C_r - 1} \tag{24}$$

The dimensionless groups remain defined as before with the exception that T_{ci} replaces T_{sat} and the addition of C_r[5].

The derivative of Eq. (24) with respect to ε is

$$\frac{\partial\Pi}{\partial\varepsilon} = \left(1 - \chi_F\right)C_r\theta + \chi_F C_r\frac{1 - \frac{1}{\tau}}{1 - \varepsilon C_r\left(1 - \frac{1}{\tau}\right)} - C_r\frac{\tau - 1}{1 + \varepsilon\left(\tau - 1\right)} - \chi_A C_r\frac{\frac{1}{\varepsilon C_r - 1} - \frac{\varepsilon - 1}{\left(\varepsilon C_r - 1\right)^2}C_r}{\varepsilon - 1}\frac{\varepsilon C_r - 1}{C_r - 1} \tag{25}$$

Graphing of Eq. (24) shows that setting Eq. (25) to zero and solving for ε will either yield no solu-

[5] In this expression, τ is the inverse of that defined by Sekulic [5]. A decision was made to be consistent between the case of an evaporator and that of an economizer or superheater, rather than Sekulic's of the ratio of temperature of the stream with the smaller heat capacity to the temperature of the stream with the larger capacity. Sekulic retained consistency between the heat capacity ratio and the temperature ratio, which was the logical choice for his work.

tion, or a local or global maximum for Π for rational values of effectiveness. (Graphs are similar in appearance to the example given for an evaporator in Figure 2.) The number of variables upon which the optimal effectiveness depends is reduced to five. The influence of τ and θ at constant χ_A , χ_F, and C_r for a heat exchanger is similar to that of an evaporator at constant χ_A and χ_F. Again, while a greater inlet temperature *ratio* favors a smaller heat exchanger, a greater inlet temperature *difference* favors a larger. Figure 6 shows the influence of C_r over a typical range for the economizers and superheaters of a HRSG. The dimensionless variables χ_A and χ_F have similar effects as for the case of an evaporator.

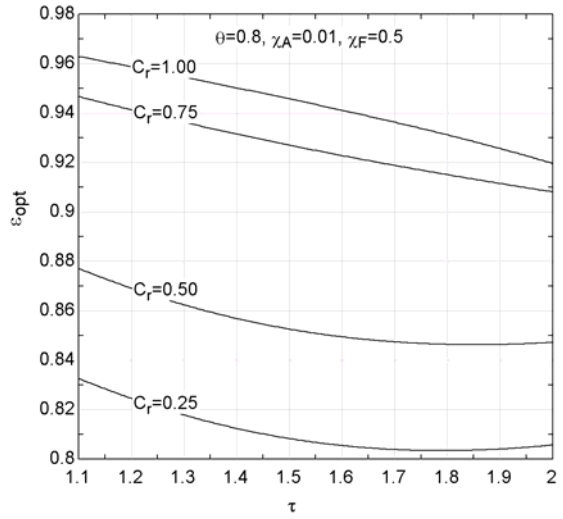

Figure 6: Influence of τ and C_r on the optimal effectiveness for a heat exchanger with the cold stream as product and having minimum *C*, constant θ, χ_A and χ_F

The f-factor is related to the effectiveness and other dimensionless groups with

$$f = \frac{\chi_A \ln\left(\frac{\varepsilon - 1}{\varepsilon C_r - 1}\right) \Big/ \left(C_r - 1\right)}{\chi_A \ln\left(\frac{\varepsilon - 1}{\varepsilon C_r - 1}\right) \Big/ \left(C_r - 1\right) + \frac{1}{C_r} \ln\left(1 - \varepsilon C_r \left(1 - \frac{1}{\tau}\right)\right) + \ln\left(1 + \varepsilon\left(\tau - 1\right)\right)} \quad (26)$$

This is again equivalent[6] to

$$f = \frac{\chi_A NTU}{\chi_A NTU + \sigma} \quad (27)$$

The optimal f-factor for an evaporator or economizer is thus not only dependent on the inlet stream temperatures, but also on the ratio of heat capacities of the streams. The graph of optimal f-factor at constant χ_A , χ_F, and C_r appears similar to that of an evaporator at constant χ_A and χ_F,.

These derivations are straightforward to repeat for other cases (i.e. different geometry, the case where the hot stream has the lower heat capacity, etc.).

NUMERICAL TESTING

In order to test the validity of the dimensionless groups, numerical optimization was undertaken. First, for an evaporator, the component profit was maximized for several different hot stream entrance temperatures. The pressure of the cold stream and the reference temperature were varied to keep the inlet temperature ratio, τ, and the dimensionless inlet temperature difference, θ, constant. This was done for a variety of values for τ and θ. The hot stream was modeled as air, using ideal gas property relations with varying specific heat. The cold stream was modeled using real properties.

It was found that (a) the resulting optimal effectiveness remained nearly constant when the relevant dimensionless groups remained constant and (b) the resulting optimal effectiveness matched the optimal effectiveness predicted by setting Eq. (15) equal to zero. The maximum discrepancy between the two calculated values over a range of hot stream entrance temperatures from 550 to 800K was 0.2%.

The calculations were repeated for a heat exchanger without a phase change. To maximize any possible effects of real fluid behavior, the heat exchanger was modeled as a superheater with the cold stream entering as a saturated liquid. The same observations were made as for an evaporator – nearly constant effectiveness resulted from the numerical optimization, and it agreed well with

[6] The difference between the term for dimensionless entropy production σ in Eq. (26) and that of Sekulic [5] is due to the inverse of definitions of τ.

the theoretical, in this case predicted by setting Eq. (25) to zero and solving for effectiveness. The maximum discrepancy in this test was 0.4%. When the calculations were repeated at lower pressures and away from the saturation point, the optimal effectiveness remained even more constant and matched the predicted value to three significant figures.

DISCUSSION

The F-Factor along the Gas Path of a HRSG

Typically, in a HRSG far more heat transfer occurs in the higher pressure evaporators than in the lower pressure units. This typically results in the lower pressure evaporators, located in areas of lower hot stream temperature, having lesser temperature inlet ratios and dimensionless inlet temperature differences. It was shown before that greater inlet temperature ratios favor lower values for the f-factors, while greater inlet temperature differences favor higher values. However, at least for a HRSG, the differences in dimensionless inlet temperature differences between high and lower-pressure evaporators are far less significant than differences in ratios, and areas of high exergetic fuel potential (temperature) favor less relative capital investment. Pinch temperatures are greater in the high pressure section than in the lower pressure sections. This matches the observations of Paulus and Tsatsaronis.

For a superheater, the situation is complicated by the effect of the heat capacity ratio, and it is difficult to state any trends of the f-factors based solely on hot-stream temperatures. The effect for the economizers is even more difficult to assess, as these are often constrained by either the maximum cold stream exit temperature (below the saturation temperature) or the hot stream exit temperature (to prevent condensation).

The work contained in this paper shows that the optimal capital investment in a heat exchanger, when investigated as a single component, depends on more than just the hot stream entrance temperature. The cold stream inlet temperature, the ratio of heat capacities and even the dead state temperatures play roles as well. And, if these variables influence the optimal size of a heat exchanger considered as a single component, they are extremely likely to play a role in the optimum sizing of a heat exchanger within a system.

The Optimal Effectiveness and Optimization

Most types of energy system components show a common relationship between exergetic efficiency and exergy destruction. As the efficiency increases, the exergy destruction *decreases*. The increased efficiency comes at the price of a greater capital investment in the component. With such components, the f-factor is a valuable tool for iterative optimization. For components showing this relationship between efficiency and exergy destruction, the f-factor will increase as the capital investment is increased and the component's efficiency improves.

Heat exchangers are unique in that an increase in efficiency can be accompanied by an *increase* in exergy destruction. When the inlet conditions are fixed, it is only possible to increase the efficiency of a heat exchanger by changing the *UA* value. Consider the case when the cold stream has the lower heat capacity: Because additional heat is transferred across a smaller temperature difference than the average for the heat exchanger, to cold stream temperatures higher than the average, the efficiency of the heat exchanger increases. However, because additional heat transfer occurs, the total exergy destruction *can* increase. This could lead to problems with the use of f-factors for optimization of a heat exchanger network: depending on the relative costs of heat transfer area and exergy destruction, the f-factor may actually decrease with increasing efficiency. Moreover, if the inlet conditions are even partially fixed, given the fact that increased efficiency comes with increased fuel exergy use, product exergy delivery and exergy destruction renders the assumption made when calculating the cost of exergy destruction – the assumption that either the exergetic fuel or product remains constant – incorrect.

The resulting dimensionless expressions derived here for optimal effectiveness might well serve as a replacement for the f-factor. Indeed, it would not be unreasonable to hypothesize that an optimally designed heat exchanger network would find all heat exchangers at their optimal component effectiveness (unless constrained by other design parameters), *as long as the fuel costs and*

product revenues were properly calculated. If this hypothesis is correct, the designer could move stepwise towards the optimum, by observing if the effectiveness of any given heat exchanger in the current iteration is greater or less than the optimum, and by making changes accordingly. The procedure would have to be iterative, and it would be unwise to make too large of a change to any heat exchanger's effectiveness in a single iteration, because (a) changes in upstream heat exchangers affect temperature ratios, etc. in the downstream heat exchangers, (b) costs and revenues will change between iterations and (c) in reality, the cost of heat exchanger area does not necessarily remain constant with varying heat exchanger size. The greatest difficulty in employing such a method would be the proper choice of exergetic costs and revenues – the average specific costs and revenues may not be the proper costs in such an optimization scheme.

The question might arise, "Why not use exergetic efficiency instead of effectiveness?" It is clear that just as the f-factor is fixed at optimal effectiveness, so is the exergetic efficiency. The advantage of the effectiveness, in the eyes of the system designer, is that it quickly specifies the heat exchanger without having to (again) resort to the use of calculations involving the inlet temperatures.

CONCLUSION

By non-dimensionalizing the expressions for component profit of two types of heat exchangers, the number of independent variables upon which these expressions depend was dramatically reduced. It was then possible to take the derivative of these expressions for dimensionless profit with respect to effectiveness, and from these derivatives the optimal heat exchanger effectiveness, considering the heat exchanger as a single component, could be found. It was found that, among other dimensionless groups, the dimensionless profit and optimal effectiveness depend on the inlet temperature ratio and the dimensionless inlet temperature difference.

Subsequently, the f-factor for the investigated heat exchanger was related to its effectiveness, the dimensionless cost of heat exchanger area and the inlet temperature ratio. Therefore, the optimal f-factor for a heat exchanger depends upon the same groups as the optimal effectiveness. As two of these groups contain the stream inlet temperatures, it is clear that the f-factor of heat exchangers in a HRSG of a cost-optimized system will vary with these temperatures. The analysis points to a situation more complicated than just a dependency of thermodynamic fuel potential, as not only the hot stream temperature, but also the cold stream inlet temperature and the ratio of heat capacities influence at least the optimal capital investment for a heat exchanger.

Beyond temperature dependency, other shortcomings in the use of the f-factor for optimizing heat exchanger networks were highlighted. These difficulties suggest that optimal effectiveness might well be an improvement on the f-factor in the iterative optimization of a heat exchanger network. Future work will center on this application.

REFERENCES

[1] Bejan A, Tsatsaronis G & Moran M. *Thermal Design and Optimization.* New York: John Wiley and Sons, 1996. Ch. 8.

[2] Paulus, DM Jr.,Tstatsaronis G. *Auxiliary Equations for the Determination of Specific Exergy Revenues*. In: Proceedings of the 17th International Conference on Efficiency, Costs, Optimization, Simulation and Environmental Impact of Energy Systems, ECOS '04 (R. Rivero, L. Monroy, R. Pulido & G. Tsatsaronis, Editors), Guanajuato, México, July 7-9, 2004, p. 561-572.

[3] Lazzaretto A, Tsatsaronis G. *On the Calculation of Efficiencies and Costs in Thermal Systems*. In: 1999 Proceedings of the ASME Advanced Energy Systems Division, AES-Vol. 39. New York: ASME. p. 421-430.

[4] Kayes WM, Crawford ME. *Convective Heat and Mass Transfer*. New York: McGraw-Hill, 1993. Ch. 18.

[5] Sekulic DP. *Thermodynamic Analysis for Thermal Design, Manufacturing, and Operation of Heat Exchangers*. In: Loknath MS et al., editor. Heat and Mass Transfer 2000. New Dehli and New York: Tata McGraw-Hill, 2000. p. 139-151.

Proceedings of ECOS 2005
Trondheim, Norway
June 20–22, 2005

A CFD-AIDED DESIGN PROCEDURE FOR COMPACT HEAT EXCHANGERS

Mauro Robbe, Enrico Sciubba[1]

Department of Mechanical and Aeronautical Engineering

University of Roma 1 "La Sapienza"

Italy

ABSTRACT

A numerical simulation of the heat exchange process within a car radiator has been performed with a CFD commercial code.
The heat exchanger is of the cross flow type, with elements composed of flattened tubes surrounded by a finned matrix; each fin has louvered surfaces, and the geometry is modular.
The fluids involved in the heat exchange are air on the cold side and a water/ethylene-glycol mixture (40%) on the hot side.
The numerical simulation was carried out on a 3D reduced model that includes a single module, consisting of one corrugation of finned matrix connected with two shells representing the upper and the lower sections of the flattened tubes respectively. The exchanger is considered to be operating in a steady-state mode. The difficulty of theoretically deriving the heat transfer coefficients on the external finned surface is overcome by imposing only a convective heat transfer boundary condition on the tube shells internal surfaces. The longitudinal variability of the heat transfer coefficient along the channels internal surfaces is accounted for by considering the hydraulic and thermal development of the flow inside of the glycol tubes: the relevant heat transfer formulae are derived by the existing literature. The external air flow is assumed to be laminar.
All results are in a good agreement with experimental data provided by tests conducted on an industrial prototype.

Keywords: Compact heat exchangers, conjugate heat transfer, louvered fins.

NOMENCLATURE

A	Surface area [m^2]	Nu	Nusselt number, $\left(=\frac{hd}{k}\right)$
D_h	Hydraulic diameter [m]		
h	Heat transfer coefficient [W/m^2C]	$Nu_{x,h}$	Local Nusselt number for constant heat transfer coefficient
H	Tube height, mm		
L_{Hy}	Hydrodynamic entry lengh [m]	Pe	Péclet number, ($=Re*Pr$)
L_{th}	Thermal entry lengh [m]		
L_{th}*	Dimensionless thermal entry length, $\left(=\frac{L_{th}}{D_h Pe}\right)$	P_f	Friction loss [W]

[1] Corresponding author: Phone:+39 06 44 58 52 44; enrico.sciubba@uniroma1.it

Pr Prandtl number, $\left(=\frac{c_p \mu}{\kappa}\right)$

Q Heat flux [W]

Re Reynolds number, $\left(=\frac{D_h v}{\nu}\right)$

T Temperature [K]

x Distance from tube inlet [m]

x* Dimensionless distance from tube inlet, $\left(=\frac{x}{D_h Pe}\right)$

v Flow velocity [m/s]

W Tube width [mm]

α Tube aspect ratio (=H/W)

μ viscosity [kg/ms]

INTRODUCTION

During the last decade, commercial CFD codes employing numerical methods for the solution of the Navier-Stokes equations have reached a high degree of reliability. Such an improvement, coupled with an exponential improvement in the hardware performance, has greatly increased the capability of numerical simulations to reproduce the details of real physical phenomena.

This capability makes it possible to substantially shorten the material prototyping phase with an important reduction of the extent of laboratory tests, and brings about corresponding monetary savings. The study reported in this paper was aimed to a verification of the accuracy of the numerical determination of the performance of the latest generation of car radiators.

Conventional design methods [8] for compact heat exchangers are based on a preliminary definition of the economical and performance requirements of the device. The so-called Mason flow chart [9], reported in figure 1, synthesizes this first stage (only the first block of the Mason diagram is reported here because economic factors or shipping problems, included in its second part, are not relevant to the present study).

According to this scheme, the "problem specification" branch represents the definition of the radiator foreseen application field: i.e., the radiator application field determines the configuration of the device.

The most common configurations for compact heat exchangers are:

1. Direct transfer heat exchangers;
2. Liquid-coupled indirect transfer h.e.;
3. Periodic flow type h.e.

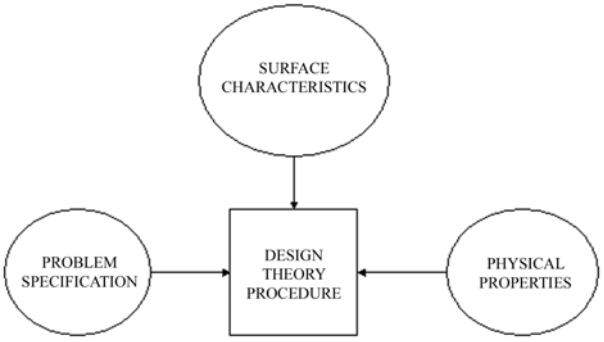

Figure 1: General methodology for heat exchanger design (first part of Mason's original chart [9])

Car radiators fall into class 2. However, in this work we are not interested in the heat exchanged inside of the engine block, and therefore we can introduce a simplification, assuming our exchanger belongs to class 1 instead. In addition, we assume that the best configuration for a car radiator is the "cross-flow finned-tube bundle".

To increase the surface-to-volume ratio, it is customary to employ low-aspect ratio (flattened) channels on the water-glycol mixture hot side and to combine them with large finned surfaces on the cold side. For what the actual (i.e., local) heat exchange coefficient is concerned, there is still a substantial lack of generally valid correlations: from an engineering design point of view the correct sizing can be easily attained by means of graphs like the one reported in figure 2.

The frontal dimensions of a compact heat exchanger result from a compromise between two contrasting requirements: an increase of the active heat exchange surface in contact with the cold fluid and the reduction of the related friction power. The friction power losses display a quadratic

dependency on the flow velocity, while the heat exchanged varies with a linear law[2].

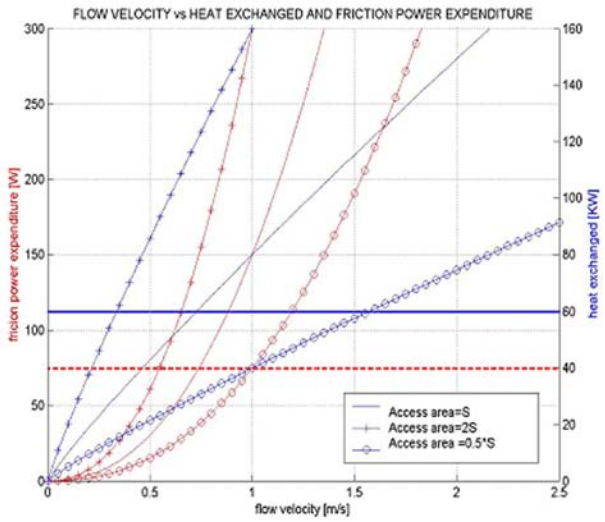

Figure 2: Radiator sizing curves

As an example, consider the situation of figure 2, where for a heat flux of 60kW (continuous horizontal thick line) and a fluid velocity of 1m/s we impose an upper limit to the pumping power of -say- 75W (dashed thick horizontal line). A radiator having an access area of 0.5 S ("o" marks) would not satisfy the thermal requirements but would instead abide by the friction power limitations. A radiator with an access area of S, on the other side, would satisfy the thermal requirements but not the friction power. The final solution consists in simultaneously reducing the fluid velocity, by changing the radiator placement within the engine compartment (for example placing it just downstream a diverging air intake) and adjusting its frontal area.

The curves displayed in figure 2 are plotted on the basis of experimental data, as compact heat exchanger performance cannot be derived with pure analytical methods: car radiator external surfaces are provided with "baroquely shaped" fins to induce boundary layer discontinuities and to improve the thermal performance on the air side; the experimental literature on louvered fins does not (and cannot) cover all existing geometries and small variations in louver inclination result in non negligible changes in radiator performance. Therefore, it is unreliable to extrapolate available data even to slightly different geometries.

This is the reason why radiator constructors must assemble a new prototype for each fin matrix geometry and for each radiator configuration.

Goal of the present work is to eliminate or strongly reduce the number of radiator prototypes to be tested. Particular attention was devoted to the modeling of the entry length development in flattened channels, that exerts a strong influence on heat transfer coefficients, especially in the case of laminar flow [12], and consequently on the overall heat exchange. Fully developed flows and turbulent flows were treated according with basic textbook literature [2,12].

THE GEOMETRIC MODEL

The radiator we will refer to hereafter is a Magneti Marelli brazed aluminium (Nocolock technology) device, with dimensions (height*width*thickness) 391.8*500*2.8 mm, a fin density of 200 fin/500mm and consisting of 40 flat parallel channels.

For the numerical simulation we considered a single element of the matrix constituting the whole radiator, figure 3.

The actual dimensions of the tubes are shown in figure 4; a frontal view of a single fin corrugation is given in figure 5.

Fin louvers belonging to adjacent corrugations are arranged at an alternate angle w.r.t. the air stream main velocity, figure 6. The fluid region surrounding the above described solid element was chosen as small as possible, to reduce the extension of the computational domain. A couple of regular volumes was added in front and behind the fin.

The downstream "plenum" is larger than the upstream one, to capture possible turbulent phenomena deriving by the interaction of the air with the fin wave. The detailed element dimensions are reported in figure 7.

To account for the presence of the solid connections due to the weldings between the corrugated fin wave and the tubes, we created small solid blocks running all along the extension of the fin-tubes contacts. The dimensions of those blocks were taken to be approximately representative of the real welding lines.

[2] Actually, the lines representing the heat exchanged in Figure 2 are not straight: the experimental evidence suggests a correlation of the type $P_f=k*V^n$, with n slightly smaller than 1.

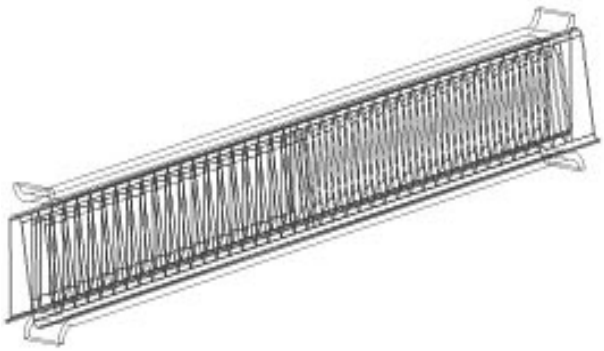

Figure 3: Geometric element for the CFD simulation

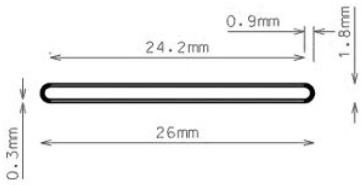

Figure 4: Single hot fluid tube section

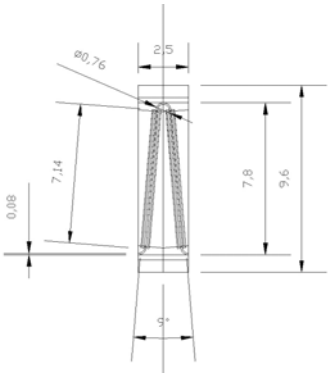

Figure 5: A single fin wave front view (mm)

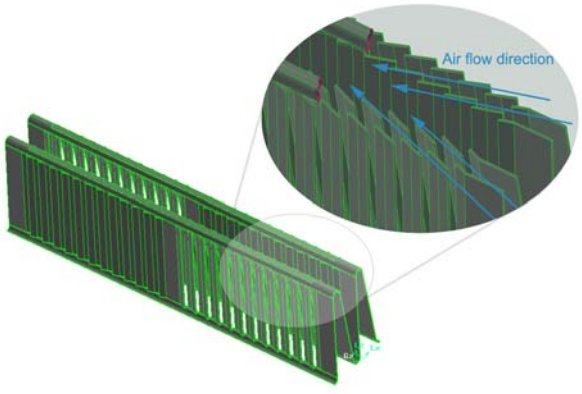

Figure 6: Detail of a pair couple of adjacent fins

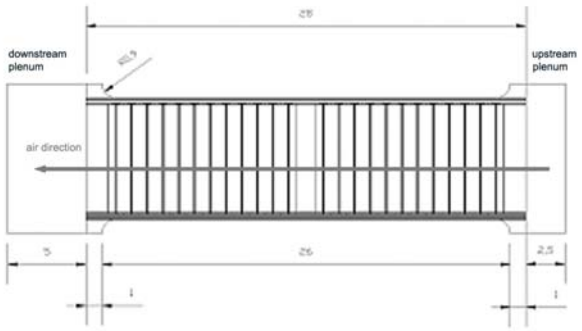

Figure 7: A complete louvered element side view (dimensions in mm)

THE FINAL MESH, THE SOLUTION PROCEDURE AND THE MATERIAL PROPERTIES

The entire domain shown in figure 3 (both solid and fluid regions) was discretised. On a hybrid-type mesh that and alternates Cooper meshing scheme zones and unstructured tetrahedral regions. Initial tests, run on a completely unstructured mesh evidenced the need for a refinement in the regions included between louvers, to adequately take into account the boundary layer development on the fin walls, allowing at the same time for a consistent reduction of cell density in less sensitive regions. The final mesh is described in table 1.

Number of Cells	Number of Faces	Number of Nodes	Number of Partitions
1860920	4210589	620440	1

Table 1: Mesh elements summary

The small hydraulic radius of the finned volumes and the relatively small air velocities result in low Reynolds numbers on the cold side, which justifies the choice of the model summarized in Table 2:

Model	Settings
Space	3D
Time	Steady
Viscous	Laminar
Wall treatment	Standard wall functions. No-slip condition
Heat Transfer	Enabled

Table 2: Model characteristics

The simulation was run using FLUENT, version5.6, the convergence of the iterative non-linear solver was accelerated (both for pressure and

for momentum) by means of the under-relaxation factors shown in Table 3:

Variable	Relaxation Factor
Pressure	0.03
Density	1
Body Forces	1
Momentum	0.07
Energy	1

Table 3: Relaxation factors

The solution scheme was:

Variable	Scheme
Pressure	Standard
Pressure-Velocity Coupling	SIMPLE algorithm
Momentum	First Order Upwind
Energy	First Order Upwind

Table 4: Solver description

For the water/ethylene-glycol mixture, temperature variable properties were assumed as shown in Table 5.

Temperature	Density [kg/m3]	Thermal conductivity [W/(mK)]	Viscosity [mPa s]	cp [KJ/(kgK)]
273	1065,00	0,396	6,50	3,36
293	1055,00	0,414	3,10	3,45
313	1042,00	0,428	1,80	3,56
333	1030,00	0,44	1,13	3,64
353	1018,00	0,45	0,80	3,71
363	1009,00	0,454	0,60	3,74
373	1002,00	0,458	0,56	3,76

Table 5: Properties of 40% vol. Water/Ethylene-Glycol mixture (adapted from[11])

BOUNDARY AND OPERATING CONDITIONS

The face through which the air impinges on the finned volume was defined "*velocity inlet*" and a single component velocity vector was assigned to it. An "outflow condition" is imposed on the downstream surface. "*Simmetry*" boundary conditions are imposed on the side walls, while adiabatic conditions are imposed on the surfaces representing the longitudinal (YZ) tube sections.

A graphical summary of the imposed boundary conditions is provided in figure 8. Planes delimiting the air volumes on the XY sections are considered to be periodic, to take into account possible vertical mass transport. The treatment of the internal tube surface ("ITS" in the following) deserves a more detailed discussion, provided in the next paragraph.

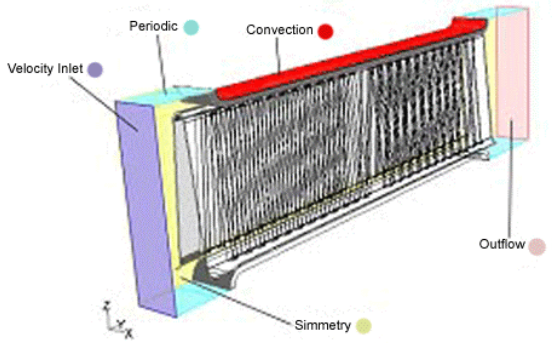

Figure 8: Boundary conditions

THERMAL BOUNDARY CONDITIONS ON THE INTERNAL TUBE SURFACE

The calculation of the temperature field established by the thermal exchange between two fluids separated by a solid matrix requires the solution of a double-conjugated problem. Each conjugate problem involves the definition of the thermal field both for fluid and solid elements. Both the temperature and heat flux at the interface between solid and fluid fields are considered continuous. The use of a numerical model with a cross flow heat exchange including both fluids results though in an extremely high CPU consumption.

To simplify this model and to reduce the physical problem to a single-conjugated one, we resolved to adopt a mathematical law to describe the behavior of the heat transfer coefficient on the internal tube surface. The existence of several concurring thermal effects on the internal tube surface, like the perturbations induced by the external fin welding, or the influence of the variation of the inlet velocity profile caused by the geometrical configuration of the water box, make though the definition of a single thermal boundary condition difficult. For these surfaces, Shah and London [12] suggest a constant temperature boundary condition, remarking that this is a valid assumption only for very high liquid flow rates. We performed some preliminary simulations with such a temperature condition on the internal duct surface, taking as "wall value" the local mixing cup temperature of the water/GE solution: the results showed an excessive thermal exchange and overestimated air-side heating; this agrees with Garimella et al. [5] experimental tests performed on a simplified tube geometry very similar to ours (α=0.05, hydraulic diameter=2.21 and Pr=10). We finally assumed a

heat transfer coefficient that is constant on the duct transversal section and varies along the tube (in the x direction, figure 9) depending on the thermal/hydraulic internal flow boundary layer development.
Neglecting the influence of the duct inlet configuration and of externally induced vibrations, we will thus assume that the laminar-to-turbulent transition takes place approximately at Re=2300: a very extensive literature of experimental data exists on this topic and shows the extreme variability of the transition Reynolds number (Pfenninger [10] pushed the laminar to turbulent transition Reynolds number value up to $1.005*10^5$), but the 2300 value is well accepted for most common cases where the tube length is much longer than the hydraulic entry length.

Laminar flow

For Re<2300, the peripheral heat transfer coefficient on the inside of the tubes is strongly influenced by the development of the temperature profile inside of the ducts and by the thermal boundary conditions. The heat transfer coefficient decreases as the velocity and thermal profiles develop and its variation affects a large portion of the tube.
To define the extension of the hydrodynamic entrance length we used Chen's equation [4] for developing flow between parallel plates:

$$\frac{L}{D} = \frac{0.315}{0.0175 * \mathrm{Re} + 1} + 0.011 * \mathrm{Re} \qquad (1)$$

The analytical definition of the dimensionless thermal entrance length shows its dependence on the Péclet number

$$L_{th}^{*} = L_{th} / (D_h Pe) \qquad (2)$$

The thermal entrance length increases with the fluid axial heat conduction (i.e. as the Pe number decreases); the lateral short walls of our almost rectangular ducts should therefore give origin to longer L_{th}^{*} higher values than a parallel plates configuration. Since the aspect ratio of the tubes is here extremely low, the parallel plates value of $L_{th}^{*} \approx 0.012$ can be regarded though as a good approximation.
For the evaluation of the heat transfer coefficient, the tube was divided into three zones:

A. Hydrodynamically-thermally developing flow
B. Hydrodynamically developed, thermally developing boundary layer
C. Completely developed thermal-hydrodynamic boundary layer

A. Hydrodynamically-thermally developing flow

A great amount of data about the values of the heat transfer coefficient is available for square and round tubes geometries; few studies exist about flattened tubes. Wibulswas [14] provides interesting analytical results about similar geometries but considers only flows with Pr=0.72. Chandrupatla [3] considers simultaneously developing flow but treats only square ducts. We used the Hwang and Fan [7] heat exchange coefficients over a simultaneously developing flow obtained for a value of Pr=10. These results are in good agreement with Garimella and al. [5] experimental data for flat tubes, for different tube lengths, different hot fluid composition (30, 40, 50% GE) and several values of the Prandtl number. Defining an axial dimensionless coordinate x* Hang and Fan's [10] experimental data provide:

x*	5*10e-5	1,25*10e-4	4,38*10e-4	7,5*10e-4
$Nu_{x,h}$	50,74	34,07	20,66	17,03

0,0015116	0,002	0,00625	0,01
14	12,6	9,5	8,8

Table 6: $Nu_{x,h}$ as a function of x* for simultaneous developing flows between parallel plates [10]

B. Thermally developing region

Adopting the same symbolism as in Table 6, and denoting by x* the distance from the duct inlet, Shah and London [12] provide the following results:

X*	0,001	0,0015	0,002	0,003
$Nu_{x,h}$	15,42	13,68	12,6	11,29

0,004	0,005	0,006	0,007
10,51	99,87	9,6	9,32

X*	0,008	0,009	0,01	0.015
$Nu_{x,h}$	9,1	8,93	8,8	8,43

0.02	0.03	0.04	0.05
8,31	8,24	8,23	8,23

Table 7: $Nu_{x,h}$ as a function of x* for fully developed velocity profile, thermally developing flow within parallel plates

Figure 9 shows the variation of the heat transfer coefficient on the internal tube surfaces for a hydraulically and thermally simultaneously developing entry length.

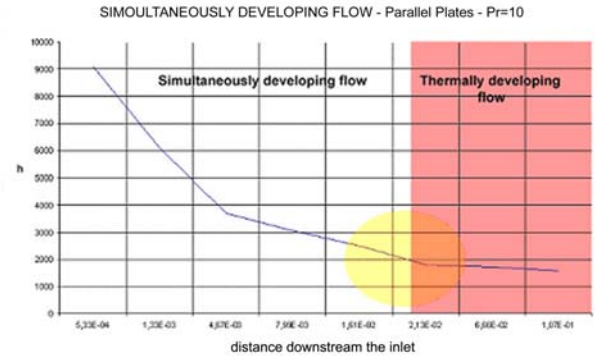

Figure 9: Heat transfer coefficient vs tube lenght along simultaneously developing entry lengths

Figure 10 clearly identifies the heat transfer coefficient for a completely developed and for thermally developing entry length.

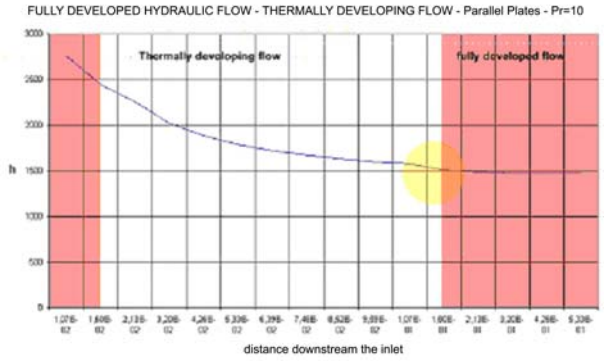

Figure 10: Heat transfer coefficient vs tube lenght along thermal developing entry length

The variation of the slopes of both curves is evidenced by the shaded areas in figure 9 and 10; such change in slope implies a variation in the thermal boundary layer configuration and confirms the results for the entry length extensions obtained with the above mentioned Chen law.
As a first step, we matched the results obtained for the simultaneously developing entry length and for the hydraulic completely developed/thermally developing entry length. Table 8 reports the values of the heat transfer coefficients calculated for real (non dimensionless) extensions of tube length along the complete boundary layer development.

x[m] 1000kg/h l	x[m] 2000kg/h l	x[m] 3000kg/h l	h [W/(m²°C)]	zone (fig.5,3)
<0,001	0,001	0,0015	9081	
0,001	0,0026	0,0039	6097	1
0,004	0,0093	0,0139	3697	
0,008	0,0159	0,0239	3047	2
0,016	0,0322	0,0483	2505	3
0,015	0,0426	0,0639	2255	4
0,021	0,0639	0,0958	2022	5
0,031	0,0852	0,1278	1882	6
0,042	0,1065	0,1597	1787	7
0,053	0,1278	0,1917	1718	8
0,063	0,1491	0,2236	1668	9
0,074	0,1704	0,2556	1628	10
0,085	0,1917	0,2875	1598	11
0,095	0,213	0,3195	1574	12
0,106	0,249	0,3374	1480	13

Table 8: Entry length real extension with corresponding heat transfer coefficient and zone identification marker

We then divided the domain in zones (Table 8, last column) with constant “h”, thus somewhat grossly approximating the heat transfer coefficient variation. Figure 11 shows, by means of different shading, the distribution of piecewise constant heat transfer coefficient regions along the tube entry length for a 1000 kg/h hot fluid flow rate

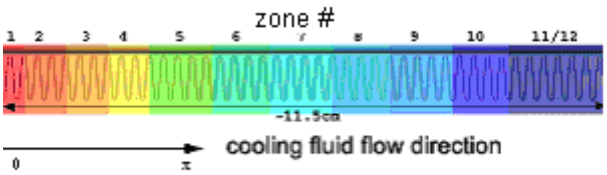

Figure 11: Zones with constant heat transfer coefficient

Turbulent region

For Re>2300 the motion transitions into turbulence.The hydraulic radius of the tubes (2.21 mm) sufficiently exceeds the 2 mm indicative value beneath which the suppression of turbulent eddy mechanism causes a reduction in the heat transfer coefficient. Bhatti and Shah [2] suggest that for practical computations of the fully developed Nusselt numbers in rectangular ducts it is possible to use the same correlations obtained for circular channels. We therefore used the Hausen [6] formula to obtain the Nusselt number for turbulent fully developed flow:

$$Nu = 0.116\left(\mathrm{Re}^{2/3} - 125\right) * \mathrm{Pr}^{1/3}\left[1 + \left(\frac{x}{D}\right)^{-2/3}\right] \qquad (3)$$

This formula takes into account the thermal entrance length effect embodied in the last bracketed factor. Figure 16 reports a comparison between the heat exchange coefficient obtained with Hausen formula and some experimental values. There is a sufficiently good agreement over the entire turbulent region.

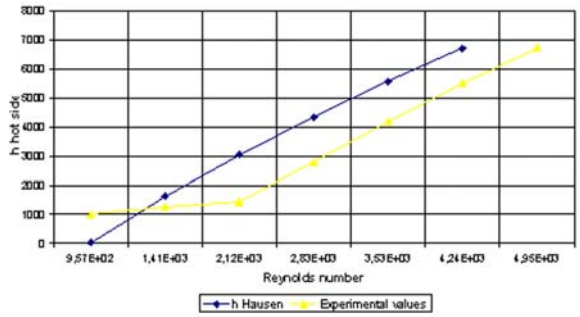

Figure 12: Cold side heat transfer coefficient vs. Reynolds number

RESULTS

Scope of the simulation was to compute the heat power exchanged in a full length (500mm) tubes radiator. Tables 9 and 10 compare the results of our Fluent® simulations with experimental data [1]. The error, defined as:

$$\frac{\varphi_{CFD} - \varphi_{EXP}}{\varphi_{EXP}} \qquad (4)$$

is reported in Table 11: it never exceeds 8% for any relevant variable.

Q [kW]		Coolant flow rate [kg/h]					
		1000	2000	3000	4000	5000	6000
Air flow rate [kg/h]	1000	11.1	11.9	12.04	12,9	14	13,3
	2000	18,1	20.64	21.61	26.2	26.5	28.5
	3000	21.9	25.8	27.9	33.4	36.4	36.7
	4000	24,1	29.54	31.96	38.8	43	44.8
	5000	26	31	34	43	48.1	52
	6000	27,2	33.1	36.4	47.1	51.6	56.2

Table 9: Heat exchanged for a 500mm radiator length - Fluent simulation

Q [kW]		Coolant flow rate [kg/h]					
		1000	2000	3000	4000	5000	6000
Air flow rate [kg/h]	1000	10,6	11,5	11,8	12,7	13	13,2
	2000	17,6	20,2	21,4	24,3	25,6	26,6
	3000	21,2	25,1	27,1	32,2	34,7	36,9
	4000	23,1	28,2	30,9	37,7	41,3	49,7
	5000	24,7	30,6	33,7	42,1	46,8	51,4
	6000	25,8	32,3	36,1	45,2	50,9	56,5

Table 10: Heat exchanged for a 500mm radiator length- Experimental data

		m-liq [kg/h]					
		1000	2000	3000	4000	5000	6000
Air flow rate [kg/h]	1000	4.50	3.36	1.99	1.55	7.14	1.50
	2000	2.76	2.13	0.97	7.25	3.39	7.71
	3000	3.19	2.71	2.86	3.59	4.67	1.90
	4000	4.14	4.53	3.31	2.83	3.95	3.12
	5000	5.00	1.29	0.88	2.09	2.70	4.42
	6000	5.14	2.41	0.82	4.03	1.35	3.55

Table 11: Heat exchange % error for a 500mm radiator length

To validate the theoretical required by our discrete model for the first zone of entrance length, we can consider experimental data derived for a 250mm radiator with the same fin geometry as the previous one.

Q [kW]		Coolant flow rate [kg/h]		
		1000	2000	3000
Air flow rate [kg/h]	1000	10,10	11.17	11,54
	2000	14,10	16,61	17,55
	3000	16,10	19,21	20,60

Table 12: Heat exchanged for a 250mm radiator - Fluent simulation

Q [kW]		Coolant flow rate [kg/h]		
		1000	2000	3000
Air flow rate [kg/h]	1000	0	0.63	0.34
	2000	0	1.33519	0.9
	3000	0	0.57	0.09

Table 13: 250 mm radiator heat exchange % error

From Tables 12 and 13 we observe that the shorter radiator exchanges a heat power much higher than the half of that exchanged by the 500mm one: this confirms that thermal transfer efficiency decreases as the entry length develops.

The graphs in figure 13 a through h report a graphic comparison between experimental and simulated results; each graph is for a single coolant flow rate over a range of air flow rates.

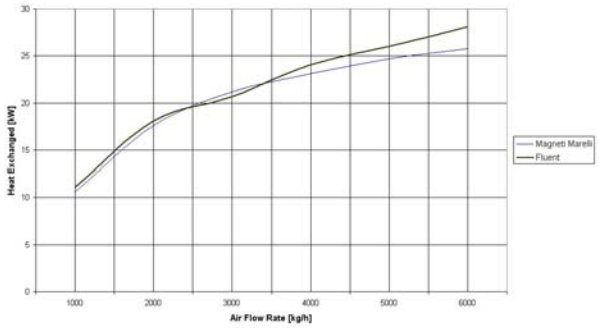

13 a: Heat exchanged within a radiator for 1000 [kg/h] hot fluid mass flow

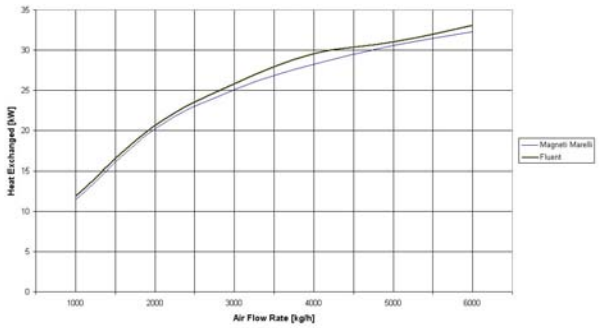

13 b: Heat exchanged within a radiator for 2000 [kg/h] hot fluid mass flow

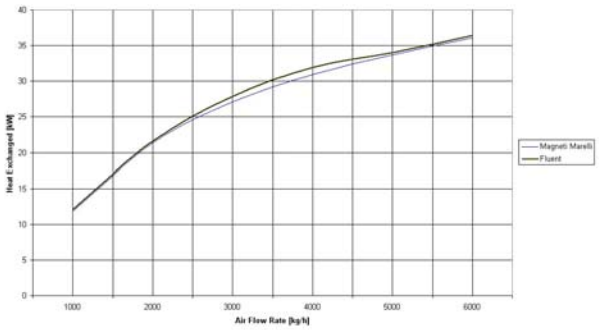

13 c: Heat exchanged within a radiator for 3000 [kg/h] hot fluid mass flow

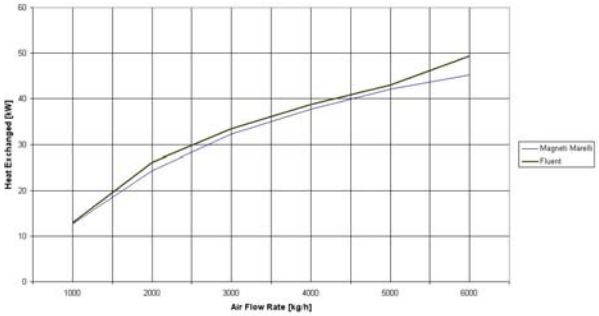

13 d: Heat exchanged within a radiator for 4000 [kg/h] hot fluid mass flow

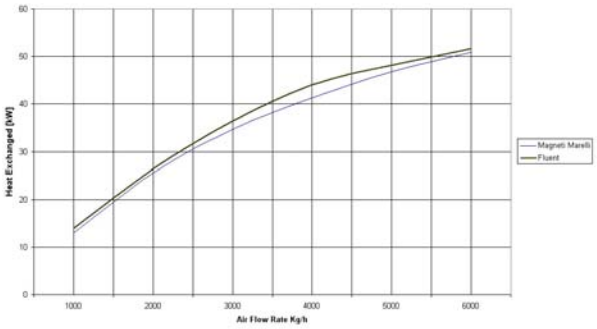

13 e: Heat exchanged within a radiator for 5000 [kg/h] hot fluid mass flow

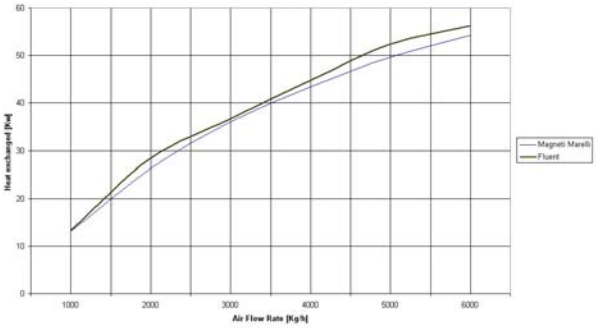

13 f: Heat exchanged within a radiator for 6000 [kg/h] hot fluid mass flow

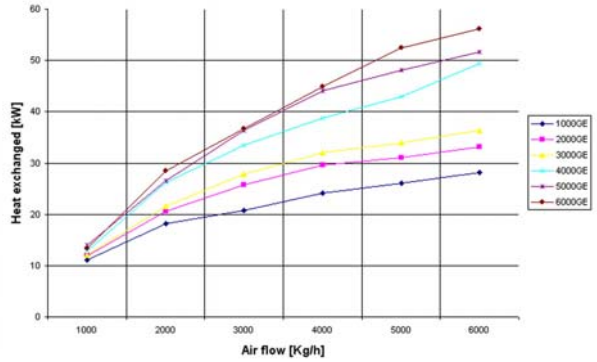

13 g: Heat exchanged vs air flow for different water flow rates

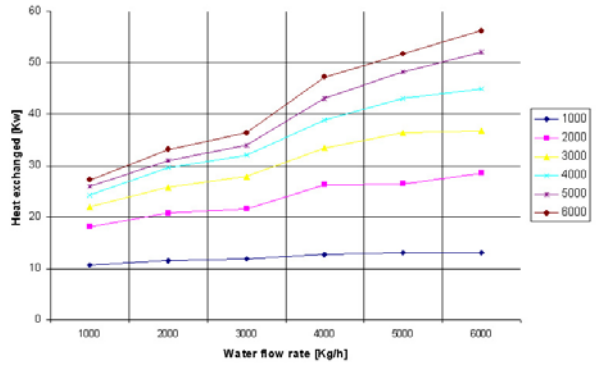

13 h: Heat exchanged vs water flow for different air flow rates

It is useful at this point to show the final temperature field on the single corrugation of the fin (figure 14) and the temperature of the cooling air for three different sections ordered according with the predominant air flow direction (figure 15): a fully three-dimensional thermal boundary development is observed, as expected. Of particular interest is the progressive reduction of the cold air core in the axial (y) direction: its asymptotic behavior suggests the existence of a practical upper limit to the axial thickness of the radiator. In correspondence of three sections of the fin like those shown in figure 15, the mean temperatures of the fin and the fluid free stream temperature were calculated. An averaged value of those ΔT was used to obtain the heat transfer coefficient for a single fin:

$$\overline{h} * A * \overline{\Delta T} = \overline{q} \qquad (5)$$

A graphical comparison between the values of global cold side heat transfer coefficient obtained with the above described method and those provided by experiments [1] are shown in figure 16.

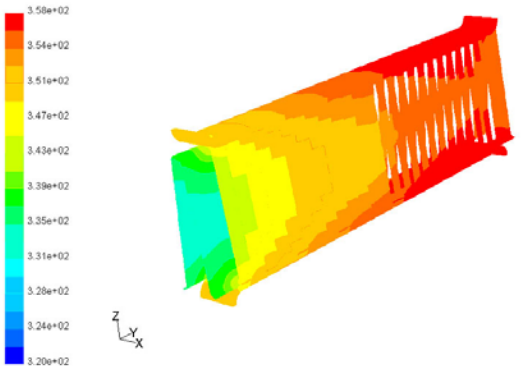

Figure 14: Temperature distribution on the single fin corrugation

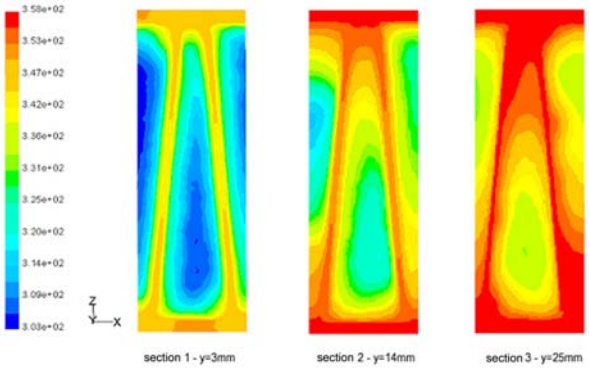

Figure 15: Cooling air temperature distribution for three sections perpendicular to the main flow

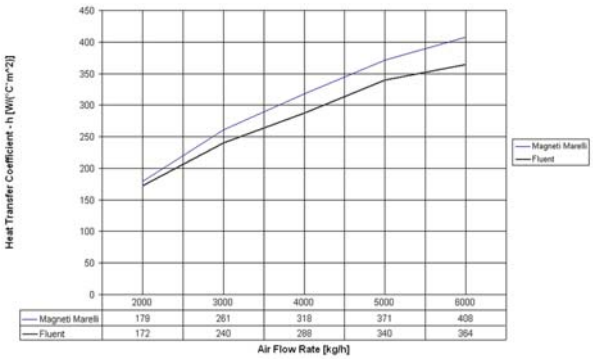

Figure 16: Cold side heat transfer coefficient vs air flow rate

SUMMARY AND CONCLUSIONS

This work presents a general procedure for predicting a compact heat exchanger performance by means of a numerical code.

As a workaround to the lack of literature data on coefficients and parameters necessary to the device performance evaluation, all simulations were performed on *ad hoc* model that implicitly calculated hard-to-predict unknown values.

A semi-empirical correlation accounting for Nusselt number variation along the hot fluid side was imposed on the internal tubes surfaces.

Values for the thermal entrance length were deduced from the parallel plates case, and this resulted in a possible underestimate of the thermal exchange.

The heat transfer coefficient was assumed to be piecewise constant for each longitudinal region of the tube, its value being calculated on the first elemental element of each slice: this caused an overestimate of the heat exchange performance. The two effects seem to balance and the numerical results agree very well with experimental data (within 8% error). The longer the slices of tubes on which the heat exchange coefficients are considered constant, the higher the error affecting the results. This is confirmed by comparisons with the results of a simulation of a 250mm lengh radiator, for which the numerical results were affected by a maximum error of 1.5%.

The values of the heat transfer coefficient on the finned surface result in good agreement with experimental data.

AKNOWLEDGMENTS

The authors acknowledge the technical support of the Magneti Marelli/Denso Thermal Division and of the Matra Automobile Engineering.

REFERENCES

[1] Biglia, M. Personal communication to M.R., 2000

[2] Bhatti, M.S., Shah, R.K., *Turbulent and transition flow convective heat transfer in ducts*, Ch. 4 in Handbook of single-phase convective heat transfer, S.Kacaç,

[3] Chandrupatla, A.R., Sastri V.M.K. *Laminar flow and heat trensfer to a non newtonian fluid in an entrance region of a square duct with prescribed constant axial wall heat flux, numer.heat transfer*, vol.1, pp. 243-254, 1974

[4] Chen, R.Y., *Flow in the entrance region at low Reynods numbers*, J.Fluids Eng.95, pp.153-158, 1973

[5] Garimella, S., Dowling, W., Van Der Veen M., Killion J.: *The effect of simultaneously developing flow on heat transfer in rectangular tubes*, Heat Transfer Engineering, vol.22,n°6, 2001,

[6] Hausen, H., *Darstellung der Wärmeüberganges in Rohren durch verallgemeinerte Potenbeziehungen*, VDI Z., N.4, pp. 91-98, 1943 (in German)

[7] Hwang, C.L., Fan, L.T. *Finite difference analysis of forced convection heat transfer in entrance region of a flat rectangular duct*, Appl.Sci.Res. Vol A.13, pp.401-422, 1964

[8] Kays, W.M., London, A.L., *Compact heat exchangers (third edition)*, McGraw Hill Book Company, 1984

[9] Mason, J.L.., *Heat Transfer in Cross-Flow,* Proc.Appl.Mechanics, 2nd US National Congress,1954

[10] Pfenninger, W., *Experiments with laminar flow in the inlet length of a tube at high Reynolds number with or without boundary layer suction*, Technical report, Northrop Aircraft INC, Hawthorne, Calif., May 1952

[11] Renault, *Manuel d'usine, Internal technical report*, 1996 (in French)

[12] Shah, R.K., London, A.L., *Laminar flow forced convection in ducts*, Academic Press, 1978, pag.22

[13] Shah, R.K., Aung, W., *Handbook of single-phase convective heat transfer*, 1987; John Wiley & sons

[14] Wibulwas, P., *Laminar flow heat transfer in non circular ducts*, Ph.D thesis, London University, London, 1966

[15] Robbe, M., Sciubba, E., *Scambio termico in un Radiatore per autovettura: Simulazione Numerica e sua Validazione Sperimentale*, Thesis, "La Sapienza" University, Rome, 2002 (in Italian)

Proceedings of ECOS 2005
Trondheim, Norway
June 20–22, 2005

EXHAUST GAS RECIRCULATION IN GAS TURBINES FOR REDUCTION OF CO_2 EMISSIONS. COMBUSTION TESTING WITH FOCUS ON STABILITY AND EMISSIONS.

Petter E. Røkke and Johan E. Hustad
Norwegian University of Science and Technology
Department of Energy and Process Engineering
N-7491 Trondheim

ABSTRACT

Exhaust gas recirculation can be applied with the intention to reduce the CO_2 emissions. When a fraction of the exhaust gas is injected in the entry of a gas turbine, the amount of CO_2 in the exhaust gas not being recirculated will be higher and less complicated to capture. However, with this change in combustion air composition, especially the reduced concentration of oxygen, the combustion process will be affected. The lower oxygen concentration decreases the stability and the increased amount of CO_2, H_2O and N_2 will decrease the combustion temperature and thus, the NO_x emissions. Testing has been performed on a 65 kW gas turbine combustor, to investigate the effect of adding N_2, CO_2 and O_2 in the combustion process, with focus on stability and emissions of NO_x. Results show that adding N_2 and CO_2 decrease the NO_x emissions, whereas O_2 addition increases the NO_x emissions. The tests have been performed both in a diffusion flame (pilot burner) and a premixed flame (main burner), and for additives being injected with the fuel or with the air stream. Addition into the fuel stream is proven to affect the NO_x emissions most. The stability limits of the flames are indicated with respect to massbased additive-to-fuel ratios.
Keywords: Exhaust gas recirculation, combustion, NO_x emissions

.

NOMENCLATURE

C_p	Specific Heat [kJ/kgK]
k	Chemical Equilibrium constant
T	Temperature [K]
w	Weighted coefficients [-]

Subscripts

0	Initial (without additives)
b	Backward reaction
f	Forward reaction

INTRODUCTION

Natural gas fired power generation facilities have always been considered as an environmental friendly power source, when compared to other fossil fuel based power sources such as for instance coal-fired power plants. The NO_x and CO emissions from natural gas fired power plants are significantly lower than when coal is applied as fuel. More recent focus has turned onto CO_2 emissions and the effect CO_2 has on the atmosphere. An increased greenhouse effect is proved to have a source in the higher concentration of CO_2 in the atmosphere. CO_2 stems from multiple human generated sources, along with more natural sources such as the photosynthesis. Combustion engines in cars, boats and planes contribute significantly, but the CO_2 from these distributed sources is difficult to handle. CO_2 from larger stationary combustion facilities, such as power plants can be handled with a CO_2 clean-up system. Several different technologies for CO_2 capture processes are being developed, as described in [1]. Especially the power demanding oil industry is interested in the development of so-called CO_2 free power generation sources. The CO_2-tax is a significant motivation for decreasing the CO_2 emissions into the atmosphere.

An alternative technology for CO_2 mitigation is to recirculate the exhaust gas of a simple cycle gas

turbine. A part of the exhaust gas can be recirculated to the entry of the gas turbine and mixed with the air. This will change the composition of the combustion air and thus, affect the combustion process. Most important with respect to NO_x emissions, the recirculated exhaust gas will decrease the O_2 concentration in the combustion air. With regards to CO_2 mitigation, the exhaust gas that is not recirculated will have a higher CO_2 concentration. One of the problems for post-combustion CO_2 separation, where the CO_2 is separated with an amine-process, is the low concentration of CO_2 in the exhaust gas. Thus, the exhaust gas from a recirculation process can give a higher CO_2 capture than for a regular gas turbine exhaust gas.

As mentioned, the combustion process is affected due to the change in combustion air composition. For gas turbines today that are operated with low emission combustion systems, most commonly so-called lean premixed systems, the flame stability will be affected by the lower O_2 concentration in the combustion air. Premixed combustion systems are highly dependent on the flame velocity of the mixture and a decrease in the O_2 concentration of the mixture lowers the flame velocity [2]. A decrease in the O_2 concentration, without further modifications of the system may then cause blowout of the flame. More conventional combustion systems that are operated with diffusion flames are less sensitive to variations in combustion air composition with regards to flame stability. NO_x emissions for such flames, however, are significantly higher than for lean premix combustion systems.

In gas burners so-called flue gas recirculation (FGR) is widely applied for reduction of NO_x emissions. Gas burners refer to 3 vol% O_2 in the exhaust gas in contrast to gas turbines that refer to 15 vol% O_2. In this paper, a gas turbine combustor has been applied for experiments on both a premixed and a diffusion flame with focus on NO_x emissions and how the addition of O_2, N_2 and CO_2 affects the NO_x emissions. O_2, N_2, CO_2 and H_2O are the main components in a hydrocarbon combustion process. Steam injection has not been applied in these experiments due to the available equipment in the laboratory, preheating to temperatures above 100ºC for the air supply has not been possible. The effect of steam is thus based on the literature. These experiments will also investigate the importance of O_2 concentration in the recirculated exhaust gas with respect to NO_x emissions.

EXPERIMENTAL SETUP

A gas turbine combustor is applied for combustion testing. The combustor has the possibility for both diffusion flame (pilot burner) and premixed flame operation (main burner).

A schematic of the rig is shown in Figure 1.

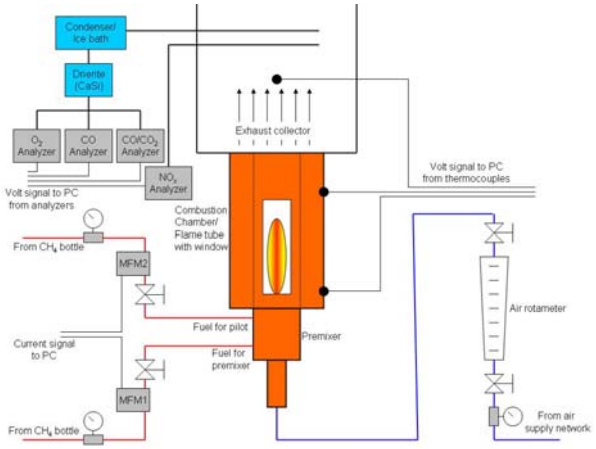

Figure 1. Experimental schematic.

Two mass flow meters are applied for the addition of two different components (fuel + additive). The additive can either be injected into the air stream or it can be premixed with the fuel. For premixing with the fuel, a mixing chamber with a fine metal grid inside it is built for efficient mixing.

A more detailed view on the premixer is shown in Figure 2. The combustion air enters vertically at (1), and flows through a section of 12 airfoil vanes (2) that creates a high swirl (tangential velocity/axial velocity~9). Premixed fuel injection is done through these vanes that are hollow and have four fuel injection holes on the pressure side of each vane. The fuel is distributed in the premix fuel manifold (5). About 2 % of the air flows through the center hollow reverse cone (3) for cooling of the perforated bluff-body (4) inside the combustor. The fuel manifold for the diffusion flame (6) distributes the fuel into the combustor through 12 holes.

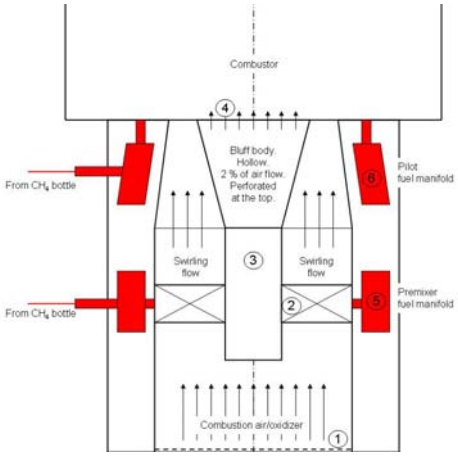

Figure 2. Premixer schematic.

A photo of the premixer and bluff-body is shown in Figure 3.

Figure 3. Premixer and bluff-body.

Measurements are performed on surface temperatures of the combustor, and the combustion gas. The concentrations of the species in the exhaust gas are measured as indicated in Figure 1. The mass flows of fuel and additive are controlled with needle valves and measured with mass flow meters, whereas the supply of air is controlled by a rotameter. The measured O_2 concentration in the exhaust gas is applied for calculation of exact air-excess ratios. As methane (CH_4) is the main component of natural gas it is applied as fuel.

EXPERIMENTAL RESULTS

First, stability limits for operation in diffusion and premixed mode is checked. In Figure 4, the indicated equivalence ratios where the flame becomes unstable is shown for operation in diffusion and premixed mode. The air supply is kept constant for each test, and the fuel supply is gradually decreased until the flame becomes unstable. The premixed flame LBO limit occurs at a 0.6 equivalence ratio, whereas the diffusion flame becomes unstable at an equivalence ratio below 0.25.

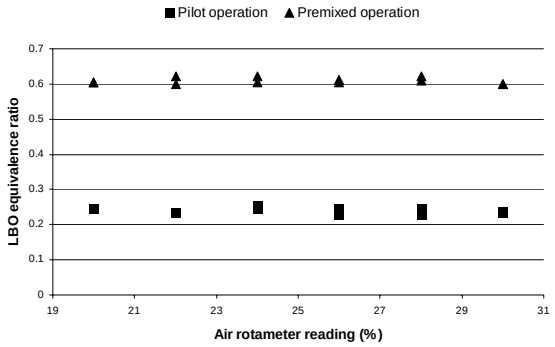

Figure 4. Lean Blowout (LBO) limits for diffusion and premixed operation.

Further, the emissions of CO and NO_x are measured for the two operation modes. The NO_x emissions are shown in Figure 5. The diffusion flame operation is a swirling co-flow flame, and the air supply to the flame is controlled. Usually, the equivalence ratio is not applied as a measure for diffusion flames, but since this is a confined system, it is an important parameter.

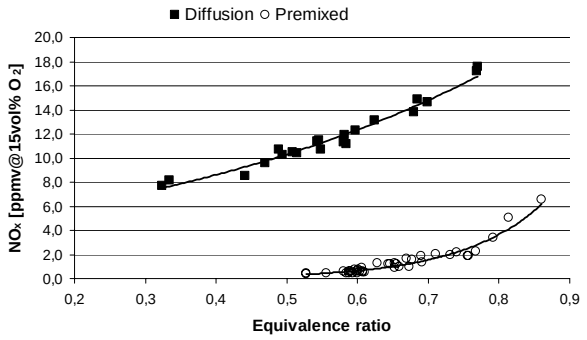

Figure 5. NO_x emissions measured for operation in diffusion and premixed mode.

The CO emissions measured were in general very low, especially for the premixed flame where the measured CO was below 3 ppmv for all equivalence ratios. For diffusion operation, the CO emissions increased significantly when approaching equivalence ratios below 0.5, as shown in Figure 6.

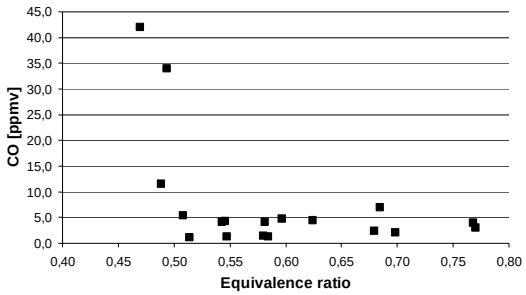

Figure 6. CO emissions for operation in diffusion mode.

Thus, the points for NO_x emissions below 0.5 equivalence ratio for diffusion operation are doubtful due to the high amounts of CO in the exhaust products. However, the higher NO_x emissions for diffusion operation than for premixed operation are not to be questioned.

The increase in NO_x emissions at higher equivalence ratios are as expected. Increasing the equivalence ratio gives a more fuel rich flame with higher flame temperature. Higher temperature affects the NO_x formation mainly through the thermal mechanism [3]. The increase in CO emissions at lean condition is caused by lower reaction ratios at lower flame temperatures.

A diffusion flame will always have a flame surface with a stoichiometric fuel-air composition. Thus, at the flame surface the temperature will be significantly higher than in a premixed flame where the overall equivalence ratio is leaner than stoichiometry. The NO_x emissions in a diffusion flame will thus be higher than in a lean premixed flame, just as the results here prove.

In the case of exhaust gas recirculation, an interesting issue is to see if the diffusion operation NO_x emissions can be reduced down to premixed operation levels.

The results given in Figure 7 show how the different additives affect the NO_x emissions in diffusion operation. The points with the highest additive-to-fuel ratio indicate stability limits where the flame becomes unstable due to the amount of additive being injected (not the actual blow-out limits). It is seen that the unstable flame occurs at lower ratios when the additive is premixed with the fuel than with the air stream. Even for O_2 enrichment of the flame, a stability limit is approached, already before an additive-to-fuel ratio at unity.

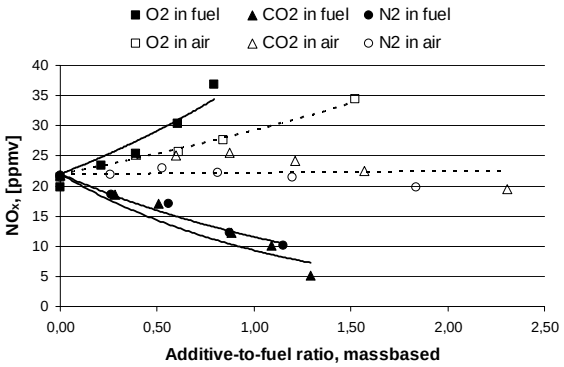

Figure 7. Additives effect on NO_x emissions in diffusion operation.

For additives being injected into the fuel stream, the flame is lifted when more additive is injected. This is due to the increased jet velocity out of the fuel nozzles. Also, the different additives have different molar weights, and thus, the molar additive-to-fuel ratio must be considered. Table 1 shows the values for the stability limits referred to Figure 7 for the massbased values.

	Mass	Molar
O_2/CH_4	0.79	0.40
CO_2/CH_4	1.29	0.47
N_2/CH_4	1.15	0.66

Table 1. Comparison of mass- and molar based stability limit additive-to-fuel ratios.

Premixing the additive with the fuel affects the NO_x emissions more than when injected with the air stream. Oxygen enrichment of the flame increases the NO_x emissions, both when injected with the fuel stream and with the air stream. When premixed with the fuel, the NO_x emissions are doubled already at an oxygen-fuel ratio below unity. CO_2 and N_2 injection seem to have quite similar effects on the NO_x emissions. A significant decrease is seen when premixed with the fuel, whereas addition into the air stream has less effect on the NO_x emissions. If steam could have been applied for the experiments, a more significant decrease in NO_x emissions would have been expected, due to a higher specific heat that would reduce the flame temperature more.

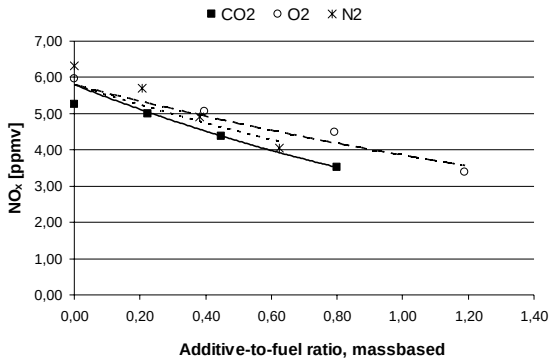

Figure 8. Additives effect on NO_x emissions in premixed operation.

The results from the experiments where the additives were injected into the flame in premixed operation are shown in Figure 8. Injection of additives into premixed operation of the flame is not affected by the injection point of the additive. The fuel and air mixture is well mixed. For all additives, the NO_x emissions decrease similarly. Even for oxygen addition to the fuel stream a decrease is seen. This is explained by the fact that for a well mixed premixed flame, operating lean, extra oxygen addition will only make the flame leaner, and the NO_x emissions will thus decrease.
The specific heat for the components of an exhaust gas is shown in Table 2.

T [K]	H_2O	CO_2	N_2	O_2
250 K	liquid	0.782	1.044	0.910
1000 K	2.267	1.232	1.167	1.085
2000 K	2.832	1.371	1.287	1.180

Table 2. Specific heat (C_p) values for H_2O, CO_2, N_2 and O_2 for different temperatures [kJ/kgK].

Steam has significantly higher specific heat than the other components and will surely affect the flame temperature in a larger degree than the other additives if evaluating only the thermal effect. The evaluation of the NO_x chemistry is similarly important. The thermal mechanism is often described by the following reaction as the rate determining step [3];

$$O + N_2 \underset{k_{1b}}{\overset{k_{1f}}{\Leftrightarrow}} NO + N \qquad (1)$$

Thus, the N_2 concentration in the flame is of main importance. It is referred to as the thermal NO_x formation mechanism because it is highly dependent on the temperature, especially at temperatures above 1850 K [4]. The prompt mechanism is determined by the sudden cracking of hydrocarbons in the flame, with the following reaction as the main [5]:

$$CH + N_2 \underset{k_{4b}}{\overset{k_{4f}}{\Leftrightarrow}} HCN + N \qquad (2)$$

The radical (CH) concentration is dependent on the temperature, and as for the thermal mechanism, the N_2 concentration is important. The principal reaction of the nitrous oxide mechanism is;

$$O + N_2 + M \underset{k_{5b}}{\overset{k_{5f}}{\rightleftharpoons}} N_2O + M \qquad (3)$$

Due to the third body dependence, this mechanism has more influence at increased pressure [6].
The results indicate that the flame being analyzed here is affected by the thermal effect when CO_2 or N_2 is added, since both have quite similar effect on the NO_x emissions. It is indicated in [7] that CO_2 may affect the NO_x formation mechanism. The CO_2 added will change the equilibrium of the $CO+OH \leftrightarrow CO_2+H$ reaction to the left, and thus compete with the $H+O_2 \leftrightarrow O+OH$ reaction for the H-atom. Fewer radicals in the flame are due to the lower temperatures, and thus less NO_x emissions. The specific heats are quite similar for the two components and thus the chemical effect is indicated to be less important for such a flame. The oxygen enrichment of the diffusion flame affects the chemical kinetics through the increased oxygen content in the flame, and also that the mixture turns towards a fuel-oxygen mixture rather than a fuel-air mixture. The properties of a CH_4-O_2 flame is significantly different than 0f a CH_4-air flame as described in Table 3.

Stoichiometric	CH_4-O_2	CH_4-Air
Flame temperature (K)	~3800	~2600
Flame velocity (cm/s)	330	40

Table 3. Different flame properties for CH_4 combustion in oxygen or in air.

The flame temperatures are calculated for atmospheric conditions [8] and the flame velocities from [2]. Thus, the thermal NO_x formation mechanism gives higher NO_x emissions with increased amount of oxygen enrichment. As

mentioned, the oxygen addition in the lean premixed flame, however, acts as a diluent.

EXHAUST GAS RECIRCULATION

The experiments performed here are with addition of the components in an exhaust gas separately. Limitations in the laboratory have excluded the possibility for injection of all components of an exhaust gas to simulate the actual combustion environment in such a process. The effect the reduction of O_2 concentration in the combustion air has on the blowout limits have been tested in [9], indicating that blow out for combustion air with less than 13.5 vol % O_2. In [10], it is said that 16-18 vol% O_2 is required for stability. The reduction in the flame velocity for some hydrocarbon fuels as a function of the oxygen concentration (in an oxygen-nitrogen mixture) is shown in [11], indicating a significant reduction when the oxygen concentration is reduced. The temperature change in the flame will also affect the combustion stability; lower temperature reduces the reaction rates and the reaction may become too slow to maintain stability. This is, however, not likely to affect the stability as much as the oxygen concentration and the flame velocity. The change in temperature is more likely to affect the NO_x emissions. As mentioned, the temperature affects both the prompt and (especially) the thermal NO_x formation mechanisms. The composition of the combustion air will have different bulk specific heats and specific heat ratio, which will give a change in the combustor inlet temperature and pressure. A change in the inlet temperature gives approximately half the change in flame temperature. This, along with the flame temperature change due to the additives, will influence the NO_x emissions.

The experiments performed with the additives being injected separately can be applied for correlating the recirculation of an exhaust gas. The trendlines can be extracted from the curves shown above and correlated in a single equation. The correlated trendlines for the different additives are as follows, based on the effect on NO_x emissions when the additive is premixed with the fuel:

$$\frac{NO_{x,O_2}}{NO_{x,0}} = e^{0.56\cdot(O_2/CH_4)_m} \quad (4)$$

$$\frac{NO_{x,N_2}}{NO_{x,0}} = e^{-0.64\cdot(N_2/CH_4)_m} \quad (5)$$

$$\frac{NO_{x,CO_2}}{NO_{x,0}} = e^{-0.86\cdot(CO_2/CH_4)_m} \quad (6)$$

Steam injection into the combustor, premixed with the fuel, has been investigated in the Cheng Low NO_x process [12]. With emphasis on homogeneity in the fuel-steam mixture, NO_x reduction has been proven without increasing the CO emissions. A decrease in the homogeneity of the fuel-steam mixture would increase the CO emissions significantly. From the results shown for NO_x emissions as a function of steam injection in [12], a trendline can be extracted as follows;

$$\frac{NO_{x,H_2O}}{NO_{x,0}} = e^{-0.90(H_2O/CH_4)} \quad (7)$$

Now, these four equations - (4), (5), (6) and (7) – can be combined into one expression for modelling of an exhaust gas recirculation process. This can be done as shown here;

$$NO_{x,total} = w_{CO_2} NO_{x,CO_2} + w_{H_2O} NO_{x,H_2O} + w_{O_2} NO_{x,O_2} + w_{N_2} NO_{x,N_2} \quad (8)$$

where w_i are coefficients for the different additives that may be adjusted due to the influence of the additives. The denominator ($NO_{x,0}$) is already eliminated since it is the same for all additives, and also for the total exhaust gas recirculation process. The w_i coefficient can be set as 0.25 if similar influence from the additives is assumed. If the recirculated exhaust gas is free of oxygen (from a stoichiometric combustion process), the coefficients for CO_2, H_2O and N_2 are set as 0.33, and the coefficient for O_2 as zero. In the case of air addition (partially premixed flame), the coefficients for O_2 and N_2 are set as 0.5 and the rest as zero.

The composition of the exhaust gas will vary due to the air excess ratio (lambda = 1/equivalence ratio) in the combustion process. Figure 9 shows how the O_2 concentration in the exhaust gas varies as a function of the air excess ratio. Gas turbines operate with an overall air excess ratio in the

range from 3-4 which gives 13-15 vol% O_2 in the exhaust gas. For the recirculation of exhaust gas the concentrations of O_2, N_2, CO_2 and H_2O are calculated, which is required for predictions based on equation (8).

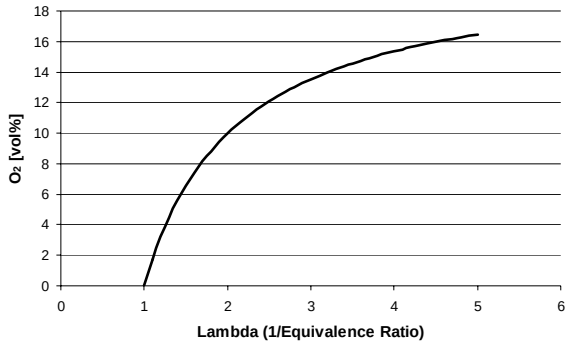

Figure 9. O_2 concentration in the exhaust gas as a function of the air excess ratio.

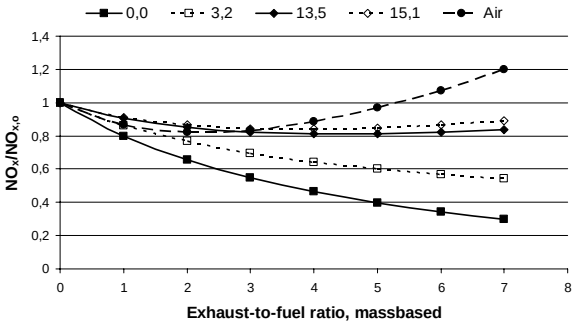

Figure 10. NO_x emissions as function of exhaust-to-fuel ratio in the combustion process. The different curves describe exhaust gas with the specified concentration of oxygen.

Applying equation (8) for varying amounts of exhaust gas being recirculated, the NO_x emissions varies as shown in Figure 10, dependent on the amount of oxygen in the recirculated gas. The lower line, with the most efficient NO_x reduction, is with exhaust gas from a complete combustion process (no oxygen). On the opposite side, applying pure air, with 20.9 vol % oxygen, gives an optimum "additional air"-to-fuel ratio (exhaust-to-fuel ratio in the figure) around 3. This is then the case for a partially premixed combustion process. The curves indicate that for the cases with higher oxygen concentrations, an optimum exhaust-to-fuel ratio can be found, approaching 3 for the partially premixed case. It is seen that for 15 vol % O_2 content in the exhaust gas, which is reference for gas turbine processes, a 20 % decrease in NO_x emissions can be achieved. A 20 % decrease in NO_x emissions in the diffusion operation mode is far from the levels achieved in premixed operation. In the case of gas burners, 3 vol % O_2 is the reference value. Thus, it is seen that a 40 % decrease in NO_x emissions can be achieved with an exhaust-to-fuel ratio at 7 for such applications. For gas turbines, the improvement potential points towards methods that can reduce the oxygen content of the recirculated exhaust gas, which will reduce the NO_x emissions further. O_2 can for instance be separated from the exhaust gas, which is a costly process. A less costly alternative is to supply additional fuel for afterburning, which then will reduce the oxygen content further.

The advantage for NO_x emissions in diffusion flames with exhaust gas recirculation is not comparable to premixed flames NO_x levels. But with the emphasis to increase the CO_2 concentration in the exhaust gas, the 20 % reduction in NO_x emissions is a positive side-effect. Post combustion CO_2 capture processes may be suited to absorb the NO_x in the exhaust gas, and thus the NO_x emissions can be avoided for such a process.

CONCLUSIONS

Experiments have been performed on a gas turbine combustor with the emphasis on stability and NO_x emissions. The combustor has been operated both in diffusion mode and premixed mode, proving that lean premixed operation is significantly more advantageous for low NO_x emissions.

To simulate the effect the components of an exhaust gas has on stability and NO_x emissions, experiments have been performed with addition of O_2, N_2 or CO_2 injected either into the fuel or into the air stream. Steam injection has been referenced from the literature. Oxygen enrichment of the diffusion flame increases the NO_x emissions, both when injected into the fuel and into the air stream, whereas N_2 and CO_2 act as diluents. For injection with the fuel on the diffusion flame, a decrease in NO_x emissions is

seen, whereas a negligible change in NO_x is seen when injected into the air stream. All additives act as diluents when injected into a lean premixed flame.

Modeling of exhaust gas recirculation has been done, based on the experiments with the additives injected separately. This indicates that the amount of O_2 in the exhaust gas plays an important role, concerning the NO_x emissions with the change in composition of the combustion air.

REFERENCES

[1] Bolland, O., Hagen, R. I., Maurstad, O., Tangen, G., Juliussen, O., Svendsen, H., "Gasskraftverk med CO_2-håndtering. Studie av alternative teknologier.", SINTEF Technical Report TR A5693, 2002. In Norwegian only.

[2] Pourkashanian, M., Yapp, L., Williams, A., Applied Energy Research, Proceedings of the Institute of Energy Conference held in Swansea, UK, 5-7 September 1989.

[3] Zel'dovich, Y. B., Sadovnikov, P. Y., Frank-Kaminetskii, D. A., M. Shelef, Trans., Academy of Sciences of USSR, Inst of Chem Physics, Moscow-Leningrad (1947).

[4] Lefebvre, A. H., "Gas Turbine Combustion", Taylor & Francis Ltd, Printed by Edwards Brothers, Ann Arbor, MI, 1998.

[5] Fenimore, C. P., 13th Symp. Comb., pp 373-379 (1971).

[6] Drake, M.C. & Blint, R.J. Comb. Flame 83:185-203 (1991)

[7] Liu, F., Guo, H., Smallwood, G. J., Comb. Flame 133:495-497, (2003).

[8] http://grashof.engr.colostate.edu/tools/, Chemical Equilibrium.

[9] Wheeler, R. V., "The Effects of Incombustible Gases", 1955, slide in course material from "Ultra Low NOx Gas Turbine Combustion" at Leeds University, January 2001.

[10] Bolland, O. and Mathieu, P., Energy Conversion and Management, 39 (16-18), p. 1653-1663, 1997.

[11] Glassmann, I., "Combustion", 3. edition, p. 159, Academic Press Inc., 1996.

[12] Sahai, V., Cheng, D.Y., ASME GT2003-38208, 2003.

Proceedings of ECOS 2005
Trondheim, Norway
June 20–22, 2005

MODIFIED THEORIES OF LAMINAR AND TURBULENT SWIRLING JETS

Siavash H. Sohrab
Robert McCormick School of Engineering and Applied Science
Department of Mechanical Engineering
Northwestern University, Evanston, Illinois 60208
UNITED STATES OF AMERICA
s-sohrab@northwestern.edu
http://www.mech.northwestern.edu/dept/people/faculty/sohrab.html

ABSTRACT

Scale-invariant forms of mass, energy, and linear momentum conservation equations in chemically reactive fields are described. The modified equation of motion is then solved for the classical problem of axisymmetric laminar rotating free jet. The results are shown to be in agreement with the classical theories of *Loitsianskii* and *Görtler*. The problem of turbulent axisymmetric rotating jet is shown to have solutions identical to those of laminar jet. Temperature distributions of axisymmetric and two-dimensional turbulent jets are determined and the latter results are found to be in agreement with the observations of *Reichardt*.

Keywords: Theory of laminar and turbulent cylindrically symmetric rotating jets. Decay of swirl.

INTRODUCTION

The universality of turbulent phenomena from stochastic quantum fields to classical hydrodynamic fields [1-26] resulted in recent introduction of a scale-invariant model of statistical mechanics and its application to the field of thermodynamics [27]. The implications of the model to the study of transport phenomena and invariant forms of conservation equations have also been addressed [28, 29]. In the present study, following the classical studies of *Loitsianskii* [39] and *Görtler* [40], the modified equation of motion is solved for the classical problem of laminar axisymmetric rotating jet. The predicted analytical solutions are found to reduce to the approximate solutions obtains from the classical form of the equation of motion. The solutions of the modified forms of the equation of motion and energy at the larger scale of laminar eddy-dynamics LED representing turbulent axi-symmetric rotating jet are also discussed.

SCALE-INVARIANT FORMS OF THE CONSERVATION EQUATIONS FOR REACTIVE FIELDS

Following the classical methods [30-32], the invariant definitions of the density ρ_β, and the velocity of *atom* $\mathbf{u}_\beta$, *element* $\mathbf{v}_\beta$, and *system* $\mathbf{w}_\beta$ at the scale β are given as [29]

$$\rho_\beta = n_\beta m_\beta = m_\beta \int f_\beta du_\beta \quad , \quad \mathbf{u}_\beta = \mathbf{v}_{\beta-1} \tag{1}$$

$$\mathbf{v}_\beta = \rho_\beta^{-1} m_\beta \int \mathbf{u}_\beta f_\beta d\mathbf{u}_\beta \quad , \quad \mathbf{w}_\beta = \mathbf{v}_{\beta+1} \tag{2}$$

Also, the invariant definitions of the peculiar and the diffusion velocities are given as [29]

$$\mathbf{V}'_\beta = \mathbf{u}_\beta - \mathbf{v}_\beta \quad , \quad \mathbf{V}_\beta = \mathbf{v}_\beta - \mathbf{w}_\beta = \mathbf{V}'_{\beta+1} \tag{3}$$

Next, following the classical methods [30-32], the scale-invariant forms of mass, thermal energy, and linear momentum conservation equations at scale β are given as [29]

$$\frac{\partial \rho_\beta}{\partial t} + \nabla.\left(\rho_\beta \mathbf{v}_\beta\right) = \Omega_\beta \tag{4}$$

$$\frac{\partial \varepsilon_\beta}{\partial t} + \nabla.\left(\varepsilon_\beta \mathbf{v}_\beta\right) = 0 \tag{5}$$

$$\frac{\partial \mathbf{p}_\beta}{\partial t} + \nabla.\left(\mathbf{p}_\beta \mathbf{v}_\beta\right) = 0 \tag{6}$$

involving the *volumetric density* of thermal energy $\varepsilon_\beta = \rho_\beta h_\beta$ and linear momentum

$\mathbf{p}_\beta = \rho_\beta \mathbf{v}_\beta$. Also, Ω_β is the chemical reaction rate and h_β is the absolute enthalpy [28].

The local velocity $\mathbf{v}_\beta$ in (4)-(6) is expressed in terms of the convective $\mathbf{w}_\beta = \langle \mathbf{v}_\beta \rangle$ and the diffusive $\mathbf{V}_\beta$ velocities [29]

$$\mathbf{v}_\beta = \mathbf{w}_\beta + \mathbf{V}_{\beta g} \quad , \quad \mathbf{V}_{\beta g} = -D_\beta \nabla \ln(\rho_\beta) \qquad (7a)$$

$$\mathbf{v}_\beta = \mathbf{w}_\beta + \mathbf{V}_{\beta tg} \quad , \quad \mathbf{V}_{\beta tg} = -\alpha_\beta \nabla \ln(\varepsilon_\beta) \qquad (7b)$$

$$\mathbf{v}_\beta = \mathbf{w}_\beta + \mathbf{V}_{\beta hg} \quad , \quad \mathbf{V}_{\beta hg} = -\nu_\beta \nabla \ln(\mathbf{p}_\beta) \qquad (7c)$$

where ($\mathbf{V}_{\beta g}$, $\mathbf{V}_{\beta tg}$, $\mathbf{V}_{\beta hg}$) are respectively the diffusive, the thermo-diffusive, and the linear hydro-diffusive velocities.

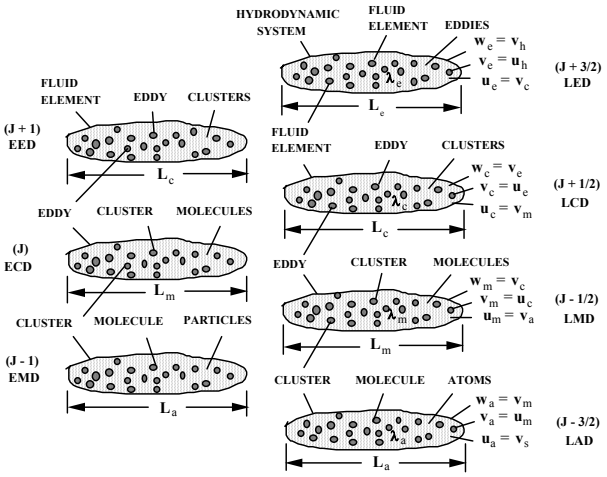

Figure 1: Hierarchy of statistical fields for equilibrium eddy-, cluster-, and molecular-dynamic scales and the associated laminar flow fields.

For unity *Schmidt* and *Prandtl* numbers, one may express

$$\mathbf{V}_{\beta tg} = \mathbf{V}_{\beta g} + \mathbf{V}_{\beta t} \quad , \quad \mathbf{V}_{\beta t} = -\alpha_\beta \nabla \ln(h_\beta) \qquad (8a)$$

$$\mathbf{V}_{\beta hg} = \mathbf{V}_{\beta g} + \mathbf{V}_{\beta h} \quad , \quad \mathbf{V}_{\beta h} = -\nu_\beta \nabla \ln(\mathbf{v}_\beta) \qquad (8b)$$

that involve the thermal $\mathbf{V}_{\beta t}$, and linear hydrodynamic $\mathbf{V}_{\beta h}$ diffusion velocities [29]. Since for an ideal gas $h_\beta = c_{p\beta} T_\beta$, when $c_{p\beta}$ is constant and $T = T_\beta$, Eq.(8a) reduces to the *Fourier* law of heat conduction

$$\mathbf{q}_\beta = \rho_\beta h_\beta \mathbf{V}_{\beta t} = -\kappa_\beta \nabla T \qquad (9)$$

where κ_β and $\alpha_\beta = \kappa_\beta / (\rho_\beta c_{p\beta})$ are the thermal conductivity and diffusivity. Similarly, (8b) may be identified as the shear stress associated with diffusional flux of linear momentum and expressed by the generalized *Newton* law of viscosity [29]

$$\boldsymbol{\tau}_{ij\beta} = \rho_\beta \mathbf{v}_{j\beta} \mathbf{V}_{ij\beta h} = -\mu_\beta \partial \mathbf{v}_{j\beta} / \partial \mathbf{x}_i \qquad (10)$$

Substitutions from (7a)-(7c) into (4)-(6), neglecting cross-diffusion terms and assuming constant transport coefficients with $Sc_\beta = Pr_\beta = 1$, result in [29]

$$\frac{\partial \rho_\beta}{\partial t} + \mathbf{w}_\beta . \nabla \rho_\beta - D_\beta \nabla^2 \rho_\beta = \Omega_\beta \qquad (11)$$

$$h_\beta \left[\frac{\partial \rho_\beta}{\partial t} + \mathbf{w}_\beta . \nabla \rho_\beta - D_\beta \nabla^2 \rho_\beta \right] + \rho_\beta \left[\frac{\partial h_\beta}{\partial t} + \mathbf{w}_\beta . \nabla h_\beta - \alpha_\beta \nabla^2 h_\beta \right] = 0 \qquad (12)$$

$$\mathbf{v}_\beta \left[\frac{\partial \rho_\beta}{\partial t} + \mathbf{w}_\beta . \nabla \rho_\beta - D_\beta \nabla^2 \rho_\beta \right] + \rho_\beta \left[\frac{\partial \mathbf{v}_\beta}{\partial t} + \mathbf{w}_\beta . \nabla \mathbf{v}_\beta - \nu_\beta \nabla^2 \mathbf{v}_\beta \right] = 0 \qquad (13)$$

In the first and second parts of (12) and (13), the *gravitational* versus the *inertial* contributions to the change in energy and momentum density are apparent. Substitutions from (11) into (12)-(13) result in the invariant forms of conservation equations in chemically reactive fields [29]

$$\frac{\partial \rho_\beta}{\partial t} + \mathbf{w}_\beta . \nabla \rho_\beta - D_\beta \nabla^2 \rho_\beta = \Omega_\beta \qquad (14)$$

$$\frac{\partial T_\beta}{\partial t} + \mathbf{w}_\beta . \nabla T_\beta - \alpha_\beta \nabla^2 T_\beta = -h_\beta \Omega_\beta / (\rho_\beta c_{p\beta}) \qquad (15)$$

$$\frac{\partial \mathbf{v}_\beta}{\partial t} + \mathbf{w}_\beta . \nabla \mathbf{v}_\beta - \nu_\beta \nabla^2 \mathbf{v}_\beta = -\mathbf{v}_\beta \Omega_\beta / \rho_\beta \qquad (16)$$

An investigation of the system (14)-(16) in the presence of chemical reactions Ω resulted in a modified hydro-thermo-diffusive theory of laminar flames presented earlier [29]. It is emphasized here that in (16) the convective velocity $\mathbf{w}_\beta$ is different from the local fluid velocity $\mathbf{v}_\beta$.

SOLUTION OF THE MODIFIED EQUATION OF MOTION FOR LAMINAR AXI-SYMMETRIC ROTATING JET

As examples of exact solutions of the modified equation of motion (16), the classical problems [32-41] of laminar [42] and turbulent [43] flow in axisymmetric and two-dimensional jets were investigated. In the present study, the modified equation of motion is solved for the classical problem of axi-symmetric laminar rotating jet investigated by *Loitsianskii* [39] and *Görtler* [40]. Therefore, one looks for the local axial, radial and azimuthal velocities (v'_x, v'_r, v'_θ) along the corresponding coordinates (x', r', θ) and introduces the dimensionless quantities

$$(v_x,\ v_r, w_x,\ w_r) = (v'_x,\ v'_r, w'_x,\ w'_r)/w'_o$$

$$v_\theta = \frac{v'_\theta}{\sqrt{\nu\omega_o}} \quad , \quad w_\theta = \frac{w'_\theta}{\sqrt{\nu\omega_o}} \quad , \quad \theta = \frac{T - T_\infty}{T_o - T_\infty}$$

$$r = \frac{r'}{l_H} \quad , \quad x = \frac{x'}{l_H} \quad , \quad l_H = l_T = \frac{\nu}{w'_o} = \frac{\alpha}{w'_o} \tag{21}$$

The initial axial convective velocity w'_o at the origin of the jet is assumed to be known and signifies the strength of the jet. Also, the initial angular frequency ω_o at the origin of the jet is known and signifies the strength of the jet angular momentum. Hence, in (21) both the local and the convective dimensionless azimuthal velocities (v_θ, w_θ) involve this initial jet angular frequency. The parameters ν and α are the kinematic viscosity and thermal diffusivity and l_H and l_T are the characteristic hydrodynamic and thermal lengths. The steady dimensionless forms of the modified equation of motion (16), energy (15), and the continuity equation (4) for incompressible fluid with the usual boundary layer assumptions and in the absence of chemical reactions Ω = 0 reduce to

$$w_x \frac{\partial \mathbf{v}_x}{\partial x} + w_r \frac{\partial \mathbf{v}_x}{\partial r} = \frac{\partial^2 \mathbf{v}_x}{\partial r^2} + \frac{1}{r}\frac{\partial \mathbf{v}_x}{\partial r} \tag{22}$$

$$w_x \frac{\partial \mathbf{v}_\theta}{\partial x} + w_r \frac{\partial \mathbf{v}_\theta}{\partial r} + \frac{w_\theta \mathbf{v}_r}{r} = \frac{\partial^2 \mathbf{v}_\theta}{\partial r^2} + \frac{1}{r}\frac{\partial \mathbf{v}_\theta}{\partial r} - \frac{\mathbf{v}_\theta}{r^2} \tag{23}$$

$$w_x \frac{\partial \theta}{\partial x} + w_r \frac{\partial \theta}{\partial r} = \frac{\partial^2 \theta}{\partial r^2} + \frac{1}{r}\frac{\partial \theta}{\partial r} \tag{24}$$

$$\frac{\partial v_x}{\partial x} + \frac{\partial v_r}{\partial r} + \frac{v_r}{r} = 0 \tag{25}$$

subject to the boundary conditions

$$r = 0 \qquad \frac{\partial v_x}{\partial r} = \frac{\partial \theta}{\partial r} = v_r = 0 \tag{26a}$$

$$r \to \infty \qquad v_r = v_\theta = v_x = \theta = 0 \tag{26b}$$

To solve equation (22), the convective velocities (w_x, w_r) that are the average of the local axial and radial velocities (v_x, v_r) are needed. Because the jet momentum is initially only in the axial direction, the radial dispersion of the jet is entirely caused by diffusion of axial momentum in the radial direction. Therefore, the jet diameter d' at any axial position will be given by the radial diffusion length

$$d'^2 = 2\nu t' \tag{27}$$

where the local diffusion time t' is related to the axial position x' and the local convective velocity w'_x by

$$t' = x'/w'_x \tag{28}$$

The dimensionless jet cross sectional area A' is given by

$$A = A'/(\nu/\omega_o) = \pi d^2/4 = \\ = (\pi/2)\, t = (\pi/2)\, x/w_x \tag{29}$$

Hence, the mass flow rate at any axial position will vary as

$$Q = \rho A' w'_x \propto \rho A w_x \propto x \tag{30}$$

where the symbol (∝) in (30) denotes proportionality. On the other hand, the total axial momentum along the jet must remain constant [32] and hence

$$J = Q w'_x \propto x\, w_x = \text{constant} \tag{31}$$

leading to the dimensionless convective velocity [35]

$$w_x = \frac{1}{2x} \tag{32}$$

Solving the global continuity equation

$$\frac{\partial w_x}{\partial x}+\frac{\partial w_r}{\partial r}+\frac{w_r}{r}=0 \tag{33}$$

after substitution from (32) results in

$$w_r=\frac{r}{4x^2} \tag{34}$$

Following *Schlichting* [32], one introduces the stream function Ψ and the similarity variable η

$$\Psi = x\,F(\eta) \qquad , \qquad \eta=\frac{r}{x} \tag{35}$$

leading to the axial velocity

$$v_x=\frac{F'(\eta)}{x} \tag{36}$$

Substitutions from (32), (34), (35), and (36) into (22) results in [42]

$$zF'''+(z^2+1)F''+2zF'=0 \tag{37}$$

$$z=0 \qquad F''=0 \tag{38}$$

$$z\to\infty \qquad F'=0 \tag{39}$$

where $z=\eta/2$ and primes denote differentiation with respect to z. The bounded solution of (37)-(39) is

$$F'=\exp(-z^2/2)]=\exp(-\eta^2/8)] \tag{40}$$

that by (36) gives

$$v_x=\frac{\exp(-\eta^2/8)}{x} \tag{41}$$

From (35) and (41), the stream function that satisfies $\Psi = 0$ at $\eta = 0$ is obtained as

$$\Psi=4x[1-\exp(-\eta^2/8)] \tag{42}$$

that in turn gives the radial velocity

$$v_r=\frac{1}{x}\left[\eta\exp(-\eta^2/8)-\frac{4}{\eta}\left(1-\exp(-\eta^2/8)\right)\right] \tag{43}$$

Since (24, 26) are similar to (22, 26), the distribution of temperature θ is similar to that of the axial velocity (41) and given by

$$\theta=\frac{\exp(-\eta^2/8)}{x} \tag{44}$$

Therefore, the ratio of the axial velocity v_x (temperature θ) to the centerline velocity v_{xc} (temperature θ_c) becomes

$$\frac{v_x}{v_{xc}}=\exp(-\eta^2/8) \tag{45}$$

$$\frac{\theta}{\theta_c}=\exp(-\eta^2/8) \tag{46}$$

The mass flow rate Q is given by [42]

$$Q=2\pi\rho\int_0^\infty v_x' r'dr'=8\pi\rho\nu x' \tag{47}$$

in exact agreement with the classical result of *Schlichting* [32]. Also, the axial momentum J

$$J=2\pi\rho\int_0^\infty v_x'^2 r'dr'=4\pi\rho\nu^2 \tag{48}$$

is a constant independent of the jet strength w'_o in accordance with the classical results [32].

At large values of x for which the present similarity solution is valid, i.e. for small values of $z=\eta/2$, (41) can be expressed as

$$v_x=\frac{\exp(-z^2/2)}{x}=\frac{1}{x}\frac{1}{\exp(-z^2/2)}$$

$$=\frac{1}{x}\frac{1}{\exp(-z^2/2)}\approx\frac{1}{x}\frac{1}{\left(1+z^2/4\right)^2} \tag{49}$$

that is in exact agreement with the classical solution [32] except for some multiplicative constants. Therefore, it is expected that the excellent agreement of the classical theory of *Schlichting* [32] with the experimental observations also extend to the modified theory [42].

The above results are now used in the azimuthal momentum conservation equation (23) to determine the angular velocity. The radial velocity can be approximated as

$$v_r=\frac{1}{x}\left[\eta\exp(-\eta^2/8)-\frac{4}{\eta}\left(1-\exp(-\eta^2/8)\right)\right]$$

$$\approx\frac{1}{x}\eta\exp(-\eta^2/8) \tag{50}$$

since under the assumption $x >>1$ ($\eta<<1$) valid for the similarity solution being considered, the second term can be neglected. Substituting (50) along with the similarity form

$$v_\theta = \frac{H(\eta)}{x^2} \tag{51}$$

and the convective velocities (32), (34), and

$$w_\theta = \frac{\eta}{4x^2} \tag{52}$$

into (23) results in

$$\eta^2 H'' + \eta(1+\eta^2/4)H' + (\eta^2 - 1)H - (\eta^3/4)\exp(-\eta^2/8) = 0 \tag{53}$$

$$\eta = 0 \qquad H = 0 \tag{54a}$$

$$\eta \to \infty \qquad H = 0 \tag{54b}$$

The solution of (53)-(54) is

$$H = \eta \exp(-\eta^2/8) \tag{55}$$

that by (51) leads to the angular velocity

$$v_\theta = \frac{\eta \exp(-\eta^2/8)}{x^2} \tag{56}$$

The rapid decay of the angular velocity with axial position in (56) is in accordance with the classical results [39-41].

The predictions of the modified theory are next compared with the classical results. As shown in (49), for z<<1 the axial velocity can be approximated as

$$v_x \approx \frac{1}{x\left(1+z^2/4\right)^2} \tag{57}$$

By substitution of (57) in the continuity equation (25) one obtains the approximate radial velocity

$$v_r \approx \frac{z(1-z^2/4)}{x(1+z^2/4)^2} \tag{58}$$

Finally, for z<<1 the angular velocity in (56) may be approximated by

$$v_\theta \approx \frac{2z}{x^2(1+z^2/4)^2} \tag{59}$$

Except for some multiplicative constants, the results (57)-(59) are in exact agreement with the classical solutions of *Loitsianskii* [39] and *Görtler* [40] discussed by *Crabtree* , *Kuchemann*, and *Sowerby* [41].

According to the classical results [39-41], the jet rotation has negligible influence on the axial and radial velocities. The weak effects occur indirectly through the pressure term that is in the parameter M signifying the total axial momentum. That is, the angular velocity v_θ in the angular momentum parameter L influences the pressure field p, that in turn influences linear momentum parameter M, thereby affecting (v_x, v_r) [41]. However, because of the small factor of 2^{-11} appearing in the expression for the dimensionless pressure in the classical theory [41], the effects of rotation on velocities (v_x, v_r) will be exceedingly small. According to the modified theory presented herein, the jet rotation does not influence either the axial or the radial velocity profiles.

SOLUTION OF THE MODIFIED EQUATION OF MOTION FOR TURBULENT AX--SYMMETRIC ROTATING JET

The scale-invariant nature of the conservation equations (14)-(16) suggests that the problem of turbulent rotating jet will be governed by the same equations (14)-(16) except at the next larger scale of laminar-eddy-dynamics LED $\beta = e$. However, the transport properties such as the momentum diffusivity ν and the thermal diffusivity α will now correspond to eddy-diffusivity for momentum ν_e and heat α_e. Therefore, as discussed in a recent study [43], the solution to the problem of turbulent rotating jet will be identical to those already found for laminar jet (41)-(43). In particular, from (45), the ratio of the axial velocity to the centerline value v_{xc} for turbulent rotating jet will be [43]

$$\frac{v_x}{v_{cx}} = \exp(-\eta^2/8) \tag{60}$$

Therefore, the transverse position where v_x is half its maximum, i.e. centerline value v_{xc} becomes

$$\eta^* = \eta(v_{cx}/2) = [-8\ln(0.5)]^{1/2} \tag{61}$$

such that (60) may be expressed as

$$\frac{v_x}{v_{cx}} = \exp[\ln(0.5)\xi^2] \quad , \quad \xi = \frac{\eta}{\eta^*} \tag{62}$$

Similarly, from (46) one obtains

$$\frac{\theta}{\theta_c} = \exp[\ln(0.5)\xi^2] \tag{63}$$

where θ_c is the temperature at the jet centerline.

The predicted axial velocity profile calculated from (62) using *Mathematica* [44] is in

excellent agreement with the experimental data of *Reichardt* [37-38] as shown in Fig.2.

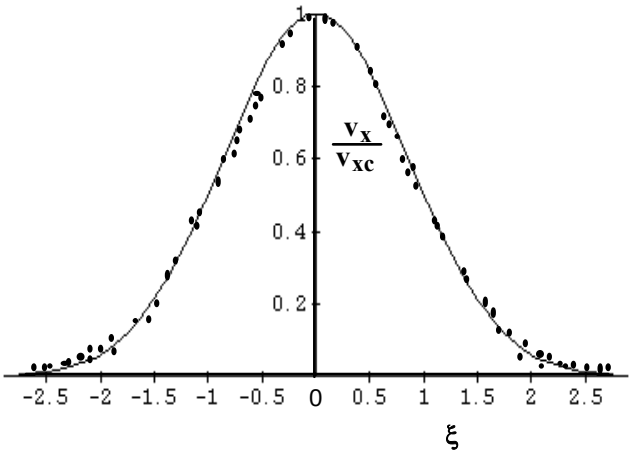

Figure 2: Comparisons of predicted velocity profile with the data of Reichardt [37] for turbulent axisymmetric jet.

It is important to note that, as opposed to the classical theories discussed in [32], the agreement with experimental data shown in Fig.2 is achieved without any empirically adjustable constants.

Comparisons between the predicted temperature profile and experiments performed on turbulent jets will be discussed next. Because the experimental data on temperature distribution in turbulent jets performed by *Reichardt* [38] involve two-dimensional jets, the problem of turbulent two-dimensional jet [43] will also be considered. Following steps parallel to (21)-(25), one arrives at the conservation equations

$$w_x \frac{\partial v_x}{\partial x} + w_y \frac{\partial v_x}{\partial y} = \frac{\partial^2 v_x}{\partial y^2} \tag{64}$$

$$w_x \frac{\partial \theta}{\partial x} + w_y \frac{\partial \theta}{\partial y} = \frac{\partial^2 \theta}{\partial y^2} \tag{65}$$

$$\frac{\partial v_x}{\partial x} + \frac{\partial v_y}{\partial y} = 0 \tag{66}$$

that are subject to the boundary conditions

$$y = 0 \qquad \frac{\partial v_x}{\partial y} = \frac{\partial \theta}{\partial y} = v_y = 0 \tag{67a}$$

$$y \to \infty \quad v_x = v_y = \theta = 0 \tag{67b}$$

Similar to the treatment of axisymmetric jet in (27)-(34) one obtains the convective field

$$w_x = \frac{1}{6x^{1/3}} \quad , \quad w_y = \frac{y}{18x^{4/3}} \tag{68}$$

Following the classical studies [32, 36], one introduces for the two-dimensional laminar jet the stream function Ψ and a similarity variable ζ as

$$\Psi \equiv x^{1/3} G(\varsigma) \quad , \quad \varsigma \equiv \frac{y}{3x^{2/3}} \tag{69}$$

that lead to the stream function

$$\Psi = \sqrt{\pi} x^{1/3} \mathrm{erf}(\varsigma / 2) \tag{70}$$

and hence the velocity components [43]

$$v_x = \frac{\exp(-\varsigma^2/4)}{x} \tag{71}$$

$$v_y = \frac{\sqrt{\pi}}{3x^{2/3}} \left[(2\varsigma/\sqrt{\pi}) \exp(-\varsigma^2/4) - \mathrm{erf}(\varsigma/2) \right] \tag{72}$$

Since under the assumption $\nu_e = \alpha_e$, the momentum and temperature equations (64) and (65) are identical and subject to identical boundary conditions (67), the temperature distribution is similar to the axial velocity (71) and given by

$$\theta = \frac{\exp(-\varsigma^2/4)}{x} \tag{73}$$

The results (71) and (73) lead to

$$\frac{v_x}{v_{xc}} = \exp(-\varsigma^2/4) \tag{74}$$

$$\frac{\theta}{\theta_c} = \exp(-\varsigma^2/4) \tag{75}$$

The predicted velocity profile (74) is in excellent agreement with the experimental observations of *Förthmann* [35, 43]. Also, the result (75) has exactly the same form as the classical solution presented by *Reichardt* [32, 38] on the basis of an entirely different theory. The classical theory is based on the assumption that the eddy diffusivity for heat is twice that for momentum

$$\alpha_e = 2\nu_e \tag{76}$$

This assumption results in the square root relation between the temperature and the axial velocity ratios [32, 38]

$$\frac{\theta}{\theta_c}=\left(\frac{v_x}{v_{xc}}\right)^{1/2}=\exp(-\eta^2/4) \qquad (77)$$

However, according to the simplified kinetic theory of ideal gas [45], (α_e,ν_e) are expected to be identical [28]

$$\alpha_e=\nu_e=l_e u_e/3=\lambda_c v_c/3 \qquad (78)$$

Of course, (α_e,ν_e) are expected to be variables in the non-equilibrium region of transition from one scale to another (Fig.1).

Because of the close agreement between the theory and experimental data achieved by the classical theory [32, 38], it is interesting to examine other possible reasons for the occurrence of the factor 2 in the classical model. According to the classical theory of *Reichardt* [32, 38], rather than solving the equation of motion directly, the first integral of this equation is considered in the form

$$\frac{\partial}{\partial x}\left(\frac{\overline{p}}{\rho}+v_x^2\right)+\frac{\partial}{\partial y}(\overline{u_x u_y})=0 \qquad (79)$$

It is suggested here that rather than (79), the integral of the equation of motion should lead to the energy, i.e. *Bernoulli* equation in the presence of turbulent diffusion expressed as

$$\frac{\partial}{\partial x}\left(\frac{\overline{p}}{\rho}+\frac{1}{2}v_x^2\right)+\frac{\partial}{\partial y}(\overline{u_x u_y})=0 \qquad (80)$$

With the *Boussinesq-Reynolds* stress expressed as

$$\overline{u_x u_y}=-\nu_e\frac{\partial v_x^2}{\partial y} \qquad (81)$$

and the assumption $\overline{p}=0$ for the free turbulent jet one obtains from (80)

$$\frac{\partial v_x^2}{\partial x}=2\nu_e\frac{\partial v_x^2}{\partial y^2} \qquad (82)$$

It is therefore suggested that the factor of 2 leading to (77) in the classical theory [32, 38] should be attributed to difference of factor ½ between (79) and (80) rather than the difference between the eddy-diffusivity for heat versus momentum (76). Another words, the factor of 2 in (82) leads to the occurrence of $1/\sqrt{2}$ in the similarity variable $\eta=y/\sqrt{2x}$ used in the analysis of the momentum as compared to the temperature field thus leading to the square root relation in (77). According to the present theory, on the other hand, the velocity and temperature ratios for axisymmetric (45)-(46) and two-dimensional (74)-(75) turbulent jets are identical.

The characteristic lengths for "atom", element, and system (l_e, λ_e, L_e) for the scales of laminar molecular-, cluster-, and eddy-dynamics (Fig.1) will be about

$$\begin{aligned}&\text{LMD} \quad (l_m=10^{-9},\ \lambda_m=10^{-7},\ L_m=10^{-5}\ \text{m})\\ &\text{LCD} \quad (l_c=10^{-7},\ \lambda_c=10^{-5},\ L_c=10^{-3}\ \text{m})\\ &\text{LED} \quad (l_e=10^{-5},\ \lambda_e=10^{-3},\ L_e=10^{-1}\ \text{m})\end{aligned} \qquad (83)$$

The field of conventional fluid mechanics will be identified as ECD scale β = c, composed of a spectrum of cluster sizes moving with Brownian motion with velocities $\mathbf{u}_c$ [29]. In a stationary fluid, molecular-clusters will be in equilibrium with suspended particles within the fluid that also undergo *Brownian* motions [28].

For LED field (Fig.1), the *Kolmogoroff* length and velocity, and the dissipation rate will be associated with the "atomic" scale and hence identified as [21-23, 26, 46, 47]

$$\eta_k=l_e=\lambda_c \quad , \quad v_k=u_e=v_c \qquad (85)$$

and

$$\varepsilon\propto\frac{u_e^3}{l_e} \qquad (85)$$

The stationary field of isotropic turbulence is identified as equilibrium-eddy-dynamic EED field shown in Fig.1 and its temperature will be expressed as [27]

$$3kT_e=m_e<u_e^2> \qquad (86)$$

Therefore, in an isolated system, as the convective and the local velocities (w_e, v_e) vanish, their kinetic energy will be dissipated into the "atomic" scales and hence manifested as heat at the temperature defined in (86).

CONCLUDING REMARKS

The solution of the modified equation of motion for the classical problem of laminar axisymmetric rotating jet studied by *Loitsianskii* and *Görtler* was determined. The analysis was also extended to velocity and temperature distributions in turbulent rotating jets as well as two-dimensional turbulent jet. The predicted velocity profiles were found to be in close agreement with the experimental observations of *Reichardt*. Also, the predicted temperature profile of two-dimensional

turbulent jet was found to be in agreement with the observations of *Reichardt.*

REFERENCES

[1] de Broglie, L., *C. R. Acad. Sci., Paris,* **183**, 447 (1926); **184**, 273 (1927); **185**, 380 (1927).

[2] de Broglie, L., *Non-Linear Wave Mechanics, A Causal Interpretation*, Elsevier, New York, 1960.

[3] de Broglie, L., *Found. Phys.***1**, 5 (1970).

[4] Madelung, E., *Z. Physik.* **40**, 332 (1926).

[5] Schrödinger, E., *Berliner Sitzungsberichte,* **144** (1931).

[6] Fürth, R., *Z. Phys.* **81**, 143 (1933).

[7] Bohm, D., *Phys. Rev.* **85**, 166 (1952).

[8] Takabayasi, T., *Prog. Theor. Phys.* **70**, 1 (1952).

[9] Bohm, D., and Vigier, J. P., *Phys. Rev.* **96**, 208 (1954).

[10] Nelson, E. *Phys. Rev.* **150**, 1079 (1966).

[11] Nelson, E. *Quantum Fluctuations*, Princeton University Press, Princeton, New Jersey, 1985.

[12] de la Peña, L., *J. Math. Phys.* **10**, 1620 (1969).

[13] de la Peña, L., and Cetto, A. M., *Found. Phys.* **12**, 1017 (1982).

[14] Barut, A. O., *Ann. Physik.* **7**, 31 (1988).

[15] Barut, A. O., and Bracken, A. J., *Phys. Rev. D* **23**, 2454 (1981).

[16] Vigier, J. P., *Lett. Nuvo Cim.* **29**, 467 (1980); Gueret, Ph., and Vigier, J. P., *Found. Phys.* **12**, 1057 (1982); Cufaro Petroni, C., and Vigier, J. P., *Found. Phys.* **13**, 253 (1983);Vigier, J. P., *Found. Phys.* **25**, 1461 (1995).

[17] Reynolds, O., *Phil. Trans. Roy. Soc.* A **186**, 123, (1895).

[18] Taylor, G. I., I-IV, *Proc. Roy. Soc.* A **151**, 421 (1935).

[19] Kármán, T. von, and Howarth, L., *Proc. Roy. Soc.* A **164**, 192 (1938).

[20] Robertson, H. P., *Proc. Camb. Phil. Soc.* **36**, 209 (1940).

[21] Kolmogoroff, A. N., *C. R. Acad. Sci. U. R. S. S.* **30**, 301 (1941); **32**, 16 (1942).

[22] Chandrasekhar, S., *Rev. Mod. Phys*. **15**, 1 (1943).

[23] Chandrasekhar, S., *Stochastic, Statistical, and Hydrodynamic Problems in Physics and Astronomy*, Selected Papers, vol.3, University of Chicago Press, Chicago, 1989.

[24] Batchelor, G. K., *The Theory of Homogeneous Turbulence,* Cambridge University Press, Cambridge, 1953.

[25] Landau, L. D., and Lifshitz, E. M., *Fluid Dynamics*, Pergamon Press, New York, 1959.

[26] Tennekes, H., and Lumley, J. L., *A First Course In Turbulence*, MIT Press, 1972.

[27] Sohrab, S. H., *Rev. Gén. Therm.* **38**, 845 (1999).

[28] Sohrab, S. H., Transport phenomena and conservation equations for multicomponent chemically-reactive ideal gas mixtures. *Proceeding of the 31st ASME National Heat Transfer Conference*, HTD-Vol. **328**, 60 (1996).

[29] Sohrab, S. H., WSEAS *Transactions on Mathemathics*, Issue **4**, Vol.3, 755 (2004).

[30] de Groot, R. S., and Mazur, P., *Nonequilibrium Thermodynamics*, North-Holland, 1962.

[31] Williams, F. A., *Combustion Theory*, 2nd Ed., Addison-Wesley, New York, 1985.

[32] Schlichting, H., *Boundary-Layer Theory*, McGraw Hill, New York, 1968.

[33] Tollmien, W., Berechnung turbulenter Ausbreitungsvorgänge. *ZAMM* **6**, 468-478 (1926).

[34] Schlichting, H., Laminare Strahlenausbreitung. *ZAAM* **13**, 260-263 (1933).

[35] Förthmann, E., Über turbulente Strahlausbreitung. *Ing.–Arch.* **5**, 42 (1934); NACA TM 789 (1936).

[36] Bickley, W., The plane jet. *Phil.. Mag.* Ser.7 **23**, 727-731 (1939).

[37] Reichardt, H., Gesetzmäβigkeiten der freien Turbulenz. VDI–Forschungsheft 414 (1942), 2nd ed. 1951.

[38] Reichardt, H., Impuls-und Wärmeaustausch in freier Turbulenz. ZAMM 24, 268 (1944).

[39] Loitsianskii, L. G., Propagation of a swirling jet in an infinite space filled with the same fluid. *Prik. Mat. Mekh.* **17**, 3-16 1953.

[40] Görtler, H., Decay of swirl in an axially symmetrical jet far from the orifice. *Revista Math. Hisp.-Amer.***IV**, Ser.14, 143-178 (1954).

[41] Crabtree, F., Kuchemann, D., and Sowerby, L., Three-Dimensional Boundary Layer. In *Laminar Boundary Layers*, L. Rosenhead (ed.) Dover, New York 1963, p.452.

[42] Sohrab, S., H., *IASME Transactions* **3**, Vol.1, 466 (2004).

[43] Sohrab, S., H., *IASME Transactions* **4**, Vol.1, 626 (2004).

[44] Wolfram, S., and Beck, G., *Mathematica The Student Book*. Addison Wesley, New York, 1994.

[45] Hirschfelder, J. O., Curtiss, C. F., and Bird, R. B., *Molecular Theory of Gases and Liquids,* Wiley, New York, 1954.

[46] Heisenberg, W., *Z. Physik*, 124 , 628 (1948).

[47] Landahl, M. T., and Mollo-Christensen, E., *Turbulent and Random Processes in Fluid Mechanics* Cambirdge University Press, New York, 1986.

Proceedings of ECOS 2005
Trondheim, Norway
June 20–22, 2005

HORIZONTAL HEAT EXCHANGERS FOR GSHPs. EFFICIENCY AND COST INVESTIGATION FOR THREE DIFFERENT APPLICATIONS

Giuseppe Starace*, Paolo Maria Congedo and Gianpiero Colangelo

Università di Lecce – CREA (research center for energy and environment)
Dipartimento di Ingegneria dell'Innovazione
Via per Arnesano – 73100 Lecce (Italy)

ABSTRACT

Ground source heat pump (GSHP) systems have a good environmental compatibility and low impact on rooms reserved to heating and cooling systems in buildings. The choice of the GSHP has to be justified in many applications, such commercial and industrial buildings, by cost advantages.

The key feature of this kind of systems is the ground heat exchanger (GHX) whose more likely configurations are vertical or horizontal. The latter can represent a good compromise solution between the cost and the effectiveness, as it can benefit to face with a heat source at quasi-constant temperature and to ask for low installation costs as can be mounted in trenches in areas adjacent to the building.

This work verifies numerically, with the help of the CFD code Fluent (Release 6.1.22), the operating conditions for horizontal heat exchangers, placed under the ground level areas of the South of Italy, that had to be provided with an air conditioning system for both winter and summer. The real operating temperatures and the heat fluxes to and from the ground have been considered in order to evaluate the environmental impact and the real advantages of this kind of heat transfer strategy compared to traditional heat pump (HP) systems, using air as heat sources and sinks. The CFD calculations showed the influence of the heat transfer process to the soil, so estimating the annual net energy flux to the ground.

A cost/benefit analysis in three different scenarios was then performed, to evaluate both GSHP vertical and horizontal GHX solutions applied to different cases. The results showed the convenience times for three different applications.

Keywords: Ground Source Heat Pump, Horizontal Heat Exchanger, Geothermal.

NOMENCLATURE

Symbol	Definition
a	Half min-max temperature difference on soil surface
b	Phase constant
c_p	Specific heat capacity
D_T	Ground thermal diffusivity
EWT	Entering water temperature
OWT	Outlet water temperature
Pr	Prandtl Number
t	Time
T(z,t)	Ground temperature
T_{2m}	Ground temperature at two meter depth
T_{cond}	Condenser operating temperature
T_{ev}	Evaporator operating temperature
T_M	Mean temperature in the period
t_M	Time needed to reach the maximum temperature on the surface
z	Depth
ν	Cinematic viscosity

*Corresponding author: Phone: +39 0832 297 366
Fax: +39 0832 325 004 E-mail: giuseppe.starace@unile.it

ρ	Density
τ	Period
ω	Angular velocity
λ	Thermal conductivity

INTRODUCTION

The needs to reduce pollutant emissions and the energy consumption, due to the growing energy demand, to the increased environmental consciousness of people in the world and to the increased price of crude oil, have been the fundamental engine for the development of innovative technologies in the field of heating and cooling systems in large buildings.

In the last decade the development of GSHP technology has registered a great interest worldwide. The first working GSHP prototype was installed in the USA in 1945 as a demonstration device, and it succeeded in showing clearly the big advantages of such an innovative solution [1]. USA is nowadays the country with the highest concentration of installed GSHPs.

For this kind of heat pumps the underground is used as heat reservoir: heat source in winter seasons and heat sink in summer. The highest number of GSHPs are located in the countries of North America and North Europe [2].

This technology gives advantages in many different fields, even if with a higher initial investment.

The main goals reached by GSHPs compared to traditional solutions can be summarized as follows:

- lower energy and overall operating costs;
- significantly reduced greenhouse emissions;
- high reliability with low maintenance;
- lower life-cycle costs;
- easier modular design that facilitates a zone-controlled approach in heating and cooling, reaches a greater comfort and increases energy efficiency;
- compactness of the equipment that reduces room reserved to heating and cooling systems;
- one single system existence that can provide heating and cooling;
- improved exterior aesthetics and environmental friendliness, as the need for external noisy units or ugly cooling towers is eliminated [3], [4].

There are different kinds of GSHPs provided with heat exchanger open or closed, ground coupled or direct expansion loop configurations, using vertical or horizontal heat exchangers.

Each solution has its own pros and cons, but the most spread ones are closed loop, ground coupled with vertical heat exchangers.

Vertical heat exchangers (borehole heat exchangers), are very efficient but expensive and the drilling costs depend on ground composition [5]. Horizontal ground heat exchangers are an alternative solution and represent a good compromise between efficiency and costs [6]. The ground coupled horizontal heat exchangers are long piping buried at a depth of 1.5-2.5 m, where the thermal vector (usually water with glycol) transfers the thermal power to and from the soil.

In North America the most common arrangements, for ground horizontal heat exchangers are linear with a single-tube or a multi-tube layouts. The most frequent solution in Europe is the one with tubes in series or parallel.

Other possible arrangements and solution enhancements are:

- ground heat exchanger spirally shaped yielding a wide surface of tubes, for heat transfer, with a compact overall volume;
- parallel tubes in trenches filled with sand or other filling material;
- providing the tubes with copper fins.

Horizontal heat exchangers are particularly suitable for use in commercial buildings heating and cooling systems, where there is the availability of a car parking or a large free open space (i.e. an open storage), where the long piping can be buried.

The lower efficiency of the horizontal heat exchangers, compared to the vertical ones, is due to the higher variability of the ground temperature. The lower the temperature daily and seasonal variations in the ground are (very smaller than the ambient air temperature variations) the better is for the ground system efficiency. Ground temperature variations are damped and phase delayed, compared to the air temperature ones, because of the ground thermal inertia and heat capacity.

The seasonal delay, that depends on the depth and the ground composition, can be as long as some weeks, so that the lowest possible temperature is encountered at the end of the cold season. This behaviour of the ground is exploited by the GSHPs for the fluid refrigeration at the beginning of the hot season with low energy consumption.

This study shows the thermal impact of a GSHP equipped with a horizontal heat exchanger on the soil interfacing the ground system. Some topics

are discussed about the energety fluxes transferred to and from the soil and the thermal modifications of the ground due to the system operation both in cold and hot seasons [7], [8].

GENERAL CONSIDERATIONS ABOUT THE USE OF GSHP IN SOUTH OF ITALY

The GSHP is mostly used in North America (USA and Canada) and North Europe (Germany, Sweden and Switzerland) [1], [9], where this devices are active in buildings mainly in the cold seasons for heating. In Italy such systems have not yet a strategic role even if some energetic, economic and geographic considerations would show they might be convenient both in cold and hot seasons with good reduction of energy consumptions and pollutant emissions. The position of the Italian peninsula, placed in a temperate climate, assures low variation of ground temperature in the year, and this is the key to success of GSHPs.

The air mean temperature variation between the cold and the hot seasons are in the order of 30-40°C; particularly in the Southern regions, heating in winter and cooling in summer are always needed. The GSHP collects the thermal power from the ground in winter rejecting heat inside the building; in summer it pumps the thermal power coming from the building into the ground.

The use in both hot and cold seasons must be guaranteed in order to keep an annual ground thermal balance not with a heat flux in one direction only. The use heating of the GSHP system all over the year is also the key feature to make it competitive as an investment. In this way, the heat pump is exploited for a longer period in the year [10].

These considerations make the GSHPs suitable for the South of Italy, where a good know-how of drilling wells made for water suction from water tables is present. Despite of that, this systems are not popular and a big effort has to be done by the Government to promote the utilization of these devices for energy and money savings. Both in winter and summer, the use of GSHP could assure savings of energy costs, if compared to traditional methane heating systems or standard air-conditioning ones, with lower pollutant emissions.

CFD SIMULATIONS OF A HORIZONTAL HEAT EXCHANGER FOR GSHPs

The numerical analysis was carried out according to the following two steps:

a) unsteady annual 2D analysis for mathematical model of temperature underground distribution validation; the boundary conditions for the simulations were experimental values at 0.1m deep and temperature at 7m deep calculated with Eq.(1). The side vertical boundary surfaces were set adiabatic as the thermal flux through them was null. A ground region smaller than the calculation domain was involved in the heat transfer process. By small changes, coefficients *a* and *b* of Eq.(1) were found for optimal fitting both in time and space, i.e. in amplitude and phase response at several depths (figure 1 and figure 2). The thermal fluxes and temperatures at different depths (from 0.2m to 7m) were also calculated for the next steps input and for the estimation of the actual involved fluxes transferred to and from the ground (figure 3);

b) unsteady annual optimized 3D analysis for the unit length pipe heat flux transferred to water in the horizontal ground heat exchanger simulated portion. Set boundary conditions were coherent with the results of previous 2D step, in terms of temperatures at two different depth level. In particular, temperatures at depth of 1m and 3m calculated by the first analysis have been used. Entering water temperatures were supposed variable with a hourly constant 7°C difference from the temperature of the ground around the pipe.

The water mass flow rate was 5.88 kg/s (with a mean velocity of 3 m/s).

Geometry and properties of materials used

The 2D analysis was made with a simple rectangle of 1m x 6.9m [length x depth]. The 3D analysis used a parallelepiped of 1m x 0.5m x 2m [length x width x depth] with a 0.05m diameter polyethylene (PE) pipe at the depth of 2m, length of 1m and thickness of 2mm. In tab.1 the main parameters of the material properties are shown, supposing a homogeneous material at all depths.

Table 1: Materials properties

	Pipe (PE)	Ground	Water
ρ [kg/m^3]	946	2723.23	998.2
λ [W/(mK)]	0.35	2.94151	0.582
c_p [J/(kgK)]	1920	837.338	4182
ν [m^2/s]			1.4E-06
Pr			10.4

Numerical model

The geometric model was created with the Gambit Preprocessor 2.1.2 with a rectangular grid. The numerical analysis was carried out using the CFD code Fluent, release 6.1.22. Tab.2 shows the input calculation parameters.

Table 2: Settings of numerical simulations

	2D	3D
Elements	Quadrangles	Tetrahedral and hexahedral elements
Cell dimension	0.01 m	0.01-0.05 m
Number of cells	69000 – 1000	30789
Solver	2D unsteady	3D unsteady
Numerical Scheme:	Segregated	Segregated
Linearization:	Implicit	Implicit
Discretizat7ion Scheme:	Second order upwind	Second order upwind

Experimental data

The experimental climatic data were temperature and velocity of the air, temperature of the underground soil at two depth (0.1 and 0.2 m) and solar radiation of the year 2002. Data were averaged hour after hour and have been recorded by an automatic station, located in Lecce (Italy), at the coordinates: Latitude 40°26'16" North and Longitude 18°14'42" East.

Ground temperature distribution

The energy balance of the ground is really complex because of the presence of all the heat transfer processes: conduction, convection and radiation [11]. The only part that concerns the soil in its depth is the conduction one, moving up and down in the surface layers depending on the instantaneous differences imposed by air temperature, sunlight, soil temperature memory, fluxes transferred to and from heat sources or sinks. The frequencies typical of the air-sun-soil interactions are the day and the annual ones (the former more influenced by casual events, the latter much more repetitive). Both can be schematized by a Fourier series with a high number of harmonics, but a schematization sufficient for the analysis of this work is that of the following equation

$$T(z,t) = T_M + a \cdot e^{-z\sqrt{\frac{\omega}{2D_T}}} sin\left(\omega t - z\sqrt{\frac{\omega}{2D_T}} + b\right) \quad \text{Eq.(1)}$$

where

$\omega = 2\pi / \tau$

$b = (\tau - 4t_M)\pi / 2\tau$

Table 3: Eq.(1) parameters values

Coefficient	Value
T_M	16.84°C
a	16.95°C
τ	1 year
t_M	218th day

Figure 1 shows the hourly average temperatures at a depth of 0.02m experimentally measured (black line) and the ones (grey line) calculated by the numerical simulation. The comparison between the two lines confirmed a good choice of the boundary condition for the numerical simulations.

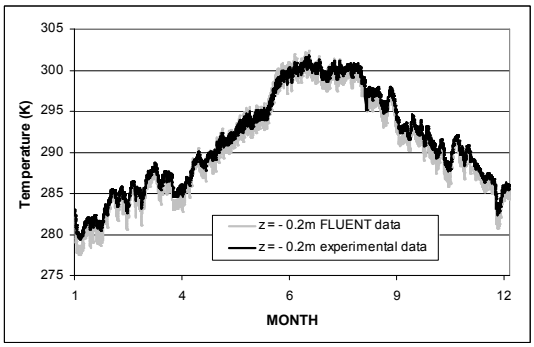

Figure 1: Comparison with the experimental data

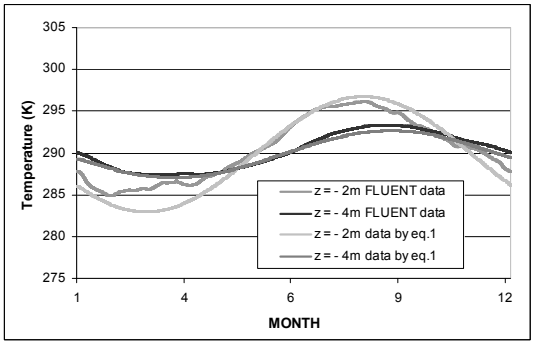

Figure 2: Comparison between data by FLUENT and Eq. 1

Figure 2 shows the correspondence between the temperature distribution at two different depths calculated both by the numerical simulations and by the Eq.1. This result underlines that the Eq.(1) can be used with a good accuracy at depths not less than 1m.

Figure 3 shows the temperature distributions at depths from 0.1m to 7m. Different considerations can be made. Moving down from the surface the temperature daily oscillations get completely dumped after 1m, the year ones disappear deeper and a phase shift due to the thermal inertia of the ground can be observed.

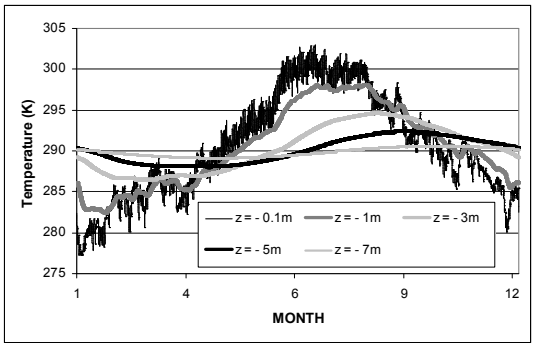

Figure 3 Temperature distribution at all depths

CFD output

No difference were taken into consideration for systems comparison about the distribution of thermal energy to the building as they were supposed the same for all the analyzed solutions. In table 4 the max and min average temperature levels of the soil, entering water, refrigerant are depicted both for winter and summer. Here the real temperature differences imposed for calculations can be observed.

Table 4: Temperature level [°C] for the CFD with a water flow rate of a 100m of pipe length at a depth of 2m

	WINTER		SUMMER	
	Min	**Max**	**Min**	**Max**
T_{2m}	12	18	17	23
EWT	5	11	24	30
OWT	5	11	24	30
T_{ev}	10	10		
T_{cond}			50	50

Refrigerant condensing temperature in winter was set at 50°C while refrigerant evaporating temperature in summer was set at 10°C.
For cost calculations and compressor efficiencies a subcooling of 5°C and a slight protection overheating were considered.
In this step a good visualization of the significant interaction pattern between pipe and ground can be observed (figure 4). In particular, the figure shows that the pipe influence is on a cylinder region around it with a diameter five times the pipe's one.

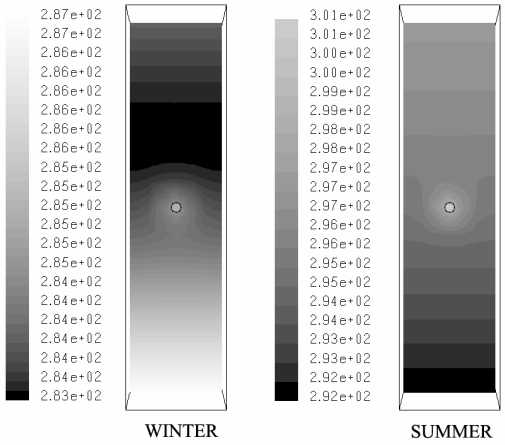

Figure 4 Examples of temperature (K) distribution around the pipe and region of influence.

In figure 5 and figure 6 the typical winter and summer heat fluxes per unit length to and from the water are shown for few days, respectively.

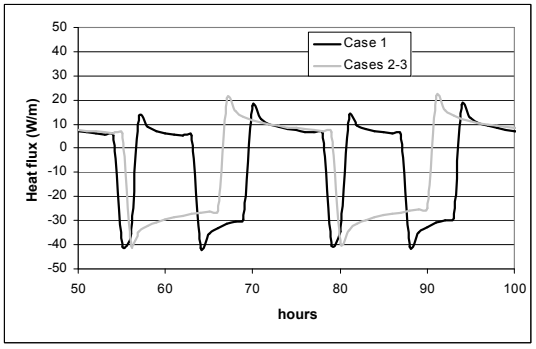

Figure 5 Typical heat flux per length unit exchanged by the water during the winter.

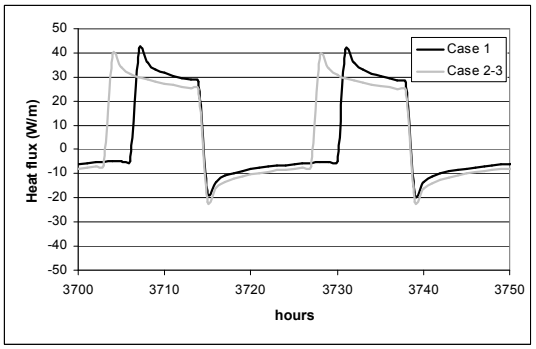

Figure 6 Typical heat flux per length unit exchanged by the water during the summer.

Environmental effects

The environmental effects of the installation of a GSHP are mainly due to the global energy balance of the ground coupled heat exchanger. The main issue of this kind of system is the heat subtraction from the ground in winter. This energy flux could be so high to cool progressively the ground till an unacceptable level, that is the origin for system performance decay and unwanted freezing effects. This problem is particularly felt in those region (North of America and Europe), where the GSHPs are used in winter only ([12], [13]). The summer use of these devices makes possible to restore to the ground a part of the heat subtracted in winter, and so, indirectly, to improve the system performance and the freezing effect. In this work it has been performed a calculation to predict the total amount of energy balance in one year between the analyzed GSHPs and the ground. The results obtained from the analyzed cases (see table 5) show that the effect of summer utilization of the horizontal GSHP, guarantee a return of energy from 21% to 28% to the ground.

Table 5: Annual ground energy [kWh] balance for a horizontal GSHP

	Winter	Summer	Net
Case 1	-5040	1416	-3624.71
Case 2	-141718	30377	-111341
Case 3	-1771470	379709	-1391761

COST EVALUATION IN DIFFERENT SCENARIOS

It is not easy to evaluate exactly the economic convenience of the GSHPs, because it depends on several variable factors such as: the geographic location, the materials price, the maintenance costs, the concurrent alternative technologies and so on [14]. In this paper a cost analysis is performed to evaluate the economic convenience for the installation of a GSHP located in South of Italy, equipped with a horizontal ground heat exchanger. This evaluation is made by comparing this solution with a vertical ground heat exchanger and a traditional air coupled heat exchanger. The main cost voices can be divided in: Capital Costs, Operating Costs and Maintenance Costs. The Capital Costs for the GSHPs are considerably higher than the equivalent traditional heat pump. In fact for the GSHPs many additional cost issues have to be taken into account apart from the particular external heat exchanger. However this cost depends on the type of GSHP. The Operating Costs are referred to estimated energy consumptions of the compared systems during winter and summer. They depend on different variable parameters such as: building type and use, duration of system working, efficiency and heat dispersion, control mode. The Maintenance Costs, on the other hand, have been considered to be the same for all the compared system. This hypothesis is not completely exact, but it comes from two main considerations: a) the Maintenance Costs for GSHPs are often lower than those referred to traditional heat pumps and so the convenience of the GSHPs is a bit better than that calculated in this paper; b) it depends on too many random parameters.

Three main cases have been analyzed to perform a consumption prevision: small, medium and large size cases.

The first system analyzed, namely Case 1, is a small size system that yields a 10 kW of thermal power in the worst design condition. This is a typical system used for a small flat or villa.

The second system analyzed, Case 2, that is medium size system, is able to generate 200 kW of thermal power. This is a system to be installed in a building hosting offices.

The last analyzed case, Case 3, is a large size system. This is able to produce 2500 kW of thermal power to be used for a commercial building.

Each case has been analyzed in three different scenarios of energy costs dynamics. In the first scenario it has been considered a constant cost of energy. The second has been built considering the hypothesis that the electricity cost in the future will have a constant growing rate equal to the present Italian average inflation rate: 2.5%. In the third scenario it is considered that the electricity cost will increase with an average constant rate of 6% per year, that is an assessment of the actual trend.

Primary overall energy consumptions (reported in table 7), seasonal efficiency, thermal energy transferred to and from buildings respectively in summer and in winter evaluations were based on a hour by hour year calculation. The used data were:

- air temperature;
- underground temperature at 2m and 7m deep;
- peak heating and cooling power respectively for winter and summer;

- mean temperature difference for water to water, soil to water, air to water, refrigerant to water heat exchangers for all the systems taken into consideration (see tab. 4);
- estimated losses due to defrosting for air-water traditional heat pump;
- on-off periods of the system and strategies of switching it on during the whole year based on a hour by hour resolution and depending on the application and size.

The calculations of the electricity consumptions and of heating and cooling energies have been carried out proportionally to the peak power data taken from the characteristic curves of popular compressors of appropriate capacity depending on the chosen working temperatures. Traditional heat pumps compressor capacity at the same input power was set higher than the GSHP one because of the former's lower efficiency. The mean temperature difference between the refrigerant and the external source (air or ground) has been set to 10°C for the traditional heat pump and to 7°C for the GSHPs. For the traditional heat pump it has also been taken into account a fraction of energy consumption due to defrosting of the external evaporator in winter. This problem, not present in the GSHPs, has been evaluated increasing the electric energy consumption for heating of 5%. The design conditions are those indicated by the Italian regulations for the design of heating and cooling system for the place where the system has been supposed to be installed. In the Case 1 the activation period in winter was from 15th November to 31st March and each day from 7.00am to 9.00am and from 4.00pm to 10.00pm (typical of flats, apartments, etc.). For the Case 2 and 3 in winter it has been set, instead, from 8.00am to 7.00pm, because of their different use (typical of offices, farms, etc.). The activation period in summer was from 1st June to 31st August and each day from 11.00am to 7.00pm for the Case 1 and from 8.00am to 7.00pm for Case 2 and 3.

Table 6: Annual electric energy consumption [kWh] for heating

	Traditional HP	Vertical GSHP	Horizontal GSHP
Case 1	2263	1553	1651
Case 2	63069	43699	46505
Case 3	785926	546232	581311

Table 7: Annual electric energy consumption [kWh] for cooling

	Traditional HP	Vertical GSHP	Horizontal GSHP
Case 1	270	132	197
Case 2	5779	2832	4209
Case 3	72237	35402	52612

The evaluation of the capital and installation costs for the GSHPs was made by evaluating the main cost voices: central unit, ground heat exchanger, circulation pump, antifreeze fluid, fittings, digging, drilling and so on. The electric energy cost was supposed to be € 0.14 per kWh, that is an average value for Italy in 2004. The cost evaluations show that the convenience of the horizontal GSHPs versus traditional air-coupled heat pump systems (shown in figure 7) is possible after 10 years for the Case 1, 6 years for Case 2 and 3 years for case 3 for the conditions considered in scenario 3. For the scenarios 1 and 2 results show that the convenience comes later, even if it remains acceptable the no. 2. The more the energy price grows, the better is the convenience of the horizontal GSHPs. Even if the vertical GSHPs guarantee higher energy savings than the horizontal ones (see table 8), on the other hand the Capital and Installation Costs are so high to double or to treble the convenience time.

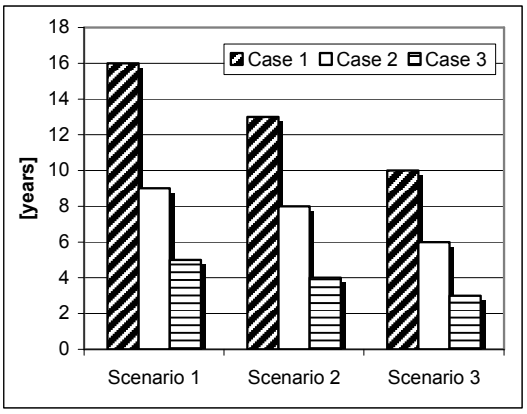

Figure 7: Convenience time of Horizontal GSHPs vs. traditional HP

Table 8: Annual electric energy savings with reference to the conventional HP

	Vertical GSHP [%]	Horizontal GSHP [%]
Case 1	33.46	27.05
Case 2	32.41	26.33
Case 3	32.22	26.13

CONCLUSIONS

An investigation on horizontal GSHPs was performed in terms of CFD simulations based on experimental data and cost comparison. Small differences between Entering and Outlet Water Temperatures assure a good exploitation of the ground heat reservoir. The area of the soil thermally influenced by the pipe presence is small enough to let the designers count on high specific heat power per square meter. The depth of 2m seems to be a good compromise between costs and increased efficiency compared to traditional solutions.

This GSHPs solution showed its convenience especially for systems of medium and big size (minimum 3.5 years) and advantages could be much more, considering that the horizontal GSHPs installation can exploit other building works, involving digging.

ACKNOWLEDGMENTS

The experimental data of the climatic conditions and ground temperature have been provided by the OCFGA group of University of Lecce and a special thanks goes to Prof. L. Ruggiero and Mr. G. Rispoli.

REFERENCES

[1] Hutter G. H., *Geothermal Heat Pumps: An Increasingly Successful Technology*, Renewable Energy, vol. 10 No. 2/3, pp. 481-488, Elsevier Science Ltd, 1996.

[2] Lund J. W., Freeston D. H., *World-wide Direct Uses of Geothermal Energy 2000*, Geothermics 30, pp 29-68, Elsevier Science Ltd, 2001.

[3] Kavanaugh S. P., Rafferty K., *Ground Source Heat Pumps - Design of Geothermal Systems for Commercial and Institutional Buildings*, ASHRAE Applications Handbook, USA, 1997.

[4] Caneta Research Inc., *Commercial/ Institutional Ground-Source Heat Pumps*. Engineering Manual, ASHRAE, USA, 1995.

[5] De Carli M., Del Bianco R., Manente M., Tonon M., Fellin F., Zecchin R., *Sviluppi nelle Pompe di Calore: il Terreno Come Sorgente Termica*, Convegno AICARR "Le moderne tecnologie negli impianti e nei componenti per il riscaldamento", Padova, Bari, Catania, AICARR, Italy, 2003.

[6] Inalli M., Esen H., *Experimental Thermal Performance Evaluation of a Horizontal Ground-Source Heat Pump System*, Applied Thermal Engineering 24, pp 2219–2232, Elsevier Science Ltd, 2004.

[7] Bi Y., Chen L., Wu C., *Ground Heat Exchanger Temperature Distribution Analysis and Experimental Verification*, Applied Thermal Engineering 22, pp 183-189, Elsevier Science Ltd, 2001.

[8] Zhao L., Zhao L. L., Zhang Q., Ding G. L., *Theoretical and Basic Experimental Analysis on Load Adjustment of Geothermal Heat Pump System*, Energy Conversion and Management 44, pp 1-9, Elsevier Science Ltd, 2002.

[9] Sanner B., Karytsas C., Mendrinos D., Rybach L., *Current Status of Ground Source Heat Pumps and Underground Thermal Energy Storage in Europe*, Geothermics 32, pp 579-588, Elsevier Science Ltd, 2003.

[10] Zogou O., Stamatelos A., *Effect of Climatic Conditions on the Design Optimization of Heat of Heat Pump Systems for Space Heating and Cooling*, Energy Conversion and Management 44, pp 1-9, Elsevier Science Ltd, 1998.

[11] Cavazza L., *Fisica del Terreno Agrario*, UTET, Torino, Italy, 1981.

[12] Starace G., *Le Pompe di Calore Geotermiche*, Convegno AICARR "Le moderne tecnologie negli impianti e nei componenti per il riscaldamento" Padova, Bari, Catania, AICARR, Italy, 2003.

[13] Lazzarin R., *Ground as a Possible Heat Pump Source*, Geothermische Energie 32/33, March/June 2001.

[14] Bloomquist R. G., *The Economics of Geothermal Heat Pump Systems for Commercial and Institutional Buildings*, Proceedings Conference on Geothermal Energy in Underground Mines, Ustron, Poland, 2001.

Proceedings of ECOS 2005
Trondheim, Norway
June 20–22, 2005

HIGH TEMPERATURE AIR COMBUSTION TECHNOLOGY IN POWER CYCLES

Andrzej Szlęk, Ryszard Wilk
Silesian University of Technology
44-100 Gliwice
Poland

Roman Weber
Technical University of Clausthal
38678 Clausthal-Zellerfeld
Germany

Abstract

HTAC (**H**igh **T**emperature **A**ir **C** ombustion) is one of the most important progress which has been done in combustion technology in recent years. It was invented about ten years ago and has been successfully applied in hundreds industrial furnaces all over the world. Authors of the present paper considered possibility of applying this technology in industrial boilers. In the paper it has been pointed out application of this technology in industrial boilers may lead to increase of thermal efficiency of power generation. Moreover possibility of gas turbines thermal efficiency improvement by has been described.
Keywords: combustion, gas turbines

INTRODUCTION

Industrial furnaces are widely used for heating, melting and in many other industrial processes. To improve thermal efficiency of the furnace usually recuperative heat exchanger is used which is presented in Fig.1. In such exchanger energy of flue gases is used for heating combustion air. Thermal efficiency

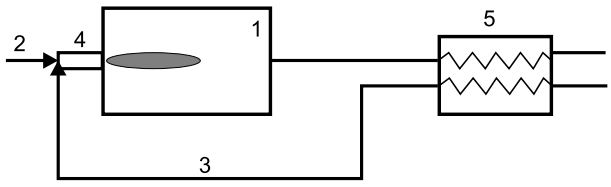

Figure 1: Scheme of the industrial furnace with recuperative heat exchanger. 1-furnace, 2-fuel supply, 3-combustion air, 4-burner, 5-recuperative heat exchanger

of such installation increases with increasing combustion air temperature [4]. Unfortunately with increasing air temperature emission of NO rises very rapidly, which is formed via thermal mechanism [8].

For many years environmental impact of NO in flue gases limited the maximal combustion air temperature. However about ten years ago it was discovered that it is possible to increase air temperature without increasing NO emission. This can be achieved when the air and fuel nozzles are separated and when sufficient in-furnace recirculation of combustion gases is present. Moreover, temperature of the air should exceed ignition temperature of fuel [2], which is about 1000^oC for the natural gas. Under such conditions combustion takes place in whole volume of combustion chamber and no visible flame can be observed. For this reason this technology is named flameless combustion or High Temperature Air Combustion (HTAC).

Today HTAC has been successfully applied in many industrial furnaces [1], [7]. In all these furnaces reduction of both specific fuel consumption and harmful species emission have been observed. Reduction of fuel consumption is the result of decreasion of

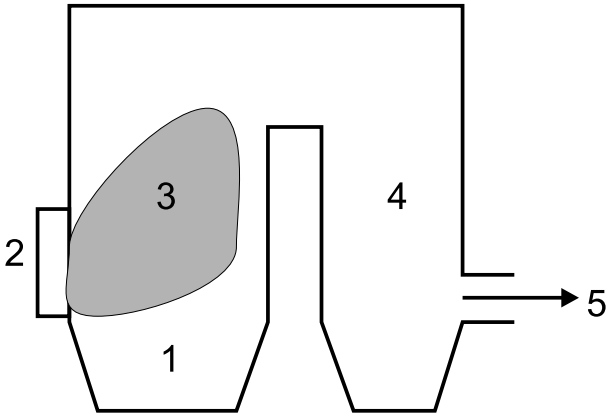

Figure 2: Classical industrial boiler. 1-combustion chamber, 2-burners, 3-flame, 4-convective section, 5-flue gas exit

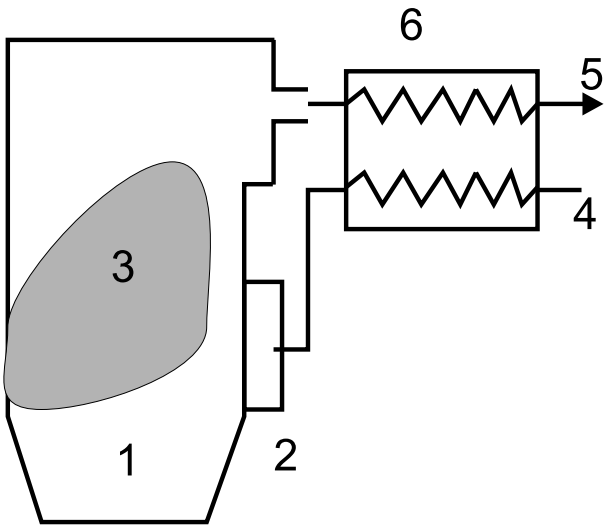

Figure 3: HTAC boiler. 1-combustion chamber, 2-burners, 3-flame, 4-air supply, 5-flue gas exit, 6 - regenerative heat exchanger

flue gas temperature and shortening of process time due to the increased radiative heat fluxes. Industrial experiences showed that thanks to HTAC technology specific fuel consumption can be reduced up to 30% comparing with conventional combustion techniques. Emission of NO is reduced due to the very uniform temperature profiles inside the combustion chamber with no peaks characteristic for classical combustion. Also emission of CO is very low which is probably result of long residence time of combustion products in the high temperature zone.
Authors of the present paper considered application of this technology in industrial boilers and in gas turbines cycles. In both cases HTAC seems to be very promising technology.

HTAC FOR INDUSTRIAL BOILERS

Combustion process and heat transfer inside the combustion chamber of boiler is different to the one taking place in furnace. First of all temperature of medium absorbing heat (water or steam) in boilers is lower than in case of furnaces (heated charge). This allows to reduce flue gas temperature in industrial boilers down to about 150^oC (limit of water condensation) which corresponds with about 8% of energy loss. For this reason introducing HTAC technology to the boiler will cause no increasion of thermal efficiency of the boiler. Nevertheless authors of the paper tried to consider what would happen if the classical boiler construction presented in Fig.2 would be replaced by the construction presented in Fig.3. In this case radiative part of the boiler is substituted by the regenerative heat exchanger preheating combustion air to the temperature high enough to run HTAC combustion. First of all heat transfer area in new boiler would be significantly reduced. This is because of increased radiative fluxes characteristic for the HTAC technology. Secondly emissions of both NO and CO would be reduced significantly. Thirdly char burn-out ratio should be increased because of the higher residence time of the combustible matter in the area of high temperatures inside the combustion chamber. Fourthly moderated combustion temperature would open possibility of dry desulphurization inside the chamber.
It was mentioned above that required air temperature for the natural gas combustion under HTAC technology is about 1000^oC. Such temperature would be very difficult to be achieved in recuperative heat exchanger. Fortunately minimal air temperature for coal combustion is significantly lower than for natural gas. It was found [5] that light fuel oil can be successfully used in HTAC boiler with air temperature equal to about 400^oC. The same result is expected for coal combustion since the minimal temperature requirements are related to fuel ignition temperature which is almost the same for oil and coal.
Reduced heat transfer area of the boiler means lower investment costs. Thus it may be reasonable to built the boiler of more expensive, heat-resistant steel.

Consequently superheated steam temperature, produced by the boiler, can be increased leading to increase in steam cycle efficiency [4]. In other words energy efficiency of the classical and HTAC boiler is almost the same, but exergy efficiency of the HTAC boiler is higher. This allows to improve thermal efficiency of the power plant. Problem of applying HTAC in boilers was discussed more widely in [5].

HTAC APPLICATION IN GAS TURBINES

The simplest gas turbine cycle consists of two isentropes and two adiabates (Fig.4. cycle A) and differs from the Carnot cycle (Fig.4. - cycle B) [3]. Energy efficiency of Carnot cycle is the highest one. Unfortunately Carnot cycle can not be applied in gas turbines because it is not possible to perform isothermal expansion of gases. In fact pseudo-isothermal expansion can be performed in multi-stage turbines with additional combustion chambers between stages.

Authors of the present paper proposed quite new method of isothermal expansion in gas turbines which is described below.

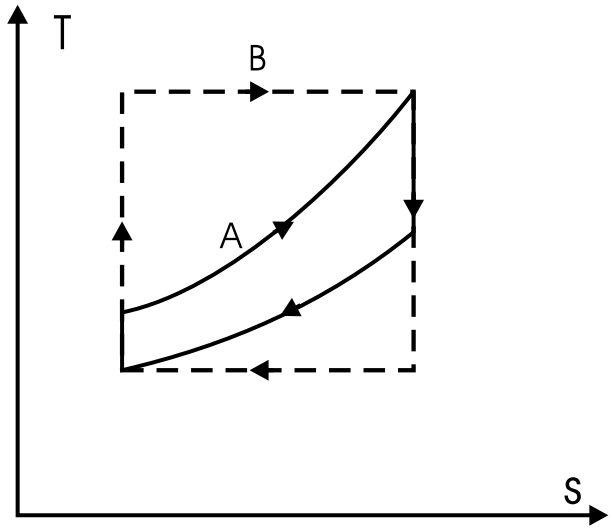

Figure 4: The simplest gas turbine cycle (A) and Carnot cycle (B)

In the HTAC industrial furnaces temperature along whole combustion chamber is almost constant, although chemical energy of the fuel is released. It is because thermal energy generated during combustion is, with almost the same intensity, radiated to the chamber walls by radiation. Gas turbines are thermally isolated and no heat can be transferred outside the turbine. But it is possible to achieve isothermal expansion of gases if heat released during combustion of gas is equal to mechanical work of expansion. In other words if mechanical energy stream transferred to the turbine's blades is equal to heat released than expansion is isothermal.

The question is how to control amount of heat released in combustion. According to authors idea it is possible by continuous supply of fuel during the expansion process. It can be done for example by introducing gas through the channels inside the blades of turbine (in such case gas can also play a cooling role for blades). Gas can be also introduced to the turbine by the nozzles located in the turbine housing.

To guarantee complete combustion of fuel and avoid stabilization problems, air temperature should be higher than self ignition temperature of the fuel. For this reason combustion air supplied to the new concept turbine should be much higher than it is used nowadays.

The idea of new turbine is presented in Fig.5. Ambient air (1) is supplied to the compressor (C) and than put to the regenerative heat exchanger (E). In the exchanger air is heated up to the temperature (3) which must be above the ignition temperature of fuel. Compressed and hot air (3) is supplied to the turbine where it expands. Fuel (6) through the channels in the rotating blades of turbine is delivered into the turbine where it mixes with hot air. Proper gas distribution along the turbine can be achieved by appropriate sizes of gas injectors located in turbine's blades. Decompressed, but hot combustion gases (4), are supplied to the heat exchanger where are cooled to the temperature (5).

Example parameters of gas in the characteristic points are listed in Table.1.

Table.1 Example parameters of the cycle

point No	pressure, bar	temperature,^oC
1	1	20
2	10	400
3	10	1150
4	1	1200
5	1	450

For the parameters listed in Tab.1 thermal efficiency of the cycle is above 65% which is much higher than the efficiency achievable by nowadays turbines. In

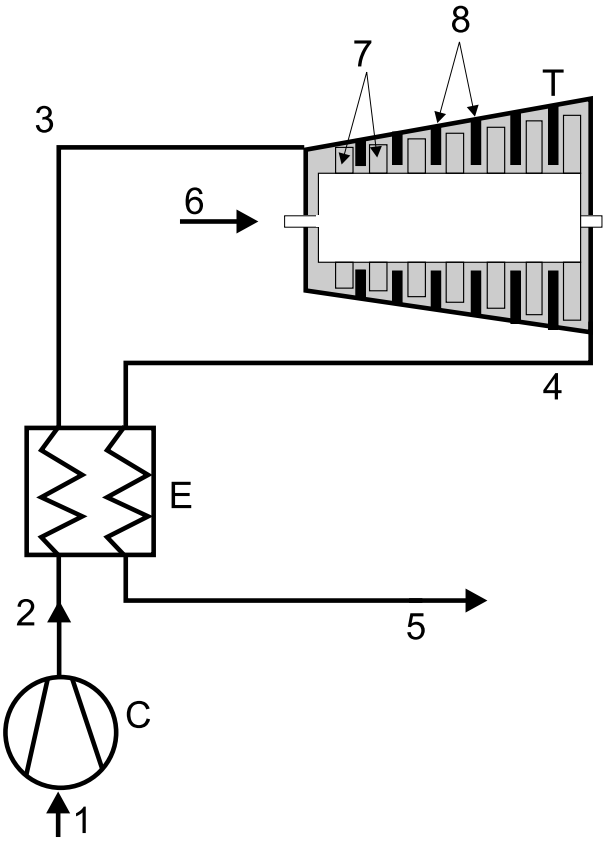

Figure 5: Scheme of the new concept of turbine. 1-air intake, 2-compressed air, 3-high temperature air, 5-flue gas exit, 6-fuel supply (through the schaft), 7-rotating blades, 8- stationary blades, C-compressor, T-turbine, E-heat exchanger)

the T-s coordinates system described turbine cycle is presented in Fig.6. This cycle is very close to the Ericson [4] cycle of the same efficiency as Carnot cycle. Described idea is protected by the international patent [6].

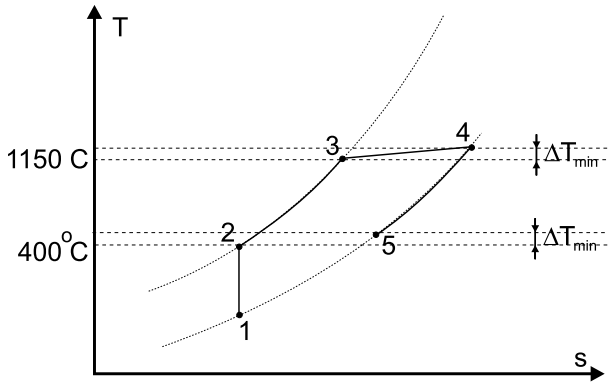

Figure 6: New turbine cycle presented in T-s coordinates

Of course this is only the idea - a lot of theoretical and experimental work has to be done before technical application. Nevertheless it indicate that by introducing combustion process into the turbine body isothermal expansion of gas can be achieved and thus Ericson or Carnot cycle performed. Consequently thermal efficiency of the cycle can be very significantly improved.

SUMMARY

High Temperature Air Combustion is one of the most important and significant progress in combustion technologies in recent years. It has developed from the laboratory scale to industrial furnaces application in only ten years which is extremely fast progress as for energy technologies. This fast progress is forced by reduction of fuel consumption and harmful species emission achievable by using HTAC technology. Authors of this paper performed preliminary considerations on using the technology in the power generation sector.

Considering application of the HTAC in industrial boilers authors pointed out that no increase in thermal efficiency is expected. Nevertheless, by reducing the boiler size increase of overheated steam parameters may be economically reasonable and thus exergy efficiency of the boiler would be achieved. As the consequence thermal efficiency of whole

power plant can be improved. Moreover reduction of harmful species emission can be achieved since the HTAC is more environment friendly technology than conventional one.
More interesting is the possibility of HTAC application in gas turbines. By introducing combustion process into the turbine body isothermal expansion can be achieved. Thus Ericson or Carnot cycle can be performed. Consequently thermal efficiency of the gas turbine cycle can be significantly improved.
Paper presents preliminary study and a lot of additional theoretical and experimental work have to be done before industrial application of presented ideas.

REFERENCES

[1] Cain B., Robertson T., Newby J., *A* review of the development and commercial application of the LNI technique, Fourth International Symposium on High Temperature Air Combustion and Gasification, Rome, November 2001

[2] Flamme M., Brune M., Konold U., Al-Halbouni A., Scherello A., Giese R., *O*ptimization of the energy efficiency of industrial furnaces, Fourth International Symposium on High Temperature Air Combustion and Gasification, Rome, November 2001

[3] Szargut J., *T*hermodynamics, Silesian University of Technology, Gliwice 1997

[4] Szargut J., Ziębik A., Principles of thermal engineering, PWN, Warszawa 1998

[5] Szlęk A., Wilk R., Malczyk K., Misztal T., *O*n HTAC application in power generation, Fifth International Symposium on High Temperature Air Combustion and Gasification, Tokyo, 2002

[6] Szlęk A., Wilk R., Weber R., *T*he method of the simultaneous combustion and expansion of gas

[7] Touzet A., Lhomme P., Quinqueneau., *N*ew efficient technologies with very low NOx emission available of the industry: two recent examples in the French metallurgy field,Fourth International Symposium on High Temperature Air Combustion and Gasification, Rome, November 2001

[8] Wilk R., *L*ow emission combustion, Polish Academy of Sciences, Katowice 200 (in polish)

Proceedings of ECOS 2005
Trondheim, Norway
June 20–22, 2005

Thermoeconomic Diagnosis of Energy Systems with Measured Data

Vittorio Verda*, Romano Borchiellini

Department of Energy Engineering
Politecnico di Torino
ITALY

ABSTRACT

The use of thermoeconomics for the diagnosis of efficiency reductions in energy systems has been widely discussed in the literature. Several procedures based on thermoeconomic analysis aiming at locating and quantifying the malfunctions have been proposed and applied to operating plants.
The correct location of anomalies is made difficult by the effects that the anomalies induce throughout the system, not only in the component where they take place. A possible approach for the correct diagnosis consists of a successive filtration of the effects induced. Diagnosis procedures are often tested on data obtained through simulators. In real applications, an additional difficulty is represented by the errors in measurements.
This paper aims at analyzing the effect of these errors on the results of the diagnosis, in particular whether the procedure still allows one identifying the malfunctioning components.
In addition, the accuracy of results is evaluated and represented through error bars associated with the indicators adopted for the diagnosis.

Keywords: Thermoeconomics, diagnosis, measurement accuracy.

NOMENCLATURE

b	Specific exergy [kJ/kg]
ECO	Economizer;
EVA	Evaporator;
E_{ij}	Flow of the productive structure [kW];
G	Mass flow rate [kg/s];
k_{ij}	Unit exergy consumption [kW/kW];
m	Number of independent variable in the model of a component;
MF	Malfunction [kW];
n	Number of components;
p	Pressure [bar];
P	Pump;
P_j	Product of the j^{th} component [kW];
$\hat{P}_j$	Expected production [kW];
SH	Super-heater;
T	Temperature [°C];
T	Turbine;

Greek

λ_{ij}	Coefficient in the linear model;

Subscripts

op	Operating condition;
ref	Reference condition.

INTRODUCTION

Diagnosis of power plants consists in detecting anomalous behaviours of the components while the system is operating and understanding their causes. This is a relevant task because of the high economic impact of failures and efficiency drops on the overall management.
Failures are generally prevented through prescriptions that include:
- avoid operating conditions outside a safe range;
- periodic check of quantities such as vibrations, metal temperatures, oil pressures, cooling fluid temperatures, etc.;
- variation in the plant load operated by following pre-determined ramps.

These prescriptions are generally integrated within a control and monitoring system that directly

* Corresponding author: Phone (+39) 011 564 44 78, Fax. (+39) 011 564 44 99, e-mail: vittorio.verda@polito.it

intervenes on the plant or signals possible problems to the operator.
Reductions in performances can be evaluated through deductive procedures. Several procedures have been proposed in the last decades and applied too gas and steam turbines; some examples are represented by: the *fault matrix* [1], the *gas path analysis* [2], the *ASME PTC-PM* [3]. Thermoeconomic analysis has been also proposed as a general tool for the diagnosis of the plant performances [4]. This tool presents several advantages: 1) it can be used not only for detecting and locating anomalies, but also for quantifying their effects, i.e. for the calculation of possible technical energy savings obtained by removing each of the anomalies [5-8]; 2) it can be applied to whatever plant, such as steam turbines [9,10], gas turbines [11,12], combined cycles [13,14], desalination plants [15], etc.
Some applications of the diagnosis procedures to real plants have been performed, providing satisfactory results [9, 14, 16]
Localization of malfunctioning components is obtained by calculating one of more indicators for all the components. These indicators are obtained by comparing some thermodynamic quantities calculated in the actual operating condition and a proper reference condition.
Diagnosis procedures need to be tested before their application to real plants can be performed. Tests are usually performed on data obtained by means of a simulator. This is the only way for testing several cases, obtained by varying the components where the anomalies are located as well as their magnitude. One of the main differences between theoretical and real applications is that, in the latter, data are affected by errors.
When diagnosis is performed by using theoretical data, the indicators are expected to assume the highest values in correspondence of the components where the anomalies have taken place.
This paper deals with the impact of measurements on the results of diagnosis. In particular, the main objective consists in investigating whether a thermoeconomic diagnosis procedure is able to detect the components where the anomalies have occurred in spite of data are affected by errors.
This topic has been tackled in some of the works available in the scientific literature (see for example, [14, 17, 18]). The approach adopted in this work allows one determining the error bars associated with the indicators.

THE DIAGNOSIS PROCEDURE

In this paragraph the diagnosis procedure is summarized. With respect to the procedure presented in a previous paper [19], some new features are introduced.
In pure thermoeconomic approaches, the physical structure of the system is substituted by a productive structure. This means that the components are represented in terms of resources required for the process and products supplied to other components or made available to the users (overall plant product). Resources and products are generally expressed in terms of exergy flows.
The concept of exergy presents several advantages in this application: 1) the objective of diagnosis consists in identifying the components where efficiency is decreased as the direct effect of the anomalies; exergy intrinsically includes the concept of performance degradation; 2) once the malfunctioning components are identified, it is likely to quantify the effects of each anomaly occurred in the system, i.e. to discriminate between the anomalies causing large impact on the fuel consumption and those not. Such evaluation, called *prognosis*, can be performed by using the concept of *fuel impact*, which is based on exergy and exergetic cost [5,6]. This aspect is not developed in this paper. Authors would like to highlight that it makes sense to use the same variables to perform diagnosis and prognosis.
Figure 1 shows the physical structure and a possible productive structure for the high pressure evaporator of the plant considered in this paper.

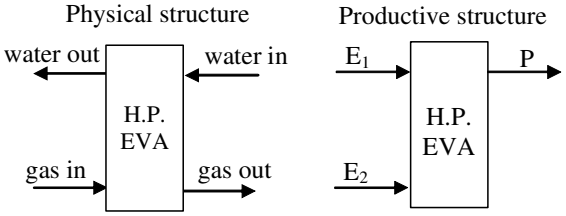

Figure 1 – Physical and productive structure of the HPSH

Resource E_1 is defined as the difference between the exergy flows of the gas entering and exiting the evaporator, while E_2 is defined as the exergy flow of the water entering the evaporator, namely:

$$E_1 = G_{gas} \cdot \left(b_{gas,in} - b_{gas,out}\right) \quad (1)$$

$$E_2 = G_{water} \cdot b_{water,in} \quad (2)$$

The product is defined as the exergy flow of the

exiting steam:

$$P = G_{water} \cdot b_{water,out} \quad (3)$$

At this point, a productive model can be built for the components. The model expresses the component product as the function of its resources, namely:

$$P_j = P_j\left(E_{1j}, E_{2j}, \mathrm{K}, E_{mj}\right) \quad (4)$$

The productive model for a component is not unique: it depends on the choice of resources and products. Some additional details related to the use of productive models instead of physical models are provided in the appendix.

A linear model is considered in this paper:

$$P_j = P_{j,ref} + \sum_{i=1}^{m} \lambda_{ij} \cdot \left(E_{ij} - E_{ij,ref}\right) \quad (5)$$

where subscript *ref* indicates a reference condition. Coefficients λ must be calculated by using plant data, measured when the plant is supposed to operate without anomalies, i.e. when it is new. At this point of the paper, errors in measurements have been still not considered; plant data are generated through a simulator by varying ambient conditions and plant load.

Equation (5) can be rewritten:

$$\Delta P_j = \sum_{i=1}^{m} \lambda_{ij} \cdot \Delta E_{ij} \quad (6)$$

Figure 2 shows the relation between ΔP and ΔE_1 ΔE_2 in the case of the high pressure evaporator. The operating conditions considered for plotting this graph refer to different values of mass flow rate, temperature and pressure of gas and water entering the component. Results show that a linear productive model is acceptable.

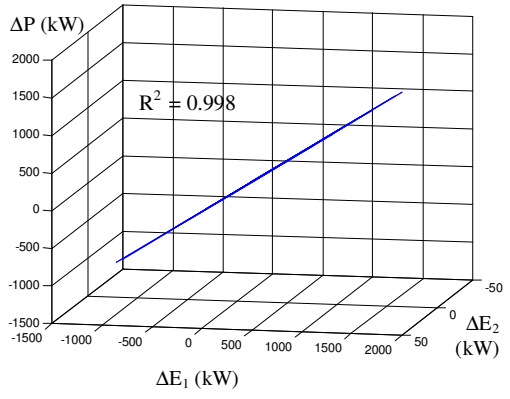

Figure 2 – Relation between resources and product of the high pressure evaporator

Curves such as the one shown in Figure 2 are sort of productive maps of the components. Non linear models can be considered as well; in particular, neural network models are suitable for the application to measured data [20].

The third step of the diagnosis procedure consists in considering two operating conditions of the plant: a reference condition (plant without anomalies) and the actual operating condition to be analyzed. For both conditions, the productive flows (resources and products) are calculated for all the components. Then, for each component, the ratio between each resource and the product is calculated. This quantity is called the unit exergy consumption:

$$k_{ij} = \frac{E_{ij}}{P_j} \quad (7)$$

Using this quantity, some performance parameters providing information about the status of the components can be calculated

1) *variation in the unit exergy consumption* between the actual operating condition and the reference condition, namely

$$\Delta k_j = k_{j\,op} - k_{j\,ref} = \frac{\sum_{i=1}^{m_j} E_{ij,op}}{P_{j,op}} - \frac{\sum_{i=1}^{m_j} E_{ij,ref}}{P_{j,ref}} \quad (8)$$

where m_j indicates the number of resources of the component j.

2) *malfunction* [7]:

$$MF_j = \sum_{i=1}^{m_j} \left(k_{ij,op} - k_{ij,ref}\right) \cdot P_{j_{ref}} \quad (9)$$

This quantity accounts for the different impact that the same anomaly would produce if it occurred in the different components, in fact, the efficiency reduction in a component has a larger overall impact in the additional fuel consumption if the component production is large.

If these parameters are different from zero for a component, it means that its performances are changed.

Before completing the analysis, it is necessary an additional step, which consists in the elimination of the induced effects. When one or more anomalies take place in the system, all components change their operating condition; for instance some of the components have to produce more since the malfunctioning component requires more resources to keep its production constant. The efficiency of components generally depends on their operating

condition, so it is possible that the two parameters introduced through equations (8) and (9) are sensibly different from zero also if in the components no anomalies have taken place. The model introduced in the second step of this procedure can be used in order to eliminate these induced effects. A possible way to reach this result consists in calculating through equation (5) the component product that would be obtained if the resources were moved from the value assumed in the operating condition to the value assumed in the reference condition (expected product). In the case of the high pressure evaporator, this component is characterized by a set of productive flows in the reference condition $\{E_1, E_2, P\}_{ref}$ and a set in the operating condition $\{E_1, E_2, P\}_{op}$. The expected production $\hat{P}$ is calculated as:

$$\hat{P} = P_{op} + \lambda_1 \cdot \left(E_{1,ref} - E_{1,op}\right) + \lambda_2 \cdot \left(E_{2,ref} - E_{2,op}\right) \quad (10)$$

If the expected production is different from the reference production, this is a symptom of anomaly in the component.
A new definition of unit exergy consumption can be introduced:

$$\hat{k}_{ij} = \frac{E_{ij,ref}}{\hat{P}_j} \quad (11)$$

This term is introduced in equations (8) and (9) in order to obtain evaluation parameters that are not affected by the induced effects:

$$\Delta\hat{k}_j = \hat{k}_j - k_{j\,ref} = \frac{\sum_{i=1}^{m_j} E_{ij,ref}}{\hat{P}_j} - \frac{\sum_{i=1}^{m_j} E_{ij,ref}}{P_{j,ref}} \quad (12)$$

$$M\hat{F}_j = \sum_{i=1}^{m_j} \left(\hat{k}_{ij} - k_{ij,ref}\right) \cdot P_{j_{ref}} \quad (13)$$

These parameters can be used for locating the anomalies.

APPLICATION TO A HEAT RECOVERY SYSTEM

In this section, the application of the diagnosis procedure to a heat recovery system is proposed. The objective of this part also consists in presenting the thermodynamic variables measured in the plant. Figure 3 shows the plant, constituted by a heat recovery steam generator and a steam turbine that are placed downstream a gas turbine. The gas turbine is not considered in this analysis.

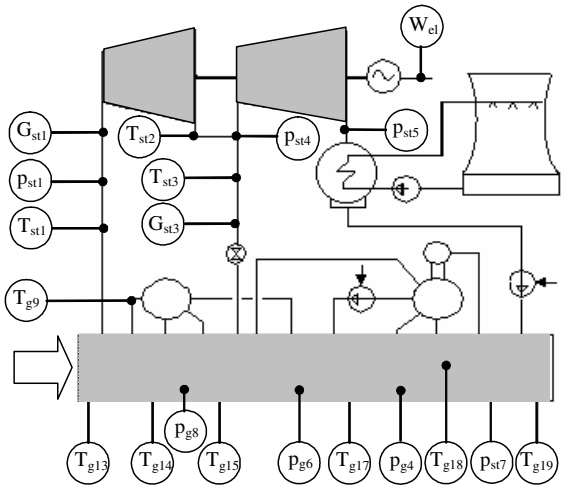

Figure 3 – Schematic of the plant with the measured thermodynamic variables

Table 1 shows the values assumed by the variables that are measured. Both the reference condition and in the actual operating condition are indicated. These values have been obtained through a simulator, without any error in the measurements. In the operating condition, the fouling in the high pressure evaporator has been simulated by reducing the heat transfer coefficient of 10%.

	Reference		Operation	
T_{g13}	509.8	°C	509.8	°C
T_{g14}	446.2	°C	446.4	°C
T_{g15}	274.4	°C	276.5	°C
T_{g17}	218.5	°C	219.6	°C
T_{g18}	174.7	°C	175	°C
T_{g19}	114.2	°C	114.1	°C
T_{st1}	490	°C	490.3	°C
T_{st3}	254	°C	254.8	°C
T_{g9}	268.8	°C	268.5	°C
T_{st2}	194.3	°C	194.9	°C
G_{st1}	49.63	kg/s	49.4	kg/s
G_{st3}	9.453	kg/s	9.719	kg/s
W_{el}	53878	kW	53774	kW
p_{st5}	0.1456	bar	0.1457	bar
p_{g8}	53.98	bar	53.75	bar
p_{g6}	64.27	bar	63.99	bar
p_{st7}	7.779	bar	7.779	bar
p_{g4}	6.534	bar	6.534	bar
p_{st4}	4.149	bar	4.149	bar
p_{st1}	52.36	bar	52.14	bar

Table 1 – Plant data

Using these data, the simulator allows one calculating all the thermodynamic data, by expressing energy and mass balances for all the components. In addition, some assumptions are made: fluid at the exit of the condenser is assumed as saturated liquid, while the fluid exiting the evaporators is assumed as saturated vapour (quality X=1). The number of measured data is in excess. In the model this fact is used in order to calculate the gas mass flow as the average value of the mass flow rates calculated in three heat exchangers.
The results obtained by applying the procedure introduced in the previous section are shown in table 2. No diagnosis can be performed for the condenser for the lack of data at cooling fluid side.
The results show that the diagnosis operated without filtering off the induced effects does not allow one to locate the anomaly correctly; in fact the largest positive variation in the unit exergy consumption takes place in the low pressure evaporator. Instead, the elimination of the induced effects through the linear model of the components highlights the high pressure evaporator as malfunctioning component, since both evaluation parameters assume the highest value in this component.

	Δk	MF	$\Delta\hat{k}$	$M\hat{F}$
HP SH	2E-05	1.31	-8E-05	-5.25
HP EVA	9E-04	89.48	0.001	96.11
LP SH	4E-04	3.03	1E-04	0.95
HP ECO	8E-04	11.32	2E-04	2.29
LP EVA	0.001	28.40	-5E-04	-13.39
LP ECO	-7E-05	-0.38	-3E-04	-2.01
HP T	-2E-04	-4.65	8E-05	2.14
LP T	1E-04	3.41	1E-04	3.38
LP P	-4E-04	-0.03	-6E-05	0.00
HP P	-5E-05	-0.29	-2E-05	-0.09

Table 2 – Diagnosis of the system without errors

THE PROBLEM OF ERRORS IN MEASUREMENTS

In this section the whole diagnosis procedure is repeated by using operating data affected by errors. These data have been also simulated, as explained hereafter. This choice has been taken in order to have complete control of the information about the anomalies occurred in the plant. The use of a simulator makes it possible to vary the number of anomalies, their location and their value, while this is not possible when real data are used. Nevertheless, the analysis has been developed in a way that makes it close to an analysis performed with real data. Only the variables actually measured in the plant have been considered. Errors have been estimated by considering real data.
A set of operating data (almost 2000 for each variable) measured in a period of about two months has been considered. These data have been first classified into groups, provided that two criteria are both satisfied: 1) the data in each group refer to operating conditions in a sufficiently short period of time; 2) the operating conditions must be characterized by close values of the gas turbine pressure ratio and its net power. Groups with abundant number of elements have been considered. After having verified the normal distribution of data for all the variables, the standard deviation has been calculated. Figure 4 shows the distribution of data for three different variables: high pressure steam pressure, outlet turbine temperature, low pressure steam mass flow rate. In the figure the normal distribution is also shown.

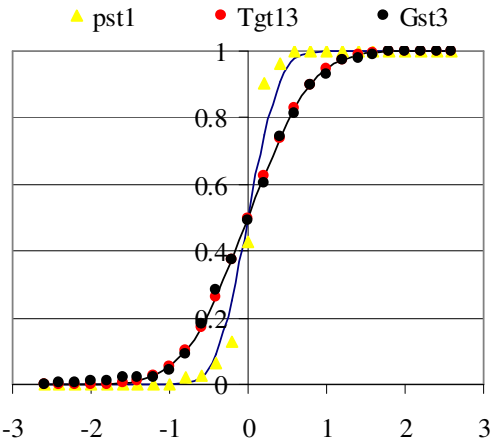

Figure 4 – Distribution of some of the measured data.

This information has been added to the simulator, so that its output is constituted by operating data affected by errors, generated according with a normal distribution. For each variable, the calculated standard deviation has been considered for generating the errors. These values are shown in Table 3.

Variable	σ		Variable	σ	
T_{g13}	0.62	°C	G_{st1}	0.2	kg/s
T_{g14}	0.34	°C	G_{st3}	0.1	kg/s
T_{g15}	0.35	°C	W_{el}	75	kW
T_{g17}	0.35	°C	p_{st5}	0.002	bar
T_{g18}	0.55	°C	p_{g8}	0.3	bar
T_{g19}	0.33	°C	p_{g6}	0.3	bar
T_{st1}	0.33	°C	p_{st7}	0.06	bar
T_{st3}	0.35	°C	p_{g4}	0.05	bar
T_{g9}	0.35	°C	p_{st4}	0.05	bar
T_{st2}	0.35	°C	p_{st1}	0.29	bar

Table 3 – standard deviation obtained for the different measured variables

The first step of the diagnosis procedure consists in determining the coefficients λ_{ij} of the linear model. For this goal, 200 data of the plant operating at different load and different ambient conditions have been generated. These data refer to the plant operating without any performance degradation. For the systems components, the accuracy of the linear models, evaluated by considering the whole set of 200 data, is shown in table 4. The average percent errors are shown as well. Errors refer to the estimation of the plant product; they account for possible non-linear behaviour and errors in measurements.

	R^2	Av err. %	Max err %
HP SH	0.992	0.05	0.19
HP EVA	0.992	0.41	1.57
LP SH	0.992	0.07	0.33
HP ECO	0.991	0.55	2.37
LP EVA	0.998	0.51	1.66
LP ECO	0.877	0.64	2.28
HP T	0.991	0.31	1.39
LP T	0.992	0.06	0.28
LP P	0.992	0.11	0.47
HP P	0.999	0.09	0.25

Table 4 – Performance of the linear model with errors in measures.

Using this model it is also possible to simulate the reference and actual operating conditions. The approach used for the diagnosis consists in simulating several times these conditions. In figure 5, the resource E1 of the high pressure evaporator in the reference and operating conditions are shown.

The number of points for the operating condition is sensibly less than for the reference condition. The reason is that some sets of the measurements do not comply the thermal balance of the components. In these cases the whole set of measures has been erased. This also means that the data distribution in the operating condition is not a normal distribution anymore.

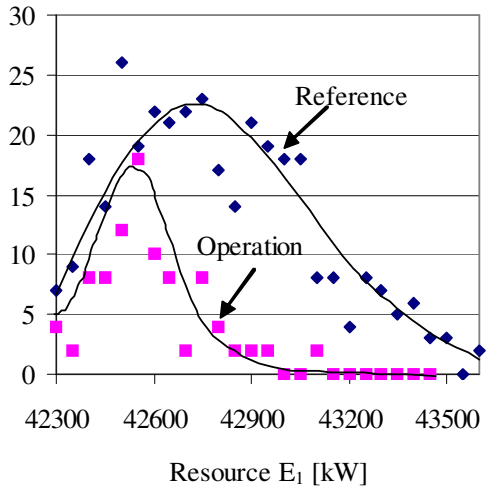

Figure 5 – Distribution of the productive resource E_1 of the high pressure evaporator.

Diagnosis is then performed by calculating the expected product and, then, the evaluation parameters for all the components. For each evaluation parameter, the average value and the error bar can be determined. Figure 5 shows the evaluation parameters obtained by considering the average values of the productive flows.

	Δk	MF	$\Delta\hat{k}$	$M\hat{F}$
HP SH	-2E-05	-1.07	-1E-04	-6.80
HP EVA	8E-04	75.00	7E-04	63.80
LP SH	2E-04	1.70	5E-06	0.04
HP ECO	0.001	19.19	0.001	16.27
LP EVA	0.001	34.30	-5E-04	-13.89
LP ECO	-4E-04	-2.52	-4E-04	-2.35
HP T	-2E-04	-5.15	2E-05	0.49
LP T	-1E-04	-3.97	-1E-04	-4.02
LP P	-4E-04	-0.04	2E-06	0.00
HP P	-3E-05	-0.17	1E-05	0.08

Table 5 – Diagnosis of the system with errors

It is possible to notice that the first parameter, the variation in the unit exergy consumption does not allow one to locate correctly the anomaly. The malfunction, instead, presents the highest value in the high pressure evaporator. This behavior is characteristic of the evaluation parameter, i.e. the malfunction is, in the authors' opinion, more suitable for the location of anomalies. A simple example can be considered in order to clarify this concept and to highlight another feature of the malfunction as an evaluation parameter.

As an example, it is possible to consider the high pressure turbine and the circulation pump of a steam power plant. The expansion is assumed between 140 bar, 450 °C and 32 bar, 262 °C and the pumping between 6 bar, 157 °C and 160 bar, 159.5 °C, while the mass flow rate is considered 1kg/s. If an error of 0.5% were committed in measuring the temperature of the flow exiting both components, it would cause a difference between calculated and expected value in the unit exergy consumption and consequently in the malfunction of both components, although no anomaly has occurred in the system. Numerical results are shown in table 6.

	Turbine	Pump
Δk [kW/kW]	0.015	0.105
MF [kW]	4.49	3.43

Table 6 – Sensitivity of the evaluation parameters to an error in measurements.

The results show that the variation in the unit exergy consumption is very different in the two components, in particular the variation occurred in the pump is larger. This different response to a similar impulse can be the origin of erroneous interpretations while diagnosing the presence of anomalies, i.e. the variation in the unit exergy consumption of the pump could be confused with an anomaly or it could impede to detect other anomalies. The malfunction seams to be less dependent on the errors in measures, in fact similar values of this parameter are obtained for both components.

A second aspect of the same problem is now considered. A general component whose productive structure is constituted by one resource and one product is considered. Once again, an error on a intensive property (pressure or temperature) is considered. An extensive quantity (e.g. mass flow rate) is made vary from 100% to 50%. Two hypotheses are made: 1) this variation just slightly affects the intensive properties required for the definition of resources and products; 2) the unit exergy consumption for this component does not depend on the resource. The variation in the unit exergy consumption and the malfunction associated with the error in measurement is computed in nominal condition (100% of the mass flow rate). These indicators are also calculated when the mass flow rate is reduced.

Figure 6 shows how the indicators vary depending on the component production; the values of the indicators are referred to the value assumed in the nominal condition. The malfunctions does not depend on the variation in the mass flow rate, while the variation in the unit exergy consumption increases as the product decreases.

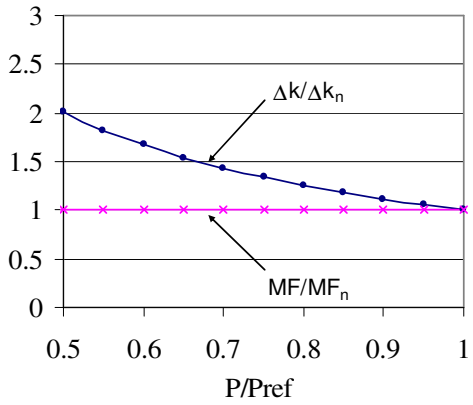

Figure 6 – Effect of the error on a intensive quantity.

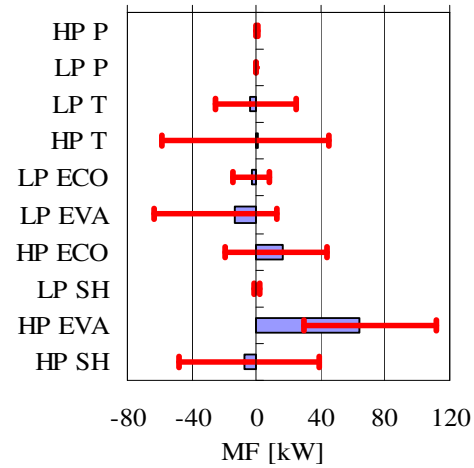

Figure 7 – Error bars associated with the corrected malfunctions.

If the error is associated with an extensive quantity, both indicators behaves in the same way, showing small variations.

At this point, an analysis of the deviation of the evaluation parameters can be performed. This analysis is conducted by considering the corrected malfunctions $M\hat{F}$ only. Figure 7 shows the average values and the error bars obtained by considering the set of data corresponding to the operating and the reference conditions.

The figure highlights that the errors induce important effects that cannot be neglected. In any case it is possible to notice that the error bar associated with the anomaly is only slightly superimposed to the error bars of the induced effects, thus the anomaly can be correctly located.

CONCLUSION

In this paper, the problems associated with the errors in measures and their impact on the results of thermoeconomic diagnosis are tackled.

Several results have been achieved. The application of a diagnosis procedure to a particular case of anomaly, occurred in the high pressure evaporator of a HRSG, shows that the impact of the errors is not negligible but it does not impede to locate correctly the anomaly, provided that a sufficiently large set of data is considered.

With respect to other diagnosis techniques, thermoeconomic diagnosis leaves to the analyst more freedom to chose among the performance indicators to use. The application here proposed highlights that the parameter called *malfunction* is less sensible to the effects of errors in measurements. In contrast, parameters such as efficiencies and unit exergy consumptions seam to be more sensitive to errors, thus less indicated for the diagnosis with real operating data.

BIBLIOGRAPHY

[1] Saravanamuttoo, H. I. H. and MacIsaac, B. D. (1983). *Thermodynamic Models for Pipeline Gas Turbine Diagnostics.* Journal of Engineering for Power. Vol. 105, October, pp. 875-884.

[2] Stamatis, A., Mathioudakis, K., Papailiou, K.D., (1990). *Adaptive Simulation of Gas Turbine Performance*. ASME Journal of Engineering for Gas Turbines and Power, 112, pp. 168-175.

[3] ASME PTC-PM (1993). *Performance Monitoring Guidelines for Steam Power Plants*. The American Society of Mechanical Engineers.

[4] Valero A., Lozano M.A. and Muñoz, M.A. (1986). *General Theory of Exergy Savings- Part I: On the Exergetic Cost, Part II: On the Thermoeconomic Cost, Part III: Energy Savings and Thermoeconomics*. Computer-Aided Engineering of Energy System, pp.1-21, A.S.M.E. W.A.M. 1986, AES-Vol. 2-3.

[5] Lozano MA, Bartolomé JL, Valero A, Reini M. (1994). *Thermoeconomic Diagnosis of Energy Systems*. Flowers 94. Florence World Energy Research Symposium. July 6-8. Florence. Italy.

[6] Lozano M.A., Valero A. (1993). *Theory of the Exergetic Cost. Energy*, The International Journal, Vol. 18, n° 9, pp. 939-960.

[7] Torres C., Valero A., Serra L., Royo J. (1999). *Structural theory and Thermoeconomic Diagnosis. Part I: On Malfunction and Dysfunction Analysis*. ECOS 99. June 8-10. Tokyo. Japan.

[8] Verda V., (2003). *Thermoeconomic approach analysis and diagnosis of energy systems: from diagnosis to prognosis.* Int. J. of Thermodynamics, Vol. 7, No. 2, pp. 73-84.

[9] Lerch F., Royo J., Serra L. (1999). *Structural theory and Thermoeconomic Diagnosis. Part II: Application to an Actual Power Plant*. ECOS 99. June 8-10. Tokyo. Japan.

[10] Reini M., Taccani R. (2002) *Improving the Energy Diagnosis of Steam Power Plants Using the Lost Work Impact Formula*. The Int. J. of Applied Thermodynamics vol.5 (No4) pp. 189-202. Dec.2002.

[11] Stoppato A., Lazzaretto A. (1996). *The Exergetic Analysis for Energy System Diagnosis*. AES. Thermodynamics and the Design, Analysis and Improvement of Energy Systems. (Ed. Duncan, A. B.; Fiszdon, J.; O'Neal, D. and Den Braven, K.) ASME Book nº H01022, 1996, pp. 191-198.

[12] Verda V., Serra L., Valero A. (2004). *The effects of the control system on the thermoeconomic diagnosis of a power plant*. Energy. 29. 3. pp 331-359.

[13] Valero A., Correas L., Zaleta A., Lazzaretto A., Verda V. , Reini M. and Rangel V., (2004). *On the thermoeconomic approach to the diagnosis of energy system malfunctions. Part-1 the TADEUS problem*. Energy, 29, pp. 1875–1887

[14] Correas L. (2001). *Thermoeconomic diagnosis of a combined cycle operation*. Ph.D. Thesis. University of Zaragoza. (In Spanish).
[15] Uche J. (2000). *Thermoeconomic Analysis and Simulation of a Combined Power Plant and Desalination Plant*. Ph. D. Thesis. University of Zaragoza.
[16] Zaleta A. (2004). *Application of thermoeconomic models to the load monitoring systems (V-SCORT) of conventional 350 MW power plants and combined cycles.* Report of the University of Guanajuato and Private Institute for Electrical System Investigation, Mexico.
[17] Stamatis A., Mathioudakis K., Papailiou K.D., (1992). *Optimal Measurement and Health Index Selection of Gas-turbine Performance Status and Fault Diagnosis*. ASME Journal of Engineering for Gas Turbines and Power, 114, pp. 209-216.
[18] Pinelli M, Spina P.R., Venturini M. (2002) *A multiple operating point minimization technique for gas turbine operating state determination*. ASME IMECE. New Orleans.
[19] Verda V., Serra L., Valero A. (2002). *Zooming Procedure for the Thermoeconomic Diagnosis of Highly Complex Energy Systems*. International Journal of Applied Thermodynamic. Vol.5 (No.2), pp.75-83, June.
[20] Verda, V. (2003). *An Improved Thermoeconomic Diagnosis Procedure for the Detection of Different Malfunctions of Complex Energy Systems*. ASME IMECE 2003-42573. Washington U.S.A.

APPENDIX. Use of productive model.

The use of a productive structure instead of the physical structure seams to involve a reduction in the number of thermodynamic variables that are used to simulate the component's behavior.

In this section, authors would like to discuss some of the effects related to the use of a productive structure to model the components in off-design conditions as well as its use in diagnosis.

All the considerations refer to the heat exchanger in figure 1, but they can be easily extended to whatever component.

The physical model is characterized by 12 variables, since there are 4 streams; for each stream the mass flow rate, pressure and enthalpy are defined. Six of these variables are independent (boundary conditions). The other variables are obtained through continuity equation, momentum equation and energy equation applied to both fluids.

If the productive structure defined by equations (1)-(3) is assumed, only two boundary conditions are imposed, i.e. the two resources. In the case of a heat exchanger, this basically means that only the thermal problem is solved. Consequently, the thermal behavior of the heat exchanger is independent on the mass flow rate of the two fluids and on their pressures.

This productive model provides the same details as a physical model with the following characteristics: 1) the transformations of the two fluids are assumed as isobaric; 2) heat transfer is expressed by using the effectiveness-NTU model with constant heat transfer coefficient.

Both physical and productive models are suitable to be expressed through linear functions. The productive model is just more compact.

Such model is expected to correctly detect anomalies affecting the heat transfer, provided that fluid dynamic and thermal behaviors are decoupled in the component. When the linear regression analysis is performed, this hypothesis is verified together with the hypothesis of linearity. The model is expected not to work properly for the diagnosis of anomalies affecting the pressure drops.

A more accurate model could be needed, both in case fluid dynamic and thermal problems are coupled, or in order to detect anomalies affecting the pressure drops. A physical model can be obtained by expressing for each flow, the outlet pressures as the function of inlet pressure and mass flow rate. A corresponding productive model can be obtained by splitting exergy flows into mechanical and thermal components.

It is also possible to obtain a productive model characterized by 6 independent resources, which is equivalent to the most possible zero-dimension physical model (it can be obtained though a change in the independent variables). For such model, the independent resources are:

$$E_1 = G_{gas} \cdot b_{Tgas,in} \tag{14}$$

$$E_2 = G_{gas} \cdot b_{Mgas,in} \tag{15}$$

$$E_3 = G_{gas} \cdot b_{Tgas,out} \tag{16}$$

$$E_4 = G_{gas} \cdot b_{Mgas,out} \tag{17}$$

$$E_5 = G_{water} \cdot b_{Twater,in} \tag{18}$$

$$E_6 = G_{water} \cdot b_{Mwater,in} \tag{19}$$

Proceedings of ECOS 2005
Trondheim, Norway
June 20–22, 2005

THREE STATEMENTS FOR A RELIABLE ON-LINE THERMOECONOMIC MONITORING AND DIAGNOSIS. DYNAMIC REFERENCE STATE, ACCEPTABLE PERFORMANCE TESTS, AND THE EQUALIZED RECONCILIATION METHOD

Alejandro Zaleta[1] , Hector Jimenez, J. Paulo Chavez
J. Jesus Pacheco, Alfonso Campos and Armando Gallegos
Department of Mechanical Engineering,
University of Guanajuato, MEXICO

ABSTRACT

The thermoeconomic diagnosis in operating power plants is more and more being demanded by the users of the same ones. Nevertheless, in spite of the efforts to unify the techniques or tactics of diagnosis, it seemed that we are even far from standardizing the analytical procedures to do it. Recently, a series of papers have been considered to compare different ways to solve a concrete problem to diagnose a power plants TADEUS part 1 to 7. In this paper, we look for to establish the minimum requirements that must fulfill the three fundamental aspects in an on-line thermoeconomic diagnosis and monitoring. Such as: *Dynamic Reference Operating State, an Acceptable Performance Test State, and an Equalized Reconciliation Method.* Where the Dynamic Reference Operating State, talks about to create a reference on the basis of the atmosphere conditions, fuel quality and present load of the plant in operation; in the Acceptable Operating State Test, we will describe to the minimum requirements of data acquisition and filtrate to have an acceptable tests and comparable with the reference; and an Equalized Reconciliation Method, talks about to the comparison of states (reference versus proves) to conditions of equal load and atmosphere, solved by a module of equation systems; respectively. An example of development and results applied to a plant of combined cycle 240 MW of third generation is presented.

Keywords: Thermoeconomic diagnosis, Anomalies, malfunctions, reconciliation.

NOMENCLATURE

GT	Gas turbine
HHV	High Heating Value [kJ/kg]
HRSG	Heat Recovery Steam Gen.
HP	High Pressure
HR	Heat Rate [kJ/kg]
h	Enthalpy [kJ/kg]
IGV	Inlet guide vanes
LHV	Low Heating value [kJ/kg]
LP	Low Pressure
$\dot{m}$	Mass flow rate [kJ/kg]
P	Pressure [kJ/kg]
ST	Steam turbine [kJ/kg]
T	Temperature [kJ/kg]
$\dot{W}$	Power [kJ/kg]

Greek

α	IGV angle
β	Pressure Ratio
Φ	Flow Mass Coefficient
η	Efficiency
ρ	Density [kJ/kg]

Subscripts

aux	Auxiliary
gen	Generated
w	Wet bulb

[1] Corresponding author: Phone: +52 464 6480911 Fax: +52 464 6472400, E-mail: azaleta@salamanca.ugto.mx

INTRODUCTION

The diagnosis in real time in existing power plants, has received in the last 10 years a special interest. Every time is clearer that the effective potential of energy saving is in the opportune detection and correction of the anomalies. The users of the plants have demonstrated that the loss of efficiency dragged during the time, creates an accumulated burst of fuel of tremendously high orders of economic magnitude. In the last decades where the operation strategy was the maximum production, without having special well-taken care of the efficiency, it seemed that this changed to always have the maximum efficiency and the maximum availability. The strategies of maintenance and control also are changing, every time that it is had better systems of data acquisition, software and hardware, and it is possible to detect the losses of efficiency or impact in the production, almost in real time. Nevertheless, it does not even exist a standardization and normalization (for example of the type ASME PTC or others) of the procedures of thermoeconomic diagnosis in operation, so that they are applicable for any power plant and can offer a clear idea of where these greater deviations and whichever time take some anomaly. A series of referring articles to the thermoeconomic diagnosis of power systems has appeared, with the intention of presenting to the scientific community the different currents to solve an example of diagnose of a case of study, call TADEUS [1-6]. The results of this series of articles have revealed the great diversity of points of view and methods of solution. In part 3 of the TADEU'S series [4], we presented the concepts of the reconciliation of a Test *versus* a Reference State, for the case described in TADEUS, based on a module of reconciliation of anomalies. Nevertheless, taking the methodology to a case in real-time (a combined cycle of third generation of 240MW), we have been new approaches in the methodology that will serve as the base to standardize the procedures of diagnose. In this sense, the objective of this work is to deepen in the foundations that a thermoeconomic diagnosis in real-time must be, and redefining the concepts of reference state *(of how it would have to be)* and test condition *(of how it is);* as well as the method reconciliation *(of how it is going to be compared).*

With the objective to give a immediately and precise answer in the diagnosis of operational thermoelectric plants, this work presents a methodology that permits opportunely inform and value Heat Rate's deviations, defined as $\left(\Delta HR = {}^{\Delta Fuel\,[kW]}\!/_{Net\ Power\,[kW]}\right)$ and Power's deviations by separated causes, in order to the user only see the anomalies of subsystems or control deviations, discriminating environment and load effects.

DYNAMIC REFERENCE OPERATING STATE

The manufacturers of power plants give to the owners the ***thermal balance*** at ISO conditions or site conditions (before project or after acceptance test), as a guarantee (reference) to the optimal state of the plant, leaving in addition a series of correction curves (by environmental conditions, fuel quality, load or degradation). Nevertheless, actually there are a few plants that have systematized this form to obtain the reference, and those that already have done; they have chosen to turn them by using parametric models (polynomials) for obtaining a reference state, losing precision and accuracy in the reference data. Moreover by considering that environment properties, fuel quality and load, change every time, it is more difficult to ensure a specific reference. For example in Figure 1, we can show a typical month of average (10 minutes) data of LHV, IGV, and environment properties, in the plant (case of study).

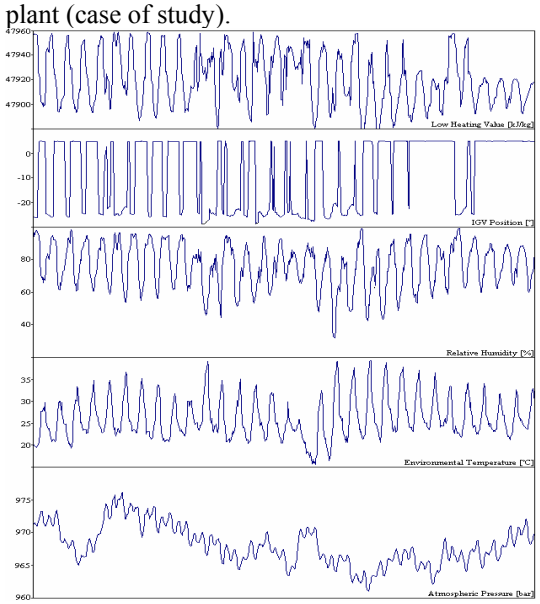

Figure 1: A typical tendency in real-time of the environmental properties, fuel quality, and IGV position (load).

Simulator Validation and a real time reference

From our point of view, the *Reference Operating State* must be based on a **simulator** able to respond to the environmental conditions, fuel quality, load and (optionally) the control of the process, with the objective to establish a (real time) dynamic and optimal reference of the systems with respect to its present operating condition, including factors like partial loads and control set-point. In this way, the ***thermal balance*** at the acceptance tests condition can serve to validate and to fit us the mathematical model (Fig. 2) of a simulator by computer, the simulator has been developed using a mathematic model based in mass and energy balances, compressor map, IGV model, model to predict steam turbine efficiencies, Stodola model to predict admission pressures. The simulator can reproduce a determinate number of thermodynamic conditions in each point of the plant (Fig. 1), the inlet independent variables are: *environmental conditions, fuel quality, IGV (Inlet Guide Vanes), temperature and pressure points control* (the objective of this paper is not show the developed of one simulator, it had been discussed in previous work [2,4]).

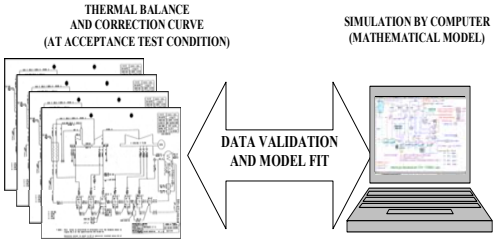

Figure 2: Comparison process and data validation of between Thermal Balance and Simulator by computer

Once validated the simulator, it is possible to execute at real time load and environmental conditions, obtaining reference thermal balances in the time (Fig. 3). In Fig. 4, it is possible to see the importance to have a dynamic variable behavior, because with this simulator any change in a specific variable represents one change for evaluating a Reference Heat Rate and Net Power. Also Fig. 4 shows a references value of Heat Rate and Power at environmental condition, fuel quality and present load, shown in Fig. 1.

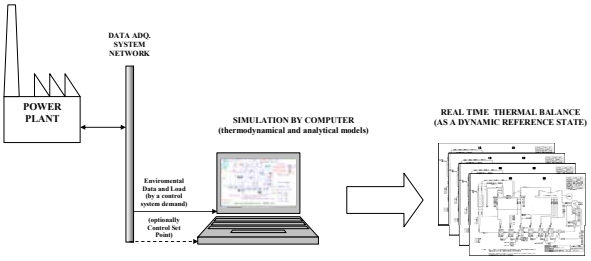

Figure 3: Scheme of data process in order to obtain a Dynamic Reference State

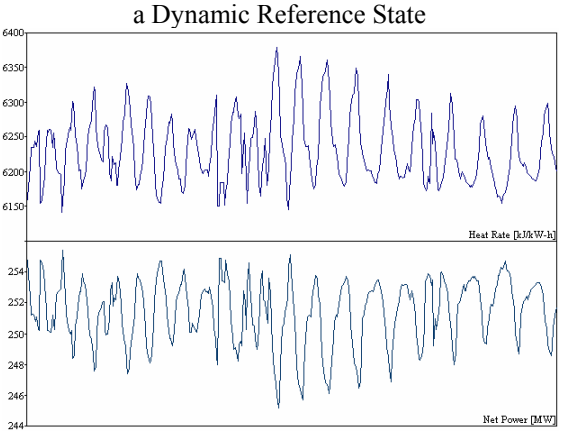

Figure 4: Reference Heat Rate and Power by Adapting in the simulator at the real-time conditions

ACCEPTABLE (DYNAMIC) PERFORMANCE TEST STATE

A performance test is defined as the data collection at determinate operation condition. The codes ASME PTC – 4, 6 and 22 *(Performance Test Code)* defined the conditions and measure points for gas turbines, steam turbine and HRSG tests. The measure data is referred to the information that can be obtained from the instrumentation in a strategic points into the plant (described in Table 1). With the objective to reproduce the same thermodynamic conditions in the reference state it is necessary additional operations using mass and energy balances, then efficiencies, heat rate and admission coefficients (Fig 5).

MEASURE POINTS	DATA
Environmental condition and compressor admition	P, T, T_w
IGV	%α
Compressor exit and air extractions	P, T
Fuel admission in the	P, T,

combustor	HHV,LHV,ρ, $\dot{m}$
Combustor (TG admission)	P
TG combustion gases exit	P, T
Gases in HRSG exit	P, T, x_i
Steam generated by HRSG	P, T, $\dot{m}$
Steam admission at AP-TV Y BP-TV	P, T
Steam exit at AP-TV and steam admission at BP-TV.	P, T
Exhaust steam	P
Condenser exit conditions and feet water.	P, T, $\dot{m}$
Suction and exit condenser and feet pumps.	P, T
Electric generator, pumps, fans and auxiliary.	Volt. and Amp.

Table 1: Measure variables (directly or indirectly) in plant

For *operating (performance) tests* state aspects like the need to data validation by a dynamic min., max., avg. values, and thermodynamic filtrate, interchange and dynamic replacement of data with the reference state, calculation of thermodynamic conditions of the test and determination of the free variables (anomalies) are necessary. First before any operation with the data, it needs a validation passing through filtrate with two limits max. and min., those limits are established by the plant operation, maxim and minimum charge. After this filter it is necessary a thermodynamic validation, that is a data compare between inlet an exit of a component, like pressure in air filters, the inlet pressure never can be less than exit pressure; with this filters it can reject any mistake. If any signal after the filter is wrong, the simulator will be replace by an optimal value for the same variable (signal). The system chose the data replace from the data base, where is update every minute by a polynomial equation.

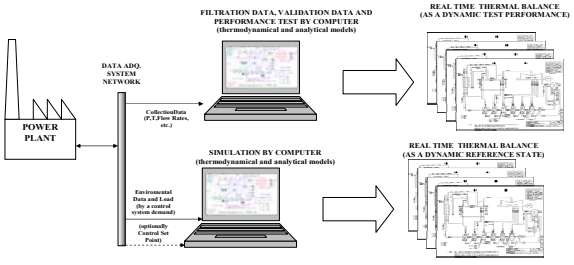

Figure 5: Scheme of data process in order to obtain an *Acceptable (dynamic) Performance Test State*

EQUALIZED RECONCILIATION METHOD

The method of diagnosis is based on reconciliation data; in other words, a comparison between test and reference; we described this method at TADEUS´ series [4]. However, this included one long list of anomalies from the external ones to the internal ones (Fig 6). In this sense, at the time of evaluating in real time the impacts to the Heat Rate and Power, the external causes can impact very strong, but they are irremediable, the question is: *is it worth really the trouble to evaluate them?.* In addition, as we discussed above, the reference must be to the same load, it is with the intention of having comparable efficiencies and operation conditions. It is the concept that we call ***Equalized Reconciliation Method,*** means a comparison of reference and test, at the same extern conditions with the intention of isolating the intrinsic effects of the components.

Anomalies Classification

The anomalies that impact to Heat Rate and Net Power are defined as internal and external (Fig. 6).

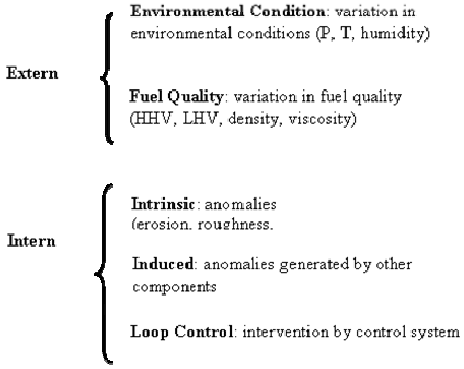

Figure 6: Anomalies Classification in Power Cycles.

In order to do reconciliation, first is necessary create one module (Figure 7), where it is determinate the Heat Rate and Net Power by mathematic models used in the simulator. Once created the module, beginning one call to evaluate in first time the test state, after every test parameter is changed by a reference parameter, until all the anomalies have been substituted. An example of a module declaration and callings of 4 anomalies (2 of control and 2 intrinsic) are shown in Fig. 7; where with a sequential replace, has been calculated ΔHR y $\Delta\dot{W}$ for each anomaly. Obtained

ΔHR is possible determinate the economic cost by every anomaly.

```
MODULE DEC LARATION
RECON (M 1,c , M 2,c , M 3,i , M 4,i , M 5,i : HR , W )
• • • {Thermodyna mic Model }• • •
HR = HR ( M 1,c , M 2,c , M 3,i , M 4,i , M 5,i : HR , W )
Ẇ = W ( M 1,c , M 2,c , M 3,i , M 4,i , M 5,i : HR , W )
END
{input data from acce ptable per formance t est }
TIT test , TSH test , η BASE ,COMP test , Δ P COMB ,test
{input data from dynamic reference state }
TIT ref , TSH ref , η BASE ,COMP ref , Δ P COMB ,ref
{CALLINGS OF MODULE }
CALL RECON (TIT test , TSH test , η BASE ,COMP test , Δ P COMB test : HR 1 , W 1 )
CALL RECON (TIT ref , TSH test , η BASE ,COMP test , Δ P COMB test : HR 2 , W 2 )
CALL RECON (TIT ref , TSH ref , η BASE ,COMP test , Δ P COMB test : HR 3 , W 3 )
CALL RECON (TIT ref , TSH ref , η BASE ,COMP ref , Δ P COMB test : HR 4 , W 4 )
CALL RECON (TIT ref , TSH ref , η BASE ,COMP ref , Δ P COMB ref : HR 5 , W 5 )
{IMPACT FOR TIT }
Δ HR TIT = HR 2 − HR 1
Δ W TIT = W 2 − W 1
{IMPACT FOR TSH }
Δ HR TSH = HR 3 − HR 2
Δ W TSH = W 3 − W 2
{IMPACT FOR η BASE ,COMP }
Δ HR η BASE ,COMP = HR 4 − HR 3
Δ W η BASE ,COMP = W 4 − W 3
{IMPACT FOR Δ P COMB }
Δ HR Δ P COMB = HR 5 − HR 4
Δ W Δ P COMB = W 5 − W 4
```

Figure 7: Simplified example of MODULE and CALL of 4 Anomalies.

On – Line Implementation

The use of this methodology has been tested by manual data acquisition, however exits the necessary to know the impact by anomaly in the moment that it occurs, so the implementation of this methodology result indispensable to offer "in real – time" diagnosis. In the actual data acquisition systems allowed the developed of "on – line" monitoring procedures, with the possibility to show the Impact of components that operate out of nominal conditions, control deviations and environment conditions.

CASE OF APPLICATION

The case of study is a combined cycle (Figure 8) with sequential combustor, two compressor stages, a steam turbine with three stages: high, intermediate and low pressure; one HRSG, one electric generator and one aerocondenser. The Table 2 shows a detail description of the plant and its principal points in the analysis.

Analysis point	Description
	GAS TURBINE
00	Atmospheric conditions
01	Air admission after air filters
02	Compressor exit, combustor EV inlet
03	Fuel to combustor EV
04	Gas Turbina inlet HP
05	Gas Turbine exit HP
06	Fuel to combustor SEV
07	Gas Turbina LP
08	Gas Turbine exit LP
09	Exhaust gases
010	Air extraction to cooler HP
011	Air exit after cooler HP
012	Air extraction to cooler LP
013	Air exit after cooler LP
020	Fuel flow to plant
	HRSG – STEAM TURBINE
1	Principal Steam inlet ST HP
2	Steam inlet ST IP
3	Steam exhaust ST HP
4	Low pressure steam
5	Steam exhaust ST IP inlet ST LP
6	Steam exhaust ST LP
71	Inlet condenser pump
70	Exit condenser pump
40	Feed water
22	Water to cooler LP
21	Water to cooler HP
32	Steam after cooler LP
31	Steam after cooler HP

Table 2: Principal analysis points in case of study

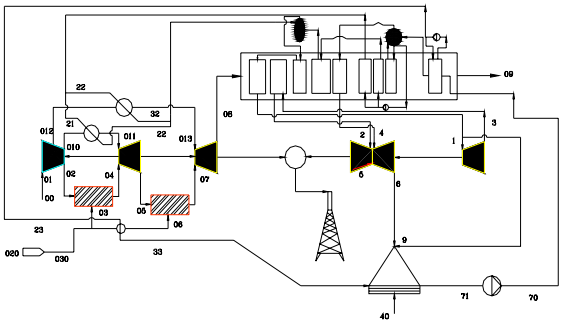

Figure 8: Plant configuration in case of study

In the next figures (Fig. 9 and Fig. 10), is possible see part of the configuration in the plant, first a layout of the same, in the second a gas turbine zoom, in this interfaces appear the most important variables with its value.

In the Thermal Flow Report (Table 3), it is presents a detail description of the most important points in the plant, including properties for each one and the operational states, actual (acceptable performance test) and optimal (dynamic references state).In the Equipment Thermal Report (Table 4), the

information given for each equipment in the plant including data like efficiency, power and heat rate, in all cases two states: optimal and actual. In the (equalized) Reconciliation Report (Table 5), presents the impact to the Net Power and Heat Rate done by a several correction factors and its economic cost.

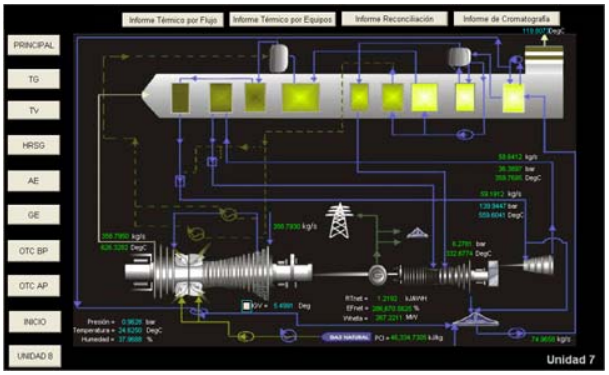

Figure 9: Combined Cycle – Principal Interface

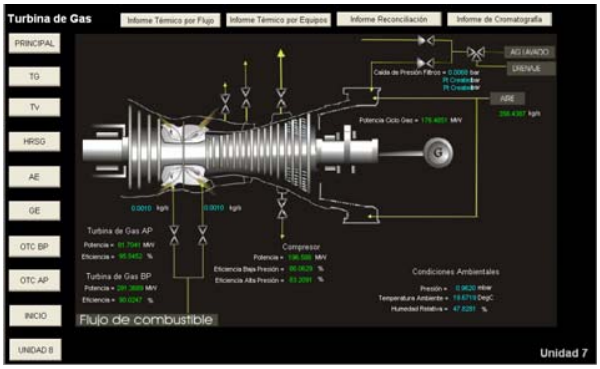

Figure 10: Gas Turbine - Interface

CONCLUSION

The opportunity knowledge of the causes that impact the efficiency in an energetic process and its economic costs, allow take decisions and corrective actions in plant, from low cost (calibration of loop control) until predictive or corrective maintenance. This actions permit save energy sources and recovery efficiency until optimal state. The "on – line" implementation of this methodology allow the detection of substantial saves in energy and the immediately correction, then avoid raise fuel consumptions and environment pollution.

REFERENCES

[1] Valero A., Correas L., Zaleta A., Lazareto A., Verda V. , Reini M. and Rangel V., "*On the thermoeconomic approach to the diagnosis of energy system malfunctions. PART-1 the TADEUS problem",* 15th International Conference on Efficiency, Costs, Optimization, Simulation and Environmental Impact of Energy Systems, ECOS 2002, Berlin, Germany. (2002).

[2] Valero A., Correas L., Zaleta A., Lazareto A., Verda V. , Reini M. and Rangel V., "*On the thermoeconomic approach to the diagnosis of energy system malfunctions. PART-2 Malfunction Definitions and Assessment"* 15th International Conference on Efficiency, Costs, Optimization, Simulation and Environmental Impact of Energy Systems, ECOS 2002, Berlin, Germany. (2002).

[3] Verda V., Valero A., Serra L., Rangel H. Zaleta A., Lazareto A., Reini M. and Tacan R. V., *On the thermoeconomic approach to the diagnosis of energy system malfunctions. PART-3 Approaches to the Diagnosis problem*. Proceedings of the 16th International Conference on Efficiency, Costs, Optimization, Simulation and Environmental Impact of Energy Systems Copenhagen, Denmark, 2003.

[4] Lazareto A, Toffolo A., "*On the thermoeconomic approach to the diagnosis of energy system malfunctions. PART-5 Indicators to Diagnose Malfunctions: Application of a New Indicator for the location of Causes*. Proceedings of the 16th International Conference on Efficiency, Costs, Optimization, Simulation and Environmental Impact of Energy Systems Copenhagen, Denmark, 2003.

[5] Zaleta A., Valero A., Rangel V., *On the thermoeconomic approach to the diagnosis of energy system malfunctions. PART-6 A reconciliation approach*. Proceedings of the 16th International Conference on Efficiency, Costs, Optimization, Simulation and Environmental Impact of Energy Systems Copenhagen, Denmark, 2003.

[6] Verda V., *On the thermoeconomic approach to the diagnosis of energy system malfunctions. PART-7 A from Diagnosis to Prognosis*. Proceedings of the 16th International Conference on Efficiency, Costs, Optimization, Simulation and Environmental Impact of Energy Systems Copenhagen, Denmark, 2003.

ANNEX 1

GAS TURBINE									
Key	**Description**	***p*[bar]**		***T*[°C]**		***h*[kJ/kg]**		**$\dot{m}$ [kg/s]**	
		Optimal	***Actual***	***Optimal***	***Actual***	***Optimal***	***Actual***	***Optimal***	***Actual***
00	Environmental Conditions	0.9687	0.9687	19.9531	19.9531	20.2385	20.2385	274.1395	268.5795
01	Compressor admition	0.9687	0.9502	19.9531	21.6406	20.2385	21.9727	274.1395	268.5795
02	Compresor exit	20.3244	19.8250	479.2276	517.8233	500.6305	543.1487	107.6584	109.5478
03	Combustor EV inlet	---	---	---	---	---	---	2.9027	3.3380
04	Expansor HP Admission	19.8244	19.1159	1190.1877	1162.1420	1385.4273	1349.7632	110.5612	112.8859
05	Expansor HP exit	8.9673	11.7578	968.0208	968.0208	1105.1069	1105.1069	112.8511	138.8969
06	Combustor SEV inlet	---	---	---	---	---	---	3.4643	3.0720
07	Expansor LP Admission	7.9673	10.7109	1129.0320	1221.7390	1307.7281	1425.5865	147.3154	141.9710
08	Expansor LP exit	0.9837	0.9799	634.8411	634.8411	699.7636	699.7636	280.5065	274.9895
09	Gas exhaust	0.9687	0.9687	94.6566	94.6566	98.8792	98.8792	280.5065	274.9895
010	Air inlet – cooler high pressure	20.3244	20.3228	479.2276	517.8233	500.6136	543.1304	33.2900	26.0131
011	Air exit – cooler high pressure	20.2562	20.2562	333.6875	333.6875	343.5631	343.5631	33.2900	26.0131
012	Air inlet – cooler low pressure	13.5479	12.9809	394.3492	394.3492	408.3841	408.3841	133.1911	133.0186
013	Air exit – cooler low pressure	11.7078	11.7078	349.2500	349.2500	360.1055	360.1055	133.1911	133.0186
STEAM TURBINE									
1	Principal Steam inlet ST HP	105.3750	105.3750	542.7188	542.7188	3477.0181	3477.0181	39.4900	39.2706
2	Steam inlet ST IP	24.1106	23.8186	552.7500	552.7500	3580.7880	3581.0565	38.9400	38.7208
3	Steam exhaust ST HP	25.5581	25.2328	334.7089	341.4063	3089.0815	3105.4307	38.9400	38.7208
4	Low pressure steam	3.2582	4.8825	323.8750	323.8750	3117.1096	3113.4470	9.4207	9.4207
6	Steam exhaust ST LP	0.0964	0.1330	45.0919	42.2012	188.8003	176.7145	48.9107	48.6914
71	Inlet condenser pump	0.0964	0.1330	45.0919	51.3859	188.8000	176.7100	50.4764	50.4764
70	Exit condenser pump	18.3936	21.4375	45.1302	41.0312	190.5587	173.7026	50.4764	50.4764
21	Water to cooler LP	238.3244	238.3244	188.9375	188.9375	813.9854	813.9854	2.0405	2.0405
31	Water to cooler HP	107.8022	107.8022	503.7500	503.7500	3127.2567	3127.2567	2.0405	2.0405
22	Steam after cooler LP	238.3244	238.3244	188.9375	188.9375	813.9854	813.9854	2.7750	2.7750
32	Steam after cooler HP	107.8022	107.8022	415.4063	415.4063	3127.2567	3127.2567	2.7750	2.7750

Table 3: Thermal Flow Report

Key	**Description**	**Efficiency [%]**		**Power [MW]**		**Heat Rate [kJ/kW-h]**	
		Optimal	***Actual***	***Optimal***	***Actual***	***Optimal***	***Actual***
CAP	Compressor High Pressure	88.2857	64.0705	---	---	---	---
CBP	Compressor Low Pressure	85.1664	85.1948	----	---	---	---
C	Compressor	87.7777	86.8601	119.3440	122.0238	---	---
AP	Expansor High Pressure	90.9000	91.5134	40.3244	33.9825	---	---
BP	Expansor Low Pressure	90.4900	91.4714	170.5380	176.5891	---	---
HP	Steam Turbine High Pressure	89.7597	85.3446	17.0229	16.3067	---	---
IP	Steam Turbine Intermediate Pressure	93.3445	90.2189	22.4782	17.4483	---	---
LP	Steam Turbine Low Pressure	92.7004	94.7489	25.2702	30.0338	---	---
BC	Condenser Pump	92.3102	92.3102	0.1050	0.1050	---	---
GE	Electric Generador	97.6709	97.5512	148.6152	144.5718	---	---
RTni	Net Heat Rate, LHV	---	---	---	---	7133.9302	7382.8075
RTnir	Net Required Heat Rate, LHV	---	---	---	---	---	7172.9893
RTns	Net Heat Rate, HHV	---	---	---	---	7906.4151	8182.4154
RTnsr	Net Required Heat Rate, HHV	---	---	---	---	---	7949.8725
EFcci	Cycle Efficiency (base LHV)	50.4631	48.7619	---	---	---	---
EFccS	Cycle Efficiency (base HHV)	45.5326	43.9968	---	---	---	---

Table 4: Components Thermal Report

Correction Factor	**Unit**	**State**		**ΔHR**	**ΔW**	**Cost**
		Optimal	***Actual***	**[kJ/kW-h]**	**[MW]**	**[usd$/h]**
Air Filtres – Drop Pression	[bar]	0.0068	0.0068	73.0092	-7.1813	265.56316
Compressor Low Pression Efficiency	[%]	89.6976	86.0629	78.7688	-8.2155	286.51323
Compressor High Pression Efficiency	[%]	89.7231	83.2091	27.2939	-2.7229	99.27872
Combustor EV – Drop Pression	[bar]	0.9419	0.9419	25.8158	-2.5292	93.90215
Combustor SEV – Drop Pression	[bar]	1.5750	1.5750	57.8192	-5.4793	210.31121
TIT – Expansor HP	[ºC]	1089.0204	1139.7842	-201.1558	20.0308	-731.68281
TIT – Expansor LP	[ºC]	1269.5566	1280.1167	-74.0467	8.2571	-269.33694
Expansor HP – Efficiency	[%]	90.9000	95.5452	-119.8195	11.5465	-435.83081
Expansor LP – Efficiency	[%]	90.4977	90.0247	25.6880	-2.5697	93.43739
Steam Turbine HP – Efficiency	[%]	89.5465	91.1942	74.6880	-7.6616	271.10789
Steam Turbine IP – Efficiency	[%]	92.7701	90.2321	13.1615	-0.5014	47.87354
Steam Turbine lP – Efficiency	[%]	92.8685	91.8964	12.3251	-0.4676	44.83118

Table 5: Reconciliation Report

Proceedings of ECOS 2005
Trondheim, Norway
June 20–22, 2005

THE NET WORK OUTPUT AND EFFICIENCY CHARACTERISTICS FOR AN IRREVERSIBLE DIESEL CYCLE

Shiyan Zheng[a, b] , Guoxing Lin[a, c,]*, Ben Hua[c]
[a] Xiamen University
Department of Physics
P. R. China

[b] Quanzhou Normal University
Department of Physics
P. R. China

[c] South China University of Technology
Chemical Engineering Research Institute
P. R. China

ABSTRACT

A cyclic model of irreversible Diesel heat engine is presented. The influences of heat transfer and irreversibility of the adiabatic processes on the net work output and the efficiency of the Diesel heat engine cycle are explored. The heat losses through cylinder walls are considered and the expansion and compression isentropic efficiencies are put forward in the present paper. The optimal relationships between the net work output or the efficiency and the isentropic efficiencies, the pressure ratio, and other parameters are derived. The optimum operating range of the pressure ratio is determined and the other optimal performance characteristics are discussed and evaluated. The conclusions obtained may provide some theoretical guidance for the optimal design of a class of internal combustion engines.

***Keywords*:** Diesel cycle, Work output, Efficiency, Pressure ratio, Irreversibility

NOMENCLATURE

A	Function defined in equation (15)
B	Function defined in equation (18)
c_P	Specific heat at constant-pressure [kJ/kg-K]
c_V	Specific heat at constant-volume [kJ/kg-K]
k	$= c_P / c_V$
$P_{1,2}$	Pressures at state 1, constant-pressure process [k Pa]

---

* Corresponding author: Fax: +86-592-2189426; E-mail: gxlin@xmu.edu.cn

q_{in} Heat added to per unit mass of the working fluid [kJ/kg]

r_e , r_p Expansion ,pressure ratio

$T_{1\sim4,2i,4i}$ Temperatures of the working fluid at state 1,2,3,4,2i and 4i [K]

$V_{1,3}$ Volumes of the working fluid at constant-volume process 4i-1 , state 3 [m^3]

w Net work output [kJ/kg]

η Efficiency

$\eta_{1,2}$ Expansion, compression isentropic efficiencies

α Parameter related to combustion [kJ/kg]

β Parameter related to heat transfer [kJ/kg-K]

INTRODUCTION

The optimum thermodynamics method has been applied successfully to a large number of engineering problems in recent decades [1-8]. Mozurkewich *et al*. [3] applied the optimal control theory to optimize piston movement for the ideal Otto cycle. Angulo-Brown *et al.* [4] optimized a non-endoreversible Otto cycle to improve power output and efficiency. Aragón-González *et al.* [5] considered the irreversible adiabatic processes in the Otto cycle. Chen *et al* [6] studied the effect of heat transfer in cylinder wall on the Otto cycle. Bhattacharyya [7] investigated the effect of compression ratio and cut-off ratio on an irreversible Diesel cycle. Akash [8] presented the effect of heat transfer on the net work output and the indicated thermal efficiency of the Diesel cycle. These research results are closer to the reality than the classical thermodynamic theory. It is significant and of practical value to investigate further the influence of the irreversibilities in the expansion and compression processes, combustion and heat transfer parameters on the performance of the Diesel heat engine cycle. In this paper, a new irreversible Diesel cycle model is established, in which the irreversibilities resulting from the non-isentropic compression and expansion processes and heat losses through the cylinder walls are taken into account. The expansion and compression isentropic efficiencies are introduced. On the basis of thermodynamic theory, the analytical expressions of the net work output and the thermal efficiency of the Diesel heat engine cycle are derived. The effects of combination parameter, heat transfer coefficient, pressure ratio on the performance of the cycle are analyzed and evaluated. Several important performance bounds are determined and discussed. The conclusions obtained may provide some theoretical instruction in the optimal design of Diesel heat engines.

THE MODEL

Figure 1 presents a pressure-volume diagram for an Diesel cycle. The process 1-2-3-4-1 is a reversible cycle while 1-2i-3-4i-1 is an irreversible one. Considering two adiabatic processes as irreversible, we define the expansion and compression isentropic efficiencies as [5]

$$\eta_1 = \frac{T_3 - T_{4i}}{T_3 - T_4} \tag{1}$$

$$\eta_2 = \frac{T_2 - T_1}{T_{2i} - T_1} \tag{2}$$

where $0 < \eta_1, \eta_2 \le 1$, and $T_1, T_2, T_{2i}, T_3, T_4$ and T_{4i} are the absolute temperatures at states 1, 2, 2i, 3, 4 and 4i, respectively. It is clear that if two adiabatic processes are reversible, $\eta_1 = \eta_2 = 1$. Moreover, the air-standard Diesel cycle is considered in the present model.

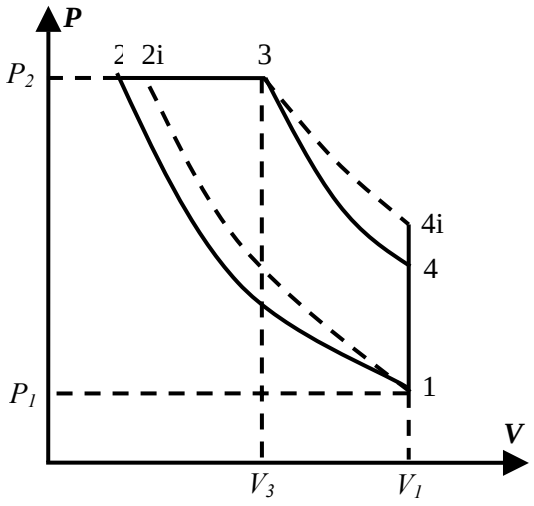

Figure 1: Schematic diagram of an irreversible Diesel cycle

According to the above model, the net work output and the efficiency are given by the following equations:

$$w = kc_v(T_3 - T_{2i}) - c_v(T_{4i} - T_1) \qquad (3)$$

$$\eta = 1 - \frac{T_{4i} - T_1}{k(T_3 - T_{2i})} \qquad (4)$$

where $k = c_p / c_v$, c_p and c_v are the constant-pressure and volume specific heats respectively and they are assumed as constant.

For the reversible processes 1-2, 3-4 and states 1 , 3 in the cycle, one has

$$T_2 / T_1 = r_p^{(k-1)/k} \qquad (5)$$

$$T_3 / T_4 = r_e^{k-1} \qquad (6)$$

$$\frac{P_1 V_1}{T_1} = \frac{P_2 V_3}{T_3} \qquad (7)$$

where $r_p = P_2/P_1$ and $r_e = V_1/V_3$ are the pressure and expansion ratios, P_1 and P_2 are the pressures at state 1 and the process 2-3, V_1 and V_3 are the volumes at the process 4i-1 and state 3.

During process 2i-3, the heat input is

$$q_{in} = c_p(T_3 - T_{2i}) \qquad (8)$$

and the heat is provided by combustion. For a real Diesel engine, heat loss between the working fluid and the cylinder wall during combustion is not negligible, and it is often assumed that the heat loss through the cylinder wall is proportional to the average temperatures of both working fluid and cylinder wall and that the cylinder wall temperature is a constant. Hence, the heat added to per unit mass of working fluid is given by [6,8-11]

$$q_{in} = \alpha - \beta(T_{2i} + T_3) \qquad (9)$$

where α and β are two parameters related to combustion and heat transfer.

By combining equations (8) with (9), it yields

$$T_3 = \frac{\alpha + (kc_v - \beta)T_{2i}}{kc_v + \beta} \qquad (10)$$

Using equations (1), (2), (5)-(7) and (10), one has

$$T_{2i} = [1 + \frac{r_p^{(k-1)/k} - 1}{\eta_2}]T_1 \qquad (11)$$

$$T_3 = A/(kc_v + \beta) \qquad (12)$$

$$T_4 = [A/(kc_v + \beta)]^k / (r_p T_1)^{k-1} \qquad (13)$$

$$T_{4i} = \frac{1 - \eta_1 + \eta_1\{A/[r_p T_1(kc_v + \beta)]\}^{k-1}}{(kc_v + \beta)/A} \qquad (14)$$

where

$$A = \alpha + (kc_v - \beta)\{1 + [r_p^{(k-1)/k} - 1]/\eta_2\}T_1 \qquad (15)$$

Then substituting equations (11), (12) and (14) into equations (3) and (4), we have

$$w = \frac{\alpha - 2\beta T_1\{1 + [r_p^{(k-1)/k} - 1]/\eta_2\}}{(kc_v + \beta)/[c_v(k - B)]} \qquad (16)$$

$$\eta = 1 - \frac{B}{k} \qquad (17)$$

where

$$B=\frac{1-\eta_1+\eta_1\{A/[r_pT_1(kc_v+\beta)]\}^{k-1}}{\{\alpha-2\beta T_1[1+(r_p{}^{(k-1)/k}-1)/\eta_2]\}/A}-\frac{(kc_v+\beta)T_1}{\alpha-2\beta T_1[1+(r_p{}^{(k-1)/k}-1)/\eta_2]} \quad (18)$$

Equations (16) and (17) are two important results in the present paper and they show clearly that the net work output and the efficiency of an irreversible Diesel heat engine cycle are dependent on not only the parameters η_1 and η_2 but also the parameters α, β and r_p. The influences of these parameters on the net work output and the efficiency will be discussed in the following sections.

NUMERICAL RESULTS AND DISCUSSION

It can be seen that both equation (16) and equation (17) are transcendental ones of the pressure ratio r_p, one can solve them by a numerical or graphical method. For example, letting $c_v=0.4372kJ/kg.K$, $k=1.4$, $T_1=300K$, $\alpha=3000kJ/kg$ and $\beta=1.5kJ/kg.K$, one can obtain that the net work output w and the efficiency η versus the pressure ratio r_p curves, as shown in figures 2 and 3. Figures 2 and 3 show clearly that when pressure ratio equal to r_{pw} and $r_{p\eta}$, the net work output and the efficiency of the Diesel heat engine cycle attain their maximum,

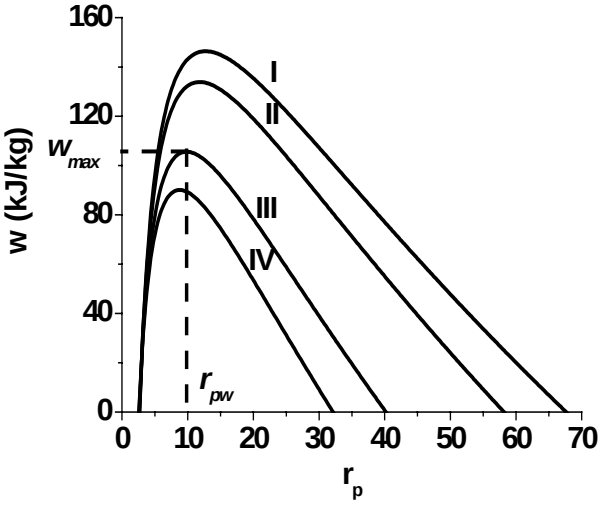

Figure 2: The net work output w versus the pressure ratio r_p curves. Curves *I, II, III* and *IV* correspond to the cases of $\eta_1=\eta_2=1$, 0.97, 0.90 and 0.86, respectively.

$w_{\max}$ and $\eta_{\max}$, respectively. Figure 2 or 3 also shows that when $r_p < r_{pw}$ or $r_{p\eta}$, both the net work output and the efficiency decreases as the pressure ratio decreases, when $r_p > r_{pw}$ or $r_{p\eta}$, the net work output or the efficiency decreases as the pressure ratio increases. It should be pointed out that the regions that the pressure ratios are located in $r_p < r_{pw}$ or $r_p > r_{p\eta}$ are not the optimal operating ones. Thus, the optimal operating range of the pressure ratio for the Diesel heat engine cycle should be

$$r_{pw} \le r_p \le r_{p\eta} \quad (19)$$

As an example, letting $\alpha=3000kJ/kg$, $\beta=1.5kJ/kg.K$ and $\eta_1=\eta_2=0.90$, we can

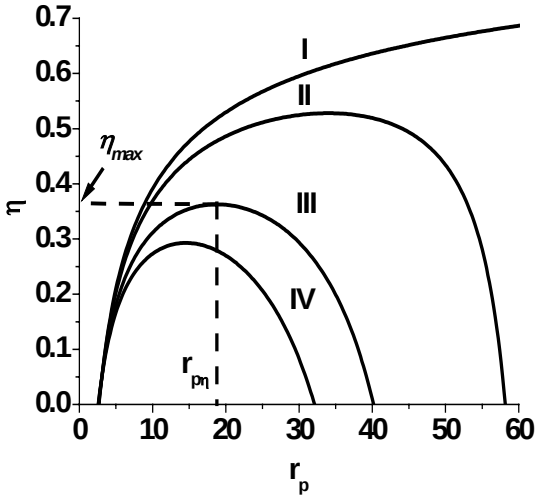

Figure 3: The efficiency η versus the pressure ratio r_p curves. Plots are presented for the same conditions as in figure 2. Curves I, II, III and IV correspond to the cases of $\eta_1 = \eta_2 = 1$, 0.97, 0.90 and 0.86, respectively.

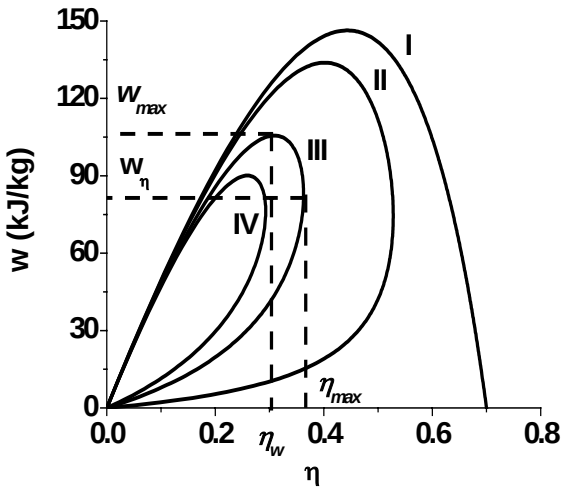

Figure 4(a): The net work output w versus the efficiency η curves. Plots are presented for the same conditions as in figure 2. Curves I, II, III and IV correspond to the cases of $\eta_1 = \eta_2 = 1$, 0.97, 0.90 and 0.86, respectively.

obtain the optimal operating range of the pressure ratio for the Diesel heat engine cycle should be $9.8 \le r_p \le 18.8$. It can be also seen from figures 2, 3 and 4(a) that the effect of parameters η_1 and η_2 on the net work output and the efficiency of the Diesel heat engine cycle is evident and they decrease with decreasing η_1 and η_2. This is natural. Because decrease of values of η_1 and η_2 implies increase of the irreversibility of the two adiabatic processes, such that the cyclic performance of the Diesel heat engine gets worse. As an example, letting $\alpha = 3000 kJ/kg$, $\beta = 1.5 kJ/kg.K$ and $\eta_1 = \eta_2 = 0.90$, we can obtain that the maximum net work output and the maximum efficiency of the cycle are, respectively, $w_{\max}$ = 105.59 kJ/kg and $\eta_{\max}$ = 0.36, and when $\alpha = 3000 kJ/kg$, $\beta = 1.5 kJ/kg.K$, $\eta_1 = \eta_2 = 0.97$, the maximum net work output and the maximum efficiency of the cycle are, respectively, $w_{\max} = 133.85$ kJ/kg and $\eta_{\max} = 0.53$.

Therefore, it is significantly important to pay great attention to the influence of irreversibilities of the adiabatic compression and expansion processes besides to heat transfer irreversibility between the working fluid and the cylinder walls on the net work output and the efficiency of the Diesel heat engine.

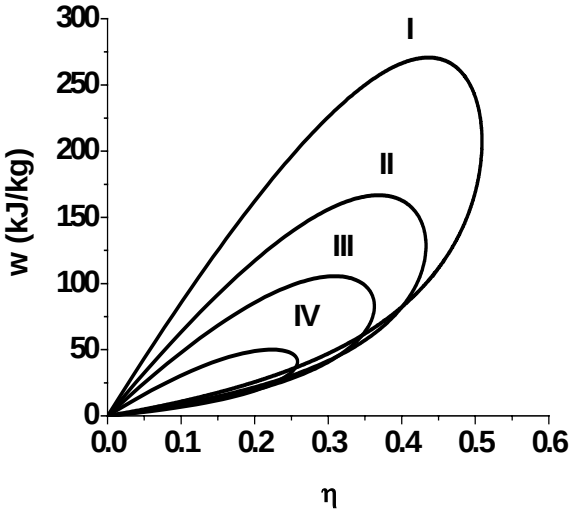

Figure 4(b): The net work output w versus the efficiency η curves. Plots are presented for the same conditions as in figure 2 except $\eta_1 = \eta_2 = 0.90$. Curves I, II, III and IV correspond to the cases of $\beta = 0.9$, 1.2, 1.5 and 2.0 $kJ/kg.K$, respectively.

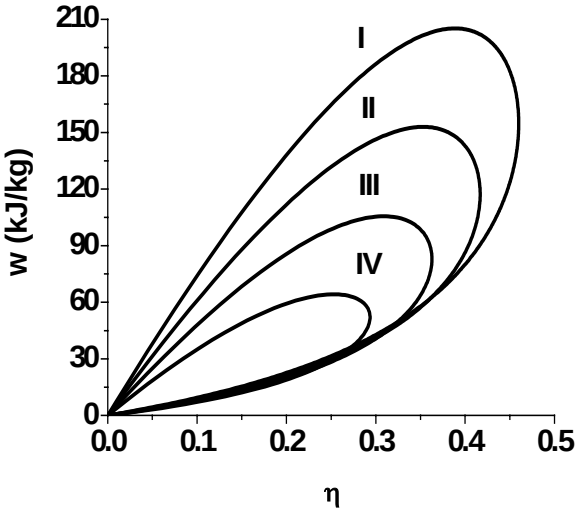

Figure 4(c): The net work output w versus the efficiency η curves. Plots are presented for the same conditions as in figure 2 except $\eta_1 = \eta_2 = 0.90$ and $\beta = 1.5 kJ/kg.K$. Curves I, II, III and IV correspond to the cases of $\alpha = 4000$, 3500, 3000 and 2500 kJ/kg, respectively.

When the Diesel heat engine is operated in those regions of the $w \sim \eta$ curves which have a positive slope, the net work output decreases with decreasing efficiency. Thus, these regions are not the optimal operating regions. Obviously, the optimal operating region of the Diesel heat engine cycle should be situated in the part of the $w \sim \eta$ curves which have a negative slope, as shown in figures 4(a), 4(b) and 4(c). When the Diesel heat engine is operated in the optimal operating region, the net work output increases with decreasing efficiency, and vice versa. Therefore, the optimal ranges of the net work output and the efficiency should satisfy the following equations:

$$w_{\max} \geq w \geq w_{\eta} \tag{20}$$

$$\eta_w \leq \eta \leq \eta_{\max} \tag{21}$$

where η_w and w_η are the efficiency at the maximum work output and the work output at the maximum efficiency. As an example, when $\alpha = 3000 kJ/kg$, $\beta = 1.5 kJ/kg.K$ and $\eta_1 = \eta_2 = 0.90$ are given, the optimal ranges of the work output and the efficiency should be 105.59kJ/kg $\geq w \geq$ 82.82kJ/kg and $0.31 \leq \eta \leq 0.36$. Similarly, using equations (11), (14) and (19), we can obtain the optimal regions of the cycle temperatures at state points 2i and 4i as

$$T_{2iw} \leq T_{2i} \leq T_{2i\eta} \tag{22}$$

and

$$T_{4iw} \geq T_{4i} \geq T_{4i\eta} \tag{23}$$

where T_{2iw} , $T_{2i\eta}$ and T_{4iw} , $T_{4i\eta}$ are the temperatures of the working fluid at state points 2i and 4i for the maximum work output or the maximum efficiency.

The heat transfer irreversibility between the working fluid and the cylinder walls during combustion has been taken into the cyclic model in the present paper and the parameter β embodies the characteristic of the irreversibility. For this reason, it is necessary to investigate the influence of parameter β on the cyclic performance of the Diesel heat engine cycle. Figure 4(b) indicates that the work output and the efficiency decrease as increase of the values of β. For example, when β =0.9, the maximum work output is about 275kJ/kg, and when β =1.2, the maximum work output is about 165kJ/kg whose value is much less than the former. Similarly, the effect of parameter α on the work output and the efficiency is plotted in figure 4(c). Evidently, the work output and efficiency increase rapidly as the values of α increase.

CONCLUSIONS

In the present paper, the effects of multi-parameters, such as combustion parameter, heat transfer parameter and irreversible adiabatic efficiencies and so on, on the performance characteristics of the Diesel heat engine cycle are investigated. Based on the obtained analytic expressions, the detailed analysis and evaluation of the optimal performance for the Diesel heat engine cycle are carried out by means of the numerical calculation and graphical method. The results obtained can provide some significant guidance for the optimal design and performance improvement of real Diesel heat engines.

ACKNOWLEDGEMENTS

This work has been supported by the Major State Basic Research Development Program (G20000 263) and the Scientific Research foundation of South China University of Technology, People's Republic of China.

REFERENCES

[1] Wu C, Chen L, Chen J. *Recent Advances in Finite-Time Thermodynamics.*New York: Nova Sci. Publishers, Inc., 1999.

[2] Bejan A. *Advanced Engineering Thermo-dynamics* 2nd edn ,New York: Wiley, 1996.

[3] Mozurkewich M, Stephen B. *Optimal paths for thermodynamic systems: The ideal Otto cycle.* J. Appl. Phys., 1982; 53(1): 34-42.

[4] Angulo-Brown F, Rocha-Martínez J, Navarrete- González T. *A non-endoreversible Otto cycle model: improving power output and efficiency.* J Phys. D: Appl. Phys., 1996; 29(1): 80-83.

[5] Aragón-González G, Canales-Palma A, León-Galicia A. *Maximum irreversible work and efficiency in power cycles.* J. Phys. D: Appl. Phys., 2000; 33: 1403-1409.

[6] Chen L, Wu C, Sun F, et al. *Heat transfer effects on the net work output and efficiency characteristics for an air-standard Otto cycle.* Energy Convers. Mgmt., 1998;39(7): 643-648.

[7] Bhattacharyya S. *Optimizing an irreversible Diesel cycle − fine tuning of compression ratio and cut-off ratio*. Energy Convers. Mgmt. 2000; 41: 847-854.

[8] Akash B. *Effect of heat transfer on the performance of an air-standard Diesel cycle*. Int. Comm. Heat Mass Transfer, 2001; 28(1): 87-95.

[9] Klein S. *An explanation for observed compression ratios in internal combustion engines.* J.Eng. Gas Turbines & Power, 1991; 113(4): 511-513.

[10] Chen L, Zheng T, Sun F, Wu C. *The power and efficiency characteristics for an irreversible Otto cycle.* Int.J. Ambient Energy, 2003; 24(4): 195-200.

[11] Parlak A. *The effect of heat transfer on performance of the Diesel cycle and exergy of the exhaust gas stream in a LHR Diesel engine atthe optimum injection timing.* Energy Convers & Mgmt, 2005; 46:167-179.

Proceedings of ECOS 2005
Trondheim, Norway
June 20–22, 2005

Renewable energy sources

Proceedings of ECOS 2005
Trondheim, Norway
June 20–22, 2005

HOME SOLAR ABSORPTION-BASED AIR CONDITIONING IN SPAIN. AN EXPERIMENTAL APPROACH.

P. Rodríguez Aumente[*] (1), M. Izquierdo Millán (2), M. C. Rodríguez Hidalgo (1) & R. Salgado Mangual (1)

(1) Universidad Carlos III de Madrid (UC3M)
Departamento de Ingeniería Térmica y de Fluidos
Avda. Universidad 30, 28911 Leganés, Madrid, Spain

(2) Instituto C. C. Eduardo Torroja (CSIC)
C/ Serrano Galvache s/nº, 28033 Madrid, Spain

(1) & (2) Unidad Asociada de Investigación en Energía y Medioambiente UC3M-CSIC

ABSTRACT

Air conditioning is spread all over the world, even more in countries like Spain where summer weather reaches temperatures above 35 ºC. That causes the increase, not only of electricity consumption, but also organic refrigerants pollution.
Experimental research is being focused on air conditioning systems able to supply the thermal load requirements of a typical house using solar thermal energy. In Spain, this load is around 6 to 8 kW, for an 80 m^2 housing, according to Spanish INE (Instituto Nacional de Estadística). An aditional advantage of the studied system is the use of refrigerants that are not organic and have no ozone deplection activity
Research has been carried out at *Universidad Carlos III de Madrid*. The facility is based on a field of 50m^2 flat-plate solar collectors and a single-effect LiBr absorption chiller. Because of this technology CO_2 emissions are greatly reduced and lessen environmental danger risks, trying to achieve Kyoto Protocol, Spain signed in 1997.
This work includes results on system performance, instantaneous thermal load calculations, economic invest, energy and economic saving and environmental impact reduction. Paper offers experimental results obtained during 2004 summer season. Absorption machine cooling power outputs about 6–10 kW have been recorded, with a required generator power input of 10-15 kW, achieving a mean time-period of 6,5 hours of complete solar autonomy on an average day.
Keywords: Solar energy. Absorption cooling. Environmental impact reduction.

NOMENCLATURE

A : Total house enclosure area [m^2].
A_p : Solar panels effective area [m^2].
A_w : House external wall area [m^2].
α : External wall absorption coefficient [].
COP : Coefficient of performance [].
c_w : Water specific heat [J/(kg·K)].
ΔT : External to internal air temperature difference [ºC].
e_i : i component of wall thickness[m].
h_e : External wall convective heat transfer coefficient [W/(m^2·K)].

[*] Corresponding author: Phone: +34 91 6249406 Fax: +34 91 624 9430 E-mail: aument@ing.uc3m.es

h_i: Internal wall convective heat transfer coefficient [W/(m^2·K)].

I_w: Instantaneous solar radiation on the outside wall surface [kW/m^2].

I: Instantaneous solar radiation on tilted surface (40º) [kW/m^2].

λ_i: Thermal conductivity coefficient of wall component *i* [W/(m·K)].

$\dot{m}_{cw}$: Cooled water mass flow rate [kg/s].

$\dot{m}_{wp}$: Solar panel's water mass flow rate [kg/s].

η_{si}: Solar collector field thermal efficiency [].

Q_w: Thermal load due to solar radiation over a sunny wall surface [kW].

Q: Instantaneous house thermal load [kW].

Q_{panel}: Instantaneous thermal power obtained from solar collector field [kW].

Q_{solar}: Instantaneous solar power available on panels surface [kW].

Q_w: Thermal load due to solar radiation over a sunny wall [kW].

$SCOP$: Solar Coefficient of Performance [].

T_a: External air temperature [ºC].

T_{icw}: Cooled water inlet (to the absorption machine) temperature [ºC].

T_{in}: Internal air temperature [ºC].

T_{ocw}: Cooled water outlet (from the sorption machine) temperature [ºC].

T_{wpi}: Water solar collector field inlet temperature [ºC].

T_{wpo}: Water solar collector field outlet temperature [ºC].

t_{pb}: Redemption period [year].

U: Overall heat transfer coefficient [W/(m^2·K)].

U_w: External wall overall heat transfer coefficient [W/(m^2·K)].

INTRODUCTION

In the past century, researchers have spent decades searching for new ways to make houses completely autonomous, working only by means of renewable energies. In the effort to reduce house electricity demand and to make "living" more environmental friendly, solar resources are gaining popularity because of its availability and its nearly zero impact to the environment.

In Spain, there is a peak in electricity consumption in summer time. This peak is due to the use of air conditioning electrically powered in most of Spanish houses, which impacts the grid and sometimes leads to black outs.

A partial solution could be found, using solar thermal panels to feed a H_2O/BrLi absorption machine [1]*. One of its advantages is that air conditioning demand is generally coupled with solar radiation. It is also a solution to the maintenance of solar installations devices during summer time, when there is no need of heating, and hot water supply demand diminishes.

Among all possible facilities, the chosen one is a 50m^2 field of flat plate solar thermal collectors and a 35kW single effect H_2O/BrLi absorption system. This kind of setup shows the lowest cost and is one of the most used accordingly to [2]. The extension of this solar collector field is able to supply a significant percentage of a typical Spanish single family house requirements [1]. Experimental set-up is located at the UC3M in Madrid.

Although H_2O/BrLi systems show the best performance in absorption machines, single effect system has a thermal COP in the range of 0.5-0.73 [2]. This value is not competitive with conventional systems, so there has to be a minimum threshold of renewable energy supply for it to be worthwhile [3].

Local climate characteristics have a significant influence not only on collector's performance but on its energy requirements, thus, it is important to use local weather conditions in order to design the system and not to over/underestimate its thermal conversion efficiency. As solar irradiation varies considerably from year to year, a large variation in the solar collector heat supply has to be expected [4]. This reason gives relevance to a detailed study on a real installation during a representative time period of use. It is useful either for daily or seasonal periods. This study takes into account that the normalized operation parameters will change along their working life.

This paper sets out an experimental approach to domestic's system operation and performance. To do that, experimental operating parameters have

* Numbers between square brackets [] are relatives to the references listed at the end of the paper.

been collected; not only the inlet and outlet collectors, heat exchangers and storage tank instantaneous temperatures, but also absorption machine components ones have been recorded during 2004 summer time in periods of 10 minutes. Weather conditions like external wet and dry bulb temperatures, solar radiation, wind velocity and direction, are also averaged over 10 minutes intervals.

FACILITY DESCRIPTION

- **Overview**

The solar facility at *Universidad Carlos III de Madrid* has the same components of an ordinary solar installation, with the difference of the incorporation of an absorption machine for cold water production for AC purposes.

The facility consists of 20 *Vitosol 100* flat-plate solar thermal collectors by Viessman, each one having 2,5 m^2 collecting surface, making a total collection surface of 50 m^2. Water is pumped from collectors to two *Alfa Laval* plate heat exchangers in a closed loop, one heat exchanger being of 22 plates and the other one of 20 plates. The heat exchagers are needed because the water flowing inside collectors incorporates antifreeze fluid for winter operating purposes. In the other side of the heat exchangers the water pumped from the thermal storage tank (tank capacity of 2,000 liters) is heated and sent to the absorption machine as the energy input into the generator. This water then comes back to the thermal storage tank to be heated again. The absorption machine is a *Yazaki LiBr-H_2O* (WFC10 model) of 35 kW cooling capacity. The condensator and absorber of this machine are cooled by a cooling tower and the cold water produced at the evaporator of the absorption machine is pumped to a fan coil to have the desired final output of cool air.

Figure 1: Configuration of the Solar Facility at Universidad Carlos III de Madrid.[1]

The facility includes an independent meteorological station which records data from solar radiation, air temperature, wind velocity, relative humidity, etc. This information and the one gathered by the Solar Facility are used as input to an in-house developed data acquisition computer software (see Figure 2).

- **Monitoring and Instrumentation**

On both facilities, solar and meteorological, data have to be processed and recorded to become a functional facility. A data acquisition program developed using *Labview* serves for this purpose.

First, calibration of instruments has been performed (thermocouples, pressure sensors, flowmeters, etc.) to record reliable measurements. Data acquisition software takes all sensor signals every 2 seconds and calculates the mean value of these signals each 10 minutes. These mean values are the ones recorded and used for off-line calculations as experimental data. Then data are processed and results are obtained for each day of summer time.

Real time experimental data from facility are available “on line” at the following web site: http://pc-134-222.uc3m.es/solar.htm

- **Interesting Details**

Following preliminary researches, the thermal storage tank was configured to work under stratification regime, thinking that this would be the best for the application, but this was not the case. Hot water was enough to feed the generator of the absorption machine but the period of time achieved producing cold water was not satisfactory. Eliminating stratification, by forcing hot water to enter at the bottom of the tank, a nearly homogeneous temperature was achieved. This behavior has given best results for the AC application because a larger autonomous working-time was recorded. Nevertheless, a lower collector

[1] Numbers in the figure refers to components of the facility. 1-Solar Collectors, 2- Heat Exchangers, 3-Storage Tank, 4-Absorption Chiller, 5-Cooling Tower, 6-Fancoil

efficiency has been detected using this configuration.

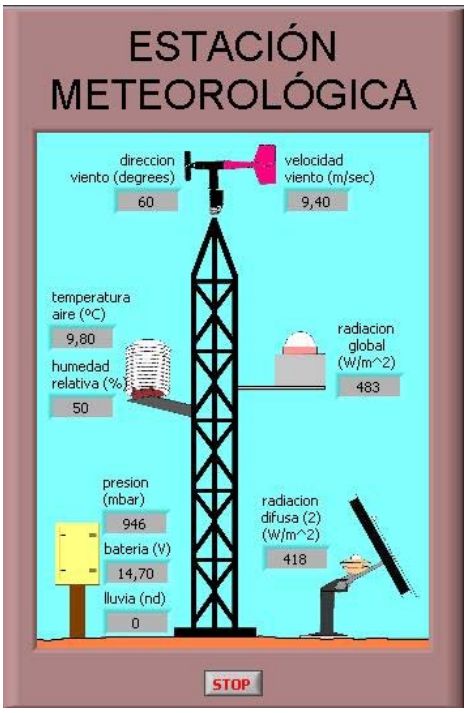

Figure 2: Meteorological Station at Universidad Carlos III de Madrid

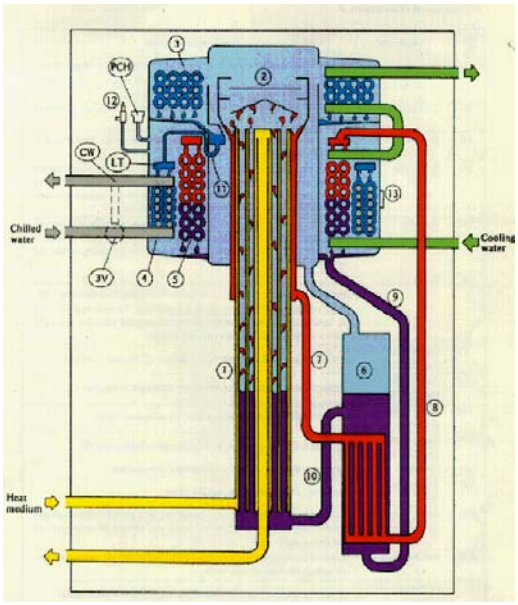

Figure 3: Yazaki LiBr-H_2O absorption machine. Taken from reference [7]

Solar facility components at a glance (see Figure 1):

- 20 Vitosol 100 flat-plate collectors.
- 2 Alfa Laval plate heat exchangers.
- Thermal Storage Tank (2000 Liters).
- Cooling Tower.
- Yazaki 35 kW Absorption Chiller.
- 1 Fan coil.
- Pumps:
  - 1 (0.50 l / s)
  - 1 (0.68 l / s)
  - 1 (0.30 l / s)
  - 1 (0.46 l / s)

EXPERIMENTAL DATA RESULTS

Data gathered from the solar facility during the 2004 summer season are exposed to be compared with the house thermal load, evaluated in the next section. As an example, results corresponding to a typical day are shown in Figure 4.

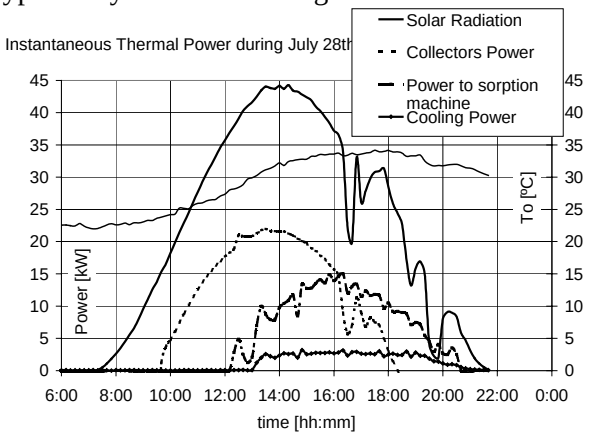

Figure 4: Instantaneous thermal power and ambient temperature corresponding to July 28th.

As it can be seen in Figure 4, due to the thermal storage tank effect, there is a delay between the collector's power and the cooling power curves. In the day shown, a significant cooling power value can be obtained for more than 2 hours in the afternoon, after the collector power is null (time between 18:00 h to 20:00 h). Accordingly to the observation of external air temperature curve, it can be concluded that this is an useful and necessary delay. During the operating period corresponding to the day shown, an averaged value of near 3 kW of cooling power has been obtained. Figures 5 to 7, show summer period (June 16th to October 14th) results. In Figures 5 and 6, daily values of total energy supplied and cooling period are shown. Summer period averaged cooling energy obtained was of 23 kWh per day; when the averaged period of useful daily cooling was of 6

hours and 30 minutes. During this time, the system was producing cooled air at a mean temperature of 15 ºC, using one fan-coil unit for this purpose.

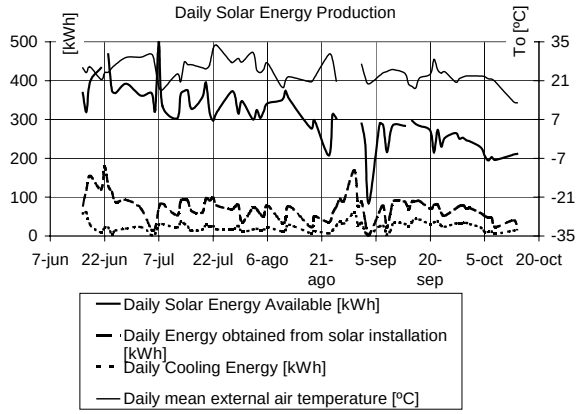

Figure 5: Daily Solar Energy Production during summer period of year 2004. Daily mean external air temperature is shown as a reference.

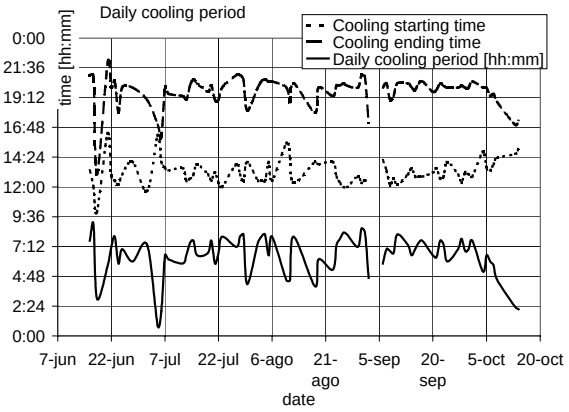

Figure 6: Daily cooling period during de summer period of year 2004.

In Figure 7, daily averaged efficiency parameters of cooling system, powered exclusively by solar energy, are shown. Definitions of those parameters are as follows:

$$COP = \frac{Q_{cool}}{Q_{panel}} \quad (1)$$

$$SCOP = \frac{Q_{cool}}{Q_{solar}} \quad (2)$$

Where:

$$Q_{cool} = \dot{m}_{cw} \cdot c_w \cdot \left(T_{icw} - T_{ocw}\right) \quad (3)$$

$$Q_{panel} = \dot{m}_{wp} \cdot c_w \cdot \left(T_{wpo} - T_{wpi}\right) \quad (4)$$

$$Q_{solar} = I \cdot A_p \quad (5)$$

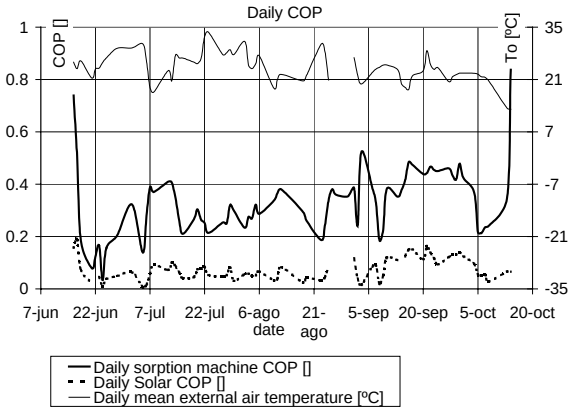

Figure 7: Daily averaged efficiency parameters of solar cooling system. Daily mean external air temperature is shown as a reference.

Averaged values of those parameters for summer time are 0,33 for *COP* and 0,07 for *SCOP*; when the averaged value of η_{si}, defined as follows, is of 0,224.

$$\eta_{si} = \frac{Q_{panel}}{Q_{solar}} \quad (6)$$

This parameter takes into account not only collector's efficiency (i.e. thermal losses in the collector itself) but also thermal losses in the solar facility (piping, pumps, thermal storage tank & heat exchangers).

THERMAL LOAD CALCULATIONS

In order to evaluate the application of solar cooling technology as previously described to a Spanish home air conditioning, its instantaneous thermal load has been calculated. That has been done using an environmental database available from UC3M meteorological installation .

House thermal load has been calculated taking into account the Spanish regulation [9] which gives an overall heat transfer coefficient U for each house wall, floor and roof.

The studied house is a single-family one, all construction element properties are well known: thickness and thermal resistances for conduction and convection and also solar radiation through the different four oriented walls, floor and roof. The latest one receives no solar radiation because of solar panels are installed there.

Regarding to thermal load calculation, it has been taken into account, radiation on wall surfaces,

accordingly to [8]. It is needed to define sunny wall temperature, different from air temperature.

$$Q_w = A_w \cdot U_w \cdot \left(T_a + \frac{\alpha \cdot I_w}{h_e} - T_{in} \right) \qquad (7)$$

where $T_a + \frac{\alpha \cdot I_w}{h_o}$ is the wall temperature under the sun radiation, and $\alpha = 0{,}6$ is the absorption wall coefficient.

The calculation process of external wall overall heat transfer coefficient is as follow:

$$U_w = \frac{1}{\frac{1}{h_e} + \sum_i \frac{e_i}{\lambda_i} + \frac{1}{h_i}} \qquad (8)$$

Repeating the process for every one of the house enclosure's walls, an overall heat transfer coefficient can be obtained for the enclosure; thus a total thermal load can be computed depending on the temperature difference ΔT:

$$Q = U \cdot A \cdot \Delta T \qquad (9)$$

Where:

$$\Delta T = T_{in} - T_a \qquad (10)$$

The calculated value for the overall house *UA* parameter was of 141 W/ºC.

The following environmental data are applied to the thermal load computation:

- Instantaneous Solar radiation on a tilted surface [W/m^2].
- Instantaneous external air temperature [ºC].
- Wind velocity [m/s] & direction.

Due to people living in the house, there are several additional thermal loads, such as, people sensitive and latent heat, about 100 W by person (4 people), thermal load from house lighting, internal air renovation (one renovation per hour), and infiltrations (considered as a 10% of total thermal load).

A constant, homogeneous indoor air temperature of 24ºC has been applied to thermal load calculations according to [10].

As an example, daily thermal load evolution, results corresponding to July 28th are shown in Figures 8 & 9.

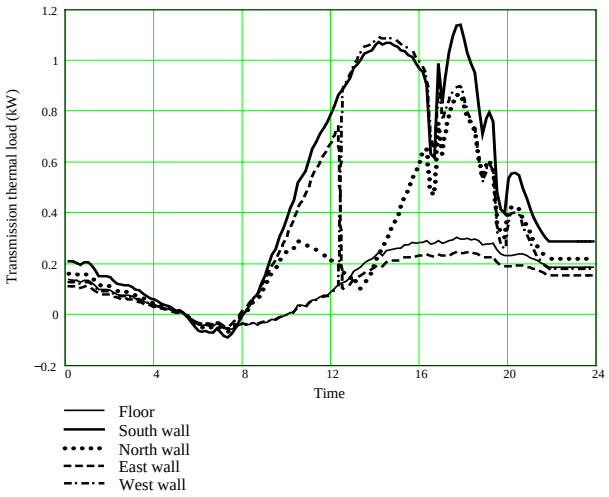

Figure 8: Instantaneous thermal load components of a single-family Spanish house corresponding to July 28th.

By integration of this instantaneous thermal load during the day, a daily thermal load has been obtained for each day of the season, giving the results shown in Figure 10.

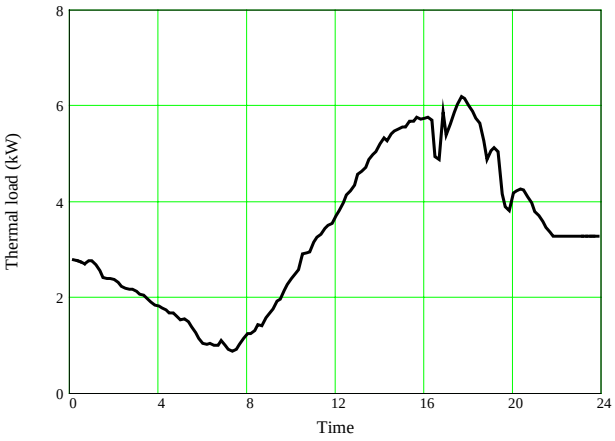

Figure 9: Total Instantaneous thermal load of a single-family Spanish house corresponding to July 28th.

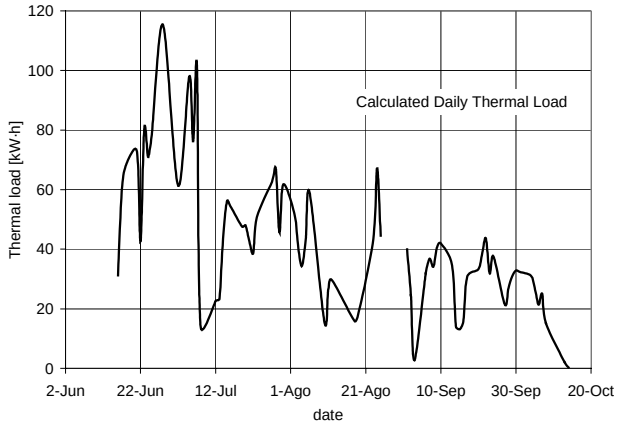

Figure 10: Daily thermal load of a single-family Spanish house corresponding to the summer season of 2004.

ECONOMIC AND ENVIRONMENTAL IMPACT

- **Economic Impact**

- Absorption chiller:

Data gathered for the study about the behaviour of the facility during summer 2004 shows that 53,6% of the total thermal load for the proposed house was delivered by renewable energy. This is 1398 kWh of the total 2938 kWh. Total thermal energy needed to supply the remaining load is 1947 kWh estimating a *COP* of 0,7 for the absorption chiller (when powered by a boiler supplying hot water at 90 ºC). Natural gas cost is estimated at 0,034 €/kWh, having a total expense of 66,20 €.

- Vapour-compression chiller:

Supplying the total thermal load with conventional vapour-compressor chiller, estimating an averaged COP of 2,4, electric energy needed reaches 1440 kWh. Total expense, estimating 0,13523 €/kWh, reaches 194,75 €.

Comparing vapour-compression chiller vs. absorption chiller, economic savings reaches 66%, i.e. 128,55 € for the totality of summer period.

- **Facility Cost**

Advantages on using equipment fed by renewable energy are noticeable. But reality is that this equipment is expensive. Nowadays, the main economical disadvantage of the facility is its initial amount. But in the future, overall costs can be lowered by means of mass production of facility components and integration. In addition to that, there are government incentives and subventions on using equipment that depends on renewable energies, and, still to come with the Kyoto agreement, savings on CO_2 emissions that can be estimated around 25 € per ton of CO_2 for the upcoming period of application 2008-2012. This is just an average between the current 6 €/t to the maximum estimated of 50 €/t for 2012.

To evaluate an estimated time of redemption for the facility, prices of main components are presented. Budget for the facility installed at UC3M is not applicable because this facility is an experimental prototype and some components are over engineered and in some cases oversized. Using gathered data, oversized components can be redesigned to the needs of a house, according to its thermal load. Another important aspect to take into account is that, to amortize the facility cost, it has to be functional around the year, not only during summer time. Because experimental data for domestic hot water and space heating are not yet available using the facility, time of redemption has to be calculated multiplying by a factor of 4/12, 4 month of summer time for the 12 month of the year. This period corresponds to that in which the air conditioning is working in a meteorologically typical Spanish summer.

Collectors	8.710 €
Heat Exchangers	500 €
Hot Water Storage Tank	2.000 €
Absorption Chiller 10kW	5.000 €
Cooling Tower	1.000 €
Fan-coil	200 €
Total	17.410 €

$$t_{pb} = \frac{17.410}{128,55}\left(\frac{4}{12}\right) = 45 years \qquad (11)$$

Resuming, facility cost reaches 17.410 € with an estimated redemption time (payback period) of 45 years, not applying any interest rates, inflation nor external subsidies for environmental protection.

- **Environmental Impact**

- Absorption chiller:

For summer 2004 total natural gas consumption to supply the remaining load would be of 125,9 kg. Estimating 0,22 kg CO_2/kWh for natural gas, total emissions, using renewable energy, reaches 428,41 kg of CO_2.

- Vapour-compression chiller:

Estimating in 0,6 kg of CO_2 by kWh of electric energy produced in the Spanish electric park during a representative year, CO_2 emission would be around 2.618,4 kg of CO_2 to supply the house thermal load.

Comparing vapour-compression chiller vs. absorption chiller, savings on natural gas consumption are of 45% and savings on CO_2 emissions are around 84% using renewable energy.

CONCLUSIONS

- An experimental facility with 50 m^2 of flat plate solar thermal collectors has been developed and fully monitored for cooling applications using absorption technologies.
- Facility has been working during 2004 summer period, producing a daily averaged cooling power of 3 kW for 6 hours and 30 minutes everyday.
- A lower value of *SCOP* has been obtained. New work has to be done in order to reduce facility thermal losses and to increase absorption cooling machine *COP*.
- Instantaneous thermal load of a single-family Spanish house has been calculated using local meteorological data. Results show that a 53,6% of summer air conditioning thermal load could be supplied by renewable source using 50 m^2 of flat plate solar thermal collectors and a 3 kW of cooling power absorption chiller.
- Thermal storage tank allows to adjust daily cooling period to the home air conditioning needs, especially later in the afternoon.
- Due to the high cost of several facility components as solar collectors and absorption chiller, the payback period for solar air conditioning applications has been estimated in 45 years.
- Compared with a conventional vapour – compression chiller, the system analyzed would provide a saving in CO_2 emissions of 84%, due to the use of a renewable energy source.

ACKNOWLEDGMENTS

This work has been partially funded by the Spanish government research grant M. C. y T. CLIMABCAR project DPI 2003-01567 & TRANSMACA project DPI 2002-02439. Their contribution is greatly appreciated.

REFERENCES

[1] Izquierdo M, Lecuona A, Rodriguez P, Venegas M, Thermal Solar Energy for Spanish houses comfort: energy saving and environmental impact reduction. ECOS 2003.

[2] Balaras C A, Grossman G, Hening H-M, Ferreira C A I, Kontoyiannidis S, Posseder E, Wang L, Wiemken E, Overview of solar assisted air-conditioning systems and applications. HPC 2004.

[3] Rodriguez P, Izquierdo M, Lecuona A, Venegas M, Sardina M, Rodriguez M C, López S, Decentralised cooling of electronic equipment using the thermal conversion of solar energy. ECEMEI 2004.

[4] Adsten M, Perers B, Wäckelgård E, The influence of climate and location on collector performance. 2001 Renewable Energy.

[5] Safarik M, Richter L, Otto M, Solar powered H2O/LiBr-Absorption chiller with low capacity. HPC 2004.

[6] Izquierdo M, Garcia N, Lecuona A, Rodriguez P, A Mobile Air Conditioning System that Reduces the Greenhouse Effect. FISITA 2004.

[7] http://www.yazakienergy.com.

[8] Pinazo Ojer, J.M. Manual de climatización Tomo II Cargas Térmicas. Universidad Politécnica Valencia.

[9] NBE-CT 79. A Spanish Basic Regulation on thermal conditions in buildings. ADAE, ASPRIMA.

[10] http://www.idae.es/revision-rite/index.html

Proceedings of ECOS 2005
Trondheim, Norway
June 20–22, 2005

RENEWABLE ENERGY IN BRAZIL

Mario Oscar Cencig*
Núcleo Interdisciplinar de Planejamento Energético (NIPE)
State University of Campinas (UNICAMP)
Campinas – São Paulo
Brazil

ABSTRACT

The Brazilian primary energy supply has a significant proportion of renewable energy (40.9 %). Brazilian Alcohol Program (PROALCOOL, started in 1975) is the major program on renewable energy in Brazil and the biggest ethanol program in the World. Growing programs: the Program for Renewable Energy – *PROINFA* (wind, biomass and small hydroelectric stations), the Probiodiesel Program (a blend of diesel with a vegetable oil), hydrogen as a fuel and fuel cells, Flex-Fuel Vehicles (with free mixing of gasoline and ethanol); also, about 22 MW from wind energy. Other issues: Brazil and the Kyoto Protocol; the Brazilian emissions of CO_2; projects concerning the Clean Development Mechanism (CDM).

THE BRAZILIAN ENERGY MATRIX

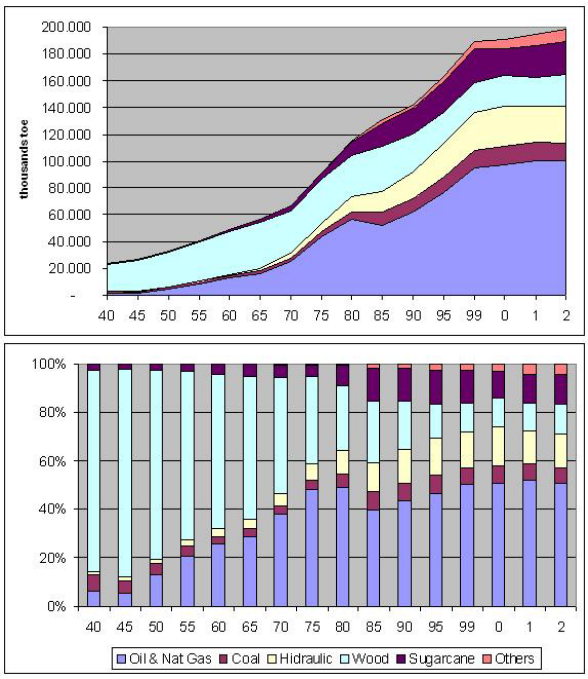

Figure 1: Brazilian energy matrix (1940-2002)

The Brazilian primary energy supply is shown for the period 1940-2002 (last data published, [1]) in the Figure 1.

It is clear the shift from biomass (wood) to oil, and an increase in hydro and sugarcane in the last 30 years. Looking in more detail, in the period 80-85 was verified an increase in renewable energies, followed by a decrease, until now. The actual situation is as Figure 2.

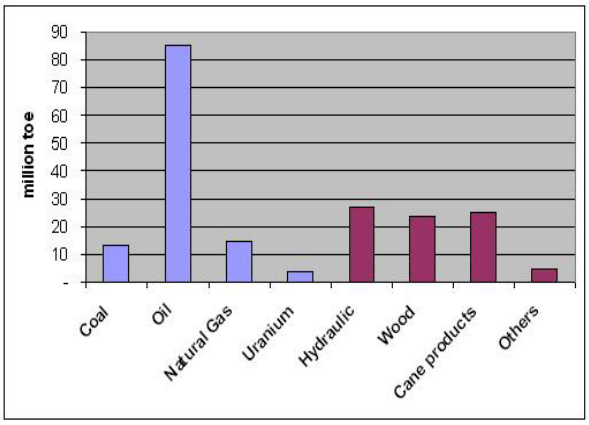

Figure 2: Brazilian primary energy supply (2002)

* Corresponding author: Phone / fax: +(55 19) 3289-3125 / 5499; e-mail: cencig@unicamp.br

The consumption (2002) was 197.9 million tons of oil equivalent, leading to 1.13 toe per capita, lower than world consumption that is about 1.65 toe per capita.
It is clear in Figure 2 the importance of renewable energy in the Brazilian case: a) non-renewable energy 59.1 % (oil 43.1 %, natural gas 7.5 %, coal 6.6 %, uranium 1.9 %), b) renewable energy 40.9 % (hydraulic 13.9 %, wood 11.9 %, products of cane 12.6 %, other 2.5 %).
Table 2 compares the Brazilian situation with selected data from the IEA data source for 2002.

	Brazil	Latin America	World	OEC countries	Non-OECD countries
Coal	6.6	4.5	23.0	20.8	26.3
Oil	43.1	47.6	35.8	40.8	28.3
Natural gas	7.5	18.8	20.9	21.3	21.0
Nuclear	1.9	1.2	6.8	11.2	2.0
Hydro	13.9	9.9	2.2	2.0	2.5
Renewable & waste	24.5	17.6	10.8	3.3	19.6
Geoth / solar / wind	2.5	0.4	0.5	0.7	0.3

Table 2: Selected IEA data [2] (in %)

Concerning the structure of electricity generation, Figure 3 shows the importance of hydro-electricity in Brazil (about 75 %), comparing with the world situation: hydraulic 17,1 %, oil 7,9 %, natural gas 17,4 %, nuclear 16,9 %, coal 39,1 %, others 1,6 %. This hydro power is mainly obtained from large plants, as for instance Itaipu, Xingó, Furnas, Ilha Solteira, between others.

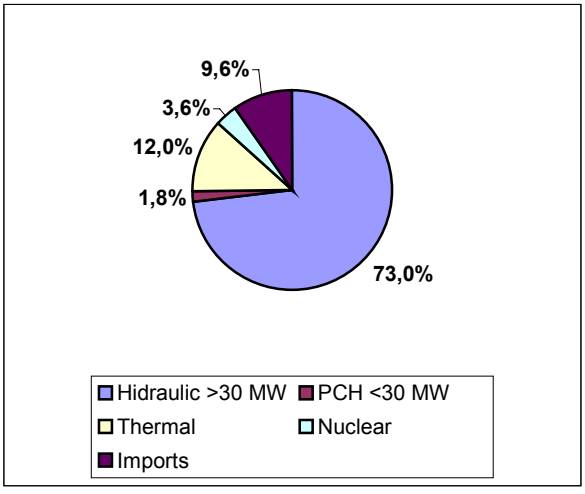

Figure 3: Electricity (Brazil, 2002)

RENEWABLE ENERGIES

Biomass programmes, ethanol and bagasse from sugarcane, biodiesel, (a blend of diesel with vegetal oil), wind power, solar and photovoltaics are at different stages of development in Brazil.

The Ethanol Program

The Brazilian Alcohol Program (PROALCOOL), started in 1975 is the major program on renewable energy in Brazil and the biggest ethanol program in the World [3], see Table 3.

Country	Million m^3
Brazil	12.50
USA	6.50
China	3.00
EU	2.00
India	1.70
Russia	1.30
Saudi Arábia	0.40
South África	0.38
Others	5.22
Total	**33.00**

Table 3: Ethanol world production (2000)

The raw sugar-cane production in Brazil was about 350 million tons in 2003 (in 5 million ha, productivity about 70 ton/ha). Production: sugar 24.82 million tons (2003/2004) and ethanol 14.28 x 10^9 liters (2003/2004). Export: sugar 14.0 million tons (2003/2004) and ethanol 1.120 x 10^9 liters (2003/2004). Figure 4 shows the situation [4].

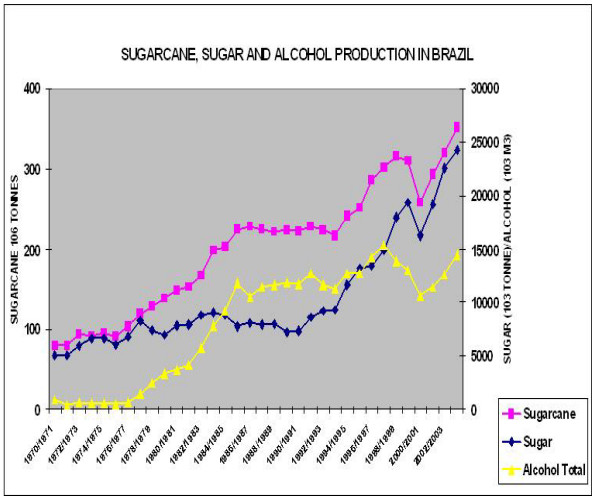

Figure 4: Sugarcane in Brazil

In Brazil, ethanol is used in one of two ways [5]:

- As octane enhancer in gasoline in the form of 22 % *anhydrous ethanol* at at 99.6 Gay-Lussac (GL) and 0.4 % water (a mixture called gasohol) or
- In neat-ethanol engines in the form of *hydrated ethanol* at 95.5 GL.

The structure of the Brazilian market of cars is shown in Figure 5.

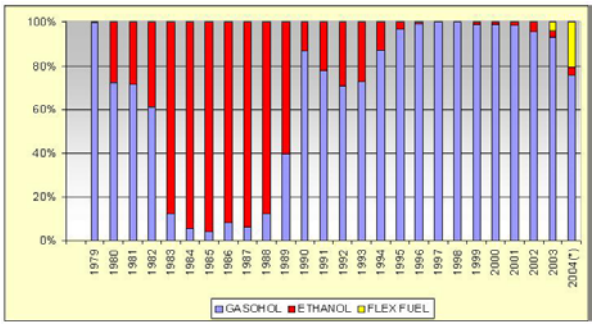

Figure 5: Sales of automobiles

Flex-Fuel Vehicles, with free mixing of gasoline and ethanol was started in March 2003. Four car makers: Fiat, Volkswagen, Ford, General Motors. Sales are growing: 11.444 units (2003), 55.346 units (January to march 2004). Figure 6 shows the actual situation for the market-share in Brazil [6].

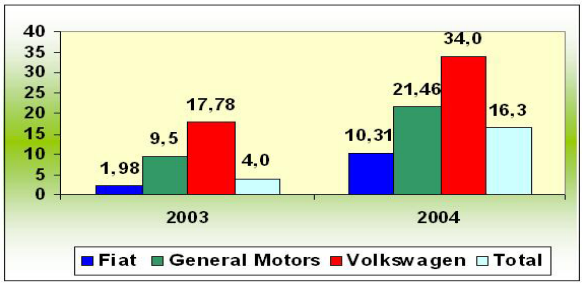

Figure 6: Flex fuel/ethanol vehicles sales (%)

A life cycle analysis of cane and ethanol production [7] show the following relationship for the energy balance: output (renewable energy) /input (non-renewable energy) = 8.3; also, there is a carbon sequestration highly significant.

The generation of electricity (cogeneration) with products of sugarcane industry (bagasse and black-liquor) is very important, the sugar and alcohol producers are auto sufficient, and the potential for fuel and electricity generation is very impressive (see Brazilian Biomass Reference Center – *CENBIO*).

The Biodiesel Program

There are several opportunities for replacing diesel fuel by vegetal oils, as is shown in Figure 7 [8]. For every region, was indicated the fuel consume (in %) and the species existent with possibilities for replacing diesel fuel.

Figure 7: Diesel fuel x vegetal oils

Nowadays, the Green Fuel Program (*Programa Combustível Verde*) expanded the concept to bio-fuel, including ethanol (PROALCOOL Program) and biodiesel (Probiodiesel Program, started October 2002), a blend of diesel with a vegetable oil, such as from soybeans, corn, *babaçu* and *dendê* palm nuts, castor beans and sugarcane. The latest program, conducted by the Ministry of Science and Technology (*Ministério da Ciência e Tecnologia – MCT*) has a target of 5% (v/v) biodiesel /conventional diesel.

The situation may be summarized as follow:

- Patent CENPES / Petrobrás (*Khalil, C.N. Processo de produção de biodiesel a partir de sementes de mamona, 2001*)
- Biodiesel plant at Charqueda (SP) looking for production 100 million liter/year
- Pilot plants at Bahia, Para, Paraná, Piauí and Natal
- University of São Paulo (Ribeirão Preto) is building the first biodiesel station of the country
- Tests are running with bus, automobiles Peugeot 206 and Xsara Picasso, truks Valtra and locomotives América Latina Logística (ALL).

Wind Energy

Brazil has a significant potential for wind energy, fundamentally at the coastal zones, research is running for a more precise determination (preliminary estimations are of 6,000 MW for the

northeast region). Figure 8 shows this potential [9].

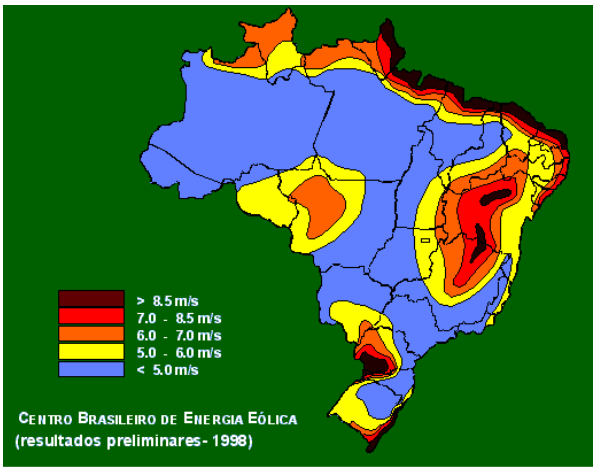

Figure 8: Brazilian wind potential

Presently, there is an electric generation (about 22 MW) at several places, in different technological stages. The most important include: Fernando de Noronha, in the State of Pernambuco, with 75 kW (started 1992); Morro do Carmelinho, with 1 MW (4 units), in the State of Minas Gerais (started 1994); Mucuripe (photo), with 2.4 MW (4 units), in the city of Fortaleza (started 1996); Palmas, with 2.5 MW (5 units) and 5,000 MWh/y, in the State of Paraná (started 1999); Taíba, with 5 MW (10 units) and 17.5 MWh/y and Prainha, with 10 MW (20 units) and 35,000 MWh/y, both in the State of Ceará (started 1999); Horizonte, with 4.8 MW, in the State of Santa Catarina (8 units, started 2003); Macau, with 1.8 MW (under construction, in the State of Rio Grande do Norte).

Figure 9: Brazilian wind projects

So, the utilization of the wind energy for electric generation purposes is more recent. The manufacturing processes are developed and there is a process of building up local capacity for manufacture. The relevant issues for expanding the wind utilization are market regulations, prices for the electricity, connection to the electric grid, so are necessary public (energy) policies for including this source in the national planning, financial questions involving financing agencies, government and private agents.

The Brazilian Wind Energy Center (*Centro Brasileiro de Energia Eólica – CBEE*) is the national reference for projects on wind energy.

Hydrogen and Fuel Cell Programs

Projects in Brazil with hydrogen as a fuel are in progress from middle of the 70´s: electrolysis of water, reforming with vapor of ethanol (from 80´s), biomass gasification (from end 90´s). The research with fuel cells (*Células a Combustível*) is more recent. In 2001 Sectorial Funds from the Science and Technology (MCT) and the Development, Industry and Trade (MDIC) Ministries and from private institutions UNICA, BALLARD, OMG and BASF for ethanol reform. In 2002, the MCT – CGEE Brazilian Fuel Cell Program (PBCaC). In 2004, the SOFC Brazilian network.

Automotive research includes the Vega, a prototype under test at the Brazilian Reference Center for Hydrogen Energy (*Centro Nacional de Referência em Energia do Hidrogênio – CENEH*), at UNICAMP.

Besides, AGRENER GD 2004 supported the organization of the 2nd International Workshop on Fuel Cells – 2nd WICaC, held on October 21st and 22nd. Although it is in its second edition, the 2nd WICaC is already the most important event about fuel cells and hydrogen in Latin America. It brought together more than 20 experts from all over the world to expose and debate the state of the art in research, development and demonstration (R&D&D) of fuel cell systems and hydrogen related technologies. Its public has reached 250 people from research centers, universities (professors and students), private companies and public organizations. In addition to the 20 conference papers, there were 15 oral presentations about the recent R&D&D activities in Brazil.

Some conclusions [10]: SOFC research in Brazil is still rather limited, about 70 people are engaged now in SOFC research; even though still limited, current skilled personnel and facilities are sufficient to head start the development of innovative solutions and bring about technological breakthroughs. Few papers are published in technological aspects, less than 70 papers in total including basic research. Even for more advanced research SOFC groups reproducibility and choice of new materials still remain a challenge.

Solar

Solar thermal has an interesting application to heating water for residential utilization. Figure 10 shows the consumption of electricity during a "typical" day at the State of São Paulo [11]; the peak of consume occurs around 7-8 pm, people take a bath and the water is mainly heated electrically.

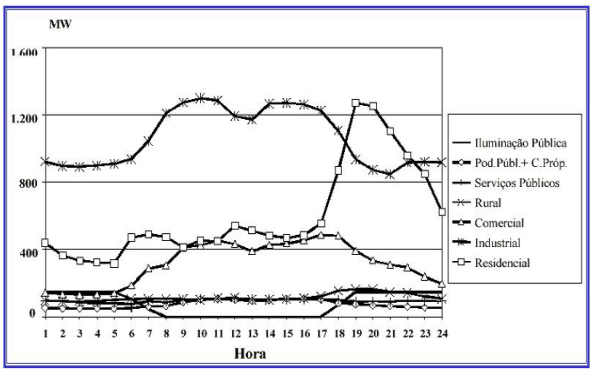

Figure 10: "Typical" day in São Paulo

There is not precise figures about the thermal utilization of solar energy, it is something like 2 million m^2 of solar collectors installed.
Concerning photovoltaic, there are thousands of units installed all over the country, basically at isolated communities (small manufacturers, schools, etc). Examples (Amazonian): Vila Campinas (124 houses), hybrid system (diesel – photovoltaic), 800 units of 64 Wp and 120 batteries; Ilha de Marajó, 10 kWp photovoltaic and 40 kW wind (hybrid system).

Brazilian Energy Policy

Several governmental programs are described. The National Electricity Conservation Program (*Programa para a Conservação de Energia Elétrica - PROCEL*) achieved savings of more than 10 TWh in electricity consumption (US$ 318 million in authorized investments between 1995 and 2000), for more details see Figure 11 [12].

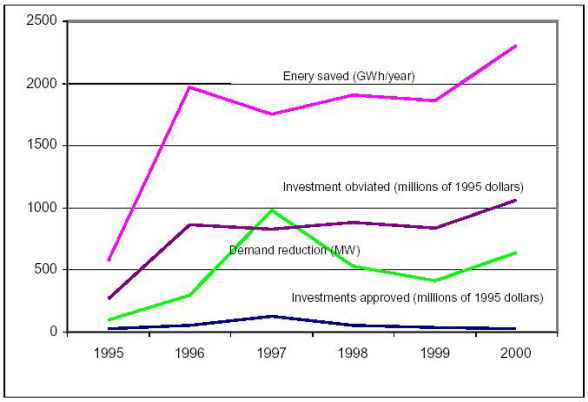

Figure 11: Performance of PROCEL

In Brazil, the PROCEL program was launched by the Federal Government in 1985 and has been run since 1991 by Eletrobrás, in coordination with the public-sector electricity companies. The current role of PROCEL is unclear.
Solar, thermal and photovoltaic are included in the Program for Energetic Development of States and Cities (*Programa para o Desenvolvimento Energético dos Estados e Municípios – PRODEEM*) from December 1994 at the Ministry of Energy (*Ministério das Minas e Energia – MME*). PCH-COM program for small hydroelectric stations (under 30 MW) is a specific program for energy policy. The Program of Incentives for Alternative Electricity Sources (*Programa de Incentivo às Fontes Alternativas de Energia Elétrica – PROINFA*) is the most recent and is a major step looking for the promotion of renewable energy sources. The potential generation for biomass is as follow: for the sugarcane sector 4,000 MW, paper and cellulose sector 1,000 MW, rise processing sector 300 MW. Two stages for the program: stage I, provides for 3,300 MW of renewable energy (wind, biomass and small hydroelectric stations) to be brought on stream before the end of 2007; stage II, once the target of 3,300 MW has been met, PROINFA will be developed with a view to increasing the share of electricity produced by the three renewable sources to 10 % of annual consumption, a target that is to be met within 20 years.

Presently, in Brazil, there are ten research centers (*Centros Nacionais de Referência em Energias Renováveis*) considered as national references for the different renewable sources that coordinate the R&D activities on renewable energies.
One general problem is the constraint on the programs by short-term priorities to the detriment of long-term priorities, as well as, the lack of national integration of different policies.

Environmental Issues

Concerning environmental issues, the Brazilian scenery has the following characteristics: Brazil is a ´Non-Annex I´ country of the Kyoto Protocol; the Brazilian emission of CO_2 (2002, estimated) is 1.7 tCO_2/tonne of oil equivalent, lower then world average, about 2.36 tCO_2/toe; about 70 % of the GHG emissions came from land use and deforestation, indicating the existence of negative questions related to the expansion of economic activities; introduction of fossil fuel-based thermoelectric power plants; several projects (ca 19 presently) concerning the Clean Development Mechanism (CDM) are under study (ranging from 95.5 to 172.5 MW, 53 million tCO_2eq for CO_2 and 38 million tCO_2eq for CH_4); also, among other initiatives, the MaB Program of Biosphere Reserves, conducted from 1993 by the Ministry of Environment (*Ministério do Meio Ambiente – MMA*) that includes the following biosphere reserves: Atlantic Rainforest (*Mata Atlântica*), Central Amazonian, *Cerrado*, *Caatinga*, *Pantanal*, the total extension of the five biosphere reserves is approximately 1.3 million km^2 (about 15 % of the territory), looking for sustainable development.
The current position of the Federal Government was explained by the Minister of Energy, Dilma Roussef, during the International Conference for Renewable Energy, which took place at Bonn (Germany, June 2004), representing the position of the Latin American and Caribbean Initiative for Sustainable Development (May 2002): a target (2010) of at least 10 % of total energy consumption with renewable energy.
The fundamental for this proposal - The Brazilian Energy Initiative – calls for expanded use of alternative sources (solar, wind, geothermal, tidal, "modern" biomass and small hydroelectric facilities), its goal is to rise the share of these sources in the total amount of world energy generated from 2.2 % today to 10 % by 2010.

REFERENCES

[1] MME, Balanço Energético Nacional 2003, Brasília, DF, 2003.

[2] IEA Energy Statistics. Available from `http://www.iea.org/statist/index.htm`

[3] Leal, R. *CO2 life cycle analysis of ethanol production and use in Brazil*. COPERSUCAR, Brazil, May 2004.

[4] Moreira, JR. *Lessons learned from bioenergy program implementation in Brazil*. Lamnet Workshop Rome, Italy, 2004.

[5] Moreira, JR, Goldemberg, J. *The alcohol program*. Energy Policy 27 (1999) 229-245.

[6] Pereira de Carvalho, E. *Brazilian sugar and ethanol market 2004*. Available from `http://www.unica.com.br`

[7] Macedo, I, Verde Leal, RL. *Estudo de caso: Projeto MDL para o setor sucroalcooleiro no Brasil*. In AGRENER GD 2004 - Fifth Brazilian Meeting on Rural Energy, Campinas, Brazil, October 19-20, 2004.

[8] Oliveira Sá, SM. *Perspectivas para o biodiesel no Brasil*. In AGRENER GD 2004 - Fifth Brazilian Meeting on Rural Energy, Campinas, Brazil, October 19-20, 2004.

[9] *Centro Brasileiro de Energia Eólica – CBEE*, January 2005, `http://www.eolica.com.br`

[10] Domínguez, RZ. *The State of the Art of SOFC in Brazil - Challenges & Prospects*. In 2nd International Workshop on Fuel Cells – 2nd WICaC, Campinas, Brazil, 2004.

[11] Rísposli, IAG, Mariotoni, CA. *Tecnologia apropriada para sistema de energia solar visando aquecimento de água para o banho humano em moradias do meio rural*. In AGRENER GD 2004 - Fifth Brazilian Meeting on Rural Energy, Campinas, Brazil, October 19-20, 2004.

[12] Altomonte, H, Coviello, M, Lutz, WF. *Renewable energy and energy efficiency in Latin America and the Caribbean: constraints and prospects*. CEPAL, Santiago, Chile, October 2003.

Proceedings of ECOS 2005
Trondheim, Norway
June 20–22, 2005

COMPRESSED AIR ENERGY STORAGE (CAES) - POSSIBILITIES IN DENMARK

Brian Elmegaard[1], Nicklas Szameitat and Wiebke Brix
Technical University of Denmark
Department of Mechanical Engineering
2800 Lyngby
Denmark

ABSTRACT

Through a systematic development of the Danish electrical supply system with wind power and Combined Heat and Power, problems with stability and electricity surplus have appeared. Therefore, the possibilities for profitably implementing a CAES plant for energy storage, peak shaving and electricity surplus reduction are investigated. Based on existing plants and the latest technology a simulation model of a 360 MW plant with an efficiency of 35 % has been developed and optimized to Danish conditions. An analysis of the economics in the plant, operating under market conditions, shows a growing potential, but the allocated investment costs require investigation of more competitive operation. The regulating-power market could be a solution.
Keywords: Energy storage, compressed air, CAES, simulation, economic analysis.

NOMENCLATURE

W_T	Turbine work [MWh]
W_C	Compression work [MWh]
Q_{in}	Energy supplied in natural gas burner [MWh]
EP	Energy price [€/MWh]
η	Thermodynamic efficiency
$\dot{C}$	Cost rate [€/s]
$\dot{Z}$	Investment cost rate [€/s]
$\dot{E}$	Exergy flow [MJ/s]
c	Exergy unit cost [€/MJ]

INTRODUCTION

Compressed air energy storage, CAES, is a method for storing power using gas turbine technology. In principle the components are the same as in an ordinary Brayton-cycle gas turbine and the configuration is nearly the same. The difference is that the compression and expansion processes do not take place at the same time, which introduces the possibility to exploit diurnal variations in electricity prices. Air is compressed and stored in a cavern while electricity is cheap, and when the electricity prices rise, the stored air is heated and expanded through a turbine, which drives a generator to produce electricity.

Today two plants operating according to this principle exist worldwide, one in Huntorf, Germany, and one in Alabama, USA. A third plant is planned in Ohio, USA [4].

The storage cavern

Construction of a CAES plant requires suitable geological conditions for the construction of a storage cavern. Air storage caverns can be constructed in rock, limestone or salt domes. Denmark does not have rocks in the underground, but in Jutland salt domes can be found. These domes are today already used as sites for natural gas storage caverns.

ELECTRICAL SYSTEM IN DENMARK

The Danish electrical supply system is unique with its large percentage of wind power and combined heat and power (CHP) plants. In the western part of Denmark, which is electrically separated from the eastern part, the total installed electrical capacity is around 7500 MW. The amount of wind

[1] Corresponding author: Phone: +45 4525 4169 Fax: +45 4593 5215 E-mail:be@mek.dtu.dk

power today is around 2400 MW (30% of the total capacity). The installed combined heat and power capacity is furthermore around 1600 MW (20% of total capacity), which means that approximately 50% of the installed capacity in western Denmark is bound production (production rates are not dictated by the grid operators).

Over the last few years the occurrence of electricity surplus has become an increasing challenge. Electricity surplus happens, when the bound production exceeds the electricity consumption, and actions have to be taken, to protect the system against overload. Electricity surplus is separated in two branches: Exportable electricity surplus and critical electricity surplus.

Exportable means that surplus electricity can be exported through cable connections with Norway, Sweden and Germany. These cable connections have a total capacity of app. 2900 MW (38% of the total installed capacity).

Critical means that the electricity cannot be exported because of physical restrictions, and may lead to shutdown of CHP plants or wind turbines.

In 2001 The Danish Energy Agency established a commission to investigate the problems with electricity surplus and the different possibilities of reducing the difficulties in an electrical system with an increasing share of wind power and CHP [3]. The investigation predicted that the electricity surplus problems would be an increasing problem for the system stability in the near future since wind power and CHP are expanding and the export options are limited.

The commission suggested a series of initiatives that would contribute to the reduction of the electricity surplus, and a long term flexible electricity storage solution was one of the options. CAES is such a long term storage initiative.

Furthermore, if the initiative can be used profitably as a flexible component in addition to the electricity surplus reduction potential, the investment is beneficial.

If the starting point is that a CAES plant will be operating under market conditions, the driving force is price variations. Charge of the storage takes place when the price is low, and discharge when the price is high. An analysis of the price variations in today's deregulated market and a preparation of these prices to use for simulations are required. As basis the system price in Denmark from the last five years is used.

DESIGN OF A CAES PLANT

In order to develop an appropriate design for a CAES plant, operating under the conditions given by the Danish electricity market, different models have been proposed using the simulation tool DNA [10]. Both static and dynamic simulations and experience from existing plants are used during the design process. A component outline of the design is shown in Figure 1.

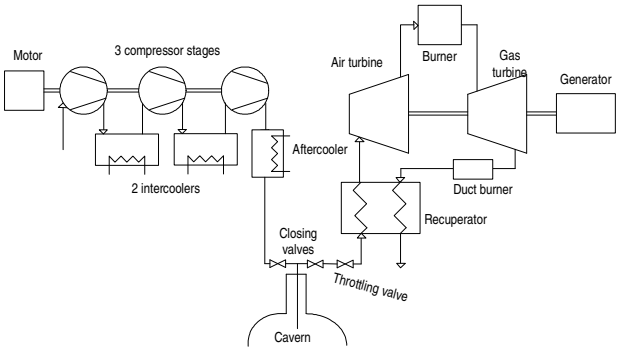

Figure 1: Component outline of the designed plant.

The three major branches, compression, storage and expansion are considered in the following.

The expansion train

The turbine required for expansion is a modified industrial gas turbine, where no compressor is needed since the compressor train has its own power shaft. Alstom Power produces such a modified gas turbine, the ET11 NM [2], and the design of the expansion train is based on the use of this turbine. The mass flow rate in the turbine is 400 kg/s, which corresponds to a power production of 360 MW.

The total expansion process is composed of the following processes: Air leaving the cavern is throttled to 56 bar to ensure constant turbine inlet conditions. Afterwards the air is heated in a regenerator and at a temperature of 550°C the air enters an air turbine, where it is expanded to 13,7 bar. In the combustion chamber natural gas is injected and ignited. The temperature is raised to 1027°C and afterwards the flue gas is expanded to atmospheric pressure. At atmospheric pressure the flue gas is reheated in a duct burner to ensure the turbine inlet temperature for the air turbine reaches 550°C in the recuperator. A T-s diagram of the expansion process is shown in Figure 2.

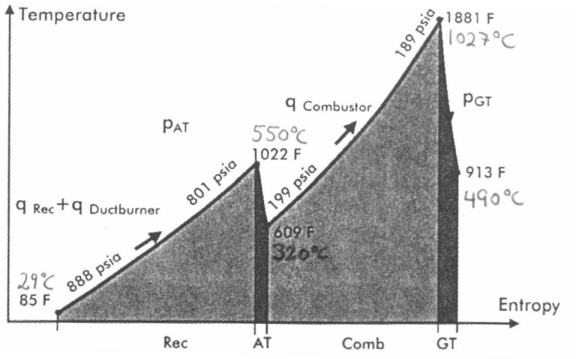

Figure 2: T-s diagram of the expansion process in the ET11 NM turbine [2].

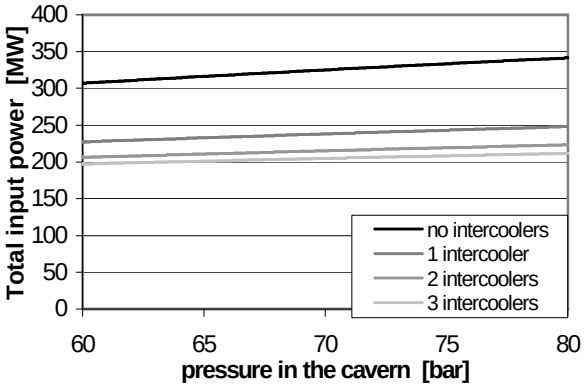

Figure 3: Power input to compressors with different numbers of intercoolers.

Pressure level in the cavern

The pressure level in the storage is an important parameter considering the thermodynamic efficiency of the plant. For gas turbines in general a large pressure ratio ensures a high thermodynamic efficiency, but since the entrance temperature into the cavern in salty environment is restricted to 35°C, an increased pressure ratio also would result in a raised heat loss in the aftercooler.

Considering a balance between efficiency improvements due to raised pressure and efficiency drop due to increased heat loss in the aftercooler at high pressure in the cavern, together with an estimate of the amount of energy, which needs to be stored, the optimal working pressure in the cavern is estimated to be 60-80 bar. Under normal operating conditions the plant will compress air up to a pressure of 80 bar in the cavern, and a full discharge of the cavern will reduce the pressure to 60 bar. To guarantee a greater flexibility the storage should be designed to be able to allow a maximum pressure of 85 bar. The depth of the cavern is chosen according to these pressure requirements.

The compression train

The compression is carried out by axial compressors. Air is compressed from atmospheric pressure to cavern pressure, which means that the compressor has to work against a varying pressure in the cavern and the power input increases during compression.

To reduce the power input to the compressor a number of intercoolers are inserted in the compressor train. Simulations of the compression with different numbers of intercoolers are carried out, and the needed power input is shown in Figure 3.

The design with two intercoolers has been chosen. The pressure ratio over each of the compressor stages varies between 3.9 and 4.3. A lower pressure ratio would not be profitable for the compressors. An additional third intercooler would not be worth the investment, taking into account the relatively low input reduction, which could be achieved.

Dimensioning

By using the ET11 NM the mass flow rate and power production is fixed to 400kg/s, 360MW for the expansion process, which is expected to be a suitable power output regarding peak-load periods in the Danish electricity system.

Running the compression with a mass flow rate of 400kg/s results in equally long compression and expansion periods. The input power for a compressor train working between 60 and 80 bar varies from 207 MW to 223 MW with an average of 216 MW as seen in Figure 3.

Taking into consideration that the plant is meant to reduce electricity surplus, a possible compression time of 10 hours would be appropriate regarding the predicted electricity surplus in the next 10 years, according to The Danish Energy Authority [3]

Dynamic simulations of the compression process running 10 hours with a mass flow rate of 400 kg/s and raising the pressure from 60 to 80 bar show that a storage capacity of 700,000 m^3 is required to suit the mentioned conditions. These simulations account for part load of the compressors and heat loss from the compressed air to cavern surroundings.

Compressing to the maximum cavern pressure of 85 bar would give the possibility to compress for

12 hours and 40 minutes. In Table 1 the optimal dimensions of the plant are listed.

Storage volume	700,000 m^3
Mass flow, compression	400 kg/s
Mass flow, expansion	400 kg/s
Power input to compressor	216 MW (avg.)
Power output from turbines	360 MW
Natural gas consumption (LHV)	416 MJ/s
Compression time	10 hours
Expansion time	9.2 hours

Table 1: Dimensions for CAES power plant in Denmark.

Operating the plant

Under normal operating conditions the plant is designed to run 10 hours of compression followed by 10 hours of expansion, with a little extra margin if necessary. In reality the plant will operate when it is economically advantageous. In Figure 4 simulation results of pressure and temperature variations in the storage cavern during a total charge/discharge period are shown. Due to a heat loss from the cavern the discharge period will be a little shorter than the charge period. Figure 5 shows the power input and output as well as the natural gas consumption.

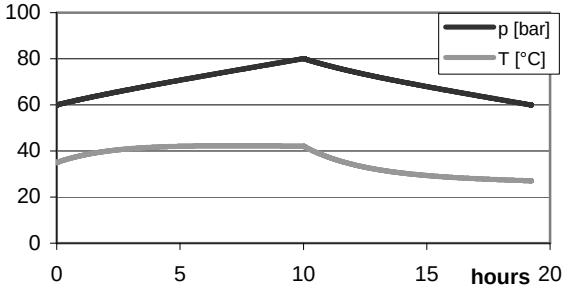

Figure 4: Pressure and temperature developments during an operating period consisting of 10 hours compression and 9.2 hours expansion.

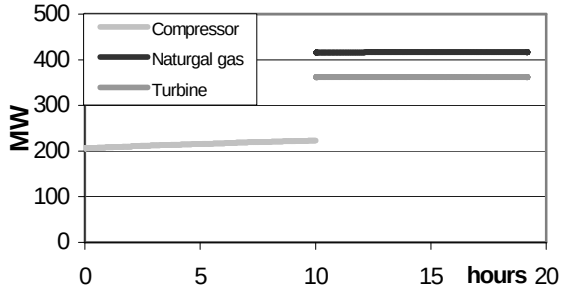

Figure 5: Compressor power input, turbine power output and natural gas consumption during a total charge/discharge period.

Thermodynamic efficiency

The efficiency of a CAES plant can be defined in different ways. The normal thermodynamic efficiency for a gas turbine process is defined by

$$\eta = \frac{W_T - W_C}{Q_{in}}. \quad (1)$$

Calculating the efficiency according to (1), where the power input and output and the natural gas energy supply is summarized over time, an efficiency of $\eta = 35.1\%$ is obtained.

Compared to this a gas turbine working under the same conditions, but without aftercooler and storage, has a thermodynamic efficiency of $\eta = 38.9\%$, this decrease in efficiency in the CAES plant occurs mainly because of heat loss in the aftercooler.

Another way of defining the efficiency for the CAES plant is based on the fact that the power used to compress is produced somewhere else, lets say in a CHP plant, which has an efficiency of 35%. The efficiency of the CAES plant can then be defined as

$$\eta_e = \frac{W_T}{Q_{in} + \frac{W_C}{0.35}} \quad (2)$$

Calculated for the designed CAES plant this efficiency is $\eta_e = 35.1\%$.

Compared to simulations of the existing plants the efficiency is increased significantly, mainly due to changes in the design and higher turbine inlet temperatures. For the Huntorf plant, which runs without recuperator, an efficiency of $\eta = 10.7$ % is found, and for the Alabama plant simulations give an efficiency of $\eta = 28.8$ %.

An exergy analysis of the system shows that exergy losses mainly occur in the burners, as expected for a gas turbine. The burner in front of the gas turbine accounts for 44 % of all losses, while the rest of the losses are quite equally distributed in the other components. The loss in the cavern with aftercooler and throttling valve accounts for 12,4% of the total losses. This is an additional loss for a CAES plant compared to a conventional gas turbine.

ALTERNATIVE DESIGNS

HP gas turbine instead of air turbine

Instead of placing a duct burner after the gas turbine in front of the recuperator a high-pressure burner could be placed in front of the first turbine,

as it is done in existing plants in Huntorf and Alabama. This would give a higher efficiency because the burner would not have to compensate for losses in the recuperator. Simulations show efficiencies of η = 36.3% and η_e = 35.5% using a high-pressure burner instead of the atmosphere-pressure duct burner.
Although a slightly better efficiency can be obtained using the high-pressure burner, the duct burner is to prefer, since NOx emissions are reduced significantly [4]. Also a high-pressure burner could require extra equipment to compress natural gas.

Throttling after the cavern
In the designed CAES plant the air exiting from the cavern is throttled, to ensure constant turbine inlet conditions. A throttling is accompanied by an exergy loss, therefore an investigation of a system working without throttle valve has been made. The varying turbine inlet temperature results in a varying mass flow and therefore a varying turbine power. The expansion time is extended to 11 hours, because of the lower mass flow.
The efficiency is 3% higher than the efficiency of the original design, but the varying turbine output is a disadvantage. Furthermore it is economically profitable to produce as much power as possible while the electricity prices are high, and this makes a throttle valve an advantage.

Higher turbine inlet temperatures
In the CAES-model the turbine inlet temperatures are 550°C and 1030°C. These temperatures are the most important parameters influencing the efficiency, and usually material properties set a limit for the maximum temperature. If both turbine inlet temperatures are raised by 20% to 660°C and 1236°C the efficiency is η = 41.8%, which is 20% higher than the original design. Higher temperatures also result in a higher turbine power output (242 MW) and higher natural gas consumption (494 MJ/s), but the ET11 NM turbine could not be used.

ECONOMIC ANALYSIS OF THE CAES PLANT

In order to evaluate the potential of the CAES concept in Denmark an analysis of the economics of the plant based on simulations with the designed model has been done. The charging and discharging intervals will at market conditions be based on the price variations of electricity. Which intervals are profitable will be investigated in the following.
On The Nordic Power Exchange – Nordpool – electrical power is traded and prices are determined for each hour of the day. The prices are fixed a day before production, and it is possible to plan the daily operation of the CAES plant based on these prices. It is assumed that the plant can start and stop quickly, so that charging or discharging can be scheduled for each hour. The electricity surplus situations are in this study assumed to be contained in the system prices.
The plant should be operating as long as it is profitable, and for simplicity the cavern has the same pressure at the end of each day. Since the mass flows in and out are equal, 12 hours of compression and 12 hours of expansion are possible on a daily basis. Each expansion hour and corresponding compression hour must respond in a positive profit contribution. Otherwise the plant has to be shut down. The equation looks like this:
Profit contribution =
$W_T \cdot EP_{HIGH} - Q_{in} \cdot EP_{GAS} - W_C \cdot EP_{LOW}$

With this method every hour in the day is arranged after price level. Then the most expensive hour is paired with the cheapest hour and the profit contribution for these two is calculated and so on. Pairs of hours with negative profit contribution mean that the plant is not in operation.
This method has been implemented in MatLab, and with input prices from the last four years, daily, monthly and annual profit contributions are calculated as well as an operating plan is worked out.
As an example the working plan for a week is shown in Figure 6. A natural gas price of app. 18€/MWh is likely in Denmark [7]

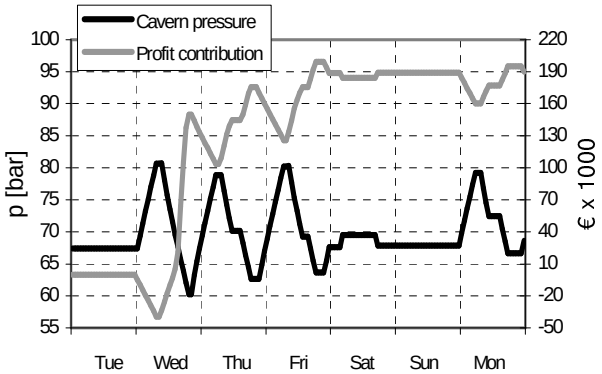

Figure 6: Seven days working plan example. Pressure and profit contribution is shown.

In this example it is seen that every day of operation leads to an increase in profit contribution. A summary of the number of operating hours over the four whole years is seen in Table 2.

Year	Production hours	Production hours /operating days
2000	49	3,5
2001	152	4,2
2002	460	8,4
2003	483	5,5
2004	27	2,3

Table 2: Number of hours with expansion with positive profit contribution.

The CAES plant can be seen as a gas turbine as well, and it is a fact that high level electricity prices make operation more profitable. A critical price that allows simultaneous compression and expansion as a normal gas turbine can be calculated from a given natural gas price. A gas price of 18€/MWh gives a critical electricity price of 52 €/MWh. Consequently, an electricity price at a general high level makes CAES very profitable. The option of operating the plant as a gas turbine also means that there should be no loss in the aftercooler. On the other hand the economics of the plant is very sensitive to variations in gas price. Regarding the system in the long term the development of the gas prices has to be considered.
For a complete evaluation of the plant knowledge of prices of the components and installation is necessary. The nature of the project is a design situation, which makes such prices hard to estimate, and furthermore only two plants of this type exist in the world.
Based on personal communication we present following price estimates:

Compression = 53 mio. € [8]
Expansion = 101 mio. € [8]
Cavern = 30 mio. € [7]
Total = 184 mio. €

These investment costs are to be paid off, and we expect that a lifetime of 20 years and an interest rate of 4% are realistic. This gives an annual payment of app. 13 Mio. Euro, which has to be subtracted from the annual profit contribution from operating the plant. The annual payment is linearly dependent on the investment cost.

The annual results from the historical prices are given in Figure 7. Maintenance costs are not included.

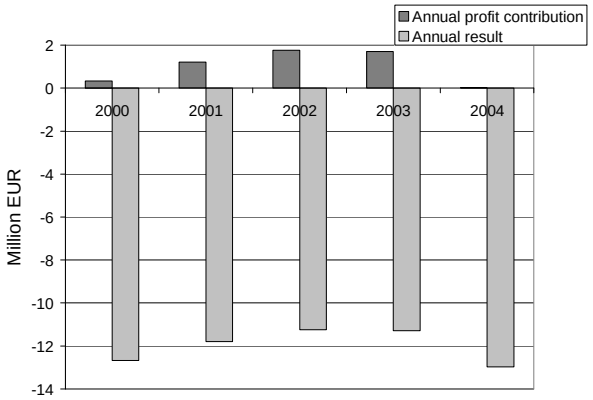

Figure 7: Annual profit contribution and result. Natural gas price is 18 €/MWh [7].

As can be seen from Figure 7 with the given prices, investing in a CAES plant and operating it on a daily basis with the system prices as the driving potential is not profitable. Even considering that installation costs are very uncertain, the profit contributions are just too small to support the high investment.

For the CAES principle to become a profitable business, other factors than operation based on the system price will have to be considered.
1) Since the CAES plant is a very flexible component in the electrical supply system, it can act as backup during power blackouts and help stabilize the grid during both surplus and demand situations.
2) There may be a subsidy to power plants, which stand by with regulating power for the grid. This is another option that has to be considered.
3) If the owners of the CAES plant are power plant companies, CAES could supplement the base load plants, and compensate for expensive regulations of the power plant.

Exergy considerations
A relationship between electricity price and operating hours can be investigated using a thermoeconomic approach. This is a more general method than using historical price data.
For each component in a system cost rates must balance [6].

$$\sum_e \dot{C}_e + \dot{C}_W = \sum_i \dot{C}_i + \dot{C}_Q + \dot{Z} \qquad (3)$$

The cost rates associated with exergy streams are calculated: $\dot{C} = \dot{E} \cdot c$

The components in the system are grouped after information about prices, and the three groups are: Compression, Cavern and Expansion. Equation (3) is applied to each group and the system of equations solved for the whole system.
With this approach it is necessary to give the investment costs as €/s, and the operating time is therefore an input. The investment is still considered to last for 20 years. The required electricity price during expansion can then be calculated with a gas price of 18 €/MWh. The compression electricity price chosen for the calculations is 21,6 €/MWh based on an average from the profit contribution calculations for 2001. For 3 compression and 3 expansion hours the cost rates through the system are seen in Figure 8. It is seen that the necessary electricity price for expansion is 7 €/s which corresponds to 69 €/MWh.

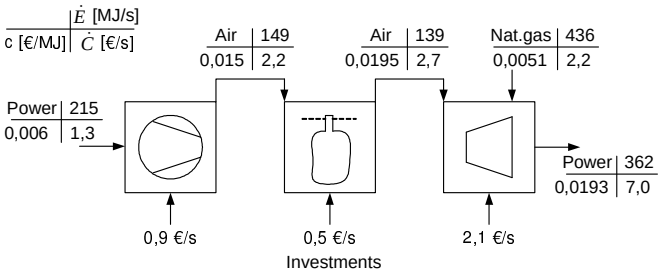

Figure 8: Cost rates in the CAES plant. Exergy streams without cost are neglected.

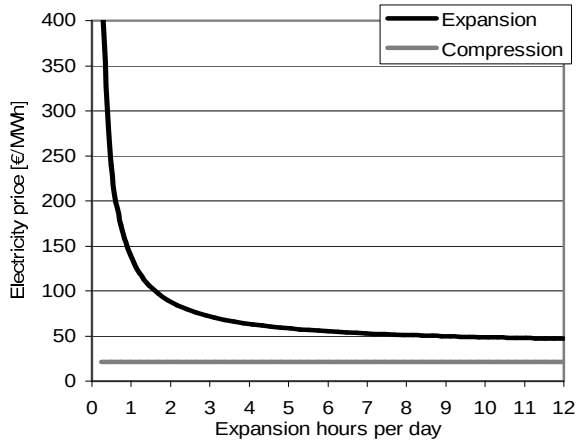

Figure 9: Required expansion price for profitable operation depending on number of operating hours.

As the investment cost rates [€/s] are highly dependent on the operating time, the important results of the thermoeconomic analysis are given as a function of this time as seen in Figure 9. A large number of operating hours is desirable to keep the needed price difference between compression and expansion electricity prices down. This requires a compromise between the needed electricity price and the number of operating hours.

PRELIMENARY ANALYSIS OF RESERVE MARKET OPERATION

If the CAES plant is operated in the reserve power market preliminary calculations show that a significantly higher annual income would be possible. The Nordpool reserve power market and production is divided into two: manual/voluntary reserve and automatic reserve.
In the automatic reserve market the plant operators obtain three income contributions. The monetary values are based on tenders of the last three quarters of 2004 [11]:
The contributions are:
Availability (annually): 8.5 mio € for 100 MW
Upward regulation: 53 €/MWh
Downward regulation: 10 €/MWh

One plant may at most contribute with 50 MW for automatic and 50 MW for manual regulation. The manual reserve market contributes about 3000 €/MW/month and plants operates at an increased power price for produced power and a decreased price for consumed power.
Only data for the reserve power market of May and June 2004 are available [9]. It is assumed that the size of the storage cavern does not give any limitations during up and down regulations, and the pressure in the cavern will be balanced when needed.
Based on calculations of the air standard cycle it is assumed that 50% of the output power comes from pressurized air and the rest is generated by the natural gas.
Based on data from May and June 2004 the annual income for automatic and manual regulation including income for availability is calculated:

Automatic regulation	14.2 mio €
Manual regulation	21.7 mio €
Total income	35.9 mio €

It seems that a CAES plant may be profitable if operated as a regulating power plant. However, it is a condition for this that the plant is able to operate under the very strong requirements for startup and load changes prescribed by Eltra.

DISCUSSION

The idea of storing power is a relevant subject in Denmark, especially because of the relatively high part of the electricity produced by wind turbines. As Denmark does not have any rivers or mountains, CAES is a solution, which is possible with existing technology.

The economical analysis shows that the development of the electricity and natural gas markets have great influence on the economical situation of a CAES plant. Based on prices from the last four years a positive profit contribution is seen for 2000-2004, but the high investment costs result in negative annual outcome. The economical analysis has been carried out from the assumption that the plant has to operate under normal market conditions, but other possibilities could exist. Letting the CAES plant operate in the regulating power market seems much more promising than operating under market conditions, but this option should be investigated further.

CONCLUSION

The possibilities of designing and operating a large scale Compressed Air Energy Storage plant for peak load support and reduction of electricity surplus in Denmark has been investigated.

A dynamic simulation model of the CAES plant has been developed, and optimization and adjustment to Danish conditions has resulted in a simulation model, which has a thermodynamic efficiency of 35,1%, can produce 360 MW of electricity during expansion, and consume 210 MW during compression. A corresponding gas turbine of the same size without the storage cavern has a thermodynamic efficiency of 38,9%.

The thermodynamic analysis is supplemented by an economic estimation of the plant as a component on market conditions in the Danish power supply. The conditions are based on the electricity price from the last four years and the estimated cost of a plant with an underground cavern. It is concluded that in Denmark this plant does not represent a profitable investment yet. The main reasons are that the investment costs are very high, and the plant is quite sensitive to natural gas price fluctuations.

If the electricity surplus increases as predicted by The Danish Energy Agency [3] it is possible that CAES can become a profitable solution in the deregulated market. On the other hand preliminary calculations show that the market for regulating power may be a more profitable alternative.

REFERENCES

[1] Brix W, Szameitat N. *CAES – Muligheder i Danmark*. Lyngby, DK: Department of Mechanichal Engineering, 2003.

[2] Van der Linden S, *The Case for CAES*, Modern Power Systems, August 2002, p. 19-21

[3] Workgroup under The Danich Energy Authority. *Rapport fra arbejdsgruppen om kraftvarme- og VE-elektricitet*, Copenhagen, DK: The Danish Energy Authority, 2001.

[4] Tuschy I. "*The Future of Compressed Air Energy Storage*", Proceedings ECOS 2002.

[5] Crotogino F. *Huntorf CAES: More than 20 years of Successful Operation*", Solution Mining Research Institute, 2001.

[6] Krane R.J. *Exergy costing*. University of Tennesee, USA.

[7] Pedersen A.H., DONG. Personal communication. 09.06.2004.

[8] Van der Linden S., Alstom. Personal communication. 08.06.2004.

[9] Parbo, Henning, Eltra, Personal Communication, January 2005

[10] DNA, Energy System Simulation Tool http://www.et.mek.dtu.dk/Software/DNA/index.html

[11] ELTRA, http://www.eltra.dk/

Proceedings of ECOS 2005
Trondheim, Norway
June 20–22, 2005

CO_2 ABATEMENT BY CO-FIRING OF NATURAL GAS AND BIOMASS DERIVED GAS IN A GAS TURBINE

Daniele Fiaschi and Riccardo Carta

Dipartimento di Energetica "Sergio Stecco"
University of Florence
Via Santa Marta, 3 – 50139 FIRENZE – ITALY
Tel. +39 055 4796436
Fax. +39 055 4796342
E – mail: danif@de.unifi.it

ABSTRACT

In this work, a possible way for partial CO_2 emissions reduction from gas turbine exhausts by linking with biomass gasification was investigated. The basic principle is the recirculation of a fraction of the exhausts (still rich in oxygen) to a gasifier, in order to have the production of a syngas to be mixed with natural gas fuel. As biomass is a CO_2 neutral fuel, the fraction of natural gas replaced with it is a measure of the CO_2 removal potential of the system.
Two solutions were investigated, the first of which only considers the gasifier, whilst the second one inquires the possibility of adding a pyrolyzer upstream the gasifier, in order to exploit the heat release of the exhausts for biomass pyrolisis to char, which is subsequently sent to the gasification section.
The produced syngas is thus sent to the cold cleaning system, recompressed and mixed with natural gas fuel. Due to the low calorific value of syngas, only a relatively reduced fraction of it should be mixed with natural gas. Encouraging results were obtained within the 10 – 30% range, with the same levels of CO_2 removal. The calculations on a target 10 MWe GT model showed only a modest reduction in efficiency, at the price of almost null modifications in machine design, which might make the solution attractive for powerplant management when carbon tax will be introduced, allowing to save 10 to 30% of energy production taxes, as well as the access to green certificates.

NOMENCLATURE

α	Moles of H per mole of biomass
β	Moles of O per mole of biomass
η_{GT}	GT efficiency
C_{tax}	Carbon tax per ton of CO_2 emission
ER	Equivalence ratio
f	Fraction of exhausts recirculated to the gasifier
F_{ren}	Fraction of syngas fuel replacing natural gas
H_P	Total energy of products
H_R	Total energy of reactants
LHV	Lower heating value
LHV_{pyr}	Lower heating value of pyrolysis gas
LHV_{syn}	Lower heating value of syngas
m_{bio}	Biomass flowrate
m_{char}	Mass flow of pyrolysis produced char
m_{pyr}	Mass flow of pyrolysis gas
m_{syn}	Syngas flowrate
PBT	Payback time
Q	Heat added or released to gasifier
R	Powerplant size scale coefficient
R_{save}	Ratio between the yearly savings due to carbon tax and that due to reduced fuel price
R_{vol}	Ratio between inlet turbine volumetric flow of gasifier integrated GT and standard GT
T_0	Reference temperature

T_g	Gasification temperature
T_{in}	Gasifier inlet temperature
T_{inpyr}	Temperature at pyrolyzer inlet
T_{outpyr}	Temperature at pyrolyzer outlet
W_{csyn}	Power demand for syngas fuel recompression

INTRODUCTION

The Kyoto Protocol subscription leaded many countries to study and propose systems and techniques for CO_2 capture and sequestration from powerplants. The major of these studies investigates in the field of very large amounts of CO_2 emissions capture (more than 80%), by applying pre or post combustion technologies [1 – 10]. Anyway, the proposed solutions often imply relevant changes in existing turbomachinery equipment, which are highly expensive and generally discourage the electricity providers in taking some measures against the growing CO_2 emissions [10]. Even the cheapest solutions, aimed to limit the existing equipment modifications (i.e. semi closed gas turbine cycles SCGT), have shown increases in the cost of electricity around 60 – 70% compared to traditional layouts with no CO_2 removal [12, 13]. Further unknowns related to costs of transportation and storage of liquid compressed CO_2 and the related environmental safety made application of CO_2 capture systems unattended [14].

It is well known that renewable fuels are globally zero CO_2 emissions to the environment, thus they might be an interesting approach to the greenhouse trouble. On the other hand, their extensive application to existing powerplants often involves deep and expensive modifications to current technologies. The most mature are those involving IGCC, which are not excessively complex to be converted to biomass fuels, even if they are applicable in the field of large power generation.

The upcoming 2006 EU carbon tax should encourage all Member States to do substantial investments in the direction of CO_2 abatement. In this way, systems with even partial CO_2 emissions reduction potential (15 to 50%) might lead to a consistent reduction in electricity production costs and encourage companies to introduce some measures to tackle CO_2 production. The partial integration of biomass fuels with natural gas may lead to the reduction of CO_2 emissions by the same proportion. Moreover, if the integration is not so high, reduced off design problems on existing turbomachinery equipment may be achieved and limited additional costs would be expectable. The present proposal deals with the possibility of an "internal" capture of CO_2 emissions, by integrating biomass fuel with natural gas fuel to a current production gas turbine: a small fraction of the exhausts, typically reach in fresh air, is recycled as the oxidizer of a gasification process, which should produce the amount of gas to replace the saved fraction of natural gas.

DESCRIPTION OF THE POWER CYCLE

The basic scheme of the proposed power cycle is shown on figure 1: The turbine exhaust gas is partially recirculated into the gasifier, in order to produce a syngas to be mixed with natural gas fuel, in a proportion which is closely related to the fraction of replaced natural gas, thus, finally, to the removed CO_2. Two options have proposed here: the first one only considers the gasifier, whereas in the second one a pyrolyzer upstream the gasifier is added (dotted lines on figure 1). The pyrolyzer takes a fraction of the exhausts heat content to do the initial pyrolysis of the entering biomass, producing char and mean LHV pyrolysis syngas. Successively, the char is sent to the downstream gasifier, where the final syngas is produced, cleaned and mixed with the pyrolysis gas, thus recompressed into the GT combustor.

Without entailed CO_2 removal systems, the saved CO_2 emission with respect to a standard turbogas corresponds to that which would be emitted by the primary replaced natural gas amount. In fact, the energy production from renewables like biomass, leads to globally zero CO_2 emission to the environment. The addiction of a downstream CO_2 removal system might further increase the biogas production (by the re-injection of a fraction of pure CO_2 into the gasifier in order to enhance

Bouduard reaction) and favour a higher CO_2 abatement, but it has not been investigated here.
The analysis was carried out referring to a biogas/natural gas integration ranging from 10 to 50%. The upper limit is very hard to exceed due to the extremely low syngas heat value, so that the gas turbine would undergo serious off design problems.

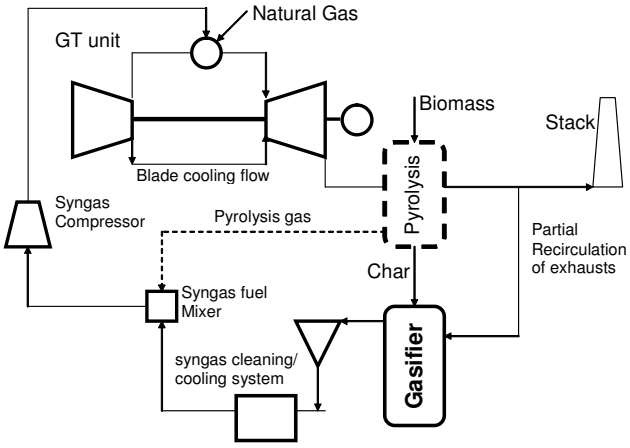

Figure 1 – Basic power cycle scheme

MODELLING GASIFIER AND POWERPLANT

Two different modules, developed with EES software, modelled the gasifier and the whole powerplant:

1 – ***gasifier/pyrolyzer***, which follows a chemical equilibrium approach for the evaluation of syngas composition, once the inlet biomass, oxidant/reducer composition and equivalence ratio (ER) are fixed. The general chemical equation, referred to one mole of biomass, is the following:

$$CH_\alpha O_\beta + a(O_2 + \frac{79}{21}N_2) + bH_2O + cCO_2 \Rightarrow$$
$$\Rightarrow n_1O_2 + n_2N_2 + n_3CO_2 + n_4CO + n_5H_2O + \quad (1)$$
$$+ n_6H_2 + n_7OH + n_8NO + n_9NO_2 + n_{10}CH_4$$

Where $CH_\alpha O_\beta$ is the chemical composition of the biomass, resulting from the ultimate analysis.
Two calculation approaches may be followed:

- Adiabatic, by fixing ER and calculating the outlet syngas equilibrium temperature T_g and composition, which follows the energy balance:
  $$H_R = H_P + Q$$
  Where H_R and H_P are the total energies of reactants and products respectively at the related temperatures, defined as:

$$H_R = LHV_{CH\alpha O\beta} + a\int_{T_0}^{T_{in}} cp_{O2}dT + \frac{79}{21}a\int_{T_0}^{T_{in}} cp_{N2}dT \quad (2)$$

$$H_P = \sum_i (n_i \int_{T_0}^{Tg} cp_i dT) + n_4 LHV_{co} + n_6 LHV_{H_2} + \quad (3)$$
$$+ n_{10} LHV_C + n_{11} LHV_{CH_4}$$

  Where LHV are the lower heating values of the combustible species; Q is the heat needed or released by the gasification process, which is set to zero in the adiabatic process.
- With fixed gasification temperature T_g and ER, by the same heat balance, determining the heat Q to be released/provided from/to the gasifier.

The number of moles of products n_1, …, n_{10} of eq. (1) is found by minimizing the Gibbs' free energy. The pyrolysis was modelled by the same module, with the addition of a semi empirical model, which is able to predict the gas composition and char production, as functions of the inlet biomass composition and the temperature of pyrolyzer.

2 – ***Gas Turbine (GT)***, which is modelled by the means of a well tested software developed at Energy Engineering Dept. of Florence (Fiaschi and Lombardi, 2001, Fiaschi and Tapinassi, 2003) with EES software, including the blade cooling.

The two modules are joined together in two different sections:

1. fuel section: the syngas coming from the gasifier may be mixed up with the natural gas and the related fuel mixture is sent to the GT combustion chamber.
2. exhausts section, where the GT exhausts are partially recirculated and sent to the gasifier as oxidisers for the gasification process.

EFFECTS OF GT EXHAUSTS ADDITION ON THE GASIFICATION REACTIONS

The basic idea of recirculating a fraction of GT exhausts to the gasifier allows the exploitation of their considerable heat content to the gasifier, where endothermic reduction reactions take place. This fraction of exhausts is mainly determined by the working conditions of the gasifier (i.e. ER). In fact, the large excess air of gas turbines makes the oxygen content of the exhausts more than enough for sustaining the gasification process. Moreover, the related CO_2 content should favour the Bouduard reaction:

$$C + CO_2 = 2CO.$$

The reference composition and temperature of exhaust gas is shown on table 1, together with the main working data of GE-5 GT, which is the reference machine here considered.

Table 1 – GE-5 gas turbine design working data

Net electric power output [kW]	5400
Compressor pressure ratio	14.8
Inlet compressor flowrate [kg/s]	19.8
Exhausts flowrate [kg/s]	20.2
Exhausts temperature [°C]	574
Heat rate [kJ/kWh]	11990
Inlet turbine volumetric flowrate [m^3/s]	4.80
Exhausts composition	
Mass fraction O_2	0.1473
Mass fraction N_2	0.735
Mass fraction CO_2	0.06868
Mass fraction H_2O	0.04902

The volumetric syngas composition vs. ER, related to the gasification with air and GT exhausts, are shown on figure 2. The gasification with exhausts leads to a syngas, which is more diluted with nitrogen for a fixed ER, due to the lower oxygen concentration of the exhausts (around 8-9%). It leads to a lower heating value of syngas (LHV_{syn}) when the exhausts are used, in spite of the higher adiabatic temperature T_g, see figure 3. On the other hand, the adoption of the hot gas stream as oxidiser suggests the possibility of working at lower equivalence ratios, as a consistent fraction of the heat needed for the endothermic gasification reactions is provided by the hot stream itself. Actually, the conversion ratios (moles of gas species per mole of inlet biomass) of the main syngas combustible species (H_2 and CO) increase in gasification with hot exhausts, as shown on figure 4. It is mainly due to the higher inlet temperature and to content of steam and CO_2 of the exhausts.

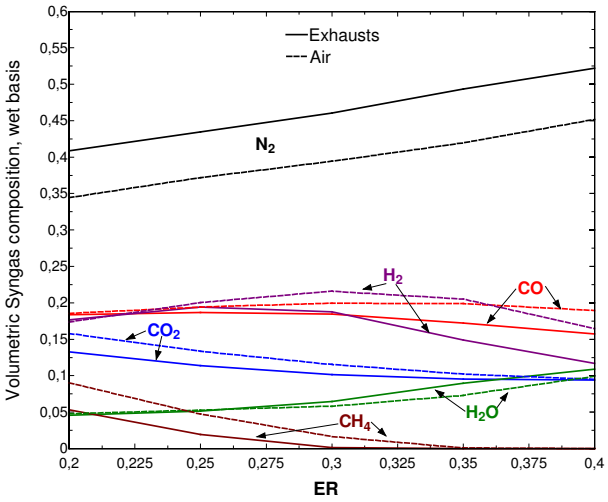

Figure 2 – syngas composition vs. ER for air and exhausts oxidisers

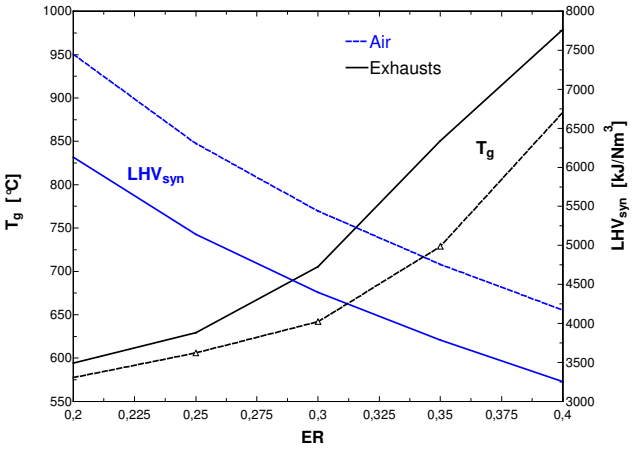

Figure 3 – syngas LHV and adiabatic gasification temperature vs. ER for air and exhausts oxidizers

PERFORMANCE ANALYSIS OF THE GT POWER CYCLE WITH INTEGRATED GASIFICATION

The proposed powerplant configuration aims to reduce part of its CO_2 emissions by replacing a

fixed fraction of natural gas fuel with biomass derived syngas. The recirculation of a fraction of the exhausts to the gasifier is advantageous because it is a hot stream, which gives an important contribution to sustain the endothermic gasification reactions, thus increasing the conversion ratio of the solid fuel. Moreover, recirculation represents a sort of "internal recycling" of a fraction of produced CO_2. In fact, an important feature of the proposed powerplant is that no additional recompression of the CO_2 and/or disposal is needed.

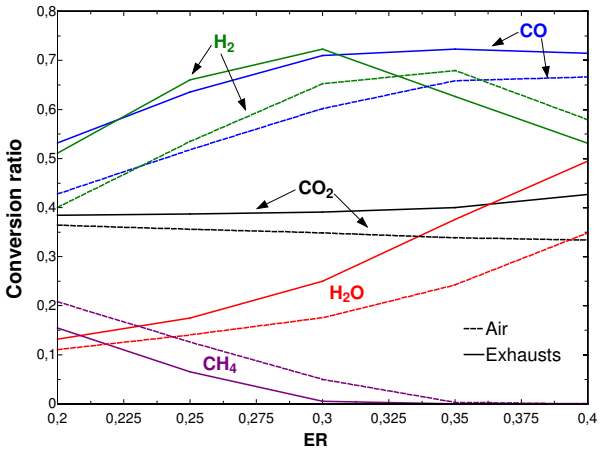

Figure 4 – conversion ratio vs. ER for air and exhausts oxidizers

The objective of this work was to assess the chances of applying this technique to remove a fraction of the CO_2 emissions from the traditional natural gas fuelled GT cycle.

The analysis was carried out referring to an integration of syngas into natural gas ranging from 10 to 50%. The upper limit is very hard to exceed, due to the extremely low heating value of the produced syngas, which would lead to a deep redesign of the GT combustor. As the main objective of this proposal is a moderate reduction of CO_2 emissions at the price of limited modifications to the existing plant with minimisation of the additional costs, the solutions involving deep modifications to the existing equipment were not considered here.

In the case of powerplant with only gasifier and no pyrolyzer, the gasification temperature is fixed at 800 °C, as well as the fraction of syngas fuel replacing natural gas (F_{ren}), which also represents the saved fraction of CO_2 emissions with respect to the standard GT, as syngas is derived from renewables, which are typically CO_2 neutral. These parameters allow the determination of the required ER and thus the fraction f of exhausts to be recirculated to the gasifier. The behaviours of f, biomass and syngas flowrates (m_{bio} and m_{syn} respectively), GT efficiency (η_{GT}) and specific CO_2 emissions are shown on figures 5 and 6 vs. F_{ren}.

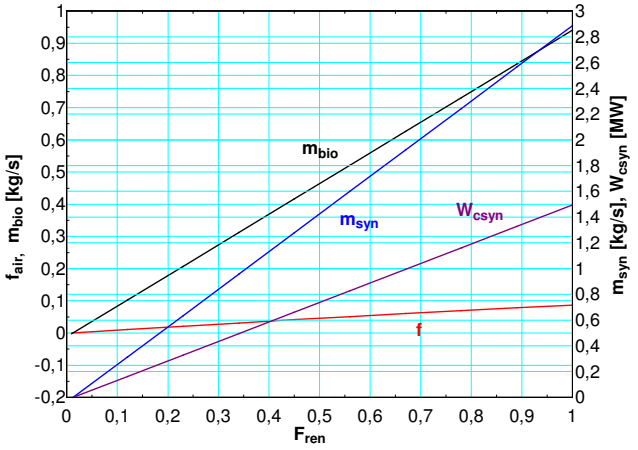

Figure 5 – syngas flowrate, biomass flowrate and fraction of exhausts recirculated to gasifier vs. ratio of renewables to natural gas fuel

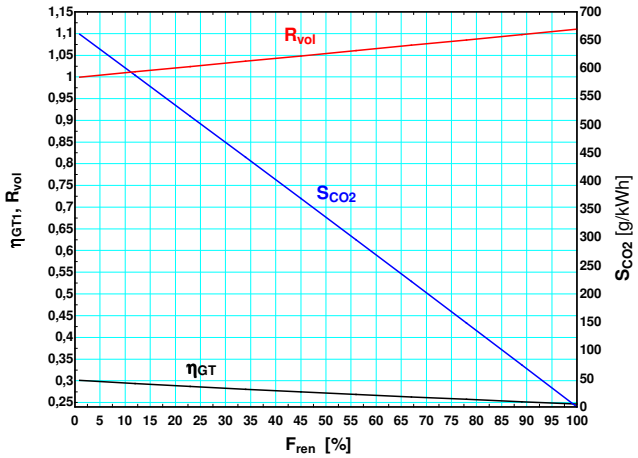

Figure 6 – GT efficiency, specific CO_2 emissions and inlet turbine volumetric ratio vs. ratio of renewables to natural gas fuel

As it is seen on figure 6, the fraction f of recirculated exhausts to the gasifier is very low, below 10%, even working with total biomass fuel (F_{ren} = 100%). The modest syngas heating value

(LHV_{syn} = 4837 kJ/Nm^3) leads to a consistent increase of fuel mass flow (m_{syn} is 6 to 10 times higher than natural gas in fuel mixture, see figure 5). It leads the expander to off design conditions, due to the higher volumetric flowrate of fuel gas mixture, which may become 10% higher than the design value at full renewable F_{ren} = 100% (see R_{vol} on figure 6). It suggests an integration of biofuel not exceeding 40 – 50%, in order to avoid high off design levels, thus maintaining the same expander and minimising the costs of modification of the existing powerplant. In this range, the CO_2 emissions of the proposed cycle may be reduced down to 350 gCO_2/kWh, which is a very interesting result for simple GT cycles. Moreover, this powerplant eliminates the problems and costs related to the CO_2 sequestration and disposal. One drawback of this powerplant is the relatively high power demand for syngas recompression (W_{csyn}, figure 5) which may reach around 20% of GT power output at F_{ren}=0.5. Anyway, it seems convenient to recompress the syngas fuel after the cleaning process and keep atmospheric gasifier to contain its costs, especially when dealing with small size plants like the one here proposed.

PERFORMANCE ANALYSIS OF THE GT POWER CYCLE WITH INTEGRATED PYROLYSIS AND GASIFICATION

The possibility of adding a pyrolyzer, downstream the gas turbine, which exploits the heat content of the exhausts to produce pyrolysis gas and char to be successively converted to syngas into the downstream gasifier, was another investigated option. Once again, the analysis was carried out versus variable ratio of biofuel to natural gas (F_{ren}), having fixed the outlet char gasification temperature at 800 °C. The main results are summarised on figures 7 and 8.

When compared to the plant with gasification only, it is evident the larger efficiency decay with F_{ren}, which is due to the higher biomass consumption (figure 7). The exhausts recirculation ratio f is reduced with respect to the case with no pyrolyzer, while an amount (m_{pyr} around 25%) of pyrolysis gas is produced and mixed with the amounts coming from the gasifier and natural gas. It leads to an increase in fuel gas heating value, due to the larger heating value (LHV_{pyr}) of pyrolysis gas (see figure 8). As a direct consequence, the volumetric flow ratio at the expander inlet of the biomass integrated GT to the standard GT (R_{vol}) is consistently reduced. It does not exceed 5% even at full biomass fuelling. It should greatly reduce the off design level of turbomachinery equipment, especially when the biomass integration level does not exceed 50%.

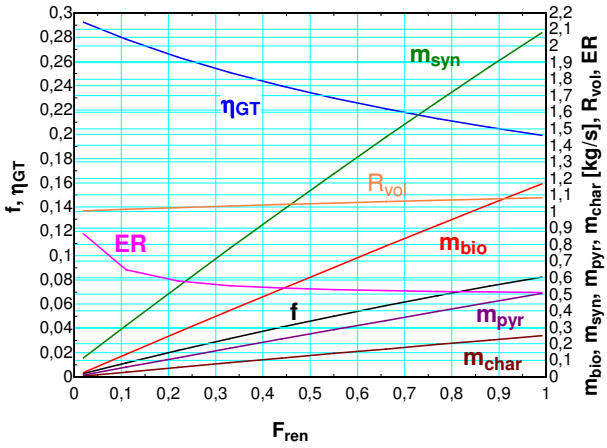

Figure 7 – GT efficiency, exhausts recirculation ratio, pyrolysis and gasification syngas flowrates, biomass and char flowrates and inlet turbine volumetric ratio vs. ratio of renewables to natural gas fuel

The temperature at pyrolyzer inlet (T_{inpyr}) is that of turbine's exhausts and is almost constant with F_{ren}, while the outlet pyrolyzer temperature T_{outpyr} decreases with increasing F_{ren}, due to the increased biomass pyrolysis level. The increase of F_{ren} also entails a slight decrease of ER, due to the larger difference between inlet biomass (m_{bio}) and produced char (m_{char}). In other words, the fraction of biomass converted by pyrolysis grows with increasing the biomass integration level. The larger extent of pyrolysis process is also responsible for the higher heat consumption. Thus, the exhausts are cooler when reach the gasifier inlet (see the behaviour of outlet pyrolyzer temperature T_{outpyr} on figure 8). It makes necessary the adoption of higher equivalence ratios to sustain the endothermic gasification reactions with respect to the plant with no pyrolyzer.

The CO_2 specific emissions may be reduced according to the fraction of natural gas replacement.

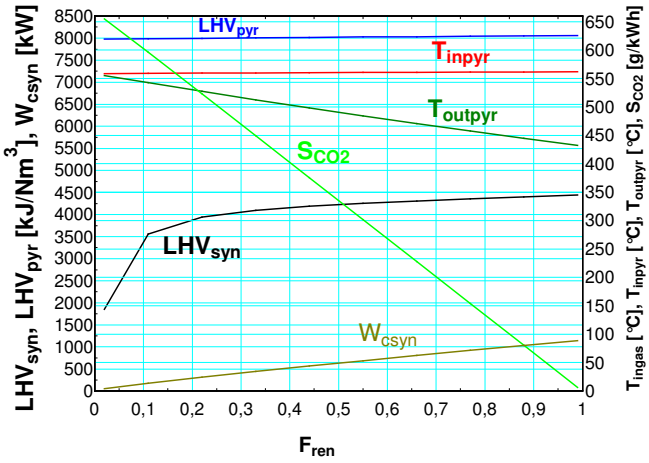

Figure 8 – Syngas and pyrolysis gas heating values, gasifier and pyrolyzer inlet temperatures, outlet pyrolyzer temperature and specific CO_2 emissions of the powerplant vs. ratio of renewables to natural gas fuel

Due to the higher heating value of syngas mixture, the additional power demand for syngas recompression is 1.5 times reduced.

EVALUATION OF ADDITIONAL COSTS DUE TO THE GASIFICATION SYSTEM

This analysis was carried out on the basis of literature data, which are referred to a nominal 30 MW powerplant size [15, 16] and later rescaled down by the following relationship:

$$cost_{size\ 2}/cost_{size\ 1} = (size_2/size_1)^R$$

where R is a scale coefficient, variable in the 0.6 - 0.85 range and depending on the specific components considered.

The costs of the main additional components required for the integration of biogas to the standard natural gas fuelled GT are reported on table 2. The analysis of costs was done at two levels of biomass fuel integration: F_{ren}=0.2 and F_{ren}=0.5. Thus, referring to the nominal 5 MWe, the power capacity of gasification system and the related devices are reduced by a factor ranging between 12 and 30 respectively.

Considering that the current cost of powerplants is around 600 €/kW, referring to the 5 MW GE5 here proposed, the cost of gasification equipment to achieve 50% natural gas replacement represents around 100% the total cost of the GT powerplant. With only 20% renewables integration level, the additional costs of gasification island are reduced to about 50% of standard powerplant cost.

Table 2 – Estimation of gasification island costs [M€]

	R	F_{ren}=0.5	F_{ren}=0.2
FUEL			
Biomass storage and distribution system	0.6	0.081	0.047
Biomass conveyors	0.8	0.044	0.021
Biomass feeding system	0.7	0.056	0.030
REACTOR			
Gasifier/Pyrolyzer	0.7	0.49	0.26
Syngas cooling	0.7	0.46	0.24
SYNGAS CLEANING SYSTEM			
Cyclones	0.7	0.19	0.10
Metal removal	0.7	0.049	0.026
Tar cracker	0.7	0.25	0.13
Condensing Scrubber	0.7	0.25	0.13
Particulate filters	0.65	0.44	0.24
SYNGAS RECOMPRESSION			
Compressor	0.85	0.24	0.11
OVERALL		**2.54**	**1.34**

The evaluation of investment profitability was carried out referring to the payback time (PBT) of the initial investment. Considering an average price of natural gas and biomass fuel of 20 c€/kg and 5 c€/kg respectively, the yearly savings due to the integration of the biofuel are closely related to the price of carbon tax and to the natural gas saving. Figure 9 shows the PBT vs. carbon tax (C_{tax}), which has been varied from current values (5 to 10 €/t) to possible future long term values (25 – 50 €/t) [17, 18], having supposed a discount rate of 10% and a plant working time of 8000 hrs/year. At current levels of carbon tax (10 €/t) the PBT is around 12 years, which is not very attractive, but even a moderate increase of C_{tax} would greatly improve the PBT of the plant with only gasifier (at 20 €/t PBT is halved to 6 years).

The ratio between the yearly saving due to carbon tax and that due to reduced fuel price, R_{save}, is

lower than one only at the lowest values of C_{tax}. The PBT here evaluated might have further consistent margins of improvement, if the contributions for use of renewable fuel (green certificates) were accounted.
In the case with pyrolyzer and gasifier, the costs of pyrolyzer plus char gasifier were supposed, at least in a first approach, the same as biomass gasifier only. It is evident that the lower efficiency of this solution, with respect to the one with gasifier only (see figure 8) leads to definitely prohibitive PBT if carbon tax is maintained below 20 €/t. For C_{tax} higher than 35 €/t, the PBT of the two proposed solutions are comparable.

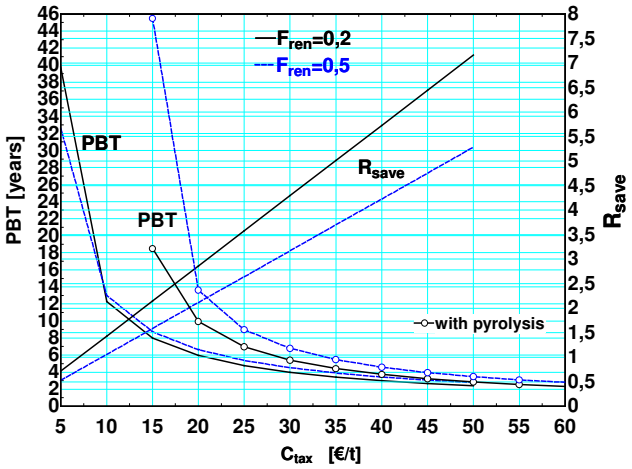

Figure 9 – PBT and R_{save} (for plant with gasifier only) vs. carbon tax price

CONCLUSIONS

A relatively simple solution for reducing a fraction ranging from 10 to 50% of CO_2 emissions from gas turbine based powerplants has been proposed. It adopts an integrated gasification/pyrolysis system, which recirculates a small fraction of the oxygen rich exhausts to the gasifier, in order to exploit their heat content and partially sustain the endothermic reduction reactions. In spite of the higher amount of gas flow required with respect to air gasification due to the lower oxygen concentration, the related heat content and, partially, the larger reducing capacity of fluegas due to presence of CO_2, lead to an increase of biomass to syngas fuel conversion ratio.

Comparing the two proposed solutions, with and without pyrolysis, the second one showed lower efficiency penalties with respect to the standard GT, but even higher volumetric flowrate to the expander, due to the lower syngas fuel heating value, which should increase the off design level of the gas turbine and the related efficiency losses. The economic analysis showed that the solution with only gasifier might be proposed in the very short time, as it allows the recuperation of the initial investment within 4 to 8 years, provided that the carbon tax was set in the range 15 – 25 €/t. The solution with pyrolyzer showed economic attractiveness only in the field of high carbon tax level (higher than 25 €/t).

REFERENCES

[1] Adelman, S.T., Hoffman, M.A., Baughn, J.W., 1995, "*A Methane-Steam Reformer for a Basic Chemically Recuperated Gas Turbine*", ASME Jnl of Engineering for Gas Turbines and Power, jan. 1995, Vol. 117, pp. 16-23.

[2] Andersen, T., Kvamsdal, M., and Bolland, O., 2000, "*Gas Turbine Combined Cycle with CO_2-capture using Auto-Thermal Reforming of natural gas*", Proceedings of ASME Turbo Expo, , May 8-11, 2000, Munich, Germany.

[3] Chiesa, P., Consonni, S., 1999, "*Shift Reactors and Physical Absorption for Low-CO_2 Emission IGCCs*", ASME Journal of Engineering for Gas Turbines and Power, Vol. 121, pp. 295-305.

[4] Lozza, G., Chiesa, P., a), "*NATURAL GAS DECARBONIZATION TO REDUCE CO_2 EMISSION FROM COMBINED CYCLES. PART A: PARTIAL OXIDATION*", Paper 2000-GT-0163, ASME IGTI Conference & Exhibition, Munich 2000.

[5] Lozza, G., Chiesa, P., b), "*NATURAL GAS DECARBONIZATION TO REDUCE CO2 EMISSION FROM COMBINED CYCLES. PART B: STEAM-METHANE REFORMING*", Paper 2000-GT-0164, ASME IGTI Conference & Exhibition, Munich 2000.

[6] Fiaschi, D., Lombardi, L. and Tapinassi, L., *The Recuperative Auto Thermal Reforming and Recuperative Reforming Gas Turbine*

Power Cycles With CO_2 Removal—Part I: The Recuperative-Auto Thermal Reforming Cycle, Journal of Engineering for Gas Turbines and Power, Vol. 125, No. 4, pp. 933–939, October 2003

[7] Fiaschi, D., Lombardi, L. and Tapinassi, L., *The Recuperative Auto Thermal Reforming and Recuperative Reforming Gas Turbine Power Cycles With CO_2 Removal—Part II: The Recuperative Reforming Cycle*, Journal of Engineering for Gas Turbines and Power, Vol. 126, No. 1, pp. 62–68, January 2004

[8] Corti, A., Failli, L., Fiaschi, D., and Manfrida, G., 1998, "Exergy Analysis of Two Second-Generation SCGT Plant Proposals," Proceedings of ASME IGTI 43rd Gas Turbine and Aeroengine Congress and Exhibition, Stockholm, Sweden.

[9] Facchini, B., Fiaschi, D., and Manfrida, G., 1997, "SCGT/CC: An Innovative Cycle With Advanced Environmental and Peakload Shaving Features," Energy Convers. Manage., 38 (15–17), pp. 1647–1653 (ScienceDirect)

[10] DOE, "Carbon Sequestration Technology Roadmap", Office of Fossil Energy, NETL, U.S. Department of Energy, 2002.

[11] Corti, A., Lombardi, L., Manfrida, G., b) "*Absorption of CO_2 with amines in a semi-closed GT cycle: Plant Performance and Operating Costs*" Proceedings of ASME IGTI 43rd Gas Turbine and Aeroengine Congress and Exhibition, Stockholm, Sweden, June, 1998.

[12] Corti, A., Manfrida, G., c) "*Economic Analysis of a Semi-Closed Gas Turbine/Combined Cycle (SCGT/CC) with CO_2 removal by amines absorption*", GHGT-4, "4th International Conference on Greenhouse Gas Control Technologies", InterLaken, Switzerland, August 30 - September 2 1998.

[13] Corti, A., Fiaschi, D., Manfrida, G., "*Thermo-Economic Evaluation of the SCGT Cycle*", Energy Conversion & Management Vol. 40 (1999), pp.1917-1929.

[14] IEA, 2000, "*Carbon Dioxide Capture and Storage*", report from Dept. of Trade and Industry, September 2000, on www.dti.gov.uk/cct.

[15] Monica Rodrigues, Andre P. C. Faaij and Arnaldo Walter, *Techno-economic analysis of co-fired biomass integrated gasification/combined cycle systems with inclusion of economies of scale*, *Energy, Volume 28, Issue 12, October 2003, Pages 1229-1258*

[16] Michiel J. A. Tijmensen, André P. C. Faaij, Carlo N. Hamelinck and Martijn R. M. van Hardeveld, *Exploration of the possibilities for production of Fischer Tropsch liquids and power via biomass gasification*, Biomass and Bioenergy, Volume 23, Issue 2, August 2002, Pages 129-152

[17] Michael Grubb, *Implications of EU ETS for Competitiveness of Energy Intensive Industry*, Presentation to IEA/IETA/EPRI Workshop on Greenhouse gas emissions trading, Paris, 4-5 Oct., 2004.

[18] Julia REINAUD, *Emissions trading and its possible mpacts: the case of energy-intensive industries in the EU-ETS*, Presentation to IEA/IETA/EPRI Workshop on Greenhouse gas emissions trading, Paris, 4-5 Oct., 2004.

Proceedings of ECOS 2005
Trondheim, Norway
June 20–22, 2005

ECONOMIC ANALYSIS OF A LICENSE TO BUILD A WIND POWER FARM

S.-E. Fleten[1], K. Krossøy, P.C. Lysaker Torgersrud
Department of Industrial Economics and Technology Management
Norwegian University of Science and Technology
NO-7491 Trondheim
Norway

B. Kvaal
TrønderEnergi
NO-7047 Trondheim
Norway

ABSTRACT

A company holding a license to build a wind farm has the right, but not the obligation, to build a certain capacity of wind power. This postponement flexibility has value when electricity prices and/or the wind speed distribution are uncertain. Assuming that long term electricity prices follow a Brownian motion dynamics, with parameters estimated by considering forward prices of the Nordic electricity market, the value of the postponement flexibility is estimated. Since this value is lost when investing, the decision rule is to invest when the value of the revenue stream from the wind farm exceeds both investment cost and flexibility value. Investment decisions and wind power values are discussed in terms of a case study from Norway. Although net present value is positive, the value of waiting is higher, so the recommendation is to postpone the investment.

NOMENCLATURE

a	Change in present value of wind farm per unit change in electricity price [MWh]
A	Scale factor in wind distribution function []
$A_{1,2}$	Parameters in the license value function [NOK]
b	Present value of wind farm with zero electricity price [NOK]
c	Construction lead time [years]
E	Expectation operator
F	Value of license to build wind farm [NOK]
G_t	Expected generation in week t [MWh]
$\overline{G}$	Expected annual generation [MWh]
h	Correction factor [], converting from annual (flat) price to a seasonally weighted average price
I	Investment cost [NOK]
k	Form factor in wind distribution
L	Economic lifetime of wind farm [years]
P_t	Expected price in week t [NOK/MWh]
r	Nominal after-tax required rate of return
$S(t)$	Long-term electricity price [NOK/MWh]
S^*	El. price level at which it is optimal to invest [NOK/MWh]
V	Present value of wind farm [NOK]
z	Brownian motion process
α	Risk-adjusted el. price growth rate [NOK/MWh/year]

[1] Corresponding author: Phone: +47 73591296 Fax: +47 73593603 E-mail: stein-erik.fleten@iot.ntnu.no

$\beta_{1,2}$	Parameters in the license value function
σ	Standard deviation parameter of long-term el. prices [NOK/MWh]

INTRODUCTION

Large areas with sparse population and relatively high yearly average wind speeds make the Norwegian coastline a favorable place to site new wind farms. The Norwegian government aims for 3 TWh yearly windpower within 2010. A new market for green certificates, and increasing electricity prices, have spurred a large number of applications for licenses to build wind farms.

Such licenses are granted freely on a first come, first served basis. Getting a license is not costless however, since formal requirements for license applications include a feasibility report, a report on environmental effects, and a duty of public consultation. We consider the case of a company holding a license to build a wind farm.

In the case considered, the regional electricity company TrønderEnergi holds a license, i.e. a deferrable right, to build a 50 MW farm on Bessakerfjellet in Nord-Trøndelag county. The profitability of this investment depends on electricity prices, green certificate prices or other subsidies, wind distribution, investment costs and operation/maintenance costs. All of these factors are uncertain, and we explicitly take into account price uncertainty by calculating the long term price level at which it is optimal to invest. Investment is optimal when the present value of revenues equal the sum of 1) investment and present value of O&M costs, and 2) the costs associated with losing the opportunity to defer investment further.

This work is an application of the theory of investment under uncertainty [1]. It is an adaptation of the model in [2]. The status of wind power in Europe is discussed in [3]. Whereas this paper considers a particular wind farm project, a related paper [4] considers choice of renewable power plant capacity under uncertainty. Also related is [5], which performs an economic analysis of the license to build a gas fired power plant.

The paper is structured as follows. Section 2 discusses technical issues surrounding the wind farm. In Section 3, the model for electricity price uncertainty is explained. Then follows two sections on subsidies and other project data. The investment decision is analysed in Section 6, followed by a discussion and a conclusion.

CAPACITY AND COST OF WIND FARM

It is common practice to measure wind speeds at the farm location over a year, and to model the uncertainty of wind speeds using a Weibull distribution. This was done also for Bessakerfjellet, based on wind measurements between June 2002 and December 2003. In addition, we used historical wind measurements for nearby locations, dating back to 1980 (a more advanced method for incorporating information from neighboring measuring stations is given in [6]). This gave us an average wind speed of 8.44 m/s, and form and scale factors of k = 1.74 and A = 9.47. These parameters enter the density function of the Weibull distribution as follows:

$$f(u) = \frac{k}{A}\left(\frac{u}{A}\right)^{k-1} \exp\left(-\left(\frac{u}{A}\right)^{k}\right) \qquad (1)$$

where u is wind speed. Form and scale factors were also found per week.

There is an economy of scale in producing, transporting, erecting and maintaining wind mills. The largest commercially available are 3 MW. The wind mills must not be located too close to each other, otherwise there will be losses due to wind shadow effects. In Norway, the license to build a wind farm is usually given with an upper bound on the total MW capacity, and for a specified geographical area. If large capacity mills are chosen, fewer mills can be bought, but at a higher cost per mill. If smaller capacity mills are chosen, more mills can be bought giving possibly a high

total cost. The optimal choice of mill type depends on their power curve, i.e. how much power they deliver given different wind speeds. A wind mill is usually operating between 4 m/s and 25 m/s, at larger speeds the mill is shut down. A power curve of a 2 MW Vestas turbine is shown in Figure 1:

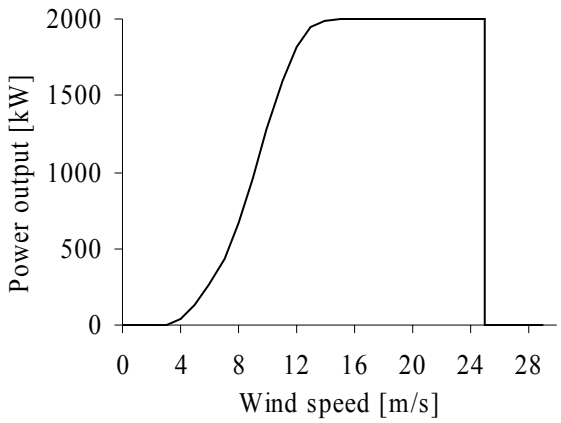

Figure 1. Power curve, showing power output as a function of wind speed.

We do not know the exact per MW cost of different turbine types before going into extensive negotiations with turbine manufacturers. For this reason we assume that the investment cost of the wind farm is independent of the type/size of turbine chosen. Thus, the optimal choice of turbine is the type/size that maximizes the yearly energy generation for the park. The expected yearly energy generated per turbine is given by

$$E = 8.76\int_{4}^{25} f(u)P(u)du \qquad (2)$$

The size of the Bessakerfjellet wind farm is set to 50 MW. Table 1 shows the annual expected energy generation per turbine, and annual expected energy generated for the whole farm, for turbines ranging from 2 MW to 3 MW. These sizes are the commercially most attractive at the time of analysis.

The calculations indicate that the Vestas 2 MW mill is a good choice. If the license holder decides to go ahead with the wind farm, an effort will be made to get more accurate investment cost data, as well as wind data. More wind data is needed for micrositing of wind mills, i.e. the exact location of the mills in the terrain and in height.

Table 1. Comparing different wind mill types. The farm can be up to 50 MW, e.g. 25 Vestas mills or 20 Nordex mills.

Manufacturer	Capacity	Energy per turbine [MWh]	Energy for farm [GWh]
Vestas	2 MW	7096	177
Bonus	2 MW	6826	171
Bonus	2,3 MW	7976	173
Nordex	2,5 MW	7898	158

ELECTRICITY PRICES

Electricity is used for heating in the Nordic area, leading to greater electricity demand in winter than in summer. Furthermore, the large share of hydropower in the region, with most inflow coming in the summer, makes for seasonality in electricity prices, with high expected prices in the winter and low summer prices. This profile is favorable for wind power, since wind speeds are greater in winter than in summer. What matters for the investment decision regarding electricity prices, is the expected future electricity prices during the lifetime of the wind farm, at the time of investment. There is uncertainty about long-term price levels, thus there is uncertainty about wind farm revenues (price times generated energy). Short term electricity prices are even more uncertain, but this does not matter for the investment decision, since such uncertainty does not influence the value of the wind farm. For the same reasons, we ignore the possibility of price spikes, price extremes, and seasonality over the day.

Another issue regarding electricity prices is their riskiness. Revenues with a high degree of systematic risk have lower value than revenues with a lower riskiness. One way of finding the present value of risky revenues is to use the information in electricity futures and forward

prices. Such contracts are traded actively in the Nordic market, and a forward curve can be constructed, based on information available in the market, revealing directly the value of future delivery of electricity. See Figure 3.

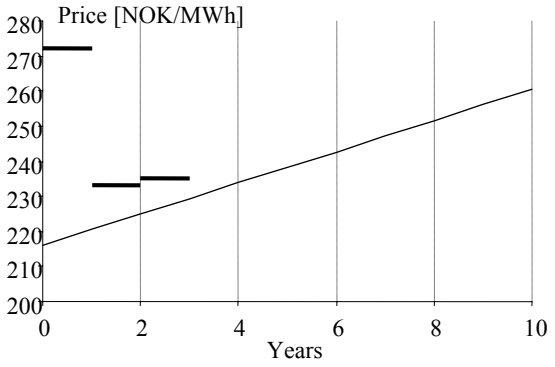

Figure 2. Forward prices on Nord Pool electricity, at the time of analysis (fall 2003). Actual market prices in bold lines, and estimated long-term relationship below.

Forward prices represent the risk-adjusted expected future electricity prices. The appropriate discount interest rate for electricity revenues, if generated energy is constant, is the risk free rate. We use the following stochastic model for long-term risk-adjusted electricity prices:

$$dS = \alpha dt + \sigma dz \qquad (3)$$

Equation (3) says that the current value of the long term price S is known, but future values of S are unknown, and are normally distributed with a variance that grows with the time horizon. Thus even though information arrives over time, with changes in market prices on forwards, future prices are always uncertain. This particular model choice is based in part on its simplicity, and in part on the empirical behavior of long-term electricity prices at Nord Pool, the Nordic power exchange. See e.g. [7] and [8] for estimation of energy price processes in this market.

This model does not account for seasonality in prices over the year. To correct for this, a correction factor h is defined. This is necessary because if expected future revenues from a wind farm is to be calculated from expected annual production, and an electricity price that does not exhibit seasonality, the revenues need to be scaled up. The power plant generates much of its annual output in the winter months, when prices usually are higher than in the summer. The correction factor h is written as

$$h = \sum_t \frac{P_t G_t}{\bar{P}} \qquad (4)$$

where $\bar{P}$ is the yearly average price. With our data it is estimated to $h = 1.046$.

Figure 3 shows how weekly local electricity prices have varied over the year, based on the average of 1996-2003. The Figure also shows weekly expected generation over the year, as a share of annual production.

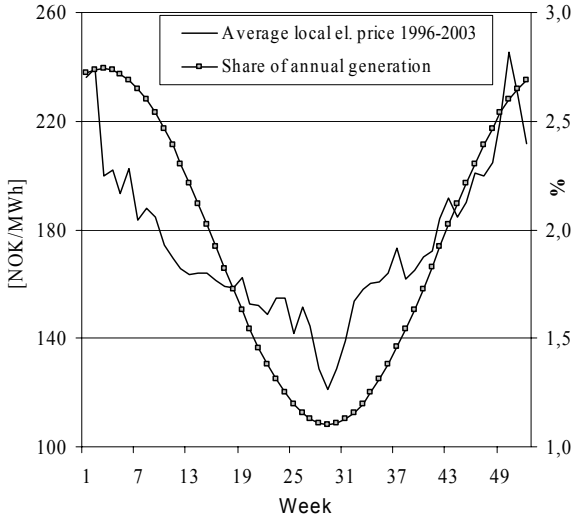

Figure 3. The relationship between expected generation and electricity price.

Based on data from Nord Pool, we estimated the current long term price to S = 216 NOK/MWh, yearly growth α = 4.4 NOK/MWh, and volatility to σ = 10.1 NOK/MWh.

SUBSIDIES

Windpower needs subsidies to be competitive. Norway has decided to adopt the Swedish model using green certificates, a market in which new renewable producers can issue certificates, and electricity retailers must buy certificates according

to certain rules. Typically, retailers must have certificates for a certain percentage of what they sell, or else they will be fined. In Sweden, there is a government-set upper and lower bound on prices, providing insurance to buyers and sellers. There is uncertainty in the future level of certificate prices, and expected price level can not be predicted with much precision. We have chosen to assume a level of 150 NOK/MWh, which is somewhat lower than average Swedish prices. This reflects the large potential Norway has for new renewable generation, particularly regarding small hydro.

As a temporary subsidy, the governmental energy fund Enova is supporting new wind power projects with up to 25% of the investment cost. The receiver of this subsidy has the option to pay it back if they find it more profitable to enter the green certificate market. We have chosen to ignore this feature of the subsidies issue since it is temporary, and instead focus on the green certificate market.

PROJECT DATA

The minimum acceptable nominal rate of return on comparable power projects has been 7-8% after tax. We choose to use $r = 8\%$, most of which is not compensation for the time value of money, but a risk premium. Above we argued that the electricity price risk in the project cash flows should not require any risk premium in the discount interest rate. We stick to that, however, there are other risks requiring a premium. We have already mentioned subsidy risk, which probably is the most important factor. Other factors include the risks in operation and maintenance cost, the level of unforeseen outage time, the exact distribution of wind speeds, and investment cost. Annual generation will vary by roughly +/- 20%. Although the mill manufacturers provide guarantees for some of the technical factors, there is no functioning market for hedging these risks. Other risks such as interest rate risk, currency risk and inflation risk, also affect profitability, but can be hedged to some extent.

The investment cost is estimated to 8 million NOK/MWh, giving a total of 400 million NOK for the 50 MW farm. Investment cost components are explained in Table 2.

Table 2. Breakdown of investment costs.

Cost component	%
Complete windmills 50 MW	83.1
Foundation	7.9
Transformer substation	2.6
Internal cables and switching station	1.6
External cabling/distribution	1.3
Access and service roads	2.6
Engineering	0.8
Total	100

The governmental license is granted for a period of 20-25 years, after which the wind mills are to be removed and the landscape restored to a natural state. However, wind mill components are designed to have a very low probability of failure within the first 20 years, and the mills can probably still be used beyond that time. We set the economic lifetime to 20 years, assuming the cost of restoring the landscape is cancelled out by the remaining value of the wind mills.

Operation and maintenance (OM) cost consist of insurance cost, periodic inspection and maintenance, damage repairs, revenue losses when units are down, and energy used in the electric motors that make the wind mill face the wind at any time. Considering experience from Denmark, we estimate the OM cost to 2% of investment cost initially, increasing with inflation thereafter. We assume inflation is 2.5%, consistent with the target for the central bank of Norway. This means the OM cost is 47.5 NOK/MWh.

Wind farms are subject to company tax and property tax, but are exempt from tax on economic rent and natural resource tax. Company tax is 28% of profit, and the investment is activated and depreciation is tax deductible. Durable assets has a depreciation rate of 4% using the balance method, except electrical equipment which is depreciated at 5%. However, the generators and other particular components are depreciated linearly over 40 years. We assume

the wind farm owner is in a tax-paying position. Yearly property tax is approximated to 0.7% of taxable value, which is 70% of investment cost.

Cost of balancing services are approximated to 10 NOK/MWh. Transmission tariffs depend on expected generation. We approximate this to 6 NOK per MWh produced, and 4% of revenues. Further, the original property owner is assumed compensated by 4 million NOK up front, and by 2.9 NOK per produced MWh. All per MWh costs are assumed to grow with inflation. The local municipality is assumed paid up front by 3 million NOK, to compensate for negative consequences e.g. connected to reduced weekend cottage building.

PROJECT ANALYSIS

The present value of revenues less costs is a function of long-term electricity prices, and is written $V(S)$. The license owner gets this value when paying investment cost I, and the net present value is $V - I$. The present value of revenues can be expressed as

$$\sum_{t=c}^{c+L} \frac{(S+\alpha t)h\bar{G}}{(1+r)^t}$$

From this we see that V is a linear function of S. We write this as

$$V(S) = a\,S + b, \qquad (5)$$

where a and b are known constants (note that the present value of costs are imbedded in b).

The value of the license equals the value of the opportunity to invest in the wind farm. We assume that the license does not expire in order to facilitate easy calculation of an upper bound on the value of the license. We assume further that holding this license is free. In this situation, the expected return on the value of the license, F, can be expressed in two ways. On the one hand this return depends on the minimum required rate of return, the value, and the size of the time interval. On the other hand, this return must equal the expected change in the value of F during the same time interval:

$$rFdt = E[dF] \qquad (6)$$

This is the Bellman equation for the value of the license [1]. We assume that long-term electricity prices are the only significant factor driving changes in F. The license value is then a function of long-term electricity prices, and the change dF can be found using Ito's lemma [1]:

$$dF = \left(\tfrac{1}{2}\sigma^2 F''(S) + \alpha F'(S)\right)dt + \sigma F'(S)dz \qquad (7)$$

By taking expectation of Eq. (7) and inserting it into Eq. (6), and dividing each term by dt, we get

$$\tfrac{1}{2}\sigma^2 F''(S) + \alpha F'(S) - rF(S) = 0 \qquad (8)$$

This is an ordinary differential equation whose solution in general is

$$F(S) = A_1 e^{\beta_1 S} + A_2 e^{\beta_2 S} \qquad (9)$$

where β_1 and β_2 are the positive and negative roots of the following quadratic expression:

$$\tfrac{1}{2}\sigma^2\beta^2 + \alpha\beta - r = 0 \qquad (10)$$

When long-term electricity prices are high enough, investment is triggered. The triggering price is denoted S^*. To determine S^*, A_1 and A_2, we use the boundary conditions associated with eq. (6):

1. Should long-term electricity prices become very low, the value of the license should approach zero. To ensure this, we must have that $A_2 = 0$. Eq. (9) now becomes

$$F(S) = A_1 e^{\beta_1 S}. \qquad (9')$$

2. When it is optimal to invest, the license is lost, but the license owner gets the net present value of the wind mill instead.

$$F(S^*) = V(S^*) - I \qquad (11)$$

By inserting Eq. (5) and (9') into Eq. (11) we obtain an equation in S^* and A_1:

$$A_1 e^{\beta_1 S^*} = aS^* + b$$

Solving that equation with respect to A_1 and substituting that expression into Eq. (9'), we obtain the value of the license as a function of the trigger price level S^*:

$$F(S, S^*) = A_1 e^{\beta_1 S} = e^{-\beta_1 S^*}(aS^* + b - I)e^{\beta_1 S} \qquad (12)$$

3. The trigger price level should be chosen to maximize the value of the license. The value of S^* maximizing the right hand side of Eq. (12) is

$$S^* = \frac{1}{\beta_1} - \frac{(b-I)}{a} \qquad (13)$$

Using Eq. (12) and (13), an approximate trigger price and value of wind farm opportunity can be calculated.

RESULTS

Net present value

The net present value depends to a large degree on the current level of long-term electricity prices, and on the price of green certificates which can be sold based on certified generation from the wind farm. Table 3 shows the net present value of the wind farm, with varying levels of electricity and certificate prices.

Table 3. Sensitivity of net present value of wind farm in million NOK, with respect to prices of green certificates in NOK/MWh and electricity prices in NOK/MWh.

	Certificate prices					
El. price	0	50	100	150	200	250
200	-192	-121	-49	22	94	165
220	-170	-98	-27	44	116	187
240	-148	-76	-5	66	138	209
260	-126	-54	17	89	160	231
280	-103	-32	39	111	182	254

Increased revenues lead to increased net present value. Given the current level of electricity prices (base case), 216 NOK/MWh, the break-even price of green certificates is 122 NOK/MWh. Given a price of green certificates of 150 NOK/MWh (base case), the break-even price of electricity is 180 NOK/MWh. The base case net present value is 40 million NOK, i.e. 800 NOK/kW or 236 NOK per annual MWh generated.

License value

The value of the license, Eq. (12), as a function of long-term electricity price level, is shown in Figure 4. Recall that the long-term electricity price level is the start level (year 0) for the forward price, i.e. 216 NOK/MWh in Figure 3. This level is stochastic and varies according to Eq. (3). As a result of an upward (downward) change in this level, the entire forward curve moves upward (downward), affecting the profitability of the investment over the whole plant lifetime[2]. As can be seen from the figure, the lower the price, the lower is the marginal value of the license – the license value tends to zero at very low prices. The base case (S = 216 NOK/MWh) license value is 47 million NOK. If the electricity price should increase enough (to S^* = 247 NOK/MWh), so that the license value becomes 75 million NOK, the license should be given up in favor of a wind farm.

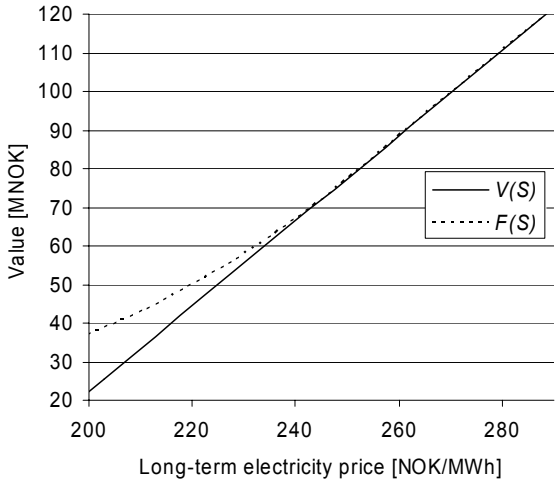

Figure 4. Net present value and license value as functions of electricity price level. Investment is optimal when net present value has reached 75 million NOK.

Trigger price

The long-term wholesale electricity price level that is high enough to trigger the investment is around 247 NOK/MWh. This is higher than the current long-term electricity price level of 216 NOK/MWh, so the conclusion is to wait for better price information. Table 4 shows how the trigger price level varies with the real price on green certificates.

[2] The forward curve from Eq. (3) is: $S + \alpha T$.

Table 4. Sensitivity of triggering electricity price level in NOK/MWh on green certificate prices in NOK/MWh.

Certificate price [NOK/MWh]	Trigger price [NOK/MWh]
0	441
50	376
100	312
150	247
200	183
250	118

The internal rate of return at the trigger level is 10.2%. This can be interpreted as a form of required rate of return, adjusted for electricity price risk.

DISCUSSION

The least realistic aspect of this model is the assumption that the license does not expire. In reality, the license is granted for around two years. At the end of this period, the license holder has a now-or-never opportunity to build a wind farm, and in that case the correct decision rule is to build the farm if the net present value is positive. The fact that the license expires, makes the trigger price level lower than with our calculations.

The cost of wind mills is constantly decreasing [9]. We have not taken this into account, but this would lead to a larger trigger price level, since it would be beneficial to wait for lower investment cost.

Long-term price uncertainty is usually modeled as having a log-normal distribution, i.e. proportional changes in price, not NOK/MWh price changes, are normally distributed. We also did the analysis with such a price model, but the main conclusion is the same, namely that it appears best to wait for better information.

CONCLUSION

We have applied the theory of investment under uncertainty to the case of an exclusive license to build a 50 MW wind power farm in Norway. Wind farms need subsidies to be viable, and Norwegian subsidies are not expected to be very high; we used a price of green certificates of 150 NOK/MWh in our analyses, or a third of expected real revenues. Given the current expected level of wholesale electricity prices, this subsidy is not enough to trigger immediate investment in the wind farm, although the net present value is around 236 NOK per generated MWh. The uncertainty in prices makes it optimal to wait and see if profitability improves.

REFERENCES

[1] Dixit A, Pindyck R, "Investment under uncertainty", Princeton University Press, 1994.

[2] McDonald R, Siegel D, "The Value of Waiting to Invest", Quarterly Journal of Economics 101 (4): 707-727, 1986

[3] Hatziargyriou N, Zervos A, "Wind power development in Europe", Proceedings of the IEEE 89 (12): 1765-1782, 2001

[4] Fleten S-E, Maribu KM, Wangensteen I, "Optimal investment strategies in renewable distributed generation under price uncertainty", Working paper, Norw Univ of Sci and Tech, 2005

[5] Dobbe T, Fleten S-E, Sigmo S, "Valuing gas power plants with CO2 capture and tradable quotas", 16th ECOS, Copenhagen, Denmark, June 30 - July 2, 2003

[6] Bechrakis DA, Sparis PD, "Correlation of wind speed between neighboring measuring stations", IEEE Transactions on Energy Conversion 19 (2): 400-406, 2004

[7] Lucia J, Schwartz E, "Electricity prices and power derivatives – evidence from the Nordic Power Exchange" Review of Derivatives Research (5): 5-50, 2002

[8] Fleten S-E, Näsäkkälä E, "Gas Fired Power Plants: Investment Timing, Operating Flexibility and Abandonment, "Working Paper 04-03, Dept of Industrial Econ and Technology Management, Norw. Univ. of Science and Technology, 2003

[9] Junginger M, Faaij A, Turkenburg WC "Global experience curves for wind farms", Energy Policy 33 (2): 133-150, 2005

Proceedings of ECOS 2005
Trondheim, Norway
June 20–22, 2005

Investigation of the Oxidation Zone in a Biomass two-stage downdraft Gasifier

Luc Gerun[*a], Jérôme Bellettre and Mohand Tazerout
Ecole des Mines de Nantes, DSEE
4, rue Alfred Kastler, B.P. 20722,
44 307 NANTES Cedex 3, France

Benny Gøbel[*b] and Ulrik Henriksen
Biomass Gasification Group,
Technical University of Denmark (DTU),
Forsøgsområde 120, Nordvej,
2800 Kongens Lyngby, Denmark

ABSTRACT

The partial combustion in a two-stage downdraft gasifier is critical for the process optimisation. Flame temperature and residence time of gas in the hot zone are indeed determining for tar cracking, the major issue in gasification. This paper presents a CFD model of the oxidation zone. Chemical reactions, including tar cracking, are treated by the "EDC" model (homogeneous reactions). Fluid flows are turbulent and simulated by the k-ε RNG turbulence model.
The validation of the model is done with the DTU 100 kW two-stage gasifier. Results fit satisfactory the data, regarding the temperature profile.
Keywords: Two-stage downdraft gasifier; partial oxidation; tar; modelling.

NOMENCLATURE

C	Concentration [kmol. m^{-3}]
c_p	Specific heat [J. kg^{-1}. K^{-1}]
d	Diameter [m]
$D_{0,r}$	Molar diffusion coefficient [kmol. m^{-3}]
E_a	Activation energy [J. kmol^{-1}]
h	Heat transfer coefficient [W. m^{-2}. K^{-1}]
h^0	Standard state enthalpy [J.kg^{-1}]
I	Radiative intensity [W. m^{-2}]
k	Thermal conductivity [W. m^{-2}. K^{-1}]
k_s	Frequency factor [s^{-1}]
k_c	Arrhenius kinetic rate [s^{-1}]
k_m	Mass diffusion coefficient [kg.m^{-2}.s^{-1}]
m	Mass [kg]
M	Molar weight [kg. kmol^{-1}]
n	Index of refraction
P	Pressure [Pa]
R	Ideal gas constant [8 314 J. kmol^{-1}]
$R_{i,r}$	Homogeneous reaction rate [kg. m^{-3}.s^{-1}]
T	Temperature [K]
u	Axial velocity [m.s^{-1}]
v	Radial velocity [m.s^{-1}]
x	Axial coordinate [m]
Y	Mass fraction, $Y_i = \frac{m_i}{m_{total}}$

Greek Letters

α	Absorption coefficient [m^{-1}]
α_{Pr}	Inverse of the turbulent Prandtl number
ε_m	Emissivity
ϕ	Hydraulic diameter [m]
ν	Kinematic viscosity [m². s^{-1}]
ρ	Density [kg. m^{-3}]
σ_S	Scattering coefficient [m^{-1}]
σ	Boltzman constant [5.67×10^{-8} W.m^{-2}.K^{-4}]

[*a] Corresponding author: E-mail: luc.gerun@emn.fr, phone number: (+33) 2 51 85 82 81, fax (+33) 2 51 85 82 99
[*b] Corresponding author: E-mail: bg@mek.dtu.dk , phone number: (+45) 45 25 41 74, fax (+45) 45 93 57 61

INTRODUCTION

The energy crisis of the 1970s sparked a renewed interest in biomass gasification systems. Nowadays environmental concerns are questioning the continued use of fossil fuels and the need for sustainable energy production has prompted new research into the possibility of gasification as a key source of energy production.
Gasification is a thermal process converting biomass feedstock into a mixture of gases that can be burnt in boilers, internal combustion engines and gas turbines.
If well designed, gasification allows an environmentally friendly energy production. Furthermore, it can help reducing the "waste disposal" constraints by using it as a feedstock to convert it into useful and valued product.
Biomass is indeed a particular kind of fuel. Its price is fixed by the collecting expenses. That is why small-scale installations are well adapted to this market. They allow valorising wastes directly on their production location.
In these perspectives downdraft gasifiers present indisputable advantages [1]. A traditional example is presented in *Figure 1* [2]. In current pilots called two-stage, drying/pyrolysis and combustion/reduction zones are physically separated. This low tar level technology only requires a small gas-cleaning unit to prevent engine fouling problems [3]. Furthermore it is well adapted to turnover and biomass diversity. Finally its utilisation is relatively easy and can be highly automated.
However available kinetics data and the theoretical comprehension of the physical phenomena remain still insufficient to build a general accurate model.

This paper presents a tool for validating two-stage downdraft gasifier design. In this type of installation, temperature field in the partial oxidation zone is crucial. Indeed gas produced during pyrolysis must pass through a hot uniform zone to crack satisfactorily tar, the main issue of gasifier. As a result, reactor diameter, throat shape and nozzle geometry have to be well designed in order to ensure an optimum process.
A CFD model is used to simulate the complex phenomena occurring in the partial oxidation zone. It includes detailed chemical mechanism with tar cracking, heat transfer with radiation and turbulent fluid flow.

Vijeu's pyrolysis model [4] is used to determine input pyrolysis gas composition, given in *Table 1* at a temperature of 650°C.
Results are then validated with the experimental data get from the DTU 100 kW_{th} two-stage gasifier [5,6]. They are finally discussed.

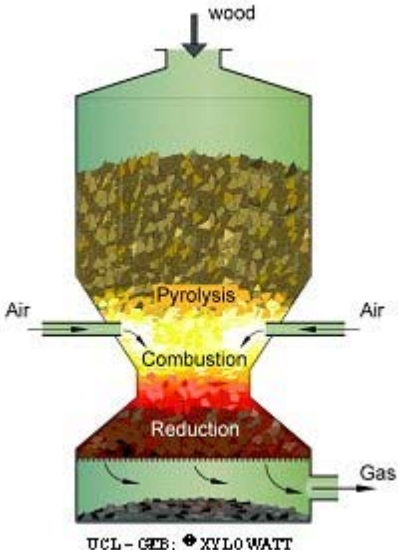

Figure 1: *Traditional downdraft gasifier [2]*

CO	CO_2	H_2	H_2O	CH_4	C_6H_6	$C_{10}H_8$
35[a]	20.8[a]	2.4[a]	7.2[a]	9.6[a]	8.7[b]	16.3[b]

a: calculated by Vijeu's pyrolysis model [4]
b: estimated [3,7]
Table 1: *Pyrolysis gas composition (mass %)*

MODEL

The model is divided into three parts: fluid flow, chemical mechanism and heat transfer. Model equations are listed in *Table 2*. *Figure 2* shows model geometry and boundary conditions.

Fluid flow

Air is injected into the reactor through three injectors with five nozzles each. Reynolds number is around 2,000 at the air injector nozzles. The flow may thus be turbulent in this zone. Moreover velocity pattern is complex as recirculation may occur.
A detailed turbulence model is thus required to simulate these phenomena. After a preliminary sensitivity study, the RNG k-ε model was chosen

Pyrolysis gas + steam inlet
u = 0.52 m/s, turbulence intensity: 3%, T=650°C, hydraulic diameter: ϕ =0.26 m.

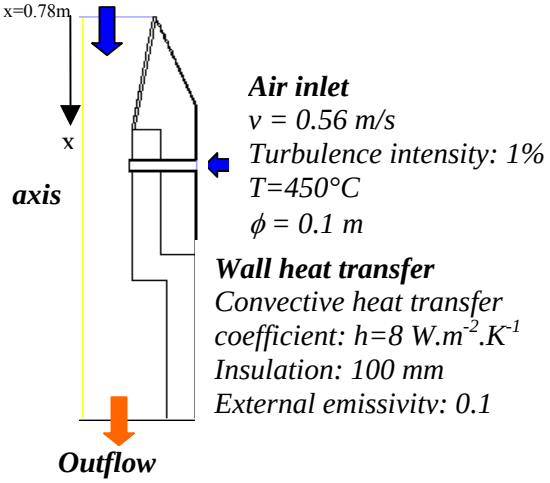

Figure 2: *Model geometry*

as the best compromise between accuracy and efficiency. It is also adequate for laminar flow that may develop inside the gasifier.
Wall boundary conditions are simulated by a low Reynolds number approach [8]. Solid phase is modelled by a Lagrangian particles tracking.

Chemical mechanism

The chemical mechanism consists in five oxidation reactions (1-5) and the water-gas shift reaction (6).

$$CO + 0.5\ O_2 \longrightarrow CO_2 \quad (1)$$
$$CH_4 + 1.5\ O_2 \longrightarrow CO + 2\ H_2O \quad (2)$$
$$H_2 + 0.5\ O_2 \longrightarrow H_2O \quad (3)$$
$$C_6H_6 + 4.5\ O_2 \longrightarrow 6\ CO + 3\ H_2O \quad (4)$$
$$C_{10}H_8 + 7\ O_2 \longrightarrow 10\ CO + 4\ H_2O \quad (5)$$
$$CO + H_2O \longleftrightarrow CO_2 + H_2 \quad (6)$$

Arrhenius rate is calculated from equation (7).

$$k_c = k_s e^{-\frac{E_a}{RT}} [A]^a [B]^b \quad (7)$$

Constants are taken from literature. They are listed in *Table 3*. The reverse term of (6) is obtained by a free Gibbs energy variation method.

Tars are modelled as a simplification of Jess works [9]. Pyrolysis, as it is slow and long, is considered to produce only secondary tar compounds, represented by benzene, and tertiary tar compounds, represented by naphthalene.
Naphthalene is indeed one of the main component of tar and 6C ring hydrocarbons are considered as the key component of thermal decomposition of aromatic hydrocarbon [9].
Further model development should include oxygenated hydrocarbons as phenol, whose concentration is not negligible particularly in steam gasification [10].
Initial tar concentration is extrapolated from literature data [3,7]. Methane includes C_2 compounds as ethane and ethylene. Tars are considered to be thermally cracked and to form soot. *Figure 2* shows the tar evolution mechanism. The kinetics constants of the five reactions are taken from Jess [9,11].

As flow is turbulent, it must be taken in consideration in the chemical reaction model. The chosen model, called "Eddy Dissipation Concept" model [12], calculates also Arrhenius rate at the turbulence time scale (18). It seems to suit well to this kind of reactive flow [13].

Besides it is observed that particles residence time is relatively short (<1s) in a two-stage downdraft gasifier. As a consequence heterogeneous reactions are negligible in the oxidation zone, as oxygen reacts far quicker with gas phase.

Heat transfer

As temperature exceeds 1000°C in the reactor core, heat transfer by radiation is predominant. They are simulated by the Discrete Ordinates model [14], a four-flux method. It integrates the Radiative Transfer Equation (13). As a result a source term S_f due to radiative transfer is included in the energy equation (12). S_f also includes the heat of the chemical reactions from equation (8).

$$S_{f,r} = -\sum_j \left(\frac{h_j^0}{M_j} + \int_{T_{ref,j}}^{T} c_{p,j} dT \right) R_{j,r} \quad (8)$$

The absorption coefficient of the fluid phase is computed by the cell-based Weighted-Sum-of-Gray-Gases model [15]. It only takes into account the concentration of CO_2 and H_2O.

Heat transfer from fluid to solid phase is calculated by equation (9).

$$m_p Cp_p \frac{dT_p}{dt} = hA_p\left(T_\infty - T_p\right) - \frac{dm_p}{dt} H_r + A_p \varepsilon_p \sigma (T_\infty^4 - T_p^4) \qquad (9)$$

Numerical solution

A segregated solver solves sequentially the continuity, momentum (Navier-Stokes equations), energy, radiation and species equations (N-1 equations for N species).

Governing equations are converted to algebraic equations that can be solved numerically by a control-volume-based technique through a power-law scheme [16]. SIMPLE algorithm couples velocity and pressure [17].

Simulation is 2D axisymmetric. In this purpose, the air injector, which is composed of five cylinders with three nozzles each, is considered as annular. Flowrate and injection surface area are conserved. Thus momentum is also conserved. Previous studies showed that this analogy was correct in this kind of problem [18].

However swirl neglecting may be a source of error.

The unstructured grid is composed of 20,000 cells. Meshing tests have been performed from 5,000 to 30,000 cells to insure independence of results.

Simulation is considered as converged when residuals remain constant at a value below 10^{-5} (10^{-4} for momentum). The calculation time is approximately fifty hours on a 3.2 GHz computer.

Mass $$\frac{\partial \rho}{\partial t} + \nabla.(\rho \vec{v}) = \mathrm{S_m} \qquad (10)$$

Momentum $$\frac{\partial}{\partial t}(\rho \vec{v}) + \nabla.(\rho \vec{v}\vec{v}) = -\nabla p + \nabla.(\bar{\bar{\tau}}) + \rho \vec{g} + \vec{F} \qquad (11)$$

Energy $$\frac{\partial}{\partial t}(\rho E) + \nabla.(\vec{v}(\rho E + p)) = \nabla.\left[k_{eff} \nabla T - (\sum_j h_h \vec{J}_j) + (\bar{\bar{\tau}}.\vec{v})\right] + S_f \qquad (12)$$

with $k_{eff} = \alpha_{\mathrm{Pr}} \mu_{eff} Cp$ [8]

Radiative transfer

$$\nabla.(I(\vec{r},\vec{s})\vec{s}) + (\alpha + \sigma_S) I(\vec{r},\vec{s}) = \alpha n^2 \frac{\sigma T^4}{\pi} + E_p + \frac{\sigma_S}{4\pi} \int_0^{4\pi} I(\vec{r},\vec{s}) \Phi(\vec{s}.\vec{s}') d\Omega' \quad) \qquad (13)$$

Turbulence $$\frac{\partial\left(\rho U_j k\right)}{\partial x_j} = \frac{\partial}{\partial x_j}\left[\rho \alpha_k \nu_{eff} \frac{\partial k}{\partial x_j}\right] + \rho \nu_t \left(\frac{\partial U_i}{\partial x_j} + \frac{\partial U_j}{\partial x_i}\right)\frac{\partial U_i}{\partial x_j} - \rho\varepsilon \qquad (14)$$

$$\frac{\partial\left(\rho U_j \varepsilon\right)}{\partial x_j} = \frac{\partial}{\partial x_j}\left(\rho \alpha_\varepsilon \nu_{eff} \frac{\partial \varepsilon}{\partial x_j}\right) + C_{\varepsilon 1} \frac{\varepsilon}{k} \rho \nu_t \left(\frac{\partial U_i}{\partial x_j} + \frac{\partial U_j}{\partial x_i}\right)\frac{\partial U_i}{\partial x_j} - C_{\varepsilon 2} \rho \frac{\varepsilon^2}{k} - R \qquad (15)$$

with $\nu_{eff} = \nu\left(1 + \sqrt{\frac{C_\mu}{\nu}} \frac{k}{\sqrt{\varepsilon}}\right)^2 = \nu\left(1 + \sqrt{\nu_t / \nu}\right)^2$

$C_\mu = 0.0845$; $C_{\varepsilon 1} = 1.42$ and $C_{\varepsilon 2} = 1.68$. α_k and α_ε are the inverse of turbulent Prandtl number for k and ε.

Species transport $$\frac{\partial}{\partial t}(\rho Y_i) + \nabla.(\rho \vec{v} Y_i) = -\nabla.\left(-\left(\rho D_{0,i} + \frac{\mu_t}{Sc_t}\right)\nabla Y_i\right) + R_i \qquad (16)$$

Homogeneous reaction rate $$R_{i,r} = \frac{(\xi^*)^2 \chi}{\tau^*}(Y_i^* - Y_i) \qquad (17)$$

With $\xi^* = C_\xi \left(\frac{\upsilon\varepsilon}{k^2}\right)^{\frac{3}{4}}$; $\tau^* = C_\tau \left(\frac{\upsilon}{\varepsilon}\right)^{\frac{1}{2}}$; $\chi = \frac{\rho}{[1 - (\xi^*)^3]}$; $C_\xi = 2{,}1377$; $C_\tau = 0{,}4082$.

Table 2: *Governing equations*

Reaction	k_s (s^{-1})	E_a (J. $kmol^{-1}$)	A	B	Reference
(1)	$1.3\times10^{11}\times[H_2O]^{0.5}$	1.256×10^{8}	1	0.5	Shin [19]
(2)	4.4×10^{11}	1.2552×10^{8}	0.5	1.25	Jones [20]
(3)	4.462×10^{12}	4.2×10^{7}	1	1	Di Blasi [21]
(4)	2.4×10^{11}	1.2552×10^{8}	1[a]	1.85	Westbrook [22]
(5)	$9.2\times10^{6}\times T$	8×10^{7}	0.5	1	Di Blasi [21]
(6)	124.03	1.26×10^{7}	1	1	Di Blasi [21]

a: modified (see Results &Discussion)

Table 3: *Reference value for kinetic constants*

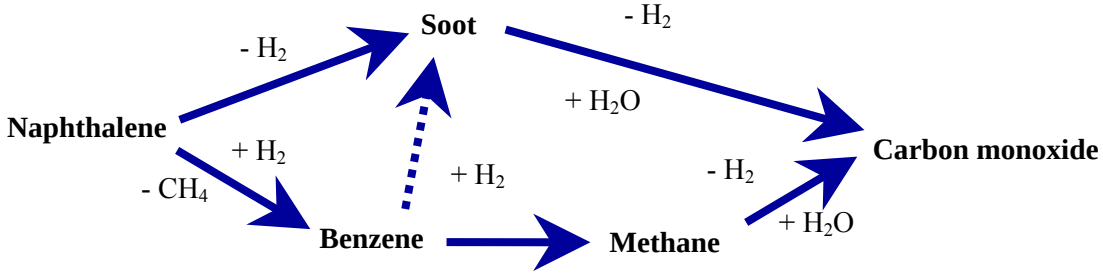

Figure 2: *Tar cracking mechanism*

EXPERIMENTAL

Facilities

The plant is a two-stage gasifier built at DTU with a thermal input of 100 kW. It consists of following components: propane heated pyrolysis unit, partial oxidation zone, air preheater, steam feeder and char bed lying on a movable grate [6]. It is showed in *Figure 3*.

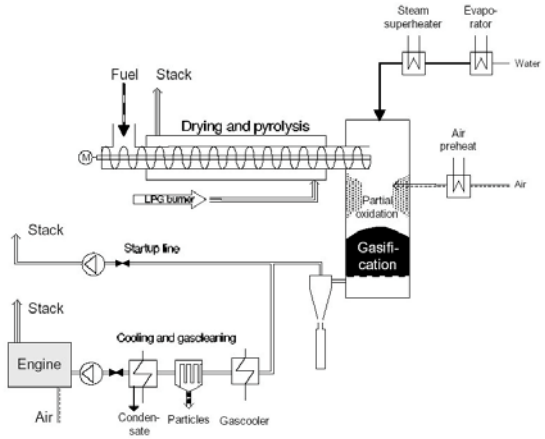

Figure 3: *100 kW_{th} two—stage gasifier*

Operating conditions

Experiments are performed with wood chips. Wood moisture is 26.5% of the total mass and the wood elementary formula is $CH_{1.4515}O_{0.66}$. Operating conditions are reported in *Table 4*.

	Wood	Air	Steam
Flowrate	24.8 kg/h	25 kg/h	7 kg/h
Initial temperature	600°C	≈450°C	600°C

Table 4: *Operating conditions*

Method of investigation

Temperature field inside the reactor was investigated through two different techniques.
A rod equipped with nine thermocouples measures the temperature along the vertical axis. It is movable and thus can inspect the radial temperature profile.
Secondly an infra red detector and a suction pyrometer are used to measure axial temperature in the symmetry axis.
Gas was analysed at the end of the process, i.e. after the reduction zone. Tar level is below 25 mg/Nm^3. The final dry gas composition is in volume-%: 17 CO, 17 CO_2, 2 CH_4 32 H_2 and 32 N_2. The soot particles concentration is around 450 mg/Nm^3 at the exit.

RESULTS & DISCUSSION

Temperature field

The *Figure 4* shows the comparison of the temperature profile along the vertical axis between the infrared measurement and the simulation

results. It fits satisfactorily the experimental data, although temperature is slightly overestimated. It may be partially due to an overestimation of the gas pyrolysis heating value.

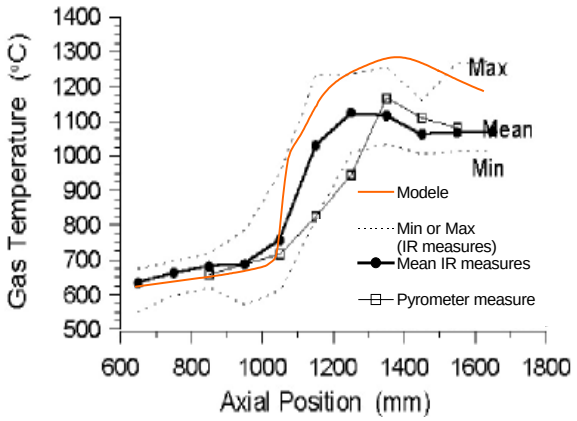

Figure 4: *Comparison modele/experiences results*

Temperature field is shown in *Figure 5*. The reaction heat is released mainly close to the injector. It induces a very hot zone in this area.

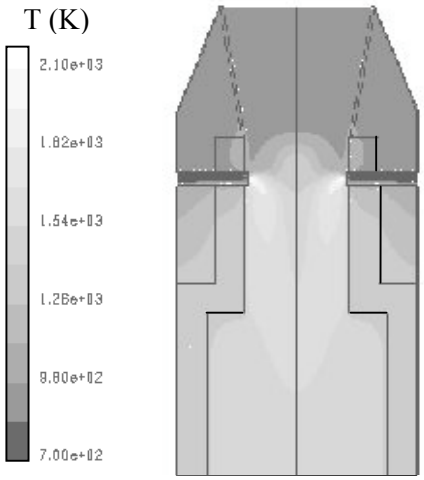

Figure 5: *Temperature field inside the reactor*

The uncertainties of measure and the operating conditions make the comparisons between experience and simulation difficult.
Indeed gasification is not a totally steady-state process. Inlet gas composition may for example vary strongly with time, as pyrolysis is also not fully stable. The effects of pyrolysis unsteadiness are studied later.

Flow pattern

The air velocity at the nozzle outlet is around 48 m/s, as the constriction accelerates the air. It implies fully developed turbulence in the flow and recirculations. These latter are shown in *Figure 6*.

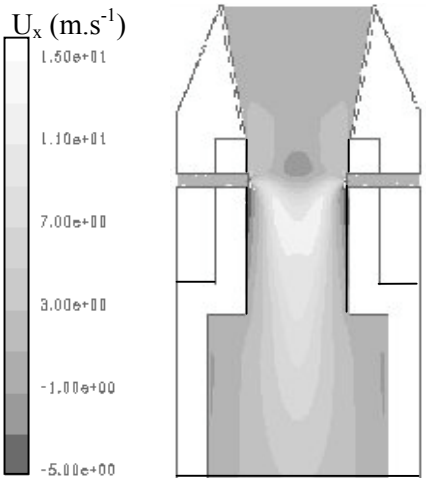

Figure 6: *Axial velocity inside the reactor*

Effect of the injection surface area

The injection surface area influences strongly the flow. Smaller nozzles induce higher air radial velocity but also higher axial gas velocity. As a result air penetrates deeper in the reactor, temperature is thus more uniform than with bigger nozzles. In the latter case the very hot zone located close to the wall is bigger. Temperature along the axis is shown in *Figure 7*.

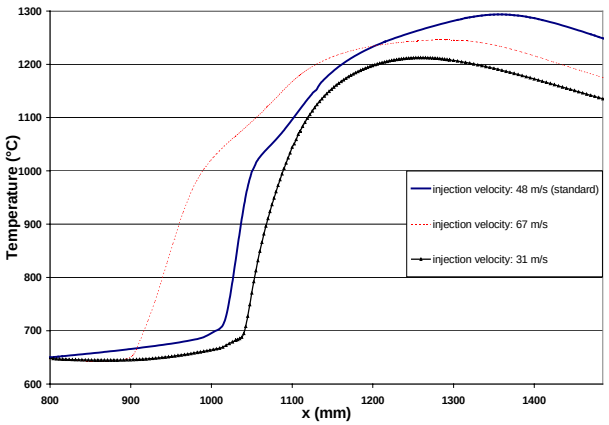

Figure 7: *Axial temperature with different nozzles*

The injector should also be carefully designed. A low opening area will induce better mixing and higher turbulence rate, necessary for a good combustion, but high gas velocity and thus smaller residence time too. This tool is also useful to find the best compromise to optimise the process.

Unsteady-state effects

The pyrolysis unsteady effects on temperature profile have been studied with the model. *Figure 8* shows a comparison of the axial temperature in the standard case, with 10% lower pyrolysis gas flowrate and with two different pyrolysis gas compositions – poorer and richer, respectively -/+ 20% [CO], [H_2], [CH_4], +/- the difference [CO_2].
It is observed that instabilities influence significantly the process. They should also be taken into account during a gasifier conception.

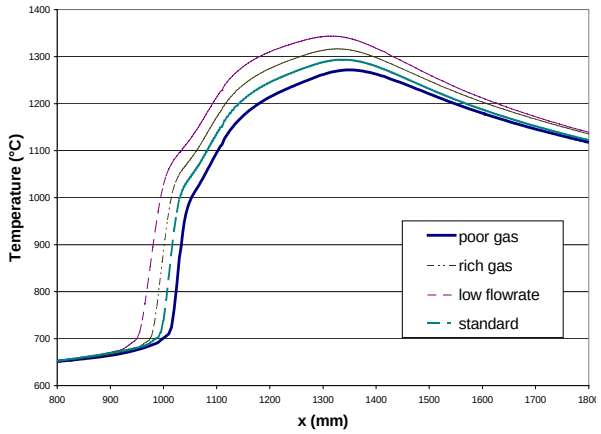

Figure 8: *Effect of pyrolysis unsteadiness on vertical axial temperature*

Chemical model discussion

The simulated final gas composition, summarised in *Table 5*, is in good agreement with experimental observations. Reduction reactions indeed convert water and char to hydrogen and carbon monoxide, diluting the mixture. Moreover the water-gas shift reaction, catalysed by the char bed, modifies the mixture composition.
It will be used in a future study as input for a reduction model to obtain a complete gasification model and then to compare numerical and experimental gas composition.

Conditions	CO	CO_2	H_2	CH_4	N_2
Standard	17.9	14.1	11.4	6.6	50
Poor gas	16.2	17.9	9.6	5.5	50.8
Rich gas	19.3	10.5	12.9	7.6	49.7
Low flowrate	16.9	13.9	10.1	6	53.1

Table 5: *Final gas dry composition (volume %)*

The modelling of competitive combustion reactions in an oxygen-limiting environment presents two main difficulties.
Firstly kinetic data are often determined for complete oxidation. Uniform sources have thus to be find or adaptations to be made.
That is why the –0.1 coefficient for benzene in its oxidation reaction (5) has been switched to 1. It implied furthermore heavy problems of solution convergence. Moreover the mechanism is very stiff and it is difficult to make it converged. It requires much time and precautions.
Besides the attempt of tar modelling is not a complete success. Naphthalene is reduced by a 5 factor during the process. It is far from the experimental results in similar case, which shows a decrease by a 100 factor. This difference can be partially explained by the neglecting of swirl effects. Residence time in simulation is thus lower than in reality.
The kinetic constants appear also to be uncertain. As already observed by Morf [10], naphthalene conversion to soot is negligible with rate of [5] used in this study. It means that either different pathways to produce soot exist or that the kinetic constants, calculated for coke-oven gas, are not adapted to biomass gasification.
To verify the later hypothesis, a try with a first order rate from Diesel combustion [23] has been performed. Naphthalene conversion to soot is then complete, whereas it was negligible with previous rate. Further kinetic study is thus required.

CONCLUSION

The oxidation zone of a two-stage downdraft gasifier has been simulated by a 2D CFD model. It takes into account turbulence, detailed chemical mechanism including tars and heat transfer.
Results fit satisfactorily to the experimental data regarding temperature pattern. However tar model requires further investigation.
Simulations enlightened several crucial point of the process:

- injector design is fundamental in gasification;
- pyrolysis unsteadiness influences significantly the process;
- kinetic data adapted to the process should be determined to ensure the tar model precision.

REFERENCES

[1] McKendry, P., *Energy production from biomass (part 3): gasification technologies*, Bioresource Technology 2002;83;55-63.

[2] Tchouate Heteu, P. M., *Feasibility of biomass gasification for decentralised rural electrification and industry in remote areas in Africa*, In: Proceedings of the First Int. Conf. and Exhibition on Biomass for energy and industry, Seville, 1999.

[3] Henriksen, U., Ahrenfeldt, J., Gøbel, B., Hindsgaul, C. and Jensen, T. K., *The Viking gasifier*, In: Proceedings of the IEA-meeting, London, 2003.

[4] Vijeu, R. and Tazerout, M., *Modélisation et dimensionnement d'une zone de pyrolyse d'un gazogène co-courant*, In: Proceedings of COFRET'04, Nancy, 2004.

[5] Gøbel, B., *Dynamisk modellering af forgasning i fixed koksbed*, Ph.D. Thesis. ET-PHD-99-04, DTU, 1999.

[6] Gøbel, B., Bentzen, J., Hindsgaul, C., Henriksen, U., Ahrenfeldt, J., Fock, F., Houbak N and Qvale, B., *High Performance Gasification with the Two-Stage Gasifier,* In proceedings of 12th European Conference and Technology Exhibition on Biomass for Energy, Industry and Climate Protection. Amsterdam 2002, 389-395.

[7] Milne, T. Abatzoglou N. and Evans, R. J., *Biomass Gasifier "TARS": Their nature, formation and conversion*, report NREL/TP-570-25357, IEA Bioenergy Biomass Utilisation, 1998

[8] Lopez-Matencio, J. L., Bellettre, J. and Lallemand, A., *Numerical prediction of turbulent heat and mass transfer above a porous wall subjected to vaporisation cooling*, I. J. Transport Phenomena, 2003;5(3);185-201.

[9] Jess, A., *Mechanisms and kinetics of thermal reactions of aromatic hydrocarbons from pyrolysis of solid fuels*. Fuel 1996;75(12);1441-1448.

[10] Morf, P., Hasler, P. and Nussbaumer, T., *Mechanisms and kinetics of homogeneous secondary reactions of tar from continuous pyrolysis of wood chips*, Fuel 2002;81(7);843-853.

[11] Jess, A., *Reaktionskinetische Untersuchungen zur thermischen Zersetzung von Modellkohlenwasserstoffen*, Erdöl Erdgas Kohle 1995;111(11);479-484.

[12] Magnussen, B. F., *On the structure of turbulence and a generalised eddy dissipation concept for chemical reaction in turbulent flow*, In: Proceedings of the Nineteenth AIAA Meeting, St Louis, 1981.

[13] Bellettre, J. and Tazerout M., *Numerical simulation of reactive flows in a wood gasifier*, In: Proceedings of the Third Mediterranean Combustion Congress, Marrakech, 2003.

[14] Chui, E. H. and Raithby, G. D., *Computation of radiant heat transfer on a non-orthogonal mesh using the finite-volume method*, Numerical Heat Transfer 1993;23;269-288.

[15] Smith, T. F. Shen Z. F. and Friedman J. N., *Evaluation of coefficients for the Weighted Sum of Gray Gas model*, J. Heat Transfer 1982;104;602-608.

[16] Patankar S. V., *Numerical Heat Transfer and Fluid Flow*, Hemisphere, Washington D.C., 1980.

[17] Ferzieger J. L. and Peric M., *Computational Methods for Fluid Dynamics*, Spinger-Verlag, Heidelberg, 1996.

[18] Bellettre, J., Bataille, F. and Lallemand, A., *A new approach for the study of the turbulent boundary layers with blowing*. International Journal of Heat and Mass Transfer, 1999;42(15);2905-2920.

[19] Shin, D. and Choi, S., *The combustion of simulated waste particles in a fixed bed,* Combustion and Flame, 2000;121;167-180.

[20] Jones, W. P. and Lindstedt R. P., *Global reaction schemes for hydrocarbon combustion*, Combustion and Flame, 1998;73;233-249.

[21] Di Blasi, C., *Dynamic behaviour of stratified downdraft gasifiers*, Chemical Engineering Science 2000;55;2931-2944.

[22] Westbrook, C. K. and Dryer, F. L., *Chemical kinetic modeling of hydrocarbon combustion*, Prog. Energy Combust. Sci. 1984(10);1-57.

[23] Tao, F., Golovitchev, V. and Chomiak, J., *A phenomenological model for the prediction of soot formation in diesel spray combustion*, Combustion and Flame, 2004;136(3);270-282.

Proceedings of ECOS 2005
Trondheim, Norway
June 20–22, 2005

A FEASIBILITY STUDY OF BLACK LIQUOR BOOSTER GASIFICATION WITH BORATE AUTOCAUSTICIZING

Sylvain Leduc*
Luleå University of Technology
Division of Energy Engineering
971 87 Luleå
Sweden

Xiaoyan Ji, Jinyue Yan
Royal Institute of Technology
Division of Energy Processes
Sweden.

ABSTRACT

Black liquor constitutes a huge energy potential. In order to improve the efficiency of a pulp mill, this study is focussed on borate autocausticizing, which has proved to work efficiently in recovery boilers. The leading idea is to complete an overloaded recovery boiler with a booster gasifier. In this configuration, the black liquor is gasified with air at low overpressure. Results regarding conventional black liquor gasification are close to the reality and very promising. Regarding black liquor gasification with borate, lack of data for orthoborate, like the Gibbs free energy, did not enable good results. The model so far is a good starting point for black liquor gasification studies, and needs to be improved as soon as new data on borates will be available.
Keywords: Black liquor, borate, orthoborate, caustisation, booster gasifier, ASPENplus.

NOMENCLATURE

BL	Black liquor
DHFORM-DH	Standard enthalpy of formation at 25˚C
DGFORM-DG	Standard free energy of formation at 25˚C
l	Liquid state
P_C	Critical pressure
P_r^{sat}	Reduced vapor pressure
P_{sat}	Saturated vapor pressure
R	The gas constant
s	Solid state
T_b	Boiling temperature
T_c	Critical temperature
tDS	Tonne per Dry solid
T_r	Reduced temperature
V_c	Critical volume
VLSTD	Standard liquid molar volume at 60˚F
Z_c	Compressibility coefficient
ω	Acentric Pitzer coefficient

* Corresponding author: Phone: +46 920 49 2178 Fax: +46 920 49 1047 E-mail: sylvain.leduc@sirius.luth.se

INTRODUCTION

Background

Black liquor gasification has been studied, developed and simulated by a large number of research organisations and universities during the past 25 years. A number of processes and gasification media have been proposed. One process configuration has gone from the laboratory experiments to the edge of commercialization. According to this solution, the black liquor is gasified with air or oxygen in a ceramic reactor. The smelt and the raw gas of the process are separated in a quench cooler under the gasification reactor (Figure 1). Gasification of this type is marketed by the Chemrec company (earlier Kvaerner Chemrec).

Two different alternatives exist for this technology: Booster gasification relieves overloaded recovery boilers. This configuration is sold on commercial

basis by Chemrec. The leading idea is to complete an overloaded recovery boiler with a small gasifier. In this configuration the black liquor is gasified with air at low overpressure. The focus lies on chemical recovery and simple design.
Another alternative of this technology is the pressurized gasification of black liquor with a gas turbine. In this configuration, all the black liquor from the pulp mill is gasified at high pressure and with oxygen. The cleaned syngas is used to drive a gas turbine to maximize power production. The gasification part has been demonstrated in laboratory experiments. The complete system with gasification integrated with a gas turbine has not yet been demonstrated anywhere on the world.
The use of sodium borates to causticize the black liquor recovery boiler smelt directly in the furnace was first suggested by Jansson in 1977 [1]. This so called autocausticizing process by Jansson involved the reaction between the sodium carbonate in the bed and the added sodium meta-borate ($NaBO_2$), to form disodium metaborate, ($Na_4B_2O_5$).The disodium borate would hydrolyze in water to sodium hydroxide (NaOH), and to the original meta-borate. This process would produce sodium hydroxide directly in the green liquor and thus eliminate the need for the recaust plant including the lime kiln.
It was demonstrated that the addition of borate to the black liquor had the potential to increase the black liquor viscosity and decrease its heating value, thus rendering the process unattractive [2].
Trans et al., 1997 [3], showed that the key borate formed in the furnace is trisodium borate, also known as orthoborate (Na_3BO_3), instead of the disodium borate as originally suggested by Jansson. In water the trisodium borate hydrolyzes to form sodium hydroxide and sodium metaborate.
The finding implies that only half a mole of boron metaborate is required to produce one mole of sodium hydroxide in the green liquor, as opposed to one mole of metaborate per mole of sodium hydroxide as in the Jansson concept. This 50% reduction in borate requirement has made the borate autocausticizing process much more attractive than previously. Especially interesting is the possibility to partially convert the carbonate in the smelt to borate with a small amount of metaborate, and then complete the causticizing of the remaining sodium carbonate in the recaust plant with a reduced amount of lime. This partial autocausticizing technology is an attractive alternative for kraft mills where the capacity of the recausticizing plant or the lime kiln is limiting the total production.
The partial borate-autocausticizing technology uses a small quantity of sodium borate to causticize a portion of sodium carbonate (Na_2CO_3), in a recovery boiler, and then completes the causticization of the remaining sodium carbonate in a conventional recaust plant with a reduced quantity of lime.

Borate autocausticizing reactions

The principal reaction that occurs in recovery boilers is the reaction between sodium meta-borate, and sodium carbonate, Na_2CO_3, in molten smelt to form tri-sodium borate (Reaction (1)).

$$NaBO_2 + Na_2CO_3 \rightarrow Na_3BO_3 + CO_2 \qquad (1)$$

In the dissolving tank, trisodium borate reacts with water to form sodium hydroxide, and regenerate sodium meta-borate (Reaction (2)).

$$Na_3BO_3 + H_2O \rightarrow NaBO_2 + 2NaOH \qquad (2)$$

If the borate make-up chemical, sodium tetraborate pentahydrate, $Na_2B_4O_7\ 5H_2O$, is introduced into the recovery cycle through mixing with green liquor or white liquor, it will react with sodium hydroxide to form sodium meta-borate in the liquor.
If the borate makeup is carried out through addition to black liquor, it will also react with residual sodium hydroxide in the liquor to form sodium meta-borate before entering the boiler. However, if the amount of $Na_2B_4O_7$ added is stoichiometrically larger than that of the residual sodium hydroxide in the black liquor, the excess $Na_2B_4O_7$ will react with sodium carbonate in molten smelt to form trisodium borate (Reaction (3), (4) and (5)).

$$Na_2B_4O_7 + Na_2CO_3 \rightarrow 4NaBO_2 + CO_2 \qquad (3)$$
$$4NaBO_2 + 2Na_2CO_3 \rightarrow 2Na_4B_2O_5 + 2CO_2 \qquad (4)$$
$$2Na_4B_2O_5 + Na_2CO_3 \rightarrow 2Na_3BO_3 + CO_2 \qquad (5)$$

Thus, several different sodium borate compounds can be formed and the overall autocausticizing efficiency depends strongly on the type of borate compounds formed in the boiler. Trisodium borate yields twice as much sodium hydroxide compared to $Na_4B_2O_5$ when hydrolysed in water (Reactions (2) and (6)).

$$Na_4B_2O_5 + H_2O \rightarrow 2NaBO_2 + 2NaOH \quad (6)$$

Sodium meta-borate does not yield any sodium hydroxide, while $Na_2B_4O_7$, if still exits in the boiler, would react with sodium hydroxide from the weak wash to form sodium meta-borate (Reaction (7)).

$$Na_2B_4O_7 + 2NaOH \rightarrow 4NaBO_2 + H_2O \quad (7)$$

Thus, if the make-up chemical is not well mixed in the liquor, or if the autocausticizing reaction in the boiler does not occur uniformly over the char bed, or if the bed temperature is not sufficiently high, the resulting smelt would contain not only trisodium borate, disodium metaborate, and sodium meta-borate, but also $Na_2B_4O_7$ which consumes sodium hydroxide. This would lower the overall autocausticizing reaction efficiency in the dissolving tank.

Recent studies from Tran et al, 2001 [4], and Cameron et al, 2001 [5], suggested a different stoichiometry and reaction product (Reaction (8) and (9)):

$$NaBO_2 + Na_2CO_3 \rightarrow Na_3BO_3 + CO_2 \quad (8)$$

$$5Na_2B_4O_7 + 2Na_2CO_3 \rightarrow 5Na_3BO_3 + 5CO_2 \quad (9)$$

The tri-sodium borate, formed by these reactions in the recovery boiler, dissolves in the smelt dissolving tank and forms caustic and metaborate (Reaction 2). Sodium metaborate remains dissolved in the liquor cycle to continue performing its autocausticizing function. No additional equipment is necessary for borate autocausticizing and the major cost involved is only the addition of makeup borate to compensate for the loss in the liquor cycle.

The major side effect is the increase in the inorganic content of the liquor due to the presence of sodium borate. This would complicate the use of borate in 100 % autocausticizing application. As a result, the initial focus of the technology was concentrated on the development of partial borate autocausticizing application, which is especially suitable in pulp mills that are recausticizing limited. By this manner the chemical species have regenerated without causticizing.

Regarding the black liquor gasification, the borate autocausticizing process is really interesting, since it is possible to avoid the immediate problem of increasing causticizing need. Black liquor gasification together with borate autocausticizing has some advantages:

The rotary kiln is the part of the process which still is dependent in many cases of fossil fuel. There are several alternative methods for heating the rotary kiln. This has proved to give either a decrease of the operating reliability, or give unwanted side-effects. With borate causticizing the production of the pulp in the mill can be totally free from fossil fuel. There are indications that the borate contributes to the delignification. This has not yet been able to be shown with experiments.

SIMULATION MODEL

Description of the system

The layout of the studied configuration represents the classical Chemrec-concept and is shown in Figure 1.

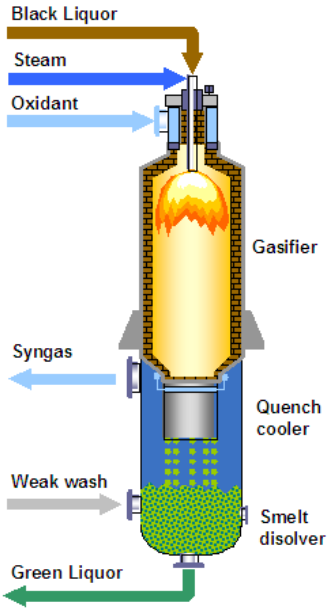

Figure 1: Basic plant configuration [6].

The gasifier is a vertically oriented entrained flow, operated at 1.3 bar, and 1000°C. Black liquor is introduced at the top, together with atomizing steam and oxidant, in this case air. The black liquor is atomized into a fine spray of droplets that undergo partial oxidation to form a combustible fuel gas and a smelt similar to that from a recovery boiler. The smelt and gas flow downwards in to the reactor and exit to the quench system.

The quench system is situated directly underneath the gasifier and is responsible for cooling the products as well as separating the smelt from the

fuel gas. The smelt falls into the quench sump, well mixed and fed with water or weak wash, to form green liquor. The fuel gas is saturated with water vapor, and passes through condensers to remove particulate matter and recover the latent heat. It then reaches a scrubber, where the gas temperature has reached 40°C. At this point, some chemical species are separated from the gas. The clean syngas is then ready to be combusted in a gas fired boiler. This gasifier has been simulated with the system process engineering software, ASPENplus. Simulations of the gasifier with usual black liquor have been studied in a first step, and with addition of borate in a second step.

Input data

The composition for black liquor and borate black liquor entering the combustor is shown in Table 1.

Elements	Without Borate [7]	With Borate[8]
C	37.18	34.71
H	3.55	3.31
O	35.09	32.77
N	0.09	0.08
S	4.86	9.07
Na	19.02	17.76
Cl	0.22	0.20
B	0	2.09

Table 1: Composition of the black liquor in mass % in dry solid.

Three different streams are needed in ASPENplus, for each stream, the flow rate of each component are as detailed on Table 2, with and without borate.

Stream	Comp.	Ordinary black liquor	Borate black liquor
Black Liquor	C	8.118	7.991
	Na	4.154	3.067
	O_2	7.663	6.121
	Cl_2	0.047	0.047
	N_2	0.019	0.019
	S	1.061	2.088
	B		2.925
H_2O	H_2O	5.557	5.499
	H_2	0.775	0.7620
Air		30	30

Table 2: Flow data in Aspen in (kg/s).

The pressure of the system is atmospheric pressure, and of the gasifier, 1.3 bar. The amount of air injected in the gasifier (30 kg/s) represents 45 % of the stoichiometric need. Dry solids content of the black liquor is 74.8%. The composition of the weak wash injected in the gasifier is shown in Table3 below.

Comp.	Min		Max	
	g/l water	kg/s	g/l water	kg/s
NaOH	5	0.20	15	0.59
Na_2CO_3	1.5	0.06	10	0.39
NaCl	0.1	0.00	0.5	0.02
Na_2S	0.5	0.02	5	0.20
Na_2SO_4	2	0.08	5	0.20
$Na_2S_2O_3$	2	0.08	5	0.20
PFG	0.1	0.00	5	0.20

Table3: Composition of the weak wash [9].

The B/Na mol ratio is over 3, which corresponds to the lower limit of complete reaction. Below this weigh ratio, the degree of completion decreases and appears to level off about 50–60 % completion [10].

Thermodynamical data

The base method used is the Redlich-Kwong-Soave equation of state with Boston-Mathias modifications (RKS-BM). ASPEN needs several input data which are not included in its data bank.
Standard enthalpy of formation at 25°C: DHFORM, and the standard free energy of formation at 25°C: DGFORM.

T (°C)	700	800	900	1000
NaCl	s	s	l	l
NaOH	l	l	l	l
Na_2SO_4	s	s	l	l
Na_2CO_3	s	s	l	l
Na_2S	s	s	s	s
$NaBO_2$	s	s	s	l
Na_3BO_3	l	l	l	l

Table 4: State of each compounds according to the temperature; (s=solid state, l=liquid state) [11].

Comp	DH (s)	DG(s)	DH(l)	DG(l)
NaCl	-411.2	-432.1	-385.2	-414.5
NaOH	-425.3	-445.39	-416.8	-439.
Na_2SO4	-1387.6	-1432.6	-1356.8	-1410.7
Na_2CO_3	-1130.7	-1172.3	-1108.1	-1155.2
Na_2S	-366.	-394.8	-323.4	-393
$NaBO_2$	-975.1	-1000.3	-960.2	-981.3
Na_3BO_3			-1966	-1700

Table 5: Enthalpy and free energy for different species [11].

For some species, such as Na_2S, $NaBO_2$, Na_3BO_3, The following parameters were estimated:

The critical temperature: for pure inorganic compounds, the method of Gambill was modified and requires only the boiling point as input [12]:

$$T_c=1,4T_b \qquad (1)$$

The acentric Pitzer coefficient (ω) is primarily a measure of the shape of a molecule. It is calculated from the reduced vapor pressure (P_r^{sat}) at a reduced temperature of 0.7 by the definition [12]:

$$\omega= -\log(P_r^{sat})_{(Tr=0.7)} -1 \qquad (2)$$

The acentric factor is used as a third parameter with the critical temperature, T_c, and the critical pressure, P_c, in cubic equations of state such as the Peng-Robinson equations. For simple spherical molecules, the acentric factor is essentially zero. For compounds of similar size and shape, the acentric factor increases slightly with increasing polarity [12].

The critical compressibility factor Z_c of a compound is calculated from the experimental or predicted values of the critical properties by the definition [12]:

$$Z_c=P_cV_c/RT_c \qquad (3)$$

The critical volume of a compound is the volume occupied by a set mass of a compound at its critical temperature and pressure [12].

$$V_c=RT_c/P_c(3,72+0,26*(4,919\omega-1,199) \qquad (4)$$

The data required in ASPEN are presented in the table below.

Data set	Unit	Na_2S	$NaBO_2$	Na_3BO_3
T_C	K	6888	2799.48	2864.4
P_C	atm	5	60	60
OMEGA		2.6	0.34746	0.70758
Z_C		0.293	0.259	0.232
V_C	m^3/kmol	3357.966	100.620	91.967
VLSTD	ml/mol	22400	22400	22400
T_b[11]	K	4200	1707	1848
T_r		0.7	0.7	0.7

Table 6: Thermodynamic data required in ASPEN. (T_c = critical temperature, P_c = critical pressure, OMEGA = acentric Pitzer coefficient, Z_c=compressibility coefficient, V_c=critical volume, VLSTD=standard liquid molar volume at 60F, T_b=boiling temperature, T_r=reduced temperature).

RESULTS

To establish a base case, the model was used to simulate gasification of non-borate black liquor. This has been done experimentally by several other authors and the results from this simulation model was compared with the results of Consonni et al., (1997) [13], see Table 7.

Components	ASPENplus	Consonni et al., 1997. [13]
Gas		
H_2O	14,632	13.100
H_2	13,977	19.200
CO	11,231	11.700
CO_2	18,646	12.500
H_2S	0,000	0.640
N_2	41,448	42.000
CH_4	0,066	0.913
COS	0,000	0.019
Smelt		
Na_2SO_4	0,677	0.000
Na_2CO_3	54,080	88.459
Na_2S	36,224	11.300
NaCl	1,100	0.000
NaOH	7,920	0.241

Table 7: Comparison of standard black liquor gasification with other reported results in mol%.

The results of the composition for the gas at the outlet of the gasifier are close to the results from Consonni et al. (1997) [13]. Species of

concentrations below 1E-3 % have been ignored, as they are considered as negligible. The reduction degree for the smelt is 100%. The results for borate gasification are shown in Table 8 and Table 9. The results were calculated with a Gibbs free energy of -1700 J/kmol.

Components	Mol %
H_2O	0.588
H_2	0.006
CO	0.007
CO_2	0.015
N_2	0.011
NaOH	39.297
NaCl	0.976
Na_2S	20.808
Na_2CO_3	2.363
Na_2SO_4	0.838
$NaBO_2$	35.092
Total	100

Table 8: Molar composition of borate green liquor flow in mol %.

Components	Rawgas	Syngas
H_2O	10.858	0.493
H_2	21.302	23.779
CO	22.836	25.491
CO_2	6.921	7.726
N_2	38.083	42.512
Total	100	100

Table 9: Mol composition of the syngas before and after gas cleaning in mol %.

From the results, it appears that autocausticizing does happen, Reactions (1) and (2). The molar fraction of CO_2 and NaOH are indeed higher for gasification with metaborate than for the case with conventional gasification. There is also sodium meta-borate in the smelt, indicating that Reaction (6) takes place in the gas phase, before the quench. This has to be verified by experiments, however. Also, effects of retention time on the completeness of Reactions (1) and (2) are still largely unexplored.

DISCUSSION

The model without borate worked properly and gave results close to the reality.

Regarding the simulation with borate, and based on the data available, it seems that an autocausticizing reaction happens in the gasifier. These results were obtained with a thermodynamic equilibrium calculation. Reaction kinetics and other reaction restraints are not considered. For simplicity, only orthoborate, has been included in the autocausticizing reactions. Other sodium borate species may well be equally important, like $Na_2B_4O_7$ and Na_3BO_3.

Recent experimental data by Sinquefield et al (2004) [14] point out that for a high temperature, low pressure gasifier, the retention time needs to be above 3 seconds.

These results have been calculated from an estimated Gibbs free energy of -1700 J/kmol for metaborate. With more data for the borate compounds that is slowly emerging, the model can be refined and improved.

The raw gas which is produced from the black liquor will contain more carbon dioxide than the usual gasified black liquor. There are some advantages and drawbacks. The concentration of CO_2 in the gas flow increases and it will be easier to separate it before the combustion. This has been chosen as a cost effective mean to decrease the CO_2 emission. Extracted CO_2 can also be used in pulp production. The drawback is that the raw gas can be less energetic and therefore will be harder to be used in a gas turbine.

The negative effects that have been identified with borate autocaustization are a possible increase of steam need in the process and possible increase of the viscosity of the black liquor at a high concentration of borate. The autocausticizing reaction is endothermic, which will influence the energy exchange for the gasification. An aspect that is not well investigated is the effect on the environment from the borate black liquor.

These calculations are based on thermodymical equilibrium and no considerations have been taken to the reaction kinetics.

CONCLUSION

The simulations concerning the gasification of black liquor without borate gave reasonable results, in line with results from other researchers, and were thus very promising.

Concerning the gasification of black liquor with borate, the model presented here is a first approximation of a thermochemical equilibrium model. Due to the lack of data for orthoborate, only a first approximation of autocausticization in a gasifier environment can be presented. Other borate compounds can also play an important part in the autocausticizing process. As soon as some data are

available, the model can be refined, for more accurate results.

ACKNOWLEDGEMENTS
This study was financed by the ÅF Research Foundation, ÅForsk., and the European Union, EU.

REFERENCES

[1] Janson J. *The Use of Unconventional Alkali in Cooking and Bleaching-Part 5. Autocausticizing reactions.* Paperi ja Puu-Papper och Trä, 61(1), p. 20-30, 1979.

[2] Janson J, and Arhippaninen. *Mill scale development of borate-based kraft pulping process.* Chemical Recovery Conference, Canada, 205.CPPA/TAPPI International 1981.

[3] Tran H, Mao X, Cameron J, Bair CM. *Autocausticizing of Smelt with Sodium Borates.* International Chemical Recovery Conference, 1998.

[4] Tran H, Mao X, Lesmana N, Kochesfahani SH, Bair CM, McBroom R. *Effects of Partial Borate Autocausticizing on Kraft Recovery Operations.* International Chemical Recovery Conference in Whistler, B.C., Canada, 2001.

[5] Cameron J, Yusuf Z. *Decarbonisation of Sodium Carbonate with Sodium Metaborate.* PAPTAC / TAPPI, International Chemical Recovery Conference, Whistler, BC, Canada, 2001,

[6] Chemrec, the world leader of black liquor gasification, 2004. See also: www.chemrec.se.

[7] Rosén E. Umeå University, personal communication, 2004

[8] Hupa M, Forssén M, Backman R, Stubbs A, Bolton R. *Fireside Behaviour of Black Liquors Containing Boron*. International Chemical Recovery, Conference, Oral Presentations, 2001.

[9] Nilsson M. ÅF, personal communication, 2004

[10] Tran, H., Mao, X., Kochesfahani, S., Bair C.M., "Occurrence of Borate Autocausticizing Reactions During Black Liquor Combustion", Tappi Fall Technical Conference, 2003.

[11] NIST Webbook, 2004. See also http://webbook.nist.gov/.

[12] Weast CR. *Handbook of Chemistry and Physics.* 70th edition, ISBN 0-8493-0470-9, 1989.1990

[13] Consonni S, Larson ED, Berglin N. *Black liquor-gasifier/gas turbine cogeneration.* Turbo-Expo, the 42nd ASME Gas Turbine and Aeroengine Congress, Exposition, and Users Symposium, Orlando, Florida, 1997.

[14] Sinquefield SA, Ball A, Zeng X, Nohlgren I. *Borate Auto-Causticizing for Low and High Temperature Black Liquor gasification.* International Chemical Recovery Conference, Charleston, South Carolina, USA, 2004.

Proceedings of ECOS 2005
Trondheim, Norway
June 20–22, 2005

SPECIAL PURPOSE SOLAR THERMAL SYSTEM AS A CLEAN DEVELOPMENT MECHANISM CANDIDATE IN GHG EMISSION REDUCTION

Paritosh Nandi*
School of Energy Studies
Jadavpur University
Calcutta-700032, India

ABSTRACT

A Solar Thermal system comprising of the concentrator, heat exchanger and the heat transfer fluid has been fabricated and an estimate has also been done of the saving in fuel and the reduction of emission. The payback period is being kept low through reduction in the initial cost outlay for setting up the system through improved designing for its better acceptability in small scale sector. With a very large number of such production units run with good profitability in the country, the reduction in emission will be appreciable and introduction of the system in numbers for regular use can be supported by Clean Development Mechanism.

Keywords: Sweetmeat, Clean Development Mechanism (CDM), Solar Parabolic Concentrator, Green House Gases (GHGs)

INTRODUCTION

Sweetmeat is a very common and popular item of the Indian sub-continental dishes. These palatable items are consumed by almost every section of people in India. As the sweetmeats are produced mainly in small-scale industries all over the country, its quantum of production generally goes unnoticed. However, the industry's annual turnover is, according to insiders, around Rs. 200 billion (more than $ 4 billion) and it provides employment, both direct and indirect, to about 1.5 million people. In the cost of production, energy, almost exclusively thermal, accounts for15% to 20% of the total and traditionally cheaper fuels like coal, fuelwood, etc. are used. Old traditional methods are still being followed and most of the items are based on milk. It needs mention here that the milk comes from semi-urban and rural areas for the urban outlets. A part of the processing is done at the milk diaries where milk is boiled to drive out a good part of water in it. There are two principal types of Indian sweetmeats: (a) Soft and semi hard products mostly from milks, and (b) Fried and crispy mostly made from flour and ground wheat and lentil. The second type has lesser shelf-life and forms a relatively small share of about twenty five per cent. This implies that most of the sweetmeats

*Corresponding author. Phone: +91 94333 19184
Email: paritoshnandy@yahoo.com
Fax: +91-33-24146853

are produced from milk. In the rural and semi-urban areas cheap traditional fuel coal and fuelwood are extensively used. In urban manufacturing units LPG and furnace oil are the major fuels, the latter having the natural preference because of its lower price.

TECHNICAL STUDY

The area of the concentrator which is made of anodized aluminium is 2.97 sq.m. and on the base of this the collector and the receiver tube is kept at an inclination of local latitude for the same purpose [1]. Tracking is employed in case of solar concentrating systems due to the movement of the sun in the sky with diurnal and seasonal position changes. For outdoor systems automatic tracking arrangement not only adds to capital cost but also requires skilled maintenance support. Essentially because of these two reasons fixed systems are preferred. However, manual and semi-automatic tracking results in an improved functioning of the system with marginal cost addition. Where grid electricity is not available automatic or semi-automatic tracking demanding interruption free electricity supply will be considerably expensive if the electricity is to be locally generated through photovoltaics or other renewable devices with storage. The concentrator and heat exchanger specifications are given here in below.

Concentrator material:	Anodized aluminium
Concentrator aperture:	1.20 m
Length of the concentrator	2.4 m
Collection area	2.88 sq.m
Reflectivity of the concentrator:	0.85
Receiver tube material:	Copper with black chrome coating
Receiver tube diameter:	40mm
Outer Glass tube (jacket) diameter:	65 mm
Amount of thermic fluid (in pipeline):	24 litre
Concentration ratio:	32

Four temperature sensors (including one sensor for recording ambient temperature) have been installed to measure the temperature at different points as given in Figure.1. For large scale application, multiplication of the same system is needed. An average temperature distribution in November 2004 of three installed RTDs on the fabricated system is shown in Figure 2.

Technological Risk

This is a supplementary system. With an average 250 sunny days in most of the regions of the country on more than two thirds of the total sunshine hours in a year the system can be put to use. With hardly any moving system the downtime will also be low.

BENEFICIAL FEATURES OF THE SYSTEM

Compared to the high cost of oil that is likely to be in future, energy conversion systems based on renewable energy technologies are much cost

effective. Renewable energy systems also have a positive impact on the various environmental, economic and political issues of the world. Benefits accruing from installation and operation of renewable energy systems can be classified into three categories, viz., saving of energy, generation of new working posts and reduction of environmental pollution [5]. Energy is saved by reduction in consumption of electricity and LPG which are the conventional energy sources. This benefit can be expressed in terms of money having regard to the corresponding production or the capital expenditure for the purchase of imported fossil fuels avoided. Further, various countries also take interest in the potential for economic development of exporting renewable energy technology expertise. The amount of emissions from solar thermal systems depends on the type of fuel used as auxiliary. In using electricity or Diesel backup in solar thermal systems, the percentage saving obtained is about 80% whereas if both electricity and Diesel are employed, the saving is 75% [6].

Electricity is uneconomical and is almost never used in the manufacturing stage. The Solar Thermal system will definitely cut down the demand of the fossil fuels like coal, oil and gas and also fuelwood. This will lead to emission reduction. The use of solar energy for heating purposes results in the reduction of emission of GHGs released through the burning of fossil fuels to produce the required thermal energy. In process industries inter-fuel substitution is often adopted for efficient system operation like replacement of coal by oil or gas. However, a substantial reduction in CO_2 emission can be achieved by utilizing solar thermal energy. A typical case of utilisation of solar thermal system and the reduction of CO_2 emission thereby can be more or less correctly estimated as shown below.

1.Emission Reduction Potential – GHG mitigation

LPG burner replaced

1kg of LPG emits 3.20 kg of CO_2, and 0.0056kg of CO in the atmosphere [2].

No of cylinders used (per day)	LPG content per cylinder (Kg)	LPG used per day (Kg)
4	17	68

Considering 250 days of operation in a year

LPG used (Kg/yr)	CO_2 emitted (yr)
17000	54.4 tons

2. Economic Analysis

LPG used per Day (Kg)	No. of pieces sweets produced (per day)	Average price (Rs.)	Daily turnover (Rs.)	Yearly turnover (Million rupees)
68	10000	2	20000	7.2

Considering total turnover is Rs. 200 billion in sweetmeat industry

Yearly turnover (Million rupees)	**CO_2 mitigated (Ton)**
7.2	54.4
200000	1510000

3. Economic Benefits:

Electrical heating system replaced [3]

Collection area	4.88 m^2
Solar insolation available	5.5 Kwh/sq.m/day
Temperature of hot milk	100 °C
Ambient temperature	25 °C
Cost of electricity	Rs.3.50 /kWh
Efficiency of electrical heater	80% ~ 90%
Efficiency of solar hot water system	50%
Life of the system	15 yrs
Heat available from Solar System	5.5×4.88×0.5 kcal/day
Saving in electricity consumption per day	13.42/0.9= 14.91
Cost of electricity saved	15×250×3.5 = Rs.13125.00
Cost of the solar system	Rs.20000.00
Pay back period	1.52 years

BARRIERS IN APPLICATION

i) Manual operation is necessary for tracking of the system which may be considered as a disadvantage in its application. Automatic tracking will deliver more energy or heat but automatic tracking is not only expensive but electric power required for tracking may also not be available in the rural areas

ii) This system is supplementary. It can not work alone throughout the year as the required amount of solar radiation that is 5.5 kWh/sq.m/ day on an average is available for 250 days only in a year. During the rainy season and for cloudy days other heating arrangements are required.

iii) As it is a new technology obviously there are some psychological barriers in its acceptance. However, adaptation of a system is better when smooth running of the system is ensured. Therefore, care is to be taken in the training of the skilled hands for its maintenance.

DESIRED PROMOTIONAL SUPPORT

It is obvious that the system cost will not be low. It is true that fuel costs are avoided but a large system cost will not make it attractive to small scale producers. Convinced of the beneficial features of such a system in eliminating to a good extent the use of oil/coal/wood and emission of CO_2, it is submitted that promotion of such systems should receive due support from government and the other agencies. Creating awareness regarding the long term benefit of the system is of course important but more important is to provide the due financial support in the form of soft loans to enable the processed food producers to invest for the installation of such

system in their work. Soft loans are to be introduced and other fiscal incentives/reliefs can be thought of. CDM is considered to be a powerful market mechanism in the emission reduction of GHGs and the extension of CDM for the application of such systems is to be seriously considered.

ELIGIBILITY FOR CDM

As per the UNFCCC the eligibility set for CDM [4] are the followings:

Baseline

In all sweetmeat manufacturing units heating is done by coal oil gas or fuel wood. If solar energy is employed the reduction in fuel consumption will surely mean a reduction in the emission of GHGs. If we start with the baseline of fuel based systems, introduction of solar thermal systems in large numbers would result in adequate emission reduction and such large deployment will qualify as a CDM candidate. As has been stated earlier it is a completely new technology and its proliferation will result in a significant reduction of emission. The system itself and its operation do not have wide variation. Amount of saving of fuel in a single day can be computed with knowledge of number of units in use in different locations/zones and an estimate of average available solar radiation in these zones from radiation measurements and thus the total fuel saving in a year can be computed. According to our computation based on recorded solar data each system can account for a reduction of emission of 50 tonnes per year. If hundreds and thousands of such systems are installed in a country it will result in a saving of around 50 MT of emission per year.

Additionalities

Additionality means to the projects which would not have taken place in absence of the crediting procedure or trading scheme. The proposed solar thermal system necessarily comes with an investment without an attractive payback period. The systems will not be used in larger numbers without any incentive. If a support comes through CDM the cost of installation will be lesser and the proposal of deployment in large number will be more realistic. It is to be admitted that there is a general reluctance in absorbing a new technology and the prices matter. It will be extremely difficult in the current volatile market of oil and gas to predict the future of solar thermal systems. However, if the systems can be made more reliable and user friendly, it will definitely be accepted by the industry. The project is yet to finalise the system design and as a result prospective customer response is yet to be had. Among the additionalities mentioned the three main additionalities are Emission, Financial and Technological additionalities. It is well clear from this case study that firstly the real measurable long term GHG mitigation is quite possible as it has already been shown. Secondly the funding for

CDM in case of solar thermal system application will not lead to diversion of official development. Thirdly it is obvious that the technology of such a solar heating system is environmentally safe and sound.

Sustainable Development Indicators:

The report is an attempt to bring to the kind notice of the policy makers in the use of a solar energy device in an industry which employ a large number of people and fairly expanding.

- ♣ It will generate employment
- ♣ It would have wider application in rural areas
- ♣ The system is as such based on the solar energy utilization and therefore sustainable in character.

A concrete evidence will demand an extensive survey in semi-urban and rural areas on the adoption of solar thermal system by the sweetmeat industries. Conduction of awareness programmes and successful demonstration will help in the desired wide-spread use. The Ministry of Non-conventional Energy Sources (MNES),

Government of India has withdrawn subsidies offered to solar thermal systems assuming that solar thermal industry can now be fully market driven. But the Ministry has taken a massive programme on the popularization of solar/renewable energy devices and solar thermal system is one. National level specifications are being framed for the purpose of standardization only in case of established products like solar cookers, solar flat plate collectors etc. Some fiscal incentives are being offered at the state level (West Bengal) but the quantum has not been fully specified. The overall policy of the government is in general highly supportive of such devices.

iv) With the introduction of this new system improvement of the quality of life of the poor people in rural areas is expected as this sweetmeat industry is mainly confined to the cottage and small scale sector employing a large number of people. Alleviation of poverty is also ensured as with the introduction of the new system in the sweetmeat industry additional employment will be generated for manufacturing of the solar systems. The introduction of the new system will not lead to any retrenchment as labour intensity will remain the same. Direct benefit from no-smoke condition with the introduction of solar heating system instead of burning conventional fuel also results in reduction of level of pollution in general.

The solar energy systems have certain negative environmental impact such as land displacement, possible air and water pollution resulting from manufacturing, normal maintenance operations and demolition of the systems. However, the limitation of land use can be done away with by mounting collectors on the roof of a building. The maintenance required is so less here that the pollution caused by demolition is not greater than the pollution caused from demolition of a conventional system of similar capacity. Similarly, in case of consumption of insignificant quantities of materials by the solar thermal system, the only potential environmental pollutant arises from the

coolant change and it can be easily controlled by good working practice. The accidental leakage of the heat transfer fluid can cause hazards to the workers' health and safety but the large-scale use of solar thermal systems would lead to significantly reduction in the burning of fossil fuels and will thus; reduce the environmental impacts associated with those.

Financial Indicators

Under the heading BENEFICIAL FEATURES OF THE SYSTEM in the paper in point (2) and point (3) it has been clearly shown that the payback period is low and the cost effectiveness of energy saving is ensured.

Manpower

In the fabrication, installation, erection and commissioning and testing of the system the following manpower will be required.

i) Skilled manpower indicates the jobs of mechanical fitter, welder, marker, mason and plumber etc. The total working hour required is around 70.

ii) Total unskilled manpower required is around 100 hours.

CONCLUSION

The governments at the centre and in the state are supportive of the development of such solar thermal system. Popularisation of the same with eventual reduction of carbon dioxide will be an humble step in meeting the objectives of the Kyoto Protocol. CDM support will mean an enormous boost to the healthy induction of a new technology in a traditional industry.

ACKNOWLEDGEMENTS

The author gratefully acknowledges the support received from the Department of Science and Technology and the CSIR, Government of India The author is also grateful to Prof. Sujay Basu and Ms. Rupanjana De for their help and encouragement.

REFERENCES

[1] Duffie J, Beckman W. *Solar engineering of thermal processes.* New York: John Wiley and Sons, 1991.

[2] Das TK, Deb C, Jash T.*Environmental consequences of parallel marketing of LPG in India.* Energy 2000; 25(1): 81-84.

[3] *Manual for Solar Thermal Systems.* Indian Renewable Energy Development Agency, New Delhi, 1997. p. 62-65.

[4] *Monitoring the Clean Development Mechanism of the Kyoto Protocol*.See also: http://www.cdmwatch.org

[5] Diakoulaki D, Zervos A, *Cost benefit analysis for solar water heating systems*. Energy Conversion and Management 2001;42(14):1727–1739

[6] Kalogirou SA. *Environmental benefits of domestic solar energy systems.* Energy Conversion and Management 2004; 45(18-19):3075–3092

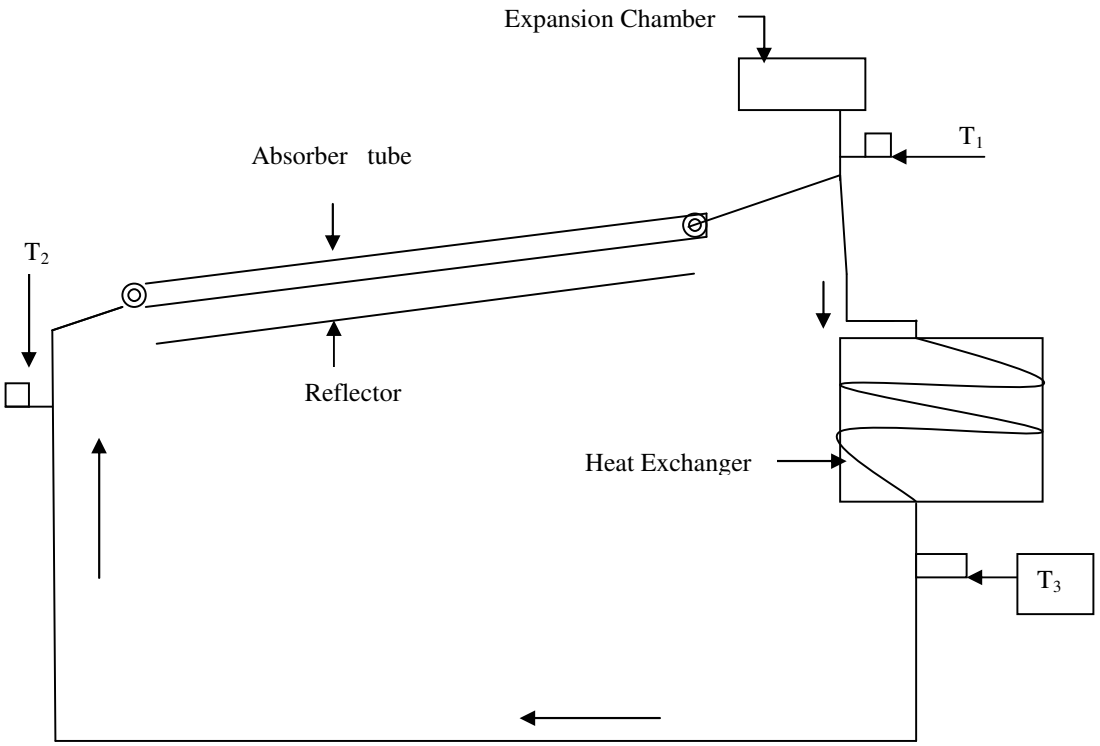

Figure 1: Flow diagram of Concentrator-Heat Exchanger System

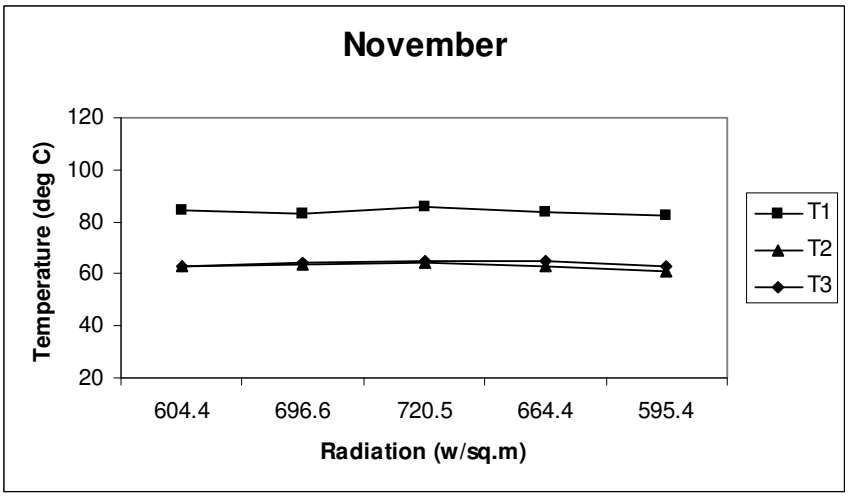

Figure 2: Temperature at three sensors against Radiation in November 2004

Proceedings of ECOS 2005
Trondheim, Norway
June 20–22, 2005

OPTIMISATION OF HEATING SYSTEM WITH RENEWABLE ENERGY SOURCES

V. Nikulshin*
Odessa National Polytechnic University
Theoretical General and Nonconventional Power Engineering Department
Ukraine

V. von Zedtwitz
ETH- Swiss Federal Institute if Technology
Department of Mechanical and Process Engineering
Switzerland

ABSTRACT

The problem of the improving efficiency is very important in the design and operation of energy intensive systems. The main way for solving this problem is an optimization. This paper describes the general approach for the thermoeconomical optimization of the system with linear structure. The suggested method is based on the creation and analysis of the special thermoeconomical expenditure graphs. This method is illustrated by an example of solar heat pump systems with season heat storage optimization.

NOMENCLATURE

c	processes flow
C	multitude of flows c
$\overline{C}$	optimal way in graph $Z = (N, D)$
$C_{i_p}^{(p)}$	node of graph $Z = (N, D)$ for element number i_p
D	multitude of arcs graph $Z = (N, D)$
E	exergy
Γ_p	display of set N_p
h	processed flow
k	number of elements and steps of optimal synthesis of system
m	mass flow
N	multitude of nodes graph $Z = (N, D)$
N_p	multitude of nodes graph $Z = (N, D)$ on p-step
n	total number of elements in system
p	number of step of optimal synthesis of system
τ	working time of system during the year
Z	thermoeconomical expenditure
$Z = (N, D)$	graph of thermoeconomical expenditure
$Z\left\{Z_{i_p}^{(p)}\right\}$	multitude of possible thermoeconomical expenditure in system on the whole
p	number of step of optimal synthesis of system
$Z_p\left\{Z_{i_p}^{(p)}\right\}$	multitude of possible thermoeconomical expenditure in system on p-step of synthesis of

Corresponding author: Phone +38 0482 288 416; Fax: +380482 250 104; e-mail: vnikul@paco.odessa.ua

system

$Z_{i_p}^{(p)}$ possible thermoeconomical expenditure in element with number i_p

Subscripts

A surface
i number of processes flow
i_p number of element (node) on p-step of optimal synthesis
ij number of element of interaction of i and j flows
j number of processed flow
min minimum
Σ sum

INTRODUCTION

Processes that are taking place in the complex energy intensive systems are characterized by mutual transformation of quantitatively different power resources. The fast growth and development of the modern technologies requests a thermodynamic analysis and optimization of these systems, based on combined application of both thermodynamics laws which request an exergy approach [1]. Exergetic methods are universal and make it possible to estimate the energy fluxes and to build up the energy balances for every element of the system using a common criterion of efficiency. Therefore, the exergetic methods are meaningful in the analysis and calculations.
Despite its usefulness, the benefits of the exergetic approach were not fully realized until recent years.
One reason for this situation is the underestimation of exergetic functions for mathematical modeling, synthesis, and optimization of the flow sheets. Another reason is the mathematical difficulty of the exergetic approach in thermodynamic analysis. Meanwhile, the increase in the complexity of optimization problems requires more effective and powerful mathematical methods. Hence, many papers have been published during the last few years, with the different applications of the exergetic methods [2,3,4].
Above mentioned papers, as well as the author's earlier investigations [5-10] show that one of the most effective mathematical methods used for exergetic analysis and optimization is the method of graph theory [8]. The benefit of the graph models can also be demonstrated by its flexibility and its wide varieties of possible applications.
Exergy topological methods include the sole use or the combination of the exergy flow graphs, exergy loss graphs, and thermoeconomical graphs [5-9].
Systems with linear structure are often used in energy technology as well as in other branches of industry. For that reason it is necessary to study the problem of linear structures systems optimization separately from the systems with arbitrary structure.

METHOD OPTIMIZATION OF LINEAR SYSTEMS

First, let us consider a homogeneous system that contains n different elements of one type (as shown in Fig. 1.)
In this system one flow h_j, j=1 interacts successively with flows C_i , i=1,2,…n.
In the problem of optimal synthesis, it could be reformulated in such a way:
It is necessary to distribute the multitude of flows
$C = \{C_1, C_2, ..., C_i, ..., C_n\}$
along the flow h_j (j=1) and the result of the interaction of these parameters of flow h_j in outlet of system will be in interval of required constrains and thermoeconomical criteria will be minimized

$$\sum_i \sum_j Z_{ij} = Z_\Sigma^{\min} \qquad (1)$$

where
Z_{ij} -thermoeconomical expenditure at i-element (j=1).
For solving this type of problem, it is necessary to build the graph of thermoeconomical expenditure as it was shown in [8]. In our case this graph will be a tree $Z = (N, D)$. The multitude of nodes N displays the possibility of distribution of flows in the system, the multitude of arcs D ,

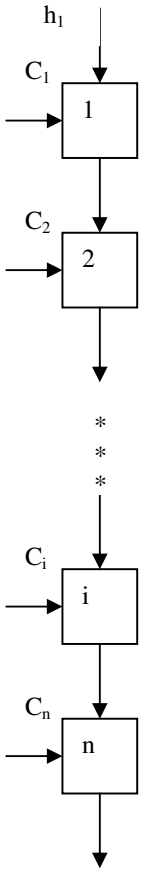

Figure1: Linear system

displays the possible meanings of thermoeconomical expenditures.

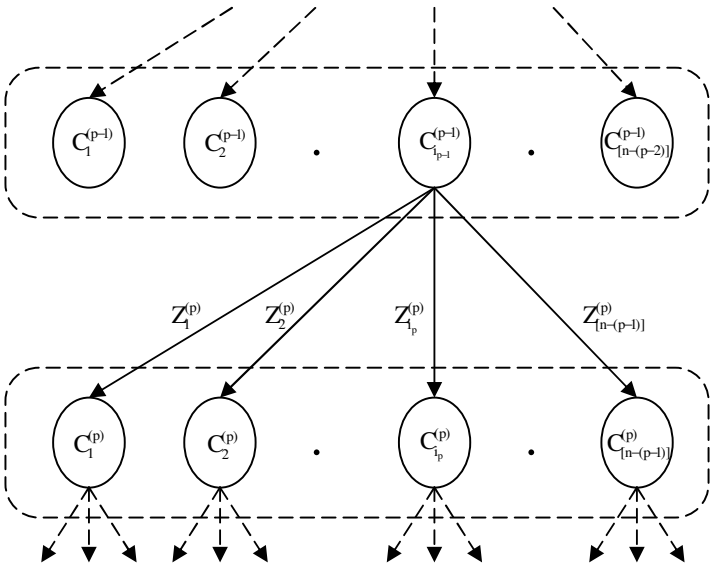

Fig.2. (P-1) and P - levels tree of thermoeconomical expenditure

The governing equation which are representing these levels are:

$$N = N_0 \mathbf{Y} N_1 \mathbf{Y} N_2 \mathbf{Y} .... \mathbf{Y} N_p ... \mathbf{Y} N_k$$

$$N_p = \left\{ C_1^{(p)}, C_2^{(p)}, ..., C_{i_p}^{(p)}, ..., C_{[n-(p-1)]}^{(p)} \right\} \quad (2)$$

$$p = 1,2,...,k; i_p = 1,2,...,\left[n - (p-1) \right]$$

where

$$N_p \subset C,\ p = 1,2,...,k,$$

$$p = 0 \Rightarrow \left| N_0 \right| = 1$$

$$p = 1 \Rightarrow \left| N_p \right| = \left| C \right|, C - N_p = \varnothing \quad (3)$$

$$1 \le p \le k \Rightarrow \left| N_p \right| \le \left| C \right|$$

$$\forall \left(C_{i_{p-1}}^{(p-1)}, C_{i_p}^{(p)} \right) \in D \Rightarrow \left(C_{i_{p-1}}^{(p-1)}, C_{i_p}^{(p)} \right) = Z_{i_p}^{(p)} \quad (4)$$

$$\forall \left(C_{i_{p-1}}^{(p-1)}, C_{i_p}^{(p)} \right) \notin D \Rightarrow \left(C_{i_{p-1}}^{(p-1)}, C_{i_p}^{(p)} \right) = \infty \quad (5)$$

where symbol ∞ shows that arcs of this type are absent.

The flow hj in graph $Z(N, D)$ is described as node $C_0^{(0)}$. Then for obtaining conditions (1) it is necessary to find an optimal way $\overline{C} \subset N$,

$$\overline{C} = \left(C_0^{(0)}, C_1^{(1)}, ..., C_{i_p}^{(p)}, ..., C_{[n-(p-1)]}^{(k)} \right) \quad (6)$$

so that

$$\sum_{i_p} \sum_{p} Z_{i_p}^{(p)} = Z_{\Sigma}^{\min} \quad (7)$$

The algorithm of Belmann-Kalaba is usually used for seeking the optimal way in graphs without contours. This algorithm is based on the matrix of expenditures analyses [8].

In our case the graph of thermoeconomical expenditure is following:

$$\Gamma_p N_p = N_{p+1} \quad (8)$$

where Γ_p is display of set N_p, and condition of Eq. (4) will be valid for elements of matrix which are located in the intersection of columns $C_{i_p}^{(p)}$ and lines

$C_{i_{p-1}}^{(p-1)}, p = 1,2,...,k;\ \ i_p = 1,2,...,\left[n - (p-1) \right]$.

This feature of graph of thermoeconomical expenditure allows one to simplify the matrix of expenditure and to reduce the number of analyzed variants in **n** times [8].

Based on features of the thermoeconomical expenditure graph, we recommend the algorithm of searching optimal variant.

Each step of seeking an optimal variant is successively compared with thermoeconomical expenditure $Z_{i_p}^{(p)}$ and $Z_{\min}^{(p)}$. In result, the flow corresponded equation (7) can be found. Then applying the procedure of seeking $Z_{\min}^{(p)}$ to all k steps, we will find the optimal flow distribution that corresponds to the condition in Eq. (1).

In case of inhomogeneous linear systems optimization, the main idea of this approach will retain.

Since inhomogeneous elements are able to change the different characteristics of flow h_j, it is necessary to consider not only the p th-step but also previous steps of the system's optimization. Consequently the method of dynamic programming has to be changed to branch- and -bound method. On this approach at each step we seek and then save expenditure $Z_{\Sigma}^{(p)\min}$, where $Z_{\Sigma}^{(p)}$ is the sum of thermoeconomical expenditure for all p steps of considered variant. Then expenditure $Z_{\Sigma}^{(p)\min}$ will be compared with the analogous sums for the previous steps $(p-1),(p-2),...,1$.

Then the variant corresponding to the following equation has to be developed

$$Z_{\Sigma}^{\min} = \min\left[Z_{\Sigma}^{(l)\min} \right], l = 1,2,..., p \qquad (9)$$

The elements for the next step of optimization have to be taken from the multitude N_{p+1}, which corresponds to equation (8).

OPTIMIZATION OF A SOLAR-HEAT PUMP SYSTEMS WITH SEASON HEAT STORAGE

The described above approach was applied to the optimization of a solar- heat pump systems with season heat storage (SHPS) with total heat productivity of 0.5 MW (see Fig. 3.) detailed description of which is given in [5].

The main difference of a SHPS from others energy intensive systems with conventional energy sources is the presence of a "charge-free" source -the sun.

However, the use of the thermoeconomical approach allows to take into account real exergy losses in the subsystem: a solar collector - the heat exchangers and to find the certain cost of the SHPS as a whole.

As it was shown above the application of the suggested method of optimization requests the presentation of the system's structure in "linear view".

For the SHPS it is possible to present this scheme as a four-sequence levels (zones) graph of thermoeconomical expenditures as it is shown in Fig.4.

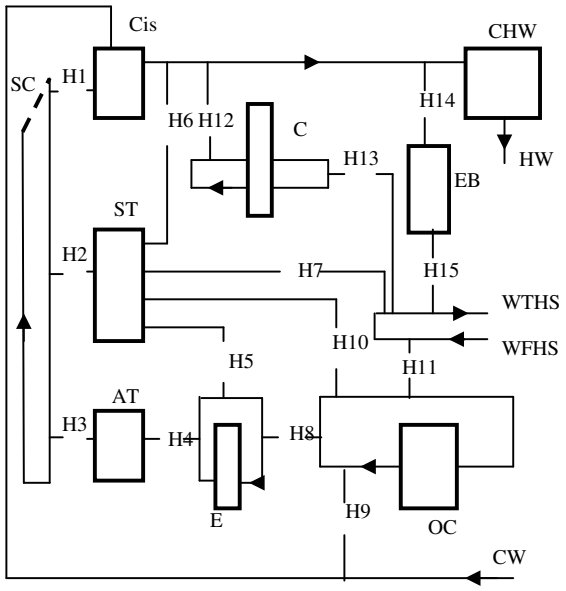

Fig. 3. Solar- heat pump systems with season heat storage.

Flows: CW - cold water; HW- hot water; WTHS - water to heating system; WFHS- water from heating system. Elements: H1-H15 - heat exchangers; SC- solar collector; Cis - cistern; ST - season storage tank; AT - antifreezes tank; E- evaporator of heat pump; C - condenser of heat pump; OC - oil cooler of heat pump; EB - electric boiler; CHW - cistern of hot water.

Numbers of indexes "i" coincide numbers of heat exchangers of the scheme in Fig.3. (e.g., Z_V - thermoeconomical expenditures the heat exchanger H5). For the other elements the correspondence of nodes of thermoeconomical graph and elements are following: solar collector (SC)- Z_{XVI}; cistern (Cis)- Z_{VII}; season storage tank (ST)- Z_{VIII}; antifreese tank (AT) - Z_{XIX}; evaporator of heat pump (E)- Z_{XX}; condenser of heat pump (C) - Z_{XXIV}; oil cooler of heat pump (OC)- Z_{XXI}; EB - electric boiler (EB)- Z_{XXII}; cistern of hot water (CHW) - Z_{XXIII}.

After transforming the initial scheme SHPS (Fig.3.) to a view of graph of thermoeconomical expenditures (Fig.4.) it is easy to build the tree of thermoeconomical expenditure shown in Fig.5.
The tree of thermoeconomical expenditure will also contain four levels ss it follows from the analysis of the graph in Fig.4.
Further consideration will be presented on an example of SHPS with a total heat production of 0.5 MW.
This system was analyzed in [5] for 64 variants:

- area of Solar Collector: A_{SK}= 1000 м^2; 2000 м^2; 3000 м^2; 4000 м^2;
- volume of Season Storage Tank :V_{ST}=3000 м^3; 4000 м^3; 11000 м^3; 15000 м^3;
- use factor for Heat Pump: n=0.2, 0.4, 0.6, 1;
- use factor for Electric Boiler Heat: s=0.2, 0.4, 0.6, 1;

with an appropriate economical estimation for each of analyzed variant.
The advantages of the suggested approach are described by solving this optimization problem.
Level I (Fig. 5.) contains four trailing tops reflecting possible thermoeconomical expenditure in a zone I (Fig.4). Zone I includes one solar collector and three heat exchangers H1, H2, H3.
The number of tops in level I is equal to four pursuant to four sizes of solar collector area A_{SK}= 1000 м^2; 2000 м^2; 3000 м^2; 4000 м^2;
Accordingly, a possible thermoeconomical expenditure at level I is:

$$Z^I_k = Z^k_I + Z^k_{II} + Z^k_{III} + Z^k_{XVI},$$

With k = 1,2,3,4 - displays four sizes of Solar Collector and correspondent heat exchangers H1, H2, H3.
With the growth of the area of solar collector not only its cost will grow, but also the cost of the heat exchangers H1, H2, H3,so $Z_1^I < Z_2^I < Z_3^I < Z_4^I$
Level II also contains four trailing tops reflecting possible thermoeconomical expenditure in a zone 2 (see Fig.4.) which includes tanks Cis, ST, AT, and heat exchangers H4, H5, H6.
As the size of the season storage tank - accumulator varies (V_{ST}=3000 м^3; 4000 м^3; 11000 м^3; 15000 м^3) different Cis, AT and heat exchangers H4, H5, H6 of correspondent size are needed. Analogically to level I:

$$Z_l^{II} = Z^l_{IV} + Z^l_V + Z^l_{VI} + Z^l_{VII} + Z^l_{VIII} + Z^l_{IX},$$

l = 1,2,3,4.

With growth of a volume V_{ST} the indispensable costs of other tanks and heat exchangers will also increase, so $Z_1^{II} < Z_2^{II} < Z_3^{II} < Z_4^{II}$.
Level III is reflecting possible thermoeconomical expenditure in a zone 3 (see Fig.4) including the heat pump and the supplementary heat exchangers. It contains 4 tops displaying the use-factor of the heat pump.
The main difference to the previous two levels is the invariable cost of the equipment, the essential factor is the costs of the electric power consumption, depending on use-factor of the heat pump n = 0,2; 0,4; 0,6; 1:

$$Z_m^{III} = Z^m_{VII} + Z^m_{IX} + Z^m_X + Z^m_{XI} + Z^m_{XII} + Z^m_{XIII} + Z^m_{IX} + Z^m_{XX} + Z^m_{XXI} + Z^m_{XXIV},$$

m = 1,2,3,4.

With growth "n" the thermoeconomical expenditure also grows in this zone, so $Z_1^{III} < Z_2^{III} < Z_3^{III} < Z_4^{III}$
Level IV reflects the possible thermoeconomical expenditure in a zone 4 (see Fig.4) including the electric boiler, heat exchangers H14 and H15, and also cistern with hot water.
This level contains the water heating after level III that increases the thermoeconomical expenditure.
Accordingly level IV also contains four tops, that increases the thermoeconomical expenditure:

$$Z_1^{IV} < Z_2^{IV} < Z_3^{IV} < Z_4^{IV},$$

Where:

$$Z_r^{IV} = Z^r_{XIV} + Z^r_{XV} + Z^r_{XXII} + Z^r_{XXIII},$$

r = 1,2,3,4.

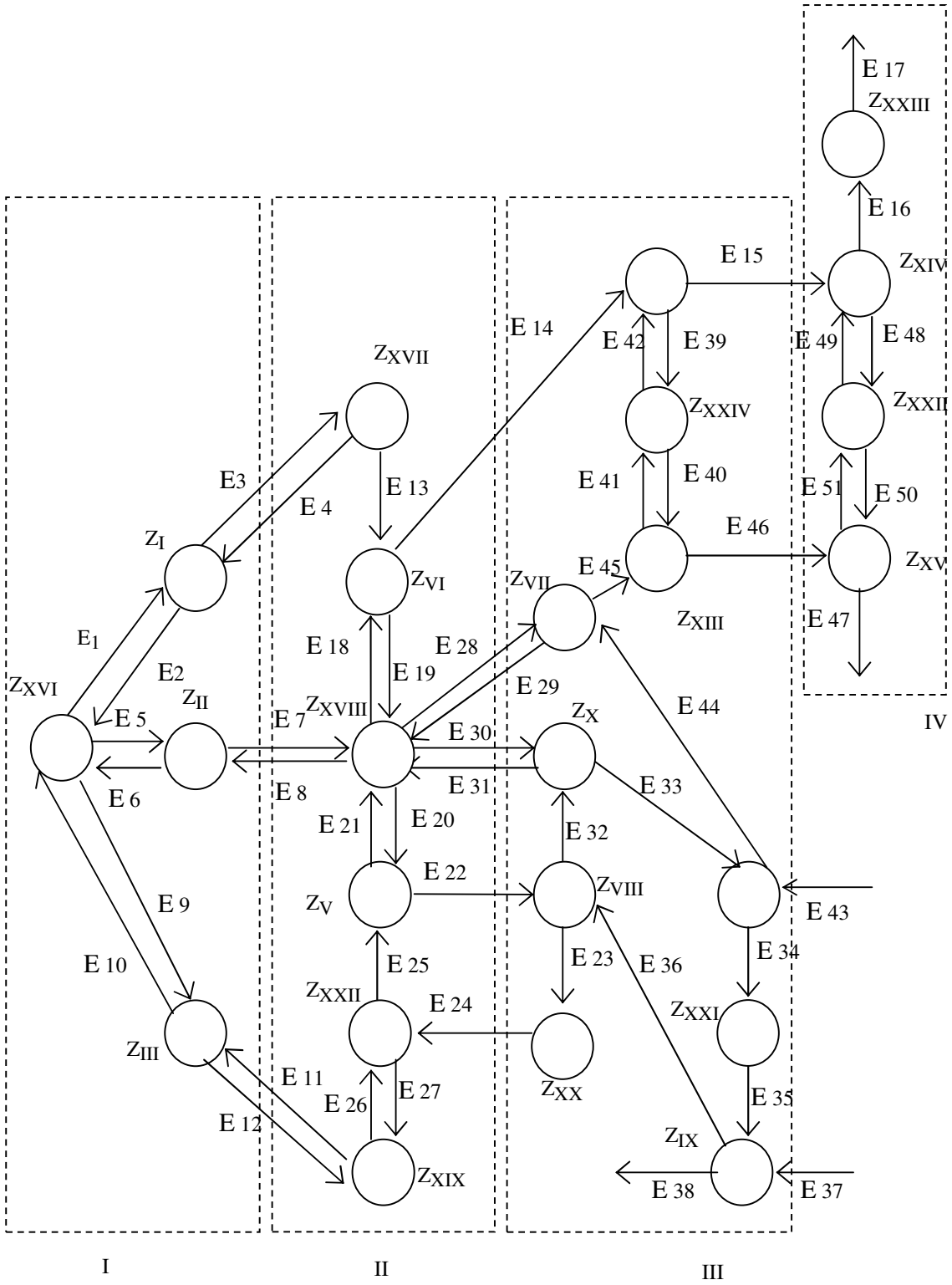

Fig.4. Graph of thermoeconomical expenditures the system shown in Fig.3.

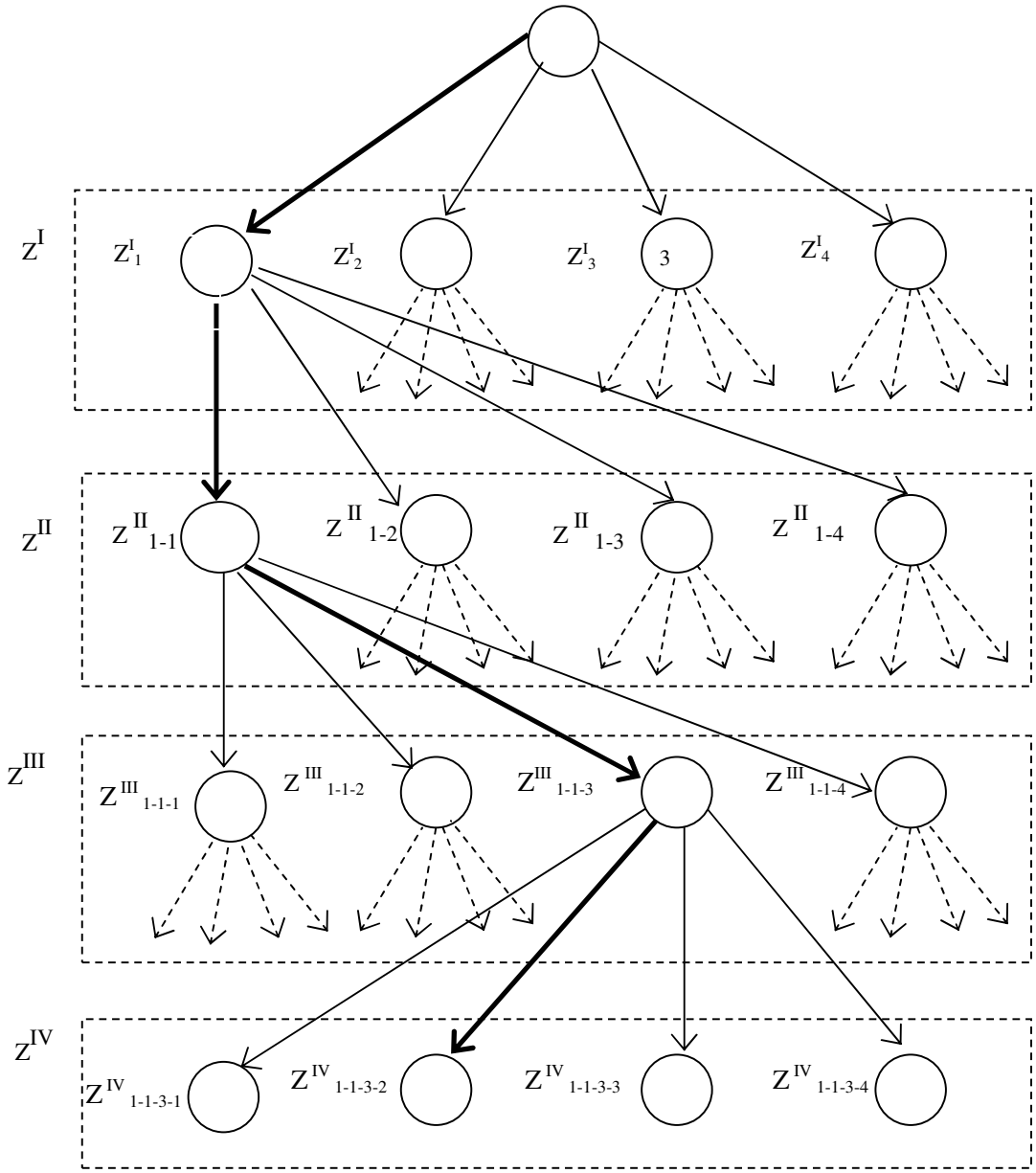

Fig.5. Tree of possible thermoeconomical expenditures

In the tree of possible thermoeconomical expenditure (Fig.5) each trailing top corresponds to the total thermoeconomical expenditure in the subsystem of the SHPS for given and the previous levels. The number of bottom indexes for trailing tops corresponds to the number of levels in the tree and also reflects the previous way to this trailing top.

For example the top $Z^{III}_{1\text{-}1\text{-}3}$ reflects the thermoeconomical expenditure of selected version 1 in a zone I, version 1 - in a zone II and version 3 - in a zone III.

The application of the described approach allows to receive the minimum value of thermoeconomical expenditures for trailing top $Z_{1\text{-}1\text{-}3\text{-}2}$. So, the optimal variant for the SHPS with total heat production of 0.5 MW is the system with a Solar Collector A_{SK}= 1000 м^2 , Season Storage Tank V_{ST}=3000 м^3 , use- - factor for the Heat Pump n=0.6, use factor for the Electric Boiler Heat s = 0.4.

So the correspondent minimum of the thermoeconomical expenditures in the system:

$$Z_{\Sigma}^{opt} = Z_{1\text{-}1\text{-}3\text{-}2} = 2502 \text{ USD/year}$$

The optimal variant is shown by bold arcs on the tree of the possible thermoeconomical expenditures (Fig.5)

It is easy to see, that in contrast to a method of direct enumeration [5] which requests the calculation of full 64 versions of a system, the suggested by us procedure of a "tree search" requests for optimization only 8 full calculations of SHPS (zone IV), 8 calculations up to a zone III and 16 calculations of zones I and II.

In result the total time for seeking an optimal variant decreased more than in 6 times.

CONCLUSION

The problem of developing the modern technologies based on optimization of linear systems has to be solved separately from the problem of optimization of systems with arbitrary structure. On the basis of features of linear systems it is possible to build the effective procedure of optimization. The suggested method based on development and analysis of the thermoeconomical expenditure graph. It allows to find the optimal variant for homogeneous systems as well as for systems with different types of elements. The method is illustrated by an example of optimization for the solar-heat pump systems with the season heat storage.

REFERENCES

[1] Bejan, A., Tsatsaronis, G., Moran, M., *Thermal Design and Optimization*, John Wiley & Sons Inc., New York, 1996.

[2] Sciubba E., Melli R., *Artificial Intellegence in Thermal Systems Design: Consept and Applications*, Nova Science Pub., 1998

[3] Sciubba E. , *Beyond thermoeconomics? The concept of Extended Exergy Accounting and its application to the analysis and design of thermal systems,* Exergy-an International Journal, 2001, Vol.1, pp. 68-85.

[4] Casarosa C., Franco A., *Thermodynamic optimization of the operative parameters for the heat recovery in combined power plants,* Int. Journal of Applied Thermodynamics Vol.4, N1, pp.43-52, 2001.

[5] Nikulshin, V., Wu, C., *Thermodynamic analysis of energy intensive systems based on exergy-topological models,* Exergy-an International Journal, Vol.1, pp. 173-180,2001.

[6] Nukulshin V., Wu C., Nikulshina V., *Exergy efficiency calculation of energy intensive systems by graphs,* Proc. of International Conference ECOS-01, Istanbul, Turkey, pp.107-115, 2001

[7] Nikulshin, V., Wu, C., *Method of thermodynamic analysis and optimization of energy intensive systems on exergy flow graphs,* Proc. of International Conference on Power and Energy Systems, Las Vegas, Nevada, USA, pp.489-491, 1999.

[8] Wu, C., Nikulshin, V., *Method of thermoeconomical optimization of energy intensive systems with linear structure on graphs,* International Journal of Energy Research, 24, pp.615-623,2000.

[9] Nikulshin V., Wu C., Bailey M., Nikulshina V., *Method of thermoeconomical optimization on graphs of energy intensive systems with pair interplay of flows,* Proc. of International Conference ECOS-02, Berlin, Germany, pp.1477-1484, 2002.

Proceedings of ECOS 2005
Trondheim, Norway
June 20–22, 2005

SOLAR STEAM-REFORMING OF HYDROCARBONS – THERMODYNAMIC ANALYSIS AND PROCESS SIMULATION

Jörg Petrasch[1] and Aldo Steinfeld[1,2]
[1]ETH - Swiss Federal Institute of Technology Zurich
Department of Mechanical and Process Engineering
CH-8092 Zürich
Switzerland

[2]Paul Scherrer Institute
Solar Technology Laboratory
CH-5232 Villigen
Switzerland

ABSTRACT

The steam-reforming of CH_4 and LPG using concentrated solar power as the source of process heat is thermodynamically examined in the temperature range 300-1300 K, pressure range 1-20 bar, and steam to hydrocarbon molar ratios range 1-3. The solar-driven process increases their LHV by over 20%. A steady state process model that includes mass and energy conservation coupled to equilibrium thermodynamic composition is formulated to predict the system performance of an idealized and a 400 kW-demonstration solar reforming plants. Process optimization predicts a peak solar-to-chemical exergy efficiency of 60%.

Keywords: solar steam-reforming, methane, LPG, solar thermo-chemistry

NOMENCLATURE

A	area [m^2]
C	solar concentration ratio [-]
G	Gibbs free energy (absolute) [J]
g	specific Gibbs free energy [J/kg]
H	enthalpy [J]
h	specific enthalpy [J/kg]
I	normal radiative flux [W/m^2]
m	mass [kg]
n	mole number [mol]
Q	thermal power [W]
S	entropy [J/K]
s	specific entropy [J/(kg K)]
T	temperature [K]
$\overline{x}$	molar basis

Greek letters

η	efficiency [-]

Abbreviations

DLR	Deutsches Zentrum für Luft und Raumfahrt
ETH	Eidgenössische Technische Hochschule
inc.	increase
LHV	lower heating value
LPG	liquid petroleum gas
WIS	Weizmann Institute of Science

Subscripts

abs	absorbed
el	electrical
en	energy
evap	evaporating
ex	exergy
in	inlet
l	liquid
out	outlet
pinch	pinch point
prod	product
react	reaction
sg	steam generation
sol	solar

INTRODUCTION

The advantages of using concentrated solar power to drive the endothermic reforming of hydrocar-

bons are three-folded: a) the discharge of pollutants is avoided; b) the gaseous products are not contaminated; and c) the calorific value of the fuel is upgraded. The solar reforming using either steam or CO_2 as partial oxidant has been extensively studied in solar concentrating facilities with small-scale solar reactor prototypes using Rh-based catalyst [1-7] Fe-based catalysts [8,9]. Recently, it has been demonstrated to proceed without added catalysis [10]. The solar reforming process has been scaled-up to power levels of 300-400 kW and tested at 1100 K and 8-10 bars in a solar tower concentrating system using two solar reforming reactor concepts: an indirect-irradiation tubular reactor [11] and a direct-irradiation volumetric reactor [12,13]. The latter is being further developed within the EU-project SOLREF [14]

This paper examines the chemical thermodynamics and process engineering of the solar reforming under the operating conditions of the 400 kW demonstration plant [15]. The chemical equilibrium compositions of methane-steam and LPG-steam systems are calculated for various stoichiometries in the pressure range 1-20 bar and temperature range 300-1300 K. Special attention is devoted to identifying the conditions that favor coking, as these will have to be avoided for preventing catalyst deactivation and carbon deposition on the reactor window. Two steady-state plant models are examined: 1) an idealized plant with theoretically minimum losses; and 2) the actual demonstration plant with measured operating parameters. Both models are compared in terms of their energy efficiency and chemical conversion for identifying irreversibility sources and optimization potential.

CHEMICAL THERMODYNAMICS

The chemical equilibrium compositions and enthalpy changes are computed using the HSC code [15] by Gibbs free enthalpy minimization. The solar steam-reforming of CH_4, represented by the overall stoichiometry reaction

$$CH_4 + H_2O = CO + 3\,H_2 \qquad (1)$$

has the potential of increasing the LHV of the feedstock (LHV_{CH4} = 797.5 kJ/mol) by 25.6 %. If CO is further water-gas shifted, 4 moles of H_2 may be obtained per mol CH_4 fed. In practice, however, a significant amount of CO_2 is co-produced while excess steam is used for avoiding coking, which decreases the energy efficiency. Further complication arises when other hydrocarbons are used as feedstock, as in the case of liquid petroleum gas (LPG) in the 400 kW solar demo plant. Typical LPG composition is listed in the Appendix. Its average C molar content per mole of the mixture is 3.682, its average molar ratio H:C is 2.54, and its average molecular mass is 53.5 g/mol. The solar steam-reforming of LPG, represented by the overall stoichiometry reaction

$$1\,LPG + 3.682\,H_2O = 3.682\,CO + 8.358\,H_2 \qquad (2)$$

has the potential of increasing the LHV of the feedstock (LHV_{LPG} = 2448 kJ/mol) by 24.3%. Table 1 shows the equilibrium composition of the CH_4-H_2O and LPG-H_2O systems at 1100 K and 1 bar, and for H_2O:CH_4 and H_2O:C molar ratios of 1, 2, and 3, respectively. For example, for a H_2O:CH_4 = 1, the solar steam-reforming of CH_4 increases its LHV by 23.1%. For H_2O:C = 1, the solar steam-reforming of LPG increases its LHV by 22.3%.

	Methane reforming H_2O:CH_4			LPG reforming H_2O:C		
	1	2	3	1	2	3
CO	0.8608	0.7996	0.6718	0.8980	0.7510	0.6264
CO_2	0.0258	0.1960	0.3268	0.0336	0.2466	0.3728
H_2	2.8111	3.1829	3.3226	2.1639	2.5098	2.6408
CH_4	0.0508	0.0044	0.0014	0.0359	0.0025	0.0009
C	0.0626	-	-	0.0325	-	-
H_2O	0.0875	0.8083	1.6746	0.0838	0.8536	1.6820
LHV inc./ %	23.1	24.3	23.7	22.3	22.6	21.8

Table 1 Equilibrium molar composition of the CH_4-H_2O and LPG-H_2O systems at 1100 K and 1 bar, and for H_2O:CH_4 and H_2O:C molar ratios of 1, 2, and 3, respectively.

Figure 1 shows the variation of the equilibrium composition of the CH_4-H_2O system as a function of temperature at a total pressure of 1, 10, and 20 bars. The parameter is the H_2O:CH_4 molar ratio: 1, 2, and 3. For H_2O:CH_4 = 1, carbon formation is thermodynamically favorable in the range 700 - 1100 K. Elevated pressures inhibit carbon formation, but at the expense of shifting the equilibrium to higher temperatures, according to Le Chatelier's principle. For H_2O:$CH_4 \geq 2$, carbon is not present in equilibrium.

The variation equilibrium composition of the LPG-H_2O system as a function of temperature at a total pressure of 1, 10, and 20 bars is shown in Figure 2. The parameter is the H_2O:C molar ratio: 1, 2, and 3. As expected carbon formation is more pronounced than in the CH_4-H_2O system because the H/C ratio is lower. For example, for H_2O:C = 1, carbon formation is thermodynamically favorable throughout the whole temperature and pressure range. Similar to the CH_4-H_2O system, the

equilibrium is shifted to higher temperatures with increasing pressure. For H_2O:C ≥ 3, carbon is not present in equilibrium.

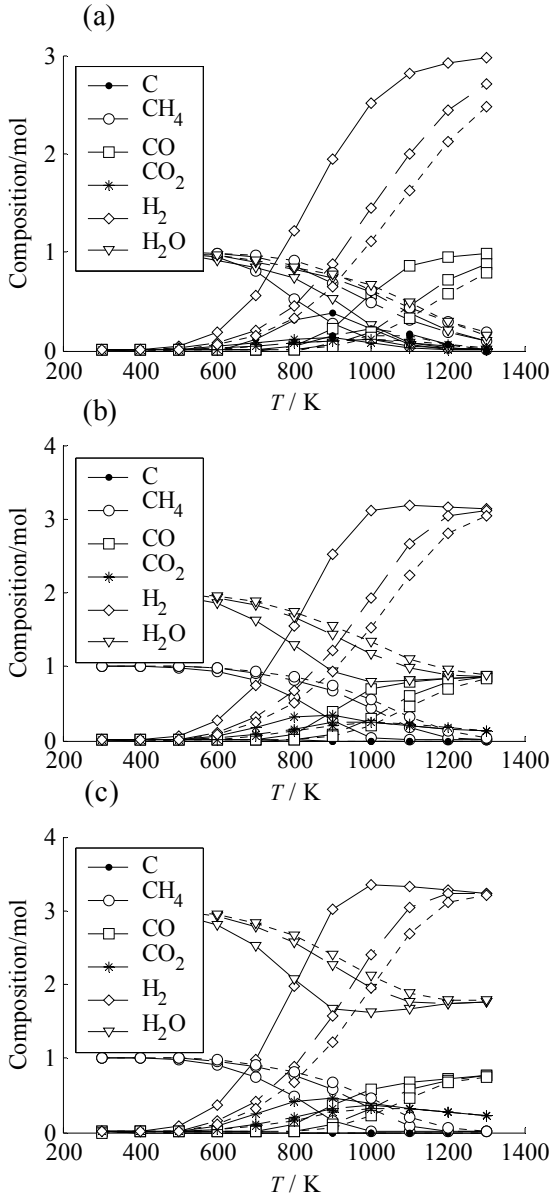

Figure 1 Equilibrium composition of the CH_4-H_2O system vs. temperature at a total pressure of 1 (solid curves), 10 (dashed curves) and 20 bars (dotted curves), for 1 mol CH_4. The parameter is the H_2O:CH_4 molar ratio: (a) H_2O:CH_4 = 1, (b) H_2O:CH_4 = 2, (c) H_2O:CH_4 = 3.

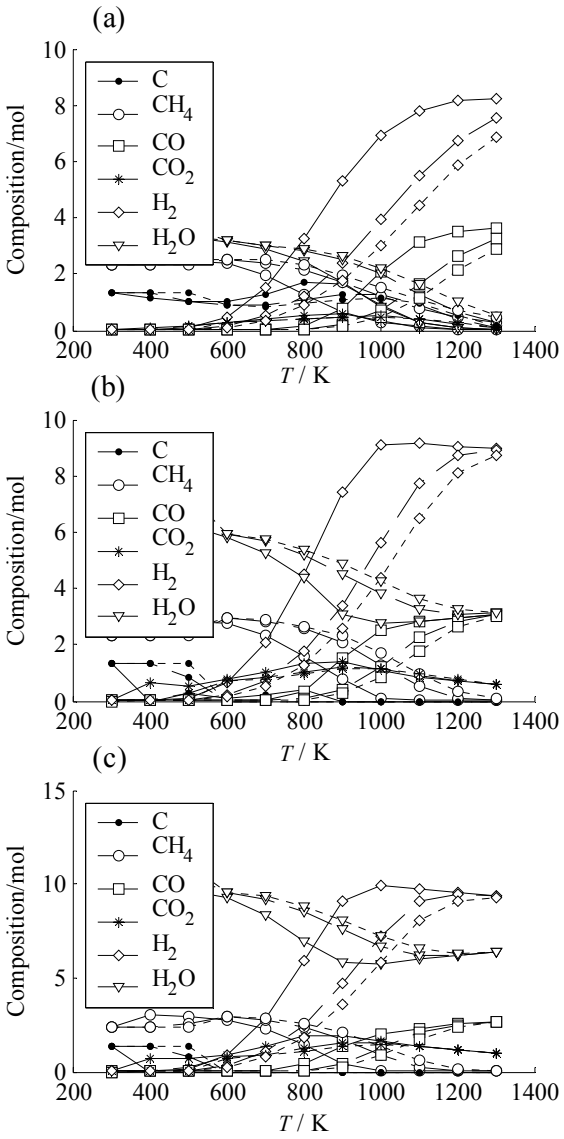

Figure 2 Equilibrium composition of the LPG-H_2O system at 1100 K and a total pressure of 1 (solid curves), 10 (dashed curves) and 20 bars (dotted curves) for 1 mol of LPG. The parameter is the H_2O:C molar ratio: (a) H_2O:C = 1, (b) H_2O:C = 2, (c) H_2O:C = 3.

STEADY STATE SYSTEM MODEL

ASPEN Plus™ [17] is applied to simulate the steady-state operation of the complete solar reforming process. Two plant models are considered: 1) an idealized plant with theoretically minimum losses, and 2) the actual demonstration plant with measured operating parameters. The methodology has been outlined elsewhere [18-19].

Idealized Plant Model

Figure 3 depicts the layout of an idealized solar reforming plant, encompassing a solar chemical reactor, a solar steam generator, and two heat exchangers: a pre-heater and a super-heater. It is assumed that Eq. (1) proceeds to completion at 1100 K and 1 bar with no excess steam, all components are perfectly insulated (no conduction or convection losses), and pumping work is negligible (no pressure drops throughout the system).

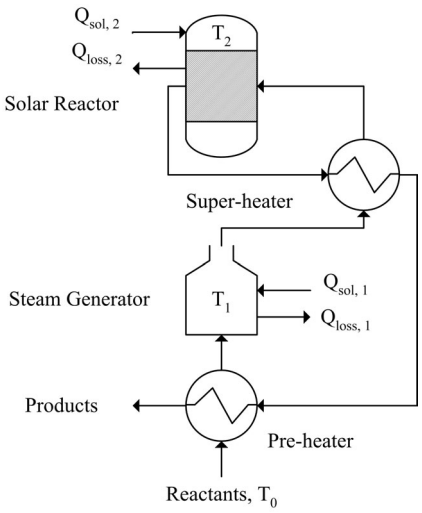

Figure 3 Scheme of idealized solar reforming plant.

Since the energy necessary for heating the reactants from 300 to 1110 K ($\Delta\bar{h}_{T_0-T_2}$ = 120.3 kJ/mol) is more than half the reaction enthalpy at 1110 K ($\Delta\bar{h}_{react}$ = 225.4 kJ/mol), heat recovery is essential. Reactants are first pre-heated to 373 K, flow through a solar-powered steam generator, and finally are super-heated using the sensible heat of the products. The solar chemical reactor and the solar steam generator are assumed to be perfectly insulated blackbody solar cavity-receivers (cavity's absorptivity and emissivity equal to 1). Their solar energy absorption efficiency, η_{abs}, is defined as the net rate at which energy is being absorbed divided by the solar power coming from the concentrator. Thus, for the solar reactor and steam generator:

$$\eta_{abs,1} = \frac{Q_{sol,1} - Q_{loss,1}}{Q_{sol,1}} = 1 - \left(\frac{\sigma T_1^4}{IC_1}\right) \quad (3)$$

$$\eta_{abs,2} = \frac{Q_{sol,2} - Q_{loss,2}}{Q_{sol,2}} = 1 - \left(\frac{\sigma T_2^4}{IC_2}\right) \quad (4)$$

where T_1 and T_2 are the nominal temperatures, $Q_{sol,1}$ and $Q_{sol,2}$ are the solar power inputs, $Q_{loss,1}$ and $Q_{loss,2}$ are the re-radiation losses, and C_1 and C_2 are the mean solar flux concentration ratios for the steam generator and reactor, respectively. η_{abs} expresses the capability of the solar receiver to absorb incoming concentrated solar energy but does not include the losses incurred in collecting and concentrating solar energy. For the solar reactor, the net energy absorbed matches the enthalpy change of the reaction,

$$\dot{Q}_{sol,1} - \dot{Q}_{loss,1} = \dot{n}\,\Delta\bar{h}_{react} = \dot{n}_{out}\,\bar{h}_{out}(T_2) - \dot{n}_{in}\,\bar{h}_{in}(T_2) \quad (5)$$

Similarly, for the steam generator, the net energy delivered to the steam generator matches the evaporation enthalpy of water:

$$\dot{Q}_{sol,2} - \dot{Q}_{loss,2} = \dot{n}\,\Delta\bar{h}_{sg} = \dot{n}\left(\bar{h}_{pinch} - \bar{h}_l(373K)\right) \quad (6)$$

where $\bar{h}_{pinch}$ is evaluated at the super-heater pinch point, since both pre-heaters and super-heaters are assumed ideal countercurrent flow heat exchangers. The overall energy conversion efficiency of the process is

$$\eta_{en} = \frac{\dot{n}_{out}\,\bar{h}_{out}(T_0) - \dot{n}_{in}\,\bar{h}_{in}(T_0)}{Q_{sol,1} + Q_{sol,2}} = \frac{\dot{n}\Delta\bar{h}_{tot}}{Q_{sol,1} + Q_{sol,2}} \quad (7)$$

The exergy efficiency is defined as

$$\eta_{ex} = \frac{\dot{n}_{out}\,\bar{g}_{out}(T_0) - \dot{n}_{in}\,\bar{g}_{in}(T_0)}{\eta_{carnot}(T_{sol})Q_{sol,1} + \eta_{carnot}(T_{sol})Q_{sol,2}} \quad (8)$$

Figure 4 shows the enthalpy change of the reaction for the system CH_4-H_2O and LPG-H_2O, with H_2O:CH_4 and H_2O:C molar ratios equal 1, respectively. Reactants are fed at T_0 = 298 K, products are obtained at 1100K. The net energy required to drive the solar reforming of CH_4 and LPG is $2.501 \cdot 10^5$ J/mol and $2.0768 \cdot 10^5$ J/mol (per mol of C), respectively.

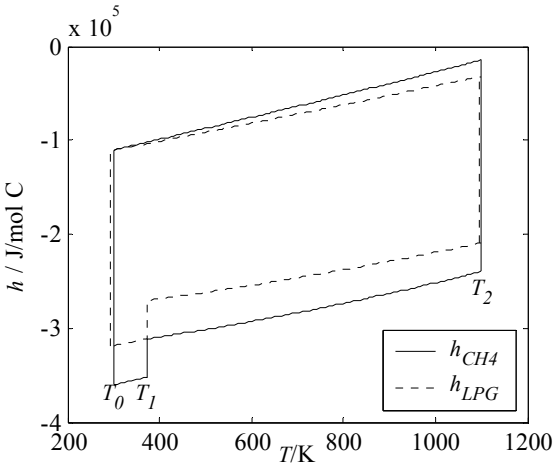

Figure 4 Enthalpy change of the reaction for the systems CH_4-H_2O and LPG-H_2O, with H_2O:CH_4 and H_2O:C molar ratios equal 1, respectively. Reactants are fed at 298 K, products are obtained at 1100 K.

Table 2 lists the baseline operating conditions and energy balances of the idealized plant, employing either CH_4 or LPG as feedstock, and for H_2O:CH_4 and H_2O:C molar ratios equal 1, respectively. η_{en} approaches 1 for both CH_4 and LPG feedstock because the only heat losses are due to re-radiation. In contrast, η_{ex} for LPG-reforming is lower than the one for CH_4-reforming because of the lower H/C ratio for LPG.

Feedstock	CH_4	LPG
Reactant stoichiometry	$H_2O:CH_4 = 1$	$H_2O:C = 1$
I	1000 W/m^2	1000 W/m^2
T_0	300 K	300 K
T_1	373 K	373 K
$T_2=T_{react}$	1110 K	1110 K
C_1	300	300
C_2	1500	1500
Δh_{react} @ T_{react}	$2.254 \cdot 10^5$ J/mol C	$1.776 \cdot 10^5$ J/mol C
Δh_{sg}	$2.468 \cdot 10^4$ J/mol C	$3.0129 \cdot 10^4$ J/mol C
Δh_{tot} @ T_0	$2.501 \cdot 10^5$ J/mol C	$2.0768 \cdot 10^5$ J/mol C
Δg_{tot} @ T_0	$1.499 \cdot 10^5$ J/mol C	$1.0474 \cdot 10^5$ J/mol C
$\eta_{abs,1}$	0.948	0.948
$\eta_{abs,2}$	0.996	0.996
η_{en}	0.949	0.951
η_{ex}	0.600	0.506

Table 2 Baseline operating conditions of the idealized plant.

Demonstration Plant Model

Figure 5 depicts the layout of the 400 kW solar reforming demonstration plant, erected at the solar tower of the Weizmann Institute. It encompasses a solar chemical reactor, a pre-reformer, a steam generator, a LPG/steam pumping system, a jet-pump for product recirculation, multiple electrical heaters for steam and reactants, and two heat exchangers. Main assumptions are: expansions in valves are adiabatic; LPG compressors operate with an isentropic efficiency 0.72; heat-exchangers are countercurrent-flow with constant overall heat-transfer coefficient times area ($U \cdot A$); and the reaction reaches chemical equilibrium in the pre-reformer and solar reactor. The solar reactor consists of a cavity-receiver with a quartz dome to enable operation at 9 bar. The reactant gas is fed through porous ceramic foam coated with Rh-catalyst directly exposed to high-flux solar irradiation, augmenting heat transfer and reaction surface [15].

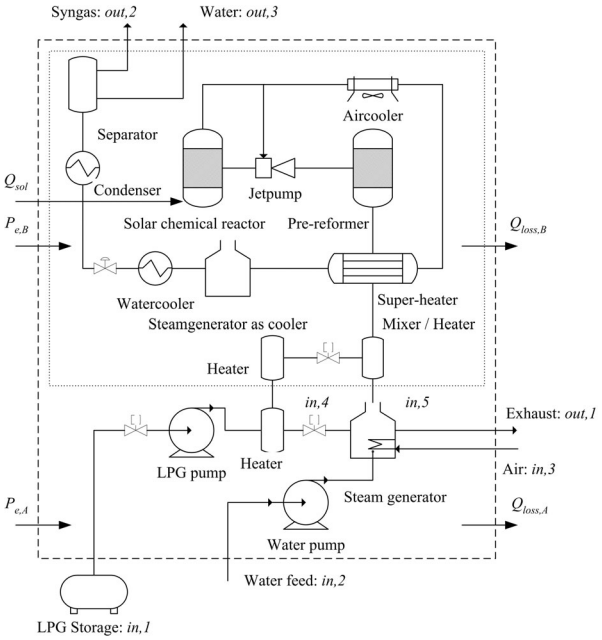

Figure 5 Scheme of the 400 kW solar reforming demonstration plant. Boundaries for system A (dashed) include steam generation; boundaries for system B (dotted) exclude steam generation and LPG preheating.

A similar reactor concept has been demonstrated for CO_2 reforming [7]. Equilibrium composition is assumed for the reactor model, as corroborated experimentally for high catalyst loading [20]. Further, the reactor is modeled as a well-insulated gray body, with an emissivity of 0.95.

LPG, at a nominal mass flow rate of 120 kg/h, is pumped to the system pressure of 17 bar, and electrically heated and evaporated to 378 K. Afterwards, the LPG-stream is splitted. 16.6% is burned to supply heat to the steam generator. The remainder is re-heated to avoid condensation and finally mixed with steam, which is electrically superheated to 498 K. The mixture undergoes a 2-stage pre-heating before entering the pre-reformer: first to 503 K by means of electrical heating, and secondly to 773 K by means of a 3.1

m^2 shell-and-tube heat exchanger. After pre-reforming to mainly CH_4, CO, and steam, the mixture flows through a jet-pump for product re-circulation at a volume ratio products-to-reactants of 3. This feature, although inefficient, is necessary for assuring stable operations conditions. The solar reactor operates at design conditions of 1100 K, 9 bar, and input solar power of 400 kW. After exiting the solar reactor, products are cooled, their sensible heat is recovered via heat exchanges, and excess steam is separated by condensation.

Steady state mass and energy conservation is applied to each of the components of Figure 5. Potential and kinetic effects are neglected. Thus,

$$0 = \sum_{i=1}^{N} \dot{m}_{in,i} - \sum_{j=1}^{M} \dot{m}_{out,j} \tag{9}$$

$$0 = \dot{Q} - P + \sum_{i=1}^{N} \dot{m}_{in,i} h_{in,i} - \sum_{j=1}^{M} \dot{m}_{out,j} h_{out,j} \tag{10}$$

The system of equations (7) and (8) are solved iteratively. Efficiencies are newly defined to account for several sources of heat loss, especially parasitical losses:

$$\eta_{en,A} = \frac{\sum_{i=1}^{3} \dot{m}_{out,i} h_{out,i} - \sum_{i=1}^{3} \dot{m}_{in,i} h_{in,i}}{Q_{sol} + P_{el,A} + P_{el,B}} \tag{11}$$

$$\eta_{en,B} = \frac{\sum_{i=1}^{3} \dot{m}_{out,i} h_{out,i} - \sum_{i=1}^{3} \dot{m}_{in,i} h_{in,i}}{Q_{sol} + P_{el,B}} \tag{12}$$

$$\eta_{ex,A} = \frac{\sum_{i=1}^{3} \dot{m}_{out,i} g_{out,i} - \sum_{i=1}^{3} \dot{m}_{in,i} g_{in,i}}{\eta_{carnot}(T_{sol}) Q_{sol} + P_{el,A} + P_{el,B}} \tag{13}$$

$$\eta_{ex,B} = \frac{\sum_{i=2}^{3} \dot{m}_{out,i} g_{out,i} - \sum_{i=4}^{5} \dot{m}_{in,i} g_{in,i}}{\eta_{carnot}(T_{sol}) Q_{sol} + P_{el,B}} \tag{14}$$

Equations (11) and (13) are valid for system *A* (Figure 5). Equations (12) and (14) are valid for system *B* (Figure 5).

Table 3 lists the baseline operating conditions and energy balances of the demonstration plant. For the baseline conditions, the exergy efficiencies of both systems A and B are negative because of the burning of LPG for supplying heat to the steam generator. Thus, fore large-scale applications, steam generation must use solar energy.

Table 4 shows the comparison between the numerically calculated temperatures and the experimentally measured ones.

Feedstock	LPG	LPG
System Boundaries	A	B
H2O:LPG mass	3	3
H2O:LPG molar	8.9	8.9
H2O:C molar	2.41	2.41
I	1000 W/m^2	1000 W/m^2
C_1	1670	1670
Q_{sol}	400 kW	300 kW
$\dot{m}_{in,1}$	0.0333 kg/s	-
$\dot{m}_{in,2}$	0.0833 kg/s	-
$\dot{m}_{in,3}$	0.1114 kg/s	-
$\dot{m}_{in,4}$	(0.0277kg/s)	0.0277 kg/s
$\dot{m}_{in,5}$	(0.0833 kg/s)	0.0833 kg/s
$\dot{m}_{out,1}$	0.11706 kg/s	-
$\dot{m}_{out,2}$	0.07132 kg/s	0.07132 kg/s
$\dot{m}_{out,3}$	0.03971 kg/s	0.03971 kg/s
$T_{in,1}$	293.15 K	-
$T_{in,2}$	293.15 K	-
$T_{in,3}$	293.15 K	-
$T_{in,4}$	413.15 K	413.15 K
$T_{in,5}$	498.15 K	498.15 K
$T_{out,1}$	473.15 K	-
$T_{out,2}$	293.15 K	293.15 K
$T_{out,3}$	293.15 K	293.15 K
T_{react}	1077 K	1077 K
$P_{el,B}$	7715 W	7715 W
$P_{el,A}$	10300 W	10300 W
η_{abs}	0.954	0.954
η_{carnot}	0.722	0.722
η_{en}	0.282	0.264
η_{ex}	-0.183	-0.0074

Table 3 Baseline operating conditions of the 400 kW demonstration plant.

The agreement at the solar reactor outlet is within 5%. Differences in the heat exchangers' temperatures are principally due to heat losses in the tubing, which are not modeled.

Location	T_{model} / K	$T_{measured}$ / K	Relative Error
Solar reactor outlet	1077	1018	0.055
Reactants at heat exchanger outlet	757	735	0.029
Products at heat exchanger outlet	554	618	0.116

Table 4 Comparison of the numerically calculated and experimentally measured temperatures

The effect of the solar power input and steam-to-LPG mass-ratio is examined for both systems A and B.

The variation of the efficiencies, reactor temperature, and the product composition as a function of the solar power input is shown in Figs. 6, 7, and 8, respectively. As expected the efficiencies and reactor temperature increase with Q_{sol} because of the higher product yield and reduced re-radiation losses for a higher solar concentration. Consequently, the product composition shifts towards CO and H_2.

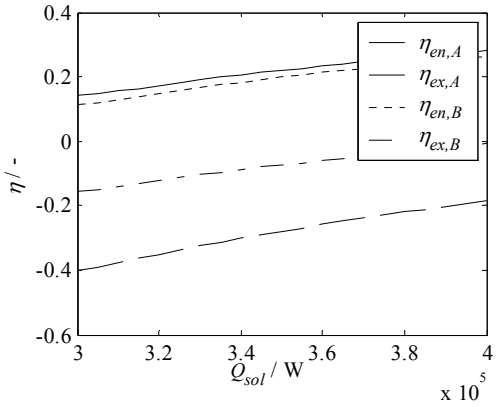

Figure 6 Variation of the energy and exergy efficiencies of systems A and B as a function of the solar power input.

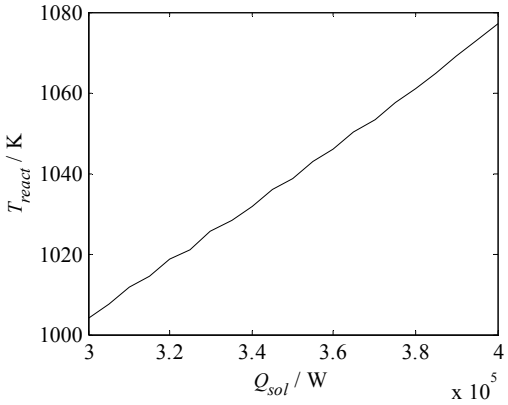

Figure 7 Variation of the reactor temperature as a function of the solar power input.

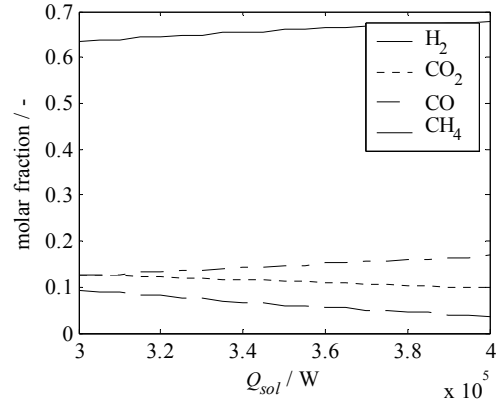

Figure 8 Variation of the molar product composition as a function of the solar power input.

The variation of the efficiencies, reactor temperature, and the product composition as a function of the steam mass flow rate is shown in Figs. 9, 10, and 11, respectively. All efficiencies decrease with increasing steam mass flow rate, except the exergy efficiency of system A. This is because the difference in Gibbs free enthalpy remains about constant (almost all LPG reacts in any case) while the parasitical losses increase (for example, more energy needed to produce and pump excess steam). As expected, the reactor temperature decreases as the steam mass flow rate increases for a given Q_{sol}. The product composition shifts towards H_2 and CO_2, because the combined effects of reduced temperature and higher steam content.

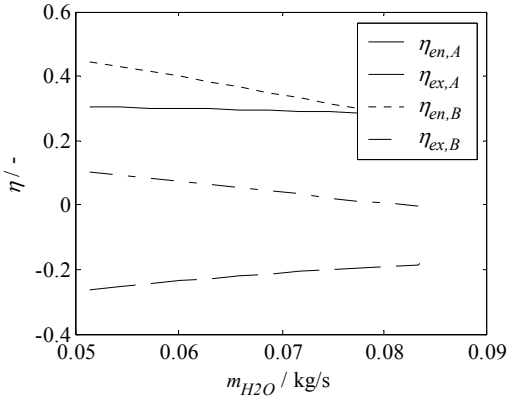

Figure 9 Variation of the energy and exergy efficiencies of systems A and B as a function of the steam mass flow rate.

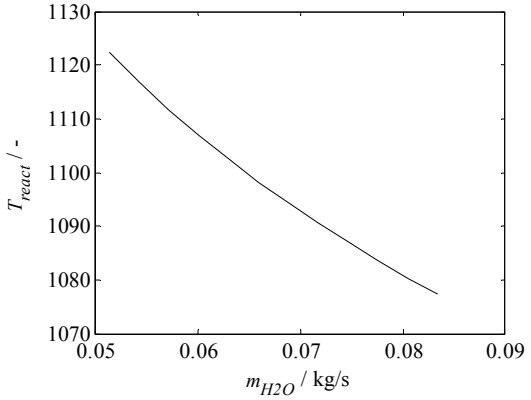

Figure 10 Variation of the reactor temperature as a function of the steam mass flow rate.

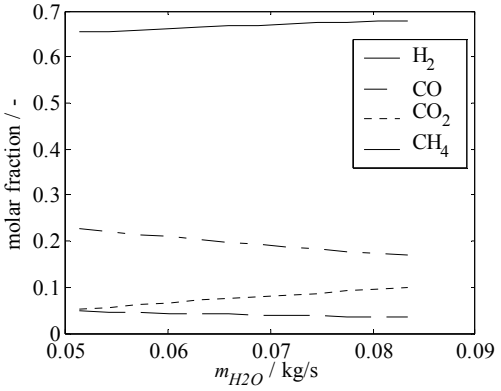

Figure 11 Variation of the product composition as a function of the steam mass flow rate.

SUMMARY AND OUTLOOK

We have computed the chemical equilibrium composition of the systems CH_4-H_2O and LPG-H_2O as a function of temperature, pressure, and

steam to hydrocarbon molar ratios. The reforming reaction proceeds in the 900-1300 K range. Low pressures and high steam to hydrocarbon molar ratios shift the equilibrium towards H_2. For CH_4-reforming using a reactant molar stoichiometry of $H_2O:CH_4 = 1$, carbon formation is thermodynamically favorable at 700 K < T < 1100 K and p < 8 bars. In contrast, for $H_2O:C \geq 2$, carbon is absent in equilibrium in the range 300-1300 K and 1-20 bar. For LPG-reforming using $H_2O:C = 1$, carbon formation is thermodynamically favorable at T < 1200 K for the whole pressure range (p < 20 bar). In contrast, for $H_2O:C \geq 3$, carbon is absent in equilibrium in the range 300-1300 K and 1-20 bar. The theoretical maximum exergy conversion efficiencies for the solar steam-reforming of CH_4 (with $H_2O:CH_4 = 1$) and LPG ($H_2O:C = 1$) are 60.0% and 50.8%, respectively. Their LHV is increased by 25.6% and 24.3%, respectively.

The model is being employed for system optimization, and will be further expanded to include dynamic behavior during transient operation such as start-ups, shut-downs, and varying solar irradiation.

Acknowledgements. This work has been conducted in the framework of the SOLREF Project, funded by the European commissions under contract No. SES6-CT-2004-502829 SOLREF.

REFERENCES

[1] Levy M., Rosin H., Levitan R. *Chemical reactions in a solar furnace by direct irradiation of the catalyst*. ASME - J. Sol. Energy Eng. 1989;111:96-97.

[2] Levy M., Rubin R., Rosin H., Levitan R. *Methane reforming by direct solar irradiation of the catalyst*. Solar Energy 1992;17:749-756.

[3] Hogan Jr. RE., Skocypec RD., Diver RB., Fish JD., Garrait M., Richardson JT. *A direct absorber reactor/receiver for solar thermal applications*. Chem. Eng. Sci. 1990;45:2751-2758.

[4] Richardson JT., and Paripatyadar SA. *Carbon dioxide reforming of methane with supported rhodium*. Appl. Catalysis 1990;61:293-309.

[5] Buck R., Muir RE., Hogan EH., Skocypec RD. *Carbon dioxide reforming of methane in a solar volumetric receiver/reactor: The CAESAR Project*. Sol. Energy Mater. 1991;24:449-463.

[6] Buck R., Abele M., Bauer H., Seitz A., and Tamme R. *Development of a volumetric receiver-reactor for solar methane reforming*. ASME - J. Sol. Energy Eng. 1994;116:449.

[7] Wörner A., Tamme R. *CO_2 reforming of methane in a solar driven volumetric receiver-reactor*. Catalysis Today 1998;46:165-174.

[8] Kodama T., Koyanagi T., Shimizu T., and Kitayama Y. *CO_2 Reforming of methane in a molten carbonate salt for use in solar thermochemical processes*. Energy & Fuels 2001;15:60-65.

[9] Gokon N., Oku Y., Kaneko H., Tamaura Y. *Methane reforming with CO_2 in molten salt using FeO catalyst*. Solar Energy 2002;72:243-250.

[10] Dahl JK., Weimer AW., Lewandowski A., Bingham C., Bruetsch F., Steinfeld A. *Dry Reforming of Methane Using a Solar-Thermal Aerosol Flow Reactor*. Industrial & Engineering Chemistry Research, 2004;43:5489 – 5495.

[11] Epstein M., Spiewak I. *Solar experiments with a tubular reformer.* In: Proceedings of the 8th Int. Symp. Solar Thermal Concentrating Technologies, p. 1209-1229, Cologne, Germany: Müller Verlag Heidelberg, 1996.

[12] Tamme R., Buck R., Epstein M., Fisher U., Sugarmen C. *Solar upgrading of fuels for generation of electricity*. J. Solar Energy Eng. 2001;123:160-163.

[13] Moeller S., Buck R., Tamme R., Epstein M., Liebermann D., Moshe M., Fisher U., Rotstein A., Sugarmen C. *Solar production of syngas for electricity generation: SOLASYS project test-phase*. In: Proceedings of the 11th SolarPACES Int. Symposium on concentrated Solar Power and Chemical Energy Technologies, Steinfeld A. (Ed.), p. 231-237, Zurich, Switzerland, 2002.

[14] http://www.pre.ethz.ch/cgi-bin/main.pl?research?project11

[15] *SOLASYS Novel solar assisted fuel drive power system*. Publishable final report EU Contract No. JOR3-CT98-0300, 2002.

[16] HSC Chemistry 5 Outokumpu Research Oy, Pori, Finland, A. Roine.

[17] Aspen engineering suite™, Aspen Technology, Inc. Ten Canal Park, Cambridge, MA 02141 USA, http://www.aspentech.com

[18] Hirsch D., Epstein M., Steinfeld A. *The solar thermal decarbonization of natural gas*. International Journal of Hydrogen Energy 2001;26:1023-1033.

[19] v. Zedtwitz P., Steinfeld A. *The solar thermal gasification of coal – energy conversion efficiency and CO_2 mitigation potential*. Energy 2003;28:441-456.

[20] Buck R. *Massenstrom-Instabilitäten bei volumetrischen Receiver-Reaktoren.* Fortschritt-Berichte VDI, Reihe 3 Verfahrenstechnik, 2002.

APPENDIX - LPG COMPOSITION

Component	Molar fraction
N-Butane	0.47608
Propane	0.27506
Iso-Butane	0.20662
Ethan	0.02684
Iso Pentane	0.01084
Cis-2-Butene	0.00198
Isobutene	0.00090
N-Pentane	0.00055
Trans-2-Butene	0.00045
Propene	0.00038
1-Butene	0.00030

Table 5 Typical molar composition of LPG.

Proceedings of ECOS 2005
Trondheim, Norway
June 20–22, 2005

RENEWABLE ENERGY IN RUSSIA: APPROPRIATE TECHNOLOGIES AND DEVOPMENT PERSPECTIVES

Irina Proshkina
Publishing House "Great Russian Encyclopedia",
Department of Physics
Russia

ABSTRACT

A brief review of renewable energy technologies in Russia is presented. High efficiency of hybrid energy systems is underlined. Minimal damage to environment is recognized as a main advantage of renewable energy technologies. Application of renewable energy technologies in Russian remote areas and hardly accessible regions is motivated now socially and economically. According to Federal Program "Energy Effective Economy", substitution of fossil fuel by local fuels and renewables will save 1 million tons of equivalent fuel annually supplied at North regions. New economic situation and increasing the environmental requirements give a new chance to renewable energy development. Some conditions for successful future of renewable energy technologies are discussed, among them the effective interaction of research institutes, developers and production companies.

INTRODUCTION

Now electric power and liquid fuel have paramount importance for life of civilisation, as these two sources represent free energy, which (in view of efficiency) can be transformed into work. Limitation of hydrocarbon fuel resources and strengthening the nature protection requirements stimulate search for alternative sources of energy in many countries.

The mankind is not threatened with an energy crisis connected to an exhaustion of stocks of petroleum, gas, coal, if it will develop technologies of use renewable energy sources (RES). In this case problems caused by harmful emissions connected with burning fuel for energy and transport will be solved, and consequently quality of life will rise. The application of RES in Russia is expedient by three reasons: inexhaustible nature, ecological acceptability and economic benefit in the removed regions of Russia. In conditions of prices growth on the organic fuel it is economically favourable for developing RES in removed areas already today. 20 millions of Russians live in regions not connected to the centralized networks of power supply. Therefore development of the renewable energy programs has the large social importance. In cities and settlements with bad ecological conditions the introduction RES in power balance helps to improve the situation.

The environmental acceptability of renewable energy can be illustrated with the following example. One RES system (wind turbine, solar photovoltaic elements, small hydroelectric power station) with capacity of 500 kW produces not less than 1 million kWh per one year. Hence it prevents emissions of equivalent coal station: carbon dioxide - 750-1250 tons, sulfur dioxide – 5-8 tons, nitrogen oxides - 3-6 tons.

Huge potential of renewable power in Russia is used unsufficiently. The share of manufacture of a thermal energy from RES (by different assessment) is 4-6 % from general ounput. The data on manufacture of the electric power from RES indicate that their share is no more than 1 %, including small hydroelectric power station. Development of renewable energy is a field of interest for many Russian

scientific institutes and industrial companies. Despite of problems with financing, the essentially new power technologies based on renewable energy sources are created in Russia.

SOLAR THERMAL SYSTEMS

After disintegration of the Soviet Union Russia began to consider as northern country, where the resources of a solar energy are unsufficient. However, last researches of Institute of high temperatures of the Russian academy of sciences (IHT RAS) prove an inconsistency of such point of view.

In laboratory of renewable energy sources of IHT RAS the Atlas of distribution of solar energy resources on Russian territory was maped, the climatic database is created especially assigned for research in the field of solar power. The laboratory specialists make cards of receipt of solar radiation on variously focused surfaces. The highest arrival of energy on a horizontal surface is characteristic for southern areas of the country (Northern Caucasus, for example). However, the resources of a solar energy are great enough also in other regions of Russia.

According to the received results the rather perspective areas are the south of Siberia and Far East. And parameters for Krasnodar region, that is rather unexpected, is the same, as for Yakutsk. As a barrier to a wide dissemination of solar termal systems serves its high cost. Therefore developers all over the world, as well as in Russia, aim to create effective solar collectors, whose use is economically competitive in different regions. Specialists of IHT RAS work actively at new models of solar collectors with application of heatproof polymeric and composit materials, that will allow to lower their cost not to the detriment of quality.

Research and development on perfection of solar collectors and concentrators are carried out in Russian Institute of electrification of an agriculture. The engineers create two essentially new solar concentrators: quasistationary and stationary types. The correction connected to change of declination of the Sun is made in quasistationary concentrator once per day; the concentrated solar radiation from separate concentrators is summarized and is directed to the receiver by optical waveguide. If the area of concentrators will reach several square kilometres, the total capacity of the concentrated solar radiation would be up to million kilowatt.

Application of solar elements with a bilaterial working surface were created in Russia in 1970s, has allowed to increase factor of concentration of stationary concentrators up to 5. Use of new stationary solar modules with concentrators for facades both roofs of buildings and reception of electrical energy and heat is especially effective.

New type of solar concentrators was offer Recently by Institute of electrification of an agriculture. Its main feature - combination of positive qualities of solar power stations to the central receiver of a modular type and opportunity of use as the receiver both traditional steam heater, and solar elements on the basis of silicon.

Application of solar concentrators makes realisable a creation of solar photo-photovoltaic systems of megawatt level of capacity at two – five reduction of their cost.

SOLAR PHOTOVOLTAIC SYSTEMS

One of the most perspective technologies of solar energy is of photovoltaic systems with solar elements on the basis of silicon. World manufacture of solar elements is increasing (up to 30 % annually) at continuous reduction of cost. Photovoltaic modules, produced in Russia, transform solar radiation to electrical energy with efficiency 11-15 %. Laboratory samples provide efficiency 23 %.

For manufacturing solar batteries the silicon is used being one of the most widespread elements of the earth's crust from firm substances. Some experts named silicon as petroleum of 21 century. The contents of silicon in the earth's crust is 29,5 % , it exceeds the contents of aluminium 3,35 times. The Russian scientists have developed new chlorine-free technology of silicon manufacture for solar photovoltaic modules. The production of “solar quality” silicon by a method of direct restoration from pure natural quartzite allows to reach an output of silicon 80-85 % of cost USD 5-15 kg. In case of wide application of this technology cost of the electric power generated by photovoltaic

modules decline to USD 0,10-0,12 kWh. In new technology the chemical methods are replaced with ecologically acceptable electrophysical methods.

There are now some enterprises in Russia having technology and capacities for manufacturing solar elements and modules up to 2 MW per year.

One more technology offered by Institute of electrification of an agriculture - technology of polymeric-free hermetic sealing of solar modules, developed together with electronic industry. It allows to doubling operational life time of solar stations from 20 to 40 years, that exceeds operation life of traditional thermal power stations.

WIND ENERGY

Russia has significant resources of wind energy in many regions, including those, where there is no electricity network (coast of Northern Ice Ocean, Kamchatka, Sakhalin, Chukotka, Yakutia). Naturally, Russia has good prospects for development of wind energy, however powerful turbines are not manufactured by domestic enterprises, and the large-scale development of this energy sector is difficult without government support. The major consumers of wind energy systems are residential users (the gardeners, vocational home owners, farmers) who require an independent provider of electric energy with the power consumption up to 1.5 — 2 kW. Other category of the consumers is the remote small technical services and automatic posts (beacons, supervision and communication, meteorological service). The smallest group of consumers includes small industrial customers (autonomous lighting, heating, water cleaning systems etc.).

Russian enterprises produce trial versions of wind turbines in very small quantities resulting in their high cost. Organization of commercial production of wind turbines and certification process requires significant investments. Wind energy systems with the capacity of 8 kW and 16 kW are commercially produced now for the individual consumers.

Manufacturers of renewable energy equipment increasingly come to a conclusion that only combined utilization of various renewable energy sources can create economically feasible alternative to traditional power sources and encourage wider use of renewable energy.

The so-called "solar" houses, getting energy from renewable sources, were built as a pilot project. For example, the first "solar" apartment building has been recently constructed in Sverdlovsk area (Ural region). Wind turbine even at a wind speed of 5 m/s can produce about 4 kW of electricity that is used to power up electrical pump in the house to get water from a well. Photovoltaic panels installed on a facade of a building have accumulators, which provide people with light and heat in case of failure on a network or during periods of increased power consumption.

Hybrid power stations (utilizing wind and diesel) seems to be most perspective for private consumers as well as for oil and gas companies at remote wells. The stations like Russian hybrid power system “Musson” can be used for lighting and household needs of the log personnel at reduced expenses for diesel fuel.

Despite a lack in demand for wind turbines and funding problem, Russian engineers continue working on improvement wind energy systems. Recently, ecologically safe wind system with no fans has been developed in the Institute of electrification of agriculture. This installation is in essence a tower, inside which air whirlwind rotates the turbine. The system is characterized by the absence of noise and vibrations.

One more way for development of wind energy in Russia is creation of joint ventures. Wind energy turbines, replaced in Europe for more powerful and modern ones, can still be at good service in Russia. For example, a wind system "Bonus-150" was set up in operation recently in the Pskov region. This turbine (having operational life time of 25 years) has already been in operation in Denmark for 10 years. This system output is about 60-70 kW. It works in an automatic mode, and does not require supporting personnel. Similar units successfully operate in Kaliningrad region.

SMALL HYDROELECTRIC POWER STATIONS

At present time a small and micro hydroelectric power stations are the most environmentally friendly systems.

In Russia, economic potential of small and micro- hydroelectric power stations is significantly underutilized. A number of small hydropower plants decreased from 5000 in 50s to 300 in 90s of the 20th century. Lately an interest to small hydroelectric power stations has been brought back to life. A process of restoration of previously destroyed and construction of new small and micro-hydroelectric power stations is on its way. During the last years, more than 20 power plants were constructed and restored in Northern Caucasus and Northwest of Russia. Micro-hydroelectric power plants can be used by small businesses, also at geological, meteorological station etc. As opposed to pressure-head hydroelectric power stations, small and micro- hydroelectric flow-through systems do not obstruct navigation, do not require deployment of expensive dams, and do not disturb the environment.

The recent product of Moscow engineers is micro-hydroelectric power station «Raduga» with capacity of 400 W, which can be used all year round, and also under ice. This station is developed for operation primarily in a channel of the flat rivers having flow speed from 0,8 m/s up to 5 m/s. Distance between a reservoir bottom and ice cover is not less than 1,5 m. The maximum submerge depth is 5 m. Such an energy unit, having a diameter of the water-wheel of 0,98 m provides electricity with capacity of 80 - 400 W (220 V, 50 Hz) with the quality comparable to standard network output.

According to market analysis micro-hydroelectric units with capacity 5-30 kW will find a market nearest time, but then small hydroelectric units with capacity 200-400 kW will be also in requisition.

BIOFUEL

The important component of renewable energy will be stations working on biomass. Biomass is pure enough as a source of energy from the ecological point of view. A process of burning biomass (as compared to coal) is not accompanied by emissions of sulphur. Also, emissions of nitrogen oxides can be reduced due to optimum technology of burning.

In Russia 20 % of the world wood resources are located. Forests cover about 40% of Russian land territory. Forest industry is an important sector of Russian economy, and utilization of the biomass (wood waste) products generated during preparation and processing of wood as an energy resource is very attractive. At present, this resource is only being minimally utilized. Alongside with valuable coniferous breeds and birch that have steady demand in traditional wood processing businesses, there are big quantities of bad quality, unusable aspens and alder.

For example, Leningrad area alone produces annually about 1100 -1200 thousand m^3 of bad quality wood that does not have any selling value, is unprofitable for business and is harmful to an environment. At the same time, this wood has significant calorie content. If this wood is effectively processed, total calorific value of this fuel will be more than 2.3 millions of GC. It is enough for operation of 750 boiler with thermal capacity 1.2 MWh. Just a single boiler is capable to provide heat to a standard 100-120 apartments building.

In case of wide spread of boiler-heated houses utilizing biofuel, there will be a replacement of oil and coal and will be a solution to a problem of wood recycling and allocation of waste. Local ecological situation will improve, due to a reduced level of environment pollution associated with acidification of ground and water, and also with methane emission, being a product of wood rotting.

Biomass can be effectively utilized in power plants as wood chips or as processed wood bio fuel (briquettes, pellets). The most perspective technology is not a direct burning (its efficiency is about 25 %), but biomass gasification using gas-vapour cycles with efficiency up to 50 %.

Russian scientists develop technology of fast pyrolysis of biomass which allow up to 80 % of organic substance to be transformed into liquid or gas fuel. From one ton of wood sawdust it is possible to obtain more than 700 kg of liquid fuel. Combining this technology with technology of cultivation of quickly

growing plants, yielding up to 40 ton of biomass in dry weight from hectare, it is possible to decentralize liquid fuel production. To supply each rural area by liquid fuel it is required less than 5 % of cultivated grounds. This technology can effectively be used in the countries importing petroleum, where today gas and oil price is high enough.

GEOTHERMAL POWER

Geothermal power is strictly not a renewable source of energy, its methods are traditional and impact on environment is essential. However, especially significant growth is observed in this sector, due to take-off of two geothermal power stations on Kamchatka with capacity 12 MW and 50 MW.

RENEABLE ENERGY TOMORROW

A decisive promotion of renewable energy sources during last years is caused in many countries by obligations to reduce GHG emissions. Russia has also acceded to Kyoto protocol. Russian government approved the Federal Target Program “Energy Efficiency Economy”. A chapter of this document named “Energy supply of remote areas, Northern and hardly accessible regions on the base of renewable energy sources and local sources of fuels” underlined a regional importance of RES. To realize great potential of renewable energy sources some problems should be solved, including lack of funds, weak coordination between researchers, providers and consumers, underestimation of RES as most appropriate energy alternative from ecological and social point of view.

REFERENCE.

First International Forum “Energy of the Future”. Moscow, Russian Academy of Sciences, 15-16 December, 2004.

Proceedings of ECOS 2005
Trondheim, Norway
June 20–22, 2005

EXERGETIC EVALUATION OF BIOMASS GASIFICATION

Krzysztof J. Ptasinski*, Mark J. Prins, Anke Pierik
Eindhoven University of Technology
Department of Chemical Engineering and Chemistry
P.O. Box 513 (Helix, STW 1.22), 5600 MB Eindhoven
The Netherlands

ABSTRACT

Biomass has great potential as a clean, renewable feedstock for producing modern energy carriers. This paper focuses on the process of biomass gasification, where the producer gas may subsequently be used for the production of electricity, fuels and chemicals. The gasifier is one of the least efficient unit operations in the whole biomass-to-energy technology chain and an analysis of the efficiency of the gasifier alone can substantially contribute to the efficiency improvement of this chain. The purpose of this paper is to compare different types of biofuels for their gasification efficiency and benchmark this against gasification of coal. In order to quantify the real value of the gasification process exergy-based efficiencies, defined as the ratio of chemical and physical exergy of the producer gas to chemical exergy of a biofuel, are proposed in this paper. Biofuels considered include various types of wood, vegetable oil, sludge, and manure. The gasification efficiencies are evaluated at the carbon boundary point, where exactly enough air is added to avoid carbon formation and achieve complete gasification. The cold gas efficiency of biofuels was found to be comparable to that of coal. It is shown that the exergy efficiencies of biofuels are lower than the corresponding energetic efficiencies. For liquid biofuels, such as sludge and manure, gasification at the optimum point is not possible, and exergy efficiency can be improved by drying the biomass using the enthalpy of producer gas.
Keywords: Biomass, Biofuels, Gasification, Exergy analysis, Process efficiency.

NOMENCLATURE

C_S	calorific value of sulfur [kJ/kg]
ΔH	enthalpy of reaction [kJ/mol]
LHV	lower heating value [kJ/kg]
LHV_{org}	LHV of organic fraction in biomass per kg of organic fraction [kJ/kg org.fr.]
LHV_{org}	LHV of organic fraction in biomass per kg of wet biomass [kJ/kg biomass]
T	temperature [^oC]
z	mass fraction [-]
β	ratio of the chemical exergy to the LHV of dry organic substances [-]
ε_{ch}	chemical exergy [kJ/kg]
ε_{ph}	physical exergy [kJ/kg]
Ψ	exergy efficiency [-]

*Corresponding author. Phone: +31(40)247-36-89, Fax: +31(40)244-66-53, E-mail: k.j.ptasinski@tue.nl

INTRODUCTION

Biomass has great potential as a renewable and relatively clean feedstock for producing modern energy carriers, such as electricity and transportation fuels. In order to compete with fossil energy sources an optimal utilization of biomass resources is desired. For biomass-based systems, a key challenge is thus to develop efficient conversion technologies. This paper focuses on the process of biomass gasification, a technology that converts biomass into gaseous products. The gas may subsequently be used for the production of electricity, fuels and chemicals.

The complete technology from solid fuel to final application involves several unit operations including grinding of fuel, drying, gasification, gas cooling, gas cleaning and final utilization of the

gas. It was previously demonstrated by Vlaswinkel [1] for gasification of coal and recently by Ptasinski et al. [2] for gasification of organic sludge that the gasifier is one of the least efficient unit operations in the whole gasification technology. Therefore an analysis of the gasifier alone can substantially contribute to the efficiency improvement of the whole gasification technology.

The main purpose of this paper is to compare different types of biofuels for their gasification efficiency and benchmark this against gasification of coal. A wide range of biomass sources, such as traditional agricultural crops, dedicated energy crops, residues from agriculture and foresting as well as organic wastes can be gasified. This is generally regarded as a real advantage, because it means that the best available and usually economically most attractive feedstock can be selected. However, these biomass types differ in chemical composition, heating value, ash and moisture content. The question is whether all the biomass types can be converted with comparable efficiencies. Biomass is not a well-defined and often inhomogeneous feedstock, whose composition may vary depending on origin, physical location, age, season and other factors. The composition of the organic matter in biomass does not vary much, e.g. wood typically contains cellulose: hemicellulose: lignin in 2:1:1 ratio. However, variations in moisture content and ash content are especially large. In this study various fuels, comprising wood, grass and vegetable oils and including wet biomass sources such as manure and sludge are studied. Coal was also chosen as a reference point for fossil fuel gasification.

The change in composition from biomass to coal can be illustrated using a diagram developed by Van Krevelen [3]. Figure 1 shows the change in atomic ratios H/C and O/C from biomass to peat, lignite, coal and anthracite. As it can be observed from this figure, biomass, e.g. wood, contains more oxygen with respect to carbon than in coal. This influences the gasification process, as gasification is a partial oxidation.

This paper starts with an evaluation of exergetic efficiencies. Focusing thereafter on biomass gasification, the question is under which gasification conditions the gasification efficiencies should be evaluated. It was shown by Desrosiers [4] and Double and Bridgwater [5] that energy-based efficiencies reach a sharp maximum at the so-called carbon boundary point where exactly the right amount of oxygen is added to the gasifier in order to achieve complete gasification. Prins et al. [6] have shown that the carbon boundary point is also the optimum for exergy-based efficiencies. The locations of the carbon boundary points with corresponding carbon boundary temperatures and gas phase compositions are calculated for a variety of biofuels. Results are presented for gasification efficiencies of these fuels, based on energy and exergy. Finally, the effect of improving gasification of wet biomass by prior drying using the enthalpy of the product gas is evaluated.

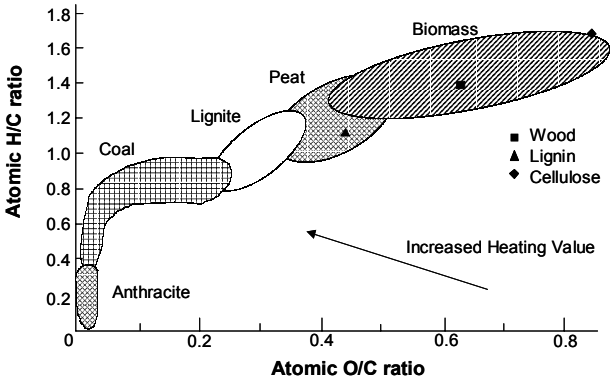

Figure 1: Van Krevelen diagram

EVALUATION OF EXERGY EFFICIENCY

The gasification process considered in this paper is schematically presented in Fig. 2. Biomass enters the gasifier at environmental temperature T_0, air at the same temperature is used as a gasifying medium. The gaseous products leave the gasifier at the reactor temperature T_R. It is assumed that the gasifier operates as adiabatic and pseudo homogeneous reactor at atmospheric pressure. Gasification entails partial oxidation of the feedstock so chemical energy of biomass is converted into that of gas and also heat.

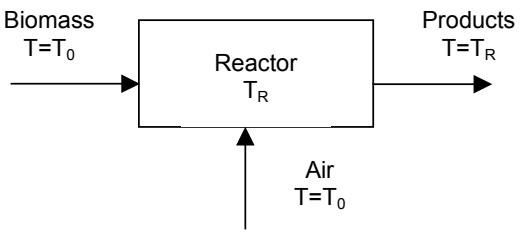

Figure 2: Schematic diagram of the gasifier

The energetic efficiency of a gasification process, generally known as the cold-gas efficiency, can be determined as:

$$\Psi_1 = \frac{LHV_{gas}}{LHV_{biomass}} \quad (1)$$

where LHV_{gas} and $LHV_{biomass}$ are the net heats of combustion (lower heating values) of gas and biomass, respectively. The lower heating values for the organic fraction of the biomass were calculated from the higher heating values, present in the Phyllis database, maintained by the Energy Research Centre of the Netherlands, ECN [7].
The exergetic efficiency may be defined as the ratio between chemical exergy of product gas and biomass feed:

$$\Psi_2 = \frac{\varepsilon_{ch,gas}}{\varepsilon_{ch,biomass}} \quad (2)$$

Both definitions have a drawback: they disregard the sensible heat contained in the product gases. Producer gas at elevated temperature is preferred over environmental temperature and therefore the calculated efficiency should be higher. However, if the sensible heat were to be added to the energetic efficiency, this efficiency would always be 100% because the gasifier operates adiabatically. This problem can be overcome by using exergetic efficiency based on chemical as well as physical exergy:

$$\Psi_3 = \frac{\varepsilon_{ch,gas} + \varepsilon_{ph,gas}}{\varepsilon_{ch,biomass}} \quad (3)$$

Exergy analysis is performed according to the method proposed by Szargut et al. [8]. Chemical exergy of the biomass is calculated from the correlations for technical fuels using the LHV, and mass fractions of organic material, sulfur, water and ash in the biomass:

$$\varepsilon_{0,total} = z_{org} \cdot (\beta \cdot LHV_{org}) + \\ + z_S(\varepsilon_{0,S} - C_S) + z_{water} \cdot \varepsilon_{0,water} + z_{ash}\varepsilon_{0,ash} \quad (4)$$

The factor β is the ratio of the chemical exergy to the LHV of the organic fraction of biomass. This factor is calculated from statistical correlations developed by Szargut and Styrylska [9]. The following correlation are used:

- for solid biofuels:

$$\beta = \frac{1.044 + 0.0160 \cdot \frac{H}{C} - 0.3493 \cdot \frac{O}{C} \cdot \left[1 + 0.0531 \cdot \frac{H}{C}\right] + 0.0493 \cdot \frac{N}{C}}{1 - 0.4124 \cdot \frac{O}{C}} \quad (5)$$

- for liquid vegetable oils:

$$\beta = 1.0374 + 0.0159 \cdot \frac{H}{C} + 0.0567 \cdot \frac{O}{C} \quad (6)$$

- for coal:

$$\beta = 1.0437 + 0.1869 \cdot \frac{z_{H_2}}{z_C} + 0.0617 \cdot \frac{z_{O_2}}{z_C} + 0.0428 \cdot \frac{z_{N_2}}{z_C} \quad (7)$$

where H/C, O/C, and N/C represent atomic ratios in the fuel.

GASIFICATION OF VARIOUS BIOFUELS AT THE CARBON BOUNDARY POINT

Table 1 shows proximate and ultimate analyses for the fossil fuel and the biofuels that were considered. The presented data were obtained from the Phyllis database [7]. Since biomass and (to a lesser degree) coal contain mainly carbon, hydrogen and oxygen, the compositions of the fuels can be indicated in a molar ternary C-H-O-diagram as shown in Fig. 3. The equilibrium composition at any point in the diagram can be computed at a given temperature and pressure by minimization of the Gibbs free energy of the system. In this work only thermodynamically stable components at temperatures above 600°C were considered, i.e. CO, CO_2, H_2, H_2O, CH_4, C(s), N_2 and H_2S. The main chemical reactions taking place in the gasifier are:

$$C + CO_2 = 2\ CO \qquad \Delta H = 172{,}6\ kJ/mol \quad (8)$$

Table 1: Proximate and ultimate analysis of various fuels

Fuel	Proximate analysis (wt%)			Ultimate analysis (wt% of organic fraction)				
	Mois-ture	Ash	Organic fraction	C	H	O	N	S
Coal	11.5	8.50	80.0	78.2	4.93	13.3	1.45	1.69
Vegetable oils	0	0	100	75.4	11.7	12.9	0	0
Straw	12.7	6.37	80.9	48.9	5.97	43.9	0.82	0.15
Treated wood	14.6	4.44	81.0	51.5	6.03	41.3	1.22	0.09
Untreated wood	19.8	1.84	78.4	50.8	6.06	42.7	0.36	0.07
Grass/plants	24.2	5.46	70.3	49.7	6.00	42.7	1.32	0.18
Sludge	32.5	25.72	41.8	50.2	7.09	34.9	5.63	1.77
Manure	43.6	17.20	39.2	50.2	6.50	34.6	5.19	0.85

Note: Ultimate analysis does not add up to exactly 100% due to presence of trace elements (e.g. chlorine).

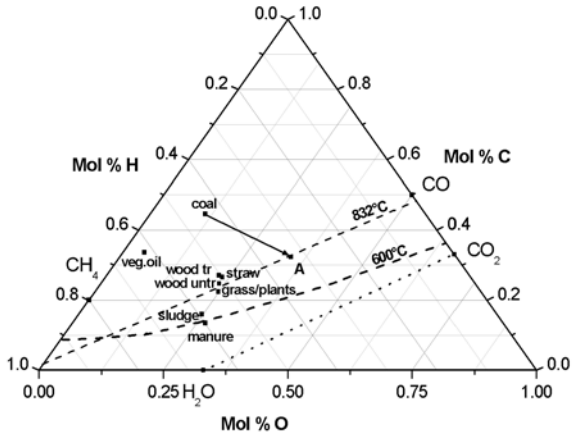

Figure 3: Location of biofuels in ternary C-H-O diagram.

$C + H_2O = CO + H_2$ $\Delta H = 131{,}4$ kJ/mol (9)

$C + 2\ H_2 = CH_4$ $\Delta H = -74{,}9$ kJ/mol (10)

$C + O_2 = CO_2$ $\Delta H = -393{,}5$ kJ/mol (11)

In Fig. 3 the indicated isotherms are the solid carbon-boundary lines (at a temperature of 600°C and 832°C). Above the carbon boundary line, solid carbon exists in heterogeneous equilibrium with gaseous components; below this line, only gaseous components are present in homogeneous equilibrium. Gasification of fuel implies adding so much oxygen until the solid carbon boundary is reached. This is indicated for coal by the arrow in Fig. 3, which points in the direction of oxygen; when point A is reached, all carbon has been gasified. The carbon-boundary point is the optimum point of the gasifier operation because exactly enough oxygen is added to achieve complete gasification. If more oxygen is added than required, the produced gas loses its heating value, until eventually the line from CO_2 to H_2O is crossed and complete combustion has taken place.

For the various biofuels considered, the optimum point of gasifier operation was calculated by the software programme Aspen Plus assuming that chemical equilibrium is attained. Table 2 shows the corresponding air/biomass ratios and carbon boundary temperatures for the optimum gasification points for the fuels. From these data, it can be observed that the solid biofuels require much less addition of air than coal or vegetable oil. The reason for this is that they already contain a large amount of oxygen in their organic matter. Since relatively little oxygen has to be added to the biomass, less oxidation reactions take place and the corresponding carbon boundary temperatures for gasification of biomass are lower than for coal and vegetable oil.

The compositions of sludge and manure lie already very close to the carbon boundary isotherm of 600°C. Because sludge and manure are very moist, they already contain a large amount of oxygen, so that oxygen addition is limited, and carbon boundary temperatures were found to be below 600°C. However, at such low temperatures, the gasification reactions become very slow and it

Table 2: Optimum gasification operating points and gas compositions for various fuels

Fuel type	T (°C)	Air flow (kg/kg biomass)	Product gas composition (mole fraction) H_2O	N_2	H_2	CO	CO_2	CH_4	H_2S
Coal	832	2.836	0.005	0.500	0.158	0.324	0.009	0.001	0.003
Vegetable oils	875	3.837	0.003	0.467	0.251	0.275	0.003	0.001	0.000
Straw	659	1.401	0.063	0.384	0.225	0.205	0.113	0.010	0.000
Treated wood	655	1.628	0.062	0.409	0.213	0.194	0.112	0.010	0.000
Untreated wood	642	1.452	0.076	0.380	0.227	0.177	0.126	0.013	0.000
Grass/plants	621	1.240	0.097	0.363	0.232	0.146	0.145	0.018	0.000
Sludge*	600	1.237	0.186	0.412	0.192	0.056	0.147	0.004	0.003
Manure*	600	1.247	0.246	0.395	0.171	0.038	0.147	0.002	0.001

* For this feedstock. the carbon boundary temperature is below 600°C. A minimum gasification temperature of 600°C was used.

would be difficult to attain chemical equilibrium in practice. A gasification temperature of at least 600°C was considered as being required in order to reach equilibrium within a reasonable reaction time. This criterion dictated the amount of air for gasification of sludge and manure, which means that these fuels are over-oxidized in order to evaporate all the moisture present.

Table 2 shows the composition of the products formed by the gasification process. As a result of the higher gasification temperature for coal and vegetable oil, more carbon monoxide and hydrogen are formed, while gasification of the other biofuels takes place at lower temperatures and the gas contains more carbon dioxide and methane. From the table, it is apparent that very moist gas streams result from gasification of sludge and manure.

RESULTS OF EXERGY ANALYSIS

Table 3 shows lower heating values, the ratio beta, and total chemical exergy of the various fuels. It is remarkable that for biomass containing a lot of oxygen, the values of beta are higher (above 1.10) than for coal and vegetable oils (around 1.07) with much lower oxygen content. This may be explained by the fact that polymers such as cellulose and hemi-cellulose are highly ordered structures, and work can be delivered if these are decomposed.

Fig. 4 shows the exergy distribution for gasification of various biofuels. The exergy contained in the biomass is converted by gasification into chemical exergy of the product gas, physical exergy of the product gas, and part of

Table 3: Lower heating value and chemical exergy of various fuels

Fuel	LHV_{org} (kJ/kg organic)	LHV_{org} (kJ/kg biomass)	β (-)	ε_{ch} (kJ/kg biomass)
Coal	31047	24839	1.067	26638
Vegetable oils	37558	37558	1.074	40338
Straw	18064	14619	1.128	16506
Treated wood	18886	15290	1.119	17129
Untreated wood	18904	14812	1.122	16634
Grass/plants	18624	13101	1.125	14760
Sludge	19617	8197	1.118	9249
Manure	19148	7506	1.116	8427

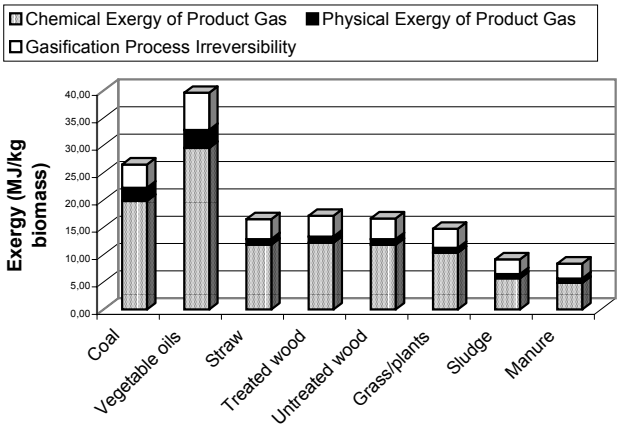

Figure 4: Exergy distribution for gasification of various fuels

the exergy of biomass is lost due to process irreversibilities. It can be seen that the largest irreversibility occurs for vegetable oil and coal gasification, which is related to the large amount of oxygen that needs to be added to vegetable oil and coal gasifiers. However, rather than the absolute irreversibility, it is more meaningful to focus on relative irreversibility, i.e. to compare the biofuels due to exergetic efficiencies.

Figure 5 shows the energetic and exergetic efficiencies for the gasification of different biofuels. The energetic efficiencies of vegetable oil, straw, treated wood, untreated wood and grass are very comparable with coal, whereas efficiencies for sludge and manure are considerably lower. This was to be expected, because gasification at the optimum operating point was not possible for these streams. In sludge and manure gasification, oxygen is added mainly to generate heat and evaporate moisture present in

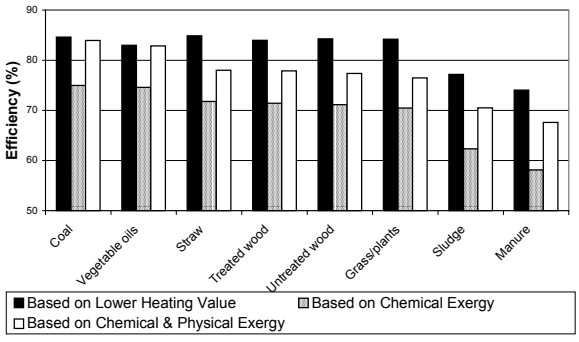

Figure 5: Comparison of gasification efficiency for various fuels

the fuel. If the exothermic oxidation reactions could drive endothermic gasification reactions, rather than endothermic evaporation of water, the gasifier would work much more efficiently.

Fig. 5 shows that the efficiency based on chemical exergy is higher for coal and vegetable oil than for the other biomass streams, i.e. around 75% versus 70-72%. This may be explained because large molecules are broken up into smaller ones. For some of the small molecules contained in the product gas, the chemical exergy is less than their lower heating value e.g. 97.6% for hydrogen and 97.2% for carbon monoxide. On the contrary, the chemical exergy for coal and biomass is higher than their heating value. Therefore, the difference in chemical exergy between feed and product is larger than the difference in lower value. This difference is smaller for coal and vegetable oils, because their chemical exergy is only 107% of their lower heating value, while for solid biomass this is 111-113%. Also, exergetic efficiencies of gasification are lower than energetic efficiencies.

Gasification efficiencies based on chemical and physical exergy are also shown in Fig. 5. The same trends are observed as before: gasification of vegetable oil and coal is better than biomass such as wood, straw or grass, while gasification of manure and sludge is much less efficient. Because coal and vegetable oil are gasified at higher temperatures, their gasification efficiencies are improved relatively much by inclusion of the physical exergy. Drier biomass such as treated wood or straw may be slightly preferred over fresh biomass such as untreated wood and grass.

Finally, it is very interesting to note that gasification of vegetable oils, which are moisture and ash-free, is comparable to gasification of coal, despite containing moisture and ash. It can be noted that chemical exergy of vegetable oils and coal is higher than that of remaining fuels (see Table 3).

IMPROVING GASIFICATION OF WET BIOMASS

It was concluded that gasification of sludge and manure is not very efficient because these contain a substantial amount of water, so that operation at the optimal gasification conditions is not possible. This is caused because extra heat must be generated at the gasification temperature (> 600°C) in order to evaporate the water at a much lower

temperature, leading to exergetic losses. In order to improve the gasification efficiency, moisture should be removed prior to the gasifier. It is possible to use the enthalpy of the gasifier product gas for drying the biomass (in the absence of alternative, external sources of heat). We have assumed that water is evaporated in the dryer at a temperature of 100°C by exchanging heat with the product stream, as shown in Fig. 6. Modeling of drier and gasifier was restricted to sludge, as this was one of the two streams containing relatively much moisture. In this new situation, the temperature of the products is lower than the temperature of the gasifier, due to the fact that heat is removed for the vaporization of the water.

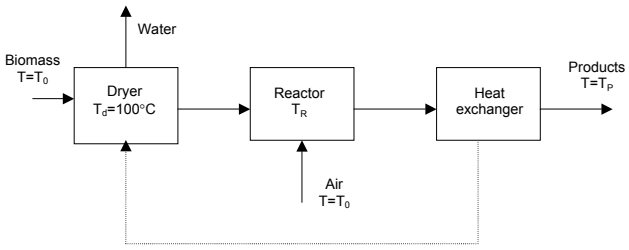

Figure 6: Process scheme for drying of biomass prior to the gasification process

Calculations were performed using Aspen Plus, and the sludge was dried from its initial moisture content of 32.5% to water percentages varying from 30% to 11%. This decreases the final temperature of the product gas from 600°C to temperatures between 514°C and 297°C. It was found that gasification of dried sludge containing 19 wt% moisture corresponded to a carbon boundary temperature of 600°C. Therefore, by drying the sludge from 32.5 wt% moisture to 19 wt% using product gas, it was possible to enable gasification at the point where not more oxygen is added than required for gasification of the carbon. This is demonstrated in the ternary C-H-O diagram in Fig. 7. By gasification of the original wet biomass at 600°C, point B is reached which is below the carbon boundary isotherm. If water is removed from the sludge by prior drying, gasification at the carbon boundary becomes possible, indicated by moving from the point indicated with 19% moisture to point A on the carbon boundary line.

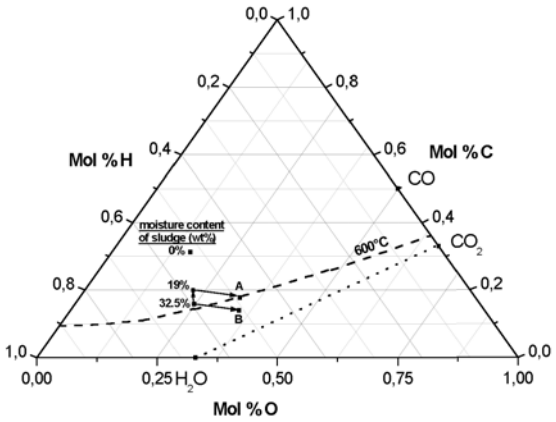

Figure 7: Drying and gasification of sludge illustrated in ternary C-H-O diagram

Figure 8 shows the effect of drying the biomass on the overall efficiency of the gasification system, including the dryer. It is obvious that the efficiency improvement by drying is less for the efficiency based on the total exergy compared to the efficiencies based on the lower heating value or the chemical exergy. The reason is that this definition takes the temperature decrease of the products into account. As the moisture content decreases, higher amounts of water have to be evaporated in the dryer. Because the heat needed to vaporize this water is removed from the hot gases leaving the gasifier, the temperature of the products decrease, thus lowering the value of the physical exergy.

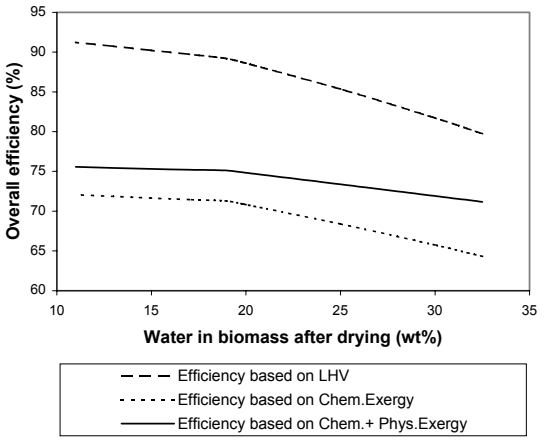

Figure 8: Improvement of gasification efficiency by drying using enthalpy of product gas

As expected, decreasing the moisture content of the biomass entering the gasifier increases the efficiencies of the process. The largest benefit is obtained when the sludge is dried from 32.5% to 19% moisture. Further drying hardly increases the chemical exergy of the product gas, but the physical exergy of the product gas is slightly increased because carbon boundary temperatures higher than 600°C can be achieved. Therefore, at increased drying levels (that is for water content in the biomass leaving the dryer lower than 19%), the efficiency based on chemical and physical exergy has the same slope as the efficiency based only on chemical exergy. Moreover, at this range the efficiency based on the total exergy (chemical and physical exergy) is only slightly higher than the efficiency based only on the chemical exergy. The reason is that the chemical exergy of the biomass is the main constituent of the total exergy and the contribution of physical exergy is much smaller.

CONCLUSIONS

In order to substitute fossil fuels by renewable fuels, solid biofuels (straw, untreated wood, treated wood, grass/plants) or liquid biofuels (vegetable oil) could replace coal as a gasification feedstock. The optimum gasification efficiencies of these fuels based on lower heating values are comparable, i.e. around 84%. However, if the efficiencies are based on chemical exergy, the solid biofuels with high oxygen content are regarded as high-quality fuels, for which a penalty is paid when decomposing them into small gaseous components. Also, the gas produced from solid biomass gasification has a lower temperature so that it contains less physical exergy. As a result of these two factors, gasification based on chemical and physical exergy shows higher efficiencies for coal than for solid biomass, i.e. almost 84% vs. 76-78%. It is interesting to note that gasification of vegetable oils is similar to the gasification of coal, and both these fuels can be considered as high quality fuels.

ACKNOWLEDGEMENT

This research project was conducted within the scope of the Incentives Programme for Energy Research, founded by NWO (Netherlands Organization for Scientific Research) and Novem (Netherlands Agency for Energy and Environment).

REFERENCES

[1] Vlaswinkel EE. *Energetic analysis and optimisation of an integrated coal gasification-combined cycle power plant*. Fuel Processing Technology 1992; 32(1-1): 47-67.

[2] Ptasinski KJ, Hamelinck C, Kerkhof PJAM. *Exergy analysis of methanol from the sewage sludge process*. Energy Conversion Management 2002; 43(9-12): 1445-1457.

[3] Van Krevelen DW. *Coal – typology – physics – chemistry - constitution*. Amsterdam: Elsevier, 1993.

[4] Desrosiers R. *Thermodynamics of gas-char reactions.* In: Reed TB, editor. A survey of biomass gasification., Solar Energy Research Institute, Colorado, 1979.

[5] Double JM, Bridgwater AV. *Sensitivity of theoretical gasifier performance to system parameters*. In: Palz W, Coombs J, Hall DO, editors. Energy from biomass, Proceedings of the 3rd EC Conference, Venice. p. 915-919, 1985.

[6] Prins MJ, Ptasinski, KJ, Janssen FJJG. *Thermodynamics of gas-char reactions: first and second law analysis*. Chem Eng Sci. 2003; 58(3-6): 1003-1011.

[7] ECN Phyllis – the composition of biomass and waste. Internet page: http://www.ecn.nl/phyllis/, 2002.

[8] Szargut J, Morris DR, Steward FR. *Exergy analysis of thermal, chemical and metallurgical processes*. Berlin: Springer Verlag, 1988.

[9] Szargut J, Styrylska T. *Approximate evaluation of the exergy of fuels* (in German). Brennst. Wärme Kraft, 1964; 16(12): 589-596.

Proceedings of ECOS 2005
Trondheim, Norway
June 20–22, 2005

BIOMASS TO BIOELECTRICITY IN CHINA: TECHNICAL ASSESSMENTS OF DIFFERENT SOLUTIONS

Rinko Rijnhout[1,2], Gang Li[1], Guanyi Chen[1,*]
[1]Tianjin University Faculty of Environmental Science and Engineering
Section of Bioenergy and Wastes Treatment
Weijin Road 92, 300072, Tianjin
China

[2]Delft University of Technology
Section of Energy Technology,
Mekelweg 2, 2628 CD, Delft
The Netherlands

ABSTRACT

The paper is a result of an EU-funded project, focusing on the feasibility study of 1 MWe biomass-fuelled power plant concentrating on using a fluidized bed gasifier coupled with a micro turbine. In total 8 technical solutions from biomass to electricity are discussed here, covering gas turbine, gasifier, pyrolyser, gas cleaning and conditioning, gas engine, Stirling engine and steam boiler. The referred biomass feedstock is local cotton stalk and sometimes rice stalk. The result indicates that, for 1 MWe power plant, fluidised bed gasifier coupled with a 500 kWe gas turbine and 500 kWe gas engine is a promising choice. The work related to environmental assessment will be of the future research.

Keywords: Biomass, Electricity, Biomass-derived gas, Micro turbine, Gasifier

INTRODUCTION

The rapid growth of the economy gives a quick increase of consumption of energy which leads meanwhile to serious pollution. Biomass is a renewable source and also a clean energy carrier thereby its extensive utilisation contributing to the national energy supply security and environmental protection. The Chinese government is therefore paying particular attention to it. Biomass can be converted into energy products (usually electricity or heating and sometimes gaseous fuel, liquid fuel, and solid fuels) through many options [1,2]. Biomass to electricity is currently mostly concerned in China and Europe as it is justified economically viable [3,4]. However, if the availability of local biomass resource is concerned and furthermore the size of biomass power plant is limited, different technical solutions for biomass to electricity may result in totally different economic advantages, even if the uncertainty regarding the technical implementation and operation of such power plant is neglected. In addition, some newly emerging technologies may be suitable for biomass-to-electricity solution, but not evidently proven. Therefore, a research addressing technical and economic aspects of biomass-to-electricity solution is necessary.

This paper is a short technical analysis of different systems, which can be used for the generation of bioelectricity from biomass in China. The work is a duty of combined EU and China funded project, targeting on a small size (around 1 MWe) biomass power plant in the vicinity of Tianjin, mainly fuelled with rice straw/cotton stalk. Different

[*]Corresponding author: Phone: +86-22-87401929 Fax: +86-22-27404833 E-mail: chen@tju.edu.cn

systems are being researched here and compared on efficiency, economics and emissions.

BIOMASS RESOURCE AND BIOELECTRICITY IN CHINA

Biomass resource in China is very abundant with the annual production of 3000Mt in total [5]. Table 1 and 2 illustrate the yearly yield of several typical biomass feedstocks in China in 2002 [6]. So much biomass feedstock is a strong driving force for developing biomass-to-energy conversion technologies in China. Up to now, a number of such technologies in terms of biomass to electricity have been developed, including a circulating fluidized bed (CFB) coupled with downstream gas engines (small scale under operation for 3 years), moving-bed pyrolyser combined with gas engines (on demonstration as of the end of 2004), fluidised bed gasifier coupled with the gas engine (on demonstration), fluidised bed boiler combined with steam turbine (under development) , fluidised bed gasifier with Stirling engine (under preparation) [7-11]. However, those technologies are usually concentrating on sawdust or rice husk and more or less being subjected to problems, such as, tar contamination, non-reliable and bad operation, less cost benefit, seriously secondary pollution, low efficiency of electricity generation.

Biomass Types	Quantity Mt	Mtce[1]	Estimated (2010)
Stalks/ straws	600	280	700
Firewood	140	80	210.5[12]
Rice husks	50	25	58
Industrial wastes	24	12	26
Bagasse	12	6	14
Total	826	403	

Table 1: Several biomass yields in China (2002)

The first CFB biomass gasification power plant using rice husk as feedstock was constructed in Putian, Fujian Province and has been continuously operated since August of 1998. The system consists of a CFB gasifier, a gas cleaner (including an inertial separator, a cyclone separator, a venturi and two water scrubbers) and power generation system, which consists of 5 x 200 kWe gas engines [7]. However this system has a total efficiency of about 17% [7]. The reliability of such system has been proven through two years of operation (about 10,000 h). The total investment is 510, 000 US$. The pay-back time for the system is no more than two years. Later another Demo-plant of 1.2MWe output was funded jointly by the Sanya Timber Factory and Guangzhou Institute of Energy Conversion [8]. The plant is based on an atmospheric circulating fluidized bed gasifier (CFBG) using wood powder as fuel in combination with a gas engine [8]. Due to the low efficiency and handing of liquid streams resulting from gas scrubbing the technology is complicated and costly.

Straw/stalk types	Quantity, Mt
Rice straw	201.8
Corn stalk	217.6
Wheat straw	102.4
Cotton stalk	18.2
Bean stalk	18.7
Others	35.7
Total	~600

Table 2: Stalk and straw output in China (2002)

The planned 1MWe Demo plant is going to be established in Tianjin. Tianjin region is available to supply rice straw and cotton stalk up to 100 MWe. Therefore, the target feedstocks here are Tianjin-origin rice straw and cotton stalk. Table 3 shows their elemental analysis under air dry basis.

Ultimate analysis	Rice straw wt %	Rice straw wt %	Cotton stalk wt%	Cotton branch[2] wt%
C	43.8	48.1	50.2	39.5
H	5.9	5.9	7.1	5.7
N	0.88	1.7	0.64	1.25
O[3]	49.1	43.6	41.9	38.1
S	0.22	0.14	0.11	0.02
Cl	-	0.58	-	-
Ash	10.6	19.1	4.6	15.43
Moisture	10	10	10	10
LHV, MJ/kg	14.5	18.4	19.3	14.7

Table 3: The ultimate analysis data and LHV

[1] Million tons of coal equivalence, Mtce.

[2] dry basis. The other data is based on dry-ash free basis

[3] by difference

TECHNICAL SOLUTIONS TO BIOELECTRICITY

Different options for generating electricity from biomass are: Ranking Cycle, Gas engine, Micro (Gas) turbine, a combination of a turbine and an engine, Stirling engine. Further next to the base system there should always be a waste heat recovery system to increase the efficiency of the plant. In this paper all these variants will be discussed except for the Fuel Cell as fuel cell at this moment is in the early developing phase for bioelectricity. However, in the coming years it would be an option.

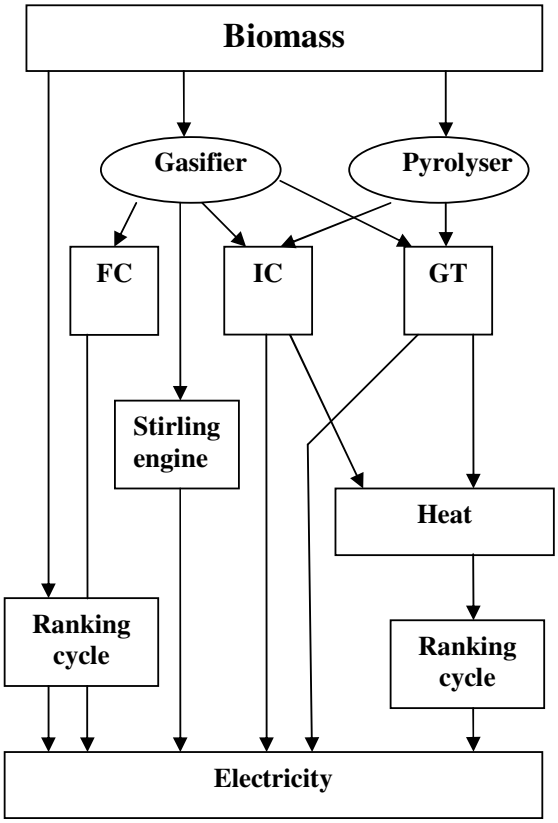

Figure 1: different solutions for electricity production from biomass

Biomass-derived gases

Biomass can first be converted to gaseous fuels and then burned in the engine or turbine to produce bioelectricity. The performances of different technical solutions are mostly dependent on the quality of gaseous fuels derived from gasification or pyrolysis of biomass. Table 4 lists the comparison of the composition of gasified and pyrolysed fuel gases. Both the gases out of the gasifiers have an approximately LHV of 3.5 to 4 MJ/kg, or 3.7~4.5MJ/Nm^3, however, the heating value of pyrolytic gas has a value of 14MJ/kg.

Gas composition at the outlet of gasifiers / pyrolysers			
Gas composition (vol. %)	AFBG	PFBG	AFBP[1]
H_2	8.55	9.30	25.50
CO	11.10	11.70	39.50
CO_2	14.95	14.50	15.55
CH_4	2.50	2.20	12.45
C_2H_n	0.82	0.43	3.50
N_2[2]	52.10	51.92	3.50
H_2O	9.98	9.95	12.63

Table 4: Gas composition at the outlet of gasifier / pyrolyser (ash and tar free)

Ranking cycle

This cycle is actually a basic steam cycle, which is being extensively used in China for producing electricity from coal for many years. The Ranking cycle fuelled by biomass is just under development now in China, and is deemed to have a few disadvantages compared to the case of coal. The lower energy density and the lower maximum temperature give a lower steam quality compared to the coal-fired case. Furthermore the scale of the plant is limited due to the availability of biomass feedstock's supply thereby resulting in a lower efficient steam turbine cycle. In addition, if rice straw and cotton stalk used as fuels, the cooling of the condenser/heat exchangers may lead to serious deposition and corrosion arising from the high content of alkali materials originated. This will reduce the system efficiency even more. In the worst case it leads to the shutdown of plant. Due to these problems the steam cycle gives an overall efficiency of around 19 to 21%, depending on the condenser values. However the system is simple in use and cheaper in cost compared to the micro (gas) turbine and even to gas engines in the middle to large scale. Further study must give a better view to this system.

Gas engine

[1] dry basis.
[2] by difference

The gas engine system used at present in China has an efficiency of nearby 17%. The problem is the low LHV and the arrangement of the different engines (5 * 200kWe). With a larger engine (1MWe) the efficiency can be further increased. For example the theoretical efficiency of the system can reach as far as 22 % to 25 % if the propoer modification to engine can be made. Another significant advantage is the local availability of the gas engine. This wouldn't increase a technical value, but significantly decrease the investment capital.

(Micro) Gas turbines

The known gas turbine, which are set to use LHV gas is the ABB Typhoon (used in Värnamo, Sweden) [13]. The Volvo VT 600, TURBEC and the Capstone gas turbines have been already designed to burn pyrolytic gas [14]. However these gas turbines are assumed that they can be rebuilt suiting for the biomass-derived gases. This involves however a higher investment than the usual gas turbine.

The main problem of a gas turbine with biomass-derived gases is that the inlet pressure of the fuel must be in comparison with the inlet pressure of the compressed air after the compressor. In normal case the natural gas or the Methane (ISO norm) is compressed in a small compressor at the inlet of the fuel. Due to the low LHV of biomass-derived gases the electricity needed for the compressor would sincerely decrease the efficiency of the total system. For example the Volvo VT 600 with a normal efficiency would go from 21.2 % around to approximately 20 %, which is a decrease in the total efficiency [14]. However due to the use of biomass-derived gas the total output of a gas turbine is increased. Due to the increase in power need of the fuel compressor the extra power output is almost totally consumed by this compressor.

There are different ways to encounter this problem. The following 2 are promising systems. The first system is a gas turbine coupled with a pressurized gasifier. This system has the advantage that the fuel gas doesn't have to be pressurized before burned in the combustion chamber of gas turbine. The intake air of the gasifier is pressurized, which, compared to the gasified fuel gas, is lower in the mass flow thereby leading to a lower electricity demand of the compressor. The advantage would be a total increase in efficiency of 2 to 3 percent. This system is already realised in Värnamo, Sweden [13]. The latter system has a pressurized system of 18 bars and uses a ABB Typhoon gas turbine with the output of 4.2 MWe.

The second option could be a gas turbine with a pyrolyser system. This system has 2 advantages compared to the former one. It could be an atmospheric system, because of the higher LHV and the need of a wet scrubber due to high ash and tar concentrations. Further the changes to the (micro) gas turbine wouldn't be significant as with the gasifier option, because of the higher LHV. However the wet scrubber invokes a series of other problems like the cleaning of the polluted waste water and the loss of sensible heat, which gives a chance to a higher environmental risk.

Combination of the gas engine and micro (gas) turbine

This combination might be slightly less efficient, because of the 2 different demanded pressures. Since the gas turbine needs a higher pressure than the gas engine, there will be a loss in energy in pressurizing the biomass-derived gases before the gas turbine or pressurizing the total air inflow of the gasifier. However this system has a few advantages that the other systems could not have. Firstly the system has the capability to be used in partial load, without lowering the efficiency when using only one gas turbine or gas engine. However further research has to be done to verify these ideas.

Stirling engine

Another option is the Stirling engine. This option has been researched at the Technical University of Denmark [15]. The electric efficiency of the system is 17.7%. Due to this low efficiency and the size of the system (35 kWe), this system can not be used in our project. However the low concentration of exhaust particles of the gasifier resulted in only the need of a bag filter, which is a huge advantage over any other gas cleaning system. The Stirling engine can also endure a larger dust and tar concentration than for example a gas engine or a gas turbine. Due to this advantage this system can be used in smaller project, which can tolerate a lower gas cleaning level not the more advanced systems.

Waste heat recovery

Most of the pilot plants in China use the waste heat only for heating the intake air of the gasifier. The waste heat (from gas cooling and flue gas) can be used in various systems. These systems can increase the efficiency of the total system substantially. The next solutions can be used in the gas turbine and gas engine variants, making them more efficient then the basic solutions.

The heat can be used to create steam in a combined cycle system. The heat of the flue gas and gas cooling can create steam of approximately 40 bars and 400 Celsius degree. Such steam can be used to drive a steam turbine, which has the potential to an additional 5 to 8 percent point of electricity. The latter value depends mostly on the condenser. Cooling water in China is not as common as in Europe where the cooling options can be more easily found for this scale. There are places in Chinese countryside where there is no open freshwater. Furthermore the temperature varies in the tropics from 20 to 40 degrees Centigrade and in the north from – 20 to 20 Celsius. These values give a not stable environment for the condenser. Combining the low isentropic efficiency of the steam turbine (due to a low power output) and the uncertain cooling option for the condenser, this option may not be as useful as in western countries.

The next option for the upgrade of the flue gas usage is the usage of a central heating system. This can be a small village or an industrial complex. Basically the heat from cooling the flue gas and the gas cooling system is the final product. It can be used for industrial steam generation, for heating or both. This option can increase the system with 60 % extra of heat efficiency. This system has some advantages in China because of the lower water dependence. The only water it needs is the water from the city heating or steam generation. It is clear this system cannot be used in the summer or in southern China because of no need for heating.

Another waste heat system can be a combination of the systems mentioned above. Using a backpressure system, this generates a lower amount of electricity, but gives the condenser a reliable cooling water supply. The last sensible option could be a seasonable use of the system. In the northern part of China the steam turbine option can be used at times when the biomass is available and electricity and heat is required. This period is the beginning of autumn and ending of spring. This leaves time for maintenance in the summer.

The usage of the waste heat is a sensible and more efficient way than the pilot plants operated at this moment. The two main disadvantages are that the capital investment is higher and the right solution for one place is not the right solution for the other. This system increases all the systems efficiencies, but it creates additional problems, which have to be solved from place to place

EMISSIONS

In contrast to woody biomass 1 year-rotation biomass like rice straw and cotton stalk have higher ash content. The ash can also contain elements like Chloride, which can be highly corrosive. Next to the efficiency and the technique the different kinds of elements have to be categorized and if needed measures have to be taken in the systems to prevent damage to the system and the environment. In addition, the N-containing pollutants should be highlighted considering the high N content of biomass feedstock.

The environmental benefit in terms of reducing carbon dioxide emission will be further investigated in later work.

CONCLUSIONS

The state of the art in the BGPG (biomass gasification power generation) in China is summarized. The size of the project is smaller compared to projects in Europe and USA. However because of lower operational cost of the gasifiers the systems can be more cost efficient at a lower level. Different systems have been selected to be researched, including gas turbines, gas engines, Ranking cycle, waste heat options and even the Stirling engine.

Different systems are being researched here and compared on efficiency, economics and emissions based on 1MWe capacity. From the technical point of view, those systems are feasible. The project is still ongoing now and therefore final results will be commissioned in the second half of 2005. The paper shows the most promising systems and interesting results in the research done so far.

Increase of efficiency compared to the 2 Pilot plants in China can certainly be done. A better cooling system or the use of a gas turbine could increase the efficiency with a few percents. A larger increase in efficiency can be created by use of a waste heat recovering system. However all these improvements will have a higher investment capital, which can make the system less economical. However further research on the relationship of efficiency and economical cost will be done in the later work.

ACKNOWLEDGMENTS

The financial support from European Commission through Asia-Pro-Eco programme is highly appreciated. The support from Jose Corella at University "Complutense" Madrid in terms of experimental results of using rice straw and cotton stalk in his test-rig should be also greatly grateful. In addition, the authors would like to thank Mohsen Assadi, Xuesong Bai, Tord Torrsion (Lund University), Umberto Desideri, Francesco Fantozi (University of Perugia), Li Sun (Energy Research Institute, Shandong Academy of Sciences) for their contribution. The support from Mengxiang Fang (Zhejiang University) should be finally acknowledged.

REFERENCES

[1] Assadi M, Bai XS, Chen G, Desideri U, Fantozzi F, Toledo JM, Torrison T: *A general Survey concerning electricity production from biomass.* In: Proceedings of Second World Biomass Conference, Rome, 2004.

[2] Larson ED, Williams RH, Regis M, Leal LV. *A review of biomass integrated-gasifier/gas turbine combined cycle technology and its application in sugarcane industries, with an analysis for Cuba.* Energy for Sustainable Development 2001; V(1):54-76.

[3] Wu C. *Economical assessment of Sanya Timber Mill for biomass gasification*. In: Proceedings of Regional Seminar on Commercialisation of Biomass Technology, Gangzhou, 2001.

[4] Bridgwater AV, Toft AJ, Brammer JG. *A techno-economic comparison of power production by biomass fast pyrolysis with gasification and combustion.* Renewable and Sustainable Energy Reviews 2002; 6:181–248.

[5] Chen G, Deng N, Zhang X, Jiao L, Spliethoff H. *Production of hydrogen-rich gas through biomass pyrolysis in a two-stage reactor.* In: Proceedings of ASME Turbo Expo 2004, Vienna, 2004.

[6] Chen G, Zhang X, Li Q, Lv X. *Development of biomass-based humidity-controlling building material*, report no. 2004-1001. Tianjin, TJU: Section of Bioenergy, 2004

[7] Yin XL, Wu C; Zheng P, Chen Y. *Design and operation of a CFB gasification and power generation system for rice husk.* Biomass and Bioenergy 23 (2002) 181–187.

[8] Wu Z, Wu C, Huang HT. *Test results and operation performance analysis of a 1MW biomass gasification electric power generation system.* Energy & Fuels 2003; 17: 619-624.

[9] Lei TY, Li ZF, Hu JJ. *Experimental study on the main technical performance of the fixed-bed biomass gasification equipment.* In: Proceedings of China Biomass Conference, Zhengzhou, 2004.

[10] Liu SY, Wang GC, DeLaquil P. *Biomass gasification for combined heat and power in Jilin Province*, report no. 2000-12. Jilin, China Modernized Biomass Energy Project Office, 2000.

[11] Ying S. *Development of the integrated biomass gasifier with Stirling engine.* Internal Communication between Liaoning Energy Research Institute and Tianjin University, 2003-2004.

[12] Li JF, H RQ. *Sustainable biomass production for energy in China.* Biomass and Bioenergy 2003; 25(12):483-499.

[13] Stahl K, Waldheim L, Morris M, Johnsson U, Gardmark L. *Biomass IGCC at Värnamo, Sweden – Past and future*. In: proceedings of GCEP Energy Workshop, Standford University, 2004.

[14] Assadi M, Bai XS, Torrison, T. *Modification of gas turbines for biomass derived gaseous fuel.* In: Proceedings of ASME Turbo Expo 2004, Vienna, 2004.

[15] Jensen N, Werling J, Carlsenb H, Henriksenb U. *CHP from updraft gasifier and stirling engine.* http://bgg.mek.dtu.dk/publications/pdf/amst02_v2_99.pdf.

Proceedings of ECOS 2005
Trondheim, Norway
June 20–22, 2005

MODEL-BASED ANALYSIS OF EFFECTS FROM LARGE-SCALE WIND POWER PRODUCTION

Johannes Rosen[1], Ingela Tietze-Stöckinger, Otto Rentz
French-German Institute for Environmental Research (DFIU)
University of Karlsruhe (TH)
Germany

ABSTRACT

For an economically and ecologically optimised integration of fluctuating renewable power generation (especially wind power) into electricity generation, a detailed consideration of fluctuation-induced effects on the existing power system is essential. A model-based approach is introduced in this paper, which comprehensively analyses the impact of such effects on power plant scheduling and facilitates their integration into the development of strategies for an optimised evolution of the future power system structure. The newly developed AEOLIUS tool for the simulation of power plant scheduling is described. In a combined analysis of long- and short-term effects it is used together with the multi-periodic cost-optimising energy system model PERSEUS-CERT. Based on the MATLAB/Simulink® package, AEOLIUS considers the challenges for plant scheduling down to a time scale of 10 minutes. Special attention is paid to the provision of stand-by capacities and control power, as well as intermediate storage. Thus, a sophisticated quantification of the actual (net) benefits of wind power feed-in is achieved. Model results for Germany show that wind mainly substitutes power from intermediate-load and base-load plants (coal-, lignite-, and nuclear-fired). However, the required provision of stand-by capacities and control power does not only limit the substitution of conventional capacities, but also the achievable net savings of fuel and emissions in conventional power generation.
Keywords: Wind power, PERSEUS-CERT, Matlab, Simulink, energy system optimisation, simulation, power plant scheduling

INTRODUCTION

To date, more than 15.000 MW of wind turbines have already been installed in Germany, able to produce roughly 30 TWh/a of electricity [1]. All of this capacity is onshore, but the German Wind Energy Institute (DEWI) estimates that in addition about 15% of electricity production could be covered by offshore wind energy in the medium term [2]. Such large amounts of fluctuating electricity feed-in, which cannot be planned in advance, are of special relevance in the context of power production planning. The fluctuations occur in a random pattern and have to be compensated by the production of the schedulable, (mostly) conventional capacities in the power system. Fluctuations in wind speed can occur quite fast [3] and the resulting problems increase with the amount of installed wind turbine capacity. Critical cases are high wind speed gradients as well as excessively high total wind speeds (as e.g. in a storm). The latter may cause that turbines producing power at their nominal capacity have to be turned out of the wind in order to prevent structural damage. This can result in a steep negative gradient of wind power production, which has to be compensated by other power plants. Sufficient amounts of reserve capacities have to be provided for this case. These can be either conventional or renewable capacities, which can be dispatched on demand. Steep positive wind power gradients can occur as well,

[1] Corresponding author: e-mail: johannes.rosen@wiwi.uni-karlsruhe.de, phone: +49 721 608-4690, fax: +49 721 758909

for which the other currently operating capacities must be prepared to reduce their production appropriately.
An increasing scale of the fluctuations is thus a challenging phenomenon and the resulting effects cannot be ignored[2], neither in power system operation, nor in long-term energy system (expansion) planning. Consequently, this requires the development of methodologies that enable an appropriate consideration of these short-term effects in long-term energy system modelling.
In the following paragraph, a brief overview of such a methodology will be given. It is based on a long-term energy system model, which is coupled with a short-term model for power plant scheduling. After explaining this context, the rest of the paper will focus on the development and application of the short-term model for power plant scheduling.

COUPLING OF LONG- AND SHORT-TERM MODELLING APPROACH

At DFIU the long-term optimising energy system model PERSEUS-CERT[3] is used for strategic energy system analysis. This multi-periodic bottom-up model of the European electricity sector has been modified to represent renewable electricity sources in a considerably more detailed way. Further, existing plants and future expansion options based on conventional technologies are modelled. The adapted version of the PERSEUS-CERT model currently covers 21 European countries, represented by 25 regions, and determines the cost-optimised development in the time period between 2000 and 2020. In addition to the installed renewable capacities in all countries, a set of detailed potential and related cost data for 15 renewable energy technologies was adapted and integrated into the model data-base for each of the EU15 countries. The realisable renewable power production options and the costs for the development and operation of the related capacities are currently represented by about 1500 new units and the same number of processes in PERSEUS, all of them with their individual technical and economic parameters (capacity, operating hours, costs, etc.). While the most important potentials are included in greater detail, smaller and less significant potentials are considered in an aggregated way to maintain an acceptable computation efficiency.
Due to the large model size and complexity, the load curve in PERSEUS-CERT is represented by eight characteristic days per year, with a total of 36 individual time slots. This temporal resolution is sufficient for the low shares of wind energy in the system that result from the model calculations when no financial incentives are taken into account. In this case, the current and expected future cost situation in the electricity sector does not allow renewable sources of electricity to become a favourable economic solution, even if CO_2 restrictions are introduced. However, the incentive mechanisms currently in place have been shown to be extremely powerful tools to stimulate a long-term growth of renewable electricity use. In this context (and in accordance with the actual developments), first model results indicate that wind energy will play a key role.

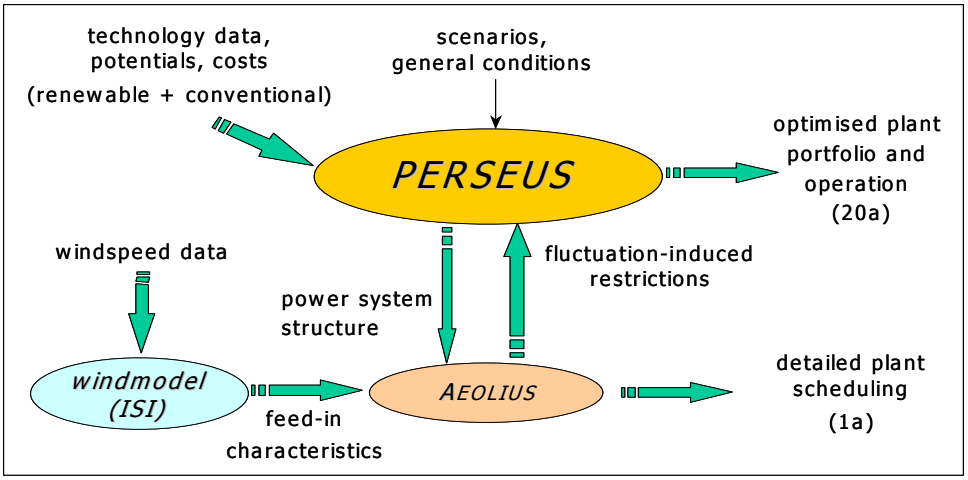

Figure 1: Interaction of models and data

[2] The interaction of large-scale wind power production with the power system, including the value of wind power in terms of fuel savings and CO_2-reductions, has been the subject of several studies, see e.g. [4], [5], [11], [14], [15].
[3] Programme-package for Emission Reduction Strategies in Energy Use and Supply – Certificate Trading. For a detailed description of the underlying PERSEUS-CERT linear optimisation approach, please refer to [6].

In order to ensure a consistent calculation of the capacity mix in future time periods also for the high wind energy shares encountered in this case, it is desirable to take into account the system requirements and interactions caused by a large-scale wind power production. This includes the secured wind turbine capacity, additional reserve capacities required, and the actual amount of fuel and emission savings. However, the temporal resolution in PERSEUS is not sufficient to represent the influence of the large resulting wind energy fluctuations, which occur randomly and do not follow a characteristic diurnal pattern. To overcome this limitation of the long-term modelling approach, it is combined with AEOLIUS, a newly developed and temporally highly resolved dynamic simulation model for power plant scheduling. It is designed to characterise the effects of an increasing contribution of fluctuating renewable electricity production on the conventional power production system, focusing especially on wind power.

The resulting complementary modelling approach is visualised in Figure 1. The future energy system structure determined by PERSEUS (without the consideration of fluctuation-induced effects) acts as input for AEOLIUS. In an iterative procedure, restrictions resulting from fluctuation-induced interdependencies between large-scale renewable power production and conventional power production are derived from AEOLIUS for individual periods of the intertemporal PERSEUS-CERT model. These restrictions can be generalised and subsequently used for an improved representation of renewable power production in PERSEUS, helping it to derive optimised long-term (20 years) energy system expansion and operation strategies on a more realistic basis.

In the following paragraphs, the newly developed dynamic AEOLIUS model is introduced in more detail.

SHORT-TERM MODELLING APPROACH

The AEOLIUS model was designed to simulate the combined medium- and short-term production planning for the entire power plant portfolio in a grid-area or a country, with the ability to account for an increasing feed-in of fluctuating renewable electricity generation. In the first model version, the German power sector is simulated for the duration of one year. Under the current market regulations, power plant schedules have to be announced 24 hours in advance (day-ahead scheduling). Beyond this, the model allows the introduction of short-term forecasts (intra-day) with better forecast quality due to the shorter forecast horizon.

AEOLIUS has been implemented in the MATLAB/Simulink® developing environment [7]. Figure 2 shows a rough overview of the simulation process with AEOLIUS. The driving force of the model is an interpolated load curve based on 8760 hourly mean values based on UCTE data for Germany [8]. For each month the weekdays are represented by the data given for the third Wednesday of this month, while the Saturdays and Sundays of each month are represented by the according data for two characteristic weekend days of the same month.

The Simulink signal corresponding to the load characteristic is depicted in the upper right of Figure 2.

The second important endogenous model variable is the feed-in of renewable electricity.

Wind power feed-in data is provided as a one-year set of hourly mean values as well. The AEOLIUS user can choose from wind power production data for good (1990), medium (1995), and bad (1996) wind years. These data sets result from the ISI wind model [9], which calculates the output of the current and the predicted future composition of wind parks in scenarios for the years 2000-2020 in 5-year intervals. The ISI model uses wind speed measurements obtained from the German meteorological service (DWD) for 22 characteristic sites in different regions on-shore (mountain, hill, near coast, coast) and off-shore. Also hydropower production data is fed into the model, but as it is much less subject to short-term fluctuations, it is easier to integrate into power production planning beforehand. Interpolated monthly mean values are thus provided as input to the model [10], which seems to be sufficiently accurate. Solar power is another type of fluctuating renewable electricity production. However, in the medium term its low efficiency and operating hours per year, resulting in a low production share, do not cause fluctuations large enough to affect the operation of the rest of the power system. Solar power production has thus not been included in the model. The same applies to schedulable renewable power sources, such as e.g. biomass or geothermal. In the simulation of future power system structures, where these

technologies can play a more important role, they can be considered in the forecasting and scheduling modules (see below) along with the conventional plant portfolio.

The level of renewable electricity feed-in determines how much of the original total demand remains to be covered by conventional power plants (Simulink signal in the middle of Figure 2). Based on this curve, load forecast simulations are conducted and a production schedule for each plant is derived. The cumulated schedule of all plants is graphically shown in the lower right Simulink signal in Figure 2. Scheduling is carried out on three different time-horizons, based on long-, medium-, and short-term forecasts. The costs and emissions resulting from the simulated schedule are computed along with further calculations and results, which all are made available for graphical and numerical analyses.

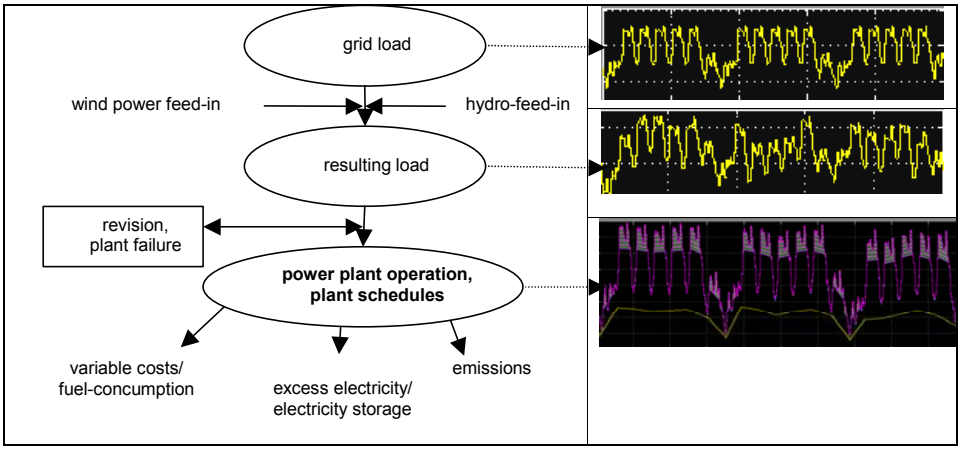

Figure 2: Schematic overview of the Aeolius fluctuation model approach

The AEOLIUS model structure is easily adaptable to the power sectors of other countries with a prospected high growth of wind energy use, as the model allows for an automated import of energy system parameters (e.g. from Excel sheets) and thus offers great flexibility for amending or changing the underlying power system specifications. This is especially advantageous with regard to the coupling with the PERSEUS-CERT model, where the parameters of future energy system structures are used to define the power plant portfolio in the short-term model.

In the following, the key aspects of the AEOLIUS simulation approach are explained in more detail.

Forecast module

The function of the forecast module is to calculate forecast data for the scheduling of the conventional plant portfolio (plus the schedulable renewable resources) for three different time horizons (24 h, 4 h, and 1 h). To account for insecurities in the forecast of the data for renewable energy production and also in electricity demand, the respective time series are varied randomly around the actual values with a Gaussian noise. This noise is more pronounced for the longer forecast horizons and decreases for the shorter forecast horizons, as the predictability for both the fluctuations in renewable energy production and demand increases for shorter time periods. While the longest forecast horizon is used to schedule the base load capacities, the medium term forecast is used to schedule intermediate load capacities. The one-hour forecast is used to schedule peak capacities and control power reserves of the other plant types currently in operation. Remaining load imbalances can be compensated by pumped storage plants, which are also modelled.

Heuristic approach for power plant scheduling

Different plant types were modelled, and in order to maintain an adequate level of technical detail, the block availability (blocks are unavailable in the case of stochastic plant failure or revision) as well as technical restrictions (e.g. start-up time, minimum times of operation and standstill, load-change characteristics, and partial load operation) were included. Besides the revision of individual blocks there are no other overall restrictions.

Similar to the approach of Krämer [11], ten different power plant types are considered (five fuel-categories, each with two different block sizes). The power plants modelled are geared to meet the technical parameters and the number of typical plants, thus creating a representative set of power stations. The pre-scheduling is based on heuristic procedures, for base, intermediate, and peak load power stations. The remaining difference between scheduled load and actual load

are balanced by stand-by capacities and pumped-storage reserves. A compensation of the arising fluctuations can thus be compensated by a sufficient supply of conventional stand-by capacities.
So-called "must-run" capacities like nuclear and lignite power plants with low specific production costs have been modelled in the base load category. They are technologically restricted to slow and relatively small changes of their output, in order to keep plant operation economical and prevent excessive material wear. In the intermediate load category, hard-coal capacities are included, with better load following characteristics and higher specific production costs than base load plants. Oil- and gas-fired plants (gas turbines and combined cycle plants), as well as pumped storage plants, all with the ability to start up and realise load changes very quickly, are considered in the peak load category. Their flexibility is, however, associated with the highest specific production costs.
Any combination of types and numbers of these plants can be combined to form a given power plant portfolio.

Capacity reserves and balancing power for security of supply

In order to provide sufficient security of supply under inherently inaccurate load forecasts or incidental power plant failures, the system must contain enough reserve capacities. Control (balancing) power in the model is provided by the activation of reserves and in order to allow for a clear and comparable quantification of fluctuation-induced effects on the scheduling of conventional capacities, it cannot be obtained from outside the system boundaries (e.g. interregional power exchange, EEX).
Basically, three different types of control power can be distinguished. They are characterised by differences in the time needed to activate the reserve and their maximum duration of deployment: primary, secondary, and tertiary reserve. Primary reserve is mainly used for an immediate correction of small power and frequency imbalances resulting from the fluctuation of electricity demand and grid operation by opening or closing turbine valves. Secondary and tertiary reserve are necessary to cover fluctuations on the power production side (wind, pv) and require the activation of additional capacity. Secondary reserve, which the grid operator must be able to activate fully within 15 minutes [12], should be taking over after 3-5 minutes. Its deployment duration is limited by technical and economic reasons to about 30 minutes. For continuing imbalances tertiary reserve must be manually activated. Gas turbines or even more quickly reacting pumped-storage plants, which can activate their full capacity within a few minutes, are counted as standing tertiary reserve, while the spinning tertiary reserve is constituted by the unused capacity margin of power plants already operating. Providing spinning reserve thus means plant operation at partial load with a reduced efficiency.
At any time, the amount of tertiary reserve is determined by the following requirements:

- coverage of possible plant failures,
- coverage of demand forecast errors, and
- compensation of output variations from fluctuating renewable power sources.

For the standing tertiary reserve, the amount necessary for the coverage of plant failures and demand forecast errors is taken into account in the model, while spinning tertiary reserve is required to balance the fluctuations from renewable electricity generation. The risk of plant failures is compensated by providing standing reserve equal to the power of the biggest block currently operated in the system. This simplification is regarded as an acceptable substitute for a probabilistic quantification of plant failures [13]. Forecast errors on the demand side are taken into account by increasing the simulated demand curve with a safety factor, which is set to 3.5% of the forecasted average load for each day.
The minimum requirement for spinning tertiary reserve is 2.5% of synchronised net plant capacity [11]. With maximum fluctuations of individual wind turbines between 75% (1 minute) up to 90% (5 minutes) of their nominal capacity, the safest solution would be to cover all capacity above the secured capacity of wind power plants by tertiary reserves. However, with an increasing penetration of wind power in electricity production, this is not an economically reasonable solution.
For the AEOLIUS simulations the probability function (frequency distribution) of hourly fluctuations is used instead to determine the required amount of tertiary reserve. As described by Sontow [14], the maximum amplitude of fluctuations expected with a 97% probability is

used as a minimum target value for the spinning reserve, which is equally distributed among all intermediate-load blocks.

Calculation of costs and emissions

Due to the limited time horizon of AEOLIUS (one year), and due to the rather long lead times for the construction of new plants, it is legitimate to assume that - unlike in the long-term PERSEUS model - the structure of the power generation system remains unchanged during this period. Thus, the amount of fixed costs (investments, interests, insurances and fixed operating costs, e.g. for staff wages, and revisions) to be accounted for is a constant figure for the time horizon of the model and does not have any influence on the scheduling of power plants. That makes it sufficient to consider only the variable costs of power generation (fuel costs and other variable operating costs, e.g. flue gas cleaning). Fuel costs depend on (world)market prices and the specific heat-demand of the plant, which varies with power output. Generally, an average specific heat demand would be sufficient, but with a growing wind power feed-in and the connected increase in necessary reserves it can be expected that plants will operate at partial load more often. Thus, load-dependent efficiency curves were used to adequately account for partial load situations. Fuel costs are calculated from the resulting thermal energy consumption of the plant and the specific fuel costs [ct/kWh]. For the fuel-prices and other variable costs fuel- and/or technology-specific values from DFIU's power plant database were used. CO_2-emissions of the plants are calculated from their respective fuel consumption using fuel-specific CO_2-emission coefficients [kg CO_2/MWh].

Simulation results

This paragraph gives an overview of how the AEOLIUS simulation model can be used to quantify the effects and the actual (net) benefits of wind power feed-in in terms of costs and emissions. In the following example, the conventional power plant portfolio installed in Germany in the year 2000 and the electricity demand are taken as a reference. Wind power is introduced into the model in three different stages based on the expansion of wind power use in Germany as anticipated by Fraunhofer ISI. While 6 GW were installed in 2000, 17.3 GW and 22.4 GW are introduced as the expected values for 2005 and 2010, respectively. A wind power production of 12 TWh, 34.9 TWh, and 50.4 TWh is introduced for the shares expected in the different years, assuming a good wind year with otherwise unchanged framework conditions in order to have a comparable basis.

Actual power production data from the year 2000 and the corresponding simulated power

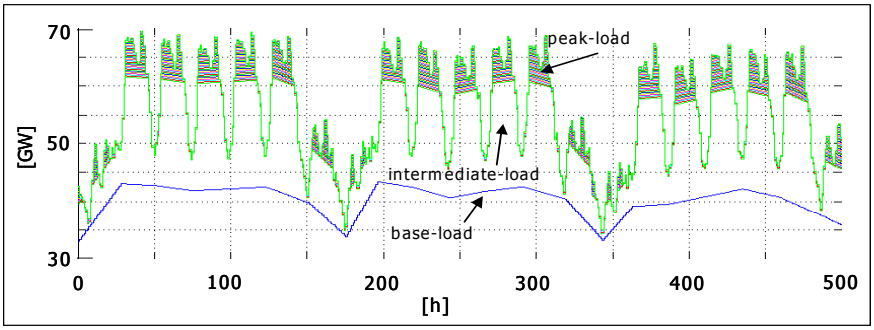

Figure 3: Load coverage by base, intermediate, and peak load during a three-week time period

production shares are in good accordance. Depending on the wind penetration results show a substitution mainly of coal-fired (about 4% in 2005 and 7% in 2010), lignite-fired (5% in 2005 up to 9.5% in 2010), as well as of nuclear production (4.5% in 2005 and nearly 10% in 2010). As quickly reacting gas-fired power plants are needed to compensate for the short-term fluctuations of wind power, the amount of gas-fired electricity displaced is negligible and, in contrast to the results above, decreases for higher shares of wind energy (from 2% in 2005 to a bit above 1% in 2010). Thus, intermediate-load generation and base-load generation are most affected. This effect can also be directly observed in the varying characteristics of base-load generation in the three-week period depicted in Figure 3.

The overall costs and CO_2-emissions of the three wind power expansion stages were compared to the costs and emissions of a reference case with the same conventional power plant structure, but without any wind power feed-in. This comparison with a purely conventional electricity system allows to calculate the average values of costs and emissions avoided per one kilowatt-hour of wind energy feed-in. This is done by relating the differences between the total costs and emissions of the reference case and those of each expansion stage to the wind power feed-in of the respective expansion stage. The calculated cost savings are used to determine the actual additional costs of wind energy feed-in, which are visualised in Figure 4. An average of 7.45 cent/kWh is paid for wind energy feed-in in Germany. Assuming that conventionally generated electricity can be replaced without efficiency losses, this would mean that about 4.3 cents/kWh could be saved by replacing electricity generated from hard coal, with remaining additional costs for wind power feed-in of 3.15 cents/kWh. However, the net cost savings resulting from AEOLIUS are much lower, for the expected wind energy feed-in in 2010, for example, only 1.14 cents/kWh of operating costs can be saved[4] in the conventional power plants, resulting in additional costs of 6.31 cents/kWh. This is due to the fact that the increasing reserve and control power requirements have to be fulfilled primarily by fossil-fuelled plants, causing losses in fuel efficiency and increased thermal wear. In addition to the reduced efficiency at partial load, the model also accounts for the emissions and fuel consumption related to plant upstarts, depending on the preceding downtime of the specific plant. Figure 4 also shows that these net savings decrease with growing shares of wind power production, with rising specific additional costs as a result. It has to be kept in mind that

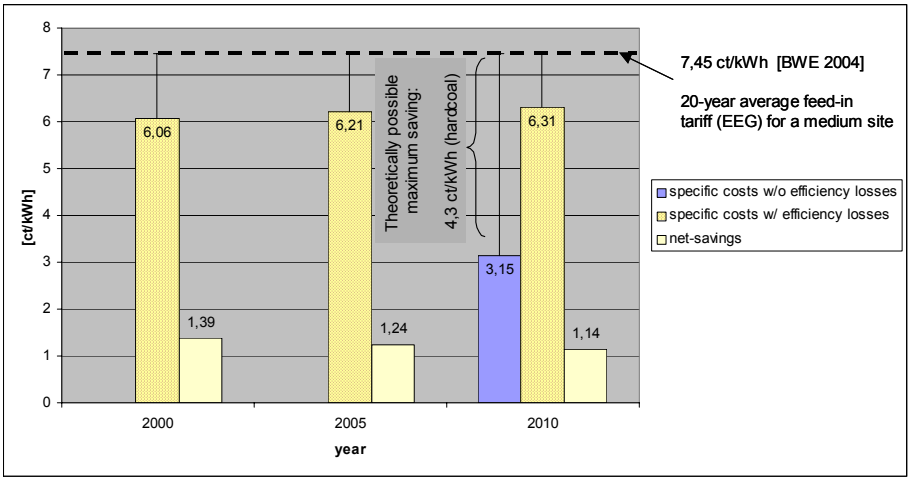

Figure 4: Theoretic and actual (net) specific costs of wind power feed-in

costs for most probably unavoidable grid expansions are not accounted for in these calculations. Along with fuel efficiency, the ecologic benefits (i.e. emission reductions) decrease with the growing share of wind energy[5]. Here the effect is even more pronounced than the influence on the costs. The reason is that in addition to the reduced fuel efficiency, wind energy does not only substitute fossil fuels, but also nearly CO_2-free electricity production from nuclear power plants, which does not save any significant amounts of emissions. The combination of these two effects causes a drastic decrease in specific emission savings.

Depending on the share of wind power in the system, only 32% (2000) down to 27% (2010) of cost savings, and between 86% (2000) and 46% (2010) of the theoretically possible emission savings can be realised. The results also depend very much on the structure of the conventional power generation capacities, whose production is partly replaced.

SUMMARY AND OUTLOOK

The aim of the newly developed AEOLIUS modelling approach was to provide a model structure for the simulation of interdependencies between increasing amounts of fluctuating electricity production (especially wind power) and the operation of the conventional plant portfolio.

[4] On the liberalised Nordic electricity market, Holttinen [4] and Nielsen [5] have calculated higher values of about 2 cents/kWh for wind power, depending on prediction accuracy and the amount of hydro power available.

[5] Similar effects have also been described by Liik [15], who modelled wind power in a unit commitment model of the Estonian electricity system, which is dominated by conventional thermal generation.

With its MATLAB/Simulink based calculation approach, the AEOLIUS model has been successfully applied to the German power sector using 60-minute average values of wind power feed-in data. The realised model allows a time-efficient plant scheduling, which accounts for the effects of a further expanding utilisation of wind energy. Typical interdependencies can be reproduced and analysed with the model, despite some simplifications. Simulations with AEOLIUS have shown that an increasing use of wind energy leads to a decrease of CO_2-emissions and lower fuel costs by substituting conventional fuels mainly in base-load and intermediate-load power production (coal, lignite, and nuclear). However, due to the increased requirements for spinning reserve (i.e. operation at reduced output level with lower plant efficiency) and more frequent load changes and/or plant upstarts, a unit of wind energy can neither avoid the entire emissions, nor the entire fuel costs associated with a unit of fossil-generated energy. Another effect limiting the achievable mitigation of greenhouse gases is the replacement of nearly CO_2-free power sources (e.g. nuclear energy) in the electricity mix.

In the further development of AEOLIUS, the modelling approach will be refined with regard to the feed-back routines between forecast horizons used for plant dispatching and the provision of control power, as well as the integration of alternative options for intermediate energy storage (e.g. hydrogen in addition to the existing pumped-storage plants). Both improvements are of special interest for the utilisation of temporally higher resolved 10 minute average values for wind power feed-in, which are currently used in a test version.

REFERENCES

[1] Ender, C.: *Wind Energy Use in Germany - Status 30.06.2004*. DEWI Magazin Nr. 25, Wilhelmshaven, August 2004

[2] Rehfeldt, K.; Gerdes, G.J.; Schreiber, M.: *Weiterer Ausbau der Windenergienutzung im Hinblick auf den Klimaschutz*. DEWI, Wilhelmshaven, 2001

[3] Boxberger, M.: *Windenergieeinspeisung und Übertragungsnetz*. Vortrag im Rahmen des Workshops „Windenergienutzung und zukünftige Entwicklung des Kraftwerksparks in Deutschland". Bremer Energie Institut, Bremen, 5-12-2002

[4] Holttinen, H.: *The impact of large wind power production on the Nordic electricity system.* VTT Publications 554, Espoo 2004

[5] Nielsen, L.H. et al.: *Wind power in a liberalised North European electricity exchange.* Proceedings of the European Wind Energy Conference 1999, Nice, France, pp. 379-382, James & James Science Publishers, 1999

[6] Enzensberger, N.: *Entwicklung und Anwendung eines Strom- und Zertifikatmarktmodells für den europäischen Energiesektor*. Karlsruhe, Univ., Diss., 2003

[7] The Mathworks, Inc.: *Using Simulink*. The Mathworks, Inc., Natick, MA, USA, 2001

[8] Union for the Coordination of Transmission of Electricity (UCTE): http://www.ucte.org/statistics/onlinedata/consumption/, 14.9.2003

[9] Sensfuß, F., Ragwitz, M., Wietschel, M. (2003): *Fluktuationen der Windenergie und deren Vorhersagbarkeit bei einem verstärkten Ausbau des Offshore Anteils in Deutschland*. Proceedings zur 3. Internationalen Energiewirtschaftstagung IEWT03, Technische Universität Wien, 2003

[10] Quaschning, V.: *Systemtechnik einer klimaverträglichen Elektrizitätsversorgung für Deutschland im 21. Jahrhundert.* VDI-Fortschritt-Beriche, Reihe 6, Nr. 437, Düsseldorf 2000

[11] Krämer, M.: *Modellanalyse zur Optimierung der Stromerzeugung bei hoher Einspeisung von Windenergie*. VDI Fortschritt-Berichte, Reihe 6 Energietechnik, Nr. 492, 2003

[12] Union for the Coordination of Transmission of Electricity (UCTE): *Summary of the current operating principles of the UCPTE*. Brussels, 1998

[13] Fischedick, M.: *Erneuerbare Energien und Blockheizkraftwerke im Kraftwerksverbund.* Technische Effekte, Kosten, Emissionen. Dissertation IER, Stuttgart, 1996

[14] Sontow, J.: *Energiewirtschaftliche Analyse großtechnischer Windstromerzeugung.* Dissertation, IER, Stuttgart, 2000

[15] Liik, O. et al.: *Co-operation of Wind Generators with Fossil Power Plants: Problems and Gains.* NordicWind Power Conference 2004, Chalmers University of Technology 2004

Proceedings of ECOS 2005
Trondheim, Norway
June 20–22, 2005

A COMPUTATIONAL FLUID DYNAMIC (CFD) STUDY OF THE WAVEPLANE DEVICE

Thomas Scanlon*
University of Strathclyde
Department of Mechanical Engineering
Glasgow G1 1XJ
Scotland

Maxime Durot and Raphael Grandin
Ecole Nationale Superieure des Mines de Paris (ENSMP)
France

Gregor MacPherson and Peter Hannah
Caley Engineering Systems
East Kilbride
Scotland

ABSTRACT

This paper describes the simulation of wave motion over a wave energy device known as the WavePlane. A general purpose computational fluid dynamics (CFD) code has been employed and modified in order to capture the physics of deep water ocean waves as well as the geometry of the WavePlane device itself. The paper describes in detail the modelling parameters employed in dealing with such a flow scenario and the results of the numerical simulation are presented which depict the flow patterns predicted and the possible energy output from the device. The results show that the CFD study has the potential to simulate such a complex scenario and can give a useful insight into possible design modifications for product improvement.
Keywords: Waves, numerical, CFD, energy conversion

INTRODUCTION

Waves, particularly those of large amplitude, contain large amounts of energy. Wave energy is in effect a stored and concentrated form of solar energy, since the winds that produce waves are caused by pressure differences in the atmosphere arising from solar heating.
The purpose of a wave energy device is to harvest the energy in the waves. Since wave energy is a renewable resource, the environmental impact is limited to the resources used for production, set-up and dismantling.
The first wave-power patent proposal was issued in 1799 by Girard, to use direct mechanical action to drive pumps, saws, mills, or other heavy machinery. Installations have been built or are under construction in a number of countries, including Scotland, Portugal, Norway, the U.S.A., China, Japan, Australia and India. The world's first

* Corresponding author: Phone +44 141 548 2842 Fax: +44 141 552 5105 E-mail tom.scanlon@strath.ac.uk

commercial wave energy plant (0.5 MW capacity) developed by WaveGen is located in Isle of Islay in Scotland.
Several studies have investigated the wave energy resource aiming to identify the best sites to deploy wave energy devices and estimate the size of the resource, including:

- 120 GW located on the west and north coasts of the United Kingdom [1]
- 320 GW around Europe [2]
- 2 TW globally [3]

Previous numerical work in this field is scarce. Dugan *et al* [4] have analysed both experimentally and numerically sloshing of water waves in a rectangular enclosure while Asavanant and van den Broeck [5] considered free surface, splashless potential flow over a two-dimensional body. It is evident that there appears to be no literature on three-dimensional, transient flow over complex bodies such as the device described in this work.
The goal of this paper is to outline some of the issues and challenges associated with CFD modelling for such a scenario and to reflect on the potential of such analyses to provide useful information in the field of wave energy generation.

WAVEPLANE BACKGROUND

The WavePlane machine was conceived in 1989 and patented in 1991 by Danish inventor Erik Skaarup. It has no moving parts except for the turbine and the generator. It is a floating device anchored to the bottom of the sea and set to face the oncoming waves. The device is equipped with large horizontal damping plates positioned under the sea surface in order to reduce as much as possible its vertical motion.
The aim of the WavePlane is to absorb the volume and the speed of the water generated by the waves and transform it into a smooth rotating flow within a tube whose energy can be converted by a turbine. A beach located at the front of the device raises the upstream wave then a series of inlet laminae collect the water and inject it tangentially in the tube in order to induce a rotating flow or vortex. The irregular motion of the waves is thus transformed into a virtually constant motion without any mechanical moving parts. Figures 1 and 2 show the design principles behind the WavePlane.

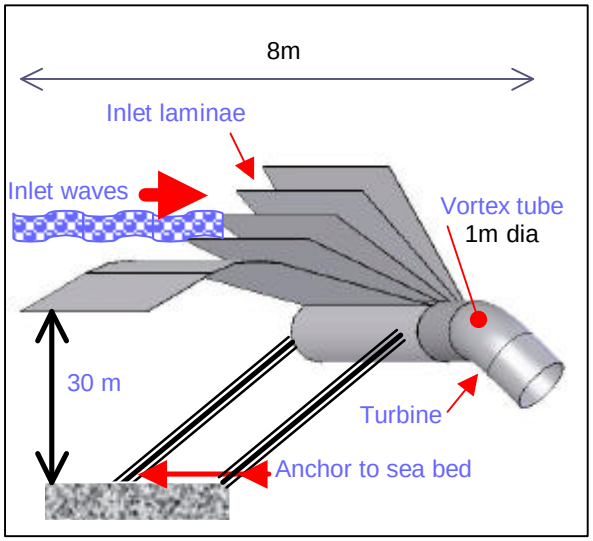

Figure 1: The WavePlane device

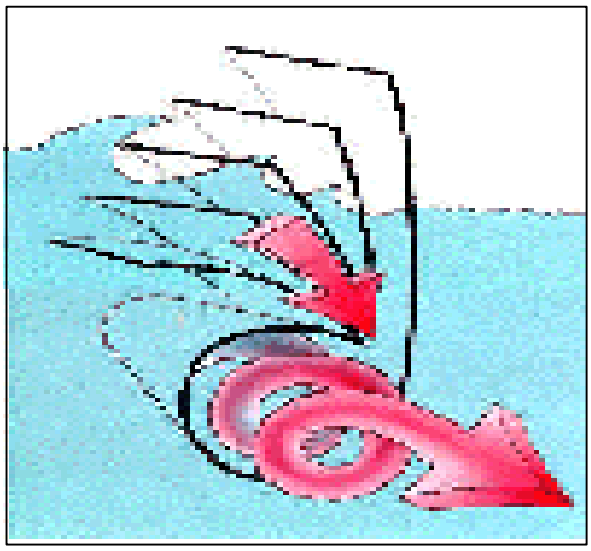

Figure 2: Vortex generation

COMPUTATIONAL FLUID DYNAMICS (CFD)

Various experiments have been performed on small-size physical models and these have improved the efficiency of the WavePlane device through the modification of the overall design. However, great care must be taken when attempting to scale up the efficiency figures for small-scale to industrial size. Physical experimentation has found that the efficiency of the energy conversion depends on numerous factors that do not behave similarly when

scaling up the problem. Amongst them are the wave height, period and speed, the movement of the WavePlane on the sea surface, the size of the tube containing the vortex and the number and the shape of the lamellas collecting the waves.

Numerical simulations using computational fluid dynamics (CFD) can produce more rapid answers to specific issues. Even if the results have to be interpreted with care, CFD is a convenient tool to obtain an idea of what will happen under real conditions. In the case of the WavePlane, CFD could then give an order of magnitude analysis of the efficiency expected for the full-size WavePlane. The main advantages of CFD are the speed of analysis and the large variety and number of results it can generate. Therefore simulating the flow in the WavePlane may provide useful information not only about its efficiency but also about the shape and the manner in which the vortex is created, the way the waves are harvested and the forces exerted by the water on the mechanical parts. Various solution parameters may also be tested in order to assess their influence on the device efficiency.

NUMERICAL MODELLING

The simulated linear wave model is based on Airy wave theory. The wave's shape is assumed to be sinusoidal, the velocities decrease with depth and the flow is taken to be irrotational and inviscid. In the physical environment of the ocean 85% of waves are of the order of 125m long or less and the ratio of wave length to height falls within that of Airy wave theory. The energy in the wave is both kinetic and potential.

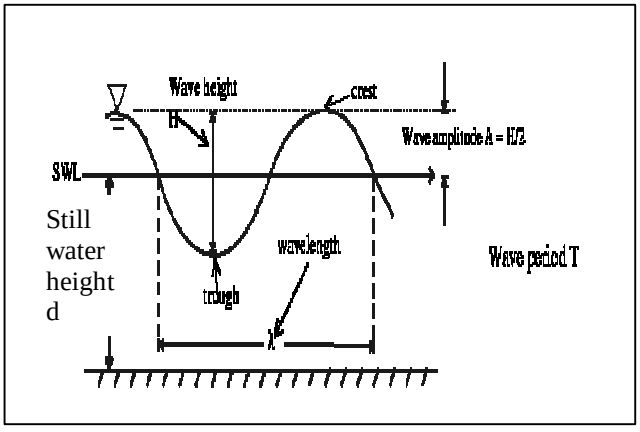

Figure 3: Theoretical Airy wave

The physical parameters involved in this numerical study were as follows:

d : still water height
L : wave length
A : wave amplitude
H : wave height
T : wave period
g : acceleration due to gravity
k : wave number

where:

$$k = 2p / L$$

and w is radian frequency where:

$$w = 2p / T$$

$$w^2 = g.k.tanh(k.d)$$

Usually, Airy waves are characterized by the ratio:

$$\frac{L}{H} \approx 25$$

The results of theory require the water surface elevation to be in the form of:

$$h(x,t) = d + \frac{H}{2}.cos(k.x - w.t)$$

and the velocity potential to be:

$$\Phi(x,y,t) = \frac{g.H}{2w}\frac{cosh(k.y)}{cosh(k.d)}sin(k.x - w.t)$$

thus giving the general form of the velocity field:

$$V_x(x,y,t) = \frac{\partial \Phi}{\partial x}(x,y,t) = \frac{H.p}{T}\frac{cosh(k.y)}{sinh(k.d)}cos(k.x - w.t)$$

$$V_y(x,y,t) = \frac{\partial \Phi}{\partial y}(x,y,t) = \frac{H.p}{T}\frac{sinh(k.y)}{sinh(k.d)}sin(k.x - w.t)$$

The average energy per meter wave width is given by:

$$E_w = \frac{r.g.H^2}{8}$$

The average mass flow rate per meter wave width is given by:

$$Q_{mw} = \frac{p.r.H^2}{4.T}$$

The average power per meter wave width is given by:

$$P_w = \frac{1}{32.p}.r.g^2.H^2.T$$

The simulated waves possess the following values:

$$H = 2m$$
$$T = 6s$$
$$L = 50m$$

The waves propagate in water of about half the wavelength in depth:

$$d \approx \frac{L}{2}$$

Therefore, to simulate open sea conditions, the computational domains in which the simulations are carried out are 30m deep, thus setting:

$$d = 30m$$

The commercially available CFD code Fluent has been employed in this study. User coding has been written by the authors to adapt the code to capture the physics of Airy waves as described above. This entails coding which describes boundary conditions for the initial, inlet and outlet conditions. The upper and lower boundary conditions for the model were assumed to be symmetric. For the inlet boundary the transient conditions of the x and y components of velocity were provided. The volume of fluid (VOF) method was used to capture the ocean-atmosphere interface so the time-dependent water surface elevation level was also prescribed at the inlet in terms of the volume fraction of water. For the outlet boundary a condition was provided that described the transient hydrostatic pressure as a wave passed through the outlet of the flow domain (at L = 50 m). A numerical grid of 220,000 unstructured cells was used to discretise space and time steps of the order of 0.1s were employed. This led to a total computational time of approximately 8 days for a simulation of 5 wave periods over the WavePlane using a PC with a P4 2.5GHz chip and 512Mb RAM.

RESULTS AND COMMENTS

Figure 4 shows the volume fraction of water as the wave encounters the WavePlane device:

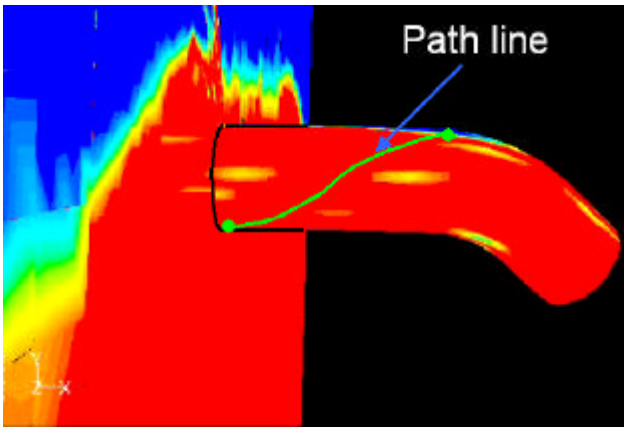

Figure 4: Contours of volume fraction and pathline in vortex tube

This figure also shows the pathline taken by a fluid element during the transient solution. This demonstrates that there exists a rotational element to the fluid flow as it passes through the vortex tube. Such a flow pattern is desirable as this will aid the rotation of the turbine.

Figure 5 shows the vortex tube outlet mass flow rate as a function of time. The average mass flow rate (horizontal line) is approximately 1500 kg/s and the flow within the tube is unconditionally positive. There is no back flow into the tube and even though the inlet conditions of the wave are periodic the CFD results predict a relatively smooth, continuous flow within the vortex tube which passes through the turbine.

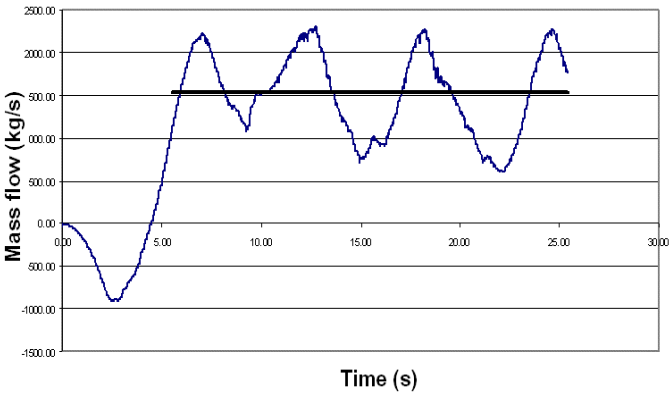

Figure 5 : Mass flow rate (kg/s) against time (s) at the outlet of the vortex tube

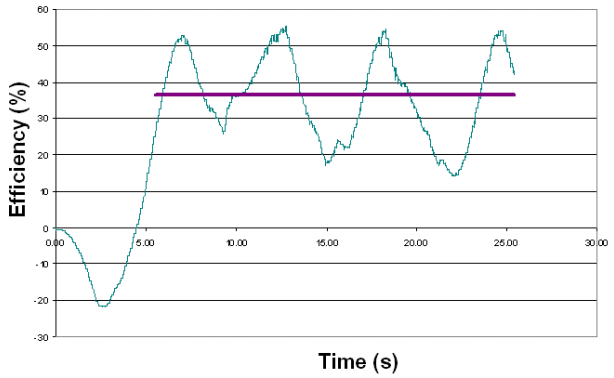

Figure 6 : Mass flow capture efficiency versus time

Figure 6 details the mass flow rate capture effeiciency which is defined as the actual mass captured by the WavePlane divided by the theoretical maximum mass flow in the oncoming wave (4181 kg/s). The results predict an average capture efficiency of 36 %.

Figure 7 shows the flow total power at the turbine location. The flow total power is the summation of the kinetic and potential energies according to:

$$P_{kin} = \int_{surf} \frac{1}{2} V^2 \times (r\vec{V}.d\vec{a})$$

$$P_{tot} = P_{kin} + \int_{surf} \frac{p}{r} \times (r\vec{V}.d\vec{a})$$

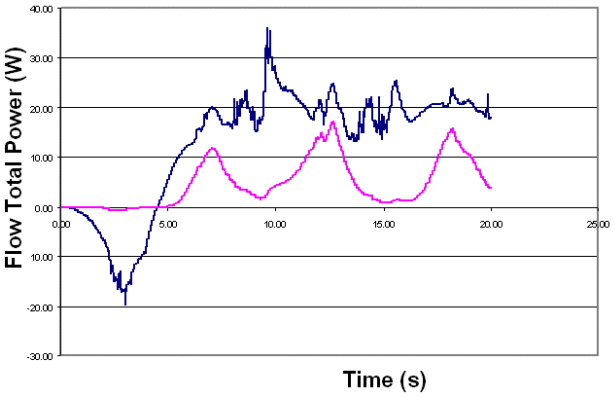

Figure 7 Transient kinetic (lower) and total (upper) powers at a plane coresponding to the turbine

The average total power is determined as 20 kW and in comparison with the maximum power available in the theoretical wave of 8m width (half of the WavePlane width – maximum power available = 184 kW) the power efficiency is calculated as 11 %.

One limiting factor of the model as it stands currently is the fact that no turbulence model has yet been incorporated in order to account for viscous losses through and over the device. This will be included in the next stage of the work. A further limitation of the model is that in order for the VOF free surface model to remain stable then very small time step sizes are necessary (0.1 s). As a results of this large computation times are required (8 days) on a high specification PC in order to obtain a solution over a reasonable time period.

CONCLUSIONS

A computational fluid dynamic (CFD) investigation of the WavePlane device has been carried out. The output shows that some useful results may be determined from such a study given that the correct physics are carefully incorporated into the model. Results from the numerical study include the flow patterns encountered and an indication of the possible efficiencies that may be generated by such a device. Further work will necessitate incorporating a turbulence model and implementing a parallel version of the code in order to reduce run times.

REFERENCES

[1] ETSU, 'The Department of Energy's R&D Programme 1974-1983', ETSU Report R-26, 1985.

[2] MT Pontes, GA Athanassoulis, S Barstow, L Bertotti, L Cavaleri, B Holmes, *et al*. The European Wave Energy Resource, 3rd EWEC, Patras, Greece, 1998.

[3] World Energy Council, 'Renewable energy resources: opportunities and constraints 1990-2020', London, 1993.

[4] Dugan J.B., Lyu M.R., Armenio V. And Rocca M.L., On the analysis of sloshing of water in rectangular containers: numerical study and experimental validation, Ocean Engineering, vol.23, no. 8, pp. 705-739(35), 1996.

[5] Asavanant J.; Vanden-Broeck J.-M., Free-surface supercritical splashless flows past a two-dimensional symmetrical rectilinear body European Journal of Mechanics - B/Fluids, vol. 17, no. 6, pp. 811-822(12), 1998.

Proceedings of ECOS 2005
Trondheim, Norway
June 20–22, 2005

A STUDY OF THE MEAT AND BONE MEAL PRODUCTION PROCESSES FOR ENERGETIC CONVERSION

José J. Segovia(*),César R. Chamorro, Miguel A. Villamañán and Carmen Martín
Universidad de Valladolid
Laboratorio de Termodinámica y Calibración TERMOCAL
E.T.S. de Ingenieros Industriales
E-47011 Valladolid
Spain

Andrés Cabanillas
CIEMAT
Dpto de Tecnologías de Combustión y Gasificación
E-28040 Madrid
Spain

ABSTRACT

This work is a study of the meat and bone meal production processes. It covers the most interesting points of the legislation that regulates the animal wastes manipulation and the different MBM production technologies. These technologies are different in the way that the cooking and sterilization stages are made, therefore there are three methods for MBM production. In this paper the productive operations are described and energy balance and processing time are calculated for them.

Keywords: Meat and bone meal, production process, energy balance

NOMENCLATURE

BSE	Bovine spongiform encephalopathy
c	Specific heat capacity [J/kgK]
c_m	Specific heat capacity of non-fat dry extract [J/kgK]
c_{pw}	Specific heat capacity of water [J/kgK]
db	Dry base
EC	European Community
HHV	Higher heating value [kJ/kg]
LHV	Lower heating value [kJ/kg]
MBM	Meat and bone meal
q	Heat transfer [kJ/kg]
t	Temperature [°C]
TSE	Transmissible spongiform encephalopathy
w	Specific humidity

* Corresponding author: Phone: +34 983 423420 Fax: : +34 983 423420 E-mail: josseg@eis.uva.es

INTRODUCTION

Animal by-products are defined as the entire bodies or parts of bodies of animals or products of animal origin not intended for human consumption, including ova, embryos and sperm. They represent more than 10 million tonnes of meat. These materials are then disposed of or processed and re-used in human food (meat-and-bone meal, fats, gelatine), the cosmetics or pharmaceuticals sectors and for other technical purposes.

Following the food crises of the 1990s, such as the bovine spongiform encephalopathy (BSE) epidemic, the role of these by-products in propagating transmissible animal diseases was brought to light. Those products derived from animals declared unfit for human consumption must not enter the food chain. Moreover, the

administration to any animal of proteins obtained by processing carcasses of the same species - or cannibalism - may constitute an additional risk of disease propagation.

Meat and Bone Meal (MBM) is produced in rendering plants where animal offal and bones are mixed, crushed and cooked together. During cooling process, tallow is extracted and the remaining material which is dried and crushed further is known as MBM. Tallow is used as a replacement for fossil fuels such as oil, or is sold to the oleochemical industry for recycling into useful products. MBM was previously a commercial product and was sold to the animal feedstuff industry, but since November 2000 the use of it in this way is no longer permitted.

Nowadays, European legislation (Regulation (EC) nº1774/2002) has established the health and surveillance rules applicable to the collection, transport, storage, handling, processing and use or disposal of animal by-products; the placing on the market and, in certain specific cases, the export and transit of animal by-products and products derived therefrom. [1].

It is necessary the development of new technologies or improved present ones in order to eliminate, in a secure way, specific risk materials and meat and bone meal.

This work is part of a project which purpose is the development of suitable technologies for secure MBM elimination whatever its origin (by-products of slaughter houses or specific risk materials). In the elimination MBM is mixed with residual biomass or mining industrial wastes of low value. This residual material will be used as a source of energy in an efficient way in order to promote energetic conversion facilities of small or average size.

This report describes briefly Spanish MBM production processes and the most interesting points of the legislation that regulates animal wastes manipulation.

Three alternative production processes are used. The purpose of this work is to chose the best production process in order to use MBM as fuel in thermoconversion plants. The study includes the composition of the raw material and a complete chemical and energetic characterization of the product (MBM): proximate analysis, ultimate analysis, lower and higher heating values and ash composition. These data are the basis for the performance of different technologies for elimination. Finally, energy balance and processing time are calculated for the three methods described.

PROCESSING PLANTS

The raw material (animal by-products), as it has been pointed out before, is very heterogeneous in composition, therefore the composition of MBM varies significantly too.

Table 1 presents some characteristics of raw material and MBM [2]:

Raw Material (30% bones)			
Moisture	Non fat-solids	Fat	
60%	24%	16%	
Meat and Bone Meal			
Moisture	Total solids	Proteins	Fat
4-8 %	92 – 96 %	80 – 86 %	8 – 12 %

Table 1: Composition of raw material and MBM

In order to study the behaviour of MBM as fuel, it has been characterized and these results are shown on the next table.

Moisture (%)		7.88
Density (kg/m^3)		178
Proximate Analysis (% db)	Fixed carbon	0.1
	Volatile	77.14
	Ash (550°C)	22.76
Ultimate Analysis (%db)	Carbon	49.5
	Hydrogen	6.36
	Nitrogen	10.75
	Sulfur	0.25
	Oxygen	9.87
	Chlorine	0.51
Heating values (kJ/kg)	HHV (dry)	20607
	HHV	19019
	LHV (dry)	19186
	LHV	17305
Analysis of ash at 550°C (% db)	Al	0.13
	Ca	10
	Fe	0.07
	K	0.07
	Mg	0.34
	Mn	0.03
	Na	1
	P	8.2

Table 2: Characterization of MBM

Table 2 summarizes proximate and ultimate analysis, lower and higher heating values, and ash composition. They have been determined by conventional methods. It can be seen that MBM from a thermal point of view is a good fuel because of its high calorific value, however MBM's nitrogen content may lead to high NO_x emissions, while its high ash content will require an efficient ash off-take system, so that those drawbacks involve a well-controlled destruction as other wastes. On the other hand, a granulometrical distribution study shows that the particle size is between 0.1 and 1mm. Its small size is good for a better combustion.

The production of MBM always requires two stages: sterilization and cooking. Sterilization consists of a thermal treatment at a temperature of 133°C and 3 bars absolute pressure for 20 minutes with a maximum particle size of 50 mm [3] to destroy infection agents.

During cooking stage at atmospheric pressure tallow melts and proteins denature and coagulate.

In Spain, three alternative production processes are used and they are different in the moment and in the way of cooking and sterilization stages. These three methods are: Sterilization and cooking in a discontinuous digester; continuous cooker and later discontinuous sterilizer and, the third, discontinuous sterilizer and continuous cooker. Now a brief description of these processes is done.

Batch Digester (Method 1)

The raw material is stored in steal hoppers and feeding screws are used. From the reception hopper the raw material is conveyed into a pre-breaker and then to a fine crusher. This reduces the particle size to 50 mm. The crushed material is again stored until its thermal treatment.

Sterilization and cooking of animal by-products are done by means of a discontinuous digester. The digester is a cylindrical vessel around 20 m^3 volume with a stirring rod. It is externally heated using a steam jacket. The steam water is produced in a conventional boiler. In a first step, digester is pressurized and sterilization takes place, raw material is treated at 133°C and a total pressure of 3-bar for 20 minutes in accordance with requirements. It produces not only the destruction of infection agents, also fat is melted and the water content of the material is vaporized. Then the system is depressurised and the steam produced in the digester is lost by evaporation. This steam is condensed and treat as waste water. Cooking process continues at atmospheric pressure and the final moisture of the material is around 6%. After cooking the tallow is separated first gravimetrically and then it is pressed. The tallow obtained is recycled as fuel in the plant or is sold for recycling into useful products. After tallow is decanted, it is filtered and pumped to a tallow storage tank. The cake of meat and bone meal, and the solid obtain in the purification of tallow are cooled and conditioned in a hammer mill. After milling MBM is re-sieved and any larger particles are then re-milled. The product is finally stored.

Continuous cooker and batch sterilization of MBM (Method 2)

In this second method, crushed raw material, is first cooked at 100°C in a continuous way. In this stage, the material is cooked and residence time is about one hour, moisture is reduced to 16%, the digestor is quite similar to the discontinuous one, it is also heated with a steam jacket but it is not closed.

One advantage of this continuous system is that it can be easily automatized and controlled and therefore energy consumption could be optimised, in addition, energy lost in feeding and discharging operations is reduced. Next the cooked product is pressed to extract the tallow and the cake is sent to a discontinuous sterilizer, where it is treated at 133°C and a steam pressure of 3-bar for 20 minutes. Before storage MBM is cooled and milled properly. A diagram of the plant is shown in Figure 1.

Batch sterilizer and continuous cooker (Method 3)

The third process, consist of a discontinuous sterilization of the crushed raw material in a tank where it is directly heated with steam water that it is in contact with the animal by-products, there is not mechanical agitation and injection of steam is also used for mixing the material to assure that all the material is kept at the desired conditions. The residence time is not enough for a good cooking and then the sterilized product is further cooked in an open continuous system, externally heated, which operates at atmospheric pressure and 100°C during one hour.

Tallow and MBM are separated by decantation and in a mechanical screw press and, finally, both are treated to be stored.

RESULTS

Energy balance and operation time have been estimated for sterilization and cooking processes. The main energy consumption is steam water whereas electric energy for stirring, crushing, pressing or feeding is neglected. It is assumed the same conditions for entering raw material and exit product, in the three methods described. It enters at 20°C with a composition of 60% water and 40% non-fat dry extract, whereas MBM produced contains 6% moisture and 94% non-fat dry extract.

The stages considered in the three methods are:

Method 1: Sterilization (heating from 20°C to 133°C); cooking at 100°C with a moisture reduction 60% to 6%.

Method 2: Heating 20°C to 100°C, cooking at 100°C, moisture reduction 60% to 16%. Intermediated stages of filtering, pressing and storing. Batch sterilization (heating 50°C to 133°C) and moisture reduction 16% to 6%.

Method 3: Sterilization (heating from 20°C to 133°C); heating 80°C to 100°C; cooking at 100°C and moisture reduction 60% to 6%. Between both treatments the material is transported and it is slight cooled.

The parameters used in the calculations and the results of energy balance are shown on Table 3, where t is the average temperature and q is the amount of heat required per kilogram treated.

The heat capacity of the material c has been estimated as:

$$c = c_{pw} \cdot w + c_m \cdot (1 - w) \quad (1)$$

where c_{pw} is the specific heat capacity of the water at the average temperature, w is the specific humidity and c_m is the specific heat capacity of the non-fat dry extract (kJ/kgK) and its temperature dependence [4] is calculated by:

$$c_m = 1.465 + 0.0067 \cdot t \quad (2)$$

where t is the temperature in °C.

Process	t (°C)	c_{pw} (kJ/kgK)	c (kJ/kgK)	q (kJ/kg)
Method 1	76.5	4.192	3.306	1589
Method 2	60	4.186	3.258	1677
	91.5	4.205	2.418	
Method 3	76.5	4.192	3.306	1656
	90	4.203	3.349	

Table 3: Results of energy balance

Energy balance indicates that method 1, where sterilization and cooking stages take place in the same batch equipment requires less energy (about 5.6%) than the other two methods per kg of raw material processed .

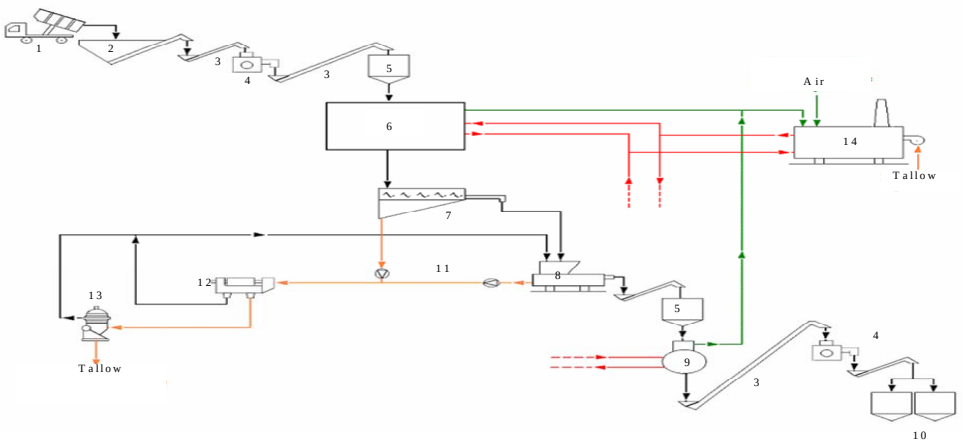

Figure 1: Production process of MBM continuous cooker and batch sterilizer (method 2).

1: Transport
2: Hopper
3: Feeding screw
4: Hammer mill
5: Intermediate storage tank
6: Continuous cooker
7: Perforated hopper
8: Press
9: Batch steriliser
10: MBM storage
11: Pumps
12: Sedimentation
13: Decanter
14: Boiler

In order to complete the study, processing time and plant dimension are evaluated for a better comparison of the three methods described.
Processing times estimated for the different stages on the three methods are:
Method 1: Feeding and preheating (10 min), sterilization (20 min) and final treatment (1 h 30 min). The typical capacity of these digesters is about 8000 kg of raw material per batch, it means that the plant processes about 4000kg/h of animal by-products.
Method 2: Cooking process takes 1 hour, and 8000 kg/h are treated. For sterilization (30 min), the capacity of this part of the plant could be reduced to 2000-2500kg/h because tallow has been separated and other part of the raw material has been lost by evaporation.
Method 3: Sterilization (30 min) and cooking (1 h). For a capacity of 8000kg/h of animal by-products in cooking stage, the capacity of the sterilizer could be reduced to 4000 kg.
These data indicate that methods 2 and 3, with a continuous cooker, can process twice animal by-products as much as batch digestor but it does not mean double the plant cost.
On the other hand, the sterilization of the MBM instead of the raw material decreases significantly the size of the sterilizer.
Therefore, the recommended process is method 2, which can be seen in detail on Figure 1.

ACKNOWLEDGEMENTS
Support for this work came from the Research Department of the Spanish Ministry of Science and Technology, Project EET2001-4573-C04-03.

REFERENCES

[1] *Regulation (EC) No 1774/2002* of the European Parliament and of the Council of 3 October 2002 laying down health rules concerning animal by-products not intended for human consumption.

[2] Madrid A. *Aprovechamiento de los subproductos cárnicos.* Madrid: Mundi-Prensa, 1999.

[3] *Council Decision of 18 July 1996.* Pressure cooking system for processing mammalian waste into MBM (inactivation of TSE agents) (D96/449/EC)

[4] Prändt O, Fisher T, Schimidhofer, Sinell H. *Tecnología e higiene de la carne*. Madrid: Acribia, 1994.

Proceedings of ECOS 2005
Trondheim, Norway
June 20–22, 2005

MAIN CHARACTERISTICS OF BIOMASS AND WASTE DURING THE DEVOLATILISATION AND COMBUSTION PROCESS

G. Skodras[1,2], P. Grammelis[2,3], P. Basinas[1], E. Kakaras [2,3] and G. P. Sakellaropoulos[1]

[1]Chemical Process Engineering Laboratory, Department of Chemical Engineering, Aristotle University of Thessaloniki, Thessaloniki, Greece
[2]Institute for Solid Fuels Technology and Applications / Centre for Reasearch & Technology Hellas, Ptolemais, Greece
[3]Laboratory of Steam Boilers and Thermal Plants, Thermal Engineering Section, Mechanical Engineering Department, National Technical University of Athens

ABSTRACT

The trend for material and energy recovery from wastes along with the need for greenhouse-gases reduction resulted in increased interest for biomass and / or wastes thermal exploitation. Combustion and pyrolysis seem to be the main route towards that direction. In this work the pyrolysis and combustion behaviour of ten biomass and waste materials was investigated. Samples tested included agricultural residues, wood processing by-products, straw and MBM (meat and bone meals). All biomass/waste species were subjected to standard proximate, ultimate and ash analyses. Both pyrolysis and combustion tests were conducted non-isothermally in a thermogravimetric analyser (TA Q600) at ambient pressure and 150-250μm particles size. The effect of the heating rate was also considered. The independent parallel, first order, reactions model was elaborated for the kinetic analysis of the pyrolysis results. The thermal degradation of the biomass/waste samples was modeled assuming three of four parallel reactions, corresponding to the decomposition of cellulose, hemicellulose and lignin for the biogenic fraction.
All samples were proven good fuels, reflection of their high volatiles and low ash content. At increased heating rates, the fuel sample reached faster higher temperatures, while enhanced pyrolysis rates were achieved. As a result, a slight decrease in total weight loss was observed accompanied with a systematic increase in pyrolysis starting temperature, and an almost linear increase in maximum pyrolysis rate. Increased combustion reactivity was found for olive kernel and willow followed by forest residue. The catalytic effect of mineral matter on char oxidation was pronounced in the MBM sample, leading to a reaction rate decrease and shifting the DTG curve to lower temperatures.

Keywords: agricultural residues, wood, MBM, thermal conversion, kinetics, ash

NOMENCLATURE

A = pre-exponential factor [sec^{-1}]
C_{total} = Total conversion [% w/w]
c_i = fraction of volatiles produced by the i^{th} component
DEV_1 = deviation between the experimental and calculated DTG curves [%]
DEV_2 = deviation between the experimental and calculated char fraction [%]
E = activation energy [KJ/mol]
M = number of parameters involved in the model
m_0 = initial dry sample mass [mg]
m_{char} = final char yield [mg]
$(m_{char})^{calc}$ = calculated final char yield [mg]
$(m_{char})^{exp}$ = experimental final char yield [mg]
$m_{char,i}$ = final char yield of the i component [mg]
m_i = actual sample mass of the i component [mg]
N = number of individual reactions
OF_{DTG} = objective function
R = gas constant [KJ $mol^{-1}K^{-1}$]
R_{max} = Maximum combustion rate [10^{-2}/min]
T = temperature [°C or K]
T_{in} = initial combustion temperature [°C]
T_{max} = temperature at max combustion rate [°C]
$T_{max\ rate}$ = temperature at max pyrolysis rate [°C]

Z = number of the measured data points
α = conversion (reacted fraction)

INTRODUCTION

The need for energy recovery from renewable sources along with the necessity for emissions reduction resulted in increased interest for biomass and / or wastes thermal conversion. Combustion constitutes one of the most important thermal treatment methods for biomasses and / or wastes. It combines the anticipation to replace the landfilling option along with energy recovery. Thus, the factors that affect the combustion procedure should be well known and studied in detail, towards the design and effective performance of industrial applications. The effect of mineral matter content in combustion and pyrolysis processes has also been investigated and identified as one of the key research areas [1].

Numerous separate studies have dealt with pyrolysis of biomass and lignocellulosic materials, while other researchers have investigated the pyrolysis of waste components. Madorsky et al, Kilzer and Broido and Chaterjje and Conrad have set the basis of the modern kinetic models [2]. Heikkinen et al studied the devolatilisation behaviour of about 50 different wastes. In order to calculate the devolatilisation of the samples, they assumed that the thermal degradation curve is obtained as a sum of the contributions of the corresponding pseudo components and found that this assumption holds for cellulosic samples [3]. Many different mechanisms have been considered, for instance the model proposed by Manya et al [4], who studied waste wood and sugarcane bagasse samples for kinetic evaluation. Waste wood pyrolysis was modeled assuming three independent parallel reactions, corresponding to the decomposition of three pseudocomponents linked hemicellulose, cellulose and lignin. In the same line, Caballero [2] tested two biomass samples including olive kernel and almond shell. He found that with three independent parallel reactions model, the agreement between calculated and experimental data is excellent. More recently, Gronly et al [5] investigated the devolatilisation behaviour of several hardwoods and softwoods. They found that devolatilisation dynamics of the wood species of the study can be described well by a simple model consisted of five parallel, first order reactions for the amounts of the volatile fractions associated with the two extractive components.

As Fisher et al [6] and Gronly et al [5] report all these derived kinetic parameters depend on the specific pyrolysis conditions that include temperature, heating rate, pressure, particle size, ambient gas environment, and the presence of ash or mineral matter deposits. Therefore, the presence of several components and the catalytic role of the inorganic matter affect the kinetic parameters. In the last two decades, extensive studies have been performed in this field of investigation by many researchers. Raveendran et al [7] examined the mineral matter of various biomass samples and reported that their main elements are Si, Ca, K, Na, and Mg followed in percentages by S, P, Fe, Mn and Al.

Serious number of research efforts has also been performed on the combustion procedure, indicating that the presence of oxygen causes many complexities. Bilbao et al [8] studied the thermal decomposition of cellulose and pine saw dust in oxidative atmosphere and found that the degradation of the material at low temperatures, causes the appearance of gas – phase reactions between the released volatiles and oxygen, and promotes the combustion of the char generated in the early stages of the solid degradation. In this line, Conesa at al [9] support that a later decomposition stage exists only when oxygen is present, maintained also by Zheng et al [10] who extensively investigated the combustion procedure.

Since, alternative fuels i.e. biomass, wastes etc. are at great importance nowadays, it is vital to understand deeply their behaviour under pyrolysis and combustion. However, there are not sufficient data available, particularly for non-conventional fuels such as MBM and wastes. To cover this need, the pyrolysis and combustion behaviour of agricultural residues, wood processing by-products, straw and MBM (meat and bone meals) was examined by thermogravimetry. The behaviour of the biomass / waste components in inert and oxidative atmosphere is compared. Kinetic parameters are calculated by using the independent parallel, first order, reactions model and the pyrolytic behaviour in the various heating rates is simulated according to the determined parameters.

The effect of mineral matter present in biomass and waste is studied and the role of feedstock properties in pyrolysis is also examined.

Samples	Proximate analysis (wt% , as received)				Ultimate analysis (wt% db)					Gross H. Val (MJ/Kg)
	Moisture	V.M.[a]	F.C.[b]	Ash	C	H	N	S	O[c]	
Olive kernel	18.1	60.8	18.5	2.6	51.6	8.5	1.08	0	38.82	29.86
Almond shell	9.7	66.9	20	3.36	49.6	6.4	0.6	0	43.4	26.21
Forest residue	21.3	63.7	13.7	1.2	51	7.9	0.3	0	40.8	28.82
MDF	6.5	74.4	17.9	1.1	47	6.4	4.6	0	42	25.29
Saw dust	14.3	73.3	11.96	0.44	51	7.9	0.3	0	40.8	28.82
Waste wood	5.63	69.53	16.08	8.76	45.99	5.67	3.82	0.05	35.44	23.91
Willow	11.3	71.47	16.1	1.14	44.7	5.7	0.2	0.03	48.21	16.97
Demolition Wood	8.6	70.69	18.8	1.92	44.5	5.6	1.1	0.09	46.52	17.87
Straw	7.9	58.54	15.8	17.74	36.4	4.8	0.9	0.29	37.03	14.88
MBM	1.35	79.66	8.61	10.38	55.67	8.03	7.15	0.05	29.1	30.64
MBMDemin	0.52	79.83	19.36	0.29	52.87	7.8	7.34	0.79	31.2	29.42

[a] Volatile matter, [b] Fixed Carbon, [c] By subtraction

Table 1: Proximate and ultimate analysis of the selected fuels

EXPERIMENTAL

Materials

Materials tested include two agricultural residues referred as almond shell and olive kernel, six woodprocessing by-products named as MDF, saw dust, willow, waste wood, forest residue and demolition wood. Meat and bone meal and straw were also added in the test matrix. The initial samples were milled and sieved and the selected particle size fraction was in the range of 150-250μm. Prior to the thermogravimetric experiments, samples were dried in the oven at 105°C in N_2 atmosphere for 3 hours. Aiming to investigate the influence of mineral matter on the thermal degradation of MBM, the specific sample was washed with three different acid solutions (5N HCl, 22N HF and 12N HCl). 18gr of sample was added in 120mL of each acid and the mixture was stirred for 1 h at 25 ± 2°C. Samples were then washed with distilled water, filtered and dried. The selected fuels were subjected to proximate analysis according to the standard ASTM D 3172-89 method. Ultimate analyses for all samples including calorific values were carried out in a Flash 1112 Series EA Thermo Finnigan CHNS elemental analyser. Proximate and ultimate analyses results are presented in Table 1. The analysis of heavy metals in the ash sample is performed by an Inductively Coupled Plasma – Atomic Emission Spectroscopy (ICP-AES) spectrophotometer.

Apparatus and Procedure

Thermogravimetric tests were performed in a TA Instruments Q600 simultaneous TGA-DSC apparatus. The weight precision of instrument is 0.1μg. Small sample weights, about 10 or occasionally 20mg were placed in an open alumina sample pan, in order to reduce the effects of eventual side reactions such as heat- and mass-transfer limitations. High purity helium and respal air (80 / 20 in N_2 / O_2) were used in the constant flow rate of 100 mL/min. Prior the heating program, system was purged for 10 min at 400 mL/min to ensure that the desired environment was established. Weight loss and the rate of weight loss were continuously recorded in a linear temperature increase from 30°C to 1000°C. Devolatilisation tests were conducted in three and in some cases in four heating regimes, i.e. 5, 20, 50 and 100°C/min.

KINETIC MODELING

The biomass and / or waste pyrolysis is a complex phenomenon and proceeds through multiple parallel or even competitive reactions. Thus, it is not possible to describe the whole process with a single reaction. Whereas that fact, DTG curves obtained by pyrolysis of biomass and waste samples can be essentially described by the relatively simple model of independent parallel reactions. More specifically, it is assumed that each component reacts independently and thus, the thermal behaviour of the sample could be described by the sum of its individual components. This approach has been successfully applied by many authors in earlier studies [4-5, 11-16]. In this work, pyrolysis of biomass and waste samples was modeled by assuming three or four independent, first order, parallel reactions.

The individual conversion rate for N reactions is described by:

$$\frac{da_i}{dt} = A_i \cdot \exp(-E_i/RT) \cdot f(a_i), \quad i=1, ..,N \qquad (1)$$

where a_i is the separate conversion, which is expressed as follows:

$$a_i = \frac{m_{0,i} - m_i}{m_{0,i} - m_{char,i}} \quad (2)$$

Assuming a first order reaction then:

$$f(a) = 1 - a \quad (3)$$

The overall conversion rate is described by

$$-\frac{dm}{dt} = \sum_i c_i \frac{da_i}{dt}, \quad i=1,..,N \quad (4)$$

The contribution of each partial process to the overall mass loss is expressed by the coefficient c_i:

$$c_i = m_{0,i} - m_{char,i} \quad (5)$$

The minimization of the objective function is used to identify the optimum kinetic parameters, as given below:

$$OF_{DTG} = \sum_{i=1}^{N} \left[\left(\frac{dm}{dt} \right)_i^{exp} - \left(\frac{dm}{dt} \right)_i^{calc} \right]^2 \quad (6)$$

The estimation of the best fitting kinetic parameters is achieved through the deviation between the experimental and calculated DTG curves, as a percentage of the maximum experimental value (dm/dt):

$$DEV_1(\%) = \frac{\sqrt{OF_{DTG}/(Z-M)}}{\max\left[\left(-dm/dt \right)_{calc} \right]} \cdot 100 \quad (7)$$

where M is the number of the model parameters (A_i, E_i, and c_i) and Z is the number of the measured data points. Also, the deviation between the observed and calculated char fraction can be used

$$DEV_2 = abs\left[\frac{(m_{char})^{exp} - (m_{char})^{calc}}{(m_{char})^{exp}} \right] \cdot 100 \quad (8)$$

where $(m_{char})^{exp}$ and $(m_{char})^{calc}$ are the experimental and calculated values of the residual mass. The latter as already reported, arise from the optimized pre-exponential factor and activation energy values computed.

RESULTS AND DISCUSSION

Pyrolysis of samples

Several characteristics of the thermal degradation of samples were used in order to evaluate its behaviour, such as the initial pyrolysis

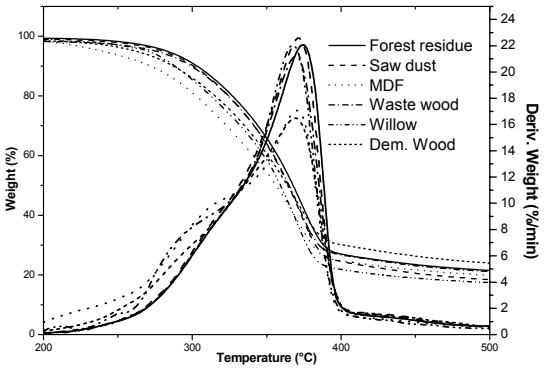

Figure 1: Weight loss and rate of weight loss as a function of temperature for several biomass samples.

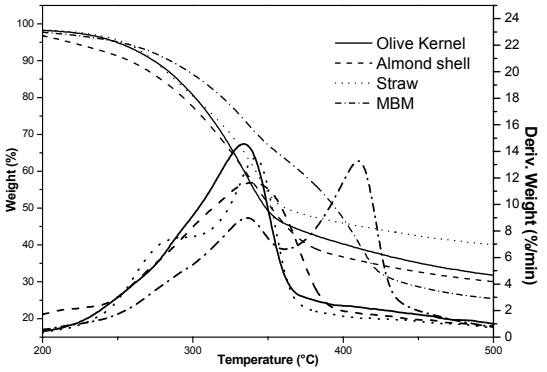

Figure 2: Weight loss and rate of weight loss as a function of temperature for several biomass and waste sample.

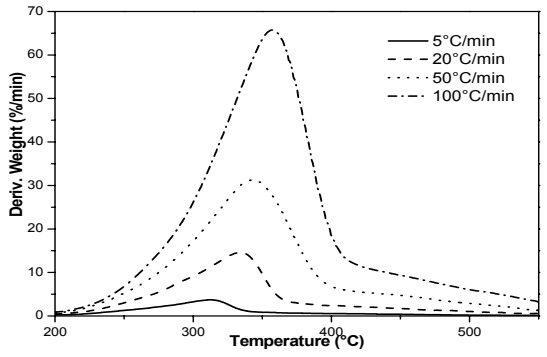

Figure 3: Effect of heating rate on the devolatilisation of olive kernel.

temperature, maximum pyrolysis rate and corresponding temperature, total conversion and contribution of various temperature intervals in total weight loss. The mass loss and the rate of mass loss are presented in figures 1 and 2 for wood based biomasses and waste samples, respectively. From the TG curves, it can be seen that pyrolysis starts at about 200°C and is essentially completed at 500°C. DTG curves of biomass and waste present a narrow peak between 330-375°C which is similar to that found by other authors [3]. Exceptional to this behaviour, MBM sample presents a maximum pyrolysis rate at 410°C. Taking into account that the reactivity is inversely proportional to the temperature corresponding to peak height, olive kernel seems to be the most reactive among the samples. In contrary, straw and MBM present the lowest peak heights and the highest peak temperature. The main devolatilisation occurs between 250-400°C in all test cases, with the exception of MBM, where the main degradation stage is completed at approximately 450°C. Significant variations of the total weight loss are observed, which are approximately between 65-85% and are in accordance with previous studies [17].
The derivatives of the weight loss for the pyrolysis of olive kernel in specific heating regimes (5, 20, 50 and 100°C/min) are presented in Figure 3. As it is obviously illustrated by the DTG curves, pyrolysis is completed at approximately the same

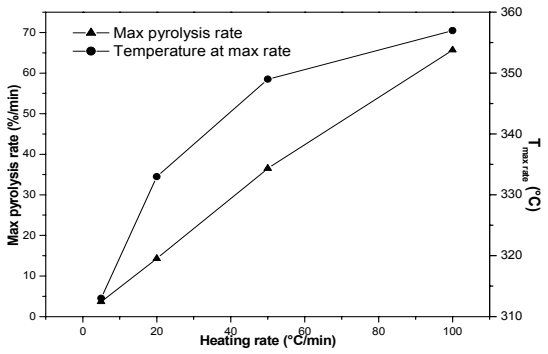

Figure 4: The maximum pyrolysis rate of olive kernel and temperature at max pyrolysis rate as function of the heating rate.

temperature region for all the heating rates. At higher heating rates a slight increase in the char yield was observed in previous studies. This has been cited to the competitive reactions that are affected by the increased heating rate [15]. An increase of the residual char between 1.3- 5.7% is obtained and thus, it is as small as it can be assumed to be practically unaffected by the heating rate. Figure 4 clearly shows that an almost linear increase in maximum pyrolysis rate is observed. At increased heating rates, sample particles reach faster higher temperatures, resulting in significantly higher DTG peaks, shifted at higher temperatures. This could be ascribed not only to the effect of the heat transfer phenomena occur at different heating histories, but also to the temperature lag of the sample.

Kinetics

Detailed reaction mechanisms are available for the kinetic evaluation of biomass and / or wastes pyrolysis. It is also adequate to take into account only the basic characteristics of the degradation process with a simplified mechanism. A relative simple approximation to determine the kinetics of the thermal decomposition consists in assuming that TG-DTG curves can be divided into three or more zones, each of them considered independently. Biomass samples can be modeled by assuming a three-step mechanism for each pseudo-component. The first pseudo-component constitutes hemicellulose, the second cellulose and lignin corresponds to the third reaction. A fourth reaction is necessary to simulate the hemicellulose decomposition. As Heikkinen et al [3] proposed lignin and xylan start decomposing at lower temperatures compared to cellulose. Lignin decomposes over a wide temperature range having

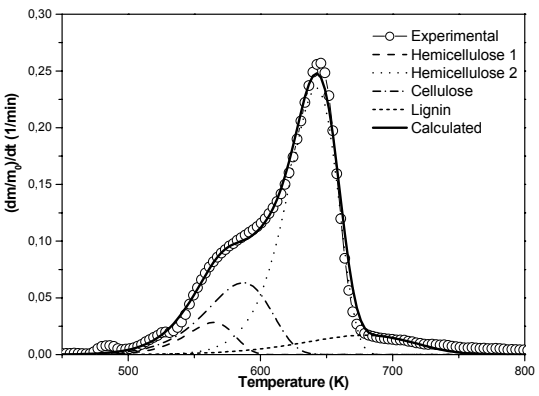

Figure 5: Modeling of the pyrolysis of willow by using four independent parallel reactions.

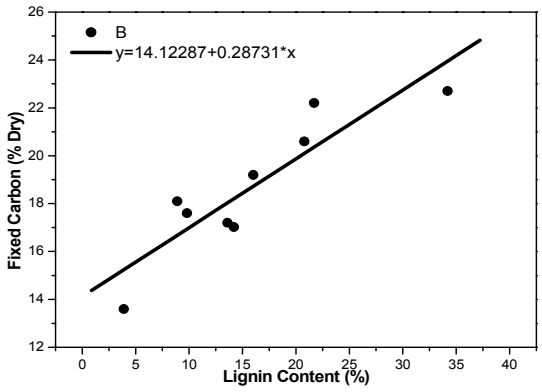

Figure 6: Fixed carbon content of lignocellulosic samples as a function of lignin content, calculated for the devolatilisation tests at 20°C/min.

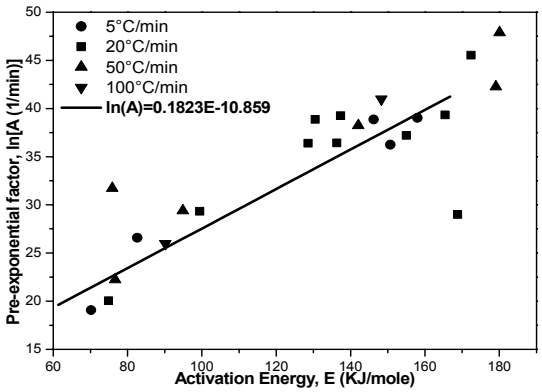

Figure 7: Kinetic parameters correlation.

a long tailing section. In literature, xylan is used instead of hemicellulose. Since many of the significant errors in kinetic estimations are derived from this assumption, hemicellulose was applied to evaluate the kinetics of the biomass samples.

Figure 5 shows the pathway that willow pyrolysis has been modeled by assuming four independent parallel reactions and using the DTG curve. The calculated kinetic parameters are listed in Table 2. MBM and four biomass samples were modeled by assuming four reactions, while the rest of the samples were efficiently modeled through three pseudo-components. It is worth mentioning that hemicellulose contributes in higher percentages, when two hemicellulose peaks are used to model accurately the thermal degradation of samples. On the other hand, cellulose is higher in samples where three independent parallel reactions are used, while lignin presents the lowest value. The average value of activation energy for the hemicellulose decomposition of biomass is 103.7 KJ/mol. This is in accordance but still lower than the values calculated by Gronly et al [16] and Sorum et al [11], being 133.5 KJ/mol and 110.3 KJ/mol, respectively. In correspondence, first reaction for meat and bone meals present a lower value (57.9 KJ/mol). The activation energy for the thermal degradation of lignin was calculated at 53 KJ/mol for the lignocellulosic materials and 31.7 KJ/mol for MBM. As resulted from the kinetic attributions pre- exponential factor values depend on the heating rate. An increase of the heating rate results in increased A values as was also shown by Bilbao et al [8].

Calculated lignin content was evaluated with respect to the fixed carbon content. Previous studies referenced to charcoal production from biomass [18, 19, 20] suggested that a correlation between lignin and fixed carbon content exists. Figure 6 shows that interrelation for the biomass samples tested. In evidence, lignin and fixed carbon content are proportional in all biomass samples. Antal et al [19] proposed a statistical **t-test** to ascertain the calculated trend of the substrates. They suggest that a **p-value** lower than 0.05 is significant for the trend existence. The calculated values for R^2 and p-value, which are 0.8 and 1.6 10^{-6} respectively, are within the margins, reflecting the linear correlation between fixed carbon and lignin content. Experimental conditions like the heating rate and sample size affect the kinetic parameters. For this reason a number of different activation energies and pre-exponential factors have been calculated in previous studies. It is important however to notice that the combined effect of kinetics in the rate constants is coherent and is known as compensation effect [16, 21]. It means that pre-exponential factor and activation energy are linearly correlated as follows:

$$\ln(A)=m\cdot E+\ln(k_0) \quad (9)$$

where the constant $m=1/RT_i$ is the slope of the linear plot. At the isokinetic temperature, T_i, all the reactions of the group proceed at the same rate k_0. Earlier research [21] suggested that this behaviour of the biomasses based on the experimental temperature measurement imprecision. In the present work kinetic data obtained for the pyrolysis

Sample	Hemicellulose 1			Hemicellulose 2			Cellulose			Lignin		
	A (1/min)	E (KJ/mol)	c (%)	A (1/min)	E (KJ/mol)	c (%)	A (1/min)	E (KJ/mol)	c (%)	A (1/min)	E (KJ/mol)	c (%)
Olive Kernel	$1.7\ 10^{10}$	108.9	9.5	-	-	-	$1.6\ 10^{11}$	130.8	56	$5.83\ 10^{2}$	46.1	34.2
Forest residue	$1.9\ 10^{11}$	128.5	24.3	$3.1\ 10^{15}$	191.2	65.1	$6.7\ 10^{6}$	95.5	6.6	$1.4\ 10^{5}$	86.6	3.9
Almond shell	$9.3\ 10^{6}$	75.4	9.1	-	-	-	$1.1\ 10^{7}$	85.8	69.1	$1.2\ 10^{2}$	40.2	21.7
MDF	$8.5\ 10^{8}$	96.9	8	$4.3\ 10^{11}$	132.7	24.7	$2.15\ 10^{14}$	176.7	51	$8.22\ 10^{1}$	35.2	16
Saw dust	$2.6\ 10^{11}$	131.1	25.3	-	-	-	$3.3\ 10^{3}$	203.2	64	$3.3\ 10^{3}$	56.7	9.8
Waste wood	$6.2\ 10^{10}$	124.3	26.3	-	-	-	$1.7\ 10^{18}$	225.1	58.8	$1.2\ 10^{3}$	51.6	14.2
Straw	$1.2\ 10^{12}$	128	14.9	$3.9\ 10^{15}$	183.6	47.9	$1.28\ 10^{9}$	101.2	19.8	$1.97\ 10^{3}$	75.2	13.6
Willow	$2.1\ 10^{13}$	144.4	6.9	$3.8\ 10^{14}$	179.9	63.2	$1.1\ 10^{10}$	114.3	20.7	$1.9\ 10^{6}$	86.6	8.9
Demol. Wood	$3.5\ 10^{8}$	99.5	34.3	-	-	-	$2.8\ 10^{15}$	191.7	44.6	$1.1\ 10^{3}$	52.2	20.8
	1st Reaction			2nd Reaction			3rd Reaction			4th Reaction		
MBM	$5.6\ 10^{4}$	57.9	20.7	$3.7\ 10^{12}$	146.9	20	$2.4\ 10^{14}$	188.1	44	$4.1\ 10^{1}$	31.7	14

Table 2: Calculated kinetic parameters for the pyrolysis of biomass samples at heating rate 20°C/min.

at various heating rates was implemented in order to calculate the isokinetic temperature value. As illustrated in Figure 7, the constant m value is 0.1823 corresponding to 387°C (660K). In this line, k_0 value is calculated at $1.9\ 10^{-5}$.

Mineral matter effect

Meat and bone meals sample is characterized by its high-ash content followed by straw as shown in Table 1. These two samples seem to be less reactive among the rest of the biomasses tested (Figures 1 and 2) and, thus, showed the lowest reaction rate. It is well known that the decomposition of cellulose in biomass is catalyzed from the mineral matter contained in the raw material [22]. Therefore, the MBM sample was demineralised in order to investigate the effect of mineral matter on the pyrolysis of the specific sample. Table 1 presents the significant effect of demineralisation on the mineral matter content. Thus, almost complete ash removal is achieved when the previously described three-stage demineralisation procedure is applied. The remaining ash in the MBM sample is too low (0.29%). Lower initial pyrolysis temperature and a decrease in maximum reaction rate were observed during the test of demineralised MBM, Figure 8.

The main elements that form biomass ashes are presented in the samples as oxides, silicates, carbonates, sulfates, chlorides and phosphates. Sample pyrolysis is mainly affected by alkali metals (K, Na), alkaline earth metals (Ca, Mg), silicon, chlorine and sulfur [1]. Ash analysis results from the ICP-AES are given in Table 3. All biomass ashes are characterized by high CaO content, which ranges from 1.2% in straw to 18.62% in the forest residue and waste wood samples. Al_2O_3 has the highest concentration in olive kernel and Fe_2O_3 in saw dust. Increased contents of MgO, Na_2O and Mn_3O_4 are present in MDF and saw dust. It is worth noting that MBM has the highest content of calcium oxide (36.7%) along with phosphorous and potassium (47.5% and 2.77%). In general, the presence of potassium is considered to increase the char yield [7]. This is also true for demineralised MBM, which has the highest total conversion. It is well established that Ca concentration increases the gasification rate [23]. This trend is also observed in pyrolysis experiments presented here. As can be seen in Figure 8 demineralised MBM present significantly lower pyrolysis rate than raw fuel. DTG curves of raw and demineralised MBM follow the same shape in the temperature region of 300-500°C, but the peak heights are reduced and shifted to lower temperatures. By noting Figure 8, a peak between 200-300 °C in demineralised MBM is presented. This could be attributed to the fact that pretreatment methods might cause affection to the chemical structure of the sample, as suggested by earlier research [11, 22].

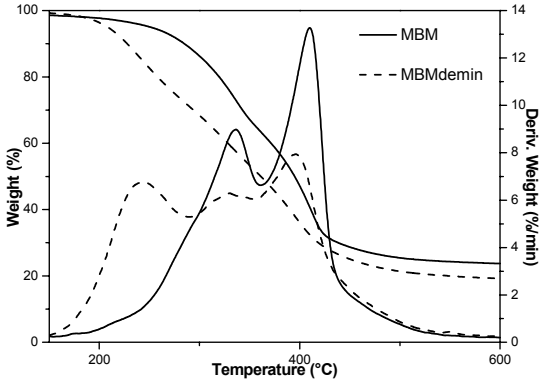

Figure 8: Comparative TG/DTG curves for the pyrolysis of MBM and demineralised MBM samples at 20°C/min.

Samples	CaO	Al_2O_3	Fe_2O_3	MgO	TiO_2	Na_2O	Mn_3O_4	K_2O	P_4O_6
	Element % w/w, ash								
Olive Kernel	13.58	3.4	3.43	3.32	0.09	1.07	0.26	-	-
Forest residue	18.62	0.93	1.43	3.15	0.05	0.57	-	-	-
Almond shell	11.20	0.95	0.87	2.32	0.05	0.74	0.04	-	-
MDF	31.36	1.47	1.84	4.15	0.14	2.48	1.19	-	-
Saw dust	24.36	1.85	4.15	4.48	0.08	1.36	2.12	-	-
Waste wood	18.62	0.93	1.43	3.15	0.05	0.57	0.05	-	-
Straw	1.2	1.1	0.48	0.61	0.03	0.43	0.02	2.6	0.1
Willow	0.55	0.004	0.004	0.06	-	0.02	0.002	0.17	0.06
Demol. Wood	0.5	0.09	0.05	0.07	0.16	0.09	-	0.09	0.01
MBM	36.7	1.43	0.7	2.22	0.014	0.78	0.06	2.77	18

Table 3: Ash composition in main oxides of biomass samples and MBM.

Samples	T_{in} (°C)	R_{max} (10^{-2}/min)	T_{max} (°C)	C_{total} (% w/w)
Olive kernel	216	34.1	284	96.2
Forest residue	243	35.1	337	99.8
Straw	219	14.1	304	79.7
Willow	239	39.3	330	100
Demol. wood	221	23	332	97.9
MBM	206	16.3	378	86.2

Table 4: Combustion characteristics of biomass samples and MBM.

Combustion of samples

The main combustion characteristic of biomass samples and MBM, i.e. the initial combustion temperature, maximum combustion rate and temperature at that rate along with the total conversion are presented in Table 4. Willow and olive kernel have the highest combustion rates at the lowest temperatures, reflecting their increased reactivity. Below 400°C, pyrolysis and combustion curves seem to follow the same behaviour with a shift of the later to lower temperatures [24], Figure 9. This behaviour indicates that mainly pyrolysis reactions take place and the presence of oxygen slightly affected the procedure actualized in the specific temperature region. The initial temperatures in all pyrolysis and combustion tests coincide. The second combustion peak represents the combustion of the generated char. Accessional attention should devote to the fact that the total conversion of MBM in pyrolysis differs in low percentage (about 6%) compared with the respective value of combustion. This fact can be explained of the low fixed carbon and high volatile content of MBM (Table 1).

Conclusions

All samples were proven good fuels, reflection of their high volatiles and low ash content. Olive kernel is most reactive among the samples. Increased heating rate results in slightly higher char yields, which are quite small. Pyrolysis is completed at approximately the same temperature region for all the heating rates. A linear increase of maximum pyrolysis rate and the corresponding temperature has been observed for all the samples. The independent parallel reactions model was employed to evaluate the kinetic parameters and was found quite effective. Three or occasionally four reactions were used to simulate the devolatilisation process. An increase of the heating rate results in increased A values, while fixed carbon content and lignin are proportionally correlated. The "compensation effect" was also examined and the isokinetic temperature was calculated at 387°C.

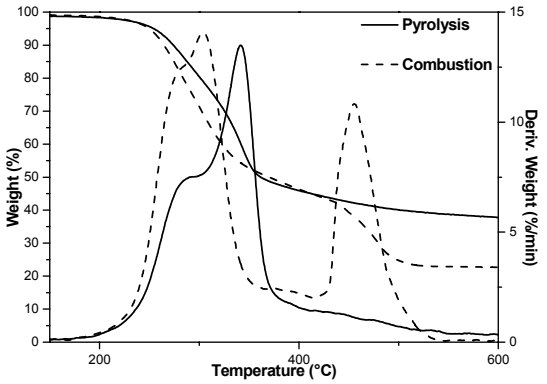

Figure 9: Comparison of pyrolysis and combustion of straw at the heating rate of 20°C/min.

MBM is the less reactive among the tested samples. Demineralization affects the pyrolysis of MBM by reducing the reaction rate and shifting the curve in lower temperatures. Demineralised MBM appears to have higher total conversion due to the reduced potassium content of the raw material. The second peak of DTG curve in the combustion test represents the incineration of the generated char. It is worth noting that the total conversion of MBM slightly differs compared to the pyrolysis char yield.

References

[1] Vamvuka D, Zografos D. *Predicting the behaviour of ash from agricultural wastes during combustion*. Fuel. 2004;83:2051-2057.

[2] Caballero J.A, Conesa J.A., Font R., Marcilla A.M.. *Pyrolysis kinetics of almond shells and olive stones considering their organic fractions*. J. Anal. Appl. Pyrol. 1997;42:159-175.

[3] Heikkinen J.M., Hordijk J.C., De Jong W., Splithoff H. *Thermogravimetry as a tool to classify waste components to be used for energy generation*. J. Anal. Appl. Pyrol. 2004;71:883-900.

[4] Manya J., Velo E., Puigjaner L. *Kinetics of Biomass Pyrolysis: a Reformulated Three-Parallel-Reactions Model*. Ind. Eng. Chem. Res. 2003;42:434-441.

[5] Gronly M. G., Varhegyi G., Di Blasi C. *Thermogravimetric analysis and devolatilisation kinetics of wood*. Ind. Eng. Chem. Res. 2002;41:4201-4208.

[6] Fisher T., Hajaligol M., Waymack B., Kellogg D. *Pyrolysis behaviour and kinetics of biomass derived materials*. J. Anal. Appl. Pyrol. 2002;62:331-349.

[7] Raveendran K., Ganesh A., Khilar K. C. *Influence of mineral matter on biomass pyrolysis characteristics*. Fuel. 1995;74(12):1812-1822.

[8] Bilbao R., Mastral J. F., Aldea M. E., Ceamanos J. *Kinetic study for the thermal decomposition of cellulose and pine sawdust in an air atmosphere*. J. Anal. Appl. Pyrol. 1997;39:53-64.

[9] Conesa J. A., Fullana A., Font R. *Thermal decomposition of meat and bone meal*. J. Anal. Appl. Pyrol. 2003;00:1-12.

[10] Zheng G., Kozinski J. A. *Thermal events occurring during the combustion of biomass residue*. Fuel. 2000;79:181-192.

[11] Sorum L., Gronly M. G., Hustad J. E. *Pyrolysis characteristics and kinetics of municipal solid wastes*. Fuel. 2001;80:1217-1227.

[12] Gronly M., Antal M. J., Varhegyi G. A *Round-Robin study of cellulose pyrolysis kinetics by thermogravimetry*. Ind. Eng. Chem. Res. 1999;38:2238-2244.

[13] Orfao J. J. M., Antunes F. J. A., Figueiredo J. L. *Pyrolysis kinetics of lignocellulosic materials-three independent reactions model*. Fuel. 1999;78:349-358.

[14] Vamvuka D., Pasadakis N., Kastanaki E., Grammelis P., Kakaras E. *Kinetic modeling of coal/Agricultural by-product blends*. Energy and Fuels. 2003;17:549-558.

[15] Varhegyi G., Antal M. J., Jr, Jakab E., Szabo P. *Kinetic modeling of biomass pyrolysis.* J. Anal. Appl. Pyrol. 1997;42:73-87.

[16] Gronly M. G. *A theoretical and experimental study of the thermal degradation of biomass*. Ph.D Thesis, The Norwegian University of science and technology, 1996.

[17] Cordero T., Rodriguez-Mirasol J., Pastrana J., Rodriguez J.J. *Improved solid fuels from co-pyrolysis of a high-sulphur content coal and different lignocellulosic wastes*. Fuel. 2004;83:1585-1590.

[18] Antal M. J., Jr, Mok W. S. L, Varhegyi G., Szekely T. *Review of methods for improving the yield of charcoal from biomass*. Energy and Fuels. 1990;4:221-225.

[19] Antal M. J., Jr, Allen S. G., Dai X., Shimizu B., Tam M. S., Gronly M. *Attainment of the theoretical yield of carbon from biomass*. Ind. Eng. Chem. Res. 2000;39:4024-4031.

[20] Mok W. S. L., Antal M. J., Jr, Szabo P., Varhegyi G., Zelei B. *Formation of charcoal from biomass in a sealed reactor*. Ind. Eng. Chem. Res. 1992;31:1162-1166.

[21] Narayan R., Antal M. J. *Thermal lag, fusion, and compensation effect during biomass pyrolysis*. Ind. Eng. Chem. Res. 1992;35:1711-1721.

[22] Antal M. J., Jr, Varhegyi G., *Cellulose pyrolysis kinetics: The current state of knowledge*. Ind. Eng. Chem. Res. 1995;34:703-717.

[23] Skodras G., Sakellaropoulos G. P. *Mineral matter effects in lignite gasification*. Fuel Processing technology. 2002;77-78:151-158.

[24] Garcia A. N., Font R., Esperanza M. M. *Thermogravimetric kinetic model of the combustion of a varnish waste based on polyurethane*. Energy and Fuels. 2001;15:848-855.

Proceedings of ECOS 2005
Trondheim, Norway
June 20–22, 2005

Thermo-ecological optimization of a solar collector

Jan SZARGUT* **and Wojciech STANEK**
Silesian University of Technology
Institute of Thermal Technology
44 100 Gliwice, Poland

ABSTRACT

The depletion of non-renewable natural exergy resources (the thermo-ecological cost) has been accepted as the objective function for thermo-ecological optimization. Its general formulation has been cited. The detailed form of the objective function has been formulated for a solar collector producing the hot water for home needs. Following design parameters have been accepted as the decision variables: the collector area per unit of the heat demand, the diameter of collector pipes, the distance of the pipe axes in the collector plate. The design parameters of the internal installation (the pipes, the hot water receiver) have not been taken into account, because they are very individual. The accumulation ability of hot water comprising one day has been assumed. The objective function contains following components: the thermo-ecological cost of copper plate, copper pipes, glass plate, steel box, thermal insulation, heat transfer liquid, electricity for driving the pump of liquid, fuel for the peak boiler. The duration curves of the flux of solar radiation and absorbed heat have been elaborated according to the meteorological data and used in the calculations. The objective function for economic optimization may have a similar form, only the cost values would be different.
Keywords: Exergy, Optimization, Non-renewable Resources, Solar Collector.

NOMENCLATURE

A — active area of the collector, m^2
b — distance between the axes of the pipes of the collector, m
c — specific thermal capacity, J/(kg K)
d — diameter of the pipes of the collector, m
$\dot{e}_r$ — energy flux of the solar radiation reaching the collector, W/m^2
E_{el} — consumption of electricity, J
G — amount of the material used to fabricate the collector, kg
K_{TE} — annual thermo-ecological cost of the useful heat, J
L — length of the pipes of the collector, m
m — coefficient characterizing the effect of the fin, m^{-1}
p — pressure, Pa
Q — amount of heat, J
Re — Reynolds number
T — temperature, K
u — coefficient of recovery of the material
U — coefficient of heat losses of the collector, $W/(m^2 K)$
$\dot{V}$ — volumetric flow rate of the liquid, m^3/s
$\dot{W}$ — driving power, W
w — flow velocity of the liquid, m/s
γ — density of the material, kg/m^3
δ — thickness of the wall, m
δp — pressure loss, Pa
ΔT_l — temperature increase of the intermediate liquid, K
ζ — correction expressing the fin effect
$\varepsilon_1, \varepsilon_2, \varepsilon_3$ — coefficient characterizing the energy efficiency of the collector, —, $W/(m^2 K)$, $W2/(m^4 K^2)$
η — energy efficiency
λ — coefficient of heat conduction, W/(m K)
λ_f — coefficient of hydraulic friction
ξ — coefficient characterizing the consumption of steel
ρ — specific thermo-ecological cost, J/kg, J/W, J/J_{el}
τ — time, s

---

*Corresponding author: Phone: (4832) 237 1661 Fax: (4832) 237 2872 E-mail: itc@itc.polsl.pl

φ — power of the absorbed heat stream, per area unit, W/m^2
χ — annual amount of the absorbed heat, J/a

Indices
A — annual demand
c — collector
Cu — copper
D — related to one day
el — electricity
f — fuel
g — glass
i — order number of the most hot day
is — thermal insulation
l — intermediate liquid
m — medium value
n — surplus over the demand
P — pump with driving electric motor
p — collector plate
s — steel
wh — peak water heater
0 — ambient value
Dot above the symbol denotes the quantity related to the time unit.

INTRODUCTION

In the field of ecological applications of exergy very important is the determination and reduction of the depletion of non-renewable natural resources. The quality of these resources may be expressed by means of exergy. The cumulative consumption of non-renewable exergy, connected with all the steps of fabrication of the considered useful product has been termed "the thermo-ecological cost" [1,2,3]. It is expressed not in monetary units, but in energy (exergy) units. An example of minimization of the thermo-ecological cost, by means of the selection of design parameters, has been presented in [4].
Sometimes an optimization of the design parameters based upon the minimization of entropy generation is recommended [5]. That method is not consequent, because it does not take into account the entropy generation in the preceding processes delivering energy carriers and semi-finished products to the considered process. On the other hand the entropy generation in the processes of extraction of the renewable exergy from the natural resources should not be taken into account, because the irreversibility of that processes has not any deleterious impact on the environment or on other fabrication processes.

The utilization of the solar energy represents a typical example of the extraction of renewable energy from the nature. Therefore, the optimization of the solar collector has been taken into account in the present paper.
The optimization problem of the solar collector has been considered, for example, in [6]. The authors apply the principle of minimization of entropy generation, including also the
irreversibility of the absorption of solar radiation. Additionally they do not take into account the changes of the energy flux of solar radiation and ambient temperature.

ASSUMPTIONS

A solar collector delivering hot water for the home use has been taken into account. It has been assumed that the annual demand for useful heat is known and the considered installation has the ability to accumulate the hot water in the scope of one day. The collector is filled with a non freezing liquid (glycol), which transports heat to the container of hot water installed inside the house. The circulation pump may be switched off when the temperature of the intermediate liquid is too low. The peak heat demand is covered by means of peak boiler fed with natural gas. The peak boiler ensures a required temperature of the hot water in the container. The collector is built of copper pipes connected in coil shape and welded to the copper plate on its bottom side [7]. The collector is covered with glass plate. The bottom wall and the side walls are made of steel and thermally insulated (Fig 1).

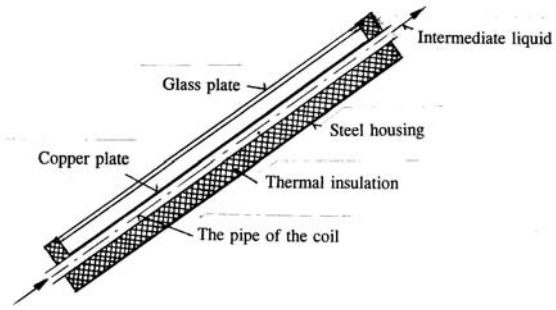

Figure 1. Scheme of the solar collector

Every optimization is partial, because it is no possible to take into account all the interactions with other processes. The considered optimization is also partial. It takes into account only the collector without the internal installation which is very individual. It has been assumed that at given heat demand the installed thermal power of the peak boiler is known because some days in winter can appear when the weather is very not friendly and the useful thermal power of the collector equals zero. On the other hand in summer very hot days can appear when the production ability of the collector is larger than the demand. The excess production should be deduced from the yearly production ability in order to determine the fuel demand in the peak boiler.

Two operation modes of the circulation pump may be applied. In the first case the flow rate of the liquid may be proportional to the heat stream absorbed in the collector. The rotation frequency of the pump should be changeable. Constant values of the liquid entering the collector and flowing out may be assumed. In the second case the flow rate of the liquid may be constant, adapted to the most warm days. The first mode of operation, accepted in the present considerations, ensures a lower consumption of electricity

Three decision variables have been accepted:

1) the active area of the collector per unit of the annual heat demand,

2) the diameter of the pipes of the collector,

3) the distance of he pipe axes of the collector.

It has been assumed that the thickness of the copper plate is determine by the required degree of its rigidity.

An optimal choice of the decision variable is possible, if the change of its value evokes opposite results. For example, an increase of the active area increases the consumption of materials, but decreases the demand of fuel in the peak boiler. The increase of diameter of pipes leads to an increase of the material consumption but decreases the flow resistance of the intermediate liquid. The increase of the distance between the axes of pipes reduces the total length of the pipes, but decreases the efficiency of the collector. The collector plate between the pipes transports the heat similarly to a fin. Its maximum temperature (in the middle between the pipes) becomes higher when the distance of pipes increases.

The total length of the pipe forming the coil results from the dependence:

$$L = \frac{A}{b} \tag{1}$$

The value of L decides about the necessary number of collectors for a given yearly heat demand.

OBJECTIVE FUNCTION

The yearly thermo-ecological cost of useful heat produced in the installation equipped in a solar collector may be expressed as follows:

$$\begin{aligned} K_{TE} = \frac{1}{\tau}\Big[& G_{\mathrm{Cu}}\,\rho_{\mathrm{Cu}}\,(1-u_{\mathrm{Cu}}) + G_g\,\rho_g + G_{is}\,\rho_{is} + \\ & G_s\,\rho_s\,(1-\mu_s) + G_l\rho_l + \dot{W}_{P\max}\rho_P + \dot{Q}_{wh\max}\rho_{wh}\Big] \\ & + \frac{\rho_{\mathrm{el}}}{\eta_{\mathrm{P}}}\int_0^{\tau_{\mathrm{P}}} \dot{V}_1 \delta p \,\mathrm{d}\tau + (Q_A - Q_c)\,\frac{\rho_{\mathrm{f}}}{\eta_{\mathrm{wh}}} \end{aligned} \tag{2}$$

The formula (2) contains two main components:

1) the investment component containing the thermo-ecological cost of the materials used for the construction of the collector and the thermo-ecological cost of the additional equipment (pump, peak boiler),

2) the operational components expressing the consumption of electricity in the circulation pump and the fuel consumption in the peak boiler.

The investment component takes into account the life time τ of the installation and the possibility to utilize copper and steel after the wear of the installation. The operational components take into account the yearly operation time τ_P of the pump, the annual demand Q_A for heat and the annual production Q_c of useful heat in the collector. The thermo-ecological cost of the peak boiler may be omitted in optimization calculations because that boiler should be able to cover the total demand for useful heat. Hence, the mentioned value is constant.

When calculating the annual production of heat in the collector, the possibility appears of some excess Q_n of the absorbed heat, which cannot be accumulated because of the assumed ability of accumulation only in the scope of one day. Hence the annual production of useful heat in the collector may be expressed as follows:

$$\begin{aligned} Q_c &= A\,\zeta \int_0^{\tau_P} \eta_c\,\dot{e}_r \,\mathrm{d}\tau - Q_n = A\,\zeta \int_0^{\tau_P} \varphi \,\mathrm{d}\tau - Q_n = \\ &= A\,\zeta\,\chi - Q_n \end{aligned} \tag{3}$$

where: η_c = energy efficiency of the collector

$\varphi = \eta_c \dot{e}_r$ = momentary thermal power per area unit of the collector

ζ (b) = correction expressing the effect of fin (efficiency of fin).

According to [8] the energy efficiency of the collector depends on its type, on the energy stream of the falling solar radiation, the mean temperature T_{lm} of the intermediate liquid and the ambient temperature:

$$\eta_c = \varepsilon_0 - \varepsilon_1 \frac{T_{lm} - T_0}{\dot{e}_r} - \varepsilon_2 \left(\frac{T_{lm} - T_0}{\dot{e}_r} \right)^2 \qquad (4)$$

Figure 2 presents after [8] the dependence (4) for some types of the collector. When the energy stream of falling solar radiation is too small, the energy efficiency has a value zero.

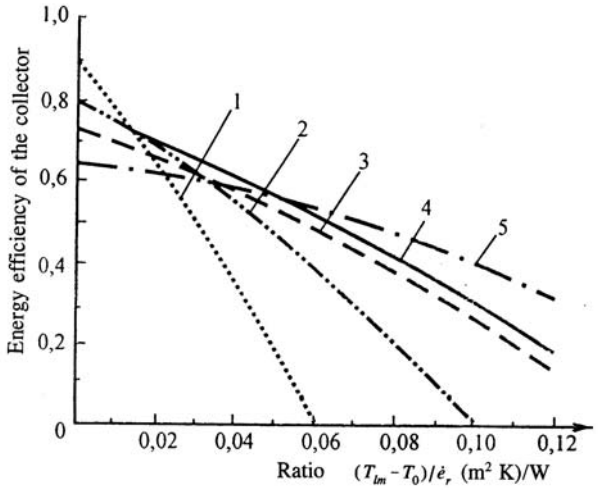

Figure 2: Energy efficiency of some types of the solar collector, after [8]

1— collector without any glass cover plate, 2 — absorber with single non-selective glass plate, 3 — absorber covered with double non-selective glass plate, 4 — absorber covered with single selective glass plate, 5 — vacuum absorber.

It has been assumed that Eq. (4) expresses the efficiency of the collector at fin efficiency near 100%. The pipes are welded to the bottom surface of the collector plate. Therefore, the correction taking into account the fin effect may be expressed more simply than in [9]:

$$\zeta = \frac{\text{tgh}\,(0{,}5\, m\, b)}{0{,}5\, m\, b} \qquad (5)$$

where:

$$m = \sqrt{\frac{U_L}{\lambda_p \delta_p}} \qquad (6)$$

where: U_L = coefficient of heat losses of the collector.

According to (4) one may introduce into (3):

$$\chi = \int_0^{\tau_P} \left[\varepsilon_0 \dot{e}_r - \varepsilon_1 (T_{lm} - T_0) - \varepsilon_2 \frac{(T_{lm} - T_0)^2}{\dot{e}_r} \right] \mathrm{d}\tau \qquad (7)$$

Only positive values of the integrated function should be taken into account. The components of that function are mutually dependent, because the ambient temperature depends on the intensity of falling solar radiation. However, that dependence is disturbed by the meteorological factors.

In order to determine the annual excess of absorbed heat, not accumulated in the system one should consider the most hot days and draw the duration curves of the absorbed heat during every of those days. Taking into account the planed heat demand per one day and the considered active area of the collector:

$$\begin{aligned} Q_n &= \sum_i Q_{ni} = \sum_i (A\zeta \int_0^{\tau_{Di}} \varphi_i \, d\tau - Q_D) = \\ &= \sum_i (A\zeta \chi_{Di} - Q_D);\ A\zeta \chi_{Di} > Q_D \end{aligned} \qquad (8)$$

where: i = order number of the hottest days

Q_D = heat demand per day

τ_{Di} = operation time of the collector in the i-th day.

The consumption of copper is expressed by following formula:

$$G_{Cu} = A \left(\frac{\pi d}{b} \delta + \delta_p \right) \gamma_{Cu} \qquad (9)$$

Similarly can be expressed other components of Eq. (2). After including also Eq. (8) the objective function takes the form:

$$K_{TE} = \frac{l}{\tau}\Big[A[(\pi \frac{d}{b}\delta + \delta_p)\gamma_{\mathrm{Cu}}\rho_{\mathrm{Cu}}(1-u_{\mathrm{Cu}}) \\ \delta_g\gamma_g\rho_g + \delta_{is}\gamma_{is}\rho_{is} + \delta_s\gamma_s(1+\xi_s)\rho_s(1-u_s) + \\ + \frac{\pi d^2}{4\,\mathrm{b}}\gamma_{\mathrm{l}}\rho_{\mathrm{l}}] + \dot{W}_{P\max}\rho_P \Big] + \\ + \frac{\rho_{\mathrm{el}}}{\eta_{\mathrm{P}}}\int_0^{\tau_P}\dot{V}_1\,\delta p\,\mathrm{d}\tau + (Q_A - A\chi\zeta + Q_n)\frac{\rho_{\mathrm{f}}}{\eta_{\mathrm{wh}}} \quad (10)$$

where ξ_s denotes the relative increase of steel consumption for side walls and supplementing parts of the collector.

The pressure loss of the intermediate liquid within the collector comprises the hydraulic resistance inside the pipes and local resistance at the inlet and outlet of the pipe. It has been assumed that the sum of local resistances equals to the dynamic pressure of the liquid:

$$\delta p = \frac{1}{2}\gamma_l w_l^2\left(\lambda_f\frac{L}{d}+1\right) = \frac{1}{2}\gamma_l w_l^2\left(\lambda_f\frac{A}{b\,d}+1\right) \quad (11)$$

Assuming:

$$\lambda_f = 0.046\,\mathrm{Re}^{-0.2} \quad (12)$$

one obtains the annual thermo-ecological cost of the consumed electricity:

$$E_{el}\rho_{el} = \frac{\rho_{el}}{\eta_P}\frac{8A^3}{\pi^2 d^4\gamma_l^2 c_l^3\Delta T_l^3}\times \\ \times\int_0^{\tau_P}\left(0.046\,\mathrm{Re}^{-0.2}\frac{A}{bd}+1\right)\varphi^3\,\mathrm{d}\tau \quad (13)$$

The Reynolds number is expressed as follows:

$$\mathrm{Re} = \frac{4\dot{V}_1\gamma_1}{\pi\, d\,\eta_l} = \frac{4\varphi A}{\pi\, dc_l\,\Delta T_1\eta_l} \quad (14)$$

The maximum driving power of the circulation pump results of (14) and maximum value $\varphi_{\max}$:

$$W_{P\max} = \frac{8A^3}{\pi^2 d^4\gamma_l^2 c_l^3\Delta T_l^3}\times \\ \times\left(0.046\,\mathrm{Re}_{\max}^{-0.2}\frac{\mathrm{A}}{bd}+1\right)\varphi_{\max}^3 \quad (15)$$

CALCULATIONS

In exemplary calculations it has been assumed that the collector is covered with single selective glass plate. Following data have been assumed :

The life time of the collector τ = 15 years

Thermo-ecological cost of the pump with driving motor ρ_P = 0.6 MJ/W

Electro-mechanical efficiency of the pump set η_P =0.7

Temperature of the intermediate liquid at the inlet and outlet of the collector T_{in} = 40 °C, T_{out} = 55 °C.

Specific thermal capacity of glycol c_l = 2.5 kJ/(kg K),

Exemplary yearly demand for useful heat Q_A = 2000 MJ/a,

Energy efficiency of the peak water heater η_{wh} = 0.8.

Coefficient of heat losses of the collector according to [9] U_L = 4.6 W/(m^2.K), coefficient of heat conductivity of copper λ_{Cu} = 372 W/(m K).

Coefficients of Eq. (4) characterizing the collector with a selective single glass plate, after Fig. 2:

$\varepsilon_0 = 0.8,\ \varepsilon_1 = 3.53\ W/(m^2K),\ \varepsilon_2 = 13.7\,W^2/(m^4K^2)$

From (5) and (6) it results m = 3.93 1/m.

Exemplary values of the correction ζ are cited in Table 1. The material parameters are given in Table 2.

RESULTS OF CALCULATIONS

Figure 3 presents the graphical interpretation of Eq. (7), according to the data taken from [10,11].

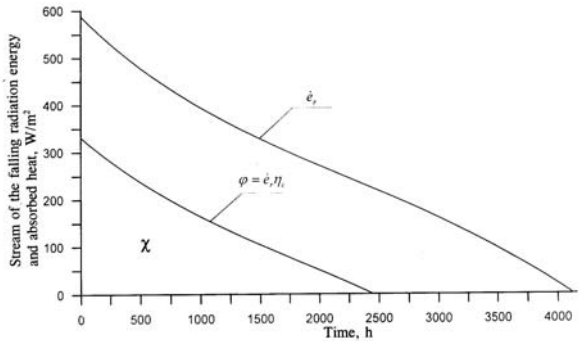

Figure 3: Results of calculations by means of Eq. (7)

b, m	0.07	0.10	0.15	0.25
ζ	0.994	0.987	0.972	0.927

Table 1: Exemplary values of the correction ζ

Material	γ kg/m^3	δ m	ρ MJ/kg or J/J$_{th}$	u
copper	8900	0.0008	151	0.5
glass	2700	0.004	33.4	0
steel	7800	0.002	59	0.3
isolation	20	0.1	165	—
intermediate liquid (glycol)	1092	—	27	—
electricity	—	—	3.13 J/J$_{th}$	—
fuel	—	—	1.04 J/J$_{th}$	—

Table 2. Material parameters

Figure 4 shows the optimization results of the pipe diameter for various values of the active collector area and constant fin effect. The optimum diameter (9 mm) does not practically depend on the active area. The nearest diameter of the produced pipes is 10 mm and, therefore, that value has been accepted for furher calculations.

Fig. 5 presents the optimization of the distance of pipe axes and the active area at a optimum active area at optimum diameter of pipes. The determined optimum parameters of the collector at giver yearly heat demand are: A_{opt} = 7.5 m^2, d_{opt} = 10 mm, b_{opt} = 0.13 m.

CONCLUSIONS

1. The optimization of the solar collector requires large meteorological data, determining the yearly duration curve of the energy stream of the falling solar radiation and the duration curves of falling energy streams during the hottest days. The meteorological data are probabilistic but deterministic. Hence the considered problem belongs to the area of deterministic optimization with probabilistic information set.

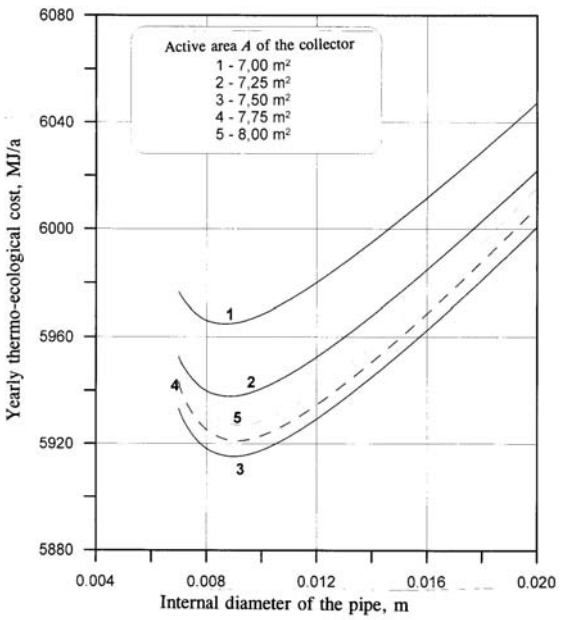

Figure 4: Optimization of pipe diameter at constant fin effect

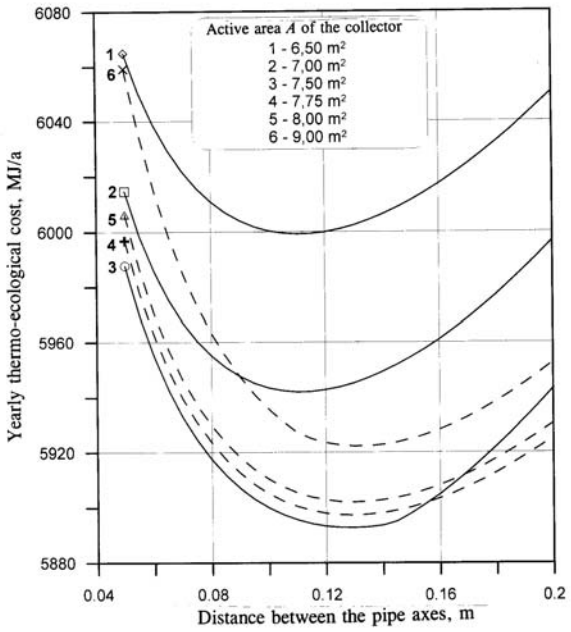

Figure 5: Optimization of the active area and distance between the pipe axes

2. The solution could be more exact when assuming an additional decision variable, namely the volume of the hot water receiver.

3. Exemplary calculations demonstrate that the optimum diameter of the collector pipe practically does not depend on the values of other decision variables.

4. The formulated objective function and the determined duration curves could be used also in an economic optimization after introducing the purchase prices instead of the values of the thermo-ecological cost.

REFERENCES

[1] Szargut J. *Minimization of the consumption of natural resources*. Bulletin of the Polish Academy of Sciences, Technical Sciences 1978;26(6):42-45.

[2] Szargut J. *Application of exergy for the calculation of ecological cost*. Bulletin of the Polish Academy of Sciences, Technical Sciences 1986;34(7-8):475-480.

[3] Szargut J. *Depletion of the unrestorable natural exergy resources*. Bulletin of the Polish Academy of Sciences, Technical Sciences 1997;45(2):241-250.

[4] Szargut J. *Minimization of the depletion of non-renewable resources by means of the optimization of design parameters*. Energy 2004;29(12-15):2161-2169.

[5] Bejan A. *Entropy generation minimization: the new thermodynamic of finite-size devices and finite-time processes*. Journ. Applied Physics Reviews, 1996;79 February.

[6] Torres-Reyers E., Navarrete-Gonzalez J.J., Zaleta-Aguilar A., Cervantes-de Gortari J.G. *Optimal process of solar to thermal energy conversion and design of irreversible flat-plate solar collectors*. Energy 2003;28(2):99-113.

[7] Pluta Z. *Solar energy installations (in Polish)*. Warszawa: Oficyna Wydawnicza Politechniki Warszawskiej, 2003.

[8] Smolec W. *Photothermal conversion of solar radiation (in Polish)*. Warszawa: Wydawnictwo Naukowe PWN, 2000.

[9] Pluta Z. *Theoretical principles of photothermal conversion of solar radiation (in Polish)*. Warszawa: Oficyna Wydawnicza Politechniki Warszawskiej, 2000.

[10] Wiśniewski G., Gołębiowski S., Gryciuk M. *Solar collectors; guide for utilization of solar energy (in Polish)*. Warszawa: Centalny Ośrodek Informacji Budownictwa, 2001.

[11] Gillet W.B., Moon J.E. *Solar collectors. Test methods and design guidelines*. Dodrecht: D. Reider Publishing Company, 1985

Proceedings of ECOS 2005
Trondheim, Norway
June 20–22, 2005

BIO-OIL PRODUCTION BY FAST PYROLYSIS OF OLIVE RESIDUE: EFFECT OF PYROLYSIS TEMPERATURE AND HEATING RATE

Basak Burcu UZUN* and Ayse Eren PÜTÜN
Anadolu University, Faculty of Architecture and Engineering, Dept. of Chemical Engineering, Iki Eylul Campus, 26555, Eskisehir, TURKEY.

Ersan PÜTÜN
Anadolu University, Faculty of Architecture and Engineering, Dept. of Material Science and Engineering, Iki Eylul Campus, 26555, Eskisehir, TURKEY.

ABSTRACT

In this study our aim is to reach high yields of bio-oil in a fixed bed tubular reactor at various pyrolysis temperatures, sweeping gas velocities, and heating rates. In these experiments, to improve heat and mass transfer, a stainless steel basket was used. Effects of different sweeping gas velocities, heating rates were examined on product yields.

Keywords: Fast Pyrolysis, Synthetic Fuels

INTRODUCTION

Fast pyrolysis of biomass is a moderate temperature process in which the feedstock is rapidly heated in the absence of oxygen [1]. While the conventional pyrolysis of wood and biomass is used essentially for making charcoal, fast pyrolysis can be controlled to give high yields of liquids (bio-oils), which can be readily stored and transported. Bio-oils can be used for the production of chemicals (food flavorings, resins, fertilizers and emission control agents) and can also substitute for fuel oils in many static applications for heat or electricity generation (boilers, furnaces, engines and turbines) [2]. For the development of effective combustion techniques, a detailed knowledge of the physico-chemical properties and the combustion characteristics are needed.

The main goal of fast pyrolysis is to convert the solid biomass into liquid bio-oil. In practice about 40-75% of the (dry) biomass is converted into oil vapour, which yields the liquid bio-oil after condensation. About 10-20% of the biomass is converted into char (solid porous carbon particles) and 10-30% is converted into an uncondensable gas.

* Corresponding author: Pnone: +90 222 335 05 80
Fax: +90 222 323 95 01 E-mail: bbuzun@anadolu.edu.tr

The water content of the fuel usually is limited to about 15 wt-%. Present fast pyrolysis reactors are based on fluidized bed, entrained flow, ablative vortex, and rotating cone technology [3].

Fast pyrolysis requires high heating rates, moderate temperatures and short residence times for liquids. Feed drying, particle size, pretreatment, reactor configuration, heat supply, heat transfer, reaction temperature, vapor residence time, secondary cracking, char and ash separation and liquid collection are very important for the creative and innovative designs. These designs are based on high heat and mass transfer rates. Heat transfer in a pyrolysis reactor occurs firstly to the reactor heat transfer medium (solid reactor wall in ablative reactors, gas and solid in fluid and transport bed reactors, gas in entrained flow reactors), secondly, from the heat transfer medium to the pyrolysing biomass. Heat is transferred from hot gas to the pyrolysing biomass particle by primarily convection and solid-solid transfer with mostly conductive heat transfer. Some radiation occurs in all reactors [4].

Particle size, sweeping gas velocity, heating rates and reactor configuration are essential for mass transfer. Since thermal conductivity of biomass is very poor, biomass particles have to be very small to fulfill the

requirements of rapid heating to give high liquid yields. As particle size increases, liquid yields reduce as secondary reactions within the particle become increasingly significant. Char removal is an essential requirement for large particle sizes. It has a catalytic activity and cracks organic vapors to secondary char. High heating rates and high heat fluxes along the reactor is important. Long vapor residence times and high temperatures cause secondary cracking of primary products reducing yields of organic liquids [5].

In the present investigation, laboratory scale results are reported about the fast pyrolytic behaviour of olive residues. The main aim of our study is to get the biofuel from olive residues. Pyrolysis experiments were conducted at pyrolysis temperature of 400-700^{o}C. In the previous study, the effects of pyrolysis temperature and reaction times on pyrolysis product yields were observed [6]. The 2.5 cm diameter of the reactor caused insufficient heat and mass transfer for the low reaction times, although it had enough space to place higher amount of raw material. Therefore some of raw material was not reacted sufficiently. For this reason, in the second part of the experiments, a stainless steel mesh basket was used to get good contact between the material and reactor walls (Figure 1.). Pyrolysis experiments were performed for various pyrolysis temperatures with using the basket. Effects of various sweeping gas velocities and heating rates were also examined.

EXPERIMENTAL

The fast pyrolysis experiments were conducted under nitrogen atmosphere in a well-swept resistively fixed-bed reactor with a length of 90 cm and an inner diameter of 2.5 cm. Experimental set-up is given in Figure 2. Heating rate and pyrolysis temperature were controlled with a PID controller. The flow of the gas released was measured by using a soap film meter, for the duration of the experiments.

The experiments were carried out placing the olive residue among a deep basket (upside down) and reactor wall, like a thin layer. In the first part of the experiments, 10g of the air-dried sample, sieved to average particle size of 1.22 mm was placed in the reactor with a sweep gas velocity of 100 cm^3min^{-1} which was controlled and measured with a rotameter and then heated with a rate of 300 ^{0}C min^{-1} to the pyrolysis temperature range of either 400,500,550 and 700 ^{o}C within a reaction time of 5 min. Released gas was collected in a gas tight Tedlar bag. The liquid phase was collected in a cold trap maintained at about 0 ^{o}C. The liquid phase consisted of aqueous and oil phases, which were separated and weighed. Particularly water was separated in a Dean &Stark apparatus. After pyrolysis, char yield was determined from weight of remained carbon residue in the reactor after pyrolysis. The gas yield was then calculated by difference.

In the second part of the experiments, various sweeping gas flow rates (50, 200, 400, and 800 cm^3 min^{-1}) were performed at optimum pyrolysis temperature (500 ^{o}C) and constant heating rate (300 ^{o}C min^{-1}) and reaction time (5min.).

At the third part of the experiments, different heating rates (5,100,500 and 1000 ^{o}C min^{-1}) were studied at optimum pyrolysis temperature (500^{o}C) and sweeping gas flow rate (400 cm^3 min^{-1}) and reaction time (5min.).

In this study, all the yields are expressed on a dry, ash-free (d.a.f) basis and the average yields from at least three experiments. All of the experimental results (product yields) were calculated according to formulas given below:

$$\text{Yield (wt.\%)} = \frac{\text{Weight of obtained product}}{\text{Weight of raw material (d.a.f.)}} \times 100 \quad (2)$$

Conversion (%)= 100 %-Char yield (%)

d.a.f. represents dry and ash free.

Figure 1. Stainless steel basket

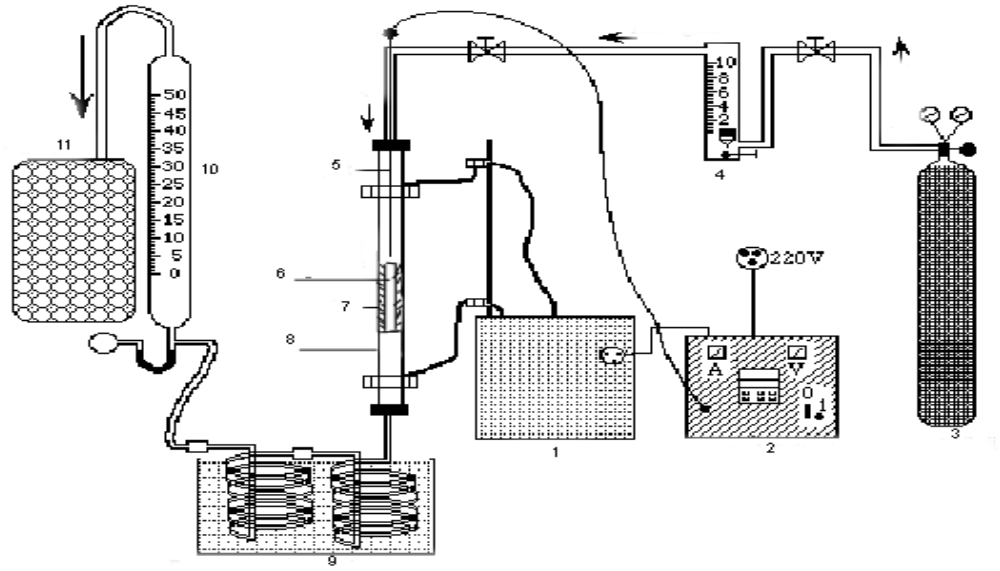

1. Power system
2. Controller
3. Nitrogen bottle
4. Rotameter
5. Thermocouple
6. Cr-Ni basket
7. Raw material
8. Reactor
9. Ice bath and liquid collecting traps
10. Soap film meter
11. Gas tight bag

Figure 2. Experimental set-up

RESULTS AND DISCUSSION

Raw Material

The sample of olive residue investigated in this study has been taken from an olive oil factory around Ayvalık located in Aegean region, western part of Turkey. The properties of raw material and proximate are given in Table 1.

Analysis	**Percentage (%)(As received)**
Moisture	8.83
Volatiles	68.75
Ash	5.12
Fixed carbon	17.30
Cellulose	66.96
Oil	5.46

Table 1. Proximate analysis and properties of olive oil residue

Product Yields

Pyrolysis experiments were conducted at pyrolysis temperature range of 400-700 ^{o}C within a constant reaction time of 5 minute. A stainless steel basket was designed to increase mass and heat transfer along the reactor walls and material. All the yields were expressed on a dry, ash-free basis and the average yields of at least three experimental errors of less then ±0.5%.

The yields of conversion were determined in relation to final temperature at 400, 500, 550 and 700 ^{o}C for the average particle size of taken 1.22 mm with a heating rate of 300 ^{o}Cmin^{-1} with sweeping gas velocity of 100 cm^{3}min^{-1}. As it is seen in Fig. 3., increasing pyrolysis temperature increases the pyrolysis conversion efficiency. Maximum oil yield was attained as 41.34% at the pyrolysis temperature of 500^{o}C. In previous study, maximum oil yield was attained at the pyrolysis temperature of 550^{o}C as 38.12% [6]. Usage of basket resulted with an increase of bio-oil 8.45%. Due to better mass and heat transfer, there is an increase of liquid yields. Experimental results are given in Fig. 3 and 4.

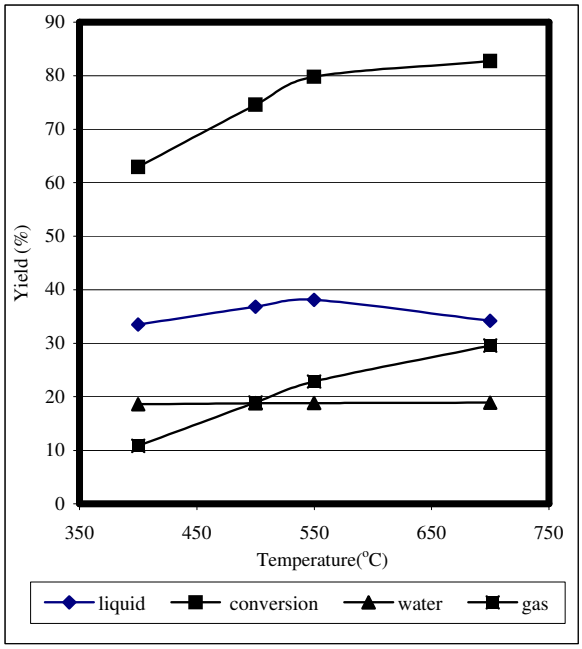

Figure 3: Pyrolysis yields of fast pyrolysis with out basket

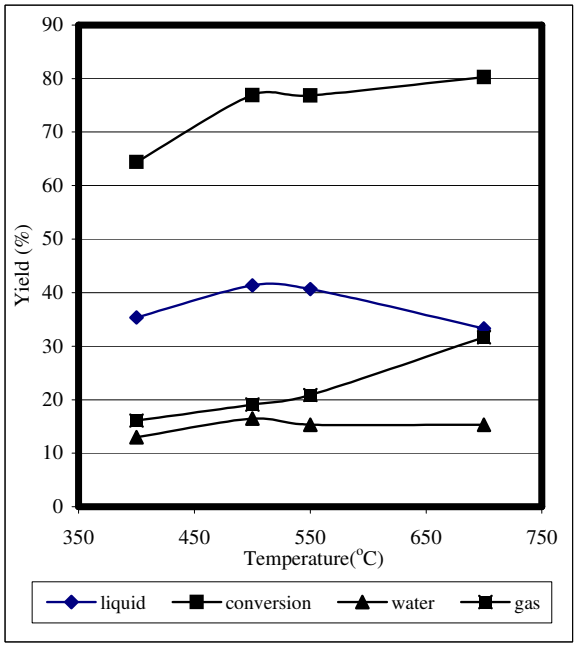

Figure 4: Pyrolysis yields of fast pyrolysis with using basket

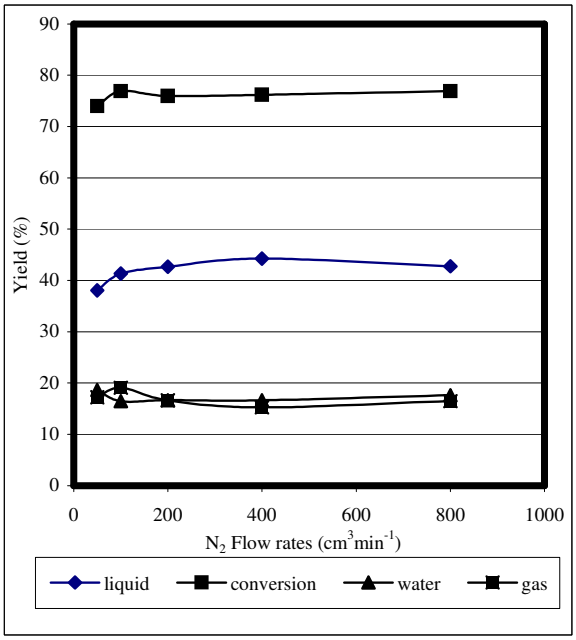

Figure 5. Effect of sweeping gas flow rates on pyrolysis yields

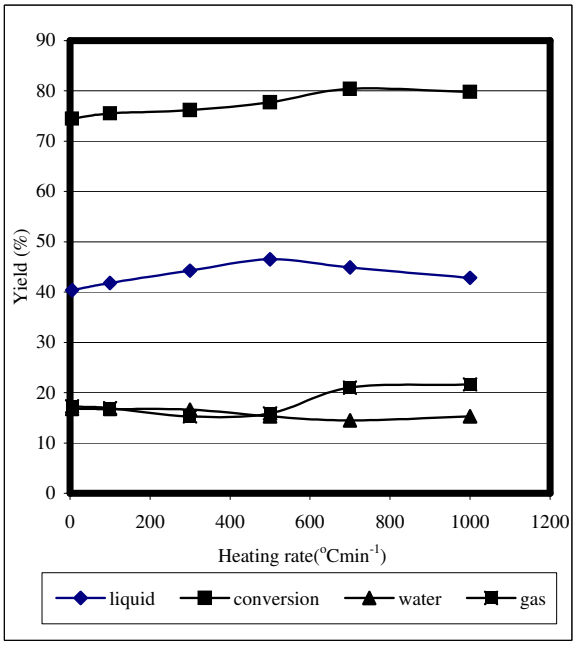

Figure 6: Effect of heating rates on pyrolysis yields

In the second set of experiments, various sweeping gas flow rates were investigated. Experimental results are given in Fig.5. According to the experimental results, 400 cm^3 min^{-1} is the most suitable flow rate to obtain maximum oil yields, due to shorten the residence times of volatiles and reduce forming secondary reactions. Liquid yields were increased from 41.34 to 44.27% (Fig. 5). As reported in the literature, the sweeping gas removed the products from the hot zone to minimize secondary reactions such as thermal cracking, repolymerization, and recondensation and to maximize the liquid yield [5]. Rapid quenching stops the chemical reactions before the valuble initial reaction products can be degraded [6]. Pyrolysis vapors are removed instantly by higher sweeping gas flow rates and if vapors are quenched sufficiently, the liquid yield has to be high. Because of sweeping gas effect, mass transfer rate is getting higher.

Experimental results of effect of heating rate are given in Fig. 6. Higher heating rates cause higher liquid yields. As it is seen, maximum oil yield was achieved as 46.52% with the heating rate of 500^oCmin^{-1}.

Comparing this study with our previous work, the main differences are in the reactor types, pyrolysis atmospheres and heating rates [7]. In the study mentioned, the maximum oil yield was found to be 32.72 % under static atmosphere, while the maximum oil yield attained was 38.98 % under nitrogen atmosphere at pyrolysis temperature of 500^oC with a sweeping gas flow rate of $200cm^3min^{-1}$ and heating rate of 7^oCmin^{-1}in Heinze retort. In that study, steam pyrolysis of olive residue in Heinze retort was also studied. The maximum oil yield was attained as 42.12% at the same pyrolysis temperature with a steam flow rate of 1.3 $cmsec^{-1}$. In this study, maximum oil yield was achieved as 46.52%. This result is better than previous results due to the reactor configuration, high heating rate and better mass and heat transfer [7].

CONCLUSION

Olive residue can be a promising candidate for the near future bio-fuel applications. Biomass decomposition rates and extents depend on the process parameters of reactor temperature, configuration, heating rate, sweeping gas velocity. Mass transfer limitations are very important for design and optimisation. In this study, for better heat and mass transfer from the reactor wall to biomass sample a stainless steel basket was used. Optimum parameters for getting maximum bio-oil in for our experimental condition were found. Maximum bio-oil was attained at pyrolysis temperature of 46.52%, with a heating rate of 500 ^oC min^{-1} and sweeping gas velocity of 400 cm^3min^{-1}. Heat and mass transfer conditions determine the selectivity of primary solid degradation reactions and thus the characteristics of pyrolysis. Therefore these affect pyrolysis yields.

REFERENCES

1. Meier D., Oasmaa A. Ad Peacocke G.V.C., *Thermochemical Biomass Conversion*, Bridgwater A.V., Boocock D.G.B. Eds. Blackie A.&P., 391(1997).

2. Milne T.A., Agblevor F., Advanced in *Thermochemical Biomass Conversion*,Bridgwater A.V., Boocock D.G.B. Eds. Blackie A.&P.,.409 (1997).

3. Bridgwater, A.V., Meier, D., Radlein, *An Overview of Fast Pyrolysis*" D.,Organic Geochemistry, 30**,** 1479-1493, (1999).

4. Bridgwater, *Principles and Practise of Biomass Fast Pyrolysis Processes for Liquids*", JAAP,51,3-22 (1999).

5. Putun A.E., Ozcan A., Gercel,H.F., Putun,E. *Production of biocrudes from biomass in a fixed-bed tubular reactor: product yields and compositions.* Fuel 80, 1371-1378 (2001).

7. Uzun, B.B., Putun A.E., Putun,E. *Biofuel productıon by fast pyrolysis of olive resıdues*, ECOS'03, Copenhagen, 1137-1142 (2003).

8. Apaydın, E.,Uzun, B.B., Putun A.E., Putun, E. *Effect of water vapour on the product yields and composition of the fixed-bed pyrolysis of olive residues*. ECOS'02, Berlin, 3-5 July, (2002)

Proceedings of ECOS 2005
Trondheim, Norway
June 20–22, 2005

AN ENERGY CROP FOR PRODUCING BIO-FUEL: EUPHORBIA RIGIDA

Basak Burcu UZUN, Ayse Eren PÜTÜN, and Esin APAYDIN
Anadolu University, Faculty of Architecture and Engineering, Dept. of Chemical Engineering, Iki Eylul Campus,26555, Eskisehir, TURKEY.

Ersan PÜTÜN
Anadolu University, Faculty of Architecture and Engineering, Dept. of Material Science and Engineering, Iki Eylul Campus,26555, Eskisehir, TURKEY.

ABSTRACT

Biomass and energy crops are the renewable energy sources, which is often believed to have the highest potential to contribute to a future sustainable energy supply to world's energy. Bioenergy is expected to become one of the best option energy sources to cope with global warming and exhaustion of fossil fuel resources. A wide range of process and routes are available for power generation. Pyrolysis is another emerging technology to convert solid wastes to char, gases and liquid fuels. In this study, our aim is to evaluate the pyrolytic behaviour of *Euphorbia rigida* known as a plant abundantly grown in arid lands by comparing the results of the previous studies at different pyrolysis conditions.

Key words: Euphorbia rigida, energy crops, bio-fuels

INTRODUCTION

Thermochemical conversion of organic residues constitutes an important way to recover energy and prepare chemicals and activated carbon. Turkey has a great potential of agricultural and forest residues. Two third of renewable energy use is provided by biomass. When thinking that more than 26 millions of people living in urban areas in Turkey, biomass energy is very important for heating and cooking [1].

The main advantages of using biomass are that it has negligible sulfur, nitrogen, and metal content and is also CO_2 neutral. Combustion is the most common way to employ biomass sources in Turkey. There are different ways to obtain heat and electricity from biomass such as liquefaction, gasification, and pyrolysis. Due to the easy application, Pyrolysis is a recommended process to convert biomass into heat, bio-oil and fine chemicals [1,2].

There is a number of biomass species can be considered as an alternative energy resource. The economics of biomass pyrolysis are generally considered to be most favorable for plant that grow abundantly and require little cultivation in arid lands. One group of plants is Euphorbiaceae, which are characterized by their ability to produce a milky latex, an emulsion of 30wt% terpenoids in water. *Euphorbia rigida* (Euphorbiaceae family) is found around the Mediterranean from Morocco through Portugal to Turkey and Iran. It is known that 80 species of Euphorbia are found in Turkey. Some species of this family have been investigated and identified as promising candidates for renewable fuels and chemical feedstocks by some researchers [3,4,5]. Also, there have been found some studies to obtain liquid products could be replaced petroleum, from *Euphorbia rigida*. Pütün et al. investigated the production of bio-fuel by pyrolysis of *Euphorbia rigida* for the first time. Further, various types of pyrolytic reactors and catalysts examined on pyrolysis of *Euphorbia rigida* by the other workers of our team. The main objective of the present study is to evaluate the aspects of Euphorbia rigida as a potential energy source, including major properties,

* Corresponding author: Pnone: +90 222 335 05
Fax: +90 222 323 95 01 E-mail: eputun@anadolu.edu.tr

pyrolytic behaviours and efficiencies of different types of pyrolytic reactors to obtain bio-fuels. For this reason the results of our previous studies were put together and compared with each other for a review study.

Proximate Analysis:

Proximate analysis was performed on the *Euphorbia rigida* sample to determine the weight fraction of volatile, ash, and fixed carbon contents. The ASTM Standart Test Method For Proximate analysis of Wood Fuels (D 870-82) was used. Then, the fixed carbon content was obtained by substracting from 100% the sum of volatile matter and ash contents in percentage.
The ultimate analysis was performed in a elementel analyzer (Carlo Erba, EA 1108). The heating values are very important thermal properties for design and evaluation of thermal conversion systems. The gross calorific values of biomass samples and bio-oils are calculated by Dulong Formula:

$$Q_{GCV}\,(MJ/kg)=33.83C+144.3(H-O/8) \quad (1)$$

Where C, H, O are respectively, the mass fraction of carbon, hydrogen, and oxygen.

Experimental Discussion:

Our previous pyrolysis experiments were performed at various pyrolysis temperatures, heating rates, with different types of atmospheres and reactors. Details of the experimental set-up were given in related papers. The general experimental procedure is given in Figure 1. In this study, due to discuss the effect of reactor configuration, experimental results of slow pyrolysis in tubular and Heinze reactors are given in Table 2 [4,5].

After that, experimental result of catalytic pyrolysis is also compared [3]. Optimum experimental results of these catalytic and non-catalytic works are discussed. These optimum results are selected for this study those obtained in maximum bio-oil yields. For slow pyrolysis in a tubular reactor, maximum oil yield was achieved at the pyrolysis temperature of 500 ^{o}C, with sweeping gas velocity of 400 cm^3 min^{-1} and heating rate of 7 ^{o}C min^{-1}. Optimum results of slow pyrolysis experiments in Heinze retort were obtained at pyrolysis temperature of 550 ^{o}C and heating rate of 7 ^{o}C min^{-1}. In catalytic study, under the same experimental conditions, Maximum oil yield was obtained with Criterion-534 (20% weight of raw material) as catalyst under static atmosphere.
After all, results of fast pyrolysis experiments performed at various pyrolysis temperatures, heating rates, and pyrolysis atmospheres such as nitrogen and pressurized hydrogen are given in Table 4. In fast pyrolysis experiments, optimum results were performed at pyrolysis temperature of 550 ^{o}C, with a sweeping gas velocity 100 $cm^3min^{-1}$of and heating rate of 300 ^{o}Cmin^{-1}[6]. In hydropyrolysis, maximum oil yield was reached at pyrolysis temperature of 550 ^{o}C, hydrogen gas velocity of 10Lmin^{-1}, 150 bar hydrogen pressure and heating rate of 300 ^{o}C min^{-1}[5]. All of the experimental results (product yields) were calculated according to formula:

$$\text{Yield (wt.\%)} = \frac{\text{Weight of obtained bio-oil}}{\text{Weight of raw material (d.a.f.)}} \times 100 \quad (2)$$

d.a.f. represents dry and ash free.

An important characteristic of the pyrolysis is residence time. Residence time of vapours mainly depend on reactor geometry and sweeping gas flow rate.

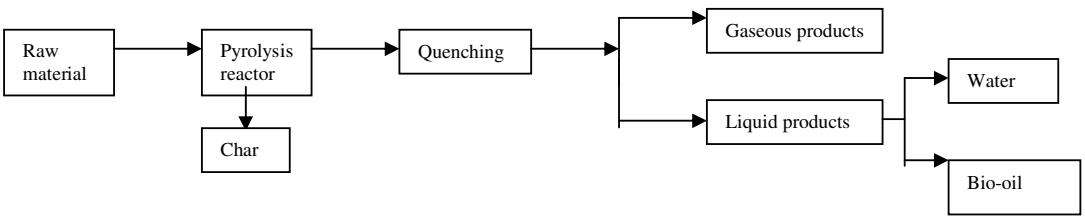

Figure 1. Pyrolysis procedure

Result of proximate analysis of Euphorbia rigida collected from Southwestern Anatolia is given in Table 1. Prior to the experiments the sample was dried and ground in a high speed rotary cutting mill 0,55mm. is found mean particle. Our sample has 3.0% moisture content.

Analysis	**Percentage (As received)**
Moisture	3.0
Volatiles	78.9
Ash	6.5
Fixed carbon	11.6

Table 1. Results of proximate analysis [3]

Elementel analysis of raw material is given in Table 2. H/C ratio of Euphorbia Rigida was found as 1.43. There was no sulphur content in this material.

Component	**(%)**
C	49.08
H	5.86
N	1.23
O*	43.83
H/C	1.43
O/C	0.67

Table 2. Results of elementel analysis [3]

In this study, our aim is to indicate maximum bio-oil yields. Optimum experimental results of Heinze retort, both catalytic and non catalytic works are given in Table 3. Whereas maximum oil yield was 31.46% for tubular reactor, Bio-oil yield was found 22.69% for Heinze retort. Selection of reactor geometry design is very important to reach desired product yields. Catalytic pyrolysis is very beneficial for product selectivity. There is a significant effect of catalyst (Criterion-534) was seen. Because of reactor geometry and sweeping gas, tubular reactor gives the highest biofuel yields among the experimental results given in Table 3.

	Slow Pyrolysis in tubular reactor [5]	**Slow Pyrolysis in Heinze reactor [4]**	**Catalytic Pyrolysis in Heinze reactor [3]**
Bio-oil(%)	31.46	22.69	30.98
Char (%)	27.98	20.40	21.38
Water(%)	16.94	24.13	26.79
Gas (%)	23.62	32.78	20.85

Table 3. Product yields of slow pyrolysis experiments

In Table 4, Experimental results of tubular reactor both nitrogen and pressurized hydrogen atmospheres are given with high heating rates. As it is expected, maximum oil yields were achieved by hydropyrolysis. Direct hydrogenation causes an increase of liquid fraction. There was a sharp decrease of char yield. Conversions of liquid and gaseous products were increased compared with fast pyrolysis results.

	Fast Pyrolysis [6]	**Hydropyrolysis [4]**
Bio-oil (%)	32.78	41.10
Char (%)	27.63	9.40
Water (%)	13.26	12.70
Gas (%)	26.33	36.80

Table 4. Yields of fast pyrolysis experiments

	C	**H**	**N**	**O**	**H/C**
Bio-oil [1]	75.50	11.10	2.80	10.60	1.76
Bio-oil [2]	74.14	9.31	2.20	14.40	1.48
Bio-oil [3]	66.24	8.95	2.10	22.71	1.62
Bio-oil [4]	68.81	8.74	1.85	20.60	1.52
Bio-oil [5]	77.30	11.70	1.80	9.20	1.82

Table 5. Elementel analysis of bio-oils

Bio-oil [1]: obtained from slow pyrolysis in a tubular reactor [5]
Bio-oil [2]: obtained from slow pyrolysis in a Heinze reactor [4]
Bio-oil [3]: obtained from catalytic pyrolysis in a Heinze reactor [3]
Bio-oil [4]: obtained from fast pyrolysis [6]
Bio-oil [5]: obtained from hydropyrolysis [4]

In Table 5, Elementel analyses of obtained bio-oils under different experimental conditions were given in Table 5. The greatest H/C was reached from bio-oil[5] obtained by Hydropyrolysis. It was found

1.82. The minimum H/C value was 1.48 from the bio-oil obtained by slow pyrolysis in Heinze retort. The heating values are very important thermal properties for the design and evaluation of thermochemical conversion systems. Gross heating values of raw material and bio-oils were calculated by Dulong formula and given in Table 6. Pyrolysis causes a double fold of heating value of raw material by converting it into liquid. Average calorific value of bituminous coal is 30 MJ/kg. While the biomass sample presents energy content nearly half of the energy content of coal. Due to abundance and content of milky latex, Euphorbia is an important energy source with the maximum calorific values of the obtained bio-oils

Material	**Gross Calorific Value (MJ/kg)**
Euphorbia Rigida	17.15
Bio-oil [1]	39.65
Bio-oil [2]	37.70
Bio-oil [3]	31.23
Bio-oil [4]	32.17
Bio-oil [5]	41.00

Table 6. Calorific values of raw material obtained bio-oils

Bio-oil [1]: obtained from slow pyrolysis in a tubular reactor
Bio-oil [2]: obtained from slow pyrolysis in a Heinze reactor
Bio-oil [3]: obtained from catalyticpyrolysis in a Heinze reactor
Bio-oil [4]: obtained from fast pyrolysis
Bio-oil [5]: obtained from hydropyrolysis

CONCLUSION

- Euphorbia Rigida can be a good candidate to produce biofuels. Because of ability to produce milky latex which is an emulsion of 30 wt.% terpenoids in water. Euphorbia species have a high potential to produce hydrocarbons by thermochemical methods. Obtained bio-oils have high energy content compared with raw material.
- After considering the experimental results hydropyrolysis seems to be the most advantageous method because of giving the maximum oil yields. Although it is a difficult and expensive process due to depending on hydrogen atmospheres with high pressures.
- While discussing the reactor geometry, selection of tubular reactor instead of Heinze retort has an advantage to reach maximum oil-yields.
- Catalytic pyrolysis in Heinze retort causes a 36.5 % increase of bio-oil yield compare with non-catalytic pyrolysis under static atmosphere. Economic feasibility depends on selection of catalyst and process.
- Selection of tubular reactor instead of Heinze retort has an advantage to reach maximum oil yields, by providing the fast pyrolysis processes, Heinze retort is more beneficial for slow pyrolysis applications. On the contrary, Fast pyrolysis is more important to reach maximum bio-oil yields in few seconds. Nevertheless cost of fast pyrolysis process is more than slow pyrolysis. Reaching higher heating rates and mass transfer rates may be feasible for optimum process parameters and reactor designs.

REFERENCES

1. Hepbaşlı, A., Ozdamar, A., Ozalp, N. *Present Status and Potential of Renewable Energy Sources in Turkey*, Energy Sorces, 23,631-648, (2001).

2. Minowa, T., Kondo, T. Dudirjo, T., *Thermochemical Liquefaction of Indonesian Biomass residues*, Biomass and Bioenergy, 14, 517-524, (1998).

3. Ateş, A., Pütün, A. E., Pütün, E., *Fixed-bed pyrolysis of Euphorbia rigida with different catalyst*, Energy conversion of Management, 46,421-432, (2005).

4. Pütün, A.E., Gercel, F.G., Kockar, O., Ege, O., Snape, C.E., Pütün, E. *Oil Production from an arid-land plant: fixed-bed pyrolysis and hydropyrolysis of Euphorbia Rigida*, Fuel, 75, 1307-1312, (1996).

5. Pütün, A.E., Ozcan, A., Gerçel, H. F., Pütün, E., *Production of biocrudes from biomass in a fixed-bed tubular reactor: product yields and compositions*, Fuel, 80, 1371-1378, (2001).

6. Gerçel, F., PhD. Thesis,Anadolu University,Institue of Fundamental and Applied Science,(1997).

Proceedings of ECOS 2005
Trondheim, Norway
June 20–22, 2005

ENERGY ANALYSIS OF TECHNOLOGICAL SYSTEMS OF COMBINED HEAT AND POWER PLANTS INTEGRATED WITH BIOMASS GASIFICATION

Bolesław Zaporowski *
Poznan University of Technology, Poznan, Poland

ABSTRACT

This paper presents a complex energy analysis of technological systems of gas and gas-steam combined heat and power (CHP) plants integrated with biomass gasification. The analysis is based on elaborated mathematical models of main elements of the technological systems of these CHP plants. The mathematical model of biomass gasification includes a system of equations, which describes chemical, physical and energy phenomena occurring in gas generator. The solution of mathematical model of gasification process allows one to determine the following quantities: the composition and lower heating value of produced gas, the gasifying agent consumption and excess ratio, the volume of gas obtained from 1 kg of biomass, and the chemical and energy efficiency of the process. In equations which describe energy processes in gas generator, heat recovery steam generator (HRSG) and gas turbine block, the physical enthalpies of the produced gas, the gasifying agent, the oxidizer (air) and the combustion gases are determined with the help of statistical physics. The paper presents the results of a computer simulation of gasification of biomass with the help of various kinds of gasifying agent and the results of simulation of the energy utilization factor, efficiency of electric energy generation and power to heat ratio for the following technological systems of gas and gas-steam CHP plants integrated with biomass gasification: gas CHP plant using simple gas turbine cycle, gas CHP plants using steam injected gas turbine (STIG) cycle, and gas-steam CHP plant using gas turbine and extraction-condensing steam turbine.
Key words: biomass gasification, gas turbine, combined heat and power (CHP) plant

NOMENCLATURE

a, b, c, d	numerical coefficients determining mass fractions of biomass, gasifying agent, steam and slag related to 1 kg of gaseous fuel
e, f, g, h	numerical coefficients determining mass fractions of gaseous fuel, oxidizer (air), nitrogen and water steam, related to 1 kg of combustion gases
B	CHP plant biomass consumption [kg/s]
M_i	molar mass of particular components of combustion gases, gaseous fuel, gasifying agent and oxidizer [kg/kmol]
n	number of components of the gasifying agent (air or oxygen)
p_{cgi}, p_{gi}, p_{gai},p_{oxi}	partial pressures of particular components of the combustion gases, gaseous fuel, gasifying agent and oxidizer
P_{elgt} , P_{elst}	electric power of the gas and steam turbine generator respectively [kW]
P_{ox}	electric power consumption of gasifying agent compressor [kW]
q_{H2O}	steam consumption per 1 kg of biomass
Q_h^g	lower heating value of gaseous fuel [kJ/Nm^3]
Q_h^b	lower heating value of biomass [kJ/kg]

* Boleslaw Zaporowski, Phone : +48 61 6652525 Fax: +48 61 6652280 E-mail: bzap@sol.put.poznan.pl

Q_c	thermal power of gas or gas-steam CHP plant produced in cogeneration [kW]
Q_{gi}	molar heating value of particular components of gaseous fuel [kJ/kmol]
$T_{cg,} T_g,$ $T_{ga,} T_{ox}$	temperature of combustion gases, gaseous fuel, gasifying agent, and oxidizer (air) [K]
T_o	reference temperature (288,15 [K])
v_g	volume of gaseous fuel obtained from 1 kg of biomass [Nm^3/kg]
v_{ga}	gasifying agent consumption per 1 kg of biomass [Nm^3/kg]
$\Delta h_{b(T_0)}$	chemical enthalpy of biomass at the reference temperature To [kJ/kg]
$\Delta h_{H_2O(T_0)}$	chemical enthalpy of water (or steam) at the reference temperature To [kJ/kg]
$\Delta H_{gi(T_0)}$	molar chemical enthalpy of particular components of gaseous fuel at the reference temperature To [kJ/kmol]
$\Delta H_{(T_0,T_g)},$ $\Delta H_{(T_0,Tga)}$	increments of molar physical enthalpy of gaseous fuel and gasifying agent related to the temperature T_0 [kJ/kmol]
$\Delta h_{A(T_0,T_g)}$	
$\Delta h_{(T_0,T_{N_2})}$	
$\Delta h_{(T_0,T_{H_2O})}$	increment of physical enthalpy of ash, nitrogen and water (or steam) related to the temperature T_0 [kJ/kg]
$\Delta H_{i(T_0,T_{cg})},$ $\Delta H_{i(T_0,T_g)},$ $\Delta H_{i(T_0,Tga)},$ $\Delta H_{i(T_0,T_{0X})}$	increments of molar physical enthalpy of particular components of combustion gases, gaseous fuel, gasifying agent and oxidizer (air) related to the temperature T_0 [kJ/kmol]
ΔQ	heat losses to the environment [kW/s]
η_{ch}	chemical efficiency of biomass gasification process
η_T	energy efficiency of biomass gasification process

INTRODUCTION

There exists a problem of the choice of energy technology from the point of view of the effective utilization of biomass chemical energy, and in terms of its impact on environment [1-12]. An energy effective and environmentally friendly technology may involve the use of biomass for cogeneration of electric energy and heat in gas combined heat and power (CHP) plants integrated with biomass gasification. In CHP plants integrated with biomass gasification there are two new elements as compared with conventional (steam) CHP plants: the application of biomass gasification instead of biomass combustion and the application of gas cycle instead of steam cycle. The technology applied in gas CHP plants integrated with biomass gasification is advantageous from the point of view of energy effectiveness and ecology.

The paper presents the analysis of four technological systems of CHP plants integrated with biomass gasification: a) gas CHP plant using simple gas turbine cycle (Fig. 1), b) two gas CHP plants using steam injected gas turbine (STIG) cycle (Fig. 2 and 3), and c) gas-steam CHP plant (Fig. 4).

The main scientific innovations of the paper are elaborated models of gas generator and of the other energy facilities of CHP plants integrated with biomass gasification with the use of statistical physics and carry out on this basis the simulation investigations of energy effectiveness of the systems of gas and gas-steam CHP plants.

MODELLING OF THE BIOMASS GASIFICATION POCESS

The mathematical model of the process of complete biomass gasification was elaborated perform multivariant calculations of energy aspects of this process with changeable parameters such as: the temperature and pressure of the process, and the kind, the excess ratio and the temperature of gasifying agent. This model allows for numerical simulation of various methods of complete, pressure gasification of various kinds of biomass, with the help of various gasifying agents.

The number of equations of the model depends on the assumed number of components of gas. The kind and the number of gas components were determined on the basis of the analysis of chemical reactions proceeding in gas generator. As a result of carried out investigations it was assumed that in

produced gas the following components were present: CH_4, NH_3, CO_2, H_2O, N_2O, NO_2, SO_2, COS, H_2S, HCN, CS_2, CO, CN, OH, NO, CS, SO, C_2, H_2, O_2, N_2, S_2, C, H, O, N, S and Ar, which means 28 components, composed of 6 elements. It was, therefore, necessary to formulate a mathematical model in the form of the system composed of 28 non-linear algebraic equations:

- 22 equations, which describe chemical reactions proceeding in gas generator,
- 5 equations of the balance of elements,
- 1 equation of the balance of partial pressures of the components of gas.

The additional 29th equation which complements the system of equations, is the equation of the balance of energy of gas generator. This equation, related to 1kg of gas, is formulated in the following form:

$$\frac{1}{\sum_{i=1}^{i=28} M_i p_{gi}} \sum_{i=1}^{i=28} p_{gi}\left(\Delta H_{i(T_0,T_g)} + \Delta H_{gi(T_0)}\right) - a\Delta h_{b(T_0)} - b\frac{1}{\sum_{i=1}^{i=n} M_i p_{gai}} \sum_{i=1}^{i=n} p_{gai}\Delta H_{i(T_o,T_{ga})} - c\left(\Delta h_{(T_0,T_{H_2O})} + \Delta h_{H_2O(T_0)}\right) + d\Delta h_{A(T_0,T_g)} + \Delta Q = 0 \quad (1)$$

The biomass gasification process may be characterized by chemical efficiency and energy efficiency of the process. The chemical efficiency of biomass gasification process is defined as the ratio of chemical energy of gaseous fuel produced in the process of gasification to chemical energy of gasified biomass. It can be determined with the help of the formula:

$$\eta_{ch} = \frac{v_g Q_h^g}{Q_h^b} \quad (2)$$

Energy efficiency of biomass gasification was defined with the help of the formula:

$$\eta_T = \frac{v_g\left(Q_h^g + \frac{1}{22{,}4136}\Delta H_{(T_0,T_g)}\right)}{Q_h^b} - \frac{v_{ga}\frac{1}{22{,}4136}\Delta H_{(T_0,T_{ga})} + q_{H_2O}\Delta h_{(T_0,T_{H_2O})}}{Q_h^b} \quad (3)$$

Gaseous fuel produced in the process of biomass gasification is cooled to the temperature required by the cleaning process. Two technologies of gaseous fuel cleaning were considered – cold gas cleanup (383K) and hot gas cleanup (811K).

ENERGY ANALYSIS OF TECHNOLOGICAL SYSTEMS OF CHP PLANTS

For the evaluation of energy effectiveness of analyzed technological systems of gas CHP plant integrated with biomass gasification there were determined: energy efficiency (energy utilization factor), efficiency of electric energy generation and cogeneration index (power to heat ratio). These quantities were determined with the help of the following relations:

- energy efficiency of gas CHP plant:

$$\eta_e = \frac{P_{elgt} + Q_c - \Delta P_{OX}}{B * Q_h^b} \quad (4)$$

- energy efficiency of gas-steam CHP plant:

$$\eta_e = \frac{P_{elgt} + P_{elst} + Q_c - \Delta P_{OX}}{B * Q_h^b} \quad (5)$$

- efficiency of electric energy generation in gas CHP plant:

$$\eta_{el} = \frac{P_{elgt} - \Delta P_{OX}}{B * Q_h^b} \quad (6)$$

- efficiency of electric energy generation in gas-steam CHP plant:

$$\eta_{el} = \frac{P_{elgt} + P_{est} - \Delta P_{OX}}{B * Q_h^b} \quad (7)$$

- cogeneration index of gas CHP plant

$$\sigma_c = \frac{P_{elgt}}{Q_c} \quad (8)$$

- cogeneration index of gas-steam CHP plant

$$\sigma_c = \frac{P_{elgt} + P_{elst}}{Q_c} \quad (9)$$

For calculations of these quantities it was very important to formulate the equation of energy balance of combustion chamber of gas turbine,

related to 1 kg of combustion gases, in the following form:

$$\frac{1}{\sum_{i=1}^{i=6} M_i p_{cgi}} \sum_{i=1}^{i=6} p_{cgi} \Delta H_{i(T_O, T_{cg})} - e \frac{1}{\sum_{i=1}^{i=28} M_i p_{gi}} \sum_{i=1}^{i=28} p_{gi} \left(Q_{gi} + \Delta H_{i(T_O, T_g)} \right) - f \frac{1}{\sum_{i=1}^{i=3} M_i p_{oxi}} \sum_{i=1}^{i=3} p_{oxi} \Delta H_{i(T_O, T_{ox})} - g \Delta h_{(T_O, T_{N_2})} + h \Delta h_{(T_O, T_{H_2O})} + \Delta Q = 0 \quad (10)$$

The formulas describing temperature functions of increments of molar physical enthalpy of particular components of combustion gases $\Delta H_{i(T_0, Tcg)}$, gaseous fuel $\Delta H_{i(T_0, T_g)}$, gasifying agent $\Delta H_{i(T_0, Tga)}$, and oxidizer $\Delta H_{i(T_0, Tox)}$ and equilibrium constants of the particular chemical reactions proceeding in gas generator have been determined with the help of the sums of states of particular components of gaseous fuel and of gasifying agent [12].

SIMULATION OF BIOMASS GASIFICATION

The simulation of biomass gasification process has been conducted for six variants (methods of biomass gasification), where the changing parameters were the temperature of gasification process and the kind of gasifying agent. The following composition of biomass: C=46.5%,

Number of biomass gasification method		1	2	3	4	5	6
Gasification pressure [MPa]		1.8	1.8	1.8	1.8	1.8	1.8
Gasification temperature [K]		1100	1100	1100	1100	1200	1000
Gasifying agent		air	air+ H_2O	oxygen	air heated to 1000 K	air	air
Gasifying agent excess ratio		0.3300	0.3417	0.2678	0.2923	0.3805	0.2286
Gasifying agent temperature [K]		695	695	695	1000	695	695
Gasifying agent consumption per 1 kg of biomass [Nm^3/kg]		1.4441	1.4953	0.2455	1.2791	1.6651	1.004
Volume of gas obtained from 1 kg of biomass [Nm^3/kg]		2.6328	3.0839	1.3751	2.4726	2.8920	2.0053
Main components of produced gas [%]	CO	22.73	16.16	40.51	24.71	22.34	21.47
	H2	16.56	19.08	25.62	17.46	16.11	11.65
	CH4	1.80	0.94	7.79	2.53	0.17	9.29
	CO2	8.83	11.38	15.57	8.28	7.86	13.04
	H2O	6.77	14.15	10.37	6.16	8.07	5.13
	N2	42.76	37.80	0.11	40.34	44.88	38.29
	Ar	0.54	0.47	0.00	0.51	0.56	0.49
	COS	0.0069	0.0054	0.0134	0.0073	0.0063	0.0093
	H2S	0.0011	0.0014	0.0019	0.0011	0.001	0.0011
Lower heating value of gaseous fuel [MJ/Nm^3]		5.303	4.438	10.673	5.913	4.625	7.298
Chemical efficiency of biomass gasification [%]		84.06	82.39	88.35	88.01	80.47	88.10
Energy efficiency of biomass gasification [%]		98.25	98.25	98.25	98.25	98.25	98.26

Table 1. The results of simulation of biomass gasification process

H=5.70%, S=0.03%, O=40.2%, N=0.19%, W=6.0% and A=0.38% was assumed in calculations. The following quantities were calculated: the composition of gas, the gasifying agent excess ratio, the gasifying agent consumption per 1 kg of biomass, the volume of gas obtained from 1 kg of biomass, the lower heating value of produced gas, the and chemical and energy efficiency of the gasification process. The results of carried out simulation of the biomass gasification process are presented in Table 1.

SIMULATION OF ENERGY EFFECTIVENESS OF CHP PLANTS INTEGRATED WITH BIOMASS GASIFICATION

Basing on the elaborated mathematical models of energy conversion processes, which take place in particular elements of the technological systems of gas CHP plant integrated with biomass gasification, and on the computer program developed on the basis of it a multivariant simulation for four elaborated technological systems of gas and gas-steam CHP plants (Fig. 1 to 4) was made. In particular variants of the simulation, cold (383 K) and hot (811 K) methods of gas cleaning were assumed. All the variants of simulation calculations were carried out for the same gas turbine with the following parameters: inlet gas temperature T_{cg1} = 1333 K, outlet gas temperature T_{cg2}=763 K The results of the simulation of energy processes in gas and gas - steam CHP plants integrated with biomass gasification are shown in Table 2 and 3.

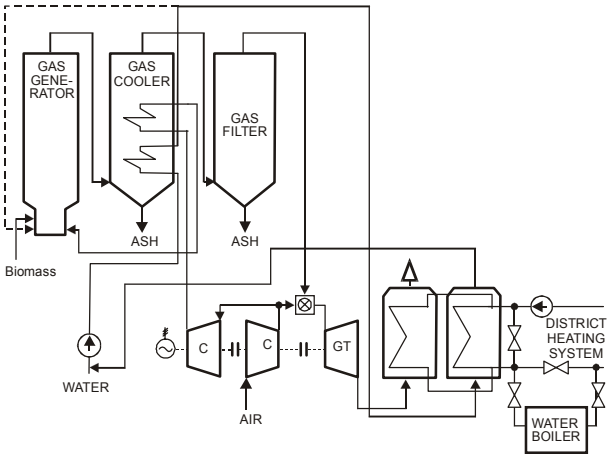

Figure 1. Technological system of gas CHP plant integrated with biomass gasification using simple gas turbine cycle

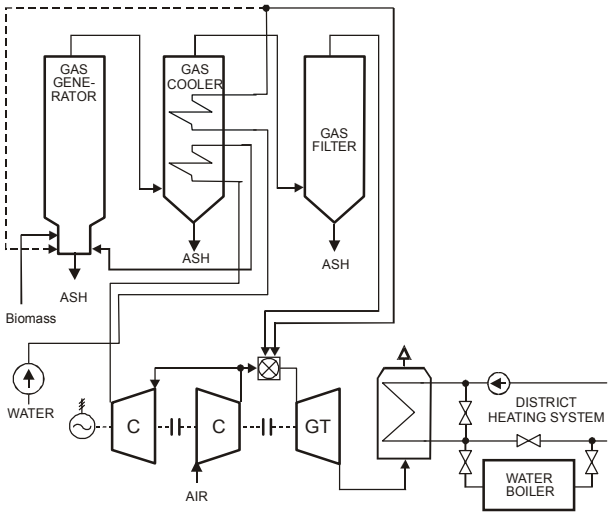

Figure 2. Technological system of gas CHP plant integrated with biomass gasification using steam injected gas turbine (STIG) cycle

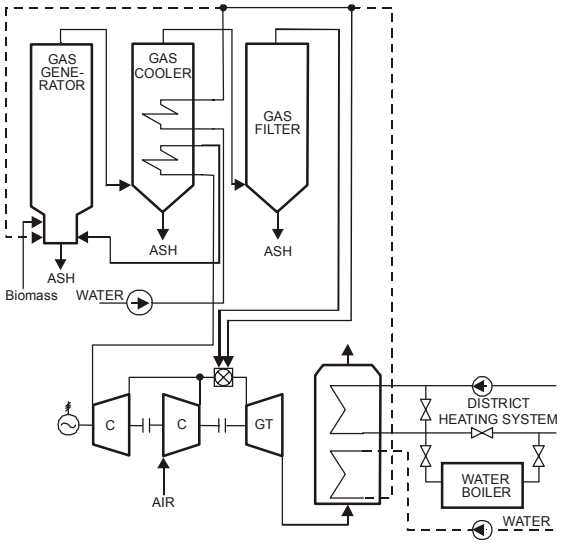

Figure 3. Technological system of gas CHP plant integrated with biomass gasification using steam injected gas turbine (STIG) cycle

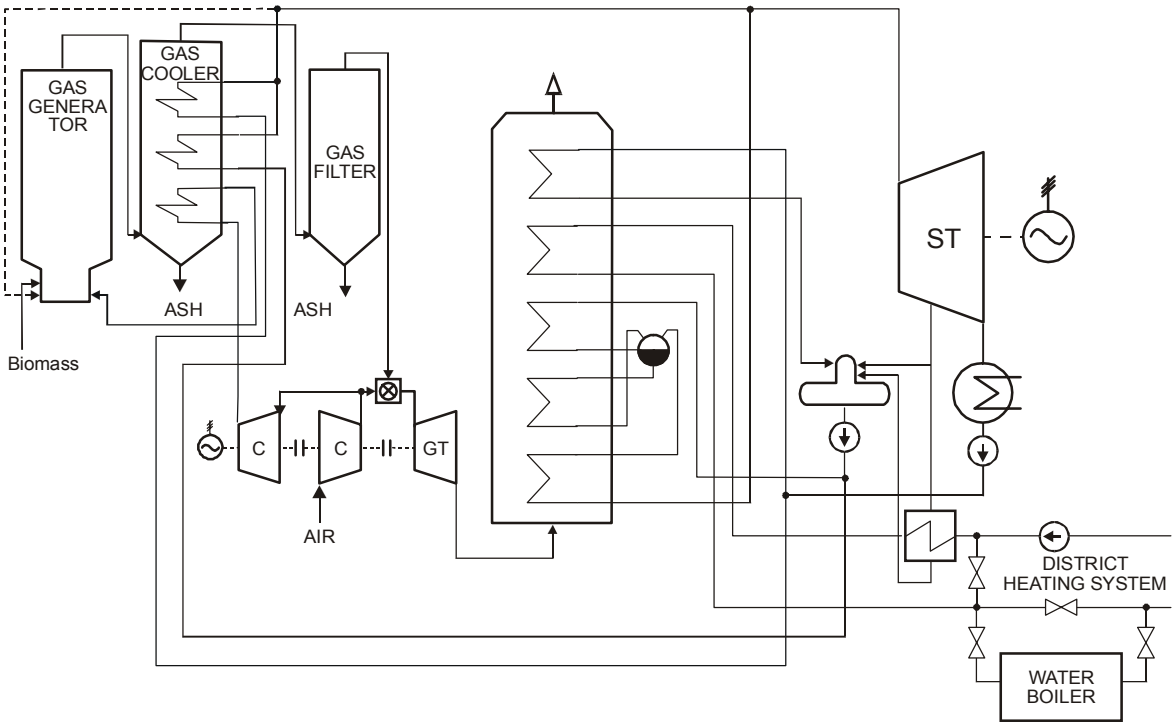

Figure 4. Technological system of gas-steam CHP plant integrated with biomass gasification

Parameter	Variant (figure) number of technological system								
	1	1	1	1	1	1	2	3	4
Number of biomass gasification method	1	2	3	4	5	6	1	1	1
Inlet gas temperature of gas turbine [K]	1333	1333	1333	1333	1333	1333	1333	1333	1333
Outlet gas temperature of gas turbine[K]	763	763	763	763	763	763	763	763	763
Biomass consumption [kg/s]	1.582	1.677	1,389	1.496	1,677	1.483	1.636	1.687	1.595
Electric power of gas turbine generator [MW]	7.81	8.43	7.64	7.74	7.90	7.72	9.24	10.60	7.82
Electric power of steam turbine generator [MW]	-	-	-	-	-	-	-	-	2.72
Thermal power produced in cogeneration [MW]	15.50	16.89	13.23	14.16	16.94	13.95	11.55	7.61	11.62
Energy efficiency (energy utilization factor)[%]	88.34	84.18	88.53	87.78	88.74	87.73	76.08	64.63	83.24
Efficiency of electric energy generation [%]	29.35	29.88	31,19	30.80	27.93	31.08	33.61	37.46	39.40
Cogeneration index (power to heat ratio)	0.504	0.499	0.577	0.547	0,466	0.553	0.800	1.393	0.907
Content of H_2O in combustion gases [%]	5.41	8.68	4.77	5.12	5.74	5.08	13.08	20.00	5.41

Table 2. The results of energy calculations of technological systems of gas and gas-steam CHP plant integrated with biomass gasification for cold gas cleaning method

Parameter	Variant (figure) number of technological system								
	1	1	1	1	1	1	2	3	4
Number of biomass gasification method	1	2	3	4	5	6	1	1	1
Inlet gas temperature of gas turbine [K]	1333	1333	1333	1333	1333	1333	1333	1333	1333
Outlet gas temperature of gas turbine[K]	763	763	763	763	763	763	763	763	763
Biomass consumption [kg/s]	1.399	1.437	1.306	1,339	1.455	1.345	1.416	1.491	1.405
Electric power of gas turbine generator [MW]	7.65	8.14	7.57	7.59	7.70	7.60	8.17	10.55	7.65
Electric power of steam turbine generator [MW]	-	-	-	-	-	-	-	-	2.10
Thermal power produced in cogeneration [MW]	12.68	13.22	11.88	11.75	13.55	11.87	11.19	4.26	9.63
Energy efficiency (energy utilization factor)[%]	87.08	82.71	87.74	86.67	87.49	86.91	81,03	59.44	82.72
Efficiency of electric energy generation [%]	32.54	33.69	32.96	33.82	31.42	33.76	34.35	42.24	42.44
Cogeneration index (power to heat ratio)	0.603	0.616	1.839	0.646	0.568	0.640	0.730	2.477	1.012
Content of H_2O in combustion gases [%]	4.79	7.44	4.48	4.58	4.98	4.60	7.64	20.00	4.79

Table 3. The results of energy calculations of technological systems of gas and gas-steam CHP plants integrated with biomass gasification for hot gas cleaning method

CONCLUSIONS

The results of the simulations allow one to formulate the following conclusions:

- The kind of gasifying agent has a significant impact on the chemical efficiency of the biomass gasification process and on the lower heating value of the produced gas. Water steam added to gas generator decreases the energy efficiency.
- The kind of gaseous fuel cleaning technology has a significant impact on the efficiency of electric energy generation. The replacement of the cold gas cleaning method with the hot gas
- Cleaning method allows the efficiency of electric energy generation to increase by around 3% in simple gas turbine cycle (Figure 1), and by around 5% in STIG cycle (Figure 3).
- Interesting simulation results were obtained for the technological system using steam injection to combustion chamber of gas turbine (STIG cycle). When the content of water steam in combustion gases is 20% (in this cycle), the efficiency of electric energy generation increases to 37.46% for cold gas cleaning method, and to 42.24% for hot gas cleaning method. However, the energy efficiency of the CHP plant decreases to 64.63% and 59.44%, respectively (Table 2).
- Among the investigated technological systems of CHP plants integrated with biomass gasification, the highest electric energy generation efficiency and a high energy efficiency is being obtained in technological systems of gas steam CHP plants (Figure 4). However, on the small scale this system has the highest investment cost.

REFERENCES

[1] Chen G., Andries J., Spliethoff Fang M.: *Kinetics of Biomass Wastes Pyrolisis for Fuel*

Gas Production. Proceedings of the 15th International Conference on Efficiency, Costs, Optimization, Simulation and Environmental Impact of Energy Systems, Berlin, 2002 Volume I, pp. 630 – 637.

[2] Corti A., Lombardi L., *Performance analysis of a Biomass Integrated Gasification Combined Cycle With Reduced CO2 Emissions*, Proceedings of the 13th International Conference on Efficiency, Costs, Optimization, Simulation and Environmental Impact of Energy Systems. 2002, Berlin, Germany Part 4, pp.781-787.

[3] Donatini F., Gigliucci G., Zamparelli C., Herzog N., Produzione-Ricerca E., *Integration of Biomass into Natural Gas Fired Combined Cycles – Thermodynamic and Economical Analyses*, Proceedings of the 13th International Conference on Efficiency, Costs, Optimization, Simulation and Environmental Impact of Energy Systems. 2002, Berlin, Germany, pp. 695-703.

[4] Knoef Ir. H.A.M., *Gasification of Biomass & Waste – Practical Experience*, III. International Slovak Biomass Forum, 2003.

[5] Morris M., Waldheim L., *Efficient Power Generation From Wood Gasification*. Proceedings of International Conference "Gasification for the Future" Noordwijk, The Netherlands, 2000.

[6] Olsson F., Torison T. *Cogeneration Based on Gasified Biomass – a Comparison of Concepts,* Proceedings of the 13th International Conference on Efficiency, Costs, Optimization, Simulation and Environmental Impact of Energy Systems. Enschede, 2000. Part 4 pp. 1945-1957

[7] Purvis C.R., Craig J.D. A *Small Scale Biomass Fueled Gas Turbine Power Plant*, The Eighth Biennial National Bioenergy Conference, Madison, 1998.

[8] Rydstrand M. C., Westmark M. O., Bartlett M. A. *An Analysis of the Efficiency and Economy of Humidified Gas Turbines in District Heating Applications*. Proceedings of the 13th International Conference on Efficiency, Costs, Optimization, Simulation and Environmental Impact of Energy Systems. 2002, Berlin, Germany Part 4, pp.781-787.

[9] Veringa H.J., Uil H. den, Mozaffarian H., *Biomass and Co-generation* , Proceedings of the 13th International Conference on Efficiency, Costs, Optimization, Simulation and Environmental Impact of Energy Systems. Enschede, 2000. Part 4 pp.1799-1812.

[10] Willeboer W., *Biomass gasification in Geertruidenberg, the Netherlands*, Proceedings of the 13th International Conference on Efficiency, Costs, Optimization, Simulation and Environmental Impact of Energy Systems. Enschede, 2000. Part 4 , pp. 1869-1875.

[11] Xiao Y.H., Cai R.X., Lin R.M. *Modeling HAT Cycle and Thermodynamic Evaluation* Proceedings of the International Conference on Efficiency, Costs, Optimization, Simulation and Environmental Aspects of Energy Systems, Stockholm, 1996.

[12] Zaporowski B. *Analysis of Coal Gasification Process for Demand of Clean Coal Technology*. Proceedings of the Second International Conference on Combustion Technologies for Clean Environment. Lisbon, 1993, Vol. I, 17.4.24-17.4.32.

Proceedings of ECOS 2005
Trondheim, Norway
June 20–22, 2005

Theoretical Analysis of a Thermodynamic Cycle for Power and Heat Production Using Supercritical Carbon Dioxide

X. R. Zhang and H. Yamaguchi
Doshisha University
Department of Mechanical Engineering
Kyoto 630-0321
Japan

K. Fujima
Mayekawa MFG. Co., Ltd.
2000 Tatsuzawa Moriya-city, Ibaraki-Pref., 302-0118
Japan

M. Enomoto
Showa Denko K. K.
1-480, Inuzuka, Oyama-city, Tochigi 323-8679
Japan

N. Sawada
Showa Tansan Co., Ltd.
7-1, Ogimachi, Kawasaki-Ku, Kawasaki-city, Kanagawa, 210-0867
Japan

ABSTRACT

A numerical study is carried out for a thermodynamic cycle — solar energy powered Rankine cycle using supercritical carbon dioxide as the working fluid for combine power and heat production. The system consists of a solar heating system, a power generating turbine, a heat recovery system, and a feed pump. A model has been developed to predict the cycle performance. The experimental data is used to verify the numerical formulation. The effects of the governing parameters on the performance are investigated numerically. The results show that the Rankine cycle has a reasonable power generation efficiency of somewhat above 20.0% and heat recovery efficiency of 68.0%, respectively. It is seen that the cycle performance is strongly dependent on the governing parameters and they can be optimized to provide maximum power, maximum heat recovery or a combination of both. The power generation and heat recovery are found to be increased with solar collector area. The power generation is also increased with water temperature of the heat recovery system, but decreased with heat exchanging area of the heat recovery system. It is also seen that the effect of the water flow rate in the heat recovery system on the cycle performance can be negligible.

Key words: Rankine Cycle, Solar Energy, Super-critical Carbon Dioxide, Power Generation, Heat Production

INTRODUCTION

Exhausting the fossil fuel leads to serious energy crisis we are about to face. Solar energy is a kind of inexhaustible energy supply. The application of solar energy to power/heat or power/refrigeration thermodynamic cycles has a potential to make solar energy competitive with fossil fuels [1−3]. Based on Kyoto Protocol, collective emissions of greenhouse gases (the period of 2008~2012) will be reduced by 5.2% compared to the year 1990. The interests in CO_2 as a working fluid increased considerably from 1990s [4, 5]. In this paper, we numerically investigate a thermodynamic cycle [6], in which both solar energy and CO_2 are used to form a Rankine cycle of power generation and heat production. Figure 1 shows a schematic diagram of the CO_2-based thermodynamic cycle.

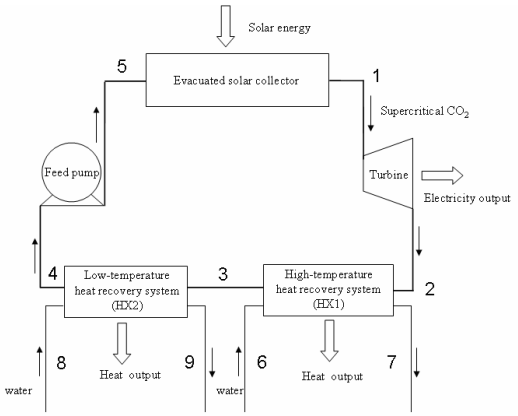

Fig. 1. A CO_2-based solar Rankine cycle for power generation and heat recovery

THEORETICAL ANALYSIS

As the first step of a basic estimation and understanding of the performance of the Rankine cycle, in this paper, a thermodynamic analysis considering a steady state is presented. It is supposed that an all-glass evacuated solar collector with a U-tube heat removal system is used in the Rankine cycle. Figure 2 shows a sketch of the solar collectors. The solar radiation passes through both the glass tubes to be absorbed by the selective surface. The surface

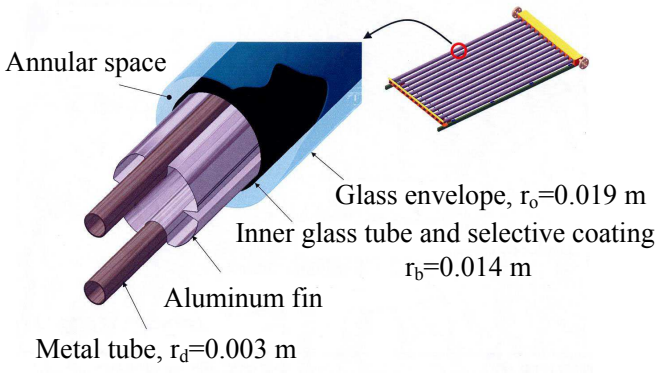

Fig. 2. A sketch of the evacuated solar collector used in the Rankine cycle

heats up and the heat is transferred by conduction to the metal tube and then by convection to the working fluid. The properties of glass are assumed to be 1.25, 0.09, and 0.05 for thermal conductivity, solar transmittance and solar absorbance, respectively. The properties of selective coating are 0.02 and 0.927 for solar transmittance and solar absorbance.

The several assumptions are made for the cycle analysis. 1. In the solar collector, thermal resistance among the selective surface, metal tube and fin is neglected. 2. In the solar collector, supercritical CO_2 is distributed uniformly in all heat removal tubes. 3. The friction loss and pressure change due to the heating or cooling processes in the collector and CO_2/water heat exchangers are neglected. 4. The CO_2 pressure at the pump outlet mainly varies with CO_2 flow rate. But the detailed relationship of this pressure and CO_2 flow rate is not clear until now. For convenience, in this study, this pressure is set as a constant value of 9.0 MPa, which may be not an optimal value, but close to the experimental value [6,7]. The pressure drop in the turbine is a constant value of 2.5 MPa. 5. The thermal loss from the CO_2 loop is neglected.

Figure 3 shows each of the differential control volumes, which is an annular region of length dx, the x axis indicating the direction of flow of the fluid inside the tube. Applying the first law of thermodynamics to each one of the differential

control volumes and assuming steady state with constant thermophysical properties except CO_2, we obtain the following equations.

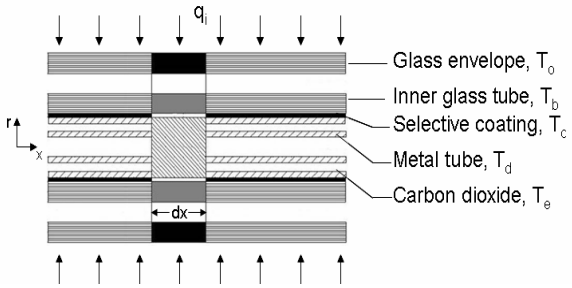

Fig. 3. The differential control volume of the solar collector used in the analysis of the model.

Solar collector

$$\alpha_g r_o q_i + r_b k_b (T_b - T_o) + \frac{r_b \sigma (T_b^4 - T_o^4)}{\frac{1}{\varepsilon_g} + (\frac{r_b}{r_o})(\frac{1}{\varepsilon_g} - 1)}$$

$$= r_o k_a (T_o - T_a) + r_o \sigma \varepsilon_o (T_o^4 - T_a^4) \quad (1)$$

$$\tau_g \alpha_g r_b q_i + \frac{\lambda_g (T_c - T_b)}{\ln\left[1 + \left(\frac{\delta}{2r_b}\right)\right]}$$

$$= r_b k_b (T_b - T_o) + \frac{r_b \sigma \left(T_b^4 - T_o^4\right)}{\frac{1}{\varepsilon_g} + \left(\frac{r_b}{r_o}\right)\left(\frac{1}{\varepsilon_g} - 1\right)} \quad (2)$$

$$\tau_g^2 \alpha_f r_b q_i = \frac{\lambda_g (T_c - T_b)}{\ln\left[1 + \left(\frac{\delta}{2r_b}\right)\right]} + 2 r_d k_c (T_c - T_e) \quad (3)$$

$$m_c C_p \frac{dT_e}{d\chi} = r_d k_c (T_c - T_e) \quad (4)$$

Turbine

$$T_2 = f1(s_2, P_1 - \Delta P) \quad (5)$$

$$P_T = m_c (h_2 - h_1) \quad (6)$$

Heat recovery system

$$Q_{H1} = m_c (h_3 - h_2) \quad (7)$$

$$Q_{H2} = m_c (h_4 - h_3) \quad (8)$$

Feed pump

$$T_5 = f3(P_5, h_5) \quad (9)$$

$$P_P = m_c (h_5 - h_4) \quad (10)$$

where, $h_2 = f2(s_2, P_1 - \Delta P)$, $h_5 = f2(s_5, P_5)$.

In this paper, a Program Package for Thermophysical Properties of Fluids database version 12.1 (PROPATH 12.1) is used in order to estimate the thermodynamic properties of CO_2. $f1$, $f2$ and $f3$ are function used in PROPATH 12.1 to calculate thermodynamic parameters of CO_2. With the available thermodynamic properties data, we modeled the components of the CO_2-based Rankine cycle. In the CO_2/water heat exchangers, the heat capacity of CO_2 is calculated based on the average temperature of CO_2-side of the heat exchangers. The outlet temperatures for CO_2 loop (T_3, T_4) and water loop (T_7, T_9) in the CO_2/water heat exchangers and heat-exchanging quantity are calculated based on the heat transfer equations and computations of heat balance [8]. The performance of the cycle is determined by solving this set of equations simultaneously. Convergent solutions are obtained based on the method of successive loops iterations in a logic manner. The convective heat transfer coefficient k_c of supercritical CO_2 in the Rankine cycle is calculated from the relations given by Hashimoto and Saikawa [9]. The heat transfer coefficient k_a (glass envelope to ambience) is calculated with expressions reported in the reference [10]. For the heat transfer coefficient between the two glass (k_b), we used the value 0.026 $W/(m^2 \cdot K)$ for very good vacuum.

The following efficiencies are defined to describe the performance of the Rankine cycle, power generation efficiency η_{power} (i.e. thermal efficiency of the Rankine cycle) and heat recovery efficiency η_{heat}:

$$\eta_{power} = \frac{P_T - P_P}{m_c (h_1 - h_5)} \quad (11)$$

$$\eta_{heat} = \frac{Q_{H1} + Q_{H2} - P_P}{m_c (h_1 - h_5)} \qquad (12)$$

RESULTS AND DISCUSSION

An examination of the problem under consideration shows that the governing parameters for the CO_2-based Rankine cycle are the climate conditions, the efficient solar collector area A_s, heat exchange area of HX1 and HX2 (A_{HX1} and A_{HX2}), inlet water temperature of HX1 and HX2 (T_6 and T_8), and water flow rate of HX1 and HX2 (m_{w1} and m_{w2}). For all simulations (in Table 1), the CO_2 flow rate m_c is assumed to be 0.0066 kg/s, which is chosen to be close to the value achieved in the experiment [6, 7].

Table 1 shows the simulated results for the typical climate of four seasons in Osaka of Japan in a year. It can be seen that during one year, the CO_2 temperatures increase with the season-averaged solar radiation and air temperature. The temperature of supercritical CO_2 at the outlet of the solar collector (T_1) can reach about 217.4 ℃ in the summer condition (from July to September), and under the winter climate (from January to March) the temperature of T_1 is about 137.0 ℃. The annual average value of T_1 is about 177.4 ℃. It can also be seen that there is about a temperature difference of 30～40 ℃ between the inlet and outlet of the turbine. At the outlet of the turbine, in the summer, CO_2 temperature T_2 is about 181.6 ℃ and the annual average value of T_2 is about 143.1 ℃, which can easily be used as a useful heat resource.

It is seen from the table 1 that the useful outputs of the Rankine cycle vary obviously with the incident solar radiation and air temperature. Contrary to the influences of the climate on the useful outputs, the higher power generation efficiency η_{power} and heat recovery efficiency η_{heat} are obtained in winter conditions. This means that in the summer conditions, the larger

Seasons	Jan-March	April-June	July-Sept	Oct-Dec
Air temp. T_a(℃)	6.6	18.9	26.5	13.0
Solar radiation. q_t(W/m^2)	510.2	773.3	851.7	593.3
CO_2 temp. T_1 (℃)	137.0	199.8	217.4	155.2
CO_2 temp. T_2 (℃)	104.1	164.9	181.6	121.8
CO_2 temp. T_3 (℃)	83.7	128.2	140.5	96.7
Electricity output (W)	337.5	399.2	416.3	355.6
Heat Output (W)	1007.3	1384.4	1494.4	1115.1
Power generation efficiency η_{power}	0.2552	0.2020	0.1906	0.2406
Heat recovery efficiency η_{heat}	0.7330	0.6516	0.6368	0.6958

Table 1 Simulated results of the Rankine cycle for the whole year (Osaka, Japan)

cycle outputs and a little lower efficiencies are obtained. It can be explained that although the electric power and heat output increase for the summer condition, the heat quantity absorbed into CO_2 in the collector also increases. Furthermore the increasing amplitude of the heat quantity is larger than that of the power output. In addition, the temperature difference between the solar collector surface and the surrounding air become greater in the summer than in winter, and then the thermal loss of the solar collector to the ambient also increases, which may also contribute to the occurrence of this phenomena. It is found that the annual averaged power generation efficiency and heat recovery efficiency are 0.222 and 0.680, respectively. It should be mentioned here that the data in Table 1 can be optimized by using variable pressures.

The formulation of numerical model in the study is expected to have a capability of reasonably dealing with the CO_2-based Rankine cycle. Therefore, for validation of the numerical model, the measured data in the reference [6] is used. The experiment was conducted under a typical summer condition in Osaka area, and the power generation efficiency η_{power} and heat output efficiency η_{heat} were measured at 0.25 and 0.65, respectively. A comparison between the experimental data and the present prediction show that the present predictions are close to the measurement values. The difference between the experimental data and numerical predictions may be due to the assumptions and simplifications made in the steady state analysis. The measured

η_{power} is 0.25, higher than the calculated value of 0.222. The reason given to this phenomena may be that the averaged CO_2 flow rate in the experiment is a little higher than the value used in the simulation, and this value of 0.25 was obtained under the summer. But to a certain extent, the agreement is found and therefore the present model can be used with confidence.

Figure 4 shows the dependence of the cycle temperatures as a function of area of evacuated solar collector for the annual-averaged incident solar radiation of 682.0 W/m^2. It is clear from the curves of Fig. 4 that the cycle temperatures increase with the area of solar collector. The reason given here is that the heat quantity absorbed into CO_2 in the solar collector greatly increases when the area of solar collector is enlarged. So when other parameters are fixed, the CO_2 temperatures increase if the collector area is increased. From Fig. 5, which shows the effect of the solar collector area on the cycle performance, it is obvious that the electric power output and heat output increases with the collector area. The reason given is that the CO_2 temperatures can be effectively raised by the increase of the collector area (from Fig. 4). It can also be seen from Fig. 5 that enlarging collector area can increase the heat output more efficiently than the electric power output. Further, from Fig. 5, it is seen that the power generation efficiency decreases with the

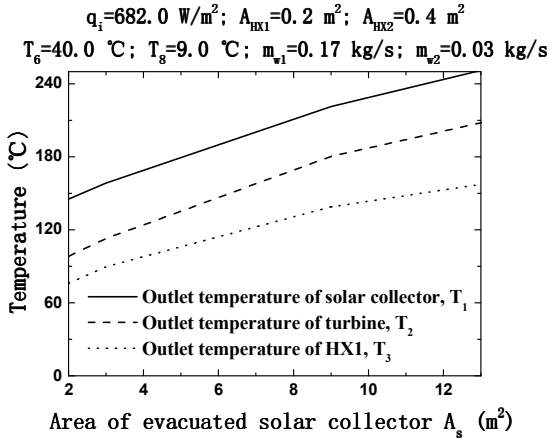

Fig. 4. Effect of area of evacuated solar collector on the CO_2 temperatures in the cycle

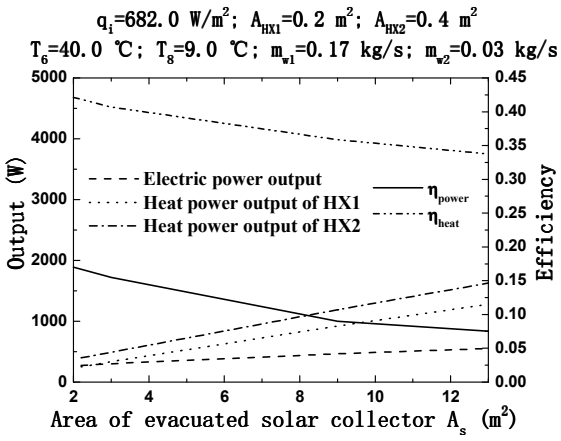

Fig. 5. Effect of collector area on the useful cycle outputs and efficiencies

increase of the collector area. It is because enlarging the collector area increases the overall quantity of heat absorbed into CO_2 in the collector. Although the electric power output is also increased by enlarging the collector area, the power generation efficiency decreases with the collector area. Another important reason is that the heat loss to the ambient environment is increased if the collector area is enlarged.

In the heat recovery systems, the heat exchanging areas (A_{HX1} and A_{HX2}), the inlet water temperature (T_6 and T_8) and the water flow rates (m_{w1} and m_{w2}) are also the governing parameters for the Rankine system. In this paper, the effect of these parameters is studied taken HX1 as an example. The effect of the heat exchanging area of HX1 A_{HX1} is shown in Figs 6 to 7 at the solar radiation of 682.0 W/m^2.

It is seen that the cycle temperature decrease with A_{HX1} increase. When the other parameters are fixed, the area increase means the more heat quantity is recovered from the cycle, which leads to the decreases of the CO_2 temperatures in the cycle. The decreases of the CO_2 temperatures result in a drop of the electric power output and heat output from the HX2, shown in Fig. 7. The heat output from the HX1 increase with the heat exchanging area A_{HX1}. The power generation efficiency η_{power} decreases with A_{HX1} increase, due to the decrease of the electric power

output. It is also sent that the heat output efficiency is almost not influenced by the heat-exchanging area A_{HX1}, since the variations of the heat outputs from HX1 and HX2, due to A_{HX1}, almost cancel each other.

Figures 8 and 9 show the variation of the cycle performance with the inlet water temperature of HX1 (T_6). Figure 8 shows that the CO_2 temperatures in the cycle go almost linearly up as the inlet water temperature of T_6 increase. It is known that heat exchanging quantity is decreased as the temperature difference drops, hence the CO_2 temperatures increase and the heat output in HX1 decrease (shown in Fig. 9). However, the heat output in HX2 increase due to the increase of the CO_2 temperature of T_3. It is obvious from Fig. 9 that the heat output efficiency is decreased with T_6 increase. It is also seen that the electric power output and power generation efficiency increase a little with T_6, which may be contributed to the CO_2 temperature increase with T_6, shown in Fig. 8.

Figures 10 to 11 show the effect of the water flow rate m_{w1} on the cycle performance. It is seen from Fig. 10 to 11 that there is no an obvious effect of m_{w1} on the CO_2 temperatures, the useful outputs from the cycle and the efficiency η_{power} and η_{heat}. It may be explained physically that although the heat exchanging process in the heat recovery system is influenced by m_{w1}, the influence is smaller and more indirect compared to those of varying heat exchanging area and inlet water temperature, since the variation of m_{w1} only can have an influence on the heat transfer coefficient, which is not only dependent on the water flow rate, but also the CO_2 flow rate etc. It should be mentioned here that the efficiencies in Fig.4～Fig.11 are somewhat lower than the efficiencies obtained in Table 1, because the CO_2 flow rate of 0.058 kg/s

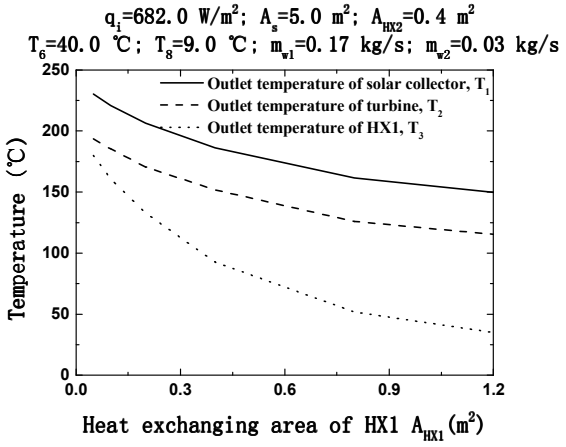

Fig. 6. Effect of heat exchanging area of HX1 on the CO_2 temperatures in the cycle

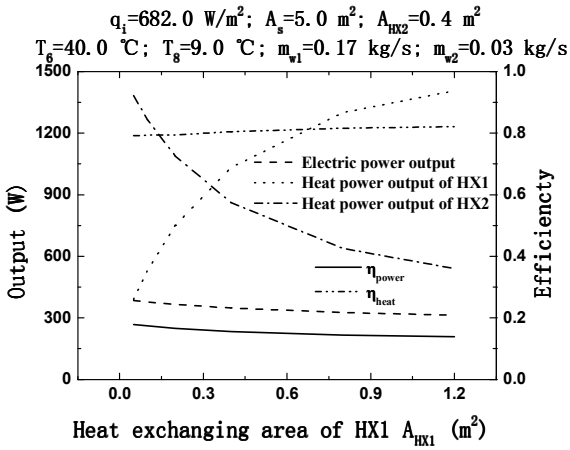

Fig. 7. Effect of heat exchanging area of HX1 on the useful cycle outputs and efficiencies

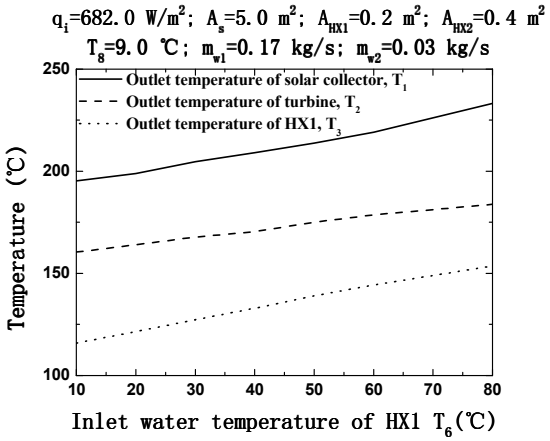

Fig. 8. Effect of inlet water temperature of HX1 on the CO_2 temperatures in the cycle

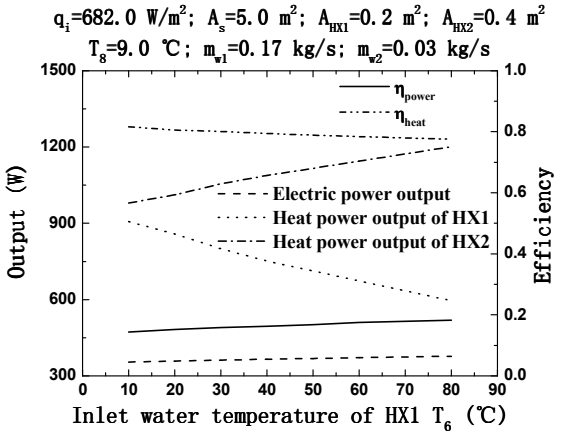

Fig. 9. Effect of inlet water temperature of HX1 on the useful cycle outputs and efficiencies

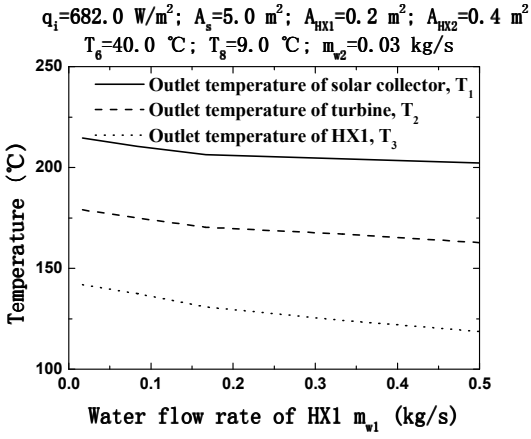

Fig. 10. Effect of water flow rate of HX1 on the CO_2 temperatures in the cycle

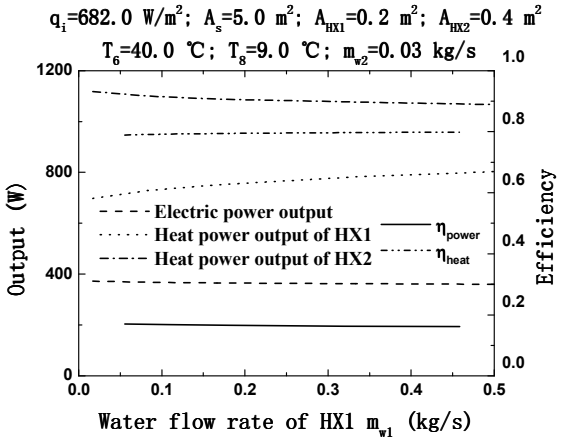

Fig. 11. Effect of water flow rate of HX1 on the useful cycle outputs and efficiencies

is used in the calculation of Fig. 4～Fig.11, which is a little lower than that used in Table 1. Furthermore, a constant pressure is assumed at the pump outlet in the present study. The pressure optimization is also needed in the future.

CONCLUSIONS

A numerical study has been made of a thermodynamic cycle — solar energy powered Rankine cycle using supercritical CO_2 as the working fluid. The following remarks are made from the results of this study:

(1) A numerical formulation of the problem considered in the study has been established and comparison of the experimental data and model prediction validates the model for predicting the cycle performance.

(2) The results show the CO_2-based Rankine cycle has a power generation efficiency and heat recovery efficiency of somewhat above 20.0 % and 68.0%, respectively.

(3) The problem considered is governed by the following independent parameters, the climate, the collector area and the heat-exchanging area, the inlet water temperature, the water flow rate of the heat recovery system. The results reveal that the electric power output is increased with the solar radiation and air temperature, the collector area and the inlet water temperature, but decreased with the increase of the heat-exchanging area. It is also seen that the influence of the water flow rate on the cycle performance can be neglected.

(4) It is recognized that a more detailed transient simulation and pressure optimization is needed to further estimate and understand the cycle performance and establish the practical usefulness of this cycle.

NOMENCLATURE

A_s Efficient area of solar colletcor [m^2]

A_{HX1}, A_{HX2} Heat exchanging area of HX1 and HX2 [m^2]

C_p Specific heat [$J/kg\cdot℃$]

$f1$, $f2$, $f3$ Functions used in PROPATH 12.1 for calculating thermodynamic parameters of carbon dioxide

h Specific enthalpy [J/kg]

k Convective heat transfer coefficient [$W/m^2\cdot K$]

L Length of metal tubes in evacuated solar colletor [m]

m_c Mass flow rate of carbon dioxide [kg/s]

m_{w1}, m_{w2} Water flow rate of HX1 and HX2 [kg/s]

P Pressure [*MPa*]

q_i Incident solar flux [W/m^2]

P_T Electric power output from the turbine [W]

Q_{H1} Heat power output from the high-temperature heat recovery system [W]

Q_{H2} Heat power output from the low-temperature heat recovery system [W]

r Radius [m]

s Specific entropy [$J/kg\cdot K$]

T Temperature [℃]

Greek Letters:

α Solar absorbtance

σ Stefan-Boltzmann constant [$W/m^2\cdot K^4$]

ε Thermal emittance

τ Solar transmittance

λ Thermal conductivity [$W/m\cdot K$]

δ Thickness of the inner glass tubes [m]

ACKNOWLEDGEMENT

This study was supported by the Academic Frontier Research Project on “Next Generation Zero-emission Energy Conversion System” of Ministry of Education, Culture, Sports, Science and Technology, Japan.

REFERENCES

[1] Mill, D. R. *Advances in Solar Thermal Electricity Technology*. Solar Energy 2004;76: 19−31.

[2] Goswami, D. Y., Xu, F. *Analysis of A New Thermodynamic Cycle for Combined Power and Cooling using Low and Mid Temperature Solar Collectors*. J. Solar Energy Eng 1999;121:91−97.

[3] Goswami, D. Y. *Solar Thermal Power Technology: Present Status and Ideas for the Future*. Energy Sources 1998;20:137−145.

[4] Lorentzen, G.. *Trans-critical Vapour Compression Cycle Device*, International Patent Publication WO 90/07683, (1990).

[5] Lorentzen, G. and Pettersen. J., *New Possibilities for Non-CFC Refrigeration*, IIR International Symposium on Refrigeration, Energy and Environment, Trondheim, Norway, 1992, 147-163.

[6] Yamaguchi. H., Zhang, X. R., Fujima, K., Enomoto, M., and Sawada, N., 2004. *A Solar Energy Powered Rankine Cycle Using Supercritical CO_2*, J. Solar Energy Eng, submitted for publication.

[7] Yamaguchi. H., Zhang, X. R., Fujima, K., Enomoto, M., and Sawada, N., 2004. *An experimental investigation on thermodynamic cycle powered by solar energy using carbon dioxide*, Solar Energy, accepted.

[8] Rohsenow, W. M., Hartnett, J. P., and Ganic. E. N. *Handbook of Heat Transfer Applications*. Washington, D. C.:Kingsport Press, 1985

[9] Hashimoto, K., Saikawa, M.. *Preliminary Experimental Result of CO_2 Gas-cooling Over-all Heat Transfer Coefficient Under Super Critical Condition*, Proceedings of IIR International Conference on Heat Transfer Issues in Natural Refrigerants, 1997, 50−58.

[10] Sawhney, R. L., Inderjit, Bansal, N. K. *Steady State Thermal Analysis of An Evacuated Tubular Collector With A CPC Booster*, Solar & Wind Technology, 1984;1: 237−244.

Proceedings of ECOS 2005
Trondheim, Norway
June 20–22, 2005

SOLAR ENERGY CONVERSION THROUGH SEAWEED PHOTOSYNTHESIS AND ZERO EMISSIONS COMBUSTION

(Toward a Life Sea near to the Dead one)

Yantovski E.*
Independent researcher
Elsass str.58, D-52068 Aachen, Germany

Nesterovski I.
Actuary
Amsterdam University, the Netherland.

ABSTRACT

Present paper is aimed at describing a "closed cycle" power plant schematics(SOFT, Solar Oxygen Fuel Turbine) with macroalgae (seaweed) cultivation in a pond, combustion of its organic matter in a fluidized bed boiler of Rankine cycle and return the combustion products to the pond to feed algae. Used for combustion oxygen is released to atmosphere in photosynthesis.

Energy efficiency is less than in Photovoltaics but energy expenditures to construct pond as solar energy receiver are much less, it gives some economic benefits. For a power unit of 100 kW the pond surface is about 3 hectare.

The cultivation of seaweeds in sea water ponds is well developed in Israel. Construction in some future of a SOFT system near to the Dead sea in Israelian desert would provide the country with needed power, chemicals and fresh water on account of solar energy. The system is protected by USPat 6,477,841 B1 of 12.11.2002 with priority in Israel of 22.03.1999.

In the paper is highlighted much more benefits to customer, than in the patent text, including fresh water by desalination. Some guesses of a desert surface for a massive scale use of ponds are given.

Introduction

Algae cultivation for electricity generation is discussed in some recent decades . All algae have been divided by microalgae (size of some microns) and macroalgae or seaweeds, which are much greater. The photosynthesis is similar in the both kinds and the early history we will start from microalgae. But the technical problems of cultivation and combustion are different, that is why we will focus on macroalgae only.

*Corresponding author: phone 49-241-9976669,
E-mail iksvotnay@aol.com

First published results of the use of open ponds with microalgae to convert carbon dioxide from power plants into methane fuel belong to Golueke and Oswald (cited in [1]). They demonstrated a small system, involving microalgae growth, digestion to methane and recycle of nutrients. They tried to catch CO2 injecting the flue gases into the pond regardless to a very small fraction of CO2 in flue gases, about 10%. Then especially active was Solar Energy Research Institute SERI (now NERL) in "Aquatic species program". After the testing of the three outdoor algae facilities in California, Hawaii and New Mexico it was concluded that it is possible to

produce microalgae in a large-scale pond at high productivity and relatively low cost.

Similar results published Alexejev et al.[2] from Moscow University, demonstrating a small microalgae system "Biosolar" with production of 40 g/sq.m dry biomass in a day. The mineralized elements from the tank of produced methane are reused by algae. CO2 is restored after burning. They stated " 1 mtce of methane might be produced from a surface of 70 sq. km annually."

Chemistry of algae pond was described by L.Brown [3,4] along with the outlook of a raceway-type pond and a paddle-wheel to move water. The overall reaction for photosynthesis by cianobacteria, micro- and macroalgae is as follows:

$$CO2 + H2O + light => CH2O + O2 \quad (1)$$

He also stated: "We estimate that microalgal biomass production can increase the productivity of desert land 160-fold (6 times that of a tropical rainforest). Microalgae require only 140-200 lb of water per pound of carbon fixed even in open ponds and this water can be low-quality, highly saline water".

If the pond water is rich with nutrients like a wasted municipal water or released from an animal farm the very high figures of dry biomass production have been published: 120 g/sq.m in a day[5]or 175 g/sq.m.day by Pulz (cited in[6]). These figures translate into 40-50 kg/sq.m annually.

In parallel to the ponds developments some schemes of relevant power plants to use produced biomass as a fuel have been proposed. Patent by Yamada [7] contains the use of dry algae as an addition to the regular fuel. A fraction of flue gases is released to atmosphere by a stack, the rest is directed to an absorption tower to be washed by water, which dissolves CO2 from the flue gases and returns it to the pond. The sore point of this scheme is rather small fraction of CO2 in flue gases, where the dominant gas is the inert nitrogen. The separation of CO2 from nitrogen turned out to be an insurmountable problem.

The radical solution, the separation of nitrogen not after, but before combustion has been described by Yantovski [8]as the cycle entitled as SOFT (Solar Oxygen Fuel Turbine). Further development of the SOFT cycle see in the subsequent sections.

Combustion of biomass in the "artificial air", the mixture of oxygen and steam or carbon dioxide, gives the flue gases without nitrogen and CO2 might be returned in the pond to feed algae.

Macroalgae cultivation in Israel

The crucial data for this paper are based on Israelian experience [9]. There are three raceway-type ponds, each surface of 1500 sq.m with the paddle-wheel sea water circulation. CO2 is supplied by a tank on a lorry and injected into water by perforated tubes. The depth of water 0.4 m, hydrogen factor pH=7. The firm figures were obtained for a seaweed *Gracilaria* only. The stable productivity of dry mass from a pond was 12 t/year or 8 kg/sq.m.year. By the use of seaweed *Ulva* the expected productivity is doubled. These ponds are located in Northern Israel, near to shore of the sea, from where the sea water is pumped into ponds. Still the produced biomass is used as raw material for chemicals and pharmaceutics. Recently some headway in seaweed cultivation had made Noritech-Seaweed Biotechnologies Ltd.

Energy flow concentration

The main obstacle of solar energy capture is its very low current density, especially annually averaged. In Israel it is about 220 W/sq.m, only 16% of the Solar constant 1368 W/sq.m. In central Europe it is a half. Thus the energy expenditure and cost of incidental energy absorber is of primary importance. In case of photovoltaics with rather high efficiency (in laboratory about 30%, in practice a half) the pure silicon absorber takes by manufacturing lots of energy and money. That is why solar cells up to now are rather expensive. As it will be shown later, efficiency of the solar energy conversion into electricity through algae pond is much less, about 3-5%. But the energy expenditure of absorber – pond is hundred times less than that of silicon.

Having been absorbed by algae the solar energy in chemical form is concentrated by water flow much better than by optical concentrator. The concentration factor of a

paraboloid concave mirror is about 500, it means the averaged focal spot energy current density is about 500x220= 110 kW/sq.m. Energy flow in the pipe from algae pond to processing is about

$\alpha \times \rho \times V \times H = 0.001 \times 1000 \times 1 \times 19.10^6 = 19\ 000$ kW/sq.m (2)

Here $\alpha = 0.001$ = mass fraction of biomass in water, ρ= 1000 kg/cub.m= water density, V = 1m/s = water velocity, H = 19 MJ/kg = dry biomass heating value.

It is evident that energy current density in the pipe is hundred times more than that in the focal point of optical concentrator. It means the equipment size for the subsequent energy conversion processes should be rather small. It is more important than large size of solar energy absorber.

Power unit outlook

Schematics is presented on Fig.1. Water with algae 6 from the pond 4 is going to the water separation unit 12, from where the pure water without algae is used as a circulating water to cool condenser 14 and absorb CO2 in 16. Wet organic matter is dried in 18 by heat of flue gases . Relatively dry fuel is directed to the fluidized bed combustor 8. After combustion in the artificial air, (the mixture of oxygen and carbon dioxide) flue gases go in the cyclon separator 20, the deflected ash is returned into the pond .CO2 with some steam go through heat exchanger 19 and fuel drier 18 to a separation point, from where a major part is mixed with oxygen, forming artificial air for fluidizer and a minor part is directed to absorber 16 to be dissolved in circulation water and returned to the pond. This minor fraction of CO2 flow is exactly equal to CO2 appeared in combustion. Oxygen is produced from air at the cryogenic or Ion Transport Membrane unit 10. Water from condenser 14 goes by a feed water pump through heat exchangers 18 and 19 into tubes of the fluidised bed combustor 8 (boiler). Produced steam expands in the turbine 22, driving generator. Low pressure steam is condensed in 14. Actually it is the ordinary Rankine cycle.

Some words on the chemicals production. It is unwise to combust the crude seaweed at power plant in the same sense as it is unwise such use of crude oil. A small mass fraction of seaweeds contains very useful organic chemicals which should be deflected along with water separation before the fuel combustion. There exist lots of methods of high organics separation, which is far from the scope of present paper. In any case the chemicals production could improve economics of the SOFT cycle.

Let us take for a numerical example the decentralized power supply by a small power plant of 100 kW [10]. In order to get the reliable figures we make rather modest assumptions :

- Fuel is wet (50% water content)
- ASU power consumption by 98% oxygen purity 0.22 kWh/kgO2
- Superheated steam before turbine 130 bar, 540 C,
- Isentropic coefficients of turbine 0.80, of feed pump 0.75.
- Seaweed productivity 16 kg/sq.m.year or 10 W(th)/sq.m
- Photosynthesis efficiency 4.6%.

Calculated results:

- Heat input 425.5 kW(th)
- Net output 107.3 kW (el)
- Cycle efficiency 25.2%
- Pond surface 4 hectar.

The graph of efficiency versus fuel moisture see in Fig.2. For quite possible figures of Rankine cycle with reheat and efficiency of 35% the needed surface of the pond is 3 ha. For an israelian kibbutz of some hundred people is enough only 4-5 such units and a pond of 15-20 ha. A local power plant of 10 MW by the cycle efficiency 40% and photosynthesis efficiency 6% the specific power per square meter is about 5 W (220x0.4x0.06=5.28) and pond size is about 2 square km. By order of magnitude it is comparable with Yatir –reservoir in the desert Negev near to Beer Sheva. The Keren Kayemeth LeIsrael[11]is planning to build 100 water reservoirs in the next fife years. One of these might be used for the SOFT demonstration.

Finally, for the national power demand of 10 GW (about 2 kW pro capita) in Israel a reasonable extrapolation is possible: expecting specific power of 10 W/sq.m due to increase

of the cycle efficiency and photosynthesis one. It means the needed pond surface is about 1000 sq.km. The surface of the Dead Sea is just the same (exactly 980 sq.km). If in some future a Life sea (with the normal, not deadly salt concentration for seaweed) would appear in the desert, not too far from the Dead one, it could give the country full electrical power along with lots of fresh water and organic chemicals. There would be no emission of combustion flue gases and no consumption of oxygen, which is consumed in combustion but released in photosynthesis. The only need is solar energy and a piece of desert. Neither terror attack could cause any serious damage.

An israelian representity at Johannesgurg Summit, Mr Jacob Keidar announced the Israel-Jordan project of a 300 km long pipeline just from Red to Dead Seas. The Life Sea might be a useful consumer of the transferred water at the middle of the pipeline.

Gasification

In the proper energy mix not only electricity , but also gaseous or liquid fuel is needed. In the SOFT cycle it is attainable by a small modification (Fig.3). The difference is the incomplete combustion (gasification) in the fluidised bed reactor, now it is a gasifier 24. Biomass gasification is well documented [12]. Fluidized bed gasification experiments with the sugarcane bagassa described by Gomez [13]. Produced gaseous fuel mixture consists of carbon monoxide, hydrogen and carbon dioxide. After cleaning in 20 it is used in a piston engine or turbine 26, producing mechanical power. The same fuel gas mixture might be converted into liquid fuel like methanol or even gasoline. After combustion in 26 the flue gases are absorbed by circulated water and returned to the pond 4 to feed seaweed 6.
The figures in brackets 0.06 and 10^3 reflect mass ratio water/CO2. Minus before the last number is a misprint.

Water desalination

For the state of Israel the problem of fresh water is not less severe as of electrical power supply. The annual demand is about 1.4 cub.km of fresh water. It rains only 50 days in a year and 60% of the land are deserts.

Let us consider what might the SOFT cycle do for a water desalination: is it possible to use low-grade heat after the turbine expansion to evaporate of a fraction of the circulating salty water (sea water) with the subsequent condensation of vapor for the fresh water production (desalination).
Assume an evaporator of a minor fraction of circulating water after turbine. Cooling and condensing this vapor by the major part of circulating water gives fresh water as condensat.
How large is its flowrate ? Assume the turbine as of back-pressure type, by exit steam pressure 1.2 bar. If in a modern high temperature steam turbine inlet is 1000 K by 200 bar, the enthalpy is 3874 kJ/kg. After expansion the steam is at 450 K and 2830 kJ/kg. For water evaporation by 1 bar the enthalpy drop of 2500 kJ/kg is enough.
In a small power unit of 100 kW the mass flowrate of cycle water of Rankine cycle is 100/0.25.1044 = 0.4 kg/s. The mass flowrate of desalinated water is the same 0.4 kg/s.
For a small demonstration plant the figures are:
Pond surface 4 ha (40 000 sq.m). Power 100 kW. Dry fuel flow 0.021 kg/s Chemicals (4%) 1 g/s . Fresh water 0.4 kg/s
Specific dry fuel consumption is 756 g/kWh. It is about twice in excess of a standard fuel consumption in microturbine power units due to lower heating value and low efficiency.

In a 1 GW power plant with cycle efficiency 40% and pond surface 10x20 km the flowrate of produced fresh water is 4 t/s or 14400t/h. Assuming 7000h/year operation the yield of water annually is about 0.1 cub km. It is evident, that if the SOFT cycle with water desalination would be used in full scale, it might meet all water demand. Contemporary practice of the use of18 power generating and desalinating plants at the West bank of Arabian Gulf[14] giving 15 GW of power and 1.9 cub.km of desalinated water annually, confirms above guesses.

Comparison with the first SOFT version of 1991.

The closed cycle power plant concept, based on algae photosynthesis in a pond, combustion of organic matter of dried algae in a zero-emission power plant and CO2 capture to return in the pond for feeding algae has been published in 1991[8] see Fig.4. Here was used air separation and expansion in a steam turbine. The difference was in the inert gas, replaced nitrogen in combustor. It was not carbon dioxide but steam. Also different was algae: not mAcro but mIcro, that is why not fluidised bed combustor but the gas-turbine one as for clean fuel was assumed. After the triple expansion in turbines together with steam the carbon dioxide was returned to the pond. Now this version is actively used by Clean Energy Systems (CES) creating a demonstration plant of 5 MW in California not for algae, but ordinary gas fuel. It might be the first Zero Emission power plant. Had it been successful, it might be added by an algae fuel system for a SOFT cycle demonstration.

Conclusion

The SOFT power cycle protected by U.S.Patent [15] is of practical interest to countries with deserts and intensive solar radiation. The concept is ready for Engineering and economical calculations. In any case, even by modest economics, it deserves of a demonstration in a small scale.

References

1. Benemann J. Utilization of carbon dioxide from fossil fuel burning power plants with biological systems. Energy Convers.Mgmt. v.34 No9-10, p.999-1009, 1993.
2. Alexejev V.V. et al. Biomass of microalgae use for solar energy conversion, Techno-economic and Ecology aspects of Ocean Energy Use. TOI Vladivostok, pp.53-58, 1985 (in Russian).
3. Brown L., Zeiler K. Aquatic biomass and carbon dioxide trapping. Energy Convers.Mgmt.,v.34 No9-10,pp1005-1013, 1993.
4. Brown L. Uptake of carbon dioxide from flue gas by microalgae. Energy Convers. Mgmt. V.37, No6-8,pp 1363-1367, 1996.
5. Lincoln E. Bull. De l'Institute Oceanografique, Monaco, 12/1993.
6. Kurano N. et al. Carbon dioxide and microalgae. In: T.Inui et al.(eds) Advances in chemical conversions. Studies in Surface Sci. and Catalysis v.114, Elsevier, 1998.
7. Yamada M. Recovery and fixation of carbon dioxide. Patent of Japan 03154616, applied 10.11.1989, publ. 02.07.1991.
8. Yantovski E. The thermodynamics of fuel-fired power plants without exhaust gases. World Clean Energy Conference CMDC, Geneva, pp 571-595, 4-7 Nov.1991.
9. Osri Uri, Seaweed cultivation project in Israel. Rosh Hanicra, 1998.
10. Iantovski E., Mathieu Ph., Nihart R. Biomass fuelled CO2 cycle with zero emission. Proc.Powergen Europe.Madrid.1997.
11. Keren Kayemeth LeIsrael. Wasser für Israel. Judisher Nationalfonds e.V. 2003
12. Olsson et al. Cogeneration based on gasified biomass, Nederlands, Proc.ECOS'2000, v.4,pp1945-1957
13. Gomez E. Preliminary tests with a sugarcan bagasse fuelled fluidised bed air gasifier. Energy Conv.Mgmt.v.40,pp205-214, 2001.
14. Azoury P.H. Power and desalination in the Arabian Gulf region. Proc, Instn. Mech. Engrs. Vol215, partA, Imech E, 2001.
15. Yantovski E. Closed Cycle Power Plant ,US Patent 6,477,841 B1, Nov.12,2002.

Fig.1.

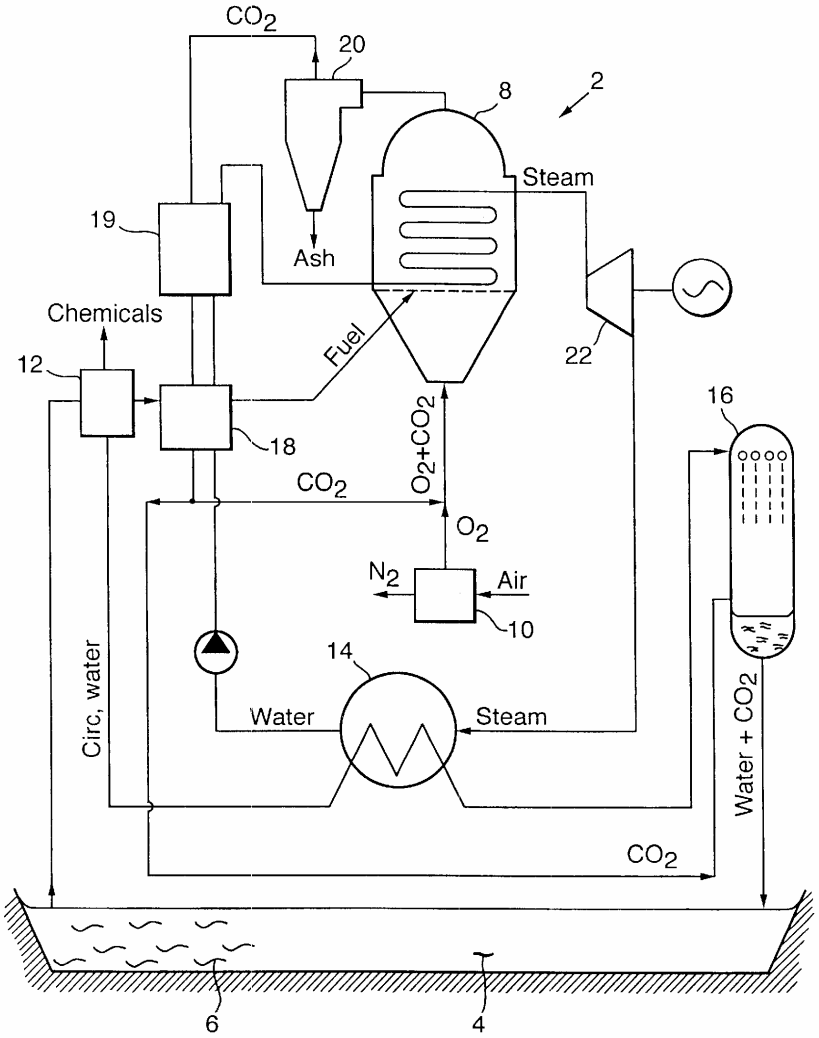
CO_2
20
8
2
Steam
19
Ash
Chemicals
Fuel
12
22
16
18
O_2+CO_2
CO_2
O_2
N_2
Air
10
14
Circ, water
Water
Steam
Water + CO_2
CO_2
6
4

Fig.2.

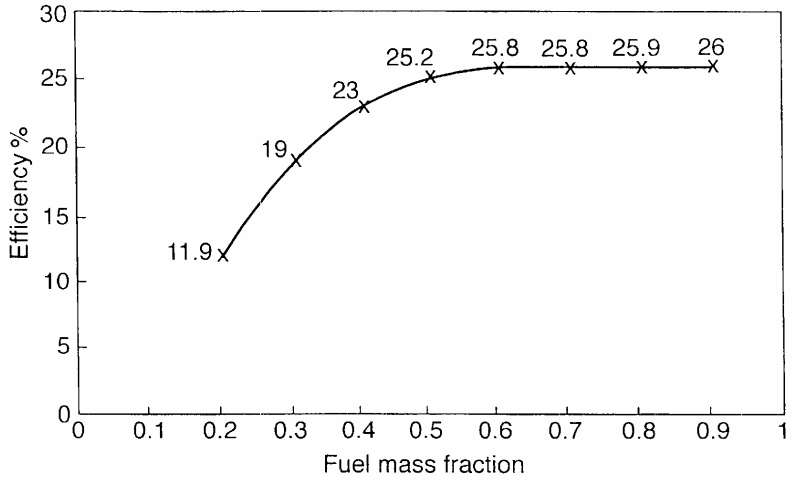
Efficiency %
Fuel mass fraction
11.9
19
23
25.2
25.8
25.8
25.9
26

Fig.3.

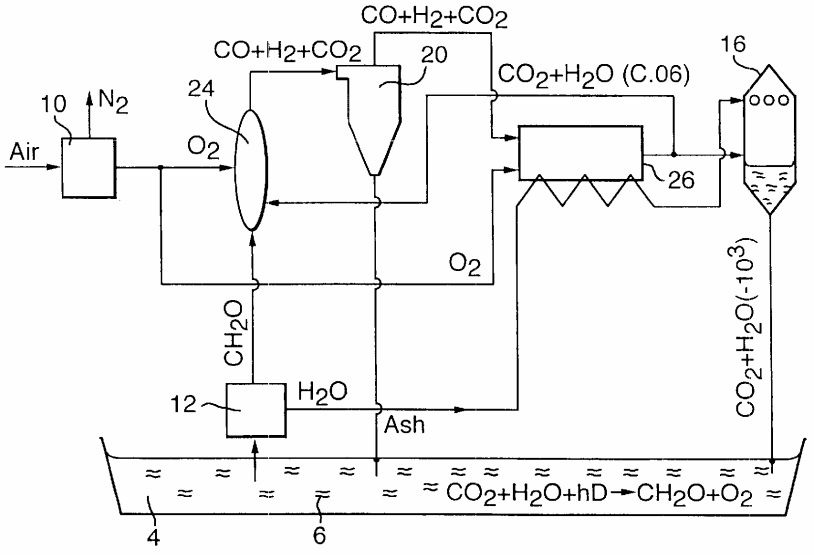
CO+H2+CO2
CO+H2+CO2
20
CO2+H2O (C.06)
16
10
N2
24
Air
O2
26
O2
CH2O
CO2+H2O(-10^3)
12
H2O
Ash
CO2+H2O+hD→CH2O+O2
4
6

Fig.4. First version of the SOFT cycle (1991).

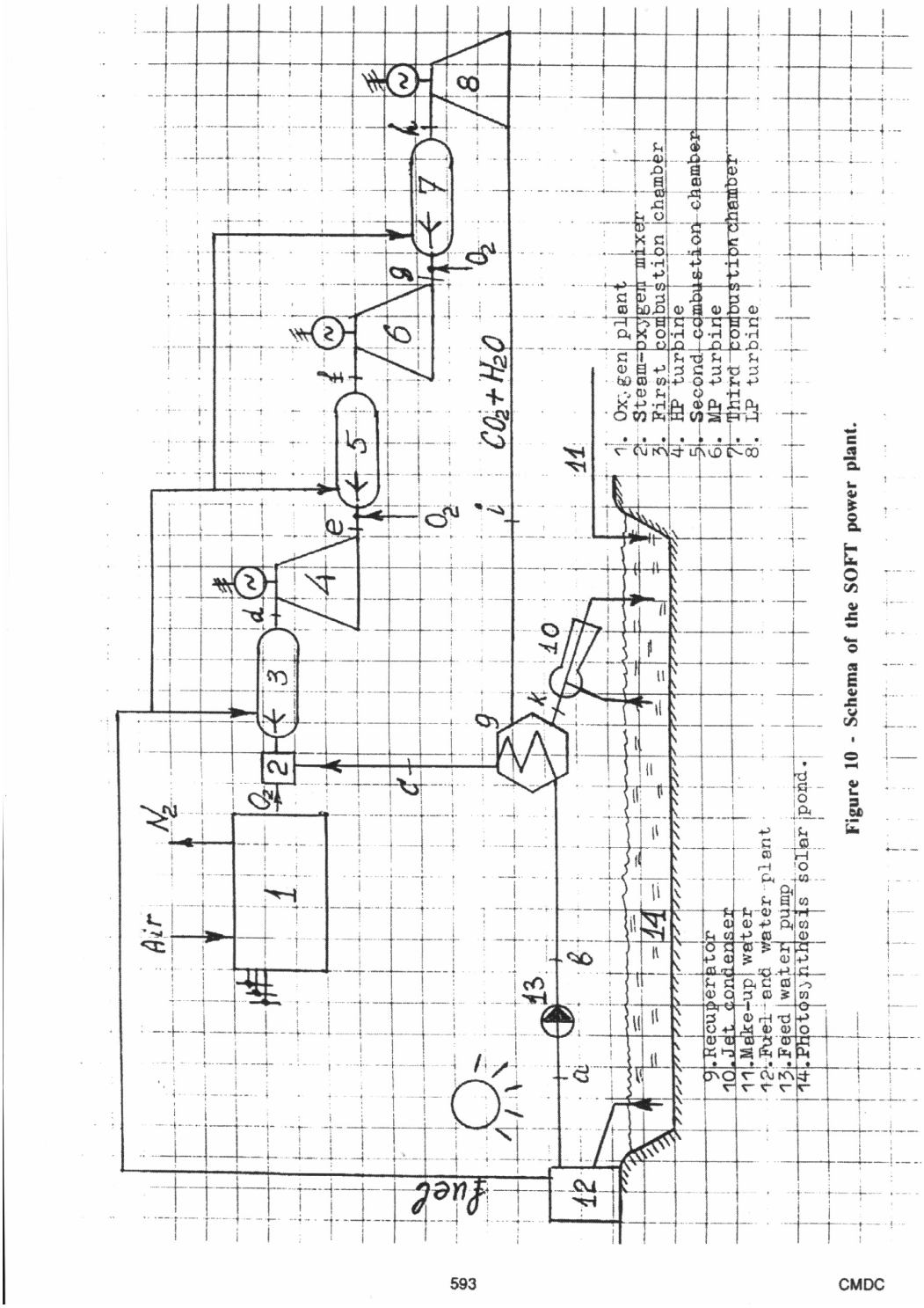

Figure 10 - Schema of the SOFT power plant.

Proceedings of ECOS 2005
Trondheim, Norway
June 20–22, 2005

PYROLYSIS OF THERMALLY THICK WOOD PARTICLES - EXPERIMENTS AND MATHEMATICAL MODELLING

Stig Møller Andersen, Søren Thaaning Pedersen,
Benny Gøbel*, Niels Houbak, Ulrik Henriksen
Technical University of Denmark, Department of Mechanical Engineering
DK-2800 Kgs. Lyngby, Denmark

Jens Dall Bentzen
COWI a/s, DK-2800 Kgs. Lyngby, Denmark

ABSTRACT

A simple, dynamic, 1-dimensional model describing heating, drying and pyrolysis of thermally thick wood particles with a 1-dimensional geometry has been developed and implemented. The model output is the dynamic evolution of both the char yield and the amount of volatiles. The model is developed in such a simple and accessible way, that it easily can be implemented in a larger model for dimensioning and optimisation of applications where pyrolysis is a part of the overall process as for instance gasification.

Experiments using a Thermo Gravimetric Analyser (TGA), built so pieces of wood can be fed into a hot atmosphere instantaneously, have been used to observe the influence of various parameters like temperature and size and wood types on the pyrolysis process.

Results from the model have been compared with results from the experiments. The comparison showed good accordance when both wood particles with a well-defined geometry (a cylinder) and when beds of wood chips and wood pellets, respectively, were pyrolysed.

The model has proven that transport of heat to the wood; internal transport and accumulation of heat inside the wood and kinetics of pyrolysis are all important parameters.

Keywords: Biomass, drying, modelling, pyrolysis, thermally thick, wood, TGA.

NOMENCLATURE

A	Frequency factor	[s^{-1}]
c_p	Heat capacity for const. pressure	[J/kg·K]
c_v	Heat capacity for const. volume	[J/kg·K]
dm	Dry mass	[g]
E	Activation energy	[J/mole]
h	Mass specific enthalpy	[J/kg]
h_k	Convective heat transfer coef.	[W/m^2·K]
HHV	Higher heating value	[MJ/kg]
k	Conductivity	[W/m·K]
m	Mass	[kg]
$\dot{m}$	Massflow	[kg/s]
$\dot{Q}$	Heat	[W]
t	Time	[s]
T	Temperature	[K]
u	Internal energy	[J]
x	Position	[m]
x	Size	[mm]
Ø	Diameter	[mm]
ε	Emission factor	[-]
ϕ	Moisture content (wet basis)	[kg/kg]
Φ	Amount of volatiles	[kg]
Φ^*	Volatiles in thermal equilibrium	[kg]
ρ_{wood}	Density of wood (wet basis)	[kg/m^3]
ρ	Density	[kg/m^3]

Subscript

evap	Evaporation
g	Gas (in the reactor)
py	Pyrolysis
sur	Surface (of wood particle)
vol	Volatiles
w	Wall (in the reactor)

Constants

$\hat{R}$	Universal gas constant	8.317 [J/mole·K]
σ	Stefan-Boltzman's constant	[W/m^2·K^4]

*Corresponding author: Phone: +45 4525 4174
Fax: +45 4593 5761 E-mail: bg@mek.dtu.dk

INTRODUCTION

A well documented and simple model calculating drying and pyrolysis under various conditions is needed to perform a successful modelling of larger energy systems like combustion and gasification plants. Most identified work has been focused on kinetics of pyrolysis, only. These analyses are accessible, but only valid for pieces of thermally thin wood, where no significant internal temperature gradients at any time are present.

Many authors have done thorough experimental work on pyrolysis of wood chips. But accessible, consistent data on the pyrolysis of thermally thick wood (e.g. wood chips or wood pellets) and the influence of variations on single parameters like particle size and temperature are rare [1]. It is assessed that such data is valuable for future construction of, among others, gasification applications. The experimental work is done under slow pyrolysis conditions with a low heating rate corresponding to the common conditions during fixed bed pyrolysis and gasification.

Some effort has been done in the past to develop models describing the simultaneous drying and pyrolysis of thermally thick wood. [2], [3], [4], [5], [6], [7], [8] have all in different ways developed models which include kinetics of drying and pyrolysis and heat balance. In particular, different approaches have been used to describe the kinetics of pyrolysis and drying, whereas both conservation of energy and mass are included in all identified models. Due to the complexity attributed to biomass in general, most models are either simplified by the geometry or by the kinetics of pyrolysis (or both).

MODELLING SECTION

The objective of this work has been to develop a simple, accessible model for implementation in a larger model of a whole gasification unit. The model is 1-dimensional. Two other important simplifications have been to neglect diffusion of volatiles and vapour and to describe the kinetics of pyrolysis to one, single first order reaction expressed in Arrhenius form.

Drying of wood is a complex phenomenon. Due to this complexity, the descriptive equation of drying [4] in the model is valid for drying below the fibre saturation point only (moisture at app. 23-30% wet basis) [3],[8].

Drying [kg/s]:

$$\frac{dm_{evap}}{dt} = \phi \cdot \rho_{wood} \cdot A_{evap} \cdot \exp\left(-\frac{E_{evap}}{\hat{R} \cdot T}\right) \quad (1)$$

The way of describing the kinetics of pyrolysis in the model developed in this study is fairly simple compared to other ways of modelling wood pyrolysis. [4], [5], [7], [9] use a more complex description where the thermal degradation is divided into the degradation of the three main polymers in wood (cellulose, hemicellulose and lignin). It has been chosen to model these processes in a more accessible and simple way.

Pyrolysis [kg/s]:

$$\frac{d\Phi_{vol}}{dt} = A_{py} \cdot \exp\left(-\frac{E_{py}}{\hat{R} \cdot T}\right) \cdot \left(\Phi^{*}_{vol} - \Phi_{vol}\right) \quad (2)$$

An analysis of combined heating, drying and pyrolysis of thermally thick wood consists basically in a control volume analysis [10]. Equations describing drying and thermal degradation are used for a differentiated control volume.

Conservation of energy [W]:

$$\sum_i \frac{\partial\left(m_i \cdot u_i\right)}{\partial t} + \sum_i d\left(\dot{m}_i \cdot h_i\right) = d\dot{Q} \quad (3)$$

Conservation of mass [kg/s]:

$$\sum_i \frac{\partial m_i}{\partial t} = -\sum_i d\dot{m} \quad (4)$$

Heat conduction [W/m^3]:

$$d\dot{Q}''' = \frac{1}{r}\frac{\partial}{\partial r}\left(k \cdot r \cdot \frac{\partial T}{\partial r}\right) \quad (5)$$

Index i in equation (3) and (4) corresponds to the different matters: wood, volatiles, vapour and char. Φ^{*}_{vol} in equation (2) is the maximum amount of volatiles pyrolyzable from biomass at one certain temperature. In other words, Φ^{*}_{vol} is a temperature dependent figure that must be experimentally evaluated for the specific type of wood. This has been done for beech, which is used in this study. Five descriptive equations are hereby valid in the differentiated control volume.

To describe the geometry of wood chips using cylindrical coordinates a transformation of length, height and width into a length and a radius is necessary. Keeping the volume and length of a wood chip constant during the transformation from Cartesian to cylindrical coordinates does this.

A combination of the five equations above given results in a system of partial differential equations, which is solved numerically. It is assumed that the heat transported to the wood by convection and radiation is conducted into the wood. An energy balance (no accumulation) applied on the surface of a particle is expressed by the equation:

$$k \cdot \left.\frac{dT}{dx}\right|_{sur} = h_k \cdot \left(T_g - T_{sur}\right) + \sigma \cdot \varepsilon \cdot \left(T_w^4 - T_{sur}^4\right) \quad (6)$$

Two important parameters to be determined are the conductivity and the heat capacity of both wood and char. With the objective of keeping the model simple, no dependency of temperature is included and the heat capacity of wood and char is assumed to be equal. Thus, the values of c_p in table 1 are used throughout this study. The conductivity for char in table 1 is the value assumed for pure charcoal. During the pyrolysis the solid fraction is not assumed as pure charcoal. In the model the conductivity of the sample decrease gradually during the thermal degradation of the material, where high degradation (low density) causes low conductivity:

$$k_{sample} = \frac{\rho}{\rho_{wood}} \cdot k_{wood} + \frac{\rho_{wood} - \rho}{\rho_{wood}} \cdot k_{char} \quad (7)$$

The pyrolysis time (reaction time) is defined as the time from when the particles were fed into the balance pan until the weight reach 98 % of the total weight loss.

Parameters describing pyrolysis and drying are found in [3],[4], (table 1).

Parameter	Value	Unit
A_{py}	$2 \cdot 10^4$	s^{-1}
E_{py}	70.4	kJ/mole
A_{evap}	$5.13 \cdot 10^6$	s^{-1}
E_{evap}	87.9	kJ/mole
c_p	1900	J/kg·K
k_{wood}	0.15	W/(m·K)
k_{char}	0.05	W/(m·K)
ε	0.9	-
ρ_{wood}	545-1200	kg/m^3
h_k	10	$W/(m^2 \cdot K)$

Table 1. Important parameters used in the model

Model assumptions

The most important assumptions are: (1) The model is 1-dimensional; (2) operating with two components: gas and wood, where the gas consist of tars, steam and other gasses (CH_4, N_2, CO, CO_2, H_2) and wood covers both wood and char; (3) ideal gases; (4) no shrinkage of the wood; (5) constant specific heat capacity; (6) no potential or kinetic energy; (7) no gas radiation; (8) no mechanical work on the system; (9) constant atmospheric pressure; (10) no diffusion limitations; (11) accumulation of gasses are neglected; and (12) the reaction enthalpy of pyrolysis is assumed to be zero [11].

EXPERIMENTAL SECTION

Apparatus

A large scale Thermo Gravimetric Analyser (TGA) operating at atmospheric pressure has been constructed [12]; an airtight, well-insulated, cylindrical reactor with adjustable electric heating elements in the isolation materials is continuously purged with N_2. Inside the reactor, a scale connected to a lever and a weight is positioned. Thus, pieces of wood can be fed into an inert, hot atmosphere instantaneously and the weight loss due to thermal degradation at various conditions can be observed. Maximum sample size is approximately 30 g. Computers do simultaneous data logging of both temperatures (T_1 - T_7) in the reactor and the mass during pyrolysis. (Figure 1).

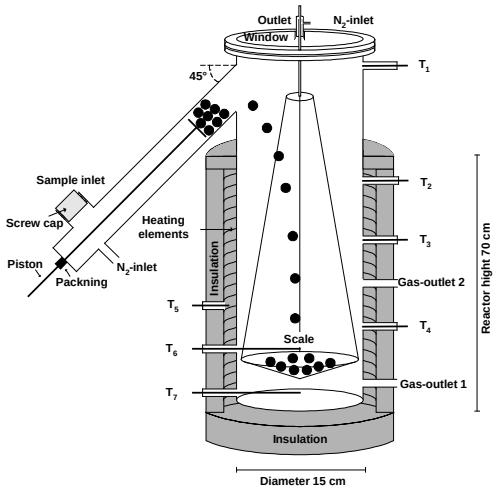

Figure 1: Thermo Gravimetric Analyser (based on [12])

In addition, a minor rearrangement on the TGA makes it possible to measure the composition of

the volatiles after water and tar components are removed. In this set up, the volatiles is removed instantly from the reactor and transported to cooling, cleaning and eventually an analyser (Servomex) detecting the gases: H_2, CO, CO_2, O_2 and CH_4.

Raw materials

A wide range of commercial wood materials for gasification and combustion was investigated: wood chips, small and large wood pellets made of sawdust (table 2).

Wood type	Species	Supplier	Diameter [mm]	Moisture (wet basis) [%]	Density [kg/m^3]
chips	beech	Danish Forest	3-100	0 - 32	545[a]
pellets, Ø6	birch	Norwegian Forest	6.25	6.9	1170
pellets, Ø10	pine	Shell	10.2	7.2	1200

Table 2: Characterisation of raw materials a: From [3]

The first type of wood pellets was made from Norwegian birch and had a diameter of 6 mm. The second type with a diameter of 10 mm was made of surplus pine from Danish furniture production.
The wood chips was produced on a commercial forestry chipper (Silvatec 478CH), sieved and tree fractions was selected together with a fraction of dried, unsieved wood chips (table 3):

Fraction	Size [mm]	Fraction of total [wt. %]	Moisture (wet basis) [%]
small	3 < x < 8	2	32
medium	8 < x < 16	19	32
large	16 < x < 45	76	32
unsieved	3 < x < 100	100	13

Table 3: Sieving of wood chips

Element		Chips[a]	Pellets Ø6	Pellets Ø10
C	[wt. %]	48.1	50.7	48[b]
O	[wt. %]	44.8	42.4	40[c]
H	[wt. %]	6.4	6.3	6.1
S	[wt. %]	-	< 0.3	0.025
N	[wt. %]	0.081	< 0.02	-
water	[wt. %]	-	-	5.6
ash	[wt. %]	0.6	0.39	0.3
HHV	[MJ/kg]	19.68	19.12	19.49

Table 4: Ultimate analysis of wood chips and wood pellets

a: previously analysis of similar wood chips
b: Source: http://www.videncenter.dk/biorakel/biorakel.asp
c: Source: http://www.ecn.nl/phyllis/

RESULTS AND DISCUSSION

The pyrolysis experiments was separated into two sessions:

1. The first session quantified the weight loss and char yield during pyrolysis when parameters such as temperature, heating conditions and size of wood particles were changed. All variations were made from a reference experiment with a set of parameters at 600°C. Emphasis has been put on the fraction of large wood chips, which is the preferred selection for combustion and gasification in fixed beds. a
2. In the second session the gasses (CO, CO_2, CH_4 and H_2) in the volatiles from the pyrolysis at different temperatures were measured.

A combination of the results from these two series of experiments gives a well-documented picture of pyrolysis of wood chips and wood pellets.

Char yield from the pyrolysis depends on the temperature. Samples of 30 g of wood have been fed into the TGA when it was preheated to a constant temperature of 400°C, 600°C and 800°C, respectively. Initially, samples of large wood chips with a well-known, uniform (app. 5·25·25 mm) size both wet and dry were pyrolysed. Then, samples of unsieved wood chips and two types of wood pellets were pyrolysed under the same conditions. The results are shown in table 5. The char yield determine by the experiments with large particles is influenced by secondary reactions as tar cracking and is by its nature not a measure of the primary char yield as seen by using small particles but a mix of both primary and secondary reactions.

		Wood chips			Wood pellets	
		large	large	unsieved	Ø6	Ø10
Initial dry mass (dm)	[g]	19.8	28.5	25.6	26.3	28.8
Moisture content	[%]	32	0	13	7	7
Time for pyrolysis	[s]	635	262	347	498	553
Char yield (% of dm)	[%]	**29**	**30**	**30**	**31**	**27**

Table 5A: Pyrolysis of samples of wood chips and wood pellets at 400 °C

		Wood chips			Wood pellets	
		large	large	unsieved	Ø6	Ø10
Initial dry mass (dm)	[g]	20.5	29.6	25.3	25.2	27.7
Moisture content	[%]	32	0	13	7	7
Time for pyrolysis	[s]	208	132	165	165	210
Char yield (% of dm)	[%]	**19**	**17**	**20**	**21**	**20**

Table 5B: Pyrolysis of samples of wood chips and wood pellets at 600 °C

		Wood chips			Wood pellets	
		large	large	unsieved	Ø6	Ø10
Initial dry mass (dm)	[g]	19.0	29.9	25.3	26.3	28.8
Moisture content	[%]	32	0	13	7	7
Time for pyrolysis	[s]	156	66	81	93	129
Char yield (% of dm)	[%]	**15**	**15**	**15**	**15**	**17**

Table 5C: Pyrolysis of samples of wood chips and wood pellets at 800 °C

The results (Table 5) show a clear trend of decreasing char yield with increasing temperature. The char yield from pyrolysis of wood chips and wood pellets showed the same magnitude of char yield independently of both size and type of wood and moisture content.
This trends correlates with results found from similar experiments with differently sized wood chips and findings identified in the literature [5],[13].

[5],[9] reports identical results for pyrolysis of pine wood cylinders and [14] on pyrolysis of beech wood cylinders

Pyrolysis of thermally thick biomass can be carried out using a preheated reactor or by heating biomass and reactor from ambient temperature.
Focusing on the heating conditions during the pyrolysis another series of experiments was conducted using the large fraction of wood chips:

- A Inserted in a hot reactor at final temperature.
- B Inserted in a 300°C warm reactor succeeded by heating to final temperature.
- C Inserted in a cold reactor (20°C) succeeded by heating to the final temperature.

Heating rate		**A**	**B**	**C**	**A**	**B**	**C**	**A**	**B**	**C**
Final temperature	**[°C]**	**400**	**400**	**400**	**600**	**600**	**600**	**800**	**800**	**800**
Initial dry mass (dm)	[g]	20.5	20.2	19.1	20.7	20.3	20.5	20.5	20.7	19.0
Char yield (% of dm)	**[%]**	**28**	**30**	**29**	**19**	**21**	**19**	**18**	**17**	**15**

Table 6: Pyrolysis of samples of large wood chips (ϕ = 32 %) using three different heating rates and three different temperatures – Determination of char yield

Results of these experiments are shown in table 6. While wood chips is thermally thick by nature the three different applied heating conditions where all limited to the conditions of slow pyrolysis, no difference in char yield were found in the tested heating conditions. A comparison to results from table 5 shows the same magnitude of char yield.

Composition of pyrolysis gas was measured after pyrolysis of samples of large wood chips in the reactor preheated to 400°C, 600°C and 800°C. The reactor was made airtight and a flow of N_2 was sucked through the reactor and sent through cooling equipment and filtering. Thus, the volatiles were removed on-line from the reactor, cleaned and sent to an analyser detecting for CO, CO_2, CH_4 and H_2. The amount of tar and water (condensed from the volatiles) was not measured but calculated by difference (Figure 2).

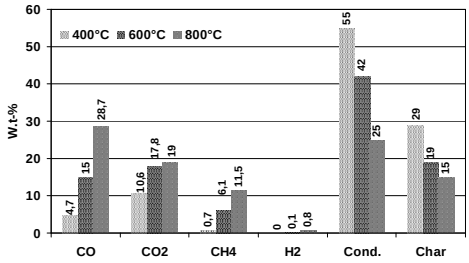

Figure 2: Composition of pyrolysis products at three different temperatures [15]

In figure 2 it is shown that the amount of tar mass decreases from 55% to 25% of the pyrolysis products.

Char

The char produced by pyrolysis of wood chips in a hot reactor at 600°C until no further mass loss, was succeeded by an ultimate analysis (table 7):

Element		
C	[wt. %]	88.9
O	[wt. %]	5.95
H	[wt. %]	2.7
S	[wt. %]	< 0.05
N	[wt. %]	0.2
water	[wt. %]	-
ash	[wt. %]	2.2

Table 7: Ultimate analysis: char of large wood chips pyrolyzed to 600 °C.

This shows clearly that a significant amount of both H and O are still present in the char even though the char has been kept in several minutes at 600°C without any further mass loss.

VERIFICATION AND USE OF MODEL

A dry, cylindrical piece of pinewood (diameter 16 mm and length 100 mm, ϕ = 0 %) with thermocouples (diameter: 0.5 mm) built into the centre and at a radius of 5.6 mm (Figure 3) was placed instantly in the TGA holding a constant temperature of 615°C. A similar cylinder was placed in the TGA to observe the mass loss under these conditions.

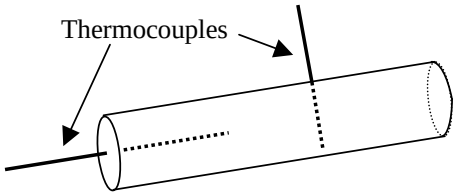

Figure 3: Wood cylinder equipped with thermocouples

Thus temperature profiles in two positions and the weight loss due to pyrolysis were measured. Due to the dimension of the cylinder, 1-dimensional geometry could easily be assumed (Figure 4).

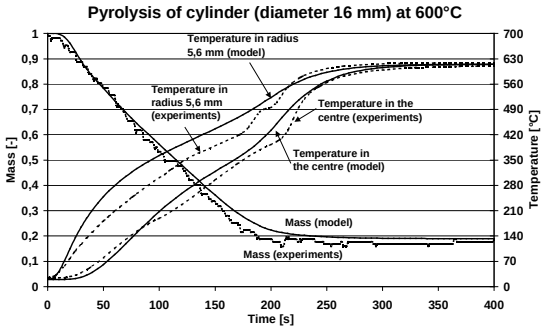

Figure 4: Pyrolysis of a cylindrical piece of pinewood. Model results and experiments. [15]

The mass decrease is well predicted by the model and the most noticeable trend, which is seen in figure 4, is the sudden rise in temperature measured in both the centre and closer to the surface in the cylinder after approximately 220 s. This can be attributed to the change from wood to char, which results in a lower heat capacity and a lower density. In the model the heat capacities for wood and char have been assumed equal and constant. Another

important finding is that the temperature profiles do not show a tendency to small exothermic reactions in the final part of the pyrolysis. This is reported in [13] with similar experiments where the maximum temperature is measured higher than the final temperature. In the model developed in this study, the enthalpy of reaction for pyrolysis is assumed to be zero [11].

Samples of 30 g large wood chips with different moisture contents (0% and 32 %) were placed in the TGA holding different, (table 5) constant temperatures, and the weight loss under thermal degradation was measured. It was hereby possible to test whether the developed, 1-dimensional model could be used for calculations on a bed of wood chips. A 1-dimensional geometry of a cylinder was found suitable (Figure 5).

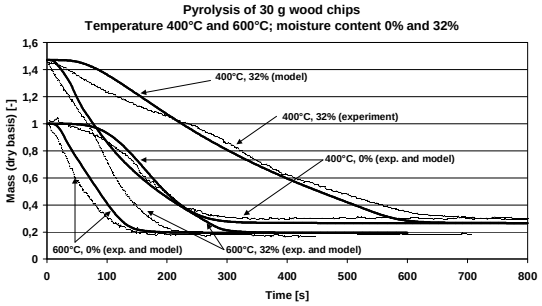

Figure 5: Pyrolysis of samples of wood chips with two different moisture contents at two different temperatures [15].

The good agreement suggests that it is enough to use a simple, 1-dimensional model to predict drying and pyrolysis of a bed of wood chips. It should be noted that a similar accordance at 800°C was not observed. This can be attributed to the constant heat capacity assumed in the model. In order to obtain a better accordance at 800°C, another value for the heat capacity should be used (see table 1).

By means of the developed and verified model, deeper investigations on the process of pyrolysis was carried out. It is investigated which of the three possible parameters: heat transfer to the particle from the surroundings, internal accumulation and transport of heat, or kinetics of pyrolysis one possibly may either neglect or see as the most important limiting part of the process.

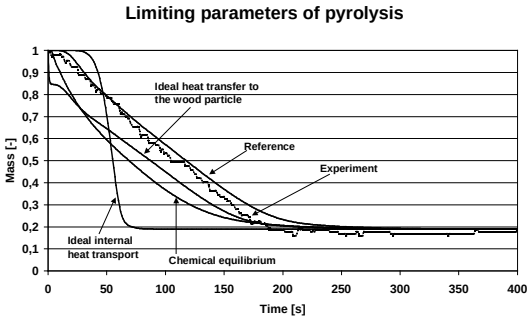

Figure 6: Investigations of the limiting parameter in pyrolysis at 615 °C [15].

The results can be found in figure 6, where these three parameters are excluded from the model one by one and the results can be compared with a reference case, where the parameters are set as normal (see table 1).

The reference line is in figure 6 also compared to the experiment, where a cylinder was pyrolysed. This experiment is the same as shown in figure 4. "Ideal heat transfer to the wood particle" in figure 6 corresponds to a simulation, where the surface temperature of the wood immediately after entering the TGA is set to the final temperature (615°C) - the limitation in external heat transfer is hereby removed. "Chemical equilibrium" corresponds to a simulation where the activation energy in the Arrhenius expression describing pyrolysis is set to 0 – Assuming chemical equilibrium. Finally, "ideal internal heat transfer" corresponds to a simulation, where the conductivity of wood and char is increased by a factor of 100, corresponding to approximated perfect internal heat transport. From figure 6 it is evident that when describing the pyrolysis of thermally thick particles none of the evaluated parameters can be assumed negligible. Therefore both internal- and external heat transfer and kinetics of pyrolysis should be included to obtain a good simulation of the pyrolysis.

CONCLUSION

Experimental investigation of slow pyrolysis of thermally thick wood was carried out on commercial wood chips and wood pellets. A decrease in char yield with increasing temperature was seen. This occurred independently of the moisture content, size and wood type.

A simple model describing drying, heating and pyrolysis of wood particles with a 1-dimensional cylinder geometry has been developed and verified.

Good agreement between calculation and experiment was obtained by comparing the 1-dimensional cylindrical model with pyrolysis experiments made on both cylinders of wood and commercial wood chips.
Model calculations showed that in order to obtain a good simulation of the pyrolysis for thermally thick particles in a pyrolysis reactor both internal and external heat transfer and kinetics of pyrolysis should be taken into account.

ACKNOWLEDGEMENT
This work was supported by the Danish Energy Agency

REFERENCES

[1] Williams PT, Besler S. *The Influence of Temperature and Heating Rate on the Slow Pyrolysis of Biomass.* Renewable Energy 1996;7(3):233-250.

[2] Bryden KM, Ragland KW, Rutland CJ. *Modeling thermally thick pyrolysis of wood.* Biomass and Bioenergy 2002;22:41-53.

[3] Grønli M. A Theoretical and Experimental *Study of the Thermal Degradation of Biomass.* Ph.D. Thesis, NTNU, 1996, Trondheim, Norway.

[4] Chan WR, Kelbon M, Krieger BB. *Modelling and Experimental Verification of Physical and Chemical Processes During Pyrolysis of a Large Biomass Particle.* Fuel 1985;64:1505-1513.

[5] Alves SS, Figueiredo JL. *A Model for Pyrolysis of wet Wood.* Chemical Engineering Science 1989;44(12):2861-2869.

[6] Pyle DL, Zaror CA. *Heat Transfer and Kinetics in the Low Temperature Pyrolysis of Solids.* Chemical Engineering Science 1984;39(1):147-158.

[7] Miller RS, Bellan J. *A Generalized Biomass Pyrolysis Model Based on Superimposed Cellulose, Hemicellulose and Lignin Kinetics.* Combust. Sci. and tech. 1997;126:97-137.

[8] Larfeldt J. *A Model Study of Drying and Pyrolysis of Biomass.* Thesis for the Degree of Licentiate of Engineering. Chalmers University of Technology, 1995.

[9] Koufopanos CA, Papayannakos N, Mashio G Lucchesi A. *Modelling of the Pyrolysis of Biomass Particles. Studies on Kinetics, Thermal and Heat Transfer Effects.* The Canadian Journal of Chemical Engineering 1991;69:907-915.

[10] Arpaci VS, Larsen PS. *Convection Heat Transfer*. Prentice-Hall, 1984.

[11] Roberts AF. *Heat of reaction during pyrolysis of wood.* Combustion and Flame 1971;17:79-86.

[12] Fock F, Henriksen U, Thomsen K. *Demonstration of the Vortex Process for Biomass Gasifiers.* In Palz, W. et al. (eds), Proceedings of the Twelfth European Biomass Conference. Amsterdam, ETA-Florence & WIP-Munich, 2002, p. 670-676.

[13] Di Blasi C, Signorelli G, Di Russo C, Rea G. *Product Distribution from Pyrolysis of Wood and Agricultural Residues.* Ind. Eng. Chem. Res. 1999;38:2216-2224.

[14] Di Blasi C, Hernandez EG, Santoro A. *Radiative Pyrolysis of Single Moist Wood Particles.* Ind. Eng. Chem. Res. 2000;39:873-882.

[15] Pedersen ST, Andersen SM. *Pyrolyse af træflis* (In Danish) (Pyrolysis of wood chips). MEK-ET-EP 2001-04, Technical University of Denmark, 2001.

Author Index

Keyword Index